Proceedings of the

XXth International Workshop on Deep-Inelastic Scattering and Related Topics DIS 2012

26–30 March 2012
Bonn, Germany

Editor: Ian C. Brock

Verlag Deutsches Elektronen-Synchrotron

Impressum

XXth International Workshop on Deep-Inelastic Scattering and Related Topics (DIS 2012)

26–30 March 2012, Bonn, Germany

Conference homepage
`http://dis2012.uni-bonn.de`

Slides at
`http://indico.cern.ch/conferenceDisplay.py?confId=153252`

Online proceedings at
`http://www-library.desy.de/preparch/desy/proc/proc12-02.html`

Editor:
Ian C. Brock
March 2013
DESY-PROC-2012-02
ISBN 978-3-935702-67-6
ISSN 1435-8077

Published by
Verlag Deutsches Elektronen-Synchrotron
Notkestraße 85
22607 Hamburg
Germany

Printed by
Kopierzentrale Deutsches Elektronen-Synchrotron

Committees

Physics Advisory Committee

- Ian C. Brock
- Jochen Dingfelder
- Friedrich Klein
- Katerina Lipka
- Sven-Olaf Moch

International Advisory Committee

- Guido Altarelli (CERN)
- Violette Brisson (Orsay)
- Dusan Bruncko (Slovak Ac.)
- Allen Cladwell (Munich)
- Giulo d'Agostini (Roma)
- John Dainton (Liverpool)
- Rolf Ent (JLAB)
- Joel Feltesse (Saclay)
- Elisabetta Gallo (Firenze)
- Rolf-Dieter Heuer (CERN)
- Robert Klanner (Hamburg)
- Max Klein (Liverpool)
- Aharon Levy (Tel Aviv) – chair
- Lev Lipatov (St. Petersburg)
- Pierre Marage (Brussel)
- Joachim Mnich (DESY)
- Hugh Montgomery (JLAB)
- Rosario Nania (Bologna)
- Jose Repond (Argonne)
- Wesley Smith (Wisconsin)
- Frank Sciulli (Columbia)
- James Stirling (Cambridge)
- Juan Terron (Madrid)
- Katsuo Tokushuku (KEK)
- Steven Vigdor (BNL)
- Albrecht Wagner (DESY)
- Matthew Wing (UCL)
- Günter Wolf (DESY)

Local Organisation

- Jens Barth
- Ian C. Brock – chair
- Resi Elßner
- Andrea Fürstenberg
- Udo Idschok
- Rainer Joosten
- Ewald Paul
- Peter Wienemann

Working Group Convenors

Working Group 1: Structure Functions

- Amanda Cooper-Sarker
- Pedro Jimenez-Delgado
- Ringailė Plačakytė

Working Group 2: Diffraction and Vector Mesons

- Dimitri Colferai
- Richard Polifka
- Marta Ruspa

Working Group 3: Electroweak and Searches

- David M. South
- Andreas Weiler
- Hwidong Yoo

Working Group 4: Hadronic Final States

- Krzysztof Nowak
- Klaus Rabbertz
- Jan-Christopher Winter

Working Group 5: Heavy Flavours

- Jolanta Brodzicka
- Massimo Corradi
- Ingo Schienbein
- Reinhard Schwienhorst

Working Group 6: Spin Physics

- Abhay Deshpande
- Kresimir Kumericki
- Marc Schlegel
- Sergei Yashchenko

Working Group 7: Future of DIS

- Elke Aschenauer
- Paul Newman

Preface

The "XXth International Workshop on Deep-Inelastic Scattering and Related Topics (DIS 2012)" was held from 26–30 March 2012 in Bonn, Germany. This was a bit earlier than usual for DIS workshops. However, the trees were all in blossom and the sun shone for most of the week, so this was not a problem. As is the tradition for these workshops, the first day consisted of plenary talks, with the ensuing three days devoted to parallel sessions, followed by a final day of summary talks from the seven working groups. Almost all of the 300 participants also gave talks: there were as many as 275 contributions, excluding the summaries.

Such a conference cannot take place and succeed without the help of a large number of people: during the planning stage, the conference itself and the putting together the proceedings.

The Physics Advisory Committee gave invaluable advice during the detailed planning of the workshop. In particular, I would like to thank Katerina Lipka who stepped in when things were not moving along quickly enough. The input from the International Advisory Committee was also very helpful in clarifying the overall goals of the workshop.

The working group convenors worked very efficiently and did an extremely good job of putting together the sessions. Topics that were relevant to more than one group were presented in joint sessions. The convenors not only ran the parallel sessions, they also worked very hard during the week to put together the comprehensive and very interesting summary talks that were given on the last day of the workshop.

I would like to warmly thank everyone in the Local Organising Committee. Udo Idschok simply took care of everything that was not associated with the talks! Without his assistance, the particpants would probably never have found the lecture halls and also not had anything to eat or drink! Peter Wienemann set up the web pages and supervised all technical aspects of the workshop. Andrea Fürstenberg looked after the registration and countless other tasks that I asked her to do. Kati Brock gave the graphics of the workshop a very distinctive and professional look.

The conference office was very professionally staffed by Raja Bernard, Valja Gebhardt, Barbara Mosblech, Jacqueline Weigelt, Rosi Wilde-Brock, Kati Brock and Sabine Kämper. The technical support during the talks was provided by Isabelle Boventer, Eike Caldeweyher, Kai Dänner, Ralf Daume, Luna Dehenn, Stefan Erbschwendner, Dustin Hebecker, Ezeda Koke, Elisa Müller, Martin Pietzka, Lara Schildgen, Jakob Seibert, Sabine Undorf and Désirée Wilde. These students also served during the coffee breaks and helped with many other aspects of the organisation. Stefan Erbschwendner deserves a special mention for the many different tasks that he did. It can fairly be said that he was Udo Idschok's right-hand man.

During the preparing of these proceedings Ozan Arslan, Jens Barth and Ewald Paul gave invaluable help. It is only due to the persistence of Ewald Paul that we actually received 226 contributions to these proceedings.

We also thank CERN, JLAB, DESY and BNL for their generous support of the workshop. The University of Bonn provided assistance in many areas, including making the lecture halls for the workshop available. The Studentwerk took care of most of the catering and were a great help in the smooth running of coffee breaks, lunches and the welcome reception.

Bonn, March 2013
Ian C. Brock

Contents

Part I

Plenary Talks

Introduction to Deep Inelastic Scattering: Past and Present

Joël Feltesse

CEA, DSM/IRFU, Centre de Saclay, 91191 Gif-sur-Yvette cedex, France

DOI: http://dx.doi.org/10.3204/DESY-PROC-2012-02/6

A brief history of Deep Inelastic Scattering (DIS) physics is presented. Going from the glorious years at SLAC 45 years ago, through the high statistics fixed experiments in the eighties and the discoveries at HERA since twenty years, without omitting Polarised Deep Inelastic Scattering, until the most recent open problems in DIS.

1 Introduction

At a moment when many of the people attending the conference have not been involved in the early DIS experiments it could be interesting to review how the field of DIS has started and evolved since 45 years. I shall start to remind the heroic years at SLAC, followed by the era of high precisions fixed target experiments before entering the new kinematic domain and its many surprises at HERA. I shall end by commenting where we are at present five years after the end of data taking at HERA.

2 Glorious years at SLAC

The heroic age of DIS opened in 1968 when a SLAC-MIT experiment [1] studied electron-proton DIS with the new commissioned linear electron accelerator at Stanford. Beam energies of up to 20 GeV were well beyond the 6 GeV peak energy of DESY, the highest electron energies then available. Two important phenomena were observed:

1. The inclusive inelastic cross-section is larger by more than one order of magnitude than expected and only weakly Q^2 dependent.

2. At an invariant hadronic mass (W) of the final state larger than 2 GeV, the structure function F_2 becomes a function of the ratio $\omega = \nu/Q^2$ over a range $0.7 < Q^2 < 2.3\,\mathrm{GeV}^2$.

The results were interpreted with a great intuition by W.K.H. Panovsky in the HEP Conference in Vienna in 1968 [2]: as *"the apparent success of the parametrization of the cross-sections in the variable νQ^2 in at least indicative that point-like interactions are becoming involved."* It was a big surprise that nobody had anticipated except a lone prophet J.D. Bjorken. In 1966 J.D. Bjorken [3] conjectured that in the limit of Q^2 and ν approaching infinity the structure function F_2 becomes function only of the ratio x. It was based on current algebra but *"a more physical description is without question needed"* [4] that J.D. Bjorken himself suggested : *"We suppose*

that the nucleon consists of a certain number of elementary constituents" [5] that behaves as free particles. However the general feeling was that *"Bjorken's results were highly esoteric"* [6].

There were in 1968 very little interest in DIS scattering. Dick Taylor in his Nobel Prize lecture [7] acknowledged that DIS was not the main focus of the experiment and should be reserved to *"subgroups"*. Nobody expected that the study of the continuum at high W would be so central in the history of high energy physics. At DESY an experiment did notice in November 1967 [8, 9] a surprising slow Q^2 dependence at high W that was tentatively attributed to resonances of high angular momentum.

The constituent model which opened the way for a simple dynamical interpretation of the deep inelastic results was the parton model of R.P. Feynman. But before the SLAC-MIT experiment there were no reasonable candidates for the constituents. Visiting SLAC in summer 1968 R.P. Feynman immediately saw in point-like partons an explanation of SLAC data. But it took many years before the theory was widely accepted. The most accepted theories were : Nuclear Democracy, Resonances Models, Regge Trajectories, VDM ... The Parton Model had to wait for decisive tests. It came first from a measurement of the ratio of longitudinal and transverse photo-absorption cross sections of the victual photon $R(\nu/Q^2) = \sigma_L/\sigma_T$ which combined SLAC and DESY experimental results [10]. R was found to be small and not increasing with Q^2 . It was an elegant indication of spin $1/2$ constituents [11]. Further stringent tests of the Quark Parton Model came from neutrino DIS scattering at CERN with the heavy liquid bubble chamber Gargamelle (which discovered later the neutral currents) :

- The Quark Parton Model (QPM) predicts that on an isoscalar target the ratio of the F_2 structure functions in electron and neutrino scattering depends only on the quark charges. When neglecting the strange quark contribution, it gives:

$$\frac{\frac{1}{2}\int [F_2^{\nu p}(x) + F_2^{\nu n}(x)]\, dx}{\frac{1}{2}\int [F_2^{ep}(x) + F_2^{en}(x)]\, dx} = \frac{2}{e_u^2 + e_d^2},$$

  where e_u and e_d are the electric charges of the u and d quarks. The ratio was found to be 3.4 ± 0.7 [12] as compared to the $18/5$ predicted value. It provided the most convincing evidence that nucleons contains fractionally charged quarks as real dynamical entities.

- For point-like constituent the total neutrino and anti-neutrino cross-sections should be proportional to the energy in the centre-of-mass (i.e. the neutrino beam energy). The linearity of the cross-section was indeed well verified by Gargamelle data. [12]

- The Gargamelle group evaluated the Gross-Llewellyn Smith Sum Rule [13] which states that :

$$\int [F_3^{\nu N}(x)]\, dx = (number\ of\ quarks) - (number\ of\ antiquarks)$$

The measured value of 3.2 ± 0.6 [12] was another significant success of the Quark Parton Model. It is worth to mention that complementary informations from e^+e^- scattering helped the QPM to emerge against strong opposition. However, in 1973, there were still several vital problems :

- The momentum sum rule, directly measured by the Gargamelle group, was strikingly small [12]:

$$\int [F_2^{\nu p}(x) + F_2^{\nu n}(x)]dx = \int x[u_p(x) + \bar{u}_p(x) + d_p(x) + \bar{d}_p(x) + s_p(x) + \bar{s}_p(x)]dx = 0.49 \pm 0.07.$$

In QPM, the sum rule represents the fraction of the nucleon's momentum carried by the quarks and the antiquarks. So, where does the other half of the nucleon's momentum comes from ?

- Why the point-like partons appear to be free during the collision?

The paradoxes were splendidly solved by the newly developed QCD in 1973. One of the early convincing tests of the correctness of QCD was the observation of the clear pattern of scaling violations in DIS with increasing Q^2: rise at small x and fall at large x due to the radiation of gluons. The scaling violations were precisely observed in a muon scattering experiment at FNAL in 1975 with a muon beam of 150 GeV [14].

3 High statistics fixed target experiments

The striking early results in DIS led to more than two decades of fixed target experiments using all available leptonic probes at SLAC, FNAL and CERN (see fig. 1). With higher beam energies the new generation of experiments extended the e-N programme of SLAC by an order of magnitude in Q^2 (see fig. 2) :

- `Electron beams`. After the pioneering SLAC-MIT experiment more DIS experiments were carried out at SLAC with unpolarised targets up to the early nineties .

- `Muon beams`. The major collaborations were BFP at FNAL with beams produced by the Tevatron and at CERN BCDMS and EMC (later replaced by NMC) with beams produced by the SPS. The beam fluxes were much lower than at SLAC but compensated by large acceptances and very long targets (up to 40 m long in BCDMS). The scattered muons were measured in an open spectrometer (BFP, EMC and NMC) or an iron toroid (BCDMS).

- `Neutrino beams`. To reach high statistics neutrino experiments at CERN (CDHSW) and at FNAL (CCFRW later replaced by NuTeV) used an heavy target calorimeter and an iron toroid to measure the scattered muon.

3.1 Inclusive measurements

With the high statistics the systematics became by far the largest source of uncertainties for structure functions measurement. Many glaring discrepancies between the muon experiments and between the neutrino experiments have generated heavy discussions for many years. The most spectacular shift was between the muon experiments BCDMS and EMC where a 10 % shift at low x and a 10 % shift at large x of opposite signs could not be compensated by shifts of normalisations [15]

A few years later, a new generation of experiments have helped to clarify the situation.The NMC experiment succeeded the EMC experiment using a large part of the EMC detector and has understood the discrepancy between BCDMS and EMC [16]. Then, more precise inclusive NMC data have superseded the EMC inclusive data. There is at present almost perfect agreement between SLAC, BCDMS and NMC experimental results. However it is still likely that the main correlated systematics of BCDMS is slightly under evaluated [17]. As to the neutrino experiments, quality of the QCD fit of the CDHSW inclusive data at CERN was

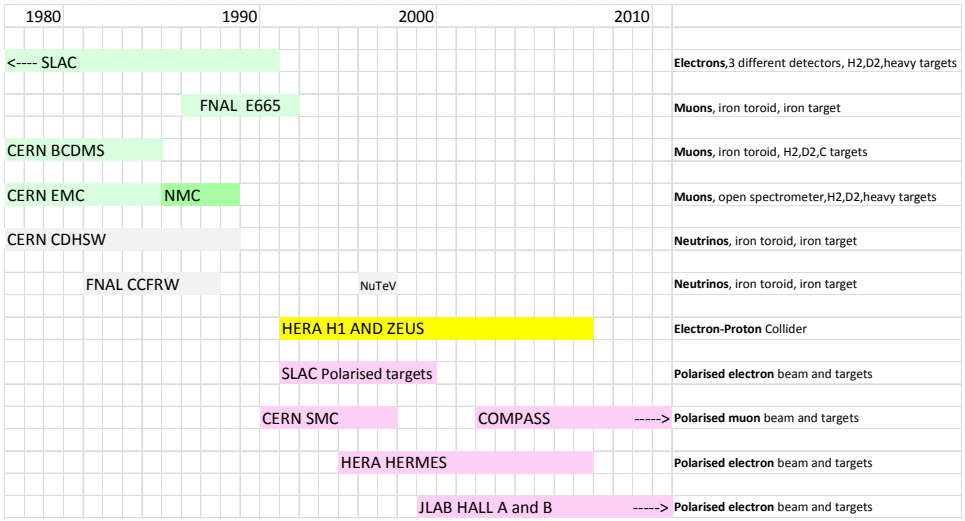

Figure 1: Time-planning of high-statistic fixed target and HERA experiments together with polarised DIS experiments.

rather poor [18]. At FNAL, after refurbishing the CCFRW detector the NuTeV experiment succeeded the CCFRW experiment. There was a large discrepancy reaching a 25 % shift at large x between NuTeV and CCFRW inclusive data. Finally NuTeV have understood the origins of the discrepancy [19]. Inclusive NuTev data have then superseded CCFRW data.

3.2 Measurements of flavour content of the sea

Estimates resting on differences or ratios of cross-sections data with the same apparatus are much less affected by systematics. They have brought new insights into the flavour content of the proton at low x. In general, the flavour content of the sea is a complex matter that does not follow the simple democratic production from gluon splitting into $q\,\bar{q}$ pairs :

- `Strange quarks`. Opposite di-muons produced in neutrino-nucleon scattering is a direct probe to measure the strange component of sea quarks in the nucleon. The high statistics neutrino experiments ([20],[21]and [22]) have found that in average the density of strange quarks is twice smaller than the density of the average of $\bar{u}$ and $\bar{d}$ quarks. The result seems to be challenged by new data at LHC [23] determined at $x = 0.023$ and $Q^2 = 1.9\,\mathrm{GeV}^2$.

An interesting situation to follow up in the coming years.

- $\bar{u}$ and $\bar{d}$. When comparing F_2 structure functions of the proton and of the neutron, SLAC, EMC and BCDMS have observed evidence that there is more $\bar{d}$ than $\bar{u}$ in the proton . More precise data came from NMC a few years later [24]:

$$\int [\bar{u}(x) - \bar{d}(x)]\, dx = -0.147 \pm 0.39$$

It is another curious asymmetry of the sea content which has been confirmed by measurements of Drell Yan pairs and production of W bosons in hadron-hadron scattering.

3.3 EMC effect

It was expected that parton distributions in a nucleon embedded in a nucleus would only differ from distributions in a free nucleon at large x due to the well known Fermi motion and at very low Q^2 due to the shadowing effect observed before in photo-productions. In 1982, it came as a surprise when the EMC experiment observed a dependence on the nuclear structure of the structure function $F_2(x, Q^2)$ in iron relative to that for deuterium at high Q^2: a rise at $x \sim 0.05$ and a strong drop at $x \sim 0.5$ [25]. Several dedicated fixed target experiments [26] confirm the effect at large x. Also a small enhancement at x around 0.05 was measured. By extending the measurement down to about $x \sim 10^{-3}$ a strong drop was observed. At present, the effect is not fully understood. So that, it is necessary to use a model to extract Parton Distribution Functions (PDF) of the nucleon from heavy target data.

3.4 Spin crisis

The proton spin sum-rule states that:

$$\frac{1}{2} = \Delta\Sigma + \Delta G + L_q + L_g$$

This means that the proton spin is the sum of the quark ($\Delta\Sigma$), plus the gluon intrinsic spins (ΔG), plus the orbital angular momentum (L_q, L_g contributions). In 1988 the EMC experiment measured the asymmetry of inclusive DIS cross-sections of a polarised muon beam off a longitudinally polarised target and obtained the surprising result that the fraction of the spin carried by the quarks is compatible with zero [27],

$$\Delta\Sigma = 12 \pm 9 \pm 14\%,$$

the so-called spin-crisis. The result has generated a lot of theoretical works and many dedicated experiments (see section 6).

4 Discoveries from HERA

With the opening of a new kinematic space by two orders of magnitude in Q^2(see fig. 2), it was clear from the early proposals of HERA that the physics interest was focused on large Q^2. In the first years of data taking the low Q^2 calorimeter of the H1 detector had a modest granularity and neither ZEUS nor H1 had a very forward proton detector for diffractive events. However at small integrated luminosity (22 nb^{-1}) two unexpected topics emerge and should stay as a part of the hard core of the HERA legacy : low x physics and diffraction.

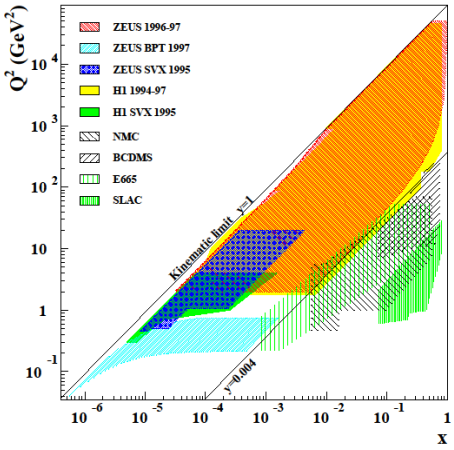

Figure 2: Kinematic regions in x and Q^2 covered by fixed target experiments and the HERA experiments.

4.1 Rise of the DIS cross-section at low x

In 1993 a few months after the end of the first period of data taking, R. Devenish [28], chairperson of the first DIS Workshop, concluded that: *"one of the moments of high drama was the presentation by H1 Collaboration of the first measurement of F_2 at HERA showing that the structure function did increase quite strongly at low x"*. It was also observed from the early data that the rise should be more pronounced as Q^2 increases [29]. Why was it such a surprise? It was commonly accepted that extrapolations at low x indicated a flattish F_2 as $x \to 0$, a Regge-like behaviour: $F_2 \sim x^{-\epsilon}$ where $\epsilon \approx 0.08$. It was however predicted in 1974 by the fathers of QCD [30], but forgotten since, that the gluon should rise at low x for Q^2 high enough and that the rise should increase with Q^2. Quoting from Frank Wilczek [31] in his comments on QCD foundational papers: *"The most dramatic of these tests, that protons viewed at ever higher resolution would appear more and more as field energy (soft glue), was only clearly verified at HERA twenty years later"* . It was later conjectured in 1983 that the rise should be tamed by saturation effects to prevent reaching the unitarity limit [32]. It is also fair to say that most of the parametrisations of the structure function F_2 had as an option the possibility of a rise at low x. The argument over the interpretation began immediately after the presentation of the data [28]. Was it an indication of the BFKL behaviour? Could it be described by the DGLAP evolution equations? Could the saturation be observed at HERA? Clear answers were given in the following years when more data were accumulated. The Q^2 evolution of the F_2 structure function is perfectly described by DGLAP evolution equations down to $x \sim 10^{-4}$ and $Q^2 \sim 2\,\mathrm{GeV}^2$ and no indication of saturation has been observed (see fig. 3). However new questions about low x physics were raised and are still open (see section 5).

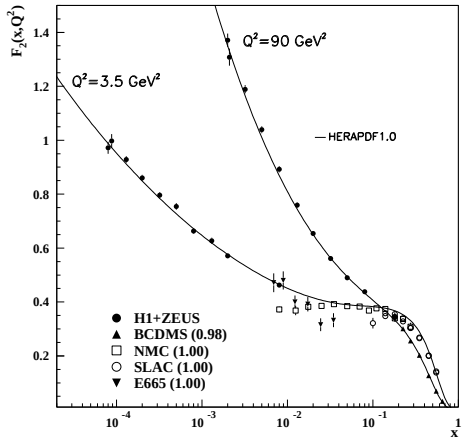

Figure 3: A recent plot of the proton structure function F_2 [33] and the HERAPDF fit [34] based on DGLAP evolution equations.

4.2 Hard diffraction

A new class of DIS events came also as a surprise. About 10 % of Neutral Current DIS events have a large rapidity gap between the proton direction and the first energy deposition in the detector. The DIS Monte Carlo programmes in use in the early years of HERA assumed that there is a colour flow between the struck quark and the proton remnants. Thus, the simulation programmes were not able to describe the data [35]. In the following years, beautiful data, where diffraction scattering can be identified via the rapidity gap or by tagging the forward proton in dedicated very forward detectors, have been accumulated by the H1 and ZEUS collaborations. At present, progresses have been made in understanding these events, but the physics of hard diffraction is not yet fully clarified.

4.3 Electroweak unification

One of the primary goals of physics at HERA was to study the neutral and the charge currents at Q^2 values sufficiently that the electromagnetic and the weak currents are of similar strength. Indeed the plot of neutral and charge currents cross-sections have shown in 1995, quoting from R.Cashmore in DIS-2001 [36]: *"the most graphic and simple demonstration of electroweak unification available"* . It provided a determination of the mass of the vector meson W in full agreement with the world average.

4.4 Gluon density

HERA is a unique facility to extract the gluon density and the running coupling constant α_s from inclusive cross-sections, jet production and heavy quarks productions. In the very first analyses in 1993, assuming that α_s takes the word average value, it has been possible to extract the gluon density from the scaling violations and in 1995 to make a direct measurement of

the gluon density from the rate of multi-jet events [37]. The full agreement at Leading Order between indirect extraction and direct measurement of the gluon density was not a surprise. It has however constituted an important test of perturbative QCD.

5 High precision and extension of the physics domain at HERA

After the early discoveries, the statistics has gradually increased until the year 2000. There have been a major upgrade of luminosity in 2001-2002. Data-taking has ended in 2007. The analysis of the data has been a permanent fight against systematics towards high precision together with searches beyond the standard model which unfortunately were not successful. Tremendous progress on the physics of DIS has been obtained over the years in theory and experiment. In DIS new domains of investigation were developed beyond the simple measurement of inclusive cross-sections. The most up-to-date status of these studies are the object of the Workshop. Let make here just a few general comments.

- `The longitudinal Structure Function` $F_L(x, Q^2)$`.` Since the early SLAC measurements in 1969, it has taken 40 years to get precise data on $F_L(x, Q^2)$ [38]. The result is in perfect agreement with the prediction of perturbative QCD down to $x \sim 10^{-4}$ and $Q^2 \sim 2$ GeV^2. Quoting from G.Altarelli in DIS-2009 :*"I had not expected that it would take such a long time to have a meaningful test of this simple prediction"* [39].

- `Physics at low` x`.` There are some hints of possible departure from standard evolution in associated production of jets in the forward direction at small x. BFKL evolution, Dipole models, Colour Glass Condensate, Geometric Scaling are appealing physics pictures of the physics but there is still no satisfactory theoretical understanding of the domain of high densities of quarks at small x.

- `Diffraction.` In addition to the measurement of Diffractive Structure Functions, measurement of Deep Virtual Compton Scattering (DVCS), production of Vector Mesons and comparison between diffractive processes at HERA and at hadron-hadron colliders have brought more insight into the study of diffraction without fully clarifying the concept of diffraction in QCD.

- `Rate of jets production.` The production of jets in DIS has become a very matured domain. It is at present one of the best tools to disentangle the value of α_s from the gluon density at NLO. The precision is so good that theoretical calculations at NNLO, as existing in inclusive processes, are highly demanded.

- `Heavy quarks productions.` In the recent years, impressive progress has been achieved by the H1 and ZEUS collaboration on the measurement of the structure functions $F_2^{c\bar{c}}$ and $F_2^{b\bar{b}}$ in DIS processes. Clear pattern of scaling violations have been observed. They are well described by perturbative QCD. The heavy quark structure functions contribute at present to the precision of the extraction of parton densities in the proton.

- `PDFs fits.` A new step in the history of DIS has been the combination of H1 and ZEUS data before any QCD fits. The precision was naturally improved by reducing the statistical errors but also by decreasing the systematic uncertainties because different experimental

techniques were used in the detectors. The gain is the production of HERAPDF fits only using the HERA DIS data with an excellent precision which rival the global fits. The precision of the parton densities is even improved when jet cross-sections and heavy quark structure functions are combined to the inclusive measurement in the QCD fit. It is anticipated that determination of PDFs with the best precision would be of growing importance for our ability to extract new physics at LHC. Conversely, measurements of Standard Physics processes at LHC should improve knowledge of parton densities in a large part of the x range.

6 Spin Physics

Since 20 years after the early measurement of EMC, in parallel to the e-p collider physics at HERA, the domain of Spin Physics in DIS has been considerably studied. Dedicated fixed target experiments at SLAC, CERN, DESY and Jlab have accumulated inclusive and semi-inclusive data on Polarised DIS. Complementary informations has been brought by experiments at RHIC. Direct measurements and NLO QCD fits have provided important information on the constituents of the nucleon. The total contribution of valence quarks, strange quarks, sea quarks and gluons do not match the $1/2$ spin value of the nucleon. At present, we still do not know where the proton spin comes from.

7 Concluding remarks

No doubt that in the history of high energy physics DIS processes have been crucial for establishing the dynamical reality of quarks and the impressive correctness of perturbative QCD. As will be shown all along the workshop the very exciting comparison between the first LHC results and the predictions mainly based on PDFs extracted from DIS processes will underline the central role of DIS.

However a few important issues remain open in the field od DIS including:

- Precise determination of the strong running constant. It is not yet clear whether determinations of α_s from DIS and from other processes do agree.
- The genuine uncertainty of PDFs is still a topic of many debates and studies [40].
- Understanding of low x physics and diffractive processes has made progress in the last years but is not yet satisfying.
- The origin of the proton spin is a mystery.

More insights into these questions are expected at the Workshop but probably not the final answer.

8 Acknowledgements

I am grateful to the organizers of the Workshop for inviting me to give this talk, thereby allowing me to revisit the glorious past and present of DIS physics. I would also like to thank L. Schoeffel for reading the manuscript and useful suggestions.

References

[1] E. D. Bloom, D. Coward, H. DeStaebler, J. Drees, G. Miller, *et al.* Phys.Rev.Lett. **23** (1969) 930–934.

[2] W. K. H. Panovsky. Conf. Proc., *14th International Conference on High-Energy Physics,* Vienna, Austria (1968) 23–39.

[3] J. Bjorken. Phys.Rev.Lett. **16** (1966) 408.

[4] J. Bjorken. Phys.Rev. **179** (1969) 1547–1553.

[5] J. Bjorken. Conf.Proc. **C670828** (1967) 490–502.

[6] J. I. Friedman. Rev.Mod.Phys. **63** (1991) 615–627.

[7] R. E. Taylor. Rev.Mod.Phys. **63** (1991) 573–595.

[8] F. Brasse, J. Engler, E. Ganssauge, and M. Schweizer. DESY-67-34 (1967) .

[9] W. Albrecht, F. Brasse, H. Dorner, W. Flauger, K. Frank, *et al.* Phys.Lett. **B28** (1968) 225–228.

[10] R. E. Taylor. Conf. Proc., *The 4th Int. Symposium on Electron and Photon Interactions at High Energies,* Liverpool, England (1969) 251–260.

[11] C. G. Callan and D. J. Gross. Phys.Rev.Lett. **22** (1969) 156–159.

[12] Gargamelle Collaboration, H. Deden, *et al.* Nucl.Phys. **B85** (1975) 269.

[13] D. J. Gross and C. H. Llewellyn Smith. Nucl.Phys. **B14** (1969) 337–347.

[14] C. Chang, K. Chen, D. Fox, A. Kotlewski, P. F. Kunz, *et al.* Phys.Rev.Lett. **35** (1975) 901.

[15] BCDMS Collaboration, A. Benvenuti, *et al.* Phys.Lett. **B223** (1989) 485.

[16] E. Kabuss. Nucl.Phys.Proc.Suppl. **29A** (1992) 1–8.

[17] A. Milsztajn, A. Staude, K. Teichert, M. Virchaux, and R. Voss. Z.Phys. **C49** (1991) 527–542.

[18] S. R. Mishra and F. Sciulli. Ann.Rev.Nucl.Part.Sci. **39** (1989) 259–310.

[19] NuTeV Collaboration, M. Tzanov, *et al.* Phys.Rev. **D74** (2006) 012008, `arXiv:hep-ex/0509010 [hep-ex]`.

[20] CDHS Collaboration, H. Abramowicz, J. de Groot, J. Knobloch, J. May, P. Palazzi, *et al.* Z.Phys. **C15** (1982) 19.

[21] CCFR Collaboration, A. Bazarko, *et al.* Z.Phys. **C65** (1995) 189–198, `arXiv:hep-ex/9406007 [hep-ex]`.

[22] NuTeV Collaboration, M. Goncharov, *et al.* Phys.Rev. **D64** (2001) 112006, `arXiv:hep-ex/0102049 [hep-ex]`.

[23] U. Klein. These Proceedings .

[24] NMC Collaboration, M. Arneodo, *et al.* Phys.Rev. **D50** (1994) 1–3.

[25] EMC Collaboration, J. Aubert, *et al.* Phys.Lett. **B123** (1983) 275.

[26] M. Arneodo. Phys.Rept. **240** (1994) 301–393.

[27] EMC Collaboration, J. Ashman, *et al.* Phys.Lett. **B206** (1988) 364.

[28] R. Devenish. J.Phys. **G19** (1993) 1425–1427.

[29] H1 Collaboration, I. Abt, *et al.* Nucl.Phys. **B407** (1993) 515–538.

[30] A. De Rujula, S. Glashow, H. D. Politzer, S. Treiman, F. Wilczek, *et al.* Phys.Rev. **D10** (1974) 1649.

[31] F. Wilczek. www.frankwilczek.com/selectedPubs20080610.pdf, Comment on QCD: Fundational Papers .

[32] L. Gribov, E. Levin, and M. Ryskin. Phys.Rept. **100** (1983) 1–150.

[33] Particle Data Group, K. Nakamura, *et al.* J.Phys.G **G37** (2010) 075021 and 2011 partial update.

[34] H1 and ZEUS Collaboration, F. Aaron, *et al.* JHEP **1001** (2010) 109, `arXiv:0911.0884 [hep-ex]`.

[35] ZEUS Collaboration, M. Derrick, *et al.* Phys.Lett. **B315** (1993) 481–493.

[36] R. Cashmore. Conf. Proc, *The 9th International Workshop on Deep Inelastic Scattering (DIS 2001),* Bologna, Italy (2001) 263–268.

[37] H1 Collaboration, S. Aid, *et al.* Nucl.Phys. **B449** (1995) 3–24, `arXiv:hep-ex/9505014 [hep-ex]`.

[38] H1 Collaboration, F. Aaron, C. Alexa, V. Andreev, S. Backovic, A. Baghdasaryan, *et al.* Eur.Phys.J. **C71** (2011) 1579, `arXiv:1012.4355 [hep-ex]`.

[39] G. Altarelli. Conf. Proc., *XVII Int. Workshop on Deep-Inelastic Scattering and Related Topics (DIS 2009),* Madrid, Spain (2009) , `arXiv:0907.1751 [hep-ph]`.

[40] S. Alekhin, S. Alioli, R. D. Ball, V. Bertone, J. Blumlein, *et al. The PDF4LHC Working Group Interim Report (*2011) , `arXiv:1101.0536 [hep-ph]`.

Precision Measurements of the Proton Structure

Iris Abt[1] on behalf of the H1 and ZEUS collaborations[2]

[1]MPI für Physik, Föhringer Ring 6, 80805 München, Germany
[2]DESY, Notkestraße 85, 22607 Hamburg, Germany

DOI: http://dx.doi.org/10.3204/DESY-PROC-2012-02/7

The "proton structure" is a wide field. Discussed are predominantly the precision measurements of the proton structure functions at HERA and some of their implications for the LHC measurements. In addition, a discussion of what a proton structure function represents is provided. Finally, a connection to nuclear physics is attempted.

1 Introduction

The proton is quite a fantastic particle. If free, it doesn't decay on any timescale people have been able to explore. It has an immense ability to heal itself, demonstrated in the high rate of diffraction even for interactions with large momentum transfer. What the author really knows, is actually quite limited. The charge was determined to be "+1", the mass was measured to be 1.6×10^{-27} kg and the spin is 1/2. Spin will not be discussed in this contribution; there are others who will write about it.

If the proton is probed with enough energy, three valance quarks are revealed. If it is probed with even more energy, the QCD affliction of the proton, i.e. the glue and the sea become visible. QCD is always used when the results of one measurement are used to make predictions for another. And one part of this *ansatz* are parton distributions functions, PDFs, of the proton. They are a very successful tool. However, their shape is entirely heuristic; QCD cannot predict them from first principle.

Protons are a vital part of nuclei. Together with neutrons, they provide the rich world of elements that we so dearly love. However, in this environment QCD is generally not the theory of choice to predict what happens. Inside a nucleus, a proton can decay because the energy to become a neutron comes from the nucleus. Nuclei are not spheres; the proton itself is often depicted as one, but that is also too simplistic.

2 Proton Structure Functions at HERA

2.1 Deep Inelastic Scattering

At HERA, the structure of the proton was probed with electrons and positrons. Figure 1 illustrates deep inelastic scattering, DIS, which is generally used to determine the proton structure. The castle is destroyed to learn about its inhabitants, i.e. the quarks and gluons, and their habits. It is interesting to note that the castle rebuilds itself in about 20 % of the interactions. However, this, i.e. diffraction, is not the subject of this contribution.

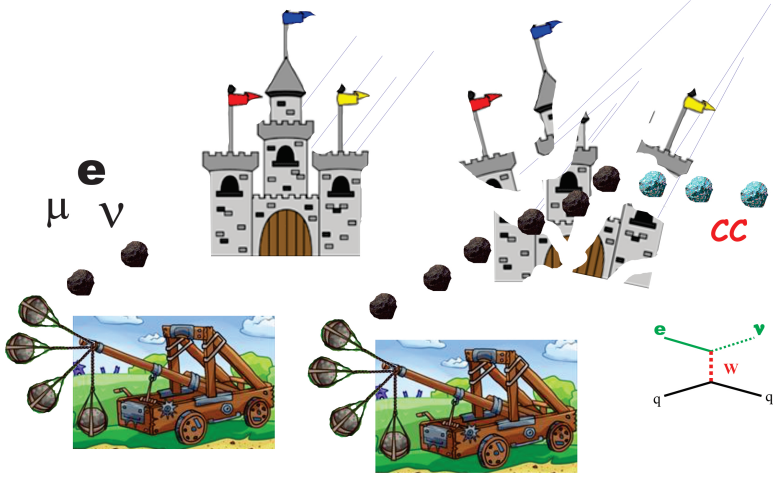

Figure 1: Illustration of deep inelastic lepton proton scattering. At HERA the lepton was an electron or positron. In this demonstration, a charged current interaction destroys the proton.

More commonly used to illustrate DIS is the Feynman diagram depicted in Figure 2. It should, however, be noted that this Feynman diagram describes the interaction in lowest order while Figure 1 includes all orders. Anyhow, the process can be described in terms of the kinematic variables x, y, and Q^2. The variable Q^2 is defined as $Q^2 = -q^2 = -(k - k')^2$, where k and k' are the four-momenta of the incoming and scattered lepton, respectively. Bjorken x is defined as $x = Q^2/2P \cdot q$, where P is the four-momentum of the incoming proton. The fraction of the lepton energy transfered to the proton in the rest frame of the proton is given by $y = P \cdot q/P \cdot k = Q^2/sx$, where s is the square of the lepton-proton centre-of-mass energy.

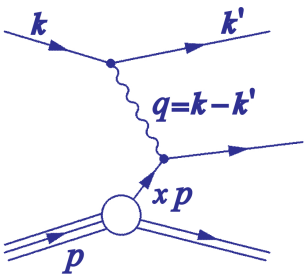

Figure 2: Feynman diagram of deep inelastic lepton proton scattering

In neutral current, NC, events, most of the information can be deduced from the deflected probe. However, quite often the hadronic system is also used in order to optimise the uncertainties. In charged current, CC, events, the outgoing neutrino evades detection and the hadronic system is all we have. This makes things are a lot more difficult.

2.2 Cross sections

All our understanding of DIS is connected to the paradigm of factorisation.

In lowest-order QCD, three processes contribute to the NC DIS cross section, namely the Born ($V^*q \to q$, with $V^* = \gamma^*, Z^*$), the boson-gluon-fusion ($V^*g \to \bar{q}q$) and QCD-Compton-scattering ($V^*q \to qg$) processes. The cross section for the production of an observed hadron,

H, in the final state in DIS can be expressed in QCD, using the factorisation theorem, as

$$\sigma(ep \to e + H + X) = \sum_{j,j'=q,\bar{q},g} f_{j/p}(x,Q) \otimes \hat{\sigma}_{jj'}(x,Q,z) \otimes F_{H/j'}(z,Q),$$

where the sum runs over all possible initial (final)-state partons j (j'), $f_{j/p}$ are the proton PDFs, which give the probability of finding a parton j with momentum fraction x in the proton, $\hat{\sigma}_{jj'}$ is the partonic cross section, which includes the matrix elements for the three processes mentioned above, and $F_{H/j'}$ are the fragmentation functions, which give the probability that a hadron H with momentum fraction z originates from parton j'.

This contribution concentrates on inclusive measurements, so that the fragmentation "only" shows up in the calculation of the systematic uncertainties connected to the acceptance and the efficiency to reconstruct an event. The cross sections are measured and their description in QCD is used to extract the PDFs which in turn are used to make predictions. This works extremely well as long as the same assumptions are made for the extraction and the predictions.

For a complete overview of neutral current, NC, and charged current, CC, cross sections, please check your favorite textbook. The electroweak Born-level cross section for the $e^{\pm}p$ NC interaction serves as an example here:

$$\frac{d^2\sigma(e^{\pm}p)}{dxdQ^2} = \frac{2\pi\alpha^2}{xQ^4}[Y_+\tilde{F}_2(x,Q^2) \mp Y_- x\tilde{F}_3(x,Q^2) - y^2\tilde{F}_L(x,Q^2)], \quad (1)$$

where α is the fine-structure constant, $Y_{\pm} = 1 \pm (1-y)^2$ and $\tilde{F}_2(x,Q^2)$, $\tilde{F}_3(x,Q^2)$ and $\tilde{F}_L(x,Q^2)$ are generalised structure functions. The contribution of the longitudinal structure function $\tilde{F}_L$ to $d^2\sigma/dxdQ^2$ is approximately 1 %, averaged over the relevant kinematic range; it contributes up to 10 % at high y. The $\tilde{F}_3$ term only starts to contribute significantly at Q^2 values of the order of the mass of the Z boson squared.

The reduced cross sections for NC $e^{\pm}p$ scattering are defined as

$$\tilde{\sigma}^{e^{\pm}p} = \frac{xQ^4}{2\pi\alpha^2}\frac{1}{Y_+}\frac{d^2\sigma(e^{\pm}p)}{dx}dQ^2 = \tilde{F}_2(x,Q^2) \mp \frac{Y_-}{Y_+}x\tilde{F}_3(x,Q^2) - \frac{y^2}{Y_+}F_L(x,Q^2). \quad (2)$$

The $x\tilde{F}_3$ can be obtained from the difference of the e^-p and e^+p cross section.

The different structure functions in the Born-level approximation are directly connected to different combinations of quark momentum distributions. The structure function $\tilde{F}_3$, for example, provides information about the u and d valence quarks.

2.3 The advent of precision

The definition of precision is certainly not objective and what it really means in this context is debatable. However, from the viewpoint of HERA, precision structure functions came about when the two experiments, H1 and ZEUS, started to combine their already individually beautiful data.

The two collaboration published their combined results on data taken in the period of 1993 – 2000 in 2010 [1]. The 10 years it took indicate that such a combination is difficult. The bins and the kinematic ranges need to be adjusted, the uncertainties evaluated according to their correlation, and, in order to do so, the team has to understand both experiments. The result is depicted in Fig. 3. Due to the careful analysis of the correlations between the systematic

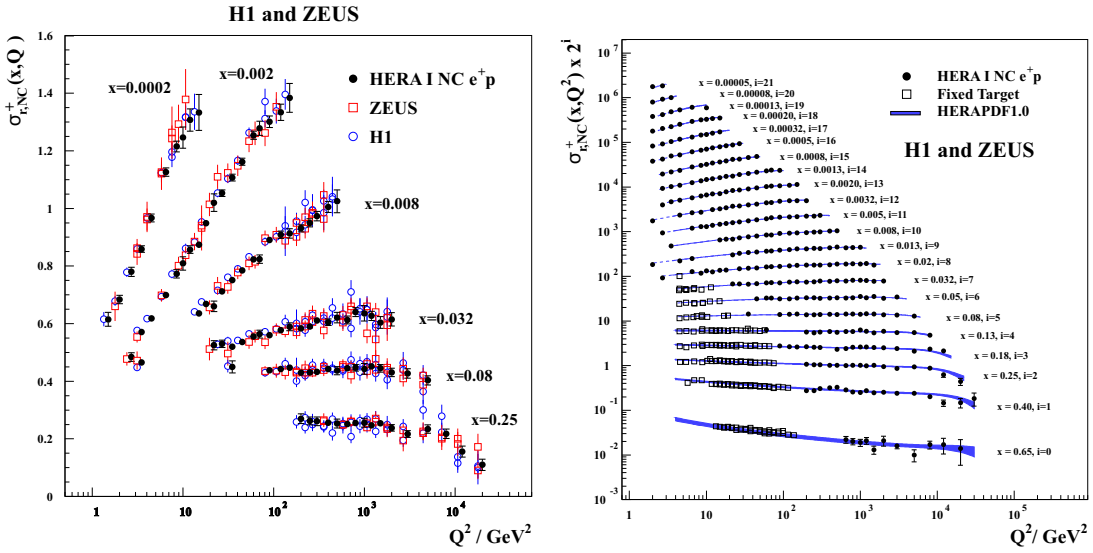

Figure 3: Combination of reduced cross section from [1]. The left panel demonstrates the power of combination for selected values of x while the right panel shows the wide kinematic range covered by HERA.

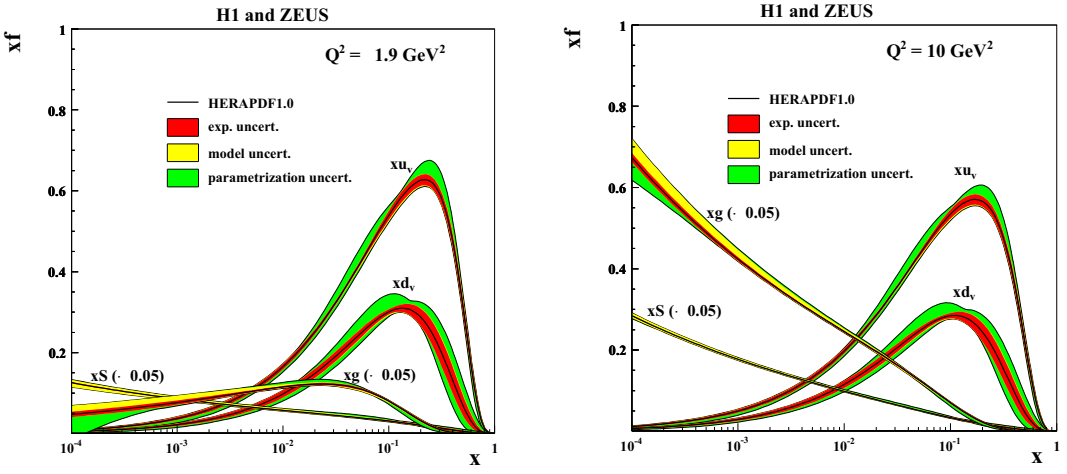

Figure 4: HERAPDF1.0: The left panel demonstrates the importance of the valence quarks at relatively low Q^2 while the right panel shows the growth of the sea and the glue with Q^2. Please note that sea and glue are scaled down by a factor 20.

uncertainties, the gain is significantly larger than expected if only the statistical precision is considered.

The results of the combination were used to produce the first HERAPDF [1], entirely deduced from HERA inclusive data, see Fig. 4.

2.4 The PDF fitting industry

There is quite a number of groups who perform fits to a wide variety of data sets in order to extract PDFs. They go by acronyms representing names or ideas, in alphabetic order: ABKM, CTEQ, HERAPDF, GJR, NNPDF, MSTW. The acronyms are usual augmented by a version number. HERAPDF was so far restricted to HERA data. Other groups use HERA data, but not exclusively.

Different PDFs can be extracted at varying order in perturbative QCD, using different flavor schemes, different parameters like charm mass and different parametrisations. It is of great importance to use the same schemes and assumptions used for the extraction when making a prediction. The predictions you see in the plots showing cross sections were of course all extracted keeping that in mind.

2.5 Towards the final HERA precision

The data taking period that will provide the final precision in cross sections and PDFs from HERA is the HERA II period from 2004 to 2007. The data are still being analysed and some results are only available as preliminary releases so far. It is expected that both the H1 and ZEUS collaborations will publish final results this summer.

Figure 5 gives a taste of the precision obtained from HERA II data. At high Q^2, the NC and CC cross sections become equal because the Z^0 starts to dominate over the photon. The difference between electron and positron data also becomes clearly visible at high Q^2.

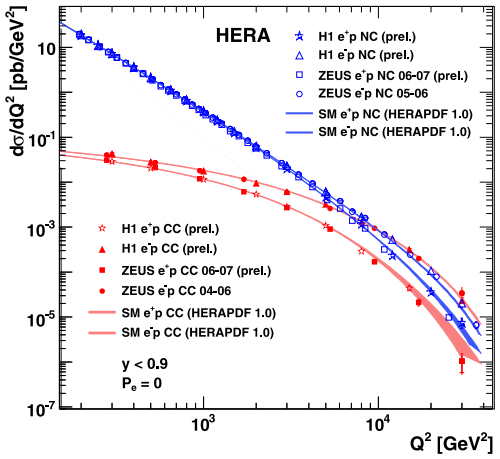

Figure 5: A demonstration how precision data reveal the unification of the electroweak force and parity violation at $Q^2 > m^2_{Z^0}$.

The CC data also provide other valuable information. As there is no interference from photon exchange, the CC process was used to check the V-A structure of the weak interaction using the polarisation of the lepton beam in HERA II [2]. However, for this contribution the access to the quark structure of the proton is more interesting. As an example, Fig. 6(left) shows the reduced cross sections for CC positron interaction as published by ZEUS [3] . These data give access to the d and s as well as $\bar{u}$ and $\bar{c}$ content of the proton.

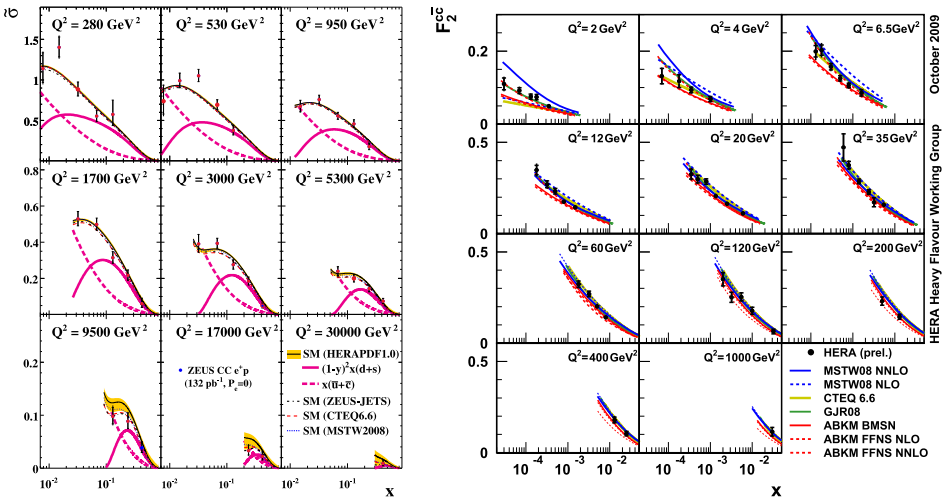

Figure 6: Access to the charm content of the proton. Left: through CC interactions, right: through D meson production.

While the CC data give a hint of charm, the production of D mesons in all varieties give a direct handle on the c content. This is used to extract the charm structure functions. A preliminary result obtained from combined ZEUS and H1 data is depicted in Fig. 6(right). The charm structure function is an important input to LHC analyses, where the knowledge or lack thereof could provide a dominating systematic uncertainty.

recommended version

NAME	NC and CC DIS	NC, lower E(p_beam)	Jets	Charm	Docu	Grids	Data comparison	Date
HERAPDF1.7 NLO	HERAI + partial HERAII	H1+ZEUS	H1 and ZEUS(1)	H1+ZEUS	Figures	N.A.		June 2011
HERAPDF1.6 NLO	HERAI + partial HERAII	---	H1 and ZEUS(1)	---	Writeup and figures	N.A.		March 2011
HERAPDF 1.5 NNLO	HERAI + partial HERAII	---	---	---	Figures	LHAPDF beta 5.8.6		March 2011
HERAPDF 1.5 NLO	HERAI + partial HERAII	---	---	---	Figures	LHAPDF beta 5.8.6		July 2010
Charm mass scan	HERAI	---	---	H1+ZEUS	Writeup and figures	---		August 2010
HERAPDF1.0 NNLO	HERAI	---	---	---	ICHEP2010 writeup and figures	Docu for LHAPDF		April 2010
	HERAI	H1+ZEUS	---	---	Writeup and figures	N.A.		April 2010
	HERAI	---	---	H1+ZEUS	DIS2010 writeup and figures	N.A.		April 2010
HERAPDF1.0 NLO PUBLISHED	HERAI	---	---	---	Paper HERAPDF1.0 page	LHAPDF	Benchmarking HERAPDF1.0	Nov. 2009

Figure 7: Available HERAPDFs as seen on the web [4].

2.6 The HERAPDF family

The HERA data was used over the past years to create a family of PDFs. Data were included as results became available. The table depicted in Fig. 7 provides an overview as given on

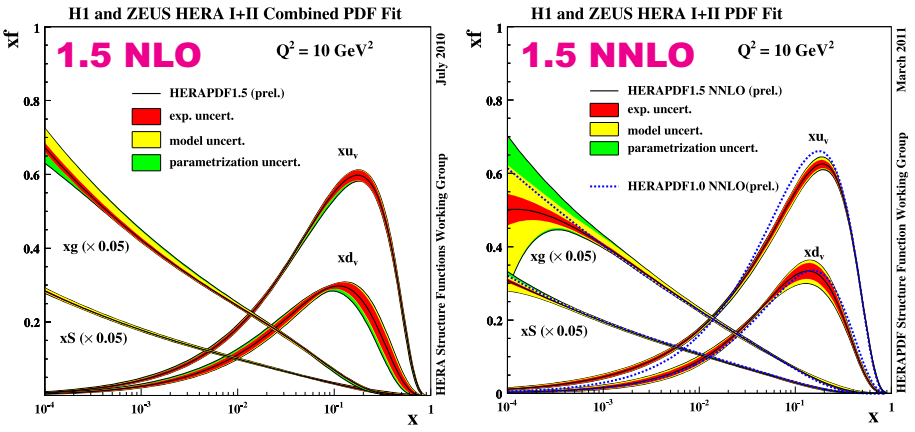

Figure 8: The currently recommended member of the HERAPDF family. The NNLO extraction has a larger uncertainty on the glue and the sea. Experimental, model and parametrisation uncertainties are given separately.

the net at the time of the conference [4]. The youngest member of the family, HERAPDF1.7, is not only based on inclusive measurements, but also on jet and charm data. Charm data was already used previously for a charm mass scan. The currently recommended version is HERAPDF1.5, available at next to leading order, NLO, and at next-to-next to leading order, NNLO, see Fig. 8. It is, as HERAPDF1.0, based on inclusive data only. As soon as the final results for the inclusive measurement of ZEUS and H1 as well as combination paper on charm will be published, a new major version of HERAPDF will be extracted.

The working group extracting, i.e. fitting, all the HERAPDFs has developed a tool named HERAfitter [5]. This tool allows the extraction of PDFs for a flexible set of input assumptions and input data. This tool has become "open source software" and is a service to the HEP community at large. It is not only used in the HERA, but also the LHC community.

3 HERAPDF goes LHC

The HERAPDFs are being used to predict the outcome of measurements done at the LHC. Figure 9 gives an example from CMS who measured the muon charge asymmetry from W decays. This is sensitive to the difference between the u and d valence quark distributions. HERAPDF1.5 is quite successful predicting this asymmetry.

LHC has also started to contribute to the PDFs. The HERAfitter tool was used to extract the strange quark content of the proton [6]. The strange quark cannot be well constrained by HERA data, as it would require a CC analysis of D mesons which so far is a "mission impossible".

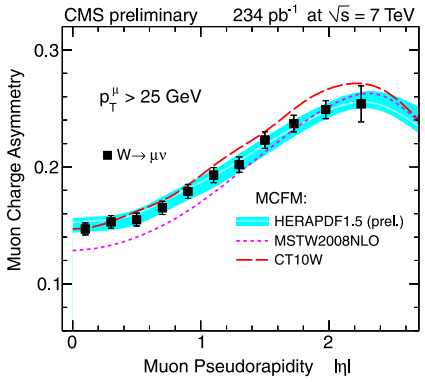

Figure 9: Muon charge asymmetry from W decays compared to predictions.

4 Low-x partons

The physical interpretation of PDFs is not clear to
the author. The parametrisations are not predicted by any theory; they are based on common sense arguments like they should be zero at $x = 1$. The variable x itself is generally interpreted as the fraction of the momentum of the proton that a parton carries. At very low x, however, the Heisenberg uncertainty principle teaches us that such a parton cannot be confined inside a proton. The interpretation is only valid in a reference frame in which the proton is fast and in the context of a scattering process with a certain momentum transfer, Q^2. In the reference frame where the proton is at rest, the variable x can be interpreted as $x \approx 0.1 \cdot l[\text{fm}]$, where l is the coherence length of fluctuations of the exchanged photon. For $x < 0.1$, l is larger than the size of the proton of about 1 fm. A detailed discussion can be found in [7]. The effect is demonstrated in Fig. 10. The photon fluctuates into a quark-antiquark pair and this fluctuates further into a hadron like object which interacts with the proton.

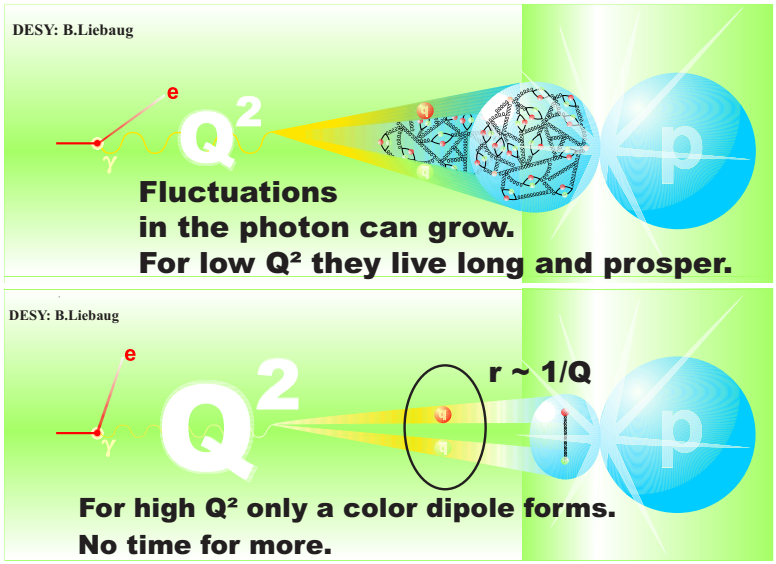

Figure 10: The ep scattering process in the rest frame of the proton. The photon looks like an extended object. At low Q^2 , top, it has time to grow into a complicated object. At high Q^2, bottom, there is only time to form a so called "color dipole".

In general, physics should not be dependent on the rest frame in which it is looked at. Therefore, the two different interpretations should only be seen as something to guide us through perturbation theory. Somehow, what me measure has to be connected to the structure of the underlying interaction. At low x, the PDFs represent more the strong and electroweak field than the proton. It would be nice to base the parametrisations that we use on some understanding of these fields. Another interesting question in this context is, whether the PDFs that could be measured in neutrino proton scattering would be the same as in electron proton scattering. After all, there is no photon to fluctuate in this case. The guess of the author is that at low x the result would be different. The photon probably just looks like a hadron. Thus, probing with a hadron would give the same results as probing with a photon(electron).

5 Test of the color dipole picture

At the very end of the HERA running, data were taken at lower proton energies. This facilitated direct measurements of the longitudinal structure function F_L [8, 9]. These measurement are tricky, because they require the identification of electrons with a relatively low energy, down to 3.4(6.0) GeV for H1(ZEUS). Both collaborations published results which clearly show that $F_L > 0$. The results on F_L can be taken as a probe of higher orders of perturbative QCD, but they can also be used to test the color dipole picture[10]. The H1 collaboration compared their results to different model predictions as depicted in Fig. 11. The predictions based on the color dipole model deviate from the PDF-based ones at low Q^2. The data seem to have a preference to fall between the two ways of looking at things. It should be noted that nature does seem to have a sense of humor.

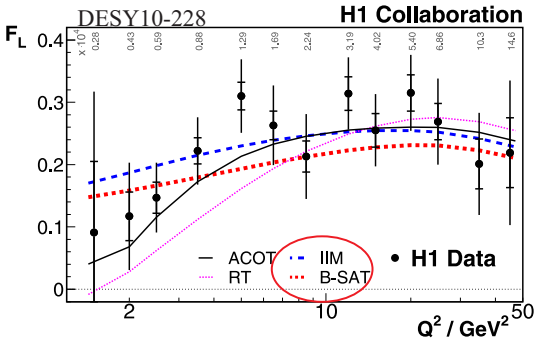

Figure 11: Measurement of the structure function F_L compared to predictions from colour dipole models, IIM and B-SAT, and others, ACOT and RT [8].

Another test of the color dipole model is provided by Deeply Virtual Compton Scattering, DVCS. The measured dependence of the cross section on the squared momentum transfer at the proton vertex, t, was compared to predictions of the colour dipole model and the model did quite well [11].

6 The looks of a proton

The PDFs as so far discussed in this contribution only give information about what happens in momentum space. It is possible to define generalised parton distribution functions which are used for two-gluon exchanges like in DVCS. The interpretation then is in longitudinal momentum and transverse position space. The aforementioned dependence of the DVCS cross section on t can be parametrised as $d\sigma/dt \sim exp(-b|t|)$ and b can be converted to an average impact parameter. The H1 collaboration has done so [11] and obtained 0.65±0.02 fm for x=0.0012. Is this the transverse expansion of the partons engaged in the interaction? Is this the size of the proton? Or the size of the photon fluctuation? Or the relevant size of the field? Anyhow, there is a quite a number of b-slope measurements available, not only for DVCS, but also for vector meson production. It might be interesting to interpret these measurements with respect to impact parameters.

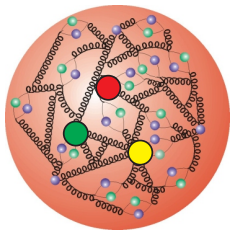

Figure 12: Standard illustration of a "HEP-proton". Three valance quarks are imbedded in a cocoon of gluons and sea quarks.

Most of the time, the "HEP-proton" is depicted as in Fig.12. The charge radius of the proton is not measured in HEP, high energy physics, but in low energy physics. The most precise

values come from electronic and muonic hydrogen [12]. The rms values are 0.8768±0.0069 fm and 0.84184±0.00067 fm. The two values disagree by four standard deviations which in itself has triggered some discussion, including discussions about physics beyond the standard model. However, the value of 0.65 fm is certainly quite different. But that is something that should not surprise too much. The author would assume that the charge radius as measured at low energies is related to the valence quarks. The "radius" measured with DVCS is connected to x=0.0012 and that should not be valence quarks at all.

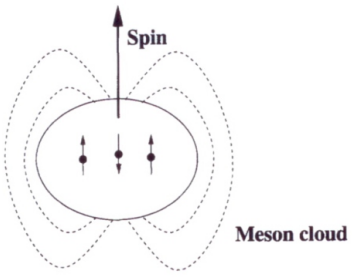

Figure 13: A proton as seen by a nuclear physicist [15]. It has a shape to support its magnetic moment and a meson cloud.

The picture of Fig.12 is in many ways misleading. Three charged objects as depicted would create an electric dipole moment, but this is known to be less than 0.54 10^{-23} ecm. And in addition, the proton cannot be spherical at all, because it has a magnetic moment, which was first measured in proton $\rightarrow \Delta$ excitations [13]; the most precise measurements come from single trapped protons [14]. The nuclear physicist's view of a proton is shown in Fig.13 [15]. Also shown is an indication of a meson cloud. This has to be there; otherwise the proton could not stick together with other baryons. This is again a completely different interpretation than typical HEP view of perturbative QCD. However, the meson cloud was observed in HEP, remember the EMC effect.

The next step in understanding the proton, or perhaps baryon or even nuclei in general, would be to match the pictures of nuclear physics with the ideas of QCD. There is some input on this from lattice QCD where the shape of baryons is actually predicted [16]. Figure 14 gives as an example the shape that is the result of a lattice QCD calculation.

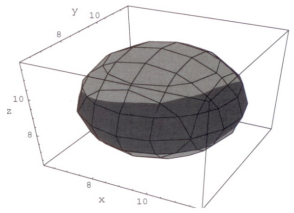

Figure 14: The shape of a Δ as predicted by lattice QCD [16].

It seems a worthwhile enterprise to think about ways how to measure such a shape and how to measure the spatial distribution of what is inside. In Fig. 1 it is shown, how we destroy the castle in order to find out what is inside and who just got married. It would be nice to open the door, have a look inside and just ask. However, many of the dynamics inside the castle might evade our observation, if we look with too much energy, because that means averaging over time; Heisenberg all over again.

7 Summary and Outlook

The proton as we know it still holds a lot of secrets. What is called the proton parton distribution functions, PDFs, was measured with excellent precision at HERA. The final results from HERA will be a very valuable legacy for a long time. They are expected within a year.

These PDFs are and will be one of the inputs to make precise Standard Model predictions for the LHC and other future experiments. The extraction of PDFs is one of the great success stories of HERA. The tools developed in this context will also survive and become part of the

HEP daily work.

The interpretation of proton PDFs in the context of understanding the proton itself is not trivial and there is more to the proton than PDFs. There are many questions about size, shape and the spatial distribution of quarks and gluons that should be addressed. In the end, it will take more than perturbative QCD to understand the proton.

References

[1] H1 and ZEUS Collab., F.D. Aaron *et al.*, JHEP **01** (2010) 109.

[2] ZEUS Collab., S. Chekanov *et al.*, Eur.Phys.J. **C61** (2009) 223.

[3] ZEUS Collab., H. Abramowicz *et al.*, Eur.Phys.J. **C70** (2010) 945.

[4] `https://www.desy.de/h1zeus/combined_results/herapdftable`

[5] `http://herafitter.hepforge.org/`

[6] ATLAS Collab., "Determination of the strange quark density of the proton from ATLAS measurements of the $W \to l\nu$ and $Z \to ll$ cross sections", 2012. `hep-ex/1203.4051`

[7] A. Caldwell and G. Grindhammer, Physik Journal **6** (2007) 39.

[8] H1 Collab., F.D. Aaron *et al.*, Eur.Phys.J. **C71** (2011) 1579.

[9] ZEUS Collab., S. Chekanov *et al.*, Phys.Lett. **B682** (2009) 8.

[10] C. Ewerz *et al.*, "The New F_l measurement from HERA and the Dipole model", 2012. `hep-ph/1206.6296`

[11] H1 Collab., F.D. Aaron *et al.*, Phys.Lett. **B659** (2008) 796.

[12] M. O. Distler *et al.*, Phys.Lett. **B696** (2011) 343.

[13] R. Beck *et al.*, Phys.Rev.Lett **78** (1997) 606.

[14] J. DiScaccia and G. Gabrielse, "Direct Measurement of the Proton Magnetic Moment", 2012. `hep-ph/1201.3038`

[15] A. Faessler, Progress in Particle and Nuclear Physics **44** (2000) 197.

[16] C. N. Papanicolas, Eur.Phys.J. **A18** (2003) 141.

α_S status

Andre Hoang[1]

[1] University of Vienna, Faculty of Physics, A-1090 Vienna

DOI: http://dx.doi.org/10.3204/DESY-PROC-2012-02/19

A write-up was not submitted for this talk. Most of the material presented can be found in: S. Bethke, A. Hoang et al., "Workshop on Precision Measurements of α_S", http://arxiv.org/abs/arXiv:1110.0016.

Status of polarized structure functions

Claude Marchand

CEA, Centre de Saclay, IRFU/SPhN, 91191 Gif-sur-Yvette, France

DOI: http://dx.doi.org/10.3204/DESY-PROC-2012-02/20

An experimental overview on polarized structure functions of the nucleon is given. It covers results from experiments performed at CERN, HERA, JLAB and RHIC. Latest results on quark and gluon helicities are discussed, as well as results on Transverse Momentum Dependent distribution functions (TMD).

1 Introduction

At leading order in pQCD, lepton-nucleon or proton-proton scattering at high energies can be interpreted as photon-quark (gluon) or quark-quark (gluon) scattering during a fragmentation phase, followed by the dress up of the quark to form a meson or a hadron in the final state. It allows thus to study quark (gluon) distribution functions (DF), given the quark fragmentation function (FF) is known. In collinear approximation (i.e. integrating over intrinsic transverse quark momentum k_T), the leading twist contribution to the quark distribution (density) function can be written as ([1]):

$$\Phi(x) = \frac{1}{2}\{q(x) + \gamma_5 \Delta q(x) S_L + \gamma_5 \Delta_T q(x) S_T \gamma_1\} n^+$$

Here, in conventional notations, $q(x)$ represent the unpolarized quark distribution function, $\Delta q(x)$ the longitudinal polarized quark distribution function (also called helicity), and $\Delta_T q(x)$ the transversely polarized quark distribution function. In the non relativistic limit, $\Delta_T q(x) = \Delta q(x)$.

One of the main goals of the current experiments studying nucleon spin structure is to determine how the total longitudinal spin projection of the nucleon, 1/2, is distributed among its constituents, quarks, gluons and orbital angular momentum:

$$\frac{S_z^N}{\hbar} = \frac{1}{2} = \frac{1}{2}\{\Delta\Sigma(= \textstyle\sum_q \Delta q) + \Delta G + L_z^q + L_z^g\}$$

We review here the recent results on the gluon and quark helicities obtained by HERMES, COMPASS, PHENIX and STAR experiments. Measurements of transverse spin asymmetries, leading to the determination of the transverse spin quark distributions and to the Sivers functions obtained by HERMES and COMPASS are also discussed, as well as their possible relation to Orbital Angular Momentum (OAM).

2 Longitudinal spin structure of the nucleon

Based on all the world data ([2, 3] and references therein) were the structure functions $g_1^p(x, Q^2)$ and $g_1^d(x, Q^2)$ have been obtained in inclusive Deep Inelastic Scattering (DIS) (Fig. 1), and

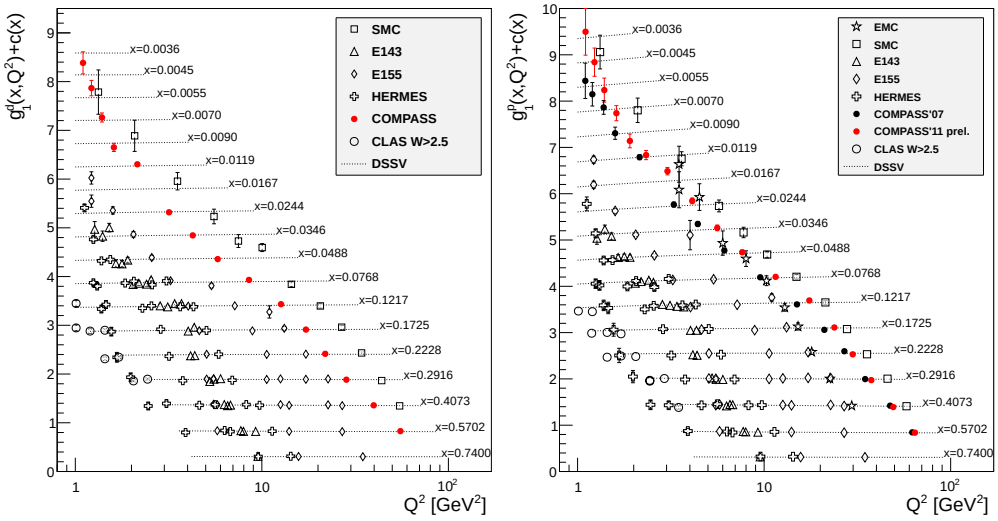

Figure 1: World data on g_1^d (left) and g_1^p (right), compared to global fit of DSSV [4]. Also shown for g_1^p are preliminary data obtained in 2011 at COMPASS with 200 GeV muon beam.

using additional information from neutron and hyperon decays (a_3, a_8), the sum of the quark contribution to the nucleon spin (in $\overline{MS}$, $\Delta\Sigma = a_0$) turns out to be about 33% [4]. In addition to the quark helicities, it is thus important to study also the gluon helicities, as well as the Orbital Angular Momentum (OAM) , in order to hope solving this so called spin crisis.

2.1 Quark helicities

As seen above, inclusive DIS gives already a lot of information on the quark helicities, allowing to measure the sum of their contribution to the nucleon spin via $\Delta\Sigma = \sum_{u,\overline{u},d,\overline{d},s,\overline{s}} \Delta q$. Using in addition SU3 flavor symmetry, were one assumes $\Delta\overline{u} = \Delta\overline{d} = \Delta\overline{s} = \Delta s$, and the DGLAP evolution equations, one can obtain separate information on the valence quark ($\Delta u_v(x)$, $\Delta d_v(x)$) and sea quark ($\Delta\overline{q}(x)$) helicities, as well as the gluon helicity $\Delta G(x)$ [5]. However, as the world coverage in Q^2 range is small, specially at low x, the accuracy on ΔG is bad. So more direct measurements of ΔG are needed. Also, from g_1^p and g_1^d alone, with the the knowledge of a_3 and a_8, one can obtain with simple algebra, the contribution of the strange quarks to the nucleon: $(\Delta s + \Delta\overline{s}) = \frac{1}{3}(a_0 - a_8) = -0.08$ [6].

Nevertheless, in order to be able to access to the quark distributions separately for u,d,s,$\bar{\text{u}}$,$\bar{\text{d}}$ and $\bar{\text{s}}$, it is necessary to study semi-inclusive DIS (SIDIS) channels, where in addition to the scattered probe, also a hadron is detected in the final state. In this case, in LO in pQCD, the measured asymmetries can be written as a sum of products of quark distribution functions $\Delta q(x, Q^2)$ and fragmentation functions $D_q^h(z, Q^2)$, z being the fraction of the probe momentum carried by the emitted hadron h.

In parallel to the polarized inclusive DIS measurements, such semi inclusive (SIDIS) events where an additional hadron tags the flavor of the struck quark, were recorded both at HERMES and COMPASS [6, 7]. These data are used to extract at LO the helicity quark distributions for

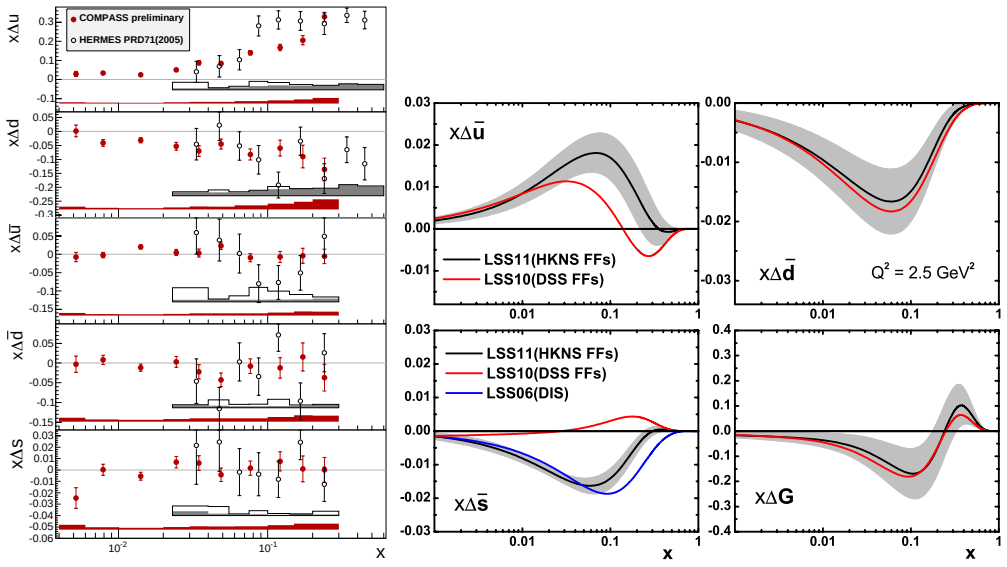

Figure 2: Left: $\Delta q(x)$ measured from SIDIS data at COMPASS [6] and HERMES [7]; Right: Results from global fit [9] using different FF's.

each quark flavor separately down to x = 0.004. This provides a wider picture of the nucleon spin, however requiring as an additional input the quark fragmentation functions. COMPASS results [6] obtained using FF's from DSS [8] are shown in Fig. 2 together with HERMES results [7] where FF's are extracted from the same HERMES data. The curve shows the global QCD fit of DSSV [4] at LO. Sea quark polarized distributions are found to be compatible with zero within the statistical errors. Concerning the strange quarks, note that the DSSV fit accommodates both the SIDIS data (COMPASS and HERMES data, shown here and compatible with zero), and the results from analyses of inclusive DIS data, which lead to a negative first moment for Δs (suggesting a negative contribution at low x). In the future, the SIDIS sector will benefit from more precise determination of quark FF's.

At RHIC, in a short exploratory run, first p-p collisions at 500 GeV were performed. By studying the parity violating reaction $u + \overline{d} \to W^+ \to e^+ + \nu$, the quantity $\Delta\overline{d}/\overline{d} - \Delta u/u$ is probed. First results from PHENIX and STAR reporting asymmetries with signs as expected from SIDIS results, are very encouraging [10, 11]. The advantage of this channel is that no FF are needed for the extraction of quark helicities.

2.2 Gluon polarization

In addition to the method of global fits on DIS data using DGLAP evolution, described in section 2.1, there are two more direct ways to experimentally determine the gluon polarization.

The first method is via polarized lepton nucleon SIDIS reactions, where the double spin asymmetry of cross sections for the photon gluon fusion (PGF) process $\gamma g \to q\overline{q}$ are measured. PGF events can be searched for in two channels: the "open charm channel" where a $c\overline{c}$ pair is produced and a charm quark is identified via the production of a D^0 meson, and the "high p_T hadron" channel, where outgoing quarks (likely light quarks) hadronize into hadrons, mainly

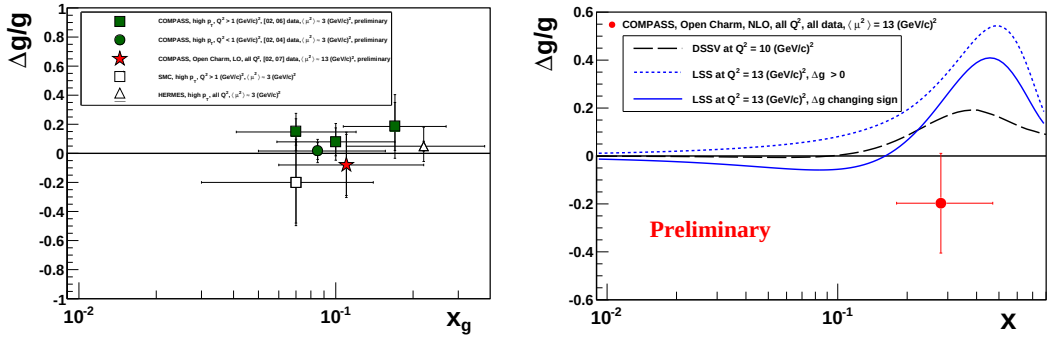

Figure 3: Direct measurements of $\Delta G/G$ via Photon GluonFusion. Left: LO extraction from open charm [12] and high p_T [13, 14, 15] PGF; Right: first NLO extraction from open charm at COMPASS [14], compared to DSSV [8] and LSS [9] global fits

pions, with high transverse momentum p_T . The open charm channel is only accessible at COMPASS [12] thanks to the high energy of the CERN polarized muon beam. It provides a clean signature of the PGF, but is a difficult channel requiring to count events with D^0 production over a large combinatorial background of πK pairs, leading to limited statistics. On the contrary, the high p_T channel, used at both COMPASS [13, 14] and HERMES [15] , benefits from high statistics but suffers from competing background processes (leading order, QCD Compton, resolved photon) which have to be simulated and accounted for.

Figure 3 left shows all existing direct measurements of the gluon polarization $\Delta G/G(x)$ extracted at leading order in QCD from the measured spin asymmetries in the high p_T and charm channels. COMPASS results from the open charm [12] (star) and high p_T [13, 14] (circle and closed square) channels are shown together with HERMES [15] (open triangle) and SMC (open square) results. Figure 3 right shows $\Delta G/G(x)$ extracted at NLO from the COMPASS charm channels [14], compared to global QCD fits from DSSV [4] and LSS [9], which do not include these data. The measurements probe x_g values of the gluon momentum fraction around 0.1-0.2 and give results compatible with zero in this kinematic range. The accuracy of these data, as well as the limited x_g range covered, do unfortunately not allow to constrain with high enough accuracy the first moment of ΔG, which enters in the nucleon spin decomposition.

The second method is via polarized hard $\vec{p}\vec{p}$ collisions, by choosing channels sensitive to ΔG and measuring double spin asymmetry of cross-sections. Such experimental studies of the gluon polarization have been performed at the RHIC collider. Collisions of protons polarized longitudinally in opposite directions have been realized mainly at $\sqrt{s} = 200$ GeV, but also at 62 GeV and more recently 500 GeV, covering various kinematics ranges. Several channels are used to pin down the gluon polarization. The most abundant channels in term of statistics are the production of π^0 at PHENIX [16] and the production of jets at STAR [17]. In both cases, three different elementary processes (gg, gq and qq) contribute to the cross-section, so that the measured double spin asymmetries A_{LL} are sensitive to a combination of three quantities: $\Delta G(x_1).\Delta G(x_2)$, $\Delta G(x_1).\Delta q(x_2)$, and $\Delta q(x_1).\Delta q(x_2)$, where x_1 and x_2 are the fractions of momentum carried by the two colliding partons. For each physical channel (π^0,

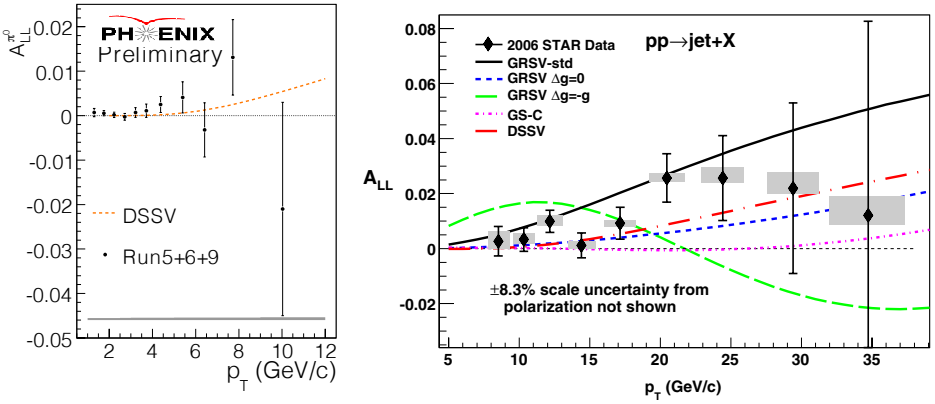

Figure 4: Double spin asymmetries measured at RHIC with $\vec{p}\vec{p}$ collisions at $\sqrt{s}$=200 GeV compared to DSSV [4]. Left: for π^0 production at Phenix [16]; Right: for single jet production at STAR [17].

jets, etc.) the measured double spin asymmetry $A_{LL}(p_T)$ is compared to calculations where a given parametrization of $\Delta G(x)$ is assumed. The results are presented in Fig. 4 left for the π^0 channel measured at PHENIX [16] and right for the single jet channel measured at STAR [17]. Both data sets favor a parametrization with a gluon polarization close to zero. When re-injected in global QCD fits including in addition world DIS and SIDIS data [4], these data provide a strong constrain on the first moment of ΔG truncated to the measured range $0.05 < x_g < 0.2$: $\Delta G^{RHIC} = 0.005^{+0.129}_{-0.164}(\Delta\chi^2/\chi^2 = 2\%)$. Without the constraint on the x_g range, ΔG obtained by theses fits turns out to be $0.013^{+0.702}_{-0.314}$, what can not fully rule out a sizeable contribution of ΔG to the nucleon spin. Data taken at higher energy (500 GeV) will be helpful to constrain the lower x_g region.

3 Transversity and TMD

The understanding of the nucleon (spin) structure obtained by studying the quark helicities Δq is basically a one-dimensional one in longitudinal momentum space. Two complementary descriptions can provide tomographic images of the structure of the nucleon in terms of partons: one in the transverse plane in momentum space, through Transverse Momentum Dependent parton distributions (TMD) [18, 19]; one in the transverse plane in coordinate space, through the generalized parton distributions (GPD) [20, 21]. We will only focus here on TMD's.

In the non collinear case, that is not integrating over the quark transverse momentum k_T, there are eight leading twist TMD's for the nucleon [1], listed in Table 1(we stick from now on to the notations of [1], notations adopted in section 2 are in parenthesis).

The unpolarized parton DF $f_1(q)$ and the polarized parton DF $g_1(\Delta q)$ have been discussed in section 2, and can be obtained in DIS. All other TMD's, including transversity TMD $h_1(\Delta_T q)$ which is chiral odd, can only be accessed in SIDIS, or polarized DY and polarized p-p collisions. Except h_1, all other TMD would vanish in absence of parton OAM and are due to the coupling of parton transverse momentum to nucleon/quark spin. In (un)polarized SIDIS, where a spinless pion or kaon is produced in the final state, they can be obtained by the study of the following

$q_{pol.} \backslash N_{pol.}$	U	L	T
U	$f_1\ (q)$		$f_{1T}^{\perp}$
L		$g_1\ (\Delta q)$	g_{1T}
T	$h_1^{\perp}$	$h_{1L}^{\perp}$	$h_1\ (\Delta_T q)$
T			$h_{1T}^{\perp}$

Table 1: Eight leading twist TMD's classified as a function of quark and Nucleon polarizations

azimuthal modulations of single (SSA) or double (DSA) spin asymmetries [22], which are each sensitive to the convolution of a TMD with the corresponding fragmentation function (FF):

- Transversity: $A_{UT}^{sin(\phi_h+\phi_S)} \propto h_1 \otimes H_1^{\perp}$
- Sivers: $A_{UT}^{sin(\phi_h-\phi_S)} \propto f_{1T}^{\perp} \otimes D_1$
- Pretzelosity: $A_{UT}^{sin(3\phi_h-\phi_S)} \propto h_{1T}^{\perp} \otimes H_1^{\perp}$
- Boer-Mulders: $A_{UU}^{cos(2\phi_h)} \propto h_1^{\perp} \otimes H_1^{\perp}$
- Worm-Gears: $A_{UL}^{sin(2\phi_h)} \propto h_{1L}^{\perp} \otimes H_1^{\perp}$; $A_{LT}^{cos(\phi_h-\phi_S)} \propto g_{1T}^{\perp} \otimes D_1$

Here, first and second subscripts in the labeling of the SSA or DSA indicate the beam and target polarization (U: unpolarized, L: longitudinal and T: transverse). ϕ_S and ϕ_h represent the azimuthal angles of the initial nucleon spin and the produced hadron momentum; they are defined w.r.t the direction of the virtual photon in the lepton scattering plane. D_1 represents the unpolarized k_T dependent FF, and $H_1^{\perp}$ the Collins FF, which describes the distribution of unpolarized hadrons in the fragmentation of a transversely polarized quark. $H_1^{\perp}$ is chiral odd, and represents the ideal partner of transversity.

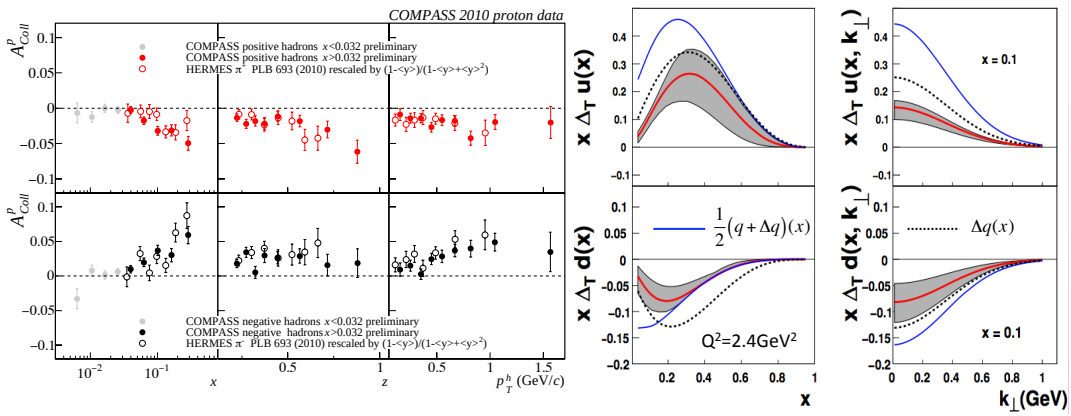

Figure 5: Left: Collins asymmetry $A_{UT}^{sin(\phi_h+\phi_S)}$ measured on the proton in 2010 at COMPASS [25] compared to the ones obtained at HERMES [23]; Right: Transversity DF obtained by global analysis [30] of Collins asymmetries [23, 26] and FF [28].

3.1 Transversity and Collins asymmetry

The only way to access the transversity distribution h_1 is by coupling it to another chiral-odd quantity. To such a purpose one can look for a chiral-odd partner either in the initial or the final state. In the first case the most promising approach, and the cleanest one from the theoretical point of view, is the study of the double transverse spin asymmetry, A_{TT} , in polarized Drell-Yan processes. Meanwhile, the most accessible and fruitful channel is the azimuthal asymmetry $A_{UT}^{sin(\phi_h+\phi_S)}$ in SIDIS processes, namely $lp^{\uparrow} \to lhX$, involving the convolution of the transversity distribution with the Collins fragmentation function. The Collins asymmetry is sensitive to the correlation between the outgoing hadron direction and the initial quark transverse spin, and can thus provide a determination of the quark transverse spin distributions $\Delta_T u$ and $\Delta_T d$.

Collins asymmetries were measured both at HERMES [23] and COMPASS [24, 25] using a transversely polarized proton target, and in addition at COMPASS [26] using a deuteron target. Mainly because of cancelations between u and d quark contributions, the data on deuteron give asymmetries compatible with zero for Collins. This is also the case for data obtained at JLAB on a transversely polarized ^{3}He target (neutron) [27] .On the contrary, signals are observed with the proton target for the Collins asymmetry for all charged hadrons, increasing as a function of x. New 2010 COMPASS data on the proton [25] are in excellent agreement with HERMES data, as can be seen if Fig. 5 (left), what implies a negligible Q^2 dependence of the Collins effect. A crucial breakthrough has been achieved thanks to the independent measurement of the Collins function (or rather, of the convolution of two Collins functions), in $e^+e^- \to h_1h_2X$ unpolarized processes by the BELLE Collaboration at KEK [28] (confirmed since by BABAR [29]). A combined fit [30] of the SIDIS data from HERMES on the proton [23] and COMPASS on the deuton [26], together with the e^+e^- BELLE data [28], allowed the simultaneous extraction of $\Delta_T u$ and $\Delta_T d$, with the interesting byproduct that the Collins unfavored fragmentation function is opposite to and as large as the favored one. As seen in Fig. 5 (right), they are opposite to each other in sign, and smaller in size than the helicity distributions. Including new 2010 COMPASS data on the proton [25] will help to improve this global fit.

An alternative method to probe quark transverse spin distributions $\Delta_T u$ and $\Delta_T d$ is to study azimuthal asymmetries from hadron pairs. Data from HERMES [31] and COMPASS [32] confirm the signal of transversity at high x observed in single hadron SIDIS. Combining these data with the Interference FF $H_1^{\sphericalangle}$ measured at BELLE [33], a first direct extraction of $(\Delta_T u - 1/4\Delta_T d)$ at LO has been performed [34], which is fully compatible with the results of the global fit on single hadron SIDIS [30]. A similar approach with hadron pair production is followed at PHENIX [35] by studying di-hadron correlations in p-p scattering at RHIC.

3.2 Sivers TMD and connection to OAM

The Sivers TMD, which correlates the nucleon spin and the transverse momentum of the parton k_T, was originally proposed to explain the large single-spin asymmetries observed in hadron-hadron scattering. The Sivers function is T-odd, namely it changes sign under naive time reversal. For a long time the Sivers function and the corresponding asymmetry were believed to vanish due to T-invariance arguments. One of the main theoretical achievements of the recent years was the discovery that the Wilson-line structure of parton distributions, which is necessary to enforce gauge invariance of QCD, provides the possibility for non-zero T-odd transverse momentum dependent (TMD) PDFs. FSI (or ISI for DY) allow for non zero Sivers functions, but they must have opposite signs in SIDIS and DY.

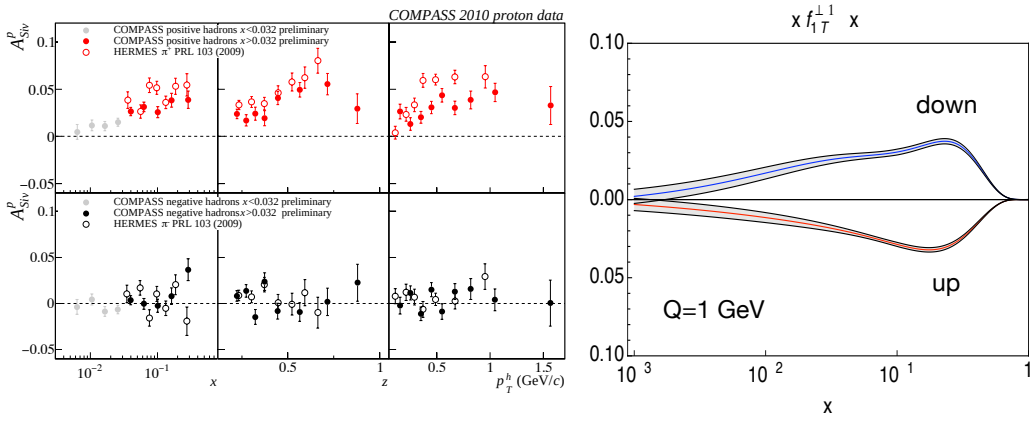

Figure 6: Left: Sivers asymmetry $A_{UT}^{sin(\phi_h-\phi_S)}$ measured on the proton at COMPASS [25] compared to the ones obtained at HERMES [36]; Right: Extracted $x.f_{1T}^{\perp}$ for u and d quarks [39].

Sivers asymmetries were measured in SIDIS at HERMES [36] and COMPASS [24] using a transversely polarized proton target, at COMPASS [26] using a deuteron target, and at at JLAB on a ^{3}He target (neutron) [27]. Mainly because of cancelations between u and d quark contributions to the isoscalar target, the data on deuteron give Sivers asymmetries compatible with zero. On the contrary, clear signals are observed on the proton target for the Sivers asymmetry for positive hadrons, while they are compatible with zero for negative hadrons. COMPASS data on the proton [25] give smaller signal then HERMES [36] (Fig. 6), which indicates a Q^2 dependence of the Sivers TMD well accounted for by recent calculation of [37].

Global analysis [38, 39] using the HERMES proton data combined with the COMPASS deuteron data led to the extraction of Sivers TMD $f_{1T}^{\perp}$ for u and d quarks, which turn out to be non zero, and of opposite sign (Fig. 6 right). Based on results of spectator models, a relation between Sivers TMD and the GPD E in the forward limit allows to constrain quark OAM using Ji's relation. Strikingly, the results are in agreement with other totally independent estimates [39].

3.3 Boer-Mulders and Worm-Gear TMD's

The Boer-Mulders TMD $h_1^{\perp}$, like the Sivers one, is naive T-odd and obeys thus the same rule that it has to change sign between SIDIS and DY. It originates from the coupling of the quark intrinsic transverse momentum and intrinsic transverse spin, a kind of spin-orbit effect, and can be accessed in conjunction with Collins FF via the $cos(2\phi)$ modulation of the unpolarized SIDIS reactions. This azimuthal asymmetry $A_{UU}^{cos(2\phi_h)}$ has been measured for positive and negative hadrons produced in SIDIS on a unpolarized proton target at HERMES [40] and on a deuteron target at COMPASS [41]. HERMES data show large non zero signals for kaons, zero for π^+ and positive for π^-. COMPASS show positive signal for both h^+ and h^-. However, it could well be that twist-4 Cahn effect has a non negligible contribution to the measured $cos(2\phi)$ asymmetry.

The Worm-Gear TMD's $g_{1T}^{\perp}$ ($h_{1L}^{\perp}$) describe the probability of finding a longitudinally (transversely) polarized quark inside a transversely (longitudinally) polarized nucleon. Interestingly,

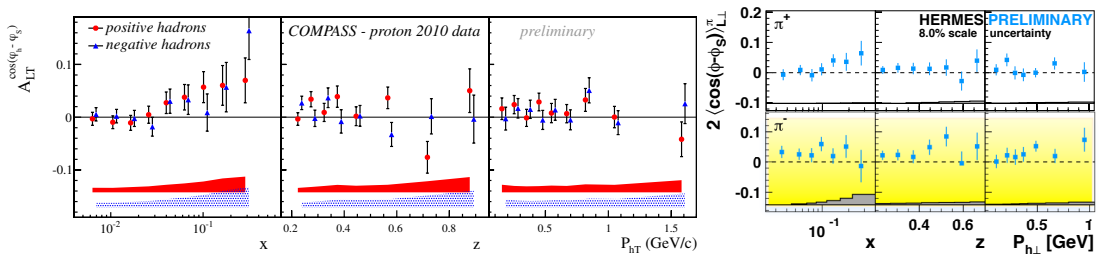

Figure 7: Preliminary $A_{LT}^{cos(\phi_h - \phi_S)}$ measured on the proton at COMPASS in 2010 (left) and at HERMES [43] (right).

they are the only two leading-twist TMD's whose corresponding GPD vanish in light-cone quark models, and are found to be one the opposite of the other in these models. These two TMD's have however a different behavior under chiral transformations: $h_{1L}^{\perp}$ is chiral-odd and can be probed in SIDIS in combination with the Collins FF, while $g_{1T}^{\perp}$ is chiral-even and can thus be accessed in SIDIS combined with the unpolarized FF. In SIDIS experiments, $g_{1T}^{\perp}$ can be accessed at leading-twist through the measurement of the DSA $A_{LT}^{cos(\phi_h - \phi_S)}$. Preliminary results exist using longitudinally polarized lepton beams on a transversely polarized proton target from COMPASS [42] and HERMES [43], and from JLAB on a ^{3}He target [44]. A clear hint of a positive signal is found for the negative pions (hadrons) in all data sets, and even for positive hadrons with the new data taken in 2010 at COMPASS.

References

[1] P. J. Mulders, Progress in Particle and Nuclear Physics **55** (2005) 243.

[2] COMPASS Collab., M. Alekseev *et al.*, Phys. Lett. **B680** (2009) 217.

[3] COMPASS Collab., M.G. Alekseev *et al.*, Phys. Lett. **B690** (2010) 466.

[4] D. de Florian, R. Sassot, M. Stratman and W. Vogelsang, Phys. Rev. **D80** (2009) 034030.

[5] J. Blümlein and H. Böttcher, arxiv:1101.0052 [hep-ph].

[6] COMPASS Collab., M.G. Alekseev *et al.*, Phys. Lett. **B693** (2010) 227.

[7] HERMES Collab., A. Airapetian *et al.*, Phys. Rev. **D71** (2005) 012003.

[8] D. de Florian, R. Sassot, and M. Stratman, Phys. Rev. **D75** (2007) 114010.

[9] E. Leader, A. V. Sidorov and D. B. Stamenov, Phys. Rev. **D84** (2011) 014002.

[10] PHENIX Collab., A. Adare *et al.*, Phys. Rev. Lett. **106** (2011) 062001.

[11] STAR Collab., M. Aggarwal *et al.*, Phys. Rev. Lett. **106** (2011) 062002.

[12] COMPASS Collab., M.G. Alekseev *et al.*, Phys. Lett. **B676** (2009) 31.

[13] COMPASS Collab., E. S. Ageev *et al.*, Phys. Lett. **B633** (2006) 25.

[14] COMPASS Collab., M. Stolarski, AIP Conf.Proc. **1441** (2012) 244.

[15] HERMES Collab., A. Airapetian et al, J. High Energy Phys. **1008** (2010) 130.

[16] PHENIX Collab., A. Manion, J. Phys. Conf. Ser. **295** (2011) 012070.

[17] STAR Collab., L. Adamczyk *et al.*, Phys. Rev. **D86** (2012) 032006.

[18] J. C. Collins and D. E. Soper, Nucl. Phys. **B194** (1982) 445.

[19] A. Bacchetta, F. Conti and M. Radici, Phys. Rev **D78** (2008) 074010.

[20] M. Burkhardt, Nuovo Cimento **35C N2** (2012) 261.
[21] M. Göckeler *et al.*, Phys. Rev. Lett. **98** (2007) 222001.
[22] A. Bacchetta, M. Diehl, K. Goeke, A. Metz, P. Mulders and M. Schlegel, JHEP **0702** (2007) 093.
[23] HERMES Collab., A. Airapetian *et al.*, Phys. Lett. **693** (2010) 11.
[24] COMPASS Collab., M.G. Alekseev *et al.*, Phys. Lett. **B692** (2010) 240.
[25] COMPASS Collab., F. Bradamante, Nuovo Cimento **35C N2** (2012) 107.
[26] COMPASS Collab., M.G. Alekseev *et al.*, Phys. Lett. **B673** (2009) 127.
[27] JLAB HallA Collab., X. Qian **et al.**, Phys. Rev. Lett. **107** (2011) 072003.
[28] BELLE Collab., R. Seidl *et al.*, Phys. Rev. **D78** (2008) 032011.
[29] BABAR Collab., I. Garzia, Nuovo Cimento **35C N2** (2012) 79.
[30] M. Anselmino *et al.*, Phys. Rev. **D75** (2007) 054032; Nucl. Phys. **B191** (2009) 98.
[31] HERMES Collab., A. Airapetian *et al.*, JHEP **0806** (2008) 017.
[32] COMPASS Collab., C. Adolf *et al.*, Phys. Lett. **B713** (2012) 10.
[33] BELLE Collab., A. Vossen *et al.*, Phys. Rev. Lett. 107 (2011) 072004.
[34] M. Radici, Nuovo Cimento **35C N2** (2012) 69.
[35] A. Vossen, Nuovo Cimento **35C N2** (2012) 59.
[36] HERMES Collab., A. Airapetian *et al.*, Phys. Rev. Lett. **103** (2009) 152002.
[37] M. Anselmino, M. Boglione and S. Mellis, `arxiv:1204.1239 [hep-ph]`
[38] M. Anselmino **et al.**, Phys. Rev. **D79** (2009) 054010.
[39] A. Bacchetta and M. Radici, Phys. Rev. Lett **107** (2011) 212001.
[40] HERMES Collab., M. Contalbrigo, AIP Conf. Proc. **1388** (2011) 471.
[41] COMPASS Collab., G. Sbrizzai, Nuovo Cimento **35C N2** (2012) 129.
[42] COMPASS Collab., B. Parsamyan, J. Phys. Conf. Ser. **295** (2011) 012046.
[43] HERMES Collab., L. L. Pappalardo, AIP Conf. Proc. **1441** (2012) 229.
[44] JLAB HallA Collab., J. Huang **et al.**, Phys. Rev. Lett. **108** (2012) 052001.

Electroweak Precision Measurements and Direct Higgs Searches at the Tevatron

David Waters for the CDF and DØ Collaborations

University College London, WC1E 6BT, UK

DOI: http://dx.doi.org/10.3204/DESY-PROC-2012-02/21

The latest electroweak precision measurements and direct Higgs boson search results from the Tevatron are reviewed. Emphasis is placed on measurements for which the Tevatron is still competitive with the LHC. In the case of certain results, notably the precision measurements of the W boson and top quark masses, the Tevatron results will remain world leading for a considerable period of time.

1 Introduction

Tevatron Run II ran from March 2001 until September 2011, delivering approximately 12 fb^{-1} of $p\bar{p}$ data at $\sqrt{s} = 1.96$ TeV to the CDF and DØ experiments. The recently released Higgs search results are based mainly on the full dataset and are almost final, with modest improvements expected for the 2012 summer conferences. Newly released measurements of the W mass use only a fraction of the total Run II dataset and, while rapidly becoming systematically limited, will be updated with the full statistics in forthcoming years.

The Tevatron is no longer at the energy frontier, and the LHC has taken over the search for the direct production of new particles. The Tevatron detectors are very well understood after more than a decade of analysis, and so they remain competitive in the precision measurement of m_W and $m_{\rm top}$. In the search for the Higgs boson the Tevatron remains competitive especially at low masses and in complementary channels to those with the greatest sensitivity at the LHC. Is is therefore particularly timely and interesting to compare the Tevatron Higgs search results with those of the LHC.

More details on many of the results discussed here can be found in parallel session contributions by Head, Knoepfel, Peters, Riddick, Soustruznik and Vellidas.

2 W Mass Measurement

The W mass receives radiative corrections quadratic in the top mass $m_{\rm top}$ and logarithmic in the Higgs mass m_H. A precise measurement of m_W, in conjunction with a precise measurement of $m_{\rm top}$ and other electroweak Standard Model observables, therefore yields information on the missing parameter m_H. In the event of a Higgs discovery at the Tevatron or LHC, a precise measurement of m_W yields a powerful consistency check that may indicate the presence of physics beyond the Standard Model.

Both CDF and DØ have recently released new measurements of m_W using much larger datasets [1, 2]. Both experiments use leptonic W decays, electrons (CDF & DØ) and muons (CDF). The key observables are the lepton 4-momentum and the hadronic recoil in the transverse plane, $\vec{u}_T$. The neutrino transverse momentum is then inferred from $\vec{p}_T^{\,\nu} = -\left(\vec{p}_T^{\,\ell} + \vec{u}_T\right)$. The greatest information on m_W comes from fitting the transverse mass, defined as :

$$m_T = \sqrt{2p_T^{\ell} p_T^{\nu} \left(1 - \cos(\Delta\phi^{\ell\nu})\right)}$$

although it should be noted that the missing-E_T and lepton p_T distributions are separately fit and combined with the m_T fit taking into account correlations, in order to extract the maximum sensitivity to m_W. The fits to the muon channel in CDF and electron channel in DØ are shown in figures 1 and 2 respectively. The CDF analysis begins with a determination of

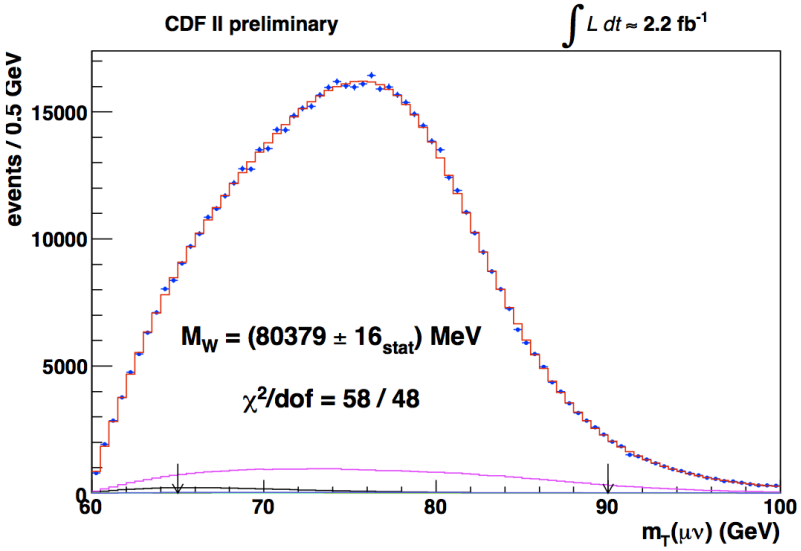

Figure 1: The transverse mass distribution in $W \to \mu\nu$ events in CDF. The data are compared to the summed signal and background (red histogram) with the background contributions indicated by the lower curves.

the momentum scale in the tracker to better than one part in 10,000 using $J/\psi \to \mu\mu$, $\Upsilon \to \mu\mu$ and $Z \to \mu\mu$ samples, where the Z data is only combined after a blinded Z mass measurement is found to be in good agreement with the World Average value. The precise momentum scale is transferred to an electron energy scale by fitting the E/p distribution in $W \to e\nu$ events. Again, the $Z \to ee$ calibration is added after a successful Z mass measurement shows that there is no bias or mid-modelled non-linearity in the electromagnetic energy scale. DØ does not have a high precision momentum scale and so the analysis proceeds only in the electron channel, using the $Z \to ee$ sample to directly calibrate the electron energy scale.

The hadronic event includes contributions from the hadrons balancing the W transverse momentum, the underlying event and any overlapping $p\bar{p}$ collisions in the same bunch crossing. A recoil model simulates the reconstructed highly smeared $\vec{u}_T$ and is calibrated from $Z \to \ell\ell$ and minimum-bias data.

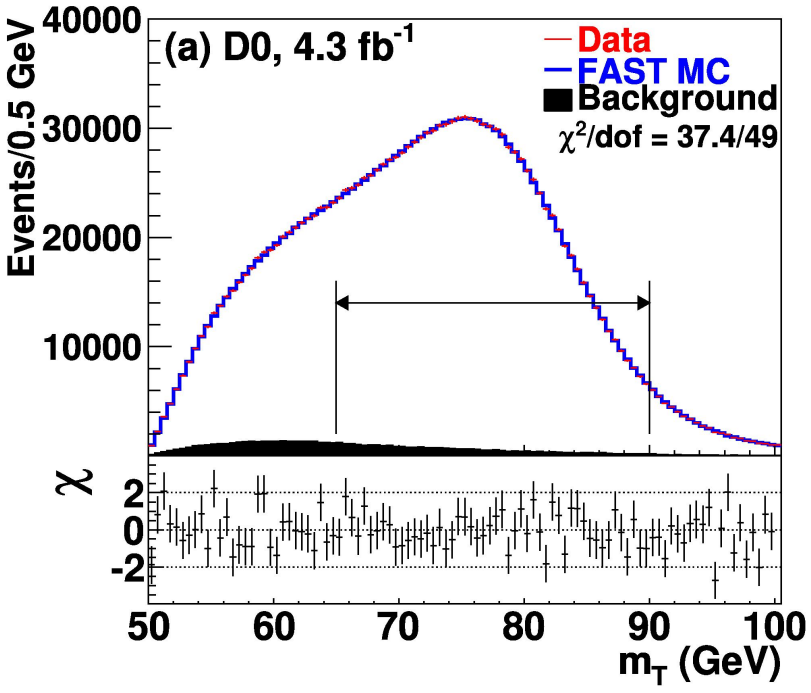

Figure 2: The transverse mass distribution in $W \to e\nu$ events in DØ. The lower signed-χ plot shows the level of agreement between data and simulation.

Signal modelling includes a description of the W and Z production in both the transverse plane (vector boson p_T due to hard and soft gluon emission) and the longitudinal axis (PDF's). QED and electroweak corrections, dominated by final state photon radiation from the charged leptons, are also modelled.

All the aspects of the analysis listed above require painstaking work to ensure that no biases are present and this has taken several years' work by both collaborations. The good χ^2 values evident in figures 1 and 2 are an indication of the success of this program, but hundreds of separate distributions in both signal and control samples are checked during the analysis.

The final results for both CDF and DØ, combined with earlier Run II results, are :

$$m_W = 80387 \pm 19 \text{ MeV} \quad \text{(CDF)}$$
$$m_W = 80375 \pm 23 \text{ MeV} \quad \text{(DØ)}$$

The CDF measurement is, by itself, more sensitive than the previous world average. These results are compared with other measurements in figure 3, which also indicates a new preliminary world average of $m_W = 80387 \pm 16$ MeV. This represents a 30% smaller uncertainty than the previous world average value of $m_W = 80399 \pm 23$ MeV. This is a major leap in precision and the Tevatron measurements are now clearly dominating the world average for this electroweak observable. The impact of this measurement on indirect determinations of the Higgs mass is discussed in the Conclusions.

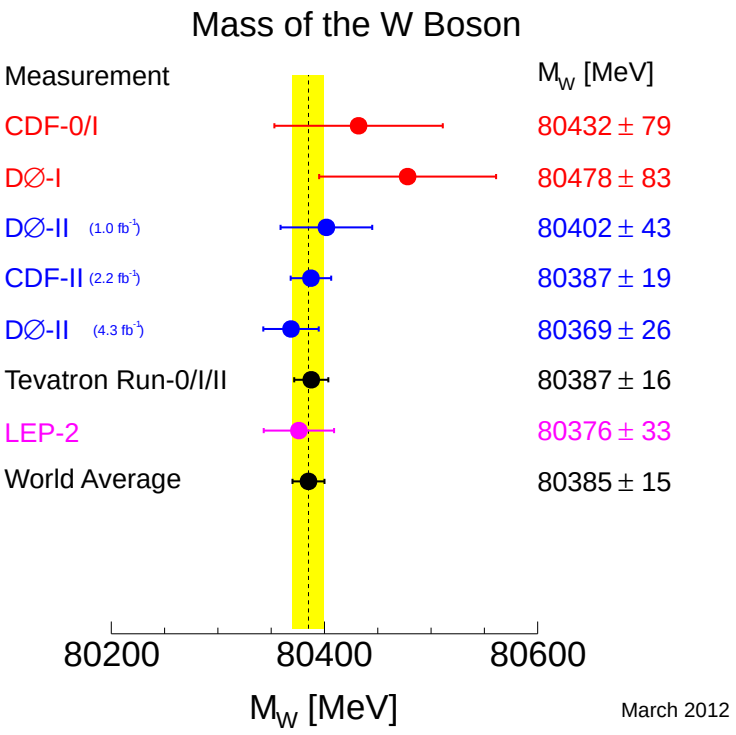

Figure 3: W mass measurements including the new measurements from CDF and DØ and with a preliminary new world average combination. From [3].

The new measurements are compared in precision with earlier Tevatron measurements in figure 4. The measurements lie broadly on a trajectory that scales statistically with a small systematic floor. The CDF Run II measurements are systematically better than the Run I measurements extrapolated to the same luminosity due to essential analysis improvements - most notably agreement between the electron energy scales determined from the W sample via E/p and the $Z \to ee$ sample. The fact that the precision is improving as would be expected statistically does *not* imply that the analyses have been easily updated with larger datasets. In reality whenever a larger dataset is analysed, all of the systematics need to be re-evaluated in order to maintain the observed scaling behaviour. Crucially, the analyses are now beginning to be dominated by production modelling systematics that cannot straightforwardly be reduced with more data. Most importantly, PDF's now represent a common systematic of 10 MeV across experiments and decay channels. Other modelling systematics such as QED are also non-negligible at the $4-7$ MeV level. Therefore future W mass measurements at the Tevatron using the full and final datasets will not continue to scale with luminosity until such systematics can be addressed. In the case of PDF's this may require new parton distributions incorporating new datasets from the Tevatron, LHCb or perhaps other experiments.

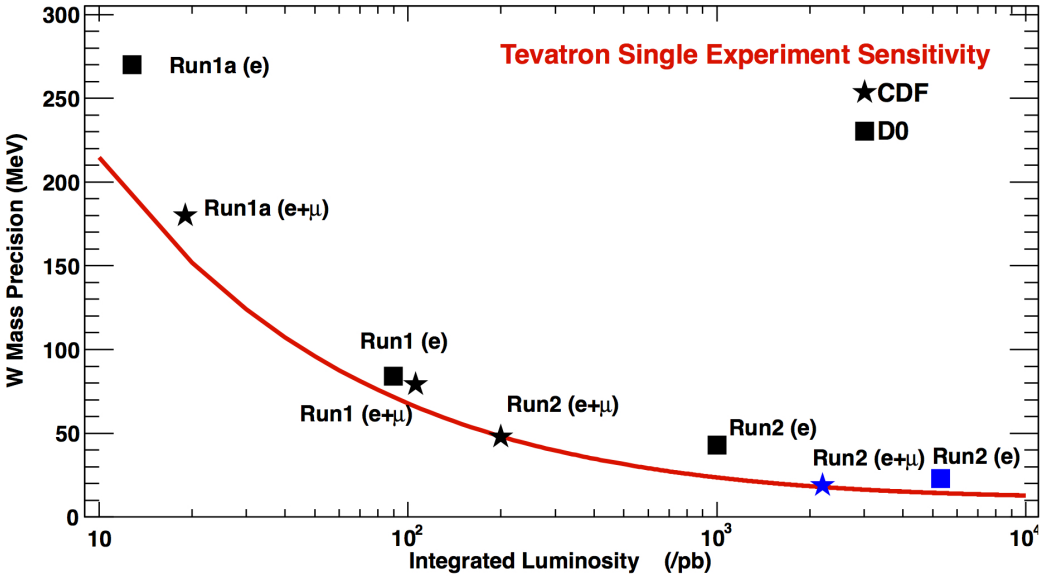

Figure 4: The precision of the measured W mass versus analysed integrated luminosity for a number of CDF and DØ Run I and Run II measurements.

3 Top Mass Measurement

The top quark mass has been directly measured at the Tevatron with significantly better accuracy than predicted at the outset of Run II, with a relative precision now approaching 0.5%. The most sensitive channel is lepton+jets, with one top decaying leptonically and the other hadronically. Dilepton events suffer from poorer statistics and weaker kinematic constraints due to the presence of two undetected neutrinos, while the all-hadronic channel suffers from poorer resolution and additional systematic uncertainties.

A major innovation in measuring the top mass at the Tevatron has been the development of an in-situ jet energy scale determination by applying the constraint that two of the jets in a hadronic top decay should have an invariant mass consistent with the mass of the decaying W boson. The additional constraint thus provided has reduced the jet energy scale systematic by a large factor. Developments have also been made over the years in fitting techniques, which broadly follow two approaches : (i) template fitting, for which a kinematic fit is performed to the $t\bar{t}$ event and a mass distribution is then compared to Monte Carlo templates similarly constructed; (ii) matrix-element methods, which determine the probability of observing kinematic configurations in data given a leading-order true kinematic distribution convolved with PDF's and detector-smearing functions.

The last combination of Tevatron top quark mass measurements was performed in the summer of 2011 and the results are shown in figure 5. The individual measurements used datasets up to 5.8 fb^{-1} in size. The Tevatron combination yields $m_{\rm top} = 173.2 \pm 0.6$ (stat) $\pm$ 0.8 (syst) $= 173.2 \pm 0.9$ GeV. In a similar fashion to the W mass measurement, many of the systematics are statistical in nature and improve with larger datasets. However signal modelling systematics - PDF's, initial & final state gluon radiation, colour-reconnection and

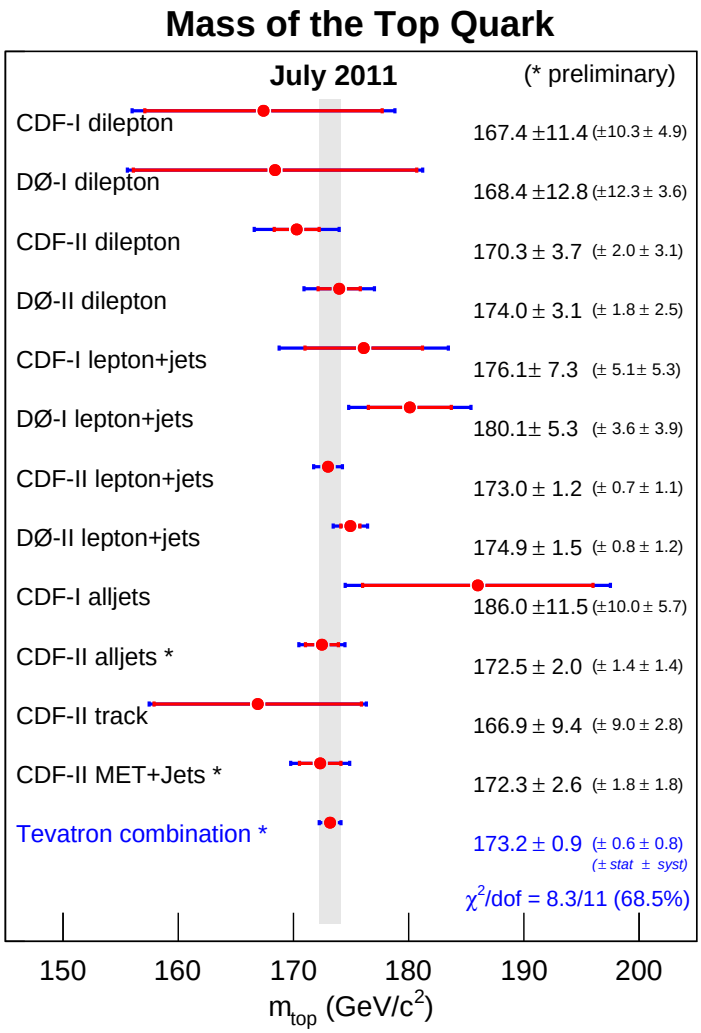

Figure 5: Top quark mass measurements including recent measurements from CDF and DØ with a preliminary world average combination. The individual measurements used datasets up to 5.8 fb^{-1} in size. From [4].

choice of generator - together account for approximately 0.5 GeV out of the total systematic of 0.8 GeV and will not improve in a straightforward way with the addition of more data.

There have been a number of updates in certain top mass measurement channels since the summer 2011 combination. For example the CDF lepton+jets analysis has been extended to 8.7 fb^{-1} and a DØ dilepton analysis on the same 4.3 fb^{-1} dataset has reduced the uncertainty using more sophisticated analysis techniques [5, 6]. Both these analyses show that improvements on the top mass uncertainty of order 10% can still be achieved, giving an indication of the likely size of the final Run II top mass precision.

4 Top Forward-Backward Asymmetry

If the top quark (anti-quark) in $t\bar{t}$ production events is reconstructed with a rapidity of y_t ($y_{\bar{t}}$) then the forward-backward asymmetry with respect to the rapidity difference $\Delta y = y_t - y_{\bar{t}}$ is defined as :

$$A_{FB} = \frac{N(\Delta y > 0) - N(\Delta y < 0)}{N(\Delta y > 0) + N(\Delta y < 0)} \ .$$

Leading-order production mechanisms should give strictly zero A_{FB}, while new physics (for example a new flavour-changing $t-$channel exchange) can easily give rise to an observable asymmetry. The picture is complicated by the fact that higher-order QCD effects *can* give a small A_{FB} up to $6-7\%$ in the Standard Model. Both CDF and DØ have persistently measured a larger asymmetry than expected, at the $\sim 2-3\sigma$ level [7, 8].

A new analysis from CDF extends the measurement to the full Run II dataset and provides useful empirical parameterisations of A_{FB} as a function of the $t\bar{t}$ invariant mass and Δy [9]. Overall it remains to be seen whether this is really evidence for new physics, or a shortcoming in the analysis or Standard Model calculation of A_{FB}. It is of course interesting to note that no new physics affecting $t\bar{t}$ production has been found *directly* either at the Tevatron or LHC, although it is still conceivable that the different parton-level production sub-processes would make an anomaly more evident in Tevatron data than at the LHC.

5 Tevatron Higgs Searches

In March 2012, the Tevatron released an almost final combined Higgs search in the full Run II dataset [10]. 20 Higgs production and decay channels have been combined, the most important ones using the full luminosity. The result is the culmination of a large number of analysis improvements that have increased signal acceptance and $b-$tagging performance and have brought to bear highly optimised multi-variate analysis techniques. Importantly, a new analysis of Standard Model WZ/ZZ diboson production in identical decay modes to the Higgs signal provides an ideal 'standard candle' and demonstrates good experimental control of relevant experimental variables [11].

For $m_H < 125$ GeV, the Tevatron sensitivity to the Higgs boson is through associated production with a W or Z boson, $VH \to \ell\nu b\bar{b}, \ell^+\ell^- b\bar{b}, \nu\bar{\nu}b\bar{b}$. For higher masses, the decay mode $H \to W^{(*)}W^{(*)}$ provides greatest sensitivity, and is sufficiently distinctive experimentally that the much larger $gg \to H$ production cross section can be exploited. All search channels are carefully combined, taking care not to dilute high-purity search regions with lower-purity regions. No significant signal is evident and therefore an upper limit on the Higgs production cross section is set across the mass range, as shown in figure 6. A particular Higgs mass hypothesis is excluded when the 95% C.L. upper limit on the cross section falls below the Standard Model cross section. This results in the following mass regions being excluded by the Tevatron :

$$100 < m_H < 106 \text{ GeV} \ ; \ 147 < m_H < 179 \text{ GeV} \quad \text{(observed)}$$
$$100 < m_H < 119 \text{ GeV} \ ; \ 141 < m_H < 184 \text{ GeV} \quad \text{(expected)}$$

As can be seen, the observed exclusion is somewhat poorer than that expected. The cross section limit is clearly worse than expected for Higgs masses in the range $\sim 110 - 140$ GeV

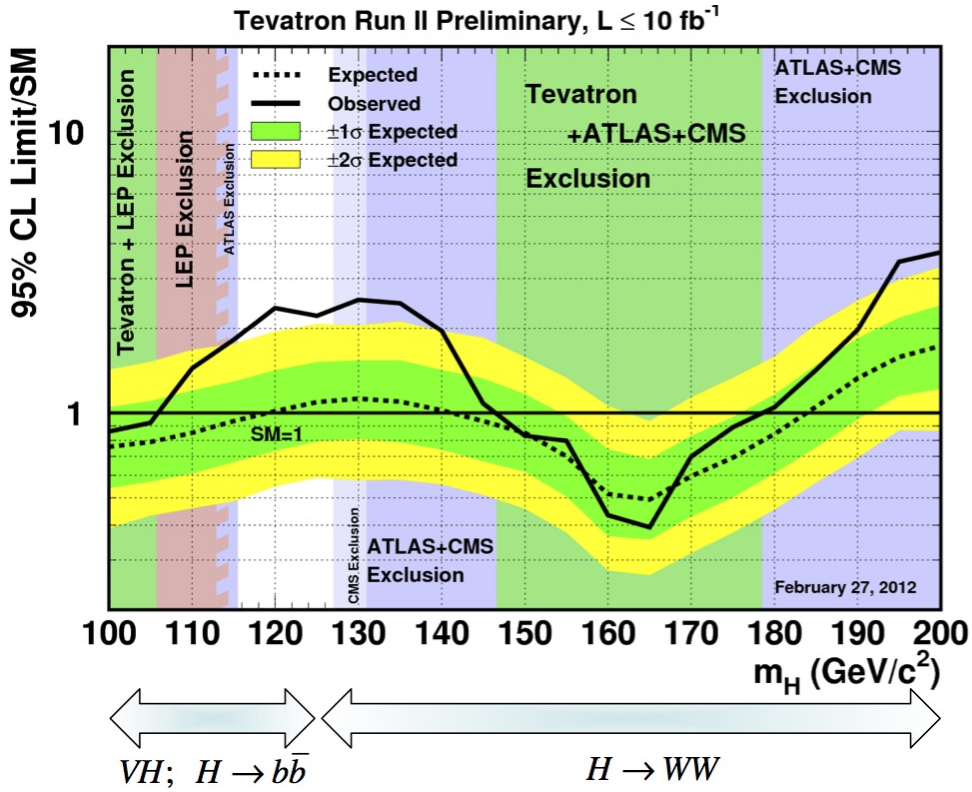

Figure 6: Combined Tevatron 95% C.L. upper limits on the Higgs boson production cross section as a function of Higgs mass, in units of the Standard Model cross section. Also indicated are mass regions already excluded by searches at LEP and the LHC. The arrows beneath the graph indicate the production and decay channels that dominate the sensitivity for different putative Higgs masses at the Tevatron. From [4], annotated.

and this of course would be expected in the presence of a signal, since the expected limits assume *no* signal. The biggest discrepancy is for a Higgs mass of 120 GeV and the probability of a background-only model fluctuating to give an excess at least as large as that observed in the data corresponds to 2.7σ. Taking account of the 'look-elsewhere effect' reduces this discrepancy to approximately 2.2σ, where it is interesting to note that because of the much poorer mass resolution of the low-mass Higgs decay channels exploited at the Tevatron, this statistical penalty is considerably smaller than at the LHC. It is of course extremely intriguing that the mass region of the Tevatron excess is similar to that observed at ATLAS and CMS.

6 Conclusions

The Tevatron era is drawing to a close, but the experiments are still generating world-leading results. New measurements of the W mass from the Tevatron now dominate the world average and the precision in the measurement of the top quark mass that has been achieved in Run II

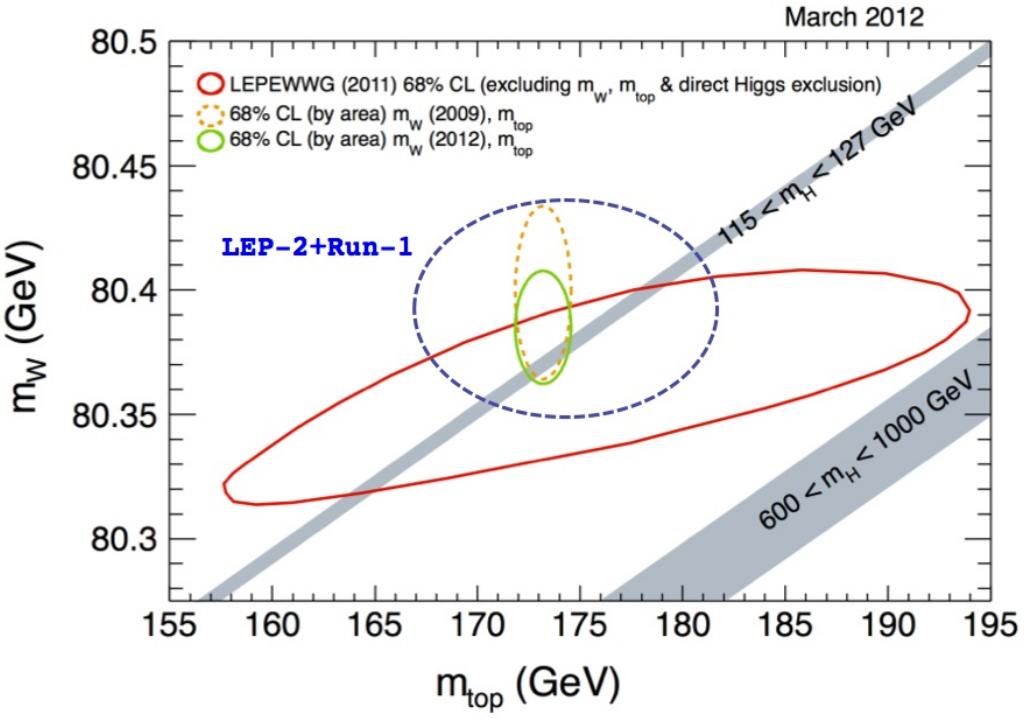

Figure 7: The small green ellipse shows the 1σ allowed region of the $m_W, m_{\rm top}$ plane including the latest direct measurements from the Tevatron. The taller yellow ellipse shows the corresponding constraint before the new 2012 measurements of the W boson mass from CDF and DØ. The large blue-dashed ellipse shows the situation that pertained with just the LEP-2 and Run I measurements, showing the dramatic improvements that have been made during Run II. The red ellipse shows the indirect constraints from other precision electroweak observables, and the grey bands show the allowed Higgs mass ranges from direct searches. All data are consistent with a light Standard Model Higgs.

is extraordinary. Figure 7 shows the impact of the latest measurements of m_W and $m_{\rm top}$ and the striking impact of Run II on these measurements is evident. Feeding the latest direct measurements of m_W and $m_{\rm top}$ into the electroweak fits results in a best fit value $m_H = 94^{+29}_{-24}$ GeV and an upper limit $m_H < 152$ GeV at 95% C.L. [12]. This mass range includes the excesses that are hinted at in direct Higgs searches at both the Tevatron and LHC.

As discussed above, there is scope for both $m_{\rm top}$ and especially m_W measurements from the Tevatron to continue to be improved, although both are now hitting quite hard theoretical systematic limits. They will remain amongst the most important and long-lived legacy measurements from the Tevatron.

7 Acknowledgements

We acknowledge especially the heroic efforts of the accelerator division and all the personnel at Fermilab that made Tevatron Run II a success. The author is grateful to STFC for supporting UK involvement in the Tevatron program and supporting his attendance at the DIS-2012 conference.

References

[1] T. Aaltonen *et al.* [CDF Collaboration], Phys. Rev. Lett. **108** (2012) 151803.

[2] V. M. Abazov *et al.* [D0 Collaboration], Phys. Rev. Lett. **108** (2012) 151804.

[3] The Tevatron Electroweak Working Group (for the CDF and DØ Collaborations), "2012 Update of the Combination of CDF and DØ Results for the Mass of the W Boson", arXiv:1204.0042v2 [hep-ex].

[4] The Tevatron Electroweak Working Group (for the CDF and DØ Collaborations), "Combination of CDF and DØ results on the mass of the top quark using up to 5.8 fb^{-1} of data", arXiv:1107.5255v3 [hep-ex].

[5] The CDF Collaboration, "Top Quark Mass Measurement in the Lepton+Jets Using 8.7 fb^{-1} of CDF Data", `http://www-cdf.fnal.gov/physics/new/top/2012/TMT_p38_public/`

[6] V. M. Abazov *et al.* [D0 Collaboration], "Measurement of the top quark mass in $p\bar{p}$ collisions using events with two leptons", arxiv:1201.5172 [hep-ex].

[7] T. Aaltonen *et al.* [CDF Collaboration], Phys. Rev. D **83** (2011) 112003.

[8] V. M. Abazov *et al.* [D0 Collaboration], Phys. Rev. D **84** (2011) 112005.

[9] The CDF Collaboration, "Study of the Top Quark Production Asymmetry and Its Mass and Rapidity Dependence in the Full Run II Tevatron Dataset", `http://www-cdf.fnal.gov/physics/new/top/2012/LepJet_AFB_Winter2012/`

[10] The Tevatron New-Phenomena and Higgs Working Group (for the CDF and DØ Collaborations), "Combined CDF and DØ Search for Standard Model Higgs Boson Production with up to 10.0 fb^{-1} of Data", arXiv:1203.3774 [hep-ex].

[11] The Tevatron New-Phenomena and Higgs Working Group (for the CDF and DØ Collaborations), "Combined CDF and D0 measurement of WZ and ZZ production in final states with b-tagged jets", arXiv:1203.3782 [hep-ex].

[12] The LEP Electroweak Working Group, `http://lepewwg.web.cern.ch/LEPEWWG/`

Precision QCD Measurements at HERA

Karin Daum[1,2] on behalf of the H1 and ZEUS collaborations

[1]Bergische Universität Wuppertal, Gaußstraße 20, 42097 Wuppertal, Germany
[2]also at DESY, Notkestraße 85, 22607 Hamburg, Germany

DOI: `http://dx.doi.org/10.3204/DESY-PROC-2012-02/23`

Recent QCD results obtained by the H1 and ZEUS collaborations at the *ep* collider HERA are presented. The high precision measurements of the inclusive deep-inelastic scattering cross section at high photon virtualities Q^2 are used to search for signs of physics beyond the Standard Model. The studies of hadronic final states such as diffraction, jet and heavy quark production as well as particle production are summarised. Predictions from perturbative QCD are confronted with these measurements and the consistency of the understanding of strong interactions tested by these processes is discussed.

1 Introduction

HERA was operated during the years 1992 to 2007 producing ep[1] interactions at centre-of-mass energies up to $\sqrt{s} = 320$ GeV. Both collider experiments H1 and ZEUS collected data corresponding to an integrated luminosity of 0.5 fb^{-1} each.

The HERA collider was an unique machine for studying strong interactions. It provides a clean environment for the precise determination of the proton structure over a wide range in Bjorken x and in virtuality Q^2 of the exchanged boson, which is either a photon or a Z-boson in case of neutral current (NC) interaction, $ep \to eX$, or a W-boson in case of charged current (CC) interactions, $ep \to \nu X$. The two high resolution multi-purpose detectors H1 and ZEUS allow for detailed analyses of the hadronic final state and thereby give access to the vast physics of diffraction and of jet, heavy quark and particle production. By all these processes different aspects of strong interactions are addressed making HERA an ideal testing ground for QCD. This talk will focus on application of parton distribution functions ($PDFs$) of the proton in searches for signals of new physics at HERA, on the strong coupling constant α_S and on fragmentation functions (FFs).

A precise knowledge of the proton PDFs is vital for interpreting the data taken at hadron colliders, especially when analysing rare Standard Model (SM) processes or when searching for signs of new physics. The backbone of all modern proton PDFs [1, 2, 3, 4, 5] are the proton structure function data from HERA [6]. In the determination of PDFs the understanding of charm production is of utmost importance. Not only that charm production contributes up to 30% to the inclusive NC cross section at HERA but also that the treatment of heavy flavour production in the calculations is a theoretical issue due to the presence of several hard scales in the problem and gives therefore rise to different PDF schemes [1, 2, 5].

[1]The term *electron* is used generically for both electrons or positrons if not otherwise stated.

The strong coupling constant α_S is a free parameter in QCD which has to be determined experimentally. Different processes are investigated to measure α_S [7], all having some experimental and/or theoretical challenges. At HERA the study of jet production with sufficiently high transverse jet momenta p_T^{jet} is best suited for the determination of α_S.

The basic concept of pQCD tightly relates the QCD evolution of PDFs to that of FFs [8] which means that the QCD vacuum as seen by studying the structure of the proton is identical to the vacuum acting in the formation of hadrons. Information on the fragmentation functions are obtained from the analysis of particle production mainly in e^+e^--annihilation. The study of particle production in ep-scattering at HERA allows testing the universality of FFs.

2 Search for physics beyond the Standard Model

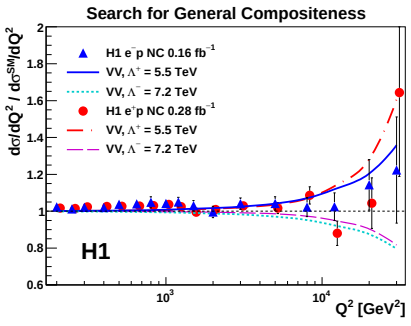

Figure 1: NC cross section $\mathrm{d}\sigma/\mathrm{d}Q^2$ normalised to the SM expectation. The H1 data are compared with the 95% C.L. limit curves for the VV compositeness scale model.

The preliminary HERA combined inclusive measurements based on the full data sets [9] are discussed in the context of the proton structure elsewhere [6]. The measured cross sections are very well described over four orders of magnitude in Q^2 and x by the SM also when using PDFs not fitted to these data. Any contribution from new physics to the DIS cross section should show up in deviations from the SM expectation. All results presented in this section are based on the full statistics taken by the experiments.

Different approaches are followed when searching for signs of new physics at HERA. The most general ansatz presented here is the search for contact interactions (CI). New phenomena with scales above the direct reach of HERA may contribute at lower scales via four-fermion-interactions[2] leading to deviations of the cross section from the SM expectation at large Q^2. This strategy allows different models of new physics to be tested. The procedure has been recently applied by H1 [10] to set lower limits on compositeness scales, on masses of heavy leptoquarks (LQ), on the gravitational scale in large extra dimensions and to set an upper limit on the quark radius. In Figure 1 the NC $e^{\pm}p$ cross sections $\mathrm{d}\sigma/\mathrm{d}Q^2$ normalised to the SM expectations are compared to the prediction corresponding to the 95% C.L. lower limits of the VV compositeness model, $\Lambda^+_{VV} > 5.6$ TeV and $\Lambda^-_{VV} > 7.2$ TeV.

Lower mass limits on heavy leptoquarks are also derived from dedicated searches for first generation LQs [11, 13], $ep \to LQ \to e(\nu)X$, as well as for lepton-flavour violating (LFV) LQs [12], $ep \to LQ \to \mu(\tau)X$. In both cases LQs may be produced either in the s-channel, leading to high sensitivity to the LQ-coupling λ_{LQ} for LQ masses M_{LQ} below the kinematic limit of HERA, $M_{LQ} \leq \sqrt{s}$, or in the u-channel which enables the search for LQs with $M_{LQ} > \sqrt{s}$ and larger values of λ_{LQ}. The searches are performed for both scalar (S) and vector-type (V) LQs.

In Fig. 2 the exclusion curves at 95% C.L. are shown for different first generation V-type LQs in the BRW model [14] in the M_{LQ}-λ_{LQ}-plane from ZEUS (preliminary). Depending on the LQ type lower mass limits up to 630 GeV (ZEUS) and 800 GeV (H1) are obtained assuming

[2]This concept was originally introduced in the Fermi theory of β decay.

a coupling λ_{LQ} of electromagnetic coupling strength ($\lambda_{LQ} = 0.3$). For LQs coupling also to neutrinos the limits obtained in the direct search are in general superior to those obtained by the CI analysis, because both NC and CC data are used.

While the search for first generation LQ is based on finding deviations from the SM in the measured inclusive NC (and CC) cross section the search for LFV LQs requires a dedicated analysis of the final state to identify individual LQ candidates. Event topologies consistent with the LQ hypothesis are selected containing exactly one high p_T well isolated muon or τ-candidate and a single high p_T jet. In the H1 analysis lower limits on M_{LQ} up to 712 GeV and 479 GeV are obtained at 95% C.L. for second or third generation LQs, respectively, assuming $\lambda_{LQ} = 0.3$.

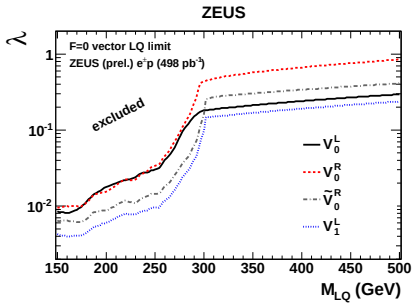

Figure 2: Preliminary exclusion curves for different first generation V-type LQs in the M_{LQ}-λ_{LQ}-plane from ZEUS. The areas above the lines are excluded at 95% C.L.

In the SM flavour changing neutral currents (*FCNC*) are strongly suppressed by the GIM mechanism. However there are extensions of the SM which predict FCNC contributions already at tree level. A possible signal for FCNC at HERA would be single top production $ep \to etX$. In the SM single top quarks are produced via the CC reaction $ep \to \nu tX$ with a cross section of less than 1 fb at HERA energies. A search for single top production is performed by ZEUS [15] with no signal above the CC background expectation being observed. In Fig. 3 the exclusion region in the plane of the top anomalous branching ratios $Br_{u\gamma}$ and Br_{uZ} from this analysis is shown together with results from other experiments. This analysis is able to extend the exclusion region at small $Br_{u\gamma}$ and Br_{uZ} values.

3 Diffraction

One of the big surprises observed at HERA at the beginning of the 90's was that about 10% of the events did not show any activity in the forward direction. These diffractive collisions, $ep \to eXp$, can be understood as resulting from processes in which the exchanged boson probes a colourless combination of partons from the proton.

To investigate the mechanism of diffraction two different methods are employed at HERA. Either the outgoing proton is directly detected in dedicated proton spectrometers, *FPS* or *LPS*, at very small angles in the direction of the proton beam and at large distance from the interaction region or a large gap in rapidity [3] (*LRG*) in the proton direction is required. The first method unambiguously identifies this process and enables the complete measurement of its kinematics but

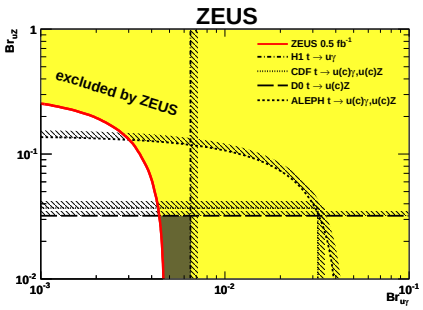

Figure 3: Exclusion boundary in the $Br_{u\gamma}$-Br_{uZ}-plane from ZEUS. The shaded region is excluded at 95% C.L.

[3] The rapidity is defined as $\eta = -\ln\tan\Theta/2$. The polar angle Θ is defined with respect to the proton direction.

suffers from small acceptance. The second method has large acceptance but also selects events with low mass excitations of the proton (proton dissociation).

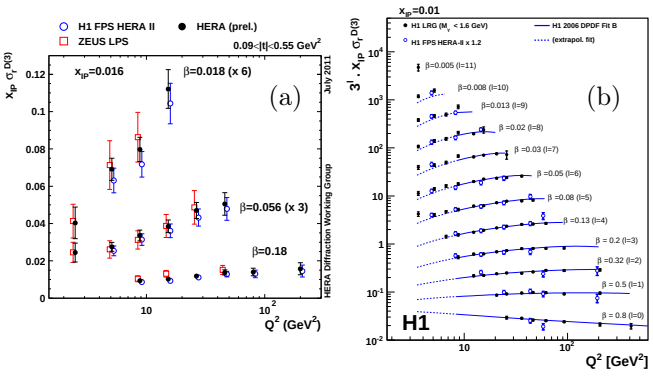

Figure 4: $x_{IP} \cdot \sigma_r^{D(3)}$ from (a) the preliminary HERA combined FPS/LPS data (black points) for $x_{IP} = 0.016$ compared to the uncombined data (open symbols) and (b) the H1 LRG data (black points) for $x_{IP} = 0.01$ in comparison to the H1 FPS data (open circles) corrected for contribution from proton dissociation.

For diffractive DIS (*DDIS*) in NC the QCD factorisation theorem holds [16], which allows DDIS to be described by diffractive PDFs (*DPDF*s) convoluted with hard scattering matrix elements. These DPDFs depend on four kinematic variables, namely the photon virtuality Q^2, the momentum transfer t at the proton vertex, the momentum fraction of the proton x_{IP} carried by the colourless exchange (*IP*) and the momentum fraction β of *IP* carried by the quark interacting with the photon. The latter two variables are related to Bjoken x via $x = x_{IP} \cdot \beta$.

The FPS and LPS DIS data measured by H1 and ZEUS have been combined using the same χ^2 minimisation procedure [17] as used previously for combining data at HERA [18]. In Fig. 4a the diffractive reduced cross section

$$\sigma_r^{D(3)}(x_{IP}, \beta, Q^2) = \frac{\beta Q^4}{2\pi\alpha_{em}^2} \frac{1}{1 - y + y^2/2} \frac{\mathrm{d}^3\sigma^{ep\to epX}}{\mathrm{d}x_{IP}\mathrm{d}\beta\mathrm{d}Q^2} = F_2^{D(3)} - \frac{y^2}{1 + (1-y)^2} F_L^{D(3)}, \quad (1)$$

with $y = Q^2/(sx)$, is shown for the preliminary HERA combined FPS/LPS data [19] for $x_{IP} = 0.016$ as a function of Q^2 and different values of β. In Eqn. 1 $F_2^{D(3)}$ and $F_L^{D(3)}$ denote the diffractive structure function and the diffractive longitudinal structure function, respectively. Also shown are the uncombined data. Due to cross calibration of the correlated systematic uncertainties of both experiments the combined data are more precise than expected from simple averaging. Scaling violations are evident from the change of the slope in Q^2 a function of β.

In Fig. 4b the diffractive reduced cross section $\sigma_r^{D(3)}$ from H1 [20] as measured by the LRG method based on the full HERA statistics is compared with pQCD predictions using the H1DPDF Fit B set [21]. The data are well described for $Q^2 > 10$ GeV^2. Also shown are the FPS measurements from H1 [22] scaled be a factor 1.20 to account for the proton dissociation contribution to the LRG data. The cross section measurements agree well with each other.

Using the LRG method H1 performed a direct measurement of the diffractive longitudinal structure function $F_L^{D(3)}$ [23]. This is the first measurement of F_L^D which became possible because of HERA running at reduced proton beam energies at the end of the HERA operation. In Fig. 5 the diffractive longitudinal structure function F_L^D divided by a parameterisation of the x_{IP} dependence of the reduced cross section $f_{IP/p}$ [21] is presented as a function of β for different Q^2. The pQCD predictions based on H1DPDF fit B included in the figure agree with data within uncertainties.

The NLO QCD analysis of inclusive DDIS cross section provides different solutions for the diffractive gluon density [21, 24]. This ambiguity can be resolved by studying diffractive di-jet production, which is directly sensitive to the diffractive gluon density [24, 25]. The H1 collaboration has performed the first measurement of the DDIS process $ep \to ejjX'p$ whit two jets and a leading proton in the final state. The differential cross section as a function of $\log_{10} x_{IP}$ is presented in Fig. 6 together with NLO QCD predictions based on the H1 DPDF fit B [21] and on the H1 2007 Jets [25] sets. Good agreement is observed between theory and data. In general the data are more precise than the predictions which have large scale uncertainties, as a measure for the importance of missing higher order contributions to the cross section.

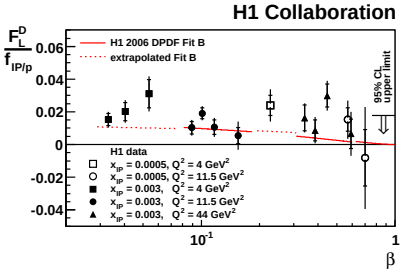

Figure 5: Diffractive longitudinal structure function F_L^D divided by a parameterisation of the x_{IP} dependence of the reduced cross section $f_{IP/p}$.

4 Jet Production

The study of jet production at HERA is very well suited for high precision measurements of the strong coupling constant α_S and to demonstrate its running over a large range in energy scale within a single experiment. Furthermore jet cross sections are valuable input for QCD analyses extracting proton PDFs because these data put significant constraints on the gluon density especially at medium x [26].

Inclusive jet production, $ep \to ejX$, is measured by ZEUS in the photoproduction regime (γp) where $Q^2 \approx 0$ for jet energies $E_T^{jet} > 17$ GeV [27]. The inclusive jet production cross section is shown in Fig. 7a as a function of η^{jet} in comparison to the NLO QCD expectation using the k_t jet algorithm [28]. In the lower part of the figure the ratio of the measured cross section to the NLO QCD calculation is shown. It is obvious that the theory does not describe the data well especially for forward η^{jet} where the prediction lies significantly below the data. This discrepancy may be resolved by either adding soft multiple interactions [29] to the theory or by using a different photon PDF set. In comparison to the data precision the theory uncertainties (hashed area) are very large mainly due to the scale variations used to estimate terms beyond NLO and due to the not well known photon PDFs. From these data the strong coupling constant is determined to be $\alpha_s(M_Z) = 0.120^{+0.0023}_{-0.0022}(exp.)^{+0.0042}_{0.0035}(th.)$. The analysis is also performed using the anti-k_t [30] and SIScone [31] jet algorithms. All results are found to be insensitive to the choice of the jet algorithm.

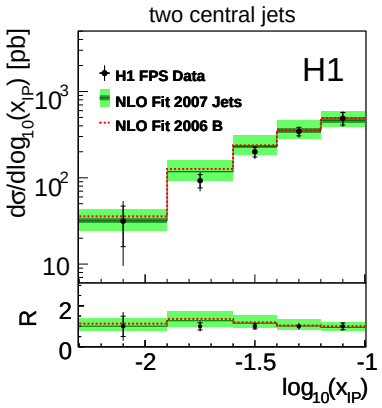

Figure 6: Diffractive dijet cross section as a function of $\log_{10} x_{IP}$ compared to NLO QCD predictions for two different DPDF sets. The theory uncertainties are indicated by the shaded band.

Normalised inclusive jet, dijet and trijet DIS cross sections for $Q^2 > 150$ GeV^2 from H1 [32] are presented in Fig 7b as a function of jet P_T for different values of Q^2. By the normalisation

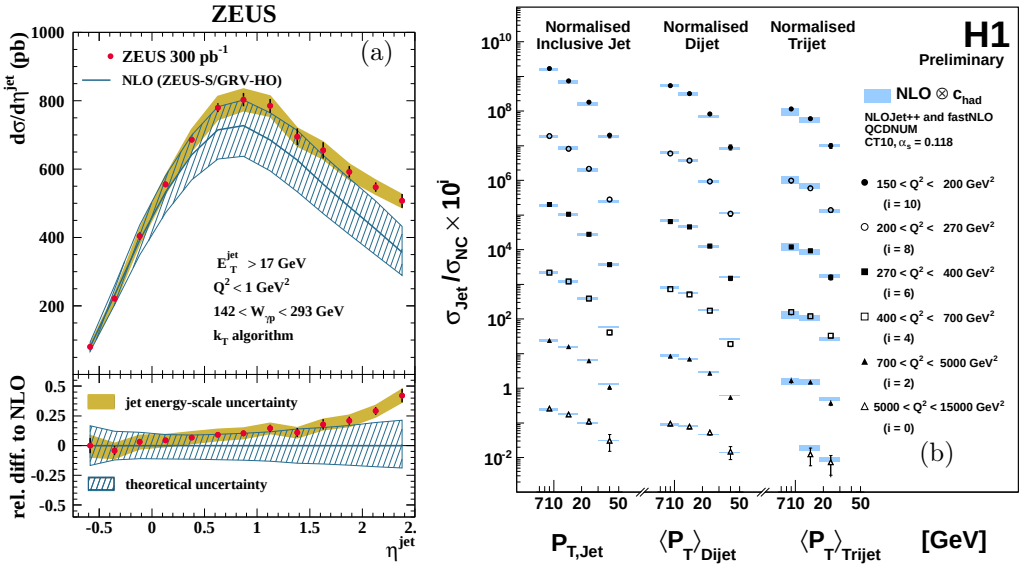

Figure 7: Jet production cross sections for (a) inclusive jet production in γp for $E_T^{jet} > 17$ GeV as a function of η^{jet} and (b) inclusive, dijet and trijet production in DIS normalised to the DIS cross section for $Q^2 > 150$ GeV^2 and $P_T^{jet} > 7$ GeV as a function of P_T for different Q^2.

to the inclusive DIS cross section the experimental systematic uncertainties are reduced. An unfolding technique is applied to properly account for correlations among the analysis bins and between the inclusive DIS, the inclusive jet, the dijet and the trijet sapmles.

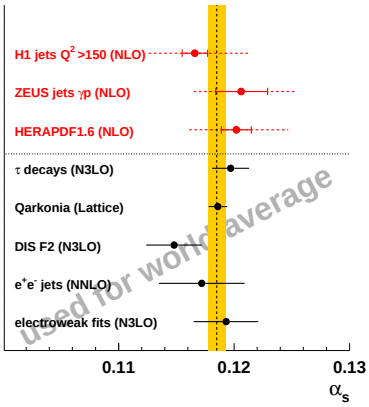

Figure 8: Compilation of α_S from different processes.

The data are also compared to NLO QCD prediction. The theory describes the data well over the full kinematic range. From these data the strong coupling constant α_S can be extracted. There is some tension observed when using the individual jet samples to determine α_S: the value obtained from the dijet sample is lower than that obtained from the other samples. This results in a poor χ^2 when fitting all samples together. The χ^2 improves significantly by restricting the phase space to the region where beyond NLO contributions are expected to be small. Using all three jet samples a value of $\alpha_S(M_Z) = 0.116 \pm 0.0011(exp.) \pm 0.0014(PDF) \pm 0.0008(had.) \pm 0.0039(theo)$ is obtained. As for jet production in γp the uncertainty on α_S is dominated by the uncertainty on the missing higher contributions.

In Fig. 8 these two α_S measurements and the preliminary result from the combined NLO QCD PDF+α_S fit to the inclusive and jet DIS data from HERA (*HERAPDF1.6*) are compared to the measurements used for the world average on α_S [7]. The HERA results are very consistent with the other measurements. The experimental uncertainties of the HERA results are comparable or superior to those from the other data apart from the error given for

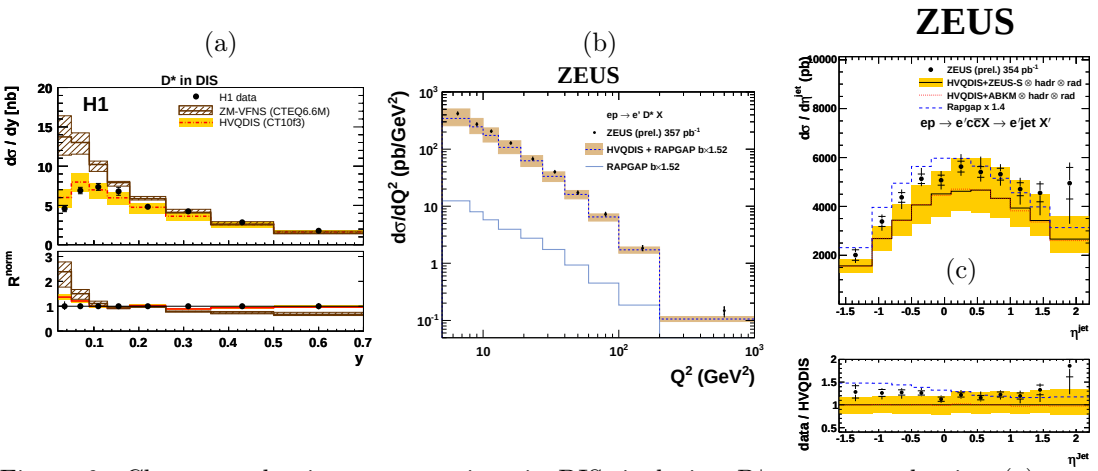

Figure 9: Charm production cross sections in DIS: inclusive D^* meson production (a) as a function of y (b) as a function of Q^2 and (c) charm jet production as a function of η^{jet}.

the lattice calculation. The precision of the HERA data is spoiled by the theory uncertainties from missing higher orders.

5 Charm Production

The dominant process for charm production at HERA is photon-gluon-fusion, $\gamma g \to c\bar{c}$, which is sensitive to the gluon density in the proton. The charm contribution to the proton structure function F_2 rises up to 30% at larger Q^2. Therefore a good understanding of this process is vital for precision PDF determinations. Due to the relative large mass m_c of the charm quark pQCD is applicable without any phase space restrictions. However the presence of several hard scales (m_c, P_T^c and Q^2) makes this process to a multiple-scale problem. Depending on the relative magnitude of m_c, P_T^c and Q^2 different approaches on pQCD have been elaborated. Precision measurements of charm production allow for the validity of these approaches to be tested.

Different experimental methods are developed for tagging charm production. Results are presented based on $D^{*\pm}$ and D meson reconstruction and on charm tagging via secondary vertices which makes use of the longevity of charmed hadrons.

The D^* meson production cross sections in DIS are presented in Fig. 9a as a function of y as measured by H1 [33] and in Fig. 9b as a function of Q^2 as measured by ZEUS [34]. In Fig. 9c the charm jet cross section as a function of η^{jet} from ZEUS [35] is shown. Charm jets are identified by requiring the presence of a secondary vertex in the events well separated from the primary vertex with a reconstructed mass consistent with the expectation for charm jets.

The measurements are compared with NLO QCD calculations in the fixed-flavour-number-scheme (*FFNS*) [36] as implemented in the HVQDIS program [37]. The predictions for the different measurements agree well with the data. Also for charm production in DIS the experimental precision of the data is significantly superior to the precision of the theory which has large uncertainties dominated by the uncertainties attributed to the missing higher order contributions. The data in Fig. 9a are also compared to calculations in the zero-mass variable-

flavour-number-scheme (*ZM-VFNS*) [38] which fails to describe the data. A similar observation has been made in a previous publication on D^* meson production at high Q^2 [39]. Therefore this calculation is not appropriate for describing the charm contribution to the proton structure function.

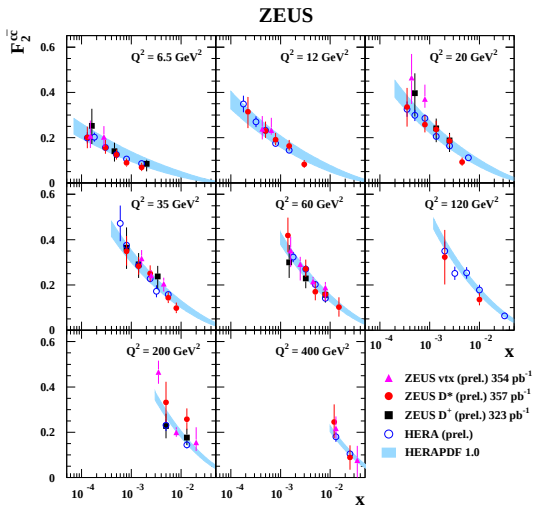

Figure 10: $F_2^{c\bar{c}}$ as a function of x for different values of Q^2 for the preliminary ZEUS measurements [34, 35] compared with the predictions based on HERAPDF1.0 (shaded band).

The measurements of charm production in DIS are used to determine the charm contribution $F_2^{c\bar{c}}$ to the proton structure function F_2. In Fig. 10 $F_2^{c\bar{c}}$ is shown as a function of x in bins of Q^2 extracted from the two preliminary ZEUS analyses discussed before. These data agree well with the preliminary HERA combined $F_2^{c\bar{c}}$ data [40]. Fig. 10 also includes the FFNS NLO QCD expectation based on HERAPDF1.0 [3] which is using only the inclusive HERA data as input. The uncertainty on the prediction is dominated by the uncertainty on m_c. The good description of the data by the calculation indicates that the gluon PDF in the proton tested by HERA processes is universal.

6 Particle Production

The study of particle production provides insight into both perturbative and non-perturbative aspects of QCD in parton fragmentation and hadronisation. The analyses of the fragmentation function into hadrons in different processes, i.e. in e^+e^-, pp or ep allows the universality of the fragmentation process to be tested.

At HERA only fragmentation into charged hadrons has been investigated so far [41, 42]. Here results from ZEUS on neutral strange particles are presented [43]. In Fig. 11a the K_s^0 scaled momentum spectrum observed in DIS is shown as a function of Q^2 in bins of x_p, with $x_p = 2P_{Breit}/Q$ and P_{Breit} being the momentum of the K_s^0 in the Breit frame[4]. Clear evidence for scaling violations is observed by the change of the Q^2 dependence from rising at small x_p to falling at large x_p. The data is compared with Monte Carlo (*MC*, lines) and with two NLO QCD calculations labeled AKK [44] and DSS [45] (shaded bands). While the MC expectations yield a fair description of the data AKK is significantly above the data except for $x_p > 0.6$ and DSS fails to describe the data for $x_p < 0.3$ at low Q^2. The better agreement of DSS may be related to the fact that this calculation is based on a global analysis of e^+e^-, pp and ep data while AKK uses e^+e^- data only. Similar deficits of the NLO QCD calculations have been observed for the charged particle production [41, 42].

In Fig. 11 new results on the production of very forward photons with $\eta_\gamma > 7.9$ in DIS from H1 [46] are also presented. These photons originate mainly from π^0 decays and therefore trace π^0 production at large η. In Fig. 11b the cross section for γ production normalised to

[4]The Breit frame is defined as the frame in which the exchanged photon's 4-vector is (0,0,0,Q).

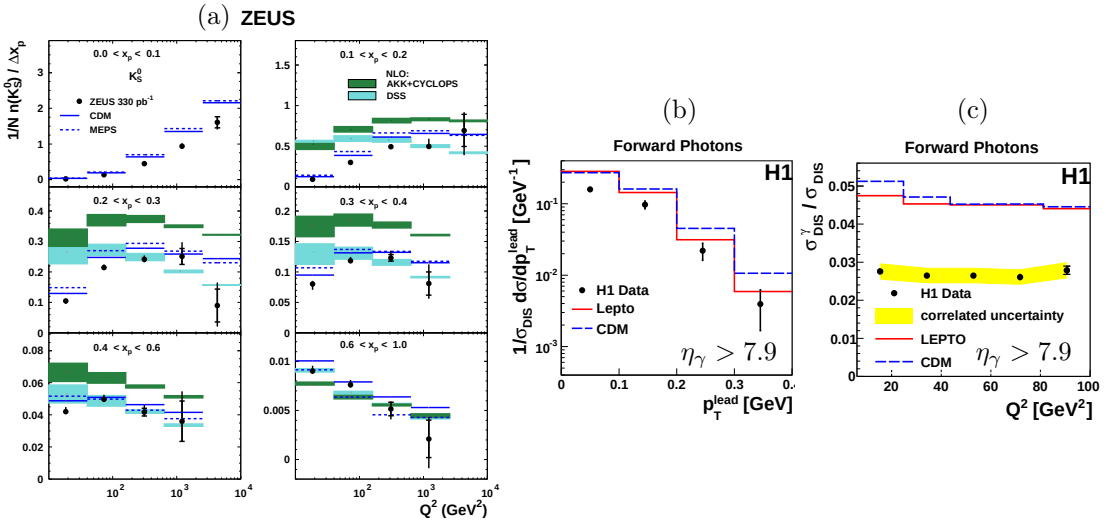

Figure 11: Particle production: (a) scaled momentum distribution for K_s^0 as a function of Q^2 in bins of x compared to MC and NLO QCD predictions, (b) normalised cross section for forward photon production as a function of p_T^{lead} and (c) forward photon yield as a function of Q^2.

the DIS cross section as a function of the transverse momentum p_T^{lead} of the leading photon is compared to two MC calculations. Both MCs predict higher cross sections than observed in data suggesting that the fragmentation of spectator quarks (proton remnant) to π^0s is not well modelled. The yield $\sigma_{DIS}^{\gamma}/\sigma_{DIS}$ shown in FIg. 11c as a function of Q^2 is found to be consistent with being independent of Q^2 similar to what is observed in MC apart from normalisation. This observation is consistent with the expectation from the limiting fragmentation hypothesis which assumes the fragmentation of the spectator quarks to be independent of the kinematics of the hard interaction.

7 Conclusion

The QCD analyses at HERA have reached very high precision and may serve as acid test for theory. In general NLO QCD gives a fair to good description of the data with the exception of fragmentations where present NLO QCD calculations have difficulties in describing the data. Unfortunately the uncertainties of the theory attributed to the missing higher orders are almost everywhere much larger than the experimental errors. Not only the interpretation of the HERA data would profit from having next-to-next-to-leading order calculations for HERA processes but also the understanding of the data from hadron colliders would be facilitated since HERA is the backbone of any modern PDF.

References

[1] H.-L. Lai *et al.*, Phys. Rev. **D82** (2010) 074024 [arXiv:1007.2241].

[2] R. S. Thorne and R. G. Roberts ; Phys. Rev **D57** (1998) 6871; R. S. Thorne, Phys. Rev **D73** (2006) 054019 [hep-ph/0601245]; A. D. Martin *et al.* Eur. Phys. J. **C70** (2010) 51[arXiv:1007.2624].

[3] H1 and ZEUS Collab., F. D. Aaron *et al.* JHEP **1**(2010) 109 [arXiv:0911.0884].
[4] NNPDF Collab. R. D. Ball *et al.* [arXiv:1107.2652].
[5] S. Alekhin, J. Blümlein and S. Moch, S. Alekhin Phys. Rev **D81** (2010) 014032 [arXiv:0908.2766]; S. Alekhin, J. Blümlein and S. Moch [arXiv:12002.2281].
[6] I. Abt, this proceedings.
[7] A. Hoang, this proceedings.
[8] G. Altarelli, Phys. Rep. **81** (1982) 1.
[9] H1 and ZEUS Collab., H1prelim-11-042, ZEUS-prel-11-002.
[10] H1 Collab., F. D. Aaron *et al.*, Phys. Lett **B705** (2011) 52, [arXiv:1107.2478].
[11] H1 Collab., F. D. Aaron *et al.*, Phys. Lett **B704** (2011) 388, [arXiv:1107.3716].
[12] H1 Collab., F. D. Aaron *et al.*, Phys. Lett **B701** (2011) 20, [arXiv:1103.4938].
[13] ZEUS collab., ZEUS-prel-11-008; S. Antonelli, this proceedings.
[14] W. Buchmüller, R. Rückl and D. Wyler, Phys. Lett **B191** (1987) 442 [Erratum ibid. **B448** (1999) 320].
[15] ZEUS Collab., H. Abramowicz *et al.*, Phys. Lett **B708** (2011) 27 [arXiv:1111.3901].
[16] J. Collins, Phys. Rev. **D57** (1998) 3051 [Erratum ibid. **D61** (2000) 019902].
[17] A. Glazov, AIP Conf. Proc. **792** (2005) 237.
[18] H1 Collab. F. D. Aaron *et al.*, Eur. Phys. J. **C63**(2009) 625 [arXiv:0904.0929].
[19] H1 and ZEUS Collab., H1prelim-11-111, ZEUS-prel-11-011; V. Sola, this proceedings.
[20] H1 Collab., F. D. Aaron *et al.*, Eur. Phys. J. **C72** (2012) 1970 [arXiv:1203.4495].
[21] H1 Collab., A. Atkas *et al.*, Eur. Phys. J. **48** (2006) 715 [hep-ex/0606004].
[22] H1 Collab., F. D. Aaron *et al.*, Eur. Phys. J. **71** (2011) 1578 [arXiv:1010.1476].
[23] H1 Collab., F. D. Aaron *et al.*, Eur. Phys. J. **72** (2012) 1838 [arXiv:1107.3420].
[24] ZEUS Collab., S. Chekanov *et al.*, Nucl. Phys. **B831** (2010) 1 [arXiv:0911.4119].
[25] H1 Collab., A. Atkas *et al.*, JHEP 0710:42 [arXiv:0708.3217].
[26] H1 and ZEUS Collab., H1prelim-11-034, ZEUS-prel-11-001; K. Nowak this proceedings.
[27] ZEUS Collab., H. Abramowicz *et al.*, to be published in Nucl. Phys. **B** , arXiv:1205.6153.
[28] S. Catani *et al.*, Nucl. Phys. **B406** (1993) 187, S. D. Ellis and D. E. Soper, Phys. Rev. **D48** (1993) 3160.
[29] T. Sjöstrand and M. van Zijl, Phys. Rev. **D36** (1987) 2019.
[30] M. Cacciari, G. P. Salam and G. Soyez, JHEP **0804** (2008) 063 [arXiv:0802.1189].
[31] G. P. Salam and G. Soyez, JHEP **0705** (2008) 086 [arXiv:0704.0292].
[32] H1 Collab., H1prelim-12-031; D. Britzger this proceedings.
[33] H1 Collab., F. D. Aaron *et al.*, Eur. Phys. J. **71** (2011) 1769,[arXiv:1106.1028].
[34] ZEUS Collab., ZEUS-prel-11-012, A. Gizhko this proceedings.
[35] ZEUS Collab., ZEUS-prel-12-002, V. Libov this proceedings.
[36] E. Laenen *et al.*, Phys. Lett. **B291** (1992) 325; Nucl. Phys. **B392** (1993) 162; Nucl. Phys. **B392** (1993) 229; S. Riemersma *et al.*, Phys. Lett. **B347** (1995) 143 [hep-ph/0611029].
[37] B. Harris and J. Smith, Nucl. Phys. **B452** (1995) 109 [hep-ph/0611029]; Phys. Rev. **D57** (1998) 2806 [hep-ph/0611029].
[38] G. Heinrich and B. A. Kniehl, Phys. Rev. **D70** (2004) 094035,[hep-ph/0611029]; C. Sandoval, Proc. of XVII International workshop on Deep-Inelastic Scattering, Madrid, 2009 [arXiv:0908.0824];
[39] H1 Collab., F. D. Aaron *et al.*, Phys. Lett. **B686** (2010)91 [arXiv:0911.3989].
[40] H1 and ZEUS Collab., H1prelim-09-171, ZEUS-prelim-09-015.
[41] H1 Collab., F. D. Aaron *et al.*, Phys. Lett. **B654** (2007)148 [arXiv:0706.2456].
[42] ZEUS Collab., H. Abramowicz *et al.*, JHEP **6** (2010) 1 [arXiv:1001.4026].
[43] ZEUS Collab., H. Abramowicz *et al.*, JHEP **03** (2012) 020 [arXiv:1111.3526].
[44] S. Albino *et al.*, Phys. Rev. **D75** (2007) 034018 [hep-ph/0611029]; S. Albino, B. A. Kniehl and G. Kramer, Nucl. Phys. **B803** (2008) 42 [arXiv:0803.2768].
[45] D. de Florian, R. Sassot and M. Stratmann, Phys. Rev. **D75** (2007) 114010 [hep-ph/0703242].
[46] H1 Collab., F. D. Aaron *et al.*, Eur. Phys. J. **C71** (2011) 1771 [arXiv:1106.5944].

Jets, W/Z and Top Quark Production at the LHC and Status of the Higgs Boson Searches at ATLAS

Oliver Kortner on behalf of the ATLAS and CMS collaborations

Max-Planck-Institut für Physik, Föhringer Ring 6, 80806 Munich, Germany

DOI: `http://dx.doi.org/10.3204/DESY-PROC-2012-02/25`

Until the end of 2011 the ATLAS and CMS experiments have each analysed up to 5 fb^{-1} of pp collision data at $\sqrt{s} = 7$ TeV. Their studies show excellent agreement between Standard Model predictions and experimental measurements for the production of jets, W/Z bosons, and top quarks. The ATLAS experiment has been able to exclude a Standard Model Higgs boson at 95% confidence level in the mass intervals 110 GeV $< m_H <$ 117.5 GeV, 118.5 GeV $< m_H <$ 122.5 GeV, 129 GeV $< m_H <$ 539 GeV.

1 Introduction

The Large Hadron Collider (LHC) has delivered about 5 fb^{-1} of pp collision data at $\sqrt{s} = 7$ TeV for each of the multipurpose detectors ATLAS and CMS [1, 2] in 2010 and 2011. The data recorded by ATLAS and CMS allow for the verification of Standard Model predictions for the production of jets, W and Z bosons as well as a detailed study of top quark production. The amount of data recorded provides sensitivity for a possible exclusion of a Standard Model Higgs boson over a wide expected mass range, from 120 GeV up to about 555 GeV at 95% confidence level. This note summarizes the status of the studies of jets, W/Z, and top quark production by ATLAS and CMS and the status of the Standard Model Higgs searches of the ATLAS experiment.

2 Jet production at the LHC

In proton proton collisions at the LHC, predominantly jets are produced via the strong interaction. The study of inclusive jet and di-jet production therefore probes next-to-leading order (NLO) perturbative QCD and the parton distribution functions. ATLAS and CMS have measured inclusive jet and di-jet cross sections. They both use the anti-k_T algorithm [3] to reconstruct jets, ATLAS with the size parameter $R = 0.4$ and $R = 0.6$, CMS with $R = 0.7$. ATLAS considers jets up to absolute values of rapidities of 4.4 while CMS stops at 2.5 in the inclusive jet and dijet studies [4, 5, 6]. ATLAS probes transverse jet momenta between 20 GeV and 1.5 TeV in the inclusive measurement and di-jet masses between 70 GeV and 5 TeV. CMS considers jets with transverse momenta between 18 GeV and 2 TeV and di-jet masses between 200 GeV and 5 TeV. The studies are therefore sensitive to values of x, the momentum fraction carried by the colliding partons, between 10^{-4} and 0.5. Both experiments express their results

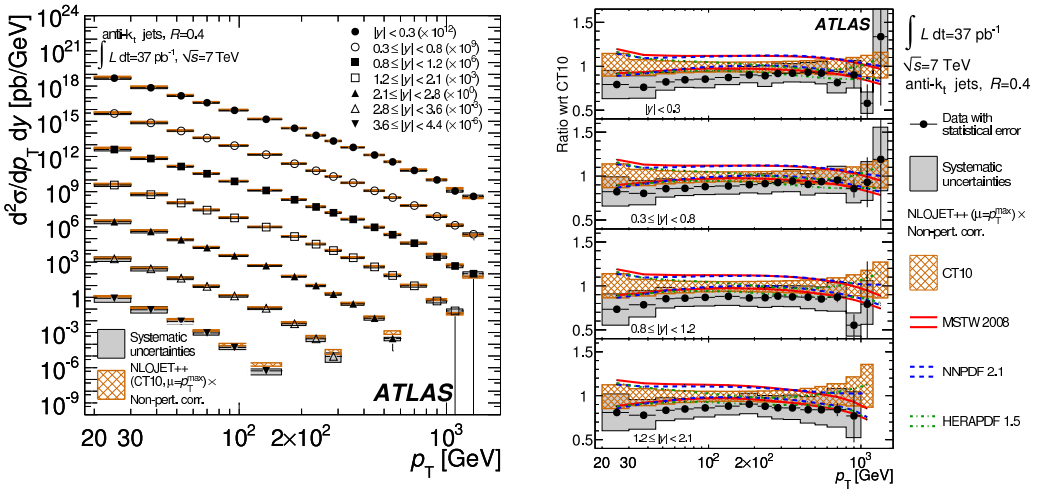

Figure 1: Left: Double differential inclusive jet production cross section measured by ATLAS. Right: Comparison of the ATLAS cross section measurements with NLO predictions corrected for non-perturbative effects [4].

in terms of jets at particle level and apply non-perturbative corrections to the NLO predictions which are important at jet transverse momenta below 100 GeV.

Figure 1 shows a comparison of the double differential inclusive jet production cross section measured by ATLAS with NLO predictions for anti-k_T jets with $R = 0.4$. The experimental data agree with NLO QCD predictions within the experimental and theoretical uncertainties in the entire phase space probed. Better agreement between experimental data and predictions is obtained for large jet sizes [4, 6].

In Figure 2 the double differential di-jet production cross section measured by CMS is compared with NLO predictions. Like in the case of the inclusive jet production cross section, the experimental data are in agreement with the theoretical predictions within the experimental and theoretical uncertainties.

3 Production of W and Z bosons at the LHC

3.1 Inclusive W and Z production mechanisms

W and Z bosons are created in quark antiquark collisions at the LHC. W^+ bosons are produced in collisions of u type quarks and d type antiquarks; in lowest order of perturbation theory, about 80% of the W^+ bosons are produced in $u\bar{d}$ collisions, about 20% in $c\bar{s}$ collisions. W^- bosons are produced in collisions of d type quarks and u type antiquarks, in about 70% of all cases in $d\bar{u}$ collisions, in the remaining case mainly in $s\bar{c}$ collisions. As a proton contains two valence u quarks and one valence d quark, roughly two times more W^+ than W^- bosons are produced in pp collisions at the LHC. Z bosons are predominantly produced in $u\bar{u}$ and $d\bar{d}$ annihilations each in about 40% of the cases and in $s\bar{s}$ and, with smaller rate, $c\bar{c}$ annihilations in the remaining cases. Given the different coupling of the quark currents to W and Z bosons

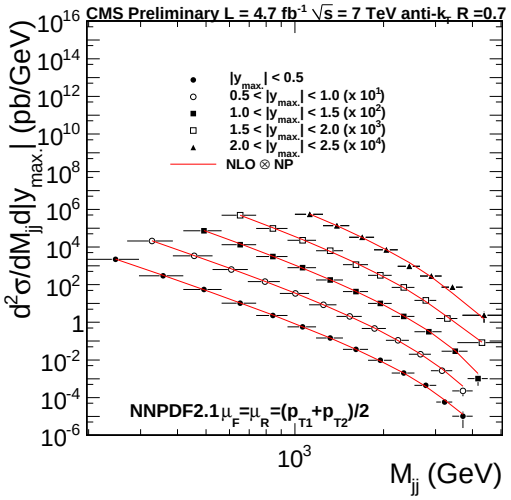

Figure 2: Comparison of double differential di-jet production cross section measured by CMS with NLO predictions corrected for non-perturbative effects [6].

more W than Z bosons are created [7]. The study of the W and Z production cross sections probes the parton densities at values of x in the interval $10^{-3} \lesssim x \lesssim 0.1$ where the momentum fractions $x_{1,2}$ of the colliding quark and antiquark are related to the W/Z rapidity by the $x_{1,2} = \frac{m_{W/Z}}{\sqrt{s}} e^{\pm y_{W/Z}}$ at tree level.

3.2 Selection of W and Z events

The ATLAS and CMS experiments use a similar selection to collect W and Z events which is driven by the final state topologies [8, 9]. W bosons are studied in their decays into a highly energetic isolated charged lepton (electron or muon) and the corresponding neutrino leading to significant missing transverse energy E_T^{miss}. The charged leptons are used to trigger the data acquisition. The E_T^{miss} distributions are used to determined the QCD background which are difficult to model with sufficient Monte-Carlo statistics. ATLAS requires $E_T^{miss} > 25$ GeV in the determination of the fiducial cross section because of the small background contribution to this phase space region. CMS does not impose an E_T^{miss} cut, but extracts the W yield from a template fit to the E_T^{miss} distribution.

Z bosons are identified by the two oppositely charged isolated high p_T decay leptons (electrons or muons). One or both charged leptons are used in the trigger. The main studies of the Z production are limited to the acceptance of the inner tracking system ($|\eta| \lesssim 2.5$); however the ATLAS experiments also considered topologies where one of the electrons is detected in the forward region ($|\eta| < 4.9$) with calorimetric coverage [8]. The results of this measurement with extended acceptance are in agreement with the main studies.

3.3 Measurements of the W and Z cross sections

Table 1 summarizes the measurements of the $W^{\pm}$ and Z productions cross sections by ATLAS and CMS based on an integrated luminosity of about 35 pb^{-1} per experiment; (Drell Yan) lepton pair production via a virtual photon are taken into account in the Z analysis. The cross sections which have been measured with similar accuracy by the two experiments agree within the quoted uncertainties. They are also in good agreement with the NNLO predictions of (6.15 ± 0.17) nb for W^+, (4.29 ± 0.11) nb for W^-, and (0.97 ± 0.03) nb for Z/γ^* [9] which are obtained with FEWZ [10] and the MSTW 2008 parton density function [11].

	$\sigma^{tot}_{W} \cdot \mathrm{BR}(W \to \ell\nu)$ [nb]	
	ATLAS	CMS
	stat sys lum acc	stat sys lum acc
W^+	$6.048 \pm 0.016 \pm 0.072 \pm 0.206 \pm 0.096$	$6.04 \pm 0.02 \pm 0.06 \pm 0.24 \pm 0.08$
W^-	$4.160 \pm 0.014 \pm 0.057 \pm 0.141 \pm 0.083$	$4.26 \pm 0.01 \pm 0.04 \pm 0.17 \pm 0.04$
$W^{\pm}$	$10.207 \pm 0.021 \pm 0.121 \pm 0.347 \pm 0.164$	$10.31 \pm 0.02 \pm 0.09 \pm 0.41 \pm 0.10$
	$\sigma^{tot}_{Z/\gamma^*} \cdot \mathrm{BR}(Z/\gamma^* \to \ell\ell)$ [nb]	
	ATLAS	CMS
	stat sys lum acc	stat sys lum acc
Z/γ^*	$0.937 \pm 0.006 \pm 0.009 \pm 0.032 \pm 0.016$	$0.974 \pm 0.007 \pm 0.007 \pm 0.039 \pm 0.018$

Table 1: Measured W and Z cross sections times branching ratios[8][9].

Higher sensitivity to the theoretical predictions is provided by differential cross sections. ATLAS and CMS find good agreement between their measured differential cross sections and the theoretical predictions. The plot on the left of Figure 3 shows the W^+ production cross section as a function of the pseudorapidity of the charged decay lepton as measured by the ATLAS experiment compared to predictions of the FEWZ [10] and DYNNLO[12] NLO calculations with different parton densities; the corresponding dependence of the Z production cross section on the rapidity of the Z boson is presented on the right of Figure 3. The measured distributions follow the predictions, but trends in the deviations of some parton density function sets are visible. The ATLAS results slightly favour MSTW08 [11] and slightly disfavour JR09 [13]. Improvements of the parton density functions by including these measurements can be expected.

3.4 Production of W and Z bosons in association with jets

W and Z bosons can be produced in association with jets (abbreviated to j in the following). Two basic processes are possible at lowest order: initial state gluon radiation of the colliding quarks and the radiation of a W or Z boson from one of the colliding quarks. The study of $W+j$ and $Z+j$ production is interesting as a test of QCD; the measurement of $W+c$ is sensitive to the s quark parton density function, the measurement of $Z+b$ to the b quark parton density function. Finally $W+j$ and $Z+j$ production is an important background to many physics processes, for instance to $pp \to t\bar{t}+X \to (W^+b)(W^-\bar{b})+X$ and $pp \to t+X \to (W^+b)+X$ or $pp \to H+X \to W^+W^-+X \to 2j+\ell\nu+X$.

Figure 4 summarizes the measurements of the $W+j$ [14] and $Z+j$ [15] cross sections and their comparisons with theoretical predictions. Good agreement with predictions of the jet multiplicity and jet kinematics by state-of-the art multi-parton matrix element generators like

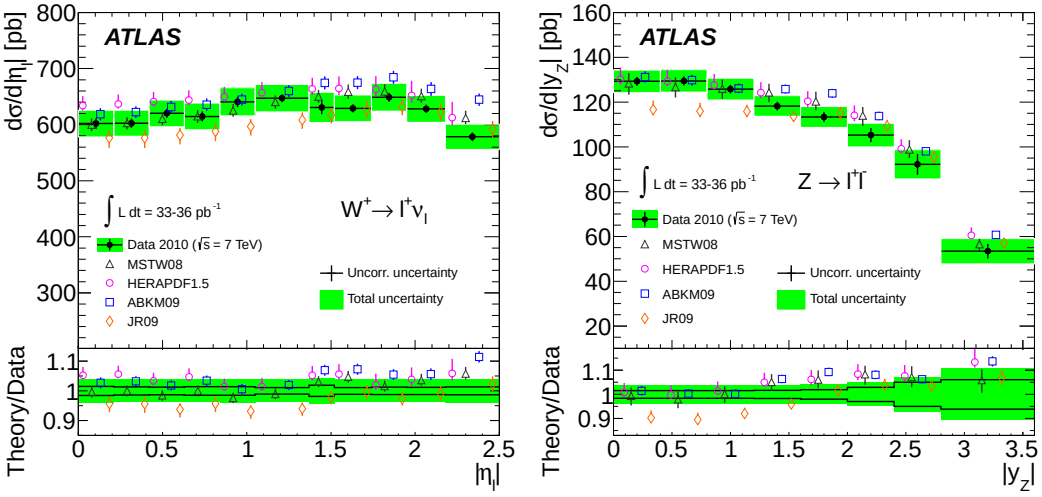

Figure 3: Comparison of differential cross sections measured by ATLAS with theoretical predictions by the FEWZ and DYNNLO calculations with different parton densities [8]. Left: W^+ production. Right: Z production.

ALPGEN [16] and SHERPA [17] is observed. PYTHIA [18] as leading order matrix element generator provides a good prediction for the production of one additional jet, but fails for higher jet multiplicities as expected.

3.5 Di-boson production

ATLAS and CMS have also studied the production of pairs of W and Z bosons. Figure 5 shows the lowest order Feynman diagrams for di-boson production. The continuum production of W and Z boson pairs is an important background to $H \to W^+W^-$ and $H \to ZZ$. In the Standard Model of electroweak interactions, the triple gauge boson vertex $Z/\gamma^* \to W^+W^-$ is allowed while the vertex $Z/\gamma^* \to ZZ$ is forbidden. Deviations of the measured ZZ production cross section could therefore be an indication for anomalous triple gauge boson couplings.

Neither ATLAS nor CMS have found deviations from the Standard Model predictions. Based on an integrated luminosity of 4.7 fb^{-1}, ATLAS measures $\sigma(W^+W^-) = [53.4 \pm 2.1(\text{stat}) \pm 4.5(\text{syst}) \pm 2.1(\text{lumi})]$ pb [19], CMS, based on an integrated luminosity of 1.1 fb^{-1}, $[55.3 \pm 3.3(\text{stat}) \pm 6.9(\text{syst}) \pm 3.3(\text{lumi})]$ pb [21] which agrees with the NLO Standard Model prediction of (45.1 ± 2.8) pb. An updated CMS measurement with the full 2011 data set can be found in [20]. The NLO Standard Model prediction of $\sigma(ZZ) = (6.5^{+0.3}_{-2.3})$ pb [22] is also consistent with the experimental measurements of $[7.2^{+1.1}_{-0.9}(\text{stat})^{+0.4}_{-0.3}(\text{syst}) \pm 0.3(\text{lumi})]$ pb by ATLAS [22] and $[3.8^{+1.5}_{-1.2}(\text{stat}) \pm 0.2(\text{syst}) \pm 0.2(\text{lumi})]$ pb by CMS [21]. It should be noted that the statistical and systematic errors of the measurements are still larger than the uncertainties of the theoretical predictions.

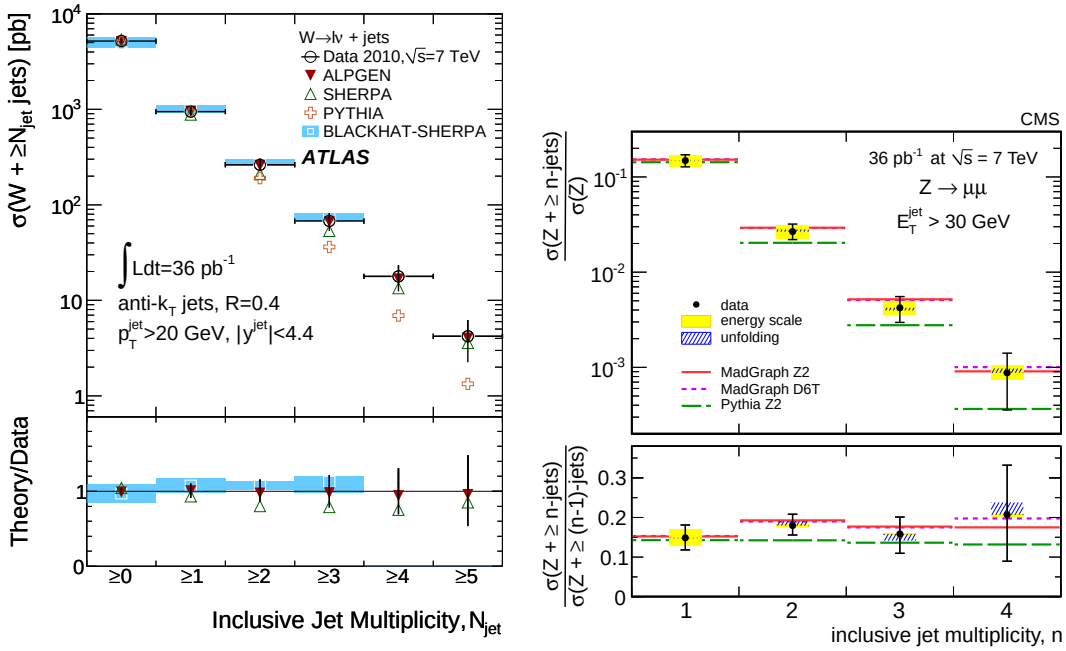

Figure 4: Comparison of the measured cross sections for the production of weak gauge bosons with jets as a function of the jet multiplicity. Left: $W + j$ as measured by ATLAS [14]. Right: $Z + j$ as measured by CMS [15].

4 Production of top quarks at the the LHC

At the LHC $t\bar{t}$ pairs are produced with a predicted cross section of 167^{+17}_{-18} pb mainly via gluon fusion [23]. Production of single top quarks is also possible at the LHC via t channel production ($64.6^{+3.3}_{-2.6}$ pb) [24], associated Wt production ($15.7^{+1.3}_{-1.4}$ pb) [25], and s channel production ((4.6 ± 0.3) pb) [26] as depicted in the Feynman diagrams of Figure 6. The experimental signature of the top quark decays is a b quark jet and the decay products of the W bosons produced in the top decay.

The LHC experiments have reached a precision of the $t\bar{t}$ cross section measurement which is smaller than the uncertainties of the theoretical predictions. Figure 7 shows a summary of the ATLAS and CMS measurements which are compatible with the theoretical predictions.

The statistics of $t\bar{t}$ pairs created at the LHC allows measurements of differential cross sections. Figure 8 shows as an example the dependence of the $t\bar{t}$ cross section of the rapidity of the $t\bar{t}$ systems. The measured cross section agrees with the theoretical predictions in all rapidity bins. The experiments have also found good agreement of the experimental measurements of the spin correlations in $t\bar{t}$ pairs [31] and the polarization of the W bosons in top quark decays [32, 33] with theoretical predictions.

ATLAS and CMS have also studied the production of single top quarks. Given the small cross sections the analysed amount of data of about 1 fb^{-1} allowed only for the measurements of the t channel and Wt production cross sections. ATLAS measures $\sigma(\text{t channel}) = 90^{+32}_{-22}$ pb [34]

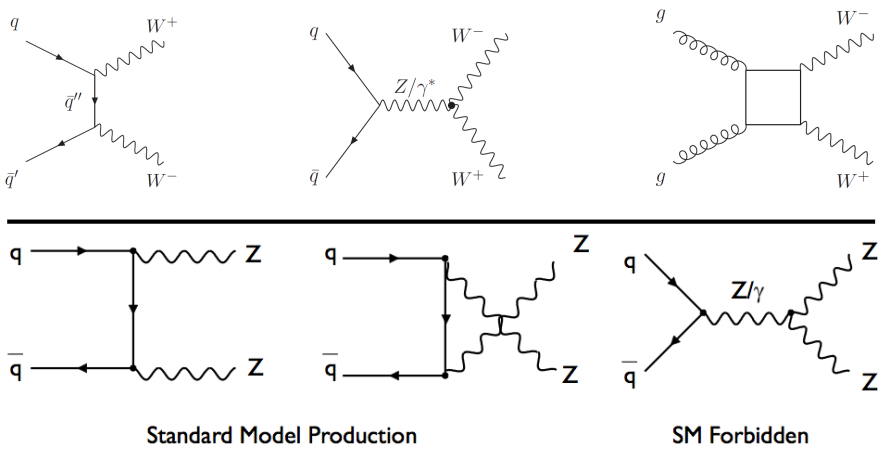

Figure 5: Lowest order Feynman diagrams for di-boson production. The graph on the bottom right is forbidden in the Standard Model.

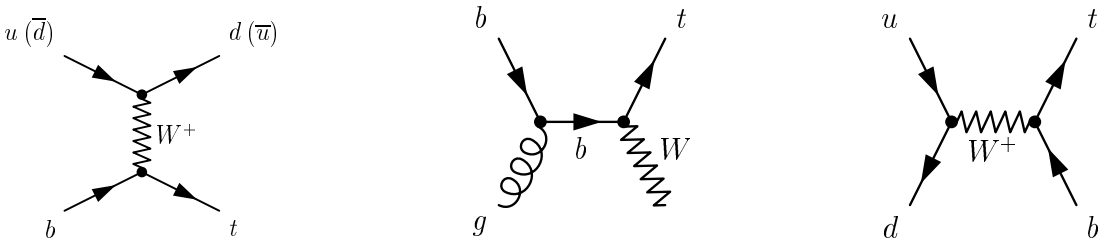

Figure 6: Lowest order Feynman diagrams of single top quark production. Left: t channel production. Middle: Wt production. Right: s channel production.

and $\sigma(Wt) < 39.1$ pb at 95% confidence level[35]; CMS finds σ(t channel) = [70.3 $\pm$ 6.15(stat) $\pm$ 9.61(syst) $\pm$ 3.36(lumi)] pb [36] and $\sigma(Wt) = 22^{+9}_{-7}$ pb at 2.7σ significance [37]. The results are compatible with the theoretical predictions.

5 Status of the search for the Standard Model Higgs boson with the ATLAS detector at the LHC

Figure 9 shows the lowest order Feynman diagrams of the Standard Model Higgs production mechanisms which are exploited by the Higgs searches of the ATLAS experiment. At the LHC Standard Model Higgs bosons are predominantly produced in gluon gluon fusion. Over a wide mass range the vector boson fusion process is an order of magnitude less frequent, but its final state topology with two high p_T forward jets with a large rapidity gap and the Higgs decay products in this gap allows for a powerful background suppression which is needed for the $H \to \tau\tau$ channel in particular. The production of Higgs bosons in association with W/Z bosons has an even lower cross section; it used in the $H \to b\bar{b}$ channel to suppress the large inclusive $b\bar{b}$ background.

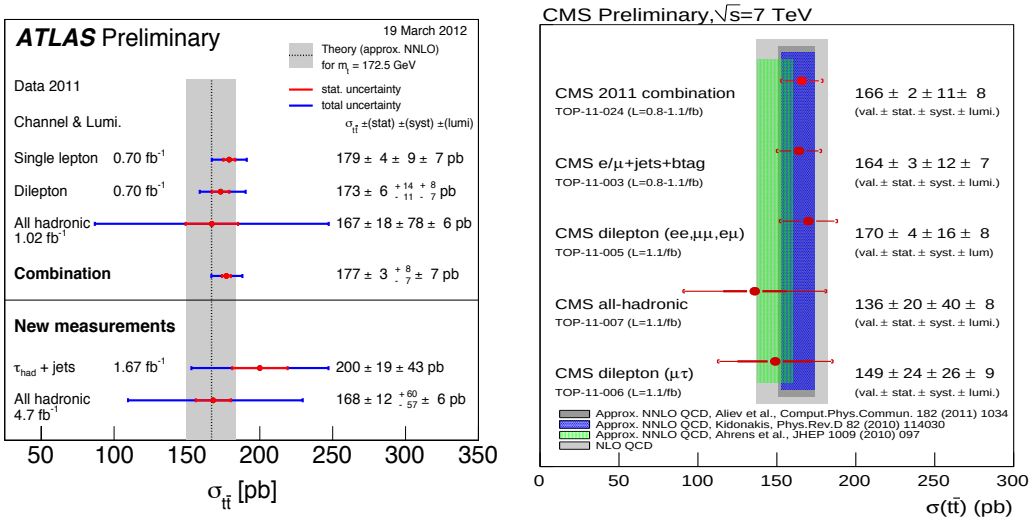

Figure 7: Summaries of the measurements of the $t\bar{t}$ production cross sections by ATLAS (left) [27, 28] and CMS [29] (right).

The integrated luminosity of 4.7 fb^{-1} collected by the ATLAS experiment makes it possible to exclude the Standard Model Higgs boson with $> 95\%$ confidence level over a wide range of Higgs masses m_H; the expected exclusion intervall is $m_H \in [120\ \text{GeV}, 555\ \text{GeV}]$ as presented in Figure 10. For $m_H \gtrsim 150$ GeV the exclusion is dominated by the following channels:

- $m_H \gtrsim 300$ GeV: $H \to ZZ \to \ell\ell\nu\nu$;
- 200 GeV $\lesssim m_H \lesssim 300$ GeV: $H \to ZZ \to 4\ell$;
- 150 GeV $\lesssim m_H \lesssim 200$ GeV: $H \to WW^* \to \ell\ell\nu\nu$.

The channel $H \to WW^* \to \ell\ell\nu\nu$ is still the most sensitive channel down to $m_H \approx$130 GeV. At lower Higgs masses, one needs to combine it with the following channels to reach sensitivity to the Standard Model cross section:

- $H \to ZZ^* \to 4\ell$;
- $H \to \gamma\gamma$;
- $H \to \tau\tau$ in vector boson fusion production;
- $H \to b\bar{b}$ in associate production with W and Z bosons.

ATLAS is able to exlude the following masses of the Standard Model Higgs boson [38]:

- 110 GeV $< m_H <$ 117.5 GeV, 118.5 GeV $< m_H <$ 122.5 GeV, 129 GeV $< m_H <$ 539 GeV at 95% confidence level;
- 130 GeV $< m_H <$ 486 GeV at 99% confidence level.

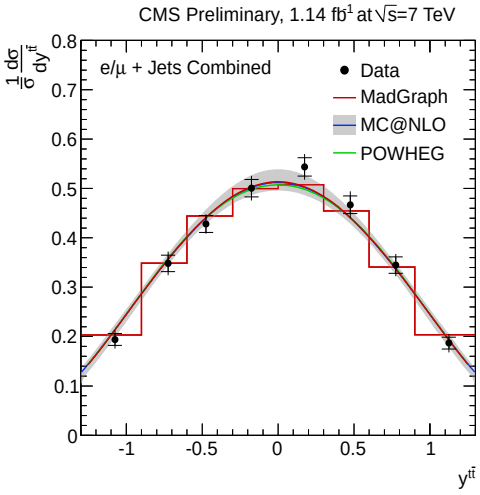

Figure 8: $t\bar{t}$ production as a function of the rapidity of the $t\bar{t}$ system as measured by CMS in comparison with NLO predictions [30].

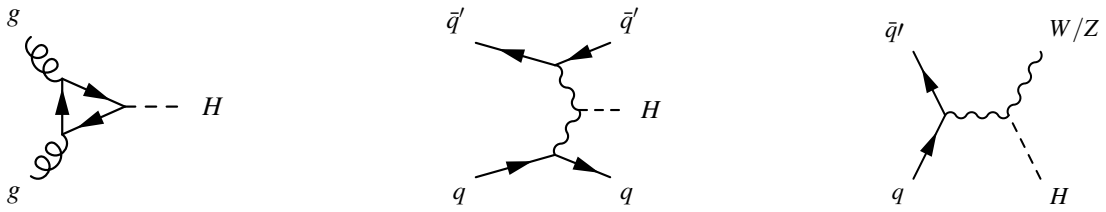

Figure 9: Lowest order Feynman diagrams of the Standard Model Higgs boson production mechanisms exploited by the ATLAS Higgs analyses. Left: Gluon gluon fusion. Middle: Vector boson production. Right: Associated Higgs production.

The observed exclusion limit around $m_H = 126$ GeV is worse than expected. This is caused by an excess of events over the background expectation in the $H \to \gamma\gamma$ and $H \to ZZ \to 4\ell$ channels. As shown in Figure 11, the excess has a 2.9 standard deviations local significance in the $H \to \gamma\gamma$ channel and a 2 standard deviations local significance in the $H \to ZZ^* \to 4\ell$ channel. As no excess is observed in the other channels, especially in the $H \to WW \to \ell\ell\nu\nu$ channel, the excess has a reduced local significance of 2.5 standard deviations. An excess of 2.9 standard deviations is expected for a Standard Model Higgs boson with $m_H = 126$ GeV. The best fit signal strength at $m_H \approx 126$ GeV is $0.9^{+0.4}_{-0.3}$ times the Standard Model cross section. The global probability of such a background fluctuation anywhere in the full explored mass range (110 GeV-600 GeV) is 30% and 10% in the mass range from 110 GeV to 146 GeV.

The triplication of the collected pp collision data in 2012 will make it possible to verify or falsify the existance of the Standard Model Higgs boson around $m_H = 126$ GeV.

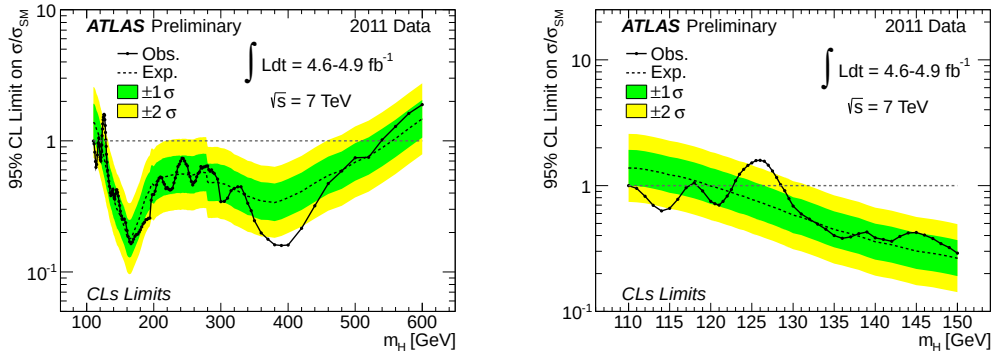

Figure 10: Exclusion limits for the Standard Model Higgs boson at 95% confidence level for Higgs boson masses m_H in the range between 100 GeV and 600 GeV [38]. The plot on the right zooms into the low mass region below $m_H = 150$ GeV.

6 Summary

The precision measurements of the production of jets, W/Z bosons and top quarks performed by ATLAS and CMS on up to 5 fb^{-1} of pp collisions data at $\sqrt{s} = 7$ TeV per experiment are in agreement with the prediction of the Standard Model. The experiment has been able to exclude a Standard Model Higgs boson at 95% confidence level in the mass intervals 110 GeV $< m_H <$ 117.5 GeV, 118.5 GeV $< m_H <$ 122.5 GeV, 129 GeV $< m_H <$ 539 GeV.

7 Bibliography

References

[1] ATLAS Collaboration, JINST 3 (2008) S08003.

[2] CMS Collaboration, JINST 3 (2008) S08004.

[3] M. Cacciari, G. Salam, and G. Soyez, JHEP 0804, 063 (2008), arXiv:0802.1189 [hep-ph].

[4] ATLAS Collaboration, arXiv:1112.6297.

[5] ATLAS Collaboration, ATLAS-CONF-2012-021, https://cdsweb.cern.ch/record/1430730.

[6] CMS Collaboration, CMS-PAS-QCD-11-004.

[7] A. D. Martin, R. G. Roberts, W. J. Stirling, R. S. Thorne, Eur.Phys.J.C14:133-145,2000.

[8] ATLAS Collaboration, Phys. Rev. D 85, 072004 (2012).

[9] CMS Collaboration, J. High Energy Phys. 10 (2011) 132.

[10] C. Anastasiou, L. J. Dixon, K. Melnikov, and F. Petriello, Phys. Rev. D 69, 094008 (2004).

[11] A. D. Martin, W. J. Stirling, R. S. Thorne, and G. Watt, Eur. Phys. J. C 63, 189 (2009).

[12] S. Catani and M. Grazzini, Phys. Rev. Lett. 98, 222002 (2007). S. Catani, L. Cieri, G. Ferrera, D. de Florian, and M. Grazzini, Phys. Rev. Lett. 103, 082001 (2009).

[13] P. Jimenez-Delgado and E. Reya, Phys. Rev. D 79, 074023 (2009).

[14] ATLAS Collaboration, Phys. Rev. D85 (2012) 092002.

[15] CMS Collaboration, J. High Energy Phys. 01 (2012) 010.

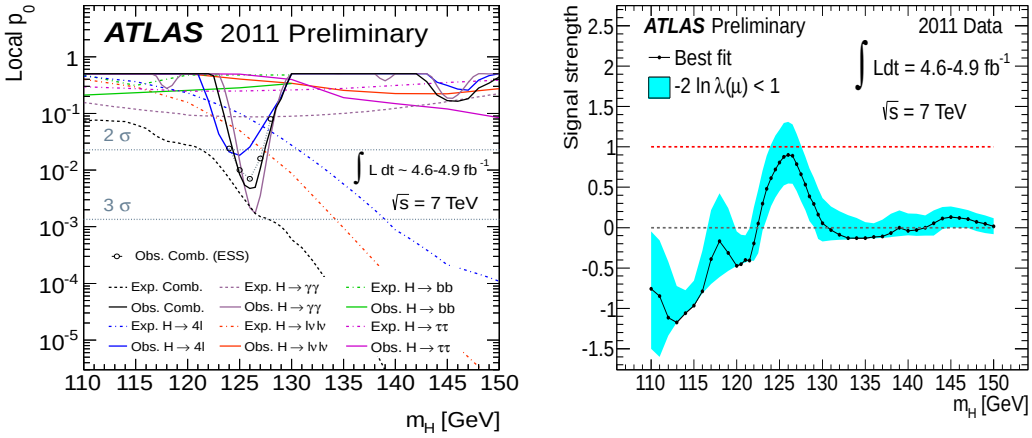

Figure 11: Left: Local statistical significance of an excess of events over the background expectation separate by Higgs decay channels. Right: Signal strength $\mu = \frac{\sigma}{\sigma_{SM}}$ best compatible with the observed excess. [38]

[16] M. L. Mangano et al., J. High Energy Phys. 07 (2003) 001.

[17] T. Gleisberg et al., J. High Energy Phys. 02 (2009) 007.

[18] T. Sjöstrand, S. Mrenna, and P. Skands, J. High Energy Phys. 05 (2006) 026.

[19] ATLAS Collaboration, ATLAS-CONF-2012-025, https://cdsweb.cern.ch/record/1430734.

[20] CMS Collaboration, CMS-PAS-SMP-12-005.

[21] CMS Collaboration, CMS-PAS-EWK-11-010.

[22] ATLAS Collaboration, ATLAS-CONF-2012-026, https://cdsweb.cern.ch/record/1430735.

[23] M. Aliev et al., Comput. Phys. Commun.182 (2011) 1034-1046, arXiv:1007:1327 [hep-ph].

[24] N. Kidonakis, Phys. Rev. D 83 (2011) 091503 [arXiv:1103.2792].

[25] N. Kidonakis, Phys. Rev. D 82 (2010) 054018 [arXiv:1005.4451].

[26] N. Kidonakis, Phys. Rev. D 81 (2010) 054028 [arXiv:1001.5034].

[27] ATLAS Collaboration, https://twiki.cern.ch/twiki/bin/view/AtlasPublic/CombinedSummaryPlots.

[28] ATLAS Collaboration, ATLAS-CONF-2012-024, https://cdsweb.cern.ch/record/1430733.

[29] CMS Collaboration, CMS-PAS-TOP-11-024.

[30] CMS Collaboration, CMS-PAS-TOP-11-013.

[31] ATLAS Collaboration, PRL 108, 212001 (2012).

[32] ATLAS Collaboration, ATLAS-CONF-2011-122, https://cdsweb.cern.ch/record/1376422.

[33] CMS Collaboration, CMS-PAS-TOP-11-020.

[34] ATLAS Collaboration, ATLAS-CONF-2011-101, https://cdsweb.cern.ch/record/1369217.

[35] ATLAS Collaboration, ATLAS-CONF-2011-104, https://cdsweb.cern.ch/record/1369829.

[36] CMS Collaboration, CMS-PAS-TOP-11-021.

[37] CMS Collaboration, CMS-PAS-TOP-11-022.

[38] ATLAS Collaboration, ATLAS-CONF-2012-019, https://cdsweb.cern.ch/record/1430033.

A Quick Tour of Ultra-Relativistic Heavy-Ion Physics at the LHC

Klaus Reygers[1] for the ALICE collaboration

[1]Physkalisches Institut, Universität Heidelberg, Im Neuenheimer Feld 226, 69120 Heidelberg, Germany

DOI: `http://dx.doi.org/10.3204/DESY-PROC-2012-02/26`

A brief summary of results on Pb+Pb collisions from ALICE, ATLAS, and CMS is presented covering global event properties, anisotropic flow, jet quenching, and quarkonia.

1 Introduction

The objective in ultra-relativistic heavy-ion physics is to study the strong interaction in the limit of high temperatures and densities. Quantum Chromodynamics, the theory of the strong interaction, is experimentally well-tested in the limit of weak coupling and low parton densities (perturbative QCD) and in the limit strong coupling for static systems at vanishing temperature (lattice QCD at $T \approx 0$). Examples are the description of jet spectra and the determination of hadron masses in lattice QCD, respectively. In heavy-ion physics one explores the regime of strong coupling at $T \gg 0$.

A prediction for this regime from first QCD principles is a transition from confined to deconfined quarks and gluons, i.e., to a quark-gluon plasma (QGP), at a temperature of $T_c \approx 150 - 160\,\mathrm{MeV}$ or roughly $1.8 \cdot 10^{12}\,\mathrm{K}$ [1]. This corresponds to an energy density of $\varepsilon_c \approx 0.5\,\mathrm{GeV/fm^3}$. This prediction from lattice QCD holds for a baryo-chemical potential $\mu_B = 0$, i.e., for systems with equal numbers of quarks and anti-quarks. These calculations indicate that the confinement/deconfinement transition at $\mu_B = 0$ is a cross-over transition.

At larger μ_B there could be a critical endpoint in the QCD phase diagram where the cross-over transition turns into a first-order transition. The search for features like this in the QCD phase diagram motivates the RHIC beam energy scan program and future experiments at FAIR. For the matter created at full RHIC energy and at the LHC $\mu_B \approx 0$.

The LHC plays a crucial role in heavy-ion physics [2]: The increase in energy by a factor ~ 14 from $\sqrt{s_{NN}} = 0.2\,\mathrm{TeV}$ at RHIC to $\sqrt{s_{NN}} = 2.76\,\mathrm{TeV}$ at the LHC provides very high initial energy densities ($\varepsilon \gtrsim 15\,\mathrm{GeV/fm^3}$) and a longer lifetime of the deconfined quark-gluon matter. Moreover, the abundant production of hard probes, like jets and heavy quarks, simplifies their use as tools to probe the medium.

The heavy-ion program at RHIC provides strong evidence for the formation of a QGP [3, 4]. The QGP at RHIC can be characterized as an almost ideal fluid, i.e., as a strongly coupled fluid with small viscosity-to-entropy density ratio η/s. Based on anisotropic flow measurement at RHIC η/s was found to be close to a conjectured theoretical lower bound of $(\eta/s)_{\mathrm{min}} = 1/4\pi$ (in natural units) with an upper limit of about $\eta/s \lesssim 2.5/(4\pi)$ [2]. Moreover, the created medium

turned out to be rather opaque to quark and gluon jets, a phenomenon called "jet quenching". After the phase of discoveries at RHIC the objective now is to characterize the medium in a quantitative way. Furthermore, the large increase in energy at the LHC allows to test models developed based on RHIC data.

The mission of heavy-ion physics may be characterized by the following two aspects: 1) Understand the complex phenomenology of A+A collisions and 2) based on that, learn something about QCD thermodynamics. In more detail, one would like to find a compelling proof of deconfinement and learn something about the equation of state, the relevant number of degrees of freedom, the viscosity, the velocity of sound, etc. As jet quenching is a prominent phenomenon the mechanism of parton energy loss is also in the focus of interest.

A standard reaction model has emerged from the study of ultra-relativistic heavy-ion collisions at the CERN SPS and at RHIC [2]. In the first stage of a A+A collision partons, mostly gluons, are liberated from the nuclear wave function. After a time of about $1\,\mathrm{fm}/c$ the system has thermalized such that the concept of temperature becomes meaningful. The large pressure of the partonic matter leads to longitudinal and transverse expansion which can be described by almost ideal hydrodynamics. At the pseudo-critical temperature of $T_c \approx 150 - 160\,\mathrm{MeV}$ the transition from the QGP to a hadron gas occurs. The hadron gas cools down further and at a temperature rather close to T_c the relative abundances of different hadron species are fixed. This is called chemical freeze-out. After the chemical freeze-out momentum spectra of the different particle species still change. At a temperature of about 100 MeV the densities become so low that the hadrons cease to interact. This is the kinetic freeze-out.

At RHIC, PHENIX and STAR continue to explore heavy-ion collisions with the aim to quantitatively characterize the created medium. At the LHC, ALICE, ATLAS, and CMS take part in the heavy-ion program. ALICE is the dedicated heavy-ion experiment at the LHC. It provides robust tracking over a larger p_T range ($\sim 0.1\,\mathrm{GeV} < p_T < 100\,\mathrm{GeV}$), good primary and secondary vertex reconstruction, and excellent particle identification, especially at low p_T where the bulk of the particles are produced. ATLAS and CMS are ideal for studying hard probes, e.g., jet production at high p_T.

2 Global Event Properties

In heavy-ion collisions the number of produced charged particles is tightly correlated with centrality, i.e., with the impact parameter of the collision. The centrality of a collision is typically defined by measuring the charged-particle multiplicity or the transverse energy a few units of pseudo-rapidity away from mid-rapidity. In order to compare experimental results with theory calculations or to compare results from different experiments the centrality is often expressed in terms of the number of participating nucleons (N_{part}) which is calculated with a geometrical Glauber model [7].

The measurement of the charged-particle multiplicity around mid-rapidity provides a first estimate of the energy density created in the central rapidity region. Fig. 1a shows the increase of $(dN_{\mathrm{ch}}/d\eta)/(N_{\mathrm{part}}/2)$ with the center-of-mass energy (per nucleon-nucleon pair) $\sqrt{s_{NN}}$ for p+p and central A+A (Au+Au, Pb+Pb) collisions. The increase in pp and A+A collisions can be described by a power law. Interestingly, the increase with $\sqrt{s_{NN}}$ in central A+A collisions ($\sim s^{0.15}$) is stronger than in pp collisions ($\sim s^{0.11}$). With the aid of the Bjorken formula

$$\varepsilon = \frac{\mathrm{d}E_T/\mathrm{d}y}{\tau_0 \pi R^2} \approx \frac{3}{2}\langle m_T \rangle \frac{\mathrm{d}N_{\mathrm{ch}}/\mathrm{d}\eta}{\tau_0 \pi R^2}, \tag{1}$$

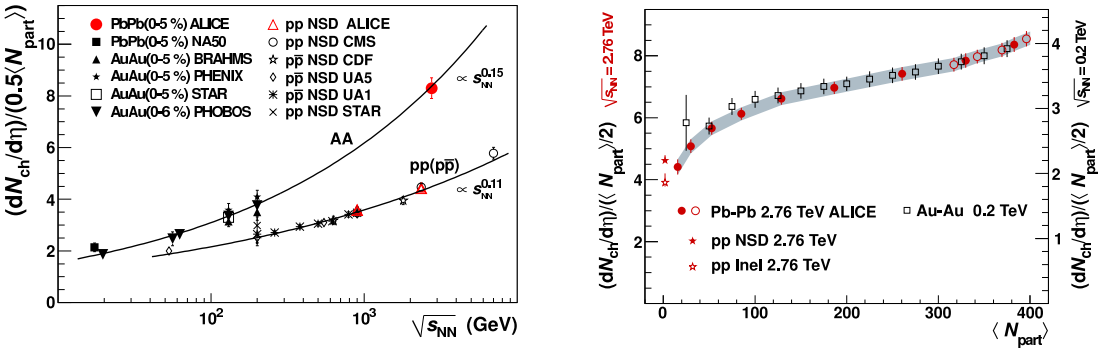

Figure 1: a) Charged-particle multiplicity normalized to $N_{\rm part}/2$ in pp and central A+A (Au+Au and Pb+Pb) collisions as a function $\sqrt{s_{NN}}$ [5]. The increase in central A+A collisions with $\sqrt{s_{NN}}$ is stronger than in pp collisions. b) The increase of the charged-particle multiplicity per participant pair with $N_{\rm part}$ at RHIC and LHC exhibits a very similar shape [6].

where $R \approx 6.62\,\mathrm{fm}$ is the radius of a Pb nucleus, the initial energy density in central Pb+Pb collisions at $\sqrt{s_{NN}} = 2.76\,\mathrm{TeV}$ can be estimated to be $\varepsilon_{\rm LHC} \approx 15\,\mathrm{GeV/fm^3} \approx 3 \times \varepsilon_{\rm RHIC}$. This is the estimate for a thermalization time of $\tau_0 = 1\,\mathrm{fm}/c$. The actual thermalization time is most likely smaller so that this estimate is considered conservative. Thus, one can conclude that the initial energy densities at RHIC and the LHC are well above the critical energy density of $\varepsilon_c \approx 0.5\,\mathrm{GeV/fm^3}$ for the transition to the QGP.

The relative increase of the charged-particle multiplicity with $N_{\rm part}$ is rather similar at RHIC and the LHC. This is shown Fig. 1b. This similarity has actually been demonstrated for an even wider energy interval of $20 \lesssim \sqrt{s_{NN}} \lesssim 2760\,\mathrm{GeV}$ [8]. The fact that the relative increase of $dN_{\rm ch}/d\eta$ is rather independent of $\sqrt{s_{NN}}$ is surprising in two-component models which assume that a soft component of the multiplicity scales with $N_{\rm part}$ and a hard scattering component with $N_{\rm coll}$, the number of inelastic nucleon-nucleon collisions. In these models the increase of the hard-scattering cross sections with $\sqrt{s_{NN}}$ needs to be balanced by shadowing of the gluon distribution function in the nucleus. Irrespective of the theoretical description, the data indicate that at a given $\sqrt{s_{NN}}$ the charged-particle multiplicity is largely determined by the geometry of the collision.

The shapes of transverse momentum spectra in central collisions for particles with different masses provide compelling evidence for radial flow, i.e., for a collective flow profile characterized by velocity vectors all pointing away from the center of the overlap zone with magnitudes independent of the azimuthal angle φ. Radial flow leads to a modification of the p_T spectrum according to $p_T^{\rm w/\ flow} = p_T^{\rm w/o\ flow} + \beta_{T,\rm flow}\gamma_{T,\rm flow} m$ where $\beta_{T,\rm flow}$ is the radial flow velocity and m the particle mass. Fig. 2 shows that the effect of radial flow is most visible for heavy particles.

The good agreement between the p_T spectra of identified particles and hydrodynamical models provides the strongest evidence for radial flow, see Fig. 2a. Essential features of complete hydro calculations are captured with so-called blast-wave fits which have the average transverse flow velocity $\langle\beta_{T,\rm flow}\rangle$ and the kinetic freeze-out temperature T_{fo} as free parameters. The p_T spectra in central Pb+Pb collisions at $\sqrt{s_{NN}} = 2.76\,\mathrm{TeV}$ are described with $\langle\beta_{T,\rm flow}\rangle_{\rm LHC} \approx 0.65\,c$ and $T_{fo} \approx 80 - 100\,\mathrm{MeV}$. The average radial flow velocity at the LHC is roughly 10 %

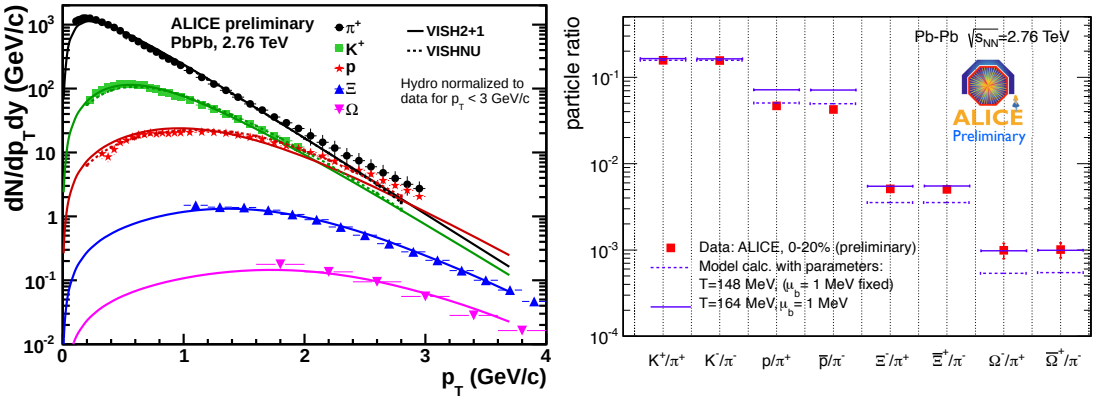

Figure 2: a) p_T spectra of identified particles measured by ALICE [2]. The data are rather well described by hydro-models which model the expansion of the fireball. b) Ratios of the yields of different particles species measured by ALICE in comparison with predictions from a statistical model. Except for the p/π ratios the data are well described with a chemical freeze-out temperature of 164 MeV and a small chemical potential of $\mu_B = 1$ MeV.

larger than in central Au+Au collisions at RHIC.

Comparisons of the p_T-integrated yields of different particles species at RHIC and LHC with predictions from statistical models show that the chemical freeze-out temperature $T_{\rm ch}$ at RHIC and LHC is close to the critical temperature T_c from lattice QCD. In statistical models for particle production the yield of a particle species depends on its mass and a chemical potential given by the baryon number, the strangeness, and the isospin of the particle. With two free parameters, $T_{\rm ch}$ and a baryo-chemical potential μ_B, particle ratios are described rather well, including the enhancement for strange particles relative to pp collisions. A fit to particle ratios at the LHC yields $T_{\rm ch} \approx 164$ MeV. The discrepancies for the p/π ratios (see Fig. 2b) remain to be understood.

3 Anisotropic Flow

In non-central A+A collisions the initial spatial anisotropy of the overlap zone is expected to lead to an anisotropy of produced particles in momentum space. The line connecting the two centers of the nuclei in the transverse plane defines the so-called reaction plane. Elliptic flow results from pressure gradients being larger in the direction of the reaction plane than perpendicular to it. It was realized that fluctuations of the initial distribution of the energy density are important. The overlap zone may, e.g., look rather like a triangle in some collisions which leads to a corresponding modulation of particles in momentum space. In general, particle production in the transverse plane as a function of the azimuthal angle φ can be described as

$$E\frac{{\rm d}^3N}{{\rm d}^3p} = \frac{1}{2\pi}\frac{{\rm d}^2N}{p_T{\rm d}p_T{\rm d}y}\left(1+2\sum_{n=1}^{\infty} v_n \cos\left[n(\varphi-\Psi_n)\right]\right) \qquad (2)$$

where v_2 describes the elliptic flow and v_3 the triangular flow.

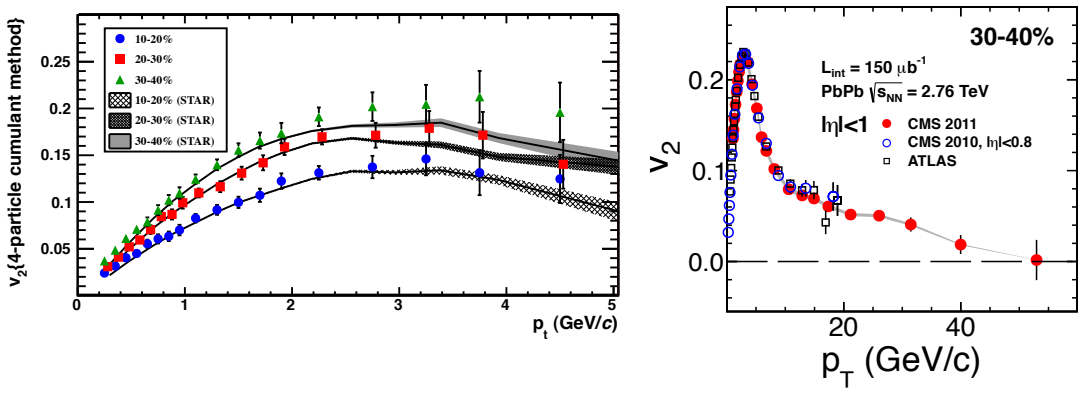

Figure 3: a) Elliptic flow coefficient v_2 for charged particles as a function of p_T for three centrality classes measured by ALICE [9]. For the shown classes v_2 decreases with increasing centrality. The p_T and centrality dependence at LHC and RHIC is remarkably similar. b) v_2 for charged particles up to $p_T \approx 50\,\mathrm{GeV}/c$ from CMS [10].

Despite the large difference in $\sqrt{s_{NN}}$ the p_T and centrality dependence of the elliptic flow at RHIC and LHC are very similar as shown in Fig. 3a. The v_2 coefficient was determined with the 4-particle cumulant method in order to minimize the contribution of non-flow effects, e.g., mini-jet production. Owing to the larger mean transverse momentum of the charged particles at the LHC the p_T-integrated v_2 at the LHC is about 30 % larger than at RHIC.

The hydro picture for v_2 is only valid at low transverse momentum ($p_T \lesssim 1.5\,\mathrm{GeV}/c$). However, a non-vanishing v_2 was measured for much larger p_T, see Fig. 3b. At large p_T the v_2 is believed to result from the path length dependence of the energy loss of quark and gluon jets in the created medium (cf. Sec. 4). The path length in the direction of the reaction plane is shorter than perpendicular to it, resulting in $v_2 > 0$.

The measurement of the Fourier coefficients v_n provides limits on the shear viscosity to entropy density ratio η/s of the created medium. In addition to v_2, flow coefficient up to v_5 have been measured (Fig. 4a). The effect of viscosity is to dissipate initial pressure gradients and to reduce collective flow. This can be seen from the hydro calculations in Fig. 4a for different η/s values. By measuring higher flow coefficients like v_3 in addition to v_2 the sensitivity for η/s is increased. Fig. 4a shows that for certain assumption about the initial distribution of energy density ("Glauber initial conditions") the data at low p_T are described with $\eta/s \approx 1/4\pi$. Based on LHC data the current upper bound is $\eta/s \lesssim 2/(4\pi) = 2 \times (\eta/s)_{\mathrm{min}}$ [2].

One of the most compelling pieces of evidence for the hydrodynamic expansion of the created medium comes from the observed mass ordering of the v_2 of identified particles. The p_T dependence of elliptic flow expected from hydro can be approximated as $v_2 \sim (p_T - \beta m_T)/T$ where β is the average transverse flow velocity and $m_T = \sqrt{p_T^2 + m^2}$ the transverse mass. The mass ordering is indeed observed and described by hydro calculations as shown in Fig. 4b.

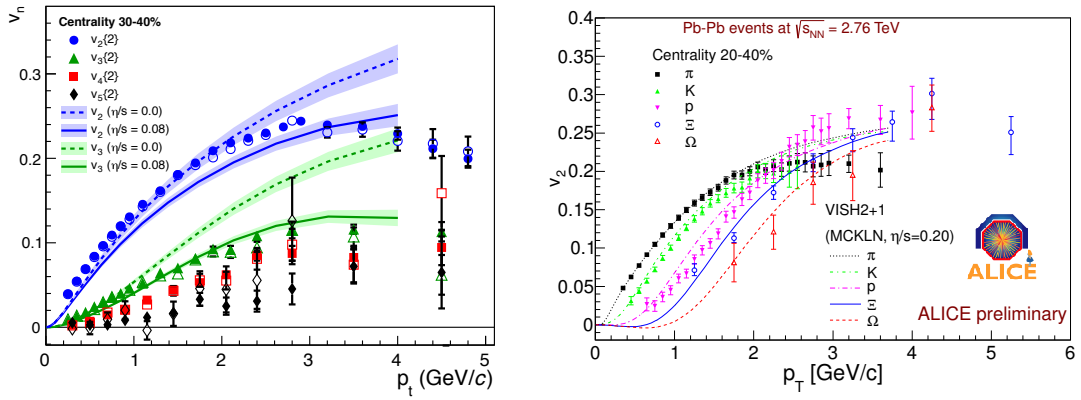

Figure 4: Fourier coefficients v_2, v_3, v_4, and v_5 of charged particles as a function of p_T in Pb+Pb collisions ($30-40\,\%$ most central class) from ALICE [11] . The p_T dependence of v_2 and v_3 is described with hydro calculations with small η/s. b) v_2 as a function of p_T for different particles species from ALICE. The v_2 shows the mass ordering expected from hydro calculations.

4 Jet Quenching

Heavy-ion physics at LHC energies benefits from the abundant production of hard probes. Hard probes are useful because they are produced in the early stage of the collisions, prior to the formation of the QGP. Moreover, their initial production rate is calculable with perturbative QCD which makes them a "calibrated" probe. Jet quenching, i.e., the energy loss of quarks and gluons from hard scattering processes, was discovered at RHIC by measuring single particle yields at high p_T. The interest in observables related to jet quenching is two-fold: one would like to 1) understand the mechanism of parton energy loss and 2) use hard probes as a tool to characterize the QGP.

Charged particles yields in central Pb+Pb collisions at $\sqrt{s_{NN}} = 2.76\,\text{TeV}$ are suppressed by more than a factor of 5 at $p_T \approx 7\,\text{GeV}/c$, see Fig. 5. The suppression is quantified with the nuclear modification factor

$$R_{AA} = \frac{\mathrm{d}N/\mathrm{d}p_T(A+A)}{\langle T_{AA}\rangle \times \mathrm{d}\sigma/\mathrm{d}p_T(p+p)} \tag{3}$$

where the nuclear overlap function $\langle T_{AA}\rangle = \langle N_{\text{coll}}\rangle/\sigma^{pp}_{\text{inel}}$ describes the increase of the parton flux from p+p to A+A. Without nuclear effects $R_{AA} = 1$ in the hard scattering regime ($p_T \gtrsim 2\,\text{GeV}/c$). R_{AA} depends on the parton energy loss as well as on the steepness of the parton spectrum. Thus, the same R_{AA} at different $\sqrt{s_{NN}}$ corresponds to a different energy loss.

The rise of R_{AA} with p_T was for the first time firmly established at the LHC. The large p_T reach of the LHC data helps unveil the dependence of the energy loss on the initial parton energy. The data are consistent with a decrease of the fractional energy loss $\Delta E/E$ with increasing parton energy E as expected in energy loss models based on perturbative QCD. The nuclear modification factor may also be affected by initial state effects like gluon shadowing. These effects will be studied in the p+Pb run in fall of 2012.

Prompt photons provide a crucial test for parton energy loss model as they do not interact

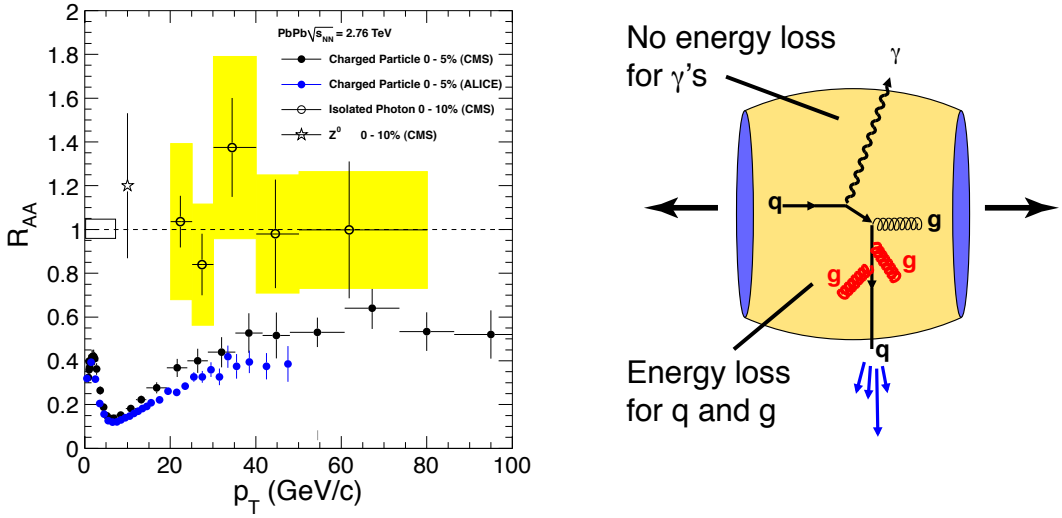

Figure 5: $R_{AA}(p_T)$ for charged particles and isolated photons in central Pb+Pb collisions at the LHC [2]. Charged particles are suppressed whereas isolated photon are not. This is expected in the parton energy loss picture because photons essentially do not interact with the medium as indicated by the sketch.

with the medium via the strong interaction. Therefore, they are expected to leave the fireball unscathed. The same holds for Z bosons. Fig. 5 shows that isolated photons and also Z bosons are indeed not suppressed ($R_{AA} \approx 1$). This provides further evidence for the parton energy loss picture.

Radiative energy loss, i.e., gluon emission induced by the medium, is expected to be the dominant energy loss mechanism in the QGP. In this picture the energy loss of gluons, light and heavy quarks in a QGP is expected to exhibit the ordering $\Delta E_g > \Delta E_{u,d,s} > \Delta E_c > \Delta E_b$ corresponding to $R_{AA}(\pi) < R_{AA}(\text{D mesons}) < R_{AA}(\text{B mesons})$. Note that for $p_T \lesssim 50\,\text{GeV}/c$ pions predominantly originate from the fragmentation of gluons jets. The larger energy loss for gluons relative to quarks is due to the different color factor, $C_F = 3$ for gluons and $C_F = 4/3$ for quarks. The smaller energy loss of heavy quarks with respect to light quarks is due to the dead-cone effect [12].

The suppression for charged hadrons, prompt D mesons, and B mesons in central Pb+Pb collisions at $\sqrt{s_{NN}} = 2.76\,\text{TeV}$ is found to be rather similar as shown in Fig. 6a. Even though the differences are small, there is at least an indication for the expected ordering. The R_{AA} of B mesons in Fig. 6a was determined by measuring the R_{AA} of non-prompt J/ψ's. The effect of shadowing is estimated in Fig. 6b with a NLO perturbative QCD calculation which employs the EPS09 parton distribution. Gluon shadowing appears to contribute to the suppression of D mesons only for $p_T \lesssim 5\,\text{GeV}/c$.

The large cross section for hard processes at the LHC provide a unique opportunity to study parton energy loss with fully reconstructed jets [14, 13]. ATLAS and CMS studied di-jet production in Pb+Pb collisions and find energy differences between the leading and sub-leading jet much larger than in pp collisions. This can be naturally explained with di-jet produced close

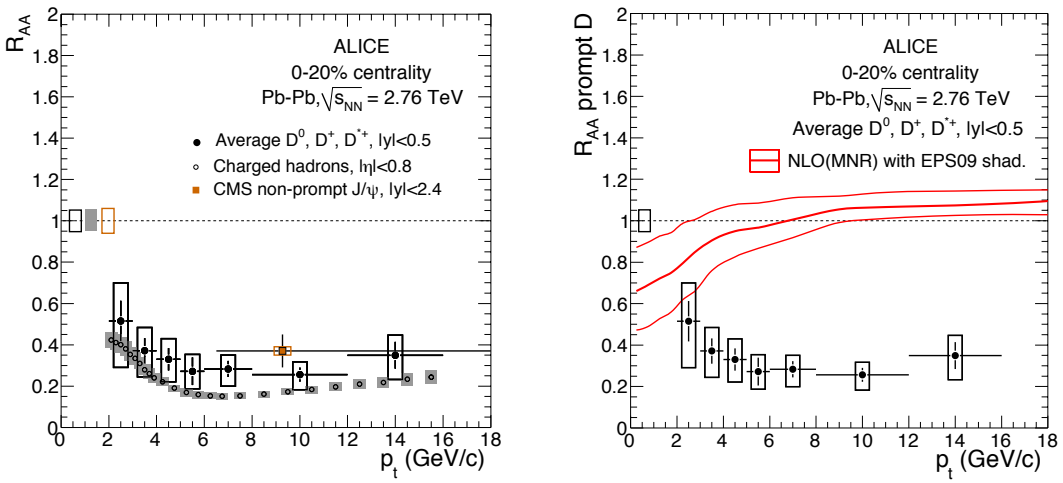

Figure 6: a) The comparison of the R_{AA} for charged hadron, D mesons, and J/ψ's from B meson decays ("non-prompt J/ψ's") tests the expected hierarchy $\Delta E_g > \Delta E_{u,d,s} > \Delta E_c > \Delta E_b$. b) Initial state effects related to modification of the gluon distribution function in the Pb nucleus (shadowing) appear to be negligible for $p_T \gtrsim 5\,\mathrm{GeV}/c$ as indicated by the NLO perturbative QCD calculation.

to the edge of the overlap zone so that one parton has a long path length in the medium and loses energy whereas the other escapes without energy loss. A closer look at di-jet production in Pb+Pb collisions reveals that the di-jets are still produced back-to-back (i.e., there is no angular decorrelation) and that the momentum distribution of jet particles transverse to the jet axis is like in pp collisions. So one has to ask: Where does the energy of jets with reduced energy go?

A first step to address this question is to study the modification of jet spectra in central Pb+Pb collisions relative to peripheral collisions with the aid of ratio $R_{CP} = N_{\mathrm{coll}}^{60-80\%}/N_{\mathrm{coll}}^{\mathrm{cent}} \times (dN_{\mathrm{jet}}^{\mathrm{cent}}/dE_T)/(dN_{\mathrm{jet}}^{60-80\%}/dE_T)$ where dN_{jet}/dE_T is the jet E_T spectrum normalized per event. ATLAS finds a factor of 2 suppression ($R_{CP} \approx 0.5$) in central Pb+Pb collisions using an anti-k_T algorithm with a radius parameter of $R = 0.4$ [15]. This indicates that with this radius parameter the full jet energy is not recovered. A detailed study by CMS in which particle tracks are correlated with the axis of the leading jet shows that the energy difference in di-jets is balanced by low p_T particles ($0.5 \lesssim p_T < 2\,\mathrm{GeV}/c$) at large angles relative to the axis of the sub-leading jet [13].

5 Quarkonia

Quarkonia belong to the classical QGP probes [18]. Considering the total J/ψ yield, the formation of a QGP in A+A collisions at low $\sqrt{s_{NN}}$ (e.g. at CERN SPS energies) is expected to result in a suppression whereas at higher $\sqrt{s_{NN}}$ the formation of a QGP may lead to a less strong suppression or even an enhancement [3]. Color screening is expected to prevent the

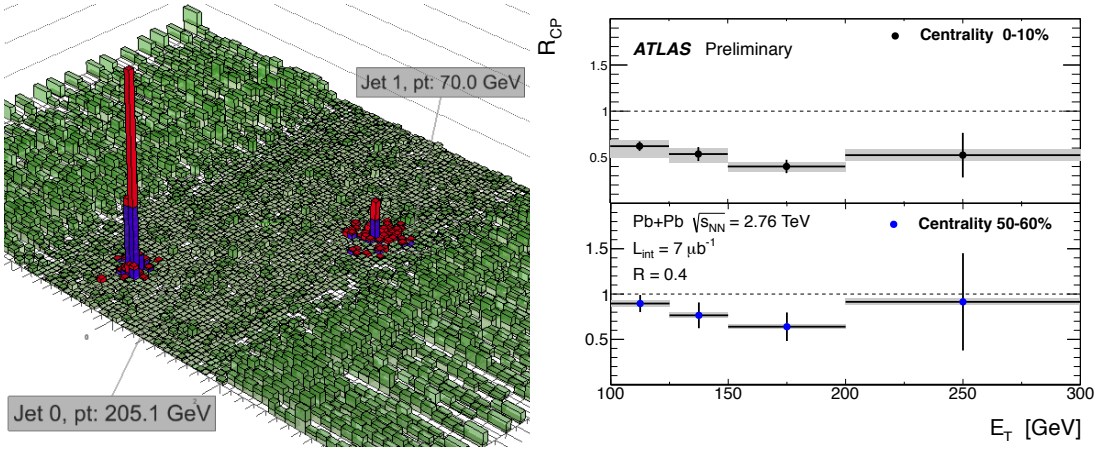

Figure 7: a) Calorimeter energy vs. η and φ in a Pb+Pb collision at $\sqrt{s_{NN}} = 2.76\,\text{TeV}$ containing a di-jet with large energy asymmetry measured by CMS [13]. b) R_{CP} (see text) of jet spectra determined with an anti-k_T algorithm with a radius parameter $R = 0.4$. For the $0 - 10\,\%$ most central Pb+Pb events the jet spectrum is suppressed indicating that with $R = 0.4$ the energy of jets suffering energy loss is not fully recovered.

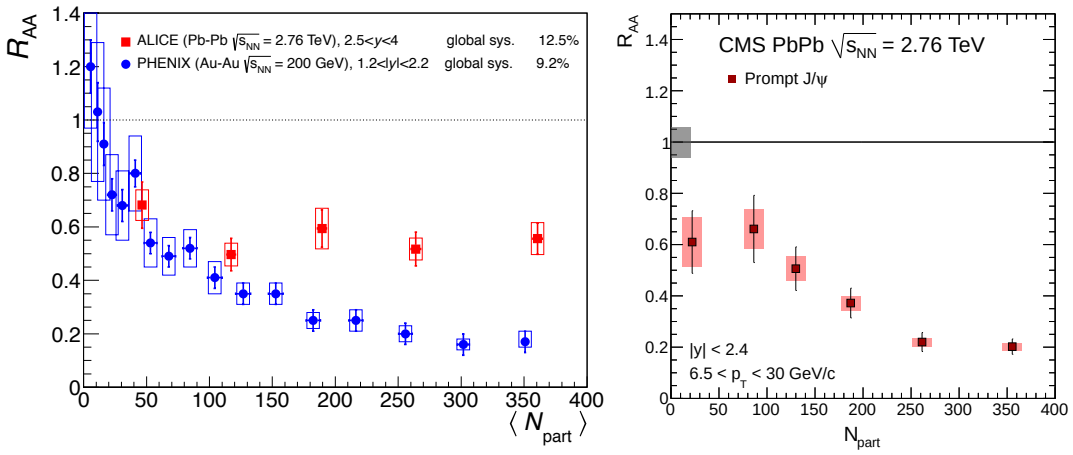

Figure 8: a) R_{AA} of inclusive J/ψ's measured by ALICE over the full p_T range ($p_T > 0$) and in $2.5 < y < 4$ as a function of centrality [16]. In central collisions the suppression ($R_{AA} \approx 0.5$–0.6) is smaller than at RHIC. b) At larger p_T ($p_T > 6.5\,\text{GeV}/c$) prompt J/ψ measured by CMS exhibit a stronger suppression in central collisions ($R_{AA} \approx 0.2$) [17].

binding of $c\bar{c}$ and $b\bar{b}$ pairs in deconfined matter. The dissociation temperature T_D is different for different quarkonium states, e.g., $T_D(J/\psi) \approx 1.2\,T_c$, $T_D(\psi') \approx T_c$, and $T_D(\Upsilon) \approx 2\,T_c$ [17]. Therefore, information about the temperature of the QGP can be obtained from the comparison of yields of different quarkonium states. At the LHC of the order of 100 $c\bar{c}$ pairs are produced in a central Pb+Pb collision. It it thus conceivable that J/ψ's in A+A collisions are produced at the phase transition due to statistical recombination of $c\bar{c}$ pairs.

For the total inclusive yields of J/ψ's (i.e., integrated over the full range $p_T > 0$) ALICE measured $R_{AA} \approx 0.6$ independent of the centrality of the Pb+Pb collision (Fig. 8a). Note that the contribution of non-prompt J/ψ's from B meson feed-down to the inclusive J/ψ yield is $\sim 15\,\%$. Gluon shadowing alone is expected to lead to a J/ψ suppression of $R_{AA} \approx 0.8$. This indicates that there is only a moderate final state suppression. Interestingly, the suppression in central Pb+Pb collisions is smaller than at RHIC. For prompt J/ψ's at larger p_T ($> 6.5\,\mathrm{GeV}/c$) the suppression increases with centrality up to $R_{AA} \approx 0.2$ in central collisions. All in all, these observations are in qualitative agreement with the recombination picture.

6 Conclusions

Owing to the large initial energy density, the long QGP lifetime, and the abundant production of hard probes the LHC is ideal for studying the QGP. Particles produced in Pb+Pb collisions at the LHC exhibit strong radial and anisotropic flow confirming the standard reaction scenario. The medium created at the LHC has the same "perfect liquid" properties as found at RHIC. The medium is opaque to jets and the large p_T reach of the R_{AA} measurements at the LHC provides constraints for parton energy loss models. The data on charmonium production are consistent with a statistical formation of J/ψ at the phase transition.

References

[1] S. Borsanyi, G. Endrodi, Z. Fodor, A. Jakovac, S. D. Katz, *et al.* JHEP **1011** (2010) 077, arXiv:1007.2580 [hep-lat].

[2] B. Muller, J. Schukraft, and B. Wyslouch. arXiv:1202.3233 [hep-ex].

[3] P. Braun-Munzinger and J. Stachel. Nature **448** (2007) 302–309.

[4] M. Tannenbaum. arXiv:1201.5900 [nucl-ex].

[5] B. Abelev *et al.* Phys.Rev.Lett. **105** (2010) 252301, arXiv:1011.3916 [nucl-ex].

[6] K. Aamodt *et al.* Phys.Rev.Lett. **106** (2011) 032301, arXiv:1012.1657 [nucl-ex].

[7] M. L. Miller, K. Reygers, S. J. Sanders, and P. Steinberg. Ann.Rev.Nucl.Part.Sci. **57** (2007) 205–243, arXiv:nucl-ex/0701025 [nucl-ex].

[8] B. Alver *et al.* Phys.Rev. **C83** (2011) 024913, arXiv:1011.1940 [nucl-ex].

[9] K. Aamodt *et al.* Phys.Rev.Lett. **105** (2010) 252302, arXiv:1011.3914 [nucl-ex].

[10] S. Chatrchyan *et al.* arXiv:1204.1850 [nucl-ex].

[11] K. Aamodt *et al.* Phys.Rev.Lett. **107** (2011) 032301, arXiv:1105.3865 [nucl-ex].

[12] Y. L. Dokshitzer and D. Kharzeev. Phys.Lett. **B519** (2001) 199–206, arXiv:hep-ph/0106202 [hep-ph].

[13] S. Chatrchyan *et al.* Phys.Rev. **C84** (2011) 024906, arXiv:1102.1957 [nucl-ex].

[14] G. Aad *et al.* Phys.Rev.Lett. **105** (2010) 252303, arXiv:1011.6182 [hep-ex].

[15] B. A. Cole. J.Phys.G **G38** (2011) 124021.

[16] B. Abelev *et al.* arXiv:1202.1383 [hep-ex].

[17] S. Chatrchyan *et al.* JHEP **1205** (2012) 063, arXiv:1201.5069 [nucl-ex].

[18] T. Matsui and H. Satz. Phys.Lett. **B178** (1986) 416.

Searches for the standard model scalar boson in CMS and for new physics in ATLAS and CMS

Barbara Clerbaux[1], on behalf of the ATLAS and CMS Collaborations

[1]IIHE(ULB-VUB), Université Libre de Bruxelles, Bd de la Plaine, 1150 Brussels, Belgium

DOI: `http://dx.doi.org/10.3204/DESY-PROC-2012-02/27`

Latest LHC results are reported focussing on the search for the standard model scalar boson, as well as a selection of searches for new physics beyond the standard model.

1 Introduction

This proceeding reports on latest results on two of the main goals of the LHC : (i) searches for the standard model (SM) Brout-Englert-Higgs scalar boson performed by the CMS Collaboration (results from ATLAS are presented separately in this proceeding) and (ii) searches for physics beyond the standard model (BSM), with a selection of results from both CMS and ATLAS. The public CMS and ATLAS results are available on the web pages given in Refs. [1, 2].

The results are based on the LHC data taken during the year 2011 at the proton-proton center of mass energy $\sqrt{s} = 7$ TeV, corresponding to an integrated luminosity delivered of more than 5 fb^{-1}, with a peak instantaneous luminosity up to 3.5 10^{33} cm^{-2}s^{-1} as shown in Fig. 1, indicating the excellent performance of the machine in 2011. With such high instantaneous luminosity the number of proton-proton interactions in each bunch crossing is in average more than 10. CMS and ATLAS are multipurpose detectors described in detail in [3, 4].

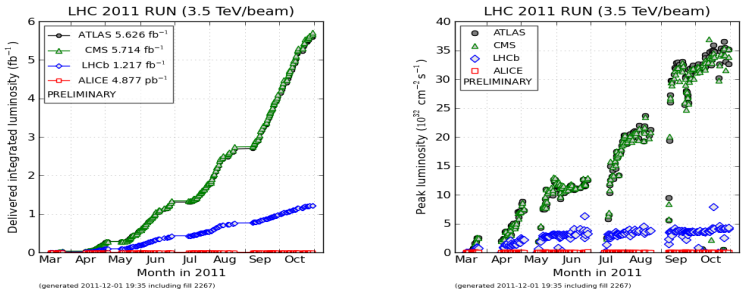

Figure 1: The integrated (left) and peak (right) luminosity delivered by the LHC machine in 2011.

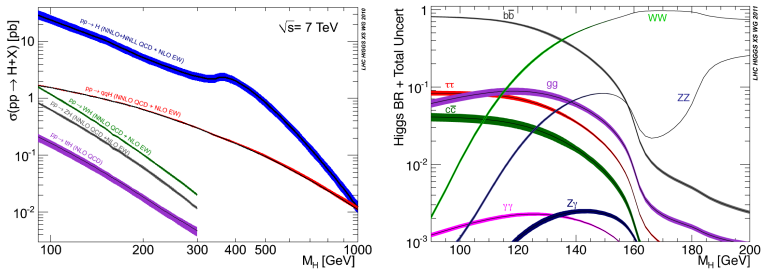

	Channel	m_H range (GeV)	Luminosity (fb^{-1})	Sub-channels	m_H resolution
new	$H \to \gamma\gamma$	110–150	4.8	2	1–2%
	$H \to \tau\tau \to e\tau_h/\mu\tau_h/e\mu + X$	110–145	4.6	9	20%
new	$H \to \tau\tau \to \mu\mu + X$	110–140	4.5	3	20%
new	$WH \to e\mu\tau_h/\mu\mu\tau_h + \nu$'s	100–140	4.7	2	20%
	$(W/Z)H \to (e\nu/\mu\nu/ee/\mu\mu/\nu\nu)(bb)$	110–135	4.7	5	10%
	$H \to WW^* \to 2\ell 2\nu$	110–600	4.6	5	20%
new	$WH \to W(WW^*) \to 3\ell 3\nu$	110–200	4.6	1	20%
	$H \to ZZ^{(*)} \to 4\ell$	110–600	4.7	3	1–2%
	$H \to ZZ^{(*)} \to 2\ell 2q$	130–164 200–600	4.6	6	3% 3%
	$H \to ZZ \to 2\ell 2\tau$	190–600	4.7	8	10–15%
	$H \to ZZ \to 2\ell 2\nu$	250–600	4.6	2	7%

Figure 2: SM scalar boson production cross sections at $\sqrt{s} = 7$ GeV (top left) and decay branching ratios (top right); the 11 decay channels analysed by CMS (bottom).

2 Searches for the standard model scalar boson in CMS

Since the introduction of a scalar field in the SM, proposed in 1964 [5, 6, 7], particle physicists have actively searched for a massive scalar (H) with no success yet. Direct searches at LEP lead to a lower limit on the scalar mass $m_H = 114.4$ GeV at 95% confidence level (CL) [8]. Latest results from indirect constraints from precision electroweak measurements give an upper limit $m_H < 152$ GeV at 95% CL [9], indicating that, if no new physics is introduced, the SM scalar boson is favored at low mass above the LEP limit. Search were also performed at the Tevatron and are reported separately in this proceeding.

The search of the scalar boson continues thanks to the LHC machine. Figure 2 presents the SM H boson production cross sections at $\sqrt{s} = 7$ GeV and the boson decay branching ratios, as a function of the boson mass. The main contributions to the production cross section come from gluon-gluon fusion and from Vector Boson Fusion (VBF). Different final state topologies are relevant for different H boson mass hypotheses. CMS studied and optimised 11 independent channels as detailed at the bottom of Fig. 2. For each channel, the table gives the corresponding m_H range, the luminosity, the number of subchannels considered and the m_H resolution.

2.1 Di-photon final state

Despite its small branching fraction, the $H \to \gamma\gamma$ channel is the most sensitive one for the low mass hypothesis (110-150 GeV). Events with two high pt photons are selected, with possibly two additional jets from outgoing quarks in the VBF production case [10]. The signature of this channel is a narrow mass peak over a large smoothly decreasing background coming from QCD production and γ+jet events. Thanks to the excellent performance of the electromagnetic

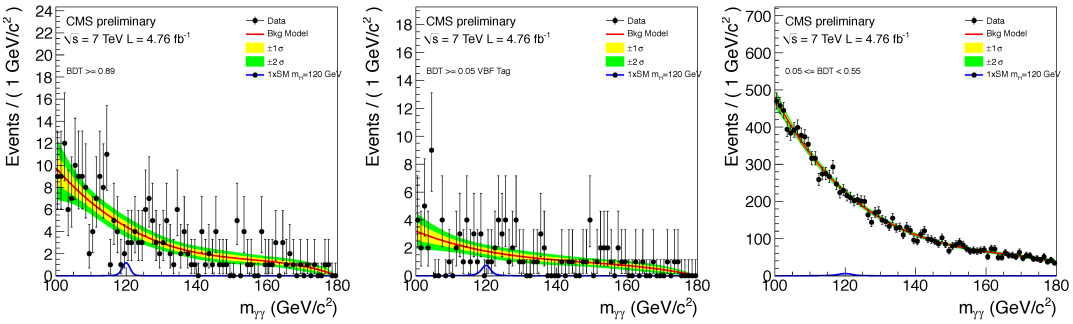

Figure 3: Background model fit to the $m_{\gamma\gamma}$ distribution for the best event class defined by a high BDT output value (left), the VBF event class (middle) and the sum of all the event classes (right). From [10].

calorimeter ECAL of CMS, a very good mass resolution of 1-2% is archieved. To improve the sensitivity of the search, selected diphoton events are subdivided into classes according to the output value of a diphoton Boosted Decision Tree (BDT) which classifies events with signal-like kinematic, good diphoton mass resolution, and good photon identification, with a high score. Five mutually exclusive event classes are defined, four defined by the diphoton BDT output, and a fifth one for the VBF candidate events. The background model is obtained by fitting polynomials to the observed diphoton mass distributions in each of the five event classes. Figure 3 presents the background model fit to the $m_{\gamma\gamma}$ distribution for different event classes, together with a simulated signal ($m_H = 120$ GeV). No significant excess is observed in the data. Figure 4 presents the exclusion limit on the cross section of a SM scalar boson decaying into two photons as a function of the boson mass and relative to the SM cross section, $\sigma/\sigma(SM)$, as well as the observed local p-values. The largest excess of events over the expected background is observed around 125 GeV. Taking into account the look-elsewhere effect in the search range 110-150 GeV, the excess has a global significance of 1.6 σ.

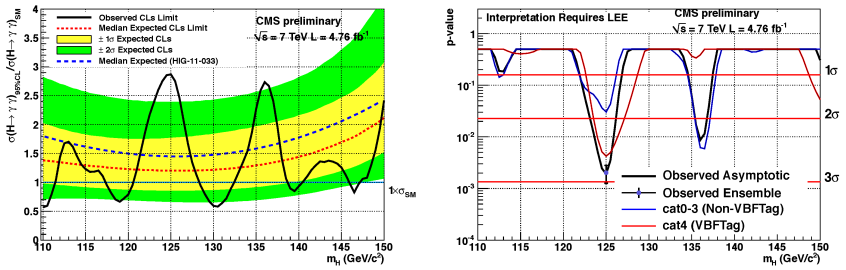

Figure 4: Exclusion limit at 95% CL on the cross section of a SM scalar boson decaying into two photons as a function of the boson mass and relative to the SM cross section, the theoretical uncertainties on the cross section have been included in the limit setting (left); the observed local p-values for the combined event class, the VBF and non-VBF classes (right). From [10].

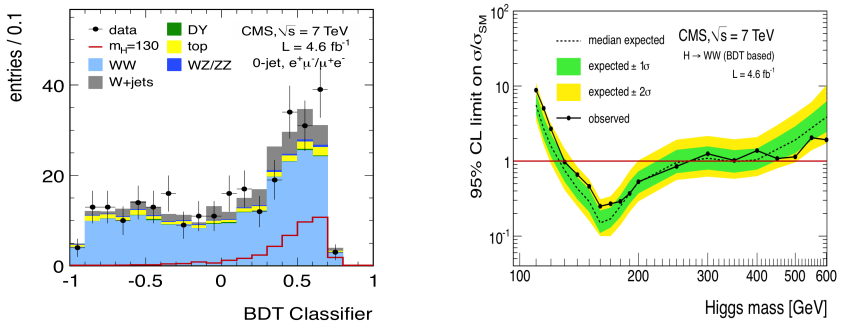

Figure 5: For the $H \to WW \to 2\ell 2\nu$ channel : BDT output in the 0-jet bin for opposite flavor final state (left) and exclusion limit at 95% CL on $\sigma/\sigma(SM)$ (right). From [11].

2.2 Di-boson final state : WW and ZZ

The $H \to WW \to 2\ell 2\nu$ channel is sensitive in a large m_H range, especially around twice the W boson mass. Events with two high pt isolated leptons are selected with additional requirement on the missing transverse energy variable (MET) in the events [11]. Due to the presence of neutrinos in the final state, the m_H resolution is poor, about 20%. Events are classified according to the exclusive jet multiplicity : 0, 1 and 2 (VBF). A multivariate (BDT) analysis is performed, optimized for each mass point. Figure 5(left) shows the BDT output in the 0-jet bin for opposite flavor final state. The main backgrounds (WW, $t\bar{t}$, Drell-Yan, W+jets) are estimated with data-driven techniques. The uncertainty on the background normalization represent the largest source of systematics of the analysis, together with the theoretical uncertainties on the scalar boson cross section. No evidence of the H boson is found and the results are interpreted as an exclusion of a wide m_H range, as shown in Fig. 5(right). Using the CLs approach, the expected exclusion mass range at 95% CL is between 127 and 270 GeV, while the observed one is 129-270 GeV.

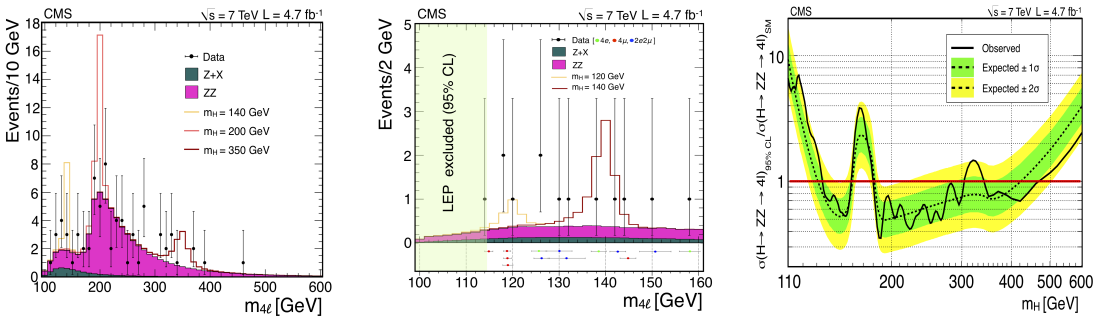

Figure 6: For the $H \to ZZ \to 4\ell$ channel : four-lepton reconstructed mass distribution (left) and a zoom at low mass (middle); exclusion limit at 95% CL on $\sigma/\sigma(SM)$(right). From [12].

The four-lepton decay channel $H \to ZZ \to 4\ell$ search [12] presents a very clear signature : two high mass pairs of isolated electrons or muons. The key point of the selection being a very good lepton identification and a selection down to low pt for the leptons, allowing a large m_H range coverage $110 < m_H < 600$ GeV. Figure 6 presents the four-lepton reconstructed mass distribution in the sum of the 4 lepton channels and a zoom at low mass. No significant excess is observed and upper limits at 95% CL exclude the SM scalar boson in the ranges 134-158 GeV, 180-305 GeV, and 340-465 GeV, see Fig. 6(right). Small excesses of events are observed around masses of 119, 126, and 320 GeV, making in these mass ranges the observed limits weaker than expected in the absence of a signal.

2.3 Channel combination

Five H boson decay modes : $\gamma\gamma$, $b\bar{b}$, $\tau\tau$, WW, and ZZ, with various final state topologies (see the bottom of Fig. 2) have been combined in the mass range 110-600 GeV [13]. The expected excluded mass range in the absence of the SM scalar boson is 114.5-543 GeV at 95% CL, and the observed exclusion mass range is 127.5-600 GeV, See Fig. 7. An excess of events above the expected SM background is observed at the low end of the explored mass range making the observed limits weaker than expected in the absence of a signal. The largest excess, with a local significance of 2.8 σ, is observed for a m_H hypothesis of 125 GeV. The global significance of observing an excess with a local significance greater than 2.8 σ anywhere in the search range 110-600 (110-145) GeV is estimated to be 0.8 σ (2.1 σ), see Fig. 7(right). More data are required to ascertain the origin of this excess.

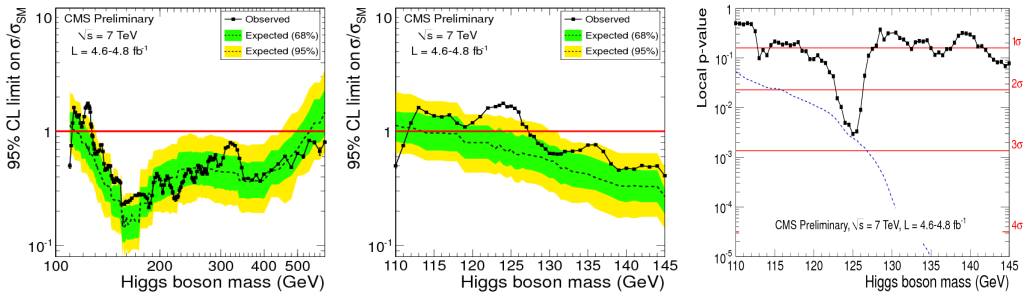

Figure 7: Combination of the 5 scalar boson decay modes : the 95% CL upper limits on the signal strength parameter $\sigma/\sigma(\mathrm{SM})$ for the SM H boson hypothesis as function of m_H (left) and a zoom at low mass (middle); the observed local p-value as a function of m_H (right). From [13].

3 Searches for scalar boson(s) beyond the standard model at the LHC

The SM scalar boson search results presented in previous section can be re-used and interpreted in the context of BSM models. For an extension of the SM including a fourth generation of fermions (SM4), the SM4 scalar boson is excluded in the mass range 120-600 GeV at 95% CL [13]. In the fermiophobic scalar boson scenario, using the $\gamma\gamma$, WW and ZZ decay channels,

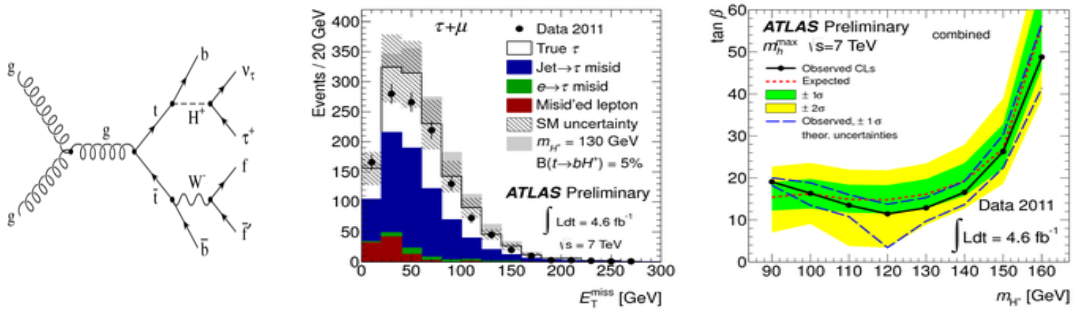

Figure 8: Example of a LO diagram for the production of a H^+ boson, followed by its decays into $\tau\nu$ (left); MET distribution in the ($b\bar{b}$+$\tau\nu$+$\mu\nu$) final state (middle). The full line corresponds to the SM-only hypothesis and the hatched area around it shows the total uncertainty for the SM backgrounds. The predicted contribution of a 130 GeV charged scalar boson with BR($t \to bH^+$) = 5% and BR($H^+ \to \tau^+\nu$) = 100% is also indicated; 95% CL exclusion limits on $\tan\beta$ as a function of m_{H^+} (right), results are shown in the context of the MSSM scenario $m_h^{\max}$ for the combination of all channels considered. ATLAS results from [15].

a fermiophobic scalar boson is excluded by CMS in the mass range 110-192 GeV at 95% CL [13]. Searches are also performed by ATLAS using the $\gamma\gamma$ decay channel [14].

Supersymmetry is a well known extension to the SM. The minimal supersymmetric SM (MSSM) contains two scalar doublets, giving rise to five physical states : a light neutral CP-even state (h), a heavy neutral CP-even state (H), a neutral CP-odd state (A) and a pair of charged states (H^+, H^-). The mass relations between these particles depend in particular on the MSSM parameter $\tan\beta$, the ratio of the scalar fields vacuum expectation values. The main H^+ production mode at the LHC is through top quark decays, for m_{H^+} smaller than the top quark mass. Search for the H^+ boson in the range 90-160 GeV, is performed by ATLAS [15] and CMS [16] using $t\bar{t}$ events, $H^+ \to \tau\nu$, with a leptonically or hadronically decaying τ lepton in the final state, see Fig. 8(left). Figure 8 (middle) shows the MET distribution in the ($b\bar{b} + \tau\nu + \mu\nu$) final state. The observed data are in agreement with the SM predictions. These results are interpreted in the context of the $m_h^{\max}$ scenario of the MSSM, and values of $\tan\beta$ above 13-26 are excluded in the mass range $90 < m_{H^+} < 150$ GeV, see Fig.8(right).

4 Searches for new physics in ATLAS and CMS

Complementary to the search for a possible scalar boson, LHC may also shed light on new physics beyond the SM. Indeed the SM is generally considered as a low energy effective model of a more fundamental theory. The motivations of new physics are numerous, one of it being the need of identification of new matter type, called the Dark Matter (DM), still unknown presently. DM candidates are proposed for example in some supersymmetry (SUSY) models. Another motivation is the wish of unification of the four fundamental interactions at high energy: the GUT (Grand Unify Theory), which generally implies the existence of new heavy resonances.

Searches are performed at the LHC to track possible new physics in many different final

state topologies, see Refs. [1, 2] for a complete list. Here three recent specific searches will be presented : SUSY searches, heavy resonance searches and dark matter searches.

4.1 Search for SUSY particles

If SUSY exists at the TeV scale, the SUSY partners of quarks and gluons, squarks and gluinos, should be abundantly produced at the LHC thanks to their large cross section production. The most sensitive search is the multijet + MET final state, as for example produced by diagram shown in Fig. 9(left). CMS has performed a search for heavy particle pairs production, sensitive to generic SUSY models provided superpartner particles are kinematically accessible, with minimal assumptions on properties of the lightest superpartner particle [17]. The kinematic consistency of the selected events is tested against the hypothesis of heavy particle pair production using the dimensionless *razor* variable R, related to the MET. The new physics signal is characterized by a broad peak in the distribution of M_R, an event-by-event indicator of the heavy particle mass scale. As no significant excess of events is found beyond the SM expectations, results are interpreted in the context of the Constrained Minimal Supersymmetric Standard Model, see Fig. 9(right).

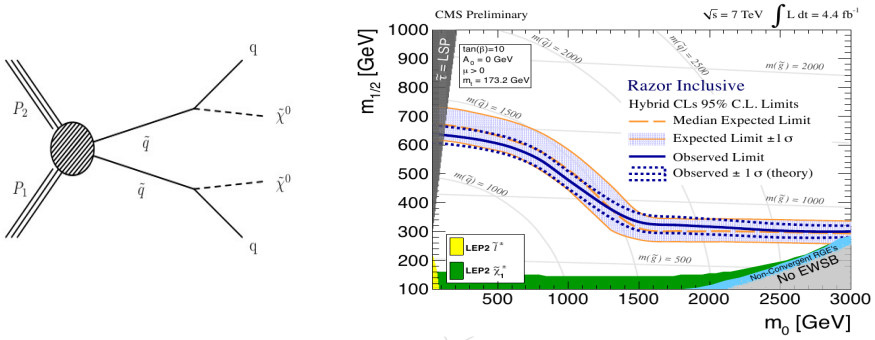

Figure 9: Example of diagram of heavy SUSY particle pair production (left); observed (solid blue curve) and median expected (dot-dashed curve) 95% CL limits in the $(m_0, m_{1/2})$ CMSSM plane with $\tan\beta = 10$, from the razor analysis. CMS results from [17].

With the large amount of luminosity collected in 2011, CMS and ATLAS become sensitive to more exclusive production modes, with lower cross section, as for example the electroweak chargino/neutralino production. Charginos $\tilde{\chi}_1^{\pm}$ and neutralinos $\tilde{\chi}_1^0$ are mass eigenstates formed from the linear superposition of the SUSY partners of the electroweak gauge bosons (W, Z, γ) and of the scalar bosons. In many SUSY models, $\tilde{\chi}_1^{\pm}$ are among the lightest SUSY particles and the $\tilde{\chi}_1^0$ is the lightest SUSY particle (LSP). Search for associated production and leptonic decays, of charginos and neutralinos are performed by ATLAS in the three lepton and MET final states [18], see Fig. 10(left). No significant excess of events is found in data. The results are interpreted in pMSSM [19] and in simplified models [20, 21]. For the simplified models, degenerate lightest chargino and next-to-lightest neutralino masses are excluded up to 300 GeV for mass differences to the lightest neutralino up to 250 GeV, see Fig. 10(right).

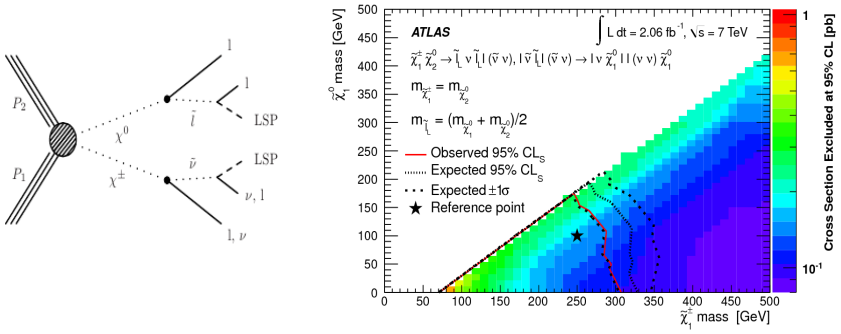

Figure 10: Example of a diagram pour chargino-neutralino production at the LHC (left); observed and expected 95% CL limit contours for chargino and neutralino production in the simplified model scenarios. ATLAS results from [18].

4.2 Search for heavy resonances

CMS and ATLAS are searching for new heavy resonances in the dilepton (ee and $\mu\mu$) decay channel. These new particles are typically predicted in GUT models (spin 1 boson noted Z'), or models proposing extra spatial dimension(s), as for example the Randall-Sundrum model (spin 2 boson noted G) [22]. Events with two isolated high pt leptons are selected [23, 24]. The dilepton mass spectrum is analysed in the high mass range, typically $M_{\ell\ell} > 500$ GeV. The main backgrounds come from Drell-Yan events (irreducible), from $t\bar{t}$ and multijet events. These later two backgrounds are estimated by data driven methods. Figure 11(left) presents the CMS dielectron invariant mass distribution, compared to the stacked sum of all expected backgrounds. Figure 11 (right) presents the expected and observed 95% CL upper limits obtained by ATLAS on $\sigma \times BR$ as a function of mass for various Z' models, with the combination of the electron and muon channels.

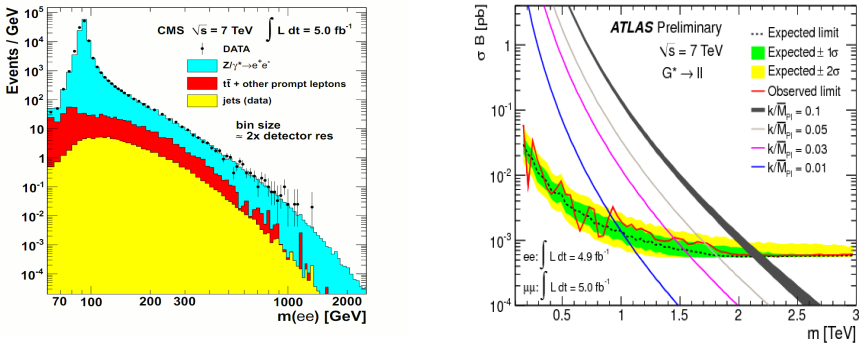

Figure 11: The CMS dielectron invariant mass distribution [23] (left); ATLAS expected and observed 95% CL upper limits on $\sigma \times BR$ as a function of mass for various Z' models (ee and $\mu\mu$ channels) combined [24].

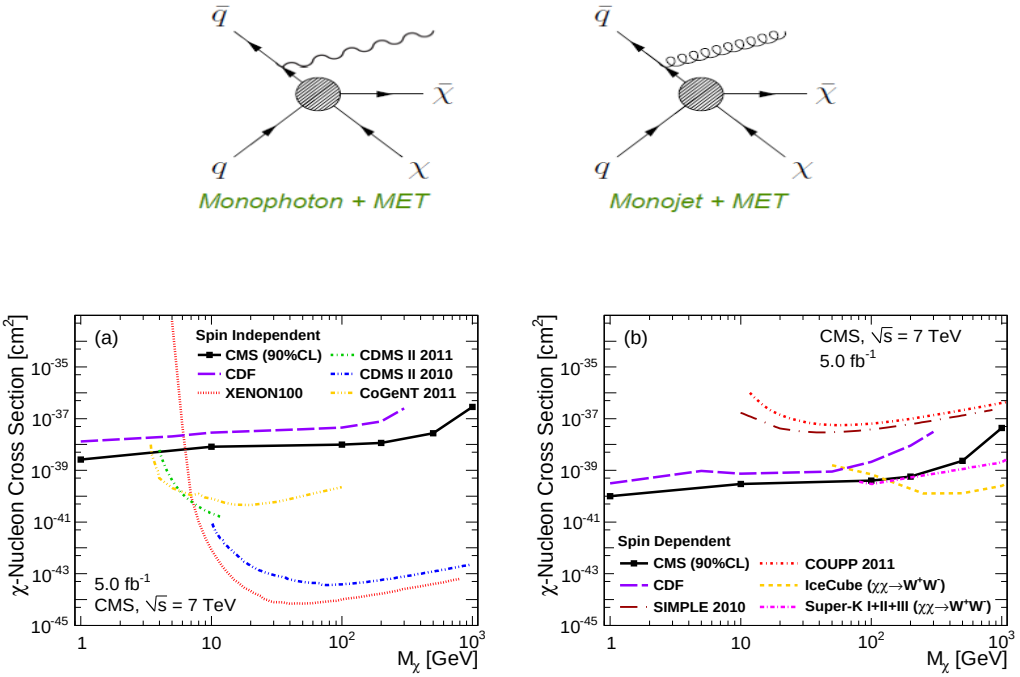

Figure 12: Diagram for mono-photon and mono-jet production with MET (top); comparison of the 90% CL upper limits on the dark matter-nucleon scattering cross section versus dark matter mass for the spin-independent (bottom left) and spin-dependent (bottom right) models, with results from various direct detection experiments. CMS results from [25].

4.3 Search for dark matter

A search for dark matter particles and large extra dimensions in events with an energetic jet or photon and an imbalance in transverse momentum is performed in CMS, the unique object in the event being the jet or the photon from ISR, see Fig. 12(top). The analyses are detailed in [25, 26]. The data are in good agreement with the expected contributions from SM processes. Using an effective operator (see Ref. [27]), constraints on the dark matter-nucleon scattering cross sections are determined, as shown in Fig. 12(bottom). For the spin-independent model, these are the best limits for a dark matter particle with mass below 3.5 GeV, a region unexplored by the direct detection experiments. For the spin-dependent model, these are the most stringent constraints over the entire 1-1000 GeV mass range studied.

5 Conclusions

This proceeding has presented the latest searches performed by CMS for the standard model scalar boson in 11 independent channels. No significant excess is found and the expected and observed 95% CL exclusion ranges in m_H are 114.5-543 and 127.5-600 GeV, respectively. A small excess of events around 125 GeV is observed, characterised by a local significance of 2.8 σ,

the global significance in the 110-145 GeV mass range and in the full mass range are 2.1 σ and 0.8 σ, respectively. The small excess is compatible with both the presence of a minimal SM scalar boson signal and the background fluctuation.

Searches for new physics by the ATLAS and CMS experiments were also performed in many topologies, more exotic final states and more exclusion production were studied. No evidence for new physics so far have been observed and limits on new physics cross section production or on new particle mass have been significantly extended.

These impressive results were possible thanks to the excellent performance of the LHC machine in 2011. A total of 15 fb^{-1} of data is expected to be collected in year 2012, 3 times more than in 2011, at a center-of-mass energy of 8 TeV. At the end of 2012, the LHC will give a final answer on the existence of the minimal SM scalar boson, and will search for new physics in a larger phase space. The data that will be collected after 2014, at the design energy of 14 TeV, will identify and study the properties of any possible new signal hopefully.

References

[1] CMS Collaboration. **https://twiki.cern.ch/twiki/bin/view/CMSPublic/PhysicsResults** (2012) .

[2] ATLAS Collaboration. **https://twiki.cern.ch/twiki/bin/view/AtlasPublic** (2012) .

[3] CMS Collaboration. JINST **03** (2008) S08004.

[4] ATLAS Collaboration. JINST **03** (2008) S08003.

[5] F. Englert and R. Brout. Phys. Rev. Lett. **13** (1964) 321.

[6] P. Higgs. Phys. Rev. Lett. **13** (1964) 508.

[7] G. Guralnik, C. Hagen, and T. Kibble. Phys. Rev. Lett. **13** (1964) 585.

[8] LEP Working Group for Higgs boson searches. CERN-EP **2003-011** (2003) 1, arXiv:1012.2367.

[9] LEP, Teavatron and SLD Electroweak Working Group. Update for Moriond 2012 (2012) http://lepewwg.web.cern.ch/LEPEWWG/.

[10] CMS Collaboration. CMS PAS **HIG-12-001** (2012) .

[11] CMS Collaboration. Phys. Lett. **B710** (2012) 91, arXiv:1202.1489.

[12] CMS Collaboration. Phys. Rev. Lett. **108** (2012) 111804, arXiv:1202.1997.

[13] CMS Collaboration. CMS PAS **HIG-12-008** (2012) .

[14] ATLAS Collaboration. Eur. Phys. J. **C72** (2012) 2157, arXiv:1205.0701.

[15] ATLAS Collaboration. JHEP **1206** (2012) 039, arXiv:1204.2760.

[16] CMS Collaboration. J. High Energy Phys. **07** (2012) 143, arXiv:1205.5736.

[17] CMS Collaboration. CMS PAS **SUS-12-005** (2012) .

[18] ATLAS Collaboration. ATLAS NOTE **2012-23** (2012) .

[19] A. Djouadi, J. Kneur, and G. Moultaka. Comput. Phys. Commun. **179** (2007) 426.

[20] J. Alwall, P. Shuster, and N. Toro. Phys. Rev. **D79** (2009) 075020.

[21] D. Alves *et al.* arXiv:1105.2838.

[22] L. Randall and R. Sundrum. Phys. Rev. Lett. **83** (1999) 3370–3373, arXiv:hep-ph/9905221.

[23] CMS Collaboration. Phys. Lett. **B714** (2012) 158, arXiv:1206.1849.

[24] ATLAS Collaboration. ATLAS CONF **2012-07** (2012) .

[25] CMS Collaboration. Phys. Rev. Lett. **108** (2012) 261803, arXiv:1204.0821.

[26] CMS Collaboration. CMS PAS **EXO-11-059** (2011) , arXiv:1206.5663.

[27] P. J. Fox *et al.* FERMILAB-PUB **487** (2011) 1, arXiv:1109.4398.

Perspectives on DIS and the LHeC

Max Klein[1]

[1]University of Liverpool, Department of Physics, United Kingdom

DOI: http://dx.doi.org/10.3204/DESY-PROC-2012-02/364

This paper is a brief summary of a plenary talk held to conclude DIS12 with considerations on the future of deep inelastic scattering. It is primarily based on the perspectives which have been obtained in a few years of study on the physics and the design concepts of a second energy frontier ep and a first eA collider, the Large Hadron Electron Collider (LHeC), which following HERA may commence operation at CERN in the early twenties.

1 Introduction

This writeup is on a concluding plenary talk [1] held at the 2012 conference on Deep Inelastic Scattering (DIS) at Bonn. The talk was devoted to perspectives in DIS as arise newly from the prospect for a TeV energy scale electron-proton and electron-ion collider, the LHeC, which relies on the unique hadron beams of the LHC. The talk was delivered at the eve of the discovery of the Higgs boson by the ATLAS and CMS experiments, which have excluded much of the expected new physics, as from SUSY, in the about $0.5-1$ TeV mass region. The three colliders, the Tevatron, LEP/SLC and HERA, which dominated particle physics for recent decades, have now all terminated operation and their data analyses are approaching completion. It had thus for various reasons been a special moment to examine perspectives of the physics of deep inelastic scattering, which has been part of the development of modern particle physics so successfully, not only by discovering quarks but also, for example, by providing the gluon distribution without which there would be no understanding of the Higgs cross section in pp at the LHC.

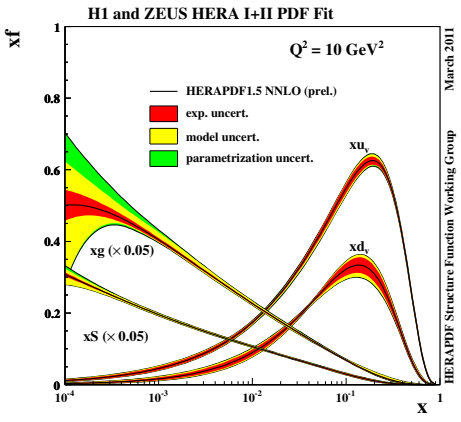

Figure 1: A determination of parton distributions at NNLO based on the HERA data.

If there was one figure to illustrate the current legacy of DIS, perhaps it is close to Fig. 1. It reveals that the proton structure at momentum fractions larger than $x \sim 0.2$ is determined by the up and down valence quarks, pointlike constituents of the proton which where discovered at SLAC in the first deep inelastic electron-proton scattering experiment, back in 1969. It then illustrates, note the downscaling factor of 0.05, that at lower

fractions of $x \lesssim 0.1$ the momentum is carried by gluons dominantly and also by sea quarks while the valence quark distributions, albeit not directly measured yet at low x, vanish. Based on the rise of F_2 and of $\partial F_2/\partial \log Q^2$, as discovered at HERA, the sea and the gluon distributions increase towards low x, with the uncertainty of the xg determination below $x \simeq 3 \cdot 10^{-4}$ becoming too large for any meaningful distinction between a steady and a tamed rise. This and similar PDF determinations from a number of well known and cooperating groups are indeed major achievements of particle physics of eminent importance, particularly when combined with the assumption of universality of PDFs which relies on the factorisation theorem. The different bands hint to the highly developed techniques of distinguishing various sources of uncertainty. And finally, the theory is now available and used to $\mathrm{N^2LO}$, which is as remarkable as the range and precision of the DIS data, mostly but not exclusively from HERA. The DIS12 workshop was yet another vivid demonstration of the richness of DIS physics, with remarkable new measurements obtained as on heavy quarks, diffraction or jets, for example. And yet, HERA is reaching its completion and thus, independently of the Higgs discovery, of the LHC physics or the termination of the Tevatron, there are intrinsic DIS reasons to newly examine its perspectives and their possible realisation.

Just at about the time of the Bonn workshop the comprehensive LHeC design report (CDR) approached completion, which is now published [2]. The talk was thus invited to coherently describe the status and development of the LHeC and its role for the future of deep inelastic scattering, as well as for particle physics from the perspective of DIS. At the workshop it was again well demonstrated that the field is not short of important initiatives and ideas to develop DIS also at medium and low energies, as with precision, with polarised and lower energy eA measurements and the development of the $3D$ view on the nucleon, for example. While an attempt had been made to include in the presentation [1] also the designs and a sketch of the physics programme of the EIC projects, under development at BNL and Jlab, this is not included in the current short writeup. Instead, reference is made to other workshop contributions and their summaries [3], and also to the extended summary of the EIC science case from a recent workshop [4]. An instructive overview on current ep collider projects, including lower energy machines, is given in the very recent issue of the ICFA Beam Newsletter [5].

The importance of the LHeC for DIS and particle physics cannot be underestimated. It exceeds the luminosity of HERA by a factor of 100 and reaches a maximum Q^2 of above $1\,\mathrm{TeV}^2$ as compared with a maximum of $0.03\,\mathrm{TeV}^2$ at HERA. Correspondingly the lowest Bjorken x covered in the DIS region with the LHeC is about 10^{-6}, where gluon saturation is expected to exist. This coverage allows a multitude of crucial DIS measurements to be performed, to complement and extend the search potential for new physics at the LHC, and it also makes the LHeC a testing ground for the Higgs boson cleanly produced in WW and ZZ fusion in ep. The extension of the kinematic coverage in DIS lepton-ion collisions amounts to nearly 4 orders of magnitude and can be expected to completely change the understanding of quark-gluon interactions in nuclei, tightly constraining the initial conditions of the formation of the quark-gluon plasma (QGP). The LHeC project represents a unique possibility to take forward the field of DIS physics as an integral part of the future high energy physics programme. It enhances the exploration of the accelerator energy frontier with the LHC. Naturally it is linked to the LHC time schedule and lifetime, which is estimated to continue for two decades hence. Therefore, a design concept has been presented which uses available, yet challenging, technology, both for the accelerator and for the detector, and time schedules are considered for realising the LHeC within about the next decade.

The following presents a brief summary of the physics, a detector and the accelerator design of the LHeC. Following the Bonn DIS workshop, at an LHeC workshop in June 2012 [6], the project had been examined in detail, a mandate been given by CERN to prototype the most crucial technical elements, and a decision has been taken, in agreement with the CERN directorate, to pursue the linac option of the LHeC in the coming years, considering the ring option as a backup, in case new technical or physics developments were suggesting to revisit that configuration.

2 Physics Perspectives with the LHeC

Basic Programme

The LHeC, with a multi-purpose detector, has a unique physics programme of deep inelastic scattering, which can be pursued with unprecedented precision over a hugely extended kinematic range. This comprises a per mille level accuracy measurement of α_s, accompanied by ultra-precise charm and beauty density measurements, the accurate mapping of the gluon field over five orders of magnitude in Bjorken x, from $x \simeq 3 \cdot 10^{-6}$ up to x close to 1, the unbiased resolution of the complete quark content of the nucleon, including first direct measurements of the Q^2 and x dependences of the strange and top quark distributions, and the resolution of the partonic structure of the photon. Neutron and nuclear structure can be explored in a vast new kinematic region, as these were uncovered by HERA, and high precision electroweak measurements can be made, for example of the scale dependence of the weak mixing angle $\sin^2\Theta_W$ and of the light-quark weak neutral current couplings. These and more exclusive measurements of e.g. jets and diffraction at high energy and mass scales, represent new challenges for the development of Quantum Chromodynamics to a new level of precision. By accessing very low x values, down to 10^{-6} at $Q^2 \simeq 1\,\mathrm{GeV}^2$, the LHeC is expected to resolve the question of whether and how partons exhibit non-linear interaction dynamics where their density is particularly high, and whether indeed there is a damping of the rise of the parton densities towards low x, a question also related to ultra-high energy neutrino physics, which probes very small x values.

Relation to QCD: Developments and Discoveries

The ultra-high precision measurements with the LHeC challenge perturbative QCD to be further developed, by preparing for a consistent DIS analysis to N^{3}LO. Precision measurements of generalised parton distributions in DVCS are necessary for the development of a parton model theory based on scattering amplitudes and the development of a 3-dimensional view of the proton. Analysis in the extended phase space will pin down the mechanism of parton emission and will determine unintegrated, transverse momentum dependent parton distributions for the description of ep as well as pp final states. The coverage of extremely low x regions at $Q^2 \geq 1\,\mathrm{GeV}^2$, both in ep and in eA, will establish the basis for the theoretical development of non-linear parton evolution physics. High energy ep scattering may be important for constructing a non-perturbative approach to QCD based on effective string theory in higher dimensions. Instantons are a basic aspect of non-perturbative QCD, which also predicts the existence of the Odderon, a dressed three-gluon state, and both are yet to be discovered. A new chapter in eA scattering will be opened with measurements of unprecedented kinematic range and precision, allowing huge progress in the understanding of partonic interactions in nuclei, which is still in its infancy. It will also probe the difference between hadronisation phenomena inside and

outside the nuclear medium. The establishment of an ultra-high parton density, "black-body" limit in DIS would change the scaling behaviour of the structure functions and the rates with which diffraction and exclusive vector meson production occur. QCD is a subtle theory which is far from being mastered and many of its areas call for a renewed and extended experimental basis.

Relations to LHC Physics

Deep inelastic scattering is the ideal process for the determination of the quark and gluon distributions in the proton. Studies of the parton substructure of the nucleon are of great interest for the development of strong interaction theory, but they are also a necessary input for new physics searches and studies at the LHC, whose potential will be correspondingly enhanced. With the increasingly apparent need to cover higher and higher new particle masses in this endeavour, it becomes ever more important to pin down the parton behaviour at large x, which governs both signal and background rates near to the LHC kinematic limit. An example is the prediction of gluino pair production cross sections from gluon-gluon fusion, which are currently not well known at masses beyond a few TeV, and for which a new level of precision on the gluon distribution will be critical. Similar situations are expected to arise in future studies of electroweak and other new physics, where large x parton distributions will play a crucial role. QCD predicts factorisation as well as resummation phenomena which can be tested with much enhanced sensitivity by combining LHC and LHeC results in inclusive and also in diffractive scattering. Certain parton distribution constraints, e.g. for the strange quark, are also derived from Drell-Yan measurements of W and Z production at the LHC, which will be verified with much extended range, accuracy and completeness at the LHeC. The eA measurements determine the parton densities and interaction dynamics in nuclei and are therefore a natural and necessary complement to the AA and pA investigations made with the LHC.

Depending on what new phenomena are found at the LHC, which has a superior cms energy compared to the LHeC (and to any of the proposed e^+e^- colliders), there are various scenarios where the cleaner ep initial state can help substantially to clarify and to investigate new physics. Key examples are the spectroscopy of leptoquarks, R-parity violating SUSY states, substructure and contact interaction phenomena, as well as the search for excited electron or neutrino states.

The Higgs particle is produced in WW and ZZ fusion in ep collisions at the LHeC. These production modes can be uniquely identified by the nature of the charged or neutral current process, and decays can be studied with low background, including the dominant decay to $b\bar{b}$ to about 4 % precision. From the WW production the contributions from CP even (SM) or odd (non-SM) Higgs quantum numbers can be unfolded.

3 LHeC Accelerator

Electron Beam Layout and Civil Engineering

The default electron beam energy is set to 60 GeV, see [2]. Two suitable configurations have been considered in the design report: a storage ring mounted on top of the LHC magnets, the ring-ring configuration (RR), and a separate linac, the linac-ring configuration (LR). In the RR case, bypasses of 1.3 km length each are considered around the existing LHC experiments, also housing the RF. This option is now treated as backup only, mainly because of its strong interference with the LHC. For the LR case, based on available cavity technology and accepting

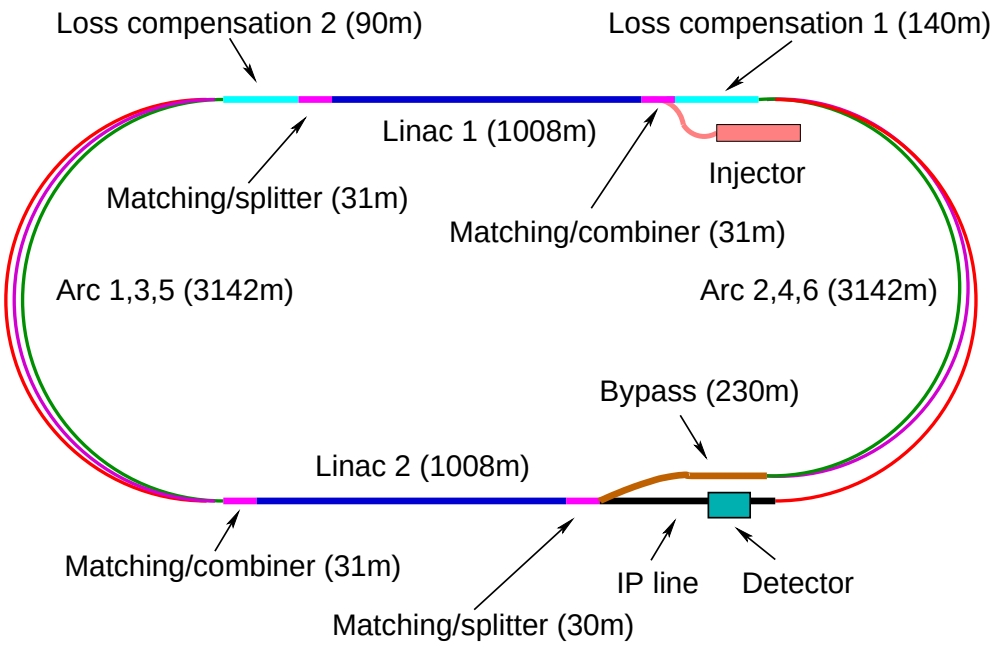

Figure 2: Schematic view on the LHeC racetrack configuration. Each linac accelerates the beam to 10 GeV, which leads to a 60 GeV electron energy at the collision point with three passes through the opposite linear structures of 60 cavity-cryo modules each. The arc radius is about 1 km, mainly determined by the synchrotron radiation loss of the 60 GeV beam which is returned from the IP and decelerated for recovering the beam power. Comprehensive design studies of the lattice, optics, beam (beam) dynamics, dump, IR and return arc magnets, as well as auxiliary systems such as RF, cryogenics or spin rotators are contained in the CDR [2], which as for physics and detector had been reviewed by referees appointed by CERN.

a synchrotron energy loss of about 1 % in the arcs, a new tunnel of racetrack shape and a length of 9 km is required, not much larger than HERA or the SPS at CERN, see Fig. 2. The tunnel is arranged tangential to IP2 (see below) and is best positioned inside the LHC, which avoids a clash with the LHC injection line TI2 and allows access shafts at the Prevessin and Meyrin sites of CERN, or in close proximity, to be erected. The civil engineering (CE) concepts were evaluated externally and no principal problem has been observed which would prevent completion of a tunnel within a few years time. For the project to begin in the early twenties, the CE efforts are considered to be strengthened by 2013/14.

Components

Designs of the magnets, RF, cryogenic and further components have been considered in some detail. Some major parameters for both the RR and the LR configurations are summarised in Tab. 1. The total number of magnets (dipoles and quadrupoles excluding the few special IR magnets) and cavities is 4160 for the ring and 5978 for the linac case. The majority are the 3080 (3504) normal conducting dipole magnets of 5.4 (4) m length for the ring (linac return arcs), for which short model prototypes have already been successfully built, testing different magnet concepts, at BINP Novosibirsk and at CERN. The number of high quality cavities for the two linacs is 960, grouped in 120 cavity-cryo modules. The cavities of 1.04 m length are

operated at a currently preferred frequency of 721 MHz, at a gradient of about 20 MV/m in CW mode, as is required for energy recovery. The cryogenics system of the ring accelerator is of modest demand. For the linac it critically depends on the cooling power per cavity, which for the draft design is assumed to be 32 W at a temperature of 2 K. This leads to a cryogenics system with a total electric grid power of 21 MW. The projected development of a cavity-cryo module for the LHeC is directed to achieve a high Q_0 value and to reduce the dissipated heat per cavity, which will reduce the dimension of the cryogenics system.

	Ring	Linac
magnets		
number of dipoles	3080	3504
dipole field [T]	$0.013 - 0.076$	$0.046 - 0.264$
number of quadrupoles	968	1514
RF and cryogenics		
number of cavities	112	960
gradient [MV/m]	11.9	20
linac grid power [MW]	–	24
synchrotron loss compensation [MW]	49	23
cavity voltage [MV]	5	20.8
cavity R/Q [Ω]	114	285
cavity Q_0	–	$2.5\ 10^{10}$
cooling power [kW]	5.4@4.2 K	30@2 K

Table 1: Selected components and parameters of the electron accelerators for the 60 GeV e beam energy.

Interaction Region and Choice of IP

Special attention is devoted to the interaction region design, which comprises beam bending, direct and secondary synchrotron radiation, vacuum and beam pipe demands. Detailed simulations are presented in [2] of synchrotron radiation effects, which will have to be pursued further. Stress simulations, geometry and material development considerations are presented for the detector beam pipe, which in the LR case is very asymmetric in order to accommodate the synchrotron radiation fan. The LR configuration requires a long dipole, currently of ± 9 m length in both directions from the interaction point, to achieve head-on ep collisions. The dipole has been integrated in the LR detector concept. The IR requires a number of focusing magnets with apertures for the two proton beams and field-free regions through which to pass the electron beam. The field requirements for the RR option (gradient of 127 T/m, beam stay-clear of 13 mm ($12\,\sigma$), aperture radius of 21 (30) mm for the p (e) beam) allow a number of different magnet designs using proven $NbTi$ superconductor technology and make use of cable (MQY) developments for the LHC. The requirements for the linac are more demanding in terms of field gradient (approximately twice as large) and tighter aperture constraints which may be better realised with Nb_3Sn superconductor technology, requiring prototyping.

The detector requires an interaction point for ep collisions while the LHC runs. There are eight points with adjacent long straight tunnel sections, called IP1-IP8, that could in principle be used for an experimental apparatus. Four of these (IP1, IP2, IP5 and IP8) house the current LHC experiments. There is no experimental cavern at IP3 nor IP7, and it is not feasible

to consider excavating a new cavern while the LHC operates. Since IP6 houses the beam extraction (dumps) and IP4 is occupied with RF equipment, the LHeC project can only be realised according to the present understanding if it uses one of the current experimental halls. The nature of the *ep* collider operation is to run synchronously with *pp* in the high luminosity phase of the LHC, which is determined primarily by the searches for ultra-rare phenomena by ATLAS (IP1) and CMS (IP5). A 9 km tunnel excavation and surface installations close to an international airport, as would be required at IP8, is considered not to be feasible. Therefore, IP2 has been used as the reference site for the CDR. IP2 appears to be well suited as it has an experimental surface hall for detector pre-assembly and with the LHeC inside the LHC ring, access to the linacs will be possible with shafts and surface installations placed on, or very close to existing CERN territory. It therefore has to be tentatively recognised that IP2 is in practice the only option for housing the LHeC detector. This would require a transition from the ALICE to the LHeC detector, for which consultations between ALICE and LHeC have recently been initiated.

The LHeC design report considers only one detector. This could possibly be built by two analysis collaborations, cooperating in its operation but otherwise ensuring independent and competing software and analysis approaches, as a "push-pull" detector philosophy is not feasible.

4 Detector Principles

The physics programme depends on a high level of precision, required for example for the measurement of α_s, and on the reconstruction of complex final states, as appear in charged current single top events or in Higgs production and decay into b final states. The detector acceptance has to extend as close as possible to the beam axis because of the interest in the physics at small and large Bjorken x. The dimensions of the detector are constrained by the radial extension of the beam pipe, in combination with maximum polar angle coverage, down to about 1° and 179° for forward going final state particles and backward scattered electrons at low Q^2, respectively. A cross section of the central, baseline detector is given in Fig. 3. In the central barrel, the following detector components are currently considered: a central silicon pixel detector surrounded by silicon tracking detectors of strip or possibly strixel technology; an electromagnetic LAr calorimeter inside a 3.5 T solenoid and a dipole magnet required to achieve head-on collisions; a hadronic tile calorimeter serving also for the solenoid flux return and a muon detector, so far for muon identification only relying on the precise inner tracking for momentum measurements. The electron at low Q^2 is scattered into the backward silicon tracker and its energy is measured in backward calorimeters. In the forward region, components are placed for tracking and for calorimetry to precisely reconstruct jets over a wide energy range up to O(TeV). Simulations of tracking and calorimeter performance are used to verify the design, although a complete simulation is not yet available. The report also contains designs for forward and backward tagging devices for diffractive and neutron physics and for photoproduction and luminosity determinations, respectively. The time schedule of the LHeC project demands a detector to be ready within about ten years. The radiation level at the LHeC is lower than in *pp*, and the *ep* cross section is low enough for the experiment not to suffer from pile-up, which are the two most demanding constraints for the ATLAS and CMS detector upgrades for the HL-LHC. The choice of components for the LHeC detector can rely on the experience obtained at HERA, at the LHC, including its detector upgrades currently being developed, and also on detector development studies for the ILC. The detector development, while requiring

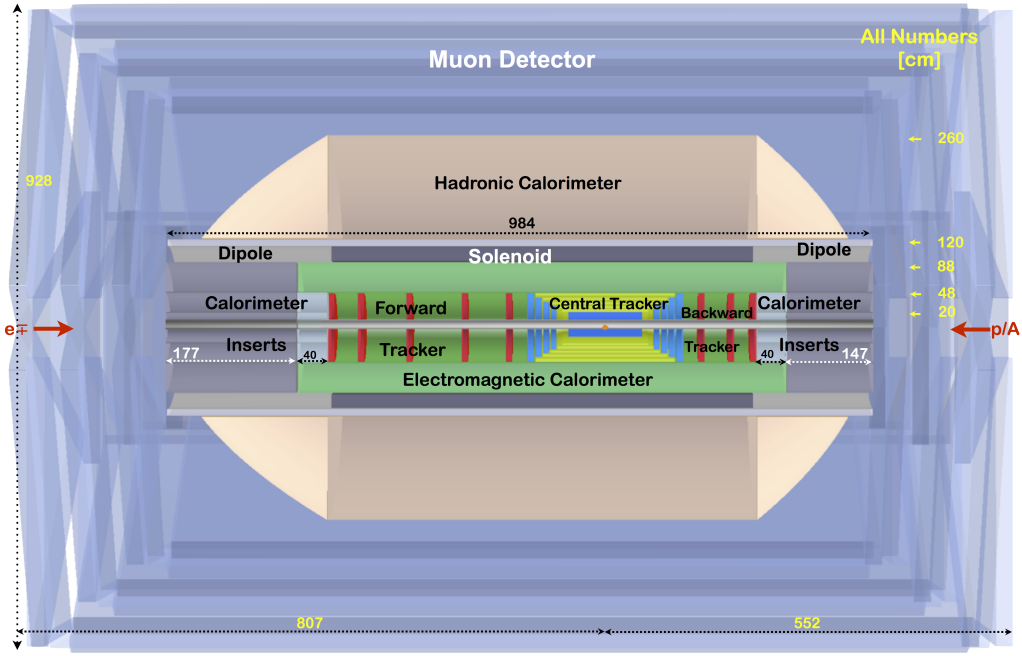

Figure 3: An rz cross section of the LHeC detector in its baseline design with the magnet configuration for LR, with the solenoid and dipoles placed between the electromagnetic and the hadronic calorimeters. The proton beam, from the right, collides with the electron beam, from the left, at the IP which is surrounded by a central tracker system, complemented by large forward and backward tracker telescopes, and followed by sets of calorimeters. The detector dimensions are ≈ 13.6 m in z and a diameter of ≈ 9.3 m, which fits in the L3 magnet structure considered for supporting the LHeC apparatus [2].

prototyping, may yet proceed without an extended R&D program.

A first study is made about the principles of pre-mounting the detector at the surface, lowering and installing it at IP2. The detector is small enough to fit into the L3 magnet structure of 11.2 m diameter, which is still resident in IP2 and is available as mechanical support. Based on the design, as detailed in the CDR, it is estimated that the whole installation can be done in 30 months, which is compliant with the operations currently foreseen in the LS3 shutdown, during which ATLAS intends to replace its complete inner tracking system.

Time Schedule and Mode of Operation

Following a CERN decision, for the next few years the LHeC design will be further pursued and collaborations are being extended or established for this purpose. The electron accelerator and new detector require a period of about a decade to be realised, based on experience from previous particle physics experiments. This duration fits with the industrialisation and production schedules, mainly determined by the required ~ 3500 approximately 5 m long warm arc dipoles and the 960 cavities for the Linac. The current lifetime estimates for the LHC predict two more decades of operation. An integrated luminosity for the LHeC of $O(100)\,\mathrm{fb}^{-1}$ may be collected in about one decade. This and the current shutdown planning of the LHC define the basic time

schedule for the LHeC project: it has to be installed during the long shutdown LS3 of the LHC, currently scheduled for 2022 and a period of about 2 years. The connection of the electron and proton beams and the detector installation can be realised in a period not significantly exceeding this tentative time window. The considerations of beam-beam tune shifts show that the ep operation may proceed synchronously with pp. Therefore with the electron beam, the LHC will be turned into a three beam facility. In the design considerations [2] it has been excluded to operate ep after the pp programme is finished, a) because this would make the LHeC as part of the LHC much more expensive by adding an extra decade of LHC operation requiring also substantial efforts to first consolidate the LHC, when the high radiation pp programme is over, and b) since one would loose the intimate and possibly crucial connection between the ep/pp and the eA/AA physics programmes, as sketched in this note.

5 Relation of the LHeC to other Projects

The LHeC represents a natural extension to the LHC, offering maximum exploitation of the existing LHC infrastructure at CERN. Physics-wise it is part of the exploration of the high energy frontier and as such linked to the LHC and the lepton-lepton colliders under consideration, a relation which resembles the intimate connection of HERA to the physics at Tevatron and LEP for the investigation of physics at the Fermi scale. As an ep and eA machine, the LHeC unites parts of the particle and nuclear physics communities for a common big project. It has a characteristic electroweak, QCD and nucleon structure physics programme which is related primarily to the LHC but also to lower energy fixed target DIS experiments operating at CERN and Jlab, and also to plans for realising lower energy electron-ion colliders at BNL and at Jlab. The superconducting (SC) IR magnets resemble HL-LHC superconducting magnet developments by the USLARP and SC magnet developments elsewhere. The LHeC linac is relevant to a variety of facilities such as the XFEL at DESY, ESS, the CEBAF upgrade at Jlab, also to the SPL at CERN and other projects for high quality cavity developments. Through the development of its high energy ERL application to particle physics, the LHeC is related to about ten lower energy projects worldwide, which are developing the energy recovery concept. The detector technology is linked mainly to the LHC experiments and some of their upgrades. It is thus evident that there are very good prospects for realising the LHeC within dedicated international collaborations at a global scale where mutual benefits can be expected at many levels.

6 Summary

The LHeC represents a new laboratory for exploring a hugely extended region of phase space with an unprecedented high luminosity in high energy DIS. It builds the link to the LHC and a future pure lepton collider, similar to the complementarity between HERA and the Tevatron and LEP, yet with much higher precision in an extended energy range. Its physics is fundamentally new, and it also is complementary especially to the LHC, for which the electron beam is an upgrade. Given the broad range of physics questions, there are various ways to classify these, partially overlapping. An attempt for a schematic overview on the LHeC physics programme as seen from today is presented in Tab. 2. The conquest of new regions of phase space and intensity has often lead to surprises, which tend to be difficult to tabulate.

QCD Discoveries	$\alpha_s < 0.12$, $q_{sea} \neq \overline{q}$, instanton, odderon, low x: (n0) saturation, $\overline{u} \neq \overline{d}$
Higgs	WW and ZZ production, $H \to b\overline{b}$, $H \to 4l$, CP eigenstate
Substructure	electromagnetic quark radius, e^*, ν^*, W?, Z?, top?, H?
New and BSM Physics	leptoquarks, RPV SUSY, Higgs CP, contact interactions, GUT through α_s
Top Quark	top PDF, $xt = x\bar{t}$?, single top in DIS, anomalous top
Relations to LHC	SUSY, high x partons and high mass SUSY, Higgs, LQs, QCD, precision PDFs
Gluon Distribution	saturation, $x \approx 1$, J/ψ, Υ, Pomeron, local spots?, F_L, F_2^c
Precision DIS	$\delta\alpha_s \simeq 0.1\,\%$, $\delta M_c \simeq 3\,\mathrm{MeV}$, $v_{u,d}$, $a_{u,d}$ to $2-3\,\%$, $\sin^2\Theta(\mu)$, F_L, F_2^b
Parton Structure	Proton, Deuteron, Neutron, Ions, Photon
Quark Distributions	valence $10^{-4} \lesssim x \lesssim 1$, light sea, d/u, $s = \overline{s}$?, charm, beauty, top
QCD	N^{3}LO, factorisation, resummation, emission, AdS/CFT, BFKL evolution
Deuteron	singlet evolution, light sea, hidden colour, neutron, diffraction-shadowing
Heavy Ions	initial QGP, nPDFs, hadronization inside media, black limit, saturation
Modified Partons	PDFs "independent" of fits, unintegrated, generalised, photonic, diffractive
HERA continuation	F_L, xF_3, $F_2^{\gamma Z}$, high x partons, α_s, nuclear structure, ..

Table 2: Schematic overview on key physics topics for investigation with the LHeC.

With its unique and precise QCD measurements the LHeC will be the necessary precision complement to ATLAS and CMS, when these run at maximum luminosity for searching at high masses, corresponding to large x. It also has its own possibilities for new physics to be observed, both in QCD and beyond the current model of particle physics. Combined with precision fixed target and medium or low energy collider measurements, the LHeC can lead the physics of DIS much beyond HERA and to its renaissance, as part of the movement of particle collider physics to smaller dimensions and higher mass scales and for the development of QCD.

Acknowledgments

The LHeC design report, on which the presentation relied, has been worked out by a large group of physicists and engineers in much of their free time. It is for that effort that one can now realistically consider a future of DIS as part of the exploration of the energy frontier. Special thanks are due to my colleagues Nestor Armesto, Armen Bunyatian, Olaf Behnke, Rohini Godbole, Paul Newman, Alessandro Polini, Daniel Schulte, Anna Stasto and RogelioTomas, who delivered detailed presentations on various aspects of the LHeC design to this workshop. DIS12 was a pleasure to attend for which I would like to express sincere thanks to the organizers.

References

[1] Slides:
`http://indico.cern.ch/contributionDisplay.py?contribId=364&sessionId=0&confId=153252`

[2] J. L. Abelleira Fernandez *et al.* [LHeC Study Group], "A Large Hadron Electron Collider at CERN" J.Phys.G. **39**(2012)075001, arXiv:1206.2913, see also `http://cern.ch/lhec`

[3] E. Aschenauer and P. Newman, Summary talks on the future of DIS session, this workshop.

[4] D. Boer, M. Diehl, R. Milner, R. Venugopalan, W. Vogelsang, D. Kaplan, H. Montgomery and S. Vigdor *et al.*, arXiv:1108.1713 [nucl-th].

[5] ICFA Beam Newsletter No 58, August 2012, to appear.

[6] CERN-ECFA-NuPECC Workshop on the LHeC, Chavannes, Switzerland, 2012, see `http://cern.ch/lhec`.

Part II

Summary Talks

Summary of the Structure Functions Working Group

Amanda Cooper-Sarkar[1], *Pedro Jimenez-Delgado*[2], *Ringailė Plačakytė*[3],

[1]Denys Wilkinson Bdg, Keble Rd, OX1 3RH OXFORD, UK
[2]Institut für Theoretische Physik, Universität Zürich, 8057 Zürich, Switzerland
Jefferson Lab, 12000 Jefferson Avenue, Newport News, VA 23606, USA
[3]DESY, Notkestraße 85, 22607 Hamburg, Germany

DOI: `http://dx.doi.org/10.3204/DESY-PROC-2012-02/357`

A summary of the recent experimental, phenomenological and theoretical results presented in the Structure Functions working group at DIS2012 workshop.

1 Introduction

In the Structure Functions working group experimental results relevant to the determination of parton distributions were presented by H1, ZEUS, ATLAS, CMS and LHCb. The HERAfitter tool, which is an open access code for fitting PDFs to relevant data, and an update of the FastNLO tool, which allows the fast computation of higher-order cross sections at hadron colliders, were presented. Progress in the determination of the parton distributions of the nucleon from most global PDF groups was reviewed and more restricted studies which focus on particular aspects of these determinations were also discussed. Analyses of nuclear PDFs were presented. Finally, phenomenological contributions within frameworks which appear as extensions or alternatives to the usual collinear factorization approach were discussed.

2 Summary of the presentations

A measurement of the integrated luminosity of HERA data collected in the years 2003 to 2007 and based on the elastic QED Compton process $ep \to e\gamma p$ has been performed by the H1 Collaboration [1]. Contrary to the standard HERA luminosity measurement which exploits Bethe-Heitler (BH) scattering with electron and the photon emitted almost collinearly to the incident electron, the particles in QED Compton scattering have a sizable transverse momentum with respect to the incident electron and are detectable in the main H1 detector. The advantage of this method is its insensitivity to the details of the beam optics, but its disadvantage is limited statistical precision. The precision of the experimental and theory uncertainties in this analysis are illustrated using the variable $(E - p_z)/(2E_e^0)$ in Fig. 1. This variable is calculated from the sum of the four-momenta of the electron and the photon (where E_e^0 is electron beam energy) and is expected to peak at unity. The tail to small values of $(E - p_z)/(2E_e^0)$ originates from initial state radiation (where theory uncertainty dominates), whereas values larger than unity occur due to resolution effects. The measured integrated luminosity is determined with a precision of 2.3% and is in agreement with the Bethe-Heitler measurement which has larger uncertainty for the second period of HERA data taking.

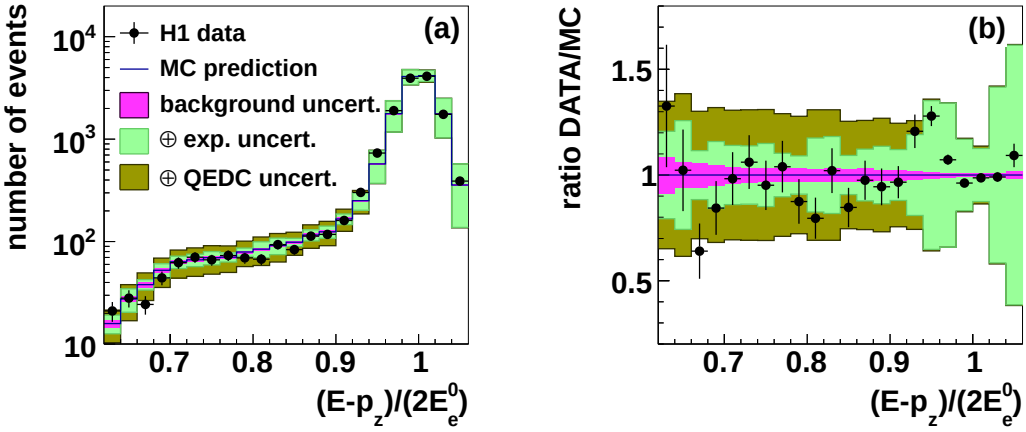

Figure 1: Distribution of the variable $(E - p_z)/(2E_e^0)$ (see text) calculated from the sum of the electron and photon four-momenta. In (a) the event counts are shown and in (b) the ratio of data to expectation is drawn. The data are shown as black dots with the statistical uncertainties indicated as vertical bars and the simulation (including background) is indicated as a solid line, with various components of the systematic uncertainty shown as shaded areas.

ZEUS have completed the measurement of inclusive cross sections from HERA-II running by finalising the Neutral Current (NC) e^+p measurement [2]. The measurements are based on an integrated luminosity of 135.5 pb^{-1} taken in 2006 and 2007 at a centre-of-mass energy of 318 GeV. The double-differential cross sections in Q^2 and x have been measured in the kinematic region $Q^2 > 185$ GeV^2 for both positively and negatively polarised positron beams. These measurements have been used to extract the polarisation asymmetry parameter $A^+ = \frac{2}{(P_+ - P_-)} \frac{(\sigma^+(P_+) - \sigma^+(P_-))}{(\sigma^+(P_+) + \sigma^+(P_-))}$, where $P_+ = +0.32$ and $P_- = -0.36$ denote the magnitude of the beam polarisations and $\sigma^+(P)$ denotes the cross section measured at polarisation P. This quantity is sensitive to the electro-weak vector couplings of the quarks and the non-zero asymmetry observed is a direct measure of parity violation. The NC e^+p data may also be averaged over positive and negative polarisations and combined with 169.9 pb^{-1} of NC e^-p measurements [4] to yield the structure function xF_3, which gives information on valence parton distribution functions. The measurement of xF_3 as a function of x in Q^2 bins is shown in Fig. 2, compared to predictions from HERAPDF1.5

The H1 and ZEUS experiments have already combined their data from HERA-I running [5] and have made preliminary combinations of HERA-II data from nominal energy and low energy running. A preliminary combination of $F_2^{c\bar{c}}$ data has also been made. These combined data sets, together with data on inclusive jet production from both H1 and ZEUS, have been used as the input to extract parton distribution functions (PDFs) in the HERAPDF1.7 NLO QCD fit [6]. These PDFs are illustrated in Fig. 2. All of the input data sets are well fit and consistent. In comparison to the published HERAPDF1.0 PDFs [5], which were based only on the HERA-I combination, the HERA-II high Q^2 cross-sections further constrain the high-x valence PDFs; the HERA-II low energy runs help to constrain the low-x gluon PDF; the charm data constrain heavy quark schemes and the jet data help to constrain $\alpha_s(M_Z)$.

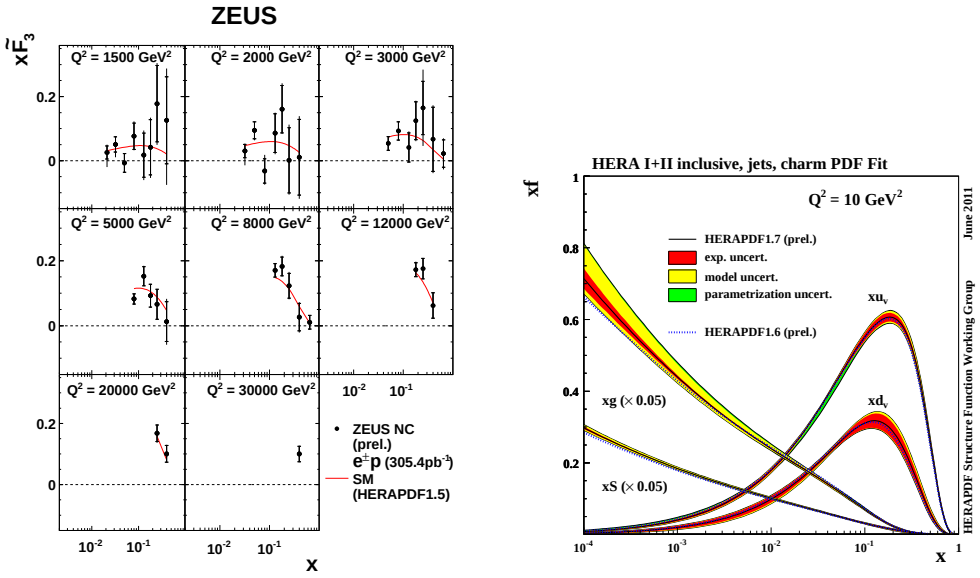

Figure 2: Left: the structure function xF_3 as a function of x in Q^2 bins, compared to the predictions of HERAPDF1.5. Right: Parton distribution functions for HERAPDF1.7

Using jet production data in PDF fitting requires fast repeated computation of NLO jet cross sections. The FastNLO [7] package provides a method to store the matrix elements calculated for such higher-order cross-sections on grids such that the cross-sections may be calculated quickly by convolution of these grids with the input PDFs. The package can be used for jet cross-sections from DIS and from hadron colliders. Typical applications of FastNLO are data and theory comparisons for various PDF sets, derivation of scale uncertainties, determination of α_s. Fig 3 shows the comparison of the inclusive jet data from various experiments to theory predictions obtained with FastNLO. Version 2 of the FastNLO project offers variaty of new features for users including largely improved technical aspects of the code (like improved reading tools) and flexibility in e.g. scale composition or scale variation. More details about new features in the version 2 of the FastNLO can be found in [8].

The HERAFitter tool has been develpoed by H1 and ZEUS as an open access code for fitting PDFs to relevant data [9]. Whereas the HERAFitter has been developed from the HERAPDF QCD fitting framework, based on QCDNUM for the NLO and NNLO QCD evolution, it goes far beyond this. The package can be used to fit all types of data used in a global PDF fit: inclusive cross sections, heavy quark structure functions, jet production data from Deep Inelastic Scattering (DIS); inclusive cross-section from fixed target data; Drell-Yan (including W, Z) cross sections from fixed target data and from Tevatron and LHC data; jet cross-sections from Tevatron and LHC data. A variety of options which facilitate benchmarking are available with the package: experimental systematic uncertainties can be treated as correlated or uncorrelated and PDF uncertainties may be evaluated from the Hessian covariance matrix or by the generation of Monte-Carlo replicas; the structure functions may be computed in a variety of heavy quark schemes; the package is interfaced to both FastNLO and to Applgrid for the fast and

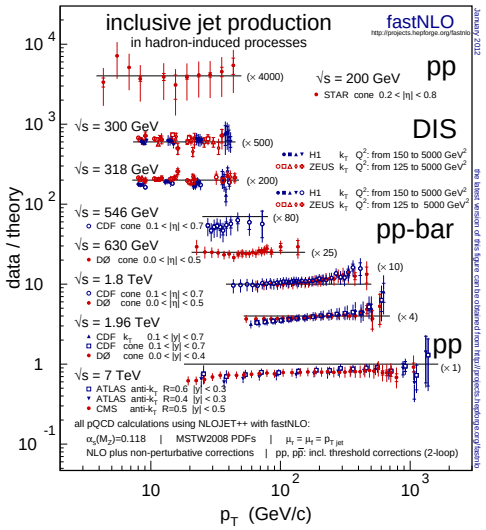

Figure 3: An overview of data over theory ratios for inclusive jet cross sections, measured in different processes at different center-of-mass energies. The data are compared to calculations obtained by FastNLO. The inner error bars represent the statistical errors and the outer error bars correspond to the quadratic sum of all experimental uncertainties.

correct input of NLO jet cross sections and Drell-Yan cross sections and the input of top cross sections via HATHOR is under development. Plotting tools are provided for the fit output and the resulting PDFs are supplied in the LHAPDF format. The package is under continuous development to provide a common platform for useful tools; for example the NNPDF reweighting tool has been included to allow fast computation of the impact of new data on existing PDFs, and the package has recently been extended to make fits to diffractive cross sections and to make fits using dipole models.

CMS has measured differential jet cross sections using $\sqrt{s} = 7$ TeV data corresponding to 4.6 pb^{-1} of 2010 data [10]. Reconstructed jets in this measurement cover rapidity up to $|y| = 2.5$, transverse momentum up to $p_T = 2$ TeV and dijet invariant mass up to $M_{JJ} = 5$ TeV. The measured cross sections are compared to perturbative QCD predictions at next-to-leading order using various sets of PDFs. Fig 4 illustrates the inclusive jet cross sections together with theoretical predictions obtained using the central value of the NNPDF set (left) and ratio of these cross sections to the NNPDF prediction with predictions from other PDF sets also shown (right). Experimental and theoretical uncertainties in the measurement are comparable in size so that these data should be able to constrain PDF uncertainties. The systematic uncertainty correlations which are necessary for the PDF fits are in preparation.

ATLAS has made a measurement of inclusive jet production using 36 pb^{-1} of data from 2010 running [11]. The data are provided with full information on correlated systematic uncertainties and this allows them to have some constraining power on PDFs. These data are well fit by most modern PDF sets such as MSTW08, CT10, NNPDF2.1 and HERAPDF1.5, however they prefer a somewhat less hard high-x gluon than the Tevatron jet data. Fig. 5 shows a comparison of these data to current PDFs. Dijet data from 4.7fb^{-1} of 2011 data are also available [11] extending the range of the di-jet mass to 4.8 TeV. These data are also illustrated in Fig. 5.

ATLAS have presented W-lepton and Z differential cross sections. as a function of (pseudo-)rapidity and as a function of p_t from 36pb^{-1} of 2010 data. The Z rapidity distribution from combined electron and muon decay channels is shown in Fig. 6. Data is also available in the τ decay channels and measurements of W and τ polarisation have been made [12]. The W, Z

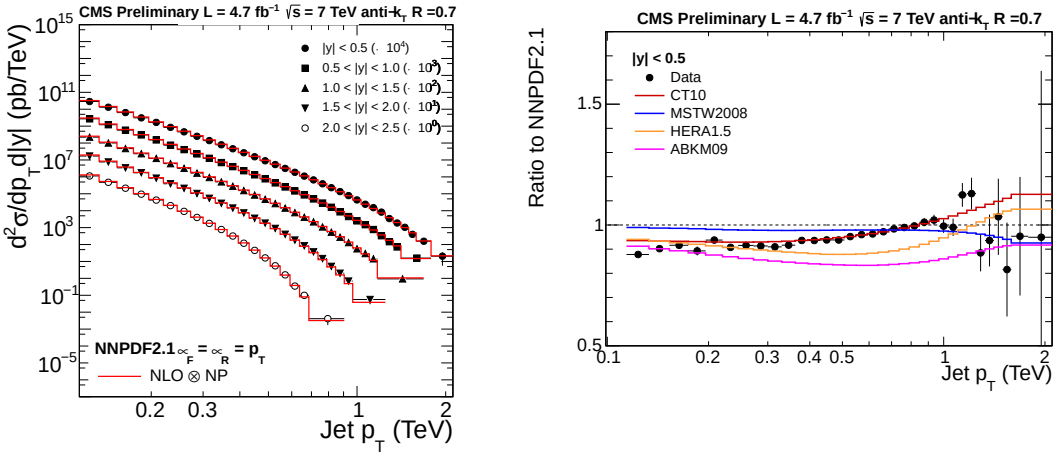

Figure 4: Inclusive jet cross sections (left) and ratio of inclusive jet (right) measured at CMS compared to theoretical prediction using the central value of the NNPDF PDF set. The solid histograms in the ratio plot also show expectations obtained with other PDF sets.

rapidity distributions are supplied with full information on correlated systematic uncertainties and this allows them to have impact on PDF fits. In particular, in Fig. 6 the Z rapidity data are presented compared to two PDF fits done using these ATLAS $W^{\pm}$ and Z data together with the HERA DIS data. The fit labelled 'epWZ fixed $\bar{s}$' has the strange quark density suppressed and fixed to 50% of the down sea quark density at the starting scale of PDF evolution $Q_0^2 \sim 2$ GeV^2 (as suggested by neutrino di-muon data). The fit labelled 'epWZ free $\bar{s}$' allows the strange quark distribution freedom in normalisation and shape, with the result that ATLAS data clearly prefer unsuppressed strangeness for $x \sim 0.01$ [13]. Fig. 6 compares the ratio of the strange to down sea quark densities at $x = 0.023$, $Q_0^2 = 1.9$ GeV^2, from the preferred epWZ free $\bar{s}$ fit to that of other PDF determinations.

Measurements of Z or W boson production associated with heavy quarks in the final state can provide important information about heavy quark densities in PDFs. The process $pp \to W + c + X$ and the cross section ratios $R_{+/-} = \sigma(W^+c + X)/\sigma(W^-c + X)$ and $R_c = \sigma(W + c + X/\sigma(W + jets + X)$ measured at CMS [14] provide information about the strange and anti-strange quark parton density functions of the proton. In these measurements muonic decays of the W-boson and lifetime tagging techniques are used to extract the charm fraction in $W + jet$ events. The measured ratios are: $R_{+/-} = 0.92 \pm 0.19(stat.) \pm 0.04(syst.)$ and $R_c = 0.143 \pm 0.015(stat.) \pm 0.024(syst.)$. Currently the 20% total uncertainty of these results limits their constraining power but higher statistics samples will significantly improve the sensitivity to the strangeness content of the PDFs. Results on the production of b jets in association with Z/γ^* were also presented by CMS collaboration [14].

The LHCb experiment has also performed measurements of W and Z production using final states containing muons, electrons and tau leptons [15]. The LHCb data provide unique constraints on both low-x and high-x PDFs beacuse of the high pseudorapidity region ($\eta > 2.5$) in which the W and Z boson cross sections are measured. Differential cross sections, W and Z cross section ratios and the lepton charge asymmetry are measured in this kinematic region. Fig. 7 shows the W-lepton asymmetry at high rapidity. The results presented use mainly

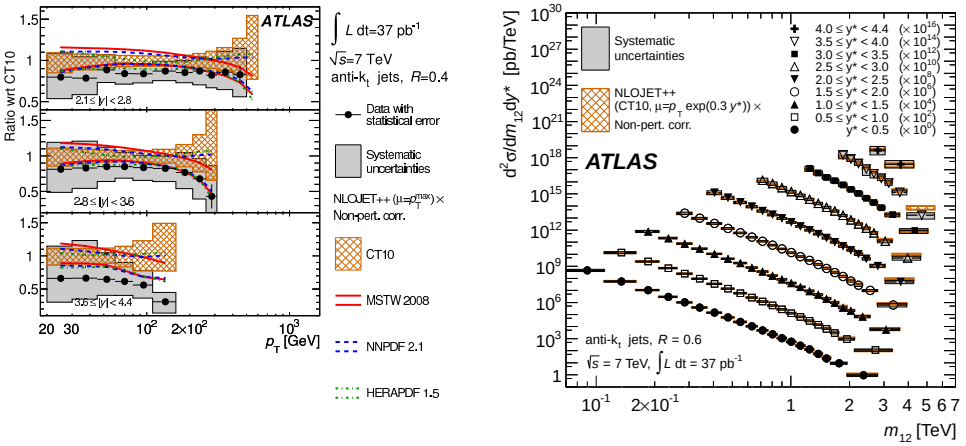

Figure 5: Left: ATLAS data on inclusive jet cross sections as a function of p_t in high rapidity bins. The data are shown in ratio to the predictions of NLOjet++ made using CT10 PDFs, with other PDF predictions shown for comparison. Right: ATLAS di-jet data as a function of di-jet invariant mass in rapidity bins

2010 data such that they are still limited by statistical precision and the uncertainty on the luminosity. Precision is expected to improve significantly with the full 2011 dataset.

LHCb have also performed the first low mass Drell-Yan cross section measurements [16] for which theoretical uncertainties (particularly scale uncertainties) and PDF uncertainties are larger compare to W and Z measurements. Differential DY cross sections are measured as a function of dimuon invariant mass (starting from 5 GeV, see Fig 7) and as a function of rapidity. This preliminary result uses background template technique [16] and currently is limited in statistical and systematic precision. Significantly smaller uncertainties in the measurement reaching even lower masses are expected with 2011 data set where luminosity is about 30 times higher.

The NNPDF collaboration have examined the impact of the LHC data on PDF fits but the early LHC data which was included in the NNPDF2.2 set are now superceded. At this meeting a preliminary examination of the impact of more recent LHC data on the NNPDF fit was presented [17]. This includes the ATLAS 2010 W-lepton and Z rapidity distributions, the higher luminosity CMS W-lepton asymmetry measurements, the LHCb Z and W-lepton high rapidity distributions, and the ATLAS and CMS inclusive jet measurements. The impact of these data has been evaluated by the technique of PDF reweighting. Of all these data sets the most discriminating is the ATLAS $W^{\pm}$-lepton and Z data. Their discriminating power is such that of 1000 initial Monte-Carlo replicas form NNPDF2.1 only 16 survive the reweighting procedure. Fig. 8 shows the impact of these data on the down quark PDF shape and uncertainty. Such a large change necessitates a fresh PDF fit which is underway.

The latest ABM11 PDF analysis [19] uses an improved treatment of heavy quark electroproduction within the fixed-flavor-number scheme at NNLO. This includes the $\overline{\rm MS}$ scheme for heavy quark masses. They find good agreement with the latest (combined) HERA charged current data, in particular no indication of *large logs* up to high Q^2. The discriminating power

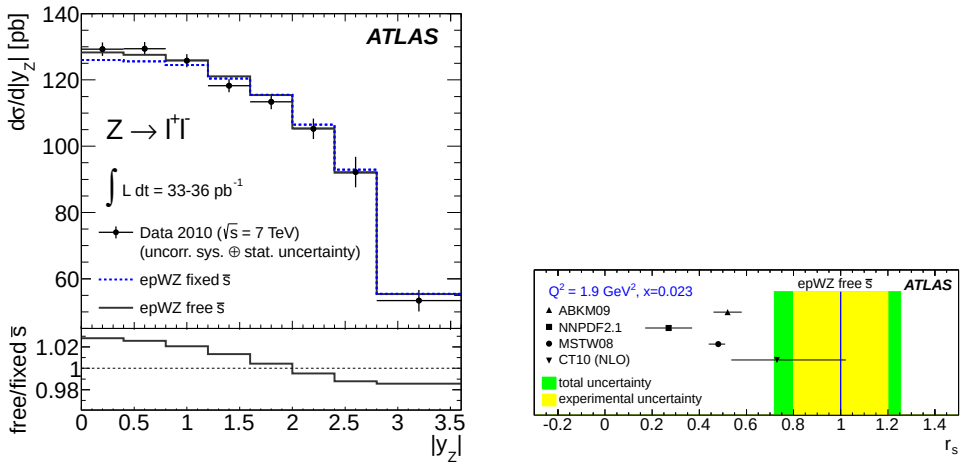

Figure 6: Left: ATLAS data on the Z rapidity distribution from combined electron and muon data. The data are compared to two PDF fits, one with fixed suppressed strangeness and the other with free unsuppressed strangeness as described in the text. Right: the ratio of strange to down quark densities in the sea, at $x = 0.023$, $Q^2 = 1.9\text{GeV}^2$, from the preferred epWZ free $\bar{s}$ fit and from other PDF determinations.

of current F_L measurements in the small x region is shown in Fig. 9. A similar situation is pointed out for dimuon production data. The ABM determination of $\alpha_s(M_Z^2)$ is lower than that reported by MSTW and/or NNPDF. It is often suggested that this is because jet data are not included in the ABM fit. However ABM find good agreement with jet data. They suggest that the higher values found by other groups could orginate in higher twist effects in the fixed target DIS data. Such power corrections are explicitly included in the ABM formalism.

The ongoing update of the NNLO *dynamical* parton distributions was presented[20]. This includes several improvements in the framework, e.g. a more careful determination of the strange-quark input parton distributions, a complete treatment of the correlations of systematic uncertainties of the data, and an improved treatment for heavy quark electroproduction from [19]; a wealth of deuteron DIS data which were not included in the JR09 analysis is also a major update. Nevertheless, there are only moderated changes of 10% or less with respect to JR09. In particular, the value of $\alpha_s(M_Z^2)$ is determined to be $\sim 0.113 \rightarrow 0.114$, depending on the value of the input scale used; the difference between these values is regarded as a genuine uncertainty of the determination [21].

The CTEQ collaboration has also presented their NNLO results [22]. There are two different sets at NNLO, one based on pre-LHC data only (CT10) and one which will include LHC data on W and Z rapidity distributions (CT12). There are ongoing investigations on the flavor structure of the quark sea at $x < 10^{-2}$; in particular the possibility of $\bar{d} \neq \bar{u}$ as $x \rightarrow 0$, as well as the relative size of the strange-quark distribution. Benchmark cross-sections at NNLO are presented for the first time.

The CTEQ-JLab Collaboration (CJ) [23] focus on the determination of PDFs in the large–x region, with the aim of using the unique capabilities of the CEBAF accelerator to measure small cross sections at extreme kinematics to reduce the large PDFs uncertainties at large x. This

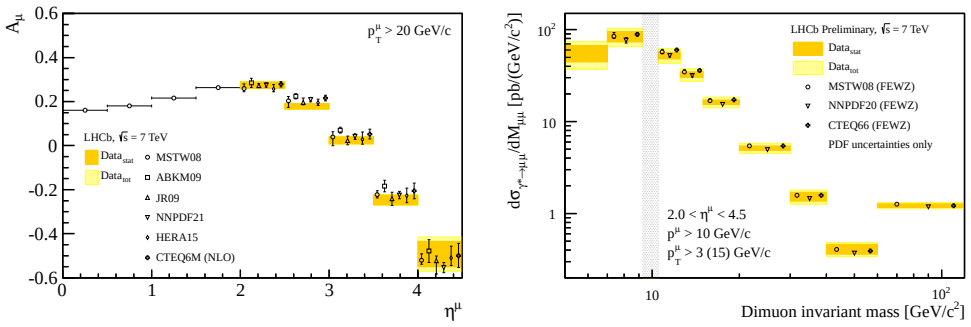

Figure 7: Left: Lepton charge asymmetry A_μ in bins of muon pseudorapidity where dark shaded bands correspond to the statistical (dark shaded/orange) and systematic (light hatched/yellow) experimental uncertainties. These are compared to NNLO and NLO predictions with different PDF sets shown by symbols with error bars where the PDF and the theoretical uncertainties are added in quadrature Right: Differential DY cross section as a function of the dimuon invariant mass. Measurements are compared to theoretical predictions calculated with FEWZ using different PDF sets.

requires a careful account of corrections which are sometimes suppressed by kinematic cuts in other analyses, e.g. higher-twist terms, target mass corrections, nuclear corrections, etc. The current focus is on different nuclear corrections in NLO predictions for parton distributions and structure functions.

A very careful re-analysis of non-singlet world data on unpolarized structure functions in the valence region was presented in ref. [24]. NLO, NNLO and even approximate N^{3}LO expressions are used in the valence region to precisely extract the value of the strong coupling constant $\alpha_s(M_Z^2)$ and the higher twist contributions. The contributions of twist $\tau = 3$ and higher to the polarized structure functions $g_1(x, Q^2)$ and $g_2(x, Q^2)$ are also investigated. At NNLO the value $\alpha_s(M_Z^2) = 0.1132 \pm 0.0022$ is obtained in good agreement with other determinations [19, 20].

An alternative approach to PDFs is based on the statistical model in which the nucleon is regarded as a gas of massless partons in equilibrium at a given temperature in a volume of finite size. Only 9 free parameters are adjusted in order to completely determine the unpolarized and polarized (helicity) distributions. This model produces a reasonable qualitative description, even for some data which were not included in the fits. Updates to include more recent data in the framework are under consideration.

Before the year 2000 prompt photon data had been used as a means of contraining the gluon distribution. However, it was dropped due to discrepancies between some of the fixed target data sets and theoretical predictions. There has recently been a suggestion to re-instate prompt photon data [18] using only high hadron collider data, which agree well with predictions made using JETPHOX. The impact of these data on the NNPDF2.1 fit has been evalaued by PDF reweighting and the data have some impact on the gluon distribution at $x \sim 0.01$, as illustrated in Fig. 8

The nCTEQ group reported [26] difficulties in describing simultaneously the commonly used charged-lepton DIS and Drell–Yan dilepton production off nuclear targets, and data on neutrino-nuclei scattering. The source of the problem involves the data/error estimates of the

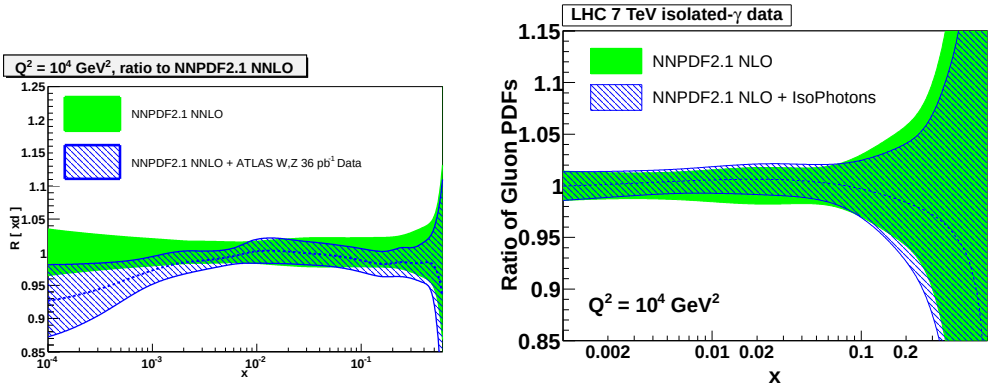

Figure 8: Left: The ratio of the NNPDF2.1 down quark PDF before and after reweighting to include the ATLAS W, Z data, including uncertainties. Right: The ratio of the NNPDF2.1 gluon PDFs before and after reweighting to include prompt photon data, including uncertainties

NuTeV neutrino data for which the correlations of systematic errors need to be taken into account. This is in contrast to the results presented in [27], where an consistent picture of universal nuclear modification factors was reported. They find it possible to describe the main features of all nuclear data, including neutrino DIS as well as inclusive pion production, without finding any significant tension among the different data sets.

An analysis of HERA data on the proton structure function F_2 in the low–x regime using BFKL evolution was presented in ref. [28]. A NLL framework which includes running coupling effects and makes use of collinear improved resummation is used to achieve a good description of the data and to study theoretical uncertainties.

The process $W/Z/DY$ + jet, where the boson is produced in the forward direction of one of the colliding protons and the jet is produced in the forward direction of the second proton, has been proposed for searches of evidence for BFKL evolution [29]. First numerical results for a number of observables which allow the isolation of BFKL effects were presented.

Another contribution within the BFKL framework was the calculation of the next-to-leading order photon impact factor for small–x DIS [30]. An analytic expression in momentum space is derived using the operator product expansion in Wilson lines.

The CCFM unintegrated PDF for the gluon has been determined [31] using the combined HERA data. For a good description of HERA data a calculation of the gluon splitting function including non-singular terms, imposition of kinematic constraints and an NLO treatment of α_s are all necessary. The analysis has been supplemented with an error estimation which allows the study of the uPDF uncertainty for processes at HERA and LHC.

Extensions of the CCFM evolution equations have been studied [32] with the aim of addressing effects like parton saturation in final states at the LHC. The question of how to combine the physics of the BK and CCFM evolution equations has been investigated and a possible non-linear extension of the CCFM equation has been obtained, as suggested by an exclusive form of the BK equation.

General bounds on the ratio of structure functions F_L/F_2 have been derived within the dipole picture [33], which are valid for any dipole cross-section and sharpened by including information on the charm structure function F_2^c. The bounds are respected by the data within

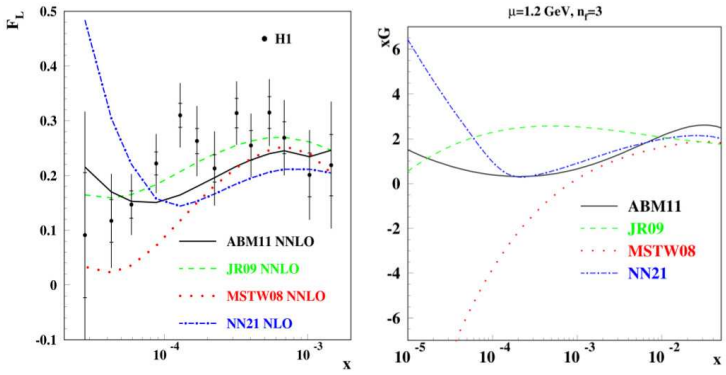

Figure 9: Discriminating power of current F_L data between different gluons at small x [19].

the experimental errors, although for $3.5\,\mathrm{GeV}^2 \leq Q^2 \leq 20\,\mathrm{GeV}^2$ the central values of the data are close to (and in some cases even above) the bounds, and thus put some strain on the validity of the dipole model.

An effort to understand the small-x behavior of the structure function F_2 on general grounds was presented [34]. It is shown that studies in field theory indicate that this behavior may be described as a *critical* phenomenon. Under the assumption of a simple power law behavior of the matrix elements in the scattering region one can derive an expression for F_2 which depends on some critical indices which should be calculable using lattice methods. A phenomenological extraction of these coefficients lead to values similar to those obtained with a two pomeron fit.

3 Conclusion

The Structure Functions session at DIS2012 was very lively with many new experimental results, especially from the LHC on Drell-Yan production, including W and Z, and on jet production, including jets with heavy flavours. There has been substantial progress in the development of tools for parton fitting. The determinations of parton distribution functions from different groups still give rise to some controversy but there is progress in understanding the differences and progress in refining the calculations which go into these analyses. All groups now present PDFs up to NNLO in the DGLAP formalism. The analysis of nuclear PDFs is coming of age. There has also been progress in calculations which extend this formalism into the BFKL regime and the high-density regime.

Acknowledgements

We thank the organisers for the invitation to convene this session and we thank all the speakers in our session for their contributions and the lively discussions. This research is supported in part by the Swiss National Science Foundation (SNF) under contract 200020-138206. Authored by Jefferson Science Associates, LLC under U.S. DOE Contract No.

DE-AC05-06OR23177. The U.S. Government retains a non-exclusive, paid-up, irrevocable, world-wide license to publish or reproduce this manuscript for U.S. Government purposes.

4 Bibliography

References

[1] **H1** Collaboration, F.D. Aaron et al, hep-ex/1205.2448, 2012.

[2] F. Januschek, these proceedings;
https://indico.cern.ch/contributionDisplay.py?sessionId=8&contribId=34&confId=153252

[3] **H1 and ZEUS** Collaborations, V. Radescu, Pos ICHEP2010(2010)168

[4] **ZEUS** Collaboration, S. Chekanov et al, EPJC62(2009)625

[5] F.D. Aaron et al, JHEP1001(2010)109.

[6] K. Nowak, these proceedings;
https://indico.cern.ch/contributionDisplay.py?sessionId=8&contribId=35&confId=153252

[7] T. Kluge, K. Rabbertz, M. Wobisch, "FastNLO: Fast pQCD Calculations for PDF Fits". hep-ph/0609285v2.

[8] D. Britzger, these proceedings;
https://indico.cern.ch/contributionDisplay.py?sessionId=25&contribId=165&confId=153252

[9] V. Radescu, these proceedings;
https://indico.cern.ch/contributionDisplay.py?sessionId=8&contribId=344&confId=153252

[10] O. Kaya, these proceedings;
https://indico.cern.ch/contributionDisplay.py?sessionId=25&contribId=312&confId=153252

[11] B. Malaescu, these proceedings;
https://indico.cern.ch/contributionDisplay.py?sessionId=25&contribId=71&confId=153252

[12] J.P. Sauvan, these proceedings;
https://indico.cern.ch/contributionDisplay.py?sessionId=23&contribId=76&confId=153252

[13] U. Klein, these proceedings;
https://indico.cern.ch/contributionDisplay.py?sessionId=8&contribId=297&confId=153252

[14] M. Musich, these proceedings;
https://indico.cern.ch/contributionDisplay.py?sessionId=23&contribId=229&confId=153252

[15] S. Farry, these proceedings;
https://indico.cern.ch/contributionDisplay.py?sessionId=23&contribId=147&confId=153252

[16] J. Anderson, these proceedings;
https://indico.cern.ch/contributionDisplay.py?sessionId=23&contribId=145&confId=153252

[17] M. Ubiali, these proceedings;
https://indico.cern.ch/contributionDisplay.py?sessionId=8&contribId=300&confId=153252

[18] D. d'Enterria nd J. Rojo, Nulc.Phys.B860(2012)311.

[19] S. Alekhin, these proceedings;
https://indico.cern.ch/contributionDisplay.py?sessionId=8&contribId=302&confId=153252

[20] P. Jimenez-Delgado, these proceedings;
https://indico.cern.ch/contributionDisplay.py?sessionId=8&contribId=299&confId=153252

[21] Pedro Jimenez-Delgado, arXiv:1206.4262 [hep-ph].

[22] P. Nadolsky, these proceedings;
https://indico.cern.ch/contributionDisplay.py?sessionId=8&contribId=301&confId=153252

[23] C. Keppel, these proceedings;
https://indico.cern.ch/contributionDisplay.py?sessionId=8&contribId=290&confId=153252

[24] J. Blümlein, these proceedings;
https://indico.cern.ch/contributionDisplay.py?sessionId=8&contribId=303&confId=153252

[25] F. Buccella, these proceedings;
https://indico.cern.ch/contributionDisplay.py?sessionId=8&contribId=95&confId=153252

[26] K. Kovarik, these proceedings;
https://indico.cern.ch/contributionDisplay.py?sessionId=8&contribId=155&confId=153252

[27] R. Sassot, these proceedings;
https://indico.cern.ch/contributionDisplay.py?sessionId=8&contribId=33&confId=153252

[28] C. Salas, these proceedings;
https://indico.cern.ch/contributionDisplay.py?sessionId=8&contribId=97&confId=153252

[29] M. Hentschinski, these proceedings;
https://indico.cern.ch/contributionDisplay.py?sessionId=23&contribId=115&confId=153252

[30] G. A. Chirilli, these proceedings;
https://indico.cern.ch/contributionDisplay.py?sessionId=8&contribId=128&confId=153252

[31] H. Jung, these proceedings;
https://indico.cern.ch/contributionDisplay.py?sessionId=8&contribId=29&confId=153252

[32] K. Kutak, these proceedings;
https://indico.cern.ch/contributionDisplay.py?sessionId=8&contribId=31&confId=153252

[33] C. Ewerz, these proceedings;
https://indico.cern.ch/contributionDisplay.py?sessionId=8&contribId=159&confId=153252

[34] O. Nachtmann, these proceedings;
https://indico.cern.ch/contributionDisplay.py?sessionId=8&contribId=118&confId=153252

Summary of the Diffraction and Vector Mesons Working Group

Dimitri Colferai[1], *Richard Polifka*[2], *Marta Ruspa*[3]

[1]University of Florence, Italy
[2]Charles University in Prague, Cezch Republic and University of Toronto, Canada
[3]University of Eastern Piedmont, Italy

DOI: http://dx.doi.org/10.3204/DESY-PROC-2012-02/360

We summarise the contributions presented in the working group "Diffraction & Vector Mesons" at the XX International Workshop on Deep Inelastic Scattering (http://www.dis2012.uni-bonn.de/).

1 Introduction

In diffractive interactions in hadron-hadron or photon-hadron collisions at least one of the beam particles emerges intact from the collision, having lost only a small fraction of its initial energy, and carrying a small transverse momentum. Therefore no color is exchanged. The signature for such processes is the presence of a large gap in rapidity (large rapidity gap, LRG) between the two hadronic final states due to the absence of color flow. At high energy this is described by the exchange of an object with the quantum numbers of the vacuum, referred to as the pomeron in the framework of Regge phenomenology [1]. Many aspects of diffraction are well understood in QCD when a hard scale is present, which allows one to use perturbative techniques and thus to formulate the dynamics in terms of quarks and gluons.

Diffractive reactions have been extensively studied at HERA and at the Tevatron and are being studied at RHIC, JLAB and LHC. Updates on the available experimental data and on their theoretical interpretation were given at this workshop. In the present summary we focus on the path from HERA to the LHC through the Tevatron and RHIC.

At HERA events of the type $ep \to eXp$, in which the virtual photon dissociates and the proton remains intact, are termed single diffractive. The final state X can be studied inclusively or requirements can be applied to it (for instance it can be asked to contain at least a dijet system). Whereas vector meson photo (elettro)-production, $ep \to eVp$, occurs when the (virtual) photon produces a vector meson. Similarly, proton (antiproton)-proton single diffractive collisions, $pp \to Xp$ ($p\bar{p} \to X\bar{p}$), can be studied inclusively or semi-inclusively. A further type of events, $pp \to pXp$, termed central exclusive, occurs when the system X is centrally produced with both hadrons intact outgoing. Though central exclusive production (CEP) is not always associated to pomeron exchange, it was discussed in our working group.

Diffractive reactions have become a valuable tool for investigating the low-x structure of the proton and the behaviour of QCD in the high density regime. Many efforts in this direction, both experimental and theoretical, were presented in our working group. Standard (fixed order

or DGLAP) approaches, which work very well in most of the perturbative regime so far explored, are expected to fail in the high-energy regime of QCD ($s \gg E_J^2, Q^2$, corresponding to large jet rapidities and small-x) due to large $\log(s/E_J^2)$ to all perturbative orders, which most probably need to be resummed. Up to now, no clear evidence of high-energy QCD dynamics has been found.

2 From HERA to hadron colliders

2.1 HERA diffractive structure function and PDFs

In the diffractive reaction $ep \to eXp$ at HERA, a photon of virtuality Q^2 dissociates interacting with the proton and produces the hadronic system X. The fraction of the proton momentum carried by the exchanged object is denoted by $x_{I\!P}$, while the fraction of the momentum of the exchanged object carried by the struck quark is denoted by β. As in the inclusive deep inelastic scattering (DIS) case, the cross section for diffractive DIS can be expressed in terms of a linear combination of structure functions, F_2^D and F_L^D. While F_2^D describes the total photon-proton process, F_L^D is only sensitive to the longitudinally polarised photon contribution. As for its inclusive counterpart, F_L^D is thus zero in the quark-parton model, but may acquire a non-zero value in QCD.

At this workshop a key step towards the completion of the measurements of the diffractive structure function F_2^D by the HERA experiments was achieved: H1 presented their final analysis with the LRG tecnique [2]. New measurements covering data taking periods 1999-2000 and 2004-2007 were combined with previously published results in order to provide a single set of diffractive cross sections. The latter are shown in Fig. 1 as a function of Q^2 for fixed values of $x_{I\!P}$ and β and compared to the ZEUS measurements and to theoretical predictions. H1 also presented the first direct measurement of F_L^D [3], shown in Fig. 1 where data points from different Q^2 and $x_{I\!P}$ values are plotted as a function of β and compared with the H1 2006 Fit B prediction (in order to remove the significant dependence on $x_{I\!P}$, the F_L^D points have been divided by the flux factor $f_{I\!P/p}$ taken from [4]). The final structure function measurements based on the proton tagged data were already published by H1 last year [5]. ZEUS published their final measurements, based on the data until the year 2000 [6].[1] With the exception of the H1 data taken with the Very Forward Proton Spectrometer (VFPS) [7], which are still under analysis, the H1 and ZEUS heritage on inclusive diffraction is settled. The next step is to combine the data and to come up with a HERA diffractive structure function. A first attempt has been taken by combining the H1 and ZEUS measurements based on the proton tagged samples [8]. Correlations of systematic uncertainties are taken into account by the combination method, leading to significantly improved precision. Figure 2 shows the combined cross section as a function of Q^2 at $x_{I\!P} = 0.05$, for different values of β in comparison with the individual measurements used for the combination. The reduction of the total uncertainty of the HERA measurement compared to the input cross sections is visible.

Measurements of particles produced at small angles to the proton beam at HERA are important for understanding the proton fragmentation and for model tuning, not only deep-inelastic scattering models but also those on the hadronic interactions of cosmic rays. H1 presented the first measurement of forward photon production in DIS [9]. All models used

[1] The forward instrumentation of the ZEUS detector was dismantled in the year 2000 before the luminosity upgrade of the HERA machine.

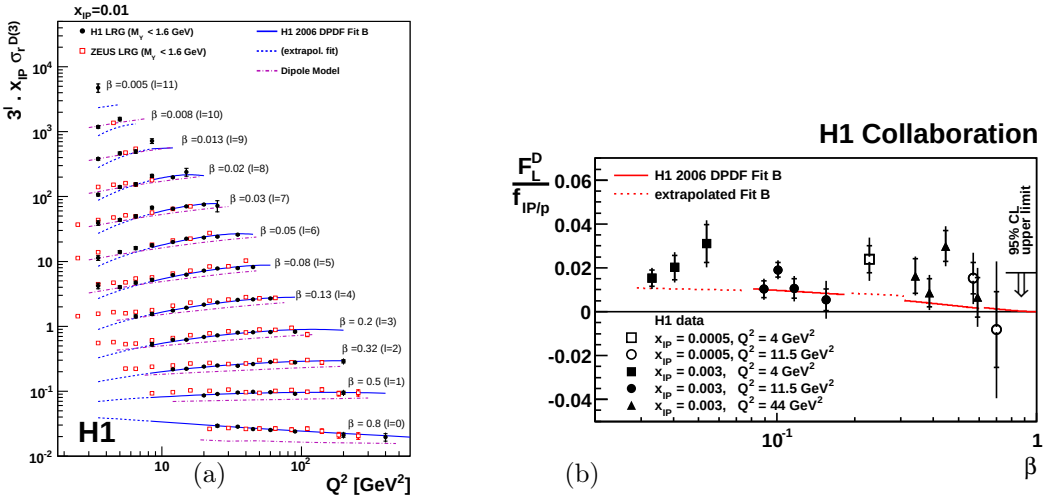

Figure 1: (a) H1 final results on the diffractive cross section measured with the LRG method (dots) compared to the ZEUS measurements (squares) and to theoretical models; (b) H1 results on the diffractive structure function F_L^D compared to the H1 2006 Fit B prediction.

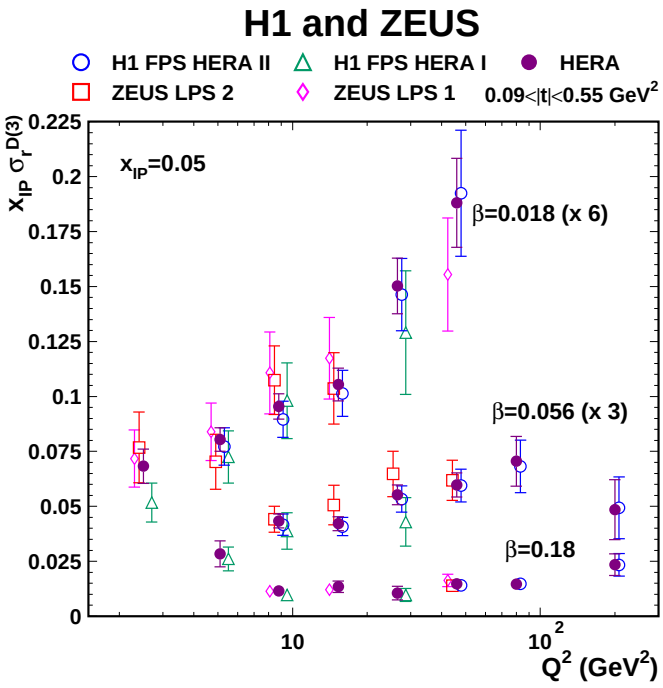

Figure 2: The diffractive cross section resulting from the combination of the H1 and ZEUS measurements as a function of Q^2 at $x_{\mathbb{P}} = 0.05$, for different values of β in comparison with the individual measurements used for the combination.

predict higher yield of photons than the data.

The HERA inclusive diffractive data were fitted repeatedly within the HERA experiments and by outside communities [10]. The new fit by S. Taheri et al. [11] is based on all the available HERA data (excluding the newest H1 results) and compared to all available HERA data, including those on F_L^D. As most of the fits on the market, it is based on the validity of a collinear factorization theorem in diffractive processes [12], which allows F_2^D to be written as a convolution of the usual partonic cross sections with diffractive parton distribution functions (DPDFs). The DPDFs, parametrised at a starting scale, are evolved according to the DGLAP equations [13] and fitted to the data. Ideally one would evolve in Q^2 for fixed values of $x_{\mathbb{P}}$ and of the four-momentum transfer t, or at least for fixed $x_{\mathbb{P}}$ if t is integrated over, but the rather limited statistics of the data makes this not trivial in most cases. Therefore an alternative approach often used is the assumption, known as "Regge factorization" hypothesis, that F_2^D can be expressed as the product of a flux, depending only on $x_{\mathbb{P}}$ and t, and the structure function of a particle-like object. Whether the data support this assumption or not is a controversial problem. In the new analysis by F. Ceccopieri [14] fit results are obtained either at fixed $x_{\mathbb{P}}$ or parameterizing the parton densities at the intial scale as a function of $x_{\mathbb{P}}$. Such approach can be extended to treat the t dependence of the cross section and will soon be tested on the final H1 data. DGLAP fits to the diffractive data deviate from the data with decreasing Q^2 below Q^2 of 5 GeV^2. These deviations have been shown by M. Sadzikowski [15] and L. Motyka [16] to be consistent with higher twist terms extracted from the saturation model (see Fig. 3). This is a first direct evidence of higher twist effects in DIS.

2.2 Factorisation tests

According to the factorization theorem, calculations based on DPDFs extracted from inclusive measurements should allow to predict cross sections for other diffractive processes. This was repeatedly proven with the HERA data on semi-inclusive final states [17]. In a recent H1 analysis [18], diffractive dijet data selected tagging the scattered proton are well described by the DPDF fits 'H1 Fit B 2006' and 'H1 Fit Jets 2007'. The factorization theorem does not hold in the case of diffractive hadron-hadron scattering [12]: indeed it has been known for years that the DPDFs extracted from the HERA data overestimate the rate of diffractive dijets at the Tevatron by one order of magnitude [19]. It was shown in [20] that this breakdown of factorization can be explained by screening effects. Because of the screening, the probability of rapidity gaps in high energy interactions to survive decreases since they may be populated by rescattering processes. The screening corrections are accounted for by the introduction of a suppression factor, which is often called the *survival probability of rapidity gaps.*

The question arises whether the breakdown of factorisation affects the distribution of the four-momentum transfer t at the proton vertex. Recent CDF data [21] show no Q^2 dependence of the exponential slope of the t-distribution from inclusive to dijet events with Q^2 up to 10000 GeV^2.

The HERA/Tevatron results are being extended by CMS [22] by studying diffractive events associated with high-p_T jets or W/Z bosons, which set the hard scale. Comparing the measured cross sections to Monte Carlo (MC) predictions based on the HERA DPDFs provides an estimate of the survival probability. The theoretical description of vector boson hadroproduction ($H_A + H_B \to B + X$, with X = W, Z, γ,...) can be improved by resumming the soft gluon emission terms into an additional factor $S(b, Q^2)$ which is universal. Such non-perturbative form factor is modified by corrections due to the intrinsic transverse momenta of partons. This is usually

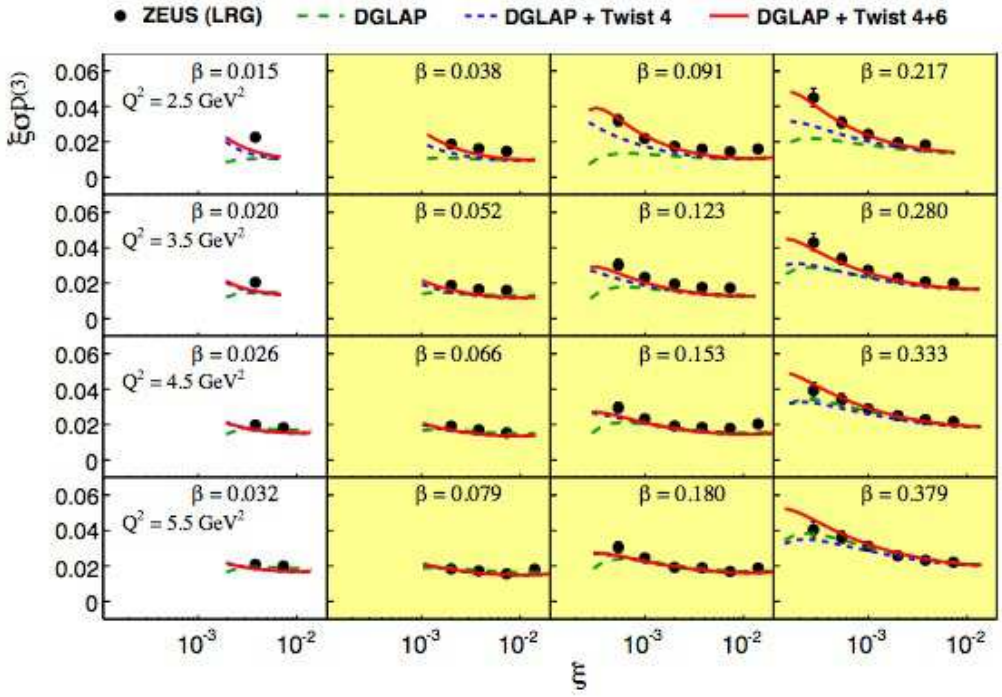

Figure 3: ZEUS diffractive cross section data compared to DGLAP predictions without and with twist 4 and 6 effects from ths saturation model.

taken into account by supplying S with yet another factor parameterised as $\exp(-gb^2)$ where $g = g_1 + g_2 \log(Q/2Q_0)$. K. Tanaka presented a first systematic determination of g_1 and g_2 by a global fit to experimental data [23].

2.3 Exclusive production

2.3.1 Vector meson production in DIS

The cross section for Υ photo-production at HERA, $\gamma p \to \Upsilon(1S)p$, was measured by ZEUS by collecting all data from 1996 to 2007 [24]. The exponential slope b ($\mathrm{d}\sigma/\mathrm{d}t \sim \exp(-b|t|)$) was measured for the first time in Υ production. For large values of the scale $Q^2 + M_{\mathrm{VM}}^2$ (around 90 GeV^2 in this case) b is related to the transverse size R_{T} of the interaction region, or, in other words, to the radius of gluons in the proton: $b \simeq R_{\mathrm{T}}^2/2$. The value $b = 4.3^{+2.0+0.5}_{-1.3-0.6}$ GeV^{-2} was found, in good agreement with the extrapolation of existing data at lower values of $Q^2 + M_{\mathrm{VM}}^2 \lesssim 40$ GeV^2.

ZEUS also reported results on the exclusive production of di-pions [25]. This measurement allows the study of radially excited 2S states and orbitally excited 2D states of the ρ meson, through the reactions $\rho'(1450) \to \pi\pi$ and $\rho''(1700) \to \pi\pi$ respectively. The large statistics makes it possible to discriminate the small peaks of the ρ' and ρ''. Apart from the mass of the

ρ', the ensuing values of masses and widths of the excited states agree well with the Particle Data Group values, and in some cases are even more precise.

The theoretical description of vector meson production is often made in the framework of the colour dipole model, where the differential cross section is given by the convolution of 3 factors: the virtual photon $\psi^{(\gamma^*)}(z, r; Q^2)$ and vector meson $\psi^{(V)}(z, r)$ wave functions, and the colour dipole cross section $N(x, r)$. The last is a non-perturbative, universal object well constrained by F_2 HERA data, and its particular functional form/parameterisation correspond to different models. The photon wave function $\psi^{(\gamma^*)}$ can be computed in QED, including QCD corrections. On the contrary, the vector meson wave function can be only parameterised in terms of a form factor, whose computation is beyond the domain of perturbative QCD.

The key observation is that such form factor formally satisfies the equation of a string living in a 5-dimensional Anti-de-Sitter space, where the would-be fifth dimensional coordinate ζ is given by a particular combination of kinematic variables: $\zeta = \sqrt{z(1-z)}r$. By solving the string equation, R. Sandapen [26] showed that the Regge-like mass spectrum of the ρ-meson, $M^2 = 4\kappa^2(n + L + S/2)$, is correctly reproduced for $\kappa = 0.55$ GeV. He found the analytic expression of the meson wave function which has no free parameters to be adjusted, and used it to describe the HERA data, by adopting the Colour-Glass-Condensate model for the dipole cross section. At low Q^2, where this approach is expected to be valid, the description is quite good, whereas at large Q^2 the cross section is underestimated.

Another method for deriving the dipole cross sections from first principles and taking into account the dependence on the impact parameter b was presented by J. Berger [27]. It is based on the evolution of the the Balitski-Kovchegov equation from a b dependent initial condition of Glauber-Mueller type. In this initial condition the skewed gluon density is used. In order to reproduce the HERA data, an additional correction to the photon wave function at low Q^2 is required, which is however universal for all mesons and processes. The data description is good for J/ψ and ϕ production, less good for ρ cross section. Quite remarkably, the main features of the inclusive F_2 measurements are also reproduced.

Diffractive neutrino-production of pions from the Minerva facility at Fermilab were presented by M. Siddikov [28]. The scattering $\nu\ T \to \mu\ \pi^+\ T$ is observed on both protonic and nuclear (C, Fe, Pb) targets T. A description of the data is then attempted by exploiting the colour dipole model, with the PCAC property to constrain the diffraction amplitude of chiral mesons. A fair description of the total cross section on protons is found for neutrino energies larger than 20 GeV, while below such values the colour dipole model fails since it does not take into account the contribution of resonances. The description on nuclear targets is made by means of a toy model based on the Gribov-Glauber approach for nuclei where only π and a_1 are present and where the Adler relation is assumed to be valid for nucleons at $Q^2 = 0$. The main result is that the Adler relation is broken on nuclei for neutrino energies larger than 10 GeV due to absorptive (shadowing) corrections.

2.3.2 Tevatron and LHC

One of the major challenges of CDF run II has been the measurement of exclusive production processes. After the study of the exclusive production of dijets, dileptons, Z, J/ψ and χ_c [29], recently CDF observed the exclusive production of two photons [30]. Whereas the lepton pairs and Z are purely QED processes, the J/ψ is produced by photo-production, mediated by photon-pomeron exchange. The exclusive dijet system, the charmonium and the diphotons are produced by double pomeron exchange via quark-loop.

Similar to the latter production mechanism, with a heavy quark loop and no other particles produced, the process termed central exclusive production (CEP) has become very attractive in the latest years looking towards the possibility of measuring an exclusive Higgs at the LHC; beyond the Higgs, the main advantage comes from the fact that any observed resonance exclusively produced in such a way must be dominantly in a spin 0, CP even state, therefore allowing a clean determination of its quantum numbers. Previous analysis are being updated taking into account the recent exclusion bounds from the LHC. Notably, M. Tasevsky [31] showed the latest updates of a study of the MSSM Higgs. At high luminosity, when the pileup events will fill the rapidity gap and make the rapidity gap requirement fail, to tag the CEP Higgs or any other central system exclusively produced forward proton detectors will be needed, the proposed installation of which at ATLAS is at the stage of LOI. CMS has a similar project at the stage of a proposal for the upcoming upgrades of the LHC. Forward proton detectors would open possibilities of searches beyond the Higgs. Studies of two photon exclusive production of Z (E. Chapon [32]) and W (E. Chapon, A. Szczurek [33]) pairs give the sensitivity to trilinear and quartic anomalous coupling between the photon and the W/Z bosons. Tagging the protons in the final state will allow to improve the reach on anomalous couplings by four orders of magnitude.

Exclusive production is already being investigated at the LHC at $\sqrt(s) = 7$ TeV. The LHCb experiment reported studies of exclusive dimuon production [34]. The production mechanism is either two photon fusion or resonance decay. Exclusive J/ψ, ψ‘ and χ_c states were observed. Two photon exclusive production of muon pairs provides an excellent tool for luminosity calibration. A similar analysis on exclusive dilepton production was presented by the CMS experiment [35]: in both the electron and muon channels the cross section was measured and compared to QED predictions. CMS is also searching for exclusive diphoton production, for which an upper limit on the cross section was set.

2.3.3 Nucleon-nucleon reactions

V. Lyuboshitz [36] showed how to parameterise the rate of the reaction $n + p \to p + n$ in terms of isospin operators and unknown scalar coefficients $c_i : i = 1, 2, 3$. By means of a series of steps involving crossing invariance, isospin covariance and the optical theorem, he found a relation for the phase of the coefficient c_1 (in front of the identity operator) in terms of the measurable cross sections $\mathrm{d}\sigma_{dp\to(pp)n}/\mathrm{d}t$, $\mathrm{d}\sigma_{np\to pn}/\mathrm{d}t$, σ_{pp} and σ_{np}. Unfortunately, at present there are no reliable experimental data for the first (deuteron dissociation) cross section, and a quantitative estimate of c_1 is not possible yet.

3 High-energy/small-x QCD

3.1 Theory

We know that the growth of the gluon density predicted by the linear DGLAP and BFKL evolution cannot go on without bounds, because saturation effects set in at high parton densities as required by unitarity. However, the kinematical region where such effects become important depends on the details of the models adopted to describe the parton evolution. D. Zaslavski presented a study of saturation where the BFKL evolution at next-to-leading logarithmic (NLL) accuracy is improved by the DGLAP resummation [37]. The regularization of the infrared has been implemented by an absorptive boundary, which means that if the gluon density reaches a

given threshold at some scale of momenta, it is set to zero for momenta lower than that scale. The outcome of the numerical evolution is that the resummation of collinear contributions and also the NLL BFKL corrections are necessary to avoid unstable behaviours (oscillations, negativity) of the gluon density. Furthermore, one observes a sizeable delay of the saturation scale $Q_s(Y)$, in the sense that it starts growing for rather large values of rapidity $Y \simeq 5$. This may have an important phenomenological impact for the onset of saturation effects.

Small-x physics can be studied also with MC techniques. Usually, the small-x information is included as a correction to standard collinear fragmentation, but it is possible to set up event generators based on the BFKL framework which directly adresses small-x processes. This is the case for the Monte Carlo proposed by C. Salas [38]. It is based on the non-forward BFKL kernel which is expected to govern the small-x evolution of diffractive events. Her implementation is very interesting, in fact it takes into account some new features like the bootstrap condition on the gluon trajectory and an analytic model for the running coupling devised by Webber, which is compatible with power-corrections. The code at leading logarithmic (LL) level is ready and shows good convergence and stability. A first study on the average number of gluons emitted versus rapidity has been done. Compared with the forward LL BFKL case, she observes less gluon emissions.

Another physical ingredient that can be included in MCs is QCD color coherence, namely the angular dependence of parton emissions on the colour charge of the emitter. In order to assess the importance of coherence effects in small-x physics, M. Deak [39] has compared two MCs: the first, devised by Webber, is based on the CCFM equation and includes coherence effects; the second, written by Sabio-Vera and Stephens, does not. The comparison has been done at fixed coupling α_s and in the LL approximation. The speaker studied the tendency of the intermediate partons to diffuse in the IR region when the rapidity distance Y of the two jets is increased at fixed p_{T}, and he found that the CCFM MC diffuses in the IR earlier (at smaller Y) than BFKL. He then showed the Y dependence of the azimuthal angular moments predicted by the two MCs, concluding that BFKL shows more azimuthal decorrelation (less angular dependence) than CCFM.

3.1.1 High-energy factorization in Mueller-Navelet jets

A process which is expected to be a gold-plated observable in revealing high-energy QCD dynamics is the production of Mueller-Navelet (MN) jets, i.e., two hard jets, one very forward and the other very backward, with any kind of radiation outside the jets. This configuration is expected to minimize the collinear partonic evolution of QCD which occurs in emissions of partons with strongly ordered transverse momenta, and to enhance the high-energy dynamics which should happen in the emission of partons with strongly ordered rapidities.

The cross section for Mueller-Navelet jets in the high-energy limit is given by the convolution of partonic PDFs $f(x)$, jet vertices $V(x, \boldsymbol{k})$ and the gluon Green's function (GGF) $G(\hat{s}, \boldsymbol{k}_1, \boldsymbol{k}_2)$. All these factors are known at next-to-leading order (NLO) and next-to-leading logarithmic (NLL) accuracy, but the actual calculation is not straightforward due to the large number of (numerical) integrations that have to be performed in the convolution and also within the jet vertices themselves.

A key observation is that the 4 integrations in $(\boldsymbol{k}_1, \boldsymbol{k}_2)$ can be reduced to one if one projects the GGF and the vertices onto the LL BFKL eigenfunctions, i.e., if one takes Mellin momenta of $|\boldsymbol{k}| \to \nu$ and computes angular Fourier momenta with respect to the relative azimuthal angle of the two jets $\phi_1 - \phi_2 \to n$. In this case we have close analytic expressions for $G_{\nu,n}$.

The computation of the Mellin transform for the vertices $V_{\nu,n}$ was done numerically [40] for the exact NLO jet vertex, however it is very time consuming.

A. Papa [41] showed that it is possible to have a compact analytic expression for the NLO jet vertex in the limit of small jet radius $R \to 0$. He provided explicit and rather compact expressions for both the quark and gluon initiated vertices, by showing that all IR singularities cancel and that the jet radius has a logarithmic dependence on R like $V_{\nu,n} = A_{\nu,n} \ln R + B_{\nu,n} + \mathcal{O}(R^{-2})$. He claims that his results can be used for fast and hopefully reliable phenomenological analysis of MN jets, since the small-cone approximation is very good up to $R \simeq 0.7$ (at least for $s \sim E_J^2$).

A more theoretical analysis has been presented by J.D. Madrigal [42] who computed the MN jet cross-section in the $N = 4$ supersymmetric Yang-Mills theory (SYM). The motivation for such a study relies in the fact that SYM is a supersymmetric version of QCD which is also conformally invariant ($\beta(\alpha) = 0$) and therefore it is expected to be solvable in the planar limit. Furthermore, it provides many informations on the analytic structure of QCD and gauge theories in general, and it coincides with QCD at tree level and in LL approximation. Thus, the hope is that we might learn something about the relations between QCD and SYM also from comparing observable quantities.

The choice of the renormalization scheme and scale is a crucial aspect. By adopting for QCD the MOM scheme and fixing the scale with the BLM procedure which absorbs the β_0 coefficients in the perturbative expansions to all orders, QCD shows a quasi-conformal behaviour. For instance, the hard pomeron exponent turns out to have a very flat dependence on the hard scale provided by the (almost) equal jet energies, but the agreement is only qualitative, the absolute values being quite different: arount 0.18 for QCD and twice as much for SYM. Closer agreement has been found in the ratio of angular moments $C_m/C_n \equiv \langle cos(m\phi)\rangle/\langle cos(n\phi)\rangle$ where ϕ is the azimuthal angle between the two jets. In this case, normalization effects almost cancel and if one restricts $m, n > 0$ then the instabilites of the BFKL series for $n = 0$ are absent, and one finds a rather good agreement between QCD and SYM estimates. The ensuing suggestion of the speaker is that such ratios should be good observables for detecting high-energy dynamics in QCD.

In the direction of developing analytical techniques for the computation of higher-order corrections to the factors entering high-energy factorization formulas, J. Madrigal [42] and M. Hentschinski [43] have computed the two-loop correction to the gluon trajectory and the one-loop corrections to the partonic impact factors, respectively, by using the Lipatov's effective action for high-energy QCD. This effective action possesses an unconventional feature, because it has additional degrees of freedom besides the fundamental fields of QCD. This is required for a correct treatment of NLL effects. Furthermore, in order to avoid overcounting of perturbative contributions, one has to perform proper subtractions. Both speakers have shown how to set up the subtraction procedure in the cases under study, reproducing eventually the known results obtained within standard BFKL resummation in perturbation theory. The method of the effective action seems promising for computing higher-order corrections or even new quantities relevant for high-energy QCD.

3.2 Experiments

Measurements of hadronic final states are a rich testing ground for QCD dynamics at small x. Recent results come from HERA, RHIC and LHC.

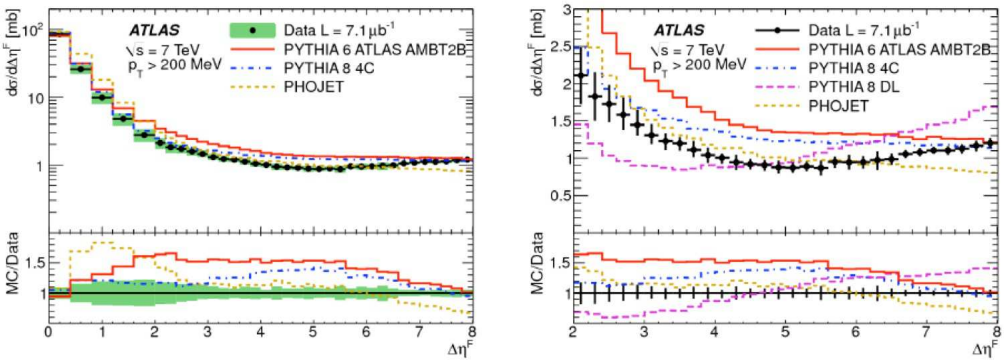

Figure 4: Cross section measured by ATLAS on a sample of inclusive minimum bias data applying the rapidity gap requirement in comparison with MC models.

- H1 data [44] on azimuthal correlations between the forward jet and the scattered positron were compared to predictions of generators based on different evolution approaches as well as to next-to-leading order calculations; cross sections are best described by a BFKL-like model; the DGLAP based RAPGAP model is substantially below the data; the CCFM-based CASCADE provides a reasonable description of the data but shows sizeable sensitivity to the unintegrated gluon density; NLO DGLAP predictions are in general below the data, but still in agreement with the large theoretical uncertainty.

- PHENIX measurements [45] on forward dihadron correlation in d-Au collisions confirm a suppression effect in comparison to the yield in proton-proton collisions depending strongly on the impact parameter (the more central the collision, the more suppressed the yield) and on the rapidity of the two hadrons (the more forward the particles, the stronger the suppression). This is a possible manifestation of saturation-like effects already observed in the BRAHMS data [46].

- ATLAS presented results [47] based on rapidity gap measurements on a sample of inclusive minimun bias data. The cross section is studied as a function of the largest distance from the edge of the detector to the first calorimeter track with p_{T} larger than a given threshold. It turns out that increasing the p_{T} cut produces larger rapidity gaps. Data have been compared to different MC models, none of which adresses all the aspects of the data (see Fig. 4). A further study consisted in fitting large rapidity gap data by using the Donnachie-Landshoff model implementation in PYTHIA 8. The result obtained for the pomeron intercept, $\alpha_P(0) = 1.059 \pm 0.003 \pm 0.035$, is consistent with the DIS value.

References

[1] P.D.B. Collins, *An Introduction to Regge Theory and High Energy Physics,* Cambridge University Press, Cambridge, 1977.

[2] E. Sauvan, these proceedings.

[3] D. Salek, these proceedings.

[4] H1 Coll., A. Aktas *et al.*, Eur. Phys. J. C 48 (2006) 715.
[5] H1 Coll., A. Aktas *et al.*, Eur. Phys. J. C 71 (2011) 1578.
[6] ZEUS Coll., S. Chekanov *et al.*, Nucl. Phys. B 816 (2009) 1.
[7] H1 Coll., F.D. Aaron *et al.*, H1prelim-10-014.
[8] V. Sola, these proceedings.
[9] H. Zohrabyan, these proceedings.
[10] ZEUS Coll., S. Chekanov *et al.*, Nucl. Phys. B 831 (2010) 1; C. Marquet, Phys. Rev. D 76 (2007) 094017; A.D. Martin, M.G. Ryskin, G. Watt, hep-ph/0609273; and references therein.
[11] S. Taheri, these proceedings.
[12] J.C. Collins. Phys. Rev. D 557 (1998) 3051; [erratum-ibid. Phys. Rev. D 61 (2000) 019902].
[13] V.N. Gribov and L.N. Lipatov., Sov. J. Nucl. Phys. 15 (1972) 438; Yu.L. Dokshitzer, Sov. Phys. JETP 46 (1977) 641; G. Altarelli and G. Parisi, Nucl. Phys. B 126 (1977) 298.
[14] F. Ceccopieri, these proceedings.
[15] M. Sadzikowski, these proceedings.
[16] L. Motyka, these proceedings.
[17] H1 Collab., F.D. Aaron et al., Eur. Phys. J. C70 (2010) 15.
[18] R. Polifka, these proceedings.
[19] CDF Coll., T. Affolder *et al.*, Phys. Rev. Lett. 84 (2000) 5043.
[20] A.B. Kaidalov *et al.*, Eur. Phys. J. C 21 (2001) 521.
[21] K. Goulianos, these proceedings.
[22] A. Vilela Pereira, these proceedings.
[23] K. Tanaka, these proceedings.
[24] J. Ciborowski, these proceedings.
[25] J. Tomaszewska, these proceedings.
[26] R. Sandapen, these proceedings.
[27] J. Berger, these proceedings.
[28] M. Siddikov, these proceedings.
[29] CDF Coll., T. Aaltonen *et al.*, Phys. Rev. D 77 (2008) 052004; CDF Coll., T. Abulencia *et al.*, Phys. Rev. Lett. 98 (2007) 112011; CDF Coll., T. Aaltonen *et al.*, Phys. Rev. Lett. 102 (2009) 242001.
[30] E. Brucken, these proceedings.
[31] M. Tasevsky, these proceedings.
[32] E. Chapon, these proceedings.
[33] A. Szczurek, these proceedings.
[34] D. Moran, these proceedings.
[35] W. Li, these proceedings.
[36] V. Lyuboshitz, these proceedings.
[37] D. Zaslavski, these proceedings.
[38] C. Salas, these proceedings.
[39] M. Deak, these proceedings.
[40] D. Colferai, F. Schwennsen, L. Szymanowski and S. Wallon, JHEP 1012 (2010) 026.
[41] A. Papa, these proceedings.
[42] J.D. Madrigal, these proceedings.
[43] M. Hentschinski, these proceedings.
[44] L. Goerlich, these proceedings.
[45] M. Chiu, these proceedings.
[46] BRAHMS Coll., I. Arsene *et al.*, Nucl.Phys. A 757 (2005) 1.
[47] M. Oreglia, these proceedings.

Summary of the Electroweak and Searches Working Group

David M. South[1], *Andreas Weiler*[1], *Hwidong Yoo*[2]

[1]DESY, Notkestraße 85, 22607 Hamburg, Germany
[2]Purdue University, West Lafayette, IN 47907, USA

DOI: http://dx.doi.org/10.3204/DESY-PROC-2012-02/359

The working group on electroweak measurements and searches for new physics at the Deep Inelastic Scattering 2012 workshop covered a wide range of results from the various experiments at the LHC (ATLAS, CMS, LHCb), the Tevatron (CDF, DØ) and HERA (H1, ZEUS), as well as results from the BaBar, NA48/62 and OPERA collaborations. In addition, invited theoretical overviews were presented and discussed in each of the sessions. A summary of a selection of the results shown at the conference is given.

1 Introduction

The electroweak and searches working group at the Deep Inelastic Scattering 2012 conference included some of the most exciting results yet in particle physics. The phenomenal performance of the LHC in 2011 allowed substantial pp data sets to be analysed at a centre-of-mass energy $\sqrt{s}$ beyond what has previously been explored. In addition, many of the results shown at the conference by the ATLAS and CMS collaborations included the full 5 fb^{-1} of 2011 data taken at $\sqrt{s} = 7$ TeV, an impressive effort. Complementing the data from the LHC, are the $p\bar{p}$ collisions at the Tevatron, where results are now emerging using the full 10 fb^{-1} Run-II data sets from the CDF and DØ collaborations. By utilising as much data as possible, the reach of searches has been significantly extended and the precision of Standard Model (SM) electroweak measurements has been greatly enhanced[1]. The final searches in $e^{\pm}p$ data from the HERA collaborations, as well as results from the BaBar, NA48/62 and OPERA collaborations, completed the picture. On the final day of the conference, collisions began again at the LHC, at an increased centre-of-mass energy of 8 TeV. The forthcoming analysis of this data will provide further insight into searches for physics beyond the SM and precision electroweak physics.

2 Standard Model Higgs searches

The search for the SM Higgs boson represents one of the most important endeavours of modern particle physics. The dominant Higgs production mechanism at hadron colliders is via gluon fusion, where other processes - associated vector boson production (VH), vector boson fusion (VBF) and top fusion - are expected to occur at a significantly lower rate. A review of the

[1]Note that these proceedings summarise the results available at the time of the conference and more recent results, in particular in the case of Higgs analyses, may be available.

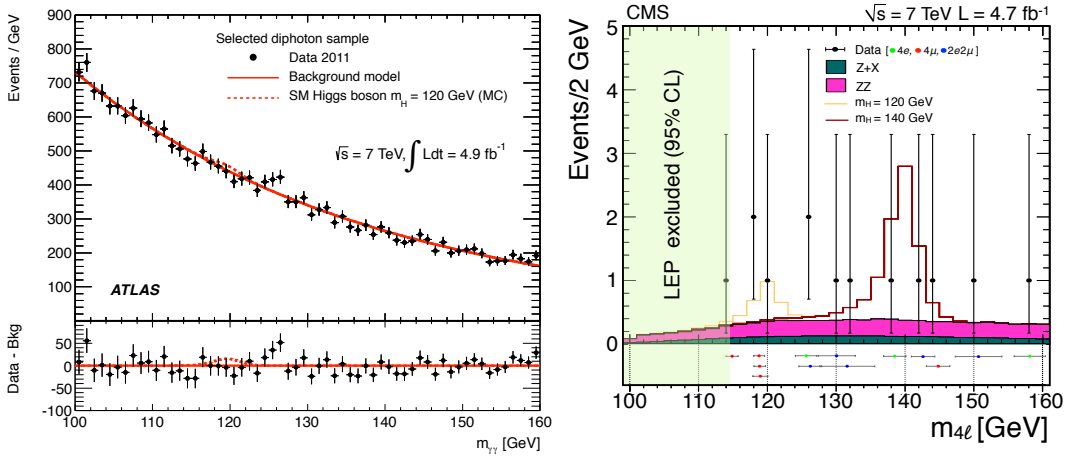

Figure 1: Left: The invariant mass distribution of the diphoton sample in the ATLAS search for $H \to \gamma\gamma$ events, where the Higgs boson expectation for a mass hypothesis of 120 GeV corresponding to the SM cross section is also shown. Right: The 4-lepton invariant mass distribution in the low mass region of the CMS search for $H \to ZZ \to 4\ell$ events. The central values and event-by-event mass measurement uncertainties are indicated, as well as the expected Higgs boson signal for two different mass hypotheses.

current theoretical predictions was presented at the conference [1], where in particular the variation in the latest PDF and scale uncertainties was discussed.

The SM Higgs boson decays via a variety of channels, where at low masses the $H \to b\bar{b}$ and $H \to \tau\tau$ decays are dominant and for Higgs masses $M_H > 135$ GeV the decays to vector boson pairs, $H \to ZZ$ and $H \to WW$ are favoured. The full spectrum of Higgs decays is investigated by dedicated ATLAS [2] and CMS [3] analyses, which often include different sub-channels, for example of the different subsequent decays of the vector bosons produced in the Higgs decay. At the LHC, the two most important channels are $H \to \gamma\gamma$, which has a relatively small branching ratio but a clean final state signature, and $H \to ZZ \to 4\ell$, where the final state contains two high-mass pairs of isolated leptons and has very little SM background. Both of these channels have good mass resolution and the invariant mass distributions in the ATLAS diphoton analysis [4] and the CMS $H \to ZZ \to 4\ell$ analysis [5] are shown in Figure 1, where a small excess of data events can be seen in both channels between 120 GeV and 130 GeV.

Combining all investigated decay channels, and using up to their complete 2011 $\sqrt{s} = 7$ TeV data sets, exclusion limits are derived as a function of the Higgs mass by ATLAS [6] and CMS [7], as shown in Figure 2. Higgs boson mass ranges of 110 GeV to 117.5 GeV, 118.5 GeV to 122.5 GeV and 129 GeV to 539 GeV (127.5 GeV to 600 GeV) are excluded by the ATLAS (CMS) analysis at the 95% confidence level (C.L.), whereas the range 120 GeV to 553 GeV (114.5 GeV to 543 GeV) is expected to be excluded by the ATLAS (CMS) analysis in the absence of a signal. The local significance of the observed excess at 126 GeV in the ATLAS combined analysis is 2.5σ, rising to 3.5σ if only the high mass resolution $H \to \gamma\gamma$ and $H \to ZZ \to 4\ell$ channels are considered. In the CMS combined analysis, an excess is observed at 124 GeV with a local significance of 2.8σ. In both experiments, the significance of the excess is considerably lower when the full mass range is taken into account, the so called "look elsewhere effect".

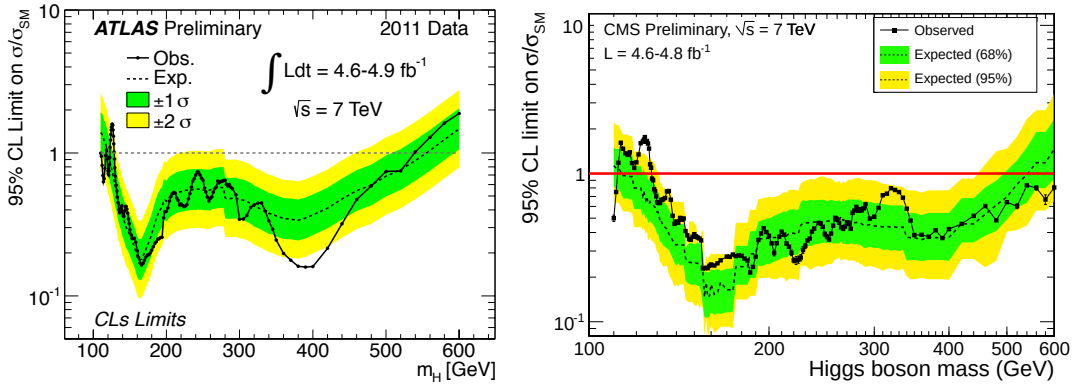

Figure 2: Combined exclusion limits from the ATLAS (left) and CMS (right) searches for the SM Higgs boson. The observed 95% C.L. combined upper limits on the production cross section divided by the SM expectation are shown by the solid line as a function of the Higgs mass. The dashed line shows the median expected limit in the absence of a signal and the green and yellow bands indicate the corresponding 68% and 95% intervals.

The focus of Higgs searches at the Tevatron is on the low mass region, $M_H < 135$ GeV, concentrating on associated vector boson (W,Z) production with subsequent $H \to b\bar{b}$ decays. Final states are categorised according to the number of charged leptons and the presence or absence of missing transverse energy (MET) in the final state, arising from the decay of the vector boson. The amount of luminosity analysed by the CDF and DØ experiments has increased, where up to 10 fb^{-1} from each experiment is now included, and several analysis improvements have been implemented [8]. Limits on Higgs production at the Tevatron are shown as a function of mass in Figure 3, where the regions 100 GeV to 106 GeV and 147 GeV to 179 GeV are excluded at the 95% C.L., compared to the expected exclusion ranges of 100 GeV to 119 GeV and 141 GeV to 184 GeV. In addition, an excess in the data with respect to the background estimation is observed in the Tevatron analysis across a broad region, which is in the same mass range as the excess observed by the LHC experiments described above. The local (global) significance of this excess is 2.7σ (2.2σ). Comparing the observed limits in the presented results from the LHC and the Tevatron, only the mass ranges $117.5 < M_H < 118.5$ GeV and $122.5 < M_H < 127.5$ GeV are currently not excluded at the 95% C.L.

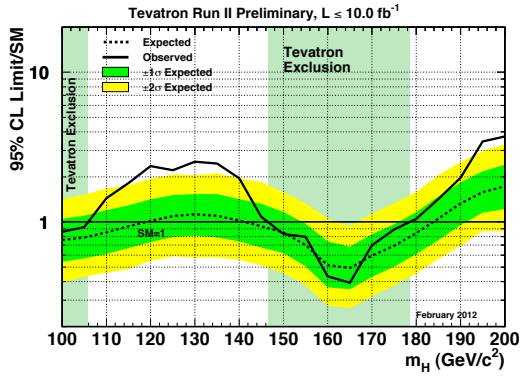

Figure 3: Observed and expected 95% C.L. upper limits on the production cross section divided by the SM expectation as a function of the Higgs mass for the combined CDF and DØ analyses. The dotted curves show the median expected limit in the absence of a signal and the green and yellow bands indicate the corresponding 68% and 95% intervals.

3 Beyond the Standard Model Higgs searches

Many models of beyond the Standard Model (BSM) physics predict Higgs-like bosons, where the coupling may be different to that of the SM Higgs, or there may be additional, neutral or charged scalars. An intriguing possibility are composite Higgs models [10], where the Higgs is a bound state of new strong dynamics close to the weak scale [11]. The Higgs is lighter than the rest of the strong states due to it being a Goldstone boson, as in the AdS/CFT inspired holographic Higgs or in little Higgs models. In such a model, new physics is expected to be be revealed via modifications to the SM Higgs couplings. Many searches for a BSM Higgs are performed at the LHC [12, 13], the Tevatron [14] and BaBar [15], and the results of two such searches are presented in the following.

Charged Higgs bosons $H^{\pm}$ are predicted by Higgs doublet models such as the Minimal Supersymmetric Standard Model (MSSM), as well as Higgs triplet models. For Higgs masses $M_{H^{\pm}} < M_t$ the dominant production mode is via top quark decay $t\bar{t} \to b\bar{b}WH^+$ and for $\tan\beta > 3$ the preferred Higgs decay mode is $H^{\pm} \to \tau^{\pm}\nu$. Searches for charged Higgs bosons are performed by the ATLAS [17] and CMS [18] collaborations, where up to four different final states are analysed according to combinations of the hadronic and leptonic decays of the W and H^+. Good agreement of the data with the SM is observed and in the absence of a signal limits are derived on the branching ratio $t \to H^+b$. Limits in the $M_{H^+} - \tan\beta$ plane from the CMS analysis are shown in Figure 4 for the combination of all examined final states.

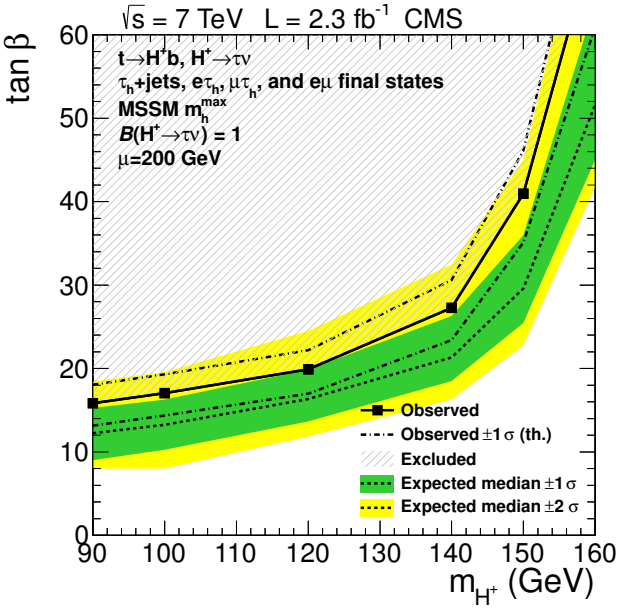

Figure 4: The exclusion region in the $M_{H^+} - \tan\beta$ MSSM parameter space obtained from the combined CMS analysis for the $M_{H^+}^{\max}$ MSSM scenario. The green and yellow bands indicate the corresponding 68% and 95% intervals.

In the case of a fermiophobic Higgs H^*, couplings to fermions are forbidden, so that production proceeds via VH and VBF only and the subsequent decays are also changed with respect to the SM Higgs. As a result, the fermiophobic Higgs decay $H^* \to \gamma\gamma$ branching ratio is considerably enhanced with respect to the SM Higgs, as can be seen in Figure 5 (left). A search by the ATLAS collaboration [16] observes a small excess in the data of order 3.0σ in the same region as the SM Higgs search, as can be seen in Figure 5 (right). With respect to the ATLAS SM Higgs search, the excluded region is extended down to Higgs masses of 110 GeV. In a similar analysis by the CMS collaboration [7] an excess is also observed at 126 GeV, although when the $H^* \to WW$ and $H^* \to ZZ$ channels are also included, this is diluted to 1.0σ with masses $M_{H^*} < 190$ GeV excluded at the 95% C.L.

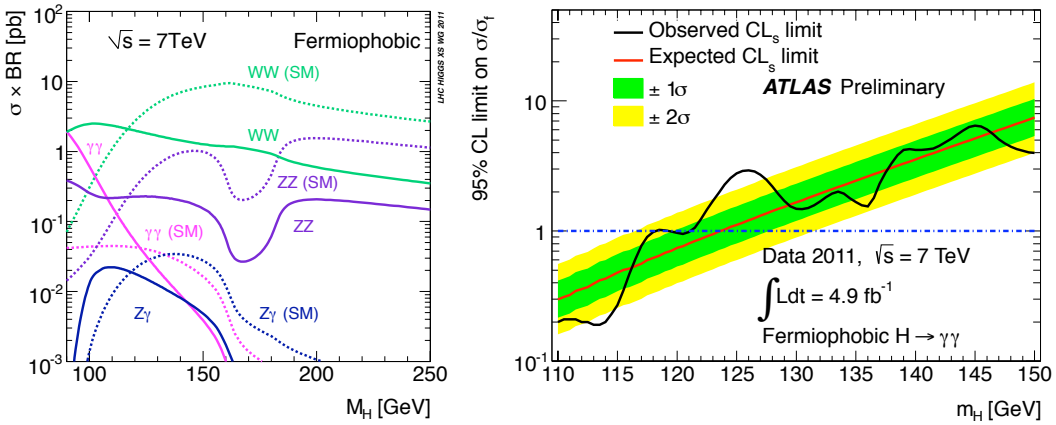

Figure 5: Left: SM (dashed lines) and fermiophobic (solid lines) Higgs production cross section × branching ratios for $\sqrt{s} = 7$ TeV as a function of the Higgs mass. Right: Observed (black line) and expected (red line) 95% C.L. limits from the ATLAS experiment for a fermiophobic Higgs boson normalised to the fermiophobic cross section × branching ratio expectation as a function of M_{H^*}. The green and yellow bands indicate the corresponding 68% and 95% intervals.

4 Searches for physics beyond the Standard Model

A large variety of searches for BSM physics are performed in high energy physics, not just at the LHC or the Tevatron, and not only within the Supersymmetry (SUSY) models described in section 5. This includes searches for signatures such as: new W' and Z' bosons, heavy neutrinos and W_R production, large extra dimensions, narrow resonances in 2 and 4-jet spectra, long lived particles and heavy stable charged particles, same sign leptons and black holes, excited quarks and leptons, leptoquarks and contact interactions, searches for $t\bar{t}$ and diboson resonances, heavy quarks and 4th generation fermions. A selection of these searches are described in the following.

Searches for new physics in events with leptons and/or jets are performed by the ATLAS [19] and CMS [20] experiments. Among many limits, in an ATLAS search for narrow resonances in dijet events, excited quarks are ruled out for masses $M_{q^*} < 3.35$ TeV [21]. A similar CMS search also looks for new physics in 4-jet final states, where the average dijet mass spectrum is shown in Figure 6 (left) and contains the expected signal from the Coloron pair production model for two alternate mass scenarios [22]. In the absence of a signal, limits are derived and Coloron masses in the range $320 < M_C < 580$ GeV are ruled out at the 95% C.L.

Event topologies with many jets in addition to a lepton would result from 4th generation fermion pair production with multiple W decays, and both CMS [23] and ATLAS [24] study such final states, requiring up to four Ws with at least one decaying leptonically. Figure 6 (right) shows the number of events observed in the ATLAS analysis [25], where the data are divided into sub-samples depending on the number of jets and Ws reconstructed in the event. A good agreement is observed between the data and the SM expectation, and a limit on a 4th generation quark mass $M_{b'} > 480$ GeV is set at the 95% C.L.

Searches for new vector bosons are also performed at the LHC [19, 20], where a dilepton search for a new Z' boson by ATLAS (CMS) sets limits of $M_{Z'} > 2.21$ (2.32) TeV at the 95%

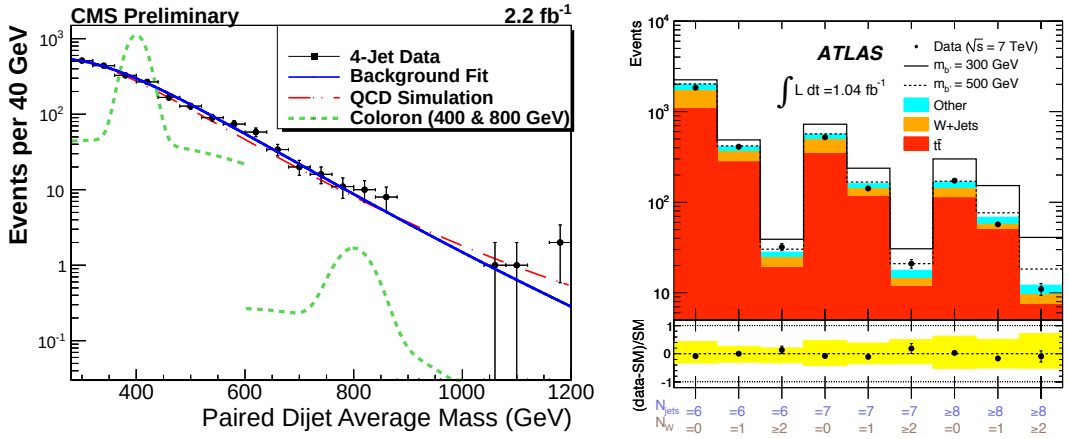

Figure 6: Left: The dijet mass distribution in the CMS data (black points) compared to a smooth background fit (solid curve) and a QCD MC based fit (dashed-dotted curve). Simulated Coloron resonances decaying to $q\bar{q}$ (green dashed curves) are also shown. Right: A distribution of the number of events observed in the ATLAS data and that expected from SM processes for $N_{\text{jets}} = 6, 7, >= 8$ and $N_W = 0, 1, >= 2$. The expected b' signal for two masses is also shown, stacked on top of the SM background prediction.

C.L. Searches for new W' bosons now also explore a region in $M^T_{W'}$ beyond 2 TeV. A theoretical review was presented at the conference which included electroweak precision limits [26].

Complimentary searches for leptoquarks (LQs) are performed at hadron colliders, where LQs are produced in pairs via the strong interaction and at HERA, where LQs are produced singly with a dependence on the coupling λ. Limits on the mass and coupling of a first generation LQ with an equal branching ratio to eq and νq ($\beta = 0.5$) are presented in Figure 7. The direct search limits from the ATLAS [19], CMS [23] and DØ [27] experiments are compared to those from H1 [28] and ZEUS [29], as well as the indirect limits from the L3 experiment at LEP [30]. The most stringent limit from hadron colliders, $M_{LQ} > 607$ GeV, is currently from ATLAS [31], although for large values of the coupling λ, the best limit is from H1 [32]. The limit from an H1 contact interaction analysis [33], which is only sensitive to $LQ \to eq$ decays, is also indicated in Figure 7.

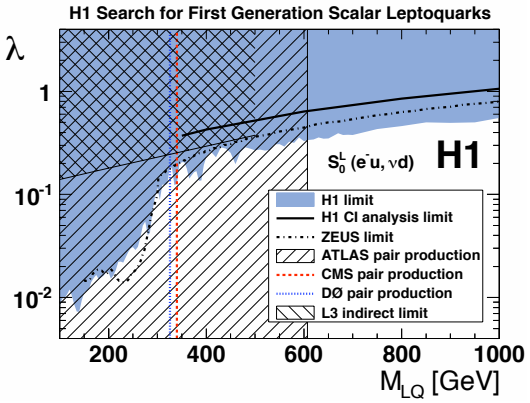

Figure 7: Exclusion limits on the coupling λ as a function of leptoquark mass M_{LQ} for the $S^L_{1/2}$ ($\beta = 0.5$) type leptoquark. The parentheses after the LQ name indicate the fermion pairs coupling to the LQ, where pairs involving anti-quarks are not shown. Domains above the curves and to the left of the horizontal lines are excluded at the 95% C.L.

5 Searches for Supersymmetry

In this section, a review is presented of the results from ATLAS and CMS on recent SUSY searches with many different final state channels, in addition to some theoretical points of view. SUSY is motivated by possible solutions to the hierarchy problem, and may be within the reach of the LHC experiments. The largest SUSY production cross sections are expected to be from gluino and squark production, and electroweak chargino and neutralino production may also be accessible. At the LHC experiments, SUSY searches look for events with the following signatures: large MET, hadronic activity, leptons (with different multiplicities from various channels), photons and heavy flavours.

$R-$parity distinguishes between SM particles ($R-$parity $= +1$) and their SUSY partners ($R-$parity $= -1$) and if conserved protects the MSSM from rapid proton decay. If $R-$parity is violated, then single SUSY particle production is possible and the lightest supersymmetric particle (LSP) can decay further, meaning that MET searches (the mainstream of SUSY searches) will not always be sensitive. A search is performed by ATLAS within the $R-$parity violating mSUGRA model, looking at 4-lepton final states [34], and excluding masses $M_{1/2} < 800$ GeV. Figure 8 shows the excluded region in the $M_{1/2} - \tan\beta$ plane at the 95% C.L. in a signal region defined as events with at least four leptons, MET > 50 GeV, as well as a Z boson veto $|M_\ell - M_Z| > 10$ GeV for all lepton pairs [35]. A search for strong $R-$parity conserving SUSY by ATLAS finds no evidence for a deviation from the SM prediction and a limit for equal mass squarks and gluinos is set at around 1.4 TeV [36]. A direct gaugino search is also performed by ATLAS, examining multi-lepton channels containing two, three, or four or more leptons in combination with MET [37] and finds no statistically significant evidence of SUSY.

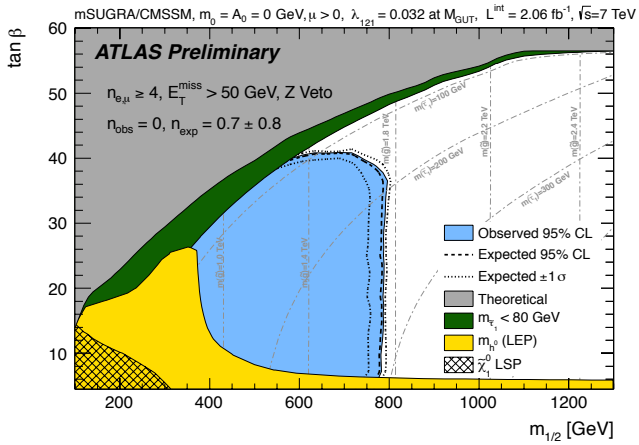

Figure 8: Limits at the 95% C.L from ATLAS in the mSUGRA/cMSSM $m_{1/2} - \beta$ plane from a search for Supersymmetry in final states with at least four isolated leptons and missing transverse momentum. The expected exclusion and its $\pm 1\sigma$ variations are indicated by dashed lines. The other solid shaded areas are excluded by LEP results on the Higgs mass or because $m_{\tilde{\tau}_1} < 80$ GeV.

CMS SUSY searches are categorised by different final states: jets+MET, jets+MET+leptons and photon decays from SUSY particles. Jets+MET is a classical signature in SUSY searches and a large branching ratio is expected in this channel. Innovative new variables are employed to suppress the QCD background in this search: M_{T2}, which is a transverse mass calculation in the case of two decay chains with missing particles and the Razor variable $R = M_R/M_T^R$, which is an approximation of the scale and distribution of the event [38]. No excess is seen in the data over the predicted SM backgrounds in the jets+MET search. Jets+MET+lepton final states are also investigated by CMS, in which leptons arise primarily from neutralino and chargino decays [39].

Various analyses with single, dilepton, and multi-lepton final states are investigated and no excess above the SM prediction is observed. CMS also performs SUSY searches for final states with photons in addition to large MET (from gravitinos) and multiple jets [40]. Both single photon and diphoton analyses observe no excess in the data compared to the SM prediction and 95% C.L. upper limits on the cross section are set as 0.01 pb for bino-like scenarios and 0.1 pb for wino-like scenarios, where squark and gluino masses less than 1 TeV are excluded. Figure 9 shows the MET distributions from the CMS single photon (left) and diphoton (right) analyses [41].

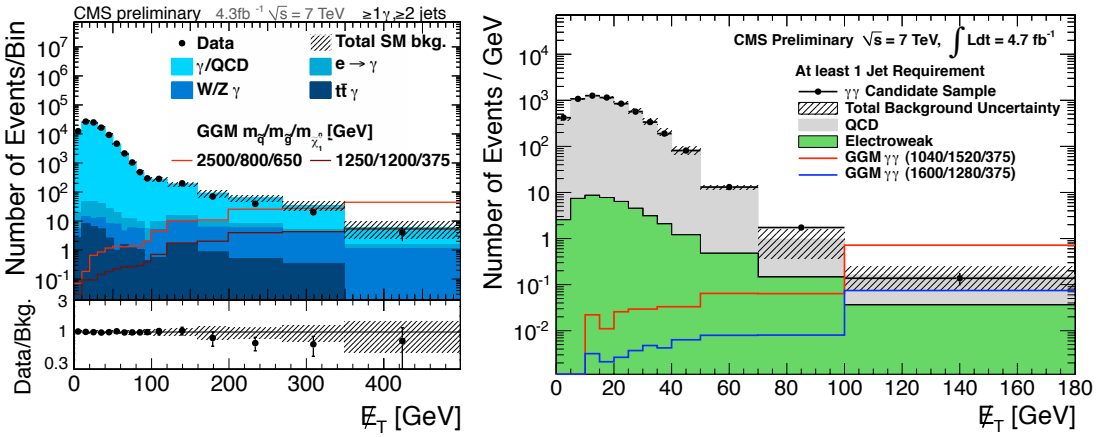

Figure 9: The missing transverse energy in the CMS single photon (left) and diphoton (right) SUSY analyses. The data events are compared to the SM background predictions, as well as the predictions from different general gauge mediation (GGM) signal benchmark points, with example squark/gluino/LSP masses as indicated in GeV.

Third generation squarks can be lighter than the other generations. This is particularly motivated by their role in solving the fine-tuning problem of the SM. Stop and sbottom masses can still be only a few hundred GeV, providing the opportunity for observing third generation squarks at the LHC. Various searches are performed by the ATLAS and CMS experiments, looking for final states with leptons, jets, MET, and b-jets, but so far no excess is observed over the SM prediction [42, 43].

Three theory reviews were presented in the SUSY session at the conference. The first two talks reviewed the status of the MSSM [44] and beyond MSSM [45] scenarios after two years of LHC data taking. Direct sparticle searches combined with a 125 GeV Higgs give strong constraints; the little hierarchy problem, constraints on neutralino dark matter (DM), and heavy stops required by the 125 GeV Higgs put some pressure on the simplest models, although a natural SUSY spectrum can still be quite light. The physics behind Z' production in the MSSM was also presented [46]. The Z' may decay to SUSY particles such as sleptons, charginos, and neutralinos, which then decay into SM particles. In such a case, two or four leptons would appear in the final state, together with large MET from the SUSY particles and the expected number of events with various scenarios and branching ratios were discussed.

6 Searches involving the top quark

The large mass of the top quark means that it has sizable coupling to the Higgs boson and explains its special role in electroweak symmetry breaking. Moreover, the experimental excess observed in the top pair ($t\bar{t}$) forward-backward asymmetry A_{FB} measurement from the Tevatron [47] may also hint at new physics. A variety of searches involving the top quark are performed at the Tevatron and the LHC, which is a top factory. The top quark decays weakly followed by leptonic or hadronic W decay, and therefore the signature from top-pairs may be either dilepton, lepton+jets, or only jets in the final state. The $t\bar{t}$ production cross section has been measured at the LHC using $\sqrt{s} = 7$ TeV data as 177 ± 3 (stat.) $^{+8}_{-7}$ (syst.) $\pm$ 7 (lumi.) pb and 165.8 ± 2.2 (stat.) $\pm$ 10.6 (syst.) $\pm$ 7.8 (lumi.) pb by the ATLAS [48] and CMS [49] experiments, respectively.

A variety of top searches are performed by ATLAS looking for $t\bar{t}$ resonances, $t\bar{t}$+MET final states and same sign top [50]. Whereas no evidence of new physics with top quarks is observed, a significant improvement of the limits from the searches has been achieved. CMS similarly performs searches for heavy resonances decaying to top pairs, boosted tops, heavy bottom-like quarks and flavour changing neutral current (FCNC) in top quark decays [51], where once again no evidence of new physics is observed. Figure 10 (left) shows the upper limits at the 95% C.L. from an ATLAS search for new phenomena in $t\bar{t}$+MET final states [52]. Similar limits from a CMS search for high mass resonances decaying to $t\bar{t}$ in the electron+jets channel are shown in Figure 10 (right).

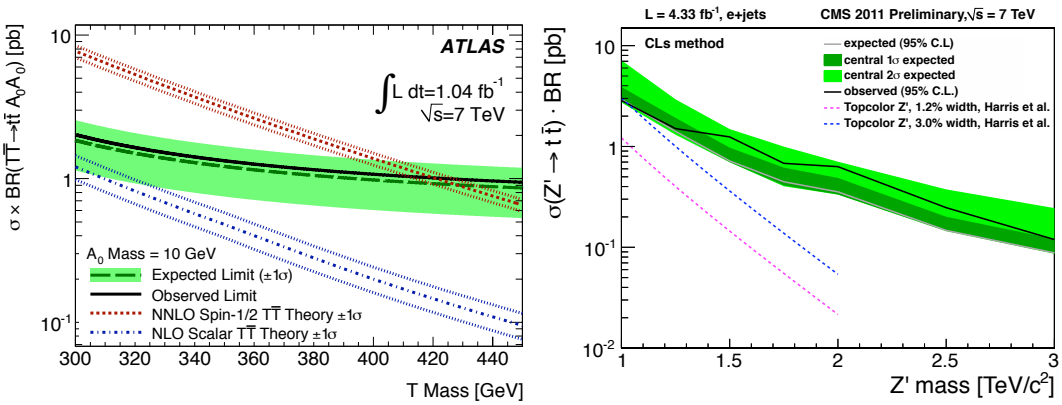

Figure 10: Left: Cross section $\times$ branching ratio excluded by ATLAS at the 95% C.L. as a function of the mass of a heavy quark like object T, for a scalar neutral mass $A_0 = 10$ GeV. Various theoretical predictions are also indicated. Right: Expected and observed upper limits at the 95% C.L. from CMS on the $\sigma(pp \to Z' \to t\bar{t})$ cross section $\times$ branching ratio as a function of the Z' mass. The expected signal from the Topcolor Z' model is also shown.

Many top based searches for new physics are also performed by the CDF and DØ experiments at the Tevatron, including among others: $t\bar{t}$ narrow resonances, top+jet resonances, dark matter candidates associated with single top, anomalous couplings, fourth generation quarks, boosted top quarks and Lorentz invariance violation. No deviation from the SM prediction is reported in this comprehensive list of searches [54].

A search is performed by the ZEUS experiment for single top production in ep collisions [29].

Single top quark production at HERA has a cross section less than 1 fb^{-1}, proceeding via the charged current interaction. However, single top may also be produced via the FCNC process, and a search is performed by ZEUS based on the measurement of W production, which examines the leptonic decay channels of the W, with an additional top-like selection. No excess above the SM prediction is observed in the data and constraints on the anomalous top branching ratios $t \to u\gamma$ and $t \to uZ$ are established.

A theoretical review of the potential for new physics in the top sector was presented at the conference, describing where significant hints of BSM physics can be found at the LHC and the Tevatron [55]. For example, a large deviation from zero in the value of A_{FB} could be due to s-channel resonances at a mass scale of the order of a TeV. At the LHC, this would manifest as an excess in the dijet and $t\bar{t}$ spectra, and such analyses can provide constraints on BSM physics. Further interesting possibilities of sub-TeV scale contributions in the u-channel or t-channel are predicted at the LHC within the $t\bar{t}$+jets signature.

7 W and Z physics

Precision measurements with W and Z bosons not only provide sensitivity to new physics but also serve as input to indirect searches for the Higgs. Diboson cross section measurements are sensitive to triple gauge couplings (TGCs), allowing limits on anomalous TGCs to be set. In addition, the diboson process is an important background in Higgs searches, particularly in the case of WW and ZZ, and therefore the production cross section needs to be known precisely. Such measurements are performed at the LHC by ATLAS [56] and CMS [57], as well as at the Tevatron, where results from the CDF and DØ experiments are combined into one set of measurements [58]. SM cross section measurements from ATLAS are shown in Figure 11 (left), where a good agreement is observed with the SM predictions, which are calculated at NLO or higher.

A measurement of the W mass gives indirect constraints on the Higgs mass and also provides a test of the SM. If the LHC discovers the Higgs, one can compare indirect and direct mass measurements for indications of BSM physics. CDF and DØ recently updated their combined W mass measurement using more data: 2.2 fb^{-1} in the case of CDF and 4.3 fb^{-1} in the case of DØ [59]. The measurement is performed using both electronic and muonic W decays, employing a template fitting method in the measurement. The momentum scale calibration is an important part of the measurement in the muon channel and is set by fits to $J/\psi, \Upsilon$ and Z data. In the electron channel, an energy scale calibration is applied: in the CDF measurement, both E/p calibrations from the momentum scale measurement and M_Z measurement are used to obtain a final energy scale, whereas in the DØ measurement, only E/p calibration from the M_Z measurement is used. The CDF result is $M_W = 80387 \pm 19$ MeV and the DØ result $M_W = 80369 \pm 26$ MeV, with a combined result of $M_W = 80387 \pm 16$ MeV, where the errors contain both statistical and systematic uncertainties. Figure 11 (right) shows the summary of the measurements of the W boson mass, including the results from the Tevatron and their average [60], as well as the measurement from LEP [61] and the resulting world average.

A measurement of elastic Z production is performed by ZEUS using their complete ep collision data set [62]. The SM cross section for Z production in ep collisions is expected to be much smaller than in pp, due to the lack of s-channel Drell-Yan production. The analysis examines the hadronic decay mode of the Z in an elastic phase space, and a cross section of $\sigma = 0.133^{+0.060}_{-0.057}$ (stat.)$^{+0.049}_{-0.038}$ (syst.) pb is measured, in good agreement with the SM prediction.

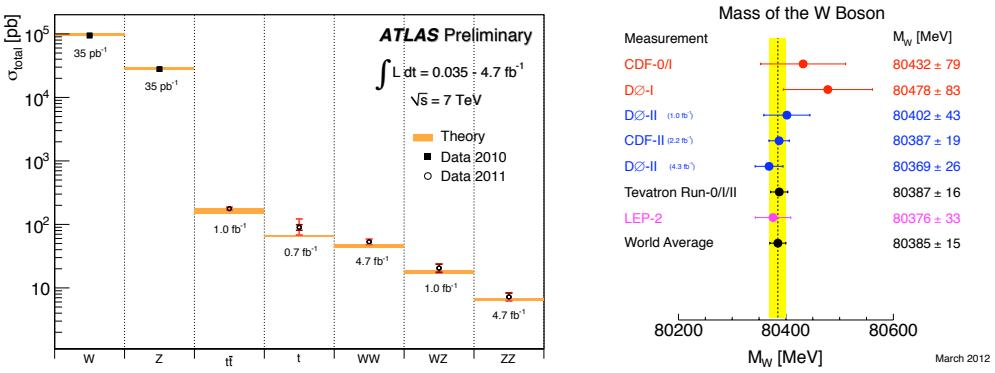

Figure 11: Left: A summary of the SM total production cross section measurements from the ATLAS experiment compared to the corresponding theoretical expectations. Right: A summary of measurements of the W boson mass, including individual and combined Tevatron results, as well as the LEP measurement. An estimate of the world average, assuming no correlations between the Tevatron and LEP results, is also included in the figure.

References

[1] F. Herzog, "SM Higgs production in theory", these proceedings; http://indico.cern.ch/contributionDisplay.py?contribId=175&confId=153252

[2] P. K. Mal, "Search for the Standard Model Higgs boson in ATLAS", these proceedings; http://indico.cern.ch/contributionDisplay.py?contribId=75&confId=153252

[3] P. Govoni, "Searches for SM Higgs at CMS", these proceedings; http://indico.cern.ch/contributionDisplay.py?contribId=219&confId=153252

[4] ATLAS Collaboration, G. Aad *et al.*, "Search for the Standard Model Higgs boson in the diphoton decay channel with 4.9 fb^{-1} of pp collisions at $\sqrt{s} = 7$ TeV with ATLAS", Phys. Rev. Lett. **108** (2012) 111803 [arXiv:1202.1414].

[5] CMS Collaboration, S. Chatrchyan *et al.*, "Search for the Standard Model Higgs boson in the decay channel H to ZZ to 4 leptons in pp collisions at $\sqrt{s} = 7$ TeV", Phys. Rev. Lett. **108** (2012) 111804 [arXiv:1202.1997].

[6] ATLAS Collaboration, "An update to the combined search for the Standard Model Higgs boson with the ATLAS detector at the LHC using up to 4.9 fb^{-1} of pp collision data at $\sqrt{s} = 7$ TeV", ATLAS-CONF-2012-019, 2012.

[7] CMS Collaboration, "Combined results of searches for a Higgs boson in the context of the Standard Model and beyond-Standard Models", CMS-HIG-12-008, 2012.

[8] K. Knoepfel, "Status of SM Higgs searches at the Tevatron", these proceedings; http://indico.cern.ch/contributionDisplay.py?contribId=278&confId=153252

[9] CDF and DØ Collaborations, "Combined CDF and DØ search for Standard Model Higgs boson production with up to 10.0 fb^{-1} of data", FERMILAB-CONF-12-065-E [arXiv:1203.3774], 2012.

[10] A. Azatov, R. Contino and J. Galloway, "Model-independent bounds on a light Higgs", JHEP **1204** (2012) 127 [arXiv:1202.3415].

[11] A. Azatov, "Theoretical review of BSM Higgs", these proceedings; http://indico.cern.ch/contributionDisplay.py?contribId=176&confId=153252

[12] J. Fernandez, "Searches for BSM Higgs at CMS", these proceedings; http://indico.cern.ch/contributionDisplay.py?contribId=220&confId=153252

[13] B. Lenzi, "Beyond Standard Model Higgs searches at ATLAS", these proceedings; http://indico.cern.ch/contributionDisplay.py?contribId=74&confId=153252

[14] E. Chapon, "BSM Higgs and other bump searches at the Tevatron", these proceedings; http://indico.cern.ch/contributionDisplay.py?contribId=279&confId=153252

[15] V. Santoro, "Searches for low-mass Higgs states at BaBar", these proceedings; http://indico.cern.ch/contributionDisplay.py?contribId=187&confId=153252

[16] ATLAS Collaboration, "Search for a fermiophobic Higgs boson in the diphoton decay channel with 4.9 fb^{-1} of ATLAS data at $\sqrt{s} = 7$ TeV", ATLAS-CONF-2012-013, 2012.

[17] ATLAS Collaboration, "Search for charged Higgs bosons decaying via $H \to \tau\nu$ in $t\bar{t}$ events using 4.6 fb^{-1} of collision data at $\sqrt{s} = 7$ TeV with the ATLAS detector", ATLAS-CONF-2012-011, 2012.

[18] CMS Collaboration, "Search for the light charged Higgs boson in top quark decays in pp collisions at $\sqrt{s} = 7$ TeV", CMS-HIG-11-019, 2011.

[19] A. Policicchio, "Searches for new physics with leptons and/or jets at ATLAS", these proceedings; http://indico.cern.ch/contributionDisplay.py?contribId=199&confId=153252

[20] M. Weber, "Searches for new physics with leptons and/or jets at CMS", these proceedings; http://indico.cern.ch/contributionDisplay.py?contribId=221&confId=153252

[21] ATLAS Collaboration, "Search for new phenomena in dijet mass and angular distributions using 4.8 fb^{-1} of pp collisions at $\sqrt{s} = 7$ TeV collected by the ATLAS detector", ATLAS-CONF-2012-038, 2012.

[22] CMS Collaboration, "Search for pair-produced dijet resonances in events with four high P_T jets in pp collisions at 7 TeV", CMS-EXO-11-016, 2011.

[23] S. Chauhan, "Searches for large extra dimensions, leptoquarks and heavy quarks at CMS", these proceedings; http://indico.cern.ch/contributionDisplay.py?contribId=222&confId=153252

[24] J. Zhong, "Searches for fourth generation heavy quarks with the ATLAS detector", these proceedings; http://indico.cern.ch/contributionDisplay.py?contribId=200&confId=153252

[25] ATLAS Collaboration, G Aad *et al.*, "Search for down-type fourth generation quarks with the ATLAS detector in events with one lepton and hadronically decaying W bosons", Phys. Rev. Lett. **109** (2012) 032001 [arXiv:1202.6540].

[26] E. Salvioni, "Some Z' and W' models facing current LHC searches", these proceedings; http://indico.cern.ch/contributionDisplay.py?contribId=177&confId=153252

[27] DØ Collaboration, V. M. Abazov *et al.*, "Search for first generation leptoquark pair production in the electron + missing energy + jets final state", Phys. Rev. **D84** (2011) 071104 [arXiv:1107.1849].

[28] H. Pirumov, "Searches at H1", these proceedings; http://indico.cern.ch/contributionDisplay.py?contribId=293&confId=153252

[29] S. Antonelli, "Searches at ZEUS", these proceedings; http://indico.cern.ch/contributionDisplay.py?contribId=294&confId=153252

[30] L3 Collaboration, M. Acciarri *et al.*, "Search for manifestations of new physics in fermion pair production at LEP", Phys. Lett. **B489** (2000) 81 [hep-ex/0005028].

[31] ATLAS Collaboration, G. Aad *et al.*, "Search for first generation scalar leptoquarks in pp collisions at $\sqrt{s} = 7$ TeV with the ATLAS detector", Phys. Lett. **B709** (2012) 158 [Erratum-ibid. **B711** (2012) 442] [arXiv:1112.4828].

[32] H1 Collaboration, F. D. Aaron *et al.*, "Search for first generation leptoquarks in ep collisions at HERA", Phys. Lett. **B704** (2011) 388 [arXiv:1107.3716].

[33] H1 Collaboration, F. D. Aaron *et al.*, "Search for contact interactions in $e^{\pm}p$ collisions at HERA", Phys. Lett. **B705** (2011) 52 [arXiv:1107.2478].

[34] C. Meyer, "Searches for $R-$parity violating Supersymmetry with the ATLAS detector in final states with leptons", these proceedings; http://indico.cern.ch/contributionDisplay.py?contribId=73&confId=153252

[35] ATLAS Collaboration, "Constraining $R-$parity violating Minimal Supergravity with $\tilde{\tau}_1$ LSP in a four lepton final state with missing transverse momentum", ATLAS-CONF-2012-035, 2012.

[36] F. Legger, "Searches for strong $R-$parity conserving SUSY production at the LHC with the ATLAS detector", these proceedings; http://indico.cern.ch/contributionDisplay.py?contribId=121&confId=153252

[37] L. Heelan, "Searches for direct Supersymmetric gaugino production with the ATLAS detector", these proceedings; http://indico.cern.ch/contributionDisplay.py?contribId=120&confId=153252

[38] S. Paktinat, "Hadronic SUSY at CMS", these proceedings;
http://indico.cern.ch/contributionDisplay.py?contribId=224&confId=153252

[39] M. Niegel, "Searches with jets + missing E_T with leptons at CMS", these proceedings;
http://indico.cern.ch/contributionDisplay.py?contribId=225&confId=153252

[40] D. W. Jang, "Search for Supersymmetry with photons at CMS", these proceedings;
http://indico.cern.ch/contributionDisplay.py?contribId=226&confId=153252

[41] CMS Collaboration, "Search for Supersymmetry in events with photons and missing transverse energy", CMS-SUS-12-001, 2012.

[42] C. Barajas, "Searches for Supersymmetry in events involving third generation squarks and sleptons with ATLAS", these proceedings; http://indico.cern.ch/contributionDisplay.py?contribId=78&confId=153252

[43] A. Kalogeropoulos, "Searches for SUSY with third-generation signatures in CMS", these proceedings;
http://indico.cern.ch/contributionDisplay.py?contribId=227&confId=153252

[44] F. Bruemmer, "The MSSM after two years of LHC running", these proceedings;
http://indico.cern.ch/contributionDisplay.py?contribId=179&confId=153252

[45] P. Lodone, "Supersymmetry phenomenology beyond the MSSM after 5/fb of LHC data," Int. J. Mod. Phys. **A27** (2012) 1230010 [arXiv:1203.6227].

[46] G. Corcella, "Z' production at the LHC in an extended MSSM", these proceedings;
http://indico.cern.ch/contributionDisplay.py?contribId=316&confId=153252

[47] CDF Collaboration, "Study of the top quark production asymmetry and its mass and rapidity dependence in the full Run II Tevatron data set", CDF Note 10807, 2012.

[48] K. Shaw, "Top quark pair production cross-section at ATLAS", these proceedings;
http://indico.cern.ch/contributionDisplay.py?contribId=89&confId=153252

[49] CMS Collaboration, "Combination of top quark pair production cross section measurements", CMS-TOP-11-024, 2012.

[50] P. Calfayan, "Search for physics beyond the Standard Model with top quarks at ATLAS", these proceedings; http://indico.cern.ch/contributionDisplay.py?contribId=305&confId=153252

[51] V. Bazterra, "Searches for physics beyond the Standard Model with top quarks at CMS", these proceedings; http://indico.cern.ch/contributionDisplay.py?contribId=258&confId=153252

[52] ATLAS Collaboration, G. Aad *et al.*, "Search for new phenomena in $t\bar{t}$ events with large missing transverse momentum in proton-proton collisions at $\sqrt{s} = 7$ TeV with the ATLAS detector", Phys. Rev. Lett. **108** (2012) 041805 [arXiv:1109.4725].

[53] CMS Collaboration, "Search for high-mass resonances decaying to $t\bar{t}$ in the electron+jets channel", CMS-PAS-EXO-11-092, 2012.

[54] Y. Peters, "Searches for new physics in the top sector at the Tevatron", these proceedings;
http://indico.cern.ch/contributionDisplay.py?contribId=208&confId=153252

[55] J. Kamenik, "Hunting for new physics in top pair production", these proceedings;
http://indico.cern.ch/contributionDisplay.py?contribId=186&confId=153252

[56] H. Skottowe, "Measurements of dibosons with the ATLAS detector and associated constraints on new physics", these proceedings; http://indico.cern.ch/contributionDisplay.py?contribId=77&confId=153252

[57] S. Folgueras, "Diboson measurements with the CMS detector", these proceedings;
http://indico.cern.ch/contributionDisplay.py?contribId=228&confId=153252

[58] M. Vesterinen, "Recent WW, WZ and ZZ results from the Tevatron", these proceedings;
http://indico.cern.ch/contributionDisplay.py?contribId=280&confId=153252

[59] T. Riddick, "W mass measurements from the Tevatron", these proceedings;
http://indico.cern.ch/contributionDisplay.py?contribId=281&confId=153252

[60] CDF and DØ Collaborations, "2012 update of the combination of CDF and DØ results for the mass of the W boson", arXiv:1204.0042, 2012.

[61] The LEP Collaborations: ALEPH, DELPHI, L3, OPAL and the LEP Electroweak Working Group, "A combination of preliminary electroweak measurements and constraints on the Standard Model", hep-ex/0612034, 2006.

[62] T. Nobe, "Elastic Z^0 production at HERA", these proceedings;
http://indico.cern.ch/contributionDisplay.py?contribId=41&confId=153252

Summary of the Hadronic Final States Working Group

Krzysztof Nowak[1,*], *Klaus Rabbertz*[2], *Jan-Christopher Winter*[7,*]

[1]DESY, Notkestraße 85, 22607 Hamburg, Germany
[2]KIT, IEKP, Wolfgang-Gaede-Str. 1, 76131 Karlsruhe, Germany
[7]CERN, PH-TH, CH-1211 Genève 23, Switzerland
[*] *Speakers*

DOI: `http://dx.doi.org/10.3204/DESY-PROC-2012-02/361`

In this summary we give a short overview of the experimental and theoretical results, which were presented during the sessions of the QCD and Hadronic Final States Working Group [1] at the DIS 2012 conference.

1 Experimental contributions

In the Hadronic Final States Working Group a large number of experimental collaborations presented their most recent updates from a broad range of QCD measurements. The covered topics include the physics of jets, prompt photons, identified particles, the underlying event as well as tuning and model development. Here, only some highlights of the talks given during the working group sessions are presented, for details please refer to the individual contributions in the workshop proceedings.

1.1 Jet production

The ZEUS collaboration has presented a new inclusive jet production measurement at the photoproduction limit [2], which is well described by NLO QCD. From these data, the strong coupling could be determined to be $\alpha_s(M_Z) = 0.1206^{+0.0023}_{-0.0022}(\text{exp})^{+0.0042}_{-0.0035}(\text{th})$, which is in agreement with the HERA and world averages. A range of further studies has been performed: the choice of the jet algorithm, the potential to restrict the proton and photon PDFs, and the sensitivity to multi-parton interaction effects.

The H1 collaboration has developed and applied a new, sophisticated unfolding method for jet measurements at high Q^2 [3]. The neutral-current DIS (deep inelastic scattering), inclusive jet, dijet and tri-jet cross sections are unfolded simultaneously preserving all the statistical and experimental correlations between them, which subsequently can be used in a fit of $\alpha_s(M_Z)$ as well as in PDF fitting programs. In addition, the unfolding procedure takes into account migrations into and out of the investigated phase space. The neutral current DIS cross sections serve to normalize the jet cross sections, which significantly reduces experimental and theoretical uncertainties. Jet cross sections are theoretically calculated up to next-to-leading order (NLO) with the help of NLOJET++ [4] and FASTNLO [5, 6]. Extracting the strong coupling constant

from these data yields $\alpha_s(M_Z) = 0.1163 \pm 0.0008(\text{exp}) \pm 0.0011(\text{had}) \pm 0.0014(\text{pdf})^{+0.0044}_{-0.0035}(\text{th})$ in agreement with previous H1 measurements.

Because of their potential for constraining the proton PDFs, the results on inclusive jet production by the ATLAS and CMS collaborations have been presented in the joint session of the Hadronic Final States and Structure Functions working groups, and are summarized elsewhere [7]. Additional jet measurements on dijets and multi-jets presented in [8] are reasonably well described by theory predictions or Monte Carlo (MC) event generators.

Jets in the forward pseudorapidity region $3.2 < |\eta| < 4.7$ were studied by CMS [9]. Events with activity in the forward region are populated by more asymmetric final-state configurations in terms of momentum fractions of the interacting partons, thus allowing studies to be extended to smaller x values. Also, the forward region is expected to be most sensitive to deviations from the DGLAP parton evolution. Both reported forward jet cross sections as well as a cross section for forward-central jet pair production have been shown, within errors, to be reasonably well described by theory predictions.

The ratio of inclusive to exclusive dijet production as a function of the rapidity separation has been studied by CMS [9]. Here, all possible jet pairings are counted within the inclusive sample, while only events with exactly one jet pair passing the selection criteria are considered in the exclusive selection. The ratio is well described by PYTHIA [10], while HERWIG [11], HEJ [12], and CASCADE [13] predictions deviate significantly.

Jets reconstructed from tracks allow a meaningful comparison to MC simulations in the soft region of very low p_T; this study was undertaken by ATLAS for jet transverse momenta down to 4 GeV [8], where events recorded with a minimum-bias trigger were used for the study. All employed MC event generators fail to describe this measurement demonstrating the need for improvements in modelling the transition region between soft and perturbative physics.

A set of measurements aiming to explore jet shapes has been presented by ATLAS [14]. The internal structure of a jet is influenced primarily by fragmentation and hadronization effects but also by hard physics, colour reconnections, the underlying event and pile-up as well as heavy particle production. Some discrepancies to the MC models have been observed for jet shapes and jet fragmentation. Nevertheless all studied models provide a reasonable description of the data. For the jet mass distributions, it was found that the "splitting and filtering" technique [15] has the potential to reduce the sensitivity to soft physics.

1.2 Weak boson plus jets production

The production of jets in association with a Z boson has been studied by the CDF collaboration combining the two channels $Z/\gamma^* \to \mu^+\mu^-$ and $Z/\gamma^* \to e^+e^-$ using the full CDF data set [16]. The results were compared to several predictions at different perturbative orders (at NLO: MCFM, BLACKHAT+SHERPA, at $\bar{n}$NLO: LOOPSIM+MCFM) and are in a very good agreement with each other. In addition, the cross section of Z+b-jet is found to be in agreement with NLO predictions from MCFM, which, however, show a large uncertainty due to the choice of the renormalization scale.

The ATLAS collaboration has presented a range of weak boson plus jet measurements based on 2010 LHC data [17]. The Z+jet and W+jet cross sections are in agreement with predictions by BLACKHAT [18] or ALPGEN [19]. PYTHIA and SHERPA [20] on the other hand fail in some details, in particular for the W+jet measurement. In addition, the W+jet to Z+jet cross section ratio, which benefits from at least partial cancellations in the experimental uncertainties, was studied as a function of the jet p_T threshold. The MCFM prediction describes the data well in

the full range of investigated p_T threshold values. Lastly, the W and Z production in association with a b-jet has been discussed. Again, the data are reasonably well described by the theory.

1.3 Photon production

Prompt photon production is another example of an environment suitable for testing the understanding of the underlying QCD process. Photons, contrary to jets, do not undergo a hadronization process leading to a direct sensitivity to the partonic hard process. Non-prompt photons coming from decays of secondary particles such as π^0 are removed to a large extent by requiring the photon to be isolated from the rest of the hadronic final state.

The ZEUS collaboration reported on the production of isolated photons with an associated jet in the range $10 < Q^2/\mathrm{GeV}^2 < 350$ [21]. The remaining background from hadronic decays is estimated by exploring differences in size and shape of the calorimetric shower. The experimental results are compared to the theory prediction at NLO assuming collinear factorization, as well as to a calculation based on the k_T-factorization approach. Both predictions do not give a satisfactory description of the data, in particular in terms of the overall normalization. The NLO result underestimates while the one based on the k_T-factorization overestimates the production rate of isolated photons.

The CDF collaboration presented a new measurement of di-photon production compared to a set of theoretical predictions, ranging from that of the LO parton shower PYTHIA to that of RESBOS, where an analytically resummed calculation at low-p_T is matched to NLO high-p_T matrix elements [22]. A pure NLO calculation cannot describe the measurements in the limit $p_T \to 0$ since resummation effects become important. Hence, RESBOS provides the best description. The LO event generator SHERPA incorporating matrix element plus parton shower merging provides the best overall description in the explored phase-space region. Both collaborations, CDF [22] and DØ [23], presented their recent studies on γ plus heavy flavour production. While the γ plus beauty production is relatively well described by theory, particularly when the gluon splitting rate is increased, the γ plus charm production is underestimated.

Finally, ATLAS has reported on inclusive photon, photon plus jet and di-photon production studied with data collected in 2010 at a centre-of-mass energy of 7 TeV [24]. The understanding of photon production at the LHC is of particular importance in view of the Higgs boson search, where the background for its photonic decay needs to be well modelled. All measurements are in agreement with the studied calculations. The NLO prediction from JETPHOX slightly overestimates the photon production rate for low transverse momenta.

1.4 Particle production

New results on the production of identified particles, important for testing and tuning hadronization and fragmentation models, were presented based on HERA and LHC data. The ZEUS collaboration has measured the scaled momentum distributions for K^0_S and $\Lambda/\bar{\Lambda}$ hadrons [25]. The scaled momentum is defined as $x_p = 2P_{\mathrm{Breit}}/\sqrt{Q^2}$ where P_{Breit} is the particle momentum in the Breit frame of reference. Measured cross sections were compared to MC predictions based on two approaches, which are the colour dipole model and matrix element plus parton shower merging. Both of which reproduce the shape of the studied distributions but fail to give the correct normalization, in particular for the K^0_S production. The results were also compared to NLO calculations using fragmentation functions (FF) tuned to previously available

data. These, in turn, do not provide a satisfactory description of the presented measurement demonstrating the potential to better constrain future FF tunes.

LHCb has measured the multiplicity of primary charged particles [26], i.e. those produced in pp collisions or from short-lived resonances. The measurement has been made in the forward region as covered by the LHCb detector. All the studied MC predictions underestimate the primary charged particle multiplicities. A better agreement can be achieved by excluding diffractive processes in PYTHIA. Also, hard events with at least one track of $p_T > 1$ GeV are better described. Furthermore, the collaboration has measured the production ratios of $\frac{\bar{p}}{p}$, $\frac{K^-}{K^+}$, $\frac{\pi^-}{\pi^+}$, $\frac{\bar{p}+p}{K^-+K^+}$, $\frac{\bar{p}+p}{\pi^-+\pi^+}$ and $\frac{K^-+K^+}{\pi^-+\pi^+}$. The best description of these ratios are provided by the NOCR (no-colour-reconnection) and LHCb PYTHIA tunes.

The spectra of charged pions, kaons and protons were measured by the CMS collaboration [27]. They are shown to be well described by fits using the Tsallis–Pareto formula [28]. In addition, studies of the multiplicity dependence of various observables have been performed, motivated by recently published CMS results showing intriguing hadron correlations at high track multiplicities [29]. Here, pion distributions are in practice independent of the collision energy $\sqrt{s}$ and average transverse momenta $\langle p_T \rangle$. Also the ratios between production rates of pions, kaons, and protons as well as $\langle p_T \rangle$ are independent of the multiplicity and $\sqrt{s}$.

The COMPASS collaboration presented pion and kaon multiplicities from deep inelastic scattering of 160 GeV muons off the deuteron target [30]. The π multiplicities as a function of the Bjørken-x and $z = E_h/E_\gamma$ are well described by existing FFs up to $z = 0.65$, the maximal z value used in the FF fit. In the case of K multiplicities on the other hand, significant discrepancies are observed over the entire kinematic region, indicating that particularly kaon measurements have the prospect of leading to significant improvements in future fits of FFs.

Pion, kaon, proton, and anti-proton multiplicities in electron scattering on neon, krypton and xenon targets were studied by the HERMES collaboration [31]. Different nuclei were used in order to investigate the space-time development of the hadronization process. A suitable experimental variable is the nuclear attenuation ratio R_A^h defined in [31]. The R_A^h distribution is qualitatively different for the K^+ mesons as compared to K^-, π^+, or π^- which might be the result of final-state interactions. The proton distributions are different to all the meson distributions and to anti-protons, which can be explained by the possibility of protons being knocked out of nuclei, while other hadrons are always produced in the hadronization process.

1.5 Minimum-bias studies and the underlying event

The CMS collaboration has determined the inelastic proton–proton cross section employing two different methods [32]. The first method with a single-sided trigger is based on counting events with as loose a selection as possible. The second method is based on the assumption that the number of inelastic pp interactions in a given bunch crossing follows a Poisson distribution. Both methods rely on MC extrapolation in order to determine the total inelastic cross section. Within the relevant uncertainties both methods give consistent results which are in agreement with previously published results from the ATLAS, ALICE and TOTEM collaborations.

The ATLAS collaboration presented three separate correlation measurements in the minimum-bias data selection [33]. The description of forward-backward multiplicity correlations vary considerably depending on the MC tune chosen. The most recent LHC tunes best describe the data. The general features of two-particle angular correlations are relatively well reproduced by the employed MC tunes, but none of them provides a satisfactory quantitative description of

the data. The presence of azimuthal ordering coming from the underlying QCD string structure is tested in a spectral analysis of correlations between longitudinal and transverse components of the momentum of charged hadrons. The measured spectra show features consistent with the fragmentation of a QCD string but the MC event generators typically produce a spectrum with more correlations than seen in data in a low-p_T depleted sample. The spectra of low-p_T particles is not well modelled.

The CMS collaboration presented three alternative approaches sensitive to the presence of the underlying event [34]. The experimentally clean Drell–Yan process has advantages of a clear separation between the hard interaction and soft components, the absence of final-state radiation, and a low probability of photon bremsstrahlung from the muons. The comparisons to theoretical models allow to conclude that MADGRAPH [35] provides an adequate description of the data while PYTHIA and HERWIG++ do not. The second analysis calculates the median of all ratios of jet p_T over the area covered by this jet in an event. This observable naturally isolates underlying event contributions by assuming that the majority of the event is dominated by soft contributions while the hard component of the interaction is well contained within the leading jets, which are treated as outliers via the median prescription. In contrast to the conventional approach, no explicit geometrical subdivision of an event is necessary. Similar to other studies it can be concluded that none of the examined MC event generator tunes provides a satisfactory description. The third analysis measures the underlying event activity by studying the energy densities at forward rapidities, where the phase space for sensitive observables is well separated from the hard interaction. The ratio of the number of events where the hard process is present to the number of events collected in minimum-bias selection is studied. In this case, the recent MC tunes to LHC data perform relatively well.

Lastly, the LHCb collaboration studies the underlying event in four distinctive classes in order to probe multiple parton interactions [36]: inclusive minimum-bias, hard scattering, diffractive, and non-diffractive enriched samples. The energy flow distributions were compared to various PYTHIA tunes and cosmic-ray models. None of the generated predictions describe all four studied samples simultaneously.

2 Theoretical contributions

There are many aspects to hadronic final states depending on the energy domains of the physics phenomena one is interested in. Accordingly we have grouped our summary of contributions into four parts reflecting jet physics at different scales: jet production and substructure, jet vetoes and intra-jet evolution. The working group covered a rich program of these topics, where we have seen a number of exciting results demonstrating progress on different frontiers, the tool-driven (progressing towards the inclusion of higher orders in MC tools), the phenomenology-driven (targetting enhanced signal from background separation) and the theory-driven frontier (aiming for better control of uncertainties). In all cases, however, thorough theory to jet-data comparisons are – and will keep – giving us feedback where models need to be refined.

2.1 Central & forward jet production

F. Siegert presented the predictions of a W+3-jet calculation at NLO matched with a parton shower (PS) using the MC@NLO technique as implemented in the SHERPA event generator [37]. This is the first application of NLO+PS matching to a final state of complexity higher than

four outgoing legs. These remarkable results (using the virtual corrections as provided by BLACKHAT) were obtained in collaboration with S. Höche, F. Krauss and M. Schönherr [38], and were shown to be in good agreement with recent data taken by the ATLAS collaboration [39]. As a difference to the original MC@NLO approach, one should stress that SHERPA's technique of using an one-step parton shower based on the exact Catani–Seymour dipole subtraction terms allows them to maintain full NLO accuracy also for the subleading colour configurations [40].

S. Prestel discussed the PYTHIA 8 implementation of tree-level matrix element plus parton shower merging based on the CKKW-L method [41, 42]. This is work he did in collaboration with L. Lönnblad, the author of the CKKW-L(önnblad) approach [43, 44]. The talk addressed two issues of particular importance to this implementation: first, how to accomplish CKKW-L merging in the context of interleaved multiple parton interactions and spacelike parton showers by preserving PYTHIA's description of the underlying event; second, how to achieve a reliable estimate for the size of effects owing to matrix element configurations occurring outside the regime of strictly ordered parton shower phase space.

J. Smillie gave a brief overview of the physics implemented in the Monte Carlo program HEJ [12] and its capabilities in describing various jet data [45]. The HEJ (High Energy Jets) project is being developed by J. Andersen, T. Hapola and J. Smillie, and provides an interesting alternative in describing multi-jet production. The approach taken in HEJ is based on the amplitude factorization present in the high energy limit. In contrast to (matched) parton showers, HEJ resums contributions that originate from large $s_{ij} = (p_i + p_j)^2$ between well-separated pairs of partons with similar p_T (i.e. soft and hard wide-angle radiation). These effects are important to consider at the LHC at high energies, as demonstrated by measurements of high H_T in W+jets production [39]. To improve the description away from the high energy limit, HEJ is flexible to be merged with LO matrix elements (MADGRAPH) and parton showers (ARIADNE) [47]. As a result HEJ's predictions agree well with measured p_T spectra at the LHC in one forward plus one central jet production [48], and measured gap fractions as a function of the rapidity separation of tagged jets [49]. As expected, deviations occur in phase-space regions governed by jet p_T hierarchy. Comparing different approaches to multi-jet emission, novel, very interesting ways to look at data have emerged. In Refs. [46, 50] it has been shown that one can distinguish predictions more clearly by plotting the average number of jets versus Δy_{fb} of the most forward and backward jet, or H_T, the scalar sum of all jet p_T in the event. An example is shown in Figure 1.

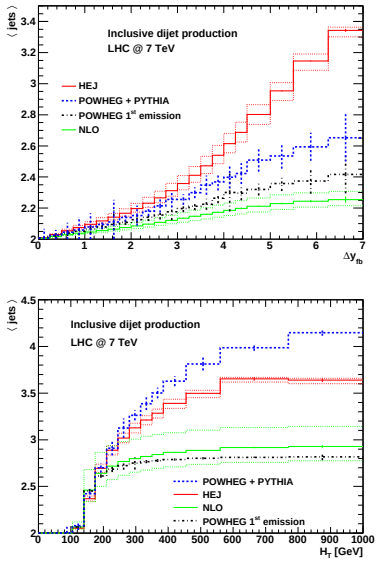

Figure 1: Average number of jets as a function of Δy_{fb} (top) and H_T, as predicted by HEJ, POWHEG+PYTHIA and to (vanilla) NLO, cf. Ref. [46]. The impact of (factor-two) scale variations is indicated as well.

In their talks M. Deák and F. Hautmann presented results of studies related to the application of the Monte Carlo program CASCADE to the interesting subject of forward high-p_T production at the LHC [51, 52]. These studies were done in collaboration with H. Jung and K. Kutak. CASCADE provides a framework for an initial-state $k_\perp$-dependent

shower based on the CCFM evolution of gluon chains. A CCFM based parton shower coupled to high energy factorized matrix elements is in principle capable of describing arbitrarily large p_T, but the inclusion of (subleading) perturbative corrections as encoded in exact matrix elements is desirable to improve the precision of the description at high transverse momenta. To avoid double counting, subtractive procedures are necessary; one of which, a vetoing technique, was discussed in more detail by M. Deák as one element towards a complete merging procedure. To validate such an approach, a suitable experimental framework has to be defined. F. Hautmann discussed, in his talk, various scenarios of how to measure correlations in azimuthal angle, rapidity and p_T in inclusive jet production with focus on forward jet hadroproduction. He emphasized the potential in measuring the rapidity and azimuthal dependence of transverse energy flows in one central plus one forward jet production [48] where CASCADE predicts, in the inter-jet region, enhanced particle and mini-jet energy flows [53, 54].

2.2 Jet substructure and jet shapes

S. Marzani, in collaboration with A. Banfi, M. Dasgupta, K. Khelifa-Kerfa and M. Spannowsky, presented their first analytical results on QCD jet mass distributions for jets produced in hadron–hadron collisions [55]. The results were obtained using traditional all-order resummation techniques, extending the application known for e^+e^- scattering to the more complicated hadronic environment. An important ingredient to Marzani et al's calculation, almost accurate to NLL, is the inclusion of non-global logarithms in the large N_C limit (where N_C denotes the number of colours). Also, comparing different jet algorithms they find the anti-k_T algorithm less prone to effects stemming from extra single logarithms, hence more robust than other algorithms like Cambridge/Aachen (C/A) or k_T. Marzani et al. applied their formalism to the phenomenologically interesting cases of Z+jet and dijet production. Although the NLL+NLO matched calculation was not quite completed at the time of the conference, they were already able to draw important conclusions using their preliminary NLL*+LO matched resummation. They showed that the effect of the non-global logarithms is crucial in describing the peak region of the $(1/\sigma)\, d\sigma/d\rho$ distribution more accurately, $\rho = m^2_{\text{jet}}/p^2_{T,\text{jet}}$. Depending on the jet size these effects will reduce the peak height bringing them in better agreement with numerical results from tuned parton shower calculations. Given Marzani et al's result [56] we now understand that the large non-perturbative corrections introduced by other groups just make up for the missing contribution of non-global logarithms. Promising as is, as an outlook, they advocate a direction of application of their formalism to the comparison of jet grooming techniques like jet filtering, pruning and trimming on a more analytic level.

M. Takeuchi presented work done mainly in collaboration with T. Plehn and M. Spannowsky on boosted, hadronically decaying top quarks in searches for new physics [57]. Hadronically decaying tops ($t \to 3$ jets) are in principle fully reconstructible. If the top quarks are boosted, they give a great handle for suppressing the large QCD and combinatorial backgrounds simply because they occur as "fat" (massive) jets with a distinct substructure. Various groups have built so-called top taggers around this idea with the aim to identify top-quark jets in a similar fashion as done for bottom-quark jets. Takeuchi et al. developed the HEPTOPTAGGER [58], which proceeds through the four steps of fat-jet finding (using the C/A algorithm for geometrically large sizes of jets: $2\, m_{\text{jet}}/p_{T,\text{jet}} \sim R \sim 1.5$), subjet identification invoking mass drop criteria, filter mass optimization for subjet triples and the implementation of constraints on 2-jet and 3-jet mass ratios. In doing so, emphasis was put on having a valid approach down to $p_{T,\text{fat-jet}} \sim 200$ GeV since the gain in cross section is huge. As one main application of

the HEPTOPTAGGER, M. Takeuchi discussed the prospects of scalar top reconstruction [59] highlighting a search strategy for the 8 TeV LHC and stop masses of ~ 400 GeV that reaches $\sim 3\,\sigma$ and $\mathcal{O}(1)$ discrimination with ~ 10 fb^{-1} of data.

Z. Li reported on results of work with H. Li and C.-P. Yuan aiming at a better analytic understanding of jet substructure related quantities at hadron colliders [60]. They established a perturbative QCD framework based on the resummation formalism of Refs. [61, 62] to calculate jet energy profiles and jet mass distributions of light-quark and gluon jets. Their novel description improves NLO predictions for both of these observables significantly [63], leading to good agreement with CDF and CMS data on jet energy profiles $\Psi(r)$ for various $p_{T,\mathrm{jet}}$ intervals without application of any further corrections, see Figure 2. To describe the jet mass spectra in the low-mass region, they however introduce non-perturbative contributions to their resummation formalism, whose realm they plan to extend to heavy-quark/boosted jets. One interesting aspect pointed out by Z. Li regards the individual knowledge of $\Psi(r)$ for both, quark and gluon jets; e.g. the latter yield steeper $\Psi(r)$. This may help enhance the sensitivity to new-physics contributions when exploring ratios between quark and gluon initiated jets in more detail.

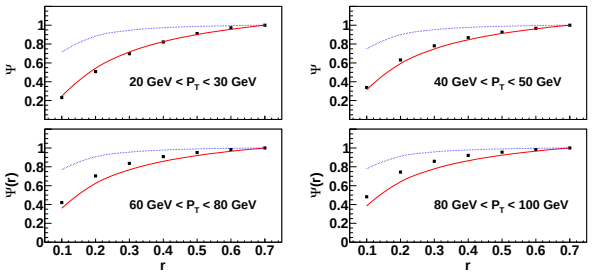

Figure 2: Examples of resummation (solid) and NLO (dashed) predictions [63] for jet energy profiles $\Psi(r)$ compared with CMS data [64].

2.3 Inclusive production versus jet vetoes

Work done in collaboration with A. Lipatov and N. Zotov was presented by M. Malyshev [65]. On the basis of the k_T-factorization approach (with its theoretical foundation given by the BFKL or CCFM equations) they calculated unpolarized Drell–Yan (DY) lepton pair production in $p\bar{p}$ and pp collisions. In a field where collinear factorization is recognized as the standard,[1] it is worthwhile to investigate what an alternative based on non-collinear factorization can do for us. As a major difference one should note that the initial gluon emissions in the k_T-factorization formalism generate the finite dilepton transverse momentum already at the Born level. The ingredients to their calculation [66] are then given by the unintegrated parton densities following the KMR prescription, and the offshell production amplitudes for Z/γ^* exchange including the Z-γ^* interference and fully spin-correlated decays into leptons. They consider offshell amplitudes at $\mathcal{O}(\alpha)$ and $\mathcal{O}(\alpha\alpha_\mathrm{s})$. Using their calculational framework they show a broad comparison with data from the Tevatron and early LHC for differential cross sections with respect to variables such as $m_{\ell\ell}$, $y_{\ell\ell}$ and $p_{T,\ell\ell}$. Generally, the agreement is found to be very reasonable. Highlights to mention are the predicted distribution for $p_{T,\ell\ell}$ featuring the low-p_T rise and turnover, and results obtained for the p_T-dependent coefficients A_1 through A_4 related to an angular analysis as recently done by the CDF collaboration [67].

Yet another approach to DY pair – or more generally gauge and Higgs boson – production was advocated by D. Wilhelm who reported on work accomplished in collaboration with

[1] Collinear factorization has been rigorously proven for DY pair production, which we nowadays control at NNLO in perturbative QCD matched to soft gluon analytic resummation at NNLL.

T. Becher and M. Neubert [68, 69]. Using methods from Soft-Collinear Effective field Theory, they developed a new, systematic framework for the evaluation of the cross section at small and very small transverse momentum of the boson, $\Lambda_{\rm QCD} \ll q_T \ll M_V$ [70]. In this framework large logarithms of the scale ratio M_V/q_T are resummed to all orders by avoiding issues with Landau pole singularities as known from the conventional/traditional resummation approach [61]. In Becher et al's approach the cross section is written as a product of a q^2-dependent hard function with a convolution of two transverse-position dependent parton distribution functions. The form of the factorization theorem is affected by an anomaly of the effective Lagrangian at the quantum level, leading to the breakdown of the naive factorization of the two collinear sectors given at the classical level. Because of this anomaly, not only the hard function encoding the virtual effects associated with the electroweak boson production, but also the product of collinear functions has a dependence on M_V. As an interesting consequence one finds that the renormalization scale μ saturates to a non-perturbative value $q^* \sim M_V \exp\{-\text{const}/\alpha_{\rm s}(M_V)\}$ for $q_T \to 0$. Numerically this amounts to $q^* \approx 1.88$ GeV for Z production. They then find their (NNLO matched) results of NNLL accuracy – including some long-distance effects for $q_T \lesssim 3$ GeV – to be in nice agreement with data on low-q_T spectra from the Tevatron and early LHC. It will be interesting to see how this approach performs in the scope of Higgs boson production where $q^* \approx 7.5$ GeV and long-distance power corrections shall be truly negligible.

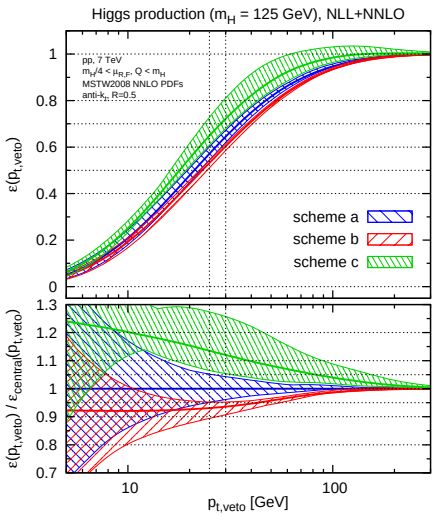

Figure 3: Jet-veto efficiency predictions at NLL+NNLO given in dependence on $p_{T,\rm veto}$ for Higgs boson production in 7 TeV pp collisions. Results are shown for three different matching schemes; for more details, cf. [71].

One of the crucial channels to explore the nature of the low-mass Higgs-like boson discovered at the 7 and 8 TeV LHC is $H \to WW^*$. Good discrimination between signal and backgrounds can be guaranteed, in particular in the 0-jet bin where the W boson contamination from the $t\bar{t}$ background is smallest. This implies a good understanding of the uncertainties related with the exclusive 0-jet cross section, $\sigma[0\,\text{jets}]$. Obtaining a reliable error estimate, however, is a tricky task, because the scale variations of the jet-vetoed NNLO result for Higgs boson production are known to underestimate the uncertainty in the region of moderate $p_{T,\rm veto} \sim 30$ GeV; on the contrary assuming uncorrelated errors the estimate $\Delta\sigma^2[0\,\text{jets}] = \Delta\sigma^2[\geq 0\,\text{jets}] + \Delta\sigma^2[\geq 1\,\text{jet}]$ is said to be too large. Results "fresh from the press" [71] regarding this subject were presented by A. Banfi during his talk at DIS 2012 [72]. Together with G. Salam and G. Zanderighi, they have been carefully studying an ansatz involving the jet-veto efficiency (i.e. the fraction of events with no jet of $p_T > p_{T,\rm veto}$): $\sigma[0\,\text{jets}] = \sigma[\geq 0\,\text{jets}] \times \varepsilon(p_{T,\rm veto})$. This allows them to discuss the uncertainties in determining the veto efficiency separately from the inclusive cross section, which has been intensely studied in the literature; for an up-to-date H physics compendium, see Refs. [73, 74]. There are two sources of uncertainties to $\varepsilon(p_{T,\rm veto})$, those related to how one defines ε at fixed order and those related to missing logarithms $\ln(M_h/p_{T,\rm veto})$ of Sudakov origin. For the former, they introduce three NNLO-equivalent schemes, which lead to very similar, precise results in their control scenario given

by Z+jet production. Owing to the poorer convergence of the perturbative series in the H case, they however see large deviations among the predictions of the different schemes. These deviations are tamed by including the logarithmic corrections to ε occurring at all orders. Using the CAESAR program, they can resum these effects to NLL accuracy, and match them with the NNLO prediction where the freedom of choosing from three equivalent schemes can be used as an additional handle in estimating the uncertainties; the results are shown in Figure 3. Comparisons with other theoretical tools (HQT+MCFM, POWHEG+PYTHIA) confirm the consistency of their results for the veto efficiency.

The discussion of jet vetoes was of importance in two other contributions: S. Marzani's second presentation within this working group [75], and P. Schichtel's contribution where he presented work accomplished together with his collaborators C. Englert, T. Plehn and S. Schumann [76, 77, 78]. One can identify two limiting cases where the scaling properties of exclusive jet cross sections are governed by two simple patterns: Poisson scaling characterized by $\sigma_{n+1}/\sigma_n = \text{const}/(n+1)$, and staircase scaling expressed as $\sigma_{n+1}/\sigma_n = \text{const}$. Using this knowledge Schichtel et al. argue in favour of achieving better control over the theoretical errors associated with exclusive n-jet production. Since this occurs as a background to an overwhelming number of searches at the LHC, they present various cases where the application of jet scaling can have an impact. They discuss the experimental laboratory of γ+jets where one can interpolate between the two patterns imposing simple kinematic cuts [78]. Furthermore, in the context of Higgs boson searches in the vector boson fusion channel, they advertise the use of fitting the n_{jets} distribution to determine the veto survival probability [79]. As an application to BSM searches, they discuss the idea of autofocus [77], a broad inclusive search that scans the parameter space using a missing transverse energy (MET) cut and two-dimensional log-likelihoods given in terms of n_{jets} and $m_{\text{eff}} = p_{T,\text{MET}} + \sum_{\text{jets}} p_{T,i}$.

Jet vetoes have also been discussed as a means to probe the colour structure of hard processes. Taking the example of dijet production under a jet veto in the inter-jet region, S. Marzani, J. Forshaw and M. Seymour worked out analytical predictions [80] based on soft gluon resummation techniques for the observable gap fraction – defined by the cross section, and normalized to the inclusive rate, where a third jet with $p_T > Q_0$ is vetoed in the rapidity region between the two jets. Choosing $Q_0 \gg \Lambda_{\text{QCD}}$ reasonably small, the impact of the underlying event is kept small. Usually one uses Monte Carlo simulations in the form of (matched/merged) parton showers to conduct these or similar studies, but this way one, at least, neglects terms subleading in N_{C}. In fact, predictions obtained by these tools show a large spread. On the contrary Marzani et al. account for the full colour structure and the effects of non-global logarithms. To gain better control over the LL resummation, they also improve the pure eikonal treatment by incorporating energy-momentum conservation at least for the first/hardest emission. A matching to fixed order beyond the leading one is foreseen for future applications.

2.4 Intra-jet evolution and hadron production

Parton showers are vital ingredients to any event-generator based Monte Carlo simulation used in collider physics. For all practical purposes, these algorithms are formulated in the limit where QCD is treated as an SU(N_{C}) gauge theory with arbitrarily large N_{C}, or $N_{\text{C}} \to \infty$.[2] S. Plätzer presented the results of a first successful attempt to include corrections to the parton shower that are beyond the large-N_{C} limit [81]. This work has been done in collaboration with M. Sjö-

[2]There is one exception: $C_{\text{F}} < C_{\text{A}}/2$ is used as the colour factor associated with gluon emission off a quark.

dahl [82]. Using the dipole-like shower framework, they can extend its capabilities such that the full colour structure of the splitting is maintained as originally formulated in the dipole factorization according to Catani and Seymour [83]. They call this a colour matrix-element correction and explain the technicalities of implementing these corrections for subsequent emissions. As a proof-of-concept, results are shown from final-state showering LEP1-like collisions where up to 6 emissions have been colour-matrix-element corrected. An event shape observable like thrust receives only marginal corrections, however specifically designed variables such as the rapidity taken with respect to the thrust axis of the three hardest partons and averaged over these partons may show 5–10% deviations. More generally, this subject constitutes a very interesting direction of research, which – in the context of jet-veto based calculations as discussed in the previous subsection – can be understood as an effort from the Monte Carlo community to improve the accuracy of e.g. gap fraction predictions.

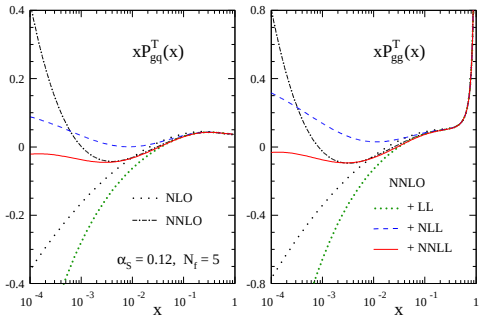

Figure 4: Timelike gluon–quark and gluon–gluon splitting functions (multiplied by x) in their NLO and NNLO approximation. Also shown is their stabilization through leading ($\alpha_s^{n-1} \ln^{2n} x$), next-to-leading and next-to-next-to-leading small-x logarithmic corrections at all orders in α_s; for more details, cf. [84].

In two thorough presentations [85], A. Vogt reviewed the status and spelled out the recent progress that has been achieved in calculating the timelike splitting functions, which govern the evolution of parton fragmentation functions in QCD. Using non-trivial relations to the spacelike DIS case and the supersymmetric limit, A. Almasy, S. Moch and A. Vogt were able to complete an indirect determination of the NNLO (i.e. third order) corrections to the timelike splitting functions, in particular the hitherto missing quark–gluon and gluon–quark quantities were derived [86]. These fixed-order results are adequate except for large ($1 - x \ll 1$) and small ($x \ll 1$) momentum fractions x where higher-order corrections generally include double logarithms that can spoil the perturbative expansions. For $x \lesssim 10^{-3} \ldots 10^{-2}$, small-$x$ effects up to N^{n}LL need to be resummed and added to the N^{n}LO results ($n = 0, 1, 2$). A. Vogt then showed that this completely removes the huge small-x instabilities present in the respective fixed-order results [84], see Figure 4 for an illustration. To accomplish the small-x resummation at N(N)LL, Vogt, Soar, Lo Presti, Kom and Almasy studied the resummation of large-x double logarithms beyond the scope of soft gluon exponentiation [87]. They realized that the same formalism can be applied to the dominant $x^{-1} \ln^{\ell} x$ terms occurring in semi-inclusive annihilation splitting and coefficient functions. Because of the importance in stabilizing the NNLO predictions, the talks also addressed the theoretical basics of these resummations.

Subject of P. Bolzoni's talk was the presentation of a new approach to the determination of the gluon to quark multiplicity ratio in dependence on the jet energy [88]. To get this ratio $r(Q^2)$, he uses the effective-N approach where the ratio can be written as $r(Q^2) \equiv \hat{r}(N_{\text{eff}}, Q^2) = D_g(N_{\text{eff}}, Q^2)/D_s(N_{\text{eff}}, Q^2)$ employing the gluon and sea-quark densities $D_{g/s}$. As a prerequisite, one needs to evaluate the first Mellin moment which implies proper knowledge of the resummation corrections. These corrections can be incorporated by an appropriate choice of $N = N_{\text{eff}}$. P. Bolzoni extended the LO treatment of the effective-N approach using the extensive theoret-

ical input on the higher-order structure of QCD splitting functions that has become available over the last years (see e.g. above). This knowledge on splitting functions can be transferred over to the $D_{g/s}$ densities applying a specific diagonalization technique to the coupled gluon–singlet system whose scale evolution is given by the DGLAP equations. As a result the perturbative series he obtains shows good convergence and the global fit to data works fairly well.

Without any doubt there is huge desire to have a reliable and robust method at hand, which tells a light-quark from a gluon jet, in other words to design a jet flavour tagger going beyond heavy-quark or b-jet identification. The concept of jet flavour however is not well defined. Nevertheless in the context of LO Monte Carlo tools a working definition for jet flavour can be adopted by invoking the (geometrical) correspondence between the jet-initiating hard parton and the emerging jet, assigning the hard parton flavour to the jet. J. Gallicchio, who presented the talk, and his collaborator M. Schwartz conducted a thorough study to identify key handles that yield the largest discriminative power in separating gluon-like from quark-like jets [89]. To pursue this task they chose a Monte Carlo simulation based "laboratory" given by fully hadronized dijet and γ+jet events, which were classified according to jet p_T windows defined at the hadron level. As for the observables, they divided them into two main classes: discrete and continuous ones where for the former, they found the number of charged particles (or, even better, all hadrons), and the latter, the linear radial moment (also known as girth) to be the strongest discriminators. The combination of these two variables into a bin-by-bin likelihood distribution led to additional, significant gain, which they also observed for other pairings of one discrete and one continuous observable. From an experimental point of view the specific ranking of the observables might differ from what Gallicchio and Schwartz established through their exhaustive search [90], but the direction and ideas they give are well testable and shall be scrutinized in an experimental environment.

On behalf of the HERWIG collaboration, C. Röhr gave a short review of the multiple parton interactions (MPI) model implemented in the HERWIG++ event generator [91]. He focused on explaining recent model refinements that were introduced as a consequence of the tuning efforts to LHC data, which can only be described if colour reconnections are properly taken into account. QCD properties such as local parton hadron duality and preconfinement disfavour the generation of massive clusters formed over large momentum distances. The core MPI model, however, enables the formation of too many heavy-mass clusters emerging during the hadronization phase of event generation. In particular those resulting from connections between beam remnants and partons of the evolving partonic interaction are problematic. C. Röhr discussed the physics and implications of two colour reconnection models implemented in newer HERWIG++ versions. The basic idea in both the plain and the statistical model is to use alternative colour connections that overlap in momentum space and lead to a reduction in cluster masses [92]. He showed examples of underlying-event/min-bias observables where good agreement between model prediction and data was achieved once colour reconnections were employed.

V. Lyuboshitz investigated the phenomenological structure of inclusive cross sections for the pair production of neutral kaons taking strangeness conservation, effects of Bose statistics and S-wave strong final-state interactions into account [93]. Similar ideas may be applied to the systems of neutral mesons involving heavy quarks, however in this case one faces difficulties due to the similar lifetimes of the associated CP-even and CP-odd decay channels.

Acknowledgements

We thank the presenters of the Hadronic Final States Session for their contributions. We also thank the conveners of *WG1: Structure Functions and Parton Densities* and *WG2: Diffraction and vector mesons* for coordinating joint sessions with our working group.

References

[1] K. Nowak, K. Rabbertz, and J. Winter, "Summary: Hadronic Final States". http://indico.cern.ch/contributionDisplay.py?contribId=361&sessionId=0&confId=153252.

[2] E. Paul, "Inclusive-Jet Photoproduction at HERA". https://indico.cern.ch/contributionDisplay.py?sessionId=11&contribId=43&confId=153252.

[3] D. Britzger, "Normalised Multi-jet Cross Sections using Regularised Unfolding and Extractions of $\alpha_s(M_Z)$ in Deep-Inelastic Scattering at high Q^2 at HERA". https://indico.cern.ch/contributionDisplay.py?sessionId=11&contribId=163&confId=153252.

[4] Z. Nagy and Z. Trocsanyi. Phys.Rev.Lett. **87** (2001) 082001, arXiv:hep-ph/0104315 [hep-ph].

[5] M. Wobisch, D. Britzger, T. Kluge, K. Rabbertz, and F. Stober. arXiv:1109.1310 [hep-ph].

[6] **fastNLO** Collaboration, D. Britzger *et al.*, *New features in version 2 of the fastNLO project*, 2012. arXiv:1208.3641 [hep-ph]. https://indico.cern.ch/contributionDisplay.py?sessionId=25&contribId=165&confId=153252.

[7] A. Sarkar, P. Jimenez-Delgado, and R. Placakyte, "Summary: Structure Functions". https://indico.cern.ch/contributionDisplay.py?sessionId=11&contribId=357&confId=153252.

[8] A. Yurkewicz, "Measurements of jet production in pp collisions with the ATLAS detector". https://indico.cern.ch/contributionDisplay.py?sessionId=11&contribId=79&confId=153252.

[9] T. Schoerner-Sadenius, "Jets and multi-jets at large rapidities in pp collisions at the LHC". https://indico.cern.ch/contributionDisplay.py?sessionId=11&contribId=184&confId=153252.

[10] T. Sjöstrand, S. Mrenna, and P. Z. Skands. Comput.Phys.Commun. **178** (2008) 852–867, arXiv:0710.3820 [hep-ph].

[11] S. Gieseke, D. Grellscheid, K. Hamilton, A. Papaefstathiou, S. Plätzer, *et al.* arXiv:1102.1672 [hep-ph].

[12] J. R. Andersen and J. M. Smillie. JHEP **1106** (2011) 010, arXiv:1101.5394 [hep-ph].

[13] H. Jung, S. Baranov, M. Deák, A. Grebenyuk, F. Hautmann, *et al.* Eur.Phys.J. **C70** (2010) 1237–1249, arXiv:1008.0152 [hep-ph].

[14] A. R. Davison, "Studies of jet shapes and substructure with ATLAS". https://indico.cern.ch/contributionDisplay.py?sessionId=11&contribId=80&confId=153252.

[15] J. M. Butterworth, A. R. Davison, M. Rubin, and G. P. Salam. Phys.Rev.Lett. **100** (2008) 242001, arXiv:0802.2470 [hep-ph].

[16] L. Ortolan, "Z+Jets results from CDF". https://indico.cern.ch/contributionDisplay.py?sessionId=11&contribId=166&confId=153252.

[17] C. Belanger-Champagne, "Studies of vector-boson+jet production with ATLAS". https://indico.cern.ch/contributionDisplay.py?sessionId=11&contribId=82&confId=153252.

[18] C. Berger, Z. Bern, L. Dixon, F. Febres Cordero, D. Forde, *et al.* Phys.Rev. **D78** (2008) 036003, arXiv:0803.4180 [hep-ph].

[19] M. L. Mangano, M. Moretti, F. Piccinini, R. Pittau, and A. D. Polosa. JHEP **0307** (2003) 001, arXiv:hep-ph/0206293 [hep-ph].

[20] T. Gleisberg, S. Höche, F. Krauss, M. Schönherr, S. Schumann, *et al.* JHEP **0902** (2009) 007, arXiv:0811.4622 [hep-ph].

[21] O. Kuprash, "Isolated photons+jet in DIS". https://indico.cern.ch/contributionDisplay.py?sessionId=11&contribId=44&confId=153252.

[22] K. Velleidis, "Photon Results from CDF".
https://indico.cern.ch/contributionDisplay.py?sessionId=11&contribId=167&confId=153252.

[23] N. Skachkov, "Photon+jets measurements in $p\bar{p}$ Collisions at DØ".
https://indico.cern.ch/contributionDisplay.py?sessionId=11&contribId=169&confId=153252.

[24] L. Carminati, "Photon and photon+jet production measured with the ATLAS detector".
https://indico.cern.ch/contributionDisplay.py?sessionId=11&contribId=81&confId=153252.

[25] I. Abt, "Scaled Momentum Distributions for K^0_s and $\Lambda/\bar{\Lambda}$ in DIS at HERA".
https://indico.cern.ch/contributionDisplay.py?sessionId=11&contribId=42&confId=153252.

[26] M. Britsch, "Inclusive particle production".
https://indico.cern.ch/contributionDisplay.py?sessionId=11&contribId=142&confId=153252.

[27] F. Sikler, "Inclusive hadron production (multiplicities and spectra) in pp collisions in CMS".
https://indico.cern.ch/contributionDisplay.py?sessionId=11&contribId=182&confId=153252.

[28] C. Tsallis. J.Statist.Phys. **52** (1988) 479–487.

[29] V. Khachatryan. JHEP **1009** (2010) 091.

[30] N. Makke, "Pion and Kaon multiplicities from muon-deuteron deep inelastic scattering at COMPASS".
https://indico.cern.ch/contributionDisplay.py?sessionId=11&contribId=100&confId=153252.

[31] G. Karyan, "Multidimensional Hadron Attenuation".
https://indico.cern.ch/contributionDisplay.py?sessionId=11&contribId=56&confId=153252.

[32] A. Zsigmond, "Inelastic cross section measurement in pp collisions in CMS".
https://indico.cern.ch/contributionDisplay.py?sessionId=11&contribId=181&confId=153252.

[33] A. Moraes, "Minimum bias and underlying event studies".
https://indico.cern.ch/contributionDisplay.py?sessionId=11&contribId=83&confId=153252.

[34] H. Haevermaet, "Characterization of the Underlying Event in pp collisions in CMS".
https://indico.cern.ch/contributionDisplay.py?sessionId=11&contribId=183&confId=153252.

[35] J. Alwall, M. Herquet, F. Maltoni, O. Mattelaer, and T. Stelzer. JHEP **1106** (2011) 128, arXiv:1106.0522 [hep-ph].

[36] D. Volanskyy, "Measurement of the forward energy flow in pp collisions at $\sqrt{s} = 7$ TeV with the LHCb experiment ".
https://indico.cern.ch/contributionDisplay.py?sessionId=11&contribId=149&confId=153252.

[37] F. Siegert, "W+n-jet predictions at NLO matched with a parton shower".
https://indico.cern.ch/contributionDisplay.py?contribId=242&sessionId=11&confId=153252.

[38] S. Höche, F. Krauss, M. Schönherr, and F. Siegert. arXiv:1201.5882 [hep-ph].

[39] G. Aad *et al.* Phys.Rev. **D85** (2012) 092002, arXiv:1201.1276 [hep-ex].

[40] S. Höche, F. Krauss, M. Schönherr, and F. Siegert. arXiv:1111.1220 [hep-ph].

[41] S. Prestel, "Matching Tree-Level Matrix Elements with Interleaved Showers".
https://indico.cern.ch/contributionDisplay.py?contribId=243&sessionId=11&confId=153252.

[42] L. Lönnblad and S. Prestel. JHEP **1203** (2012) 019, arXiv:1109.4829 [hep-ph].

[43] L. Lönnblad. JHEP **0205** (2002) 046, arXiv:hep-ph/0112284 [hep-ph].

[44] S. Catani, F. Krauss, R. Kuhn, and B. Webber. JHEP **0111** (2001) 063, arXiv:hep-ph/0109231 [hep-ph].

[45] J. Smillie, "The High-Energy-Jets framework applied to multi-jet production".
https://indico.cern.ch/contributionDisplay.py?contribId=233&sessionId=11&confId=153252.

[46] S. Alioli, J. R. Andersen, C. Oleari, E. Re, and J. M. Smillie. Phys.Rev. **D85** (2012) 114034, arXiv:1202.1475 [hep-ph].

[47] J. R. Andersen, L. Lönnblad, and J. M. Smillie. JHEP **1107** (2011) 110, arXiv:1104.1316 [hep-ph].

[48] S. Chatrchyan *et al.* JHEP **1206** (2012) 036, arXiv:1202.0704 [hep-ex].

[49] G. Aad *et al.* JHEP **1109** (2011) 053, arXiv:1107.1641 [hep-ex].

[50] J. Alcaraz Maestre *et al.* arXiv:1203.6803 [hep-ph].

[51] M. Deák, "Subtraction method for parton shower to $2 \to 2$ matrix element matching in k_t-factorisation". https://indico.cern.ch/contributionDisplay.py?contribId=1&sessionId=11&confId=153252.

[52] F. Hautmann, "Forward jets and small-x physics at the LHC". https://indico.cern.ch/contributionDisplay.py?contribId=271&sessionId=11&confId=153252.

[53] M. Deák, F. Hautmann, H. Jung, and K. Kutak. arXiv:1012.6037 [hep-ph].

[54] M. Deák, F. Hautmann, H. Jung, and K. Kutak. Eur.Phys.J. **C72** (2012) 1982, arXiv:1112.6354 [hep-ph].

[55] S. Marzani, "QCD resummation for jet-mass distributions". https://indico.cern.ch/contributionDisplay.py?contribId=172&sessionId=11&confId=153252.

[56] M. Dasgupta, K. Khelifa-Kerfa, S. Marzani, and M. Spannowsky. arXiv:1207.1640 [hep-ph].

[57] M. Takeuchi, "Boosted hadronically decaying tops in new physics searches". https://indico.cern.ch/contributionDisplay.py?contribId=270&sessionId=11&confId=153252.

[58] T. Plehn, M. Spannowsky, M. Takeuchi, and D. Zerwas. JHEP **1010** (2010) 078, arXiv:1006.2833 [hep-ph].

[59] T. Plehn, M. Spannowsky, and M. Takeuchi. JHEP **1208** (2012) 091, arXiv:1205.2696 [hep-ph].

[60] Z. Li, "Jet Substructure at Hadron Colliders". https://indico.cern.ch/contributionDisplay.py?contribId=164&sessionId=11&confId=153252.

[61] J. C. Collins, D. E. Soper, and G. F. Sterman. Nucl.Phys. **B250** (1985) 199.

[62] L. G. Almeida, S. J. Lee, G. Perez, G. F. Sterman, I. Sung, *et al.* Phys.Rev. **D79** (2009) 074017, arXiv:0807.0234 [hep-ph].

[63] H.-n. Li, Z. Li, and C.-P. Yuan. Phys.Rev.Lett. **107** (2011) 152001, arXiv:1107.4535 [hep-ph].

[64] **CMS** Collaboration, "Jet Transverse Structure and Momentum Distribution in pp Collisions at 7 TeV", Tech. Rep. CMS-PAS-QCD-10-014, CERN, Geneva, July, 2010.

[65] M. Malyshev, "Drell–Yan lepton pair production in the k_t-factorization approach". https://indico.cern.ch/contributionDisplay.py?contribId=3&sessionId=11&confId=153252.

[66] A. Lipatov, M. Malyshev, and N. Zotov. JHEP **1112** (2011) 117, arXiv:1110.6582 [hep-ph].

[67] T. Aaltonen *et al.* Phys.Rev.Lett. **106** (2011) 241801, arXiv:1103.5699 [hep-ex].

[68] D. Wilhelm, "Electroweak Gauge-Boson and Higgs Production at Small q_T: Infrared Safety from the Collinear Anomaly". https://indico.cern.ch/contributionDisplay.py?contribId=314&sessionId=11&confId=153252.

[69] T. Becher, M. Neubert, and D. Wilhelm. JHEP **1202** (2012) 124, arXiv:1109.6027 [hep-ph].

[70] T. Becher and M. Neubert. Eur.Phys.J. **C71** (2011) 1665, arXiv:1007.4005 [hep-ph].

[71] A. Banfi, G. P. Salam, and G. Zanderighi. JHEP **1206** (2012) 159, arXiv:1203.5773 [hep-ph].

[72] A. Banfi, "Jet-veto efficiencies at all orders in QCD". https://indico.cern.ch/contributionDisplay.py?contribId=269&sessionId=11&confId=153252.

[73] S. Dittmaier *et al.* arXiv:1101.0593 [hep-ph].

[74] S. Dittmaier, C. Mariotti, G. Passarino, R. Tanaka, *et al.* arXiv:1201.3084 [hep-ph].

[75] S. Marzani, "Probing colour flow with jet vetoes". https://indico.cern.ch/contributionDisplay.py?contribId=264&sessionId=11&confId=153252.

[76] P. Schichtel, "From Jet Counting to Jet Vetoes". https://indico.cern.ch/contributionDisplay.py?contribId=230&sessionId=11&confId=153252.

[77] C. Englert, T. Plehn, P. Schichtel, and S. Schumann. Phys.Rev. **D83** (2011) 095009, arXiv:1102.4615 [hep-ph].

[78] C. Englert, T. Plehn, P. Schichtel, and S. Schumann. JHEP **1202** (2012) 030, arXiv:1108.5473 [hep-ph].

[79] E. Gerwick, T. Plehn, and S. Schumann. Phys.Rev.Lett. **108** (2012) 032003, arXiv:1108.3335 [hep-ph].

[80] R. M. Duran Delgado, J. R. Forshaw, S. Marzani, and M. H. Seymour. JHEP **1108** (2011) 157, arXiv:1107.2084 [hep-ph].

[81] S. Plätzer, "Subleading N_C improved Parton Showers".
https://indico.cern.ch/contributionDisplay.py?contribId=234&sessionId=11&confId=153252.

[82] S. Plätzer and M. Sjödahl. JHEP **1207** (2012) 042, arXiv:1201.0260 [hep-ph].

[83] S. Catani and M. Seymour. Nucl.Phys. **B485** (1997) 291–419, arXiv:hep-ph/9605323 [hep-ph].

[84] A. Vogt. JHEP **1110** (2011) 025, arXiv:1108.2993 [hep-ph].

[85] A. Vogt, "On the timelike splitting functions at NNLO and beyond & Resummation of large-x and small-x double logarithms in DIS and semi-inclusive e^+e^- annihilation".
https://indico.cern.ch/contributionDisplay.py?contribId=267&sessionId=11&confId=153252,
https://indico.cern.ch/contributionDisplay.py?contribId=268&sessionId=11&confId=153252.

[86] A. Almasy, S. Moch, and A. Vogt. Nucl.Phys. **B854** (2012) 133–152, arXiv:1107.2263 [hep-ph].

[87] A. Almasy, G. Soar, and A. Vogt. JHEP **1103** (2011) 030, arXiv:1012.3352 [hep-ph].

[88] P. Bolzoni, "A new approach to hadron multiplicity ratio".
https://indico.cern.ch/contributionDisplay.py?contribId=96&sessionId=11&confId=153252.

[89] J. Gallicchio, "Quark and Gluon Tagging at the LHC".
https://indico.cern.ch/contributionDisplay.py?contribId=287&sessionId=11&confId=153252.

[90] J. Gallicchio and M. D. Schwartz. Phys.Rev.Lett. **107** (2011) 172001, arXiv:1106.3076 [hep-ph].

[91] C. Röhr, "The Underlying Event in HERWIG++".
https://indico.cern.ch/contributionDisplay.py?contribId=367&sessionId=11&confId=153252.

[92] S. Gieseke, C. Röhr, and A. Siodmok. arXiv:1206.0041 [hep-ph].

[93] V. Lyuboshitz, "On the pair correlations of neutral K, D, B and B_s mesons with close momenta produced in inclusive multiparticle processes".
https://indico.cern.ch/contributionDisplay.py?contribId=17&sessionId=11&confId=153252.

Summary of the Heavy Flavour Working Group

Jolanta Brodzicka[1], *Massimo Corradi*[2], *Ingo Schienbein*[3], *Reinhard Schwienhorst*[4]

[1] Krakow University, [2] INFN Bologna, [3] LPSC Grenoble, [4] Michigan State University

DOI: http://dx.doi.org/10.3204/DESY-PROC-2012-02/362

We review theoretical and phenomenological aspects of heavy flavour production as discussed in the heavy flavour working group of the DIS 2012. Recent theoretical progress includes approximate NNLO calculations for heavy quark structure functions in deep inelastic scattering, the extension of the ACOT heavy flavour scheme to jet production, and advances in top physics where the highlight is clearly the first complete NNLO QCD prediction for top pair production in the $q\bar{q}$ annihilation channel. Furthermore, state of the art phenomenological predictions for open charm and bottom, charmonium, and single top and top pair production are discussed in addition to other topics such as the effect of double parton scattering on heavy quark production. New measurements on charm and beauty production presented in the heavy flavor working group are summarized and discussed in comparison with QCD predictions. Top quark strong and weak couplings as well as top quark properties are being measured with precision at the LHC and the Tevatron. We summarize also recent results on spectroscopy of charmonia, bottomonia and b-hadrons, along with studies of their decays and properties. Searches for physics beyond Standard Model through precise measurements of rare decays of heavy flavours are discussed as well.

1 Introduction

The measurement of heavy quark production provides a test of many aspect of QCD. A considerable progress in the QCD calculations for heavy-quark production has been done in the recent years. The theoretical results presented at this workshop are reviewed in Section 2. Many new results have been presented on the production of heavy quarks from different types of collisions: deep inelastic scattering, photoproduction, pp and $p\bar{p}$, and nuclear collisions (PbPb, AuAu, CuCu, dAu). Results on charm and beauty production are summarized in Section 3. Due to space constraints the results from heavy-ion collisions, which would deserve a dedicated summary, are not discussed. The measurements of top quark production are discussed in Section 4 with the new results on top properties. Finally Section 5 summarizes the updates in heavy hadron spectroscopy and on searches beyond the Standard Model exploiting B-hadron decays.

2 Theory

2.1 Deep inelastic scattering

Deep inelastic scattering (DIS) data form the backbone of global analyses of parton distribution functions (PDFs). Precise determinations of PDFs require the inclusion of heavy (charm,

bottom) quark mass terms in the calculation of DIS structure functions at higher orders in perturbation theory. In fixed order perturbation theory the charm contribution F_a^c to the inclusive DIS structure function F_a $(a = 2, L)$ is given as a convolution of PDFs f_j with heavy quark Wilson coefficients H_j $(j = g, u, d, s)$:

$$F_a^c(x, Q^2) = H_{a,j}(x, \frac{Q^2}{\mu^2}, \frac{m^2}{\mu^2}) \otimes f_j(x, \mu^2)\,, \tag{1}$$

where m is the charm quark mass and μ the factorization scale (which has been identified with the renormalization scale). For neutral current DIS, the coefficients $H_{a,j}$ are currently known to order $\mathcal{O}(\alpha_s^2)$. At this conference, progress has been reported to construct approximate heavy quark Wilson coefficients at order $\mathcal{O}(\alpha_s^3)$ using the information from different kinematic limits.

Due to mass factorization, in the limit $Q^2 \gg m^2$ the $H_{a,j}$ can be written as a convolution of light flavor Wilson coefficients $C_{a,i}$ with universal operator matrix elements (OMEs) A_{ij}:

$$H_{a,j} \simeq C_{a,i}(x, \frac{Q^2}{\mu^2}) \otimes A_{ij}(x, \frac{m^2}{\mu^2})\,. \tag{2}$$

Indicating the loop order as upper index one can write generically

$$H^{(3)} \simeq C^{(0)} \otimes A^{(3)} + C^{(1)} \otimes A^{(2)} + C^{(2)} \otimes A^{(1)}\,, \tag{3}$$

where the light flavor Wilson coefficients are available up to order $\mathcal{O}(\alpha_s^3)$ [1]. In order to construct the heavy quark Wilson coefficient functions $H_{a,j}^{(3)}$ in the asymptotic limit, the OMEs are needed up to the same order $\mathcal{O}(\alpha_s^3)$ and partial results for certain color factors have been obtained very recently [2]. As an important application, the OMEs are needed for the definition of variable flavor number schemes since they enter the matching conditions for the PDFs with n_f and $n_f + 1$ active flavours.

In addition to the asymptotic limit $Q^2 \gg m^2$, it is possible to exploit universal features in the threshold region $\beta = \sqrt{1 - 4m^2/s} \simeq 0$ where Sudakov logarithms $\ln \beta$ can be resummed and in the high energy limit where information on leading and next-to-leading small-x logarithms is available in order to construct improved heavy quark coefficient functions at order $\mathcal{O}(\alpha_s^3)$ [3, 4].

As is well-known, the heavy quark coefficient functions H_i are not IR-safe: $H_i \to \infty$ for $\frac{Q^2}{m^2} \to \infty$. Therefore, most of the modern global analyses of PDFs use so called general mass variable flavor number schemes (GM-VFNS) where the large logarithms $\ln \frac{Q^2}{m^2}$ are removed from the coefficients H_i and resummed by heavy quark initiated subprocesses with evolved heavy quark parton distributions. At the same time, finite mass terms $\frac{m^2}{Q^2}$ are retained in the subtracted IR-safe Wilson coefficients $\hat{H}_i$. For use in precision determinations of PDFs, these GM-VFNS have to be formulated at NNLO and F. Olness presented approximate results for the neutral current structure functions F_2 and F_L in the ACOT GM-VFNS [5] up to order $\mathcal{O}(\alpha_s^3)$ [6].

2.2 Open charm and beauty

Most of the heavy flavour schemes have been formulated for inclusive DIS processes and are used in global analyses of PDFs. On the other hand, less inclusive processes provide many additional tests of pQCD in various kinematic regions and are closer to the experimental measurements.

However, theoretical calculations are much more challenging and even more so if heavy quark mass effects have to be taken into account. Nevertheless, any heavy flavour scheme should also be applicable to less inclusive observables in order to be considered a general formalism of perturbative QCD (pQCD) including heavy quark masses [7]. Relying on a factorization theorem with heavy quarks [8], ACOT-like variants of the GM-VFNS have been applied to inclusive heavy meson production in DIS [9], photoproduction [10], hadroproduction [11, 12], and electron-positron annihilation [13]. At this conference updated numerical results for inclusive D and B meson production in the GM-VFNS at the LHC have been presented [14]. Furthermore, a new method for calculating DIS jet production in the ACOT scheme has been reported extending the dipole subtraction formalism to all possible QCD splitting processes with heavy quarks including splittings of coloured, massive particles in the initial state [15].

An interesting feature of exclusive processes with a heavy quark in the final state is that they are useful to probe heavy flavour PDFs. In most global analyses of PDFs the charm and bottom distributions are generated "radiatively" using perturbatively calculated boundary conditions. With other words, no new fit parameters are associated to the charm and bottom PDFs. However, a purely perturbative treatment might not be adequate, in particular for the charm quark with mass $m_c \simeq 1.5$ GeV, and in fact non-perturbative models exist that predict an intrinsic charm (IC) component in the nucleon [16]. Clearly, the heavy quark PDFs should be tested since they play an important role in some key processes at the LHC [17]. A promising way to constrain models on IC is the measurement of inclusive D meson production at RHIC or with the LHCb detector at the LHC where at forward rapidities the differential cross section can be enhanced by a factor of up to 5 compared to the prediction with a radiatively generated charm PDF [14]. Another process which is very sensitive to the heavy quark PDF is direct photon production in association with a heavy quark jet [18]. Data from the D0 experiment at the Tevatron [19, 20] overshoot the standard NLO QCD predictions [21] at large transverse photon momenta and the inclusion of an intrinsic heavy quark component in the nucleon can reduce the difference between data and theory but not fully resolve it. Measurements of this process at RHIC and the LHC probe the heavy quark PDFs in different regions of the momentum fraction x and would be useful to shed more light on the current situation. In addition, the measurements at the LHC would provide a baseline for $\gamma + Q$ production in pA [22] and AA collisions [23].

Finally, work has been presented on $c\bar{c}$ production in the k_T-factorization formalism. The predictions for D meson production at the LHC somehow undershoot the data of ALICE and LHCb (preliminary). Furthermore, the production of two $c\bar{c}$ pairs in a formalism with double-parton scattering has been discussed. The predicted cross sections for $c\bar{c}c\bar{c}$ at the LHC receive similar contributions from single-parton and from double-parton scattering [24].

2.3 Charmonium production

The charmonium J/ψ has been extensively studied experimentally ever since its discovery in 1973. However, theoretically, heavy quarkonium production and decay are still not well understood. A rigorous framework for theoretical studies is provided by the factorization theorem of nonrelativistic QCD (NRQCD) [25] where the charmonium production cross section factorizes into calculable short distance cross sections for the production of a heavy quark pair $c\bar{c}[n]$ in a Fock state n and nonperturbative long distance matrix elements (LDMEs) $\langle \mathcal{O}^{J/\psi}[n] \rangle$ which have to be extracted from experiment. The Fock states are described by quantum numbers for spin, orbital and total angular momentum and color, $n = {}^{2s+1}L_J^{[c]}$. For J/ψ production

the following states are considered: $n = {}^3S_1^{[1]}, {}^1S_0^{[8]}, {}^3S_1^{[8]}, {}^3P_J^{[1]}$ including color-octet (CO) states $[c] = [8]$ in addition to color singlet (CS) states $[c] = 1$.

A NLO NRQCD analysis of the J/ψ yield and polarization based on the results in [26] can be summarized as follows [27, 28]: (i) A global analysis of unpolarized world J/ψ data from hadroproduction, photoproduction, two-photon scattering and electron-positron annihilation experiments allows to determine the three CO LDMEs $\langle \mathcal{O}^{J/\psi}({}^3S_1^{[1]})\rangle, \langle \mathcal{O}^{J/\psi}({}^1S_0^{[8]})\rangle, \langle \mathcal{O}^{J/\psi}({}^3S_1^{[8]})\rangle$ and the data are well described. Here it is important to note that hadroproduction data alone can not constrain all three matrix elements even including polarization data. (ii) The predictions from the NLO NRQCD global analysis of unpolarized world data do not agree with J/ψ polarization data from CDF I and the new measurements from CDF II. With other words it is not possible to describe the unpolarized hadro- and photoproduction data and the CDF polarization measurements with one set of CO LDMEs. Conversely, the new measurements from ALICE agree with NLO NRQCD within errors. Future precise polarization measurements at the LHC will have the potential to confirm or dismiss the universality of the LDMEs.

2.4 Top quark physics

In the past few years, there has been impressive theoretical progress in the calculation of top quark pair production beyond NLO. A highlight has certainly been the completion of the exact NNLO QCD corrections to $q\bar{q} \to t\bar{t} + X$ which represents a theoretical breakthrough because it is the first ever NNLO calculation involving more than two coloured particles and/or massive fermions [29, 30]. As a last missing piece for this calculation, suitable counter terms needed to regulate infrared divergences in the interference terms of tree-level and one-loop amplitudes with three particles in the final state (of which two are massive) have been derived in [31, 32]. For $\mu_R = \mu_F =: \mu$ the partonic cross section reads in NNLO ($k \leq 2$):

$$\hat{\sigma}_{q\bar{q}}(\beta, m^2, \mu^2) = \frac{\alpha_s^2}{m^2} \sum_{k=0}^{2} \sum_{l=0}^{k} \alpha_s^k \sigma_{q\bar{q}}^{(k,l)}(\beta) L^l \,, \tag{4}$$

where $L = \ln(\mu^2/m^2)$. The scale-dependent terms $\sigma_{q\bar{q}}^{(k,l)} L^l$ with $l \geq 1$ can be generally computed from the lower order functions $\sigma_{q\bar{q}}^{(k'<k,l=0)}$ by renormalization group methods [33] so the new information resides in the function $\sigma_{q\bar{q}}^{(2,0)}(\beta)$. Furthermore, it is possible to perform an all order resummation of universal Sudakov logarithms $\ln \beta$, which become dominant close to the production threshold ($\beta \to 0$), at next-to-next-to-leading logarithmic (NNLL) accuracy. The NNLO+NNLL result allows one to predict the $t\bar{t}$ production cross section at the Tevatron with significantly improved precision at the level of 3% [30]. A C++ program for the calculation of the $t\bar{t}$ total cross section including the full NNLO corrections is publicly available [34].

In addition to the production threshold ($\beta = \sqrt{1 - 4m_t^2/\hat{s}} \to 0$) all order resummations can also be performed for the pair invariant mass (PIM) threshold $z = M_{t\bar{t}}^2/\hat{s} \to 1$ treating the $t\bar{t}$ system as a pair and the one particle inclusive (1PI) threshold $s_4 = \hat{s} + \hat{t}_1 + \hat{u}_1 \to 0$ where one integrates over the phase space of one of the heavy quarks. The latter two thresholds are relevant for differential distributions in the pair invariant mass and for the transverse momentum or rapidity of the observed heavy quark, respectively, in addition to the total cross section and different approaches to resum them exist in the literature [35, 36, 37]. The differences between the methods concern formally subleading terms which, however, can be numerically important. Alternatively, approximate NNLO theories can be constructed by combining the

information from the exact NLO calculation with all universal (soft and collinear) logarithmic terms appearing at NNLO, see also Sec. 2.1.

Within the approach based on soft-collinear-effective theory (SCET), phenomenological predictions for the total cross section [38] and various differential distributions [39] at the Tevatron and the LHC have been discussed [35]. Furthermore, using standard momentum-space resummation in pQCD, a large number of numerical results for the differential and total cross sections for both, top pair [40] and single top production [41], have been presented by N. Kidonakis [36]. One observable which has received a lot of attention recently is the top quark charge asymmetry. It was shown, that the higher order predictions are consistent with NLO and hence do not resolve the discrepancy with the Tevatron data at high invariant mass and rapidity [42].

More exclusive top observables are important because they can have sizable production cross sections or constitute important backgrounds for Higgs searches. Here theoretical progress has been achieved by merging exact NLO calculations with parton showers. At this conference, results have been presented for the production of top quark pairs with one jet ($t\bar{t}+j$) [43, 44]. In addition, several processes ($t\bar{t}+j$ [45], $t\bar{t}+Z$ [46], $t\bar{t}+H/A$ [47] and $W^+W^-b\bar{b}$) have been implemented into the PowHel framework as has been discussed in a talk by A. Kardos [48].

3 Charm and beauty production

3.1 Heavy quarkonium production

Measurements of the production cross sections of prompt J/ψ have been performed by the four LHC collaborations. In addition CMS [49] and LHCb [50] also presented measurements of $\psi(2S)$ production which is less influenced by feed-down from the decays of heavier states. These results are reasonably well described by the NRQCD predictions including CS+CO contributions at NLO as discussed in the theory section 2. Calculations based on the k_T factorization approach including only CS diagrams are also able to describe the data.

The situation is less clear when the polarization of the produced state is considered. The new measurements of the J/ψ and $\Upsilon(nS)$ helicity, presented respectively by the ALICE [51] and CDF [52, 53] collaborations, agree marginally with the NRQCD NLO prediction. The CDF Υ result, obtained with a integrated luminosity of 5.7 fb^{-1}, is in good agreement with previous CDF data obtained with lower luminosity while the disagreement with the measurement by the D0 collaboration persists.

3.2 Charm production in DIS and $F_2^{c\bar{c}}$

The H1 and ZEUS collaborations are finalizing their effort to measure charm and beauty production in DIS and to provide the best possible measurement of $F_2^{c\bar{c}}$, the component of the inclusive structure function F_2 with charm in the final state. The H1 collaboration published their final measurement of D^{*+} production in DIS [54], while ZEUS presented preliminary results on D^{*+} production and on charmed jets tagged using secondary vertices [55, 56]. These results are reasonably well described by NLO QCD calculations as shown in Fig. 1 (left) for the D^{*+} case. Charm cross section measurements obtained with different techniques are used to extract $F_2^{c\bar{c}}$. Figure 1 (right) shows the ZEUS preliminary measurements compared to a preliminary combination including H1 data and ZEUS measurements from older data sets. Once combined, these data will improve the knowledge of $F_2^{c\bar{c}}$, reaching a precision of about 5% over a wide range of x and Q^2.

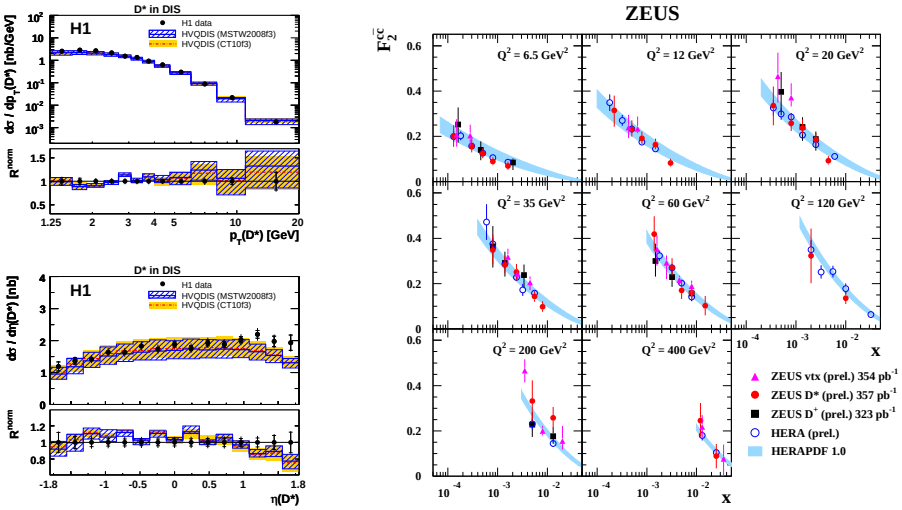

Figure 1: Left: H1 measurement of the D^{*+} meson production in DIS for $Q^2 > 5$ GeV^2, $p_T > 1.25$ GeV and $|\eta| < 1.8$ as a function of p_T and η, compared to NLO QCD calculations. Right: the charm structure function $F_2^{c\bar{c}}$. Recent preliminary ZEUS results based on secondary vertex tagging, on D^{*+} and D^+ mesons are compared to the preliminary combination of H1 and previous ZEUS data and to a GM-VFNS prediction based on the HERAPDF1.0 PDFs.

3.3 Charm photo- and hadro-production

The H1 collaboration presented a new measurement of the D^{*+} photoproduction cross sections [57] that has been compared to various QCD calculations: fixed-order NLO, the NLO Monte-Carlo matched to parton-shower (MC@NLO) [58] and GM-VFNS. They all describe well the data within their theoretical uncertainties. The ZEUS collaboration presented a precise measurement of the charm fragmentation fractions into different charmed hadrons, based on photoproduction data [59]. The good agreement with e^+e^- results supports the universality of charm fragmentation.

The ATLAS and ALICE collaborations presented differential cross sections for the production of D mesons [60, 61]. The results are in agreement with QCD predictions at NLO matched to next-to-leading-log resummation (FONLL) [62] and, at transverse momenta larger than the charm mass, also to GM-VFNS calculations [14]. Compared to FONLL, data are in general on the upper edge of the theoretical uncertainty, which is particularly large at low transverse momenta, as shown e.g. in Fig. 2 (left). Less inclusive observables do not match completely the standard expectations. This is the case of the measurement of D^* jets by ATLAS [63], in which the fraction of the jet momentum carried by the associated D^* is on average lower than the predictions based on standard QCD programs and on the charm fragmentation functions measured in e^+e^- experiments. The measurement of double charm (CC) and charmonium-charm ($J/\psi C$) production made by the LHCb collaboration [64] is also challenging our understanding of heavy-flavour production. The rate of CC meson pairs is $\approx 10\%$ of the $C\bar{C}$ rate, as shown in Fig. 2 (right). Considering that cc production occurs at $O(\alpha_s^4)$, while $c\bar{c}$ pairs are produced at

$O(\alpha_s^2)$, this result appears unexpected at a first sight. Anyway a comparison with detailed QCD calculations is needed to understand the origin of this large CC fraction. Proposed explanations are multiparton interactions or the excitation of intrinsic charm in the proton.

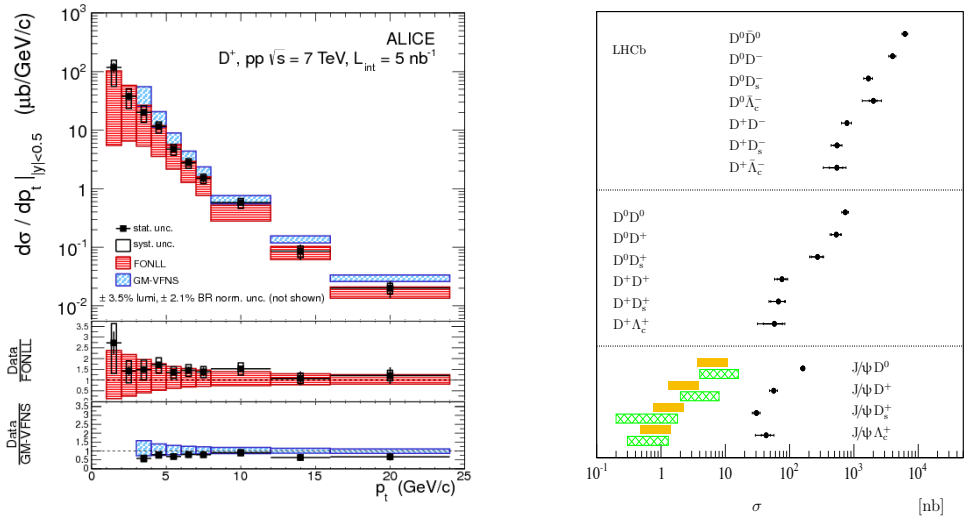

Figure 2: Left: D^+ meson production cross section differential in p_T as measured by ALICE in pp collisions compared to FONLL and GM-VFNS predictions. Right: cross section for the production of two hadrons containing charm quarks as measured by LHCb for $2 < y < 4$ and $3 < p_T < 12$ GeV: $C\bar{C}$ (up), CC (middle), $J/\psi C$ (bottom). Filled areas correspond to theoretical calculations for gluon-gluon processes.

3.4 Beauty production

New measurements of open beauty production at the LHC have been presented, using different techniques in different kinematic ranges. All the four LHC experiments measured beauty production by tagging non-prompt J/ψ or $\psi(2S)$ from B-hadron decays, covering a large range in p_T (from zero to tens of GeV) and in rapidity ($0 < y < 4.5$). The results are in good agreement with the FONLL theory within relatively large theoretical uncertainties, as shown in Fig. 3 (left) for the CMS case. They CMS collaboration also presented a measurement of the cross section for di-muons originating from the decays of $b\bar{b}$ pairs [65] which provides precise data in the low-p_T regime. The measured cross section is in agreement with the MC@NLO prediction within the $\approx 30\%$ theoretical uncertainty.

At high p_T, the measurement of beauty production has been extended by the ATLAS and CMS collaborations using b-jet tagging algorithms [66, 67]. Figure 3 (right) shows, as an example, the ATLAS inclusive b-jet cross section in bins of p_T and rapidity, measured using 2010 data and compared to the predictions from the MC@NLO and the POWEG+Pythia [68] NLO Monte Carlos. The agreement is good, especially with POWEG+Pythia which features a better treatment of beauty fragmentation and decays. The uncertainty is dominated by the experimental systematics on b-tagging efficiency and on b-jet energy scale that sum up to $\approx 16\%$ at $p_T = 100$ GeV and central rapidity.

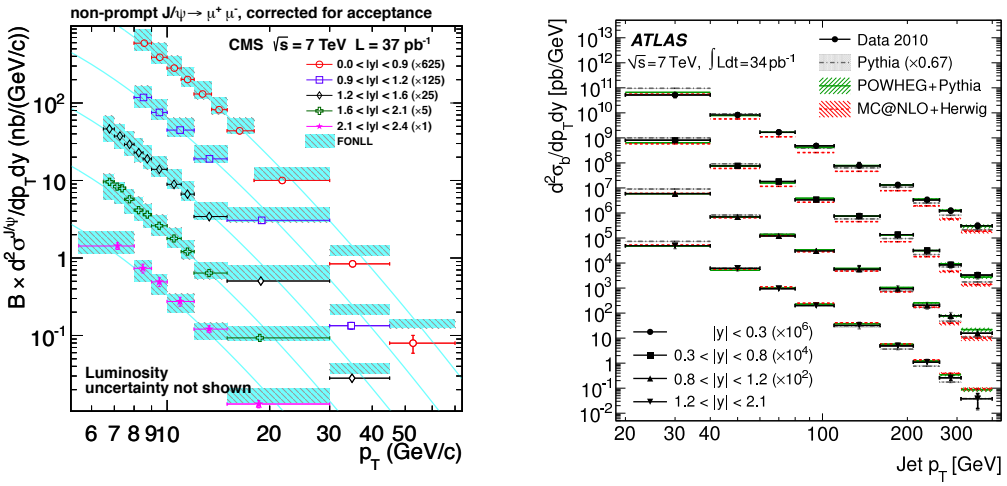

Figure 3: Left: non-prompt J/ψ production from b-hadron decays measured by CMS compared to FONLL predictions. Right: comparison of the inclusive b-jet cross section measured by ATLAS to various QCD predictions.

4 Top quark physics

Many top quark measurements have been made at the Tevatron and the LHC, both in top quark pair and single top production. At the Tevatron, results using half or all of the final data set have been released, and results from the LHC with 2011 data collected at 7 TeV are available.

4.1 Top quark pair production

The top quark pair production cross section has been measured in different final states. Cross section measurements from the CDF and D0 collaborations with up to 5 fb^{-1} of 1.96 TeV proton-antiproton data utilize electrons, muons, taus and all-hadronic final states. Each experiment has measured the cross section with an uncertainty of better than 8% [69, 70].

The LHC collaborations ATLAS [71, 72] and CMS [73, 74] have measured the top quark pair production cross section in several different final state configurations, summarized in Fig. 4. This includes tau lepton final states, and for ATLAS even the tau+jets and all-hadronic final states. All measurements show good agreement with the SM expectation.

CMS additionally has a preliminary measurement of the differential cross section as a function of p_T and rapidity of the $t\bar{t}$ system [75]. ATLAS has preliminary measurements of the $t\bar{t}$ cross section with a veto on forward jets [76] and of the cross section for $t\bar{t}$ production in association with a photon [77].

4.2 Single top quark production

Single top quark production has been observed both at the Tevatron and the LHC. D0 has measured the cross section for the t-channel production mode [78] as well as the total single

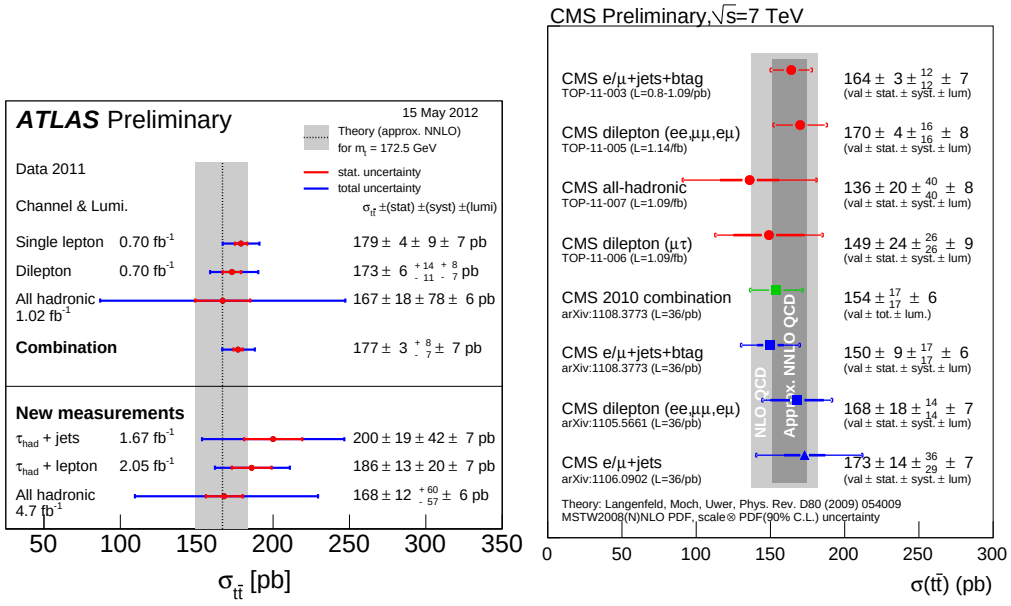

Figure 4: Summary of top quark pair production cross section measurements (left) by ATLAS and (right) by CMS.

top production cross section [79]. CDF has a preliminary measurement of single top quark production based on 7.5 fb^{-1} of data [80]. Figure 5 (left) shows the 2d contour of t-channel vs s-channel cross sections measured by CDF and compares them to the SM.

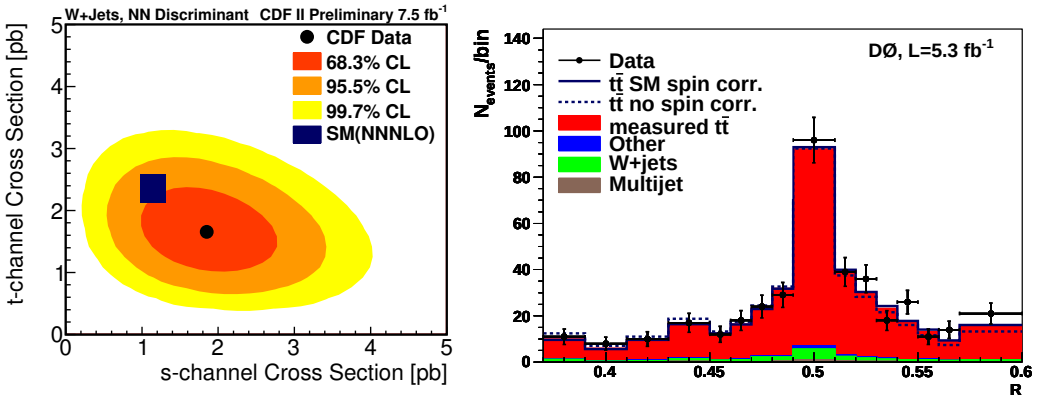

Figure 5: (left) Single top quark production cross section for s-channel and t-channel from CDF and (right) top quark spin correlation measurement by D0.

ATLAS has measured the t-channel cross section to be 83 ± 20 pb using 1 fb^{-1} of 7 TeV data using a neural network approach [81]. A cut-based measurement also provides separate

top and antitop quark t-channel cross sections [81]. CMS has measured a t-channel cross section of 70.3 ± 11.5 pb [82]. ATLAS and CMS also have first searches for Wt associated production [83, 84], but have not yet measured the cross section. ATLAS also has searched for s-channel single top quark production [85].

The single top quark cross section is proportional to the CKM matrix element $|V_{tb}|^2$, and all collaborations have derived lower limits on $|V_{tb}|$. D0 has also extracted a measurement of the top quark width from the t-channel cross section through a combination with the flavour composition measurement in top quark decays [86].

The single top quark final state is sensitive to many models of new physics. Recent searches for flavor-changing neutral currents [87] and new heavy bosons by ATLAS [88], and for anomalous couplings by D0 [89, 90] have not found any evidence for new physics and set stringent limits.

4.3 Top quark mass

The mass of the top quark has been measured with high precision at both the Tevatron and the LHC. D0 has a new top quark mass measurement in the dilepton channel [91] and CDF has a new measurement in the lepton+jets channel [92] with an uncertainty of 1.3 GeV. The Tevatron average of 173.2 GeV has an uncertainty of only 1.0 GeV [93].

ATLAS and CMS have not yet reached that level of precision but have also produced first results. The ATLAS top quark mass measurement has an uncertainty of 2.4 GeV and the CMS measurement has an uncertainty of 1.3 GeV. CMS also measures the mass difference between top and antitop quarks [94].

4.4 Top quark properties

Abundant top quark samples are now available making measurements such as spin correlation in top quark pair production possible. D0 has reported evidence for spin correlation [95], shown in Fig. 5 (right). A preliminary CDF study finds a value consistent with no spin correlation in a similar size data set [96]. ATLAS also observes spin correlation [97].

Since the Tevatron is a proton-antiproton collider, a forward/backward asymmetry in top quark pair production can be measured in the rapidity difference between the top and antitop quark. CDF has a preliminary result for the full Tevatron data set [98], finding a significant deviation from the SM. D0 also sees a deviation from the SM expectation [99].

At the LHC proton-proton collider, a possible asymmetry is reflected as a charge asymmetry which is more difficult to measure. The ATLAS measurement of the charge asymmetry is consistent with the SM expectation [100]. The CMS measurement is also consistent with the SM [101].

5 Spectroscopy and rare decays

5.1 Spectroscopy of heavy quarkonia and b-hadrons

Comprehensive study of heavy quarkonia is an important test of the QCD. The goal is to complete the predicted $c\bar{c}$ and $b\bar{b}$ spectra, measure their properties and transitions. Such an experimental information allows validating the QCD predictions obtained either in the theoretical approach, where the $Q\bar{Q}$ multiplets are calculated on the lattice, or in the phenomenological

one i.e. from the potential models which attempt to model QCD features by describing the interquark potential.

In the charmonium landscape, all the states lying below the threshold for decays to open charm were discovered. Agreement with predictions of the potential models is quite good, whereas the lattice usually underestimates some of the splittings, for instance the $J/\psi - \eta_c(1S)$ hyperfine one [102]. The era of precise lattice QCD calculations for charmonia above the $D\bar{D}$ threshold has only begun. There are only a few such charmonia observed, whereas most of the missing states (except for ground D-wave states) are expected to decay dominantly into $D^{(*)}\bar{D}^{(*)}$-like final states and to have quite large widths. Over the last decade many $c\bar{c}$-like states, called the X, Y, Z, were observed by experiments at e^+e^- as well as hadron colliders [102]. Their properties are either unusual for conventional charmonia (large widths for hadronic transitions, non-zero electric charge) or simply don't match any empty slots in the $c\bar{c}$ spectrum. Therefore they are considered as candidates for exotic hadrons, like molecules, tetraquarks or hybrids, which are also predicted within the QCD framework. The experiments continue their efforts to confirm and/or further study properties of these resonances. Belle have investigated the properties of the most famous $c\bar{c}$-like state, the $X(3872)$ in its discovery decay mode $J/\psi\pi^+\pi^-$. The world best upper limit on its width was set at 1.2 MeV/c^2 [103]. Neither the charged partner $X^\pm \to J/\psi\pi^\pm\pi^0$ nor the C-odd partner searched for in $J/\psi\eta$ and $\chi_{c1}\gamma$ final states have been observed. Instead, Belle found the first evidence of the narrow $\psi_2(1D)$ charmonium decaying to the $\chi_{c1}\gamma$ at the mass of 3823 ± 3 MeV/c^2 [104]. Babar have reported study of the $\eta_c\pi^+\pi^-$ produced in two-photon annihilation. Such a study is important to test an interpretation of the $X(3872)$ as the $\eta_{c2}(1D)$ or to search for the $\eta_{c2}(1D)$ itself, but no significant signal for neither of them has been found. Charged $c\bar{c}$-like states play a special role, as they must consist of at least four quarks. Belle observed three such resonances, the $Z(4430)^\pm \to \psi'\pi^\pm$ and $Z(4050)^\pm, Z(4250)^\pm \to \chi_{c1}\pi^\pm$ produced in $B \to Z^\pm K$ decays [105], however Babar have not confirmed any of them [106]. Since the upper limits set by Babar on the product branching fractions do not contradict the Belle measurements, the conclusive results are expected to come from the LHC experiments. Both LHCb and CMS have demonstrated that they will play an important role in studies of $c\bar{c}$ spectroscopy. Using only a small fraction of their data, they measured precisely mass and pp production of the $X(3872)$ [107, 108]. The $X(3872) \to J/\psi\pi^+\pi^-$ yield expected with the 2011 Run data will hopefully allow them to discriminate between the two possible spin-parities of the $X(3872)$, 1^{++} and 2^{-+}.

Experimental data on the bottomonium spectrum remain even more incomplete. The field has become lively once B-factories took data at $\Upsilon(\mathrm{n}S)$'s other than $\Upsilon(4S)$, which allowed Babar to discover the ground bottomonium $\eta_b(1S)$ in the $\Upsilon(2,3S) \to \eta_b(1S)\gamma$ transitions [109]. Belle studies of the data collected at the $\Upsilon(5S)$ have revealed that its properties differ from other $\Upsilon(\mathrm{n}S)$'s. A reason for abnormally large transitions $\Upsilon(5S) \to \Upsilon(1,2,3S)\pi^+\pi^-$ [110] are two charged $b\bar{b}$-like states $Z_b(10610)^\pm, Z_b(10650)^\pm \to \Upsilon(1,2,3S)\pi^\pm$ that mediate these transitions [111]. The $\Upsilon(5S) \to h_b(1,2P)\pi^+\pi^-$ transitions have been found to be as large and also saturated with the $Z_b(10610)^\pm, Z_b(10650)^\pm \to h_b(1,2P)\pi^\pm$ amplitudes. Interpretation of the $Z_b^\pm$ states as $B^{(*)}\bar{B}^*$ molecules seems to be supported by their masses and decay amplitude pattern [112]. The $\Upsilon(5S) \to h_b(1,2P)\pi^+\pi^-$ transitions allowed the first observation of the spin-singlet $h_b(1P)$ and $h_b(2P)$ bottomonia [113]. Belle have also reported a measurement of the mass and the first measurement of the width of the $\eta_b(1S)$ produced in $h_b(1P) \to \eta_b(1S)\gamma$. Measured $\eta_b(1S) - \Upsilon(1S)$ hyperfine splitting improved agreement with the theoretical predictions [102]. The $b\bar{b}$ spectroscopy is also studied at the hadron colliders. The first particle observed at the LHC has been a candidate for $\chi_b(3P)$ found at 10530 ± 51 MeV/c^2 by Atlas in

$\chi_b(3P) \to \Upsilon(1,2S)\gamma$ transitions [115]; it has been soon confirmed by DØ [116].

LHCb has taken over a leading role in studies of b-hadrons being out of reach of the B-Factories. The presented results on B_c mesons, such as a mass measurement using the $B_c^+ \to J/\psi\pi^+$ decays, their production relative to topologically similar $B^+ \to J/\psi K^+$ reference decays, as well as the first observation of the $B_c^+ \to J/\psi\pi^+\pi^-\pi^+$ decays, comprise an important experimental input on this heaviest b-meson observed so far [117]. The world best mass measurements of b-baryons: Λ_b^0, Ξ_b^- and Ω_b^- and study of the Λ_b production allowing extraction of the $\frac{f_{\Lambda_b}}{f_d+f_u}$ production fraction, nicely improve previous Tevatron measurements.

5.2 Rare decays of heavy flavours

Search for physics beyond the Standard Model (SM) is nowadays one of the main goals of particle physics. Precision studies of the $B_{(s)}$, $D_{(s)}$ and τ decays which in the SM are either suppressed or forbidden, allow one to search for New Physics (NP) effects. Virtual contributions of NP particles can enter the diagrams underlying the studied processes and modify the SM predictions for various observables, like decay rate, CP violation or polarization. The deviation of a given observable from the SM will be a sign of NP, whereas the study of correlations between observables will allow one to identify the nature of NP. Such indirect searches are complementary to the direct ones performed at the LHC. All the measurements performed so far to overconstrain the unitarity triangle (UT) describing B meson system seem to be consistent with each other within their uncertainties [118] and thus constrain NP corrections to be at most at the 10% level. Numerous tensions between the measurements and the SM predictions reported over the last few years encourage to investigate them further with increased precision.

The asymmetry of same-sign muon pairs from semileptonic $B_{(s)}$ decays was found by D to be larger than the SM prediction by 3.9σ [119]. This asymmetry is related to CP violation in $B^0-\bar{B}^0$ and $B_s^0-\bar{B}_s^0$ mixing. A phase entering the latter, the ϕ_s, can be independently measured via a time dependent analysis of $B_s^0 \to J/\psi\phi$, where CP violation occurs via interference between the decay proceeding with and without B_s mixing. Updated measurements of the ϕ_s and $\Delta\Gamma_s$ by CDF [120] and LHCb [121] show that the overall agreement with the SM is good. This might suggest the NP contribution in the $B^0 - \bar{B}^0$ mixing, and such a picture seems to be supported by a 2.5σ discrepancy between the $\sin 2\beta$ UT parameter measured directly from the $B^0 \to c\bar{c}K^0$ decays and indirectly determined from the global fit to all the remaining UT measurements [118].

The golden mode for NP searches, the $B_s^0 \to \mu^+\mu^-$, is very clean from the theoretical as well as the experimental point of view. The SM prediction for its branching ratio is only $(3.2 \pm 0.2) \times 10^{-9}$, while a broad class of NP models can enhance it up to 10^{-7}. A global effort has been made to find the $B_s^0 \to \mu^+\mu^-$ signal and the strongest constraint of $\mathcal{BR}(B_s^0 \to \mu^+\mu^-) < 3.8 \times 10^{-9}$ comes from LHCb [122]. CDF measurement updated with their full data sample [123] has not reinforced previously found signal increase.

Contrary to the $D^0 - \bar{D}^0$ mixing, where any NP effects would be obscured by long distance contributions, CP violation in D meson decays has been over last the years suggested to be a good place for NP searches. In the SM it is expected to be very small, at the level of 10^{-3} at most, and experimental measurements have reached that precision only recently. First evidence of CP violation in charm decays has been found by LHCb in the measurement of $\Delta A_{CP} = A_{CP}(D0 \to K^+K^-) - A_{CP}(D0 \to \pi^+\pi^-) = (-0.82 \pm 0.21 \pm 0.11)\%$ [124], which in a first approximation corresponds to the difference of direct CP violation. Together with the result reported by CDF [125], no CP violation scenario is excluded at the 4σ level. However,

according to the revised theoretical calculations such an increased CP violation can be still accommodated within the SM [126].

Indirect searches for NP in the heavy flavour sector have been very lively. Many rare processes only come within reach thanks to increasing sensitivity obtained with data from LHC and full data samples from B-Factories and Tevatron experiments being analyzed. Some of the important studies, like precision $\mathcal{BR}(B \to \tau\nu)$, polarization measurements in $B \to \bar{D}^{(*)}\tau\nu$, lepton flavour violation in τ decays will be feasible only with Super$B$-Factories being under construction.

6 Conclusions

There has been theoretical progress concerning approximate NNLO calculations for heavy quark structure functions in deep inelastic scattering, the extension of the ACOT heavy flavour scheme to jet production, and advances in top physics (soft gluon resummations, merging with parton showers) where the highlight is clearly the first complete NNLO QCD prediction for top pair production in the $q\bar{q}$ annihilation channel. Furthermore, state of the art phenomenological predictions for open charm and bottom, charmonium, and single top and top pair production have been discussed in addition to other topics such as the effect of double parton scattering on heavy quark production.

A huge amount of measurements of heavy-quarkonium and of open charm and beauty production has been produced from HERA, LHC, Tevatron, and RHIC. These measurements challenge the QCD predictions that are typically less precise than experimental data. The agreement between data and theory is in general good. Some measurements, for which the agreement is marginal, deserve further studies: the polarization of heavy quarkonium, the measurement of jets associated to a D^{*+} presented by ATLAS, and the measurement of double charm production performed by LHCb.

The top quark is being scrutinized with unparalleled precision at both the Tevatron and the LHC. The D0 and CDF experiments are measuring the strong and electroweak production cross section as well as the top quark mass very precisely.

New $c\bar{c}$ and $b\bar{b}$ states have been observed and exotic quarkonia extensively studied by B-Factories as well as LHC and Tevatron experiments. LHCb have performed the world best measurements of properties of B_c and b-baryons.

Rare decays of $D_{(s)}$, $B_{(s)}$ and τ have been measured with increased sensitivity. Some of them show tensions with Standard Model predictions and thus give hints of New Physics.

References

[1] J. A. M. Vermaseren, A. Vogt, and S. Moch. Nucl. Phys. **B724** (2005) 3–182.

[2] J. Blumlein. these proceedings.
J. Blumlein, A. Hasselhuhn, S. Klein, and C. Schneider. arXiv:1205.4184 [hep-ph].
J. Ablinger, J. Blumlein, A. Hasselhuhn, S. Klein, C. Schneider, *et al.* arXiv:1206.2252 [hep-ph].

[3] S. Moch. these proceedings.

[4] H. Kawamura, N. Lo Presti, S. Moch, and A. Vogt. arXiv:1205.5727 [hep-ph].

[5] M. A. G. Aivazis, J. C. Collins, F. I. Olness, and W. K. Tung. Phys. Rev. **D50** (1994) 3102–3118.

[6] T. Stavreva, F. Olness, I. Schienbein, T. Jezo, A. Kusina, *et al.* arXiv:1206.2325 [hep-ph].
T. Stavreva, F. Olness, I. Schienbein, T. Jezo, A. Kusina, *et al.* Phys.Rev. **D85** (2012) 114014.

[7] R. Thorne and W. Tung. arXiv:0809.0714 [hep-ph].
F. Olness and I. Schienbein. Nucl.Phys.Proc.Suppl. **191** (2009) 44–53.

[8] J. C. Collins. Phys. Rev. **D58** (1998) 094002.

[9] S. Kretzer and I. Schienbein. Phys.Rev. **D56** (1997) 1804–1807; Phys.Rev. **D59** (1999) 054004.

[10] G. Kramer and H. Spiesberger. Eur.Phys.J. **C22** (2001) 289–301; Eur.Phys.J. **C28** (2003) 495–513; Eur.Phys.J. **C38** (2004) 309–318; Phys.Lett. **B679** (2009) 223–227.
B. Kniehl, G. Kramer, I. Schienbein, and H. Spiesberger. Eur.Phys.J. **C62** (2009) 365–374.

[11] F. I. Olness, R. Scalise, and W.-K. Tung. Phys.Rev. **D59** (1999) 014506.

[12] B. Kniehl, G. Kramer, I. Schienbein, and H. Spiesberger. Phys.Rev. **D71** (2005) 014018; Eur.Phys.J. **C41** (2005) 199–212; AIP Conf.Proc. **792** (2005) 867–870; Phys.Rev.Lett. **96** (2006) 012001; Phys.Rev. **D77** (2008) 014011.

[13] T. Kneesch, B. Kniehl, G. Kramer, and I. Schienbein. Nucl.Phys. **B799** (2008) 34–59.

[14] H. Spiesberger. arXiv:1205.7000 [hep-ph].
B. Kniehl, G. Kramer, I. Schienbein, and H. Spiesberger. arXiv:1202.0439 [hep-ph]; Phys.Rev. **D84** (2011) 094026; Phys.Rev. **D79** (2009) 094009.

[15] P. Kotko and W. Slominski. arXiv:1206.3517 [hep-ph]; arXiv:1206.4024 [hep-ph].

[16] J. Pumplin, H. Lai, and W. Tung. Phys.Rev. **D75** (2007) 054029 and references therein.

[17] F. Maltoni, G. Ridolfi, and M. Ubiali. JHEP **1207** (2012) 022.

[18] K. Kovarik and T. Stavreva. arXiv:1206.2175 [hep-ph].

[19] V. M. Abazov *et al.* Phys. Rev. Lett. **102** (2009) 192002.

[20] V. M. Abazov *et al.* Phys.Lett. **B714** (2012) 32–39.

[21] T. Stavreva and J. Owens. Phys.Rev. **D79** (2009) 054017.

[22] T. Stavreva, I. Schienbein, F. Arleo, K. Kovarik, F. Olness, *et al.* JHEP **1101** (2011) 152.

[23] T. Stavreva, F. Arleo, and I. Schienbein. J.Phys.G **G38** (2011) 124187.

[24] A. Szczurek. arXiv:1206.0274 [hep-ph].
M. Luszczak, R. Maciula, and A. Szczurek. Phys.Rev. **D85** (2012) 094034.
W. Schafer and A. Szczurek. Phys.Rev. **D85** (2012) 094029.

[25] G. T. Bodwin, E. Braaten, and G. P. Lepage. Phys.Rev. **D51** (1995) 1125–1171. Erratum-ibid. D **55, 5853 (1997)**.

[26] M. Butenschoen and B. A. Kniehl. Phys.Rev.Lett. **108** (2012) 172002; Phys.Rev.Lett. **107** (2011) 232001; Phys.Rev.Lett. **106** (2011) 022003; Phys.Rev.Lett. **104** (2010) 072001.

[27] B. Kniehl. these proceedings.

[28] M. Butenschoen and B. A. Kniehl. Nucl.Phys.Proc.Suppl. **222-224** (2012) 151–161.

[29] A. Mitov. these proceedings.

[30] P. Baernreuther, M. Czakon, and A. Mitov. arXiv:1204.5201 [hep-ph].

[31] I. Bierenbaum. these proceedings.

[32] I. Bierenbaum, M. Czakon, and A. Mitov. Nucl.Phys. **B856** (2012) 228–246.

[33] U. Langenfeld, S. Moch, and P. Uwer. Phys.Rev. **D80** (2009) 054009.

[34] M. Czakon and A. Mitov. arXiv:1112.5675 [hep-ph].

[35] L. L. Yang. these proceedings.

[36] N. Kidonakis. these proceedings, arXiv:1205.3453 [hep-ph].

[37] N. Kidonakis and B. D. Pecjak. arXiv:1108.6063 [hep-ph].

[38] V. Ahrens, A. Ferroglia, M. Neubert, B. D. Pecjak, and L. L. Yang. Phys.Lett. **B703** (2011) 135–141.

[39] V. Ahrens, A. Ferroglia, M. Neubert, B. D. Pecjak, and L. L. Yang. JHEP **1009** (2010) 097.
V. Ahrens, A. Ferroglia, M. Neubert, B. D. Pecjak, and L.-L. Yang. JHEP **1109** (2011) 070.

[40] N. Kidonakis. Phys.Rev. **D84** (2011) 011504; Phys.Rev. **D82** (2010) 114030.

[41] N. Kidonakis. Phys.Rev. **D81** (2010) 054028; Phys.Rev. **D82** (2010) 054018; Phys.Rev. **D83** (2011) 091503.

[42] V. Ahrens, A. Ferroglia, M. Neubert, B. D. Pecjak, and L. L. Yang. Phys.Rev. **D84** (2011) 074004.

[43] S. Alioli, J. Fuster, A. Irles, S.-O. Moch, P. Uwer, *et al.* arXiv:1206.1750 [hep-ph].

[44] S. Alioli, S.-O. Moch, and P. Uwer. JHEP **1201** (2012) 137.

[45] A. Kardos, C. Papadopoulos, and Z. Trocsanyi. Phys.Lett. **B705** (2011) 76–81.

[46] A. Kardos, Z. Trocsanyi, and C. Papadopoulos. Phys.Rev. **D85** (2012) 054015.
M. Garzelli, A. Kardos, C. Papadopoulos, and Z. Trocsanyi. Phys.Rev. **D85** (2012) 074022.

[47] M. Garzelli, A. Kardos, C. Papadopoulos, and Z. Trocsanyi. Europhys.Lett. **96** (2011) 11001.

[48] A. Kardos. these proceedings.

[49] S. Chatrchyan *et al.* JHEP **1202** (2012) 011, arXiv:1111.1557 [hep-ex].

[50] R. Aaij *et al.* arXiv:1204.1258 [hep-ex].

[51] B. Abelev *et al.* Phys.Rev.Lett. **108** (2012) 082001, arXiv:1111.1630 [hep-ex].

[52] T. Aaltonen *et al.* Phys.Rev.Lett. **108** (2012) 151802, arXiv:1112.1591 [hep-ex].

[53] M. Kambeitz. these proceedings.

[54] H1 Collab., F. Aaron *et al.* Eur.Phys.J. **C72** (2012) 1995, arXiv:1106.1028 [hep-ex].

[55] A. Gizhko. these proceedings.

[56] V. Libov. these proceedings.

[57] H1 Collab., F. Aaron *et al.* Eur.Phys.J. **C72** (2012) 1970, arXiv:1111.0584 [hep-ex].

[58] S. Frixione, P. Nason, and B. R. Webber. JHEP **0308** (2003) 007, arXiv:hep-ph/0305252 [hep-ph].

[59] G. Dolinska. these proceedings.

[60] A. Barton. these proceedings.

[61] Alice Collab., B. Abelev *et al.* JHEP **1201** (2012) 128, arXiv:1111.1553 [hep-ex].

[62] M. Cacciari, M. Greco, and P. Nason. JHEP **9805** (1998) 007, arXiv:hep-ph/9803400 [hep-ph].

[63] ATLAS Collab., G. Aad *et al.* Phys.Rev. **D85** (2012) 052005, arXiv:1112.4432 [hep-ex].

[64] LHCb Collab., JHEP **1206** (2012) 141, arXiv:1205.0975 [hep-ex].

[65] CMS Collab., S. Chatrchyan *et al.* JHEP **1206** (2012) 110, arXiv:1203.3458 [hep-ex].

[66] ATLAS Collab., G. Aad *et al.* Eur.Phys.J. **C71** (2011) 1846, arXiv:1109.6833 [hep-ex].

[67] CMS Collab., S. Chatrchyan *et al.* JHEP **1204** (2012) 084, arXiv:1202.4617 [hep-ex].

[68] S. Frixione, P. Nason, and G. Ridolfi. JHEP **0709** (2007) 126, arXiv:0707.3088 [hep-ph].

[69] CDF Collab., T. Aaltonen *et al.* Phys.Rev.Lett. **105** (2010) 012001, arXiv:1004.3224 [hep-ex].

[70] D0 Collab., V. M. Abazov *et al.* Phys.Rev. **D84** (2011) 012008, arXiv:1101.0124 [hep-ex].

[71] ATLAS Collab., G. Aad *et al.* arXiv:1205.2067 [hep-ex].

[72] ATLAS Collab, G. Aad *et al.* JHEP **1205** (2012) 059, arXiv:1202.4892 [hep-ex].

[73] CMS Collab., S. Chatrchyan *et al.* arXiv:1203.6810 [hep-ex].

[74] CMS Collab., S. Chatrchyan *et al.* Phys.Rev. **D84** (2011) 092004, arXiv:1108.3773 [hep-ex].

[75] CMS Collab., S. Chatrchyan *et al.* CMS-TOP-11-030.

[76] ATLAS Collab., G. Aad *et al.* Eur.Phys.J. **C72** (2012) 2043, arXiv:1203.5015 [hep-ex].

[77] ATLAS Collab., G. Aad *et al.* ATLAS-CONF-2011-153.

[78] D0 Collab., V. M. Abazov *et al.* Phys.Lett. **B705** (2011) 313–319, arXiv:1105.2788 [hep-ex].

[79] D0 Collab., V. M. Abazov *et al.* Phys.Rev. **D84** (2011) 112001, arXiv:1108.3091 [hep-ex].

[80] CDF Collab., T. Aaltonen *et al.* CDF/PUB/TOP/PUBLIC/10793.

[81] ATLAS Collab., G. Aad *et al.* arXiv:1205.3130 [hep-ex].
[82] CMS Collab., S. Chatrchyan *et al.* CMS-TOP-11-021.
[83] ATLAS Collab., G. Aad *et al.* ATLAS-CONF-2011-104.
[84] CMS Collab., S. Chatrchyan *et al.* CMS-TOP-11-022.
[85] ATLAS Collab., G. Aad *et al.* ATLAS-CONF-2011-118.
[86] D0 Collab., V. M. Abazov *et al.* Phys.Rev. **D85** (2012) 091104, arXiv:1201.4156 [hep-ex].
[87] ATLAS Collab., G. Aad *et al.* Phys.Lett. **B712** (2012) 351, arXiv:1203.0529 [hep-ex].
[88] ATLAS Collab., G. Aad *et al.* arXiv:1205.1016 [hep-ex].
[89] D0 Collab., V. M. Abazov *et al.* Phys.Lett. **B708** (2012) 21–26, arXiv:1110.4592 [hep-ex].
[90] D0 Collab., V. M. Abazov *et al.* Phys.Lett. **B713** (2012) 165–171, arXiv:1204.2332 [hep-ex].
[91] D0 Collab., V. M. Abazov *et al.* arXiv:1201.5172 [hep-ex].
[92] CDF Collab., T. Aaltonen *et al.* CDF/PUB/TOP/PUBLIC/10761.
[93] CDF and D0 Collaborations, arXiv:1107.5255 [hep-ex].
[94] CMS Collab., S. Chatrchyan *et al.* JHEP **1206** (2012) 109, arXiv:1204.2807 [hep-ex].
[95] D0 Collab., V. M. Abazov *et al.* Phys.Rev.Lett. **108** (2012) 032004, arXiv:1110.4194 [hep-ex].
[96] CDF Collab., T. Aaltonen *et al.* CDF/PUB/TOP/PUBLIC/10719.
[97] ATLAS Collab., G. Aad *et al.* Phys.Rev.Lett. **108** (2012) 212001 arXiv:1203.4081 [hep-ex].
[98] CDF Collab., T. Aaltonen *et al.* CDF/PUB/TOP/PUBLIC/10807.
[99] D0 Collab., V. M. Abazov *et al.* Phys.Rev. **D84** (2011) 112005, arXiv:1107.4995 [hep-ex].
[100] ATLAS Collab., G. Aad *et al.* Eur.Phys.J. **C72** (2012) 2039, arXiv:1203.4211 [hep-ex].
[101] CMS Collab., S. Chatrchyan *et al.* Phys.Lett. **B709** (2012) 28–49, arXiv:1112.5100 [hep-ex].
[102] Quarkonium Working Group, N. Brambilla *et al.* Eur. Phys. J. **C71** (2011) 1534.
[103] Belle Collab., S.-K. Choi *et al.* Phys. Rev. **D84**, 052004 (2011).
[104] J. Brodzicka. these proceedings.
[105] Belle Collab., R. Mizuk *et al.* Phys. Rev. **D 80**, 031104 (2009); Phys. Rev. **D78**, 072004 (2008).
[106] Babar Collab., B. Aubert *et al.* Phys. Rev. **D 79**, 112001 (2009); Phys. Rev. **D 85**, 052003 (2012).
[107] LHCb Collab., R. Aaij *et al.* Eur. Phys. J. **C 72** (2012) 1972.
[108] CMS Collab., CMS-PAS-BPH-10-018.
[109] Babar Collab., B. Aubert *et al.* Phys. Rev. Lett. **101**, 071801 (2008).
[110] Belle Collab., K.-F. Chen *et al.* Phys. Rev. **D 82**, 091106 (2010).
[111] Belle Collab., A. Bondar *et al.* Phys. Rev. Lett. **108**, 122001 (2012).
[112] A. Bondar *et al.* arXiv:1105.4473.
[113] Belle Collab., I. Adachi *et al.* Phys. Rev. Lett. **108**, 032001 (2012).
[114] Belle Collab., I. Adachi *et al.* arXiv:1110.3934.
[115] Atlas Collab., G. Aad *et al.* Phys. Rev. Lett. **108**, 152001 (2012).
[116] D Collab., V.M. Abazov *et al.* arXiv:1203.6034.
[117] Z. Yang. these proceedings.
[118] CKMfitter Group, http://ckmfitter.in2p3.fr/
[119] DØCollab., V. M. Abazov *et al.* Phys. Rev. **D84**, 052007 (2011).
[120] CDF Collab., CDF Note 10778.
[121] LHCb Collab., R. Aaij *et al.* Phys. Rev. Lett. **108**, 101803 (2012).
[122] LHCb Collab., R. Aaij *et al.* arXiv:1203.4493.
[123] CDF Collab., www-cdf.fnal.gov/physics/new/bottom/120209.bmumu10fb
[124] LHCb Collab., R. Aaij *et al.* Phys. Rev. Lett. **108**, 111602 (2012).
[125] CDF Collab., CDF Note 10784.
[126] J. Brod *et al.* arXiv:1111.5000.

Part III

Combined Sessions

WG1: Structure Functions and WG3: Electroweak and Searches

Z' bosons at the LHC in a modified MSSM

G. Corcella

INFN, Laboratori Nazionali di Frascati,
Via E. Fermi 40, I-00044, Italy

DOI: http://dx.doi.org/10.3204/DESY-PROC-2012-02/316

I study the production of heavy neutral gauge bosons Z' at the LHC in U(1)$'$ models, inspired by Grand Unification Theories, as well as in the Sequential Standard Model, accounting for possible decays into supersymmetric channels. I shall consider the MSSM and present results on branching ratios and event rates with sparticle production at the LHC, taking particular care about final states with charged leptons and missing energy.

Heavy neutral bosons Z' are predicted in U(1)$'$ gauge groups, inspired by Grand Unification Theories (GUTs), and in the Sequential Standard Model (SSM), wherein the Z' has the same coupling to fermions and gauge bosons as the Z in the Standard Model (SM) (see, e.g., the reviews in Refs. [1, 2]). From the experimental viewpoint, searches for Z' bosons have been performed at the Tevatron [3] and at the LHC [4]. The latest LHC analyses excluded a U(1)$'$-based Z' with mass below 2.32 TeV (CMS) and 2.21 TeV (ATLAS), whereas the lower mass limits for the SSM Z' are currently about 1.49-1.69 TeV (CMS) and 1.77-1.96 TeV (ATLAS). Such results crucially rely on the assumption that the new neutral gauge bosons only decay into Standard Model final states. In this talk, following the lines of [5], I wish to investigate the possibility that the Z' can decay according to modes Beyond the Standard Model (BSM). In particular, I will consider supersymmetry and the Minimal Supersymmetric Standard Model, extending the work carried out in [6] by varying the Z' mass and scanning thoroughly the U(1)$'$ and MSSM parameter space. With respect to Refs. [7, 8], which also studied Z' decays in supersymmetry, the so-called D-term correction, due to the extra U(1)$'$ group, is added to the sfermion masses and the supersymmetric particle masses are not treated as free parameters, but they are obtained diagonalizing the corresponding mass matrices. If the branching ratios into BSM modes were to be relevant, one may have to reconsider the current exclusion limits on the Z' boson. From the point of view of supersymmetry, the production of charged-slepton or chargino pairs in Z' decays has the advantage, with respect to other production channels, that the Z' mass sets a kinematic constrain on the final-state invariant mass.

The U(1)$'$ models originate from the breaking of a rank-6 GUT group E_6 according to $E_6 \to SO(10) \times U(1)'_\psi$, followed by $SO(10) \to SU(5) \times U(1)'_\chi$. The heavy neutral bosons associated with $U(1)'_\psi$ and $U(1)'_\chi$ are thus named Z'_ψ and Z'_χ, respectively, whereas a generic Z' boson is a combination of Z'_ψ and Z'_χ, with a mixing angle θ:

$$Z'(\theta) = Z'_\psi \cos\theta - Z'_\chi \sin\theta. \tag{1}$$

Following [5], the models and the Z' bosons which will be investigated are listed in Table 1. The model Z'_η comes from the breaking of the GUT group in the SM, i.e. $E_6 \to SM \times U(1)'_\eta$; the Z'_S is present in the secluded model, wherein the SM is extended by means

of a singlet field S; the $Z'_{\rm N}$ is equivalent to the Z'_χ model, but with the 'unconventional' assignment of SM, MSSM and exotic fields in the SU(5) representations, as debated in [9]. When studying supersymmetric contributions to Z' decays, it is necessary to modify the particle content of the MSSM. First, besides the MSSM Higgs doublets, one needs an extra scalar Higgs boson to break the U(1)$'$ gauge symmetry and give mass to the Z'. After symmetry breaking, one is left with two charged Higgs bosons $H^\pm$, one neutral CP-odd A and three neutral CP-even, i.e. h and H, already present in the MSSM, and a novel H'. In the gaugino sector, two new neutralinos are to be included, for a total of six, corresponding to the supersymmetric partners of the Z' and of the extra Higgs. However, as pointed out in [5], the novel Higgs and neutralinos are typically too heavy to contribute to Z' phenomenology.

Model	θ
Z'_ψ	0
Z'_χ	$-\pi/2$
Z'_η	$\arccos\sqrt{5/8}$
$Z'_{\rm S}$	$\arctan(\sqrt{15}/9)-\pi/2$
$Z'_{\rm I}$	$\arccos\sqrt{5/8}-\pi/2$
$Z'_{\rm N}$	$\arctan\sqrt{15}-\pi/2$

Table 1: Z' bosons in the U(1)$'$ models along with the mixing angles.

In the extended MSSM, besides the SM modes, one has to consider Z' decays into slepton, squark, chargino, neutralino and Higgs pairs, as well as final states with Higgs bosons associated with a W or a Z. As in [5], I shall pay special attention to supersymmetric decays yielding charged leptons, as they are the golden channel for the experimental searches. Final states with two charged leptons and missing energy may come from primary decays into charged sleptons $Z' \to \tilde{\ell}^+\tilde{\ell}^-$, with the sleptons decaying according to $\tilde{\ell}^\pm \to \ell^\pm\tilde{\chi}^0$, with $\tilde{\chi}^0$ being a neutralino, or from primary decays into charginos $Z' \to \tilde{\chi}_2^+\tilde{\chi}_2^-$, followed by $\tilde{\chi}_2^\pm \to \ell^\pm\tilde{\chi}_1^0$. A decay chain, leading to four leptons and missing energy, is also yielded by decays into neutralinos $Z' \to \tilde{\chi}_2^0\chi_2^0$, with subsequent $\tilde{\chi}_2^0 \to \ell^\pm\tilde{\ell}^\mp$ and $\tilde{\ell}^\pm \to \ell^\pm\tilde{\chi}_1^0$. Finally, the decay into sneutrino pairs, such as $Z' \to \tilde{\nu}_2\tilde{\nu}_2^*$, followed by $\tilde{\nu}_2 \to \tilde{\chi}_2^0\nu$ and $\tilde{\chi}_2^0 \to \ell^+\ell^-\tilde{\chi}_1^0$, with an intermediate charged slepton, gives four charged leptons and missing energy, due to both neutrinos and neutralinos.

Following [5], I explore the Z' branching ratios by varying the Z' and slepton masses, while fixing the other parameters to the following 'Reference Point':

$$\begin{aligned} &\mu = 200\ ,\ \tan\beta = 20\ ,\ A_q = A_\ell = A_f = 500\ \text{GeV}\ , \\ &m_{\tilde{q}}^0 = 5\ \text{TeV}\ ,\ M_1 = 150\ \text{GeV}\ ,\ M_2 = 300\ \text{GeV}\ ,\ M' = 1\ \text{TeV}. \end{aligned} \tag{2}$$

In Eq. (2), μ is the parameter contained in the Higgs superpotential, $\tan\beta = v_2/v_1$ is the ratio of the vacuum expectation values of the two MSSM Higgs doublets, A_f is the coupling of the Higgs with the fermions. Furthermore, $m_{\tilde{q}}^0$ is the squark mass, assumed to be the same for all flavours at the Z' scale, before the addition of the D-term, M_1, M_2 and M' are the soft masses of the gauginos $\tilde{B}$, $\tilde{W}_3$ and $\tilde{B}'$. As for the U(1)$'$ coupling g', we shall adopt the GUT-driven convention that it is proportional to the coupling constant g_1 of U(1) via $g' = \sqrt{5/3}g_1$. In the Sequential Standard Model, the coupling of the $Z'_{\rm SSM}$ to sfermions is instead the same as in the SM, i.e. $g_{\rm SSM} = g_2/(2\cos\theta_W)$, where g_2 is the SU(2) coupling and θ_W the Weinberg angle.

An extensive analysis for all the models quoted in Table 1 has been carried out in [5]: here I just report the branching ratios for the GUT-inspired model Z'_ψ (Table 2) and for the $Z'_{\rm SSM}$ (Table 3), since they are the ones yielding the highest rates into supersymmetric channels. The branching ratios are listed for 1 TeV$< m_{Z'} <$5 TeV and for the values of $m_{\tilde{\ell}}^0$ which minimize and maximize the slepton rate, with $m_{\tilde{\ell}}^0$ being the slepton mass, assumed to be the same for all

$m_{Z'}$	$m^0_{\tilde{\ell}}$	$\mathrm{BR}_{q\bar{q}}$	$\mathrm{BR}_{\ell\ell}$	$\mathrm{BR}_{\nu\bar{\nu}}$	BR_{WW}	BR_{Zh}	$\mathrm{BR}_{\tilde{\chi}^+\tilde{\chi}^-}$	$\mathrm{BR}_{\tilde{\chi}^0\tilde{\chi}^0}$	$\mathrm{BR}_{\tilde{\nu}\tilde{\nu}^*}$	$\mathrm{BR}_{\tilde{\ell}\tilde{\ell}}$	$\mathrm{BR}_{\mathrm{BSM}}$
1.0	0.4	48.16	8.26	8.26	3.00	2.89	9.13	16.53	1.91	1.90	35.31
1.0	0.7	50.07	8.59	8.59	3.08	2.99	9.49	17.18	0.00	0.00	32.75
1.5	0.6	46.78	7.90	7.90	2.71	2.69	9.73	18.64	1.83	1.83	37.43
1.5	1.0	48.55	8.20	8.20	2.81	2.79	10.10	19.35	0.00	0.00	35.05
2.0	0.8	46.30	7.77	7.77	2.62	2.62	9.92	19.37	1.80	1.80	38.15
2.0	1.3	48.03	8.06	8.06	2.72	2.72	10.29	20.10	0.00	0.00	35.84
2.5	1.0	46.01	7.70	7.70	2.58	2.59	9.99	19.68	1.79	1.78	38.58
2.5	1.6	47.72	7.99	7.99	2.67	2.68	10.36	20.41	0.00	0.00	36.30
3.0	1.1	45.35	7.58	7.58	2.53	2.54	9.92	19.63	1.86	1.86	39.49
3.0	1.9	47.10	7.88	7.88	2.62	2.64	10.30	20.39	0.00	0.00	37.15
3.5	1.3	44.91	7.50	7.50	2.49	2.51	9.86	19.58	1.83	1.83	40.08
3.5	2.2	46.61	7.79	7.79	2.59	2.61	10.24	20.32	0.00	0.00	37.81
4.0	1.5	44.60	7.45	7.45	2.47	2.49	9.82	19.53	1.80	1.80	40.51
4.0	2.5	46.26	7.72	7.72	2.56	2.58	10.19	20.26	0.00	0.00	38.29
4.5	1.6	44.32	7.40	7.40	2.45	2.47	9.78	19.47	1.84	1.84	40.89
4.5	2.8	46.01	7.68	7.68	2.54	2.57	10.15	20.21	0.00	0.00	38.63
5.0	1.8	44.16	7.37	7.37	2.44	2.46	9.76	19.44	1.82	1.82	41.11
5.0	3.1	45.83	7.65	7.65	2.53	2.55	10.13	20.18	0.00	0.00	38.88

Table 2: Z'_ψ branching ratios for a few values of Z' and slepton masses, expressed in TeV. $\mathrm{BR}_{\mathrm{BSM}}$ is the total decay rate in BSM channels.

flavours, before the D-term addition. In the Z'_ψ case, both SM and BSM branching fractions are reported; for the SSM, only the BSM channels are quoted. From such tables, one can learn that, in the Z'_ψ scenario, the BSM modes account for about 35-40% of the total width, whereas in the SSM they can be up to 60-65%. In both cases, the dominant BSM contributions are the ones into neutralinos and charginos, whereas the slepton modes, i.e. charged sleptons or sneutrinos, can reach 4% for the Z'_ψ and 5-6% for the Z'_{SSM}. Ref. [5] also presents the branching ratios as a function of m^0_ℓ: as expected, the slepton rates rapidly decrease as $m^0_{\tilde{\ell}}$ increases. Such spectra are not shown here for the sake of brevity.

Before concluding, in Table 4 I present the expected number of events with supersymmetric cascades (N_{casc}), i.e. production of neutralinos, charginos or sleptons, and the charged-slepton rates (N_{slep}), in the high-luminosity phase of the LHC, i.e. $\mathcal{L} = 100$ fb^{-1}, and at the centre-of-mass energy $\sqrt{s} = 14$ TeV. The parameters are fixed to the Reference Point (2), whereas the Z' is set either to 1.5 or to 2 TeV and $m^0_{\tilde{\ell}}$ to the value maximizing the slepton rate. The numbers in Table 4 are obtained in the narrow-width approximation and calculating the $pp \to Z'$ cross section at leading order, as in [5]. One finds that the cascade events can be up to $\mathcal{O}(10^5)$ and the charged sleptons up to $\mathcal{O}(10^4)$: the highest rate of production of supersymmetric particles occurs in the SSM, but even the U(1)$'$ models yield meaningful sparticle production.

In summary, I reviewed the main issues discussed in Ref. [5] and presented some results on Z' decays in the MSSM, extended by means of an extra GUT-inspired U(1)$'$ group, as well as in the SSM. In order to reconsider the Z' exclusion limits or draw a conclusive statement on the feasibility to discover supersymmetry in Z' decays at the LHC, however, it will be compulsory implementing this modelling in the framework of a Monte Carlo generator. This is in progress.

$m_{Z'}$	$m^0_{\tilde{\ell}}$	$\mathrm{BR}_{H^+H^-}$	BR_{Zh}	B_{hA}	$\mathrm{BR}_{\tilde{\chi}^+\tilde{\chi}^-}$	$\mathrm{BR}_{\tilde{\chi}^0\tilde{\chi}^0}$	$\mathrm{BR}_{\tilde{\ell}\tilde{\ell}}$	$\mathrm{BR}_{\tilde{\nu}\tilde{\nu}^*}$	$\mathrm{BR}_{\mathrm{BSM}}$
1.0	0.10	0.00	$\sim 10^{-6}$	0.00	18.31	29.30	1.89	3.77	53.27
1.0	0.50	0.00	$\sim 10^{-6}$	0.00	19.41	31.06	0.00	0.00	50.47
1.5	0.10	0.00	0.87	0.76	17.84	32.52	1.75	3.48	57.21
1.5	0.75	0.00	0.92	0.80	18.82	34.31	0.00	0.00	54.55
2.0	0.10	0.00	1.93	1.85	17.37	33.01	1.67	3.33	59.17
2.0	1.00	0.00	2.04	1.95	18.28	34.75	0.00	0.00	57.02
2.5	0.10	0.91	2.59	2.53	16.93	32.78	1.62	3.22	60.58
2.5	1.25	0.95	2.72	2.66	17.79	34.45	0.00	0.00	58.57
3.0	0.10	1.72	2.98	2.94	16.62	32.51	1.58	3.15	61.49
3.0	1.50	1.81	3.13	3.08	17.44	34.12	0.00	0.00	59.58
3.5	0.10	2.27	3.23	3.20	16.42	32.30	1.56	3.10	62.08
3.5	1.75	2.38	3.38	3.35	17.22	33.88	0.00	0.00	60.22
4.0	0.10	2.65	3.39	3.37	16.28	32.16	1.54	3.07	62.46
4.0	2.00	2.78	3.56	3.53	17.07	33.71	0.00	0.00	60.65
4.5	0.10	2.91	3.51	3.49	16.19	32.06	1.53	3.05	62.73
4.5	2.25	3.05	3.67	3.65	16.96	33.59	0.00	0.00	60.94
5.0	0.10	3.11	3.59	3.57	16.12	31.98	1.52	3.03	62.93
5.0	2.50	3.26	3.76	3.74	16.89	33.51	0.00	0.00	61.16

Table 3: As in Table 2, but for the Sequential Standard Model, including only the BSM modes.

References

[1] J.L. Hewett and T.G. Rizzo, Phys. Rep. **183** (1989) 193.

[2] P. Langacker, Rev. Mod. Phys. **81** (2009) 1199.

[3] CDF Collaboration, Phys. Rev. Lett. **106** (2011) 121801; D0 Collaboration, *Phys. Lett.* **B695** (2011) 88.

[4] ATLAS Collaboration, Phys. Rev. Lett. **107** (2011) 272002; CMS Collaboration, JHEP **1105** (2011) 093.

[5] G. Corcella and S. Gentile, arXiv:1205.5780 [hep-ph].

[6] T. Gherghetta, T. A. Kaeding, and G. L. Kane, Phys. Rev. **D57** (1998) 3178.

[7] M. Baumgart, T. Hartman, C. Kilic and L.-T. Wang, JHEP **0711** (2007) 084.

[8] C.-F. Chang, K. Cheung and T.-C. Yuan, JHEP **1109** (2011) 058.

[9] E. Nardi and T.G. Rizzo, Phys. Rev. **D50** (1994) 203.

Model	$m_{Z'}$	$\mathrm{N}_{\mathrm{casc}}$	$\mathrm{N}_{\mathrm{slep}}$
Z'_η	1.5	13650	–
Z'_η	2.0	2344	–
Z'_ψ	1.5	10241	622
Z'_ψ	2.0	2784	162
Z'_{N}	1.5	9979	414
Z'_{N}	2.0	2705	104
Z'_{I}	1.5	8507	–
Z'_{I}	2.0	2230	–
Z'_{S}	1.5	8242	65
Z'_{S}	2.0	2146	16
Z'_{SSM}	1.5	775715	24774
Z'_{SSM}	2	19570	606

Table 4: Rates of supersymmetric cascades and charged sleptons at the LHC for an integrated luminosity of 100 fb^{-1} and a centre-of-mass energy of 14 TeV. The Z' mass is given in TeV.

Measurements of dibosons with the ATLAS detector and associated constraints on new physics

Hugh Skottowe on behalf of the ATLAS collaboration

skottowe@physics.harvard.edu
Harvard University, 18 Hammond Street, Cambridge MA 02138, USA

DOI: http://dx.doi.org/10.3204/DESY-PROC-2012-02/77

Diboson cross sections have been measured for all combinations of W,Z and isolated photons, using the ATLAS detector at the LHC. The cross sections are measured in kinematic regions defined by the decay kinematics, in some cases including vetoes on additional jets. The measurements are also extrapolated to the full phase space using theoretical calculations of the acceptance, and are additionally used to place constraints on triple-gauge boson couplings.

1 Introduction

At the end of the 2011 proton-proton run of the LHC, the delivered luminosity was increased by a factor of $\sim$5 from the $\sim$1 fb^{-1} dataset used for summer 2011 conference results. New measurements using the full $\sim$5 fb^{-1} dataset are presented here. The larger dataset implies a significant reduction of statistical errors, and therefore more precise tests of the Standard Model.

The diboson production processes presented here are sensitive to triple gauge couplings (TGCs), which are allowed in the Standard Model only for specific vertices. Anomalous triple gauge couplings, differing from those expected in the Standard Model, could manifest as modifications of the cross section or kinematics of diboson production. These diboson production processes are also important backgrounds in searches for the Higgs boson. The WW and ZZ processes could happen both through decays of a Standard Model Higgs boson, or through direct production, which acts a large background in the search for the Higgs.

2 The ATLAS experiment

The ATLAS detector is a general purpose detector at the LHC, CERN. It consists of an inner detector for charged tracking, surrounded by electromagnetic and hadronic calorimeters, and finally a muon detector system. The detector and its performance are described in detail in [1].

3 Event selection and cross-section measurements

The production of a high p_{T} photon in association with a W or Z boson is the highest cross-section process considered here. As with the other diboson channels, measurements of this

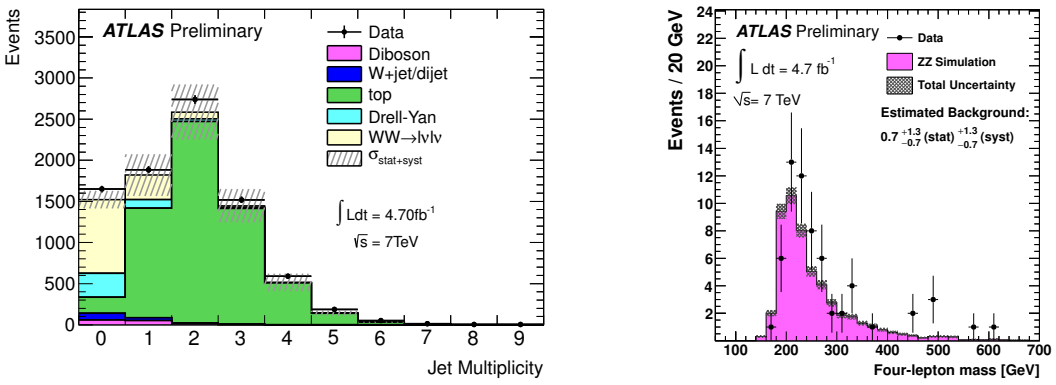

(a) (b)

Figure 1: (a) Jet multiplicity distribution for candidate WW events, before the final jet veto cuts [4] (b) Four-lepton invariant mass distribution for ZZ events after the full selection [7].

process can probe anomalous TGCs. The analysis is performed only for the case of the W/Z boson decaying fully leptonically, and the main backgrounds consist of jets produced in association with a W or Z boson, where a jet fakes either a photon or a charged lepton [2]. Events are selected by requiring one (for the Wγ case) or two (for the Zγ case) leptons (electron or muon, denoted ℓ) with transverse momentum (p_{T}) of at least 15 GeV. In addition, an isolated photon must be reconstructed, with transverse energy (E_{T}) of at least 15 GeV. The photon must be separated from each lepton[1] by $\Delta R > 0.7$. Finally, for the Wγ channel, missing transverse energy ($E_{\mathrm{T}}^{\mathrm{miss}}$) of at least 25 GeV is required, and the transverse mass of the W must exceed 40 GeV; for Zγ, the dilepton invariant mass must be greater than 40 GeV. The results of the cross-section measurements will be given at the end of this section.

The production of two W bosons of opposite charge, with both W bosons decaying leptonically, is another process which has been measured using the ATLAS dataset from 2011 [4]. This is again sensitive to anomalous TGCs, and is one of the most important backgrounds in the search for a Standard Model Higgs boson via the H→WW decay. The main backgrounds are the production of jets in association with a Z boson, and top quark production. The former is reduced by vetoing dilepton masses within 15 GeV of the nominal Z mass and by requiring large missing transverse energy[2]; the latter is reduced by requiring events to contain zero jets with $p_{\mathrm{T}} > 25$ GeV, and zero jets with $p_{\mathrm{T}} > 20$ GeV that contain a b-hadron. Figure 1(a) shows the jet multiplicity after the missing transverse energy cut, and before the jet veto cuts.

Increasing the required number of leptons from two to three, the diboson production process WZ has also been measured [5]. This analysis is again sensitive to anomalous TGCs, and searches for a charged Higgs boson. The analysis is much cleaner than the WW analysis, with the main backgrounds being caused by the reconstruction of a jet as a charged lepton, or by a true charged lepton not being detected. These main backgrounds are production of jets in association with a single Z boson, and ZZ diboson production, and top quark production. Events are selected by first requiring two isolated leptons (either two electrons or two muons)

[1] ΔR is the sum in quadrature of the separation in azimuth and pseudorapidity, $(\Delta R)^2 = (\Delta\phi)^2 + (\Delta\eta)^2$

[2] We use the variable $E_{\mathrm{T,rel}}^{\mathrm{miss}}$, which is the component of the $E_{\mathrm{T}}^{\mathrm{miss}}$ vector which is perpendicular to the closest lepton or jet if this closest object is separated by $\Delta\phi \leq \frac{\pi}{2}$; otherwise, if $\Delta\phi > \frac{\pi}{2}$, then $E_{\mathrm{T}}^{\mathrm{miss}}$ is used.

Process	$\int \mathcal{L} dt$	σ_{fid} [fb]	(stat.)	(syst.)	(lumi.)	σ_{tot} [pb]	(stat.)	(syst.)	(lumi.)	Reference
$W\gamma$	$1\,\text{fb}^{-1}$	4.60	± 0.11	± 0.64	± 0.17					[2]
$Z\gamma$	$1\,\text{fb}^{-1}$	1.29	± 0.05	± 0.15	± 0.05					[2]
WW	$1\,\text{fb}^{-1}$	*by channel: see reference*				54.4	± 4.0	± 3.9	± 2.0	[3]
WW	$5\,\text{fb}^{-1}$	*by channel: see reference*				53.4	± 2.1	± 4.5	± 2.1	[4]
WZ	$1\,\text{fb}^{-1}$	102	$^{+15}_{-14}$	$^{+7}_{-6}$	$^{+4}_{-4}$	20.5	$^{+3.1}_{-2.8}$	$^{+1.4}_{-1.3}$	$^{+0.9}_{-0.8}$	[5]
$ZZ \to \ell\ell\ell\ell$	$1\,\text{fb}^{-1}$	19.4	$^{+6.3}_{-5.2}$	$^{+0.9}_{-0.7}$	± 0.7	8.5	$^{+2.7}_{-2.3}$	$^{+0.4}_{-0.3}$	± 0.3	[6]
$ZZ \to \ell\ell\ell\ell$	$5\,\text{fb}^{-1}$	21.2	$^{+3.2}_{-2.7}$	$^{+1.0}_{-0.9}$	± 0.8	7.2	$^{+1.1}_{-0.9}$	$^{+0.4}_{-0.3}$	± 0.3	[7]
$ZZ \to \ell\ell\nu\nu$	$5\,\text{fb}^{-1}$	12.2	$^{+3.0}_{-2.8}$	± 1.9	± 0.5	5.4	$^{+1.3}_{-1.2}$	$^{+1.4}_{-1.0}$	± 0.2	[8]

Table 1: Summary table of cross-section measurements. Results are given both for the fiducial volume defined by the selection cuts, σ_{fid}, and extrapolated to the total cross section, σ_{tot}.

with $p_{\text{T}} > 15\,\text{GeV}$, with a dilepton mass within 10 GeV of the nominal Z mass, then requiring a third lepton with $p_{\text{T}} > 20\,\text{GeV}$ attributed to the W. In addition, $E_{\text{T}}^{\text{miss}} > 25\,\text{GeV}$ is required, and the transverse mass of the W boson is required to be greater than 40 GeV.

Measurements have been made of ZZ diboson production in two final states: firstly with both Z bosons decaying into charged leptons, and secondly with one Z decaying into charged leptons and the other Z boson decaying to a pair of neutrinos (sharing the final state with the WW diboson measurement described above). The latter final state gives a gain in branching fraction compared to the former, but also suffers from increased background.

For the $\ell^-\ell^+\ell^-\ell^+$ final state, four isolated leptons are required, with $p_{\text{T}}>7\,\text{GeV}$ [7]. The leptons are required to form two pairs, each with dilepton invariant mass within 15 GeV of the nominal Z mass. The four-lepton mass distribution of selected events is shown in figure 1(b).

For the $\ell^-\ell^+\nu^-\nu^+$ final state, two leptons with $p_{\text{T}} >20\,\text{GeV}$ and with $m_{\ell\ell}$ within 15 GeV of the nominal Z mass are required [8]. Large missing transverse energy is also required. For this the axial $E_{\text{T}}^{\text{miss}}$ is used, requiring the component of the $E_{\text{T}}^{\text{miss}}$ parallel to the dilepton vector in the plane transverse to the beam to be greater than 80 GeV. Finally, the events are required to contain zero jets with $p_{\text{T}}>25\,\text{GeV}$, and the fractional p_{T} difference between $E_{\text{T}}^{\text{miss}}$ and dilepton is required to be small: $|E_{\text{T}}^{\text{miss}} - p_{\text{T}}^{\ell\ell}|/p_{\text{T}}^{\ell\ell}<0.6$.

The results of all the above cross-section measurements are presented in table 1. For each analysis, the most recent ATLAS result is given. All measurements agree with the Standard Model prediction within the respective uncertainties. In the case of WW and $ZZ \to \ell^-\ell^+\ell^-\ell^+$, the previous cross-section result is also given, as these have been used to derive the TGC limits discussed in the next section. More details on the measurements can be found in the reference for each analysis in the table.

4 Limits on anomalous triple gauge couplings

The final selected events in each of the analyses described above can be used further, to derive limits on anomalous triple gauge couplings (TGCs). Anomalous TGCs can result in deviations of the cross sections and kinematics of these processes, and therefore cross-section measurements, or kinematic distributions, can be used to impose limits on these couplings. Figure 2(a) shows the example of the WW analysis, where the leading-lepton p_{T} spectrum is very sensitive to anomalous TGCs, particularly at large values. The distribution observed in data is used

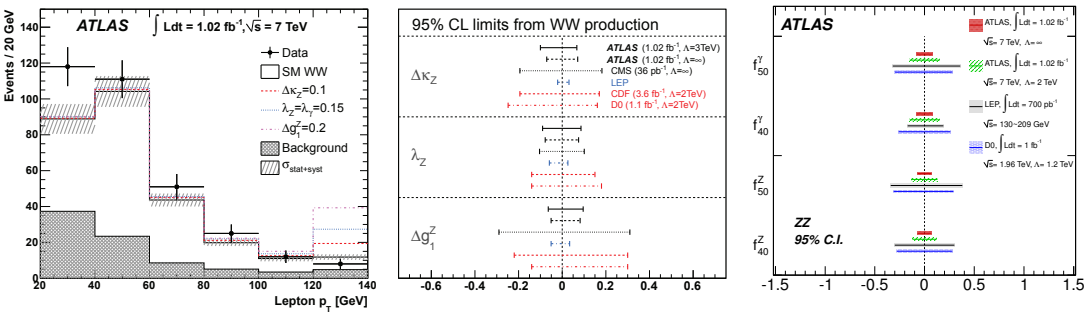

(a) (b) (c)

Figure 2: (a) Leading-lepton p_{T} spectrum of WW events, for data and MC with various TGCs ($\Delta\kappa_z$, λ_z and Δg_1^z are all equal to zero in the SM) [3]. This spectrum is used to derive the limits on anomalous TGCs shown in (b). (c) Limits on anomalous TGCs computed from the cross-section measurement of ZZ$\rightarrow\ell^-\ell^+\ell^-\ell^+$ [6].

to compute the limits on anomalous TGCs shown in figure 2(b). Figure 2(c) shows the limits computed using ZZ$\rightarrow\ell^-\ell^+\ell^-\ell^+$ events. Anomalous TGC limits have also been derived using Wγ, Zγ [2] and WZ [5] events.

5 Summary

Cross sections have been measured for a number of diboson production processes, both extrapolated to the total phase space, and within a fiducial volume given by the detector acceptance and event selection cuts. These measurements have been made for production of Wγ, Zγ, WW, WZ and ZZ, using part or all of the ATLAS dataset from the 2011 run of the LHC at $\sqrt{s} = 7\,\mathrm{TeV}$. These analyses form precise tests of the Standard Model, and have been used to place stringent limits on anomalous triple gauge couplings.

References

[1] The ATLAS Collaboration, 2008, JINST **3** S08003, doi:10.1088/1748-0221/3/08/S08003

[2] The ATLAS Collaboration, arXiv:1205.2531, submitted to Phys. Lett. B

[3] The ATLAS Collaboration, Phys. Lett. **B 712** (2012) 289, arXiv:1203.6232

[4] The ATLAS Collaboration, ATLAS-CONF-2012-025, http://cdsweb.cern.ch/record/1430734

[5] The ATLAS Collaboration, Phys. Lett. **B 709** (2012) 341, arXiv:1111.5570

[6] The ATLAS Collaboration, Phys. Rev. Lett. **108** (2012) 041804, arXiv:1110.5016

[7] The ATLAS Collaboration, ATLAS-CONF-2012-026, http://cdsweb.cern.ch/record/1430735

[8] The ATLAS Collaboration, ATLAS-CONF-2012-027, http://cdsweb.cern.ch/record/1430736

Diboson measurements with the CMS detector

Santiago Folgueras[1] on behalf of the CMS Collaboration

[1]Universidad de Oviedo, Spain

DOI: http://dx.doi.org/10.3204/DESY-PROC-2012-02/228

We present studies of diboson production in pp collisions at 7 TeV center-of-mass energy based on data recorded by the CMS detector at the LHC in 2010 and 2011. These include precise measurements of W and Z production in association with a photon and of WW production, WZ and ZZ productions at the LHC. The leptonic decay modes of the W and Z bosons are used. The results are interpreted in terms of constraints on anomalous triple gauge couplings.

1 Introduction

The gauge boson self-interactions appear as vertices involving three or four gauge bosons. The study of diboson production in proton-proton collisions is an important test of the standard model (SM) because of its sensitivity to the self-interaction between gauge bosons via trilinear gauge couplings (TGC). The values of these couplings are fully fixed in the SM by the gauge structure of the $SU(2) \times U(1)$ Lagrangian. Any deviation, manifested as an increased cross section, would indicate new physics. Understanding diboson production is also important for Higgs boson searches, because electroweak WW and ZZ production are irreducible backgrounds for high mass Higgs.

The measurement here described were performed using data recorded by the CMS detector at the LHC in 2010 and 2011. A detailed description of the CMS detector can be found elsewhere [1].

2 WW, WZ, ZZ cross section measurements with 1.1 fb^{-1}

This measurements are based on data taken in 2011 corresponding to an integrated luminosity ($\mathcal{L}$) of 1.1 fb^{-1} and are fully described in Ref. [2].

2.1 Measurement of the $WW \rightarrow l^+\nu l^-\bar{\nu}$ cross section

The fully leptonic W^+W^- final state consists of two oppositely charged leptons and large missing energy from the two undetectable neutrinos. Events are selected using triggers that require the presence of one or two high-p_T leptons (electrons or muons). Lepton candidates are then reconstructed offline and events with two oppositely charged (and only two), isolated leptons (ee, $\mu\mu$, $e\mu$) are chosen with extra requirements on E_T^{miss} and invariant mass to reject Drell-Yan. The background from top quarks decays is reduced rejecting events with one jet

or more, or that have been tagged as a top-like event using b-jet tagging techniques. A more detailed description can be found here, [2].

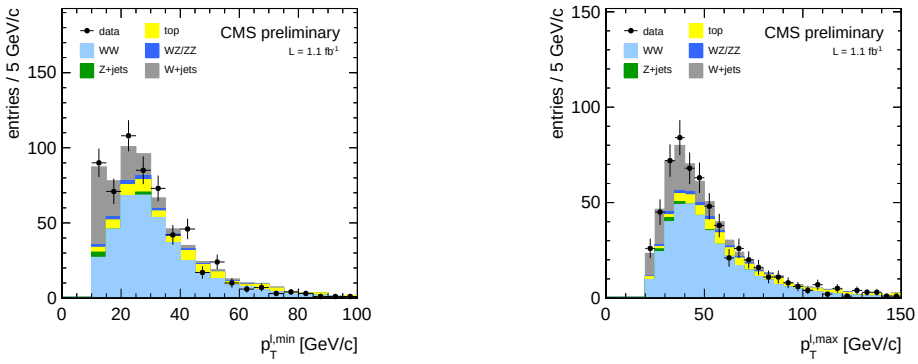

Figure 1: Leading (left) and trailing (right) lepton p_T. Each component in simulation is scaled to data-driven estimates.

The backgrounds include: $W + jets$ and QCD multi-jet events where at least one of the jets is misidentified as a lepton, top production ($t\bar{t}$ and tW), the $Z/\gamma^* \rightarrow ll$ process, and other diboson processes (WZ, ZZ and $W\gamma$). All the backgrounds are estimated from data, except $W\gamma$ and $Z/\gamma^* \rightarrow \tau\tau$ that are estimated from simulation. The W^+W^- yield is calculated from the number of events in the signal region, after subtracting the expected contributions of the various SM background processes. From this yield and the $W \rightarrow l\nu$ branching fraction [3], the W^+W^- production cross section in pp collisions at $\sqrt{s} = 7$ TeV is found to be $\sigma_{W^+W^-} = 55.3 \pm 3.3\,(\text{stat}) \pm 6.9\,(\text{syst}) \pm 3.3\,(\text{lumi})$ pb. This is consistent with the SM expectation of 43.0 $\pm$ 2.0 pb at NLO [4] within one standard deviation. An update of this measurement using 4.9 fb^{-1} can be found in Ref. [5].

2.2 Measurement of the $WZ \rightarrow l\nu l^+l^-$ cross section

The $WZ \rightarrow l\nu l^+l^-$ decay is characterized by a pair of same-flavor, opposite-charge isolated leptons with an invariant mass corresponding to the Z boson, together with a third isolated lepton and large E_T^{miss}.

Candidate events are selected using a double electron or double muon trigger. The Z boson is reconstructed from two opposite sign, same flavor leptons passing loose identification criteria. We look for the W boson decay by requiring a third isolated lepton and requiring E_T^{miss} in the event to be larger than 30 GeV. In a data sample corresponding to $\mathcal{L} = 1.1$ fb^{-1}, 75 events pass these selection criteria. The invariant mass of the Z candidates for the selected events is shown in Fig. 2. We estimate the $Z + jets$ background using the data sidebands, and the fake-lepton originated backgrounds

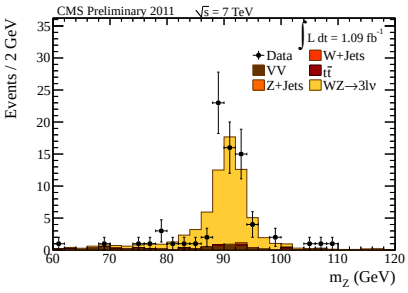

Figure 2: Dilepton invariant mass for events passing the full selection.

by computing the jet to lepton fake rate from $W + jets$ events in data. Similarly, we estimate the tt background contamination within the signal region using data. All other backgrounds are estimated from simulation.

This results in the cross section measurement: $\sigma(pp \to WZ + X) = 17.0 \pm 2.4(\text{stat.}) \pm 1.1(\text{syst.}) \pm 1.0(\text{lumi.})$ pb..The theoretical NLO prediction is 19.79 ± 0.09 [4], which is in good agreement with the measured value. Cross section measurements in the individual channels are consistent with the central value. More details on this measurement are given in Ref [2].

2.3 Measurement of the $ZZ \to l^+l^-l^+l^-$ cross section

The $ZZ \to l^+l^-l'^+l'^-$ process with $l, l' = e, \mu, \text{or } \tau$ is characterized by two pairs of same flavor, opposite charge, high p_T , isolated leptons, coming from the primary vertex, with an invariant mass corresponding to a Z boson. The process has a clean signature with very little experimental background. We reconstruct each Z boson in the mass range $60 < m_Z < 120$ GeV. One Z is required to decay into a pair of electrons or muons, and the second Z can decay to $\mu\mu, ee$ or $\tau\tau$.

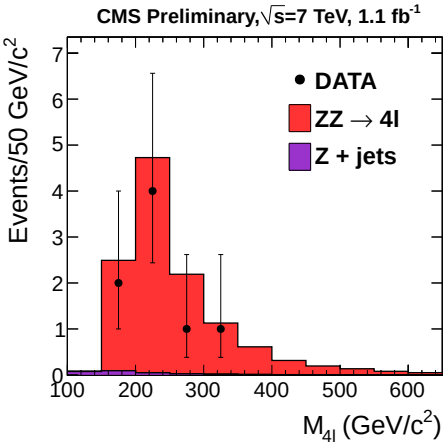

Figure 3: Invariant mass of the 4 leptons ($2e2\mu, 4\mu, 4e$).

For the 4l final state with $l = e, \mu$, we require the that the first Z is reconstructed using a pair of loose identified leptons an invariant mass greater than 60 GeV. For the second lepton pair we require opposite charge and matching flavor with an invariant mass $60 < m_Z < 120$ GeV and such that the reconstructed four-lepton mass satisfies $m_{4l} > 100$ GeV. For the $2l2\tau$ final state, the first Z boson is required to decay to $\mu\mu$or ee as described above, and the second Z decays into a pair of taus. Each tau candidate can decay leptonically, or hadronically. In case the decay is leptonic the p_T should be greater than 10 GeV, we require the hadronic τ to have $p_T > 20$ GeV. The two leptons should be isolated and should have opposite charge. The visible mass should be between 30 and 80 GeV.

The reducible instrumental background is very small or negligible. We estimate any residual background and the associated systematic uncertainty using empirical methods based on experimental data. In the 4l final state, we observe 8 events compared to 12.5 ± 1.1 events expected from the SM. The reconstructed four-lepton invariant mass distribution is shown in Fig. 3. The resulting cross section is $\sigma(pp \to ZZ + X) = 3.8^{+1.5}_{-1.2}(\text{stat.}) \pm 0.2(\text{sys.}) \pm 0.2(\text{lumi.})$ pb, which can be compared to the theoretical NLO prediction 6.4 ± 0.6 pb computed with MCFM[4]. More details on this measurement are given in Ref. [2].

3 Wγ and Zγ measurements

We present a measurement of $W\gamma$ and $Z\gamma$ production in proton-proton collisions at $\sqrt{s} = 7$TeV, based on a data sample recorded by the CMS experiment at the LHC, and corresponding to an integrated luminosity of 36 pb^{-1}. The electron and muon decay channels of the W and Z are used. The total cross sections are measured for photon transverse energy greater than 10 GeV and spatial separation from charged leptons in the plane of pseudorapidity and azimuthal angle greater than 0.7, and with an additional dilepton invariant mass requirement of > 50 GeV for the $Z\gamma$ process. The following cross section times branching fraction values are found: $\sigma(pp \to W\gamma + X)B(W \to l\nu) = 56.3 \pm 5.0$ (stat.) ± 5.0 (syst.) ± 2.3 (lumi.) pb and $\sigma(pp \to Z\gamma + X)B(W \to ll) = 9.4 \pm 1.0$ (stat.) ± 0.6 (syst.) ± 0.4 (lumi.) pb. These measurements are in agreement with standard model predictions. The first limits on anomalous $WW\gamma$, $ZZ\gamma$, and $Z\gamma\gamma$ trilinear gauge couplings at $\sqrt{s} = 7$ TeV are set. The details of this analysis are fully documented in Ref. [6].

4 Z to 4l measurements

We present the first observation of the Z boson decaying to 4 leptons in proton-proton collisions. The analyzed dataset corresponds to an integrated luminosity of 4.7 fb^{-1}. We observe a pronounced resonance peak, with the statistical significance of 8.9σ in the distribution of invariant mass of four leptons with its mean and width consistent with the Z boson. With the kinematic requirements imposed in the analysis, we observe 26 events in the mass window of $80-100$ GeV, in agreement with the expected rate of 25.0 events, comprised of 24.6 ± 2.2 $Z \to 4l$ events and 0.4 ± 0.1 events from backgrounds. The measured branching fraction of $Z \to 4l$ decays with a cut on the minimum dilepton mass $m_{2l} > 4GeV$ is $BR(Z \to 4l) = 4.4^{+1.0}_{-0.8}$ (stat) ± 0.2 (syst) $\times 10^6$ and agrees with the standard model prediction of 4.45×10^6. The measured cross section times branching fraction is $\sigma \times BR(Z \to 4l) = 125^{+26}_{-23}$ (stat)$^{+9}_{-6}$(syst)$^{+7}_{-5}$(lumi) fb, also consistent with the standard model prediction of 120 fb. The four-lepton mass peak arising from $Z \to 4l$ decays provides a natural standard candle for the Higgs boson search in the $H \to ZZ \to 4l$ decay mode. The details of this analysis are described in Ref.[7].

References

[1] **CMS** Collaboration, "The CMS experiment at the CERN LHC", JINST **3** (2008) S08004.

[2] **CMS** Collaboration, "Measurement of the WW, WZ and ZZ cross sections at CMS", 201

[3] K. Nakamura *et al.* (Particle Data Group), J. Phys. G 37, 075021 (2010).

[4] J. Campbell, K. Ellis, and C. Williams, "MCFM - Monte Carlo for FeMtobarn processes", 2011

[5] **CMS** Collaboration, "Measurement of WW production rate", 2012

[6] **CMS** Collaboration, Phys. Lett. B **701**, 535 (2011) [arXiv:1105.2758 [hep-ex]].

[7] **CMS** Collaboration, "Observation of Z to 4l production in pp collisions at 7 TeV", 2012

Recent WW, WZ and ZZ Results from the Tevatron

Mika Vesterinen

CERN, 1211 Genève 23, Switzerland

DOI: http://dx.doi.org/10.3204/DESY-PROC-2012-02/280

Recent results on WW,WZ and ZZ production from the CDF and D0 experiments are presented. Measurements of $WZ \to \ell\nu\ell\ell$ production are consistent with predictions of the standard model. For the first time in the $\ell\nu jj$ final state, the WZ and WW signals are disentangled. Measurements of ZZ/WZ production with final states including b-tagged jets provide an excellent validation of searches for the low mass Higgs boson.

1 Introduction

The pair production of electroweak vector bosons (only combinations of W and Z [1] bosons are discussed here) is a powerful testing ground for the predictions of the standard model, and the measured cross sections can be enhanced in many new physics scenarios. The non-Abelian structure of the electroweak sector implies a specific set of triple gauge couplings, that maintain unitarity in WW and WZ production. However, the standard model does not contains any such tree level couplings that contribute to ZZ production. Whilst these diboson processes are of interest in their own right, they also contribute significant background in searches for a standard model Higgs boson, and thus need to be understood to a high degree of accuracy. In $p\bar{p}$ collisions at $\sqrt{s} = 1.96$ TeV, the standard model predicts production cross sections of; $\sigma(WW) = 11.3 \pm 0.8$ pb, $\sigma(WZ) = 3.2 \pm 0.2$ pb, $\sigma(ZZ) = 1.2 \pm 0.1$ pb, computed at next-to-leading order in the strong coupling [1, 2]. These cross sections correspond to the decay $Z \to \ell\ell$ with the dilepton invariant mass satisfying, $75 < M_{\ell\ell} < 105$ GeV. These processes are already well established at hadron colliders, with ZZ production being the most recent observation in 2008 [3], using 2.7 fb^{-1}. With roughly 10 fb^{-1} of data per experiment, the emphasis now moves towards precision measurements of the cleanest (leptonic) modes, and to the exploration of more challenging final states, in particular those that are common to searches for a Higgs boson.

2 Production of WZ in fully leptonic final states

For WZ production, the golden decay mode is into the $\ell\nu\ell\ell$ ($\ell = e$ or μ) final state, that is easily triggered on and isolated from QCD backgrounds. The D0 Collaboration recently updated the study of this mode with 8.6 fb^{-1} [4], measuring a cross section of $\sigma(WZ) = 4.5^{+0.6}_{-0.7}$ pb, which

[1] For decays into charged fermions, Z implies Z/γ^*.

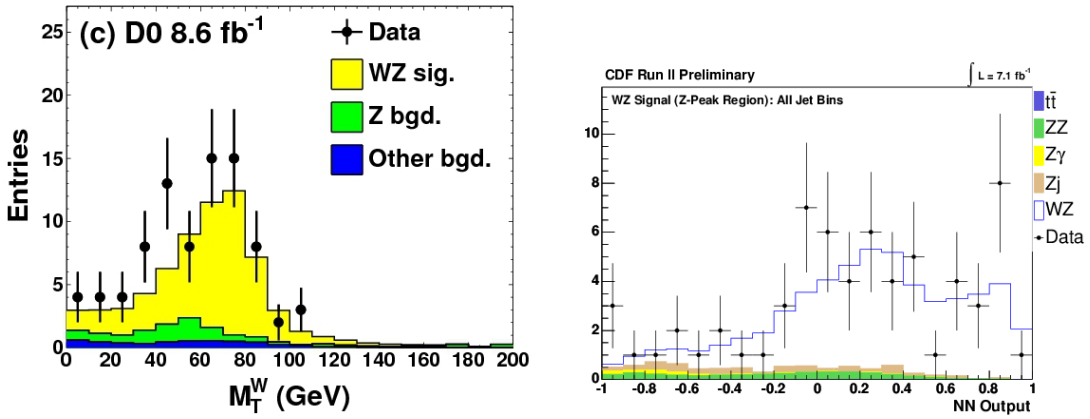

Figure 1: Left: The W transverse mass distribution of the candidate $WZ \to \ell\nu\ell\ell$ events in the D0 analysis of this channel. Right: the neural network output distribution of the candidate $WZ \to \ell\nu\ell\ell$ events in the CDF analysis

.

is higher than, but still compatible with the standard model prediction. The left-hand panel of Figure 1 shows the W transverse mass [2] distribution of the selected $WZ \to \ell\nu\ell\ell$ candidate events. This analysis actually measures the ratio of cross sections for WZ production relative to Z production. A next-to-next-to-leading-order calculation [5, 6] of the Z cross section is used to translate this ratio into a WZ cross section. This approach has the advantage of largely canceling systematic uncertainties in, for example, the luminosity and the lepton reconstruction efficiencies.

The CDF Collaboration also recently released an updated study of this channel using 7.1 fb^{-1} [7], measuring a cross section of $\sigma(WZ) = 3.9^{+0.8}_{-0.7}$ pb, in agreement with the D0 measurement and with the standard model prediction. The right-hand panel of Figure 1 shows the distribution of a neural network output, that helps to separate the signal from the backgrounds. Stringent limits are set on anomalous WWZ couplings.

3 WW/WZ production in semi-leptonic final states

The production of WW/WZ with decays into the $\ell\nu jj$ final state was first observed by the CDF Collaboration in 3.5 fb^{-1} [8]. The D0 Collaboration recently published an updated study of this channel using 4.3 fb^{-1} [9], that measures a cross section of $\sigma(WW + WZ) = 19.6 \pm 3.2$ pb. Neither experiment has sufficient dijet invariant mass resolution to directly resolve the decay $W \to jj$ from the decay $Z \to jj$. By dividing the sample into categories with 0, and and 2 b-tagged jets, the D0 analysis [9] manages to de-correlate the WW and WZ cross sections. Figure 2 shows the dijet invariant mass distributions in the 0 and 2 b-tag samples, after background subtraction. The b-tagging tends to enrich the sample with the decays

[2] The transverse mass is defined as $M_T = \sqrt{p_T^\ell p_T^\nu (1 - \cos\phi)}$, where p_T^ℓ and p_T^ν are the transverse momenta of the charged lepton and the neutrino, respectively. The opening angle between the charged lepton and the neutrino, in the plane transverse to the beam direction is denoted ϕ.

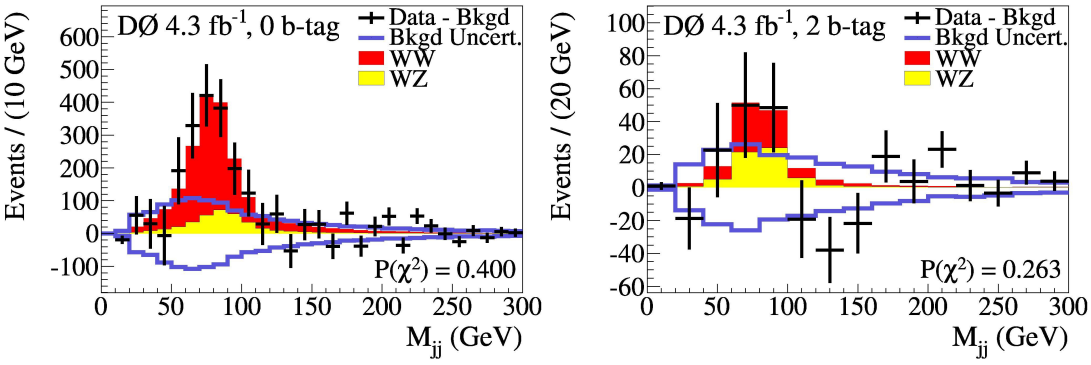

Figure 2: The background subtracted dijet invariant mass distribution in a sample of $WW/WZ \to \ell\nu jj$ events. Left: events in which neither jet is b-tagged. Right: events in which both jets are b-tagged.

$Z \to bb$ and $Z \to cc$. A simultaneous fit to the WW and WZ cross sections reveals a WW cross section of $\sigma(WW) = 15.9^{+3.7}_{-3.2}$ pb, but no significant WZ signal is measured. However, by constraining the WW cross section to the standard model value, a WZ cross section of $\sigma(WZ) = 6.5 \pm 0.9(\text{stat}) \pm 3.0(\text{syst})$ pb is measured, corresponding to an observed(expected) significance of 2.2(1.2) standard deviations.

4 ZZ/WZ production with heavy flavour jets

Three of the most sensitive search channels for a low mass standard model Higgs boson at the Tevatron are; $ZH \to \nu\nu bb$, $ZH \to \ell\ell bb$ and $WH \to \ell\nu bb$. All three search channels are contaminated by VZ ($V = W$ or Z) with the decay $Z \to bb$, and to a lesser extend $Z \to cc$. A powerful validation of these analyses is to actually attempt to observe a significant VZ signal. Diboson interpretations for each of these channels have been reported by the CDF Collaboration [10, 11, 12], and by the D0 Collaboration [13, 14, 15]. In all of these analyses, the event selection and background modeling is identical to the corresponding standard model Higgs search. Recently, a combination of results from the two experiments was performed [16]. The left hand panel of Figure 3 shows the background subtracted dijet invariant mass distribution of this combination. A significant VZ signal can be seen in this event sample that requires at least one b-tagged jet. Each of the input analyses uses a multivariate classifier to improve sensitivity to the signal. The D0 analyses use boosted decision trees, whilst the CDF analyses use neural networks. An optimal combination of inputs groups together bins of similar S/B, as shown in the right hand panel of Figure 3. This yields a cross section of $\sigma(WZ + ZZ) = 4.47 \pm 0.64(\text{stat}) \pm 0.73(\text{syst})$, corresponding to a significance of 4.6 standard deviations, and in agreement with the standard model predictions.

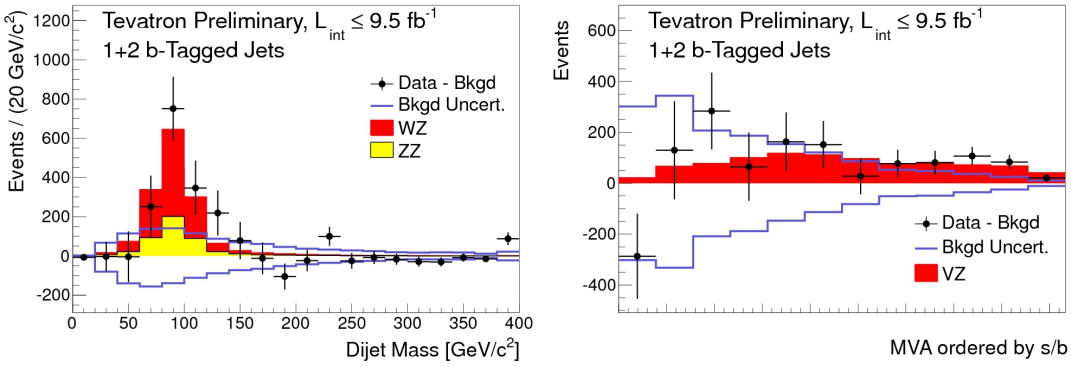

Figure 3: Left: The background subtracted dijet invariant mass distribution of the combination of CDF and D0 inputs for VZ production with heavy flavour jets. Right: The background subtracted distribution, binned by expected S/B.

5 Conclusions

Updated measurements are reported for $WZ \to \ell\nu\ell\ell$ production and $WW/WZ \to \ell\nu jj$ production. The measured cross sections are in agreement with predictions of the standard model. For the first time, separate measurements are made for WW and WZ cross sections using the $\ell\nu jj$ final state. A combined Tevatron search for VZ production in final states with b-tagged jets obtains a signal significance of 4.6 standard deviations, that is consistent with predictions of the standard model. This demonstrates the sensitivity of the Tevatron searches for a low mass Higgs boson.

References

[1] J. M. Campbell and R. K. Ellis. Phys. Rev. D **60** (1999) 113006.

[2] A. Martin, W. Stirling, R. Thorne, and G. Watt. Eur. Phys. J. C **63** (2009) 189–285.

[3] V. Abazov *et al.* Phys. Rev. Lett. **101** (2008) 171803.

[4] D0 Collaboration, V.M Abazov *et al.*, arXiv:1201.5652[hep-ex], *accepted by Phys. Rev. D* (2012).

[5] R. Hamberg, W. van Neerven, and T. Matsuura. Nucl. Phys. B **359** (1991) 343.

[6] A. D. Martin, R. G. Roberts, W. J. Stirling, and R. S. Thorne. Phys. Lett. B **604** (2004) 61.

[7] CDF Collaboration, T. Aaltonen *et al.*, arXiv:1202.6629v1[hep-ex], *submitted to Phys. Rev. Lett.* (2012).

[8] T. Aaltonen *et al.* Phys. Rev. Lett. **103** (2009) 091803.

[9] V. Abazov *et al.* Phys. Rev. Lett. **108** (2012) 181803.

[10] CDF Collaboration, T. Aaltonen *et al.*, CDF Conference Note 10796 (2012).

[11] CDF Collaboration, T. Aaltonen *et al.*, CDF Conference Note 10798 (2012).

[12] CDF Collaboration, T. Aaltonen *et al.*, CDF Conference Note 10799 (2012).

[13] D0 Collaboration, V.M. Abazov *et al.*, D0 Note 6220-CONF (2011).

[14] D0 Collaboration, V.M. Abazov *et al.*, D0 Note 6223-CONF (2011).

[15] D0 Collaboration, V.M. Abazov *et al.*, D0 Note 6256-CONF (2011).

[16] Tevatron New Phenomina and Higgs Working Group, CDF Collaboration, D0 Collaboration, FERMILAB-CONF-12-068-E, CDF-NOTE-10802, D0-NOTE-6311, arXiv:1203.3782[hep-ex] (2012).

W Mass Measurements from the Tevatron

Thomas Riddick for the CDF and DØ Collaborations
University College London, WC1E 6BT, UK

DOI: http://dx.doi.org/10.3204/DESY-PROC-2012-02/281

The CDF collaboration has analysed 2.2 fb^{-1} of Run II electron and muon data for a new precise determination of the mass of the W boson; the result obtained is $m_W = 80.387 \pm 0.019$ MeV/c^2. The DØ collaboration has analysed 4.3 fb^{-1} of Run II electron data for a new precise determination of the mass of the W boson; when combined with a previous DØ collaboration measurement using 1 fb^{-1}, the result obtained is $m_W = 80375 \pm 23$ MeV/c^2. The new world average value for the W mass including both these new results is $m_W = 80385 \pm 15$ MeV/c^2 and the new (95 %CL) indirect Higgs constraint from this updated value of m_W is $m_H < 152$ MeV/c^2.

1 Introduction

The three principle motivations for measuring the W mass are: as a test of the Standard Model; as an indirect constraint on the mass of the Higgs boson; and if the Higgs boson is discovered, as a probe for indication of new physics through the comparison of direct and indirect Higgs mass measurement. The number of W events available for analysis at the two Tevatron experiments is about two orders of magnitude greater than for the final measurements of the W mass at any of the four LEP II experiments; thus allowing for greater statistical precision in Tevatron W mass analyses than those from LEP II. Though precision measurements at the Tevatron are impeded by the 'messy' collision environment, by combined bespoke detector simulation with careful study the Tevatron experiments can produce W mass analyses with competitive systematic uncertainties.

2 Technique

The DØ analysis uses the decay channel $W \to e\nu$ for its W mass measurement; the CDF analysis also uses this channel and considers the channel $W \to \mu\nu$. The hadronic decay channels of the W produce events that are too 'messy' to accurately determine the W mass from and events in the τ leptonic decay channel are difficult to reconstruct. Tight cuts are used to give high purity samples of W decays and to ensure only events falling into well instrumented regions of the detector are used.

Because of the missing energy of the neutrino it is not possible to fully reconstruct W decay events in three dimensions. Instead the W mass (m_W) is determined by fitting Monte-Carlo templates to data. The main distribution fitted is the transverse mass distribution:

$$m_T = \sqrt{2p_T^{\ell} p_T^{\nu} \left(1 - \cos(\Delta\phi^{\ell\nu})\right)} \tag{1}$$

where p_T^ℓ is the transverse momentum (energy) of the muon (electron), p_T^ν is the transverse momentum of the neutrino reconstructed from the missing transverse energy and $\Delta\phi^{\ell\nu}$ is the angle between $\vec{p}_T^{\,\ell}$ and $\vec{p}_T^{\,\nu}$. The CDF analysis momentum is measured in the CDF MWPC gaseous tracker (the COT) and energy is measured in the various calorimeters; the silicon tracker is not used in this the CDF analysis. In the DØ analysis energy is measured in the calorimeter. Simulated background distributions are added to the Monte-Carlo templates. The p_T^ℓ distribution is also fitted; the final m_W is obtained by combining the results of these fits correctly accounting for statistical correlations. (The CDF analysis also determines m_W by fitting the p_T^ν distribution and adds this to the combination too.)

For both analyses samples of W decay events are simulated using the event generator RESBOS. NLO QCD correction are calculated by tuning the parameters of RESBOS for the non-perturbative region by fitting the Z invariant mass in $Z \to \ell^+\ell^-$ data. Both analyses calculate NLO QED corrections using PHOTOS. CDF have studied QED effects extensively in HORACE and then validated PHOTOS against HORACE; DØ have validated PHOTOS against WGRAD/ZGRAD.

CDF uses momentum measurements from the tracker both directly in the muon channel and indirectly in the electron channel. Thus it is necessary to calibrate the momentum scale; the level of accuracy required for W mass measurement being greater than that provided by collaboration wide calibrations. The procedure for calibrating the momentum scale in the CDF analysis begins with a precise alignment of the COT using cosmic ray data. Fits of J/ψ mass distribution of $J/\psi \to \mu^+\mu^-$ in bins of $< 1/p_T >$ are used to tuning the thickness of ionising material modelled in the inner detector. The overall momentum scale is set using a combined fits to the J/ψ, Υ and Z mass distributions in $J/\psi \to \mu^+\mu^-$, $\Upsilon \to \mu^+\mu^-$ and $Z \to \mu^+\mu^-$ events. As a cross check the momentum scale fitted using just the J/ψ and Υ mass distribution is compared to that fitted using just the Z mass distribution; these two measurement are consistent to within the statistical uncertainty on the fits.

Both analyses use energy measurements from their detectors electromagnetic calorimeter to measured the energy of electrons. DØ fits the calorimeter energy scale using the boson invariant mass distribution from $Z \to e^+e^-$. CDF fits the calorimeter scale separately using two different techniques. The first is boson invariant mass distribution from $Z \to e^+e^-$ events. The second is the E/p (energy over momentum) distribution from $W \to e\nu$ events; this transfers the precise momentum calibration to calorimeter energy measurements. The two techniques produced results that are consistent to within the statistical uncertainty of the fits; the two results are combined to produced an overall calorimeter energy scale.

The p_T of the neutrino is reconstructed from the measured p_T of the lepton and the measured hadronic recoil using the relation $p_T = -(\vec{p}_T^{\,\ell} + \vec{u}_T)$, where u_T is the hadronic recoil, the vector sum of all energy measured in the calorimeters (both electromagnetic and hadronic) not associated with the lepton. The recoil is modelled in these analyses Monte-Carlo simulations using parameterisations of minimum bias data and fully leptonic Z decay data.

3 Results

The new CDF result [1] analyses 2.2 fb^{-1} of data in both the electron and muon channels. The final combined result for both channels (fitting all of m_T, p_T^ℓ and p_T^ν in each) is:

$$m_W = 80387 \pm 19 \text{ MeV/c}^2. \tag{2}$$

The m_T distribution fit for m_W is given in figure 1.

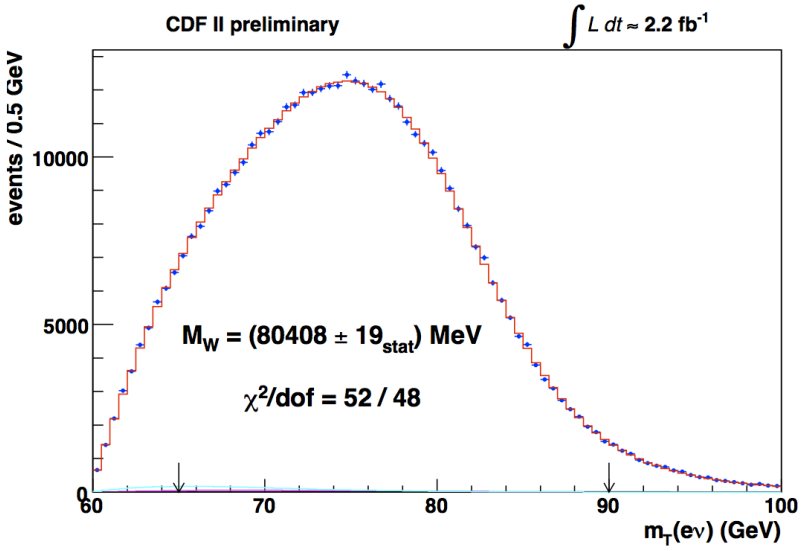

Figure 1: Comparison of best fit template m_T distribution (red histogram) to data (blue points) for $W \to e\nu$ events from the new CDF W mass analysis.

The new DØ result [2] analyses 4.3 fb^{-1} of data in the electron channel. The final result (fitting both m_T, p_T^ℓ) is:

$$m_W = 80367 \pm 26 \text{ MeV/c}^2. \quad (3)$$

The m_T distribution fit for m_W is given in figure 2. This can be combined with a previous independent DØ measurement using 1 fb^{-1} to give:

$$m_W = 80375 \pm 23 \text{ MeV/c}^2. \quad (4)$$

The uncertainties on both the DØ and CDF analyses are given in table 1. Combining these results with the old world average ($m_W = 80.399 \pm 0.023$) give a new world average of:

$$m_W = 80385 \pm 15 \text{ MeV/c}^2. \quad (5)$$

The new (95 %CL) indirect Higgs constraint from combining this updated value of m_W with the current world average top quark mass is $m_H < 152$ MeV/c^2.

References

[1] T. Aaltonen *et al.* [CDF Collaboration], Phys. Rev. Lett. **108** (2012) 151803.

[2] V. M. Abazov *et al.* [D0 Collaboration], Phys. Rev. Lett. **108** (2012) 151804.

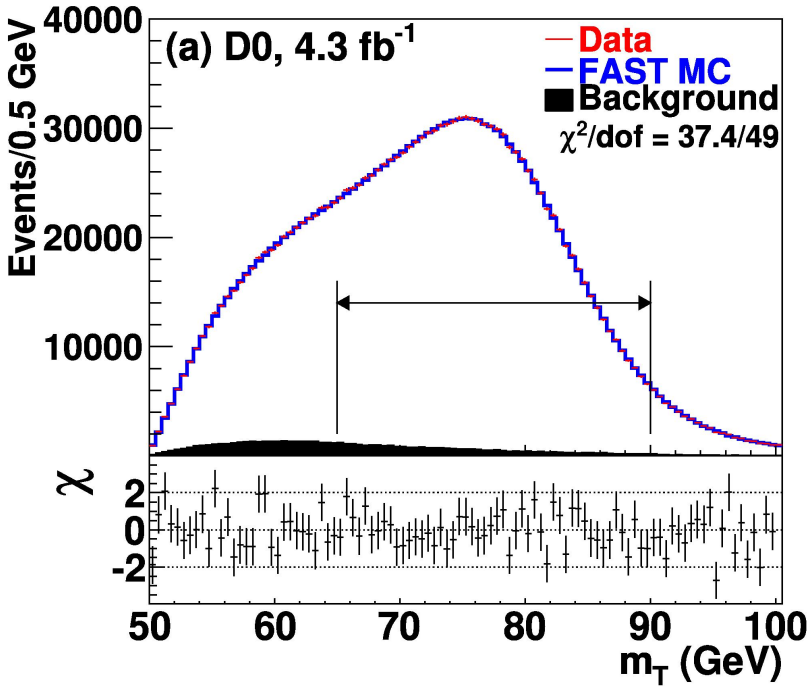

Figure 2: Comparison of best fit template m_T distribution (red histogram) to data (blue points) for $W \to e\nu$ events from the new DØ W mass analysis.

Uncertainty Source	CDF Uncertainty (MeV/c^2)	DØ Uncertainty (MeV/c^2)
Energy (and Momentum) Scale Calibration and Resolution	7	17
Recoil Model	6	5
Efficiencies	-	2
Backgrounds	3	2
Experimental Sub Total	**10**	**18**
PDFs	10	11
QED	4	7
Boson p_T	5	2
Production Sub Total	12	13
Total Systematics	15	22
W **Sample Statistics**	12	13
Overall Total	19	26

Table 1: Systematic and Statistical Uncertainties on the new Tevatron W mass analyses.

Elastic Z^0 production at HERA

Takuya Nobe on behalf of the ZEUS collaboration

Department of Physics, Tokyo Institute of Technology, Tokyo 152-8551 Japan

DOI: http://dx.doi.org/10.3204/DESY-PROC-2012-02/41

Elastic Z^0 events $ep \to eZ^0p^{(*)}$ have been measured in ep collisions at HERA using the ZEUS detector. The analysis is based on the data collected between 1996 and 2007, amounting to 496 pb^{-1} of integrated luminosity. The Z^0 was measured in hadronic decay mode with elastic condition defined by $\eta_{max} < 3.0$, where η_{max} is defined as the pseudorapidity of the energy deposit in the calorimeter closest to the proton beam direction. An excess of events was observed at the Z^0 mass. The cross section was obtaind by fitting the data with signal (MC)+background shapes templates. The shape of the background templates were estimated with a data-driven method. The cross section, $\sigma_{(ep\to eZ^0p^{(*)})} = 0.133^{+0.060}_{-0.057}\,(\text{stat.})^{+0.049}_{-0.038}\,(\text{syst.})$ pb, was found to be in agreement with the Standard Model prediction of 0.16 pb.

1 Introduction

The cross section for $W^{\pm}$ production has been measured by H1 and ZEUS [1] to be:

$$\sigma_{(ep\to l\nu X)} = 1.06 \pm 0.16\,(\text{stat.}) \pm 0.07\,(\text{syst.})\ \text{pb}.$$

In contrast, the cross section for Z^0 production in ep collision is expected to be much smaller in the Standard Model (SM), about 0.4 pb, making it difficult to use leptonic decay modes which have very small branching ratios ($BR \simeq 0.03$). In this analysis, the hadronic decay mode ($BR \simeq 0.7$) is used, although the QCD di-jet background is quite large. In order to discriminate signal events from the QCD di-jet background, the measurement of Z^0 production was performed in the elastic regime. A peak in the invariant mass distribution is expected at the Z^0 mass above a broad background from hadronic jets.

2 Datasets and Monte Carlo

Data collected between 1996 and 2007 with total integrated luminosity of 496 pb^{-1} were used. The luminosity was measured using the Bethe-Heitler reaction $ep \to e\gamma p$ by a luminosity detector which consisted of a lead-scintillator calorimeter [2] and an independent magnetic spectrometer [3].

A Monte Carlo (MC) simulation generated by EPVEC [4] interfaced to Pythia hadronic fragmentation was exploited. The cross section of Z^0 production predicted by the SM is 0.16 pb for elastic and quasi-elastic processes and 0.24 pb for deep inelastic scattering and resolved photoproduction.

3 Event selection

The trigger requirements were optimized by MC efficiency studies and imposed on data events.

As the primary cut, at least two jets with high transverse energies, E_T, greater than 25 GeV are required in the event and the invariant mass is calculated by using all jets with $E_T > 4$ GeV and an absolute value of the pseudorapidity, $\eta = -log\left(\tan\frac{\theta}{2}\right)$, less than 2.0. The two jets from the Z^0 decay should be back-to-back in the x-y plane, so that $|\Delta\phi| > 2$ rad is required, where $\Delta\phi$ is the azimuthal difference between the first and second E_T jet. In order to select the elastic process preferentially, a cut on $\eta_{max} < 3.0$ was applied, where eta_{max} is defined as the pseudorapidity of the energy deposit in the calorimeter closest to the proton beam direction calculated by calorimeter cells with $E > 400$ MeV. Due to large mass of the final-state hadronic system, the electron is back scattered to the forward calorimeter or forward beam pipe. Therefore $\theta_e < 80°$ (if electron found), $E_{RCAL} < 2$ GeV and $50 < E - p_Z < 64$ GeV[1] are required in order to suppress low-Q^2 NC background events.

Additionally, some cosmic and beam-gas rejection cuts are applied. If the direction of the selected jet is compatible with that of an electron candidate, then the jet is treated as a misidentified electron and the remaining jet candidates are used to reconstruct M_{jets}.

The total selection efficiency is estimated by MC to be 9% for all processes, and 22% for (quasi-)elastic process. Number of events expected in the final sample is 18.3.

4 Background shape study

Figure 1 shows the invariant mass distributions of the data for various η_{max} slices. No significant η_{max} dependence of M_{jets} was found within the statistical uncertainties of the non-signal region ($\eta_{max} > 3.0$). In addition, the M_{jets} shape outside of the Z^0 mass window in the signal region ($\eta_{max} < 3.0$) is consistent with that in the non-signal region. Therefore, we adopted the shape of M_{jets} in the non-signal region data as a background template in the fit by introducing the term of $N_{bg,i}^{data,\eta_{max}>3.0}$.

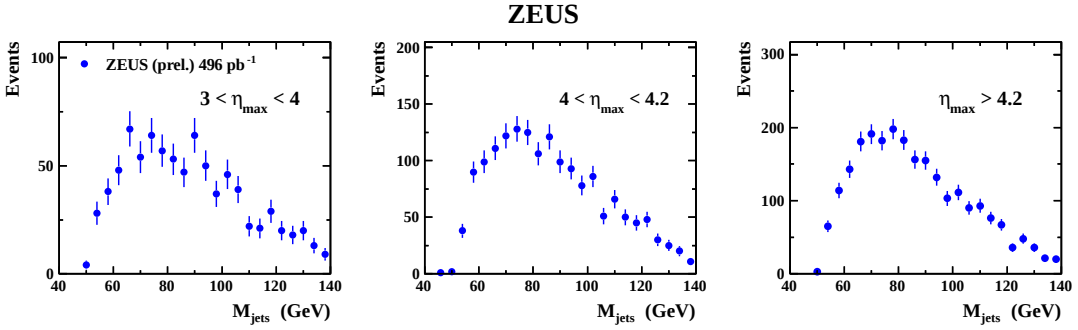

Figure 1: M_{jets} distribution in several η_{max} slices

[1] The nominal value of $E - p_z$ is twice the electron beam energy, 55 GeV.

5 Cross section extraction

First, the signal+background M_{jets} shape template is defined according to;

$$N_{ref,i} = aN_{sg,i}^{MC,\eta_{max}<3.0}(e) + bN_{bg,i}^{data,\eta_{max}>3.0}$$

where i is the bin number and e is a parameter to account for energy shift i.e. $M_{jets} = (1+e)\,M_{jets}^{MC}$. The quantity $N_{sg,i}^{MC,\eta_{max}<3.0}$ is a signal template estimated from the Z^0 MC and $N_{bg,i}^{data,\eta_{max}>3.0}$ is the data shape outside of the signal region($\eta_{max} > 3.0$), which corresponds to the background shape in the signal region (see section 5). a and b are normalization factors for the signal and background, respectively. Then, the χ^2 is calculated by summing over all bins;

$$\chi^2 = -2\sum_i log\frac{\mathcal{L}\left(N_{ref,i}, N_{obs,i}\right)}{\mathcal{L}\left(N_{obs,i}, N_{obs,i}\right)} + \left(\frac{e}{\sigma_e}\right)^2$$

$$log\frac{\mathcal{L}\left(N_{ref,i}, N_{obs,i}\right)}{\mathcal{L}\left(N_{obs,i}, N_{obs,i}\right)} = \begin{cases} N_{ref,i} - N_{obs,i} + N_{obs,i}log\left(N_{obs,i}/N_{ref,i}\right) & (\text{if } N_{obs,i} > 0) \\ N_{ref,i} - N_{obs,i} & (\text{if } N_{obs,i} = 0) \end{cases}$$

where $(e/\sigma_e)^2$ is a penalty term of allowed energy shifts with an assigned systematic uncertainty of 3% ($\sigma_e = 0.03$). The best combination of (a,b,e) is found by minimising the χ^2. The best fit 'a' corresponds to the ratio between the observed and expected cross section, i.e. $\sigma_{obs} = a\,\sigma_{SM}$. The maximum and minimum values of 'a' in the interval $\Delta\chi^2 < 1$ define the range of statistical uncertainty.

6 Systematic errors

Several sources of systematic uncertainties were considered and their impact on the measurement was estimated as follows:

- An uncertainty of 3% on $E_{T,jet}$ was assigned to the energy scale of the jets and the effect on the acceptance correction was estimated using the signal MC.
- An uncertainty associated with elastic selection cut was estimated. The acceptance of $\eta_{max} < 3.0$ cut for (quasi-)elastic process was found to be 67%. In this analysis, the lower side of systematic error was estimated very conservatively by assuming 100% acceptance of this cut for (quasi-)elastic process. We found that the acceptance changed by +40%. The upper side of the systematic error was estimated by omitting the energy cut in the selection of the calorimeter cells used to calculate η_{max} with the MC. With this method, the effect was estimated to cause a 26.8% acceptance loss.
- The background shape uncertainty was estimated by using different slices of η_{max} in the fit. The background shape in the region of $3.0 < \eta_{max} < 4.0$ was not used to estimate the systematic error as a small fraction of signal events exist in this η_{max} region. The ratio of signal-to-background in this region is estimated to be 2.6% for $80 < M_{jets} < 100\,\text{GeV}$ while that in the other slices is less than 0.4%.
- The uncertainty associated with the luminosity was estimated to be 1.9%.

All systematics are listed in Table 1.

Source	Errors on cross-section
$E_{T,jet}$	(+2.1%, -1.7%)
η_{max}	(+36.5%, -28.6%)
b.g. shape	± 1.5%
lumi.	± 1.9%
Total	(+36.6%, -28.8%)

Table 1: List of systematic errors on Z^0 production cross-section measurement

7 Results

Figure 2 shows the invariant mass distribution in the signal region(blue points) together with the best fit result(solid line is signal+b.g. and dashed line is b.g. only). The best fit parameter 'a' is equal to 0.82 (the energy scale shift e was 0.028), so that $15.0^{+6.8}_{-6.4}$(stat.) events were observed. The extracted Z^0 elastic production cross-section and uncertainties are:

$$\sigma_{\left(ep\to eZ^0p^{(*)}\right)} = 0.133^{+0.060}_{-0.057}\,(\text{stat.})^{+0.049}_{-0.038}\,(\text{syst.})\ \text{pb}.$$

This result is consistent with the SM cross section of 0.16 pb. This is the first measurement of Z^0 production in ep collisions.

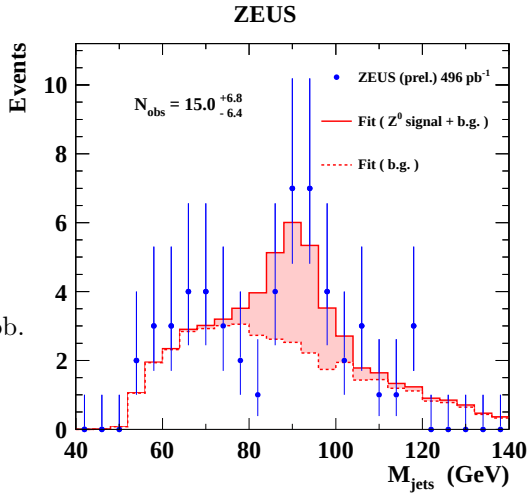

Figure 2: M_{jets} in signal region and best fit result

References

[1] The H1 and ZEUS collaborations, JHEP **3** (2010) 035.

[2] J. Andruszkóow et al., Preprint DESY-92, 1992;
ZEUS Collaboration, M. Derrick et al., Z. Phys. **C 63**, 391 (1994);
J. Andruszków et al., Acta Phys. Pol. **B 32**, 2025 (2001).

[3] M. Helbich et al., Nucl. Inst. Meth. **A 565**, 572 (2006).

[4] U. Baur, J. A. Vermaseren and D. Zeppenfeld, Nucl. Phys. **B 375** 3 (1992).

Forward Drell-Yan plus backward jet as a test of BFKL evolution

Martin Hentschinski, Clara Salas

Instituto de Física Teórica UAM/CSIC, C/ Nicolás Cabrera 13-15,
Universidad Autónoma de Madrid, Cantoblanco, E-28049 Madrid, Spain

DOI: http://dx.doi.org/10.3204/DESY-PROC-2012-02/115

We study Drell-Yan plus jet events where the gauge boson is produced in the forward direction of one of the colliding protons and a jet is produced in the forward direction of the second proton. The resulting large rapidity difference between the final states then opens up the phase space for BFKL evolution. First numerical results on partonic level are provided.

1 Introduction

Due to its large center of mass energy the LHC allows for the study of forward physics using methods of perturbative QCD. Among them we find forward production of different systems such as high p_T jets, heavy quark pairs [1] and Drell-Yan (DY) processes where a virtual photon or Z boson decays into a pair of leptons [2, 3]. The study of these type of processes is interesting as they allow to probe parton distribution functions at very small values of x which have not been reached in so-far collider experiments. It therefore provides a possibility to test formalisms which have been especially developed for the description of small x processes and which go beyond the standard formulation in terms of collinear factorization by including additional small x enhanced contributions. The starting point of such studies is given by BFKL evolution which resums small x logarithms on the level of partonic scattering amplitudes at leading logarithmic (LL) [4, 5] and next-to-leading-logarithmic (NLL) [6, 7] accuracy. Extensions of BFKL evolution comprise on the one hand additional resummation of collinear logarithms [8, 9, 10, 11, 12] which cure the instability of pure NLL BFKL evolution and on the other hand the inclusion of saturation effects which refer to the presence of high parton densities at small x.

A proper identification of relevant effects at small x seems almost impossible at the level of inclusive cross-sections. Cancellations between different final states minimize the sensitivity to the particular feature of the employed method and deviations from inclusive evolution equations due to small x effects may be partly hidden into the chosen initial conditions. It is therefore necessary to turn to the study of more exclusive observables in order to distinguish different effects at small x and to identify the correct description. Among these exclusive observables there is a class of events where the entire dependence of the process on the non-perturbative dynamics is factorized by conventional collinear factorization. These observables typically involve hard events in the forward region of both scattering protons, while the large difference in rapidity difference between the hard final states opens up the phase space for BFKL evolution.

Among the best explored processes of this type are 'Mueller-Navelet' jets which consist of a high p_T-jets in the forward regions of each proton. Currently this process is one of the little examples where a complete NLL description exists [13], with both BFKL evolution and impact factors at NLL [14, 15, 16, 17]. In contrast to naïve expectations, the result of [13] revealed a strong dependence t on the next-to-leading order corrections to the jet impact factors. At the same time, the numerical differences between the NLL resummed result and a pure collinear NLO result remain small for a large class of observables, once NLO corrections to impact factors are included.

This observation motivates the study of a new type of forward-backward observable, where a DY pair is produced in the forward direction of one of the particles instead of a jet. The hope is that this observable is able to better distinguish between standard NLO results and NLL BFKL resummed predictions. Even though the large virtuality of the photon and/or the mass of the Z diminish at first the value of the strong coupling constant α_s, the rapidity difference between lepton pair and backward jet remains large at the Large Hadron Collider, $\Delta Y < 7$ and a study of BFKL evolution seems meaningful. In particular with the DY final state in the color singlet, this observable can be expected to be less sensitive to hadronization effects. In addition, study of new final states may also trigger new theoretical efforts for an improved definition of impact factors and lead to the identification of new BFKL observables. In the following we present some partial results of our study, for details we refer to the paper in preparation [18].

2 The leading-order DY impact factor

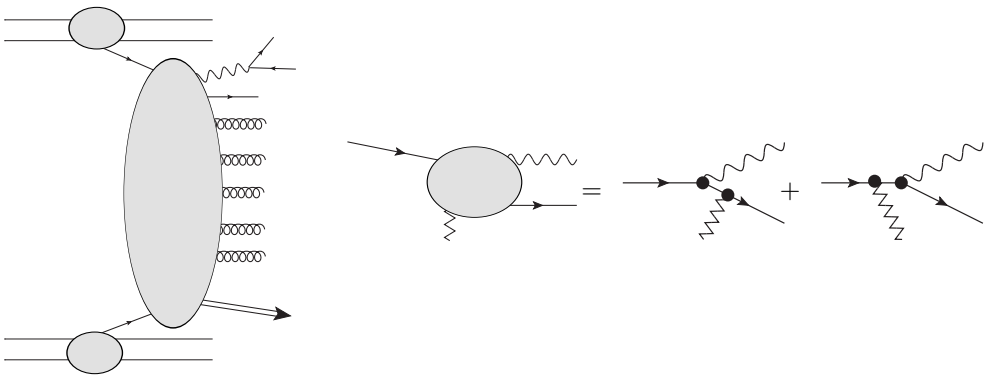

(a) (b)

Figure 1: a) A large difference in rapidity between the forward gauge boson (γ^*, Z) and the backward jet opens up the phase space for BFKL evolution. b) The leading order DY impact factor is obtained as the sum of two effective diagrams where the t-channel gluon carries eikonal polarizations.

In the current study we restrict to the LO impact factor, where relevant diagrams can be found in Fig. 1.b. A complete NLO study seems possible using Lipatov's effective action [19]

which is currently explored at NLO [20, 21, 22, 23]. The leading order impact factor reads

$$\Phi_{Zq} = \frac{c_f \alpha_s \sqrt{N_c^2 - 1}}{\pi \boldsymbol{k}^2 N_c} \left[\frac{z\boldsymbol{k}^2\big((1-z)^2+1\big) + 2M^2(1-z)z}{D_1 D_2} - \frac{M^2 z(1-z)}{D_1^2} - \frac{M^2(1-z)z}{D_2^2} \right]$$
$$D_1 = (\boldsymbol{q} - z\boldsymbol{k})^2 + (1-z)M^2 \qquad D_2 = \boldsymbol{q}^2 + (1-z)M^2 \tag{1}$$

Here M denotes the mass of the Z boson and the virtuality of the photon respectively, while c_f yields the corresponding coupling to the quark. $\boldsymbol{q}$ and $\boldsymbol{k}$ are the transverse momenta of the final state gauge boson and initial gluon, while z is the momentum fraction of the initial quark momentum carried on by the gauge boson.

3 Preliminary numerical results at partonic level

The above impact factor carries a logarithmic singularity if the final state quark turns to be soft. To avoid this singularity we study ratios of angular coefficients $\mathcal{C}_n = \langle \cos n\phi \rangle$, where ϕ denotes the azimuthal angle between the jet and the gauge boson. In a preliminary study

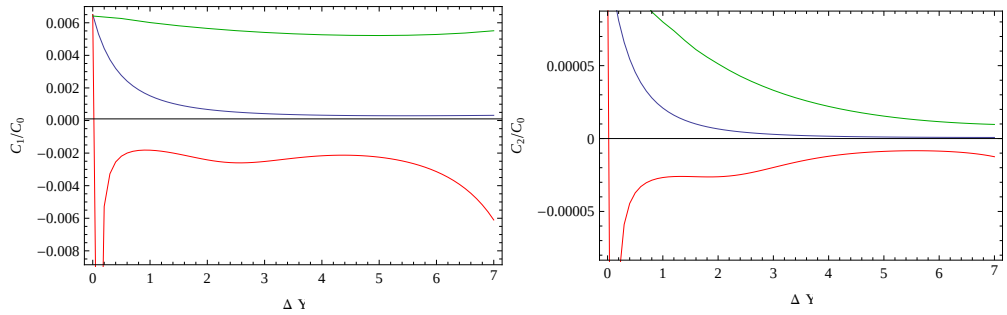

(a) (b)

Figure 2: Comparison on partonic level with fixed running coupling of LL (green), NLL (red) and NLL RG improved (blue) BFKL Green's function [12]. Both ratios $\mathcal{C}_1/\mathcal{C}_0$ (a) and $\mathcal{C}_2/\mathcal{C}_0$ are highly sensitive to the Green's function

which restricts to the partonic level and fixed coupling, we find a rather poor convergence of the BFKL evolution for the ratios $\mathcal{C}_n/\mathcal{C}_0$. It is notable that a similar effect occurs in the NLL jet study of [13] where the NLO impact factor corrections dominate the corresponding observable. The ratio $\mathcal{C}_1/\mathcal{C}_2$ shows on the other hand very good convergence and promises to be a good candidate for future phenomenological studies.

Acknowledgments

We are grateful for financial support from the German Academic Exchange Service (DAAD), the MICINN under grant FPA2010-17747, the Research Executive Agency (REA) of the European Union under the Grant Agreement number PITN-GA-2010-264564 (LHCPhenoNet) and Comunidad de Madrid (HEPHACOS ESP-1473).

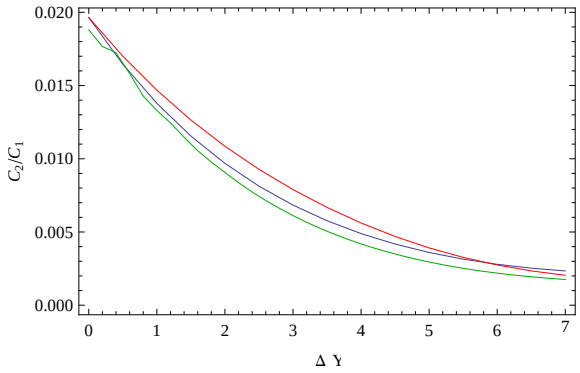

Figure 3: Comparison on partonic level with fixed running coupling of LL (green), NLL (red) and NLL RG improved (blue) BFKL Green's function [12]. The ratio $\mathcal{C}_2/\mathcal{C}_1$ reveals excellent convergence at this level of accuracy.

References

[1] C. Salas and J. Stirling. in preparation.

[2] S. Marzani and R. D. Ball. Nucl.Phys. **B814** (2009) 246–264, arXiv:0812.3602 [hep-ph].

[3] F. Hautmann, M. Hentschinski, and H. Jung. arXiv:1205.1759 [hep-ph].

[4] V. S. Fadin, E. A. Kuraev, and L. N. Lipatov. Phys. Lett. **B60** (1975) 50–52.

[5] I. I. Balitsky and L. N. Lipatov. Sov. J. Nucl. Phys. **28** (1978) 822–829.

[6] V. S. Fadin and L. N. Lipatov. Phys. Lett. **B429** (1998) 127–134, arXiv:hep-ph/9802290.

[7] M. Ciafaloni and G. Camici. Phys. Lett. **B430** (1998) 349–354, arXiv:hep-ph/9803389.

[8] G. Salam. JHEP **9807** (1998) 019, arXiv:hep-ph/9806482 [hep-ph].

[9] M. Ciafaloni, D. Colferai, and G. Salam. Phys.Rev. **D60** (1999) 114036, arXiv:hep-ph/9905566 [hep-ph].

[10] M. Ciafaloni, D. Colferai, G. Salam, and A. Stasto. Phys.Rev. **D68** (2003) 114003, arXiv:hep-ph/0307188 [hep-ph].

[11] G. Altarelli, R. D. Ball, and S. Forte. Nucl.Phys. **B742** (2006) 1–40, arXiv:hep-ph/0512237 [hep-ph].

[12] A. Sabio Vera. Nucl.Phys. **B722** (2005) 65–80, arXiv:hep-ph/0505128 [hep-ph].

[13] D. Colferai, F. Schwennsen, L. Szymanowski, and S. Wallon. JHEP **1012** (2010) 026, arXiv:1002.1365 [hep-ph].

[14] J. Bartels, D. Colferai, and G. Vacca. Eur.Phys.J. **C24** (2002) 83–99, arXiv:hep-ph/0112283 [hep-ph].

[15] J. Bartels, D. Colferai, and G. Vacca. Eur.Phys.J. **C29** (2003) 235–249, arXiv:hep-ph/0206290 [hep-ph].

[16] F. Caporale, D. Y. Ivanov, B. Murdaca, A. Papa, and A. Perri. JHEP **1202** (2012) 101, arXiv:1112.3752 [hep-ph].

[17] D. Y. Ivanov and A. Papa. JHEP **1205** (2012) 086, arXiv:1202.1082 [hep-ph].

[18] M. Hentschinski and C. Salas. in preparation.

[19] L. N. Lipatov. Nucl. Phys. **B452** (1995) 369–400, hep-ph/9502308.

[20] M. Hentschinski and A. S. Vera. Phys.Rev. **D85** (2012) 056006, arXiv:1110.6741 [hep-ph].

[21] M. Hentschinski. Nucl.Phys. **B859** (2012) 129–142, arXiv:1112.4509 [hep-ph].

[22] G. Chachamis, M. Hentschinski, J. M. Martinez, and A. Sabio Vera. Nucl.Phys. **B861** (2012) 133–144, arXiv:1202.0649 [hep-ph].

[23] G. Chachamis, M. Hentschinski, J. D. Madrigal Martinez, and A. Sabio Vera. in preparation.

Measurement of W/Z production with the ATLAS detector

Jean-Baptiste Sauvan on behalf of the ATLAS Collaboration

Laboratoire de l'Accélérateur Linéaire, IN2P3/CNRS, Université Paris-Sud 11, Orsay, France

DOI: http://dx.doi.org/10.3204/DESY-PROC-2012-02/76

The production of W and Z bosons at the LHC has been measured with the ATLAS detector. These measurements include inclusive and differential cross sections, W polarisation, and the polarisation of τ leptons from W decays. They show sensitivity to the proton structure and are also used to test predictions from perturbative QCD and phenomenological models.

Introduction

A large number of W and Z bosons have been produced at the LHC and recorded by the ATLAS detector [1] during the years 2010 and 2011. These datasets allowed for the precise measurement of inclusive and differential production rates as well as other important physical quantities such as the W polarisation. These measurements are key ingredients that can be used to constrain parton distribution functions (PDFs) and test various predictions from perturbative QCD (pQCD) and Monte Carlo generators. A short overview of these measurements is given in the present proceedings. All of them are based on the dataset recorded in 2010, corresponding to an integrated luminosity of about 35 pb^{-1}, with the exception of the inclusive $Z \to \tau\tau$ cross section measurement that makes use of up to 1.55 fb^{-1} of 2011 data.

1 Inclusive cross section measurements

The production cross sections of the inclusive Drell-Yan processes $W^{\pm} \to \ell\nu$ and $Z/\gamma^* \to \ell\ell$ ($\ell = e, \mu$) have been measured and compared with pQCD calculations based on a number of different PDF sets available at NNLO [2]. They have been measured within a restricted phase space defined by cuts on the charged leptons and the neutrino transverse momenta (i.e., fiducial cross-section measurements), and have also been extrapolated to the full kinematic range to obtain the total W and Z/γ^* cross sections.

The measurements in the electron and in the muon decay channels have been found to be consistent with each other. They have been combined using a method which accounts for the correlations among the different sources of systematic uncertainty [3, 4]. The precision of the integrated cross sections in the fiducial region is about 1.2 %, with an additional uncertainty of 3.4 % resulting from the luminosity measurement. The uncertainties on the total cross sections are about twice as large because they include the uncertainties arising from the determination

of the acceptance correction. A broad agreement of the theory predictions with the data is observed (see Figure 1).

Ratios of cross sections have been computed accounting for the correlations between uncertainties [2]. The precision of these measurements is very high, with a total uncertainty of 0.9 % for the W^+/W^- ratio and of 1.3 % for the $W^\pm/Z$ ratio due to the cancellation of the luminosity uncertainty. The $W^\pm/Z$ ratio measures a rather PDF-insensitive quantity, provided that the parton sea is flavour-symmetric, and the agreement with the measurement supports the assumption of a flavour-independent light-quark sea at the W and Z scale. On the other hand, charge-dependent ratios are more sensitive to up-down quark distribution differences and exhibit more significant deviations. Again, a broad agreement between the predictions and the data is observed.

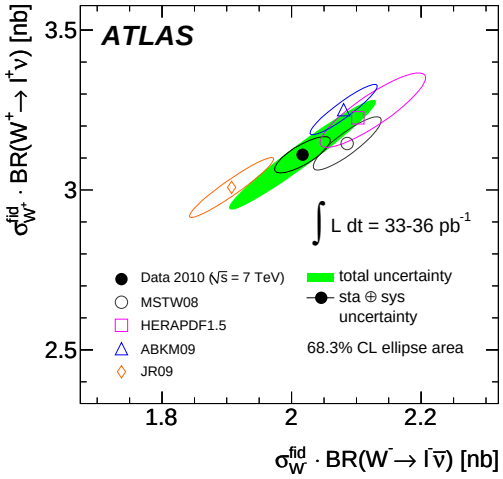

Figure 1: Measured and predicted fiducial cross sections times leptonic branching ratios: σ_{W^+} vs σ_{W^-} [2]. The ellipses illustrate the 68 % CL coverage for total uncertainties (full green) and excluding the luminosity uncertainty (open black). The uncertainties of the theoretical predictions correspond to the PDF uncertainties only.

Inclusive W and Z cross sections have also been measured in the τ-lepton decay channel [5, 6]. Since these processes constitute a major background for many searches, it is important to characterise them as precisely as possible. The latest $Z \to \tau\tau$ measurement uses about 1.5 fb^{-1} of 2011 data and combines three different pairs of τ decay channels. The systematic uncertainty estimated for this measurement is at the 10 % level. Both the $W \to \tau\nu$ and the $Z \to \tau\tau$ measurements are consistent with the ones that use electrons or muons, providing a validation of the τ reconstruction and identification algorithms.

2 Differential cross section measurements

In addition to the integrated cross sections, the $W^\pm$ cross sections have been measured differentially as a function of the lepton (electron or muon) pseudorapidity in the region $|\eta_\ell| \leq 2.5$ [2]. The Z/γ^* cross section has been measured as a function of the boson rapidity $|y_Z|$ up to 2.4 and an extension to $|y_Z| \leq 3.6$ has been obtained in the electron channel, with the inclusion of the forward detector region [2]. These measurements allow one to probe a large range of parton momentum fraction due to its dependence on the rapidity of the vector bosons.

The measured y_Z (see Figure 2–left) and η_ℓ dependencies are broadly described by the predictions of the PDF sets considered. However, some deviations are visible; for example, the JR09 PDF set predicts a lower Z cross section, at central rapidities, than the measurement, and almost all predictions tend to overestimate the Z and W cross sections at large y_Z and η_ℓ. These measurements can therefore provide additional constraints on PDFs, especially on the strange-quark density [7], for which very little is known.

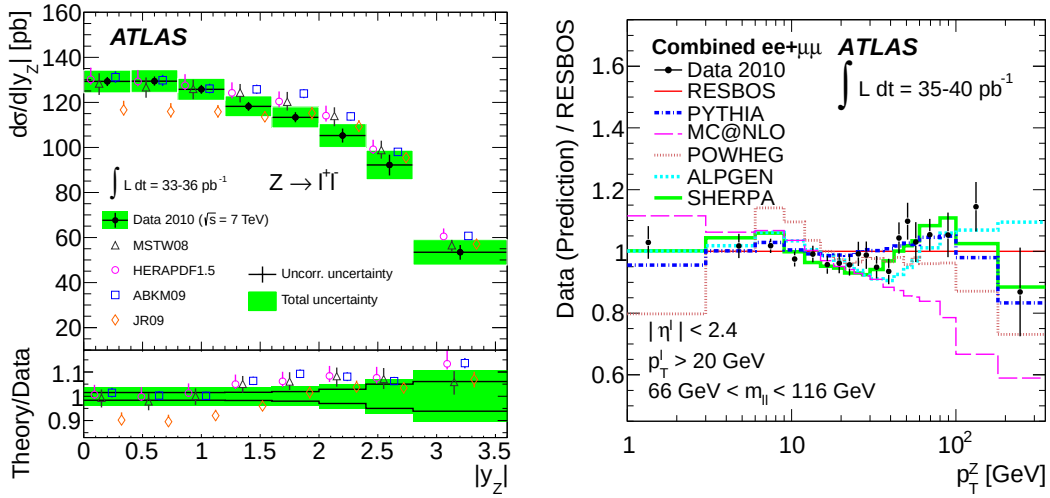

Figure 2: (Left) Differential $d\sigma/d|y_Z|$ cross section measurement for $Z \to \ell\ell$ compared to NNLO theory predictions using various PDF sets [2]. (Right) Ratios of the combined data and various predictions to the RESBOS prediction for the normalised differential cross section as a function of p_{T}^{Z} [8].

The W and Z production cross sections have also been measured as a function of the vector boson p_{T} in the electron and muon channels, and the two channels have been combined [8, 9] (see Figure 2–right). These measurements are used to test pQCD predictions and the phenomenological models used in Monte Carlo generators. Two regimes are particularly interesting: the low-p_{T} regime, which is dominated by soft and collinear parton emission, and the high-p_{T} regime, which corresponds to events containing at least one hard parton. The low-p_{T} region can be modeled by logarithmic resummations or parton shower algorithms. On the other hand, pQCD calculations and generators using NLO matrix elements or tree-level $2 \to n$ matrix elements can be tested at high p_{T}.

The RESBOS prediction, which combines resummed and fixed-order pQCD calculations, shows good agreement with the measurement over the entire p_{T} range, indicating the importance of resummation (the RESBOS prediction is used as a reference in Figure 2). The ALPGEN+HERWIG, SHERPA, and PYTHIA predictions also give a good description of the data. On the other hand, NLO generators such as MC@NLO or POWHEG+PYTHIA underestimate the data at high transverse momentum. Fixed-order pQCD calculations predict too few events at high p_{T} at $\mathcal{O}(\alpha_S)$ but the agreement with the measured distributions is significantly improved by the $\mathcal{O}(\alpha_S^2)$ calculations [8, 9].

3 Polarisation measurements

Using the decay-lepton transverse momentum and the missing transverse momentum, the W decay angular distribution projected onto the transverse plane has been measured and analysed in terms of the helicity fractions f_0, f_L and f_R [10]. These helicity fractions have been obtained in two different kinematic ranges ($35\ \mathrm{GeV} < p_{\mathrm{T}}^{W} < 50\ \mathrm{GeV}$ and $p_{\mathrm{T}}^{W} > 50\ \mathrm{GeV}$) by fitting

distributions of the cosine of the "transverse helicity" angle $\cos\theta_{2D}$ with templates representing longitudinal, left- and right-handed W bosons. The measurements of $f_L - f_R$ and f_0 have been compared to the values obtained from the MC@NLO and POWHEG generators (see Figure 3). No stringent constraints nor clear inconsistencies can be deduced, due to large uncertainties on the measurements, especially on f_0.

The polarisation of τ leptons has been measured for the first time at a hadron collider, using $W \to \tau\nu$ decays [11]. Hadronic 1-prong τ decays have been used, and the τ polarisation has been obtained from the energy sharing between charged and neutral pions. The measured value $P_\tau = -1.06 \pm 0.04\,(\text{stat})^{+0.05}_{-0.07}\,(\text{syst})$ is in agreement with the Standard Model prediction.

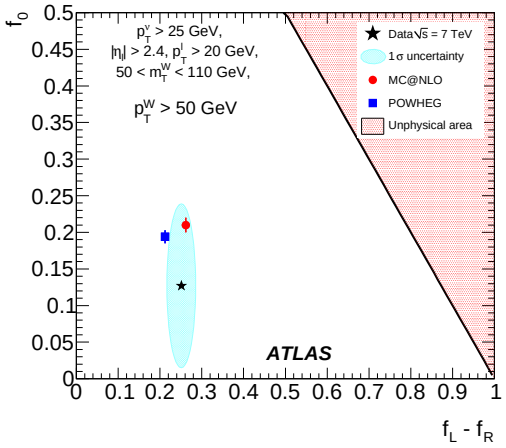

Figure 3: Measured values of f_0 and $f_L - f_R$ for $p_T^W > 50$ GeV compared with the predictions of MC@NLO and POWHEG [10]. The ellipse around the data point corresponds to one standard deviation.

Conclusion

The high production rate of W and Z bosons at the LHC enables detailed studies such as precise total and differential cross-section measurements or polarisation measurements. These measurements can be used to further refine our knowledge of the proton structure, and test predictions from perturbative QCD and various phenomenological models. $W \to \tau\nu$ and $Z \to \tau\tau$ decays have also been measured, proving the ability of ATLAS to measure τ observables (e.g. polarisation), which are key ingredients for searches and the characterisation of new phenomena.

Most of the measurements presented in these proceedings have been performed using the dataset recorded in the year 2010. Efforts are ongoing to publish results using the larger 2011 dataset.

References

[1] ATLAS Collaboration. JINST **3** (2008) S08003.
[2] ATLAS Collaboration. Phys. Rev. D **85** (2012) 072004, arXiv:1109.5141 [hep-ex].
[3] A. Glazov, "Averaging of DIS cross section data", in *AIP Conf. Proc.*, vol. 792, pp. 237–240. 2005.
[4] H1 Collaboration. Eur. Phys. J. C **63** (2009) 625–678, arXiv:0904.0929 [hep-ex].
[5] ATLAS Collaboration. Phys. Lett. B **706** (2012) 276–294, arXiv:1108.4101 [hep-ex].
[6] ATLAS Collaboration. Tech. Rep. ATLAS-CONF-2012-006, 2012.
[7] ATLAS Collaboration, submitted to PRL. arXiv:1203.4051 [hep-ex].
[8] ATLAS Collaboration. Phys. Lett. B **705** (2011) 415–434, arXiv:1107.2381 [hep-ex].
[9] ATLAS Collaboration. Phys. Rev. D **85** (2012) 012005, arXiv:1108.6308 [hep-ex].
[10] ATLAS Collaboration, submitted to EPJC. arXiv:1203.2165 [hep-ex].
[11] ATLAS Collaboration, submitted to EPJC. arXiv:1204.6720 [hep-ex].

Measurement of W and Z production in the forward region with LHCb

Stephen Farry[1] on behalf of the LHCb collaboration

[1]University College Dublin, Belfield, Dublin 4, Dublin, Ireland

DOI: http://dx.doi.org/10.3204/DESY-PROC-2012-02/147

We report on measurements of W and Z production in the forward region, using data collected at the LHCb experiment with a centre of mass energy of $\sqrt{s} = 7$ TeV with an integrated luminosity of up to 1 fb^{-1}. W and Z bosons are reconstructed in leptonic decay channels, and their cross-sections determined using data-driven techniques. Results are presented inclusively (within the fiducial region considered), and differentially as a function of boson rapidity (Z) and lepton pseudorapidity (W). The ratio of W to Z production, W^+/W^- production and the W charge asymmetry (for three lepton p_T thresholds) is also given. All results are compared to NNLO predictions.

1 Introduction

The LHCb detector is a single arm spectrometer fully instrumented in the pseudorapidity region $2.0 \leq \eta \leq 5.0$. It has been designed to study heavy flavour physics in the forward region where B mesons are predominantly produced in proton proton collisions. While it shares some of its pseudorapidity range with the ATLAS and CMS general purpose detectors ($|\eta| > 2.5$), the remaining coverage is unique to LHCb. Further information about the detector can be found in [1].

Measurements of W and Z production cross-sections at the LHC constitute an important test of the Standard Model. While the partonic cross-sections are well understood and known to the percent level, additional theoretical uncertainties arise due to the knowledge of the Parton Density Functions (PDFs) which parameterise the behaviour of the colliding protons. This results in an overall uncertainty of between 3 and 10% [2]. LHCb's pseudorapidity range allows it to probe these PDFs in a distinct region of (x, Q^2) space, where x is the fractional momentum carried by the struck quark, and Q^2 is the energy transfer of the interaction. Thus measurements of the W and Z cross-sections at LHCb can provide important constraints to these PDFs in a unique kinematic region.

2 Event Selection

2.1 $Z \to \mu\mu$

The $Z \to \mu\mu$ analysis is performed on the full dataset collected by LHCb in 2010, corresponding to a luminosity of 37.1 pb^{-1}. Events are triggered on a single high momentum muon trigger

requiring a transverse momentum, $p_T > 10$ GeV. Events are then selected which contain two well reconstructed muons with $p_T > 20$ GeV with a pseudorapidity in the range $2.0 < \eta^\mu < 4.5$ and with a di-muon invariant mass in the range $60 < M_{\mu\mu} < 120$ GeV. The backgrounds considered are from $Z \to \tau\tau$ events where both tau leptons decay to muons, heavy flavor decays with two semi-leptonic muonic decays and generic QCD events, where pions or kaons either decay in flight to muons, or punch through the detector and are falsely identified. The total number of selected events is 1966 with an estimated purity of 99.7%.

2.2 $Z \to ee$

For the $Z \to ee$ analysis, the 2011 dataset is used, with a luminosity of 945 pb^{-1} . Events are triggered on a high momentum electron trigger which passes events containing electrons with $p_T > 15$ GeV. Events are then selected containing two identified electrons with a transverse momentum greater than 20 GeV and lying within the pseudorapidity region $2 < \eta^e < 4.5$. Due to saturation of the electromagnetic calorimeter and incomplete Bremsstrahlung recovery, the $Z \to ee$ mass peak is spread to lower values, and so the mass window is chosen to be $M_{ee} > 40$ GeV. The backgrounds considered are $Z \to \tau\tau$ where both tau leptons decay to electrons, and generic QCD events. In total, 21535 events are selected with an estimated purity of 97.8%.

2.3 $Z \to \tau\tau$

Two different final states are considered to measure the $Z \to \tau\tau$ cross-section, which is performed on both the the 2010 and 2011 datasets, with a combined luminosity of up to 247 pb^{-1}. Both final states contain a high momentum muon with a transverse momentum greater than 20 GeV that is required to pass the trigger, while the second candidate can be either a muon ($\mu\mu$) or an electron (μe) with a transverse momentum exceeding 5 GeV. In all cases the tracks are required to have a pseudorapidity in the range $2 < \eta < 4.5$, with a visible mass greater than 20 GeV, where the visible mass is the mass of the combined momentum of the visible decay products. Due to large backgrounds a number of different requirements are placed on the events. In both cases, the tracks are required to be isolated and have a separation of greater than 2.7 radians in the transverse plane. In addition, due to a large background from Drell-Yan produced di-muon pairs in the ($\mu\mu$) final state, the tracks are required to have a large summed impact parameter, and a p_T asymmetry between the two candidates of greater than 0.2. A total of 81 events are selected in the (μe) channel with a purity of 85% while 33 events are selected in the ($\mu\mu$) channel with a purity of 78%.

2.4 $W \to \mu\nu$

In the $W \to \mu\nu$ analysis, performed with the full 2010 dataset of 37.1 pb^{-1}, events are selected which trigger on a high momentum single muon trigger and possess a well reconstructed muon with p_T >20 GeV in the pseudorapidity region $2.0 < \eta^\mu < 4.5$. Further restrictions are placed on the event to reject backgrounds. The muons are isolated and prompt, have a small impact parameter, and deposit less than 4% of their momentum in the calorimetry system. In addition the events contain no other muons with a p_T >5 GeV. The backgrounds considered are from the decay-in-flight and punch-through of kaons and pions, $Z \to \mu\mu$ events where one of the muons is not reconstructed in the LHCb acceptance, the decay of W and Z bosons through tau decay modes producing a single muon in the final state, and the decay of heavy quarks. The signal

Source	$\Delta\sigma^Z(\%)$ $\mu\mu$	ee	$\tau\tau(\mu e)$	$\tau\tau(\mu\mu)$	$\Delta\sigma^W(\%)$ W^+	W^-
Systematic	4.3	3.1	16	10	3.2	2.9
Luminosity	3.5	3.5	5.1	5.1	3.5	3.5
Statistical	2.2	0.7	17	12	1.1	1.2
Luminosity(pb^{-1})	37.1	945	247	246	37.1	37.1

Table 1: Summary of the uncertainties on the measurements made by LHCb.

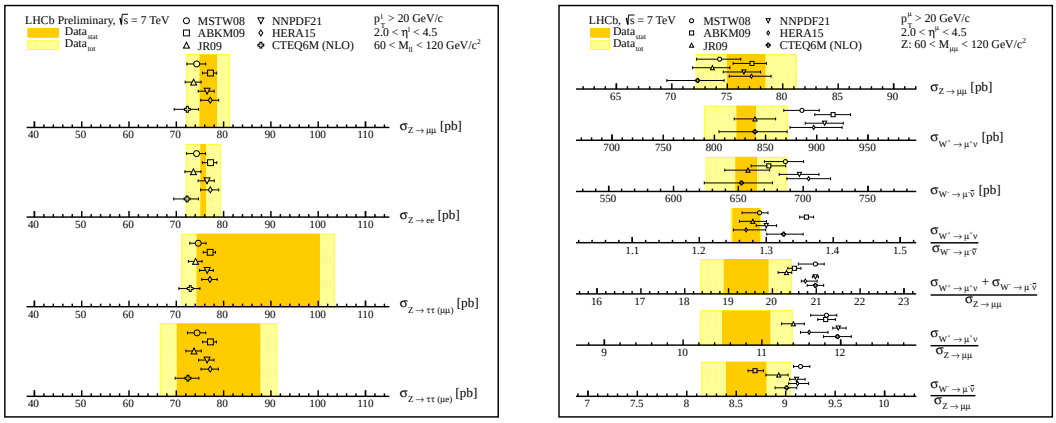

Figure 1: Summary and comparison to theory for the Z cross-section measurements (left) and W and Z cross-section and ratio measurements (right)

purity is obtained by fitting signal and background templates to the p_T spectrum of the muon in data, where templates are obtained from a combination of data and simulation. A total of 14660 (11618) $W^+(W^-)$ events are selected with a purity of 78.8%(78.4%).

3 Cross-Section Determination

The cross section is determined from the number of events selected, N, through the formula

$$\sigma = \frac{\rho \cdot N}{A \cdot \varepsilon \cdot \int \mathcal{L}} \cdot f_{FSR} \tag{1}$$

where ρ represents the purity of the selected events. The integrated luminosity, $\int \mathcal{L}$ is determined using both a Van Der Meer scan [3] and a beam gas method [4] and is known to a precision of 3.5%. The efficiency, ε, is the product of the trigger, track finding, muon identification and selection efficiencies and is estimated primarily using data driven methods; more details can be found in [5, 6, 7]. All cross-sections are quoted in the kinematic regions defined by the selection of the $Z \to \mu\mu$ and $W \to \mu\nu$ selections, where the leptonic product of the W or Z are required to have transverse momenta exceeding 20 GeV and pseudorapidites between 2

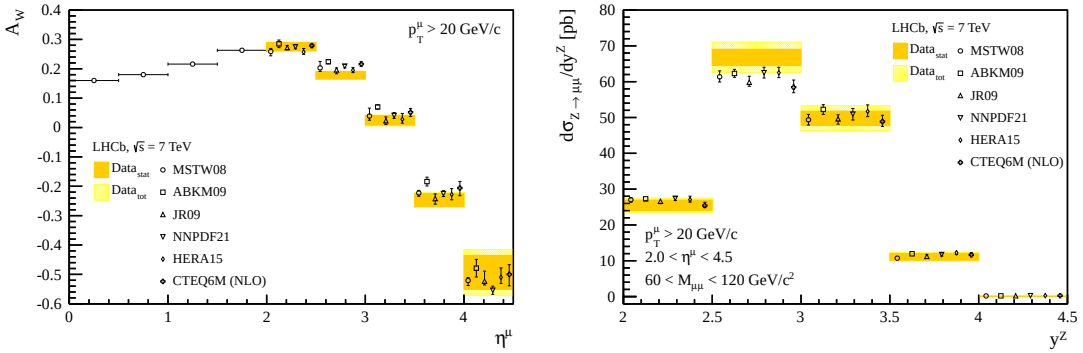

Figure 2: Summary and comparison to theory for the W asymmetry differential cross-section as a function of lepton pseudorapidity (left) and Z differential cross-section as a function of boson rapidity (right).

and 4.5, and in the case of the Z the di-lepton mass is between 60 and 120 GeV. The acceptance factor, A, is used when necessary to correct to this kinematic region, while the factor f_{fsr}, is used to correct the measurements for final state radiation. Both of these factors are calculated from simulation.

3.1 Results

The results are presented both as overall cross-section in Fig. 1 and as differential cross-sections in Fig. 2 as a function of boson rapidity, in the case of the Z measurements, and lepton pseudorapidity, in the case of the W. All results are consistent with the theoretical predictions calculated using DYNNLO[8] at NNLO and a number of different PDF sets. A summary of the uncertainties is given in Table 1. The $Z \to \mu\mu$ measurement is limited by the statistical determination of the efficiencies in 2010 data, with $Z \to \tau\tau$ limited by statistics, and the $W \to \mu$ and $Z \to ee$ measurements are limited by the luminosity determination.

References

[1] The LHCb Collaboration, 2008 JINST 3 S08005.

[2] Martin, A.D. et al. Eur.Phys.J., C63, 2009

[3] S. Van Der Meer, ISR-PO/68-31 (1968)

[4] M. Ferro-Luzzi, Nucl. Instrum. Methods A 553, 388 (2005)

[5] The LHCb Collaboration, LHCb-PAPER-2012-008.

[6] The LHCb Collaboration, LHCb-CONF-2012-012.

[7] The LHCb Collaboration, LHCb-CONF-2011-041.

[8] S. Catani et al. arXiv:0903.2120 [hep-ph]

Inclusive low mass Drell-Yan production in the forward region at $\sqrt{s} = 7$ TeV

Jonathon Anderson[1] on behalf of the LHCb collaboration

[1]Physik-Institut der Universität Zürich, Switzerland.

DOI: http://dx.doi.org/10.3204/DESY-PROC-2012-02/145

A measurement of the Drell-Yan cross-section in dimuon final states for muons within pseudorapidities of 2 to 4.5, in the mass range $5 < \mathrm{M} < 120$ GeV/c^2, is presented. The muons are required to have a momenta larger than 10 GeV/c and a transverse momenta larger that 3 GeV/c. The cross section is measured differentially, in mass, and in rapidity of the virtual photon in two distinct mass regions. The analysis uses the full dataset collected by the LHCb experiment during 2010 with an integrated luminosity of 37 pb^{-1}.

1 Introduction

The LHCb detector [1] is a single-arm forward spectrometer at the LHC covering the pseudorapdity range $2 < \eta < 5$, primarily designed for the study of particles containing b or c quarks. In addition to its main flavor physics programme, LHCb can make precision measurements of electroweak bosons at high rapidities. This document describes measurements of the differential cross-section of low mass Drell-Yan production with the LHCb detector at $\sqrt{s} = 7$ TeV using about 37 pb^{-1} of data collected in 2010 [2].

These measurements are an important test of the Standard Model at LHC energies. Perturbative QCD predictions of these processes are available at next-to-next-to-leading order (NNLO). The measurements of the low mass Drell-Yan cross-sections at LHCb are sensitive to Bjorken-x values as low as 8×10^{-6} for four-momentum transfer $\mathrm{Q}^2 = 25$ GeV^2/c^4, where x is the momentum fraction carried by the struck quark. They will provide important input to the knowledge of the parton density functions and the understanding of the theoretical calculations.

2 Analysis overview

Candidate $\gamma^\star \to \mu\mu$ events are selected via a dimuon trigger and an offline selection that requires that each muon has momenta $\mathrm{p} > 10$ GeV/c, transverse momenta $\mathrm{p}_T > 3$ GeV/c, pseudorapidity $2 < \eta < 4.5$ and, combined, that the dimuon pair has an invariant mass in the range $5 < M_{\mu\mu} < 120$ GeV/c^2. The mass range $9 < M_{\mu\mu} < 10.5$ GeV/c^2, where the $\Upsilon \to \mu\mu$ contribution dominates, is excluded. While the high mass region is very pure, the background increases significantly towards low masses. Four sources of background have been evaluated: semileptonic decays of hadrons containing b and c quarks; pions and kaons that have been mis-identified as muons; $\gamma^\star/Z \to \tau\tau$ events where both taus decay to muons; and, for the mass bins below 10 GeV/c^2, the contribution due to the radiative tail of $\Upsilon \to \mu\mu$ events.

The signal yield is extracted by a template fit to the minimum muon isolation distribution of the two muons using the TFractionFitter ROOT package. Here the muon isolation is defined as the fraction of the transverse momenta of the muon-jet carried by the muon, $z = p_T^{\mu}/p_T^{Jet}$. The muon-jet is defined as the jet which contains the muon, and is reconstructed with the anti-kt algorithm [3] with the size R = 0.5. Signal events are expected to have an isolation distribution close to unity while the background events tend to have lower values since they are usually produced in the same direction as the other fragmentation products. Fits are performed in nine different mass bins and in five rapidity bins in two mass regions. The signal template used in the fits is obtained from simulation. This is validated by comparing the isolation distribution for $\Upsilon \to \mu\mu$ and $Z \to \mu\mu$ events in data and simulation where good agreement is seen. The template for backgrounds due to misidentified pions and kaons is obtained from data by taking opposite sign di-track combinations (assumed to be pions and kaons) in events that pass the minimum bias trigger and weighting each combination by the probability that both tracks are misidentified as muons. This probability is taken to be the fraction of tracks identified as muons in randomly triggered events and is parametrised as a function of the longitudinal momentum. The template for the heavy quark background is taken from data by selecting the events in our sample that have two muons that do not come from the proton-proton interaction vertex and do not form a common vertex. This sample also contains a contribution from $\gamma^{\star}/Z \to \tau\tau$ decays. For the mass bins below 10 GeV/c^2, a template describing the component due to the radiative tail of Υ decays is also included in the fit. This template is taken from simulation and the normalization in the fit is fixed to the number of expected Υ events extracted from a fit to the Υ mass distribution in data. The extracted sample purity varies between 7% and 100% depending on the mass and rapidity bin. To estimate the uncertainty on the fits due to our understanding of these templates, cross-check fits are performed using different templates. Here the mis-id template is taken from events containing two muons with the same charge, the heavy quark template is taken from simulation, and the signal template from simulation is distorted by applying a scale factor of 0.95 or 1.05. The resulting differences in the extracted signal yield are taken as the systematic uncertainties due to the template shapes. Here the largest uncertainty is due to the shape of the heavy quark template and varies depending on the mass bin, being 24% in the lowest mass bin and less than 1% for masses above 20 GeV/c^2.

The experimental efficiencies due to reconstruction and triggering are all determined from data using dimuon resonances (J/ψ, Υ and Z) and tag-and-probe techniques. The event yield is then corrected on an event by event basis as a function of the transverse momentum and pseudorapidity of the two muons. The systematic uncertainty on this correction is dominated by the uncertainty on the determination of the tracking efficiencies which is limited by the available statistics and varies between 4% and 10% depending on the mass and rapidity bin.

Two methods are used to determine the integrated luminosity, a Van der Meer scan [4] where the colliding beams are moved transversely across each other to determine the beam profile, and a beam gas method [5], where reconstructed beam-gas interaction vertices near the beam crossing point determine the beam profile. Both methods give similar results and have a precision of 3.5%.

Since the cross-section is measured in the kinematic range of the measurement, the only acceptance correction comes from migrations into and out of the phase space. The acceptance is determined from simulation and is consistent with one. Corrections are applied for bin-to-bin migrations. They are estimated from MC and found to be small, below 1% for most of the bins. No corrections are yet applied for final state radiation.

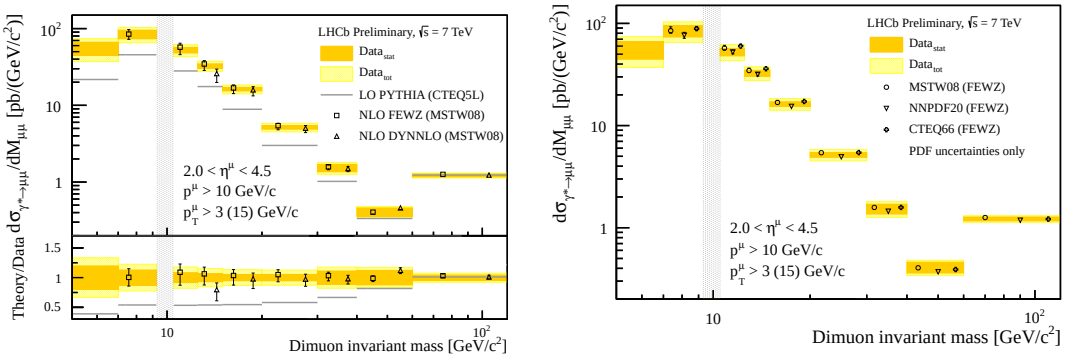

(a) (b)

Figure 1: $\gamma^\star \to \mu\mu$ cross section as a function of dimuon mass. The orange bands correspond to the statistical uncertainties, the yellow band to the statistical and systematic uncertainties added in quadrature. (a): Superimposed are the PYTHIA predictions and the NLO predictions from FEWZ and DYNNLO. The lower plot shows the ratio of the predictions or the uncertainties to the data. (b): Superimposed are NLO predictions from FEWZ with the PDF sets from MSTW08, NNPDF and CTEQ. The uncertainties of the NLO predictions contain the PDF uncertainties evaluated at the 68% confidence level and the theoretical errors added in quadrature.

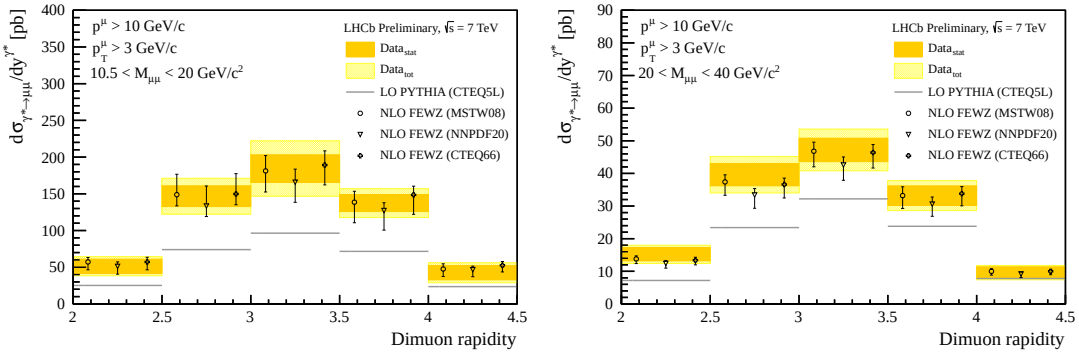

(a) (b)

Figure 2: Differential cross section for $\gamma^\star \to \mu\mu$ as a function of rapidity for two different dimuon mass regions (a: $10.5 < M < 20 GeV/c^2$, b: $20 < M < 40 GeV/c^2$). The orange bands correspond to the statistical uncertainties, the yellow band to the statistical and systematic uncertainties added in quadrature. Superimposed are NLO predictions from FEWZ with the PDF sets from MSTW08, NNPDF and CTEQ; they are displaced horizontally for presentation. The NLO uncertainties correspond to the PDF uncertainties evaluated at the 68% confidence level.

3 Results

Figure 1(a) shows the differential cross-section as a function of the invariant mass of the dimuons together with predictions from PYTHIA [6] (normalised to the cross-section measured in the highest mass bin) and NLO calculations. NLO predictions are only available for FEWZ [7] for masses larger than 7 GeV/c^2 and for DYNNLO [8] for masses larger than 12.5 GeV/c^2. Figure 1(b) shows the same data in comparison with FEWZ predictions with three different PDF sets: MSTW08 [9], NNPDF20 [10] and CTEQ66 [11]. Here, only the uncertainties due to the PDF uncertainty is shown; these are smaller than the theory uncertainties at NLO. Figure 2 shows the differential cross-section as a function of the rapidity of the dimuons in two different mass bins. PYTHIA underestimates the Drell-Yan cross-section by more than a factor two but describes the shapes in y and mass reasonably well. The FEWZ predictions with three different PDFs describe all the shapes and also the normalisation over the mass region where the calculation is valid.

4 Conclusions

The Drell-Yan cross-section has been measured for dimuon invariant masses $5 < M_{\mu\mu} < 120$ GeV/c^2 using 37 pb^{-1} of data collected in 2010. The signal is extracted by fitting signal and background templates to the isolation distribution of the muons. At low masses the dominant systematic uncertainty comes from the uncertainty of the shapes of the templates. The cross-section is measured as a function of the invariant dimuon mass and as a function of the dimuon rapidity in two different invariant mass regions. While the PYTHIA predictions agree in shape but are too low in normalisation, reasonable agreement is found with NLO predictions in those mass regions where the calculations are available.

References

[1] The LHCb collaboration, *The LHCb Detector at the LHC*, JINST **3** S08005 (2008).

[2] The LHCb collaboration, *Inclusive low mass Drell-Yan production in the forward region at $\sqrt{s}$ = 7 TeV*, LHCb-CONF-2012-013.

[3] M. Cacciari and G. P. Salam, Dispelling the N3 myth for the k(t) jet-finder, Phys. Lett. B641 (2006) 57, arXiv:hep-ph/0512210.

[4] S. van der Meer, *Calibration of the effective beam height in the ISR*, ISR-PO/68-31, 1968.

[5] The LHCb collaboration, R. Aaij et al., *Absolute luminosity measurements with the LHCb detector at the LHC*, JINST 7 (2012) P01010, arXiv:1110.2866.

[6] T. Sjostrand, S. Mrenna, and P. Skands, PYTHIA 6.4 physics and manual, JHEP 05 (2006) 026, arXiv:hep-ph/0603175.

[7] R. Gavin, Y. Li, F. Petriello, and S. Quackenbush, FEWZ 2.0: A code for hadronic Z production at next-to-next-to-leading order, Comput. Phys. Commun. 182 (2011) 2388, arXiv:1011.3540.

[8] S. Catani, L. Cieri, G. Ferrera, D. de Florian, M. Grazzini, Phys. Rev. Lett. 103 (2009) 082001, arXiv:0903.2120.

[9] A. Martin, W. Stirling, R. Thorne, and G. Watt, Parton distributions for the LHC, Eur. Phys. J. C63 (2009) 189, arXiv:0901.0002.

[10] R. D. Ball et al., A first unbiased global NLO determination of parton distributions and their uncertainties, Nucl. Phys. B838 (2010) 136, arXiv:1002.4407.

[11] P. M. Nadolsky et al., Implications of CTEQ global analysis for collider observables, Phys. Rev. D78 (2008) 013004, arXiv:0802.0007.

WG1: Structure Functions and WG4: Hadronic Final States

New features in version 2 of the fastNLO project

Daniel Britzger[1], *Klaus Rabbertz*[2], *Fred Stober*[2], *Markus Wobisch*[3]
(The fastNLO Collaboration)

[1]DESY, Hamburg, Germany
[2]KIT, Karlsruhe, Germany
[3]Louisiana Tech University, Ruston, Louisiana, USA

DOI: `http://dx.doi.org/10.3204/DESY-PROC-2012-02/165`

Standard methods for higher-order calculations of QCD cross sections in hadron-induced collisions are time-consuming. The fastNLO project uses multi-dimensional interpolation techniques to convert the convolutions of perturbative coefficients with parton distribution functions and the strong coupling into simple products. By integrating the perturbative coefficients for a given observable with interpolation kernels, fastNLO can store the results of the time-consuming folding integrals in tables, which subsequently are used for very fast rederivations of the same observable for arbitrary parton distribution functions, different scale choices, or $\alpha_s(M_Z)$. Various tables with code for their evaluation are available for numerous jet measurements at the LHC, the TeVatron, and HERA. FastNLO is used in publications of experimental results by the ATLAS, CMS, CDF, DØ, and H1 collaborations, and in all recent global PDF analyses by MSTW, CTEQ, and NNPDF. This article focuses on developments implemented in the new version 2 of fastNLO, enhancing and broadening its functionality.

1 Introduction and the fastNLO concept

Precision measurements in high energy physics reveal their full power only if they are compared to accurate theoretical predictions. For the interpretation of experimental data or the extraction or tuning of model parameters reasonably fast theory calculations are needed. For measurements defined in published cross sections, repeated computations of (almost) the same cross sections have to be performed. Typical examples where calculations have to be repeated more often for the same observable are:

- Comparisons of data vs. theory, where e.g. different sets of parton distribution functions (PDFs) are used, like those provided by the global fitting collaborations.
- Determination of the PDF uncertainty on theory predictions. As an example, the uncertainty on the cross sections arising from the NNPDF [1] PDF set require 100 to 1000 rederivations of the same cross sections where only the PDFs differ.
- Fitting of PDFs where for each step in the iterative procedure the cross sections have to be recalculated for the corresponding temporary PDF. FastNLO is used by various global PDF fitting groups, like MSTW [2], CTEQ [3], NNPDF [1], ABM [4], or HERAPDF [5].

- Determination of model parameters, or the determination of the strong coupling constant in iterative fits.
- Determination of the theory uncertainty of cross sections from missing higher orders, where conventionally the calculations are repeated for different choices of the renormalization and/or factorization scale.
- Studies of the scale dependence of the theory cross sections. For processes involving multiple scales it is not clear, which scale setting to choose.

Some observables in next-to-leading order (NLO) or even higher-order calculations can be computed rather fast like e.g. DIS structure functions. Other observables like Drell-Yan and jet cross sections, however, are very slow to compute. Especially the latter ones are the current focus of fastNLO. FastNLO provides computer code and precalculated tables of perturbative coefficients for various observables in hadron-induced processes. The calculation of the fundamental cross sections or matrix elements is performed by flexible computer code like `NLOJet++` [6, 7, 8, 9], which has been used here.

For illustrating the ideas in this document, all formulae are shown for jet production cross sections in deep-inelastic scattering. All concepts and formulae can be generalized to hadron-hadron collisions like at the LHC or the TeVatron [10].

1.1 The fastNLO concept

Perturbative QCD predictions for observables in hadron-induced processes depend on the strong coupling constant α_s and on the PDFs of the hadron(s). Any cross section in lepton-hadron or hadron-hadron collisions can be written as the multiplication of the strong coupling constant to the power of n, α_s^n , the perturbative coefficients $c_{i,n}$ for the partonic subprocess i, and the corresponding linear combination of PDFs from the one or two hadrons f_i, which is a function of the fractional hadron momenta x_a, x_b carried by the respective partons, as:

$$\sigma_{ep\to\text{jets}}(\mu_r,\mu_f) = \sum_{i,n} \int_0^1 dx \alpha_s^n(\mu_r) c_{i,n}(\frac{x_{Bj}}{x},\mu_r,\mu_f) f_i(x,\mu_f) \tag{1}$$

The calculation of this cross section with reasonable statistical precision is very slow due to the necessary Monte Carlo integration of the accessible phase space. The idea of fastNLO is to separate the PDFs and the α_s factors from the perturbative coefficients $c_{i,n}$ and to convert this integration into a sum [11, 12]. This discretization introduces a set of eigenfunctions $E_i(x)$ (with $\sum_i E_i(x) \equiv 1$) around a defined number of x-values. The PDF in eq. 1 can then be replaced by $f_i \simeq \sum_i f_a(x_i)E_i(x)$ and is removed from the integral. When calculating the perturbative coefficients the nodes receive fractional contributions of each event within the x-range of each eigenfunction. The perturbative coefficients are calculated once with very high statistical precision and are stored in a *table*. The remaining integration over x to compute the cross section is turned into a sum over the n perturbative orders, i parton flavors, and all the x-nodes. To respect the scale dependence, a similar procedure is employed. The multiplication of the PDF, α_s, and the perturbative factors are performed when reading the table of all $c_{i,n}$ values, which is very fast and gives the opportunity to change the PDFs and α_s as required. When calculating hadron-hadron cross sections, the two x integrations are replaced by two sums instead of only one like in the depicted DIS case.

2 New features in fastNLO version 2

Here, new features of the fastNLO version 2 are presented in comparison to the previous version 1.4 [10]. The fastNLO project comprises three main elements, the *table* format, *creator* code to create and *reader* code to read and evaluate the tables with an interface to PDFs.
A new *table* format features more flexibility and foresees to incorporate multiple additive or multiplicative contributions to the cross sections. Threshold corrections, which were already available previously for hadron-hadron induced inclusive jet production [13], higher-order calculations, electroweak corrections, or new physics contributions can be implemented in a similar way as soon as they are available. Further multiplicative correction factors like non-perturbative corrections can be stored together with their uncertainties. Also data can be included within the new table format together with their correlated and uncorrelated uncertainties.
The computation of the tables has been optimized. An automated scan to determine the covered x-range is performed first. The now flexible number of x-nodes for each analysis bin respects their different x-coverage. The scale dependence is stored as a separate array and also the interpolation of the scale nodes is optimized.
The fastNLO *reader* code for evaluating the fastNLO tables is now available in Fortran as well as in independently developed `C++` classes with an agreement of $\mathcal{O}(10^{-10})$ between the two. It is distributed in one package [14] as open source code, which is installable following the GNU autotools procedure with the only dependence on some external functionality to access PDFs like in LHAPDF [15]. Previously released tables keep their validity and can be converted into the new format.

3 The generalized concept of flexible-scale tables

A generalized concept for even more flexible tables was also released in fastNLO version 2. These are called *flexible-scale* tables and are based on two principles.
The dependence on the renormalization and factorization scales $\mu_{r/f}$ can be factorized when calculating the perturbative coefficients $c_{i,n}$, like

$$c_{i,n}(\mu_r, \mu_f) = c^0_{i,n} + \log(\mu_r) c^r_{i,n} + \log(\mu_f) c^f_{i,n}. \tag{2}$$

This way, only scale independent weights c^0, c^r, and c^f are stored in three scale independent fastNLO tables. The multiplication of the scale dependent log terms are performed only when evaluating the table. Similarly to the α_s term in eq. 1, where $a_s(\mu_r)$ can be regarded as an arbitrary function of the scale μ_r, also the scales μ_r and μ_f can be regarded as functions of any relevant k observables s_k, like $\mu_{r/f} = \mu_{r/f}(s_1, s_2)$. FastNLO examples employ $k = 2$ since each observable needs a separate interpolation array and increases the required evaluation time.
This method gives the opportunity to store multiple possible scale definitions, like e.g. the jet momentum p_{T} and the event virtuality Q^2. When evaluating the fastNLO table it is now possible to choose any function of these two scale settings for the definition of the renormalization and factorization scale. Typical examples are e.g. $\mu_r^2 = (Q^2 + p_{\mathrm{T}}^2)/2$ and $\mu_f^2 = Q^2$, but also definitions like $\mu = s_1 \cdot \exp(0.3 \cdot s_2)$ are possible. Further, the scales can be varied independently and by arbitrary scale factors. This gives new opportunities to study the scale dependence of cross sections. The concept is also available for pp and $p\overline{p}$ calculations. For future applications, the *flexible-scale* concept is valid also for higher-order calculations like NNLO without any significant loss in speed.

4 Showcase application

Numerous fastNLO tables are available on the fastNLO website [14] for various measurements by ATLAS, CDF, CMS, DØ, H1, STAR, and ZEUS. All calculations were performed using the `NLOJet++` program [6, 7, 8, 9], for calculating the matrix elements. A data/theory comparison of global inclusive jet data in hadron induced processes as a function of the transverse jet momentum for various center-of-mass energies is shown in fig. 1 employing the MSTW2008 PDF sets. Hadron-hadron induced processes further include 2-loop threshold corrections, which represent a part of NNLO. An updated version of this plot is available through the arXiv article [16].

References

[1] R. D. Ball, V. Bertone, F. Cerutti, L. Del Debbio, S. Forte, *et al.* Nucl.Phys. **B849** (2011) 296–363, arXiv:1101.1300 [hep-ph].

[2] A. Martin, W. Stirling, R. Thorne, and G. Watt. Eur.Phys.J. **C63** (2009) 189–285, arXiv:0901.0002 [hep-ph].

[3] H.-L. Lai, M. Guzzi, J. Huston, Z. Li, P. M. Nadolsky, *et al.* Phys.Rev. **D82** (2010) 074024, arXiv:1007.2241 [hep-ph].

[4] S. Alekhin, J. Blümlein, and S. Moch. arXiv:1202.2281 [hep-ph].

[5] K. Nowak *et al.*, 2012. to appear in these proceedings.

[6] Z. Nagy and Z. Trocsanyi. Phys. Rev. **D59** (1999) 014020, arXiv:hep-ph/9806317.

[7] Z. Nagy and Z. Trocsanyi. Phys. Rev. Lett. **87** (2001) 082001, arXiv:hep-ph/0104315.

[8] Z. Nagy. Phys. Rev. Lett. **88** (2002) 122003, arXiv:hep-ph/0110315.

[9] Z. Nagy. Phys. Rev. **D68** (2003) 094002, arXiv:hep-ph/0307268.

[10] T. Kluge, K. Rabbertz, and M. Wobisch. arXiv:hep-ph/0609285 [hep-ph].

[11] C. Pascaud and F. Zomer. LAL-94-42 (1994) .

[12] M. Wobisch. Dissertation, RWTH Aachen, DESY-THESIS-2000-049, 2000.

[13] N. Kidonakis and J. Owens. Phys.Rev. **D63** (2001) 054019, arXiv:hep-ph/0007268 [hep-ph].

[14] D. Britzger, T. Kluge, K. Rabbertz, F. Stober, and M. Wobisch, "The fastNLO homepage at HepForge". http://fastnlo.hepforge.org/.

[15] M. Whalley, D. Bourilkov, and R. Group. arXiv:hep-ph/0508110 [hep-ph].

[16] M. Wobisch, D. Britzger, T. Kluge, K. Rabbertz, and F. Stober. arXiv:1109.1310 [hep-ph].

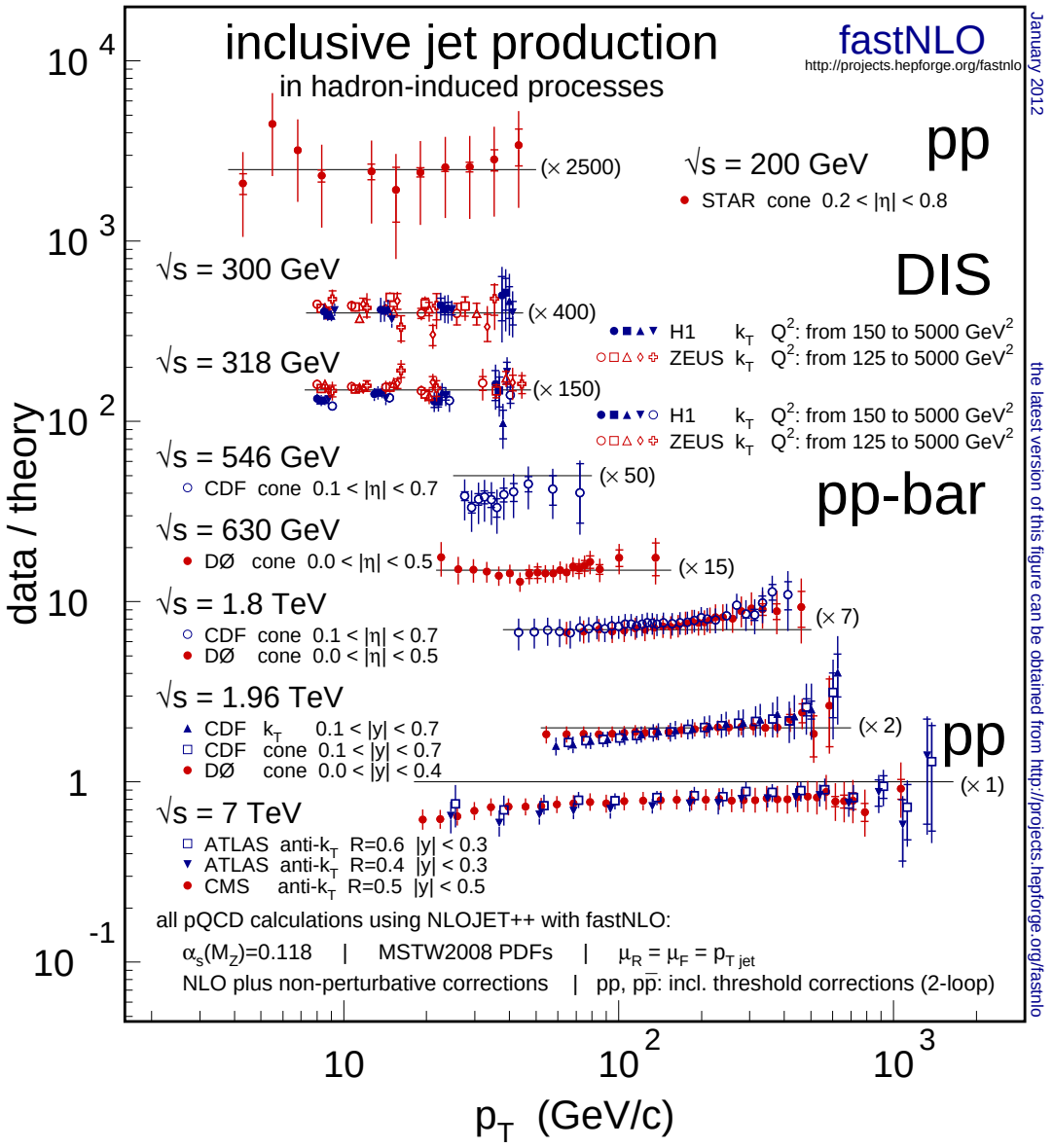

Figure 1: Ratios of data and theory for inclusive jet cross section measured in hadron-hadron collisions and in deeply inelastic scattering at different center-of-mass energies. The ratios are shown as a function of jet transverse momentum p_T. The theory results are computed for MSTW2008 PDFs.

Inclusive Jet Production Measured with ATLAS and Constraints on PDFs

Bogdan Malaescu on behalf of the ATLAS Collaboration

CERN, CH-1211, Geneva 23, Switzerland

DOI: http://dx.doi.org/10.3204/DESY-PROC-2012-02/71

Inclusive jet and dijet double-differential cross sections have been measured in proton-proton collisions at a centre-of-mass energy of 7 TeV using the ATLAS detector at the LHC. The cross sections were measured using jets clustered with the anti-k_t algorithm. The measurements are performed in the jet rapidity range $|y| < 4.4$, covering jet transverse momenta from 20 GeV to 1.5 TeV and dijet invariant masses from 70 GeV to 5 TeV. The data are compared to expectations based on next-to-leading order QCD calculations corrected for non-perturbative effects, as well as to next-to-leading order Monte Carlo predictions. The data test the theory in a new kinematic regime, and provide sensitivity to parton distribution functions in a region where they are currently not well constrained.

1 Introduction

The inclusive jet and dijet cross sections are important tools for testing Quantum Chromodynamics (QCD) and searching for physics beyond the Standard Model at the LHC. The ATLAS Collaboration has published a first measurement of these cross sections at $\sqrt{s} = 7$ TeV, using an integrated luminosity of 17 nb^{-1} [1]. A second measurement, using the full 2010 data sample of 37.3 pb^{-1} [2], significantly extended the covered phase space: in the jet transverse momentum p_T (from 60 GeV down to 20 GeV, and from 600 GeV up to 1.5 TeV), in rapidity (from $|y| < 2.8$ to $|y| < 4.4$), as well as in dijet mass (from 1.8 up to 4.8 TeV). A preliminary measurement of the dijet cross section using 4.7 fb^{-1} in the full 2011 data sample [3] shows an improved precision comparing to the previous measurements. These analyses probe next-to-leading order (NLO) perturbative QCD and parton distribution functions (PDFs) in a kinematic regime not explored before.

2 Jet definition, reconstruction and calibration

For the ATLAS inclusive jet and dijet cross section measurements, jets are defined using the anti-k_t algorithm [4]. The measurements are performed for two different values of the distance parameter R (0.4 and 0.6).

Jets are reconstructed at the electromagnetic (EM) scale [1], the inputs being three-dimensional topological clusters built from calorimeter cells. The four-momentum of the uncalibrated, EM-scale jet is defined as the sum of the four-momenta of its constituent calorimeter energy clus-

[1] The EM-scale correctly reconstructs the energy of the electromagnetic showers deposited in the calorimeter.

ters. Additional energy due to pile-up interactions is subtracted by applying a correction depending on the number of reconstructed vertices in the event. The energy of the jet is then corrected for instrumental effects like energy lost in the dead material or due to calorimeter non-compensation. This jet energy scale (JES) correction, as a function of the energy and pseudorapidity of the reconstructed jet, is derived using isolated jets in the Monte Carlo simulation (MC) [5].

The JES uncertainty is the dominant uncertainty for the inclusive jet and dijet measurements [2]. Comparing to the previous measurement [1], this uncertainty has been strongly reduced, due to an improved calibration of the calorimeter response at the EM-scale using $Z \to ee$ *in-situ* data, as well as using the single hadron energy measurement from *in-situ* and test-beam data. The improved precision is confirmed by independent *in-situ* measurements in collision data, like the comparison of calorimeter jet energy to the sum of track p_T associated to the jet, and transverse momentum balance in γ+jet, dijet and multijet events [5].

In order to allow for a reliable treatment of the bin-to-bin correlations of the uncertainties, it is important to separate the different uncertainty components. Therefore the JES uncertainty has beed split in several components, and the calorimeter component (dominant in the central region) has been split in several sources. All the uncertainty components (sources) are treated as fully correlated in p_T and rapidity, and independent between each other.

3 Data correction to particle level

The measured cross sections are corrected for the experimental effects and are hence obtained for the *particle level* final state. In MC particle jets are built from stable particles, including muons and neutrinos from decaying hadrons.

The inclusive jet and dijet measurements are corrected from detector to particle level using a matrix based unfolding [2]. A transfer matrix relating particle level and reconstructed quantities is built from MC, using a geometrical matching between particle level and reconstructed level jets. The matching efficiency is taken into account in a three step unfolding procedure. The first step applies the matching efficiency at the reconstructed level to the data spectrum, so that it can be directly compared with the spectrum of MC matched reconstructed jets. The second step performs the actual unfolding, correcting for the transfer of jets (events) between the bins. Finally, the third step corrects for the matching efficiency at the particle level.

The bin-by-bin, SVD [6] and IDS [7] unfolding methods have been tested at the second step of the procedure. These methods differ by the correction strategy, the way they rely on the shape of the MC spectrum at the particle level (the SVD and IDS methods rely much less on this shape compared to the bin-by-bin method), as well as by their respective regularisation methods (a local, significance-based regularization is used in IDS, while a regularisation based on a singular value decomposition plus a constraint on the global curvature of the unfolded spectrum are used for SVD).

The potential bias of each of these unfolding methods has been studied using a data-driven closure test, relying on the shape comparison between data and MC at the reconstructed level. For this test, a reweighting of the particle level MC spectrum (used to build the transfer matrix) by a smooth function is performed, such that, after projection on the reconstructed MC axis, a better agreement with data is observed. The reweighted reconstructed MC is unfolded with each of the three methods, using the original transfer matrix (without reweighting, like for the unfolding of the data) as input of the methods. The comparison of the corresponding results

with the reweighted particle level MC provides an estimation of the *MC shape uncertainty* for each unfolding method. The smallest uncertainty, at the 1% level, is obtained using the IDS method, while a larger uncertainty is obtained with SVD. After a NLO/LO reweighting of the particle level MC shape in the input transfer matrix, the bin-by-bin method has an uncertainty similar to the one of IDS, while it was larger before. The IDS method is used for performing the nominal correction of the data spectra.

The full set of uncertainties are propagated from the reconstructed to the unfolded level. The statistical uncertainties are propagated using pseudo-experiments, where both the input data spectrum and the MC transfer matrix are statistically fluctuated and a covariance matrix is obtained. Each component of the systematic uncertainty is propagated by performing shifts of the reconstructed spectrum by one standard deviation in the positive and negative direction respectively, redoing the unfolding and comparing the results with the nominal unfolded spectrum. The resolution uncertainty is propagated by performing a smearing of the nominal transfer matrix by the resolution uncertainty, re-doing the unfolding and comparing with the nominal result.

4 Theoretical predictions and comparison with the data

The unfolded experimental cross sections are compared with the NLO QCD prediction, corrected for non-perturbative effects. Both the NLOJET++ [8] and the POWHEG [9, 10] (with parton shower switched off) generators were used for the hard scattering. The CT10 [11] NLO parton distribution functions and the same values for the renormalization and factorization scales (the transverse momentum of the leading jet) were used for both programs. An agreement between the results of the two programs at the few percent level was observed for the inclusive jet cross section, over all the rapidity regions. They are also consistent for dijet events with both jets in the central region. However, large differences are observed for dijet events with large rapidity separations between the two leading jets, for which the NLOJET++ prediction is unstable. This prediction is much more stable when using a scale taking into account the rapidity difference between the two leading jets. The results were also compared with predictions obtained using alternative PDFs: MSTW 2008 [12], NNPDF 2.1 [13] and HERAPDF 1.5 [14].

The non-perturbative correction factors are derived using PYTHIA [15], while the uncertainties are obtained from comparisons between different PYTHIA tunes, as well as from the comparison with HERWIG++ [16]. These correction factors have been applied to the NLO predictions, in view of the comparison with the experimental cross sections.

Figure 1 shows the relative comparison between the 2010 inclusive jet cross section, for jets with R=0.6, and the theoretical predictions obtained using NLOJET++, with non-perturbative corrections. Within the quoted uncertainties, the general agreement is good, except in the high transverse momentum region where the data start to be sensitive to the various PDF sets.

Comparisons have also been performed with the POWHEG prediction, showered with PYTHIA and respectively HERWIG. Important differences between these two are observed, both for the inclusive and dijet cross sections.

5 Conclusions

The ATLAS experiment has performed several measurements of the inclusive jet and dijet cross sections, using data taken during 2010 as well as 2011. These measurements, provided with the

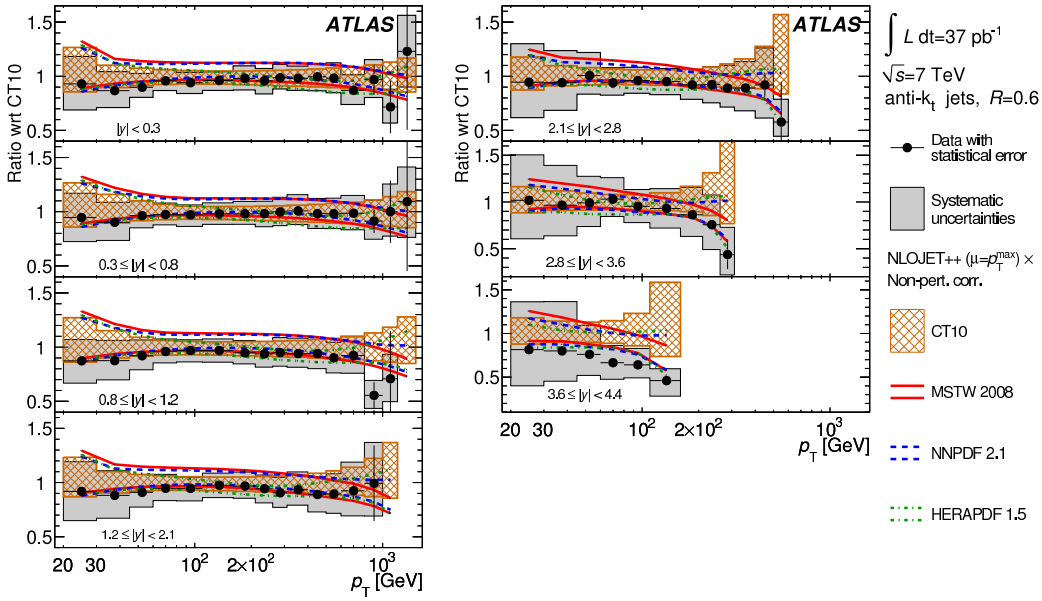

Figure 1: Relative comparison between the experimental inclusive jet cross section [2] and the theoretical predictions obtained using NLOJET++ with various PDF sets.

full information on uncertainties and correlations, allow for tests of QCD in phase space regions that were not covered previously.

References

[1] ATLAS Collaboration, Eur. Phys. J. C **71**, 1512 (2011) [arXiv:1009.5908 [hep-ex]].

[2] ATLAS Collaboration, arXiv:1112.6297 [hep-ex], accepted for publication in Physical Review D.

[3] ATLAS Collaboration, ATLAS-CONF-2012-021, https://cdsweb.cern.ch/record/1430730.

[4] M. Cacciari, G. P. Salam and G. Soyez, JHEP **0804**, 063 (2008) [arXiv:0802.1189 [hep-ph]].

[5] ATLAS Collaboration, arXiv:1112.6426 [hep-ex].

[6] A. Hoecker and V. Kartvelishvili, Nucl. Instrum. Meth. A **372**, 469 (1996) [hep-ph/9509307].

[7] B. Malaescu, arXiv:0907.3791 [physics.data-an].

[8] Z. Nagy, Phys. Rev. D **68**, 094002 (2003) [hep-ph/0307268].

[9] S. Alioli, P. Nason, C. Oleari and E. Re, JHEP **1101**, 095 (2011) [arXiv:1009.5594 [hep-ph]].

[10] P. Nason, arXiv:0709.2085 [hep-ph].

[11] H. -L. Lai *et al.*, Phys. Rev. D **82**, 074024 (2010) [arXiv:1007.2241 [hep-ph]].

[12] A. D. Martin, W. J. Stirling, R. S. Thorne and G. Watt, Eur. Phys. J. C **63**, 189 (2009) [arXiv:0901.0002 [hep-ph]].

[13] R. D. Ball *et al.*, Nucl. Phys. B **838**, 136 (2010) [arXiv:1002.4407 [hep-ph]].

[14] H1 and ZEUS Collaborations, H1prelim-10-142, ZEUS-prel-10-018.

[15] T. Sjostrand, S. Mrenna and P. Z. Skands, JHEP **0605**, 026 (2006) [hep-ph/0603175].

[16] M. Bahr *et al.*, Eur. Phys. J. C **58**, 639 (2008) [arXiv:0803.0883 [hep-ph]].

Jet Cross Section Measurements With CMS

Özlem Kaya on behalf of the CMS Collaboration

Kafkas University, Kars, Turkey (Member through Bogazici University, Istanbul, Turkey)

DOI: http://dx.doi.org/10.3204/DESY-PROC-2012-02/312

A measurement of inclusive jet production cross section is presented. Data from LHC proton-proton collisions at $\sqrt{s} = 7$ TeV, corresponding to 4.7 fb^{-1} of integrated luminosity, have been collected with the CMS detector. Jets are reconstructed with the anti-k_T clustering algorithm of size parameter $R = 0.7$, extending to rapidity $|y| = 2.5$, and transverse momentum $p_T = 2$ TeV. The measured cross section is corrected for detector effects and compared to perturbative QCD predictions at next-to-leading order, using various sets of parton distribution functions.

1 Introduction

Events with high transverse momentum jets in proton-proton collisions are explained in Quantum Chromodynamics (QCD) in terms of parton-parton scattering, where the outgoing scattered partons manifest themselves as hadronic jets. The inclusive jet and dijet cross sections are calculated precisely in perturbative QCD and can be used to constrain the parton distribution functions. In this Physics Analysis Summary, the measurement of the double-differential inclusive jet (p + p $\rightarrow$ jet + X) and dijet (p + p $\rightarrow$ jet + jet + X) production cross sections are reported as a function of the jet transverse momentum or the dijet invariant mass, and jet rapidity at $\sqrt{s} = 7$ TeV [1]. The data are collected with the Compact Muon Solenoid (CMS) detector [2] at the CERN Large Hadron Collider (LHC) during the 2011 run and correspond to an integrated luminosity of 4.7 fb^{-1}, two orders of magnitude larger than the published LHC results from the 2010 run [3],[4],[5]. The measured cross sections are corrected for detector effects and compared to the QCD predictions. The parton transverse momentum fractions $x_T = \frac{2p_T}{\sqrt{s}}$ probed in this measurement cover the range $0.033 < x_T < 0.57$.

2 Jet Reconstruction and Event Selection

Jets are reconstructed using the anti-k_T clustering algorithm [6] with size parameter $R = 0.7$. Each particle is reconstructed with the particle-flow technique [7] which combines the information from several subdetectors. The jet energy corrections are derived using simulated events, generated by PYTHIA6.4.22 (PYTHIA6) [8] and processed through the CMS detector simulation based on GEANT4 [9], and *in situ* measurements with dijet and photon+jet events [10]. An offset correction is also applied to take into account the extra energy clustered in jets due to additional proton-proton interactions within the same bunch crossing (pile-up).

The data samples are collected with single-jet high level triggers (HLT) [11] which require at least one jet in the event to satisfy the condition $p_T > 60$, 110, 190, 270 and 340 GeV,

respectively. In order to suppress non-physical jets, they are required to satisfy tight identification criteria: each jet should contain at least two particles, one of which is a charged hadron. Furthermore, the jet energy fraction carried by neutral hadrons and photons should be less than 90%. For the inclusive jet measurement, events are required to contain at least one tight jet with $p_T > 114$GeV, 196GeV, 300GeV, 362GeV, and 507GeV for the five single-jet HLT triggers used respectively. The inclusive measurement is performed in five rapidity regions of $\Delta|y| = 0.5$, up to $|y| = 2.5$. For the dijet measurement, at least two tight reconstructed jets with $p_{T1} > 60$GeV and $p_{T2} > 30$GeV are required. The dijet measurement is performed in five rapidity regions, defined by the maximum absolute rapidity $|y_{\max}| = \max(|y_1|, |y_2|)$ of the two leading jets in the event. The online jets are reconstructed using only calo clusters and non calibrated.

3 Experimental Measurements

The measured double-differential inclusive jet cross section and dijet mass cross sections are defined as $\frac{\mathrm{d}^2\sigma}{\mathrm{d}p_T\mathrm{d}|y|} = \frac{1}{\epsilon\mathcal{L}_{\mathrm{eff}}}\frac{N}{\Delta p_T \Delta|y|}$, and $\frac{\mathrm{d}^2\sigma}{\mathrm{d}M_{\mathrm{JJ}}\mathrm{d}|y_{\max}|} = \frac{1}{\epsilon\mathcal{L}_{\mathrm{eff}}}\frac{N}{\Delta M_{\mathrm{JJ}}\Delta|y_{\max}|}$, respectively, where N is the number of jets in the bin, ϵ is the product of the trigger and event selection efficiencies, $\mathcal{L}_{\mathrm{eff}}$ is the integrated luminosity of the data sample used for the analysis, Δp_T, ΔM_{JJ}, $\Delta|y|$, and $\Delta|y_{\max}|$ are the transverse momentum, invariant mass and rapidity bin widths for inclusive jet and dijet mass, respectively.

The measured spectra are then corrected for detector smearing effects (unfolded to the particle level), using the iterative (D'Agostini) method [12], as implemented in the RooUnfold package [13]. The response matrix is taken from the simulation, and the final statistical errors include the correlations between the bins. Figure 1 shows the unfolded double-differential cross sections as a function of jet p_T and M_{JJ}, compared to the QCD prediction.

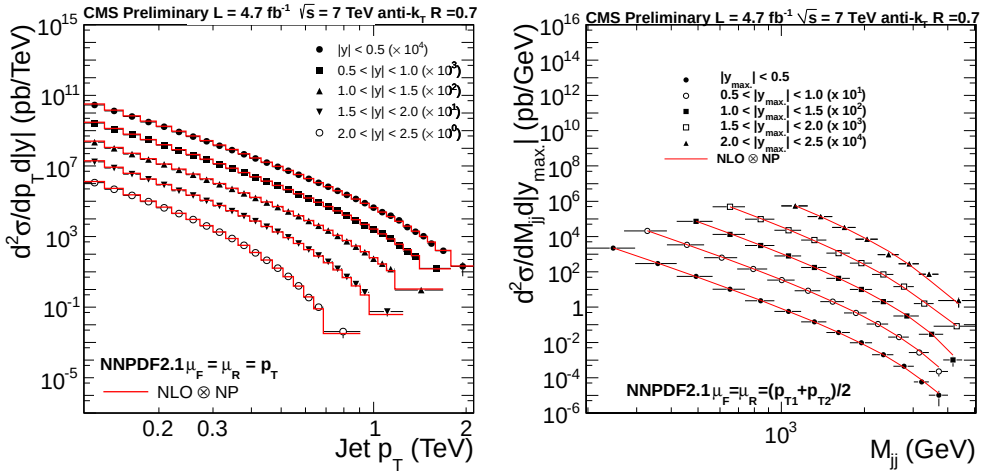

Figure 1: Inclusive jet (left) and dijet (right) cross sections compared to the theory prediction using the central value of the NNPDF PDF set.

4 Theory Predictions

The theoretical predictions for the jet cross sections consist of a next-to-leading-order (NLO) QCD calculation and a nonperturbative correction to account for the multiparton interactions (MPI) and hadronisation effects. The NLO calculations are done using the NLOJet++ program (v2.0.1) within the framework of the fastNLO package (v1.4) [14] The NLO calculation is performed using five different PDF sets: CT10 [15], MSTW2008NLO [16], NNPDF2.1 [17], HERAPDF1.5 [18], and ABKM09 [19] at the corresponding default values of the strong coupling constant $\alpha_S(M_Z) = 0.1180, 0.120, 0.119, 0.1176$, and 0.1179 respectively. The non-perturbative effects are estimated from the simulation, using the event generators PYTHIA6 (tune Z2) and HERWIG++ 2.4.2 [20]. The central value of the non-perturbative correction is calculated from the average of the two models considered, and ranges from 1% to 20%.

5 Measurement-Theory Comparison

In order to reveal the details of the agreement between the CMS data and the theory prediction, the ratio of the two is taken. Figures 2 shows the ratio to the prediction using the central value of the NNPDF PDF set.

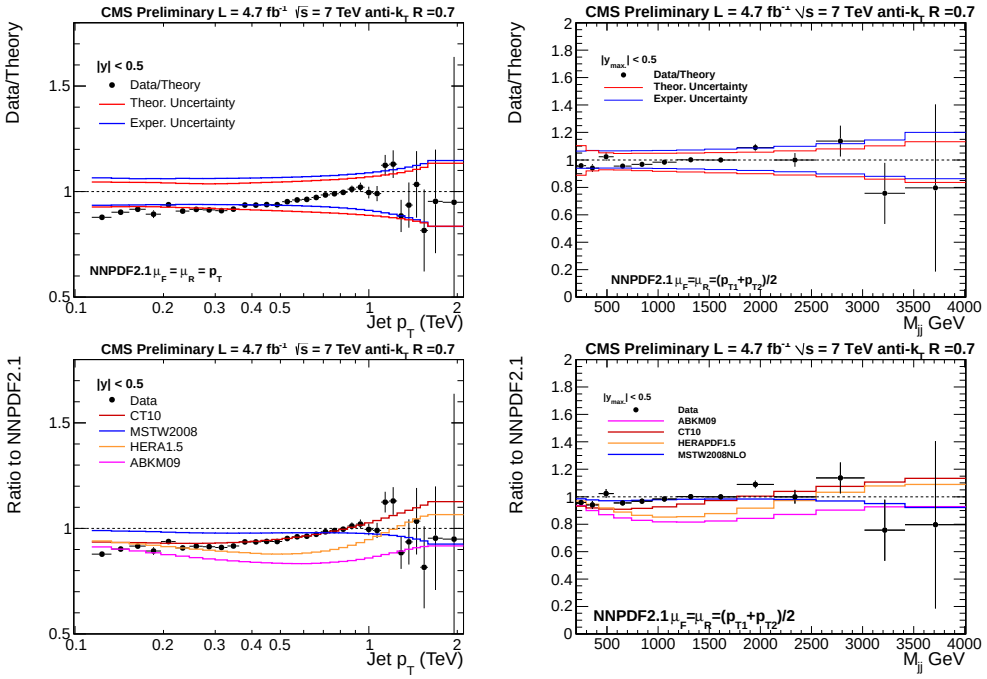

Figure 2: Top:Ratio of inclusive jet (left) and dijet (right) cross sections in $|y| < 0.5$ to the theory prediction of different PDF sets.

The additional curves represent the ratio of the other PDF set's central values. An overall good agreement is observed in all rapidity bins, with the various theory predictions showing differences of otypically 10 to 20%.

6 Summary

A measurement of the double-differential inclusive jet and dijet cross sections has been presented. Using 4.7 fb^{-1} of data from proton-proton collisions at $\sqrt{s} = 7$ TeV collected with the CMS detector, the measurement covers the jet p_T range from 0.1 TeV to 2 TeV, and the dijet mass range from 0.3 TeV to 5 TeV, in five rapidity bins, up to $|y| = 2.5$. Detailed comparisons to perturbative QCD predictions show good agreement with the theoretical predictions from five PDF sets. The size of the experimental uncertainties is comparable to the theoretical uncertainties, and in particular at the limits of the phase space, which allows for these data to be used in the global PDF fits and constrain their uncertainties.

References

[1] **CMS** Collaboration, "Measurement of Differential Jet Cross Sections at $\sqrt{s} = 7$ TeV with the CMS Detector", **CMS PAS QCD-11-004**.

[2] **CMS** Collaboration, "The CMS experiment at the CERN LHC", JINST 3:S08004,2008.

[3] **ATLAS** Collaboration, "Measurement of inclusive jet and dijet production in pp collisions at 7 TeV using the ATLAS detector", arXiv:hep-ex/1112.6297. Submitted to Physical Review D.

[4] **CMS** Collaboration, "Measuprement of the differential dijet mass cross section in proton-proton collisions at $\sqrt{s} = 7$ TeV", Phys.Lett. **B700** (2011) 187.

[5] **CMS** Collaboration, "Measurement of the Inclusive Jet Cross Section in pp Collisions at 7 TeV", Phys.Rev.Lett. **107** (2011) 132001. doi:10.1103/PhysRevLett.107.132001.

[6] M. Cacciari, G. P. Salam, and G. Soyez, "The anti-kt jet clustering algorithm", JHEP 04 (2008) 063. doi:10.1088/1126-6708/2008/04/063.

[7] **CMS** Collaboration, "Particle–Flow Event Reconstruction in CMS and Performance for Jets, Taus, and Emiss", CMS Physics Analysis Summary CMS-PAS-PFT-09-001 (2009).

[8] T. Sjöstrand, S. Mrenna, and P. Skands, "PYTHIA 6.4 physics and manual", JHEP 05 (2006) 026. doi:10.1088/1126-6708/2006/05/026.

[9] S. Agostinelli *et al.*, "Geant 4 – A Simulation Toolkit", Nucl. Inst. Meth. **A506** (2003) 250. doi:10.1016/S0168-9002(03)01368-8.

[10] **CMS** Collaboration, "Determination of Jet Energy Calibration and Transverse Momentum Resolution in CMS", JINST 6 (2011) P11002. doi:10.1088/1748-0221/6/11/P11002.

[11] **CMS** Collaboration, "The CMS High Level Trigger", Eur. Phys. J. **C46** (2006) 605. doi:10.1140/epjc/s2006-02495-8.

[12] G. D'Agostini, "A Multidimensional unfolding method based on Bayes' theorem.", Nucl.Instrum.Meth. **A362** (1995) 487.

[13] T. Adye, "Unfolding algorithms and tests using RooUnfold", arXiv:physics.data-an/1105.1160.

[14] T. Kluge, K. Rabbertz, and M. Wobisch, "fastNLO: Fast pQCD calculations for PDF fits", arXiv:hep-ph/0609285v2.

[15] H. -L. Lai *et al.*, "New parton distributions for collider physics", Phys. Rev. **D82** (2010) 074024. doi:10.1103/PhysRevD.82.074024.

[16] A. D. Martin *et al.*, "Parton distributions for the LHC", Eur. Phys. J. **C63** (2009) 189. doi:10.1140/epjc/s10052-009-1072-5.

[17] R. D. Ball *et al.*, "A first unbiased global NLO determination of parton distributions and their uncertainties", Nucl. Phys. B838 (2010) 136. doi:10.1016/j.nuclphysb.2010.05.008.

[18] **H1** and **ZEUS** Collaboration, "Combined Measurement and QCD Analysis of the Inclusive ep Scattering Cross Sections at HERA", JHEP 01 (2010) 109. doi:10.1007/JHEP01(2010)109.

[19] S. Alekhin, J. Blumlein and S.Klein et al, "The3-, 4-, and 5-flavor NNLO Parton from Deep-Inelastic-Scattering Data and at Hadron Colliders",Phys. Rev. **D81** (2010) 014032. doi:10.1103/PhysRevD.81.014032.

[20] M. Bähr *et al.*, "Herwig++ Physics and Manual", Eur. Phys. J.**C58** (2008) 639. doi:10.1140/epjc/s10052-008-0798-9.

A new approach to gluon-quark multiplicity ratio

Paolo Bolzoni[1]

[1]II. Institut für Theoretische Physik, Luruper Chaussee 149, 22761 Hamburg, Germany

DOI: http://dx.doi.org/10.3204/DESY-PROC-2012-02/96

We present a new approach in considering and including both the perturbative and the nonperturbative contributions to the multiplicity ratio r of gluon and quark jets. The new method is motivated by recent developments in timelike small-x resummation obtained in the $\overline{\rm MS}$ factorization scheme. A global analysis to fit the available data is also presented.

1 Introduction

The gluon-quark multiplicity ratio is defined as $r = N_g/N_q$, where $N_{g(q)}$ is the number of hadrons produced in a gluon(quark) jet. A purely perturbative and analytical prediction has been achieved by a solution to the equations for the generating functionals in the modified leading logarithmic approximation (MLLA) in Ref.[1] up to the so called N^{3}LOr in the expansion parameter $\gamma_0 = \sqrt{2N_c\alpha_s/\pi}$ *i.e.* γ_0^3. Here the theoretical prediction is about 10% higher than the data at the scale of the Z^0 vector boson and the difference with the data becomes even larger at lower scales. Among the many attempts to predict r numerically, the most successfull refers to numerical sulutions to the coupled system of equations of the generating functionals for the quark (Z_F) and the gluon (Z_G) in the MLLA framework (see *e.g.* [2]). These numerical solutions describe well the data only above at relatively high energies [3, 4, 5]. This shows that the slope of the multiplicity ratio predicted by this approach tends to be smaller than its experimental value. An alternative approach was given in Ref. [6] where equations for the derivative of the ratio of the multiplicities are obtained in the MLLA within the framework of the colour dipole model. There a constant of integration which encodes nonperturbative contributions is fixed by the data. Here a new approach is presented.

2 The multiplicity ratio in the effective-ω approach

We consider the standard Mellin-space moments of the coupled gluon-singlet system whose evolution in the scale μ^2 is governed in QCD by the DGLAP equations:

$$\mu^2\frac{d}{d\mu^2}\left(\begin{array}{c} D_g \\ D_s \end{array}\right) = \left(\begin{array}{cc} P_{qq} & P_{gq} \\ P_{qg} & P_{gg} \end{array}\right)\left(\begin{array}{c} D_g \\ D_s \end{array}\right). \tag{1}$$

The timelike splitting functions P_{ij} can be computed perturbatively in the strong coupling constant:

$$P_{ij}(\omega,\mu^2) = \left(\frac{\alpha_s(\mu^2)}{4\pi}\right)P_{ij}^{(0)}(\omega)+\left(\frac{\alpha_s(\mu^2)}{4\pi}\right)^2 P_{ij}^{(1)}(\omega)+\left(\frac{\alpha_s(\mu^2)}{4\pi}\right)^3 P_{ij}^{(2)}(\omega)+O(\alpha_s^4), \quad i,j=g,q, \tag{2}$$

where $\omega = N - 1$ with N the usual Mellin conjugate variable to the fraction of longitudinal momentum x. The functions $P_{ij}^{(k)}(\omega)$ with $k = 0, 1, 2$ appearing in Eq.(2) in the $\overline{MS}$ scheme can be found in Ref.[7, 8, 9] up to NNLO and in Ref.[10] the NNLL contributions up to $O(\alpha_s^{16})$ in the same scheme. Fully analytical resummed results in a closed form in the $\overline{MS}$ scheme are known at NLL for the eigenvalues of the siglet-gluon matrix [10, 11].

It would be desiderable to fully diagonalize Eq.(1). However in general this is not possible because the contributions to the splitting function matrix do not commute at different orders. One is hence enforced to write a series expansion about the LO which in turn can be diagonalized. Therefore we start choosing a basis where the LO is diagonal (see *e.g.* [12]) with the timelike splitting function matrix taking the form:

$$P(\omega) = \begin{pmatrix} P_{++}(\omega) & P_{+-}(\omega) \\ P_{-+}(\omega) & P_{--}(\omega) \end{pmatrix}, \tag{3}$$

where by definition

$$P_{+-}^{(0)}(\omega) = P_{-+}^{(0)}(\omega) = 0, \tag{4}$$

and where $P_{\pm\pm}^{(0)}(\omega)$ are the eigenvalues of the LO splitting matrix.

Now relating the (g, s) basis to this new $(+, -)$ basis, we can decompose the singlet and the gluon fragmentation function symbolically in the following way:

$$D_a(\omega, \mu^2) = D_a^+(\omega, \mu^2) + D_a^-(\omega, \mu^2); \qquad a = s, g. \tag{5}$$

According to Eq.(1) the plus and minus components have the form

$$D_a^\pm(\omega, \mu^2) = \tilde{D}_a^\pm(\omega, \mu_0^2) \left[\frac{\alpha_s(\mu^2)}{\alpha_s(\mu_0^2)}\right]^{-\frac{P_{\pm\pm}^{(0)}}{2\beta_0}} H_a^\pm(\omega, \mu^2), \tag{6}$$

where the normalization factors $\tilde{D}_a^\pm(\omega, \mu_0^2)$ satisfy

$$\tilde{D}_g^+(\omega, \mu_0^2) = -\frac{\alpha_\omega}{\epsilon_\omega}\, \tilde{D}_s^+(\omega, \mu_0^2)\,; \qquad \tilde{D}_g^-(\omega, \mu_0^2) = \frac{1 - \alpha_\omega}{\epsilon_\omega}\, \tilde{D}_s^-(\omega, \mu_0^2), \tag{7}$$

with

$$\alpha_\omega = \frac{P_{qq}^{(0)}(\omega) - P_{++}^{(0)}(\omega)}{P_{--}^{(0)}(\omega) - P_{++}^{(0)}(\omega)}, \quad \epsilon_\omega = \frac{P_{gq}^{(0)}(\omega)}{P_{--}^{(0)}(\omega) - P_{++}^{(0)}(\omega)}. \tag{8}$$

The perturbative functions $H_a^\pm(\omega, \mu^2)$ in Eq.(6) up to NNLO may be represented as

$$\begin{aligned} H_a^\pm(\omega, \mu^2) &= 1 + \left(\frac{\alpha_s(\mu^2)}{4\pi}\right) \left(Z_{\pm\pm,a}^{(1)}(\omega) - Z_{\pm\mp,a}^{(1)}(\omega)\right) \\ &\quad + \left(\frac{\alpha_s(\mu^2)}{4\pi}\right)^2 \left(\tilde{Z}_{\pm\pm,a}^{(2)}(\omega) - \tilde{Z}_{\pm\mp,a}^{(2)}(\omega)\right), \end{aligned} \tag{9}$$

where the functions $Z_{\pm\pm,a}^{(1)}$, $Z_{\pm\mp,a}^{(1)}$, $\tilde{Z}_{\pm\pm,a}^{(2)}$ and $\tilde{Z}_{\pm\mp,a}^{(2)}$ with $a = g, s$ in terms of the timelike splitting functions up to NNLO in the $(+, -)$ basis are given by:

$$Z_{\pm\pm,s}^{(1)}(\omega) = Z_{\pm\pm,g}^{(1)}(\omega) = \frac{1}{2\beta_0}\left[P_{\pm\pm}^{(1)}(\omega) - P_{\pm\pm}^{(0)}(\omega)\frac{\beta_1}{\beta_0}\right], \tag{10}$$

$$Z_{\pm\mp,s}^{(1)}(\omega) = \frac{P_{\pm\mp}^{(1)}(\omega)}{2\beta_0 + P_{\pm\pm}^{(0)}(\omega) - P_{\mp\mp}^{(0)}(\omega)}, \quad Z_{\pm\mp,g}^{(1)}(\omega) = Z_{\pm\mp,s}^{(1)}(\omega)\, \frac{P_{qq}^{(0)}(\omega) - P_{\mp\mp}^{(0)}(\omega)}{P_{qq}^{(0)}(\omega) - P_{\pm\pm}^{(0)}(\omega)},$$

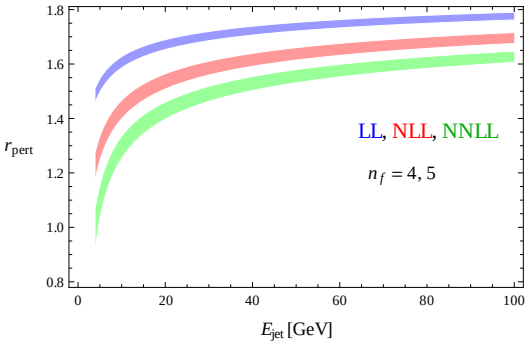

Figure 1: $r_{pert}^{N^kLL}(Q^2)$ with $k = 0, 1, 2$ (blue,red,green) according to Eq.(15). The bands correspond to $n_f = 4, 5$.

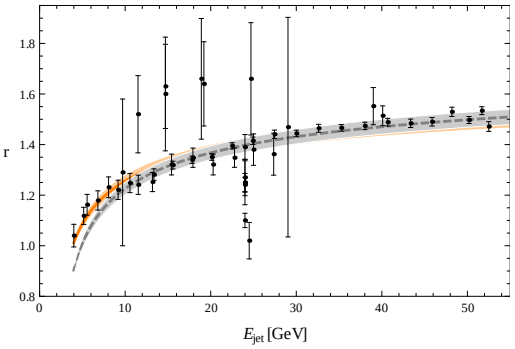

Figure 2: The multilicity ratio r according to Eq.(14) with $K(n_f = 4) = 0.941 \pm 0.019$ (orange) and $K(n_f = 5) = 0.978 \pm 0.020$ (dashed grey).

and

$$
\begin{aligned}
\tilde{Z}^{(2)}_{\pm\pm,s}(\omega) &= \tilde{Z}^{(2)}_{\pm\pm,g}(\omega) = \frac{1}{4\beta_0}\left[P^{(2)}_{\pm\pm}(\omega) - \left(P^{(1)}_{\pm\pm}(\omega) - P^{(0)}_{\pm\pm}(\omega)Z^{(1)}_{\pm\pm,s}(\omega)\right)\frac{\beta_1}{\beta_0}\right. \\
&\left. + P^{(0)}_{\pm\pm}(\omega)\left(\frac{\beta_1^2}{\beta_0^2} - \frac{\beta_2}{\beta_0}\right) - \sum_{i=\pm} P^{(1)}_{\pm i}(\omega)Z^{(1)}_{i\pm,s}(\omega)\right] + \sum_{i=\pm} Z^{(1)}_{\pm i,s}(\omega)Z^{(1)}_{i\pm,s}(\omega), \\
\tilde{Z}^{(2)}_{\pm\mp,s}(\omega) &= \frac{1}{4\beta_0 + P^{(0)}_{\pm\pm}(\omega) - P^{(2)}_{\mp\mp}(\omega)}\left[P^{(2)}_{\pm\mp}(\omega) - \left(P^{(1)}_{\pm\mp}(\omega) - P^{(0)}_{\pm\pm}(\omega)Z^{(1)}_{\pm\mp,s}(\omega)\right)\frac{\beta_1}{\beta_0}\right. \\
&\left. - \sum_{i=\pm} P^{(1)}_{\pm i}(\omega)Z^{(1)}_{i\mp,s}(\omega)\right] + \sum_{i=\pm} Z^{(1)}_{\pm i,s}(\omega)Z^{(1)}_{i\mp,s}(\omega), \\
\tilde{Z}^{(2)}_{\pm\mp,g}(\omega) &= \tilde{Z}^{(2)}_{\pm\mp,s}(\omega)\,\frac{P^{(0)}_{qq}(\omega) - P^{(0)}_{\mp\mp}(\omega)}{P^{(0)}_{qq}(\omega) - P^{(0)}_{\pm\pm}(\omega)}.
\end{aligned}
\tag{11}
$$

It is a well known fact that the multiplicity can be obtained from the DGLAP evolution equations Eq.(1) once one is able to take its first Mellin moment $\omega = N - 1 = 0$. This is not possible using a fixed order computation because of the presence of singularitues at $\omega = 0$ due to multiple soft emissions. Resummation of these divergences has been shown to be the appropriate thing to do to avoid this problem. This has been shown a long time ago in [13] at leading logarithmic accuracy (LL). The algebraic relations in Ref. [14] show that the first Mellin moment of the resummed leading logarithmic splitting function $P^{LL}_{++}(\omega)$ can be obtained by taking the LO leading singular term and assign an effective value to ω:

$$
P^{LL}_{++}(\omega = 0) = \frac{\alpha_s C_A}{\pi\omega^{LL}_{eff}}; \quad \omega^{LL}_{eff} = 2\,P^{LL}_{++}(\omega = 0) = \sqrt{\frac{2C_A\alpha_s}{\pi}} = 1.382\,\sqrt{\alpha_s} \tag{12}
$$

Our approach consists in adopting the same procedure also to fix $P^{NLL}_{++}(\omega = 0)$ and $P^{NNLL}_{++}(\omega = 0)$. The former quantity is analytically known [10, 11], while the last one is known up to the 16th order [10]. In this case we have obtained a numerical estimation of the

first Mellin moment of $P_{++}^{NNLL}(\omega)$ performing a numerical extrapolation. Our result is:

$$\omega_{eff}^{NNLL} = 1.3820\,\sqrt{\alpha_s} + (0.0059\,n_f + 0.8754)\alpha_s + (0.0300\,n_f + 1.0881)\alpha_s^{3/2}, \tag{13}$$

which is valid for $n_f = 4, 5$ number of active flavors.

Neglecting the evolution of the minus component in Eq.(5) and using Eq.(7) we arrive at our definition of the gluon-quark multiplocity ratio which is given by

$$r^{N^kLL}(Q^2) \equiv \frac{D_g(\omega_{eff}^{N^kLL}, Q^2)}{D_s(\omega_{eff}^{N^kLL}, Q^2)} = K\, r_{pert}^{N^kLL}(Q^2), \tag{14}$$

where

$$r_{pert}^{N^kLL}(Q^2) = \frac{D_g^+(\omega_{eff}^{N^kLL}, Q^2)}{D_s^+(\omega_{eff}^{N^kLL}, Q^2)} = -\frac{\alpha_\omega}{\epsilon_\omega}\frac{H_g^+(\omega_{eff}^{N^kLL}, Q^2)}{H_s^+(\omega_{eff}^{N^kLL}, Q^2)}; \quad K = \frac{D_s^+(\omega_{eff}^{N^kLL}, Q^2)}{D_s^+(\omega_{eff}^{N^kLL}, Q^2) + \bar{D}_s}, \tag{15}$$

by use of Eq.(6). Fig.1 shows our results for $r_{pert}^{LL}(Q^2)$,$r_{pert}^{NLL}(Q^2)$ and $r_{pert}^{NNLL}(Q^2)$ for $n_f = 4, 5$ and Fig.2 shows our 90% C.L. fit of K in Eqs.(14,15) using the NNLL result for r_{pert}. In our analysis we have used the first three terms of the ω expansion for the splitting functions and the double counted terms due to resummation have been subtracted. The running of α_s has been evaluated at NNLO with $n_f = 5$ and with $\alpha_s(M_Z) = 0.118$. The data are taken from the summary tables of [15] and references therein and from [16].

References

[1] A. Capella, I. M. Dremin, J. W. Gary, V. A. Nechitailo, and J. Tran Thanh Van. Phys. Rev. **D61** (2000) 074009, arXiv:hep-ph/9910226.

[2] Y. L. Dokshitzer, V. A. Khoze, A. H. Mueller, and S. I. Troian. Gif-sur-Yvette, France: Ed. Frontieres 274 p. (Basics of perturbative QCD).

[3] E. D. Malaza and B. R. Webber. Nucl. Phys. **B267** (1986) 702.

[4] S. Catani, Y. L. Dokshitzer, F. Fiorani, and B. R. Webber. Nucl. Phys. **B377** (1992) 445–460.

[5] S. Lupia and W. Ochs. Phys. Lett. **B418** (1998) 214–222, arXiv:hep-ph/9707393.

[6] P. Eden and G. Gustafson. JHEP **09** (1998) 015, arXiv:hep-ph/9805228.

[7] M. Gluck, E. Reya, and A. Vogt. Phys. Rev. **D48** (1993) 116.

[8] S. Moch and A. Vogt. Phys. Lett. **B659** (2008) 290–296, arXiv:0709.3899 [hep-ph].

[9] A. A. Almasy, A. Vogt, and S. Moch. arXiv:1107.2263 [hep-ph].

[10] A. Vogt. JHEP **10** (2011) 025, arXiv:1108.2993 [hep-ph].

[11] S. Albino, P. Bolzoni, B. A. Kniehl, and A. V. Kotikov. Nucl. Phys. **B855** (2012) 801–814, arXiv:1108.3948 [hep-ph].

[12] A. J. Buras. Rev. Mod. Phys. **52** (1980) 199.

[13] A. H. Mueller. Phys. Lett. **B104** (1981) 161–164.

[14] A. H. Mueller. Nucl. Phys. **B213** (1983) 85.

[15] M. Siebel. WU-B-DIS-2003-11.

[16] D. Acosta *et al.* Phys.Rev.Lett. **94** (2005) 171802.

WG1: Structure Functions and WG5: Heavy Flavours

Higher Twist contributions to the Structure Functions $F_2(x, Q^2)$ and $g_2(x, Q^2)$

Johannes Blümlein[1], *Helmut Böttcher*[1]

[1]Deutsches Elektronen-Synchrotron, DESY, Platanenallee 6, D-15738 Zeuthen, Germany

DOI: http://dx.doi.org/10.3204/DESY-PROC-2012-02/252

We report on recent results on higher twist contributions to the unpolarized structure functions $F_2^{p,d}(x, Q^2)$ at N^{3}LO in the large x region and constraints on the twist–3 contribution to polarized structure function $g_2(x, Q^2)$.

1 Introduction

Higher twist terms contribute to the nucleon structure functions at lower scales Q^2. The range in which these terms may be safely neglected against the leading twist contributions, partly depends on the size of the experimental errors in the respective measurement. Highly precise data at low values of Q^2 allow to access these contributions, the detailed physical understanding of which is presently still in an early stage. It has been outlined in Refs. [1, 2] how the higher twist contributions can be extracted in a phenomenological way in case of the structure functions $F_2(x, Q^2)$ and $F_L(x, Q^2)$ in the valence quark region. In this note we report on recent results of an improved analysis. Another interesting question concerns the structure function $g_2(x, Q^2)$ in the polarized case, which has been measured to a higher precision during the last years [3]. Here we try to extract first information on the twist-3 contributions to $g_2(x, Q^2)$.

2 Higher Twist Contributions to $F_2^{p,d}(x, Q^2)$

We have carried out a QCD analysis in the valence region including more recent data from JLAB following earlier work [1]. In the present analysis tails from sea-quarks and the gluon in the valence region were dealt with based on the ABKM distributions [4]. Both the valence quark distributions $xu_v(x, Q_0^2)$ and $xd_v(x, Q_0^2)$ at $Q_0^2 = 4$ GeV^2 are effected only very little. The values of $\alpha_s(M_Z^2)$ change marginally w.r.t. the earlier analysis [1]. We obtain : $\alpha_s(M_Z^2) = 0.1148 \pm 0.0019$ NLO, $= 0.1134 \pm 0.0020$ NNLO; 0.1141 ± 0.0021 N^{3}LO*. Here, the N^{3}LO*-analysis accounts for the three-loop Wilson coefficients and a Padé-model for the non-singlet four-loop anomalous dimension, to which we attached a $\pm 100\%$ uncertainty, cf. [1] for details. Furthermore, we found that the response of the individual deep-inelastic data sets in the valence region respond stable values, which are in accordance with the central value obtained moving from NLO to N^{3}LO*. The present result agrees very well with determinations of $\alpha_s(M_Z^2)$ in Refs. [4–6], see also [7]. A survey on the current status of $\alpha_s(M_Z^2)$ based on precision measurements in different reactions has been given in [8]. In the present analysis we obtain a lower value of α_s than the world average, cf. [8], and values being obtained in [9, 10] at NNLO.

Reasons for the difference to the values given in [9, 10] have been discussed in Refs. [6, 7] in detail. In particular, the partial response of α_s in case of the BCDMS and SLAC data in [9, 10] turns out to be partly different comparing to the results in [4–6]. There are also differences between the analyses [9] and [10] w.r.t. several data sets contributing.

The higher twist contributions can be determined by extrapolating the fit-results at leading twist for $W^2 > 12.5$ GeV^2 to the region $4 < W^2 < 12.5$ GeV$^2, Q^2 \geq 4$ GeV^2, cf. [2, 11]. The results for the coefficients $C_{\rm HT}^{p,d}(x)$

$$F_2(x,Q^2) = F_2(x,Q^2)\left[\frac{O^{\rm TM}[F_2(x,Q^2)]}{F_2(x,Q^2)} + \frac{C_{\rm HT}(x)}{Q^2[{\rm GeV}^2]}\right] \tag{1}$$

are shown in Figure 1, where we averaged over the respective range in Q^2. We applied the target mass corrections [12] to the leading twist contributions.[1] The result for the higher twist coefficients for proton and deuteron targets depends on the order to which the leading twist distribution is described. The higher twist terms become smaller moving from NLO to N^{3}LO*. Within the present theoretical and experimental accuracy the curves stabilize for $x < 0.65$, while at larger values there are still differences.

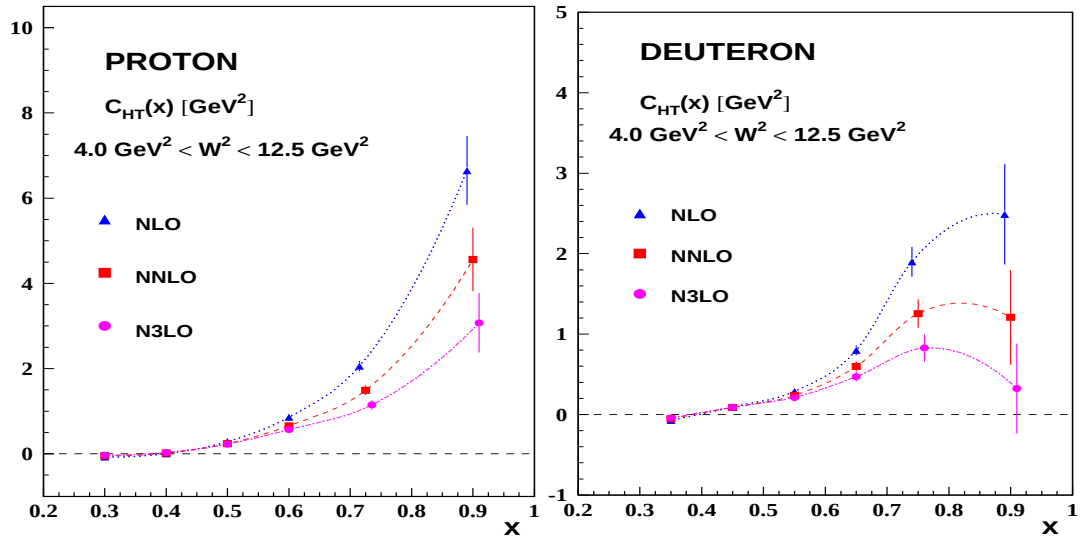

Figure 1: The empiric higher twist contributions to $F_2^{p,d}(x,Q^2)$ in the valence region, Eq. (1), extracted by calculating the leading twist part at NLO, NNLO, and N^{3}LO*, [11].

3 $g_2^{\rm tw3}(x,Q^2)$

Higher twist contributions to the polarized structure function $g_1(x,Q^2)$ have been studied in Refs. [14, 15] in phenomenological approaches aiming on the twist-4 contributions. However, the structure function $g_2(x,Q^2)$, together with other polarized electro-weak structure functions

[1] An unfolding of the target mass corrections of the DIS world data for F_2 and F_L including the JLAB data, has been performed in [13] recently.

[16–18], receives also twist-3 contributions. $g_2(x, Q^2)$ obeys the Burkhardt-Cottingham relation [19]

$$\int_0^1 dx g_2(x, Q^2) = 0 \ . \tag{2}$$

Since the Wandzura-Wilczek relation [20] implies, that the first moment of the twist-2 part vanishes separately also

$$\int_0^1 dx g_2^{\mathrm{tw3}}(x, Q^2) = 0 \tag{3}$$

holds. The errors on the present world data from E143, E155, HERMES and NMC [3] on $g_2(x, Q^2)$ are still large but yet one may try the fit of a profile in x. In Ref. [21] the parameterization

$$g_2^{\mathrm{tw3}}(x) = A\left[\ln(x) + (1-x) + \frac{1}{2}(1-x)^2\right] + (1-x)^3\left[B - C(1-x) + D(1-x)^2\right] \tag{4}$$

has been proposed. Since the data points are measured at different values of Q^2 an evolution has to be performed to a common scale. Furthermore, the target mass corrections [18] have to be taken into account. In Figure 2 the results of the fit to $g_2^{\mathrm{tw3}}(x, Q^2)$ are presented for $Q^2 = 3$ GeV^2. We limited the analysis to the region $Q^2 > 1$ GeV^2. The present errors are still large and the data of E155 dominate in the fit. We may compare with a theoretical prediction given in [21]. Indeed both results are quite similar.

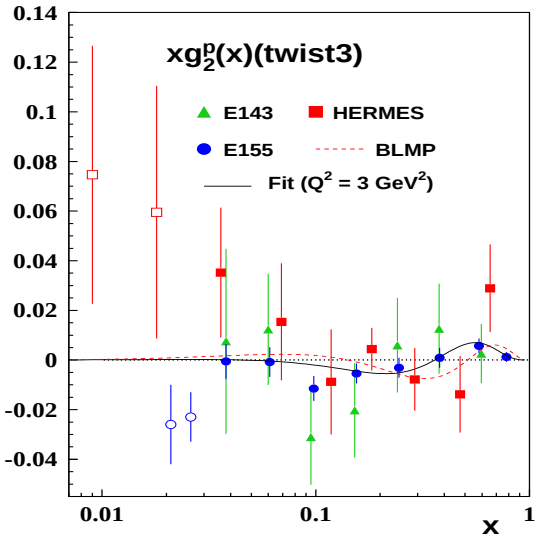

Figure 2: The twist-3 contributions to $g_2(x, Q^2)$ subtracting the twist-2 part according to the Wandzura-Wilczek relation [20] using the result of [15] for the twist-2 contribution to $g_1(x, Q^2)$ on experimental data from E143, E155, and HERMES [3] fitting the shape (4) (full line). Open symbols refer to data in the region $Q^2 < 1$ GeV^2. The dashed line shows the result of a calculation at $Q^2 = 1$ GeV^2 given in [21].

The twist-3 contribution to the structure function $g_1(x,Q^2)$ can be obtained from that to $g_2(x,Q^2)$ by the integral-relation [18]

$$g_1^{\rm tw3}(x,Q^2) = \frac{4x^2M^2}{Q^2}\left[g_2^{\rm tw3}(x,Q^2) - 2\int_x^1 \frac{dy}{y} g_2^{\rm tw3}(y,Q^2)\right] , \tag{5}$$

cf. [22]. Due to the large errors of the data the present results are of more qualitative character. To study the twist-3 contributions both to the structure functions $g_2(x,Q^2)$ and $g_1(x,Q^2)$ in detail, a high luminosity machine, like the planned EIC [23], is needed.

4 Conclusions

We performed a re-analysis of the present deep-inelastic world data on proton and deuteron targets for the structure function $F_2(x,Q^2)$ in the valence region $x > 0.3$ accounting for remaining non-valence tails, which were calculated using the ABKM09 distributions [4]. We obtain a slightly lower value of $\alpha_s(M_Z^2)$ than in our previous analysis [1] at N^{3}LO*, however, far within the 1σ error range. Very stable predictions are obtained going from NLO to N^{3}LO*, both for the valence distribution functions and $\alpha_s(M_Z^2)$. The values being obtained for the different subsets of experimental data in the present fit are well in accordance with our global result. We do not confirm the significant differences reported by MSTW between the SLAC *ep* and *ed* data at NNLO [9]. We also disagree with the large value of NNPDF [10] for the BCDMS data at NLO, which also contradicts the corresponding result by MSTW [9]. Our results are in agreement with those of the GJR collaboration [5] and the singlet analyses [4, 6]. We obtained an update of the dynamical higher twist contributions to $F_2^{p,d}(x,Q^2)$ in the valence region, which depends on the order to which the leading twist contributions were calculated. The effect stabilizes including corrections up to N^{3}LO* in the range $0.3 < x \lesssim 0.65$. At larger values of x still higher order corrections may be needed. A first estimate on the quarkonic twist-3 contributions to the polarized structure function $g_2(x,Q^2)$ is given in a fit to the available world data on $g_2(x,Q^2)$. The contributions to $g_1(x,Q^2)$ are obtained by an integral relation, cf. Ref. [18].

5 Acknowlededgments

For discussions we would like to thank S. Alekhin. This work has been supported in part by DFG Sonderforschungsbereich Transregio 9, Computergestützte Theoretische Teilchenphysik, and EU Network LHCPHENOnet PITN-GA-2010-264564.

References

[1] J. Blümlein, H. Böttcher and A. Guffanti, Nucl. Phys. B **774** (2007) 182 [hep-ph/0607200]; Nucl. Phys. Proc. Suppl. **135** (2004) 152 [hep-ph/0407089].

[2] J. Blümlein and H. Böttcher, Phys. Lett. B **662** (2008) 336 [arXiv:0802.0408 [hep-ph]].

[3] E143 Coll., K. Abe et al., Phys. Rev. D 58, 112003 (1998);
E155 Coll., P. L. Anthony et al., Phys. Lett. B 553, 18 (2003);
A. Airapetian, N. Akopov, Z. Akopov, E. C. Aschenauer, W. Augustyniak, R. Avakian, A. Avetissian and E. Avetisyan *et al.*, Eur. Phys. J. C **72** (2012) 1921 [arXiv:1112.5584 [hep-ex]].

[4] S. Alekhin, J. Blümlein, S. Klein and S. Moch, Phys. Rev. D **81** (2010) 014032 [arXiv:0908.2766 [hep-ph]].

[5] M. Glück, E. Reya and C. Schuck, Nucl. Phys. **B754** (2006) 178 [arXiv:hep-ph/0604116];
P. Jimenez-Delgado and E. Reya, Phys. Rev. **D79** (2009) 074023 [arXiv:0810.4274 [hep-ph]].

[6] S. Alekhin, J. Blümlein and S. Moch, arXiv:1202.2281 [hep-ph].

[7] S. Alekhin, J. Blümlein and S. Moch, Eur. Phys. J. C **71** (2011) 1723 [arXiv:1101.5261 [hep-ph]].

[8] S. Bethke *et al.*, Proceedings of the Workshop on Precision Measurements of α_s, arXiv:1110.0016 [hep-ph].

[9] A. D. Martin, W. J. Stirling, R. S. Thorne, G. Watt, Eur. Phys. J. **C64** (2009) 653 [arXiv:0905.3531 [hep-ph]].

[10] S. Lionetti *et al.*, Phys. Lett. B **701** (2011) 346 [arXiv:1103.2369 [hep-ph]].

[11] J. Blümlein and H. Böttcher, in preparation.

[12] H. Georgi and H. D. Politzer, Phys. Rev. D **14** (1976) 1829.

[13] M. E. Christy, J. Blümlein and H. Böttcher, arXiv:1201.0576 [hep-ph].

[14] E. Leader, A. V. Sidorov and D. B. Stamenov, Phys. Rev. D **80** (2009) 054026 [arXiv:0908.2390 [hep-ph]].

[15] J. Blümlein and H. Böttcher, Nucl. Phys. B **841** (2010) 205 [arXiv:1005.3113 [hep-ph]].

[16] J. Blümlein and N. Kochelev, Phys. Lett. B **381** (1996) 296 [hep-ph/9603397].

[17] J. Blümlein and N. Kochelev, Nucl. Phys. B **498** (1997) 285 [hep-ph/9612318].

[18] J. Blümlein and A. Tkabladze, Nucl. Phys. B **553** (1999) 427 [hep-ph/9812478].

[19] H. Burkhardt and W. N. Cottingham, Annals Phys. **56** (1970) 453.

[20] S. Wandzura and F. Wilczek, Phys. Lett. B **72** (1977) 195.

[21] V. M. Braun, T. Lautenschlager, A. N. Manashov and B. Pirnay, Phys. Rev. D **83** (2011) 094023 [arXiv:1103.1269 [hep-ph]].

[22] J. Blümlein, H. Böttcher, and A. De Freitas, in preparation.

[23] D. Boer, M. Diehl, R. Milner, R. Venugopalan, W. Vogelsang, D. Kaplan, H. Montgomery and S. Vigdor *et al.*, arXiv:1108.1713 [nucl-th].

Heavy Quark Production in the ACOT Scheme Beyond NLO

T. Stavreva[1], *F. I. Olness*[2]*, *I. Schienbein*[1], *T. Ježo*[1], *A. Kusina*[2], *K. Kovařík*[3], *J. Y. Yu*[1,2]

[1]Laboratoire de Physique Subatomique et de Cosmologie, Université Joseph Fourier/CNRS-IN2P3/INPG, 53 Avenue des Martyrs, 38026 Grenoble, France
[2]Southern Methodist University, Dallas, TX 75275, USA
[3]Institute for Theoretical Physics, Karlsruhe Institute of Technology, Karlsruhe, D-76128, Germany

DOI: http://dx.doi.org/10.3204/DESY-PROC-2012-02/272

We analyze the properties of the ACOT scheme for heavy quark production and make use of the $\overline{MS}$ massless results at NNLO and N^{3}LO for the structure functions F_2 and F_L in neutral current deep-inelastic scattering to estimate the higher order corrections. The dominant heavy quark mass effects at higher orders can be taken into account using the massless Wilson coefficients together with an appropriate slow-rescaling prescription implementing the phase space constraints. Combining the exact ACOT scheme at NLO with these expressions should provide a good approximation to the full calculation in the ACOT scheme at NNLO and N^{3}LO.

1 Introduction

With the ever-increasing precision of the experimental data, the production of heavy quarks in high energy processes has become an increasingly important subject. As theoretical calculations and parton distribution function (PDF) evolution are progressing to next-to-next-to-leading order (NNLO) of QCD, there is a clear need to formulate and also implement the heavy quark schemes at this order and beyond. The most important case is arguably the heavy quark treatment in inclusive deep-inelastic scattering (DIS) since the very precise HERA data for DIS structure functions and cross sections form the backbone of any modern global analysis of PDFs. Here, the heavy quarks contribute up to 30% or 40% to the structure functions at small momentum fractions x. Extending the heavy quark schemes to higher orders is therefore necessary for extracting precise PDFs and hence for precise predictions of observables at the LHC. Additionally, it is theoretically important to have a general pQCD framework including heavy quarks which is valid to all orders in perturbation theory over a wide range of hard energy scales. The results of this study form the basis for using the ACOT scheme in NNLO global analyses and for future comparisons with precision data for DIS structure functions.

*Presented by F.I. Olness.

2 ACOT Scheme

The ACOT renormalization scheme [1] provides a mechanism to incorporate the heavy quark mass into the theoretical calculation of heavy quark production both kinematically and dynamically. In 1998 Collins [2] extended the factorization theorem to address the case of heavy quarks; this work provided the theoretical foundation that allows us to reliably compute heavy quark processes throughout the full kinematic realm.

The ACOT prescription is to just calculate the massive partonic cross sections and perform the factorization using the quark mass as regulator. The ACOT scheme does not need any observable–dependent extra contributions or any regulators to smooth the transition between the high and low scale regions.

In Ref. [3] we demonstrated using the NLO full ACOT scheme that the dominant mass effects are those coming from the phase space which can be taken into account via a generalized slow-rescaling $\chi(n)$-prescription.[1] Assuming that a similar relation remains true at higher orders, one can construct the following approximation to the ACOT result up to N^{3}LO ($\mathcal{O}(\alpha_S^3)$):

$$\text{ACOT}[\mathcal{O}(\alpha_S^{0+1+2+3})] \quad \simeq \quad \text{ACOT}[\mathcal{O}(\alpha_S^{0+1})] + \text{ZMVFNS}_{\chi(\text{n})}[\mathcal{O}(\alpha_\text{S}^{2+3})] \tag{1}$$

In this equation, "ACOT" generically represents any variant of the ACOT scheme (ACOT, S-ACOT, S-ACOT$_\chi$); for the results presented in Sec. 3, we will use the fully massive ACOT scheme with all masses retained out to NLO. The ZMVFNS$_{\chi(\text{n})}$ term uses the massless Wilson coefficients at $\mathcal{O}(\alpha\,\alpha_S^2)$ and $\mathcal{O}(\alpha\,\alpha_S^3)$. This approximation is necessary as not all the necessary massive Wilson coefficients at $\mathcal{O}(\alpha\,\alpha_S^2)$ and $\mathcal{O}(\alpha\,\alpha_S^3)$ have been computed.

3 Results

We now present the results of our calculation extending the ACOT scheme to NNLO and N^{3}LO. The details of the numerical calculations are presented in Ref. [3]. We have used the QCDNUM program [4] for the DGLAP evolution, and the Fortran subroutines provided by Andreas Vogt for the higher order Wilson coefficients. We choose $m_c = 1.3$ GeV, $m_b = 4.5$ GeV, $\alpha_S(M_Z) = 0.118$.

In Figures 1a and 1b we display the fractional contributions for the final-state quarks to the structure functions F_2 and F_L, respectively, for selected x values as a function of Q. We observe that for large x and low Q the heavy flavor contributions are minimal. but these can grow quickly as we move to smaller x and larger Q. For example, at $x = 10^{-5}$ and large Q we see the F_2 contributions of the u-quark and c-quark are comparable (as they both couple with a factor 4/9), and the d-quark and s-quark are comparable (as they both couple with a factor 1/9).

In Figure 2a we display the results for F_2 vs. Q computed at various orders. For large x (c.f. $x = 0.1$) we find the perturbative calculation is particularly stable; we see that the LO result is within 20% of the others at small Q, and within 5% at large Q. The NLO is within 2% at small Q, and indistinguishable from the NNLO and N^{3}LO for Q values above ~ 10 GeV. The NNLO and N^{3}LO results are essentially identical throughout the kinematic range.

In Figure 2b we display the results for F_L vs. Q computed at various orders. In contrast to F_2, we find the NLO corrections are large for F_L; this is because the LO F_L contribution

[1] Specifically, $\chi(n) = x[1 + (n\,m/Q)^2]$, where m is the quark mass.

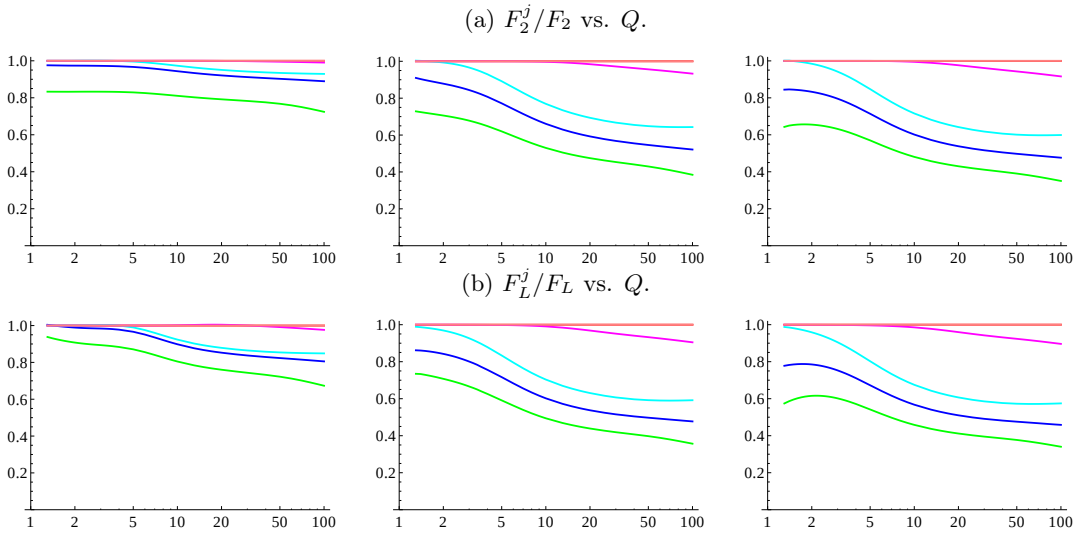

Figure 1: Fractional contribution for each quark flavor to $F_{2,L}^j/F_{2,L}$ vs. Q at N^{3}LO for fixed $x = \{10^{-1}, 10^{-3}, 10^{-5}\}$ (left to right). Results are displayed for $n = 2$ scaling. Reading from the bottom, we have the cumulative contributions from the $j = \{u, d, s, c, b\}$ (green, blue, cyan, magenta, pink).

(which violates the Callan-Gross relation) is suppressed by (m^2/Q^2) compared to the dominant gluon contributions which enter at NLO. Consequently, we observe (as expected) that the LO result for F_L receives large contributions from the higher order terms. Essentially, the NLO is the first non-trivial order for F_L, and the subsequent contributions then converge. While the calculation of F_L is certainly more challenging, the relevant kinematic range probed by HERA the theoretical calculation is generally stable.

4 Conclusions

We extended the ACOT calculation for DIS structure functions to N^{3}LO by combining the exact ACOT result at NLO with a $\chi(n)$-rescaling for the higher order terms; this allows us to include the leading mass dependence at NNLO and N^{3}LO.

We studied the F_2 and F_L structure functions as a function of x and Q. We examined the flavor decomposition of these structure functions, and verified that the heavy quarks were appropriately suppressed in the low Q region. We found the results for F_2 were very stable across the full kinematic range for $\{x, Q\}$, and the contributions from the NNLO and N^{3}LO terms were small. For F_L, the higher order terms gave a proportionally larger contribution (due to the suppression of the LO term from the Callan-Gross relation); nevertheless, the contributions from the NNLO and N^{3}LO terms were generally small in the region probed by HERA. Using the results of this calculation we can obtain precise predictions for the inclusive F_2 and F_L structure functions which can be used to analyze the HERA data.

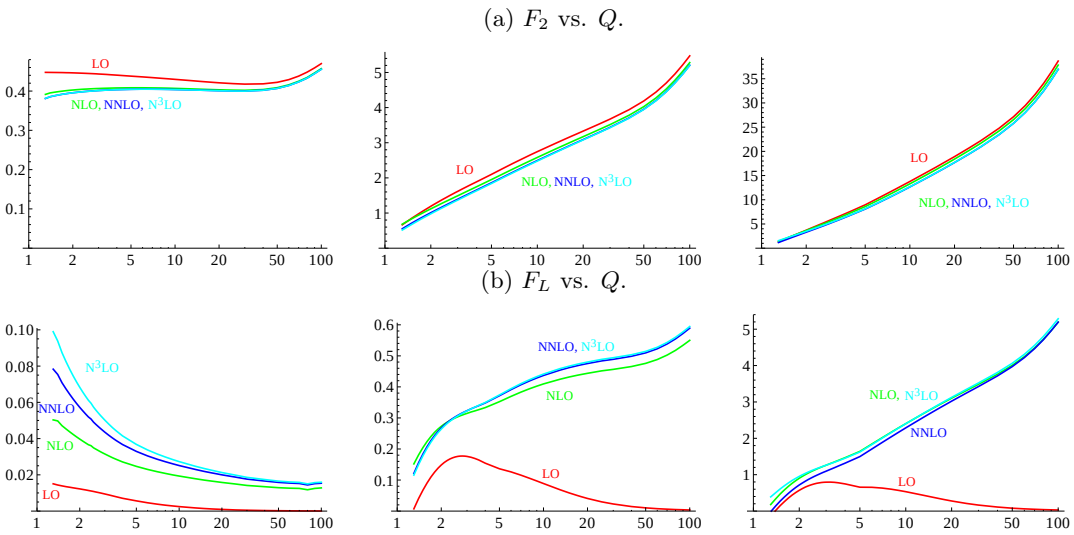

Figure 2: $F_{2,L}$ vs. Q at {LO, NLO, NNLO, N^{3}LO} (red, green, blue, cyan) for fixed $x = \{10^{-1}, 10^{-3}, 10^{-5}\}$ (left to right) for $n = 2$ scaling.

Acknowledgments

We thank M. Botje, A. M. Cooper-Sarkar, A. Glazov, C. Keppel, J. G. Morfín, P. Nadolsky, M. Guzzi, J. F. Owens, V. A. Radescu, and A. Vogt for discussions. We acknowledge the hospitality of CERN, DESY, Fermilab, Les Houches, Galileo Galilei Institute and the INFN. This work was partially supported by the U.S. Department of Energy under grant DE-FG02-04ER41299, the Lightner-Sams Foundation, the Théorie LHC France initiative funded by the CNRS/IN2P3, and by *Projet international de cooperation scientifique* PICS05854 between France and the USA.

References

[1] M. A. G. Aivazis, J. C. Collins, F. I. Olness, and W. K. Tung. Phys. Rev. **D50** (1994) 3102–3118, hep-ph/9312319.

[2] J. C. Collins. Phys. Rev. **D58** (1998) 094002, hep-ph/9806259.

[3] T. Stavreva, F. Olness, I. Schienbein, T. Jezo, A. Kusina, *et al.* arXiv:1203.0282 [hep-ph].

[4] M. Botje. Comput. Phys. Commun. **182** (2011) 490–532, arXiv:1005.1481 [hep-ph].

Measurement of charm production in DIS with D^* mesons and extraction of $F_2^{c\bar{c}}$

Andrii Gizhko[1] on behalf of the ZEUS Collaboration

[1]National University "Kyiv-Mohyla Academy", Kyiv, Ukraine.

DOI: http://dx.doi.org/10.3204/DESY-PROC-2012-02/45

Charm production has been measured with the ZEUS detector in deep inelastic *ep* scattering at HERA. The measurement is based on the full reconstruction of the decay chain $D^* \to D^0\,\pi$, $D^0 \to$ K π and exploits the full HERA II statistics with integrated luminosity $L = 357$ pb^{-1} . Differential cross-sections have been measured. The kinematic range is 1.5 GeV $< P_t$(D*) < 20 GeV, $|\eta$(D*)$| < 1.5$, $5 < Q^2 < 1000$ GeV^2 and $0.02 <$ y < 0.7. The observed cross sections were extrapolated to the full P_t(D*) and η(D*) range in order to determine the open-charm contribution, $F_2^{c\bar{c}}$(x,Q^2) to the proton structure function F_2.

1 Introduction

The production of heavy quarks at HERA proceeds dominantly via the direct boson-gluon fusion (BGF) process $\gamma g \to c\bar{c}\,(\gamma g \to b\bar{b})$. The measurement of processes involving heavy flavour production gives a test of perturbative QCD calculations and information on the gluon content of proton. The measurement of the charm contribution $F_2^{c\bar{c}}$ to the proton structure function allows to test parton density functions. Information about gluon and heavy quark distribution in the region of low Bjorken x is important for measurement of Standard Model and new physics processes at hadron-hadron colliders such as LHC.

In this paper recent measurements on the charm production in neutral current deep inelastic scattering (NC DIS) obtained from the reconstruction of D* mesons at HERA by the ZEUS experiment are presented. The analysis is based on e^+p and e^-p data collected by ZEUS from 2004 to 2007 at a center of mass energy $\sqrt{s} = 318$ GeV .

2 Analysis Techniques

In this analysis charmed hadrons were detected by reconstructing the decay products of $D^{*\pm}$ mesons in the central tracking detector using $D^* \to K\pi\pi$ decay channel. The kinematic range of measurement is $5 < Q^2 < 1000$ GeV^2, $|\eta(D^*)| <$1.5, 1.5 $< P_t$ (D*) $<$ 20 GeV, 0.02 $<$ y < 0.7. The invariant mass difference M(K$\pi\pi$) - M(Kπ) for D^0 candidates in the range 1.8 $<$ M(Kπ) $<$1.92 GeV is shown in Fig.1. Background was estimated by using combination of tracks with wrong charge of reconstructed D^0. Both combinations, right and wrong charge were normalized in background region [150,168] MeV. The shaded area indicates the signal mass window. D* mesons can also originate from beauty hadrons, but contribution is only a

few %. For acceptance calculation RAPGAP Monte Carlo samples (charm and beuaty) were used.

3 D* differential cross-sections

On Fig.2 measured double-differential cross-sections (black dots) are compared to NLO QCD calculation made with the HVQDIS program [1] (dashed line) and measurements of the H1 collaboration [2] (empty symbols). The beauty contribution to $D^{*\pm}$ production (continuous line) was calculated with the RAPGAP [3] Monte Carlo, scaled by 1.52 in agreement with ZEUS measurements. For all cross-sections QED corrections were applied. Presented measurements are in good agreement with theoretical prediction.

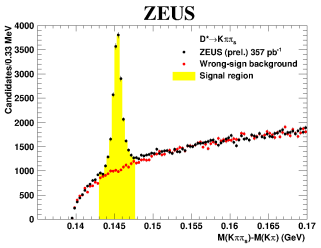

Figure 1: D* signal

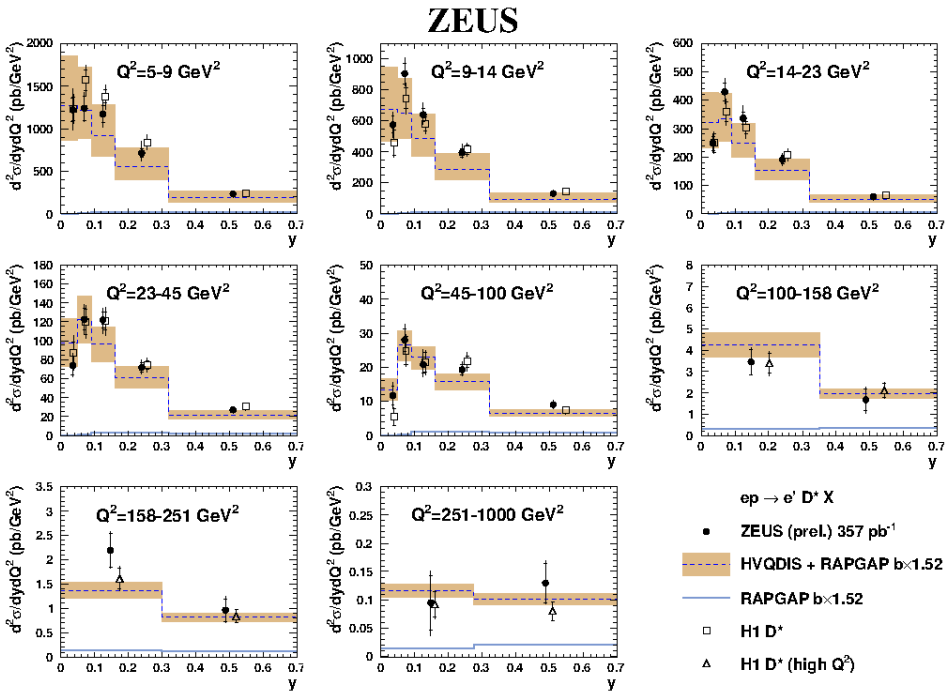

Figure 2: Double-differential cross-sections in bins of Q^2 and y, compared to recent H1 data [**?**] and to the HVQDIS calculation.

4 $F_2^{c\bar{c}}$ measurement

The $F_2^{c\bar{c}}$ ratio was evaluated as :

$$F_2^{c\bar{c}} = \sigma_{bin}^{vis} \times \left(\frac{F_2^{c\bar{c}}(x,Q^2)}{\sigma_{bin}^{vis}} \right)_{theory}$$

where σ_{bin}^{vis} is the D* visible cross-section in a Q^2, y bin after substraction of the beauty contribution. On Fig.3 is measured charm structure function $F_2^{c\bar{c}}$ (filled circles) compared to the recent D^+ [4] ZEUS result (filled squares) and preliminary combination of H1 and ZEUS data [5] (empty circles).

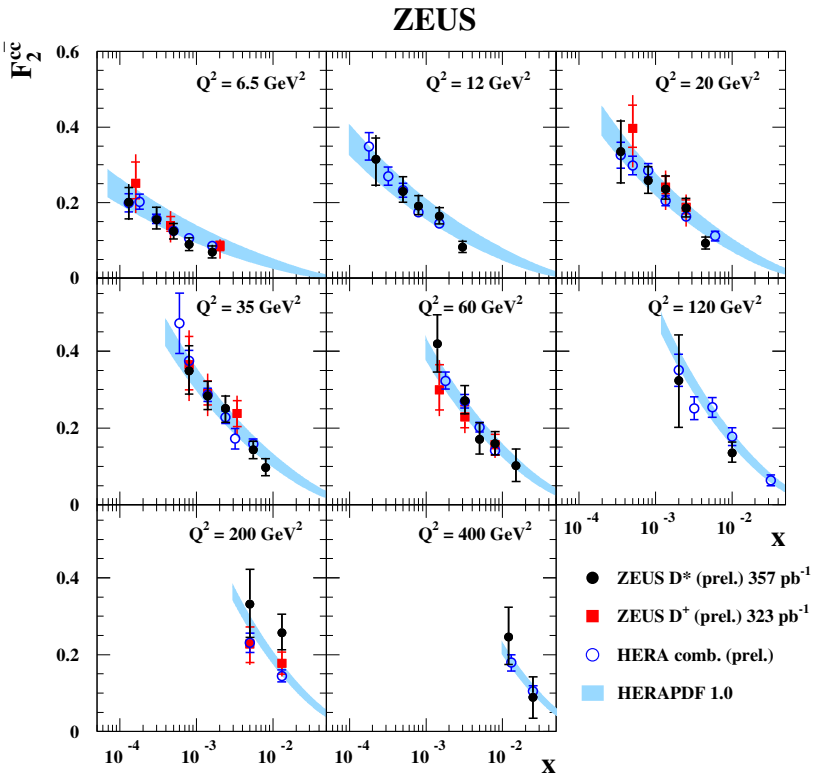

Figure 3: Measured charmed structure function $F_2^{c\bar{c}}$ compared to previous HERA results and HERAPDF 1.0

$\left(\frac{F_2^{c\bar{c}}(x,Q^2)}{\sigma_{bin}^{vis}} \right)_{theory}$ ratio were obtained using HVQDIS program and cross-section extrapolation on full phase space were performed with following parameters :

Scales: the renormalization (μ_R) and factorization (μ_F) scales set to μ_F=μ_R=$\sqrt{Q^2 + 4m_c^2}$

and varied simultaneously by a factor two up and down. The scales were varied both in HVQDIS and in the PDF fit.

Mass: the charm quark mass (m_c) is set to 1.5 ± 0.15 GeV, varied simultaneously in HVQDIS and in the PDF fit.

PDF: the HERAPDF 1.0 PDF fit performed with the fixed flavour number scheme (FFNS) , with scales and masses in agreement with those used in HVQDIS.

Fragmentation function: fragmentation is performed in the γ^* - p frame using Kartvelishvili fragmentation function with the parameter α_K dependent on the photon-parton center of mass energy squared, based on [6] and [7].

Fragmentation fraction: the probability that a c quark produces a D^{*+} meson is set to f(c $\rightarrow D^{*+}$) = 0.2287.

The theoretical band shown in Fig.3 is RT GM-VFNS heavy flavour scheme at NLO based on the HERAPDF 1.0 densities. The band corresponds to a variation of m_c from 1.3 to 1.65 GeV.

5 Summary

A measurement of the heavy flavour content of the proton in DIS at HERA have been presented. D* cross-sections and $F_2^{c\bar{c}}$ measurements were made using information from ZEUS detector with D* $\rightarrow$ K π π_{slow} decay channel. The D* cross-sections are found to be well described by the predictions of perturbative QCD at NLO. Measured $F_2^{c\bar{c}}$ are in good agreement with previous HERA measurements and HERAPDF 1.0. Measured $F_2^{c\bar{c}}$ will improve precision of H1-ZEUS combination.

References

[1] B. W. Harris and J. Smith, Nucl. Phys. **B 452** (1995) 109.

[2] F. D. Aaron *et al.* [H1 Collaboration],[arXiv:1106.1028[hex-ex]];F.D.Aaron *et al.* [H1 Collaboration], Phys. Lett. B **686** (2010) 91.

[3] H. Jung, Comp. Phys. Comm. **86** (1995) 147.

[4] ZEUS Collaboration, *Measurement of charm production with $D^{\pm}$ in DIS at HERAII*, ZEUS-prel-10-005,

[5] H1 and ZEUS collaborations, *Combination of F_2 c from DIS measurements at HERA*, H1prelim-09-171, ZEUS-prel-09-015,

[6] F. D. Aaron *et al.*[H1 Collaboration],Eur. Phys. J. C **59** (2009) 589.

[7] S. Chekanov *et al.*[ZEUS Collaboration], JHEP **0904** (2009) 082.

Measurement of charm production in DIS with inclusive secondary vertices and determination of $F_2^{c\bar{c}}$ with the ZEUS detector at HERA

Vladyslav Libov[1] on behalf of the ZEUS Collaboration

[1]DESY, Notkestraße 85, 22607 Hamburg, Germany

DOI: http://dx.doi.org/10.3204/DESY-PROC-2012-02/46

Charm production in deep inelastic scattering has been measured with the ZEUS detector using the full HERA II data set. The charm content in events with a jet has been extracted using the decay length significance and invariant mass of secondary vertices. Differential cross sections as a function of the photon virtuality Q^2, Bjorken x, jet transverse energy E_T^{jet} and jet pseudorapidity η^{jet} were measured and compared to theoretical predictions. The open charm contribution to the proton structure function F_2 was extracted from double differential cross sections.

1 Introduction

The production of charm quarks at HERA, an electron-proton collider with a center-of-mass energy of 318 GeV, is interesting in several aspects. In the lowest order, heavy quarks are produced via boson-gluon fusion, hence this process is sensitive to the gluon content of the proton and provides means to check the validity of the gluon density determined from scaling violations of the inclusive F_2 structure function. Charm production allows studies of the multiple-hard-scale problem in QCD which arises because the charm mass is not the only hard scale in the process: at very high photon virtuality Q^2 or charm quark momentum the perturbative expansion can diverge due to presence of large logarithmic terms. Several schemes exist to perform perturbative calculations, such as massive, massless or mixed schemes. They treat differently heavy quark mass and hence the multi-scale problem. Charm data are also sensitive to the value of the charm quark mass.

This work reports a preliminary measurement [1] of charm jet production differential cross-sections in DIS and the determination of the charm contribution to the F_2 proton structure function, $F_2^{c\bar{c}}$.

2 Experimental procedure

After production in the hard interaction, charm quarks hadronize into charm hadrons, which due to their long lifetime travel detectable distances before they decay. This feature allows the usage of lifetime-tagging techniques in order to distinguish charm quark production from

background processes. The measurement reported here employs a method where the charm quarks are tagged by a secondary vertex associated with a jet.

The kinematic region considered was:

- $5 < Q^2 < 1000$ GeV^2, where Q^2 is the negative 4-momentum squared of the virtual photon;
- $0.02 < y < 0.7$, where y is the fraction of the electron energy lost in the interaction in the proton rest frame (inelasticity);
- jets were required to have $E_T > 4.2$ GeV and $-1.6 < \eta < 2.2$.

Tracks belonging to each jet were considered. If at least two tracks with $p_T > 0.5$ GeV were found within the cone of $\Delta R = \sqrt{\Delta\phi^2 + \Delta\eta^2} < 1$ w.r.t. to the jet axis, a secondary vertex was fitted, otherwise the jet was discarded. For each fitted secondary vertex, its decay length significance was calculated using the formula: $S = L_{xy}/\sigma(L_{xy})$, where L_{xy} is the decay length projected onto the jet axis in the plane perpendicular to the beam, and $\sigma(L_{xy})$ is its uncertainty. The decay length signifance was used as a discriminating variable. The distributions for data and charm, beauty and light flavor (LF) Monte Carlo are shown in Fig. 1. The dominant contribution comes from LF production. This background was reduced by mirroring, that is subtraction of the negative significance part from the positive part. After the mirroring, template fits were performed to obtain the charm fraction in the data. The secondary vertex mass was used in addition for separation: the fits were done simultaneously in three vertex mass bins (1-1.4 GeV, 1.4-2 GeV, 2-6 GeV). This is done mainly to enhance the sensitivity to beauty, since the mass is larger for b-quarks than for charm or LF. The procedure was repeated for each bin in the differential cross-sections. $F_2^{c\bar{c}}$ was determined by extrapolation of $Q^2 - x$ double-differential cross-sections to the full phase space using NLO QCD calculations described below.

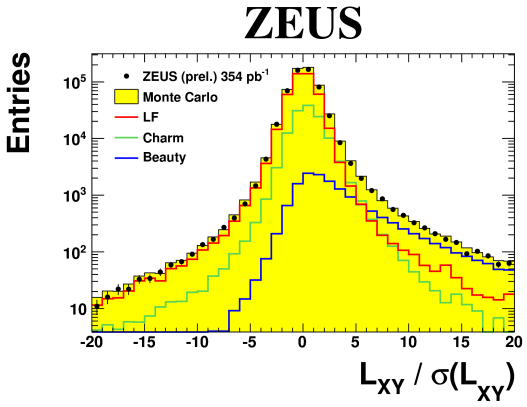

Figure 1: Decay length significance for data, charm, beauty and light flavors Monte Carlo for vertex mass in range $[2, 6]$ GeV. The Monte Carlo distributions were scaled according to the fit results.

3 Theory predictions

NLO QCD calculations were performed with the HVQDIS [2] program (fixed-flavor number scheme). The ZEUS-S [3] and ABKM NLO [4] parton density functions (PDF) were used. The renormalization and factorization scales were set to $\mu_R = \mu_F = \sqrt{Q^2 + 4m_c^2}$. The charm quark mass was set to $m_c = 1.5$ GeV. As HVQDIS provides parton cross-sections at QED Born level, hadronization and QED corrections were applied as determined from the RAPGAP [5] Monte Carlo (LO+parton shower). Uncertainties on the theory predictions were estimated by

variation of HVQDIS settings: μ_R and μ_F independently by factors 0.5 and 2; m_c to 1.3 and 1.7 GeV and by variation of the PDFs within uncertainties.

4 Results

Fig. 2 shows measured differential cross sections as a function of E_T^{jet} and η^{jet} together with NLO QCD calculations. Predictions from RAPGAP Monte Carlo, scaled according to the fit are also shown. The overall agreement between data and theoretical predictions is reasonable, although the data tend to lie above the NLO predictions. Predictions with ZEUS-S and ABKM PDF sets are practically the same. Conclusions for differential cross sections as a function of Q^2 and x (not shown) are very similar.

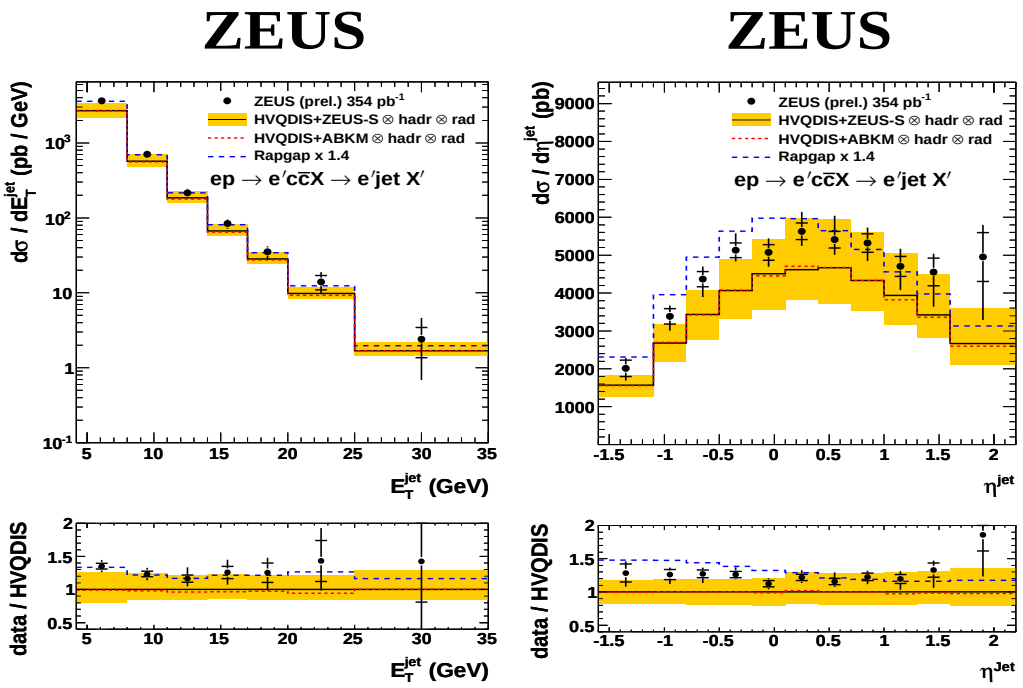

Figure 2: Measured differential cross-sections as a function of E_T^{jet} and η^{jet}.

Fig. 3 shows the contribution to the proton structure function $F_2^{c\bar{c}}$ as a function of x for different values of Q^2. Data are compared to recent ZEUS preliminary measurements [6] with D^* and D^+ tags and also to the preliminary combination [7] of H1 and ZEUS data. All results are consistent, albeit using different techniques. The precision of the new measurement is competitive at moderate and high Q^2. The precision at low Q^2 can still be improved by extending the phase space to lower jet energies. The prediction from HERAPDF 1.0 [8] is also shown. The uncertainty band is determined by the charm mass variation. Charm data are not included in the HERAPDF 1.0 fit hence the nice agreement confirms the QCD factorization theorem.

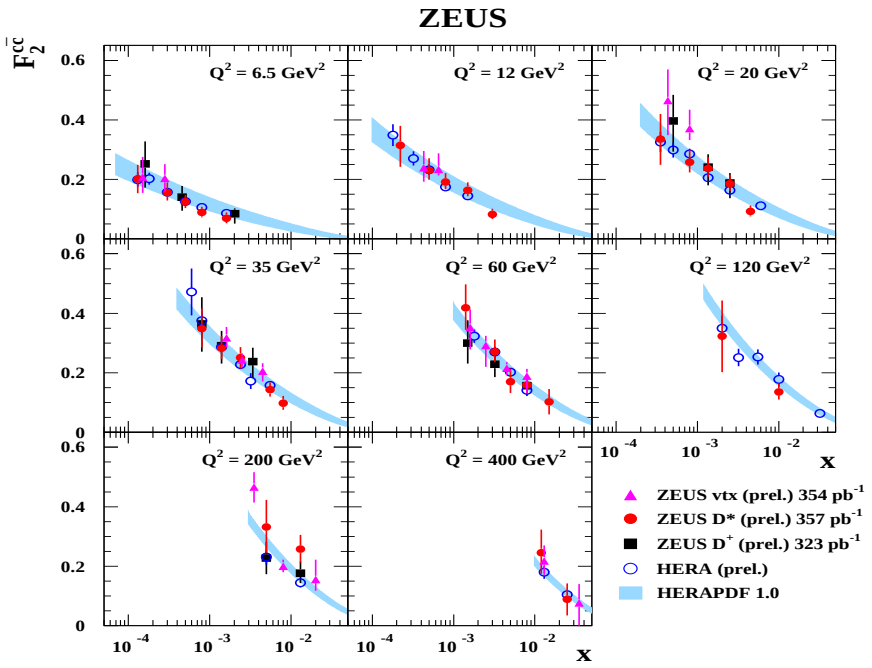

Figure 3: $F_2^{c\bar{c}}$ results compared to previous measurements and QCD predictions based on HERAPDF 1.0

5 Conclusions

The measurement of charm production differential cross-sections in deep inelastic scattering and charm contribution to the proton structure function $F_2^{c\bar{c}}$ with inclusive secondary vertices at ZEUS has been reported. The overall agreement between data and QCD calculations is reasonable, with the theory lying slightly below the data. The precision of $F_2^{c\bar{c}}$ is competitive compared to previous measurements. There are ongoing studies to reduce the extrapolation uncertainty at low Q^2.

References

[1] ZEUS Collab., ZEUS-prel-12-002
[2] B.W. Harris and J. Smith, Phys. Rev. D 57, 2806 (1998)
[3] ZEUS Collab., S. Chekanov et al., Phys. Rev. D 67, 012007 (2003)
[4] S. Alekhin et al., Phys. Rev. D 81, 014032 (2010)
[5] H. Jung, Comp. Phys. Comm. 86, 147 (1995)
[6] ZEUS-prel-11-012, ZEUS-prel-10-005
[7] H1prelim-09-171, ZEUS-prel-09-015
[8] H1 and ZEUS Collab., F.D. Aaron et al., JHEP 01, 1-63 (2010)

Measurement of $D^{*\pm}$ Meson Production and Determination of $F_2^{c\bar{c}}$ at low Q^2 in Deep-Inelastic Scattering at HERA

Eva Hennekemper on behalf of the H1 Collaboration

Kirchhoff-Institut für Physik, Universität Heidelberg, Germany

DOI: http://dx.doi.org/10.3204/DESY-PROC-2012-02/191

Inclusive production of D* mesons in deep-inelastic *ep* scattering at HERA is studied in the range $5 < Q^2 < 100$ GeV^2 of the photon virtuality and $0.02 < y < 0.7$ of the inelasticity of the scattering process. The observed phase space for the D* meson is $p_T(D*) > 1.25$ GeV and $|\eta(D*)| < 1.8$. The data sample corresponds to an integrated luminosity of 348 pb^{-1} collected with the H1 detector. Single and double differential cross sections are measured and the charm contribution $F_2^{c\bar{c}}$ to the proton structure function F_2 is determined. The results are compared to perturbative QCD predictions at next-to-leading order implementing different schemes for the charm mass treatment and with Monte Carlo models based on leading order matrix elements with parton showers.

1 Introduction

A measurement of charm production in deep-inelastic scattering at HERA based on the reconstruction of a D^* meson [1] is presented. At HERA protons of 920 GeV have been collided with electrons of 27.6 GeV. D^* meson production at HERA happens predominantly in the following way: a charm-anticharm quark pair is produced in boson gluon fusion via the interaction of a photon from the electron and a gluon from the proton. The charm quark fragments then further into a D^* meson and hadrons. The events containing D^* mesons have been measured with the H1 detector. The kinematic range in the photon virtuality Q^2 is $5 < Q^2 < 100$ GeV^2, and in the inelasticity $0.02 < y < 0.7$. In comparison to earlier H1 analysis [2] the range in transverse momentum and pseudorapidity of the D^* is extended to $p_T(D*) > 1.25$ GeV and $|\eta(D*)| > 1.8$, such that the phase space is now about a factor of two larger. The D^* meson decays in the so-called golden decay channel $D^{*\pm} \to D^0\pi_s^\pm \to K^\mp\pi^\pm\pi_s^\pm$. The three final state

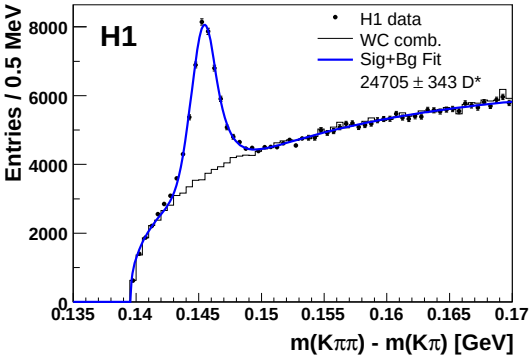

Figure 1: The mass difference of the reconstructed D^* and D^0 mesons. Data points are presented as black dots, the fit result as solid line.

particles are charged so that their tracks can be reconstructed in the central jet chambers. The D^* mesons are reconstructed with the mass difference method, where ΔM is the mass difference of the reconstructed D^* and D^0. The analysis sample comprises the full HERAII statistics and the total integrated luminosity amounts to 348 pb^{-1}. The D^* signal is shown in figure 1. In total 24705 D^* have been found, which means an increase of statistics by a factor 10 in comparison to the earlier H1 analysis [2]. In this analysis the cross sections have been determined on Born-level, the radiative effects have been corrected with using the HERACLES [3] interface. Detector effects like migrations and efficiencies have been corrected with regularized matrix unfolding. The total systematic uncertainty amounts to 7.6%, where the largest part results from the track finding efficiency with 4.1%.

1.1 QCD calculations

In this analysis the Monte Carlo (MC) generators RAPGAP [4] and CASCADE [5] have been used, which are leading order (LO) α_s QCD calculations with additional parton showers [6]. Both MCs are calculated in the fixed flavor number scheme (FFNS). The main difference of these MC generators is, that RAPGAP uses the collinear factorization with DGLAP evolution equations, while CASCADE has implemented k_T-factorization with CCFM evolution equations. In addition next-to-leading order (NLO) QCD calculations have been used in this measurement: First from HVQDIS [7], which is a FFNS calculation with collinear factorization and DGLAP evolution equations. And secondly a zero-mass variable flavor number scheme (ZM-VFNS) calculation [8] with collinear factorization and DGLAP evolution equations. In this calculation the charm quark is treated above the charm-threshold as massless parton of the proton.

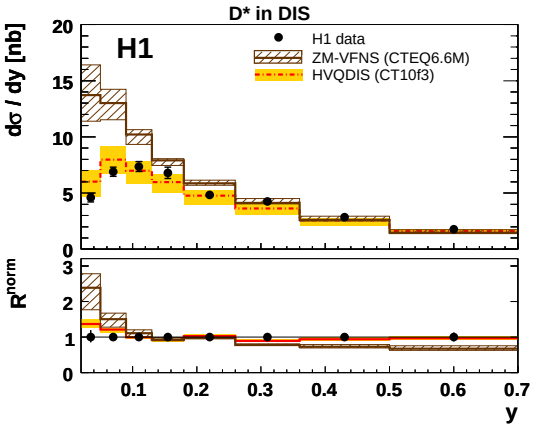

Figure 2: Single differential cross section in the inelasticity y. The H1 measurement is shown with black points with error bars denoting the systematic and statistical uncertainty of the analysis. In addition the predictions of the HVQDIS and the ZM-VFNS calculations are presented.

2 Results

The LO and NLO calculations in the FFNS give a good description of the measured D^* meson cross sections as a function of the kinematic variables of the D^* meson and of the event kinematics. The ZM-VFNS calculation fails to describe the data. In figure 2 the single differential cross section in y is presented in comparison to HVQDIS and the ZM-VFNS calculation. The uncertainty band of HVQDIS comes from the variation of the renormalization- and factorization scale, the charm mass and the fragmentation parameters, whereas the uncertainty band of the ZM-VFNS calculation includes only the scale uncertainties.

The charm cross section and $F_2^{c\bar{c}}$ are connected by the formula

$$\frac{\mathrm{d}^2\sigma^{c\bar{c}}}{\mathrm{d}x\,\mathrm{d}Q^2} = \frac{2\pi\alpha_{em}^2}{Q^4 x}\left([1+(1-y)^2]\,F_2^{c\bar{c}}(x,Q^2) - y^2 F_L^{c\bar{c}}(x,Q^2)\right) \quad . \tag{1}$$

The H1 measurement comprises 50% of the total charm production phase space. The extrapolation to the full phase space was performed with

$$F_2^{c\bar{c}\,\mathrm{exp}}(\langle x\rangle,\langle Q^2\rangle) = \frac{\sigma_{\mathrm{vis}}^{\mathrm{exp}}(y,Q^2)}{\sigma_{\mathrm{vis}}^{\mathrm{theo}}(y,Q^2)} \cdot F_2^{c\bar{c}\,\mathrm{theo}}(\langle x\rangle,\langle Q^2\rangle) \quad , \tag{2}$$

where $\sigma_{vis}^{theo}(y,Q^2)$ and $F_2^{c\bar{c}theo}(x,Q^2)$ are taken from the HVQDIS prediction. This extrapolation introduces two additional uncertainties to the measurement. To determine the 'extrapolation-' uncertainty the theory parameters within HVQDIS have been varied and the 'model-' uncertainty was estimated by performing the extrapolation procedure with another model, here from CASCADE. Figure 3 (left) displays the extracted $F_2^{c\bar{c}}$. An independent H1 measurement [9]

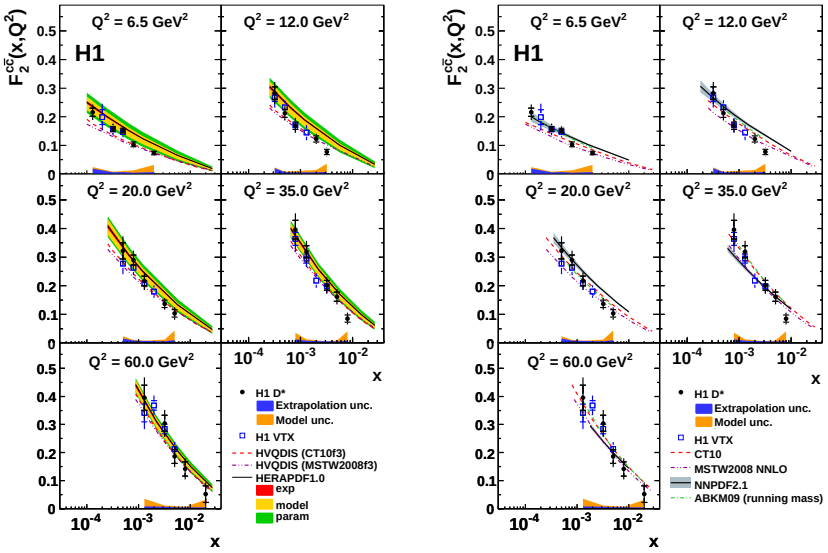

Figure 3: The extracted $F_2^{c\bar{c}}$ (black points), compared to H1 lifetime measurement (blue squares), HVQDIS and HERAPDF1.0 (on the left) and to global fit PDFs (on the right).

using lifetime information is shown too. These two H1 measurements are in good agreement. In addition the data is compared to HVQDIS predictions with two different parton density functions (PDFs) and to the HERAPDF1.0 expectation [10] in this figure. Both predictions fit well the measurement. This implies that the gluon PDF found in scaling violations of inclusive DIS cross section measurements agrees well with the gluon density from the D^* measurement. In figure 3 (right) the data is further compared to different PDFs from global fits of CT10 [11], MSTW2008 NNLO [12], NNPDF2.1 [13] in the general mass variable flavor number scheme (GMVFNS) and of ABKM09 [14] in the FFNS. The experimental uncertainty of the analysis are of the same size as the spread of the predictions. Overall, these predictions show good agreement with the H1 measurement.

2.1 Conclusion

The H1 measurement of inclusive D^* cross sections in DIS in an increased phase space and using the full HERAII statistics has been presented. The data is well described by the FFNS calculations, but not by the ZM-VFNS calculation. The charm contribution to the proton structure function $F_2^{c\bar{c}}$ has been extracted. The extrapolation to the full phase space was performed with two predictions from HVQDIS and CASCADE. This D^* measurement is in good agreement with an independent H1 measurement using lifetime informations. $F_2^{c\bar{c}}$ is well described by all of the NLO calculations, so that one can conclude that the gluon PDF found in scaling violations of inclusive DIS cross section measurements agrees well with the gluon density in this measurement.

References

[1] F. D. Aaron *et al.* [H1 Collaboration], "Measurement of $D^{*\pm}$ Meson Production and Determination of F_2^{ccbar} at low Q2 in Deep-Inelastic Scattering at HERA," Eur. Phys. J. C **71** (2011) 1769 [arXiv:1106.1028 [hep-ex]].

[2] A. Aktas *et al.* [H1 Collaboration], Eur. Phys. J. **C51** (2007) 271 [hep-ex/0701023].

[3] A. Kwiatkowski, H. Spiesberger, and H.J. Mohring, HERACLES V4.6, Comp. Phys. Commun. **69** (1992) 155.

[4] H. Jung, RAPGAP V3.1, Comp. Phys. Commun. **86** (1995) 147.

[5] H. Jung, CASCADE V2.0, Comp. Phys. Commun. **143** (2002) 100.

[6] M. Bengtsson and T. Sjostrand, Z. Phys. **C37** (1988) 465.

[7] B.W. Harris and J. Smith, Nucl. Phys. **B452** (1995) 109 [hep-ph/9503484];
B.W. Harris and J. Smith, Phys. Rev. **D57** (1998) 2806 [hep-ph/9706334].

[8] G. Heinrich, B. A. Kniehl, Phys. Rev. **D70** (2004) 094035 [hep-ph/0409303];
C. Sandoval, Proc. of XVII International Workshop on Deep-Inelastic Scattering (DIS 2009), Madrid, 2009, arXiv:0908.0824;
C. Sandoval, "Inclusive Production of Hadrons in Neutral and Charged Current Deep Inelastic Scattering", Ph.D. Thesis, Univ. Hamburg (2009), DESY-THESIS-2009-044.

[9] F.D. Aaron *et al.* [H1 Collaboration], Eur. Phys. J. **C65** (2010) 89 [arXiv:0907.2643].

[10] F.D. Aaron *et al.* [H1 and ZEUS Collaboration], JHEP **1001** (2010) 109 [arXiv:0911.0884].

[11] H.L. Lai *et al.* [CTEQ Collaboration], Phys. Rev. **D82** (2010) 074024 [arXiv:1007.2241].

[12] A.D. Martin, W.J. Stirling, R.S. Thorne and G. Watt, Eur. Phys. J. **C63** (2009) 189 [arXiv:0901.0002].

[13] R.D. Ball *et al.*, Nucl. Phys. **B849** (2011) 296 [arXiv:1101.1300].

[14] S. Alekhin, J. Blümlein, S. Klein and S. Moch, Phys. Rev. **D81** (2010) 014032 [arXiv:0908.2766].

WG1: Structure Functions and WG7: Future of DIS

Precision QCD and electroweak physics at LHeC

Olaf Behnke

DESY, Hamburg - Germany
obehnke@mail.desy.de

DOI: http://dx.doi.org/10.3204/DESY-PROC-2012-02/340

A brief review is presented of the precision QCD and electroweak physics potentials at a possible future Large Hadron electron Collider (LHeC). All presented results are taken from the recently released conceptional design report [1] (CDR), in which further references can be found.

1 Introduction

The $e^{\pm}p$ collider LHeC with (about) 60 GeV times 7 TeV beam energies, an integrated luminosity of 1-100 fb^{-1}, and lepton beam polarisation up to $\pm$ 0.9, is one of the most interesting options for future particle physics colliders. The LHeC would provide ample opportunities to continue and extend precision QCD and electroweak studies much beyond what has been achieved at HERA. Among other things the LHeC will reveal all kind of facets of the proton structure, as represented by the Parton Distribution Functions (PDF), which parametrise the quark and gluon densities in the proton. This will be crucial for the understanding (and predictions) of LHC results. The large asymmetry of the two beam energies necessitates an excellent forward hadron calorimetry and calibration in order to explore the full kinematic phasespace up to large values of the *Bjorken* scaling variable $x \simeq 0.8$. The next sessions describe some selected physics studies from the CDR.

2 Proton structure and α_s

A set of neutral (γ, Z-exchange) and charged current (W-exchange) pseudodata have been simulated. The simulations were performed according to accelerator and detector scenarios that seem realistic and include also expected systematic uncertainties. At HERA, the exchange of the W and Z weak gauge bosons contributed only in a small phase space of highest accessible boson virtualities Q^2. In contrast the LHeC will be the first genuine "electroweak electron proton collider" machine. The integrated neutral (NC) and charged current (CC) event rates obtained from the simulations are about two order of magnitude larger at LHeC than at HERA and values of Q^2 are reached of up to $Q^2 \sim 10^6$ GeV. For the NC case, precise data are expected from smallest $x \approx 0.000008$ to largest $x \approx 0.8$. In a seizable fraction of the Q^2 phase space the photon and Z^0 exchanges are 1:1. Running with two lepton beam charges (electrons and positrons) and positive and negative lepton longitudinal polarisations will be crucial for electroweak precision physics as well as for the exploration of the proton structure. For the latter the Z and W exchanges assist the photon exchange for a complete *quark flavour*

decomposition. Subtracting the NC cross sections for positron beams from those for electron beams isolates the $\gamma - Z$ interference term, as expressed by the structure function $xF_3^{\gamma Z}$, and provides direct information on the valence quarks from $x \sim 0.001$ to $x \sim 0.8$. The CC data for electron beams with W^- exchange and those for positron beams with W^+ exchange allow to unfold the u, d and also the $\bar{u}, \bar{d}$ densities in the proton. The longstanding question: "is the strange sea equal to the anti-strange sea?" can be answered by studying the charged current processes $W^+ s \to c$ and $W^- \bar{s} \to \bar{c}$ and tagging the charm (or anti-charm) quark in the final state. Studies with corresponding pseudodata indicate that a precise measurement of strange and anti-strange densities in the proton is possible over a wide range in Q^2 and x.

The knowledge of the gluon density is crucial at the LHC, for instance for the SM Higgs production which is dominated by the gg fusion process. The current knowledge comes mainly from the observed scaling violations of the structure function F_2 at HERA (as visible in the inclusive NC data). It is rather precise in the region relevant for Higgs production at LHC but diverges towards smaller values of gg centre-of-mass energy.

Figure 1 show the projected error bands of selected PDFs: valence quarks and gluon, as determined from a Next-to-Leading Order (NLO) QCD analysis of inclusive NC and CC data. The results using the LHeC simulated pseudodata in addition to real HERA data are compared to those using only HERA or using HERA and fixed target data from BCDMS. A huge improvement in precision and also an extension of effective coverage to much smaller x values and towards large values $x \sim 0.8$ is demonstrated. Among other things this will be helpful to pin down the not so well known ratio u/d for $x \to 1$. One nice feature (not shown here) is that, using the LHeC data, one can relax many assumptions that were made for PDF fits to the HERA data alone, for instance $\bar{u} = \bar{d}$ for $x \to 0$. Relaxing this constraint, the PDF error bands for fitting the HERA data alone increase drastically, showing the insensitivity of the HERA data, while those for LHeC plus HERA stay reasonably small, due to the much better flavour decomposition capabilities at LHeC. The u/d flavour decomposition at LHeC can be further improved with the planned deuteron runs.

Inclusive deep inelastic NC data allow a precision determination of the strong coupling constant α_s, mainly via the scaling violations of F_2. Projections show that it will be possible, by fitting simultaneously LHeC and HERA data to reach a precision of 1 permille, which is a factor ~ 10 better than fitting only HERA data.

3 Jet and heavy flavour production

Jets are produced in ep collisions in leading order $o(\alpha_s)$ via the Boson Gluon Fusion (BGF) process $\gamma^* g \to q\bar{q}$, and the QCD compton process $\gamma^* q \to qg$. Here q and g denote initial (from the proton) or outgoing hard partons, the latter producing jets. The BGF process rate is proportional to the product of the gluon density and α_s, while the QCD compton is proportional to the product of the quark densities and α_s. Thus the analysis of jet production helps to disentangle the gluon density and α_s. The jet data at LHeC cover a kinematic range up to 500 GeV transverse momenta (compared to ~ 100 GeV at HERA). This will allow to study for the first time with good precision the running od α_s to such high scales where the onset of *top loop diagrams* are expected to influence the running behaviour. This will provide a unique test of the SM strong interactions. Currently the precision of predictions for jet productions in ep collisions is limited to order $o(\alpha_s^2)$. At the time of the LHeC, order $o(\alpha_s^3)$ calculations should be available which will be crucial to exploit the full physics potential of jet measurements at

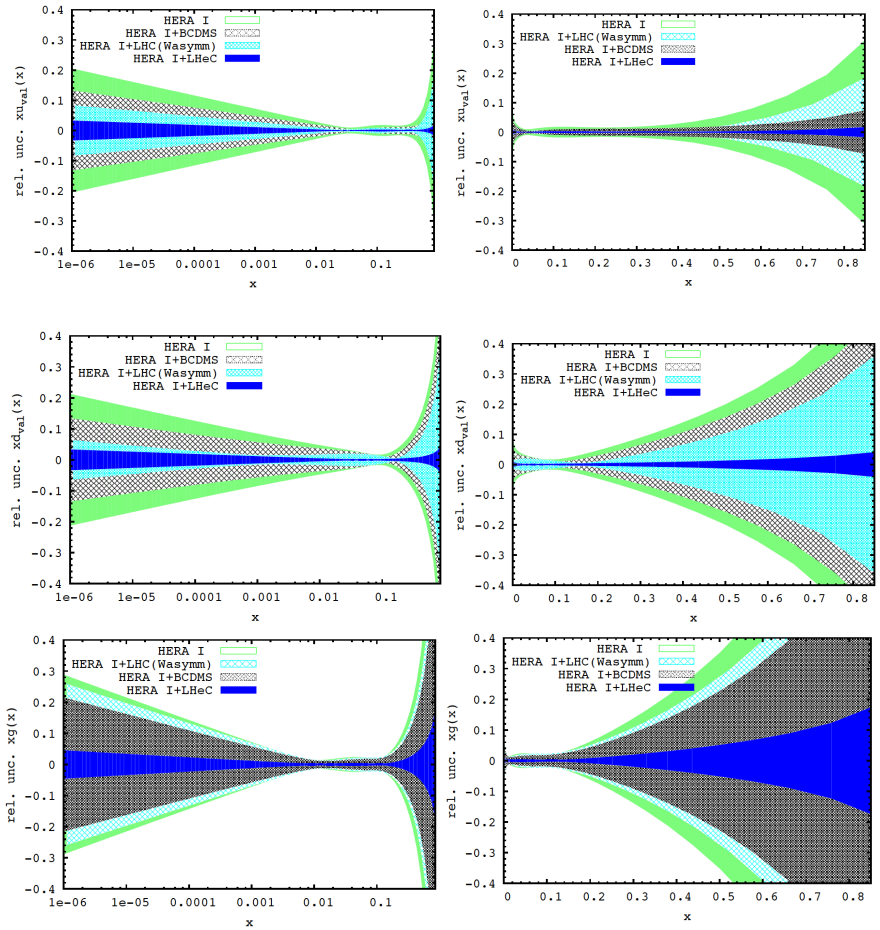

Figure 1: Uncertainty of selected parton distributions, at $Q^2 = 1.9\,\mathrm{GeV}^2$, as resulting from an NLO QCD fit to selected data (see text). Top: up valence quark; Middle: down valence quark; Down: gluon; left: logarithmic x, right: linear x.

the LHeC.

Charm and beauty quarks are produced in ep collisions in leading order via the BGF process $\gamma^* g \to c\bar{c}$ (or $b\bar{b}$). This process provides direct sensitivity to the gluon density in the proton. Charm and beauty production contribute up to 35% and 9% of the inclusive deep inelastic scattering cross sections. Thus a direct measurement of this contribution, represented by the structure functions $F_2^{c\bar{c}}$ and $F_2^{b\bar{b}}$, is of great importance for the understanding of the whole proton structure in terms of light quarks, heavy quarks and gluons. Projections for $F_2^{c\bar{c}}$ and $F_2^{b\bar{b}}$ have been obtained using RAPGAP Monte Carlo simulations and are shown in Figure 3. They indicate a huge phase space extension and improvement in precision compared to representative HERA results which are also shown. The extension to low x values will be important for the study of the gluon density, while the mapping from low to high Q^2 for the precision determination of the charm and beauty quark masses and more generally for the treatment of mass

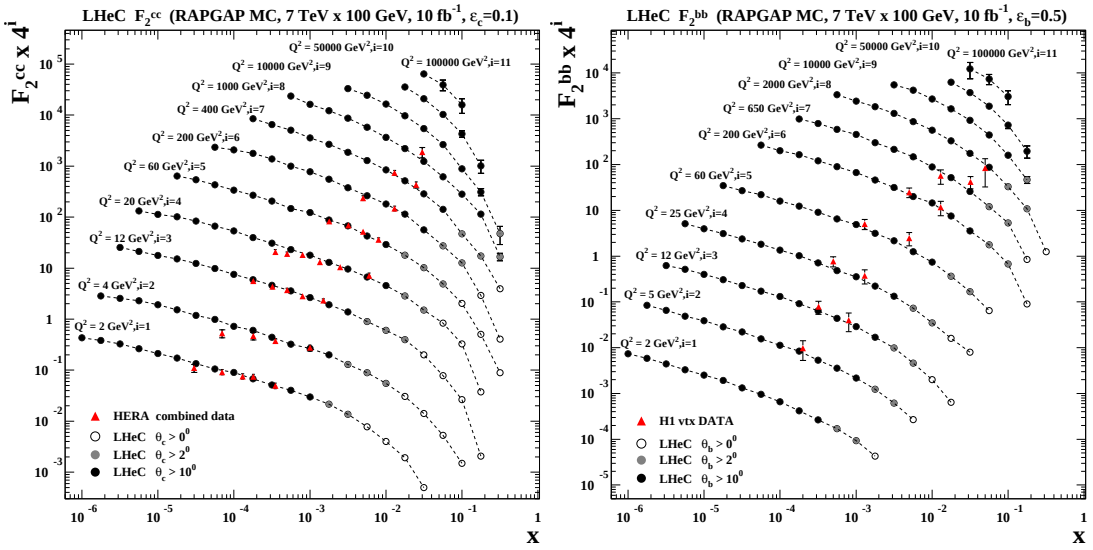

Figure 2: LHeC Projections for structure functions F_2^{cc} (left) and F_2^{bb} (right), compared to HERA data, shown as a function of x for various Q^2 values.

dependent terms in pQCD. With very good forward charm and beauty tagging capabilities of the LHeC detector, it will be possible to reach large x-values $x \geq 0.1$ where one can test the hypothesis of an *intrinsic* charm (or beauty) component in the proton wave function.

At LHeC one can also study for the first time at an ep collider top production, which is dominated by the reaction $bW^+ \to t$ (and $\bar{b}W^-\bar{t}$). In general LHeC will be the first multiflavour factory ep collider, allowing to do studies related to all six quark flavours.

4 Electroweak measurements

The LheC provides a rich potential for electroweak precision measuremnts from which here only a few are reported. Studies with $e^{\pm}p$ NC and CC pseudodata of positive and negative lepton beam polarisations show that there is a good sensitivity to determine the light quark axial and vector couplings to the Z boson. It will be possible to provide from these data a few relatively precise points for the running of the Weinberg angle $\sin^2\theta_W(\mu)$, for scales μ between 10 and 400 GeV, which are complementary and/or extend determinations from other type of experiments and colliders.

The interesting prospects of Higgs production were presented in another talk [2].

References

[1] The LHEC study group, "A Large Hadron Electron Collider at CERN: Report on the Physics and Design Concepts for Machine and Detector", arXiv:1206.2913v1.

[2] Rohini Godbole, "Higgs CP properties and the LHeC", these proceedings.

Diffractive and exclusive processes at small x at the Large Hadron-electron Collider

Anna M. Staśto[1,2,3]

[1] The Pennsylvania State University, University Park, 16802 PA, USA
[2] RIKEN BNL, Upton, 11793 NY, USA
[3] H. Niewodniczański Institute of Nuclear Physics, Polish Academy of Sciences, Kraków, Poland

DOI: `http://dx.doi.org/10.3204/DESY-PROC-2012-02/339`

In this talk, I will discuss the opportunities for the exploration of physics phenomena at low values of Bjorken x at the Large Hadron-electron Collider. In particular, the prospects for the measurements of the diffractive and exclusive processes will be outlined.

Small x physics at the LHeC. Large Hadron-electron Collider (LHeC) is a proposed facility for the electron - hadron and nucleus scattering at CERN which would utilize existing high energy beams from the LHC. The projected energy for the electron beam is in the range of $60 - 140$ GeV. In addition to the deep inelastic electron-proton scattering, the LHeC proposal includes also collisions of electrons with lead nuclei. This machine would greatly expand the kinematic range previously explored by the HERA collider thus allowing to probe the details of strong and electroweak interactions.

Of particular interest is the huge physics potential of the LHeC of exploring the region of small values of Bjorken x. Large center-of-mass energy, of the order of $\sqrt{s} \sim 1 - 2$ TeV, would allow to extend the range in x by at least an order of magnitude compared to the HERA collider. In this regime novel phenomena are expected which are related to the occurrence of the high parton density. An alternative way of probing the high parton density is through the collisions of electrons with heavy nuclei thus providing a unique insight into the structure of nuclei at high energies, and furnishing valuable input for the heavy ion collisions probed at the LHC. The LHeC would be characterized by the large instantaneous luminosity, of the order of 10^{33} cm^{-2}s^{-1}, which would allow for the high precision measurements.

Wide range of physics possibilities at the LHeC have been discussed in other talks in this workshop. In particular, prospects for the precision QCD and Electroweak measurements have been reviewed by O. Behnke [1] and the inclusive measurements essential for the exploration of the small x physics have been discussed by N. Armesto [2] including the DIS off nuclei. This talk focuses on the diffractive and exclusive processes at small x which could be explored at the LHeC. All the material presented in this talk can be found in the Conceptual Design Report for the LHeC [3].

Inclusive diffraction. It was discovered at HERA that a large fraction, i.e. about 10%, of DIS interactions are diffractive events. These events are of type $ep \to eXp$, where the interacting proton stays intact. It emerges in the final state well separated from the rest of the hadronic final state X by a rapidity gap. From a variety of theoretical studies it has become clear that

the diffraction is closely linked with the partonic saturation. The phenomenological studies based on dipole models at small x suggest that the diffractive DIS events involve significantly softer scales as compared with the non-diffractive events at the same values of Q^2. Thus a study of diffraction offers a unique opportunity to investigate the transition between perturbative and non-perturbative dynamics and the onset of non-linear effects in parton density.

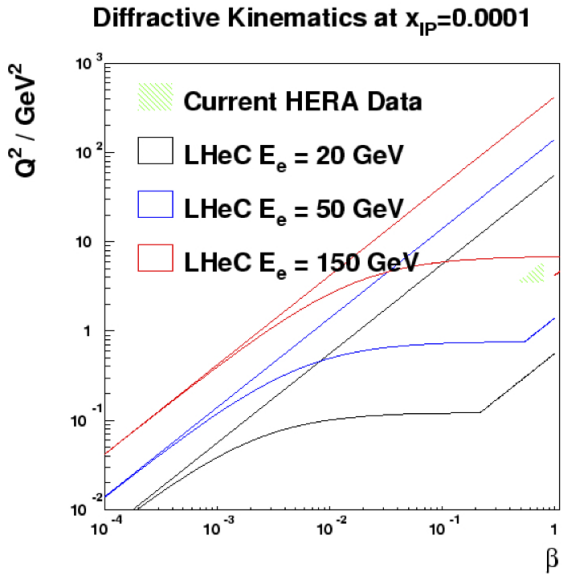

Figure 1: Diffractive DIS ranges in Q^2 and β of HERA and of the LHeC for electron energies $E_e = 20, 50, 150$ GeV and $x_{I\!P} = 0.0001$. Scattered electron acceptance is taken to be 1°.

The LHeC will offer ample opportunities to perform the measurements of the diffractive DIS in an unprecedented kinematic range. The diffractive kinematic plane is shown in Fig. 1 for a value of the Pomeron momentum fraction $x_{I\!P} = 0.0001$. The accessible kinematic ranges are shown for three electron energies, $E_e = 20, 50, 150$ GeV. The kinematic coverage of HERA is superimposed in this plot. It is clear that the LHeC will have a much increased reach for the diffractive events compared with HERA towards low values of both $x_{I\!P}$ and β. The kinematic range of diffractive DIS measurements at the LHeC is also illustrated in Fig. 2 (left plot) for the example of a 150 GeV electron beam compared with an estimation of the final HERA performance. The pseudodata for F_2^D diffractive structure function are simulated for the LHeC together with the range accessible at HERA. The dependence of the kinematical ranges on the backward acceptance cuts of 1° and 10° of the detector is also illustrated.

The diffractive DIS region of very low β is of particular interest since the diffractively produced systems will be created with very large invariant masses. This is clearly illustrated in Fig.2 (right plot). This figure compares the expected M_X distributions for one year of running at three LHeC electron beam energy choices. LHeC will enable to experimentally access the region of very large diffractive masses, up to several hundred GeV. Therefore it will be possible to study diffractive final states involving beauty quarks and W and Z bosons. If existing, the exotic states with 1^- quantum numbers, could be produced.

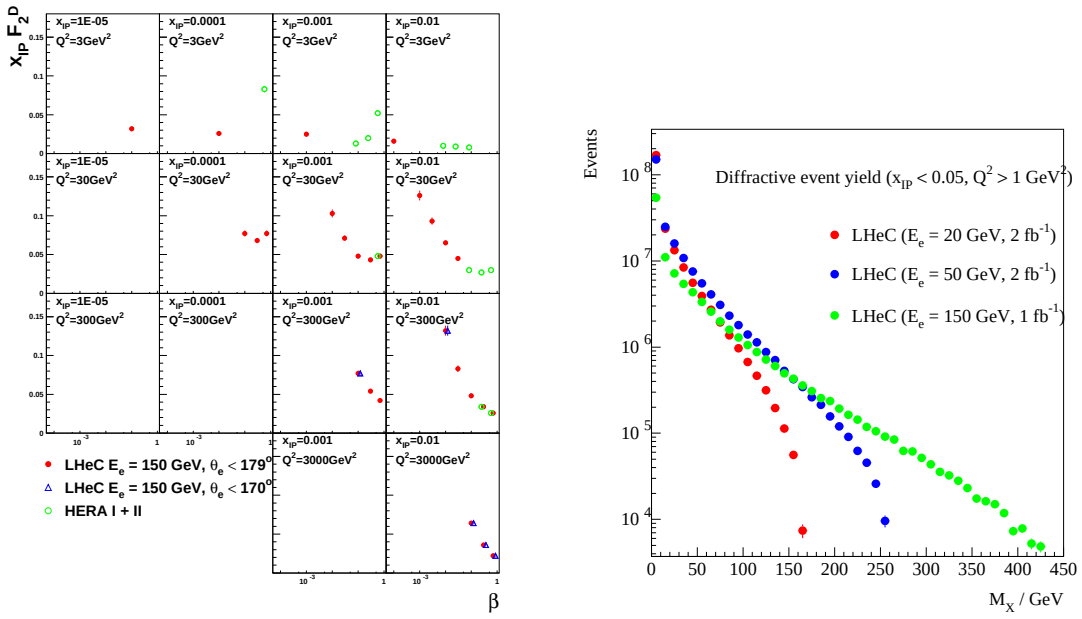

Figure 2: Left: simulation of an LHeC measurement of the diffractive structure function, F_2^D using a 2 fb^{-1} sample, compared with an estimate of the results achievable at HERA. Luminosity for an experiment is taken to be 500 pb^{-1}. The loss of kinematic region if the LHeC scattered electron acceptance extends to within 10° of the beam-pipe, rather than 1° is also illustrated. Right: simulated distributions in the invariant mass M_X from the RAPGAP Monte Carlo for $x_{I\!P} < 0.05$.

Measurements of the inclusive diffraction at the LHeC will allow large improvements in extraction and constraining of the diffractive PDFs. In addition, the assumption about the proton vertex factorisation can be tested precisely by comparing the β and Q^2 dependences at different small $x_{I\!P}$ values in their considerable regions of overlap. Furthermore, the ample production of dijets or heavy quarks as components of the diffractive system X will allow for the precision tests of QCD collinear factorisation in diffraction.

Inclusive diffraction can also be explored in electron-ion scattering, where it is expected to be enhanced over the proton case. In the nuclear case two types of processes can occur, the fully coherent diffraction, where the nucleus stays intact ($eA \to eXA$) and incoherent diffraction, where the nucleons within the nucleus are resolved and the nucleus breaks up. Dedicated forward instrumentation will be implemented to distinguish between these two scenarios.

Exclusive processes. Exclusive processes such as the electroproduction of vector mesons and photons or photoproduction of heavy quarkonia provide a valuable information on nucleon structure and small-x dynamics. Diffractive channels are of particular interest since the underlying exchange is dominated by the gluons, and the cross section for this process is proportional to the square of the gluon density (unlike the inclusive non-diffractive case). Thus, the study of these processes could provide us with the better understanding of the gluon saturation. The same exclusive processes can be measured in electron scattering off nuclei, where the gluon

density is modified by nuclear effects.

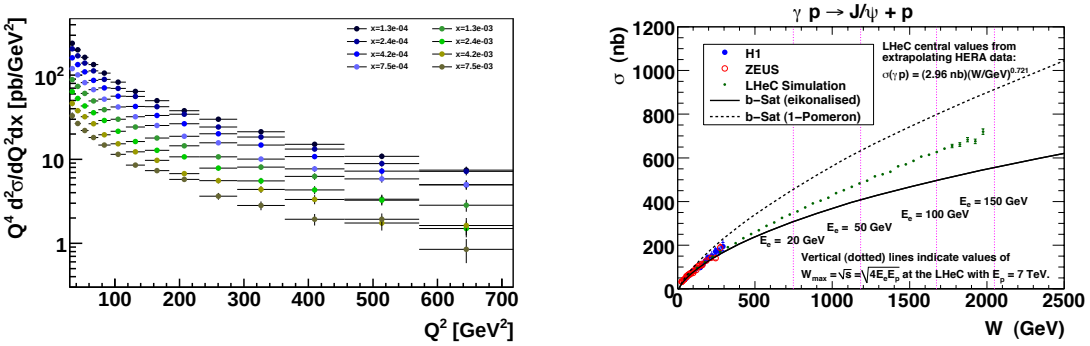

Figure 3: Left: Simulated LHeC measurement of the DVCS cross section multiplied by Q^4 for different x values for a luminosity of 100 fb^{-1}, with $E_e = 50$ GeV, and electron and photon acceptance extending to within 10° of the beampipe with a cut at $P_T^\gamma = 5$ GeV. Right: LHeC exclusive diffractive J/ψ photoproduction pseudodata, as a function of the γp centre-of-mass energy W. The difference between the solid and dashed curves indicates the size of unitarity corrections.

The exclusive processes give access to the spatial distribution of the gluon density, parametrized by the impact parameter of the collision. They can be used to extract the Generalised Parton Densities (GPDs) which encode the information on the three-dimensional structure of the hadron. At the LHeC the Q^2-dependence of these processes can be studied and different channels compared in order to test the universality of GPDs. Vector meson production probes the gluon GPD of the target, while the Deeply Virtual Compton Scattering (DVCS) involves also the singlet quark GPD.

A simulation of the DVCS process at the LHeC is shown in Fig. 3 (left plot). Precise measurements extending to $Q^2 > 500$ GeV^2 are possible, well beyond the range previously explored for DVCS or other GPD-sensitive processes. The right plot in Fig. 3 shows the predictions for exclusive J/ψ photoproduction obtained within the dipole model which includes parton saturation effects. Comparison between the single-Pomeron exchange contribution and the calculation which includes non-linear effects is shown. It is clear from Fig. 3 that the errors on the LHeC pseudodata are much smaller than the difference between the two predictions. Therefore, exclusive J/ψ photoproduction at the LHeC may be an ideal observable for investigating unitarity corrections at small x.

Acknowledgements The author acknowledges the support by the Polish NCN grant DEC-2011/01/B/ST2/03915, the DOE OJI grant No. DE - SC0002145 and by the Sloan Foundation.

References

[1] O. Behnke, talk at DIS2012.

[2] N. Armesto, talk at DIS2012.

[3] *A Large Hadron-electron Collider at CERN*, Report on Physics and Design. Concepts for Machine and Detector (*to be published*).

WG2: Diffraction and Vector Mesons and WG5: Heavy Flavours

Jet Reconstruction in LHCb

Albert Bursche[1] on behalf of the LHCb Collaboration

[1] Universität Zürich – Physik-Institut Winterthurerstrasse 190, CH 8057 Zürich, Switzerland

DOI: http://dx.doi.org/10.3204/DESY-PROC-2012-02/146

We report on the jet reconstruction in LHCb. An overview of the LHCb jet reconstruction is presented and the performance of the jet reconstruction is evaluated.

1 Introduction

The LHCb detector [1] was designed and built to study the properties of charmed and beauty hadrons but it is also used to perform a rich programme of electroweak physics and QCD. In order to reach the LHCb acceptance the produced particles must be moving in the forward direction. This leads to an constraint on the interacting partons, which have to have a large difference in Björken–x. LHCb is able to probe partons in the proton Björken–x as low as 8×10^{-6} at $Q^2 = 25$ GeV [2]. Most of the studies have been carried out using lepton final states. Reconstruction of jets enables LHCb to extend this programme to include studies like Z production in association with jets [3].

2 LHCb detector

The LHCb detector is a single-arm forward spectrometer covering the pseudo-rapidity range $2 < \eta < 5$, designed for the study of particles containing b or c quarks. The detector includes a high precision tracking system consisting of a silicon-strip vertex detector (VELO) surrounding the pp interaction region, a large-area silicon-strip detector (TT) located upstream of a dipole magnet with a bending power of about 4 Tm, and three stations of silicon-strip detectors (IT) and straw drift-tubes (OT) placed downstream. The combined tracking system has a momentum resolution $\Delta p/p$ that varies from 0.4% at 5 GeV to 0.6% at 100 GeV, and an impact parameter resolution of 20μm for tracks with high transverse momentum. Charged hadrons are identified using two ring-imaging Cerenkov detectors (RICH). Photon, electron and hadron candidates are identified by a calorimeter system consisting of scintillating-pad and pre-shower detectors, an electromagnetic calorimeter (ECAL) and a hadronic calorimeter (HCAL). Muons are identified by a muon system composed of alternating layers of iron and multiwire proportional chambers.

3 Jet Reconstruction

Jets are clustered using the anti–k_T algorithm [4, 5] in the energy recombination mode with an R–parameter of one half. The jets on truth level are defined for *stable particles*[1].

[1] Stable particles in this sense are $p, n, \pi^{\pm}, K^0, K^{\pm}, e^{\pm}, \mu^{\pm}$ and γ.

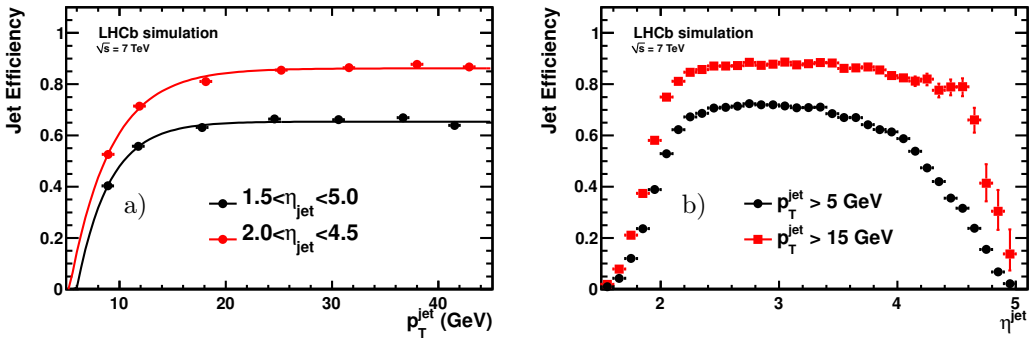

Figure 1: Efficiency of the jet reconstruction and identification as function of the transverse momentum and of η.

The jet reconstruction is optimised to use the precise tracking information wherever possible, since the energy recorded in the individual calorimeter cells saturates at transverse energies about 10 GeV. Therefore the measured jets are reconstructed from charged particle candidates from tracks; reconstructed Λ^0 and K_S^0 candidates as two track combinations; π^0 and photon candidates from the ECAL and neutral hadron candidates from the HCAL. No track in the jet is allowed to carry more than 80% of the jet momentum. Otherwise the jet candidate is rejected. In order to minimise the dependence on pileup the jets are reconstructed for each primary vertex separately and are required to contain at least four particles reconstructed from tracks containing VELO segments that are associated to a primary vertex.

4 Performance of the Jet Reconstruction

The efficiency of the jet reconstruction and identification in simulation(Pythia) is shown in Figures 1a as function of transverse momentum p_T and in Figure 1b as function of η. The efficiency for 15 GeV is well above 80% in the central η region: $2 < \eta < 4.5$. Most of the inefficiency originates from the jet identification selection.

Figure 2 shows the fraction of the jet energy measured by the tracking system, the ECAL and the HCAL respectively. About 70% of the jet energy is carried by stable charged particles and thus can be measured precisely by the tracking system. The second largest component of about 20% of the jets energy is carried by photons and measured in the ECAL. Only a small fraction of about 10% of the jet energy is measured with the HCAL.

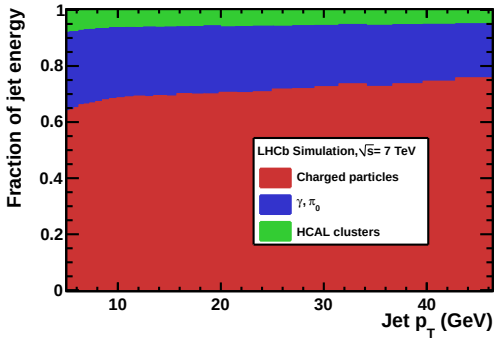

Figure 2: Measured particle content of the jets.

$Z \to \mu\mu$ production in association with jets is used to study the jet reconstruction in data.[2] A candidate event is shown in Figure 3.

Z candidates are selected using the selection defined in [6]. This selection requires two identified muons with opposite charge, a $p_T > 20$ GeV, and pseudorapidity $2 < \eta < 4.5$, that have an invariant mass between 60 and 120 GeV. Additionally, one jet originating from the Z vertex with $p_T > 10$ GeV is required and the Z p_T should exceed 10 GeV as well. Events with a second jet satisfying $\frac{p_{T,\text{Next to leading Jet}}}{p_{T,\text{Leading Jet}}} > 0.25$ are rejected.

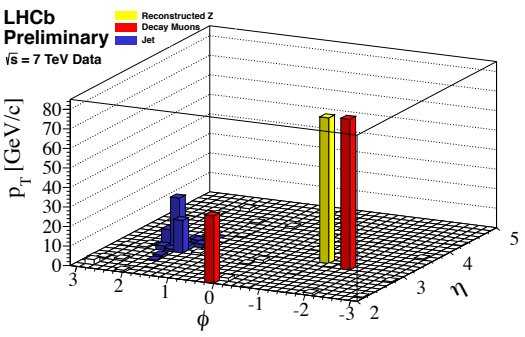

Figure 3: Candidate event of associated production of a Z boson and a jet. ($p_{T,\text{jet}} = 75$ GeV, $p_{T,\mu^+} = 35$ GeV, $p_{T,\mu^-} = 77$ GeV and $m_{\mu^+\mu^-} = 97.1$ GeV)

Figure 4a shows the angle $\Delta\phi$ of to Z and the jet in the transverse plane. There is a clear peak of events being back–to–back. In those events any transverse momentum from the Z boson must be roughly balanced by the jet. Thus the p_T measurement contains information about the jet p_T.

For further studies we require the Z boson to recoil collinearly ($|\Delta\phi(Z, \text{Leading Jet})| < \frac{7\pi}{8}$) against the jet. Figure 4b shows the Z–jet p_T balance. This provides a control sample to study the jet energy scale. Both the mean value and the shape of the distribution are nicely described by the simulation. This means the jet energy correction factors can be extracted from simulation with a small uncertainty.

5 Conclusion and Outlook

LHCb is able to reconstruct jets and to correct their energy to the level of stable particles. This jet reconstruction has extended the LHCb electroweak and QCD programme. A full Z plus jet measurement is now available [3].

References

[1] A. A. Alves, Jr. *et al.* [LHCb Collaboration], JINST **3** (2008) S08005.

[2] R. Aaij *et al.* [LHCb Collaboration] LHCb-CONF-2012-013.

[3] R. Aaij *et al.* [LHCb Collaboration] LHCb-CONF-2012-016.

[4] M. Cacciari, G. P. Salam and G. Soyez, Eur. Phys. J. C **72** (2012) 1896 [arXiv:1111.6097 [hep-ph]].

[5] M. Cacciari, G. P. Salam and G. Soyez, JHEP **0804** (2008) 063 [arXiv:0802.1189 [hep-ph]].

[6] R. Aaij *et al.* [LHCb Collaboration], arXiv:1204.1620 [hep-ex].

[2] With $Z \to \mu\mu$ the contribution of the virtual photon is included in this notation.

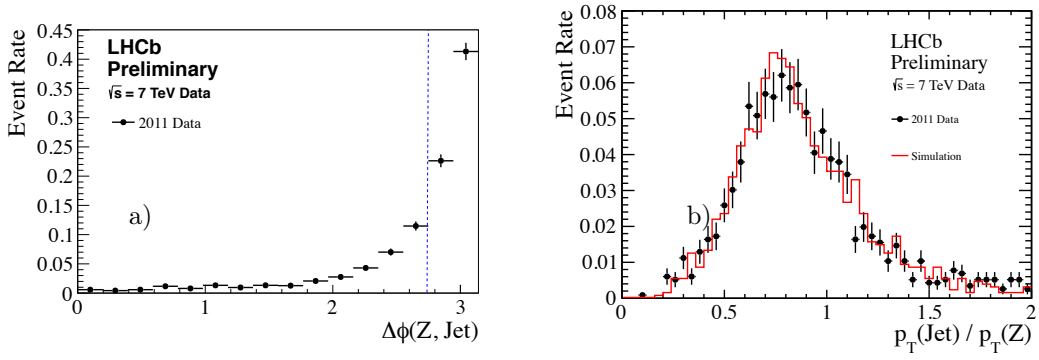

Figure 4: Angle $\Delta\phi$ of the Z and the jet in the transverse plane (a). Events above the dashed line at $7\pi/8$ are considered back to back in this analysis and shown in the Z–jet p_T balance plot (b).

Measurement of Photon Production in the Very Forward Direction in Deep-Inelastic Scattering at HERA

Hamlet Zohrabyan on behalf of the H1 Collaboration

DESY, Notkestraße 85, 22607 Hamburg, Germany

DOI: http://dx.doi.org/10.3204/DESY-PROC-2012-02/58

Recent measurements of the forward photon production in Deep Inelastic Scattering obtained by the H1 Collaboration using the Forward Neutron Calorimeter are presented. Results are compared with Monte Carlo models used in inclusive DIS analyses and with several Cosmic Ray hadronic interaction models.

1 Introduction

Measurements of particle production at very small angles with respect to the proton beam direction (forward direction) in *ep* colisions are important for the theoretical understanding of proton fragmentation. Measurements of forward particle production also provide important constraints for the modeling of the high energy air showers and thereby are very valuable for the understanding of high energy cosmic ray data.
The production of forward photons is studied in deep-inelastic positron-proton scattering (DIS) at HERA [1]. The data are taken with the H1 detector in the years 2006 and 2007 and correspond to an integrated luminosity of 126 pb^{-1}. The analysis covers the kinematic range of negative four momentum transfer squared at the positron vertex $6 < Q^2 < 100$ GeV^2 and inelasticity $0.05 < y < 0.6$. The photons are detected in the Forward Neutron Calorimeter (FNC), which is situated at a polar angle of 0^o at $z = 106m$ from the interaction point. The acceptance of the FNC is defined by the aperture of the HERA beam-line magnets and is limited to scatering angles of $\theta \lesssim 0.8$ mrad, corresponding to the pseudorapidity range $\eta > 7.9$.

2 Forward Photon Spectra in DIS

The measured differential cross sections for the production of very forward photon, normalised to the total inclusive DIS cross sections in the kinematic range defined above, are presented Figures 1 - 3. Figures 1 and 2 show the measurement as a function of longitudinal momentum fraction of the leading photon to the incoming proton, x_L^{lead}, and the transverse momentum of leading photon, p_T^{lead}.

In the Figure 3 the cross section is also presented as a function of the sum of longitudinal momentum fraction x_L^{sum} of all photons in the acceptance of the FNC. Two or more photons entering the FNC are reconstructed as a single cluster due to the relatively large size of the FNC

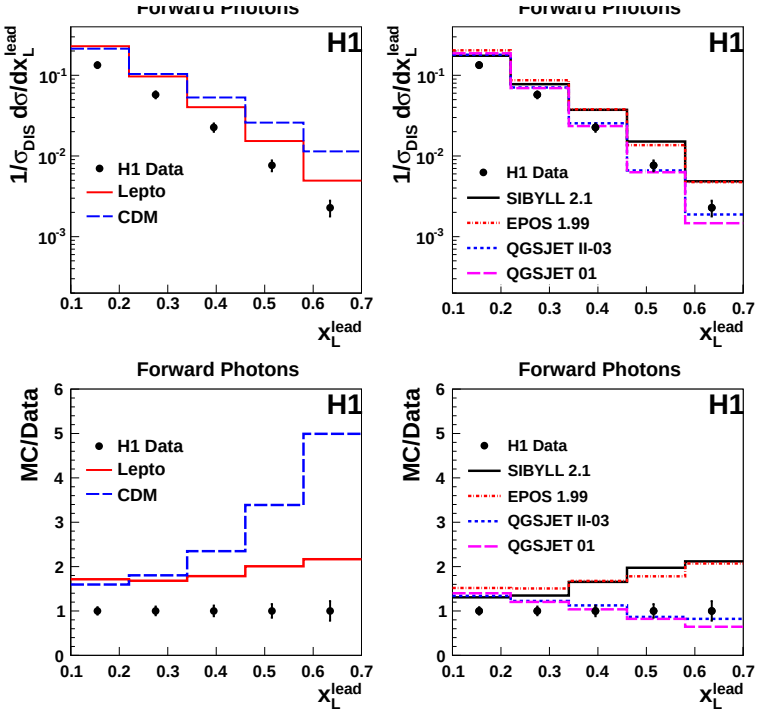

Figure 1: The DIS normalized cross sections for the production of forward photons as a function of x_L^{lead} for the data and the MC model predictions (upper row) and normalised to data distributions (lower row). The left side plots show the comparision with LEPTO and CDM models. The right side plots show the comparision with CR models.

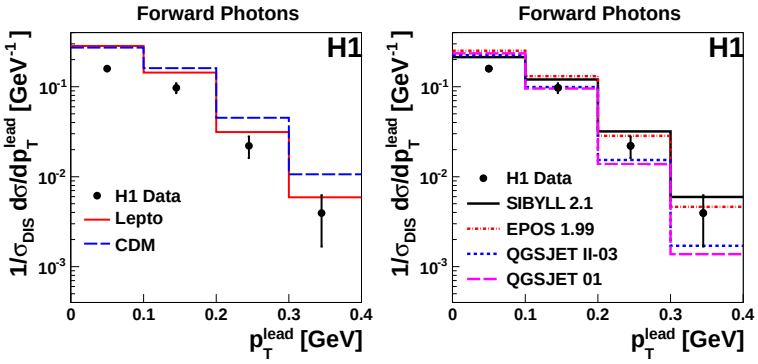

Figure 2: The DIS normalized cross sections for the production of forward photons as a function of p_T^{lead} for the data and the MC model predictions.

readout moduls and the small geometrical acceptance window. According to the Monte Carlo (MC) simulation, low energetic clusters ($x_L < 0.7$) reconstructed in the FNC mainly originate from single photons,while at high energies two or more photons may form a cluster. Therefore,

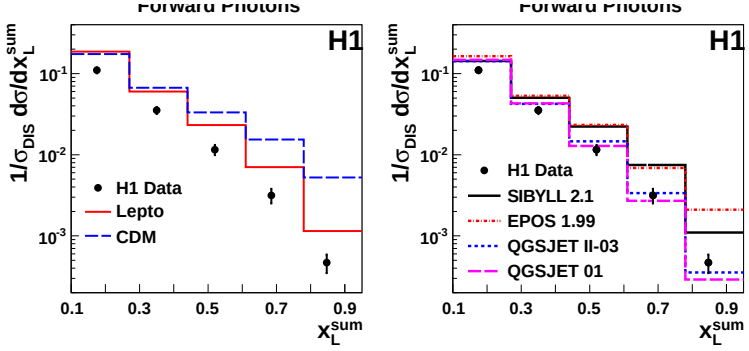

Figure 3: The normalized cross sections for the production of forward photons as a function of x_L^{sum} for the data and the MC model predictions.

the measurement of the cross section of single photon production is limited to $x_L^{lead} < 0.7$, while the measurement of the total forward photon production cross section is extended to larger $x_L^{sum} < 0.95$.

The data are compared with the predictions of different MC models. The DJANGOH [2] program is used to generate inclusive DIS events. Higher order QCD effects are simulated using leading log parton showers as implemented in LEPTO [3], or using the Colour Dipole Model (CDM) as implemented in ARIADNE [4]. The measurements are also compared to the predictions of several hadronic interaction models which are commonly used for the simulation of Cosmic Ray (CR) air shower cascades: EPOS [5], QGSJET 01 [6], QGSJET II [7] and SIBYLL [8].In all these models the main source of forward photons is the $\pi^0 \to 2\gamma$ decay. All models overestimate the total rate of forward photons. The LEPTO and CDM models predict by about 70% more photons than are measured, while the CR models (EPOS, SIBILL and QGSJET) overestimate the rate of photons by about $30 - 50\%$. The shapes of all measured distributions are well described by LEPTO. The CDM predicts harder x_L and p_T spectra. The QGSJET models overestimate the measured cross sections by about 40% at lowest x_L and p_T, but are consistent with the data within the experimental uncertainties elsewhere. The EPOS and SIBYLL models predict harder x_L spectra, but describe reasonably well the shape of the p_T distribution.

3 Fraction of DIS events with forward photon

The measurement of forward photons allows a test of the limiting fragmentation hypothesis, which implies that the production of forward photons in DIS is insensitive to Q^2 and the Bjorken x variable, x_{Bj}. To investigate this prediction, the ratio of the forward photon production cross section to the inclusive DIS cross section is studied as a function of Q^2 and x_{Bj} (Figure 4).

Within the uncertainties the fraction of DIS events with photons is independent from Q^2 and x_{Bj}. The LEPTO and CDM models display significant differences in normalization compared to the data as well as slight dependences as a function of Q^2 and x_{Bj}.

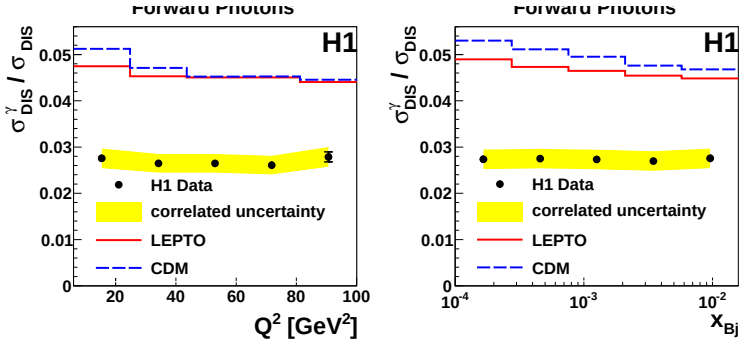

Figure 4: Fraction of the DIS events with the forward photons as a function of Q^2 and x_{Bj}

4 Summary

The production of forward photons has been studied in DIS positron-proton scattering in the kinematic region $6 < Q^2 < 100$ GeV^2, $0.05 < y < 0.6$ in the pseudorapidity rang $\eta > 7.9$. The DIS normalized cross sections are presented for the production of the most energetic photons as a function of the longitudinal momentum fraction in the range $0.1 < x_L^{lead} < 0.7$ and transverse momentum p_T^{lead} and as a fraction of the sum of all forward photons in the range $0.1 < x_L^{sum} < 0.95$. The predictions of Monte Carlo models overestimate the rate of photons. LEPTO describe the shapes well, while CDM predict harder spectra for x_L and p_T. The measurements also compared with CR models commonly used for simulation of air shower cascades. None of them can describe the data in rate and in shape. Within the measured kinematic range, the relative rate of forward photons in DIS events is observed to be independent of Q^2 and x_{Bj}, in agreement with the hypothesis of limiting fragmentation.

The measurements may lead to further understanding of proton fragmentation and can be used for model tuning.

References

[1] F.D.Aaron et al.[H1 Collaboration], Eur.Phys.J. **C71** (2011) 1771 [arXiv:1106.5944]

[2] K.Charchula,G.A.Schuler and H.Spiesberger, DJANGOH 1.4, Comput.Phys.Commun. 81, 381 (1994)

[3] G.Ingelman, A.Edin and J.Rathsman, LEPTO 6.5, Comput.Phys.Commun. 101 (1997) 108 [hep-ph/9605286]

[4] L.Lonnblad, ARIADNE 4.10, Comput.Phys.Commun. 71 (1992) 15

[5] K.Werner,F.-M.Liu and T.Pierog, Phys.Rev. **C74** (2006) 044902 [hep-ph/0506232]

[6] N.N.Kalmykov, S.S.Ostapchenko, A.I.Pavlov, Nucl.Phys.Proc.Suppl.52B (1997) 17

[7] S.S.Ostapchenko, AIP Conf.Proc. 928 (2007) 118 [arXiv:0706.3784]

[8] E.-J.Ahn et al., Phys.Rev. **D80** (2009) 094003 [arXiv:0906.4113]

Measurement of the Azimuthal Correlation between the most Forward Jet and the Scattered Positron in Deep-Inelastic Scattering at HERA

Lidia Goerlich on behalf of the H1 Collaboration

Institute of Nuclear Physics PAN, Radzikowskiego 152, 31-342 Kraków, Poland

DOI: http://dx.doi.org/10.3204/DESY-PROC-2012-02/59

Deep-inelastic positron-proton scattering events at low Q^2 with a forward jet, produced at small angles with respect to the proton beam, are measured with the H1 detector at HERA. A subsample of events with an additional jet in the central region is also studied. For both samples differential cross sections and normalised distributions are measured as a function of the azimuthal angle difference, $\Delta\phi$, between the forward jet and the scattered positron in bins of the rapidity distance, Y, between them. The data are used to discriminate between QCD models with different parton evolution schemes.

1 Introduction

The HERA *ep* collider has extended the available kinematic range for deep-inelastic scattering (DIS) to regions of the Bjorken scaling variable, x, as small as 10^{-5} at moderate Q^2 of a few GeV^2. At low x a parton in the proton can induce a QCD cascade before an interaction with the virtual photon. Several perturbative QCD-based approaches are available to describe the dynamics of the parton evolution process. In the standard DGLAP evolution [1] partons emitted in the cascade are strongly ordered in transverse momentum, k_T, measured with respect to the proton direction. At small values of x a transition is expected from DGLAP to BFKL dynamics [2] in which there is no ordering in k_T of the partons along the ladder.

Measurements of DIS events with energetic jets of high transverse momentum produced close to the proton direction in the laboratory frame, referred to as the forward region, are considered to be especially sensitive to the QCD dynamics at low x [3]. The distribution of the azimuthal angle difference, $\Delta\phi$, between the forward jet and the scattered electron may show sensitivity to the underlying physics in the evolution of the parton cascade [4]. In this talk the study of the H1 Collaboration on the azimuthal correlation between the forward jet and the scattered positron in DIS at low x is presented [5].

2 QCD calculations

The measurements presented are compared with predictions of Monte Carlo (MC) generators which implement various QCD models. RAPGAP [6], labeled DGLAP, matches first order QCD matrix elements to DGLAP based leading-log parton showers with k_T ordering. The

factorisation and renormalisation scales are set to $\mu_f = \mu_r = \sqrt{Q^2 + p_{\mathrm{T}}^2}$, where p_{T} is the transverse momentum of the two outgoing hard partons in the centre-of-mass of the hard subsystem. DJANGO/ARIADNE is an implementation of the Colour Dipole Model (CDM) [7] in which the parton emissions perform a random walk in k_T such that CDM provides a BFKL-like approach. CASCADE [8] uses off-shell QCD matrix elements, supplemented with gluon emissions based on the CCFM evolution [9] which aims to unify the DGLAP and BFKL approaches. In this analysis two different sets of unintegrated gluon density (uPDF) are used: set A0 with only singular terms of the gluon splitting function and J2003-set 2 including also non-singular terms.

The data are also compared to the fixed order NLO DGLAP predictions of the NLOJET++ program [10] used here to calculate dijet production at parton level in DIS at NLO(α_S^2) accuracy. The parton level cross sections are corrected for hadronisation effects using the RAPGAP model.

3 Results

The data used in this work were collected with the H1 detector in 2000 and correspond to an integrated luminosity of 38.2 pb^{-1}. The analysis phase space is restricted in Q^2, x and inelasticty y: $5 < Q^2 < 85$ GeV^2, $0.0001 < x < 0.004$, $0.1 < y < 0.7$.

Jets are identified using the k_T cluster algorithm in the Breit frame. Events with at least one forward jet satisfying the following cuts in the laboratory frame are selected: $P_{\mathrm{T,fwdjet}} > 6$ GeV, $1.73 < \eta_{\mathrm{fwdjet}} < 2.79$, $x_{\mathrm{fwdjet}} = E_{fwdjet}/E_p > 0.035$ and $0.5 < P^2_{\mathrm{T,fwdjet}}/Q^2 < 6$. Here η_{fwdjet} is the pseudorapidity of the forward jet.

The last two cuts aim to enhance the effects of BFKL dynamics and suppress the standard DGLAP evolution. If more than one jet satisfies these criteria then the jet with the largest pseudorapidity is chosen.

The forward jet cross section $d\sigma/d\Delta\phi$ as a function of the azimuthal angle difference $\Delta\phi$ between the most forward jet and the scattered positron is shown in Figure 1 for three intervals of the positron-jet rapidity distance Y, defined as $Y = \ln(x_{\mathrm{fwdjet}}/x)$. At higher values of Y the forward jet is more decorrelated from the scattered positron. The predictions of three QCD-based models with different underlying parton dynamics are compared with the data. The cross sections are well described in shape and normalisation by CDM which has a BFKL-like approach. Predictions of RAPGAP, which implements DGLAP

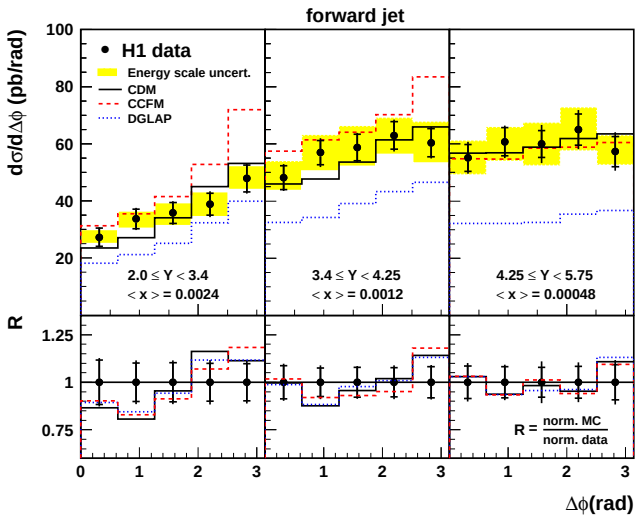

Figure 1: Differential forward jet cross section as a function of $\Delta\phi$ in three intervals of Y compared with the predictions of different QCD-based models. The systematic error due to the uncertainty of the hadronic energy scale is shown as a bound around the data points.

evolution, fall below the data, particularly at large Y. Calculations in the CCFM scheme as implemented in CASCADE using the uPDF set A0 overestimate the measured cross section for large $\Delta\phi$ values in the two lowest Y intervals. However, this model provides as good a description as CDM of the data in the highest Y interval.

In the lower part of Figure 1 the shape of the $\Delta\phi$ distributions, $1/\sigma \cdot d\sigma/d\Delta\phi$, is compared to the different MC predictions. The ratio R of MC to data for normalised cross sections is shown. The ratio plots show that in the analysed phase space region the shape of the $\Delta\phi$ distributions is well described by all MC models and this observable alone cannot discriminate between different QCD dynamics.

Predictions of the CCFM model presented in Figure 2 indicate a significant sensitivity to the choice of the uPDF. The set A0 is the same as in the previous figure. Predictions using J2003-set 2, marked set 2, do not describe the data in normalisation especially at high Y and in shape especially at low Y.

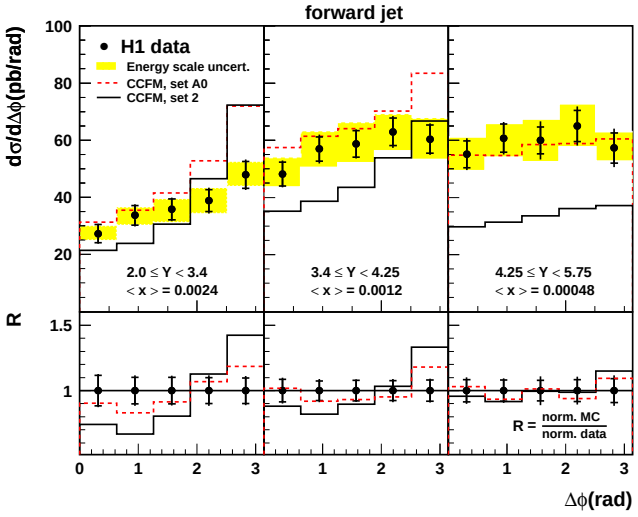

Figure 2: Differential forward jet cross section as a function of $\Delta\phi$ in three intervals of Y compared to the predictions of CASCADE(CCFM) with two different uPDF.

Comparison of the measured $\Delta\phi$ distributions with NLO DGLAP predictions is shown in Figure 3.

Large theoretical uncertainties of up to 50% from the variation of factorisation and renormalisation scales are observed indicating that in this phase space region higher order contributions are expected to be important.

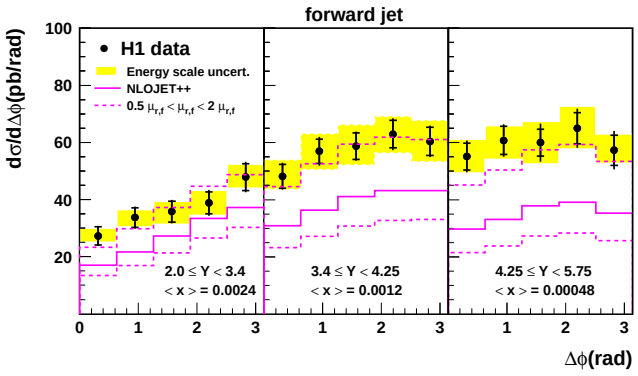

Figure 3: Differential forward jet cross section as a function of $\Delta\phi$ compared to NLO QCD predictions.

The cross section $d\sigma/dY$ as a function of the rapidity separation Y is shown on Figure 4. The data are best described by the BFKL-like CDM model. The DGLAP predictions fall below the data, but approach them at small Y. The predictions of the CCFM model are above the data at small Y but describe them well at larger Y.

A subsample of events with an additional jet in the central region of the laboratory frame is also studied. The central jet is

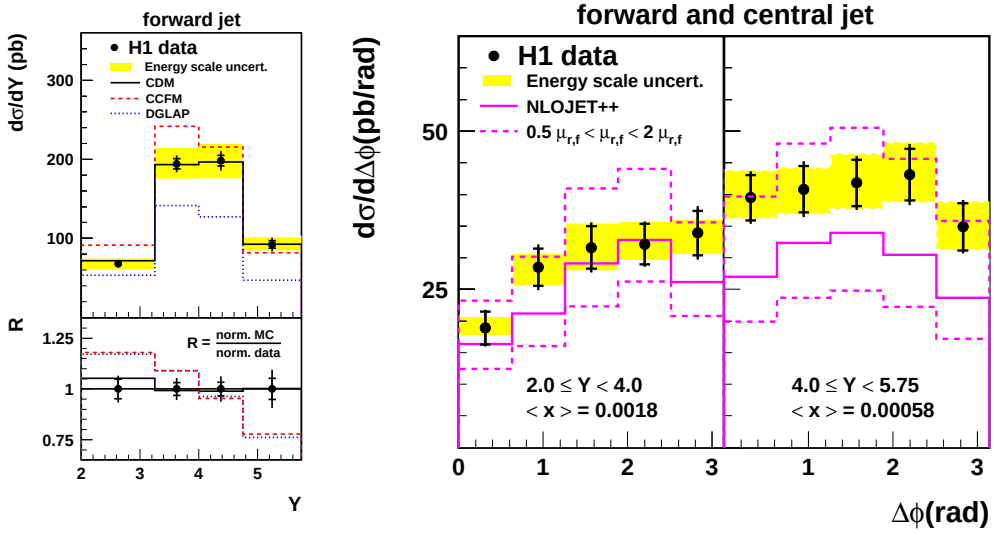

Figure 4: Differential forward jet cross section as a function of Y (left plot) and differential forward and central jet cross section as a function of $\Delta\phi$ in two intervals of Y (right plot).

selected with $P_{\mathrm{T,cenjet}} > 4$ GeV, in the region $-1 < \eta_{\mathrm{cenjet}} < 1$ and with a large rapidity separation from the most forward jet $\Delta\eta = (\eta_{\mathrm{fwdjet}} - \eta_{\mathrm{cenjet}}) > 2$. The measured $\Delta\phi$ distributions are compared with NLO DGLAP predictions on the right side of Figure 4. The NLO calculation provides a reasonable description of the data at low Y, at high Y it is below the data, but within the large theoretical uncertainty.

In summary, measurements of the cross sections as a function of $\Delta\phi$ and Y are best described by the BFKL-like CDM model, while the DGLAP model is substantially below the data. The CCFM model provides a reasonable description of the data but shows sizeable sensitivity to the unintegrated gluon density. The shape of the $\Delta\phi$ distributions does not discriminate further between different evolution schemes. The fixed order NLO DGLAP predictions are in general below the data, but still in agreement within the large theoretical uncertainties.

References

[1] G. Altarelli and G. Parisi. Nucl. Phys. **B126** (1977) 298.

[2] E. Kuraev, L. Lipatov and V. Fadin. Sov. Phys. JETP **45** (1977) 199.

[3] A. H. Mueller. Nucl. Phys. B, Proc. Suppl. **18C** (1990) 125.

[4] J. Bartels *et al.* Phys. Lett. **B384** (1996) 300.

[5] H1 Collab., F. D. Aaron *et al.*, Eur. Phys. J. **C72** (2012) 1910.

[6] H. Jung. Comput. Phys. Commun. **86** (1995) 147.

[7] L. Lönnblad. Comput. Phys. Commun. **71** (1992) 15.

[8] H. Jung. Comput. Phys. Commun. **143** (2002) 100.

[9] S. Catani, F. Fiorani and G. Marchesisni. Nucl. Phys. **B336** (1990) 18.

[10] Z. Nagy and Z. Trocsanyi. Phys. Lett. **87** (2001) 82001.

Parton shower contributions to jets from high rapidities at the LHC

M. Deák[1], *F. Hautmann*[2], *H. Jung*[3,4], *K. Kutak*[5]

[1]Universidade de Santiago de Compostela, E-15782 Santiago de Compostela
[2]Theoretical Physics, University of Oxford, Oxford OX1 3NP
[3]Deutsches Elektronen Synchrotron, D-22603 Hamburg
[4]CERN, Physics Department, CH-1211 Geneva 23
[5]Instytut Fizyki Jadrowej im H. Niewodniczanskiego, PL 31-342 Krakow

DOI: http://dx.doi.org/10.3204/DESY-PROC-2012-02/271

We discuss current issues associated with the dependence of jet distributions at the LHC on the behavior of QCD parton showers for high rapidities.

At the LHC, due to the phase space opening up at high center-of-mass energy, hadronic jets are accessed for the first time in a region sensitive to contributions of high rapidities [1], in which the forward kinematics forces the hard process into a regime characterized by multiple hard scales [2]. In this multi-scale region the production cross section is affected by high-energy logarithmically-enhanced corrections to all orders in the strong coupling, requiring resummation methods [3] to go beyond finite-order perturbation theory. Moreover, with increasing center-of-mass energies and rapidities the nonperturbative parton distributions are probed for smaller longitudinal momentum fractions. This implies that effects on jet distributions from multiple parton collisions [4] become more pronounced [5] due to the increase in the parton density.

Measurements of inclusive jet production are being carried out at the LHC [6, 7] over a kinematic range in transverse momentum and rapidity much larger than at the Tevatron and previous colliders. Comparisons with standard model theoretical predictions are based either on next-to-leading-order (NLO) QCD calculations, supplemented with nonperturbative (NP) corrections [6, 7] estimated from Monte Carlo event generators, or on NLO-matched parton shower event generators of the kind described in [8].

This article considers effects of QCD parton showers on jet production for increasing rapidity. As discussed in [2, 9] such multi-scale processes are sensitive to effects of the finite transverse-momentum tail of QCD multi-parton matrix elements. The theoretical framework to take these effects into account is based on using partonic matrix element and initial-state distributions unintegrated in both longitudinal and transverse momenta [10, 11, 12]. On the other hand, in NLO event generators finite-$k_\perp$ terms are taken into account only partially, through the higher-order correction at fixed α_s order. Parton shower generators based on collinear evolution, which are either matched to NLO calculations [8] or used to extract the NP corrections [6, 7], do not include finite-$k_\perp$ terms, as these terms correspond to modifications to angular or transverse-momentum ordering [10, 11, 12]. In what follows we illustrate parton showering effects using three Monte Carlo event generators: the $k_\perp$-shower CASCADE generator [13], the NLO matched POWHEG generator [14], and PYTHIA shower Monte Carlo [15], used in two different modes: with

the tune P1 [15] including multiple parton collisions, and with single parton collision (PYTHIA-nompi). As emphasized in [16], effects coming from noncollinear multi-parton emission influence jets at large rapidities as well as jets produced centrally but in association with observed forward final states.

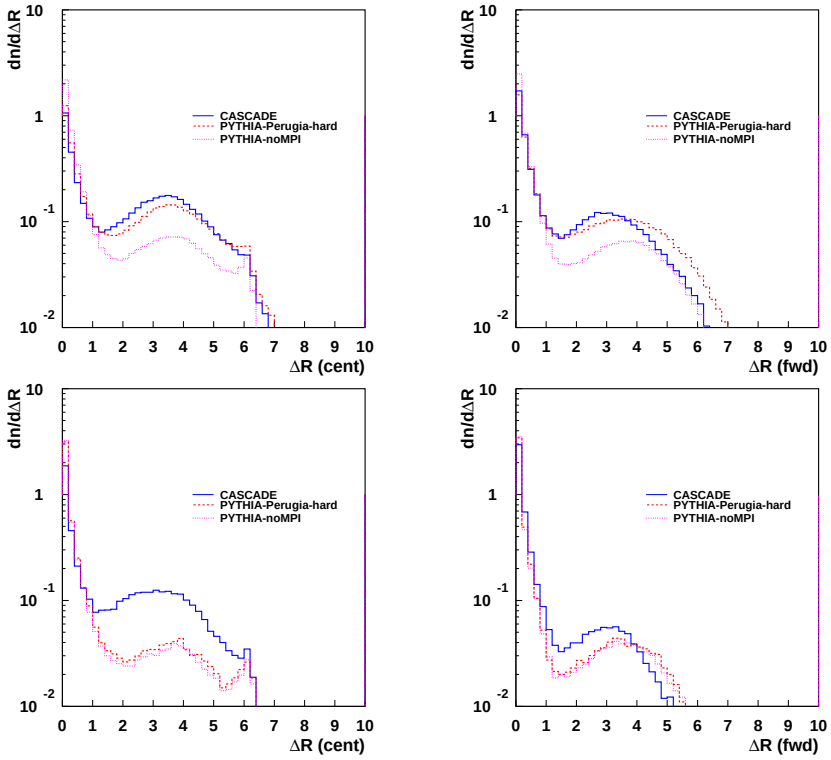

Figure 1: ΔR distribution of central ($|\eta_c| < 2$, left) and forward jets ($3 < |\eta_f| < 5$, right) for $E_T > 10$ GeV (upper row) and $E_T > 30$ GeV (lower row) [16]. The curves correspond to the $k_\perp$-shower Monte Carlo generator CASCADE and to the PYTHIA shower Monte Carlo generator used in two modes, one in which multiple parton interactions are included and one in which they are switched off.

In Fig. 1 we consider final states associated with production of a forward and a central jet [16] reconstructed via the Siscone algorithm [17] ($R = 0.4$) and report the $\Delta R = \sqrt{\Delta\phi^2 + \Delta\eta^2}$ distribution, where $\Delta\phi = \phi_{jet} - \phi_{part}$ ($\Delta\eta = \eta_{jet} - \eta_{part}$) is the azimuthal (rapidity) difference between the jet and the corresponding parton from the matrix element. This distribution probes to what extent jets are dominated by hard partons in the matrix element or originate from the showering. The large-ΔR region, corresponding to sizeable contributions to jets from showers, is seen to be enhanced by noncollinear corrections. While this effect can be also produced by multi-parton interactions for low E_T jets, this no longer applies as E_T increases. It is noteworthy that as a consequence of high-rapidity correlations the enhanced dependence of jet distributions on features of the parton showers is especially pronounced for central jets.

In Fig. 2 this issue is examined using the NLO event generator POWHEG matched with parton showers PYTHIA and HERWIG. We show the central jet transverse energy spectrum

for the two cases, normalized to the result obtained by switching off parton showering. The marked differences between the two cases are consistent with the findings in [18], and with the large contribution to jets from showering indicated by Fig. 1. In particular this suggests that high-rapidity correlations affect the behavior of jet distributions in the central region.

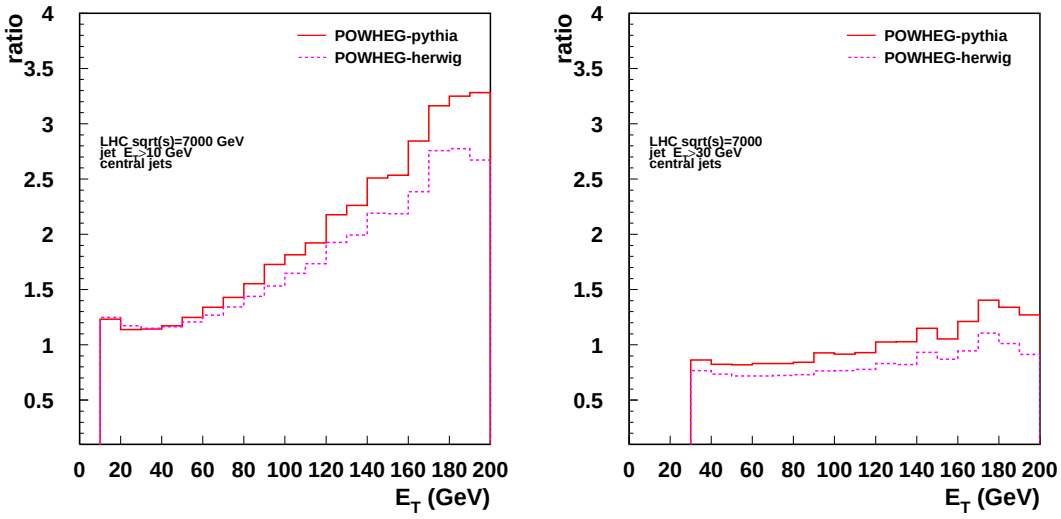

Figure 2: Ratio of central jet transverse energy spectra from the NLO-matched Monte Carlo generator POWHEG, interfaced with PYTHIA and HERWIG parton showers, to the no-showering result. (left) $E_T > 10$ GeV; (right) $E_T > 30$ GeV.

We observe that while first measurements of forward jet spectra [18] are roughly in agreement with Monte Carlo simulations, detailed aspects of production rates and correlations [18, 19] are not well understood yet. Also, hadronic event shapes measured at the LHC [20] suggest that parton showering effects dominate contributions of hard matrix elements evaluated at high multiplicity. The numerical results [16] for the large rapidity region underline especially the significance of contributions to showering from transverse momentum dependent branching [21] and parton distributions [22]. This region is relevant to many aspects of LHC physics, including studies of jets from decays of highly boosted new particles [23], new particle searches using vector boson fusion channels [24], relationship of forward particle production and cosmic ray physics [25], high-density QCD and heavy ion collisions [26]. The treatment in terms of unintegrated distributions may in particular be useful to investigate effects of gluon rescattering [27] within parton branching approaches.

Acknowledgments. We thank the conveners for the invitation and excellent organization of the meeting.

References

[1] S. Baranov et al., in Z. Ajaltouni et al., Proc. *HERA and the LHC*, arXiv:0903.3861 [hep-ph] (CERN/DESY 2008).

[2] M. Deak, F. Hautmann, H. Jung and K. Kutak, JHEP **0909** (2009) 121; arXiv:0908.1870.

[3] S. Catani, M. Ciafaloni and F. Hautmann, Nucl. Phys. B**366** (1991) 135.

[4] N. Paver and D. Treleani, Nuovo Cim. **A**70 (1982) 215.

[5] P. Bartalini and L. Fanò (eds.), arXiv:1003.4220 [hep-ex], Proc. 1st Workshop on Multiple Parton Interactions (Perugia, 2008); P. Bartalini et al., arXiv:1111.0469 [hep-ph].

[6] ATLAS Coll. (G. Aad et al.), arXiv:1112.6297 [hep-ex].

[7] CMS Coll., preprint CMS PAS QCD-11-004.

[8] P. Nason and B.R. Webber, arXiv:1202.1251 [hep-ph].

[9] F. Hautmann and H. Jung, JHEP **0810** (2008) 113.

[10] G. Marchesini and B.R. Webber, Nucl. Phys. **B386** (1992) 215.

[11] M. Ciafaloni, Nucl. Phys. B**296** (1988) 49.

[12] S. Catani et al., Phys. Lett. B**242** (1990) 97; Nucl. Phys. B Proc. Suppl. **29A** (1992) 182; Phys. Lett. B**307** (1993) 147; S. Catani and F. Hautmann, Phys. Lett. B**315**(1993)157; Nucl. Phys. B**427** (1994) 475.

[13] H. Jung et al., Eur. Phys. J. C **70** (2010) 1237.

[14] S. Alioli, P. Nason, C. Oleari and E. Re, JHEP **1104** (2011) 081.

[15] P. Skands, Phys. Rev. D**82** (2010) 074018.

[16] M. Deak, F. Hautmann, H. Jung and K. Kutak, arXiv:1012.6037 [hep-ph]; arXiv:1112.6386 [hep-ph]; Eur. Phys. J. C **72** (2012) 1982; arXiv:1206.1745 [hep-ph].

[17] M. Cacciari and G.P. Salam, Phys. Lett. B **641** (2006) 57; M. Cacciari, G.P. Salam and G. Soyez, http://fastjet.fr; G.P. Salam and G. Soyez, JHEP **0705** (2007) 086.

[18] CMS Coll. (S. Chatrchyan et al.), JHEP **1206** (2012) 036.

[19] ATLAS Coll. (G. Aad et al.), JHEP **1109** (2011) 053; CMS Coll. (S. Chatrchyan et al.), arXiv:1204.0696 [hep-ex].

[20] CMS Coll. (V. Khachatryan et al.), Phys. Lett. B**699** (2011) 48.

[21] F. Hautmann and H. Jung, arXiv:0712.0568; arXiv:0808.0873; arXiv:1206.1796; F. Hautmann, Acta Phys. Polon. B **40** (2009) 2139; F. Hautmann, M. Hentschinski and H. Jung, arXiv:1205.6358 [hep-ph].

[22] F. Hautmann, Phys. Lett. B**655**(2007)26; arXiv:0708.1319; Nucl. Phys. B**604**(2001)391; hep-ph/0011381; hep-ph/0101006; J.C. Collins and F. Hautmann, JHEP **0103** (2001) 016; Phys. Lett. B**472** (2000) 129.

[23] A. Altheimer et al., arXiv:1201.0008 [hep-ph].

[24] CMS Coll. (S. Chatrchyan et al.), Phys. Lett. B**713** (2012) 68; Phys. Lett. B**710** (2012) 403; ATLAS Coll. (G. Aad et al.), Phys. Rev. Lett. **108** (2012) 111803; arXiv:1206.5971 [hep-ex].

[25] M. Grothe et al., arXiv:1103.6008 [hep-ph].

[26] D. d'Enterria, arXiv:0911.1273 [hep-ex].

[27] F. Hautmann and D.E. Soper, Phys. Rev. D**75** (2007) 074020; Phys. Rev. D**63** (2000) 011501; F. Hautmann et al., hep-ph/9906284; hep-ph/9806298; F. Hautmann, Phys. Lett. B**643** (2006) 171.

Probing colour flow with jet vetoes

Simone Marzani

Institute for Particle Physics Phenomenology, Durham University,
Durham DH1 3LE, United Kingdom

DOI: `http://dx.doi.org/10.3204/DESY-PROC-2012-02/264`

We discuss jet vetoes as a means of probing colour flow in hard-scattering processes in hadronic collisions. As an example, we describe a calculation of the dijet cross-section with a jet veto, which resums the leading logarithms of the veto scale and is matched to a fixed-order computation. We compare this prediction to the measurement performed by the ATLAS collaboration. Finally, we outline future developments in this research area.

1 Introduction

The phenomenology of strong interactions and, in particular, jet physics are playing a central role in the physics program during these first years of the LHC [1, 2, 3, 4, 5, 6, 7, 8]. In the basic picture of perturbative QCD, hard partons are produced in high-energy collisions and hadronise into colour-neutral particles, which are typically highly collimated into jets. In reality, QCD provides us with a much richer picture, which potentially leads to interesting phenomenology. Studies of inter-jet radiation and colour connections between jets can unveil non-trivial information about the underlying hard-scattering process. Beyond their own interest as pure QCD effects, these correlations play an important role in many analyses and can be used, for instance, to reduce overwhelming backgrounds.

Jet vetoes appear often in particle physics analyses as tool to keep jet multiplicity fixed. They can also be used to select or suppress certain contributions in specific processes, such as Higgs production in association with two jets, where one can enhance the vector-boson-fusion (VBF) component with respect to the gluon-gluon fusion (GF) one by applying a central jet veto [9].

Jet vetoes can also be used a means to probe the colour structure of hard processes. For instance, in Refs. [10, 11], the problem of identifying the colour of a heavy resonance decaying into a $t\bar{t}$ pair was considered. Clearly, the radiation emitted by this new particle depends on its colour charge. However, this poses difficulties, since the amount of relatively soft radiation is heavily influenced by the underlying event. One can instead study the response of such radiation to the presence of a jet veto and, if the veto scale Q_0 is kept large enough, one can minimise contaminations from non-perturbative physics.

Another interesting analysis [12] suggests studying the cross-section as function of the veto scale for associated Higgs production with two jets and a jet veto, in order to simultaneously determine the effective coupling of Higgs to the gluons and to the vector bosons. This analysis shows that the biggest theoretical uncertainty comes from the Q_0 dependence of the GF channel.

If jet vetoes are to be used to extract information on the colour flow of hard processes,

possibly involving new physics, the Q_0 dependence needs to be under good theoretical control. Unfortunately, performing accurate predictions in perturbative QCD in the presence of jet-vetoes is far from trivial: large logarithms of the ratio of veto scale over the hard scale of the process Q_0/Q contaminate the perturbative expansion and they need to be resummed to all orders (for recent theoretical work see, for instance, Refs. [13, 14]). Moreover, if the veto is applied only in given regions of phase-space, the observable becomes non-global and the resummation more complex [15]. Monte Carlo parton showers are often used in these studies, but they neglect sub-leading N_c terms, so a better theoretical treatment is needed.

We start by considering the simplest process, i.e. dijets events, with a veto on the emission of additional radiation in the inter-jet region. This measurement has already been performed [3], so we have been able to use data to validate our theoretical predictions [16, 17].

2 The dijet cross-section with a jet veto

We are interested in dijet production in proton-proton collisions at $\sqrt{S} = 7$ TeV, where we veto the emission of a third jet with transverse momentum bigger than Q_0 in the rapidity region between the two jets. The veto scale is chosen to be $Q_0 = 20$ GeV. We define the gap fraction as the ratio of the cross-section for this process over the inclusive rate:

$$f^{\text{gap}} = \frac{\mathrm{d}^2\sigma^{\text{gap}}}{\mathrm{d}Q\mathrm{d}\Delta y} \Big/ \frac{\mathrm{d}^2\sigma}{\mathrm{d}Q\mathrm{d}\Delta y}; \tag{1}$$

clearly, in the Born approximation, every event is a gap event and so $f^{\text{gap}} = 1$. Beyond the Born approximation, the leading jets are no longer balanced in transverse momentum. We choose Q as the mean of the transverse momenta of the leading jets. This choice, in contrast for instance to the transverse momentum of the leading jet, is more stable under the inclusion of radiative corrections. The rapidity separation Δy is measured from the centres of the leading jets.

The technique for resumming logarithms of the ratio Q/Q_0 for the gaps-between-jets cross section has been known for quite a long time, see for instance [18, 19, 20]. The observable we are studying is non-global and for this reason "in-gap" virtual corrections are not enough to capture the single logarithmic accuracy. Radiation outside the gap is forbidden to re-emit back into the gap, inducing non-global logarithms [15]. Currently, these contributions can be resummed only in the large N_c approximation. Here, instead, we adopt a different approach: we keep the full colour structure but we expand in the number of gluons, real or virtual, outside the gap; it was argued in [16] that this way of proceeding is a reasonable one. We resum the contributions arising from allowing zero and one gluons outside the gap:

$$\frac{\mathrm{d}^2\sigma^{\text{gap}}_{\text{res}}}{\mathrm{d}Q\mathrm{d}\Delta y} = \frac{\mathrm{d}^2\sigma^{(0)}}{\mathrm{d}Q\mathrm{d}\Delta y} + \frac{\mathrm{d}^2\sigma^{(1)}}{\mathrm{d}Q\mathrm{d}\Delta y} + \dots \tag{2}$$

The first contribution to this expansion is obtained by considering the original four-parton matrix element, dressed by in-gap virtual gluons, with transverse momenta above Q_0. No out-of-gap gluons are included. The resummed partonic cross section has the form

$$|\mathcal{M}^{(0)}|^2 = \text{tr}\left(H e^{-\xi(Q_0,Q)\Gamma^\dagger} e^{-\xi(Q_0,Q)\Gamma}\right), \quad \text{with} \quad \xi(k_1,k_2) = \frac{2}{\pi}\int_{k_1}^{k_2}\frac{dk_t}{k_t}\alpha_s(k_t), \tag{3}$$

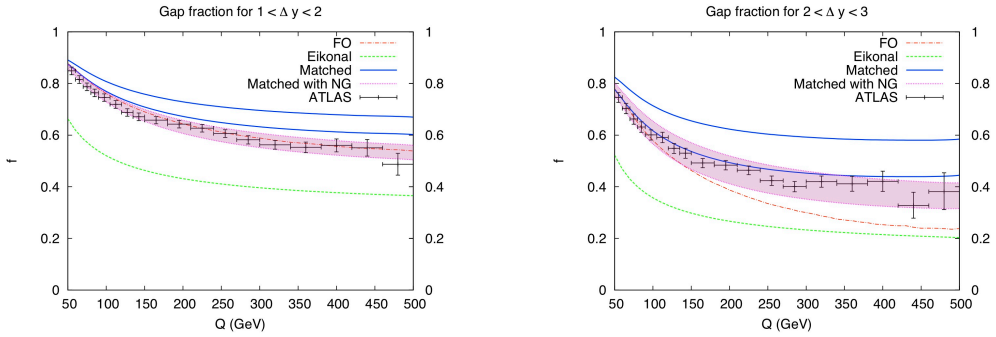

Figure 1: The matched gap fraction as a function of the transverse momentum Q in different rapidity bins.

where H is a matrix describing the hard-scattering and Γ is the soft anomalous dimension matrix, which describes the evolution of a four-parton system. We also aim to resum the non-global logarithms that arise as a result of allowing one soft gluon outside the rapidity gap. The general framework in which this calculation is performed is described in [19, 20]. We must now consider both real (Ω_R) and virtual (Ω_V) corrections to the four-parton scattering, each dressed with any number of soft gluons:

$$|\mathcal{M}^{(1)}|^2 = -\frac{2}{\pi}\int_{Q_0}^{Q}\frac{dk_t}{k_t}\alpha_s(k_t)\int_{\text{out}}(\Omega_R+\Omega_V)\ . \tag{4}$$

In the case that the out-of-gap gluon is virtual, the subsequent evolution is still given by Γ; in the case of real emission, we have to consider the colour evolution of a five parton system. It has been shown [19, 20] that QCD coherence is violated in this process at sufficiently high perturbative orders, because of Coulomb gluon exchange. As a consequence super-leading logarithms originate when the out-of-gap gluon becomes collinear with one of the initial-state partons. This affects the gap fraction at $O(\alpha_s^4)$ and beyond. The numerical impact of these contributions has been studied in [16] and was found to be generally modest.

One of the findings of Ref. [16] was that the gap fraction is under-estimated when it is computed purely with soft gluon techniques. In the eikonal approximation energy-momentum is not conserved and there is no recoil of the hard lines against the emissions, which are considered soft. Emissions of "soft" gluons with $k_t \gtrsim Q_0$ do not cost any energy and if they end up in the rapidity region between the leading jets, they spoil the gap. Thus, a pure eikonal calculation tends to produce too small a gap fraction. The result can be improved by matching to a fixed order calculation. We have performed the leading-order (LO) matching to the full $2 \to 3$ tree-level matrix elements in Ref. [17], where we have also approximately taken into account energy-momentum conservation in the resummation by shifting the argument x of the parton distribution functions.

The plots in Figs. 1 and 2 show the gap fraction as a function of Q in four different rapidity bins. The black crosses are the data points measured by the ATLAS collaboration [3] with the

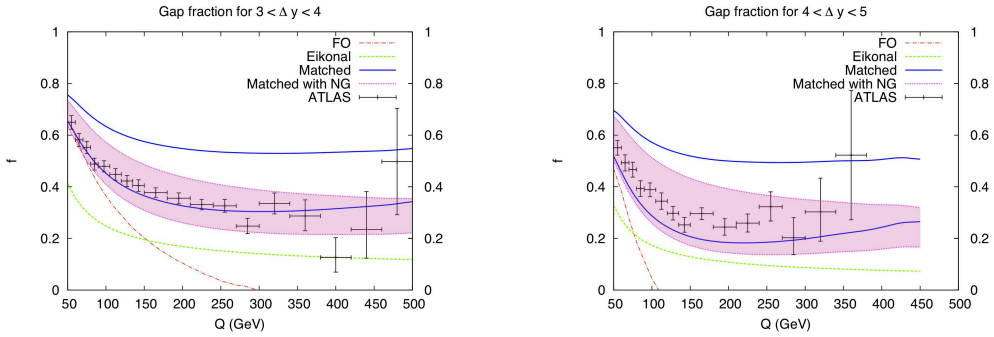

Figure 2: The matched gap fraction as a function of the transverse momentum Q in different rapidity bins.

gap defined by the two highest p_T jets. The LO calculation (dash-dotted red line) is clearly only sensible in the first rapidity bin and for $\Delta y > 2$, it decreases very rapidly as a function of Q and eventually becomes negative. This unphysical behaviour is driven by a large logarithmic term $\sim \alpha_s \Delta y \ln \frac{Q}{Q_0}$, which needs to be resummed. The eikonal resummation (dashed-green line) restores the physical behaviour but, as we have previously discussed, completely ignores the issue of energy-momentum conservation and produces too small a gap fraction. Our matched curves (blue band), with the inclusion of non-global logarithms (magenta band), do seem to capture most of the salient physics. However, our results are affected by large theoretical uncertainties due to the fact that the calculation is accurate only at the leading logarithmic level.

3 Conclusion and Outlook

We have discussed jet vetoes as a probe of colour flow in hard scatterings. Perturbative choices for the veto scale Q_0 reduce the influence of the underlying event and yield good agreement between the dijet data and resummed perturbation theory, although theoretical predictions are affected by large uncertainties. Nevertheless, the situation can be improved by matching to NLO [21].

Having validated the theoretical framework with a process with a relatively simple final state, our interest now lies in exploring more complicated processes, within and beyond the Standard Model. The ATLAS collaboration have recently measured the $t\bar{t}$ cross-section in the presence of a jet veto [22]. The process $Z + 2\,\text{jets} + \text{veto}$ is also interesting [23] and we plan to study this in the near future as an important step towards understanding Higgs production in association with two jets [24].

References

[1] G. Aad *et al.* [ATLAS Collaboration], Eur. Phys. J. **C71** (2011) 1512. [arXiv:1009.5908 [hep-ex]].

[2] G. Aad *et al.* [ATLAS Collaboration], Phys. Rev. Lett. 106, 172002 (2011). [arXiv:1102.2696 [hep-ex]].

[3] G. Aad *et al.* [ATLAS Collaboration], JHEP **1109** (2011) 053 [arXiv:1107.1641 [hep-ex]].

[4] G. Aad *et al.* [ATLAS Collaboration], arXiv:1203.4606 [hep-ex].

[5] V. Khachatryan *et al.* [CMS Collaboration], Phys. Rev. Lett. **106** (2011) 122003. [arXiv:1101.5029 [hep-ex]].

[6] S. Chatrchyan *et al.* [CMS Collaboration], Phys. Lett. **B700** (2011) 187-206. [arXiv:1104.1693 [hep-ex]].

[7] S. Chatrchyan *et al.* [CMS Collaboration], Phys. Rev. Lett. **107** (2011) 132001 [arXiv:1106.0208 [hep-ex]].

[8] S. Chatrchyan *et al.* [CMS Collaboration], Phys. Lett. B **702** (2011) 336 [arXiv:1106.0647 [hep-ex]].

[9] V. D. Barger, R. J. N. Phillips and D. Zeppenfeld, Phys. Lett. B **346** (1995) 106 [hep-ph/9412276].

[10] I. Sung, Phys. Rev. D **80** (2009) 094020 [arXiv:0908.3688 [hep-ph]].

[11] S. Ask, J. H. Collins, J. R. Forshaw, K. Joshi and A. D. Pilkington, JHEP **1201** (2012) 018 [arXiv:1108.2396 [hep-ph]].

[12] B. E. Cox, J. R. Forshaw and A. D. Pilkington, Phys. Lett. B **696** (2011) 87 [arXiv:1006.0986 [hep-ph]].

[13] A. Banfi, G. P. Salam and G. Zanderighi, arXiv:1203.5773 [hep-ph].

[14] T. Becher and M. Neubert, arXiv:1205.3806 [hep-ph].

[15] M. Dasgupta and G. P. Salam, Phys. Lett. B **512** (2001) 323 [arXiv:hep-ph/0104277].

[16] J. Forshaw, J. Keates and S. Marzani, JHEP **0907** (2009) 023 [arXiv:0905.1350 [hep-ph]].

[17] R. M. Duran Delgado, J. R. Forshaw, S. Marzani and M. H. Seymour, JHEP **1108** (2011) 157 [arXiv:1107.2084 [hep-ph]].

[18] N. Kidonakis, G. Oderda and G. Sterman, Nucl. Phys. B **531** (1998) 365 [arXiv:hep-ph/9803241].

[19] J. R. Forshaw, A. Kyrieleis and M. H. Seymour, JHEP **0608** (2006) 059 [arXiv:hep-ph/0604094].

[20] J. R. Forshaw, A. Kyrieleis and M. H. Seymour, JHEP **0809** (2008) 128 [arXiv:0808.1269 [hep-ph]].

[21] Z. Nagy, Phys. Rev. D **68** (2003) 094002 [arXiv:hep-ph/0307268].

[22] G. Aad *et al.* [ATLAS Collaboration], arXiv:1203.5015 [hep-ex].

[23] D. L. Rainwater, R. Szalapski and D. Zeppenfeld, Phys. Rev. D **54** (1996) 6680 [arXiv:hep-ph/9605444].

[24] J. R. Forshaw and M. Sjödahl, JHEP **0709** (2007) 119 [arXiv:0705.1504 [hep-ph]].

Dijet Production in QCD and $\mathcal{N} = 4$ SYM

Grigorios Chachamis[1], *José Daniel Madrigal*[2], *Agustín Sabio Vera*[2]

[1]Paul Scherrer Institut, CH-5232 Villigen PSI, Switzerland
[2]Instituto de Física Teórica UAM/CSIC,U. Autónoma de Madrid, E-28049 Madrid, Spain.

DOI: http://dx.doi.org/10.3204/DESY-PROC-2012-02/131

We investigate dijet production at large rapidity separation in QCD and $\mathcal{N} = 4$ SYM, showing that both theories give similar predictions for observables only sensitive to conformal properties of the scattering such as ratios of azimuthal angle correlations. Renormalization prescriptions are important in this comparison.

1 Introduction

In spite of real-world QCD being neither supersymmetric nor conformal invariant, it shares many features with $\mathcal{N} = 4$ SYM. Both theories are identical when loops of quarks and scalars do not appear, i.e. at tree-level, and in the leading $\ln s$ term of the high-energy limit, where the scattering is dominated by exchange of a gluon ladder in the t-channel. The infrared structure of both theories is similar at the level of soft divergences. It is interesting to look for regimes where QCD and $\mathcal{N} = 4$ give similar predictions. With this target in mind we will study both theories in the Regge limit $s \gg -t$, with s and t the usual Mandelstam invariants.

2 Ratios of Azimuthal Correlations in High-Energy Dijets

To define the observables of interest, we consider the kinematic configuration of Fig. 1, the well-known Mueller-Navelet jets [1]. Two forward jets with similar transverse scales $q_{1,2}^2 \simeq p^2$ are tagged at a large rapidity separation $Y = \ln \frac{x_1 x_2 s}{\sqrt{\boldsymbol{q}_1^2 \boldsymbol{q}_2^2}}$ and relative azimuthal angle $\phi = \vartheta_1 - \vartheta_2$, where $x_{1,2}$ are the fractions of longitudinal momenta of the parent hadrons carried by the jet[1]. Such a configuration is particularly suited to unveil QCD dynamics in the high-energy limit, specifically through the study of dijet azimuthal correlation [3, 4].

The large value of Y calls for a resummation of high-energy logarithms of the form $(\alpha_s \ln(s/q^2))^n$. This resummation is performed in the BFKL approach [5], and the differential cross section for dijet production at the parton level[2] is given by

$$\frac{d\hat{\sigma}}{d^2\boldsymbol{q}_1 d^2\boldsymbol{q}^2} = \frac{\pi^2 \bar{\alpha}_s^2}{2} \frac{f(\boldsymbol{q}_1, \boldsymbol{q}_2, Y)}{\boldsymbol{q}_1^2 \boldsymbol{q}_2^2}; \quad f(\boldsymbol{q}_1, \boldsymbol{q}_2, Y) = \int \frac{d\omega}{2\pi i} e^{\omega Y} f(\boldsymbol{q}_1, \boldsymbol{q}_2, \omega), \quad \bar{\alpha}_s \equiv \frac{\alpha_s N_c}{\pi}, \quad (1)$$

in terms of the Mellin transform of the solution to the BFKL equation

[1]Partons are here identified with jets, as we consider for simplicity the jet vertex only to leading order [2].
[2]Dependences on PDFs cancel in our observables, allowing for sound comparison between QCD and $\mathcal{N} = 4$.

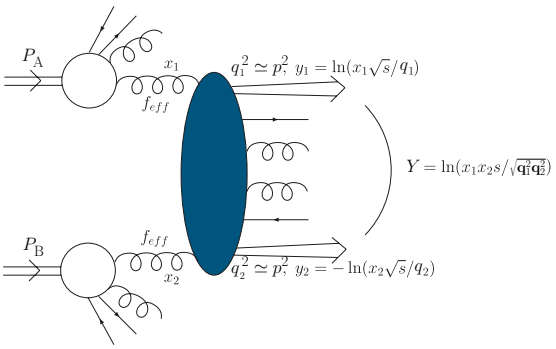

Figure 1: Mueller-Navelet Jets.

$$\omega f(\boldsymbol{q}_1^2, \boldsymbol{q}_2^2, \omega) = \delta^2(\boldsymbol{q}_1^2 - \boldsymbol{q}_2^2) + \int d^2\boldsymbol{\kappa}\, \mathcal{K}_{\rm NLL}(\boldsymbol{q}_1, \boldsymbol{\kappa}) f(\boldsymbol{\kappa}, \boldsymbol{q}_2, \omega). \tag{2}$$

In the leading log approximation, this equation enjoys conformal SL(2,$\mathbb{C}$) invariance in the plane transverse to the colliding partons [6], and the integral kernel $\mathcal{K}$ is diagonalised by the eigenfunctions $\psi_{n,\nu} = \frac{1}{2\sqrt{\pi}}(\boldsymbol{q}^2)^{i\nu-1/2}e^{in\vartheta}$. The discrete quantum number $n = 0, 1, 2\cdots$ controls the azimuthal behaviour in the transverse plane and corresponds to a conformal spin, since it carries a representation of SL(2,$\mathbb{C}$). It turns out [7] that the asympotic intercepts of the kernel corresponding to $n \geq 1$ are very similar at LL and NLL, not having the weak convergence problem of the $n = 0$ case —corresponding to the pomeron intercept— which needs an all-orders collinear resummation [8]. This motivates us to look for observables insensitive to the conformal spin $n = 0$.

We consider the Fourier expansion of the differential cross section (1) in the azimuthal angle

$$\begin{aligned} \frac{d\hat{\sigma}(\bar{\alpha}_s, Y, p^2)}{d\phi} &= \frac{\pi\bar{\alpha}_s^2}{4p^2}\sum_{n=-\infty}^{\infty} e^{in\phi}\mathcal{C}_n(Y); \\ \mathcal{C}_n^{\rm QCD}(Y) &= \int_{-\infty}^{\infty}\frac{d\nu}{2\pi}\frac{\exp\left[\bar{\alpha}_s(p^2)Y\left(\chi_0(|n|,\nu)+\bar{\alpha}_s(p^2)\left(\chi_1(|n|,\nu)-\frac{\beta_0}{8N_c}\frac{\chi_0(|n|,\nu)}{\left(\frac{1}{4}+\nu^2\right)}\right)\right)\right]}{1/4+\nu^2}. \end{aligned} \tag{3}$$

The label n for each of the moments is the conformal spin. The functions $\chi_{0,1}$ in the definition of the coefficients $\mathcal{C}_n$ are the building blocks of the NLL BFKL kernel [9]. A similar formula for $\mathcal{C}_n$ holds in the supersymmetric case with $\beta_0 = 0$ and $\bar{\alpha}_s$ replaced by the corresponding 't Hooft coupling a, see [2] for details. Different observables can be built out of the coefficients $\mathcal{C}_n$. The total (averaged over ϕ) cross-section is $\hat{\sigma} = \frac{\pi^3\bar{\alpha}_s^2}{2p^2}\mathcal{C}_0$, while contributions of higher conformal spins are projected in the moments $\langle\cos(n\phi)\rangle = \mathcal{C}_n/\mathcal{C}_0$. The dependence on $n = 0$ cancels when constructing the ratios $\mathcal{R}_{m,n} = \frac{\langle\cos(m\phi)\rangle}{\langle\cos(n\phi)\rangle} = \frac{\mathcal{C}_m}{\mathcal{C}_n}$. These ratios $\mathcal{R}_{m,n}$ have a good perturbative convergence, and are clean observables to test the properties of the Regge limit, in particular conformal invariance, without interference of collinear contributions. They were computed in [2] in QCD and $\mathcal{N} = 4$ SYM for different renormalisation prescriptions.

3 Comparing QCD and $\mathcal{N} = 4$ SYM

The results found in [2] are summarised in Fig. 2. $\mathcal{N} = 4$ results are showed in a yellow band since the non-running coupling was allowed to take values in a given range. One can see that the predictions of the two theories for $\mathcal{R}_{m,n}$ lie very close, in particular when choosing the Brodsky-Lepage-Mackenzie (BLM) procedure [10]. The BLM procedure effectively resums the effects of a non-zero β-function and has a conformal behaviour like the one exhibited by $\mathcal{N} = 4$ theory. In [11] it was shown to give a more sensible result than $\overline{\text{MS}}$ scheme for the pomeron intercept. The appearance of an unnaturally high BLM scale for the coupling in this case is relaxed when studying observables insensitive to $n = 0$ [12]. It is interesting to note that only when considering clean and perturbatively convergent observables for the high-energy limit, the BLM prescription is systematically closer than the other renormalization schemes to the supersymmetric result.

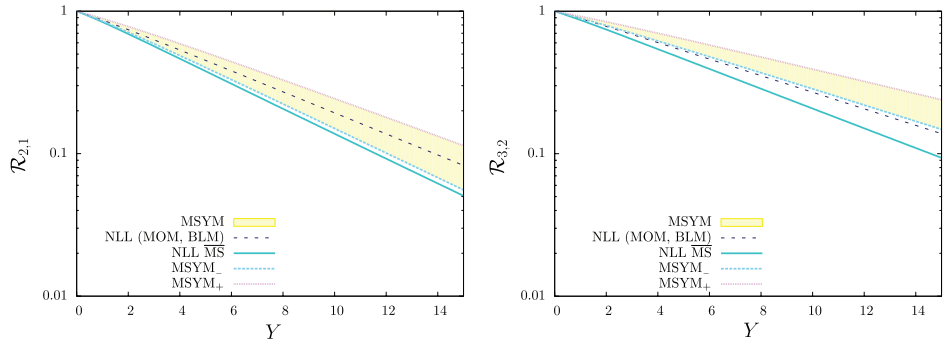

Figure 2: Evolution of ratios $\mathcal{R}_{2,1}$ (left) and $\mathcal{R}_{3,2}$ (right) with jet rapidity separation in QCD and $\mathcal{N} = 4$ SYM for different renormalisation schemes ($\overline{\text{MS}}$ vs BLM).

Research supported by E. Comission [LHCPhenoNet (PITN-GA-2010-264564)] & C. Madrid (HEPHACOS ESP-1473).

References

[1] A. H. Mueller and H. Navelet, Nucl. Phys. B **282** (1987) 727.

[2] M. Angioni, G. Chachamis, J. D. Madrigal and A. Sabio Vera, Phys. Rev. Lett. **107** (2011) 191601 [arXiv:1106.6172 [hep-th]].

[3] V. Del Duca and C. R. Schmidt, Phys. Rev. D **49** (1994) 4510 [hep-ph/9311290]; W. J. Stirling, Nucl. Phys. B **423** (1994) 56 [hep-ph/9401266]; A. Sabio Vera and F. Schwennsen, Nucl. Phys. B **776** (2007) 170 [hep-ph/0702158]; C. Marquet and C. Royon, Phys. Rev. D **79** (2009) 034028 [arXiv:0704.3409 [hep-ph]]; D. Colferai, F. Schwennsen, L. Szymanowski and S. Wallon, JHEP **1012** (2010) 026 [arXiv:1002.1365 [hep-ph]]; F. Caporale, D. Yu. Ivanov, B. Murdaca, A. Papa and A. Perri, JHEP **1202** (2012) 101 [arXiv:1112.3752 [hep-ph]].

[4] L. Goerlich, these Proceedings.

[5] L. N. Lipatov, Sov. J. Nucl. Phys. **23** (1976) 338 [Yad. Fiz. **23** (1976) 642]; E. A. Kuraev, L. N. Lipatov and V. S. Fadin, Sov. Phys. JETP **45** (1977) 199 [Zh. Eksp. Teor. Fiz. **72** (1977) 377]; I. I. Balitsky and L. N. Lipatov, Sov. J. Nucl. Phys. **28** (1978) 822 [Yad. Fiz. **28** (1978) 1597].

[6] L. N. Lipatov, Sov. Phys. JETP **63** (1986) 904 [Zh. Eksp. Teor. Fiz. **90** (1986) 1536].

[7] A. V. Kotikov and L. N. Lipatov, Nucl. Phys. B **582** (2000) 19 [hep-ph/0004008]; A. Sabio Vera, Nucl. Phys. B **746** (2006) 1 [hep-ph/0602250].

[8] G. P. Salam, JHEP **9807** (1998) 019 [hep-ph/9806482]; A. Sabio Vera, Nucl. Phys. B **722** (2005) 65 [hep-ph/0505128].

[9] V. S. Fadin and L. N. Lipatov, Phys. Lett. B **429** (1998) 127 [hep-ph/9802290]; M. Ciafaloni and G. Camici, Phys. Lett. B **430** (1998) 349 [hep-ph/9803389].

[10] S. J. Brodsky, G. P. Lepage and P. B. Mackenzie, Phys. Rev. D **28** (1983) 228.

[11] S. J. Brodsky, V. S. Fadin, V. T. Kim, L. N. Lipatov and G. B. Pivovarov, hep-ph/0111390.

[12] G. Chachamis, J. D. Madrigal and A. Sabio Vera, arXiv:1110.5830 [hep-ph].

Next-to-leading and Resummed BFKL Evolution with Saturation Boundary

David Zaslavsky

Pennsylvania State University, University Park, PA 16802 USA

DOI: http://dx.doi.org/10.3204/DESY-PROC-2012-02/215

We have simulated BFKL evolution using collinear resummation to address the instabilities arising from the NLL kernel, and a saturation boundary instead of the nonlinear term to tame the growth of the solution at low momenta. Our results establish that the saturation boundary alone does not cure the NLL instabilities, but with the resummation, it allows us to extract the rapidity dependence of the saturation scale and demonstrates some possibly important pre-asymptotic behavior.

1 BFKL Evolution

In the calculations of scattering amplitudes for strongly bound systems, one of the key components is the fundamental QCD dipole amplitude. When the rapidity $Y = \ln \frac{1}{x}$ is large, this amplitude is governed by the BFKL equation [1, 2, 3], which is a linear equation that gives the evolution in rapidity of the dipole amplitude.

For purposes of this project [4], the BFKL equation can be written in the form

$$\omega F(\omega, \mathbf{k}) = F_0(\mathbf{k}) + \int \frac{\mathrm{d}^2\mathbf{k}'}{\pi^2} K(\mathbf{k}, \mathbf{k}') F(\omega, \mathbf{k}')$$

where ω is the Mellin variable conjugate to x, $F(\omega, \mathbf{k})$ is a convolution of the gluon Green's function with one impact factor, and the kernel $K(\mathbf{k}, \mathbf{k}')$ is known to NLL order.

Of particular interest in these analyses are the singularity structures of the kernel in double Mellin space: where are the poles in γ, the Mellin variable conjugate to $\ln k^2$, and what orders are they? For the leading term, we can write the singularity structure as

$$K_0 \sim \frac{1}{\gamma} + \frac{1}{1-\gamma}$$

(single poles at $\gamma = 0, 1$), and for the NLL term,

$$K_1 \to \chi_1(\gamma) \sim -\frac{1}{2\gamma^3} - \frac{1}{2(1-\gamma)^3} - \frac{11/12}{\gamma^2} - \frac{11/12 + b}{(1-\gamma)^2} + \mathcal{O}\left(\frac{1}{\gamma}\right)$$

This expression contains triple poles which arise from kinematical constraints, and double poles which come from the running of the strong coupling and from the nonsingular terms in the DGLAP splitting function. With the NLL term included, the BFKL evolution is unstable: it gives rise to negative or oscillating cross sections.

Fortunately, it is possible to cure these instabilities by using a resummation procedure to incorporate certain higher-order terms into the BFKL kernel. There are various procedures one can use; this project employs the renormalization-group improved kernel, scheme B from [5]. This scheme basically amounts to shifting the locations of the poles in the Mellin-space kernel, and once we no longer have the double and triple poles at 0 and 1, the instabilities in the evolution which lead to nonsensical cross sections are no longer present.

2 Traveling Waves and Saturation

Another problem with the BFKL evolution is that, at low momenta, the solution exhibits runaway growth, to the point where it violates the unitarity bound on the cross-section. To deal with this, one needs to account for gluon self-interactions by adding a negative nonlinear term. The rapidity-dependent threshold momentum at which the self-interactions become important is called the saturation scale, $Q_s(Y)$.

One can make an analogy between the BFKL equation with the nonlinear term and the general class of diffusive equations of the form

$$\partial_t u(x,t) = \mathbb{D}_x \cdot u(x,t) + f\big(u(x,t)\big)$$

where $\mathbb{D}_x$ is a differential operator in x. These equations admit solutions which depend only on the combination $x - vt$, thus containing an advancing wavefront, in the region where the nonlinear term is negligible. This wavefront manifests itself in BFKL evolution as geometric scaling: the cross section depends on k^2 and Y in the combination $\frac{k^2}{Q_s^2(Y)}$. [6]

We can exploit this "flow" of the solution towards higher momenta to avoid solving the nonlinear equation directly, which would be very computationally intensive. Instead of actually including the nonlinear term, we use the pure linear equation with a saturation boundary: simply replace the normal BFKL evolution below some threshold momentum with some other evolution that keeps the solution well bounded. Imposing the boundary should ideally simulate the effect the nonlinear term has at $k^2 \gtrsim Q_s^2(Y)$, including preserving the wavefront, thereby allowing us to determine the form of $Q_s(Y)$ without having to do the full nonlinear calculation.

It turns out that the rapidity dependence of the saturation scale is, to a large extent, independent of the exact nature of how this boundary is implemented. In this work we use two schemes, the frozen boundary and the absorptive boundary. In both cases, we begin by identifying the saturation momentum, up to an arbitrary constant factor, as the value Q_s satisfying $F(Q_s) = c$, where c is a fixed cutoff value. At each step of the simulation, we replace the region of the solution at $k < Q_s - \delta$ with either 0 (for the absorptive boundary) or $F(Q_s - \delta)$ (for the frozen boundary). We then run the evolution in rapidity for one step. The propagation of the wavefront increases the saturation scale, and we repeat the application of the boundary.

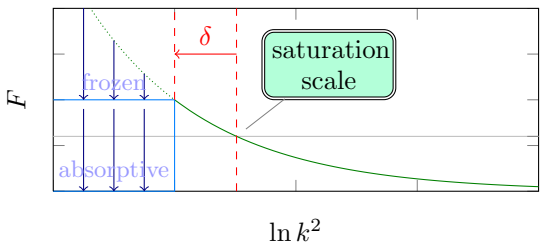

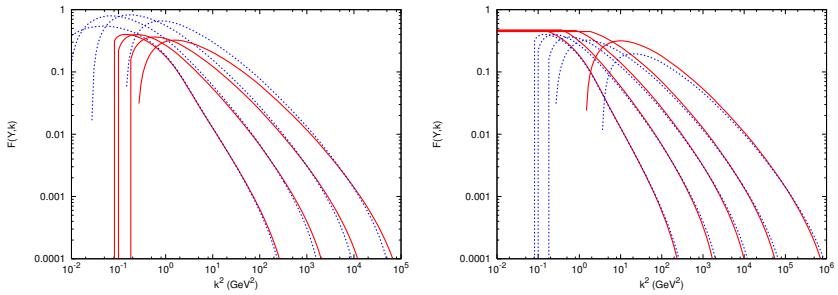

Figure 1: Solutions to the BFKL equation with the NLL kernel using a fixed coupling. On the left, the dotted lines show the solution computed without any saturation boundary at rapidities $Y = 2, 6, 10, 14$. The solid lines show the solution, computed with an absorptive boundary, at the same rapidities. The plot on the right compares the absorptive boundary (now the dotted lines) with the frozen boundary (solid lines), at $Y = 2, 6, 10, 14, 20$.

3 Results

The main objective of all this is to understand the interaction between the saturation boundary and the resummed kernel. We have analyzed the LL, NLL, and resummed kernels, solving the momentum-space BFKL equation with the saturation boundary in each case.

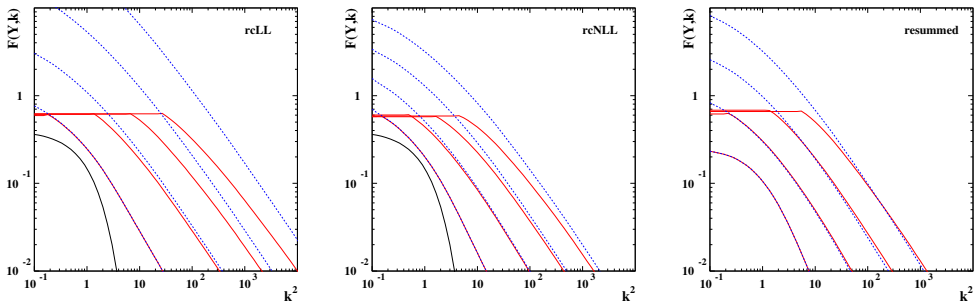

Figure 2: Solution to the BFKL equation with (solid) and without (dotted) the saturation boundary, here applied as the frozen boundary. From left to right, the kernels used are (1) LL with running coupling, (2) NLL with running coupling, and (3) collinear resummed.

Figure 1 shows the solution for F computed using the NLL kernel with fixed coupling. These results show evidence of the instabilities that occur at low momenta without the boundary, and we can also see the traveling wave behavior at larger momenta, which is only slightly affected by the application of the boundary in this case. However, at large values of Y as shown in the right hand plot, the solution eventually fails to reach sufficiently large values of F to satisfy $F(Q_s) = c$, meaning that we cannot continuously extract a saturation scale for $Y \gtrsim 15$. Evidently the saturation boundary is not enough to prevent the problems with BFKL evolution; we will need to incorporate higher-order terms, including and beyond the running coupling.

In figure 2, we have the solutions computed with the running coupling. These display the untamed growth at low momenta and, again, the traveling wave behavior at large momenta. However, in this case there is a noticeable difference in the propagation speed of the wavefront depending on which kernel is used and whether the saturation boundary is present.

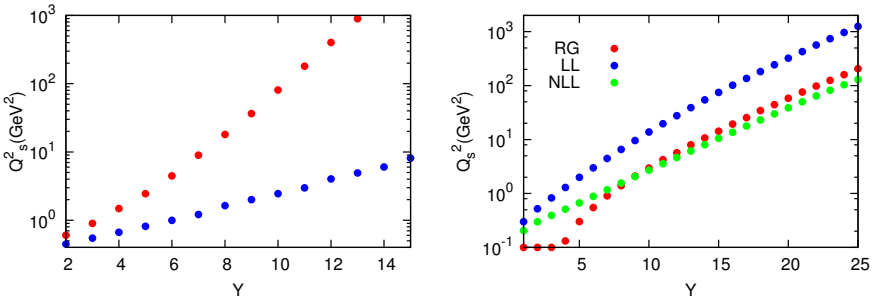

Figure 3: Evolution of the saturation scale with rapidity. On the left is fixed coupling, the upper dots being for the LL kernel and the lower dots for the NLL kernel, and on the right are the running coupling results. The rcLL kernel is the highest set of dots, rcNLL is the next one below it at the left edge of the plot, and the resummed kernel is the set of dots that starts out flat and rises sharply at $Y \sim 4$.

Finally, figure 3 shows the main result, the evolution of the saturation scale. With the fixed coupling, we see an essentially exponential growth in the saturation scale at LL, as predicted in [6, 7], which is suppressed by the NLL corrections. With the running coupling, the asymptotic trend in Q_s is roughly similar for all three kernels, which also agrees with predictions.

An interesting feature of the saturation scale dependence is that, with the resummed kernel, we see a characteristic plateau at low rapidity. This is related to a dip in the DGLAP splitting function described in [5]. The presence of this plateau indicates that the pre-asymptotic behavior of $Q_s(Y)$ may have important consequences for future phenomenological studies.

Acknowledgements

The research described here was partially supported by US D.O.E. and MNiSW grants. The presentation was partially supported by a travel grant from Stack Exchange Inc.

References

[1] V. S. Fadin, E. A. Kuraev and L. N. Lipatov, Phys. Lett. B **60**, 50 (1975).

[2] I. I. Balitsky and L. N. Lipatov, Sov. J. Nucl. Phys. **28**, 822 (1978) [Yad. Fiz. **28**, 1597 (1978)].

[3] L. N. Lipatov, Sov. Phys. JETP **63**, 904 (1986) [Zh. Eksp. Teor. Fiz. **90**, 1536 (1986)].

[4] E. Avsar, A. M. Stasto, D. N. Triantafyllopoulos and D. Zaslavsky, JHEP **1110**, 138 (2011) [arXiv:1107.1252 [hep-ph]].

[5] M. Ciafaloni, D. Colferai, G. P. Salam and A. M. Stasto, Phys. Rev. D **68**, 114003 (2003) [hep-ph/0307188].

[6] S. Munier and R. B. Peschanski, Phys. Rev. D **69**, 034008 (2004) [hep-ph/0310357].

[7] A. H. Mueller and D. N. Triantafyllopoulos, Nucl. Phys. B **640**, 331 (2002) [hep-ph/0205167].

Applications of Lipatov's high energy effective action to NLO BFKL jet phenomenology

Martin Hentschinski[1], *Beatrice Murdaca*[2], *Agustín Sabio Vera*[1]

[1] Instituto de Física Teórica UAM/CSIC, C/ Nicolás Cabrera 13-15,
Universidad Autónoma de Madrid, Cantoblanco, E-28049 Madrid, Spain

[2] Dipartimento di Fisica, Universitá della Calabria, and
Istituto Nazionale di Fisica Nucleare, Gruppo collegato di Cosenza,
I-87036 Arcavacata di Rende, Cosenza, Italy

DOI: `http://dx.doi.org/10.3204/DESY-PROC-2012-02/53`

We report on recent progress in the evaluation of next-to-leading order observables using Lipatov's QCD high energy effective action. We calculate both real and virtual corrections to the quark induced forward jet vertex at NLO, making use of a new regularization method and a subtraction mechanism. As a new result we determine the real part of the NLO Mueller-Tang impact factor which is the only missing element for a complete NLO BFKL description of dijet events with a rapidity gap.

1 Introduction

Due to its large center of mass energy the LHC provides an ideal opportunity to test BFKL-driven observables [1, 2]. Among them we find both central production processes, such as heavy quark production (see *e.g.* [3]) and forward production of different systems such as high p_T jets, heavy quark pairs [4] or Drell-Yan pairs [5, 6]. In the case of two tagged forward/backward jets there might be a rapidity gap between them ('Mueller-Tang') or not ('Mueller-Navelet'). These jet events allow then to test the forward (Mueller-Navelet) and non-forward (Mueller-Tang) BFKL kernel. While Mueller-Navelet jet events are currently one of the few examples where a complete description at next-to-leading logarithmic (NLL) accuracy exists [7, 8, 9, 10, 11, 12], for Mueller-Tang jets we so far have at NLO accuracy the non-forward BFKL kernel [13], while impact factors are known only to leading order (LO). The limitation to LO impact factors is currently one of the main drawbacks of BFKL phenomenology. A promising tool to overcome this limitation is given by Lipatov's effective action [14]. So far this action has been mainly applied for the determination of LO transition kernels [15, 16, 17, 18]. In this contribution we show that it can be further used to calculate NLO correction. In particular, we re-derive the NLO Mueller-Navelet quark-jet impact factor and determine the missing real NLO correction to the Mueller-Tang quark-initiated jet impact factors. For details we refer to [19, 20].

2 The high energy effective action

The effective action adds to the QCD action an induced term, $S_{\text{eff}} = S_{\text{QCD}} + S_{\text{ind.}}$, which describes the coupling of the reggeized gluon field $A_\pm(x) = -it^a A^a_\pm(x)$ to the usual gluonic field $v_\mu(x) = -it^a v^a_\mu(x)$. This induced term reads

$$S_{\text{ind.}}[v_\mu, A_\pm] = \int \mathrm{d}^4x \,\mathrm{tr}\Big[\Big(W_+[v(x)] - A_+(x)\Big)\partial_\perp^2 A_-(x)\Big] + \int \mathrm{d}^4x \,\mathrm{tr}\Big[\Big(W_-[v(x)] - A_-(x)\Big)\partial_\perp^2 A_+(x)\Big]. \tag{1}$$

The infinite number of couplings of the gluon field to the reggeized gluon field are encoded in two functionals $W_\pm[v] = v_\pm \frac{1}{D_\pm}\partial_\pm$ where $D_\pm = \partial_\pm + g v_\pm$. Note that the reggeized gluon fields are special in the sense that they are invariant under local gauge transformations, while they transform globally in the adjoint representation of the $\mathrm{SU}(N_c)$ gauge group. In addition, strong ordering of longitudinal momenta in high energy factorized amplitudes leads to the kinematical constraint of the reggeized gluon fields,

$$\partial_+ A_-(x) = \partial_- A_+(x) = 0, \tag{2}$$

which is always implied. Quantization of the gluonic field requires to add gauge fixing and ghost terms, which we have included in the QCD action. Feynman rules have been derived in [21]. We

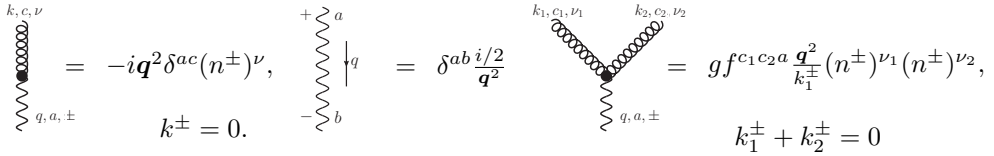

(a) (b) (c)

Figure 1: The direct transition vertex (a), the reggeized gluon propagator (b) and the unregulated order g induced vertex (c)

show them using curly lines for the conventional QCD gluon field and wavy (photon-like) lines for the reggeized gluon field. There exist an infinite number of higher order induced vertices. For the present analysis only the order g induced vertex in fig. 1.c is needed. In the determination of loop corrections we must fix a regularization of the light-cone singularity present in fig. 1.c. As suggested by one of us in [22] this pole should be treated as a Cauchy principal value.

3 NLO quark jet impact factors

When calculating quantum corrections new divergences in longitudinal components appear. As it was demonstrated in [19, 23] these can be regularized by deforming the light cone using a parameter ρ which is considered in the limit $\rho \to \infty$. In this new setup, the Sudakov projections take place on the vectors $n_a = e^{-\rho} n^+ + n^-$ and $n_b = n^+ + e^{-\rho} n^-$. To obtain the virtual

corrections we are seeking for it is needed to calculate the one-loop self energy corrections to the reggeized gluon propagator. Diagrammatically, these are

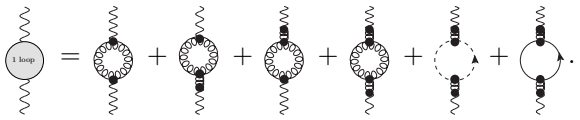

(3)

The 1-loop corrections to the quark-quark-reggeized gluon vertex are

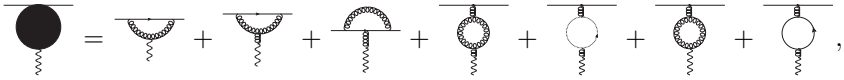

(4)

from which it is needed to subtract the factorizing contribution

(5)

The one-loop quark-quark scattering amplitude in the high energy limit is then given by the following sum

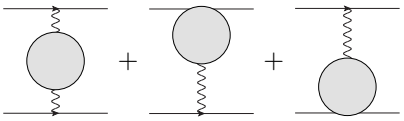

(6)

The sum of this three contributions is finite in the limit $\rho \to \infty$ and the dependence on the regulator vanishes. The result is in agreement with calculations using more standard techniques, performed in [24] and confirmed in [25]. A similar result holds for the real corrections, see [19] for details. All of these results are needed for Mueller-Navelet jets. The determination of the Mueller-Tang impact factor requires to consider diagrams where two reggeized gluons couple to the quark induced jet, see Fig. 2.a. Due to the condition Eq. (2), the integration over the minus component of the loop momentum of the reggeized gluon loop is absorbed into the definition of the impact factor. With the virtual NLO corrections already known [26], we focus on the real NLO corrections. The relevant diagrams split into two groups: the two reggeized gluon

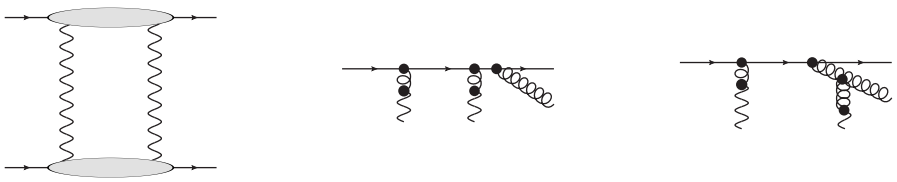

(a) (b) (c)

Figure 2:

state couples either to a single parton (Fig. 2.b) or to two different partons (Fig. 2.c). While the integration over the longitudinal loop momentum is divergent for individual diagrams, this divergence is found to cancel for their sum.

Our results show the use of the high energy effective action in the determination of higher order corrections in multi-Regge and quasi-multi-Regge kinematics. In addition to the calculations here presented, these methods have been successfully applied to the determination of the quark contributions to the two-loop gluon Regge trajectory [23]. Determination of the gluonic NLO corrections to jet impact factor and gluon trajectory are currently in progress [27].

Acknowledgments

We are grateful for financial support from the German Academic Exchange Service (DAAD), the MICINN under grant FPA2010-17747, the Research Executive Agency (REA) of the European Union under the Grant Agreement number PITN-GA-2010-264564 (LHCPhenoNet) and Comunidad de Madrid (HEPHACOS ESP-1473).

References

[1] V. S. Fadin, E. A. Kuraev, and L. N. Lipatov. Phys. Lett. **B60** (1975) 50–52.

[2] I. I. Balitsky and L. N. Lipatov. Sov. J. Nucl. Phys. **28** (1978) 822–829.

[3] G. Chachamis, M. Hentschinski, A. Sabio Vera, and C. Salas. arXiv:0911.2662 [hep-ph].

[4] C. Salas and J. Stirling. in preparation.

[5] F. Hautmann, M. Hentschinski, and H. Jung. arXiv:1205.1759 [hep-ph].

[6] M. Hentschinski and C. Salas. in preparation.

[7] V. S. Fadin and L. N. Lipatov. Phys. Lett. **B429** (1998) 127–134, arXiv:hep-ph/9802290.

[8] J. Bartels, D. Colferai, and G. Vacca. Eur.Phys.J. **C24** (2002) 83–99, arXiv:hep-ph/0112283 [hep-ph].

[9] J. Bartels, D. Colferai, and G. Vacca. Eur.Phys.J. **C29** (2003) 235–249, arXiv:hep-ph/0206290 [hep-ph].

[10] D. Colferai, F. Schwennsen, L. Szymanowski, and S. Wallon. JHEP **1012** (2010) 026, arXiv:1002.1365 [hep-ph].

[11] F. Caporale, D. Y. Ivanov, B. Murdaca, A. Papa, and A. Perri. JHEP **1202** (2012) 101, arXiv:1112.3752 [hep-ph].

[12] D. Y. Ivanov and A. Papa. JHEP **1205** (2012) 086, arXiv:1202.1082 [hep-ph].

[13] V. Fadin and R. Fiore. Phys.Rev. **D72** (2005) 014018, arXiv:hep-ph/0502045 [hep-ph].

[14] L. N. Lipatov. Nucl. Phys. **B452** (1995) 369–400, hep-ph/9502308.

[15] M. Hentschinski. Nucl.Phys.Proc.Suppl. **198** (2010) 108–111, arXiv:0910.2981 [hep-ph].

[16] M. Hentschinski. arXiv:0908.2576 [hep-ph].

[17] M. Hentschinski. Acta Phys. Polon. **B39** (2008) 2567–2570, arXiv:0808.3082 [hep-ph].

[18] M. Hentschinski, J. Bartels, and L. Lipatov. arXiv:0809.4146 [hep-ph].

[19] M. Hentschinski and A. S. Vera. Phys.Rev. **D85** (2012) 056006, arXiv:1110.6741 [hep-ph].

[20] M. Hentschinski, B. Murdaca, and A. Sabio Vera. in preparation.

[21] E. N. Antonov, L. N. Lipatov, E. A. Kuraev, and I. O. Cherednikov. Nucl. Phys. **B721** (2005) 111–135, hep-ph/0411185.

[22] M. Hentschinski. Nucl.Phys. **B859** (2012) 129–142, arXiv:1112.4509 [hep-ph].

[23] G. Chachamis, M. Hentschinski, J. Madrigal Martinez, and A. Sabio Vera. Nucl.Phys. **B861** (2012) 133–144, arXiv:1202.0649 [hep-ph].

[24] V. S. Fadin, R. Fiore, and A. Quartarolo. Phys.Rev. **D50** (1994) 2265–2276, arXiv:hep-ph/9310252 [hep-ph].

[25] V. Del Duca and C. R. Schmidt. Phys.Rev. **D57** (1998) 4069–4079, arXiv:hep-ph/9711309 [hep-ph].

[26] V. S. Fadin, R. Fiore, M. Kotsky, and A. Papa. Phys.Rev. **D61** (2000) 094006, arXiv:hep-ph/9908265 [hep-ph].

[27] G. Chachamis, M. Hentschinski, J. D. Madrigal Martinez, and A. Sabio Vera. in preparation.

WG2: Diffraction and Vector Mesons and WG6: Spin Physics

Imaging partons in exclusive scattering processes

Markus Diehl

DESY, Notkestraße 85, 22607 Hamburg, Germany

DOI: http://dx.doi.org/10.3204/DESY-PROC-2012-02/98

The spatial distribution of partons in the proton can be probed in suitable exclusive scattering processes. I report on recent performance estimates for parton imaging at a proposed Electron-Ion Collider.

Deeply virtual Compton scattering (DVCS) and exclusive meson production in lepton-proton collisions offer unique possibilities for determining the spatial distribution of quarks, antiquarks and gluons as a function of their longitudinal momentum inside the proton. Such "tomographic images" of the proton can provide insight into key aspects of QCD dynamics, such as the interplay between sea quarks and gluons, the relation between sea and valence quarks, and the orbital angular momentum carried by these partons.

To obtain such images one needs to measure the transverse momentum transfer $\boldsymbol{\Delta}$ to the proton. A Fourier transform then gives the distribution in impact parameter $\boldsymbol{b}$, which is the position of the struck parton in the plane transverse to the proton direction of movement. In the scattering amplitude the longitudinal momentum fraction x of the parton is integrated over, with typical values around $\frac{1}{2}x_B$ for DVCS and $\frac{1}{2}x_V = \frac{1}{2}x_B\,(1 + M^2/Q^2)$ for the production of a meson with mass M. The reconstruction of a joint density in x and $\boldsymbol{b}$ can be envisaged in the framework of generalized parton distributions (GPDs) by making use of their evolution in the resolution scale, which is given by Q^2 in DVCS and by $Q^2 + M^2$ in meson production. This requires precise data in a very wide range of x_B and Q^2.

Measurements from HERA suggest that at x around 10^{-3} gluons have a more narrow impact parameter distribution than sea quarks. Information about the spatial distribution of valence quarks can be inferred from electromagnetic form factors and from lattice calculations, and a direct study of quarks with large momentum fraction x will be possible with the 12 GeV upgrade at Jefferson Lab. The planned DVCS measurement by COMPASS will give us a first glimpse into the x region between 10^{-1} and 10^{-2}. To realize the full physics potential of parton imaging will, however, require a new facility. Here I report on a study of parton imaging at a proposed electron-ion collider (EIC) [1]. For complementary information see [2, 3].

Pseudo-data for $ep \to ep\gamma$ have been generated according to a GPD model that reproduces the existing DVCS measurements of H1 and ZEUS. Technically, the unpolarized distributions H for gluons and for sea quarks are modeled with two SO(3) partial waves each, as described in [3] and in Sec. 3 of [4]. The t dependence of the distributions is $\exp\bigl[\,t\,(\frac{B}{2} + \alpha' \log\frac{1}{x})\bigr]$, with different slopes B for gluons and sea quarks and with a small shrinkage parameter α' as suggested by HERA measurements. In DVCS, the invariant momentum transfer t to the proton and its transverse component are related by $-t = (\boldsymbol{\Delta}^2 + x_B^2\, m_p^2)/(1 - x_B)$, where m_p is the proton mass. In the simulation [2] acceptance cuts for the final-state electron, photon and proton have been imposed, and the data have been smeared for the expected resolution in x_B, Q^2 and t.

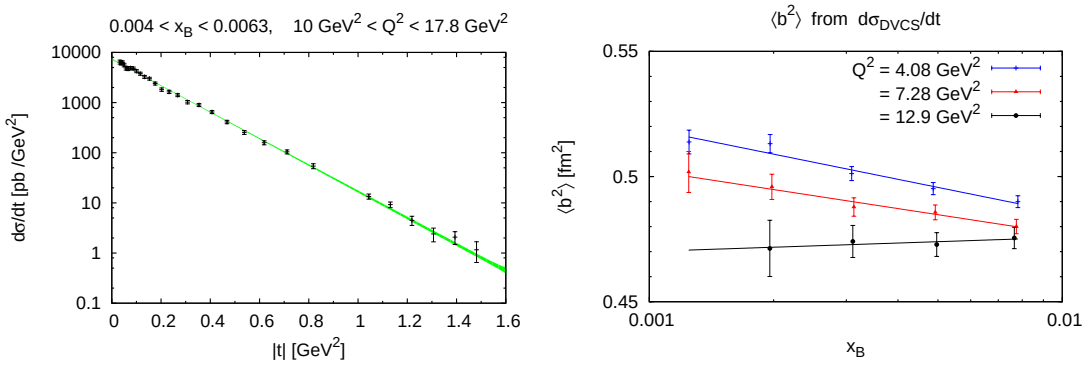

Figure 1: Left: simulated DVCS cross section at EIC for a bin in x_B and Q^2. Right: average squared impact parameter obtained from $d\sigma/dt_{\rm DVCS}$ for different bins in x_B and Q^2.

An assumed 5% uncorrelated systematic error has been added in quadrature to the statistical error in the cross section. The cross section $d\sigma/dt$ for DVCS ($\gamma^* p \to \gamma p$) is obtained after subtraction of the cross section for the Bethe-Heitler process, with an uncertainty of 3% taken on the latter. Beam energies are $E_e = 20\,\text{GeV}$ and $E_p = 250\,\text{GeV}$. Statistical errors are for an integrated luminosity of $10\,\text{fb}^{-1}$ for the $|t|$ range from $0.03\,\text{GeV}^2$ to $1\,\text{GeV}^2$ and for $100\,\text{fb}^{-1}$ for $|t|$ above $1\,\text{GeV}^2$. Here and in the following the uncertainty in the overall luminosity is not included in the errors, because it does not affect the form of the spectra which are at the center of our interest.

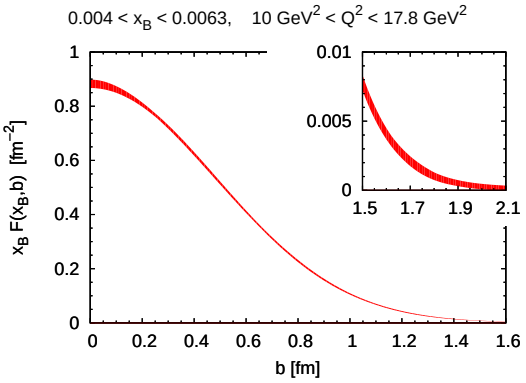

Figure 2: Impact parameter distribution in DVCS obtained from the left panel of Fig. 1. The band reflects the uncertainty in fitting $d\sigma/dt$ and in extrapolating it to the unmeasured t region as specified in Sec. 3.6.1 of [1].

The left panel of Fig. 1 shows the resulting t spectrum for DVCS in a bin of x_B and Q^2, together with an exponential fit. From the t slope one obtains the average squared impact parameter $\langle \boldsymbol{b}^2 \rangle$ for the particular combination of quarks, antiquarks and gluons "seen" in DVCS. The right panel of Fig. 1 shows that with the expected accuracy one can resolve the separate dependence of $\langle \boldsymbol{b}^2 \rangle$ on Q^2 and x_B, which has never been possible so far. In the model used for generating the data, both dependences are small logarithmic effects, which reflect both perturbative and non-perturbative dynamics of sea quarks and gluons in the proton. From $d\sigma/dt$ one obtains the Compton scattering amplitude $|\mathcal{A}_{\gamma^* p \to \gamma p}|$, whose Fourier transform w.r.t. $\boldsymbol{\Delta}$ gives an impact parameter distribution $F(x_B, \boldsymbol{b})$ of partons with momentum fraction of order $\frac{1}{2} x_B$. Figure 2 shows that precise imaging is possible in a wide range of b. Of particular interest at large b is the prediction of an exponential falloff with an x dependent slope of typical size $1/(2m_\pi) \approx 0.7\,\text{fm}$ [5]. Due to partons inside virtual pions, which

because of their small mass can fluctuate to large distances, this predicted behavior is a consequence of chiral symmetry breaking in QCD and awaits experimental verification.

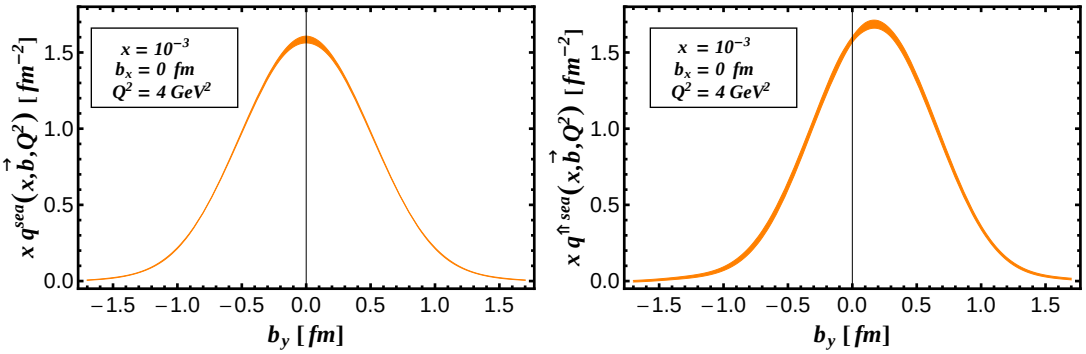

Figure 3: Impact parameter densities of unpolarized sea quarks in an unpolarized proton (left) and in a proton polarized along the x axis (right), obtained from a fit to pseudo-data for the DVCS cross section and the transverse proton spin asymmetry [2, 3].

With transverse proton polarization one gains access to distributions E, which carry characteristic information about orbital angular momentum of partons in the proton. Transformed to b space, these distributions describe how the impact parameter distribution of partons is shifted sideways in a transversely polarized proton. Pseudo-data for the DVCS cross section and for the transverse proton spin asymmetry have been generated [2] assuming a model of E for sea quarks and for gluons of the same type as the model of H described above. Parameter are chosen to satisfy the positivity requirements on E. The simulation is for $E_e = 20\,\mathrm{GeV}$ and $E_p = 250\,\mathrm{GeV}$, with errors for an integrated luminosity of $100\,\mathrm{fb}^{-1}$ and for 80% transverse proton polarization measured with 5% accuracy. Systematic uncertainties of 5% are added in quadrature. As shown in Fig. 3, a fit of the generated data for the DVCS cross section and the transverse proton spin asymmetry allows the simultaneous extraction of the GPDs H and E for sea quarks. The fitted data covers the kinematic range $3.2\,\mathrm{GeV}^2 < Q^2 < 17.8\,\mathrm{GeV}^2$, $10^{-4} < x_B < 10^{-2}$ and $0.03\,\mathrm{GeV}^2 < |t| < 1.5\,\mathrm{GeV}^2$. Thanks to the effect of logarithmic scaling violations, even the extraction of H for gluons is possible in this fit, as shown in Fig. 4, whereas the errors on E for gluons are very large.

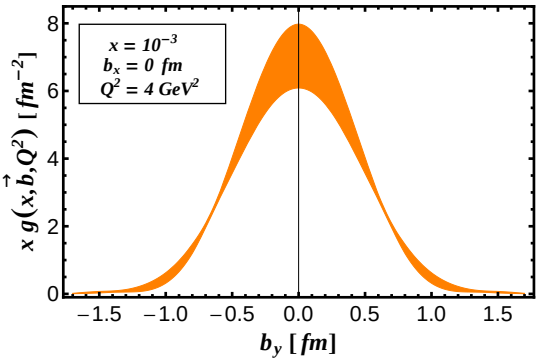

Figure 4: As Fig. 3, but for unpolarized gluons in an unpolarized proton.

Selective information about gluons can be obtained in exclusive J/Ψ production. We have generated pseudo-data for $e^- p \to e^- J/\Psi\, p \to e^-(e^+e^-)\, p$ with a version of PYTHIA modified to describe the H1 and ZEUS measurements of this process. We assume an acceptance in pseudorapidity of $\eta < 5$ for all final-state leptons and an acceptance for the recoil proton as in

the DVCS studies above. The t spectra and corresponding impact parameter distributions in Fig. 5 show that EIC can provide accurate images of gluons in the proton over two orders of magnitude in x.

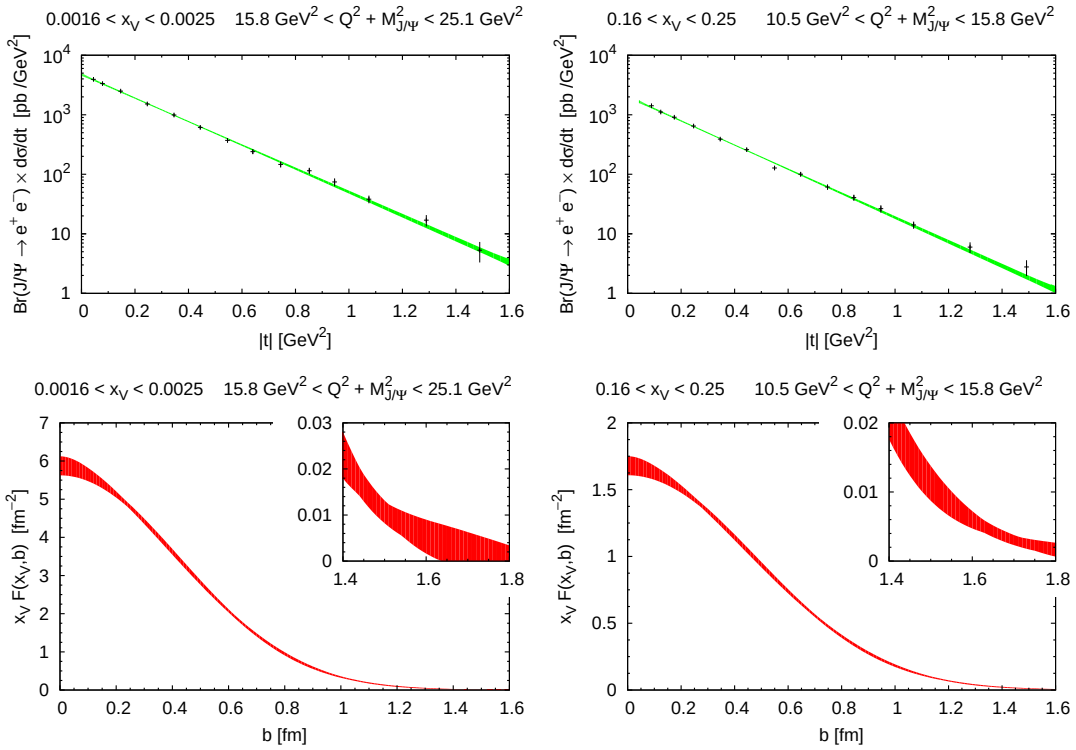

Figure 5: Simulated cross sections for $\gamma^* p \to J/\Psi\, p$ and the corresponding impact parameter distributions for gluons. The left panels are for $E_e = 20\,\text{GeV}$, $E_p = 250\,\text{GeV}$ and the right panels for $E_e = 5\,\text{GeV}$, $E_p = 100\,\text{GeV}$, with $10\,\text{fb}^{-1}$ integrated luminosity in both cases.

Acknowledgments

I gratefully acknowledge collaboration with E.-C. Aschenauer, S. Fazio, K. Kumerčki and D. Müller, who performed the simulations and fits on which the result presented here are based.

References

[1] D. Boer *et al.*, arXiv:1108.1713 [nucl-th].

[2] S. Fazio, talk and proceedings at this conference.

[3] D. Müller, talk and proceedings at this conference, arXiv:1205.6967 [hep-ph].

[4] K. Kumerički and D. Müller, Nucl. Phys. B **841** (2010) 1 [arXiv:0904.0458 [hep-ph]].

[5] M. Strikman and C. Weiss, Phys. Rev. D **69** (2004) 054012 [hep-ph/0308191].

Spacelike and Timelike Compton Scattering: Progress report

H. Moutarde[1], *F. Sabatié*[1]

[1]IRFU/Service de Physique Nucléaire, CEA, Centre de Saclay, F-91191 Gif-sur-Yvette, FRANCE

DOI: http://dx.doi.org/10.3204/DESY-PROC-2012-02/154

We present some recent results on the analysis of hard scattering processes in the framework of Generalized Parton Distributions. In particular we compute DVCS observables on unpolarized targets with the Kroll - Goloskokov model (suited to DVMP analysis). We also discuss NLO contributions to DVCS and TCS processes for various kinematic settings.

1 Introduction

The Deeply Virtual Compton Scattering (DVCS) process is the theoretically cleanest way to access Generalized Parton Distributions (GPD). However Deeply Virtual Meson Production (DVMP) and Timelike Compton Scattering (TCS) measurements will bring further constraints on our experimental knowledge of GPDs (see reviews [1, 2, 3, 4] and references therein).

First we outline some results on exclusive processes and describe a GPD model used for the evaluations presented in this work. Then we estimate the phenomenological impact of Next-to-Leading Order (NLO) corrections to Leading Order (LO) evaluations. The following section confront this GPD model to DVCS measurements. We finish with some technical remarks.

2 Theoretical framework

2.1 Exclusive processes

The partonic interpretation of electroproduction of mesons or real photon relies on the use of factorization theorems. They express observables in terms of Compton Form Factors (CFF), which are convolutions of known kernels with GPDs. That GPDs are universal quantities should be checked to ensure the consistency of this partonic picture. One first step towards this aim consists in confronting a GPD model tailored to study DVMP to DVCS.

2.2 Kroll - Goloskokov GPD model

The Kroll - Goloskokov (KG) model was designed to interpret meson electroproduction. Details about this model can be found in [5, 6, 7]. The GPD H (main contribution to the DVCS observables discussed here) is classically described by a double distribution and a profile function. It is Regge behaved and possesses an exponential dependence in Mandelstam variable t, uncorrelated to the longitudinal momentum transfer x. Its corresponding CFF is denoted $\mathcal{H}$.

3 DVCS and TCS at LO and NLO

3.1 LO and NLO Compton Form Factors

Since the integration kernel of CFFs is singular in the vicinity of the skewness ξ, a CFF a is complex function. At LO the imaginary part of a CFF is simply the singlet GPD evaluated at $x = \xi$, but at NLO both real and imaginary parts involve integrals with logarithmic integrable singularities. Their numerical treatment requires some care, espacially at small ξ [11]. Expressions for CFFs at LO and NLO for DVCS and TCS may be found in [8, 9, 10].

3.2 Estimates for the DVCS and TCS processes

Figure 1 displays the real and imaginary parts of the CFF $\mathcal{H}$ at LO and NLO evaluated at factorization scale 4 GeV^2 and vanishing t for Bjorken $x_B = 2\xi/(1+\xi)$ ranging between 10^{-4} and 1. Although the comparison is model dependent, the typical discrepancy between LO and NLO is 40 % at small ξ. It is maximum around $\xi = 0.1$ (COMPASS - HERMES kinematics).

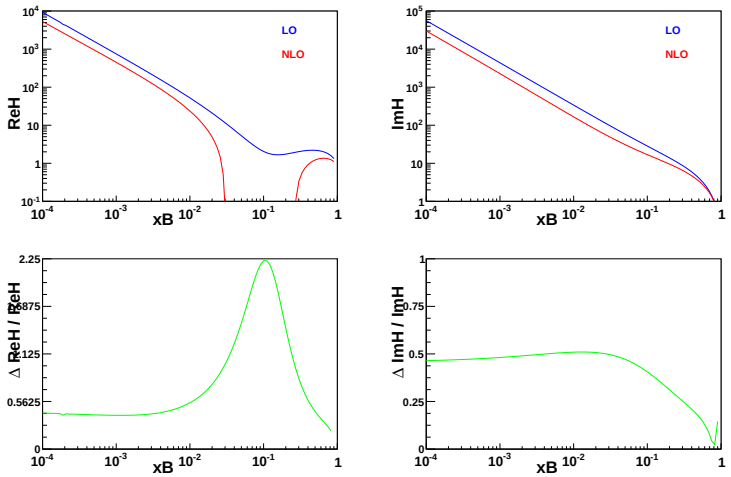

Figure 1: Upper plots: $\mathcal{H}$ at LO and NLO. Lower plots: relative discrepancy at LO and NLO.

4 Computation of DVCS observables

4.1 HERMES observables

The HERMES Collaboration released a great wealth of observables in recent years [12]. Figure 2 shows the $\sin\phi$ harmonics of the Beam Spin Asymmetry (BSA), mostly sensitive to the imaginary part of $\mathcal{H}$ and the $\cos\phi$ harmonics of the Beam Charge Asymmetry (BCA), mostly sensitive to the real part of $\mathcal{H}$. The GK model is in a reasonable agreement with the data.

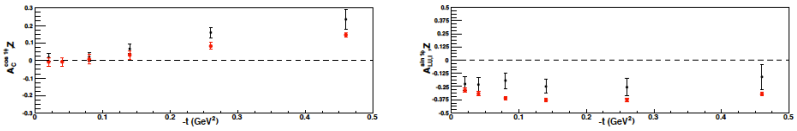

Figure 2: Left: BCA $\cos\phi$ harmonics; Right: BSA $\sin\phi$ harmonics.

4.2 JLab observables

JLab 6 GeV DVCS observables on unpolarized targets [13, 14] cover a wide kinematic range or are highly precise. Figure 3 shows that the GK model tends to underestimate helicity-independent cross sections near $\phi = 180°$. It also overestimates the helicity-dependent cross-sections and BSAs near $\phi = 90°$, see [15] for details.

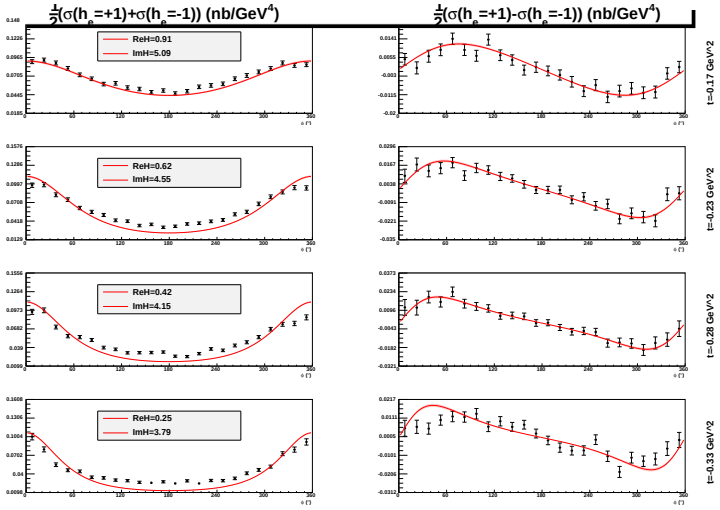

Figure 3: JLab Hall A helicity-dependent and independent cross sections.

5 Technical remarks

5.1 Phenomenology toolkit

Systematic comparisons of GPD models and data require databases of experimental results and theoretical predictions, a fitting engine, tools to propagate statistic and systematic uncertainties and a flexible visualizing software. Ideally the same building blocks should be used for fits to data and designs of new experiments. Part of these building blocks are used here.

5.2 Constraints

After JLab's 12 GeV upgrade, phenomenologists will deal with observables with an advertised statistical accuracy of $\simeq 1\,\%$. It induces some constraints on the aforementioned phenomenology

toolkit. For example the evaluation of CFFs should have an accuracy better than 0.1 % on this kinematic region, which precludes naive integration routines.

6 Conclusions

Some software components for global GPD phenomenology have been developed and extensively tested. The treatment of NLO contributions shows a surprisingly large gluon contribution in the HERMES and COMPASS kinematics, and raises the question of resummation. This study also shows how the expected accuracy of forthcoming data influences the design of software components devoted to GPD phenomenology.

Acknowledgements

The authors would like to thank P. Kroll, B. Pire, L. Szymanowski and J. Wagner who contributed to different parts of the work presented here. The authors also thank the organizers of the 20th International Workshop on Deep-Inelastic Scattering and Related Subjects held in Bonn (March 26 - 30, 2012). This work was supported in part by the Commissariat à l'Energie Atomique and the GDR n° 3034 "Chromodynamique Quantique et Physique des Hadrons".

References

[1] K. Goeke, M.V. Polyakov and M. Vanderhaeghen, Prog. Part. Nucl. Phys. **47**, 401 (2001).

[2] M. Diehl, Phys. Rept. **388**, 41 (2003).

[3] A.V. Belitsky and A.V. Radyushkin, Phys. Rept. **418**, 1 (2005).

[4] S. Boffi and B. Pasquini, Riv. Nuovo Cim. **30**, 387 (2007).

[5] S. Goloskokov and P. Kroll, Eur. Phys. J. C. **42**, 281 (2005).

[6] S. Goloskokov and P. Kroll, Eur. Phys. J. C. **59**, 809 (2009).

[7] M. Diehl, Th. Feldmann, R. Jakob and P. Kroll, Eur. Phys. J. C. **39**, 1 (2005).

[8] A. Belistky, D. Mueller, L. Niedermeier and A. Schaefer, Phys. Lett. B **437**, 160 (1998).

[9] A. Belistky, D. Mueller, L. Niedermeier and A. Schaefer, Nucl. Phys. B **546**, 279 (1999).

[10] B. Pire, L. Szymanowski and J. Wagner, Phys. ReV. D **83**, 2011 (034009).

[11] H. Moutarde, B. Pire, F. Sabatié, L. Szymanowski, J. Wagner, *in preparation.*

[12] M. Murray, *these proceedings.*

[13] C. Muñoz Camacho *et al.*, Phys. Rev. Lett. **97**, 262002 (2006).

[14] F.X. Girod *et al.*, Phys. Rev. Lett. **100**, 162002 (2008).

[15] P. Kroll, H. Moutarde and F. Sabatié, *in preparation.*

Spin structure of the "forward" nucleon charge-exchange reaction $n + p \to p + n$ and the deuteron charge-exchange breakup

Valery V. Lyuboshitz[†], *Vladimir L. Lyuboshitz*

Joint Institute for Nuclear Research, 141980 Dubna, Moscow Region, Russia
[†] E-mail: Valery.Lyuboshitz@jinr.ru

DOI: http://dx.doi.org/10.3204/DESY-PROC-2012-02/18

The structure of the nucleon charge-exchange process $n + p \to p + n$ is investigated basing on the isotopic invariance of the nucleon-nucleon scattering. Using the operator of permutation of the spin projections of the neutron and proton, the connection between the spin matrices, describing the amplitude of the nucleon charge-exchange process at zero angle and the amplitude of the neutron elastic scattering on the proton in the "backward" direction, has been obtained. Due to the optical theorem, the spin-independent part of the differential cross-section of the process $n + p \to p + n$ at zero angle for unpolarized particles is expressed through the difference of total cross-sections of unpolarized proton-proton and neutron-proton scattering. Meantime, the spin-dependent part of this cross-section is proportional to the differential cross-section of the deuteron charge-exchange breakup $d + p \to (pp) + n$ at zero angle at the deuteron momentum $\mathbf{k}_d = 2\,\mathbf{k}_n$ ($\mathbf{k}_n$ is the initial neutron momentum). Analysis shows that, in the wide range of neutron laboratory momenta $k_n > 700\,MeV/c$, the main contribution into the differential cross-section of the process $n + p \to p + n$ at zero angle is provided namely by the spin-dependent term.

1 Isotopic structure of NN-scattering

Taking into account the isotopic invariance, the matrices of amplitudes of proton-proton elastic scattering, neutron-proton elastic scattering and charge transfer process $n + p \to p + n$ are connected by the following relation:

$$\hat{f}_{np\to pn}(\mathbf{p}, \mathbf{p}') = \hat{f}_{pp\to pp}(\mathbf{p}, \mathbf{p}') - \hat{f}_{np\to np}(\mathbf{p}, \mathbf{p}')\,. \tag{1}$$

Here $\mathbf{p}$ and $\mathbf{p}'$ are the initial and final momenta in the c.m. frame, the directions of $\mathbf{p}'$ are defined within the solid angle in the c.m. frame, corresponding to the front hemisphere.

It should be stressed that the differential cross-section of the charge-exchange reaction, defined in the front hemisphere $0 \le \theta \le \frac{\pi}{2}$, $0 \le \phi \le 2\pi$ (here θ is the angle between the momenta of initial neutron and final proton, ϕ is the azimuthal angle), should coincide with the differential cross-section of the elastic neutron-proton scattering into the back hemisphere by the angle $\widetilde{\theta} = \pi - \theta$ at the azimuthal angle $\widetilde{\phi} = \pi + \phi$ in the c.m. frame. Due to the antisymmetry of the state of two fermions with respect to the total permutation, including the permutation of momenta ($\mathbf{p}' \to -\mathbf{p}'$), permutation of spin projections and permutation of

isotopic projections ($p \leftrightarrows n$), the following relation between the amplitudes $\hat{f}_{np\to pn}(\mathbf{p},\mathbf{p}')$ and $\hat{f}_{np\to np}(\mathbf{p},-\mathbf{p}')$ holds [1–4] :

$$\hat{f}_{np\to pn}(\mathbf{p},\mathbf{p}') = -\hat{P}^{(1,2)}\hat{f}_{np\to np}(\mathbf{p},-\mathbf{p}')\,, \tag{2}$$

where $\hat{P}^{(1,2)}$ is the operator of permutation of spin projections of two particles with equal spins; the matrix elements of this operator are [5]:
$\langle m_1' m_2' \mid \hat{P}^{(1,2)} \mid m_1 m_2\rangle = \delta_{m_1' m_2}\delta_{m_2' m_1}$. For particles with spin 1/2 [1–5]

$$\hat{P}^{(1,2)} = \frac{1}{2}(\hat{I}^{(1,2)} + \hat{\boldsymbol{\sigma}}^{(1)}\hat{\boldsymbol{\sigma}}^{(2)}), \tag{3}$$

where $\hat{I}^{(1,2)}$ is the four-row unit matrix, $\hat{\boldsymbol{\sigma}}^{(1)}$, $\hat{\boldsymbol{\sigma}}^{(2)}$ – vector Pauli operators. It is evident that $\hat{P}^{(1,2)}$ is the unitary and Hermitian operator.

Taking into account the relations (2) and (3), the differential cross-sections of the charge-exchange process $n+p\to p+n$ and the elastic np-scattering in the corresponding back hemisphere coincide at any polarizations of initial nucleons:

$$\frac{d\sigma_{np\to pn}}{d\Omega}(\mathbf{p},\mathbf{p}') = \frac{d\sigma_{np\to np}}{d\Omega}(\mathbf{p},-\mathbf{p}'). \tag{4}$$

However, the separation into the spin-dependent and spin-independent parts is <u>different</u> for the amplitudes $\hat{f}_{np\to pn}(\mathbf{p},\mathbf{p}')$ and $\hat{f}_{np\to np}(\mathbf{p},-\mathbf{p}')$!

2 Nucleon charge-exchange process at zero angle

Now let us investigate in detail the nucleon charge transfer reaction $n+p\to p+n$ at zero angle. In the c.m. frame of the (np)-system, the amplitude of the nucleon charge transfer in the "forward" direction $\hat{f}_{np\to pn}(0)$ has the following spin structure:

$$\hat{f}_{np\to pn}(0) = c_1\hat{I}^{(1,2)} + c_2\,[\hat{\boldsymbol{\sigma}}^{(1)}\hat{\boldsymbol{\sigma}}^{(2)} - (\hat{\boldsymbol{\sigma}}^{(1)}\mathbf{l})(\hat{\boldsymbol{\sigma}}^{(2)}\mathbf{l})] + c_3\,(\hat{\boldsymbol{\sigma}}^{(1)}\mathbf{l})(\hat{\boldsymbol{\sigma}}^{(2)}\mathbf{l})\,, \tag{5}$$

where $\mathbf{l}$ is the unit vector directed along the incident neutron momentum. In so doing, the second term in Eq. (5) describes the spin-flip effect, and the third term characterizes the difference between the amplitudes with the parallel and antiparallel orientations of the neutron and proton spins.

The spin structure of the amplitude of the elastic neutron-proton scattering in the "backward" direction $\hat{f}_{np\to np}(\pi)$ is analogous:

$$\hat{f}_{np\to np}(\pi) = \widetilde{c}_1\hat{I}^{(1,2)} + \widetilde{c}_2\,[\hat{\boldsymbol{\sigma}}^{(1)}\hat{\boldsymbol{\sigma}}^{(2)} - (\hat{\boldsymbol{\sigma}}^{(1)}\mathbf{l})(\hat{\boldsymbol{\sigma}}^{(2)}\mathbf{l})] + \widetilde{c}_3\,(\hat{\boldsymbol{\sigma}}^{(1)}\mathbf{l})(\hat{\boldsymbol{\sigma}}^{(2)}\mathbf{l}). \tag{6}$$

However, the coefficients $\widetilde{c}$ in Eq.(6) <u>do not coincide</u> with the coefficients c in Eq.(5). According to Eq.(2), the connection between the amplitudes $\hat{f}_{np\to pn}(0)$ and $\hat{f}_{np\to np}(\pi)$ is the following:

$$\hat{f}_{np\to pn}(0) = -\hat{P}^{(1,2)}\hat{f}_{np\to np}(\pi)\,, \tag{7}$$

where the unitary operator $\hat{P}^{(1,2)}$ is determined by Eq.(3).

As a result of calculations with Pauli matrices, we obtain:

$$c_1 = -\frac{1}{2}\,(\widetilde{c}_1 + 2\widetilde{c}_2 + \widetilde{c}_3); \quad c_2 = -\frac{1}{2}\,(\widetilde{c}_1 - \widetilde{c}_3); \quad c_3 = -\frac{1}{2}\,(\widetilde{c}_1 - 2\widetilde{c}_2 + \widetilde{c}_3). \tag{8}$$

Hence, it follows from here that the "forward" differential cross-section of the nucleon charge-exchange reaction $n+p \to p+n$ for unpolarized initial nucleons is described by the expression:

$$\frac{d\sigma_{np\to pn}}{d\Omega}(0) = |c_1|^2 + 2|c_2|^2 + |c_3|^2 =$$

$$= \frac{1}{4}\,|\widetilde{c}_1 + 2\widetilde{c}_2 + \widetilde{c}_3|^2 + \frac{1}{2}\,|\widetilde{c}_1 - \widetilde{c}_3|^2 + \frac{1}{4}\,|\widetilde{c}_1 - 2\widetilde{c}_2 + \widetilde{c}_3|^2 = |\widetilde{c}_1|^2 + 2|\widetilde{c}_2|^2 + |\widetilde{c}_3|^2. \tag{9}$$

Thus, $\frac{d\sigma_{np\to pn}}{d\Omega}(0) = \frac{d\sigma_{np\to np}}{d\Omega}\ (\pi)$, just as it must be in accordance with the relation (4).

The differential cross-section of the process $n + p \to p + n$ in the "forward" direction for unpolarized nucleons can be presented in the following form, distinguishing the spin-independent and spin-dependent parts:

$$\frac{d\sigma_{np\to pn}}{d\Omega}(0) = \frac{d\sigma^{(si)}_{np\to pn}}{d\Omega}(0) + \frac{d\sigma^{(sd)}_{np\to pn}}{d\Omega}(0)\,. \tag{10}$$

In doing so, in accordance with the optical theorem, the spin-independent part $\frac{d\sigma^{(si)}_{np\to pn}}{d\Omega}(0)$ in Eq.(10) is determined by the difference of total cross-sections of the unpolarized proton-proton and neutron-proton interaction:

$$\frac{d\sigma^{(si)}_{np\to pn}}{d\Omega}(0) = |c_1|^2 = \frac{k^2}{16\pi^2}(\sigma_{pp} - \sigma_{np})^2(1+\alpha^2)\,, \tag{11}$$

where $k = |\mathbf{p}| = |\mathbf{p}'|$ is the modulus of neutron momentum in the c.m. frame of the colliding nucleons [1)], $\alpha = \mathrm{Re}\ c_1/\mathrm{Im}\ c_1$. The spin-dependent part of the cross-section of the "forward" charge-exchange process is

$$\frac{d\sigma^{(sd)}_{np\to pn}}{d\Omega}(0) = 2|c_2|^2 + |c_3|^2. \tag{12}$$

Meantime, according to Eqs. (6), (8) and (9), the spin-dependent part of the cross-section of the "backward" elastic np-scattering is

$$\frac{d\sigma^{(sd)}_{np\to np}}{d\Omega}(\pi) = 2|\widetilde{c}_2|^2 + |\widetilde{c}_3|^2. \tag{13}$$

We see that $\frac{d\sigma^{(sd)}_{np\to pn}}{d\Omega}(0) \neq \frac{d\sigma^{(sd)}_{np\to np}}{d\Omega}(\pi)$.

Further it is advisable to deal with the differential cross-section $\left.\frac{d\sigma}{dt}\right|_{t=0}$, being a relativistic invariant ($t = -(p_1 - p_2)^2 = (\mathbf{p} - \mathbf{p}')^2 - (E - E')^2 = 2k^2(1 - \cos\theta)$). In this representation, the spin-independent and spin-dependent parts of the differential cross-section of the "forward"

[1)] We use the unit system with $\hbar = c = 1$.

charge transfer process $\left.\frac{d\sigma_{np\to pn}}{dt}\right|_{t=0}$ are as follows: $\left.\frac{d\sigma^{(si)}_{np\to pn}}{dt}\right|_{t=0} = (\pi/k^2)\,|c_1|^2$, $\left.\frac{d\sigma^{(sd)}_{np\to pn}}{dt}\right|_{t=0}$ $= (\pi/k^2)\,(2|c_2|^2 + |c_3|^2)$.

Now it should be noted that, in the framework of the impulse approach, there exists a simple connection between the spin-dependent part of the differential cross-section of the charge-exchange reaction $n + p \to p + n$ at zero angle $\left.\frac{d\sigma^{(sd)}_{np\to pn}}{dt}\right|_{t=0}$ (not the "backward" elastic neutron-proton scattering, that would be an error !) and the differential cross-section of the deuteron charge-exchange breakup $d + p \to (pp) + n$ in the "forward" direction $\left.\frac{d\sigma_{dp\to(pp)n}}{dt}\right|_{t=0}$ at the deuteron momentum $\mathbf{k}_d = 2\mathbf{k}_n$ ($\mathbf{k}_n$ is the the initial neutron momentum) . In the case of unpolarized particles we have [6–8]:

$$\left.\frac{d\sigma_{dp\to(pp)n}}{dt}\right|_{t=0} = \frac{2}{3}\left.\frac{d\sigma^{(sd)}_{np\to pn}}{dt}\right|_{t=0}. \tag{14}$$

In doing so, this formula remains still valid if one takes into account the deuteron D-wave state [8].

It is easy to understand also that, due to the isotopic invariance, the same relation (like Eq. (14)) takes place for the process $p + d \to n + (pp)$ at the proton laboratory momentum $\mathbf{k}_p = \mathbf{k}_n$ and for the process $n + d \to p + (nn)$ at the neutron laboratory momentum $\mathbf{k}_n$.

As a result, it follows from Eqs. (10),(11) and (14) that

$$\left.\frac{d\sigma_{np\to pn}}{dt}\right|_{t=0} = \frac{3}{2}\left.\frac{d\sigma_{dp\to(pp)n}}{dt}\right|_{t=0} + \frac{1}{16\pi}(\sigma_{pp} - \sigma_{np})^2(1 + \alpha^2)\,. \tag{15}$$

Thus, in principle, taking into account Eqs. (14) and (15), the modulus of the ratio of the real and imaginary parts of the spin-independent charge transfer amplitude at zero angle ($|\,\alpha\,|$) may be determined using the experimental data on the cross-sections.

The analysis shows: if we suppose that the real part of the spin-independent amplitude of charge transfer $n+p \to p+n$ at zero angle is smaller or of the same order as compared with the imaginary part ($\alpha^2 \lesssim 1$), then it follows from the available experimental data on the differential cross-section of charge transfer $\left.\frac{d\sigma_{np\to pn}}{dt}\right|_{t=0}$ and the data on the total cross-sections σ_{pp} and σ_{np} that the main contribution into the cross-section $\left.\frac{d\sigma_{np\to pn}}{dt}\right|_{t=0}$ is provided namely by the spin-dependent part $\left.\frac{d\sigma^{(sd)}_{np\to pn}}{dt}\right|_{t=0}$.

If the differential cross-section $\frac{d\sigma}{dt}$ is given in the units of $mbn/\left(\frac{GeV}{c}\right)^2$ and the total cross-sections are given in mbn, then the spin-independent part of the "forward" charge transfer cross-section may be expressed in the form :

$$\left.\frac{d\sigma^{(si)}_{np\to pn}}{dt}\right|_{t=0} \approx 0.0512\,(\sigma_{pp} - \sigma_{np})^2(1 + \alpha^2). \tag{16}$$

Using (16) and the data from the works [9–11], we obtain – assuming $\alpha^2 \lesssim 1$ – the estimates of the ratio $\left.\frac{d\sigma^{(si)}_{np\to pn}}{dt}\right|_{t=0} \Big/ \left.\frac{d\sigma_{np\to pn}}{dt}\right|_{t=0}$, for different values of the neutron laboratory

momentum $k_n = (0.7 \div 2.5)\ \frac{GeV}{c}$, at the level of $(10 \div 20)\%$, i.e. the spin-dependent part provides at least $(80 \div 90)\%$ of the total magnitude of the "forward" charge transfer cross section (see also [1–4]) .

The experimental data on the differential cross-sections of "forward" deuteron charge-exchange breakup processes $d + p \to (pp) + n$ and $n + d \to (nn) + p$ (see [4] and references therein), obtained recently in Dubna (JINR, Laboratory of High Energy Physics), also confirm the conclusion about the predominant role of the spin-dependent part of the differential cross-section of the nucleon charge-exchange reaction $n + p \to p + n$ in the "forward" direction.

References

[1] V. L. Lyuboshitz, V. V. Lyuboshitz, in Proceedings of the XI International Conference on Elastic and Diffractive Scattering (Blois, France, May 15 - 20, 2005), Gioi Publishers, 2006, p.223 .

[2] V. L. Lyuboshitz and V. V. Lyuboshitz, in Proceedings of the 17-th International Spin Physics Symposium – SPIN2006 (Kyoto, Japan, October 2 - 7, 2006), AIP Conf. Proc. **915** (2007) 789 .

[3] V. L. Lyuboshitz and V. V. Lyuboshitz, in Proceedings of the 20-th European Conference on Few-Body Problems in Physics – EFB20 (Pisa, Italy, September 10 - 14, 2007), Few-Body Systems **44** (2008) 61 .

[4] V. L. Lyuboshitz, V. V. Lyuboshitz. Yad. Fiz. **74** (2011) 324 [Phys. At. Nucl. **74** (2011) 306].

[5] V. L. Lyuboshitz and M. I. Podgoretsky, Phys. At. Nucl. **59** (1996) 449 .

[6] N. W. Dean, Phys. Rev. **D5** (1972) 1661; Phys. Rev. **D5** (1972) 2832 .

[7] V. V. Glagolev, V. L. Lyuboshitz, V. V. Lyuboshitz, N. M. Piskunov, JINR Communication **E1-99-280**, Dubna, 1999 .

[8] R. Lednicky, V. L. Lyuboshitz, V. V. Lyuboshitz, in Proceedings of the XVI International Baldin Seminar on High Energy Physics Problems (JINR **E1,2-2004-76**, Dubna, 2004), vol.I, p.199.

[9] P. F. Shepard *et al.*, Phys. Rev. **D10** (1974) 2735 .

[10] T. J. Delvin *et al.*, Phys. Rev. **D8** (1973) 136 .

[11] J. L. Friedes *et al.*, Phys. Rev. Lett. **15** (1965) 38 .

Overview of Deeply Virtual Compton Scattering at HERMES

Morgan Murray[1] on behalf of the HERMES Collaboration.

[1] Rm.514b, University of Glasgow, Glasgow, G12 8QQ, Scotland

DOI: http://dx.doi.org/10.3204/DESY-PROC-2012-02/4

Deeply Virtual Compton Scattering represents the best experimental channel through which to understand Generalised Parton Distributions. The HERMES experiment measured the most diverse set of DVCS results of any experiment; this talk discusses the most recent sets of DVCS results released by HERMES and the unique experimental conditions found at HERMES that facilitated the measurements. We also examine the various ways in which the HERMES experimental measurements are being used to constrain GPDs and how future experiments can learn from the HERMES program.

1 Introduction

The HERMES experiment at DESY ran from 1995 to 2007 as a forward spectrometer on the HERA electron/positron beam. Its original *raison d'être* was the investigation of the spin structure of the nucleon, a purpose continued in the later years of the experiment's lifetime with its focus on exclusive physics. These proceedings report briefly on selected HERMES results on Deeply Virtual Compton Scattering, i.e. the electroproduction of real photons on typically a Hydrogen target.

The study of exclusive physics is performed with a view to obtaining information on Generalised Parton Distributions (GPDs). These theoretical objects contain a wealth of information on nucleonic structure, including a way to access the total angular momentum of the constituent partons [1] and correlated information pertaining to the distribution of partons in the transverse spatial plane of the nucleon with the fraction of the nucleon's longitudinal momentum carried by that parton [2]. There are four distributions of interest that are expected to enter into typical scattering experiments at leading twist with the least kinematical suppression: $H, E, \widetilde{H}$ and $\widetilde{E}$. Generalised Parton Distributions only describe the soft part of the diagram and thus appear in data from lepton scattering experiments convoluted with a hard scattering kernel [3]. The resultant distribution is referred to a Compton Form Factor (CFF) and is typically denoted $\mathcal{H}, \mathcal{E}, \widetilde{\mathcal{H}}$ and $\widetilde{\mathcal{E}}$ for GPDs $H, E, \widetilde{H}$ and $\widetilde{E}$ respectively.

The process $ep \to ep\gamma$ has two contributors; alongside the DVCS process there is a contribution from the Bethe-Heitler process (ep scattering with a Bremsstrahlung photon). The scattering amplitudes from each process interfere and provide the cross-section with three contributory terms: one term from the squared amplitude from each process and one from the interference between the two processes. Typically at the kinematic space covered by HERMES the BH process dominates but access to the large interference term can provide information

derived from CFFs and thus GPDs.

2 The HERMES Experiment

The HERMES experiment has been covered in detail in the literature, eg. [4], and no such detailed description will be repeated here. This work will refer solely to BH/DVCS detected by scattering a positron or electron off a proton target, with the produced photon being detected in the electromagnetic calorimeter. Bethe Heitler/Deeply Virtual Compton Scattering events are traditionally selected at HERMES by use of a missing mass technique — the recoiling proton is scattered outside of the HERMES acceptance, so the final data sample comprises the desired BH/DVCS candidate events and some background processes [5]–[13]. The largest contributor to these background processes is BH involving a proton resonance which typically makes up approx. 10% of the data sample. The HERMES spectrometer was upgraded in 2006 with a recoil proton detector in the target region [14] in order to eliminate this background process. The HERMES set of DVCS results now includes a beam helicity measurement made using this procedure.

3 Deeply Virtual Compton Scattering

HERMES was designed to measure asymmetries. Asymmetries in the azimuthal distribution (ϕ) of the produced real photon in DVCS are measured to provide information that can be used to constrain Generalised Parton Distributions [3]. As a consequence of the unique HERMES setup, there are several different combinations of beam and target states that can supply useful information for DVCS:

$$\mathcal{A}_{\mathrm{C}}(\phi) \equiv \frac{\mathrm{d}\sigma^{+}(\phi)-\mathrm{d}\sigma^{-}(\phi)}{\mathrm{d}\sigma^{+}(\phi)+\mathrm{d}\sigma^{-}(\phi)} \tag{1}$$

$$\mathcal{A}_{\mathrm{LU}}(\phi) \equiv \frac{\mathrm{d}\sigma^{\rightarrow}(\phi)-\mathrm{d}\sigma^{\leftarrow}(\phi)}{\mathrm{d}\sigma^{\rightarrow}(\phi)+\mathrm{d}\sigma^{\leftarrow}(\phi)} \tag{2}$$

$$\mathcal{A}_{\mathrm{UT}}(\phi) \equiv \frac{\mathrm{d}\sigma^{\Uparrow}(\phi)-\mathrm{d}\sigma^{\Downarrow}(\phi)}{\mathrm{d}\sigma^{\Uparrow}(\phi)+\mathrm{d}\sigma^{\Downarrow}(\phi)} \tag{3}$$

$$\mathcal{A}_{\mathrm{LT}}(\phi) \equiv \frac{\left(\mathrm{d}\sigma^{\vec{\Uparrow}}(\phi)+\mathrm{d}\sigma^{\overleftarrow{\Downarrow}}(\phi)\right)-\left(\mathrm{d}\sigma^{\vec{\Downarrow}}(\phi)+\mathrm{d}\sigma^{\overleftarrow{\Uparrow}}(\phi)\right)}{\left(\mathrm{d}\sigma^{\vec{\Uparrow}}(\phi)+\mathrm{d}\sigma^{\overleftarrow{\Downarrow}}(\phi)\right)+\left(\mathrm{d}\sigma^{\vec{\Downarrow}}(\phi)+\mathrm{d}\sigma^{\overleftarrow{\Uparrow}}(\phi)\right)} \tag{4}$$

$$\mathcal{A}_{\mathrm{UL}}(\phi) \equiv \frac{\mathrm{d}\sigma^{\Rightarrow}(\phi)-\mathrm{d}\sigma^{\Leftarrow}(\phi)}{\mathrm{d}\sigma^{\Rightarrow}(\phi)+\mathrm{d}\sigma^{\Leftarrow}(\phi)} \tag{5}$$

$$\mathcal{A}_{\mathrm{LL}}(\phi) \equiv \frac{\left(\mathrm{d}\sigma^{\vec{\Rightarrow}}(\phi)+\mathrm{d}\sigma^{\overleftarrow{\Leftarrow}}(\phi)\right)-\left(\mathrm{d}\sigma^{\vec{\Leftarrow}}(\phi)+\mathrm{d}\sigma^{\overleftarrow{\Rightarrow}}(\phi)\right)}{\left(\mathrm{d}\sigma^{\vec{\Rightarrow}}(\phi)+\mathrm{d}\sigma^{\overleftarrow{\Leftarrow}}(\phi)\right)+\left(\mathrm{d}\sigma^{\vec{\Leftarrow}}(\phi)+\mathrm{d}\sigma^{\overleftarrow{\Rightarrow}}(\phi)\right)} \tag{6}$$

Here $\rightarrow$ ($\leftarrow$) refers to the direction of the beam helicity and $\Uparrow$ ($\Downarrow$, $\Rightarrow$, $\Leftarrow$) refers to the direction of the target helicity. The beam charge asymmetry in Eq. 1 is sensitive mostly to the real part of CFF $\mathcal{H}$, the beam helicity asymmetry in Eq. 2 is sensitive mostly to the imaginary part of CFF $\mathcal{H}$, the longitudinal target spin asymmetry in Eq. 5 provides access to the imaginary part of $\widetilde{\mathcal{H}}$ and the double spin asymmetry in Eq. 6 provides access to the real part of $\widetilde{\mathcal{H}}$. Since

HERA supplied both beam charges, the interference and DVCS contributions to Eq. 2 can be extracted separately.

There are currently two approaches for obtaining GPD information from experimental data. One approach is to fit the CFFs from experimental measurements of asymmetries simultaneously, thus revealing information on the CFFs but not the underlying GPDs [16]. The second approach is to postulate GPDs from first principles and work through the detailed calculations to produce predictions for asymmetries. The underlying calculations can then be revised to provide predictions that are more consistent with the observed data [17], [18]. There have also recently been explorations into the extraction of GPDs from HERMES data using neural networks [19].

4 DVCS Measurements @ HERMES

Two of the DVCS measurements made at HERMES are presented in Fig. 1. They correspond to the asymmetries in Eqs. 1 and 2. The lower panel in each of the figures shows the expected contamination in the data sample from resonance events. Asymmetries with a leading twist contribution from GPD H are given by the $\cos\phi$ harmonic in the upper plot in Fig. 1 and the $\sin\phi$ harmonic in the lower plot in Fig. 1. The other harmonics in the plots show sub-leading twist contributions or harmonics that are expected to be significantly suppressed at HERMES kinematics. All of these higher-twist amplitudes are compatible with zero.

The beam helicity asymmetry has also been measured at HERMES using a kinematically complete event selection technique [15]. Extractions of the asymmetry amplitudes of Eqs. 3, 4, 5 and 6 have also been published by HERMES [7, 11, 13].

References

[1] X. Ji Phys. Rev. Lett. **78** (1997) 610.

[2] M. Burkardt Phys. Rev. **D62** (2000) 071503.

[3] A. Belitsky, A. Kirchner and D. M'uller Nucl. Phys. **B629** (2002) 323.

[4] K. Ackerstaff *et al.* Nucl. Instrum. Meth. **A417** (1998) 230.

[5] A. Airapetian *et al.* Phys. Rev. Lett. **87** (2001) 182001.

[6] A. Airapetian *et al.* Phys. Rev. **D75** (2007) 011103.

[7] A. Airapetian *et al.* JHEP **06** (2008) 066.

[8] A. Airapetian *et al.* JHEP **11** (2009) 083.

[9] A. Airapetian *et al.* Nucl. Phys. **B829** (2010) 001.

[10] A. Airapetian *et al.* Phys. Rev. **C81** (2010) 035202.

[11] A. Airapetian *et al.* JHEP **06** (2010) 019.

[12] A. Airapetian *et al.* Nucl. Phys. **B842** (2011) 265.

[13] A. Airapetian *et al.* Phys. Lett. **B704** (2011) 015.

[14] R. Kaiser *et al.* HERMES 02-003 (2002)

[15] J. Bowles, C. Riedl and S. Yaschenko DIS Procs. (2011)

[16] M. Guidal and H. Moutarde Eur. Phys. J. **A42** (2009) 071.

[17] K. Kumerički and D. Müller Nuc. Phys. **B841** (2010) 001.

[18] G. Goldstein, O. Gonzalez and S. Liuti Phys. Rev. **D84** (2011) 034007.

[19] K. Kumerički, D. Müller and A. Schäfer JHEP **07** (2011) 073.

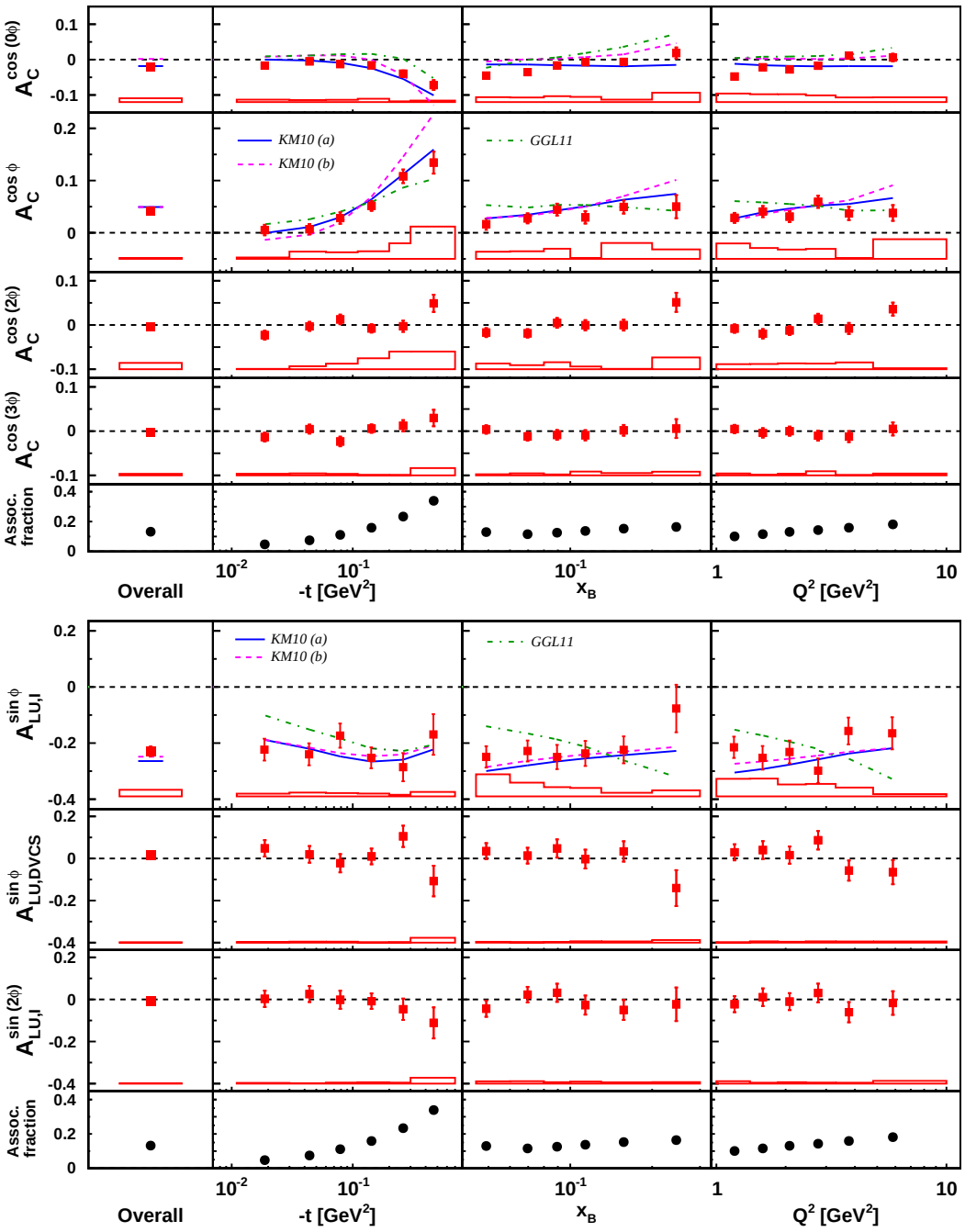

Figure 1: The Beam Charge Asymmetry (top) and Beam Helicity Asymmetry (bottom) measured using a missing-mass technique at HERMES. See text for details.

Deeply Virtual Compton Scattering with CLAS and CLAS12

Daria Sokhan[1] on behalf of the CLAS Collaboration

[1]IPN Orsay, Bat 100 - M053, Orsay 91406, France

DOI: http://dx.doi.org/10.3204/DESY-PROC-2012-02/355

Two very effective means of accessing Generalised Parton Distributions of the nucleon are Deeply Virtual Compton Scattering (DVCS) and Meson Production (DVMP). Jefferson Laboratory, USA, previously operational with a 6 GeV electron beam and currently undergoing an upgrade to 12 GeV, is ideally suited for measuring these processes. This paper focuses on a selection of recent results from the very active DVCS experimental programme with the large angle spectrometer CLAS, and introduces the exciting programme planned for its successor suite of detectors, CLAS12, in the vast, as yet unprobed kinematic region opening up to experiment.

1 Introduction

Studying the nucleon via the scattering of a high energy electron reveals different facets of its structure depending on the reaction observed. A three-dimensional image of the nucleon can be produced from measurements in deep exclusive reactions, which, for example, give access to Generalised Parton Distributions (GPDs), functions relating the transverse position of quarks to their longitudinal momentum.

Two powerful experimental methods for accessing GPDs are via Deeply Virtual Compton Scattering (DVCS) and Meson Production (DVMP), where a high energy electron scatters from a single quark in the nucleon and a high energy real photon or meson is produced as a result. The process is determined by the variables Q^2 (the virtuality of the photon exchanged between the scattered electron and the quark), x (the fractional longitudinal momentum of the struck quark), ξ (the fractional change in the longitudinal momentum of the struck quark) and t (the squared momentum change of the nucleon). In the kinematic regime of high Q^2 and low t, DVCS and DVMP give access to four GPDs: H, $\tilde{H}$, E and $\tilde{E}$ for each quark flavour.

In DVCS, the sensitivity of the experiment to different GPDs can be vastly increased if — in addition to measuring cross-sections — the polarisation of either beam or target (or both) is a controlled parameter: by measuring spin asymmetries (differences of cross-sections for opposite polarisation states divided by their sum). By applying fits to the measured asymmetries, it is possible to extract, in a model-independent way, Compton Form Factors (CFFs), which form the real and imaginary parts of combinations of GPD functions at certain x-values or their integrals along x. Since x is not an experimentally-accessible parameter in DVCS, model-application is then required to extract GPDs from the CFFs. The contributions of certain GPDs to some spin asymmetries are kinematically suppressed, depending on which polarisation states and nucleon target are used. Thus, for example, the beam-spin asymmetry on the proton is dominated by

GPD H, while on the neutron by GPD E. To enable a full extraction of GPDs it is therefore necessary to measure a wide range of observables, on both the proton and the neutron, and across maximally wide regions of phase space.

A significant advantage of meson production is that it gives additional access to quark-flavour decomposition, although the extraction of GPDs is made more complicated than in the case of DVCS by the stronger higher-twist contributions. Cross-sections for the production of vector mesons are sensitive to GPDs H and E, while those for pseudo-scalar mesons have high sensitivity to $\tilde{H}$ and $\tilde{E}$. Due to length constraints, we do not discuss DVMP results in the section below.

2 DVCS experiments with CLAS at Jefferson Lab — 6 GeV era

A very rich experimental programme in measurements of DVCS has been underway at Jefferson Laboratory, using its high intensity electron beam accelerator, which has just come to the end of its 6 GeV era, and the large angle spectrometer CLAS positioned in Hall B. In the past years, following a number of first measurements from early electroproduction experiments [1, 2], two dedicated experiments — both using polarised electron beams — have been carried out using CLAS. The first of these had an unpolarised H_2 target and allowed measurements of cross-sections and beam-spin asymmetries to be extracted on the proton (Figure 1), the second used a polarised H_2 target and also took a small pilot data sample with a liquid D_2 target. These data are currently under analysis for the extraction of cross-sections, beam-spin (Figure 2(a)), target-spin (Figure 2(b)) and double-spin asymmetries in DVCS on the proton and neutron, and for cross-section measurements of DVMP on the proton.

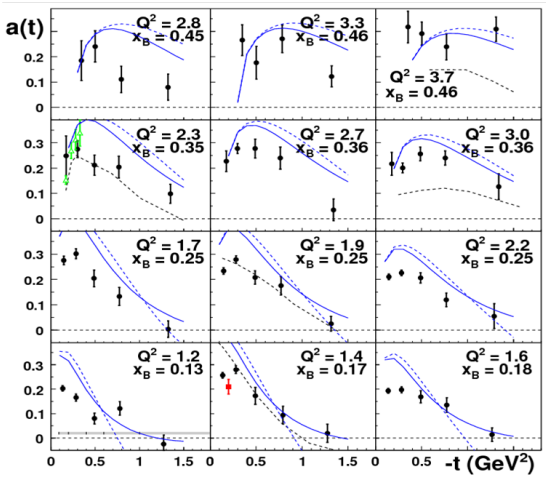

Figure 1: Beam-spin asymmetry (a(t)) in $ep \to e'p'\gamma$ [3] (round points), compared to model predictions: the solid line in each plot is VGG twist-2 [4], the dashed line above it is VGG twist-3, the darker dashed line below the solid one is the Regge model prediction. Points — square: previous CLAS result, triangle: Jefferson Lab Hall A result.

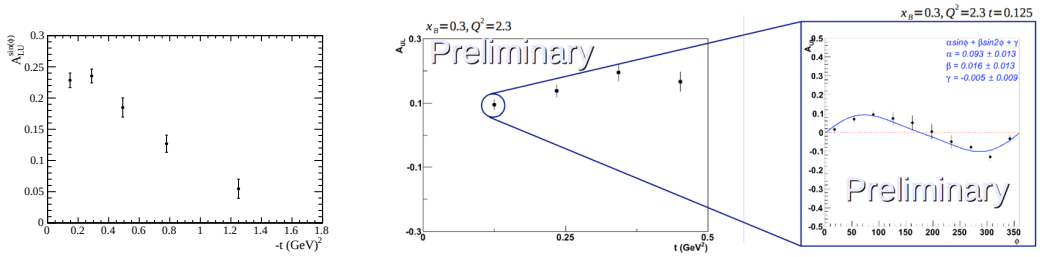

(a) (b)

Figure 2: Preliminary extraction of beam-spin, A_{LU} (left) and target-spin, A_{UL} (right) asymmetry in $ep \to e'p'\gamma$, uncorrected for background, from the recent CLAS experiment "eg1-dvcs" (*E. Seder, G. Smith, private communication 2012.*) The graph on the right shows how a single value of A_{UL} is determined from a fit to the ϕ-asymmetry.

The published beam-spin and target-spin asymmetries from CLAS have been analysed, in an almost model-independent way, for the extraction of the $\Im\mathfrak{m}H$ and $\Im\mathfrak{m}\tilde{H}$ CFFs (Figure 3). One of the resulting conclusions of their observed slopes in the dependence on t suggests that the axial charge may be more concentrated in the proton than the electromagnetic charge.

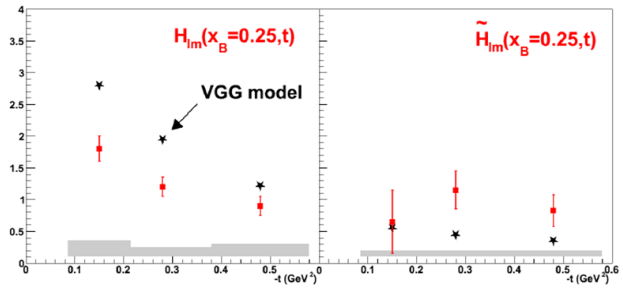

Figure 3: Comparison of CFF extracted with the technique of ref. [4] from data measured by CLAS (square) and predicted by the VGG model (star) as a function of t.

3 CLAS12 at Jefferson Lab — 12 GeV era

The Jefferson Lab accelerator is currently undergoing an upgrade to double its maximum energy of operation to 12 GeV, with 11 GeV deliverable to Hall B, where the design and construction of CLAS12 — a new set of detectors optimised for reconstruction of electroproduction events in the vast new region of phase space being opened to experiment (Figure 4) — is underway. The rich experimental programme proposed for CLAS12 includes, amongst others, experiments to measure DVCS and DVMP in the totally new kinematic region.

Specifically, the experimental DVCS programme approved includes 85 days with a polarised beam (expected degree of polarisation $\approx 85\%$) and an unpolarised H_2 target and 120 days with

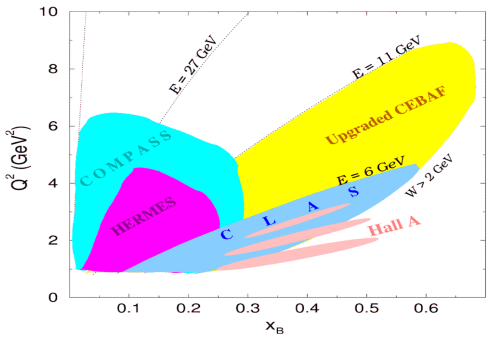

Figure 4: Regions of phase space covered by the existing facilities for electroproduction experiments, showing the vast new kinematic region covered by CLAS12.

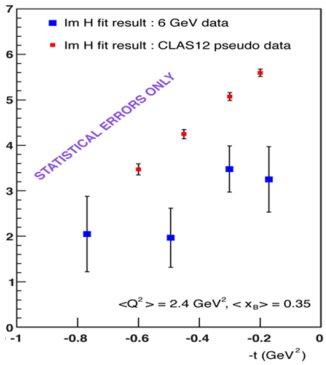

Figure 5: Comparison of the statistical error-bars on $\Im\mathrm{m}H$ extracted from fits to CLAS data (big squares) and expected from the proposed CLAS12 experiment (H. Moutarde).

a longitudinally polarised H_2 target to measure beam- and target-spin asymmetries in DVCS on the proton, covering the kinematic regions $1 < Q^2 < 10$ GeV^2, $0.1 < x_B < 0.65$ and $t < 2.5$ GeV^2. As an example, the projected effect on the model-dependent extraction of $\Im\mathrm{m}H$ can be seen in Figure 5, where the great reduction in the error-bars on the CFF is evident. Additionally, a proposal to measure exclusive DVCS on the neutron has been accepted last year [5], which will be the first extensive measurement of this reaction. The experiment has been accorded 80 days of beam-time on an unpolarised deuterium target. In this kinematic regime, neutron DVCS is extremely sensitive to GPD E, which is the least known and least constrained of the four GPDs. It is particularly important, however, as it features prominently in Ji's so-called "Sum Rule", which relates the total angular momentum of the quarks to the GPDs E and H. A measurement of E, therefore, has the potential to shed important light on the puzzle of nucleon spin. To enable exclusive measurements of neutron DVCS, a neutron detector optimised for the DVCS kinematics at 11 GeV and for the space and technical constraints of CLAS12 has been designed – and is currently under construction – at IPN Orsay.

Other opportunities at CLAS12 for 11 GeV include DVCS with a transversely polarised proton target, which would allow measurement of the transverse-spin asymmetries highly sensitive to the GPD E (and as a result to the up-quark contributions to proton spin), as well as measurements of the polarised and unpolarised DVCS cross-sections and both vector and pseudo-scalar meson production. CLAS12 will be the world's only full acceptance, general purpose detector for high luminosity electron scattering experiments, and will be perfectly suited for the GPD programme.

References

[1] **CLAS** Collaboration, S. Stepanyan *et al.* Phys. Rev. Lett. **87** (2001) 182002.

[2] **CLAS** Collaboration, S. Chen *et al.* Phys. Rev. Lett. **97** (2006) 072002.

[3] **CLAS** Collaboration, F.-X. Girod *et al.* Phys. Rev. Lett. **100** (2008) 162002.

[4] M. Guidal Phys. Lett. B **689** (2010) 156-162.

[5] JLAB PR12-11-003, Spokesperson: S. Niccolai (2011).

Hard Exclusive ρ^0-Meson Production at COMPASS

Heiner Wollny for the COMPASS collaboration

CEA Saclay, 91191 Gif-sur-Yvette, France

DOI: http://dx.doi.org/10.3204/DESY-PROC-2012-02/127

New results for the transverse target spin azimuthal asymmetry $A_{UT}^{\sin(\phi-\phi_S)}$ for hard exclusive ρ^0-meson production on a transversely polarised ^{6}LiD and NH_3 target will be presented. The measurement was performed with the COMPASS detector using the 160 GeV/c muon beam of the SPS at CERN. The asymmetry is sensitive to the nucleon helicity-flip generalised parton distribution E, which is related to the orbital angular momentum of quarks in the nucleon.

1 Introduction

Hard exclusive vector meson production on nucleons is an important tool to study strong interactions. Moreover, in Bjorken kinematics it provides access to generalised parton distributions (GPDs) [1, 2, 3]. The GPDs contain a wealth of information on the structure of the nucleon. In particular, they embody both nucleon electromagnetic form factors and parton distribution functions. Furthermore GPDs correlate longitudinal momenta and transverse spatial position of partons referred to as 3-dimensional nucleon tomography [4] .

At leading twist, vector meson production is described by the GPDs H^f and E^f, where f denotes a quark of flavour f or a gluon. The GPDs are functions of t, x and ξ, where t is the squared four-momentum transfer to the nucleon, x is the average and ξ is half the difference of the longitudinal momenta carried by the struck parton in the initial and final state. The GPDs H^f describe the case where the nucleon-helicity is conserved in the scattering process, whereas the GPDs E^f describe the case of nucleon-helicity flip. Hence, in the latter case angular momentum must be involved in order to conserve total angular momentum. The Ji relation, connects the total angular momentum of a given parton species f to the second moment of the sum of GPDs H^f and E^f [3]:

$$J^f = \frac{1}{2}\lim_{t\to 0}\int_{-1}^{1} \mathrm{d}x\, x\left[H^f(x,\xi,t) + E^f(x,\xi,t)\right]. \tag{1}$$

This relation attracted much attention since it is the only known way to constrain the quark angular momentum to the nucleon spin budget. In vector meson production on unpolarised nucleons the GPDs E^f are suppressed in COMPASS kinematics and one is only sensitive to the GPDs H^f. However, in the cross-section for transversely polarised nucleons the GPDs E^f appear at leading twist in the azimuthal asymmetry $A_{UT}^{\sin(\phi-\phi_S)}$. Here, the indices U and T refer to the unpolarised beam and transversely polarised target, respectively. The superscript $\sin(\phi-\phi_S)$ indicates the type of azimuthal modulation of the cross-section, where ϕ is the azimuthal angle between lepton scattering plane and the plane defined by the virtual photon

and the produced meson, and ϕ_S is the azimuthal angle of the target spin vector relative to the lepton scattering plane. In this paper the asymmetry $A_{UT}^{\sin(\phi-\phi_S)}$ for exclusive ρ^0-meson production on transversely polarised deuterons and protons is presented.

2 Data sample and event selection

The presented analysis is performed on data taken with the COMPASS spectrometer [5] by scattering positive muons of 160 GeV/c from the CERN SPS off transversely polarised solid state targets. The data taken in 2003 and 2004 with a ^{6}LiD target and the data taken in 2007 and 2010 with a NH_3 target were analysed. For the ^{6}LiD material the average target polarisation is about 0.5, while for NH_3 it is about 0.8. The target dilution factor for exclusive ρ^0 production is typically 0.45 and 0.25 for the ^{6}LiD and NH_3 target, respectively. Before 2006 the target consisted of two separated cells of equal length, which were oppositely polarised. Since 2006 three target cells were used, where neighbouring cells were oppositely polarised and the length of the two outer cells matches the length of the middle one. This ensures a better balanced acceptance for cells with opposite polarisation. Both target layouts allow a simultaneous measurement of both target spin directions compensating flux dependent systematic uncertainties. In addition, to reduce systematic effects of the acceptance the polarisation of the target cells were reversed about every week.

A new solenoid magnet installed during the shut down in 2005 increased the angular acceptance of the experiment from ±70 mrad to the design value of ±180 mrad.

Events in the DIS regime are selected by cuts on squared four-momentum transfer $Q^2 > 1\,(\mathrm{GeV}/c)^2$, on the fractional energy lost of the muon $0.1 < y < 0.9$ and on the invariant mass of the $\gamma^* - N$ system $W > 5\,\mathrm{GeV}/c^2$. An upper cut on $Q^2 < 10\,(\mathrm{GeV}/c)^2$ is applied to remove the region where the fraction of non-exclusive background is large. The interaction vertex is required to be inside the polarised target material and the extrapolated track of the beam muon must traverse the full length of the target, in order to ensure equal flux in all target cells. The ρ^0-meson is detected via its decay into a $\pi^+\pi^-$ pair, with invariant mass $0.5\,\mathrm{GeV}/c^2 < M_{\pi\pi} < 1.1\,\mathrm{GeV}/c^2$. Only events with an incident muon track, a scattered muon track and two additional tracks with opposite charge are considered. Suppression of semi-inclusive deep-inelastic (SIDIS) production is achieved by a cut on the energy of the ρ^0-meson and on the missing energy $E_{\mathrm{miss}} = (M_X^2 - M_P^2)/(2M_P)$, where M_X is the invariant mass of the undetected system and M_P is the proton mass: $E_{\rho^0} > 15\,\mathrm{GeV}$ and $-2.5\,\mathrm{GeV} < E_{\mathrm{miss}} < 2.5\,\mathrm{GeV}$. In order to suppress background of coherent production of exclusive ρ^0 production on nuclei of the target a lower cut on the transverse momentum p_T of the ρ^0-meson is applied: $0.1\,(\mathrm{GeV}/c)^2 < p_T^2 < 0.5\,(\mathrm{GeV}/c)^2$ for ^{6}LiD and $0.05\,(\mathrm{GeV}/c)^2 < p_T^2 < 0.5\,(\mathrm{GeV}/c)^2$ for NH_3, where the upper cut on p_T^2 is applied to remove the region, where non-exclusive production dominates.

After all cuts the final samples of incoherent exclusive ρ^0 production consist of about 97000 and 797000 events for the ^{6}LiD and NH_3 target, respectively. Still, about 20 % of the events originate from SIDIS production. In order to correct for this contribution fits to the E_{miss} distribution are performed in each bin required for the asymmetry extraction. This means in bins in x_{Bj}, Q^2, or p_T^2 per target cell, and also in $\phi - \phi_S$ and according to the target spin orientation. For the signal a Gaussian distribution is fitted. The shape for the background is obtained from a parameterisation of SIDIS Monte Carlo (MC) data generated with LEPTO binned in the same way as the real data, except in polarisation state and $\phi - \phi_S$, since no

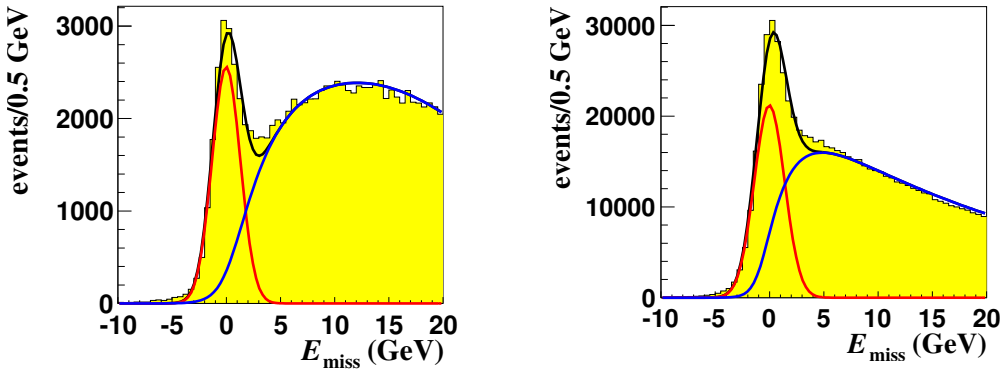

Figure 1: Signal plus background fit to the E_{miss} distribution for the ^{6}LiD data (left) and NH_3 data (right) in the region $2.4\,(\text{GeV}/c)^2 < Q^2 < 10\,(\text{GeV}/c)^2$ where the SIDIS background is the largest. The different shapes of the two distributions for large E_{miss} is explained by the increased angular acceptance of the COMPASS detector due to the new target magnet installed in 2005.

polarisation effects are simulated. The shape obtained from MC is fixed and only the normalisation is fitted to the data. This is exemplarily shown in Fig. 1 for both the ^{6}LiD and NH_3 data in the region $2.4\,(\text{GeV}/c)^2 < Q^2 < 10\,(\text{GeV}/c)^2$ integrated over the target cells, polarisation state and angle $\phi - \phi_S$. The resolution in E_{miss} is not sufficient to resolve ρ^0 production with diffractive dissociation of the target nucleon. It is visible in Fig. 1 right of the exclusive peak as a slight enhancement over the SIDIS background. The amount was estimated using Monte Carlo generated with HEPGEN [6] to be $\approx 14\,\%$. No attempt was made to remove this background. This is motivated by HERA results for unpolarised protons, which demonstrated that the angular distributions for proton-dissociative production are consistent with those of exclusive ρ^0 production [7, 8, 9]. The asymmetry is extracted from the numbers of exclusive events, after subtraction of SIDIS background, using a binned maximum likelihood fit in 12 bins of $\phi - \phi_S$.

3 Results

The results for the transverse target spin asymmetries $A_{UT}^{\sin(\phi-\phi_S)}$ measured on proton and deuteron as a function of x_{Bj}, Q^2 or p_T^2, are shown in Fig. 2. For both targets the asymmetries are found to be small and compatible with zero within statistical uncertainties. For transversely polarised deuterons it is the first measurement. The proton results are compatible with the results measured by HERMES [10]. Note that the COMPASS proton results are more precise by a factor of about 3 and cover a larger kinematic domain. The results are compared with predictions of the GPD model by Goloskokov and Kroll [11], taking into account only contributions from valence quark GPDs E^u and E^d. A reasonable agreement is achieved. The small value of the asymmetry can be explained by an approximate cancellation of comparable contributions of opposite signs from GPDs E^u and E^d: $E^u \approx -E^d$. For proton the asymmetry is sensitive to $2/3E^u + 1/3E^d$, while for deuteron it depends on $E^u + E^d$.

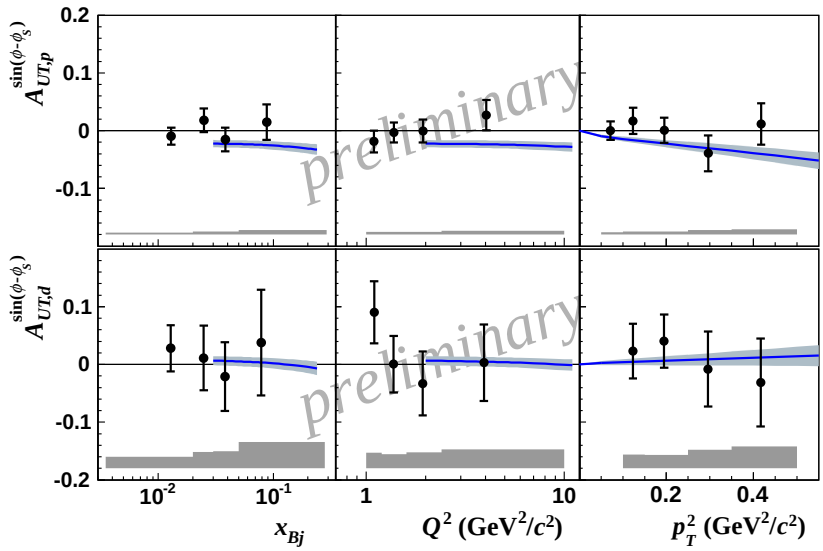

Figure 2: Results for $A_{UT}^{\sin(\phi-\phi_S)}$ measured on proton (upper) and deuteron (lower) as a function of x_{Bj}, Q^2 and p_T^2. The systematic uncertainties are indicated by grey bands. The curves show the predictions of the GPD model [11] using the set of parameters called 'variant 1'. The theoretical error bands take into account uncertainties of GPD parameterisations.

References

[1] D. Mueller, D. Robaschik, B. Geyer, F. Dittes, and J. Horejsi. Fortsch.Phys. **42** (1994) 101, arXiv:hep-ph/9812448 [hep-ph].

[2] A. Radyushkin. Phys.Lett. **B385** (1996) 333–342, arXiv:hep-ph/9605431 [hep-ph].

[3] X.-D. Ji. Phys.Rev.Lett. **78** (1997) 610–613, arXiv:hep-ph/9603249 [hep-ph].

[4] M. Burkardt. Phys.Rev. **D62** (2000) 071503, erratum ibid. **D66** (2002) 119903, arXiv:hep-ph/0005108 [hep-ph].

[5] P. Abbon *et al.* Nucl. Instrum. Meth. **A577** (2007) 455–518, arXiv:hep-ex/0703049.

[6] A. Sandacz. http://project-gpd-full-chain-mc.web.cern.ch/project-gpd-full-chain-mc/hepgen.

[7] J. Breitweg *et al.* Eur.Phys.J. **C12** (2000) 393–410, arXiv:hep-ex/9908026 [hep-ex].

[8] S. Chekanov *et al.* PMC Phys. **A1** (2007) 6, arXiv:0708.1478 [hep-ex].

[9] F. Aaron *et al.* JHEP **1005** (2010) 032, arXiv:0910.5831 [hep-ex].

[10] A. Rostomyan and J. Dreschler. arXiv:0707.2486 [hep-ex].

[11] S. Goloskokov and P. Kroll. Eur.Phys.J. **C59** (2009) 809–819, arXiv:0809.4126 [hep-ph].

WG3: Electroweak and Searches and WG5: Heavy Flavours

Top Quark Pair Production beyond the Next-to-Leading Order

Valentin Ahrens[1], *Andrea Ferroglia*[2], *Matthias Neubert*[1], *Ben D. Pecjak*[1], *Li Lin Yang*[3]

[1]Institut für Physik (THEP), Johannes Gutenberg-Universität, D-55099 Mainz, Germany
[2]New York City College of Technology, 300 Jay Street, Brooklyn, NY 11201, USA
[3]Institute for Theoretical Physics, University of Zürich, CH-8057 Zürich, Switzerland

DOI: http://dx.doi.org/10.3204/DESY-PROC-2012-02/185

We report on recent calculations of the total cross section and differential distributions of top quark pair production at hardon colliders, including the invariant mass distribution, the transverse momentum and rapidity distributions, as well as the forward-backward asymmetry. The calculations are based on soft gluon resummation at the next-to-next-to-leading logarithmic accuracy.

1 Introduction

Top quark pair production is a benchmark process at hadron colliders such as the Tevatron and the LHC. Its special role in the physics program of these experiments makes it crucial to have precise QCD predictions for the total and differential cross sections. The starting point for such predictions is the next-to-leading order (NLO) calculations of the total and differential cross sections carried out more than two decades ago [1]. Since higher-order corrections to these results as estimated through scale variations are expected to be as large as 10-15%, it would be desirable to extend the calculations beyond NLO. Here there are two paths. One is to calculate the full next-to-next-to-leading order (NNLO) cross section. This is indeed an active area of research and was discussed at this conference by Alexander Mitov, with the first numerical result for the total cross section in the $q\bar{q}$ channel available in [2]. Another is to use techniques from soft gluon resummation to calculate what are argued to be the dominant corrections at NNLO and beyond. Such resummed calculations are the subject of this talk.

2 Soft gluon resummation and approximate NNLO

Soft gluon resummation is a rich field with a long history and it is far beyond the scope of this talk to give a detailed review. Instead, we will briefly explain the main ideas and the different conventions used in the literature.

The basic idea of resummation can be conveyed through the following schematic picture. In certain kinematic regions (the so-called "threshold" regions), the differential partonic cross sections $d\hat{\sigma}$ receive logarithmically enhanced corrections in the form $\alpha_s^n L^m$ at each order in perturbation theory, where $m \leq 2n$ and L represent some logarithms[1] which become large in

[1]usually of some conjugate variable in the Mellin or Laplace moment space

the limit of soft gluon emission. When L is so large such that $\alpha_s L \sim 1$, the perturbation series needs to be re-organized so that these large terms are resummed to all orders in α_s. This is achieved using techniques of re-factorization and renormalization-group evolution, and in the end one can show that the partonic cross section can be written in the form (with L counted as $1/\alpha_s$)

$$d\hat{\sigma} = (c_0 + \alpha_s c_1 + \cdots) \exp\left[\frac{g_0}{\alpha_s} + g_1 + \alpha_s g_2 + \cdots\right],$$

where the coefficients c_i and g_i do not contain any large logarithms. The number of terms included in the exponent and in the prefactor defines a certain "logarithmic accuracy", with the terms shown above being the next-to-next-to-leading logarithmic (NNLL) order. Alternative to resummation, one can also use the knowledge to recover the leading terms at higher orders. With the information from the exact NLO result and the NNLL resummation (as is the case for top quark pair production), one can determine the terms $\alpha_s^2 L^m$ with $m = 1, 2, 3, 4$ in the NNLO corrections. These "NLO+NNLL resummed" and "approximate NNLO" results are the starting point of our phenomenological analyses in [4], which will be presented in the next section. Finally, a method to obtain some information about the missing constant term $\alpha_s^2 L^0$ was proposed in [5], with numerical results in preparation.

Name	Observable	Threshold limit
production threshold	σ	$\beta = \sqrt{1 - 4m_t^2/\hat{s}} \to 0$
pair-invariant-mass (PIM)	$d\sigma/dM_{t\bar{t}}d\theta$	$(1-z) \equiv (1 - M_{t\bar{t}}^2/\hat{s}) \to 0$
single-particle-inclusive (1PI)	$d\sigma/dp_T dy$	$s_4 \equiv \hat{s} + \hat{t}_1 + \hat{u}_1 \to 0$

Table 1: The three cases in which soft gluon resummation has been applied in top quark pair production.

Before going into numerics, let us emphasize that soft gluon resummation is a very generic method which can be applied to many observables, where each observable is associated with a specific definition of "threshold". In top quark pair production at hadron colliders, all applications in the literature can be grouped into one of the three cases listed in Table 1. The production threshold is the limit where the top and anti-top quarks are nearly at rest, which can only be applied for the total inclusive cross section. Besides logarithmic enhancement from soft gluon emissions, one must take into account Coulomb gluon exchanges in this case, which result in terms of the form $\ln \beta^m/\beta^n$. A simultaneous resummation of both type of contributions at NNLL accuracy has been performed in [3]. The PIM and 1PI threshold, on the other hand, can be applied to certain differential distributions as indicated in Table 1. Of course, starting from these two distributions, one may also perform a partial integration or full integration to obtain observables such as the forward-backward asymmetry and the total cross section. In the following, we will employ PIM and 1PI kinematics, whichever is appropriate for the specific observables.

3 Total and differential cross sections

In this section we present our predictions for the total and differential cross sections, which are based on the series of works in [4]. In all numerical results we adopt $m_t = 173.1$ GeV, and use

	Tevatron	LHC7	LHC8	LHC14
NLO	$6.72^{+0.41+0.47}_{-0.76-0.45}$	159^{+20+14}_{-21-13}	228^{+28+19}_{-30-17}	$889^{+107+66}_{-106-58}$
NNLO approx.	$6.63^{+0.07+0.63}_{-0.41-0.48}$	155^{+8+14}_{-9-14}	221^{+12+19}_{-12-19}	855^{+52+60}_{-38-59}

Table 2: The total cross sections (in pb) at the Tevatron and the LHC for different collider energies. The first errors are perturbative uncertainties, and the second errors are PDF+α_s uncertainties.

MSTW2008 PDF sets.

We first show our results for the total cross sections[2] in Table 2. The approximate NNLO results are computed by combining the approximate NNLO formula from PIM and 1PI kinematics. The first errors are perturbative uncertainties, which for the NLO results are estimated by varying μ_f and μ_r up and down by a factor of 2, with the default being $\mu_f = \mu_r = m_t$. For the approximate NNLO results, besides scale variation, we also use the difference between PIM and 1PI kinematics as an additional source of perturbative uncertainties. We also show the uncertainties associated with the experimental determination of the PDFs and the strong coupling constant, which are estimated following the prescription in [6] at 90% CL. Compared to the NLO results, the approximate NNLO corrections do not change the central values very much, while the perturbative uncertainties are reduced a lot.

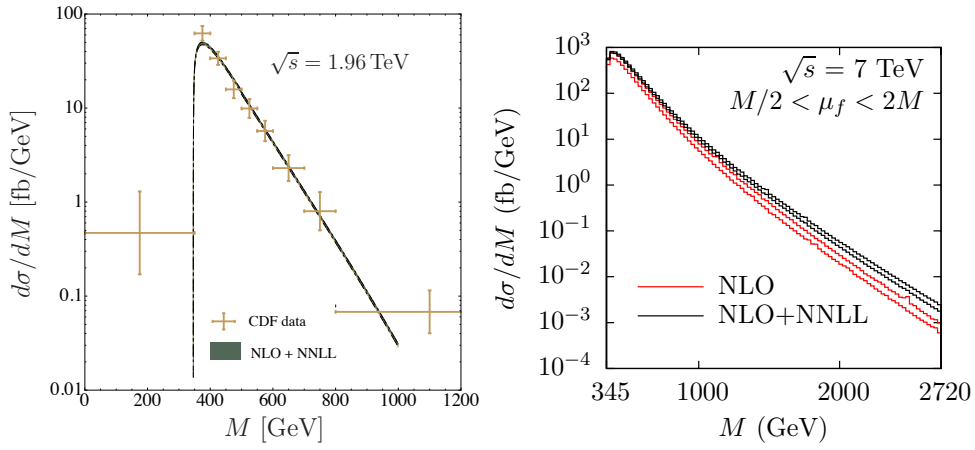

Figure 1: The invariant mass distributions at the Tevatron compared with CDF data (left) and at the LHC with $\sqrt{s} = 7$ TeV (right).

We now turn to differential distributions. A particularly interesting observable is the invariant mass distribution of the $t\bar{t}$ pair, which is very sensitive to contributions from new heavy resonances. We show in Figure 1 our NLO+NNLL predictions at the Tevatron (left) and the LHC with $\sqrt{s} = 7$ TeV (right). Our predictions at the Tevatron agree quite well with the measurements from the CDF collaboration [7]. For the LHC, we observe large corrections over

[2]These are obtained using the numerical program TopNNLO, which can be downloaded at `http://www.physik.uzh.ch/~llyang/TopNNLO.tar.gz`

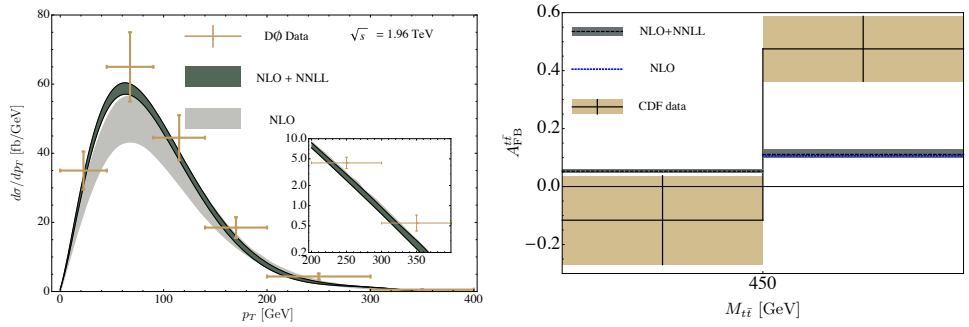

Figure 2: Left: the transverse momentum distribution of the top quark at the Tevatron compared with D0 data. Right: The invariant mass dependent forward-backward asymmetry at the Tevatron.

the NLO predictions in the high invariant mass region, with the shape being slightly distorted, which is important for new physics searches. In Figure 2 we show another two distributions at the Tevatron: the transverse momentum (p_T) distribution of the top quark, and the invariant-mass-dependent forward-backward asymmetry. Our result for the p_T distribution is shown together with the NLO result and the D0 data [8]. It is apparent that the NNLL resummation improves the agreement between the theoretical prediction and the experimental measurement. The forward-backward asymmetry, on the other hand, was found by the CDF and D0 collaborations [9] to be in tension with theoretical predictions, especially in the high invariant mass region. Here resummation only mildly increases the asymmetry, so that the discrepancy between theory and experiment calls for other explanations.

References

[1] P. Nason, S. Dawson and R. K. Ellis, Nucl. Phys. B **303**, 607 (1988); Nucl. Phys. B **327**, 49 (1989) [Erratum-ibid. B **335**, 260 (1990)]; W. Beenakker, H. Kuijf, W. L. van Neerven and J. Smith, Phys. Rev. D **40**, 54 (1989); W. Beenakker, W. L. van Neerven, R. Meng, G. A. Schuler and J. Smith, Nucl. Phys. B **351**, 507 (1991).

[2] P. Baernreuther, M. Czakon and A. Mitov, arXiv:1204.5201 [hep-ph].

[3] M. Beneke, P. Falgari, S. Klein and C. Schwinn, Nucl. Phys. B **855**, 695 (2012), [arXiv:1109.1536 [hep-ph]]; M. Cacciari, M. Czakon, M. L. Mangano, A. Mitov and P. Nason, Phys. Lett. B **710**, 612 (2012), [arXiv:1111.5869 [hep-ph]].

[4] V. Ahrens, A. Ferroglia, M. Neubert, B. D. Pecjak and L. L. Yang, Phys. Lett. B **687**, 331 (2010), [arXiv:0912.3375 [hep-ph]]; JHEP **1009**, 097 (2010), [arXiv:1003.5827 [hep-ph]]; JHEP **1109**, 070 (2011), [arXiv:1103.0550 [hep-ph]]; Phys. Lett. B **703**, 135 (2011), [arXiv:1105.5824 [hep-ph]]; Phys. Rev. D **84**, 074004 (2011), [arXiv:1106.6051 [hep-ph]].

[5] A. Ferroglia, B. D. Pecjak and L. L. Yang, arXiv:1205.3662 [hep-ph].

[6] A. D. Martin, W. J. Stirling, R. S. Thorne and G. Watt, Eur. Phys. J. C **64**, 653 (2009), [arXiv:0905.3531 [hep-ph]].

[7] T. Aaltonen *et al.* [CDF Collaboration], Phys. Rev. Lett. **102**, 222003 (2009), [arXiv:0903.2850 [hep-ex]].

[8] V. M. Abazov *et al.* [D0 Collaboration], Phys. Lett. B **693**, 515 (2010), [arXiv:1001.1900 [hep-ex]].

[9] T. Aaltonen *et al.* [CDF Collaboration], Phys. Rev. D **83**, 112003 (2011), [arXiv:1101.0034 [hep-ex]]; V. M. Abazov *et al.* [D0 Collaboration], Phys. Rev. D **84**, 112005 (2011), [arXiv:1107.4995 [hep-ex]].

Measurements of single top-quark production with the ATLAS detector

W. H. Bell[1] on behalf of the ATLAS Collaboration

[1]Université de Genève, Section de Physique, 24 rue Ernest Ansermet, CH-1211 Genève 4

DOI: http://dx.doi.org/10.3204/DESY-PROC-2012-02/90

These proceedings summarise the single top-quark production cross-section results obtained with the ATLAS [1] detector at a centre-of-mass energy of 7 TeV. Cross-section results for the t, Wt and s-channels are presented. These results are interpreted in terms of the CKM matrix element $|V_{\mathrm{tb}}|$ assuming $|V_{\mathrm{tb}}| \gg |V_{\mathrm{ts}}|$ and $|V_{\mathrm{td}}|$. Searches for flavour changing neutral-currents and right-handed W' in single top-quark events are also presented.

1 Introduction

Top-quark production in proton-proton collisions at the LHC [2] is dominated by top anti-top production processes. In contrast to the dominant production via flavour-conserving strong interactions, single top quarks are produced through the electroweak interaction. In the Standard Model (SM) three processes are responsible for single top-quark production: the exchange of a virtual W-boson in the t and s channels, and the associate production of a top quark and a real W-boson (Wt).

Experimental measurements of the single top-quark production cross-section directly probe the W-t-b vertex, constraining possible sources of beyond the SM physics processes [3]. Cross-section measurements set constraints on the absolute value of V_{tb}, without an assumption on the number of quark generations. The same results can alternatively be used to constrain the b-quark parton density function (PDF) using the t-channel measurements. Within the SM, production of a single top-quark via flavour changing neutral currents (FCNC) is forbidden at the tree-level and suppressed at higher orders [4]. However, beyond the standard model theories, which include exotic quarks [5], new scalars [6], supersymmetry [7] and technicolour [8] predict higher FCNC rates.

2 Event selection

Data were selected using a high transverse momentum (p_{T}) inclusive single lepton trigger. Electrons were then required to have cluster E_{T} greater than 25 GeV and an absolute pseudorapidity ($|\eta|$) less than 2.47. Electron clusters within the barrel-endcap transition region $1.37 < |\eta| < 1.52$ were excluded. Muons candidates were required to be within $p_{\mathrm{T}} > 25$ GeV and $|\eta| < 2.5$. Tight isolation requirements around the lepton candidate were made using the inner detector tracker and calorimeter, to reduce the QCD-multijet background contribution.

Jets were reconstructed using the anti-k$_t$ algorithm [9] and a radius parameter of 0.4. A tagging algorithm based on the combination of secondary vertex and combined lifetime information was used to tag jets from b-quark decays. The missing transverse momentum ($E_{\mathrm{T}}^{\mathrm{miss}}$) was then calculated from the reconstructed objects and unclustered calorimeter cells.

The event sample for the t-channel analysis [10] was defined by requiring exactly two or three jets $p_{\mathrm{T}} > 25$ GeV and $|\eta| < 4.5$. Exactly one jet $p_{\mathrm{T}} > 25$ GeV and $|\eta| < 2.5$ was required to be b-tagged, with an efficiency of 57% and a light jet rejection factor of 520 (reciprocal of light jet tagging efficiency). Events with more than one selected lepton were rejected. The QCD-multijet background was reduced by requiring $E_{\mathrm{T}}^{\mathrm{miss}} > 25$ GeV and the sum of the $E_{\mathrm{T}}^{\mathrm{miss}}$ and transverse W mass $m_{\mathrm{T}}(W)$ [1] to be greater than 60 GeV. Events were selected for the FCNC [11] and right-handed W' [12] searches using the same lepton, b-tagging, jet p_{T}, $E_{\mathrm{T}}^{\mathrm{miss}}$ and $E_{\mathrm{T}}^{\mathrm{miss}} + m_{\mathrm{T}}(W)$ requirements. For both searches, jets were required to be within $|\eta| < 2.5$. In the case of the FCNC analysis, events with exactly one b-jets were selected, whereas the W' analysis required two jets and exactly one b-tag. The s-channel analysis [13] used a b-tagging efficiency of 50% with a corresponding light jet rejection rate of 270. Exactly two jets ($|\eta| < 2.5$) and one or two b-tagged jets $|\eta| < 2.5$ were required.

Dilepton events were selected for the Wt analysis [14] by requiring exactly two selected leptons with opposite charge. The backgrounds from Z boson processes were reduced by rejecting events with a dilepton mass $81 < m_{\mathrm{ll}} < 101$ GeV and by requiring an azimuthal separation $\Delta\phi(l_1, E_{\mathrm{T}}^{\mathrm{miss}}) + \Delta\phi(l_2, E_{\mathrm{T}}^{\mathrm{miss}}) > 2.5$. The QCD-multijet background was reduced by requiring $E_{\mathrm{T}}^{\mathrm{miss}} > 50$ GeV.

3 Analyses and results

The t-channel analysis was performed using multivariate and cut-based signal discrimination techniques. The dominant systematic uncertainties were found to be the initial and final state radiation (14%) and the b-tagging efficiency (13%). In comparison, the statistical uncertainty was found to be 5%. The t-channel cross-section was determined to be $\sigma_t = 83 \pm 4(\mathrm{stat.})\ ^{+20}_{-19}(\mathrm{syst.})$ pb from the simultaneous measurement in the two and three jet channels. A value of $|V_{\mathrm{tb}}|^2$ was extracted by assuming $|V_{\mathrm{tb}}| \gg |V_{\mathrm{td}}|$, $|V_{\mathrm{ts}}|$ and that the W-t-b interaction is a SM-like left-handed weak coupling. The cross-section measurement from the neural network analysis was divided by the SM expectation to determine $|V_{\mathrm{tb}}|^2$. Using the constraint $0 < |V_{\mathrm{tb}}| < 1$, $|V_{\mathrm{tb}}|$ was found to be greater than 0.75 at the 95% confidence level (CL). The separation between signal and background contributions for the output of the neural network is shown in Fig. 1(a). The results of the multivariate and cut based analyses are summarised in Fig. 1(b), and are found to be consistent with SM predictions.

The Wt analysis was performed using an integrated luminosity of 0.70 fb^{-1}. The dominant systematic uncertainties were found to be the jet energy scale (35%), jet reconstruction efficiency (33%), jet energy resolution (32%) and the top anti-top background (24%). The statistical uncertainty was found to be 37%. The 95% CL observed (expected) cross-section limit was found to be $\sigma(pp \to Wt + X) < 39(41)$ pb.

The s-channel analysis was carried out for an integrated luminosity of 0.70 fb^{-1}. The dominant uncertainties were found to be statistical (100%), MC generator modelling (60%) and

[1] $m_{\mathrm{T}}(W)$ is defined as $\sqrt{2p_{\mathrm{T}}^{l}p_{\mathrm{T}}^{\nu}(1-\cos(\phi^{l}-\phi^{\nu}))}$, where l and ν refer to the lepton and neutrino terms respectively. In the event selection the neutrino terms were replaced with the $E_{\mathrm{T}}^{\mathrm{miss}}$ and its azimuthal angle.

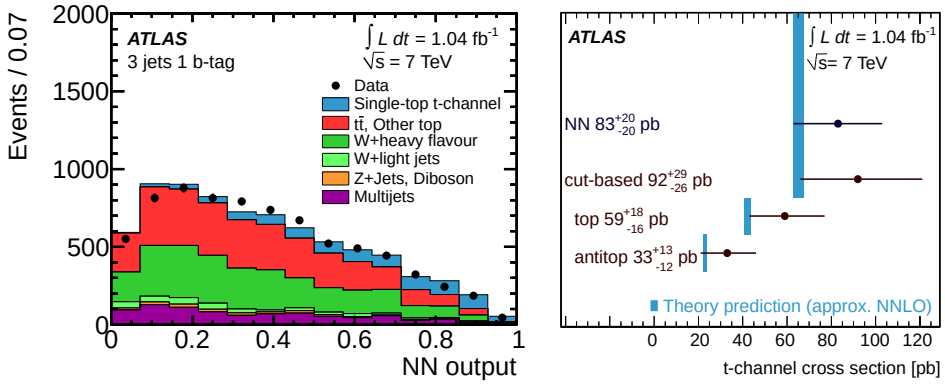

(a) (b)

Figure 1: (a) Neural network output distribution in the 3-jet b-tagged sample [10]. All component distributions are normalised to the result of the maximum-likelihood fit. (b) Summary of the ATLAS single top-quark t-channel cross-section results [15]. Theoretical predictions obtained from N. Kidonakis, Phys. Rev. D 83 (2011) 091503 (approximate NNLO) are shown by the vertical bands.

luminosity (50%). A cross-section limit was extracted using a likelihood function, including the statistical uncertainties, nuisance parameters for the systematic uncertainties, and a Gaussian constraint on the luminosity. The observed (expected) cross-section limit was found to be $\sigma(pp \to Wt + X) < 26.5(20.5)$ pb.

The FCNC search was carried out in the framework of the t-channel analysis using an integrated luminosity of 2.05 fb^{-1}. The largest systematic uncertainties were the jet p_{T} and η-dependent scale factors (23–45%). A binned likelihood method was applied to the neutral network output distributions, including the systematic and statistical uncertainties. Since no significant rate of FCNC is observed, an upper limit on the production cross-section was determined to be 3.9 pb at 95% CL. The resulting limit on the branching fractions $t \to ug$ and $t \to cg$ is shown in Fig. 2(a).

A right-handed W' search was performed within the framework of the s-channel analysis, and an integrated luminosity of 1.04 fb^{-1}. Following the event selection, the m_{tb} mass shown in Fig 2(b) was used to discriminate between signal and background events. The dominant systematic uncertainties were found to be the jet energy scale and the b-tagging scale factors (8-20%). No statistically significant excess was observed in the selected data. Upper limits on the cross-section times branching ratio were found to be 6.1–1.0pb at the 95% CL for W' masses of 0.5–2.0 TeV. The limits were translated into a lower bound on the allowed right-handed W' mass of greater than 1.13 TeV at the 95% CL.

4 Conclusion

The ATLAS collaboration has performed a complete set of single top-quark analyses, using data collected from pp collisions at a centre-of-mass energy of 7 TeV. The measurements and limits on each of the components of the single-top production cross-section have been performed and

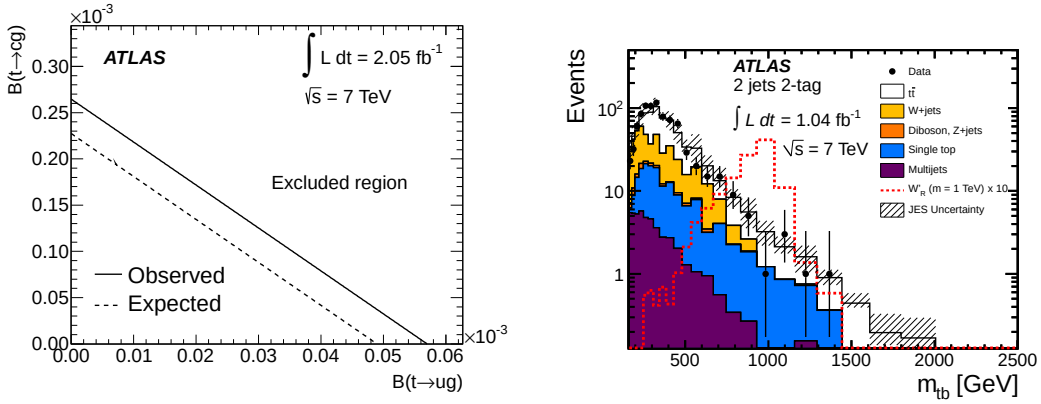

(a) (b)

Figure 2: (a) Upper limit on the branching fractions $t \to ug$ and $t \to cg$ [11]. (b) The distribution of m_{tb} for double-tagged two-jet events compared to Standard Model expectations [12]. The expected W' signal was normalised to the theoretical cross-section and then scaled by a factor of 10.

found to be in agreement with standard model predictions. Limits on the production of single top quarks via FCNC and right-handed W' have been established.

References

[1] The ATLAS Collaboration. JINST **3** (2008) S08003.

[2] L. Evans, (ed.) and P. Bryant, (ed.). JINST **3** (2008) S08001.

[3] T. M. Tait and C.-P. Yuan. Phys.Rev. **D63** (2000) 014018, `arXiv:hep-ph/0007298 [hep-ph]`.

[4] S. Glashow, J. Iliopoulos, and L. Maiani. Phys.Rev. **D2** (1970) 1285–1292.

[5] J. Aguilar-Saavedra. Phys.Rev. **D67** (2003) 035003, `arXiv:hep-ph/0210112 [hep-ph]`.

[6] S. Bejar, J. Guasch, and J. Sola. Nucl.Phys. **B600** (2001) 21–38, `arXiv:hep-ph/0011091 [hep-ph]`.

[7] J. M. Yang, B.-L. Young, and X. Zhang. Phys.Rev. **D58** (1998) 055001, `arXiv:hep-ph/9705341 [hep-ph]`.

[8] G.-r. Lu, F.-r. Yin, X.-l. Wang, and L.-d. Wan. Phys.Rev. **D68** (2003) 015002, `arXiv:hep-ph/0303122 [hep-ph]`.

[9] M. Cacciari, G. P. Salam, and G. Soyez. JHEP **0804** (2008) 063, `arXiv:0802.1189[hep-ph]`.

[10] The ATLAS Collaboration. `arXiv:1205.3130 [hep-ex]`.

[11] The ATLAS Collaboration. Phys.Lett. **B712** (2012) 351–369, `arXiv:1203.0529 [hep-ex]`.

[12] The ATLAS Collaboration. `arXiv:1205.1016 [hep-ex]`.

[13] The ATLAS Collaboration. `ATLAS-CONF-2011-118`.

[14] The ATLAS Collaboration. `ATLAS-CONF-2011-104`.

[15] "Measurement of the t-channel single top-quark production cross section in pp collisions at $\sqrt{s} = 7$ TeV with the ATLAS detector". https://atlas.web.cern.ch/Atlas/GROUPS/PHYSICS/PAPERS/TOPQ-2011-14/.

Search for physics beyond the Standard Model with top quarks at ATLAS

Philippe Calfayan[1] on behalf of the ATLAS Collaboration

[1]Ludwig-Maximilians-Universität, Munich, Germany

DOI: http://dx.doi.org/10.3204/DESY-PROC-2012-02/305

This document reports on recent searches for new physics involving top quarks in proton-proton collisions at the center-of-mass energy $\sqrt{s} = 7$ TeV. Analyses using data samples with integrated luminosities up to 2 fb^{-1} recorded with the ATLAS detector are presented.

1 Introduction

With a mass close to the scale of the electroweak symmetry breaking, the top quark plays a special role in some models of new physics by coupling to new particles.

The $t\bar{t}$ forward-backward asymmetry (A_{FB}) has recently been measured at the Tevatron [1, 2] and was found to be significantly larger than the prediction from the SM, which further motivates the search for physics beyond the Standard Model (SM) with top quarks.

Using data sets of proton-proton collisions collected by the ATLAS detector [3] at the Large Hadron Collider (LHC), we present searches for resonances decaying to opposite or same-sign top-quark pairs, or top-quark partners with decay products resulting in an excess of missing transverse momentum ($\not{E}_T$).

2 Top pairs and top quark decays

As predicted in the SM, the top quark decays to a W boson and a b quark, and may lead to a leptonic or hadronic final state, according to the subsequent decay of the W boson.

As a consequence, the $t\bar{t}$ decays are characterized by the di-lepton, lepton plus jets, and all jets signatures. While the di-lepton final state has the cleanest topology and a low branching ratio, the all jet signature is produced with a large branching ratio and suffers from a significant background contamination. The lepton plus jet final state thus constitutes a compromise in terms of branching ratio and associated background.

3 Searches for $t\bar{t}$ resonances

3.1 The di-lepton final state

The search for $t\bar{t}$ resonances in the di-lepton final state has been carried out using a data sample of 1.04 fb^{-1} [4]. Three final state topologies have been considered: di-electron, di-muon, and

electron-muon. The signal is interpreted in terms of the production of top pairs via a Kaluza-Klein gluon (KK-gluon) in the Randall-Sundrum (RS) Model [5].

The main background is the SM production of top pairs, while the second largest one originates from Drell-Yan processes and is estimated by normalizing simulation to data in the mass window of the Z boson. The scalar sum $H_T + \not{E}_T$ is used as the main discriminant between signal and background due to the presence of two neutrinos, with H_T defined as the scalar sum of the transverse momenta of the two final state leptons and of all the jets in the event above a given momentum threshold.

Upper limits on the signal production cross section times branching ratio are derived as function of the KK-gluon mass, using bins of the $H_T + \not{E}_T$ variable. As shown in Figure 1, these experimental limits are compared to the theoretical production cross sections and interpreted as lower bounds on the mass of the KK gluon. Four different values for the coupling of light quarks to the KK gluon are considered by scaling the strong coupling parameter $g_{qqg_{KK}}/g_s$ from 0.2 to 0.35. Observed lower bounds on the KK-gluon mass from 0.8 to 1.02 TeV are found. All limits reported in this proceedings are at 95% confidence level.

3.2 The lepton plus jets final state

The search for $t\bar{t}$ resonances in the electron plus jets and in the muon plus jets final states has been performed with a data sample corresponding to 2.05 fb^{-1} [6]. The signal is assumed to originate from the resonance of a leptophobic Z' [7] or a KK-gluon.

The main irreducible background from the SM is the $t\bar{t}$ production. The background consisting of the W boson production in association with jets is modeled using simulation and data-driven corrections. The multi-jet background, which contains fake leptons, is estimated with data-driven templates. The selection of candidate events requires at least one b-tagged jet, and a minimal requirement on the number of jets that depends on whether the event contains a jet with a large mass. The reconstructed $t\bar{t}$ invariant mass is used to distinguish between signal and background, and its shape is taken into account to derive upper limits on the signal production cross section times branching ratio. The limits are compared to the theory.

Leptophobic Z' with masses between 500 and 860 GeV are excluded, as illustrated in Figure 2. In the case of standard RS couplings between the KK-gluon and quarks, KK-gluon with masses between 500 and 1025 GeV are discarded.

4 Search for new phenomena in the $t\bar{t}$ plus $\not{E}_T$ final state

A search for new phenomena in events consisting of $t\bar{t}$ pairs and large $\not{E}_T$ has been published [8] using 1.04 fb^{-1} of data. The analysis investigates the pair production of fourth generation spin-$\frac{1}{2}$ quarks (T) which would decay to a SM top quark and stable, neutral, and weakly-interacting new particle (A_0) [9]. $T\bar{T}$ pairs are assumed to only decay to the final state $t\bar{t}A_0A_0$, and the search is performed in the case where the $t\bar{t}$ pair decays to a lepton plus jets.

The main background arises from SM $t\bar{t}$ di-lepton events where one lepton is not reconstructed, is outside the detector acceptance, or is a tau lepton decaying hadronically. The second largest background is due to W+jets and semi-leptonic $t\bar{t}$ decays, for which the normalization and shape are extracted from the data. To isolate the signal, events with an additional lepton or isolated track are excluded. The track veto reduces single prong hadronic tau decays in $t\bar{t}$ events.

Figure 3 represents the region of excluded signal as function of the masses of the new particles T and A_0. The mass of T is excluded up to 420 GeV assuming that the mass of A_0 is less than 10 GeV. In the case where the mass of A_0 does not exceed 140 GeV, masses of T between 330 and 390 GeV are ruled out. Currently, this analysis is not sensitive to scalar T quarks due to their smaller production cross section.

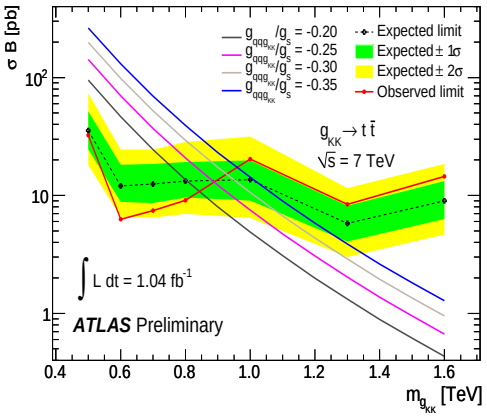

Figure 1: Search for $t\bar{t}$ resonance in the di-lepton final state [4]. Expected and observed upper limits on the signal cross section times branching ratio are compared to the theory in the case of a KK-gluon (g_{KK}) mediator.

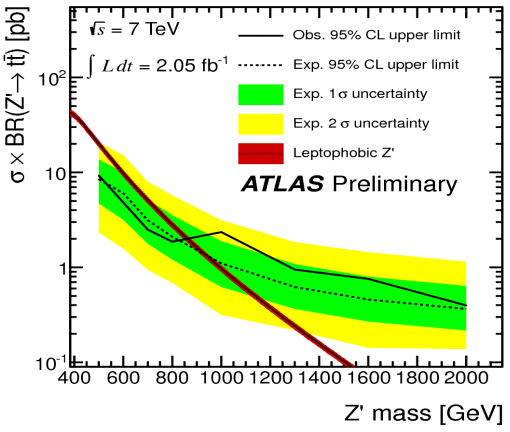

Figure 2: Search for $t\bar{t}$ resonance in the lepton plus jets final state [6]. Expected and observed upper limits on the signal cross section times branching ratio are compared to the theoretical prediction in the case of a a leptophobic $Z^{'}$ mediator.

5 Search for same-sign top-quark production

A search for same-sign top-quark (tt) production based on 1.04 fb^{-1} of data has recently been published [10]. Various generic heavy vector bosons and scalars are considered as mediators. Both top quarks are assumed to decay leptonically, which results in a final state consisting of two same-sign leptons. The di-electron and di-muon channels are explored.

The main background from the SM is due to the associated production of W and Z bosons. The contribution of events with fake leptons from hardonic decays or photon conversions is estimated from the data. Another source of background is the misidentification of the lepton charge, which is accounted for using a data-driven approach. The event selection includes a requirement on the variable H_T depending on the mass of the assumed mediator.

The production of tt pairs via a flavour-changing $Z^{'}$ [11] could explain the $t\bar{t}$ A_{FB} measured at the Tevatron. Upper limits on the tt production cross section from 1.4 to 2.0 pb are obtained, depending on the mass of the assumed mediator. Figure 4 provides the Tevatron measurements of A_{FB}, together with the tt production cross section for different masses of $Z^{'}$ as function of A_{FB} [12], and with the associated upper limit measured at ATLAS. As shown, a flavour-changing $Z^{'}$ is excluded as the source of the large A_{FB} asymmetry observed at the Tevatron.

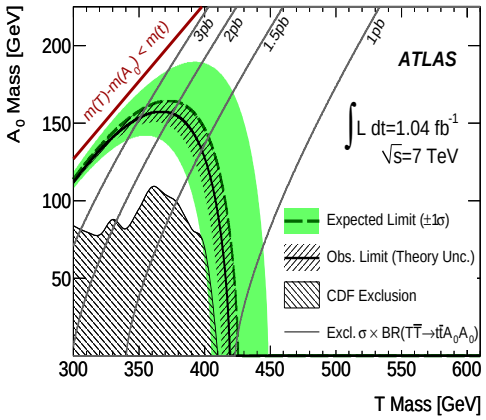

Figure 3: Search for new phenomena in the $t\bar{t}$ plus $\not{E}_T$ final state [8]. The mass exclusion region is parametrized as function of the masses of the hypothetic particles T and A_0.

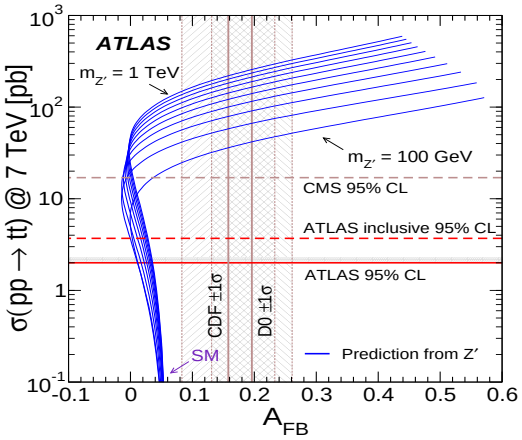

Figure 4: Search for same-sign top-quark production (1.04 fb^{-1}) [10]. Allowed regions for new physics contributions to inclusive $t\bar{t}$ A_{FB}, and contribution from Z' exchange versus tt production cross section at the LHC [12].

6 Conclusions and perspectives

The ATLAS experiment carried out seaches for physics beyond the SM with top quarks using data samples of proton-proton collision at $\sqrt{s} = 7$ TeV with integrated luminosities up to 2 fb^{-1}. Diverse final states have been explored but no evidence of new phenomena has been observed. Limits on production cross section and mass of new particles and mediators have however significantly been improved. Results are to be revised using the complete 2011 data set of 5 fb^{-1}, yet updates are expected based on the large data sets the LHC is planned to collect at $\sqrt{s} = 8$ TeV in 2012.

References

[1] CDF Collaboration, Phys. Rev. **D83** (2011) 112003.
[2] DØ Collaboration, Phys. Rev. **D84** (2011) 112005.
[3] ATLAS Collaboration, JINST **3** (2008) S08003.
[4] ATLAS Collaboration, ATLAS-CONF-2011-123, http://cdsweb.cern.ch/record/1376423.
[5] B. Lillie *et al.*, JHEP **09** (2007) 074.
[6] ATLAS Collaboration, ATLAS-CONF-2012-029, http://cdsweb.cern.ch/record/1430738.
[7] R. M. Harris *et al.*, hep-ex/9911288 (1999).
[8] ATLAS Collaboration, PRL **108** (2012) 041805.
[9] J. Alwall *et al.*, Phys. Rev. **D81** (2010) 114027.
[10] ATLAS Collaboration, JHEP **1204** (2012) 069.
[11] E. L. Berger *et al.*, Phys. Rev. Letter. **106** (2011) 201801.
[12] J. A. Aguilar-Saavedra and M. Pérez-Victoria, Phys. Rev. **D84** (2011) 115013.

Searches for New Physics in the Top Sector at the Tevatron

Yvonne Peters[1]

[1]University of Manchester, Manchester, M13 9PL, England

DOI: http://dx.doi.org/10.3204/DESY-PROC-2012-02/208

The top quark, discovered in 1995 by the CDF and D0 collaborations at the Tevatron collider at Fermilab, is the heaviest known elementary particle today. Due to its high mass and short lifetime, the top quark plays a special role in searching for physics beyond the Standard Model. In this article, recent results of searches for new physics in the top sector, performed by CDF and D0, are presented. In particular, we discuss the search for $t\bar{t}$ resonances, for tj resonances, the search for heavy fourth generation quarks, for dark matter produced in association with single tops, the study of anomalous couplings, the search for boosted top quarks as well as the analysis of Lorentz Invariance violation in the top quark sector.

1 Introduction

Discovered in 1995 by the CDF and D0 collaborations, the top quark [1, 2] is the heaviest known elementary particle today, with a mass of $m_t = 173.18 \pm 0.94$ GeV [3]. The top quark decays before hadronization, therefore being the only particle to study bare quarks. Furthermore, the Yukawa coupling of the top quark and the Higgs boson is expected to be large due to its high mass. The special properties of the top quark make it an interesting particle to study and as windwo to new physics.

In the following, recent searches for physics beyond the Standard Model (SM) in the top quark sector, performed by the CDF and D0 collaborations using Tevatron Run II data, are presented.

2 Searches for New Physics in Top Quark Production

At the Fermilab Tevatron, a proton-antiproton collider with a center of mass energy of $\sqrt{=}1.96$ TeV, top quark production occurs dominantly in pairs ($t\bar{t}$) through the strong interaction, with about 85% via $q\bar{q}$ annihilation and about 15% via gluon-gluon fusion. At about half the production cross section of $t\bar{t}$, single top quark production via the electroweak interaction takes place.

For measurements of the $t\bar{t}$ production cross section and top quark properties, the $t\bar{t}$ final states are classified according to the decays of the two W bosons from the top and anti-top decay. We separate the final states into dileptonic, semileptonic and allhadronic channels according to the number of leptons in the final state. If the lepton is a hadronic decaying tau, the events are treated as separate channels (τ+lepton and τ+jets).

In the SM, no $t\bar{t}$ resonances exist, while many models beyond the SM predict production via a resonance, as for example Topcolor assisted technicolor models. Using events in the semileptonic final state, both bthe CDF and D0 collaboration searched for a narrow resonance X, with $\Gamma_X = 1.2\% M_X$, by searching for a bump in the spectrum of the invariant $t\bar{t}$ mass, $m_{t\bar{t}}$. Using events with at least four jets and 4.8 fb^{-1} of data at CDF and at least three jets and 5.4 fb^{-1} at D0, limits on $\sigma(p\bar{p} \to X) \times B(X \to t\bar{t})$ versus M_X have been extracted. In the benchmark model of topcolor assisted technicolor, a $Z^{'}$ for masses below 835 GeV is excluded by D0 [4] and below 900 GeV by CDF [5] at the 95% confidence level (CL).

Recently, CDF performed a search for a top plus jet (tj) resonance M using the full Run II data set of 8.7 fb^{-1} by looking for a tj resonance in the $t\bar{t}j$ system. A kinematic fitter is applied on events with at least five jets, of which at least one has to be identified as a b-jet, in the semileptonic final state, and a bump search in the tj invariant mass is performed. Limits are set on $\sigma(p\bar{p} \to Mt\bar{t})$, resulting in upper limits between 0.61 pb and 0.02 pb at the 95% CL. These can be translated into limits on the mass of M assuming M to be part of a new color singlet or color triplet model [6].

Another search recently performed by CDF using 7.7 fb^{-1} investigates the possibility of a dark matter candidate D produced in association with a top quark. Single top events, where the top quark decays fully hadronically and the dark matter candidate leaves high missing transverse energy in the detector, are used for this search. A template fit of the missing transverse energy spectrum is performed in events with at least three jets and no leptons, inspecting dark matter candidates with masses of up to 150 GeV. Upper limts on $\sigma(p\bar{p} \to Mt\bar{t})$ can be set as function of m_D [7], which are about 0.5 pb over the investigated mass range.

3 Searches for New Physics in Top Quark Decay

In the SM, the top quark decays with a probability of almost 100% into a W-boson and a b-quark. The coupling of the W boson to fermions has the $V-A$ form of a left-handed vector interaction. Possible new physics could occur if the coupling of the W boson to the top and bottom quark (tWb coupling) is of the form of right-handed vector couplings, or left- or right-handed tensor couplings. In an effective Lagrangian approach, the different couplings can be introduced as form factors f_V^L, f_V^R, f_T^L, f_T^R, describing the left (L) and right (R) handed vector (V) and tensor (T) couplings, respectively. In the SM, $f_V^L = 1$ and all others are zero.

Recently, the D0 collaboration performed a search for anomalous couplings using information from single top quark production and the measurement of the W helicity in top quark decays. Using single top quark events, mutlivariate discriminants are trained on a single top sample with either f_V^R, f_T^L, or f_T^R set to one as the signal sample, while SM single top ($f_V^L = 1$) is considered as part of the background. For each trained multivariate discriminant, the pair of one of the anomalous couplings form factors and the coupling form factor f_V^L are then considered simultaneously, and limits can be extracted in the plane of (f_V^R, f_V^L) , (f_T^L, f_V^L), or (f_T^R, f_V^L) [8]. Furthermore, the W helicity in top quark decays can be measured using the distribution of the angle between the direction opposite to the top quark and the direction of the down-type fermion (charged lepton or down-type quark) from the decay of the W boson, both in the W boson rest frame [9]. The extracted W helicity fractions can be interpreted as limits on f_V^R, f_T^L, or f_T^R. By combining the analysis of anomalous couplings in single top events with information from the W helicity analysis, posterior probability density distributions for the anomalous coupling form factors are obtained. This provides 95% CL limits on anomalous tWb

couplings of $|f_V^R|^2 < 0.30$, $|f_T^L|^2 < 0.05$, and $|f_T^R|^2 < 0.12$ [10].

4 Top-related Searches for New Physics

Until today, three generations of quarks and leptons are known in the SM. A simple extension would be the inclusion of a fourth generation of fermions. Both collaborations, D0 and CDF, searched for pair production of massive fourth generation quarks, t', assuming the decay into a W boson and a down-type quark. CDF allows this down-type quark to be d, s or b, while D0 assumes a b-quark. The search is performed in the semileptonic final state with at least four jets, of which at least one has to be an identified b-jet at D0. The $t'\bar{t}'$ sample is expected to have a higher fitted top mass and a larger scalar sum of the lepton and jet p_Ts, thus the search is performed as a template fit of these two observables. Upper limts on $\sigma(p\bar{p} \to t'\bar{t}')$ are extracted as function of the t' mass $m_{t'}$, resulting in lower limits on $m_{t'}$ at the 95% CL of $m_{t'} > 285$ GeV at D0 [11] using 5.3 fb^{-1} and $m_{t'} > 358$ GeV by CDF [12] using 5.6 fb^{-1}.

Another top related search recently performed by the CDF collaboration is a search for massive, collimated jets, which serves as a test of quantum chromodynamics and can give insights into parton showering models. The search aims to select events where the decay products of the top quark are collimated into one single, massive jet. Using 6.0 fb^{-1}, CDF requires events with at least one jet cluster with $p_T > 400$ GeV, and high jet masses [13]. The search is performed in the lepton+jets final state, where high missing transverse energy is required, and the allhadronic final state, where for each event two jets are required to have high jet mass and the event has no missing transverse energy. Upper limits can be set on the $t\bar{t}$ production cross section for two cases. The resulting upper limit is $\sigma_{t\bar{t}} < 38$ fb at the 95% CL for events where at least one top is produced with $p_T > 400$ GeV, and $\sigma_{t\bar{t}} < 20$ fb for the pair production of massive objects produced with $p_T > 400$ GeV.

At D0, the possibility of Lorentz invariance violation in the top quark sector has been considered, by searching for a time dependent $t\bar{t}$ production cross section in the lepton plus jets final state, using 5.3 fb^{-1} of data. Lorentz-violating terms can be introduced to the SM Lagrangian via an effective field theory in the standard-model extension (SME) framework [14]. The SME predicts $\sigma_{t\bar{t}}$ to depend on the sidereal time, due to the change of the orientation of the D0 detector with the rotation of the Earth relative to fixed stars. No indication for a time dependent $\sigma_{t\bar{t}}$ can be observed, and first constraints on Lorentz invariance violation in the top quark sector are set [15].

5 Conclusion and Outlook

In this report, a collection of recent searches for physics beyond the SM in the top quark sector by the CDF and D0 collaborations has been discussed. New models have been tested using up to the full Tevatron data set. No evidence for physics beyond the SM has been seen yet.

Acknowledgements

I thank my collaborators from CDF and D0 for their help in preparing the presentation and this article. I also thank the staffs at Fermilab and collaborating institutions, and acknowledge the support from STFC.

References

[1] F. Abe *et al.* [CDF Collaboration], Phys. Rev. Lett. **74**, 2626 (1995) [arXiv:hep-ex/9503002].

[2] S. Abachi *et al.* [D0 Collaboration], Phys. Rev. Lett. **74**, 2632 (1995) [arXiv:hep-ex/9503003].

[3] [Tevatron Electroweak Working Group and CDF Collaboration and D0 Collab], arXiv:1107.5255 [hep-ex].

[4] V. M. Abazov *et al.* [D0 Collaboration], Phys. Rev. D **85**, 051101 (2012).

[5] T. Aaltonen *et al.* [CDF Collaboration], Phys. Rev. D **84**, 072004 (2011).

[6] T. Aaltonen *et al.* [CDF Collaboration], CDF Conf. Note 10776 (2012).

[7] T. Aaltonen *et al.* [CDF Collaboration], arXiv:1202.5653v1 (2012).

[8] V. M. Abazov *et al.* [D0 Collaboration], Phys. Lett. B **703**, 21 (2012).

[9] V. M. Abazov *et al.* [D0 Collaboration], Phys. Rev. D **83**, 032009 (2011).

[10] V. M. Abazov *et al.* [D0 Collaboration], arXiv:1204.2332 [hep-ex] (2012).

[11] V. M. Abazov *et al.* [D0 Collaboration], Phys. Rev. D **85**, 051101 (2012).

[12] T. Aaltonen *et al.* [CDF Collaboration], arxiv:1107.3875 (2011).

[13] T. Aaltonen *et al.* [CDF Collaboration], Conf. Note 10234 (2011).

[14] D. Colladay and V.A. Kostelecky, Phys. Rev. D **58**, 116002 (1998); V.A. Kostelecky, Phys. Rev. D **69**, 105009 (2004).

[15] V. M. Abazov *et al.* [D0 Collaboration], arXiv:1203.6106 (2012).

Hunting New Physics in Top Pair Production

Jernej F. Kamenik[1,2]

[1]Jožef Stefan Institute, Jamova 39, 1000 Ljubljana, Slovenia
[2]Faculty of Mathematics and Physics, University of Ljubljana, Jadranska 19, 1000 Ljubljana, Slovenia

DOI: `http://dx.doi.org/10.3204/DESY-PROC-2012-02/186`

Measurements of the forward-backward asymmetry (FBA) in $t\bar{t}$ production at the Tevatron significantly deviate from expectations within the standard model. Several new physics (NP) scenarios have been proposed as explanations of this anomaly. I briefly review the $t\bar{t}$ production observables at the LHC which could shed light on to the origin of the large FBA, whether it is mostly due to NP resonances exchanged in the $s-$, $t-$ or $u-$ channel, or even due to incoherent effects.

1 Introduction

The forward-backward asymmetry (FBA) in $t\bar{t}$ production at the Tevatron has been measured by both the CDF [1, 2] and DØ [3] collaborations and found to be significantly larger than the standard model (SM) predictions. The naïve average of the inclusive FBA, adding the uncertainties in quadrature, is

$$A_{FB} = 0.187 \pm 0.037\,, \tag{1}$$

while the NLO QCD prediction [1, 4] including leading electroweak (EW) contributions [5] is $A_{FB}^{\rm SM} = 0.07(2)$. Both CDF and DØ have also measured the FBA in bins of $m_{t\bar{t}}$ and t-$\bar{t}$ rapidity differences. Only CDF [1, 2], however, unfolds to the partonic ("truth") level obtaining

$$\begin{aligned} A_{FB}^{\rm lo} &\equiv A_{FB}(m_{t\bar{t}} < 450\ {\rm GeV}) = 0.078 \pm 0.054\,,\\ A_{FB}^{\rm hi} &\equiv A_{FB}(m_{t\bar{t}} > 450\ {\rm GeV}) = 0.296 \pm 0.067\,, \end{aligned} \tag{2}$$

to be compared with the SM (NLO QCD and EW) predictions $(A_{FB}^{\rm lo})^{\rm SM} = 0.05(1)$ and $(A_{FB}^{\rm hi})^{\rm SM} = 0.11(2)$ [1, 4, 5].

A related observable at the LHC is the charge asymmetry (CA) in $t\bar{t}$ production, A_C. In contrast to the FBA, the measurements of the CA at the LHC agree with the SM expectations. The average of ATLAS [6] and CMS [7] results,

$$A_C = 0.001 \pm 0.014\,, \tag{3}$$

agrees within errors with the SM prediction $A_C^{\rm SM} = 0.007(1)$ [6, 4, 5]. Recently, the ATLAS collaboration also presented the first results for the CA binned in $m_{t\bar{t}}$ [8]

$$\begin{aligned} A_C^{\rm lo} &\equiv A_C(m_{t\bar{t}} < 450\ {\rm GeV}) = -0.053 \pm 0.088\,,\\ A_C^{\rm hi} &\equiv A_C(m_{t\bar{t}} > 450\ {\rm GeV}) = -0.008 \pm 0.047\,, \end{aligned} \tag{4}$$

in agreement with the corresponding SM predictions, $A_C^{\rm lo} = 0.002(2)$ and $A_C^{\rm hi} = 0.009(2)$ [6, 4, 5]. Together with inclusive $t\bar{t}$ production cross-section and $m_{t\bar{t}}$ spectrum measurements at the Tevatron and the LHC, the measured CA already represents a significant constraint on NP models trying to address the anomalously large FBA values.

2 New physics models for the FBA

The large size of the observed non standard contributions to the FBA, points to NP affecting the $t\bar{t}$ production at hadronic colliders at the tree level and typically requires on-shell new degrees of freedom below the TeV scale. A reliable model-independent analysis of NP effects in $t\bar{t}$ production using effective field theory methods is thus not possible [9]. Alternatively, one can consider a single NP amplitude interfering with the SM contributions at a time. Such scenarios can then be classified according to the new resonances coupling to quarks and exchanged in $s-$, $t-$ or $u-$channel. Among the plethora of possible spin, weak isospin, charge and color assignments, only a few of such states can produce a sizable positive FBA at the Tevatron without being in gross conflict with the measurements of the total cross-section and/or the $m_{t\bar{t}}$ spectrum [10]. These include an $s-$channel exchanged (axial-)vector color octet boson (axigluon) [11, 12, 13], neutral (Z') [14] or charged (W') [15] vector bosons, coupling chirally to quarks and exchanged in the $t-$channel, a scalar isodoublet [16] whose neutral component contributes in the $t-$channel, as well as scalar color triplet [17, 18] or sextet [17] bosons coupling chirally to up-type quarks and contributing in the $u-$channel (c.f. [19] for a recent review).

3 LHC constraints

In $t-$ and $u-$channel models, the new FBA contributions are mainly driven by kinematics. In particular, they exhibit a forward Rutherford scattering peak. Due to the resulting strong correlations between the FBA and CA, the existing LHC CA measurements alone already exclude the Z' and W' models from addressing the FBA puzzle [20]. Another consequence is an enhanced $t\bar{t}$ production cross-section in the forward region, which could be probed with dedicated analyses at ATLAS and CMS [21] or even at the LHCb [22]. On the other hand, while same-sign top pair production [23] as well as electroweak [24, 25] and precision flavor observables [24, 26, 27] can be a problem, the relevance of such constraints is model-dependent and dangerous effects can be suppressed systematically e.g. by use of symmetries [27]. Similarly, if the new resonances are massive enough and not too broad, sizable flavor violating $t+$jet resonance production can be expected in $t\bar{t}+$jet final states [18, 28].

With $s-$channel NP, the FBA is essentially due to spin interference effects. Close to threshold, top quark spins effectively probe initial parton chiralities and possible non-standard contributions can be tested for using angular lepton asymmetries in leptonic top decay channels [29]. In general one expects strong correlations with $t\bar{t}$ spin correlation observables (c.f. [20] and references therein). On the other hand the singular features in the $m_{t\bar{t}}$ spectrum expected from $s-$channel NP (resonance in the cross-section and a flip in sign of the FBA and CA) can be suppressed if the resonance appears below $t\bar{t}$ production threshold [12, 13] and/or if it is very broad, as also required by dijet (resonance) constraints [13, 30, 31]. Another interesting related channel is (resonant) four top production at the LHC [32] which already provides a significant constraint [33].

4 Incoherent NP $t\bar{t}$ production

At present, the $t\bar{t}$ production cross-section at the Tevatron and the LHC is still subject to significant $\mathcal{O}(10\%)$ uncertainty. Thus, inclusive $t\bar{t}$ production observables like the FBA and CA could also be affected by NP contributions not interfering with the leading QCD $t\bar{t}$ amplitudes. An example is the production of "top partners" ($\tilde{t}$) decaying to top quarks and additional light invisible particles (χ^0) [34]. In order to pass experimental $t\bar{t}$ reconstruction and escape searches for $t\bar{t}$+ MET (missing transverse energy) $\tilde{t}$ should be almost degenerate with the top and χ^0 approximately massless. This puts strong preference for scalar $\tilde{t}$ candidates whose QCD production cross-section is mostly p-wave and is thus suppressed close to threshold [35]. The FBA is in this case driven by strongly asymmetric $t-$channel χ^0 mediated contributions [34]. Since the relevant interactions are flavor violating and involve couplings to light quarks, one would generically also expect effects in jets+MET final states.

5 Conclusions

The most significant hints of physics beyond the standard model at the Tevatron have been reported in the top sector. The large observed value of the FBA could still be due to new $\mathcal{O}$(TeV) ($s-$channel) resonances, in which case one generically expects excesses in the $t\bar{t}$ and di-jet (pair) spectra. Alternative interesting possibilities are represented by sub TeV NP contributions in the $u-$ or $t-$channel, in which case one predicts interesting signatures in $t\bar{t}$+jets final states. At the LHC, the FBA is manifested in terms of a rapidity dependent CA. Presently measured inclusive values are well consistent with SM predictions, introducing some tension in almost all existing NP proposals (see however [31]). In the near future top spin correlation and polarization observables could provide more complementary constraints. Finally, an enhanced $t\bar{t}$ production cross-section in the forward region in such NP scenarios represents an opportunity for an interesting top physics program at the LHCb.

Acknowledgements

This work was supported in part by the Slovenian Research Agency.

References

[1] T. Aaltonen *et al.* [CDF Collaboration], Phys. Rev. D **83**, 112003 (2011);

[2] Y. Takeuchi *et al.* [CDF Collaboration] (2011), http://www- cdf.fnal.gov/physics/new/top/2011/DilAfb/, Note10398; T. Schwarz *et al.* [CDF Collaboration] (2011), CDF Note 10584; S. Leone [CDF Collaboration], Talk given at Moriond EWK, March 9, 2012.

[3] V. M. Abazov *et al.* [D0 Collaboration], Phys. Rev. D **84**, 112005 (2011).

[4] S. Frixione and B. R. Webber, JHEP **0206**, 029 (2002); S. Frixione, P. Nason and B. R. Webber, JHEP **0308**, 007 (2003).

[5] W. Hollik and D. Pagani, Phys. Rev. D **84**, 093003 (2011); J. H. Kuhn and G. Rodrigo, JHEP **1201** (2012) 063; A. V. Manohar and M. Trott, Phys. Lett. B **711** (2012) 313.

[6] [ATLAS Collaboration], (2011), ATLAS-CONF-2011-106; [arXiv:1203.4211 [hep-ex]].

[7] [CMS Collaboration], (2011), CMS-PAS-TOP-11-030.

[8] A. Krasznahorkay, [ATLAS Collaboration], presented at ASPEN 2012 Winter Conference, 12 February, 2012.

[9] C. Delaunay, O. Gedalia, Y. Hochberg, G. Perez and Y. Soreq, JHEP **1108** (2011) 031.

[10] J. A. Aguilar-Saavedra and M. Perez-Victoria, JHEP **1105**, 034 (2011); J. A. Aguilar-Saavedra and M. Perez-Victoria, Phys. Rev. D **84**, 115013 (2011).

[11] O. Antunano, J. H. Kuhn and G. Rodrigo, Phys. Rev. D **77**, 014003 (2008); P. Ferrario and G. Rodrigo, Phys. Rev. D **80**, 051701 (2009); P. H. Frampton, J. Shu and K. Wang, Phys. Lett. B **683**, 294 (2010).

[12] R. Barcelo, A. Carmona, M. Masip and J. Santiago, Phys. Rev. D **84** (2011) 014024; R. Barcelo, A. Carmona, M. Masip and J. Santiago, arXiv:1106.4054 [hep-ph].

[13] G. M. Tavares and M. Schmaltz, Phys. Rev. D **84**, 054008 (2011); J. A. Aguilar-Saavedra and M. Perez-Victoria, Phys. Lett. B **705**, 228 (2011).

[14] S. Jung, H. Murayama, A. Pierce and J. D. Wells, Phys. Rev. D **81**, 015004 (2010).

[15] K. Cheung, W. -Y. Keung and T. -C. Yuan, Phys. Lett. B **682**, 287 (2009).

[16] K. Blum, Y. Hochberg and Y. Nir, JHEP **1110**, 124 (2011).

[17] J. Shu, T. M. P. Tait and K. Wang, Phys. Rev. D **81**, 034012 (2010); A. Arhrib, R. Benbrik and C. -H. Chen, Phys. Rev. D **82**, 034034 (2010); K. M. Patel and P. Sharma, JHEP **1104**, 085 (2011); Z. Ligeti, G. M. Tavares and M. Schmaltz, JHEP **1106** (2011) 109.

[18] I. Dorsner, S. Fajfer, J. F. Kamenik and N. Kosnik, Phys. Rev. D **81**, 055009 (2010).

[19] J. F. Kamenik, J. Shu and J. Zupan, arXiv:1107.5257 [hep-ph].

[20] S. Fajfer, J. F. Kamenik and B. Melic, arXiv:1205.0264 [hep-ph].

[21] O. Antunano, J. H. Kuhn and G. Rodrigo, Phys. Rev. D **77**, 014003 (2008); J. L. Hewett, J. Shelton, M. Spannowsky, T. M. P. Tait and M. Takeuchi, Phys. Rev. D **84** (2011) 054005; J. -F. Arguin, M. Freytsis and Z. Ligeti, Phys. Rev. D **84**, 071504 (2011).

[22] A. L. Kagan, J. F. Kamenik, G. Perez and S. Stone, Phys. Rev. Lett. **107**, 082003 (2011).

[23] J. A. Aguilar-Saavedra and M. Perez-Victoria, Phys. Lett. B **701**, 93 (2011); C. Degrande, J. -M. Gerard, C. Grojean, F. Maltoni and G. Servant, Phys. Lett. B **703**, 306 (2011).

[24] U. Haisch and S. Westhoff, JHEP **1108**, 088 (2011).

[25] M. I. Gresham, I. -W. Kim, S. Tulin and K. M. Zurek, arXiv:1203.1320 [hep-ph].

[26] I. Dorsner, S. Fajfer, J. F. Kamenik and N. Kosnik, Phys. Rev. D **82**, 094015 (2010).

[27] B. Grinstein, A. L. Kagan, M. Trott and J. Zupan, Phys. Rev. Lett. **107**, 012002 (2011); JHEP **1110**, 072 (2011).

[28] M. I. Gresham, I. -W. Kim and K. M. Zurek, Phys. Rev. D **84**, 034025 (2011).

[29] A. Falkowski, G. Perez and M. Schmaltz, arXiv:1110.3796 [hep-ph].

[30] R. S. Chivukula, E. H. Simmons and C. -P. Yuan, Phys. Rev. D **82**, 094009 (2010); C. Delaunay, O. Gedalia, S. J. Lee, G. Perez and E. Ponton, Phys. Lett. B **703**, 486 (2011); Y. Bai, J. L. Hewett, J. Kaplan and T. G. Rizzo, JHEP **1103** (2011) 003; A. Djouadi, G. Moreau and F. Richard, Phys. Lett. B **701**, 458 (2011);

[31] J. Drobnak, J. F. Kamenik and J. Zupan, arXiv:1205.4721 [hep-ph].

[32] J. A. Aguilar-Saavedra and J. Santiago, Phys. Rev. D **85**, 034021 (2012).

[33] N. Zhou, D. Whiteson and T. M. P. Tait, Phys. Rev. D **85**, 091501 (2012).

[34] G. Isidori and J. F. Kamenik, Phys. Lett. B **700**, 145 (2011).

[35] W. Beenakker, S. Brensing, M. Kramer, A. Kulesza, E. Laenen and I. Niessen, JHEP **1008**, 098 (2010).

Exclusive and Rare B Decays in ATLAS

Elisa Musto[1,2] on behalf of the ATLAS Collaboration

[1]INFN Sezione di Napoli
[2]Dipartimento di Scienze Fisiche, Università di Napoli, Napoli, Italy.

DOI: http://dx.doi.org/10.3204/DESY-PROC-2012-02/309

The ATLAS experiment at LHC presented a variety of B-Physics results obtained by analyzing data collected during 2010 and 2011. B meson properties are investigated in the exclusive decays involving a J/ψ. A brief overview of these measurements is given; then, the blind analysis search for the decay $B_s \to \mu^+\mu^-$ is described.

1 Introduction

The ATLAS B-Physics program is mainly based on exclusive and rare B-hadron decays as they allow to perform interesting studies in the Heavy Flavor sector and to search for New Physics. Several measurements have been done by using proton-proton collisions at a center-of-mass energy of 7 TeV recorded with the ATLAS [1] detector at the LHC during 2010 and 2011. These measurements rely mainly on the Inner Detector (ID) tracker and on the Muon Spectrometer (MS) systems, which achieved very good performance despite the challenging pile-up conditions due to the high luminosity reached. Dedicated B-physics triggers based on di-muons were developed and were kept unprescaled without having to raise the $p_T(\mu)$ threshold.

2 Exclusive B mesons decays

B mesons in ATLAS are reconstructed in exclusive channels involving a J/ψ which further decays to a di-muon final state [2, 3, 4, 5, 6, 7]. The analysis of these decays is important to study the B meson properties, to test the theoretical predictions, or to be used as reference in future important measurements.

In particular, some decays serve as reference for other decay channels, like $B^\pm \to J/\psi K^\pm$ for $B_s \to \mu^+\mu^-$. The $B_d^0 \to J/\psi K^{*0}$ and $B_s^0 \to J/\psi\phi(K^+K^-)$ decays are studied to evaluate B_d^0 and B_s^0 lifetimes; the latter allows the measurement of the B_s^0 mixing phase which generates CP violation. $B_d^0 \to J/\psi K_s^0(\pi^+\pi^-)$ and $\Lambda_b^0 \to J/\psi\Lambda^0(p^+\pi^-)$ serve to measure the lifetime ratio of Λ_b^0 and B_d^0, predicted by Heavy Quark Expansion (HQE) [8] and perturbative QCD. Also the study of the Λ_b^0 polarization is relevant to test these models. Finally, the study of $B_c^\pm \to J/\psi\pi^\pm$ is useful to probe heavy quark dynamics.

The J/ψ selection requires a pair of good quality oppositely charged tracks identified as muons fitted to a common vertex. Depending on the exclusive decay, the tracks belonging to the di-muon candidate and one or two additional tracks are again fitted to a common vertex; this time the di-muon tracks are constrained to the J/ψ world average mass while to the other tracks a mass hypothesis is assigned. All B hadron mass measurements agree with PDG values;

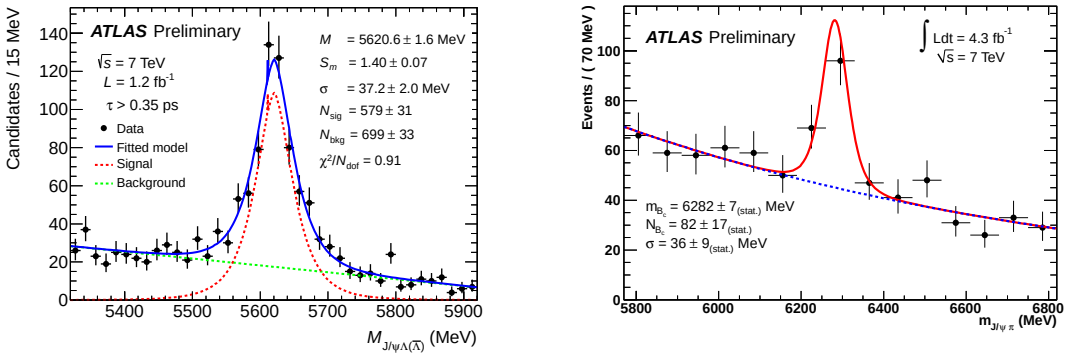

Figure 1: Invariant mass distributions of $\Lambda_b^0 \to J/\psi\Lambda^0(p^+\pi^-)$ and charge conjugate (left) and $B_c^\pm \to J/\psi\pi^\pm$ (right) candidates found in ATLAS data.

two examples of invariant mass distributions are shown in Figure 1 for $\Lambda_b^0 \to J/\psi\Lambda^0(p^+\pi^-)$) (left) [6] and for $B_c^\pm \to J/\psi\pi^\pm$ (right) [7] decays.

3 The $B_s \to \mu^+\mu^-$ decay

The $B_s \to \mu^+\mu^-$ decay is a Flavor Changing Neutral Current process involving a $b \to s$ quark transition. It is highly suppressed in the Standard Model picture and occurs at the lowest order through one-loop diagrams, so that the theoretical estimation of the branching ratio is $(3.55 \pm 0.28) \times 10^{-9}$ [9, 10]. Contributions from New Physics can significantly increase this branching ratio. Recently the CDF collaboration reported an excess of $B_s \to \mu^+\mu^-$ candidates [11] , which has not been confirmed by the latest results of the LHCb [12] and the CMS [13] collaborations.

The ATLAS analysis [14] is based on data collected up to July 2011 with stable LHC beams, corresponding to 2.4 fb^{-1} of integrated luminosity. In order to minimize the systematic uncertainties the $B_s \to \mu^+\mu^-$ branching ratio is normalized to the branching ratio of another high-yield B meson decay channel taken as reference; for this purpose the $B^\pm \to J/\psi K^\pm \to \mu^+\mu^- K^\pm$ decay has been used. The expression of the $B_s \to \mu^+\mu^-$ branching ratio reads

$$Br(B_s \to \mu^+\mu^-) = \frac{N_{\mu\mu}}{N_{B^\pm}} \times R_{\alpha\epsilon} \times \frac{\mathcal{L}_{ref}}{\mathcal{L}_{\mu\mu}} \times \frac{f_u}{f_s} \times Br(B^\pm \to J/\psi K^\pm) \times Br(J/\psi \to \mu^+\mu^-) \quad (1)$$

where $R_{\alpha\epsilon} = \frac{\epsilon_{B^\pm}\alpha_{B^\pm}}{\epsilon_{\mu\mu}\alpha_{\mu\mu}}$ and for each decay mode, N is the number of observed events, ϵ and α are, respectively, the efficiencies and acceptances, $\mathcal{L}$ is the integrated luminosity and f_u/f_s is the relative p-p production rate of $B^\pm$and B_s mesons. In Equation 1 the luminosity factors cancel out since the same integrated luminosity has been used. Equation 1, when setting $N_{\mu\mu} = 1$, provides the so-called *Single Event Sensitivity* (SES). A blind search is performed, meaning that all the quantities entering the SES have been evaluated by excluding in the data sample the signal region, corresponding to a mass window of $\pm$ 300 MeV around the B_s mass, until the analysis was considered finalized and approved by the Collaboration.

Monte Carlo (MC) samples [1]were used to model both signal and reference channels. In particular, for each decay mode N is evaluated from data after background subtraction while the ratio $R_{\alpha\epsilon}$ is evaluated from MC; for the remaining quantities the values $\frac{f_u}{f_s} = 0.267 \pm 0.021$ [2] , and $Br(B^{\pm} \to J/\psi K^{\pm} \to \mu^+\mu^- K^{\pm}) = (6.01 \pm 0.21) \times 10^{-5}$ [17] are used. The main background is expected to originate from true di-muon events, dominated by (prompt) Drell-Yan pairs ($pp \to \mu^+\mu^-$) and non-prompt heavy flavor semi-leptonic decays ($pp \to b\bar{b} \to \mu^+\mu^- X$). To model this *continuum* background the data belonging to the sidebands of the signal region ($4766\ MeV < m_{\mu\mu} < 5066\ MeV \bigcup 5666\ MeV < m_{\mu\mu} < 5966\ MeV$), as shown in Figure 2, were used. In order to avoid biases, the sidebands data have been split in 2 equal populated parts: one was used in the optimization of the cuts, the other for the estimation of the background in the signal region after the optimization. In addition, the irreducible background which originates from neutral B meson two-body decays with charged hadrons in final state misidentified as prompt muons[3], has been evaluated using MC and accounted in the upper limit extraction[4]. To improve the signal/background separation, the samples were split in three mass resolution categories ($\sigma_{m_{\mu\mu}} \sim 60/80/120\ MeV$) depending on the maximum absolute value of the muons pseudorapidity in the di-muon candidate, η_{max}. A multivariate analysis (MVA) has been used to combine the separation power of 14 different variables, selected according to their discriminating power and avoiding correlations; the chosen multivariate classifier was the Boosted Decision Tree (BDT) algorithm. In particular, these variables exploit the signal features, like the separation between the primary and the secondary vertex, the symmetry of the final state (pointing angle, impact parameters, etc.) and the B meson hadronization features

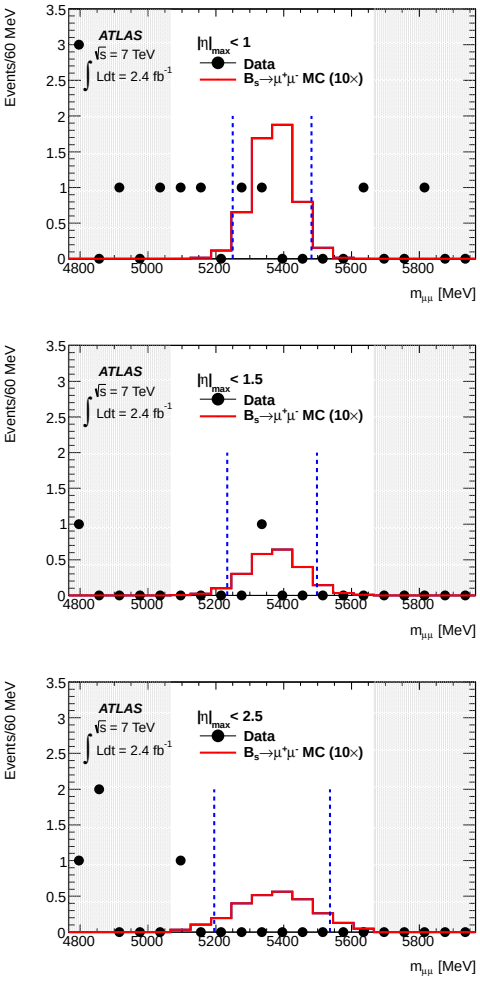

Figure 2: Invariant mass distributions for the three resolution categories (top to bottom).

[1]MC samples were corrected by using per event weights in order to account for the differences between B_s and B^+spectra and for the discrepancies found from comparison with data.

[2]This value is obtained from Reference [15] assuming $f_u = f_d$ (following Reference [16]) and no kinematic dependence of $\frac{f_u}{f_s}$.

[3]The probability to misidentify a final state hadron as muon either due to punch-through or decay in flight (*muon fake rate*) has been estimated to be $\sim 10^{-3}$.

[4]Additional sources of background have been estimated to be negligible.

(transverse momentum, isolation[5], etc). For each mass resolution category, the selection has been optimized as a function of the width of the search window in mass Δm and of the lower cut on the BDT output[6]. To obtain a limit at 95% CL, the estimator [18] $\mathcal{P} = \epsilon_S/(1+\sqrt{N_{bkg}})$ is maximized, where ϵ_S is the signal efficiency and N_{bkg} is the number of background events. To avoid the introduction of additional systematic uncertainties, the same BDT classification optimized on the $B_s \to \mu^+\mu^-$ signal has been used for the $B^\pm \to J/\psi K^\pm$ selection. For each resolution category, the invariant mass distribution is shown in Figure 2: each plot shows the invariant mass distribution for the selected candidates in data (dots) compared to the signal (continuous line) as predicted by MC, assuming a branching ratio 10 times greater than the SM expectation. The two vertical lines correspond to the optimized Δm cut, while the grey areas correspond to the sidebands used. No excess of events has been found, therefore an upper limit on the $B_s \to \mu^+\mu^-$ branching ratio is set. The observed limit, obtained by means of an implementation [19] of the CL_s method [20], is < 2.2 (1.9) $\times 10^{-8}$ at 95% (90%) CL.

4 Conclusions

The ATLAS Collaboration presented interesting results in the B-Physics sector, mainly concerning masses and lifetimes of various B hadrons, which allow to test the theoretical prediction, to perform future measurements of CP violation or to search for New Physics. For this purpose the $B_s \to \mu^+\mu^-$ decay has been studied and an upper limit has been set.

References

[1] The ATLAS Collaboration, JINST **3** (2008) S08003.
[2] The ATLAS Collaboration, ATLAS-CONF-2010-098 `http://cdsweb.cern.ch/record/1307530`.
[3] The ATLAS Collaboration, ATLAS-CONF-2011-050 `https://cdsweb.cern.ch/record/1341815`.
[4] The ATLAS Collaboration, ATLAS-CONF-2011-092 `http://cdsweb.cern.ch/record/1363779`.
[5] The ATLAS Collaboration, ATLAS-CONF-2011-105 `http://cdsweb.cern.ch/record/1369830`.
[6] The ATLAS Collaboration, ATLAS-CONF-2011-124 `http://cdsweb.cern.ch/record/1378514`.
[7] The ATLAS Collaboration, ATLAS-CONF-2012-028 `http://cdsweb.cern.ch/record/1430737`.
[8] I. Bigi, T. Mannel, S. Turczyk and N. Uraltsev, JHEP **1004** (2010) 073.
[9] A. J. Buras, M. Nagai and P. Paradisi, JHEP **1105** (2011) 005.
[10] UTfit Collaboration, M. Bona *et al.*, PoS(EPS-HEP2011) 185.
[11] The CDF Collaboration, Phys.Rev.Lett. **107** (2011) 191801.
[12] The LHCb Collaboration, `hep-ex/1203.449` .
[13] The CMS Collaboration, `hep-ex/1203.3976` .
[14] The ATLAS Collaboration, `hep-ex/1204.0735v2` .
[15] The LHCb Collaboration, Phys. Rev. **D 85** (2012) 032008.
[16] Heavy Flavor Averaging Group, D. Asner *et al.*, `hep-ex/1010.1589` .
[17] Particle Data Group, K. Nakamura *et al.*, J. Phys. **G 37** (7A) (2010) 075021.
[18] G. Punzi, `physics.data-an/0308063`.
[19] T. Junk, Nucl. Instrum. Meth.**A434** (1999) 435-443.
[20] A. L. Read, J. Phys. **G28** (2002) 2693-2704.

[5]The isolation is track based, and the dependence on pile-up is reduced by using only tracks associated with the same primary vertex as the B candidate.

[6]The mass dependence of the BDT output has been checked with a test signal, where the signal mass has been shifted to the value of 6.5 GeV: no significant correlation between the two has been found.

Searches for BSM physics using flavor transitions at the Tevatron

Lucia Grillo[1] on behalf of the CDF and DØ Collaborations

[1] University of Trieste and INFN Trieste, Italy, now Physikalisches Institut, Ruprecht-Karls-Universität, Im Neunheimer Feld 226, 69120 Heidelberg, Germany

DOI: http://dx.doi.org/10.3204/DESY-PROC-2012-02/203

The CDF and DØ experiments at the Tevatron $p\bar{p}$ collider continue to produce important results on the benchmark channels for the indirect searches for Beyond Standard Model (BSM) physics using flavor transitions, now exploiting the full Run II dataset. We report three final CDF results: new bounds on the B_s^0 mixing phase and on the B_s^0 mass eigenstates decay width difference, a measurement of the difference of CP asymmetries in K^+K^- and $\pi^+\pi^-$ decays of D^0 mesons, and an update of the search for $B_{(s)}^0$ mesons decaying into pairs of muons. We also present the $B_s \to D_s^{(*)+} D_s^{(*)-}$ decays brunching ratio measurements using 6.8 fb^{-1} of data, and a search for CP violation in $D^0 \to K_S^0\pi^+\pi^-$decays in 6.0 fb^{-1} of data.

1 Searches for BSM physics through CP violation

The understanding of CP violation in the B_s sector still offers room for possible non-SM contributions, as indicated by the anomaly in the dimuon charge asymmetry reported by the DØ Collaboration [1]. CDF has updated the time-dependent CP violation measurement in $B_s^0 \to J/\psi\phi$ decays, since this is widely recognized as the most effective experimental probe of New Physics (NP) entering B_s mixing. Along with this result, we present the measurement of the $B_s^0 \to D_s^{(*)+} D_s^{(*)-}$ brunching fractions, which helps to constrain the B_s^0 mass eigenstates decay width difference. In the case of charmed mesons, CP violation is not so well established as for B mesons and kaons. The first evidence of CP violation in two-body singly-Cabibbo-suppressed D^0 decays has been recently reported by the LHCb Collaboration [2], suggesting a possible hint of NP. It is important both to have an independent confirmation of this result in a different environment such as $p\bar{p}$ collisions where no production asymmetries are expected, and to search for and measure CP violation in other charmed meson decays.

1.1 Measurement of the $B_s^0 \to J/\psi\phi$ time-evolution

New dynamics entering the B_s^0 sector would significantly alter the phase difference ϕ_s between the B_s^0–$\bar{B}_s^0$ mixing amplitude and the amplitude of B_s^0 and $\bar{B}_s^0$ decays into common final states, with respect to its nearly vanishing value expected in the SM. A non-CKM enhancement of ϕ_s can also decrease the decay width difference between the heavy and light mass-eigenstate of the B_s^0 meson, $\Delta\Gamma_s$. Since the decay is dominated by a single real amplitude, the phase difference equals the mixing phase to a good approximation. Early Tevatron measurements have shown a

mild discrepancy of about 2σ with the SM expectation [3]. The latest updates by CDF and DØ are in better agreement with the SM, as well as first measurements provided by LHCb [4, 5, 6]. Here we report the new CDF update using the final dataset of 10 fb^{-1} which includes about 11000 flavor-tagged $B_s^0 \to J/\psi\phi$ decays collected by a low-momentum dimuon trigger [7]. The decays are fully reconstructed through four tracks that fit to a common displaced vertex, two matched to muon pairs consistent with a J/ψ decay, and two consistent with a $\phi \to K^+K^-$ decay. A joint fit that exploits the candidate-specific information given by the B mass, decay time and production flavor, along with the decay angles of kaons and muons, is used to determine both ϕ_s and $\Delta\Gamma_s$. The analysis closely follows the previous measurement [4]. The only major difference is the use of an updated calibration of the tagging algorithm that uses information from the decay of the "opposite side" bottom hadron in the event to determine the flavor of the B_s^0 at its production, with tagging power $(1.39 \pm 0.01)\%$. The information of the tagger that exploits charge-flavor correlations of the neighboring kaon to the B_s^0 is instead restricted to only half of the sample, with tagging power $(3.2 \pm 1.4)\%$, degrading the statistical resolution on ϕ_s by no more than 15%. A decay resolution of ~ 90 fs allows resolving the fast B_s^0 oscillations to increase sensitivity on the mixing phase. The 68% and 95% confidence regions in the plane $(\phi_s, \Delta\Gamma_s)$ obtained from the profile-likelihood of the CDF data are reported in Fig. 1 (left). The confidence interval for the mixing phase is $\phi_s \in [-0.60, 0.12]$ rad at 68% C.L., in agreement with the CKM value and recent D0 and LHCb determinations [5, 8]. This is the final CDF measurement on the B_s^0 mixing phase, and provides a factor of 35% improvement in resolution with respect to the latest determination. CDF also reports $\Delta\Gamma_s = (0.068 \pm 0.026 \pm 0.007)$ ps^{-1} under the hypothesis of a SM value for ϕ_s, along with the measurement of the B_s^0 lifetime, $\tau_s = (1.528 \pm 0.019 \pm 0.009)$ ps, in agreement with other experiments' results [5, 8].

1.2 Measurement of $B_s \to D_s^{(*)+} D_s^{(*)-}$ brunching ratios

Using 6.8 fb^{-1} of data collected by the displaced track trigger we performed the world's most precise measurement of $B_s \to D_s^{(*)+} D_s^{(*)-}$ brunching ratios [9], that could be used to infer indirect information about $\Delta\Gamma_s$. We measure the B_s production rate times the $B_s \to D_s^{(*)+} D_s^{(*)-}$ brunching ratio relative to the normalization mode $B^0 \to D_s^+ D^-$. The relative brunching fractions are determined in a simultaneous mass fit to two signal and two normalization samples. The measured values depend on the yields observed on the four samples and the relative efficiency of signal and normalization modes. An accurate determination of the relative efficiencies is achieved by taking into account the Dalitz structure of the D_s^+ decay. Using measured values of production and relative brunching fractions, the following absolute brunching fractions are derived: $\mathcal{B}(B_s \to D_s^+ D_s^-) = (0.49 \pm 0.06 \pm 0.05 \pm 0.08)\%$, $\mathcal{B}(B_s \to D_s^{*\pm} D_s^{\mp}) = (1.13 \pm 0.12 \pm 0.09 \pm 0.19)\%$, $\mathcal{B}(B_s \to D_s^{*+} D_s^{*-}) = (1.75 \pm 0.19 \pm 0.17 \pm 0.29)\%$, $\mathcal{B}(B_s \to D_s^{(*)+} D_s^{(*)-}) = (3.38 \pm 0.25 \pm 0.30 \pm 0.56)\%$. Statistical, systematic and normalization uncertainties are reported.

1.3 Measurement of CP violation in $D^0 \to h^+h^-$ decays

In singly-Cabibbo-suppressed transitions such as $D^0 \to h^+h^-$ ($h = K, \pi$) decays, any time-integrated CP asymmetry significantly larger than the 1% expected in the CKM hierarchy can be due to the presence of new dynamics that can enhance both the D^0–$\bar{D}^0$ mixing amplitude and the SM-suppressed penguin amplitude. In 2011, using 5.9 fb^{-1} of data, CDF

produced the world's most precise measurements of the CP asymmetries in $D^0 \to K^+K^-$ decays, $A_{CP}(KK) = (-0.24 \pm 0.22 \pm 0.09)\%$, and in $D^0 \to \pi^+\pi^-$ decays, $A_{CP}(\pi\pi) = (0.22 \pm 0.24 \pm 0.11)\%$ [10]. The difference between the individual asymmetries: $\Delta A_{CP} = A_{CP}(KK) - A_{CP}(\pi\pi)$ is maximally sensitive to the presence of direct CP violation and highly suppresses systematic uncertainties from instrumental asymmetries. CDF presents the ΔA_{CP} measurement using the full CDF Run II dataset collected by the trigger on displaced tracks [11]. We use the charge of the soft pion in the $D^{\star+} \to D^0\pi^+$ decay to identify the D^0 flavor at production. The presence of the soft pion causes a bias in the measurement of the asymmetry induced by a few percent difference in reconstruction efficiency between positive and negative tracks at low momentum. However, provided that the relevant kinematic distributions are equalized in the two decay channels, this spurious asymmetry cancels to an excellent level of accuracy in ΔA_{CP}. The cancellation of instrumental asymmetries allows a looser selection criteria with respect to the measurement of individual asymmetries and the larger statistics increases the sensitivity on ΔA_{CP}. The number of decays for D^0 and $\bar{D}^0$ candidates has been determined with a simultaneous fit to the $D^0\pi$ mass distribution of positive and negative D^* decays. Using final samples of 550 thousands $D^0 \to \pi^+\pi^-$ decays and 1.21 million $D^0 \to K^+K^-$ decays, CDF measures $\Delta A_{CP} = (-0.62 \pm 0.21 \pm 0.10)\%$ which is 2.7σ from zero. Such a result provides a strong indication of CP violation in CDF charm data confirming the LHCb evidence [2] with the same resolution. The combination of CDF, LHCb and B-factory measurements deviates by approximately 3.8σ from the no CP violation point.

1.4 Search for CP violation in $D^0 \to K^0_S\pi^+\pi^-$decays

In a sample corresponding to an integrated luminosity of 6.0 fb^{-1} of data we search for time-integrated CP asymmetries in the resonant substructure of the three-body decay $D^0 \to K^0_S\pi^+\pi^-$ decays. As the SM expectation of these CP asymmetries is of the order 10^{-6} and thus well below the experimental sensitivity, an observation of CP violation would be a clear hint for NP. The production flavor of the D^0 is determined, by the charge of the soft pion from the $D^{*+} \to D^0\pi^+$ decay. Two complementary approaches are used, namely a full Dalitz fit employing the isobar model for the involved resonances and a model-independent bin-by-bin comparison of the D^0 and $\bar{D}^0$ Dalitz plots. Our analysis represents a big improvement in terms of precision with respect to CLEO [12], but still no hints of any CP violating effects are found. Individual asymmetries are reported in [13]; the measured value for the overall integrated CP asymmetry is $A_{CP} = (-0.05 \pm 0.57 \pm 0.54)\%$.

2 Searches for BSM physics through rare B decays

In the SM all neutral currents conserve flavor so transitions as $B^0 \to \mu^+\mu^-$ and $B^0_s \to \mu^+\mu^-$ can occur only through higher order loop diagrams. The brunching fractions are predicted in the SM to be $(3.2\pm0.2)\times10^{-9}$ and $(1.0\pm0.1)\times10^{-10}$ respectively for the B^0_s and the B^0 mesons. A wide class of BSM theories predict significantly higher brunching ratio values. This makes these decays one of the most sensitive indirect searches for NP. Last summer CDF reported an intriguing $\sim2.5\sigma$ fluctuation over background in 7 fb^{-1} of data. Even though compatible with the SM and other experiments' results, it allowed the first two-sided bound on the $B^0_s \to \mu^+\mu^-$ rate [14]. Here we report the CDF update of the analysis with the final 10 fb^{-1} dataset [15]. The analysis methods are not changed from the previous iteration to ensure the unbiased inclusion

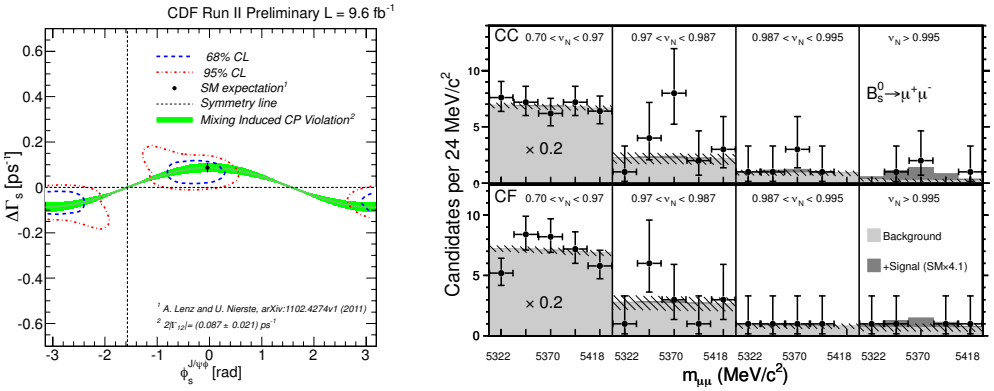

Figure 1: Left: 68% and 95% confidence regions in the plane $(\phi_s, \Delta\Gamma_s)$ from profile-likelihood of CDF data. Right: CDF $B_s^0 \to \mu^+\mu^-$ data compared with the expected background, for "Central Central (CC)" and "Central Forward (CF)" muons, according to the detector region.

of new data. Combinatorial and hadronic B-decay background predictions have been checked with many control samples and an optimized neural net (NN) has been used to eliminate these backgrounds while keeping the signal efficiency high. The search has been performed in mass and NN bins, and the observed signal has been normalized to the $B^+ \to J/\psi K^+$ channel. The data are found to be consistent with the background expectations for the $B^0 \to \mu^+\mu^-$ decay and yield the observed limit $< 4.6 \times 10^{-9}$ (expected limit: $< 4.2 \times 10^{-9}$). For $B_s^0 \to \mu^+\mu^-$ (Fig. 1 right) the summer 2011 deviation has not been reinforced by adding new data, the final double sided limit from CDF is $0.8 \times 10^{-9} < \mathcal{B}(B_s \to \mu^+\mu^-) < 3.4 \times 10^{-8}$ at 95% C.L., which is still compatible both with the SM expectation and the latest limits from LHC experiments. [16].

References

[1] V. M. Abazov *et al.* (DØ Collaboration), *Phys. Rev.* D **84**, 052007 (2011).
[2] R. Aaij *et al.* (LHCb Collaboration), *Phys. Rev. Lett.* **108**, 111602 (2012).
[3] CDF and D0 Collaborations, CDF Note 9787, D0 Note 5928 (2009).
[4] T. Aaltonen *et al.* (CDF Collaboration), *Phys. Rev.* D **85**, 072002 (2012).
[5] V. M. Abazov *et al.* (D0 Collaboration), *Phys. Rev.* D **85**, 032006 (2012).
[6] R. Aaij *et al.* (LHCb Collaboration), *Phys. Rev. Lett.* **108**, 101803 (2012)
[7] T. Aaltonen *et al.* (CDF Collaboration), CDF Note 10778 (2012).
[8] R. Aaij *et al.* (LHCb Collaboration), LHCb-CONF-2012-002.
[9] T. Aaltonen *et al.* (CDF Collaboration), CDF Note 10721.
[10] T. Aaltonen *et al.* (CDF Collaboration), *Phys. Rev.* D **85**, 012009 (2012).
[11] T. Aaltonen *et al.* (CDF Collaboration), CDF Note 10784 (2012).
[12] D. M. Asner *et al.* (CLEO Collaboration), *Phys. Rev. Lett.* **70**, 091101 (2004).
[13] http://www-cdf.fnal.gov/physics/new/bottom/111013.blessed-D0KSpipi_ACP.
[14] T. Aaltonen *et al.* (CDF Collaboration), *Phys. Rev. Lett.* **107**, 191801 (2011).
[15] http://www-cdf.fnal.gov/physics/new/bottom/120209.blessed-bmumu10fb.
[16] CMS PAS BPH-11-020, ATLAS-CONF-2012-010, LHCb-PAPER-2012-007.

Beyond Standard Model searches through heavy flavors at *BABAR*

Marco Bomben[1] on behalf of the *BABAR* Collaboration

[1]LPNHE - Barre 12-22, 1er Étage - 4 place Jussieu - 75252 PARIS CEDEX 05

DOI: http://dx.doi.org/10.3204/DESY-PROC-2012-02/304

The *BABAR* experiment recorded 471×10^6 $B\overline{B}$ pairs at the $\Upsilon(4S)$ resonance (corresponding to an integrated luminosity of 429 fb^{-1}). We present here a selection of recent results from the *BABAR* collaboration: search for lepton-number violation in the decay $B^+ \to h^-\ell^+\ell^+$, search for lepton-flavor violation in $B^\pm \to h^\pm\tau\ell$ and *CP*-violation in $\tau^- \to K^0_S(\geq 0\pi^0)\nu_\tau$.

1 Search for lepton-number violation in the decay $B^+ \to h^-\ell^+\ell^+$

In the Standard Model (SM), the lepton number L is conserved in low-energy collisions and decays. Through neutrino oscillation L-conservation can be violated, for example in the process $B^+ \to h^-\ell^+\ell^+$; highly suppressed in the SM, this lepton-number violating process can be enhanced in several Beyond SM scenarios, such as left-right symmetric gauge theories, SO(10) supersymmetry, R-parity violating models, or extra-dimensions.

In this analysis [1], four final states are considered: the decay channel is $B^+ \to h^-\ell^+\ell^+$ with $h = K, \pi$ and $l = e, \mu$. The continuum and $B\overline{B}$ backgrounds are rejected using bagged decision trees (BDT), based on ΔE (the difference between the expected B energy and the reconstructed B energy), event shape and vertexing variables. A likelihood ratio R is constructed from the $B\overline{B}$ BDT. Unbinned maximum likelihood fits of $m_{\rm ES}$ and R, the likelihood ratio, are performed for each of the four modes. We use the $B^+ \to J/\psi h^+$ data control sample to obtain the $m_{\rm ES}$ fit parameters. The fits are shown in Fig. 1, where we observe that no signal is seen. From these negative results, we obtain upper limits at 90% confidence level (CL) on the four channels: $\mathcal{B}(B^+ \to K^-e^+e^+) < 3.0 \times 10^{-8}$, $\mathcal{B}(B^+ \to K^-\mu^+\mu^+) < 6.7 \times 10^{-8}$, $\mathcal{B}(B^+ \to \pi^-e^+e^+) < 2.3 \times 10^{-8}$, and $\mathcal{B}(B^+ \to \pi^-\mu^+\mu^+) < 10.7 \times 10^{-8}$. These upper limits are 40-70 times more stringent than previous limits set by other experiments.

2 A search for the decay modes $B^\pm \to h^\pm\tau\ell$

FCNC and charged lepton flavor violation are forbidden in the SM at tree level. However, in many extensions of the SM, these effects could be enhanced, especially for the second and third generation [2]. We study [3] the eight final states $B^\pm \to h^\pm\tau\ell$, with $h = K, \pi$ and $\ell = e, \mu$. The final states $B^\pm \to K^\pm\tau e$, $B^\pm \to \pi^\pm\tau\mu$, and $B^\pm \to \pi^\pm\tau e$ have never been done before. We fully reconstruct the hadronic B on one side (the "tag" B) using final states of the type

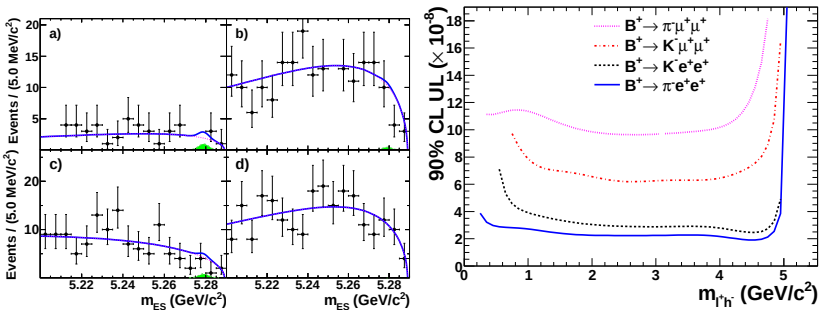

Figure 1: Left: $m_{\rm ES}$ distributions for a) $B^+ \to K^- e^+ e^+$, b) $B^+ \to K^- \mu^+ \mu^+$, c) $B^+ \to \pi^- e^+ e^+$, and d) $B^+ \to \pi^- \mu^+ \mu^+$. The solid blue line is the total fit, the dotted magenta line is the background, the solid green histogram is the signal. Right: 90% CL upper limits on the branching fractions as a function of the mass $m_{\ell^+ h^-}$.

$B^- \to D^{(*)0} X^-$, where X^- is composed of $\pi^\pm$, $K^\pm$, K^0_S, and π^0. This determines the three-momentum of the other B (the "signal" B) on the other side and thus allows us to indirectly reconstruct the τ lepton through:

$$\vec{p}_\tau = -\vec{p}_{\rm tag} - \vec{p}_h - \vec{p}_\ell; \;\; E_\tau = E_{\rm beam} - E_h - E_\ell; \;\; m_\tau = \sqrt{E_\tau^2 - |\vec{p}_\tau|^2},$$

where $(E_\tau, \vec{p}_\tau)$, $(E_h, \vec{p}_h)$, and $(E_\ell, \vec{p}_\ell)$ are the corresponding four-momenta of the reconstructed signal objects, and where $\vec{p}_{\rm tag}$ is the three-momentum of the tag B, and $E_{\rm beam}$ the beam energy. The τ is required to decay to a "one-prong" final state: $\tau \to e\nu\overline{\nu}$, $\tau \to \mu\nu\overline{\nu}$, and $\tau \to (n\pi^0)\pi\nu$ with $n \geq 0$. The signal branching fraction is determined by using the ratio of the number of $B^\pm \to h^\pm \tau \ell$ signal candidates to the yield of control samples of $B^+ \to \overline{D}^{(*)0} \ell^+ \nu; \overline{D}^0 \to K^+ \pi^-$ events from a fully reconstructed hadronic $B^\pm$ decay sample.

The background is mainly coming from semileptonic B decays and from semileptonic D decays. We remove these backgrounds by rejecting the signal B candidates where two of their daughters are kinematically compatible with originating from a charm decay. After this requirement, we reject the continuum background using a cut on the likelihood ratio R, based on particle identification and event shape variables.

The signal region is defined as $\pm 60\,{\rm MeV}/c^2$ around the indirectly reconstructed τ mass m_τ. Figure 2 show an example of m_τ distributions for the data, for the background, and for the signal MC. No signal is observed, which allows us to put 90% CL limit on the branching fractions. Assuming $\mathcal{B}(B^+ \to h^+ \tau^- \ell^+) = \mathcal{B}(B^+ \to h^+ \tau^+ \ell^-)$, we obtain the combined limits shown in Table 1. These limits can be translated into model-independent bounds on the energy scale of new physics in flavor-changing operators [4]: $\Lambda_{\bar{b}d} > 11$ TeV and $\Lambda_{\bar{b}s} > 15$ TeV (at 90% CL), which improved the previous limits of 2.2 and 2.6 TeV, respectively.

3 Search for CP violation in the decays $\tau^- \to \pi^- K^0_S \left(\geq 0\pi^0\right) \nu_\tau$

CP violation, until now, has only been observed in hadronic decays (K, B, and D systems). However, Bigi and Sanda predict [5] a non-zero decay rate asymmetry for τ decays to final

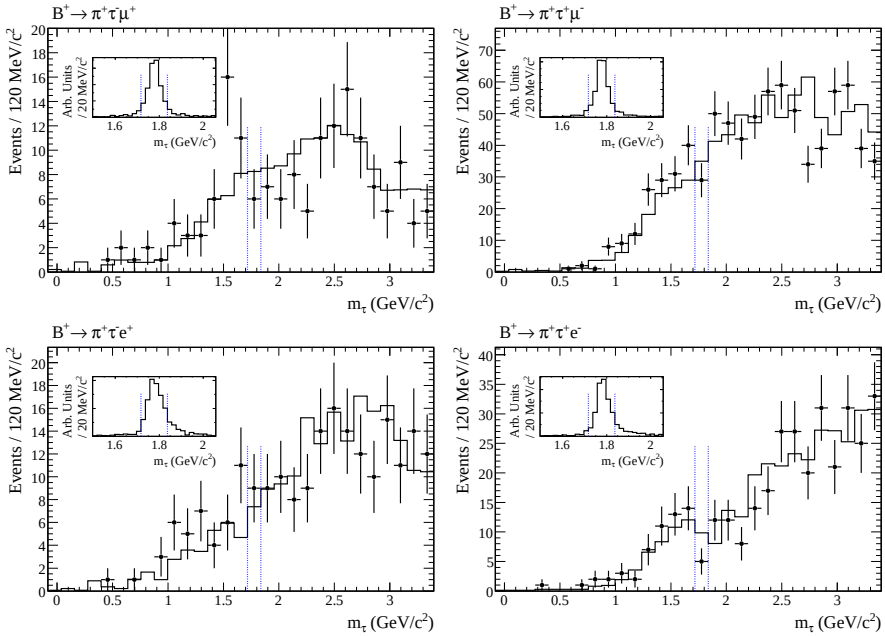

Figure 2: Observed distributions of the τ invariant mass for the $B \to \pi\tau\ell$ modes. The distributions show the sum of the three τ channels (e, μ, π). The points with error bars are the data. The solid line is the background MC which has been normalized to the area of the data distribution. The dashed vertical lines indicate the m_τ signal window range. The inset shows the m_τ distribution for signal MC.

Table 1: Branching fraction central values and 90% CL upper limits (UL) for the combination $\mathcal{B}(B^+ \to h^+\tau\ell) \equiv \mathcal{B}(B^+ \to h^+\tau^-\ell^+) + \mathcal{B}(B^+ \to h^+\tau^+\ell^-)$.

Mode	$\mathcal{B}(B \to h\tau\ell)$ $(\times 10^{-5})$ central value	90% CL UL
$B^+ \to K^+\tau\mu$	$0.0\ ^{+2.7}_{-1.4}$	< 4.8
$B^+ \to K^+\tau e$	$-0.6\ ^{+1.7}_{-1.4}$	< 3.0
$B^+ \to \pi^+\tau\mu$	$0.5\ ^{+3.8}_{-3.2}$	< 7.2
$B^+ \to \pi^+\tau e$	$2.3\ ^{+2.8}_{-1.7}$	< 7.5

states containing a K^0_S meson, due to the CP violation in the kaon sector. The decay rate asymmetry is:

$$A_Q = \frac{\Gamma\left(\tau^+ \to \pi^+ K^0_S\, \overline{\nu}_\tau\right) - \Gamma\left(\tau^- \to \pi^- K^0_S\, \nu_\tau\right)}{\Gamma\left(\tau^+ \to \pi^+ K^0_S\, \overline{\nu}_\tau\right) + \Gamma\left(\tau^- \to \pi^- K^0_S\, \nu_\tau\right)},$$

and is predicted to be equal to $(0.33 \pm 0.01)\%$. Any deviation from the SM prediction could be a sign of new physics. It has to be noted that A_Q is independent of the number of neutral pions in the final state. Recently, Grossman and Nir [6] noticed that the calculation needs to take

into account interferences between the amplitudes of intermediate K^0_S and K^0_L mesons, which are as important as the pure K^0_S amplitude. This means that A_Q depends on the reconstruction efficiency as a function of the $K^0_S \to \pi^+\pi^-$ decay time.

We study here [7] the decay channel $\tau^- \to \pi^- K^0_S \left(\geq 0\pi^0\right) \nu_\tau$. The event is divided into two hemispheres, one corresponding to the signal side, and one to the tag side with $\tau^- \to \ell^- \overline{\nu}_\ell \nu_\tau$, $\ell = e, \mu$. The selection of the signal events requires that the invariant mass of the reconstructed τ lepton is smaller than $1.8\,\mathrm{GeV}/c^2$. After a two-stage likelihood selection (reducing mainly continuum background and K^0_S one, respectively), we obtain 199064 candidates for the electron tag channel (e-tag), and 140602 for the muon tag channel (μ-tag). The composition of the sample in term of signal and background events is presented in Table 2.

Table 2: Composition of the sample after all selection criteria have been applied.

Source	Fractions (%)	
	e-tag	μ-tag
$\tau^- \to \pi^- K^0_S(\geq 0\pi^0)\,\nu_\tau$	78.7 ± 4.0	78.4 ± 4.0
$\tau^- \to K^- K^0_S(\geq 0\pi^0)\,\nu_\tau$	4.2 ± 0.3	4.1 ± 0.3
$\tau^- \to \pi^- K^0 \overline{K}^0 \nu_\tau$	15.7 ± 3.7	15.9 ± 3.7
Other background	1.40 ± 0.06	1.55 ± 0.07

We need to correct the raw asymmetry from the pollution of the other modes shown in Table 2. For the mode $\tau^- \to K^- K^0_S(\geq 0\pi^0)\,\nu_\tau$, the expected asymmetry is opposite to the one from the signal, and for the mode $\tau^- \to \pi^- K^0 \overline{K}^0 \nu_\tau$, the expected asymmetry is zero. Furthermore, an additional correction was pointed out recently [8]: we need to take into account a correction on the asymmetry A_Q due to the different nuclear-interaction cross-section of the K^0 and $\overline{K}^0$ mesons with the material in the detector. We calculate this correction to be $(0.07 \pm 0.01)\%$ and we subtract it from the measured asymmetry. After all corrections are applied, and after combining the results from the e-tag and μ-tag, we obtain $A_Q = (-0.36 \pm 0.23 \pm 0.11)\%$.

As we mentioned, this result should be compared with the prediction of the SM, corrected by the $K^0_S \to \pi^+\pi^-$ decay time dependence. Using the MC sample, we find a multiplicative factor of 1.08 ± 0.01. The SM decay-rate asymmetry, after correction, is then predicted to be $A_Q^{\mathrm{SM}} = (0.36 \pm 0.01)\%$. We observe that our measurement is 2.8 standard deviations away from the SM prediction.

References

[1] J. P. Lees *et al.* (*BABAR* Collaboration), Phys. Rev. D **85**, 071103 (2012).

[2] M. Sher and Y. Yuan, Phys. Rev. **D44**, 1461 (1991).

[3] *BABAR* collaboration, submitted to Phys. Rev. **D**, arXiv:1204.2852 (2012).

[4] D. Black, T. Han, H.-J. He, and M. Sher, Phys. Rev. **D66**, 053002 (2002).

[5] I. I. Bigi and A. I. Sanda, Phys. Lett. B **625**, 47 (2005).

[6] Y. Grossman and Y. Nir, arXiv:1110.3790 [hep-ph]

[7] J.-P. Lees *et al.* (*BABAR* collaboration), Phys. Rev. **D85**, 031102 (2012).

[8] B. R. Ko *et al.*, arXiv:1006.1938 (2010).

Search for the rare decays $B \to \mu^+\mu^-$ with the CMS detector

Franco Simonetto

INFN and Universita' di Padova, via Marzolo 8, Italy

DOI: http://dx.doi.org/10.3204/DESY-PROC-2012-02/239

I summarize here the results of a search for the rare decays $B^0 \to \mu^+\mu^-$ and $B_s^0 \to \mu^+\mu^-$, based on a sample of data collected by the CMS detector from pp collisions at $\sqrt{s} = 7$ TeV, corresponding to an integrated luminosity of 4.9 fb^{-1}. No excess of events over the expected background is observed. The resulting upper limits on the branching fractions are $\mathcal{B}(B_s^0 \to \mu^+\mu^-) < 7.7 \times 10^{-9}$ and $\mathcal{B}(B^0 \to \mu^+\mu^-) < 1.8 \times 10^{-9}$ at 95 % confidence level.

1 Introduction

In the Standard Model (SM) of electroweak interaction the leptonic decays $B_{(s)}^0 \to \mu^+\mu^-$ proceed through high order terms involving penguin or box diagrams. The decay rate is further depressed by the small values of the Cabibbo-Kobaiashi-Maskawa terms involved in the transition, $|V_{td(s)}|^2$, by the helicty related factor m_μ^2/m_B^2 (where m_μ, m_B are the muon and B mesons masses respectively), and by the ratio $(f_b/m_B)^2$, where $f_b \sim 200MeV$ is the $B_{(s)}^0$ -meson decay constant parameterizing the contribution of the quark annihilation diagram. Therefore, very low decay rates are expected in the SM : $\mathcal{B}(B_s^0 \to \mu^+\mu^-) = (3.2 \pm 0.2) \times 10^{-9}$ and $\mathcal{B}(B^0 \to \mu^+\mu^-) = (1.0 \pm 0.1) \times 10^{-9}$ [1], where the uncertainty is due mostly to the limited knowledge of the f_B factors.

Several extension of the SM introduce new diagrams which can enhance the rates quite sizeably [2, 3, 4, 5]. Destructive interference, however, can also result in a further depression of the decay rates for some choice of the model parameters [6].

The CMS collaboration has performed a search [7] based on 4.9 fb^{-1} of data from pp interactions at $\sqrt{s} = 7$ TeV produced by the LHC collider. Thanks to the excellent operations of LHC, the high efficiency in track reconstruction and muon identification, and to the great accuracy in the reconstruction of charged particle trajectories, the results are competitive with those from the other LHC collaborations [8], [9], and from Tevatron experiments [10],[11]. I present below a brief description of this search.

2 Data analysis

The CMS detector is described at length elsewhere [12]. Muons with rapidity $|\eta| < 2.4$ are identified matching track segments from the inner silicon tracker with those reconstructed independently in the self-triggering muon chambers, placed in the return yoke of the solenoidal

3.8 T magnetic field. The muon identification efficiency for signal events is 70% in the barrel ($|\eta| < 1.4$) and 85% in the forward region.

A dimuon trigger was used, requiring a $\mu^+\mu^-$ pair with invariant mass $4.8 < m_{\mu\mu} < 6.0$ GeV: this interval includes the signal region and two side-bands used to subtract the combinatorial background. The other trigger requirements, (track quality, muon momenta in the plane orthogonal to the beam axis, p_T) were tightened as the luminosity increased. A sample of $B^+ \to K^+ J/\Psi(\to \mu^+\mu^-)$ was also selected to compute the normalization and the efficiency corrections. In addition, a control sample of $B_s \to \phi J/\Psi$ decays, with $\phi \to K^+K^-$ and $J/\Psi \to \mu^+\mu^-$ was selected to correct for potential differences in B^+ and B_s production and fragmentation.

Large samples of simulated events were produced, representing the signal, the normalization and control samples, and the background from rare B decays with one or two hadron mis-identified as muons, like $B \to h\mu\nu_\mu$ or $B \to hh'$ $(h, h' = \pi, K, p)$. A detailed simulation of the CMS detector was used; simulated events were analysed as the real data, including trigger requirements.

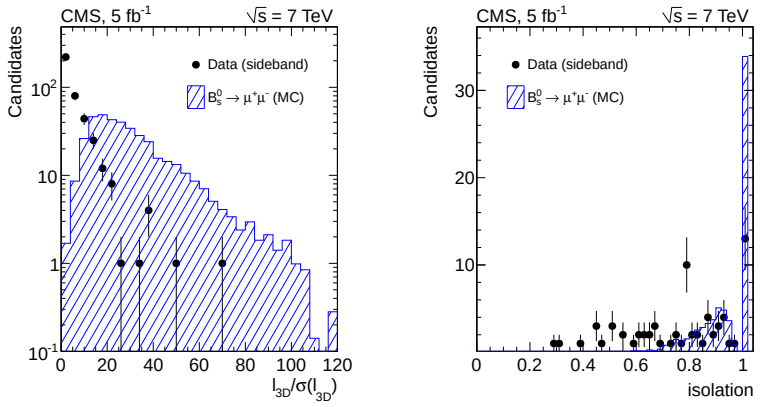

Figure 1: Rigth: $\ell_{3D}/\sigma(\ell_{3D})$; left : isolation parameter. Points with error bars: data side bands; histogram: signal Monte Carlo

At the analysis stage, a slightly tighter request was applied to the dimuon mass: $4.9 < m_{\mu\mu} < 5.9$ GeV. The two muons were combined to form a B candidate. Its trajectory was extrapolated back to the beam line to compute the projection δ_z of the distance of closest approach from each primary vertex (up to 30 collisions per event were registered) along the beam (z) axis. The muons were then assigned to the vertex with the minimum value of δ_z, and the vertex fit was repeated without the muons. Finally, a kinematic fit was applied to the two muon trajectories, requiring a common production point (secondary vertex). To select the signal, requirements were applied on the secondary vertex fit (χ^2/dof), on the transverse momentum of each muon and of the B candidate, on the 3D impact parameter of the B candidate (δ_{3D}) and on its significance ($\delta_{3D}/\sigma(\delta_{3D})$), on the significance of the distance between the secondary and the primary vertex ($\ell_{3D}/\sigma(\ell_{3D})$), and on the angle α between the B momentum and the line joining the primary to the secondary vertex. Three isolation requirements (I, d^0_{cs}, N_{close}) were also applied. Figure 1 shows for illustratrion the distributions of $\ell_{3D}/\sigma(\ell_{3D})$ and of the

isolation parameter I for the simulated signal (histogram) and for the data side bands (points with error bars).

Simulated signal events and the data side bands were used to optimize the selections so as to obtain the best 95% C.L. exclusion limit assuming the SM branching ratios. A different set of cuts was applied in the barrell (both tracks with $|\eta| < 1.4$) and in the forward. The complete set of requirements applied at the analysis stage is summarized in tab. 1.

A study performed in the simulated events and in the data normalization samples showed that the selection efficiency does not depend on the multiplicty of primary vertex (pileup). The efficiency for the signal was $(2.9 \pm 0.2) \times 10^{-4}$ in the barrell and $(1.6 \pm 0.2) \times 10^{-4}$ in the endcaps. A blind analysis was performed: the signal region, defined by $5.20 < m_{\mu\mu} < 5.45$, was not inspected until the completion of the study of the systematic uncertainties.

Variable	Barrell	Endcap	Units
$p_T(\mu_1)$	> 4.5	> 4.5	GeV
$p_T(\mu_2)$	> 4.0	> 4.2	GeV
$p_T(B)$	> 6.5	> 8.5	GeV
χ^2/dof	<2.2	<1.8	
δ_{3D}	< 0.008	< 0.008	cm
$\delta_{3D}/\sigma(\delta_{3D})$	< 2	< 2	
α	<50	<30	mrad
$\ell_{3D}/\sigma(\ell_{3D})$	> 13	> 15	
I	> 0.8	> 0.8	
d^0_{ca}	> 0.05	> 0.05	cm
N_{close}	< 2	< 2	

Table 1: Selection criteria applied at the analysis stage

3 Results

The branching ratio was computed separately in the barrell and in the forward regions according to the formula:

$$\mathcal{B}(B^0 \to \mu^+\mu^-) = \frac{N_S}{N_{B^+}} \frac{f_u}{f_s} \frac{\epsilon^+}{\epsilon_s} \mathcal{B}(B^+ \to KJ/\Psi) \times \mathcal{B}(J/\Psi \to \mu^+\mu^-) \quad (1)$$

where N_S is the number of signal events after background subtraction, N_{B^+} is the number of events in the normaliztion sample ($82700 \pm 415o$ in the barrell and 23800 ± 1200 in the forward region), ϵ_s, ϵ^+ the corresponding efficiencies, $f_{u(s)}$ the probability that a b quark hadronizes to a $B^+(B_s)$ meson.

Figure 2 shows the search result: six events were found in the $B_s \to \mu^+\mu^-$ signal window, while 5.9 ± 0.8 background events were expected, and two in the $B^0 \to \mu^+\mu^-$ region, with an expected background of 2.0 ± 0.5. As no signal excess was observed , the following upper limits at 95% C.L. were computed:

$$\mathcal{B}(B^0_s \to \mu^+\mu^-) < 7.7 \times 10^{-9} \quad (2)$$

$$\mathcal{B}(B^0 \to \mu^+\mu^-) < 1.8 \times 10^{-9} \quad (3)$$

These results include the systematic unertainties in acceptance and efficiency computation for the signal and normalization samples, those due to the limited knowledge of the production rates for the background from rare B decays, and the statistical error from side-band subtraction.

References

[1] A. J. Buras, "Minimal flavour violation and beyond: Towards a flavour code for short distance dynamics", Acta Phys. Polon. B 41 (2010) 2487, arXiv:1012.1447.

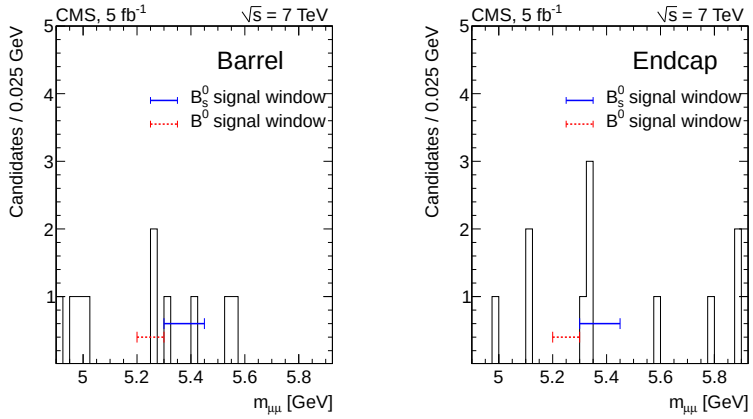

Figure 2: Dimuon invariant mass distributions in the barrel (left) and endcap (right) channels. The signal windows for B_s^0 and B^0 are indicated by horizontal lines.

[2] J. R. Ellis, K. A. Olive, Y. Santoso et al., "On $B_s \to \mu^+\mu^-$ and cold dark matter scattering in the MSSM with non-universal Higgs masses", JHEP 05 (2006) 063, arXiv:hep-ph/0603136.

[3] S. Davidson and S. Descotes-Genon, "Minimal Flavour Violation for Leptoquarks", JHEP 11 (2010) 073, arXiv:1009.1998.

[4] S. R. Choudhury, A. S. Cornell, N. Gaur et al., "Signatures of new physics in dileptonic B-decays", Int. J. Mod. Phys. A21 (2006) 2617–2634, arXiv:hep-ph/0504193.

[5] J. Parry, "Lepton flavor violating Higgs boson decays, $\tau \to \mu\gamma$ and $B_s \to \mu^+\mu^-$ in the constrained MSSM+NR with large $\tan\beta$", Nucl.Phys. B760 (2007) 38–63, arXiv:hep-ph/0510305.

[6] J. R. Ellis, J. S. Lee, and A. Pilaftsis, "B-Meson Observables in the Maximally CP-Violating MSSM with Minimal Flavour Violation", Phys. Rev. D76 (2007) 115011, arXiv:0708.2079.

[7] CMS Collaboration Collaboration, "Search for $B_s^0 \to \mu^+\mu^-$ and $B^0 \to \mu^+\mu^-$ decays", JHEP 1204 (2012) 033, arXiv:1203.3976.

[8] ATLAS Collaboration Collaboration, "Search for the decay $B_s^0 \to \mu^+\mu^-$ with the ATLAS detector", arXiv:1204.0735.

[9] LHCb Collab., "Strong constraints on the rare decays $B_s^0 \to \mu^+\mu^-$ and $B^0 \to \mu^+\mu^-$", Phys. Rev. Lett. 108 (2012) 231801, arXiv:1203.4493.

[10] DØ Collab., "Search for the rare decay $B_s^0 \to \mu^+\mu^-$", Phys. Lett. B693 (2010) 539–544, arXiv:1006.3469.

[11] CDF Collab., "Search for $B_s^0 \to \mu^+\mu^-$ and $B^0 \to \mu^+\mu^-$ Decays with CDF II", Phys.Rev.Lett. 107 (2011) 239903, arXiv:1107.2304.

[12] CMS Collab., "The CMS experiment at the CERN LHC", JINST 3 (2008) S08004.

WG6: Spin Physics and
WG7: Future of DIS

Transverse Momentum Dependent Parton Distributions at an Electron-Ion Collider

Feng Yuan[1]

[1]Nuclear Science Division, Lawrence Berkeley National Laboratory, Berkeley, CA 94720, USA

DOI: http://dx.doi.org/10.3204/DESY-PROC-2012-02/322

We summarize the current status and future perspective of the transverse momentum dependent parton distributions at an electron-ion collider.

Transverse momentum dependent (TMD) parton distributions have attracted great attentions from both experiment and theory sides in recent years [1]. They open a new window to investigate the strong interaction physics and the fundamental properties of QCD theory. At the leading order, there are eight independent TMD quark distributions: three $k_\perp$-even distributions (unpolarized, longitudinal polarized quark distributions, and the quark transversity), and five $k_\perp$-odd distributions. Because of the correlations between the quark transverse momentum and the nucleon spin, the TMDs naturally provide important information on the dynamics of partons in the transverse plane in momentum space. Measurements of the $k_\perp$-odd quark distributions provide information about the correlation between the quark orbital angular momentum and the nucleon/quark spin because they require wave function components with nonzero orbital angular momentum.

One particular example is the quark Sivers function $f_{1T}^{\perp q}$ which describes the transverse momentum distribution correlated with the transverse polarization vector of the nucleon. There have been strong evidence of the Sivers effect in the DIS experiments observed by the HERMES, COMPASS, and JLab Hall A collaborations [2, 3, 4] (see Fig. 1). An important aspect of the Sivers functions which has been revealed theoretically in last few years is the process dependence and the color gauge invariance [5, 6]. Together with the Boer-Mulders function, they are denoted as naive time-reversal odd (T-odd) functions. In the semi-inclusive DIS (SIDIS), where a leading hadron is detected in coincidence with the scattered lepton, the quark Sivers function arises due to the exchange of (infinitely many) gluons between the active struck quark and the remnants of the target, which is referred as the final state interaction effects in DIS. On the other hand, for the Drell-Yan lepton pair production process, it is the initial state interaction effects. As a consequence, the quark Sivers functions differ by a sign in these two processes. This non-universality is a fundamental prediction from the gauge invariance of QCD [6]. The experimental check of this sign change is currently one of the outstanding topics in hadronic physics, and Sivers functions from Drell-Yan process can be measured at RHIC.

In high energy hadronic processes where we hope to study the transverse momentum dependent parton distributions, besides the transverse momentum, an additional hard momentum scale is essential to make the proper use of the TMD parton distributions and fragmentation functions. This hard momentum scale needs to be much larger than the transverse momentum scale. At the electron-ion collider, DIS processes naturally provide a hard momentum scale: Q, the virtuality for the virtual photon. More importantly, the EIC design has a wide range

of Q^2 values, which will provide a unique opportunity to systematically investigate the strong interaction dynamics associated with the TMD physics.

There have been tremendous progresses in understanding TMDs and the related physics. However, without a new lepton-hadron collider many aspects of this fascinating field will remain unexplored or at best only on a qualitative level. Existing facilities either suffer from a much too restricted kinematic coverage or from low luminosity or from both. The advantage of the semi-inclusive DIS measurement discussed below is to have the two planes defined as the lepton plane and hadron plane, which allows to access to different angular dependences in the hadron production. These angular distributions are important to extract the TMDs since each of them has a unique angular dependence. Precision measurements of the various angular modulations are only possible with a dedicated detector at the EIC.

Based on the present status of research we see the following potentials in an EIC:

- precise, quantitative measurements of TMDs in the valence region due to high luminosity, and the ability to go to sufficiently large values of Q^2 in order to suppress potential higher twist contaminations;
- related to the wide kinematic coverage and the high luminosity, the ability to provide multi-dimensional representations of the observables, which is impossible on the basis of current experiments;
- measurements of the TMDs for antiquarks and gluons at an unprecedented level;
- systematic studies of perturbative QCD techniques (for polarization observables) and studies of QCD evolution properties of TMDs.

In the following, we will take semi-inclusive DIS as an example for the quark Sivers function and highlight the impact of the EIC machine. For the gluon Sivers function, we refer to the talk by Tom Burton [7].

In general, SIDIS depends on six kinematic variables. In addition to the variables for inclusive DIS, x, $y = (P\cdot q)/(P\cdot l)$, and the azimuthal angle ϕ_S describing the orientation of the target spin vector for transverse polarization, one has three variables for the final state hadron, which we denote by $z = (P\cdot P_h)/(P\cdot q)$ (longitudinal hadron momentum), P_{hT} (magnitude of transverse hadron momentum), and the angle ϕ_h for the orientation of $\boldsymbol{P}_{hT}$. In the one-photon exchange approximation, the SIDIS cross section can be decomposed in terms of structure functions. For example, for the spin-average and single-spin dependent contributions, we have

$$\frac{d\sigma}{dx_B\, dy\, d\phi_S\, dz\, d\phi_h\, dP_{hT}^2} \propto F_{UU,T} + |\boldsymbol{S}_\perp| \sin(\phi_h-\phi_S) F_{UT,T}^{\sin(\phi_h-\phi_S)} + ... \qquad (1)$$

To extract the quark Sivers function, experimentally, we measure the $\sin(\phi_h-\phi_s)$ modulation of the single transverse spin asymmetry (SSA), which is defined by the ratio of the two cross section terms in Eq. (1). This asymmetry depends on four kinematics: Q^2, x_B, z_h, P_{hT}.

In the following, we illustrate the expected impact of data from the EIC using the parameterization from Ref. [8] as an arbitrarily chosen model of the Sivers function. This parameterization, denoted $theor_i = F(x_i, z_i, P_{hT}^i, Q_i^2; \mathbf{a_0})$ with the M parameters $\mathbf{a_0} = \{a_1^0, ..., a_M^0\}$ fitted to existing data, serves to generate a set of pseudo-data in each kinematic bin i. In each x_i, Q_i^2, z_i and P_{hT}^i bin, the obtained values, $value_i$, for the Sivers function are distributed using a Gaussian smearing with a width σ_i corresponding to the simulated event rate at an center-of-mass energy of $\sqrt{s} = 45$ GeV obtained with an integrated luminosity of 10 fb^{-1}. To illustrate

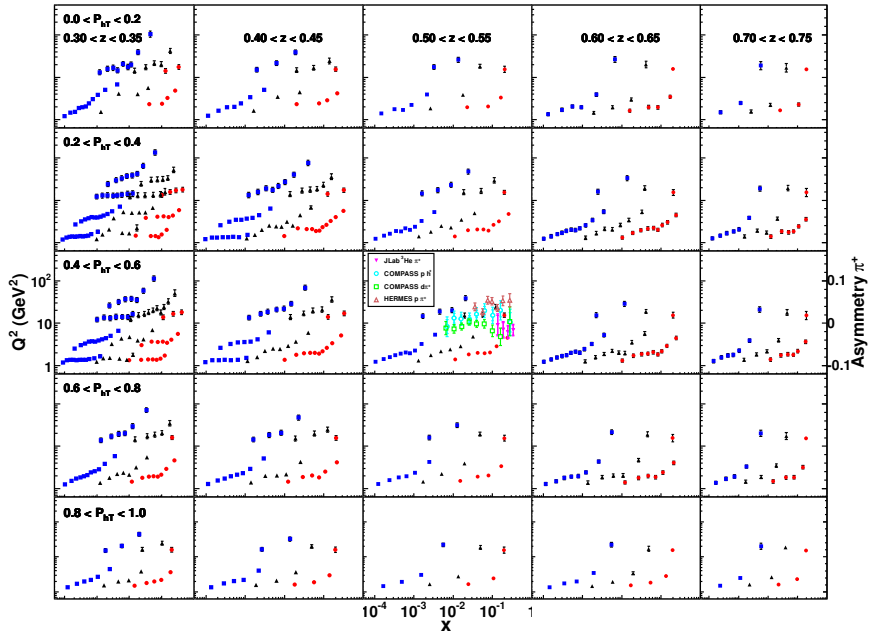

Figure 1: Four-dimensional representation of the projected accuracy for π^+ production in semi-inclusive DIS off the proton. Each panel corresponds to a specific z bin with increasing value from left to right and a specific P_{hT} bin with increasing value from top to bottom, with values given in the figure. The position of each point is according to its Q^2 and x value, within the range $0.05 < y < 0.9$. The projected event rate, represented by the error bar, is scaled to the (arbitrarily chosen) asymmetry value at the right axis. Blue squares, black triangles and red dots represent the $\sqrt{s} = 140$ GeV, $\sqrt{s} = 45$ GeV and $\sqrt{s} = 15$ GeV EIC configurations, respectively. Event counts correspond to an integrated luminosity of 10 fb^{-1} for each of the three configurations. Also shown in the center panel are the x-Q^2 distributions of current experimental data from HERMES, COMPASS, and JLab Hall A and their asymmetries, where z_h and P_{hT} have been integrated out for the appropriate kinematics.

the obtainable statistical precision the event rate for the production of π^+ in semi-inclusive DIS was used, see, for example, Fig. 1.

This new set of pseudo-data was then analysed like the real data in Ref. [8]. Figure 2 shows the result for the extraction of the Sivers function for the valence and sea u quarks. Similar results are obtained for the down quarks as well. The central value of $f_{1T}^{\perp u}$, represented by the red line, follows by construction the underlying model. The 2-sigma uncertainty of this extraction, valid for the specifically chosen functional form, is indicated by the dark grey area, which is hardly seen around the red line. This precision, obtainable with an integrated luminosity of 10 fb^{-1}, is compared with the uncertainty of the extraction from existing data, represented by the light grey band. Our current knowledge is restricted to an essentially qualitative picture of the Sivers function (and TMDs in general) only. From this comparison, we can clearly see that the EIC will be the unique facility for accessing the Sivers function (and TMDs in general) with unprecedented precision, and particularly in the currently unexplored sea quark region.

A more important kinematic reach of an EIC machine is the transverse momentum distri-

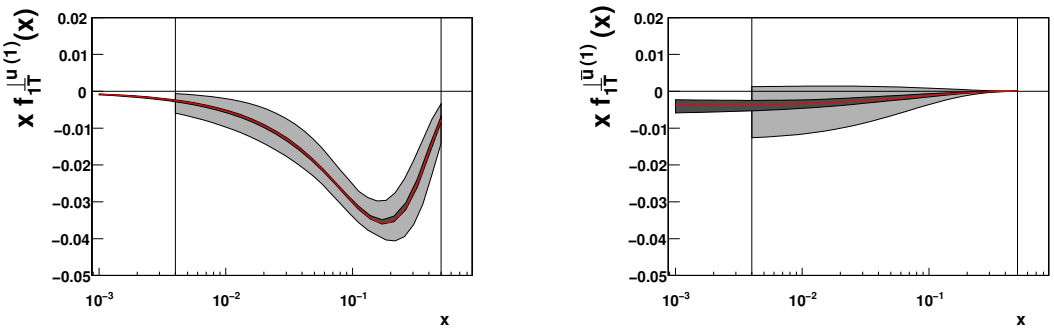

Figure 2: [color online] Comparison of the precision (2-σ uncertainty) of extractions of the Sivers function for the valence (left) and sea (right) u quarks from currently available data [8] (grey band) and from pseudo-data generated for the EIC with energy setting of $\sqrt{s} = 45$ GeV and an integrated luminosity of 10 fb^{-1} (dark grey band around the red line). The uncertainty estimates are for the specifically chosen underlying functional form.

butions of the physical observables. This is particularly important to connect to the collinear factorization approach in hadron physics to understand the long standing open question, which is the underlying mechanism giving rise to single spin asymmetry. Recent theoretical developments have revealed that the transverse momentum dependent Sivers mechanism and the twist-three collinear mechanism are unified to describe the same physics in the overlap region where both approaches apply [9]. High luminosities at the EIC machine provide a golden opportunity to explore the rich physics of the transverse momentum dependence of the SIDIS measurements.

We thank H. Gao, D. Hasch, A. Prokudin, and all the authors who contributed to the TMD chapter of Ref. [1] for their help and support of this document. This work was partially supported by the U.S. Department of Energy via grants DE-AC02-05CH11231.

References

[1] D. Boer, *et al.*, arXiv:1108.1713 [nucl-th].

[2] A. Airapetian *et al.* [HERMES Collaboration], Phys. Rev. Lett. **94**, 012002 (2005).

[3] M. Alekseev *et al.* [COMPASS Collaboration], Phys. Lett. B **673**, 127 (2009). [arXiv:0802.2160 [hep-ex]].

[4] X. Qian *et al.* [The Jefferson Lab Hall A Collaboration], Phys. Rev. Lett. **107**, 072003 (2011).

[5] S. J. Brodsky, D. S. Hwang and I. Schmidt, Phys. Lett. B **530**, 99 (2002); Nucl. Phys. B **642**, 344 (2002).

[6] J. C. Collins, Phys. Lett. B **536**, 43 (2002); X. Ji and F. Yuan, Phys. Lett. B **543**, 66 (2002); A.V. Belitsky, X. Ji, and F. Yuan, Nucl. Phys. B **656**, 165 (2003); D. Boer, P. J. Mulders and F. Pijlman, Nucl. Phys. B **667**, 201 (2003).

[7] T. Burton, these proceedings.

[8] M. Anselmino, M. Boglione, U. D'Alesio, S. Melis, F. Murgia and A. Prokudin, arXiv:1012.3565 [hep-ph].

[9] X. Ji, J-W. Qiu, W. Vogelsang and F. Yuan, Phys. Rev. Lett. **97**, 082002 (2006); Phys. Rev. D **73**, 094017 (2006); Phys. Lett. **B638**, 178-186 (2006); Y. Koike, W. Vogelsang, F. Yuan, Phys. Lett. **B659**, 878-884 (2008); A. Bacchetta, D. Boer, M. Diehl and P. Mulders, JHEP **08**, 023 (2008).

Gluon Sivers and experimental considerations for TMDs

Thomas Burton

Brookhaven National Laboratory, Upton, NY 11973, USA

DOI: http://dx.doi.org/10.3204/DESY-PROC-2012-02/323

The study and characterisation of transverse-momentum-dependent distribution functions (TMDs) is a major goal of the Electron-Ion Collider (EIC) physics programme. The study of gluon TMDs poses a greater challenge than for quark TMDs in DIS measurements, as gluons do not directly couple to photons. The study of D meson pairs has been proposed to provide access to gluon TMDs, but is demanding due to the rarity of D production. Here, we discuss the feasibility of such a measurement, and touch upon wider issues to be considered when measuring TMDs at the EIC.

1 Introduction

The EIC is proposed as a next-generation collider facility, with unprecedented luminosity and the ability to study both nucleons and nuclei at a variety of energies. There are two proposed realisations: eRHIC at Brookhaven National Lab (BNL), and ELIC at Jefferson Lab. Building on the legacy of HERA, RHIC, CERN and others, it will deliver a broad programme of nucleon and nucleon structure studies with extremely high precision. One of the key topics of interest at the EIC is the family of distribution functions known as TMDs. TMDs add a transverse momentum component to conventional (one-dimensional) parton distribution functions (PDFs), providing a "3D" picture of partons in the the nucleon: TMDs essentially allow a tomographic imaging of the motion of partons at the femtoscale. Work at HERMES and COMPASS, among others, has provided tantalising hints about these distributions. However, data remains relatively scarce and a detailed understanding is far from achieved. The high luminosity and broad kinematic reach of the EIC will provide the perfect environment for not just exploring these functions, but characterising them in exquisite detail.

The TMDs of quarks and gluons are of equal importance, but studying gluon distributions in electron-proton collisions is more challenging. Unlike electrically charged quarks, gluons do not directly couple to photons, which mediate the e-p interaction. A potential route to access gluon distributions is to study the production of pairs of D mesons. Here, we discuss the potential of such a method in measuring the gluon *Sivers distribution*. The Sivers distribution is a member of the TMD family that correlates the transverse momentum of partons in a nucleon with the transverse spin of the nucleon. It has enjoyed a great deal of theoretical and experimental study in recent years, and as such stands as an exemplar for the wider TMD family.

2 Studying the gluon Sivers function with D meson pairs

The methodology for studying the gluon Sivers function with D mesons is detailed extensively in section 2.3 of [1]. For certain kinematics, a charm-anticharm pair produced from a gluon (via the process $\gamma^* g \to q\bar{q}$) interacts like a single gluon. Thus, the QCD interactions that give rise to the Sivers distribution in gluons will give rise to the same Sivers distribution in the charm quark pairs. Quarks are not themselves detected, but their kinematics can be at least partly reconstructed from those of the D mesons they produce. As the Sivers distribution correlates spin and transverse momentum, a non-zero distribution results in a spin-dependent azimuthal asymmetry in the D pair transverse momentum distribution around the virtual photon mediating the DIS interaction. Measuring this asymmetry would allow the gluon Sivers distribution to be extracted.

This signature is exciting as it provides an avenue to measuring the Sivers function where few (or no) others are currently known to exist. For example, dijet or dihadron production in proton-proton collisions, which would provide a natural environment for measuring gluon distributions due to the dominance of gluon interactions, are excluded due to the demonstration of factorisation breaking, precluding theoretical treatment.

While exciting, the measurement is not without its difficulties. The rarity of D meson production, coupled with the necessity to detect and reconstruct not one but two in a single event, makes it statistically challenging. To investigate the feasibility of such a measurement, PYTHIA simulations were run to determine the event rates that could be expected at an EIC.

3 PYTHIA simulation

Charm events were generated with PYTHIA 6.416 for a high-energy EIC configuration: a 20 GeV/c electron beam colliding with a 250 GeV/c proton beam. This configuration is most favourable for two reasons: an enhancement in the charm production cross section, and, at least in the BNL eRHIC design for the EIC, the maximum beam luminosity (see table 1).

Energy	eRHIC luminosity	σ_{cc}
5 x 100	0.62×10^{33} cm^{-2} s^{-1}	7.7 nb
5 x 250	9.70×10^{33} cm^{-2} s^{-1}	13.3 nb
20 x 250	9.70×10^{33} cm^{-2} s^{-1}	25.2 nb

Table 1: eRHIC design luminosities and charm cross sections (from PYTHIA) for different eRHIC energy configurations ($E_{electron}$ x E_{proton}). Luminosity depends on the proton beam energy, but not the electron beam energy.

The CT10 NLO PDF parameterisations [2] were used. Radiative corrections were not explicitly included. A cut on the DIS inelasticity of $0.01 < y < 0.95$ was imposed and a single Q^2 bin of 1 to 10 GeV^2 was used. Events were required to contain at least two D^0 mesons. The $D^0 \to \pi$K decay channel was used, due to the large branching ratio (3.87% [3]) and the relative ease of experimentally reconstructing it. Other D^0 decays are typically semileptonic or multi-hadon decays with three or more final-state products, significantly increasing the difficulty of, or excluding, reconstruction. While other D mesons (D^+, D^-, D^{0*}) could be used in an actual experiment, the increase in statistics from such decays was not sufficient to change the basic message of the Monte Carlo study: whether the analysis is feasible or not. Therefore, the $D^0 \to \pi K$ decay channel alone was used for simplicity. D^0s generated directly from the DIS interaction and those generated via feed-down from heavier D mesons, for example D^{*+}, were

not distinguished. Studies of the kinematics of a D^0 compared to that of the heavier D generating it found little difference. Thus, a feed-down D^0 is considered to provide as good a proxy for the charm quark kinematics as its parent. The correlation between charm quark and D meson kinematics was also examined. They were typically found to be closely correlated in azimuth, by $\Delta\phi$ <0.5 rad in the virtual photon frame.

No detailed simulation of the effect of detector performance was done, but a simple acceptance cut, requiring all particles to be more than one degree from the beam direction, was imposed.

4 Results and discussion

D^0 pairs were binned simultaneously in azimuthal angle around the virtual photon direction and transverse momentum, and the statistical uncertainty in each bin estimated as $\sqrt{N}$ (for N counts). Uncertainties were rescaled to represent 100 fb^{-1} of data. As the measurement is a single-spin asymmetry, error bars were also divided by proton beam polarisation, which was assumed to be 70% (the eRHIC design polarisation). The resulting statistical uncertainties are shown in Figure 1 for two bins in D meson pair transverse momentum and 10 bins in azimuthal angle.

As seen in the figure, uncertainties of a few to several percent can be anticipated, depending on the pair transverse momentum range. The potential asymmetries derived from the model in [1] depend on the the pair transverse momentum and can exceed 20% for k_{perp} >1 GeV/c. This indicates that measuring D pair production is indeed feasible as an avenue to measuring the gluon Sivers function. At its maximum luminosity, and conservatively assuming an operational efficiency of 50%, eRHIC would accumulate about 3 fb^{-1} per week. 100 fb^{-1} would therefore require close to entire year of running at eRHIC. The eRHIC physics programme would generally demand multiple energy configurations to be run in each year, so such an amount would likely represent a multi-year goal.

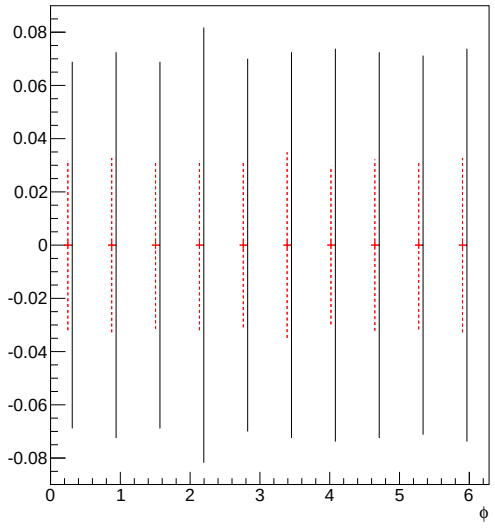

Figure 1: Estimated statistical uncertainties on the spin asymmetry in D meson pair production with 100 fb^{-1} integrated luminosity for two bins in pair transverse momentum: 0.5 to 1 GeV/c (red, dashed) and 1 to 2 GeV/c (black, solid). Bin-to-bin variations are due to limited statistics in the Monte Carlo sample.

The measurement of D mesons highlights key performance requirements for an EIC detector that apply more generally to other semi-inclusive and exclusive measurements at an EIC. Perhaps most important is the requirement for precise tracking and particle identification (PID) over a wide range in rapidity. As is seen in Figure 2, not only are hadrons produced in the proton beam direction, but also at significant rates in the

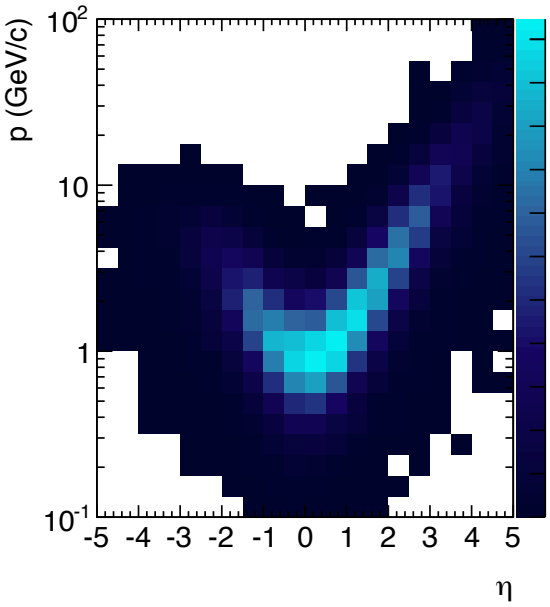

Figure 2: Distriubution of π from D^0 decays in momentum and pseudorapidity (colour online).

central region and the electron beam direction. Hadron momenta are typically modest in the central region (less than a few GeV/c), but extend to to several tens of GeV/c in the proton beam direction. Therefore PID detectors capable of distinguishing hadrons up to high momentum will be required in this region. Furthermore, in common with inclusive events, the scattered electron should be detected and measured precisely to determine the DIS kinematics. An EIC detector should therefore provide high momentum and angular resolution and hadron-electron separation over a several units of rapidity. Whilst doing so, the material budget of the tracking detectors must be kept low enough to allow measurement of electrons down to low momenta (less than 1 GeV/c), where multiple scattering becomes an issue.

References

[1] D. Boer, M. Diehl, R. Milner, R. Venugopalan, W. Vogelsang, *et al.* `arXiv:1108.1713 [nucl-th]`.

[2] H.-L. Lai, M. Guzzi, J. Huston, Z. Li, P. M. Nadolsky, *et al.* Phys. Rev. **D82** (2010) 074024, `arXiv:1007.2241 [hep-ph]`.

[3] Particle Data Group, K. Nakamura, *et al.* Journal of Physics G: Nuclear and Particle Physics **37** no. 7A, (2010) 075021. `http://stacks.iop.org/0954-3899/37/i=7A/a=075021`.

GPDs at an EIC

Salvatore Fazio[1]

[1]Brookhaven National Laboratory, PO Box 5000, 11973 Upton NY, USA

DOI: http://dx.doi.org/10.3204/DESY-PROC-2012-02/324

The feasibility for a measurement of the exclusive production of a real photon, a process although known as Deeply Virtual Compton Scattering (DVCS) at an Electron Ion Collider (EIC) has been explored. DVCS is universally believed to be a golden measurement toward the determination of the Generalized Parton Distribution (GPDs) functions. The high luminosity of the machine, expected in the order of $10^{34} cm^{-2} s^{-1}$ at the highest center-of-mass energy, together with the large resolution and rapidity acceptance of a newly designed dedicated detector, will open a opportunity for very high precision measurements of DVCS, and thus for the determination of GPDs, providing an important tool toward a 2+1 dimensional picture of the internal structure of the proton and nuclei.

1 GPDs and DVCS

In order to open a new window into a kinematic regime that allows the systematic study of quarks and gluons, the world's most versatile nuclear microscope, the Electron Ion Collider (EIC), has been proposed. With its wide range in energy, nuclear beams and high luminosity, the EIC will offer an unprecedented opportunity for discovery and precision measurements, allowing us to study the momentum and space-time distribution of gluons and sea quarks in nucleons and nuclei.

One of the main goals of an EIC will be a precise determination of the Generalized Parton Distribution functions (GPDs), which lead to a 2+1 dimensional imaging of the protons/nuclei in the impact parameter space. GPDs are functions describing the distribution of quarks and gluons in the nucleon with respect to both position and momentum. Moreover, GPDs allow us to study how the orbital motion of quarks in the nucleon contributes to the nucleon spin - a question of crucial importance for nucleon structure.

It is universally believed that the golden measurement toward the determination of the whole set of GPDs is Deeply Virtual Compton Scattering (DVCS), which is the exclusive production of a real photon. This process is sensitive to both quarks and gluons and, unlikely the exclusive production on Vector Mesons, it is not affected by the uncertainty on the VM wave-function. Furthermore it shows a very clean experimental signature consisting of two clusters in the calorimeter with a track matching one of the clusters and a leading proton eventually measured in the forward detectors (Roman Pot spectrometer).

The important observables sensitive to the GPDs are the differential cross section as a function of the four-momentum transfer at the proton vertex, $|t|$, and the charge- and spin-asymmetries. For the purpose of the cross section measurement it is important to remove from the signal the background coming from the Bethe-Heithler (BH) events. The latter is essentially a QED process, known to an uncertainty in the order of $\sim 3\%$ coming from the uncertainty

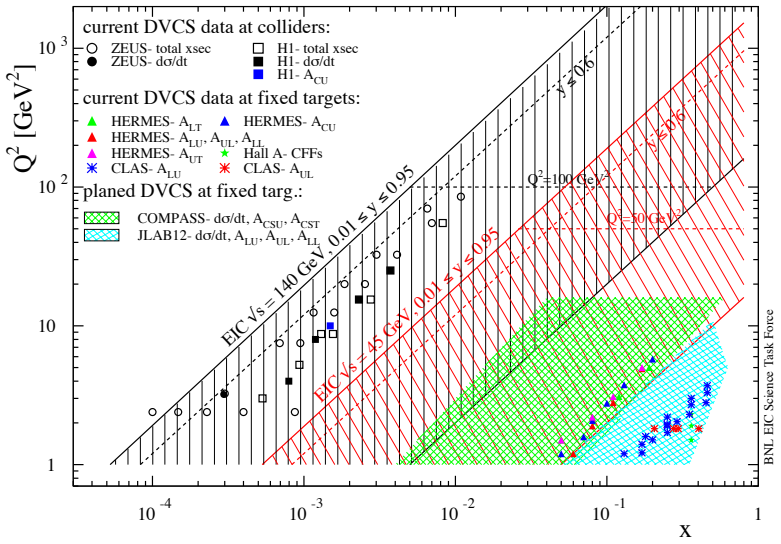

Figure 1: The EIC phase space for stage-1 (red) and stage-2 (black) compared with available data and expected future experiments.

on the proton form factor, with the same final state topology of DVCS and can be subtracted from the signal by the means of MC technique. Thus, especially for an EIC where systematics will dominate the measurements, it is important to minimize the BH contribution, particularly at low energy configurations where BH tends to dominate over the DVCS. Presently available DVCS measurements provide some limited information on GPDs and more precise data, in a wider phase space and including transversely polarized target spin asymmetry, are required to pin them down. For more informations read D. Mueller contribution in this book of proceedings. New fixed target measurements are planned at COMPASS II using a polarized muon beam, extending HERMES kinematics to lower x_{Bj}, and at JLAB@12 GeV, see Fig. 1. EIC will cover a much larger phase-space and help quantify QCD phenomena at small x_{Bj} [1]. An access to GPDs requires a large data set with small errors. In the following we would like to illustrate the potential of an EIC machine for DVCS studies.

2 MC simulation

The Monte Carlo generator used for the present study is MILOU [2], which simulates both the DVCS and the BH processes together with their interference term. The simulated Q^2 and x_{Bj} range corresponds to the phase space achievable with an EIC. The electron and proton beam-energy configuration considered for the present study are: 5x100 GeV (stage-1) and 20x250 GeV (stage-2), as in Fig. 1.

The BH contamination has been investigated for each Q^2, x_{Bj}, $|t|$ bin as a function of y. After all BH suppression criteria have been applied it was found that for stage-2 the BH

contamination grows from negligible (at low-y) to about 70% at $y \sim 0.6$. For stage-1, the BH contribution grows faster and can be dominant at large-y depending on the x_{Bj}-bin, nevertheless most of the statistics at this low center-of-mass energy is contained in the safe region: $y < 0.3$. It is then crucial to have a detector which makes the experimentalists fully capable to apply all the selection criteria required for a BH suppression (tracker: excellent angular resolution, em Cal: fine granularity and goos resolution at lower energies).

The data coming from MC simulation have been used as mock data to measure the $|t|$-differential cross section and the charge- and spin-asymmetries. Results are based on the EIC version in consideration at BNL and known as eRHIC. Simulated data samples correspond to a luminosity of 100 fb^{-1} for stage-2 and 10 fb^{-1} for stage-1 configurations, both corresponding to approximately 1 year of data taking assuming a 50% operational efficiency. Tha variables have been smeared according to the expected resolution. A logarithmic fine binning of x_{Bj} and Q^2 has been applied, whereas in the case of the cross section measurement, $|t|$ has been binned three times larger than the expected resolution form the Roman Pot spectrometer, which can measure proton momentum in the range $0.03 < |t| < 0.88\ GeV^2$. For large values of $|t| > 1.0\ GeV^2$ the proton can be measured in the main detector.

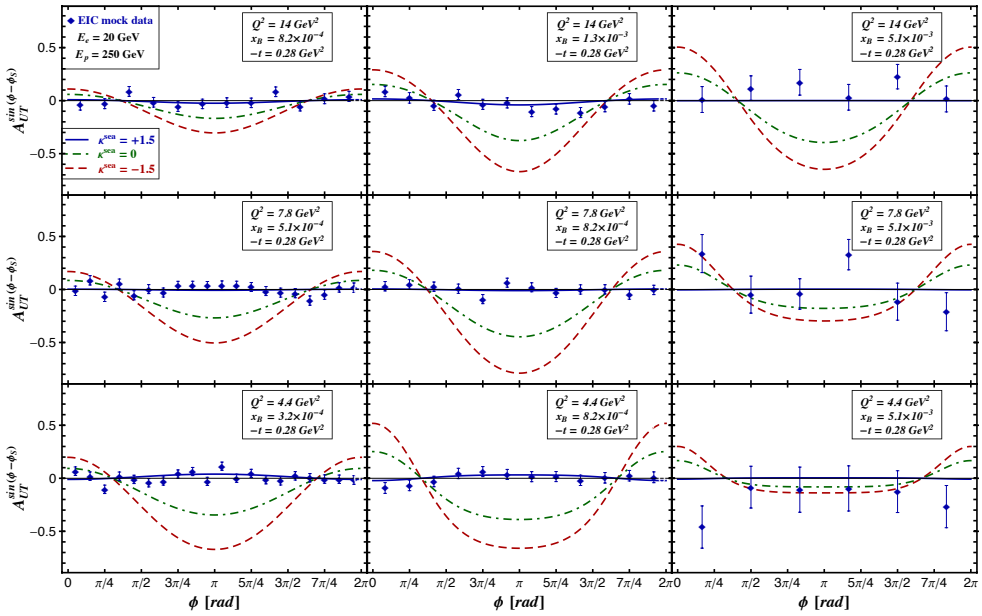

Figure 2: Transverse target-spin asymmetry uncertainties for EIC stage-2 mock data (*diamonds*) compared to theory model with large positive (*solid*), vanishing (*dot − dashed*), and large negative (*dashed*) E^{sea} contributions.

The simulation proves that an EIC can perform accurate measurements of cross sections and asymmetries in a very fine binning and with a statistical acceptance often as low as a few percent. For more details and figures see the D. Mueller's and M. Diehl' contributions. This implies that the measurement is actually limited by systematics. For the purposes of the present study, a systematic uncertainty of 5% has been assumed, based on the experience achieved at HERA and the expected acceptance and technology improvements of a EIC new detector. The

overall systematic uncertainty due to the uncertainty on the measurement of luminosity was not considered here, since it simply affects the normalization of the cross section measurement. As an example of the precision achievable at an EIC, Fig. 2 shows the expected uncertainty for the transverse target-spin asymmetry (A_{UT}) as a function of the azimuthal angle ϕ between the production and the scattering planes for a particular $x_{Bj}, Q^2, |t|$ bin, compared to theoretical expectations.

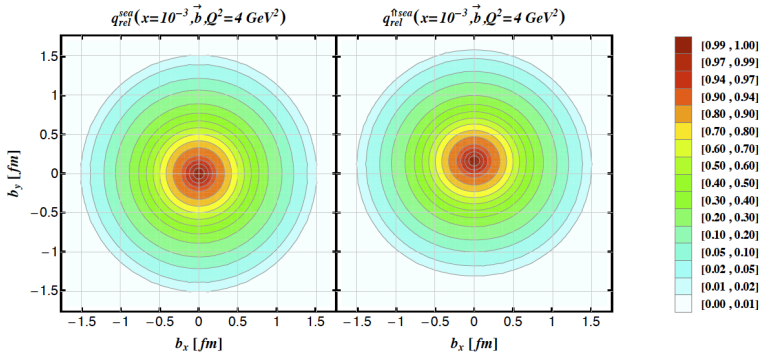

Figure 3: Tomographical picture of the sea-quuarks distribution in the impact parameter space for an unpolarized ($left$) and a polarized ($right$) proton beam.

Mock data have been then used, together with the data presently available, to constrain the GPDs. It was found that an EIC would have a great impact on the knowledge of GPDs, especially of GPD E, which at the moment remains unconstrained. For more details and discussion see D. Mueller's contribution. Fig. 3 shows an example of a tomographic picture of the see-quarks distribution in the nucleon in the impact parameter space, as resulting from EIC mock data analysis, for a particular x_{Bj}, Q^2 bin, for the case of an unpolarized and a polarized target-beam.

3 Conclusions

To conclude, an EIC will be a unique facility to study DVCS with high precision and accuracy. The very high luminosity of the machine together with the precision of $|t|$ measurement from a dedicated spectrometer and the tracker acceptance at large rapidities opens the possibility of a fine binning in Q^2 and x_{Bj} and $|t|$ with a very low uncertainty. This will give a precious contribution to the GPDs extraction and will help to discriminate among different theoretical models.

References

[1] D. Boer et al., "Gluons and the quark sea at high energies: Distributions, polarization, tomography", 2011, arXiv:1108.1713.

[2] E. Perez, L. Schoeffel, and L. Favart, (2004), hep-ph/0411389.

GPDs from present and future measurements

Krešimir Kumerički[1], *Dieter Müller*[2]

[1]Department of Physics, University of Zagreb, Zagreb, HR-10002, Croatia
[2]Ruhr-University Bochum, Bochum, D-44780, Germany

DOI: http://dx.doi.org/10.3204/DESY-PROC-2012-02/236

We report on the access of generalized parton distributions (GPDs) from deeply virtual Compton scattering (DVCS) measurements. We also point out that such measurements at a proposed high-luminosity electron-ion collider (EIC) provide insight in both the transverse distribution of sea quarks and gluons as well as the proton spin decomposition.

1 Introduction

During the last decade the HERA and JLAB collaborations have spent much effort to measure exclusive processes such as electroproduction of photon, vector mesons, and pseudoscalar mesons in the deeply virtual region in which the virtuality $\mathcal{Q}^2 \gtrsim 1\text{GeV}^2$ of the exchanged space-like photon allows to resolve the internal structure of the proton. In such processes one can access GPDs which can be viewed as a non-diagonal overlap of light-cone wave functions. These GPDs are intricate functions $F(x, \eta, t, \mu^2)$ that depend on the momentum fraction x, the skewness η, the t-channel momentum transfer t, and the factorization scale μ^2. Phenomenologically, they are most directly accessible at the crossover line $\eta = x$ (see below). Moreover, GPDs are related to (generalized) form factors and standard parton densities. The GPD framework opens a complementary window to address the partonic content of the nucleon. In particular, it offers the possibility to access the transverse distribution of partons and to address the decomposition of the nucleon spin in terms of quark and gluon degrees of freedom, see reviews [1].

In Sect. 2 we shortly report on the GPD extraction from present DVCS data and in Sect. 3 we study the possible impact of an proposed EIC. Finally, we conclude.

2 GPDs from present DVCS experiments

The DVCS amplitude is mostly dominated by the Compton form factor (CFF) $\mathcal{H}$ and to extract information on the associated GPD H we consider DVCS off an unpolarized proton target. The leading twist-two dominated beam spin $A_{\text{LU}}^{\sin\phi}$, beam charge $A_{\text{BC}}^{\cos\phi}$ and $A_{\text{BC}}^{\cos(0\phi)}$ as well as azimuthal angle $\Sigma_{\text{UU},w}^{\cos\phi}$ asymmetry data from fixed target experiments together with fit results [5] and model predictions [6] are displayed in Fig. 1. Here, *KM10*$_{...}$ arise from DVCS fits that include also H1/ZEUS collider data and utilize hybrid models where sea quarks and gluons are described by flexible GPD models while the valence quark GPDs are only modeled on the crossover line and dispersion relations are used for the later to evaluate the corresponding real part of the CFFs [5]. It turns out that the unpolarized cross section measurements of Hall A at

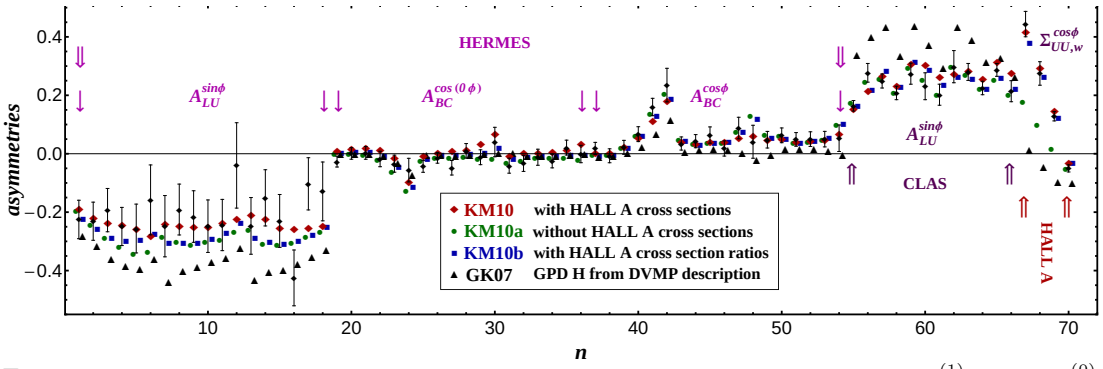

Figure 1: Measurements for fixed target kinematics labeled by data point number n: $A_{\rm LU}^{(1)}$ (1-18), $A_{\rm BC}^{(0)}$ (19-36), $A_{\rm BC}^{(1)}$ (37-54) from [2]; $A_{\rm LU}^{(1)}$ (55-66) and $\Sigma_{\rm LU}^{(1),w}$ (67-70) are derived from Refs. [3] and [4]. Hybrid model fits *KM10a* (circles, slightly shifted to the l.h.s.) *KM10b* (squares, slightly shifted to the r.h.s.) and *KM10* (diamonds) and a model prediction *GK07* (triangles-up, slightly shifted to the r.h.s.) [6].

rather large $x_{\rm B} = 0.36$ indicate a larger DVCS amplitude, which is not expected from "standard" GPD models. In the *KM10a* fit we simply neglect this data, in *KM10b* fit we form azimuthal angle asymmetries from these cross sections, and finally in the KM10 model we take these cross sections explicitly into account. All fits have χ^2/d.o.f. ≈ 1 and, especially, we describe with the *KM10* model the Hall A cross sections, where the DVCS amplitude enhancement at large $x_{\rm B}$ arises from an effective contribution that is pragmatically associated with $\widetilde{\mathcal{H}}$ and $\widetilde{\mathcal{E}}$. The results are available as executable code, providing the photon electroproduction cross section off unpolarized proton, on http://calculon.phy.pmf.unizg.hr/gpd/.

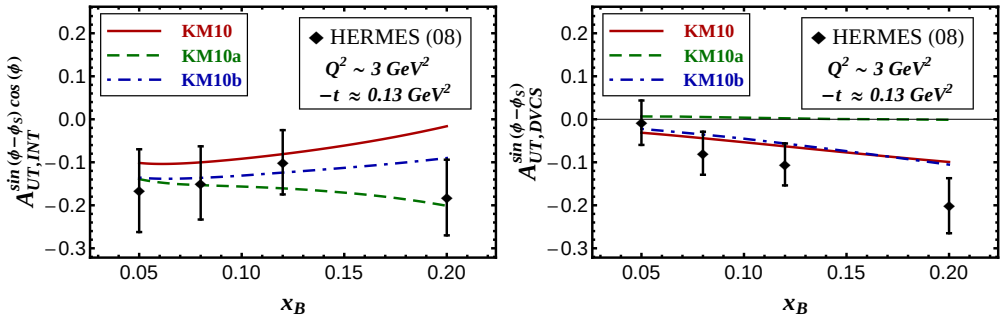

Figure 2: DVCS predictions for the single transverse target spin asymmetries from HERMES [8].

A more detailed model analysis of DVCS data, including measurements on polarized proton, is feasible and should be performed in near future. It has been illustrated in CFF fits [7] that the inclusion of measurements with a longitudinal polarized proton target provide access to the GPD $\widetilde{H}$ and simultaneously reduce the GPD H uncertainties. On the other hand, the target helicity flip GPDs E and $\widetilde{E}$ remain hidden in present measurements. The most promising observable to access GPD E is the single transverse target spin asymmetry. However, although the HERMES collaboration was able to disentangle the interference and DVCS squared terms [8], we might conclude from the fact that these measurements are partially describable with our unpolarized fits, where GPD E enters only in the real part of CFF $\mathcal{E}$, that GPD E extraction from present data suffers strongly from the correlation with the other GPDs, see Fig. 2.

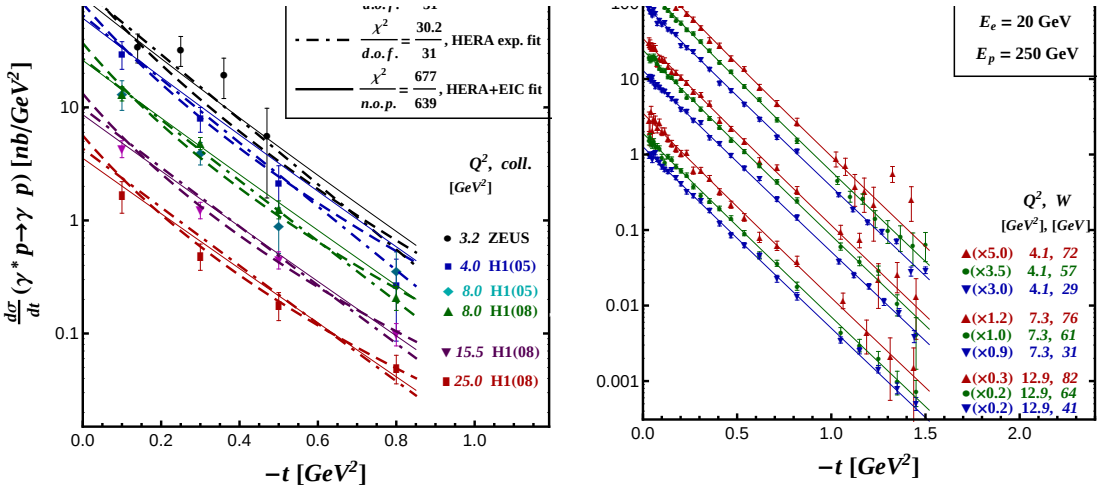

Figure 3: DVCS measurements from H1 [9] and ZEUS [10] (left) and EIC pseudo data (right).

3 Impact of planned and proposed DVCS experiments

In nearest future it is expected that new DVCS measurements will be released: beam spin asymmetry from HERMES, taken with a recoil detector, longitudinal target spin asymmetries from CLAS, and cross sections from CLAS and Hall A, see the contributions of M. Murray and D. Sokhan in these proceedings. These results will provide more constraints in a global GPD analysis; however, they will not give a full solution of the decomposition problem. Certainly, the planned high luminosity experiments at JLAB@12 GeV will help to access GPDs in the valence region. The planned COMPASS II experiments will improve the knowledge of GPD H in the region where sea quarks and gluons are getting dominant, and, hopefully, measurements on a polarized target might give insight in the small x-behavior of other twist-two GPDs. Thereby, the interesting point is whether GPD E possesses a "pomeron"-like behavior.

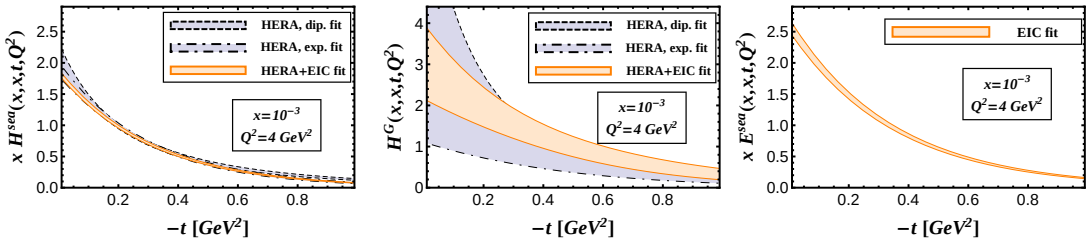

Figure 4: Fit results to H1/ZEUS (dashed and dash-dotted surrounded areas) and EIC pseudo (solid surrounded areas) DVCS cross sections, shown in Fig. 3.

In Fig. 3 we display DVCS cross section data from H1/ZEUS (left) and EIC pseudo data for an electron and proton beam energy of $E_e = 20\ GeV$ and $E_p = 250\ GeV$, respectively (right). The cross section is obtained by subtracting the BH contribution, where the interference term is negligibly small. Due to the exponential t-dependence of the CFFs, the subtraction errors are rather large at $1\ GeV^2 \lesssim -t$. For more details on data simulation, see the contributions of E. Aschenhauer and S. Fazio in these proceedings. In Fig. 4 we display the outcome of our

H1/ZEUS (dashed and dash-dotted surrounded areas) and simultaneous H1/ZEUS/EIC (solid surrounded areas) fits with flexible GPD models. Thereby, we also took EIC pseudo data for the transverse polarized target spin asymmetry $A_{\rm UT}^{\sin(\phi-\phi_S)}(\phi)$, which allows for a decomposition of GPD H and E contributions. As explained in the proceedings contribution of M. Diehl, such measurements allow for a 2D imaging of the partonic content at small x of the unpolarized and transverse polarized proton. We add that an access of GPD E in this region will provide a qualitative estimate of the angular momentum carried by sea quarks.

4 Conclusions

The first generation of hard exclusive experiments at HERA and JLAB provided us insight into the GPD description of DVCS, where GPD H could be accessed with some uncertainty. The biggest portion of these uncertainties is related to the fact that measurements on unpolarized proton do not allow for a GPD decomposition. In future GPD analyses this problem might be partially overcome, however, we expect that it cannot be fully solved. Planned and proposed experiments will have a big impact to reveal GPDs from measurements. Especially, a high-luminosity EIC offers the possibility to resolve the transverse distribution of quarks and to give a qualitative insight into the angular momentum of sea quarks.

Acknowledgements: This work is partly supported by MZOS grant no. 119- 0982930-1016, BMBF grant no. 06BO9012 and the HadronPhysics3 Grant Agreement no. 283286.

References

[1] M. Diehl. Phys. Rept. **388** (2003) 41, hep-ph/0307382; A. V. Belitsky and A. V. Radyushkin. Phys. Rept. **418** (2005) 1–387, hep-ph/0504030.

[2] A. Airapetian *et al.* JHEP **11** (2009) 083, arXiv:0909.3587 [hep-ex].

[3] F. X. Girod *et al.* Phys. Rev. Lett. **100** (2008) 162002, arXiv:0711.4805 [hep-ex].

[4] C. M. Camacho *et al.* Phys. Rev. Lett. **97** (2006) 262002, arXiv:nucl-ex/0607029.

[5] K. Kumerički and D. Müller. Nucl. Phys. **B841** (2010) 1–58, arXiv:0904.0458 [hep-ph]; K. Kumerički *et al.* arXiv:1105.0899 [hep-ph].

[6] S. V. Goloskokov and P. Kroll. Eur. Phys. J. **C53** (2008) 367–384, arXiv:0708.3569 [hep-ph].

[7] M. Guidal. Phys. Lett. **B689** (2010) 156–162, arXiv:1003.0307 [hep-ph]; Phys. Lett. **B693** (2010) 17–23, arXiv:1005.4922 [hep-ph].

[8] A. Airapetian *et al.* JHEP **06** (2008) 066, arXiv:0802.2499 [hep-ex].

[9] A. Aktas *et al.* Eur. Phys. J. **C44** (2005) 1–11, arXiv:hep-ex/0505061; F. Aaron *et al.* Phys.Lett. **B681** (2009) 391–399, arXiv:0907.5289 [hep-ex].

[10] S. Chekanov *et al.* Phys. Lett. **B573** (2003) 46–62, arXiv:hep-ex/0305028; JHEP **05** (2009) 108, arXiv:0812.2517 [hep-ex].

Helicity Parton Distributions at an EIC*

Elke C. Aschenauer[1], *Rodolfo Sassot*[2], *Marco Stratmann*[1]

[1]Physics Department, Brookhaven National Laboratory, Upton, NY 11973, USA
[2]Departamento de Física and IFIBA, Facultad de Ciencias Exactas y Naturales, Universidad de Buenos Aires, Ciudad Universitaria, Pabellón 1 (1428) Buenos Aires, Argentina

DOI: http://dx.doi.org/10.3204/DESY-PROC-2012-02/326

We present a quantitative assessment of the impact of a future EIC on determinations of helicity quark and gluon densities and their contributions to the proton spin. Our results are obtained by performing global QCD analyses at NLO accuracy based on realistic sets of pseudo-data for various conceivable center-of-mass system energies.

1 Motivation and Framework

Despite the impressive progress made both experimentally and theoretically in the past two decades, many fundamental questions related to the proton's helicity structure, including a quantitative understanding of the decomposition of the proton's spin, still remain unanswered. An accurate determination of the first moments of polarized quark and gluon densities entering the proton's spin sum rule or elucidating the flavor dependence of helicity PDFs to quantify, e.g., a potential SU(3) symmetry breaking in the light quark sea, cannot be achieved without considerably enlarging the kinematic coverage of spin-dependent data towards smaller momentum fractions x in the future. All the required measurements to address and answer these questions are unique to a polarized, high energy lepton-nucleon collider such as the proposed electron-ion collider (EIC) project [1].

To assess the impact of a future EIC in determining helicity PDFs we will consider two sets of energies conceivable at the first stage of the eRHIC option of an EIC [2] which is based on colliding an $E_e = 5\,\mathrm{GeV}$ electron beam with the existing RHIC proton beam of $E_p = 100 - 250\,\mathrm{GeV}$. Simulations based on pseudo-data generated with an electron energy of $20\,\mathrm{GeV}$ are used to estimate the impact of a later stage of an EIC; for details, see [3]. The resulting c.m.s. energies $\sqrt{s}$ range from about $45\,\mathrm{GeV}$ to $141\,\mathrm{GeV}$ and allow one to access x values down to 5.3×10^{-4} and 5.3×10^{-5}, respectively, in DIS with $Q^2 > 1\,\mathrm{GeV}^2$. Figure 1 illustrates the dramatically extended $x - Q^2$ coverage of an EIC for both stages as compared to existing fixed-target DIS experiments and data from polarized pp collisions.

We use the PEPSI MC generator [4] to produce fictitious EIC data for the inclusive and semi-inclusive DIS of longitudinally polarized electrons and protons with identified charged pions and kaons in the final-state. We demand a minimum Q^2 of $1\,\mathrm{GeV}^2$, a squared invariant mass of the virtual photon-proton system larger than $W^2 = 10\,\mathrm{GeV}^2$, and $0.01 \leq y \leq 0.95$.

*talk presented by M. Stratmann

The range of y is further restricted from below by constraining the depolarization factor of the virtual photon to be larger than 0.1. To ensure detection of the scattered lepton we require a minimum momentum of 0.5 GeV, and, in case of SIDIS, only hadrons with a momentum larger than 1 GeV and a fractional energy in the range $0.2 \leq z \leq 0.9$ are accepted. All particles detected in the final-state should be at least 1 degree away from the beam directions. The statistical accuracy of each DIS and SIDIS data set corresponds to a modest accumulated integrated luminosity of $10\,\text{fb}^{-1}$, equivalent to about one to two months of operations for the anticipated luminosities for eRHIC [2], except for the $5 \times 100\,\text{GeV}$ option which requires about a year of running.

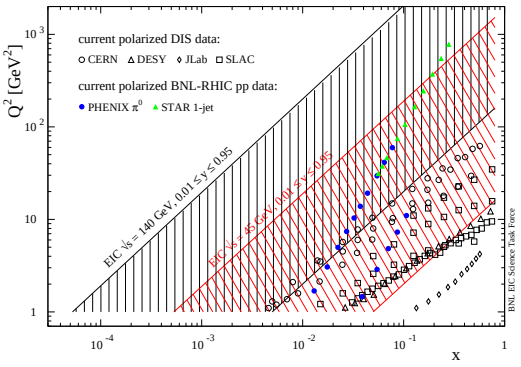

Figure 1: Kinematic range in x and Q^2 accessible with two different c.m.s. energies at an EIC for $0.01 \leq y \leq 0.95$.

Monte Carlo data for the ratio g_1/F_1 in DIS and SIDIS are generated in 4 [5] bins per decade in Q^2 [x] spaced logarithmically. As the actual pseudo-data used in our global analyses, we take the ratio g_1/F_1 computed at NLO accuracy using the DSSV+ [5] and MRST [6] polarized and unpolarized PDFs, respectively, and assign to each (x, Q^2)-bin the same relative statistical uncertainties as obtained with the MC event generator and assuming 70% beam polarizations. In addition, we randomize the pseudo-data in each bin within these one-sigma uncertainties. For the SIDIS data with identified charged pions and kaons we assign an additional, conservative 5 and 10% relative uncertainty to the EIC pseudo-data to reflect our current incomplete knowledge of parton-to-pion and parton-to-kaon fragmentation functions, respectively, based on uncertainty estimates for the DSS sets of FFs [7]. In total we add 234 data points for DIS and about 800 points for SIDIS to the existing DSSV+ global analysis framework [5] based on 570 DIS, SIDIS, and pp data. We note that the typical size of the double spin asymmetry $A_{LL} \simeq g_1/F_1$ at the lowest x values accessible at an EIC can be as small as a few times 10^{-4}, depending on the yet unknown behavior of $\Delta g(x, Q^2)$ in this kinematic regime. This size sets the scale at which one needs to control systematic uncertainties due to detector performance or luminosity measurements.

2 Impact of EIC DIS and SIDIS data

As an example, the l.h.s. of Fig. 2 illustrates our simulated data sets for inclusive polarized DIS at an EIC for three different c.m.s. energies assuming an integrated luminosity of $10\,\text{fb}^{-1}$. The solid lines are the result of the DSSV+ best fit, and the shaded bands illustrate the current uncertainty estimate. While DIS measurements for $20 \times 250\,\text{GeV}$ collisions are crucial to reach x values of a few times 10^{-5}, one can already cover momentum fractions down to 5×10^{-4} for $Q^2 \gtrsim 2.5\,\text{GeV}^2$ with c.m.s. energies envisioned in the first stage of eRHIC. Having available an as large as possible range in Q^2 for any given fixed value of x is of outmost importance for studying scaling violations $dg_1/d\log Q^2$ which, for small enough x, are closely related to the yet unknown polarized gluon density. Our projected SIDIS data for identified charged pions and kaons share the same x and Q^2 binning as the DIS data presented in Fig. 2.

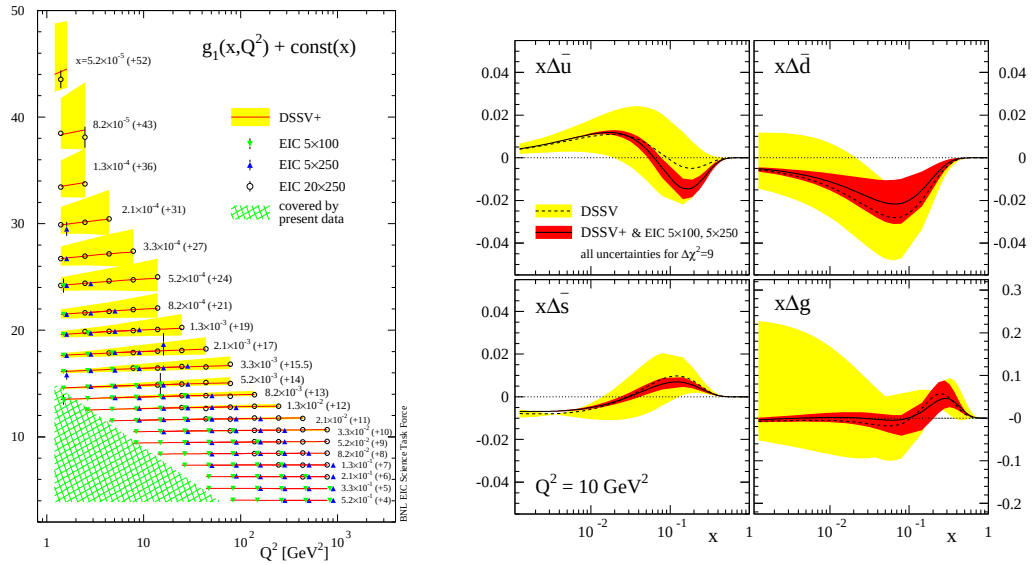

Figure 2: **left:** projected EIC data for $g_1(x, Q^2)$ for three different c.m.s. energies; constants are added to g_1 to separate the different x bins. The solid lines and shaded bands reflect our current knowledge [5]. **right:** impact of projected DIS and SIDIS data for 5×100 and $5 \times 250\,\mathrm{GeV}$ collisions on the determination of helicity sea quark PDFs and the gluon. The outer bands illustrate present uncertainty estimates and the inner bands the improvements expected due to EIC data.

The r.h.s. of Fig. 2 demonstrates the impact of the projected combined EIC data for DIS and SIDIS on extractions of the polarized sea quark and gluon densities, utilizing only data which can be obtained with the initial stage of the eRHIC option. The outer bands in each panel refer to the present ambiguities for helicity PDFs as determined in the DSSV analysis [5]. The smaller, inner bands are obtained with the same global analysis framework, functional form for the PDFs, number of free fit parameters, and $\Delta\chi^2$ criterion but now include also the projected EIC data. As can be seen, the expected improvements are dramatic, in particular, for the polarized gluon density below $x \simeq 0.01$ but also for the individual sea quark flavors. More detailed studies and χ^2 profiles can be found in [3]. It should also be stressed that only the relative improvement of the uncertainties in Fig. 2, i.e., the differences between the inner and outer error bands, is of significance here since the generation of the pseudo-data requires to assume a certain set of polarized PDFs. Of course, only real EIC data will eventually reveal the actual functional form of the helicity PDFs at small x. We note, that at an EIC one can for the first time systematically study the validity of the leading twist pQCD framework assumed in global QCD analyses of helicity PDFs so far by varying the lower cut-off scale $Q_{\min}$ above which one starts to include data in the fit.

Finally, we look into what can be achieved for the first moments of the flavor singlet combination $\Delta\Sigma$ and the gluon helicity density Δg which both enter the proton spin rule. Figure 3 shows the correlated uncertainties for the truncated moments computed in the region $0.001 \leq x \leq 1$ with and without including projected EIC data sets. As can be seen, $\Delta g(Q^2, 0.001, 1)$ and

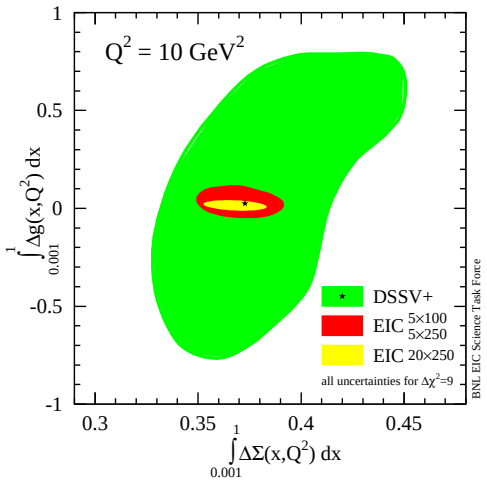

Figure 3: Correlated uncertainties for the first moments of the flavor singlet combination $\Delta\Sigma$ and the gluon helicity density Δg computed in the region $0.001 \leq x \leq 1$. The green, red, and yellow shaded areas are based on fits to current data and to projected EIC data with 5 GeV and 20 GeV electron beams, respectively. The symbol denotes the DSSV+ best fit.

$\Delta\Sigma(Q^2, 0.001, 1)$ can be constrained up to about ± 0.05 and ± 0.02, respectively, if 20×250 GeV data are included in the PDF analyses. However, already at the initial stage of an EIC a very significant reduction of uncertainties can be achieved. Quantifying the relevance of orbital angular momenta of quarks and gluons will be part of another suite of unique measurements at an EIC aiming at the nucleon's spatial structure [1].

Acknowledgements

E.C.A. and M.S. are supported by the U.S. Department of Energy under contract number DE-AC02-98CH10886. The work of R.S. is supported by CONICET, ANPCyT, and UBACyT. We acknowledge additional support from a BNL "Laboratory Directed Research and Development" grant (LDRD 12-034).

References

[1] D. Boer *et al.*, "INT report on EIC Science", arXiv:1108.1713.

[2] For information on the eRHIC project, see, `http://www.bnl.gov/cad/eRhic/` and `https://wiki.bnl.gov/eic`

[3] E. C. Aschenauer, R. Sassot, and M. Stratmann, arXiv:1206.6014 [hep-ph].

[4] L. Mankiewicz, A. Schafer, and M. Veltri, Comput. Phys. Commun. **71**, 305 (1992).

[5] D. de Florian, R. Sassot, M. Stratmann, and W. Vogelsang, Phys. Rev. Lett. **101**, 072001 (2008); Phys. Rev. D **80**, 034030 (2009); Prog. Part. Nucl. Phys. **67**, 251 (2012).

[6] A. D. Martin, R. G. Roberts, W. J. Stirling, and R. S. Thorne, Eur. Phys. J. C **28**, 455 (2003).

[7] D. de Florian, R. Sassot, and M. Stratmann, Phys. Rev. D **75**, 114010 (2007).

Part IV

Working Group 1
Structure Functions

Convenors:

Amanda Cooper-Sarker, Pedro Jimenez-Delgado,

Ringailė Plačakytė

Measurement of high-Q^2 e^+p neutral current cross sections at HERA and determination of the structure function $x\tilde{F}_3$

Friederike Januschek[1] on behalf of the ZEUS collaboration

[1]DESY, Notkestraße 85, 22607 Hamburg, Germany

DOI: http://dx.doi.org/10.3204/DESY-PROC-2012-02/34

The cross sections for neutral current deep inelastic scattering in e^+p collisions with a longitudinally polarised positron beam were measured using the ZEUS detector at HERA. The single-differential cross-sections $d\sigma/dQ^2$, $d\sigma/dx$ and $d\sigma/dy$ and the double-differential cross sections in Q^2 and x are presented in the kinematic region $Q^2 > 185$ GeV^2 and $y < 0.9$ for both positively and negatively polarised positron beams and for each polarisation state separately. The measurements are based on an integrated luminosity of 135.5 pb^{-1} taken in 2006 and 2007 at a centre-of-mass energy of 318 GeV. The structure function $x\tilde{F}_3$ is determined by combining these e^+p results with previously measured e^-p neutral current data. The measured cross sections are compared to the predictions.

1 Introduction

At the ep collider HERA electrons and positrons with an energy of 27.5 GeV collided with protons of an energy of predominantly 920 GeV, leading to a centre-of-mass energy of about 320 GeV. During the HERA II running period (2002-2007), the instantaneous luminosity was higher and the lepton beam was longitudinally polarised. This made it possible to study the polarisation dependence of deep inelastic scattering (DIS) in $e^{\pm}p$ neutral current (NC) and charged current (CC) interactions. The higher integrated luminosity of the HERA II data also improves the precision of measurements of the proton structure functions and makes these measurements a key input to the fits of the parton distribution functions (PDFs).

The NC DIS measurement presented here [1] is from e^+p data collected in 2006–2007. The sample corresponds to an integrated luminosity of 135.5 pb^{-1}, where 78.8 pb^{-1} were collected with a positive polarisation of the positron beam, while for the remaining 56.7 pb^{-1} the polarisation of the beam was negative. The mean polarisation of the two data sets is 0.32 and -0.36, leading to a mean polarisation of 0.03 for the combined set.

2 Neutral Current cross sections with longitudinally polarised leptons

The electroweak Born-level cross section of the NC process $e^{\pm}p \to e^{\pm}X$ can be written as

$$\frac{d^2\sigma(e^{\pm}p)}{dxdQ^2} = \frac{2\pi\alpha^2}{xQ^4}\left[Y_+\tilde{F}_2(x,Q^2) \mp Y_- x\tilde{F}_3(x,Q^2) \ -y^2\tilde{F}_L(x,Q^2)\right] = \frac{2\pi\alpha^2}{xQ^4}\tilde{\sigma} \ .$$

At HERA, of the (generalised) proton structure functions, $\tilde{F}_2$ is dominant in most of the phase space and $x\tilde{F}_3$ is sizable at high Q^2. $\tilde{F}_L$ gives a sizable contribution only at high y. Taking into account the lepton-beam polarisation, P_e, $\tilde{F}_2$ and $x\tilde{F}_3$ can be expressed as:

$$\tilde{F}_2{}^{\pm} = F_2^{\gamma} - (v_e \pm P_e a_e)\chi_Z F_2^{\gamma Z} + (v_e^2 + a_e^2 \pm 2P_e v_e a_e)\chi_Z^2 F_2^Z$$

and

$$x\tilde{F}_3{}^{\pm} = -(a_e \pm P_e v_e)\chi_Z x F_3^{\gamma Z} + (2v_e a_e \pm P_e(v_e^2 + a_e^2))\chi_Z^2 x F_3^Z \ ,$$

where $\chi_Z = \frac{1}{\sin^2\theta_W}\frac{Q^2}{M_Z^2+Q^2}$, v_e and a_e being the vector and axial-vector couplings of the electron to the Z boson and θ_W is the electroweak mixing angle.

At leading order in QCD, F_2^{γ}, $F_2^{\gamma Z}$ and F_2^Z can be written as linear combinations of the sum and $F_3^{\gamma Z}$ and F_3^Z as linear combinations of the difference of quarks and anti-quarks distributions in the proton:

$$[F_2^{\gamma}, F_2^{\gamma Z}, F_2^Z] = \sum_q [e_q^2, 2e_q v_q, v_q^2 + a_q^2]x(q+\bar{q})$$

and

$$[xF_3^{\gamma Z}, xF_3^Z] = \sum_q [e_q a_q, v_q a_q]x(q-\bar{q}) \ .$$

The difference of the e^+p and e^-p cross sections at zero polarisation of the lepton beam can be used to extract the structure function $x\tilde{F}_3$.

If the NC cross sections is measured separately for positive and negative lepton-beam polarisation, the polarisation asymmetry

$$A^{\pm} = \frac{2}{P_e^+ - P_e^-}\frac{\sigma^{\pm}(P_e^+) - \sigma^{\pm}(P_e^-)}{\sigma^{\pm}(P_e^+) + \sigma^{\pm}(P_e^-)} = \mp 2\chi_Z a_e v_q e_q / e_q^2 \propto a_e v_q$$

can be extracted. The asymmetry is proportional to the products $a_e v_q$ of the axial-vector coupling of the electron and the vector coupling of the quarks to the Z boson. Thus a measurement of A^+ can give direct evidence of parity violation with minimal assumptions on the proton structure.

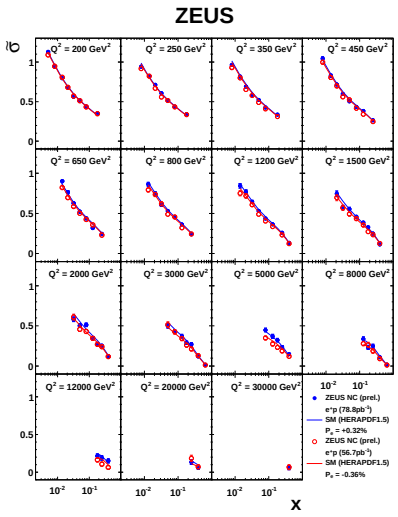

Figure 1: The NC reduced cross sections $\tilde{\sigma}_{NC}$ as a function of x at fixed Q^2 values: shown are e^+p ZEUS data with positive polarisation (closed circles) and the corresponding SM predictions obtained using the HERAPDF1.5 PDFs (solid lines) as well as the data with negative polarisation (open circles) and the corresponding SM predictions obtained using the HERAPDF1.5 PDFs (dashed lines).

3 Results

3.1 Polarised cross sections and polarisation asymmetry

The single-differential and the reduced cross sections (shown in Figure 1) were measured for negative and positive polarisation and agree with the Standard Model (SM) expectation evaluated using the HERAPDF1.5 [2, 3] PDFs. At high Q^2, the cross sections for the two polarisations differ, as expected, and from this difference the polarisation asymmetry A^+ was extracted showing parity violation (see Figure 2).

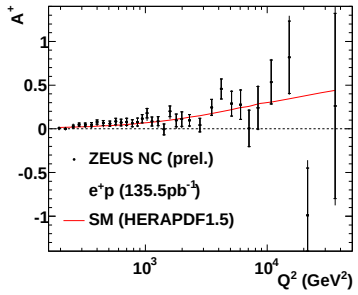

Figure 2: The Q^2 dependence of the polarisation asymmetry A^+, from e^+p scattering. The ZEUS data points are compared to the SM expectation obtained using the HERAPDF1.5 PDFs (solid red line).

3.2 Unpolarised cross sections and $x\tilde{F}_3$

The complete data set was also analysed and the single-differential cross sections $d\sigma/dQ^2$, $d\sigma/dx$ and $d\sigma/dy$ were measured and corrected to $P_e = 0$ for the residual polarisation. They are presented in Figure 3. From the reduced cross sections at zero polarisation in combination with the previously published results of e^-p data [4] the structure function $x\tilde{F}_3$ was extracted and is shown in Figure 4. These e^-p and e^+p data sets are the largest from ZEUS giving the most precise ZEUS $x\tilde{F}_3$ measurement to date.

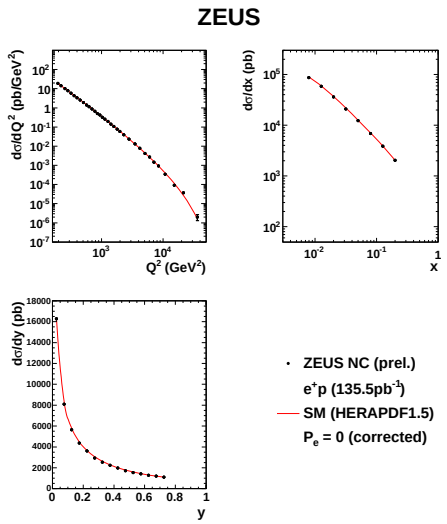

Figure 3: The single-differential NC e^+p cross sections $d\sigma/dQ^2$ (top left), $d\sigma/dx$ (top right) and $d\sigma/dy$ (bottom left) for $Q^2 > 185$ GeV^2 and $y < 0.9$.

4 Summary

The e^+p NC cross sections were measured with a longitudinally polarised lepton beam using the HERA II 2006–2007 data sample. The polarisation asymmetry of the NC cross section was measured showing parity violation directly with minimal dependence on the PDFs. Exploiting the dependence of the NC cross section on the charge of the lepton beam, the structure function $x\tilde{F}_3$, sensitive to the valence quark distributions, was extracted. The measurements are in agreement with the SM and have the potential to constrain the PDFs.

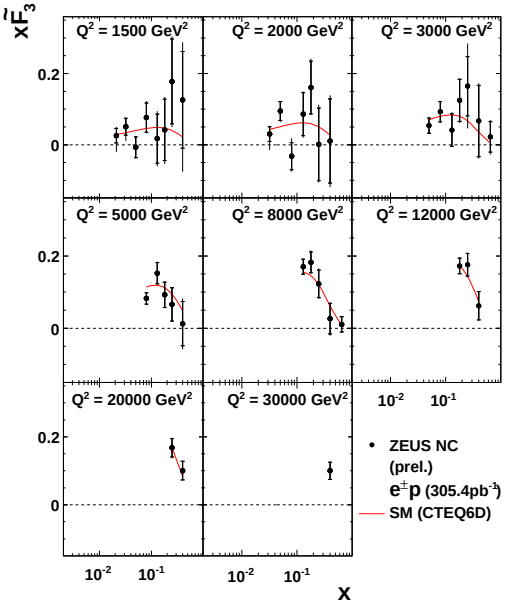

Figure 4: The structure function $x\tilde{F}_3$ evaluated using e^+p and e^-p data (solid points) compared to the SM expectations obtained using the CTEQ6D PDF set (solid line).

References

[1] **ZEUS** Collaboration, H. Abramowicz *et al.*, "Measurement of high-q^2 neutral current deep inelastic e^+p scattering cross sections with a longitudinally polarised positron beam at HERA". ZEUS-prel-11-003.

[2] **ZEUS and H1** Collaboration, H. Abramowicz *et al.*, "QCD NLO analysis of inclusive data (HERAPDF 1.5) ". H1prelim-10-142, ZEUS-prel-10-018, 2010.

[3] V. Radescu. PoS **ICHEP2010** (2010) 168.

[4] S. Chekanov *et al.* Eur. Phys. J. **C62** (2009) 625–658, `arXiv:0901.2385 [hep-ex]`.

Determination of the Integrated Luminosity at HERA using Elastic QED Compton Events

Stefan Schmitt on behalf of the H1 Collaboration

DESY, Notkestraße 85, 22607 Hamburg, Germany, sschmitt@mail.desy.de

DOI: http://dx.doi.org/10.3204/DESY-PROC-2012-02/109

A measurement of the integrated luminosity at the ep collider HERA is presented, exploiting the elastic QED Compton process $ep \to e\gamma p$. The electron and the photon are detected in the backward calorimeter of the H1 experiment. The integrated luminosity of the data recorded in 2003 to 2007 is determined with a precision of 2.3%. The measurement is found to be compatible with the corresponding result obtained using the Bethe-Heitler process.

1 Introduction

For particle collider experiments, the precise knowledge of the integrated luminosity is essential for any type of cross section measurement. The time-integrated luminosity is often determined from the event count N observed in a process with well-known cross section σ as $\mathcal{L} = N/\sigma$. At the ep collider HERA, electrons[1] and protons were colliding head-on at energies $E_e^0 = 27.5\,\mathrm{GeV}$ and $E_p^0 = 920\,\mathrm{GeV}$, respectively. The reaction used to determine the integrated luminosity is the production of a radiative photon in elastic ep scattering, $ep \to e\gamma p$. Depending on the phase space considered, this process is referred to as Bethe-Heitler (BH) scattering or QED Compton (QEDC) scattering. In the BH process [1] both the electron and the photon are emitted almost collinearly to the incident electron. The corresponding cross section is very large, $\mathcal{O}(100\,\mathrm{mb})$. For QEDC scattering [2] the particles have a sizable transverse momentum with respect to the incident electron and can be detected in the main detector. The momentum transfer squared at the proton vertex, t, is generally small. At very small momentum transfer $|t| \ll 1\,\mathrm{GeV}^2$, elastic scattering dominates. At $|t| \gtrsim 1\,\mathrm{GeV}^2$, inelastic processes are relevant and the reaction is sensitive to the proton structure. In addition, there are quasi-elastic contributions to the cross section, where the outgoing proton forms an excited state, like Δ or $N^\star$, which then decays to a low mass hadronic system. Within the phase space considered in this analysis, the elastic QEDC cross section is $\mathcal{O}(50\,\mathrm{pb})$. The Compton process, including quasi-elastic and inelastic contributions, is simulated using the COMPTON22 event generator [3].

At HERA, the integrated luminosity is usually measured in the BH process, using dedicated detectors located at small angles. The advantage of this process is its very large cross section, thus negligible statistical uncertainties are achieved for small amounts of integrated luminosity. However, there are various sources of possibly large systematic uncertainty, like acceptance limitations for the small angle detectors and details of the HERA beam optics.

[1] The term "electron" is used generically to refer to both electrons and positrons.

Here, a determination of the integrated luminosity is presented, based on the elastic QEDC process, which is measured in the H1 main detector [4]. Both the scattered electron and photon are detected in the H1 rear calorimeter (SpaCal) [5]. The position of the interaction vertex along the beam direction is determined using the central inner proportional chambers (CIP) [6]. This method is insensitive to details of the beam optics. However, the smallness of the cross section leads to limited statistical precision.

2 Event selection

Elastic QEDC events are selected by requiring two clusters in the electromagnetic section of the SpaCal. The transverse sizes of the SpaCal clusters are restricted to $R_{\log} < 6\,\text{cm}$, where $R_{\log}$ is calculated from the SpaCal cell centres using logarithmic energy weighting [7]. The cluster energies are required to be larger than 2.2 GeV. In the range $30 \leq R < 72\,\text{cm}$ of the radial distance from the beam, R, exactly two such clusters are required, whereas for $20 \leq R < 30\,\text{cm}$ no cluster is allowed. The restriction $R \geq 30\,\text{cm}$ on the two clusters ensures that the particles are within the CIP acceptance. Electron trajectories and the position of the vertex are reconstructed using the SpaCal cluster position together with position information from the CIP chambers. If there is only one SpaCal cluster with CIP hits, that cluster is taken as electron while the other cluster is taken as photon. If both SpaCal clusters have CIP hits, it is assumed that the photon has converted into an electron-positron pair while passing the material in front of the CIP detector and the particle assignment is done according to the hypothesis yielding an azimuthal opening angle of the two particles closest to 180°. Only events with longitudinal vertex position $|z_{\text{vtx}}| < 35\,\text{cm}$ are selected in the analysis. In addition, the following cuts are applied: energy of the most (least) energetic particle greater than 10 (7) GeV, polar angles θ_e, θ_γ within 155.9° and 169.5°, difference in azimuth between 170° and 190°. Inelastic background sources are further suppressed by using conditions on additional activity in the detector, such as limited energy in the forward part of the LAr calorimeter, and a veto on the number of tracks in the central tracking detectors. Finally, the modulus of the transverse component of the missing momentum, P_T^{miss}, is used as the main discriminating variable. Figure 1 shows the composition of the event sample differential in the variable P_T^{miss}, where the signal and various background processes are indicated. The elastic QEDC process dominates at small P_T^{miss}. At high P_T^{miss}, quasi-elastic and inelastic QEDC processes are dominant. Other background sources include electron-positron pair production, $ep \to ep\,e^-e^+$, simulated with GRAPE [8] and various diffractive processes like deeply virtual Compton scattering, modelled with MILOU [9], diffractive vector meson production, simulated with DIFFVM [10] and non-resonant diffrac-

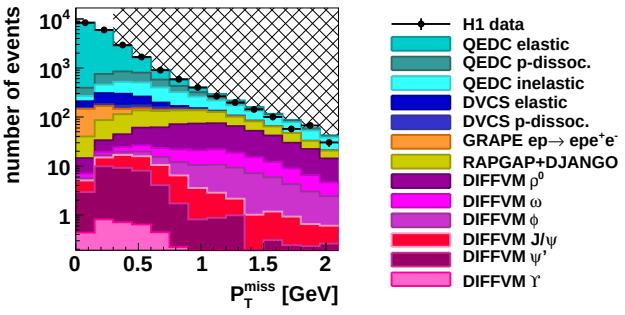

Figure 1: distribution of the missing transverse momentum. The data are shown as black dots. The total prediction and contributions from various background sources are indicated. The region $P_T^{\text{miss}} > 0.3\,\text{GeV}$ is excluded.

tion, modelled with RAPGAP [11].
A selection criterion $P_T^{\text{miss}} < 0.3\,\text{GeV}$ is applied. Within the selected region 14277 candidate events are observed and the fraction of background amounts to 8%.

3 Systematic uncertainties

Table 1 summarises the contributions to the uncertainties of the luminosity measurement. Systematic effects dominate over statistical uncertainties. The contributions to the uncertainty from experimental conditions, background normalisation and QEDC theory are similar in size.

Experimental uncertainties	**1.4%**
Background uncertainties	**1.2%**
QEDC theory uncertainties	**1.1%**
Statistical uncertainty	**0.8%**
Total uncertainty	**2.3%**

Table 1: Summary of the uncertainties on the determination of the integrated luminosity using elastic QEDC events.

The experimental uncertainties are dominated by the SpaCal energy resolution. The energy resolution is monitored using the double-angle reconstruction method [12] for the transverse momentum, P_T^{DA}. Distributions of the ratio of measured transverse momentum over P_T^{DA} are used to calibrate the energy resolution in the simulation. The calibration is repeated for electrons, non-coverted photons and converted photons, respectively.

The background uncertainties are dominated by the normalisation of the quasi-elastic and inelastic QEDC contributions. These are monitored using fits to the distribution of the components of the total transverse momentum parallel and perpendicular to the electron transverse momentum. The fits are performed outside the signal region, for $P_T^{\text{miss}} > 0.3\,\text{GeV}$

The uncertainties to the elastic QEDC theory are dominated by higher order effects. Initial state radiation is modelled as described in [13] using a photon radiator [14]. As an alternative the peaking approximation [15] as implemented in the COMPTON22 generator is considered. The difference between these models dominates the theory uncertainty.

The distribution of $\sum(E - p_z)/(2E_e^0)$, calculated from the sum of the electron and photon four-momenta, is shown in figure 2. This variable estimates the momentum fraction of the electron entering the hard collision after initial state radiation. The systematic uncertainties are shown differential in $\sum(E - p_z)/(2E_e^0)$. The width of the peak near 1 is dominated by energy resolution effects. The tail towards lower $\sum(E - p_z)/(2E_e^0)$ is sensitive to initial state radiation and to background processes. The simulation is capable to describe the data within uncertainties.

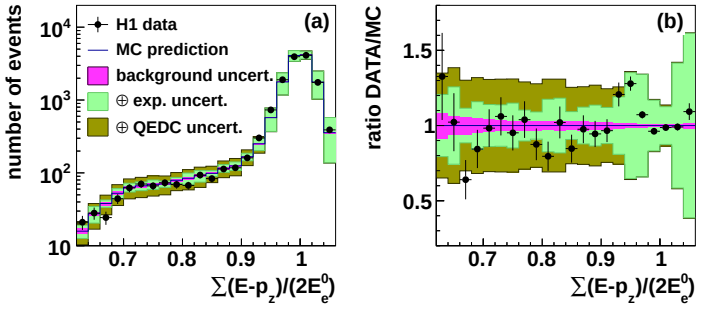

Figure 2: distribution of the variable $\sum \frac{E-p_z}{2E_e^0}$. The data are shown as black dots. The total prediction and contributions from various sources of systematic uncertainty are indicated.

4 Results

The integrated luminosity of the H1 data collected in the years 2003 to 2007 is determined using elastic QED Compton events. For the data sample as used in this paper, an integrated luminosity of $\mathcal{L}^{\mathrm{QEDC}} = 351.6 \pm 8.0\,\mathrm{pb}^{-1}$ is measured. The statistical uncertainty amounts to 0.8%, whereas the total systematic error is 2.1%. The integrated luminosity is in agreement with the Bethe-Heitler measurement, $\mathcal{L}^{\mathrm{BH}} = 338.9 \pm 10.2\,\mathrm{pb}^{-1}$.

References

[1] H. Bethe and W. Heitler, Proc. Roy. Soc. Lond. **A146** (1934) 83.

[2] W. Beenakker, F. A. Berends and W. L. van Neerven, Proc. of Workshop on Radiative Corrections for e^+e^- collisions, ed. J. H. Kühn, Ringberg Castle, Tegernsee (1989);
J. Blümlein, Z. Phys. **C47** (1990) 89;
J. Blumlein, G. Levman and H. Spiesberger, J. Phys. **G19** (1993) 1695;
J. Blumlein, Z. Phys. **C65** (1995) 293 [hep-ph/9403342].

[3] A. Courau and P. Kessler, Phys. Rev. **D46** (1992) 117;
V. Lendermann, H. C. Schultz-Coulon and D. Wegener, Eur. Phys. J. **C31** (2003) 343 [hep-ph/0307116].

[4] I. Abt *et al.* [H1 Collaboration], Nucl. Instrum. Meth. **A386** (1997) 310;
I. Abt *et al.* [H1 Collaboration], Nucl. Instrum. Meth. **A386** (1997) 348.

[5] R. Appuhn *et al.* [H1 SpaCal Group], Nucl. Instrum. Meth. **A386** (1997) 397.

[6] J. Becker *et al.*, Nucl. Instrum. Meth. **A586** (2008) 190 [physics/0701002].

[7] A. Glazov, N. Raicevic and A. Zhokin, Comput. Phys. Commun. **181** (2010) 1008.

[8] T. Abe, GRAPE-Dilepton version 1.1, Comput. Phys. Commun. **136** (2001) 126 [hep-ph/0012029].

[9] E. Perez, L. Schoeffel and L. Favart, hep-ph/0411389.

[10] B. List, A. Mastroberardino, Proc. of the Workshop on Monte Carlo Generators for HERA Physics, eds. A. Doyle *et al.*, DESY-PROC-1999-02 (1999) 396.

[11] RAPGAP 3.1: H. Jung, Comput. Phys. Commun. **86** (1995) 147.

[12] S. Bentvelsen, J. Engelen and P. Kooijman, Proc. of the Workshop on Physics at HERA, eds. W. Buchmüller, G. Ingelman, Hamburg, DESY (1992) 23;
K. C. Hoeger, *ibid.* 43.

[13] H. Anlauf *et. al* [Darmstadt-Siegen Collaboration], Z. Phys. **C52** (1991) 655.

[14] G. Montagna, O. Nicrosini and L. Trentadue, Nucl. Phys. **B357** (1991) 390.

[15] E. Etim, G. Pancheri and B. Touschek, Nuovo Cim. **B51** (1967) 276;
G. Pancheri, Nuovo Cim. **A60** (1969) 321.

QCD NLO analysis of inclusive, charm and jet data (HERAPDF 1.7)

Krzysztof Nowak on behalf of the H1 and ZEUS Collaborations

DESY, Notkestraße 85, 22607 Hamburg, Germany

DOI: http://dx.doi.org/10.3204/DESY-PROC-2012-02/35

A preliminary global NLO QCD analysis of the HERA data is presented. The following data sets are used in this analysis: the NC and CC inclusive DIS cross sections obtained from preliminary combination of the measurements from H1 and ZEUS based on HERA I and HERA II data at the nominal proton beam energy, the preliminary combined inclusive NC DIS cross sections at reduced proton beam energies, the inclusive jet cross sections from H1 and ZEUS and the preliminary combined HERA results on the charm contribution $F_2^{c\bar{c}}$ to the proton structure.

1 Introduction

Electron-proton collisions performed at the HERA collider provide a perfect environment for precise determination of parton density functions (PDFs) of the proton. They are determined by global fitting groups which base their fits on measurements performed at HERA as well as proton-antiproton data from Tevatron and fixed-target data from various experiments. The HERAPDF fitting group restricts used data to measurements based only on HERA data.

Both the H1 and ZEUS collaborations have performed PDF fits based on solely their data [1, 2]. The precision in the PDF determination has been improved by the combination of the H1 and ZEUS data collected in the period 1994-2000, resulting in the HERAPDF 1.0 fit [3]. The preliminary combination of the high statistics H1 and ZEUS data collected in years 2004-2007 was used in a more precise QCD analysis, named HERAPDF 1.5 [4]. The inclusion of the preliminary combined charm contribution $F_2^{c\bar{c}}$ to the proton structure in the PDF analysis has been used for the determination of the charm mass model parameter m_c^{model} for the different heavy flavour treatments in the evolution code [5]. Finally, several H1 and ZEUS results on inclusive jet production were used together with combined inclusive DIS data in the QCD analysis for a simultaneous determination of the PDFs and the strong coupling constant $\alpha_S(M_Z)$, termed HERAPDF 1.6 [6]. This document presents an analysis combining all these developments in a single fit which will be referred to as HERAPDF 1.7. In addition fit uses data collected during last months of HERA operation taken with reduced proton beam energy. This analysis tests the internal compatibility of different HERA data sets.

2 Data Sets

The QCD analysis presented in this document is based on four main components:

- **Preliminary combined H1 and ZEUS Neutral and Charged Current high Q^2 data**, which is crucial for the determination of PDFs. The combination of H1 and ZEUS measurements provide the most precise data spanning over the wide kinematic range $0.045 < Q^2 < 30000$ GeV^2 and $6 \times 10^{-5} < x < 0.65$. This data alone allows for the determination of PDFs with high precision, as was shown in [4].

- **Preliminary combined H1 and ZEUS data measured at reduced proton beam energy** measured in the last few months of HERA operation provide additional constrain on PDFs in the low Q^2 and low x region [7].

- **Preliminary combined H1 and ZEUS measurement of $F_2^{c\bar{c}}$ structure function**, which is directly sensitive to m_c^{model} parameter related to mass of the charm quark (for more detailed discussion see [5]).

- **Inclusive jet results in DIS from H1 and ZEUS:** high Q^2 DIS normalised inclusive jet data (HERA I+II) from H1 [8], low Q^2 DIS inclusive jet data (HERA I) from H1 [9], high Q^2 DIS inclusive jet data (HERA I, 96/97) from ZEUS [10] and high Q^2 DIS inclusive jet data (HERA I, 98-00) from ZEUS [11]. The inclusion of the jet data allows for a simultaneous determination of the strong coupling constant $\alpha_s(M_Z)$ and PDFs as has been demonstrated in [6]. It also leads to a small uncertainty reduction for the high-x gluon PDF.

All previously mentioned data sets have been already used as input to QCD analyses performed by HERAPDF fitting group. In this presentation we use all of them simultaneously in order to demonstrate the high level of consistency between different areas of HERA-based studies.

3 Theoretical predictions

For the inclusive DIS cross sections, for both the nominal and reduced proton beam energies, the QCDNUM 17 program [12] is used. The factorisation and renormalisation scales are chosen as $\mu_f = \mu_r = \sqrt{Q^2}$. Heavy quarks are treated as massive at threshold using the Thorne-Roberts general mass variable flavour number scheme [13], which also provided prediction for the $F_2^{c\bar{c}}$. The Thorne-Roberts program is used in its *optimal* version rather than *standard* which was previously used in HERAPDF fits. The *optimal* scheme is preferred due to a smooth threshold transition (see [14]).

The predictions for jet cross sections are calculated using the NLOJET++ program [15]. The fast convolution of the matrix elements with PDFs and α_s is preformed by the FASTNLO program [16]. Renormalisation and factorisation scale choices follow those in the relevant publications, using a combination of Q^2 and transverse jet energy measured in the Breit frame E_T.

Value of the m_c^{model} parameter is taken as $m_c^{model} = 1.5$ GeV which is obtained to be optimal for Thorne-Roberts scheme in [5]. The strong coupling constant is fixed to value of $\alpha_s(M_Z) = 0.119$, which is obtained from a fit with free $\alpha_s(M_Z)$. The other model parameters and uncertainties due to the assumptions made follow closely approach described in HERAPDF 1.0 publication [3].

4 PDF parametrisation

The parametrisation of PDFs at the starting scale of $Q_0^2 = 1.9$ GeV^2 follows the general approach taken in the previous HERAPDF fits. Five PDFs are parametrised, including gluon (g), valence quarks (u_v, d_v) and sea quarks ($\bar{U}$, $\bar{D}$) taking following functional form:

$$\begin{aligned} xg(x) &= A_g x^{B_g} \cdot (1-x)^{C_g} - A'_g x^{B'_g} (1-x)^{C'_g} \\ xu_v(x) &= A_{u_v} x^{B_{u_v}} \cdot (1-x)^{C_{u_v}} \cdot (1 + E_{u_v} x^2) \\ xd_v(x) &= A_{d_v} x^{B_{d_v}} \cdot (1-x)^{C_{d_v}} \\ x\bar{U}(x) &= A_{\bar{U}} x^{B_{\bar{U}}} \cdot (1-x)^{C_{\bar{U}}} \\ x\bar{D}(x) &= A_{\bar{D}} x^{B_{\bar{D}}} \cdot (1-x)^{C_{\bar{D}}} \end{aligned}$$

.

The parameters A_g, A_{u_v}, A_{d_v} are constrained by quark counting and momentum sum rules. It is assumed that $B_{\bar{U}} = B_{\bar{D}}$, $C'_g = 25$, $A_{\bar{U}} = A_{\bar{D}}(1-f_s)$, where f_s is the strangeness fraction at the starting scale Q_0 (assumed to be $f_s = 0.31$). The inclusion of these constraints results in a 13-parameter fit, while further parameters are considered when evaluating the parametrisation uncertainty. Assumption on the starting scale Q_0 lead to additional parametrisation uncertainty which is taken into account as well.

The parametrisation used in this study is slightly different from the parametrisation used for HERAPDF 1.6 where 14 free parameters were considered. In addition to the parameters introduced here, a non-vanishing linear term $D_{u_v} x$ is allowed which is considered as part of the parametrisation uncertainty in this study.

5 Results

The inclusion of all the previously used HERA data into a single fit allows a determination of PDFs with a very good precision. The resulting fit is called HERAPDF 1.7. In figure 1 HERAPDF1.6 (a) and HERAPDF1.7 (b) are shown evaluated at the scale $Q^2 = 10$ GeV^2. In Fig. 1 (b) also HERAPDF 1.6 is plotted as a reference.

Overall only small differences are observed for the quark PDFs. HERAPDF 1.7 exhibits slightly higher parametrisation uncertainties, particularly visible for u_v in the mid-x range between 10^{-2} and 10^{-1} which previously was assigned to model uncertainty. This is a direct consequence of a transition from 14-parameters fit to 13-parameters fit which was discussed earlier.

HERAPDF 1.7 has a significantly steeper gluon distribution. This is due to use of *optimal* rather than *standard* Thorne-Roberts scheme together with increased m_c^{model} value. The effect is reduced by the usage of higher $\alpha_s(M_Z)$ value which in general lead to a more gentle slope of gluon distribution. Also the experimental uncertainties are slightly reduced for HERAPDF 1.7 fit.

The usage of all previously studied data sets in a simultaneous fit is an important exercise to verify the consistency of all used HERA measurements. The study proves the high level of consistency between data sets, particularly if optimal values of model parameters like m_c^{model} and $\alpha_s(M_Z)$ are used.

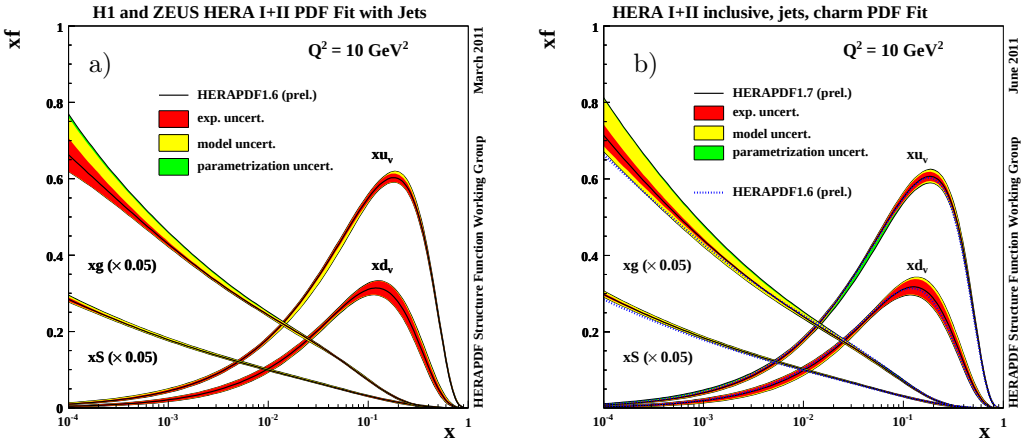

Figure 1: Gluon (g), valence quarks (u_v and d_v) and sea quarks ($S = \bar{U} + \bar{D}$) parton density functions at $Q^2 = 10$ GeV with their experimental, model and parametrisation uncertainties for HERAPDF 1.6 (a) and HERAPDF 1.7 (b) fits.

References

[1] F. D. Aaron *et al.* Eur. Phys. J. **C64** (2009) 561–587, arXiv:0904.3513 [hep-ex].

[2] S. Chekanov *et al.* Eur.Phys.J. **C42** (2005) 1–16, arXiv:hep-ph/0503274 [hep-ph].

[3] F. D. Aaron *et al.* JHEP **01** (2010) 109, arXiv:0911.0884 [hep-ex].

[4] V. Radescu. PoS **ICHEP2010** (2010) 168.

[5] R. Placakyte. proceedings **DIS2011** (2011) .

[6] K. Nowak. proceedings **DIS2011** (2011) .

[7] H1 prelim-10-044, ZEUSprelim-10-008 (2010) .

[8] F. Aaron *et al.* Eur.Phys.J. **C65** (2010) 363–383, arXiv:0904.3870 [hep-ex].

[9] F. Aaron *et al.* Eur.Phys.J. **C67** (2010) 1–24, arXiv:0911.5678 [hep-ex].

[10] S. Chekanov *et al.* Phys.Lett. **B547** (2002) 164–180, arXiv:hep-ex/0208037 [hep-ex].

[11] S. Chekanov *et al.* Nucl.Phys. **B765** (2007) 1–30, arXiv:hep-ex/0608048 [hep-ex].

[12] M. Botje. Comput.Phys.Commun. **182** (2011) 490–532, arXiv:1005.1481 [hep-ph].

[13] R. Thorne. Phys.Rev. **D73** (2006) 054019, arXiv:hep-ph/0601245 [hep-ph].

[14] R. Thorne. PoS **DIS2010** (2010) 053, arXiv:1006.5925 [hep-ph].

[15] Z. Nagy and Z. Trocsanyi. Phys.Rev.Lett. **87** (2001) 082001, arXiv:hep-ph/0104315 [hep-ph].

[16] T. Kluge, K. Rabbertz, and M. Wobisch. DIS 2006 proceedings (2006) 483–486, arXiv:hep-ph/0609285 [hep-ph].

ABM11 parton distributions and benchmarks

Sergey Alekhin[1,2], *Johannes Blümlein*[1], *Sven-Olaf Moch*[1]

[1]DESY, Platanenallee 6, D–15738 Zeuthen, Germany
[2]Institute for High Energy Physics, 142281 Protvino, Moscow region, Russia

DOI: http://dx.doi.org/10.3204/DESY-PROC-2012-02/302

We present a determination of the nucleon parton distribution functions (PDFs) and of the strong coupling constant α_s at next-to-next-to-leading order (NNLO) in QCD based on the world data for deep-inelastic scattering and the fixed-target data for the Drell-Yan process. The analysis is performed in the fixed-flavor number scheme for $n_f = 3, 4, 5$ and uses the $\overline{MS}$ scheme for α_s and the heavy quark masses. The fit results are compared with other PDFs and used to compute the benchmark cross sections at hadron colliders to the NNLO accuracy.

The nucleon PDFs play crucial role in the collider phenomenology and very often they put a limit on theoretical prediction accuracy, particularly for the calculations in the next-to -next-to-leading order (NNLO) in QCD. To meet quick accumulation of the data and steady progress in reduction of the systematic uncertainties in the LHC experiment we provide the NNLO nucleon PDF set with improved accuracy [5]. These PDFs are obtained from the updated version of the ABKM09 analysis [6] performed in the fixed-flavor number (FFN) scheme with the number of fermions taken as $n_f = 3, 4, 5$, depending on the process used to constrain the PDFs. In the present analysis we replace the inclusive neutral-current (NC) DIS data of the H1 and ZEUS experiments by the combined HERA data set, which are obtained from merging those of separate experiments [7]. The data are substantially improved by cross-calibration of the separate experiments and by merging both statistical and systematic errors. Due to these improvements the combined HERA data provide a better constraint on the small-x gluon and quark distributions. We also add to our analysis the inclusive charged-current (CC) DIS HERA data obtained by merging the H1 and ZEUS samples. The CC HERA data provide a supplementary constraint on the PDFs helping to disentangle the small-x quark distributions. Finally, we include the H1 data obtained in a spe-

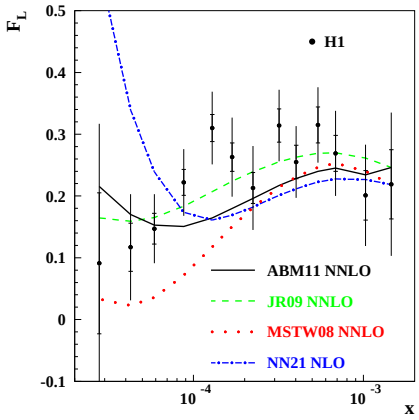

Figure 1: The data on F_L versus x obtained by the H1 collaboration [1] confronted with the 3-flavor scheme NNLO predictions based on the different PDFs (solid line: this analysis, dashes: JR09 [2], dots: MSTW [3]). The NLO predictions based on the 3-flavor NN21 PDFs [4] are given for comparison (dashed dots). The value of Q^2 for the data points and the curves in the plot rises with x in the range of $1.5 \div 45$ GeV^2.

cial HERA run at reduced collision energy, which are particularly sensitive to the contribution of longitudinal structure function F_L at small x [1]. This run was motivated by a particular sensitivity of the small-x F_L to the resummation effects and collinear factorization violation. Besides, F_L is quite sensitive to the gluon distribution therefore the data of Ref. [1] can help to consolidate the small-x gluon distributions provided by different groups, cf. Fig. 1.

In our analysis the DIS data are described within the 3-flavour FFN scheme, as well as in the ABKM09 case. However, in the present fit we employ the heavy-quark Wilson coefficients with the $\overline{MS}$ definition for the c- and b-quark masses, as suggested in Ref. [8]. For the case of $\overline{MS}$ definition the perturbative stability of the calculations is substantially improved. Moreover, in this case the constraints on the heavy-quark masses coming from the e^+e^- data, which are commonly obtained in the $\overline{MS}$ definition, can be consistently imposed in the PDF fit. This leads to a reduction of the PDF uncertainties due to the heavy-quark masses. In particular, the errors in the 4(5)-flavour heavy-quark PDFs, which are generated from the 3-flavour ones using the matching conditions, are significantly improved as compared to the earlier ABKM09 PDFs, cf. Fig. 2.

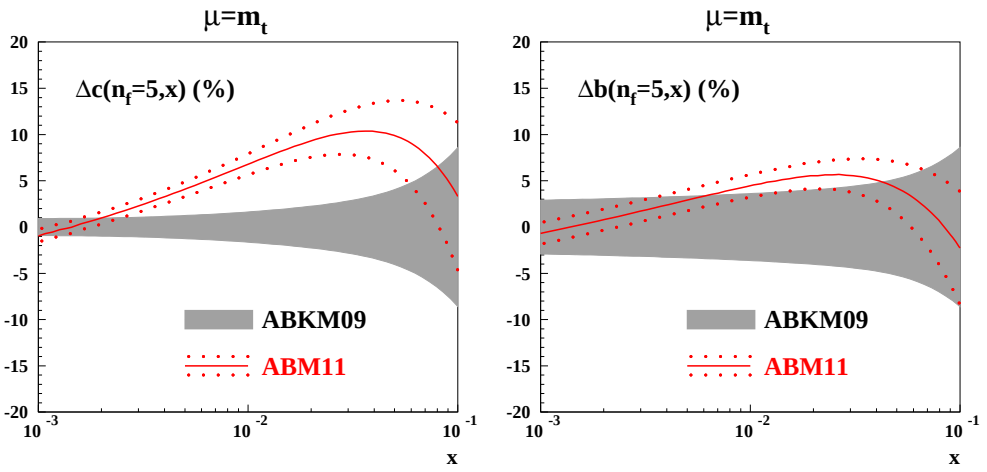

Figure 2: The charm- (left) and the bottom-quark (right) PDFs obtained in the fit: The dotted (red) lines denote the $\pm 1\sigma$ band of relative uncertainties (in percent) and the solid (red) line indicates the central prediction resulting from the fit with the running masses taken at the PDG values [9]. For comparison the shaded (grey) area represents the results of ABKM09 [6].

The value of strong coupling constant $\alpha_s(M_Z)$ is determined in our fit simultaneously with the PDFs. This approach provides a straightforward treatment of their correlation that is important for calculation of the uncertainties in the hadronic cross section predictions. At NNLO the ABM11 fit obtains the value of $\alpha_s(M_Z) = 0.1134 \pm 0.0011(\text{exp.})$. This is comparable with our earlier determination $\alpha_s(M_Z) = 0.1135 \pm 0.0014(\text{exp.})$ [6], while the error is improved due to more accurate data employed in the present analysis. It is also in a good agreement with $\alpha_s(M_Z) = 0.1141^{+0.0020}_{-0.0022}$ obtained in the analysis of the non-singlet DIS data with account of the QCD corrections up to the N^{3}LO [10]. In the ABM11 analysis the value of α_s is constrained both by the non-singlet and the singlet DIS data, cf. Fig. 3. For the kinematics of the SLAC and NMC experiments the χ^2-profile is sensitive to the power corrections including target

mass effects and the dynamical twist-4 terms. The latter are poorly defined by the strong interaction theory and therfore put limit on the accuracy of α_s determined in our fit. On the other hand, the BCDMS and HERA data are insensitive to the power term due to kinematics peculiarities. Moreover, these data sets provide complementary constraints in determining α_s [11]. Performing the NNLO variant of our fit with the SLAC and NMC data dropped we obtain $\alpha_s(M_Z) = 0.1133 \pm 0.0011(\text{exp.})$, which is not affected by the power corrections. Furthermore, it is in nice agreement with one obtained in the nominal ABM11 fit that gives confidence in the consistent treatment of the power terms in our analysis (cf. also discussion in Ref. [12]).

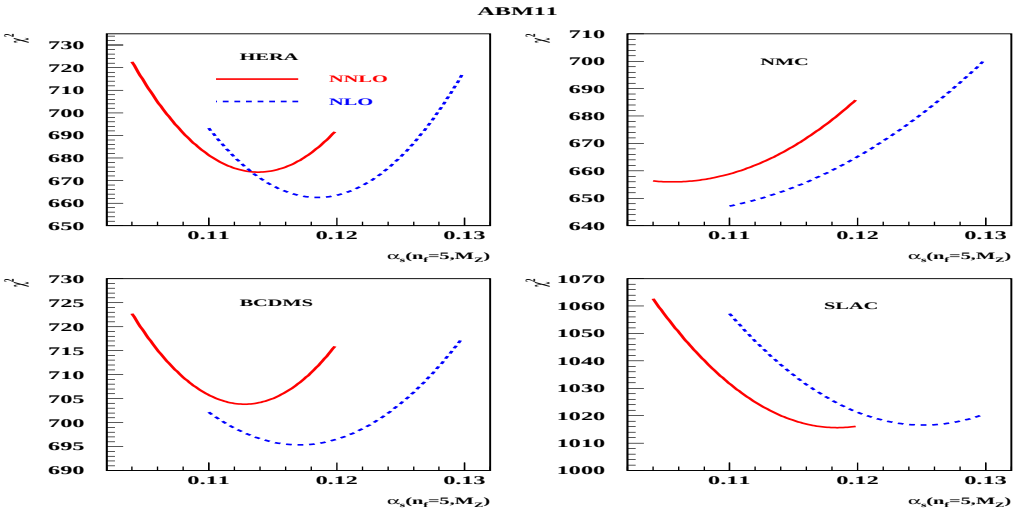

Figure 3: The χ^2-profile versus the value of $\alpha_s(M_Z)$, for the separate data subsets, all obtained in variants of the present analysis with the value of α_s fixed and all other parameters fitted (solid lines: NNLO fit, dashes: NLO fit).

Predictions for the charged-lepton asymmetry and the inclusive jet production cross sections at the energy of LHC are in a good agreement with the first data collected by the CMS and ATLAS experiments [13, 14, 15, 16], cf. Figs. 5, 4, despite these data are not used in ABM11 fit. Moreover, the value of $\alpha_s = 0.1151 \pm 0.0001$ (stata.) ± 0.0047(sys.) extracted from the ATLAS data of Ref. [15] in the NLO [17] is in agreement with our results. In contrast, the jet Tevatron data go above our predictions and the large-x gluon distribution rises significantly once they are included in the analysis. Note that the MSTW PDFs systematically overshoot the LHC jet data (cf. Fig. 5) as well as other PDFs tuned to the Tevatron data [16, 15]. On the whole, this leads to the conclusion that the LHC data prefer softer gluons as compared to the Tevatron case.

The Higgs production rates at the LHC and Tevatron are widely defined by the gluon distribution shape and the value of α_s. The NNLO predictions for the cross section of Higgs production in the proton-proton collisions at the LHC energies calculated with different NNLO PDFs are displayed in Table . At smaller collision energy, when the production rate is more sensitive to the large-x gluon distribution tail, the ABM11 calculations go lower than the MSTW08 and NN21 ones, while at high energies the difference between the predictions is

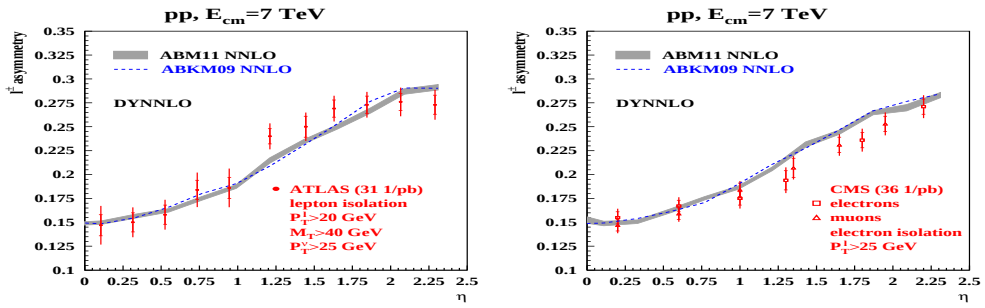

Figure 4: The data on charged-lepton asymmetry versus the lepton pseudo-rapidity η obtained by the ATLAS [13] (left panel) and CMS [14] (right panel) experiments compared to the NNLO predictions based on the DYNNLO code [18] and the ABM11 NNLO PDFs with the shaded area showing the integration uncertainties. The ABKM09 NNLO predictions are given for comparison by dashes, without the integration uncertainties shown.

smaller.

$\sqrt{s}$ (TeV)	ABM11	ABKM09 [6]	JR09 [2, 19]	MSTW08 [3]	NN21 [20]
7	$13.23^{+1.35+0.30}_{-1.31-0.30}$	$13.12^{+1.34+0.38}_{-1.31-0.38}$	$13.02^{+1.24+0.41}_{-1.17-0.41}$	$14.39^{+1.54+0.17}_{-1.47-0.22}$	$15.14^{+1.68+0.21}_{-1.53-0.21}$
8	$16.99^{+1.69+0.37}_{-1.63-0.37}$	$16.87^{+1.68+0.47}_{-1.63-0.47}$	$16.53^{+1.54+0.53}_{-1.44-0.53}$	$18.36^{+1.92+0.21}_{-1.82-0.28}$	$19.30^{+2.09+0.26}_{-1.89-0.26}$
14	$44.68^{+4.02+0.85}_{-3.78-0.85}$	$44.75^{+4.07+1.16}_{-3.85-1.16}$	$42.13^{+3.60+1.59}_{-3.26-1.59}$	$47.47^{+4.52+0.50}_{-4.18-0.71}$	$49.77^{+4.91+0.54}_{-4.30-0.54}$

Table 1: The total NNLO cross sections in pb for Higgs production in the gluon-gluon fusion obtained with different PDF sets at the mass of Higgs boson $M_H = 125$ GeV. The errors shown are the scale uncertainty are based on the shifts $\mu = m_H/2$ and $\mu = 2m_H$ and the 1σ PDF uncertainty, respectively.

In summary, we have produced the new NNLO PDF set with improved accuracy at small x due to new input from the HERA data and refined theoretical treatment of the heavy-quark electro-production in the running-mass definition. The predictions based on these PDFs are in a good agreement with the first LHC data, which can be used in future to improve the PDF accuracy further. A benchmarking w.r.t. to other PDFs is performed; the differences found can be also reduced with the help of new HERA and LHC data.

Acknowledgment

This work has been supported in part by DFG Sonderforschungsbereich Transregio 9, Computergestützte Theoretische Teilchenphysik, and EU Network LHCPHENOnet PITN-GA-2010-264564.

References

[1] F. Aaron, C. Alexa, V. Andreev, S. Backovic, A. Baghdasaryan, *et al.* Eur.Phys.J. **C71** (2011) 1579, arXiv:1012.4355 [hep-ex].

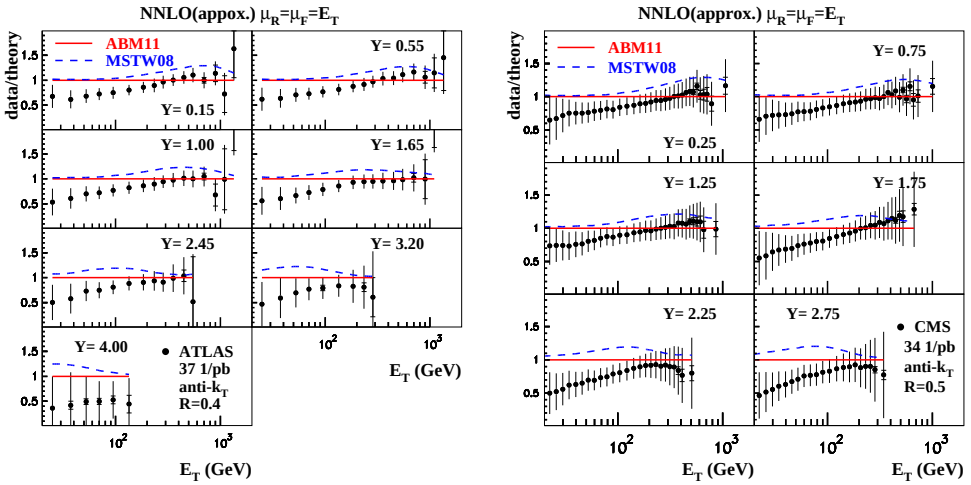

Figure 5: Cross section data for 1-jet inclusive production from the ATLAS collaboration [15] (left panel) and from the CMS collaboration [16] (right panel) as a function of the jet's transverse energy ET for $\mu_R = \mu_F = E_T$ compared to the result of the present analysis (solid) and to MSTW [3] (dashed). The theory predictions include the NNLO threshold resummation corrections to the jet production.

[2] P. Jimenez-Delgado and E. Reya. Phys.Rev. **D79** (2009) 074023, arXiv:0810.4274 [hep-ph].

[3] A. Martin, W. Stirling, R. Thorne, and G. Watt. Eur.Phys.J. **C63** (2009) 189–285, arXiv:0901.0002 [hep-ph].

[4] R. D. Ball, V. Bertone, F. Cerutti, L. Del Debbio, S. Forte, *et al.* Nucl.Phys. **B849** (2011) 296–363, arXiv:1101.1300 [hep-ph].

[5] S. Alekhin, J. Blümlein, and S. Moch. arXiv:1202.2281 [hep-ph].

[6] S. Alekhin, J. Blumlein, S. Klein, and S. Moch. Phys.Rev. **D81** (2010) 014032, arXiv:0908.2766 [hep-ph].

[7] F. Aaron *et al.* JHEP **1001** (2010) 109, arXiv:0911.0884 [hep-ex].

[8] S. Alekhin and S. Moch. Phys.Lett. **B699** (2011) 345–353, arXiv:1011.5790 [hep-ph].

[9] K. Nakamura *et al.* J.Phys.G **G37** (2010) 075021.

[10] J. Blumlein, H. Bottcher, and A. Guffanti. Nucl.Phys. **B774** (2007) 182–207, arXiv:hep-ph/0607200 [hep-ph].

[11] C. Adloff *et al.* Eur.Phys.J. **C21** (2001) 33–61, arXiv:hep-ex/0012053 [hep-ex].

[12] S. Alekhin, J. Blumlein, and S. Moch. Eur.Phys.J. **C71** (2011) 1723, arXiv:1101.5261 [hep-ph].

[13] G. Aad *et al.* Phys.Lett. **B701** (2011) 31–49, arXiv:1103.2929 [hep-ex].

[14] S. Chatrchyan *et al.* JHEP **1104** (2011) 050, arXiv:1103.3470 [hep-ex].

[15] G. Aad *et al.* Phys. Rev. **D86** (2012) 014022, arXiv:1112.6297 [hep-ex].

[16] S. Chatrchyan *et al.* Phys.Rev.Lett. **107** (2011) 132001, arXiv:1106.0208 [hep-ex].

[17] B. Malaescu and P. Starovoitov. arXiv:1203.5416 [hep-ph].

[18] S. Catani, L. Cieri, G. Ferrera, D. de Florian, and M. Grazzini. Phys.Rev.Lett. **103** (2009) 082001, arXiv:0903.2120 [hep-ph].

[19] P. Jimenez-Delgado and E. Reya. Phys.Rev. **D80** (2009) 114011, arXiv:0909.1711 [hep-ph].

[20] R. D. Ball *et al.* Nucl.Phys. **B855** (2012) 153–221, arXiv:1107.2652 [hep-ph].

Progress in the dynamical parton distributions

Pedro Jimenez-Delgado

Institut für Theoretische Physik, Universität Zürich, 8057 Zürich, Switzerland
Jefferson Lab, 12000 Jefferson Avenue, Newport News, VA 23606, USA

DOI: `http://dx.doi.org/10.3204/DESY-PROC-2012-02/299`

The present status of the (JR) dynamical parton distribution functions is reported. Different theoretical improvements, including the determination of the strange sea input distribution, the treatment of correlated errors and the inclusion of alternative data sets, are discussed. Highlights in the ongoing developments as well as (very) preliminary results in the determination of the strong coupling constant are presented.

The *dynamical* parton distributions of the nucleon at $Q^2 \gtrsim 1$ GeV^2 are QCD radiatively generated from *valencelike*[1] positive definite input distributions at an optimally determined low input scale $Q_0^2 < 1$ GeV^2. Thus the *steep* small-Bjorken-x behavior of structure functions, and consequently of the gluon and sea distributions, appears within the dynamical (radiative) approach mainly as a consequence of QCD-dynamics at $x \lesssim 10^{-2}$ [1]. Alternatively, in the common "standard" approach the input scale is fixed at some arbitrarily chosen $Q_0^2 > 1$ GeV^2, and the corresponding input distributions are less restricted; for example, the mentioned *steep* small-x behavior has to be *fitted*.

Following the radiative approach, the well-known LO/NLO GRV98 dynamical parton distribution functions of [2] have been updated in [3], and the analysis extended to the NNLO of perturbative QCD in [4]. In addition, in [3, 4] a series of "standard" fits were produced in (for the rest) exactly the same conditions as their dynamical counterparts. This allows us to compare the features of both approaches and to test the the dependence in model assumptions. The associated uncertainties encountered in the determination of the parton distributions turn out, as expected, to be larger in the "standard" case, particularly in the small-x region, than in the more restricted dynamical radiative approach where, moreover, the "evolution distance" (starting at $Q_0^2 < 1$ GeV^2) is sizably larger [3, 4].

The strong coupling constant $\alpha_s(M_Z^2)$ was determined in our analyses together with the parton distributions, in particular it is closely related to the gluon distribution which drives the QCD evolution and consequently its uncertainty is also smaller in the dynamical case. We obtained $\alpha_s(M_Z^2) = 0.1124 \pm 0.0020$ at NNLO, and 0.1145 ± 0.0018 at NLO in the dynamical case; to be compared with $\alpha_s(M_Z^2) = 0.1158 \pm 0.0035$ at NNLO, and 0.1178 ± 0.0021 at NLO in the "standard" one. The difference between these values is to be interpreted as a genuine uncertainty stemming from parameterization dependence, e.g. our contribution to the next PDG determination will be an average over NNLO dynamical and standard results. We consider this approach to be more realistic than considering only the reduced errors stemming exclusively from experimental uncertainties in each single analysis.

[1] Valencelike refers to $a_f > 0$ for *all* input distributions $xf(x, Q_0^2) \propto x^{a_f}(1-x)^{b_f}$, i.e., not only the valence but also the sea and gluon input densities vanish at small x.

The dynamical predictions for $F_L(x, Q^2)$ become perturbatively stable already at $Q^2 = 2$ - 3 GeV^2, where precision measurements could even delineate NNLO effects in the very small-x region. Moreover they are positive and in excellent agreement with the latest H1 data [8]. This is in contrast to the results based in the common "standard" approach, which are less precise and in some cases turn negative at the lower Q^2 values.

The inclusive production cross sections for W^+, W^- and Z^0-bosons form important benchmarks for the physics at hadron colliders. Our NLO [5] and NNLO [6] predictions for these standard candles processes were presented not long ago, and a detailed comparison of the predictions predictions based on the available NNLO parton parameterizations was performed in [7]. According to these studies the rates for gauge boson production at the LHC can be predicted with an accuracy of better than about 10% at NNLO. NNLO predictions for the Higgs boson production cross sections for Tevatron and LHC energies were also considered; the production rates could be predicted with an accuracy of about 10–20% at the LHC. The inclusion of the NNLO contributions is mandatory for achieving such accuracies since the total uncertainties are substantially larger at NLO.

During the time passed since the last determination of our PDFs there have been experimental and theoretical developments which deserve consideration. From the experimental side, besides results coming from LHC which we will not discuss here, the combined HERA data on neutral current and charge current DIS has been published [9]; the combination of the charm production data is ready but unfortunately still not publicly available. For the older fixed-target data in our analyses we use now directly the measured cross-sections (instead of the extracted structure functions) since potential problems with some of these extractions have been pointed out [10]. A wealth of deuteron data have also been included, for which description we use the nuclear corrections of [11]. Further theoretical improvements include the use of the running mass definition for DIS charm and bottom production [12].

In this proceeding we will concentrate in several concrete aspects of the ongoing update, modifications in the ansatz for the strangeness input distributions, and some consequences of the treatment of correlated systematic errors, in particular of the normalization uncertainties. Some preliminary results on determinations of $\alpha_s(M_Z^2)$ and the (future) inclusion of higher-twist terms in our analyses are also briefly discussed.

As in previous dynamical determinations [1, 2], since the data sets used are insensitive to the specific choice of the strange quark distributions, the strange densities of the *dynamical* distributions in [3, 4] have been generated entirely radiatively starting from vanishing strange input distributions:

$$s(x, Q_0^2) = \bar{s}(x, Q_0^2) = 0 \tag{1}$$

at the *low* input scale[2]. The plausibility of these *assumptions* was investigated in [13] by confronting the predictions derived from dynamical distributions determined in this way with the most precise dimuon production data [14], which were the most sensitive to the strangeness content of the nucleon until the recent ATLAS measurements [15]. A good agreement was found at NLO. Since the NNLO corrections (thus the experimental acceptance corrections) for these process are not known, a consistent study of these data at NNLO is not possible. However it is apparent that unless the NNLO corrections were very large (which seems unlikely) our JR09 NNLO distributions would generally undershoot the data. Indeed the would-be NNLO results favor $\bar{s} \simeq 0.1(\bar{u} + \bar{d})$ at the input scale. In order to estimate the implications which this

[2] In the "standard" case, where $Q_0^2 > 1$ GeV^2, the strange input distributions were chosen $s(x, Q_0^2) = \bar{s}(x, Q_0^2) = \frac{1}{4}(\bar{u}(x, Q_0^2) + \bar{d}(x, Q_0^2))$, as is conventional [3, 4].

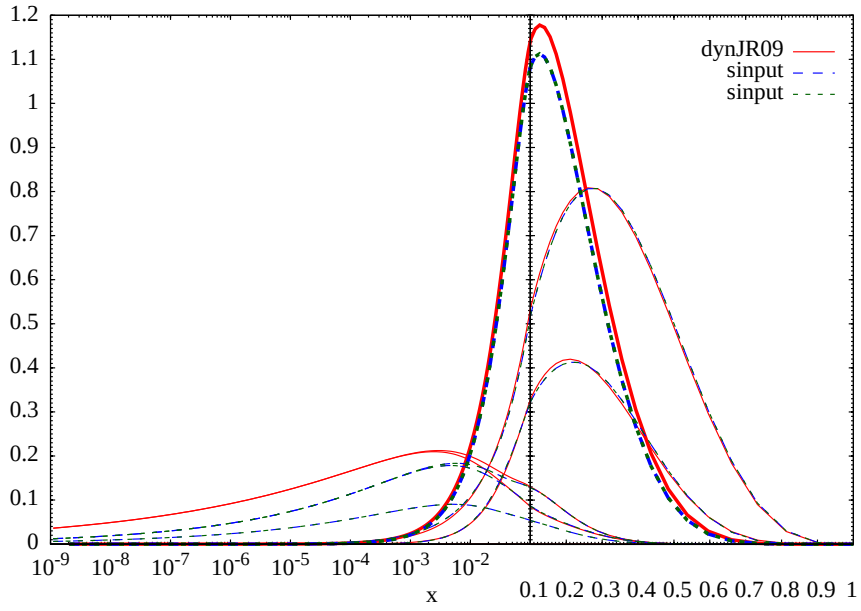

Figure 1: DIS2012 Proceedings.

could have for our predictions for benchmark processes at the LHC we have repeated our JR09 dynamical analysis using $s(x,Q_0^2) = \bar{s}(x,Q_0^2) = \frac{1}{4}(\bar{u}(x,Q_0^2) + \bar{d}(x,Q_0^2))$ as in our "standard" fits. The resulting input distributions are compared with the original JR09 input in Fig. 1. It can be observed that the increase in the strange distributions is *compensated* by a decrease in the light sea, while the other distributions remain practically unaltered. The mentioned benchmark cross-sections for W and Z production are practically identical in both cases. Nevertheless the determinations of strange input distributions will have to be revisited in light of the mentioned ATLAS measurements [15], which seem to imply a greater strange content of the nucleon.

Another aspect of our analyses in which we have been working is a more complete treatment of the correlated systematic uncertainties of the data. The least-squares estimator that we use to take them into account has been explicitly written down in Appendix B of [16]. This is used as well for normalization uncertainties, and implies that data and theory are relatively shifted by amounts which are determined by the minimization but not restricted further. This is in contrast to the treatment that we used in our (G)JR analyses, where the normalization shifts were limited by the experimental normalization uncertainties, and has resulted in small shifts on the valence distributions in the medium x region.

Yet another issue raised by the ABM collaboration is the necessity of including higher twist for the description of fixed target data [17]; even if moderate kinematical cuts are used to select the data included in the fits; in particular for SLAC and NMC data. The kinematical cuts in our G(JR) analyses were $Q^2 \geq 4$ GeV^2 and $W^2 \geq 10$ GeV^2, and were applied to the F_2 values extracted from different beam energies and combined. The description was good for NMC data and rather poor for SLAC data. However since the number of points for these experiments was rather small (about 100 data points for NMC and 50 for SLAC), the values of the cuts did not affect very much the results of the fits.

This picture changes if, as the ABM collaboration does, data on the cross sections for individual energies are used, which amounts to hundreds of data points for each experiment. As mentioned in the introduction, we also use these data in our current preliminary analyses, for which the virtuality cut has been raised to $Q^2 \geq 9$ GeV^2. We find results which are rather similar to our JR09 analyses, with $\alpha_s(M_Z^2)$ values about 0.113 to 0.114, depending on the input scale. If the usual cut of $Q^2 \geq 4$ GeV^2 is applied to these data $\alpha_s(M_Z^2)$ raises to 0.1176; a tendency in agreement with the ABM observations [17]. The inclusion of higher twist terms in the theoretical description should strongly reduce the dependence of the outcome of the fits and is currently under consideration.

To summarize, we have discussed several aspects of the ongoing update of the JR dynamical parton distributions, in particular the determination of strangeness input distributions, the treatment of normalizations, and results on $\alpha_s(M_Z^2)$ and their dependence on kinematical cuts and the treatment of higher-twist contributions. Changes in the parton distributions induced by all this modifications in the analysis and in the data have been, until now, quite modest.

References

[1] M. Glück, E. Reya and A. Vogt, *Z. Phys.* **C67** (1995) 433.

[2] M. Glück, E. Reya and A. Vogt, *Eur. Phys. J.* **C5** (1998) 461.

[3] M. Glück, P. Jimenez-Delgado and E. Reya, *Eur. Phys. J.* **C53** (2008) 355.

[4] P. Jimenez-Delgado and E. Reya, *Phys. Rev.* **D79** (2009) 074023.

[5] M. Glück, P. Jimenez-Delgado, E. Reya and C. Schuck, *Phys. Lett.* **B664** (2008) 133.

[6] P. Jimenez-Delgado and E. Reya, *Phys. Rev.* **D80** (2009) 114011.

[7] S. Alekhin, J. Blumlein, P. Jimenez-Delgado, S. Moch and E. Reya, Phys. Lett. B **697** (2011) 127

[8] F. D. Aaron, C. Alexa, V. Andreev, S. Backovic, A. Baghdasaryan, S. Baghdasaryan, E. Barrelet and W. Bartel *et al.*, Eur. Phys. J. C **71** (2011) 1579

[9] F. D. Aaron *et al.* [H1 and ZEUS Collaboration], JHEP **1001** (2010) 109

[10] S. Alekhin, J. Blumlein and S. Moch, Eur. Phys. J. C **71** (2011) 1723

[11] A. Accardi, W. Melnitchouk, J. F. Owens, M. E. Christy, C. E. Keppel, L. Zhu and J. G. Morfin, Phys. Rev. D **84** (2011) 014008

[12] S. Alekhin and S. Moch, Phys. Lett. B **699** (2011) 345

[13] P. Jimenez-Delgado, Phys. Lett. B **689** (2010) 177

[14] D. Mason *et al.*, *Phys. Rev. Lett.* **99** (2007) 192001.

[15] G. Aad *et al.* [ATLAS Collaboration], arXiv:1203.4051 [hep-ex].

[16] D. Stump, J. Pumplin, R. Brock, D. Casey, J. Huston, J. Kalk, H. L. Lai and W. K. Tung, Phys. Rev. D **65** (2001) 014012

[17] S. Alekhin, J. Blumlein and S. Moch, arXiv:1202.2281 [hep-ph].

Progress in CTEQ-TEA PDF analysis

Pavel Nadolsky[1,5], *Jun Gao*[1], *Marco Guzzi*[1], *Joey Huston*[2], *Hung-Liang Lai*[3], *Zhao Li*[2], *Jon Pumplin*[2], *Dan Stump*[2], *C.-P. Yuan*[2,4]

[1]Department of Physics, Southern Methodist University, Dallas, TX 75275, USA
[2]Department of Physics and Astronomy, Michigan State University, E. Lansing, MI 48824, USA
[3]Taipei Municipal University of Education, Taipei, Taiwan
[4]Center for High Energy Physics, Peking University, Beijing, China
[5]Presenter

DOI: http://dx.doi.org/10.3204/DESY-PROC-2012-02/301

Recent developments in the CTEQ-TEA global QCD analysis are presented. The parton distribution functions CT10-NNLO are described, constructed by comparing data from many experiments to NNLO approximations of QCD.

The global analysis of QCD makes use of experimental data from many short-distance scattering processes to construct, within some approximations, universal parton distribution functions (PDFs) for the proton. Then these functions can be used to calculate hadronic cross sections in the Standard Model and other theories. Global analysis and the resulting PDFs are necessary for the interpretation of experimental results at hadron colliders.

Recently published PDFs are based on next-to-next-to-leading order (NNLO) approximations for perturbative QCD [1]. Complete calculations for this order of approximation are available for the running coupling $\alpha_s(Q)$, PDF evolution in Q, matrix elements in deep-inelastic scattering [2] and vector boson production [3]. The CTEQ analysis treats quark-mass effects in the S-ACOT-χ factorization scheme, which has been recently extended to two-loop, or NNLO, accuracy [4]. Though the NNLO matrix elements are still unknown for some important processes, such as the inclusive jet production in $pp/p\overline{p}$ collisions, it is important to use NNLO approximations, where available.

CTEQ has developed PDFs for general-purpose computations and estimates of PDF-driven uncertainties over many years [5]. The most recent PDFs in this class, named CT10 and CT10W, were published in 2010 [6]. We now present a new family of CTEQ parton distributions, named CT10 NNLO. There are several reasons for publishing them. First, the CT10 NNLO global analysis is based on the NNLO approximation of perturbative QCD, whereas the CT10 and earlier analyses were based on NLO. Second, benchmarking of NLO jet cross sections [7]and DIS cross sections was performed to quantify theoretical uncertainties, and an in-depth study of the treatment of correlated experimental errors has been completed. Third, selection of experimental data sets has been revisited. The new NNLO PDFs are closely related to both CT10 and CT10W NLO PDFs and can be matched to either of two NLO PDF sets when comparing the NLO and NNLO cross sections. In all three cases, only data from pre-LHC experiments were used in the global fit. The same values of the QCD coupling and heavy-quark masses as in CT10 NLO were assumed. Some results concerning CT10 NNLO PDFs were presented at DIS2012 [8] and will be described here. A longer paper on CT10 NNLO is

in preparation. The CT10 NNLO PDFs are now available in the LHAPDF library.

In the near future, a new release of NLO and NNLO PDFs, named CT12, will include available data from LHC experiments. Some preliminary results of the CT12 analysis were also presented at DIS2012 [8].

Selection of data. At NLO, the main distinction between CT10 and CT10W sets concerns the inclusion of the D0 Run-2 W electron and muon asymmetry [11], $A_\ell(y_\ell)$, that constrains the behavior of the ratio $d(x,Q/u(x,Q)$ at $x > 0.1$. The CT10 NLO set does not include the D0 Run-2 A_ℓ data, while the CT10W NLO set includes 4 $p_{T\ell}$ bins of A_ℓ. The CT10 NNLO analysis includes all data sets that were used in the NLO fits, with the exception of the Tevatron Run-1 inclusive jet cross sections [9] that have been superceded by more precise Tevatron Run-2 jet cross sections [10]; and the D0 Run-2 A_ℓ data sets, of which only most inclusive (best understood) bins of $p_{T\ell}$ are included in both the electron and muon channel. Since CT10 NNLO includes only a part of the D0 A_ℓ data that distinguishes between CT10 NLO and CT10W NLO, it can be treated as a counterpart of either the CT10 NLO or CT10W NLO PDF set.

Overview of the PDFs. Figure 1 gives an overview of the CT10 NNLO PDFs. Four PDFs are shown: $u_{\rm valence}(x,Q) = (u-\overline{u})(x,Q)$; $d_{\rm valence}(x,Q) = (d-\overline{d})(x,Q)$; $g(x,Q)$; and $q_{sea}(x,Q) = 2(\overline{d}+\overline{u}+\overline{s})(x,Q)$. The vertical axis is $x\,f(x,Q)$. The CT10 NNLO PDFs are illustrated by plotting all the error PDFs; hence the figure shows not only the central fit but also the uncertainty ranges. The dashed curves are the central-fit CT10 NLO PDFs.

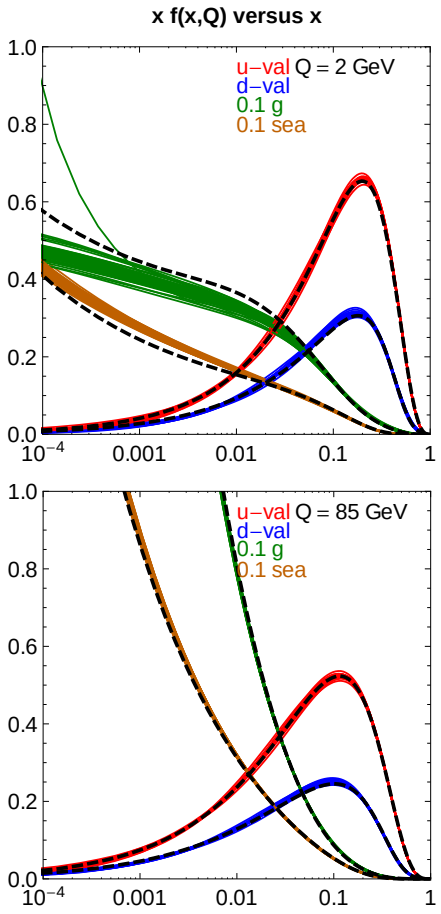

Figure 1: CT10 NNLO (solid color) and NLO (dashed) parton distribution functions.

Both NLO and NNLO fits have about the same $\chi^2/N_{pt} \approx 1.1$ for $N_{pt} = 2700$ data points. Slide 5 in Ref. [8] shows a more complete comparison of CT10 NNLO to CT10W NLO, for $Q = 2\,\text{GeV}$ and for thre parton flavors, g, u, and $\bar{u}$. The various PDFs are plotted as a ratio to the central CT10W NLO. The curves are the ratios of the central CT10 NNLO to CT10W NLO. The shaded regions are the *error bands* for the PDFs (both NLO and NNLO). The central NNLO PDFs differ from the central NLO PDFs, but the difference is comparable in size to the error bands. The error band for NNLO is slightly smaller than for NLO.

Compared to CT10W NLO, the NNLO PDF set at a small scale Q has a suppressed gluon and increased sea quarks at $x < 10^{-2}$, reduced $g(x,Q)$ and $d(x,Q)$ at $x > 0.1$, and very different charm and bottom PDFs (slide 6 in [8]). The reduction in $g(x,Q)$ Compared to MSTW'08 NNLO, the central CT10 NNLO gluon PDF is somewhat harder at $x < 10^{-3}$ and $x = 0.1-0.5$, and softer at $x > 0.5$ (slide 9 in [8]). The strangeness PDF is larger at $x \sim 10^{-2}$ in CT10 NNLO than in MSTW'08 NLO, producing a good agreement with the ATLAS measurement of

the $\bar{s}(x)/\bar{u}(x)$ at this x value.

Boson/collider	CT10 NLO	CT10 NNLO	MSTW'08 NNLO
W^+ LHC14 (nb)	12.2 ± 0.5	12.7 ± 0.5	12.4 ± 0.2
W^+ LHC7 (nb)	6.0 ± 0.2	6.3 ± 0.2	6.2 ± 0.1
W^+ Tevatron (nb)	1.35 ± 0.05	1.38 ± 0.05	1.38 ± 0.02
W^- LHC'14 (nb)	8.9 ± 0.4	9.4 ± 0.4	9.3 ± 0.2
W^- LHC'7 (nb)	4.10 ± 0.15	4.29 ± 0.16	4.31 ± 0.07
Z LHC14 (nb)	2.07 ± 0.08	2.17 ± 0.08	2.13 ± 0.03
Z LHC7 (nb)	0.96 ± 0.03	1.00 ± 0.03	0.99 ± 0.02
Z Tevatron (pb)	260 ± 9	263 ± 8	261 ± 5
H^0_{SM} LHC14 (pb)	101 ± 9	99 ± 8	102 ± 7
H^0_{SM} LHC7 (pb)	31.2 ± 1.9	29.7 ± 1.7	29.8 ± 1.3
H^0_{SM} Tevatron (pb)	1.77 ± 0.12	1.77 ± 0.12	1.80 ± 0.11

Table 1: Total cross sections for production of electroweak bosons.

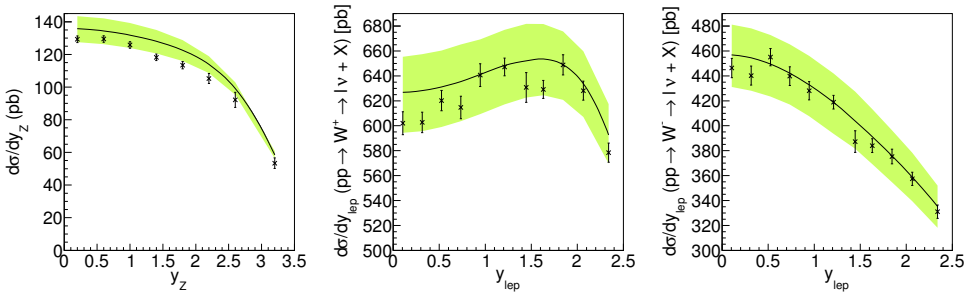

Figure 2: Comparisons of ATLAS data with ResBos predictions for Z^0 and $W^\pm$ lepton rapidity distributions.

Predictions for the LHC. In a future paper we will provide detailed comparisons of theory and data, where the theory is calculated from the CT10 NNLO PDFs. Here we collect some representative cross sections for the hadron colliders. Table 1 compares predictions for total cross sections for W, Z and Higgs boson production via gluon fusion (with Higgs mass of 125 GeV) at the Tevatron and the LHC (with $\sqrt{s}$ =7 and 14 TeV). The comparison is between CT10 NLO, CT10 NNLO, and MSTW'08 NNLO. The CT10 NNLO central PDF increases the total cross sections by a few percent compared with CT10 NLO accuracy and is close to MSTW'08. Theoretical uncertainties from alternative PDF sets for CT10 NNLO are similar to those for CT10, and in W/Z production they are about twice as those for MSTW'08.

Fig. 2 shows the comparison of ATLAS data [14] with ResBos [15] predictions for Z and W-lepton rapidity distributions at the LHC ($\sqrt{s} = 7$ TeV) using CT10 NNLO PDFs. Theoretical uncertainty bands were calculated using the error PDF sets. The ResBos prediction of Z and W^+-lepton rapidity distribution, using the central PDF set, is higher than ATLAS data by a few percent. However, for W^--lepton rapidity distribution, the ResBos prediction is more consistent with ATLAS data. It is expected that these data could further refine the PDFs at the NNLO accuracy.

Fig. 3 compares the ATLAS data for inclusive jet transverse momentum distribution with

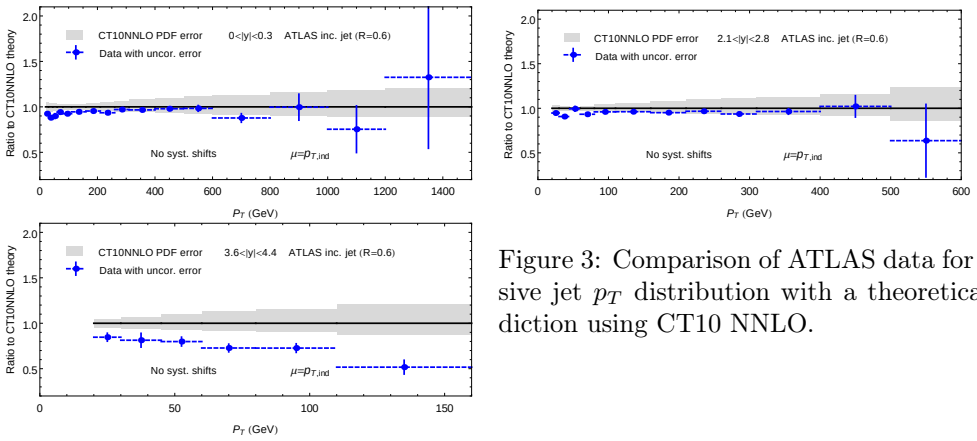

Figure 3: Comparison of ATLAS data for inclusive jet p_T distribution with a theoretical prediction using CT10 NNLO.

theoretical predictions based on the NLO matrix elements and CT10 NNLO PDFs. They agree well even without including the systematic shifts, except for the large rapidity region. After accounting for the systematic shifts, the reduced χ^2 is 0.78 for the measurement with R=0.4 and 0.76 for the one with R=0.6. The effect of the LHC data on the PDFs will be explored in the CT12 analysis.

This work was supported by the U.S. DOE Early Career Research Award DE-SC0003870 and by the U.S. NSF under grant No. PHY-0855561.

References

[1] A. D. Martin, W. J. Stirling, R. S. Thorne, G. Watt, Eur. Phys. J. C63 (2009) 189; R. D. Ball et al, Nucl. Phys. B855 (2012) 153; S. Alekhin, J. Blumlein, S. Moch, arXiv:1202.2281 [hep-ph].

[2] S. Moch, J. A. M. Vermaseren and A. Vogt, Nucl. Phys. B 688 (2004) 101; A. Vogt, S. Moch and J. A. M. Vermaseren, Nucl. Phys. B 691 (2004) 129.

[3] C. Anastasiou, L. J. Dixon, K. Melnikov, and F. Petriello, Phys. Rev. Lett., 91, (2003) 182002; Phys. Rev. D 69, (2004) 094008.

[4] M. Guzzi, P. M. Nadolsky, H.-L. Lai, C.-P. Yuan, arXiv:1108.5112 [hep-ph].

[5] J. Pumplin, *et al.*, JHEP 0207:012 (2002); D. Stump, *et al.*, JHEP 0310:046 (2003); P. M. Nadolsky, *et al.*, Phys. Rev. D78 (2008) 013004.

[6] H.-L. Lai, et al., Phys. Rev. D82 (2010) 074024.

[7] J. Gao, Z. Liang, P. Nadolsky, in J. A. Maestre, *et al.*, arXiv:1203.6803 [hep-ph], p. 77.

[8] Slides: http://bit.ly/CT10DIS2012 .

[9] T. Affolder, *et al.* (CDF Coll.) Phys.Rev. D64 (2001) 032001; B. Abbott, *et al.* (D0 Coll.), Phys.Rev. D64 (2001) 032003.

[10] T. Aaltonen, *et al.* (CDF Coll.), Phys.Rev. D78 (2008) 052006; V. M. Abazov, *et al.* (D0 Coll.), Phys.Rev.Lett. 101 (2008) 062001.

[11] V. M. Abazov, et al. (D0 Coll.), Phys.Rev.Lett. 101 (2008) 211801; Phys.Rev. D77 (2008) 011106.

[12] ATLAS Coll., arXiv:1203.4051 [hep-ex].

[13] D. Stump, *et al.*, Phys. Rev. D65 (2001) 014012; J. Pumplin, *et al.*, Phys. Rev. D65 (2001) 014013; A. D. Martin, et al.,, Eur. Phys. J. C28 (2003) 455; *ibid.*, C35 (2004) 325; A.M.Cooper-Sarkar, J. Phys. G28 (2002) 2669; S. Alekhin, Phys. Rev. D68 (2003) 014002; R. D. Ball, *et al.*, Nucl. Phys. B809 (2009) 1.

[14] G. Aad, *et al.* [ATLAS Collaboration], Phys. Rev. D85 (2012) 072004.

[15] C. Balazs, C.-P. Yuan, Phys. Rev. D56 (1997) 5558; F. Landry, *et al.*, Phys. Rev. D 67 (2003) 073016.

Global Analysis of Nuclear PDFs

Daniel de Florian[1], *Rodolfo Sassot*[1], *Marco Stratmann*[2], *Pia Zurita*[1]

[1]Departamento de Física and IFIBA, FCEyN, Universidad de Buenos Aires,
Ciudad Universitaria, Pabellón 1 (1428) Buenos Aires, Argentina
[2]Physics Department, Brookhaven National Laboratory, Upton, NY 11973, USA

DOI: `http://dx.doi.org/10.3204/DESY-PROC-2012-02/33`

We present a new global QCD analysis of nuclear parton distribution functions. In addition to the most commonly analyzed data sets for deep inelastic scattering of charged leptons off nuclei and Drell Yan di-lepton production, we include also measurements for neutrino-nuclei scattering as well as inclusive pion production in deuteron-gold collisions. The emerging picture is one of consistency, where universal nuclear modification factors for each parton flavor reproduce the main features of all data without any significant tension among the different sets.

1 Motivation

In the last few years, significant progress has been made in obtaining nuclear PDFs (nPDFs) from data. In addition to the theoretical improvements routinely used in modern extractions of free proton PDFs, such as the consistent implementation of QCD corrections beyond the LO [1] and uncertainty estimates [2, 3], the most recent determinations of nPDFs have also extended the types of data sets taken into account, moving towards truly global QCD analyses of nuclear effects [3, 4, 5, 6]. The addition of novel hard probes to the fit does not only lead to better constrained sets of nPDFs and allows one to study the nuclear modification to the different parton species individually, but also tests the assumed process independence of nuclear effects.

The deep inelastic scattering (DIS) of charged leptons off nuclear targets not only initiated all studies of nPDFs but still provides the best constraints on nuclear modifications for quark distributions. Upon combination with available data on Drell Yan (DY) di-lepton production off nuclear targets, a better discrimination between valence and sea quarks can be achieved. However, DIS and DY data only loosely constrain the nuclear modifications to the gluon density because they cover a too small range in the hard energy scale Q. To remedy this situation, data from BNL-RHIC for inclusive pion production in deuteron-gold (dAu) collisions have been included in the analysis of nPDFs performed in Ref. [3]. Not surprisingly, these data have a significant impact in the determination of the gluon distribution. The corresponding nuclear modification for gluons turned out to be much more pronounced than in previous estimates and also much larger than those found for all the other partonic species.

Another promising avenue for significant improvements is neutrino induced DIS off iron and lead targets, with results available from NuTeV, CDHSW, and CHORUS [7]. These data receive their importance from their discriminating power between nuclear modifications for quarks and antiquarks and have been included in a series of analyses in Refs. [4, 6]. Unexpectedly, the

correction factors obtained from neutrino scattering data are found to differ significantly from those extracted with charged lepton probes [4, 6]. At variance with these results, Ref. [5] confronts the neutrino DIS cross sections with nPDFs obtained in [3] without any refitting and finds no apparent disagreement.

The novel global QCD analysis of nPDFs presented here [7] incorporates in a comprehensive way all of the above mentioned improvements and data sets. The resulting nPDFs at next-to-leading order accuracy supersede previous work presented in [1]. We adopt a contemporary set of free nucleon PDFs [8] as our reference distribution to quantify modifications of PDFs in nuclei. As in [8], we use a general mass variable flavor number scheme to treat charm and bottom quark contributions in our analysis. We use the Hessian method [9] to estimate the uncertainties of the nuclear modification factors and examine critically their range of validity.

2 Framework

Throughout the analysis, we make the usual assumption that theoretical expressions for measured cross sections involving a nucleus factorize into calculable partonic hard scattering cross sections, identical to those used for processes involving free nucleons, and appropriate combinations of non-perturbative collinear parton densities and fragmentation functions. The nPDFs $f_i^A(x,Q_0)$ at an initial scale $Q_0 = 1\,\mathrm{GeV}$ are related to proton distributions $f_i^p(x,Q_0)$ through a multiplicative nuclear modification factor $R_i^A(x,Q_0)$ as

$$f_i^A(x,Q_0) = R_i^A(x,Q_0)\, f_i^p(x,Q_0)\,, \tag{1}$$

where x is the usual DIS scaling variable for free nucleons. Both valence quark distributions are assigned the same nuclear modification factor $R_v^A(x,Q_0^2)$ which we parametrize as

$$R_v^A(x,Q_0^2) = \epsilon_1\, x^{\alpha_v}(1-x)^{\beta_1}\,(1+\epsilon_2(1-x)^{\beta_2})\,(1+a_v(1-x)^{\beta_3})\,. \tag{2}$$

We also assume that the light sea quarks and antiquarks share the same correction factor $R_s^A(x,Q_0^2)$. No significant improvement in the quality of the fit to data is found by relaxing this assumption. We choose another factor $R_g^A(x,Q_0^2)$ to parametrize medium effects for gluons. An excellent description of the data is achieved by relating both R_s^A and R_g^A to R_v^A specified in Eq. (2), allowing only for a different normalization and modifications in the low-x behavior. Hence we choose, without any loss in the quality of the fit,

$$R_s^A(x,Q_0^2) = R_v^A(x,Q_0^2)\,\frac{\epsilon_s}{\epsilon_1}\,\frac{1+a_s x^{\alpha_s}}{a_s+1}\,, \qquad R_g^A(x,Q_0^2) = R_v^A(x,Q_0^2)\,\frac{\epsilon_g}{\epsilon_1}\,\frac{1+a_g x^{\alpha_g}}{a_g+1}\,. \tag{3}$$

We note that the coefficients ϵ_1 and ϵ_2 in Eq. (2) are fixed by charge conservation, and if we further constrain ϵ_s and ϵ_g to be equal, which, again, has no impact on the quality of the fit, ϵ_s is fixed by momentum conservation. The A dependence of the remaining free parameters $\xi \in \{\alpha_v, \alpha_s, \alpha_g, \beta_1, \beta_2, \beta_3, a_v, a_s, a_g\}$ is parametrized in the usual way [1] as $\xi = \gamma_\xi + \lambda_\xi A^{\delta_\xi}$. The very mild A dependence found for some of the ξ's allows us to further reduce the number of additional parameters by setting $\delta_{a_g} = \delta_{a_s}$ and $\delta_{\alpha_g} = \delta_{\alpha_s}$, leaving a total of 25 free parameters, which are obtained by a standard χ^2 minimization, without artificial weights for certain data sets, i.e. $\omega_i = 1$, and with statistical and systematic errors added in quadrature in Δ_i^2:

$$\chi^2 \equiv \sum_i \omega_i\,\frac{(d\sigma_i^{\mathrm{exp}} - d\sigma_i^{\mathrm{th}})^2}{\Delta_i^2} \tag{4}$$

3 Results

The total χ^2 for the optimum fit was found to be 1544.7 for 1579 data points ($\chi^2/d.o.f. = 0.994$). All data sets are adequately reproduced, well within the nominal statistical range $\chi^2 = n \pm \sqrt{2n}$ with n the number of data. More specifically, the partial contribution to χ^2 of all the charged lepton DIS data amounts to 897.52 units for 894 data points, for neutrino DIS we find 488.20 units compared to 532 data points, DY observables amount to 90.72 units for 92 points, and pion production in dAu collisions adds another 68.26 units to χ^2 for 61 data points.

In Figs. 1-3 we show some examples of the good agreement between the fit and charged lepton DIS, neutrino DIS, and hadroproduction data, respectively; see Ref. [7] for details. The remarkable agreement with charged lepton DIS data, shown in Fig. 1, is a common feature of all nPDFs analyses.

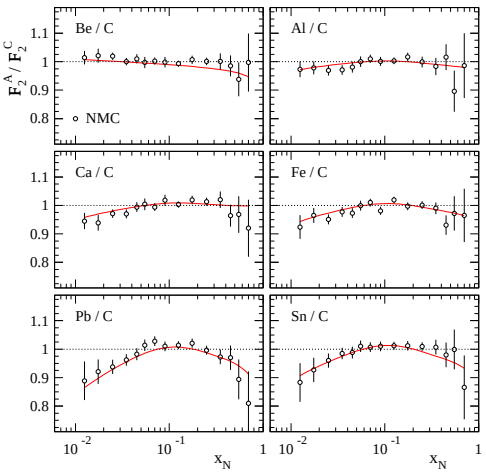

Figure 1: Comparison to charged lepton DIS

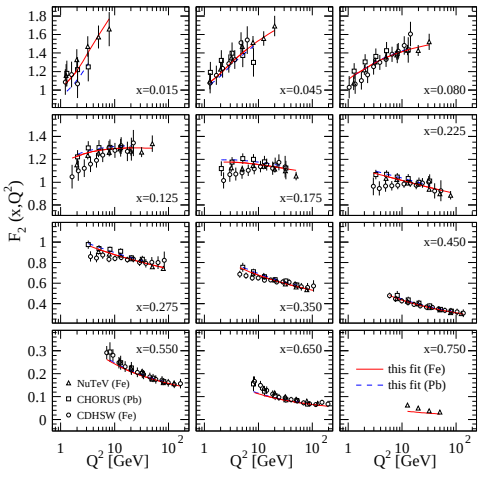

Figure 2: Comparison to neutrino DIS data

Neutrino DIS data for the averaged structure function $(F_2^{\nu A} + F_2^{\bar{\nu} A})/2$ are well reproduced within the experimental uncertainties both in shape and in magnitude, see Fig. 2. The only noticeable exception are the CDHSW data at Q^2 values below $10\,\mathrm{GeV}^2$ where they exhibit a rather different slope than the other data. In fact, in this Q^2 region it appears to be impossible to simultaneously fit all data sets equally well, suggesting some systematic discrepancy among the different neutrino data which needs to be investigated further. Data for the averaged structure function F_3 are also well described by our fit [7].

In general, results from dAu collisions are significantly less straightforward to interpret in terms of nuclear modification factors. Each value of p_T samples different fractions of the contributing partonic hard scattering processes, integrated over a range of x. Furthermore, since p_T sets the magnitude for the factorization scale, the ratios reflect also the energy scale dependence of the effects. Apart from the nuclear modifications of parton densities, accounted for by the nPDFs, the cross sections are in principle also sensitive to medium induced effects in the hadronization process.

Assuming factorizability for a given nucleus, such final-state effects can be absorbed into effective nuclear parton-to-hadron fragmentation functions (nFFs). The solid lines in Fig. 3 represent the result of our best fit of nPDFs using the nFFs of Ref. [10]. The fit follows well the

rise and fall of the ratio at small and high p_T, respectively, but falls somewhat short in reproducing the enhancement found at medium p_T. Owing to the large experimental uncertainties, the χ^2 for this subset of data is nevertheless good, $\chi^2_{dAu}/n = 1.12$, in particular, if compared to the outcome of an otherwise similar fit using vacuum FFs [11] where $\chi^2_{dAu}/n = 1.37$. Data for π^0 yields in dAu collisions were first incorporated by EPS [3] and found to provide a vital constraint on R_g^{Au}. At variance with our approach, the authors in [3] disregard any medium modifications in the hadronization and assign a large weight ω_{dAu} in Eq. (4), which drives their observed large nuclear modifications of the gluon density. Our R_g^{Au} exhibits only moderate nuclear corrections.

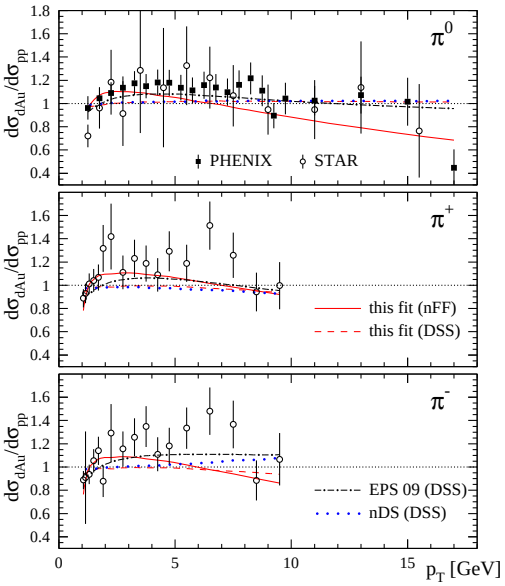

Figure 3: Pion production in dAu collisions

Uncertainties in the extraction of our nPDFs have been estimated with the Hessian method [9] for a tolerance criterion of $\Delta\chi^2 = 30$ and found to be rather large [7], in particular, when compared to the present knowledge of free proton PDFs. As always, these estimates are only trustworthy in the region constrained by data, i.e., $x > 0.01$. In particular, prompt photon and DY di-lepton production in dAu and pPb collisions at RHIC and the LHC, respectively, will help to further constrain nPDFs in the future; see, e.g., Ref. [7] for some quantitative expectations.

Acknowledgements

M.S. acknowledges support by the U.S. DOE under contract no. DE-AC02-98CH10886. This work was supported in part by CONICET, ANPCyT, UBACyT, and the E.U. under grant no. PITN-GA-2010-264564 (LHCPhenoNet).

References

[1] D. de Florian and R. Sassot, Phys. Rev. **D69** (2004) 074028.
[2] M. Hirai, S. Kumano, and T. H. Nagai, Phys. Rev. **C76** (2007) 065207.
[3] K. J. Eskola, H. Paukkunen, and C. A. Salgado, JHEP **0904** (2009) 065.
[4] I. Schienbein *et al.*, Phys. Rev. **D77** (2008) 054013; **D80** (2009) 094004.
[5] H. Paukkunen and C. A. Salgado, JHEP **1007** (2010) 032.
[6] K. Kovarik *et al.*, Phys. Rev. Lett. **106** (2011) 122301.
[7] D. de Florian, R. Sassot, M. Stratmann, and P. Zurita, arXiv:1112.6324 and references therein.
[8] A. D. Martin, W. J. Stirling, R. S. Thorne, and G. Watt, Eur. Phys. J. **C63** (2009) 189.
[9] J. Pumplin *et al.*, Phys. Rev. **D65** (2001) 014011; Phys. Rev. **D65** (2001) 014013.
[10] R. Sassot, M. Stratmann, and P. Zurita, Phys. Rev. **D81** (2010) 054001.
[11] D. de Florian, R. Sassot, and M. Stratmann, Phys. Rev. **D75** (2007) 114010.

Update and Comparison of Nuclear Parton Distribution Functions and Neutrino DIS.

K. Kovařík

Institute for Theoretical Physics, Karlsruhe Institute of Technology, Karlsruhe, 76128,Germany

DOI: http://dx.doi.org/10.3204/DESY-PROC-2012-02/155

We compare the nuclear corrections factors from neutrino deep-inelastic scattering (DIS) with the ones coming from a standard analysis of nuclear parton distribution functions (nPDF). We focus on a discrepancy between the most precise neutrino DIS data from NuTeV and the nuclear PDF coming from the analysis of charged lepton DIS and Drell-Yan data.

1 Introduction

An indispensable part of any prediction for a process measured at a hadron collider such as the LHC are the parton distribution functions (PDFs). Because of the importance of PDFs, many groups perform and update global analyses of PDFs for protons [1, 2, 3] and for nuclei [4, 5, 6]. Proton PDF are determined from data taken not only on protons but from some data taken on nuclear targets, mainly deuterium but also heavy nuclei such as lead and iron in case of neutrino DIS. Neutrino DIS data is sensitive to the strange quark content of the proton and complements newly available LHC data from W- or Z-boson production.

In order to include the neutrino DIS data in a global fit to help constrain the proton PDF, we have to apply a nuclear correction factor. The nuclear correction factor can be obtained either from a specific model of nuclear interactions or from an analysis of nuclear parton distribution functions (NPDF) based on experimental data.

Here, we discuss a compatibility of neutrino DIS data with the nuclear correction factors obtained from NPDF analysis focusing on the neutrino DIS data from the NuTeV experiment.

2 Nuclear correction factors from nuclear PDF

Nuclear correction factors are in general defined as a ratio of an observable in a nuclear process and the same observable in a process involving protons. In the following, we discuss two nuclear correction factors both related either to the F_2 structure function in neutrino DIS

$$R^{\nu}_{CC}(F_2; x, Q^2) \simeq \frac{d^A + \bar{u}^A + \ldots}{d^{A,0} + \bar{u}^{A,0} + \ldots}\,, \tag{1}$$

or to the F_2 structure function in charged lepton DIS

$$R^{e,\mu}_{NC}(F_2; x, Q^2) \simeq \frac{[d^A + \bar{d}^A + \ldots] + 4[u^A + \bar{u}^A + \ldots]}{[d^{A,0} + \bar{d}^{A,0} + \ldots] + 4[u^{A,0} + \bar{u}^{A,0} + \ldots]}\,. \tag{2}$$

The superscript '0′ stands for using the free nucleon PDFs $f_i^{p,n}(x,Q)$ as given below in Eq. (5).

Nuclear correction factors such as those defined by Eqs. 1,2 can be either extracted from the data or calculated using the extracted parton distribution functions. Here we use the nuclear PDF from [7] and [8] where the parameterizations of the nuclear parton distributions of partons in bound protons at the input scale of $Q_0 = 1.3$ GeV are

$$\begin{aligned} x\, f_k(x,Q_0) &= c_0 x^{c_1}(1-x)^{c_2} e^{c_3 x}(1+e^{c_4}x)^{c_5}\,, \\ \bar{d}(x,Q_0)/\bar{u}(x,Q_0) &= c_0 x^{c_1}(1-x)^{c_2} + (1+c_3 x)(1-x)^{c_4}\,, \end{aligned} \tag{3}$$

where $f_k = u_v, d_v, g, \bar{u}+\bar{d}, s, \bar{s}$ and $\bar{u}, \bar{d}$ are a generalization of the parton parameterizations in free protons used in the CTEQ proton analysis [9]. To account for different nuclear targets, the coefficients c_k are made to be functions of the nucleon number A

$$c_k \to c_k(A) \equiv c_{k,0} + c_{k,1}\left(1 - A^{-c_{k,2}}\right),\ k = \{1,\ldots,5\}\,. \tag{4}$$

From the input distributions, we can construct the PDFs for a general (A,Z)-nucleus

$$f_i^{(A,Z)}(x,Q) = \frac{Z}{A}\, f_i^{p/A}(x,Q) + \frac{(A-Z)}{A}\, f_i^{n/A}(x,Q), \tag{5}$$

where we relate the distributions of a bound neutron, $f_i^{n/A}(x,Q)$, to those of a proton by isospin symmetry.

In the analysis, the same standard kinematic cuts $Q > 2$ GeV and $W > 3.5$ GeV were applied as in [9] and we obtain a fit with χ^2/dof of 0.946 to 708 data points with 32 free parameters (for further details see [7]). In Fig. 1 (solid line), we show how the result of our global analysis

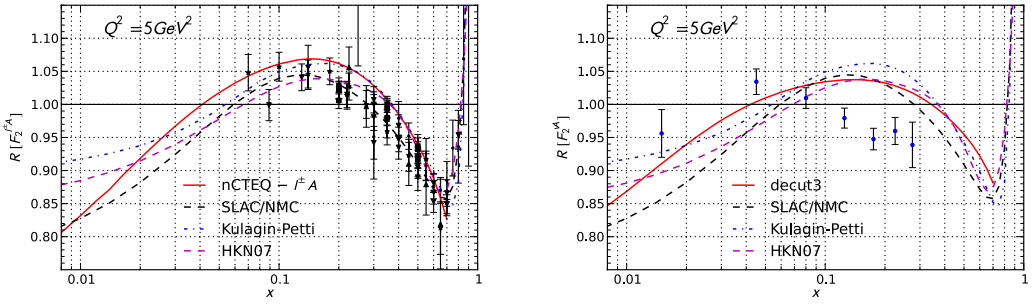

Figure 1: Nuclear correction factors $R_{NC}^{e,\mu}(F_2;x,Q^2)$ and $R_{CC}^{\nu}(F_2;x,Q^2)$ from the global NPDF analysis compared with the corresponding data for iron target.

of charged lepton data translates into nuclear correction factors and how the nuclear correction factors compare with experimental data. As first observed in [10], the $R_{CC}^{\nu}(F_2;x,Q^2)$ correction factor calculated using Eq. 1 with parton densities from the fit to the charged lepton nuclear data, does not describe the NuTeV data well which raises the question if including neutrino DIS data in the global analysis corrects this behavior without spoiling the $R_{NC}^{e,\mu}(F_2;x,Q^2)$ correction factor which fits the charged lepton DIS and DY data well.

w	$\chi^2_{l^\pm A}$ (/pt)	$\chi^2_{\nu A}$ (/pt)	total χ^2(/pt)
0	638 (0.90)	-	638 (0.90)
1/7	645 (0.91)	4710 (1.50)	5355 (1.39)
1/2	680 (0.96)	4405 (1.40)	5085 (1.32)
1	736 (1.04)	4277 (1.36)	5014 (1.30)
∞	-	4192 (1.33)	4192 (1.33)

Table 1: Summary table of a family of compromise fits.

3 Neutrino DIS

To analyze the possible discrepancy between the nuclear correction factor $R^{\nu}_{CC}(F_2; x, Q^2)$ from the fit to charged lepton data and the neutrino DIS data, we have included the NuTeV and Chorus neutrino DIS cross-section data in the global fit. The 3134 neutrino DIS cross-section data points would clearly dominate 708 charged lepton data in the global fit. That is why, we have introduced the weight to the neutrino data and set up a series of fits in order to find a compromise fit. χ^2/dof for each compromise fit with a different weight of neutrino DIS data is listed in Tab. 1. Each global fit with a different weight results in a different nuclear correction factor and in Fig. 2 we see that the weight is a suitable parameter which interpolates between the fit using only charged lepton data and the fit using only neutrino data (for further details see [8]). In order to decide on how well the compromise fits describe the data we use the χ^2

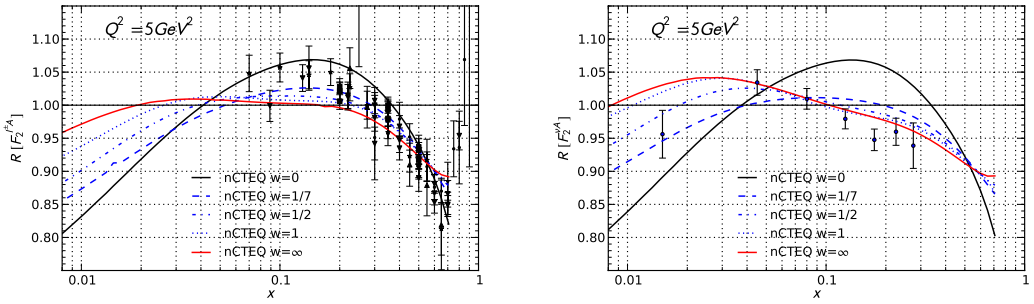

Figure 2: Nuclear correction factors $R^{e,\mu}_{NC}(F_2; x, Q^2)$ and $R^{\nu}_{CC}(F_2; x, Q^2)$ for all fits in Tab. 1.

goodness-of-fit criterion used in [11, 2]. We consider a fit a good compromise if its χ^2 for both data subsets, the charged lepton DIS and DY data and the neutrino DIS data, is within 90% confidence level of the fits to only charged lepton or neutrino data.

We define the 90% percentile ξ_{90} used to define the 90% confidence level, by

$$\int_0^{\xi_{90}} P(\chi^2, N) d\chi^2 = 0.90\,, \tag{6}$$

where N is the number of degrees of freedom and $P(\chi^2, N) = \frac{(\chi^2)^{N/2-1} e^{-\chi^2/2}}{2^{N/2}\Gamma(N/2)}$ is the probability distribution. We can assign a 90% confidence level error band to the χ^2 of the fits to the charged lepton DIS and DY data and to the neutrino DIS data. By looking at the overall χ^2/dof values

and at the plots in Fig. 2, one might conclude that the global fit with $w = 1/2$ describes both data well to constitute a compromise fit. The conclusion changes however when we inspect separate contributions to the χ^2/dof from different experiments. The change in global χ^2 is mostly due to change in χ^2 of the DIS scattering on iron which makes all the compromise fits incompatible. The conclusion about incompatibility of the fits rests on NuTeV data having

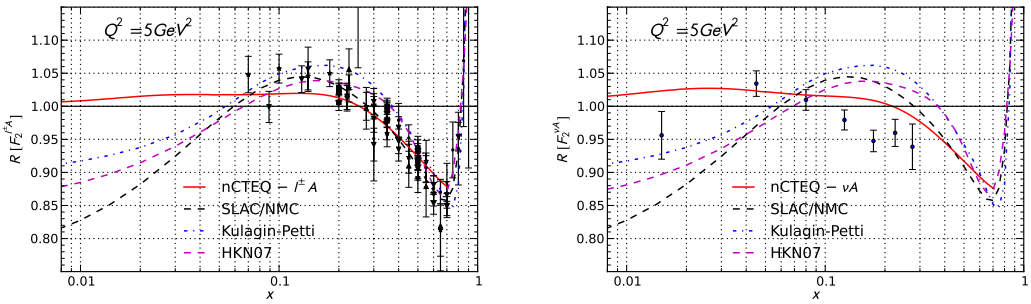

Figure 3: Nuclear correction factors $R^{e,\mu}_{NC}(F_2; x, Q^2)$ and $R^{\nu}_{CC}(F_2; x, Q^2)$ where neutrino data were included with uncorrelated systematic errors.

small errors which can be demonstrated by neglecting the correlations in systematic errors which results in a compatible fit of all the data (see Fig. 3).

4 Conclusion

A thorough global NPDF analysis of the combined charged lepton and neutrino data leads us to conclude that there is no good compromise description of both the data sets simultaneously. The differences can be seen in the low and intermediate x regions where the neutrino DIS (NuTeV) do not show a strong shadowing effect as the charged lepton data do. The inability to describe all data by one consistent framework poses problems for including the NuTeV data to the proton PDF analysis.

References

[1] R. D. Ball *et al.* Nucl. Phys. **B823** (2009) 195–233, arXiv:0906.1958 [hep-ph].

[2] A. D. Martin, W. J. Stirling, R. S. Thorne, and G. Watt. Eur. Phys. J. **C63** (2009) 189–285, arXiv:0901.0002 [hep-ph].

[3] P. M. Nadolsky *et al.* Phys. Rev. **D78** (2008) 013004, arXiv:0802.0007 [hep-ph].

[4] M. Hirai, S. Kumano, and T. H. Nagai. Phys. Rev. **C76** (2007) 065207, arXiv:0709.3038 [hep-ph].

[5] K. J. Eskola, H. Paukkunen, and C. A. Salgado. JHEP **04** (2009) 065, arXiv:0902.4154 [hep-ph].

[6] D. de Florian, R. Sassot, P. Zurita, and M. Stratmann. Phys.Rev. **D85** (2012) 074028, arXiv:1112.6324 [hep-ph].

[7] I. Schienbein *et al.* Phys. Rev. **D80** (2009) 094004, arXiv:0907.2357 [hep-ph].

[8] K. Kovařík *et al.* Phys.Rev.Lett. **106** (2010) 122301, arXiv:1012.0286 [hep-ph].

[9] J. Pumplin *et al.* JHEP **07** (2002) 012, hep-ph/0201195.

[10] I. Schienbein *et al.* Phys. Rev. **D77** (2008) 054013, arXiv:0710.4897 [hep-ph].

[11] D. Stump *et al.* Phys. Rev. **D65** (2001) 014012, arXiv:hep-ph/0101051.

Using the BFKL resummation to fit DIS data: collinear and running coupling effects

Martin Hentschinski, Agustín Sabio Vera, Clara Salas

Instituto de Física Teórica UAM/CSIC, U. Autónoma de Madrid, E-28049 Madrid, Spain

DOI: http://dx.doi.org/10.3204/DESY-PROC-2012-02/97

The proton structure function F_2 is studied in the low x regime using BFKL evolution. The next to leading logarithmic (NLL) analysis requires the inclusion of running coupling effects which lead to off-diagonal terms in the evolution kernel. An all-orders resummation is used to improve the collinear behavior of the NLL BFKL result. We emphasize the theoretical uncertainties that appear throughout the analysis and give a comparison to the combined HERA data.

1 Introduction

In 2010 HERA made public the combined results [1] obtained by H1 [2] and ZEUS [3] Collaborations for the proton structure function $F_2(x, Q^2)$ at low values of the Bjorken x variable and a quite broad range of values of the photon virtuality Q^2. This observable became specially convenient to test the region of applicability of the theory based on the high energy or Regge limit, which corresponds to the center of mass energy of the system $\sqrt{s}$ being asymptotically larger than any other scale involved. In Deep Inelastic Scattering (DIS) a hard scale is provided by the high virtuality of the photon. Since the x variable is given within very good approximation by the ratio between the photon virtuality and the center of mass energy squared, we can refer to the Regge limit as the limit of low Bjorken x. In this regime large logarithms of energy appear, dominating the scattering amplitude, and they need to be resummed to all orders. Such a resummation is achieved by the so-called BFKL evolution equation [4–8].

The aim of the present study is to analyze the theoretical uncertainties encountered in the determination of F_2 at NLL accuracy using high energy factorization [9]. Care has to be taken when introducing running coupling effects and it is also needed to resum to all orders the leading collinear singularities which are numerically large in this kinematical region [10–14]. Concerning the running of the coupling, we compare the results obtained using a running with a Landau pole with a model which freezes in the infrared and is compatible with power corrections to jet observables [15]. A numerical analysis of the gluon Green function in the kinematic region of interest is provided. We conclude with a preliminary comparison of our theoretical calculation for F_2 with HERA data.

2 Analyzing the proton structure function

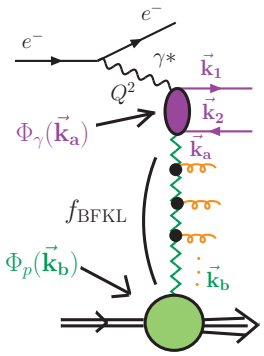

Figure 1

High energy factorization allows to write the proton structure function as a convolution in transverse momentum space of a nonperturbative object describing the proton (proton impact factor Φ_p) with the photon (photon impact factor Φ_γ), calculated using perturbation theory, together with a gluon Green function f, linking both process-dependent components and accounting for the BFKL evolution:

$$F_2(x,Q^2) = \frac{F_c}{(2\pi)^4}\int \frac{\mathrm{d}^2\mathbf{k}_a}{\mathbf{k}_a^2}\int \frac{\mathrm{d}^2\mathbf{k}_b^2}{\mathbf{k}_b}\Phi_\gamma(\mathbf{k}_a)\, f(x,\mathbf{k}_a,\mathbf{k}_b)\,\Phi_p(\mathbf{k}_b)\ .$$

Fig. 1 shows the different parts involved. Although an analytic expression for the photon impact factor at next to leading order accuracy [16–18] has been recently calculated [19] we use for simplicity in our analysis the leading order result as presented in [20]. The proton impact factor needs to be modeled. Our results are based on a simple choice which introduces just a few parameters to be determined by the experiment and it presents a Poissonian-like distribution in transverse momentum space with its maximum around the confinement scale. Finally, the gluon Green function is governed by the BFKL equation. Its LL solution is smooth and convergent but not sufficient to explain the DIS data. The first attempt to have a good description of F_2 would consist on studying the next order of accuracy. However it is known that the NLL kernel is unstable in collinear regions. We have found that by introducing an all-orders collinear resummation consistent with the NLL solution following the procedure given in [14] we not only eliminate the collinear instabilities but also get a good preliminary description of the data. Figs. 2 and 3 compare the LL gluon Green function to the collinearly improved one. Since this formalism does not modify the NLL results but only gives higher order corrections there is certain freedom in the way of performing the resummation. In the present analysis we use an expression for the NLL eigenvalues which includes the action on the impact factors of the differential operators breaking the scale invariance of the kernel.

At NLL accuracy one needs to account for the running of the coupling. This gives an analytical expression for the kernel which contains a differential operator in the Mellin variable γ [21]. There is in principle no theoretical restriction (other than having an hermitian hamiltonian) on whether to act with this operator in a symmetric way [22], *i.e.* on both proton and photon impact factors or in an asymmetric way (only on one of them). Nevertheless, it turns out that each option produce very different results, as shown in fig. 2. The reason for this is that each of them naturally leads to a different scale for the running coupling due to the scale of the logarithm accompanying the term in β_0 of the kernel, responsible for the running. This is, however, an assumption about higher order terms again. We could have decided to leave the logarithms without absorbing them into the expression for the running coupling. We have also compared the results obtained for two different models of the running, a perturbative one, with a Landau pole, and the one presented in [15] and described

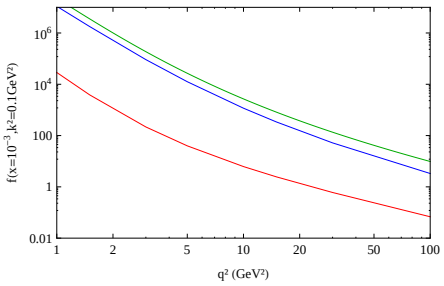

Figure 2: Action of the differential operator. Upper curve: LL; mid curve: asymmetric differential operator acting on the photon; and lower curve: symmetric choice.

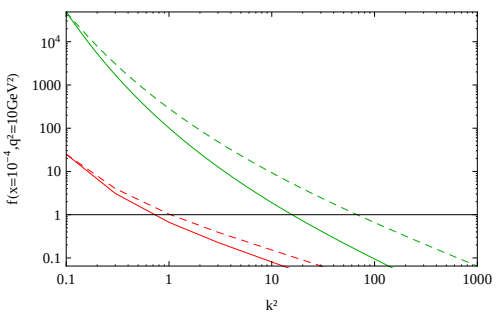

(a) Dependence on $\mathbf{k}^2$ for $s_0 = Q^2$ (solid lines) and $s_0 = kq$ (dashed lines) at LL (upper set, green) and NLL collinear improved (lower set, red) accuracy.

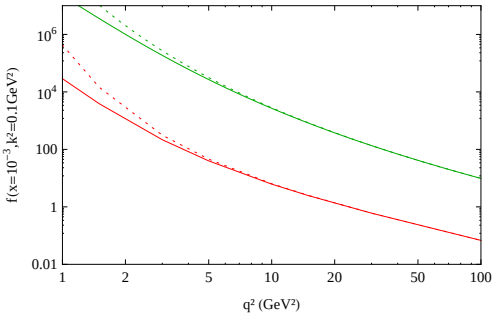

(b) Dependence on the model for the running: the solid lines correspond to the IR finite running and the dotted ones to the perturbative one at LL (upper set, green) and NLL collinear improved (lower set, red) accuracy.

Figure 3: Numerical analysis of the gluon Green function.

earlier in the introduction. However, as it can be seen in fig. 3b we are studying a region in which these are minor effects, since we ask the transverse scale to be perturbative.

The last important point of discussion in this analysis is what to do with the choice of energy scale s_0 appearing in the gluon Green function:

$$f(s,\mathbf{k},\mathbf{q}) = \frac{1}{2\pi^2}\sum_n \int_{-\infty}^{\infty} \mathrm{d}\nu \int_{\delta-i\infty}^{\delta+i\infty} \frac{\mathrm{d}\omega}{2\pi i}\, \frac{\mathrm{e}^{\mathrm{in}(\theta_\mathrm{q}-\theta_\mathrm{k})}}{\omega - \mathcal{K}(\bar{\alpha}_s, 1/2+i\nu)}\, \frac{1}{\mathbf{q}^2}\left(\frac{\mathbf{q}^2}{\mathbf{k}^2}\right)^{1/2+i\nu}\left(\frac{s}{s_0}\right)^{\omega} .$$

It is known that any dependence of the cross section on this scale must cancel at NLL accuracy. However, if we want to express f as a function of x a shift in ω is produced leading to a remaining dependence on it that appear as higher order corrections. A natural choice in this case would be the DIS scale, $s_0 = Q^2$, so that $(s/s_0)^\omega = x^{-\omega}$. The symmetric choice as a product of the internal scales $s_0 = kq$ was used to calculate the NLL BFKL solution [21]. As it can be seen in fig. 3a there is a difference in the results obtained with each version.

Figure 4 shows one of the possible preliminary fits that can be done of F_2 within this theoretical framework. In particular, a symmetric version of the differential operator has been used together with the symmetric energy scale $s_0 = kq$, the perturbative running coupling and proton impact factor given by

$$\Phi_p(\mathbf{k}^2) = A\left(\mathbf{k}^2/Q_0^2\right)^\delta \mathrm{e}^{\mathbf{k}^2/\mathrm{Q}_0^2} .$$

The expression for the photon impact factor used can be found in [23].

A detailed analysis of the work here presented can be found in [24].

Acknowledgements

The European Comission (LHCPhenoNet PITN-GA-2010-264564) is acknowledged for funding the expenses of the conference.

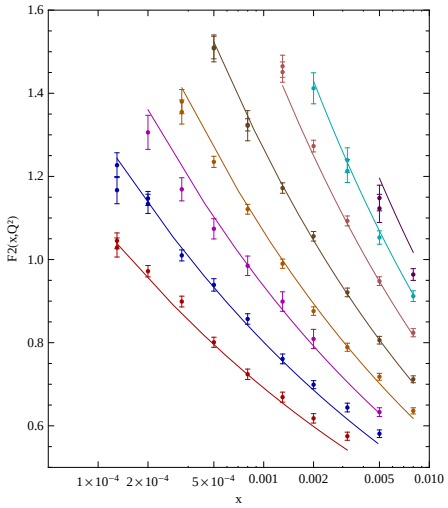

Figure 4: Preliminary fit to F_2 with $\delta = 1.246$, $Q_0^2 = 0.368\text{GeV}^2$ and $A_p = 0.07346$.

References

[1] F. Aaron *et al.* JHEP **1001** (2010) 109, arXiv:0911.0884 [hep-ex].

[2] T. Ahmed *et al.* Nucl.Phys. **B439** (1995) 471–502, arXiv:hep-ex/9503001 [hep-ex].

[3] M. Derrick *et al.* Z.Phys. **C69** (1996) 607–620, arXiv:hep-ex/9510009 [hep-ex].

[4] V. S. Fadin, E. Kuraev, and L. Lipatov. Phys.Lett. **B60** (1975) 50–52.

[5] L. Lipatov. Sov.J.Nucl.Phys. **23** (1976) 338–345.

[6] E. Kuraev, L. Lipatov, and V. S. Fadin. Sov.Phys.JETP **44** (1976) 443–450.

[7] E. Kuraev, L. Lipatov, and V. S. Fadin. Sov.Phys.JETP **45** (1977) 199–204.

[8] I. Balitsky and L. Lipatov. Sov.J.Nucl.Phys. **28** (1978) 822–829.

[9] S. Catani, M. Ciafaloni, and F. Hautmann. Nucl.Phys. **B366** (1991) 135–188.

[10] G. Salam. JHEP **9807** (1998) 019, arXiv:hep-ph/9806482 [hep-ph].

[11] M. Ciafaloni, D. Colferai, and G. Salam. Phys.Rev. **D60** (1999) 114036, arXiv:hep-ph/9905566 [hep-ph].

[12] M. Ciafaloni, D. Colferai, G. Salam, and A. Stasto. Phys.Rev. **D68** (2003) 114003, arXiv:hep-ph/0307188 [hep-ph].

[13] G. Altarelli, R. D. Ball, and S. Forte. Nucl.Phys. **B742** (2006) 1–40, arXiv:hep-ph/0512237 [hep-ph].

[14] A. Sabio Vera. Nucl.Phys. **B722** (2005) 65–80, arXiv:hep-ph/0505128 [hep-ph].

[15] B. R. Webber. JHEP **9810** (1998) 012, arXiv:hep-ph/9805484 [hep-ph].

[16] V. Fadin, D. Y. Ivanov, and M. Kotsky. Nucl.Phys. **B658** (2003) 156–174, arXiv:hep-ph/0210406 [hep-ph].

[17] J. Bartels, D. Colferai, S. Gieseke, and A. Kyrieleis. Phys.Rev. **D66** (2002) 094017, arXiv:hep-ph/0208130 [hep-ph].

[18] I. Balitsky and G. A. Chirilli. Phys.Rev. **D83** (2011) 031502, arXiv:1009.4729 [hep-ph].

[19] G. Chirilli *et al.* To appear in the proceedings of DIS 2012 .

[20] J. R. Forshaw and D. Ross. Cambridge Lect.Notes Phys. **9** (1997) 1–248.

[21] A. Kotikov and L. Lipatov. Nucl.Phys. **B582** (2000) 19–43, arXiv:hep-ph/0004008 [hep-ph].

[22] F. Schwennsen. arXiv:hep-ph/0703198 [HEP-PH].

[23] A. Bialas, H. Navelet, and R. B. Peschanski. Nucl.Phys. **B603** (2001) 218–230, arXiv:hep-ph/0101179 [hep-ph].

[24] G. Chachamis, M. Hentschinski, A. Sabio Vera, and C. Salas. In preparation .

Determination of transverse momentum dependent gluon density from HERA structure function measurements

Hannes Jung[1,2], *Francesco Hautmann*[3]

[1]DESY, Notkestraße 85, 22607 Hamburg, Germany
[2]CERN, 1211 Genève 23, Switzerland
[3]Theoretical Physics Department, University of Oxford, Oxford OX1 3NP, GB

DOI: `http://dx.doi.org/10.3204/DESY-PROC-2012-02/29`

The transverse momentum dependent gluon density obtained with CCFM evolution is determined from a fit to the latest combined HERA structure function measurements.

1 Introduction

The combined measurements of the structure function at HERA [1] allow the determination of parton distribution functions to be carried out to high precision. While these data have been used to determine the collinear parton densities, the transverse momentum distributions (TMD) or unintegrated gluon distributions were only based on older and much less precise measurements [2, 3].

In high energy factorization [4] the cross section is written as a convolution of the partonic cross section $\hat{\sigma}(k_t)$ which depends on the transverse momentum k_t of the incoming parton with the k_t-dependent parton density function $\tilde{\mathcal{A}}(x, k_t, p)$:

$$\sigma = \int \frac{dz}{z} d^2k_t \hat{\sigma}(\frac{x}{z}, k_t) \tilde{\mathcal{A}}(x, k_t, p) \tag{1}$$

where p is the factorization scale. The evolution of $\tilde{\mathcal{A}}(x, k_t, p)$ can proceed via the BFKL, DGLAP or via the CCFM evolution equations. Here, an extension of the CCFM evolution is applied (to be also used in the parton shower Monte Carlo event generator CASCADE [5]) which includes the use of two loop α_s as well as applying a consistency constraint [6, 7, 8] in the $g \to gg$ splitting function [9]:

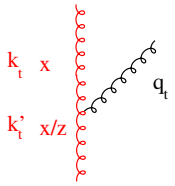

Figure 1: Gluon branching

$$P_{gg}(z, p, k_t) = \bar{\alpha}_s\left(k_t^2\right)\left(\frac{(1-z)}{z} + \frac{z(1-z)}{2}\right)\Delta_{ns} + \bar{\alpha}_s(p^2)\left(\frac{z}{1-z} + \frac{z(1-z)}{2}\right), \tag{2}$$

with Δ_{ns} being the non-Sudakov form factor. The consistency constraint is given by [6] (see Fig. 1):

$$q_t^2 < \frac{(1-z)k_t^2}{z} \tag{3}$$

2 Evolution

Since the CCFM evolution cannot be easily written in an analytic closed form, a Monte Carlo method, based on [10, 11], is used. However, the Monte Carlo solution is time consuming, and cannot be used in a straightforward way in a fit program. For a realistic solution, first a kernel $\tilde{\mathcal{A}}(x'', k_t, p)$ is determined from the MC solution of the CCFM evolution equation, and then is folded with the non-perturbative starting distribution $\mathcal{A}_0(x)$:

$$x\mathcal{A}(x,k_t,p) = x\int dx' \int dx'' \mathcal{A}_0(x)\tilde{\mathcal{A}}(x'',k_t,p)\,\delta(x'\cdot x''-x) \quad (4)$$

$$= \int dx' \int dx'' \mathcal{A}_0(x)\tilde{\mathcal{A}}(x'',k_t,p)\,\frac{x}{x'}\delta(x''-\frac{x}{x'}) \quad (5)$$

$$= \int dx' \mathcal{A}_0(x')\cdot\frac{x}{x'}\tilde{\mathcal{A}}\left(\frac{x}{x'},k_t,p\right) \quad (6)$$

The kernel $\tilde{\mathcal{A}}$ includes all the dynamics of the evolution, Sudakov form factors and splitting functions and is determined in a grid of $50\otimes 50\otimes 50$ bins in x, k_t, p.

The calculation of the cross section according to eq.(1) involves a multidimensional Monte Carlo integration which is time consuming and suffers from numerical fluctuations, and cannot be used directly in a fit procedure involving the calculation of numerical derivates in the search for the minimum. Instead the following procedure is applied:

$$\sigma_r(x,Q^2) = \int_x^1 dx_g \mathcal{A}(x_g,k_t,p)\hat{\sigma}(x,x_g,Q^2) \quad (7)$$

$$= \int dx_g\, dx'\, dx'' \mathcal{A}_0(x')\tilde{\mathcal{A}}(x'',k_t,p)\cdot\hat{\sigma}(x,x_g,Q^2)\cdot\delta(x'\,x''-x_g) \quad (8)$$

$$= \int dx'\, dx'' \mathcal{A}_0(x')\cdot\tilde{\mathcal{A}}(x'',k_t,p)\cdot\hat{\sigma}(x,x'\,x'',Q^2) \quad (9)$$

$$= \int_x^1 dx' \mathcal{A}_0(x')\cdot\int_{x/x'}^1 dx''\tilde{\mathcal{A}}(x'',k_t,p)\cdot\hat{\sigma}(x,x'\,x'',Q^2) \quad (10)$$

$$= \int_x^1 dx' \mathcal{A}_0(x')\cdot\tilde{\sigma}(x/x',Q^2) \quad (11)$$

Here, first $\tilde{\sigma}(x',Q^2)$ is calculated numerically with a Monte Carlo integration on a grid in x for the values of Q^2 used in the fit. Then the last step (i.e. eq.(11)) is performed with a fast numerical gauss integration, which can be used in standard fit procedures.

The fit to the HERA structure function measurements is performed applying the `herafitter` program [1, 12, 13] to determine the parameters of the starting distribution $\mathcal{A}_0$ at the starting scale Q_0:

$$x\mathcal{A}_0(x,k_t) = Nx^{-B_g}\cdot(1-x)^{C_g}(1-D_g x) \quad (12)$$

3 Fit to HERA structure function

The parameters N, B_g, C_g, D_g in eq.(12) are determined from a fit to the combined structure function measurement [1] in the range $x < 0.01$ and $Q^2 > 5$ GeV. In addition to the gluon

induced process $\gamma^* g^* \to q\bar{q}$ the contribution from valence quarks is included via $\gamma^* q \to q$ using a CCFM evolution of valence quarks as described in [14]. The results presented here are obtained with the `herafitter` package, treating the correlated systematic uncertainties separately from the uncorrelated statistical and systematic uncertainties. To obtain a reasonable fit to the structure function data, the starting scale Q_0 as well as Λ_{qcd} has been varied. An acceptable χ^2/ndf could only be achieved when applying the consistency constraint eq.(3): without consistency constraint the best $\chi^2/ndf \sim 14 - 28$, depending on which form of the splitting function is used. With consistency constraint and the splitting function eq.(2) the best fit gives $\chi^2/ndf \sim 1.5$ for $Q_0 = 1.8$ GeV and $\Lambda_{qcd} = 0.17$ GeV at $n_f = 4$ flavours. It has been checked, that the χ^2/ndf does not change significantly when using 3 instead of 4 parameters for the initial starting distribution $\mathcal{A}_0$.

In fig.2 the resulting unintegrated gluon density **JH-set0** is shown for 2 values of p^2 compared to **set A0** [15].

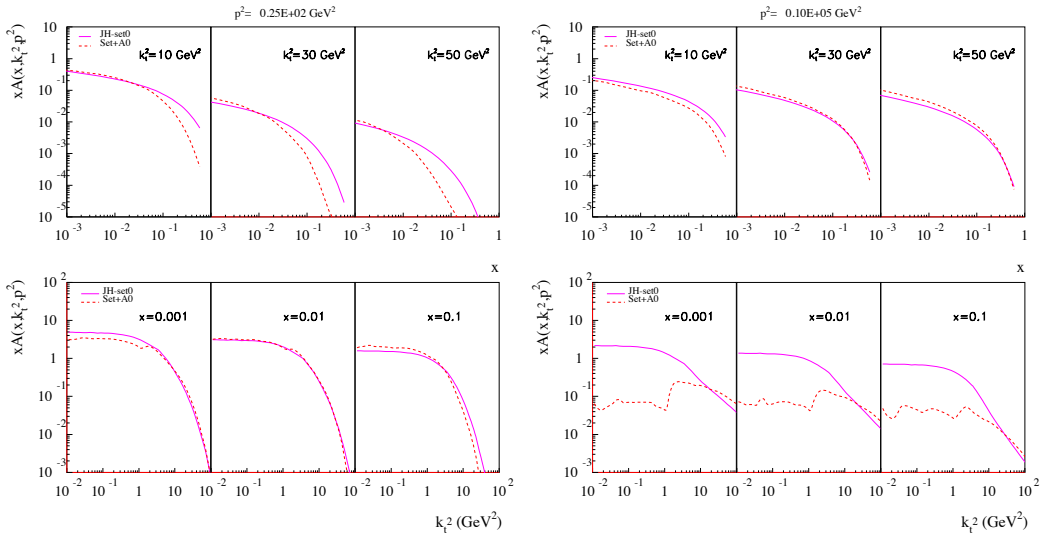

Figure 2: Unintegrated gluon density **JH-set0** for $p^2 = 25$ GeV^2 (left) and $p^2 = 10^5$ GeV^2 (right) as a function of x for different values of k_t^2 and as a function of k_t^2 for different values of x compared to **set A0** [15]

The uncertainties of the pdf are obtained within the `herafitter` package from a variation of the individual parameter uncertainties following the procedure described in [16] applying $\Delta\chi^2 = 1$. The uncertainties on the gluon are small (much smaller than obtained in standard fits), since only the gluon density is fitted. The uncertainty bands for the gluon density are shown in fig. 3(left). In fig. 3(right) the prediction for b-jet cross section as calculated from CASCADE [5] using the gluon density described here (labeled as **set0**) is shown together with a prediction using an older set (labeled as **setA 0** [15]) in comparison with a measurement from CMS [17].

Acknowledgments. We thank the conveners for the invitation and excellent organization of the meeting.

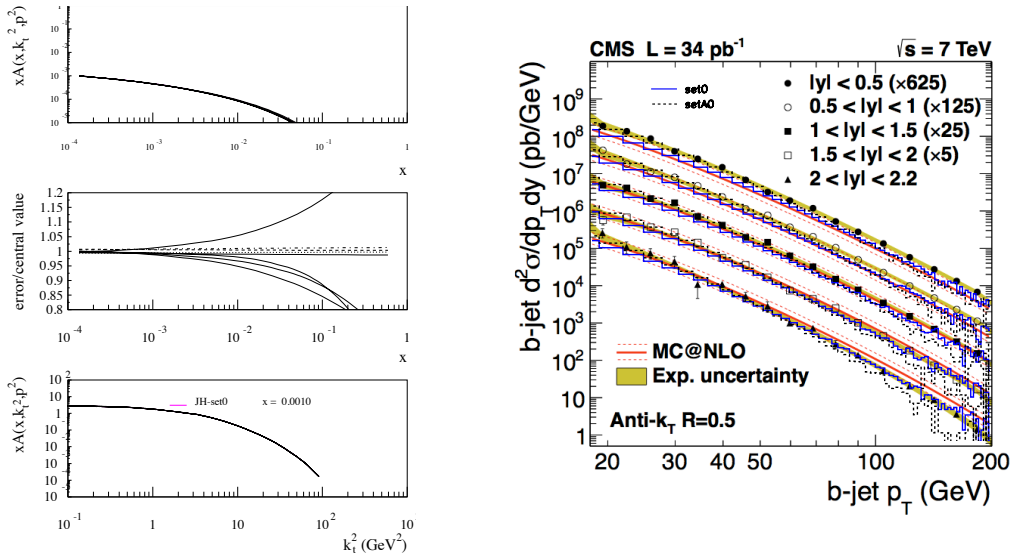

Figure 3: (left): Uncertainties of the uPDF at $p^2 = 25$ GeV^2. (right): Cross section of b-jet production as a function of p_t for different bins in y as measured by CMS [17] compared to predictions from CASCADE [5] using the unintegrated gluon density described here

References

[1] F. Aaron *et al.* JHEP **1001** (2010) 109, arXiv:0911.0884 [hep-ex]. 61 pages, 21 figures.

[2] H. Jung. Acta Phys. Polon. **B33** (2002) 2995–3000, arXiv:hep-ph/0207239.

[3] M. Hansson and H. Jung. arXiv:hep-ph/0309009.

[4] S. Catani, M. Ciafaloni, and F. Hautmann. Nucl. Phys. **B366** (1991) 135.

[5] H. Jung, S. Baranov, M. Deak, A. Grebenyuk, F. Hautmann, *et al.* Eur.Phys.J. **C70** (2010) 1237, arXiv:1008.0152 [hep-ph].

[6] J. Kwiecinski, A. D. Martin, and P. Sutton. Z.Phys. **C71** (1996) 585, arXiv:hep-ph/9602320 [hep-ph].

[7] M. Ciafaloni. Nucl. Phys. **B296** (1988) 49.

[8] B. Andersson, G. Gustafson, and J. Samuelsson. Nucl.Phys. **B467** (1996) 443. Revised version.

[9] B. Andersson *et al.* Eur. Phys. J. **C25** (2002) 771, arXiv:hep-ph/0204115.

[10] G. Marchesini and B. R. Webber. Nucl. Phys. **B349** (1991) 617.

[11] G. Marchesini and B. R. Webber. Nucl. Phys. **B386** (1992) 215.

[12] F. Aaron *et al.* Eur.Phys.J. **C64** (2009) 561, arXiv:0904.3513 [hep-ex]. 35 pages, 10 figures.

[13] "HERAFitter", 2012. http://herafitter.hepforge.org/.

[14] M. Deak, F. Hautmann, H. Jung, and K. Kutak. arXiv:1012.6037 [hep-ph].

[15] H. Jung. arXiv:hep-ph/0411287.

[16] J. Pumplin, D. Stump, R. Brock, D. Casey, J. Huston, *et al.* Phys.Rev. **D65** (2001) 014013, arXiv:hep-ph/0101032 [hep-ph].

[17] S. Chatrchyan *et al.* JHEP **1204** (2012) 084, arXiv:1202.4617 [hep-ex].

Photon impact factor for BFKL pomeron at next-to-leading order

Giovanni Antonio Chirilli
Lawrence Berkeley National Laboratory, Nuclear Science Division,
Berkeley, CA 94720, USA,
gchirilli@lbl.gov

DOI: http://dx.doi.org/10.3204/DESY-PROC-2012-02/128

An analytic expression in momentum space of the next-to-leading order photon impact factor for small-x deep inelastic scattering will be presented. The result is obtained using the operator product expansion in Wilson lines.

1 Introduction

In order to obtain an analytic expression of the NLO photon impact factor for BFKL pomeron, we use the high-energy Operator Product Expansion (OPE) in terms of Wilson lines. Our calculation mainly consist of three steps: we first obtain an analytic expression in coordinate space of the NLO impact factor, then, we obtain its Mellin representation, and finally we perform the Fourier transform in momentum space.

The logic of the high-energy OPE is the same as the one for the usual OPE. In order to find a certain asymptotical behavior of an amplitude using the OPE technique one introduces a factorization scale which factorize the amplitude into a product of coefficient functions and matrix elements of the relevant operators. Then, one has to find the evolution equations of the operators with respect to the factorization scale, solve the evolution equation and finally, convolute the solution with the initial conditions for the evolution and get the amplitude.

At high energy the scattering amplitude of the process is strongly ordered in rapidity space. For this reason it is natural to introduce a factorization parameter in rapidity space which factorize, order by order in perturbation theory, the scattering amplitude in coefficient functions and matrix elements of the relevant operator. The evolution of the matrix element with respect to the factorization scale is the non-linear BK equation [1, 2]. The linearization of this non-linear equation reproduce the BFKL equation [3]. Both, the BK equation and the BFKL equation are known at NLO accuracy in QCD and in $\mathcal{N}$=4 SYM theory [5, 6, 7, 8].

2 NLO Impact Factor for DIS

To better illustrate the logic of the OPE, let us consider the T-product of two electromagnetic currents which will be relevant for Deep Inelastic scattering (DIS) when evaluated in the target (nucleon or nucleus) state. The technique we are using is the background field technique: we consider the T-product of two electromagnetic currents in a background of gluon field. In the

spectator frame the background field reduces to shock wave (for a review see [4]). In DIS, in the dipole model, the virtual photon which mediate the interaction between the lepton and the nucleon, splits in a quark anti-quark pair long before the interaction with the target. The propagation of the quark anti-quark pair in the background of a shock wave, reduces to two Wilson lines. If the quark fluctuate perturbatively in a quark and a gluon before interacting with the target, then the number of Wilson lines increases. Formally, we can write down the expansion of the T-product of two electromagnetic currents in the following way

$$T\{\hat{j}_\mu(x)\hat{j}_\nu(y)\} = \int d^2z_1 d^2z_2 \; I^{\rm LO}_{\mu\nu}(z_1,z_2,x,y)[{\rm Tr}\{\hat{U}^\eta_{z_1}\hat{U}^{\dagger\eta}_{z_2}\}]^{\rm comp.}$$
$$+\int d^2z_1 d^2z_2 d^2z_3 \; I^{\rm NLO}_{\mu\nu}(z_1,z_2,z_3,x,y)[{\rm tr}\{\hat{U}^\eta_{z_1}\hat{U}^{\dagger\eta}_{z_3}\}{\rm tr}\{\hat{U}^\eta_{z_3}\hat{U}^{\dagger\eta}_{z_2}\} - N_c{\rm tr}\{\hat{U}^\eta_{z_1}\hat{U}^{\dagger\eta}_{z_2}\}] + \cdots \quad (1)$$

where $U_x = {\rm Pexp}({\rm ig}\int {\rm dx}^+{\rm A}^-({\rm x}^+ + {\rm x}_\perp)$ is the Wilson line. In Eq. (1), the coefficient $I^{\rm LO}_{\mu\nu}$ represents the leading order impact factor, while the NLO impact factor is given by the coefficient $I^{\rm NLO}_{\mu\nu}$. In QCD Feynmann diagrams at tree level are conformal invariant. The LO impact factor is indeed conformal invariant and it can be written in terms of conformal vectors [9] $\kappa = \frac{\sqrt{s}}{2x_*}(\frac{p_1}{s} - x^2p_2 + x_\perp) - \frac{\sqrt{s}}{2y_*}(\frac{p_1}{s} - y^2p_2 + y_\perp)$ and $\zeta_i = \left(\frac{p_1}{s} + z^2_{i\perp}p_2 + z_{i\perp}\right)$

$$\langle T\{\hat{j}_\mu(x)\hat{j}_\nu(y)\}\rangle_A = \frac{s^2}{2^9\pi^6x_*^2y_*^2}\int d^2z_{1\perp}d^2z_{2\perp}\frac{{\rm tr}\{U_{z_1}U^\dagger_{z_2}\}}{(\kappa\cdot\zeta_1)^3(\kappa\cdot\zeta_2)^3}\times$$
$$\frac{\partial^2}{\partial x^\mu\partial y^\nu}\left[2(\kappa\cdot\zeta_1)(\kappa\cdot\zeta_2) - \kappa^2(\zeta_1\cdot\zeta_2)\right] + O(\alpha_s) \quad (2)$$

The NLO impact factor is also a tree level diagram, but it is not conformal invariant due to the rapidity divergence present at this order. Since we regularize such divergence by rigid cut-off, we introduce terms which violate the conformal invariance. In order to restore the symmetry we introduce counterterms which form the composite operator. The procedure of restoring the loss of conformal symmetry due to the regularization of the rapidity divergence by rigid cut-off, is analog to the procedure of restoring gauge invariance by adding counterterms to local operator when the rigid cut-off is used instead of dimensional regularization, which automatically preserve gauge symmetry, to regulate ultraviolet divergence at one loop order. In Eq. (1), the composite operator is

$$\left[{\rm Tr}\{\hat{U}^\eta_{z_1}\hat{U}^{\dagger\eta}_{z_2}\}\right]^{\rm conf} = {\rm Tr}\{\hat{U}^\eta_{z_1}\hat{U}^{\dagger\eta}_{z_2}\}$$
$$+\frac{\alpha_s}{4\pi}\int d^2z_3\;\frac{z_{12}^2}{z_{13}^2z_{23}^2}[\frac{1}{N_c}{\rm tr}\{\hat{U}^\eta_{z_1}\hat{U}^{\dagger\eta}_{z_3}\}{\rm tr}\{\hat{U}^\eta_{z_3}\hat{U}^{\dagger\eta}_{z_2}\} - {\rm Tr}\{\hat{U}^\eta_{z_1}\hat{U}^{\dagger\eta}_{z_2}\}]\ln\frac{az_{12}^2}{z_{13}^2z_{23}^2} + O(\alpha_s^2) \quad (3)$$

The parameter a is analog to μ_F in the usual OPE. Note also that at this order the operator proportional to the NLO impact factor does not need to be modified. It would get a counterterm at NNLO accuracy. Using, then, the composite operator the NLO impact factor is conformal invariant and it can be written entirely in terms of the conformal vectors we defined above. See Ref. [10] for its explicit expression. Such result is an analytic expression of the photon impact factor in coordinate space which is relevant for DIS off a large nucleus where the non linear operator appearing at NLO level is relevant at high parton density regime. What we are interested in is the NLO impact factor for BFKL pomeron. Thus, our next step, before proceeding to the calculation of the Mellin representation, is to obtain the linearization of result

in coordinate space in the non-linear case. It turns out that the coordinate representation of the NLO impact factor in the linearized case can be written as a linear combination of five conformal tensor structures [10]. In Ref. [9] it was indeed predicted that any impact factor can be written as a linear combination of the same conformal tensor structures. The projection of the impact factor on the Lipatov eigenfunctions with conformal spin 0 is related to the unpolarized structure function for DIS. While the projection on the Lipatov eigenfunction with conformal spin 2 is related to the polarized structure function. The result of the Mellin representation can be found in Ref. [11]. Once we have performed the Mellin representation, we are ready to perform the Fourier transform in momentum space. The result is

$$
\begin{aligned}
I^{\mu\nu}(q,k_\perp) &= \frac{N_c}{32}\int\frac{d\nu}{\pi\nu}\frac{\sinh\pi\nu}{(1+\nu^2)\cosh^2\pi\nu}\Big(\frac{k_\perp^2}{Q^2}\Big)^{\frac{1}{2}-i\nu}\Big\{\Big[\Big(\frac{9}{4}+\nu^2\Big)\Big(1+\frac{\alpha_s}{\pi}+\frac{\alpha_s N_c}{2\pi}\mathcal{F}_1(\nu)\Big)P_1^{\mu\nu}\\
&+\Big(\frac{11}{4}+3\nu^2\Big)\Big(1+\frac{\alpha_s}{\pi}+\frac{\alpha_s N_c}{2\pi}\mathcal{F}_2(\nu)\Big)P_2^{\mu\nu}\Big]\\
&+\frac{\frac{1}{4}+\nu^2}{2k_\perp^2}\Big(1+\frac{\alpha_s}{\pi}+\frac{\alpha_s N_c}{2\pi}\mathcal{F}_3(\nu)\Big)\big[\tilde{P}^{\mu\nu}\bar{k}^2+\bar{P}^{\mu\nu}\tilde{k}^2\big]\Big\} \qquad (4)
\end{aligned}
$$

where

$$
\begin{aligned}
P_1^{\mu\nu} &= g^{\mu\nu}-\frac{q_\mu q_\nu}{q^2}; \qquad P_2^{\mu\nu} = \frac{1}{q^2}\Big(q^\mu-\frac{p_2^\mu q^2}{q\cdot p_2}\Big)\Big(q^\nu-\frac{p_2^\nu q^2}{q\cdot p_2}\Big)\\
\bar{P}^{\mu\nu} &= \big(g^{\mu 1}-ig^{\mu 2}-p_2^\mu\frac{\bar{q}}{q\cdot p_2}\big)\big(g^{\nu 1}-ig^{\nu 2}-p_2^\nu\frac{\bar{q}}{q\cdot p_2}\big)\\
\tilde{P}^{\mu\nu} &= \big(g^{\mu 1}+ig^{\mu 2}-p_2^\mu\frac{\tilde{q}}{q\cdot p_2}\big)\big(g^{\nu 1}+ig^{\nu 2}-p_2^\nu\frac{\tilde{q}}{q\cdot p_2}\big)
\end{aligned}
$$

$$
\begin{aligned}
\mathcal{F}_{1(2)}(\nu) &= \Phi_{1(2)}(\nu)+\chi_\gamma\Psi(\nu), \qquad \mathcal{F}_3(\nu) = F_6(\nu)+\Big(\chi_\gamma-\frac{1}{\bar{\gamma}\gamma}\Big)\Psi(\nu),\\
\Psi(\nu) &\equiv \psi(\bar{\gamma})+2\psi(2-\gamma)-2\psi(4-2\gamma)-\psi(2+\gamma),\\
F_6(\gamma) &= F(\gamma)-\frac{2C}{\bar{\gamma}\gamma}-1-\frac{2}{\gamma^2}-\frac{2}{\bar{\gamma}^2}-3\frac{1+\chi_\gamma-\frac{1}{\gamma\bar{\gamma}}}{2+\bar{\gamma}\gamma},\\
\Phi_1(\nu) &= F(\gamma)+\frac{3\chi_\gamma}{2+\bar{\gamma}\gamma}+1+\frac{25}{18(2-\gamma)}+\frac{1}{2\bar{\gamma}}-\frac{1}{2\gamma}-\frac{7}{18(1+\gamma)}+\frac{10}{3(1+\gamma)^2}\\
\Phi_2(\nu) &= F(\gamma)+\frac{3\chi_\gamma}{2+\bar{\gamma}\gamma}+1+\frac{1}{2\bar{\gamma}\gamma}-\frac{7}{2(2+3\bar{\gamma}\gamma)}+\frac{\chi_\gamma}{1+\gamma}+\frac{\chi_\gamma(1+3\gamma)}{2+3\bar{\gamma}\gamma},\\
F(\gamma) &= \frac{2\pi^2}{3}-\frac{2\pi^2}{\sin^2\pi\gamma}-2C\chi_\gamma+\frac{\chi_\gamma-2}{\bar{\gamma}\gamma}
\end{aligned}
$$

In order to obtain the full expression in momentum space of the NLO DIS amplitude, we need to perform also the Fourier transform of the NLO linearized BK equation for the dipole form of the unitegrated gluon distribution $\mathcal{V}(z)=z^{-2}\mathcal{U}(z)$ where $\mathcal{U}(x,y)=1-N_c^{-1}\mathrm{tr}\{U(x_\perp U^\dagger(y_\perp)\}$ [11]. The k_T factorized form of the NLO amplitude for DIS can be found in Ref. [11].

3 Conclusions

An analytic expression of the NLO photon impact factor in momentum space for the pomeron contribution, given in formula (4), and the k_T factorization formula, up to NLO accuracy, of

the NLO DIS amplitude, given in [11], has been presented. So far the NLO impact factor was available only as a combination of numerical and analytical expressions [12]. The $k_{\rm T}$ factorization formula given in [11] is intimately related to the two-gluon (pomeron) exchange. In order, then, to obtain a factorized form of the DIS amplitude in $k_{\rm T}$ space, we considered the linearized case. We then obtained first a Mellin representation of the NLO impact factor and finally performed the Fourier transform in momentum space and obtained the first main result presented here, formula (4). A $k_{\rm T}$ factorization formula can be obtained also for the NLO amplitude of the γ^*-γ^* scattering (see Ref. [13] for the $\mathcal{N}$=4 SYM theory case). One simply needs to perform the Fourier transform of the NLO evolution equation for the $\mathcal{U}(x)$ operator. This would represent a proof, for the first time, of the validity of the factorization in $k_{\rm T}$ space at NLO accuracy also for γ^*-γ^* scattering, since an analytic expression of the NLO photon impact factor in momentum space was not known before. The $k_{\rm T}$ factorization form of DIS amplitude [11] as well as the one for γ^*-γ^* scattering are simply a consequence of the success of the high-energy OPE.

The author is grateful to the organizers of DIS 2012 conference for financial support.

References

[1] I. Balitsky, Nucl. Phys. B **463**, 99 (1996) [hep-ph/9509348].

[2] Y. V. Kovchegov, Phys. Rev. D **60**, 034008 (1999) [hep-ph/9901281]; Phys. Rev. D **61**, 074018 (2000) [hep-ph/9905214].

[3] E. A. Kuraev, L. N. Lipatov and V. S. Fadin, Sov. Phys. JETP **45**, 199 (1977) [Zh. Eksp. Teor. Fiz. **72**, 377 (1977)]; I. I. Balitsky and L. N. Lipatov, Sov. J. Nucl. Phys. **28**, 822 (1978) [Yad. Fiz. **28**, 1597 (1978)].

[4] I. Balitsky, In "Shifman, M. (ed.): At the frontier of particle physics, vol. 2" 1237-1342 [hep-ph/0101042].

[5] I. Balitsky and G. A. Chirilli, Phys. Rev. D **77**, 014019 (2008) [arXiv:0710.4330 [hep-ph]].

[6] I. Balitsky and G. A. Chirilli, Nucl. Phys. B **822**, 45 (2009) [arXiv:0903.5326 [hep-ph]].

[7] I. Balitsky and G. A. Chirilli, Phys. Rev. D **79**, 031502 (2009) [arXiv:0812.3416 [hep-ph]].

[8] V. S. Fadin and L. N. Lipatov, Phys. Lett. B **429**, 127 (1998) [hep-ph/9802290]; M. Ciafaloni and G. Camici, Phys. Lett. B **430**, 349 (1998) [hep-ph/9803389].

[9] L. Cornalba, M. S. Costa and J. Penedones, JHEP **1003**, 133 (2010).

[10] I. Balitsky and G. A. Chirilli, Phys. Rev. D **83**, 031502 (2011) [arXiv:1009.4729 [hep-ph]].

[11] I. Balitsky and G. A. Chirilli, arXiv:1207.3844 [hep-ph].

[12] J. Bartels and A. Kyrieleis, *Phys. Rev.* **D70**,114003(2004); J. Bartels, D. Colferai, S. Gieseke, and A. Kyrieleis, *Phys. Rev.* **D66**, 094017 (2002). J. Bartels, S. Gieseke, and A. Kyrieleis, *Phys. Rev.* **D65**, 014006 (2002).

[13] I. Balitsky and G. A. Chirilli, Phys. Lett. B **687**, 204 (2010) [arXiv:0911.5192 [hep-ph]].

Low x physics: a critical phenomenon?

Otto Nachtmann[1]

[1] Institute for Theoretical Physics, University of Heidelberg

DOI: http://dx.doi.org/10.3204/DESY-PROC-2012-02/118

A write-up was not submitted for this talk. Most of the material in presented can be found in: O. Nachtmann, "Effective field theory approach to structure functions at small x", Eur. Phys. J. C 26, 579-596 (2003) http://arxiv.org/abs/hep-ph/0206284.

Nonlinear extension of the CCFM equation

Krzysztof Kutak

Instytut Fizyki Jądrowej im. H. Niewodniczańskiego
Radzikowskiego 152, 31-342 Krakow, Poland

DOI: http://dx.doi.org/10.3204/DESY-PROC-2012-02/31

Motivated by the regime of QCD explored nowadays at LHC, where both the total energy of collision and momenta transfers are high, evolution equations of high energy factorization are investigated. In order to study such effects like parton saturation in final states one is inevitably led to investigate how to combine physics of the BK and CCFM evolution equations. We report on recently obtained resummed form of the BK equation and nonlinear extension of the CCFM equation.

1 Introduction

The Large Hadron Collider (LHC) is already operational and Quantum Chromodynamics (QCD) is the basic theory which is used to set up the initial conditions for the collisions at the LHC as well as to calculate hadronic observables. The application of perturbative QCD relies on factorization theorems which allow to decompose a given process into a long distance part, called parton density, and a short distance part, called matrix element. Here we will focus on high energy factorization [1, 2]. The evolution equations of high energy factorization sum up logarithms of energy accompanied by a strong coupling constant, i.e. terms proportional to $\alpha_s^n \ln^m s/s_0$, which applies when the total energy of a scattering process is much bigger than any other hard scale involved in a process.
Until now, in principle, the BFKL, BK [3–5] and CCFM [6–8] evolution equations were used on equal footing since the energy ranges did not allow to discriminate between these frameworks. However, there were indications already at HERA [9] for the need to account for nonlinear effects in gluon density. These observation are supported by recent results obtained in [10, 12]. On top of this, the results from [13] point at the need to use the framework which incorporates hardness of the collision into BFKL like description. With the LHC one entered into a region of phase space where both the energy and momentum transfers are high and formed systems of partons dense. Recently a framework has been provided in [14] where both dense systems and hard processes at high energies can be studied.

2 Exclusive form of the Balitsky-Kovchegov equation

At the leading order in $\ln 1/x$ the Balitsky-Kovchegov equation for the dipole amplitude in the momentum space is written as an integral equation reads [14]:

$$\begin{aligned}\Phi(x,k^2) &= \Phi_0(x,k^2) \\ &+ \overline{\alpha}_s \int_x^1 \frac{dz}{z} \int_0^\infty \frac{dl^2}{l^2} \left[\frac{l^2\Phi(x/z,l^2) - k^2\Phi(x/z,k^2)}{|k^2-l^2|} + \frac{k^2\Phi(x/z,k)}{\sqrt{(4l^4+k^4)}} \right] \\ &- \overline{\alpha}_s \int_x^1 \frac{dz}{z} \Phi^2(x/z,k)\end{aligned} \tag{1}$$

where the lengths of transverse vectors lying in transversal plane to the collision axis are $k \equiv |\mathbf{k}|$, $l \equiv |\mathbf{l}|$ ($\mathbf{k}$ is a vector sum of transversal momenta of emitted gluons during evolution), $z = x/x'$(see Fig. (1), $\overline{\alpha}_s = N_c\alpha_s/\pi$. The linear term in eq. (1) can be linked to the process of creation of gluons while the nonlinear term can be linked to fusion of gluons and therefore introduces gluon saturation effects.

The unintegrated gluon density obeying the high energy factorization theorem [1] is obtained from [18, 19]:

$$\mathcal{F}_{BK}(x,k^2) = \frac{N_c}{\alpha_s\pi^2} k^2 \nabla_k^2 \Phi(x,k^2) \tag{2}$$

where the angle independent Laplace operator is given by $\nabla_k^2 = 4\frac{\partial}{\partial k^2} k^2 \frac{\partial}{\partial k^2}$.
As explained in [14] this equation can be rewritten in a resummed form:

$$\begin{aligned}\Phi(x,k^2) \;&=\; \tilde{\Phi}^0(x,k^2) \\ &+\; \overline{\alpha}_s \int_x^1 d\,z \int \frac{d^2\mathbf{q}}{\pi q^2}\, \theta(q^2-\mu^2) \frac{\Delta_R(z,k,\mu)}{z} \left[\Phi(\frac{x}{z}, |\mathbf{k}+\mathbf{q}|^2) - q^2\delta(q^2-k^2)\,\Phi^2(\frac{x}{z},q^2) \right].\end{aligned} \tag{3}$$

where $\mathbf{q} = \mathbf{l} - \mathbf{k}$ and $\Delta_R(z,k,\mu) \equiv \exp\left(-\overline{\alpha}_s \ln\frac{1}{z} \ln\frac{k^2}{\mu^2}\right)$ is a Regge form factor.

Eq. (3) is a new form of the BK equation in which the resummed terms in a form of Regge form factor are the same for the linear and nonlinear part. This form will serve as a guiding equation to generalize the CCFM equation to include nonlinear effects which allow for recombination of partons with constraint on angle of emission.

2.1 Nonlinear extension of the CCFM equation

As it has already been stated the motivation to extend the CCFM to account for nonlinearity is to be able to study the impact of saturation of partons on exclusive observables. There are indications [15, 23] that such effects might be significant in for instance production of charged particles at HERA or in forward production of di-jets [10, 11].
The nonlinear extension of CCFM has been recently proposed in [14] and its extension changes the interpretation of the quantity for which the equation is written. It is not longer high energy factorizable gluon density but should be interpreted as the dipole amplitude in momentum space Φ, denoted from now on by $\mathcal{E}$, which besides x and k^2 depends also on a hard scale p. The peculiar structure of the nonlinear term of the equation written below is motivated by the following requirements:

- the second argument of the $\mathcal{E}$ should be k^2 as motivated by the analogy to BK

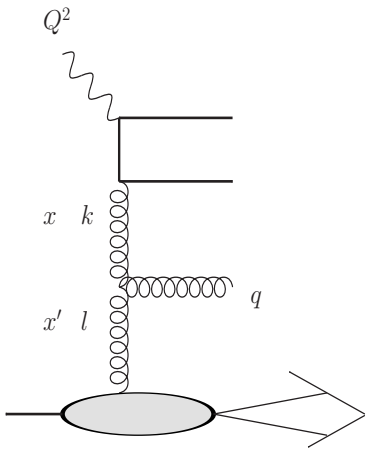

Figure 1: Plot explaining meaning of variables in BK and CCFM evolution equations.

- the third argument should reflect locally the angular ordering

$$\begin{aligned}\mathcal{E}(x,k^2,p) &= \mathcal{E}_0(x,k^2,p) \\ &+ \bar{\alpha}_s \int_x^1 dz \int \frac{d^2\bar{\mathbf{q}}}{\pi\bar{q}^2}\,\theta(p-z\bar{q})\Delta_s(p,z\bar{q})\left(\frac{\Delta_{ns}(z,k,q)}{z}+\frac{1}{1-z}\right)\Bigg[\mathcal{E}\left(\frac{x}{z},k'^2,\bar{q}\right) \\ &- \bar{q}^2\delta(\bar{q}^2-k^2)\,\mathcal{E}^2(\frac{x}{z},\bar{q}^2,\bar{q})\Bigg].\end{aligned} \tag{4}$$

The momentum vector associated with i-th emitted gluon is

$$q_i = \alpha_i\, p_P + \beta_i\, p_e + q_{t\,i} \tag{5}$$

The variable p in (4) is defined via $\bar{\xi} = p^2/(x^2 s)$ where $\frac{1}{2}\ln(\bar{\xi})$ is a maximal rapidity which is determined by the kinematics of hard scattering, $\sqrt{s}$ is the total energy of the collision and $k' = |\boldsymbol{k} + (1-z)\bar{\boldsymbol{q}}|$. The momentum $\bar{\mathbf{q}}$ is the transverse rescaled momentum of the real gluon, and is related to $\mathbf{q}$ by $\bar{\mathbf{q}} = \mathbf{q}/(1-z)$ and $\bar{q} \equiv |\bar{\mathbf{q}}|$.
The form factor Δ_s screens the $1-z$ singularity while form factor Δ_{ns} screens the $1/z$ singularity, in a similar form as the Regge form factor but also accounts for angular ordering:

$$\Delta_{ns}(z,k,q) = \exp\left(-\alpha_s \ln\frac{1}{z}\ln\frac{k^2}{zq^2}\right). \tag{6}$$

where for the lowest value of zq^2 we use a cut off μ.

Similarly as in case of the BK equation in order to obtain high energy factorizable unintegrated gluon density one applies relation (2). The nonlinear term in (4), apart from allowing for recombination of gluons might be understood as a way to introduce the decoherence into the emission pattern of gluons. This is because the gluon density is build up due to coherent gluon emission and since the nonlinear term comes with the negative sign it slows down the

growth of gluon density and therefore it introduces the decoherence. We expect the nonlinear term to be of main importance at low x similarly as in case of the BK equation. In this limit it will be of special interest to check whether in this formulation of the nonlinear extension of the CCFM equation one obtains an effect of saturation of the saturation scale as observed in [17]. This effect is of great importance since it has a consequences for example for imposing a bound on amount of production of entropy from saturated part of gluon density as observed in [24].

3 Conclusions and outlook

We reported on recently obtained new form of the BK equation written in a resummed form and on extension of CCFM to account for nonlinearity. The obtained extension of CCFM will be useful for studies of impact saturation of gluons on exclusive observables.

Acknowledgements

I would like to thank organizers of DIS 2012 and in particular Dimitri Colferai for inviting me to give a talk. This research has been supported by grant LIDER/02/35/L-2/10/NCBiR/2011

References

[1] S. Catani, M. Ciafaloni, F. Hautmann, Nucl. Phys. **B366** (1991) 135-188.
[2] L. V. Gribov, E. M. Levin and M. G. Ryskin, Phys. Rept. **100** (1983) 1.
[3] I. Balitsky, Nucl. Phys. B **463** (1996) 99.
[4] Y. V. Kovchegov, Phys. Rev. D **60** (1999) 034008.
[5] Y. V. Kovchegov, Phys. Rev. D **61** (2000) 074018.
[6] M. Ciafaloni, Nucl. Phys. B **296**, 49 (1988).
[7] S. Catani, F. Fiorani and G. Marchesini, Nucl. Phys. B **336**, 18 (1990).
[8] S. Catani, F. Fiorani and G. Marchesini, Phys. Lett. B **234**, 339 (1990).
[9] A. M. Stasto, K. J. Golec-Biernat, J. Kwiecinski, Phys. Rev. Lett. **86** (2001) 596-599.
[10] J. L. Albacete, C. Marquet, Phys. Rev. Lett. **105** (2010) 162301.
[11] K. Kutak and S. Sapeta, arXiv:1205.5035 [hep-ph].
[12] A. Dumitru, K. Dusling, F. Gelis *et al.*, Phys. Lett. **B697** (2011) 21-25.
[13] M. Deak, F. Hautmann, H. Jung, K. Kutak, [arXiv:1012.6037.
[14] K. Kutak, K. Golec-Biernat, S. Jadach and M. Skrzypek, JHEP **1202** (2012) 117.
[15] K. Kutak, H. Jung, Acta Phys. Polon. **B40** (2009) 2063-2070.
[16] E. Avsar and E. Iancu, Nucl. Phys. A **829** (2009) 31.
[17] E. Avsar and A. M. Stasto, JHEP **1006** (2010) 112.
[18] M. Braun, Eur. Phys. J. C **16**, 337 (2000).
[19] K. Kutak and J. Kwiecinski, Eur. Phys. J. C **29** (2003) 521.
[20] J. Bartels, M. Wusthoff, Z. Phys. **C66** (1995) 157-180.
[21] J. Bartels, K. Kutak, Eur. Phys. J. **C53** (2008) 533-548.
[22] J. Kwiecinski, A. D. Martin and P. J. Sutton, Phys. Rev. D **52** (1995) 1445.
[23] C. Adloff *et al.* [H1 Collaboration], Nucl. Phys. **B485** (1997) 3-24.
[24] K. Kutak, Phys. Lett. B **705** (2011) 217.

The statistical model for parton distributions

Claude Bourrely[1], *Franco Buccella*[2], *Jacques Soffer*[3]

[1] Aix-Marseille Université, Département de Physique, Faculté des Sciences de Luminy, 13288 Marseille, Cedex 09, France
[2] INFN, Sezione di Napoli, via Cintia, I-80126, Napoli
[3] Physics Department, Temple University Barton Hall, 1900 N, 13th Street Philadelphia, PA 19122-6082, USA

DOI: `http://dx.doi.org/10.3204/DESY-PROC-2012-02/95`

The phenomenological motivations, the expressions and the comparison with experiment of the parton distributions inspired by the quantum statistics are described. The Fermi-Dirac expressions for the quarks and their antiparticles automatically account for the correlation between the shape and the first moments of the valence partons, as well as the flavor and spin asymmetries of the sea. One is able to describe with a small number of parameters both unpolarized and polarized structure functions.

Let us first recall some of the basic ingredients for building up the parton distribution functions (PDF) in the statistical approach, as oppose to the standard polynomial type parametrizations, based on Regge theory at low x and counting rules at large x. The fermion distributions are given by the sum of two terms [1], the first one, a quasi Fermi-Dirac function and the second one, a flavor and helicity independent diffractive contribution equal for light quarks. So we have, at the input energy scale $Q_0^2 = 4\text{GeV}^2$,

$$xq^h(x,Q_0^2) = \frac{AX_{0q}^h x^b}{\exp[(x-X_{0q}^h)/\bar{x}]+1} + \frac{\tilde{A}x^{\tilde{b}}}{\exp(x/\bar{x})+1}\ , \tag{1}$$

$$x\bar{q}^h(x,Q_0^2) = \frac{\bar{A}(X_{0q}^{-h})^{-1}x^{2b}}{\exp[(x+X_{0q}^{-h})/\bar{x}]+1} + \frac{\tilde{A}x^{\tilde{b}}}{\exp(x/\bar{x})+1}\ . \tag{2}$$

Notice the change of sign of the potentials and helicity for the antiquarks. The parameter $\bar{x}$ plays the role of a *universal temperature* and $X_{0q}^{\pm}$ are the two *thermodynamical potentials* of the quark q, with helicity $h = \pm$. It is important to remark that the diffractive contribution occurs only in the unpolarized distributions $q(x) = q_+(x) + q_-(x)$ and it is absent in the valence $q_v(x) = q(x) - \bar{q}(x)$ and in the helicity distributions $\Delta q(x) = q_+(x) - q_-(x)$ (similarly for antiquarks). The *eight* free parameters[1] in Eqs. (1,2) were determined at the input scale from the comparison with a selected set of very precise unpolarized and polarized Deep-Inelastic Scattering (DIS) data [1]. They have the following values

$$\bar{x} = 0.09907,\ b = 0.40962,\ \tilde{b} = -0.25347,\ \tilde{A} = 0.08318, \tag{3}$$

$$X_{0u}^+ = 0.46128,\ X_{0u}^- = 0.29766,\ X_{0d}^- = 0.30174,\ X_{0d}^+ = 0.22775\ . \tag{4}$$

[1] $A = 1.74938$ and $\bar{A}\ = 1.90801$ are fixed by the following normalization conditions $u - \bar{u} = 2$, $d - \bar{d} = 1$.

For the gluons we consider the black-body inspired expression

$$xG(x,Q_0^2) = \frac{A_G x^{b_G}}{\exp(x/\bar{x}) - 1} \ , \tag{5}$$

a quasi Bose-Einstein function, with $b_G = 0.90$, the only free parameter [2], since $A_G = 20.53$ is determined by the momentum sum rule. We also assume that, at the input energy scale, the polarized gluon distribution vanishes, so $x\Delta G(x,Q_0^2) = 0$. For the strange quark distributions, the simple choice made in Ref. [1] was greatly improved in Ref. [2]. More recently, new tests against experimental (unpolarized and polarized) data turned out to be very satisfactory, in particular in hadronic collisions, as reported in Refs. [3, 4]. For illustration, we will just give

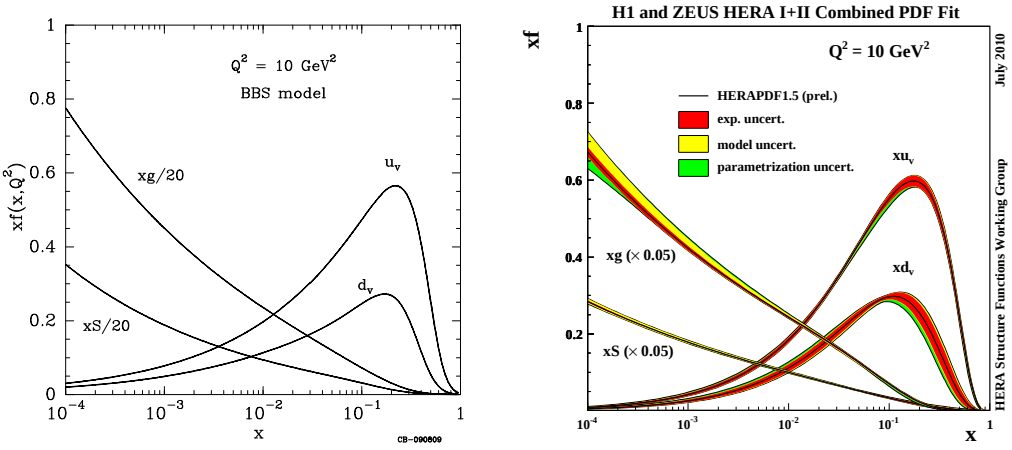

Figure 1: *Left* : BBS predictions for various statistical unpolarized parton distributions versus x at $Q^2 = 10\text{GeV}^2$. *Right* : Parton distributions at $Q^2 = 10\text{GeV}^2$, as determined by the HERAPDF fit, with different uncertainties (Taken from Ref. [5]).

one recent result, directly related to the determination of the quark distributions from unpolarized DIS. We display on Fig. 1 (*Left*), the resulting unpolarized statistical PDF versus x at Q^2=10 GeV^2, where xu_v is the u-quark valence, xd_v the d-quark valence, with their characteristic maximum around $x = 0.3$, xG the gluon and xS stands for twice the total antiquark contributions, *i.e.* $xS(x) = 2x(\bar{u}(x)+\bar{d}(x)+\bar{s}(x))+\bar{c}(x))$. Note that xG and xS are downscaled by a factor 0.05. They can be compared with the parton distributions as determined by the HERAPDF1.5 QCD NLO fit, shown also in Fig. 1 (*Right*), and there is a good agreement. The results are based on recent ep collider data from HERA, combined with previously published data and the accuracy is typically in the range of 1.3 - 2%. Another interesting point concerns the behavior of the ratio $d(x)/u(x)$, which depends on the mathematical properties of the ratio of two Fermi-Dirac factors, outside the region dominated by the diffractive contribution. So for $x > 0.1$, this ratio is expected to decrease faster for $X_{0d}^+ - \bar{x} < x < X_{0u}^+ + \bar{x}$ and then above, for $x > 0.6$ it flattens out. This change of slope is clearly visible in Fig. 2 (*Left*), with a very

[2] In Ref. [1] we were assuming that, for very small x, $xG(x,Q_0^2)$ has the same behavior as $x\bar{q}(x,Q_0^2)$, so we took $b_G = 1 + \tilde{b}$. However this choice leads to a too much rapid rise of the gluon distribution, compared to its recent determination from HERA data, which requires $b_G = 0.90$.

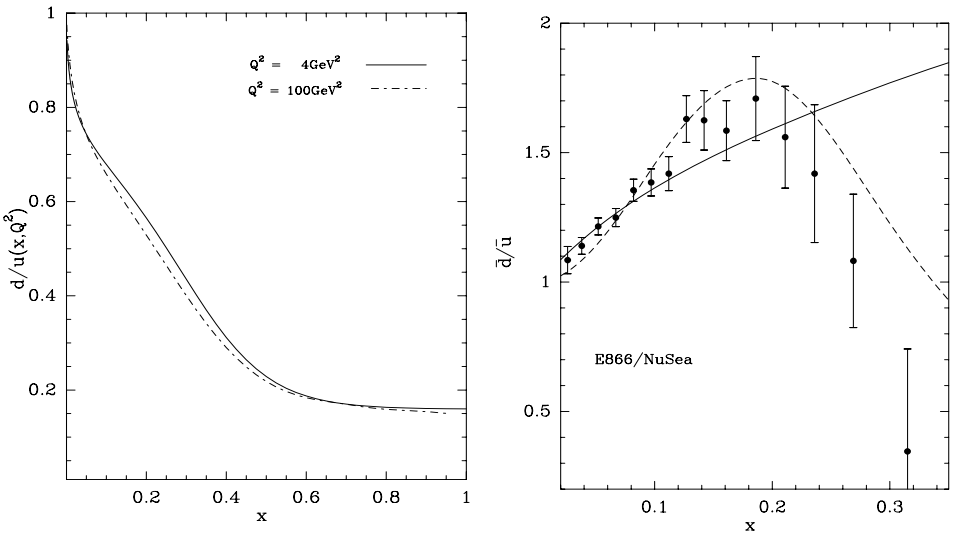

Figure 2: *Left* : The ratio $d(x)/u(x)$ as function of x for $Q^2 = 4\text{GeV}^2$ (solid line) and $Q^2 = 100\text{GeV}^2$ (dashed-dotted line). *Right* : Comparison of the data on $\bar{d}/\bar{u}$ versus x, from E866/NuSea at $Q^2 = 54\text{GeV}^2$ [7], with the prediction of the statistical model (solid curve) and the set 1 of the parametrization proposed in Ref. [8] (dashed curve).

little Q^2 dependence. Note that our prediction for the large x behavior, differs from most of the current literature, namely $d(x)/u(x) \to 0$ for $x \to 1$, but we find $d(x)/u(x) \to 0.16$ near the value 1/5, a prediction originally formulated in Ref. [6]. This is a very challenging question, since the very high-x region remains poorly known.

To continue our tests of the unpolarized parton distributions, we must come back to the important question of the flavor asymmetry of the light antiquarks. Our determination of $\bar{u}(x, Q^2)$ and $\bar{d}(x, Q^2)$ is perfectly consistent with the violation of the Gottfried sum rule, for which we found the value $I_G = 0.2493$ for $Q^2 = 4\text{GeV}^2$. Nevertheless there remains an open problem with the x distribution of the ratio $\bar{d}/\bar{u}$ for $x \geq 0.2$. According to the Pauli principle, this ratio is expected to remain above 1 for any value of x. However, the E866/NuSea Collaboration [7] has released the final results corresponding to the analysis of their full data set of Drell-Yan yields from an 800 GeV/c proton beam on hydrogen and deuterium targets and, for $Q^2 = 54\text{GeV}^2$, they obtain the ratio $\bar{d}/\bar{u}$ shown in Fig. 2 (*Right*). Although the errors are rather large in the high-x region, the statistical approach disagrees with the trend of the data. Clearly by increasing the number of free parameters, it is possible to build up a scenario which leads to the drop off of this ratio for $x \geq 0.2$. For example this was achieved in Ref. [8], as shown by the dashed curve in Fig. 2 (*Right*). There is no such freedom in the statistical approach, since quark and antiquark distributions are strongly related. On the experimental side, there are now new opportunities for extending the $\bar{d}/\bar{u}$ measurement to larger x up to $x = 0.7$, with the running E906 experiment at the 120 GeV Main Injector at Fermilab [9] and a proposed experiment at the new 30-50 GeV proton accelerator at J-PARC [10].

Analogous considerations can be made for the corresponding helicity distributions, whose most recent determinations are shown in Fig. 3 (*Left*). By using a similar argument as above, the ratio $\Delta u(x)/u(x)$ is predicted to have a rather fast increase in the x range $(X_{0u}^- - \bar{x}, X_{0u}^+ + \bar{x})$

and a smoother behaviour above, while $\Delta d(x)/d(x)$, which is negative, has a fast decrease in the x range $(X^+_{0d} - \bar{x}, X^-_{0d} + \bar{x})$ and a smooth one above. This is exactly the trends displayed in Fig. 3 (*Right*) and our predictions are in perfect agreement with the accurate high-x data. We note the behavior near $x = 1$, another typical property of the statistical approach, is also at variance with predictions of the current literature. The fact that $\Delta u(x)$ is more concentrated in the higher x region than $\Delta d(x)$, accounts for the change of sign of $g_1^n(x)$, which becomes positive for $x > 0.5$, as first observed at Jefferson Lab [13]. Concerning the light antiquark helicity

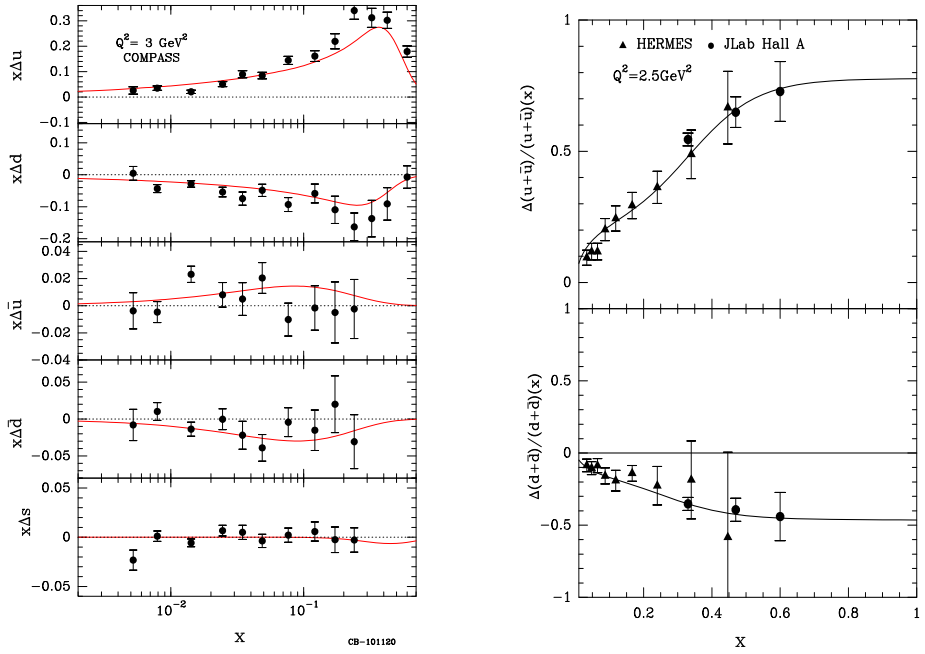

Figure 3: *Left* : Quark and antiquark helicity distributions as a function of x for $Q^2 = 3\text{GeV}^2$. Data from COMPASS [11]. The curves are predictions from the statistical approach. *Right* : Ratios $(\Delta u + \Delta\bar{u})/(u + \bar{u})$ and $(\Delta d + \Delta\bar{d})/(d + \bar{d})$ as a function of x. Data from Hermes for $Q^2 = 2.5\text{GeV}^2$ [12] and a JLab Hall A experiment [13]. The curves are predictions from the statistical approach.

distributions, the statistical approach imposes a strong relationship to the corresponding quark helicity distributions. In particular, it predicts $\Delta\bar{u}(x) > 0$ and $\Delta\bar{d}(x) < 0$, with almost the same magnitude, in contrast with the simplifying assumption $\Delta\bar{u}(x) = \Delta\bar{d}(x)$, often adopted in the literature. The COMPASS data [14] give $\Delta\bar{u}(x) + \Delta\bar{d}(x) \simeq 0$, which implies either small or opposite values for $\Delta\bar{u}(x)$ and $\Delta\bar{d}(x)$. Indeed $\Delta\bar{u}(x) > 0$ and $\Delta\bar{d}(x) < 0$, predicted by the statistical approach [1] (see Fig. 3 (*Left*), lead to a non negligible positive contribution of the sea to the Bjorken sum rule, an interesting consequence. For lack of space we only mention the extension to the transverse momentum dependence (TMD), an important aspect of the statistical PDF and we refer the reader to Ref. [15].

A new set of PDF was constructed in the framework of a statistical approach of the nucleon. All unpolarized and polarized distributions depend upon *nine* free parameters for light quarks

and gluon, with some physical meaning. New tests against experimental (unpolarized and polarized) data on DIS, Semi-inclusive DIS and also hadronic processes, are very satisfactory. It has a good predictive power, but some special features remain to be verified, specially in the high-x region, a serious challenge for the future.

References

[1] C. Bourrely, F. Buccella and J. Soffer, Eur. Phys. J. **C23**, 487 (2002).

[2] C. Bourrely, F. Buccella and J. Soffer, Phys. Lett. **B648**, 39 (2007).

[3] C. Bourrely, F. Buccella and J. Soffer, Mod. Phys. Lett. **A18**, 771 (2003).

[4] C. Bourrely, F. Buccella and J. Soffer, Eur. Phys. J. **C41**, 327 (2005).

[5] F.D. Aaron *et al.*, JHEP **1001**, 109 (2010).

[6] G.R. Farrar and D.R. Jackson, Phys. Rev. Lett. **35**, 1416 (1975).

[7] R.S. Towell *et al.*, [FNAL E866/Nusea Collaboration], Phys. Rev. **D64**, 052002 (2001).

[8] A. Daleo, C.A. García Canal, G.A. Navarro and R. Sassot, Int. J. Mod. Phys. **A17**, 269 (2002).

[9] D.F. Geesaman *et al.* [E906 Collaboration], FNAL Proposal E906, April 1, 2001.

[10] J.C.. Peng *et al.*, hep-ph/0007341.

[11] M. Alekseev *et al.* [COMPASS Collaboration], Phys. Lett. **B693**, 227 (2010).

[12] K. Ackerstaff *et al.*, [Hermes Collaboration], Phys. Lett. **B464**, 123 (1999).

[13] X. Zheng *et al.*, [Jefferson Lab Hall A Collaboration], Phys. Rev. **C70**, 065207 (2004).

[14] M. Alekseev *et al.* [COMPASS Collaboration], Phys. Lett. **B660**, 458 (2008).

[15] C. Bourrely, F. Buccella and J. Soffer, Phys. Rev. **D83**, 074008 (2011).

Part V

Working Group 2
Diffraction and Vector Mesons

Convenors:

Dimitri Colferai, Richard Polifka, Marta Ruspa

Combination of the Inclusive Diffractive Cross Sections at HERA

Valentina Sola[1] on behalf of the H1 and ZEUS Collaborations

[1]Hamburg Universität, Luruper Chaussee 149, 22761 Hamburg, Germany

DOI: http://dx.doi.org/10.3204/DESY-PROC-2012-02/36

A combination of the inclusive diffractive cross section measurements made by the H1 and ZEUS Collaborations at HERA is presented. The analysis uses samples of diffractive deep-inelastic ep scattering data at $\sqrt{s} = 318$ GeV where leading protons are detected by special spectrometers. Correlations of systematic uncertainties are taken into account by the combination method, resulting in improved precision.

1 Inclusive Diffraction at HERA

Diffractive processes have been studied extensively in deep-inelastic ep scattering (DIS) at the HERA collider. Such interactions, $ep \to eXp$, are characterised by the presence of a leading proton in the final state carrying most of the initial energy and by the presence of a large gap in rapidity between the proton and the rest of the hadronic system, X. The kinematic variables used to describe diffractive DIS are the four-momentum squared of the exchanged photon, Q^2, the squared four-momentum transfer at the proton vertex, t, the longitudinal momentum fraction of the proton carried by the diffractive exchange, $x_{I\!P}$, and the longitudinal momentum fraction of the struck parton with respect to the diffractive exchange, β. The latter two are related to the Bjorken scaling variable, x, by $x = x_{I\!P}\beta$.

The experimental signatures of diffractive interactions have been widely exploited at HERA to select diffractive events by tagging the outgoing proton in the H1 Forward Proton Spectrometer (FPS) [1, 2], in the H1 Very Forward Proton Spectrometer (VFPS) [3] and in the ZEUS Leading Proton Spectrometer (LPS) [4, 5] or by requiring the presence of a Large Rapidity Gap (LRG) [5, 6, 7] between the proton and the system X. The methods differ in the kinematic coverage and in their dominant sources of systematic uncertainty. The LRG method is limited to relatively low $x_{I\!P}$ by the need to contain the system X in the central detector components. The largest uncertainty arise from proton dissociative events, i.e. events where the proton dissociates into a low mass state that escapes entirely undetected into the beam-pipe. These events affect the global normalization of the measured LRG cross section. On the other hand, LPS and FPS data extend to $x_{I\!P} \sim 0.1$. They have little or no proton dissociation background, but are subject to small acceptance and large uncertainties in the proton tagging efficiency, which is strongly dependent on the proton-beam optics.

Combining the H1 and ZEUS diffractive data leads to the most accurate measurements of diffractive cross sections in deep inelastic scattering. These data provide high precision input for the extraction of diffractive parton distribution functions (DPDFs). A first step, presented

here [8], is taken towards such long term perspective by combining the H1 FPS [2] and the ZEUS LPS [5] proton-tagged data, for which both experiments published their final results.

2 Combination of the H1 and ZEUS Diffractive Cross Sections

2.1 Combined Data Sets

The H1 FPS data [2] correspond to an integrated luminosity of 156.6 pb^{-1} and were collected in the years from 2005 to 2007, after the HERA luminosity upgrade. The ZEUS LPS sample [5] was collected in the years 1999 and 2000 and corresponds to an integrated luminosity of 32.6 pb^{-1}. Since the H1 and ZEUS measurements were made with different binning, the ZEUS points are swum to the H1 bin centers by using the NLO QCD fit ZEUS SJ [9].

In the original analyses [2, 5] the reduced cross sections $\sigma_r^{D(3)}$ are directly measured in the t range visible to the proton taggers ($0.09 < |t| < 0.55$ GeV^2 for ZEUS and $0.1 < |t| < 0.7$ GeV^2 for H1) and extrapolated to the full range $0 < |t| < 1$ GeV^2. For the extrapolations an exponential t dependence is assumed with a slope parameter b between 5 and 6 GeV^{-2} depending on $x_{I\!P}$ for H1 and $b = 7.0 \pm 0.3$ GeV^{-2} for ZEUS as extracted from the diffractive cross sections in the visible ranges of the analyses. These extrapolations introduce extra uncertainties of the cross sections. In order to minimize such systematic effect the H1 and ZEUS cross sections are combined in the ZEUS visible t range $0.09 < |t| < 0.55$ GeV^2, common to both acceptances. In this range the normalization uncertainties are smaller and the ratio of the H1 FPS to ZEUS LPS data averaged over the measured kinematic range is $0.91 \pm 0.01(stat) \pm 0.03(sys) \pm 0.08(norm)$, consistent with unity. The resulting kinematic range of the combined data is $0.09 < |t| < 0.55$ GeV^2, $2.5 < Q^2 < 200$ GeV^2, $0.0018 < \beta < 0.56$ and $0.0009 < x_{I\!P} < 0.09$.

2.2 Combination Method

The combination is based on the χ^2 minimization method described in [10] and already used for previous combined HERA results [11]. The averaging procedure is based on the assumption that at a given kinematic point the H1 and ZEUS experiments are measuring the same cross section. The correlated systematic uncertainties are treated as free parameters and thereby enable a cross-calibration of the two experiments. It allows a model independent check of the data consistency and leads to a significant reduction of the correlated uncertainty. For an individual data set, the χ^2 function is defined as:

$$\chi^2_{exp}(\mathbf{m}, \mathbf{b}) = \sum_i \frac{[m^i - \sum_j \gamma^i_j m^i b_j - \mu^i]^2}{\delta^2_{i,stat}\mu^i(m^i - \sum_j \gamma^i_j m^i b_j) + (\delta_{i,uncor} m^i)^2} + \sum_j b_j^2. \quad (1)$$

Here μ^i is the measured value at a point i and γ^i_j, $\delta_{i,stat}$ and $\delta_{i,uncor}$ are relative correlated systematic, relative statistical and relative uncorrelated systematic uncertainties, respectively. The function χ^2_{exp} depends on the true values m^i of the measurements and the shift b_j of the correlated systematic error sources. The total χ^2 function, χ^2_{tot}, is built from the sum of the χ^2_{exp} functions for each data set.

2.3 Procedural Uncertainties

A series of uncertainties that may affect the combined measurement due to the combination procedure are studied. All the following effects are considered and treated as correlated procedural errors and for each data point their value is estimated and summed in quadrature to the total uncertainty.

The χ^2 function given by Eq. 1 treats all systematic uncertainties as multiplicative, i.e. proportional to the expected central values. To study the sensitivity of the average result to this error treatment, an alternative averaging is performed, for which only normalization uncertainties are taken as multiplicative while all other uncertainties are treated as additive. The difference between this average and the nominal average result is of the order of 4%.

The H1 and ZEUS experiments use similar methods for detector calibration, apply similar reweighting to the Monte Carlo for the acceptance corrections and employ similar Monte Carlo simulation models for radiative corrections, for the hadronic final state simulation and for the proton dissociation backgound subtraction. Such similarities may lead to correlations between the H1 and ZEUS measurements. To investigate the effect of correlations, 4 sources of similar systematic uncertainties of the two experiments are identified. These are related to the electromagnetic energy scale of the caloriemter of the main detector, the proton dissociation backgound and the $x_{I\!P}$ and t reweighting. Averages are formed for each of the 2^4 possible assumptions on whether these systematics are correlated or uncorrelated between the experiments and are compared with the nominal average for which all sources are assumed to be uncorrelated. The maximum difference between the nominal and the alternative averages is taken as an additional uncertainty.

In the nominal average the systematic error sources of the H1 FPS measurement [2] are all considered as point-to-point correlated. An alternative average is performed considering the hadronic energy scale, the event vertex reconstruction, the bin centre corrections and the background subtraction as uncorrelated errors. The difference with the nominal case is on average below 1%, increasing up to 10% for the lowest $x_{I\!P}$ bin.

The bias introduced by extrapolating the ZEUS data to the H1 binning scheme has been studied. An alternative average was performed once the ZEUS cross sections are swum according to an altrernative NLO QCD fit, the H1 'Fit B' [6]. The estimated overall effect is of the order of 1%.

3 Results

In the minimization procedure 227 data points were combined to 169 cross section measurements. The data show good consistency with $\chi^2/ndof = 52/58$. In Fig. 1 the combined data are compared to the input H1 FPS and ZEUS LPS data. The combination is driven by the H1 results, which are statistically more powerful. The combined measurement shows though an average improvement in precision of about 20% with respect to the original H1 data.

A total of 20 sources of correlated systematic uncertainties are considered, which shift by up to 1σ of the nominal value in the averaging procedure, with the exception of the H1 hadronic energy scale which shifts by 1.6σ. Several correlated systematic uncertainties are reduced significantly by the averaging procedure; notably, the contribution of the H1 uncertainty in the leading proton energy is reduced by a factor of 2.

These combined data are very valuable in the scenario of inclusive diffraction at HERA and beyond. They can provide the absolute normalization of the diffractive reduced cross section in

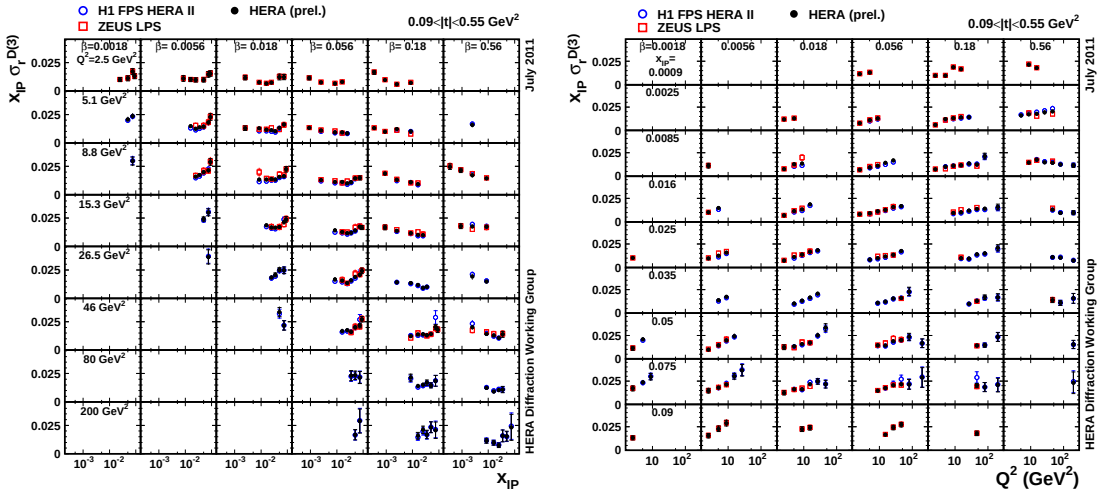

Figure 1: HERA diffractive reduced cross section as a function of $x_{I\!P}$ for different β and Q^2 (left) and as a function of Q^2 for different β and $x_{I\!P}$, compared to the H1 FPS and ZEUS LPS measurements.

deep inelastic scattering and they can help to quantify the proton dissociation contributions in the samples selected with the LRG method.

4 Conclusions

The H1 and ZEUS diffractive cross sections based on proton-tagged data are combined for the first time, resulting in a unique HERA diffractive DIS data set with improved precision. This result fixes the absolute normalization of the DIS diffractive reduced cross section and can be used as input for a QCD analysis to extract a unique set of HERA DPDFs.

References

[1] H1 Collaboration, A. Atkas *et al.*, Eur. Phys. J. **C48** (2006) 749.

[2] H1 Collaboration, F.D. Aaron *et al.*, Eur. Phys. J. **C71** (2011) 1578.

[3] H1 Collaboration, F.D. Aaron *et al.*, H1prelim-10-014 (2010).

[4] ZEUS Collaboration, S. Chekanov *et al.*, Eur. Phys. J. **C38** (2004) 43.

[5] ZEUS Collaboration, S. Chekanov *et al.*, Nucl. Phys. **B816** (2009) 1.

[6] H1 Collaboration, A. Aktas *et al.*, Eur. Phys. J. **C48** (2006) 715.

[7] H1 Collaboration, F.D. Aaron *et al.*, submitted to Eur. Phys. J. **C** (2011) `hep-ex/1203.4495`.

[8] H1 and ZEUS Collaborations, F.D. Aaron *et al.*, H1prelim-11-111, ZEUS-prel-11-011 (2011).

[9] ZEUS Collaboration, S. Chekanov *et al.*, Nucl. Phys. **B831** (2010) 1.

[10] H1 Collaboration, F.D. Aaron *et al.*, Eur. Phys. J. **C63** (2009) 625.

[11] H1 and ZEUS Collaborations, F.D. Aaron *et al.*, JHEP **01** (2010) 109.

Inclusive Measurement of Diffractive Deep Inelastic Scattering at HERA

Emmanuel Sauvan[1] on behalf of the H1 Collaboration

[1] LAPP, CNRS/IN2P3 et Université de Savoie, Annecy-le-Vieux, France

DOI: http://dx.doi.org/10.3204/DESY-PROC-2012-02/209

The diffractive process $ep \to eXY$, where Y denotes a proton or its low mass excitation having $M_Y < 1.6$ GeV, is studied with the H1 experiment at HERA. Triple differential cross sections are measured as a function of the photon virtuality Q^2, the longitudinal momentum fraction of the incident proton carried by the colourless exchange $x_{I\!P}$ and $\beta = x/x_{I\!P}$, where x is the Bjorken scaling variable. These measurements are made after selecting diffractive events by demanding a large empty rapidity interval separating the final state hadronic systems X and Y. High statistics measurements covering the data taking periods 1999-2000 and 2004-2007 are combined with previously published results. The combined data represent a factor between three and thirty increase in statistics with respect to the previously published results. The measurements are compared with predictions from NLO QCD calculations based on diffractive parton densities and from a dipole model. The proton vertex factorisation hypothesis is tested.

1 Introduction

At low x in deep inelastic scattering (DIS) at HERA, approximately 10% of the events are of the type $ep \to eXp$, where the final state proton carries more than 95% of the proton beam energy. For these processes, a photon virtuality Q^2, coupled to the incoming lepton, undergoes a strong interaction with the proton to form an hadronic final state system X of mass M_X separated by a large rapidity gap (LRG) from the leading proton. In such a reaction no net quantum number are exchanged and a fraction $x_{I\!P}$ of the proton longitudinal momentum is transferred to the system X. In addition the virtual photon couples to a quark carrying a fraction $\beta = x/x_{I\!P}$ of the exchanged momentum. The study and interpretation of diffraction at HERA provides essential inputs for the understanding of quantum chromodynamics (QCD) at high parton densities.

2 Large rapidity gap measurements and combination

High statistics data with an integrated luminosity of up to 366 pb^{-1} recorded with the H1 detector in the years 1999-2000 and 2004-2007, when HERA collided protons of 920 GeV energy with 27.6 GeV electrons and positrons have been analysed [1]. Diffractive neutral current DIS events are selected by requiring an absence of hadronic activity in a large rapidity region extending close to the outgoing proton beam direction. The measurement is integrated over

the region $M_Y < 1.6$ GeV, $|t| < 1$ GeV^2. Triple differential reduced cross sections are measured, as defined by $\sigma_r^{D(3)}(Q^2, \beta, x_{I\!P}) = \frac{\beta Q^4}{4\pi\alpha_{em}^2} \frac{1}{(1-y-\frac{y^2}{2})} \frac{\mathrm{d}^3\sigma^{ep\to eXY}}{\mathrm{d}Q^2\,\mathrm{d}\beta\,\mathrm{d}x_{I\!P}} = F_2^{D(3)} - \frac{y^2}{1+(1-y)^2} F_L^{D(3)}$, where $F_2^{D(3)}$ and $F_L^{D(3)}$ are diffractive structure functions, $F_L^{D(3)}$ corresponding to longitudinal polarisation of the virtual photon.

A combination with previous measurements obtained by H1, also using LRG events and based on low and medium Q^2 data from 1997 and high Q^2 data from 1999-2000 [2], is performed in order to provide a single set of diffractive cross sections from all H1 data. The combination is performed taking into account correlated systematic uncertainties by using the χ^2 minimisation method developed for the combination of inclusive DIS cross sections [3, 4, 5]. A reasonable consistency of the different data sets is found, confirming with a larger statistic previous H1 measurements. The combined data span more than two orders of magnitude in Q^2 from 3.5 GeV^2 to 1600 GeV^2 and cover the range $0.0017 \leq \beta \leq 0.8$ for five fixed values of $x_{I\!P}$ in the range $0.0003 \leq x_{I\!P} \leq 0.03$. A significant reduction of statistical errors is observed. In the best measured region for $Q^2 \geq 12$ GeV^2, the statistical and systematic uncertainties are at the level of 1% and 5%, respectively, with an additional overall normalisation uncertainty of 4%. An example of the β dependence of the reduced cross section $\sigma_r^{D(3)}$ from combined H1 data is presented in Fig. 1 at a fixed $x_{I\!P} = 0.003$ value. It is compared to previous published H1 results [2] and to predictions from the H1 2006 DPDF Fit B [2]. Similar figures for other $x_{I\!P}$ bins and for Q^2 dependences can be found in [1].

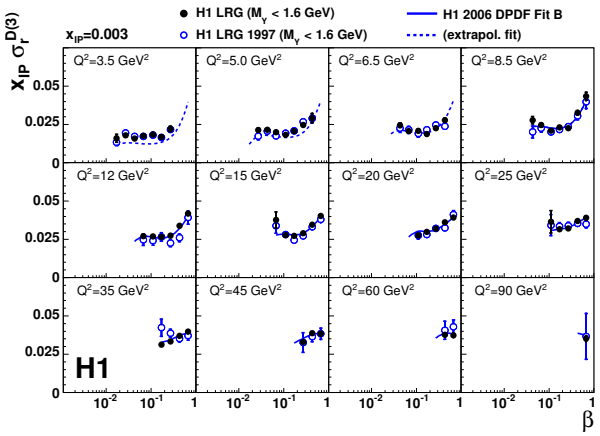

Figure 1: The β dependence of the reduced diffractive cross section, multiplied by $x_{I\!P}$, for $x_{I\!P} = 0.003$, for combined H1 data, compared to previously published H1 measurements [2]. Overall normalisation uncertainties of 4% and 6.2% on the combined and previous data, respectively, are not shown.

The combined reduced cross section $\sigma_r^{D(3)}$ can be compared with other H1 measurements obtained by a direct measurement of the outgoing proton using the H1 Forward Proton Spectrometer (FPS) [6]. The cross section $ep \to eXY$ measured here with the LRG data includes proton dissociation to any system Y with a mass in the range $M_Y < 1.6$ GeV, whereas in the cross section measured with the FPS the system Y is defined to be a proton. Therefore, the cross section ratio LRG/FPS provides an experimental determination of the fraction of proton dissociative events, $ep \to eXY$, where the proton dissociation system has a small mass M_Y, in LRG events. The global weighted average of the cross section ratio LRG/FPS is found to be $\frac{\sigma(M_Y<1.6\,\mathrm{GeV})}{\sigma(Y=p)} = 1.203 \pm 0.019(\mathrm{exp.}) \pm 0.087(\mathrm{norm.})$.

The combined H1 LRG cross section are also compared with the most recent measurements by the ZEUS experiment using a similar LRG selection [7]. These ZEUS diffractive data have been determined for identical β and $x_{I\!P}$ values, but at different Q^2 values to H1. In order to match the $M_Y < 1.6$ GeV range of the H1 data, a global factor of 0.91 ± 0.07 is applied to the ZEUS LRG data [7]. The comparison for $M_Y < 1.6$ GeV between the H1 data and the rescaled

ZEUS data is shown in Fig. 2. The ZEUS data tend to remain higher than those of H1 by $\sim 10\%$ on average. Deviations are observed between the β dependence of the two measurements at the highest and lowest β values. However a good agreement of the Q^2 dependence is observed throughout most of the phase space.

3 Comparison with models

In Fig. 2 the data are compared also with predictions of the H1 2006 DPDF Fit B [2] and of a dipole model [8]. As the dipole model predictions correspond to the process $ep \to eXp$, they are rescaled by a factor of 1.20 according to the comparison of FPS and LRG H1 data. Both approaches give a good overall description of the measurements. In the low Q^2 range, for $Q^2 < 8.5$ GeV^2, the dipole model, which includes saturation effects, seems to better describe the data, whereas for larger β and for $x_{I\!P} = 0.01$ it tends to underestimate the measured cross section.

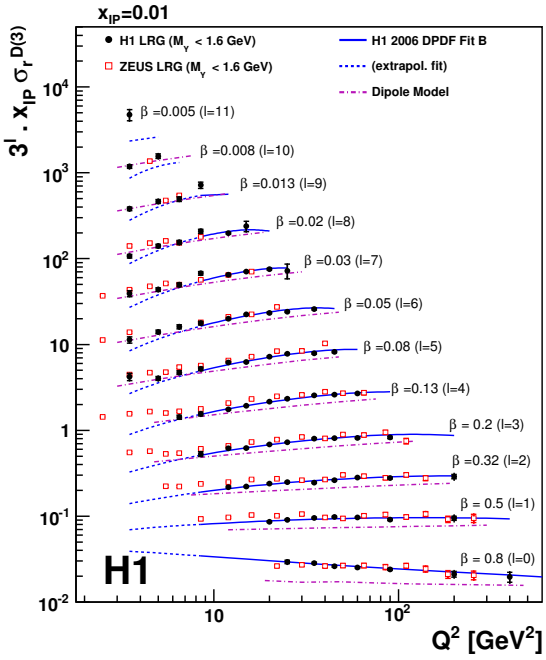

Figure 2: The Q^2 dependence of the reduced diffractive cross section from combined H1 data, multiplied by $x_{I\!P}$, for $x_{I\!P}$= 0.01. The overall normalisation uncertainties of H1 and ZEUS data are not shown. Predictions from the H1 2006 DPDF Fit B and dipole model are displayed.

The diffractive structure function can also be investigated in the framework of Regge phenomenology and is usually expressed as a sum of two factorised contributions corresponding to Pomeron and secondary Reggeon trajectories $F_2^{D(3)}(Q^2, \beta, x_{I\!P}) = f_{I\!P/p}(x_{I\!P})\, F_2^{I\!P}(Q^2, \beta) + n_{I\!R}\, f_{I\!R/p}(x_{I\!P})\, F_2^{I\!R}(Q^2, \beta)$. In this parametrisation, $F_2^{I\!P}$ can be interpreted as the Pomeron structure function and $F_2^{I\!R}$ as an effective Reggeon structure function. The Pomeron and Reggeon fluxes are assumed to follow a Regge behaviour with linear trajectories $\alpha_{I\!P,I\!R}(t) = \alpha_{I\!P,I\!R}(0) + \alpha'_{I\!P,I\!R} t$, such that $f_{I\!P/p,I\!R/p}(x_{I\!P}) = \int_{t_{cut}}^{t_{min}} \frac{e^{B_{I\!P,I\!R} t}}{x_{I\!P}^{2\alpha_{I\!P,I\!R}(t)-1}} \mathrm{d}t$. In previous publications [6, 7, 9, 10], it has already been shown that fits of this form provide a good description of the data. This supports the proton vertex factorisation hypothesis whereby the $x_{I\!P}$ and t dependences are decoupled from the Q^2 and β dependences for each of the Pomeron and sub-leading contributions. This global conclusion can be refined using the advantage of the improved statistical precision of the new data, by dividing the full range in Q^2 into six intervals. For each interval i, a free Pomeron intercept $\alpha_{I\!P}(0)[Q_i^2]$ is introduced, allowing thus to test differentially in Q^2 the factorisation assumption. The fit performed in such a way provides a good description of the data and results on the Pomeron intercept are presented in Fig. 3. No significant Q^2 dependence of the Pomeron intercept is observed, which supports the pro-

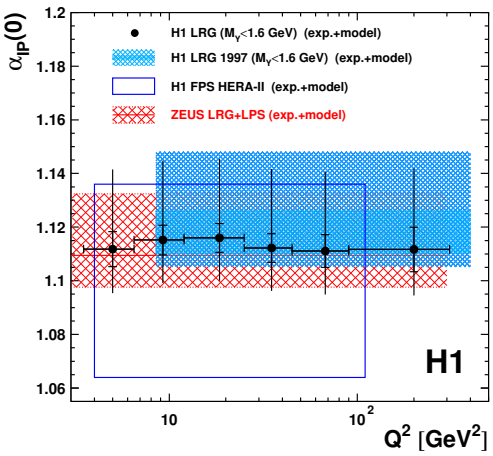

Figure 3: Pomeron intercept values obtained from Regge fits in different Q^2 bins (dots). The inner error bars represent the statistical and systematic errors added in quadrature and the outer error bars include model uncertainties in addition. Previous determinations of the Pomeron intercept [2, 6, 7, 10] are also displayed for comparison. For these previous results the bands or boxes represent the combination of experimental and model uncertainties, always dominated by the model error.

ton vertex factorisation hypothesis, as discussed above. The average value is found to be $\alpha_{I\!P}(0) = 1.113 \pm 0.002$ (exp.) $^{+0.029}_{-0.015}$ (model).

4 Conclusion

A measurement of the reduced inclusive diffractive cross section $\sigma_r^{D(3)}(Q^2, \beta, x_{I\!P})$ for the process $ep \to eXY$ with $M_Y < 1.6$ GeV and $|t| < 1$ GeV^2 is presented. New results obtained from the selection of LRG events using high statistics data taken from 1999 to 2007 by the H1 detector at HERA are combined with previous H1 results obtained with the same technique. By comparison to proton-tagged cross section, a contribution of 20% of proton dissociation is found to be present in LRG data. The combined H1 LRG data are compared with predictions from the dipole and DPDF approaches and a reasonable description of the data is achieved by both models. The $x_{I\!P}$ dependence of $\sigma_r^{D(3)}$ is described using a model motivated by Regge phenomenology, in which a leading Pomeron and a sub-leading exchange contribute. A possible Q^2 dependence of the Pomeron intercept was tested with increased sensitivity. The result is compatible with previous determinations and do not exhibit any dependence on Q^2, which supports the proton vertex factorisation hypothesis.

References

[1] H1 Collaboration, submitted to EPJC. arXiv:1203.4495 [hep-ex].
[2] H1 Collaboration. Eur. Phys. J. C **48** (2006) 715, hep-ex/0606004.
[3] A. Glazov, "Averaging of DIS cross section data", AIP Conf. Proc. vol 792 (2005) 237.
[4] H1 Collaboration. Eur. Phys. J. **C63** (2009) 625, arXiv:0904.0929 [hep-ex].
[5] H1 and ZEUS Collaborations. JHEP **1001** (2010) 109, arXiv:0911.0884 [hep-ex].
[6] H1 Collaboration. Eur. Phys. J. **C71** (2011) 1578, arXiv:1010.1476 [hep-ex].
[7] ZEUS Collaboration. Nucl. Phys. B **816** (2009) 1, arXiv:0812.2003 [hep-ex].
[8] C. Marquet, Phys. Rev. D **76** (2007) 094017, arXiv:0706.2682 [hep-ex].
[9] H1 Collaboration. Z. Phys. C **76** (1997) 613, hep-ex/9708016.
[10] H1 Collaboration. Eur. Phys. J. C **48** (2006) 749, hep-ex/0606003.

Measurement of Dijet Production in Diffractive Deep-Inelastic Scattering with a Leading Proton at HERA

Richard Polifka on behalf of the H1 Collaboration*

Charles University in Prague
E-mail: Richard.Polifka@cern.ch

DOI: http://dx.doi.org/10.3204/DESY-PROC-2012-02/211

The latest results from the H1 experiment on the diffractive dijet production in deep-inelastic scattering are presented. The first jet measurements with a tagged leading proton are described. The results are discussed in terms of diffractive parton densities and Regge factorisation.

1 Introduction

Measurements of di-jets in diffractive deep inelastic scattering (DIS) provide an unique tool to investigate the gluonic part of the object exchanged in the diffractive interactions - the Pomeron [1]. The presence of a hard scale - the transverse momenta of the jets - allows to compare the measured data with next-to-leading order QCD calculations. This provides the possibility to test the QCD factorization in diffractive DIS as well as to look for effects of parton evolution beyond the DGLAP approach. In the following sections, the diffractive jet production with a proton measured with the H1 experiment at the HERA collider will be described and the latest results will be presented.

2 Jets in Diffractive DIS at HERA

In the low x_{Bj} region in the high energy electron[1]-proton collisions at HERA, events of the type $ep \to eXY$, where the final state consists of two systems X and Y, comprise approximately 10% of all deep-inelastic scattering events (DIS). The products of the hard interaction with the photon emitted by the electron are contained in the system X, the system Y contains the outgoing proton (elastic processes) or its low mass excitations (proton dissociation). Both systems are clearly separated by a region without energy flow (Large Rapidity Gap). These events are called diffractive. Diffractive interactions are described according to the Regge phenomenology in terms of the exchange of a colourless object which carries the quantum numbers of the vacuum, the so called Pomeron. At HERA, extensive measurements of inclusive diffractive DIS have been performed using two experimental methods of detecting diffraction - the Large Rapidity Gap (LRG) method [2] and the tagging of the outgoing proton with dedicated detectors

*The work was supported by the grant SVV-2010-261 309.

[1]The term "electron" is used here to denote both electron and positron.

(FPS and VFPS for H1, LPS for ZEUS) [1]. In addition to the standard DIS variables Q^2 (photon virtuality) and x_{Bj} (the longitudinal momentum fraction of the interacting parton with respect to the incoming proton), the following additional variables are used to describe diffractive processes: the fractional longitudinal momentum loss of the proton $x_{I\!P} = 1 - E'_p/E_p$, the momentum fraction of the interacting parton with respect to the Pomeron β, defined similar to x_{Bj}, and the squared four-momentum transfer at the proton vertex t. In the following analysis, the events tagged by the FPS are analysed. As proven by Collins [3], the diffractive DIS cross section can be factorized into a hard process (denoted as $d\hat{\sigma}^{ei}$) calculable within the pQCD framework and the diffractive parton distribution functions f_i^D (DPDF) which have to be determined experimentally: $d\sigma(Q^2, |t|, \beta, x_{I\!P}) = \sum_i f_i^D(Q^2, |t|, \beta, x_{I\!P}) \otimes d\hat{\sigma}^{ei}(Q^2, x_{Bj} = x_{I\!P} \cdot \beta)$, where the sum runs over all partons. Regge factorization (also called proton vertex factorization) is usually assumed in addition, where the dependence on the variables characterizing the proton vertex ($x_{I\!P}$ and t) factorizes from the hard interaction depending on β and Q^2: $f_i^D(Q^2, |t|, \beta, x_{I\!P}) = f_{I\!P/p}(x_{I\!P}, t) \cdot f_i(\beta, Q^2)$, where the $f_{I\!P/p}$ stands for the Pomeron flux and f_i is the probability of finding a parton i in the Pomeron. The quark densities within the Pomeron are well constrained by the inclusive diffractive DIS measurements, whereas a better constraint on the gluon density in the Pomeron is provided by measurement of jets in the final state. In addition, dijet measurements allow tests of perturbative QCD calculations, various models for modelling diffractive processes and serve as a tool for studying the parton evolution. The measurement of jet production in diffraction with the *FPS* method has been performed for the first time [4]. The cross section is corrected to the level of stable hadrons with a matrix unfolding. It is compared to pNLO DGLAP QCD calculations, DPDF-based RAPGAP Monte Carlo, two-gluon Pomeron RAPGAP Monte Carlo and soft colour interaction (SCI) model as implemented in the LEPTO Monte Carlo. The jet cross section is measured for two topologies. The 'two central jets' topology (see Table 1) is used for testing the proton vertex factorisation and the DPDFs in processes with a leading proton in the final state, whereas the 'one central + one forward jet' topology is motivated by the search for deviations from DGLAP parton evolution. In contrary to non-diffractive DIS, jets reconstructed in the forward region are not spoiled by the presence of the proton remnant and can be therefore directly related to partons emitted during the interaction.

Selection	two central jets	one central + one forward jet
DIS	$4 < Q^2 < 110$ GeV^2 $0.05 < y < 0.7$	
Leading Proton	$x_{I\!P} < 0.1$ $\lvert t \rvert < 1$ GeV^2	
Jets	$P^*_{T,1} > 5$ GeV $P^*_{T,2} > 4$ GeV $-1 < \eta_{1,2} < 2.5$	$P^*_{T,c}, P^*_{T,f} > 3.5$ GeV $M_{jj} > 12$ GeV $-1 < \eta_c < 2.5$ $1 < \eta_f < 2.8, \eta_f > \eta_c$

Table 1: Phase space of the diffractive dijet FPS measurements, The asterisk marks variables reconstructed in the hadronic centre-of-mass system while other quantities are reconstructed in the lab frame.

The Figures 1 and 2 present the comparison of the measured hadron level cross sections to the NLO QCD DGLAP predictions as well as Monte Carlo Models for the 'two central jets' topology. The NLO predictions describe the data within quoted uncertainties. From the

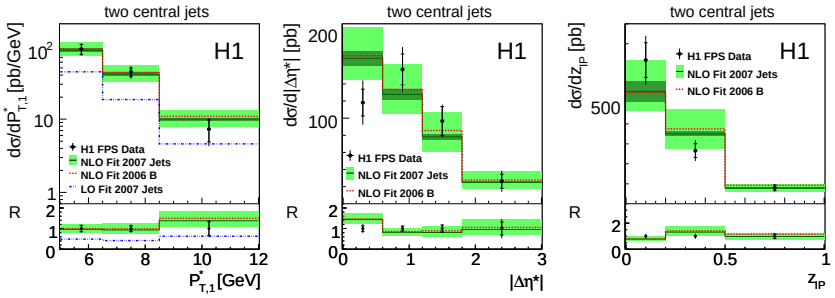

Figure 1: The sinlge differential cross section for the production of two central jets shown as a function of $p^*_{T,1}$, $|\Delta\eta^*|$ and $z_{I\!P}$ (Pomeron momentum fraction which goes into the di-jet system) compared to the NLO QCD DGLAP predictions based on DPDFs H1 2007 Jets and H1 2006 Fit B.

Monte Carlo Models, only the DPDF based RAPGAP MC is able to describe all shape aspects of the kinematic distributions. The Figure 3 left presents the comparison of the *FPS* and *LRG* methods and the extension of the phase space for the *FPS* method. Both methods agree well within errors, the *LRG* measurement is corrected for proton dissociation by a constant factor of 1.2. The measured B slope of the t distribution (middle) is compared to the inclusive *FPS* measurement [1] (right), the result is consistent with the assumption of the proton vertex factorisation being independent on the diffractive final state. Figure 4 presents the comparison of the data to NLO QCD DGLAP in the phase space enhancing effects beyond DGLAP. No deviations were observed within the uncertainties.

3 Conclusion

The latest results on the measurements of diffractive di-jet production with the scattered proton tagged in the Forward Proton Spectrometer at HERA have been presented. The cross sections are well described by the NLO DGLAP QCD predictions even in the phase space enhancing possible deviations from the DGLAP parton evolution. A good agreement between the LRG and FPS methods as well as consistency with proton vertex factorisation assumption has been shown. The DPDF based RAPGAP Monte Carlo describes the kinematical distributions in shape, whereas the two-gluon pomeron and scoft colour interaction models fail.

References

[1] A. Aktas *et al.* [H1 Collaboration], Eur. Phys. J. **C 71** (2011) 1578 [arXiv:1010.1476].

[2] C. Adloff *et al.* [H1 Collaboration], Z. Phys. **C 76** (1997) 613 [hep-ex/9708016].

[3] J. Collins,Phys. Rev. **D 57** (1998) 3051; [Erratum-ibid. **D 61** (2000) 019902]; [hep-ph/9709499].

[4] F. D. Aaron *et al.* [H1 Collaboration], Eur. Phys. J. **C 72** (2012) 1970 [arXiv:1111.0584].

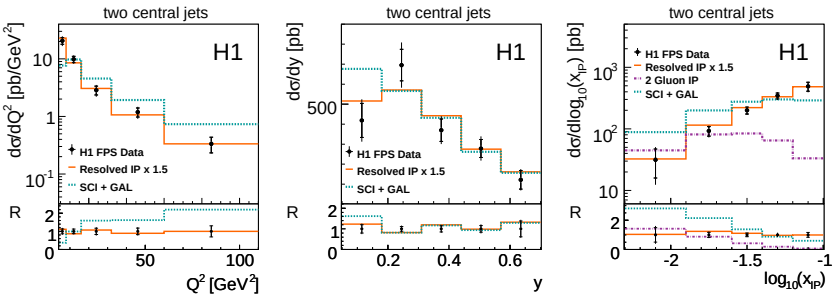

Figure 2: The sinlge differential cross section for the production of two central jets shown as a function of Q^2, y and $\log(x_{I\!P})$ compared to the DPDF based RAPGAP, 2 gluon $I\!P$ RAPGAP and SCI LEPTO Monte Carlo Models.

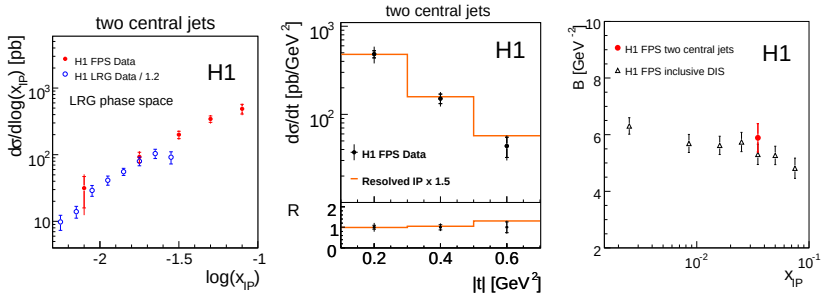

Figure 3: The comparison of the FPS and LRG method as a fuction of $\log(x_{I\!P})$ (left), the sinlge differential cross section for the production of two central jets shown as a function of t (middle) and comparison of the fitted B slope parameter in the inclusive (black open) and dijet (full red) diffractive measurements with tagged leading proton (right).

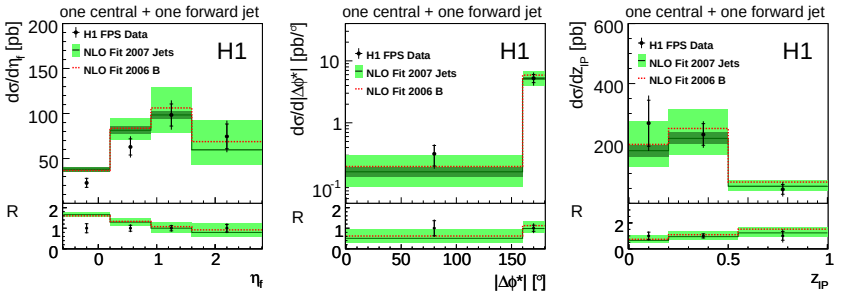

Figure 4: The sinlge differential cross section for the production of one central + one forward jet shown as a function of η_f^*, $|\Delta\phi^*|$ and $z_{I\!P}$ compared to the NLO QCD DGLAP predictions based on DPDFs H1 2007 Jets and H1 2006 Fit B.

Revisiting QCD Fits in Diffractive DIS

Federico A. Ceccopieri[1,2], *Laurent Favart*[2]

[1]IFPA, Université de Liège, Allée du 6 août, Bât B5a, 4000 Liège, Belgium.
[2]Université Libre de Bruxelles, Boulevard du Triomphe, 1050 Bruxelles, Belgium.

DOI: `http://dx.doi.org/10.3204/DESY-PROC-2012-02/282`

A new method of extracting diffractive parton distributions is presented which avoids the use of Regge theory ansatz and is in much closer relation with the factorisation theorem for diffractive hard processes.

1 Introduction

Diffractive parton distributions functions (DPDF's) [1] are essential ingredients in the understanding and description of hard diffractive processes. The factorisation theorem for diffractive Deep Inelastic Scattering (DIS) [2] enables one to factorise the diffractive DIS cross-section into a long-distance contribution, parametrised by DPDF's, from a short-distance one, pertubatively calculable. Although DPDF's encode non-perturbative effects of QCD dynamics and therefore must be extracted from data, their dependence on the factorisation scale is predicted by pQCD [1]. Moreover the short distance cross-section is the same as inclusive DIS [2] so that higher order corrections can be systematically accounted for. Due to the factorisation theorem, DPDF's are universal distributions in the context of diffractive DIS and diffractive dijet cross-sections are well described by next-to-leading order predictions based on DPDF's [3]. The commonly used approach [3, 4, 5, 6] to extract DPDF's is to assume proton vertex factorisation, *i.e.* that DPDF's can be factorised into a flux factor depending only on $x_{I\!P}$ and t and a term depending only on the lepton variables β and Q^2:

$$f_i^D(\beta, Q^2, x_{I\!P}, t) = f_{I\!P/P}(x_{I\!P}, t)\; f_i^{I\!P}(\beta, Q^2) + f_{I\!R/P}(x_{I\!P}, t)\; f_i^{I\!R}(\beta, Q^2) + ...$$

Each term in the expansion, according to Regge theory, is supposed to give a dominant contribution in a given range of $x_{I\!P}$, the pomeron ($I\!P$) at low $x_{I\!P}$, the reggeon ($I\!R$) at higher value of $x_{I\!P}$ and so on. The flux factor $f_{I\!P/P}$ ($f_{I\!R/P}$) can be interpreted as the probability that a pomeron (reggeon) with a given value of $x_{I\!P}$ and t couples to the proton. This approach assumes an arbitrary truncation of the trajectory expansion and requires that parton distributions of each trajectory ($f_i^{I\!P}$, $f_i^{I\!R}$, ...) should be simultaneously extracted from data. It therefore introduces a large number of parameters in the fit and it is potentially biased by the choices of the flux factors. Although it has been proven to be supported by phenomenological analyses within HERA-I data precision, it is not routed in perturbative QCD and might be not entirely satisfactory with the expected precision increase of HERA-II data.

2 The new method

The alternative method we propose is instead inspired by the factorisation theorem [2] for diffractive DIS itself. The latter states that factorisation holds at fixed values of $x_{I\!P}$ and t so that the parton content described by f_i^D is uniquely fixed by the kinematics of the outgoing proton and it is in principle different for different values of $x_{I\!P}$ (and t, eventually). This idea is realised in practice by performing a series of pQCD fits at fixed values of $x_{I\!P}$ with a common initial condition controlled by a set of parameters $\{p_i\}$. This procedure guides us to infere the approximate dependence of parameters $\{p_i\}$ on $x_{I\!P}$ allowing the construction of initial condition in the $\{\beta, x_{I\!P}\}$ space to be used in a global fit, without any further model dependent assumption. For the fits at fixed $x_{I\!P}$ we choose the following singlet and gluon distributions at the arbitrary scale Q_0^2:

$$\begin{aligned} \beta\,\Sigma(\beta,Q_0^2) &= A_q\,\beta^{B_q}\,(1-\beta)^{C_q}\,e^{-\frac{0.01}{1-z}}\,, \\ \beta\,g(\beta,Q_0^2) &= A_g\,e^{-\frac{0.01}{1-z}}\,, \end{aligned}$$

which have four free parameters. We further assume that all lights quark distributions are equal to each other. The exponential dumping exponential factor allows more freedom in the variation of the parameters C_q at large β and we choose the gluon distribution to be a simply a costant at Q_0^2 [4]. Such distributions are then evolved with the `QCDNUM17` [7] program within a fixed flavour number scheme to next-to-leading order accuracy. Heavy flavours contributions are taken into account in the general massive scheme. The convolution engine of `QCDNUM17` is used to obtain $F_2^{D(3)}$ and $F_L^{D(3)}$ structure functions at next-to-leading order which are then minimised against H1 data [4]. In order to avoid the resonance region, a cut on the invariant mass of the hadronic system X is applied, $M_{\rm X}^2 \geq 4\,\mathrm{GeV}^2$. Fixed $x_{I\!P}$-fit results are sensitive to the choice of the mininum Q^2 value of data to be included in the fits. The inclusion in the fits of data for which $Q^2 < 8.5\,\mathrm{GeV}^2$ in general worsens the χ^2 and induce large fluctuation in the gluon distribution. This effect has been already noticed in Ref. [4] and avoided by including in the fit only data for which $Q^2 \geq 8.5\,\mathrm{GeV}^2$. The same strategy will be adopted here. Good quality fits have been obtained with the common initial condition for all values of $x_{I\!P}$-bins [8]. The dependence of the parameters (as returned by the fits at fixed $x_{I\!P}$) on $x_{I\!P}$ is shown in Fig. [1]. Red dots are the results from pQCD fits at fixed $x_{I\!P}$. The singlet normalisation A_q behaves as an inverse power of $x_{I\!P}$. In order to improve the description at higher $x_{I\!P}$, however, an additional term is also included:

$$A_q(x_{I\!P}) = A_{q,0}\,(x_{I\!P})^{A_{q,1}}\,(1-x_{I\!P})^{A_{q,2}}\,.$$

The gluon normalisation is compatible with a single inverse power behaviour of the type:

$$A_g(x_{I\!P}) = A_{g,0}\,(x_{I\!P})^{A_{g,1}}\,.$$

The coefficients B_q and C_q which control the β-shape of the singlet distribution are well described by:

$$\begin{aligned} B_q(x_{I\!P}) &= B_{q,0} + B_{q,1}\,x_{I\!P}\,, \\ C_q(x_{I\!P}) &= C_{q,0} + C_{q,1}\,x_{I\!P}\,. \end{aligned}$$

The following generalised initial condition

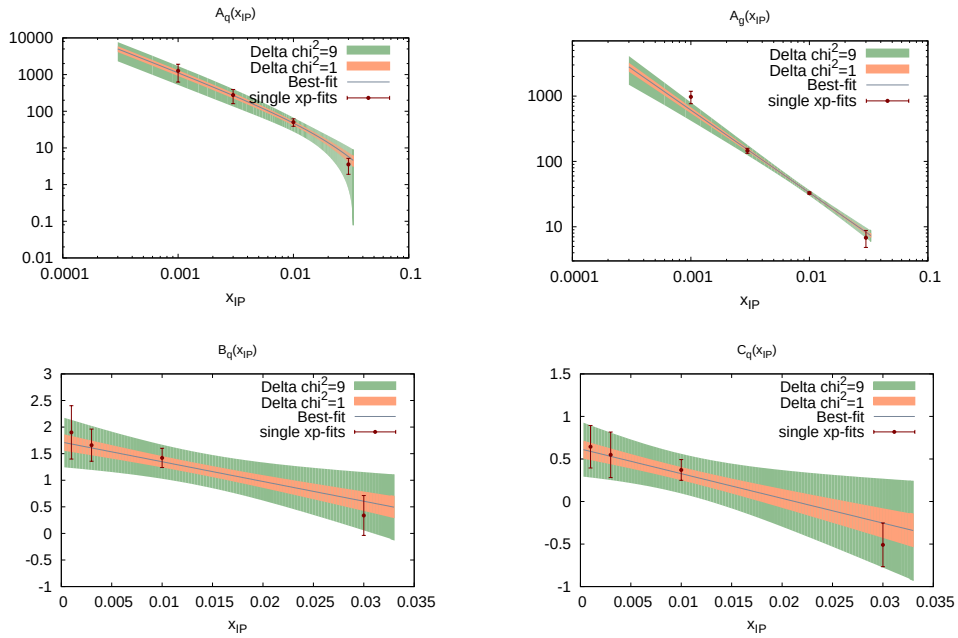

Figure 1: Parameters as a function of $x_{I\!P}$. Red dots are the results from pQCD fits at fixed $x_{I\!P}$. The grey line are best-fit prediction from $x_{I\!P}$-combined fit. The bands represent the propagation of experimental uncertainties by using the Hessian method [10].

$$\begin{aligned} \beta\,\Sigma(\beta,Q_0^2,x_{I\!P}) &= A_q(x_{I\!P})\,\beta^{B_q(x_{I\!P})}\,(1-\beta)^{C_q(x_{I\!P})}\,e^{-\frac{0.01}{1-z}}\,, \\ \beta\,g(\beta,Q_0^2,x_{I\!P}) &= A_g(x_{I\!P})\,e^{-\frac{0.01}{1-z}}\,, \end{aligned}$$

is then used to perform a $x_{I\!P}$-bin combined fit. The combined fit has nine free parameters. Following the procedure described in Ref. [9], to each systematic errors quoted in the experimental analysis is assigned a free systematic parameters which is then minimised in the fit along with theory parameters. As for the single-$x_{I\!P}$ fits, only data points for which $M_{\rm x}^2 \geq 4\,{\rm GeV}^2$ and $Q^2 \geq 8.5\,{\rm GeV}^2$ are included in the fit. The latter has an appreciable sensitivity on the scale Q_0^2 due to the relative stiffness of the initial condition. The choice of Q_0^2 is then optimised performing a scan which gives the best χ^2 value for $Q_0^2 = 2.3\,{\rm GeV}^2$. The best fit returns a $\chi^2 = 166$ for 182 degrees of freedom which is of comparable quality as the one presented in Ref. [4]. The initial condition allows the singlet and gluon normalisation, A_q and A_g respectively, to have a different power behaviour. It is therefore interesting to notice that if the condition $A_{q,1} = A_{g,1}$ is enforced, this results in a global increase of the χ^2 to 171 units for 183 degree of freedom. If one further neglects the $x_{I\!P}$-dependence of B_q and C_q by setting $B_{q,1} = C_{q,1} = 0$ the χ^2 increases to 188 units for 185 degree of freedom. This is an *a posteriori* confirmation that not only diffractive parton distributions change their magnitude versus $x_{I\!P}$ but also that a modulation in their β-shape (for the singlet, in this case) is necessary to better fit the data. The initial condition at $Q_0^2 = 2.3\,{\rm GeV}^2$ as a function of β for different values of $x_{I\!P}$ are shown in Fig. [2].

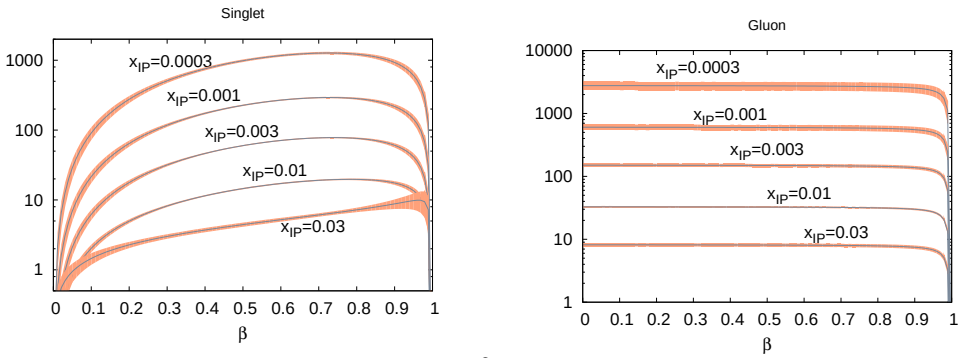

Figure 2: Singlet and gluon initial condition at Q_0^2 as a function of β for different $x_{I\!P}$-values. The bands represent the propagation of experimental uncertainties by using the Hessian method [10].

3 Conclusions

We have outlined a new method to extract diffractive PDF's inspired by the factorisation theorem for diffractive DIS. From a series of pQCD fits at fixed $x_{I\!P}$ we were able to infere the dependence of parameters on such a variable and this allowed us to construct a generalised initial condition without assuming neither proton vertex factorisation nor the existence of a series of Regge trajectories. The best-fit returns a χ^2/d.o.f. close to unity, as the Regge-based pQCD fit of Ref. [4], but in our opinion the new procedure treats the non-perturbative $x_{I\!P}$-dependence of the cross-section in a controlled and less model dependent way and it might be capable (or even necessary) to fully exploit the expected improved precision of HERA-II data [11, 12, 13].

F.A.C. would like to thank Dimitri Colferai and Ian Brock for their kind invitation to DIS12 Conference and the University of Bonn for support. L.F. is supported by the Fonds National de la Recherche Scientifique Belge (FNRS).

References

[1] L. Trentadue, G. Veneziano. Phys. Lett. **B323** (1994) 201;
G. Camici, M. Grazzini, L. Trentadue. Phys. Lett. **B439** (1998) 382.

[2] M. Grazzini, L. Trentadue, G. Veneziano. Nucl. Phys. **B519** (1998) 394;
J. C. Collins. Phys. Rev. **D57** (1998) 3051.

[3] H1 Collaboration (A. Aktas *et al.*) JHEP (2007) 0710:042;
ZEUS Collaboration (S. Chekanov *et al.*) Eur. Phys. J. **C52** (2007) 813.

[4] H1 Collaboration (A. Aktas *et al.*) Eur. Phys. J. **C48** (2006) 715.

[5] ZEUS Collaboration (S. Chekanov *et al.*) Nucl. Phys. **B831** (2010) 1.

[6] S. Taheri Monfared *et al.* e-Print: `arXiv`:1109.0912 [hep-ph]

[7] M. Botje. Comput. Phys. Commun. **182** (2011) 490.

[8] F. A. Ceccopieri, L. Favart. e-Print: `arXiv`:1110.4829 [hep-ph]

[9] C. Pascaud and F. Zomer. LAL-95-05.

[10] J. Pumplin *et al.* Phys. Rev. **D65** (2001) 014011.

[11] H1 Collaboration (F.D. Aaron *et al.*) Eur. Phys. J. **C71** (2011) 1578.

[12] H1 Collaboration (F.D. Aaron *et al.*) e-Print: `arXiv`:1203.4495 [hep-ex]

[13] T. Hreus. [H1prelim-10-014] PoS DIS2010 (2010) 068.

Uncertainties on diffractive parton distribution functions from fit to the HERA data

S. Taheri Monfared[1], *Ali N. Khorramian*[2,1], *S. Atashbar Tehrani*[1]

[1]School of Particles and Accelerators, Institute for Research in Fundamental Sciences (IPM), P.O.Box 19395-5531, Tehran, Iran
[2]Physics Department, Semnan University, Semnan, Iran

DOI: http://dx.doi.org/10.3204/DESY-PROC-2012-02/52

In the present QCD analysis, we use a wide range of the inclusive diffractive deep inelastic scattering observable based on different methods of data selections. Diffractive parton distribution and their uncertainty bands are determined from a global fit in the next-to-leading order (NLO). Predictions based on the extracted diffractive parton densities are compared to the available theoretical models. Satisfactory agreement exists.

1 Introduction

The diffractive deep inelastic scattering (DDIS) at HERA provide a very interesting sample of the interplay between hard and soft aspects of QCD interactions. On one side virtuality of the photon probe is large, while on the other side, the scattered proton remains almost intact, missing just a small fraction of its initial momentum.

The concept of diffractive parton distribution functions (DPDFs) plays an important role in the study of diffractive reactions in DIS and is essential input to calculations of hard diffractive processes at the LHC.

In this paper, we briefly reports the uncertainties of DPDFs extracted from the H1 and ZEUS data. An effective χ^2 function is used not only to obtain the best fit, but also to find the neighborhood of the global minimum in order to quantify the uncertainties. The need to quantify the uncertainties for new physics searches in the next generation of collider experiments has stimulated much interest among phenomenological groups in developing new approaches [1, 2]. We followed the approach introduced in Ref. [3].

2 Diffractive data

At HERA, diffractive events were selected either by the detection of the final state proton [4, 5, 6, 7, 8] or on the basis of a large rapidity gap between the system X and the outgoing proton [7, 9]. The diffractive contribution was also identified by the M_X method [10, 11] based on the shape of the mass distribution of the system X. Within the normalization uncertainties the results from the different methods agree reasonably well.

3 Uncertainties of DPDFs

We analyzed almost all HERA diffractive deep inelastic scattering data in the standard NLO parton model approach of the perturbative QCD. Our detailed fit procedure is available in Ref. [12, 13, 14]. Here, we focus on the propagation of uncertainty bands. The quality of fit is traditionally determined by the χ^2 of the fit to the data [15], which is minimized using the MINUIT package [16]. $\chi^2_{\rm global}$ is defined by

$$\chi^2_{\rm global}(p) = \sum_{i=1}^{n^{data}} \left[\left(\frac{1-\mathcal{N}_i}{\Delta\mathcal{N}_i} \right)^2 + \sum_{j=1}^{n^{data}} \left(\frac{\mathcal{N}_j\, F_{2,j}^{D,data} - F_{2,j}^{D,theor}(p)}{\mathcal{N}_j\, \Delta F_{2,j}^{D,data}} \right)^2 \right] , \tag{1}$$

where p denotes the set of independent parameters in the fit and n^{data} is the number of data points included. For the i^{th} experiment, $F_{2,j}^{D,data}$, $\Delta F_{2,j}^{D,data}$ and $F_{2,j}^{D,theor}$ denote the data value, measurement uncertainty and theoretical value for n^{th} data point. $\Delta\mathcal{N}_i$ is the experimental normalization uncertainty and $\mathcal{N}_i$ is an overall normalization factor for the data of experiment i. We allow for a relative normalization shift $\mathcal{N}_i$ between different data sets within uncertainties $\Delta\mathcal{N}_i$ quoted by the experiments.

The errors include systematic and statistical uncertainties, being the total experimental error evaluated in quadrature. We check the fit stability by performing the two approaches with statistical and systematics errors added in quadrature or with statistical errors only. For a given set of data, the results based on the fit with statistical or total errors are very close. When moving to a combined fit of all data sets, although DPDFs show small differences between both fits, using statistical errors lead to fit with a large χ^2.

There are clear procedures for propagating experimental uncertainties on the fitted data points through to the PDF uncertainties. The most common is the Hessian approach. In this case we can consider

$$\Delta\chi^2_{\rm global} \equiv \chi^2_{\rm global} - \chi^2_{\rm min} = \sum_{i,j} H_{ij}(a_i - a_i^{(0)})(a_j - a_j^{(0)}), \tag{2}$$

where the Hessian matrix is defined as

$$H_{ij} = \frac{1}{2} \frac{\partial^2\, \chi^2_{\rm global}}{\partial a_i \partial a_j} \bigg|_{\rm min} . \tag{3}$$

The standard formula for linear error propagation is

$$(\Delta F)^2 = \Delta\chi^2 \sum_{i,j} \frac{\partial F}{\partial a_i} (H_{ij})^{-1} \frac{\partial F}{\partial a_j}. \tag{4}$$

Since the derivative of F with respect to each parameter a_i is required, this formula is not easily calculable. It can be improved by finding and rescaling the eigenvectors of H [17, 18, 3]. In term of the rescaled eigenvectors z_i, the increase in χ^2 is given by

$$\chi^2_{\rm global} - \chi^2_{\rm min} = \sum_i z_i^2. \tag{5}$$

The uncertainty on a quantity is then obtained applying

$$(\Delta F)^2 = \frac{1}{2}\sum_i \left[F(S_i^+) - F(S_i^-)\right]^2, \tag{6}$$

where S_i^+ and S_i^- are PDF sets displaced along eigenvector directions by the given $\Delta\chi^2$. The uncertainties on our DPDFs following this method are presented in Figure 1. Our predictions are in fair agreement with the others.

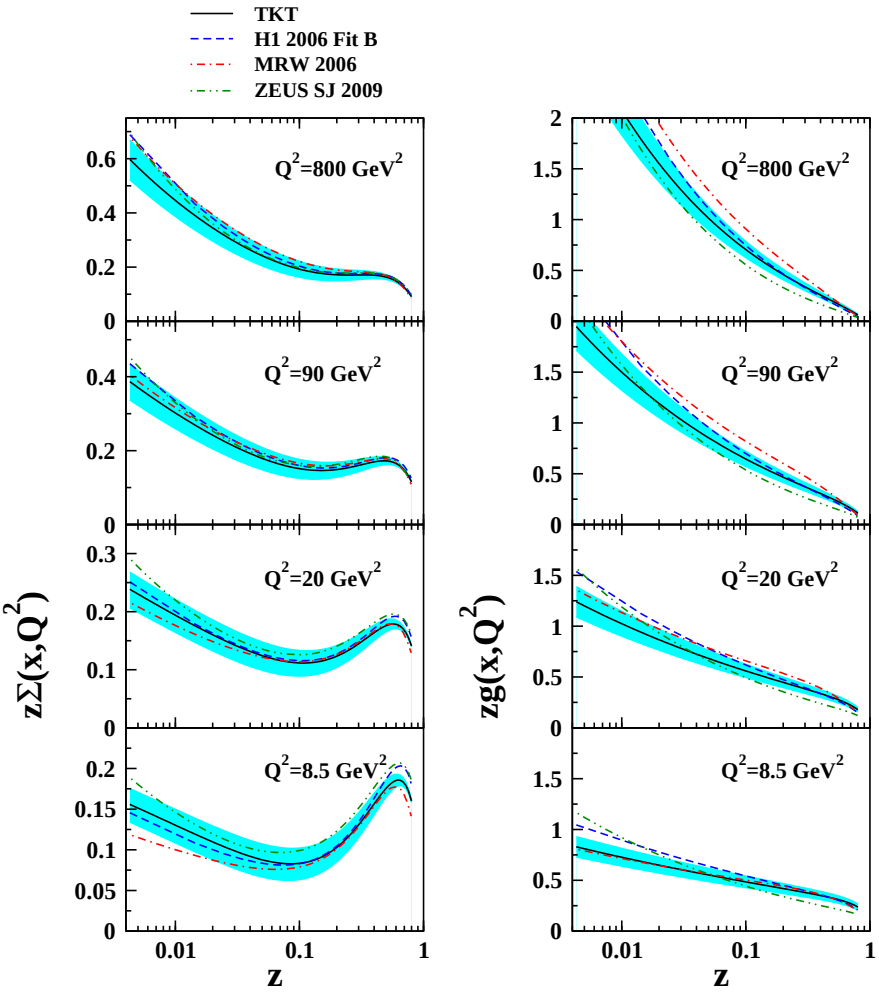

Figure 1: Comparison between the total quark singlet and gluon distributions obtained from our model (solid curve), H1 2006 DPDF Fit B (dashed curve) [9], ZEUS SJ (dashesd-dotted-dotted curve) [19] and MRW (dashesd-dotted curve) [20] at four different values of Q^2 as a function of z.

4 Conclusion

The cross sections and structure functions of the diffractive reaction from HERA have been measured in a very wide range of Q^2, β. Our predictions for all DPDFs using QCD fits to the almost all available HERA experimental data are in very good agreement with the other theoretical models. Our DPDF uncertainty bands are also calculated in different energy scales.

A FORTRAN package containing our Pomeron densities Σ and g with their errors at NLO in the $\overline{\text{MS}}$ scheme can be found in `http://particles.ipm.ir/links/QCD.htm`.

5 Acknowledgements

S. T. M. gratefully acknowledges the generous support of the organizing committee of DIS 2012 for providing the opportunity to attend the conference.

References

[1] U. Baur, (ed.), R. K. Ellis, (ed.) and D. Zeppenfeld, (ed.), FERMILAB-PUB-00-297.

[2] S. Catani, M. Dittmar, J. Huston, D. E. Soper, S. Tapprogge, P. Aurenche, C. Balazs and R. D. Ball *et al.*, hep-ph/0005114.

[3] A. D. Martin, W. J. Stirling, R. S. Thorne and G. Watt, Eur. Phys. J. C **63**, 189 (2009) [arXiv:0901.0002 [hep-ph]].

[4] A. Aktas *et al.* [H1 Collaboration], Eur. Phys. J. C **48**, 749 (2006) [arXiv:hep-ex/0606003].

[5] F. D. Aaron *et al.*, Eur. Phys. J. C **71**, 1578 (2011) [arXiv:1010.1476 [hep-ex]].

[6] S. Chekanov *et al.* [ZEUS Collaboration], Nucl. Phys. B **713**, 3 (2005) [arXiv:hep-ex/0501060].

[7] S. Chekanov [ZEUS Collaboration], Nucl. Phys. B **800**, 1 (2008) [arXiv:0802.3017 [hep-ex]].

[8] H1. Collaboration, arXiv:1107.3420 [hep-ex].

[9] A. Aktas *et al.* [H1 Collaboration], Eur. Phys. J. C **48**, 715 (2006) [arXiv:hep-ex/0606004].

[10] S. Chekanov *et al.* [ZEUS Collaboration], Eur. Phys. J. C **38**, 43 (2004) [arXiv:hep-ex/0408009].

[11] S. Chekanov *et al.* [ZEUS Collaboration], Nucl. Phys. B **816**, 1 (2009) [arXiv:0812.2003 [hep-ex]].

[12] S. T. Monfared, A. N. Khorramian and S. A. Tehrani, arXiv:1109.0912 [hep-ph].

[13] S. Taheri Monfared and A. N. Khorramian, Int. J. Mod. Phys. A **26**, 692 (2011).

[14] S. Taheri Monfared, Ali. N. Khorramian, S. Atashbar Tehrani, Proceedings of the Conference in Honor of Murray Gell-Mann's 80th Birthday, World Scientific, 503-510 (2010).

[15] D. Stump *et al.*, Phys. Rev. D **65**, 014012 (2001) [arXiv:hep-ph/0101051].

[16] F. James and M. Roos, Comput. Phys. Commun. **10**, 343 (1975).

[17] J. Pumplin *et al.*, Phys. Rev. D **65**, 014013 (2001) [arXiv:hep-ph/0101032].

[18] A. D. Martin, R. G. Roberts, W. J. Stirling and R. S. Thorne, Eur. Phys. J. C **28**, 455 (2003) [arXiv:hep-ph/0211080].

[19] S. Chekanov *et al.* [ZEUS Collaboration], Nucl. Phys. B **831**, 1 (2010) [arXiv:0911.4119 [hep-ex]].

[20] A. D. Martin, M. G. Ryskin and G. Watt, Phys. Lett. B **644**, 131 (2007) [arXiv:hep-ph/0609273].

Evidence for breakdown of the DGLAP description in diffractive DIS at HERA

Mariusz Sadzikowski, Leszek Motyka, Wojciech Slominski

Institute of Physics, Jagiellonian University, Reymonta 4, 30-059 Kraków, Poland

DOI: http://dx.doi.org/10.3204/DESY-PROC-2012-02/134

HERA data on diffractive DIS show deviations from twist 2 DGLAP predictions below $Q^2 \sim 5$ GeV^2 at low pomeron ξ, which may reach up to 100 %. These deviations are consistent with higher twists effects extracted from the saturation model. It is a first direct evidence for the higher twists in DIS. This finding affects determination of the diffractive parton densities that are used for the predictions at the LHC.

1 Introduction

A large fraction of the deep inelastic scattering (DIS) HERA data are produced due to the processes of diffractive dissociation of virtual photons $\gamma^* p \to Xp$ (DDIS). In those reactions, viewed from the proton rest frame, the virtual photon γ^* fluctuates into the strongly interacting debris which scatter off the proton target and eventually create a final hadronic state X. The proton target remains intact. The conventional description of DDIS is based on the leading twist DGLAP evolution equations which characterize the QCD hard scale dependence of the diffractive parton distribution functions (DPDFs). This approach is justified by Collins factorization theorem [1]. Despite of clear success such description faces an important limitation that follows from neglecting higher twists. The higher twists contribution becomes relevant below some energy scale which depends on the process. In the case of the inclusive DIS, a leading twist description of the data is reasonable down to the photon virtuality $Q^2 \sim 1$ GeV^2 [2], however, in the case of DDIS such description breaks down already at higher scale $Q^2 \sim 5$ GeV^2. In this presentation we would like to show, that the deviations of the extrapolated DGLAP description from the DDIS date at low Q^2 are consistent with emergence of the higher twists contribution. This provides a first evidence of the higher twists effects in DIS data and opens a new window for studying the physics beyond leading twist, both at the experimental and theoretical level.

2 Cross section and the breakdown of twist-2 description

The DDIS is an quasi-elastic electron - proton scattering process $e(k)p(P) \to e(k')p(P')X(P_X)$ in which the final hadronic state X with four-momentum P_X is separated in rapidity from the proton, that scatters elastically. The t-integrated ep cross-section reads:

$$\frac{d\sigma}{d\beta dQ^2 d\xi} = \frac{2\pi\alpha_{\rm em}^2}{\beta Q^4}[1 + (1-y)^2]\sigma_r^{D(3)}(\beta, Q^2, \xi) \tag{1}$$

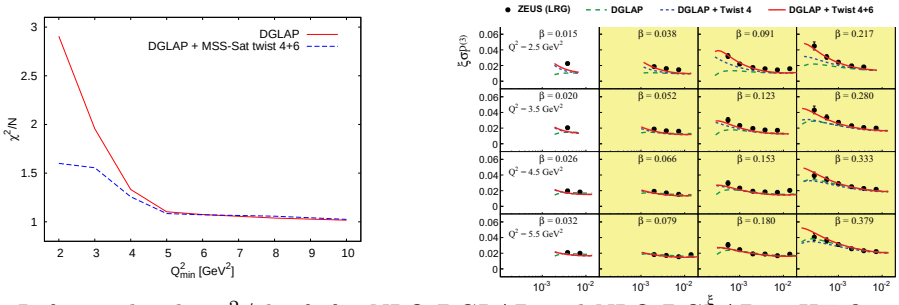

Figure 1: Left panel - the $\chi^2/\text{d.o.f.}$ for NLO DGLAP and NLO DGLAP + HT fits to ZEUS LRG data [3] with $Q^2 > Q^2_{\rm min}$. Right panel - the LRG ZEUS data for $\xi\sigma_r^{D(3)}$ at low Q^2 compared to a DGLAP fit [3] and the DGLAP fit with included twist-4 and twist-4 and 6 corrections from the saturation model. In yellow (gray) — the region of β where the correction due to $q\bar{q}gg$ may be neglected.

where the invariants read $y = (kq)/(kP)$, $Q^2 = -q^2$, $\xi = (Q^2 + M_X^2)/(W^2 + Q^2)$ and $t = (P' - P)^2$. The quantity $W^2 = (P + q)^2$ is the invariant mass squared in photon-proton scattering, and M_X^2 is the invariant mass of the hadronic state X. The reduced-cross-section may be expressed in terms of the diffractive structure functions $\sigma_r^{D(3)}(\beta, Q^2, \xi) = F_L^{D(3)} + F_T^{D(3)}$, whereas the structure functions T, L may be, respectively, expressed through transversally and longitudinally polarized γ^* - proton cross sections $F_{L,T}^{D(3)} = (Q^4/4\pi^2\alpha_{em}\beta\xi)\, d\sigma_{L,T}^{\gamma^* p}/dM_X^2$.

In recent analysis [3] the ZEUS diffractive data were fitted within NLO DGLAP approximation. A satisfactory good description was found only for $Q^2 > Q^2_{min} = 5$ GeV^2. The ZEUS fits were performed above Q^2_{min} and then extrapolated to lower photon virtualities. The deviations of the fits rapidly grow with decreasing ξ and Q^2 reaching 100 percent effect at the minimal $Q^2 = 2.5$ GeV^2 and $\xi \simeq 4 \cdot 10^{-4}$. We confirmed this result calculated $\chi^2/\text{d.o.f.}$ for subsets of ZEUS LRG data with $Q^2 > Q^2_{min}$ and $\beta > 0.035$ [4] (see Fig. 1, left panel). The cut off in β serves to reject contributions from highly resolved projectiles. It is clear from this discussion that the leading twist DGLAP evolution is unable to describe the DDIS data below $Q^2 \simeq 5$ GeV^2 and at the low ξ.

3 Estimation of the higher twist contributions

The large energy limit of the DDIS scattering may be described within the framework of the colour dipole model [5, 6]. In this approach the $\gamma^* p$ process is factorized into an amplitude of photon fluctuation into the partonic debris and then scattering of these states off the proton by the multiple gluon exchange. We take into account the contributions from the fluctuation of the photon into a colour singlet quark-antiquark pair $q\bar{q}$ and into $q\bar{q}$-gluon triple. We neglect the contribution from the higher Fock states. This gives the t-integrated $\gamma^* p$ cross section $d\sigma_{L,T}^{\gamma^* p}/dM_X^2 = d\sigma_{L,T}^{q\bar{q}}/dM_X^2 + d\sigma_{L,T}^{q\bar{q}g}/dM_X^2$. Assuming an exponential t-dependence of diffractive cross-section, one finds for the $q\bar{q}$ component

$$\frac{d\sigma_{L,T}^{q\bar{q}}}{dM_x^2} = \frac{1}{16\pi b_D} \int \frac{d^2p}{(2\pi)^2} \int_0^1 dz\; \delta\left(\frac{p^2}{z\bar{z}} - M_x^2\right) \sum_f \sum_{spin} \left| \int d^2r e^{i\vec{p}\cdot\vec{r}} \psi^f_{h\bar{h},\lambda}(Q, z, \vec{r}) \sigma_d(r, \xi) \right|^2 . \tag{2}$$

where b_D is a diffractive slope, $z\bar{z} = z(1-z)$ and the first sum runs over the three light flavours. The second sum of (2) means summation over massless (anti)quark helicities $(\bar{h})h$ in the case of longitudinal photons whereas for transverse photons there is an additional average over initial photon polarizations λ. The squared photon wave functions reads, e.g. [7]

$$\sum_{spin} \psi^f_{h\bar{h},\lambda}(Q,z,\vec{r})\psi^{f\,*}_{h\bar{h},\lambda}(Q,z,\vec{r}\,') = \frac{N_c\alpha e_f^2}{2\pi^2}\left\{\begin{array}{ll} 4Q^2(z\bar{z})^2K_0(\epsilon r)K_0(\epsilon r') & (L) \\ \epsilon^2(z^2+\bar{z}^2)\frac{\vec{r}\cdot\vec{r}\,'}{rr'}K_1(\epsilon r)K_1(\epsilon r') & (T)\end{array}\right. \tag{3}$$

where K_0, K_1 are McDonald-Bessel functions and $\epsilon = \sqrt{z\bar{z}}Q$. We use the GBW parametrization [6] for the dipole-proton cross section $\sigma_d(r,\xi) = \sigma_0(1-\exp(-r^2/4R_\xi^2))$. The saturation radius in DDIS depends on ξ, $R_\xi = (\xi/x_0)^{\lambda/2}$ GeV^{-1} and $\sigma_0 = 23.03$ mb, $\lambda = 0.288$, $x_0 = 3.04\cdot 10^{-4}$.

The contribution of the $q\bar{q}g$ component of γ^* is calculated at $\beta = 0$ and in the soft gluon approximation (the longitudinal momentum carried by a gluon is much lower then carried by the $q\bar{q}$ pair). This approximation is valid in the crucial region of $M_X^2 \gg Q^2$ or $\beta \ll 1$, where the deviations from DGLAP are observed. The correct β-dependence is then restored using a method described in [8], with kinematically accurate calculations of Ref. [9]. With these approximations one obtains:

$$\begin{aligned}\frac{d\sigma^{q\bar{q}g}_{L,T}}{dM_x^2} &= \frac{1}{16\pi b_D}\frac{N_c\alpha_s}{2\pi^2}\frac{\sigma_0^2}{M_x^2}\int d^2r_{01}N^2_{q\bar{q}g}(r_{01},\xi)\sum_f\sum_{spin}\int_0^1 dz|\psi^f_{h\bar{h},\lambda}(Q,z,r_{01})|^2, \quad (4)\\ N^2_{q\bar{q}g}(r_{01}) &= \int d^2r_{02}\frac{r_{01}^2}{r_{02}^2r_{12}^2}\left(N_{02}+N_{12}-N_{02}N_{12}-N_{01}\right)^2\end{aligned}$$

where $N_{ij} = N(\vec{r}_j - \vec{r}_i)$, $\vec{r}_{01}, \vec{r}_{02}, \vec{r}_{12} = \vec{r}_{02} - \vec{r}_{01}$ denote the relative positions of quark and antiquark (01), quark and gluon (02) in the transverse plain. The form of N^2_{qqg} follows from the Good-Walker picture of the diffractive dissociation of the photon [10]. The factor $1/M_X^2$ is a remnant of the phase space integration under the soft gluon assumption. The twist decomposition of (4) is performed using the Mellin transform in the r_{01} variable:

$$\frac{d\sigma^{q\bar{q}g}_{L,T}}{dM_X^2} = \frac{N_c\sigma_0^2\alpha_s}{32\pi^3 b_D M_X^2}\int\frac{ds}{2\pi i}\left(\frac{4Q_0^2}{Q^2}\right)^{-s}\tilde{H}_{L,T}(-s)\,\tilde{N}^2_{qqg}(s), \tag{5}$$

The Mellin transform of $N^2_{q\bar{q}g}(r_{01})$ can be done in two steps. First one defines new integrals

$$\begin{aligned} I_1 &= \frac{(Q_0^2)^s}{\pi}\int d^2r_{01}(r_{01}^2)^{s-1}\int d^2r_{02}\frac{r_{01}^2}{r_{02}^2r_{12}^2}\left[\left(N_{02}+N_{12}-N_{02}N_{12}\right)^2 - N_{01}^2\right], \quad (6)\\ I_2 &= \frac{(Q_0^2)^s}{\pi}\int d^2r_{01}(r_{01}^2)^{s-1}\int d^2r_{02}\frac{r_{01}^2}{r_{02}^2r_{12}^2}2N_{01}\left[N_{02}+N_{12}-N_{02}N_{12}-N_{01}\right].\end{aligned}$$

where $\tilde{N}^2_{q\bar{q}g}(s) = I_1 - I_2$. The integral I_1 can be performed exactly,

$$I_1 = \pi\left(Q_0R_\xi\right)^{2s}2^{1+s}\left(2^{1+s}-1\right)\Gamma(s)\times\left[H_s - {}_3F_2(1,1,1-s;2,2;-1)s\right],\ H_s = \sum_{k=1}^{s}\frac{1}{k}, \tag{7}$$

and for I_2 we use the large daughter dipole approximation $r_{02} \gg r_{01}, \vec{r}_{12} \approx \vec{r}_{02}$ and obtain,

$$I_2 = \pi\left(Q_0R_\xi\right)^{2s}2^{1+2s}\Gamma(s)\left\{1-2^{1-s}+3^{-s}+\frac{2^{-s}s}{1+s}\left[1-{}_2F_1\left(1+s,1+s;2+s;-\frac{1}{2}\right)\right]\right\}. \tag{8}$$

The twist decomposition follows from (5) as a sum over residues at the negative integer values of s. Accuracy of this approximation is at the level of 5 per cent.

4 Discussion

In Fig. 1, right panel we compare selected results with data: the extrapolated DGLAP results, DGLAP plus twist-4, DGLAP plus twist-4 and twist-6. The saturation model results are obtained using the original GBW parameters λ and σ_0, and three massless quark flavours. In our approach we modified the GBW parameter x_0 to $\xi_0 = 2x_0$ in order to account for the difference between Bjorken x and ξ, the variables used in GBW dipole cross-section in DIS and DDIS respectively. We chose $\alpha_s = 0.4$ that provides a good description of data. The conclusions from the analysis and from the Fig. 1 are the following: (i) at twist-2 the DGLAP fit and the twist-2 components of the model are reasonably consistent, but all fail to describe the data below $Q^2 = 5$ GeV^2 and at low ξ; (ii) a combination of the DGLAP fit and twist-4 and twist-6 components of the model gives a good description of the data at low Q^2. Inclusion of the higher twists terms improves the fit quality in the low Q^2 region (see the dashed curve at Fig. 1, left panel). Indded, the maximal value of χ^2/d.o.f. $\simeq 1.5$ at $Q^2_{min} = 2$ GeV^2 is significantly lower then χ^2/d.o.f. $\simeq 3$ of the DGLAP fit. However, it is important to stress that a truncation of the twist series (up to twist-6) is required to have a good description of the data. Such truncation, however, may be motivated in QCD. Let us recall that in BFKL, at the leading logarithmic approximation, only one reggeized gluon may couple to a fundamental colour line. Since DGLAP and BFKL approximations have the same double logarithmic ($\ln x \ln Q^2$) limit, one concludes that also in DGLAP couplings of more than two gluons to a colour dipole is much weaker than in the eikonal picture. Thus one can couple only 2 gluons to a colour dipole and up to four gluons to $q\bar{q}g$ component (two colour dipoles in the large N_c limit) without violating BFKL constraint. This means that one may expect a suppression beyond twist-8 if only the $q\bar{q}$ and $q\bar{q}g$ components are included in the calculations. This qualitative argument requires, obviously, further detailed studies.

5 Acknowledgements

The work is supported by the Polish National Science Centre grant no. DEC-2011/01/B/ST2/03643.

References

[1] J. Collins, Phys. Rev. **D57** (1998) 3051.

[2] J. Bartels, K. Golec-Biernat and L. Motyka, Phys. Rev. **D81** (2010) 054017.

[3] S. Chekanov et al. [ZEUS Collaboration], Nucl. Phys. **B831** (2010) 1; Nucl. Phys. **B816** (2009) 1.

[4] L. Motyka, M. Sadzikowski and W. Slominski, arXiv:1203.5461 (2012).

[5] N. N. Nikolaev and B. G. Zakharov, Z. Phys. **C49** (1991) 607;

[6] K. J. Golec-Biernat and M. Wüsthoff, Phys. Rev. **D59** (1998) 014017, Phys. Rev. **D60** (1999) 114023.

[7] H. Kowalski, L. Motyka and G. Watt, Phys. Rev. **D74** (2006) 074016.

[8] C. Marquet, Phys. Rev. **D76** (2007) 094017.

[9] M. Wüsthoff, Phys. Rev. **D56** (1997) 4311.

[10] S. Munier and A. Shoshi, Phys. Rev. **D69** (2004) 074022.

Central Exclusive Production in $p\bar{p}$ Collisions at CDF II

Erik Brücken[1] on behalf of the CDF Collaboration

[1]University of Helsinki and Helsinki Institute of Physics, Gustaf Hällströmin katu 2a, 00560 Helsinki, Finland

DOI: `http://dx.doi.org/10.3204/DESY-PROC-2012-02/254`

We report central exclusive production results studied at the Run II Collider Detector at Fermilab with focus on our recently published paper on the first observation of exclusive $\gamma\gamma$ production in $p\bar{p}$ collisions at $\sqrt{s}$ =1.96 TeV at the Tevatron. In particular, starting from earlier studies by the CDF collaboration, we discuss exclusive dijet, dilepton, Z, J/Ψ and χ_c productions and finally our recent observation of exclusive diphoton production. Whereas the lepton pairs are purely QED produced, the J/Ψ and the Z boson are produced by photo-production, mediated by photon-pomeron exchange ($\gamma + I\!P$). The double pomeron exchange producing the exclusive dijet, charmonium and diphotons via quark-loop is of great interest looking towards the possibilities of finding an exclusive Higgs at the Large Hadron Collider (if it exists). The production mechanism for an exclusive Higgs is similar via a heavy quark-loop with no other particles produced.

1 Introduction

At the Run II Collider Detector at Fermilab (CDF II) central exclusive production (CEP) has been studied extensively with great success. CEP belongs to the class of diffractive processes here with a centrally produced system X and both proton and antiproton staying intact after the collision. This can happen via a strong exchange of a colorless object (Pomeron $I\!P$, see Fig:1 (left))[1] or a purely QED exchange of virtual photons or a mixture of both (photoproduction). Large observable pseudorapidity gaps on both sides are characteristic for such processes.

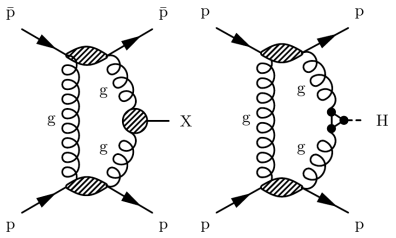

Figure 1: Leading order diagrams for (left) CEP via double pomeron exchange and (right) CEP of a Higgs boson in $p\bar{p}$ collisions.

At CDF II we are equipped with forward detectors to study CEP. In addition to the central, azimuthal and forward-backward symmetric, multipurpose detector with its excellent tracking system and projective calorimetry, we find: the Miniplug, a liquid scintillator calorimeter covering a pseudorapidity region of $3.6 < |\eta| < 5.2$; beam shower counter stations (BSC) from $5.4 < |\eta| < 7.4$; and Roman pot spectrometers (RPS) at 57 m from the interaction point on the antiproton side, accepting momentum fraction losses of $0.02 < \xi < 0.1$.

In addition to the general interest in CEP a motivation boost comes from the possibility of

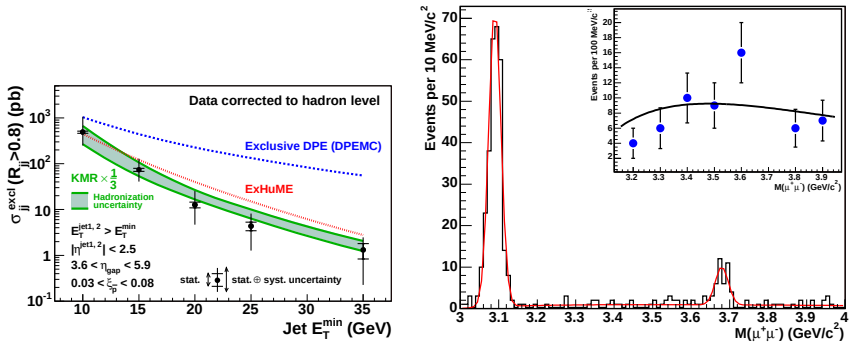

Figure 2: Exclusive dijet cross sections compared to Monte Carlo and LO analytical predictions (left). Invariant exclusive dimuon mass distribution with two Gaussian fits of the J/Ψ and $\Psi(2s)$ peak (right). The inlay graphic shows the exclusive dimuon QED continuum with the $\Psi(2s)$ peak excluded.

observing a standard model Higgs boson at LHC in the same way (see Fig:1 (right)) with direct access to its quantum numbers. Although not possible at Tevatron, several similar processes can and have been studied at CDF II to test and calibrate theoretical predictions. In particular we observed QED production of e^+e^- and $\mu^+\mu^-$, searched for Photoproduction of the Z boson and J/Ψ concluding in an observation of the latter, and observed double pomeron exchange (DPE) processes such as exclusive dijets, charmonium, χ_c and our most recent, the CEP of diphotons, observed for the first time in hadron-hadron collisions.

2 Review of earlier results

2.1 Exclusive dijet production

Exclusive dijets have been observed in CDF II data [2]. Exclusive dijets have been extracted from data of 310 pb^{-1} integrated luminosity using the ratio of the dijet mass to the total mass $R_{jj} = M_{jj}/M_x$ of the final state. At high $R_{jj} > 0.8$ exclusive dijets can be separated from inclusive diffractive dijets. Protons tagged by the RPS ensure a good separation of diffractive and non-diffractive events. The cross sections measured (see Fig. 2 left) clearly favor the KMR prediction [3].

2.2 Exclusive e^+e^- production

Introducing a special trigger requiring two EM showers in the calorimeter and a void of particles in the forward using BSC-1, we observed for the first time QED production of exclusive e^+e^- via virtual radiated photons in data of 532 pb^{-1} integrated luminosity in $p\bar{p}$ collisions [4]. A special method to ensure exclusiveness is used. The calorimetry including the forward detectors are divided into sections. For each section the noise level is defined. After subtracting the signal each event is filtered for additional activity above noise within $|\eta| < 7.4$. We found 16 exclusive e^+e^- candidates with $E_T > 5$ GeV and $|\eta| < 2$ The measured cross section of $\sigma = 1.6^{+0.5}_{-0.3}(\text{stat}) \pm 0.3(\text{syst})$ pb is in good agreement with theoretical predictions.

2.3 Exclusive charmonium and $\mu^+\mu^-$ production

In parallel we started to look at exclusive dimuon states [5]. With a special trigger for central muons and forward gaps we extracted 402 back to back $\mu^+\mu^-$ candidates with $M_{\mu\mu}$ between 3 and 4 GeV and $|\eta| < 0.6$ in $p\bar{p}$ collisions of 1.48 fb^{-1} integrated luminosity. The invariant mass distribution is shown in Fig. 2 on the right. Clearly seen are the J/Ψ and $\Psi(2s)$ peaks and the QED continuum in the inlay graphic. The first observations of the exclusive photoproduction of charmonium and the exclusive QED production of $\mu^+\mu^-$ in hadron-hadron collisions are also in good agreement with theoretical predictions. Allowing an additional photon in the final state we find an increase of 66 events in the J/Ψ compared to only one event in the $\Psi(2s)$ peak. This is clear evidence for exclusive χ_c production via DPE, decaying to J/Ψ plus photon.

2.4 Search for exclusive Z production

We did a search for exclusive photoproduction of the Z boson [6]. Due to its small cross section we did not expect to find this process at Tevatron. Any sign would have been an indication for beyond standard model physics. We set an upper limit on the production cross section. As a side product we measured exclusive high mass dilepton production ($40 < M_{ll} < 75$ GeV/c^2) that is in good agreement with theoretical predictions.

3 Exclusive $\gamma\gamma$ production

Our latest result is the first observation of exclusive $\gamma\gamma$ production in hadron-hadron collisions [8]. Similar to the exclusive Higgs (see Fig. 1 (left)), the diphoton system is produced via gluon-gluon fusion through a quark loop ($gg \to \gamma\gamma$). The other so-called *screening* gluon cancels the color-flow such that the (anti)proton stays intact and no soft hadronization occurs. In an earlier study in Run II we already found evidence for this process [7], but with only three candidate events. With an updated trigger with lower threshold for EM showers in the calorimeter and an forward gap-trigger we could record data of 1.11 fb^{-1} integrated luminosity. We selected events with exact two back to back EM object with $E_T > 2.5$ GeV in the central detector region of $|\eta| < 1.0$. No other activity above noise was allowed in the entire calorimetry including the forward detectors covering $|\eta| < 7.4$. First a subset of 34 events having exactly two charged particle tracks was extracted. Those events are consistent with exclusive e^+e^- and serve as a control channel to the diphoton study. Up to the tracking cut electrons and photons do not show any difference at the detector level. The number of exclusive e^+e^- events and the measured cross section is in perfect agreement with theoretical predictions and our earlier observation study [4]. A class of 43 events with no charged tracks are identified as exclusive $\gamma\gamma$ candidates. The invariant mass and $\Delta\phi$ distribution is shown in Fig. 3 (left, middle). Possible background contamination was discussed. Non negligible backgrounds has been identified as a small fraction of undetected proton dissociation (0.14 events) due to limited forward coverage and exclusive $\pi^0\pi^0$ production. The latter was be estimated using proportional wire

Table 1: Parameters for the exclusive $\gamma\gamma$ cross section ($E_T(\gamma) > 2.5$ GeV, $|\eta(\gamma)| < 1$).

$\gamma\gamma$ CEP	Value
Events	43
$\mathcal{L}_{\text{int}}$	1.11 ± 0.07fb^{-1}
$\varepsilon_{\text{exclusive}}$	0.068 ± 0.004 (syst)
$\varepsilon_{\text{photon-pair}}$	0.40 ± 0.02 (stat) ± 0.03 (syst)
$\varepsilon_{\text{no conversion}}$	0.57 ± 0.06 (syst)
$\pi^0\pi^0$ b/g	0.0, < 15 (95% C.L.) events
Dissoc. b/g	0.14 ± 0.14 (syst) events

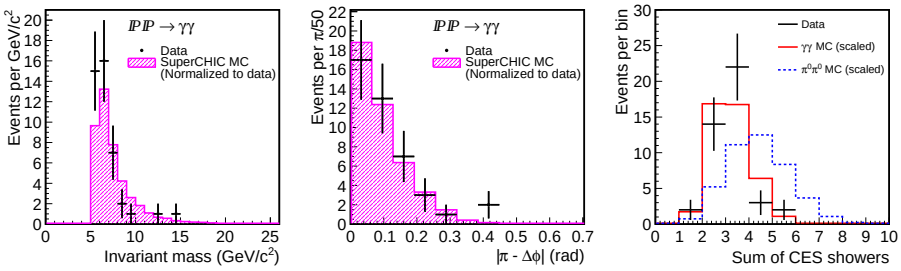

Figure 3: Two-photon candidates: invariant mass distribution (left), $|\pi - \Delta\phi|$ distribution (middle) compared to MC prediction. Distribution of reconstructed CES showers per events for data and $\gamma\gamma$ and $\pi^0\pi^0$ MC simulations (right).

chambers at shower maximum position in the EM calorimeter (CES). Neutral pions decay to two photons with a minimal opening angle of around 3° in our energy region. With the CES detector we reconstructed the number of showers to distinguish two close-by photons from π^0 decays with single signal photons. The most probable fraction of exclusive $\pi^0\pi^0$ was found to be zero with an upper limit of 15 events at 95%CL. Other possible backgrounds were found to be negligible. We measured a cross section of $\sigma(|\eta| < 1, \mathrm{E_T} > 2.5\mathrm{GeV}) = 2.48\,^{+0.40}_{-0.35}(\mathrm{stat})\,^{+0.40}_{-0.51}(\mathrm{syst})\,\mathrm{pb}$ using the parameters listed in Tab. 1. A comparison to KMR model predictions [9] using different parton density functions is shown in Fig. 4. We find a good agreement to the theoretical prediction and can create some constraint on the PDF's used.

4 Conclusions

CEP results of the CDF collaboration are presented. They certainly constraint theoretical predictions and help understanding non-perturbative soft QCD dynamics. Especially the exclusive $\gamma\gamma$ production is helpful as the cleanest DPE process. Recently we published successfully the exclusive $\gamma\gamma$ result as *first observation*. The Higgs boson produced by DPE, if it exists, could be found at the LHC. Our results help tuning and calibrating forward detectors and analysis tools at LHC.

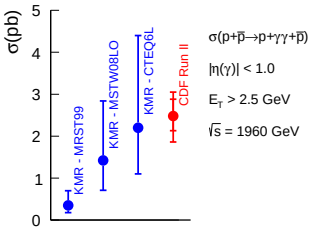

Figure 4: Comparison of measured to predicted cross sections.

References

[1] S. Donnachie, G. Dosch, P.V. Landshoff, and O. Nachtmann, *Pomeron Physics and QCD*, (Cambridge University Press, Cambridge, U.K., 2002).

[2] T. Aaltonen *et al.* (CDF Collaboration), Phys. Rev. D **77**, 052004 (2008).

[3] V.A. Khoze, A.D. Martin and M.G. Ryskin, Eur. Phys. J. C **14**, 525 (2000).

[4] A. Abulencia *et al.* (CDF Collaboration), Phys. Rev. Lett. **98**, 112001 (2007).

[5] T. Aaltonen *et al.* (CDF Collaboration), Phys. Rev. Lett. **102**, 242001 (2009).

[6] T. Aaltonen *et al.* (CDF Collaboration), Phys. Rev. Lett. **102**, 222002 (2009).

[7] T. Aaltonen *et al.* (CDF Collaboration), Phys. Rev. Lett. **99**, 242002 (2007).

[8] T. Aaltonen *et al.* (CDF Collaboration), Phys. Rev. Lett. **108**, 081801 (2012).

[9] L.A. Harland-Lang, V.A. Khoze, M.G. Ryskin, and W. J. Stirling, Eur. Phys. J. C **69**, 179 (2010).

Exclusive Dimuon production at LHCb

Dermot Moran[1] on behalf of the LHCb Collaboration

[1]University of Manchester, Oxford Road, Manchester, M13 9PL

DOI: http://dx.doi.org/10.3204/DESY-PROC-2012-02/148

We report on preliminary results for the measurement of exclusive dimuon production at LHCb. Cross-section measurements for exclusive J/ψ, $\psi\prime$ and for non-resonant production $p + p \to p + \mu^+\mu^- + p$ are presented and comparisons made with theory. The additional requirement of a single photon allows the the cross-section for exclusive χ_c production to be measured and also the relative contribution of χ_c^0,χ_c^1,χ_c^2 to be determined.

1 Introduction

LHCb is one of the experiments located on the Large Hadron Collider at CERN [1]. It is a forward arm spectrometer covering a pseudorapidity of $1.9 < \eta < 4.9$, with some backward acceptance to charged particles in the region $-4 < \eta < -1.5$. Collisions with a centre of mass energy of 7 TeV began at the LHC in March 2010 with a total integrated luminosity of 37 ± 3.7 pb^{-1} collected in that year.

Exclusive production in proton-proton collisions are elastic processes in which the protons remain intact, and the additional particles are created through photon and/or pomeron propagators. Dimuons can be produced by diphoton fusion giving rise to a continuous dimuon invariant mass spectrum, while photon-pomeron fusion can produce $J/\psi, \psi\prime$ which decay to two muons. Double pomeron fusion can produce χ_c that decay to J/ψ plus a photon. The final state protons are only marginally deflected, go down the beam-pipe, and remain undetected. The experimental signal therefore in LHCb is a completely empty event except for two muons and possibly a photon. As LHCb is not hermetic, there will be sizeable backgrounds from inelastic processes where the other particles travel outside the detector acceptance. However the transverse momentum (Pt) of the centrally produced object is generally smaller in an elastic collision. Therefore the Pt distribution of exclusive candidates should display a peak at low momentum values corresponding to elastic production and a tail at higher momentum values corresponding to inelastic production.

In the following we outline cross-section measurements of the exclusive processes mentioned above where the final state particles have pseudorapidities between 2 and 4.5. The full data sample collected in 2010 is used in this study. However as we are interested in events with a single primary vertex the data under consideration is limited to beam crossings without multiple interactions. The average number of interactions per beam crossing, μ, was generally high ($\mu = 2$) in 2010 with the result that much of the data is unusable for this study. The exclusive trigger used in 2010 required a dimuon in coincidence with a low charged particle multiplicity (< 20).

2 Exclusive J/ψ and $\psi\prime$ selection

We select J/ψ and $\psi\prime$ candidates as those dimuons with a mass within 65 MeV of the PDG value. Exclusive candidates are selected by requiring no backward tracks, just two forward tracks and no photons in the event. The left hand plot in Figure 1 displays the Pt spectrum for the J/ψ candidates. We have fit the spectrum with two shapes representing the elastic (green) and inelastic (red) contributions. The shape for the elastic signal is taken from the Starlight generator [2] while the shape for the inelastic background is taken from data by requiring greater than two forward tracks. The dimuon Pt is required to be less than 900 MeV/c giving a signal purity of 80 ± 3 %.

Exclusive $\psi\prime$ decays such as $\psi\prime \to J/\psi\pi^+\pi^-$ contribute a significant background to the exclusive J/ψ measurement. The amount of feed down from the $\psi\prime$ is estimated from simulation using the number of observed exclusive $\psi\prime \to \mu^+\mu^-$ candidates in data. Other exclusive resonances which can feed down to give J/ψ in the final state are the χ_c family, via the decay $\chi_c \to J/\psi\gamma$ where the photon is outside the LHCb acceptance or is undetected. The χ_c feeddown is estimated from simulation using the number of observed exclusive $\chi_c \to J/\psi\gamma$ candidates. Non-resonant backgrounds are estimated by fitting crystal ball functions to the mass peaks and exponentials to the background.

3 Exclusive diphoton dimuon selection

To select exclusive dimuon events in the continuum, a cut is placed requiring the invariant mass of the dimuons to be further than 100 MeV/c^2 away from the J/ψ and $\psi\prime$. The signal events, produced through di-photon fusion, are peaked to low invariant masses where the background from pion kaon mis-identification is significant. Even though LHCb can trigger down to a mass of 1 GeV/c^2, a higher mass cut of 2.5 GeV/c^2 is used to suppress mis-id to a negligible level. As for the J/ψ and $\psi\prime$, exclusive candidates are selected by requiring no backward tracks, just two forward tracks and no photons in the event. The right hand plot in Figure 1 displays the Pt spectrum for the diphoton dimuon candidates. The spectrum is fit to the elastic signal shape as provided by the LPAIR generator [3] and the inelastic background shape provided from data by requiring greater than two forward tracks. A clear excess of signal events is observed below 100 MeV/c where a cut is placed in order to select events with a purity of $97 \pm 1\%$.

4 Exclusive χ_c selection

Exclusive χ_c candidates are selected by requiring dimuons with masses within 65 MeV of the J/ψ PDG value in events with no backward tracks, just two forward tracks and a single photon. The plot in Figure 2 shows the invariant mass of the photon plus J/ψ system. A fit is performed to the spectrum using the shapes as given by the SuperChiC generator [4] for χ_c^0,χ_c^1,χ_c^2 aswell as the feed-down from the $\psi\prime$. The ratio of χ_c^0:χ_c^1:χ_c^2 is 1: 2.2±0.8: 3.9±1.1. The inelastic contribution is determined in the same way as for the J/ψ. The fraction of exclusive events below 900 MeV/c is 0.39 ± 0.13.

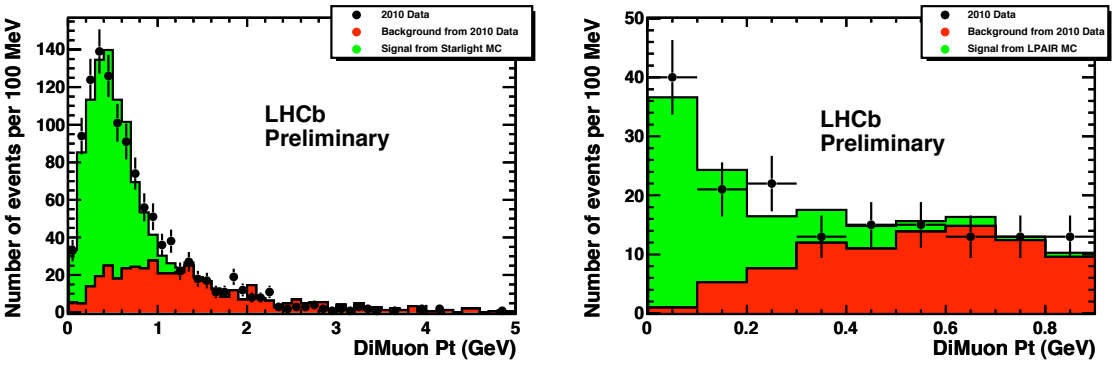

Figure 1: Left: Transverse momentum distribution for exclusive J/ψ candidates. Right: Transverse momentum distribution for exclusive diphoton dimuon candidates.

	J/ψ	$\psi\prime$	χ_c^0	χ_c^1	χ_c^2	diγ diμ
Efficiency	0.71 ± 0.07	0.71 ± 0.07	0.34 ± 0.06	0.43 ± 0.05	0.44 ± 0.04	0.25 ± 0.03
#Events	1468 ± 38	40 ± 6	25 ± 6	56 ± 18	99 ± 29	40 ± 6
Purity	0.71 ± 0.03	0.67 ± 0.03	0.39 ± 0.13	0.39 ± 0.13	0.39 ± 0.13	0.97 ± 0.01
$L_{eff}(\text{pb}^{-1})$	3.1 ± 0.6	3.1 ± 0.6	3.1 ± 0.6	3.1 ± 0.6	3.1 ± 0.6	2.3 ± 0.5
Cross-section	474 ± 12	12.2 ± 1.8	9.3 ± 2.2	16.4 ± 5.3	28.0 ± 5.4	67 ± 10
x BR (pb)	$\pm 51 \pm 92$	$\pm 1.3 \pm 2.4$	$\pm 3.5 \pm 1.8$	$\pm 5.8 \pm 3.2$	$\pm 9.7 \pm 5.4$	$\pm 7 \pm 15$

Table 1: Summary of cross-section calculation. The uncertainty on the cross-section measurement is split into three parts, the first is statistical, the second is systematic and the third relates to the luminosity estimate.

5 Cross-section calculations

The selection, reconstruction and trigger efficiencies have been determined from simulation, with systematic uncertainties applied based on data MC comparison studies [5]. The effective luminosity is determined by the trigger efficiencies and by the μ factor. The evaluation of μ leads to a large systematic uncertainty on the luminosity for this study. The number of events, efficiency, purity, luminosity and cross-section are summarised in Table 1. The uncertainty on the cross-section measurement is split into three parts, the first is statistical, the second is systematic and the third relates to the luminosity estimate.

We have found our measurements to be consistent with the predictions of Starlight, Motyka and Watt [6] , Schafer and Szczurek [7] (J/ψ and $\psi\prime$ predictions), SuperChiC (J/ψ and χ_c predictions) and LPAIR (diphoton dimuon prediction). The LPAIR theoretical prediction for diphoton dimuon production has an uncertainty of less than 1%. However the uncertainties on the other predictions are quite large.

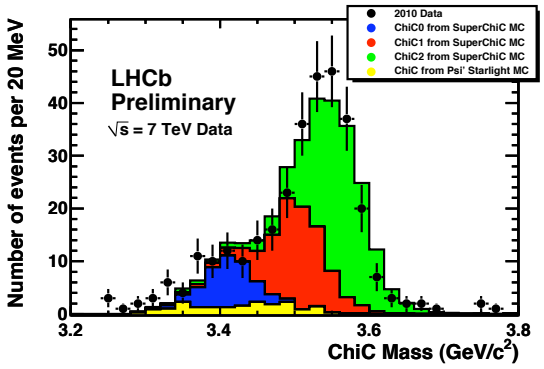

Figure 2: Invariant mass of J/ψ plus photon system. Also shown is a fit to the spectrum using the SuperChic predictions for χ_c^0,χ_c^1,χ_c^2 aswell as the feed-down from the $\psi\prime$.

6 Conclusion

We have observed clear signals for exclusive J/ψ ,$\psi\prime$ and χ_c. Preliminary results show the measured cross-sections to be in agreement with the theoretical predictions which have large uncertainties. The measured cross-section for diphoton produced dimuons is consistent with the theoretical estimate.

We wish to thank Valery Khoze, Lucien Harland-Lang, Wolfgang Schafer, James Stirling, Graeme Watt and Joakim Nystrand for many helpful communications and illuminating discussions.

References

[1] The LHCb Collaboration, A.A. Alves Jr. et al, "The LHCb Detector at the LHC", 2008 JINST 3 S08005.

[2] S. Klein and J. Nystrand, "Exclusive vector meson production in relativistic heavy ion collisions", Phys. Rev. C 60, 014903 (1999)

[3] J. Vermaseren, it Two-photon processes at very high energies, Nucl. Phys. B229, 347, 1983.

[4] L.A. Harland-Lang, V.A. Khoze, M.G. Ryskin, W.J. Stirling, "Central Exclusive χ_c Meson Production at the Tevatron Revisited", arXiv:0909.4748 [hep-ph].

[5] LHCb-CONF-2011-0222

[6] L. Motyka, G. Watt "Exclusive photoproduction at the Fermilab Tevatron and CERN LHC within the dipole picture", Phys. Rev. D 78, 014023 (2008)

[7] W. Schafer,"Exclusive photoproduction of vector mesons and Z-bosons (in hadronic collisions)". Presentation at "Diffractive and electromagnetic processes at the LHC", 4-8 January, 2010. http://diff2010-lhc.physi.uni-heidelberg.de/Talks/schaefer ect10.pdf

Search for central exclusive $\gamma\gamma$ production and observation of central exclusive e^+e^- production in pp collisions at $\sqrt{s} = 7$ TeV

Wenbo Li on behalf of the CMS Collaboration

School of Physics, and State Key Laboratory of Nuclear Physics & Technology, Peking University, Beijing, China

DOI: http://dx.doi.org/10.3204/DESY-PROC-2012-02/343

We present a search for central exclusive $\gamma\gamma$ production, $pp \to p + \gamma\gamma + p$, and the observation of central exclusive e^+e^- production, $pp \to p + e^+e^- + p$, in proton-proton collisions at $\sqrt{s} = 7$ TeV, for an integrated luminosity of 36 pb^{-1}. No diphoton candidate satisfies the selection criteria. An upper limit on the cross section for $E_T(\gamma) > 5.5$ GeV and $|\eta(\gamma)| < 2.5$ is set at 1.30 pb with 95% confidence level. Seventeen exclusive e^+e^- candidates are observed, along with an estimated background of 0.84 ± 0.28 (stat.) events, in agreement with the QED-based prediction of 16.5 ± 1.2 (syst.) events.

1 Introduction

In central exclusive production, $pp \to p + X + p$, the colliding protons emerge intact from the interaction, and all the energy transferred from the protons goes into a central color-singlet system. No other particles are produced aside from the central system, and large rapidity gaps are present. The three main types of exclusive processes are ascribed to $\gamma\gamma$ interactions (e.g. exclusive e^+e^- production), $\gamma\mathbb{P}$ fusion (e.g. exclusive Υ production) and $\mathbb{P}\mathbb{P}$ exchange (e.g. exclusive $\gamma\gamma$ or Higgs boson production), where $\mathbb{P}$ denotes a pomeron. This article presents a search for exclusive $\gamma\gamma$ production, and the observation of exclusive e^+e^- production in pp collisions at $\sqrt{s} = 7$ TeV [1]. The analysis is based on a data sample corresponding to an integrated luminosity of 36 pb^{-1} recorded in 2010 by the CMS experiment.

Exclusive $\gamma\gamma$ events can be produced via the $gg \to \gamma\gamma$ process through a quark loop, with an additional "screening" gluon exchanged to cancel the color of the interacting gluons, and so allow the protons to stay intact. The quantum chromodynamics (QCD) calculation of this diagram is difficult because the screening gluon has low squared-four-momentum-transfer Q^2, and extra soft interactions between the protons may produce particles that destroy the rapidity gaps — an effect quantified by the so-called rapidity-gap survival probability, which is poorly known theoretically. The study of exclusive $\gamma\gamma$ production may shed light on diffraction and the dynamics of pomeron exchange. In addition, exclusive $\gamma\gamma$ production provides an excellent test of the theoretical predictions for exclusive Higgs boson production.

Exclusive e^+e^- production is a quantum electrodynamics (QED) process, and the cross section is known with an accuracy better than 1%. Detailed theoretical studies have shown that in this case the corrections due to the rapidity-gap survival probability are well below 1%

and can be safely neglected [2]. Exclusive e^+e^- events provide an excellent control sample for other exclusive processes whose theoretical predictions are less certain, such as exclusive $\gamma\gamma$ production. Semi-exclusive e^+e^- production, involving single or double proton dissociation, is also considered as signal in this analysis. This process has larger theoretical uncertainties, and requires the knowledge of the rapidity-gap survival probability. In the rest of this article, exclusive events will be referred to as "el-el" events, while semi-exclusive events with either or both protons dissociated will be referred to as "inel-el" and "inel-inel" events, respectively.

The EXHUME event generator [3] is used to simulate exclusive diphoton events and to calculate their production cross section, which is an implementation of the perturbative calculation of the Durham KMR model [4]. The LPAIR event generator [5] is used to simulate both exclusive and semi-exclusive e^+e^- events. The rapidity-gap survival probability is not included in LPAIR. In order to simulate the fragmentation of the excited protons in the semi-exclusive case, the LUND shower routine implemented in the JETSET package [6] is used.

2 The CMS Detector

The central feature of the CMS apparatus is a superconducting solenoid, providing a field of 3.8 T. Within the field volume are the silicon pixel and strip tracker, the crystal electromagnetic calorimeter (ECAL) and the brass/scintillator hadron calorimeter (HCAL). The ECAL provides coverage in the pseudorapidity range $|\eta| < 1.479$ in the barrel region (EB) and $1.479 < |\eta| < 3.0$ in the two endcap regions (EE). The HCAL provides coverage for $|\eta| < 1.3$ in the barrel region (HB) and $1.3 < |\eta| < 3.0$ in the two endcap regions (HE). Muons are measured in gas-ionization detectors, which are made by using three technologies: Drift Tubes (DT), Cathode Strip Chambers (CSC), and Resistive Plate Chambers (RPC). In addition to the barrel and endcap detectors, the two hadronic forward calorimeters (HF) cover the region of $2.9 < |\eta| < 5.2$.

3 Event Selection

The selection of signal events proceeds in three steps. Exactly two photons or two electrons of opposite charge, each with $E_{\mathrm{T}} > 5.5$ GeV and $|\eta| < 2.5$, are required to be present in the triggered events. Photon or electron identification criteria are subsequently applied. Then, the events are required to satisfy the cosmic-ray rejection criteria. Finally, the exclusivity selection is performed in order to reject non-exclusive events as well as pileup events (events with any other inelastic pp interaction overlapping with the exclusive interaction).

Both exclusive diphoton and dielectron events were selected online by requiring the presence of two electromagnetic showers with a minimum E_{T} of 5 GeV. The first offline selection step is to require the presence of exactly two photon candidates or two electron candidates of opposite charge, each with $E_{\mathrm{T}} > 5.5$ GeV and $|\eta| < 2.5$, for the diphoton and dielectron analyses, respectively. These photon (electron) candidates are subsequently required to satisfy the identification criteria described in Ref. [1].

In order to remove cosmic-ray events, the two photons (electrons) are required to have timing consistent with that of particles originating from a collision. Furthermore, the two candidates are required to be separated by more than 2.5 rad in ϕ.

Exclusivity selection criteria are designed to select exclusive events by rejecting events having particles in the range $|\eta| < 5.2$ not associated with the two photon (electron) candidates. More specifically, it is required that there should be no additional tracks in the tracker, no additional

towers above noise thresholds in the calorimeters (EB, EE, HB, HE, and HF), and no track segments in the DTs and CSCs, where 'additional' means 'not associated to the two photons (electrons)'. The exclusivity selection efficiency for the used data sample is only 0.145, and is dominated by the losses due to the no-pileup requirement.

4 Results

No diphoton candidate survives the selection criteria. An upper limit on the production cross section is set employing a Bayesian approach at 95% confidence level:

$$\sigma^{E_T(\gamma)>5.5\text{ GeV},\,|\eta(\gamma)|<2.5}_{\text{exclusive and semi-exclusive }\gamma\gamma\text{ production}} < 1.30\text{ pb}$$

The upper limit is on the sum of the exclusive (el-el) and semi-exclusive (inel-el and inel-inel) $\gamma\gamma$ production cross sections, with no particles from the proton dissociation having $|\eta| < 5.2$ for the semi-exclusive case. A comparison between the present upper limit and four theoretical predictions (el-el only) is shown in Fig. 1. Two different PDF sets, MRST01 and MSTW08, from both leading-order and next-to-leading-order fits, are considered. The difference between leading-order and next-to-leading-order predictions reflects mostly the difference in the low-x gluon density ($\sigma \sim (xg)^4$ [8]). The upper limit measured in this analysis is an order of magnitude above the predicted cross sections with next-to-leading-order PDFs, while it provides some constraint on the predictions with leading-order PDFs. If the MSTW08-LO PDF is used, the probability of finding no candidate in the present data is less than 23%. The semi-exclusive $\gamma\gamma$ production cross section is much less known theoretically, but is expected to be of magnitude similar to that of the fully exclusive process [7].

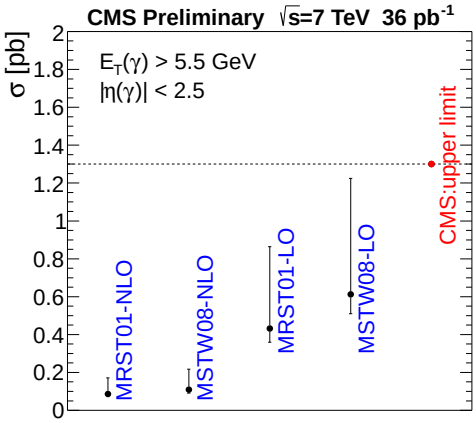

Figure 1: Comparison of the upper limit derived with the present data and four theoretical predictions (el-el only). If the contributions from semi-exclusive production are included, the predictions can increase by a factor of ∼2 [7].

Process	$\mathcal{L}$	σ	ε	Yield
el-el	$36.2 \pm 1.4\text{ pb}^{-1}$	3.74 pb	0.0488 ± 0.0056	6.57 ± 0.80 (syst.) events
inel-el		6.68 pb	0.0348 ± 0.0035	8.37 ± 0.90 (syst.) events
inel-inel		3.52 pb	0.0119 ± 0.0011	1.51 ± 0.15 (syst.) events
Total				16.5 ± 1.2 (syst.) events

Table 1: Predicted e^+e^- yields for both exclusive and semi-exclusive e^+e^- production. The integrated luminosity $\mathcal{L}$ has a relative uncertainty of 4% [9], and ε is the overall selection efficiency. The production cross sections σ are calculated with the LPAIR generator, and the poorly-known rapidity-gap survival probability is not included.

Seventeen exclusive e^+e^- candidates are observed with an expected background of 0.84 ± 0.28 (stat.) events, consistent with the theoretical prediction for the combined el-el, inel-el and inel-inel e^+e^- yields of 16.5 ± 1.2 (syst.) events (Table 1). Figure 2 shows the comparison of the

measured invariant-mass, p_{T} and $\Delta\phi$ distributions of the e^+e^- pairs with the MC simulation. Both the yield and the kinematic distributions are in good agreement with the assumption of exclusive e^+e^- production via the $\gamma\gamma \to e^+e^-$ process, which validates the analysis technique, notably the exclusivity selection. The good agreement between the measurement and the simulation lends further support to the result of the exclusive $\gamma\gamma$ production search.

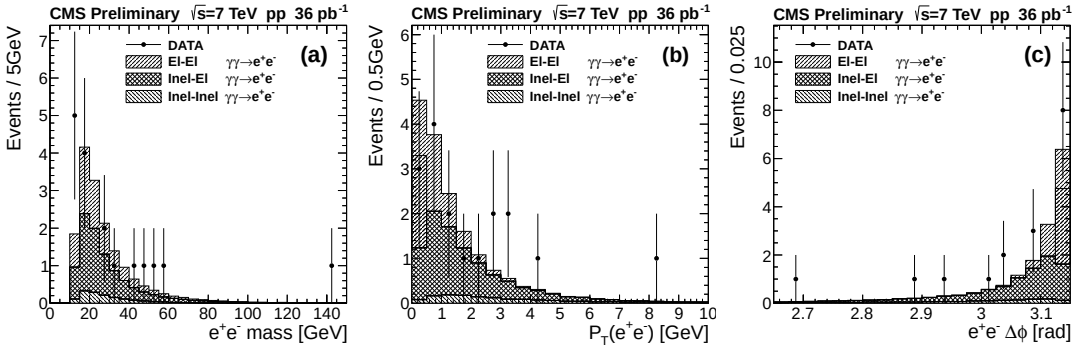

Figure 2: Distributions of the invariant mass (a), the transverse momentum (b), and the azimuthal angle difference (c) of the e^+e^- pairs, compared to the LPAIR predictions. The simulation is normalized to an integrated luminosity of 36 pb^{-1} and does not include the estimated 0.84 ± 0.28 background events.

5 Acknowledgements

The author would like to thank the National Natural Science Foundation of China and the China Scholarship Council for support.

References

[1] CMS Collaboration. CMS Physics Analysis Summary **FWD-11-004** (2012) . http://cdsweb.cern.ch/record/1427001.

[2] V. A. Khoze, A. D. Martin, M. G. Ryskin and R. Orava. Eur. Phys. J. **C19** (2001) 313–322, arXiv:hep-ph/0010163.

[3] J. Monk and A. Pilkington. Comput. Phys. Commun. **175** (2006) 232–239, arXiv:hep-ph/0502077.

[4] V. A. Khoze, A. D. Martin and M. G. Ryskin. Eur. Phys. J. **C23** (2002) 311–327, arXiv:hep-ph/0111078.

[5] S. P. Baranov et al. Physics at HERA, Proceedings of the Workshop (1991) 1478–1482.

[6] T. Sjostrand and M. Bengtsson. Comput. Phys. Commun. **43** (1987) 367–379. Especially Section 6.3: The Coherent Evolution Case.

[7] L. A. Harland-Lang, V. A. Khoze, M. G. Ryskin and W. J. Stirling. arXiv:1204.4803.

[8] L. A. Harland-Lang, V. A. Khoze, M. G. Ryskin and W. J. Stirling. Eur. Phys. J. **C69** (2010) 179–199, arXiv:1005.0695.

[9] CMS Collaboration. CMS Detector Performance Summary **DP-2011-002** (2011) . http://cdsweb.cern.ch/record/1335668.

Exclusive Production of the MSSM Higgs Bosons at the LHC

S. Heinemeyer[1], *V.A. Khoze*[2], *Marek Tasevsky*[3], *Georg Weiglein*[4]

[1]Instituto de Física de Cantabria (CSIC-UC), Santander, Spain
[2]Department of Physics, Durham University, Durham DH1 3LE, U.K.
[3]Institute of Physics, ASCR, Na Slovance 2, 182 21 Prague, Czech republic
[4]DESY, Notkestraße 85, D–22603 Hamburg, Germany

DOI: http://dx.doi.org/10.3204/DESY-PROC-2012-02/262

We review the prospects for Central Exclusive Production (CEP) of BSM Higgs bosons at the LHC using forward proton detectors proposed to be installed at 220 m and 420 m from the ATLAS and/ or CMS. Results are presented for MSSM in standard benchmark scenarios and in scenarios compatible with the Cold Dark Matter relic abundance and other precision measurements. Following results of the LHC Higgs boson searches, we investigate a hypothesis that candidates found at a mass of 125 GeV are compatible with light CP-even MSSM Higgs bosons. We show that CEP can give a valuable information about spin-parity properties of the Higgs bosons.

1 Introduction

The central exclusive production of new particles has received a great deal of attention in recent years (see [1] and references therein). The process is defined as $pp \to p \oplus \phi \oplus p$ and all of the energy lost by the protons during the interaction (a few per cent) goes into the production of the central system, ϕ. The final state therefore consists of a centrally produced system (e.g. dijet, heavy particle or Higgs boson) coming from a hard subprocess, two very forward protons and no other activity. The '$\oplus$' sign denotes the regions devoid of activity, often called rapidity gaps. Studies of the Higgs boson produced in CEP used to form a core of the physics motivation for upgrade projects to install forward proton detectors at 220 m and 420 m from the ATLAS [2] and CMS [3] detectors, see [1]. At the moment, only 220 m stations are considered to be installed in ATLAS [4]. Proving that the detected central system is the Higgs boson coming from the SM, MSSM or other BSM theories will require measuring precisely its spin, CP properties, mass, width and couplings.

In [5] we have presented detailed results on signal and background predictions of CEP production (based on calculations in [6] and the FeynHiggs code [7, 8]) of the light (h) and heavy (H) Higgs bosons which have then been updated in [9]. Changes between these two publications are described in [9] and summarized in [10]. Four luminosity scenarios are considered: "60 fb^{-1}" and "600 fb^{-1}" refer to running at low and high instantaneous luminosity, respectively, using conservative assumptions for the signal rates and the experimental efficiencies (taken from [11]); possible improvements on the side of theory and experiment could allow for scenarios where the

event rates are enhanced by a factor 2, denoted by "60 fb^{-1} eff×2" and "600 fb^{-1} eff×2".

2 Results and LHC exclusion regions

Standard benchmark scenarios designed to highlight specific characteristics of the MSSM Higgs sector, so called M_h^{max} and no-mixing scenarios, do not necessarily comply with other than MSSM Higgs sector constraints. Scenarios which fulfill constraints also from electroweak precision data, B physics data and abundance of Cold Dark Matter (CDM) are the so called CDM benchmark scenarios [12]. As observed and discussed in [9], the 5σ discovery and 3σ contours show in general similar qualitative features as the results in the M_h^{max} and no-mixing scenario. Since publications [9] and [10], the results have been updated by adding the exclusion regions coming from LHC searches for MSSM signal (see Fig. 1). These exclusion regions are obtained using the code HiggsBounds version 3.6.0 [13]. Compared to previous results with Tevatron exclusion regions ([9, 10]), the allowed region for MSSM has now significantly shrunk.

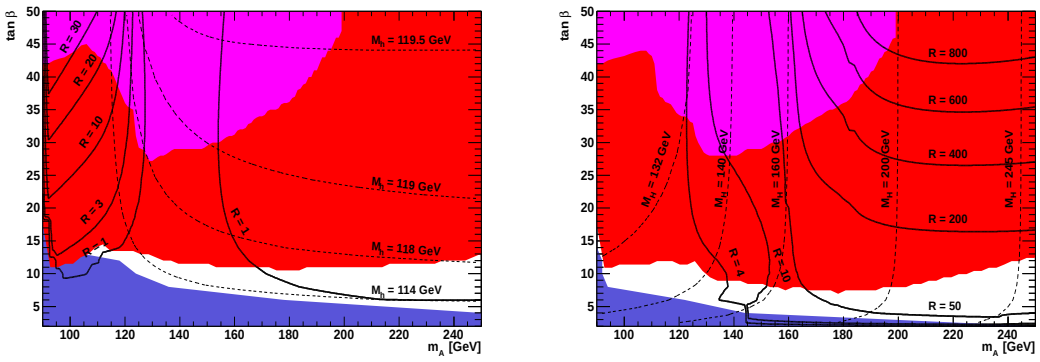

Figure 1: Ratios of MSSM to SM cross sections and mass M_h (M_H) contours for $h(H) \to b\bar{b}$ channel in CEP production in the $M_A - \tan\beta$ plane of the MSSM are shown on left (right) within the no-mixing (M_h^{max}) benchmark scenario. The lighter (dark) shaded region corresponds to the parameter region excluded by the LEP (Tevatron) Higgs boson searches, the smaller region on top corresponds to the Tevatron Higgs boson search.

3 Hypothesis of a Higgs boson at 125 GeV

Presently a big effort is put into Higgs boson searches at the LHC, both at SM and beyond SM. While the MSSM exclusion regions are already accounted for in our results (see e.g. Fig. 1), the results of the SM Higgs boson search on the data samples collected in 2011 (up to 4.9 fb^{-1}) are as follows: both ATLAS ([14]) and CMS ([15]) exclude similar mass regions and both observe an excess of the signal over background in the same mass region. After combining all decay channels, ATLAS (CMS) declare the excess at M_h=126 GeV (125 GeV) with a local significance of 2.5σ (2.8σ). The global probability for such an excess found in the search range $110 < M_h < 600$ GeV, in the absence of a signal, is 2.2σ (2.1σ). A natural question then is how

the observation of Higgs candidates in this mass range would affect our results. Let us work with a hypothesis that Higgs candidates are found at the mass of 125 ±3 GeV (1.5 GeV corresponds to the experimental uncertainty thanks to the fact that most of the signal comes from the $\gamma\gamma$ decay channel, being the most precise in the mass measurement; the theory uncertainty is estimated in [16]). This SM Higgs mass range $122 < M_h < 128$ GeV is compatible with the allowed mass range $122.5 < M_h < 127.5$ GeV when combining exclusion limits found at 95% C.L. by both experiments. The effect of this hypothesis is shown in Fig. 2 (now with the y-axis in the logarithmic scale) from which two main facts may be drawn: i) CEP MSSM signal still survives the as yet provided exclusion limits. In the allowed region, a significance of 3σ may be achieved for the highest luminosity scenario, ii) MSSM is in agreement with the tentative hints at 125 GeV, although the allowed region may shrink further with time.

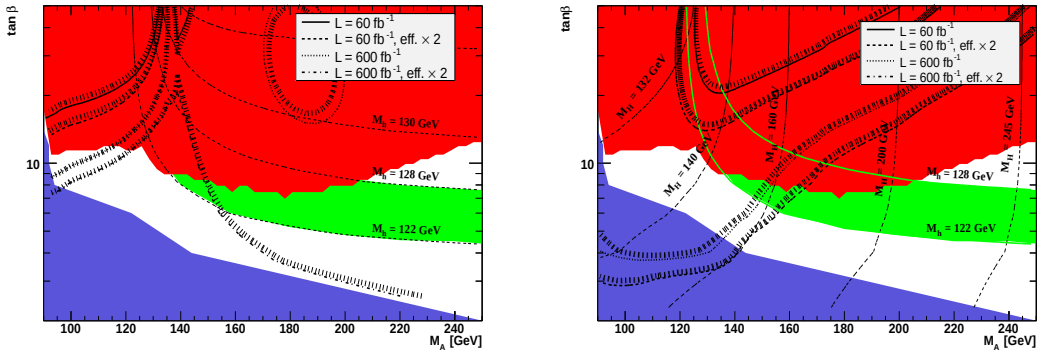

Figure 2: 3σ evidence and mass M_h (M_H) contours for $h(H) \to b\bar{b}$ channel in CEP production in the $M_A - \tan\beta$ plane of the MSSM are shown on left (right) within the M_h^{max} benchmark scenario. The results are shown for four assumed effective luminosities (see the text). The lighter (dark) shaded region corresponds to the parameter region excluded by the LEP (Tevatron) Higgs boson searches. The region $122 < M_h < 128$ GeV refers to the hypothesis of Higgs bosons found at 125 GeV with assumed theory and experimental uncertainties.

4 Coupling structure and spin-parity determination

Standard methods to determine the spin and the CP properties of Higgs bosons at the LHC rely to a large extent on the coupling of a relatively heavy Higgs boson to two gauge bosons. In particular, the channel $H \to ZZ \to 4l$ - if it is open - offers good prospects [17]. In a study [18] of the Higgs production in the weak vector boson fusion it was found that for M_H =160 GeV the W^+W^- decay mode allows the discrimination between a pure CP-even (as in the SM) and a pure CP-odd tensor structure at a level of 4.5–5.3σ using about 10 fb^{-1} of data (assuming the production rate is that of the SM, which is in conflict with the latest search limits from the Tevatron [19]). A discriminating power of 2σ was declared in the $\tau^+\tau^-$ decay mode at M_H =120 GeV and luminosity of 30 fb^{-1} .

The situation is different in MSSM: for $M_H \approx M_A \gtrsim 2M_W$ the lightest MSSM Higgs boson couples to gauge bosons with about SM strength, but its mass is bounded to a region $M_h \lesssim$

135 GeV [8], where the decay to $WW^{(*)}$ or $ZZ^{(*)}$ is difficult to exploit. On the other hand, the heavy MSSM Higgs bosons decouple from the gauge bosons. Consequently, since the usually quoted results for the $H \to ZZ/WW \to 4l$ channels assume a relatively heavy ($M_H \gtrsim$135 GeV) SM-like Higgs, these results are not applicable to the case of the MSSM. The above-mentioned analysis of the weak boson fusion with $H \to \tau^+\tau^-$ is applicable to the light CP-even Higgs boson in MSSM but due to insignificant enhancements compared to the SM case no improvement can be expected.

An alternative method which does not rely on the decay into a pair of gauge bosons or on the production in weak boson fusion would therefore be of great interest. Thanks to the $J_z = 0$, C-even, P-even selection rule, the CEP Higss boson production in MSSM can yield a direct information about spin and CP properties of the detected Higgs boson candidate and in addition, a small number of such events is sufficient [9].

Acknowledgments

The work of M.T. supported by the projects LA08032 and LA08015 of the Ministry of Education of the Czech republic. The work of S.H. supported in part by CICYT (grant FPA 2010–22163-C02-01) and by the Spanish MICINN's Consolider-Ingenio 2010 Program under grant MultiDark CSD2009-00064.

References

[1] FP420 R&D Collab., *J. Inst.* **4** (2009) T10001, arXiv:0806.0302 [hep-ex].

[2] ATLAS Collab., *J. Inst.* **3** (2008) S08003.

[3] CMS Collab., *J. Phys.* **G 34** (2007) 995, CERN-LHCC-2006-021, CMS-TDR-008-2 (2007).

[4] ATLAS Collab., Letter of Intent of the Phase-I Upgrade, http://cdsweb.cern.ch/record/1402470.

[5] S. Heinemeyer *et al.*, *Eur. Phys. J.* **C 53** (2008) 231.

[6] V.A. Khoze, A.D. Martin and M.G. Ryskin, *Eur. Phys. J.* **C 23** (2002) 311; *Eur. Phys. J.* **C 55** (2008) 363; V.A. Khoze *et al.*, *Eur. Phys. J.* **C 33** (2004) 261.

[7] S. Heinemeyer, W. Hollik and G. Weiglein, *Comp. Phys. Commun.* **124** (2000) 76.

[8] G. Degrassi, S. Heinemeyer, W. Hollik, P. Slavich and G. Weiglein, *Eur. Phys. J.* **C 28** (2003) 133.

[9] S. Heinemeyer *et al.*, Eur. Phys. J. **C71** (2011) 1649.

[10] S. Heinemeyer *et al.*, arXiv:1106.3450[hep-ph].

[11] M. Albrow *et al.*, CERN-LHCC-2006-039/G-124 (2006), CMS Note 2007/002, TOTEM Note 06-5.

[12] J. Ellis *et al.*, *JHEP* **0710** (2007) 092, arXiv:0709.0098 [hep-ph].

[13] P. Bechtle *et al.*, *Comput. Phys. Commun.* **181** (2010) 138, arXiv:0811.4169 [hep-ph].

[14] O. Kortner, these proceedings.

[15] B. Clerbaux, these proceedings.

[16] S. Heinemeyer *et al.*, Phys. Lett **B710** (2012) 201.

[17] V. Buescher and K. Jakobs, *Int. J. Mod. Phys.* **A 20** (2005) 2523.

[18] C. Ruwiedel, N. Wermes and M. Schumacher, *Eur. Phys. J.* **C 51** (2007) 385.

[19] CDF abd D0 collaborations, *Phys. Rev. Lett.* **104** (2010) 061802, arXiv:1007.4587 [hep-ex].

High Energy Exclusive Leptoproduction of the ρ-meson: Theory and Phenomenology

I. V. Anikin[1,2], *Adrien Besse*[3], *D.Yu. Ivanov* [4], *B. Pire*[5], *L. Szymanowski*[6], *S. Wallon*[3,7]

[1]Bogoliubov Laboratory of Theoretical Physics, JINR, 141980 Dubna, Russia
[2]Institute for Theoretical Physics, University of Regensburg, D-93040 Regensburg, Germany
[3]LPT, Université Paris-Sud, CNRS, 91405, Orsay, France
[4]Sobolev Institute of Mathematics and Novosibirsk State University, 630090 Novosibirsk, Russia
[5]CPHT, École Polytechnique, CNRS, 91128 Palaiseau Cedex, France
[6]National Center for Nuclear Research (NCBJ), Warsaw, Poland
[7]UPMC Univ. Paris 06, faculté de physique, 4 place Jussieu, 75252 Paris Cedex 05, France

DOI: `http://dx.doi.org/10.3204/DESY-PROC-2012-02/63`

We describe the hard leptoproduction of transversally polarized rho-meson, up to twist 3 accuracy, including 2- and 3- particles Fock-states, in the HERA kinematics of high center-of-mass energy. We first build a model based on a simple approach to the unintegrated gluon density (the parton impact factor) that we compare with H1 and ZEUS data for the ratios of helicity amplitudes $T(\gamma_T^* \to \rho_T)/T(\gamma_L^* \to \rho_L)$ and $T(\gamma_T^* \to \rho_L)/T(\gamma_L^* \to \rho_L)$ and get a good description of the data. We also show how saturation effects can be included in this model by extending the dipole representation of the scattering amplitude in coordinate space up to twist 3.

1 Ratios of helicity amplitudes of the hard leptoproduction of the $\rho-$meson: a theoretical approach

In the Regge inspired factorization scheme, helicity amplitudes of the hard diffractive $\rho-$meson production

$$\gamma^*(q,\lambda_\gamma)\, N(p_2) \to \rho(p_\rho,\lambda_\rho)\, N(p_2)$$

are expressed in terms of the $\gamma^*(\lambda_\gamma) \to \rho(\lambda_\rho)$ impact factor ($\Phi^{\gamma^*(\lambda_\gamma)\to\rho(\lambda_\rho)}$) and the nucleon transition impact factor ($\Phi^{N\to N}$). At Born order, the helicity amplitudes read (using underlined letters for the euclideans two dimensional transverse vectors):

$$T_{\lambda_\rho\lambda_\gamma}(\underline{r};Q,M) = is\int \frac{d^2\underline{k}}{(2\pi)^2}\,\frac{1}{\underline{k}^2(\underline{k}-\underline{r})^2}\,\Phi^{N\to N}(\underline{k},\underline{r};M^2)\,\Phi^{\gamma^*(\lambda_\gamma)\to\rho(\lambda_\rho)}(\underline{k},\underline{r};Q^2)\,. \qquad (1)$$

The momenta q and p_ρ are parameterized using the Sudakov decompositions in terms of two light cone vectors p_1 and p_2 as $q = p_1 - \frac{Q^2}{s}p_2$ and $p_\rho \equiv p_1 + \frac{m_\rho^2 - t + t_{min}}{s}p_2 + r_\perp$ with $2p_1\cdot p_2 = s$ and $q^2 = -Q^2$ is the virtuality of the photon. The computation of the $\gamma^*(\lambda_\gamma) \to \rho(\lambda_\rho)$ impact factor is performed within collinear factorization of QCD. The dominant contribution (twist 2) $\gamma_L^* \to \rho_L$ transition (twist 2) has been computed long time ago [1] while a consistent

treatment of the twist 3 $\gamma_T^* \to \rho_T$ transition has been performed only recently in references [2, 3]. Impact factors involve a hard part where the hard photon decays into partons that interact with the $t-$channel gluons and soft parts where these partons hadronize into a $\rho-$meson. Soft and hard parts are factorized in momentum space by expanding the hard parts around the longitudinal components of the momenta of the partons, collinear to the direction of the $\rho-$meson momentum. Fierz identity applied to spinor and color spaces, is used to factorize color and spinor indices linking hard and soft parts. Up to twist 3, the amplitude involves the contributions of the 2- and 3-parton exchanges between the hard part and the soft part of the impact factor, Figure 1 shows the 3 types of terms involved. Soft parts correspond to the Fourier

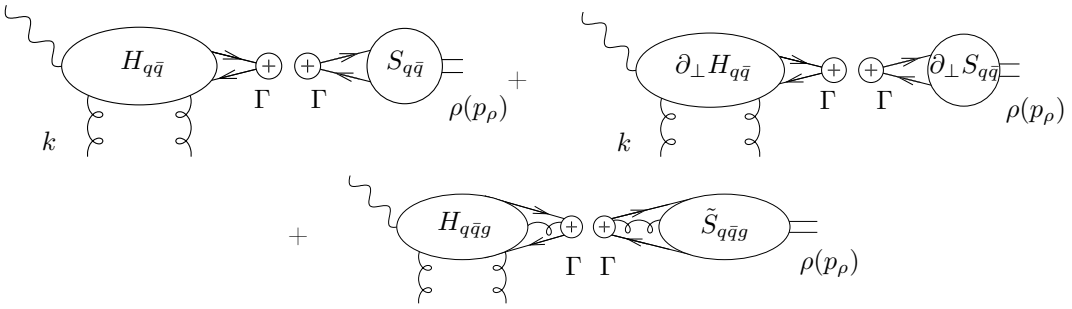

Figure 1: Illustration of the 3 different types of terms entering the computation up to twist 3. From left to right: the 2-parton collinear contribution, the 2-parton first order contribution in $\ell_\perp$, the collinear term of the 3-parton contribution. Γ stands for the set of Dirac matrices inserted using Fierz identity in the spinor space.

transforms of the vacuum to $\rho-$meson matrix elements that are parameterized by five 2-parton distribution amplitudes (DAs) and two 3-parton DAs. Due to the equation of motion of QCD and the so-called condition of the $n-$independence (c.f [3] for details), the DAs are expressed in terms of a single pure 2-parton DA and two pure 3-parton DAs. Results can be then split into the 2-parton contribution, so-called Wandzura-Wilczek (WW) contributions, and the genuine 3-parton contribution. In our model we take the explicit solutions of the ERBL equations up to the first term involving the factorization scale dependence μ_F. A first phenomenological approach [4] consists in choosing a simple model for the proton impact factor [5], depending on two free parameters M and A,

$$\Phi_{N\to N}(\underline{k},\underline{r};M^2)=A\delta_{ab}\left[\frac{1}{M^2+(\frac{r}{2})^2}-\frac{1}{M^2+(\underline{k}-\frac{r}{2})^2}\right].$$

Figure 2 shows the results for the ratios of the helicity amplitudes that we obtain with this approach, compared to the data of H1 [6] depending on the free parameter M and on an infrared cut off λ for the integral over the transverse momenta of the $t-$channel gluons. Similarly, ZEUS [7] data were compared to the results. Predictions are in fairly good agreement with the data for a value of M between 0.9 GeV and 5 GeV and the result depends weakly of the value of M and μ_F. The dependence in the cut-off λ shows that soft gluons with momenta smaller than Λ_{QCD}, $|\underline{k}| \leq \Lambda_{QCD}$, have a small contribution to the result while the contribution of the gluons with $|\underline{k}| \sim$1 GeV cannot be neglected and thus calls for an inclusion of the saturation dynamics of the nucleon.

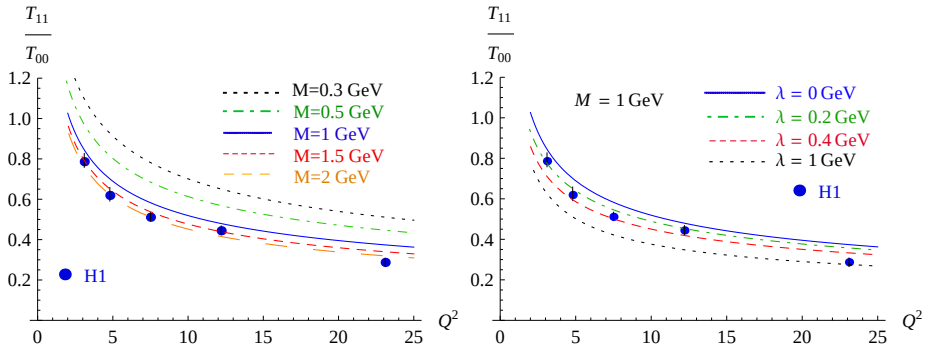

Figure 2: Predictions for the ratio T_{11}/T_{00} as a function of Q^2, compared to the data from H1 [6]. Left: fixed $\lambda = 0$, and various values for M. Right: fixed scale M = 1 GeV, and various values of λ.

2 Dipole representation of the scattering amplitude in coordinate space up to twist 3

In the Ref. [8], we show that performing the collinear approximation up to twist 3 after expressing the hard and soft parts of the impact factor $\gamma_T^* \to \rho_T$ in term of their transverse Fourier transforms, the color dipole interaction with the $t-$channel gluons factorizes out in the scattering amplitude of the full process. In the WW approximation, the result exhibits the wave function of the tranversally polarized photon $\Psi^{\gamma_T^*}_{\lambda\gamma(\lambda)}$ [9, 10, 11, 12] and the relevant combination of DAs $\phi^{WW}_{\lambda_\rho(\lambda)}$,

$$\Phi^{\gamma_T^* \to \rho_T, WW} = \frac{m_\rho f_\rho}{\sqrt{2}} \int dy \int d^2\underline{x}\, g^2\, \delta^{ab}\, \mathcal{N}(\underline{x},\underline{k}) \sum_{(\lambda)} \phi^{WW}_{\lambda_\rho(\lambda)}\, \Psi^{\gamma_T^*}_{\lambda\gamma(\lambda)}\,, \tag{2}$$

where λ denotes the helicity of the exchanged quark. In Eq. 2, $\mathcal{N}(\underline{x},\underline{k})$ is proportional to the scattering amplitude of a color dipole with the two $t-$channel gluons. Let us emphazise that

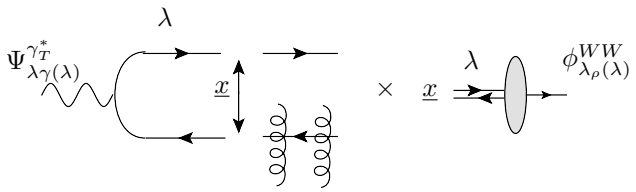

Figure 3: Illustration of the $\gamma_T^* \to \rho_T$ in the WW approximation in the dipole factorized form after using the equation of motion of QCD.

the appearance in Eq. 2 of the scattering amplitude of the dipole with the $t-$channel gluons $\mathcal{N}(\underline{x},\underline{k})$ is not a straightforward consequence of the Fourier transform of the hard part. The factorized form in Eq. 2 appears only after using the equation of motion of QCD.

Beyond the WW approximation, the 3-parton contribution leads to a similar result where the dipole scattering amplitude factorizes out after using the equation of motion of QCD. However, since the 3-body wave function of the photon is still unknown, a clear interpretation of this factorized form is still required.

3 Conclusion

We have first shown [4] that a model à la Gunion and Soper gives a good description of the data, however saturation effects are needed. We then proved in Ref. [8] that the twist 3 impact factor of the transition $\gamma_T^* \to \rho_T$ exhibits the color dipole scattering amplitude with the target. The next step is now to compare H1 and ZEUS data with the ratio T_{11}/T_{00} obtained by combining our results of the impact factor up to twist 3 computed in the collinear approximation with a model for the color dipole/target amplitude. Another perspective would be to extend our computations to the nonforward kinematics, in particular in order to investigate saturation effects at fixed impact parameter.

4 Acknowledgements

We thank K. Golec-Biernat and L. Motyka for stimulating discussions. This work is supported in part by the Polish NCN grant DEC-2011/01/B/ST2/03915, by the French-Polish Collaboration Agreement Polonium, by the Russian grant RFBR-11-02-00242 and by the P2IO consortium.

References

[1] I. F. Ginzburg, S. L. Panfil, V. G. Serbo, Nucl. Phys. B284, 685-705 (1987).

[2] I. V. Anikin, D. Yu. Ivanov, B. Pire, L. Szymanowski, S. Wallon, Phys. Lett. B682, 413 - 418 (2010).

[3] I. V. Anikin, D. Yu. Ivanov, B. Pire, L. Szymanowski, S. Wallon, Nucl. Phys. B828, 1 - 68 (2010).

[4] I. Anikin, A. Besse, D. Yu. Ivanov, B. Pire, L. Szymanowski, S. Wallon, Phys. Rev. D84, 054004 (2011).

[5] J. F. Gunion and D. E. Soper, Phys. Rev. D15, 2617 (1977).

[6] F. D. Aaron et al. [H1 Collaboration], JHEP 1005, 032 (2010).

[7] S. Chekanov et al. [ZEUS Collaboration], PMC Phys. A1, 6 (2007).

[8] A. Besse, L. Szymanowski, S. Wallon, arXiv:1204.2281v1 [hep-ph] (2012).

[9] A. H. Mueller, Nucl. Phys. B335, 115 (1990).

[10] N. Nikolaev, B. G. Zakharov, Z. Phys. C 49, 607 (1990).

[11] D. Yu. Ivanov and M. Wüsthoff, Eur. Phys. J. C 8, 107 (1999).

[12] S. Gieseke and C. F. Qiao, Phys. Rev. D 61, 074028 (2000).

W, Z and jet central exclusive production at the LHC

O. Kepka[1], *A. Dechambre*[2,3], *M. Trzebinski*[4], *R. Staszewski*[4,3], *É. Chapon*[4], *C. Royon*[4]

[1] Center for Particle Physics, Institute of Physics, Academy of Science, Prague
[2] IFPA, Dept. AGO, Université de Liège
[3] CEA/IRFU/Service de physique des particules, CEA/Saclay
[4] Institute of Nuclear Physics, Polish Academy of Sciences, Krakow

DOI: `http://dx.doi.org/10.3204/DESY-PROC-2012-02/218`

We study the W/Z pair production via two-photon exchange at the LHC and give the sensitivities on trilinear and quartic gauge anomalous couplings between photons and W/Z bosons. Tagging the protons in the final state in the ATLAS Forward Physics detectors as an example allows to improve the reach on anomalous couplings by four orders of magnitude reaching the values predicted by extra-dimension theories. The measurement of the exclusive jet production using the same detectors at the LHC will also be described.

1 Probing Anomalous Couplings

The studies presented in this section involve exclusive diffractive processes at the LHC. Diffractive events are characterized by an object produced in the central detector, two intact protons after interaction and nothing else (no energy loss or remnants). Events are generated using FPMC, a generator implementing diffractive or photon induced processes. We also make use of the ATLAS Forward Physics project (AFP), which is an upgrade of the ATLAS experiment. It will consist of forward proton detectors to be installed on both sides of the ATLAS detector, at about 220 meters from the interaction point, in movable beam pipes. Each station will welcome both silicon and timing detectors, that respectively measure the position and the time of flight to remove pile-up.

We study the QED process $pp \to ppWW$, in which the W boson pair is produced *via* a photon exchange between the two protons. We use the photon equivalent approximation (Budnev flux). Photons have typically a low virtuality Q^2 but can have a high energy. In particular we can have a high missing mass $M_{\gamma\gamma} = \sqrt{s\xi_1\xi_2}$ (where ξ is the momentum fraction loss of the proton). The cross section for this process is fairly large in the Standard Model ($\sigma_{pp\to ppWW} = 95.6$ fb), even at high missing mass ($\sigma_{pp\to ppWW}(W = M_X > 1\,\text{TeV}) = 5.9$ fb). As we will see, this process is highly sensitive to beyond Standard Model effects, especially anomalous gauge couplings.

We consider dimension 6 operators for the implementation of the anomalous quartic $\gamma\gamma WW$ and $\gamma\gamma ZZ$ couplings:

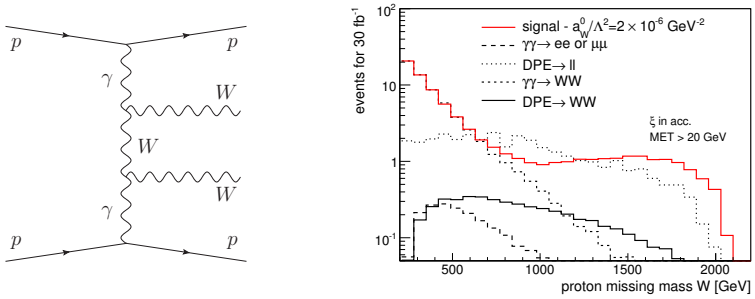

Figure 1: Left: Feynman diagram for $pp \to ppWW$. Right: proton missing mass distribution for signal ($a_0^W/\Lambda^2 = 2 \times 10^{-6}\,\mathrm{GeV}^{-2}$) and background.

$$\mathcal{L}_6^0 = \frac{-e^2}{8}\frac{a_0^W}{\Lambda^2}F_{\mu\nu}F^{\mu\nu}W^{+\alpha}W^-_\alpha - \frac{e^2}{16\cos^2\Theta_W}\frac{a_0^Z}{\Lambda^2}F_{\mu\nu}F^{\mu\nu}Z^\alpha Z_\alpha \quad (1)$$

$$\mathcal{L}_6^C = \frac{-e^2}{16}\frac{a_C^W}{\Lambda^2}F_{\mu\alpha}F^{\mu\beta}(W^{+\alpha}W^-_\beta + W^{-\alpha}W^+_\beta) - \frac{e^2}{16\cos^2\Theta_W}\frac{a_C^Z}{\Lambda^2}F_{\mu\alpha}F^{\mu\beta}Z^\alpha Z_\beta \quad (2)$$

All anomalous parameters (a_0^W, a_0^Z, a_C^W, a_C^Z) are equal to zero in the Standard Model. We only consider $\gamma\gamma WW$ and $\gamma\gamma ZZ$ anomalous parameters (the latter being not discussed here), but many more are possible ($\gamma\gamma$, Higgs, etc.). It is worth noting that because these are dimension 6 operators, they violate unitarity at high energy, so that we need the introduction of form factors to avoid quadratical divergences of scattering amplitudes: $a_0^W/\Lambda^2 \to \frac{a_0^W/\Lambda^2}{(1+W_{\gamma\gamma}/\Lambda_{\mathrm{cutoff}})^2}$ where $\Lambda_{\mathrm{cutoff}} \sim 2\,\mathrm{TeV}$ is the scale of new physics.

We focus on events where both W bosons decay leptonically. Our experimental signature is therefore two leptons, two tagged protons in the forward detectors, and nothing else in the detector. The possible backgrounds are inelastic WW production, dilepton through photon exchange, dilepton through double pomeron exchange (DPE), and WW through DPE. However dilepton production involves back-to-back leptons and no missing transverse energy ($\not\!\!E_T$); and DPE induces some energy flow in the forward regions as well as a higher number of tracks, because of the pomeron remnants.

More precisely, at preselection we require two reconstructed leptons (ee, $e\mu$ or $\mu\mu$) with $|\eta^{e,\mu}| < 2.5$ and $p_T^{e,\mu} > 10\,\mathrm{GeV}$, two tagged protons ($\xi \in [0.0015, 0.15]$), and nothing else. Additional cuts on $\not\!\!E_T$ and the opening angle between the two leptons ($\Delta\phi_{ll}$) help reject dilepton production. In order to reject DPE WW as well as increase the sensitivity to anomalous couplings, we also cut on the mass W of the central system reconstructed using AFP and on the leading lepton transverse impulsion. Our final selection is defined as $\not\!\!E_T > 20\,\mathrm{GeV}$, $W > 800\,\mathrm{GeV}$, $M_{ll} \notin [80, 100]$, $\Delta\phi_{ll} < 3.13$ and $p_T^{\mathrm{lep1}} > 160\,\mathrm{GeV}$. A yield table is given in Table 1.

Results obtained with fast simulation (ATLFAST++) are up to four orders of magnitude more sensitive than the LEP limits, or two orders of magnitude more sensitive than "standard" searches using $pp \to l^\pm\nu\gamma\gamma$ [3].

However, fast simulation does not allow to study the effect of pile-up and the rejection of non-diffractive backgrounds. This is why the analysis was also performed using the ATLAS full

cut / process	$\gamma\gamma \to ll$	$\gamma\gamma \to WW$	DPE $\to ll$	$\lvert a_0^W/\Lambda^2\rvert = 5.4 \cdot 10^{-6}\,\mathrm{GeV}^{-2}$
$p_T^{\mathrm{lep}1,2} > 10\,\mathrm{GeV}$	50619	99	18464	202
Final selection	0	0.69	0.20	17

Table 1: Cut flow table. Events for 30fb^{-1} (fast simulation ATLFAST++).

a_0^W/Λ^2 Sensitivity	5σ	95% C.L.	OPAL limits
$\mathcal{L} = 40\,\mathrm{fb}^{-1}$, $\mu = 23$	$5.5 \cdot 10^{-6}$	$2.4 \cdot 10^{-6}$	$[-0.020, 0.020]$
$\mathcal{L} = 300\,\mathrm{fb}^{-1}$, $\mu = 46$	$3.2 \cdot 10^{-6}$	$1.3 \cdot 10^{-6}$	

Table 2: Sensitivity with full simulation.

simulation. The exclusivity of the event is defined thanks to the proton time of flight, but also the number of tracks fitted to the vertex. Indeed, for signal two tracks are expected from the vertex (from the leptonic decay of the W bosons), while for background (e.g. $t\bar{t}$) much more tracks are expected. In addition to the previously mentioned backgrounds considered with fast simulation, we also considered single-diffractive WW production and non diffractive backgrounds ($t\bar{t}$, diboson, $W/Z + jets$, Drell-Yan, single top). The simulation assumes a 10 ps resolution for the proton timing detectors, and two luminosity scenarios: respectively 40 (200) fb^{-1} of data with $\mu = 23$ (46) interactions per bunch crossing. Results from full simulation [4] are shown in Table 2 and are very similar to the prediction of fast simulation.

2 Exclusive Models Uncertainties

We study the sources of uncertainties on gluon-mediated exclusive diffractive processes, in the case of diffractive Higgs production and jets production at the LHC. Several models are available with similar predictions, such as Khoze, Martin, Ryskin (KMR [5]), or the one on which we focused: Cudell, Hernández, Ivanov, Dechambre exclusive (CHIDe [6]). The main sources of uncertainty are the rapidity gap survival probability (measured to be 0.1 at the Tevatron, not measured at the LHC and assumed to be 0.03), the gluon distributions and the Sudakov form-factors.

The choice of the gluon distribution parametrization contributes to the model uncertainty both at the Tevatron (Figure 2) and at the LHC. For instance it gives an uncertainty of a factor about 3.5 on exclusive dijet and about 2 on exclusive Higgs cross section at the LHC.

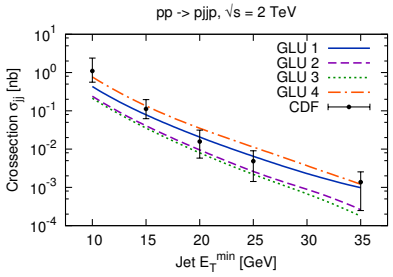

Figure 2: Exclusive diffractive jet production at the Tevatron for different gluon distribution parametrizations.

The Sudakov form-factor takes the following form in the CHIDe model:

$$T(l_i, \mu) = \exp\left[-\int_{l_i^2/x'}^{\mu^2/x} \frac{\mathrm{d}\mathbf{q}^2}{\mathbf{q}^2} \frac{\alpha_s(\mathbf{q}^2)}{2\pi} \int_0^{1-\Delta} \left(zP_{gg} + \sum_q P_{qg}(z) \right) \mathrm{d}z \right] \tag{3}$$

The uncertainty comes from the limits of the integral, x and x' (the latter having a bigger impact), which have not yet been fixed by a theoretical calculation. They are constrained, to some extent, by the exclusive jet cross section measurement from CDF. However varying x' by a reasonable factor 2 can change the cross section by a factor up to 5, as shown on Figure 3. When propagated to the LHC, the uncertainty using the CDF constraint alone is even more sizable: a factor about 10 for jets or even 25 for Higgs exclusive production. Fortunately, a $100\,\mathrm{pb}^{-1}$measurement of the exclusive jet cross section at the LHC (easily doable with AFP) would help constrain the uncertainties, which would go down to a factor about 5 for Higgs.

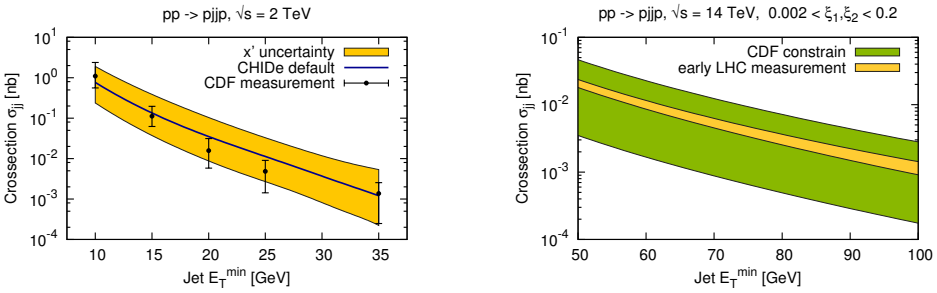

Figure 3: Left: impact of the uncertainty on x' on the exclusive diffractive jet cross section at the Tevatron. Right: impact of this uncertainty on the exclusive jet cross section at the LHC, with the CDF constrain alone and with the constrain of an early exclusive jet cross section measurement at the LHC.

Conclusion

We have presented two central exclusive studies possible at the LHC. Concerning anomalous couplings in two-photon processes, the analysis takes advantage of the AFP forward proton detectors, and improves the sensitivity of up to 4 orders of magnitude compared to the LEP. For uncertainties on exclusive diffractive Higgs and jets production, the main sources of theoretical uncertainties are coming from the gluon distributions parametrization and the Sudakov form-factors. An exclusive jet cross section at the LHC could improve a lot the constraint from CDF measurement.

Regarding AFP, the letter of intent has been approved in ATLAS and by the LHCC, and if the project is definitely approved, movable beam pipes, silicon detectors and timing detectors will be installed in 2014.

References

[1] E. Chapon, C. Royon, O. Kepka, Phys. Rev. **D81** (2010) 074003.
[2] A. Dechambre, O. Kepka, C. Royon, R. Staszewski, Phys. Rev. **D83** (2011) 054013.
[3] J.P. Bell, Eur. Phys. J. **C64** (2009) 25.
[4] C. Royon, LHCC Meeting (March 2012), http://indico.cern.ch/conferenceDisplay.py?confId=182599
[5] V.A. Khoze, A.D. Martin and M.G. Ryskin, Eur. Phys. J. **C14** (2000) 525.
[6] J.R. Cudell, A. Dechambre, O.F. Hernandez and I.P Ivanov, Eur. Phys. J. **C61** (2009) 369.

New Results on Diffractive *t*-Distributions from CDF

Konstantin Goulianos on behalf of the CDF Collaboration.

The Rockefeller University, 1230 York Avenue, New York, NY 10065, USA

DOI: http://dx.doi.org/10.3204/DESY-PROC-2012-02/255

We present a measurement of antiproton ($\bar{p}$) four-momentum transfer distributions, $t_{\bar{p}}$, for inclusive and dijet single-diffractive production at $\sqrt{s}$ =1.96 TeV at the Fermilab Tevatron $\bar{p}p$ Collider. We use data collected by the CDF II detector equipped with a Roman Pot Spectrometer that measures $t_{\bar{p}}$ and the $\bar{p}$ forward momentum loss, $\xi_{\bar{p}}$. We report results for $0.05 < \xi_{\bar{p}} < 0.08$, $-t_{\bar{p}} \leq 4$ GeV^2, and jet transverse energies, $E_T^{\rm jet}$, of $10^2 < Q^2 \approx (E_T^{\rm jet})^2 < 10^4$ GeV^2. In addition, we search for diffractive dips in both the inclusive and dijet distributions, and compare all results with theoretical expectations.

1 Introduction

We present a measurement of four-momentum-transfer (t) distributions for inclusive and dijet single-diffractive (SD) production in $\bar{p}p$ collisions at $\sqrt{s} = 1.96$ TeV, $\bar{p}+p \to \bar{p}+G_{\bar{p}}+X_p$, where $G_{\bar{p}}$ is a region of pseudorapidity[1] devoid of particles (rapidity gap), and X represents particles from the dissociation of the proton [1]. The rapidity gap, presumed to be caused by a color-singlet exchange with vacuum quantum numbers between the $\bar{p}$ and the dissociated proton, traditionally referred to as Pomeron ($I\!P$) exchange, is related to $\xi_{\bar{p}}$, the forward momentum loss of the surviving $\bar{p}$, by $G_{\bar{p}} = -\ln \xi_{\bar{p}}$. Using data collected by the CDF II detector, equipped with a Roman Pot Spectrometer (RPS) that measures $t_{\bar{p}}$ and $\xi_{\bar{p}}$ for each event, we extract $t_{\bar{p}}$ distributions for events within $0.05 < \xi_{\bar{p}} < 0.08$. We cover the ranges of $-t_{\bar{p}} \leq 4$ GeV^2 and jet transverse energy, $E_T^{\rm jet}$, of $10^2 < Q^2 \approx (E_T^{\rm jet})^2 < 10^4$ GeV^2, search for diffractive dips, and compare all results with theoretical expectetions.

2 Measurement

Detector. Figure 1 is a schematic plan view of the detector used in this measurement, showing the main detector (CDF II) and the forward detector-components used in the diffractive-physics measurements. The forward detectors include a Roman Pot Spectrometer (RPS), which measures $\xi_{\bar{p}}$ and $t_{\bar{p}}$ with resolutions $\delta\xi_{\bar{p}} = 0.001$ and $\delta t_{\bar{p}} = \pm 0.07$ GeV^2 at $\langle -t_{\bar{p}} \rangle \approx 0.05$ GeV^2, where $\delta t_{\bar{p}}$ increases with $t_{\bar{p}}$ with a $\propto \sqrt{-t_{\bar{p}}}$ dependence.

[1] Rapidity, $y = \frac{1}{2} \ln \frac{E+p_L}{E-p_L}$, and pseudorapidity, $\eta = -\ln \tan \frac{\theta}{2}$, where θ is the polar angle of a particle with respect to the proton beam ($+\hat{z}$ direction), are used interchangeably for particles detected in the calorimeters, since in the kinematic range of interest in this analysis they are approximately equal.

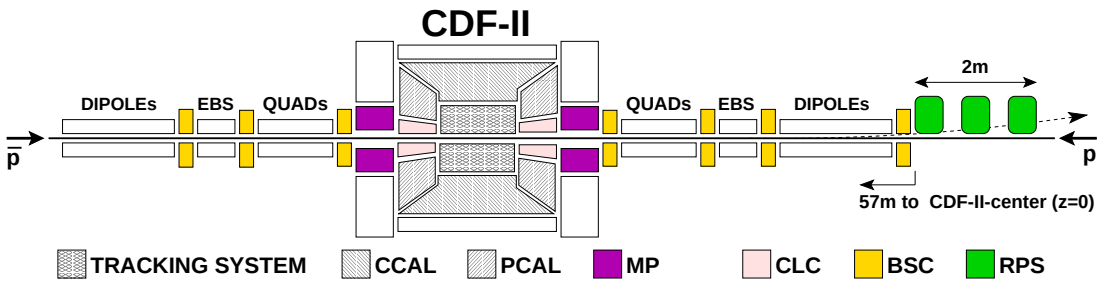

Figure 1: Schematic plan view of the detector, showing the main detector (CDF II) with the tracking system and calorimeters (central, CCAL; plug, PCAL), and the forward components (Cerenkov Luminosity Counters, CLC; MiniPlugs, MP; Roman Pot Spectrometer, RPS). The beamline elements labeled EBS are the electrostatic beam separators.

Data samples. This analysis is based on data corresponding to an integrated luminosity $\mathcal{L}\approx$ 310 pb^{-1} collected in 2002–2003. Events are selected online with a three-level prescaled triggering system, which accepts RPS-triggered inclusive events, as well as jet-enriched events, by requiring at least one calorimeter tower with $E_T > 5$, 20, or 50 GeV within $|\eta| < 3.5$. Jets are reconstructed using the midpoint algorithm [2].

The following trigger definitions are used for measuring $t_{\bar{p}}$ distributions:

- RPS: requires the RPS trigger counters to be in time with a $\bar{p}$ crossing the CDF II nominal interaction region;
- J5 (J20, J50): jet with $E_T^{\rm jet} \geq 5$ (20, 50) GeV in CCAL or PCAL;
- RPS $\cdot$ Jet5 (Jet20, Jet50): RPS trigger in coincidence with J5 (J20, J50).

RPS alignment. The measurements of $t_{\bar{p}}$ require precise alignment of the RPS detectors relative to the actual position of the beam at the time of data collection. We developed a *dynamic alignment* method that is applied offline to the collected data samples. The method consists of introducing offsets in the nominal x and y coordinates of the RPS detectors relative to the beam, fitting data for $-t \leq 1$ GeV^2 with a form composed of two exponential terms,

$$\frac{dN_{\rm events}}{dt} = N_{norm}\left(A_1 e^{b_1 t} + A_2 e^{b_2 t}\right), \qquad (1)$$

where N_{norm} is a normalization factor, and iteratively adjusting the offsets until a maximum for $dN_{\rm events}/dt$ at $t_{\bar{p}} = 0$ is obtained. To improve the fits, we set $A_2/A_1 = 0.11$, which is the average value over all data subsamples, and repeat the iterative fitting. This method yields an accuracy of ± 60 μm in the beam position, which leads to a systematic uncertainty of $\pm 5\%$ in b_1 and b_2.

3 Results

$t_{\bar{p}}$ distributions for $-t_{\bar{p}} \leq 1$ GeV^2. Inclusive and jet-enriched data of $10^2 < Q^2 \approx (E_T^{\rm jet})^2 < 10^4$ GeV^2 have been studied. Results for $t_{\bar{p}}-$distribution shapes are shown in Fig. 2

and in table 1. No significant Q^2 dependence is observed from $\langle Q^2 \rangle \approx 1$ GeV^2 (inclusive) to $Q^2 \approx 10^4$ GeV^2. The mean values of b_1 and b_2 over all the data samples are 5.27 ± 0.33 GeV^{-2} and 1.17 ± 0.17 GeV^{-2}, respectively. Systematic uncertainties in b_1 and b_2 are due to RPS-tracker thresholds(1%), instantaneous luminosity (2%), beam conditions (4%), and RPS alignment (5%). These uncertainties are correlated among all data points, and when added in quadrature yield an overall total uncertainty of $\delta b_{1,2}^{\rm syst} = \pm 9.7\%$. The measured slopes of the inclusive sample are in agreement with expectations from the Donnachie-Landshoff (DL) model [3]. The Q^2 near-independence of the $t_{\bar{p}}$ distributions favors models of hard-diffractive production in which the hard scattering is controlled by the parton distribution function of the recoil antiproton, while the rapidity-gap formation is governed by a color-neutral soft exchange [4]-[7].

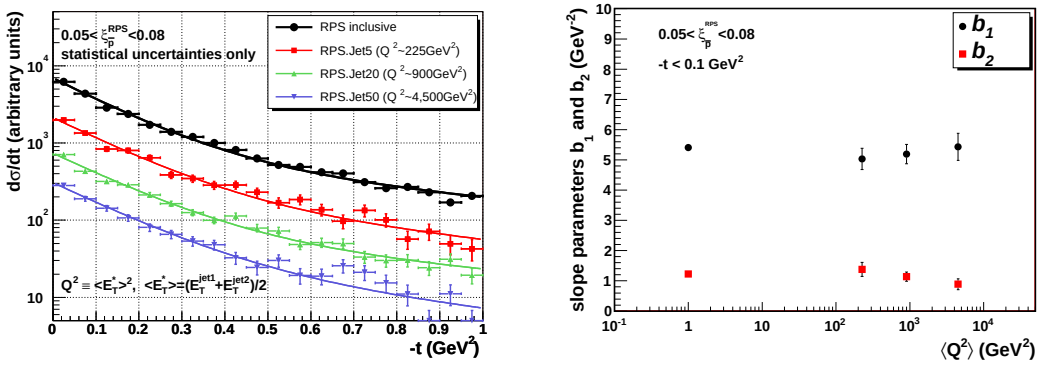

Figure 2: *(left)* $t_{\bar{p}}$ distributions for SD RPS data of various average Q^2 values within $0.05 < \xi_{\bar{p}}^{\rm RPS} < 0.08$; *(right)* the slope parameters b_1 and b_2 vs $\langle Q^2 \rangle$ of a fit to the form $dN_{\rm events}/dt = N_{\rm norm}(A_1 e^{b_1 t} + A_2 e^{b_2 t})$, with $A_2/A_1 = 0.11$ (average over all data subsamples). The RPS inclusive points have been placed arbitrarily at $\langle Q^2 \rangle$=1 GeV^2.

Table 1: Slopes of $t_{\bar{p}}$ distributions of SD RPS data within $0.05 < \xi_{\bar{p}}^{\rm RPS} < 0.08$ for inclusive and dijet event samples of various $\langle E_T^* \rangle$ or $Q^2 \equiv \langle E_T^* \rangle^2$ values obtained from fits to the form $dN_{\rm events}/dt = N_{\rm norm}(A_1 e^{b_1 t} + A_2 e^{b_2 t})$ with $A_2/A_1 = 0.11$, fixed at the average value obtained in the dynamic alignment of all different event subsamples. The uncertainties listed are statistical.

Event sample	$\langle E_T^* \rangle$ (GeV)	Q^2 (GeV^2)	b_1 (GeV^{-2})	b_2 (GeV^{-2})	$b_1/\ b_1^{\rm incl}$	$b_2/\ b_2^{\rm incl}$
RPS	incl	≈ 1	5.4 ± 0.1	1.2 ± 0.1	1	1
RPS $\cdot$ Jet5	15	225	5.0 ± 0.3	1.4 ± 0.2	0.93 ± 0.08	1.12 ± 0.23
RPS $\cdot$ Jet20	30	900	5.2 ± 0.3	1.1 ± 0.1	0.96 ± 0.07	0.93 ± 0.16
RPS $\cdot$ Jet50	67	4500	5.5 ± 0.5	0.9 ± 0.2	1.00 ± 0.10	0.72 ± 0.18

$t_{\bar{p}}$ distributions for $-t_{\bar{p}} \leq 4$ GeV^2 and search for diffractive dips. Figure 3 *(left)* shows $t_{\bar{p}}$ distributions in the region of $-t_{\bar{p}} \leq 4$ GeV^2 for the inclusive and the RPS $\cdot$ jet20 data of $\langle Q^2 \rangle \simeq 900$ GeV^2. The following prominent features are observed: (i) the two distributions

are similar in shape, (ii) the inclusive distribution follows the DL prediction for $-t_{\bar{p}} \lesssim 0.5$ GeV^2, but lies increasingly higher than the DL curve as $-t_{\bar{p}}$ increases, becoming approximately flat for $-t_{\bar{p}} \gtrsim 2$ GeV^2. As the $t_{\bar{p}}$ acceptance, shown in Fig. 3 *(right)*, varies slowly in this region, and the overall $t_{\bar{p}}$ resolution at $-t_{\bar{p}} \approx 2.5$ GeV^2 is $\approx \pm 1$ GeV^2, we conclude that the observed flattening-out of the distributions is physics-based, possibly caused by an underlying diffractive dip at $t_{\bar{p}} \approx 2.5$ GeV^2 filled-out by resolution effects.

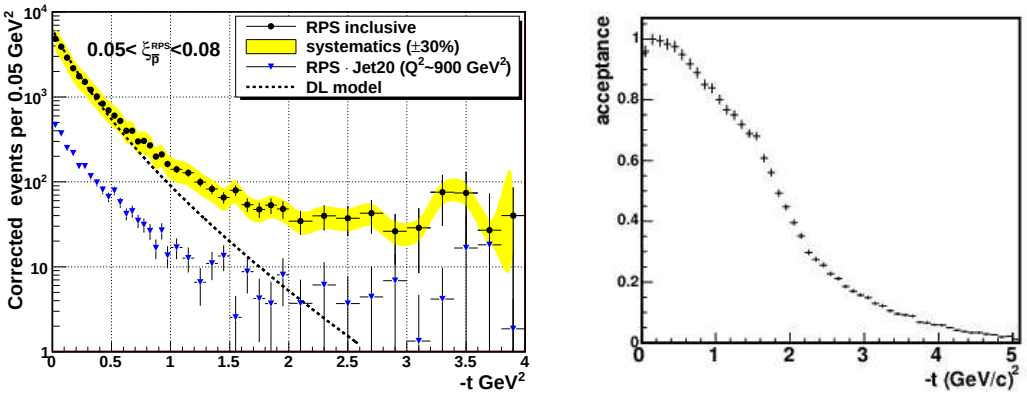

Figure 3: *(left)* t distributions of two data samples of SD RPS events within $0.05 < \xi_{\bar{p}}^{\rm RPS} < 0.08$ corrected for RPS acceptance after background subtraction: RPS inclusive, $\langle Q^2 \rangle \simeq 1$ GeV^2 (circles), and RPS $\cdot$ Jet20, $\langle Q^2 \rangle \simeq 900$ GeV^2 (triangles); the curve is the expectation of the DL model normalized to the RPS inclusive data within $-t \lesssim 0.5$ GeV^2. *(right)* RPS acceptance vs $-t_{\bar{p}}$, integrated over the region of $0.05 < \xi_{\bar{p}} < 0.08$.

4 Acknowledgments

I would like to thank Michele Gallinaro, Koji Terashi, Mary Convery, and Christina Mesropian for invaluable contributions to this analysis, my colleagues at the CDF Collaboration, and the Office of Science of the Department of Energy for its generous financial support.

References

[1] V. Barone and E. Predazzi, "High-Energy Particle Diffraction", Springer Press, Berlin, (2002).

[2] G. C. Blazey *et al.*, "Run II Jet Physics", in *Proceedings of the Run II QCD and Weak Boson Physics Workshop*. arXiv:hep-ex/0005012, 2000.

[3] A. Donnachie and P. Landshoff, Phys. Lett. **B518** (2001) 63.

[4] K. Goulianos, "Renormalized Diffractive Parton Densities," in *Diffraction 06, International Workshop on Diffraction in High-Energy Physics*, Adamantas, Milos island, Greece (2006). PoS (DIFF2006) 044.

[5] S. J. Brodsky *et al.,* Phys. Rev. D **71** (2005) 074020.

[6] A. B. Kaidalov *et al.,* Eur. Phys. J. C **21** (2001) 521. Eur. Phys. J. C **21** (2001) 521.

[7] B. Z. Kopeliovic *et al.,* Phys. Rev. D **76**, 034019 (2007).

Probing hard diffraction with CMS

Antonio Vilela Pereira[1] for the CMS Collaboration

[1]INFN Torino, Via Pietro Giuria 1, 10125, Torino, Italy

DOI: http://dx.doi.org/10.3204/DESY-PROC-2012-02/342

The cross section for dijet production in pp collisions at $\sqrt{s} = 7$ TeV is presented as a function of $\tilde{\xi}$, a variable that approximates the fractional momentum loss of the scattered proton in single-diffractive events. The observation of W and Z boson production with a pseudorapidity gap in the final state is also presented.

1 Introduction

This paper presents a measurement of the dijet production cross section as a function of a variable, denoted $\tilde{\xi}$, which approximates the fractional momentum loss of the scattered proton in single-diffractive (SD) reactions, $pp \to Xp$ [1]. The observation of W and Z events associated with pseudorapidity gaps is also discussed. According to a Monte Carlo model, these events can be interpreted as due to diffractive W/Z production [2].

The analysis is based on the data collected by the CMS experiment during the year 2010, at a centre-of-mass energy of 7 TeV. The data are compared to simulated events obtained from the Pythia6 [5] and Pythia8 [6] event generators. Diffractive events with a hard sub-process are simulated with the Pompyt [7] and Pomwig [8] generators, as well as Pythia8. Diffractive dijet events were also generated at next-to-leading (NLO) accuracy using the Pomweg [9] framework. These generators were used with diffractive parton distributions (dPDFs) from the same fit to diffractive deep inelastic scattering data (H1 Fit B) [10].

A detailed description of the Compact Muon Solenoid (CMS) experiment can be found elsewhere [4]. The central feature of the CMS apparatus is a superconducting solenoid, of 6 m internal diameter. Within the field volume are the silicon pixel and strip tracker, the crystal electromagnetic calorimeter (ECAL) and the brass-scintillator hadronic calorimeter (HCAL). Muons are measured in gaseous detectors embedded in the iron return yoke. CMS has extensive forward calorimetry. The forward part of the hadron calorimeter, HF, covers the pseudorapidity region $2.9 < |\eta| < 5.2$. In the current analysis only the region $3.0 < |\eta| < 4.9$ was used, thus restricting the data to a region of well understood reconstruction efficiency.

2 Event selection

To select dijet events, at least one jet with uncorrected transverse momentum (p_T) greater than 6 GeV was required at the trigger level. Offline, events were selected with two jets with $p_T > 20$ GeV, in the pseudorapidity region $-4.4 < \eta^{\mathrm{jet}(1,2)} < 4.4$. Jets were reconstructed with the anti-k_T jet-finding algorithm with radius parameter $R = 0.5$. The diffractive contribution was enhanced by requiring the pseudorapidity of the event most forward (backward) reconstructed

object $\eta_{\max}$ ($\eta_{\min}$), using a particle-flow algorithm which combines measurements from the tracker and the calorimeters [3], to be $\eta_{\max} < 3$ ($\eta_{\min} > -3$). This selection corresponds to imposing a pseudorapidity gap of at least 1.9 units in the HF acceptance. It rejects most of events with additional pp interactions in the same bunch crossing (i.e. *pile-up*).

The identification of W bosons required the presence of isolated electrons and muons with transverse-momentum (p_T) greater than 25 GeV with pseudorapidity $|\eta| < 1.4$, and the missing transverse momentum, reconstructed from a particle-flow algorithm, greater than 30 GeV. The transverse mass was further required to be greater than 60 GeV. Analogously, the selection of Z bosons required two isolated electrons or muons with opposite charge with $p_T > 25$ GeV, at least one of them at $|\eta| < 1.4$. The reconstructed invariant mass of the di-lepton system was further required to lie between 60 and 120 GeV. Events were selected online by requiring a high transverse momentum electron or muon. The trigger efficiency for signal events is above 99%. In order to reject pile-up events, a single reconstructed vertex was required.

3 Results

The dijet production cross section is measured as a function of the variables $\tilde{\xi}^+$ and $\tilde{\xi}^-$, defined as $\tilde{\xi}^{\pm} = C \, \frac{\sum\left(E^i \pm p_z^i\right)}{\sqrt{s}}$, where E^i and p_z^i are the energy and longitudinal momentum of each reconstructed particle-flow object, respectively, and the sum runs over all objets measured in the detector. The constant C is a correction factor determined from the MC. The results as a function of $\tilde{\xi}^+$ and $\tilde{\xi}^-$ were averaged, and presented as a function of $\tilde{\xi}$. The reconstructed $\tilde{\xi}$ distribution is shown in the left panel of Figure 1. The results are presented both when not applying the $\eta_{\max} < 3$ ($\eta_{\min} > -3$) selection and when this condition was required. This pseudorapidity gap selection rejects events at high values of $\tilde{\xi}$, while the region of low $\tilde{\xi}$, where the diffractive contribution dominates, is only marginally affected. The shape of the distributions can be described by a combination of diffractive (POMPYT) and non-diffractive (PYTHIA6, Tune Z2) MC simulated events. The data collected correspond to an integrated luminosity of 2.7 nb^{-1}.

The right panel of Fig. 1 shows the differential cross section for dijet production as a function of $\tilde{\xi}$, where the measured number of dijet events in each bin was corrected by a factor which includes the effects of the geometric acceptance of the apparatus as well as unfolding corrections to account for the finite resolution of $\tilde{\xi}$, as well as p_T^{jet} and η^{jet}, and the trigger efficiency. A correction for the effect of pile-up was also applied. At hadron-level, $\tilde{\xi}^+$ and $\tilde{\xi}^-$ are defined analogously from the energy and longitudinal momentum of each final-state particle with $-\infty < \eta < 4.9$ for $\tilde{\xi}^+$ and $-4.9 < \eta < +\infty$ for $\tilde{\xi}^-$. In the region of low $\tilde{\xi}^{\pm}$ this variable is a good approximation of ξ for single-diffractive events. The data are compared to the predictions of non-diffractive (PYTHIA6, Tune Z2 and PYTHIA8, Tune 1) and diffractive (POMPYT SD, POMWIG SD, PYTHIA8 SD+DD) MC models, as well as the NLO calculation based on POMWEG. The contribution of SD MCs is needed to describe the low-$\tilde{\xi}$ data. They predict however more events than are observed, by a factor of about 5 in the lowest $\tilde{\xi}$ bin[1]. The ratio of the measured cross section to that expected by diffractive MCs in Fig. 1 can be taken as an upper limit of the rapidity-gap survival probability.

[1]The normalisation of the SD+DD PYTHIA8 prediction disagrees with that of POMPYT and POMWIG. This is a consequence of the different modelling of diffraction in these generators: while they all use the same H1 dPDFs, the parametrisation of the Pomeron flux in PYTHIA8 is different, and notably not that used in [10].

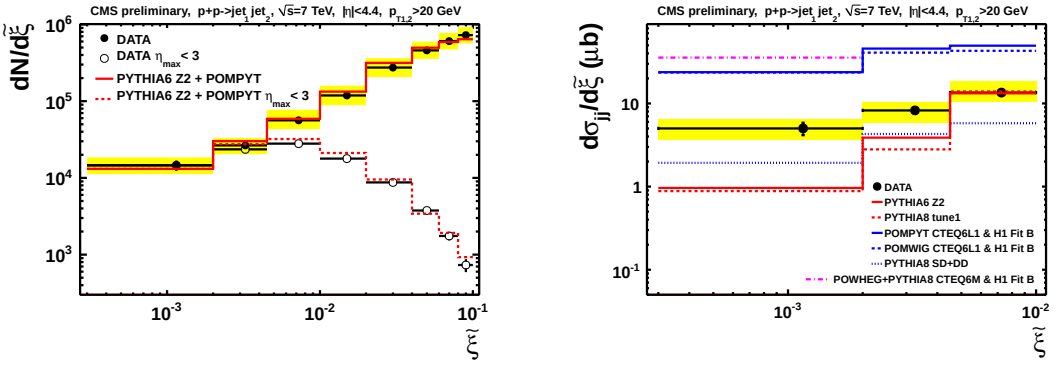

Figure 1: Left: Reconstructed $\tilde{\xi}$ distributions compared to MC predictions including diffractive dijet production (PYTHIA6 + POMPYT) without (solid line) and with (dashed line) the $\eta_{\max} < 3$ ($\eta_{\min} > -3$) condition. The MC diffractive dijet contribution has been scaled by a factor of 0.23, obtained from a fit to the data. Right: The differential cross section for dijet production as a function of $\tilde{\xi}$ for jets with $-4.4 < \eta < 4.4$ and $p_T > 20$ GeV. The points are plotted at the centre of the bins. The predictions of non-diffractive and diffractive MC generators are also shown (see text). The error bars indicate the statistical uncertainty and the band represents the jet and calorimeter energy-scale uncertainties added in quadrature.

In the left panel of Figure 2, the distribution of the energy deposited in HF is shown for events in which a W boson decaying in the muon channel is observed. The data are compared with the predictions of PYTHIA6, as well as PYTHIA8. Large discrepancies between the data and the different models are observed. Events with zero energy deposition reflect the presence of a pseudorapidity gap extending over HF. The fractions of W and Z events with a pseudorapidity gap are found to be, respectively, $[1.46 \pm 0.09(\text{stat.}) \pm 0.38(\text{syst.})]\%$ and $[1.57 \pm 0.25(\text{stat.}) \pm 0.42(\text{syst.})]\%$, where a data-driven pile-up correction has been applied. The results for the electron and muon decay channels are combined. The data collected correspond to an integrated luminosity of 36 pb^{-1}.

The distribution of the selected W candidate events with a pseudorapidity gap is shown in the right panel of Fig. 2 as a function of the signed charged lepton pseudorapidity η_ℓ, defined to be positive when the observed gap and the lepton are in the same hemisphere and negative otherwise. The data show that charged leptons from W decays are found more often in the hemisphere opposite to the gap. The corresponding asymmetry is $[-21.0 \pm 6.4]\%$. In the case of Z events, the rapidity of the lepton pair is used instead and an asymmetry of $[-20 \pm 16]\%$ is observed. The asymmetry seen in the data agrees well with the POMPYT simulation of diffractive W/Z events. A fit of the predictions of POMPYT and the PYTHIA6 non-diffractive simulation results in a fraction of diffractive events of $[50.0 \pm 9.3(\text{stat.}) \pm 5.2(\text{syst.})]\%$ in the selected sample.

4 Summary

The differential cross section for dijet production as a function of $\tilde{\xi}$, a variable that approximates the fractional momentum loss of one of the protons in single-diffractive processes, has

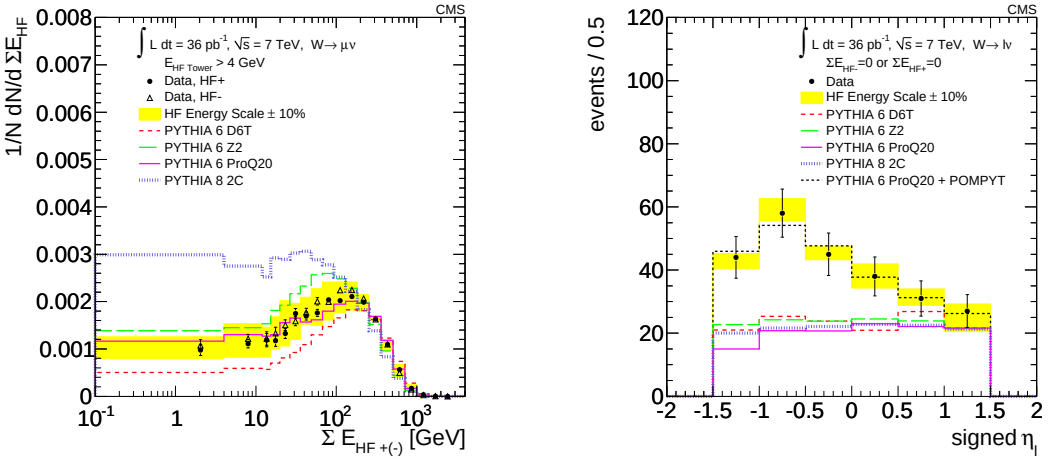

Figure 2: Left: Distribution of the $W \to \mu\nu$ candidate events as a function of the energy deposition in HF. The predictions of PYTHIA6, with different tunes, and PYTHIA8 are also shown. Right: Signed lepton pseudorapidity distribution in W events with a pseudorapidity gap (see text). Electron and muon channels are combined. The fit result for the combination of the PYTHIA6 (ProQ20 tune) and POMPYT predictions is shown as the dotted line. Fit results of the non-diffractive component using different PYTHIA6 tunes are also shown.

been measured with the CMS detector for events with at least two jets with $p_T > 20$ GeV in the pseudorapidity region $-4.4 < \eta < 4.4$. The results are compared to diffractive and non-diffractive MC models. The low-$\tilde{\xi}$ data are dominated by diffractive dijet production. Diffractive generators based on dPDFs from the HERA experiments overestimate the measured cross section and their normalisation needs to be scaled down by a factor which can be interpreted as the effect of the rapidity-gap survival probability.

The production of W and Z bosons with a pseudorapidity gap in the final state has been observed. In these events, a large asymmetry in the signed charged lepton (η_ℓ) distribution is seen. This asymmetry is well described by the prediction of the POMPYT generator. The diffractive component in the rapidity-gap event sample is determined to be $[50.0 \pm 9.3(\text{stat.}) \pm 5.2(\text{syst.})]\%$ and provides the first evidence of diffractive W/Z production at the LHC.

References

[1] CMS Collaboration, PAS-FWD-10-004 (2011).

[2] CMS Collaboration, Eur. Phys. J. C **72** (2012) 1839 [arXiv:1110.0181 [hep-ex]].

[3] CMS Collaboration, PAS-PFT-10-002 (2010).

[4] CMS Collaboration, JINST **3** (2008) S08004.

[5] T. Sjostrand, S. Mrenna and P. Skands, JHEP **0605** (2006) 026.

[6] T. Sjostrand, S. Mrenna and P. Z. Skands, Comput. Phys. Commun. **178** (2008) 852.

[7] P. Bruni and G. Ingelman, Phys. Lett. B **311**, 317 (1993).

[8] B. E. Cox and J. R. Forshaw, Comput. Phys. Commun. **144** (2002) 104 [hep-ph/0010303].

[9] S. Alioli, K. Hamilton, P. Nason, C. Oleari and E. Re, JHEP **1104** (2011) 081 [arXiv:1012.3380 [hep-ph]].

[10] A. Aktas *et al.* [H1 Collaboration], Eur. Phys. J. C **48** (2006) 715 [hep-ex/0606004].

Probing the Low-x Structure of the Nucleus with the PHENIX Detector

Mickey Chiu

Brookhaven National Lab, Upton, NY 11973 USA

DOI: http://dx.doi.org/10.3204/DESY-PROC-2012-02/133

One of the fundamental goals of the PHENIX experiment is to understand the structure of cold nuclear matter, since this serves as the initial state for heavy-ion collisions. Knowing the initial state is vital for interpreting measurements from heavy-ion collisions. Moreover, the structure of the cold nucleus by itself is interesting since it is a test-bed for our understanding of QCD. In particular there is the possibility of novel QCD effects such as gluon saturation at low-x in the nucleus. At RHIC we can probe the behavior of gluons at low-x by measuring the pair cross-section of di-hadrons from di-jets in d+Au collisions. Our results show a systematic decrease in the pair cross-section as one goes to smaller impact parameters of the nucleus, and also as one goes to lower Bjorken x. There is a possibility that these interesting effects come from gluon recombination at low x in the Au nucleus.

1 Introduction

Deuteron-gold collisions at RHIC provide a means to explore nuclear effects on the initial-state parton densities in the nucleus, which is vitally important to understanding the baseline production for Quark-Gluon Plasma studies in heavy-ion collisions. RHIC experiments have shown that single inclusive hadron yields in the forward (deuteron) rapidity direction for $\sqrt{s_{NN}} = 200$ GeV d+Au collisions are suppressed relative to p+p collisions [1, 2, 3]. The mechanism for the suppression has not been firmly established. Many effects have been proposed for this suppression, such as gluon saturation [4, 5], initial state energy loss [6, 7], parton recombination [8], multi-parton interactions [9], and leading and higher-twist shadowing [10, 11].

One set of measurements that might help to distinguish between the competing models is forward azimuthally correlated di-hadron correlation functions, which directly probe di-jet production through their 2→2 back-to-back peak at $\Delta\phi = \pi$. This technique has been used extensively at RHIC and is described in detail elsewhere [12, 13, 14]. The di-hadron results presented here were obtained from p+p and d+Au runs in 2008 with the PHENIX detector and include a new electromagnetic calorimeter, the Muon Piston Calorimeter (MPC), with an acceptance of $3.1 < \eta < 3.8$ in pseudorapidity and $0 < \phi < 2\pi$.

Di-hadron measurements can probe more precise ranges of parton x in a gold nucleus than do single hadron probes (e.g., $R_{\rm dA}$). At forward rapidities, a single hadron probe will cover a very broad range of x, $10^{-3} < x_{Au} < 0.5$, thus mixing together the shadowing, anti-shadowing, and even EMC effects [10]. Azimuthally correlated di-hadron measurements also enhance the di-jet fraction in the event selection, since one selects only the back-to-back hadrons.

By performing several correlation measurements with particles at different p_T and rapidities,

one can systematically scan different x ranges with an observable that is enhanced for the leading-order perturbative QCD component. Probing the x dependence of the effect is an important test since most models predict that any effects should be stronger at smaller x. Particles at higher pseudorapidities are produced from smaller x, so measuring hadrons from more forward rapidities should probe smaller x.

2 PHENIX MPC d+Au di-Hadron Correlations

For this analysis, back-to-back π^0-π^0 or hadron-π^0 pairs are measured with one particle at mid-rapidity, and the other at forward rapidity. Back-to-back cluster-π^0 pairs are also measured where both are in the forward rapidity region. The clusters are reconstructed from the energy deposit of photons in the MPC, and are estimated to be at least 80% dominated by π^0's, with the remainder coming from single photons from decays of η's and from direct photons. Further details of the analysis are available in [14].

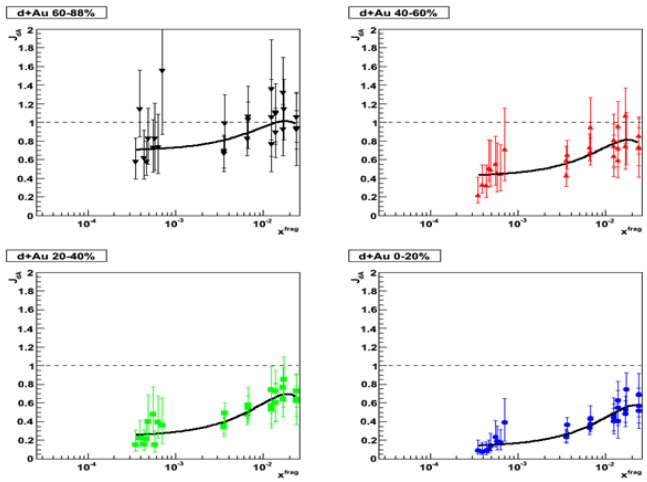

Figure 1: $J_{\rm dA}$ vs x_{Au}^{frag} for 4 different centrality bins. The points are fit with the same parametric function as those used for the EPS09 set of nuclear pdf's [16].

From the pairs we extract the relative yield, $J_{\rm dA}$, of correlated back-to-back hadrons in d+Au collisions compared to p+p collisions scaled with the average number of binary nucleon collisions $\langle N_{coll}\rangle$, where

$$J_{\rm dA} = \frac{1}{\langle N_{coll}\rangle}\frac{\sigma_{dA}^{pair}/\sigma_{dA}}{\sigma_{pp}^{pair}/\sigma_{pp}}$$

and is explained in detail in [15]. $J_{\rm dA}$ is simply the analog of the usual nuclear modification factor $R_{\rm dA}$ but for hadron pairs. The $\sigma_{dA,pp}$ are the p+p or d+Au inelastic cross-sections, while $\sigma_{dA,pp}^{pair}$ are the cross-sections for di-hadron pair production, and is used as a proxy for di-jets in PHENIX.

In Fig. 1, we have plotted the values of $J_{\rm dA}$ versus x_{Au}^{frag} for four different d+Au centrality selections. x_{Au}^{frag} is defined as

$$x_{Au}^{frag} = (\langle p_{T1}\rangle e^{-\langle\eta_1\rangle} + \langle p_{T2}\rangle e^{-\langle\eta_2\rangle})/\sqrt{s_{NN}}$$

and can be directly measured experimentally. x_{Au}^{frag} should be correlated with the Bjorken x that is probed in the nucleus, assuming that a normal leading order (LO) perturbative QCD framework applies for this data. In the case of 2→2 LO processes, the variable x_{Au}^{frag} is lower than x_{Au} by the mean fragmentation fraction, $\langle z\rangle$, of the struck parton in the Au nucleus. From the plot, one can see that $J_{\rm dA}$ decreases with increasing centrality, or equivalently with

increasing nuclear thickness. The suppression also increases as one goes to lower x_{Au}^{frag} in the nucleus probed by the deuteron.

In Fig. 2, the $J_{\rm dA}$ values for three different x_{Au}^{frag} are plotted versus $\langle N_{\rm coll}\rangle$, the mean number of binary collisions, in the four centrality classes depicted in Fig. 1. One can clearly see from this plot a systematic decrease of $J_{\rm dA}$ with greater $\langle N_{\rm coll}\rangle$, as well as with decreasing x. The decrease is approximately linear.

3 Discussion

In a leading order pQCD picture, the variable $J_{\rm dA}$ is

$$J_{dA} = \frac{\sigma_{dA}^{pair}/\sigma_{dA}}{\langle N_{coll}\rangle\, \sigma_{pp}^{pair}/\sigma_{pp}} \approx \frac{f_d^a(x_d^a) \otimes f_{Au}^b(x_{Au}^b) \otimes \hat{\sigma}^{ab\to cd} \otimes \mathcal{D}(z_c, z_d)}{\langle N_{coll}\rangle\, f_p^a(x_p^a) \otimes f_p^b(x_p^b) \otimes \hat{\sigma}^{ab\to cd} \otimes \mathcal{D}(z_c, z_d)} \tag{1}$$

for partons a+b going to outgoing jets c+d, which then fragment to hadrons with longitudinal fractions z_c, z_d. In the above convolutions over the parton distribution functions (f), the parton-parton cross-section $\hat{\sigma}$, and fragmentation functions $\mathcal{D}$, most of the terms are expected to be roughly similar between p+p and d+Au except for the nuclear gluon parton distribution (pdf).

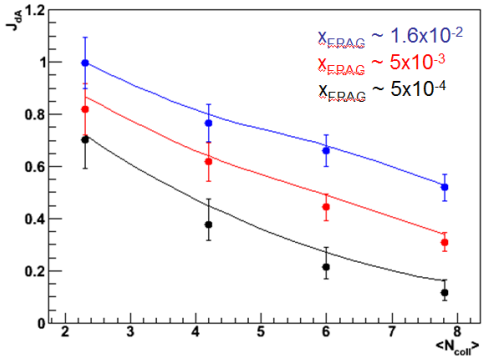

Figure 2: $J_{\rm dA}$ vs $\langle N_{\rm coll}\rangle$, the mean number of binary collisions, for different x_{Au}^{frag} values.

Naively, $J_{\rm dA}$ might be largely dominated by the modification to the nuclear gluon pdf, since most of the events with di-hadrons at forward rapidities consist of a high-x parton from the deuteron and a low-x gluon from the gold nucleus. Assuming this to be true, one can then associate $J_{\rm dA}$ with the relative modification of the nuclear gluon distribution, R_g^{Au}, i.e.,

$$J_{\rm dA} \sim R_g^{Au} = G_{Au}(x, Q^2)/A\, G_p(x, Q^2)$$

One can then interpret Fig. 2 as a systematic decrease in the gluon distribution when one goes to the thicker parts of the nucleus, perhaps due to recombination of the gluons, and that the recombination creates a proportional decrease in the number of gluons with increasing number of nucleons along a line in the nucleus. This is schematically illustrated in Fig. 3. This decrease is stronger at lower x, which one might expect since the transverse size of the gluons are larger for lower x.

If nature is kind and this data can be interpreted in terms of a simple LO pQCD picture, then this data may provide valuable information on how gluons recombine in the nucleus as a function of the thickness of the nucleus and Bjorken x of the gluon. Furthermore, it may be possible to extract R_g^{Au}, which is extremely important for understanding the quark gluon plasma since it forms the main ingredient for production in heavy ion collisions.

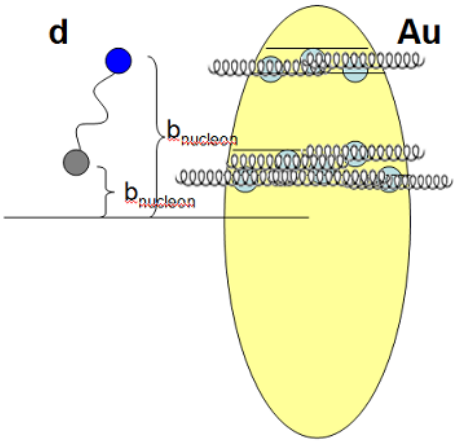

Figure 3: Schematic illustration depicting the increasing overlapping of gluons with smaller impact parameter.

References

[1] I. Arsene *et al.*[BRAHMS Collaboration], Phys. Rev. Lett. **93** (2004) 242303
[2] J. Adams *et al.*[Star Collaboration], Phys. Rev. Lett. **97** (2006) 152302
[3] S. Adler *et al.*[PHENIX Collaboration], Phys. Rev. Lett. **94** (2005) 082302
[4] L. D. McLerran and R. Venugopalan, Phys. Rev. D **49** (1994) 3352
[5] D. Kharzeev, E. Levin and L. McLerran, Nucl. Phys. A **748** (2005) 627
[6] I. Vitev Phys. Rev. C **75** (2007) 064906
[7] L. Frankfurt and M. Strikman, Phys. Lett. B **645** (2007) 412
[8] R. C. Hwa, C. B. Yang and R. J. Fries, Phys. Rev. C **71** (2005) 024902
[9] M. Strikman and W. Vogelsang, Phys. Rev. D **83**, 034029 (2011)
[10] V. Guzey, M. Strikman and W. Vogelsang, Phys. Lett. B **603**, 173 (2004)
[11] J. w. Qiu and I. Vitev, Phys. Lett. B **632** (2006) 507
[12] S. Adler *et al.*[PHENIX Collaboration], Phys. Rev. C. **73** (2006) 054903
[13] S. Adler *et al.*[PHENIX Collaboration], Phys. Rev. Lett. **96** (2006) 222301
[14] A. Adare *et al.* [PHENIX Collaboration], Phys. Rev. Lett. **107**, 172301 (2011)
[15] A. Adare *et al.*[PHENIX Collaboration], Phys. Rev. C. **78** (2008) 014901
[16] K. J. Eskola, H. Paukkunen and C. A. Salgado, JHEP **0904** (2009) 065

Diffractive pQCD mechanisms of exclusive production of $b\bar{b}$ dijets and W^+W^- pairs in proton-proton collisions

Antoni Szczurek[1,2]

[1]Institute of Nuclear Physics PAN, ul. Radzikowskiego 152, PL-31-342 Kraków, Poland
[2]Rzeszów University, ul. Rejtana 16, PL-35-959 Rzeszów, Poland

DOI: http://dx.doi.org/10.3204/DESY-PROC-2012-02/261

We discuss central exclusive production of W^+W^- pairs in proton-proton collisions at LHC. Predictions for the total cross section and differential distributions in transverse momentum of $W^\pm$ and WW invariant mass are presented. We discuss both $\gamma\gamma \to W^+W^-$ mechanism as well as a new mechanism of exclusive diffractive production. The amplitude for the latter process is calculated in the Durham model. We compare the two (QED and QCD) types of contributions. The diffractive contribution is only a small fraction of fb compared to the $\gamma\gamma$ contribution which is of the order of 100 fb. This opens a possibility of searches for anomalous four-boson $\gamma\gamma W^+W^-$ coupling due to physics beyond Standard Model.

1 Introduction

The $\gamma\gamma \to W^+W^-$ process is interesting reaction to test the Standard Model and any other theory beyond the Standard Model. The linear collider would be a good option to study the couplings of gauge bosons in the future. For instance in Ref.[1] the anomalous coupling in locally SU(2) $\times$ U(1) invariant effective Lagrangian was studied. Other models also lead to anomalous gauge boson coupling.

It was discussed recently [3, 4, 5] that the $pp \to ppW^+W^-$ reaction is a good case to study experimentally the γW^+W^- and $\gamma\gamma W^+W^-$ couplings almost at present. Only photon-photon contribution for the purely exclusive production case was considered so far.

Central exlusive production has been recently an active field of research [6]. The exclusive reaction $pp \to pHp$ has been intensively studied by the Durham group [7]. This study was motivated by the clean environment and largely reduced background due to a suppression of $b\bar{b}$ production as a consequence of the $J_z = 0$ rule in the forward limit. During the conference some results for the $b\bar{b}$ production were shown.

In this communication, we discuss exclusive production of W^+W^- pairs in high-energy proton-proton collisions. The original results have been presented recently in [2]. The $pp \to pW^+W^-p$ process going through the diffractive QCD mechanism with the $gg \to W^+W^-$ subprocess naturally constitutes an irreducible background for the exclusive electromagnetic $pp \to p(\gamma\gamma \to W^+W^-)p$ process. We discuss the contribution of the diffractive mechanism which could potentially shadow the photon-photon fusion.

2 Diffractive mechanism

A schematic diagram for central exclusive diffractive production of $W^{\pm}W^{\mp}$ pairs in proton-proton scattering $pp \to pW^{\pm}W^{\mp}p$ is shown in Fig. 1.

The amplitude of the diffractive process at high energy is written as:

$$\mathcal{M}_{\lambda_+\lambda_-}(s,t_1,t_2) \;\simeq\; is\frac{\pi^2}{2}\int d^2\mathbf{q}_{0\perp}V_{\lambda_+\lambda_-}(q_1,q_2,k_+,k_-)\frac{f_g(q_0,q_1;t_1)f_g(q_0,q_2;t_2)}{\mathbf{q}_{0\perp}^2\,\mathbf{q}_{1\perp}^2\,\mathbf{q}_{2\perp}^2}\,, \quad (1)$$

where $\lambda_{\pm} = \pm 1,\, 0$ are the polarisation states of the produced $W^{\pm}$ bosons, respectively, $f_g(r_1,r_2;t)$ is the off-diagonal unintegrated gluon distribution function (UGDF).

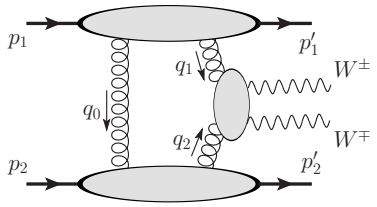

Figure 1: Diagram for the central exclusive diffractive WW pair production in pp collisions.

The $gg \to W^+_{\lambda_+}W^-_{\lambda_-}$ hard subprocess amplitude $V_{\lambda_+\lambda_-}(q_1,q_2,k_+,k_-)$ can be formally written as

$$V_{\lambda_+\lambda_-} = n_\mu^+ n_\nu^- V^{\mu\nu}_{\lambda_+\lambda_-} = \frac{4}{s}\frac{q_{1\perp}^\nu}{x_1}\frac{q_{2\perp}^\mu}{x_2}V_{\lambda_+\lambda_-,\mu\nu}, \quad q_1^\nu V_{\lambda_+\lambda_-,\mu\nu} = q_2^\mu V_{\lambda_+\lambda_-,\mu\nu} = 0\,, \quad (2)$$

where $n_\mu^{\pm} = p_{1,2}^\mu/E_{p,cms}$ and the center-of-mass proton energy $E_{p,cms} = \sqrt{s}/2$.

There are two types of diagrams entering the hard subprocess amplitude: triangles and boxes [2]. The corresponding amplitudes have been calculated using the Mathematica-based `FormCalc` (FC) package. The details are explained in [2].

The bare amplitude above is subjected to absorption corrections that depend on the collision energy and typical proton transverse momenta. The bare cross section is usually multiplied by a rapidity gap survival factor which we take the same as for the Higgs boson and $b\bar{b}$ production to be $S_g = 0.03$ at the LHC energy.

The diffractive WW CEP amplitude (1) described above is used to calculate the corresponding cross section. In order to make the calculation feasible we simplify the calculation limiting to the forward region. The calculation in the full phase space is obtained by assuming exponential dependence in t_1 and t_2 and assuming no correlation between outgoing protons. In such an approximate calculation the phase space integral reduces to four dimensions [2].

3 Electromagnetic mechanism

In this section we briefly discuss the $\gamma\gamma \to W^+W^-$ mechanism. Here we limit to only Standard Model amplitude. The relevant subprocess diagrams are shown in Fig. 2. The cross section for the subprocess can be expressed in terms of Mandelstam variables.

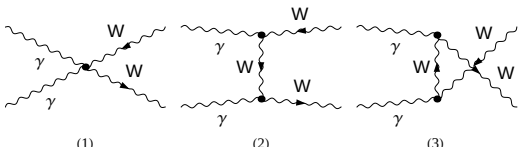

Figure 2: The Born diagrams for the $\gamma\gamma \to W^{\pm}W^{\mp}$ subprocess.

Since we concentrate on the diffractive mechanism the cross section for the $\gamma\gamma$ mechanism is calculated in approximate way.

To calculate differential distributions the following parton formula is used

$$\frac{d\sigma}{dy_+ dy_- d^2p_{W\perp}} = \frac{1}{16\pi^2 \hat{s}^2}\, x_1 f_1^{WW}(x_1)\, x_2 f_2^{WW}(x_2)\, \overline{|\mathcal{M}_{\gamma\gamma\to W^+W^-}(\hat{s},\hat{t},\hat{u})|^2}\,, \tag{3}$$

where $x_{1,2}$ are momentum fractions of the fusing gluons.

In our evaluations we use the Weizsäcker-Williams equivalent photon fluxes of protons from Ref. [8].

4 Results

In Fig. 3 we show distribution in W^+ (W^-) transverse momentum. The distribution for exclusive diffractive production is much steeper than that for the electromagnetic contribution. The diffractive contribution peaks at $p_{t,W} \sim 25$ GeV. This is somewhat smaller than for the $\gamma\gamma \to W^+W^-$ mechanism where the maximum is at $p_{t,W} \sim 40$ GeV. The exclusive cross section for photon-photon contribution is at large transverse momenta ~ 1 TeV smaller only by one order of magnitude than the inclusive $gg \to W^+W^-$ component shown for comparision.

Fig. 4 shows distribution in the W^+W^- invariant mass which is particularly important for the New Physics searches at the LHC [3]. The distribution for the diffractive component drops quickly with the M_{WW} invariant mass. For reference and illustration, we show also distribution when the Sudakov form factors in off-diagonal UGDF's is set to one. As can be seen from the figure, the Sudakov form factor lowers the cross section by a large factor. The damping is M_{WW}-dependent as can be seen by comparison of the two curves. We show the full result (boxes + triangles) and the result with boxes only which would be complete if the Higgs boson does not exist. At high invariant masses, the interference of boxes and triangles decreases the cross section even more. The distribution for the photon-photon component drops very slowly with M_{WW} and at $M_{WW} > 1$ TeV the corresponding cross section is even bigger than the $gg \to W^+W^-$ component to inclusive production of W^+W^-.

5 Summary

Recently ([2]) we have calculated the QCD diffractive contribution to the exclusive $pp \to pW^+W^-p$ process for the first time in the literature with the full one-loop $gg \to W^+W^-$

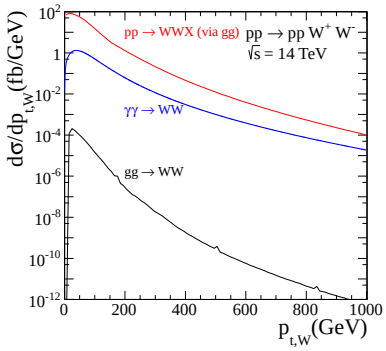

Figure 3: Distribution in transverse momentum of one of the W bosons. The diffractive contribution is shown by the bottom solid line while the $\gamma\gamma \to W^+W^-$ contribution by the middle solid line. The top solid line corresponds to the inclusive gluon-initiated $pp \to W^+W^-X$ component.

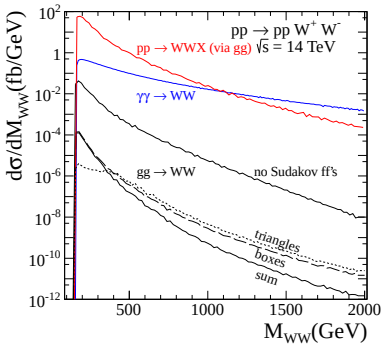

Figure 4: Distribution in W^+W^- invariant mass. We show both the QCD diffractive contribution and the $\gamma\gamma \to^+ W^-$ contribution. The result when the Sudakov form factor is put to one is shown for illustration. The most upper curve is for the inclusive gluon-initiated $pp \to W^+W^-X$ component.

matrix element. The full amplitude is a sum of two mechanisms. First component is a virtual (highly off-shell) Higgs boson production and its subsequent transformation into real W^+W^- pair. Second component relies on the formation of intermediate quark boxes.

We have made first evaluation of differential distributions using amplitudes in the forward limit "corrected" off-forward via a simple exponential (slope dependent) extrapolation. Distributions in W-boson transverse momentum and W^+W^- pair invariant mass has been presented here for illustration. The contribution of triangles (with the intermediate s-channel Higgs boson) turned out to be smaller than the contribution of boxes. These results have been compared with the results obtained for purely electromagnetic photon-photon fusion. We have shown that the diffractive contribution is much smaller than the electromagnetic one. There are several reasons of the suppression. Since here we have focused on large invariant masses of the W^+W^- system, rather large x gluon distributions enter the calculation of the diffractive amplitude.

The gluon densities at such large invariant masses, i.e. large x_1 and x_2, are rather small. Furthermore relative to the electromagnetic process the diffractive contribution is strongly damped by the Sudakov form factor, soft gap survival probability and optionally (if Higgs boson exists) by the interference of box and triangle diagrams.

In summary, we have given a new argument for the recent idea that the $pp \to ppW^+W^-$ reaction is a good place for searches beyond Standard Model as far as four-boson (anomalous) coupling is considered.

6 Acknowledgements

I am indebted to Piotr Lebiedowicz and Roman Pasechnik for collaboration on the issues presented here. I wish to thank the organizers for perfect organization of DIS2012. My stay during the conference in Bonn was supported from a polish grant DEC-2011/01/B/ST2/04535.

References

[1] O. Nachtmann, F. Nagel, M. Pospischil and A. Utermann, Eur. Phys. J. **C45** (2005) 679; Eur. Phys. J. **C46** (2006) 93.

[2] P. Lebiedowicz, R. Pasechnik and A. Szczurek, arXiv.1203.1832 [hep-ph].

[3] O. Kepka and C. Royon, Phys. Rev. **D78** (2008) 073005;
E. Chapon, C. Royon and O. Kepka, Phys. Rev. **D81** (2010) 074003.

[4] N. Schul and K. Piotrzkowski, Nucl. Phys. B (Proc. Suppl.) **179-180** (2008) 289;
T. Pierzchała and K. Piotrzkowski, Nucl. Phys. B (Proc. Suppl.) **179-180** (2008) 257.

[5] M. Maniatis, A. v. Manteuffel and O. Nachtmann, Nucl. Phys. B (Proc. Suppl.) **179-180** (2008) 104.

[6] M. G. Albrow, T. D. Coughlin and J. R. Forshaw, Prog. Part. Nucl. Phys. **65** (2010) 149.

[7] V. A. Khoze, A. D. Martin and M. G. Ryskin, Phys. Lett. **B401** (1997) 330;
V. A. Khoze, A. D. Martin and M. G. Ryskin, Eur. Phys. J. **C14** (2000) 525;
V. A. Khoze, A. D. Martin and M. G. Ryskin, Eur. Phys. J. **C19** (2001) 477 [Erratum-ibid. **C20** (2001) 599];
V. A. Khoze, A. D. Martin and M. G. Ryskin, Eur. Phys. J. **C23** (2002) 311;

[8] M. Drees and D. Zeppenfeld, Phys. Rev. **D39** (1989) 2536.

Measurement of the t-dependence in Exclusive Photoproduction of $\Upsilon(1S)$ Mesons at HERA

Jacek Ciborowski for the ZEUS Collaboration

University of Warsaw, Faculty of Physics, Hoża 69, 00681 Warsaw, Poland

DOI: http://dx.doi.org/10.3204/DESY-PROC-2012-02/37

The exclusive photoproduction reaction $\gamma p \to \Upsilon(1S)p$ has been studied with the ZEUS detector in ep collisions at HERA using an integrated luminosity of 468 pb^{-1}. The measurement covers the kinematic range $60 < W < 220$ GeV and $Q^2 < 1$ GeV^2, where W is the photon-proton c.m.s. energy and Q^2 is the photon virtuality. The exponential slope, b, of the t dependence of the cross section, where t is the squared four-momentum transfer at the proton vertex, has been measured, yielding $b = 4.3^{+2.0}_{-1.3}(stat.)^{+0.5}_{-0.6}(syst.)$ GeV^{-2}. This constitutes the first measurement of the t dependence of the $\gamma p \to \Upsilon(1S)p$ cross section.

1 Introduction

In exclusive photoproduction of heavy vector mesons (VM), the mass of the the heavy quark provides a hard scale and the process can be described by models based on perturbative QCD (pQCD) [1, 2]. At leading order (Fig. 1) the photon fluctuates into a $q\bar{q}$ state of small transverse size, which interacts with partons in the proton through a two-gluon colour-singlet state, forming a heavy VM. The cross section is proportional to the square of the gluon density in the proton thus heavy vector meson photoproduction exhibits rapid rise of the cross section with the photon-proton c.m.s. energy, W, explained through the increasing gluon density with decreasing fractional momentum, $x \propto 1/W^2$ (at HERA $10^{-4} < x < 10^{-2}$). Prior to this measurement, the ZEUS Collaboration measured the W-dependence of the exclusive photoproduction of $\Upsilon(1S)$ mesons, $\gamma p \to \Upsilon(1S)p$, parametrised as $\sigma^{\gamma p}(W) \propto W^{\delta}$, yielding $\delta = 1.2 \pm 0.8$ [3] (Fig. 2), consistent with predictions for exclusive photoproduction of $\Upsilon(1S)$ mesons in leading-order pQCD [4]. Studies of the exclusive photoproduction of vector mesons [5] have shown that the

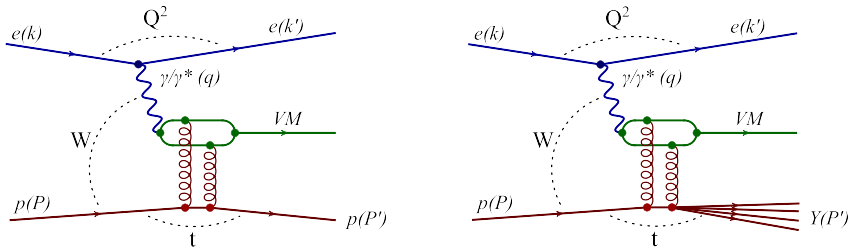

Figure 1: Diagrams for exclusive (left) and proton-dissociative (right) vector-meson photoproduction in ep interactions (see text for description of kinematic variables).

t dependence of the differential cross section may be approximated in the region of small t ($|t| < 1\,\mathrm{GeV}^2$) with a single exponential: $\mathrm{d}\sigma/\mathrm{d}|t| \propto \exp(-b|t|)$, where t is the four-momentum transfer squared at the proton vertex. The slope parameter, b, measured at ZEUS for exclusive J/ψ production at $W_0 = 90\,\mathrm{GeV}$ is $b = 4.15 \pm 0.05(\mathrm{stat.})^{+0.30}_{-0.18}(\mathrm{syst.})\,\mathrm{GeV}^{-2}$ [6] (and exhibits a logarithmic W variation). In an optical model approach for exclusive production of vector mesons, the slope parameter b is related to the radii of the proton, R_p, and the vector meson, R_{VM}, according to the formula: $b \approx (R_p^2 + R_{VM}^2)/4$. The value of b measured for J/ψ production is approximately equal to that expected from the size of the proton, $b \approx 4\,\mathrm{GeV}^{-2}$, in agreement with calculations based on pQCD [7]. This suggests that the size of the J/ψ meson is small compared to that of the proton. A similar picture is expected in the case of exclusive $\Upsilon(1S)$ production [8, 9].

This contribution reports on the first measurement of b in exclusive $\Upsilon(1S)$ photoproduction, observed in the $\mu^+\mu^-$ decay channel in the kinematic range $60 < W < 220\,\mathrm{GeV}$, using data collected with the ZEUS detector [10], corresponding to an integrated luminosity of $468\ \mathrm{pb}^{-1}$ (1996-2007). In the quoted period HERA provided electron and positron beams of energy $E_e = 27.5\,\mathrm{GeV}$ and proton beams of energy $E_p = 920(820)\,\mathrm{GeV}$ (c.m.s. energy $\sqrt{s} = 318(300)\,\mathrm{GeV}$). The four-momenta of the incoming and outgoing electron and proton are

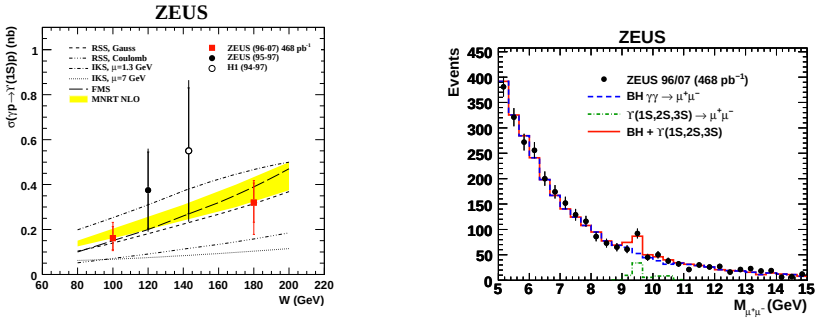

Figure 2: Left: W-dependence of the exclusive photoproduction of $\Upsilon(1S)$ Mesons, $\gamma p \to \Upsilon(1S)p$, and predictions in leading-order pQCD [4]; right: this analysis - invariant mass distribution of $\mu^+\mu^-$ pairs. The dashed line shows the simulated Bethe-Heitler (BH) (exclusive and proton dissociative) distribution, normalised to the data points in the range $[5-15]\,\mathrm{GeV}$ with exclusion of the $[9-11]\,\mathrm{GeV}$ mass window. Simulated contributions of the $\Upsilon(1S)$, $\Upsilon(2S)$ and $\Upsilon(3S)$ resonances is shown as a histogram on the mass axis (dashed-dotted line). The solid line shows the sum of all contributions.

denoted by k, k', P and P', respectively. The exclusive reaction $ep \to e\Upsilon(1S)p$ is described by the following variables (Fig. 1): $s = (k+P)^2$, the c.m.s. energy squared of the electron-proton system; $Q^2 = -q^2 = -(k-k')^2$, the negative four-momentum squared of the exchanged photon; $y = (q \cdot P)/(k \cdot P)$, the fraction of the electron energy transferred to the hadronic final state in the rest frame of the initial-state proton; $W^2 = (q+P)^2 = -Q^2 + 2y(k \cdot P) + m_p^2$, the c.m.s. energy squared of the photon–proton system, where m_p is the proton mass; $M_{\mu^+\mu^-}$, the invariant mass of the $\mu^+\mu^-$ pair; $t = (P-P')^2$, the squared four-momentum transfer at the proton vertex, determined from the approximate formula: $t \approx -(p_x^+ + p_x^-)^2 - (p_y^+ + p_y^-)^2$ where $p_{x,y}^{\pm}$ are the components of the transverse momentum of the decay muons.

The details of the present analysis can be found elsewhere [11]. Events were restricted to Q^2 values from the kinematic minimum, $Q^2 \approx 10^{-9}$ GeV^2 to a value at which the scattered electron starts to be observed in the calorimeter (CAL), $Q^2 \approx 1$ GeV^2, with an estimated median Q^2 value of 10^{-3} GeV^2. Exclusive $\mu^+\mu^-$ events in photoproduction were selected online by requiring at least one track associated with a deposit in muon detectors. The main offline selections were as follows: two oppositely charged tracks forming a vertex and no other tracks present in the central tracking system; position of the vertex consistent with an ep interaction; transverse momentum of each track $p_T > 1.5$ GeV; at least one track identified as a muon in muon detectors, if not explicitly identified as a muon, the second track had to be associated with a minimum-ionising energy deposit in the CAL; the energy of each CAL cluster not associated to any of the final-state muons was required to be less than 0.5 GeV, in order to be above the noise level of the CAL. It implicitly selected exclusive events with an effective cut $Q^2 < 1$ GeV^2; the sum of the energy in the forward CAL modules surrounding the beam hole had to be smaller than 1 GeV to suppress the contamination from proton-dissociative events, $ep \to e\Upsilon Y$ (Fig. 1). According to a Monte Carlo study, this corresponds to an effective cut on the mass M_Y of the dissociated system originating from the proton, $M_Y < 4$ GeV; four-momentum-transfer squared $|t| < 5$ GeV^2. The total number of selected $\mu^+\mu^-$ pairs was 2769 (contamination with cosmic ray muons is below 1%).

The invariant-mass distribution of $\mu^+\mu^-$ pairs is shown in Fig. 2 including the simulated contributions from the Bethe-Heitler (exclusive and proton dissociative) process and from the $\Upsilon(1S)$, $\Upsilon(2S)$ and $\Upsilon(3S)$ resonances. The BH distributions were normalised to the data in the range $[5-15]$ GeV excluding the $[9-11]$ GeV mass window. For the determination of the slope parameter for exclusive $\Upsilon(1S)$ production, only events in the mass window $[9.33-9.66]$GeV were considered. The width of the mass window was chosen in order to avoid excessive smearing of the t variable and to retain a good signal-to-background ratio (71% of all reconstructed $\Upsilon(1S)$ events are expected in this window and the relative contaminations of $\Upsilon(2S)$ and $\Upsilon(3S)$ states with respect to $\Upsilon(1S)$ are 1.3% and 0.1%, respectively). The contribution from the $\Upsilon(2S)$ and $\Upsilon(3S)$ states was neglected for the extraction of the slope parameter b. The value of the slope parameter for exclusive $\Upsilon(1S)$ production was determined as follows: the sum of simulated distributions of all contributing processes was fitted to the observed event yields in the signal mass window $[9.33 - 9.66]$ GeV in the four t bins shown in Fig. 3. A binned Poissonian log-likelihood function was used. The expected number of Bethe-Heitler background events was fixed to the value obtained from the $\mu^+\mu^-$ spectrum outside the signal region. In view of insufficient statistics for a standalone measurement, the contribution of proton-dissociative $\Upsilon(1S)$ events in the final sample was adopted from diffractive J/ψ production [6], 0.25 ± 0.05.

The values of the slope parameter for the proton dissociative $\Upsilon(1S)$ production in the MC was taken to be 0.65 ± 0.1 GeV^2 [6]. The fit was performed with two free parameters: the slope b and the number of expected $\Upsilon(1S)$ events in the signal mass window. After evaluation of systematic uncertainties, the slope parameter b for the exclusive production of $\Upsilon(1S)$ mesons was measured to be $b = 4.3^{+2.0}_{-1.3}(stat.)^{+0.5}_{-0.6}(syst.)$ GeV^{-2}.

A comparison of all HERA measurements of the slope parameter b for exclusive light and heavy vector meson production and for deeply virtual Compton scattering (DVCS) is shown in Fig. 3. This analysis doubles the range covered by previous measurements in terms of $Q^2+M_{VM}^2$, where M_{VM} denotes the mass of a vector meson, extending the value of the scale to ≈ 90 GeV^2, the highest achieved to date in the measurement of the t-slope parameter for a vector meson. The measured value is in agreement with an asymptotic behaviour of this dependence, reflecting the proton radius. This was already suggested by earlier measurements and is consistent with

predictions based on pQCD models ($b = 3.68\,\mathrm{GeV}^{-2}$) [12].

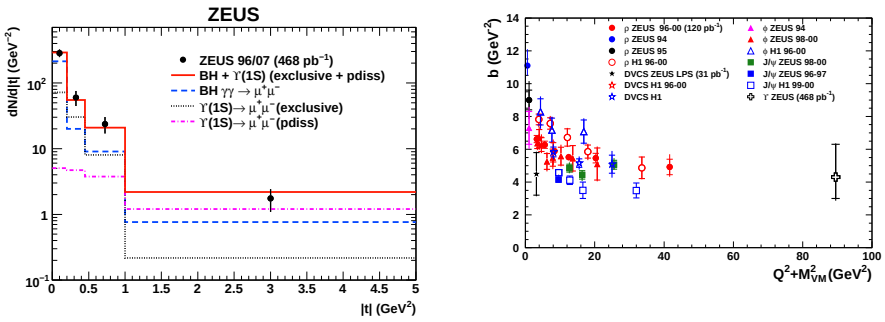

Figure 3: Left: Measured $|t|$ distribution (full dots) with error bars denoting statistical uncertainties. Fitted distributions for simulated events are shown for the Bethe-Heitler (dashed line), exclusive $\Upsilon(1S)$ (dotted line) and proton dissociative $\Upsilon(1S)$ (dashed-dotted line) processes. The solid line shows the sum of all contributions; right: compilation of the HERA measurements of the slope parameter b as a function of the scale $Q^2 + M^2_{VM}$, for exclusive $\Upsilon(1S)$ production (the rightmost data point), for other exclusive vector-meson production and for deeply virtual Compton scattering (DVCS) (see [11] for references).

References

[1] H. Kowalski, L. Motyka and G. Watt. Phys. Rev. **D74** (2006) 074016.

[2] L. Frankfurt, W. Koepf and M. Strikman. Phys. Rev. **D54** (1996) 3194.

[3] ZEUS Collaboration, S. Chekanov *et al.* Phys. Lett. **B680** (2009) 4.

[4] L.L. Frankfurt, M.F. McDermott and M. Strikman. JHEP **9902** (1999) 002.

[5] G. Wolf. Rep. Prog. Phys. **73** (2010) 116202, and references therein.

[6] ZEUS Collaboration, S. Chekanov *et al.* Eur. Phys. J. **C24** (2002) 345.

[7] L. Frankfurt, W. Koepf and M. Strikman. Phys. Rev. **D57** (1998) 512.

[8] Ji-Huan Pan *et al.* Comm. Theor. Phys. **52** (2009) 108.

[9] B.E. Cox, J.R. Forshaw and R. Sandapen. JHEP **0906** (2009) 034.

[10] ZEUS Collaboration, U. Holm (Ed.), The ZEUS detector, status report (unpublished), DESY, 1993, available on http://www-zeus.desy.de/bluebook/bluebook.html.

[11] ZEUS Collaboration, H. Abramowicz, et al., Phys. Lett. **B708** (2012) 14.

[12] B.E. Cox, J.R. Forshaw and R. Sandapen. JHEP **0906** (2009) 034.

Exclusive dipion production

Justyna Tomaszewska on behalf of the ZEUS Collaboration

Universität Hamburg, Luruper Chaussee 149, D-22761 Hamburg

DOI: http://dx.doi.org/10.3204/DESY-PROC-2012-02/38

The exclusive electroproduction of two pions in the mass range $0.4 < \mathrm{M}_{\pi\pi} < 2.5$ GeV has been studied with the ZEUS detector at HERA using an integrated luminosity of 82 pb^{-1}. The two-pion invariant-mass distribution is interpreted in terms of the pion electromagnetic form factor, $|F(M_{\pi\pi})|$, assuming that the studied mass range includes the contributions of the ρ, ρ' and ρ" vector-meson states.

1 Exclusive dipion production

Exclusive electroproduction of vector mesons takes place through a virtual photon γ^* by means of the process $\gamma^* p \to Vp$. At large values of the centre-of-mass energy, W, this is usually viewed as a three-step process; the virtual photon γ^* fluctuates into a $q\bar{q}$ pair which interacts with the proton through a two-gluon ladder and hadronizes into a vector meson, V.
Exclusive $\pi^+\pi^-$ production has been measured at HERA [1] experiments: ZEUS [2, 3] and H1 [4] as well as in the annihilation process $e^+e^- \to \pi^+\pi^-$ [5, 6]. The $\pi^+\pi^-$ mass distribution shows a complex structure in the mass range 1–2 GeV. Evidence for two excited vector-meson states has been established [7]; the $\rho'(1450)$ is assumed to be predominantly a radially excited $2S$ state and the $\rho''(1700)$ is an orbitally excited $2D$ state, with some mixture of the S and D waves [8]. In addition there is also the $\rho_3(1690)$ spin-3 meson [9] which has a $\pi\pi$ decay mode.

1.1 Data selection

The data used in this analysis were collected at the HERA ep collider during 1998-2000 with the ZEUS detector. At that time HERA operated at a proton energy of 920 GeV and at a positron energy of 27.5 GeV. The integrated luminosity used was 82 pb^{-1}.

The data are selected in the two-pion mass range $0.4 < \mathrm{M}(\pi\pi) < 2.5$ GeV, in the kinematic range $2.5 < \mathrm{Q}^2 < 80$ GeV^2, 32<W<180 GeV and |t|<0.6 GeV^2, where Q^2 is the virtuality of the photon and t is the squared four-momentum transfer at the proton vertex. The $M_{\pi\pi}$ system consists of a resonance part and a non-resonant background.

1.2 Pion Form Factor

The resonances (ρ, ρ' and ρ'') are described by the pion form factor,F_π. It can be related to the $\pi\pi$ invariant-mass distribution through the following relation [10]:

$$\frac{dN(M(\pi\pi))}{dM_{\pi\pi}} \propto |F_\pi(M_{\pi\pi})|^2$$

In the mass range $M_{\pi\pi} < 2.5$ GeV, Kuhn-Santamaria (KS) [11] include contributions from the $\rho(770)$, $\rho'(1450)$ and ρ"(1700) resonances,

$$F_\pi = \frac{BW_\rho(M_{\pi\pi}) + \beta BW_{\rho'}(M_{\pi\pi}) + \gamma BW_{\rho"}(M_{\pi\pi})}{1+\beta+\gamma}.$$

Here β and γ are relative amplitudes and BW_V is the Breit-Wigner distribution of the vector meson V.

The $\pi^+\pi^-$ mass distribution, after acceptance correction, is shown in Figure 1. A clear peak is seen in the ρ mass range. A small shoulder is apparent around 1.3 GeV and a secondary peak at about 1.8 GeV.

The two-pion invariant-mass distribution was fitted, using the least-square method, as a sum of two terms,

$$\frac{dN(M_{\pi\pi})}{dM_{\pi\pi}} = A\left(1-\frac{4M_\pi^2}{M_{\pi\pi}^2}\right)\left[F_\pi + B\left(\frac{M_0}{M_{\pi\pi}}\right)^n\right],$$

where A is an overall normalization constant. The second term is a parameterization of the non-resonant background, with constant parameters B, n and $M_0 = 1$ GeV. The other parameters, the masses and widths of the three resonances and their relative contributions β and γ, enter through the pion form factor, F_π. The fit, which includes 11 parameters, gives a good description of the data.

The result of the fit is shown in Figure 1 together with the contribution of each of the two terms. The ρ and the ρ" signals are clearly visible. The negative interference between all the resonances results in the ρ' signal appearing as a shoulder.

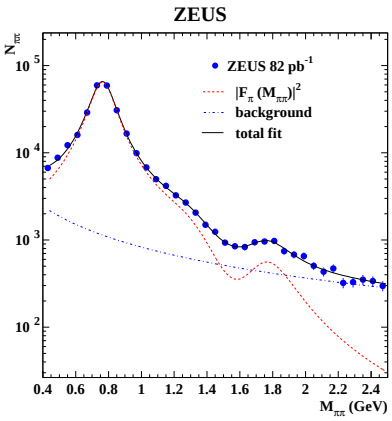

Figure 1: The two-pion invariant-mass distribution, $M_{\pi\pi}$, where $N_{\pi\pi}$ is the acceptance-corrected number of events in each bin of 60 MeV. The dots are the data and the full line is the result of a fit using the Kuhn-Santamaria parameterization. The dashed line is the result of the pion form factor normalized to the data, and the dash-dotted line denotes the background contribution.

1.3 Q^2 dependence

The Q^2 dependence of the relative amplitudes was determined by performing the fit to $M_{\pi\pi}$ in three Q^2 regions, 2–5, 5–10 and 10–80 GeV^2. The results are shown in Figure 2. A reasonable description of the data is achieved in all three Q^2 regions. The absolute value of β increases with Q^2, while the value of γ is consistent with no Q^2 dependence, within large uncertainties.

The Q^2 dependence of the ρ by itself is given elsewhere [2]. Since the $\pi\pi$ branching ratios of ρ' and ρ" are poorly known, the ratio R_V defined as

$$R_V = \frac{\sigma(V)\cdot Br(V\to\pi\pi)}{\sigma(\rho)},$$

has been measured, where σ is the cross section for vector-meson production, and $Br(V\to\pi\pi)$ is the branching ratio of the vector meson $V(\rho', \rho")$ into $\pi\pi$.

The ratio R_V for $V = \rho', \rho"$, as a function of Q^2 is presented in Figure 3.

Owing to the large uncertainties of $R_{\rho"}$, no conclusion on its Q^2 behaviour can be deduced, whereas $R_{\rho'}$ clearly increases with Q^2. This rise has been predicted by several models [12, 13, 14, 15, 16]. The suppression of the $2S$ state (ρ') is connected to a node effect, which results

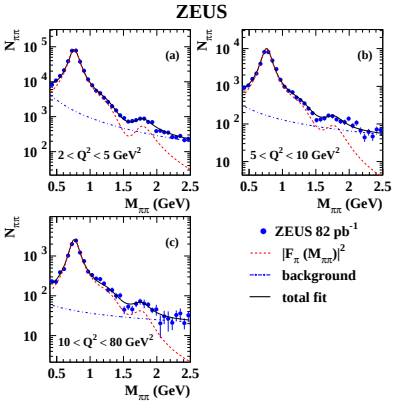

Figure 2: The two-pion invariant-mass distribution, $M_{\pi\pi}$ for three regions of Q^2, as denoted in the figure.

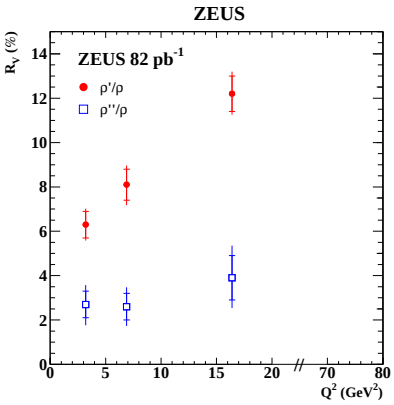

Figure 3: The ratio R_V as a function of Q^2 for $V = \rho'$ (full circles) and ρ" (open squares). The inner error bars indicate the statistical uncertainty, the outer error bars represent the statistical and systematic uncertainty added in quadrature.

in cancellations of contributions from different impact-parameter regions at lower Q^2, while at higher Q^2 the effect vanishes.

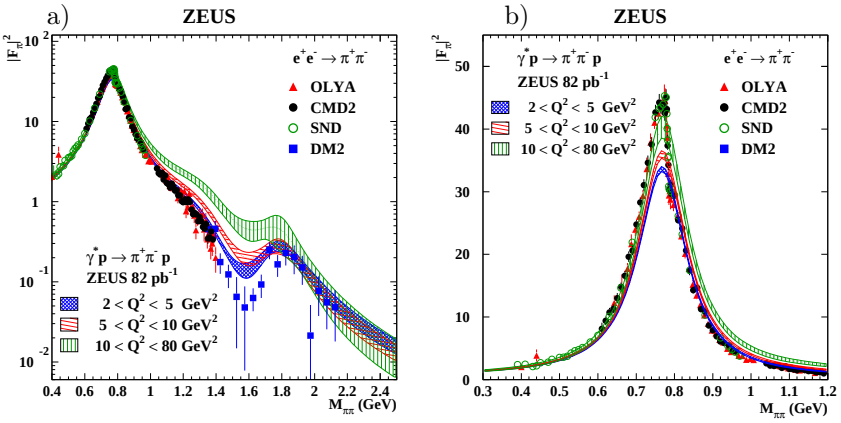

Figure 4: The pion form factor squared, $|F_\pi|^2$, in the whole mass range (a)) and in the ρ mass region (b)), as a function of the $\pi^+\pi^-$ invariant mass, $M_{\pi\pi}$, as obtained from the reaction $e^+e^- \to \pi^+\pi^-$ [5, 17, 18, 19, 20]. The shaded bands represent the square of the pion form factor and its total uncertainty obtained in the present analysis for three ranges of Q^2: 2–5 GeV^2(crossed lines), 5–10 GeV^2(horizontal lines) and 10–80 GeV^2 (vertical lines).

Figure 4 a) shows the curves representing the pion form factor, $|F_\pi(M_{\pi\pi})|^2$, as obtained in the present analysis for the three Q^2 ranges: 2–5, 5–10, 10–80 GeV^2. Also shown are results

obtained in the time-like regime from the reaction $e^+e^- \to \pi^+\pi^-$. In general, the features of the $|F_\pi(M_{\pi\pi})|^2$ distribution observed here are also observed in e^+e^-, i.e., the prominent ρ peak, a shoulder around the ρ' and a dip followed by an enhancement in the ρ" region. Above the ρ region, where the interference between the ρ' and the ρ" starts to dominate, there is a dependence of $|F_\pi(M_{\pi\pi})|^2$ on Q^2, with the results from the lowest Q^2 range closest to those from e^+e^-. However, in the region of the ρ peak, shown in Figure 4 *b*), the pion form-factor $|F_\pi(M_{\pi\pi})|^2$ is highest at the highest Q^2, as in the ρ'-ρ" interference region, while the e^+e^- data are higher than those in the highest Q^2 range. They are equal within errors for $M_{\pi\pi} > 1.8$ GeV.

2 Summary

Exclusive two-pion electroproduction has been studied by ZEUS at HERA. The mass distribution is well described by the pion electromagnetic form factor, $|F_\pi(M_{\pi\pi})|^2$, which includes three resonances, ρ, $\rho'(1450)$ and $\rho''(1700)$.

A Q^2 dependence of $|F_\pi(M_{\pi\pi})|^2$ is observed, visible in particular in the interference region between ρ' and ρ''. The electromagnetic pion form factor obtained from the present analysis is lower (higher) than that obtained from $e^+e^- \to \pi^+\pi^-$ for $M_{\pi\pi} < 0.8$ GeV ($0.8 < M_{\pi\pi} < 1.8$ GeV). They are equal within errors for $M_{\pi\pi} > 1.8$ GeV.

The Q^2 dependence of the cross-section ratios $R_{\rho'} = \sigma(\rho' \to \pi\pi)/\sigma(\rho)$ and $R_{\rho''} = \sigma(\rho'' \to \pi\pi)/\sigma(\rho)$, has been studied. The ratio $R_{\rho'}$ rises strongly with Q^2, as expected in QCD-inspired models in which the wave-function of the vector meson is calculated within the constituent quark model, which allows for nodes in the wave-function to be present.

References

[1] A Proposal for a Large Electron-Proton Colliding Beam Facility at DESY, DESY HERA 81-10 (1981).

[2] ZEUS Coll., S. Chekanov et al.,PMC Phys. **A 1** (2007) 6.

[3] ZEUS Coll., H. Abramowicz et al.,Eur. Phys. J. C **72** (2012) 1869.

[4] H1 Coll., F.D. Aaron et al.,JHEP **05** (2010) 032.

[5] L.M. Barkov et al.,Nucl. Phys. **B 256** (1985) 365.

[6] D. Aston et al., Phys. Lett. **B 92** (1980) 215.

[7] A. Donnachie and H. Mirzaie, Z. Phys. **C 33** (1987) 407.

[8] I.P. Ivanov and N.N. Nikolaev, JETP Lett. **69** (1999) 294.

[9] Omega Photon Coll., M. Atkinson et al., Z.Phys. **C 26** (1985) 499.

[10] B. Clerbaux and M.V. Polyakov, Nucl. Phys. **A 79** (2000) 185.

[11] J.H. Kuhn and A. Santamaria, Z. Phys. **C 48** (1990) 445.

[12] J. Nemchik, N.N. Nikolaev and B.G. Zakharov, Phys. Lett. **B 339** (1994) 194.

[13] L. Frankfurt, W. Koepf and M. Strikman, Phys. Rev. **D 54** (1996) 3194.

[14] I.P. Ivanov and N.N. Nikolaev, Acta Phys. Polon. **B 33** (2002) 3517.

[15] H. Abramowicz, L. Frankfurt and M. Strikman, Surveys High Energy Phys. 11 (1997) 51.

[16] I.P. Ivanov, PhD Thesis (Bonn University), hep-ph/0303035 (2003).

[17] DM2 Coll., D. Bisello et al., Phys. Lett. **B 220** (1989) 312.

[18] CMD2 Coll., R.R. Akhmetshin et al., Phys. Lett. **B 527** (2002) 161.

[19] CMD2 Coll. V.M. Aul'chenko et al., JETP Lett., **82** (2005) 743.

[20] SND Coll., M.N. Achasov et al., J. Exp. Theor. Phys. **101** (2005) 1053.

An AdS/QCD holographic wavefunction for the ρ meson

Jeff Forshaw[1], *Ruben Sandapen*[2]

[1]University of Manchester, Oxford Road, Manchester M13 9PL, UK.
[2]Université de Moncton, Moncton, N-B, E1A 3E9, Canada.

DOI: http://dx.doi.org/10.3204/DESY-PROC-2012-02/265

We use an AdS/QCD holographic wavefunction to generate predictions for the rate of diffractive ρ-meson electroproduction that are in reasonable agreement with data collected at the HERA electron-proton collider.

1 Introduction

In the dipole model of high-energy scattering [1, 2, 3, 4], the scattering amplitude for diffractive ρ meson production is a convolution of the photon and vector meson $q\bar{q}$ light-front wavefunctions with the total cross-section to scatter a $q\bar{q}$ dipole off a proton. QED is used to determine the photon wavefunction and the dipole cross-section can be extracted from the precise data on the deep-inelastic structure function F_2 [5, 6]. This formalism can then be used to predict rates for vector meson production and diffractive DIS [7, 8] or to to extract information on the ρ meson wavefunction using the HERA data on diffractive ρ production [9, 10]. Here we use it to predict the cross-sections for diffractive ρ production using an AdS/QCD holographic wavefunction proposed by Brodsky and de Téramond [11]. We also compute the second moment of the twist-2 distribution amplitude and find it to be in agreement with Sum Rules and lattice predictions.

2 The AdS/QCD holographic wavefunction

In a semiclassical approximation to light-front QCD the meson wavefunction can be written in the following factorized form [11]

$$\phi(x,\zeta,\varphi) = \frac{\Phi(\zeta)}{\sqrt{2\pi\zeta}} f(x) \mathrm{e}^{iL\varphi} \tag{1}$$

where L is the orbital quantum number and $\zeta = \sqrt{x(1-x)}b$ (x is the light-front longitudinal momentum fraction of the quark and b the quark-antiquark transverse separation). The function $\Phi(\zeta)$ satisfies a Schrödinger-like wave equation

$$\left(-\frac{\mathrm{d}^2}{\mathrm{d}\zeta^2} - \frac{1-4L^2}{4\zeta^2} + U(\zeta)\right)\Phi(\zeta) = M^2\Phi(\zeta)\ , \tag{2}$$

where $U(\zeta)$ is the confining potential defined at equal light-front time. After identifying ζ with the co-ordinate in the fifth dimension in AdS space, Eq. (2) describes the propagation of spin-J string modes, in which case $U(\zeta)$ is determined by the choice for the dilaton field. We use here the soft-wall model [12], in which

$$U(\zeta) = \kappa^4\zeta^2 + 2\kappa^2(J-1) \ . \tag{3}$$

The eigenvalues of Eq. (2) are then given as

$$M^2 = 4\kappa^2(n + J/2 + L/2) \ , \tag{4}$$

so that the parameter κ can then be fixed as the best fit value to the Regge slope for vector mesons. Here we use $\kappa = 0.55$ GeV. After solving Eq. (2) with $L = 0$ and $S = 1$ to obtain $\Phi(\zeta)$, it remains to specify the function $f(x)$ in equation (1). This is done by comparing the expressions for the pion EM form factor obtained in the light-front formalism and in AdS space [13]. After accounting for non zero quark masses [14], the final form of the AdS/QCD wavefunction is [15]

$$\phi(x,\zeta) = N\frac{\kappa}{\sqrt{\pi}}\sqrt{x(1-x)}\exp\left(-\frac{\kappa^2\zeta^2}{2}\right)\exp\left(-\frac{m_f^2}{2\kappa^2 x(1-x)}\right) \ , \tag{5}$$

where N is fixed so that

$$\int \mathrm{d}^2\mathbf{b}\ \mathrm{d}x\ |\phi(x,\zeta)|^2 = 1 \ . \tag{6}$$

The meson's light-front wavefunctions can be written in terms of the AdS/QCD wavefunction $\phi(x,\zeta)$ [10]. For longitudinally polarized mesons:

$$\Psi^L_{h,\bar{h}}(b,x) = \frac{1}{2\sqrt{2}}\delta_{h,-\bar{h}}\left(1 + \frac{m_f^2 - \nabla^2}{M_\rho^2\ x(1-x)}\right)\phi(x,\zeta) \ , \tag{7}$$

where $\nabla^2 \equiv \frac{1}{b}\partial_b + \partial_b^2$ and h ($\bar{h}$) are the helicities of the quark (anti-quark). The imposition of current conservation implies that this can be replaced by

$$\Psi^L_{h,\bar{h}}(b,x) = \frac{1}{\sqrt{2}}\delta_{h,-\bar{h}}\ \phi(x,\zeta) \ . \tag{8}$$

We choose to normalize $\phi(x,\zeta)$ using

$$\sum_{h,\bar{h}}\int \mathrm{d}^2\mathbf{b}\,\mathrm{d}x\,|\Psi^L_{h,\bar{h}}(b,x)|^2 = 1 \tag{9}$$

using either Eq. (7) or Eq. (8) and refering to them as Method B or Method A respectively. Note that Method A implies that Eq. (6) is satisfied exactly whereas Method B is equivalent to assuming that the integral in Eq. (6) is a little larger than unity.

For transversely polarized mesons:

$$\Psi^{T=\pm}_{h,\bar{h}}(b,x) = \pm[ie^{\pm i\theta}(x\delta_{h\pm,\bar{h}\mp} - (1-x)\delta_{h\mp,\bar{h}\pm})\partial_b + m_f\delta_{h\pm,\bar{h}\pm}]\frac{\phi(x,\zeta)}{2x(1-x)} \ , \tag{10}$$

where $be^{i\theta}$ is the complex form of the transverse separation, $\mathbf{b}$.

3 Comparing to data, sum rules and the lattice

Our predictions for the total cross-section and the ratio of longitudinal to transverse cross-section are compared to the HERA data in Fig. 1. As can be seen, the agreement is quite good given that our predictions do not contain any free parameters. The disagreement at high Q^2 is expected since this is the region where perturbative evolution of the wavefunction will be relevant and the AdS/QCD wavefunction we use is clearly not able to describe that.

We also compute the second moment of the corresponding twist-2 Distribution Amplitude and find our predictions to be in agreement with those made using Sum Rules and lattice QCD. We obtain a value of 0.217 for Method A and 0.228 for Method B, which is to be compared with the Sum Rule result of 0.24 ± 0.02 at $\mu = 3$ GeV [16] and the lattice result of 0.24 ± 0.04 at $\mu = 2$ GeV [17]. The AdS/QCD wavefunction neglects the perturbatively known evolution with the scale μ and should be viewed as a parametrization of the DA at some low scale $\mu \sim 1$ GeV. Viewed as such, the agreement is good.

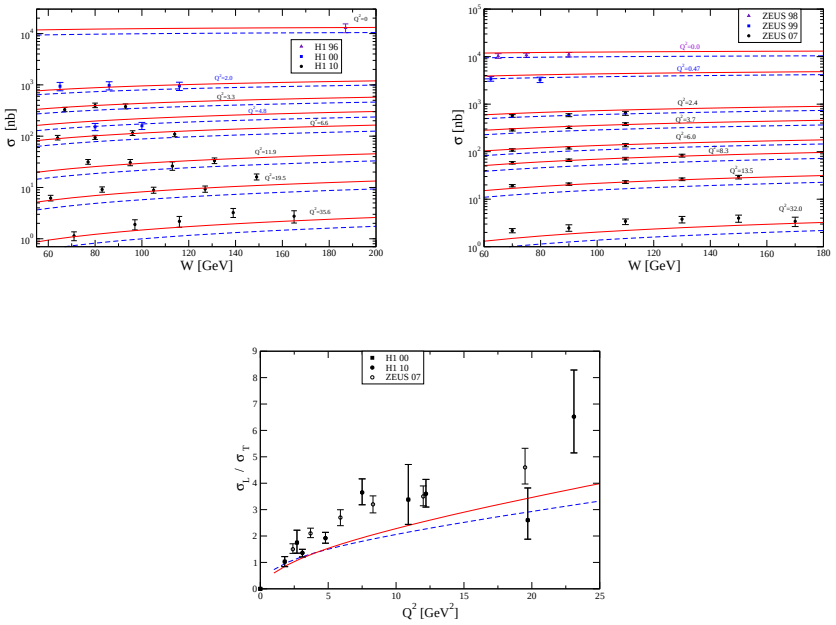

Figure 1: Comparison to the HERA data [18, 19]. Solid red curve is for Method B and the dashed blue curve is for Method A.

4 Acknowledgements

R.S thanks the organisers for a very pleasant workshop and the Faculté des Sciences of the Université de Moncton as well as the Faculté des Études Superieures et de la Recherche (FESR) of the Université de Moncton for financial support.

References

[1] N. N. Nikolaev and B. G. Zakharov. Z. Phys. **C49** (1991) 607–618.

[2] N. N. Nikolaev and B. G. Zakharov. Z. Phys. **C53** (1992) 331–346.

[3] A. H. Mueller. Nucl. Phys. **B415** (1994) 373–385.

[4] A. H. Mueller and B. Patel. Nucl. Phys. **B425** (1994) 471–488, arXiv:hep-ph/9403256.

[5] G. Soyez. Phys. Lett. **B655** (2007) 32–38, arXiv:0705.3672 [hep-ph].

[6] J. R. Forshaw and G. Shaw. JHEP **12** (2004) 052, arXiv:hep-ph/0411337.

[7] J. R. Forshaw, R. Sandapen, and G. Shaw. Phys. Rev. **D69** (2004) 094013, arXiv:hep-ph/0312172.

[8] J. R. Forshaw, R. Sandapen, and G. Shaw. JHEP **11** (2006) 025, arXiv:hep-ph/0608161.

[9] J. R. Forshaw and R. Sandapen. JHEP **11** (2010) 037, arXiv:1007.1990 [hep-ph].

[10] J. R. Forshaw and R. Sandapen. JHEP **1110** (2011) 093, arXiv:1104.4753 [hep-ph].

[11] G. F. de Teramond and S. J. Brodsky. Phys.Rev.Lett. **102** (2009) 081601, arXiv:0809.4899 [hep-ph].

[12] A. Karch, E. Katz, D. T. Son, and M. A. Stephanov. Phys.Rev. **D74** (2006) 015005, arXiv:hep-ph/0602229 [hep-ph].

[13] S. J. Brodsky and G. F. de Teramond. Phys.Rev. **D77** (2008) 056007, arXiv:0707.3859 [hep-ph].

[14] S. J. Brodsky and G. F. de Teramond. arXiv:0802.0514 [hep-ph].

[15] J. Forshaw and R. Sandapen. arXiv:1203.6088 [hep-ph].

[16] P. Ball, V. M. Braun, and A. Lenz. JHEP **08** (2007) 090, arXiv:0707.1201 [hep-ph].

[17] P. A. Boyle *et al.* PoS **LATTICE2008** (2008) 165, arXiv:0810.1669 [hep-lat].

[18] S. Chekanov *et al.* PMC Phys. **A1** (2007) 6, arXiv:0708.1478 [hep-ex].

[19] The H1 Collaboration. JHEP **05** (2010) 032, arXiv:0910.5831 [hep-ex].

New determination of the nonperturbative form factor in QCD transverse-momentum resummation for vector boson production

Masanori Hirai[1], *Hiroyuki Kawamura*[2], *Kazuhiro Tanaka*[3]

[1]Department of Physics, Tokyo University of Science, Noda, Chiba 278-8510, Japan
[2]KEK Theory Center, Tsukuba, Ibaraki 305-0801, Japan
[3]Department of Physics, Juntendo University, Inzai, Chiba 270-1695, Japan

DOI: `http://dx.doi.org/10.3204/DESY-PROC-2012-02/136`

In the b_* model for the Collins-Soper-Sterman (CSS) resummation, the resummed form factor is accompanied by the nonperturbative gaussian form factor, which is known to exhibit strong dependence on the the vector boson mass. The nonperturbative form factor of similar nature arises in another approach for the CSS resummation, the "minimal prescription (MP)" based on analytic continuation to treat the impact parameter transform. We perform a global fit of the nonperturbative form factor in the MP resummation at the next-to-leading logarithmic accuracy, with the Z boson production data at the Tevatron and the low energy Drell-Yan data, and find weak dependence on the vector boson mass.

We consider the hadroproduction of vector bosons, $h_1 + h_2 \to V(Q, y, \cdots) + X$, where the vector bosons $V = \gamma^*, Z, W$ have momentum Q^μ and rapidity y. The differential cross section with the center of mass energy $\sqrt{S}$ of the two colliding hadrons $h_{1,2}$ is given as ($x_{1,2} = Qe^{\pm y}/\sqrt{S}$),

$$d\sigma \propto \sum\nolimits_q e_q^2 \left[q_{h_1}(x_1, Q^2)\bar{q}_{h_2}(x_2, Q^2) + \bar{q}_{h_1}(x_1, Q^2) q_{h_2}(x_2, Q^2) \right] + \cdots, \tag{1}$$

with the product of the (anti-)quark distributions for $h_{1,2}$ and the ellipses standing for the perturbative corrections, the contributions associated with the gluon distributions, etc. This is a benchmark process at the LHC; the comparison with experimental data gives constraints for the PDFs; this is also important for the new physics search. Thus, precise theoretical predictions are desirable. Now the perturbative QCD corrections are known up to NNLO not only for the total cross sections and the rapidity distributions, but also for fully differential cross sections [1].

We note that the vector bosons $V = \gamma^*, Z, W$ are mostly produced at small transverse momentum Q_T of typically a few GeV: the vector bosons with the large Q_T are obtained by the recoil from the hard emission and can be treated by the fixed-order perturbation theory. On the other hand, the large cross section at the small Q_T is obtained by the recoil from the emission of the soft gluons, whose contributions are accompanied by the logarithms $\alpha_s \ln^2 Q^2/Q_T^2$, $\alpha_s \ln Q^2/Q_T^2$, which become very large and diverge for small Q_T and have to be resummed to all orders in α_s to obtain meaningful results. The contributions due to the multiple gluon emission, where the total sum of the gluon's transverse momenta equals Q_T, are conveniently treated in the impact parameter b space conjugate to the transverse-momentum space with

$\delta^{(2)}(Q_T - k_{1T} - k_{2T} - \cdots - k_{nT}) = \int d^2b e^{ib\cdot Q_T} \prod_n e^{-ib\cdot k_T}$. According to the Collins-Soper-Sterman (CSS) resummation formalism [2], the resummed contributions to all orders can be reorganized in terms of the quark and gluon PDFs, the perturbatively calculable coefficient functions, the hard vertex to produce the vector boson V, and the Sudakov factor due to the contributions of soft gluon radiation, which is given as exponentiation of the corresponding all-orders perturbation series. The resummation replaces the RHS of (1) by

$$\int d^2b e^{i\mathbf{b}\cdot\mathbf{Q}_T} e^{S(b,Q)} \sum\nolimits_q e_q^2 \left[q_{h_1}\left(x_1, \frac{b_0^2}{b^2}\right) \bar{q}_{h_2}\left(x_2, \frac{b_0^2}{b^2}\right) + \bar{q}_{h_1}\left(x_1, \frac{b_0^2}{b^2}\right) q_{h_2}\left(x_2, \frac{b_0^2}{b^2}\right) \right] + \cdots , \tag{2}$$

as the b-space Fourier transform back to the Q_T space. Here, $b_0 = 2e^{-\gamma_E}$ with γ_E being the Euler constant and the optimal scale for the PDFs is given by the order of $1/b$. We do not show explicitly the coefficient functions and the hard production vertex, with the corresponding higher-order perturbative corrections being contained in the ellipses, while we show the Sudakov factor $e^{S(b,Q)}$, which is universal with ($X(\alpha_s) = \sum_{n=1}^{\infty} (\alpha_s/2\pi)^n X^{(n)}$ with $X = A, B$)

$$S(b,Q) = -\int_{b_0^2/b^2}^{Q^2} \frac{d\mu^2}{\mu^2} \left\{ \left(\ln \frac{Q^2}{\mu^2} \right) A\left(\alpha_s(\mu^2)\right) + B\left(\alpha_s(\mu^2)\right) \right\},$$

where $A^{(1)} = 2C_F$ is the leading logarithmic (LL) contribution, and $A^{(2)} = 2C_F[(67/18 - \pi^2/6)C_G - 5N_f/9]$ and $B^{(1)} = -3C_F$ are the next-to-leading (NLL) level contributions, with $C_F = (N_c^2 - 1)/(2N_c)$, $C_G = N_c$, and N_f being the number of QCD massless flavors. In this work we employ the resummation at the NLL accuracy. The importance of the NLL accuracy is demonstrated in, e.g., Fig. 1 in the first paper in [8].

The Sudakov factor associated with all-orders resummation should be eventually accompanied by the nonperturbative form factor, which is usually taken as a gaussian form and would be considered as originating from the intrinsic k_T of partons inside hadron. This implies the following replacement in (2), with Q_0 denoting a certain fixed momentum,

$$e^{S(b,Q)} \to e^{S(b,Q)} e^{-g_{NP} b^2}, \qquad g_{NP} = g_1 + g_2 \ln \frac{Q}{2Q_0}, \tag{3}$$

where the linear dependence of g_{NP} on $\ln Q$ is obeyed by the renormalization group. We have, at least, two nonperturbative parameters g_1, g_2 associated with the resummed form factor.

The participation of the nonperturbative form factor is also signaled by the infrared Landau pole arising in the integrand of (2) at $b \simeq (1/Q)e^{1/[2\beta_0 \alpha_s(Q^2)]}$ from the all-orders resummation embodied by the Sudakov factor, where β_0 is the first coefficient of the QCD β function. A conventional approach to avoid the Landau pole is to introduce the cut-off $b_{\max}$ in the b integration: making the replacement $b \to b_* = b/\sqrt{1 + b^2/b_{\max}^2}$ with $b_{\max} \simeq 0.5$ GeV^{-1} in the Sudakov factor and the PDFs in (2), the b integration is effectively frozen before reaching the Landau pole. Based on this, the resummed cross sections are fitted to the experimental data and the results of this global fit give $g_1 \simeq -0.08$ GeV^2, $g_2 \simeq 0.67$ GeV^2 [3] and $g_1 \simeq 0.016$ GeV^2, $g_2 \simeq 0.54$ GeV^2 [4] for $Q_0 = 1.6$ GeV, exhibiting the strong $\ln Q$ dependence of g_{NP}.

Another approach to circumvent the Landau pole is based on the deformation of the b-integration contour in the complex b space [5, 6, 7, 8, 9]. Its advantages are that it leaves unchanged the perturbative expansion to any (and arbitrarily-high) fixed order in α_s, and that it does not require any infrared cut-off, like $b_{\max}$, in the b-space integration, so this approach is often called the "minimal prescription (MP)". However, now we need the PDFs at the complex

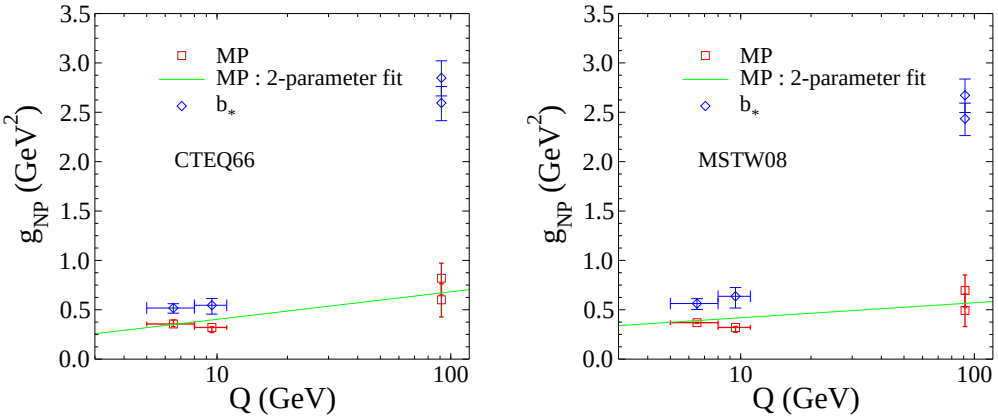

Figure 1: Fit of g_{NP} to R209, and CDF and D0 Z data, using CTEQ6.6M (left panel) and MSTW2008 (right panel) sets for the input PDFs to calculate the NLL resummed cross sections.

scale b_0/b (see (2)) and the numerical calculations become complicated. The values of g_1, g_2 based on the global fit have been unknown in the MP. Performing the matching of, e.g., the Q_T-integrated cross section, $\int dQ_T d\sigma/dQ_T$, and the average Q_T, $\int dQ_T Q_T d\sigma/dQ_T$, between the above two schemes, the b_* model and the MP, the results indicate that the values of g_1, g_2 in the MP are largely different from those in the b_* model [10].

We perform a global fit of the nonperturbative form factor in the MP. We calculate the Q_T-differential and y-integrated cross sections at the NLL accuracy in the MP using the method described in Appendix in [6]. The experimental data sets we use are the available rapidity-integrated cross section data: the low-energy Drell-Yan data (R209 measured at CERN in the different Q ranges, $5 < Q < 8$ GeV and $8 < Q < 11$ GeV) and the Tevatron Z-boson production data (CDF Run-0, Run-1 and D0 Run-1). The cross section calculated with the nonperturbative form factor $e^{-g_{NP}b^2}$ in (3) is compared with each of the above data sets, associated with different Q ranges, and we perform the 1-parameter fit of g_{NP} for each data sets, allowing us to adjust overall normalization factor of the calculated cross section [10]. Plotting the results as a function of the vector boson mass Q, we can extract the Q-dependence of g_{NP}. The symbol $\square$ in Fig. 1 shows the fitted results of g_{NP} as a function of Q: the two symbols at low Q are obtained using the R209 data, while the upper and lower symbols at high Q are obtained using the CDF and D0 data, respectively [10]. We perform those fits using the two different sets of NLO PDFs, CTEQ6.6M and MSTW2008. For comparison, we also plot the results of the similar fits in the b_* model by the symbol $\diamondsuit$, which show the strong $\ln Q$ dependence corresponding to the above-mentioned values [3, 4] of g_1, g_2 in the b_* model. We see that the results in the MP have rather mild $\ln Q$ dependence, with some dependence on the PDFs.

We also use the 2-paramater form (3) of the nonperturbative form factor and perform the 2-parameter fit of g_1, g_2 using all the above-mentioned data sets, allowing us to adjust the overall normalization factor of the calculated cross section similarly as in the case of the 1-parameter fit [10]. We obtain good description of the Q_T distributions for Drell-Yan and Z-boson productions using the 2-paramater form (3), with $g_1 = 0.241^{+0.026}_{-0.028}$ GeV^2, $g_2 = 0.121^{+0.041}_{-0.038}$ GeV^2 for the CTEQ6.6M PDF and $g_1 = 0.330^{+0.024}_{-0.026}$ GeV^2, $g_2 = 0.066^{+0.039}_{-0.037}$ GeV^2 for the MSTW2008 PDF; here, the errors in the results of g_1, g_2 corresponds to the 1-σ deviation

from the χ^2 minimum. Our best fit value of g_1, g_2 gives the solid line in Fig. 1, and the mild $\ln Q$ dependence in the MP reflects that the value of g_2 in the MP is smaller than that in the b_* model by the factor 4 or more.

We note that the Fourier transform of the nonperturbative form factor in (3) gives the intrinsic transverse-momentum distribution $e^{-k_T^2/(4g_{NP})}$, which implies $\langle k_T^2 \rangle = 4g_{NP}$ for the average k_T^2. The mild Q dependence in the MP gives $\langle k_T^2 \rangle = 4g_{NP} \lesssim 2$ GeV^2 over wide range of Q. Because this represents the combined contributions from the two protons $h_{1,2}$, we obtain $\langle k_T^2 \rangle_{\text{1-proton}} \lesssim 1$ GeV^2. This suggests that the nonperturbative form factor in the MP can be naturally interpreted as arising from the intrinsic k_T of partons inside hadrons.

To summarize, we have discussed the NLL resummation in the vector boson production, which is crucial for reliable prediction of the transverse-momentum Q_T distribution. We have the Sudakov factor and the associated nonperturbative form factor which is parameterized by the two nonperturbative parameters g_1, g_2. We employed the MP based on analytic continuation procedure in the impact-parameter space, instead of using the conventional b_* model. In the MP, we performed a first systematic determination of g_1, g_2 by the global fit of the NLL-resummed cross section to experimental data. The results are obtained for the two popular sets of the PDFs, and exhibit the significantly weaker $\ln Q$ dependence of the nonperturbative form factor than that in the b_* model. We mention that the so-called "revised b_* model" using the cut-off $b_{\max}$ which is three times larger than the usual choice $b_{\max} \simeq 0.5$ GeV^{-1} gives the small value of g_2 [11] similar to the present result, so the investigation of the relation between the MP and the revised b_* model would be interesting. We also found that the nonperturbative form factor in the MP can be naturally interpreted as arising from the intrinsic k_T. For more detailed analysis, more data, in particular, the low energy Drell-Yan data, are desirable. g_1, g_2 in the MP determined by us are applicable to the production of the colorless final states, W, Higgs, diboson, etc.

Acknowledgements

This work was supported by the Grant-in-Aid for Scientific Research No. B-19340063. The work of K. T. was supported in part by the Grant-in-Aid for Scientific Research No. 23540292 and by the Grant-in-Aid for Scientific Research on Priority Areas No. 22011012. H. K. acknowledges the Grant-in-Aid for Scientific Research on Priority Areas No. 21105006.

References

[1] S. Catani *et al.* Phys. Rev. Lett. **103** (2009) 082001, and references therein.
[2] J. C. Collins, D. E. Soper and G. F. Sterman. Nucl. Phys. **B250** (1985) 199.
[3] A. Kulesza and W. J. Stirling. JHEP **0312** (2003) 056.
[4] F. Landry, R. Brock, P. M. Nadolsky and C. P. Yuan. Phys. Rev. **D67** (2003) 073016.
[5] E. Laenen, G. F. Sterman and W. Vogelsang. Phys. Rev. Lett. **84** (2000) 4296.
[6] A. Kulesza, G. F. Sterman and W. Vogelsang. Phys. Rev. **D66** (2002) 014011.
[7] G. Bozzi, S. Catani, D. de Florian and M. Grazzini. Nucl. Phys. **B737** (2006) 73.
[8] H. Kawamura, J. Kodaira and K. Tanaka. Nucl. Phys. **B777** (2007) 203; Phys. Lett. **B662** (2008) 139.
[9] H. Kawamura, J. Kodaira and K. Tanaka. Prog. Theor. Phys. **118** (2007) 581.
[10] M. Hirai, H. Kawamura and K. Tanaka, in preparation.
[11] A. V. Konychev and P. M. Nadolsky. Phys. Lett. **B633** (2006) 710.

The NLO jet vertex for Mueller-Navelet and forward jets in the small-cone approximation

Dmitry Yu. Ivanov[1], *Alessandro Papa*[2]

[1]Sobolev Institute of Mathematics and Novosibirsk State University, 630090 Novosibirsk, Russia
[2]Dipartimento di Fisica, Università della Calabria, and Istituto Nazionale di Fisica Nucleare, Gruppo collegato di Cosenza, Arcavacata di Rende, I-87036 Cosenza, Italy

DOI: `http://dx.doi.org/10.3204/DESY-PROC-2012-02/260`

We calculate in the next-to-leading order the impact factor (vertex) for the production of a forward high-p_T jet, in the approximation of small aperture of the jet cone in the pseudorapidity-azimuthal angle plane. The final expression for the vertex turns out to be simple and easy to implement in numerical calculations.

1 Introduction

We consider the process proton(p_1)+proton(p_2) $\to$ jet(k_1)+jet(k_2)+X. Introducing the Sudakov decomposition ($s = 2p_1 \cdot p_2$),

$$k_1 = \alpha_1 p_1 + \frac{\vec{k}_1^{\,2}}{\alpha_1 s} p_2 + k_{1,\perp} \,, \quad k_{1,\perp}^2 = -\vec{k}_1^{\,2} \,,$$

$$k_2 = \alpha_2 p_2 + \frac{\vec{k}_2^{\,2}}{\alpha_2 s} p_1 + k_{2,\perp} \,, \quad k_{2,\perp}^2 = -\vec{k}_2^{\,2} \,,$$

we take the kinematics when jet transverse momenta are large, $\vec{k}_1^{\,2} \sim \vec{k}_2^{\,2} \gg \Lambda_{\rm QCD}^2$, and there is a large rapidity gap between jets, $\Delta y = \ln \frac{\alpha_1 \alpha_2 s}{|\vec{k}_1||\vec{k}_2|}$, which requires large c.m. energy of the proton collisions, $s = 2p_1 \cdot p_2 \gg \vec{k}_{1,2}^{\,2}$. In the perturbative QCD description of the process, the hard scale is provided by the jet transverse momenta, $Q^2 \sim \vec{k}_{1,2}^{\,2} \gg \Lambda_{\rm QCD}^2$; moreover, we neglect power-suppressed contributions $\sim 1/Q$, thus allowing the use of leading-twist PDFs, $f_g(x)$ and $f_q(x)$. We still need to resum the QCD perturbative series, according to DGLAP [1], $\sum_n a_n(\alpha_s^n \ln^n Q^2 + b_n \alpha_s^n \ln^{n-1} Q^2)$ and BFKL [2], $\sum_n (c_n \alpha_s^n \ln^n s + d_n \alpha_s^n \ln^{n-1} s)$. Mueller and Navelet [3] proposed that, for $\Delta y \gg 1$, the BFKL approach is more adequate and leads to a *faster* energy dependence and more decorrelation in the relative jet azimuthal angle $\phi = \phi_1 - \phi_2 - \pi$.

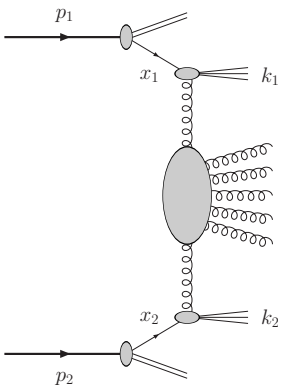

Figure 1: Schematic representation of the Mueller-Navelet jet production.

In the BFKL approach, valid in the Regge limit $s \to \infty$, the total cross section of a hard process $A + B \to X$, via the optical theorem, $\sigma = \frac{{\rm Im}_s \mathcal{A}}{s}$, can be written as the convolution of the Green's function of two interacting Reggeized gluons and of the impact factors of the

colliding particles. This is valid both in the LLA (resummation of all terms $(\alpha_s \ln s)^n$) and in the NLA (resummation of all terms $\alpha_s(\alpha_s \ln s)^n$). In formulae,

$$\mathrm{Im}_s \mathcal{A} = \frac{s}{(2\pi)^{D-2}} \int \frac{d^{D-2}\vec{q}_1}{\vec{q}_1^{\,2}} \Phi_A(\vec{q}_1, s_0) \int \frac{d^{D-2}\vec{q}_2}{\vec{q}_2^{\,2}} \Phi_B(-\vec{q}_2, s_0) \int\limits_{\delta - i\infty}^{\delta + i\infty} \frac{d\omega}{2\pi i} \left(\frac{s}{s_0}\right)^{\omega} G_\omega(\vec{q}_1, \vec{q}_2) \; .$$

The Green's function is process-independent and is determined through the BFKL equation,

$$\omega \, G_\omega(\vec{q}_1, \vec{q}_2) = \delta^{D-2}(\vec{q}_1 - \vec{q}_2) + \int d^{D-2}\vec{q} \, K(\vec{q}_1, \vec{q}) \, G_\omega(\vec{q}, \vec{q}_1) \; ,$$

whereas impact factors are process-dependent and only very few of them have been calculated in the NLA. For the process under consideration, the starting point is provided by the impact factors for colliding partons [4, 5] (see Fig. 2).

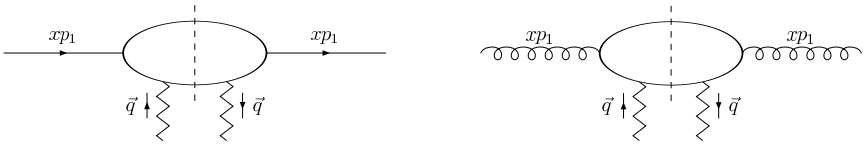

Figure 2: Schematic representation of quark (left) and gluon (right) impact factors.

In the LLA one needs leading-order (LO) impact factors, which take contribution only from a one-particle intermediate state in the parton-Reggeon collision; in the NLA one needs next-to-LO (NLO) impact factors, which take contributions from virtual corrections (one-particle intermediate states) and real particle production (two-particle intermediate states). The steps to get the quark(gluon) jet vertex from the quark(gluon) parton impact factor are: (1) *open* one of the integrations over the phase space of the intermediate state to *allow* one parton to generate the jet, (2) take the convolution with PDFs, $\sum_{a=q,\bar{q}} f_a \otimes$ (quark jet vertex) + $f_g \otimes$ (gluon jet vertex), (3) project onto the eigenfunctions of the LO BFKL kernel, i.e. transfer to the (ν, n)-representation

$$\Phi(\nu, n) = \int d^2\vec{q} \, \frac{\Phi(\vec{q})}{\vec{q}^{\,2}} \frac{1}{\pi\sqrt{2}} \left(\vec{q}^{\,2}\right)^{\gamma - \frac{n}{2}} \left(\vec{q} \cdot \vec{l}\right)^n \; , \quad \gamma = i\nu - \frac{1}{2} \; , \quad \vec{l}^{\,2} = 0 \; .$$

The NLO jet vertices have been calculated in the transverse momentum space (no step (3)) in [6] and cross-checked in [7]. They are given by complicated expression, to be transferred numerically to the (ν, n)-representation, as it was done in [8], where they were used to study Mueller-Navelet jets in the NLA with LHC kinematics.

Here we want to sketch the derivation of an approximated expression for jet vertices, valid for jets with small aperture of the cone in the pseudorapidity - azimuthal angle plane. The details of the calculation are given in [9].

2 Jet definition, small-cone approximation (SCA) and outline of the calculation

In the LO we have a one-particle intermediate state and the kinematics of the produced parton a is completely fixed by the jet kinematics (see Fig. 3).

In the NLO, when real corrections are considered, we have two-particle intermediate states. Then, we can have the following cases: (i) the parton a generates the jet, while the parton b can have arbitrary kinematics, provided that it lies *outside* the jet cone; (ii) similarly with $a \leftrightarrow b$; (iii) the two partons a and b both generate the jet (see Fig. 4(left)).

The case in which one parton (say a) generates the jet and the other parton is outside the jet cone can also be written as the contribution when the parton a is produced with the same jet kinematics while the parton b can have any kinematics (*inclusive* jet production by the parton a) *minus* the contribution when the parton b lies *inside* the jet cone (see Fig. 4(right)).

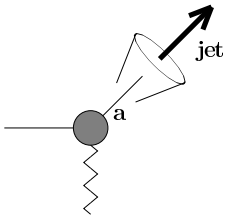

Figure 3: Parton-Reggeon collision, the jet is formed by a single parton.

The SCA [10] means that all cones which appear in the jet definition given above are to be taken with aperture (in the pseudorapidity - azimuthal angle plane) smaller than a fixed value R. For $s \sim Q^2$, very good agreement between SCA and Monte Carlo calculations was found for cone sizes up to $R = 0.7$ [10].

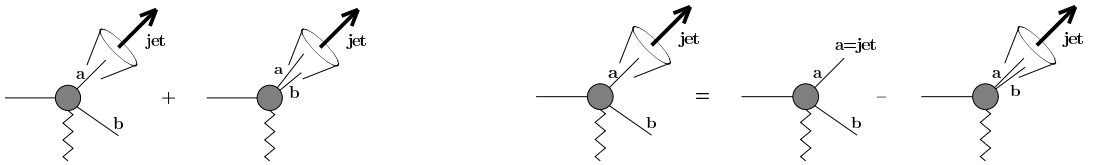

Figure 4: (Left) Parton-Reggeon collision, two partons are produced and the jet is formed either by one of the partons or by both partons. (Right) The production of the jet by one parton when the second one is outside the cone can be seen as the *inclusive* production minus the contribution when the second parton is inside the cone.

For the jet vertex in the LLA the starting point is given by the *inclusive* LO parton impact factors, $\Phi_q = g^2 \frac{\sqrt{N^2-1}}{2N}$ and $\Phi_g = \frac{C_A}{C_F}\Phi_q$. Then we have to *open* the integration over the one-particle intermediate state, i.e. introduce suitable delta functions, and take the convolution with the PDFs, getting (α and $\vec{k}$ are the jet kinematic variables)

$$\frac{d\Phi^J}{\vec{q}^{\,2}} = \mathcal{C} \int d\alpha \frac{d^2\vec{k}}{\vec{k}^{\,2}}\, dx\, \delta^{(2)}\left(\vec{k} - \vec{q}\right) \delta(\alpha - x) \left(\frac{C_A}{C_F} f_g(x) + \sum_{a=q,\bar{q}} f_a(x) \right) .$$

This expression can be used to construct the collinear and QCD coupling counterterms in the NLA, arising when the renormalization of the PDFs and of the QCD coupling are taken into account.

For the jet vertex in the NLA, we separate the cases of quark- and gluon-iniziated subprocesses. For incoming quark, we have the following contributions: (a) virtual corrections, (b) real corrections from the quark-gluon state. The contribution (b) can be separated into the following pieces: (b_1) both quark and gluon generate the jet, (b_2) gluon *inclusive* jet generation minus gluon *inclusive* jet generation with the quark in the jet cone, (b_3) quark *inclusive* jet generation minus quark *inclusive* jet generation with the gluon in the jet cone. For incoming gluon, we have the following contributions: (a) virtual corrections, (b) real corrections from quark-antiquark state, (c) real corrections from two-gluon state. The contribution (b) can be separated into the following pieces: (b_1) both quark and antiquark generate the jet, (b_2) (anti)quark *inclusive*

jet generation minus (anti)quark *inclusive* jet generation with the antiquark(quark) in the jet cone. The contribution (c) can be separated into the following pieces: (c_1) both gluons generate the jet, (c_2) gluon *inclusive* jet generation minus gluon *inclusive* jet generation with the other gluon in the jet cone.

The final result for the jet vertex (see [9]) in the (ν, n)-representation is free of IR and UV divergences and is of the form $A \ln R + B + \mathcal{O}(R^2)$, as discussed in [11].

3 Summary

The NLO vertex for the forward production of a high-p_T jet from an incoming quark or gluon, emitted by a proton, has been calculated in the SCA. The result has been presented in the so called (ν, n)-representation, which turns to be very convenient for numerical implementation, as discussed in [12]. Besides Mueller-Navelet jets, the vertex can be used also for forward-jet electroproduction, $\gamma^* p \to \text{jet} + X$, in combination with the NLO photon impact factor [13].

References

[1] V.N. Gribov, L.N. Lipatov, Sov. J. Nucl. Phys. **15** (1972) 438; G. Altarelli, G. Parisi, Nucl. Phys. B **126** (1977) 298; Y.L. Dokshitzer, Sov. Phys. JETP **46** (1977) 641.

[2] V.S. Fadin, E.A. Kuraev, L.N. Lipatov, Phys. Lett. B **60** (1975) 50; E.A. Kuraev, L.N. Lipatov and V.S. Fadin, Zh. Eksp. Teor. Fiz. **71** (1976) 840 [Sov. Phys. JETP **44** (1976) 443]; **72** (1977) 377 [**45** (1977) 199]; Ya.Ya. Balitskii and L.N. Lipatov, Sov. J. Nucl. Phys. **28** (1978) 822.

[3] A.H. Mueller, H. Navelet, Nucl. Phys. B **282** (1987) 727.

[4] V.S. Fadin, R. Fiore, M.I. Kotsky and A. Papa, Phys. Rev. D **61** (2000) 094005; Phys. Rev. D **61** (2000) 094006.

[5] M. Ciafaloni and G. Rodrigo, JHEP **0005** (2000) 042.

[6] J. Bartels, D. Colferai and G.P. Vacca, Eur. Phys. J. C **24** (2002) 83; Eur. Phys. J. C **29** (2003) 235;

[7] F. Caporale, D.Yu. Ivanov, B. Murdaca, A. Papa and A. Perri, JHEP **1202** (2012) 101.

[8] D. Colferai, F. Schwennsen, L. Szymanowski, S. Wallon, JHEP **1012** (2010) 026.

[9] D.Yu. Ivanov and A. Papa, arXiv:1202.1082.

[10] B. Jäger, M. Stratmann, W. Vogelsang, Phys. Rev. D **70** (2004) 034010.

[11] M. Furman, Nucl. Phys. B **197** (1982) 413.

[12] D.Yu. Ivanov and A. Papa, Nucl. Phys. B **732** (2006) 183; Eur. Phys. J. C **49** (2007) 947; F. Caporale, A. Papa and A. Sabio Vera, Eur. Phys. J. C **53** (2008) 525.

[13] G. Chirilli, these proceedings and references therein.

The non-forward BFKL equation and infrared effects

Grigorios Chachamis[1], *Agustín Sabio Vera*[2], *Clara Salas*[2]

[1]Paul Scherrer Institut, CH-5232 Villigen PSI, Switzerland
[2]Instituto de Física Teórica UAM/CSIC, Nicolás Cabrera 15, UAM, E-28049 Madrid, Spain

DOI: http://dx.doi.org/10.3204/DESY-PROC-2012-02/214

An iterative solution best suited for a Monte Carlo implementation is presented for the non-forward BFKL equation in a generic color representation. We introduce running coupling effects compatible with bootstrap to all orders in perturbation theory. A numerical analysis is given showing a smooth transition from a hard to a soft pomeron when accounting for running effects.

1 Introduction

The solution to the LL BFKL equation projected in the color singlet in the non-forward case was first calculated in the seventies by Balitski, Fadin, Kuraev and Lipatov [1–5]. Three decades later a solution based on a sum of iterations of the kernel in transverse momentum space was proposed at LL [6] and Next to Leading Logarithmic(NLL) [7] accuracy and used to build up a Monte Carlo code to provide numerical studies of it. Similar studies for the color octet representation were given in [8–10].

The present work is based on the formalism given in [6]. The study is extended to give a solution in a general color group representation $\mathcal{R}$ and presented in a way such that all the infrared divergences appear as an overall factor in the gluon Green function so that a finite piece can be identified and treated numerically. In order to account for higher order corrections and study the properties of the infrared the running of the coupling is introduced. How to account for it is a non well-defined problem. There is no theoretical strong restriction on it and different possibilities have been suggested in the literature [11–16]. We insert it in a way consistent with gluon reggeization, as proposed in [14–16], which naturally leads to the appearance of renormalon singularities in the infrared. The fact that the solution is given in transverse momentum and rapidity space makes possible to study diffusion properties, analyzed in Sec. 3.1. The aim of this review is to give a very short qualitative explanation of the main points of the work presented. We refer the reader to the article in preparation [17] and the references given here for the calculation.

2 Non-forward BFKL equation in a generic color representation

The infrared divergences that appear in a general color representation can be written as an overall factor in the gluon Green function. To show this one has to regularize half of the divergences in the gluon Regge trajectory using dimensional regularization ($D = 4 - 2\,\epsilon$) and introduce a mass parameter λ for the remaining ones. In doing it, the dependence on λ cancels out with the contribution of the real emissions while the one on ϵ remains in the factorized term, leading to a solution to the non-forward BFKL equation independent of λ for $\lambda \to 0$.

The divergent term depends on the choice of the color projection. In the singlet representation, for example, $c_1 = 1$ and all infrared divergences cancel out. The non-forward equation for the color singlet can be solved in an iterative way by going back to momentum space using a Mellin transform. Details on how this is down are given in [7]. The result obtained is the product of an exponential term depending on the λ and $1/\epsilon$ parameters and a finite part that we denote by $\mathcal{H}\,(\mathbf{q}_1, \mathbf{q}_2; \mathbf{q}; \mathrm{Y})$. We analyze this function in sec. 3. It is convenient for the numerical study to express the gluon Green function $\mathcal{F}(\mathbf{q}_1, \mathbf{q}_2; Y)$ as a function of the azimuthal angle between the two-dimensional vectors $\mathbf{q}_1$ and $\mathbf{q}_2$, its Fourier conjugate variable or conformal spin n and the anomalous dimension γ.

2.1 Infrared effects

A way to introduce running coupling effects at in the analysis of a $2 \to 2$ partonic process at LL accuracy is to replace the reggeized gluon propagating in the t-channel by a gluon (or renormalon) chain [18]. Our choice of accounting for the running is based on this approach. A comparison of the LL gluon trajectory with the new one tells us that the only needed change to be done in the analytic expressions is the replacement $\mathbf{k}^2 \to \eta(\mathbf{k})$, with $\eta(\mathbf{k}) \equiv \mathbf{k}^2/\bar{\alpha}_s(\mathbf{k}^2)$. In order to define the new BFKL kernel the bootstrap condition is imposed so that gluon reggeization is still justified. This procedure naturally leads to the appearance of renormalons as power corrections that could let us learn about the properties of the infrared. Details on this setup can be found in [14–16].

Concerning the choice for the running we use a parametrization which freezes in the infrared and it is consistent with global data of infrared power corrections to perturbative observables [19]. When the external transverse momentum scales in the gluon Green function are perturbative enough, this model for the running cannot be distinguished with a perturbative one with a Landau pole. Nonetheless, we do find sensitivity to the IR finite model for sufficient small values of these scales.

3 Numerical analysis for the color singlet

Figures 2a show the convergence of the sum defining the function $\mathcal{H}(\mathbf{q}_1, \mathbf{q}_2; \mathbf{q}; \mathrm{Y})$. In can be seen how for a fixed value of Y and the coupling $\bar{\alpha}_s$ a finite number of terms in the sum is enough to have a good accuracy for the gluon Green function. As the value of the effective parameter $\bar{\alpha}_s \mathrm{Y}$ gets larger the Green function is more sensitive to high multiplicity terms, following a Poissonian distribution. It can also be noticed how the distribution in the number of iterations of the kernel gets broader for larger center of mass energies although the convergence is always good.

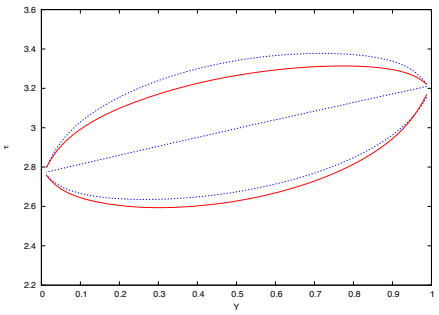

Figure 1: Diffusion pattern for fixed coupling (blue, dotted line) and running coupling (red, solid line).

It is also instructive to study the solution in terms of the different Fourier components in the azimuthal angle between the two momenta $\mathbf{q}_1$ and $\mathbf{q}_2$. A complete analysis is shown in Figs. 2b for both forward and non-. It can be seen how the only rising component is the $n = 0$ one. For completeness, fig. 2c shows the dependence of the solution on the azimuthal angle for the sum of all Fourier components. The collinear limit is investigated in Fig. 2d.

3.1 Diffusion

The diffusion [20, 21] of the transverse scales in the BFKL ladder has been studied in terms of the average value $\langle\tau\rangle$ of $\tau = \log\left((\mathbf{q}_1 + \sum \mathbf{k}_i)^2\right)$ as a function of the rapidity Y' along the gluon ladder. For each set $[\mathbf{q}_1, \mathbf{q}_2, Y]$ (where $\mathbf{q}_1$ and $\mathbf{q}_2$ are the transverse momenta of the edges of the ladder) the non-forward BFKL equation is solved numerically allowing the study of the evolution of $\langle\tau\rangle$ along the ladder as well as the weight of each configuration point in n-momenta phase space to the total solution. Fig. 1 compares the diffusion pattern found for a fixed choice of the strong coupling and a version with running coupling inserted as explained in the previous section. The straight line in the middle corresponds to $\langle\tau\rangle$ while the upper/lower curves are the mean plus/minus the standard deviation. The set of values taken for the plot are $k_a = 5$ GeV, $k_b = 4$ GeV and $Y = 1$. The figure shows how the version with running is shifted to the infrared providing a smooth transition from the hard to the soft pomeron.

Acknowledgements

The European Comission (LHCPhenoNet PITN-GA-2010-264564) is acknowledged for funding the expenses of the conference.

References

[1] V. S. Fadin, E. Kuraev, and L. Lipatov. Phys.Lett. **B60** (1975) 50–52.

[2] L. Lipatov. Sov.J.Nucl.Phys. **23** (1976) 338–345.

[3] E. Kuraev, L. Lipatov, and V. S. Fadin. Sov.Phys.JETP **44** (1976) 443–450.

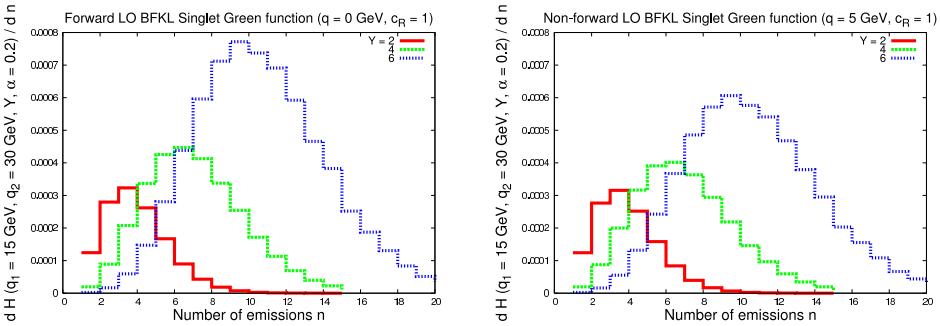

(a) Distribution in the contributions to the BFKL gluon Green function with a fixed number of iterations of the kernel, plotted for different values of the center-of-mass energy, and a fixed $\bar{\alpha}_s = 0.2$. Left: forward case; right: non-forward case with $q = 5$ GeV.

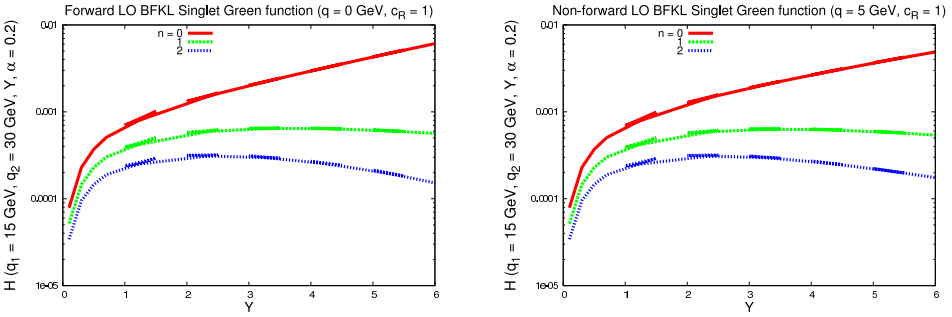

(b) Projection of the gluon Green function on different Fourier components in the azimuthal angle between the $\mathbf{q}_1$ and $\mathbf{q}_2$ transverse momenta. Left: forward case; right: non-forward case with $q = 5$ GeV.

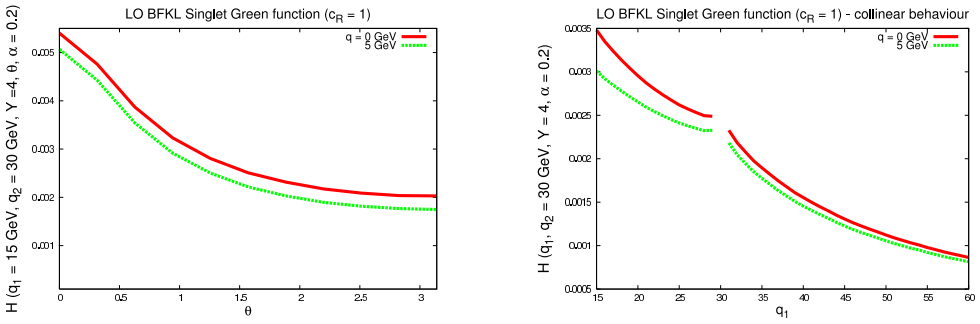

(c) Gluon Green function dependence for the full range in azimuthal angles.

(d) Collinear behavior of the gluon Green function.

Figure 2: Numerical analysis

[4] E. Kuraev, L. Lipatov, and V. S. Fadin. Sov.Phys.JETP **45** (1977) 199–204.

[5] I. Balitsky and L. Lipatov. Sov.J.Nucl.Phys. **28** (1978) 822–829.

[6] J. R. Andersen and A. Sabio Vera. JHEP **0501** (2005) 045, arXiv:hep-ph/0411231 [hep-ph].

[7] J. R. Andersen and A. Sabio Vera. Nucl.Phys. **B679** (2004) 345–362, arXiv:hep-ph/0309331 [hep-ph].

[8] J. Kwiecinski, C. Lewis, and A. D. Martin. Phys.Rev. **D54** (1996) 6664–6673, arXiv:hep-ph/9606375 [hep-ph].

[9] C. R. Schmidt. Phys.Rev.Lett. **78** (1997) 4531–4535, arXiv:hep-ph/9612454 [hep-ph].

[10] L. H. Orr and W. J. Stirling. Phys.Rev. **D56** (1997) 5875–5884, arXiv:hep-ph/9706529 [hep-ph].

[11] V. S. Fadin and L. Lipatov. Phys.Lett. **B429** (1998) 127–134, arXiv:hep-ph/9802290 [hep-ph].

[12] Y. V. Kovchegov and A. H. Mueller. Phys.Lett. **B439** (1998) 428–436, arXiv:hep-ph/9805208 [hep-ph].

[13] R. S. Thorne. Phys.Rev. **D60** (1999) 054031, arXiv:hep-ph/9901331 [hep-ph].

[14] M. Braun. Phys.Lett. **B348** (1995) 190–195, arXiv:hep-ph/9408261 [hep-ph].

[15] E. Levin. Nucl.Phys. **B453** (1995) 303–333, arXiv:hep-ph/9412345 [hep-ph].

[16] Y. V. Kovchegov and H. Weigert. Nucl.Phys. **A784** (2007) 188–226, arXiv:hep-ph/0609090 [hep-ph].

[17] G. Chachamis, A. Sabio Vera, and C. Salas. In preparation .

[18] V. I. Zakharov. Nucl.Phys. **B385** (1992) 452–480.

[19] B. R. Webber. JHEP **9810** (1998) 012, arXiv:hep-ph/9805484 [hep-ph].

[20] J. R. Forshaw and D. Ross. Cambridge Lect.Notes Phys. **9** (1997) 1–248.

[21] J. Bartels, H. Lotter, and M. Vogt. Phys.Lett. **B373** (1996) 215–222, arXiv:hep-ph/9511399 [hep-ph].

Diffraction and rapidity gap measurements in ATLAS

Pavel Ruzicka[1] on behalf of the ATLAS Collaboration

[1]Institute of Physics of the Academy of Sciences of the Czech Republic

DOI: http://dx.doi.org/10.3204/DESY-PROC-2012-02/72

Pseudorapidity gap distributions in Large Hadron Collider proton-proton collisions at $\sqrt{s} = 7$ TeV are studied using a minimum bias data sample of integrated luminosity 7.1 μb^{-1}. Cross sections are measured differentially in the size $\Delta\eta^F$ of the larger of the pseudorapidity regions extending to the limits of the ATLAS acceptance, at $\eta = \pm 4.9$, in which no final state particles are produced above a transverse momentum threshold $p_{\mathrm{T}}^{\mathrm{cut}}$. The measurements span the region $0 < \Delta\eta^F < 8$ for $200 < p_{\mathrm{T}}^{\mathrm{cut}} < 800$ MeV. The measured data, at large $\Delta\eta^F$, constrain value of pomeron intercept appropriate to triple Regge models while at small $\Delta\eta^F$, data test reliability of hadronisation models in describing rapidity and transverse momentum fluctuations in final state particle production.

1 Introduction

This report is based on the ATLAS article [1] to which a reader is referred for further information. In the Minimum Bias collisions at a center-of-mass energy of $\sqrt{s} = 7$ TeV an average distance between two neighboring charged particles with transverse momentum $p_{\mathrm{T}} > 100$ MeV is typically around 0.15 units in pseudorapidity [2]. Larger gaps between the particles can be created due to statistical fluctuations in the hadronisation process, which are exponentially suppressed [3] as a function of gap size, or by t-channel colour singlet exchange. The colour singlet exchange can be provided by electroweak or more frequently by strongly interacting states. The later processes are termed as diffractive and their phenomenological description is inspired by Regge theory where the colour singlet object is associated with pomeron [4, 5].

The Minimum Bias processes are usually decomposed into non-diffractive contribution and three different diffractive components: Single Diffractive dissociation (SD) $pp \to pX$ producing forward gap between the intact proton and dissociated system X, Double Diffractive dissociation (DD) $pp \to XY$ where central gap is produced between the two dissociated systems X and Y and Central Diffractive contribution (CD) in which final state particles are produced in the central region with intact forward protons emerging on both sides. The kinematics of the diffractive dissociation is commonly described in terms of invariant masses M_X and M_Y of the dissociated systems X and Y respectively and squared four momentum transfer t. Alternative variables to the M_X and M_Y are

$$\xi_X = \frac{M_X^2}{s}\,, \qquad\qquad \xi_Y = \frac{M_Y^2}{s},$$

where s is the square of the center-of-mass energy. The size of rapidity gap is closely correlated with the variables ξ_X and ξ_Y. In case of SD, ξ_X is equal to momentum fraction loss of the

intact proton and the size $\Delta\eta$ of the rapidity gap between the final state proton and the X system satisfies

$$\Delta\eta \approx -\ln \xi_X .$$

This correlation has great importance for the measurement because it enables to constrain diffractive models by measurement of the rapidity gap spectra.

2 Reconstruction of rapidity gaps

Rapidity gaps were reconstructed using the ATLAS calorimeter system and inner detector tracker. Calorimeter has been used for its large coverage $|\eta| < 4.9$. It consists of highly segmented electromagnetic ($|\eta| < 3.2$), hadronic end-cap ($1.5 < |\eta| < 3.2$) and electromagnetic/hadronic forward ($3.1 < |\eta| < 4.9$) calorimeters all of which are liquid argon sampling calorimeters. In addition, steel/scintillator hadronic tile calorimeter covers central region ($|\eta| < 1.7$).

Energy depositions of individual particles traversing material are reconstructed in the calorimeter using clustering algorithm which combines energy deposits in individual calorimeter cells. Due to electronic noise in read-out system, cell energies exhibit random fluctuations. They are well described by Gaussian distributions parameterized by standard deviation σ_{noise} for all calorimeter subsystems with the exception of the tile calorimeter, which shows non-Gaussian tails. The default clustering algorithm [6] is seeded by cells satisfying $S = E/\sigma_{\text{noise}} > 4$, implying that on average, six noisy clusters per event are reconstructed. As the rapidity gaps can extend over many units of pseudorapidity, the gap identification relies crucially on the suppression of the noise contribution. To suppress noise to acceptable levels, the clusters are considered only if they contain at least one cell outside the tile calorimeter with $S > S_{\text{th}}(\eta)$, where $S_{\text{th}}(\eta)$ is η-dependent threshold increasing from 4.8 in the forward region to 5.8 in the central region where the cell density is high. The calorimeter information is combined with the information from the Inner Detector for $|\eta| < 2.5$.

An interval in η is deemed to contain final state particles if at least one cluster in that interval passes the noise suppression requirements and has a transverse momentum above $p_{\text{T}}^{\text{cut}}$, or if there is at least one good track in the inner detector with transverse momentum above $p_{\text{T}}^{\text{cut}}$. Detector simulation showed that the lowest accessible energy with a good acceptance is for clusters with $p_{\text{T}} > 200$ MeV.

Events with colliding protons bunch crossing are selected using the Minimum Bias Trigger Scintillator (MBTS) which consists of two discs symmetrically situated 3 m away from the interaction point and covers $2.1 < |\eta| < 3.8$. The trigger has large efficiency > 99 % for events with particle produced in the MBTS acceptance region.

The reconstructed forward gap size, $\Delta\eta^F$, is defined by the larger of the two empty pseudorapidity regions extending between the edges of the detector acceptance at $\eta = 4.9$ or $\eta = -4.9$ and the nearest track or calorimeter cluster passing the selection requirements at smaller $|\eta|$. The rapidity gap size relative to $\eta = \pm 4.9$ lies in the range $0 < \Delta\eta^F < 8$, where the upper limit on the gap size is dictated by a requirement of a high trigger efficiency $> 50\%$, which rapidly decreases once the gap extends over both positive/negative MBTS counters at the same time.

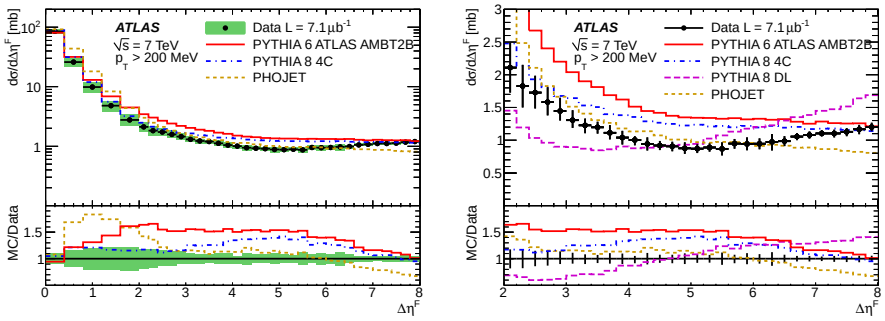

Figure 1: Inelastic cross section differential in forward gap size $\Delta\eta^F$ for particles with $p_{\mathrm{T}} > 200$ MeV [1]. Right plot zooms into large rapidity gap region, $\Delta\eta^F > 2$.

3 Results

All the results are corrected for the detector effects to level of stable particles. Inelastic cross section differential in forward rapidity gap size, $\Delta\eta^F$, for $p_{\mathrm{T}}^{\mathrm{cut}} = 200$ MeV is shown in Fig. 1. The uncertainty of the measurement is around 8 % for large gaps, $\Delta\eta^F > 3$, and 20 % for small at $\Delta\eta^F = 1.5$. At small gaps, $\Delta\eta < 2.5$, both data and Monte Carlo (MC) models follow exponential decrease which is typical for ND events dominating this region according to all MCs. PYTHIA8 has the best agreement with the data while PHOJET overshoots the data almost by factor two due to wrong ND normalization. For large gaps, $\Delta\eta^F > 3$, a plateau in data is presented, which is attributed mainly to diffractive processes. Although the MCs reproduce the diffractive plateau, none of them describes both shape and normalization precisely over the whole range. PHOJET and PYTHIA predict that only diffractive processes contribute to cross section in the large gap region. From the right plot of the Fig. 1, which zooms into the large gaps region, it can be seen that data exhibits smaller slope than PYTHIA8 with Donnachie-Landshoff (DL) [7] but higher slope than the rest of the MCs models. The slope of the distribution for large rapidity gaps is strongly correlated with the pomeron intercept $\alpha_{I\!P}(0)$. Hence, distribution for DL model, which sets the $\alpha_{I\!P}(0) = 1.085$, grows faster for large $\Delta\eta^F$ than for the other models with $\alpha_{I\!P}(0) = 1$. This observation can be used for the determination of the pomeron intercept from data. The DL model in the PYTHIA8 has been used to fit the data in the large rapidity gaps $\Delta\eta^F > 5$. Obtained value [1]

$$\alpha_{I\!P}(0) = 1.058 \pm 0.003(\mathrm{stat.})^{+0.034}_{-0.039}(\mathrm{syst})$$

is compatible with default DL value due to large systematic uncertainty.

The distribution at small rapidity gaps is sensitive to fluctuation in hadronisation processes thus it is interesting to compare the data to other hadronisation models than Lund String model implemented in PYTHIA and PHOJET. An alternative is a cluster hadronisation model which is available in HERWIG++. The HERWIG++ Minimum Bias model tune UE7-2 is compared with data in left plot of Fig. 2. It should be emphasized that the model of minimum bias production does not contain diffraction processes and thus only exponential fall off the rapidity gap distribution is expected. Even though not containing an explicit diffractive component, HERWIG++ produces large gaps with non-exponential behavior and bump around $\Delta\eta^F = 6$. This behavior persists also when the colour reconnection (CR) model is switched-off or when

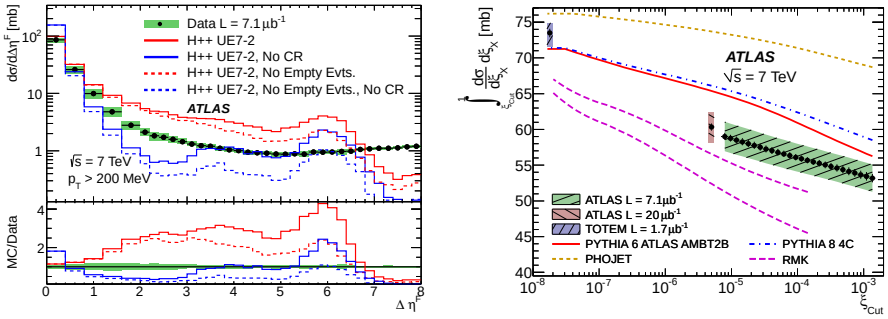

Figure 2: (Left) Inelastic differential cross section as a function of forward gap size $\Delta\eta^F$ for particles with $p_{\mathrm{T}} > 200$ MeV in HERWIG++ UE7-2 minimum bias model [1], see text for explanation. (Right) Inelastic integrated cross section as a function of minimum ξ denoted as ξ_{Cut} [1].

events with no scatterings of either the soft or semi-hard are excluded (No Empty Evts.).

The strong correlation between rapidity gaps and ξ_X makes it possible to convert the inelastic integrated cross section as a function of $\Delta\eta^F$ into an integral over the inelastic pp cross section down to some minimum value ξ_{Cut} of ξ_X i.e. perform a following transformation

$$\int_0^{\Delta\eta^F_{\mathrm{Cut}}} \frac{\mathrm{d}\sigma}{\mathrm{d}\Delta\eta^F}\mathrm{d}\Delta\eta^F \rightarrow \int_{\xi_{\mathrm{Cut}}}^1 \frac{\mathrm{d}\sigma}{\mathrm{d}\xi_X}\,\mathrm{d}\xi_X \ .$$

This is done only by applying small correction for hadronisation effects and for including particles below $p_{\mathrm{T}} = 200$ MeV. The integrated inelastic cross section is shown as a function of ξ_{Cut} in right plot of Fig. 2. The data are compared with a previous ATLAS result [8] and with the TOTEM extraction of the full inelastic cross section [9], derived from a measurement of the elastic cross section via the optical theorem. Apart from the standard MCs models, the plot shows two versions of the KMR model [10]. PYTHIA and PHOJET fail to describe evolution of data from low to large ξ value; the fraction of low mass diffractive events is under-estimated. On the other hand, although the normalization of the KMR model is not correct, its shape exhibits better agreement with data than the rest of the models.

References

[1] ATLAS Collaboration, Eur. Phys. J., **C72** (2012) 1926.

[2] ATLAS Collaboration, New J. Phys., **13** (2011) 053033.

[3] J. Bjorken, S. Brodsky, H. J. Lu, Phys. Lett., **B286** (1992) 153.

[4] E. Feinberg, I. Pomerančuk, Suppl. Nuovo Cimento, **3** (1952) 652.

[5] G. Chew, S. Frautschi, Phys. Rev. Lett., **7** (1961) 394.

[6] W. Lampl and others, ATL-LARG-PUB-2008-002. ATL-COM-LARG-2008-003(2008).

[7] A. Donnachie, P. Landshoff, Nucl. Phys. **B244** (1984) 322.

[8] ATLAS Collaboration, Nature Comm., **2** (2011) 463.

[9] TOTEM Collaboration, EPL (Europhysics Letters), **96** (2011) 21002.

[10] M. G. Ryskin, A. D. Martin, V. A. Khoze, Eur. Phys. J., **C71** (2011) 1617.

Two-Loop Gluon Regge Trajectory from Lipatov's Effective Action

Grigorios Chachamis[1], *Martin Hentschinski*[2], *José Daniel Madrigal*[2], *Agustín Sabio Vera*[2]

[1]Paul Scherrer Institut, CH-5232 Villigen PSI, Switzerland
[2]Instituto de Física Teórica UAM/CSIC; U. Autónoma de Madrid, E-28049 Madrid, Spain.

DOI: `http://dx.doi.org/10.3204/DESY-PROC-2012-02/129`

Lipatov's high-energy effective action is a useful tool for computations in the Regge limit beyond leading order. Recently, a regularisation/subtraction prescription has been proposed that allows to apply this formalism to calculate next-to-leading order corrections in a consistent way. We illustrate this procedure with the computation of the gluon Regge trajectory at two loops.

1 The High-Energy Effective Action (HEA)

Effective field theories provide a useful framework to treat problems involving a hierarchy of scales in quantum field theory, and are widely used in the context of QCD (e.g. chiral perturbation theory or heavy-quark effective theory). A hierarchy of scales is also present in the Regge or high-energy limit, since the centre-of-mass energy squared s is asymptotically larger than the momentum transfer $-t$ in a scattering process, hence we expect the effective theory approach to be applicable to this case. Besides making computations simpler, a hermitian HEA incorporates unitarity. The reggeized gluon [1] plays a key role as the effective degree of freedom. The HEA has already been used to calculate reggeon vertices [2, 3]. It was introduced by Lipatov for leading order computations [4].

We work with a HEA [5] which is gauge invariant and valid beyond multi-Regge kinematics, as it includes interactions of arbitrary numbers of reggeized gluons with QCD particles. The procedure to compute loop calculations is explained in the following [6, 7]. Interactions take place in quasi-multi-Regge kinematics (Fig. 1(a)) [8]. Emissions gather in different clusters strongly ordered in rapidity, $y_0 \gg y_1 \gg \cdots \gg y_{n+1}$, $y_k = \frac{1}{2}\ln\frac{k^+}{k^-}$, while all particles produced in each cluster have approximately the same rapidity. This strong ordering simplifies the polarisation tensor of t-channel reggeized gluons, $g_{\mu\nu} \to \frac{1}{2}(n^+)_\mu(n^-)_\nu + \mathcal{O}(s^{-1})$, and makes their propagators essentially transverse, $q_i^2 = -\boldsymbol{q}_i^2$. Light-cone vectors are defined by $n^{+,-} = 2p_{A,B}/\sqrt{s}$, $k = \frac{1}{2}(k^+n^- + k^-n^+) + \boldsymbol{k}$.

Effective vertices between reggeized quarks and gluons and particles, like the one shown in Fig. 1(c), consist of two pieces: a projection of the usual QCD vertex on QMRK, and a so-called induced contribution. This structure is given by

$$S_{\text{eff}} = S_{\text{QCD}} + S_{\text{ind}}; \quad S_{\text{ind}} = \int d^4x\, \text{Tr}[(W_+[v(x)] - \mathscr{A}_+(x))\partial_\perp^2 \mathscr{A}_-(x)] + \{+ \leftrightarrow -\}, \qquad (1)$$

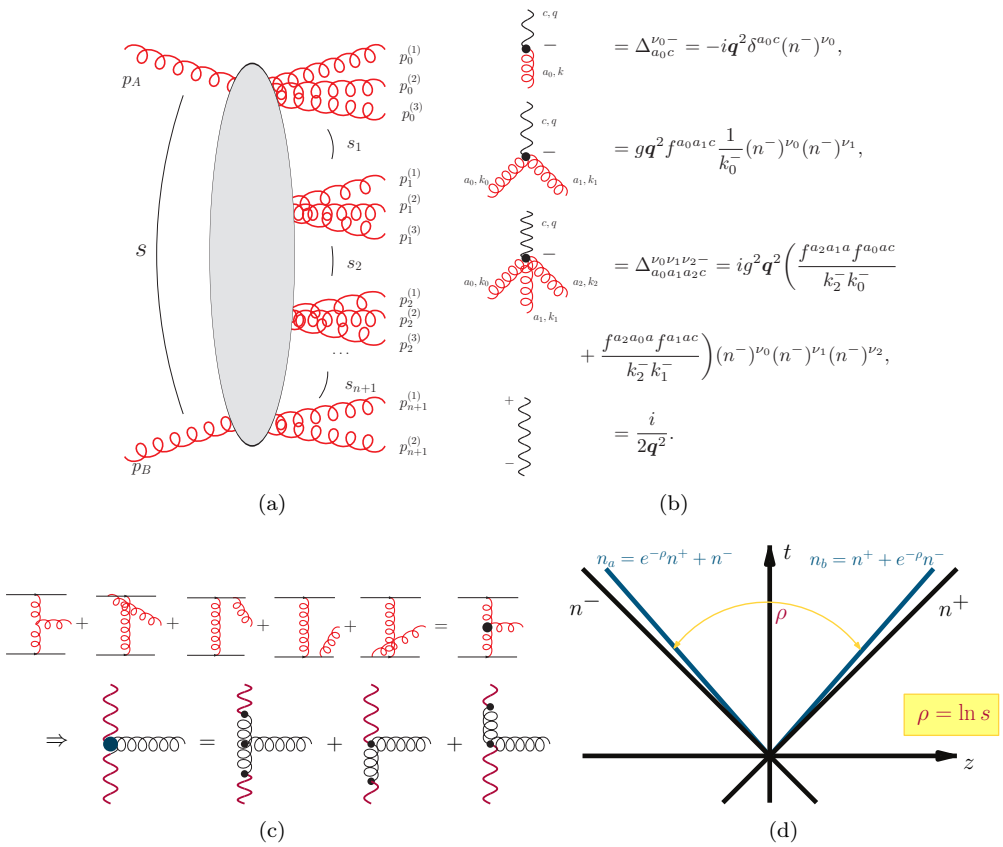

Figure 1: (a) quasi-multi-Regge kinematics; (b) Feynman rules for low-order effective vertices; (c) Reggeon-Reggeon-Gluon effective vertex; (d) Light-cone tilting regularisation.

where $\mathscr{A}_\pm$ are the gauge-invariant reggeon fields, which interact non-trivially with gauge invariant currents of quark and gluon fields that can be written in terms of Wilson lines $W_\pm[v] = v_\pm \frac{1}{D_\pm}\partial_\pm = v_\pm - g v_\pm \frac{1}{\partial_\pm} v_\pm + \cdots$. The projection of the reggeon polarisation tensor translates into the kinematical constraints $\partial_\pm \mathscr{A}_\mp(x) = 0$ and $\sum_{i=0}^{r} k_i^\pm = 0$.

2 Regularisation and Subtraction

The Feynman rules for Lipatov's HEA [2] are shown in Fig. 1(b). Poles of the form $1/k^\pm$, coming from the non-local operator $1/\partial_\pm$, are ubiquitous, and a prescription to regulate them must be taken, since they cause divergences in the longitudinal sector of loop integrals. A tilting of the light-cone by a hyperbolic angle ρ was chosen in [6](Fig. 1(d)).[1] A technicality when using the HEA beyond tree-level is that the locality in rapidity, assumed in the derivation of

[1] These poles can be considered as principal values [9]. This does not affect the terms proportional to $\ln s$, but it is necessary for instance to recover the subleading pieces.

(1), must be now enforced by hand. An alternative to the imposition of a rapidity cutoff [10], is the subtraction of non-local contributions, mediated by reggeon exchange (see, e.g. Fig. 2).

3 Computation of NLO Gluon Regge Trajectory

This regularisation/subtraction procedure was put into work in [7] with the computation of the quark piece of the NLO gluon Regge trajectory, already known in QCD [11] and $\mathcal{N}=4$ SYM [12]. The Regge trajectory is the factor $\omega(t)$ appearing in the effective propagators of reggeons, $s^{\omega(t)}$, and is a key piece in the BFKL evolution equation [1], related to the virtual contributions. In the HEA framework, it corresponds to the diagrams in Fig. 2.

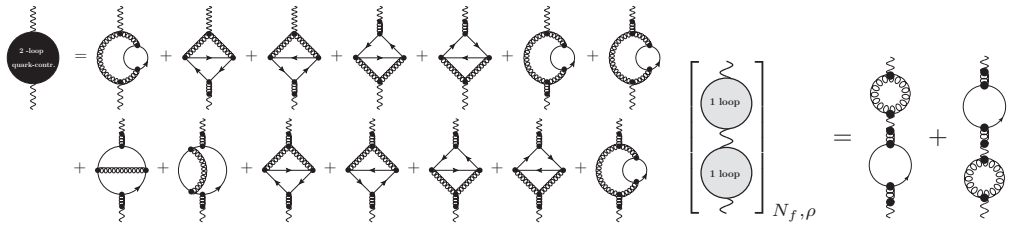

(a) (b)

Figure 2: Contributions to the quark piece of the 2-loop gluon trajectory: (a) unsubtracted gluon self-energy (only the first diagram is ρ-enhanced); (b) subtractions.

In order to compute the 2-loop gluon trajectory $\omega^{(2)}$, the following steps must be carried out [7]: 1) determine the high-energy limit of the 2-loop parton-parton scattering amplitude by dropping terms suppressed when $\rho\to\infty$; 2) subtract non-local contributions to reggeised gluon self-energy; 3) divide by the tree-level result; 4) remove all terms corresponding to combinations of 1-loop trajectory and 1-loop impact factors; 5) remove a term $\frac{1}{2}\ln^2(s/s_0)[\omega^{(1)}(t)]^2$. With some modifications, the procedure is general for any other computation. For the quark piece of the two-loop trajectory, $\omega_q^{(2)}$, actually only two diagrams are ρ-enhanced and must be computed (one of them is the subtraction). With no rapidity cutoff, the usual techniques for computing loop integrals can be applied, and one finds exact agreement with the result in the literature

$$\omega_q^{(2)}\left(\frac{\boldsymbol{q}^2}{\mu^2}\right)=\bar{g}^4\left(\frac{\boldsymbol{q}^2}{\mu^2}\right)^{2\epsilon}\frac{4N_f}{\epsilon N_c}\frac{\Gamma^2(2+\epsilon)}{\Gamma(4+2\epsilon)}\left[\frac{2\Gamma^2(1+\epsilon)}{\epsilon\Gamma(1+2\epsilon)}-\frac{3\Gamma(1-2\epsilon)\Gamma(1+\epsilon)\Gamma(1+2\epsilon)}{\epsilon\Gamma^2(1-\epsilon)\Gamma(1+3\epsilon)}\right];\qquad(2)$$

with $\bar{g}^2=\frac{g^2N_c\Gamma(1-\epsilon)}{(4\pi)^{2+\epsilon}}$ and $d=4+2\epsilon$.

The gluon piece of $\omega^{(2)}$ is currently under study. More powerful technology is needed there to reduce the diagrams to master integrals and to compute the integrals themselves. It is expected however that future developments along these lines will make Lipatov's action become a useful tool for computations in the Regge limit.

Research supported by E. Comission [LHCPhenoNet (PITN-GA-2010-264564)] & C. Madrid (HEPHACOS ESP-1473).

References

[1] L. N. Lipatov, Sov. J. Nucl. Phys. **23** (1976) 338 [Yad. Fiz. **23** (1976) 642]; E. A. Kuraev, L. N. Lipatov and V. S. Fadin, Sov. Phys. JETP **45** (1977) 199 [Zh. Eksp. Teor. Fiz. **72** (1977) 377]; I. I. Balitsky and L. N. Lipatov, Sov. J. Nucl. Phys. **28** (1978) 822 [Yad. Fiz. **28** (1978) 1597].

[2] E. N. Antonov, L. N. Lipatov, E. A. Kuraev and I. O. Cherednikov, Nucl. Phys. B **721** (2005) 111 [hep-ph/0411185].

[3] M. A. Braun and M. I. Vyazovsky, Eur. Phys. J. C **51** (2007) 103 [hep-ph/0612323]; M. A. Braun, L. N. Lipatov, M. Y. Salykin and M. I. Vyazovsky, Eur. Phys. J. C **71** (2011) 1639 [arXiv:1103.3618 [hep-ph]].

[4] L. N. Lipatov, Nucl. Phys. B **365** (1991) 614.

[5] L. N. Lipatov, Nucl. Phys. B **452** (1995) 369 [hep-ph/9502308]; L. N. Lipatov, Phys. Rept. **286** (1997) 131 [hep-ph/9610276].

[6] M. Hentschinski and A. S. Vera, Phys. Rev. D **85** (2012) 056006 [arXiv:1110.6741 [hep-ph]].

[7] G. Chachamis, M. Hentschinski, J. D. Madrigal and A. Sabio Vera, Nucl. Phys. B **861** (2012) 133 [arXiv:1202.0649 [hep-ph]].

[8] V. S. Fadin and L. N. Lipatov, JETP Lett. **49** (1989) 352 [Yad. Fiz. **50** (1989) 1141] [Sov. J. Nucl. Phys. **50** (1989) 712].

[9] M. Hentschinski, Nucl. Phys. B **859** (2012) 129 [arXiv:1112.4509 [hep-ph]].

[10] M. Hentschinski, J. Bartels and L. N. Lipatov, arXiv:0809.4146 [hep-ph].

[11] V. S. Fadin, R. Fiore and M. I. Kotsky, Phys. Lett. B **387** (1996) 593 [hep-ph/9605357]; V. S. Fadin, R. Fiore and A. Quartarolo, Phys. Rev. D **53** (1996) 2729 [hep-ph/9506432]; J. Blümlein, V. Ravindran and W. L. van Neerven, Phys. Rev. D **58** (1998) 091502 [hep-ph/9806357]; V. Del Duca and E. W. N. Glover, JHEP **0110** (2001) 035 [hep-ph/0109028].

[12] A. V. Kotikov and L. N. Lipatov, Nucl. Phys. B **582** (2000) 19 [hep-ph/0004008]; J. Bartels, L. N. Lipatov and A. Sabio Vera, Phys. Rev. D **80** (2009) 045002 [arXiv:0802.2065 [hep-th]]; J. Bartels, L. N. Lipatov and A. Sabio Vera, Eur. Phys. J. C **65** (2010) 587 [arXiv:0807.0894 [hep-th]].

Single-pion production in neutrino interactions

B.Z. Kopeliovich, Iván Schmidt, M. Siddikov

Departamento de Física Universidad Técnica Federico Santa María; and
Instituto de Estudios Avanzados en Ciencias e Ingeniería; and
Centro Científico-Tecnológico de Valparaíso;
Casilla 110-V, Valparaíso, Chile

DOI: `http://dx.doi.org/10.3204/DESY-PROC-2012-02/28`

We study diffractive neutrino-proton and neutrino-nuclear collisions in the framework of the color dipole model and evaluate the single-pion production differential cross-section for the kinematics of the ongoing experiment Minerva at Fermilab [1]

1 Introduction

Due to its V-A form the neutrino-hadron interactions possess a rich structures. However, because of smallness of the cross-sections experimental data have been scarce until recently, mostly being restricted to total cross-sections. With the launch of the new high-statistics experiments like MINERνA at Fermilab [1], the neutrino-hadron interactions can be studied with a better precision and at higher energies than before. The V-A structure of the neutrino-quark amplitudes enables us to study simultaneously $\langle VV\rangle$, $\langle AA\rangle$ and $\langle VA\rangle$ correlators in the same process.

The properties of the vector current have been well studied in interactions of charged leptons and photons with protons and nuclei. For the axial current the situation is more complicated and interesting than for the vector current, especially at small Q^2, because the chiral symmetry breaking generates the near-massless pseudo-goldstone mesons (pions). For this reason the chiral symmetry is vital and should be embedded into any dynamical model used for calculation of the cross section at small Q^2.

In this paper we present the results for diffractive pion production obtained within the color dipole description with axial distribution amplitudes derived in the Instanton Vacuum Model (IVM). Full details of evaluations may be found in our recent papers [2, 3].

2 Results and discussion

Most of the data on neutrino-production of pions on protons have been available so far only at energies close to the resonance region [4]. Data at higher energies are scarce and have rather low statistics [6, 7]. Because the dipole formalism should not be trusted at low energies, we provide predictions for the high energies, which can be accessed in the ongoing experiment Minerva at Fermilab [1, 8].

The Q^2 dependence of the diffractive cross section deserves special attention. It would be very steep at small Q^2, if the pion dominance were real. However, since the pion pole is

terminated due to conservation of the lepton current (up to the lepton mass), the Q^2 dependence is controlled by the heavier singularities. In the approximation of an effective singularity at $Q^2 = -M^2$ [9] one should expect the Q^2 dependence to have the dipole form $\propto (Q^2 + M^2)^{-2}$.

The numerical results of the dipole model indeed confirm the dipole-like form of the cross section at small Q^2 with the effective mass $M \approx 0.91$ GeV, which is not far from the mass extracted from data $M \approx 1.1$ GeV [4].

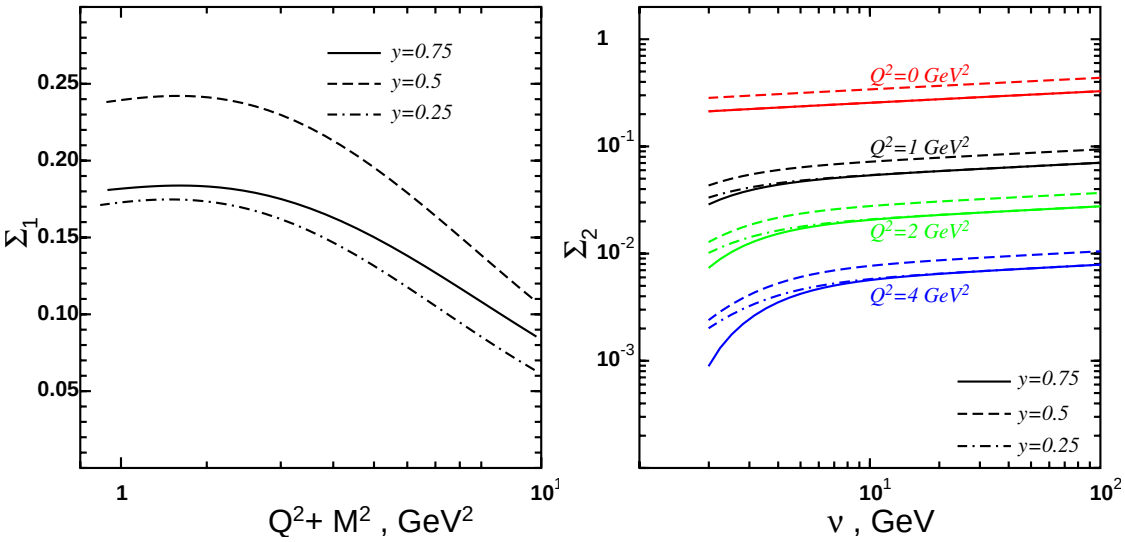

Figure 1: Left: The Q^2-dependence of the cross section of diffractive neutrino-production of pions scaled by factor $(Q^2 + M^2)^2$. Neutrino energy $E_\nu = 20$ GeV, $y = \nu/E_\nu = 0.5$, $\Sigma_1 = (Q^2 + M^2)^2 \nu d^3\sigma/dt\, d\nu\, dQ^2$ [in units $10^{-38} cm^2$]. The mass parameter $M = 0.91$ GeV is adjusted to minimize the variations of the scaled cross section at small Q^2. Right: Forward neutrino-production cross-section of pions as function of ν at several fixed values of y and Q^2, $\Sigma_2 = \nu d^3\sigma/dt\, d\nu\, dQ^2$ [in units $10^{-38} cm^2/GeV^4$].

The forward invariant cross-section of diffractive neutrino-production of pions on protons is depicted in the right pane of the Fig. (1) as function of ν at several fixed values of y and Q^2.

For the nuclei, in the Figure 2 we compare the results for the ratio

$$R^{coh}_{A/N}(\nu, Q^2) = \frac{1}{A} \frac{d^2\sigma_A/d\nu\, dQ^2}{d^2\sigma_N/d\nu\, dQ^2}, \tag{1}$$

is plotted in the Figure 2 by solid curves vs energy ν. These results of the dipole model are compared with the expectations based on the Adler relation [10, 11] shown by dashed lines. Our results significantly underestimate the Adler relation predictions at all energies. At low energies the Adler relation is trivially broken [5, 12] because the longitudinal momentum transfer is large and the amplitudes of pion production on different nucleons are out of coherence. At high energies the lifetime of the intermediate heavy states (a_1 meson, $\rho\pi$, etc.) is long, and absorptive corrections suppress the coherent cross section, leading to a dramatic breakdown of the Adler relation [12].

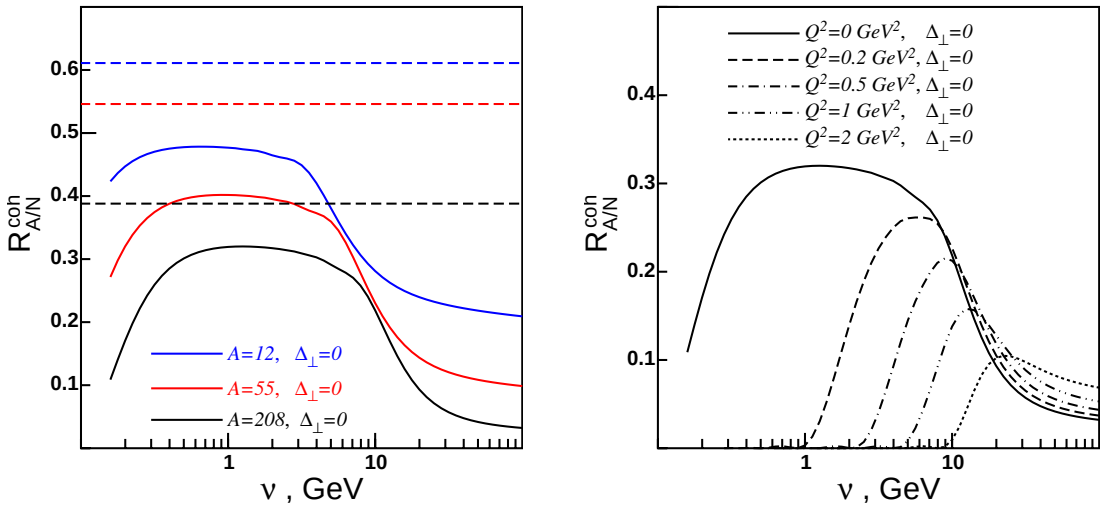

Figure 2: ν-dependence of the ratio of the coherent forward neutrino-pion production cross-sections on nuclear and proton targets. *Left:* ν-dependence of the ratio for different nuclei at $Q^2 = 0$. Solid curves correspond to the color dipole model, dashed lines show the predictions of the Adler relation. *Right:* ν-dependence of the nuclear ratio vs Q^2 for lead ($A = 208$).

There is, however, a wide energy interval from few hundreds MeV up to about 10 GeV, where the Adler relation was expected to be valid [12]. Now we see that even at these energies the Adler relation is broken. To understand why this happens notice that an effective two-channel model used in [12] assumed dominance of two states in the dispersion relation for the axial current, the pion and an effective axial vector pole a with the mass of the order of 1GeV. The condition of validity of the Adler relation was shortness of the coherence length related to the mass of the a-state compared to the nuclear size,

$$l_c^a = \frac{2\nu}{Q^2 + m_a^2} \ll R_A. \tag{2}$$

In contrast to this simple model, the invariant mass of a $\bar{q}q$ dipole is not fixed, $m^2_{\bar{q}q} = (m_q^2 + k_T^2)/\alpha(1-\alpha)$, where α is the fractional light-cone momentum of the quark. Correspondingly, the related coherence length, $l_c^{\bar{q}q}$ is distributed over a wide mass range, and while the center of the distribution and large masses lead to a short $l_c^{\bar{q}q}$, the low-mass tail of this distribution results in a long $l_c^{\bar{q}q} \gg R_A$. For this reason the absorption corrections suppress the cross section, even at moderate energies.

In Fig. 3 the ratio of the incoherent nuclear-to-nucleon cross-sections

$$R^{inc}_{A/N}(t,\nu,Q^2) = \frac{d\sigma_{\nu A\to l\pi A^*}/dtd\nu dQ^2}{A\, d\sigma_{\nu N\to l\pi N}/dtd\nu dQ^2}, \tag{3}$$

is plotted versus energy ν. As was discussed in [2, 12] the energy dependence of the incoherent cross-section is controlled only by the coherence length l_c^a, related to the heavy axial states, so there are only two regimes: $l_c^a \le R_A$ and $l_c^a > R_A$. Our numerical calculations confirm such a behavior.

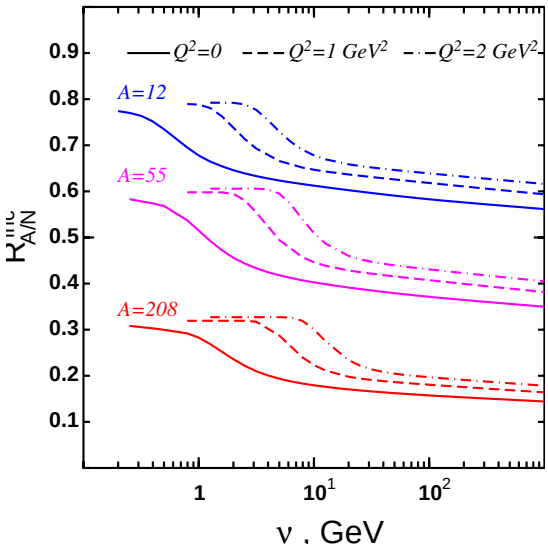

Figure 3: ν-dependence of the ratio of the incoherent forward pion neutrino-production cross-sections on nuclear and proton targets at different virtualities Q^2.

Acknowledgements

This work was supported in part by Fondecyt (Chile) grants No. 1090291, 1100287 and 1120920, and by Conicyt-DFG grant No. 084-2009. M. S. also acknowledges partial support of DIS 2012 organizing committee in the form of waiving the conference fee.

References

[1] D. Drakoulakos *et al.* [Minerva Collaboration], arXiv:hep-ex/0405002.

[2] B. Z. Kopeliovich, I. Schmidt and M. Siddikov, Phys. Rev. D **84** (2011) 033012 [arXiv:1107.2845 [hep-ph]].

[3] B. Z. Kopeliovich, I. Schmidt and M. Siddikov, arXiv:1201.4053 [hep-ph], to appear in PRD

[4] B. Z. Kopeliovich and P. Marage, Int. J. Mod. Phys. A **8** (1993) 1513.

[5] A. A. Belkov and B. Z. Kopeliovich, Sov. J. Nucl. Phys. **46** (1987) 499 [Yad. Fiz. **46** (1987) 874].

[6] J. Bell *et al.*, Phys. Rev. Lett. **41** (1978) 1008.

[7] P. Allen *et al.*, Nucl. Phys. B **264** (1986) 221.

[8] K. S. McFarland [MINERvA Collaboration], Nucl. Phys. Proc. Suppl. **159** (2006) 107 [arXiv:physics/0605088].

[9] B. Z. Kopeliovich, I. Potashnikova, M. Siddikov, I. Schmidt, Phys. Rev. C **84** (2011) 024608 [arXiv:1105.1711 [hep-ph]].

[10] S. L. Adler, Phys. Rev. **135** (1964) B963.

[11] S. L. Adler and Y. Dothan, Phys. Rev. **151** (1966) 1267.

[12] B. Z. Kopeliovich, I. Potashnikova, M. Siddikov, I. Schmidt, Phys. Rev. C **84** (2011) 024608 [arXiv:1105.1711 [hep-ph]].

Diffractive Vector Meson Cross Sections from BK evolution with Impact Parameter

Jeffrey Berger

Penn State University, Physics Department, University Park, PA 16802, USA

DOI: http://dx.doi.org/10.3204/DESY-PROC-2012-02/266

The solution of the Balitsky-Kovchegov evolution equation with impact parameter dependence is used to compute cross sections for $J/\Psi, \rho$ and ϕ vector meson production. These calculations are then compared with data from HERA and good agreement is found for the J/Ψ and ϕ mesons while the ρ has a low normalization. The phenomenological corrections needed to bring the calculations into agreement with the data are discussed. The work presented here may be found in the publication [1].

1 Introduction

The Balitsky-Kovchegov (BK) equation [2, 3, 4, 5] is a non-linear evolution equation in Bjorken x (denoted x_{bj}) whose solution describes the scattering of a color dipole ($q\,\bar{q}$ pair) on a target. The BK equation has the form

$$\frac{\partial N_{\mathbf{x_0 x_1}}}{\partial Y} = \int \frac{d^2\mathbf{x_2}}{2\pi}\,\mathcal{K}(x_{01}, x_{12}, x_{02}; \alpha_s, m)\left[N_{\mathbf{x_0 x_2}} + N_{\mathbf{x_2 x_1}} - N_{\mathbf{x_0 x_1}} - N_{\mathbf{x_0 x_2}} N_{\mathbf{x_2 x_1}}\right] . \quad (1)$$

The scattering amplitude $N_{\mathbf{x_0 x_1}}$ depends on the rapidity $Y = \ln(1/x_{bj})$ and the coordinates of the color charges of the dipole $\mathbf{x_0}$ and $\mathbf{x_1}$ [1]. We shall not make the assumption that the scattering amplitude depends on only the dipole size $x_{01} = |\mathbf{x_0} - \mathbf{x_1}|$ but instead include the dependences on impact parameter $b_{01} = |\mathbf{x_0} + \mathbf{x_1}|/2$ and the angle θ between the impact parameter and the dipole size. More details on the numerical solution are given in [6]. The kernel $\mathcal{K}(x_{01}, x_{12}, x_{02}; \alpha_s, m)$ determines the dipole splitting and the form which behaves in a manner that best describes the F_2 data [7] is

$$\mathcal{K} = \bar{\alpha}_s(x_{01}^2)\left[\frac{1}{x_{02}^2}\left(\frac{\alpha_s(x_{02}^2)}{\alpha_s(x_{12}^2)} - 1\right) + \frac{1}{x_{12}^2}\left(\frac{\alpha_s(x_{12}^2)}{\alpha_s(x_{02}^2)} - 1\right) + \frac{x_{01}^2}{x_{12}^2 x_{02}^2}\right]\Theta(\frac{1}{m^2} - x_{02}^2)\Theta(\frac{1}{m^2} - x_{12}^2) . \quad (2)$$

In the above equation, we use $\alpha_s(x^2) = \frac{1}{b\,\ln\left[\Lambda_{\rm QCD}^{-2}\left(\frac{1}{x^2}+\mu^2\right)\right]}$ for the form of the running coupling with $b = \frac{33-2n_f}{12\pi}$ and n_f is the number of active flavors. The μ parameter effectively freezes the coupling at large dipole sizes and the massive parameter m cuts off large non-perturbative

[1] A note on notation : bold-faced variables represent two-dimensional vectors, otherwise they are to be understood as magnitudes.

dipoles. The value of these parameters as well as others mentioned can be found in [1]. The initial condition of the evolution is described in [1] as well.

2 Phenomenological corrections

Several corrections must be made in order to bring the calculation using the dipole scattering amplitude into agreement with the HERA data. One of these corrections is a skewed unintegrated gluon distribution. There is no gluon distribution in the formalism used for the evolution but it is present in the initial condition. Additionally the real part of the scattering amplitude is corrected for (this correction is much more modest compared to the large correction that the skewed gluon distribution gives). Both of these corrections are described in more depth in [1].

A correction to the photon wavefunction is also required. This correction has the form

$$|\Psi_\gamma|^2 \to |\Psi_\gamma|^2 \left(\frac{1 + Be^{-\omega^2 (x_{01} - R)^2}}{1 + Be^{-\omega^2 R^2}} \right) , \tag{3}$$

where B, R and ω are parameters which are fit to the data. This correction gives an enhancement at small Q^2, which corresponds to large dipole sizes. This can be thought of as a contribution stemming from the photon having a hadronic component at these large sizes.

3 Comparison to vector meson cross sections

The differential cross section for exclusive vector meson production has been measured by H1 [8, 9, 10] and ZEUS [11, 12, 13, 14] collaborations at HERA. In computing the differential cross section the vector meson wavefunction used is known as the NNPZ prescription [15, 16].

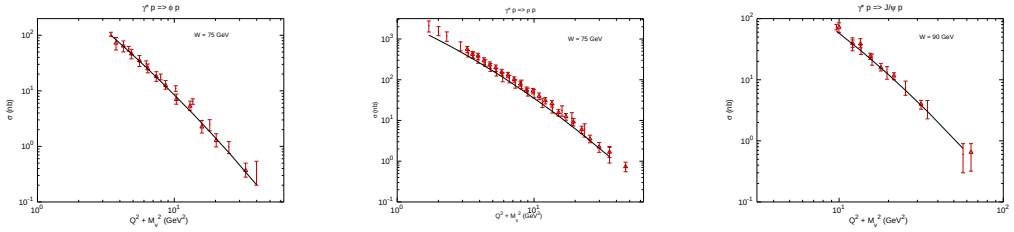

Figure 1: $Q^2 + M_V^2$ dependence of the vector meson cross section for elastic production of J/Ψ,ρ, and ϕ.

The integrated cross section is shown plotted in Fig 1 versus Q^2 and in Fig 2 versus W^2. The data is well explained by our calculations in the case of both J/Ψ and ϕ vector mesons. However the ρ vector meson has a normalization which is consistently low.

The dependence on the momentum transfer t is important in that it is conjugate to the impact parameter, so information on the measurement of the momentum transfer dependence also gives information about the dependence on the interaction on impact parameter. The differential cross section for J/Ψ versus the momentum transfer t and the energy W can be seen

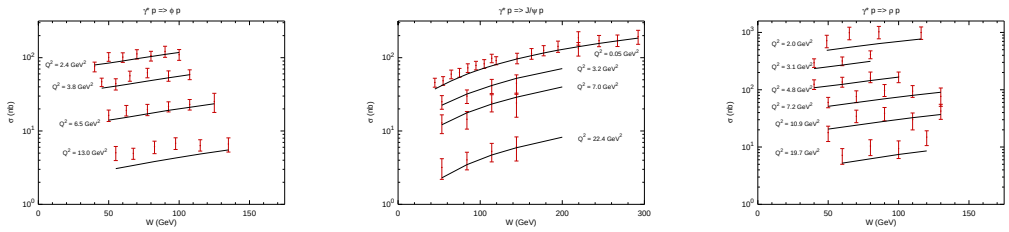

Figure 2: W dependence of the vector meson cross section for elastic production of J/Ψ,ρ, and ϕ.

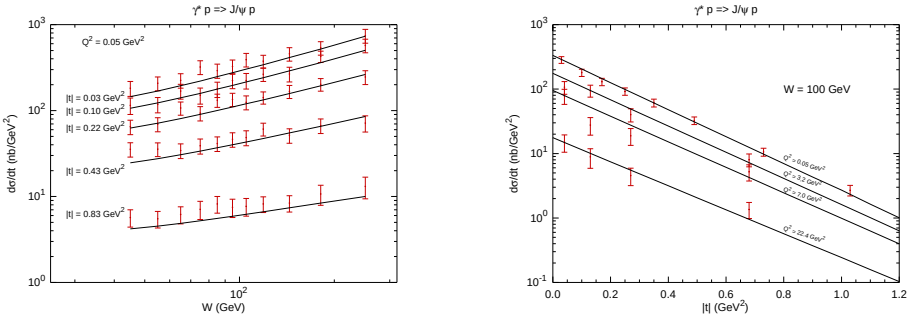

Figure 3: Differential cross section plots of J/Ψ production

in Fig 3. The differential cross section is well explained by the calculation. On a logarithmic plot the differential cross section versus t falls along linear paths which suggests a parameterization of $d\sigma/dt \sim \exp(-B_D|t|)$ where B_D is a slope parameter.

The plots for B_D versus both $Q^2 + M^2$ and W can be found in Fig 4 for J/Ψ production. The slope B_D describes the interaction area in impact parameter space and it was found that there is a slope in B_D versus W. This feature is not present in other models and arises naturally from the inclusion of impact parameter in our calculation. The rise of the slope with energy corresponds to the diffusion of the interaction region in impact parameter space. The slope B_D is sensitive to the initial distribution size in impact parameter, which determines the intercept, as well as the mass cutoff in the kernel (2) determining the slope.

4 Conclusions

The BK equation with impact parameter dependence describes well the data for exclusive vector meson production for J/Ψ and ϕ mesons. The ρ meson has a chronic low normalization which is possibly due to an additional soft correction. The effects of the phenomenological corrections is large and cannot be neglected, especially the skewed gluon distribution. The photon wavefunction correction (3) is a universal correction and does not only apply to vector

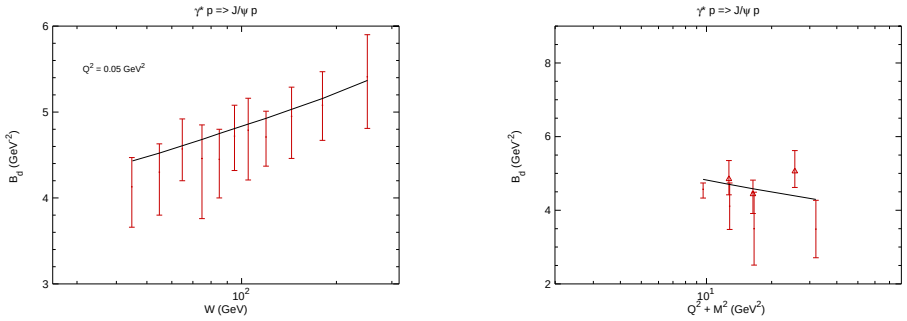

Figure 4: Dependence of the slope parameter BD versus W and $Q^2 + M_V^2$ for J/Ψ production.

meson production but inclusive measurements as well. It was found that the F_2 structure function did not find good agreement with the data, while the trends of the data were described the normalization was, in general, too large. This indicates that the photon wavefunction correction is too large, however lowering it worsens the vector meson fits, implying there is more to be done with the vector meson wavefunctions or that there is a soft correction which affects only the vector mesons which is not taken into account. Despite the fact that there are some normalization issues in fitting both inclusive and exclusive data simultaneously the solution to the BK equation with impact parameter does describe the trends of the data, as well as producing an energy dependence of B_D which arises purely from the impact parameter dependence of our model.

References

[1] J. Berger and A. M. Stasto. arXiv:1205.2037 [hep-ph].

[2] I. Balitsky. Nucl. Phys. **B463** (1996) 99–160, arXiv:hep-ph/9509348.

[3] I. Balitsky. Phys. Rev. **D60** (1999) 014020, arXiv:hep-ph/9812311.

[4] Y. V. Kovchegov. Phys. Rev. **D60** (1999) 034008, arXiv:hep-ph/9901281.

[5] Y. V. Kovchegov. Phys. Rev. **D61** (2000) 074018, arXiv:hep-ph/9905214.

[6] J. Berger and A. Stasto. Phys. Rev. **D83** (2011) 034015, arXiv:1010.0671 [hep-ph].

[7] J. Berger and A. M. Stasto. arXiv:1106.5740 [hep-ph]. * Temporary entry *.

[8] C. Adloff *et al.* Eur.Phys.J. **C13** (2000) 371–396, arXiv:hep-ex/9902019 [hep-ex].

[9] A. Aktas *et al.* Eur.Phys.J. **C46** (2006) 585–603, arXiv:hep-ex/0510016 [hep-ex].

[10] F. Aaron *et al.* JHEP **1005** (2010) 032, arXiv:arXiv:0910.5831 [hep-ex].

[11] S. Chekanov *et al.* Eur. Phys. J. **C24** (2002) 345–360, arXiv:hep-ex/0201043.

[12] S. Chekanov *et al.* Nucl.Phys. **B695** (2004) 3–37, arXiv:hep-ex/0404008 [hep-ex].

[13] S. Chekanov *et al.* Nucl.Phys. **B718** (2005) 3–31, arXiv:hep-ex/0504010 [hep-ex].

[14] S. Chekanov *et al.* PMC Phys. **A1** (2007) 6, arXiv:0708.1478 [hep-ex].

[15] J. Nemchik, N. N. Nikolaev, and B. Zakharov. Phys.Lett. **B341** (1994) 228–237, arXiv:hep-ph/9405355 [hep-ph].

[16] J. Nemchik, N. N. Nikolaev, E. Predazzi, and B. Zakharov. Z.Phys. **C75** (1997) 71–87, arXiv:hep-ph/9605231 [hep-ph].

Nonlinear extension of the CCFM equation

Krzysztof Kutak

Instytut Fizyki Jądrowej im. H. Niewodniczańskiego
Radzikowskiego 152, 31-342 Krakow, Poland

DOI: http://dx.doi.org/10.3204/DESY-PROC-2012-02/54

Motivated by the regime of QCD explored nowadays at LHC, where both the total energy of collision and momenta transfers are high, evolution equations of high energy factorization are investigated. In order to study such effects like parton saturation in final states one is inevitably led to investigate how to combine physics of the BK and CCFM evolution equations. We report on recently obtained resummed form of the BK equation and nonlinear extension of the CCFM equation.

1 Introduction

The Large Hadron Collider (LHC) is already operational and Quantum Chromodynamics (QCD) is the basic theory which is used to set up the initial conditions for the collisions at the LHC as well as to calculate hadronic observables. The application of perturbative QCD relies on factorization theorems which allow to decompose a given process into a long distance part, called parton density, and a short distance part, called matrix element. Here we will focus on high energy factorization [1, 2]. The evolution equations of high energy factorization sum up logarithms of energy accompanied by a strong coupling constant, i.e. terms proportional to $\alpha_s^n \ln^m s/s_0$, which applies when the total energy of a scattering process is much bigger than any other hard scale involved in a process.
Until now, in principle, the BFKL, BK [3–5] and CCFM [6–8] evolution equations were used on equal footing since the energy ranges did not allow to discriminate between these frameworks. However, there were indications already at HERA [9] for the need to account for nonlinear effects in gluon density. These observation are supported by recent results obtained in [10, 12]. On top of this, the results from [13] point at the need to use the framework which incorporates hardness of the collision into BFKL like description. With the LHC one entered into a region of phase space where both the energy and momentum transfers are high and formed systems of partons dense. Recently a framework has been provided in [14] where both dense systems and hard processes at high energies can be studied.

2 Exclusive form of the Balitsky-Kovchegov equation

At the leading order in $\ln 1/x$ the Balitsky-Kovchegov equation for the dipole amplitude in the momentum space is written as an integral equation reads [14]:

$$\begin{aligned}\Phi(x,k^2) &= \Phi_0(x,k^2) \\ &+ \overline{\alpha}_s \int_x^1 \frac{dz}{z} \int_0^\infty \frac{dl^2}{l^2} \left[\frac{l^2\Phi(x/z,l^2) - k^2\Phi(x/z,k^2)}{|k^2-l^2|} + \frac{k^2\Phi(x/z,k)}{\sqrt{(4l^4+k^4)}} \right] \\ &- \overline{\alpha}_s \int_x^1 \frac{dz}{z} \Phi^2(x/z,k)\end{aligned} \tag{1}$$

where the lengths of transverse vectors lying in transversal plane to the collision axis are $k \equiv |\mathbf{k}|$, $l \equiv |\mathbf{l}|$ ($\mathbf{k}$ is a vector sum of transversal momenta of emitted gluons during evolution), $z = x/x'$(see Fig. (1), $\overline{\alpha}_s = N_c\alpha_s/\pi$. The linear term in eq. (1) can be linked to the process of creation of gluons while the nonlinear term can be linked to fusion of gluons and therefore introduces gluon saturation effects.

The unintegrated gluon density obeying the high energy factorization theorem [1] is obtained from [18, 19]:

$$\mathcal{F}_{BK}(x,k^2) = \frac{N_c}{\alpha_s\pi^2} k^2 \nabla_k^2 \Phi(x,k^2) \tag{2}$$

where the angle independent Laplace operator is given by $\nabla_k^2 = 4\frac{\partial}{\partial k^2} k^2 \frac{\partial}{\partial k^2}$.
As explained in [14] this equation can be rewritten in a resummed form:

$$\begin{aligned}\Phi(x,k^2) \;&=\; \tilde{\Phi}^0(x,k^2) \\ &+\; \overline{\alpha}_s \int_x^1 d\,z \int \frac{d^2\mathbf{q}}{\pi q^2}\, \theta(q^2-\mu^2) \frac{\Delta_R(z,k,\mu)}{z} \left[\Phi(\frac{x}{z}, |\mathbf{k}+\mathbf{q}|^2) - q^2\delta(q^2-k^2)\,\Phi^2(\frac{x}{z},q^2) \right].\end{aligned} \tag{3}$$

where $\mathbf{q} = \mathbf{l} - \mathbf{k}$ and $\Delta_R(z,k,\mu) \equiv \exp\left(-\overline{\alpha}_s \ln\frac{1}{z} \ln\frac{k^2}{\mu^2}\right)$ is a Regge form factor.

Eq. (3) is a new form of the BK equation in which the resummed terms in a form of Regge form factor are the same for the linear and nonlinear part. This form will serve as a guiding equation to generalize the CCFM equation to include nonlinear effects which allow for recombination of partons with constraint on angle of emission.

2.1 Nonlinear extension of the CCFM equation

As it has already been stated the motivation to extend the CCFM to account for nonlinearity is to be able to study the impact of saturation of partons on exclusive observables. There are indications [15, 23] that such effects might be significant in for instance production of charged particles at HERA or in forward production of di-jets [10, 11].
The nonlinear extension of CCFM has been recently proposed in [14] and its extension changes the interpretation of the quantity for which the equation is written. It is not longer high energy factorizable gluon density but should be interpreted as the dipole amplitude in momentum space Φ, denoted from now on by $\mathcal{E}$, which besides x and k^2 depends also on a hard scale p. The peculiar structure of the nonlinear term of the equation written below is motivated by the following requirements:

- the second argument of the $\mathcal{E}$ should be k^2 as motivated by the analogy to BK

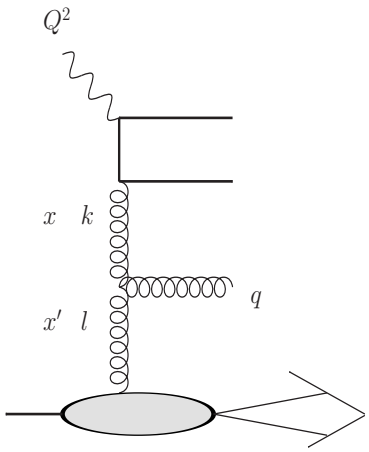

Figure 1: Plot explaining meaning of variables in BK and CCFM evolution equations.

- the third argument should reflect locally the angular ordering

$$\begin{aligned}\mathcal{E}(x,k^2,p) &= \mathcal{E}_0(x,k^2,p) \\ &+ \bar{\alpha}_s \int_x^1 dz \int \frac{d^2\bar{\mathbf{q}}}{\pi\bar{q}^2}\,\theta(p-z\bar{q})\Delta_s(p,z\bar{q})\left(\frac{\Delta_{ns}(z,k,q)}{z}+\frac{1}{1-z}\right)\Bigg[\mathcal{E}\left(\frac{x}{z},k'^2,\bar{q}\right) \\ &- \bar{q}^2\delta(\bar{q}^2-k^2)\,\mathcal{E}^2(\frac{x}{z},\bar{q}^2,\bar{q})\Bigg].\end{aligned} \tag{4}$$

The momentum vector associated with i-th emitted gluon is

$$q_i = \alpha_i\, p_P + \beta_i\, p_e + q_{t\,i} \tag{5}$$

The variable p in (4) is defined via $\bar{\xi} = p^2/(x^2 s)$ where $\frac{1}{2}\ln(\bar{\xi})$ is a maximal rapidity which is determined by the kinematics of hard scattering, $\sqrt{s}$ is the total energy of the collision and $k' = |\boldsymbol{k} + (1-z)\bar{\boldsymbol{q}}|$. The momentum $\bar{\mathbf{q}}$ is the transverse rescaled momentum of the real gluon, and is related to $\mathbf{q}$ by $\bar{\mathbf{q}} = \mathbf{q}/(1-z)$ and $\bar{q} \equiv |\bar{\mathbf{q}}|$.
The form factor Δ_s screens the $1-z$ singularity while form factor Δ_{ns} screens the $1/z$ singularity, in a similar form as the Regge form factor but also accounts for angular ordering:

$$\Delta_{ns}(z,k,q) = \exp\left(-\alpha_s \ln\frac{1}{z}\ln\frac{k^2}{zq^2}\right). \tag{6}$$

where for the lowest value of zq^2 we use a cut off μ.

Similarly as in case of the BK equation in order to obtain high energy factorizable unintegrated gluon density one applies relation (2). The nonlinear term in (4), apart from allowing for recombination of gluons might be understood as a way to introduce the decoherence into the emission pattern of gluons. This is because the gluon density is build up due to coherent gluon emission and since the nonlinear term comes with the negative sign it slows down the

growth of gluon density and therefore it introduces the decoherence. We expect the nonlinear term to be of main importance at low x similarly as in case of the BK equation. In this limit it will be of special interest to check whether in this formulation of the nonlinear extension of the CCFM equation one obtains an effect of saturation of the saturation scale as observed in [17]. This effect is of great importance since it has a consequences for example for imposing a bound on amount of production of entropy from saturated part of gluon density as observed in [24].

3 Conclusions and outlook

We reported on recently obtained new form of the BK equation written in a resummed form and on extension of CCFM to account for nonlinearity. The obtained extension of CCFM will be useful for studies of impact saturation of gluons on exclusive observables.

Acknowledgements

I would like to thank organizers of DIS 2012 and in particular Dimitri Colferai for inviting me to give a talk. This research has been supported by grant LIDER/02/35/L-2/10/NCBiR/2011

References

[1] S. Catani, M. Ciafaloni, F. Hautmann, Nucl. Phys. **B366** (1991) 135-188.
[2] L. V. Gribov, E. M. Levin and M. G. Ryskin, Phys. Rept. **100** (1983) 1.
[3] I. Balitsky, Nucl. Phys. B **463** (1996) 99.
[4] Y. V. Kovchegov, Phys. Rev. D **60** (1999) 034008.
[5] Y. V. Kovchegov, Phys. Rev. D **61** (2000) 074018.
[6] M. Ciafaloni, Nucl. Phys. B **296**, 49 (1988).
[7] S. Catani, F. Fiorani and G. Marchesini, Nucl. Phys. B **336**, 18 (1990).
[8] S. Catani, F. Fiorani and G. Marchesini, Phys. Lett. B **234**, 339 (1990).
[9] A. M. Stasto, K. J. Golec-Biernat, J. Kwiecinski, Phys. Rev. Lett. **86** (2001) 596-599.
[10] J. L. Albacete, C. Marquet, Phys. Rev. Lett. **105** (2010) 162301.
[11] K. Kutak and S. Sapeta, arXiv:1205.5035 [hep-ph].
[12] A. Dumitru, K. Dusling, F. Gelis *et al.*, Phys. Lett. **B697** (2011) 21-25.
[13] M. Deak, F. Hautmann, H. Jung, K. Kutak, [arXiv:1012.6037.
[14] K. Kutak, K. Golec-Biernat, S. Jadach and M. Skrzypek, JHEP **1202** (2012) 117.
[15] K. Kutak, H. Jung, Acta Phys. Polon. **B40** (2009) 2063-2070.
[16] E. Avsar and E. Iancu, Nucl. Phys. A **829** (2009) 31.
[17] E. Avsar and A. M. Stasto, JHEP **1006** (2010) 112.
[18] M. Braun, Eur. Phys. J. C **16**, 337 (2000).
[19] K. Kutak and J. Kwiecinski, Eur. Phys. J. C **29** (2003) 521.
[20] J. Bartels, M. Wusthoff, Z. Phys. **C66** (1995) 157-180.
[21] J. Bartels, K. Kutak, Eur. Phys. J. **C53** (2008) 533-548.
[22] J. Kwiecinski, A. D. Martin and P. J. Sutton, Phys. Rev. D **52** (1995) 1445.
[23] C. Adloff *et al.* [H1 Collaboration], Nucl. Phys. **B485** (1997) 3-24.
[24] K. Kutak, Phys. Lett. B **705** (2011) 217.

Comparison of two small x Monte Carlos with and without coherence effects.

M. Deák

Departamento de Física de Partículas, Facultade de Física,
Universidade de Santiago de Compostela, Campus Sur,
15706 Santiago de Compostela, Spain

DOI: `http://dx.doi.org/10.3204/DESY-PROC-2012-02/2`

We compare two Monte Carlo implementations of resummation schemes for the description of parton evolution at small values of Bjorken x. One of them is based on the BFKL evolution equation and generates fully differential parton distributions in momentum space making use of reggeized gluons. The other one is based on the CCFM partonic kernel where QCD coherence effects are introduced. It has been argued that both approaches agree with each other in the $x \to 0$ limit. We show that for azimuthal angle dependent quantities, although at high energies the BFKL approach is dominated by its zero conformal spin component, the CCFM gluon Green function receives contributions from all conformal spins even at very small x.

1 Introduction

An important challenge in the phenomenology of Quantum Chromodynamics (QCD) is to understand what are the dominant effective degrees of freedom underlying the strong interaction at high energies. In the limit where the center–of–mass energy $\sqrt{s}$ in a collision is much larger than any of the relevant mass scales the Balitsky–Fadin–Kuraev–Lipatov (BFKL) approach [1, 2, 3] appears to be a very useful framework to describe the scattering. In its original formulation this approach is based on the exchange of "reggeized" gluons in the t–channel. The interaction among them takes place via a gauge invariant (reggeized gluon)-(reggeized gluon)-(gluon) vertex. This simple effective structure stems from the dominance of the so-called multi–Regge kinematics where gluon cascades are only ordered in longitudinal components.

The simplicity of the final integral equation should not shadow the strong self-consistency of the full BFKL program where tight bootstrap conditions linking the reggeization of the gluon with the pomeron wavefunction, dominant in diffractive interactions, are fulfilled. The regime of applicability of the leading order BFKL approach to phenomenology is limited since it should be valid in a certain window of center-of-mass energies and perturbative scales. To extend its range of applicability one should include either higher order corrections, going beyond the 'multi-Regge" kinematics, include non-linear corrections responsible for the restauration of unitarity at very small x[1] or, as we are going to discuss in this paper, to include a more global treatment of collinear regions in phase space using the Catani-Ciafaloni-Fiorani-Marchesini

[1] In this work we consider equivalent variables the center-of-mass energy s, the DIS Bjorken x and the rapidity Y linking them by $Y \simeq \ln s \simeq \ln 1/x$.

(CCFM) equation, which provides a good matching from BFKL to the $x \to 1$ regime, at least, as we are going to show in this work, as long as anomalous dimensions and k_t-diffusion properties are concerned.

2 Results

We use Monte Carlo program SMALLX to calculate observables related to the CCFM Green and the Monte Carlo implementation of the BFKL equation described in [4].

We compare the diffusion picture in the t-channel transversal momentum k_t – rapidity y plane and angular angle correlation dependence of the BFKL and the CCFM Green's functions.

In the CCFM case, instead of a symmetric diffusion like in the BFKL case, the diffusion is asymmetric with extra soft emissions, fig. 1.

We quantify the angular correlation dependence by calculating Fourier moments of Green's functions with respect to the angle between the transversal momenta $\mathbf{k}_a$ and $\mathbf{k}_b$. As one can see from figures 2 and 3 the maximum rapidity Y dependence of the moments is much stronger in the CCFM case than in the BFKL case. The stronger correlation is especially prominent for $n > 0$ moments, where in the CCFM case the moments for $n = 1$ and 2 grow with rapidity, in the BFKL case they show constant or decreasing tendency.

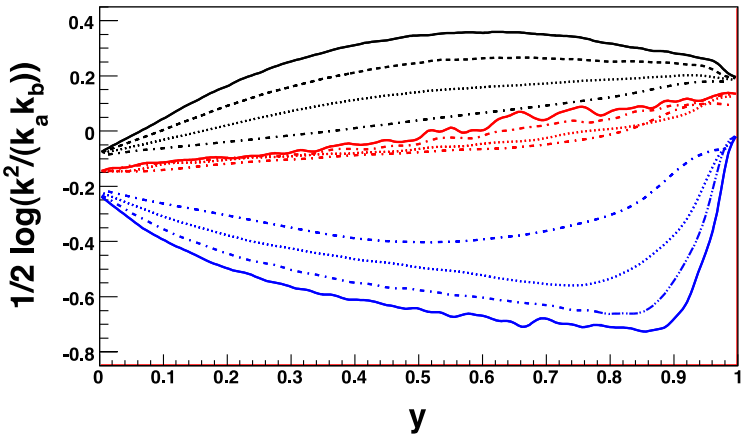

Figure 1: Distribution of transverse scales in the evolution with x of the CCFM equation.

3 Conclusions and scope

In this letter we have compared two Monte Carlo implementations of the CCFM and BFKL formalisms for the description of small x observables. The main difference between them from the theoretical point of view is the introduction of QCD coherence effects in the CCFM equation. We have found that the symmetric diffusion into infrared and ultraviolet regions of phase space characteristic of the BFKL parton evolution is broken in the CCFM case, where the

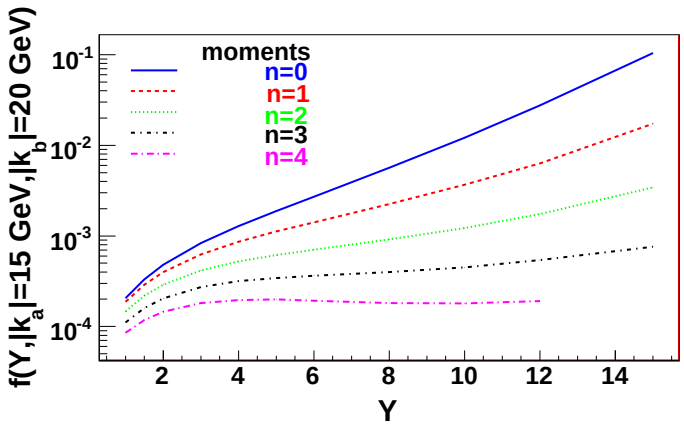

Figure 2: Variation with rapidity of the different components of the Fourier expansion on the azimuthal angle of the CCFM gluon Green function.

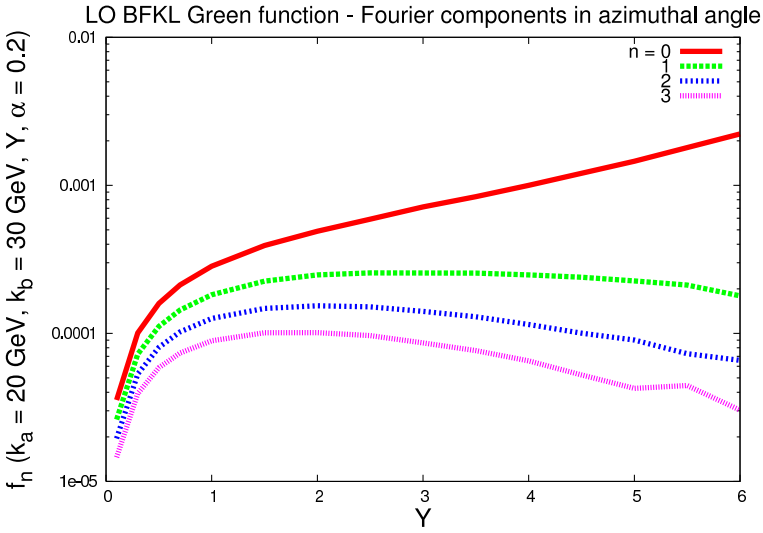

Figure 3: Variation with rapidity of the different components of the Fourier expansion on the azimuthal angle of the BFKL gluon Green function.

infrared scales play a dominant role. As our main result we have found that the higher Fourier components in the gluon Green function have a very different behaviour in both theories, rising with energy in the CCFM case and decreasing in the BFKL one. It will be very interesting to trace these differences at an observable level [5, 6, 7, 8] and to implement higher order corrections [10, 11, 12, 13, 14, 15, 16, 17, 18, 19, 9] to evaluate their effects on them. These lines of research will be the subject of our future investigations.

References

[1] L. N. Lipatov, Sov. J. Nucl. Phys. **23** (1976) 338.

[2] E. A. Kuraev, L. N. Lipatov, V. S. Fadin, Phys. Lett. B **60** (1975) 50, Sov. Phys. JETP **44** (1976) 443, Sov. Phys. JETP **45** (1977) 199.

[3] I. I. Balitsky, L. N. Lipatov, Sov. J. Nucl. Phys. **28** (1978) 822.

[4] A. Sabio Vera, arXiv:hep-ph/0307046, arXiv:hep-ph/0408008, arXiv:hep-ph/0510046.
A. Sabio Vera and P. Stephens, PoS D **IFF2006** (2006) 030.

[5] M. Deak, F. Schwennsen, JHEP **0809** (2008) 035. [arXiv:0805.3763 [hep-ph]].

[6] M. Deak, F. Hautmann, H. Jung *et al.*, JHEP **0909** (2009) 121. [arXiv:0908.0538 [hep-ph]].

[7] M. Deak, A. Grebenyuk, F. Hautmann *et al.*, [arXiv:1006.5401 [hep-ph]].

[8] M. Deak, F. Hautmann, H. Jung *et al.*, [arXiv:1012.6037 [hep-ph]].

[9] A. Sabio Vera, Acta Phys. Polon. B **39** (2008) 2213 [arXiv:0803.4485 [hep-ph]].

[10] G. Chachamis, M. Hentschinski, A. Sabio Vera and C. Salas, arXiv:0911.2662 [hep-ph].

[11] V. S. Fadin and L. N. Lipatov, Phys. Lett. B **429** (1998) 127.

[12] M. Ciafaloni and G. Camici, Phys. Lett. B **430** (1998) 349.

[13] G. P. Salam, JHEP **9807**, 019 (1998).

[14] A. Sabio Vera, Nucl. Phys. B **722** (2005) 65.

[15] C. R. Schmidt, Phys. Rev. D **60** (1999) 074003.

[16] J. R. Forshaw, D. A. Ross and A. Sabio Vera, Phys. Lett. B **455** (1999) 273, Phys. Lett. B **498** (2001) 149,

[17] G. Chachamis, M. Lublinsky and A. Sabio Vera, Nucl. Phys. A **748** (2005) 649.

[18] J. Bartels, A. Sabio Vera and F. Schwennsen, JHEP **0611** (2006) 051, PoS D **IFF2006** (2006) 029, arXiv:0709.3249 [hep-ph].

[19] F. Caporale, A. Papa and A. Sabio Vera, Eur. Phys. J. C **53** (2008) 525, Acta Phys. Polon. B **39** (2008) 2571.

Part VI

Working Group 3
Electroweak and Searches

Convenors:

David M. South, Andreas Weiler, Hwidong Yoo

Search for the Standard Model Higgs Boson in ATLAS

Prolay Mal on behalf of the ATLAS Collaboration

SPP/IRFU, CEA Saclay, Gif-sur-Yvette 91191, France

DOI: http://dx.doi.org/10.3204/DESY-PROC-2012-02/75

The search for the Standard Model (SM) Higgs boson based on 4.7-4.9 fb^{-1} of pp collision data at $\sqrt{s} = 7$ TeV recorded with the ATLAS detector is presented here. The combined ATLAS results exclude the SM Higgs boson masses (m_H) of 110.0-117.5, 118.5-122.5 and 129-539 GeV at 95% confidence level. An excess of events has been observed around $m_H \sim 126$ GeV with the global probability of 30% (10%) to occur anywhere in $110 < m_H < 600$ ($110 < m_H < 146$) GeV.

1 Introduction

The Higgs mechanism [1] provides a general framework to explain the observed masses of the W and Z gauge bosons through electroweak symmetry breaking. Within the Standard Model (SM), this mechanism posits the existence of a scalar boson, the Higgs boson, with an a priori unknown mass (m_H). The direct searches for the SM Higgs boson at the LEP experiments have excluded $m_H < 114.4$ GeV [2], while the searches at the Tevatron exclude $156 < m_H < 177$ GeV [3]. However, a global fit of the electroweak measurements performed at LEP, SLD and the Tevatron experiments, predicts a SM Higgs boson mass of 94^{+29}_{-24} GeV.

2 Individual Search Channels

The SM Higgs searches in ATLAS have been performed over a wide range of Higgs boson masses (110-600 GeV) considering different SM production mechanisms (gluon fusion, vector boson fusion and vector boson associated production) and their subsequent decay modes. The detector resolution for the reconstructed Higgs boson mass plays a crucial role in classifying the searches into numerous channels having different selection criteria as detailed below. The SM Higgs boson signal events have been simulated using PowHeg and Pythia generators, while the background contributions have been estimated either using simulation, or directly from data as appropriate.

2.1 $H \to ZZ \to l^+l^-\nu\bar{\nu}$, $H \to ZZ \to l^+l^-q\bar{q}$, $H \to WW \to l\nu q\bar{q}'$

Searches in these channels are focused on high mass Higgs boson searches over a typical Higgs mass range of 200-600 GeV. In the ZZ channels the events are required to have a lepton pair (e^+e^- or $\mu^+\mu^-$) with reconstructed M_{ll} close to the Z boson mass. The selected events for the $H \to ZZ \to l^+l^-\nu\bar{\nu}$ [4] search are further classified into two subcategories considering the pile-up effects ('low' and 'high') on the reconstructed missing transverse energies ($\not{E}_T$), while

the H $\rightarrow$ ZZ $\rightarrow$ $l^+l^-q\bar{q}$ [5] search considers 'tagged' (2 b-tagged jets) and 'untagged' (< 2 b-tagged jets) events separately. Figures 1 (a) and 1 (b) show the transverse mass distribution for H $\rightarrow$ ZZ $\rightarrow$ $l^+l^-\nu\bar{\nu}$ candidates in the 'low' pile-up data, and $m_{l^+l^-q\bar{q}}$ distribution for H $\rightarrow$ ZZ $\rightarrow$ $l^+l^-q\bar{q}$ in 'tagged' selection respectively. The selection criteria for the H $\rightarrow$ WW $\rightarrow$ $l\nu q\bar{q}'$ search [6] are optimized over a Higgs boson mass range of 300-600 GeV considering 'H+0jet', 'H+1jet' and 'H+2jets' (mostly from the vector boson fusion processes).

2.2 $H \rightarrow ZZ^{(*)} \rightarrow l^+l^-l'^+l'^-$

The search in this channel [7] consists of event categories with different lepton flavor combinations, while the SM $ZZ^{(*)}$ production processes remain irreducible background at the final level of event selection. Full reconstruction of the Higgs boson mass is possible for this channel with excellent mass resolution (2% and 1.5% for 4e and 4μ at $m_H \sim 120$ GeV). The 4-lepton invariant mass (m_{4l}) distribution is displayed in Figure 1 (c).

2.3 $H \rightarrow \gamma\gamma$

Although H $\rightarrow \gamma\gamma$ decays have small branching ratio (about 0.2%), search in this channel [8] has the potential to discover the Higgs boson in the low mass range (110-150 GeV). The analysis is split into nine independent sub-channels based on the photon pseudorapidity, conversion status, and the momentum component of the diphoton system transverse to the thrust axis (p_{Tt}). The background distribution is obtained by fitting the $m_{\gamma\gamma}$ distribution in data with a smoothly falling exponential function, while the ATLAS $m_{\gamma\gamma}$ mass resolution is approximately 1.4% for $m_H = 120$ GeV. The diphoton invariant mass distribution is shown in Figure 1 (d).

2.4 $H \rightarrow WW^{(*)} \rightarrow l^+\nu l'^-\bar{\nu}$

The searches in this channel [9] cover a wide range of 110 < m_H < 600 GeV consisting of different number of jets (0, 1 and 2 jets) and lepton flavor combinations (ee, $\mu\mu$ and eμ) in the final states. The reconstructed WW transverse mass (m_T) has been utilized in this analysis as a discriminating variable as shown in Figure 1(e) for the 'H+0jet' sub-channel.

2.5 $(W/Z)H \rightarrow (l\nu/l^+l^-, \nu\bar{\nu})b\bar{b}$

The searches in (W/Z)H $\rightarrow$ ($l\nu/l^+l^-, \nu\bar{\nu}$)$b\bar{b}$ channels [10] are optimized for m_H of 110-130 GeV. The main advantage with these channels is due to the large BR(H $\rightarrow b\bar{b}$) at low m_H, along with the possibility to fully reconstruct the Higgs boson mass through $m_{b\bar{b}}$. The final states with one or two charged leptons are sub-categorized depending on the transverse momentum of the reconstructed vector boson, and the lepton flavors. Figure 1 (f) shows the $m_{b\bar{b}}$ distribution for the WH $\rightarrow l\nu b\bar{b}$ sub-channel.

2.6 $H \rightarrow \tau^+\tau^- \rightarrow l^+l^-\nu\nu\nu\nu$, $l\tau_{had}\nu\nu\nu$, $\tau_{had}\tau_{had}\nu\nu$

H $\rightarrow \tau^+\tau^-$ searches [11] consist of all possible leptonic and hadronic (τ_{had}) decay modes of the τ-leptons originating from the Higgs boson decay. For the H $\rightarrow \tau^+\tau^- \rightarrow l^+l^-\nu\nu\nu\nu$ and H $\rightarrow \tau_{had}\tau_{had}\nu\nu$ channels, invariant mass of the $\tau^+\tau^-$ system is reconstructed assuming collinear

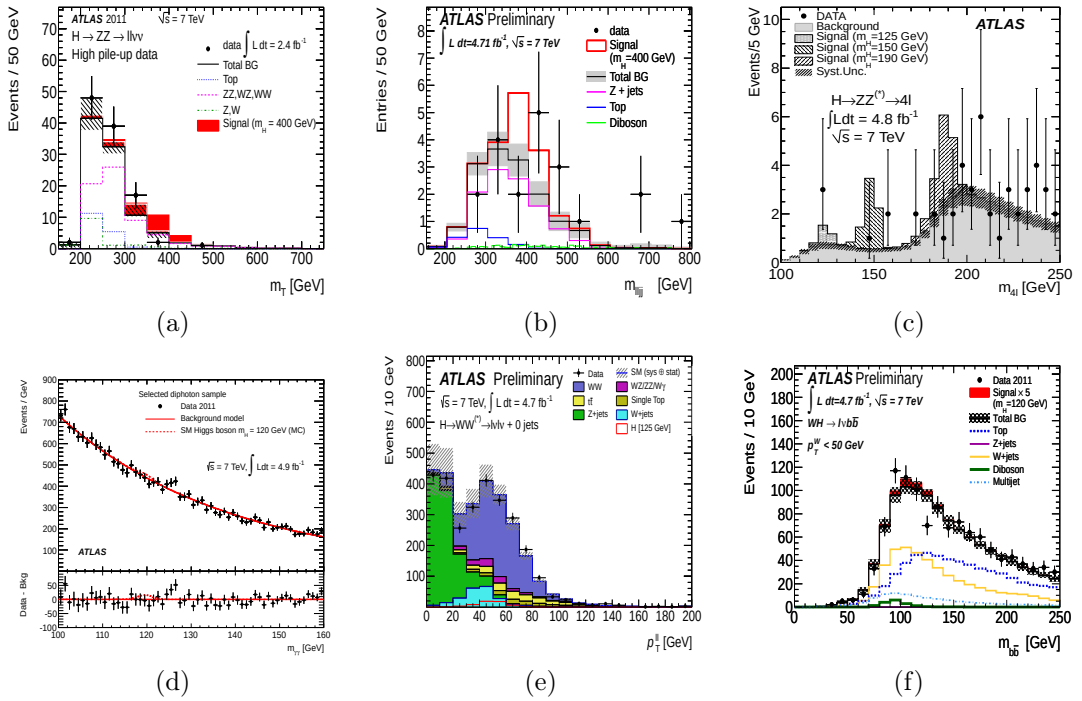

Figure 1: ATLAS SM Higgs Search observables in different channels: (a) the transverse mass distribution in $H \to ZZ \to l^+l^-\nu\bar{\nu}$ channel, (b) the invariant mass distribution of the llqq system for the $H \to ZZ \to l^+l^-q\bar{q}$ search, (c) the m_{4l} distribution for the $H \to ZZ^{(*)} \to l^+l^-l'^+l'^-$ candidate events, (d)the $m_{\gamma\gamma}$ spectrum in $H \to \gamma\gamma$ search, (e) the m_T distribution in the $H \to WW^{(*)} \to l^+\nu l'^-\bar{\nu}$, and (f) the $m_{b\bar{b}}$ distribution for the $WH \to l\nu b\bar{b}$ analysis.

approximation. The searches in $H \to l\tau_{had}\nu\nu\nu$ channel reconstruct the $m_{\tau^+\tau^-}$ using the Missing Mass Calculator techniques [12] where the full event topology is reconstructed using the kinematics of the τ-lepton decay products.

3 Exclusion limits

The results from the aforesaid search channels have been utilized to set an upper limit on the SM Higgs boson production cross section as a function of the m_H. The limits are conveniently expressed in terms of the signal strength ($\mu = \sigma/\sigma_{SM}$), the ratio of a given Higgs boson production cross section (σ) to its SM predicted value (σ_{SM}). The CL_s prescription[13] with a profile likelihood ratio test statistic, $\lambda(\mu)$ [14] has been utilized here to derive the exclusion limits. Figure 2 shows the exclusion limits on μ at 95% confidence level (CL) for individual search channels, along with the combined ones from all search channels over the m_H range of 110-150 GeV. A small excess of events near $m_H \sim 126$ GeV is observed in $H \to \gamma\gamma$ and $H \to ZZ^{(*)} \to l^+l^-l'^+l'^-$ search channels, both of which fully reconstruct the Higgs boson mass with high resolution.

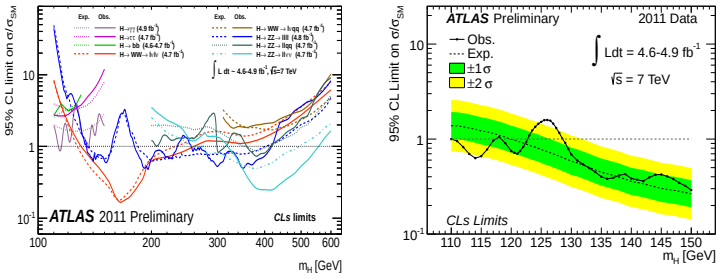

Figure 2: Exclusion limits on the SM Higgs production cross-sections at 95% CL for individual search channels (left), and for the combination of all search channels in m_H range of 110-150 GeV (right).

4 Conclusions

ATLAS has performed extensive searches for the SM Higgs boson utilizing the full 4.7-4.9 fb^{-1} dataset recorded during the 2011 LHC operations. The ATLAS combination [15] from numerous search channels excludes the SM Higgs boson mass in ranges of 110.0-117.5 GeV, 118.5-122.5 GeV, and 129-539 GeV at the 95% CL, while an exclusion of 120 GeV$< m_H <$555 GeV is expected in the absence of Higgs signal. Furthermore, the exclusion limits have been recalculated at 99% CL and the SM Higgs boson over a mass range of 130-486 GeV has been excluded. The excess in the observed data has a local significance of 2.5σ, where the expected significance in the presence of a SM Higgs boson with $m_H = 126$ GeV is 2.9σ. The global probability for such an excess to occur across the entire SM Higgs mass range (110-600 GeV) is estimated to be 30%. However, the said probability reduces to nearly 10% if a 110-146 GeV mass range for the SM Higgs boson is considered.

References

[1] P. Higgs, Phys. Lett. **12** 132 (1964); P. Higgs, Phys. Lett. **13** 508 (1964); P. Higgs, Phys. Rev. **145** 1156 (1966); F. Englert and R. Brout, Phys. Lett. **13** 321 (1964).

[2] The LEP Working Group for Higgs Boson Searches, Phys. Lett. B **565** 61 (2003).

[3] The TEVNPH Working Group, arXiv:1107.5518v2 [hep-ex] (2011).

[4] ATLAS Collaboration, ATLAS-CONF-2012-016, http://cdsweb.cern.ch/record/1429665.

[5] ATLAS Collaboration, ATLAS-CONF-2012-017, http://cdsweb.cern.ch/record/1429666.

[6] ATLAS Collaboration, ATLAS-CONF-2012-018, http://cdsweb.cern.ch/record/1429667.

[7] ATLAS Collaboration, Phys. Lett. B **710** 383 (2012).

[8] ATLAS Collaboration, Phys. Rev. Lett. **108** 111803 (2012).

[9] ATLAS Collaboration, ATLAS-CONF-2012-012, http://cdsweb.cern.ch/record/1429660.

[10] ATLAS Collaboration, ATLAS-CONF-2012-015, http://cdsweb.cern.ch/record/1429664.

[11] ATLAS Collaboration, ATLAS-CONF-2012-014, http://cdsweb.cern.ch/record/1429662.

[12] A. Elagin *et al.*, Nucl. Instrum. Meth. **A654** 481 (2011), arXiv:1012.4686 [hep-ex].

[13] A. Read, J. Phys. **G28** 2693 (2002).

[14] G. Cowan *et al.*, Eur. Phys. J. **C71** 1554 (2011).

[15] ATLAS Collaboration, ATLAS-CONF-2012-019, http://cdsweb.cern.ch/record/1430033.

Searches for Standard Model Higgs boson at CMS

Pietro Govoni[1] for the CMS Collaboration

[1]CERN, 1211 Genève 23, Switzerland

DOI: http://dx.doi.org/10.3204/DESY-PROC-2012-02/219

A search for the Standard Model Higgs boson has been performed by the CMS Collaboration, with the full dataset delivered by the LHC during the 2011, in a wide spectrum of channels. The statistical combination of the results allows to exclude a wide region of its mass at 95% confidence level: 127.5 – 600 GeV/c^2. A modest excess at about 125 GeV/c^2 is observed, with a significance of 1.6 σ in the range 110 – 150 GeV/c^2. More data are needed to ascertain the origin of the observed excess.

Standard Model (SM) Higgs boson (H) searches are of primary importance in the analysis of the first data delivered by the LHC, since they can lead to the understanding of the electroweak symmetry breaking mechanism, which gives elementary particles their mass [1, 2, 3, 4].

The CMS experiment [5], one of the two multi-purpose detectors installed at the LHC pp collider at CERN, features a 3.8 T magnetic field parallel to the beam axis, generated by a super-conducting solenoid of 6 m diameter and 13 m length, which hosts the central tracking and calorimetry detectors of the experiment. The former is composed by ten layers of silicon pixels or strips, while the latter is subdivided into a fine-grained scintillating crystals homogeneous detector to detect electromagnetic showers, and a segmented brass-plastic scintillators calorimeter, measuring hadronic showers. Outside the solenoid, and placed in the iron return yoke of the magnetic field, gas detectors measure the passage of muons produced in the interactions.

Events produced by the beam collisions are triggered by means of a two-layers system: the first one reduces the rate by three orders of magnitude by means of dedicated electronics; the second one, running on a farm of commercial PCs, selects the events after a fast reconstruction and event analysis, and by gaining other three orders of magnitude brings the rate at the level of few hundreds events per second.

During the offline analysis and the last phase of the triggering, physics objects produced by the collisions are reconstructed in the detector from the measurement of each single particle flowing in the CMS volume, with a particle flow approach [6].

The CMS experiment collected about 5 fb^{-1} of data, that have been analyzed to search for the Higgs boson in its decay into several final states, which cover a wide range of the expected Higgs boson mass: in case it does not exist, the corresponding expected exclusion range with the available statistics is 114.5 – 543 GeV/c^2 at 95% confidence level. Such a large coverage is obtained thanks to the statistical combination of the results obtained in each of the sub-channels studied, where a modified CL$_S$ technique is applied to extract limits [7].

At low mass, above the 114.4 GeV/c^2 limit set by LEP [8], the most sensitive channel is H $\to \gamma\gamma$ [9, 10], which despite the low expected rate is very well identified using the characteristic signature of two isolated photons resonating in a narrow peak, thanks to the excellent energy

resolution of the electromagnetic calorimeter. The two decay products are selected vetoing charged activity in their neighborhood, from the shape of their energy deposit and with p_T cuts relative to their invariant mass. The vertex they originate from is chosen, among the various interactions that happen during a LHC bunch crossing, by looking at tracks in the event. The collected events are divided into five different categories, four of which are chosen as a function of photon reconstruction resolution, goodness of identification and kinematics of the di-photon system. The last one exploits the vector boson fusion (VBF) signature, where the Higgs boson is produced together with two energetic jets well separated in pseudorapidity. The continuum background to the Higgs signal, mainly due to QCD di-photon or photon+jet production, is modeled using a polynomial fit to the observed di-photon mass spectrum. As the expected sensitivity of the analysis does not allow to exclude the SM Higgs, the observed exclusion range at 95% confidence level depends on the statistical fluctuations of data with respect to the predictions, and translates into several disjoint intervals: 110.0 – 111.0, 117.5 – 120.5, 128.5 – 132.0, 139.0 – 140.0, 146.0 – 147.0 GeV/c^2 (see Figure 1). Among the non-excluded sections, around the value of 125 GeV the probability that the background fluctuation produces a signal (the p-value) corresponds to a local discovery significance of 2.8 σ.

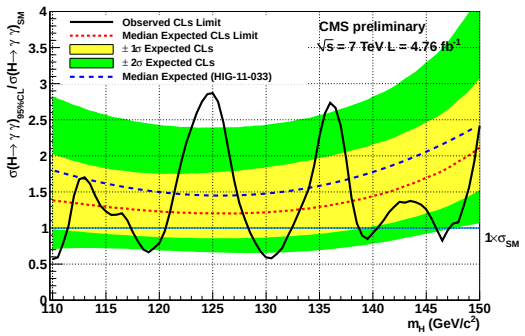

Figure 1: The exclusion limit obtained with the H $\rightarrow \gamma\gamma$ search.

Another resonance searched in the low Higgs mass range is the decay into two τ leptons, in the fully- and semi-leptonic τ final states [11]. Events are selected with a p_T selection on the τ candidates and the major background due to Z boson production is measured by selecting Z bosons decaying into muons and substituting the muons for simulated τs. Also in this case, events are subdivided into categories, depending on the number of observed jets: no jets, one boosted jet ($p_T > 150$ GeV) and two jets in the VBF topology. The most sensitive channel is the VBF one. The $\tau\tau$ channel alone is not able and exclude the SM higgs boson, but it contributes to final exclusion in combination with the other analyses.

Also the Higgs decay into two b quarks has been exploited [12], selecting the two b candidates by tagging tracks with large impact parameter in the jets detected in each event. The huge QCD di-jet background is reduced by searching for the associated production of a Higgs boson with a W or Z boson, the decay products of which have to be present in the event (electrons, muons or neutrinos as unbalanced energy in the transverse plane with respect to the beam direction). In addition, the vector boson is required to be boosted. As for the $\tau\tau$ channel, results obtained from this study do not put an exclusion limit to the SM Higgs boson, but contribute to the global CMS limit.

As its mass increases, the Higgs boson primarily decays into a pair of vector bosons. Similarly to the $\gamma\gamma$ case, the final state with two Z bosons decaying leptonically [13] shows a very clean signature, characterized by four isolated leptons with appropriate flavour and charge combinations, so that one of the two pairs can be required not to be on-shell. Also in this case, the invariant mass resolution of the Higgs resonance is very good. The main background to fight is the electro-weak production of Z boson pairs, which is estimated from simulation. The low background level of this channel makes it a powerful probe to test a very wide mass range, resulting in an observed exclusion at 95% confidence level in the following intervals: 134 –158, 180 – 305 and 340 – 465 GeV/c^2. The inaccessible window between 158 and 180 GeV/c^2 is due to the decrease in cross section for this channel, because of the competition with the decay into WW, while the other inaccessible window is determined by a statistical fluctuation of data with respect to the expectations. The largest excess is observed at 119.5 GeV/c^2, that corresponds to a local significance of 2.5 σ.

The H $\rightarrow$ WW $\rightarrow \ell\nu\ell\nu$ analysis [14] complements the ZZ one along the Higgs mass spectrum. The final state is characterized by the presence of two oppositely charged, isolated leptons and missing energy due to neutrinos escaping CMS. The main backgrounds are due to the electroweak production of WW pairs and top pairs, as well as Z production with jets. Besides this, QCD dijet and W + jets production can contaminate the signal region, because of misidentification of jets as leptons: the huge cross section of the backgrounds balances the small misidentification probability. Dedicated treatment of the missing energy reconstruction is necessary to suppress the Z + jets background. The analysis is performed separately in the no-jets case, one jet case and two jets case with VBF topology. While profiting of the highest cross-section over a wide mass range, this study suffers from the presence of the two neutrinos in the final state, that prevents the invariant mass reconstruction of the Higgs resonance. Therefore, the resolution in the exclusion limit is much worse with respect to the ZZ or $\gamma\gamma$ cases, and all the backgrounds have been carefully measured in signal-free regions in data, as no invariant mass fit can be performed to identify the signal. The Higgs mass range excluded at 95% confidence level by this study is 129 – 270 GeV/c^2.

The most powerful exclusion at higher Higgs masses is provided by the H $\rightarrow$ ZZ $\rightarrow 2\ell 2\nu$ [15]. The final state of this analysis is identified as a same-flavour, opposite-charge high-p_T leptons pair consistent with the Z boson mass, and large missing energy due to neutrinos. The WW and ZZ backgrounds that contaminate the signal region are estimated from control regions with opposite-flavour lepton pairs, while the Z + jets one, which depends on the missing energy reconstruction in the detector, is modeled by kinematically reweighting a γ + jets sample. The resulting excluded 95% confidence level range is 270 – 440 GeV/c^2. Also the H $\rightarrow$ WW $\rightarrow \ell\nu\ell\nu$, the H $\rightarrow$ ZZ $\rightarrow 4\ell$ and the H $\rightarrow$ ZZ $\rightarrow 2\ell 2q$ [16] play an important role in the high mass regime. In particular, the latter searches for a pair of opposite charge same flavour leptons, together with two jets resonating at the Z mass, and the Z+jets background is evaulated from sidebands in the m_{jj} spectrum.

The results of all the CMS Higgs analyses [17, 18] have been combined with the frequentist LHC-type CL$_S$ with profiled likelihood test-statistics and log-normal treatment of nuisance parameters. The obtained exclusion limits are, for 95% confidence level, 127.5 – 600 GeV/c^2, and for 99% confidence level 129 – 525 GeV/c^2, as shown in Figure 2 on the left.

The observed limit on the high mass side is larger than expected, because of a down-fluctuation of data, while the lower limit is higher than expected because of excess in data at low mass. The smallest p-value observed is situated at 125 GeV/c^2 and corresponds to a global significance of 0.8 σ when considering the full investigated range for the look-elsewhere effect

(110 – 600 GeV/c^2), while it becomes 1.6 σ in a narrower range (100 – 150 GeV/c^2). To check the compatibility of this deviation with the SM, a global fit is performed on the results of all the analyses with signal-plus-background hypothesis, where the free parameter is a multiplicative factor to the signal cross section (the signal strength). The result of the fit is shown in Figure 2 on the right, as a function of the Higgs mass. when looking at the 125 GeV/c^2 point, the fit has been also performed in single channels and the maximum of the signal strengths compared. All the final states are compatible with the SM hypothesis.

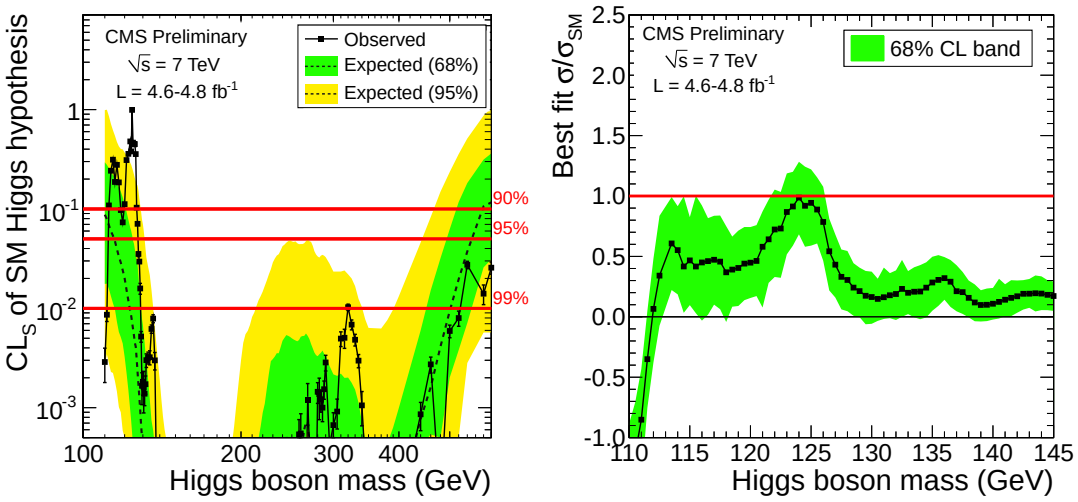

Figure 2: The confidence level of exclusion for the SM Higgs as a function of its mass (left), and the best fit of the signal strength, in the low region of the investigated invariant mass spectrum (right).

In conclusion, the full dataset acquired by CMS during 2011 has been studied searching for the SM Higgs boson, with a broad range of Higgs decay channels. The global combination of the analyses outcomes excludes the Higgs boson at 95% confidence level in the 127.5 – 600 GeV/c^2 mass range. A modest excess at about 125 GeV/c^2 is observed, with a local significance 2.8 σ, and a global one of 0.8 σ (1.6 σ) in the full search range (in 100 – 150 GeV/c^2 range). More data are required to ascertain the origin of the observed excess.

References

[1] S. Weinberg, *Phys. Rev.Lett.* **19** (1967) 1264.

[2] A. Salam, p. 367. Almquist and Wiksells, Stockholm, 1968.

[3] F. Englert and R. Brout, *Phys. Rev. Lett.* **13** (1964) 321.

[4] P. W. Higgs, *Phys. Rev. Lett.* **13** (1964) 508.

[5] CMS Collaboration, *JINST* **3** (2008) S08004.

[6] CMS Collaboration, CMS Physics Analysis Summary CMS-PAS-PFT-10-002 (2010).

[7] ATLAS and CMS Collaborations, ATLAS-CONF-2011-157, CMS HIG-11-023 (2011).

[8] R. Barate *et al.*, *Phys. Lett.* **B565** (2003) 61–75.

[9] S. Chatrchyan *et al.* [CMS Collaboration], Phys. Lett. B **710**, 403 (2012) [arXiv:1202.1487 [hep-ex]].
[10] CMS Collaboration, CMS Physics Analysis Summary CMS-PAS-HIG-12-001 (2012).
[11] S. Chatrchyan *et al.* [CMS Collaboration], arXiv:1202.4083 [hep-ex].
[12] S. Chatrchyan *et al.* [CMS Collaboration], Phys. Lett. B **710**, 284 (2012) [arXiv:1202.4195 [hep-ex]].
[13] S. Chatrchyan *et al.* [CMS Collaboration], arXiv:1202.1997 [hep-ex].
[14] S. Chatrchyan *et al.* [CMS Collaboration], Phys. Lett. B **710**, 91 (2012) [arXiv:1202.1489 [hep-ex]].
[15] S. Chatrchyan *et al.* [CMS Collaboration], JHEP **1203**, 040 (2012) [arXiv:1202.3478 [hep-ex]].
[16] S. Chatrchyan *et al.* [CMS Collaboration], arXiv:1202.1416 [hep-ex].
[17] S. Chatrchyan *et al.* [CMS Collaboration], Phys. Lett. B **710**, 26 (2012) [arXiv:1202.1488 [hep-ex]].
[18] CMS Collaboration, CMS Physics Analysis Summary CMS-PAS-HIG-12-008 (2012).

Standard Model Higgs Searches at the Tevatron

Kyle J. Knoepfel on behalf of the CDF and D0 collaborations

Fermi National Accelerator Laboratory, P.O. Box 500, Batavia, IL

DOI: http://dx.doi.org/10.3204/DESY-PROC-2012-02/278

We present results from the search for a standard model Higgs boson using data corresponding up to 10 fb^{-1} of proton-antiproton collision data produced by the Fermilab Tevatron at a center-of-mass energy of 1.96 TeV. The data were recorded by the CDF and D0 detectors between March 2001 and September of 2011. A broad excess is observed between $105 < m_H < 145$ GeV/c^2 with a global significance of 2.2 standard deviations relative to the background-only hypothesis.

1 Introduction

The Higgs boson is the only standard model (SM) particle yet to be found. Within the SM, it is the particle responsible for giving the W and Z bosons and fermions their masses [1]. Although the value of the Higgs mass is a parameter, and is therefore formally unconstrained, measurements of electroweak observables such as m_W and m_t, indirectly constrain it to be less than roughly 150 GeV/c^2 at 95% confidence level (C.L.).

In December of 2011, the CMS and ATLAS collaborations released results indicating excesses in the $H \to \gamma\gamma$ channel relative to the background-only hypothesis. Along with the $H \to \gamma\gamma$ channel, the $H \to W^+W^-$ and $H \to ZZ$ diboson channels have the most sensitivity to Higgs production [2, 3]. On the other hand, the sensitivity to the Higgs through the $H \to b\bar{b}$ channel is a bit less — as of the Moriond 2012 conference, the expected sensitivities to the $H \to b\bar{b}$ final states were roughly $4.3 \times \sigma_{\mathrm{SM}}$ [4] and $3.5 \times \sigma_{\mathrm{SM}}$ [5], respectively, for the CMS and ATLAS Higgs searches. In contrast, the expected sensitivities at the Tevatron at low-mass are predominantly through the $H \to b\bar{b}$ associated production modes, and on the order of $1.7 \times \sigma_{\mathrm{SM}}$ [6] and $2.2 \times \sigma_{\mathrm{SM}}$ [7], respectively, for the CDF and D0 searches. The low-mass Higgs searches at the Tevatron and LHC are therefore complementary. The $H \to b\bar{b}$ searches at the Tevatron are therefore the focus of this presentation.

2 Low-Mass Higgs Searches at the Tevatron

Low-Mass Higgs searches use a typical analysis selection, summarized in Table 1. Requiring the two leading jets in the event to be b-tagged substantially reduces the background relative to the Higgs signal. Additional sensitivity can be gained by also considering events where one but not both leading jets are tagged. Note that analyses that have zero and one leptons in the final state are also sensitive to $\ell\nu b\bar{b}$ and $\ell^+\ell^- b\bar{b}$ final states, respectively, due to losing a lepton from detector inefficiencies. Multivariate techniques are implemented to separate signal from QCD and electroweak backgrounds.

To obtain the best expected sensitivities to SM Higgs production, the b-tagging and lepton identification algorithms must be optimized. Also, variables that discriminate between signal and background processes can be improved, such as the dijet invariant mass m_{jj}, which improves the ability of multivariate discriminants to separate the Higgs signal from background processes.

Analysis Channel	No. of Leptons	$\not\!\!E_T$	No. of b-jets
$ZH \to \nu\bar{\nu}b\bar{b}$	0	Yes	2
$WH \to \ell\nu b\bar{b}$	1	Yes	2
$ZH \to \ell^+\ell^- b\bar{b}$	2	No	2

Table 1: Basic selection for $H \to b\bar{b}$ final states produced in association with a W or Z boson.

2.1 Analysis Improvements

The results presented here are given in Ref. [8] and the references therein. Many Higgs analyses at CDF and D0 have implemented several improvements, consisting of increased luminosity (roughly 10% gain in sensitivity), improved b-tagging, improved m_{jj} resolution, and various improvements in analysis methods. At CDF, an improved b-tagging algorithm called HOBIT [9] was used in most of the mainstream $H \to b\bar{b}$ search channels. This multivariate algorithm, trained on $H \to b\bar{b}$ events for a Higgs mass of $m_H = 120$ GeV/c^2, increased Higgs sensitivity by roughly 10% for a given search channel. Various analysis improvements were made by the D0 searches, including increasing signal acceptance by relaxing some of the variable definitions.

3 Tevatron Combinations

To determine upper limits on SM Higgs production at 95% C.L., two approaches are taken: a frequentist profile likelihood approach where the minimum of the likelihood is used to determine the nuisance parameters; a modified frequentist (or Bayesian) approach where the nuisance parameters are integrated out to determine posterior probabilities. Both approaches yield agreement better than 10% for all Higgs mass hypotheses in the range $100 < m_H < 200$ GeV/c^2, and better than 1% on average. The Bayesian limits are adopted as the Tevatron results.

Systematic uncertainties such as the jet-energy scale, luminosity, and pdf's are incorporated as nuisance parameters. Care is taken to ensure that all appropriate correlations are taken into account between the CDF and D0 experiments.

3.1 All Channels

The complete list of channels that goes into the Higgs Tevatron combination is given in Ref. [8], along with a complete description of the limit-setting procedure and handling of systematic uncertainties. The 95% C.L. limits on Higgs production are shown in Fig. 1, along with the best-fit value assuming the existence of signal in the data. The expected upper limit is better than $1.15 \times \sigma_{\rm SM}$ across the entire Higgs mass range. The expected exclusion regions are $100 < m_H < 119$ GeV/c^2 and $141 < m_H < 184$ GeV/c^2, whereas the observed exclusion regions are $100 < m_H < 106$ GeV/c^2 and $147 < m_H < 179$ GeV/c^2. A broad excess is observed in the mass range $105 < m_H < 145$ GeV/c^2, where the minimum local p-value (p_0) at $m_H = 120$ GeV/c^2 corresponds to a 2.7-standard-deviation departure from the background-only hypothesis. Assuming a jet-energy resolution of about 10%, the estimated correction from the look-elsewhere effect gives $p_{\rm global} \approx 4 \times p_0$, which corresponds to a 2.2 standard-deviation

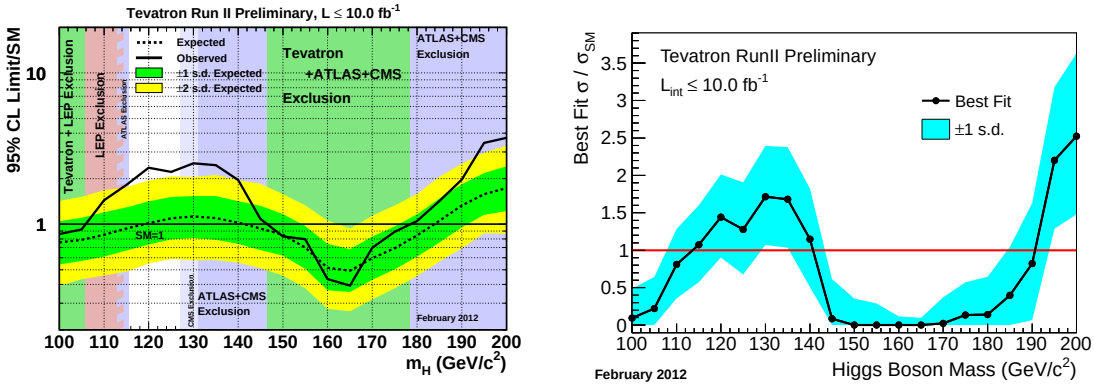

Figure 1: (Left) Upper limits on SM Higgs production at 95% C.L. assuming the background-only hypothesis. (Right) Best fit value for SM Higgs production, assuming the signal plus background hypothesis.

effect relative to the background-only hypothesis. The best-fit value of the Higgs production cross-section is consistent with the SM prediction in the mass region $110 < m_H < 140$ GeV/c^2.

3.2 $H \to b\bar{b}$ Channels

Upper limits on SM Higgs production have also been obtained by looking at only $H \to b\bar{b}$ final states. The 95% C.L. limits, and associated best-fit value for Higgs production are shown in Fig. 2.

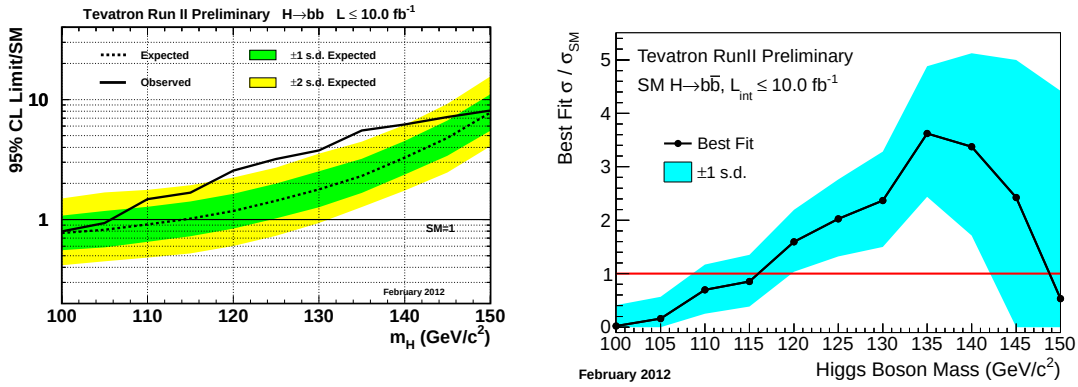

Figure 2: (Left) Upper limits on $H \to b\bar{b}$ production at 95% C.L. assuming the background-only hypothesis. (Right) Best fit value for $H \to b\bar{b}$ production, assuming the signal plus background hypothesis.

The broad excess in the low-mass range results in a minimum p-value of 2.8 standard deviations away from the background-only hypothesis at a Higgs mass of $m_H = 135$ GeV/c^2. Using a look-elsewhere effect correction of 2 (based on the assumed jet-energy resolution), the global p-value is diluted to a 2.6 standard-deviation effect. The best-fit value is consistent with the SM prediction in the region $110 < m_H < 120$ GeV/c^2. The significant departure from the SM prediction in the region $120 < m_H < 145$ GeV/c^2 results from the signal component of the fit needing to compensate for the excess of data events relative not only to the background-only prediction, but also to the signal-plus-background prediction.

4 Conclusions

The CDF and D0 collaborations have combined their results to give a Tevatron-wide combination of the upper limits of the SM Higgs production at 95% C.L. After combining all channels across the range $100 < m_H < 200$ GeV/c^2, a broad excess is observed in data relative to the background-only hypothesis, corresponding to a 2.2 standard-deviation effect. Considering only the $H \to b\bar{b}$ search channels yields an excess in data, corresponding to a 2.6 standard-deviation departure from the background-only prediction. An update of the Tevatron combination is expected in the summer of 2012.

5 Acknowledgments

The author wishes to thank the DIS workshop organizers and conveners for an enjoyable and rewarding experience. He acknowledges support from Fermi National Accelerator Laboratory and the CDF experiment.

References

[1] F. Englert and R. Brout, Phys. Rev. Lett. **13** 321 (1964); P. W. Higgs, Phys. Rev. Lett. **13** 508 (1964); G. S. Guralnik *et al.*, Phys. Rev. Lett. **13** 585 (1964)

[2] CMS Collaboration, S. Chatrchyan *et al.*, "Combined results of searches for the standard model Higgs boson in pp collisions at $\sqrt{s} = 7$ TeV", 2012. `arXiv:1202.1488v1 [hep-ex]`

[3] ATLAS Collaboration, "An update to the combined search for the Standard Model Higgs boson with the ATLAS detector at the LHC using up to 4.9 fb^{-1} of pp collision data at $\sqrt{s} = 7$ TeV", 2012. ATLAS-CONF-2012-019

[4] CMS Collaboration, S. Chatrchyan *et al.*, "Search for the standard model Higgs boson decaying to bottom quarks in pp collisions at $\sqrt{s} = 7$ TeV", 2012. `arXiv:1202.1488v1 [hep-ex]`

[5] ATLAS Collaboration, "Search for the Standard Model Higgs boson produced in association with a vector boson and decaying to a b-quark pair using up to 4.7 fb^{-1} of pp collision data at $\sqrt{s} = 7$ TeV with the ATLAS detector at the LHC", 2012. ATLAS-CONF-2012-015

[6] CDF Collaboration, "Combination of CDF's searches for the standard model Higgs boson with up to 10.0 fb^{-1} of data", 2012. CDF Note 10804

[7] D0 Collaboration, "Combined Search for the Standard Model Higgs Boson from the D0 Experiment in up to 9.7 fb^{-1} of Data", 2012. D0 Note 6304-CONF

[8] The TEVNPH Working Group, for the CDF and D0 Collaborations,"Combined CDF and D0 Search for Standard Model Higgs Boson Production with up to 10.0 fb^{-1} of Data", 2012. `arXiv:1203.3774v1 [hep-ex]`

[9] J. Freeman *et al.*, "Introduction to HOBIT, a b-Jet Identification Tagger at the CDF Experiment Optimized for Light Higgs Boson Searches", 2012. `arXiv:1205.1812v1 [hep-ex]`

The Higgs boson beyond Standard Model

Aleksandr Azatov[1]

[1]Dipartimento di Fisica, Università di Roma "La Sapienza"
and INFN Sezione di Roma; I-00185 Rome, Italy

DOI: `http://dx.doi.org/10.3204/DESY-PROC-2012-02/176`

We will review the status of the Higgs boson beyond Standard Model. This proceeding will be focused on the experimental and theoretical status of the Higgs boson in the Composite Higgs models. In particular we will discuss implications on the beyond Standard Model (BSM) Higgs coming from the observed excess at 125 GeV.

1 Introduction

Higgs fields is the only missing element of the Electroweak Symmetry breaking mechanism. With the recent hints from LHC about excess at 125 GeV [1, 2] it becomes crucial to understand the nature of this candidate for the Higgs boson and the mechanism that stabilizes its mass at the electroweak scale. One of the most attractive explanations of the Higgs mass stability is given in the models, where the Higgs appears as a composite field of some new strong dynamics [3]. However masses of the composite states in such framework are generically around TeV, so that we need additional mechanism to explain, why the Higgs is much lighter than the rest of the composite states. Such mass hierarchy can be naturally explained in the models, where Higgs is a pseudo Nambu-Goldstone boson of some larger global symmetry group[3, 4]. Recently this idea attracted more attention because this setup is dual to the extra dimensional models in warped geometry[5], where Higgs comes as a fifth component of the five dimensional gauge field [6]. Generically in such models the rest of the composite resonances are much heavier than the Higgs field, which makes them hard to produce directly at the LHC, however their indirect effects might be seen in the modifications of the Higgs couplings to the Standard Model(SM) fields. Within this framework first hints of new physics might be observed in the deviations of the Higgs couplings from their Standard Model expectations. In this note we will review generic predictions of the composite models as well as current constraints on the Higgs couplings.

2 Single Higgs effective theory

As we argued in the previous section, for the BSM Higgs we expect modifications of the Higgs couplings. To parametrize such interactions the Higgs field h, it is convenient to use Electroweak (EW) chiral lagrangian with all the possible additional interactions involving h[7, 8]. LEP constraints on $\Delta\rho$ parameter force our lagrangian to be symmetric under custodial $SU(2)_L \times SU(2)_R$ symmetry. Longitudinal polarizations of the W and Z correspond to the Nambu-Goldstone (NG) bosons of $SU(2)_L \times SU(2)_R/SU(2)_V$ symmetry breaking, and can be described

by the 2×2 matrix

$$\Sigma(x) = \exp\left(i\sigma^a \chi^a(x)/v\right) , \tag{1}$$

where σ^a are the Pauli matrices and $v = 246\,\text{GeV}$. The scalar h is assumed to be a singlet of the custodial $SU(2)_V$. The Lagrangian thus reads:

$$\mathcal{L} = -V(h) + \mathcal{L}^{(2)} + \mathcal{L}^{(4)} + \dots \tag{2}$$

where $\mathcal{L}^{(n)}$ includes the terms with n derivatives and $V(h)$ is the potential for h. At the level of two derivatives one has [7]

$$\begin{aligned}\mathcal{L}^{(2)} =& \frac{1}{2}(\partial_\mu h)^2 + \frac{v^2}{4} Tr\left(D_\mu \Sigma^\dagger D^\mu \Sigma\right)\left(1 + 2a\,\frac{h}{v} + b\,\frac{h^2}{v^2} + \cdots\right) \\ & - \frac{v}{\sqrt{2}} \lambda^u_{ij}\left(\bar{u}^{(i)}_L, \bar{d}^{(i)}_L\right)\Sigma\left(u^{(i)}_R, 0\right)^T\left(1 + c_u\,\frac{h}{v} + c_{2u}\,\frac{h^2}{v^2} + \cdots\right) + h.c. \\ & + (u_R \Leftrightarrow d_R, c_u \Leftrightarrow c_d) + ((u, d \Leftrightarrow \nu, e), c_u \Leftrightarrow c_l)\end{aligned} \tag{3}$$

Standard Model corresponds to the point where all $a = b = c_i = 1$ and $c_{2i} = 0$ At the level of four derivatives one can write the lagrangian as a sum of operators O_i

$$\mathcal{L}^{(4)} = \sum_i O_i \tag{4}$$

where O_i are defined in the following way

$$\begin{aligned}& O_1 = \mathrm{Tr}\left[(D_\mu\Sigma)^\dagger (D^\mu \Sigma)\right](\partial_\nu F_1(h))^2, \quad O_2 = \mathrm{Tr}\left[(D_\mu\Sigma)^\dagger (D_\nu \Sigma)\right]\partial^\mu\partial^\nu F_2(h) \\ & O_{GG} = G_{\mu\nu}G^{\mu\nu}\,F_{GG}(h), \quad O_{BB} = B_{\mu\nu}B^{\mu\nu}\,F_{BB}(h) \\ & O_W = D_\mu W^a_{\mu\nu}\,\mathrm{Tr}\left[\Sigma^\dagger \sigma^a i\overleftrightarrow{D}_\nu \Sigma\right] F_W(h), \quad O_B = -\partial_\mu B_{\mu\nu}\,\mathrm{Tr}\left[\Sigma^\dagger i\overleftrightarrow{D}_\nu \Sigma\,\sigma^3\right] F_B(h) \\ & O_{WH} = i\,W^a_{\mu\nu}\,\mathrm{Tr}\left[(D^\mu\Sigma)^\dagger \sigma^a D^\nu \Sigma\right] F_{WH}(h), \quad O_{BH} = -i\,B_{\mu\nu}\,\mathrm{Tr}\left[(D^\mu\Sigma)^\dagger (D^\nu\Sigma)\sigma^3\right] F_{BH}(h) \\ & O_{W\partial H} = \frac{1}{2}\,W^a_{\mu\nu}\,\mathrm{Tr}\left[\Sigma^\dagger \sigma^a i\overleftrightarrow{D}^\mu \Sigma\right]\partial^\nu F_{W\partial H}(h), \quad O_{B\partial H} = -\frac{1}{2}\,B_{\mu\nu}\,\mathrm{Tr}\left[\Sigma^\dagger i\overleftrightarrow{D}^\mu \Sigma\sigma^3\right]\partial^\nu F_{W\partial B}(h) \\ & F_i(h) = \alpha_i^{(0)} + \alpha_i^{(1)} h + \alpha_i^{(2)} h^2 + ...\end{aligned} \tag{5}$$

The operators O_W, O_B contribute to the S parameter and the operators O_{GG}, O_{BB} are important for the contribution of the Higgs couplings to gluons and photons. Generically all these operators have independent coefficients, which have to be determined during the experiment.

3 Current constraints on the Higgs couplings

In this section we will derive the current bounds on the Higgs couplings. Instead of considering the whole set of operators presented in the previous section we will focus on the following scenario

$$c_u = c_d = c_l \equiv c \tag{6}$$

and all the operators O_i vanish.[1] We will assume that couplings of the Higgs to gluons and photons are modified only due to the modification of the Higgs couplings to W and t no direct contribution to these vertices. Note that assumption Eq. 6 is realized in type I 2HDM and also in the composite Higgs scenarios, where both top and bottom mix with the same representations of composite group, for example in the models (MCHM4,5) based on the $SO(5)/SO(4)$ coset we have

$$\begin{aligned} \text{MCHM 4}: \quad & a = c = \sqrt{1-\xi} \\ \text{MCHM 5}: \quad & a = \sqrt{1-\xi},\ c = \frac{1-2\xi}{\sqrt{1-\xi}}, \end{aligned} \tag{7}$$

where ($\xi = \frac{v^2}{f^2}$) and f is analogue of pion decay constant. To derive current constraints on the (a, c) parameters we assumed Bayesian approach and extracted likelihoods following the method suggested in [8]. The results are presented on the Figure 1.

We can see that for the Higgs mass above 130 GeV large part of the parameter space is excluded. Also note that for the light Higgs $m_h = 120, 130$ GeV iso-contours are not symmetric in $(c \Leftrightarrow -c)$, this is because of the $\gamma\gamma$ channel where we can probe the relative sign between a and c due to the interference of the diagrams with loops of W and loops of t.

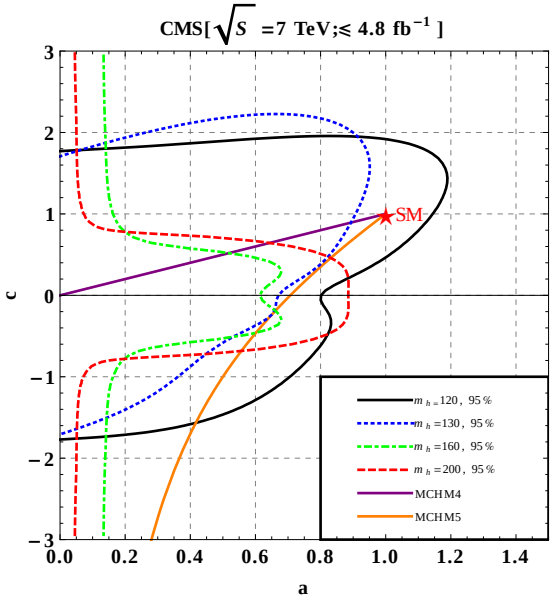

Figure 1: Current exclusions in the plane (a, c) for various Higgs masses as obtained with our method: the area to the right of each curve is excluded at 95% CL. These exclusions combine all search channels at CMS, with the full 2011 data set, purple and orange lines indicate MCHM4 and MCHM5 contours in the (a, c) plane

4 Excess at 125 GeV

Recently both collaborations ATLAS and CMS reported excess of events at $m_h \approx 125$ GeV, so it is interesting to know what we can learn about the couplings of this resonance with the current LHC data. On the Fig. 2 we plotted posterior probability fixed contours in the (a, c) plane. We can see that so far SM Higgs is well in agreement with the current data. Also note that due to the $\gamma\gamma$ channel probability contours are asymmetric in $(c \Leftrightarrow -c)$, and there is always a solution with negative c. Another interesting feature is a big difference between CMS and ATLAS plots near the fermiophobic line $c = 0$. This is due to the fact that CMS collaboration presents results for the exclusive searches in $\gamma\gamma$ and WW channels. For example, cuts requiring

[1] Note that this assumption is not as bad as it might seem, because only $O_{GG}, O_{BB}, O_{W,B}, O_{W(B)\partial H}$ are important for the single Higgs production, however constraints from S parameter require $O_{W,B}$ to be small. Also in the case when Higgs is a pNGB field, operators $O_{GG,(BB)}$ explicitly break shift symmetry and should be suppressed.

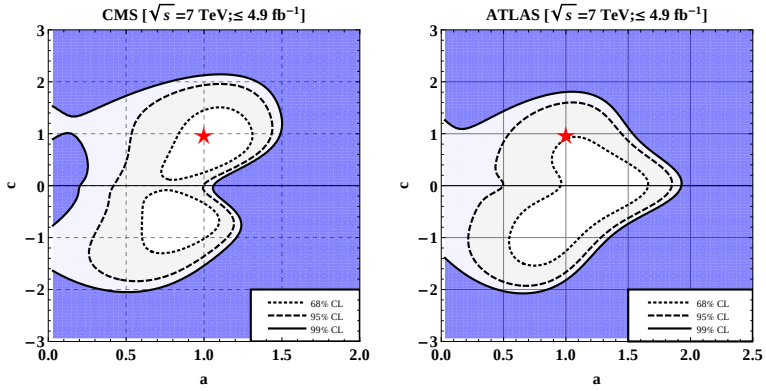

Figure 2: Isocontours of 68%, 95%, 99% probability in the (a, c) plane for 125 GeV Higgs coming from CMS (left) and ATLAS (right), Standard Model is indicated by star

two extra high p_T jets in the forward region in the final state help to select events produced mainly through the vector boson fusion mechanism, this allows us to probe a region of parameter space in the $c = 0$ region. This illustrates explicitly, how important exclusive analysis is for determining Higgs couplings in the future.

5 Summary

We reviewed current status of the BSM Higgs at LHC and analysed current constraints on the Higgs couplings from ATLAS and CMS at 5 fb^{-1}. Even now at low luminosity we can extract some information about the Higgs couplings, and constrain the parameter space of the composite models. This exercise demonstrates that exclusive analysis is essential in understanding the nature of the Higgs boson.

References

[1] ATLAS Collaboration, "Combined search for the Standard Model Higgs boson using up to 4.9 fb-1 of pp collision data at sqrt(s) = 7 TeV with the ATLAS detector at the LHC," arXiv:1202.1408 [hep-ex].

[2] CMS Collaboration, "Combination of CMS searches for a Standard Model Higgs boson" CMS-PAS HIG-11-032

[3] D. B. Kaplan, H. Georgi and S. Dimopoulos, Phys. Lett. B **136**, 187 (1984).

[4] G. F. Giudice, C. Grojean, A. Pomarol and R. Rattazzi, JHEP **0706**, 045 (2007) [hep-ph/0703164].

[5] L. Randall and R. Sundrum, Phys. Rev. Lett. **83**, 3370 (1999) [hep-ph/9905221].

[6] K. Agashe, R. Contino and A. Pomarol, Nucl. Phys. B **719**, 165 (2005) [hep-ph/0412089].

[7] R. Contino, C. Grojean, M. Moretti, F. Piccinini and R. Rattazzi, JHEP **1005**, 089 (2010) [arXiv:1002.1011 [hep-ph]].

[8] A. Azatov, R. Contino and J. Galloway, JHEP **1204**, 127 (2012) [arXiv:1202.3415 [hep-ph]].

Searches for BSM Higgs at CMS

J. Germander[1] on behalf of the CMS Collaboration

[1]Univ. of Oviedo, Spain

DOI: http://dx.doi.org/10.3204/DESY-PROC-2012-02/220

These proceedings report the results on the Higgs Searches beyond the standard model at the CMS experiment with data collected during the 2011 LHC run at 7 TeV, corresponding to an integrated luminosity of about 5 fb^{-1}. Results for several models are shown from analyses performed by the CMS collaboration. No significant deviation from the standard model is found and limits on the Higgs mass are set for each physics scenario.

1 Introduction

The standard model (SM) of Particle Physics describes very precisely the experimental measurements up to now but one of its key ingredient has not yet been observed: the Higgs boson, which is at the source of the electro-weak symmetry breaking and provides a mechanism to assign mass to particles. It is clear, however, that the SM theory breaks at larger scales and some major open points are the unification of couplings, hierarchy problem, dark matter issue and neutrino masses. Theories have been proposed that attempt to answer some of these open questions such as supersymmetry (SUSY) or other beyond standard model (BSM) scenarios and are currently under experimental test. The CMS experiment, a multi-purpose detector [1] operating at the CERN LHC pp collider, has been designed to investigate a wide range of physical phenomena. In these proceedings, the latest BSM Higgs searches at the CMS experiment will be briefly described. These results are achieved by the CMS collaboration with data collected in 2011 corresponding luminosity of about 5 fb^{-1}.

2 Minimal supersymmetric standard model Higgs

In the MSSM, the standard scalar Higgs boson is substituted by three neutral ϕ = (h,H,A) and two charged ($H^{\pm}$) Higgs particles and all decays to *down-type* fermions are enhanced by a factor of $tan\ \beta$. For relatively high $tan\ \beta$ the BR ($\phi \rightarrow \tau^{+}\tau^{-}$) is about 10% which is much lower than the corresponding branching ratio of the b-decay mode. Neutral MSSM Higgs bosons are searched in the di-tau final state which is preferred for its clear signature in the two leptons final states (electrons or muons) and in the lepton plus an hadronic decaying τ final state. The dilepton channel was searched in dimuons and in electron-muon final states. The hadronic τ is reconstructed in 1 and 3 prongs ($+N\pi^{0}$). To extract the di-tau mass a kinematic fit is applied to the measured components, including the missing energy, with an improvement of about 20% on the measured mass [2]. In Figure 1(left) is shown the exclusion plot for the neutral MSSM Higgs mass versus tan β. For $tan\ \beta = 20$ Higgs masses up to 300 GeV/$c^2$are excluded.

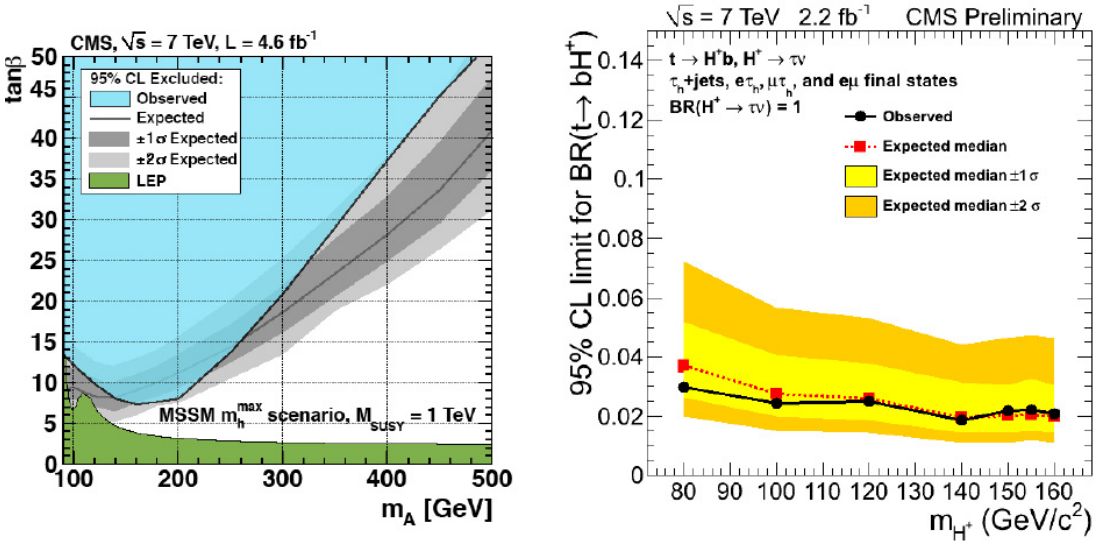

Figure 1: Left: Region in the parameter space of tan β versus m_A excluded at 95% CL in the context of the MSSM scenario. 95% CL upper limit and the expected one- and two-standard-deviation ranges are shown together with the observed excluded region. Right: Upper limit on BR($t \to bH^+$) assuming BR($H^+ \to \tau^+\nu$)=1 as a function of m_{H^+}). The yellow bands show the one and two sigma bands around the expected limit.

The charged MSSM Higgs bosons are searched in the top decays $t \to bH^\pm$ with the tau final states $H^+ \to \tau^+\nu$. The $t\bar{t}$ production yields with tau final states are modified by Higgs diagrams if the Higgs mass is lower than the top mass. The Higgs particle is searched in isolated τ decays plus b-jets and possibly an isolated lepton in the final state, depending on the second top decay chain in the $t\bar{t}$ events. Results from this analysis [3] on BR($t \to bH^+$) are shown in Figure 1(right). Values of BR($t \to bH^+$) $> 4\%$ are excluded for all the possible Higgs mass values.

3 Light pseudoscalar Higgs boson

The presence of a light pseudoscalar CP-odd Higgs a is predicted within the next to minimal supersymmetric extension to the standard model. This search [4] has been performed in the sidebands of the $\Upsilon \to \mu^+\mu^-$ dimuon decays, namely $5.5 < M(\mu\mu) < 9$ GeV/c^2 and $11.5 < M(\mu\mu) < 14$ GeV/c^2. A special high level trigger conceived for charmonium states studies was set up and this analysis was performed with a data sample corresponding to a luminosity of 1.3 fb^{-1}. Results are shown in Figure 2 with no excess found in the dimuon spectrum. An upper limit on the cross-section $\sigma(pp \to a \to \mu^+\mu^-)$ below 5 pb is set for all the masses in the two search intervals.

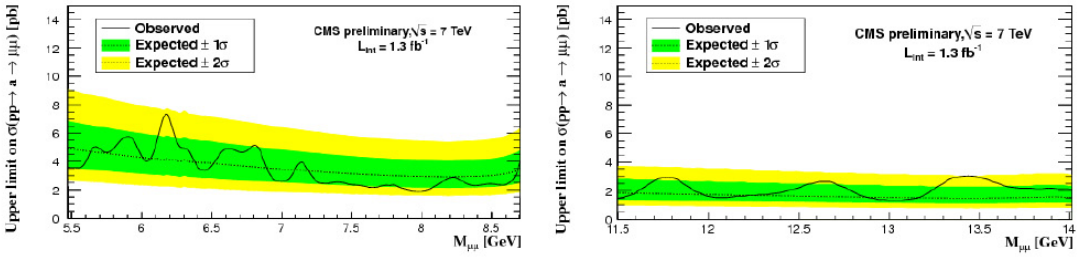

Figure 2: Limits on the cross-section $\sigma(pp \to a \to \mu^+\mu^-)$ for the two mass intervals in the Υ sidebands.

4 Doubly charged H^{++}

These exotic Higgs bosons are predicted within the *type II* see-saw model and are related to the presence of a light neutrino mass. H^{++} decay to two same charged leptons and obviously do not have any physical background in the SM. They are produced in pairs or together with a single charged Higgs through the processes: $Z/\gamma \to H^{++}H^{--}$ and $W^+ \to H^{++}H^-$ (charge conjugates included), giving a final states with four or three leptons, same charge resonant. No excess is observed in the CMS data. In Figure 3(left) are shown the mass limits for the different leptonic final states and four benchmark points of the see-saw mechanism [5].

5 Fermiophobic Higgs boson decays

In the Fermiophobic model the gluon-gluon process of Higgs production is forbidden and the production cross-section is suppressed by an order of magnitude with the Vector Boson Fusion (VBF) and the Higgs-strahlung (VH) that become the two most important contributions to Higgs production. On the other hand, the diphoton decay $H \to \gamma\gamma$ is enhanced by another order of magnitude. This analysis is based on the selection of two high p_T photons and three tag classes with electron, muon or dijets in the final states [6] corresponding to different decays in the associate production. The results are presented in Figure 3(right) and show a small excess at 126 GeV/c^2 which is diluted when the diphoton channel is combined [7] with $H \to WW, ZZ$. Two intervals of Higgs mass are excluded at 95% of C.L.: $110 < M_H < 124$ GeV/c^2 and $128 < M_H < 136$ GeV/c^2.

6 Other results

Other result to be mentioned here are the standard model SM4 extensions searches obtained including a fourth quark generation [7] that significantly increase the Higgs bosons production rate. The SM4 model is excluded at 95% CL from 120 up to 600 GeV/c^2 of Higgs masses.

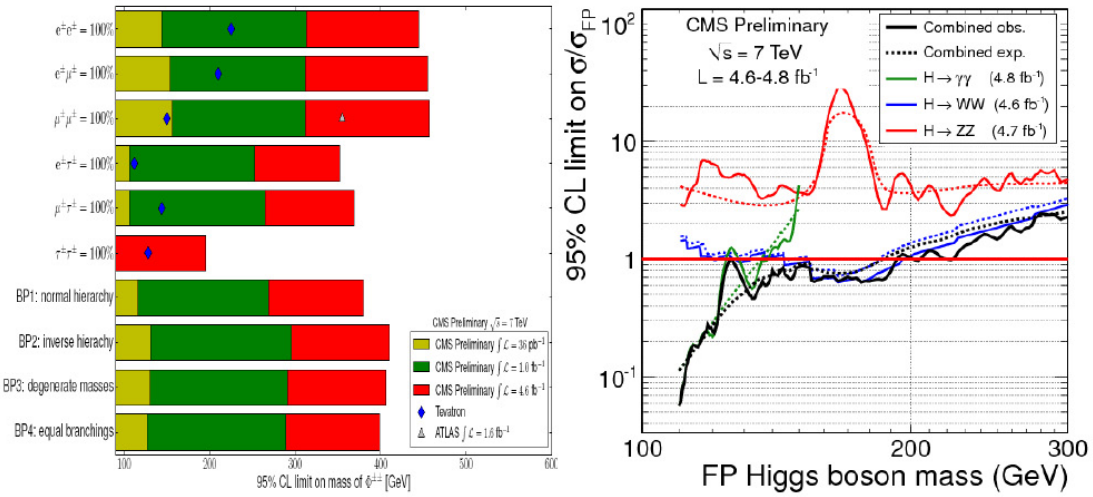

Figure 3: Left: Limits on the mass of the doubly charged Higgs bosons for different final states. Right: The 95% CL upper limits on the signal strength parameter $\mu = \sigma/\sigma_{FP}$ for the fermiophobic Higgs boson hypothesis as function of the Higgs boson mass with the contribution for the three explored Higgs boson decay modes in the full mass range.

7 Conclusions

A broad program of BSM Higgs bosons searches with CMS has been presented. Model independent inclusive searches together with well defined new physics scenarios have been probed during 2011 with a luminosity of about 5 fb^{-1}. A large fraction of the MSSM Higgs parameters are constrained by the $H \to \tau^+\tau^-$ analysis. A small excess on the $H \to \gamma\gamma$ is registered, compatible with a statistical fluctuation. No evidence for new BSM Higgs bosons is observed. The 2012 run, with about 15 fb^{-1} of data collected, will help to improve these searches.

References

[1] S. Chatrchyan *et al.* [CMS Collaboration], JINST **3** (2008) S08004.

[2] S. Chatrchyan *et al.* [CMS Collaboration], arXiv:1202.4083 [hep-ex], submitted to PLB.

[3] S. Chatrchyan *et al.* [CMS Collaboration], "Search for the light charged Higgs boson in top quark decays in pp collisions at sqrts = 7 TeV," CMS-PAS-HIG-11-019

[4] S. Chatrchyan *et al.* [CMS Collaboration], "Search of a light pseudoscalar Higgs boson in the dimuon channel," CMS-PAS-HIG-12-004

[5] S. Chatrchyan *et al.* [CMS Collaboration], "Search for Doubly Charged Higgs," CMS-PAS-HIG-12-005

[6] S. Chatrchyan *et al.* [CMS Collaboration], "Search for the fermiophobic model Higgs boson decaying into two photons," CMS-PAS-HIG-12-002

[7] S. Chatrchyan *et al.* [CMS Collaboration], "Combination of SM, SM4, FP Higgs boson searches," CMS-PASHIG-12-008

Searches for Beyond-Standard Model Higgs bosons at ATLAS

Bruno Lenzi[1] on behalf of the ATLAS Collaboration

[1]CERN, 1211 Genève 23, Switzerland

DOI: http://dx.doi.org/10.3204/DESY-PROC-2012-02/74

The results of the searches for Higgs bosons beyond the Standard Model with the ATLAS detector, based on the 2011 proton-proton collision data recorded at the Large Hadron Collider (LHC) at a centre-of-mass energy of 7 TeV are reported. No significant excess is observed and exclusion limits are set on the production cross section times branching ratio of neutral Higgs bosons from a fermiophobic benchmark model and the minimal supersymmetric model (MSSM), as well as singly and doubly-charged Higgs bosons.

Introduction

In order to reveal the mechanism responsible for the electroweak symmetry breaking, the ATLAS experiment [1] has carried out an extensive program of searches for Higgs bosons using LHC collision data recorded in 2011. In addition to the search for the Standard Model (SM) scalar boson, the existence of Higgs particles predicted by two Higgs doublet [2] (in particular the MSSM [3]), Higgs triplet [4] models and others was investigated. Results of the searches for fermiophobic Higgs bosons, neutral MSSM Higgs bosons, charged and doubly-charged Higgs bosons are presented below.

1 Fermiophobic Higgs boson

A fermiophobic benchmark model, in which the Higgs field does not couple to fermions while the couplings to bosons are kept at their SM values, allows a generic investigation of scenarios in which the Higgs field couplings to some or all fermion generations are suppressed. ATLAS has looked for fermiophobic Higgs bosons, produced via vector boson fusion or associated with W or Z bosons, in the diphoton decay channel using 4.9 fb^{-1} of collision data [5].

The overal sensitivity is dominated by events with high diphoton transverse momentum with respect to the thrust axis ($p_{\mathrm{Tt}} > 40$ GeV). The corresponding diphoton invariant mass spectrum in the range 100 – 160 GeV is shown in Fig. 1a. The background model from an exponential function and the expected signal (with a resolution of about 1.5 GeV), modelled by the sum of a Crystal-Ball and a wide Gaussian, are also shown. The largest excess with respect to the background-only hypothesis is found at 125.5 GeV (Fig. 1b), with a local significance of 2.9 standard deviations, which reduces to 1.6 standard deviations when taking into account the look-elsewhere effect. The data exclude the fermiophobic Higgs model in the ranges 110.0 – 118.0 GeV and 119.5 – 121.0 GeV at 95% confidence level (CL), as shown in Fig. 1c.

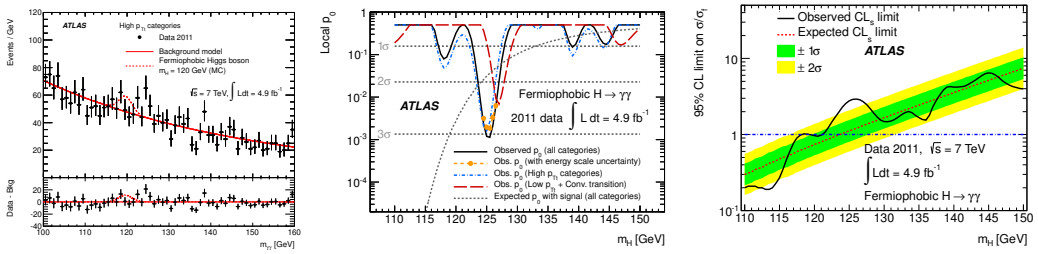

(a) (b) (c)

Figure 1: (a) Diphoton invariant mass spectrum for the high p_{Tt} categories, overlaid with the background model and the expected fermiophobic Higgs boson signal ($m_H = 120$ GeV) [5]. (b) Observed and median expected local p_0 and (c) 95% CL exclusion limits normalised to the fermiophobic cross section times branching ratio expectation σ_{f} as a function of the fermiophobic Higgs boson mass m_H [5].

2 Neutral MSSM Higgs bosons

A search for neutral MSSM Higgs bosons ($A/H/h$) decaying to pairs of τ-leptons was performed using 1.06 fb^{-1} of integrated luminosity [6]. Four final states with opposite-charged τ-lepton candidates, reconstructed by their decays to leptons (electrons or muons, $\ell = e, \mu$) or hadrons (τ_{had} in the following), were considered ($e\mu$, $e\tau_{\mathrm{had}}$, $\mu\tau_{\mathrm{had}}$ and $\tau_{\mathrm{had}} + \tau_{\mathrm{had}}$).

Background events from QCD processes and Z boson decays were suppressed by requiring a minimum amount missing transverse energy, while specific cuts depending on the final state were applied to reject processes like W + jets, diboson and top-quark decays. Data-driven techniques were used in the estimation of the background from QCD processes and the irreducible background from $Z \to \tau\tau$ decays. The presence of a possible signal was investigated using the di-τ invariant mass spectrum, reconstructed using different techniques for each final state. The sum of the spectra of the $e\tau_{\mathrm{had}}$ and $\mu\tau_{\mathrm{had}}$ final states, reconstructed using the Missing Mass Calculator (MMC), is shown in Fig. 2a.

The observed number of events in each final state and their sum are consistent with the expected background. Exclusion limits for the production of MSSM $A/H/h$ bosons as a function of the parameters m_A and $\tan\beta$ in the maximal mixing scenario ($m_{\mathrm{h}}^{\mathrm{max}}$) [7] are shown in Fig. 2b.

3 Charged Higgs bosons

ATLAS has performed a model-independent search for charged Higgs bosons ($H^{\pm}$) using 4.6 fb^{-1} of collision data [8]. Charged Higgs bosons with masses in the range 90 – 160 GeV could be produced in top-quark pair events ($t\bar{t} \to b\bar{b}H^{\pm}W^{\mp}$) and can decay via $H^+ \to \tau\nu$. Both leptonically or hadronically decaying τ-leptons and W bosons were considered, except for both τ and W decaying leptonically, leading to the final states e/μ + jets, $\tau_{\mathrm{had}} + e/\mu$ and τ_{had}+ jets.

A dedicated event selection for each final state was applied in order to reject non-$t\bar{t}$ backgrounds. The discrimination between W and H^+ decays relied on the amount of missing transverse energy ($E_{\mathrm{T}}^{\mathrm{miss}}$) or on the transverse mass (m_{T}) of the τ-lepton and the $E_{\mathrm{T}}^{\mathrm{miss}}$. The

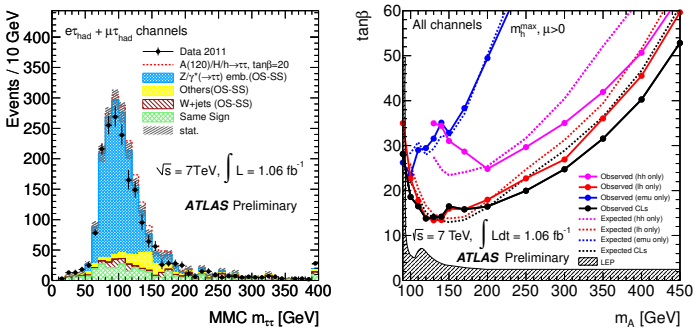

(a) (b)

Figure 2: (a) MMC mass distribution for the sum of the $e\tau_{\rm had}$ and $\mu\tau_{\rm had}$ final states, compared with the background expectation and overlaid with the expected MSSM signal for $m_A = 120$ GeV, $\tan\beta = 20$ [6]. (b) Expected and observed 95% CL exclusion limits in the $m_A - \tan\beta$ plane of the MSSM for the individual $e\mu$, $e\tau_{\rm had} + \mu\tau_{\rm had}$ (ℓh) and $\tau_{\rm had}\tau_{\rm had}$ (hh) analyses and their combination [6].

$m_{\rm T}$ distribution for the $\tau_{\rm had}$+ jets final state is shown in Fig. 3a. Data-driven methods were used in the estimation of the multi-jet background, backgrounds with misidentified leptons or hadronically decaying τ-leptons, as well as backgrounds with true τ-leptons.

Assuming a branching ratio of the charged Higgs boson to a τ-lepton and a neutrino $B(H^+ \to \tau\nu) = 100\%$, upper limits on the branching ratio of top-quark decays to a b-quark and a charged Higgs boson are set between 5% and 1% for charged Higgs boson masses ranging from 90 GeV to 160 GeV, respectively (Fig. 3b). In the context of the MSSM $m_{\rm h}^{\rm max}$ scenario, values of $\tan\beta$ above 12 – 26, as well as between 1 and 2 – 6, are excluded for charged Higgs boson masses between 90 GeV and 150 GeV (Fig. 3c).

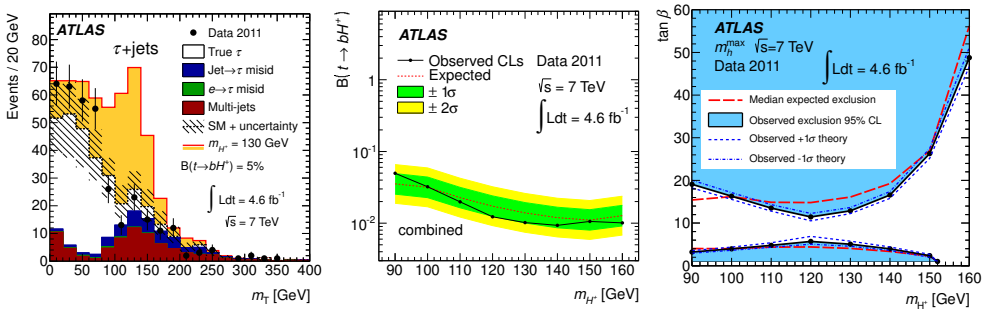

(a) (b) (c)

Figure 3: (a) Distribution of $m_{\rm T}$ in the τ+jets channel, overlaid with the expected background and signal ($m_{H^+} = 130$ GeV, $B(t \to bH^+) = 5\%$) [8]. (b) Expected and observed 95% CL exclusion limits as a function of m_{H^+} on $B(t \to bH^+)$ assuming $B(H^+ \to \tau\nu) = 100\%$ [8]. (c) Expected and observed 95% CL limits on $\tan\beta$ for the $m_{\rm h}^{\rm max}$ scenario [8].

4 Doubly-charged Higgs bosons

A search for doubly-charged Higgs bosons decaying to same-sign dimuons was performed using 1.6 fb^{-1} of collision data [9], looking for a narrow resonance in the dimuon invariant mass spectrum. The contribution of SM processes giving rise to high-p_{T} prompt (from τ-lepton, W or Z-boson decays) like-sign dimuons, such as WZ, ZZ, $W^{\pm}W^{\pm}$ and $t\bar{t}W$, was estimated using Monte Carlo simulations. The background from semi-leptonic b- or c-hadron decays, muons from pion or kaon decays in flight, and misidentified muons from hadronic showers in the calorimeter was estimated from data. Backgrounds where the charge of one of the two muons is misidentified are negligible in the relevant mass range.

The distribution of the invariant mass of the muon pair $m(\mu\mu)$, shown in Fig. 4a, is found to agree well with the background expectation. Limits on the cross section times branching ratio of pair production of doubly-charged Higgs bosons ($pp \to H^{++}H^{--}$) via a virtual Z/γ^* exchange are shown in Fig. 4b, for the doubly-charged Higgs boson mass range 100 – 400 GeV. The observed upper limit is 11 fb (1.7 fb) at $m(H^{++}) = 100$ GeV (400 GeV). The lower mass limit on doubly-charged Higgs bosons with a 100% (33%) branching ratio to muons is 355 (244) GeV and 251 (209) GeV for H^{++} bosons coupling to left-handed and right-handed fermions, respectively.

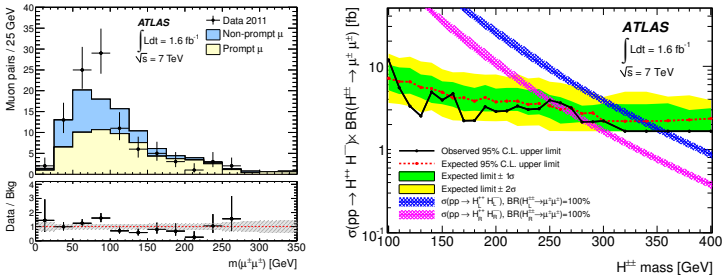

(a) (b)

Figure 4: (a) Distribution of the dimuon invariant mass for $\mu^{\pm}\mu^{\pm}$ pairs [9]. (b) Upper limit at 95% CL on the cross section times branching ratio for pair production of doubly-charged Higgs bosons decaying to two muons [9].

References

[1] ATLAS Collaboration. JINST **3** (2008) S08003.

[2] T. D. Lee. Phys. Rev. D **8** (1973) 1226–1239.

[3] H. Haber and G. Kane. Phys. Rep. **117** (1985) 75 – 263.

[4] T. P. Cheng and L.-F. Li. Phys. Rev. D **22** (1980) 2860–2868.

[5] ATLAS Collaboration. `arXiv:1205.0701 [hep-ex]`.

[6] ATLAS Collaboration. ATLAS-CONF-2011-132, https://cdsweb.cern.ch/record/1383835 .

[7] M. S. Carena *et al.* Eur.Phys. J. C. **26** (2003) 601–607, `arXiv:hep-ph/0202167 [hep-ph]`.

[8] ATLAS Collaboration. `arXiv:1204.2760 [hep-ex]`.

[9] ATLAS Collaboration. Phys. Rev. D **88** (2012) 032004, `arXiv:1201.1091 [hep-ex]`.

Search for low-mass Higgs states @ *BABAR*

Valentina Santoro[1]

[1]INFN Ferrara, via Saragat 1, 44122 Ferrara, Italy

DOI: http://dx.doi.org/10.3204/DESY-PROC-2012-02/187

Several types of new-physics models predict the existence of light dark matter candidates and low-mass Higgs states. Previous *BABAR* searches for invisible light-Higgs decays have excluded large regions of model parameter space. We present searches for a dark-sector Higgs produced in association with a dark gauge boson and searches for a light Higgs in $\Upsilon(nS)$ decays.

1 Search for Low-Mass Dark Matter at *BABAR*

We have now an overwhelming astrophysical evidence of dark matter. To explain this experimental evidence many theoretical models [1] introducing new dark forces mediated by new gauge boson have been introduced. These models propose Weakly Interacting Massive Particles (WIMPs) that can annihilate into pairs of dark bosons, which subsequently annihilate to lepton pairs (protons are kinematically forbidden). One of this model [2, 3] introduce a new dark sector that couples to the SM with a dark boson (i.e. the dark photon A') through a small kinetic mixing term. Thanks to their large luminosities and low-background environment the B-factories offer an ideal place to probe for MeV-GeV dark matter, complementing searches from LHC. The dark boson mass is generated via the Higgs mechanism, adding a dark Higgs boson ($h^{'}$) to the theory. The dark photon and the Higgs bosons could have a comparable mass (GeV-scale). A very minimal scenario has a single dark photon and a single dark Higgs boson. In the *BABAR* analysis [4] we make use of the *Higgsstrahlung* process $e^+e^- \to A^{'*} \to A^{'}h^{'}$, $h^{'} \to A^{'}A^{'}$ using 521 fb^{-1}. The signal is either fully reconstructed into lepton or pion pair (exclusively mode), or partially reconstructed (inclusive mode). Only two of the three hidden photons are reconstructed in the latter case, and the four-momentum of the third one is identified to that of the recoiling system.

In these searches no significant signal is observed. Using uniform priors in the cross section upper limits on the $e^+e^- \to A^{'*} \to A^{'}h^{'}$, $h^{'} \to A^{'}A^{'}$ cross section are obtained as a function of the hidden Higgs and hidden photon masses. These limits on the cross section are translated into 90 % upper limit on $\alpha_{\rm D}\epsilon^2$ shown in Fig. 1, where $\alpha_{\rm D} = g_{\rm D}2/4\pi$, $g_{\rm D}$ is the dark sector gauge coupling, ϵ is the mixing strength. Values down to 10^{-10} - 10^{-8} are excluded for a large range of hidden photon and hidden Higgs masses, assuming prompt decay. Assuming $\alpha_{\rm D} = \alpha \simeq 1/137$, limits on the mixing strength in the range 10^{-4} - 10^{-3} are derived as shown in Fig. 2, these limits are an order of magnitude smaller than the current experimental bounds extracted from direct photon production in this mass range.

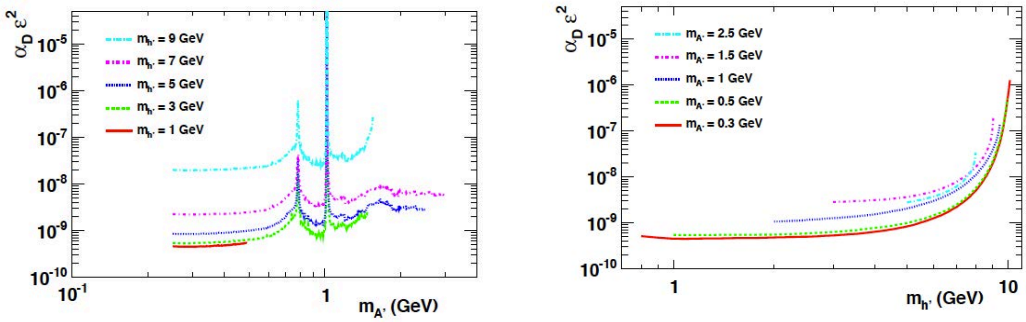

Figure 1: Limits on $\alpha_D \epsilon^2$ for the Dark Photon (left) and Dark Higgs (right).

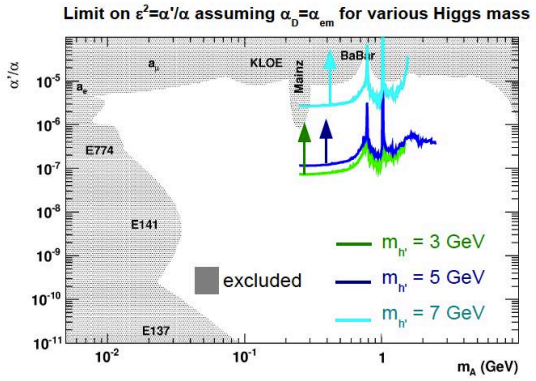

Figure 2: Limit on the mixing strength, ϵ^2, for various Higgs masses.

2 Search for light Higgs @ *BABAR*

In recent years a number of theoretical models [5] predicted for the existence of a light CP-odd Higgs boson A^0 related to the Next-to-Minimal Supersymmetric Model (NMSSM). Direct searches constrain the mass of $m_{A^0} < 2m_b$, where m_b is the b quark and the decay of $A^0 \to b\bar{b}$ is forbidden. Of particular interest is to search the lightest CP-odd Higgs boson in Υ decays such as $\Upsilon(nS) \to \gamma A^0$, where $A^0 \to SM$ particles. In these $\Upsilon(nS)$ transitions low mass Dark Matter Candidate (χ) can be also directly produced (i.e. $\Upsilon(nS) \to \chi\chi$). The large data sets available at *BABAR* experiment with more than 500 fb^{-1} of data at the $\Upsilon(4S)$, $\Upsilon(3S), \Upsilon(2S)$ resonances and just below the $\Upsilon(4S)$ resonance allow us to place stringent constraints on such theoretical models.
We searched for light Higgs in *BABAR* using two-body-radiative decay on Υ states. The key experimental signature is the monochromatic photon in the CM frame $E^*_\gamma = \frac{m_\Upsilon - m^2_{A^0}}{2m_\Upsilon}$. With this analysis technique we searched for the following transitions:

- $\Upsilon(2S, 3S) \to \gamma A^0,\ A^0 \to \mu^+\mu^-$ [6]

- $\Upsilon(2S,3S) \to \gamma A^0,\ A^0 \to \tau^+\tau^-$[7]
- $\Upsilon(2S,3S) \to \gamma A^0,\ A^0 \to$ hadrons[8]

In all the searches we did not find any evidence of signals but upper limits versus hypothesis mass have been extracted the results are shown in Fig. 3 for the $A^0 \to \mu^+\mu^-$, in Fig. 4 for the $A^0 \to \tau^+\tau^-$ (where τ is reconstructed both in $\tau \to e\nu\bar{\nu}$ and $\tau \to \mu\nu\bar{\nu}$) and in Fig. 5 for the $A^0 \to$ hadrons.

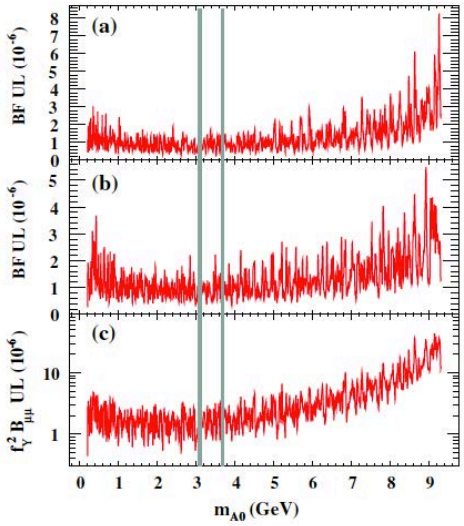

Figure 3: 90 % C.L. upper limits on (a) $\mathcal{B}(\Upsilon(2S) \to \gamma A^0) \times \mathcal{B}_{\mu^+\mu^-}$, (b) $\mathcal{B}(\Upsilon(3S) \to \gamma A^0) \times \mathcal{B}_{\mu^+\mu^-}$ and (c) effective coupling $f_\Upsilon^2 \times \mathcal{B}_{\mu^+\mu^-}$ as a function of m_{A^0}. The shaded areas show the regions around the J/ψ and the $\psi(2S)$ resonances excluded from the search.

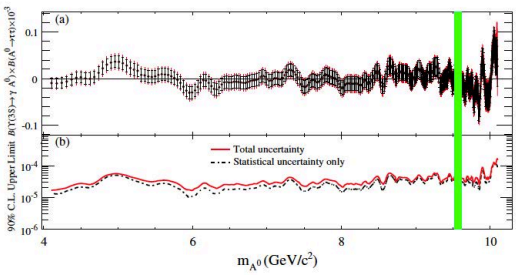

Figure 4: (a) Product branching fractions as a function of the Higgs mass. (b) The corresponding 90% C.L. upper limits on the product of the branching fractions versus the Higgs mass values.

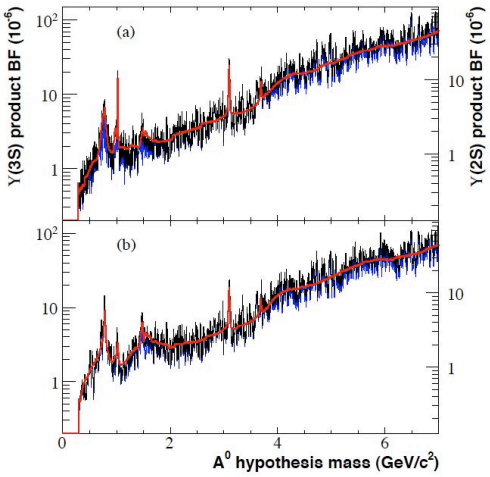

Figure 5: 90 % C.L. upper limits on product branching fractions (BF) (left axis) $\mathcal{B}(\Upsilon(3S) \to \gamma A^0)\ \mathcal{B}(A^0 \to hadrons)$ and (right axis) $\mathcal{B}(\Upsilon(2S) \to \gamma A^0)\ \mathcal{B}(A^0 \to hadrons)$ for (a) CP-all analysis and (b) CP-odd analysis.

3 Conclusion

We have searched for evidence of dark sector candidates and evidence of CP-odd light Higgs in the $\Upsilon(2S)$ and $\Upsilon(3S)$ data sample at *BABAR* . We did not observe any significant signal but more stringent limit have been set on space parameters of NP model.

References

[1] B. Batell, M. Pospelov and A. Ritz, Phys. Rev. D **79**, 115008 (2009)

[2] N. Arkani-Hamed, D. P. Finkbeiner, T. R. Slatyer and N. Weiner, Phys. Rev. D **79**, 015014 (2009)

[3] R. Essig, P. Schuster and N. Toro, Phys. Rev. D **80**, 015003 (2009)

[4] arXiv:1202.1313 [hep-ex]]

[5] R. Dermisek, J. F. Gunion and B. McElrath, Phys. Rev. D **76**, 051105 (2007)

[6] B. Aubert *et al.* , Phys. Rev. Lett. **103**, 081803 (2009)

[7] B. Aubert *et al.*, Phys. Rev. Lett. **103**, 181801 (2009)

[8] J. P. Lees *et al.* , Phys. Rev. Lett. **107**, 221803 (2011)

BSM Higgs and other Bump Searches at the Tevatron

Émilien Chapon[1] on behalf of the CDF and DØ collaborations

[1]CEA, F91191 Gif-sur-Yvette, France

DOI: http://dx.doi.org/10.3204/DESY-PROC-2012-02/279

In Beyond Standard Model (BSM) theories such as supersymmetry, the electroweak symmetry breaking mechanism predicts one or several Higgs bosons with different masses and couplings to other particles compared to the Standard Model (SM) one. We present the constraints on BSM theories originating from searches for exotic Higgs bosons from the CDF and D0 collaborations at the Tevatron. In addition, searches for excesses in other channels will also be presented, such as in the dijet mass spectrum in W+2jets events.

The Minimum Supersymmetric Standard Model (MSSM) requires two Higgs doublets, which couple to respectively up-type and down-type quarks, with vacuum expectation values (vev) of respectively v_u and v_d. The ratio of the two vevs is denoted $\tan\beta = \frac{v_u}{v_d}$. It is worth noting that large values of $\tan\beta$ look natural, as for instance $\tan\beta \approx \frac{m_t}{m_b} \approx 35$.

In the MSSM, there are five physical Higgs bosons: three neutral (denoted H, h and A) and two charged (H^+ and H^-). The three neutral Higgs bosons are collectively denoted ϕ.

A nice feature of the coupling of the Higgs boson to b quarks is that it is enhanced with $\tan\beta$, which leads to an enhanced production cross section $\sigma(p\bar{p} \to \phi)$ compared to the Standard Model. In addition to this effect, two of the three neutral Higgs bosons become degenerate in mass, which effectively doubles the production cross-section. Finally, the branching ratio is also modified: at high $\tan\beta$, we have $\mathcal{B}(\phi \to b\bar{b}) \approx 90\%$ and $\mathcal{B}(\phi \to \tau^+\tau^-) \approx 10\%$, while other decay modes are suppressed compared to the SM.

At tree level, the MSSM Higgs sector is fully described by two parameters: $\{m_A, \tan\beta\}$. However, radiative corrections make it more model-dependent for the $\phi \to b\bar{b}$ decay mode.

1 MSSM

Searches for a MSSM neutral Higgs boson are performed by both the CDF and DØ experiments in its main decay channels.

$\phi \to \tau\tau$ **(inclusive):** An inclusive $\phi \to \tau\tau$ search has been performed by both the CDF (in the $\tau_\mu\tau_{\rm had}$, $\tau_e\tau_{\rm had}$, $\tau_e\tau_\mu$ final states [1]) and DØ (in the $\tau_e\tau_\mu$, $\tau_\mu\tau_{\rm had}$ [2] and $\tau_\mu\tau_{\rm had}$ [3] final states) experiments. Both experiments did not find any excess in the visible mass spectrum $M_{\rm vis} = \sqrt{(P_{\tau_{\rm h}} + P_{\tau_\mu} + \not\!\!E_T)^2}$. The dominant backgrounds are Z+jets, but also multijet and $t\bar{t}$.

$b\phi \to b\bar{b}b$ **(associated production):** At high $\tan\beta$, the coupling of the Higgs boson to b quarks is such that $\mathcal{B}(\phi \to b\bar{b}) \approx 90\%$. However, despite of this large branching ratio, and hence relatively large signal, this channel suffers from a very large multijet background, which is also challenging to model because of the large theoretical uncertainties on multijet processes

cross sections. To make this analysis possible, both CDF [4] and DØ [5] experiments actually look for the associated production of the MSSM Higgs boson with a b quark (respectively with $2.6\,\mathrm{fb}^{-1}$ and $5.2\,\mathrm{fb}^{-1}$ of data), so that the experimental signature is three to four jets with high transverse momentum p_T, out of which at least three must be b-tagged. The flavor composition of the multijet background is fit using data.

Both experiments use the invariant mass of two of the b-tagged jets to set limits on the production cross section times branching ratio $\sigma(p\bar{p} \to \phi + b_{\mathrm{jet}}) \times \mathcal{B}(\phi \to b\bar{b})$. CDF chooses to consider the two jets with the highest transverse momentum, while DØ uses a likelihood to discriminate signal from background and choose the pair which most likely comes from a Higgs boson decay.

Both experiments see an excess, CDF around 120 GeV with a local significance of $2.0\,\sigma$ and DØ with a local significance of $1.9\,\sigma$. In order to further investigate this excess, a Tevatron combination is in progress, as well as updates to these analyses.

$b\phi \to b\tau\tau$ **(associated production):** There are several motivations for performing a search for $b\phi \to b\tau\tau$. Compared to $b\phi \to b\bar{b}b$, the results obtained are much less sensitive to model parameters. Moreover this final state benefits from a lower $Z \to \tau\tau$ background compared to the inclusive $\phi \to \tau\tau$ search, thanks to the use of b-tagging.

For these reasons the DØ experiment has performed this analysis in the $\tau_e\tau_{\mathrm{had}}$ ($3.7\,\mathrm{fb}^{-1}$, Preliminary) and $\tau_\mu\tau_{\mathrm{had}}$ ($7.3\,\mathrm{fb}^{-1}$ [6]) final states. To get the best sensitivity from data, the analyzers use multivariate techniques: the multijet and $t\bar{t}$ backgrounds are rejected using two dedicated discriminants, while, because no excess over background is found, limits are set using a final discriminant.

Combination: The DØ experiment has done a combination of different MSSM Higgs searches [3], combining $b\phi \to b\bar{b}b$ ($5.2\,\mathrm{fb}^{-1}$), $b\phi \to b\tau_\mu\tau_{\mathrm{had}}$ ($7.3\,\mathrm{fb}^{-1}$) and $\phi \to \tau_\mu\tau_{\mathrm{had}}$ ($7.3\,\mathrm{fb}^{-1}$).

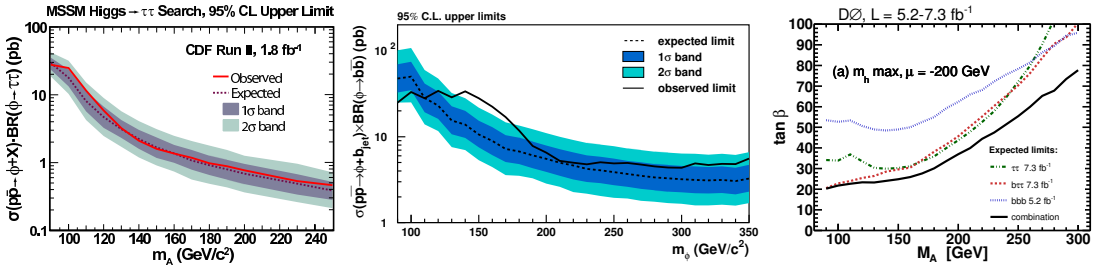

Figure 1: Left: Expected and observed limits on $\sigma(p\bar{p} \to \phi + X) \times \mathcal{B}(\phi \to \tau\tau)$ from CDF [1]. Middle: Expected and observed limits on $\sigma(p\bar{p} \to b + \phi) \times \mathcal{B}(\phi \to b\bar{b})$ from CDF [4]. Right: expected limits on MSSM parameters in the $(m_A, \tan\beta)$ plan from DØ [3]. The contributions from the channels entering the combination are also shown.

2 Looking for excesses in other channels

Analyzers have also looked for resonances predicted by other models.

Hidden Valley: The CDF experiment has looked for Hidden Valley particles ($5.8\,\mathrm{fb}^{-1}$, Preliminary [7]), denoted HV. These are long-lived heavy particles ($c\tau \approx 1\,\mathrm{cm}$), which decay into a pair of b quarks: HV $\to b\bar{b}$. Displaced vertex variables are used, relying on the b-jets

impact parameter and the reconstructed HV particle decay length. No excess is found and limits are set on the production cross section.

Doubly-charged Higgs: The models implementing two Higgs triplets predict doubly-charged Higgs bosons, which have been considered by the DØ experiment [8] using up to 7.0 fb^{-1} of data. The branching ratio of such particle depends on the model, but the analysis requires two hadronic taus and one muon in the final state, making it the first analysis looking for $H^{\pm\pm} \to \tau_{\rm had}\tau_{\rm had}X$ at a hadronic collider. The analysis is split into four channels, depending on the nature of the two same-sign leptons and on the presence or not of additional leptons. No evidence for signal has been found.

Fermiophobic Higgs search: Various models predict a Higgs boson with reduced, or even forbidden, couplings to fermions. In particular, assuming no coupling to fermions the gluon fusion mode $gg \to H_f$ is forbidden, because of the absence of coupling to heavy quarks. Another feature is that only decays to bosons are allowed (there is no $H_f \to ff$ decay), and hence the branching ratio $\mathcal{B} \to \gamma\gamma$ is greatly enhanced, making this channel dominate the exclusion.

Both the CDF and DØ experiments have released a preliminary result [9, 10] in this model in the $\gamma\gamma$ final state using the full Tevatron dataset (9.7-10 fb^{-1}). DØ uses a decision tree to set limits, and models the background using Monte-Carlo simulations. CDF uses the invariant mass $M_{\gamma\gamma}$ of the two photons to set limits, and estimates the background via a sideband fitting, with a sliding window shadowing the signal region. No excess is found and the Tevatron combination [11] excludes a fermiophobic Higgs mass below 119 GeV/c^2 at 95% C.L.

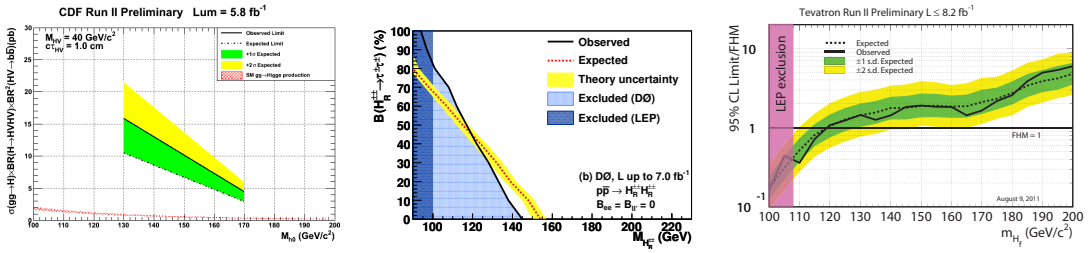

Figure 2: Left: limits on $\sigma gg \to H \times \mathcal{B}(H \to \mathrm{HVHV}) \times \mathcal{B}^2(\mathrm{HV} \to b\bar{b})$ as a function of M_{h_0} as measured from CDF. Middle: limits on $\mathcal{B}(H_R^{\pm\pm} \to \tau^\pm\tau^\pm)$ as a function of M_H, from DØ [8]. Right: Combined Tevatron limits [11] on the fermiophobic Higgs production cross-section, divided by the prediction of the fermiophobic Higgs model, as a function of m_{h_f}.

Dijet mass spectrum in $W + jj$ events: The CDF experiment has found an excess in the dijet mass spectrum in $W + jj$ events, published with 4.3 fb^{-1} [12] and updated to 7.3 fb^{-1}, which they can fit by a Gaussian resonance with cross section $\sigma = 3.1 \pm 0.8$ pb. The DØ experiment, however, has done the same analysis [13] and has excluded the presence of a resonance in this final state that would have a cross-section greater than 4 pb.

Despite many studies, this disagreement between both experiments has not been fully understood yet. CDF is performing several independent analyses with the full dataset to make a final statement on the subject. If the excess is confirmed, DØ will also update its result with the full dataset.

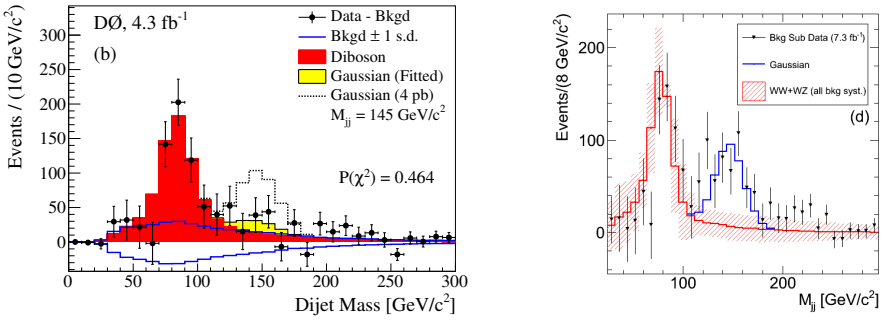

Figure 3: Left: background-subtracted dijet mass spectrum measured by DØ in $W + jj$ events [13], showing the diboson contribution in red. The contribution from a Gaussian signal, which cross-section times branching ratio is either fitted to the data or fixed to 4 pb, is also shown. Right: similar plot from CDF [12], with the fitted contribution from the Gaussian signal.

Conclusion

We have reported selected results from the CDF and DØ BSM Higgs searches. The Higgs sector is a good place to look for new physics, because BSM theories predict Higgs bosons with different properties than the Standard Model one. In the case of the MSSM, analyzers look for its main decay channels at high $\tan\beta$, i.e. $\phi \to b\bar{b}$ and $\phi \to \tau^+\tau^-$. The results from these different analyses can be combined in order to obtain the best sensitivity possible. We have also presented the results in other BSM theories: Hidden Valley, doubly-charged Higgs and fermiophobic Higgs. At last, we have reported the status of the bump search in the dijet mass spectrum of $W + jj$ events.

Most of these results will be legacy results from the Tevatron. However there are still updates to come, for instance from the $b\phi \to b\bar{b}b$ analysis or from a fermiophobic Higgs Tevatron combination with the full Run II dataset.

References

[1] CDF Collaboration, Phys. Rev. Lett. **103** (2009) 201801.
[2] DØ Collaboration, Phys. Lett. **B707** (2011) 323.
[3] DØ Collaboration, Phys. Lett. **B710** (2012) 569.
[4] CDF Collaboration, Phys. Rev. **D85** (2012) 032005.
[5] DØ Collaboration, Phys. Lett. **B698** (2011) 97.
[6] DØ Collaboration, Phys. Rev. Lett. **107** (2011) 121801.
[7] CDF Public Note 10356.
[8] DØ Collaboration, Phys. Rev. Lett. **108** (2012) 021801.
[9] CDF Public Note 10731.
[10] DØ Conference Note 6297-CONF.
[11] Tevatron New Phenomena & Higgs Working Group, `hep-ex/1109.0576`
[12] CDF Collaboration, Phys. Rev. Lett. **106** (2011) 171801.
[13] DØ Collaboration, Phys. Rev. Lett. **107** (2011) 011804.

Some Z' and W' Models facing current LHC Searches

Ennio Salvioni[1,2]

[1]Theory Division, Physics Department, CERN, CH-1211 Geneva 23, Switzerland
[2]Dipartimento di Fisica e Astronomia, Università di Padova and INFN,
Via Marzolo 8, I-35131 Padova, Italy

DOI: `http://dx.doi.org/10.3204/DESY-PROC-2012-02/177`

We present the implications of data collected by ATLAS and CMS in 2011 on some classes of Z' and W' models. We remark how the strongest bounds, coming for example from searches in final states containing leptons, do not apply to some theoretically well-motivated resonances, and discuss where signals from such states would appear.

1 Introduction and summary

Heavy vectors appear in an extremely large variety of New Physics models, with very different motivations, properties, and signatures. This implies that many interesting cases need to be left out of this short review, including all colored states. In this contribution we will discuss the implications of the data recorded by ATLAS and CMS in 2011[1] on some classes of Z' and W', which can be broadly defined as color-neutral spin-1 states with electric charge zero and one respectively.

The absence of any signal in data (except perhaps the hints of a Higgs boson with mass around 125 GeV, see Refs. [1, 2]) implies that strong bounds can be set on some models. An example is given by heavy vectors that are sizably coupled to light quarks and decay into experimentally straightforward final states, such as $\ell^+\ell^-$ or $\ell\,\nu\,(\ell = e, \mu)$. We will discuss in Sec. 2 a class of models, known as *minimal* Z' [3], which satisfy these conditions and point out that, in agreement with the estimate of Refs. [4, 5], the LHC has already started probing regions of its parameter space which are allowed by Electroweak Precision Tests (EWPT) and at the same time are compatible with a Grand Unified Theory (GUT) origin of the Z'. While this type of Z' appears in many motivated New Physics models, including GUTs and string constructions with intersecting D-branes, in these theories there is no compelling reason that forces the resonances to be at the TeV scale. This is not the case in strongly-coupled extensions of the Standard Model (SM), where a new strong interaction is involved in the breaking of the EW symmetry. An interesting possibility is that the Higgs be a pseudo-Goldstone boson of a spontaneously broken global symmetry in the strong sector, as this would explain the Little Hierarchy between the scale of the strong sector and the Higgs mass. See Ref. [6] for an introduction and an extensive list of references. In this framework, naturalness forces the scale of resonances to be not too far from the EW scale, otherwise the fine-tuning in the Higgs mass becomes inacceptable. Although these are welcome news for the LHC, the properties of vectors arising as resonances of a strong sector are very different from those of the "standard" weakly

[1]We will sometimes use the self-explanatory abbreviations LHC7, LHC8 and LHC14 in this note.

coupled Z' and W' (of which minimal Z' are an example), and make their discovery challenging. In fact, following the idea of partial compositeness the couplings of composite resonances to light fermions are expected to be small, since the latter, being light, are mostly elementary states. This implies that the Drell-Yan production of composite Z' and W' is suppressed, while the main decay channels contain Goldstone bosons (the Higgs and the longitudinal polarizations of W and Z) and third-generation fermions, for example for a neutral resonance $Z' \to Z_L h, W_L^+ W_L^-, t\bar{t}$ typically dominate. In addition the electroweak S parameter constrains such resonances to be heavier than about 2.5 TeV, placing them out of the reach of the first two runs of the LHC. Dedicated studies [7, 8, 9] show that these resonances can be discovered at LHC14 with large luminosity up to masses of roughly 3 TeV.

Still keeping the compositeness idea in mind, it is interesting to ask whether there could be resonances light enough to give signals at LHC7/8, while at the same time satisfying all current electroweak and collider bounds. In Sec. 3 we discuss an example, a *weakly constrained* W' [10], whose main manifestation would be the observation of a bump in the dijet invariant mass spectrum. While in Ref. [10] the phenomenology of this resonance was discussed adopting an effective, model-independent approach, we notice an interesting similarity with the phenomenological implications of a flavor-symmetric strong sector, which was proposed in Ref. [11]. In this case Minimal Flavor Violation can be implemented, alleviating the tension with flavor bounds that is generically present in composite Higgs models with partial compositeness. This in turn implies that some chiralities of light quarks are largely composite and thus sizably coupled to resonances, giving rise for example to large Drell-Yan production of spin-1 composites and subsequent decay into the dijet final state.

2 Minimal Z'

This class of models is based on a minimal extension of the SM gauge group, consisting in an extra $U(1)'$ factor, and of the SM matter content, which is enlarged to include one right-handed neutrino per family (this allows the implementation of the see-saw mechanism for neutrino masses at the renormalizable level). It can be easily seen that with the specified fermion content all anomalies cancel, provided the generator of $U(1)'$ is a linear combination of Y and $B-L$. The class of models thus defined "continuously interpolates" among several specific models frequently discussed in the literature, such as Z'_χ, which arises from $SO(10)$ grand unification, Z'_{3R}, which appears in Left-Right models, and Z'_{B-L}, the 'pure $B-L$' model. Following the notation of Ref. [4], the coupling of the mass-eigenstate Z' to fermion $f = u_L, d_L, u_R, \ldots$ reads

$$\mathcal{L} \,=\, g_Z \sum_f Q_{Z'}(f) \overline{f} \gamma^\mu f \, Z'_\mu \,,$$

$$Q_{Z'}(f) = \sin\theta' [T_{3L}(f) - \sin^2\theta_W Q(f)] + \cos\theta' [\widetilde{g}_Y Y(f) + \widetilde{g}_{BL}(f)] \,, \qquad \left(\tan\theta' \simeq -\widetilde{g}_Y \frac{M_{Z^0}^2}{M_{Z'}^2} \right) .$$

θ' is the Z-Z' mixing angle, and we defined $\widetilde{g}_{Y,BL} \equiv g_{Y,BL}/g_Z$ and $M_{Z^0}^2 = g_Z^2 v^2/4$. In first approximation, the three parameters $M_{Z'}$, $\widetilde{g}_Y, \widetilde{g}_{BL}$ are sufficient to describe the phenomenology of the Z'. In Ref. [4] a comparison of the LHC7 reach with the strong bounds coming from EWPT and with the constraints imposed by a GUT origin of the Z' was performed. Here we update such comparison making use of the results of the ATLAS [12] and CMS [13] searches for resonances in the dilepton final state, based on $\sim 5\,\text{fb}^{-1}$ of LHC collisions at 7 TeV. As can be

seen from the left panel of Fig. 1, for a relatively light Z' with mass of 1 TeV the current LHC constraints are much more powerful than those coming from EWPT. On the other hand, for larger masses the LHC has started probing regions of parameter space that were both allowed by EWPT and GUT-compatible, represented by the orange region in the right panel of Fig. 1.

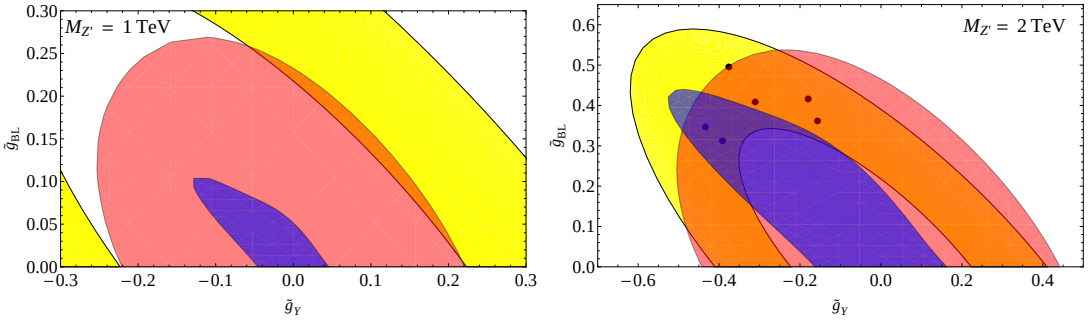

Figure 1: Comparison of the region allowed by LHC7 with $\sim 5\text{fb}^{-1}$ (blue) with those compatible with EWPT (red) and with GUTs (yellow), in the plane $(\widetilde{g}_Y, \widetilde{g}_{BL})$. The black dots appearing in the right panel are specific supersymmetric GUT models, see Ref. [4].

3 A weakly constrained W'

In Ref. [10] an isospin-singlet W' was studied in a model-independent approach, by writing an effective Lagrangian containing all the dimension-four operators compatible with the SM gauge symmetry and involving the SM fields plus the resonance. The absence of an associated neutral resonance in the effective theory implies that the bounds on Z' from EW data and from colliders can be avoided. Furthermore, gauge invariance forces the W' to be leptophobic, its dominant couplings to fermions being

$$\mathcal{L} = \frac{g_q}{\sqrt{2}}(V_R)_{ij}\overline{u}^i_R\gamma^\mu d^j_R W'^+_\mu + \text{h.c.}\,,$$

where $i, j = 1, 2, 3$ are flavor indexes and V_R is a matrix that in the effective approach is arbitrary. For suitable choices of V_R, constraints from flavor data are very weak. In Ref. [10] the LHC phenomenology of the resonance was discussed assuming the least constrained among these special forms, namely $(V_R)_{ij} = \delta_{ij}$. If the W-W' mixing is neglected, only two parameters are relevant, the mass $M_{W'}$ and coupling to quarks g_q. The null results of LHC searches in the dijet final state then place bounds on these parameters, as shown in the left panel of Fig. 2 (see also Ref. [16]). We make use of the latest searches for resonances in the dijet invariant mass spectrum [14, 15], and of the CMS search for quark compositeness in dijet angular distributions [17]. The bound from the latter is obtained applying the results of Ref. [18] [2], and is more relevant for strongly coupled resonances. In the right panel of Fig. 2 we compare the discovery prospects for the W' at LHC8 with the current exclusion from LHC7 (based on 1 fb^{-1} of data [3]),

[2] We thank J. Serra for providing the update of the numerical bounds given in Ref. [18].

[3] Rescaling the exclusion to the full $\sim 5\,\text{fb}^{-1}$ luminosity collected in 2011 increases the bound to about $M_{W'} \gtrsim 2\,\text{TeV}$.

assuming a coupling $g_q = g$. We find that a W' with mass up to 2.2 TeV can be discovered with 15 fb^{-1}. See Ref. [10] for details on how this estimate was derived.

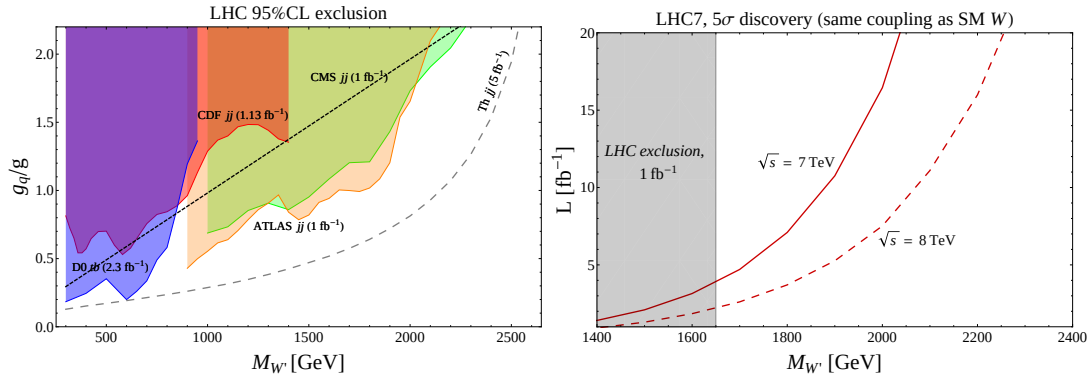

Figure 2: (*Left panel*) Current bounds in the plane $(M_{W'}, g_q/g)$ from Tevatron searches in the tb (blue) and dijet channel (red), from LHC searches for resonances decaying into dijets (brown and pink) and from LHC searches for quark compositeness (dashed straight line, corresponding to $M_{W'}/g_q > (2.2\,\text{TeV})/\sqrt{2}$). The exclusion expected from LHC dijet resonance searches after 5 fb^{-1}, computed in Ref. [10], is also shown as a dashed line. (*Right panel*) Discovery luminosity as a function of the W' mass, assuming a coupling $g_q = g$, at LHC7 and LHC8.

References

[1] ATLAS Collaboration, Phys. Lett. B **710** (2012) 49 [arXiv:1202.1408 [hep-ex]].

[2] CMS Collaboration, Phys. Lett. B **710** (2012) 26 [arXiv:1202.1488 [hep-ex]].

[3] T. Appelquist, B. A. Dobrescu and A. R. Hopper, Phys. Rev. D **68** (2003) 035012 [arXiv:hep-ph/0212073].

[4] E. Salvioni, G. Villadoro and F. Zwirner, JHEP **0911** (2009) 068 [arXiv:0909.1320 [hep-ph]].

[5] E. Salvioni *et al.*, JHEP **1003** (2010) 010 [arXiv:0911.1450 [hep-ph]].

[6] R. Contino, [arXiv:1005.4269 [hep-ph]].

[7] K. Agashe *et al.*, Phys. Rev. D **76** (2007) 115015 [arXiv:0709.0007 [hep-ph]].

[8] K. Agashe *et al.*, Phys. Rev. D **80** (2009) 075007 [arXiv:0810.1497 [hep-ph]].

[9] A. Katz, M. Son and B. Tweedie, JHEP **1103** (2011) 011 [arXiv:1010.5253 [hep-ph]].

[10] C. Grojean, E. Salvioni and R. Torre, JHEP **1107** (2011) 002 [arXiv:1103.2761 [hep-ph]].

[11] M. Redi and A. Weiler, JHEP **1111** (2011) 108 [arXiv:1106.6357 [hep-ph]].

[12] ATLAS Collaboration, ATLAS-CONF-2012-007.

[13] CMS Collaboration, CMS-EXO-11-019.

[14] ATLAS Collaboration, Phys. Lett. B **708** (2012) 37 [arXiv:1108.6311 [hep-ex]].

[15] CMS Collaboration, Phys. Lett. B **704** (2011) 123 [arXiv:1107.4771 [hep-ex]].

[16] R. Torre, arXiv:1109.0890 [hep-ph].

[17] CMS Collaboration, JHEP **1205** (2012) 055 [arXiv:1202.5535 [hep-ex]].

[18] O. Domenech, A. Pomarol and J. Serra, Phys. Rev. D **85** (2012) 074030 [arXiv:1201.6510 [hep-ph]].

Searches for new Physics with Leptons and/or Jets at CMS

Martin Weber on behalf of the CMS collaboration

RWTH Aachen, III. Physikalisches Institut A, 52056 Aachen, Germany

DOI: http://dx.doi.org/10.3204/DESY-PROC-2012-02/221

Using up to $4.98\,\mathrm{fb}^{-1}$ of proton-proton collision data accumulated at a center-of-mass energy of 7 TeV in 2011, CMS has searched for signs of new physics in final states with leptons and jets. Many different production and decay signatures have been investigated, showing good agreement with Standard Model predictions. Mass limits for the production of new, heavy particles have been set ranging from few hundred GeV up to several TeV, including limits on the mass of the Z' and W' of the Sequential Standard Model of $M(Z') > 2.3\,\mathrm{TeV}$ and $M(W') > 2.5\,\mathrm{TeV}$ at 95% confidence level.

1 Introduction

The CMS [1] experiment at the CERN LHC [2] successfully recorded proton-proton collisions with an integrated luminosity of $\mathcal{L} = 4.98\ \mathrm{fb}^{-1}$ during data taking in 2011. These data have been used to search for signs of new physics beyond the Standard Model.

We report the progress on searches for new heavy electroweak gauge bosons (Z', W') with leptons in the final state, searches for a right-handed W_R-Boson and heavy neutrino in the leptons+jets final state, and on searches for particles produced and decaying through the strong force in final states with two or more jets.

2 Searches for resonances decaying to leptons

A new, neutral, heavy Boson Z' naturally arises in Grand Unified Theories and is a prime candidate for these searches [3]. Under the assumption of couplings equal to those of the Z Boson, the decay to leptons $\ell = e, \mu$ is an experimentally sensitive search channel. Here, two well isolated electrons or muons are required, with a vertex requirement for the muons in order to reduce background from cosmic muons. The muons need to be oppositely charged, whereas this requirement is not applied for electrons due to the worse momentum resolution and thus difficult charge measurement at high transverse momenta. In order to reduce fakes, one electron is required to be in the barrel region. The dominating background in this search is Drell-Yan production, which is estimated from simulation and scaled to the data in a region 80–120 GeV around the Z peak. Systematic uncertainties due to a p_T dependent k-factor have been estimated with FEWZ [4] and are below 10%. Top-Pair production and other background with prompt lepton pairs have been taken from simulation, and the signal-free distribution of $e\mu$ pairs shows a good agreement between data and simulation. QCD jet data has been estimated

from data outside the signal region. PDF uncertainties contribute less than 10% to the total systematic uncertainty of ≈ 12% in the range 200 GeV–2 TeV.

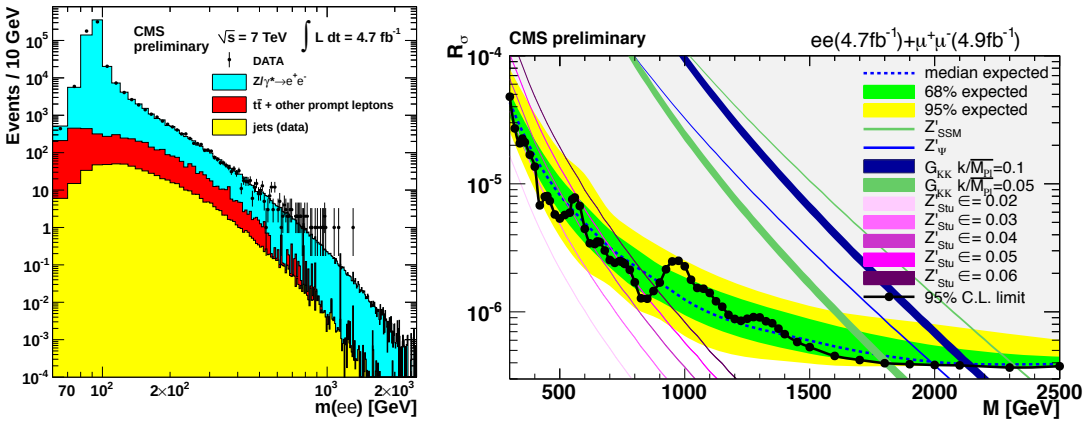

Figure 1: Search for resonances in dileptons (ee, $\mu^+\mu^-$). Left: Invariant mass of two electrons after selection. Right: Exclusion limits on Z' and other models.

Figure 1 (left) shows the invariant mass of the two electrons for the electron selection, and a good agreement between simulation and data is found, whereas the right part shows exclusion limits for some Z' and other physics models. A Z' with mass $M > 2.3$ TeV in the Sequential Standard Model can be excluded with 95% confidence level (CL).

Searches for a new charged heavy W' Boson with couplings equal to those in the Standard Model have been performed in the lepton and missing energy channel [5]. In this search, an isolated electron or muon is required. In the r-ϕ-plane, the neutrino from the W' carries away an amount of energy approximately equal to the lepton momentum p_T^ℓ but in opposite direction. The selection therefore requires the transverse missing energy E_T^{miss} to be in the range $0.4 < p_T^\ell / E_T^{miss} < 1.5$ and $\Delta\phi > 2.5$ between lepton and E_T^{miss}.

The transverse mass $M_T = \sqrt{2 \cdot E_T^{miss} \cdot p_T^\ell (1 - \cos\Delta\phi)}$ is used as a test distribution, shown in the left part of Figure 2. A good agreement between data and simulation is observed. In order to be independent from possible interference effects, the function $f(M_T) = a/(M_T + b)^c$ is fitted to simulation and scaled to data in the range 200 GeV $< M_T <$ 500 GeV. This function is used to determine the number of background events above an optimized M_T threshold. The limits are obtained from a Bayesian single-bin counting experiment with event numbers taken above the M_T threshold. Systematic uncertainties mainly arise from the measurement of E_T^{miss} and are about 2% on the number of events above the M_T threshold. Expected and observed limits on the W' mass are shown in Figure 2 on the right, and $M(W') > 2.5$ TeV at 95% CL. Considering constructive interference between W and W', the exclusion limit changes to $M(W') > 2.63$ TeV and to $M(W') > 2.43$ TeV for destructive interference.

3 Searches with leptons and jets

A fully left-right symmetric extension of the Standard Model predicts the existence of both right-handed charged gauge bosons W_R and heavy neutrinos N_ℓ. Under quite general assumptions,

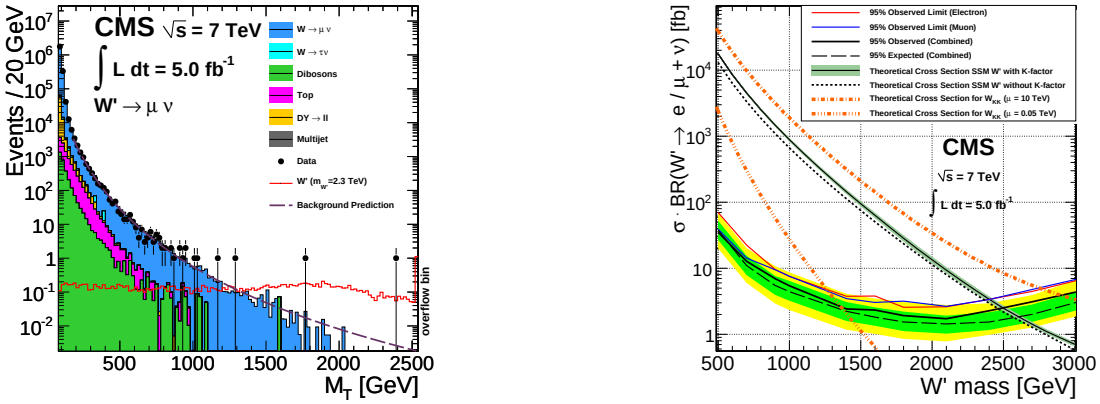

Figure 2: Search for W'. Left: Transverse mass of W' candidates in the $e\nu_e$ channel after selection. Right: Exclusion limits on W' and other models for the $e\nu_e + \mu\nu_\mu$ channels combined.

the W_R can be resonantly produced and decays via a heavy Neutrino N_ℓ in a two jet two lepton final state. In this search [6], a pair of isolated same-flavour leptons $\ell = e, \mu$ is required. The two highest p_T jets in the events are considered as candidates from the W_R decay. Contribution from Z+jets is reduced by requiring the invariant mass $M_{\ell\ell} > 200$ GeV $\gg M_Z$. The cross-section for the Z+jets process has been estimated at the Z-peak, and QCD jets background is estimated from the data themselves. A further reduction of Standard Model backgrounds is achieved by requiring a high dijet invariant mass $M_{jj} > 520$ GeV.

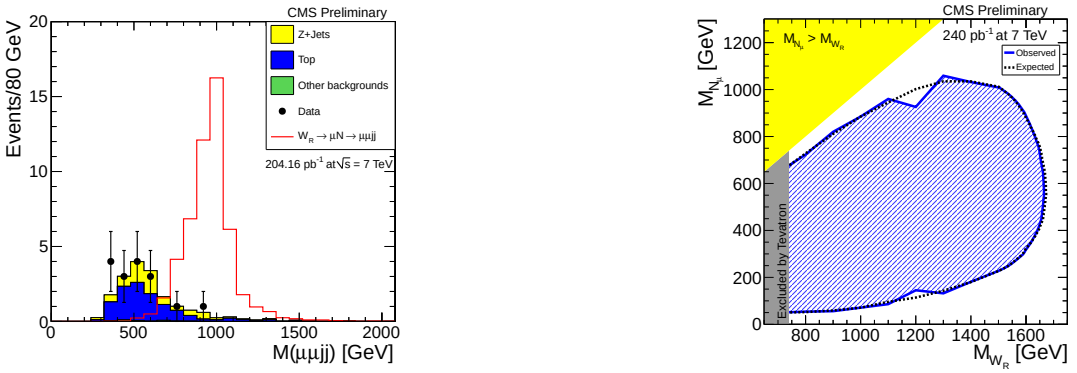

Figure 3: Search for a right-handed W_R Boson. Left: $M_{\mu\mu jj}$ mass after selection. Right: Expected and measured exclusion contour in the $M(W_R)$-$M(N_\ell)$ plane.

Figure 3 (left) shows the distribution of the $M_{\mu\mu jj}$ mass after selection, with a signal $M(W_R) = 1$ TeV and $M(N_\ell) = 600$ GeV overlaid. The figure shows a good agreement between data and simulation and no signs for a signal. Systematic uncertainties on event numbers are 10-25% with large contributions from the jet energy scale and the QCD jets background estimate. Exclusion limits, which are shown in Figure 3 (right) in the $M(W_R)$-$M(N_\mu)$ plane, have

been set with a multibin Bayesian counting experiment including systematic uncertainties. A very similar exclusion is obtained for the W_R decay to N_e.

4 Searches with jets

Searches for new physics have also been performed in a two-jet final state [7]. Here the assumption is the resonant production of strongly coupling and decaying new narrow resonances. Two "wide jets" are formed and their invariant mass is used for the search for new physics. Detector effects dominate the mass resolution and thus generic templates are used for excluding resonances decaying to quark-quark, quark-gluon and gluon-gluon final states. Exclusion limits at 95% CL are shown in Figure 4 (left). The observed limits at 95% CL are $M > 4.00$ TeV for string resonances, $M > 2.49$ TeV for excited quarks, $M > 2.47$ TeV for axigluons/colorons, $M > 3.52$ TeV for E_6 diquarks and $M > 1.51$ TeV for W'. The largest systematic uncertainties are the jet energy resolution and scale with approximately 15% uncertainty on the number of background events.

Figure 4 (right) shows the 95% CL exclusion limits obtained from the search for pair-produced particles in the four-jet final state [7], with the example of a coloron exclusion in the range 320 GeV $< M(C) <$ 580 GeV.

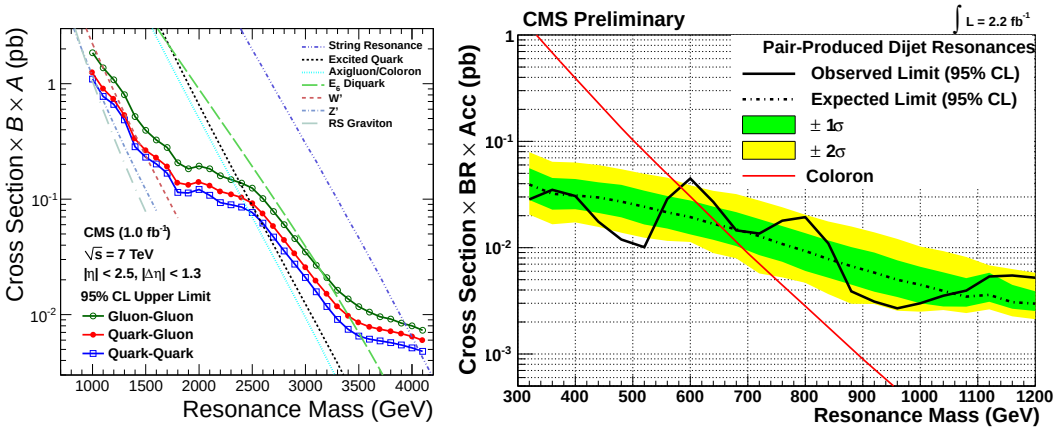

Figure 4: Exclusion limits on various models in the di-jet (left) and four-jet final state (right).

References

[1] CMS collaboration, 2008 JINST **3** S08004 (2008).

[2] L. Evans and P Bryant (eds.), 2008 JINST **3** S08001 (2008).

[3] CMS collaboration, CMS PAS EXO-11-019 (2011).

[4] K. Melnikov and F. Petriello, arXiv:hep-ph/0609070v1, doi:10.1103/PhysRevD.74.114017.

[5] CMS collaboration, arXiv:1204.4764 [hep-ex] (2012), submitted to JHEP.

[6] CMS collaboration, CMS PAS EXO-11-002 (2011).

[7] CMS collaboration, Phys. Lett. **B 704** 3 (2011).

[8] CMS collaboration, CMS PAS EXO-11-016 (2012).

Search for New Physics with leptons and/or jets at ATLAS

Antonio Policicchio[1] on behalf of the ATLAS Collaboration

[1]INFN Cosenza, c/o Dipartimento di Fisica, Universitá della Calabria, I-87036 Rende (Cs), Italy

DOI: http://dx.doi.org/10.3204/DESY-PROC-2012-02/199

Data taken in 2011 with the ATLAS detector at the Large Hadron Collider (LHC) have been used to search for physics beyond the Standard Model. Results are presented based on between 1 and 5 fb^{-1} of $\sqrt(s) = 7$ TeV proton-proton collisions mainly focussing on final states with jets and/or leptons. No evidence of new physics is found.

1 Introduction

The CERN LHC delivered more than 5 fb^{-1} of proton-proton collisions at $\sqrt{s} = 7$ TeV to the ATLAS [1] detector in 2011. Selected results on Beyond Standard Model (BSM) searches are summarized in this paper. The emphasis here is on *exotic* physics mainly focussing on final states with leptons and/or jets: new gauge bosons, composite objets, extra dimensions and other exotica. Results are presented by final state, showing how each search can be used to constrain different models. Some cross-section limit plots are also shown.

2 Results

Di-jets resonances are signatures for many BSM models and include string balls, GUT diquarks, excited quarks, W' and Z'. Searches are based on 5 fb^{-1} of data [2]. Additional sensitivity to new physics is obtained by studying the dijet angular distribution: high mass BSM objects are expected to be produced nearly at rest and therefore to produce a central angular distribution [2]. ATLAS sets the following limits at 95% CL (bayesian approach) $m_{q^*} > 3.35$ TeV for a generic Gaussian resonance such as for an excited quark, $m_{s_8} > 1.94$ TeV for color octet scalars, $m_{BH} > 3.96$ TeV for mini quantum black holes assuming six extra space-time dimensions for quantum gravity, and excludes quark contact interactions below a compositeness scale of 7.8 TeV. Fig. 1 (left) shows the obtained limit on the cross section times acceptance for a narrow dijet resonance, as a function of its mass. Also shown is the theoretical curve for a model of excited quark.

ATLAS searches for resonances in the dilepton (electrons and muons) invariant mass spectrum. BSM physics signals used as benchmarks include different models of Z' and graviton resonance. The search [3] is based on 5 fb^{-1} and sets mass limits $m_{Z'} > 2.11$ TeV on SSM Z' production and $m_{G^*} > 2.16$ TeV on Randall-Sandrum RS1 graviton production for coupling strength $k/\bar{M}_{Pl} = 0.1$. Fig. 1 (right) shows the cross section limits for Z' as a function of

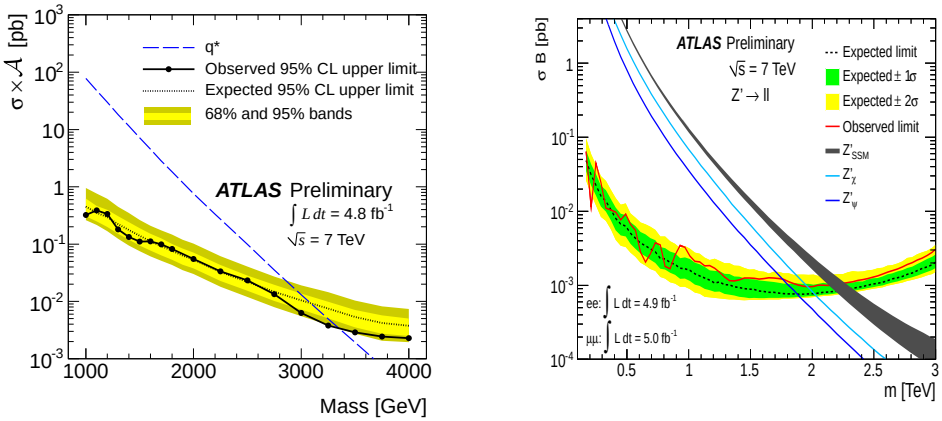

Figure 1: Left: dijet resonance limit on a generic Gaussian signal [2]; right: expected and observed cross section limits on dilepton resonances as a function of invariant dilepton mass [3].

dilepton resonance mass. The shape of the high mass tail is also sensitive to BSM physics. Limits, with 1.2 fb^{-1} of integrated luminosiy, are set on quark-lepton compositeness scales Λ^- > 10.1 TeV (8.0 TeV) and $\Lambda^+ > 9.4$ TeV (7.0 TeV) in the electron (muon) channel assuming destructive and constructive interference with Drell-Yan distribution, respectively [4].

ATLAS has carried out same-sign dileptons and multilepton searches looking for a variety of new physics signatures: doubly-charged Higgs, excited neutrinos, extra dimensions. The search for same-sign dimuons is based on 1.6 fb^{-1} and sets limits on doubly-charged Higgs production at $m_{H^{\pm\pm}} > 355$ GeV, assuming pair production via the exchange of a virtual Z/γ^* and 100% branching ratio to muons, and on like-sign top quark production cross section of 3.7 pb [5]. A search for two like-sign muons in events with high track multiplicity in 1.3 fb^{-1} sets a model independent limit on the new physics contribution to the signal region at 0.018 pb [6].

Inclusive searches in events with three or more leptons are based on 1 fb^{-1}. Data are consistent with Standard Model (SM) expectation. Fiducial limits are extracted on models predicting excesses of multi-lepton events using pair production of doubly-charged Higgs bosons as a benchmark model. The observed fiducial cross-section limit is 38 fb. Cross-section upper limits are also set at $\sigma < 41$, 34 fb for 200, 300 GeV mass, assuming decay to either a neutrino and a Z boson or an electron and a W boson [7].

ATLAS has searched for pair-produced leptoquarks decaying to either $lqlq$ or $lq\nu q$. Searches are restricted to one generation, i.e. e, μ or τ. A first generation search [8] in the $eejj$ and $e\nu jj$ channels using 1.1 fb^{-1} sets mass limits $m_{LQ} > 660$ GeV for $\beta = 1$ and $m_{LQ} > 607$ GeV for $\beta = 0.5$, where β is the branching ratio of a leptoquark to the channel with a charged lepton. The limits in the $\beta - m_{LQ}$ plane are shown in Fig. 2 (left), where β is the branching ratio of a leptoquark to the channel with a charged lepton. A search for a second generation using the $\mu\mu jj$ and $\mu\nu jj$ channels has been performed in 1 fb^{-1}: the mass limits are $m_{LQ} > 685$ GeV for $\beta = 1$ and $m_{LQ} > 594$ GeV for $\beta = 0.5$ [9]. The limits in the $\beta - m_{LQ}$ plane are shown in Fig. 2 (right).

A search has been performed for singly produced excited leptons by contact interaction and decaying to $e\gamma$ or $\mu\gamma$ resonance in events with $ee\gamma$ or $\mu\mu\gamma$, based on 5 fb^{-1} of data [10]. Fig. 3

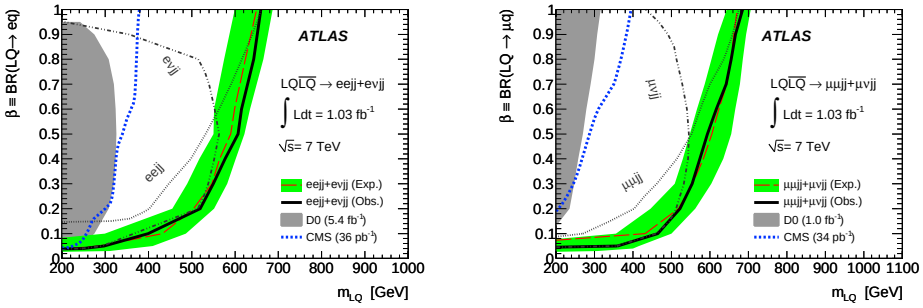

Figure 2: Expected and observed limit on leptoquark production. Left is for first generation limit in the $\beta - m_{LQ}$ plane [8] and right is for second generation [9].

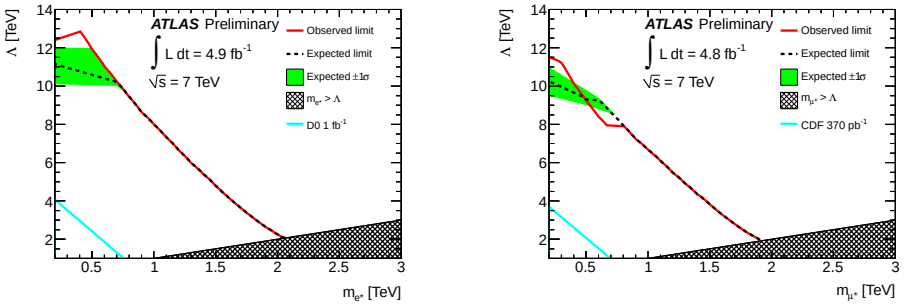

Figure 3: Expected and observed limits on excited electron (left) and muon (right) production [10].

shows the two-dimensional limits on compositeness scale Λ and excited lepton mass m_{l^*}. At $\Lambda = m_{l^*}$, the mass limits are $m_{e^*} > 2.0$ TeV and $m_{\mu^*} > 1.9$ TeV.

A search for diboson resonances has been performed in the channel $ZZ \to llll$ and $ZZ \to lljj$ in 1 fb^{-1} and a limit has been set at $m_{G^*} > 845$ GeV on the spin-2 RS1 graviton with coupling strength $k/\bar{M}_{Pl} = 0.1$ [11].

A heavy neutrinos N coupling to a right-handed boson W_R via the decay chain $qq \to W_R \to Nl \to W_R^* ll \to lljj$ lead to a mass resonance in both ljj and $lljj$. A search in 2.1 fb^{-1} assumes similar masses for heavy electron and muon neutrinos, and sets a mass limit $m_{W_R} > 1.8$ TeV for $m_{W_R} - m_N > 300$ GeV [12]. Separate limits have been set for Dirac and Majorana neutrinos and results are very similar.

Decays far from the interaction point are signatures of long-lived neutral particles. ATLAS has performed a search based on 1.9 fb^{-1} for pairs of back-to-back particles decaying in the muon system [13]. A dedicated trigger algorithm and a vertex finding routine in the muon system have been developed. Such decays are signatures, for example, of Higgs decays to pairs of long-lived neutral particles $h \to \pi_v \pi_v$, where π_v is a pseudoscalar from an Hidden Sector weakly coupled to the SM sector. Limits have been set as a function of the proper decay length of the π_v excluding the range 0.5-23 m depending on the Higgs mass (120-140 GeV) and on the π_v mass (20-40 GeV). Exclusion limits are shown in Fig. 4.

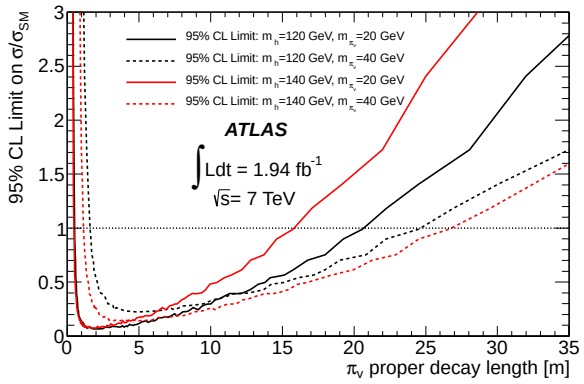

Figure 4: Observed 95% upper limits on the process $h \to \pi_v\pi_v$ as a function of the π_v proper decay length, expressed as a multiple of the SM cross section for Higgs production. Exclusion limits assume 100% branching ratio for the Higgs decaying to π_v's [13].

3 Conclusions

ATLAS has searched in a wide range of final states for signal of new physics BSM. No evidence for new physics has (yet) been found. Important constraints have been set on a variety of BSM models.

4 Acknowledgements

I would like to thank to the organizers of the DIS2012 conference.

References

[1] The ATLAS Collaboration, JINST 3 (2008) S08003
[2] The ATLAS Collaboration, ATLAS-CONF-2012-038 (2012), https://cdsweb.cern.ch/record/1432206
[3] The ATLAS Collaboration, ATLAS-CONF-2012-007 (2012), https://cdsweb.cern.ch/record/1428547
[4] The ATLAS Collaboration, arXiv:1112.4462 (2011), accepted by Phys. Lett. B
[5] The ATLAS Collaboration, arXiv:1201.1091, submitted to Phys. Rev. D
[6] The ATLAS Collaboration, Phys. Lett. B 709 (2012) 322
[7] The ATLAS Collaboration, ATLAS-CONF-2011-158 (2012), https://cdsweb.cern.ch/record/1399618
[8] The ATLAS Collaboration, Phys. Lett. B 709 (2012) 158
[9] The ATLAS Collaboration, arXiv:1203.3172 (2012), submitted to Eur. Phys. J. C
[10] The ATLAS Collaboration, ATLAS-CONF-2012-008 (2012), https://cdsweb.cern.ch/record/1428548
[11] The ATLAS Collaboration, arXiv:1203.0718 (2012), submitted to Phys. Lett. B
[12] The ATLAS Collaboration, arXiv:1203.5420 (2012), submitted Eur. Phys. J. C
[13] The ATLAS Collaboration, arXiv:1203.1303 (2012), submitted to Phys. Rev. Lett.

Searches for Large Extra Dimensions, Leptoquarks and Heavy Quarks at CMS

Sushil Singh Chauhan on behalf of the CMS Collaboration
University of California, Davis, USA

DOI: http://dx.doi.org/10.3204/DESY-PROC-2012-02/222

We present results from several searches for physics beyond the standard model involving large extra dimensions, leptoquarks, and heavy quarks at $\sqrt{s}$ = 7 TeV with the CMS experiment. Many different final states are analyzed using the data collected in 2010 and 2011 corresponding to an integrated luminosity up to $5.0 fb^{-1}$. The results are used to set new limits on the scale of large extra dimensions and on the masses of leptoquarks and heavy quarks.

1 Introduction

The CMS experiment has been designed to look for new physics beyond the Standard Model(SM). This includes searches for large extra dimensions, leptoquarks and heavy quarks production. The measurements described here were performed using data recorded by the CMS detector [1] at the LHC in 2010 and 2011[1].

2 Large Extra Dimensions (LED) Searches

In the framework of the ADD model proposed by **A**rkani-Hamed, **D**imopoulos, and **D**vali, the gravitational and gauge interactions unify at the electroweak scale so that there is only one fundamental length scale. The observed weakness of gravity is explained as a consequence of the universe having "large" (mm) extra dimensions, where gravity could propagate. The number of extra dimensions (n_D) and the effective scale (M_D) are the main parameters of the ADD model.

The ADD model predicts a number of possible signatures within the reach of LHC. Production of monophoton ($\gamma + \not{E}_{\mathrm{T}}$) and monojet (jet+$\not{E}_{\mathrm{T}}$) are the clean channels to search for existence of LED where $\not{E}_{\mathrm{T}}$ originate from graviton as it escapes detection. If LED exists, it will manifest itself as an excess of events in the previously mentioned final states. The monophoton study is done in the phase space defined by $p_T^{\gamma} > 145$ GeV, $|\eta^{\gamma}| < 1.44$ and $\not{E}_{\mathrm{T}} > 130$ GeV, while monojet uses $p_T^{jet} > 110$ GeV with $|\eta^{jet}| < 2.4$. Both analyses optmized their selections for better sensitivity and used other vetoes to reduce potential background contributions mainly arising from QCD and $W/Z + X$ production [2, 3]. Figure 1 shows p_T distributions from these analyses after the full selection criteria is applied. The new lower limits from monophoton and monojet studies are $1.64 - 1.73$ TeV ($n_D = 3 - 6$), $2.49 - 4.44$ TeV ($n_D = 2 - 6$) at 95%CL with $5.0 fb^{-1}$ and $4.7 fb^{-1}$ of integrated luminosity respectively [2, 3].

[1] some of the results are recently updated with a slightly higher luminosity and are presented here

For a search in the diphoton channel, both γs are required to have $E_T > 70$GeV and $|\eta^\gamma| < 1.44$. The reducible backgrounds from QCD and γ+jets are estimated from data using the fake ratio method. The observed events yield and background expectations are compared in different ranges of $M_{\gamma\gamma}$ for any signal excess. A new lower limits of $2.3 - 3.8$ TeV is set by this analysis on the scale of LED for $2.2fb^{-1}$ of data [4]. In the dilepton search isolated leptons are required to be $p_T^e > 35$ GeV(40 GeV for μ). The Drell-Yan production is the largest background here and is estimated from simulation and NLO corrections are applied. These corrections, along with the PDF uncertainties, dominate the systematic uncertainty for the background prediction [5]. The observed lmit on LED scale from this analysis is $2.5 - 3.8$ TeV for $n_D \geq 3 - 7$.

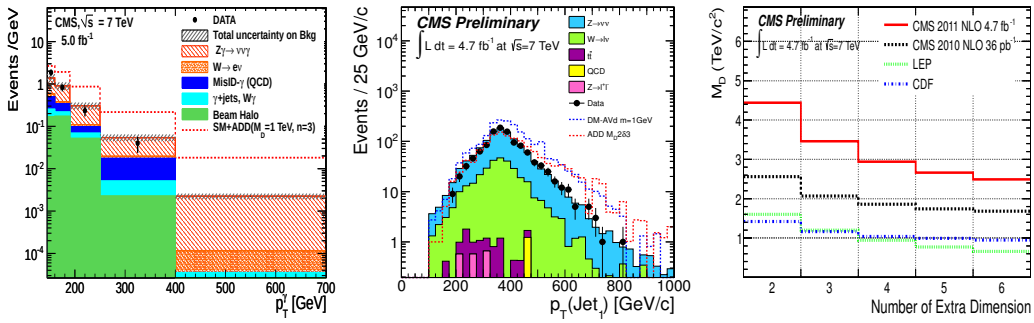

Figure 1: The p_T spectrum of γ from $\gamma+\not{E}_{\rm T}$ final state (left) and jet p_T distribution from jet$+\not{E}_{\rm T}$ final states(middle) after full selection. The observed limits for different n_D from monojet study are also shown(right).

3 Leptoquark Searches

The Standard Model shows a remarkable symmetry between quarks and leptons. This symmetry may imply a more fundamental relation between the two. It is natural to think of a theory which relates quarks and leptons and predicts new particles called leptoquarks which carry both lepton and baryon number.

CMS has searched for leptoquark production for first and second generation with $llqq$ (with branching fraction $\beta = 1.0$) and $l\nu qq$ ($\beta = 0.5$) final states production [6, 7, 8]. For this observation, the scaler sum of transverse momentum (S_T) of leptons and jets (and $\not{E}_{\rm T}$ for $l\nu qq$) is studied as the key variable (see Fig. 2). The main backgrounds comes from W/Z+jets and $t\bar{t}$ for first generation searches, and from Z/γ^*+jet and $t\bar{t}+VV$ for second generation searches. The new limits on M_{LQ} obtained from these analyses are 339 (384) GeV for $ee\nu\nu$ ($e\nu qq$) with $\sim 36pb^{-1}$, and 632 (523) GeV for $\mu\mu qq$ ($\mu\nu qq$) final state with $2.0fb^{-1}$ of integrated luminosity. These limits are obtained for β or $\beta^2 \times \sigma$ as a function of M_{LQ}(see Fig. 2(right)).

In the search for third generation scalar leptoquarks, a final state with two tagged $b-$jets and $\not{E}_{\rm T}$ is analyzed [9]. A special variable called *razor*, designed to search for a pair of heavy particles, is used in this study. It is defined as ratio of $M_T^R = \sqrt{(E_{j1}+E_{j2})^2 - (p_z^{j1}+p_z^{j2})^2}$ and $M_R = \sqrt{\not{E}_{\rm T}(\vec{p_T^{j1}}+\vec{p_T^{j2}}) - \not{E}_{\rm T}(\vec{p_T^{j1}}+\vec{p_T^{j2}})}$. The main background for this final state comes from SM heavy flavor multijets, $W/Z+$ heavy flavor jets, and $t\bar{t}$+jets production. This analysis is performed with $1.8fb^{-1}$ of data collected at the beginning of 2011 and gives a lower bound of $M_{LQ} > 350$ GeV at 95%CL.

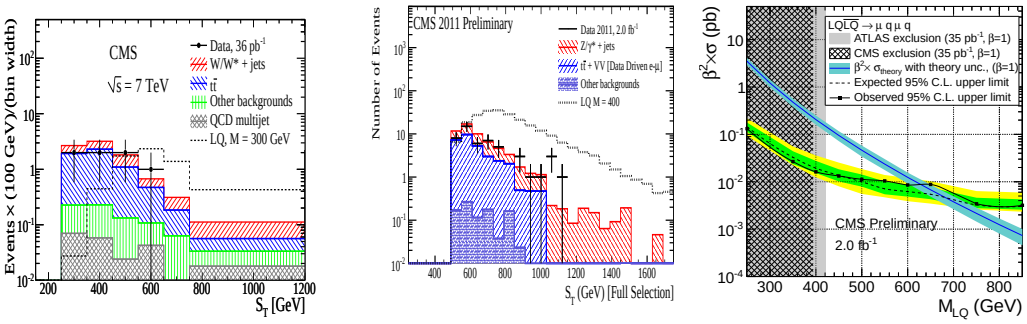

Figure 2: S_T distribution for $e\nu qq$ final state (left) and $\mu\mu qq$ final states (middle) for scalar leptoquark search. The signal expectation is also shown for a given leptoquark mass M_{LQ}. The limits for $\beta^2 \times \sigma$ as a function of M_{LQ} are also shown (right) from $\mu\mu qq$ channel.

4 Heavy Quark Searches

An obvious extension of SM is the prediction of a new generation of heavy quarks. The presence of such heavy quarks could solve some of the known problems of particle physics. For example, the existence of such a new generation could enhance the CP violation by a large factor and hence could explain the observed matter-antimatter asymmetry in the universe.

The $t'\bar{t'}$ pair production search has been performed for the dilepton and lepton+jets final states. For the $t'\bar{t'} \rightarrow (l^+\nu b)(l^-\bar{\nu}\bar{b})$ production search the mass of "$b-$jet+lepton" is reconstructed from different b and l combinations. The lowest mass (M_{lb}^{min}) of these combinations is considered for a comparision of the SM prediction with data. The main backgrounds $t\bar{t}$ tends to accumulate at lower M_{lb}^{min} values thus providing a way to reduce it by a large fraction [10](see Fig. 3 (left)). The signal region is defined by $M_{lb}^{min} > 170$ GeV. For the lepton+jets final state the $H_T (= p_T^l + p_T^{miss} + \sum p_T^{jet})$ and reconstructed mass from kinematical fit(M_{fit}) are used as discriminating variables. Here the $t'\bar{t'}$ signal is expected to be at high H_T while the SM $t\bar{t}$ ends up at low H_T and M_{fit} values [11]. The new limit of $M_{t'} > 557$ (560) GeV is obtained from dilepton (lepton+jets) final state with $5.0 fb^{-1}$ ($4.9 fb^{-1}$) of integrated luminosity.

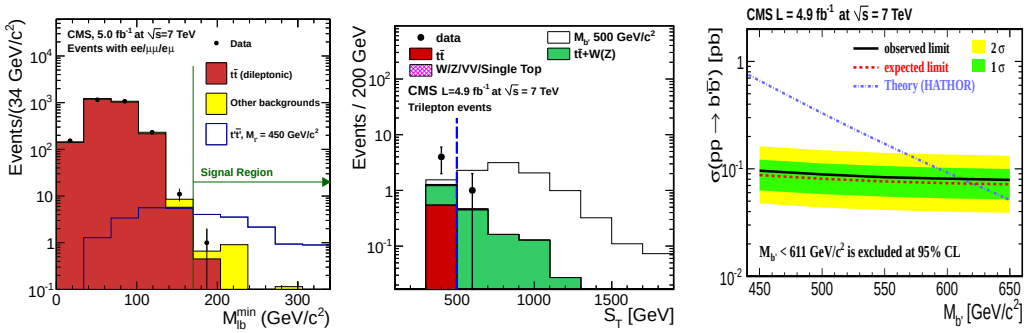

Figure 3: The M_{lb}^{min} spectrum of $b-$jet+lepton for t' search(left). The S_T distribution (middle) and cross section limits as a function of $M_{b'}$ (right) for trilepton search.

The $b'\bar{b}'$ pair production searches are done with 3−leptons+2−jets or same sign 2−lepton+4 jets final states with very low SM background. The event selection requires $p_T^l > 20$GeV and at least 1 b−jet ($p_T > 25$ GeV). The S_T distribution is examined for any b' signal in the S_T region above the SM prediction (see Fig. 3). A final selection of $S_T > 500$ GeV is used to reduce the $t\bar{t}$ background [12]. Based on this study the b' are excluded with mass below 611 GeV at 95%CL.

Inclusive search for t' and b' are also done and details can be found in Ref. [13]. The pair production of vector-like heavy quarks with $T \to tZ$ has been studied at CMS assuming a 100% branching fraction. This analysis is performed for a final state of $Z(ll) + 1-\text{lepton} + \geq 2-\text{jets}$. A more detail of the analysis can be found in Ref. [14].

5 Conclusion

The lower limits on the large extra dimension scale in the ADD framework are extended to $M_D \geq 2.49 - 4.44$ TeV for $n_D = 2 - 6$ from the monojet study. The search for leptoquarks for second generation at CMS have set new lower bound of $M_{LQ} > 632$ (523) GeV for $\beta = 1.0$ (0.5). The CMS searches for heavy quarks have excluded $M_{t'}(M_{b'})$ below 560 GeV (611 GeV).

References

[1] CMS Collaboration, "The CMS experiment at the CERN LHC", JINST **3** (2008) S08004.

[2] Search for Dark Matter and Large Extra Dimensions in pp Collisions Yielding a Photon and Missing Transverse Energy , arXiv:1204.0821, *CMS EXO-11-096*.

[3] Search for Dark Matter and Large Extra Dimensions in Monojet Events in pp Collisions at $\sqrt{s} = 7$ TeV, `https://twiki.cern.ch/twiki/bin/view/CMSPublic/PhysicsResultsEXO11059Winter2012`, *CMS PAS EXO-11-059*, Phys. Rev. Lett. **107**, 201804 (2011).

[4] Search for Signatures of Extra Dimensions in the Diphoton Mass Spectrum at the Large Hadron Collider, CMS Collaboration, Phys. Rev. Lett. **108**, 111801 (2012)

[5] Search for large extra dimensions in dimuon and dielectron events in pp collisions at $\sqrt{s} = 7$ TeV, CMS Collaboration, Physics Letters **B** 711, 15-30(2012).

[6] Search for Pair Production of First-Generation Scalar Leptoquarks in pp Collisions at $\sqrt{s} = 7$ TeV, CMS Collaboration. Phys. Rev. Lett. **106**, 201802(2011).

[7] Search for first generation scalar leptoquarks in the eνjj Channel in pp Collisions at $\sqrt{s} = 7$ TeV, CMS Collaboration, Physics Letters **B** 703, 246-266 (2011).

[8] Search for Second Generation Scalar Leptoquarks, *CMS PAS EXO-11-028*

[9] Search for Pair Production of Third-Generation Scalar Leptoquark, *CMS PAS EXO-11-030*.

[10] Search for heavy, top-like quark pair production in the dilepton final state in pp collisions at $\sqrt{s} = 7$ TeV, arXiv:1203.5410, *CMS EXO-11-050*.

[11] Search for the pair production of a fourth-generation up-type quark (t') in events with a lepton and at least 4 jets, *CMS PAS EXO-11-099*.

[12] Search for heavy bottom-like quarks in 4.9 inverse femtobarns of pp collisions at $\sqrt{s} = 7$ TeV , arXiv:1204.1088, *CMS EXO-11-036*.

[13] Inclussive Search for a Fourth Generation of Quarks, *CMS PAS EXO-11-054*.

[14] Search for a Vectorlike Quark with Charge 2/3 in $t + Z$ Events from pp Collisions at $\sqrt{s} = 7$ TeV, CMS Collaboration, Phys. Rev. Lett. **107**, 271802 (2011).

Search for Heavy Stable Charged Particles with the CMS detector at the LHC

Loïc Quertenmont[1]

[1]CERN, 1211 Genève 23, Switzerland

DOI: http://dx.doi.org/10.3204/DESY-PROC-2012-02/223

Heavy Stable (or quasi-stable) Charged Particles (HSCP) are predicted by various extensions to the Standard Model of the fundamental interactions among elementary particles. If this prediction reveals to be true, such particles should be produced at the Large Hadron Collider (LHC) and observable with the Compact Muon Solenoid (CMS) detector. Results of the search for slowly moving (or stopped) HSCP with an integrated luminosity of 4.7 fb^{-1} (0.9 fb^{-1}) is described.

1 Introduction

Heavy Stable (or quasi-stable) Charged Particles (HSCP) are predicted by various extensions to the Standard Model of the fundamental interactions among elementary particles. If this prediction reveals to be true, such particles should be produced at the Large Hadron Collider (LHC) and observable with the Compact Muon Solenoid (CMS) detector [1].

Given their large mass and the limited energy available in LHC collisions, the HSCP will be significantly slower than light ($\beta < 1$). Consequently, they will have an anomalously high ionization energy loss (dE/dx) that could be measured by the CMS Silicon Strip Tracker. A large fraction of these highly penetrating particles are also expected to reach the CMS Muon System, which could therefore be used to measure the time-of-flight (TOF) of the particles. The typical signature of an HSCP is therefore a high momentum track reaching the muon system that have an anomalously high dE/dx and TOF.

The interactions with matter experienced by a strongly-interacting HSCP, which is expected to form a bound state (R-hadron) in the process of hadronization, can lead to a change of its electric charge. A recent study on the modelling of the interaction of the HSCP with matter claims that certain species of HSCPs will always be neutral, and therefore undetectable, in the muon system. A complementary search, which does not require the HSCP to reach the muon system is therefore also presented. For low-β R-hadrons, the energy loss is sufficient to bring 20% to 40% of the produced particles to rest inside the detector volume. These stopped R-hadrons could decay seconds, days, or weeks later. These decays would be out-of-time with respect to LHC collisions and may well occur at times when there are no collisions or when there is no beam in the LHC machine. The observation of such decays, in what should be a quiet detector would be yet another unambiguous signature for the discovery of new physics.

2 Search for HSCP

This search for slowly-moving HSCP uses events from 7 TeV pp collisions produced by the LHC during the 2011 Run corresponding to an integrated luminosity of 4.7 fb^{-1} [2]. The events where selected using transverse missing energy (MET>150 GeV) and muon (muon pT>40GeV) triggers. The HSCP candidates are selected based on their pT, dE/dx and TOF. The absence of correlation between these three variables is exploited to predict the background in the signal region (high pT, high dE/dx and long TOF). Mass of the candidates, reconstructed from their momentum and dE/dx, is also used to further select the candidates. The Fig.1 [4] shows the reconstructed and predicted mass spectrum for a loose signal selection. A similar search not using the TOF information was also performed in order to be sensitive to HSCP being unobservable in the muon system. In both case, a good agreement between the observation and the prediction was found. A lower limit at the 95% confidence level (C.L.) on the mass of stable gluinos (stops) is set at 1091(734) GeV/c^2, using a conventional model of nuclear interactions that allows charged hadrons containing this particle to reach the muon detectors. A lower limit of 923 (623) GeV/c^2 is also set for a stable gluinos (stops) in a conservative scenario of complete charge suppression, where any R-hadron becomes neutral before reaching the muon detectors. Pair-Produced (GMSB-SP7) staus with mass lower than 306 (221) GeV/c^2 are also excluded at 95% C.L., see Fig.1.

3 Search for stopped HSCP

The search looks for the subsequent decay, of long-lived particles which have stopped in CMS, during time intervals where there were no pp collisions in the CMS experiment like during gaps between crossings in the LHC beam structure [3]. Such decays where recorded with a dedicated calorimeter trigger. In a dataset that is sensitive to an integrated luminosity of up to 0.9 fb^{-1}, depending on the particle lifetime, and a search interval corresponding to 168 hours of LHC operation. The background rate is estimated using data taken in 2010 with a low peaked luminosity and corresponding to more than 300 hours of LHC operation. No significant excess above background was observed, therefore 95% C.L. on gluino and stop production where set. These limits range over 13 orders of magnitude of particle lifetime as shown on Fig.2 [4]. These limits can be translated in limits on the mass of long-lived gluinos (stops) of 601 (337) GeV/c^2 for models in which the mass difference between the gluinos (stops) and the LSP is of 100 (200) GeV/c^2.

References

[1] The CMS Collaboration, "The CMS experiment at the CERN LHC",JINST,0803,S08004, 2008.

[2] The CMS Collaboration, "Search for heavy long-lived charged particles in pp collisions at $\sqrt{s}$ =7 TeV", CMS-EXO-11-022, arXiv:1205.0272, 2011.

[3] The CMS Collaboration, "Search for Stopped HSCP in pp collisions at $\sqrt{s}$ =7 TeV", CMS-PAS-EXO-11-020, 2011.

[4] The CMS Collaboration, "Public CMS Exotica Results", `https://twiki.cern.ch/twiki/bin/view/CMSPublic/PhysicsResultsEXO`.

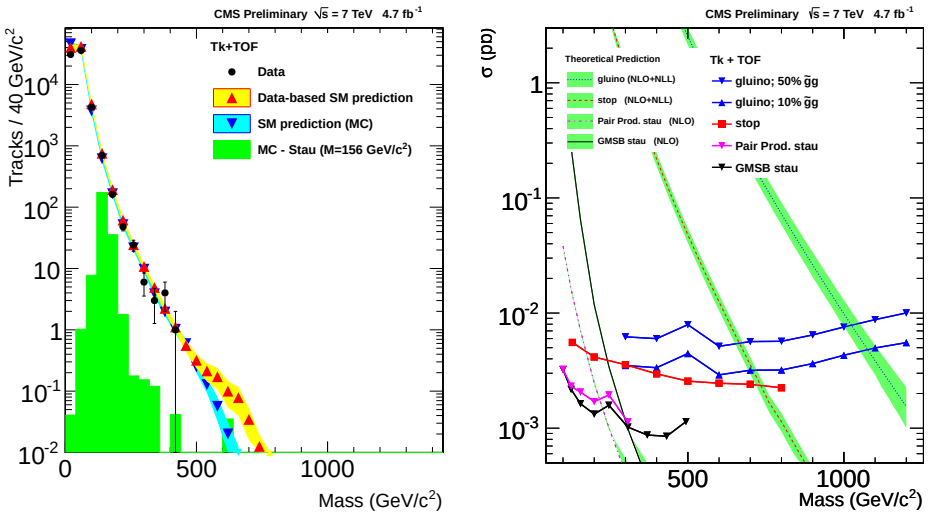

Figure 1: Left: Distribution of candidate mass for the loose selection of the tracker+TOF analysis. Shown are: data (black dots with the error bars), data-driven background estimate (red triangles) with its uncertainty (yellow band), simulated signal (green shaded histogram) and background prediction from MC using the same method as for data (blue inverted triangles). Right: Predicted theoretical cross section and observed 95% CL upper limits on the cross section for the different signal models considered: production of stops, gluinos, and staus; different fractions (f) of R-gluonball states produced after hadronization; standard and charge suppression (ch. suppr.) scenario for nuclear interactions experienced by R-hadrons. The uncertainties on the theoretical cross section are illustrated as bands around the central values.

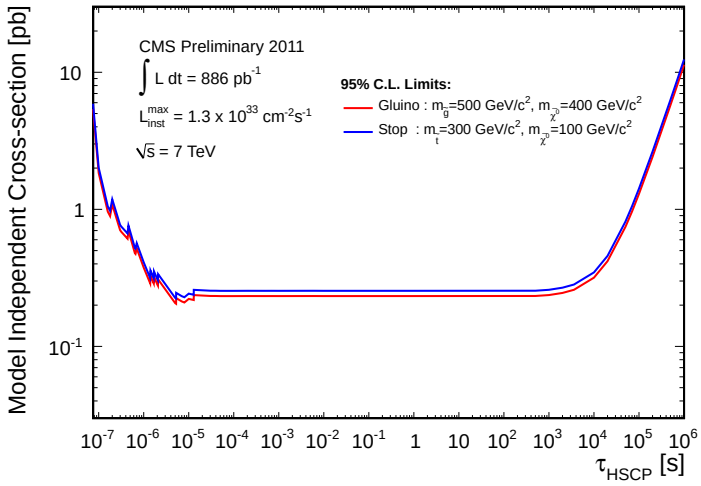

Figure 2: Observed 95%C.L. limits on HSCP pair production cross section times branching fraction times stopping probability, from the counting experiment. This is a reasonably model independent result. Separate curves are shown for gluino and stop, with masses detailed on the plot.

Searches for Fourth Generation Heavy Quarks with the ATLAS Detector

Jiahang Zhong[1] on behalf of the ATLAS Collaboration

[1]University of Oxford, OX13RH Oxford , United Kingdom

DOI: http://dx.doi.org/10.3204/DESY-PROC-2012-02/200

The addition of one or more generations of heavy fermions is a natural extension to the Standard Model. Fourth generation heavy quarks can be produced at the LHC at rates that can be observed in the 2011 data samples, depending on the quark mass. The talk presents results from searches performed by the ATLAS collaboration for fourth generation quarks decaying via several potential decay channels.

Introduction

The addition of one or more generations of heavy fermions is a natural extension to the Standard Model (SM). New physics models with such heavy quarks can accommodate a heavier Higgs boson within the constraint of precision electroweak data, and extend the CKM matrix to provide new sources of CP violation [1, 2]. Here we presents several studies carried out with the ATLAS detector [3], using 7 TeV proton-proton collision data delivered by the LHC in 2011.

$t'\bar{t}'$ in the lepton+jets channel

This study searches for pair production of t', assuming it decays exclusively into Wb [4]. Signature expected here is an isolated lepton (e, μ), high missing transverse momentum ($E_{\mathrm{T}}^{\mathrm{miss}}$), and at least three energetic jets, one of which must be tagged as b-jet. The primary discriminant from SM top quark pair production is the t' mass (m_{recon}) reconstructed from the jets.

The m_{recon} distribution was analyzed by a binned log-likelihood ratio as test-statistic. With 1.04 fb^{-1} data, no excess was observed over the m_{recon} distribution. Using the CLs method [5, 6], upper limit on the $t'\bar{t}'$ cross-section is set as in figure 1. Comparing with theoretical prediction, t' with mass below 404 GeV is excluded at 95% confidence level.

$Q\bar{Q}$ in the opposite-sign di-lepton channel

This study searches for heavy quark (Q) pair production, under the assumption that Q decays to Wq ($q = u, d, c, s, b$) [7]. This is applicable to both up-type and down-type fourth generation quarks and other exotic models. The expected final state contains two isolated leptons (e, μ) with opposite charges, and at least two energetic jets. In the $ee/\mu\mu$ channels, the Drell-Yan background is suppressed by imposing constraints on the di-lepton invariant mass and $E_{\mathrm{T}}^{\mathrm{miss}}$. In the $e\mu$ channel, a high value of H_T, defined as the scalar sum of E_T from all selected leptons and jets, is required.

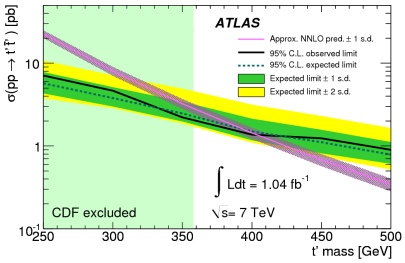

Figure 1: 95% C.L. upper limits on the $t'\bar{t}'$ cross-section as a function of the t' mass, in the lepton+jets channel.

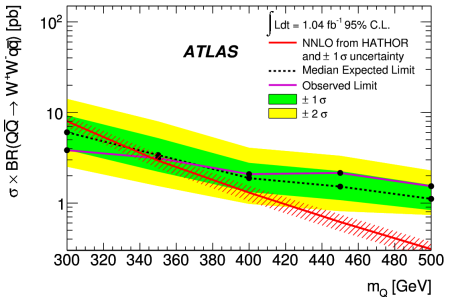

Figure 2: 95% C.L. upper limits on the $Q\bar{Q}$ cross-section as a function of the Q mass, in the di-lepton channel.

The observable in this analysis is again the reconstructed mass of Q. The $E_{\mathrm{T}}^{\mathrm{miss}}$ is solved into two neutrinos, by exploiting the small angular separation between the lepton and neutrino from the boosted W. The optimal directions of the neutrinos are solved by minimizing the mass difference between the two reconstructed heavy quarks. The final reconstructed mass ($m_{Collinear}$) of each event is the average of m_Q and $m_{\bar{Q}}$.

To enhance sensitivity, additional mass-dependent cuts are further applied on the several variables, including leading jet p_T, $E_{\mathrm{T}}^{\mathrm{miss}}$, and H_T+$E_{\mathrm{T}}^{\mathrm{miss}}$ v.s. $m_{Collinear}$ plane. The observed $m_{Collinear}$ distribution are in good agreement with the expected background, using 1.04 fb^{-1} data. Assuming 100% branching ratio of $Q \to Wq$, this analysis set a lower limit of m_Q at 350 GeV at 95% confidence level (figure 2).

$b'\bar{b}'$ in the same-sign di-lepton channel

This analysis is carried out in a model-independent approach, searching for new physics in the same-sign (SS) di-lepton (e, μ) final state [8]. A down-type heavy quark b' is assumed to decay exclusively to Wt. Thus, up to four W bosons are expected, giving a good chance of SS di-lepton final state. Besides two energetic leptons, at least two energetic jets and high $E_{\mathrm{T}}^{\mathrm{miss}}$ are required. Again, cuts on the di-lepton invariant mass and H_T are applied to suppress SM backgrounds. Most backgrounds in this analysis are derived by data-driven techniques.

In the end, observed numbers of events in 1.04 fb^{-1} data were compared to the background expectation, in six bins of different lepton flavors and charges. No excess was observed, and a lower bound of 450 GeV for the b' mass is derived at 95% confidence level (figure 3).

$b'\bar{b}'$ in the lepton+jets channel

This study searches for b' pair production in the single-lepton final state [9], again assuming 100% branching ratio for $b' \to Wt$. In addition to the lepton, the presence of at least six energetic jets and high $E_{\mathrm{T}}^{\mathrm{miss}}$ are required.

The hadronically-decayed W bosons are reconstructed from jet pairs with ΔR <1.0 and invariant mass within W mass window. Such selection has an efficiency as high as 80%, for energetic W bosons with p_T around 250 GeV.

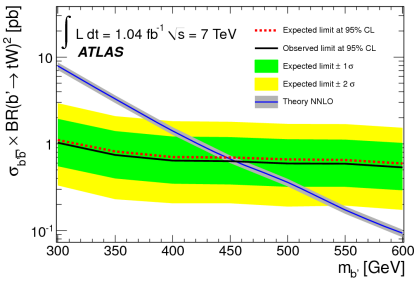

Figure 3: 95% C.L. upper limits on the $b'\bar{b}'$ cross-section as a function of the b' mass, in the same-sign di-lepton channel.

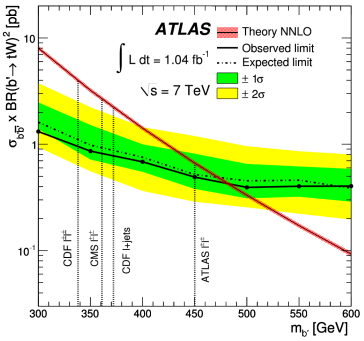

Figure 4: 95% C.L. upper limits on the $b'\bar{b}'$ cross-section as a function of the b' mass, in the lepton+jets channel.

Nine exclusive bins are examined, split by the multiplicity of hadronic W ($N_W = 0, 1, \geq 2$) and jet multiplicity ($N_{jet} = 6, 7, \geq 8$). A binned maximum likelihood fit is performed to derive the most likely cross-section of $b'\bar{b}'$. No evidence of b' production is observed with 1.04 fb^{-1} data. The b' masses below 480 GeV are excluded at 95% confidence level (figure 4).

$b'\bar{b}'$ in the $Z + b$ channel

This analysis looks for b' pair production with at least one b' decaying to a Z boson and a b quark [10]. It complements the above-mentioned searches in the $b' \to Wt$ decay mode, and is particularly relevant for the vector-like quarks in the high mass region.

The expected signature here is a Z boson and at least one b-tagged jet, with a high transverse momentum of the Z+b system. The Z boson is reconstructed from opposite charge electron pair, with invariant mass within Z mass window.

The observable here is the invariant mass of the Z+b system. The distribution of m_{Zb} from 2.0 fb^{-1} data is consistent with SM prediction, against all b' mass values considered. The cross-section limits can be seen in figure 5. This result can be interpreted as a b' mass limit of 400 GeV assuming 100% branching ratio of $b' \to Zb$. Alternatively, for a vector-like singlet b' mixing solely with the third SM generation, masses below 358 GeV are excluded from this search.

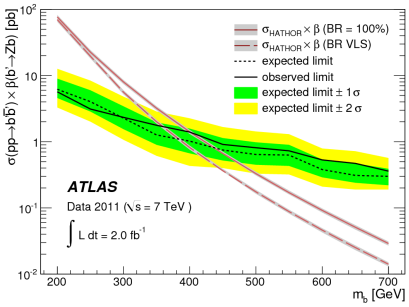

Figure 5: 95% C.L. upper limits on the $b'\bar{b}'$ cross-section as a function of the b' mass, in the $Z + b$ channel.

Vector-like quarks in the V+jets channel

This analysis searches for single production of vector-like quarks (VLQ), assuming full coupling to a vector boson and light quarks [11]. Both the

charged current (CC) channel and the neutral current (NC) channel are studied.

In the CC channel, the W boson is reconstructed from one isolated lepton (e, μ) and a high $E_{\mathrm{T}}^{\mathrm{miss}}$, with their transverse mass above certain threshold. As the W boson is highly boosted, angular separation between the lepton and the $E_{\mathrm{T}}^{\mathrm{miss}}$ should not be too large in the transverse plane. In addition, at least one jet in the event must be very energetic. In the NC channel, the Z boson is reconstructed from two same-flavor opposite-sign leptons. The invariant mass of the lepton pair must be within Z mass window, and the p_T of the di-lepton system should be large. In both channel, the presence of at least two jets are required. As a forward jet is expected, a minimum pseudo-rapidity separation is required between the leading-p_T jet and the second or third-leading jet.

The observable in this analysis is the mass of the VLQ, reconstructed from the vector boson and the leading jet. With 1.04 fb^{-1} data, no significant excess over background expectation is observed. This leads to 95% C.L. lower limit for the VLQ mass as 900 GeV in the CC channel and 760 GeV in the NC channel (figure 6).

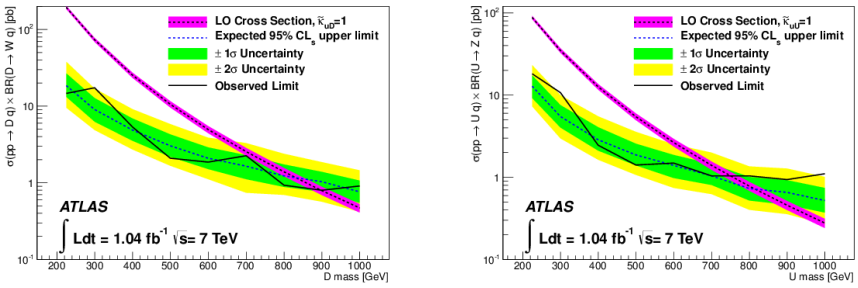

(a) (b)

Figure 6: 95% C.L. upper limits on the single VLQ production cross-section as a function of the VLQ mass, in the charged current channel (a) and the neutral current channel (b).

References

[1] B. Holdom, W. Hou, T. Hurth, M. Mangano, S. Sultansoy, *et al.* PMC Phys. **A3** (2009) 4, arXiv:0904.4698 [hep-ph].

[2] A. K. Alok, A. Dighe, and D. London. Phys.Rev. **D83** (2011) 073008, arXiv:1011.2634 [hep-ph].

[3] ATLAS Collaboration. JINST **3** (2008) S08003.

[4] ATLAS Collaboration. arXiv:1202.3076 [hep-ex].

[5] T. Junk. Nucl.Instrum.Meth. **A434** (1999) 435–443, arXiv:hep-ex/9902006 [hep-ex].

[6] A. L. Read. J.Phys.G **G28** (2002) 2693–2704.

[7] ATLAS Collaboration. arXiv:1202.3389 [hep-ex].

[8] ATLAS Collaboration. JHEP **1204** (2012) 069, arXiv:1202.5520 [hep-ex].

[9] ATLAS Collaboration. arXiv:1202.6540 [hep-ex].

[10] ATLAS Collaboration. Phys.Rev.Lett. (2012) , arXiv:1204.1265 [hep-ex].

[11] ATLAS Collaboration. arXiv:1112.5755 [hep-ex].

Searches at ZEUS

Stefano Antonelli[1]

[1]CNAF, viale Berti Pichat 6/2, 40127 Bologna, Italy

DOI: `http://dx.doi.org/10.3204/DESY-PROC-2012-02/294`

The results of recent searches for scalar and vector leptoquarks and anomalous single top production in $e^{\pm}$ collisions at HERA are presented. The searches make use of the full ZEUS data set corresponding to 0.5 fb^{-1}. No evidence for leptoquarks signals is found and limits are set on the Yukawa coupling, λ, as a function of the leptoquark mass for different leptoquark types within the Buchmüller-Rückl-Wyler model. No evidence for top production is found and upper limits on the single top cross section via flavour changing neutral current and on the anomalous coupling $\kappa_{tu\gamma}$ are set.

1 Search for leptoquarks

Many extensions of the Standard Model (SM) predict the existence of particles, such as leptoquarks (LQs), carrying both lepton and baryon numbers [1]. At HERA, LQs could be resonantly produced in the s-channel or exchanged in the u-channel between the initial state lepton of energy 27.6 GeV and a quark coming from the proton of energy up to 920 GeV with subsequent decays into electron and quark or neutrino and quark, Fig. 1. These decays have a topology similar to deep-inelastic scattering (DIS) neutral current (NC) or charged current (CC).

Analysis searches for deviations from the SM in the lepton-jet invariant mass spectrum at different lepton scattering angle (θ^*) in the lepton-jet scattering frame to reduce DIS background. Two plots of mass spectra measured for NC-like and CC-like events for 106 pb^{-1} data set are showed in Fig. 2.

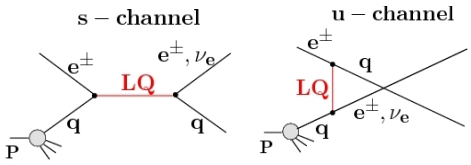

Figure 1: Leptoquark diagrams: s-channel LQ production (left) and u-channel LQ exchange (right).

Since no evidence for any leptoquark signal is found, limits are derived on the Yukawa coupling λ as a function of the mass for different leptoquark states as described by the Buchmüller-Rückl-Wyler model (BRW) [1]. Limits are evaluated including also data recorded with the ZEUS detector in 1994-2000, as published in [2], for a total of 0.5 fb^{-1}. Table 3 shows mass limit for the 14 BRW LQs at $\lambda = 0.3$. Figures 4 show the limits on the S_0^L and $S_{1/2}^L$ compared to the limits from CMS [3], D0 [4] and L3 [5]. Assuming $\lambda = 0.3$, the mass limits range from 291 to 629 GeV.

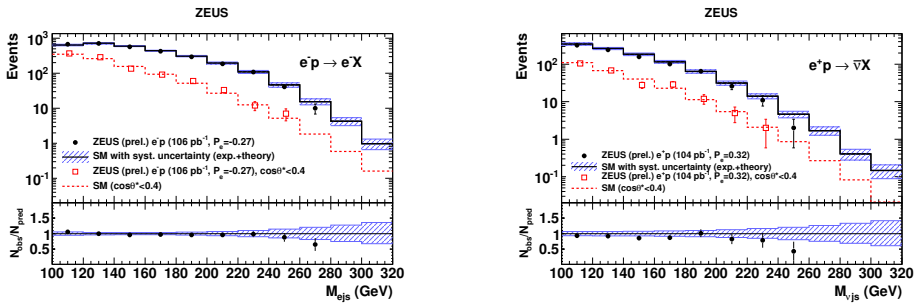

Figure 2: On the left: comparison of the left-handed e^-p sample (dots) and the NC SM expectation (solid histogram) for the reconstructed invariant mass M_{ejs} in the $e^-p \to e^-X$ topology. On the right: comparison of the right-handed e^+p sample (dots) and the CC SM expectation (solid histogram) for the reconstructed invariant mass $M_{\nu js}$ in the $e^+p \to \nu X$ topology. The data (open squares) and SM expectation (dashed histogram) after the $cos\theta^* < 0.4$ are also shown. The shaded area shows the overall uncertainty of the SM MC expectation. The lower half of the plot shows the ratio between the data and the SM expectation before the $cos\theta^*$ cut.

LQ Type (F=0)	V_0^L	V_0^R	$\tilde{V}_0^R$	V_1^L	$S_{1/2}^L$	$S_{1/2}^R$	$\tilde{S}_{1/2}^L$
M_{LQ}(GeV) ZEUS (prel.)	504	293	343	629	322	300	293
LQ Type (F=2)	S_0^L	S_0^R	$\tilde{S}_0^R$	S_1^L	$V_{1/2}^L$	$V_{1/2}^R$	$\tilde{V}_{1/2}^L$
M_{LQ}(GeV) ZEUS (prel.)	435	326	291	466	292	324	409

Figure 3: Limits for 7 scalar + 7 vector states assuming em coupling $\lambda = \sqrt{4\pi\alpha} = 0.3$.

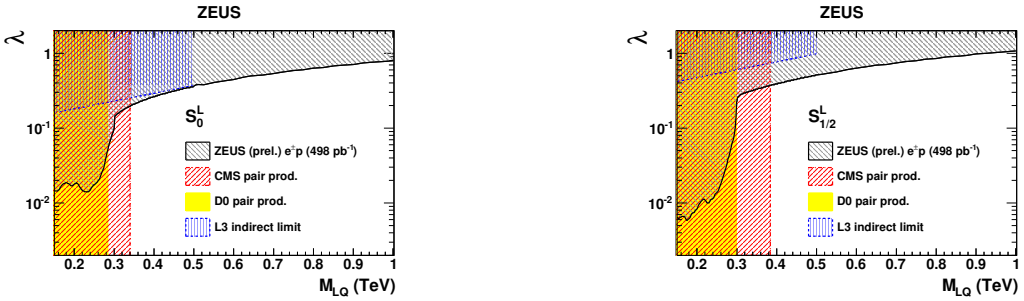

Figure 4: Coupling limit as a function of LQ mass for the S_0^L (left) and $S_{1/2}^L$ (right) from ZEUS, CMS, D0, L3 .

2 Search for single top production

In ep collisions at HERA, the production of single top quarks is possible due to the large centre of mass energy, $\sqrt{s} = 318$ GeV. The dominant process for SM single top production, charged cur-

rent process $ep \to \nu tX$, has a cross section of less than 1 fb [6, 7] so no sizeable production is expected and any excess can be attributed to new physics. In several extensions of the SM [8], single top production can happen via a flavour changing neutral current (FCNC) process mediated by an effective coupling which allows a $u-t$ transition via a neutral vector boson γ ($tu\gamma$) or Z (tuZ), see Fig. 5 Due to the large Z mass the process is more sensitive to a coupling $tq\gamma$. Furthermore, the production of single top quark is most sensitive to the $tu\gamma$ coupling because large values of x, the fraction of the proton momentum carried by the struck quark, are needed to produce a top quark and, at large x, u-quark parton distribution function (PDF) of the proton is dominant.

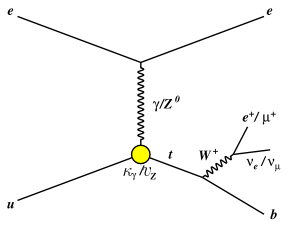

Figure 5: Anomalous single-top production via flavour changing neutral current transitions at HERA with subsequent decays $t \to bW^+$ and $W^+ \to \nu_e(\nu_\mu)e^+(\mu+)$.

The search has been performed in the electron and muon channels. Figure 6 shows the preselection plots in the muon (left) and electron (right) channels.

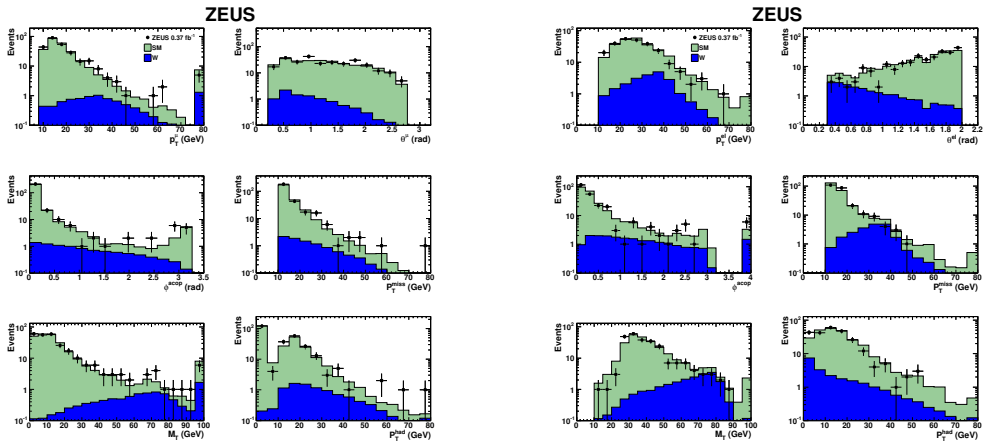

Figure 6: Preselection plots in the muon (left) and electron (right) channels.

Since no excess of events above the SM expectations is observed, a further selection is made to improve the limit on FCNC cross section under the assumption of no signals. The 95% C.L. limit on the cross section is found to be: $\sigma < 0.24$ pb at $\sqrt{s} = 318$ GeV. The limit on the cross section is converted into a limit on the coupling κ_γ: $\kappa_\gamma < 0.18$ (95% C.L.). This result has been combined with a previous ZEUS result [9] giving the following results: $\sigma < 0.13$ pb and $\kappa_\gamma < 0.13$ (95 % C.L.) [10]. Constraints on the anomalous top branching ratios (Br) $t \to u\gamma$ and $t \to uZ$ were also evaluated assuming a non-zero v_Z. Figure 7 shows the ZEUS boundary in the $(\mathrm{Br_{u\gamma}}, \mathrm{Br_{uZ}})$ plane compared to limits from H1 [11], ALEPH [14], CDF [12], D0 [13]. For low values of v_Z , resulting in branching ratios of $t \to uZ$ of less than 4%, this paper provides the current best limits.

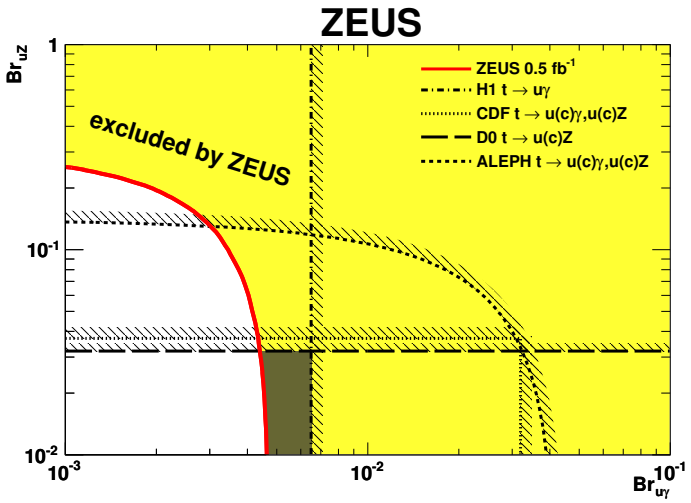

Figure 7: ZEUS boundary in the $(\mathrm{Br}_{u\gamma}, \mathrm{Br}_{uZ})$ plane. Also shown are boundaries of H1 [11], CDF [12], D0 [13] and ALEPH [14]. The shaded area is excluded. The dark shaded region denotes the area uniquely excluded by ZEUS.

References

[1] W. Buchmüller, R. Rückl, D. Wyler, "Leptoquarks in lepton-quark collisions", Phys. Lett. **B191** (1987) 442. Erratum in Phys. Lett **B448**, (1999) 320.

[2] ZEUS Coll., S. Chekanov et al. , "Search for resonant decays to lepton+jet at DESY HERA and limits on leptoquarks", Phys. Rev. **D68** (2003) 052004.

[3] Chatrchyan, Serguei and others , "Search for first generation scalar leptoquarks in the $e\nu$ jj channel in pp collisions at sqrt(s)=7 TeV", Phys. Lett. **B703** (2003) 246.

[4] Abazov, V.M. and others , "Search for pair production of first-generation leptoquarks in p pbar collisions at sqrt(s)=1.96 TeV", Phys. Lett. **B681** (2009) 224.

[5] Acciarri, M. and others , "Search for manifestations of new physics in fermion pair production at LEP", Phys. Lett. **B489** (2000) 81.

[6] T. Stelzer, D. Sullivan and S. Willenbrock, Phys. Rev. **D56** (1997) 5919.

[7] T. Moretti and K. Odagiri, Phys. Rev. **D57** (1998) 3040.

[8] T.Han, J.L.Hewett, Phys. Rev. **D60** (1999) 074015.

[9] ZEUS Coll., S. Chekanov et al., Phys. Lett. **B559** (2003) 153

[10] ZEUS Coll., H. Abramowicz et al., Phys. Lett. **B708** (2012) 27

[11] H1 Coll., F.D. Aaron et al., Phys. Lett. **B678** (2009) 450

[12] CDF Coll., F. Abe et al., Phys. Rev. Lett. **80** (1998) 2525

[13] D0 Coll., V.M. Abazov et al., Phys. Lett. **B701** (2011) 313

[14] Aleph Coll., A. Heister et al., Phys. Lett. **B543** (2002) 173

Results from the NA48 experiment on the semileptonic decays of charged kaons

Mauro Piccini[1]

[1] INFN - Sezione di Perugia, 06123 Perugia, Italy

DOI: http://dx.doi.org/10.3204/DESY-PROC-2012-02/295

In the 2003 and 2004 years the NA48/2 experiment collected a large sample of $K^{\pm}$ decays. Using a run with minimal trigger conditions a sample of 2.5×10^6 $K^{\pm} \to \pi^0 \mu^{\pm} \nu_{\mu}$ ($K^{\pm}_{\mu 3}$) events and 4.0×10^6 $K^{\pm} \to \pi^0 e^{\pm} \nu_e$ ($K^{\pm}_{e3}$) were collected. These samples allow a precise measurement of the form factors according to various parameterisations. In this report the event selections and the fitting procedure are described and preliminary results are presented.

1 Introduction

Semileptonic decays of charged and neutral Kaons provide the most accurate and theoretically cleanest way to measure the CKM matrix element $|V_{us}|$. In addition, also a stringent constraint on new physics can be given by testing lepton universality. The hadronic matrix element of these decays is described by two dimensionless form factors $f^{\pm}(t)$, which depend on the squared four-momentum $t = (p_K - p_{\pi})^2$ transferred to the lepton system. These form factors are important input parameters to the phase space integral of those decays for the determination of $|V_{us}|$. The $K^{\pm}_l$ ($l = e, \mu$) decays are usually described in terms of the vector form factor f_+ and the scalar form factor f_0 defined as:

$$f_0(t) = f_+(t) + \frac{t}{m_K^2 - m_{\pi}^2} f_-(t). \tag{1}$$

The function f_+ and f_0 are related to the vector (1^-) and scalar (0^+) exchange to the lepton system, respectively. Being proportional to the lepton mass squared, the contribution of f^- can be neglected in K_{e3} decays. By construction, $f_0(0) = f_+(0)$ and, since $f_+(0)$ is not directly measurable, it is customary to factor out $f_+(0)$ and to normalize to this quantity all the form factors:

$$\overline{f}_+(t) = \frac{f_+(t)}{f_+(0)}, \quad \overline{f}_0(t) = \frac{f_0(t)}{f_0(0)}, \quad \overline{f}_+(0) = \overline{f}_-(0). \tag{2}$$

To describe the form factors, two different parameterisations are used in this study. The most used one is the Taylor expansion:

$$\overline{f}_{+,0}(t) = 1 + \lambda'_{+,0} \frac{t}{m_{\pi^2}} + \lambda''_{+,0} \frac{t^2}{m_{\pi^4}}, \tag{3}$$

where $\lambda'_{+,0}$ and $\lambda''_{+,0}$ are the slope and the curvature of the form factors, respectively. The disadvantage of this parameterisation is related to the strong correlations between parameters

and the absence of physical constraints. To reduce the parameters and to add a physical motivation the pole parameterisation is also used:

$$\overline{f}_{+,0}(t) = \frac{M_{V,S}^2}{M_{V,S}^2 - t} \tag{4}$$

In this parameterisation the dominance of a single resonance is assumed and the corresponding pole masses $M_{V,S}$ are the only free parameters.

2 The NA48/II experiment: beam and detector

In the 2003 and 2004 years the NA48/2 experiment has collected data from charged kaon decays. Two simultaneous K^+ and K^- beams were produced by a 400 GeV/c proton beam delivered by the CERN SPS and impinging on a berillium target. The layout of beams and detectors is shown in figure 1. The NA48/2 beamline was designed to select kaons with a momentum range of (60 $\pm$ 3) GeV/c. The data used for the $K^{\pm}_{l3}$ form factor analysis were collected in 2004 during a dedicated run with a special trigger setup which only requires one or more tracks in the magnetic spectrometer and at least a energy deposit of 10 GeV/c in the electromagnetic calorimeter. Also the intensity of the beam was lowered and the momentum spread was reduced to obtain an acceptable rate of events to be recorded. The main components

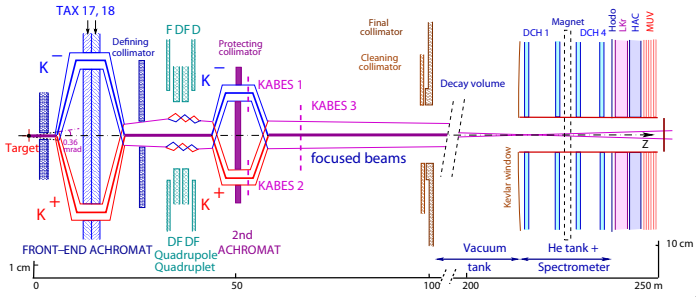

Figure 1: Schematic side view of the beam line, the decay volume and the detector of the NA48/II experiment.

of the NA48/2 detector were a magnetic spectrometer, composed by four drift chambers and a dipole magnet deflecting the charged particles in the horizontal plane, providing a resolution on the momentum measurement of 1.4% for 20 GeV/c charged tracks, and a liquid krypton electromagnetic calorimeter (LKr) with an energy resolution of about 1% for 20 GeV photons and electrons. For the selection of $K^{\pm}_{\mu 3}$ decays, the muon veto system (MUV) was essential to distinguish muons from pions. It consisted out of three planes of alternating horizontal and vertical scintillator strips. Each plane was shielded by a 80 cm thick iron wall. The inefficiency of the system was at the level of one per mill for muons with momentum greater than 10 GeV/c and the time resolution was below 1 ns. The NA48 detector is described in detail elsewhere [1].

3 Event selection

The topologic of the decays allowed the detector to measure only the lepton and the two photons coming from the instant decay of the neutral pion, the neutrino leaves the detector unseen. To select the decay, one track in the magnetic spectrometer and at least two clusters in the electromagnetic calorimeter are necessary. The track has to be inside the geometrical acceptance of the detector, need a good reconstructed decay vertex, proper timing cuts and a momentum $p > 5$ GeV/c for electrons. For muons the momentum need to be greater than 10 GeV/c to ensure proper efficiency of MUV system. To identify the track as a muon an associated hit in the MUV system and $E/p > 0.2$ is required, where E is the energy deposited in the electromagnetic calorimeter and p the track momentum. For electrons a cut range between $0.95 > E/p > 1.05$ is used. For the electron identification no associated hit in the MUV system is required. At least two photon clusters are needed to reconstruct the neutral pion. They need to be well isolated from any track hitting the calorimeter, to have an energy $E_\gamma > 3$ GeV/c, and to be in time with the track in the spectrometer. Finally a kinematical constraint is applied, requiring the missing mass squared (in the lepton mass hypothesis) to satisfy $m^2_{miss} < 10$ MeV^2. For $K^\pm_{\mu 3}$ the background from $K^\pm \to \pi^\pm\pi^0$ events with charged $\pi^\pm$ that decay in flight are suppressed by using a combined cut on the invariant mass $m^2_{\pi^\pm\pi 0}$ and on the π^0 transverse momentum. This cut reduces the contamination to 0.5% causing a loss of statistics of about 24%. Another source of background is due to $K^\pm \to \pi^\pm\pi^0\pi^0$ events with $\pi^\pm$ decaying in flight and a π^0 not reconstructed. The estimated contamination amounts to about 0.1% and no specific cut is applied. For $K^\pm_{e3}$ only the background from $K^\pm \to \pi^\pm\pi^0$ significantly contributes to the signal. A cut in the transvers momentum of the event reduce this background to less than 0.1% by only lossing about 3% of signal events. The selected samples amount to 2.5×10^6 $K^\pm_{\mu 3}$ events and 4.0×10^6 $K^\pm_{e3}$ events.

4 Fitting procedure

To extract the form factors a two dimensional fit is performed to the Dalitz plot density. The reconstructed four-momenta of the pion and the lepton are boosted into the kaon rest frame by using the calculated energy of the charged kaon. The calculation is done by assuming no transverse component of the momentum of the kaon. This leaves only two solution for the longitudinal component of the momentum of the neutrino. In this way the energy resolution in the Dalitz plot is improved, especially for high pion energies. The reconstructed data Dalitz plot is corrected for the remaining background, the acceptance and the distortions induced by radiative effects. The radiative effects were simulated by using a special Monte Carlo generator developed by the KLOE collaboration [2]. For the fit, the Dalitz plot is subdivided into 5×5 MeV^2 cells. Cells which cross or are outside of the kinematical border are not used in the fit.

5 Preliminary results

The results of the fits for quadratic and pole parameterisations are listed in Table 1. The comparison between K_{l3} quadratic fit results by recent experiments is shown in Figure 2. The 68% confidence level contours are displayed for both K^0_{l3} (KLOE, KTeV and NA48) and charged K decays (ISTRA+ studied K^-_{l3} only). The preliminary NA48/2 results presented here are the first high precision measurements done with both K^+ and K^- decays. The values of the

Quadratic $(\times 10^{-3})$	λ'_+	λ''_+	λ_0
$K^{\pm}_{\mu 3}$	$26.3 \pm 3.0_{stat} \pm 2.2_{sys}$	$1.2 \pm 1.1_{stat} \pm 1.1_{sys}$	$15.7 \pm 1.4_{stat} \pm 1.0_{sys}$
$K^{\pm}_{e3}$	$27.2 \pm 0.7_{stat} \pm 1.1_{sys}$	$0.7 \pm 0.3_{stat} \pm 0.4_{sys}$	
Combined	26.98 ± 1.11	0.81 ± 0.46	16.23 ± 0.95
Pole (MeV/c^2)	M_V		M_S
$K^{\pm}_{\mu 3}$	$873 \pm 8_{stat} \pm 9_{sys}$		$1183 \pm 31_{stat} \pm 16_{sys}$
$K^{\pm}_{e3}$	$879 \pm 3_{stat} \pm 7_{sys}$		
Combined	877 ± 6		1176 ± 31

Table 1: NA48/2 preliminary form factors fit results for quadratic and pole parameterisations. In the combined results the statistical and systematical uncertainties are combined.

parameters of the vector form factor λ'_+ and λ''_+ are compatible with the combined fit done by FlaviaNet[3] (also shown in figure 2). All the measured parameters are in good agreement with the measurements done by the other experiments. For this preliminary result, the systematic uncertainty has been evaluated by changing the cuts defining the vertex quality and the geometrical acceptance by small amounts. In addition, variations are applied to the resolutions of pion and muon energies in the kaon center of mass system, and to the cuts applied to reject backgrounds related to $\pi \to \mu$ decays. The systematic error also took into account for the differences in the results of two independent analyses that were realized in parallel.

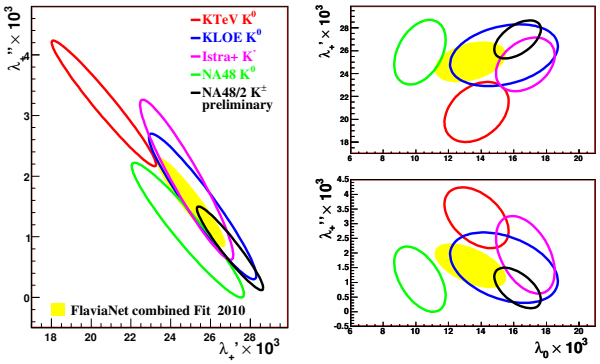

Figure 2: Quadratic fit results for K_{l3} decays. The ellipses are the 68% confidence level contours. For comparison the combined fit from FlaviaNet Working Group 1 is also shown.

6 Bibliography

References

[1] V. Fanti *et al.* **NA48** Collaboration, Nucl. Instrum. Methods **A 574** (2007) 433.

[2] C. Gatti, Eur. Phys. J. **C 45** (2006) 417.

[3] M. Antonelli *et al.* , Eur. Phys. J. **C 69** (2010) 399.

The MSSM After Two Years of LHC Running

Felix Brümmer

DESY, Notkestraße 85, 22607 Hamburg, Germany

DOI: http://dx.doi.org/10.3204/DESY-PROC-2012-02/179

The Minimal Supersymmetric Standard Model is increasingly getting constrained by the null results from squark and gluino searches at the LHC, and by the indications for a Higgs around 125 GeV. This talk presents a theorist's (biased) view of the impact of these constraints, with a focus on recent work.

1 Introduction

The Minimal Supersymmetric Standard Model (MSSM) is obtained by promoting all Standard Model (SM) fields to superfields, *i.e.* by adding adding scalar *squark* and *slepton* superpartners for all SM fermions and fermionic *gaugino* superpartners for all SM gauge bosons. Moreover, the scalar Higgs doublet of the SM is replaced by two Higgs doublets H_u and H_d and their fermionic *higgsino* superpartners. If the superparticle masses are close to the electroweak scale, this model can solve the electroweak hierarchy problem, lead to gauge coupling unification at high energies, and (if the lightest superparticle is stable) provide a dark matter candidate.

The MSSM has around 100 free parameters more than the SM. They should be fixed by augmenting it with a predictive mechanism for supersymmetry breaking and its mediation. However, many such mechanisms have been proposed (and many more might be conceivable), and it is difficult to assess which of them should be preferred. To study the MSSM phenomenology with a manageable number of parameters, the following approaches are common:

- Appealing to more or less motivated universality principles, one can just reduce the independent UV-scale parameters *ad hoc* to a small subset which still gives a viable phenomenology. The most common example is the CMSSM with parameters m_0, $M_{1/2}$, A_0, $\tan\beta$, and $\mathrm{sgn}(\mu)$. This gives a self-consistent particle spectrum which is useful for phenomenological benchmarks, but is hard to justify theoretically.

- In so-called simplified models, the spectrum is truncated to a few states relevant for a particular collider signature. Bounds *e.g.* on superparticle masses can then be obtained relatively easily, although they are usually stronger than they would be in realistic models. A related approach, the pMSSM, retains the full MSSM spectrum but prescribes the 19 most relevant parameters at the electroweak scale without referring to their UV-scale origins. It is often not clear if such a simplified spectrum can resemble an actual model.

- It is also worthwile to study full realistic models, but as mentioned there is a multitude of models on the market, and insights gained in one specific framework often cannot easily be carried over to another.

2 Constraints

In the R-parity conserving MSSM, supersymmetric particles are pair-produced at the LHC. The production channels with the largest cross-sections are $pp \to \tilde{g}\tilde{g}$, $\tilde{g}\tilde{q}$, $\tilde{q}\tilde{q}^*$, $\tilde{q}\tilde{q}$; here $\tilde{g}$ is the gluino and $\tilde{q}$ is any first-generation squark. Squarks and gluinos decay via cascade decays into Standard Model particles and the lightest supersymmetric particle, which escapes the detector as missing transverse energy (MET). This gives rise to the characteristic jets + MET (+ possibly leptons) signatures at ATLAS and CMS. The null results with the first 4.7 fb^{-1} of data at $\sqrt{s} = 7$ TeV allow to set stringent exclusion bounds on the superparticle masses [1, 2]. For instance, in the CMSSM with $\tan\beta = 10$, $A_0 = 0$, at the point where the squark and gluino masses are equal, masses below 1.4 TeV are excluded [1]. For $m_{\tilde{q}} \gtrsim 1500$ GeV, the gluino mass bound is somewhat weaker, $m_{\tilde{g}} \gtrsim 900$ GeV. These bounds do not necessarily carry over to less restrictive models; *e.g.* they become significantly weaker if the mass ratio $m_{\tilde{g}} : m_{\tilde{B}}$ between the gluino and the bino, which is about 6 : 1 in the CMSSM, is reduced.

Further constraints come from the recent indications for a 124–126 GeV Higgs boson [3, 4]. Should these be confirmed, the Higgs mass would be rather high for the MSSM. More precisely, at large $\tan\beta$ and in the decoupling limit $m_{A^0} \gg m_Z$, including the dominant one-loop corrections, the Higgs mass is

$$m_{h^0}^2 = m_Z^2 + \frac{3}{4\pi^2} y_t^4 v^2 \left(\log \frac{m_{\tilde{t}}^2}{m_t^2} + \frac{A_t^2}{m_{\tilde{t}}^2} \left(1 - \frac{A_t^2}{12\, m_{\tilde{t}}^2} \right) \right) + \dots \tag{1}$$

where $m_{\tilde{t}}$ is the average stop mass and A_t is the stop trilinear coupling. To increase m_{h^0} above m_Z, the terms in parentheses should be large, which requires either $m_{\tilde{t}} \gg m_t$ or $|A_t/m_{\tilde{t}}| \approx 2$ (see *e.g.* [5, 6] and Fig. 1). The former implies a large fine-tuning of parameters, whereas the latter, the *maximal stop mixing scenario*, is nontrivial to realize in UV-scale models [7, 8, 9].

In addition, there are constraints from flavour physics and from cosmology. For instance, one often asserts that the lightest supersymmetric particle should be the lightest neutralino and that its thermal relic density should reproduce the WMAP measurement for the dark matter abundance [10]. This is increasingly difficult to realize in constrained scenarios such as the CMSSM [11]. However, dark matter might also consist of other particles such as gravitinos, axions, or axinos, whose abundance cannot readily be computed without further model assumptions.

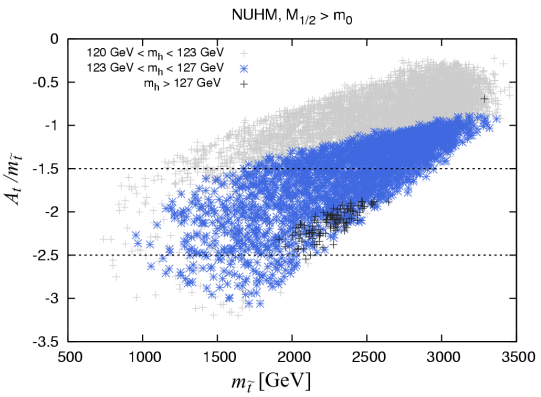

Figure 1: Higgs masses around 125 GeV (blue points) require $|A_t|/m_{\tilde{t}}$ around 2–2.5, or very large $m_{\tilde{t}}$ (from scans over non-universal Higgs mass models with large GUT-scale $M_{1/2}$ [9]).

3 Light stops

While the first-generation squarks and gluinos must be heavy to evade the direct search bounds, the stops could still be relatively light, $m_{\tilde{t}} < 1$ TeV. This is favoured by naturalness: The stops couple to H_u with a

large Yukawa coupling, and consequently the stop masses and Higgs mass parameters are naturally of similar order of magnitude. However, the parameters of the Higgs potential also set the electroweak scale, which therefore cannot be much smaller without considerable fine-tuning. Explicitly, for large $\tan\beta$ one obtains

$$m_Z^2 = -2(m_{H_u}^2 + |\mu|^2)\,, \tag{2}$$

so $|m_{H_u}^2| \gg m_Z^2$ requires a large cancellation between the two terms on the right-hand side. Furthermore, also the higgsino mass μ cannot be too large. A minimal spectrum, in which only those states are light that are required to be light by naturalness [12, 13], is sketched in Fig. 2.

The stops and the left-handed sbottom, as well as two higgsino-like neutralinos and a higgsino-like chargino, are below a TeV. The gluino should not be much heavier. All other superparticles can be heavy enough to be of LHC reach. The Higgs mass should be accounted for by large stop mixing. Several models have recently been proposed in order to obtain a superparticle spectrum of this kind [14].

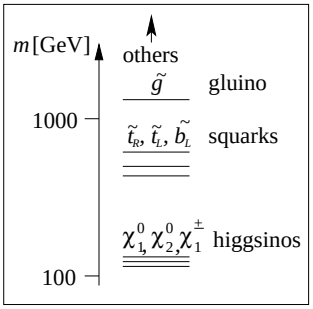

Figure 2: A "natural" mass spectrum with light stops.

4 Heavy stops

A different approach is to try to reconcile heavy stops with naturalness. With $m_{\tilde{t}} \gtrsim 3$ TeV, the Higgs mass in Eq. (1) can be increased to around 125 GeV, even without large mixing contributions. In a generic setting this would require large fine-tuning, as discussed above and as is also evident from Eq. (2) when expressing its RHS in terms of UV-scale boundary values for the soft terms (quoted here for large $\tan\beta \approx 50$ and $m_{\tilde{t}} \approx 1$ TeV [15]):

$$\begin{aligned} m_Z^2 \approx \Big(& 2.25\, M_3^2 - 0.45\, M_2^2 - 0.01\, M_1^2 + 0.19\, M_2 M_3 + 0.03\, M_1 M_3 \\ & + 0.74\, m_{\tilde{t}_R}^2 + 0.65\, m_{\tilde{t}_L}^2 - 0.04\, m_{\tilde{b}_R}^2 - 1.32\, m_{H_u}^2 - 0.09\, m_{H_d}^2 \\ & + 0.19\, A_0^2 - 0.40\, A_0 M_3 - 0.11\, A_0 M_2 - 0.02\, A_0 M_1 - 1.42\, |\mu|^2 \Big)\Big|_{M_{\rm GUT}} . \end{aligned} \tag{3}$$

Here $M_{1,2.3}$ are the gaugino masses, m_ϕ^2 are the various scalar soft masses, and A_0 is the trilinear coupling (assumed to be universal for simplicity). Clearly, if the typical soft mass scale is $\gg 1$ TeV, large cancellations are required for the RHS to sum up to $m_Z^2 = (91\ \text{GeV})^2$.

In certain models these cancellations are actually enforced by relations between the parameters. For instance, in the original *focus point* scenario [16, 17], the gaugino and higgsino masses M_i and μ as well as A_0 are of the order of the electroweak scale. The GUT-scale scalar masses are universal, $m_{\tilde{t}_R} = m_{\tilde{t}_L} = m_{\tilde{b}_R} = m_{H_u} = m_{H_d} \equiv m_0$. Because the coefficients in the second line of Eq. (3) happen to approximately sum up to zero, m_0 can be several TeV without worsening the fine-tuning.

Focus point supersymmetry is coming under pressure, because it requires relatively small gluino masses which are now in conflict with direct search bounds. However, variations are possible which also involve relations between the gaugino masses [18]. Examples are given by the models of [15, 19], which rely on a combination of high-scale gauge mediation and gravity

mediation. The spectrum is largely determined in terms of three integers $N_{1,2,3}$, with Eq. (3) becoming

$$m_Z^2 = \left(2.25\,N_3^2 - 0.45\,N_2^2 - 0.01\,N_1^2 + 0.19\,N_2N_3 + 0.04\,N_1N_3 + 3.80\,N_3 - 1.16\,N_2\right) m_{\rm GM}^2 - 1.42\,|\mu|^2\,;$$

here $m_{\rm GM}$ is of the order of the electroweak scale, GUT-scale gaugino masses are given by $M_i = N_i m_{\rm GM}$, and scalar soft masses scale like $m_\phi^2 \sim N m_{\rm GM}^2$. A model with, for instance, $(N_1, N_2, N_3) = (28, 28, 11)$ gives a realistic value for m_Z despite the individual soft masses being multi-TeV.

Should a scenario like this be realized in Nature, all coloured states would probably be too heavy to be produced at the LHC. The only electroweak-scale superparticles would be three almost mass-degenerate higgsinos which are difficult to detect at the LHC [20, 21]. Signals for them might show up in LHC monojet searches or at a future linear collider. This situation is sketched in Fig. 3.

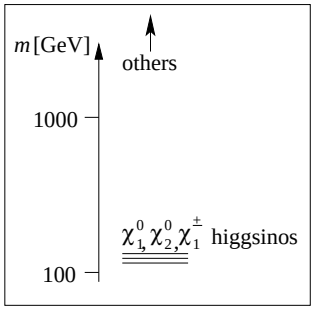

Figure 3: A spectrum where only the higgsinos are light.

References

[1] ATLAS Collaboration, ATLAS-CONF-2012-033, ATLAS-CONF-2012-037, ATLAS-CONF-2012-041.

[2] CMS Collaboration, PAS-SUS-12-005; S. Paktinat, presentation at this conference; M. Niegel, presentation at this conference.

[3] ATLAS Collaboration, G. Aad *et al.*, Phys. Lett. B **710** (2012) 49.

[4] CMS Collaboration, S. Chatrchyan *et al.*, arXiv:1202.1488 [hep-ex].

[5] A. Arbey, M. Battaglia, A. Djouadi, F. Mahmoudi and J. Quevillon, Phys. Lett. B **708** (2012) 162.

[6] S. Heinemeyer, O. Stål and G. Weiglein, Phys. Lett. B **710** (2012) 201.

[7] P. Draper, P. Meade, M. Reece and D. Shih, arXiv:1112.3068 [hep-ph].

[8] L. Aparicio, D. G. Cerdeño and L. E. Ibáñez, arXiv:1202.0822 [hep-ph].

[9] F. Brümmer, S. Kraml and S. Kulkarni, arXiv:1204.5977 [hep-ph].

[10] WMAP collaboration, E. Komatsu *et al.*, Astrophys. J. Suppl. **192** (2011) 18.

[11] H. Baer, V. Barger and A. Mustafayev, arXiv:1202.4038 [hep-ph].

[12] R. Barbieri and D. Pappadopulo, JHEP **0910** (2009) 061.

[13] M. Papucci, J. T. Ruderman and A. Weiler, arXiv:1110.6926 [hep-ph].

[14] C. Csáki, L. Randall and J. Terning, arXiv:1201.1293 [hep-ph]; S. Krippendorf, H. P. Nilles, M. Ratz and M. W. Winkler, arXiv:1201.4857 [hep-ph]; G. Larsen, Y. Nomura and H. L. L. Roberts, arXiv:1202.6339 [hep-ph]; N. Craig, S. Dimopoulos and T. Gherghetta, JHEP **1204** (2012) 116; N. Craig, M. McCullough and J. Thaler, arXiv:1203.1622 [hep-ph].

[15] F. Brümmer and W. Buchmüller, JHEP **1107** (2011) 010.

[16] K. L. Chan, U. Chattopadhyay and P. Nath, Phys. Rev. D **58** (1998) 096004.

[17] J. L. Feng, K. T. Matchev and T. Moroi, Phys. Rev. Lett. **84** (2000) 2322; Phys. Rev. D **61** (2000) 075005.

[18] D. Horton and G. G. Ross, Nucl. Phys. B **830** (2010) 221.

[19] F. Brümmer and W. Buchmüller, arXiv:1201.4338 [hep-ph].

[20] H. Baer, V. Barger and P. Huang, JHEP **1111** (2011) 031.

[21] S. Bobrovskyi, F. Brümmer, W. Buchmüller and J. Hajer, JHEP **1201** (2012) 122.

Searches for Jets + missing Et without leptons at CMS

Saeid Paktinat Mehdiabadi for the CMS Collaboration

School of Particles and Accelerators
Institute for Research in Fundamental Sciences (IPM)
P.O.Box 19395-5531, Tehran, Iran

DOI: http://dx.doi.org/10.3204/DESY-PROC-2012-02/224

We present results of searches for SUSY production at CMS in events containing hadronic jets and missing energy. Various discriminants based on the event kinematics are employed to suppress standard-model backgrounds. The results are interpreted in the context of the Constrained Minimal Supersymmetric Standard Model, and of a number of *simplified models*.

1 Introduction

The CMS [1] experiment at the Large Hadron Collider (LHC) has a reach program to search for the Supersymmetry (SUSY). The evolving list of the analyses and their results can be found at [2]. In this note, the searches with the fully hadronic final states are reviewed. This channel has the largest branching ratio but at the same time faces a huge background from Standard Model (SM) processes with the same signature, such as $Z \to \nu\bar{\nu}$+jets events as well as $t\bar{t}$+jets and W+jets events, where the W either decays into light leptons which are not identified or into hadronically decaying τ leptons. In these processes, genuine missing transverse energy (MET) is caused by neutrinos. A different major background arises from QCD multijet events where one or more jets are severely mismeasured. To estimate the backgrounds, the main focus of the analyses is on the data driven methods. Apart from the classical signature of *Jets + MET*, some new variables are defined which make the separation of the signal and background much more easier. Most of the analyses have used the full collision data from 2011 which is close to 5 fb^{-1} of pp collisions in 7 TeV center of mass energy.

2 Jets + MET

If the colored sparticles are not too heavy, a lot of them can be produced in the LHC. Their decay chain can be ended up to a multijet event plus two stable sparticles which escape from the detection and appear as the missing transverse momentum. So a highly unbalanced event with a large jet multiplicity is known as a classical signature of SUSY. The main backgrounds of this search are the QCD multijet events with highly mismeasured jets [3]. To estimate this background, a multijet control sample, where the jets are rebalanced by maximizing a likelihood using the measured jet resolution is used. The MET is forced to be vanished in all events.

This rebalanced sample can be compared to generated QCD multijet events. Because of the rebalancing and the huge QCD cross-section the method is safe against signal contamination. In a second step, the jets of the rebalanced sample are smeared according to the jet resolution including non-Gaussian tails measured in γ-jet and di-jet data events. To estimate the $Z \to \nu\bar{\nu}$ background, the high P_T γ+jets events when the photon is ignored are used. The background from $t\bar{t}$ and W+jets with a hadronically decaying tau is modeled using a data control sample with one isolated muon. The simulation is used to replace the muon by a hadronic tau. The similar isolated muon or electron data sample can be used to evaluate the $t\bar{t}$ and W+jets events which have a lost lepton. The sample is reweighted according to the muon or electron reconstruction and isolation efficiencies as measured on the Z-peak in data. Figure 1 shows the

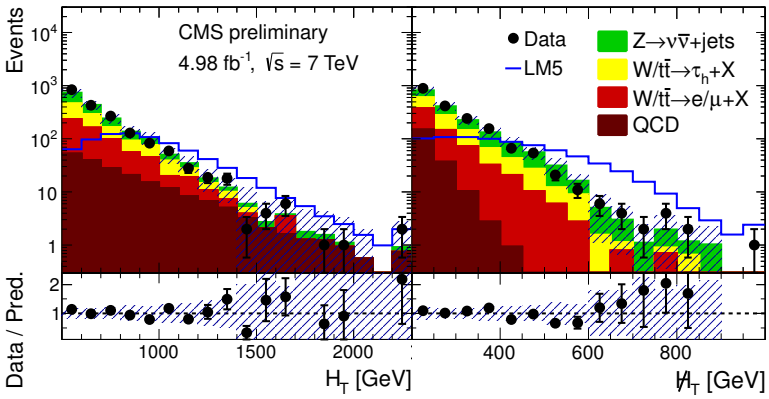

Figure 1: H_T and $\not{H}_T$. The ratio of the data to sum of the backgrounds is shown at the bottom.

scalar (H_T) and vectorial ($\not{H}_T$) sum of the P_T of the jets in the events that survive the cuts. The SM backgrounds predict the data in a good precision and no excess is seen in the data.

3 α_T analysis

The α_T analysis [4] tries to use a search variable which is QCD safe by definition. In a dijet event, α_T is defined as the ratio of the E_T of the next to leading jet and the transverse mass (M_T) of the system of two jets. For the multijet events, the jets are assigned to two mega-jets by minimizing the H_T difference. Figure 2 (left) shows the α_T distribution after applying all cuts for 1.1 fb^{-1} of data. It can be seen that QCD events can not go beyond $\alpha_T = 0.55$. Above this value the distribution is dominated by the SM events with a genuine MET. The residual QCD contribution and the other SM backgrounds in the search region ($\alpha_T > 0.55$) are predicted by scaling the yields for $\alpha_T < 0.55$ in different control samples by R_{α_T}, the ratio of the number of events with $\alpha_T > 0.55$ and $\alpha_T < 0.55$. The control sample for $t\bar{t}$ and W+jets backgrounds is a muon+jets sample and a γ+jets sample is used to model the contribution from Z+jet. In case of QCD multijet events, R_{α_T} is expected to fall with increasing H_T because the jet P_T resolution improves with H_T . Figure 2 (right) shows the dependence of R_{α_T} on H_T. The distribution is flat as expected for events with real MET, demonstrating the QCD depletion in the search region. The distributions for two examples of SUSY contributions are also shown. The data points are consistent with the SM only distribution within the uncertainties.

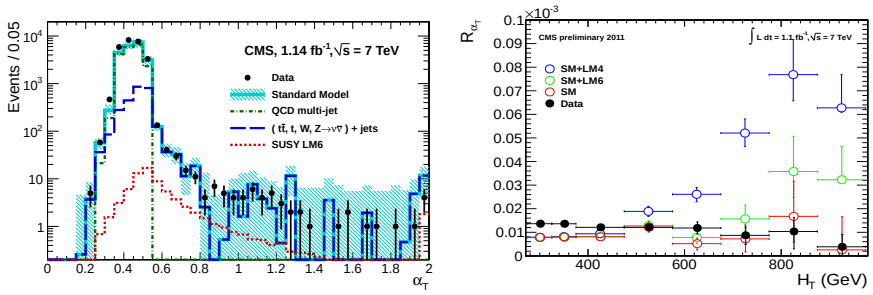

Figure 2: α_T (left), R_{α_T} versus H_T (right), data shows only the expected SM background.

4 Razor analysis

Another QCD safe analysis in CMS which is known as Razor analysis [5] relies on the mass scale and average transverse mass of the events. The search variables are defined as follow:

$$M_R \equiv \sqrt{(E_{j_1} + E_{j_2})^2 - (p_z^{j_1} + p_z^{j_2})^2}\ , M_T^R \equiv \sqrt{\frac{\not{E}_T(p_T^{j1} + p_T^{j2}) - \not{\vec{E}}_T \cdot (\vec{p}_T^{\,j1} + \vec{p}_T^{\,j2})}{2}}\ .$$

given a scale estimator M_R and a transverse estimator M_T^R, the razor dimensionless ratio is defined as $R \equiv \frac{M_T^R}{M_R}$. To make two mega-jets in a multijet event, the combination minimizing the sum of the squared invariant masses is selected. Different SM backgrounds are predicted by a 2 dimensional template in the (M_R, R^2) plane. Figure 3 (left) shows the R^2 distribution for different backgrounds and their sum. No evidence of any new physics is seen.

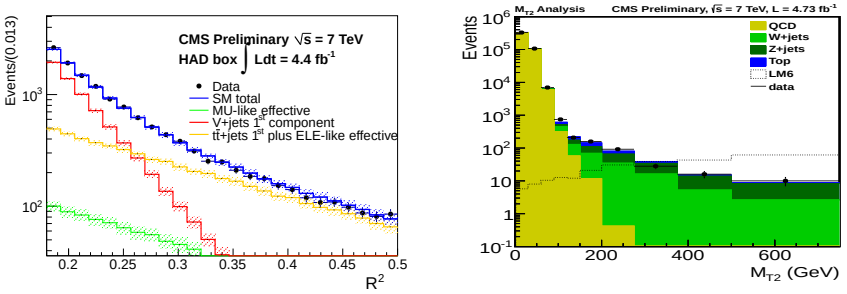

Figure 3: R^2 and M_{T2} distributions for data and different components of the backgrounds.

5 M_{T2} analysis

In the M_{T2} analysis [6] an extension of the well known transverse mass is used to look for the production of the pair produced heavy particles that their decay end up to heavy stable particles. To estimate the QCD contribution a special data driven method is used. Contribution of the $t\bar{t}$ and W+jets is estimated by using a muon+jets control sample. γ+jets is used to predict the

Z+jets background. Figure 3 (right) compares the M_{T2} distribution for different backgrounds, their sum and the real data. There is a good agreement between the data and backgrounds.

6 Interpretation

Looking for new physics with different search variables does not show any evidence for an excess over the predicted SM backgrounds. Statistical methods are used to interpret this lack of evidence numerically and restrict the allowed phase space for SUSY. Exclusion limits at 95% C.L. have been determined in the mSUGRA/CMSSM (m_0, $m_{1/2}$) plane. The results are shown in Figure 4 (left) for $A_0 = 0$, $\mu > 0$ and $\tan\beta = 10$. Besides the exclusion in the

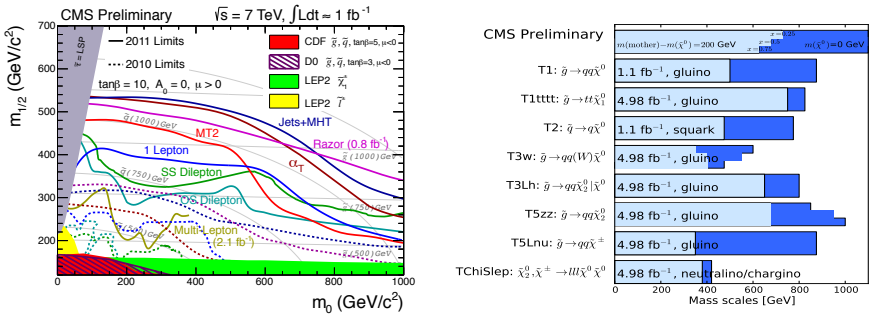

Figure 4: Exclusion limits in mSUGRA/CMSSM plane (left) and the simplified models (right).

mSUGRA/CMSSM plane the results are interpreted in so-called Simplified Models topologies. These are simple signal models each one has exactly one decay mode which is only constrained by the kinematics and the masses of the participating particles. In Figure 4 (right) the excluded masses in different models are shown for m(χ^0) = 0 GeV (dark blue) and m(mother)-m(χ^0) = 200 GeV (light blue).

7 Acknowledgments

The author would like to thank the management and staff of the school of particles and accelerators of IPM, especially Prof. Arfaei for their support. Thanks to all of the members of the CMS collaboration for their outstanding results discussed partly here and thanks to the organizing committee in the University of Bonn for their warm hospitality. Credit: Copyright CERN for the benefit of the CMS Collaboration.

References

[1] S. Chatrchyan *et al.* [CMS Collaboration], JINST **3**, S08004 (2008).
[2] https://twiki.cern.ch/twiki/bin/view/CMSPublic/PhysicsResultsSUS.
[3] S. Chatrchyan *et al.* [CMS Collaboration], (2012) CMS-PAS-SUS-12-011.
[4] S. Chatrchyan *et al.* [CMS Collaboration], Phys. Rev. Lett. **107**, 221804 (2011) [arXiv:1109.2352 [hep-ex]].
[5] S. Chatrchyan *et al.* [CMS Collaboration], (2012) CMS-PAS-SUS-12-005.
[6] S. Chatrchyan *et al.* [CMS Collaboration], (2012) CMS-PAS-SUS-12-002.

Search for R-parity violating SUSY signatures with the ATLAS detector

Carsten Meyer on behalf of the ATLAS Collaboration

University of Mainz, Germany

DOI: http://dx.doi.org/10.3204/DESY-PROC-2012-02/73

Searches for supersymmetry at the LHC also cover signatures from R-parity violating processes. These can be final states with resonant or non-resonant lepton flavour violation or multiple leptons. The talk presents recent results from searches for R-parity violation in events containing leptons based on data recorded in 2011 by the ATLAS detector.

1 Introduction

In general supersymmetry can lead to a large variety of signatures [1]. If R-parity is not conserved, the lightest supersymmetric particle (LSP) can decay further into standard model particles via R-parity violating Yukawa couplings. These new Yukawa couplings can either violate lepton number conservation (λ,λ') or baryon number conservation (λ") [2]. The results presented here show searches for R-parity violating supersymmetry in different final states containing leptons with the ATLAS detector using data recorded in 2011 [3]. In none of the searches an excess of data above the standard model background is observed and limits were set on the masses of new particles, the R-parity violating couplings itself and the parameter space of certain R-parity violating SUSY models.

2 Searches for heavy neutral particles in the eμ final state

A lot of standard model extensions predict new short-lived, heavy particles that can decay into two oppositely signed leptons of different flavours. In R-parity violating supersymmetry a heavy tau sneutrino can undergo this decay. The search for a heavy neutral particle decaying into an electron and a muon based on 1.07 fb^{-1} [4] is an update of the same analysis performed on 35 pb^{-1} presented in [5]. A single lepton trigger is used to collect the data sample analyzed in this search. The trigger efficiency is measured to be 100% with a precision of 1% for all $e\mu$ candidates that pass the offline selection. Electrons are required to have a transverse momentum of larger than 25 GeV, with a pseudorapidity of $|\eta| < 1.37$ or $1.52 < |\eta| < 2.47$. Quality criteria based on shower shapes, track quality, track matching with the calorimeter cluster and calorimeter isolation are imposed. Muons are reconstructed using the inner detector and the muon system. The transverse momentum must be larger than 25 GeV with a pseudorapidity of $|\eta| < 2.4$. Track isolation is imposed to reduce the background from non isolated muons. Each event is required to have exactly one electron and one muon passing the listed selection criteria. The invariant mass of the electron and muon - as the final discriminant - is examined for the presence

of a heavy tau sneutrino. The distribution is divided into 11 search regions, which depend on the simulated mass resolution defined as ($m_{\tilde{\nu}_\tau}$ + 3σ,$m_{\tilde{\nu}_\tau}$ - 3σ), where σ is the expected $m_{e\mu}$ resolution. In each search region, the number of observed and simulated background and signal events is used to calculate upper limits on $\sigma(\mathrm{pp} \longrightarrow \tilde{\nu}_\tau) \times BR(\tilde{\nu}_\tau \longrightarrow \mathrm{e}\mu)$, probing assumed $m_{\tilde{\nu}_\tau}$ in the range between 100 GeV up to 2 TeV. Figure 1 shows the 95% CL limits on $\sigma \times$ BR(eμ) as a function of the tau sneutrino mass. For R-parity violating couplings $\lambda'_{311} = 0.11$ (0.1) and $\lambda_{312} = 0.07$ (0.05) tau sneutrinos with masses up to 1.32 (1.45) TeV are excluded. Figure 2 shows the 95 % C.L. upper limit on λ'_{311} for different values of λ_{312} as a function of $m_{\tilde{\nu}_\tau}$.

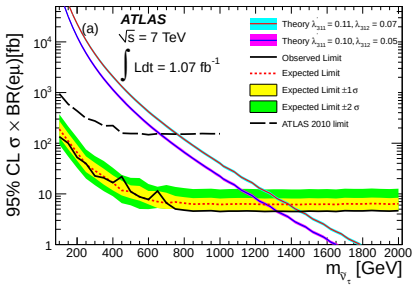

Figure 1: 95% C.L. upper limits on $\sigma \times$ BR(eμ) as a function of the tau sneutrino mass [4]. Also shown are the ± 1 and ± 2 standard deviation uncertainty bands and the previous ATLAS result from 2010

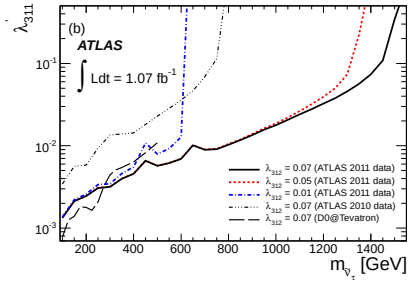

Figure 2: 95% C.L. upper limits on λ'_{311} as a function of the tau sneutrino mass for three different values of λ_{312} [4]. Also shown are the exclusion regions obtained from the D0 experiment and the previously published ATLAS analysis

3 Constraining R-parity violating mSUGRA in a four lepton final state

Events with a high multiplicity of leptons can occur in a large variety of standard model extensions. The search presented in [6] is based on 2.06 fb^{-1} and targets a R-parity violating

mSUGRA model with a $\tilde{\tau}_1$ as the lightest supersymmetric particle undergoing a four body decay into a tau, a neutrino and two charged leptons. This search is a reinterpretation of the previously performed search for supersymmetry in four lepton final states [7] aiming at R-parity violating decays. The RPV coupling $\lambda_{121} = 0.032$ at the grand unification scale is small enough that SUSY particle pair production still dominates leading to final states with at least 4 charged leptons and missing transverse momentum. Single lepton triggers are used to collect the data and the simulated events are weighted by the trigger efficiencies measured on data. In order to obtain a high and stable trigger efficiency, an electron (muon) with a transverse momentum of 25 GeV (20 GeV) must be present in the event. Electrons are required to have a transverse energy of at least 10 GeV, with a pseudorapidity of $|\eta| < 2.47$. In the barrel/endcap region the cut on the transverse energy is tightened to 15 GeV. A track isolation is imposed to reduce the background from non prompt electrons. Muons are required to have a transverse momentum of at least 10 GeV with a pseudorapidity of $|\eta| < 2.4$. Again a track isolation requirement is introduced to reduce the background arising from non prompt muons. A signal region is examined for the presence of a SUSY signal. Events with at least four electrons or muons passing the listed selection criteria and $E_T^{miss} > 50$ GeV are selected. An additional Z boson veto of 10 GeV around the Z boson mass is imposed for each opposite sign-same flavour lepton pair. No data event is observed with a background expectation of 0.7 ± 0.8. Figure 3 shows the 95% C.L. exclusion in the $m_{1/2}$ $\tan(\beta)$ plane. The region for $m_{1/2} < 800$ GeV is excluded except for high values of $\tan(\beta) > 40$, where the LSP lifetime rapidly increases and the four body branching ratio rapidly decreases.

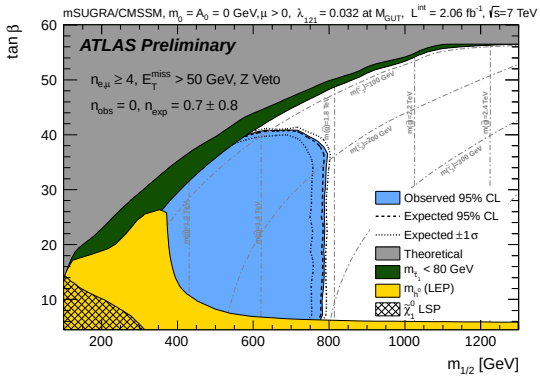

Figure 3: 95 % C.L. exclusion in the $m_{1/2}$ $\tan(\beta)$ plane [6]. Also shown are previous limits from LEP

4 Constraining bilinear R-parity violation in a one lepton final state

The analysis presented in [8] is based on 1.04 fb^{-1} and aims at bilinear R-parity violation in final states with jets, missing transverse momentum and exactly one charged and isolated muon [9]. Tight cuts on the jet transverse momenta, the missing energy and the transverse mass are applied in order to enhance the signal and suppress the background. Backgrounds were

estimated in dedicated control regions and extrapolated into the signal region with transfer factors derived from the Monte Carlo. After applying all selection criteria, 7 events were observed with a background expectation of 6 ± 2.7. 95% C.L. limits were set in the m_0 $m_{1/2}$ plane as shown in figure 4.

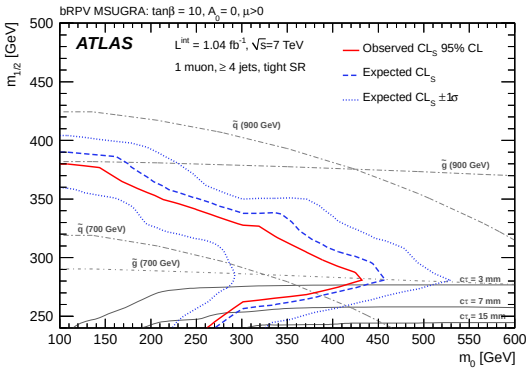

Figure 4: 95 % C.L. exclusion in the m_0 $m_{1/2}$ plane. The region below $m_{1/2} = 240$ GeV, where the LSP lifetime exceeds $c\tau > 15$ mm is not shown. [8]

5 Conclusion

Three searches for R-parity violating supersymmetry in different final states using ATLAS data collected in 2011 were presented. All analyses show good agreement between observed data and standard model predictions. Limits on SUSY particle masses and R-parity violating couplings were strongly improved compared to previous ATLAS and TeVatron limits.

References

[1] "A Supersymmetry Primer" S. Martin http://arxiv.org/abs/hep-ph/9709356

[2] "About R-parity and the Supersymmetric Standard Model" P. Fayet arXiv:hep-ph/9912413v1

[3] ATLAS Collaboration, JINST 3 (2008) S08003

[4] ATLAS Collaboration EPJC 71 (2011) 1809

[5] ATLAS Collaboration PRL 106 (2011) 251801

[6] ATLAS collaboration "Constraining R-parity violating Minimal Supergravity with stau_1 LSP in a four lepton final state with missing transverse momentum" ATLAS-CONF-2012-035 https://cdsweb.cern.ch/record/1432202

[7] ATLAS collaboration "Search for supersymmetry in events with four or more leptons and missing transverse momentum in pp collisions at $\sqrt{s} = 7$ TeV with the ATLAS detector" ATLAS-CONF-2012-001 https://cdsweb.cern.ch/record/1418920

[8] ATLAS Collaboration "Search for supersymmetry in final states with jets, missing transverse momentum and one isolated lepton in $\sqrt{s} = 7$ TeV pp collisions using 1fb^{-1} of ATLAS data" PRD 85 (2012) 012006

[9] W. Porod, M. Hirsch, J. Romao, and J. W. F. Valle, "Testing neutrino mixing at future collider experiments" Phys. Rev. D63 (2001) 115004, arXiv:hep-ph/0011248

Searches for strong R-parity conserving SUSY production at the LHC with the ATLAS detector

Federica Legger[1] on behalf of the ATLAS collaboration

[1]Ludwig-Maximilians-Universität Geschwister-Scholl-Platz 1, 80539 München, Germany

DOI: http://dx.doi.org/10.3204/DESY-PROC-2012-02/121

Searches for supersymmetric squarks and gluinos in events containing jets, missing transverse momentum, and one or zero lepton are presented. The results are based on the full data sample (5 fb^{-1}) recorded in 2011 at $\sqrt{s} = 7$ TeV centre-of-mass energy by the ATLAS experiment at the LHC.

1 Introduction

The search for physics beyond the Standard Model (SM) is one of the main tasks of Large Hadron Collider (LHC) experiments. SuperSymmetry (SUSY) is one of the most promising extensions of the SM. At a proton-proton collider, the strong production of supersymmetric particles (squark-squark, gluino-gluino, gluino-squark) is the preferred mechanism, if those particles are within the energy reach of the LHC. In R-parity conserving SUSY models [1, 2, 3, 4, 5, 6, 7, 8, 9], sparticles are produced in pairs, and the Lightest Supersymmetric particle (LSP) is stable and weakly interacting, therefore escaping detection. The experimental signature of such events is therefore several energetic jets and/or leptons, originating from the cascade decays of the initial squarks and gluinos, and large missing transverse momentum, $E_T^{\rm miss}$ coming from the LSP. Typical SM backgrounds to such searches are multi-jet, $t\bar{t}$, W, Z, and single top production. In this paper, a search for supersymmetry in events with several jets, large $E_T^{\rm miss}$, and 1 or 0 lepton is presented, using the full data sample collected in 2011 by the ATLAS experiment [10] at the LHC in $p-p$ collisions at a center-of-mass energy of 7 TeV, corresponding to an integrated luminosity of $\sim$4.7 fb^{-1} after the application of basic data quality requirements. Three analyses are presented, covering squark-squark and gluino-gluino production. In the first case, 1 (or more) jet is produced from each squark decay, therefore the analysis focuses on events with 2 or more energetic jets, and no lepton (see section 2). In the second case, longer decay chains are possible and a separate analysis focus on events with larger jet multiplicity (more than 5) and no lepton (described in section 3). The case where the squark or gluino decays producing one light (e or μ) lepton (and several jets) is presented in section 4.

2 The 0-lepton analysis

The effective mass $m_{\rm eff}$ (defined as the sum of $E_T^{\rm miss}$ and the transverse momentum p_T of all jets) is used in the 0-lepton analysis to discriminate SUSY signal from SM backgrounds. The background originating from multi-jet production is kept under control through a cut on the

minimum azimuthal angle ($\Delta\phi$) between the jets and the $E_T^{\rm miss}$ vector. In total, 11 signal regions with various jet multiplicities (ranging from 2 to 6) and different cuts on $m_{\rm eff}$ have been defined, in order to achieve maximal coverage in the squark-gluino mass plane, and to enhance sensitivity to models with compressed spectra (small mass splitting). The contribution in the signal regions from SM backgrounds from mismeasured multi-jet events, W and $Z(\rightarrow \nu\nu)$+jets, $t\bar{t}$ are estimated from background-enriched control regions through transfer factors taken from Monte Carlo (MC) or data (for multi-jet events). The 0-lepton analysis is described in [11]. No evidence is found for physics beyond the Standard Model. The results are interpreted in the context of a MSUGRA/CMSSM model with $tan(\beta) = 10$, $A_0 = 0$ and $\mu > 0$ (see Fig. 1) and a simplified MSSM scenario with only strong production of gluinos and first- and second-generation squarks, and direct decays to jets and neutralinos (see Fig. 2). Gluino masses below 940 GeV, and squark masses below 1380 GeV (for gluino masses up to 2 TeV) are excluded at the 95% confidence level in the simplified model, whereas squarks and gluinos of equal mass are excluded for masses below 1400 GeV in the MSUGRA/CMSSM model.

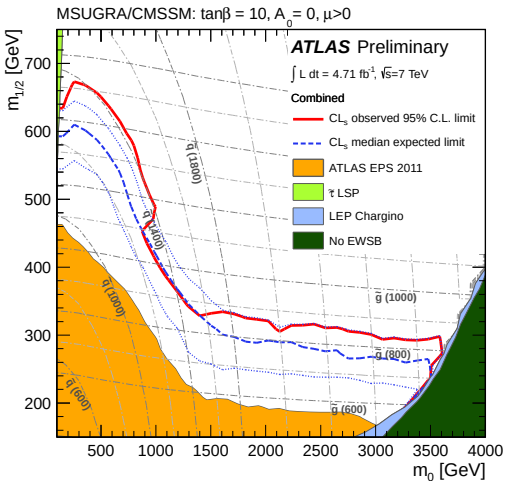

Figure 1: 95% CL_s exclusion limits in the MSUGRA/CMSSM model for the 0-lepton analysis [11].

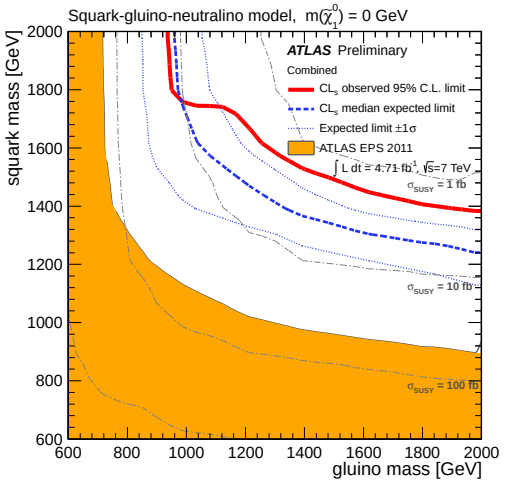

Figure 2: 95% CL_s exclusion limits in the simplified MSSM scenario for the 0-lepton analysis [11].

3 The 0-lepton multi-jet analysis

In the 0-lepton multi-jet analysis, searches for events containing from more than 5 to more than 8 jets are performed. The signal/background discriminating variable is H_T, defined as the scalar sum of the transverse momenta of all jets. 6 non-exclusive signal regions are defined according to various jet multiplicities and different cuts on the $E_T^{\rm miss}$ significance, defined as $E_T^{\rm miss}/\sqrt{H_T}$. The main SM backgrounds are multi-jet processes (including fully hadronic $t\bar{t}$), estimated from data in control regions with lower jet multiplicities and $E_T^{\rm miss}$, and *leptonic* processes in which the lepton is out of the detector acceptance or misidentified: $t\bar{t}$ (semi and full-leptonic) and W/Z+jets, estimated from data (when possible) in control regions, and extrapolated to signal

regions using MC (similar to the 0-lepton analysis). The 0-lepton multi-jet analysis is described in detail in [12]. A global fit for the normalisation of each background from the control regions is simultaneously performed in each signal region. No significant excess of data over SM prediction is found, therefore limits are set to a MSUGRA/CMSSM supersymmetric model where, for large m_0, gluino masses smaller than 850 GeV are excluded at the 95% C.L (see Fig. 3). Within a simplified model containing only a gluino octet and a neutralino (and assuming that the gluino decays with 100% branching fraction to $t\bar{t}$ and a neutralino), gluino masses smaller than 880 GeV are excluded for neutralino masses less than 100 GeV (see Fig. 4).

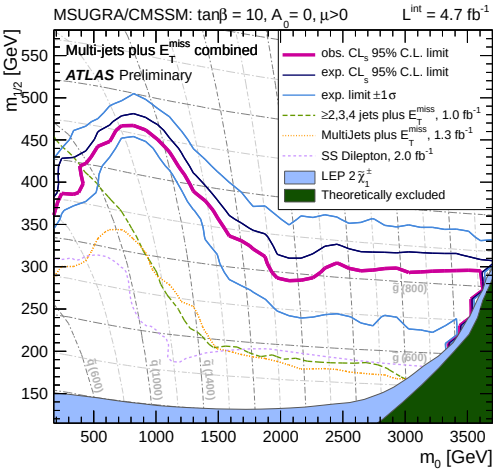

Figure 3: 95% CL_s exclusion limits in the MSUGRA/CMSSM model for the multijet analysis [12].

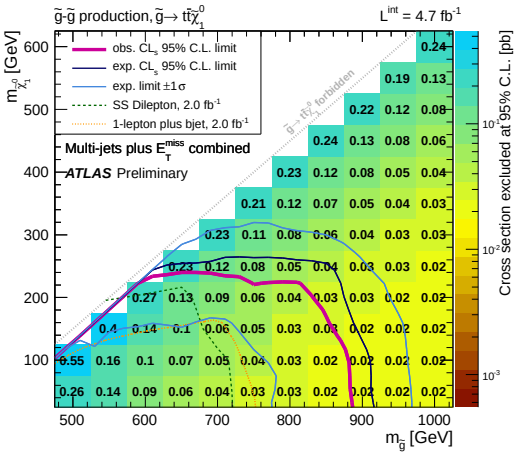

Figure 4: 95% CL_s exclusion limits in the simplified model scenario for the multijet analysis [12].

4 The 1-lepton analysis

The search for strong production of squarks and gluinos in events containing jets, $E_T^{\rm miss}$, and one isolated lepton (e or μ) from chargino decays is the aim of the 1-lepton analysis. Three orthogonal signal regions are defined: one requiring one soft lepton (with transverse momentum smaller than 20 GeV for muons and 25 GeV for electrons) to enhance sensitivity to compressed spectra models, and two with one hard lepton and 3 or 4-jet multiplicities to probe higher SUSY mass scales. SUSY signal is separated from SM backgrounds (mainly multi-jet, $t\bar{t}$ and W) using $m_{\rm eff}$. The background in the signal regions is estimated with an (over-constrained) simultaneous fit based on the profile likelihood method, with as inputs the contributions of the various background sources in appropriate control regions, and transfer functions to the signal regions taken from data or MC [13]. No hint of new physics is found, therefore limits are set in the MSUGRA/CMSSM model, where squarks and gluinos of equal masses below approximately 1200 GeV are excluded at 95% CL (see Fig. 5). In a simplified model with gluino-gluino pair production with several jets, W's and neutralinos in the final state (where the gluino decays to the LSP via the intermediate step - one-step - of the lightest chargino, and with the chargino

mass set halfway, $x = 1/2$, in between the gluino and neutralino masses), gluino masses below approximately 900 GeV are excluded for LSP masses below 200 GeV. The soft 1-lepton search is more powerful along the diagonal region where the masses of the gluino and LSP become quasi-degenerate, while the hard-lepton analyses are more powerful in the rest of the phase space (see Fig. 6).

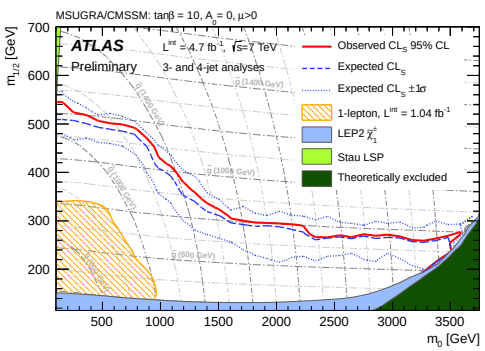

Figure 5: 95% CL_s exclusion limits in the MSUGRA/CMSSM model for the 1 (hard) lepton analysis [13].

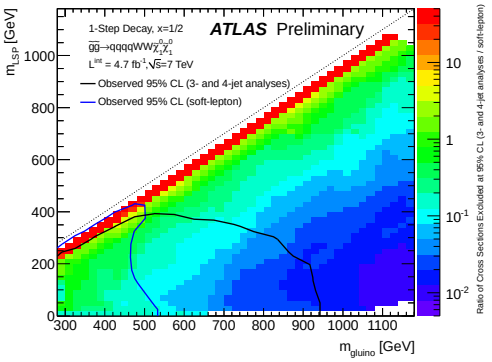

Figure 6: Ratio of the excluded cross sections by the hard-lepton (numerator) versus the soft-lepton (denominator) analyses, in the gluino production simplified model [13].

5 Conclusion

Three searches for strong production of SUSY particles using the ATLAS detector with the full 2011 dataset have been presented. No excess of data over SM expectation is found. Squarks and gluinos of equal mass are excluded up to 1400 GeV in the MSUGRA/CMSSM model. These limits considerably extend the exclusion limits by previous ATLAS measurements.

References

[1] Yu.A. Golfand, E.P. Likhtman, JETP Lett. **13**, (1971) 323-326
[2] A. Neveu, J.H. Schwartz, Nucl. Phys. B **31**, (1971) 86-112
[3] A. Neveu, J.H. Schwartz, Phys. Rev. D **4**, (1971) 1109-1111
[4] P. Ramond, Phys. Rev. D **3**, (1971) 2415-2418
[5] D.V. Volkov, V.P. Akulov, Phys. Lett. B **46**, (1973) 109-130
[6] J. Wess, B. Zumino, Phys. Lett. B **49**, (1974) 52-60
[7] J. Wess, B. Zumino, Nucl. Phys. B **70**, (1974) 39-50
[8] P. Fayet, Phys. Lett. B **69**, (1977) 489
[9] G.R. Farrar, P. Fayet, Phys. Lett. B **76**, (1978) 575
[10] ATLAS Collaboration, J. Instrum. **3**, S08003 (2008)
[11] ATLAS Collaboration, ATLAS-CONF-2012-033, http://cdsweb.cern.ch/record/1432199 (2012)
[12] ATLAS Collaboration, ATLAS-CONF-2012-037, http://cdsweb.cern.ch/record/1432204 (2012)
[13] ATLAS Collaboration, ATLAS-CONF-2012-041, http://cdsweb.cern.ch/record/1435195 (2012)

Searches for SUSY with third-generation signatures in CMS

Alexis Kalogeropoulos[1] for the CMS Collaboration

[1]Vrije Universiteit Brussel, Pleinlaan 2, B-1050 Brussel, Belgium

DOI: http://dx.doi.org/10.3204/DESY-PROC-2012-02/227

We present results of searches for SUSY production at CMS in events containing hadronic jets and missing energy. The tagging of heavy flavor in the jets is used both to distinguish standard-model components, and for sensitivity to those SUSY models that lead to final states rich in heavy-flavored particles.

1 Search for new physics in events with same-sign dileptons, b-tagged jets and missing energy

This is a search for anomalous production with same-sign (SS) dilepton final state with at least 2 b-jets and missing energy. Such topologies resulted from SM processes are rare, thus their anomalous production could be an indication of new physics. Events including 2 to 4 b-quark jets could be signatures of SUSY where bottom and top-quark superpartners are lighter than other $\tilde{q}$. Although is not discussed explicitly here, this study links to other exotic models, like maximal flavour violation (MxFV) and Z'-boson, which would lead to like-sign top pair production. Although here we present results for $4.7fb^{-1}$, more recent result for $4.98fb^{-1}$ have been recently published [1].

1.1 Event selection and Background estimation

Two SS lepton are required to have $p_T \geqslant 20$ GeV $|\eta| < 2.4$ and an invariant mass $m_{\ell\ell} > 8$GeV. Jets and missing transverse energy (E_T^{miss}) were reconstructed with using the particle flow algorithm. At least 2 b-tagged jets were required with $p_T > 40$GeV , $|\eta| < 2.5$, while only events with $E_T^{miss} > 30$GeV were considered.The background constitutes from fake leptons, while rare SM processes that can give 2 isolated SS leptons, and misconstructed opposite-sign lepton pair, as SS pairs. The background from fakes is based on events with one or both leptons failing the isolation and identification selection, but still passing a looser selection. The full data-driven techniques for background estimation are analytically discussed here [1]. While the contribution from rare processes like ttW and ttZ represents more than 90% of all, others where considered as well, like WZ, ZZZ which were estimated from Monte Carlo simulation. In general they are strongly suppressed by the b-tagging requirement.

1.2 Models

SUSY models of gluon pair production were considered, with decays to on and off-shell top quarks. Model A1 depicts a 3-body $\tilde{g}$ decay mediated by virtual stop : $\tilde{g} \to t\bar{t}\tilde{\chi}_1^0$ (Figure 1), with the assumption that the stop is the lightest squark. Other models were also considered, like when stop quarks are light enough to be on-shell, with 2-body $\tilde{g}$ decays to a top-stop pair $\tilde{g} \to \bar{t}\tilde{t}_1$, $\tilde{t}_1 \to t\chi_1^0$. Those models give final states with as many as 4 isolated high p_T leptons, 4 b-quarks, several light quark jets, and E_T^{miss}. Also, models with multiple tops and W-boson from decays of sbottom quarks were also considered, and for all the above, upper limits on the $m(\chi_1^0$-$\tilde{g}$) plane were obtained at 95 % C.L. Such an example is Figure 2 for model A1.

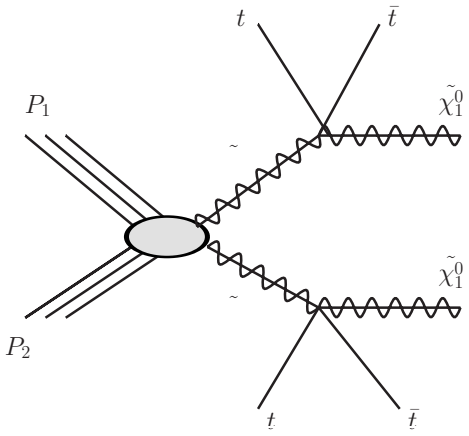

Figure 1: Model A1 with three body decays.

1.3 Results

No significant deviations from the SM expectations was observed, while limits were put at 95% CL on the parameter space for several models of SS top pair production, two models of $\tilde{g}$ decay into virtual or real stop quarks, a model of $\tilde{b}$ pair production, and a model of $\tilde{b}$ production from $\tilde{g}$ decay.

2 Search for supersymmetry in hadronic final states using M_{T2} in 7 TeV pp collisions at the LHC

Hadronic final states are usually imply large E_T^{miss}. In this analysis, the stransverse mass variable, M_{T2} is used purely as a discovery variable, and therefore, is found to be very sensitive to the presence of new physics. Since M_{T2} must depict the produced particle masses which in general are much lighter if they are counted for the SM background processes rather than SUSY ones, evidence of new physics is expected to show up, as an excess in the tail of the M_{T2} distribution.Although we present here results for $1.1fb^{-1}$ of collected data at sqrt(s) = 7TeV , a recent update of the analysis for $4.73fb^{-1}$ can be found [2].

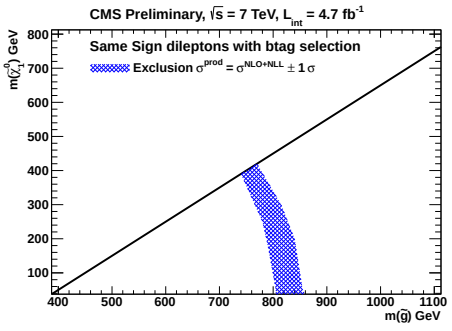

Figure 2: Exclusion limit at 95 % CL on m($\tilde{\chi}_1^0$) - m($\tilde{g}$) plane for model A1

2.1 Event selection and Background estimation

Two different approaches were used, the High M_{T2} analysis aiming on heavy sparticle production decays, which is more sensitive to the case where $\tilde{q}$ are heavy and $\tilde{g}$ are light where $\tilde{g}$-$\tilde{g}$ are dominating, and the $\tilde{g}$, giving rise to 3-body decays with relative small E_T^{miss}. At least 3 Jets were required, where the two leading ones are required to have $p_T \geqslant 100$ GeV and $|\eta| < 2.4$, while the scalar sum of all Jets p_T defined as HT has to be $\geqslant 600$ GeV and a veto on isolated electrons and muons is put as well. Signal region (SR), was defined where M_{T2} >400 GeV, while the Control Region (CR) was defined to be 200 GeV $\leqslant M_{T2} \leqslant$ 400 GeV.

To cover cases where $\tilde{g}$ decay is mediated by virtual $\tilde{q}$ exchange, and the $\tilde{t}$ and $\tilde{b}$ are expected to be lighter than all $\tilde{q}$, the Low M_{T2} analysis was introduced. In this case, at least 4 Jets were selected with at least 1 b-tagged (in order to further suppress the QCD background), while p_T of the leading Jet $\geqslant 150$ GeV and for the second leading Jet $\geqslant 100$ GeV, while the SR is defined where $M_{T2} > 150$ GeV and the CR. The exact selection criteria are discussed analytically [2].

For the background estimation for the High M_{T2} case, a data-driven method was used based on $\Delta\Phi_{min}$ which is the difference in azimuth, between the E_T^{miss} vector and the closest jet, and M_{T2}. For the Low M_{T2} however, the ratio between events before and after b-tagging as a function of M_{T2} was found compatible with a flat distribution. Thus, the QCD contribution in the pre-tagged sample was estimated following the High M_{T2} approach.

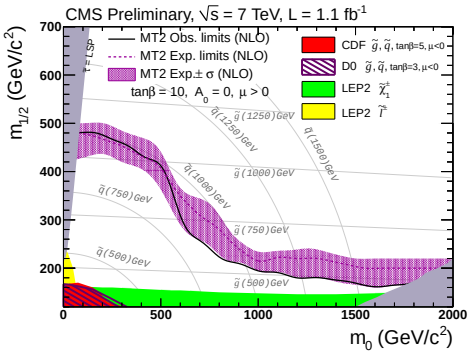

Figure 3: Exclusion limit in the CMSSM $m_0 - m_{1/2}$ plane from the combined High/Low M_{T2} analyses.

2.2 Results

No excess over the SM predictions was observed and data is in good agreement with the Monte Carlo description. Nevertheless, combining both Low and High M_{T2}, upper limits at 95%CL on the mSUGRA / CMSS plane were put after taking into account corrections for efficiencies and systematic uncertainties as in shown in Figure 3.

3 Search for New Physics in Events with b-quark Jets and Missing Transverse Energy in pp Collisions at 7 TeV

Experimental signatures including large E_T^{miss} and multiple Jets with high p_T, are excellent candidates for NP. Also, events including b-jets, usually are accompanied by different background composition which implies also different sensitivity to NP. In this analysis, a search for NP in events with large E_T^{miss} , no identified leptons, at least 3 high p_T Jets, and at least 1 b-jet was performed. Results are based on data equivalent to $1.1 fb^{-1}$. The full analysis can be found here [3].

3.1 Event selection and Background estimation

At least 3 Jets were required with $p_T > 50$GeV , $|\eta| < 2.4$, at least 1 b-tagged Jet with $p_T >$ 30 GeV , in events with no identified nor isolated $el(mu)$ candidate with $p_T > 10$ GeV and $|\eta| < 2.5(2.4)$. Two different set of selections were used, namely loose(tight) selection which require $H_T > 350$ (500) GeV and $E_T^{miss} > 200$ (300) GeV.

Main background in the lower p_T region, comes from QCD and is estimated in a data-driven way using $\Delta\Phi_N^{min}$ and E_T^{miss} levels of correlation, while events with a Z+jets where one of more b-jets is present, form an irreducible background when the Z decays to two ν. This is however evaluated by reconstructing $Z \to \ell + \ell-$. However, the dominant background at high E_T^{miss} comes from top quark (either $t\bar{t}$ or single-top), while $W + jets$ constitute a smaller background with similar signatures coming from semi or full hadronic decays. A template method then was introduced, in which the shape of the E_T^{miss} distribution is measured in a single-lepton data control sample and was used to describe the shape of the E_T^{miss} spectrum for Top and W background events. All relevant plots can be found [3].

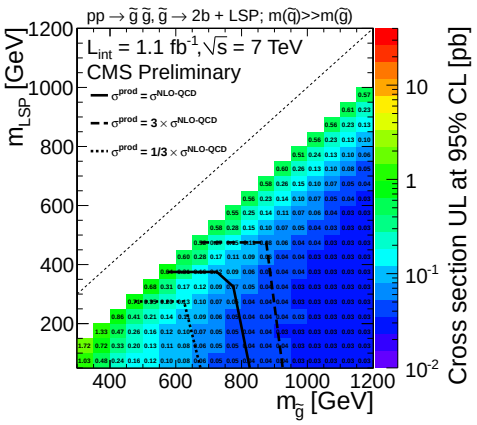

Figure 4: 95% CL cross section upper limits for the T1bbbb Simplified Model

4 Results

In this study, no evidence for an excess of events above the expectation from the standard model was observed. Nevertheless, both in the context of the CMSSM and in the framework of different Simplified Model (like T1bbbb or T1tttt) limits were set. As an example, the 95% CL cross section upper limit for the T1bbbb Simplified Model is shown in Figure 4.

References

[1] CMS collaboration, JINST, 0803 (2008) S08004 . *Search for new physics in events with same-sign dileptons and b-tagged jets in pp collisions at $\sqrt{s}$ = 7 TeV.*
`https://twiki.cern.ch/twiki/bin/view/CMSPublic/PhysicsResultsSUS11020` `hep-ex/1205.3933`
`http://cdsweb.cern.ch/record/1449950`

[2] CMS collaboration, JINST, 0803 (2008) S08004 *Search for SUSY in all-hadronic events with MT2.*
`https://twiki.cern.ch/twiki/bin/view/CMSPublic/PhysicsResultsSUS12002`
`http://cdsweb.cern.ch/record/1444892`

[3] CMS collaboration, JINST, 0803 (2008) S08004 *Search for New Physics in Events with b-quark Jets and Missing Transverse Energy in p-p Collisions at 7 TeV.*
`https://twiki.cern.ch/twiki/bin/view/CMSPublic/PhysicsResultsSUS11006`
`http://cdsweb.cern.ch/record/1390493`

Part VII

Working Group 4
Hadronic Final States

Convenors:

Krzysztof Nowak, Klaus Rabbertz, Jan-Christopher Winter

Production of isolated photons with jets in deep inelastic *ep* scattering at the ZEUS detector

Oleg Kuprash for the ZEUS collaboration

DESY, Notkestraße 85, 22607 Hamburg, Germany

DOI: `http://dx.doi.org/10.3204/DESY-PROC-2012-02/44`

Inclusive cross sections for the production of isolated photons accompanied by jets have been measured in neutral current deep inelastic scattering, for virtualities of the exchanged boson in the range $10 < Q^2 < 350\,\mathrm{GeV}^2$. The cross sections are compared to fixed-order perturbative QCD calculations and to the calculations based on k_T factorisation approach.

1 Introduction

This report presents measurements of isolated photons accompanied by jets in neutral current (NC) deep inelastic scattering (DIS) [1] performed with the ZEUS detector.

Isolated photons are photons emitted directly by quarks or leptons that take part in a hard scattering process. Photons emitted by leptons are called LL-photons, by quark - QQ-photons respectively. Example diagrams of these different processes are shown on Figure 1. Events with isolated photons provide a clean test of QCD since such photons do not undergo the hadronisation process and arrive in the detector unchanged after their production. The requirement for an accompanying jet enhances the QQ component of the cross section relative to LL and provides a test of perturbative QCD with two hard scales.

Figure 1: LL (left) and QQ (right) mechanisms of isolated photon production

2 Event Selection and extraction of the signal

The measurements are based on e^+p and e^-p data taken at HERA with integrated luminosities of $134\,\mathrm{pb}^{-1}$ and $198\,\mathrm{pb}^{-1}$, respectively. Events were selected by requiring a scattered-electron candidate with the polar angle $\theta^e > 140^\circ$ and energy $E^e > 10\,\mathrm{GeV}$. The kinematic quantity Q^2 was reconstructed from the scattered electron as $Q^2 = -(k - k')^2$, where k (k') is the four-momentum of the incoming (outgoing) lepton. The kinematic region $10 < Q^2 < 350\,\mathrm{GeV}^2$ was

selected. To remove background from the photoproduction regime, where $Q^2 \approx 0\,\mathrm{GeV}^2$, events were required to have $35 < E - p_Z < 65\,\mathrm{GeV}$. Here $E - p_Z = \sum_i E_i(1 - \cos\theta_i)$, E_i is the energy deposited in i-th calorimeter cell, θ_i is its polar angle and the sum runs over all cells. A set of further cleaning cuts was applied.

The photon candidate, which is measured as a cluster of cells with signals in the calorimeter (CAL), was required to have a transverse energy in the range $4 < E_T^\gamma < 15\,\mathrm{GeV}$. In order to measure well-understood shower shapes in the calorimeter, the photon was required to be recorded in the barrel section, with pseudorapidity in the range $-0.7 < \eta^\gamma < 0.9$. To reduce the background from neutral mesons, isolation criteria were applied: there should not be any track with momentum greater than 250 MeV within a cone of $\Delta R = 0.2$ around the photon candidate, where $\Delta R = \sqrt{(\Delta\phi)^2 + (\Delta\eta)^2}$ is the distance in the pseudorapidity-azimuthal plane. It was required that at least 90% of the measured photon energy should be deposited in the electromagnetic sections of the CAL. In order to reduce the fraction of events with quark-to-photon fragmenation (which is not discussed in this report), the ratio of the photon energy to the energy of the jet containing the photon was required to be greater than 0.9, thereby isolating the photon.

Jets were selected with transverse energies $E_T^{\mathrm{jet}} > 2.5\,\mathrm{GeV}$ and pseudorapidities in the range $-1.5 < \eta^{\mathrm{jet}} < 1.8$. The jets were clustered using the k_T algorithm in the longitudinally invariant inclusive mode as implemented in the HEPFORGE KTJET package [2].

For the signal extraction of isolated photons a shower shape technique was utilised. The variable $\langle \delta Z \rangle = \sum_i |Z_i - Z_{\mathrm{cluster}}|/(w_{\mathrm{cell}} \sum_i E_i)$ was used to describe the shower shape; its distribution is shown in Figure 2. Here Z_i is the Z position of the centre of the $i-$th cell, Z_{cluster} is the Z position of the centre of the CAL cluster where the photon candidate deposited its energy, w_{cell} is the cell width in the Z direction, and E_i is the energy deposited in the cell. The sum runs over the barrel CAL cells of the cluster.

Separate Monte Carlo samples were used for the simulation of the LL- and QQ-photon production. The $\langle \delta Z \rangle$ distribution in data was fitted by the sum of the Monte Carlo distributions in the range $0 < \langle \delta Z \rangle < 0.8$.

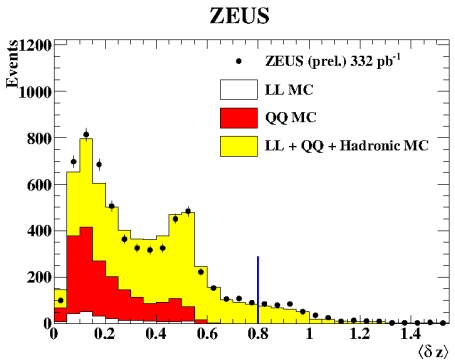

Figure 2: Distribution of $\langle \delta Z \rangle$

3 Theoretical predictions

The results are compared to new theoretical calculations. The GKS predictions [3] are fixed-order NLO calculations at order $\alpha^3\alpha_s$ in the electromagnetic and strong couplings. They take into account both LL and QQ contributions as well as the LQ interference term. The LQ interference term gives an effect of $\approx 3\%$ on the cross sections and this effect is reduced to $\approx 1\%$ when e^+p and e^-p data are combined since the sign of the term is different for e^+p and e^-p. The calculations were obtained using the HERAPDF1.0 [4] parameterisations for the proton PDFs with the factorisation and renormalisation scales set to $\mu_F = \mu_R = \sqrt{Q^2 + (p_T^{\rm jet})^2}$. The uncertainty due to the choice of the renormalisation and factorisation scales, which is the largest source of the overall theoretical uncertainty, were evaluated by scaling μ_R and μ_F by a factor 2 up and down independently. The total uncertainty on the integrated cross section is about 5% rising to approximately $\pm 10\%$ at large negative jet pseudorapidities.

The BLZ predictions [5] are made in the framework of the QCD k_T factorisation approach based on the off-shell partonic amplitude $eq^\star \to e\gamma q$. Photon radiation from the quarks as well as from the leptons are taken into account. Unintegrated proton parton densities are used in the KMR model. Uncertainties are mainly due to the procedure for the setting of the accompanying jet rapidity and are up to 20%.

4 Results

The phase space of the measurements was defined by $10 < Q^2 < 350\,\mathrm{GeV}^2$; the selected events were required to have a well reconstructed electron with energy $E^e > 10\,\mathrm{GeV}$ and scattering angle $\theta > 140^\circ$. The photon was required to have transverse energy in the range $4 < E_T^\gamma < 15\,\mathrm{GeV}$ and pseudorapidity $-0.7 < \eta^\gamma < 0.9$. If the photon belongs to a jet, photon energy must be greater than $0.9E^{\text{jet containing }\gamma}$. The transverse energy of the accompanying jet was greater than 2.5 GeV and its pseudorapidity was in range $-1.5 < \eta^{\rm jet} < 1.8$. The jets were reconstructed using the k_T clustering algorithm in the $E-$scheme in the longitudinally invariant inclusive mode with the R parameter set to 1.0.

In Figure 3 differential cross sections as function of E_T^γ, η^γ, Q^2, x, $E_T^{\rm jet}$ and $\eta^{\rm jet}$ are presented. For the QQ-events x is the fraction of the proton momentum carried by the incoming parton, x is defined as $Q^2/(2P(k-k'))$, where P is the four-momentum of the incoming proton.

Both theories provide a reasonable description of the data in shape, however the GKS theory agrees better with the cross sections as functions of jet variables. The GKS predictions systematically underestimate the data by typically 20% while the BLZ predictions overestimate them by about 20%.

The results indicate the necessity for further improved QCD calculations.

References

[1] H. Abramowicz *et al.* [ZEUS Collaboration], arXiv:1206.2270 [hep-ex].

[2] J. M. Butterworth, J. P. Couchman, B. E. Cox and B. M. Waugh, Comput. Phys. Commun. **153** (2003) 85 [hep-ph/0210022].

[3] A. Gehrmann-De Ridder, G. Kramer and H. Spiesberger, Nucl. Phys. B **578** (2000) 326 [hep-ph/0003082].

[4] F. D. Aaron *et al.* [H1 and ZEUS Collaboration], JHEP **1001** (2010) 109 [arXiv:0911.0884 [hep-ex]].

[5] S. P. Baranov, A. V. Lipatov and N. P. Zotov, Phys. Rev. D **81** (2010) 094034 [arXiv:1001.4782 [hep-ph]].

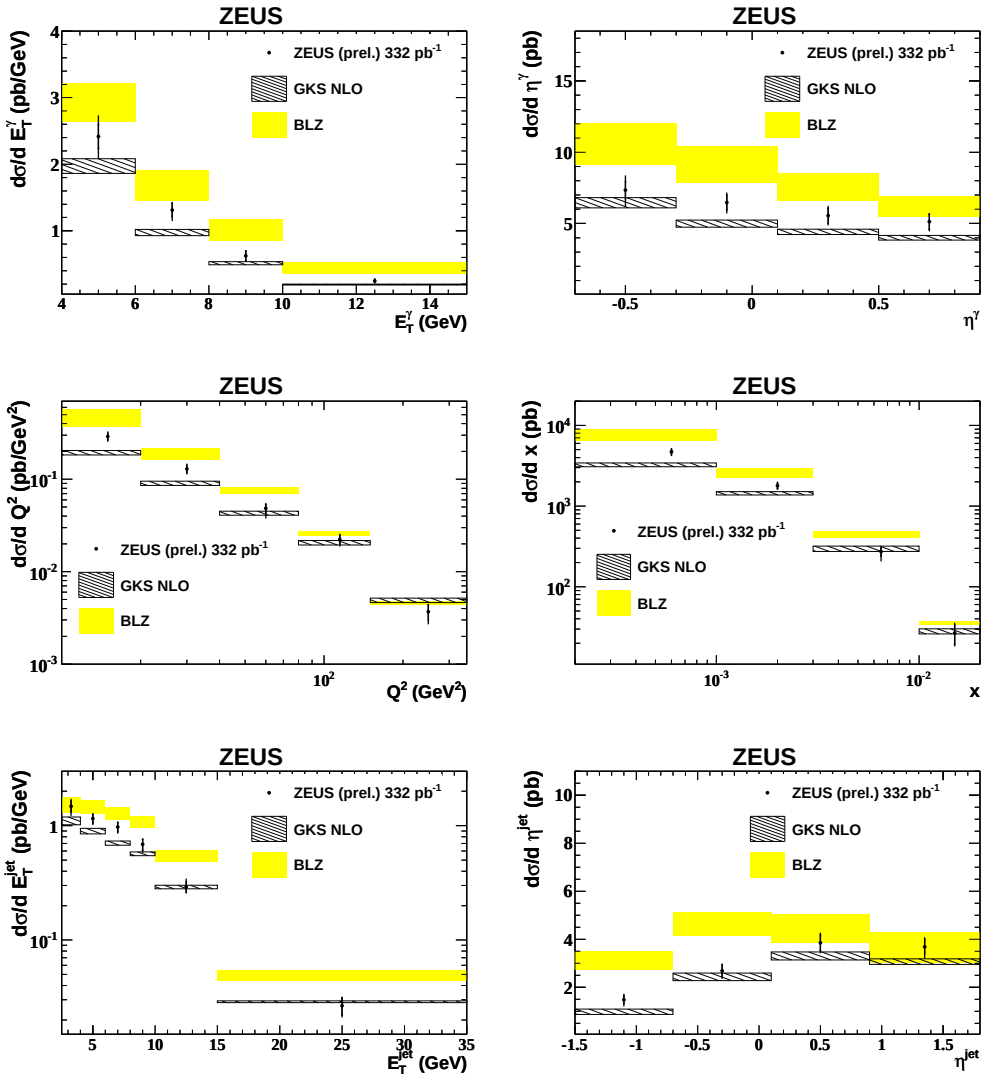

Figure 3: Differential cross sections as functions (from left to right, top to bottom) of the photon energy, the photon pseudorapidity, x, Q^2, the jet energy and the jet pseudorapidity

Photon measurements with the full CDF data set

Costas Vellidis[1], *Ray Culbertson*[1], *Tingjun Yang*[1]

[1]FNAL, Batavia, IL 60510, USA

DOI: http://dx.doi.org/10.3204/DESY-PROC-2012-02/167

We present results of the cross section measurement of photon production associated with bottom- and charm-quark production and of the cross section measurement for diphoton production. The measurements involve the full CDF data sample and they are compared with state-of-the-art calculations. The comparisons show only partial agreement between data and calculations.

1 Introduction

CDF has an extensive active program of prompt photon measurements using of the full data set. The measurements benefit from the clean identification and precise measurement of the energy and direction of photons with the CDF detector. For the reported measurements the candidate prompt photons are selected offline from tower clusters of the electromagnetic calorimeter and reconstructed in a cone of radius R=0.4 in the $\eta-\phi$ plane. The photons are required to be central $|\eta| < 1$, and to have a transverse energy $E_T = E \sin\theta > 30$ GeV for the photon+heavy flavor measurements and $E_T > 17, 15$ GeV (for the 1^{st} and 2^{nd} photon in the event, respectively) in the diphoton measurements, where E is the total energy of the photon. For the photon+heavy flavor measurements a secondary vertex algorithm is also used to select heavy flavor jets. This is done by fitting the invariant mass of the selected jet to derive the light flavor, charm, and bottom fractions.

2 Photon+heavy flavor production

The measurements are compared with LO calculations from the PYTHIA [1] parton shower Monte Carlo and with a NLO calculation from [2]. The latter calculation includes pointlike photon subprocesses through $O(\alpha\alpha_s^2)$ and fragmentation subprocesses through O (α_s^3). Predictions from PYTHIA are obtained for two cases: One with the default gluon splitting rate into heavy flavor quark pairs and one with the gluon splitting rate increased by a factor of 2. The kinematic cuts applied on both

	$\sigma_{total}(\gamma$+b) (pb)	$\sigma_{total}(\gamma$+c) (pb)
Data	$19.7\pm0.7_{\text{stat}}$ $(+5.0-4.2)_{\text{syst}}$	$132.2\pm4.6_{\text{stat}}$ $(+13.2-19.2)_{\text{syst}}$
PYTHIA	17.0	101.4
PYTHIA ($\times 2$ g$\rightarrow$ Q$\bar{\text{Q}}$)	19.5	106.0

Table 1: Total cross sections for photon+b/c production.

the data and the calculations are $|y| < 1$, $30 < p_T < 300$ GeV/c for the photon and $|y| < 1.5$, $p_T > 20$ GeV/c for the b or c quark, where y is the rapidity and p_T the transverse momentum. The photons are required to be isolated in a cone of radius R=0.4, with an isolation energy <2 GeV, and the angular distance between the photon and the b or c quark is required to be ΔR>0.4.

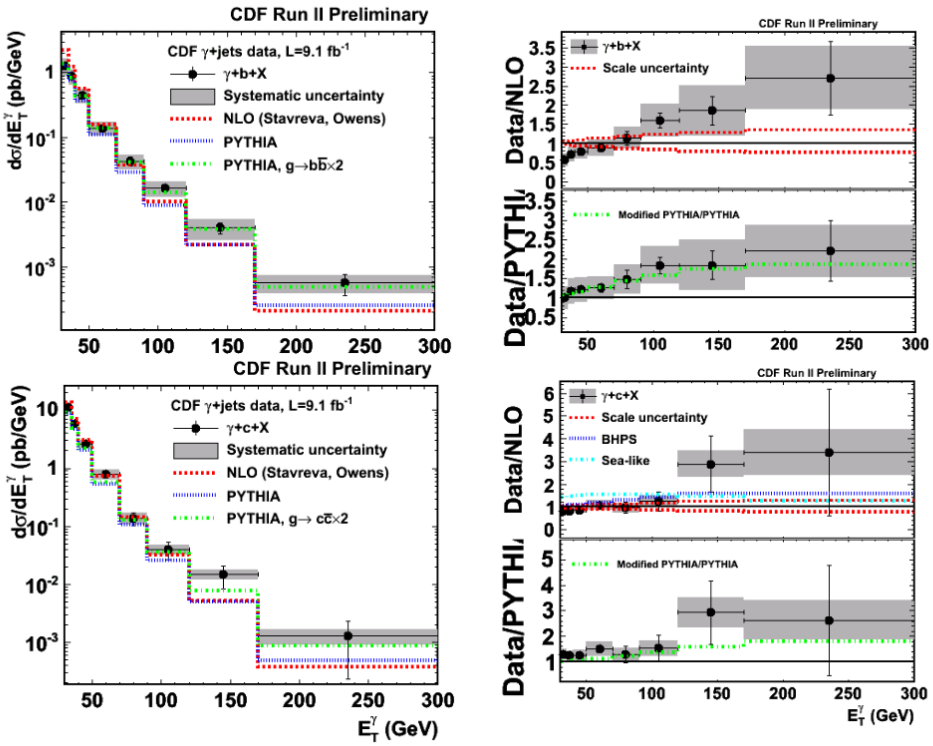

Figure 1: Differential cross sections and data/theory ratios for photon+heavy flavor production. The shaded band depicts the total systematic uncertainty of the measurement.

Table 1 shows the total cross sections from the data and from the two PYTHIA calculations. The γ+b calculation is in relatively good agreement with the data, especially when the gluon splitting rate is increased. The γ+c calculation underestimates the data. Figure 1 shows the measured and predicted cross sections and the data/theory ratios differential in the photon transverse energy. A scale uncertainty is estimated for the NLO calculations. The ratio of data to PYTHIA is taken with respect to the default calculation and then the ratio of the modified to the default PYTHIA calculation is also plotted. In the case of γ+c production two variations of the NLO calculation using intrinsic charm hadron models are also compared with the data. The NLO calculations do not reproduce the shapes of the data. The PYTHIA predictions are in better agreement with the shapes of the data when the gluon splitting rate is increased.

3 Diphoton production

The measurements are compared with five calculations: (i) Predictions from the LO parton shower program PYTHIA [1]. (ii) Predictions from the LO parton shower program SHERPA [3]. (iii) Fixed-order NLO predictions including non-perturbative fragmentation processes at LO from the program MCFM [4]. (iv) Fixed-order NLO predictions including non-perturbative fragmentation processes at NLO from the program DIPHOX [5]. (v) Predictions from the program RESBOS [6] performing a low-p_T analytically resummed calculation which is then matched to the high-p_T NLO matrix element calculation. The RESBOS calculation is constrained by a cut on the diphoton invariant mass $M_{\gamma\gamma} < 350$ GeV/c^2. PYTHIA is run in a mode that combines $\gamma\gamma$ and γ+jet production from which events with at least two prompt photons are selected during the simulation, thus including in part real NLO contributions from initial and final state radiation. Table 2 shows the total cross sections from the data and from calculations. Theoretical uncertainties from the choice of scale and the parton distribution functions (PDF) are included for NLO parton-level calculations, where such uncertainties are better defined. All predictions are consistent with the data. Figure 2 shows the relative deviations, in the form of (data−theory)/theory, between measured and predicted cross sections differential in the diphoton transverse momentum p_T and in the azimuthal distance $\Delta\phi$ between the two photons in the event. The fixed-order NLO calculations fail to describe the data in the limit $p_T \to 0$. The RESBOS calculation provides the best description of the data in the limit of low diphoton p_T, where resummation is most important. The best overall agreement is achieved by the SHERPA prediction, although this one too underestimates the data in the region of $\Delta\phi < 1.5$ rad.

	$\sigma_{total}(\gamma\gamma)$ (pb)
Data	$12.3\pm0.2_{\rm stat}\pm3.5_{\rm syst}$
RESBOS	11.3±2.4
DIPHOX	10.6±0.6
MCFM	11.6±0.3
SHERPA	10.9
PYTHIA	9.2

Table 2: Total cross sections for diphoton production.

4 Summary

We reported high precision measurements of the cross sections for prompt photon production associated with heavy quark flavor and for prompt diphoton production, both using the full CDF data sample. The measurements are compared with state-of-the-art calculations. The comparisons show only partial agreement between data and calculations.

5 Bibliography

References

[1] T. Sjöstrand *et al.* Comp. Phys. Comm. **135** (2001) 238.

[2] J. Owens and T. Stavreva. Phys. Rev. **D79** (2009) 054017.

[3] T. Glesiberg *et al.* J. High En. Phys. **02** (2009) 007.

[4] J. M. Campbell *et al.* Phys. Rev. **D60** (1999) 113006.

[5] T. Binoth *et al.* Phys. Rev. **D63** (2001) 114016.

[6] T. Balazs *et al.* Phys. Rev. **D76** (2007) 013008.

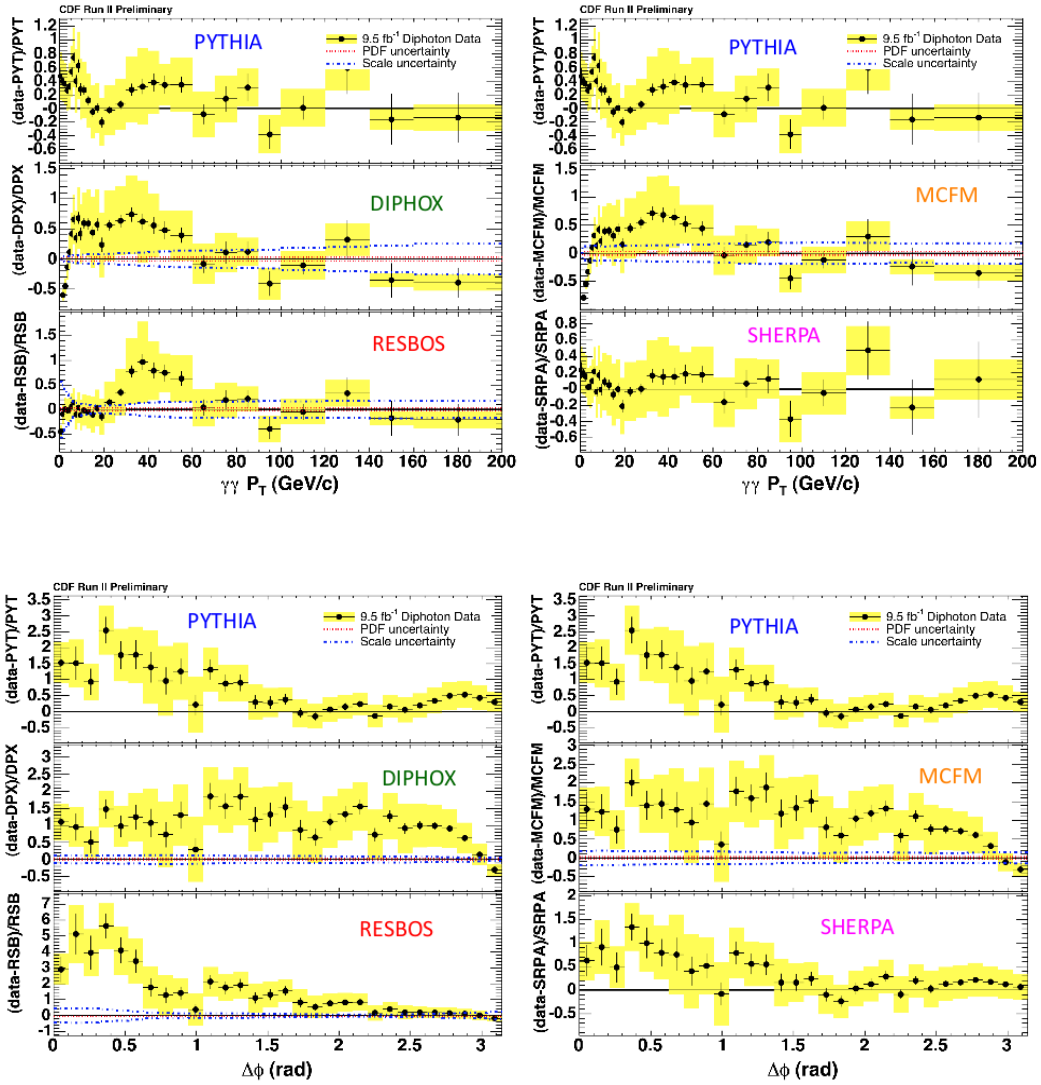

Figure 2: (Data−theory)/theory differential cross section ratios for diphoton production. The shaded band depicts the total systematic uncertainty of the measurement.

Prompt photon measurements with the ATLAS detector

Leonardo Carminati[1] on behalf of the ATLAS Collaboration

[1]Università e sezione INFN di Milano, via G. Celoria 16, 20133 Milano, Italy

DOI: `http://dx.doi.org/10.3204/DESY-PROC-2012-02/81`

An overview of the main prompt photon measurements with the ATLAS detector is presented. The production cross sections for inclusive photons, photon plus jets and diphotons have been measured with 37 pb^{-1} of pp collisions at $\sqrt{s}$=7 TeV collected at the LHC in 2010. Data have been found to be in fair agreement with next-to-leading order perturbative QCD calculations. The overall picture confirms that QCD photons are well understood in ATLAS laying solid foundations for discovery physics involving photons.

1 Introduction

The study of the production of prompt photons at hadron colliders is an important test of perturbative QCD (pQCD) predictions [1], providing a colorless probe of the hard scattering process. Moreover, the measurements of the prompt photon production cross section, inclusive or in association with jets, can be used to constrain the parton density functions [2]. In particular they are sensitive to the gluon content of the proton through the $qg \rightarrow q\gamma$ subprocess, which at leading-order dominates the inclusive prompt photon cross section at the LHC. Finally the diphoton and photon plus jet production represent irreducible and reducible backgrounds respectively for some discovery physics searches, such as the Higgs boson decay into photon pairs [3]. In ATLAS, photons are reconstructed from electromagnetic clusters in the calorimeter and from tracking information provided by the inner detector. Both unconverted and converted photon candidates are considered for this measurement. Photon candidates are required to pass identification criteria based on shower shapes in the calorimeters [4]. In the following "isolated" photons are considered, *i.e.* photons whose transverse energy $E_{\mathrm{T}}^{\mathrm{iso}}$, within a cone of radius $R = \sqrt{\Delta\eta^2 + \Delta\phi^2} = 0.4$ centered around the photon direction in the pseudo-rapidity (η) and azimuthal angle (ϕ) plane, is smaller than typically 4 GeV [1]. The background for all these analyses mainly comes from jets containing high energy π^0s faking photons : the isolation requirement is useful to reject the fake photons since they are usually accompanied by hadronic activity around the leading particle direction. For the same reason, the isolation cut also reduces the contribution due to real photons produced in partons fragmentation which is desirable since it cannot be calculated in pQCD. All the results presented here are based on 2010 data collected by the ATLAS experiment at a center-of-mass energy of 7 TeV.

[1]The energy associated to the photon candidate itself is subtracted from the isolation energy.

2 Inclusive photon production cross section

A first measurement of the isolated prompt photon production cross section [4] used 0.88 pb^{-1} of data and covered the kinematic region 15 GeV $\leq E_{\mathrm{T}} <$ 100 GeV in three different pseudorapidity bins: $0.0 \leq |\eta| < 0.6$,$0.6 \leq |\eta| < 1.37$ and $1.52 \leq |\eta| < 1.81$. The most recent measurement [5] explored a higher E_{T} regime, 45 GeV $\leq E_{\mathrm{T}} <$ 400 GeV, and expanded the coverage to include the $1.81 \leq |\eta| < 2.37$ region by using the full 35 pb^{-1} of data from 2010 run. In both analyses, the JETPHOX [6] program was used to compute the NLO cross sections with different sets of parton density functions (PDFs). The measured cross sections are compared in Fig. 1 to the theoretical predictions obtained with the CTEQ6.6 PDF set. The four η bins are included, scaled by an arbitrary factor for the sake of clarity. A very good agreement can be observed, within uncertainties, between the two measurements in the overlapping region. The NLO pQCD predictions agree in all cases with the observed cross sections for transverse energies > 25 GeV, while for transverse energies < 25 GeV the cross sections predicted by JETPHOX are higher than the measured ones. Similar results have been obtained using both MSTW2008 and NNPDF 2.0 PDF sets. The theoretical uncertainty is dominated by the scale uncertainty (10%), which presently limits the discrimination between PDFs. From the experimental side the statistical uncertainty is negligible, the systematic being dominated by the purity and photon efficiency estimations.

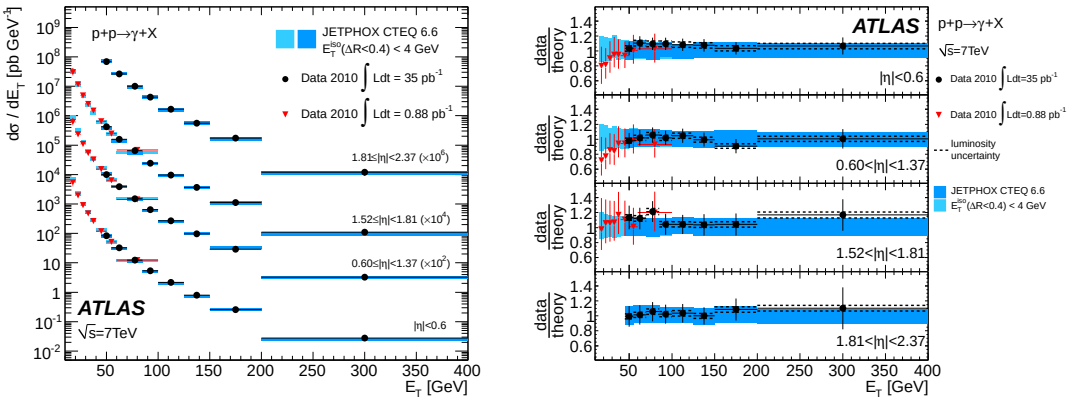

Figure 1: Inclusive photon production cross section [7] compared with NLO predictions obtained using JETPHOX with CTEQ6.6 for the four photon $|\eta|$ ranges described in the text.

3 Photon plus jets production cross section

The differential cross section $d\sigma/dE_{\mathrm{T}}^{\gamma}$, as a function of the photon transverse energy, has been determined [8] for isolated photons in the pseudorapidity range $|\eta^{\gamma}| < 1.37$ and transverse energy $E_{\mathrm{T}}^{\gamma} > 25$ GeV, after integration over the jet transverse momenta for $p_{\mathrm{T}}^{\mathrm{jet}} > 20$ GeV. A minimum separation of $\Delta R > 1.0$ in the $\{\eta, \phi\}$ plane is required between the leading jet and the photon. The cross sections are presented separately for the three jet rapidity intervals $|y^{\mathrm{jet}}| < 1.2$, $1.2 \leq |y^{\mathrm{jet}}| < 2.8$ and $2.8 \leq |y^{\mathrm{jet}}| < 4.4$, distinguishing between the same-sign

($\eta^\gamma y^{\rm jet} \geq 0$) and opposite-sign ($\eta^\gamma y^{\rm jet} < 0$) configurations. This subdivision allows the comparison between data and NLO pQCD predictions in configurations where the relative contribution of the fragmentation component to the cross section and the explored ranges of the incoming parton momentum fraction x are different. As shown in Fig. 2 the NLO pQCD cross sections provided by JETPHOX are in fair agreement with the measured ones considering the typical (10% to 30%) experimental and theoretical systematic uncertainties. In the $E_{\rm T}^\gamma < 45$ GeV region, the NLO QCD calculation consistently overestimates the measured cross section, as in Sec. 2.

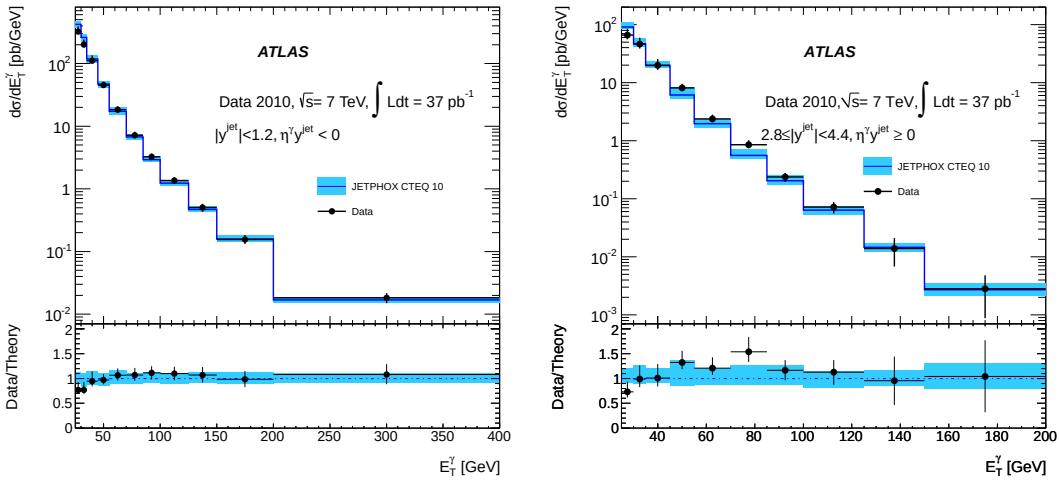

Figure 2: Experimental (black dots) [8] and theoretical (blue line) photon + jet production cross sections, for $|y^{\rm jet}| < 1.2$ same-sign configuration (left) and $2.8 \leq |y^{\rm jet}| < 4.4$ opposite-sign configuration. The black error bars represent the total experimental uncertainty. The blue bands show the total uncertainties on the theoretical predictions obtained with JETPHOX.

4 Diphoton production cross section

Finally the measurement of the production cross section of isolated diphotons in pp collisions was performed [9]: candidate events were selected requiring two photons, with transverse momenta $p_{\rm T} > 16$ GeV and satisfying experimental identification and isolation requirements. The two candidates were also required to have a separation $\Delta R > 0.4$. In Fig. 3, the differential cross sections as a function of the invariant mass $m_{\gamma\gamma}$ and the azimuthal separation $\Delta\phi_{\gamma\gamma}$ of the photon pair are presented. The experimental results are compared with NLO predictions obtained with the DIPHOX [10] and ResBos [11] generators. More photon pairs are seen in data at low $\Delta\phi_{\gamma\gamma}$ values, while fixed order NLO theoretical predictions favour a larger back-to-back production ($\Delta\phi_{\gamma\gamma} \simeq \pi$). In the $\Delta\phi_{\gamma\gamma} \simeq \pi$ region multiple soft gluon emission is important and fixed-order calculations break down because of infrared divergences. A recent NNLO calculation [12] is expected to improve the agreement in the low $\Delta\phi_{\gamma\gamma}$ region. The distribution of $d\sigma/dm_{\gamma\gamma}$ is in good agreement with both the DIPHOX and ResBos predictions, apart from the low mass region which corresponds to the low $\Delta\phi_{\gamma\gamma}$ region discussed previously.

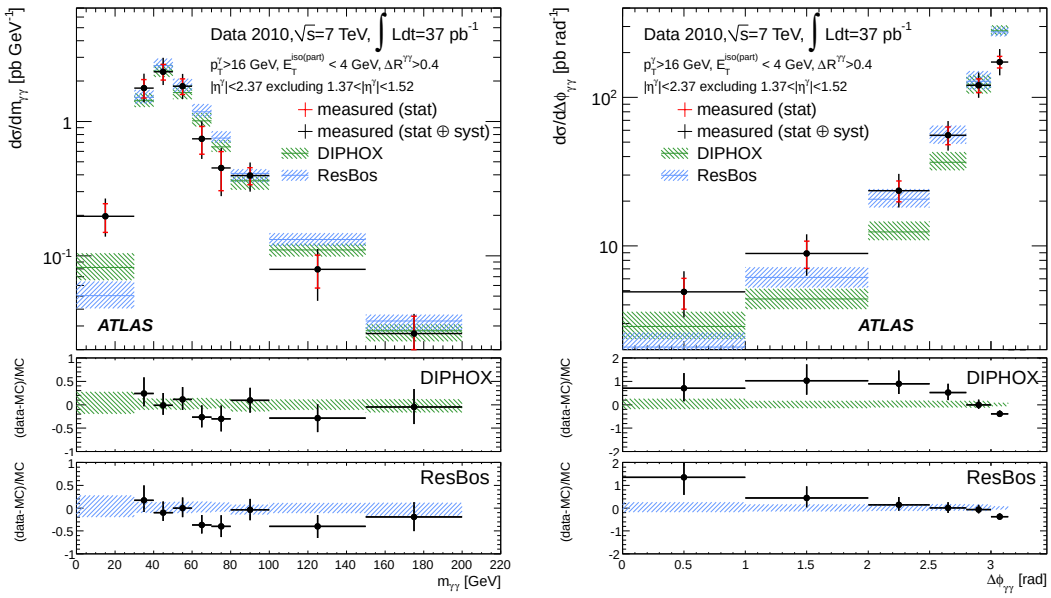

Figure 3: Diphoton production cross section as a function of the invariant mass $m_{\gamma\gamma}$ (left) and the azimuthal separation $\Delta\phi_{\gamma\gamma}$ of the two photons (right). The measurements [9] are compared with DIPHOX and ResBos predictions using the CTEQ6.6 PDF set.

5 Conclusion

The production cross sections for inclusive photons, photons plus jets and diphotons have been measured with 37 pb^{-1} of data collected by the ATLAS detector in 2010 and found to be in fair agreement with NLO predictions. Analyses are ongoing to look into 2011 and 2012 data in order to stress further the reliability of the QCD predictions.

References

[1] P. Aurenche *et al.* Nucl. Phys. **B297** (1988) 661.

[2] D. d'Enterria and J. Rojo. Nucl. Phys. **B860** (2012) 311–338.

[3] ATLAS Collaboration. Phys. Rev. Lett. **108** (2012) 111803, arXiv:1202.1414 [hep-ex].

[4] ATLAS Collaboration. Phys. Rev. **D83** (2011) 052005, arXiv:1012.4389 [hep-ex].

[5] ATLAS Collaboration. Phys. Lett. **B706** (2011) 150–167, arXiv:1108.0253 [hep-ex].

[6] P. Aurenche *et al.* Phys. Rev. D **73** (2006) 094007.

[7] ATLAS Collaboration. ATL-PHYS-PUB-2011-013 (2011) . https://cdsweb.cern.ch/record/1395049.

[8] ATLAS Collaboration. Phys. Rev. **D85** (2012) 092014, arXiv:1203.3161 [hep-ex].

[9] ATLAS Collaboration. Phys. Rev. **D85** (2012) 012003, arXiv:1107.0581 [hep-ex].

[10] T. Binoth *et al.* Eur. Phys. J. **C16** (2000) 311–33.

[11] C. Balazs *et al.* Phys.Rev. **D76** (2007) 013009, arXiv:0704.0001 [hep-ph].

[12] S. Catani *et al.* Phys. Rev. Lett. **108** (2012) 072001.

Jet-veto efficiencies at all orders in QCD

Andrea Banfi[1]

[1] University of Freiburg, Hermann-Herder-Strasse 3, 79104 Freiburg, Germany

DOI: http://dx.doi.org/10.3204/DESY-PROC-2012-02/269

We present a next-to-leading logarithmic resummation for the jet-veto efficiency in Higgs production. We then discuss how this prediction affects the theoretical uncertainties in the region of transverse momenta of interest for Higgs searches at the LHC.

In searches of a Standard Model Higgs boson decaying into a pair of W bosons, it is customary to divide events with the requested signature into bins corresponding to different jet multiplicities [1, 2]. In particular, we concentrate on the 0-jet cross section, obtained by requiring that there are no jets with transverse momentum p_t larger than $p_{\mathrm{t,veto}}$. This 0-jet bin turns out to be less contaminated by W's originated from top-antitop production.

The 0-jet cross section can be computed at next-to-next-to-leading order (NNLO) thanks to the fully differential calculations for Higgs production of Refs. [3, 4]. The question then arises on how to estimate the theoretical uncertainties of the 0-jet cross section. It was already observed in Ref. [5] that simultaneous variation of renormalisation and factorisation scales leads to underestimating theoretical uncertainties, which even vanish for $p_{\mathrm{t,veto}} \simeq 25\mathrm{GeV}$. Therefore, the authors of that paper propose a more sophisticated way to asses uncertainties based on those of the inclusive cross section. The authors of Ref. [6] argued further that the small scale uncertainty in the 0-jet cross section was due to cancellations between two effects of different physical origin. Indeed, $\sigma_{0-\mathrm{jets}}(p_{\mathrm{t,veto}}) = \sigma_{\mathrm{inclusive}} - \sigma_{\geq 1-\mathrm{jet}}(p_{\mathrm{t,veto}})$. While the inclusive cross section $\sigma_{\mathrm{inclusive}}$ is affected by a large K-factor, the one for having more than one jet $\sigma_{\geq 1-\mathrm{jet}}(p_{\mathrm{t,veto}})$ contains logarithmically enhanced contributions $\alpha_s^n \ln^m(M_H/p_{\mathrm{t,veto}})$, with $m \leq 2n$. Since these two effects are uncorrelated, they propose to estimate the uncertainties on $\sigma_{0-\mathrm{jets}}$ by just adding in quadrature the uncertainties on $\sigma_{\mathrm{inclusive}}$ and $\sigma_{\geq 1-\mathrm{jet}}$. We elaborate further on this idea and write the 0-jet cross section as the product of $\sigma_{\mathrm{inclusive}}$ and the jet-veto efficiency $\epsilon(p_{\mathrm{t,veto}})$, defined as the fraction of events such that all jets have a transverse momentum less than $p_{\mathrm{t,veto}}$. We argue that the knowledge of higher and higher orders for $\sigma_{\mathrm{inclusive}}$ does not help in reducing the uncertainty in $\epsilon(p_{\mathrm{t,veto}})$, which rather reflects our ignorance about logarithms $\alpha_s^n \ln^m(M_H/p_{\mathrm{t,veto}})$ of Sudakov origin, arising from a veto condition on real radiation. In the following we then consider the uncertainties on $\sigma_{\mathrm{inclusive}}$ and $\epsilon(p_{\mathrm{t,veto}})$ as uncorrelated and we concentrate on the efficiency only [7].

At fixed order, the efficiency is defined in terms of the following cross sections:

$$\begin{aligned} &\sigma_{\mathrm{inclusive}} \equiv \sigma = \sigma_0 + \sigma_1 + \sigma_2 + \dots\,, \\ &\sigma_{0-\mathrm{jets}}(p_{\mathrm{t,veto}}) = \Sigma(p_{\mathrm{t,veto}}) = \sigma_0 + \Sigma_1(p_{\mathrm{t,veto}}) + \Sigma_2(p_{\mathrm{t,veto}}) + \dots\,, \end{aligned} \tag{1}$$

where σ_i and $\Sigma_i(p_{\mathrm{t,veto}})$ are of relative order α_s^i with respect to the Born cross section σ_0. It is

also useful to introduce the "complementary" cross sections $\bar{\Sigma}_i(p_{\rm t,veto})$ as follows

$$\bar{\Sigma}_i(p_{\rm t,veto}) = -\int_{p_{\rm t,veto}}^{\infty} dp_t \frac{d\Sigma_i(p_t)}{dp_t}\,, \qquad \Sigma_i(p_{\rm t,veto}) = \sigma_i + \bar{\Sigma}_i(p_{\rm t,veto})\,. \tag{2}$$

We remark that at the moment the perturbative expansion of these cross section is known up to relative order α_s^2. We now identify three schemes that we believe cover the possibilities to construct a jet-veto efficiency starting from the above cross sections:

$$\begin{aligned}
\epsilon^{(a)}(p_{t,\rm veto}) &= \frac{\sigma_0 + \Sigma_1(p_{t,\rm veto}) + \Sigma_2(p_{t,\rm veto})}{\sigma_0+\sigma_1+\sigma_2}\,,\\
\epsilon^{(b)}(p_{t,\rm veto}) &= \frac{\sigma_0 + \Sigma_1(p_{t,\rm veto}) + \bar{\Sigma}_2(p_{t,\rm veto})}{\sigma_0+\sigma_1}\,,\\
\epsilon^{(c)}(p_{t,\rm veto}) &= 1 + \left(1-\frac{\sigma_1}{\sigma_0}\right)\frac{\bar{\Sigma}_1(p_{t,\rm veto})}{\sigma_0} + \frac{\bar{\Sigma}_2(p_{t,\rm veto})}{\sigma_0}\,.
\end{aligned} \tag{3}$$

We observe that all these prescriptions differ only at order α_s^3. Each of them has its own meaning. Scheme (a) is the naive definition of the efficiency as the ratio between the 0-jet cross section and the inclusive cross section. Scheme (b) can be motivated by the fact that the jet-veto efficiency can be seen as one minus the probability of having one jet with $p_t > p_{\rm t,veto}$. This gives, at present accuracy, $\epsilon^{(b)}(p_{\rm t,veto}) = 1 - \sigma_{\geq 1-\rm jet}(p_{\rm t,veto})^{\rm NLO}/\sigma^{\rm NLO}_{inclusive}$. Finally, scheme (c) corresponds to the strict fixed order expansion of the efficiency.

In the following we use these three schemes as an extra handle, besides renormalisation and factorisation scale variations, to quantify the uncertainties on the jet-veto efficiency. Indeed, if we compute $\epsilon(p_{\rm t,veto})$ for the three schemes, we obtain very different predictions. Namely, including also independent variation of renormalisation and factorisation scale in the range $M_H/4 \leq \mu_R, \mu_F \leq M_H$ with $1/2 \leq \mu_R/\mu_F \leq 2$, in the region of interest for experimental studies ($p_{\rm t,veto} = 25$GeV for ATLAS and $p_{\rm t,veto} = 30$GeV for CMS), the spread in fixed-order predictions for the jet-veto efficiency is around 30% [7, 8]. This is not observed in Z production, where all three schemes basically coincide.

Since part of this bad convergence can be attributed to the presence of large logarithms of soft-collinear origin, it is useful to see how the uncertainty changes when performing an all-order resummation of such logarithms. At next-to-leading logarithmic (NLL) accuracy, which amounts in controlling all terms $\alpha_s^n \ln^n(M_H/p_{\rm t,veto})$ in $\ln \epsilon(p_{\rm t,veto})$, this is possible with the automated resummation program CAESAR [9]. In particular, if jets are to be found everywhere in rapidity, CAESAR tells us that the jet-veto efficiency is resummable within NLL accuracy, and has the form

$$\epsilon(p_{t,\rm veto}) \sim \mathcal{L}_{gg}(p_{t,\rm veto})\, e^{-R(p_{t,\rm veto})}\, \mathcal{F}(R')\,, \qquad R' = -\,p_{t,\rm veto}\,\frac{dR(p_{t,\rm veto})}{dp_{t,\rm veto}}\,, \tag{4}$$

where $\mathcal{L}_{gg}(p_{t,\rm veto})$ is the gluon-gluon luminosity, evaluated at the factorisation scale $p_{\rm t,veto}$, and $R(p_{\rm t,veto})$ is the Sudakov exponent

$$R(p_{t,\rm veto}) = 2C_A \int_{p_{t,\rm veto}^2}^{M_H^2} \frac{dk_t^2}{k_t^2}\,\frac{\alpha_s^{\rm CMW}(k_t)}{\pi}\left[\ln\frac{M_H}{k_t} - \frac{4\pi\beta_0}{C_A}\right], \quad \beta_0 = \frac{11C_A - 4T_R n_f}{12\pi}\,, \tag{5}$$

where $\alpha_s^{\rm CMW}(k_t)$ is the physical coupling of Ref. [10]. While $R(p_{\rm t,veto})$ contains virtual corrections only, the function $\mathcal{F}(R')$ accounts for multiple soft-collinear real emissions. For a perfectly

factorisable observable $V(k_1, \ldots, k_n) = \max_i\{V(k_i)\}$ we have $\mathcal{F}(R') = 1$. It turns out that, for small $p_{\mathrm{t,veto}}$, if jets are defined with a k_t^{2p}-algorithm (anti-k_t, Cambridge-Aachen, k_t), for emissions widely separated in rapidity no recombination can occur. Therefore, it is only the hardest gluon that contributes to the jet-veto efficiency, and therefore $\mathcal{F}(R') = 1$. A resummed prediction as the one in Eq. (4) contains an extra source of theoretical uncertainties. Indeed one can decide to resum $\ln(Q/p_{\mathrm{t,veto}})$ instead of $\ln(M_H/p_{\mathrm{t,veto}})$, where Q is an arbitrary "resummation" scale we choose to vary in the range $M_H/4 \leq Q \leq M_H$. Finally, to be able to present resummed predictions for the jet-veto efficiency, we have to match the efficiency in Eq. (4) with its expression at order α_s^2. Therefore, we introduce three matching schemes, defined in such a way that for $p_{\mathrm{t,veto}} \ll M_H$ the matched efficiency reduces to the expression in Eq. (4), whilst for $p_{\mathrm{t,veto}} \sim M_H$, it approaches its fixed order expression in any of the three schemes introduced in Eq. (3). The matching scheme gives us then an extra handle to estimate theoretical uncertainties.

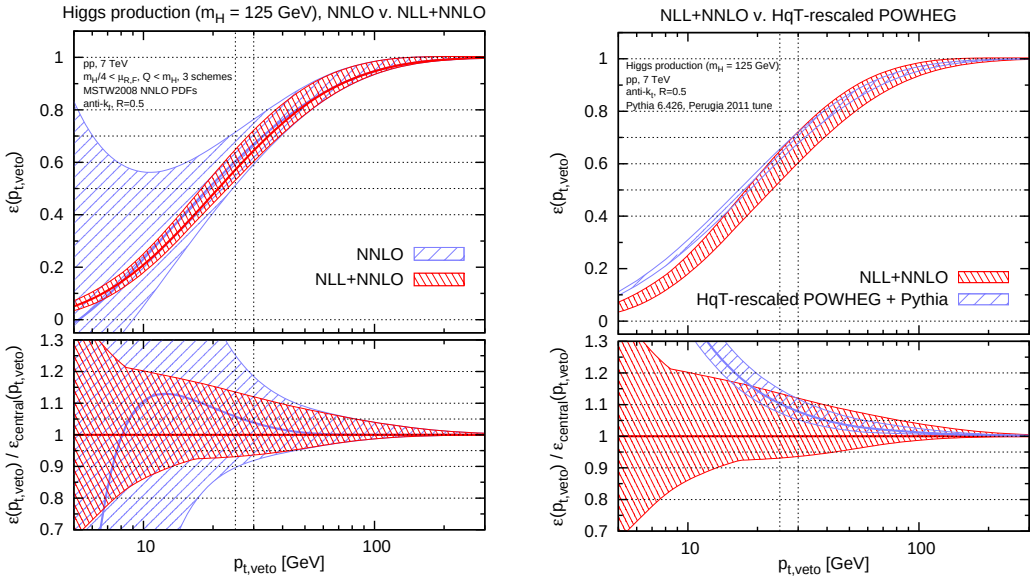

Figure 1: Left: the jet-veto efficiency for Higgs production at order α_s^2 (NNLO) and matched to NLL resummation (NLL+NNLO). Right: NLL+NNLO efficiency compared to POWHEG rescaled using HqT.

We now present results for the matched jet-veto efficiency, at the LHC with $\sqrt{s} = 7$ TeV, with jets clustered using the anti-k_t algorithm with $R = 0.5$, and for $M_H = 125$ GeV. In order to estimate theoretical uncertainties, we identify a "central" prediction, the efficiency computed with matching scheme (a) and with all scales Q, μ_R, μ_F equal to $M_H/2$. We then vary one scale at a time for scheme (a) in the range $[M_H/4, M_H]$, and vary the matching schemes using $Q = \mu_R = \mu_F = M_H/2$. In this way we believe we do not double count uncertainties. The predictions corresponding to this choice are shown in Fig. 1. We observe that NLL resummation helps reducing the uncertainties in the jet-veto effiency. Indeed, for $p_{\mathrm{t,veto}}$ between 25 and 30 GeV, they move from 20% (pure NNLO) down to 10% (NLL+NNLO). This improvement is not as huge, as is for lower values of $p_{\mathrm{t,veto}}$, and reflects the fact that in this

intermediate region $\ln(M_H/p_{\mathrm{t,veto}})$ is not large enough to guarantee that resummation effects dominate. We notice also that here the uncertainty is dominated by the difference between matching schemes. Since this difference is formally NNNLL, we do not expect that a NNLL resummation could considerably help to reduce the theoretical uncertainty. Finally, we compare our predictions with the Monte Carlo event generator that is currently used by CMS and ATLAS to estimate the jet-veto efficiency. This is POWHEG [11] interfaced to PYTHIA [12], rescaled in such a way that it agrees with the Higgs p_t spectrum computed at NNLL+NNLO accuracy with the program HqT [13]. The uncertainties in POWHEG+PYTHIA are estimated by following the recommendation of Refs. [8, 14], i.e. varying renormalisation and factorisation scales independently around $M_H/2$ and fixing the parameter `hfact` to $h = M_H/1.2$. We observe good agreement between our NLL+NNLO and POWHEG+PYTHIA in the region of $p_{\mathrm{t,veto}}$ of interest. However, at lower values of $p_{\mathrm{t,veto}}$, we find that NLL+NNLO predictions tend to give lower efficiency than that obtained with POWHEG+PYTHIA. We remark that the same trend is observed when comparing NLL+NLLO to predictions obtained with other Monte Carlo event generators.

To conclude, we have investigated how a NLL resummation for the jet-veto efficiency affects the theoretical uncertainty on this quantity. It would be very interesting to see how these findings change after a NNLL resummation. In Ref. [7] we have computed (for $R < \pi$) the part of NNLL resummation that depends on the jet radius. The remaining NNLL contributions could be obtained by relating the jet-veto efficiency to the Higgs p_t spectrum (see for instance [15]). We hope to complete this study soon.

Note Added. The NNLL resummation for the jet-veto efficiency in Higgs and Drell-Yan production has been recently completed in Ref. [16].

Acknowledgements

This work presented here has been done in collaboration with Gavin Salam and Giulia Zanderighi. I am also grateful to Ian Winter for the invitation to the Workshop.

References

[1] G. Aad *et al.* [ATLAS Collaboration], Phys. Rev. Lett. **108** (2012) 111802.
[2] S. Chatrchyan *et al.* [CMS Collaboration], Phys. Lett. B **710** (2012) 91.
[3] C. Anastasiou, K. Melnikov, F. Petriello, Nucl. Phys. **B724** (2005) 197-246.
[4] M. Grazzini, JHEP **0802** (2008) 043.
[5] C. Anastasiou, G. Dissertori, F. Stockli and B. R. Webber, JHEP **0803** (2008) 017.
[6] I. W. Stewart and F. J. Tackmann, Phys. Rev. D **85** (2012) 034011.
[7] A. Banfi, G. P. Salam and G. Zanderighi, JHEP **1206** (2012) 159.
[8] S. Dittmaier, S. Dittmaier, C. Mariotti, G. Passarino, R. Tanaka, S. Alekhin, J. Alwall and E. A. Bagnaschi *et al.*, arXiv:1201.3084 [hep-ph].
[9] A. Banfi, G. P. Salam and G. Zanderighi, JHEP **0503** (2005) 073.
[10] S. Catani, B. R. Webber and G. Marchesini, Nucl. Phys. B **349** (1991) 635.
[11] S. Alioli, P. Nason, C. Oleari and E. Re, JHEP **0904** (2009) 002.
[12] P. Z. Skands, Phys. Rev. D **82** (2010) 074018.
[13] G. Bozzi, S. Catani, D. de Florian and M. Grazzini, Nucl. Phys. B **737** (2006) 73.
[14] J. M. Campbell, R. K. Ellis, R. Frederix, P. Nason, C. Oleari and C. Williams, JHEP **1207** (2012) 092.
[15] T. Becher and M. Neubert, JHEP **1207** (2012) 108.
[16] A. Banfi, P. F. Monni, G. P. Salam and G. Zanderighi, arXiv:1206.4998 [hep-ph].

From Jet Counting to Jet Vetoes

Peter Schichtel[1,*], *Christoph Englert*[2], *Erik Gerwick*[3], *Tilman Plehn*[1], *Steffen Schumann*[3]

[1] Institut für Theoretische Physik, Universität Heidelberg, Germany
[2] Institute for Particle Physics Phenomenology, Durham University, United Kingdom
[3] II. Physikalisches Institut, Universität Göttingen, Germany
[*] *Speaker*

DOI: `http://dx.doi.org/10.3204/DESY-PROC-2012-02/230`

The properties of multi-jet events impact many LHC analysis. The exclusive number of jets at hadron colliders can be described in terms of two simple patterns: staircase scaling and Poisson scaling. In photon plus jets production we can interpolate between the two patterns using simple kinematic cuts. The associated theoretical errors are well under control. Understanding such exclusive jet multiplicities significantly impacts Higgs searches and searches for supersymmetry at the LHC.

1 Introduction

In LHC searches jets and their properties play an important role for our understanding of hadron collisions. Jets in association with W/Z bosons as well as pure QCD jets not only help us to understand the theory, but also pose important backgrounds to new physics searches. Currently, the Higgs searches are certainly the most exciting LHC analysis. In the weak boson fusion (WBF) channel these searches rely on central jet vetoes, where jet radiation between two hard tagging jets is forbidden [1]. This idea is based on the color structure in WBF processes. Nowadays, for example the $H \to WW$ searches are divided into *exclusive* $0, 1$ and 2 jet bins. Whenever new physics scenarios introduce new heavy colored particles [2] their search relies on jets which appear as decay and radiation jets. The production scale for such heavy objects is encoded in the effective mass $m_{\text{eff}} = \not{p}_T + \sum_{\text{jets}} p_{T,\text{jet}}$, which is essentially proportional to the number of jets.

We propose the *exclusive* number of jets n_{jets} as the proper observable to study jets at the LHC. If we control this observable we can in addition use many multi-jet observables, like m_{eff}, whose uncertainties are otherwise notorious. There are, however, some issues in the definition of *exclusive* as compared to *inclusive* multi-jet observables. To gain higher precision we usually rely on higher order calculations, which in QCD predict inclusive observables. This means that once we include parton densities obeying the DGLAP equation any number of collinear jets is automatically included. On the other hand, exclusive jet bins are statistically independent. We use Sherpa [3] and its CKKW [4] algorithm to generate matched LO events to study exclusive jet cross-section ratios. In general we observe two distinct patterns: Poisson and staircase scaling.

2 Scaling patterns

2.1 Poisson scaling

Poisson processes are well known for example when we rely on the eikonal approximation [5, 6]. There, the matrix element factorizes for example from soft photon emission

$$\mathcal{M}_{n+1} = g_s T^3 \epsilon_\mu^* \bar{u}(q) \frac{q^\mu + \mathcal{O}(\not{k})}{qk + \mathcal{O}(k^2)} \mathcal{M}_n \,. \tag{1}$$

This relation can be used to resum emissions to all orders. It leads to a Poisson distribution for visible emissions

$$\sigma_n \propto \frac{\bar{n}^n}{n!} e^{-\bar{n}} \qquad \text{with} \quad \bar{n} \propto \frac{\alpha}{\pi} \log \frac{E_\text{hard}}{E_\text{soft}} \,. \tag{2}$$

The numerator is just the exponentiation of n emission probabilities, while the $n!$ factor takes care of the bosonic phase space. The exponential factor normalizes the distribution correctly. This way we find the logarithmic dependence of $\bar{n}$, where E_soft is the minimum resolution for soft photons. The cross-section ratios for Poisson processes immediately follow as

$$R_{(n+1)/n} \equiv \frac{\sigma_{n+1}}{\sigma_n} = \frac{\bar{n}}{n+1} \,. \tag{3}$$

We observe this behavior in all QED processes in the soft limit.

2.2 Staircase scaling

In contrast to Eq.(3) we find constant values for QCD and W/Z plus jets at hadron colliders. This behavior is called staircase scaling and follows [7, 8]

$$R_{(n+1)/n} \equiv \frac{\sigma_{n+1}}{\sigma_n} = R \,. \tag{4}$$

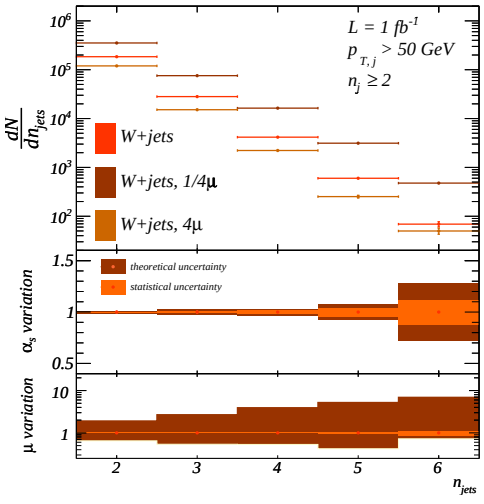

Figure 1: Theory uncertainties for W plus jets production. Figure from Ref.[7].

Staircase scaling is a well established fact known since UA1 [8] and has been observed by ATLAS and CMS [9, 10]. Using SHERPA [3] we simulate exclusive n_jets rates for W/Z plus jets and for QCD jets up to $n_\text{jets} = 8$ and reproduce this pattern. A major issue in the prediction of exclusive observables is the estimation of theoretical uncertainties. We rely on two handles: the value of the strong coupling $\alpha_S(m_Z)$ and a free overall scale parameter connected to the factorization scale. The uncertainties we estimate by varying $\alpha_s(m_Z)$ within its allowed values and by multiplying the default scale by 1/4 and 4. In Fig. 1 we show the n_jets distribution including uncertainties for W plus jets. While the variation of α_s only gives a small error bar the impact of changing μ is very large. However, the actual staircase pattern is not altered. Interpreting the large scale variation as an effect beyond the expected accuracy we can treat it as a MC tuning parameter, which happens to be close to unity for SHERPA [7].

3 Photon laboratory

The perfect place to study Poisson and staircase scaling in more detail is photon plus jets [11]. It has a high cross section and is therefore accessible for early LHC data. At first glance neither Poisson nor staircase scaling is observed in this channel. In contrast to the W/Z case the photon has no mass to define a hard process.

Inspired by the staircase pattern in W/Z plus jets we propose the following cut scenario: count only jets and isolated photons above $p_T^{\min}$, then impose a wide separation cut between the photon and all the counted jets either in terms of the invariant mass or equivalently in terms of R. In Fig. 2 we observe staircase scaling for values of $R > 1.0$ and for invariant masses around 90 GeV, given $p_T^{\min} = 50$ GeV.

To see Poisson scaling we induce a large logarithm as in Eq.(2) by asking for one jet with $p_T > 100$ GeV and lowering $p_T^{\min} = 20$ GeV. As we can see in Fig. 2 the cross section ratios follow a Poisson distribution. For high jet multiplicities the logarithm runs out of steam and we return to staircase scaling, with a constant ratio R determined by $p_T^{\min} = 20$ GeV. The quantitative description of the staircase and Poisson scaling in the photon plus jets can be directly linked to the W/Z plus jets case [11].

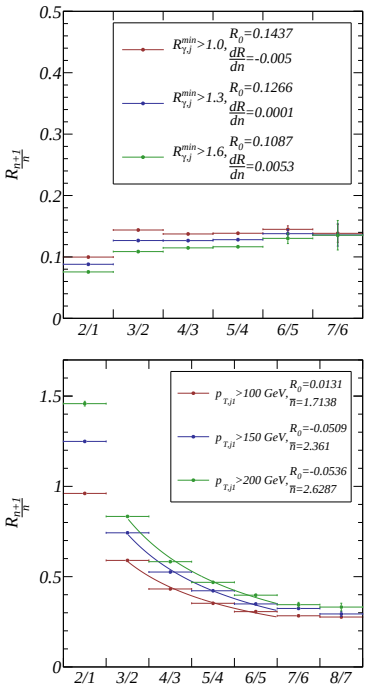

Figure 2: Kinematic regimes showing staircase and Poisson scaling. Figure from Ref. [11].

4 Applications

4.1 Higgs searches

In WBF Higgs searches we use a jet veto to suppress QCD backgrounds. The prediction of the jet veto probability is notorious [12]. In Fig. 3 we show how the WBF cuts drive the backgrounds into the Poisson regime while the signal stays approximately staircase. A simple fit to the n_{jets} distribution gives the veto survival probability.

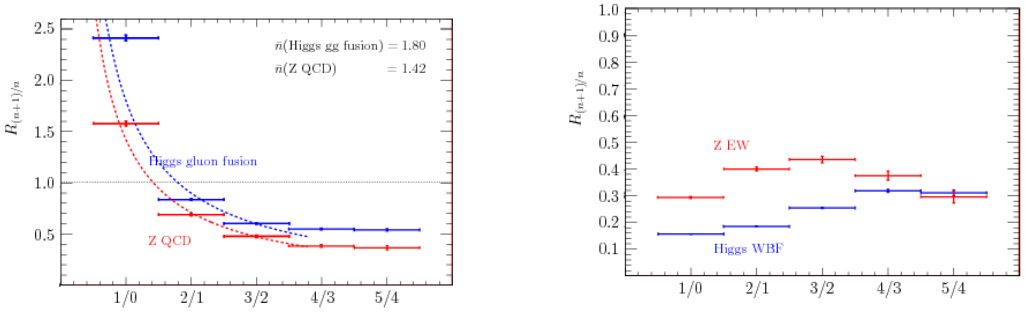

Figure 3: Poisson backgrounds (left) and staircase signal (right) for Higgs production. Figure from Ref. [12].

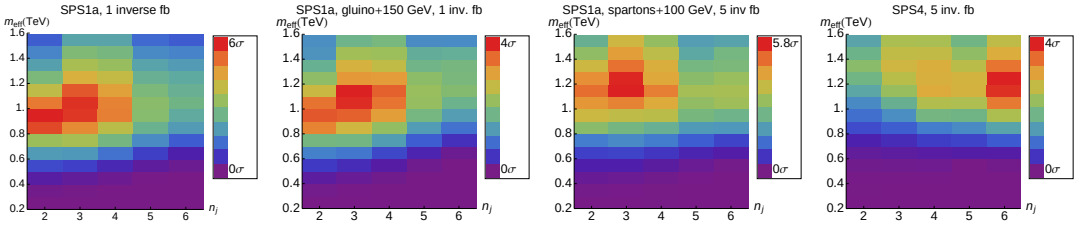

Figure 4: Two-dimensional likelihood for an SPS1a and SPS4 SUSY signal over backgrounds. Figure from Ref. [7].

4.2 Inclusive searches and autofocus

Searches for new physics focus on heavy colored states, for example decaying to dark matter. Contrary to tuned cuts searches, which rely on model spectra, we propose an inclusive ansatz, where we only count jets and apply a missing energy cut [7]. Information about the heavy mass scale is encoded in the effective mass. Due to its close connection to $n_{\rm jets}$ this mass observable is well controlled and can be used in our analysis. It yields complementary information to the number of jets. While $n_{\rm jets}$ is sensitive to deviations mostly in the high multiplicity regime, the effective mass also is sensitive for low multiplicities.

For a simple supersymmetric spectrum we use both observables to perform a log-likelihood test of the SM and SUSY hypotheses. The two-dimensional likelihoods for the different squark and gluino channels we show in Fig. 4. While the $m_{\rm eff}$ axis reflects the mass of the pair of heavy new states, the $n_{\rm jets}$ axis is sensitive to the color charge of the squarks and gluinos.

5 Acknowledgments

P.S. acknowledges support by the International Max Planck Research School for Precision Tests of Fundamental Symmetries.

References

[1] D. L. Rainwater and D. Zeppenfeld. Phys.Rev. **D60** (1999) 113004, arXiv:hep-ph/9906218 [hep-ph].

[2] D. E. Morrissey, T. Plehn, and T. M. Tait. Phys.Rept. **515** (2012) 1–113, arXiv:0912.3259 [hep-ph].

[3] T. Gleisberg, S. Hoeche, F. Krauss, M. Schonherr, S. Schumann, *et al.* JHEP **0902** (2009) 007, arXiv:0811.4622 [hep-ph].

[4] S. Catani, F. Krauss, R. Kuhn, and B. Webber. JHEP **0111** (2001) 063.

[5] M. E. Peskin and D. V. Schroeder. Westview Press (1995) .

[6] E. Laenen, L. Magnea, G. Stavenga, and C. D. White. JHEP **1101** (2011) 141, arXiv:1010.1860 [hep-ph].

[7] C. Englert, T. Plehn, P. Schichtel, and S. Schumann. Phys.Rev. **D83** (2011) 095009, arXiv:1102.4615 [hep-ph].

[8] S. Ellis, R. Kleiss, and W. J. Stirling. Phys.Lett. **B154** (1985) 435.

[9] G. Aad *et al.* Phys.Lett. **B698** (2011) 325–345, arXiv:1012.5382 [hep-ex].

[10] CMS-PAS-EWK-10-012 (2011) .

[11] C. Englert, T. Plehn, P. Schichtel, and S. Schumann. JHEP **1202** (2012) 030, arXiv:1108.5473 [hep-ph].

[12] E. Gerwick, T. Plehn, and S. Schumann. Phys.Rev.Lett. **108** (2012) 032003, arXiv:1108.3335 [hep-ph].

Measurements of Jet Production in pp Collisions with the ATLAS Detector

Adam Yurkewicz on behalf of the ATLAS Collaboration

Northern Illinois University, DeKalb, IL, United States of America

DOI: http://dx.doi.org/10.3204/DESY-PROC-2012-02/79

Differential jet cross sections are measured in inclusive jet, dijet, and multijet events at a center-of-mass energy of 7 TeV using information from the ATLAS calorimeters and tracking detectors. The inclusive jet measurements use jets with transverse momenta from 20 GeV to 1.5 TeV, and the dijet measurements extend up to masses of 5 TeV. Measurements using jets builts from charged tracks are only sensitive to the charged-particle content of the jet, but allow measurements at low transverse momenta. A wide range of QCD-based calculations is compared with measurements, testing the predictions of QCD in a new kinematic regime.

1 Introduction

At the Large Hadron Collider, jet production is the dominant high transverse-momentum (p_T) process. Jet cross sections are one of the main observables in high-energy physics, providing precise information about the structure of the proton, and allowing tests of predictions from QCD calculations.

This note summarizes several of the measurements of inclusive jet, dijet, and multijet differential cross sections made using the ATLAS detector with up to 4.8 fb^{-1} of data collected in 2010 and 2011. The measured jets cover a large p_T and rapidity range. At high rapidities and high dijet masses, this allows tests of QCD in new kinematic regimes. At low p_T, the measurements are more sensitive to non-perturbative effects from hadronization and the underlying event. Measurements of jets reconstructed from charged tracks allow comparisons to theoretical models down to 4 GeV in p_T.

All measurements are made using jets reconstructed with the anti-k_T jet-finding algorithm [1], and are corrected for detector effects using Monte Carlo simulations. Results presented here use jets with distance parameter $R = 0.6$ (cited results also use R=0.4 jets).

2 Inclusive Jet and Dijet Production

Measurements of inclusive jet and dijet differential cross sections are made over a large kinematic range and compared to MC predictions [2, 3]. In order to compare the data to the predictions, the measured jets are corrected for all detector inefficiencies and resolutions using an iterative unfolding procedure. They are then compared to "particle-level" jets built from stable particles using MC simulations. The dominant systematic uncertainty comes from the knowledge of the

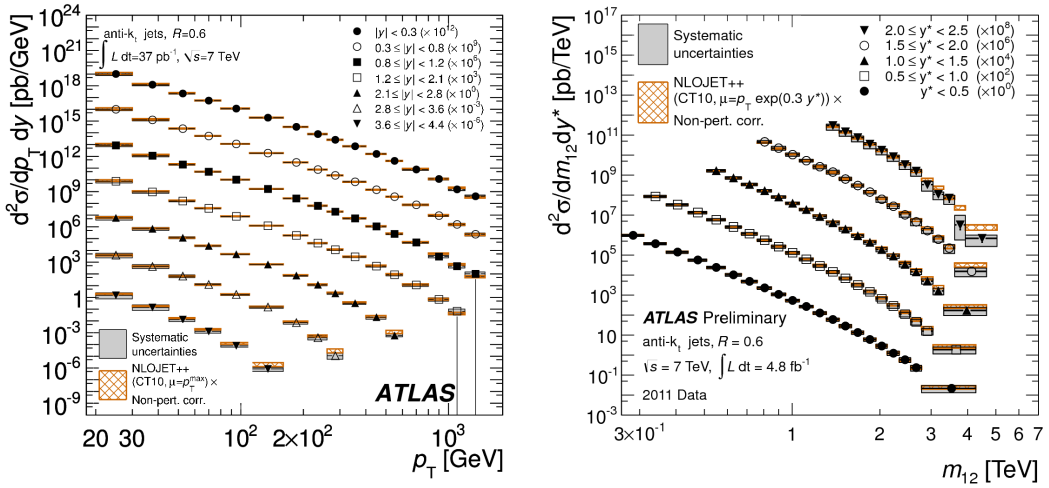

Figure 1: The double differential cross sections for the inclusive jet measurement (using 37 pb^{-1} of data) as a function of p_T in bins of rapidity (left) and for the dijet measurement (using 4.8 fb^{-1} of data) as a function of mass in bins of y* (defined in text) compared to NLO predictions (right).

jet energy scale. This uncertainty is less than 2.5(4.6)% for jets with p_T >60(20) GeV in the central region and rises to ≈12% at low p_T in the forward region. Uncertainties from the jet reconstruction efficiency, jet resolution, and pileup are also included. The uncertainty on the luminosity measurement is 3.4%.

Cross section measurements are compared to NLO pQCD predictions from NLOJET++, corrected for non-perturbative effects, and also to NLO predictions from the POWHEG generator. Comparisons using several different PDF sets are made. Figure 1 shows the double differential cross sections for the inclusive jet cross section measurement as a function of p_T in bins of rapidity, and for the dijet cross section measurement as a function of dijet mass, binned in half the absolute rapidity difference between the two leading jets, $y^* = |y_1 - y_2|/2$. Good agreement is observed between the observed cross sections and the predictions from the Monte Caro simulations.

3 Multijet Production

Measurements of multijet differential cross sections [4] are used for shape comparisons to leading-order simulations as well as comparisons to next-to-leading order perturbative calculations. Measurements are corrected using a bin-by-bin unfolding procedure with MC simulation. Systematic uncertainties on the unfolding procedure are derived from comparisons to unfolding factors calculated using other MC simulations, and by varying the jet resolution and energy scale within their uncertainties.

The dominant systematic uncertainty comes from the jet energy scale uncertainty. For this measurement, additional contributions which may alter the jet energy scale are considered including a difference in the admixture of light-quark and gluon jets relative the MC simulation, the presence of nearby jets, and the presence of additional proton-proton interactions. Uncer-

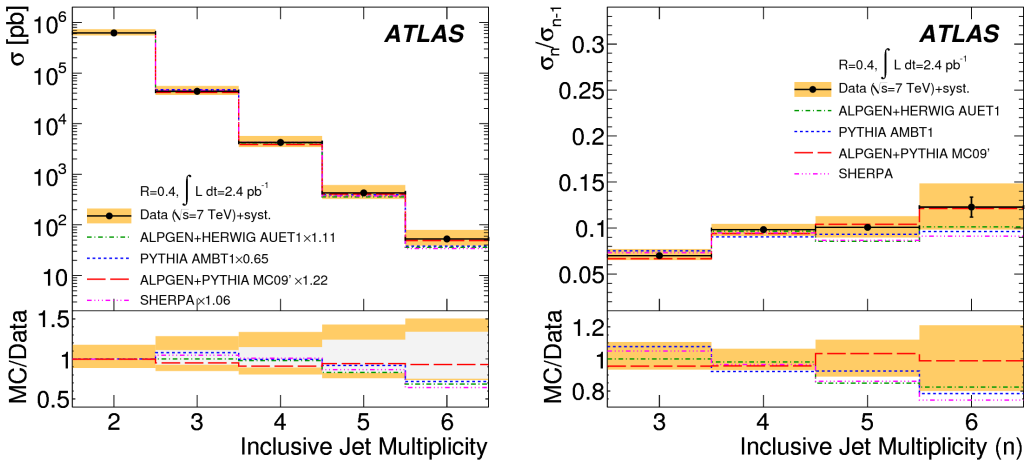

Figure 2: The total inclusive jet cross section as a function of jet multiplicity (left) and the ratio of n-jet to (n-1)-jet cross sections. The data are compared to several MC simulations, which have been normalized to the measured two-jet cross section (right). Jets with p_T >60 GeV are counted.

tainties from the jet reconstruction efficiency, jet resolution, and pileup are included in the total systematic uncertainty.

Figure 2 shows the total inclusive jet cross section as a function of jet multiplicity and the ratio of n-jet to (n-1)-jet cross sections. The data are compared to several MC simulations, which have been normalized to the measured two-jet cross section. The simulations agree with the measured results across the full jet multiplicity spectrum.

Other differential distributions, including the p_T spectra of jets, have also been made. The MC predictions show significant differences between leading order calculations. The measurements are also compared to NLO pQCD calculations corrected for non-perturbative effects. The calculations describe the data well, except in the lowest p_T bin.

4 Measurements with Jets from Tracks

Measurements with jets reconstructed from charged tracks allow comparisons to MC simulations at very low p_T [5], a region inaccessible with jets reconstructed in the calorimeters. Events are recorded with a minimum-bias trigger. Charged tracks with p_T >400 MeV are used as input to the anti-k_T jet finder. Jet properties are studied for jets with $|y| < 1.9$. Five quantities are measured: $\frac{d^2\sigma_{jet}}{dp_{T\,jet}dy_{jet}}$; $\frac{1}{N_{jet}}\frac{dN_{jet}}{dN^{ch}_{jet}}$; $\frac{1}{N_{jet}}\frac{dN_{ch}}{dz}$; $\frac{1}{N_{jet}}\frac{dN_{ch}}{dp^{rel}_T}$; and $\rho_{ch}(r)$.

Figure 3 shows the cross section for charged particle jets as a function of p_T for jets with $|y| < 0.5$, and the multiplicity of particles per jet over the full measured rapidity range in bins of p_T, compared to several MC predictions. None of the compared tunes or models agrees with all quantities measured within their uncertainties. Difficulty in modeling the transition between soft and perturbative physics is indicated by disagreements between data and all MC

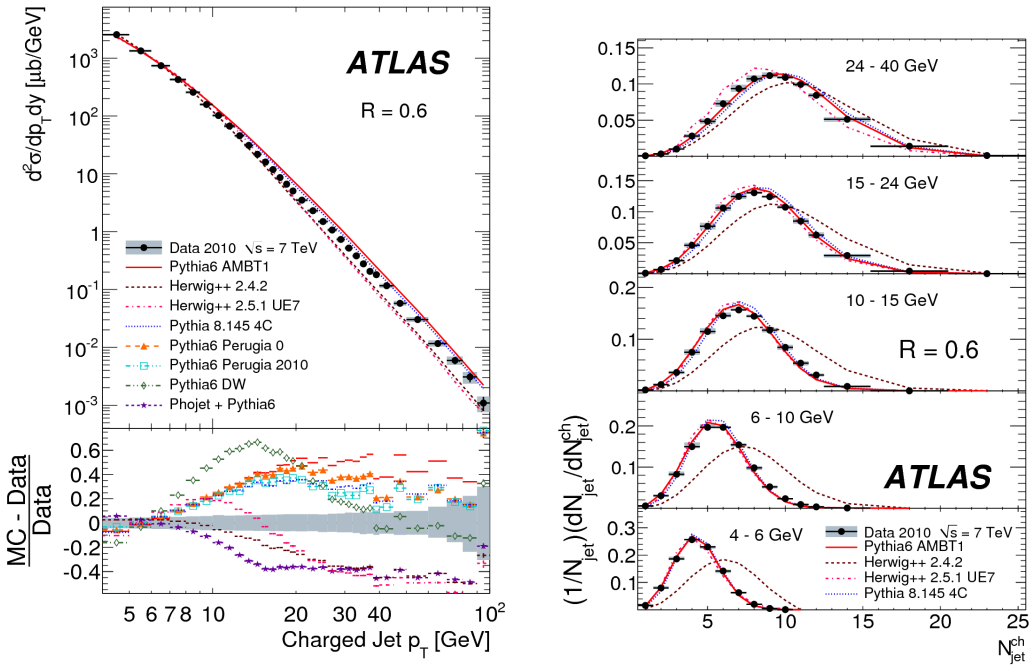

Figure 3: The cross section for charged particle jets as a function of p_T, with $|y| < 0.5$ (left), and the multiplicity of particles per jet, over the full measured rapidity range, in bins of p_T (right), compared to several MC predictions.

distributions in the 10–20 GeV range.

5 Conclusions

ATLAS measurements of jet cross sections in inclusive jet, dijet, and multijet events at a center-of-mass energy of 7 TeV cover a large, new kinematic range. Detailed understanding of the detector performance has precisely determined systematic uncertainties, in particular those arising from the jet energy scale. Comparisons to MC simulations show good agreement.

Measurements of jets reconstructed from charged tracks allow comparisons to many different MC event generators and tunes in an interesting kinematic regime. No tune or model is able to reproduce the charged jet measurements, and they can be used to improve future simulations.

References

[1] M. Cacciari, G. P. Salam and G. Soyez, JHEP **0804**, 063 (2008) [arXiv:0802.1189 [hep-ph]].
[2] ATLAS Collaboration, Phys. Rev. D (accepted) [arXiv:1112.6297 [hep-ex]].
[3] ATLAS Collaboration, ATLAS-CONF-2012-021 [https://cdsweb.cern.ch/record/1430730].
[4] ATLAS Collaboration, Eur. Phys. J. C **71** (2011) 1763 [arXiv:1107.2092 [hep-ex]].
[5] ATLAS Collaboration, Phys. Rev. D **84** (2011) 054001 [arXiv:1107.3311 [hep-ex]].

Jet and Multi-Jet Production at Large Rapidity (Separation) with the CMS Experiment

Thomas Schörner-Sadenius on behalf of the CMS collaboration
DESY, Notkestraße 85, 22607 Hamburg, Germany

DOI: http://dx.doi.org/10.3204/DESY-PROC-2012-02/184

Recent CMS results on the production of forward jets, of forward–central dijet systems and of dijet systems with large rapidity separation are reported. The measurements are intended to shed additional light on the long-standing question of parton evolution in the proton and to provide separation power between the various approximations.

1 Introduction

Hadronic jets have for a long time been a vital tool for investigations of the theory of strong interactions, quantum chromodynamics (QCD). At the LHC (as before at HERA and at the Tevatron), jet and multi-jet measurements especially at central rapidity values ($|y| < 2.5$) are well described by QCD calculations at next-to-leading order (NLO) based on collinear factorisation and the DGLAP approximation [1]. However, these jets offer access only to limited regions of phase space, in particular to not too small values of parton momentum fraction x and not too large rapidity separations $|\Delta y|$ of the hard jets created in the collision. In contrast, the behaviour of the proton and QCD jet phenomenology at smaller values of x are still to a certain extent *terra incognita*. Previous collider experiments — e.g. at HERA and the Tevatron — have endeavoured to explore this region, to look for signs of deviations from the collinear-factorisation DGLAP picture and to establish the necessity of alternative approaches to parton evolution like the BFKL [2] or CCFM [3] evolution approximations. Also phenomena like gluon saturation [4] and k_T factorisation [5] have been topics of many studies.

A particularly promising region to look for the breakdown of DGLAP assumptions is the "forward region", i.e. the regime of large (pseudo)rapidities: Here, in the vicinity of the beams, highly energetic parton radiation is suppressed in the DGLAP picture. Furthermore, in proton–proton collisions the forward region — compared to the central region — is populated by more asymmetric events in terms of the momentum fractions $x_{1,2}$ of the two incoming partons, thus potentially allowing for an extension of the phase space to smaller x values. Finally, a large rapidity reach opens up a large phase space (a long parton ladder) between the scattering protons, thus giving a lot of room for parton emissions and for the realisation of the underlying evolution mechanisms. It is due to its extended rapidity reach and its increased centre-of-mass energy that measurements in the forward region at the LHC promise results and insights beyond those achieved in (for example) forward-jet measurements at HERA or measurements of Mueller–Navelet jet events at the Tevatron. Furthermore, the increased reach in x is interesting also for studies of the proton PDFs.

2 CMS, jets and the event samples

The measurements presented here were performed with the CMS experiment in 33 nb^{-1} to 5 pb^{-1} of data recorded in 2010 at centre-of-mass energies of 7 TeV, when there was still little pile-up contamination for the collected event samples. Jets in CMS can be reconstructed either using calorimeter energy deposits, tracks from the inner detector or a so-called "particle flow" algorithm which maximises the resolution by optimally combining calorimeter and tracking information. For the presented measurements, calorimeter jets have been used. The anti-k_T algorithm with a radius parameter of 0.5 was chosen. Jets are categorised as "central" or "forward" according to their pseudorapidity η, with the central region being defined by $|\eta| < 2.8$ and the forward region by $3.2 < |\eta| < 4.7$.

Events were typically triggered with a single-jet trigger with an uncalibrated threshold of the transverse momentum p_T of 15 GeV; in case of dijet selections, dedicated dijet triggers were also employed. Trigger efficiencies were studied using minimum-bias events and lower-threshold triggers; all triggers were found to be fully efficient for calibrated transverse jet momenta p_T of at least 35 GeV. The typical selection of the events also comprised — among other requirements — a well-reconstructed primary vertex.

3 Forward jets

A forward-jet analysis was performed in 3.14 pb^{-1} of data [6]. The data were corrected for the dependence of the jet response on the transverse momentum and the pseudorapidity, p_T and η, and for pile-up effects using MC simulations ad p_T balancing in dijet and photon–jet events [7]. The corrected data are well described by leading-order MC predictions from both HERWIG and PYTHIA. The good description of the data enables an unfolding of the data using a bin-by-bin method. The correction factors determined with PYTHIA and HERWIG are averaged to yield the actually used correction, and the difference to an ansatz method is taken as a systematic uncertainty on the correction procedure. The corrections are of the order of 10% (40%) for p_T values of 35 (140) GeV, and the uncertainty is below 10% for all p_T bins.

The experimental systematic uncertainties of the measurement are typically of the order of 20%; the dominant contribution is the jet energy scale uncertainty. The theory uncertainties are typically of the order of 10% and driven by the model uncertainty at low p_T and the PDF uncertainty at high p_T.

Figure 1 (left) shows the result of the analysis — the corrected and unfolded inclusive forward-jet cross section as a function of the jet transverse momentum, p_T, compared to various predictions (NLO calculations and various MC models). The data are in general described by all predictions within the considerable uncertainties, as can be seen from the ratios of the predicted cross sections to the measured one in the right side of the figure.

Particular emphasis was given to the effect of different PDF parametrisations. It was found that all PDF sets used are similar and consistent with the data, even if on average the data points are overshot by about 20% by the NLO calculations.

In a further analysis in the same data set [6], a dijet sample consisting of one central and one forward jet is selected (in case of more than one sufficiently hard jet in either region, the hardest one is chosen). The selection and correction procedure for this dijet analysis follows closely that of the forward-jet analysis just discussed, and also the size of the corrections and their uncertainties, the quality of the description of the data by the MC models and the

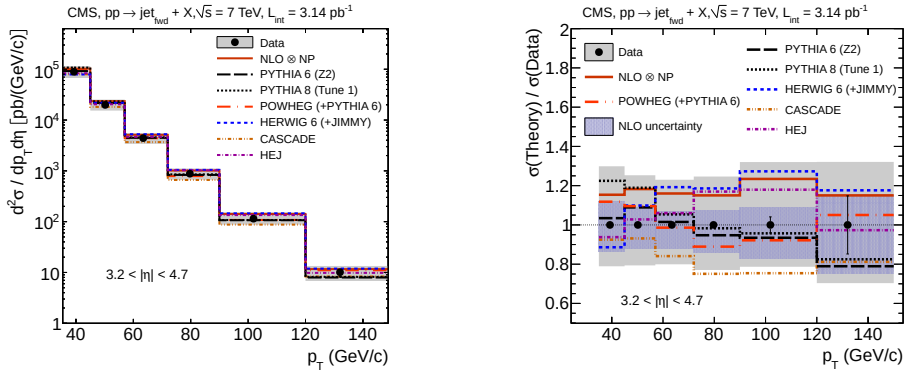

Figure 1: Left: inclusive forward-jet cross section as a function of p_T. The data points are compared to various models and predictions. Right: ratios of the predictions to the data.

experimental and systematic uncertainties are similar.

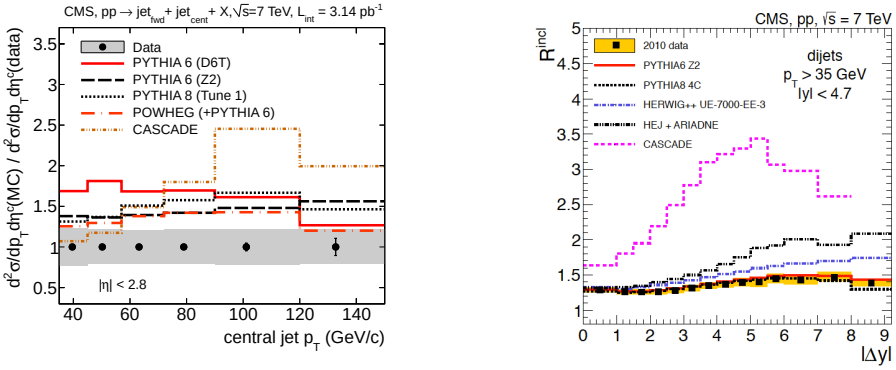

Figure 2: Left: the cross section of central–forward dijet production as a function of the central jet p_T. Shown are ratios between various predictions and the data. Right: R^{incl} for data and various models.

Figure 2 (left) shows the ratio of various predictions of the dijet cross section to the measured one as a function of the p_T of the central jet. HERWIG, HERWIG++, POWHEG+HERWIG and the HEJ generator describe the data slightly better than the models shown in the figure. The forward jet in the dijet system is typically better described than the central one, although at low p_T PYTHIA, POWHEG+PYTHIA and CASCADE are all too high and the POWHEG+HERWIG prediction is significantly to high for all p_T bins.

4 Dijet ratios at large rapidity separation

A third measurement by CMS also focused on dijet systems and used 33 nb^{-1} and 5 pb^{-1}, respectively, for dijets with small and large rapidity separation, $|\Delta y|$ [8]. Dijet events were studied as a function of this observable, and the quantity studied is the ratio of the inclusive

to the exclusive dijet cross section, $\sigma^{incl}/\sigma^{excl}$ [9]. Here, events with exactly one pair of jets passing the selection criteria (mainly the already well-known minimum p_T cut of 35 GeV) are counted for the "exclusive" sample; for the "inclusive" sample, each pairwise combination of jets above that threshold is counted. The Mueller-Navelet (MN) sample is a subset of the inclusive sample and considers only the jet at highest (most forward) and that at lowest (most backward) rapidity [10]. The ratio of inclusive (MN) to exclusive dijets is called R^{incl} (R^{MN}).

Figure 2 (right) displays the experimental situation. The plot shows R^{incl} as a function of $|\Delta y|$ (note that the inclusive and the Mueller-Navelet cases are quite similar, and that — as expected — at large rapidity separations the two quantities agree). R^{incl} increases with increasing $|\Delta y|$ because of increasing phase space; for kinematic reasons the quantity decreases again at the highest rapidity separations.

The data are well described by the various PYTHIA models, whereas HERWIG overshoots the data especially at medium and high rapidity separation values. The HEJ and CASCADE predictions are significantly off.

5 Summary and conclusions

The large rapidity range and large available phase space at the LHC offer excellent opportunities for detailed studies of parton dynamics. Many relevant measurements have already been performed in this very active field. Here, measurements of inclusive forward-jet cross sections, of central–forward dijet systems and of the ratio of inclusive to exclusive dijet production have been presented.

The data and their description by the various predictions do not give a consistent picture of forward physics and of parton evolution. Depending on the phase space, different models fail or succeed in describing the data, and no firm conclusions on the necessity for alternatives to the DGLAP evolution scheme can be drawn. For progress in this direction, a more consistent and more complete understanding of parton dynamics is required.

References

[1] V. N. Gribov and L. N. Lipatov, Sov. J. Nucl. Phys. **15** (1972) 438 and 675.
L. N. Lipatov, Sov. J. Nucl. Phys. **20** (1975) 94.
G. Altarelli and G. Parisi, Nucl. Phys. B **126** (1977) 298.
Y. L. Dokshitzer, Sov. Phys. JETP **46** (1977) 641.

[2] E. A. Kuraev *et. al.*, Sov. Phys. JETP **44** (1976) 443 and Sov. Phys. JETP **45** (1977) 199.
I. I. Balitsky and L. N. Lipatov, Sov. J. Nucl. Phys. **28** (1978) 822.

[3] M. Ciafaloni, Nucl. Phys. B **296** (1988) 49.
S. Catani *et al.*, Phys. Lett. B **234** (1990) 339 and Nucl. Phys. B **336** (1990) 18.
G. Marchesini, Nucl. Phys. B **445** (1995) 49.

[4] F. Gelis *et al.*, Ann. Rec. Nucl. Part. Sci. **60** (2010) 463.

[5] E. M. Levin *et al.*, Sov. J. Nucl. Phys. **53** (1991) 657.
S. Catani *et al.*, Nucl. Phys. B **366** (1991) 135.
J. C. Collins and R. K. Ellis, Nucl. Phys. B **360** (1991) 3.

[6] CMS collab., S. Chatrchyan *et al.*, submitted to JHEP; arXiv:1202.0704 [hep-ex].

[7] CMS collab., S. Chatrchyan *et al.*, JINST **6** (2011) P11002; arXiv:1107.4277.

[8] CMS collab., S. Chatrchyan *et al.*, submitted to Eur. Phys. J.; arXiv:1204.0696 [hep-ex].

[9] V. T. Kim and G. B. Pivovarov, Phys. Rev. D **53** (1996) 6, arXiv:hep-ph/9506381.

[10] A. H. Mueller and H. Navelet, Nucl. Phys. B **282** (1987) 727.

The High Energy Jets Framework

Jennifer M. Smillie

University of Edinburgh, Mayfield Road, Edinburgh, EH9 3JZ, UK

DOI: http://dx.doi.org/10.3204/DESY-PROC-2012-02/233

High Energy Jets provides an all-order description of wide-angle QCD emissions, resumming the leading-logarithmic contributions in the high-energy limit. In this contribution, we briefly summarise the approach and its implementation in a flexible Monte Carlo event generator. We discuss comparisons between HEJ and recent LHC data and then go on to probe the similarities and differences in the results obtained from High Energy Jets and other theoretical frameworks in inclusive dijet and W+dijet production.

1 Introduction to High Energy Jets (HEJ)

Accurate theoretical descriptions of multi-jet production are of key importance to physics at the Large Hadron Collider. This is our first opportunity to test our theoretical understanding of QCD at these high energies, and this will be key to reaching the full potential of the LHC physics programme. For example, the results of comprehensive analyses of multi-jet radiation with current data will be used when applying a jet veto to the production of a Higgs boson in association with jets.

It has already been seen in the 7 TeV LHC data that the ratio between inclusive $(n+1)$-jet rates and inclusive n-jet rates can be large. While this is true for the ratios of the cross sections, the effect is particularly large in certain key regions of phase space including high momentum regions (see e.g. high H_T in [1]) or events where there is a large rapidity separation between jets (see e.g. [2]).

Motivated by the large impact of higher order corrections, the High Energy Jets (HEJ) framework [3, 4, 5] provides an all-order resummation of the dominant (leading-log) contributions to wide-angle, hard QCD radiation in the High Energy limit. In this limit, scattering amplitudes factorise into rapidity-ordered pieces. This structure allows an extremely efficient description of many-particle hard-scattering matrix elements. This forms the basis of the HEJ description which has been developed for the production of jets, and also W, Z and Higgs boson production in association with jets. The High Energy limit can be stated as

$$s_{ij} \to \infty \ \forall \ \{i,j\}, \quad |p_{\perp,i}| \text{ fixed}, \tag{1}$$

where i, j label outgoing quarks and gluons. In practice this corresponds to wide-angle QCD emissions and may be stated equivalently in terms of pairwise rapidity differences becoming large while transverse momenta components remain finite. This is in contrast to the soft and collinear emissions which are included in a parton shower resummation. A complete jet description can be achieved by consistently merging the two approaches [6].

The derivation of the building blocks of the HEJ framework has been described in detail in [3, 4]. The implementation of these for multi-jet production in a fully flexible event generator is described further in [5], and the generator itself is publicly available at `www.cern.ch/hej`.

Predictions from HEJ have been used in analyses by ATLAS [2] and by CMS [7, 8]. The ATLAS study was a study of jet radiation with a jet veto across a wide range of transverse momenta and rapidities. HEJ gave a consistently good description of data throughout. Discrepancies were only seen in cases where cuts had induced a large hierarchy of transverse momentum scales, as this evolution is not systematically included in the parton-level predictions. In the central-forward CMS study [7] which separated the jets in rapidity, HEJ again gave a good description of data where more traditional approaches performed less well. In a subsequent jet study [8], the HEJ predictions showed slight deviation from data at large rapidity differences; work is ongoing to evaluate the uncertainties in this case.

Overall, HEJ has given an excellent description of early data, and in some cases has outperformed other more standard approaches. This underlines the importance of the higher order contributions included in HEJ. In the rest of this contribution, we probe to what extent data could probe the differences between the HEJ approach and that of other theoretical frameworks which are built upon fixed-order matrix elements.

2 Comparisons Between Theoretical Approaches

We begin by comparing HEJ and POWHEG [9, 10] predictions for dijet production. The HEJ framework is an all-order resummation of wide-angle QCD radiation which includes, for events which result in four or fewer jets, matching to leading-order matrix elements. In contrast, the POWHEG description of multi-jet production begins with a next-to-leading order (NLO) matrix element, which is then supplemented with a resummation from a parton shower. It is surprising, then, that the predictions from the two approaches have been seen to be very similar (see [2]). The extent to which these descriptions can be distinguished was studied recently in [11].

In order to implement cuts which do not induce a large hierarchy in transverse momentum between the jets, a minimal set is used:

$$p_{\perp,j} > 35 \text{ GeV}, \quad p_{\perp,j_1} > 45 \text{ GeV}, \quad |y_j| < 4.7. \tag{2}$$

The additional cut on the hardest jet is in order to allow a meaningful comparison with the pure NLO calculation. Neither the POWHEG or HEJ descriptions suffer from an instability in the presence of symmetric cuts.

The left plot in figure 1 shows the predictions for the average number of jets as a function of the rapidity difference between the most forward and most backward jet in each event, Δy_{fb}. The bands around the HEJ and NLO predictions indicate the result of varying the renormalisation and factorisation scales by a factor of two in each direction. The vertical lines indicate statistical uncertainty. In this plot, all the predictions show an increase in the average number of jets with Δy_{fb}, with the largest increase being seen in the HEJ prediction, as expected. The lowest prediction comes from the pure NLO calculation, followed by the POWHEG first emission, then the full POWHEG+PYTHIA shower, which increases to a value around 2.6 for $\Delta y_{fb} = 7$.

The same variable is shown in the right plot in figure 1, but now as a function of H_T. It is immediately clear from the different behaviour that a different region of phase space is now being probed. As H_T increases, the largest prediction now comes from the POWHEG+PYTHIA

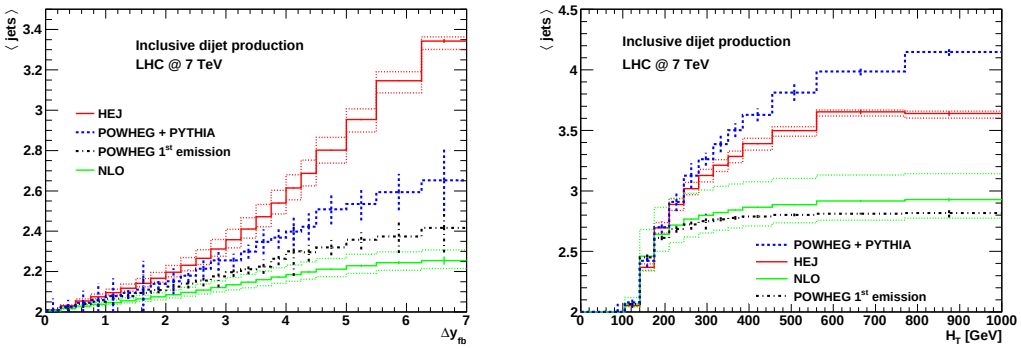

Figure 1: The average number of jets as a function of (left) the difference in rapidity between most forward and most backward jet, and (right) as a function of H_T. Plots taken from [11].

prediction which peaks above an *average* value of 4 jets per event, which is remarkably high for an inclusive dijet sample. The HEJ prediction levels off a little below this around 3.6. The NLO and POWHEG 1st emission predictions are restricted to lie below 3, and both reach values close to that.

The differences in the predictions here appear to be significant enough that one could hope to distinguish between the approaches with LHC data. Other variables were also studied in [11], which showed smaller differences. For example, when a measure of the azimuthal decorrelation of the jets (which results from hard radiation) is studied as a function of Δy_{fb}, the predictions from HEJ and POWHEG+PYTHIA are extremely similar until values of $\Delta y_{fb} > 6$.

A related study has been performed in the context of W boson production in association with jets in [12]. Here, predictions from four theoretical approaches were compared: NLO and a merged NLO sample both from BlackHat [13, 14, 15], a merged matrix-element plus parton shower sample from Sherpa [16, 17, 18] and HEJ [19]. Figure 2 shows the predictions for the average number of jets now for this process. In the left plot, it can again be clearly seen that the predictions all rise with Δy_{fb}. In this case, there is a high level of agreement between the predictions until large values of Δy, with only the pure NLO prediction lying slightly below.

In the right-hand plot of figure 2, the average number of jets for W+jets is shown as a function now of H_T. Here, the SHERPA and Exclusive NLO sums predictions give the highest value for large H_T, peaking around a value of 4. The HEJ prediction here is lower, and closer to the pure NLO result around 3. It should be possible to distinguish between these with data.

3 Summary

The High Energy Jets framework provides an alternative method to describing multi-jet production, which is based on an all-order resummation of hard, wide-angle QCD radiation. It has already been seen to give a good description of early LHC data. Analyses which may be able to distinguish between different theoretical descriptions in jets and W+jets have been discussed. For example, the average number of jets as a function of H_T shows large differences between different theoretical approaches for both processes.

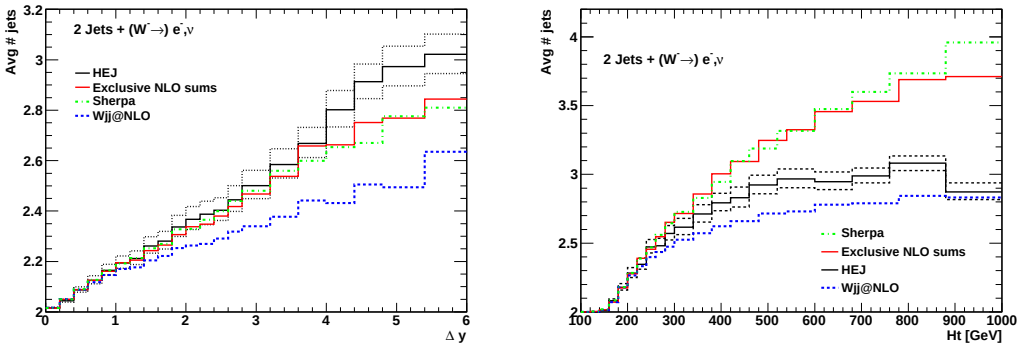

Figure 2: A comparison of the predictions for the average number of jets in an inclusive W+dijet sample from different theoretical descriptions as a function of (left) the difference in rapidity between most forward and most backward jet, and (right) as a function of H_T. Plots taken from [12].

Acknowledgements

JMS thanks the conference organisers and the conveners of the *Hadronic Final States* Working Group for an interesting and fruitful week. JMS is funded by the UK Science and Technology Facilities Council (STFC).

References

[1] G. Aad *et al.* Phys.Rev. **D85** (2012) 092002, arXiv:1201.1276 [hep-ex].

[2] G. Aad *et al.* JHEP **1109** (2011) 053, arXiv:1107.1641 [hep-ex].

[3] J. R. Andersen and J. M. Smillie. JHEP **1001** (2010) 039, arXiv:0908.2786 [hep-ph].

[4] J. R. Andersen and J. M. Smillie. Phys.Rev. **D81** (2010) 114021, arXiv:0910.5113 [hep-ph].

[5] J. R. Andersen and J. M. Smillie. JHEP **1106** (2011) 010, arXiv:1101.5394 [hep-ph].

[6] J. R. Andersen, L. Lönnblad, and J. M. Smillie. JHEP **1107** (2011) 110, arXiv:1104.1316 [hep-ph].

[7] S. Chatrchyan *et al.* arXiv:1202.0704 [hep-ex].

[8] S. Chatrchyan *et al.* arXiv:1204.0696 [hep-ex].

[9] S. Alioli, P. Nason, C. Oleari, and E. Re. JHEP **1006** (2010) 043, arXiv:1002.2581 [hep-ph].

[10] S. Alioli, K. Hamilton, P. Nason, C. Oleari, and E. Re. JHEP **1104** (2011) 081, arXiv:1012.3380.

[11] S. Alioli, J. R. Andersen, C. Oleari, E. Re, and J. M. Smillie. Phys. Rev. D. to appear, arXiv:1202.1475.

[12] J. A. Maestre, S. Alioli, J. Andersen, R. Ball, A. Buckley, *et al.* arXiv:1203.6803 [hep-ph].

[13] C. Berger, Z. Bern, *et al.* Phys.Rev.Lett. **102** (2009) 222001, arXiv:0902.2760 [hep-ph].

[14] C. Berger, Z. Bern, *et al.* Phys.Rev. **D80** (2009) 074036, arXiv:0907.1984 [hep-ph].

[15] C. Berger, Z. Bern, *et al.* Phys.Rev.Lett. **106** (2011) 092001, arXiv:1009.2338 [hep-ph].

[16] S. Hoeche, F. Krauss, S. Schumann, and F. Siegert. JHEP **0905** (2009) 053, arXiv:0903.1219 [hep-ph].

[17] S. Hoeche, S. Schumann, and F. Siegert. Phys.Rev. **D81** (2010) 034026, arXiv:0912.3501 [hep-ph].

[18] T. Carli, T. Gehrmann, and S. Hoeche. Eur.Phys.J. **C67** (2010) 73–97, arXiv:0912.3715 [hep-ph].

[19] J. R. Andersen, T. Hapola and J. M. Smillie. JHEP **1209** (2012) 047, arXiv:1206.6763 [hep-ph].

Z+jets Results from CDF

Lorenzo Ortolan

IFAE Barcelona

DOI: http://dx.doi.org/10.3204/DESY-PROC-2012-02/166

The CDF collaboration has an interesting and comprehensive program on the study of jet production in association with a Z/γ^* boson. These measurements are important because Z/γ^*+jets events are a background in many searches of new physics and in particular $Z/\gamma^* + b-$jet represents the main and irreducible background for Higgs boson produced in association with a Z/γ^* where the Higgs decays in two b quarks.
In this contribution new measurements of Z/γ^*+jets differential cross section and the $Z/\gamma^* + b-$jet cross section ratio with respect to the Z inclusive cross section are presented. The results are performed with the complete dataset collected at CDF and are compared with the next-to-leading order predictions.

1 Introduction

The study of jet production in association with a Z boson at hadron colliders is fundamental not only because it allows to test the perturbative QCD predictions but also because it represents an important background to many searches of new physics, for example Higgs and SUSY. For this reason dedicated measurements of Z/γ^*+jet and $Z/\gamma^* + b-$jet cross sections are crucial to improve the understanding and the modeling of these processes.

2 Z/γ^*+jet Cross section measurement

The CDF collaboration recently presented updated results for Z/γ^*+jet in $Z/\gamma^* \to \mu^+\mu^-$ muon [1] and $Z/\gamma^* \to e^+e^-$ electron [2] channels. Here the measurement is presented combining the two channels using the complete dataset collected at CDF. For both channels the same kinematics cuts are used and the measurements are defined in the same phase space.
Events are required to have two high p_T ($p_T \geq 25\ GeV/c$) central ($|\eta| \leq 1.0$) leptons with an invariant mass between 66 and 116 GeV/c^2. The jets are reconstructed with the MidPoint[3] algorithm in a cone of 0.7 and are required to have $p_T \geq 30\ GeV/c$ and $|Y^{jet}| \leq 2.1$. The background is estimated using data driven techniques and Monte Carlo programs. In particular fakes contributions (QCD dijet, W+jets and decay in flight) are estimated with data driven sample while backgrounds coming from $t\bar{t}$, diboson (ZZ, WW, ZW) are evaluated with PYTHIA Monte Carlo. The global contribution from background represents less than 10 %.
The measurement at calorimetric level is unfolded back to hadron level to take into account resolution effects and the detector acceptance of $Z \to l^+l^-$. The unfolding is done using ALP-

GEN+PYTHIA Monte Carlo with Tune Perugia 2011[4]. The results are compared with several predictions at different perturbative orders (NLO evaluated by MCFM, NLO by BLACKHAT+SHERPA, $\bar{n}NLO$ by LOOPSIM+MCFM) and corrected for non perturbative effects (underlying events and hadronization) using ALPGEN+PYTHIA. Differential cross section distributions (Figure 1) are well described by theory predictions. The main systematic uncertainty is due to the error in the jet energy scale and varies between 3-15 %. The renormalization and factorization scale and PDF uncertainties are calculated for the theoretical predictions.

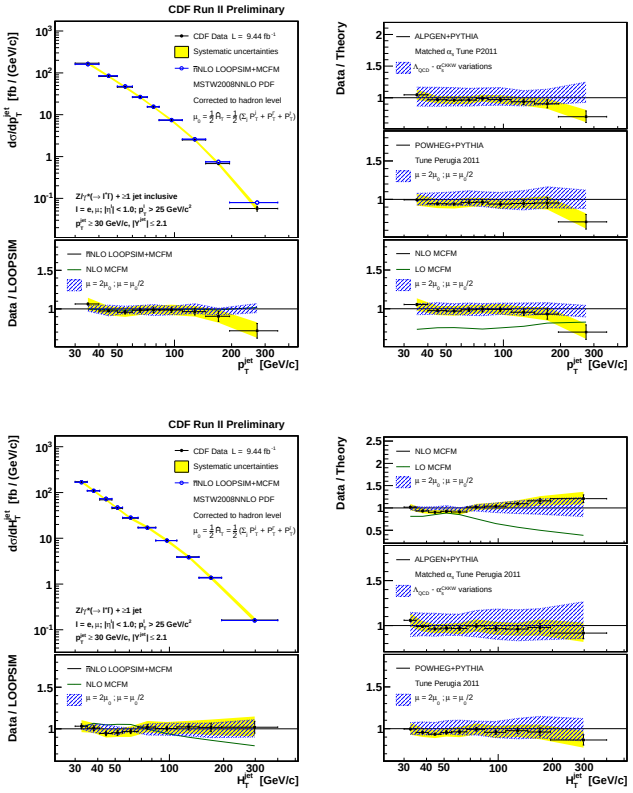

Figure 1: Measured inclusive jet differential cross sections as a function of jet transverse momentum and H_T^{jet} in $Z+ \geqslant 1$ jet events. Data (black dots) are compared to $\bar{n}NLO$ predictions (open circles). The shaded bands show the total systematic uncertainty, except for the 5.8% luminosity uncertainty.

3 $Z/\gamma^* + b-$jet Cross section measurement

The $Z/\gamma^* + b-$jet cross section measurement at CDF was previously published with 2 fb^{-1} of integrated luminosity [5]. Here an update of this measurement based on 9 fb^{-1}[6] (the full

CDF dataset) is presented. It is performed as a per-jet cross section measurement ratio with respect to Z/γ^* inclusive cross section and Z/γ^*+jet cross section. This is done because in this way some systematics (luminosity uncertainty, lepton ID) are largely canceling in the ratio.
The events are required to have two high energy leptons (electrons or muons) with an invariant mass between 66 and 116 GeV/c^2 and a central ($|Y^{jet}| \leq 1.5$) high p_T ($p_T \geq 20$ GeV/c) jet clustered with MidPoint 0.7. The $Z/\gamma^* \rightarrow l^+l^-$ selection is improved to optimize the lepton identification efficiency. This is done using cuts on the outputs of two artificial neural networks trained to separate fake signals from real leptons. The improvement on the Z acceptance is $\sim$30/40 % respectively for muon and electron channel.
The identification of the b jet is done with a Secondary Vertex Tagger. Since the tagged sample is not pure, the b quark composition is extracted from a fit to the mass of a displaced secondary vertex reconstructed within the jet. The measurement is unfolded back to the hadron level to the total phase space and normalized to the Z/γ^* inclusive and Z/γ^*+jet cross section. The main systematics is coming from the variation of the template shape due to a track reconstruction inefficiency and due to b-tagging efficiency uncertainty.
The results obtained is $\frac{\sigma(Z+\mathrm{b})}{\sigma(Z)} = 2.61 \pm 0.23 \pm 0.29 \times 10^{-3}$ and $\frac{\sigma(Z+\mathrm{b})}{\sigma(Z+\mathrm{jet})} = 2.08 \pm 0.18 \pm 0.27 \times 10^{-2}$.
These are compared (Table 1) to NLO predictions evaluated with MCFM and corrected for non perturbative effects, at different re-normalization scales. Within the uncertainty the measured cross section is in agreement with the theory, but a large uncertainty is present due to the choice of the re-normalization scale.

	Measured	NLO $Q^2 = m_Z^2 + p_{T,Z}^2$	NLO $Q^2 = < p_{T,jet}^2 >$
$\frac{\sigma(Z+\mathrm{b})}{\sigma(Z)}$	$2.61 \pm 0.23 \pm 0.29 \times 10^{-3}$	2.3×10^{-3}	2.8×10^{-3}
$\frac{\sigma(Z+\mathrm{b})}{\sigma(Z+\mathrm{jet})}$	$2.08 \pm 0.18 \pm 0.27 \times 10^{-2}$	1.8×10^{-2}	2.2×10^{-2}

Table 1: The results of per jet $Z + b-$jet cross section ratio with respect to Z/γ^* inclusive and Z/γ^*+jet cross section. These results are compared with the predictions done at NLO with MCFM at different re-normalization/factorization scales.

Using the same analysis strategy the $Z/\gamma^* + b-$jet differential cross sections as a function of jet rapidity and jet p_T are performed and the results are shown in Figure 2.

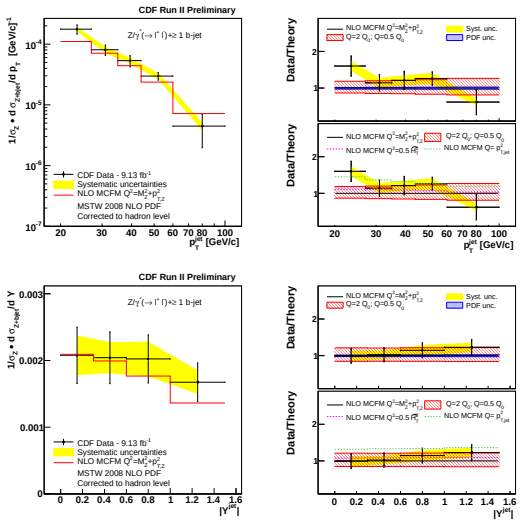

Figure 2: Differential cross section as a function of jet p_T and jet rapidity compared with NLO prediction by MCFM. In the ratio there is the comparison at different renormalization and factorization scales. The predictions are affected by large scale uncertainty.

4 Summary

In this report, measurements of Z/γ^*+jet differential cross section have been presented using the complete dataset available at CDF. It was found that the data is well described by the theoretical predictions corrected by non perturbative effects.
It has been also reported the per-jet $Z/\gamma^* + b-$jet cross section ratio measurement with respect to the Z/γ^* inclusive and Z/γ^*+jet cross section and the differential cross section distribution as a function of jet p_T and jet rapidity. Results are in agreement with NLO predictions.

References

[1] CDF Collaboration, *CDF Conference Note 10216*.

[2] CDF Collaboration, *CDF Conference Note 10394*.

[3] A. Abulencia et al. (CDF Collaboration), *Measurement of the inclusive jet cross section in $p\bar{p}$ interactions at $\sqrt{(s)} = 1.96$ TeV using a cone-based jet algorithm*, *Phys. Rev. D* **74**, 071103(R) (2006).

[4] Cooper et al., *Monte Carlo tuning in the presence of the Matching*, PH-CERN-TH/2011-228

[5] T. Aaltonen et al., *Phys. Rev. D.* **79**, 052008 (2009).

[6] CDF Collaboration, *CDF Conference Note 10594*.

Studies of vector boson+jet production with the ATLAS detector

Camille Bélanger-Champagne[1] on behalf of the ATLAS collaboration

[1]McGill University, Montréal, Québec, Canada

DOI: http://dx.doi.org/10.3204/DESY-PROC-2012-02/82

The production of jets or b-jets in association with a W or Z boson in proton-proton collisions at 7 TeV at the LHC is an important test of quantum chromodynamics (QCD). Electron and muon decay channels of the Z and W bosons are studied. Cross sections have been measured up to high jet multiplicities with the ATLAS detector on data samples with integrated luminosities between 33 pb^{-1} and 37 pb^{-1}. These measurements were compared to new higher-order QCD calculations. The ratio of (W + a single jet)/(Z + a single jet) has also been measured. Overall, the cross sections demonstrate the need for the inclusion of higher-multiplicity matrix elements in the calculations.

1 Introduction and motivation

Measurements of the production of jets in association with a W or Z boson constitute a stringent set of tests of our understanding of the Standard Model and quantum chromodynamics (QCD). It is particularly interesting to perform such measurements in the high energy regime of the LHC and compare them to both leading-order (LO) and next-to-leading-order (NLO) predictions. Measurements of vector boson+jets cross sections with improved precision also benefit other measurements for which they are important backgrounds, such as measurements in the top sector and searches for new phenomena beyond the Standard Model.

2 Data and Monte Carlo event samples

The data used for all measurements discussed here was collected with the ATLAS detector [1] in 2010. In all cases here, the vector bosons decay via leptonic channels, where "lepton" is taken to mean electron or muon. The data event samples were collected via single lepton triggers in the ATLAS trigger system. Electrons are chosen to have transverse momentum $p_T > 20$ GeV and pseudorapidity ($|\eta| < 1.37$ or $1.52 < |\eta| < 2.47$) to avoid the calorimeter transition region. Muons are chosen to have $p_T > 20$ GeV and $|\eta| < 2.4$. Jet candidates are reconstructed using an anti-k_T algorithm with radius parameter R=0.4 and are chosen to have $p_T > 30$ GeV and rapidity $|y| < 4.4$. A minimal distance requirement given by $\Delta R = \sqrt{(\Delta\eta)^2 + (\Delta\phi)^2}$ >0.5 or 0.6, according to the analysis, is applied between the jets and the leptons. In cases with a Z boson decaying to a lepton pair, the invariant mass of the pair of leptons is restricted to a mass window around the Z mass of 66 GeV $< m_{ll} <$ 116 GeV. In cases with a W boson decaying

to a lepton l and a neutrino ν, events are further required to have missing transverse energy $E_T^{miss} > 25$ GeV and a transverse mass $m_T = \sqrt{2p_T^l p_T^\nu (1 - \cos(\phi^l - \phi^\nu))} > 40$ GeV.

Results are compared to the predictions at LO from Monte Carlo event generators PYTHIA [2], SHERPA [3] and ALPGEN [4] and at NLO from Monte Carlo generators BlackHat(+SHERPA)[5] and MCFM [6], as well as calculations in the 5 flavour number scheme (5FNS) [7].

3 Z+jets and W+jets cross sections

Cross section measurements of the production of jets in association with Z and W bosons were performed as a function of many variables [8, 9]. The experimental cross section measured as a function of any one of many variables, here denoted generically as ξ, is given by

$$\frac{d\sigma}{d\xi} = \frac{1}{\mathcal{L}} \frac{1}{\Delta\xi} (N_{data} - N_{backg}) \times U(\xi),$$

where $\mathcal{L}$ is the integrated luminosity of the data sample, N_{data} is the number of observed events in an interval $\Delta\xi$, N_{backg} is the estimated number of background events in this interval and $U(\xi)$ is an unfolding factor. Background contributions from Standard Model processes are estimated using a combination of LO Monte Carlo event samples with the exception of the multijet background from QCD, which is estimated from data. The cross section measurements are unfolded bin-by-bin to particle level, using LO Monte Carlo signal samples to derive the values of the correction factors $U(\xi)$. These factors range in value from 0.9 to 1.5. Dominant systematic uncertainties on these measurements come from the jet energy scale and resolution (10-20%) and the uncertainty on the unfolding factor, which goes up to 5% at high jet p_T and multiplicity.

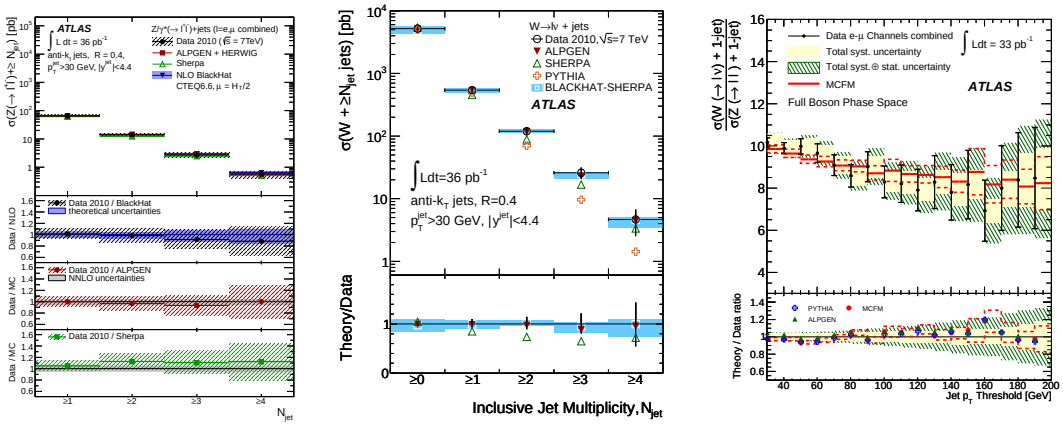

Figure 1: (left) Measured cross section $\sigma_{N_{jet}}$ for Z/gamma* ($\rightarrow l^+l^-$)+jets production as a function of the inclusive jet multiplicity for the combined electron and muon channels [8]. (centre) W+jets cross section for the combined electron and muon channels as a function of corrected jet multiplicity [9]. (right) Ratio of the vector boson + 1 jet cross sections extrapolated to the total phase space [10]. All the measurements are compared to theoretical predictions.

In Figure 1 (left), the measured cross section $\sigma_{N_{jet}}$ for Z/gamma* ($\rightarrow l^+l^-$)+jets production as a function of the inclusive jet multiplicity is compared to predictions. It is well-matched by all the theoretical predictions from Monte Carlo generators. Cross sections with respect to other variables such as jet transverse momenta and rapidities are also well-described by Monte Carlo models, in particular BlackHat.

In Figure 1 (centre), the measured W+jets cross section for the combined electron and muon channels as a function of corrected jet multiplicity is compared to predictions. BlackHat-SHERPA and ALPGEN provide good descriptions of the behaviour of the data while SHERPA and PYTHIA fall off more steeply than data.

4 Ratio of vector boson + single jet cross sections

The ratio of (W+single jet) cross section to the (Z+single jet) cross section was measured as a function of the jet p_T threshold [10]. This measurement is designed to maximize the cancellation of experimental systematic uncertainties. Here, the jet pseudorapidity is limited to the region $|\eta| < 2.8$ and the range of allowed dilepton invariant masses is 71 GeV $< m_{ll} <$ 111 GeV. Estimated background event yields are subtracted from the observed event counts to obtain the signal estimate $N_{sig}^{l,V}$ for each lepton l and each boson V. The particle level event count $N_{part}^{l,V}$, is obtained by applying a correction that accounts for the trigger, lepton reconstruction and boson reconstruction efficiencies, and the boson resolution. The cross section ratio is then given by $R_{jet} = (N_{part}^{l,W}/N_{part}^{l,Z}) \times C_{jet}^{l}$ where C_{jet}^{l} is a correction factor accounting for all remaining non-cancelling effects related to lepton and jet selection criteria. Systematic uncertainties on the measurement of the ratio range from 4% at low jet p_T to 15% at high p_T. The main contribution comes from systematic uncertainties on the boson reconstruction.

The measurement of the cross section ratio as a function of jet p_T threshold, extrapolated to the full boson phase space, is shown in Figure 1 (right). It is compared to an NLO prediction from MCFM. The prediction is found to be in good agreement with data over the range of jet p_T thresholds investigated.

5 Z+b jets and W+b jets cross sections

Cross sections were also measured in the particular case of the production of a Z or W boson in association with b-jets [11, 12], of particular interest as probes into the heavy sector. To perform these measurements, in addition to the data selection highlighted above for leptons, events were required to contain at least one jet with $p_T > 25$ GeV in the rapidity region $|y| < 2.1$, tagged as a b-jet by a secondary vertex tagger (SV0) [13], calibrated to give 50% b-tagging efficiency. The b-jet signal yield is extracted from template fits to the behaviour of the tagger. The systematic uncertainty associated to the b-tagging efficiency, approximately $\pm$10%, is a dominant systematic uncertainty for the measurements in both the Z and W cases. Acceptance and/or unfolding factors were extracted from leading-order signal Monte Carlo samples. The uncertainty on the model dependence of the correction factors is the other dominant systematic uncertainty in the Z boson case, while in the W boson case the systematic uncertainty on the background estimate forms the other dominant systematic uncertainty.

The measurements of the inclusive cross section for the production of a Z boson in association with b-jets as well as the average number of b-jets produced per Z boson (i.e. the ratio of this cross section to the inclusive Z+jets cross section) are given in Table 1. The measurements are

	Cross section (pb)	Number of b-jets per Z boson
Experiment	$3.55^{+0.82}_{-0.74}(\text{stat})^{+0.73}_{-0.55}(\text{syst})\pm 0.12(\text{lumi})$	$(7.6^{+1.8}_{-1.6}(\text{stat})^{+1.5}_{-1.2}(\text{syst}))\times 10^{-3}$
MCFM	3.88 ± 0.58	$(8.8\pm 1.1)\times 10^{-3}$
ALPGEN	2.23 ± 0.01(stat only)	$(6.2\pm 0.1$(stat only))$\times 10^{-3}$
SHERPA	3.29 ± 0.04(stat only)	$(9.3\pm 0.1$(stat only))$\times 10^{-3}$

Table 1: Experimental measurement and predictions of σ_b, the fiducial cross section for inclusive b-jet production in association with a Z boson and of the average number of b-jets produced per Z boson [11].

	Experiment (pb)	NLO 5FNS (pb)
1 b-jet	$4.5 \pm 1.3(\text{stat})\pm 1.3(\text{syst})$	$2.9^{+0.4}_{-0.8}(\text{scale})^{+0.2}_{-0.0}(\text{PDF})^{+0.2}_{-0.1} m_b \pm 0.2$ NP
2 b-jet	$5.7 \pm 1.3(\text{stat})\pm 1.4(\text{syst})$	$1.9^{+0.8}_{-0.4}(\text{scale})^{+0.1}_{-0.0}(\text{PDF})^{+0.1}_{-0.1} m_b \pm 0.1$ NP

Table 2: Experimental measurement and predictions of the fiducial cross section for the production of a W boson in association with b-jets, converted to one lepton flavour. The uncertainties on the prediction arise from the choice of factorization and renormalisation scales (scale), parton distribution functions (PDF) and b-quark mass (m_b), and from non-perturative corrections (NP) [12].

compared to NLO predictions from MCFM and LO predictions from ALPGEN and SHERPA. MCFM provides predictions that are compatible with the experimental measurements whereas the LO predictions, being also compatible within the uncertainties of the measurement, differ significantly from each other.

The measurements of the cross section for the production of a W boson in association with 1 or with 2 b-jets are presented in Table 2 and compared to 5FNS NLO predictions. The predictions fall below the observed cross section, but are compatible within the uncertainty.

6 Summary and conclusions

The ATLAS experiment has performed many measurements of the production of jets in association with vector bosons. These constitute a series of precision tests of the Standard Model. Overall, these measurements show good agreement with LO predictions and improved agreement when higher-order matrix elements are included in the calculation of these predictions.

References

[1] ATLAS Collaboration. JINST **3** (2008) S08003.

[2] T. Sjostrand, S. Mrenna, and P. Z. Skands. JHEP **0605** (2006) 026, arXiv:hep-ph/0603175 [hep-ph].

[3] T. Gleisberg, S. Hoeche, F. Krauss, M. Schönherr, S. Schumann, *et al.* JHEP **0902** (2009) 007, arXiv:0811.4622 [hep-ph].

[4] M. L. Mangano, M. Moretti, F. Piccinini, R. Pittau, and A. D. Polosa. JHEP **0307** (2003) 001, arXiv:hep-ph/0206293 [hep-ph].

[5] C. Berger, Z. Bern, L. J. Dixon, F. Febres Cordero, D. Forde, *et al.* Nucl.Phys.Proc.Suppl. **205-206** (2010) 92–97, arXiv:1005.3728 [hep-ph].

[6] J. M. Campbell and R. Ellis. Nucl.Phys.Proc.Suppl. **205-206** (2010) 10–15, arXiv:1007.3492 [hep-ph].

[7] J. M. Campbell, R. K. Ellis, F. Febres Cordero, F. Maltoni, L. Reina, *et al.* Phys.Rev.D **79** (2009) 034023, arXiv:0809.3003 [hep-ph].

[8] ATLAS Collaboration. Phys.Rev.D **85** (2012) 032009, arXiv:1111.2690 [hep-ex].

[9] ATLAS Collaboration. Phys.Rev.D **85** (2012) 092002, arXiv:1201.1276 [hep-ex].

[10] ATLAS Collaboration. Phys.Lett.B **708** (2012) 221–240, arXiv:1108.4908 [hep-ex].

[11] ATLAS Collaboration. Phys.Lett.D **706** (2012) 295–313, arXiv:1109.1403 [hep-ex].

[12] ATLAS Collaboration. Phys.Lett.B **707** (2012) 418–437, arXiv:1109.1470 [hep-ex].

[13] ATLAS Collaboration. ATLAS-CONF-2010-042 (2010) . http://cdsweb.cern.ch/record/1277682.

W+n-jet predictions at NLO matched with a parton shower

Frank Siegert[1], *Stefan Höche*[2], *Frank Krauss*[3], *Marek Schönherr*[3]

[1]Physikalisches Institut, Albert-Ludwigs-Universität Freiburg, D-79104 Freiburg, Germany
[2]SLAC National Accelerator Laboratory, Menlo Park, CA 94025, USA
[3]Institute for Particle Physics Phenomenology, Durham University, Durham DH1 3LE, UK

DOI: `http://dx.doi.org/10.3204/DESY-PROC-2012-02/242`

The MC@NLO method as implemented in the Sherpa MC generator is presented using the production of W-bosons in conjunction with up to three jets as an example. Corresponding results computed at next-to leading order in QCD and including parton shower corrections are compared to recent experimental data from the Large Hadron Collider.

1 Introduction

To make the LHC a discovery machine we have to acknowledge the fact that it is a QCD machine. Many signals suffer from large backgrounds largely due to QCD multi-jet production which have to be under good theoretical control to interpret the measurements.

There are mainly two approaches to include higher-order QCD corrections in theoretical calculations of scattering matrix elements (ME):

Fixed-order ME calculations put an emphasis on the exact evaluation of a finite number of terms in the perturbation series. Apart from being exact to the given order this also has the benefit of including all interference terms from different diagrams and working with a number of colours $N_C = 3$. Last, but not least, it becomes possible to include also the exact finite part of virtual contributions in a fixed-order calculation.

Their disadvantages appear when an observable becomes sensitive to logarithmically enhanced regions. It is not sufficient to truncate the perturbation series at a fixed order anymore, if the perturbative nature of the coupling constant α_s is countered by large logarithms which appear when partons become soft or collinear to each other. This problem is solved in the **parton shower** approach (PS), where the logarithmically enhanced contributions are resummed to all orders, albeit only in an approximation valid in the collinear limit of the matrix element and in the large N_C limit. This allows to generate events with partons at the hadronisation scale and thus enables exclusive hadron-level event generation.

It is thus a worthwhile goal to combine the two approaches and keep the advantages: Include the virtual contributions and first hard emission from the exact next-to-leading order matrix element, and add further parton evolution using a parton shower approach.

2 Recap: Resummation and NLO calculations

The basic property of QCD allowing a parton shower resummation is the universal factorisation of real emission matrix elements in the collinear limit:

$$\mathcal{R} \overset{ij \text{ collinear}}{\longrightarrow} \mathcal{D}_{ij}^{(\mathrm{PS})} = \mathcal{B} \times \left(\frac{1}{2p_i p_j} \, 8\pi\alpha_s \, \mathcal{K}_{ij}(p_i, p_j) \right) \tag{1}$$

With the approximation that multiple emissions happen independently of each other (thus yielding Poisson statistics) the corresponding branching probability can be exponentiated to give the total no-branching probability down to an evolution scale t:

$$\Delta^{(\mathrm{PS})}(t) \;=\; \prod_{\tilde{ij}} \exp\left\{ - \sum_{f_i = q,g} \int \mathrm{d}\Phi_{R|B}^{ij} \, \Theta\left(t(\Phi_{R|B}^{ij}) - t \right) \, \frac{\mathcal{D}_{ij}^{(\mathrm{PS})}}{\mathcal{B}} \right\} \tag{2}$$

To understand the implications of the no-branching probability Δ, let us look at the expectation value of an observable O taking into account up to one emission from the parton shower on top of a Born-level event:

$$\langle O \rangle^{(\mathrm{PS})} \;=\; \int \mathrm{d}\Phi_B \, \mathcal{B} \left[\underbrace{\Delta^{(\mathrm{PS})}(t_0) \, O(\Phi_B)}_{\text{unresolved}} \;+\; \underbrace{\sum_{\tilde{ij}} \sum_{f_i} \int_{t_0}^{\mu_F^2} \mathrm{d}\Phi_{R|B}^{ij} \, \frac{\mathcal{D}_{ij}^{(\mathrm{PS})}}{\mathcal{B}} \Delta^{(\mathrm{PS})}(t) \, O\left(r_{\tilde{ij}}(\Phi_B)\right)}_{\text{resolved}} \right] \tag{3}$$

The "unresolved" contribution corresponds to the event generation case where no emission above the parton shower cut-off scale t_0 has been generated and is thus proportional to the no-branching probability $\Delta(t_0)$. The "resolved" contribution on the other hand represents the integration over events which had an emission with evolution scale $t > t_0$.

As a reminder and to fix some notation, the contributions of an NLO calculation for the expectation value of O are briefly recalled:

$$\begin{aligned} \langle O \rangle^{(\mathrm{NLO})} \;=\; & \sum_{\vec{f}_{\mathrm{B}}} \int \mathrm{d}\Phi_B \left[\mathcal{B}(\Phi_B) + \tilde{\mathcal{V}}(\Phi_B) + \sum_{\tilde{ij}} \mathcal{I}_{\tilde{ij}}^{(\mathrm{S})}(\Phi_B) \right] O(\Phi_B) \\ & + \sum_{\vec{f}_{\mathrm{R}}} \int \mathrm{d}\Phi_R \left[\mathcal{R}(\Phi_R) \, O(\Phi_R) - \sum_{\{ij\}} \mathcal{D}_{ij}^{(\mathrm{S})}(\Phi_R) \, O(b_{ij}(\Phi_R)) \right] \end{aligned} \tag{4}$$

Here, the Born ($\mathcal{B}$), virtual ($\mathcal{V}$) and real emission ($\mathcal{R}$) pieces are denoted accordingly. Since $\mathcal{V}$ and $\mathcal{R}$ are oppositely divergent in separate phase space integrations, one needs to employ a subtraction procedure: The real subtraction terms $\mathcal{D}$ are linked to their integrated form $\mathcal{I}$ by a phase space integration over the 1-emission phase space and can be calculated e.g. in the scheme of [1].

3 Combining NLO and PS

Applying PS resummation on top of such NLO events is not straightforward: The observable has to be evaluated at different kinematics in the $\mathcal{R}$ and $\mathcal{D}$ terms. But if that is taken into

account, and they are thus showered separately, one generates an additional term at $\mathcal{O}(\alpha_s)$ [2] which is not present in the NLO calculation ("double counting"). To counter that term a solution was proposed in [2] introducing an additional set of "modified" subtraction terms $\mathcal{D}^{(\mathrm{A})}$. When generating events according to that modified NLO cross section, they will have either Φ_R kinematics (resolved, non-singular term) and are kept as they are or Φ_B kinematics. In the latter case, they are processed through a one-step PS with $\Delta^{(\mathrm{A})}$, i.e. using the modified subtraction terms as PS kernels, either generating an emission (resolved, singular) or no emission (unresolved, singular) above t_0. The result of this procedure,

$$\langle O\rangle^{(\mathrm{NLO+PS})} = \sum_{\vec{f}_B}\int \mathrm{d}\Phi_B \bar{\mathcal{B}}^{(\mathrm{A})}(\Phi_B)\left[\underbrace{\Delta^{(\mathrm{A})}(t_0)}_{\text{unresolved}} O(\Phi_B) + \sum_{\{\widetilde{ij},f_i\}}\int_{t_0}\mathrm{d}\Phi^{ij}_{R|B}\underbrace{\frac{\mathcal{D}^{(\mathrm{A})}_{ij}(r_{\widetilde{ij}}(\Phi_B))}{\mathcal{B}(\Phi_B)}\Delta^{(\mathrm{A})}(t)}_{\text{resolved, singular}} O(r_{\widetilde{ij}}(\Phi_B))\right]$$
$$+\sum_{\vec{f}_R}\int \mathrm{d}\Phi_R \underbrace{\left[\mathcal{R}(\Phi_R)-\sum_{ij}\mathcal{D}^{(\mathrm{A})}_{ij}(\Phi_R)\right]}_{\text{resolved, non-singular}} O(\Phi_R),$$

with $\bar{\mathcal{B}}^{(\mathrm{A})}(\Phi_B)$ defined as

$$\bar{\mathcal{B}}^{(\mathrm{A})}(\Phi_B) = \mathcal{B}(\Phi_B)+\tilde{\mathcal{V}}(\Phi_B)+\sum_{\{\widetilde{ij}\}}\mathcal{I}^{(\mathrm{S})}_{\widetilde{ij}}(\Phi_B)+\sum_{\{\widetilde{ij}\}}\sum_{f_i=q,g}\int \mathrm{d}\Phi^{ij}_{R|B}\left[\mathcal{D}^{(\mathrm{A})}_{ij}(r_{\widetilde{ij}}(\Phi_B))-\mathcal{D}^{(\mathrm{S})}_{ij}(r_{\widetilde{ij}}(\Phi_B))\right]$$

can be shown to reproduce $\langle O\rangle^{(\mathrm{NLO})}$ to $\mathcal{O}(\alpha_s)$.

This procedure still leaves the freedom of choosing $\Delta^{(\mathrm{A})}$. The original approach [2] uses the parton shower splitting kernels as additional subtraction terms, $\mathcal{D}^{(\mathrm{A})}_{ij} \to \mathcal{D}^{(\mathrm{PS})}_{ij}$. This option has the advantage that the exponentiation in the "resolved, singular" contribution is naturally bounded by the factorisation scale μ_F. Problems appear though with soft divergences in the "resolved, non-singular" integration, since the parton shower splitting kernels do not cover soft divergences.

An alternative approach was suggested in [3] and implemented in SHERPA [4], where the full Catani-Seymour dipoles are used $\mathcal{D}^{(\mathrm{A})}_{ij} \to \mathcal{D}^{(\mathrm{S})}_{ij}$. With this, $\bar{\mathcal{B}}^{(\mathrm{A})}$ simplifies significantly, but at a cost: $\mathcal{D}^{(\mathrm{S})}$ can become negative, resulting in $\Delta > 1$. This is generated in SHERPA by a weighted $N_C = 3$ one-step PS based on the subtraction terms $\mathcal{D}^{(\mathrm{S})}$. With this approach, exact NLO accuracy also for sub-leading colour configurations is achieved. The phase space boundary for the exponentiation though has to be imposed "artificially" by cuts in the dipole phase space.

4 Results

Results for $W + n$-jet production at the LHC are presented here in comparison to ATLAS data [5]. Events are simulated using SHERPA's MC@NLO for $W+0$, $W+1$, $W+2$ and $W+3$-jet production with virtual corrections from BLACKHAT [6] including a leading-colour approximation for the $W + 3$-jet virtual ME. For $n > 0$ events are generated requiring k_T jets with $p_\perp > 10$ GeV, and the exponentiation region was restricted using an $\alpha = 0.01$-cut in the dipole terms [7]. The comparison comprises of three levels of event simulation: "NLO" as fixed-order calculation, "MC@NLO 1em" as MC@NLO including the hardest emission only and "MC@NLO PL" as MC@NLO including the full PS. All distributions are simulated at NLO accuracy and the theoretical predictions describe data very well.

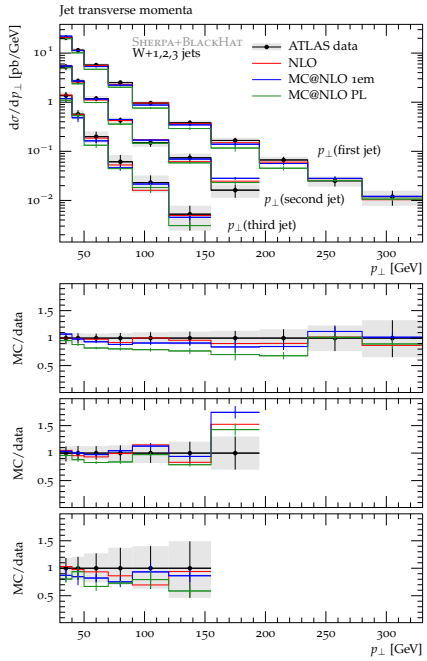

Fig. 1: Transverse momentum of the first, second and third jet (from top to bottom).

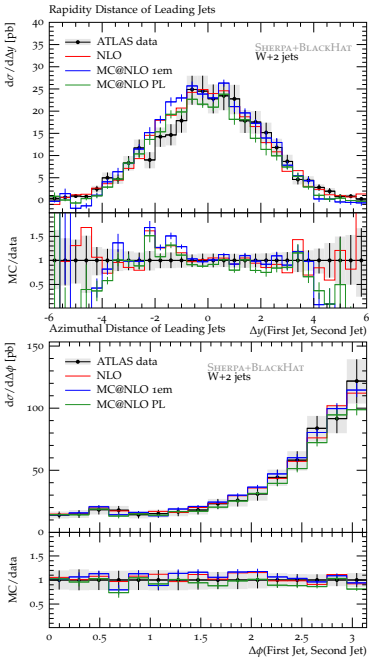

Fig. 2: Angular correlations of the two leading jets in $W^\pm + \geq 2$ jet production.

5 Conclusions and outlook

The concept of NLO+PS matching was presented in a common formalism, and MC@NLO was developed as a special case. It was emphasised that an exact treatment of sub-leading colour configurations can be achieved by exponentiating Catani-Seymour subtraction terms. The first NLO+PS predictions for W+3 jets were presented and showed good agreement with experimental data from ATLAS. With this method at hand, it becomes now possible to generate exclusive hadron-level event samples at NLO accuracy.

In the future, an improved functional form of the phase-space cut α will allow for a better limitation of the exponentiation region. Also, by merging NLO+PS with higher-multiplicity tree-level MEs one can already provide an improved description of multi-jet final states in the MENLOPS approach [8]. Ultimately, it remains a goal to achieve the merging of NLO+PS predictions at different multiplicities into one inclusive sample.

References

[1] S. Catani and M. H. Seymour. Nucl. Phys. **B485** (1997) 291–419, arXiv:hep-ph/9605323.
[2] S. Frixione and B. R. Webber. JHEP **06** (2002) 029, hep-ph/0204244.
[3] S. Höche, F. Krauss, M. Schönherr, and F. Siegert. arXiv:1111.1220 [hep-ph].
[4] T. Gleisberg *et al.* JHEP **02** (2009) 007, arXiv:0811.4622 [hep-ph].
[5] G. Aad *et al.* arXiv:1201.1276 [hep-ex].
[6] C. F. Berger *et al.* Phys. Rev. **D78** (2008) 036003, arXiv:0803.4180 [hep-ph].
[7] Z. Nagy. Phys. Rev. **D68** (2003) 094002, arXiv:hep-ph/0307268.
[8] S. Höche, F. Krauss, M. Schönherr, and F. Siegert. JHEP **08** (2011) 123, arXiv:1009.1127 [hep-ph].

Subleading-N_c improved parton showers

Simon Plätzer[1], *Malin Sjödahl*[2]

[1]DESY, Notkestraße 85, 22607 Hamburg, Germany
[2]Lund University, Sölvegatan 14A, SE-223 62 Lund, Sweden

DOI: http://dx.doi.org/10.3204/DESY-PROC-2012-02/234

We present an algorithm for improving subsequent parton shower emissions by full SU(3) colour correlations in the framework of a dipole-type shower. As a proof of concept, we present results from the first implementation of such an algorithm for a final state shower.

1 Introduction and motivation

Parton showers and event generators are indispensable tools for predicting and understanding collider results [1, 2, 3]. Considering their importance for interpreting LHC results, it is essential to have a good understanding of their approximations and limitations. These simulations have up to now all been based on QCD as an $SU(N_c)$ gauge theory in the limit of large N_c. For $N_c = 3$, this approximation seems to work remarkably well despite the fact that $1/N_c = 1/3$, in the general case, and $1/N_c^2 = 1/9$ in most cases are not truly small parameters. Otherwise, significant deviations from parton shower predictions as compared to experimentally measured observables would have already hinted towards a severe underestimate of colour suppressed terms.

Including colour suppressed terms in parton shower simulations has so far been an unexplored continent, and investigating effects caused by colour correlations beyond the large-N_c limit is mandatory in the age of ever improving simulations, particularly when including higher-order QCD corrections. Especially when considering the matching of parton showers to NLO QCD corrections, subleading-N_c improved parton showers provide a valuable input in making these matchings more precise such that the matching conditions are indeed satisfied exactly, and not only modulo colour suppressed terms.[1]

We here present an approach to subleading colour contributions [5] which is simple in the sense that it fits very well into the framework of existing Monte Carlo event generators. We note that this is not the end of the story, as for the general case an evolution at amplitude level would have to be considered. Our approach of colour matrix element corrections is a first step towards quantifying the size of the expected effects.

2 From dipole factorization to dipole showering

Dipole factorization, [6], states that the behaviour of QCD tree-level matrix elements squared in any singly unresolved limit involving two partons i, j (*i.e.* whenever i and j become collinear

[1]In this context an independent approach, considering only one emission, has been presented in [4].

or one of them soft), can be cast into the form

$$|\mathcal{M}_{n+1}(...,p_i,...,p_j,...,p_k,...)|^2 \approx \sum_{k\neq i,j} \frac{1}{2p_i\cdot p_j}\langle \mathcal{M}_n(...,p_{\tilde{ij}},...,p_{\tilde{k}},...)|\mathbf{V}_{ij,k}(p_i,p_j,p_k)|\mathcal{M}_n(...,p_{\tilde{ij}},...,p_{\tilde{k}},...)\rangle \ , \quad (1)$$

where $|\mathcal{M}_n\rangle$ – which is a vector in the space of helicity and colour configurations – denotes the amplitude for an n-parton final state. Here an emitter $\tilde{ij}$ undergoes splitting to two partons i and j in the presence of a spectator $\tilde{k}$ which absorbs the longitudinal recoil of the splitting, $\tilde{k}\to k$. This factorization formula, which is well established to provide a subtraction scheme for NLO calculations, can actually be used to derive a dipole-type shower algorithm [7]. Results of an implementation have been reported in [8], and similar approaches have been considered in [9, 10]. In these cases, the colour correlations present in $\mathbf{V}_{ij,k}$ are approximated in the large-N_c limit, while keeping the colour factor for gluon emission off quarks, $C_F=\mathbf{T}^2_{q_i}$, exact. In turn, chains of colour connected dipoles evolve through subsequent emissions generating more dipoles in a chain or leading to a breakup of the chain in case a gluon splits into a $q\bar{q}$ pair until eventually the transverse momentum of potential emissions is below an infrared cutoff in the region of one GeV.

3 Colour matrix element corrections

The dipole factorization formula eq. 1 implies a factorization at the level of cross sections; here, the differential cross section for $n+1$ partons factorizes into the cross section for producing n partons times a radiation density as the sum over all dipole configurations $\tilde{ij},\tilde{k}$, which undergo radiation, $\tilde{ij},\tilde{k}\to i,j,k$:

$$dP_{ij,k}(p_\perp^2,z) = V_{ij,k}(p_\perp^2,z)\frac{d\phi_{n+1}(p_\perp^2,z)}{d\phi_n}\times\frac{-1}{\mathbf{T}^2_{\tilde{ij}}}\frac{\langle\mathcal{M}_n|\mathbf{T}_{\tilde{ij}}\cdot\mathbf{T}_k|\mathcal{M}_n\rangle}{|\mathcal{M}_n|^2} \quad (2)$$

Here, we have used the spin-averaged version of the dipole kernels including the product of colour charges encoding the colour correlations, $\mathbf{V}_{ij,k}=-V_{ij,k}\mathbf{T}_{\tilde{ij}}\cdot\mathbf{T}_k/\mathbf{T}^2_{\tilde{ij}}$, and $\mathrm{d}\phi_k$ denotes the k-parton phase space. In the large-N_c limit, this formula yields the basis for the dipole shower considered so far: $-\mathbf{T}_{\tilde{ij}}\cdot\mathbf{T}_k/\mathbf{T}^2_{\tilde{ij}}\to\delta(\tilde{ij},k\text{ colour connected})/(1+\delta_{\tilde{ij}})$, where $\delta_{\tilde{ij}}=1(0)$ for $\tilde{ij}=g(q/\bar{q})$. To obtain an algorithm which instead keeps the full colour correlations, we do not consider this approximation but keep the second factor in eq. 2 exactly. Owing to the similarity of matrix element corrections present in parton showers so far, we refer to this improvement as 'colour matrix element corrections'.

Eq. 2 describes how a single emission incorporates colour correlations. Indeed, for the first emission off the hard subprocess, $|\mathcal{M}_n\rangle$ is known, though it has to be recalculated after each subsequent emission to define the colour matrix element correction for the next emission. Instead of directly calculating the next amplitude, which would only be possible if we had derived splitting amplitudes in the singly unresolved limits, we observe that

$$|\mathcal{M}_n|^2=\mathcal{M}_n^\dagger S_n\mathcal{M}_n=\mathrm{Tr}\left(S_n\times\mathcal{M}_n\mathcal{M}_n^\dagger\right) \quad (3)$$

and

$$\langle\mathcal{M}_n|\mathbf{T}_{\tilde{ij}}\cdot\mathbf{T}_{\tilde{k}}|\mathcal{M}_n\rangle=\mathrm{Tr}\left(S_{n+1}\times T_{\tilde{k},n}\mathcal{M}_n\mathcal{M}_n^\dagger T^\dagger_{\tilde{ij},n}\right) \ , \quad (4)$$

where we have chosen a definite basis $\{|\alpha\rangle\}$ for the colour space, $|\mathcal{M}_n\rangle = \sum_{\alpha=1}^{d_n} c_{n,\alpha}|\alpha_n\rangle \quad \leftrightarrow$ $\mathcal{M}_n = (c_{n,1}, ..., c_{n,d_n})^T$ and introduced the scalar product matrix $S_n = \{\langle\alpha_n|\beta_n\rangle\}$ as well as matrix representations of the colour charge operators for n partons, $\mathbf{T}_i \to T_{i,n}$.

These representations then imply that we can work with an amplitude matrix M_n as the fundamental object,

$$M_{n+1} = -\sum_{i\neq j}\sum_{k\neq i,j} \frac{4\pi\alpha_s}{p_i\cdot p_j}\frac{V_{ij,k}(p_i,p_j,p_k)}{\mathbf{T}^2_{\tilde{ij}}}\; T_{\tilde{k},n} M_n T^\dagger_{\tilde{ij},n}\;, \tag{5}$$

where the initial matrix for the hard subprocess is given by $M_{n_{\text{hard}}} = \mathcal{M}_{n_{\text{hard}}}\mathcal{M}^\dagger_{n_{\text{hard}}}$.

4 Technicalities

Having outlined the principle of the algorithm for including colour correlations for subsequent parton shower emissions, two major technical issues have to be addressed: On the one hand, an general treatment of the colour basis for an arbitrary number of partons is required. On the other hand, sampling from the probability (Sudakov-type) density driving the next parton shower emission has to be generalized to the case of non-positive splitting rates as typically encountered for $1/N_c$ suppressed contributions.

For the first task, we have implemented a C++ library ColorFull [11] implementing the trace bases of colour space, [12]. This library is interfaced to the Matchbox framework presented in [8]. The colour matrix element corrections calculated in this part of the simulations, are inserted as correction weights into an existing dipole shower implementation, which uses the ExSample library [13] to sample Sudakov-type densities derived from the absolute value of the colour-corrected splitting rates. For the second task, we then employ the interleaved competition/veto algorithm outlined in [14] to arrive at events distributed according to the desired density (note that the sum of all splitting rates approximates a squared matrix element and is thus positive).

5 Results

As a proof-of-concept, we present results from the subleading-N_c improved parton shower for final state radiation, more precisely considering $e^+e^- \to q\bar{q}$ at LEP1 energies. We compare three different approximations: 'full' colour correlations, the 'shower' approximation where the $\mathbf{T}_i\cdot\mathbf{T}_j/\mathbf{T}_i^2$ are taken in the large-N_c limit, and a 'strict' large-N_C approximation, where also $C_F \approx C_A/2$. Interestingly, the 'shower' approximation does not exactly reproduce the shower implementation; from four partons onwards, this evolution is sensitive to the emission history, though matches the shower implementation if one sequence of dipoles has dominated. Indeed, the differences between the 'shower' approximation and the default shower implementation are at the per-mille level as one would expect from strong ordering in the emission history.

In the results presented here, we include up to six improved shower emissions. $g \to q\bar{q}$ splittings are neglected, as there are no associated colour correlations; we also do not include hadronization. For event shapes and jet rates we find small subleading-N_c effects when considering the shower approximation; for tailored observables, probing the dynamics of soft radiation with respect to a hard subsystem of the event, larger effects are seen. The strict approximation shows larger deviations. This fact can mainly be attributed to the change in the Sudakov exponent for gluon emission off a quark. A few sample results are shown in figure 1.

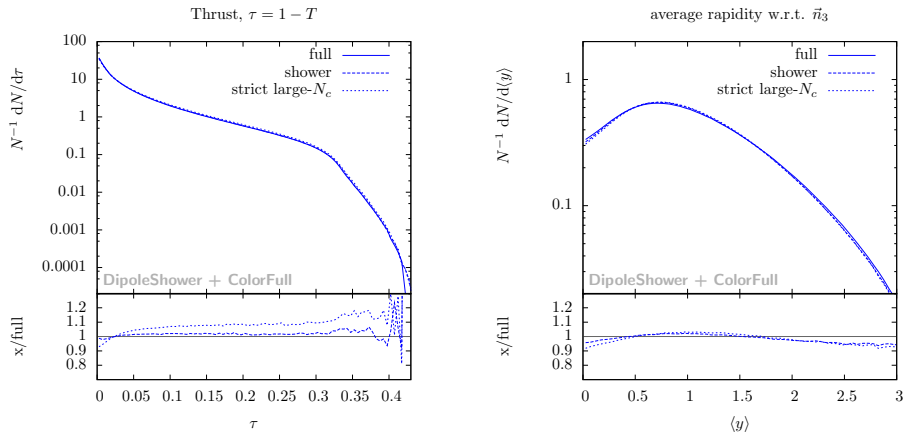

Figure 1: The thrust distribution (left) and the average rapidity w.r.t the thrust axis defined by the three hardest partons using the different approximations.

6 Conclusions

We have presented the first implementation of a subleading-N_c improved parton showers. For $e^+e^- \to$ jets small effects are seen except for very special observables. The technical issues associated with the implementation, particularly the treatment of the colour basis and the presence of negative splitting kernels will serve as input for related and future work; we also anticipate that larger effects can be seen in hadron collisions, *e.g.* $pp \to$ jets.

References

[1] T. Sjöstrand, S. Mrenna, and P. Skands. Comput. Phys. Commun. **178** (2008) 852–867, arXiv:0710.3820 [hep-ph].

[2] M. Bähr et al. Eur. Phys. J. **C58** (2008) 639–707, arXiv:0803.0883 [hep-ph].

[3] T. Gleisberg *et al.* JHEP **02** (2004) 056, arXiv:hep-ph/0311263.

[4] S. Hoeche, F. Krauss, M. Schonherr, and F. Siegert. arXiv:1111.1220 [hep-ph].

[5] S. Platzer and M. Sjodahl. arXiv:1201.0260 [hep-ph].

[6] S. Catani and M.H. Seymour. Nucl. Phys. **B485** (1997) 291–419, arXiv:hep-ph/9605323.

[7] S. Platzer and S. Gieseke. JHEP **01** (2011) 024, arXiv:0909.5593 [hep-ph].

[8] S. Platzer and S. Gieseke. arXiv:1109.6256 [hep-ph].

[9] M. Dinsdale, M. Ternick and S. Weinzierl. Phys. Rev. **D76** (2007) 094003, arXiv:0709.1026 [hep-ph].

[10] S. Schumann and F. Krauss. JHEP **03** (2008) 038, arXiv:0709.1027 [hep-ph].

[11] M. Sjödahl. work in progress .

[12] M. Sjodahl. JHEP **0909** (2009) 087, arXiv:0906.1121 [hep-ph].

[13] S. Platzer. Eur.Phys.J. **C72** (2012) 1929, arXiv:1108.6182 [hep-ph].

[14] S. Platzer and M. Sjodahl. Eur.Phys.J.Plus **127** (2012) 26, arXiv:1108.6180 [hep-ph].

Matrix Elements with Vetoes in the CASCADE Monte Carlo Event Generator

M. Deák[1], *F. Hautmann*[2], *H. Jung*[3,4], *K. Kutak*[5]

[1]Universidade de Santiago de Compostela, E-15782 Santiago de Compostela
[2]Theoretical Physics, University of Oxford, Oxford OX1 3NP
[3]Deutsches Elektronen Synchrotron, D-22603 Hamburg
[4]CERN, Physics Department, CH-1211 Geneva 23
[5]Instytut Fizyki Jadrowej im H. Niewodniczanskiego, PL 31-342 Krakow

DOI: http://dx.doi.org/10.3204/DESY-PROC-2012-02/1

We illustrate a study based on a veto technique to match parton showers and matrix elements in the CASCADE Monte Carlo event generator, and present a numerical application to gluon matrix elements for jet production.

Baseline studies of final states containing multiple jets at the Large Hadron Collider use Monte Carlo event generators — see e.g. [1] for a recent review — based on collinear evolution of parton showers combined with hard matrix elements. These are either high-multiplicity tree-level matrix elements [2], or next-to-leading-order matrix elements [3] including virtual emission processes, or possibly, in the future, a combination of both [4, 5]. The parton showers take into account collinear small-angle QCD radiation, while the matrix elements take into account hard large-angle radiation.

When the longitudinal momentum fractions involved in the production of jets become small, however, new effects on jet final states arise from noncollinear corrections to parton branching processes [6], due to soft but finite-angle multi-gluon emission. An example of this occurs at the LHC when jets are produced at increasingly high rapidities [7]. In order to take these corrections into account one needs [8] transverse-momentum dependent showering algorithms coupled [9] to hard matrix elements at fixed transverse momentum.

The CASCADE Monte Carlo event generator [10] provides an implementation of this framework. Applications of this to hard production in the LHC forward region [11] have been investigated in [12], where studies of forward-central jet correlations have been proposed. First LHC measurements of jets at wide rapidity separations have appeared in [13, 14]. The approach of CASCADE is based on a small-x expansion, so that in order to apply it to the highest jet $p_\perp$ it is relevant to match it with perturbative fixed-order terms. In this article we describe a study based on a vetoing procedure to combine shower and matrix element contributions to jet production. The technique discussed is one of the elements needed to improve the accuracy of CASCADE at high transverse momenta.

To illustrate this, we focus on the partonic $q\bar{q}$ production process in the gg^* channel. This can occur by direct production from gluon-gluon annihilation or by decay $g \to q\bar{q}$ following elastic gluon scattering. When the quarks have small relative transverse momentum the two mechanisms are effectively of the same order in the strong coupling. The question of properly

simulating these processes also arises in the case of collinear shower Monte Carlo; but the case of the transverse momentum dependent shower involves an additional (semi)hard scale set by the off-shellness of the incoming parton. Different behaviors may be expected depending on the ratio $|k^2|/\mu^2$, where $|k^2|$ is the off-shellness and μ^2 is the merging scale used for combining the different production processes. An approach to treat this is based on the subtractive method [15] (see [16] and [17] for further applications of the method). An analysis along these lines is reported in [18]. In this article we describe the result of another type of calculation [12], based on introducing a veto on $g \to q\bar{q}$ splitting above a given transverse momentum scale $\mu = \mathrm{p}_\perp^{(V)}$. In this calculation the gluonic matrix element is combined with the vetoed branching, and added to the hard production contribution.

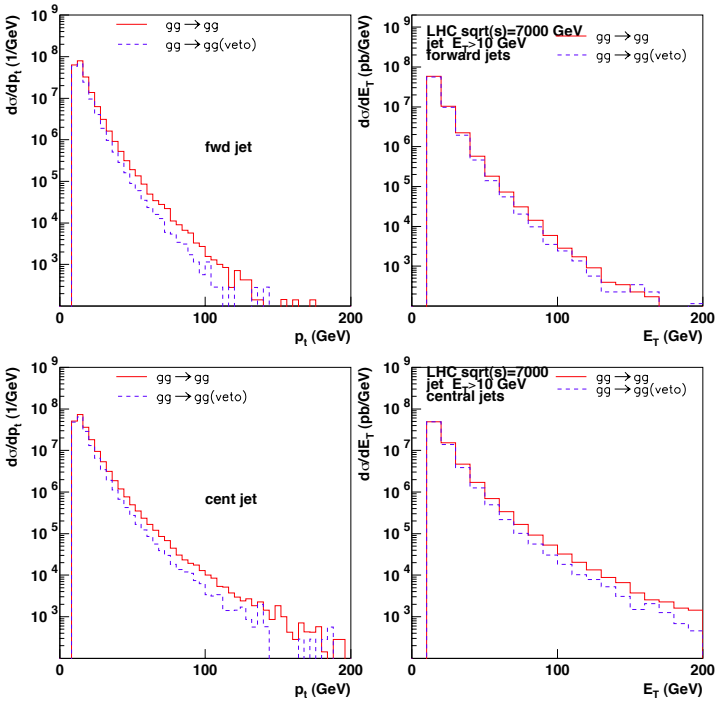

Figure 1: The effect of the veto at forward (top) and central (bottom) rapidities: (left) parton-level; (right) jet-level.

In Fig. 1 we consider the kinematic region [12] for production of jets at forward and central rapidities, and we examine numerically the effect of the veto on the gluon scattering contribution both at the level of final state partons and at the level of reconstructed jets. We see that in both cases the shape of transverse spectra is changed by the veto. In Fig. 2 we include all partonic channels, in the same kinematic region, combining the previous contribution with hard production. Then the shape of the transverse distribution is not changed much as an effect of the veto, while this results into a change in normalization. For reference we also include the result from the PYTHIA Monte Carlo generator [19] used in the LHC tune Z1 [20].

In summary, the study discussed in this contribution introduces vetoed decays coupled with finite-$\mathrm{k}_\perp$ matrix elements as an approach to matching in the case of transverse momentum

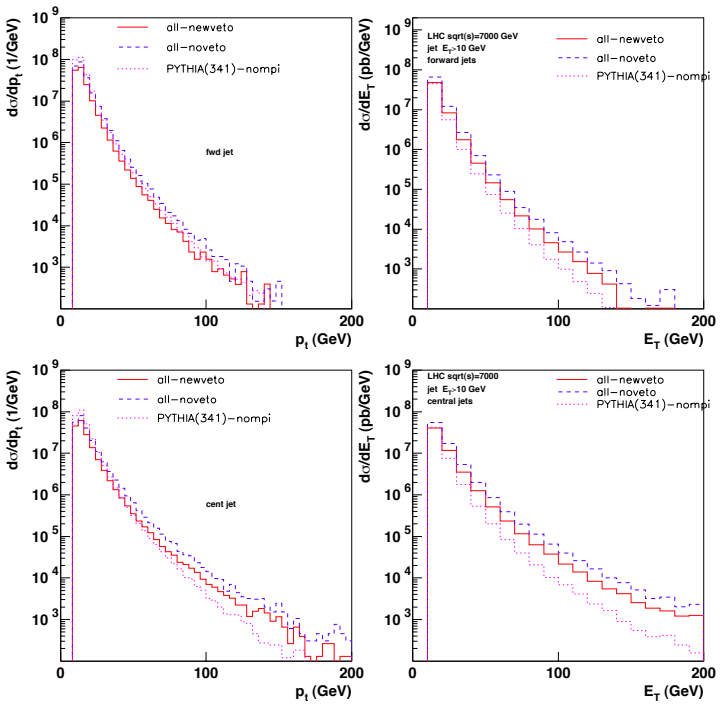

Figure 2: Comparison of transverse momentum spectra at forward (top) and central (bottom) rapidities: (left) parton-level; (right) jet-level.

dependent parton showers. This is one of the ingredients to extend results of the CASCADE Monte Carlo generator toward higher $p_\perp$ jets. Other physical effects will also be important in this region. One is the behavior of the gluon distribution for large x at transverse momentum dependent level. At present this is not very well constrained in fits to experimental data [21]. Another is the inclusion of subleading quark contributions [22] to the evolution of the small-x parton shower. In the intermediate to low $p_\perp$ range, studies of the associated mini-jet energy flow [12, 23] as a function of rapidity and azimuthal distance will be helpful to investigate showering and possibly gluon rescattering [24] effects. We expect this to be relevant especially to analyze multiple parton interactions [25] and their role in multi-jet production at the LHC.

Acknowledgments. We thank the conveners for the invitation and excellent organization of the meeting.

References

[1] S. Höche, SLAC preprint SLAC-PUB-14498 (2011).

[2] J. Alwall et al., Eur. Phys. J. C **53** (2008) 473.

[3] P. Nason and B.R. Webber, arXiv:1202.1251 [hep-ph].

[4] C.W. Bauer, F.J. Tackmann and J. Thaler, JHEP **0812** (2008) 010; JHEP **0812** (2008) 011.

[5] N. Lavesson and L. Lönnblad, JHEP **0812** (2008) 070.

[6] F. Hautmann and H. Jung, arXiv:0712.0568 [hep-ph]; JHEP **0810** (2008) 113.

[7] M. Deak, F. Hautmann, H. Jung and K. Kutak, JHEP **0909** (2009) 121; arXiv:0908.1870.

[8] G. Marchesini and B.R. Webber, Nucl. Phys. **B386** (1992) 215.

[9] S. Catani et al., Phys. Lett. B**242** (1990) 97; Nucl. Phys. B**366** (1991) 135; Nucl. Phys. B Proc. Suppl. **29A** (1992) 182; Phys. Lett. B**307** (1993) 147; S. Catani and F. Hautmann, Nucl. Phys. B**427** (1994) 475.

[10] H. Jung, Comput. Phys. Commun. **143** (2002) 100; H. Jung et al., Eur. Phys. J. C **70** (2010) 1237.

[11] Z. Ajaltouni et al., arXiv:0903.3861 [hep-ph]; D. d'Enterria, arXiv:0911.1273 [hep-ex]; M. Grothe et al., arXiv:1103.6008 [hep-ph].

[12] M. Deak, F. Hautmann, H. Jung and K. Kutak, arXiv:1012.6037 [hep-ph]; arXiv:1112.6386 [hep-ph]; Eur. Phys. J. C **72** (2012) 1982; in preparation.

[13] CMS Coll. (S. Chatrchyan et al.), arXiv:1202.0704 [hep-ex].

[14] ATLAS Coll. (G. Aad et al.), JHEP **1109** (2011) 053; CMS Coll. (S. Chatrchyan et al.), arXiv:1204.0696 [hep-ex].

[15] J.C. Collins and F. Hautmann, JHEP **0103** (2001) 016; Phys. Lett. B**472** (2000) 129.

[16] Y. Chen, J.C. Collins and X. Zu, JHEP **0204** (2002) 041; J.C. Collins and X. Zu, hep-ph/0212053, JHEP **0503** (2005) 059.

[17] F. Hautmann, Phys. Lett. B**655** (2007) 26; arXiv:0708.1319; Nucl. Phys. B**604** (2001) 391; hep-ph/0105098; hep-ph/0101006; hep-ph/0011381.

[18] M. Deak, talk at Rencontres de Moriond 2012 (La Thuile, March 2012).

[19] P. Skands, Phys. Rev. D**82** (2010) 074018.

[20] R.D. Field, arXiv:1010.3558 [hep-ph].

[21] H. Jung, talk at DIS2012 Workshop (Bonn, April 2012).

[22] F. Hautmann, Acta Phys. Polon. B **40** (2009) 2139; PoS ICHEP2010 (2010) 150; F. Hautmann, M. Hentschinski and H. Jung, arXiv:1205.1759 [hep-ph]; arXiv:1205.6358 [hep-ph].

[23] F. Hautmann, arXiv:1205.5411 [hep-ph]; arXiv:1101.2656 [hep-ph]; PoS ICHEP2010 (2010) 108.

[24] F. Hautmann and D.E. Soper, Phys. Rev. D**75** (2007) 074020; arXiv:0712.0526 [hep-ph]; Phys. Rev. D**63** (2000) 011501; F. Hautmann, JHEP **0210** (2002) 025; hep-ph/0105082; Phys. Lett. B**643** (2006) 171; arXiv:0812.2873 [hep-ph]; F. Hautmann, Z. Kunszt and D.E. Soper, hep-ph/9906284; hep-ph/9806298.

[25] P. Bartalini and L. Fanò (eds.), Proc. 1st MPI Workshop (Perugia, 2008), arXiv:1003.4220 [hep-ex]; P. Bartalini et al., arXiv:1111.0469 [hep-ph].

Drell-Yan Lepton Pair Production at the Tevatron and LHC in the k_T-factorization Approach

Artem Lipatov, Maxim Malyshev, Nikolai Zotov

Skobeltsyn Institute of Nuclear Physics, Lomonosov Moscow State University, 119991 Moscow, Russia

DOI: http://dx.doi.org/10.3204/DESY-PROC-2012-02/3

We present the results of the numerical calculations of Drell-Yan lepton pair production at Tevatron and LHC in the framework of the k_T-factorization approach. Our predictions are compared with the D0, CDF and CMS experimental data.

Our study is motivated by recent measurements of the Drell-Yan lepton pair production performed by the CMS collaboration at LHC [1], taken at the center-of mass energy 7 TeV.

We use the k_T-factorization approach, which previously was successfully applied to various high energy physics processes, such as the heavy flavour [2, 3], prompt photon [4] and top [5] production at the Tevatron and LHC energies.

According to the k_T-factorization theorem, to calculate the cross section of the Drell-Yan lepton pair production one should convolute the off-shell partonic cross sections with the relevant unintegrated quark and/or gluon distributions in the proton:

$$\sigma = \sum_{i,j=q,\,g} \int \hat{\sigma}^*_{ij}(x_1, x_2, \mathbf{k}^2_{1T}, \mathbf{k}^2_{2T})\, f_i(x_1, \mathbf{k}^2_{1T}, \mu^2) f_j(x_2, \mathbf{k}^2_{2T}, \mu^2)\, dx_1 dx_2\, d\mathbf{k}^2_{1T} d\mathbf{k}^2_{2T},$$

where $\hat{\sigma}^*_{ij}(x_1, x_2, \mathbf{k}^2_{1T}, \mathbf{k}^2_{2T})$ is the relevant partonic cross section. The initial off-shell partons have fractions x_1 and x_2 of initial protons longitudinal momenta and non-zero transverse momenta $\mathbf{k}_{1T}$ and $\mathbf{k}_{2T}$.

Concerning the unintegrated parton distributions we use the KMR prescription [6, 7]. It represents an approximate treatment of the parton evolution mainly based on the DGLAP equation and incorpotating the BFKL effects at the last step of the parton ladder only, in the form of the properly defined Sudakov formfactors $T_q(\mathbf{k}^2_T, \mu^2)$ and $T_q(\mathbf{k}^2_T, \mu^2)$, including logarithmic loops. In this approach both gluon and quark distributions can be obtained.

We have calculated matrix elements for $q\bar{q} \to \gamma/Z \to l^+l^-$ and $qg^* \to \gamma/Z + q \to l^+l^-q$. In the k_T-factorization approach the contribution from another subprocess, $q\bar{q} \to \gamma/Z + g \to l^+l^-g$ is already taken into account by the quark-antiquark annihilation due to the initial state radiation. So this subprocess has been taken out of our consideration in order to avoid double counting, which is in contrast with the collinear QCD factorization.

The calculation implies a modification of gluon polarization density matrix. It takes so called BFKL form: $\sum \epsilon^\mu \epsilon^{*\nu} = k^\mu_T k^\nu_T / \mathbf{k}^2_T$. In all other respects the evaluation follows the standard QCD Feynman rules.

To take into account the non-logarithmic loop corrections we use the approximation proposed in [8]. It was demonstrated that the main part of the non-logarithmic loop corrections to the

quark-antiquark annihilation cross section can be absorbed in the effective K-factor: $K = \exp(C_F \pi^2 \alpha_S(\mu^2)/2\pi)$, where the color factor $C_F = 4/3$. A particular choice $\mu^2 = \mathbf{p}_T^{4/3} M_{ll}^{2/3}$ has been proposed [8, 9] to eliminate sub-leading logarithmic terms. We chose this scale to evaluate the strong coupling constant in the expression for K.

In KMR unintegrated parton distributions we used the standard MSTW'2008 (LO) set [10] as an input. We took the renormalization and factorization scales $\mu_R^2 = \mu_F^2 = \xi^2 M_{ll}^2$. In order to evaluate theoretical uncertainties, we varied ξ between $1/2$ and 2 about the default value $\xi = 1$. Following to [11], we set $M_Z = 91.1876$ GeV, Γ_Z =2.4952 GeV, $\sin^2\theta_W = 0.23122$. We used the LO formula for the strong coupling constant $\alpha_s(\mu^2)$ with $n_f = 4$ active quark flavours at Λ_{QCD} =200 MeV, so that $\alpha_S(M_Z) = 0.1232$.

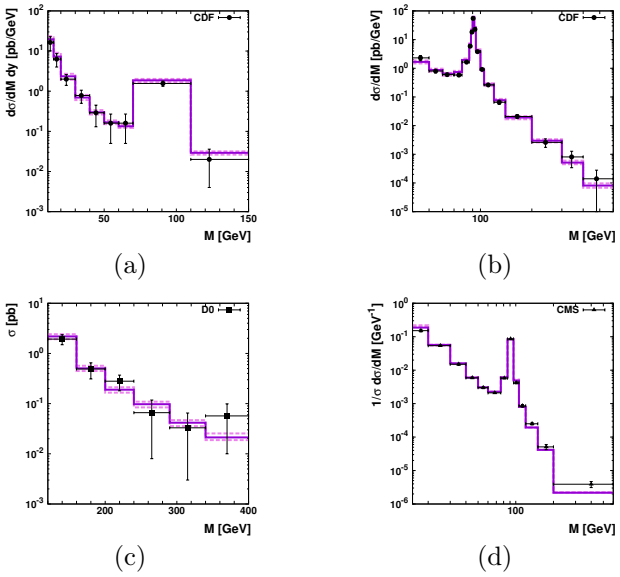

Figure 1: The differential cross sections of the Drell-Yan lepton production in hadron collisions as a function of M_{ll} calculated at $\sqrt{s}$ =1.8 TeV (a—c) and 7 TeV (d). The experimental data are from D0, CDF and CMS.

The results of our calculations [12] for Drell-Yan lepton pair production are presented in Fig. 1 in comparison with the D0 [13], CDF [14, 15] and CMS data [1]. Solid histograms are obtained by fixing both the factorization and renormalization scales at the default value $\mu = M_{ll}$, whereas the upper and lower dashed histograms correspond to the scale variation as it was described above. One can see that the Tevatron and LHC experimental data are reasonably well described by the k_T-factorization approach in the whole range of invariant masses.

Now we turn to an analysis of angular distributions in dilepton production. The general expression can be described by the polar θ and azimuthal ϕ angles of the produced particles in the dilepton rest frame. When integrated over ϕ or $\cos\theta$, respectively, the angular distribution can be presented as follows:

$$\frac{d\sigma}{d\cos\theta} \sim (1+\cos^2\theta) + \frac{1}{2}A_0(1-3\cos^2\theta) + A_4\cos\theta, \tag{1}$$

$$\frac{d\sigma}{d\phi} \sim 1 + \beta_3\cos\phi + \beta_2\cos 2\phi, \tag{2}$$

where $\beta_3 = 3\pi A_3/16$ and $\beta_2 = A_2/4$. Note that the angular coefficients A_0 and A_2 are the same for the γ^* or Z boson exchange, and A_3 and A_4 originate from the $\gamma^* - Z$ interference. The Lam-Tung relation [16] $A_0 = A_2$ is valid for both quark-antiquark annihilation and QCD Compton subprocesses at $\mathcal{O}(\alpha\alpha_s)$ order. Higher-order QCD calculations [17, 18] as well as QCD

resummation up to all orders [19] indicate that violations of the Lam-Tung relation are small. Very recently the CDF collaboration reported [20] the first measurement of the angular coefficients A_0, A_2, A_3 and A_4 in the Z peak region ($66 < M_{ll} < 116$ GeV) at $\sqrt{s}$ =1960 GeV. Below we estimate these coefficients regarding the CDF measurements. Our evaluation generally followed the experimental procedure. We have collected the simulated events in the specified bins of dilepton transverse momentum, generated the decay lepton angular distributions according to the calculated matrix elements and then applied a two-parametric fit based on 1. The estimated values of angular coefficients in the Collins-Soper frame are shown in Fig. 2. Solid and two dashed histograms represent fitted values of angular coefficients and corresponding uncertainties of fitting procedure. The default scale $\mu = M$ has been applied. We find that our predictions agree well with the CDF data as well as collinear QCD predictions listed in [20]. We would like to only remark that the latter predict a flat behaviour of A_3 in a whole p_T range whereas CDF data tends to support our predictions (slight decreasing of A_3 when we move to large p_T values).

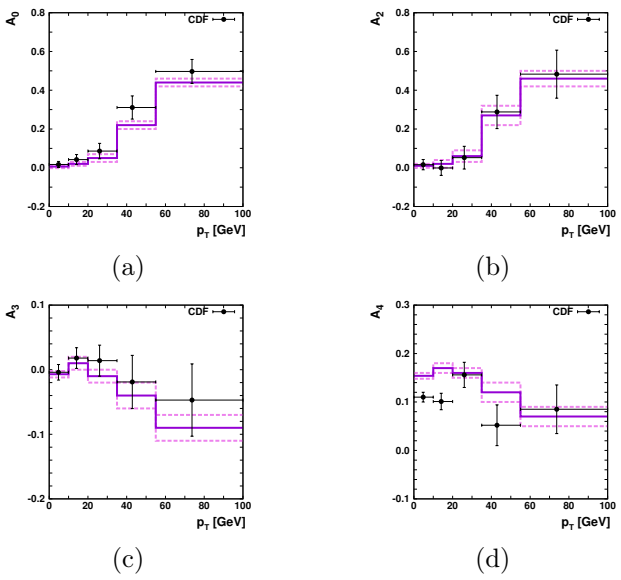

Figure 2: Angular coefficients A_0, A_2, A_3 and A_4 of dilepton production as a function of p_T calculated at $\sqrt{s}$ =1.96 TeV. The experimental data are from CDF.

In summary, we have studied the Drell-Yan lepton pair production in the k_T-factorization QCD approach at LHC energies. The matrix elements for $q\bar{q} \to \gamma/Z \to l^+l^-$ and $qg^* \to \gamma/Z + q \to l^+l^-q$ have been evaluated. A reasonably good description of D0, CDF and CMS data for the Drell-Yan lepton pair production at Tevatron and LHC has been obtained. A theoretical uncertainties investigation has been studied and a predictive power of the used approach has been shown. The CDF data for A_3 tend to support our predictions.

Acknowledgments

The presented research was supported by RF FASI grant NS-4142.2010.2, RF FASI state contract 02.740.11.0244 and RFBR grant 11-02-01454-a. A.L. and M.M. were supported by the grant of President of Russian Federation (MK-3977.2011.2) and A.L. also was supported by DESY Directorate in the framework of Moscow — DESY project on Monte-Carlo implementation for HERA — LHC. M.M. is very grateful to the organizing committee, especially to Ian Brock, Andrea Fürstenberg and Désirée Wilde for their support.

References

[1] CMS collab., S. Chatrchyan *et al.*, JHEP **1110** (2011) 007.

[2] H. Jung, M. Krämer, A. V. Lipatov and N. P. Zotov. JHEP **1101** (2011) 085.

[3] H. Jung, M. Krämer, A. V. Lipatov and N. P. Zotov. Phys. Rev. **D85** (2012) 034035.

[4] A. V. Lipatov, M. A. Malyshev and N. P. Zotov. Phys. Lett. **B699** (2011) 93.

[5] A. V. Lipatov and N. P. Zotov. Phys. Lett. **B704** (2011) 189.

[6] M. A. Kimber, A. D. Martin and M. G. Ryskin. Phys. Rev. **D63** (2001) 114027.

[7] G. Watt, A. D. Martin and M. G. Ryskin. Eur. Phys. J. **C31** (2003) 73.

[8] G. Watt, A. D. Martin and M. G. Ryskin. Phys. Rev. **D70** (2004) 014012.

[9] A. Kulesza and W. J. Stirling. Nucl. Phys. **B555** (1999) 279.

[10] A. D. Martin, W. J. Stirling, R. S. Thorne and G. Watt. Eur. Phys. J. **C63** (2009) 189.

[11] PDG collab., C. Amster *et al.*, Phys. Lett. **B667** (2008) 1.

[12] A. V. Lipatov, M. A. Malyshev and N. P. Zotov. JHEP **1112** (2011) 117.

[13] D0 collab., B. Abbott *et al.*, Phys. Rev. Lett **82** (1999) 4769.

[14] CDF collab., F. Abe *et al.*, Phys. Rev. **D49** (1994) 1.

[15] CDF collab., T. Affolder *et al.*, Phys. Rev. Lett. **87** (2001) 131802.

[16] C. S. Lam and W. K. Tung. Phys. Lett. **B80** (1979) 228.

[17] E. Mirkes and J. Ohnemus. Phys. Rev. **D50** (1994) 5692.

[18] E. Mirkes and J. Ohnemus. Phys. Rev. **D51** (1995) 4891.

[19] E.L. Berger, J. Qiu, and R.A. Rodriguez-Pedraza. Phys. Lett. **B656** (2007) 74.

[20] CDF collab. T. Aaltonen *et al.*, Phys. Rev. Lett. **106** (2011) 241801.

Electroweak Gauge-Boson and Higgs Production at Small q_T
Infrared Safety from the Collinear Anomaly

Thomas Becher[1], *Matthias Neubert*[2], *Daniel Wilhelm*[2,3]

[1]Institut für Theoretische Physik, Universität Bern, Switzerland
[2]Institut für Physik (THEP), Johannes Gutenberg-Universität Mainz, Germany
[3]Presenter

DOI: http://dx.doi.org/10.3204/DESY-PROC-2012-02/314

We study the differential cross sections for electroweak gauge-boson and Higgs production at small and very small transverse-momentum q_T. Large logarithms are resummed using soft-collinear effective theory. The collinear anomaly generates a non-perturbative scale q_*, which protects the processes from receiving large long-distance hadronic contributions. A numerical comparison of our predictions with data on the transverse-momentum distribution in Z-boson production at the Tevatron and LHC is given.

1 Introduction

In multi-scale processes with several disparate scales, large logarithms of scale ratios spoil the perturbative expansion of fixed-order calculations. To obtain a reliable theory prediction one has to resum these logarithms to all orders. Traditional resummation approaches often suffer from cut-off effects originating from the regularization of Landau-pole singularities. One way to avoid such complications is to factorize the observable via an appropriate effective field theory (EFT), describing the low-energy degrees of freedom using effective quark and gluon fields and resum large logarithms using renormalization group (RG) techniques.

We studied the differential cross section for Drell-Yan like gauge-boson production at hadron colliders [1][2], in the regime where the transverse-momentum q_T of the produced boson (or lepton pair) is small compared to its invariant mass M. We considered in detail real production of W- and Z-bosons and the decay of massive ($M \gg q_T$) virtual photons into lepton pairs. The region of small q_T is of great phenomenological importance, since it has the largest cross section and is used e.g. to extract the W-boson mass and width. Pioneering work in this field was done in [3], but this is the first time the resummation was done directly in momentum space. The extension of the used formalism to Higgs-boson production via gluon-fusion can be achieved in a straightforward manner. Here the region of small q_T is important because one usually vetoes hard jets in order to enhance the signal over background ratio.

2 Factorization in soft-collinear effective theory

In contrast to the naive expectation, the underlying scale of the needed EFT for Drell-Yan like processes is not only the small scale q_T. The appearance of Sudakov double logarithms [4] at 1-loop-order automatically generates a new soft scale w, correlated to the hard and collinear scales M and q_T, which becomes obvious by decomposing such a logarithm:

$$\ln^2 \tfrac{M^2}{q_T^2} = \tfrac{1}{2}\left[\ln^2 \tfrac{M^2}{\mu^2} - \ln^2 \tfrac{q_T^2}{\mu^2} - \ln^2 \tfrac{q_T^2}{\mu^2} + \ln^2 \tfrac{w^2}{\mu^2}\right] , \quad w = \tfrac{q_T^2}{M} .$$

The appropriate EFT describing these degrees of freedom is the soft-collinear effective theory (SCET). In general SCET contains any number of “collinear" fields describing high-energetic lightlike particles (or jets) and soft fields, which mediate the only interactions between the different collinear modes. In our case there are two collinear particles, the two colliding hadrons, whose momenta are characterized best in lightcone coordinates. Therefore we introduce two lightlike reference vectors n and $\bar{n}$ along the beam axis. Now every 4-vector k can be decomposed into its collinear k_+, anticollinear k_- and transverse component $k_\perp (k_T^2 = -k_\perp^2)$, by projecting it onto n and $\bar{n}$. The values of interest are the scalings of momenta in these components and their virtuality $\sqrt{k^2}$, described by the small expansion parameter $\lambda = \frac{q_T}{M}$ (Table 1). To receive the SCET Lagrangian one integrates out all hard modes, defined by their virtuality, in our case the produced boson. After a field redefinition even the soft modes decouple from the two collinear modes and one can match hadronic matrix-elements onto operators in SCET, which leads directly to a factorized cross section:

Mode	$\frac{1}{M}(k_+, k_-, k_T)$	Virtuality
Hard	$q \sim (\,1\,,\,1\,,\lambda\,)$	M
Collinear	$p \sim (\,1\,,\lambda^2\,,\lambda\,)$	$M\lambda \sim q_T$
Anticollinear	$\bar{p} \sim (\lambda^2,\,1\,,\lambda\,)$	$M\lambda \sim q_T$
Soft	$k \sim (\lambda^2, \lambda^2, \lambda^2)$	$M\lambda^2 \sim w$

Table 1: Scaling of involved particles.

$$\frac{\mathrm{d}^2\sigma}{\mathrm{d}q_T \mathrm{d}y} = A \cdot H \cdot \sum_{ij} Q_{ij} \cdot \tfrac{1}{4\pi} \int \mathrm{d}^2\vec{x}_\perp \mathrm{e}^{-i\vec{q}_\perp \vec{x}_\perp} \cdot W \cdot \mathcal{B}_{i/P_1} \mathcal{B}_{j/P_2} + \mathcal{O}\left(\lambda^2\right) . \tag{1}$$

The kinematic prefactor A is not affected by the matching and can contain the leptonic part describing the decay of the boson. H denotes the hard function depending only on the hard scale M and containing the Wilson coefficients. The hadronic matrix element factorizes in a soft function W and two collinear functions $\mathcal{B}$, which are summed over contributing partons with effective charges Q. The Wilson coefficients and thus the hard functions are known at least to two-loop order. The soft modes do not contribute, since the soft function is equal to $W = 1 + \mathcal{O}(\lambda)$ for all orders. The collinear functions $\mathcal{B}$ are generalized, x_T dependent parton-distribution-functions (PDF), and can be matched at the partonic level onto ordinary PDFs. So the cross section seems to be calculable straightforwardly, but there are more subtle obstacles due to the collinear anomaly, which will be discussed in the next section.

3 Collinear anomaly and infrared safety

Two problems appear in the factorized formula (1). The first one is related to the renormalization invariance. As a physical observable, the cross section should be invariant under the change of μ, thus its derivative with respect to μ has to give zero. The derivative of the hard

function is known and leads to terms proportional to logarithms of the hard scale M, which should be compensated by the derivatives of the other factors. But, in the absence of the soft contribution, there is no term depending on M, thus the cross section seems to be not scale invariant. The second problem appears in the matching of the generalized PDFs $\mathcal{B}$ onto ordinary PDFs, because they lead to integrals which cannot be regularized in dimensional regularization.

Both problems originate directly from the collinear anomaly (CA), a real quantum anomaly in SCET, in the sense that a symmetry is broken by quantum corrections. At LO the two collinear Lagrangians are invariant under the so-called rescaling transformation, which is given by multiplying all (anti-)collinear momenta by a real factor $(\bar{a})a$. But at higher orders, this symmetry is broken and restricted to $\bar{a} \cdot a \equiv 1$, thus the product $p \cdot \bar{p}$ proportional to M^2 is a new invariant in the EFT. Knowing the origin of the divergences, one can analytically regulate the one-loop diagrams in the matching procedure. A gauge invariant way is to change the phasespace integral according to [5]. One collinear function $\mathcal{B}$ alone is not well-defined, only their product is regulator independent and an anomalous dependency on the hard scale factors out, which ensures the RG invariance of the whole cross section:

$$\mathcal{B}_{i/P_1} \cdot \mathcal{B}_{j/P_2} \to \left(x_T^2 M^2\right)^{-F_{ij}\left(x_T^2,\mu\right)} \cdot B_{i/P_1}\left(x_T^2,\mu\right) \cdot B_{j/P_2}\left(x_T^2,\mu\right)$$

Now the two problems are solved, the only remaining question is the choice of the renormalization scale μ. The idea is of course to choose μ such that the not resummed logarithms remain small. The collinear functions B depend on μ via $L_\perp = \ln\left(x_T^2\mu^2\right)$, so the choice of the renormalization scale similar to the reciprocal transverse displacement $\mu \sim \frac{1}{x_T}$ would lead to small logarithms. But as an integration variable of the Fourier transformation, x_T is not an underlying scale of the process. The next idea could be to choose μ similar to the conjugate variable of x_T: $\mu \sim q_T$. To verify this choice one has to evaluate the Fourier integral. At LO this leads to the analytically solvable integral K_0 (2). At higher orders the only difference is the appearance of powers of $L_\perp$, so these integrals K_n can be written as derivatives of K_0 with respect to η (3), which makes obvious that the choice $\mu \sim q_T$ leads to small logarithms:

$$K_0 \sim \int \mathrm{d}^2\vec{x}_\perp \mathrm{e}^{-i\vec{q}_\perp\vec{x}_\perp} \cdot \mathrm{e}^{-\eta L_\perp} \sim \left(\frac{q_T^2}{\mu^2}\right)^\eta \frac{\Gamma(1-\eta)}{\Gamma(\eta)} \tag{2}$$

$$K_n = (-\partial_\eta)^n K_0 \sim \ln^n\left(\frac{q_T^2}{\mu^2}\right) \qquad \eta = \frac{\alpha_s}{4\pi}\Gamma_0 \ln\frac{M^2}{\mu^2} \tag{3}$$

The parameter η in the exponent of K_0 represents the M dependence originating from the CA. Choosing $\mu \sim q_T$, η is a small number at high q_T and increases as one lowers q_T. The solution of K_0 introduces a new scale q_*, where η becomes equal to 1 and K_0 diverges (Gamma function in 2). For the Z-boson this scale is around $q_*^Z \approx 1.8$ GeV and for the Higgs $q_*^H \approx 7.7$ GeV, so it lies in the perturbative domain $q_* > \Lambda_{NP}$.

To lower q_T beyond q_*, one has to dismiss the demand of small logarithms $\alpha_s L_\perp \sim \mathcal{O}(\alpha_s)$, so even at LO one has to take more terms in the exponent of K_0 into account. The next term is quadratic in $L_\perp$ and negative, so the integral becomes a Gaussian. Considering this integral at $\mu \sim q_*$ the Gaussian regulates it with an expectation value of $L_\perp \sim \mathcal{O}(1)$ and a standard deviation of $\mathcal{O}\left(1/\sqrt{\alpha_s}\right)$. By adopting a new power-counting with $\alpha_s^2 L_\perp \sim \mathcal{O}(1)$ and setting $\mu \sim \max[q_T, q_*]$, the terms of the CA lead to finite, resummed results, independent of the restriction $q_T > q_*$ or even $q_T > \Lambda_{NP}$. Thus the CA leads to infrared safety, in the sense that it gives the possibility to calculate the intercept at $q_T = 0$.

4 Conclusion and Outlook

The transverse-momentum distribution of Drell-Yan like processes is one of the most basic observables at hadron colliders. It nevertheless manifests a number of remarkable properties at low transverse-momentum. Our approach using SCET to factorize the differential cross section and resum large logarithms via RG-techniques, leads for the first time to an analytical result in momentum space, free of unphysical Landau-pole singularities. The CA creates a new scale q_*, which protects the cross section at vanishing transverse-momentum from non-perturbative effects, so it leads to infrared safety.

Numerical comparisons of our predictions with data on the transverse-momentum distribution in Z-boson production at the Tevatron and LHC are given in Fig. 1. They include the matching to NLO fixed-order calculations and the influence of long-distance effects, which are suppressed by q_*. The hard function is resummed using the π^2-resummation. The error bands are calculated by varying μ by a factor of two. All effects are discussed in detail in [2].

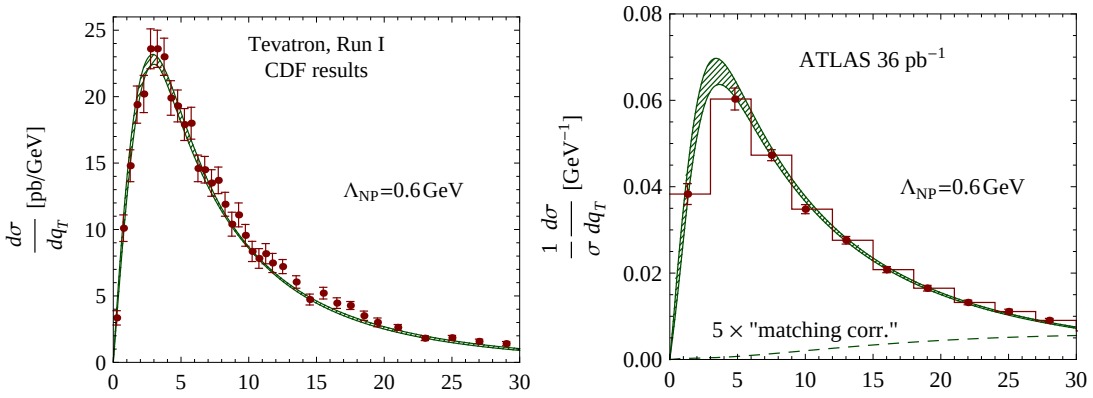

Figure 1: Transverse-momentum distribution compared with Tevatron Run I data from CDF [6] and LHC data from ATLAS [7].

Work in progress is the implementation of the lepton-tensor, in order to regard the experimental cuts and the extension to the Higgs-boson. In addition we need to match our resummed cross section to NNLO fixed-order results to extend our prediction to higher q_T. The next milestone in future will be to match the generalized PDFs at two-loop order, to improve our accuracy to the actual level of fixed-order calculations.

References

[1] T. Becher and M. Neubert. Eur.Phys.J. **C71** (2011) 1665, arXiv:1007.4005 [hep-ph].

[2] T. Becher, M. Neubert, and D. Wilhelm. JHEP **1202** (2012) 124, arXiv:1109.6027 [hep-ph].

[3] J. C. Collins, D. E. Soper, and G. F. Sterman. Nucl.Phys. **B250** (1985) 199.

[4] V. Sudakov. Sov.Phys.JETP **3** (1956) 65–71.

[5] T. Becher and G. Bell. arXiv:1112.3907 [hep-ph].

[6] T. Affolder *et al.* Phys.Rev.Lett. **84** (2000) 845–850, arXiv:hep-ex/0001021 [hep-ex].

[7] G. Aad *et al.* Phys.Lett. **B705** (2011) 415–434, arXiv:1107.2381 [hep-ex].

Measurement of Normalised Multi-jet Cross Sections using Regularised Unfolding and Extraction of $\alpha_s(M_Z)$ in DIS at High Q^2

Daniel Britzger[1] on behalf of the H1 Collaboration

[1]DESY, Notkestraße 85, 22607 Hamburg, Germany

DOI: http://dx.doi.org/10.3204/DESY-PROC-2012-02/163

New results on normalised inclusive jet, dijet and trijet differential cross sections in neutral current DIS based on a regularised unfolding procedure are presented. Compared to a previously published result on normalised multi-jet cross sections, the new features are an extended range in jet pseudorapidity, an improved hadronic energy scale uncertainty of 1% and the application of an unfolding procedure. The normalised jet cross sections are compared to QCD calculations at NLO. The value of the strong coupling determined from the normalised inclusive jet, dijet and trijet measurements simultaneously is $\alpha_s(M_Z) = 0.1163 \pm 0.0008\,\text{(exp.)} \pm 0.0011\,\text{(sys.)}^{+0.0044}_{-0.0035}\,\text{(theo.)} \pm 0.0014\,\text{(PDF)}$.

1 Introduction

Jet production in neutral current DIS at HERA provides an important testing ground for QCD. The measurement of jet quantities is directly sensitive to the strong coupling α_s and can give constraints on the gluon density in the proton. Furthermore, it is a valuable benchmark process for Monte Carlo event generators, particularly with regard to parton showers. Two different kinds of jet measurements can be distinguished. Inclusive jet measurements, where each single jet is counted, and jet measurements like dijet and trijet measurements, where each event that fulfills topological and kinematic criteria on jet quantities contributes to the cross section once. Both approaches allow to extract the strong coupling by comparing to perturbative QCD predictions.

The measurement presented here is based on data with an integrated luminosity of 361 pb^{-1} collected in the years 2003 - 2007 with the H1 detector [1]. The data are identical to a previous H1 analysis of absolute jet cross sections [2]. This analysis is extended to normalised cross sections, where the normalisation is performed with respect to the NC DIS cross section. In [2] and in the analysis reported here, improvements on the reconstruction of tracks and the calorimetric energy were applied [3]. The correction of detector effects to determine the particle level cross section is performed using a regularised unfolding procedure and is presented in more detail in this document.

2 Phase space definition

The NC DIS events are selected by requiring an identified scattered electron, a virtuality of the exchanged boson (γ/Z^0) of $150 < Q^2 < 15000\,\mathrm{GeV}^2$ and an inelasticity of the interaction of $0.2 < y < 0.7$. The jet finding is performed in the Breit frame of reference where the exchanged boson is completely space-like. Particle candidates of the hadronic final state are clustered into jets using the inclusive k_T algorithm [4] with a distance parameter $R_0 = 1$, as implemented in the FastJet package [5]. The jets are required to be in the pseudorapidity range in the laboratory rest frame between $-1.0 < \eta^\mathrm{jet}_\mathrm{lab} < 2.5$, and the jet momentum in the Breit frame is required to be $7 < P_\mathrm{T} < 50$ GeV. Events with at least two (three) jets with transverse momentum larger than 5 GeV are considered as dijet (trijet) events if the two leading jets of the measured observables have an invariant mass M_{jj} exceeding 16 GeV. For events that fulfill the dijet (trijet) criteria, the average transverse momentum is $\langle P_\mathrm{T}\rangle = \frac{1}{N}\sum_i^N P_\mathrm{T}^{\mathrm{jet},i}$, with $N = 2(3)$. All three double differential jet measurements are normalised to the inclusive NC DIS measurement as function of Q^2. The advantage of the normalised jet cross sections compared to absolute jet cross sections [2] are reduced systematic uncertainties on the experimental as well as on the theoretical side.

3 Detector correction using regularised unfolding

Due to kinematic migrations because of resolution and other effects and due to the limited acceptance of the detector, the data have to be corrected. For this purpose a multidimensional regularised unfolding procedure, including all correlations, is applied. This procedure makes use of a migration matrix A that connects the *particle level*, represented by the vector x, with the *detector level*, represented by the vector y, such that the equation $y = Ax$ holds. The particle level distribution x is determined using the TUNFOLD package [6]. The χ^2-function

$$\chi^2(x) = (y - A\cdot x)^T\ V_{yy}^{-1}\ (y - A\cdot x) + \tau^2(x - x_0)^T(L^TL)(x - x_0) \tag{1}$$

is minimised analytically as a function of x, where V_{yy} is the covariance matrix, and x_0 is the bias distribution. The Tikhonov regularisation parameter τ protects the result from large fluctuations, and a regularisation condition for the matrix L the unit matrix is chosen.

The unfolding is performed using a single matrix A with an overall 4×4 structure that allows to unfold four measurements (NC DIS, inclusive jets, dijet, trijet) all at once and further gives the possibility to determine the normalised cross sections taking all correlations into account (see sec. 4). The four diagonal elements are submatrices that describe the migrations of just one single measurement.

NC DIS submatrix: The migrations of the NC DIS measurements are described in two dimensions, i.e. in the kinematic variables y and Q^2. The NC DIS data are used to determine the normalised jet cross sections.

Inclusive jets submatrix: The inclusive jet measurement is a measurement of jet multiplicities, where jets are defined by the jet algorithm independently on particle level and on detector level. This implies that jets have to be connected between both levels. A geometric jet matching method based on a closest pair algorithm with a distant measure $R = \sqrt{\Delta\phi^2 + \Delta\eta^2}$ and a maximum distance of $R < 0.9$ is applied. This ensures that no kinematical biases are introduced.

Matched jets are filled into the submatrix of the inclusive jets in a three-dimensional unfolding scheme in the variables P_{T}, Q^2 and y. Jets that appear on generator level only are treated as inefficiencies. Jets that appear on detector level only are difficult to handle and cause a large error on the overall normalisation if not handled properly. Detector-level-only jets do not have particle level jet quantities, but still event observables on particle level are known. These jets are filled into the submatrix that connects the detector level inclusive jets to the particle level NC DIS measurement. The normalisation of the NC DIS measurement is preserved by adding negative weights to the efficiency accordingly.

Dijet and trijet submatrices: The unfolding of the dijet and trijet measurement is performed in a three dimensional unfolding scheme in the kinematic variables $\langle P_{\mathrm{T}} \rangle$, Q^2 and y. Additional bins describe migrations in and out of the dijet and trijet phase space. Migrations in the kinematic variables $M_{jj} > 16$ GeV, $P_{\mathrm{T}}^{\mathrm{jet2}} > 5$ GeV and requirements on $\eta_{\mathrm{lab}}^{\mathrm{jet}}$ are taken into account. Similarly as for the inclusive jets, events that do not fulfill the dijet (trijet) requirements on particle level but on detector level are estimated by the NC DIS events.

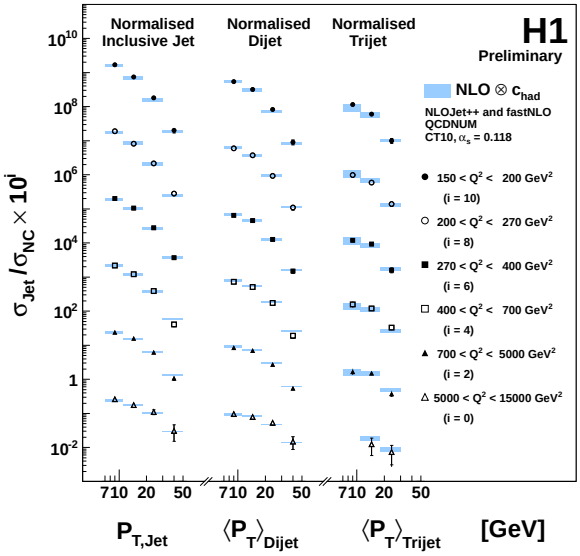

Figure 1: Normalised inclusive jet, dijet and trijet measurements in six bins of the virtuality of the exchanged boson Q^2 and in bins of the transverse jet momentum P_{T} in the Breit frame or the average transverse momentum of the two (three) leading jets $\langle P_{\mathrm{T}} \rangle$, respectively. The correlated statistical errors are shown by the inner error bars which are mostly smaller than the marker size. The outer error bar shows the total experimental uncertainty, incorporating all systematic experimental uncertainties. The data are corrected for detector effects using a regularised unfolding technique. The measurements are compared to next-to-leading order QCD calculations using the CT10 PDF set. They are corrected for hadronisation effects. The theory predictions include uncertainties determined by scale variations of a factor 2 up and down.

The covariance matrix on detector level V_{yy} is determined by data and contains the statistical uncertainty and all correlations between the four measurements. The unfolded covariance matrix V_{xx} on particle level is determined by error propagation through the unfolding process and holds information on the correlations resulting from detector effects as well as the propagated correlations between the single measurements.

4 Result

4.1 Normalised multijet cross sections

Each bin of the jet measurements is normalised with the corresponding bin of the inclusive NC DIS measurement. The covariance matrix of all three normalised jet measurements is determined by a full error propagation using the covariance matrix V_{xx}. Also the systematic errors are determined by a full error propagation. This procedure is equivalent to a direct measure of normalised jet cross sections. The normalised inclusive jet, dijet and trijet measurements are shown in Fig. 1, where they are compared to pQCD predictions which show a good agreement over the full phase space.

4.2 Determination of the strong coupling constant

The strong coupling is determined by performing a χ^2-minimisation procedure to all three normalised jet measurements simultaneously with $\alpha_s(M_Z)$ as a free parameter. The theory calculations are performed using the QCDNUM program [7] for the NC DIS cross sections and the NLOJET++ program [8, 9] interfaced to FASTNLO [10, 11] for a fast repeated calculation of the jet cross sections using the CT10 PDF set [12]. The χ^2-definition includes the full covariance matrix after the unfolding and takes into account systematic uncertainties using nuisance parameters. In order to consider only bins that show a fast convergence, bins with large k-factors of $k > 1.3$ are excluded from the fit, where $k = \sigma_{\mathrm{NLO}}/\sigma_{\mathrm{LO}}$. The resulting fit takes contributions from 42 out of 65 bins into account and shows a reasonable χ^2/ndf of 53/41. The resulting $\alpha_s(M_Z)$ is determined to be

$$\alpha_s(M_Z) = 0.1163 \pm 0.0008\ (\mathrm{exp.}) \pm 0.0011\ (\mathrm{had.}) \pm 0.0014\ (\mathrm{pdf})\ ^{+0.0044}_{-0.0035}\ (\mathrm{theo.}).$$

This result is consistent with previous H1 publications of normalised multi-jet cross sections [13]. The uncertainties from hadronisation corrections (had.), the PDF uncertainty (pdf) and theoretical uncertainties from missing higher orders (theo.) are determined by repeating the fit with shifted theory cross sections. Each of the theoretical uncertainties is larger than the total experimental uncertainty. The result is consistent with the world average within the errors [14].

References

[1] H1 Collaboration. preliminary result: H1prelim-12-031 (2012) .

[2] H1 Collaboration. preliminary result: H1prelim-11-032 (2011) .

[3] R. Kogler. PhD thesis, Universität Hamburg, DESY-THESIS-2011-003, MPP-2010-175, 2011.

[4] S. D. Ellis and D. E. Soper. Phys. Rev. D **48** (1993) 3160.

[5] M. Cacciari, G. P. Salam, and G. Soyez. Eur.Phys.J. **C72** (2012) 1896, arXiv:1111.6097 [hep-ph].

[6] S. Schmitt. arXiv:1205.6201 [physics.data-an].

[7] M. Botje. Comput.Phys.Commun. **182** (2011) , arXiv:1005.1481 [hep-ph].

[8] Z. Nagy and Z. Trocsanyi. Phys. Rev. D **59** (1999) 14020.

[9] Z. Nagy and Z. Trocsanyi. Phys. Rev. Lett. **87** (2001) 82001.

[10] M. Wobisch *et al.* arXiv:1109.1310 [hep-ph].

[11] D. Britzger *et al.* these proceedings (2012) .

[12] H.-L. Lai *et al.* Phys.Rev. **D82** (2010) 074024, arXiv:1007.2241 [hep-ph].

[13] F. Aaron *et al.* Eur.Phys.J. **C65** (2010) , arXiv:0904.3870 [hep-ex].

[14] S. Bethke. Eur. Phys. J. C **64** (2009) 689.

Inclusive-jet photoproduction at HERA and determination of α_s

Ewald Paul[1] on behalf of the ZEUS Collaboration

[1]Physikalisches Institut Bonn, Germany

DOI: http://dx.doi.org/10.3204/DESY-PROC-2012-02/43

Differential inclusive-jet cross sections have been measured in photoproduction with the ZEUS detector at HERA at a centre-of-mass energy of 318 GeV using an integrated luminosity of 300 pb^{-1}. Cross sections are presented as functions of the jet pseudorapidity, η^{jet}, and the jet transverse energy, E_T^{jet}. of η^{jet}. The cross sections have the potential to constrain the gluon density in the proton and the photon when included as input to fits to extract the proton parton distribution functions. Next-to-leading order QCD calculations give a good description of the measurements. The value of the strong coupling constant $\alpha_S(M_Z)$ has been extracted from the measurement. The energy-scale dependence of α_S has been determined in the range $17 < E_T^{\mathrm{jet}} < 71$ GeV.

1 Introduction

The study of jet production in ep collisions at HERA has been well established as a testing ground of perturbative QCD. Jet cross sections provide precise determinations of the strong coupling constant, α_S, and its scale dependence.

2 Cross sections in comparison to NLO-QCD predictions

Cross sections of inclusive-jet photoproduction were measured as functions of E_T^{jet} and η^{jet} in the kinematic range $Q^2 < 1\,\mathrm{GeV}^2$, $142 < W_{\gamma p} < 293$ GeV, $E_T^{\mathrm{jet}} > 17$ GeV and $-1 < \eta^{\mathrm{jet}} < 2.5$. Jets were identified in the laboratory system using the k_T cluster algorithm [4] in the longitudinally invariant inclusive mode [5] with the radius set to unity. Differential cross sections $d\sigma/dE_T^{\mathrm{jet}}$ and $d\sigma/d\eta^{\mathrm{jet}}$ are shown in figs. 1 and 2 respectively. The experimental errors include statistical and systematic errors except the jet-energy uncertainty which is shown separately. The cross sections are compared to NLO QCD predictions based on a program witten by M. Klasen, T. Kleinwort and G. Kramer [1]. In this program, renormalisation and factorisation scale were set to E_T^{jet}. The implemeted parton densities were ZEUS-S for the proton[2] and GRV-HO for the photon [3]. The predictions were calculated on parton level, and corrected to hadron level using Monte Carlo simulations (PYTHIA and HERWIG). In general the data are well described by the predictions. However, some differences are visible at small E_T^{jet} and large η^{jet}. The differences seen for η^{jet} are reduced if the cut on E_T^{jet} is raised to 21 GeV [6].

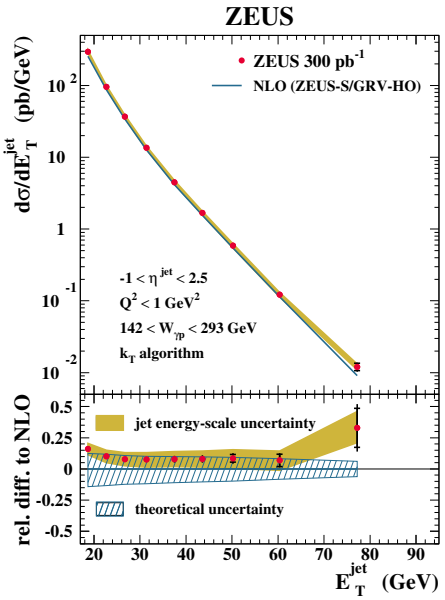

Figure 1: The cross section $d\sigma/dE_T^{\rm jet}$ compared to NLO QCD predictions. Shaded band: energy scale uncertainty of the jets. Hatched band: total theoretical uncertainty.

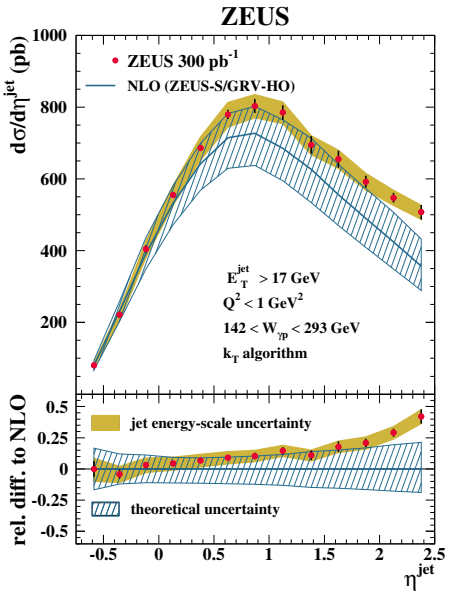

Figure 2: The cross section $d\sigma/d\eta^{\rm jet}$. Other details are the same as in Fig. 1.

3 Dependence on model asumptions

To access the influence of the jet algorithm , cross sections were also studied with the jet algorithms anti-k_T [7] and SIScone [8]. It has been noticed that no significant differences in the comparison between data and predcitions were observed.

Another study was carried out using the Monte-Carlo program PYTHIA-MI for hadronisation corrections. This program includes non-perturbative multi-parton interactions [9]. As can be seen in Fig. 3, the prediction for the $\eta^{\rm jet}$ distribution can be improved by including multi-parton interactions with an appropriate cut on the transverse momentum of the scattered parton. The prediction with $p_{T,\rm min}^{\rm sec} = 1.5\,\text{GeV}$ is closest to the data.

4 Dependence on the choice of PDFs

Predictions were caculated using the AFG04[10] and CJK[11] photon PDFs instead of GRV-HO. Figure 4 shows the comparison between the measured cross sections and the predictions based on different photon PDFs. The uncertainty coming from the photon PDFs is largest at low $E_T^{\rm jet}$ and high $\eta^{\rm jet}$ and approximately ofthe order of the theoretical uncertainty. The measured cross sections are, on a similar level, sensitive to proton PDFs[6]. This implies that the measured cross sections have the potential to constrain the gluon density in photon and proton when used as input to a global fit.

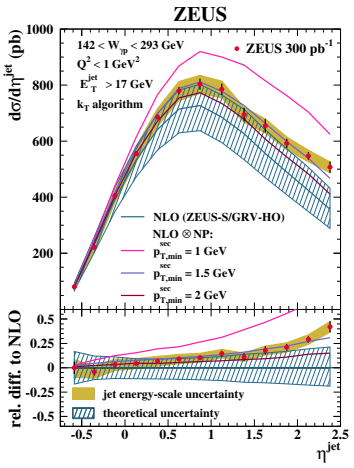

Figure 3: The cross section $d\sigma/d\eta^{\text{jet}}$ compated to NLO QCD predictions including multi-parton interactions.

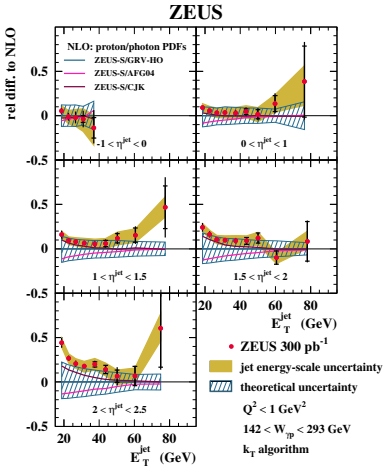

Figure 4: Relative differences between measured and predicted cross sections for several photon PDFs. (Default: GRV-HO).

5 Measurement of $\alpha_S(M_Z)$ and the α_S energy scale dependence

Differential cross sections $d\sigma/dE_T^{\text{jet}}$ measured in the range $21 < E_T^{\text{jet}} < 71\,\text{GeV}$ were used to determine values of the strong coupling constant α_S using the method presented previously [12]. The fit was restricted to $E_T^{\text{jet}} < 71\,\text{GeV}$ because of the uncertainty coming from the photon PDFs for higher E_T^{jet} values. The value of $\alpha_S(M_Z)$ was determined by fitting NLO QCD predictions to the $d\sigma/dE_T^{\text{jet}}$ distribution [6]. The fit obtained with the k_T algorithm yielded: $\alpha_S(M_Z) = 0.1206^{+0.0023}_{-0.0022}(exp.)^{+0.0042}_{-0.0035}(th.)$. The value is in good agreement with the world and HERA averages and the errors are comparable to those of other recent measurements.

The energy scale dependence of α_S was determined from NLO QCD fits without assumung the running of α_S [6]. The result, shown in fig. 5, demonstrates the running of α_S over a large range in E_T^{jet}. The predicted running calculated in two loops [13] is in good agreement with the data.

6 Summary

Inclusive-jet photoproduction was measured with the ZEUS detector at the *ep* collider HERA. Cross sections were calculated as functions of E_T^{jet} and η^{jet}. In general they are well described by NLO QCD predictions. Three jet algorithms were studied with respect to the comparison of data and predictions showing that the observed differences are small. Studies of multi-parton interactions have shown that their inclusion improves the description of the jet rates at low E_T^{jet} and high η^{jet}. The measured cross sections have the potential to improve PDFs of photon and proton when included in a global fit. The strong coupling constant α_S was determined at the mass of the Z boson and energy scaling was observed over a wide range of E_T^{jet}.

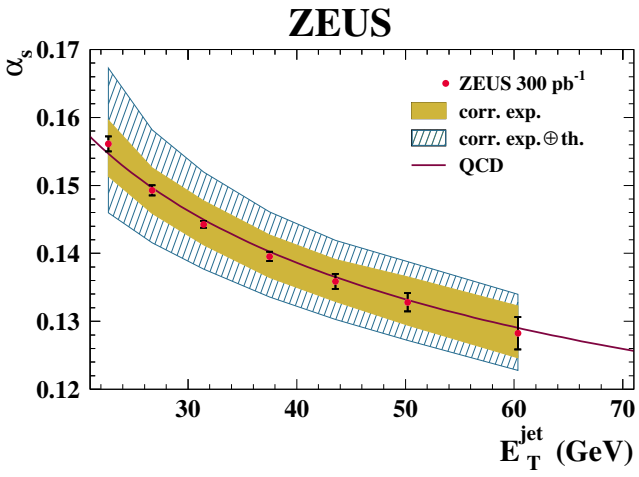

Figure 5: Dependence of α_S on $E_T^{\rm jet}$ as scaling variable. Solid line: normalisation group prediction. Error bars: uncorrelated experimetnal errors. Shaded band: correlated experimental errors. Hatched band: correlated experimental and theoretical errors added in quadrature.

References

[1] M. Klasen *et al.* Eur. Phys. J. Direct **C1** (1998) 1.

[2] ZEUS Collaboration, S. Chekanov *et al.* Phys. Rev. **D67** (2003) 012007.

[3] M. Glück *et al.* Phys. Rev. **D45** (1992) 3986; M. Glück *et al.* Phys. Rev. **D46** (1992) 1973.

[4] S. Catani *et al.* Nucl. Phys. **B406** (1993) 87.

[5] S. D. Ellis and D. E. Soper, Phys. Rev. **D48** (1993) 3160.

[6] ZEUS Collaboration, H. Abramovicz *et al.* DESY 12-045 (March 2012.

[7] M. Cacciari *et al.* JHEP **0804** (2008) 063.

[8] G. P. Salam and G. Soyez, JHEP **0705** (2007) 086.

[9] T. Sjöstrand and M. van Zijl, Phys. Rev. **D36** (1987) 2019.

[10] P. Aurenche *et al.* Eur. Phys. J. **C44** (2005) 395.

[11] F. Cornet *et al.* Phys. Rev. **D70** (2004) 093004.

[12] ZEUS Collaboration, S. Chekanov *et al.* Phys. Lett. **B547** (2002) 164.

[13] D. J. Gross and F. Wilczek, Phys. Rev. Lett. **30** (1973) 1343; H. D. Politzer, Phys. Rev. Lett. **30** (1973) 3633; D. J. Gross and F. Wilczek, Phys. Rev. **D8** (1973) 3633; H. D. Politzer, Phys. Rep. **14** (1974) 129.

Spectra of Charged Pions, Kaons, and Protons Identified via Tracker Energy Loss from CMS

Ferenc Siklér[1] for the CMS Collaboration

[1]Wigner RCP, Budapest, Hungary

DOI: http://dx.doi.org/10.3204/DESY-PROC-2012-02/182

Measured spectra of identified charged hadrons produced in pp collisions at $\sqrt{s} = 0.9$, 2.76, and 7 TeV are presented in the transverse momentum range $p_{\mathrm{T}} \approx 0.1$–$1.7$ GeV/c at midrapidity ($|y| < 1$). The charged pions, kaons, and protons are identified using the measured energy loss in the silicon tracker and other track information. The fully corrected primary p_{T} spectra and integrated yields are compared to various tunes of the PYTHIA6 and PYTHIA8 event generators. The average p_{T} for pions, kaons, and protons increases rapidly with the mass of the hadron and the event charged-particle multiplicity, independent of the center-of-mass energy.

1 Introduction

The study of particle production in hadronic collisions has a long history in high energy physics, nuclear physics, and cosmic-ray physics. The measurement of particle spectra is important for studying the scaling properties of particle production and to test predictions of models and Monte Carlo event generators. Details of the analysis can be found in [1].

2 Data analysis

The CMS detector is described in [2]. Particle reconstruction is bounded by the acceptance of the tracker, while particle identification capabilities are limited to $p < 0.16$ GeV/c for electrons, $p < 1.20$ GeV/c for pions, $p < 1.05$ GeV/c for kaons, and $p < 1.70$ GeV/c for protons. The physics results will be presented in the range $-1 < y < 1$. The statistical uncertainties of the measurement are negligible.

The selected event sample is corrected to a well-defined particle-level selection to ease comparison with generator-level predictions. In this study a double-sided (DS) selection was chosen. It is close to the actual hardware trigger and software selections: at least one particle with $E > 3$ GeV on each side ($-5 < \eta < -3$ and $3 < \eta < 5$). According to several PYTHIA tunes, the overall efficiency of this double-sided selection to the total inelastic cross-section is about 66-72% (0.9 TeV), 70-76% (2.76 TeV), and 73-78% (7 TeV). Mostly non-diffractive events are selected, but a smaller fraction of single- or double-diffractive events are accepted as well.

The special tracking and the agglomerative vertex-reconstruction algorithm used in the analysis are the same as for the previous papers on unidentified spectra [3, 4] which provides high reconstruction efficiency with low background rate.

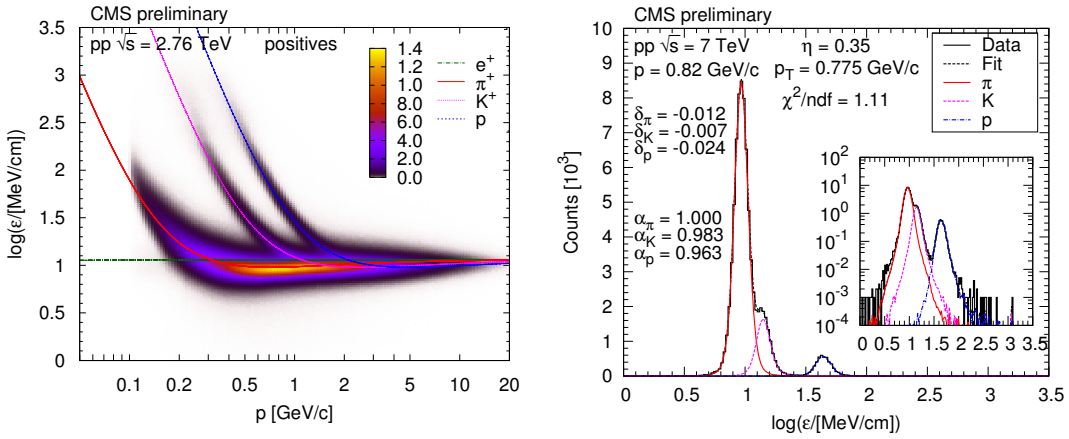

Figure 1: Left: Distribution of $\log \varepsilon$ values as a function of total momentum p in case of the 2.76 TeV dataset, for positives particles. Right: Example $\log \varepsilon$ distribution for the 7 TeV inclusive dataset. The curves are the results of template fits.

The silicon layers are thin and the individual energy deposits are not Gaussian-distributed but show a long tail of higher values. The energy loss of charged particles in silicon can be approximated by a simple analytical model [5]. It gives the probability density $p(y|\varepsilon, l)$ of energy deposit y, if the *most probable energy loss rate* ε at a reference path length of l_0, and the path length l inside the silicon are known. In this analysis the model is used in connection with maximum likelihood estimation to calibrate the gain of the detector elements, in our case the readout chips, and is applied to the energy loss rate estimation of tracks (Fig. 1). For details see [1].

3 Results

In previously published measurements of unidentified and identified particles, the following form of the Tsallis-Pareto-type distribution [6, 7] was used:

$$\frac{d^2N}{dydp_{\mathrm{T}}} = \frac{dN}{dy} \cdot C \cdot p_{\mathrm{T}} \left[1 + \frac{(m_{\mathrm{T}} - m)}{nT}\right]^{-n}$$

where C is a normalization constant, and $m_{\mathrm{T}} = \sqrt{m^2 + p_{\mathrm{T}}^2}$. The above formula is a useful parametrization of the data for extrapolating the spectra to $p_{\mathrm{T}} = 0$ and for obtaining $\langle p_{\mathrm{T}} \rangle$ and dN/dy.

The fully corrected transverse momentum distributions of positive and negative hadrons (pions, kaons, protons) are shown in Fig. 2, plotted with fits to the Tsallis-Pareto parametrization. Comparisons to PYTHIA tunes show that tunes D6T and 4C are systematically below or above the spectra, whereas Z2 is generally closer to the measurements (except for low-p_{T} protons). The ratios of oppositely charged particles are around one as expected for pair-produced particles at midrapidity.

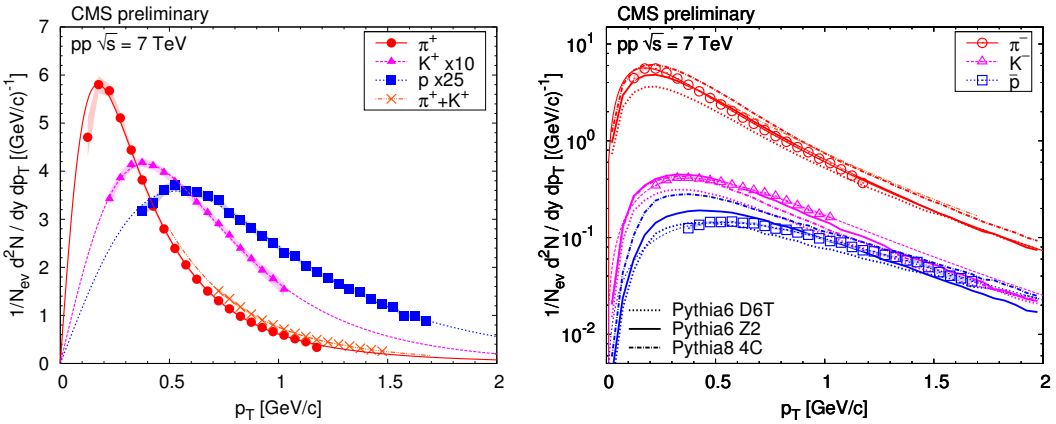

Figure 2: Transverse momentum distributions of identified charged hadrons (pions, kaons, protons) in the range $|y| < 1$, for positives (left) and negatives (right), at $\sqrt{s} = 7$ TeV. Kaons and protons are scaled as shown. Fits to Eq. (3) or predictions of PYTHIA tunes are superimposed.

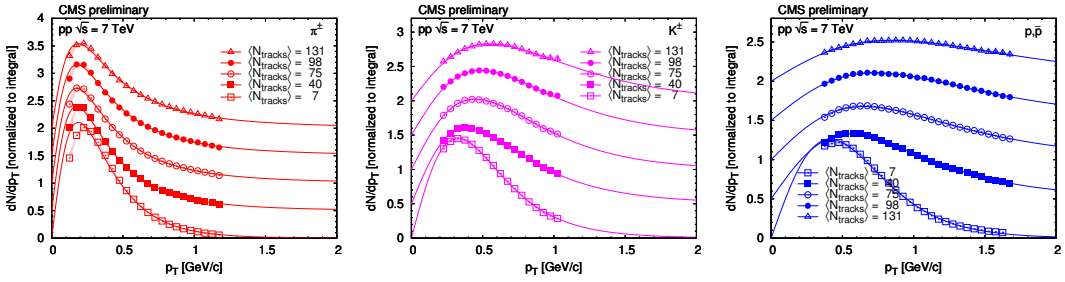

Figure 3: Normalized transverse momentum distributions of charged pions, kaons, protons in a few representative multiplicity classes, in the range $|y| < 1$, at $\sqrt{s} = 7$ TeV, fitted to the Tsallis-Pareto parametrization (solid lines). For visibility, the values with increasing multiplicity are successively shifted by 0.5 units along the vertical axis.

The study of the multiplicity dependence of the various observables considered here is motivated by the intriguing hadron correlations observed in pp collisions at high track multiplicities [8]. To this end, 12 event classes are defined, according to the number of reconstructed particles. In order to facilitate comparisons with models, the corresponding true track multiplicity in the range $|\eta| < 2.4$ (N_{tracks}) was determined from models. Normalized transverse momentum distributions of identified charged hadrons in selected multiplicity classes, in the range $|y| < 1$, at $\sqrt{s} = 7$ TeV are shown in Fig. 3. In case of pions the distributions are remarkably similar, in practice independent of $\sqrt{s}$ and multiplicity. For kaons and protons there is a clear evolution as the multiplicity increases.

Ratios of particle yields as a function of multiplicity in $|\eta| < 2.4$ reveal that K/π and p/π ratios are flat as a function of N_{tracks}. The universality of $\langle p_{\text{T}} \rangle$ and particle ratios versus track

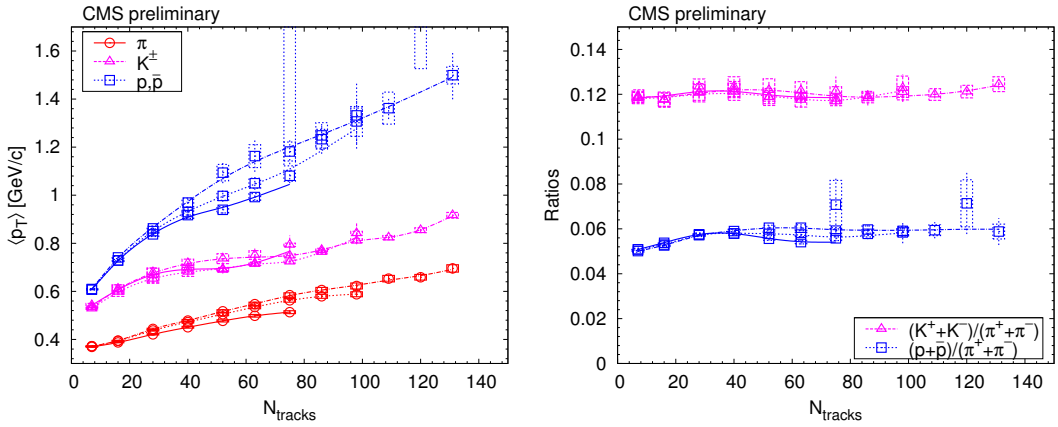

Figure 4: Left: Average transverse momentum of identified charged hadrons (pions, kaons, protons) in the range $|y| < 1$, for all particle types. Right: Ratios of particle yields. Both plots are given as a function of particle multiplicity in $|\eta| < 2.4$.

multiplicity, independent of the collision energy, is demonstrated in Fig. 4.

4 Summary

Measured spectra of identified charged hadrons produced in pp collisions at $\sqrt{s} = 0.9$, 2.76, and 7 TeV were presented. The obtained p_{T} spectra and integrated yields were compared to models. The multiplicity dependence of the rapidity-density and the average transverse momentum indicates that particle production at LHC energies is strongly correlated with event multiplicity rather than with the center-of-mass energy of the collision. This correlation can have a common deeper reason: at TeV energies, the characteristics of particle production in hadronic collisions are constrained by the amount of initial parton energy that is available in any given collision.

The author wishes to thank to the Hungarian Scientific Research Fund (K 81614), and the Swiss National Science Foundation (128079) for support.

References

[1] CMS Collab., CMS PAS FSQ-12-014 (2012).

[2] CMS Collab., S. Chatrchyan *et al.*, JINST **3** (2008) S08004.

[3] CMS Collab., V. Khachatryan *et al.*, JHEP **1002** (2010) 041.

[4] CMS Collab., V. Khachatryan *et al.*, Phys. Rev. Lett. **105** (2010) 022002.

[5] F. Sikler, "A simple energy loss model and its applications for silicon detectors," `arXiv:1111.3213`.

[6] C. Tsallis, J. Statist. Phys. **52** (1988) 479.

[7] T. S. Biro, G. Purcsel and K. Urmossy, Eur. Phys. J. A **40** (2009) 325.

[8] CMS Collab., V. Khachatryan *et al.*, JHEP **1009** (2010) 091.

Inclusive Particle Production

Markward Britsch[1] on behalf of LHCb collaboration

[1]Max-Planck-Institut für Kernphysik, Saupfercheckweg 1, 69117 Heidelberg, Germany

DOI: http://dx.doi.org/10.3204/DESY-PROC-2012-02/142

The LHCb detector has a unique pseudorapidity coverage and low transverse momentum theshold. These properties allow for measurements providing unique insight into particle production in the forward region at the LHC. The latest LHCb soft-QCD results, the measurements of charged particle multiplicity at 7 TeV and the measurement of the $\bar{p}/p$, K^-/K^+, π^-/π^+, $(\bar{p}+p)/(\pi^-+\pi^+)$, $(K^-+K^+)/(\pi^-+\pi^+)$ production ratios at 0.9 TeV and 7 TeV are presented. These results offer an important input to the understanding of baryon transport and of the hadronization process in a kinematical range where QCD models have large uncertainties.

1 Introduction

The LHCb detector [1] at the LHC at CERN covers a unique kinematic range for tracks of $2 < \eta < 5$ and down to $p_{\mathrm{T}} \approx 0$. It is a forward spectrometer optimized for b- and c-physics, has an excellent vertex resolution due to its vertex detector (VELO) and good $\pi/K/p$ separation due to its two RICH detectors. The trigger used in the analyses presented in this contribution is a trigger with minimal bias, requiring just one track in the VELO.

The measurement of inclusive particle production delivers important input to models of pp interactions. Measurements provide essential input for the tuning of event generators and the modeling of the underlying event. They can also be used to test predictions of particle production and hadronization models. Finally they can probe baryon number transport mechanisms. The forward region is of special interest as it is much less covered by other experiments and QCD models have large uncertainties.

In the remainder of this contribution the measurements of charged particle multiplicities and densities will be discussed in Section 2. This will be followed by the description of the measurements of the hadron ratios in Section 3. Note that measurements of strange particle production [2, 3, 4] are not included in this summary.

2 Charged particle multiplicity

LHCb has measured the multiplicity of primary charged particles [5], i.e., those directly produced in pp-collisions, or from short lived decays. In this measurement only information from the VELO, the silicon vertex detector which has a low material budget, was used (except for defining hard events, see below). The measurement is performed in a uniform acceptance and high efficiency range of $2 < \eta < 4.5$ ("forward"), $-2.5 < \eta < -2$ ("backward"). There is no magnetic field in the VELO, thus tracks are straight lines and we apply no explicit momentum

cut. We used $1.5 \cdot 10^6$ pp events of each magnet polarity at $\sqrt{s} = 7$ TeV from the low luminosity running phase in 2010 with a low pile up of 3.7 %. To select primary particles from pp-collisions we cut on the minimal track distance to the beam line and select only particles from the "luminous region" in beam line direction. In addition to suppress fake tracks we apply track quality cuts. There are two background sources that have to be corrected for. We carry out per event corrections for remaining fake tracks [5] and for remaining non-prompt particles, i.e., gamma conversions and V^0s. Using unfolding we correct for migrations due to reconstruction efficiency. Finally we do a correction for the small pile up to get the result for single interactions.

Figure 1 shows the multiplicity distribution in the forward range with comparison to different MC tunes. Only events with at least one track in the forward range are accepted. All generators underestimate the charged particle multiplicity. Agreement is improved if diffractive processes are excluded in Pythia.

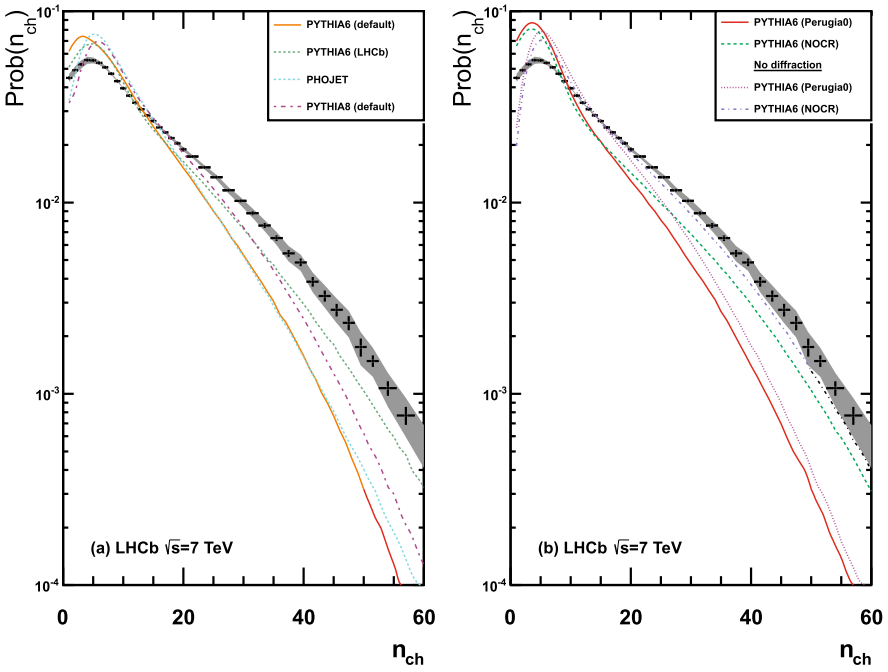

Figure 1: Charged particle multiplicity in the forward region in comparison to MC tunes.

The multiplicity distribution in the forward range for hard events, i.e., events with at least one track with $p_T > 1$ GeV, are better described by MC, where the best agreement is achieved with PYTHIA in LHCb [6] and NOCR [7] tuning. Figure 2 shows the particle densities where only events with at least one track in the forward direction were accepted in data as well as in MC. The charged particle density is larger than in the standard MC prediction. The models without diffractive processes provide a better quantitative description but fail to describe the shape. The details of this analysis are given in [5].

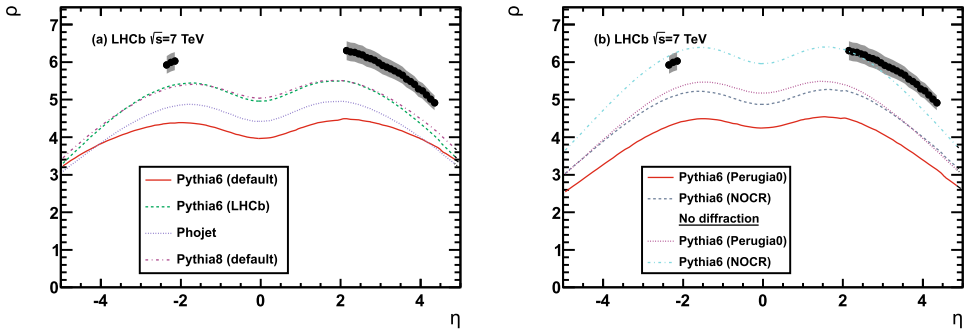

Figure 2: Charged particle densities with at least one track in the forward region.

3 Hadron production ratios

LHCb has measured the production ratios of $\frac{\overline{p}}{p}$, $\frac{K^-}{K^+}$, $\frac{\pi^-}{\pi^+}$, $\frac{\overline{p}+p}{K^-+K^+}$, $\frac{\overline{p}+p}{\pi^-+\pi^+}$ and $\frac{K^-+K^+}{\pi^-+\pi^+}$. The measurements are performed at $\sqrt{s} = 900$ GeV (0.3 nb^{-1}) and $\sqrt{s} = 7$ TeV (1.8 nb^{-1}). Prompt particles with $p > 5$ GeV are selected with particle identification (PID) requirements. The efficiency and purity of the PID are evaluated on data using a tag and probe method on $\phi \to K^+K^-$, $K^0_{\rm s} \to \pi^+\pi^-$ and $\Lambda \to \pi p$. The measurements are done in bins of $p_{\rm T}$ and η. The cross contamination effect due to PID misidentification is taken from the calibration samples. The correction of particle losses due to interaction with material is extracted from MC.

Figures 3 and 4 show a sample of the results in comparison to different MC tunes. There are some disagreements while the NOCR [7] and LHCb [6] tunes describe the data best. The complete plots can be found in the slides of the talk [8]. Using the rapidity loss $\Delta y = y_{\rm beam} - y$ used to compare data from different $\sqrt{s}$, was used to compare our results with those from other experiments. The LHCb data is consistent with previous experiments but significantly more precise. The full details of the analysis and the results will be give in a paper [9].

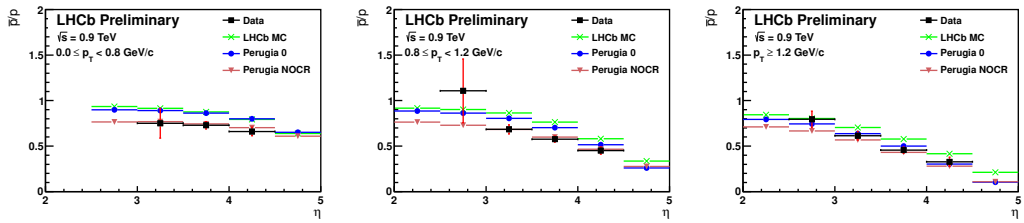

Figure 3: $\frac{\overline{p}}{p}$, $\sqrt{s} = 900$ GeV Left to right: $0 < p_{\rm T} < 0.8$ GeV, $0.8 < p_{\rm T} < 1.2$ GeVand $p_{\rm T} > 1.2$ GeV. Black is data where the black error bars are the statistical errors (mostly invisible) and the red (grey) error bars are systematic errors.

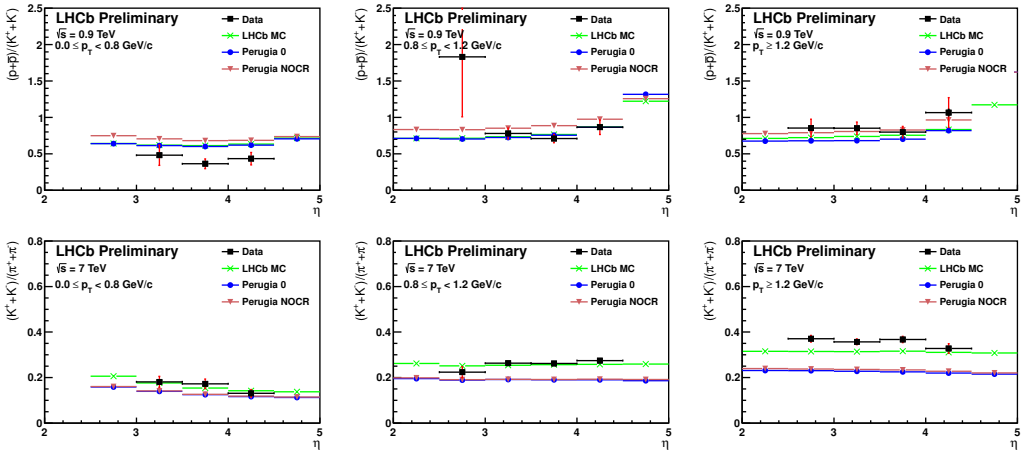

Figure 4: $\frac{\bar{p}+p}{K^-+K^+}$ $\sqrt{s} = 900$ GeV, and $\frac{K^-+K^+}{\pi^-+\pi^+}$ $\sqrt{s} = 7$ TeV. Left to right: $0 < p_{\mathrm{T}} < 0.8$ GeV, $0.8 < p_{\mathrm{T}} < 1.2$ GeVand $p_{\mathrm{T}} > 1.2$ GeV. Black is data where the black error bars are the statistical errors (mostly invisible) and the red (grey) error bars are systematic errors.

4 Summary

LHCb is an excellent environment for particle production measurements in the forward region. The charged particle multiplicities are underestimated by MC generators, which better describe hard events especially the NOCR and LHCb tunes. The light flavor hadron ratios need MC-tuning and are again best described by the NOCR and LHCb tunes. Future analysis will include the $\sqrt{s} = 2.76$ TeV data already taken and the $\sqrt{s} = 8$ TeV data that is about to be taken.

References

[1] A. A. Alves *et al.* JINST **3** (2008) S08005.

[2] R. Aaij *et al.* Phys. Lett. **B693** (2010) 69–80, `arXiv:1008.3105 [hep-ex]`.

[3] R. Aaij *et al.* J. High Energy Phys. **08** (2011) 034.

[4] R. Aaij *et al.* Phys. Lett. B **703** (2011) 267–273.

[5] R. Aaij *et al.* Eur. Phys. J. C **72** (2012) 1947.

[6] M. Clemencic *et al.* Journal of Physics: Conference Series **331** (2011) 3.

[7] P. Skands. Phys. Rev. D **82** (2010) 074018.

[8] M. Britsch, "`https://indico.cern.ch/contributionDisplay.py?contribId=142&sessionId=11&confId=153252`".

[9] R. Aaij *et al.*, "Lhcb-paper-2011-037 (in preparation)", 2012.

Pion and Kaon Multiplicities from muon-deuteron Deep Inelastic Scattering at COMPASS

Nour Makke[1]

[1] University and INFN section of Trieste, Piazzale Europa 1, I-34127 TS, Italy

DOI: http://dx.doi.org/10.3204/DESY-PROC-2012-02/100

The hadronization process, which turns partons into non-perturbative hadronic bound states in hard-scattering reactions, plays a fundamental role in our understanding of the proton structure. Currently, our knowledge of quark Fragmentation Functions into hadrons (FFs) originates mainly from existing global QCD analyzes which are mostly based on inclusive measurements in electron-positron annihilation process. While the latter, with current available data, mainly fixes the flavor singlet combinations of FFs, semi-inclusive DIS measurements give access to the flavor structure of FFs via hadron multiplicities. The COMPASS collaboration has recently measured charge separated pion and kaon multiplicities using 160 GeV/c muons off deuteron target. This measurement makes a fundamental experimental contribution towards a deeper understanding of the hadronization process.

1 Introduction

Within the framework of leading-twist collinear QCD, processes with observed final-state hadrons can be described in terms of perturbative hard scattering cross sections and non-perturbative universal functions: parton distributions and fragmentation functions. While parton distributions, which describe the quark structure of initial-state hadrons, are nowadays precisely known except for strange quark distribution which still carries a large uncertainty, fragmentation functions which encode details of the hadronization process are poorly known. Current parametrizations for fragmentation functions are mainly based on single-inclusive measurements in e^+e^- annihilation (see quark fragmentation chapter in [3]). While current available e^+e^- data are very precise, they do not allow to disentangle quark from anti-quark fragmentation and allow only flavor singlet combinations of fragmentation functions [1]. Semi-inclusive lepton-nucleon scattering data have the advantage of disentangling the charge and the flavor structure of fragmentation functions by weighting differently contributions of quark flavors in the subsequent hadronization process. A direct access to the FFs is provided in semi-inclusive DIS via the hadron multiplicities (Eq.1), defined, in the QCD improved quark-parton model, by the averaged number of final-state hadrons produced per deep inelastic scattering event.

$$\frac{1}{\sigma^{DIS}}\frac{d\sigma^h}{dxdQ^2dz} = \frac{\sum_q e_q^2 q(x,Q^2) D_q^h(z,Q^2)}{\sum_q e_q^2 q(x,Q^2)} \tag{1}$$

Here the sum runs over active quark flavors. $q(x,Q^2)$ denotes Parton Distribution Function (PDF) of flavor q and $D_q^h(z,Q^2)$ denotes fragmentation function of a quark of flavor q into a

final-state hadron of type h. D_q^h is defined as the mean number of hadrons of type h produced from the fragmentation of q with fractional energies z ($= E_h/E_\gamma$) in the range $[z, z + dz]$.

2 The COMPASS Experiment

COMPASS is a fixed target experiment [2] located at CERN. It uses a high energy hadron or muon beam provided by the CERN Super Proton Synchrotron (SPS). The muon beam originates from the decay of positive pions which in turn come from the scattering of a primary proton beam on a Beryllium target. The COMPASS spectrometer is 50 m long and consists of two stages designed to detect hadrons produced at small and large angles. Each stage is equipped with a magnet and a set of tracking detectors of different types. COMPASS provides particle identification through the use of a RICH detector, which is crucial for this analysis.

3 Experimental Data Analysis

Pion and Kaon multiplicities have been extracted using data recorded by the COMPASS experiment by scattering a 160 GeV/c polarized μ^+ beam off a two cell polarized deuteron (^{6}LiD) target. The raw hadron multiplicities are first extracted from experimental data by averaging over the two target polarizations and then corrected for the acceptance of the spectrometer. This factor correction takes into account the limited geometrical and angular acceptance of the experimental apparatus, the detection inefficiency as well as the kinematic smearing. The acceptance correction factors have been estimated with a Monte Carlo (MC) simulation of μ−N scattering at the COMPASS kinematics. The LEPTO generator has been used with parton shower simulation and MSTW08 parametrization for parton distributions. The COMPASS apparatus was simulated using Geant3 toolkits and finally, the hadronization process has been simulated using the Lund string model in which the intrinsic k_T of quarks inside the nucleon and the hadronization parameters were tuned for a best description of COMPASS data. The Monte Carlo data are reconstruted with the same software as the experimental data. A good description of data by the produced MC sample is observed for inclusive and semi-inclusive DIS events (Fig.1).

The measurement covers a wide kinematic domain defined by cuts on the photon virtuality $Q^2 > 1$ [GeV/c]^2 and on the energy fraction of the lepton carried by the exchanged virtual photon y ($= E_\gamma/E_\mu$). The latter is restricted to the range [0.1, 0.9] to suppress DIS events with small energy transfer and to avoid the region the most affected by radiative effects. A cut on the invariant mass of the hadronic system $W > 7$ GeV is applied to avoid kinematic regions where acceptance corrections are smaller than 5%, in particular for the kaon case. The selected DIS event sample covers a wide range of the Bjorken variable $x \in [4.10^{-3}, 0.7]$. Produced final-state hadrons are required to have a fractional energy z in the range [0.2, 0.85]. The lower cut selects only hadrons produced in the current fragmentation region (to avoid the fragmentation of the target remnant) and the upper one suppresses hadrons produced from diffractive processes. The hadron identification is ensured in the momentum range [3 (10), 50 GeV] for pions (kaons). For $P > 50$ GeV/c, the separation between pions and kaons becomes problematic. A total sample of 5.10^6 DIS events is selected, with 10^6 (9.10^5) π^+ (π^-) and 2.10^5 ($1.3.10^5$) K^+ (K^-). The analysis [3] has been performed in different combinations of bins in x, z and Q^2. The radiative corrections were estimated and found to be of the order of 15% in the region $x < 0.01$ and negligible for the remaining x domain. The acceptance was estimated to be $\sim 60\%$ in the covered kinematic domain, with a statistical precision of $3 - 5\%$.

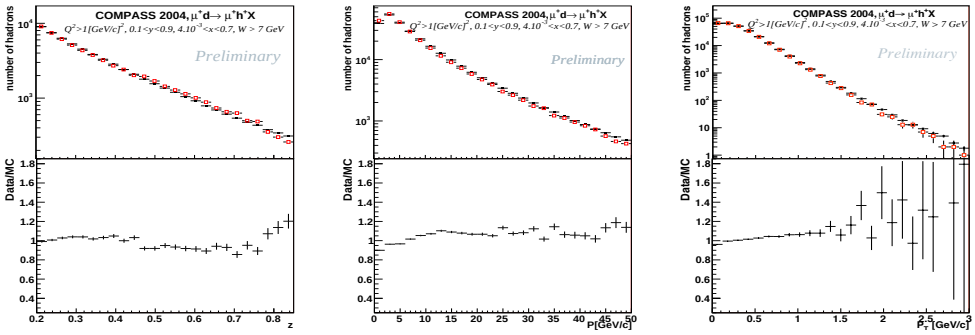

(a) fractional energy z (b) Hadron Momentum P (c) Transverse momentun P_T

Figure 1: Kinematical distributions for experimental data (black markers) and simulated Monte Carlo sample (red markers) (Upper row) as well as the ratio of data to Monte Carlo (lower row).

4 Results

Pion and kaon multiplicities versus (x,z) are shown in Fig.2 in comparison with LO theoretical calculations performed using Eq.1, MRST04 and DSS LO parametrizations for PDFs and fragmentation functions respectively. A good agreement is observed for pions in the entire range except for $z > 0.65$. However this observation is not surprising since DSS includes semi-inclusive DIS data only up to $z = 0.65$. In the kaon case, significant discrepancies are observed in nearly the entire kinematic domain, indicating that COMPASS kaon multiplicities may have an important impact on QCD global fits of fragmentation functions and even on the determination of the unpolarized strange quark distribution function.

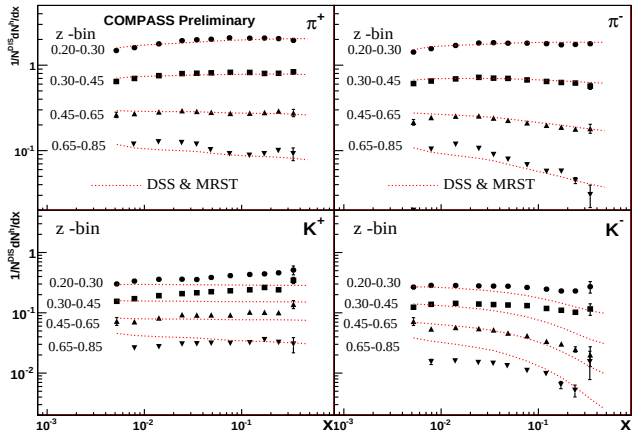

Figure 2: Charged pion (top) and kaon (bottom) multiplicities versus x in four z bins. Only statistical errors are shown, systematic uncertainties reache 5% for pions and 10 % for kaons.

Fig.3(a) shows pion and kaon multiplicities versus (Q^2,z). COMPASS data have the advantage of covering wide z and Q^2 ranges. The Q^2 dependence is found to be more pronounced for

negative hadrons than for positive ones for $z > 0.4$. This dependence originates mainly from the x-dependence of the PDFs and is in agreement with LO predictions. Fig.3(b) shows a first preliminary NLO fit of COMPASS pion multiplicities performed by de Florian et al. and shown in [4]. Results for kaons are also presented in [4]. While the NLO fit works well for pions, some issues have been encountered for kaons and are currently under investigations.

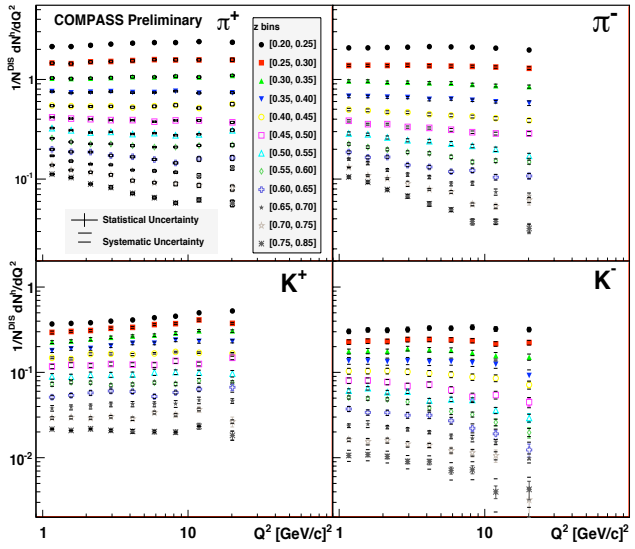

(a) COMPASS multiplicities versus Q^2

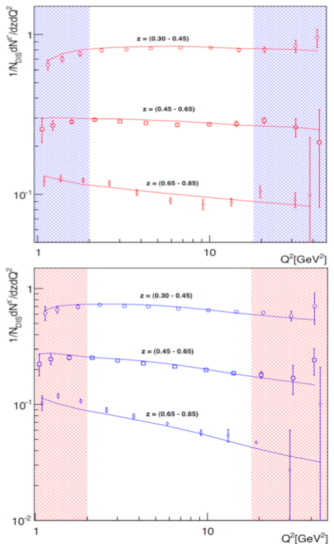

(b) A preliminary NLO fit to COMPASS pion multiplicities.

Figure 3: (a) Charged pion (top) and kaon (bottom) multiplicities as a function of z in nine Q^2 bins. Statistical and systematic errors are shown. (b)Preliminary NLO fit of π^+ (top) and π^- (bottom) multiplicities. Data points in the dashed region have not been included into the fit.

In conclusion, pion and kaon multiplicities have been measured by the COMPASS collaboration, using deep inelastic scattering of muons off deuteron target, in the kinematic domain $Q^2 > 1$ (GeV/c)^2, $0.1 < y < 0.9$, $4.10^{-4} < x < 0.7$ and $W > 7$ (GeV/c). These data have been used for a LO extraction of quark fragmentation functions [3] and are highly required for NLO global QCD analysis of fragmentation functions [4]. In the near future, the COMPASS collaboration will perform the same measurement using proton target in order to better constrain the strange quark distribution in the nucleon. The corresponding data set will be collected during this year of COMPASS data taking.

References

[1] D. de Florian *et al.* Phys. Rev. D75 (2007) 114010; Phys. Rev. D76 (2007) 074033

[2] COMPASS Collaboration, The Compass Experiment at CERN Nucl. Intrum. Meth. A577 (2007) 455–518

[3] N. Makke, "Measurement of polarisation of strange quark in the nucleon and determination of quark fragmentation functions", *Ph.D. thesis, Paris Sud University and CEA centre de Saclay*, Orsay, France, 2011.

[4] W. Vogelsang, "QCD SPIN Physics: Some Recent Highlights", in *International Workshop on Hadron Structure and Spectroscopy, Lisbon, Portugal, 2012.*

Multidimensional study of the hadron attenuation at HERMES

Gevorg Karyan[1] on behalf of the HERMES collaboration

[1]A.I. Alikhanyan National Science Laboratory, Alikhanian Brothers 2, 0036 Yerevan, Armenia

DOI: http://dx.doi.org/10.3204/DESY-PROC-2012-02/56

Hadron multiplicity ratios in semi-inclusive deep-inelastic scattering have been measured on neon, krypton and xenon targets relative to deuterium using 27.6 GeV positron or electron beam at the HERMES experiment. They are presented for pions (π^+, π^-), kaons (K^+, K^-), protons and anti-protons as a function of the virtual photon energy ν, its virtuality Q^2, the fractional hadron energy z and the transverse component of hadron momentum p_t with respect to the direction of the virtual photon. Dependences are presented in a two-dimensional representation, i.e. in the form of detailed binning over one variable and three slices over the other variable. These results may help to understand some aspects of hadronization process.

1 Introduction

Semi-inclusive deep-inelastic scattering (SIDIS) of leptons off nuclei provides a tool to investigate a quark hadronization or fragmentation into hadrons[1][2]. In such a process, lepton transfers a certain amount of energy (ν) to the "struck" quark which then propagates through the nuclear medium, and looses part of it's energy by emiting a gluon. The time needed for this propagation is called the production time. After this time a colorless pre-hadron has formed, which evolves to the final hadron during the so-called formation time. To investigate a space-time development of this process, nuclei with different mass and size can be used. The suitable experimental observable is the nuclear attenuation ratio, which is a ratio between hadron multiplicities from a nuclear target with atomic mass (A) to those on the deuterium[3][4][5].

$$R_A^h(\nu, Q^2, z, p_t^2) = \frac{(\frac{N^h(\nu,Q^2,z,p_t^2)}{N^e(\nu,Q^2)})_A}{(\frac{N^h(\nu,Q^2,z,p_t^2)}{N^e(\nu,Q^2)})_D} \tag{1}$$

where N^h is the number of semi-inclusive hadrons in a given (ν,Q^2,z,p_t^2) bin and N^e is the number of inclusive deep-inelastic scattered leptons in the same (ν,Q^2) bin.
This ratio depends on leptonic variables such as the energy of virtual photon ν and it's virtuality Q^2 and on hadronic variables like the fraction z of the virtual photon energy carried by the hadron and the square of the hadron momentum component p_t^2 transverse to the virtual photon direction. The attenuation ratio, in general, depends also on azimuthal angle ϕ, which is the angle between the lepton-scattering plane and the hadron-production plane. In this measurement no ϕ dependence was observed within statistical accuracy. Thus the integration over ϕ

was performed. In order to study the nuclear attenuation effect in more detail the dependencies of R_A^h are presented in a two-dimensional form, using a detailed binning over one variable and a coarser binning in another variable.

2 Data Extraction and Results

The data were collected with the HERMES spectrometer using 27.6 GeV electron or positron beams stored in HERA at DESY[6]. To select deep-inelastic scattered (DIS) leptons the following requirements were used : $Q^2 > 1\ GeV^2$, $W^2 > 4\ GeV^2$ and $y = \nu/E < 0.85$, where W is the invariant mass of virtual photon-nucleon system and E is the beam energy. The cut on the invariant mass is imposed to suppress the resonance contribution and the constrain on y limits the magnitude of radiative corrections.
For charged hadron identification, dual-radiator ring-imaging Čerenkov detector (RICH) was used[7], which allows to identify charge separeted pions, kaons and (anti)proton in momentum range : $2 < p_h < 15.0\ GeV$. Hadrons were selected within the cuts : $x_F > 0$ and $z > 0.2$, where x_F is the Feynman variable which is defined as a ratio of the longitudinal momentum transferred to the hadron in the photon-nucleon centre-of-mass system to it's maximum possible value and z is the ratio of the hadron energy devided by ν.

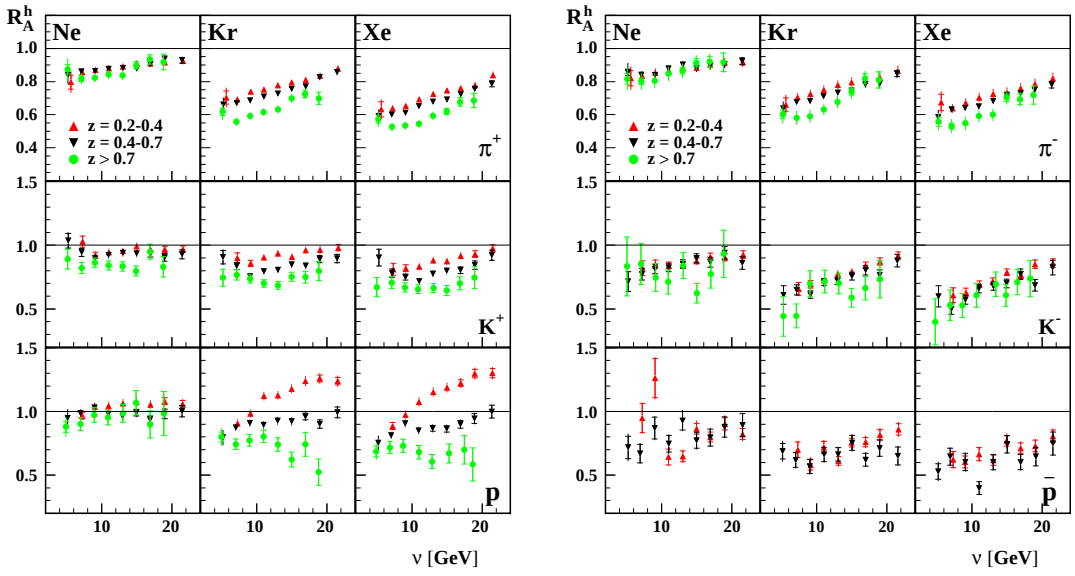

Figure 1: Dependence of R_A^h on ν for three slices in z.

In figure 1, the ν dependence of R_A^h is shown in three z slices. The scale uncertainties are estimated to be 3%, 5%, 4%, and 10% for pions, kaons, protons and atiprotons, respectively. With increasing ν a rise of R_A^h was observed for pions(π^+, π^-) and negatively charged kaons(K^-) which is consistent with fragmentation models that explain such a behaviour as a result of Lorentz dilation and/or a modification of the fragmentation function[8]. Compared to negatively charged kaons (K^-), the ν dependence of R_A^h for positively charged kaons (K^+) shows

an enhancement for the lowest z-slice and it seems to be flatter for the high z values. For protons the behaviour of R_A^h is very different from those of the other hadrons. Particularly for the lowest z-slice it exceeds the unity at large ν values. This phenomena might be caused by the fact that protons can be knocked out off the nucleus while other hadrons are always the result of hadronization. This effect is stronger for heavy nuclei which is consistent with the assumption of large contribution from knock-out processes. Unlike protons, antiprotons are produced by hadronization only and show a similar behaviour as mesons.

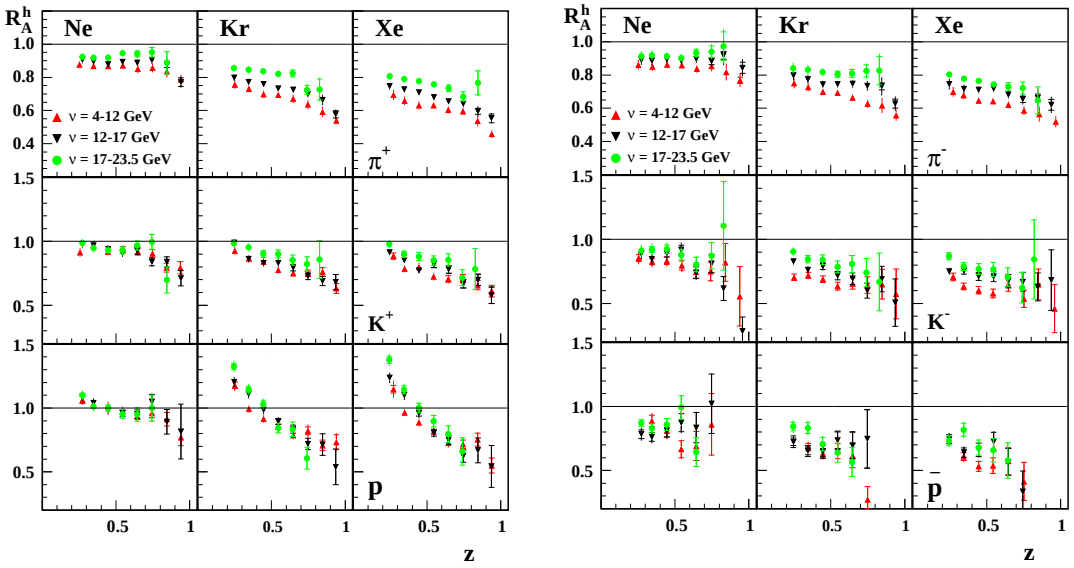

Figure 2: Dependence of R_A^h on z for three slices in ν.

In figure 2, the dependence of R_A^h on z for three slices in ν is presented. The R_A^h shows a slight change in different ν slices for π^+ and π^- and a strong dependence for protons on krypton and xenon targets. This behaviour for protons can be explained by a large contribution from final-state interaction at low z values.
The dependence of R_A^h on p_t^2 is shown in figure 3 for three slices in z. An increase of R_A^h was observed at high p_t^2 (the Cronin effect) which is larger for protons compared to mesons. For the highest z slice the Cronin effect is suppressed for mesons while the protons show a significant rise with p_t^2.

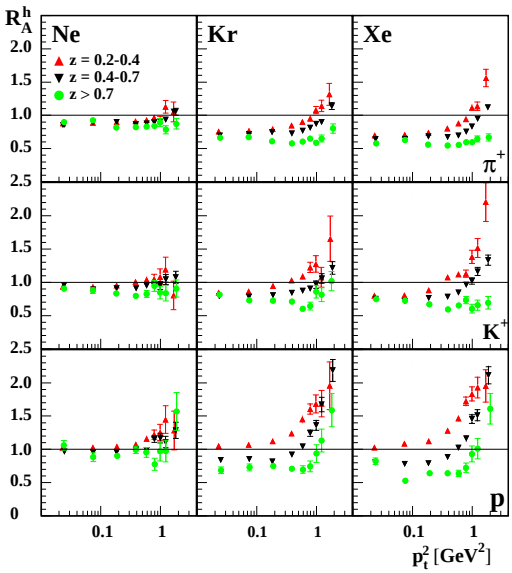

Figure 3: Dependence of R_A^h on p_t^2 for three slices in z.

3 Conclusions

The first two dimensional kinematic dependencies for hadron multiplicity ratio R_A^h have been presented for pions(π^+, π^-), kaons(K^+, K^-) and protons(p, $\bar{p}$) on neon, krypton and xenon targets relative to deuterium. For π^+ and π^- the behaviour of R_A^h is about the same within the experimental uncertainties. The dependence of $R_A^{K^+}$ on ν for positevely charged kaons was found to be different from $R_A^{\pi^+}$, $R_A^{\pi^-}$ and $R_A^{K^-}$ at high values of z which might be the result of final-state interactions. Proton data show a significant difference from the other hadrons which can be explained by a contribution of knock-out processes, in addition to the fragmentation process.

References

[1] L. Osborne et al., Phys. Rev. Lett. 40, 1624 (1978).

[2] J. Ashman et al. [EMC], Z. Phys. C 52, 1 (1991).

[3] A. Airapetian et al. [HERMES], Eur. Phys. J. C 20, 479 (2001).

[4] A. Airapetian et al. [HERMES], Phys. Lett. B 577, 37 (2003).

[5] A. Airapetian et al. [HERMES], Nucl. Phys. B 780, 1(2007).

[6] K. Akertaff et al., HERMES coll., Nucl. Instrum. Methods A417 239 (1998).

[7] N. Akopov et al. NIM A479 (2002) 511.

[8] A. Accardi et al., Riv. Nuovo Cim. 32, 439 (2010).

Scaled momentum distributions for K^0_S and $\Lambda/\bar{\Lambda}$

Iris Abt

Max-Planck-Institute for Physics, Föhringer Ring 6, 80805 Munich, Germany

DOI: http://dx.doi.org/10.3204/DESY-PROC-2012-02/42

Scaled momentum distributions for the strange hadrons K^0_S and $\Lambda/\bar{\Lambda}$ were measured in deep inelastic ep scattering with the ZEUS detector at HERA using an integrated luminosity of 330 pb^{-1} in the kinematic region $10 < Q^2 < 40000$ GeV^2 and $0.001 < x < 0.75$. Predictions based on different approaches to fragmentation were compared to the measurements. Next-to-leading-order QCD calculations based on fragmentation functions, FFs, extracted from e^+e^- data alone, fail to describe the measurements. The measurements presented in this paper have the potential to further constrain the fragmentation functions of quarks, anti-quarks and gluons yielding K^0_S and $\Lambda/\bar{\Lambda}$ strange hadrons.

1 Motivation

Perturbative QCD allows to calculate processes involving coloured partons. To compare to experimental results, one needs to take into account jet fragmentation and hadronization in order to predict final states consisting of colour-neutral hadrons. In Monte-Carlo(MC) models, this is usually done by using the Lund string model. The other method is to use fragmentation functions (FFs) within the standard framework of leading-twist collinear QCD factorization. In both cases, one needs to tune parameters to obtain a good desription of the data. This has been done extensively for inclusive charged-particle final-states using electron-positron, pp, $\bar{p}p$ and ep data. However, no attempt has been carried out so far to use a subset of strange hadrons for such a tuning.

The analysis presented in this talk is based on data from the HERA collider using the ZEUS detector. The ability of previously tuned MC models and of calculations using FFs to describe scaled momentum distributions for K^0_S and $\Lambda/\bar{\Lambda}$ strange hadrons is tested. To this end, the data are compared to the color dipole model (CDM) of the Ariadne MC and to the matrix-element parton shower (MEPS) of the Lepto MC, as well as to the next-to-leading-order (NLO) calculations.

In this study, the scaled momentum distributions for K^0_S and Λ hadrons[1] are presented for the first time in DIS. The scaled momentum is defined as $x_p = 2P^{\text{Breit}}/\sqrt{Q^2}$, where P^{Breit} is the particle momentum in the Breit frame and Q^2 is the virtuality of the exchanged photon. The Breit frame [1] is the frame in which the exchanged virtual boson is purely space-like, with 3-momentum $\mathbf{q} = (0, 0, -Q)$. It provides a maximal separation between the products of the beam fragmentation and the hard interaction. The measurements were performed in the

[1]Here and in the following, the notation Λ includes both the particle and its antiparticle unless otherwise stated.

current region of the Breit frame, which is equivalent to one hemisphere in e^+e^- annihilations, as functions of Q^2 and x_p.

2 Experimental details

The data used in this analysis were collected during the running period 2005–2007, when HERA operated with protons of energy $E_p = 920$ GeV and electrons of energy $E_e = 27.5$ GeV, and correspond to an integrated luminosity of 330 pb^{-1}. The data passed through a standard neutral-current (NC) deep inelastic scattering (DIS) selection [6] in the kinematic region $10 < Q^2 < 40000$ GeV^2 and $0.001 < x < 0.75$, where x is the Bjorken scaling variable.

The strange hadrons K^0_S and Λ were identified via the charged-decay channels $K^0_S \to \pi^+\pi^-$ and $\Lambda \to p\pi^-$ ($\bar{\Lambda} \to \bar{p}\pi^+$). The candidates were reconstructed using two oppositely charged tracks associated with a displaced secondary vertex.

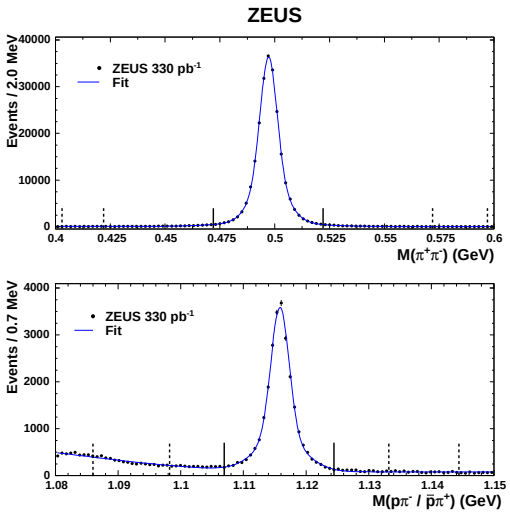

Figure 1: (a) The $\pi^+\pi^-$ invariant-mass distribution for K^0_S candidates (dots). (b) The $p\pi^-/\bar{p}\pi^+$ invariant-mass distribution for $\Lambda/\bar{\Lambda}$ candidates (dots). In both (a) and (b), the solid line represents an indicative fit by two Gaussians and a (a) linear and (b) quadratic background function. The solid vertical lines indicate the signal window used in the analysis. The dashed lines indicate the two sideband regions used for the background subtraction in each kinematic bin.

Figure 1 shows the $M(\pi^+\pi^-)$ and $M(p\pi)$ distributions. A small amount of background is observed. The fit shown in Fig. 1 is for illustration only. The number of K^0_S (Λ) candidates in each bin of x_p and Q^2 was estimated by counting the entries in the signal region, $472 - 522$ ($1107.0 - 1124.5$) MeV, and subtracting the number of expected background entries. The latter was determined from a linear fit to the sideband regions $403 - 422$ and $572 - 597$ ($1086.0 - 1098.2$ and $1133.2 - 1144.4$) MeV, also indicated in Fig. 1. There were 806 505 (165 875) K^0_S (Λ) candidates in the data sample. In the current region of the Breit frame, there were 238 153 K^0_S and 40 728 Λ candidates. A Monte Carlo study showed that 6% of the selected Λ candidates come from higher-baryon decays.

3 Comparison of the predictions with the data

Next-to-leading-order predictions, based on different FFs, and leading-logarithm parton-shower Monte Carlo calculations, interfaced with the Lund string fragmentation model, were compared to the measurements.

Two sets of calculations based on different parameterisations of the FFs were used. The first set was obtained from fits to e^+e^- data and based on the program CYCLOPS [2], called "AKK+CYCLOPS" [3, 4]. The second set was obtained from a global fit to e^+e^-, pp and ep data, called "DSS" [5]. It was only available for K^0_S predictions.

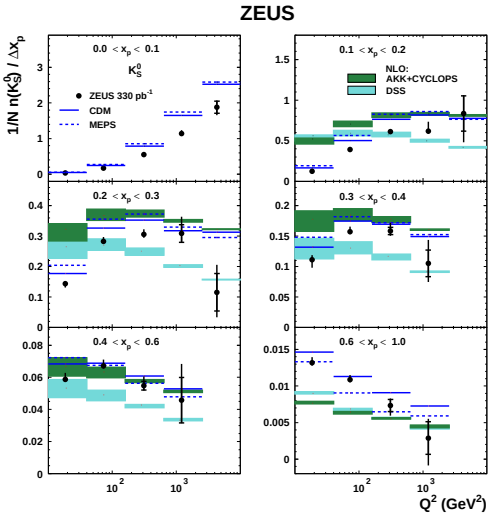

Figure 2: The measured scaled momentum distributions $(1/N)(n(K^0_S)/\Delta x_p)$ as functions of Q^2 in different regions of x_p (dots). For comparison, the NLO predictions of AKK+CYCLOPS (dark-shaded band) and DSS (light-shaded band) are also presented. The bands represent the theoretical uncertainty. The predictions from CDM (solid lines) and MEPS (dashed lines) are also shown.

Figure 2 shows the scaled momentum distributions for K^0_S as functions of Q^2 in different regions of x_p. The data show clear scaling violation. This behaviour is expected on the basis of the QCD description of the parton evolution with increasing Q: the phase space for soft gluon radiation increases, leading to a rise of the number of soft particles with small x_p.

The predictions from the CDM and MEPS models, based on leading-logarithmic matrix elements plus parton shower and the Lund fragmentation model are compared to the measurements in Fig. 2. They describe the shapes of the distributions fairly well while overestimating the overall production of K^0_S by 10 to 20%.

The NLO QCD calculations, based on full NLO matrix elements and the fragmentation-function approach are also compared to the measurements in Fig. 2 for $x_p > 0.1$. The AKK+CYCLOPS calculations, based on FFs extracted from e^+e^- data alone, fail to describe the measurements. These calculations predict a much too high K^0_S rate but for $x_p > 0.6$. These discrepancies might come from the fact that the FFs used in these predictions have a poorly constrained gluon contribution, which is dominant at low x_p.

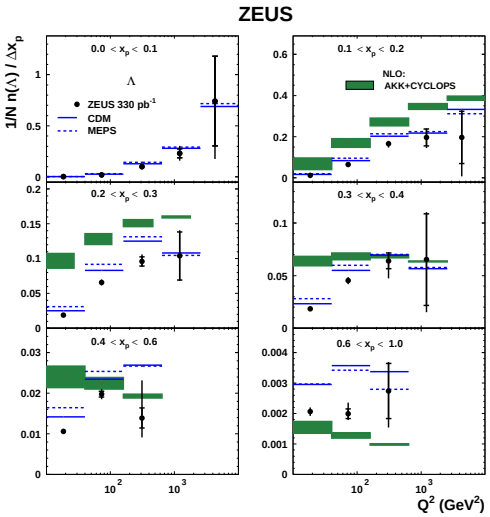

Figure 3: The measured scaled momentum distributions $(1/N)(n(\Lambda)/\Delta x_p)$ as functions of Q^2 in different regions of x_p (dots). Other details as in the caption to Fig. 2.

The DSS calculations, based on FFs extracted from a global analysis, give a good description of the measurements for $x_p > 0.3$ and $10 < Q^2 < 40000$ GeV^2. The prediction for this region of phase space is mainly constrained by pp data, which sufficiently constrain the FFs at high x_p. At lower x_p, the DSS calculations fail to describe the data. This can be explained by the fact that the DSS fit in this region of phase space is mostly unconstrained by the available data. Thus, the measurements presented in this paper will help to improve significantly such global fits in this region of phase space.

Figures 3 shows the scaled momentum distributions for Λ. Scaling violations are clearly observed. The predictions of CDM and MEPS give a reasonable description of the measurements, but overestimate the overall Λ rate by $\approx 20\%$. The AKK+CYCLOPS NLO calculations fail to describe the measurements.

ZEUS has previously published measurements of scaled momentum distributions for inclusive charged particles in DIS [6]. These measurements are dominated by the contribution from charged pions. Figure 4 shows the scaled momentum distributions presented in this paper together with those from the inclusive charged particles analysis in the kinematic region of $0.1 < x_p < 0.4$ as functions of Q^2. For $Q^2 > 100$ GeV^2, all distributions show a plateau. At lower Q^2, and especially at low x_p, sizeable mass effects are expected. This is clearly visible. For $0.1 < x_p < 0.2$, the value of $(1/N)(n(H)/\Delta x_p)$ drops to 10 (20)% of its maximum value for Λ (K^0_S), while for inclusive charged particles, the $(1/N)(n(H)/\Delta x_p)$ value is still 40% of the plateau value at the lowest Q^2 accessible.

4 Summary and conclusions

Scaled momentum distributions for K^0_S and Λ hadrons were measured for the first time in ep DIS. The distributions were measured in the Q^2 range from 10 to 40000 GeV^2 and $0.001 < x < 0.75$.

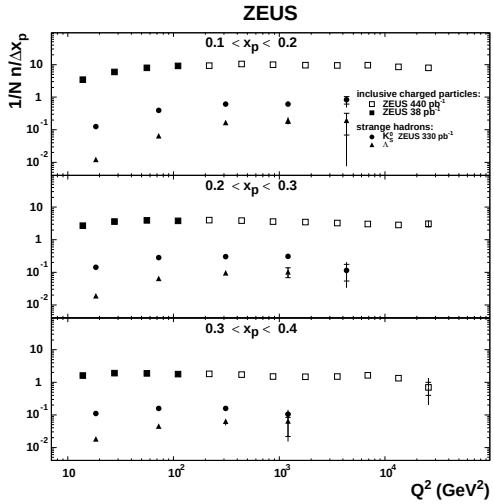

Figure 4: The measured scaled momentum distributions $(1/N)(n(H)/\Delta x_p)$ for $H = K^0_S$ (dots), Λ (triangles) and light charged particles (squares) as functions of Q^2 in different regions of x_p. Other details as in the caption to Fig. 2.

Scaling violations were clearly observed for both the K^0_S and Λ hadrons.

Next-to-leading-order QCD calculations, based on different parameterisations of the FFs, were compared to the measurements. The predictions based on FFs extracted from e^+e^- data alone fail to describe the measurements. Those predictions based on a global analysis which include e^+e^-, *pp* and *ep* data give an improved description of the measurements. However, they predict a too high production rate of K^0_S and Λ hadrons at low x_p and Q^2. The measurements presented in this paper have the potential to constrain significantly the FFs for the strange hadrons K^0_S and Λ.

References

[1] R.P. Feynman, *Photon-Hadron Interactions*. Benjamin, New York, (1972)

[2] D. Graudenz, Phys. Lett. B 406 (1997) 178

[3] S. Albino et al., Phys. Rev. D 75 (2007) 034018

[4] S. Albino, B.A. Kniehl and G. Kramer, Nucl. Phys. B 803 (2008) 42

[5] D. de Florian, R. Sassot and M. Stratmann, Phys. Rev. D 75 (2007) 114010

[6] ZEUS Collaboration, H. Abramowicz et al., JHEP 1006 (2010) 009

On the pair correlations of neutral K, D, B and B_s mesons with close momenta produced in inclusive multiparticle processes

Valery V. Lyuboshitz †, *Vladimir L. Lyuboshitz*

Joint Institute for Nuclear Research, 141980 Dubna, Moscow Region, Russia
† E-mail: Valery.Lyuboshitz@jinr.ru

DOI: http://dx.doi.org/10.3204/DESY-PROC-2012-02/17

The phenomenological structure of inclusive cross-sections of the production of two neutral K mesons in collisions of hadrons and nuclei is investigated taking into account the strangeness conservation in strong and electromagnetic interactions. Relations describing the dependence of the correlations of two short-lived and two long-lived neutral kaons $K^0_S K^0_S$, $K^0_L K^0_L$ and the correlations of "mixed" pairs $K^0_S K^0_L$ at small relative momenta upon the space-time parameters of the generation region of K^0 and $\bar{K}^0$ mesons have been obtained. It is shown that under the strangeness conservation the correlation functions of the pairs $K^0_S K^0_S$ and $K^0_L K^0_L$, produced in the same inclusive process, coincide, and the difference between the correlation functions of the pairs $K^0_S K^0_S$ and $K^0_S K^0_L$ is conditioned by the production of the pairs of non-identical neutral kaons $K^0\bar{K}^0$. Analogous correlations for the pairs of neutral heavy mesons D^0, B^0 and B^0_s, generated in multiple processes with the charm (beauty) conservation, are analyzed, and differences from the case of neutral K mesons are discussed .

1 Consequences of the strangeness conservation for neutral kaons

In the work [1] the properties of the density matrix of two neutral K mesons, following from the strangeness conservation in strong and electromagnetic interactions, have been investigated. By definition, the diagonal elements of the non-normalized two-particle density matrix coincide with the two-particle structure functions, which are proportional to the double inclusive cross-sections.

Strangeness is the additive quantum number. Taking into account the strangeness conservation, the pairs of neutral kaons K^0K^0 (strangeness $S=+2$), $\bar{K}^0\bar{K}^0$ (strangeness $S=-2$) and $K^0\bar{K}^0$ (strangeness $S=0$) are produced incoherently. This means that in the K^0-$\bar{K}^0$- representation the non-diagonal elements of the density matrix between the states K^0K^0 and $\bar{K}^0\bar{K}^0$, K^0K^0 and $K^0\bar{K}^0$, $\bar{K}^0\bar{K}^0$ and $K^0\bar{K}^0$ are equal to zero. However, the non-diagonal elements of the two-kaon density matrix between the two states $|K^0\rangle^{(\mathbf{p}_1)}|\bar{K}^0\rangle^{(\mathbf{p}_2)}$ and $|\bar{K}^0\rangle^{(\mathbf{p}_1)}|K^0\rangle^{(\mathbf{p}_2)}$ with the zero strangeness are not equal to zero, in general. Here $\mathbf{p}_1$ and $\mathbf{p}_2$ are the momenta of the first and second kaons.

The internal states of K^0 meson ($S=1$) and $\bar{K}^0$ meson ($S=-1$) are the superpositions of

the states $|K_S^0\rangle$ and $|K_L^0\rangle$, where K_S^0 is the short-lived neutral kaon and K_L^0 is the long-lived one. Neglecting the small effect of CP non-invariance, the CP-parity of the state K_S^0 is equal to $(+1)$, and the CP-parity of the state K_L^0 is equal to (-1); in doing so,

$$|K^0\rangle = \frac{1}{\sqrt{2}}(|K_S^0\rangle + |K_L^0\rangle), \quad |\bar{K}^0\rangle = \frac{1}{\sqrt{2}}(|K_S^0\rangle - |K_L^0\rangle).$$

It is clear that both the quasistationary states of the neutral kaon have no definite strangeness.

It follows from the Bose-symmetry of the wave function of two neutral kaons with respect to the total permutation of internal states and momenta that the CP-parity of the system $K^0\bar{K}^0$ is always positive [2] (the C-parity is $(-1)^L$, the space parity is $P = (-1)^L$, where L is the orbital momentum).

The system of two non-identical neutral kaons $K^0\bar{K}^0$ in the symmetric internal state, corresponding to even orbital momenta, is decomposed into the schemes $|K_S^0\rangle|K_S^0\rangle$ and $|K_L^0\rangle|K_L^0\rangle$ [2]:

$$|\psi^+\rangle = \frac{1}{\sqrt{2}}(|K^0\rangle^{(\mathbf{p}_1)} \otimes |\bar{K}^0\rangle^{(\mathbf{p}_2)} + |\bar{K}^0\rangle^{(\mathbf{p}_1)} \otimes |K^0\rangle^{(\mathbf{p}_2)}) =$$

$$= \frac{1}{\sqrt{2}}(|K_S^0\rangle^{(\mathbf{p}_1)} \otimes |K_S^0\rangle^{(\mathbf{p}_2)} - |K_L^0\rangle^{(\mathbf{p}_1)} \otimes |K_L^0\rangle^{(\mathbf{p}_2)}); \tag{1}$$

meantime, the system $K^0\bar{K}^0$ in the antisymmetric internal state, corresponding to odd orbital momenta, is decomposed into the scheme $|K_S^0\rangle|K_L^0\rangle$ [2]:

$$|\psi^-\rangle = \frac{1}{\sqrt{2}}(|K^0\rangle^{(\mathbf{p}_1)} \otimes |\bar{K}^0\rangle^{(\mathbf{p}_2)} - |\bar{K}^0\rangle^{(\mathbf{p}_1)} \otimes |K^0\rangle^{(\mathbf{p}_2)}) =$$

$$= \frac{1}{\sqrt{2}}(|K_S^0\rangle^{(\mathbf{p}_1)} \otimes |K_L^0\rangle^{(\mathbf{p}_2)} - |K_L^0\rangle^{(\mathbf{p}_1)} \otimes |K_S^0\rangle^{(\mathbf{p}_2)}). \tag{2}$$

The strangeness conservation leads to the fact that all the double inclusive cross-sections of production of pairs $K_S^0K_S^0$, $K_L^0K_L^0$ and $K_S^0K_L^0$ (two-particle structure functions) prove to be symmetric with respect to the permutation of momenta $\mathbf{p}_1$ and $\mathbf{p}_2$.

Besides, due to the strangeness conservation, the structure functions of neutral K mesons produced in inclusive processes are invariant with respect to the replacement of the short-lived state K_S^0 by the long-lived state K_L^0, and *vice versa* [1]:

$$f_{SS}(\mathbf{p}_1, \mathbf{p}_2) = f_{LL}(\mathbf{p}_1, \mathbf{p}_2) = \frac{1}{4}\,[f_{K^0K^0}(\mathbf{p}_1, \mathbf{p}_2) + f_{\bar{K}^0\bar{K}^0}(\mathbf{p}_1, \mathbf{p}_2) +$$

$$+ f_{K^0\bar{K}^0}(\mathbf{p}_1, \mathbf{p}_2) + f_{\bar{K}^0K^0}(\mathbf{p}_1, \mathbf{p}_2)] + \frac{1}{2}\,\mathrm{Re}\,\rho_{K^0\bar{K}^0\to\bar{K}^0K^0}(\mathbf{p}_1, \mathbf{p}_2), \tag{3}$$

$$f_{SL}(\mathbf{p}_1, \mathbf{p}_2) = f_{LS}(\mathbf{p}_1, \mathbf{p}_2) = \frac{1}{4}\,[f_{K^0K^0}(\mathbf{p}_1, \mathbf{p}_2) + f_{\bar{K}^0\bar{K}^0}(\mathbf{p}_1, \mathbf{p}_2) +$$

$$+ f_{K^0\bar{K}^0}(\mathbf{p}_1, \mathbf{p}_2) + f_{\bar{K}^0K^0}(\mathbf{p}_1, \mathbf{p}_2)] - \frac{1}{2}\,\mathrm{Re}\,\rho_{K^0\bar{K}^0\to\bar{K}^0K^0}(\mathbf{p}_1, \mathbf{p}_2), \tag{4}$$

where $\rho_{K^0\bar{K}^0\to\bar{K}^0K^0}(\mathbf{p}_1, \mathbf{p}_2) = (\rho_{\bar{K}^0K^0\to K^0\bar{K}^0}(\mathbf{p}_1, \mathbf{p}_2))^*$ are the non-diagonal elements of the two-kaon density matrix. The difference between the two-particle structure functions f_{SS} and f_{SL} is connected just with the contribution of these non-diagonal elements.

2 Structure of pair correlations of identical and non-identical neutral kaons with close momenta

Now let us consider, within the model of one-particle sources [2-7], the correlations of pairs of neutral K mesons with close momenta (see also [8-10]). In the case of the identical states $K^0_S K^0_S$ and $K^0_L K^0_L$ we obtain the following expressions for the correlation functions R_{SS}, R_{LL} (proportional to the structure functions), normalized to unity at large relative momenta:

$$R_{SS}(\mathbf{k}) = R_{LL}(\mathbf{k}) = \lambda_{K^0K^0}\,[1 + F_{K^0}(2\mathbf{k}) + 2\,b_{\rm int}(\mathbf{k})] +$$

$$+ \lambda_{\bar{K}^0\bar{K}^0}\left[1 + F_{\bar{K}^0}(2\mathbf{k}) + 2\,\tilde{b}_{\rm int}(\mathbf{k})\right] + \lambda_{K^0\bar{K}^0}\,[1 + F_{K^0\bar{K}^0}(2\mathbf{k}) + 2\,B_{\rm int}(\mathbf{k})]\,. \qquad (5)$$

Here $\mathbf{k}$ is the momentum of one of the kaons in the c.m. frame of the pair, and the quantities $\lambda_{K^0K^0}$, $\lambda_{\bar{K}^0\bar{K}^0}$ and $\lambda_{K^0\bar{K}^0}$ are the relative fractions of the average numbers of produced pairs K^0K^0, $\bar{K}^0\bar{K}^0$ and $K^0\bar{K}^0$, respectively ($\lambda_{K^0K^0} + \lambda_{\bar{K}^0\bar{K}^0} + \lambda_{K^0\bar{K}^0} = 1$) . The "formfactors" $F_{K^0}(2\mathbf{k})$, $F_{\bar{K}^0}(2\mathbf{k})$ and $F_{K^0\bar{K}^0}(2\mathbf{k})$ appear due to the contribution of Bose-statistics:

$$F_{K^0}(2\mathbf{k}) = \int W_{K^0}(\mathbf{r})\,\cos(2\mathbf{kr})\,d^3\mathbf{r}, \qquad F_{\bar{K}^0}(2\mathbf{k}) = \int W_{\bar{K}^0}(\mathbf{r})\,\cos(2\mathbf{kr})\,d^3\mathbf{r},$$

$$F_{K^0\bar{K}^0}(2\mathbf{k}) = \int W_{K^0\bar{K}^0}(\mathbf{r})\,\cos(2\mathbf{kr})\,d^3\mathbf{r}. \qquad (6)$$

where $W_{K^0}(\mathbf{r})$, $W_{\bar{K}^0}(\mathbf{r})$ and $W_{K^0\bar{K}^0}(\mathbf{r})$ are the probability distributions of distances between the sources of emission of two K^0 mesons, between the sources of emission of two $\bar{K}^0$ mesons and between the sources of emission of the K^0 meson and $\bar{K}^0$ meson, respectively, in the c.m. frame of the kaon pair. Meantime, the quantity $b_{\rm int}(\mathbf{k})$ describes the contribution of the S-wave interaction of two K^0 mesons, the quantity $\tilde{b}_{\rm int}(\mathbf{k})$ describes the contribution of the S-wave interaction of two $\bar{K}^0$ mesons and the quantity $B_{\rm int}(\mathbf{k})$ describes the contribution of the S-wave interaction of the K^0 meson with the $\bar{K}^0$ meson. Due to the CP invariance, the quantities $b_{\rm int}(\mathbf{k})$ and $\tilde{b}_{\rm int}(\mathbf{k})$ can be expressed by means of averaging the same function $b(\mathbf{k},\mathbf{r})$ over the different distributions:

$$b_{\rm int}(\mathbf{k}) = \int W_{K^0}(\mathbf{r}) b(\mathbf{k},\mathbf{r}) d^3\mathbf{r}, \quad \tilde{b}_{\rm int}(\mathbf{k}) = \int W_{\bar{K}^0}(\mathbf{r}) b(\mathbf{k},\mathbf{r}) d^3\mathbf{r}.$$

The quantity $B_{\rm int}(\mathbf{k})$ has the structure : $B_{\rm int}(\mathbf{k}) = \int W_{K^0\bar{K}^0}(\mathbf{r}) B(\mathbf{k},\mathbf{r}) d^3\mathbf{r}$, where $B(\mathbf{k},\mathbf{r}) \neq b(\mathbf{k},\mathbf{r})$.

Let us emphasize that when the pair of non-identical neutral kaons $K^0\bar{K}^0$ is produced but the pair of identical quasistationary states $K^0_S K^0_S$ (or $K^0_L K^0_L$) is registered over decays, the two-particle correlations at small relative momenta have the same character as in the case of usual identical bosons with zero spin [2].

For the pairs of non-identical kaon states $K^0_S K^0_L$ the correlation functions at small relative momenta have the form:

$$R_{SL}(\mathbf{k}) = R_{LS}(\mathbf{k}) = \lambda_{K^0K^0}\,[1 + F_{K^0}(2\mathbf{k}) + 2\,b_{\rm int}(\mathbf{k})] +$$

$$+ \lambda_{\bar{K}^0\bar{K}^0}\left[1 + F_{\bar{K}^0}(2\mathbf{k}) + 2\,\tilde{b}_{\rm int}(\mathbf{k})\right] + \lambda_{K^0\bar{K}^0}\,[1 - F_{K^0\bar{K}^0}(2\mathbf{k})]\,. \qquad (7)$$

It follows from Eqs.(5) and (7) that the correlation functions of pairs of neutral K mesons with close momenta, which are created in inclusive processes, satisfy the relation

$$R_{SS}(\mathbf{k}) + R_{LL}(\mathbf{k}) - R_{SL}(\mathbf{k}) - R_{LS}(\mathbf{k}) = 2\left[R_{SS}(\mathbf{k}) - R_{SL}(\mathbf{k})\right] = \\ = 4\lambda_{K^0\bar{K}^0}\left[F_{K^0\bar{K}^0}(2\mathbf{k}) + B_{\rm int}(\mathbf{k})\right]. \quad (8)$$

We see that the difference between the correlation functions of the pairs of identical neutral kaons $K^0_S K^0_S$ and pairs of non-identical neutral kaons $K^0_S K^0_L$ is conditioned exclusively by the generation of $K^0\bar{K}^0$-pairs.

The relations connecting the contribution of the S-wave strong interaction into the pair correlations of particles at small relative momenta with the parameters of low-energy scattering were obtained earlier in the papers [4-7]. It is essential that the "formfactors" (6) and the functions $b_{\rm int}(\mathbf{k})$, $\tilde{b}_{\rm int}(\mathbf{k})$ and $B_{\rm int}(\mathbf{k})$ depend on the space-time parameters of the generation region of neutral kaons and tend to zero at high values of the relative momentum $q = 2|\mathbf{k}|$ of two neutral kaons. Concretely, the expression for the function $B(\mathbf{k}, \mathbf{r})$ in the case of the $K^0\bar{K}^0$ system has been obtained in the paper [10]. In the same paper, the estimate of contribution of the transition $K^+K^- \to K^0\bar{K}^0$ has also been presented .

3 Correlations of neutral heavy mesons

Formally, analogous relations are valid also for the neutral heavy mesons D^0, B^0 and B^0_s . In doing so, the role of strangeness conservation is played, respectively, by the conservation of charm and beauty in inclusive multiple processes with production of these mesons . In these cases the quasistationary states are also states with definite CP parity, neglecting the effects of CP nonconservation. For example,

$$|B^0_S\rangle = \frac{1}{\sqrt{2}}(|B^0\rangle + |\bar{B}^0\rangle),\ CP \text{ parity } (+1); \quad |B^0_L\rangle = \frac{1}{\sqrt{2}}(|B^0\rangle - |\bar{B}^0\rangle),\ CP \text{ parity } (-1).$$

The difference of masses between the respective CP-odd and CP-even states is very insignificant in all the cases, ranging from 10^{-12} MeV for K^0 mesons up to 10^{-8} MeV for B^0_s mesons . Concerning the lifetimes of these states, in the case of K^0 mesons they differ by 600 times, but for D^0, B^0 and B^0_s mesons the respective lifetimes are almost the same. In connection with this, it is practically impossible to distinguish the states of D^0, B^0 and B^0_s mesons with definite CP parity by the difference in their lifetimes. These states, in principle, can be identified through the purely CP-even and purely CP-odd decay channels ; however, in fact the branching ratio for such decays is very small . For example,

$$Br\,(D^0 \to \pi^+\pi^-) = 1.62 \cdot 10^{-3}\ (\ CP = +1\ ); \quad Br\,(D^0 \to K^+K^-) = 4.25 \cdot 10^{-3}\ (\ CP = +1\ )\ ;$$

$$Br\,(B^0_s \to J/\Psi\ \pi^0) < 1.2 \cdot 10^{-3}\ (\ CP = +1\ ); \quad Br\,(B^0 \to J/\Psi\ K^0_S) = 9 \cdot 10^{-4}\ (\ CP = -1\ )\ .$$

Just as in the case of neutral K mesons, the correlation functions for the pairs of states of neutral D, B and B_s mesons with the same CP parity ($R_{SS} = R_{LL}$) and for the pairs of states with different CP parity (R_{SL}) do not coincide, and the difference between them is conditioned exclusively by the production of pairs $D^0\bar{D}^0$, $B^0\bar{B}^0$ and $B^0_s\bar{B}^0_s$, respectively. In particular, for B^0_s mesons the following relation holds:

$$R_{SS}(\mathbf{k}) - R_{SL}(\mathbf{k}) = 2\lambda_{B^0_s\bar{B}^0_s}\left[F_{B^0_s\bar{B}^0_s}(2\mathbf{k}) + B_{\rm int}(\mathbf{k})\right]; \quad (9)$$

here $\lambda_{B_s^0\bar{B}_s^0}$ is the relative fraction of generated pairs $B_s^0\bar{B}_s^0$,

$$F_{B_s^0\bar{B}_s^0}(2\mathbf{k}) = \int W_{B_s^0\bar{B}_s^0}(\mathbf{r})\,\cos(2\mathbf{kr})\,d^3\mathbf{r}, \qquad B_{\rm int}(\mathbf{k}) = \int W_{B_s^0\bar{B}_s^0}(\mathbf{r})\,B(\mathbf{k},\mathbf{r})\,d^3\mathbf{r},$$

$$B(\mathbf{k},\mathbf{r}) = |A_{B_s^0\bar{B}_s^0}(k)|^2\frac{1}{r^2} + 2\,{\rm Re}\left(A_{B_s^0\bar{B}_s^0}(k)\frac{\exp(ikr)\cos\mathbf{kr}}{r}\right),$$

where $A_{B_s^0\bar{B}_s^0}(k) \equiv A_{B_s^0\bar{B}_s^0\to B_s^0\bar{B}_s^0}(k)$ is the amplitude of S-wave $B_s^0\bar{B}_s^0$ - scattering, $k = |\,\mathbf{k}\,|$, $r = |\,\mathbf{r}\,|$. Let us remark that the B_s^0 and $\bar{B}_s^0$ mesons do not have charged partners (the isotopic spin equals zero) and, on account of that, in the given case the transition similar to $K^+K^- \to K^0\bar{K}^0$ is absent .

4 Summary

1. It is shown that, taking into account the strangeness conservation, the correlation functions for two short-lived neutral K mesons (R_{SS}) and two long-lived neutral K mesons (R_{LL}) are equal to each other. This result is the direct consequence of the strangeness conservation.
2. It is shown that the production of $K^0\bar{K}^0$-pairs with the zero strangeness leads to the difference between the correlation functions R_{SS} and R_{SL} of two neutral kaons.
3. The character of analogous correlations for neutral heavy mesons D^0 , B^0, B_s^0 with nonzero charm and beauty is discussed . Contrary to the case of K^0 mesons, here the distinction of respective CP-even and CP-odd states encounters difficulties, which are connected with the insignificant difference of their lifetimes and the relatively small probability of purely CP -even and purely CP-odd decay channels .

References

[1] V. L. Lyuboshitz. Yad. Fiz. **23** (1976) 1266 [Sov. J. Nucl. Phys. **23** (1976) 673].

[2] V. L. Lyuboshitz and M. I. Podgoretsky. Yad. Fiz. **30** (1979) 789 [Sov. J. Nucl. Phys. **30** (1979) 407].

[3] M. I. Podgoretsky. Fiz. Elem. Chast. At. Yadra **20** (1989) 628 [Sov. J. Part. Nucl. **20** (1989) 266].

[4] R. Lednicky and V. L. Lyuboshitz. Yad. Fiz. **35** (1982) 1316 [Sov. J. Nucl. Phys. **35** (1982) 770].

[5] V. L. Lyuboshitz. Yad. Fiz. **41** (1985) 820 [Sov. J. Nucl. Phys. **41** (1985) 523].

[6] V. L. Lyuboshitz. Yad. Fiz. **48** (1988) 1501 [Sov. J. Nucl. Phys. **48** (1988) 956].

[7] R. Lednicky, V. V. Lyuboshitz and V. L. Lyuboshitz. Yad. Fiz. **61** (1998) 2161 [Phys. At. Nucl. **61** (1998) 2050].

[8] V. L. Lyuboshitz and V. V. Lyuboshitz. Nukleonika, v.**51**, Suppl. 3 (2006), p.S69 - in Proceedings of Quark Matter 2005 Conference (Budapest, Hungary, August 4 - 9, 2005).

[9] V. L. Lyuboshitz and V. V. Lyuboshitz, in Proceedings of the IV International Conference on Quarks and Nuclear Physics – QNP-06 (Madrid, Spain, June 5 - 10, 2006), Berlin - Heidelberg, 2007, p.109 .

[10] V. L. Lyuboshitz and V. V. Lyuboshitz. Pis'ma v EchaYa, **4** (2007) 654 [Physics of Particles and Nuclei Letters, **4** (2007) 388] .

Studies of Jet Shapes and Substructure with the ATLAS Experiment

Adam Davison[1] on behalf of the ATLAS Collaboration

[1]University College London, Gower Street, London, United Kingdom

DOI: http://dx.doi.org/10.3204/DESY-PROC-2012-02/80

The internal structure of jets produced in proton-proton collisions at 7 TeV centre-of-mass energy provides a direct test of QCD which is largely orthogonal to other measurements of jets. The ATLAS experiment at the CERN LHC has measured a number of distributions related to the distribution of energy inside jets including jet shapes, fragmentation functions, masses and substructure variables.

1 Introduction

The ATLAS detector observes proton-proton collisions provided by the CERN Large Hadron Collider [1]. The results presented here use the 2010 ATLAS dataset, consisting of 35 pb^{-1} of collisions with a centre-of-mass energy of 7 TeV. A key feature of the ATLAS detector is excellent calorimeter granularity. The electromagnetic calorimeter has granularity ranging from 0.025×0.025 to 0.1×0.1 in the $\eta - \phi$ plane. The finest region of the hadronic calorimeter has granularity of 0.1×0.1.

Measurements of jet production at ATLAS have contributed to the understanding of QCD at higher energies than ever before explored at a hadron collider. In addition to testing the production of jets however, it is also informative to look inside jets at their internal structure. The structure of jets is influenced by a wide range of physics, such as fragmentation and hadronisation, and also hard physics, colour connections, underlying-event, pile-up and heavy particle production. Measurements of the internal structure of jets therefore help test models of all these processes. Additionally, for the first time at the LHC heavy particle production in jets can often include W and Z-bosons and top quarks.

2 Jet Shapes

Jet shapes determine the fraction of the p_{T} of a jet which is within an annulus centred on the jet radius. Formally quantities are defined such as:

$$\rho(r) = \frac{1}{\Delta r} \frac{1}{N^{\text{jet}}} \sum_{\text{jets}} \frac{p_T(r - \Delta r/2, r + \Delta r/2)}{p_T(0, R)}.$$

Where R is the radius of the jet and r is a distance from the jet axis, both defined in the $y - \phi$ plane. $p_T(a, b)$ is a function which gives the total p_T of particles which are between a and

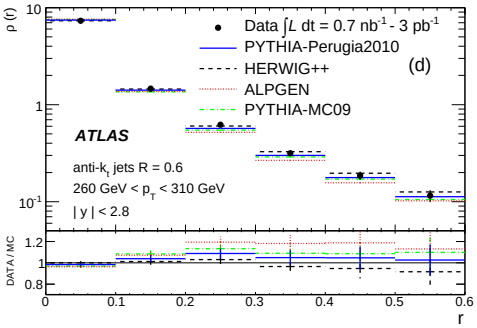

Figure 1: The measured differential jet shape, $\rho(r)$, in inclusive jet production. Error bars indicate the statistical and systematic uncertainties added in quadrature [3].

b away from the jet axis. It can be seen from this definition that ρ is the density of energy at a certain distance from the jet axis in $y - \phi$ space.

ATLAS has measured $\rho(r)$ for anti-k_t [2] jets with R-parameters of 0.4 and 0.6, corrected for detector effects and compared the resulting distributions to a number of predictions from Monte Carlo packages [3]. Figure 1 shows some of these results. Although there is clearly variation between different Monte Carlo models and tunings, the distributions are generally well reproduced.

3 Jet Fragmentation

An alternative way to study the internal structure of jets is to study the momenta of individual particles inside jets. Specifically, for a jet with four-momentum $\overline{p}_{\text{jet}}$ and a charged particle inside the jet with four-momentum $\overline{p}_{\text{ch}}$, the following variables are defined:

$$z = \frac{\overline{p}_{\text{jet}} \cdot \overline{p}_{\text{ch}}}{|\overline{p}_{\text{jet}}|^2} \qquad p_{\text{T}}^{\text{rel}} = \frac{|\overline{p}_{\text{ch}} \times \overline{p}_{\text{jet}}|}{|\overline{p}_{\text{jet}}|} .$$

These quantities represent the projection of the momentum of the charged particle along and transverse to the jet axis respectively. Differential cross-sections are defined as:

$$F(z, p_{\text{Tjet}}) = \frac{1}{N_{\text{jet}}} \frac{dN_{\text{ch}}}{dz} \quad \text{and} \quad f(p_{\text{T}}^{\text{rel}}, p_{\text{Tjet}}) = \frac{1}{N_{\text{jet}}} \frac{dN_{\text{ch}}}{dp_{\text{T}}^{\text{rel}}} .$$

ATLAS has measured these differential cross-sections for anti-k_t jets with and R-parameter of 0.6, corrected for detector effects [4]. Figure 2 shows a sample of these measurements compared to predictions from Monte Carlo packages. Again there are differences between the predictions of different Monte Carlo generators and tunings however all models correctly predict the overall shape of the distributions.

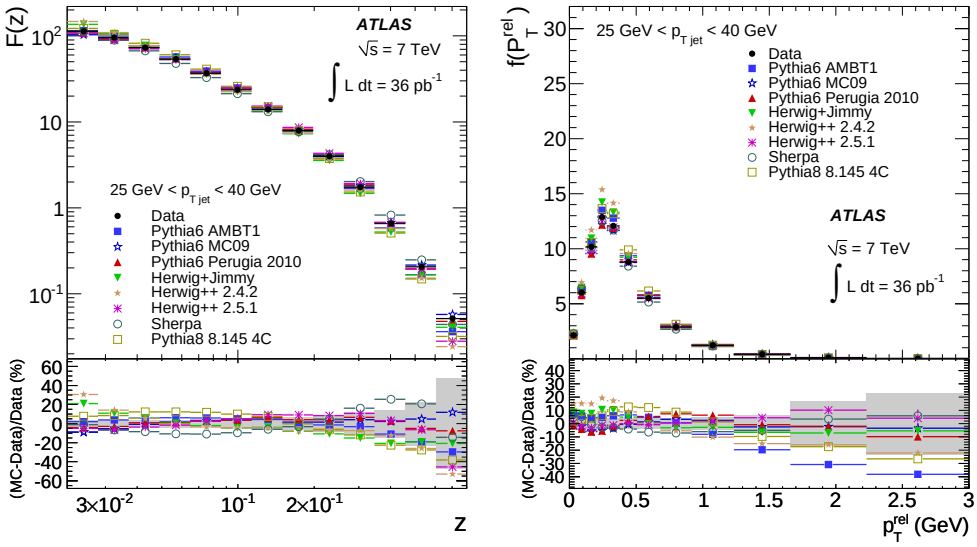

Figure 2: The measured differential cross-sections as a function of z (left) and p_{T}^{rel} (right) for anti-k_t jets with R-parameter 0.6 in the p_{T} range 25 to 40 GeV[4].

4 Jet Mass and Substructure

Recent phenomenological studies [5] have highlighted the potential for studies of jet mass and substructure in searches for new physics. Generally these searches centre on the idea that heavy particles such as W and Z bosons, top quarks and Higgs bosons could be produced with large Lorentz boosts at the LHC. At sufficiently large boosts, the decay products are collimated such that they are identified as a single jet in a detector. This type of jet has an invariant mass close to that of the parent particle and also distinctive internal structure which can be used to discriminate against jets from purely light QCD processes. Often these searches focus on larger radius jet algorithms in order to capture a whole heavy-particle decay.

ATLAS has measured a number of quantities related to this topic in anti-k_t jets with R-parameter of 1.0 and Cambridge-Aachen [6, 7] jets with R-parameter of 1.2 [8]. Jet mass is defined simply as the mass component of the jet four-momentum. Also measured was jet mass after the jet had been subjected to a procedure known as "splitting and filtering" [9]. This procedure searches through the clustering history of a jet to identify interesting structure and retains only radiation likely to relate to this structure, reducing the effective area of the jet. Additionally two variables designed to identify jets containing heavy particles, N-subjettiness [10] and k_t splitting scales [11] were measured. Finally the pile-up dependence of mean mass was also explored.

Two example results can be seen in Figure 3, which shows the jet mass distributions for Cambridge-Aachen jets with an R-parameter of 1.2 before and after applying the splitting and filtering procedure. HERWIG++ 2.4.2 does not describe the jet mass before splitting and filtering. However, differences between Monte Carlo generators and the data are significantly reduced by the application of the splitting and filtering procedure, implying that this procedure reduces sensitivity to soft physics.

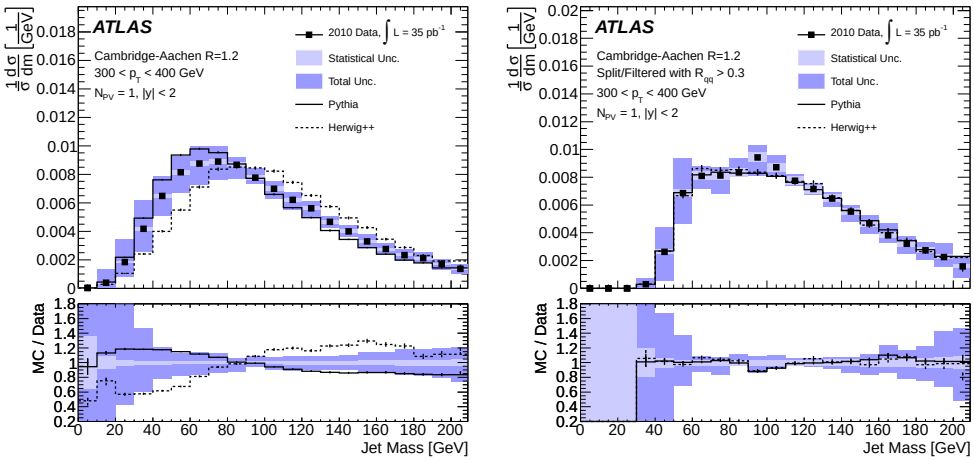

Figure 3: The measured differential cross-sections as a function of jet mass for Cambridge-Aachen jets with R-parameter 1.2 (left) and the same jets after the application of splitting and filtering (right) in the p_{T} range 300 to 400 GeV[8].

5 Conclusions

The study of the internal structure of jets is an interesting opportunity to test our understanding of QCD in new ways. ATLAS has measured a number of quantities relating to the internal structure of jets, including jet shapes, fragmentation functions, mass and substructure variables. These measurements make it possible to improve Monte Carlo models and tunings which is crucial for ATLAS as many new physics searches rely on accurate models of QCD backgrounds.

References

[1] **ATLAS** Collaboration, JINST **3** (2008) S08003.

[2] M. Cacciari, G. P. Salam and G. Soyez, JHEP **04** (2008) 063.

[3] **ATLAS** Collaboration, Phys. Rev. **D 83** (2011) 052003.

[4] **ATLAS** Collaboration, Eur. Phys. J. **C 71** (2011) 1795.

[5] A. Abdessalam *et al.* Eur. Phys. J. **C 71** (2011) 1661.

[6] Y. L. Dokshitzer *et al.* JHEP **08** (1997) 001.

[7] M. Wobisch and T. Wengler, PITHA **16** (1999).

[8] **ATLAS** Collaboration, `arXiv:1203.4606`.

[9] J. M. Butterworth *et al.* Phys. Rev. Lett. **100** (2008) 242001.

[10] J. Thaler and K. Van Tilburg, JHEP **03** (2011) 015.

[11] J. M. Butterworth, B. E. Cox and J. R. Forshaw, Phys. Rev. Lett. **100** (2008) 242001.

Boosted Hadronically Decaying Tops in New Physics Searches

Michihisa Takeuchi

Universität Heidelberg, Heidelberg, Germany

DOI: http://dx.doi.org/10.3204/DESY-PROC-2012-02/270

Top momentum reconstruction often plays an important role for new physics signal reconstruction at the LHC. In principle, it is possible to reconstruct hadronically decaying top momentum fully but suffering from large QCD and combinatorics background. Starting from geometrically large size of jets and looking into their substructure, we can efficiently reduce these background. We develop HEPTopTagger by adopting combination of Cambridge/Aachen algorithm and mass drop criterion. For physics applications, we illustrate scalar top reconstruction and top forward-backward asymmetry at the LHC.

1 Moderately Boosted Tops at the LHC

For the fine tuning problem of the Higgs sector, top quark plays a important role due to large top yukawa coupling and a top partner particle plausibly exists for the solution. Thus, analyzing top sector is strongly related with revealing the origin of electro-weak symmetry breaking. Additionally, several anomalies related with tops are reported by Tevatron, for example, A^t_{FB} [1, 2, 3], single top cross sections etc. These facts motivate us to study top sector.

At the LHC we expect top pairs copiously generated via the strong interactions and it is time to start the precision physics. For hadronic tops, we can reconstruct the top momentum in principle unlike leptonic decays, where we need to infer at least neutrino momentum from missing momentum. The disadvantage for using hadronic decaying tops is that we need to address tremendous QCD combinatorial background. For this purpose, focusing on boosted top is one of the effective strategies. Many works have been done in this direction using substructures of geometrically large jets, and several top taggers have been developed. However, most of the taggers mainly focus on highly boosted tops, typically tops with $p_T > 500$ GeV.

We developed top tagger focusing on more specific regime, so-called *moderately boosted tops*, which are tops with 200 GeV $< p_T <$ 500 GeV. In the region we have larger number of tops in the Standard Model, which makes our top tagger testable by data. Moreover, the momentum range is also the same as tops expected from light scalar top decays. In the following we shortly explain our top tagging algorithm HEPTopTagger and its applications [4, 5, 6, 7, 8].

2 HEPTopTagger

Since we focus on lower p_T tops we need to enlarge the effective jet size to capture three decay products from a top. We show ΔR_{bjj} vs. p_T distribution, where ΔR_{bjj} is geometrical separation

of them, for a $t\bar{t}$ sample in the left panel of Figure 1. As seen in the plot we need to start with $R = 1.5$ to capture a top with $p_T \sim 200$ GeV. The following steps show the HEPTOPTAGGER algorithm [4, 5, 6]:

1. **fat jets** define a fat jet using the Cambridge/Aachen algorithm with $R = 1.5$.

2. **find all subjets using a mass drop criterion**

   During unclustering a jet j into two subjets j_1, j_2 ($m_{j_2} < m_{j_1}$), keep both j_1 and j_2 only if $m_{j_1} < 0.8\ m_j$, otherwise keep only j_1. Each subjet j_i we either further decompose if $m_{j_i} > 50$ GeV or add to the list of relevant subjets.

3. **choose three subjets with best filtered mass**

   choose three subjets with best filtered mass m_{jjj}^{filt} in all pairings: the filtering parameters we choose $R_{\text{filter}} = \min(0.3, \Delta R_{jk}/2), n_{\text{filter}} = 5$. We regard it as a top candidate when $|m_{jjj}^{\text{filt}} - m_t| < 25$ GeV.

4. **check mass ratios**

   construct exactly three subjets j_1, j_2, j_3 from the five filtered constituents, ordered by p_T. If the masses (m_{12}, m_{13}, m_{23}) satisfy one of the following three criteria, accept them as a tagged top:

$$0.2 < \arctan\frac{m_{13}}{m_{12}} < 1.3 \text{ and } \quad R_{\text{min}} < \frac{m_{23}}{m_{123}} < R_{\text{max}}$$

$$R_{\text{min}}^2\left(1+\left(\frac{m_{13}}{m_{12}}\right)^2\right) < 1-\left(\frac{m_{23}}{m_{123}}\right)^2 < R_{\text{max}}^2\left(1+\left(\frac{m_{13}}{m_{12}}\right)^2\right) \text{ and } \quad \frac{m_{23}}{m_{123}} > 0.35$$

$$R_{\text{min}}^2\left(1+\left(\frac{m_{12}}{m_{13}}\right)^2\right) < 1-\left(\frac{m_{23}}{m_{123}}\right)^2 < R_{\text{max}}^2\left(1+\left(\frac{m_{12}}{m_{13}}\right)^2\right) \text{ and } \quad \frac{m_{23}}{m_{123}} > 0.35$$

   with $R_{\text{min}} = 85\% \times m_W/m_t$ and $R_{\text{max}} = 115\% \times m_W/m_t$. The numerical soft cutoff at 0.35 is independent of the masses involved and only removes QCD events.

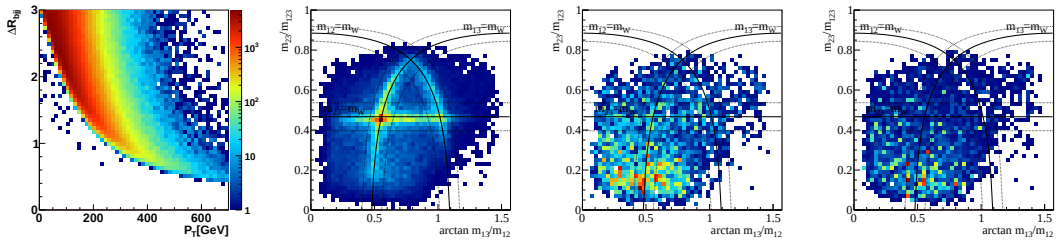

Figure 1: Left: ΔR_{bjj} vs p_T distribution for a $t\bar{t}$ sample. Distributions in the $\arctan m_{13}/m_{12}$ vs m_{23}/m_{123} plane for $t\bar{t}$, W+jets and pure QCD jets samples from second left to right.

As a result, tagging efficiency relative to all hadronic tops is 20% to 40% and mis-tagging rates for QCD and W+jets relative to all fat jets are 2% to 4% depending on p_T. We also check the tagged top momentum is well reconstructed.

3 Application for scalar top partner searches

For illustrating a benefit of the top tagger we show searches for stop pairs in purely hadronic top decays at the LHC. With the top tagging we can use reconstructed top momentum and analyze the angular correlations directly. We consider the following process with assuming $m_{\tilde{\chi}_1^0} = 98$ GeV and 100% branching ratio for $\tilde{t}_1 \to t\tilde{\chi}_1^0$:

$$pp \to \tilde{t}_1\tilde{t}_1^* \to (t\tilde{\chi}_1^0)\,(\bar{t}\tilde{\chi}_1^0) \to (bjj\tilde{\chi}_1^0)\,(\bar{b}jj\tilde{\chi}_1^0)\,.$$

Main Standard Model backgrounds are $t\bar{t}$+jets, W+jets and QCD after usual supersymmetric particle search cuts. A set of cuts used for selecting scalar top pair signal is listed in the following table.

no lepton, $\not{E}_T > 150$ GeV	
two fat jets	
two tagged tops	W+jets, Z+jets negligible
b-tag for 1st tagged top	QCD negligible
$m_{T2} > 250$GeV	$t\bar{t}$+jets controllable

After requiring two tagged tops in a event we efficiently drop the background contributions from W+jets and Z+jets. For reducing QCD contribution we require b-tagged jet inside a first tagged top, which doesn't work for reducing $t\bar{t}$ background. For reducing $t\bar{t}$ background we require m_{T2} variable should exceed a certain threshold. For the detailed numbers see Ref. [4]. As a result, for stop mass $m_{\tilde{t}} = 340$ GeV we achieve $S/B \sim 1$ and $S/\sqrt{B} > 5$ for 10 fb^{-1} at 14 TeV run of the LHC. Scalar top mass measurement using m_{T2} endpoint is also possible due to good momentum reconstruction for two tagged tops. We also achieved $S/B \sim 2$ with $S/\sqrt{B} > 5$ for the semi-leptonic mode by requiring one top tag and one isolated lepton [5].

Scalar top search at 8 TeV run of the LHC [7] would be more interesting. We need to improve the search strategy due to small scalar top production cross section compared with 14 TeV run. Since two tops from two scalar top decays are not produced in back-to-back they have no correlation in p_T unlike $t\bar{t}$ production, thus both tops hardly have $p_T > 200$ GeV. Hence, we should aim the events with one top boosted and the other top not boosted.

We mainly work on three modes: one boosted tops with one bottom jet, one boosted tops with one isolated lepton, and two isolated leptons. By requiring selection cuts on $m_T^{(b)}$, m_T^{ℓ}, and $m_{T2}^{\ell\ell}$ respectively for the three modes we can reduce effectively $t\bar{t}$ background, which is the dominant background at the end. The detailed descriptions of the cuts and resulting numbers are seen in Ref. [7]. As a result, we achieve $S/B \sim 1$ and $S/\sqrt{B} = 3$ in hadronic mode with one top tag for $m_{\tilde{t}} = 400$ GeV. In the semi-leptonic mode we achieve $S/B \sim 2$ and $S/\sqrt{B} = 5.4$ with one top tag. In the di-lepton mode, we achieve $S/B = 5.8$ and $S/\sqrt{B} = 15.8$ although it would not be a direct discovery for scalar tops. All $S/\sqrt{B}$ values quoted is for 10 fb^{-1}. We can also exclude scalar top existence up to ~ 600 GeV at 95% C.L.

4 Application for top forward backward asymmetry A_{FB}^t

We also utilize our top tagger for measuring top forward-backward asymmetry A_{FB}^t, where some discrepancy with Standard Model expectations seen according to the recent Tevatron measurement, in particular in large $m_{t\bar{t}}$ regime [1, 2, 3]. Thus, more investigation of A_{FB}^t in

large $m_{t\bar{t}}$ regime, in other word, boosted top regime is desirable. For this purpose it is suit to use our top tagging algorithm [8].

Our event selection is basically one top tag and one isolated lepton. We can determine the corresponding top charge from the isolated lepton charge. Once top and lepton momenta are given we reconstruct the observable

$$\mathcal{A}_C(y_0) = \frac{N_t(|y| < y_0) - N_{\bar{t}}(|y| < y_0)}{N_t(|y| < y_0) + N_{\bar{t}}(|y| < y_0)},$$

where $N_{t/\bar{t}}(|y| < y_0)$ is the number of (anti-)tops with absolute value of its rapidity y satisfying $|y| < y_0$. In the Standard Model, due to the difference of parton distribution functions between quarks and anti-quarks anti-top rapidity distribution is expected more central than top, leading $\mathcal{A}_C < 0$. According to the efficiency of the tagger we can estimate how much integrated luminosity is needed to see non-zero NLO effect predicted by the Standard Model QCD. As a result we see it at 5σ level with 60 fb^{-1} at 14 TeV run of the LHC.

Adding the four-fermi quark interactions to the Standard Model Lagrangian for reproducing the Tevatron results predicts more significant effect at the LHC. We can see the effect at 5σ level only with 2 fb^{-1} at 14 TeV run and at 2.8σ level with 10 fb^{-1} at 7 TeV run.

5 Summary

We focus on top tagging for moderately boosted tops down to $p_T \sim 200$ GeV, which makes the tagger testable using Standard Model top data. One of the general idea behind our work is to treat tops at the LHC just like bottoms. By using jet substructure, which is information previously thrown away, we can enhance S/B ratio against QCD combinatorial backgrounds even in fully hadronic mode. To utilize data at the LHC maximally we should make an effort to use more information available.

We have shown the possible applications using HEPTOPTAGGER for scalar top pair searches and for top forward-backward asymmetry measurement. The results for light scalar top searches with moderately boosted tops show enough chance to discover it at the LHC even at a center-of-mass energy of 8 TeV.

References

[1] V. M. Abazov *et al.* [D0 Collaboration], Phys. Rev. Lett. **100**, 142002 (2008)

[2] T. Aaltonen *et al.* [CDF Collaboration], Phys. Rev. Lett. **101**, 202001 (2008)

[3] T. Aaltonen *et al.* [CDF Collaboration], Phys. Rev. Lett. **102**, 222003 (2009)

[4] T. Plehn, M. Spannowsky, M. Takeuchi and D. Zerwas, JHEP **1010**, 078 (2010)

[5] T. Plehn, M. Spannowsky and M. Takeuchi, JHEP **1105**, 135 (2011)

[6] T. Plehn, M. Spannowsky and M. Takeuchi, Phys. Rev. **D85**, 034029 (2012)

[7] T. Plehn, M. Spannowsky and M. Takeuchi, arXiv:1205.2696 [hep-ph].

[8] J. L. Hewett, J. Shelton, M. Spannowsky, T. M. P. Tait and M. Takeuchi, Phys. Rev. **D84**, 054005 (2011)

Characterization of the Underlying Event in p-p collisions in CMS

Hans Van Haevermaet for the CMS Collaboration

University of Antwerp, Groenenborgerlaan 171, 2020 Antwerpen, Belgium

DOI: http://dx.doi.org/10.3204/DESY-PROC-2012-02/183

We present measurements of the Underlying Event (UE) in proton-proton collisions in CMS at the LHC at $\sqrt{s} = 0.9$, 2.76 and 7 TeV using different methods to distinguish the hard scatter system. Charged particle and energy densities are determined in the central ($|\eta| < 2$) and forward ($5.2 < |\eta| < 6.6$) regions as a function of the transverse momentum of the hard interaction characterized by central track-jets or Drell-Yan processes. In addition a novel technique using jet area/median properties to study the UE is presented. All results are corrected to hadron level and compared to various Monte Carlo (MC) models embedding different UE tunes.

1 Introduction

The Underlying Event in proton-proton collisions is everything except the hard scattering between the two high-p_T partons. Elements of this are the presence of Initial State Radiation (ISR), Final State Radiation (FSR), Multiple Partonic Interactions (MPI) and Beam Remnants (BR). The understanding of these phenomena in proton-proton collisions at the LHC is crucial for precision measurements of Standard Model processes and accordingly for the search for new physics. Unfortunately however, its dynamics are not well understood since they are governed by soft and semi-hard interactions which can not be fully described with perturbative QCD. This leads to the need of phenomenological models in MC generators containing parameters which must be tuned using existing data. Given the new unexplored energy domain at the LHC, its data is ideal to do further studies of the UE properties at $\sqrt{s}$ values of up to 7 TeV and constrain the existing models.

When describing collisions, a typical Minimum Bias (MB) event can be regarded as a peripheral collision which is characterised by a small overlap between the interacting protons while an event with a hard scale present is a more central collision with the interacting protons having a bigger overlap. One can thus expect more MPI in events with a high $\hat{p}_T$ than in MB events. The number of interactions in a collisions then thus not only depend on the centre-of-mass energy - the increase of particle densities gives a rise in interactions - but also on the hard scale of the event. This behaviour is reflected in existing phenomenological MPI models developed to describe these soft interactions. To achieve this one has to extend the hard scatter cross section to low $\hat{p}_T$ values and to avoid the divergence a regularisation value $\hat{p}_{T,0}$ has to be introduced: $1/\hat{p}_T^4 \rightarrow 1/(\hat{p}_T^2 + \hat{p}_{T,0}^2)^2$, which is also energy dependent: $\hat{p}_{T,0}(\sqrt{s}) = \hat{p}_{T,0}(\sqrt{s_0}) \cdot (\sqrt{s}/\sqrt{s_0})^{\epsilon}$. In these models more MPI activity is then predicted for smaller values of the $\hat{p}_{T,0}$ and ϵ param-

eters. The study of new data as a function of the hard scale and the centre-of-mass energy of the event can thus help to improve and tune the current models. [1] [2]

2 Underlying Event activity in the Drell-Yan process

One possibility is to study the UE activity using the experimentally clean Drell-Yan interaction. This is a complementary approach to already existing studies [3] and has the additional advantages of providing a clean separation of the hard interaction from the soft components, the absence of FSR and a low probability of photon brehmsstrahlung from the muons. The analysis strategy presented here is to measure the charged particle - and energy densities ($p_T > 0.5$ GeV/c, $|\eta| < 2$, muons from DY excluded) as a function of the di-muon p_T and the di-muon mass in the different geometrical *Towards*, *Transverse* and *Away* regions [4] with respect to the di-muon pair (81 GeV$/c^2 < M_{\mu\mu} < 101$ GeV$/c^2$). Analysing the di-muon p_T dependence enables us to probe the ISR spectrum while the studying the di-muon mass behaviour verifies the MPI saturation. The *Away* region is dominated by the hardest ISR that balances the di-muon system while the *Towards* and *Transverse* regions are sensitive to soft emissions due to MPI. Figure 1 shows the results of the energy densities as a function of the di-muon p_T. In the *Towards* and *Transverse* regions a slow growth of the densities is observed with increasing di-muon p_T. POWHEG Z2 and PYTHIA8 4C fail to describe the data while MADGRAPH with tune Z2 succeeds rather well. The *Away* region, sensitive to the spectrum of the hardest emission, is equally well described by all models and tunes. [5]

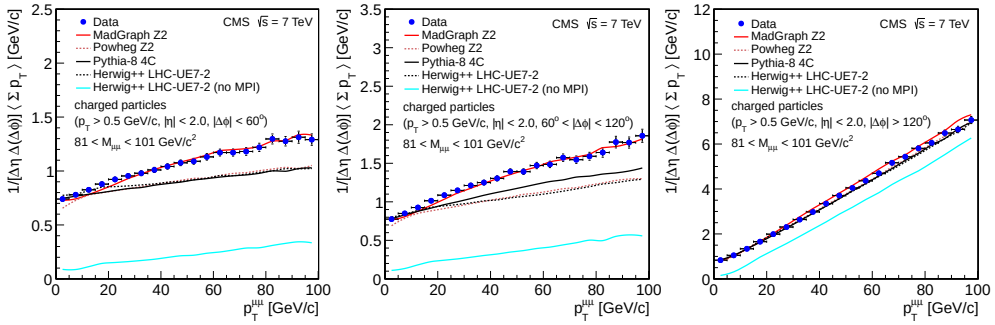

Figure 1: The energy density in the towards (left), transverse (middle), and away (right) regions as a function of $p_T^{\mu\mu}$ for events satisfying $81 < M_{\mu\mu} < 101$ GeV$/c^2$. Predictions of MADGRAPH Z2, POWHEG Z2, PYTHIA8 4C, and HERWIG++ LHC-UE7-2 (with and without MPIs) are superimposed. [5]

3 Jet area/median approach

The second analysis presented uses an alternative approach to study the UE activity at central rapidity. The soft hadronic activity in the event is measured by calculating the ratio of the jet p_T and the area covered by this jet in the (η, ϕ) plane for all jets in the event.

To quantify this we introduce the event variable:

$$\rho = \underset{j\in\text{jets}}{\text{median}} \left[\left\{ \frac{p_{T,j}}{A_j} \right\} \right]$$

This variable naturally isolates the UE contributions assuming that the majority of the event is dominated by soft interactions and has the additional advantage that no geometrical slicing of the phase space is needed. The usage of the median in the definition makes it robust to outliers in the distributions which can be hard interactions. To avoid problems with limited detector acceptance, an adjusted observable ρ' is introduced which uses only jets containing at least one physical particle [6]. The jets to then calculate ρ' are track-jets reconstructed with the k_T algorithm (R = 0.6) within $|\eta| < 1.8$. The input tracks to the jets have $p_T > 0.3$ GeV/c and $|\eta| < 2.3$. One can then study the jet area/median behaviour as a function of the leading jet found in the event. Figure 2 shows the results for $\sqrt{s} = 0.9$ and 7 TeV fully corrected to hadron level. Tunes Z1, Z2 and 4C of PYTHIA are too low at 7 TeV and one can generally see that the amount of events with very high activity is underestimated by the current models. [6]

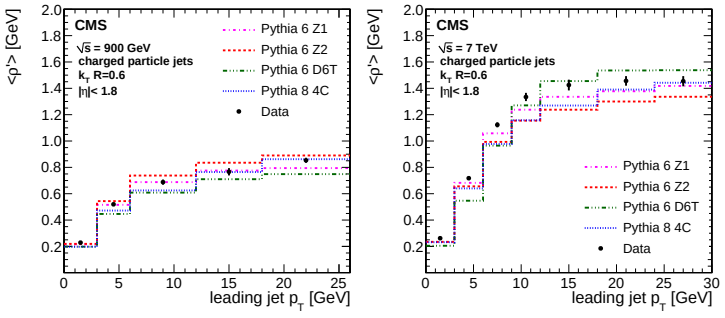

Figure 2: Mean values of the corrected ρ' distributions versus leading charged-particle jet transverse momentum at $\sqrt{s} = 0.9$ TeV (left) and $\sqrt{s} = 7$ TeV (right) in comparison to the predictions by the different generator tunes. [6]

4 Study of the Underlying Event at forward rapidity

The last analysis presented measures the UE activity by studying the energy densities at forward rapidity $5.2 < |\eta| < 6.6$. In this case the UE observables are separated with a large $\Delta\eta$ from the hard interaction and again no division of the phase space is needed. The analysis strategy is to look at the behaviour of the ratio of the energy deposited in inclusive MB events and the energy deposited in events with a hard scale $\hat{p}_T$ as a function of the leading jet of the event with $p_T > 1$ GeV/c and $|\eta| < 2$. The additional advantages of using a ratio of energy densities are that the results are more robust to systematic uncertainties and absolute energy calibration. Figure 3 then shows the hard-to-inclusive ratio as a function of the leading charged jet p_T at $\sqrt{s} = 0.9$, 2.76 and 7 TeV. At 7 TeV the well known UE behaviour of a fast increase at low p_T followed by a plateau above $p_T = 8$ GeV/c is visible while at 2.76 TeV the increase of the ratio is much reduced. At 0.9 TeV however the ratio goes below unity which can be understood

as follows: the production of central hard jets accompanied with higher UE activity depletes the energy of the proton remnant which fragments in the rapidity range of the measurement. Although the older D6T tune fails to describe the data, recent models tuned to LHC data (Z2*, 4C, HERWIG 2.5) reproduce the results rather well. [7]

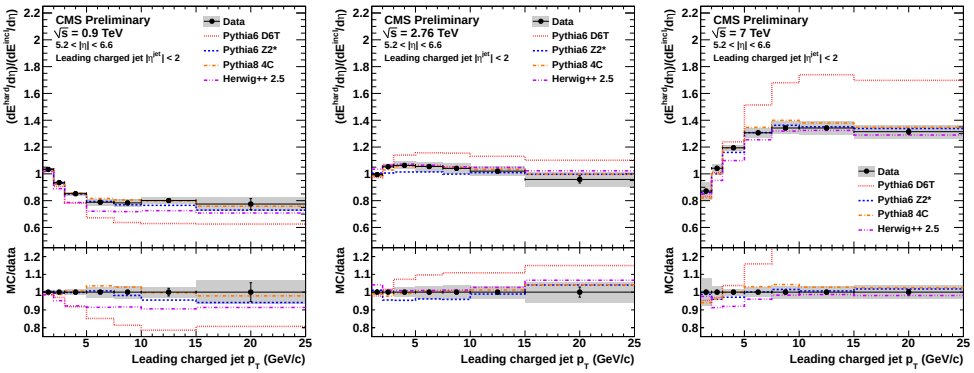

Figure 3: Ratio of the energy deposited in the pseudorapidity range $5.2 < |\eta| < 6.6$ for events with a charged particle jet with $|\eta^{jet}| < 2$ with respect to the energy in inclusive events, as a function of charged particle jet transverse momentum for $\sqrt{s} = 0.9$ (left), 2.76 (middle) and 7 TeV (right). [7]

5 Conclusions

The UE activity is studied in many ways with the CMS experiment at the LHC by measuring energy densities and jet area/median values at central or forward rapidity using leading jets or Drell-Yan processes to determine the hard scale of the event. Models tuned to early LHC data can describe many aspects of the UE, i.e. the evolution of both central & forward energy densities and the behaviour of the jet area/median as a function of the hard scale of the event. Notable discrepancies of the UE activity are observed in the *Towards* & *Transverse* regions in Drell-Yan at high p_T.

References

[1] S. Alekhin, G. Altarelli, N. Amapane, J. Andersen, V. Andreev, M. Arneodo, V. Avati and J. Baines *et al.*, "HERA and the LHC: A Workshop on the implications of HERA for LHC physics: Proceedings Part A," hep-ph/0601012.

[2] L. Frankfurt, M. Strikman and C. Weiss, Phys. Rev. D **83** (2011) 054012 [arXiv:1009.2559 [hep-ph]].

[3] S. Chatrchyan *et al.* [CMS Collaboration], JHEP **1109** (2011) 109 [arXiv:1107.0330 [hep-ex]].

[4] R. Field, "Early LHC Underlying Event Data - Findings and Surprises," arXiv:1010.3558 [hep-ph].

[5] S. Chatrchyan *et al.* [CMS Collaboration], "Measurement of the underlying event in the Drell-Yan process in proton-proton collisions at sqrt(s) = 7 TeV," arXiv:1204.1411 [hep-ex].

[6] The CMS Collaboration, "Measurement of the underlying event activity in pp collisions at $\sqrt{s} = 0.9$ and 7 TeV with the novel jet-area/median approach," CMS-QCD-10-021, CERN-PH-EP-2012-152.

[7] The CMS Collaboration, "Study of the Underlying Event at Forward Rapidity in Proton-Proton Collisions at the LHC," CMS-PAS-FWD-11-003, [http://cdsweb.cern.ch/record/1434458].

Measurements of Correlations in Minimum Bias Interactions with the ATLAS Detector

Arthur Moraes[1] on behalf of the ATLAS Collaboration

[1]University of Glasgow, Kelvin Building, Glasgow G12 8QQ, UK

DOI: http://dx.doi.org/10.3204/DESY-PROC-2012-02/83

This report presents a brief summary of recent minimum bias measurements using data recorded with the ATLAS detector at the LHC. Measurements done with inelastic proton-proton collisions at different centre-of-mass energies are shown and discussed. In this report we present results on forward-backward multiplicity correlations, two-particle angular correlation and the azimuthal ordering of charged particles.

1 Introduction

Inclusive charged-particle distributions have been measured in proton-proton (pp) collisions at the Large Hadron Collider (LHC) for different centre-of-mass energies [1, 2, 3]. These measurements provide insight into the strong interaction (QCD) at low energy scales and show that predictions of current phenomenological models cannot fully describe the measured observables in all regions of phase-space.

Some of these discrepancies may be reduced through the development of parametrisations for the models of non-perturbative QCD, or tunes, that better match model predictions to the latest measurements of particles produced at very low-p_T. Nevertheless, it is also possible that a new formulation of certain components of these phenomenological models is needed. Many of the difficulties in accurately describing observables dominated by low-p_T QCD phenomena stem from the fact that there is often a combination of non-perturbative effects, including soft diffraction, low-p_T parton scattering and hadronisation. These effects act simultaneously in a given region of phase-space and are difficult to separate experimentally.

This report presents a brief summary of recent minimum bias measurements using data recorded with the ATLAS detector [4] at the LHC. We will discuss ATLAS results on forward-backward multiplicity correlations [5], two-particle angular correlation [6] and the azimuthal ordering of charged hadrons [7].

2 Results

2.1 Forward-backward correlation

Using inelastic pp interactions at $\sqrt{s}$ = 900 GeV and 7 TeV measurements have been made of the correlations between forward and backward charged-particle multiplicities in intervals of pseudorapidity (η).

The forward-backward (FB) multiplicity correlation, ρ^n_{fb}, between two particle multiplicities is the normalised covariance between the two distributions, relative to the mean value of each. For a given data sample or Monte Carlo (MC) sample, it is defined as

$$\rho^n_{fb} = \frac{\langle (n_f - \langle n_f \rangle)(n_b - \langle n_b \rangle) \rangle}{\sqrt{\langle (n_f - \langle n_f \rangle)^2 \rangle \langle (n_b - \langle n_b \rangle)^2 \rangle}}. \quad (1)$$

Here, n_f and n_b are the respective charged-particle multiplicities in two chosen forward and backward η intervals in an event, $\langle\rangle$ denotes a mean over the events in the sample. Charged-particle multiplicities are obtained for particles with transverse momentum (p_T) above a given minimum (p_T^{min}). Figure 1 shows the FB multiplicity correlation in symmetrically opposite η intervals for events with at least two charged particles with $p_T > 100$ MeV and $|\eta| < 2.5$. Corrected data at 7 TeV (a) and 900 GeV (b) is compared to a selection of MC simulations [5]. The systematic uncertainties are indicated by a grey band; the statistical uncertainties are too small to be visible on the figure. The multiplicity correlations are substantially lower at 900 GeV than at 7 TeV. The comparisons indicate that model predictions vary considerably depending on the tune chosen; the shapes of the distributions are generally similar but some of the tunes show systematically different trends from the data. The correlations given by Pythia 6 AMBT2B are the most consistent with the data; AMBT2B was tuned to these event samples using different variables but not these correlations.

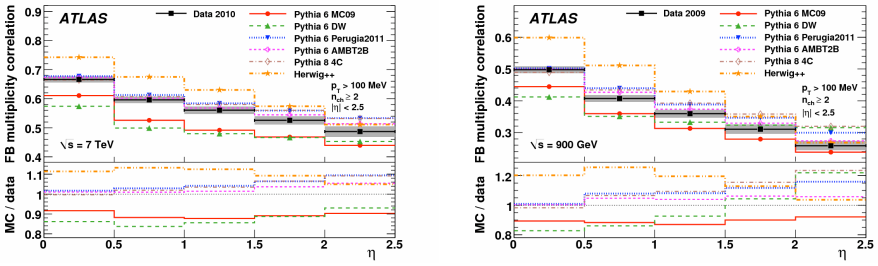

(a) (b)

Figure 1: Forward-backward multiplicity correlation in symmetrically opposite η intervals for events with at least two charged particles with $p_T > 100$ MeV and $|\eta| < 2.5$. Data at 7 TeV (a) and 900 GeV (b), compared to a selection of MC simulations [5].

2.2 Inclusive two-particle angular correlation

Two-particle angular correlations in pp collisions at $\sqrt{s} = 900$ GeV and 7 TeV were also measured with the ATLAS detector [6]. The two-particle angular correlation is defined as

$$R(\Delta\eta, \Delta\phi) = \frac{\langle (n_{ch} - 1) F(n_{ch}, \Delta\eta, \Delta\phi) \rangle_{ch}}{B(\Delta\eta, \Delta\phi)} - \langle n_{ch} - 1 \rangle_{ch}. \quad (2)$$

In eq. (2), the foreground distribution, $F(n_{ch}, \Delta\eta, \Delta\phi)$, describes the angular separation in azimuth ($\Delta\phi$) and pseudorapidity ($\Delta\eta$) between pairs of particles emitted in the same event of charged multiplicity n_{ch} and $B(\Delta\eta, \Delta\phi)$ is a multiplicity independent background distribution

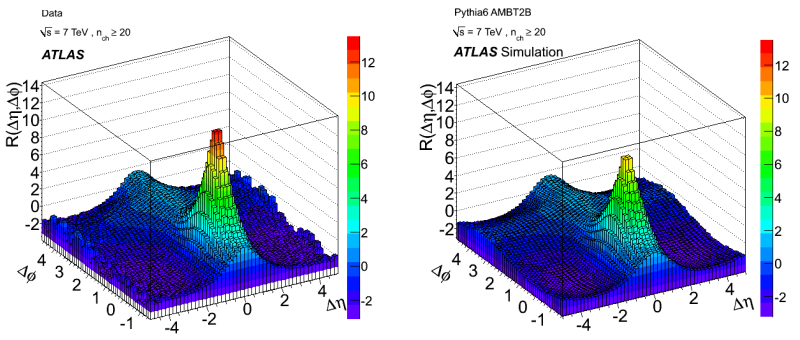

(a) (b)

Figure 2: Corrected $R(\Delta\eta, \Delta\phi)$ two-particle correlation functions at $\sqrt{s} = 7$ TeV for $n_{ch} \geqslant 20$ (a) data and (b) Monte Carlo (Pythia 6 - AMBT2B). These plots are symmetric around $\Delta\eta = 0$ by construction [6].

of uncorrelated pairs from different events. The correlations were measured for charged particles produced in the kinematic range of $p_T > 100$ MeV and $|\eta| < 2.5$. Figure 2 shows the corrected $R(\Delta\eta, \Delta\phi)$ two-particle correlation functions at $\sqrt{s} = 7$ TeV for $n_{ch} \geqslant 20$ for both data (a) and MC Pythia 6 AMBT2B (b). While Pythia 6 AMBT2B and many of the models investigated in this study reproduce the general features of the two-particle correlation function, none of them provide a good quantitative description of the strength of the correlations. In order to properly describe the correlations, the phenomenology of soft particle production needs further improvement. Similar results are obtained for comparisons between data and MC at $\sqrt{s} = 900$ GeV [6].

2.3 Measurement of the azimuthal ordering of charged hadrons

The presence of azimuthal ordering, stemming from the underlying QCD string structure formed during hadronisation, should be observable with the help of a power spectrum suitably defined to expose the properties of the string fragmentation. The ordering of charged hadrons in the azimuthal angle relative to the beam axis (ϕ) in high-energy pp collisions at the LHC was recently measured by the ATLAS Collaboration [7]. A spectral analysis of correlations between longitudinal and transverse components of the momentum of the charged hadrons was performed with the power spectrum defined as

$$S(\xi) = \frac{1}{N_{ev}} \sum_{event} \frac{1}{n_{ch}} |\sum_{j}^{n_{ch}} \exp(i(\xi\eta_j - \phi_j))|^2, \tag{3}$$

where ξ is a parameter and η_j (ϕ_j) is the pseudorapidity (azimuthal angle) of the j-th hadron, N_{ev} is the number of events, and n_{ch} is the number of charged hadrons in the event. The inner sum runs over charged hadrons in the event and the outer sum over events in the sample.

Figure 3 shows the measured S_η distribution (corrected for detector effects) compared to particle level predictions from various MC models using conventional hadronisation algorithms.

The comparisons are made for two samples with different particle selection cuts: (a) low-p_T depleted sample (particle p_T cut-off: $p_T > 500$ MeV) and (b) low-p_T enhanced sample ($p_T > 100$ MeV, and selection of events with no particles with $p_T^{max} > 1$ GeV).

Predictions generated with MC tunes typically produce a spectrum with more correlations than seen in data for the low-p_T depleted sample as shown in fig. 3(a). The correlations measured in a phase space region dominated by low-p_T particles are not well described by conventional models of hadron production, as shown in fig. 3(b). The measured spectra show features consistent with the fragmentation of a QCD string represented by a helix-like gluon chain [7].

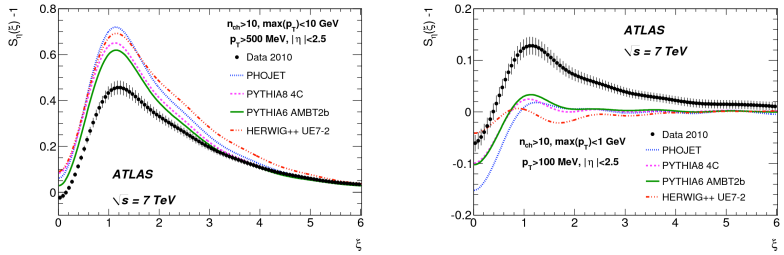

(a) (b)

Figure 3: Measured S_η distribution compared to particle level predictions from various MC models using conventional hadronisation algorithms. The error bars correspond to the combined statistical and systematic uncertainties: (a) low-p_T depleted sample and (b) low-p_T enhanced sample [7].

3 Summary

Recent measurements of correlations in minimum bias interactions with the ATLAS Detector have been presented and indicate that the phenomenology of soft particle production needs further improvement. In many cases this can be addressed by re-tuning the MC generators, but the data suggest fundamental re-thinking of the models is also necessary.

References

[1] ATLAS Collaboration, New J. Phys. **13** (2011) 053033.

[2] ALICE Collaboration, Eur. Phys. J. C **68** (2010) 345.

[3] CMS Collaboration, J. High Energy Phys. **01** (2011) 079.

[4] ATLAS Collaboration, JINST **8** (2008) S08003.

[5] ATLAS Collaboration, "Forward-backward correlations and charged-particle azimuthal distributions in pp interactions using the ATLAS detector", 2012. `[hep-ex] 1203.3100`

[6] ATLAS Collaboration,"Measurement of inclusive two-particle angular correlations in pp collisions with the ATLAS detector at the LHC", 2012. `[hep-ex] 1203.3549`

[7] ATLAS Collaboration, "Measurement of the azimuthal ordering of charged hadrons with the ATLAS detector", 2012. `[hep-ex] 1203.0419`

Measurement of the forward energy flow in pp collisions at $\sqrt{s} = 7$ TeV with the LHCb detector

Dmytro Volyanskyy, Michael Schmelling on behalf of the LHCb collaboration

Max-Planck-Institut für Kernphysik, 69117 Heidelberg, Deutschland

DOI: http://dx.doi.org/10.3204/DESY-PROC-2012-02/149

We present the results on the energy flow measured with minimum-bias data collected by the LHCb experiment in pp collisions at $\sqrt{s} = 7$ TeV for inclusive minimum-bias interactions, hard scattering processes and events with enhanced or suppressed diffractive contribution. The measurements are performed in the pseudorapidity range $1.9 < \eta < 4.9$, which corresponds to the main detector acceptance of the LHCb spectrometer. The data are compared to predictions given by the PYTHIA-based and cosmic-ray Monte Carlo event generators, which model the underlying event activity in different ways.

1 Introduction

The energy flow created in inelastic hadron-hadron interactions at large values of the pseudorapidity $\eta = -\ln\tan\theta/2$ with θ being the polar angle of particles w.r.t. the beam axis, is expected to be directly sensitive to the amount of parton radiation and multi-parton interactions (MPI) [1]. The latter mainly arise in the region of a very low $x = p_{\text{parton}}/p_{\text{hadron}} \to 0$, where parton densities are large so that the probability of more than a single parton-parton interaction per hadron-hadron collision is high. MPI represent a predominant contribution to the soft component of a hadron-hadron collision, called the underlying event (UE). Its precise theoretical description still remains a challenge as MPI phenomenon is currently weakly known.

In this study, experimental results on the energy flow are compared to predictions given by the PYTHIA-based [2, 3, 4] and cosmic-ray Monte Carlo (MC) event generators [5], which model the UE activity in different ways. The analysis was performed using a sample of minimum-bias data collected by the LHCb experiment [6] in pp collisions at $\sqrt{s} = 7$ TeV during the low luminosity running period in 2010. The events were recorded using a trigger that has required the presence of at least one reconstructed track segment in the spectrometer. For a particular pseudorapidity bin with the width $\Delta\eta$, the total energy and total number of stable particles E_{tot} and $N_{part,\eta}$, the energy flow is defined as

$$\frac{1}{N_{\text{int}}}\frac{dE_{tot}}{d\eta} = \frac{1}{\Delta\eta}\left(\frac{1}{N_{\text{int}}}\sum_{i=1}^{N_{part,\eta}} E_{i,\eta}\right) , \tag{1}$$

where N_{int} is the number of inelastic pp interactions and $E_{i,\eta}$ is the energy of an individual particle.

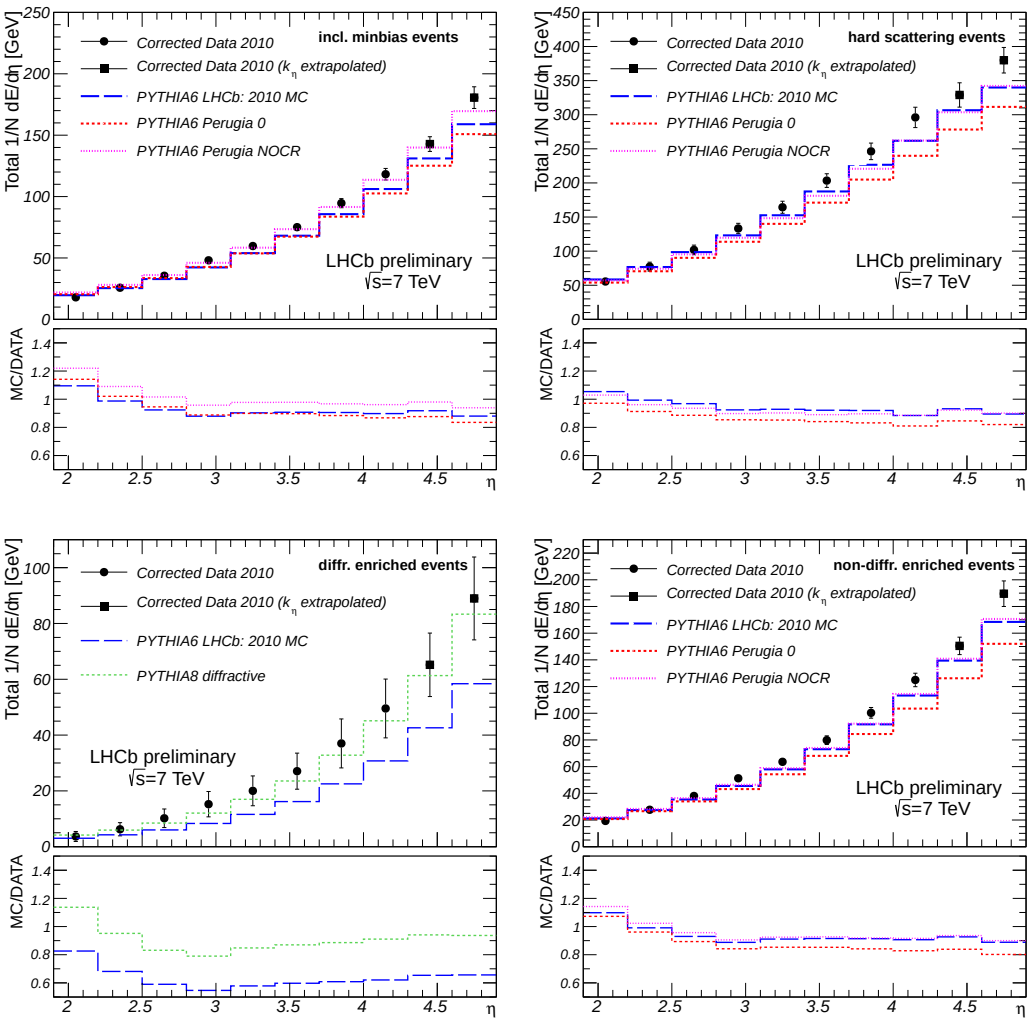

Figure 1: *Total corrected energy flow obtained for all event classes under consideration. The measurements are indicated by points with error bars representing the systematic uncertainties, while the generator level predictions given by the PYTHIA-based models are shown as histograms. The ratios between the model predictions and corrected data are demonstrated in addition.*

2 Analysis Strategy

In this analysis, the energy flow carried by the charged stable particles was measured using good quality reconstructed tracks traversing the full LHCb tracking setup with a momentum in the range $2 < p < 1000$ GeV/c and $1.9 < \eta < 4.9$. Particle identification was not used in this study. Instead, the energy was simply estimated from the reconstructed momentum. The reconstructed charged energy flow was corrected for detector effects using the average of correction factors

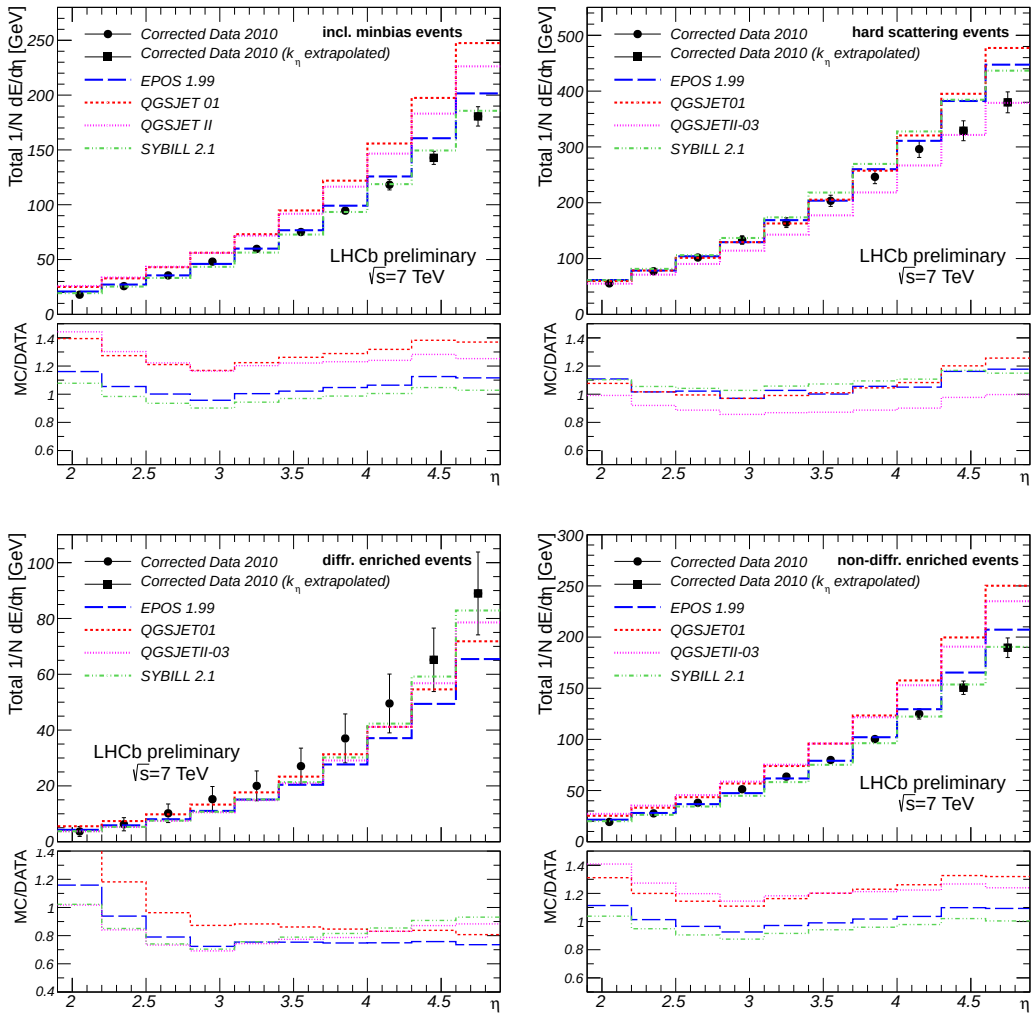

Figure 2: *Total corrected energy flow obtained for all event classes under consideration. The measurements are indicated by points with error bars representing the systematic uncertainties, while the predictions given by the cosmic-ray interaction models are shown as histograms. The ratios between the model predictions and corrected data are demonstrated in addition.*

obtained from various MC models as the ratio of the predictions at generator and detector levels for each η bin. The total energy flow was estimated from the corrected charged one by using a data-constrained MC estimate of the neutral component. For the two highest η bins the data-constrained measurements of the neutral energy flow were extrapolated from the more central region as the LHCb Electromagnetic Calorimeter has no detection coverage for that region of phase space.

In order to probe various aspects of multi-particle production in high-energy hadron-hadron collisions, the measurements were performed for the following four event classes: inclusive

minimum-bias (containing at least one track with $p > 2$ GeV/c in $1.9 < \eta < 4.9$), hard scattering (having at least one track with $p_{\mathrm{T}} > 3$ GeV/c in $1.9 < \eta < 4.9$), diffractive and non-diffractive enriched interactions. The last two event types were selected among the inclusive minimum-bias ones requiring the absence and presence of at least one backward track reconstructed by the LHCb Vertex Locator in $-3.5 < \eta < -1.5$, respectively. A detailed description of the whole analysis procedure can be found in [7].

3 Results

The computed total corrected energy flow is illustrated for every event class in Fig. 1 and Fig. 2 along with the PYTHIA-based and cosmic-ray model predictions, respectively. As can be seen, the energy flow increases with the momentum transfer in an underlying pp inelastic interaction. The development of the energy flow as a function of η is reasonably well reproduced by the MC models. Nevertheless, the PYTHIA-based generators underestimate the corrected data at large η, while most of the cosmic-ray interaction models overestimate it, except for the diffractive enriched events. The predictions given by the SIBYLL 2.1 cosmic-ray generator [8] for the inclusive minimum-bias and non-diffractive enriched events provide the best description of the corresponding energy flows across the entire η range of the measurements. In the forward region the total uncertainties for most of the event classes are around 5%. For the diffractive enriched events, the uncertainties are about 3 times larger mainly because of the strong model dependency of the correction factors. None of the MC models used in this analysis are able to describe the energy flow measurements for all event classes that have been studied. It follows that the results obtained in this analysis can be used to improve the existing MC models by further constraining the parameters describing the partonic stage of high-energy hadronic interactions, diffractive particle production and hard QCD processes.

4 Acknowledgements

We are thankful to Colin Baus and Ralf Ulrich from the Karlsruhe Institute of Technology for providing the predictions of the cosmic-ray MC generators.

References

[1] T. Sjostrand, M. van Zijl, Phys. Rev. D **36** (1987) 2019.

[2] P. Skands, Phys. Rev. **D82** (2010) 074018.

[3] M. Clemencic *et al.*, Journal of Physics: Conference Series 331 (2011), no. 3 032023.

[4] T. Sjostrand *et al.*, Comput. Phys. Commun. **178** (2008) 852.

[5] D. d'Enterria *et al.*, Astropart.Phys. **35** (2011) 98-113 and references therein.

[6] LHCb Collaboration. JINST **3** (2008) S08005.

[7] LHCb Collaboration. CERN-LHCb-CONF-2012-012.

[8] E.-J. Ahn *et al.*, Phys. Rev. **D80** (2009) 094003.

Inelastic proton-proton cross section measurements in CMS at $\sqrt{s} = 7$ TeV

Anna Julia Zsigmond[1,2] on behalf of the CMS Collaboration

[1]Eötvös Loránd University, Budapest, Hungary
[2]Institute for Particle and Nuclear Physics, Wigner RCP, Budapest, Hungary

DOI: http://dx.doi.org/10.3204/DESY-PROC-2012-02/181

We present measurements of the total inelastic pp cross section at 7 TeV obtained with the CMS detector. Two different methods are used. In runs with low event pile-up, we exploit the large pseudorapidity coverage ($|\eta| < 5.2$) of the CMS calorimeters to obtain the cross section for events with any activity in the acceptance range. In addition, runs with high event pile-up are used by fitting a Poisson distribution with the total visible cross section as parameter to the number of reconstructed primary vertices. Both measurements are corrected to a hadron level definition of the inelastic cross section.

1 Introduction

The cross sections of hadronic collisions are important and fundamental quantities in high energy particle and nuclear physics and have been studied in the last 40 years in experiments covering many orders of magnitude in center-of-mass energies.

In this report we present two methods for measuring the inelastic proton-proton cross section with the CMS detector. Data collected in 2010 were used in both analyses but with different luminosity and pile-up conditions. Low pile-up data were used to count events with activity in either of the Hadron Forward Calorimeters (HF) in the first method presented. The other method used high luminosity data to count pile-up events in a given bunch crossing as a function of bunch luminosity and fitted with a Poisson distribution to evaluate the cross section.

Both measurements are corrected to hadron level definitions of the inelastic *pp* cross section. From these definitions, extrapolations are performed to the total inelastic *pp* cross section with various Monte Carlo models also used in cosmic-rays physics.

2 Event counting method with single-sided trigger

The goal of the first method [1] is to count events with as loose selection as possible to detect the largest possible cross section which translates to the smallest possible extrapolation. In the event counting, we required one reconstructed energy deposit in either side of the HF Calorimeters with at least 5 GeV total energy. The possible signal events were triggered by two proton bunches entering CMS and the background was estimated from the number of selected events triggered by a single bunch entering CMS. With the HF detectors only, more than one

inelastic interaction in the same bunch- crossing cannot be separated, which means the need of low pile-up data ($\lambda < 12\%$) for small pile-up correction factor.

Using generator level Monte Carlo, the inelastic interactions can be characterized with the variable ξ. The final state particles are ordered in rapidity and the largest rapidity gap is used to assign the particles into two systems. The invariant masses of the two systems are calculated and the higher mass system is called X, then the variable ξ is given by $\xi = M_X^2/s$. In case of single diffractive events, ξ is the fractional momentum loss of the scattered proton. Studying the HF selection efficiency as a function of ξ showed that events with small ξ can escape detection. For $\xi > 5 \times 10^{-6}$, the efficiency of detection is more than 98%.

The definition of the inelastic *pp* cross section with $\xi > 5 \times 10^{-6}$ is

$$\sigma_{\text{inel}}(\xi > 5 \times 10^{-6}) = \frac{N_{\text{inel}}(1 - f_\xi)F_{\text{pile-up}}}{\epsilon_\xi \int \mathcal{L}\text{dt}}$$

where N_{inel} is the number of events selected by the HF calorimeters after subtracting the background, f_ξ is the fraction of selected events that are low mass (contamination), $F_{\text{pile-up}}$ is the pile-up correction factor, $\int \mathcal{L}\text{dt}$ is the integrated luminosity and ϵ_ξ is the efficiency to detect an inelastic event with $\xi > 5 \times 10^{-6}$, namely the fraction of high mass events that are selected.

The efficiency (ϵ_ξ) and contamination (f_ξ) correction factors were determined from three Monte Carlo generators using the full detector simulation of CMS: PYTHIA 6 [2], PYTHIA 8 [3] and PHOJET [4]. To calculate the pile-up correction factor ($F_{\text{pile-up}}$) an iterative method was used where the average number of collisions per bunch-crossing, the pile-up (λ) was measured from the data directly. Several low pile-up datasets were used to obtain the cross section. The integrated luminosity values for these datasets were obtained on the basis of Van der Meer scans, which carry a 4% normalization uncertainty dominating the uncertainties in the present analyses.

The result of the analysis for events with ($\xi > 5 \times 10^{-6}$) is obtained by averaging the 5 GeV HF threshold cross section values measured at different pile-up conditions. The systematic uncertainties of the result take into account noisy tower exclusion, run-by-run luminosity variations, varying the HF energy threshold and the model dependence.

The final result for the inelastic *pp* cross section with ($\xi > 5 \times 10^{-6}$):

$$\sigma_{\text{inel}}(\xi > 5 \times 10^{-6}) = 60.2 \pm 0.2(\text{stat.}) \pm 1.1(\text{syst.}) \pm 2.4(\text{lumi.}) \text{ mb.}$$

3 Pile-up counting method

The second method [5] is based on the assumption that the number of inelastic *pp* interactions in a given bunch crossing follows a Poisson probability distribution:

$$P(n) = \frac{(\mathcal{L}\sigma_{\text{inel}})^n}{n!} e^{-\mathcal{L}\sigma_{\text{inel}}}$$

where $\mathcal{L}$ is the bunch crossing luminosity and σ_{inel} is the total inelastic *pp* cross section.

Two data samples, an inclusive di-electron and a single muon, were collected with the CMS triggers. The specific trigger requirements are not important as long as their efficiencies do not depend on the instantaneous luminosity. Using these data samples the number of reconstructed vertices were counted in each bunch crossing in bins of luminosity. Every vertex had to fulfill the quality requirements to be counted as a visible vertex. The quality requirements are the

following: the transverse position of the vertex between ± 0.06 cm, the minimum distance between two vertices 0.1 cm, $NDOF = 2 \times \Sigma_{tracks}(weights) - 3 > 0.5$ where the $weights$ are the quality of the tracks associated with the vertex, at least 2, 3 or 4 tracks with $p_T > 200$ MeV/c in $|\eta| < 2.4$ associated with the vertex and each track should have at least 2 pixel and 5 strip hits. To obtain the true number of vertices from the visible number of vertices a bin-by-bin correction factor was applied using the full simulation of the CMS detector accounting for vertex reconstruction efficiency, vertex merging and fakes.

After the corrections applied, the distributions of the fraction of pile-up events as a function of the single bunch luminosity for $n = 0, ..., 8$ pile-up events are well fitted with a Poisson distribution. The 9 values of the cross section are fitted together to get the visible inelastic pp cross section. The main sources of systematic uncertainties are the use of different datasets, change in the fit limits, the minimum distance between vertices, the vertex quality requirement and the application of an analytic method for the corrections.

The final results with at least 2, 3 or 4 charged particles with $|\eta| < 2.4$ and $p_T > 200$ MeV/c of the visible inelastic pp cross section are the following:

$$\sigma_{\text{vis}}(\geq 2 \text{ charged particles}) = 58.7 \pm 2.0(\text{syst.}) \pm 2.4(\text{lumi.}) \text{ mb.}$$

$$\sigma_{\text{vis}}(\geq 3 \text{ charged particles}) = 57.2 \pm 2.0(\text{syst.}) \pm 2.4(\text{lumi.}) \text{ mb.}$$

$$\sigma_{\text{vis}}(\geq 4 \text{ charged particles}) = 55.4 \pm 2.0(\text{syst.}) \pm 2.4(\text{lumi.}) \text{ mb.}$$

4 Extrapolation to the total inelastic cross section

Additional Monte Carlo models were used for the extrapolation from the different hadron level definitions of the cross section to the total inelastic pp cross section. The considered models were PYTHIA 6 [2], PYTHIA 8 [3], PHOJET [4], EPOS 1.99 [6], SYBILL 2.1 [7], QGSJET 1 and QGSJET-II [8] which use different models/tunings for the hard parton-parton and for the diffractive scattering cross sections. Every model show a similar trend for the measured hadron level cross sections but there are substancial differences in the expextations for the total inelastic pp cross section.

For the extrapolation from the inelastic pp cross section with ($\xi > 5 \times 10^{-6}$) to the total inelastic pp cross section all generators were considered except QGSJET 1 since this model used in cosmic-rays physics is only describing one of the hemispheres of the collision, which is not suitable for efficiency calculations when a single energy deposit in either one of the two HF calorimeters is required. The final result of the first analysis is

$$\sigma_{\text{inel}} = 64.5 \pm 0.2(\text{stat.}) \pm 1.1(\text{syst.}) \pm 2.6(\text{lumi.}) \pm 1.5(\text{extr.}) \text{ mb.}$$

The extrapolation from the visible cross section with at least 2,3 or 4 charged particles with $p_T > 200$ MeV/c and $|\eta| < 2.4$ has been computed using only the models in agreement with the measured points (not PHOJET or SYBILL). The final result of the second analysis is

$$\sigma_{\text{inel}} = 68 \pm 2.0(\text{syst.}) \pm 2.4(\text{lumi.}) \pm 4(\text{extr.}) \text{ mb.}$$

5 Summary

CMS measured the inelastic pp cross section at $\sqrt{s} = 7$ TeV with two independent method using two different subdetectors. The results for the inelastic pp cross section with ($\xi > 5 \times 10^{-6}$) are in very good agreement with the result of the ATLAS Collaboration in the same kinematic range [9].

The extrapolations to the total inelastic pp cross section rely entirely on the models and their description of the low mass region. Within the large extrapolation uncertainties the results of CMS presented here are in agreement with the results from ATLAS, ALICE and TOTEM collaborations as shown in Figure 1.

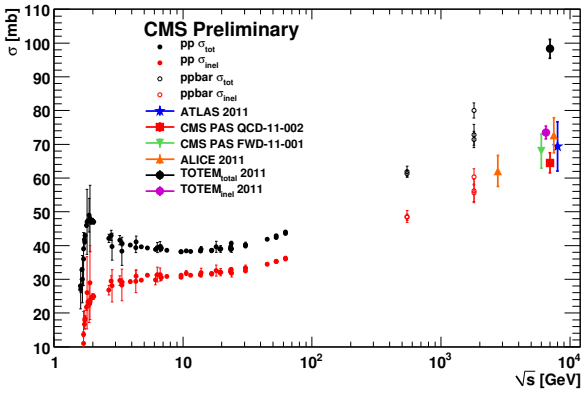

Figure 1: The total inelastic pp cross section at $\sqrt{s} = 7$ TeV from CMS compared with ATLAS, ALICE, TOTEM and lower energy pp and $p\bar{p}$ data from PDG.

Acknowledgements

The author wishes to thank to the Hungarian Scientific Research Fund (K 81614) for support.

References

[1] CMS Collaboration, CMS Physics Analysis Summary, **CMS-PAS-QCD-11-002** cdsweb.cern.ch/record/1433413

[2] T. Sjostrand, S. Mrenna and P. Z. Skands, JHEP **0605** (2006) 026 hep-ph/0603175

[3] T. Sjostrand, S. Mrenna and P. Z. Skands, Comput. Phys. Commun. **178** (2008) 852 arXiv:0710.3820

[4] R. Engel, J. Ranft and S. Roesler, Phys. Rev. D **52** (1995) 1459 hep-ph/9502319

[5] CMS Collaboration, CMS Physics Analysis Summary, **CMS-PAS-FWD-11-001** cdsweb.cern.ch/record/1373466

[6] K. Werner, F. -M. Liu and T. Pierog, Phys. Rev. C **74** (2006) 044902 hep-ph/0506232

[7] E. -J. Ahn, R. Engel, T. K. Gaisser, P. Lipari and T. Stanev, Phys. Rev. D **80** (2009) 094003 arXiv:0906.4113

[8] S. Ostapchenko, Phys. Rev. D **83** (2011) 014018 arXiv:1010.1869

[9] ATLAS Collaboration, G. Aad *et al.*, Nature Commun. **2** (2011) 46 arXiv:1104.0326

[10] M. G. Poghosyan, J. Phys. G G **38** (2011) 124044 arXiv:1109.4510

[11] G. Antchev, P. Aspell, I. Atanassov, V. Avati, J. Baechler, V. Berardi, M. Berretti and E. Bossini *et al.*, Europhys. Lett. **96** (2011) 21002 arXiv:1110.1395

The Underlying Event in Herwig++

Stefan Gieseke[1], *Christian Röhr*[1]*, *Andrzej Siódmok*[1,2]

[1]Karlsruhe Institute of Technology (KIT), 76128 Karlsruhe, Germany
[2]The University of Manchester, Manchester, United Kingdom

DOI: http://dx.doi.org/10.3204/DESY-PROC-2012-02/367

We review the modelling of multiple interactions in the event generator Herwig++ and study implications of recent tuning efforts to LHC data. A crucial ingredient to a successful description of minimum-bias and underlying-event observables is a model for colour reconnection. Improvements to this model, inspired by statistical physics, are presented.

1 Introduction

Multiple partonic interactions (MPI) are vital for a successful description of the underlying event (UE) in hard hadronic collisions and of minimum-bias (MB) data from the Tevatron and the Large Hadron Collider (LHC). A model of independent multiple partonic interactions was first implemented in Pythia [1], where its relevance for a description of hadron collider data was immediately shown. Meanwhile, all major event generators for LHC physics, Herwig [2], Pythia [3, 4] and Sherpa [5], contain MPI models. The core MPI model in Herwig++, which is similar to the Jimmy add-on [6] to the Fortran version of Herwig, was introduced in Ref. [7]. Additional hard parton-parton scatters unitarize the hard jet cross section. Also the jet-like structure of the underlying event is reproduced by this model. With soft components in multiple parton interactions included, which is described in Ref. [8], this model is sufficient to describe the UE data collected at the Tevatron. First MB data from ATLAS [9], however, e.g. the pseudorapidity distribution of charged particles, cannot be reproduced with the core MPI model discussed so far.

As shown in Ref. [10], which we summarize in this work, we can significantly improve the description of MB and UE data from the LHC if we include a model for colour reconnections (CR). The idea of CR is based on colour preconfinement [11], which implies that parton jets emerging from different partonic interactions are colour-connected if they overlap in momentum space. As the core MPI model does not take that into account, those colour connections have to be adapted afterwards by means of a CR procedure.

The colour connections between partons define colour singlet objects, the clusters. The cluster hadronization model [12], which is implemented in Herwig++, generates hadronic final states based on clusters. Figure 1a shows that in events with multiple parton scatters clusters can be discriminated by the origin of their partonic constituents. We define three classes of clusters. h-type clusters consist of partons generated perturbatively in a single partonic subprocess. The second type of clusters are the subprocesses-interconnecting ones, which

*Speaker

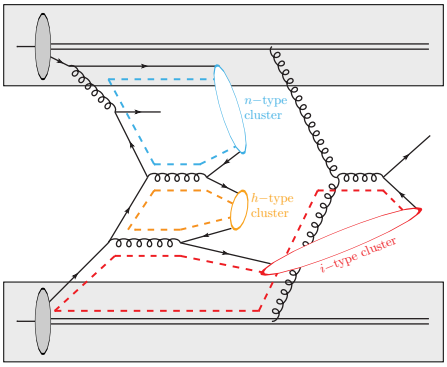

(a) Sketch of cluster classes in a simple pp event. The classes are defined in the text.

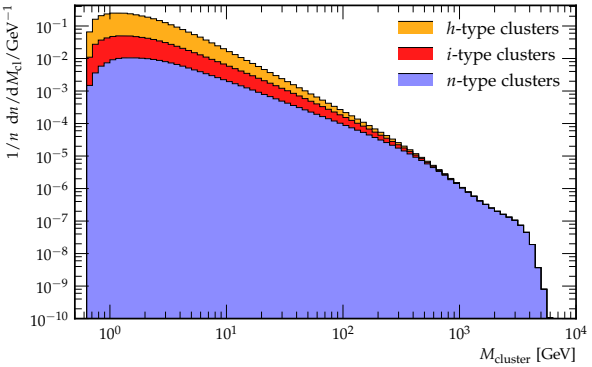

(b) Contributions of the cluster classes to the invariant cluster mass distribution in soft-inclusive pp collisions at 7 TeV.

Figure 1: Classification of clusters in hadron collision events.

combine partons generated perturbatively in different subprocesses. These clusters are labelled as i-type. The remaining clusters, which we call n-type, contain one parton which was created non-perturbatively, i.e. during the extraction of partons from the hadrons or in soft scatters. Using this classification, we see in Fig. 1b that n-type clusters contribute most to the high-mass tail in the invariant mass distribution of the clusters. This observation is easily interpreted: The non-perturbative extraction of the partons from the protons, denoted by the grey-shaded area in Fig. 1a, may yield colour connections between partons which are distant in momentum space and thus have large invariant masses. To restore the physical picture of preconfinement, a colour reconnection model must be applied which helps to avoid these heavy clusters.

2 Colour reconnection models

A colour reconnection model has been included in HERWIG++ as of version 2.5 [13]. This model iterates over all cluster pairs in a random order. Whenever a swap of colours is preferable, i.e. when the new cluster masses are smaller, this is done with a given probability, which is the only model parameter. This *plain* model has shown to give the desired results. As the clusters are presented to the model only in a given sequence, though, it is hard to assess which clusters are affected and to what extent the sequence is physically relevant.

For these reasons, we implemented another CR model, which adopts the Metropolis [14] and the Simulated-Annealing algorithm [15]. The *statistical* colour reconnection model has been implemented as of HERWIG++ 2.6 [16] and is discussed in detail in Ref. [10]. The new CR model reduces the colour length $\lambda \equiv \sum_{i=1}^{N_{\mathrm{cl}}} m_i^2$ statistically, where N_{cl} is the number of clusters in an event and m_i is the invariant mass of cluster i.

For both the plain and the statistical CR model we observe an extreme drop in the colour length, $\Delta_{\mathrm{if}} \equiv 1 - \lambda_{\mathrm{final}}/\lambda_{\mathrm{init}}$, as shown in Fig. 2a. Here, λ_{init} and λ_{final} denote the colour length λ before and after the colour reconnection procedure, respectively. The change in the cluster mass spectrum is directly visible in Fig. 2b. For these plots, a set of typical values for the model parameters was used, which we obtained from tunes to experimental data.

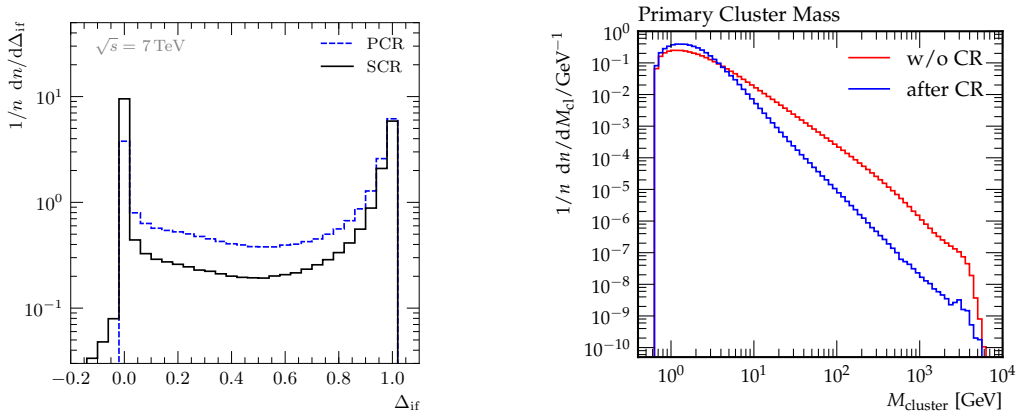

(a) Colour length drop in soft-inclusive pp collisions. PCR denotes the plain CR model, whereas SCR stands for the statistical model.

(b) Effect of colour reconnection on the cluster mass spectrum.

Figure 2: Impact of colour reconnection on the colour length and the cluster mass spectrum.

3 Results

We find that CR improves the description of MB data from ATLAS. As an example, we show in Fig. 3a the pseudorapidity distribution of charged particles at $\sqrt{s} = 900$ GeV, compared to ATLAS data from [17]. This analysis suppresses contributions from diffractive events by cutting on the transverse momentum of the charged particles, $p_\perp > 500$ MeV, and on the charged-particle multiplicity, $N_{\text{ch}} \geq 6$. As HERWIG++ contains no model for soft diffraction, a comparison to samples with looser cuts, $p_\perp > 100$ MeV and $N_{\text{ch}} \geq 1$, which contain diffractive contributions, yields less agreement. We expand on this in more detail in [10].

The model also enables a good description of the underlying event. In Fig. 3b we see, as an example, the charged-particle multiplicity density at $\sqrt{s} = 7$ TeV, in a region *transverse* to the leading track in azimuth, $60° < |\Delta\phi| < 120°$, which is most sensitive to underlying-event activity. The model results are compared to ATLAS data from [18].

4 Conclusions

We have summarized the latest developments in the MPI model in HERWIG++ and expanded on the motivation and modelling of colour reconnection. Furthermore, we have shown that (sufficiently diffraction-suppressed) minimum-bias data from the LHC and underlying-event observables are well described by the present model.

Acknowledgements

We are grateful to the other members of the HERWIG collaboration for critical discussions and support. Moreover, we wish to thank the organizers for this pleasant workshop. We acknowledge financial support from the Helmholtz Alliance "Physics at the Terascale".

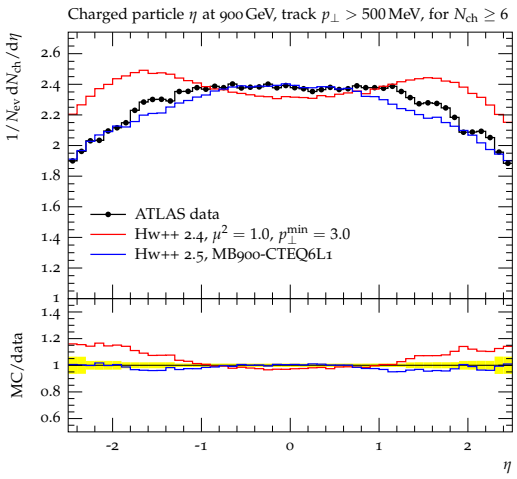

(a) Pseudorapidity distribution of charged particles. The HERWIG 2.4 model contains no CR. MB900-CTEQ6L1 is a dedicated tune of the model with PCR to 900 GeV MB data.

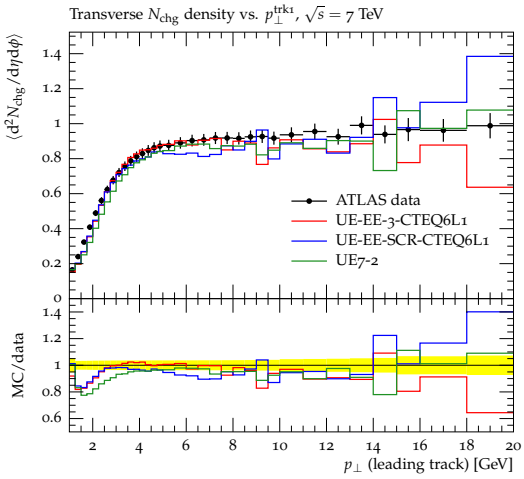

(b) Charged-particle multiplicity density in the transverse area as a function of the $p_\perp$ of the leading track. All histograms show HERWIG UE tunes including CR.

Figure 3: HERWIG results compared to ATLAS data.

References

[1] T. Sjöstrand and M. van Zijl. Phys.Rev. **D36** (1987) 2019.

[2] M. Bähr *et al.* Eur. Phys. J. **C58** (2008) 639–707, arXiv:0803.0883 [hep-ph].

[3] T. Sjöstrand, S. Mrenna, and P. Skands. JHEP **05** (2006) 026, arXiv:hep-ph/0603175.

[4] T. Sjöstrand, S. Mrenna, and P. Skands. Comput. Phys. Commun. **178** (2008) 852–867, arXiv:0710.3820 [hep-ph].

[5] T. Gleisberg *et al.* JHEP **02** (2009) 007, arXiv:0811.4622 [hep-ph].

[6] J. Butterworth, J. R. Forshaw, and M. Seymour. Z.Phys. **C72** (1996) 637–646, arXiv:hep-ph/9601371 [hep-ph].

[7] M. Bähr, S. Gieseke, and M. H. Seymour. JHEP **07** (2008) 076, arXiv:0803.3633 [hep-ph].

[8] M. Bähr, J. M. Butterworth, S. Gieseke, and M. H. Seymour. arXiv:0905.4671 [hep-ph].

[9] G. Aad *et al.* Phys.Lett. **B688** (2010) 21–42, arXiv:1003.3124 [hep-ex].

[10] S. Gieseke, C. Röhr, and A. Siódmok. arXiv:1206.0041 [hep-ph].

[11] D. Amati and G. Veneziano. Phys. Lett. **B83** (1979) 87.

[12] B. R. Webber. Nucl. Phys. **B238** (1984) 492.

[13] S. Gieseke, D. Grellscheid, K. Hamilton, A. Papaefstathiou, S. Plätzer, *et al.* arXiv:1102.1672 [hep-ph].

[14] N. Metropolis, A. Rosenbluth, M. Rosenbluth, A. Teller, and E. Teller. J.Chem.Phys. **21** (1953) 1087–1092.

[15] S. Kirkpatrick, C. D. Gelatt, and M. P. Vecchi. Science **220** (1983) 671–680.

[16] K. Arnold *et al.* arXiv:1205.4902 [hep-ph].

[17] G. Aad *et al.* New J.Phys. **13** (2011) 053033, arXiv:1012.5104 [hep-ex].

[18] G. Aad *et al.* Phys. Rev. D **83** (2011) 112001, arXiv:1012.0791 [hep-ex].

Part VIII

Working Group 5
Heavy Flavours

Convenors:

Jolanta Brodzicka, Massimo Corradi, Ingo Schienbein,

Reinhard Schwienhorst

Inclusive D-Meson Production at the LHC

Hubert Spiesberger

Johannes-Gutenberg-Universität, 55099 Mainz, Germany

DOI: http://dx.doi.org/10.3204/DESY-PROC-2012-02/249

I present predictions for the inclusive production of D mesons at the CERN LHC in the general-mass variable-flavor-number scheme at next-to-leading order. Numerical results are compared to data where available, and uncertainties to scale variations, parton distribution functions and charm mass are discussed. I point out that measurements at large rapidity have the potential to pin down models of intrinsic charm.

D-meson production at the LHC was studied by the ALICE [1], ATLAS [2], and LHCb Collaborations [3]. Here I present predictions for the inclusive production of D mesons at the LHC within the general-mass variable-flavor-number scheme (GM-VFNS) [4]. More results and additional details of the calculation can be found in [5]. In a recent paper [6], we have also considered the inclusive production of B mesons, for which experimental results from the CMS Collaboration are available [7]. For an alternative approach, see Ref. [8].

Figure 1 shows a comparison of the GM-VFNS predictions for the transverse momentum distribution with data from ALICE. Here the renormalization (μ_R) and factorization scales for initial state (μ_I) and final state (μ_F) singularities are fixed by $\mu_i = \xi_i \sqrt{p_T^2 + m_c^2}$, where m_c is the charm quark mass, and the scale parameters ξ_i ($i = R, F, I$) are varied about the default values of 1 by factors of 2 up and down to obtain an estimate of a theory uncertainty band (dotted lines in the figure). The data are reasonably well described by theory at the larger values of p_T, where data are available, but theory starts to overshoot at $p_T < 5$ GeV. There, the fixed flavor number scheme (FFNS) [9] works better (see the dashed lines in Fig. 1). The GM-VFNS is preferred at large p_T since it includes resummed contributions from large logarithms by virtue of the DGLAP evolution equations for the parton distribution (PDFs) and fragmentation functions (FFs). The GM-VFNS also predicts smaller scale uncertainties than the FFNS. We have used CTEQ6.6 PDFs [15] and, in the case of the GM-VFNS, FFs of Ref. [10]. The FFNS calculation is performed without including a FF; the transition from the

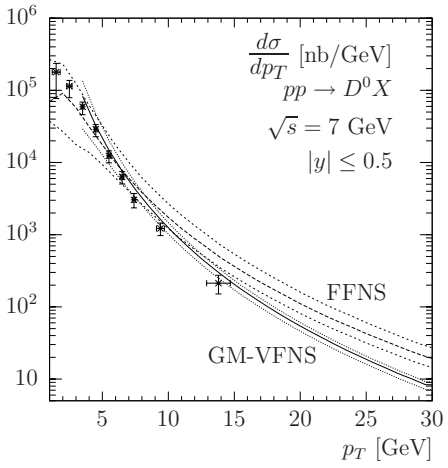

Figure 1: $\mathrm{d}\sigma/\mathrm{d}p_T$ for $p + p \to D^0 + X$ integrated over rapidity in the range $-0.5 \leq y \leq 0.5$ for $\sqrt{s} = 7$ TeV at NLO in the GM-VFNS (solid line) and the FFNS (dashed line). Dotted lines describe the corresponding error bands from scale variations. The ALICE data were taken from [1].

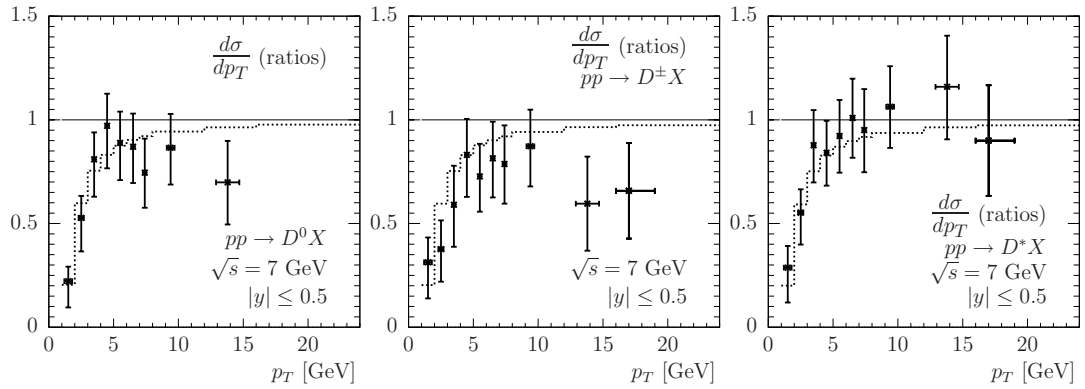

Figure 2: Ratios of $d\sigma/dp_T$ for D-meson production at ALICE at $\sqrt{s} = 7$ TeV using $\xi_I = \xi_F = 0.8$ and $\xi_R = 1$. All cross sections and the data from Ref. [1] are normalized to the GM-VFNS prediction with $\xi_i = 1$. The PDFs are taken from MSTW08-NLO [13] and the charm quark mass is $m_c = 1.5$ GeV.

charm quark to the charmed meson is taken into account by multiplying the parton level result with the branching ratio $BR(c \to D^0) = 0.628$.

The uncertainties due to variations of the factorization scales are dominant. It is interesting to see that the scale parameters can be chosen to bring the GM-VFNS predictions into agreement with the data also at low values of p_T. This is shown in Fig. 2 for MSTW08-NLO PDFs [13] and using $m_c = 1.5$ GeV for the charm quark mass. The differential cross sections $d\sigma/dp_T$ are shown here for $\xi_I = \xi_F = 0.8$, $\xi_R = 1$ in p_T bins and compared with data points from the ALICE collaboration [1]. All results are normalized to the GM-VFNS prediction with $\xi_i = 1$. One can see that a proper choice of the factorization scales can help to ensure that the

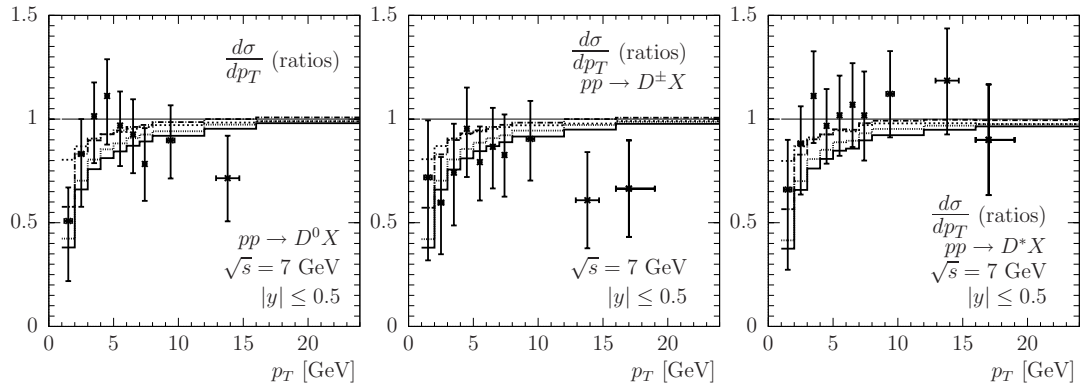

Figure 3: $d\sigma/dp_T$ for D-meson production at ALICE at $\sqrt{s} = 7$ TeV for different PDFs. All cross sections are calculated with $\xi_I = \xi_F = 0.7$, $\xi_R = 1$ and normalized to the GM-VFNS prediction with CTEQ6.6 PDFs. The histograms from top down correspond to CT10 [11], HERAPDF 1.5 (NLO) [12], MSTW08-NLO [13] and NNPDF 2.1 [14].

resummed contributions due to incoming heavy quarks, and those due to light-parton fragmentation, fade out in a controlled manner as $p_T/m \to 0$, i.e. in the kinematic region where the FFNS should be appropriate.

In Figure 3 an attempt is made to show the uncertainties coming from using different PDF input. The results for most of the bins lie within the error bars of the experimental data and do not prefer one PDF set over another. Actually, due to the different values of m_c used in the PDF fits, there is some residual m_c dependence of the predicted cross sections at low values of p_T. The value $m_c = 1.5$ GeV used in our calculation agrees with the one in the fragmentation functions of Ref. [10], but not with the one in the parton distribution functions used here. While the CTEQ6.6 and CT10 sets use $m_c = 1.3$ GeV, in the MSTW08-NLO, NNPDF 2.1, and HERAPDF 1.5 (NLO) sets $m_c = 1.4$ GeV was chosen. A consistent calculation would require the same value of m_c in all components of the cross section formula. However, separate fits of the fragmentation functions for different values of m_c are not available. The dependence on the heavy quark mass is, however, not very strong and non-negligible only in the low p_T range, see Fig. 4.

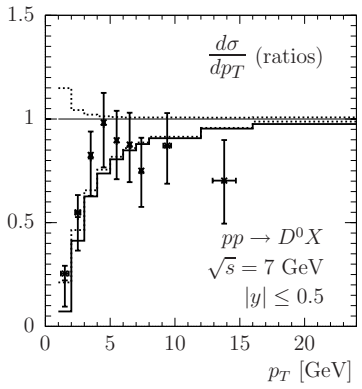

Figure 4: $d\sigma/dp_T$ for D^0-meson production at ALICE [1] with MSTW08-NLO PDFs [13] normalized to the GM-VFNS prediction with $\xi_{I,F,R} = 1$ and $m_c = 1.5$ GeV. The lower two histograms are obtained using $\xi_{I,F} = 0.7$ and $\xi_R = 1$ and the two dashed histograms are for $m_c = 1.4$ GeV.

Non-perturbative contributions to the charm quark content of the proton may lead to enhanced charm parton distributions $c(x, \mu_F)$ at $x > 0.1$. This can become visible in the cross section for D meson production at large rapidities. Parametrizations of this so-called intrinsic charm are available from the CTEQ collaboration, based on various models and compatible with the global data samples. In Ref. [17], we have studied the impact of these models on possible measurements at the Tevatron and at BNL RHIC. Here, I present results of a calculation using the parametrization CTEQ6.6 [15] to obtain an estimate of the expected relative enhancements of the p_T distributions in bins of rapidity. Figure 5 shows typical results for D^0 production; for other D mesons, the results are very similar. Two models have been selected among the possible options in CTEQ6.6 (see Ref. [16] for details): Fig. 5a shows the calculation using the BHPS model with a 3.5 % $(c + \bar{c})$ content in the proton (at the scale $\mu_F = 1.3$ GeV), Fig. 5b refers to the model of a high strength sea-like charm component. In both cases, one observes large enhancements, increasing with rapidity, and in the first model also with p_T. Thus one can expect that forthcoming data from the LHCb experiment should be able to exclude or narrow down models for intrinsic charm.

References

[1] B. Abelev *et al.* (ALICE Collaboration), JHEP **1201**, 128 (2012).

[2] The ATLAS Collaboration, ATL-PHYS-PUB-2011-012; ATLAS-CONF-2011-017.

[3] The LHCb Collaboration, LHCb-CONF-2010-013.

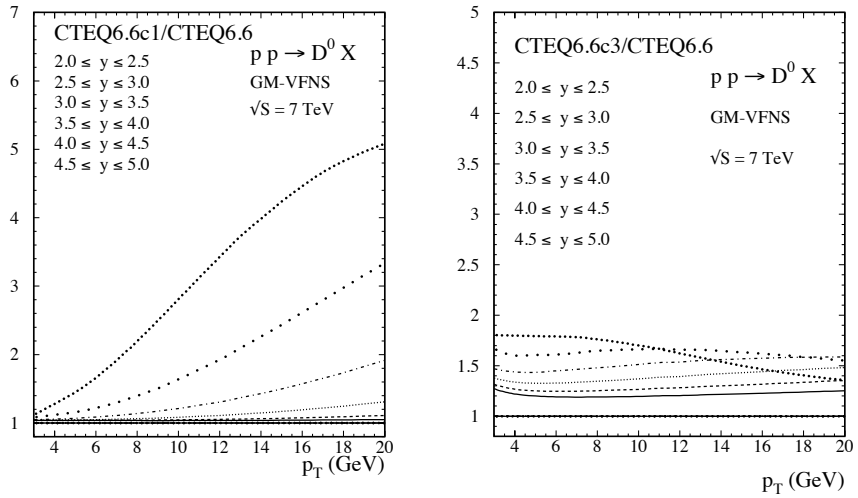

Figure 5: Ratio of the p_T distributions $\mathrm{d}\sigma/\mathrm{d}p_T$ for $p+p \to D^0 + X$ at NLO in the GM-VFNS at $\sqrt{s} = 7$ TeV, using two different models of intrinsic charm: (a) BHPS model with 3.5 % $(c+\bar{c})$ content (at $\mu_F = 1.3$ GeV), (b) model with a high strength sea-like charm component. The FFs are taken from Ref. [10]. The various lines represent the default predictions for $\xi_R = \xi_I = \xi_F = 1$, integrated over the rapidity regions indicated in the figures (larger rapidities correspond to larger cross section ratios everywhere in (a) and at small p_T in (b)).

[4] B. A. Kniehl, G. Kramer, I. Schienbein, and H. Spiesberger, Phys. Rev. D **71**, 014018 (2005); Eur. Phys. J. C **41**, 199 (2005); AIP Conf. Proc. **792**, 867 (2005); Phys. Rev. Lett. **96**, 012001 (2006); Phys. Rev. D **79**, 094009 (2009).

[5] B. A. Kniehl, G. Kramer, I. Schienbein and H. Spiesberger, arXiv:1202.0439.

[6] B. A. Kniehl, G. Kramer, I. Schienbein, and H. Spiesberger, Phys. Rev. D **84**, 094026 (2011).

[7] V. Khachatryan *et al.* (CMS Collaboration), Phys. Rev. Lett. **106**, 112001 (2011); Phys. Rev. Lett. **106**, 252001 (2011); Phys. Rev. D **84**, 052008 (2011).

[8] M. Cacciari, S. Frixione, N. Houdeau, M. L. Mangano, P. Nason and G. Ridolfi, arXiv:1205.6344 [hep-ph].

[9] P. Nason, S. Dawson, and R. K. Ellis, Nucl. Phys. B **303**, 607 (1988); B **327**, 49 (1989); B **335**, 260(E) (1989); W. Beenakker, H. Kuijf, W. L. van Neerven, and J. Smith, Phys. Rev. D **40**, 54 (1989); W. Beenakker, W. L. van Neerven, R. Meng, G. A. Schuler, and J. Smith, Nucl. Phys. B **351**, 507 (1991); S. Frixione, M. Mangano, P. Nason and G. Ridolfi, Phys. Lett. B **348**, 633 (1995); S. Frixione, P. Nason and G. Ridolfi, Nucl. Phys. B **545**, 3 (1995); I. Bojak and M. Stratmann, Phys. Rev. D **67**, 034010 (2003).

[10] T. Kneesch, B. A. Kniehl, G. Kramer, and I. Schienbein, Nucl. Phys. B **799**, 34 (2008).

[11] H. L. Lai, M. Guzzi, J. Huston, Z. Li, P. M. Nadolsky, J. Pumplin, and C. P. Yuan, Phys. Rev. D **82**, 074024 (2010).

[12] H1 and ZEUS Collaborations, ZEUS-prel-10-018 and H1prelim-10-142; ZEUS-prel-11-001 and H1prelim-11-034; ZEUS-prel-11-002 and H1prelim-11-042; A. M. Cooper-Sarkar, arXiv:1112.2107. To be published in: Proceedings of the 2011 Europhysics Conference on High Energy Physics-HEP-2011.

[13] A. D. Martin, W. J. Stirling, R. S. Thorne, and G. Watt, Eur. Phys. J. C **63**, 189 (2009) .

[14] R. D. Ball, V. Bertone, F. Cerutti, L. Del Debbio, S. Forte, A. Guffanti, J. I. Latorre, and J. Rojo *et al.*, Nucl. Phys. B **849**, 296 (2011).

[15] P. M. Nadolsky *et al.* (CTEQ Collaboration), Phys. Rev. D **78**, 013004 (2008).

[16] J. Pumplin, H. L. Lai, and W. K. Tung, Phys. Rev. D **75**, 054029 (2007).

[17] B. A. Kniehl, G. Kramer, I. Schienbein, and H. Spiesberger, Phys. Rev. D **79**, 094009 (2009).

Heavy Flavour Production in ATLAS

Adam Barton[1]

[1]Lancaster University UK

DOI: http://dx.doi.org/10.3204/DESY-PROC-2012-02/86

ATLAS has studied heavy flavour production in a variety of decay channels and inclusive signatures including charmed mesons, jets originating from b-quarks and inclusive muons and electrons. Differential production cross sections for beauty and charm are extracted from these signatures and compared with a variety of theoretical predictions.

1 Introduction

The goals of the heavy-flavour physics program at ATLAS are to test theoretical models for heavy-flavour production within the Standard Model (SM) and to search for new physics through rare decays or new sources of CP violation. The proceedings present a selection of analyses that completed during 2011 based on 2010 data and include cross-section and lifetime measurements. The quarkonium cross-sections are presenting in a separate article.

Details of the ATLAS detector may be found in [1]. The sub-detectors used in these analyses are the Inner Detector Tracker (ID) and Muon Spectrometer (MS). In many cases the data collection relied on specific B-physics triggers selection implemented in the Higher Level Trigger (HLT).

2 D meson cross-section measurements

Using an integrated luminosity of 1.1 nb^{-1}, $D^{*\pm}$, $D^{\pm}$ and $D_S^{\pm}$ charmed meson with $p_T > 3.5\ GeV$ and $|y| < 2.1$ are reconstructed using tracks measured in the ATLAS ID [2]. Using the example of the $D^{*\pm}$, which is identified in the decay channel $D^{*\pm} \to D^0\pi_s^{\pm} \to (K^-\pi^+)\pi_s^{\pm}$, where the $\pi_s^{\pm}$ is the slow pion in the $D^{*\pm}$ decay frame, pairs of oppositely-charged tracks with $p_T > 1.0\ GeV$ are combined to form D^0 candidates, with kaon and pion masses assumed for the appropriate track to calculate the invariant mass. Any additional track, with $p_T > 0.25\ GeV$ and a charge opposite to that of the kaon track, is assigned the pion mass and combined with the D^0 candidate to form a $D^{*\pm}$ candidate. A clear signal in Fig. 1 in the distribution of the mass difference $\Delta M = M(K\pi\pi_s) - M(K\pi)$ at the nominal value of $M(D^{*\pm} - M(D^0)$. From a fit to the ΔM distribution, a $D^{*\pm}$ yield of 2310 ± 130 is obtained and its mass was fitted as $145.41 \pm 0.03\ MeV$ in agreement with the PDG world average. The results for the $D^{\pm}$ (yield 1546 ± 81) and $D_S^{\pm}$ (yield 304 ± 51 mesons are also found to be consistent with PDG world averages. Using Monte Carlo to correct for the detector response, the $D^{*\pm}$ and $D^{\pm}$ production cross-sections (in the kinematic acceptance for the D-mesons of $p_T > 3.5\ GeV$ and $|y| < 2.1$) are found and shown in Fig. 1 for the $D^{*\pm}$ meson. The cross section appears to be generally larger than theories predict, especially at low p_T.

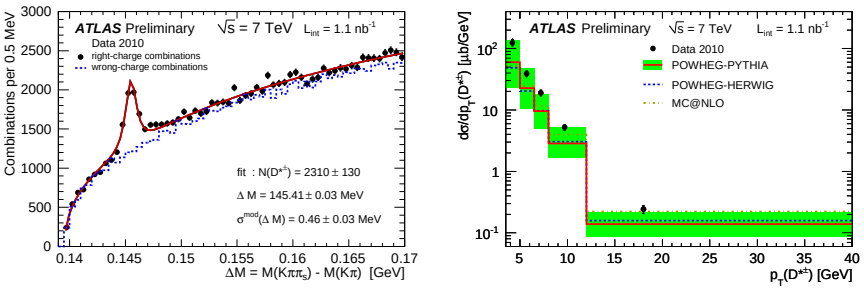

Figure 1: (Left) The distribution of the mass difference, $\Delta M = M(K\pi\pi_s) - M(K\pi)$, for $D^{*\pm}$ candidates. The dashed lines show the distribution for wrong-charge combinations and the solid curves represent the fit results. (Right) Differential cross-section for $D^{*\pm}$ mesons as a function of pT for data compared to the NLO QCD calculations of POWHEG-PYTHIA, POWHEG-HERWIG and MC@NLO for D mesons produced within $|y| < 2.1$. The bands show the estimated theoretical uncertainty of the POWHEG-PYTHIA calculation.

3 Lifetime measurements

Precise measurements of B-hadron lifetimes allow tests of theoretical predictions from the Heavy Quark Expansion framework, which can predict lifetime ratios for different B-hadron species with per cent level accuracy. An average lifetime measurement of the inclusive decay $B \to J/\psi X \to \mu\mu X$ is made on the full 2010 dataset (totalling 35 pb^{-1}) [3]. Since the inclusive decay has orders of magnitude higher statistics than an individual exclusive decay this measurements allows a details investigation of the decay length resolution and the impact of residual misalignment of the tracking system. The inclusive lifetime measurement is of the average lifetime of the admixture of B-hadrons produced at the LHC and decaying to final states including a J/ψ. J/ψ mesons produced from the decays of B-hadrons are non-prompt, having a displayed decay vertex due to the B-hadron lifetime. The average B-lifetime is extracted from the data by performing an unbinned maximum likelihood fit simultaneously to the J/ψ invariant mass and the pseudo-proper decay time. To extract the real lifetime of the B-hadrons, a correction for the smearing introduced by the use of the pseudo-proper lifetime is used. This correction, called the "F-factor" is obtained using Monte Carlo with the J/ψ spectrum re-weighted to match BaBar data. The invariant mass and pseudo-proper decay time projections of the fit are shown in Fig. 3. The average B-lifetime is measured to be:

$$\langle \tau_B \rangle = 1.1489 \pm 0.016(\text{stat.}) \pm 0.043(\text{syst.}) \text{ ps} \quad (1)$$

with the main systematic uncertainty due to the radial alignment of the inner detector. This source of uncertainty can be improved in future analyses. These results agree with recent measurements from CDF and the PDG lifetimes calculated from average lifetime.

4 $B \to J/\psi X$ exclusive decays

The masses of the B_d^0 and Λ_b mesons are reconstructed through the exclusive decays $B_d^0 \to J/\psi K_s$ and $\Lambda_b \to J/\psi \mu^+\mu^-\Lambda(p^+\pi^-)$. These decays will be expanded upon in future analyses

investigating heavy quark effective theory, QCD and the $B_d^0 \to J/\psi K_s$ can be used to investigate CP violation. The mass spectrum for each decay can be seen in Fig. 2.

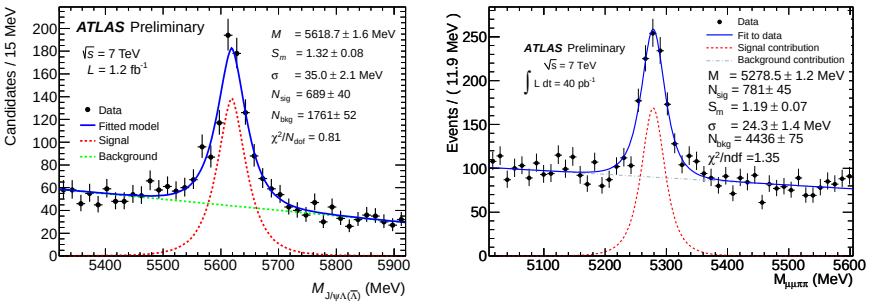

Figure 2: (Left) the reconstructed mass of the $\Lambda_b \to J/\psi\mu^+\mu^-\Lambda(p^+\pi^-)$ decay without a proper decay time cut (Right) The reconstructed mass of the $B_d^0 \to J/\psi K_s$ without a proper decay time cut

The lifetimes of the B_d^0 and B_S^0 mesons are determined from their exclusive decays modes $B_d^0 \to J/\psi K^{*0}$ and $B_S^0 \to J/\psi\phi$, using the J/ψ decay to a di-muon state, the $K^{*0} \to K^+\pi^-$ and the $\phi \to K^+K^-$. The currently published analyses is based on an integrated luminosity of 40 pb^-1 [4]. The study of the $B_s \to J/\psi\phi$ decay is of special interest because it allows the measurement of the B_S^0 mixing phase which can generate CP violation in this channel. The standard model prediction for this phase is small meaning an excess would be a clear indication of new physics. The light (B_L) and heavy (B_H) mass eigenstates have two distinct decay widths Γ_L and Γ_H which have been determined at the Tevatron using a technique of time dependant angular analyses that simultaneously extracts the CP-even and CP-odd amplitudes. The B_d^0 decay provides a testing ground thanks to its similar topology and larger statistics.

The candidates are reconstructed by selecting all pairs of oppositely charged tracks not identified as muons for the K^{*0} or ϕ and tracks identified as muons by the muon spectrometer are used for the J/ψ. The four final state tracks that pass certain selection cut have their decay vertex calculated and the proper decay time extracted. The mass and decay time are used in an unbinned maximum likelihood fit using event by event errors. The B_d^0 lifetime is found to be

$$\tau_{B_d} = 1.51 \pm 0.04(\text{stat.}) \pm 0.04(\text{syst.}) \text{ ps} \quad (2)$$

$$\tau_{B_s} = 1.41 \pm 0.08(\text{stat.}) \pm 0.05(\text{syst.}) \text{ ps} \quad (3)$$

References

[1] The ATLAS Collaboration, JINST, 3, (2008), S08003
[2] The ATLAS Collaboration, ATLAS-CONF-2011-017 (2011)
[3] The ATLAS Collaboration, ATLAS-CONF-2011-145 (2011)
[4] The ATLAS Collaboration, ATLAS-CONF-2011-092 (2011)
[5] The ATLAS Collaboration, ATLAS-CONF-2011-124 (2011)
[6] The ATLAS Collaboration, ATLAS-CONF-2011-105 (2011)

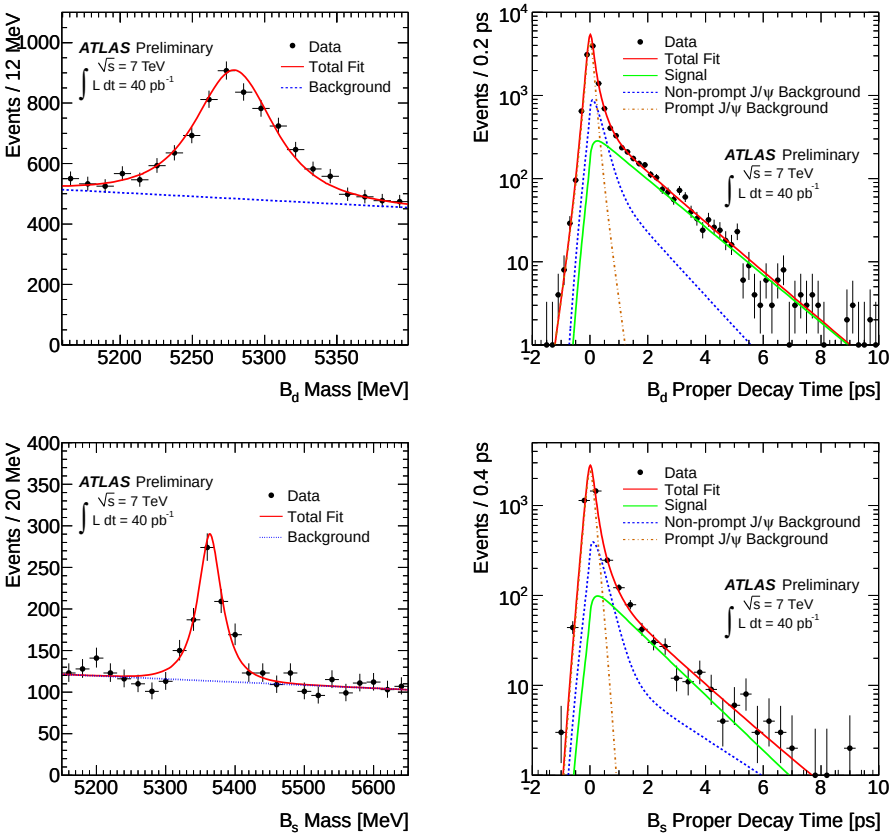

Figure 3: (Top) The simultaneous mass lifetime fit of the $B_d^0 \to J/\psi K^{*0}$ decay, using per candidate errors. (Bottom) The simultaneous mass lifetime fit of the $B_S^0 \to J/\psi\phi$ decay, using per candidate errors

Measurements of beauty quark production at CMS

Wolfram Erdmann[1] for the CMS collaboration

[1]Paul Scherrer Institut, 5232 Villigen-PSI, Switzerland

DOI: http://dx.doi.org/10.3204/DESY-PROC-2012-02/237

The CMS collaboration has measured the production of b-quarks in pp collisions at a center-of-mass energy of $\sqrt{s} = 7$ TeV at the LHC. The measurement of the production cross section for Λ_b baryons are shown and results for jets containing b-quarks and for b-anti-b-pairs decaying into muons are compared to NLO QCD predictions.

1 Introduction

The production of b quarks in proton-proton collisions at the Large Hadron Collider (LHC) is expected to be dominated by gluon-fusion processes. With the center of mass energy of $\sqrt{s} = 7$ TeV, QCD based predictions of the production cross-sections are tested in a new kinematical regime. The CMS detector[1] is well equipped for b-physics in the central rapidity region, $|\eta| \lesssim 2.4$, with muon reconstruction and triggering as well as precise tracking and vertexing for b-tagging and excellent mass resolution. The running period in 2010 with relatively low instantaneous luminosity and negligible pile-up permitted data taking with low trigger thresholds and is very well suited for low p_T production cross section measurements. The single inclusive production of beauty quarks ($pp \to b + X$) has already been measured by CMS through the inclusive $b \to \mu X$ and fully reconstructed B mesons. In this note we present recent measurements of the inclusive b-jet cross section, $b\bar{b}$-pair production and differential cross sections for the production of the b-baryon Λ_b .

2 Inclusive b-jet production

The comparison of jet cross sections with theoretical predictions is less affected by details of the hadronization and decay than measurements based on identified hadrons. On the other hand, the calibration of the b-tagging efficiency introduces a sizeable systematic uncertainty.

The CMS collaboration has recently published two b-jet cross section measurements based on inclusive b-tagged jets and on b-tagged jets with muons[2]. The latter measurement is based on a data sample collected with a single muon trigger while the former is based on inclusive jet triggers. Both measurements reconstruct jets with the anti-kt jet-algorithm with radius parameter $R = 0.5$ applied identified objects (particle flow algorithm). Using simulated events, the reconstructed jet energy is corrected to the corresponding "generator-level" jet by applying the same anti-kt algorithm to all stable particles produced by the event generator. The fraction of events with b-quarks in the samples is increased by b-tagging, requiring the presence of a secondary vertex with a minimum number of tracks and separation from the primary collision vertex.

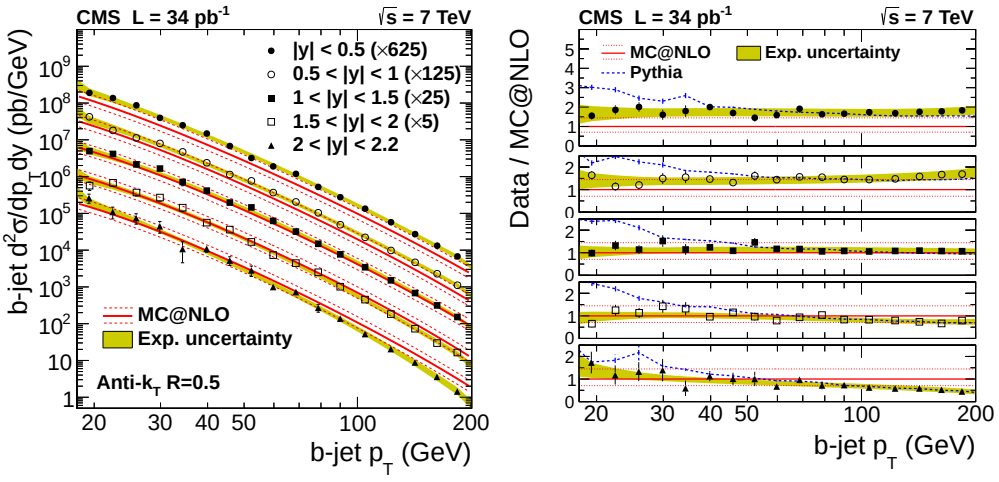

Figure 1: Differential b-jet cross section as a function of jet transverse momentum in five rapidity bins. The symbols with error bars are the meausrement. The ratio of data divided by the MC@NLOprediction is shown on the right hand side, the five curves correspond to the rapidity bins from central (top) to forward (bottom).

The jet analysis uses 34 pb^{-1} of data collected in 2010 with a combination of minimum bias and jet triggers. A high purity b-tag requiring a secondary vertex with at least three tracks is used to reject non-b events. The tagging efficiency rises from 5% for the lowest jet transverse momenta (18 GeV) to 56% at 100 GeV The invariant mass of the tracks forming the secondary vertices is higher for jets with b-quarks than for lighter quark and gluon jets. The b-fraction of the tagged sample is determined is a function of jet transverse momentum from fitting the invariant vertex mass distribution with templates obtained from simulated events. The observed purity is of the order of 75%.

The muon analysis uses 3.0 pb^{-1} of data collected early in 2010 for which the muon trigger with a transverse momentum threshold of 9 GeV was not prescaled. The muon-event sample is already b-enriched and a lower purity version of the b-tagging requiring a two-track vertex is applied. This maintains a high tagging efficiency ranging from 50% at 30 GeV to 75% at 100 GeV jet p_T. Muon and b-tagged jet are accepted if their angular separation $\sqrt{\Delta\eta^2 + \Delta\phi^2}$ is 0.3 or less. The transverse momentum of the muon relative to the jet axis, p_T^{rel}, is on average higher for b–jets than for light jets. The b-fraction in the muon sample is determined by fitting the observed p_T^{rel} distribution with templates from simulated events. The cross section for b-jets with a muon with rapidity $|\eta_\mu| < 2.4$ and transverse momentum $p_T^\mu > 9$ GeV has been compared with predictions from PYTHIA and MC@NLO. Total rate and jet p_T spectrum are found to be in good agreement with the MC@NLO prediction. The shape of the rapidity distribution on the other hand is described better by PYTHIA, which overestimates the normalization. A similar observation was made in previous b-production measurements.

Figure (1) shows the double differential jet cross section obtained with the jet-based analysis. The MC@NLO prediction tends to lie below the data for central rapidities, but agrees within the theoretical uncertainties. At high rapidities, the slope of the p_T dependent cross section is not well described by MC@NLO. PYTHIA overestimates the cross section at low p_T but agrees well

at high p_T.

The muon acceptance for a jet with rapidity $|\eta| < 2.2$ varies with jet p_T between 5% and 20 %. After correcting for this, the muon cross section is found to be consistent with the jet cross section integrated over rapidities. Both measurements lie above the MC@NLO prediction but are consistent with it within uncertainties.

3 Measurement of $\sigma(pp \to b\bar{b}X \to \mu\mu Y)$

The production of $b\bar{b}$ pairs in pp collisions has been inferred from the detection of lepton pairs from semileptonic b-hadron decays in 27.9 pb^{-1} of data collected with a dimuon trigger[3]. The backgrounds from single b-hadron decays producing two muons, $Z \to \mu\mu$, and Υ decays can be removed by appropriate cuts on the invariant mass, e.g. $m(\mu\mu) > 5$ GeV. Remaining source of muons are charm production (C), prompt muons (P) from Drell Yan events and muons from light hadron decaying to muons inside the detector (D). The precise measurement of the impact parameter of the muon with respect to the collision point, d_{xy}, permits separating these source because of the different lifetimes involved. A fit to the two-dimensional distribution $(d_{xy}(\mu_1), d_{xy}(\mu_2))$ is used to determine the b-fraction of a sample of muon pairs with both muons inside $|\eta| < 2.1$ and $p_T > 4(6)\ GeV$. The impact parameter template for prompt muons is measured in data, using Υ decays, while other templates are obtained from simulated events. The 1d projection of the fit result is shown in figure 2. The result is a very precise measurement with less than 10% systematic uncertainty, dominated by efficiency determination for finding the two muons: 25.7 ± 0.1 (stat.) ± 2.2 (syst.) ± 1.0 (lumi.) nb for $p_T >$ 4 GeV and 5.03 ± 0.05 (stat.) ± 0.46 (syst.) ± 0.20 (lumi.) for $p_T > 6$ GeV. The corresponding MC@NLO predictions are 19.7 ± 0.3 (stat.) $^{+6.5}_{-4.1}$ (syst.) nb and 4.40 ± 0.14 (stat.) $^{+1.10}_{-0.84}$ (syst).

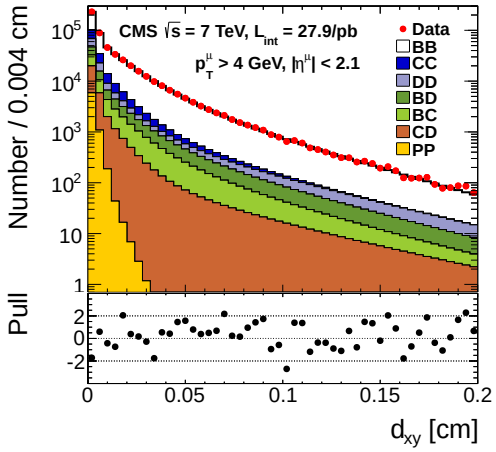

Figure 2: One-dimensional projection of the muon impact parameter fit. Points are data, the histograms show the templates for combinations of muons from b-decays (B) and other sources (see text).

4 Λ_b production

CMS has measured the production of the Λ_b baryon [4] through reconstruction of the decays $\Lambda_b \to \Lambda J/\psi$ followed by $\Lambda \to p\pi$ and $J/\psi \to \mu^+\mu^-$. The measurement is based on 1.9 fb^{-1} of data collected in 2011 using a displaced dimuon trigger. Clean samples of $J\psi$ and Λ candidates are obtained by requiring a good secondary vertex significantly displaced from the collision point. A total of 1252 ± 42 (stat. error only) signal events is found on top of a low background. The rates of $\bar{\Lambda}_b$ and Λ_b are in good agreement with each other, taking into account the expected

reconstruction efficiency is 15% lower than for $\bar{\Lambda}_b$ because of the different nuclear interactions of anti-protons.

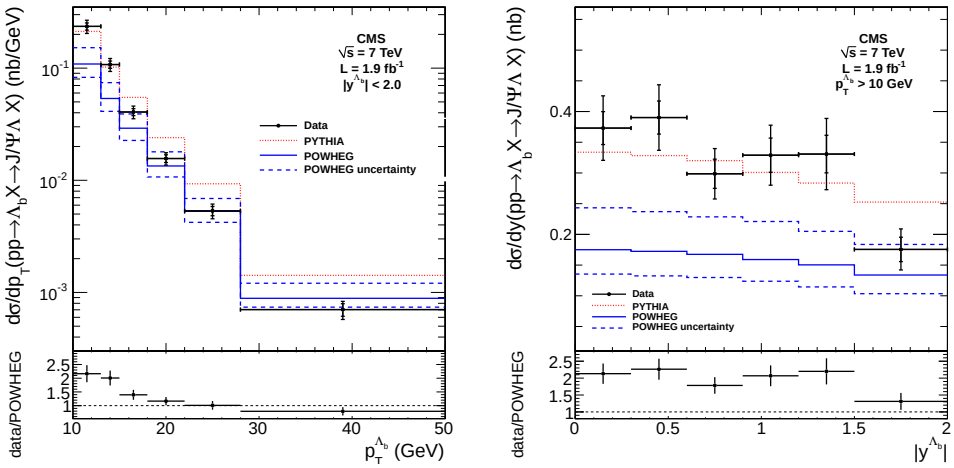

Figure 3: Differential Λ_b cross sections times branching fractions. Error bars and theoretical uncertainties do not contain the contribution from the branching fractions (e.g. 54% from $BR(\Lambda_b \to \Lambda J/\psi)$). The shape of the rapidity distribution (right) is well described by theoretical predictions, while the cross section falls faster as a function of p_T than predicted. The small figures at the bottom show the ratio of the data and POWHEG prediction.

The cross section is found to have a steeper p_T dependence than predicted by calculations. It is also found to be softer than the measured B-meson spectra in a similar pseudorapidity range.

5 Conclusion

Recent CMS results on b-production in pp collisions at $\sqrt{s} = 7$ TeV have been reported and compared with QCD predictions. The NLO-QCD Monte Carlo MC@NLO tends to underestimate inclusive production cross sections but is generally in agreement within the large theoretical uncertainties. The the shape of the rapidity distributions at low p_T and the p_T distribution of jets at high rapidity are not well described. The production of Λ_b baryons has been measured and the p_T spectrum is found to be steeper than predicted and steeper than for B mesons.

6 Bibliography

References

[1] S. Chatrchyan *et al.* JINST **3** (2008) S08004.

[2] S. Chatrchyan *et al.* JHEP **1204** (2012) 084, `arXiv:1202.4617 [hep-ex]`.

[3] S. Chatrchyan *et al.* `arXiv:1203.3458 [hep-ex]`.

[4] C. Collaboration *et al.* `arXiv:1205.0594 [hep-ex]`.

Open heavy flavour production in pp collisions at $\sqrt{s} = 7$ TeV with ALICE at the LHC

Rosa Romita for the ALICE Collaboration

GSI, Darmstadt, Germany

DOI: http://dx.doi.org/10.3204/DESY-PROC-2012-02/130

ALICE (A Large Ion Collider Experiment) is the LHC experiment dedicated to the study of the Quark Gluon Plasma (QGP) in Pb-Pb collisions. Heavy quarks are ideal probes to explore the QGP formation and properties, since they experience the full collision history and are expected to be abundantly produced at the LHC. It is of great importance to measure the heavy flavour cross section not only in Pb–Pb collisions, but also in pp collisions. ALICE measures heavy quark production both at central and forward rapidity, using hadronic decays of D mesons and semi-leptonic decays of D and B mesons. We report on the measurements of heavy quark production in pp collisions at $\sqrt{s} = 7$ TeV.

1 Introduction

Heavy quarks are a well-suited tool to probe the high-density state of strongly-interacting matter formed in heavy ions collisions at ultra-relativistic energies, because they are produced in the early stage of the collision and they can subsequently interact with the medium, via the mechanisms of elastic and inelastic parton energy loss [1]. In pp collisions, besides providing the reference for the Pb–Pb results, the measurement of charm and beauty cross sections has a great interest per se, as a test of perturbative QCD calcualtions of heavy quark production at LHC energies. The design of ALICE [2] allows for the measurement of open heavy flavour down to low momenta, both in the hadronic (at central rapidity, $-0.5 < y < 0.5$) and leptonic decay channels (at forward rapidity, $2.5 < y < 4$). We describe heavy-flavour production measurements for 7 TeV pp collisions. Measurements have been performed also for pp collisions at $\sqrt{s} = 2.76$ TeV [3], but are not covered here. In section 2 the detector, its performance and the data samples relevant for the analyses presented here are briefly described. Section 3 presents the results of open charm reconstruction and the inclusive cross section measurement via hadronic channels at central rapidity. In sections 4 and 5 the heavy-flavour inclusive cross section measurement in leptonic channels are summarized: electrons in the central rapidity region, muons at forward rapidity.

2 ALICE detector and data taking

The ALICE detector is composed of a central barrel, with tracking, vertexing and particle identification (PID) detectors, and a forward muon spectrometer, where muons are reconstructed and identified. The detectors of the central barrel ($-0.9 < \eta < 0.9$) used for the heavy-flavour

analyses presented here are the Inner Tracking System (ITS), the Time Projection Chamber (TPC), the Time Of Flight (TOF), the Transition Radiation Detector (TRD) and the ElectroMagnetic CALorimeter (EMCAL). The main goal of the ALICE muon spectrometer is the study of quarkonia states and inclusive heavy-flavour production in the muon channel. It covers the rapidity range -4.0 $< \eta <$-2.5 and provides a muon trigger. The following data samples are used for the analyses described here: 5 nb^{-1} integrated luminosity at 7 TeV for D mesons analysis; 2.6 nb^{-1} integrated luminosity at 7 TeV for single electrons; 16.5 nb^{-1} at 7 TeV for single muons.

3 Open charm via hadronic decay channels

Open charm mesons ($\text{D}^0 \to \text{K}^-\pi^+$, $\text{D}^+ \to \text{K}^-\pi^+\pi^+$, $\text{D}^* \to \text{D}^0\pi^+$ and $\text{D}_\text{s} \to \text{K}^-\text{K}^+\pi^+$ and baryon (Λ_c) have a very short mean proper decay lenght $c\tau$, that ranges from 60 μm for Λ_c to 300 μm for D^+. The decay length of these particles is very small and the combinatorial background is high already in pp collisions, making the measurement challenging. These particles are exclusively reconstructed using their hadronic decay channels into 2, 3 or 4 charged particle final states. D mesons candidates are selected both applying topological cuts and identifying their charged decay pions and kaons with TPC and TOF. From the resulting invariant mass distrubution, the raw yield is obtained. The corrections for efficiency and acceptance are determined using Monte Carlo simulations. The measured fraction of prompt charm is inferred from FONLL predictions, that reproduce well beauty production measured in the CMS [5] and LHCb [6] experiments. The p_t differential cross section for the charmed meson $\text{D}^+ \to \text{K}^-\pi^+\pi^+$ is shown in the left panel of figure 1 [9], in the momentum range $1 < p_\text{t} < 24$ GeV/c, together with the comparison with two different pQCD based calculations [7, 8]: the agreement is good within the uncertainties. The p_t differential cross section for the charmed mesons D^0, D^+, D^* and D_s are shown in the right panel of figure 1.

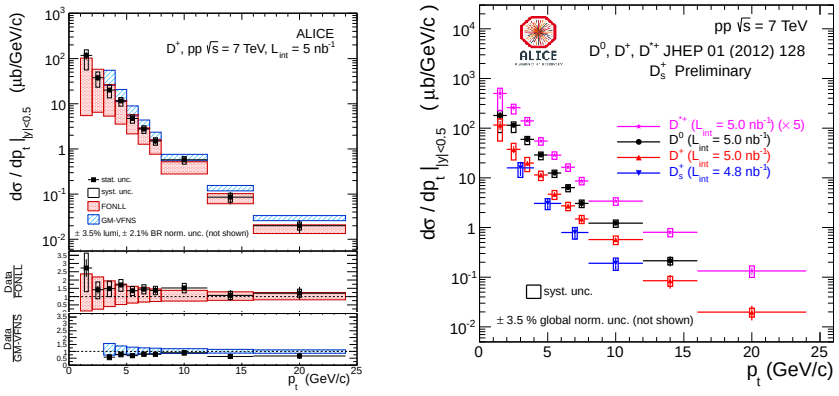

Figure 1: Left panel: Differential production cross section for D^+ in pp collisions at $\sqrt{s} = 7$ TeV (points), compared with two different pQCD based calcutations (blue and red bands [7−9].Right Panel: Cross section for the four D mesons in pp collisions at $\sqrt{s} = 7$ TeV.

4 Electrons from heavy-flavour hadron decays

The inclusive heavy-flavour cross section can be obtained using electrons in the central barrel, since heavy flavour hadrons have a large branching ratio to leptons (about 10%). The electron identification strategy [10] is based on the TPC and TOF detectors and is effective for tracks with momentum up to 6 GeV/c. To extend the p_{t} range of the measurement up to 8 GeV/c, the PID is exploited also in the TRD, bringing the hadron contamination down to 2% in the whole momentum range. An alternative approach is to combine the information coming from the TPC with the energy deposit in the EMCAL to identify electrons. This PID strategy allows to obtain a good electron sample in the range $3 < p_{\mathrm{t}} < 7$ GeV/c. The charm and beauty decays are not the only sources that contribute to the inclusive electron spectrum. The background sources can be modeled in a cocktail which allows to obtain a sample dominated by beauty-decay electrons, from which a small contribution of background and charm-decay electrons is subsequently subtracted. The inclusive cross section for heavy-flavour decay electron production in pp collisions at $\sqrt{s} = 7$ TeV is shown in the left panel of figure 2, compared to the FONLL prediction for charm and beauty production in the electron channel [11]. The beauty contribution can be estimated in two independent ways. A cut on high values of the electrons impact parameter can distinguish c and b decay products. As a consistency test, the charm cross section measured with the charmed mesons decays is used to produce a pure charm electron spectrum. The difference between the two spectra at high p_{t} can be attributed to the contribution from beauty decays. In the right panel of figure 2, the measurement is shown in the range $1.5 < p_{\mathrm{t}} < 6$ GeV/c and compared to FONLL predictions.

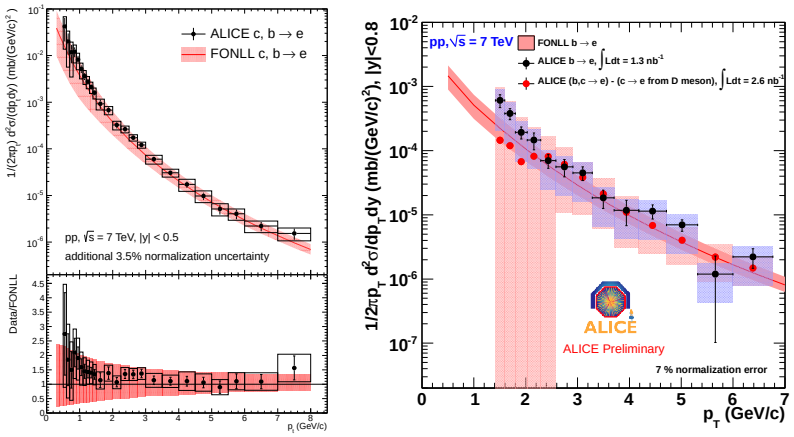

Figure 2: Left panel: Differential production cross section of electrons from heavy-flavour decays for pp collisions at $\sqrt{s} = 7$ TeV (black points), compared with FONLL predictions for c, b $\rightarrow$ e (red line and band) [10, 11]. Right panel: Transverse momentum differential production cross section of electrons from beauty decay obtained with the impact parameter analysis (black points) and from the inclusive electron spectrum (red points). They are compared to FONLL predictions for b $\rightarrow$ e (red band).

5 Muons from heavy-flavour hadron decays

Open heavy-flavour production is measured at forward rapidity in the semi-muonic decay channel [12]. In the inclusive muon p_{t} distribution there are several contributions, that can be removed in order to isolate muons from charm and beauty decays. Hadrons that do not reach the trigger chambers at the end of the spectrometer are removed. A Monte Carlo simulation is used to estimate and subtract residual decay muons, originating from decays of light mesons before the front absorber. The p_{t} differential cross section of muons from heavy flavour decays

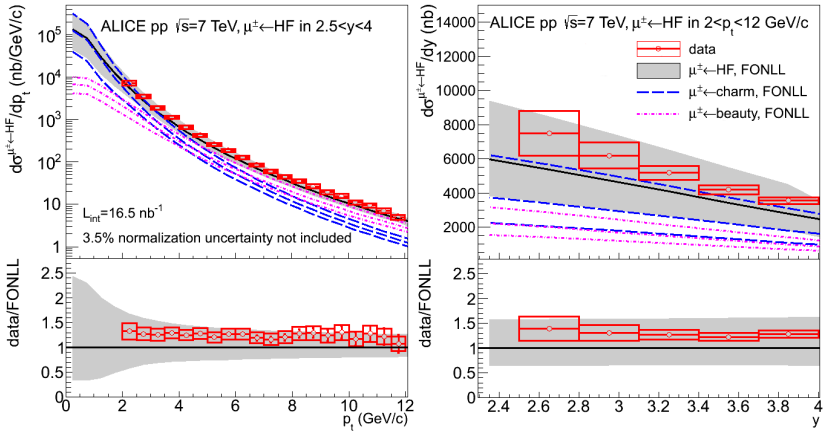

Figure 3: p_{t} (left panel) and y (right panel) differential cross section for muons from heavy flavour decays for pp collisions at $\sqrt{s} = 7$ TeV (points), compared to FONLL predictions (bands) [12, 7].

in $2.5 < y < 4$ and $2 < p_{\mathrm{t}} < 12$ GeV/c is shown in figure 3 [12]. The measurement is compared compared FONLL predictions [7], which provide a fair description within uncertainties.

6 Conclusions

We have presented results on heavy-flavour cross sections measured with the ALICE detector in pp collisions at $\sqrt{s} = 7$ TeV. These results agree well with pQCD based model predictions and represent the essential baseline to understand heavy flavour production in heavy-ion collisions.

References

[1] ALICE Collaboration, arXiv:1203.2160 [nucl-ex].

[2] ALICE Collaboration, K. Aamodt et al., J. Instrum 3, S08002 (2008).

[3] ALICE Collaboration, arXiv:1205.4007v1 [hep-ex].

[4] ALICE Collaboration, J. Alme et al., Nuclear Instruments and Methods, Volume 622, Issue 1, arXiv:1001.1950.

[5] V. Khachatryan *et al.* [CMS Collaboration], Eur. Phys. J. C **71** (2011) 1575 [arXiv:1011.4193 [hep-ex]].

[6] R. Aaij *et al.* [LHCb Collaboration], Phys. Lett. B **694** (2010) 209 [arXiv:1009.2731 [hep-ex]].

[7] M. Cacciari, M. Greco, P. Nason, JHEP 9805 (1998) 007.

[8] B.A. Kniehl et al., Phys. Rev. Lett. 96 (2006) 012001.
[9] B. Abelev *et al.* [ALICE Collaboration], JHEP01(2012)128 [arXiv:1111.1553 [hep-ex]].
[10] ALICE Collaboration, arXiv:1205.5423 [hep-ex].
[11] P.M. Nadolsky et al. Phys.Rev., D78:013004, 2008.
[12] B. Abelev *et al.* [ALICE Collaboration], Phys. Lett. B **708** (2012) 265 [arXiv:1201.3791v1 [hep-ex]].

Production of $c\bar{c}$ pairs at LHC: k_t-factorization and double-parton scattering

Antoni Szczurek[1,2]

[1]Institute of Nuclear Physics PAN, ul. Radzikowskiego 152, PL-31-342 Kraków, Poland
[2]Rzeszów University, ul. Rejtana 16, PL-35-959 Rzeszów, Poland

DOI: `http://dx.doi.org/10.3204/DESY-PROC-2012-02/213`

We discuss charm production at LHC. The production of single $c\bar{c}$ pairs is calculated in the k_t-factorization approach. We use several unintegrated gluon distributions from the literature. Differential distributions for several charmed mesons are presented and compared to recent results of the ALICE and LHCb collaborations. Some missing strength can be observed. Furthermore we discuss production of two $c\bar{c}$ pairs within a simple formalism of double-parton scattering (DPS). Surprisingly large cross sections, comparable to single-parton scattering (SPS) contribution to $c\bar{c}$ production, are predicted for LHC energies.

1 Introduction

The cross section for open charm production at the LHC is very large. Different mesons are measured [1, 2]. Some other experiments are preparing their experimental cross sections. Different theoretical approaches for heavy quark production are used in the literature. In the present communication we present briefly some results for charmed meson production within k_t-factorization approach. A more detailed analysis will be presented elsewhere [3]. Similar analysis within next-to-leading order aproach was presented very recently [4]. Previously we have used the k_t-factorization approach for charm production at the Tevatron [5] and for non-photonic electron production at RHIC [6, 7]. The k_t-factorization approach was also successfully used for beauty [8] and top [9] quark (antiquark) inclusive production.

Recently we have made first estimates for the production of two $c\bar{c}$ pairs [10, 11]. We have considered both double-parton scattering (DPS) mechanism [10] as well as single-parton scattering (SPS) mechanism [11]. By comparison of contributions of both mechanisms we come to the conclusion that the production of two $c\bar{c}$ pairs is a favourite place to study and identify double-parton scattering effects. The double-parton scattering was studied recently for different high-energy processes.

2 Inclusive charmed meson production

In the leading-order (LO) approximation within the k_t-factorization approach the quadruply differential cross section in the rapidity of Q (y_1), in the rapidity of $\bar{Q}$ (y_2) and in the transverse

momentum of Q ($p_{1,t}$) and $\bar{Q}$ ($p_{2,t}$) can be written as

$$\frac{d\sigma}{dy_1 dy_2 d^2p_{1,t} d^2p_{2,t}} = \sum_{i,j} \int \frac{d^2\kappa_{1,t}}{\pi} \frac{d^2\kappa_{2,t}}{\pi} \frac{1}{16\pi^2 (x_1 x_2 s)^2} \overline{|\mathcal{M}_{ij\to Q\bar{Q}}|^2} \tag{1}$$
$$\delta^2\left(\vec{\kappa}_{1,t} + \vec{\kappa}_{2,t} - \vec{p}_{1,t} - \vec{p}_{2,t}\right)\ \mathcal{F}_i(x_1, \kappa_{1,t}^2)\ \mathcal{F}_j(x_2, \kappa_{2,t}^2)\ ,$$

where $\mathcal{F}_i(x_1, \kappa_{1,t}^2)$ and $\mathcal{F}_j(x_2, \kappa_{2,t}^2)$ are so-called unintegrated gluon (parton) distributions. The unintegrated parton distributions are evaluated at: $x_1 = \frac{m_{1,t}}{\sqrt{s}} \exp(y_1) + \frac{m_{2,t}}{\sqrt{s}} \exp(y_2)$, $x_2 = \frac{m_{1,t}}{\sqrt{s}} \exp(-y_1) + \frac{m_{2,t}}{\sqrt{s}} \exp(-y_2)$, where $m_{i,t} = \sqrt{p_{i,t}^2 + m_Q^2}$.

The hadronization is done in the way explained in Ref.[6]. In Fig. 1 we show two examples how we describe LHC experimental data [1, 2]. There seems to be some strength missing. A possible explanation of that observation will be discussed in the next section.

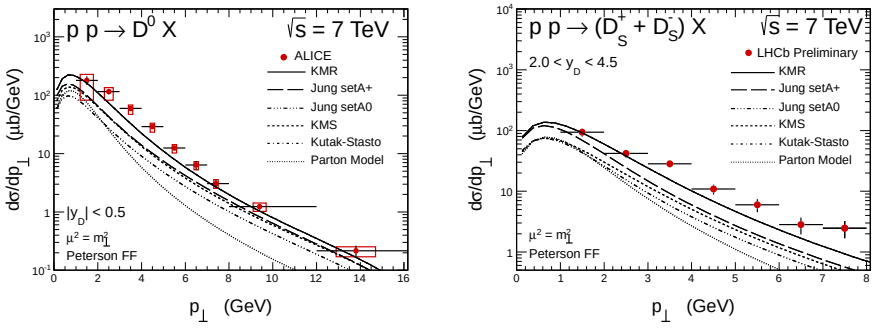

Figure 1: Two examples of transverse momentum distribution of charmed mesons compared to ALICE (left panel) and LHCb (right panel) experimental data. The calculations were done for different unintegrated gluon distributions.

3 Production of two $c\bar{c}$ pairs

Two possible mechanisms of the production of two $c\bar{c}$ pairs are shown in Fig. 2.

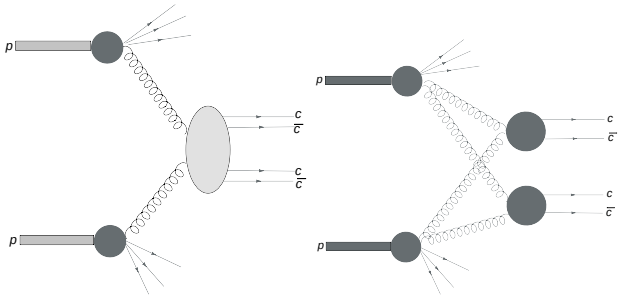

Figure 2: SPS (left) and DPS (right) mechanisms of $(c\bar{c})(c\bar{c})$ production.

The cross section for differential distribution in a simple double-parton scattering in leading-order collinear approximation can be written as

$$\frac{d\sigma}{dy_1 dy_2 d^2p_{1t} dy_3 dy_4 d^2p_{2t}} = \frac{1}{2\sigma_{eff}} \frac{d\sigma}{dy_1 dy_2 d^2p_{1t}} \cdot \frac{d\sigma}{dy_3 dy_4 d^2p_{2t}} \tag{2}$$

which by construction reproduces the formula for integrated cross section [10]. This cross section is formally differential in 8 dimensions but can be easily reduced to 7 dimensions noting that physics of unpolarized scattering cannot depend on azimuthal angle of the pair or on azimuthal angle of one of the produced c ($\bar{c}$) quark (antiquark). This can be easily generalized by including QCD evolution effects [10].

In Fig. 3 we compare cross sections for the single $c\bar{c}$ pair production as well as for single-parton and double-parton scattering $c\bar{c}c\bar{c}$ production as a function of proton-proton center-of-mass energy. At low energies the conventional single $c\bar{c}$ pair production cross section is much larger. The cross section for SPS production of $c\bar{c}c\bar{c}$ system is more than two orders of magnitude smaller than that for single $c\bar{c}$ production. For reference we show the proton-proton total cross section as a function of energy. At higher energies the DPS contribution of $c\bar{c}c\bar{c}$ quickly approaches that for single $c\bar{c}$ production as well as the total cross section.

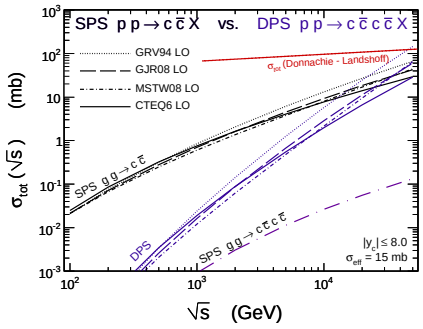

Figure 3: Total LO cross section for single $c\bar{c}$ pair and SPS and DPS $c\bar{c}c\bar{c}$ production as a function of center-of-mass energy.

In Ref.[10] we have also considered several correlation observables between different c quarks and $\bar{c}$ antiquarks. Particularly interesting are correlations between c-c and $\bar{c}$-$\bar{c}$. Two examples are shown in Fig. 4. We show both terms: when $c\bar{c}$ are emitted in the same parton scattering ($c_1\bar{c}_2$ or $c_3\bar{c}_4$) and when they are emitted from different parton scatterings ($c_1\bar{c}_4$ or $c_2\bar{c}_3$). In the latter case we observe a long tail for large rapidity difference as well as at large invariant masses of $c\bar{c}$.

In Ref.[11] we have calculated cross section for $c\bar{c}c\bar{c}$ production in single-parton scattering in high-energy approximation. In Fig. 5 we compare the SPS contribution with the DPS one. Clearly the SPS contribution at large rapidity difference between cc or $\bar{c}\bar{c}$ is much smaller than the DPS contribution.

In Ref.[10] we have discussed that the sum of transverse momenta of two c (or two $\bar{c}$) has a hard tail. This is of course not an observable. In Fig. 6 we show instead distribution in transverse momentum of the D^0D^0 pair (or $\bar{D}^0\bar{D}^0$ pair) for the rapidity interval relevant for

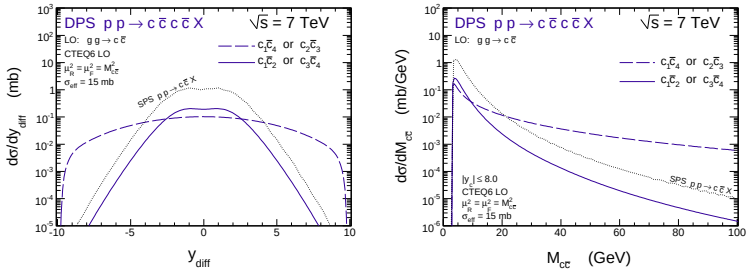

Figure 4: Distribution in rapidity difference (left panel) and in invariant mass of the $c\bar{c}$ pair (right panel) at $\sqrt{s} = 7$ TeV.

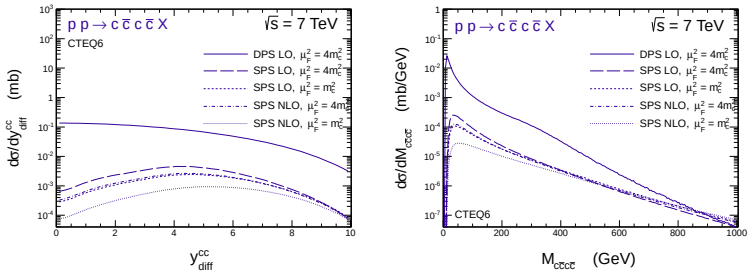

Figure 5: Comparison of SPS and DPS contributions for two correlation distributions.

a given experiment. This distribution has surprisingly long tail. For comparison we show transverse momentum distribution of one D^0 (or $\bar{D}^0$).

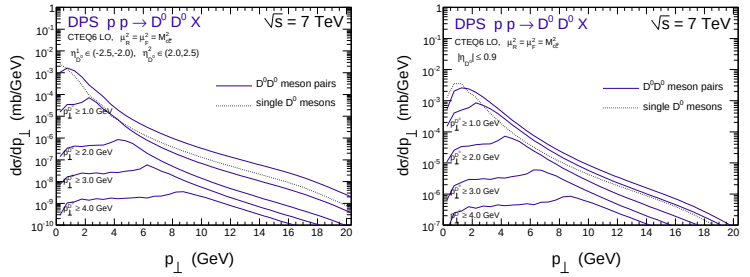

Figure 6: Transverse momentum distribution of the D^0D^0 (or $\bar{D}^0\bar{D}^0$) pairs for the rapidity interval of ATLAS or CMS (left) and ALICE (right) experiments for different cuts on transverse momenta of each meson in the pair. The distribution in transverse momentum of single D^0 is shown for comparison (dashed line). All distributions are shown for $\sqrt{s} = 7$ TeV.

4 Summary

We have presented our selected new results for charmed meson production at LHC. Results of our calculation have been compared with recent ALICE and LHCb experimental data for transverse momentum distribution of D mesons. There seems to be a missing strength, especially for the LHCb kinematics.

One of possible explanation is a presence of double-parton scattering contributions. Therefore the second topic discussed during the conference was the production of two $c\bar{c}$ pairs. We have compared energy dependence of the DPS contribution to the $c\bar{c}c\bar{c}$ production with that for the $c\bar{c}$ production. The cross section for two pair production grows much faster than that for single pair production. At high energies the two cross sections become comparable. We have also discussed some correlation observables that could be used to identify double-parton scattering contribution. The rapidity difference is one of the good examples.

We have also estimated corresponding single-parton scattering contributions in a high energy approach. The latter turned out to be much smaller than the double-parton scattering contributions.

In summary, we have found that the production of two $c\bar{c}$ pairs is one of the best places to study and identify double-parton scattering effects. For example a good possibility would be to measure two D^0D^0 or two $\bar{D}^0\bar{D}^0$ mesons. The LHCb collaboration has started already such studies [12].

5 Acknowledgements

I am indebted to Marta Łuszczak, Rafał Maciuła and Wolfgang Schäfer for collaboration on the issues presented here. I wish to thank the organizers for perfect organization of DIS2012. My stay during the conference in Bonn was supported from a polish grant DEC-2011/01/B/ST2/04535.

References

[1] B. Abelev et al. (ALICE Collaboration), JHEP **01** (2012) 128.

[2] LHCb Collaboration, LHCb-CONF-2010-013.

[3] R. Maciuła and A. Szczurek, a paper in preparation.

[4] B.A. Kniehl, G. Kramer, I. Schienbein and H. Spiesberger, arXiv:1202.0439 [hep-ph].

[5] M. Łuszczak and A. Szczurek, Phys. Rev. **D73** (2006) 054028.

[6] M. Łuszczak, R. Maciuła and A. Szczurek, Phys. Rev. **D79** (2009) 034009.

[7] R. Maciuła, A. Szczurek and G. Ślipek, Phys. Rev. **D83** (2011) 054014.

[8] H. Jung, M. Kraemer, A.V. Lipatov and N.P. Zotov, arXiv:1111.1942.

[9] A.V. Lipatov and N.P. Zotov, Phys. Lett. **B704** (2011) 189.

[10] M. Łuszczak, R. Maciuła and A. Szczurek, Phys. Rev. **D85** (2012) 094034, arXiv:1111.3255 [hep-ph].

[11] W. Schäfer and A. Szczurek, Phys. Rev. **D85** (2012) 094029, arXiv:1203.4129 [hep-ph].

[12] R. Aaij et al. (LHCb Collaboration), arXiv:1205.0975 [hep-ex].

Constraining the Intrinsic Heavy Quark PDF via Direct Photon Production in Association with a Heavy Quark Jet.

Karol Kovařík[1], *Tzvetalina Stavreva*[2]

[1]Institute for Theoretical Physics, Karlsruhe Institute of Technology, Karlsruhe, 76128,Germany
[2]Laboratoire de Physique Subatomique et de cosmologie, Grenoble, 38026, France

DOI: http://dx.doi.org/10.3204/DESY-PROC-2012-02/250

We investigate a possible use of direct photon production in association with a heavy quark to test different models of intrinsic heavy quark parton distribution function (PDF) at the Tevatron, at the large hadron collider (LHC) and at RHIC.

1 Introduction

Parton distribution functions (PDFs) are an essential component of any prediction involving colliding hadrons. In view of their importance, the proton PDFs have been a focus of long and dedicated global analyses performed by various groups [1, 2, 3]. Most PDF analyses assume five active quark flavours with corresponding parton distributions $u(x,Q^2), d(x,Q^2), c(x,Q^2), s(x,Q^2)$ and $b(x,Q^2)$ but only the light quark parton distribution functions u, d and s are non-zero at the input scale Q_0. The massive quark PDF are normally generated only radiatively from the gluon through a radiation of a quark-anti-quark pair. This however does not have to be the case and there exist models predicting an intrinsic contribution to the charm quark PDF [4]. Depending on the model, the intrinsic component changes the charm PDF at a higher scale as shown in Fig. 1. The BHPS model (shown as CTEQ6.6C2 in Fig. 1) is a light-cone model which enhances the charm PDF at large values of x as opposed to the sea-like model (shown as CTEQ6.6C4 in Fig. 1) where the charm intrinsic contribution is proportional to the light flavour sea quark distributions and modifies the radiative charm PDF at all values of x.

The direct photon production in association with a heavy quark jet is one of only a few processes one can use to probe a possible intrinsic heavy quark component at high-x. As is shown in Fig. 1 for the direct photon production process at the Tevatron [5], the different models of intrinsic charm modify the prediction for this specific process at high transverse momenta of the photon. We discuss similar predictions for different collider scenarios.

2 Direct photon production

Single direct photons have long been considered an excellent probe of the structure of the proton due to their point-like electromagnetic coupling to quarks and due to the fact that they escape confinement. Concentrating on a double inclusive production of a direct photon with a heavy

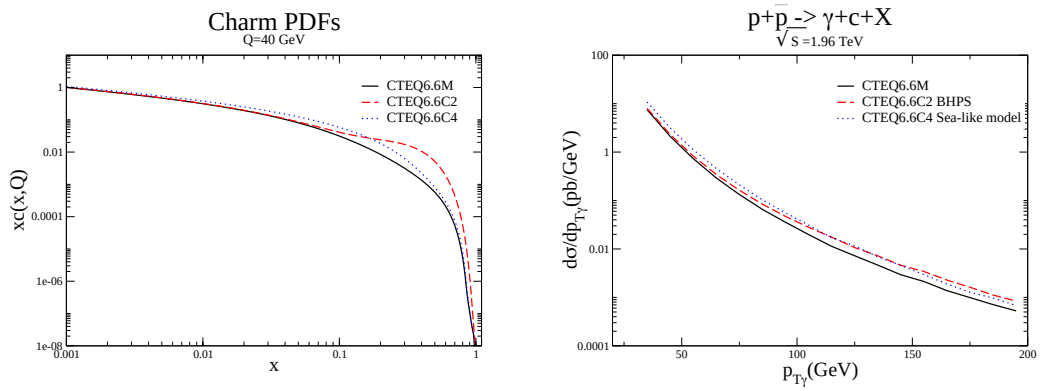

Figure 1: Charm parton distribution function $c(x, Q)$ at $Q = 40$ GeV and the differential cross-section for the direct photon production with a charm quark jet.

quark allows access to different PDF components. Single direct photons couple mostly to valence quarks in the proton. By investigating direct photons accompanied by heavy quark jets, one gains access to the gluon and the heavy quark PDF. That is because, at leading order $\mathcal{O}(\alpha\alpha_s)$, the direct photon with a heavy quark arises only from $gQ \to \gamma Q$ Compton scattering process as opposed to the single photon in which case a Compton scattering contribution $gq \to \gamma q$ competes against a contribution from quark annihilation $q\bar{q} \to \gamma g$.

At leading order, we see that the initial state for the direct photon production with a heavy quark jet depends only on gluon PDF and heavy quark PDF where also the latter is often radiatively generated from the gluon leading to even stronger dependence of this process on the gluon PDF.

At next-to-leading order (NLO), the dependence of the direct photon production even with a heavy quark jet lessens due to the radiation subprocesses which include a light quark initial

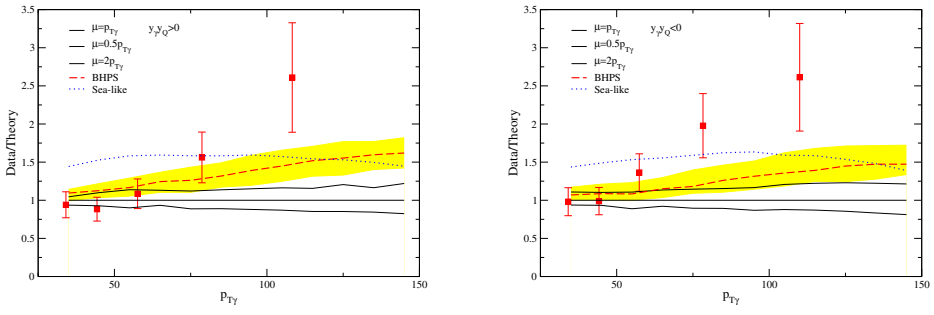

Figure 2: Data/Theory plot for NLO direct photon production in association with a charm quark jet at the Tevatron.

states as well. Especially at the Tevatron, these subprocesses can even dominate the total cross-section (for details see [5]).

3 Predictions for Tevatron, RHIC and the LHC

Here we present predictions mostly in the form of differential cross-section over the transverse momentum of the photon for three different colliders - the Tevatron, RHIC and the LHC. We use specific cuts for minimal transverse momenta of the photon and the heavy quark jet, rapidity of the photon and we use isolation criteria for a direct photon specified by each experiment. All cuts are given in Tab. 1.

Data are already available for the process from the D0 experiment at the Tevatron and as can be seen in Fig. 2, data at high transverse momentum of the photon do not agree with the standard NLO prediction and are also outside the uncertainty band shown in the Fig. 2.

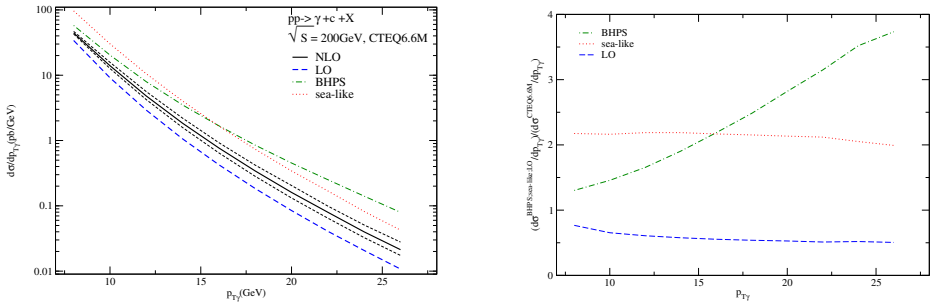

Figure 3: Differential cross-section for direct photon production with a charm quark jet at RHIC showing the LO prediction (blue dashed), NLO prediction with the uncertainty (solid black) and prediction for two models of intrinsic charm - BPHS (green dash-dotted), sea-like (red dotted).

Exp.		p_T min.	y	Isolation
RHIC-Phenix	photon	7 GeV	$\lvert y_\gamma \rvert < 0.35$	$R = 0.5$, $p_T = 0.7$ GeV
	heavy quark	5 GeV	$\lvert y_Q \rvert < 0.8$	—
LHC-CMS	photon	20 GeV	$1.56 < \lvert y_\gamma \rvert < 2.5$	$R = 0.4$, $p_T = 4.2$ GeV
	heavy quark	18 GeV	$\lvert y_Q \rvert < 2.0$	—

Table 1: Kinematic cuts for all collider scenarios.

The BHPS model of intrinsic charm enhances the cross-section at high x which corresponds exactly to the region of large p_T where data deviate from the theory prediction. Unfortunately not even the BHPS model can fully explain the data but it may indicate the presence of intrinsic component of the charm quark PDF.

A similar predictions to the one for Tevatron can be made for RHIC and the LHC. As can be seen from Figs. 3, 4, a possible measurement of the direct photon production with a heavy

quark at RHIC is more sensitive to different models of intrinsic charm because $\sqrt{s}$ at RHIC is smaller than at the LHC. That is why the direct photon production at RHIC probes a higher x of the PDF of the colliding particles which is sensitive to the BHPS model of intrinsic charm.

4 Conclusions

We have showed predictions for direct photon production process in association with a heavy quark jet. Based on the discrepancy between data and theory at NLO at the Tevatron, we focused on the case of a charm jet because the charm intrinsic contribution is less suppressed in comparison to a possible bottom quark intrinsic contribution. We have shown that using the studied process, one can test models of intrinsic charm such as the BPHS model which modify the charm PDF at large x beyond the reach of DIS measurements.

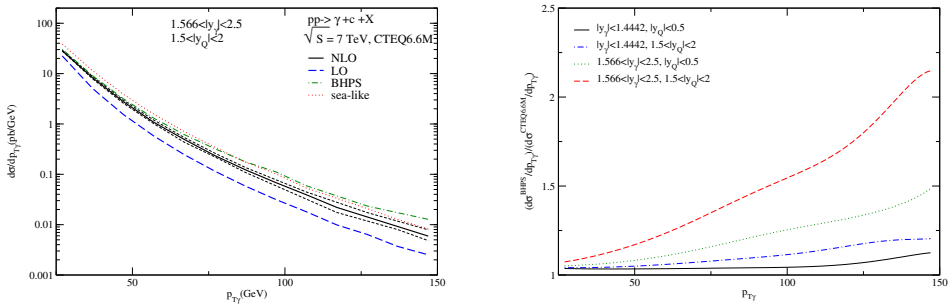

Figure 4: Differential cross-section for direct photon production with a charm quark jet at the LHC showing the same curves as in Fig. 3.

References

[1] R. D. Ball *et al.* Nucl. Phys. **B823** (2009) 195–233, arXiv:0906.1958 [hep-ph].

[2] A. D. Martin, W. J. Stirling, R. S. Thorne, and G. Watt. Eur. Phys. J. **C63** (2009) 189–285, arXiv:0901.0002 [hep-ph].

[3] P. M. Nadolsky *et al.* Phys. Rev. **D78** (2008) 013004, arXiv:0802.0007 [hep-ph].

[4] J. Pumplin, H. L. Lai, and W. K. Tung. Phys. Rev. **D75** (2007) 054029, arXiv:hep-ph/0701220.

[5] T. Stavreva and J. Owens. Phys.Rev. **D79** (2009) 054017, arXiv:0901.3791 [hep-ph].

Fully massive Scheme for Jet Production in DIS

Piotr Kotko, Wojciech Slominski

M. Smoluchowski Institute of Physics, Jagiellonian Univ., Cracow*

DOI: http://dx.doi.org/10.3204/DESY-PROC-2012-02/116

We present a consistent treatment of heavy quarks for jet production in DIS at NLO accuracy. The method is based on the ACOT massive factorization scheme and dipole subtraction method for jets. The last had to be however extended in order to take into account initial state splittings with heavy quarks. We constructed relevant kinematics and dipole splitting functions together with their integrals. We partially implemented the method in a MC program and checked against the known inclusive result for charm structure function.

1 Introduction

There are two basic approaches to heavy quarks production in DIS. First is so called zero-mass variable flavor number scheme (ZM-VFNS), which treats heavy quarks as massless partons with corresponding parton distribution functions (PDF). This scheme is applicable when the hard scale (taken here as the virtuality of the exchanged boson Q^2) is much larger then the mass $m_{\mathbf{Q}}$ of a given heavy quark $\mathbf{Q}$. On the other hand, when Q^2 is of the order of $m_{\mathbf{Q}}$, so called fixed flavor number scheme (FFNS) is applicable. It retains the full mass dependence in the coefficient function and there is no PDF for $\mathbf{Q}$ as to the leading power it cannot appear in the soft part.

Increasing precision of the data forces us to control also the intermediate region of Q^2. The methods that address this problem are called general mass schemes (GM) [1, 2, 3, 4]. They are however formulated for inclusive processes only and similar method relevant for jets is highly desirable.

In the following we briefly describe our solution to this problem [5, 6]. It is based on the ACOT massive factorization theorem [1, 7] and massive dipole subtraction method (DSM) [8, 9, 10], which however had to be reformulated in order to match with the former.

2 Dipole subtraction method with massive partons

Consider NLO calculation of a cross section for producing n jets in lepton-hadron reaction. The LO cross section is schematically written as

$$\sigma_n^{(\mathrm{LO})} = \mathcal{N} \sum_a f_a \otimes \int d\Phi_{n,a} \; |\mathcal{M}_{n,a}|^2 \, F_{n,a}, \tag{1}$$

*The work supported by the Polish National Science Centre grant No. DEC-2011/01/B/ST2/03643.

where $\mathcal{N}$ is a normalization factor, f_a are PDFs, $d\Phi_{n,a}$ is n-parton phase space (PS) and $\mathcal{M}_{n,a}$ is a tree-level matrix element (ME) with n final state partons and one QCD initial state parton a. The jet function $F_{n,a}$ determines the actual observable and is realized by a suitable jet algorithm. It satisfies $F_{n+1,a} = F_{n,a}$ in the singular regions of PS. At NLO the corrections involve loop diagrams living on n-particle PS and additional real emission belonging to $(n+1)$-particle PS. Both contain IR singularities which ultimately cancel, however the cancellation is non-trivial as the singularities have different origin. An elegant and exact solution is provided by DSM. One adds and subtracts an auxiliary contribution $\mathcal{D}_{n,a}$, such that it mimics all the singularities of $\mathcal{M}_{n+1,a}$ and at the same time can be analytically integrated over singular regions of PS. To be more specific we have

$$\sigma_n^{(\mathrm{NLO})} = \mathcal{N} \sum_a f_a \otimes \left\{ \int d\Phi_{n+1,a} \left[\left|\mathcal{M}_{n+1,a}\right|^2 F_{n+1,a} - \mathcal{D}_{n,a} F_{n,a} \right] + \int d\Phi_{n,a} \left[\mathcal{M}_{n,a}^{(\mathrm{loop})} + \int d\phi_a \, \mathcal{D}_{n,a} - \mathcal{C}_{n,a} \right] F_{n,a} \right\}, \quad (2)$$

where virtual corrections to $\left|\mathcal{M}_{n,a}\right|^2$ are symbolically denoted as $\mathcal{M}_{n,a}^{(\mathrm{loop})}$. The subspace leading to singularities is $d\phi_a$ and fulfils PS factorization formula $d\Phi_{n+1,a} = d\Phi_{n,a} \otimes d\phi_a$. Thanks to the properties of $\mathcal{D}_{n,a}$ and $F_{n+1,a}$ the first square bracket is integrable in four dimensions, while in the second, the poles resulting from integral $\int d\phi_a \, \mathcal{D}_{n,a}$ are cancelled against the ones in $\mathcal{M}_{n,a}^{(\mathrm{loop})}$. However, not all singularities cancel in this way – there are also collinear poles connected with initial state splittings of massless partons. They are removed by means of collinear subtraction term $\mathcal{C}_{n,a}$. It has the form

$$\mathcal{C}_{n,a} = \sum_b \mathcal{F}_{ab} \otimes \left|\mathcal{M}_{n,b}\right|^2, \quad (3)$$

where $\mathcal{F}_{ab}$ are renormalized partonic PDFs, i.e. the densities of partons b inside parton a. For instance in the $\overline{\mathrm{MS}}$ scheme $\mathcal{F}_{ab}(z) = -\frac{1}{\varepsilon} \frac{\alpha_s}{2\pi} P_{ab}(z)$, where $P_{ab}(z)$ are standard splitting functions.

Within DSM the dipole function is realized as a sum of contributions corresponding to single emissions with different combinations of "emitter" and "spectator"partons[1]. Each such term D has a general form

$$D = \hat{V} \hat{C} \left| \hat{\mathcal{M}}_{n,a} \right|^2, \quad (4)$$

where $\hat{V}$ is so called dipole splitting matrix (in helicity space) and encodes the information about some of the singularities of $\mathcal{M}_{n+1,a}$. The matrix $\hat{C}$ corresponds to color operators for parton emissions, which act on the matrix element. The notation above is symbolic and means that both quantities are correlated in the color and spin space. For DIS, there are three different classes of dipoles D, depending on whether emitter or spectator are in the initial or final states. Here we are mainly interested in the case of initial state emitter and final state spectator as they contain factorization-related information.

When heavy quarks are present, the above general picture remains the same. If however a massive parton takes part in a splitting process there is no collinear singularity. Nevertheless

[1]The notion "emitter" and "spectator" are explained in [11]

there are IR sensitive logarithms which become harmful when the external scale becomes large. We shall refer to such terms as *quasi-collinear singularities* [12] and abbreviate as q-singularities.

The first step towards GM scheme for jets is to construct dipole functions controlling q-singularities for initial state emissions. Moreover we want to have possibly massive initial states as it is allowed by the ACOT scheme. It was partially done in [8] (for $\mathbf{Q} \to \mathbf{Q}g$ splitting), while in [10] the splitting processes with heavy quarks are considered in the final states only.

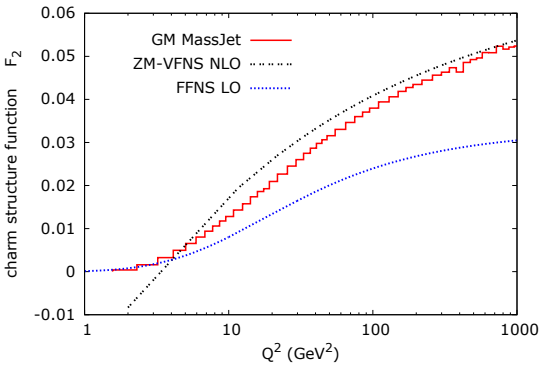

Figure 1: ACOT charm structure function calculated using MC implementation of our method (`MassJet`). The calculations are done for $x_B = 0.05$ and CTEQ5 PDFs.

Let us look at the particular example. Consider the initial state $g \to \mathbf{Q}\overline{\mathbf{Q}}$ splitting. Let us assign the momentum p_a to the gluon, p_i to the emitted final state quark (or anti-quark), and p_j to the spectator. Using these, we construct new momenta which enter $\mathcal{M}_{n,a}$ in (4): $\tilde{p}_j^\mu = \tilde{w}\left(p_i^\mu + p_j^\mu\right) - \tilde{u}p_a^\mu$ becomes a new final state and $\tilde{p}_{\underline{ai}}^\mu = (\tilde{w}-1)\left(p_i^\mu + p_j^\mu\right) - (\tilde{u}-1)\,p_a^\mu$ becomes a new initial state. The variables $\tilde{u}$, $\tilde{w}$ can be determined from on-shell conditions for $\tilde{p}_j$ and $\tilde{p}_{\underline{ai}}$. Our dipole splitting function reads

$$\hat{V}_{g\to\mathbf{Q}\overline{\mathbf{Q}},\,j} = 8\pi\mu_{\mathrm{r}}^{2\varepsilon}\alpha_s T_R\left[1 - \frac{1}{1-\varepsilon}\left(2\tilde{u}\,(1-\tilde{u}) - \frac{(1-\tilde{u})\,m_{\mathbf{Q}}^2}{p_i\cdot p_a}\right)\right], \tag{5}$$

where μ_r is a mass scale needed in $D = 4 - 2\varepsilon$ dimensions. In this case $\hat{V}$ is just diagonal in helicity space.

Consider next the integral of (5) over one-particle subspace. It can be conveniently expressed in terms of rescaled masses $\eta_l^2 = m_l^2/2\tilde{p}_j\cdot p_a$ for some parton l. In the limit of small $\eta_{\mathbf{Q}}$ we get

$$\int d\phi\,\hat{V}_{g\to\mathbf{Q}\overline{\mathbf{Q}},\,j}\,(u) = \frac{\alpha_s}{2\pi}\left[P_{gq}\,(u)\left(\log\frac{u^2}{u+\eta_j^2} - \log\eta_{\mathbf{Q}}^2\right) + 2T_R\,u\,(1-u)\right] + \mathcal{O}\left(\eta_{\mathbf{Q}}^2\right). \tag{6}$$

We see that there is a term of the form $P_{gq}\,(u)\log\eta_{\mathbf{Q}}^2$ which becomes harmful when the scale becomes large (in massless case there would be a pole $1/\varepsilon$). Similar terms appear also in other dipoles for the initial state emissions.

3 General mass scheme for jets

In the spirit of the ACOT scheme, the initial state q-singularities have to be factorized out. It is accomplished by $\mathcal{C}_{n,a}$ term with partonic PDFs $\mathcal{F}_{ab}$ calculated in a special way. Let us recall at this point, that the latter are defined as certain ME of light-cone operators and can be calculated order by order using special Feynman rules (see e.g. [13]). The results contain UV singularities which have to be renormalized, leading to evolution equations. For the present application we calculate $\mathcal{F}_{ab}$ to one loop with full mass dependence and renormalize them using

the $\overline{\text{MS}}$ scheme[2]. Since counterterms are mass independent in this scheme, we assure that hadronic PDFs evolve according to standard massless DGLAP equations. For instance we get

$$\mathcal{F}_{g\mathbf{Q}}(z) = \frac{\alpha_s}{2\pi} T_R \left(1 - 2z(1-z)\right) \log \frac{\mu_r^2}{m_{\mathbf{Q}}^2}, \tag{7}$$

$$\mathcal{F}_{\mathbf{Q}g}(z) = \frac{\alpha_s}{2\pi} C_F \frac{1 + (1-z)^2}{z} \left[\log \frac{\mu_r^2}{m_{\mathbf{Q}}^2} - 2\log z - 1\right], \tag{8}$$

$$\mathcal{F}_{\mathbf{QQ}}(z) = \frac{\alpha_s}{2\pi} C_F \left\{\frac{1+z^2}{1-z} \left[\log \frac{\mu_r^2}{m_{\mathbf{Q}}^2} - 2\log(1-z) - 1\right]\right\}_+ . \tag{9}$$

We have checked that the above procedure leads to IR safe dipoles in the limit of vanishing $\eta_{\mathbf{Q}}$. Moreover, the results coincide with those Ref. [10] in the $\overline{\text{MS}}$ scheme.

In order to perform numerical tests we have partially implemented our method in a dedicated C++ program based on FOAM [14]. Using the program, we have calculated the charm structure function F_2 and compared it with semi-analytical calculation in the ACOT scheme. This exercise uses three dipoles and two collinear subtraction terms. The virtual corrections are taken from [15]. We find that the soft poles are indeed cancelled by the corresponding poles coming from the integrated dipoles. Moreover, we find agreement with the semi-analytical calculation and observe that our result properly interpolates between the two limiting solutions of the ZM-VFNS and FFNS schemes, as depicted in Fig. 1.

Let us stress that the result is obtained by a numerical integration of a fully differential cross section, which provides a severe test on the implementation of our massive dipole formalism.

References

[1] M. A. G. Aivazis, J. C. Collins, F. I. Olness, and W.-K. Tung. Phys. Rev. **D50** (1994) 3102–3118, arXiv:hep-ph/9312319.

[2] M. Buza, Y. Matiounine, J. Smith, and W. L. van Neerven. Eur. Phys. J. **C1** (1998) 301–320, arXiv:hep-ph/9612398.

[3] R. S. Thorne and R. G. Roberts. Phys. Rev. **D57** (1998) 6871–6898, arXiv:hep-ph/9709442.

[4] S. Forte, E. Laenen, P. Nason, and J. Rojo. Nucl.Phys. **B834** (2010) 116–162, arXiv:1001.2312 [hep-ph].

[5] P. Kotko, *General Mass Scheme for Jet production in QCD*. PhD thesis, Jagiellonian Univ., 2012.

[6] P. Kotko and W. Slominski. In preparation.

[7] J. C. Collins. Phys. Rev. **D58** (1998) 094002, arXiv:hep-ph/9806259.

[8] S. Dittmaier. Nucl. Phys. **B565** (2000) 69–122, arXiv:hep-ph/9904440.

[9] L. Phaf and S. Weinzierl. JHEP **0104** (2001) 006, arXiv:hep-ph/0102207 [hep-ph].

[10] S. Catani, S. Dittmaier, M. H. Seymour, and Z. Trocsanyi. Nucl. Phys. **B627** (2002) 189–265, arXiv:hep-ph/0201036.

[11] S. Catani and M. H. Seymour. Nucl. Phys. **B485** (1997) 291–419, arXiv:hep-ph/9605323. Erratum: *ibid.* **B510**:503-504,1998; [arXiv:hep-ph/9605323v3] includes changes from the Erratum.

[12] S. Catani, S. Dittmaier, and Z. Trocsanyi. Phys. Lett. **B500** (2001) 149–160, arXiv:hep-ph/0011222.

[13] J. Collins, *Foundations of perturbative QCD*, vol. 32. Cambridge Univ. Press, 2011.

[14] S. Jadach. Comput. Phys. Commun. **152** (2003) 55–100, arXiv:physics/0203033.

[15] S. Kretzer and I. Schienbein. Phys. Rev. **D58** (1998) 094035, arXiv:hep-ph/9805233.

[2] More precisely we use the Collins-Wilczek-Zee renormalization scheme which assumes the $\overline{\text{MS}}$ above certain threshold and zero momentum subtraction below it.

Measurements of Jets containing Charm and Bottom Quarks with the ATLAS Detector

David Calvet[1] on behalf of the ATLAS Collaboration

[1]LPC Clermont-Ferrand, BP80026, 63171 Aubière cedex, France

DOI: http://dx.doi.org/10.3204/DESY-PROC-2012-02/88

The inclusive and dijet production cross-sections have been measured for jets containing b-hadrons (b-jets) in proton-proton collisions at the LHC using the ATLAS detector. The b-jets are identified using either a lifetime-based method or a muon-based method. $D^{*\pm}$ meson production in jets is also measured, with fully reconstructed $D^{*\pm}$ mesons. The results are compared to next-to-leading-order QCD predictions.

1 Introduction

Heavy flavour production in high-energy interactions provides an important test of perturbative QCD (pQCD). Calculations of the b-quark production cross-section have been performed at next-to-leading order (NLO) in pQCD and can be matched to different parton-shower and hadronisation models to produce final states that can be compared to those measured in collision data. Another method to study the production of heavy quarks is to measure $D^{*\pm}$ mesons produced inside jets. With collisions at higher center-of-mass energy at the CERN Large Hadron Collider (LHC), the kinematical range accessible to experiment has been significantly extended. It is therefore of great interest to test the theoretical predictions at $\sqrt{s}$ =7 TeV. This contribution reports a measurement of the inclusive b-jet and $b\bar{b}$-dijet production cross-sections, and a measurement of $D^{*\pm}$ meson production in jets, both with the ATLAS detector [1].

2 Measurement of the inclusive and dijet cross-sections of b-jets

The inclusive b-jet and $b\bar{b}$-dijet production cross-sections are measured using data recorded in 2010 with an integrated luminosity of 34.0 pb^{-1}. They are compared to next-to-leading order QCD predictions derived using POWHEG and MC@NLO [2]. To perform the parton-showering, POWHEG is interfaced to Pythia 6 and MC@NLO to Herwig 6 [2].

The relatively long lifetime of hadrons containing b-quarks is exploited to obtain a jet sample enriched in b-jets by selecting jets with a reconstructed secondary vertex significantly displaced from the primary vertex. The efficiency of the b-tagging is estimated with a data-driven method that uses jets containing a muon. The number of b-jets before and after b-tagging is obtained using the variable p_T^{rel}, which is defined as the momentum of the muon transverse to the combined muon plus jet axis. Muons originating from b-hadron decays having a harder p_T^{rel} spectrum than

muons in other jets, it is possible to obtain the fraction of b-jets in a given sample by fitting the p_T^{rel} spectrum using templates for b-, c- and light-flavour jets. Then, to estimate the number of b-jets in this enriched sample (the purity) a fit to the invariant mass distribution of the charged particle tracks in the secondary vertex is performed.

The p_T^{rel} method can also be used as a discriminant variable to measure the inclusive b-jet cross-section directly. The muon-based cross-section measurement relies on this method in the range $30 < p_T < 140$ GeV and shows good agreement with the measurement obtained with the lifetime method.

The inclusive b-jet cross-section measurement as a function of jet p_T in the range $20 < p_T < 400$ GeV and rapidity in the range $|y| < 2.1$ is presented in Figure 1.

The normalized leading-order Pythia prediction shows broad agreement with the measured cross-section. As can be seen in Figure 2, the inclusive b-jet cross-section is found to be in good agreement with the POWHEG+Pythia prediction over the full kinematic range. MC@NLO+Herwig, however, predicts a significantly different behaviour of the double-differential cross section that is not observed in the data.

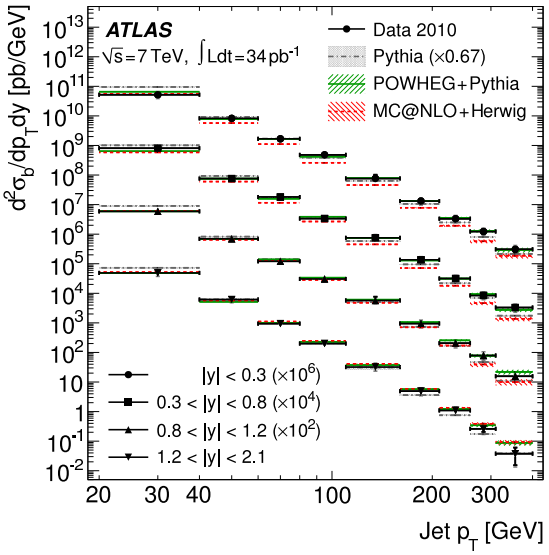

Figure 1: Inclusive double-differential b-jet cross-section as a function of p_T for different rapidity ranges [1]. The data are compared to the predictions of Pythia, POWHEG and MC@NLO.

The $b\bar{b}$-dijet cross-section was measured as a function of dijet invariant mass in the range $110 < m_{jj} < 760$ GeV, as a function of the azimuthal angle difference between the jets and of the angular variable $\chi = \exp|y_1 - y_2|$ (see Ref. [1]). POWHEG+Pythia and MC@NLO+Herwig show good agreement with the measured $b\bar{b}$-dijet cross-sections, as does the normalized leading-order Pythia generator.

Both cross-section measurements are dominated by systematic uncertainties, mainly coming from the b-jet energy scale and the determination of the b-jet tagging efficiency and purity.

3 Measurement of $D^{*\pm}$ meson production in jets

The production of $D^{*\pm}$ mesons inside jets is measured using data recorded between April and July 2010 with an integrated luminosity of 0.30 pb^{-1}.

Candidates for $D^{*\pm}$ mesons inside jets are reconstructed in the decay chain: $D^{*+} \to D^0\pi^+$, $D^0 \to K^-\pi^+$ and its charge conjugate. A D^0 ($\bar{D}^0$) candidate – combining two oppositely-charged tracks with $p_T > 1$ GeV – whose mass is within 50 MeV of the PDG value is then combined with a third track with $p_T > 0.5$ GeV having the same charge as the pion of the D^0 ($\bar{D}^0$) candidate. This $D^{*\pm}$ candidate is required to have $p_T > 7.5$ GeV, and the measured

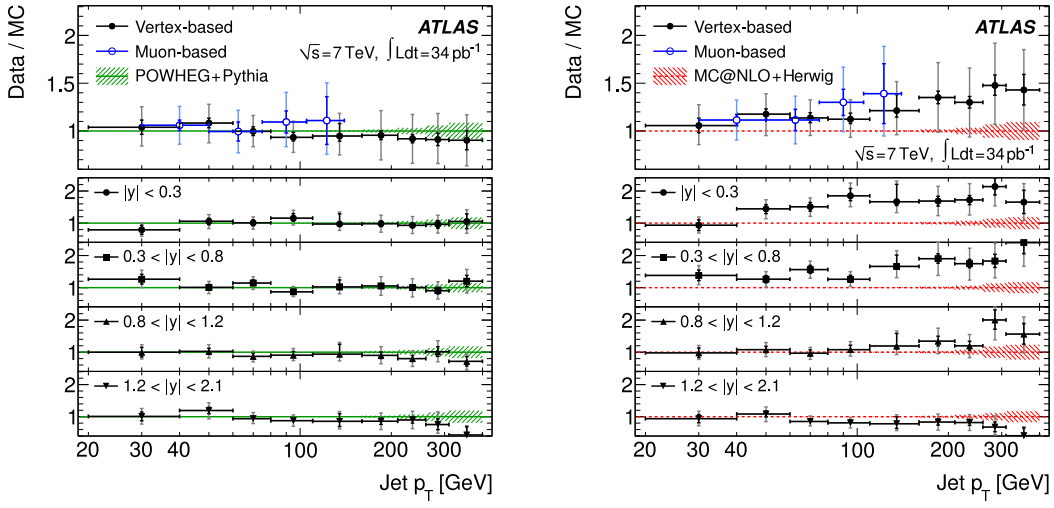

Figure 2: Ratio of the measured cross-sections to the theory predictions of POWHEG (left) and MC@NLO (right) [1]. In the region where the lifetime-based measurement overlaps with the muon $p_T^{\rm rel}$ measurement both results are shown. The top plot shows the full rapidity acceptance, while the four smaller plots show the comparison for each of the rapidity ranges separately. The data points show both the statistical uncertainty (dark colour) and the combination of the statistical and systematic uncertainties (light colour). The shaded regions around the theoretical predictions reflect the statistical uncertainty only.

D^0 ($\bar{D}^0$) transverse decay length is required to be greater than zero. The reconstructed $D^{*\pm}$ candidates are matched with the reconstructed jets in the event. The momentum fraction $z = p_{||}(D^{*\pm})/E(\text{jet})$ of these candidates is required to be larger than 0.3. The $D^{*\pm}$ jet yield is extracted from the distribution of the difference of the masses of the $D^{*\pm}$ and D^0 ($\bar{D}^0$) candidates in bins of the jet p_T and z. After applying all the event selection and criteria, a total of 4282±93 $D^{*\pm}$ jet signal candidates are obtained. The distribution for the data integrated over all bins of p_T and z, together with the fit result, is shown in Figure 3.

The ratio $\mathcal{R}(p_T, z) = N_{D^{*\pm}}(p_T, z)/N_{jet}(p_T)$ is calculated after a Bayesian iterative unfolding algorithm is applied to correct for the detector efficiency and bin-to-bin migration due to the detector resolution – $N_{D^{*\pm}}$ is also corrected for the branching fraction $\mathcal{B}(D^{*\pm} \to K^{\mp}\pi^{\pm}\pi^{\pm})$. The unfolding algorithm has been validated using Monte-Carlo (MC) simulated events and no bias is observed. The main systematic uncertainties come from trigger efficiency, track reconstruction efficiency and jet energy scale, see Ref. [1] for more details.

The measured $D^{*\pm}$ jet production rate integrated over all the p_T and z bins is found to be $\mathcal{R} = 0.025 \pm 0.001(\text{stat.}) \pm 0.004(\text{syst.})$ for $D^{*\pm}$ jets with $25 < p_T < 70$ GeV, in the range $|\eta| < 2.5$ and with momentum fraction $0.3 < z < 1$. Measurements for different bins in p_T and z are available in Ref. [1]. Comparisons between the measurement and predictions from various MC calculations are shown in Figure 3 as a function z. The values of $\mathcal{R}$ predicted by MC calculations are lower than the data by a factor 2 to 3 in the bins with lowest z, and this is especially significant at low p_T. The predictions are consistent with the data for $z > 0.7$

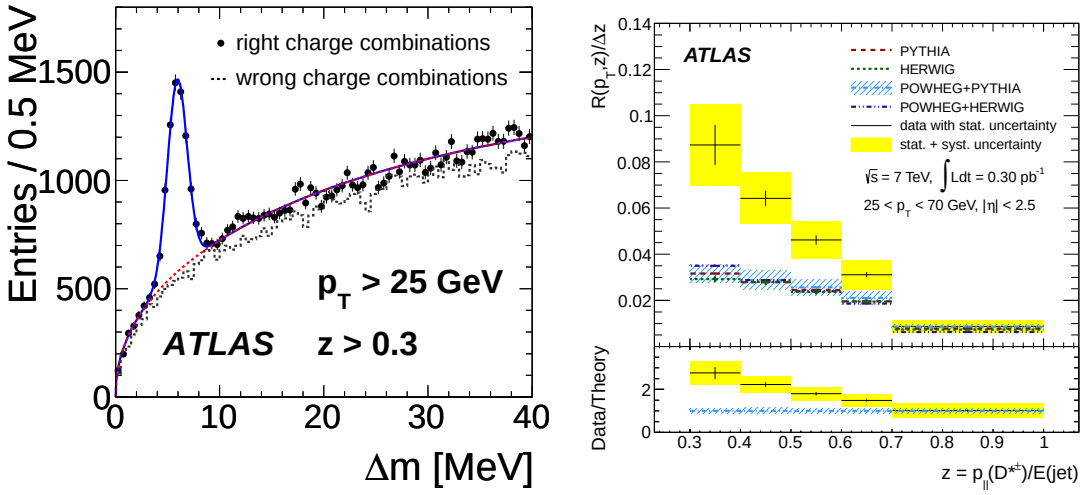

Figure 3: Left: distribution of the mass difference of the $D^{*+} \to D^0\pi^+$ and its charge conjugate inside jets [1]. The solid line is the fit result. The dotted line represents the background component. Right: comparison of the $D^{*\pm}$ production rate $\mathcal{R}(p_T, z)/\Delta z$ in different z bins between the measurement and the MC predictions of Pythia, Herwig, POWHEG+Pythia and POWHEG+Herwig [1]. The inset shows the ratio of the measurement to the POWHEG+Pythia prediction.

at all p_T. Integrating over all the p_T and z bins, the production rate $\mathcal{R}$ is estimated to be 0.0133 ± 0.0008 by POWHEG+Pythia, which is just about half of the measured value.

4 Conclusions

The inclusive b-jet and $b\bar{b}$-dijet production cross-sections are found to be in good agreement with the POWHEG+Pythia predictions over the full kinematic range. MC@NLO+Herwig, however, predicts a significantly different behaviour for the inclusive b-jet double-differential cross section which is not present in the data. Nevertheless, it shows good agreement with the measured $b\bar{b}$-dijet cross-section.

In contrast, the measured production of $D^{*\pm}$ mesons inside jets is not well modeled in any of the current MC generators. These results show the need of further QCD refinements to improve the description of high transverse momentum D-meson production in this new energy range of hadron collisions.

References

[1] ATLAS Collaboration, EPJ **C71** (2011) 1846; ATLAS Collaboation, Phys. Rev. **D85** (2012) 052005.

[2] [Pythia] T. Sjöstrand, S. Mrenna, P. Z. Skands, JHEP **05** (2006) 026; [Herwig] G. Corcella *et al*, JHEP **01** (2001) 010; [POWHEG] P. Nason, JHEP **11** (2004) 040; S. Frixione, P. Nason, C. Oleari, JHEP **11** (2007) 070; S. Alioli, K. Hamilton, P. Nason, C. Oleari, E. Re, JHEP **04** (2011) 081; [MC@NLO] S.Frixione, B. R. Webber, JHEP **06** (2002) 029; S. Frixione, P.Nason, B. R. Webber, JHEP **08** (2003) 007

Measurement of charm fragmentation fractions in photoproduction at HERA

Ganna Dolinska[1] on behalf of the ZEUS Collaboration

[1]Taras Shevtchenko National University Of Kyiv, Volodymyrska str. 60, Kyiv, Ukraine

DOI: http://dx.doi.org/10.3204/DESY-PROC-2012-02/47

The production of D^*, D^+, D^0, D_s and Λ_c charm hadrons in ep scattering at HERA was studied with the ZEUS detector, and the fractions of c quarks hadronizing as a particular charm hadron were derived. The measurement has been performed in the photoproduction regime, using the full HERA II data set with a total integrated luminosity of 372 pb^{-1}. The obtained fractions are compared to previous results from HERA and from e^+e^- experiments.

1 Introduction

Charm quark production provides an important testing of perturbative QCD (pQCD) and has been extensively studied in *ep* collisions at HERA. One thing which cannot be predicted by pQCD are the fragmentation fractions of charm quarks into specific charmed hadrons. It is usually assumed that these fractions are universal, i.e. the same for charm quarks produced in e+e- annihilation, in *ep* collisions and also in *pp* or other hadronic collisions. However, the charm production mechanisms are not the same. In e+e- collisions, cc pairs are produced dominantly in a colour-singlet state, which is not the case for *ep* scattering. Thus, measurements of charm fragmentation characteristics at HERA can provide important input to a stringent test of charm-fragmentation universality.

The fractions of quarks hadronizing as a particular charm hadron have been measured in previous studies at HERA [1, 2, 3, 4, 5]. In this paper the measurement of fragmentation fractions in photoproduction with the ZEUS detector is presented with much improved statistics compared to a previous ZEUS publication [1].

2 Hadron reconstruction

The production of D^*, D^+, D^0, D_s and Λ_c charm hadrons was measured in the range of transverse momentum $p_T(D, \Lambda_c) > 3.8GeV$ and pseudorapidity $|\eta(D, \Lambda_c)| < 1.6$.

Charm hadrons were reconstructed using tracks from ZEUS tracking system. The tracks were assigned to the reconstructed event vertex. The hadrons were reconstructed from the following decays: $D^0 \to K^-\pi^+$, $D^{*+} \to D^0\pi_s^+$, $D^+ \to K^-\pi^+\pi^+$, $D_s^+ \to \phi\pi^+$ with $\phi \to K^+K^-$ and $\Lambda_c^+ \to K^-p\pi^+$.

The relatively long life time of the D can result in a decay vertex that is spatially separated from the primary interaction point. This property can be used to improve the statistical

precision of the D mesons' signal by reducing the combinatorial background. The corresponding variable was the decay length significance $S_l = l/\sigma_l$ where l is a decay length in the transverse plane and σ_l is the uncertainty assosiated with the distance. The cut on the decay length significance was chosen to maximize the signal-to-background ratio. For the D^0 meson it was chosen as $S_l > 1$, for the D^+ - $S_l > 3$ and for the D_s - $S_l > 0$.

Reflections from D_s^+ and Λ_c^+ decays to three charged particles were subtracted from the D^+ mass spectrum using the simulated reflection shapes normalized to the measured D_s^+ and Λ_c^+ production rates. The same was done also for $M(KK\pi)$ distribution for D_s^+ candidates and for $M(Kp\pi)$ distribution for Λ_c^+ candidates.

3 Charm fragmentation fractions

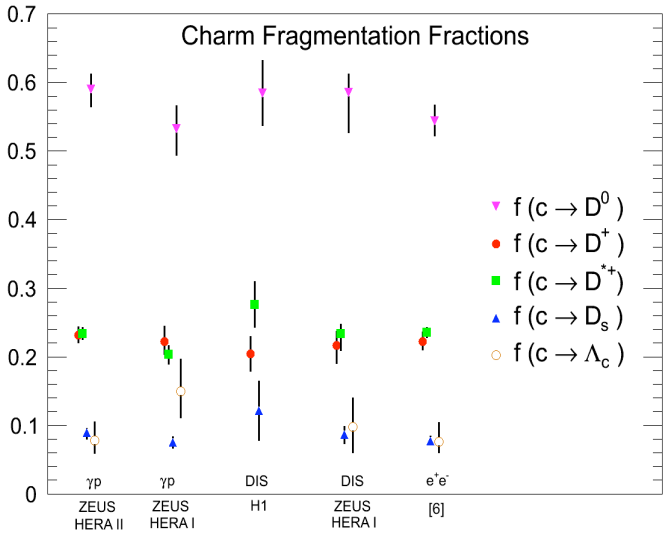

Figure 1: The fractions of c-quark hadronizing as a particular charmhadron. The photoproduction measurements presented here are shown (first column) and compared to previous HERA results in photoproduction (second column) and DIS (third and fourth column) and to e^+e^- data (last column)

The fragmentation fraction $f(h)$ for a specific charm hadron h was computed from

$$f(h) = \sigma(h)/\sigma_g \tag{1}$$

where $\sigma(h)$ is the cross section of the charm hadron and σ_g is the sum

$$\sigma_g = \sigma(D^+) + \sigma(D^0) + \sigma(D_s) + 1.14 \cdot \sigma(\Lambda_c) \tag{2}$$

The factor 1.14 accounts for unobserved heavier charm baryons, and $\sigma(D^0)$ and $\sigma(D^+)$ include both direct decays plus decays originating from D^*.

Figure 1 shows the result. A comparison with other HERA experiments from H1 [2] and ZEUS in DIS [3, 4] and in photoproduction [1] and with experiments at e^+e^- storage rings [5, 6] is also shown. The date support the hypothesis that fragmentation proceeds independently of the hard sub-process.

4 Conclusions

The production of charm hadrons D^{*+}, D^+, D^0, D_s^+ and Λ_c^+ has been measured in the kinematic range $p_T(D, \Lambda_c) > 3.8GeV$ and $|\eta(D, \Lambda_c)| < 1.6$.

The fractions of c quarks hadronizing as D^{*+}, D^+, D^0, D_s^+ and Λ_c^+ hadrons have been calculated in the accepted kinematic range. The measured open-charm fragmentation fractions are consistent with previous HERA results [1, 2, 3, 4] and with those obtained in e^+e^- annihilations [5, 6].

These measurements support the hypothesis that fragmentation proceeds independently of the hard sub-process.

References

[1] ZEUS Collab.,S.Chekanov et al.,Eur.Phys.J.C44(2005)351

[2] H1 Collab.,A.Aktas et al.,Eur.Phys.J.C38(2005)447

[3] ZEUS Collab.,S.Chekanov et al.,JHEP 07(2007)74

[4] ZEUS Collab.,H.Abramowicz et al., JHEP11(2010)009

[5] L.Gladilin, Preprint hep-ex/9912064,1999

[6] ATLAS Collaboration, ATLAS-CONF-2011-017,2011

Differential and total cross sections for top pair and single top production

Nikolaos Kidonakis

Kennesaw State University, Physics #1202, Kennesaw, GA 30144, USA

DOI: http://dx.doi.org/10.3204/DESY-PROC-2012-02/251

I present theoretical results at approximate NNLO from NNLL resummation for top quark production at the LHC and the Tevatron, including new results at 8 TeV LHC energy. Total cross sections are shown for $t\bar{t}$ production, for single top production in the t and s channels and via associated tW production, and for associated tH^- production. Top quark transverse momentum and rapidity distributions in $t\bar{t}$ production are also presented, as well as new results for t-channel single top and single antitop p_T distributions.

1 Introduction

The top quark is a centerpiece of LHC and Tevatron physics, and both $t\bar{t}$ and single top production are being studied. The LO partonic processes for top-antitop pair production are $q\bar{q} \to t\bar{t}$, dominant at the Tevatron, and $gg \to t\bar{t}$, dominant at LHC energies. For single top quark production the partonic channels are the t channel: $qb \to q't$ and $\bar{q}b \to \bar{q}'t$; the s channel: $q\bar{q}' \to \bar{b}t$; and associated tW production: $bg \to tW^-$. A related process is the associated production of a top quark with a charged Higgs, $bg \to tH^-$.

Higher-order QCD corrections are significant for top quark production. Soft-gluon emission corrections are dominant and have been resummed through NNLL accuracy [1, 2]. Approximate NNLO (and even higher-order [3]) differential cross sections have been derived from the expansion of the NNLL resummed result for $t\bar{t}$ [1] and single top [2] production.

There are several different approaches to resummation (for a detailed review see [4]; yet another approach appeared later in [5]). The approach used here is the only NNLL calculation at the differential cross-section level using the standard moment-space resummation in pQCD.

We note that the threshold approximation works very well not only for Tevatron but also for LHC energies because partonic threshold is still important. There is less than 1% difference between NLO approximate and exact cross sections, and this is also true for differential distributions, see the left plot in Fig. 1.

2 $t\bar{t}$ production

We begin with top-antitop pair production [1]. The NNLO approximate $t\bar{t}$ cross section at the Tevatron, with a top quark mass $m_t = 173$ GeV and using MSTW2008 NNLO pdf [6], is $7.08^{+0.00\,+0.36}_{-0.24\,-0.27}$ pb, where the first uncertainty is from scale variation $m_t/2 < \mu < 2m_t$ and the second is from the pdf at 90% C.L.

The $t\bar{t}$ cross section at the LHC at 7 TeV energy is $163^{+7}_{-5} \pm 9$ pb; at 14 TeV it is 920^{+50+33}_{-39-35} pb. The new result for the current 8 TeV LHC energy is

$$\sigma_{t\bar{t}}^{\rm NNLOapprox}(m_t = 173\,{\rm GeV},\, 8\,{\rm TeV}) \quad = \quad 234^{+10}_{-7} \pm 12\ {\rm pb}\,.$$

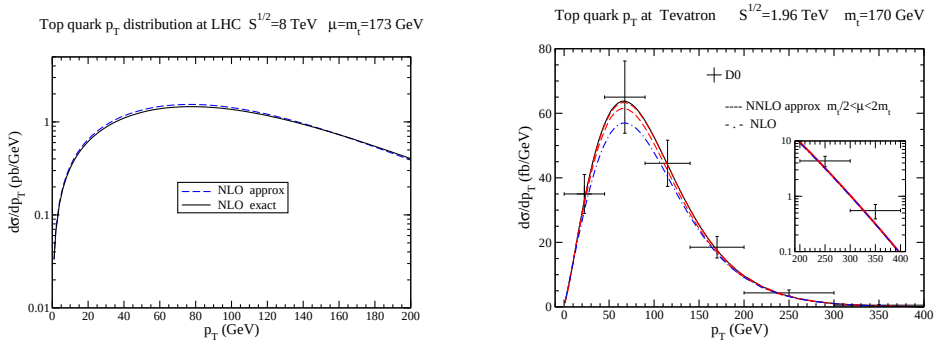

Figure 1: Top quark p_T distribution at the LHC (left) and the Tevatron (right).

The top quark p_T distribution at the Tevatron is shown in the right plot of Fig. 1. We note the excellent agreement of the NNLO approximate results with D0 data [7]. The top quark p_T distributions at the LHC at 7 and 8 TeV energies are shown in the left plot of Fig. 2.

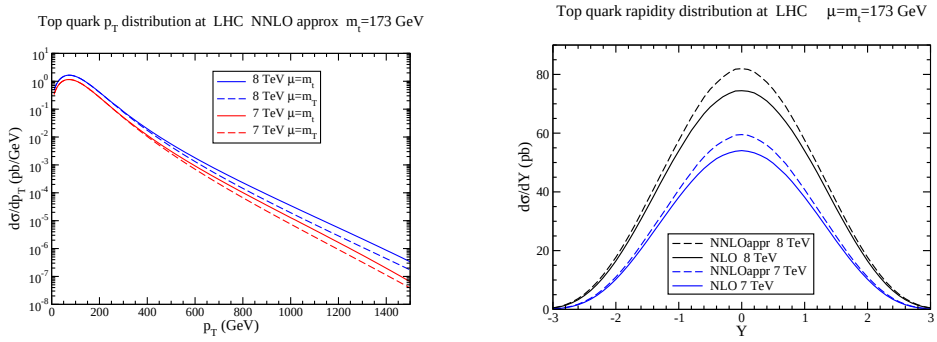

Figure 2: Top quark p_T (left) and rapidity (right) distributions at the LHC [$m_T = \sqrt{p_T^2 + m_t^2}$].

The top quark rapidity distribution at the LHC at 7 and 8 TeV energies is shown in the right plot of Fig. 2. The top quark rapidity distribution at the Tevatron displays a significant forward-backward asymmetry, $A_{\rm FB} = [\sigma(Y > 0) - \sigma(Y < 0)]/[\sigma(Y > 0) + \sigma(Y < 0)] = 0.052^{+0.000}_{-0.006}$, which is smaller than observed values (see also the review in [4] and recently [8, 9]).

3 Single top quark production

We continue with single top production [2], and start with updated results for the t channel.

The t-channel cross sections at LHC energies for single top production, single antitop production, and their sum are given in Table 1. The t-channel single top quark production at the Tevatron is $1.04^{+0.00}_{-0.02} \pm 0.06$ pb; the result for antitop at the Tevatron is the same.

t-channel LHC	t	$\bar{t}$	Total
7 TeV	$43.0^{+1.6}_{-0.2} \pm 0.8$	$22.9 \pm 0.5^{+0.7}_{-0.9}$	$65.9^{+2.1+1.5}_{-0.7-1.7}$
8 TeV	$56.4^{+2.1}_{-0.3} \pm 1.1$	$30.7 \pm 0.7^{+0.9}_{-1.1}$	$87.2^{+2.8+2.0}_{-1.0-2.2}$
14 TeV	$154^{+4}_{-1} \pm 3$	94^{+2+2}_{-1-3}	248^{+6+5}_{-2-6}

Table 1: t-channel cross sections in pb at the LHC for $m_t = 173$ GeV.

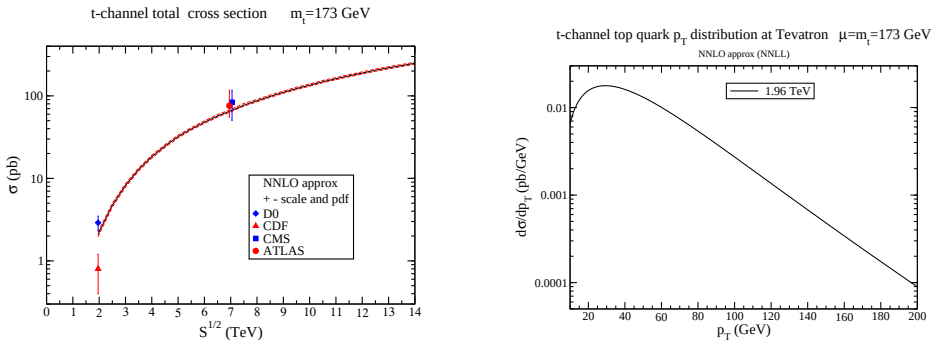

Figure 3: t-channel total cross section versus collider energy (left) and t-channel top quark p_T distribution at the Tevatron (right).

Results for the t-channel total cross section are shown versus collider energy in the left plot of Fig. 3. The right plot of Fig. 3 displays new results for the t-channel top quark p_T distribution at the Tevatron.

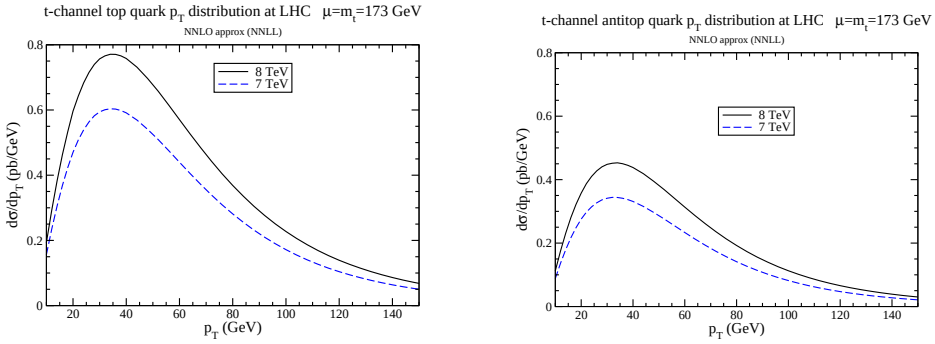

Figure 4: t-channel top (left) and antitop (right) p_T distributions at the LHC.

New results for t-channel top and antitop p_T distributions at the LHC are shown in Fig. 4.

Next we present s-channel results. Table 2 shows the s-channel cross sections at the LHC. The s-channel total cross section versus LHC energy in shown in the left plot of Fig. 5. The s-channel single top cross section at the Tevatron is $0.523^{+0.001+0.030}_{-0.005-0.028}$ pb; the result for antitop production at the Tevatron is identical to that for top.

Next we study the associated tW^- production at the LHC. The tW^- cross section at 7 TeV is $7.8 \pm 0.2^{+0.5}_{-0.6}$ pb; at 8 TeV it is $11.1 \pm 0.3 \pm 0.7$ pb; and at 14 TeV it is $41.8 \pm 1.0^{+1.5}_{-2.4}$ pb.

s-channel LHC	t	$\bar{t}$	Total
7 TeV	$3.14 \pm 0.06^{+0.12}_{-0.10}$	$1.42 \pm 0.01^{+0.06}_{-0.07}$	$4.56 \pm 0.07^{+0.18}_{-0.17}$
8 TeV	$3.79 \pm 0.07 \pm 0.13$	$1.76 \pm 0.01 \pm 0.08$	$5.55 \pm 0.08 \pm 0.21$
14 TeV	$7.87 \pm 0.14^{+0.31}_{-0.28}$	$3.99 \pm 0.05^{+0.14}_{-0.21}$	$11.86 \pm 0.19^{+0.45}_{-0.49}$

Table 2: s-channel cross sections in pb at the LHC for $m_t = 173$ GeV.

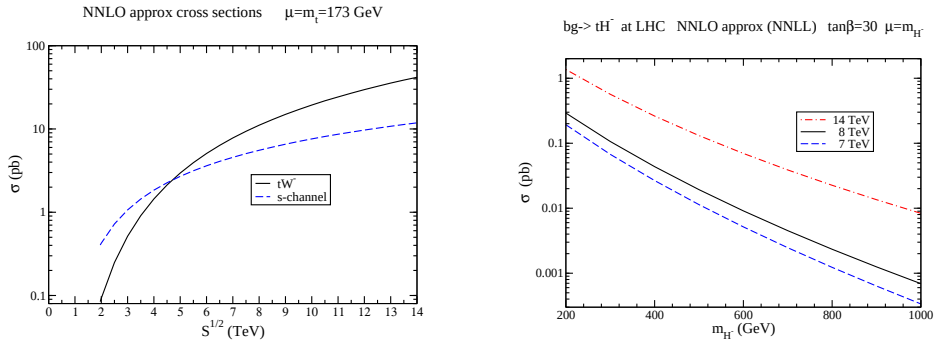

Figure 5: s-channel total and tW^- (left) and tH^- (right) production cross sections.

The cross section for $\bar{t}W^+$ production is identical. The tW^- cross section versus LHC energy in shown in the left plot of Fig. 5.

Finally, we study the associated production of a top quark with a charged Higgs. The right plot of Fig. 5 shows results at LHC energies versus charged Higgs mass with $\tan\beta = 30$.

Acknowledgements

The work of N.K. was supported by the National Science Foundation under Grant No. PHY 0855421.

References

[1] N. Kidonakis. Phys. Rev. **D82** (2010) 114030; Phys. Rev. **D84** (2011) 011504.

[2] N. Kidonakis. Phys. Rev. **D81** (2010) 054028; Phys. Rev. **D82** (2010) 054018; Phys. Rev. **D83** (2011) 091503.

[3] N. Kidonakis. Mod. Phys. Lett. **A19** (2004) 405; Phys. Rev. **D73** (2006) 034001.

[4] N. Kidonakis and B. D. Pecjak. arXiv:1108.6063 [hep-ph].

[5] M. Beneke, P. Falgari, S. Klein, and C. Schwinn. Nucl. Phys. **B855** (2012) 695.

[6] A. D. Martin, W. J. Stirling, R. S. Thorne, and G. Watt. Eur. Phys. J. **C63** (2009) 189.

[7] D0 Collaboration. Phys. Lett. **B693** (2010) 515.

[8] S. J. Brodsky and X.-G. Wu. arXiv:1205.1232 [hep-ph].

[9] P. Skands, B. Webber, and J. Winter. arXiv:1205.1466 [hep-ph].

Top Quark Pair Production Cross-Section at ATLAS

Kate Shaw on behalf of the ATLAS Collaboration

ICTP INFN Gruppo Collegato di Udine

DOI: http://dx.doi.org/10.3204/DESY-PROC-2012-02/89

Measurements of the top quark pair ($t\bar{t}$) production cross-section in proton-proton collisions at $\sqrt{s} = 7$ TeV are presented using data recorded with the ATLAS detector at the Large Hadron Collider (LHC). The statistical combination of $t\bar{t}$ production cross-section ($\sigma_{t\bar{t}}$) measurements is presented using the lepton+jets, dilepton and all-hadronic channel. A new measurement of $\sigma_{t\bar{t}}$ with a hadronically decaying tau lepton and jets is also shown, together with an updated measurement in the all-hadronic channel. Finally a measurement of the jet activity in $t\bar{t}$ events using a veto on additional central jet activity is presented.

1 Introduction

The precision measurement of the top quark pair ($t\bar{t}$) production cross-section ($\sigma_{t\bar{t}}$) provides not only a vital test of perturbative QCD, but also an important variable to observe deviations from Standard Model (SM) predictions, that could indicate new physics.

In the SM, for pp collisions at $\sqrt{s} = 7$ TeV $\sigma_{t\bar{t}}$ is calculated to be 167^{+17}_{-18} pb [2]. The lifetime of the top quark is shorter than the hadronisation time scale, thus it decays almost 100% of the time to a W boson and a b-quark. The decay topologies are determined by the decay of the W boson, either into a lepton-neutrino pair ($W \to lv$), or into a pair of quarks ($W \to qq'$). In the lepton+jets mode, with a branching ratio (BR) of 37.9%, one top quark decays leptonically and the other hadronically, whereas in the dilepton mode (BR = 6.5%), both top quarks decay leptonically. These channels have a final state signature involving one or two leptons, missing transverse momentum (E_T^{miss}) and jets. In the all-hadronic mode (BR = 46%), both top quarks decay hadronically producing a final state signature of 6 jets where two originate from b-quarks.

2 Statistical Combination

A combination of $\sigma_{t\bar{t}}$ measurements [3] is presented in the lepton + jets [4] and dilepton [5] channels, both using 0.70 fb^{-1} of data, and the all-hadronic channel [6] using 1.02 fb^{-1} of data.

In the lepton + jets channel events are selected with exactly one lepton (electron (e) or muon (μ)), at least three jets and large E_T^{miss}. The backgrounds include W+jets (dominant), single top, diboson, Z+jets, and QCD multijet production. Kinematic variables are selected to distinguish between the $t\bar{t}$ signal and background, and a likelihood discriminant is constructed. The cross-section is extracted from a maximum likelihood fit to these discriminant distributions.

In the dilepton channel final states comprise of two oppositely-charged leptons (ee, $\mu\mu$, eμ), E_T^{miss} and at least two jets. The background includes Z/γ^* events, W+jets, diboson, $t\bar{t}$

lepton+jets, and single top quark production. The cross-section is measured using a cut-based analysis with a profile likelihood fit to the number of observed events.

The all-hadronic channel event selection applies a veto on isolated leptons, requires at least five jets of which two are b-tagged. The dominant background is from QCD multijets which is modelled using a data-driven approach to reproduce the shapes of various kinematic and topological distributions from alternative data samples. The cross-section is extracted using a binned maximum-likelihood fit of signal and background templates using the χ^2 of a kinematic fit to the top mass as a discriminant. Section 4 presents an update of this measurement.

A combination is obtained from the product of the individual likelihoods of each analysis and measured as $\sigma_{t\bar{t}} = 177 \pm 3(\text{stat.})^{+8}_{-7}(\text{syst.}) \pm 7(\text{lumi.})$ pb, showing good agreement with the SM prediction and the uncertainty is smaller than the theoretical uncertainty. The main systematics are from uncertainties associated with the Monte Carlo (MC) generator, Jet Energy Scale (JES), Initial and Final State Radiation (ISR/FSR) and lepton identification. The individual and combined cross-section measurements are shown on the upper part of the left plot of Figure 1.

3 Cross-section measurement in $t\bar{t} \to \tau_{\text{had}}$+jets channel

A new measurement of $\sigma_{t\bar{t}}$ based on 1.67 fb^{-1} of data is presented, where one top quark decays into a tau lepton, a b-quark and a neutrino, and the other decays hadronically [7], resulting in a final state consisting of a hadronically decaying tau lepton and jets ($t\bar{t} \to \tau_{\text{had}}$+jets).

The data sample is selected using a b-jet trigger requiring more than three jets where two are identified as b-jets using a dedicated high-level trigger b-tagging algorithm. Events are selected with at least five jets (two b-tagged) where one is selected as a tau (τ_{had}) candidate. The hadronic top quark is reconstructed using the combination of three jets where one is b-tagged, that have the highest 4-vector p_T sum (with a reconstruction efficiency $\epsilon \sim 70\%$). The τ_{had} candidate is chosen from the remaining non-b-tagged jets that has the highest p_T ($\epsilon \sim 50\%$).

The tau lepton decays hadronically 65% of the time, $\sim$77% ($\sim$23%) of these decays produce one (three) charged hadron(s) (i.e. one (three) track(s)). This characteristic track multiplicity (n_{track}) distribution provides an excellent variable to separate the signal from the background, which is dominated by multijet events.

The data sample n_{track} distribution is fitted with three templates and the τ_{had} signal is extracted using an extended binned-likelihood fit. The cross-section is measured to be $\sigma_{t\bar{t}} = 200 \pm 19(\text{stat.}) \pm 43(\text{syst.})$ pb, shown in the lower part of the left plot in Figure 1. The main systematics arise from ISR/FSR uncertainty and b-tagging efficiency.

4 Cross-section measurement in the all-hadronic channel

The measurement of $\sigma_{t\bar{t}}$ in the all-hadronic channel has the advantage of a large BR but suffers from a large multijet background. Events are selected with at least six jets where two are b-tagged and a veto on events with isolated leptons. Starting from the reconstructed jets a likelihood approach is used to perform a kinematic fit to reconstruct the top quark mass (m_t).

The m_t distribution for the multijet background is modelled from events passing event selection with no b-tagged jets. An unbinned likelihood fit to the m_t distribution obtained from the kinematic fit is used to determine the event yield and background normalisation. The dominate systematic uncertainties include ISR/FSR, b-tagging efficiency and mistag rate,

and JES uncertainties. The cross-section is measured using 4.7 fb^{-1} of data [8] to be $\sigma_{t\bar{t}} = 168 \pm 12(\text{stat.})^{+60}_{-57}(\text{syst.}) \pm 7(\text{lumi.})$ pb, shown in the lower part of the left hand plot in Figure 1.

5 Measurement of $t\bar{t}$ production with a veto on additional central jet activity

A measurement is presented of the jet activity arising from hard, wide angle QCD emission from $t\bar{t}$ events using 2.05 fb^{-1} of data in the dilepton channel [9]. Events are selected with two opposite sign leptons (e or μ), E_T^{miss} and two b-tagged jets. A veto is then applied to events which contain an additional jet with a p_T above a defined threshold in a central rapidity region. The background to this signal includes single top, W+jets and multijet events. The measurement of jet activity is presented as the fraction of events surviving the jet veto, known as the gap fraction defined as $f(Q_0) = \frac{n(Q_0)}{N} \equiv \frac{\sigma(Q_0)}{\sigma}$ where N is the number of selected $t\bar{t}$ events passing selection, $n(Q_0)$ is the subset of these events that do not contain an additional jet with a $p_T > Q_0$, σ is the fiducial cross-section for inclusive $t\bar{t}$ production, and $\sigma(Q_0)$ is the fiducial cross-section for events passing the jet veto.

The measured $f(Q_0)$ from data is compared to multi-leg LO and NLO generator predictions, and reasonable agreement is seen in the full rapidity interval. However in the most central (forward) rapidity region the $f(Q_0)$ predicted by MC@NLO [10] is larger (smaller) than that measured in data. Furthermore the predictions from the ACERMC [11] generator with varied PYTHIA [12] parton shower parameters are compared to data, and is shown on the right plot in Figure 1 where the data points and therefore the statistical uncertainties are correlated. As a results of this measurement ATLAS has updated it's ISR systematic prescriptions, which will lead to all future ISR systematic uncertainties associated with future measurements being approximately 50% smaller.

6 Summary

These proceedings present various measurements of $\sigma_{t\bar{t}}$, including a statistical combination of the lepton+jets, dilepton and all-hadronic channels, and measurements in the $t\bar{t} \to \tau_{had}$+jets and all-hadronic channels, all agreeing well with SM predictaions. A study on the jet activity in $t\bar{t}$ events was performed resulting in a 50% reduction in future measurements' ISR systematic uncertainties.

References

[1] ATLAS Collaboration, "The ATLAS Experiment at the CERN Large Hadron Collider", *JINST* **3** S08003 (2008).

[2] M. Aliev *et al.*, "HAdronic Top and Heavy quarks crOss section calculatoR", arXiv:1007:1327.

[3] ATLAS Collaboration, "Statistical combination of top quark pair production cross-section measurements using dilepton, single-lepton and all-hadronic final states at $\sqrt{s} = 7$ TeVwith the the ATLAS detector", ATLAS-CONF-2012-024, https://cdsweb.cern.ch/record/1430733.

[4] ATLAS Collaboration, "Measurement of the $t\bar{t}$ production cross-section in pp collisions at $\sqrt{s} = 7$ TeV using kinematic information of lepton+jets events", ATLAS-CONF-2011-121, https://cdsweb.cern.ch/record/1376413.

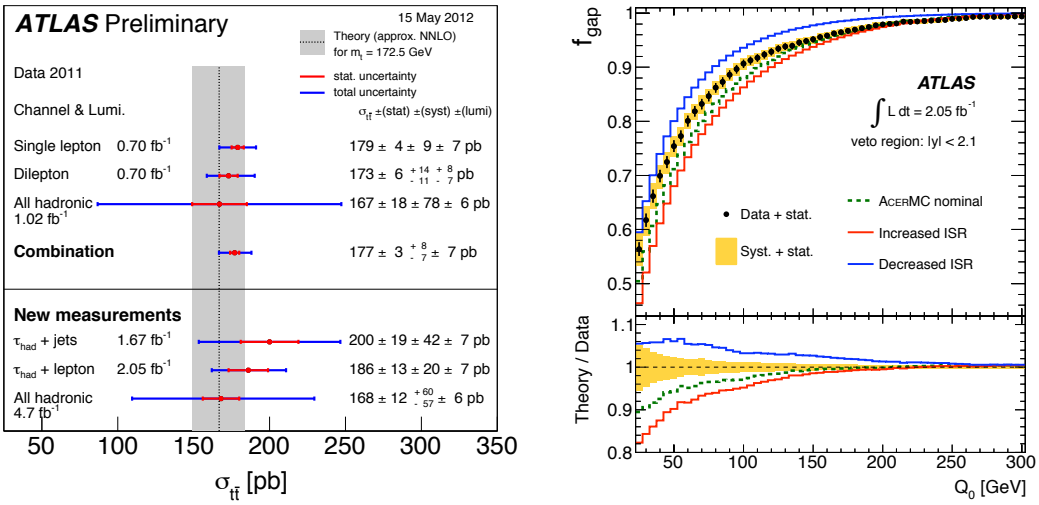

Figure 1: The left plot [3][13] shows a summary of $\sigma_{t\bar{t}}$ measurements compared to the theoretical expectation, including the individual and combined measurements (upper part) and the new measurements (lower part) including the $\tau_{\rm had}$+lepton [14] channel. The right plot [9] shows the measured $f(Q_0)$ compared with the ACERMC prediction, where PYTHIA parton shower parameters are varied to produce samples with nominal, increased and decreased ISR.

[5] ATLAS Collaboration, "Measurement of the cross section for top-quark pair production in pp collisions at $\sqrt{s} = 7$ TeV with the ATLAS detector using final states with two high-pt leptons", JHEP 1205 (2012) 059, arXiv:1202.4892.

[6] ATLAS Collaboration, "Measurement of the $t\bar{t}$ production in the all-hadronic channel in 1.02 fb^{-1} of pp collisions at $\sqrt{s} = 7$ TeV with the ATLAS detector", ATLAS-CONF-2011-140, https://cdsweb.cern.ch/record/1385033.

[7] ATLAS Collaboration, "Measurement of the $t\bar{t}$ production cross section in the final state with a hadronically decaying tau lepton and jets using the ATLAS detector", ATLAS-CONF-2012-032, https://cdsweb.cern.ch/record/1432198.

[8] ATLAS Collaboration, "Measurement of the $t\bar{t}$ production cross section in the all-hadronic channel in 4.7 fb^{-1} of pp collisions at $\sqrt{s} = 7$ TeV with the ATLAS detector", ATLAS-CONF-2012-031, https://cdsweb.cern.ch/record/1432196.

[9] ATLAS Collaboration, "Measurement of $t\bar{t}$ production with a veto on additional central jet activity in pp collisions at $\sqrt{s} = 7$ TeV using the ATLAS detector", Eur.Phys.J C72 (2012) 2043, arXiv:1203.5015.

[10] S. Frixione and B.R. Webber, "Matching NLO QCD computations and parton shower simulations", JHEP 0206 (2002) 029 , arXiv:hep-ph0204244].

[11] B. Kersevan and E. Richter-Was, "The Monte Carlo Event Generator AcerMC 2.0 with Interfaces to PYTHIA 6.2 and HERWIG 6.5", arXiv:hep-ph/0405247.

[12] T. Sjöstrand, S. Mrenna, P. Skands, "PYTHIA 6.4 Physics and Manual", JHEP 05 (2006) 026.

[13] ATLAS Collaboration, https://twiki.cern.ch/twiki/bin/view/AtlasPublic/TopPublicResults#Summary_plots_of_cross_sections.

[14] ATLAS Collaboration, "Measurement of the top quark pair production corss section with ATLAS in pp collisions at $\sqrt{s} = 7$ TeV using final states with an electron or a muon and a hadronically decaying τ lepton", Submitted to Physics Letters B, arXiv:1205.2067.

Measurements of total and differential top-production cross sections with the CMS experiment

Antonio Tropiano[1]

[1]Università degli Studi di Firenze, Via Sansone 1, 50019 Sesto Fiorentino (FI), Italy

DOI: http://dx.doi.org/10.3204/DESY-PROC-2012-02/257

Precise measurements of the top quark pair production cross section at 7 TeV, performed using CMS data collected in 2011, are presented. The total cross section is measured in the lepton+jets, dilepton and fully hadronic channels, including the tau-dilepton mode. The results are combined and confronted with precise theory calculations. An indirect constraint on the top quark mass through its relation to the cross section is also obtained. Various differential cross sections are measured as well and compared with theoretical models. Further results include measurements of single top production cross section.

1 Introduction

Measurements of the top quark pair production cross section in proton-proton collisions at the LHC provide important tests for understanding the top quark production mechanism, studying perturbative QCD and can also be used in new physics searches. At the LHC the top pairs are mostly produced through gluon-gluon fusion and the different final states result from the combinatorics of the W boson decays, since the top quark decays mostly in the $t \to Wb$ channel. The $t\bar{t}$ decay channels comprise therefore fully-hadronic (46%), lepton+jets (45%) and dileptonic (9%) final states. Recent CMS [1] measurements have been carried out in all these decay channels where the most precise measurement is obtained in the lepton+jets channel [2]. Inclusive and differential cross section measurements have been performed, both for top pair and single top production [3]. The results of these measurements will be shown and discussed.

2 Inclusive cross section measurements

The cleanest channel and the most suitable one for precise measurements of the $t\bar{t}$ production cross section is the lepton+jets channel. The analysis is performed by selecting different categories of events according to the jet multiplicity and the number of b-tagged jets. The cross section is then extracted with a fit to a simple and robust variable, the mass of the secondary vertex of the jets. The fit takes into account not only the normalisation of the background processes but also how it can be affected by the different systematic uncertainties such as jet energy scale, b-tag or mistag efficiencies, the contamination from initial/final state radiation (ISR/FSR) and the factorisation and renormalization scales used to model the signal and some of the backgrounds (i.e. Q^2 scale). The relative uncertainty in the measurement of the $t\bar{t}$ cross

section is ≈7% and it is dominated by the uncertainty in modeling of the signal component and by the measurement of the luminosity.

In the remaining channels the $t\bar{t}$ production cross section has been carried out through counting experiment for the dilepton channel, while in the fully hadronic channel a fit to the distribution of the reconstructed top mass with a kinematic fit was used. Overall the results in these channels are compatible with the theoretical predictions but their uncertainties are larger with respect to the measurement in the lepton+jets channel due to systematic effects such as jet energy scale or background estimations.

Fig. 1 summarises the results obtained in the different channels and the final combination. The total uncertainty attained by each experiment has now surpassed the theoretical uncertainty at approx. NNLO.

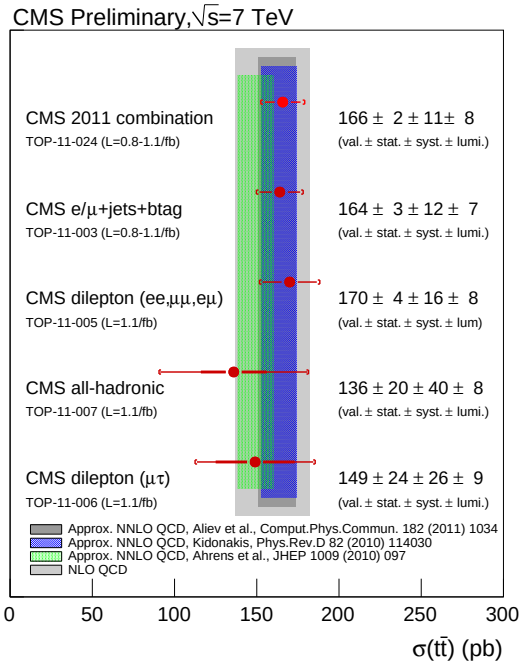

Figure 1: Summary of CMS measurements and their combination overlaid with three theory predictions.

3 Differential cross section measurements

With the large statistics sample acquired in 2011 the inclusive measurements where expanded to measure differential cross sections. Differential measurements were carried out in the lepton+jets and dilepton channels after the reconstruction of the $t\bar{t}$ kinematics, unfolded to parton level. The differential cross section is measured after background subtraction and unfolding the observed value. Overall there is a very good agreement between the unfolded data and the simulation within the uncertainty of the measurement. One distribution of particular interest

is $p_T^{t\bar{t}}$ and it is shown in Figure 2 (left).

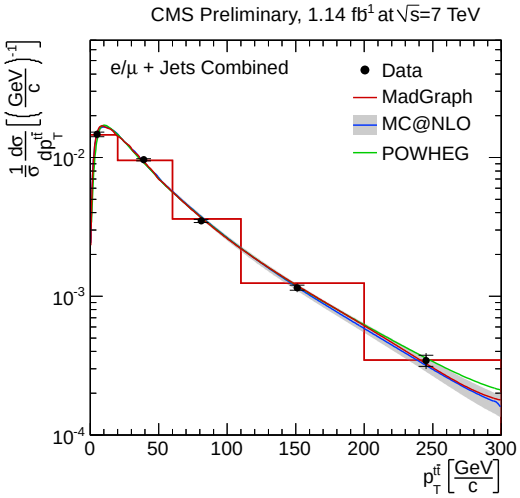

Figure 2: p_T of the $t\bar{t}$ system in the lepton+jets channel. The measurements are compared to predictions from MadGraph, POWHEG, and MC@NLO Monte Carlo generators.

4 Top quark mass extraction from the cross section

The top quark mass has also been extracted by comparing the measured inclusive $t\bar{t}$ production cross section to fully inclusive calculations at high-order QCD that involve an unambiguous definition of m_t. This extraction provides an important test of the mass scheme as applied in simulations and gives complementary information, with different sensitivity to theoretical and experimental uncertainties than the direct measurements of m_t, which rely on the kinematic details of the mass reconstruction.

Three different approaches to calculate the higher-order corrections to the next-to-leading order (NLO) calculations of top quark pair production have been used [4, 5, 6], where the cross section of $t\bar{t}$ production is obtained by a combination of measurements in the dilepton channel. Data are compared with different approximate NNLO predictions in Fig. 3. The uncertainty on the theoretical predictions includes the variation of the scales, parton luminosity and the variation of the $\alpha_S(M_Z)$ in the PDF.

5 Single top production

Single top quarks can be produced through the s and t-channels and in association with a W boson. The dominant production mode is the t-channel and its final state consists of one central isolated lepton accompanied by E_T^{miss}, a b-jet and a forward high p_T recoiling jet. The most recent results use a fit to the pseudo-rapidity of the recoil jet to extract the production of single

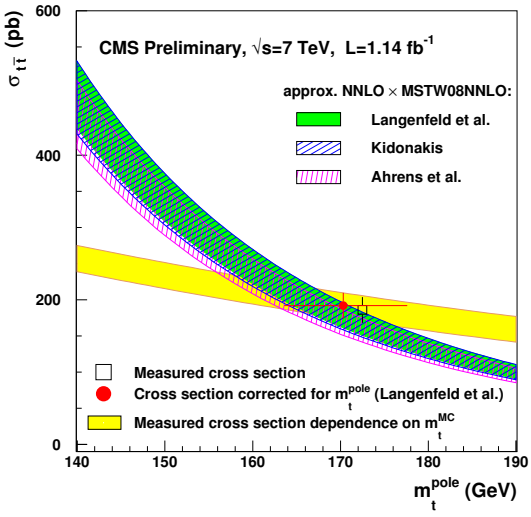

Figure 3: The cross section (open square) of $t\bar{t}$ production in the dilepton channel. The closed circle represents the measured cross section corrected for the m_t^{pole} dependence at the determined value of m_t^{pole} using three different calculations. The dependence of the measured cross section on m_t^{MC} is shown as a light shaded band. Different approximate NNLO predictions are shown as differently hatched bands. The uncertainty on the theoretical predictions includes the variation of the scales, parton luminosity and the variation of the $\alpha_S(M_Z)$ in the PDF.

top in the t-channel [7]. The cross section measurement gives $\sigma(t) = 70.2 \pm 11.5(stat. + syst.) + \pm 3.4(lumi.)$ pb, where the most important source of uncertainty is due to the Jet Energy Scale.

6 Conclusions

Inclusive and differential top quark production cross section measurements with the CMS experiment has been presented. In particular for the differential cross section measurement and for the mass extraction from the cross section, data have been compared with different theoretical predictions and they have been found to agree with the predictions within the theoretical uncertainties.

References

[1] CMS Collaboration, J. Inst. **3** (2008) 361.
[2] CMS Collaboration, **CMS-PAS-TOP-11-003** (2011)
[3] CMS Collaboration, **CMS-PAS-TOP-11-013** (2011)
[4] Ahrens *et al.*, JHEP **1009** (2011) 97.
[5] M. Aliev *et al.*, Phys. Rev. D **80** (2009).
[6] N. Kidonakis, Phys. Rev. D **82** (2010).
[7] CMS Collaboration, **CMS-PAS-TOP-11-021** (2012)

Top Quark Production at D0

Karel Soustružník on behalf of D0 Collaboration

Charles University in Prague

DOI: http://dx.doi.org/10.3204/DESY-PROC-2012-02/205

We present measurements of the production cross sections of top-antitop quark pair via the strong interaction and of single top quark via the weak interaction in proton-antiproton collisions at sqrt(s)=1.96 TeV using data corresponding to integrated luminosities up to 5.4 fb^{-1}. The data were collected with the D0 detector at the Fermilab Tevatron collider. We also present measurements of the forward-backward asymmetry in the top-antitop quark final states.

1 Tevatron and D0

Top quark, the heaviest known elementary particle, was discovered by CDF and D0 collaborations at the Fermilab Tevatron collider in 1995 [1],[2]. Tevatron provided proton-antiproton beams with the center of mass energy of 1.96 TeV and until its shutdown on September 30th 2011 10.5 fb^{-1} of data was recorded per experiment.

D0 detector is a multipurpose detector with high resolution inner detectors for precise tracking and vertex reconstruction, electromagnetic and hadronic calorimeters and outer muon system.

2 Top quark pair production

Top quark is produced at Tevatron mainly in pairs in strong interaction via quark-antiquark annihilation ($\sim 85\,\%$) and gluon-gluon fusion ($\sim 15\,\%$).

The theoretical value of top quark pair production cross section for the Tevatron at approximately next-to-next-to leading order (NNLO_{approx}) is $\sigma_{t\bar{t}} = 7.46$ pb (at $m_t = 172.5$ GeV) [3].

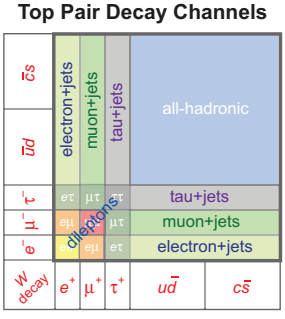

Figure 1: Top quark pair decay channels.

Because the top quark decays almost entirely to W boson and b quark, top quark pair final states are categorized according to W boson decay. The dilepton final state corresponds to both W bosons decaying leptonically. It has small background, but also small branching ratio of $\sim 10\,\%$. The lepton+jets final state corresponds to one W boson decaying leptonically and the other hadronically. This channel has moderate background and large branching ratio of $\sim 44\,\%$ and provides analyzers the highest sensitivity to signal. The all hadronic final state corresponds to both W bosons decaying hadronically. This channel has the advantage of large branching fraction of $\sim 46\,\%$ and absence

of undetectable neutrinos in the final state, but QCD multi-jet background dominates the signal by several orders of magnitude in cross section.

The measurement of top quark pair production cross section in lepton+jets channel is based on data with an integrated luminosity of 5.3 fb^{-1}. Events are required to contain one isolated electron or muon, at least two jets and large missing transverse energy due to escaping neutrino.

Main background processes contributing to this channel are W+jets, QCD multijet production, Z+jets and diboson events.

Top pair production cross section is measured using three methods: a *kinematic* method based on $t\bar{t}$ event kinematics, a *counting* method using identification of b-jets, and a method combining both techniques. Kinematic method uses a multivariate discriminant, shown in Figure 2, constructed from kinematic variables providing the best discrimination between signal and background. Cross section is extracted by performing a maximum likelihood fit of the distributions in the discriminant to data. Counting method exploits b-jet identification to further reduce background and top pair production cross section is obtained from maximum likelihood fit to data for the predicted number of events.

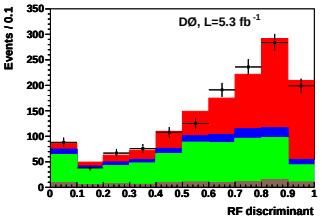

Figure 2: Multivariate discriminant.

Assuming the value of the top quark mass of 172.5 GeV the top quark pair production cross section was measured to be $\sigma_{t\bar{t}} = 7.78^{+0.77}_{-0.64}$ (stat + syst) pb [4].

The measurement of top quark pair production cross section in dilepton final state is divided into four channels ($ee+2j$, $\mu\mu + 2j$, $e\mu + 1, 2j$) and is based on data with an integrated luminosity of 5.4 fb^{-1}.

Selected events have two isolated leptons, at least one or two jets and a large missing transverse energy coming from neutrinos. Main backgrounds contributing to this channel are Drell-Yan, Z boson and diboson production and instrumental background.

In order to enhance the separation between signal and background the neural network (NN) based b-tagging discriminants are constructed. Figure 3 shows the NN b-tagging discriminant distribution for $ee + 2j$ channel. Top quark pair production cross section, $\sigma_{t\bar{t}}$, is extracted from the fit to these b-tagging discriminants and maximizing likelihood function for observed number of events. The cross section measured in dilepton channel is $\sigma_{t\bar{t}} = 7.36^{+0.90}_{-0.79}$ (stat + syst) pb [5].

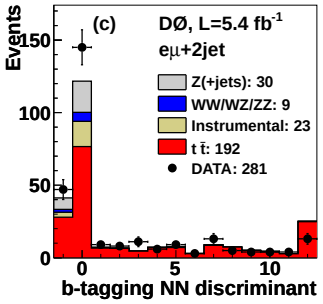

Figure 3: B-tagging discriminant.

The top pair production cross section measurements in lepton+jets and dilepton channels were combined by maximizing the product of likelihood function for both final states leading to relative precision of 8 %. The combined cross section is $\sigma_{t\bar{t}} = 7.56^{+0.63}_{-0.56}$ (stat + syst) pb [5].

3 Single top quark production

Unlike the top quark pairs single top quarks are produced via electroweak interaction. Single top quark production was observed by CDF and D0 collaborations in 2009 [6], [7]. Theoretical values of single top production cross section in s-channel, t-channel and associated production for Tevatron are $\sigma_{s-ch} = 1.04$ pb, $\sigma_{t-ch} = 2.26$ pb and $\sigma_{tW} = 0.28$ pb assuming the top quark

mass of 172.5 GeV [8].

Measurement of production cross sections of single top quarks is based on data sample corresponding to the integrated luminosity of 5.4 fb^{-1}. Selected events are required to have one isolated electron or muon, large missing transverse energy, two to four jets, where one or two of them have to be b-tagged. Main backgrounds are W+jets, $t\bar{t}$ and multijet production.

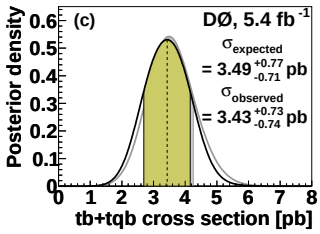

Figure 4: Single top quark production cross section.

Because the expected signal is smaller than the uncertainty on the background, three multivariate analysis (MVA) methods are used to construct a multivariate discriminant to extract the signal from data. All three methods are combined to increase the sensitivity. Bayesian approach is then used to obtain the s- and t-channel production cross sections together and separately from combined discriminant. Constructed Bayesian posterior probability density for combined s- and t-channel cross sections is shown in Figure 4. The measured cross sections are $\sigma_{s+t} = 3.43^{+0.73}_{-0.74}$ pb, $\sigma_{s-ch} = 0.68^{+0.38}_{-0.35}$ pb and $\sigma_{t-ch} = 2.86^{+0.69}_{-0.63}$ pb [9].

Data sample corresponding to the integrated luminosity of 5.4 fb^{-1} was used to perform a model-independent measurement of t-channel single top quark production cross section with no assumptions about tb production rate.

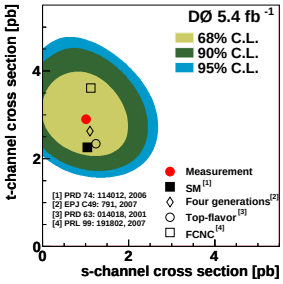

Figure 5: The 2D posterior probability density.

Three multivariate analysis techniques are combined to make a discriminant for improved separation of signal and background. The single top quark production cross section is measured using a Bayesian approach when a two-dimensional (2D) posterior probability density is constructed as a function of the cross sections for the tb and tqb processes. The 2D posterior probability density for combined discriminant is shown in Figure 5. No constraint is applied on relative rates of s-channel and t-channel production. The t-channel cross section is then extracted from a one-dimensional (1D) posterior probability by integrating over s-channel cross section values and thus without any assumptions about s-channel cross section. The s-channel cross section is obtained in a similar way. The measured cross sections of t-channel and s-channel are $\sigma_{t-ch} = 2.90 \pm 0.59$ pb, $\sigma_{s-ch} = 0.98 \pm 0.63$ pb [10].

4 Forward-backward asymmetry

The forward-backward asymmetry in top quark pair production is predicted by QCD at higher orders. The QCD predicts a small asymmetry ($\sim$ 5-9 %) at next-to-leading order (NLO) while it predicts no asymmetry at leading order (LO). The forward-backward asymmetry in $t\bar{t}$ events is defined as $A_{fb} = \frac{N(\Delta y>0) - N(\Delta y<0)}{N(\Delta y>0) + N(\Delta y<0)}$, where Δy is a difference of top and antitop quark rapidities. Using the lepton charge to distinguish between top and antitop quarks, the rapidity difference Δy is reconstructed as $\Delta y = q_l(y_{t,lep} - y_{t,had})$. The asymmetry based on charge and rapidity of the lepton from top quark decay is defined as $A^l_{fb} = \frac{N(q_l y_l>0) - N(q_l y_l<0)}{N(q_l y_l>0) - N(q_l y_l<0)}$. In order to compare the measured asymmetry with a theoretical prediction, the *reconstruction* level asymmetry (after

event selection, reconstruction and background subtraction) has to be corrected for detector effects to *production* level.

The forward-backward asymmetry in top quark pair production was measured in lepton+jets channel using data sample corresponding to the integrated luminosity of 5.4 fb^{-1}.

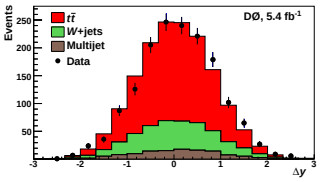

Figure 6: The top and antitop rapidity difference.

Selected events are required to have one isolated electron or muon, large missing transverse energy, at least four jets where at least one of them is b-tagged. Main background is from W+jets and multijet production. A likelihood discriminant is constructed using variables providing separation between signal and background. The reconstructed asymmetry is extracted from maximum likelihood fit of the discriminant. To obtain the asymmetry at the production level the reconstructed asymmetry has to be corrected (*unfolded*) for detector resolution and acceptance effects using regularized unfolding. The measured values of the top quark pair production asymmetry at reconstruction and production level are $A_{fb} = (9.2 \pm 3.7)\,\%$ and $A_{fb} = (19.6 \pm 6.5)\,\%$. The lepton based asymmetry is $A^l_{fb} = (14.2 \pm 3.8)\,\%$ at reconstruction level and $A^l_{fb} = (15.2 \pm 4.0)\,\%$ after unfolding [11].

5 Summary

The top quark pair production cross section was measured with 8 % relative precision. Both top quark pair and single top quark production cross sections are consistent with standard model prediction. The measured production forward-backward asymmetry in $t\bar{t}$ events is significantly higher than prediction.

References

[1] CDF Collaboration, F. Abe *et al.*, Phys. Rev. Lett. **74**, 2626 (1995).

[2] D0 Collaboration, S. Abachi *et al.*, Phys. Rev. Lett. **74**, 2632 (1995).

[3] S. Moch and P. Uwer, Phys. Rev. D **78**, 034003 (2008).

[4] D0 Collaboration, V. M. Abazov *et al.*, Phys. Rev. D **84**, 012008 (2011).

[5] D0 Collaboration, V. M. Abazov *et al.*, Phys. Lett. B **704**, 403 (2011).

[6] D0 Collaboration, V. M. Abazov *et al.*, Phys. Rev. Lett. **103**, 092001 (2009).

[7] CDF Collaboration, T. Aaltonen *et al.*, Phys. Rev. Lett. **103**, 092002 (2009).

[8] N. Kidonakis, Phys. Rev. D **74**, 114012 (2006).

[9] D0 Collaboration, V. M. Abazov *et al.*, Phys. Rev. D **84**, 112001 (2011).

[10] D0 Collaboration, V. M. Abazov *et al.*, Phys. Lett. B **705**, 313 (2011).

[11] D0 Collaboration, V. M. Abazov *et al.*, Phys. Rev. D **84**, 112005 (2011).

Top quark physics at CDF

Costas Vellidis[1]

[1]FNAL, Batavia, IL 60510, USA

DOI: http://dx.doi.org/10.3204/DESY-PROC-2012-02/204

We present recent measurements from CDF of spin correlations, of the top decay relative branching ratio BR(t→Wb)/Σ_qBR(t→Wq) and the derived indirect constraint on the $|V_{tb}|$ CKM matrix element, of the single top production cross section and the derived direct constraint on $|V_{tb}|$, and of the forward-backward asymmetry in top pair production.

1 Measurements

In the standard model (SM) top quark pairs are produced in a definite spin state depending on the production mechanism: in a spin 1 state via quark pair annihilation (∼85% at the Tevatron) or in a spin 0 state via gluon fusion (∼15% at the Tevatron). Since the top quark decays before hadronization, the spin information is passed to the decay products and thus the spin correlation of the top quark pair can be measured from decay product angular distributions. The (frame dependent) correlation strength, in a frame with spin quantization axis in the direction of the colliding beams, is predicted by the SM to be $\kappa^{SM}_{beam} = 0.78^{+0.03}_{-0.04}$ [1] and is measured at CDF to be $\kappa^{ll}_{beam} = 0.04 \pm 0.56$ [2] in the dilepton channel and $\kappa^{lj}_{beam} = 0.72 \pm 0.69$ [3] in the lepton+jets channel. The measurements are done by fitting Monte Carlo (MC) angular distribution templates to data corresponding to 5.1 fb^{-1} and 5.3 fb^{-1} of integrated luminosity, respectively.

In the SM the top quark decays into a W boson and a b quark almost 100% of the time. Therefore, two b quarks are expected in each top pair event. The finite b-tagging efficiency determines the size of top pair event samples with 0, 1, or 2 tagged jets. The ratio R = BR(t→Wb)/Σ_qBR(t→Wq), where q = d, s, or b, is measured at CDF from the size of each subsample via a 2D likelihood fit to data corresponding to the full integrated luminosity of 8.7 fb^{-1}, simultaneosuly with the top pair production cross section $\sigma(p\bar{p} \to t\bar{t})$. The results are R = 0.94±0.09 and $\sigma(p\bar{p} \to t\bar{t})$ = 7.5±1.0 pb [4]. Then R is used to constrain the CKM matrix element $|V_{tb}|$ to be 0.97±0.05 or $|V_{tb}|$>0.89 at 95% confidence level (CL), assuming a unitary 3×3 CKM matrix [4].

Single top quarks are produced via electroweak (EW) interaction mechanisms, by the exchange of a W boson in the s or t channel. Single top production in association with a W boson is very suppressed at the Tevatron but is included for consistency in the signal model. The measurement of the single top production cross section is an important test of the SM as it is sensitive to new physics, such as flavor-changing neutral currents, heavy weak bosons W′ and CP violation, and also provides a direct measurement of $|V_{tb}|$. It is experimentally challenging because it requires the extraction of a small signal out of a large background with large uncertainty. The measurement is based on the use of neural network to discriminate

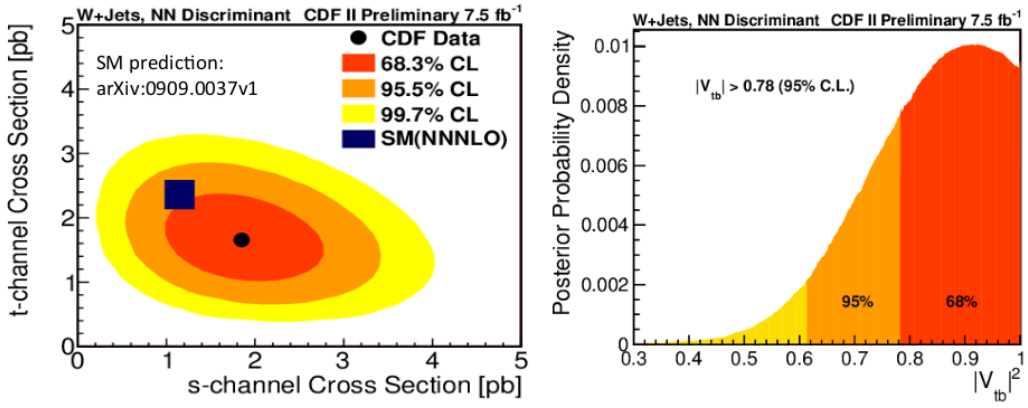

Figure 1: **Left:** 1-, 2- and 3-σ contour plots of the 2D single top cross section fit to the data, compared with the SM prediction. **Right:** 1- and 2-σ exclusion of $|V_{tb}|^2$ values.

the signal from the background assuming a top quark mass of 172.5 GeV/c^2 and using data corresponding to 7.5 fb^{-1} of integrated luminosity. Figure 1 shows the 2D fit result of the s- and t-channel production cross section, compared with the SM prediction [5], and the 68% and 95% CL limits on $|V_{tb}|$ derived from the 1D fit of the combined s+t-channel cross section [6]. The results are $\sigma_s = 1.81^{+0.63}_{-0.58}$ pb, $\sigma_t = 1.49^{+0.47}_{-0.42}$ pb, $\sigma_{s+t} = 3.04^{+0.57}_{-0.53}$ pb and $|V_{tb}| = 0.92^{+0.10}_{-0.08}$(stat.+syst.)$\pm$0.05(theory).

In the SM top pairs are produced isotropically in leading order (LO). Next-to-leading order (NLO) quantum chromodynamics (QCD) predicts a small forward-backward asymmetry A_{FB} in the rapidity difference $\Delta y = y_t - y_{\bar{t}}$ distribution. A calculation using the NLO QCD program POWHEG [7], corrected for EW terms at NLO [8], gives an inclusive asymmetry of 6.6%. The forward-backward asymmetry has been measured at the Tevatron using about half the data set, with the results summarized in Table 1. The results show an unexpectedly large asymmetry.

Measurement	Parton Level A_{FB} (%)
CDF Lepton+Jets[9]	15.8$\pm$7.4
CDF Dilepton[10]	42$\pm$16
CDF Dilepton[11]	20.1$\pm$6.7
D0 Lepton+Jets[12]	19.6$\pm$6.5

Table 1: Tevatron A_{FB} measurements using data corresponding to $\sim$5 fb^{-1} of integrated luminosity.

To investigate further this property of top pair production, particularly the dependencies on sensitive kinematic variables, CDF measured the asymmetry using the full data set corresponding to 8.7 fb^{-1} of integrated luminosity [13].The inclusive result is shown in Figure 2. The kinematic dependencies of the asymmetry are shown in Figure 3. Parton level shape corrections use a regularized unfolding algorithm to avoid instabilities arising from the statistical fluctuations. The dependencies are well approximated by a linear model. Both the magnitude of

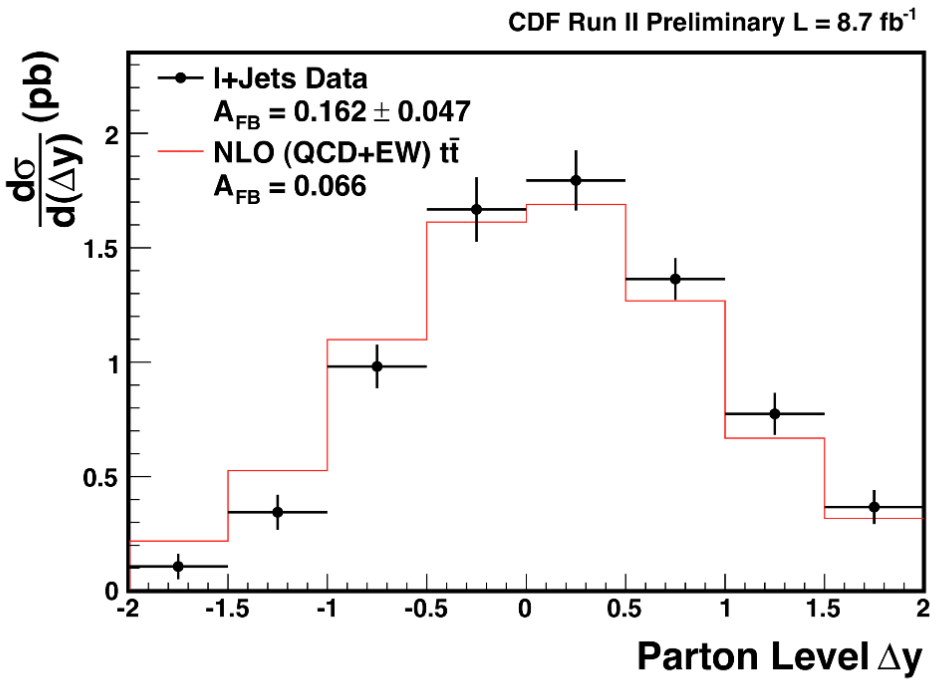

Figure 2: The $t\bar{t}$ production cross sectionin the lepton+jets channel, differential in the $t - \bar{t}$ rapidity difference, measured with the full CDF data set and compared with a NLO QCD+EW calculation.

inclusive result and the slopes of the differential asymmetries are stronger than the predictions of the NLO QCD+EW calculations at the level of 2.0σ - 2.5σ.

Several possibilities are examined to explain the discrepancy between the predicted and observed asymmetry. One possibility is a mismodeling within the SM such as mismodeled top pair transverse momentum spectrum or missing higher order corrections. Another possibility is new physics: many models have been proposed to interpret the measured asymmetry such as axigluon or heavy boson (Z', W') exhange models. Measurements of other top quark properties, such as differential cross sections and spin observables, can help differentiate between the various possibilities and are currently pursued at CDF.

2 Summary

We reported high precision measurements of spin correlations, branching ratio, single top production cross section and forward-backward asymmetry in top pair production from CDF.

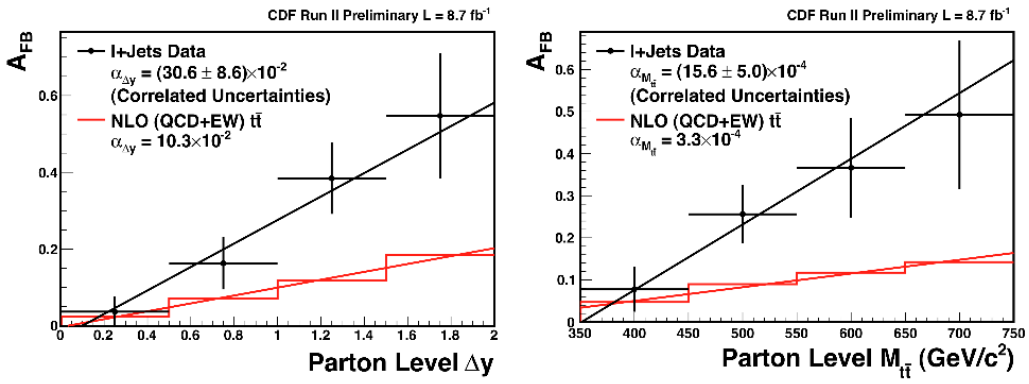

Figure 3: The forward-backward asymmetry, differential in the $t - \bar{t}$ rapidity difference (left) and in the $t\bar{t}$ invariant mass (right), measured with the full CDF data set and compared with NLO QCD+EW calculations.

Constraints on the $|V_{tb}|$ CKM matrix element are also imposed by the single top and branching ratio measurements. In general, good agreement with the standard model is observed. Exception is the asymmetry which appears stronger in magnitude and with stronger kinematic dependencies than the NLO QCD+EW predictions at the level of 2σ.

References

[1] W. Bernreuther *et al.* Nucl. Phys. **B 690** (2004) 81.

[2] CDF Conference Note 10719.

[3] CDF Conference Note 10211.

[4] CDF Conference Note 10887.

[5] N. Kidonakis arXiv:0909.0037v1.

[6] CDF Conference Note 10793.

[7] S. Frixione *et al.* J. High Energy Phys. **0709** (2007) 126.

[8] W. Hollik and D. Pagani Phys. Rev. **D84** (2011) 093003; J. Kühn and G. Rodrigo J. High Energy Phys. **1201** (2012) 063; A. Manohar and M. Trott arXiv:1201.3926[hep-ph].

[9] T. Aaltonen *et al.* (CDF Collaboration) Phys. Rev. **D83** (2011) 112003.

[10] CDF Conference Note 10436.

[11] CDF Conference Note 10584.

[12] V. M. Abazov *et al.* (D0 Collaboration) Phys. Rev. **D84** (2011) 112055.

[13] CDF Conference Note 10807.

Measurements of the top quark mass with the ATLAS Experiment

Christian Jung[1] on behalf of the ATLAS collaboration

[1]TU Dortmund, Otto-Hahn-Strasse 4, 44221 Dortmund, Germany

DOI: http://dx.doi.org/10.3204/DESY-PROC-2012-02/91

Three measurements of the mass of the top quark performed with the ATLAS detector in proton-proton collision at the LHC are presented. Two of them employ the decay mode where one of the pair-produced top quarks decays in either an electron or a muon and the other one into jets while the third measurement is performed in the decay mode where both top quarks decay into jets. Finally a combination of the two channels of the most precise measurement is presented which leads to the result of $m_{\mathrm{top}} = 174.5 \pm 0.6_{\mathrm{stat.}} \pm 2.3_{\mathrm{syst.}}$ GeV.

1 Introduction

A precise measurement of the top quark mass is an important part of the LHC physics program. Because of its high mass the top quark plays an important role in precision fits of the standard model as well as in several models of physics beyond the standard model [1].

The most precise measurement to date is the combination of measurements of the two Tevatron experiments CDF and D0 with a result of $m_{\mathrm{top}} = 173.2 \pm 0.6_{\mathrm{stat.}} \pm 0.8_{\mathrm{syst.}}$ GeV[2] yielding a total uncertainty of 0.9 GeV.

In the following, three measurements of the top quark mass using ATLAS data are presented:

- A 1D template method which uses the lepton + jets decay channel
- A 2D template method using the same events as the 1D analysis
- A measurement using the fully hadronic top decay channel

2 1D Template Method

Candidate events are required to contain exactly one isolated lepton (electron or muon) with transverse momentum of more than 25 GeV, at least four jets with transverse momentum larger than 25 GeV and different cuts on missing energy and transverse mass of the lepton and the missing energy. Additionally, at least one of the selected jets has to be tagged by a high-performance b-tagger.

As all three methods presented use the three-jet invariant mass in the measurement, one of the dominating systematic uncertainties is the knowledge of the jet energy scale. In order to lessen the size of the jet energy scale systematic uncertainty it is possible to refine the approach

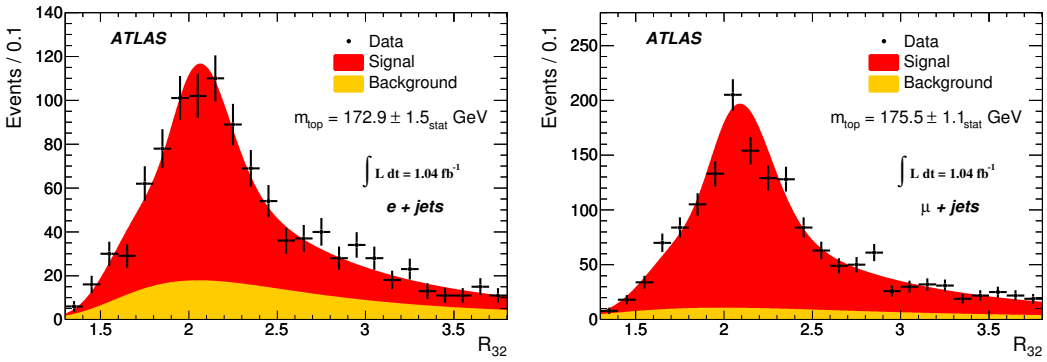

Figure 1: The R_{32} variable in data together with the fit result for the 1D template analysis in the e+jets channel (left) and the μ+jets channel (right). [3]

a bit. One possibility is to fit the so-called R_{32} variable which is the ratio of the three-jet-mass and the two-jet-mass of the two light jets from the W boson decay. Since numerator and denominator are both affected by the same jet energy scale the effect on the fitted top mass is dampened.

A kinematic fit using the full event topology is performed to assign jets to partons. To ensure the convergence of the fit only events with a certain likelihood value are kept. Also all jets used in the fit are required to have a transverse momentum of more then 40 GeV. Finally the reconstructed W boson mass must be in the range between $60-100$ GeV. From the two jets assigned as originating from the W decay and the hadronic b-jet the invariant masses of the W boson and the top quark are reconstructed and from the ratio of these the R_{32} variable is built. A likelihood fit to the data using templates of the R_{32} distribution for different generated top quark masses is performed to extract the top quark mass. Figure 1 shows the distribution of R_{32} in data together with the fitted signal and background contributions.

3 2D Template Method

Another approach for mitigating the effect of the jet energy scale uncertainty is to do a multidimensional analysis. This analysis measures the top mass together with a Jet Scale Factor (JSF) which is a correction factor to the jet energies. In addition to the top candidate invariant mass distribution it fits the W candidate invariant mass distribution to gain information on the JSF.

The candidate events are selected in the same way as in the 1D analysis. The assignment of the jets to partons is done combining each pair of untagged jets which fulfill $50\,\text{GeV} < M_{12} < 110\,\text{GeV}$ with the b-tagged jet. Events which do not fulfill this requirement are discarded. As these cuts are less stringent than the additional cuts performed in the 1D analysis this analysis has a higher number of candidates. The combination with the highest transverse momentum is chosen. Similarly to the 1D analysis templates of the reconstructed W boson and the top quark masses for different configurations of top quark mass and JSF are produced. The measured values in data are then used in a two-dimensional likelihood fit to extract the top quark mass and the JSF.

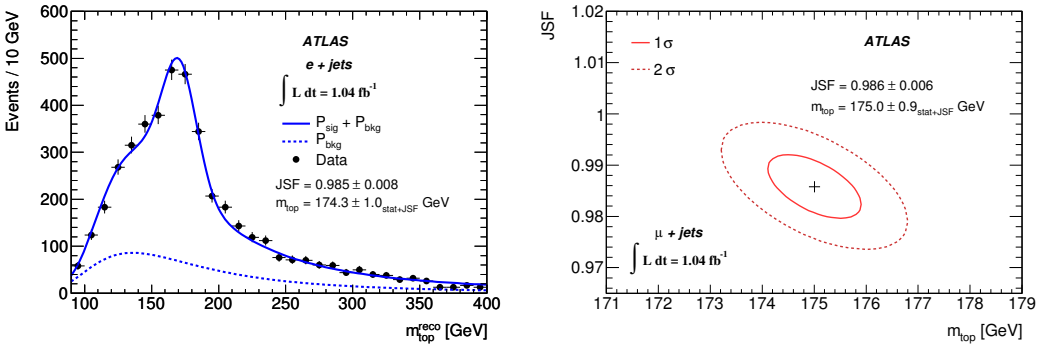

Figure 2: The invariant mass of the top candidates in data together with the fit result for the 2D template analysis in the e+jets channel (left) and correlation between the top mass and the JSF in the muon channel (right). [3]

In figure 2 the reconstructed top mass and the fit result of the template analysis is shown for the electron channel. It also shows the correlation between the top quark mass and the JSF in the muon channel.

4 Measurement in the All-hadronic Channel

In this channel, the main challenge for a top mass measurement is the reduction and the estimate of the multijet background. The reduction of the background is performed by choosing higher transverse momentum cuts on the jets and by requiring two b-tagged jets. The background template is obtained by selecting QCD multijet events which contain 5 jets, two of which must be b-tagged. Then, from a different event a jet with a lower transverse momentum than any of the five jets is added. To validate this approach, several validations have been made for example modeling six-jet events with five-jet event-mixed data but using no b-tagging requirement. Figure 3 shows the three-jet invariant mass for this crosscheck together with the estimate from this technique.

A χ^2-fit is performed to assign the jets to W boson and top quark decays. Additionally events with a $\chi^2 > 8$ are discarded from the analysis.

Figure 3 shows the obtained invariant mass of the top candidates. For the background fit only the normalization has been fitted as the shape was obtained with the data-driven technique.

5 Results

Table 1 shows the results for the three analyses. All measurements agree within statistical errors and are limited by the systematic uncertainties. For all three analyses, the dominating systematic uncertainties are the light jet energy scale, the b-jet energy scale and the uncertainty on additional initial or final state radiation. The all-hadronic analysis also has an additional contribution from the uncertainty of the background shape estimation technique.

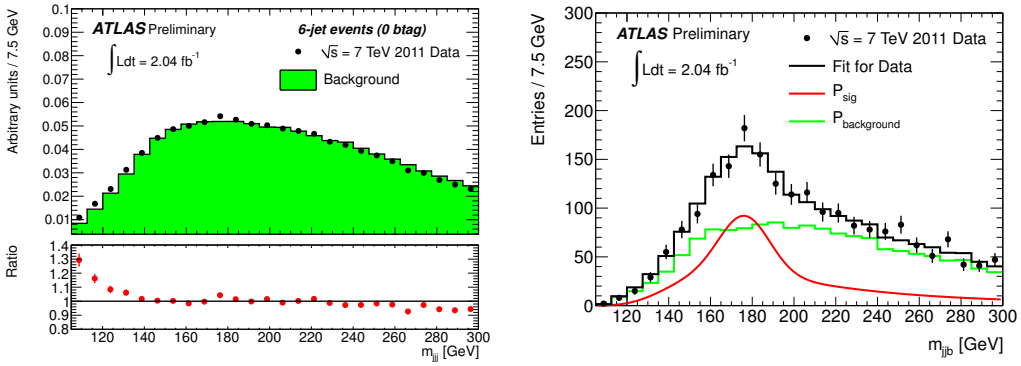

Figure 3: The three-jet invariant mass of the six-jet background with no b-tagging requirement. The green area represents five-jet event-mixed background (left) and the invariant mass of the top candidates in data together with the fit result for the analysis in the all-hadronic channel (right).[4]

The 2D method also measures the JSF, with values equal to 0.985 ± 0.008 (electron channel) and 0.986 ± 0.006 (muon channel) suggesting that the jet energies are described with an accuracy of about 1%. The correlation between the top mass and the JSF is estimated to be -0.6 for both channels.

All results are compatible with the current world average. Finally, the two channels of the lepton+jets 2D analysis are combined to give the following result for the top mass: $m_{\text{top}} = 174.5 \pm 0.6_{\text{stat.}} \pm 2.3_{\text{syst.}}$ GeV.

Method	m_{top}[GeV]
1D electron	$172.9 \pm 1.5_{\text{stat.}} \pm 2.5_{\text{syst.}}$
1D muon	$175.5 \pm 1.1_{\text{stat.}} \pm 2.6_{\text{syst.}}$
2D electron	$174.3 \pm 1.0_{\text{stat.}} \pm 2.2_{\text{syst.}}$
2D muon	$175.0 \pm 0.9_{\text{stat.}} \pm 2.5_{\text{syst.}}$
1D All Hadronic	$174.9 \pm 2.1_{\text{stat.}} \pm 3.8_{\text{syst.}}$
World average [2]	$173.2 \pm 0.6_{\text{stat.}} \pm 0.8_{\text{syst.}}$

Table 1: The fitted top mass for all 5 measurements together with the current world average top mass.

6 Acknowledgments

The work presented here is carried out within the framework of Forschungsschwerpunkt FSP 101 and also supported by the Bundesministerium für Bildung und Forschung BMBF under grant 05HA9PEA.

References

[1] S. Heinemeyer, W. Hollik, and G. Weiglein. Phys. Rept. **425** (2006) 265–368, `arXiv:hep-ph/0412214`.

[2] Tevatron Electroweak Working Group, for the CDF and D0 Collaborations, "Combination of CDF and D0 results on the mass of the top quark using up to 5.8 fb^{-1} of data", `arXiv:1107.5255 [hep-ex]`.

[3] **ATLAS** Collaboration, "Measurement of the top quark mass with the template method in the top antitop $\rightarrow$ lepton + jets channel using ATLAS data", `arXiv:1203.5755 [hep-ex]`.

[4] **ATLAS** Collaboration, "Determination of the top quark mass with a template method in the all-hadronic decay channel using 2.04 fb^{-1} of ATLAS data", ATLAS-CONF-2012-030, CERN, Geneva.

D0 top quark mass and properties

Tim Head for the D0 collaboration

The University of Manchester, Manchester M13 9PL, United Kingdom

DOI: http://dx.doi.org/10.3204/DESY-PROC-2012-02/310

We present measurements of the top quark mass, the top quark width and the ratio, f, of events with correlated t and $\bar{t}$ spins to the total number of $t\bar{t}$ events. The analyzed $p\bar{p}$ collision data correspond to an integrated luminosity of 5.3-5.4 fb^{-1} collected by the D0 Collaboration at the Tevatron Collider. The top quark mass is measured in the dilepton final state resulting in $m_t = 174.0 \pm 2.4(\text{stat}) \pm 1.4(\text{syst})$ GeV. The dominant systematic uncertainty from jet energy calibration is reduced by using a correction obtained from $t\bar{t} \to \ell$+jets events. The total width is extracted from the partial width $\Gamma(t \to Wb)$ and the branching fraction $B(t \to Wb)$. The resulting width is $\Gamma_t = 2.00^{+0.47}_{-0.43}$. The ratio f is evaluated using a matrix-element-based approach in both the ℓ+jets and dilepton final state. The combination provides evidence for the presence of spin correlation in $t\bar{t}$ events with a significance of more than 3 standard deviations.

1 Introduction

The top quark is the heaviest known elementary particle and completes the quark sector of the standard model (SM). It differs from the other quarks not only by its much larger mass, but also by its lifetime that is expected to be shorter than the QCD scale typical of the formation of hadronic bound states. Since the top quark decays through the electroweak interaction before it can interact through the strong interaction the spin orientation of the top quark at production is reflected in the angular distributions of the final state particles. This allows a measurement of the degree to which the spins of the top and antitop quarks are correlated, which is expected to be large in the SM.

In $p\bar{p}$ collisions, top quarks t are primarily produced in $t\bar{t}$ pairs, with each t quark decaying to a b quark with $\mathcal{B}(t \to Wb) \approx 100\%$. These events yield final states with either 0, 1, or 2 leptons from the decays of the two W bosons coming from $t\bar{t}$ decay. For the measurement of the t quark mass we consider the dilepton channel where the two leptons are electrons or muons. In addition the ℓ+jets channel, where the lepton is an electron or muon from a W boson and the second W boson decays to quarks, is used in the measurement of the degree to which the spins of the t and $\bar{t}$ quarks are correlated. The top quark width Γ_t is determined from a measurement in the dilepton and ℓ+jets channel as well as a measurement of the t-channel single top quark production cross section.

2 Event selection

The three analyses discussed in this note use common event selections for the three final states considered. In the dilepton final state events are selected to have two leptons (ee, $e\mu$, $\mu\mu$) and two or more jets. The leptons must have transverse momentum $p_T > 15$ GeV and the jets must satisfy $p_T > 20$ GeV. Electrons and jets are required to satisfy pseudorapidity $|\eta| < 2.5$, while muons must have $|\eta| < 2$. The $e\mu$ events must satisfy $H_T > 120$ GeV, where H_T is the sum of the p_T of jets and the leading lepton. In $\mu\mu$ and ee events, we further require $\not\!\!E_T$ to be significantly different from values typically found in the distribution from Z+jets events. Additionally, events in the $\mu\mu$ final state have to satisfy $\not\!\!E_T > 40$ GeV. These and all other selection criteria are detailed in [1].

In the ℓ+jets final state we require one isolated electron with $p_T > 20$ GeV and $|\eta| < 1.1$, or one isolated muon with $p_T > 20$ GeV and $|\eta| < 2.0$, as well as an imbalance in transverse momentum $\not\!\!E_T > 20(25)$ GeV for the e+jets (μ+jets) channel. In addition we require at least four jets with $p_T > 20$ GeV and $|\eta| < 2.5$; the jet with the largest transverse momentum must have $p_T > 40$ GeV. Full details are given in [2].

In order to measure the t-channel cross section events containing an isolated electron or muon, missing transverse energy and at least two jets are selected. Backgrounds is suppressed by requiring that one or two of the jets is identified as a b-jet. The discrimination between signal and background is further improved by employing multivariate analysis techniques as described in [3].

3 Measurement of the top quark mass

We analyze dilepton events using the neutrino weighting (νWT) approach. While the dilepton channel has low backgrounds, the small branching ratio into leptons means that m_t measurements from these events were statistically limited until recently [4]. Additionally, the dominant systematic uncertainty from jet energy calibration have been large compared to the ℓ+jets channel.

In ℓ+jets events two quarks originating from W boson decay yield a dijet mass signature that permits a precise calibration of jet energies [5]. Here we use the calibration obtained in the ℓ+jets channel to reduce this uncertainty. We carefully evaluate uncertainties arising from the use of this calibration in a different environment.

The consequence of two neutrinos being present in dilepton events is that the kinematics are under-constrained. The νWT technique is used to extract m_t [6]. To solve the event kinematics we integrate over the η distributions of the two neutrinos. By comparing the measured $\not\!\!E_T$ with the $\not\!\!E_T$ calculated from the assumed neutrino ηs we assign a weight to each sampling.

The probability distributions of the mean and RMS values (μ_W and σ_w) of the event weight distributions are constructed for background samples. For $t\bar{t}$ the probability distributions are generated as a function of μ_w, σ_w and m_t. We perform a binned maximum likelihood fit of the selected data events to these probability distributions.

The measurement is calibrated by performing the same extraction on pseudo experiments drawn from MC events. Systematic uncertainties are evaluated for jet energy calibration, effects of modelling of initial and final state radiation, color reconnection, higher order QCD evolution, parton distribution functions and uncertainties arising from the uncertainties on the offset and slope of the calibration from pseudo experiments.

Combining the measurements in the three dilepton channels gives

$$m_t = 173.7 \pm 2.8(\text{stat}) \pm 1.5(\text{syst}) \text{ GeV}.$$

This is the most precise measurement of m_t in the dilepton channel to date [7].

4 Determination of the top quark width

We determine the $\Gamma(t \to Wb)$ from a measurement of the t-channel single top quark production cross section. This process involves a Wtb vertex and is thus proportional to $\Gamma(t \to Wb)$. Beyond the SM contributions may have different effects on the s- and t-channel cross sections. Here the t-channel cross section was chosen as it has the highest production cross section. The s-channel production rate is not assumed to be equal to the SM prediction.

The partial decay width $\Gamma(t \to Wb)$ can be expressed in terms of the t-channel single top quark production cross section as

$$\Gamma(t \to Wb) = \sigma(t\text{−channel}) \frac{\Gamma(t \to Wb)_{\text{SM}}}{\sigma(t\text{−channel})_{\text{SM}}}. \quad (1)$$

The total decay width Γ_t can be written in terms of the partial decay width and the branching fraction $\mathcal{B}(t \to Wb)$ as

$$\Gamma_t = \frac{\Gamma(t \to Wb)}{\mathcal{B}(t \to Wb)}. \quad (2)$$

The total decay width can be calculated by combining Eqs. 1 and 2.

The branching fraction $\mathcal{B}(t \to Wb)$ is measured by distinguishing between the standard decay mode of the t quark, $t\bar{t} \to W^+bW^-\bar{b}$, and decay modes that include light quarks. We use a neural network b-tagging algorithm [8] to identify jets that originate from the hadronization of long-lived b hadrons (b-tagged jet) and distinguish between the bb, bq and qq' final states in $t\bar{t}$ decay.

The t-channel cross section is extracted from a fit to a discriminant trained to separate the t-channel signal from the backgrounds in 6 independent analysis channels, defined according to jet multiplicity (2,3 or 4), and number of b-tagged jets (1 or 2) [9].

The main systematic uncertainties affect both the t-channel output discriminant and the measured branching fraction $\mathcal{B}(t \to Wb)$. The main systematic uncertainties arise from b-jet identification, jet energy resolution and background normalization.

The partial width is extracted using a Bayesian approach. The most probable value for the total width is defined by the peak of the probability density function and corresponds to

$$\Gamma_t = 2.00^{+0.47}_{-0.43}\text{GeV}.$$

This is the most precise determination of the width to date [10].

5 Evidence for spin correlation

A significant correlation between the direction of the spin of the top and antitop quark is expected in the SM. We present the first measurement in the ℓ+jets channel of the ratio of events, f, with correlated t and $\bar{t}$ spins to the total number of $t\bar{t}$ events. The ratio f is

measured using a matrix-element-based approach in which Monte Carlo simulations with SM spin correlation and without spin correlation are compared to data.

The $t\bar{t}$ signal is modelled using the MC@NLO [11] event generator, which allows generation of $t\bar{t}$ MC samples both with and without the expected spin correlation.

To make optimal use of the kinematic information in $t\bar{t}$ events, we calculate signal probabilities P_sgn for each event using the leading-order (LO) matrix element for the hypothesis of correlated ($H = c$) and for the hypothesis of uncorrelated ($H = u$) spins. Writing P_sgn as a function of the hypotheses H as:

$$P_{\rm sgn}(x;\, H) = \frac{1}{\sigma_{obs}} \int f_{\rm PDF}(q_1) f_{\rm PDF}(q_2)\, dq_1\, dq_2 \times \frac{(2\pi)^4 |\mathcal{M}(y,H)|^2}{q_1 q_2 s} W(x,y)\, d\Phi_6,$$

with $\sigma_{\rm obs}$ being the LO $q\bar{q} \to t\bar{t}$ production cross section including selection efficiency and acceptance effects, q_1 and q_2 denoting the fraction of the proton and antiproton momentum carried by the partons, $f_{\rm PDF}$ representing the parton distribution functions, s the square of the center-of-mass energy of the colliding $p\bar{p}$ system, and $d\Phi_6$ the infinitesimal volume element of the six-body phase space. Detector resolution effects are taken into account by introducing transfer functions $W(x,y)$ that describe the probability of a partonic final state y to be measured as x. Additional details of the $P_{\rm sgn}$ calculation can be found in Ref. [12].

To distinguish between correlated and uncorrelated top quark spin hypotheses, we define, a discriminant R:

$$R = \frac{P_{\rm sgn}(x, H = c)}{P_{\rm sgn}(x, H = c) + P_{\rm sgn}(x, H = u)}.$$

The ratio f is measured by comparing templates from distributions of R for $t\bar{t}$ MC events with and without spin correlation, as well as background MC, to data. The binned maximum likelihood fit to the data is performed independently in several sub samples of varying sensitivity.

The main systematic uncertainty is the finite number of MC events used in the templates. Combining the dilepton and ℓ+jets channels we obtain

$$f = 0.85 \pm 0.29(\text{stat} + \text{syst}).$$

We can exclude $f < 0.052$ at 99.7% C.L., therefore this represents first evidence of SM spin correlation at 3.1 standard deviations [13].

6 Summary

We have presented three results measuring properties of the heaviest elementary particle, the top quark. Using dilepton events the top quark mass is measured to be $m_t = ...$ GeV [7], consistent with measurements in other channels. By combining results of two previous measurements [9, 14] we obtain the most precise determination of the top quark width $\Gamma_t = 2.00^{+0.47}_{-0.43}$ GeV [10]. Distinguishing correlated and uncorrelated $t\bar{t}$ spins using a matrix-element-based approach we obtain evidence for SM like correlation of the spins [13].

References

[1] V. M. Abazov *et al.* Phys.Lett. **B704** (2011) 403–410, arXiv:1105.5384 [hep-ex].

[2] V. M. Abazov *et al.* Phys.Rev. **D84** (2011) 012008, arXiv:1101.0124 [hep-ex].

[3] V. Abazov *et al.* Phys.Rev. **D78** (2008) 012005, arXiv:0803.0739 [hep-ex].

[4] V. Abazov *et al.* Phys.Lett. **B655** (2007) 7–14, arXiv:hep-ex/0609056 [hep-ex].

[5] V. Abazov *et al.* Nature **429** (2004) 638–642, arXiv:hep-ex/0406031 [hep-ex].

[6] B. Abbott *et al.* Phys.Rev.Lett. **80** (1998) 2063–2068, arXiv:hep-ex/9706014 [hep-ex].

[7] V. M. Abazov *et al.* arXiv:1201.5172 [hep-ex].

[8] V. Abazov *et al.* Nucl.Instrum.Meth. **A620** (2010) 490–517, arXiv:1002.4224 [hep-ex].

[9] V. M. Abazov *et al.* Phys.Lett. **B705** (2011) 313–319, arXiv:1105.2788 [hep-ex].

[10] V. M. Abazov *et al.* Phys.Rev. **D85** (2012) 091104, arXiv:1201.4156 [hep-ex].

[11] S. Frixione and B. R. Webber. JHEP **0206** (2002) 029, arXiv:hep-ph/0204244 [hep-ph].

[12] F. Fiedler, A. Grohsjean, P. Haefner, and P. Schieferdecker. Nucl.Instrum.Meth. **A624** (2010) 203–218, arXiv:1003.1316 [hep-ex].

[13] V. M. Abazov *et al.* Phys.Rev.Lett. **108** (2012) 032004, arXiv:1110.4194 [hep-ex].

[14] V. Abazov *et al.* Phys.Rev.Lett. **107** (2011) 121802, arXiv:1106.5436 [hep-ex].

Top quark properties at ATLAS

Minoru Hirose[1] on behalf of the ATLAS Collaboration

[1]Osaka University, 1-1 Machikaneyama, Toyonaka, Osaka 560-0043, Japan

DOI: http://dx.doi.org/10.3204/DESY-PROC-2012-02/308

Discovered in 1995 by the CDF and D experiments at Tevatron, the top quark is the heaviest known elementary particle. Its properties might offer a hint of physics beyond the Standard Model. It is thus of interest to measure them as precisely as possible. We present a summary of property measurements of the top quarks which are produced in pp collisions with $\sqrt{s} = 7$ TeV at the LHC. Measurements of the top quark charge, the inclusive $t\bar{t}\gamma$ cross section, the W boson polarisation in top quark decays, the spin correlation in $t\bar{t}$ production and the charge asymmetry in $t\bar{t}$ production were performed with the ATLAS experiment. All measurements are in good agreement with the Standard Model predictions.

1 Introduction

The top quark was discovered in 1995 [1, 2], but many of its properties have been measured only with large uncertainties or not at all. Since a large number of top quarks from pp collisions with $\sqrt{s} = 7$ TeV at the LHC was already recorded by the ATLAS experiment, measurements with much higher precision can be performed to investigate the properties of the top quark. These precise measurements might give us a clue to catch physics beyond the Standard Model. Top quarks are produced mainly in pairs via the strong interaction and are predicted to decay via the electroweak interaction into a W boson and a bottom quark with nearly 100% branching ratio. Events are classified according to the decay of the W bosons. Each boson can either decay into a pair of quarks or into a charged lepton and a neutrino. Single lepton and dilepton topologies (one and two charged leptons in the final state respectively) were used in the analyses presented below. Only electrons and muons, including those from tau decays, were considered.

2 Top quark charge

The top quark charge was measured using 0.70 fb^{-1} of data. This measurement relies on the charge reconstruction of the top quark decay products. While the charge of the W boson can be determined through its leptonic decay, the b-quark charge is not directly measurable, as the b-quark hadronisation process results in a jet of hadronic particles (b-jet). It is possible however to establish a correlation between the charge of the b-quark and a weighted sum of the electric charges of the particles belonging to the b-jet. This weighted sum was used as the b-jet charge. The combined b-jet charge, $\mathcal{Q}_{comb}$ was defined as the product of the b-jet charge and the lepton charge for the b-jet associated with the leptonically decaying W. The measured average value of $\mathcal{Q}_{comb}$ was found to be in good agreement with the SM prediction. Also, the result was

compared with the expectation for a "top-like" quark with an exotic charge of -4/3e. The exotic scenario is excluded at more than five standard deviations [3].

3 Inclusive $t\bar{t}\gamma$ cross section

Top quark pair events with additional photons in the final state are directly sensitive to the $t\bar{t}\gamma$ vertex. A first measurement of the $t\bar{t}\gamma$ cross section in pp collisions at $\sqrt{s}$ =7 TeV was performed using 1.04 fb^{-1} of data. Events are selected that contain a large transverse momentum electron or muon and a large transverse momentum photon. In the electron and muon samples, 52 and 70 candidate events were identified, respectively. The amount of the signal contribution was extracted using the template fitting method. The resulting cross section times branching ratio into the single and dilepton channel $t\bar{t}\gamma$ production with a photon with transverse momentum above 8 GeV is

$$\sigma_{t\bar{t}\gamma} \times \mathrm{BR} = 2.0 \pm 0.5(\mathrm{stat.}) \pm 0.7(\mathrm{syst.}) \pm 0.08(\mathrm{lumi.})\mathrm{pb}\ [4].$$

This result is consistent with the theoretical calculation which yields 2.1 ± 0.4 pb [5, 6] for the same phase space and decay channels.

4 W boson polarisation in top quark decays

A measurement of the helicity of W bosons and angular asymmetries in top quark decays was performed using final states with one or two charged leptons, missing transverse energy and at least four or two jets, respectively, with an integrated luminosity of 1.04 fb^{-1}. The fraction of each W boson helicity state (longitudinal, right- and left-handed. Each of them are called F_0, F_R and F_L, respectively) was extracted using the template fitting method for both single lepton and dilepton channel. The results obtained by fitting the three helicity fractions and from the asymmetry measurement are compatible with each other in all channels. Since F_R was found to be compatible with zero within uncertainty, the fit was repeated for a fixed F_R.

A combination of the measurements in the single lepton and dilepton channels with the right-handed fraction set to zero yields:

$$\begin{aligned} F_0 &= 0.66 \pm 0.03(\mathrm{stat.}) \pm 0.04(\mathrm{stat.}), \\ F_L &= 0.34 \pm 0.03(\mathrm{stat.}) \pm 0.04(\mathrm{stat.})\ [7]. \end{aligned}$$

This result is in agreement with the NNLO QCD prediction. As the polarisation of the W bosons in top quark decays is sensitive to the structure of the Wtb-vertex, the measurements were used to set limits on anomalous contributions to the Wtb-Lagrangian [8]. There are four couplings in the Lagrangian (V_L, V_R, g_L and g_R) and V_R, g_L and g_R are absent in the SM at the tree level. Figure 1 shows the allowed region of the anomalous couplings g_L and g_R with V_R set to zero.

5 Spin correlation in $t\bar{t}$ production

A measurement of the spin correlation in $t\bar{t}$ production was performed using data corresponding to an integrated luminosity of 2.1 fb^{-1}. The lifetime of the top quark is at least an order of

magnitude shorter than the timescale for strong interactions, implying that the top quark decays before hadronisation. Therefore the spin of the top quark at production is transferred to its decay products and can be measured directly via their angular distributions. In this analysis, candidate events were selected in the dilepton topology with large missing transverse energy and at least two jets. The difference in azimuthal angle between the two charged leptons in the laboratory frame was used to extract the correlation between the top and antitop quark spins. In the helicity basis the measured degree of correlation corresponds to

$$A_{\text{helicity}} = 0.40 \pm 0.04(\text{stat.})^{+0.08}_{-0.07}(\text{syst.}) \text{ [9]},$$

in agreement with the NLO SM prediction. The hypothesis of zero spin correlation is excluded at 5.1 standard deviations.

6 Charge asymmetry in $t\bar{t}$ production

Due to the asymmetry in the production via $q\bar{q}$ and qg, QCD predicts at the LHC a small excess of centrally produced antitop quarks while top quarks are produced, on average, at higher absolute rapidities. Thus, a measurement of the top-antitop production charge asymmetry A_C was performed using data corresponding to an integrated luminosity of 1.04 fb^{-1}. A_C is defined as

$$A_C = \frac{N(\Delta|y| > 0) - N(\Delta|y| < 0)}{N(\Delta|y| > 0) + N(\Delta|y| < 0)}$$

where $\Delta|y| \equiv |y_t| - |y_{\bar{t}}|$ is the difference between the absolute values of the top and antitop rapidities ($|y_t|$ and $|y_{\bar{t}}|$) and N is the number of events with $\Delta|y|$ positive or negative. Events were selected with exactly one isolated lepton, missing transverse momentum and at least four jets of which at least one identified as coming from a b-quark. A kinematic fit was used to reconstruct the $t\bar{t}$ event topology. After background subtraction, a Bayesian unfolding procedure was performed to correct for acceptance and detector effects. Measurement yields

$$A_C = -0.018 \pm 0.028(\text{stat.}) \pm 0.023(\text{syst.}) \text{ [10]},$$

consistent with the prediction from the MC@NLO [11] Monte Carlo generator $A_C = 0.006 \pm 0.002$. Also, Figure 2 summarises the measurements of A_C in two ranges of invariant mass of the top-antitop pair. These results are compatible with the prediction from the MC@NLO Monte Carlo generator, showing no evidence for an enhancement from physics beyond the Standard Model.

7 Summary

Several top properties measurements were performed with the ATLAS experiment. Spin correlations in $t\bar{t}$ production were observed with 5.1 sigma significance. All results are in good agreement with the SM predictions. Most of them will profit from the higher luminosity.

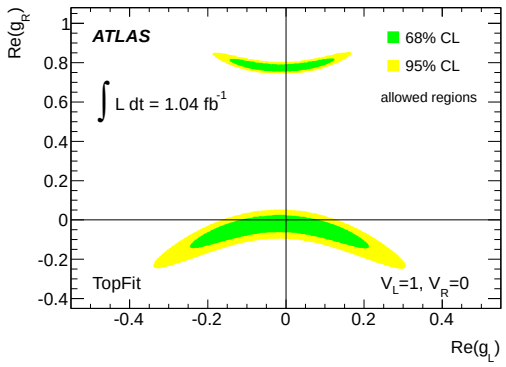

Figure 1: Allowed regions at 68% CL (green) and at 95% CL (green+yellow) for the Wtb anomalous couplings [7].

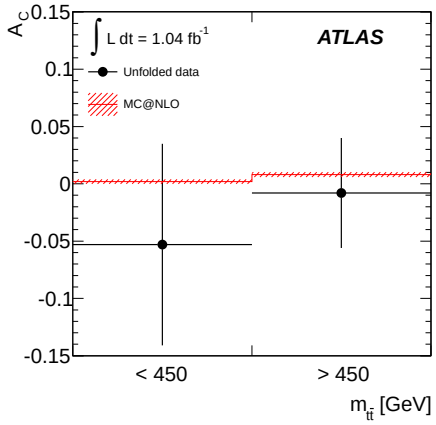

Figure 2: Unfolded asymmetries in two regions of $m_{t\bar{t}}$ compared to the prediction from MC@NLO. The error bands on the prediction include uncertainties from parton distribution functions and renormalisation and factorisation scales [10].

References

[1] CDF Collaboration, F. Abe et al., Phys. Rev. Lett. **74** (1995) 2626-2631, arXiv/9503002

[2] DØ Collaboration, S. Abachi et al., Phys. Rev. Lett. **74** (1995) 2632-2637, arXiv/9503003

[3] ATLAS Collaboration, ATLAS-CONF-2011-141 (https://cdsweb.cern.ch/record/1385517)

[4] ATLAS Collaboration, ATLAS-CONF-2011-153 (https://cdsweb.cern.ch/record/1398197)

[5] K. Melnikov, M. Schulze and A. Scharf, Phys. Rev. D83 (2011) 074013 arXiv:1102.1967

[6] A. Scharf, private communication.

[7] ATLAS Collaboration, submitted to JHEP, arXiv:1205.2484

[8] J. A. Aguilar-Saavedra, Nucl. Phys. B821 (2009) 215–227 arXiv:0904.2387

[9] ATLAS Collaboration, Phys. Rev. Lett. **108**, 212001 (2012), arXiv/1203.4081

[10] ATLAS Collaboration, submitted to Eur. Phys. J. C, arXiv/1203.4211

[11] S. Frixione and B.R. Webber, JHEP 0206 (2002) 029 arXiv:0204244

Top-quark pair-production with one jet and parton showering at hadron colliders

Simone Alioli[1], *Juan Fuster*[2], *Adrian Irles*[2], *Sven-Olaf Moch*[3], *Peter Uwer*[4], *Marcel Vos*[2]

[1]LBNL & UC Berkeley, 1 Cyclotron Road, Berkeley, CA 94720, USA
[3]IFIC, Universitat de Valencia – CSIC, Catedratico Jose Beltran 2, E-46980 Paterna, Spain
[3]DESY, Platanenalle 6, D-15738 Zeuthen, Germany
[4]Humboldt-Universität, Newtonstraße 15, D-12489 Berlin, Germany

DOI: `http://dx.doi.org/10.3204/DESY-PROC-2012-02/231`

We present heavy-flavor production in association with one jet in hadronic collisions matched to parton shower Monte Carlo predictions at next-to-leading order QCD with account of top-quark decays and spin correlations. We use the `POWHEG BOX` for the interface to the parton shower programs `PYTHIA` or `HERWIG`. Phenomenological studies for the LHC and the Tevatron are presented with particular emphasis on the inclusion of spin-correlation effects in top decay and the impact of the parton shower on the top-quark charge asymmetries. As a novel application of the present calculation the measurement of the top-quark mass is discussed.

1 Introduction

The Large Hadron Collider (LHC) and the Tevatron provide an experimental environment allowing for top-quark measurements with percent level accuracy. Precise measurements for top-quark production demand theoretical predictions with comparable precision. This requires the knowledge of the hard scattering process beyond the leading order (LO) in perturbation theory. Furthermore, for the direct comparison with experimental data, fully exclusive events are needed, that take into account all-order logarithmic enhancements of soft and collinear regions of phase space and hadronization effects by means of Shower Monte Carlo (SMC) programs. Both approaches can be combined systematically by merging NLO computations with parton showers, in the `MC@NLO` [1] or `POWHEG` [2] approach.

2 $t\bar{t}$ + 1-jet hadroproduction in `POWHEG`

In the following we concentrate on the recent implementation of the $t\bar{t}+1$-jet hadroproduction in the `POWHEG` approach, presented in Ref. [3]. A large fraction of the inclusive $t\bar{t}$ production does indeed actually contain events with one or even more additional jets. Furthermore, due to the larger phase space available, the relative importance of data samples with $t\bar{t}$+jets is larger at the LHC with respect to the Tevatron, increasing the need of an accurate theoretical description of this process. Top-quark pair-production associated with jets is also an important background to Higgs boson production in vector boson fusion and for many signals of new

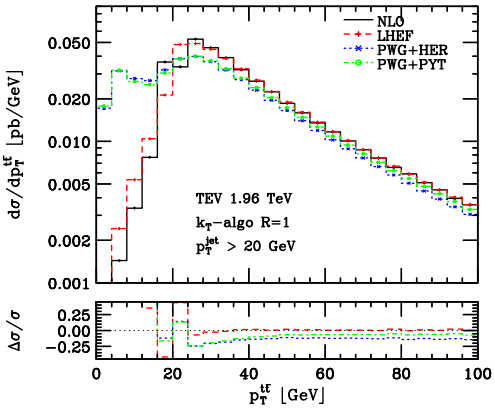

Figure 1: Differential cross section as a function of the $t\bar{t}$-pair transverse momentum at the Tevatron ($\sqrt{s} = 1.96$ TeV)

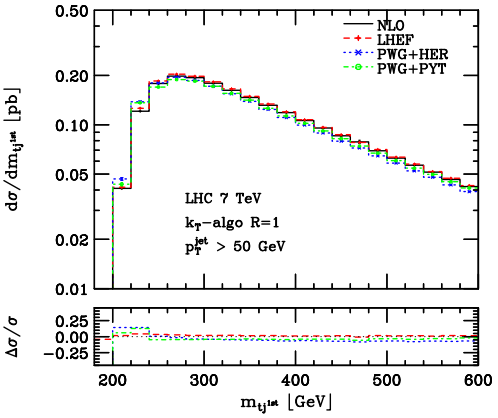

Figure 2: Differential cross section as a function of the (tj_1) invariant mass at the LHC ($\sqrt{s} = 7$ TeV)

physics. The implementation reported here is based on the NLO QCD corrections evaluated in Ref. [4, 5], merged with HERWIG [6] and PYTHIA [7] SMC programs, using the POWHEG BOX [8].

We present results for both Tevatron and LHC colliders, having assumed a jet reconstruction cut in the analysis of $p_{\mathrm{T}} > 20$ GeV and 50 GeV, respectively. We have used the inclusive-k_T jet algorithm with $R = 1$ and the E_T-recombination scheme. Renormalization and factorization scales have been set to $\mu_R = \mu_F = m_t = 174$ GeV, we have used the PDF set CTEQ6M [9], and we have not imposed any extra acceptance cut, other than those necessary to define the hard jet. In Fig. 1 we show the differential cross section as a function of the transverse momentum of the $t\bar{t}$-pair at the Tevatron, while in Fig. 2 we plot the invariant mass of the system made by the top-quark and the hardest jet at the 7 TeV LHC. The different curves appearing on each plot refer respectively to the fixed order results (NLO), to the results after the first emission has been performed by POWHEG (LHEF) and to the fully showered events, with HERWIG (PWG+HER) or PYTHIA (PWG+PYT) showers. Shower effects are visible in the low-$p_{\mathrm{T}}^{t\bar{t}}$ region, while more inclusive observables like the invariant mass of the system made by the top-quark and the hardest jet, $m_{(tj_1)}$, are basically unaffected by the shower.

3 Spin correlations in top-quark decays

In our implementation we have also included the spin-correlations. In doing so, we have neglected off-shell effects and non-resonant production mechanisms. We proceeded by first generating events with stable top-quarks (un-decayed events) through the usual POWHEG machinery and then generating the decay products according to the matrix element for the full production and decay process (decayed events), following Ref. [10]. In our study we always assumed the double-leptonic top-quark decay channel $t \to W^+ b \to \ell^+ \nu b$. In Fig. 3 we draw the differential distribution $\frac{1}{\sigma} \frac{d^2\sigma}{d\cos\theta_1 d\cos\theta_2}$ after the HERWIG shower, at the Tevatron collider, where the angles θ_1 and θ_2 between the directions of flight of the leptons coming from the decayed top-quark in the t ($\bar{t}$) rest frame and the beam axis can be interpreted in the context of spin correlations as the quantization axis for the (anti-)top-quark spin. No extra acceptance cut is imposed on the

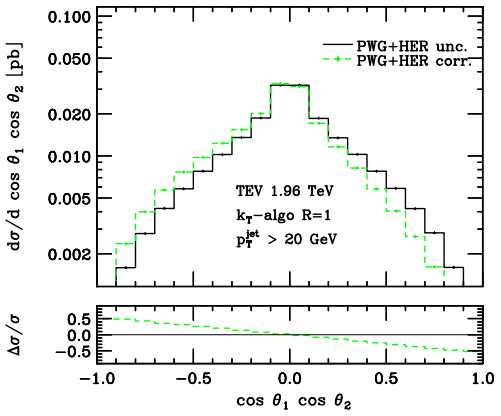

Figure 3: Effect of the inclusion of spin correlations when interfacing to HERWIG.

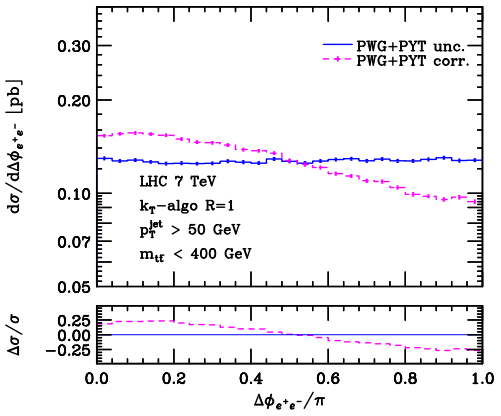

Figure 4: Effect of the inclusion of spin correlations when interfacing to PYTHIA.

leptons. In Fig. 4 we show instead the differential cross section as a function of the azimuthal distance between the two leptons coming from the top-quarks decays, for the LHC collider configuration and after the PYTHIA shower. An extra cut $m_{t\bar{t}} < 400$ GeV has been imposed here to enhance the effect. A similar observable has recently been used in $t\bar{t}$-production to observe spin-correlations [11]. The plots in Fig. 4 clearly demonstrate the differences between spin-correlated results and those obtained by letting the respective SMC program performing uncorrelated top-quark decays.

4 Asymmetries

We have also investigated the $t\bar{t}$ charge asymmetry in presence of a hard jet, finding that the inclusion of the parton shower changes significantly the fixed-order predictions in the low $p_T^{t\bar{t}}$ region, where shower effects are known to be large. Away from this region the parton shower leads only to a marginal change of the charge asymmetry binned in $p_T^{t\bar{t}}$. This quantity is now available at NLO accuracy, supplemented by the shower. For more details and for complete tables including results obtained with different cuts and at various stages of the simulation, we refer to Ref. [3].

5 Top-quark mass measurement

As a novel application the differential cross section for $t\bar{t}+1$-jet production can be used for a determination of the top-quark mass. To that end, we consider the differential $t\bar{t}+1$-jet rate,

$$\frac{dn_3}{d\rho_s}(m^p_{top},\mu,\rho_s) = \frac{1}{\sigma_{t\bar{t}j}}\frac{d\sigma_{t\bar{t}j}}{d\rho_s}(m^p_{top},\mu,\rho_s), \tag{1}$$

where $\sigma_{t\bar{t}j}$ denotes the cross section for the process $pp \to t\bar{t}$+1-jet+X. The variable ρ_s is defined as $\rho_s = \frac{2\cdot m_0}{\sqrt{s_{t\bar{t}j}}}$ with $m_0 = 170$ GeV and $s_{t\bar{t}j}$ is the invariant mass squared of the final state. In Fig. 5 a clear separation between the distributions for different top-quark masses is observed except in the region of $0.55 < \rho_s < 0.62$ where the curves cross due to the normalization of

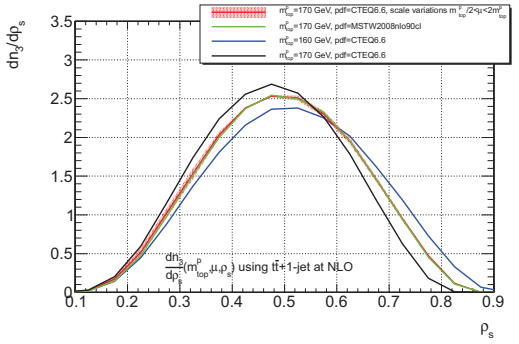

Figure 5: $dn_3/d\rho_s(m^p_{top}, \mu)$ calculated at NLO for different masses $m^p_{top} = 160$, 170 and 180 GeV. For $m^p_{top} = 170\,\text{GeV}$ the scale uncertainty is shown and two PDF sets [13, 14] for comparison.

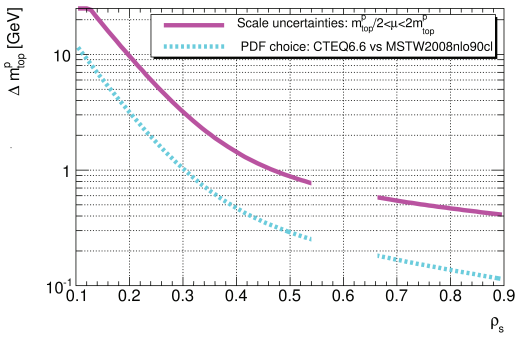

Figure 6: Sensitivity on value of the top-quark mass (for $m^p_{top} = 170\,\text{GeV}$) along with scale uncertainty (magenta solid line) and effect of PDF choice [13, 14]. The crossing region is excluded.

$\frac{dn_3}{d\rho_s}(m^p_{top}, \mu, \rho_s)$. As a consequence a decrease of sensitivity is observed in the crossing region. The approach of Eq. (1) nicely complements top-quark mass measurements from the $t\bar{t}$ total cross section, see Ref. [12] for the first measurement of the $\overline{\text{MS}}$ mass. The impact of the conventionally estimated scale variation (solid line) and the PDF choice (dashed line) on the top mass value (for $m_{top} = 170\,\text{GeV}$) is displayed in Fig. 6. It demonstrates that a theoretical uncertainty of $500-600$ MeV can be reached with a mass measurement in the interval $\rho_s > 0.62$ based on the scale uncertainty and the dependence on the PDF choice. Additional sources of systematic uncertainities have been investigated and have led to error estimates below 1 GeV. The crossing region is again excluded due to the vanishing sensitivity. The curves in Fig. 6 have been obtained assuming a linear dependence of n_3 on the top-quark mass for intervals of $\Delta m^p_{top} = 5$ GeV.

References

[1] S. Frixione and B. R. Webber. JHEP **0206** (2002) 029, arXiv:hep-ph/0204244 .

[2] P. Nason. JHEP **0411** (2004) 040, arXiv:hep-ph/0409146 .

[3] S. Alioli, S. Moch, and P. Uwer. JHEP **1201** (2012) 137, arXiv:1110.5251.

[4] S. Dittmaier, P. Uwer, and S. Weinzierl. Phys.Rev.Lett. **98** (2007) 262002, arXiv:hep-ph/0703120 .

[5] S. Dittmaier, P. Uwer, and S. Weinzierl. Eur.Phys.J. **C59** (2009) 625–646, arXiv:0810.0452.

[6] G. Corcella *et al.* JHEP **0101** (2001) 010, arXiv:hep-ph/0011363 .

[7] T. Sjostrand, S. Mrenna, and P. Z. Skands. JHEP **0605** (2006) 026, arXiv:hep-ph/0603175 .

[8] S. Alioli *et al.* JHEP **1006** (2010) 043, arXiv:1002.2581.

[9] J. Pumplin *et al.* JHEP **0207** (2002) 012, arXiv:hep-ph/0201195 .

[10] S. Frixione *et al.* JHEP **0704** (2007) 081, arXiv:hep-ph/0702198 .

[11] G. Aad *et al.* Phys.Rev.Lett. **108** (2012) 212001, arXiv:1203.4081 [hep-ex].

[12] U. Langenfeld, S. Moch, and P. Uwer. Phys.Rev. **D80** (2009) 054009, arXiv:0906.5273.

[13] P. M. Nadolsky *et al.* Phys.Rev. **D78** (2008) 013004, arXiv:0802.0007.

[14] A. Martin *et al.* Eur.Phys.J. **C63** (2009) 189–285, arXiv:0901.0002.

$\mathrm{t\bar{t}} + X$ hadroproduction at NLO accuracy with decay and evolution to the hadron level

Adam Kardos[1], *Maria Vittoria Garzelli*[2], *Zoltán Trócsányi*[1]

[1]Institute of Physics and MTA-DE Particle Physics Research Group, University of Debrecen, H-4010 Debrecen P.O.Box 105, Hungary
[2]Laboratory for Astroparticle Physics, University of Nova Gorica, SI-5000 Nova Gorica, Slovenia

DOI: `http://dx.doi.org/10.3204/DESY-PROC-2012-02/232`

We discuss how the hadroproduction of $\mathrm{t\bar{t}}$-pairs in association with jets, vector and/or scalar bosons is implemented in the `PowHel` framework. In this framework matrix elements obtained from the `HELAC-NLO` package are used to provide predictions of distributions at the hadron level that are correct up to next-to-leading order accuracy in perturbation theory. We also show first predictions for $W^+W^-\mathrm{b\bar{b}}$-hadroproduction.

Accurate predictions for the production of $\mathrm{t\bar{t}}$-pairs alone or in association with jets, vector and/or scalar bosons are important for many experimental studies at hadron colliders both aiming at better understanding of the Standard Model (SM) and searches for new physics. However, the t-quarks and heavy bosons decay quickly and their decay products are detected. The experimental analyses often concentrate on the leptonic decay channels because these offer a much cleaner final state than the hadronic ones. Thus it is important not only to predict cross sections for the production of the heavy quarks and bosons, but also for the spectra of the leptons that emerge in their decays. While the theoretical description of such final states is straightforward at leading-order accuracy using the state-of-the art calculational tools, such predictions are known to suffer from large scale ambiguities and corrections from parton showers and hadronization. In order to improve the accuracy of the theoretical description during the last decade a lot of effort has been invested to match perturbative predictions at the next-to-leading order (NLO) accuracy with shower Monte Carlo (SMC) programs. One such approach is the POWHEG method [1, 2] that was implemented in a process independent framework in the `POWHEG-BOX` program [3].

To write the POWHEG cross section, one defines the NLO-corrected fully differential cross section belonging to the underlying Born configuration

$$\tilde{B}(\Phi_B) = B(\Phi_B) + V(\Phi_B) + \int \mathrm{d}\Phi_{\mathrm{rad}} \hat{R}(\Phi_R)\,,$$

and the POWHEG Sudakov form factor

$$\Delta(\Phi_B, p_\perp) = \exp\left\{ - \int \frac{\mathrm{d}\Phi_{\mathrm{rad}} R(\Phi_R) \Theta(k_\perp(\Phi_R) - p_\perp)}{B(\Phi_B)} \right\}.$$

In these equations $\mathrm{d}\Phi_B$ denotes the phase space measure of the Born computation, while $\mathrm{d}\Phi_R$ is that for the real radiation process. The latter is parametrized as $\mathrm{d}\Phi_R = \mathrm{d}\Phi_B \mathrm{d}\Phi_{\mathrm{rad}}$, where

$\mathrm{d}\Phi_{\mathrm{rad}}$ includes the measure for the three variables that describe the radiation process of the extra parton and the corresponding Jacobian factor. The functions $B(\Phi_B)$ and $V(\Phi_B)$ denote the Born contribution and the finite part of the virtual corrections, respectively. Finally, $\hat{R}(\Phi_R)$ is the regularized real radiation contribution that is also defined in the FKS subtraction scheme. In the `POWHEG-BOX` the latter two are defined in the FKS subtraction scheme [4].

In the Sudakov form factor, the function $k_\perp(\Phi_R)$ has to be equal to the transverse momentum of the emitted parton relative to the emitting one near the region of singular emission. Then the POWHEG fully differential cross section is defined as

$$\mathrm{d}\sigma_{\mathrm{LHE}} = \tilde{B}(\Phi_B)\mathrm{d}\Phi_B \left[\Delta(\Phi_B, p_\perp^{\min}) + \mathrm{d}\Phi_{\mathrm{rad}}\Delta\Big(\Phi_B, k_\perp(\Phi_R)\Big)\frac{R(\Phi_R)}{B(\Phi_B)}\Theta(k_\perp(\Phi_R) - p_\perp^{\min})\right] . \quad (1)$$

The advantage of this formula is that it can be used to generate equal weight events with Born configuration (first term) or including first radiation (second term). These events, termed LHE's, are stored in files according to the Les Houches accord [5].

The `POWHEG-BOX` provides a general framework to implement the POWHEG cross section in Eq. (1). In this framework, the following ingredients are needed:

- The flavor structures of the Born and real radiation emission subprocesses.
- The Born-level phase space, that we generate to emphasize the resonant kinematics of the decaying t- and $\bar{\mathrm{t}}$-quark.
- We obtain the squared matrix elements for the Born and the real-emission processes and color-correlated Born amplitudes with all incoming momenta using amplitudes computed by codes included in the `HELAC-NLO` package [6], in particular `HELAC-1LOOP` based on the OPP method [7] complemented by Feynman-rules for the computation of the QCD R_2 rational terms [8]. The matrix elements in the physical channels were obtained by crossing. In order to treat the numerical instabilities, we implemented `dd`-precision numerics by developing a `HELAC-1LOOP@dd` version of the `HELAC-1LOOP` program.
- We project spin-correlated Born amplitudes from the helicity basis to the Lorentz one by using the polarization vectors.

The generation of the matrix elements is straightforward using the `HELAC-NLO` code. There are two problems that arise during integration. The first one is that for vanishing transverse momentum of massless partons or vanishing invariant mass of a massless parton pair the Born cross section becomes singular. While this can never happen in a LO computation due to the selection cuts, it is a problem in the POWHEG method because the selection cuts can only be applied after event generation. The traditional way of treating this problem is the introduction of a generation cut. With this cut the LO cross section becomes finite, but the generation of the events is still rather inefficient because most of the events are generated in the region of small $p_\perp$ of the massless parton, thus they are lost when the physical selection cuts are applied (usually much higher, in the region of 20 – 30 GeV). In order to make the generation of events more efficient, we introduce suppression factors. As we want to suppress the region of small $p_\perp$, our choice for the suppression factor is

$$\mathcal{F} = \left(\frac{p_\perp^2}{p_\perp^2 + p_{\perp,\,\mathrm{supp}}^2}\right)^i ,$$

with $i = 3$ in our calculation.

The second problem is a purely numerical one and is related to the numerical computation of one-loop amplitudes as implemented in `CutTools` [10]. In order to control numerical instabilities an $\mathcal{N} = \mathcal{N}$ test was implemented. For a given numerator we determine the scalar-integral coefficients using double precision arithmetics. We check the accuracy of the integrand by reconstructing it using all coefficients (and spurious terms) with a randomly chosen loop momentum. If the reached relative accuracy is worse than 10^{-4}, we pass the same phase space point in double-double precision (computed at the first place) to `HELAC-1LOOP@dd` to recalculate all the coefficients. The `HELAC-1LOOP@dd` code is a straightforward extension of `HELAC-1LOOP` to double-double precision using `QD` [9]. If the $\mathcal{N} = \mathcal{N}$ test fails, `CutTools` turns on its multi-precision version and calls the corresponding double-double precision version subroutines of `HELAC-1LOOP@dd`. This way we avoided all numerical instabilities in the computation of the virtual corrections.

We implemented all these improvements in the `PowHel` framework that can be used to generate LHE's for the following final states in hadroproduction: (i) a $t\bar{t}$-pair, (ii) a $t\bar{t}$-pair in association with a jet [11], (iii) a $t\bar{t}$-pair in association with a scalar [12] and a pseudoscalar Higgs boson [13], (iv) a $t\bar{t}$-pair in association with a SM Z^0-boson [14, 15], (v) $W^+W^-b\bar{b}$, and three more processes that are not yet published. In this proceedings we discuss item (v) briefly.

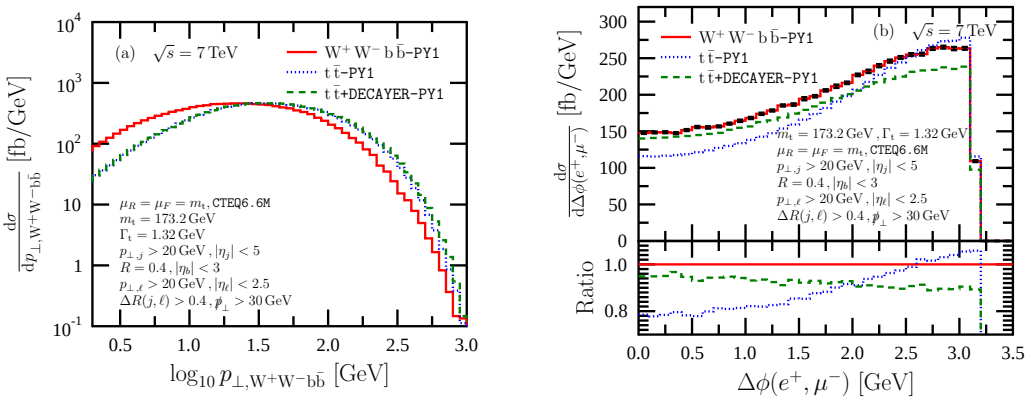

Figure 1: Distribution of the a) transverse momentum of the $W^+W^-b\bar{b}$-system; b) azimuthal separation between the hardest isolated positron and muon. The lower inset in the right panel shows the ratio of the predictions with approximate decays of the t-quarks as compared to the complete $W^+W^-b\bar{b}$-prediction. Selection cuts are specified in the plots.

Fig. 1.a shows the distribution of the transverse momentum of the $W^+W^-b\bar{b}$ system. Our selection cuts are shown in the figure. In a fixed-order computation this distribution diverges for vanishing transverse momentum. In the POWHEG cross section this divergence is smeared by the Sudakov form factor as can be seen in the figure. In addition to the $W^+W^-b\bar{b}$ final state computed at the NLO accuracy and matched to the `PYTHIA` SMC [16], we also show the prediction obtained by computing the $t\bar{t}$ final state and letting the SMC decay the heavy quarks (line marked as $t\bar{t}$-`PY1`). The third line (marked as $t\bar{t}$-`DECAYER-PY1`) shows the predictions obtained by performing the decays of the heavy particles according to the method descibed by Ref. [17] and implemented in a general way in our code `DECAYER`. The large difference between

the $W^+W^-\mathrm{b}\,\bar{\mathrm{b}}$-prediction is due to the different source of first emission in the two approaches: for the $W^+W^-\mathrm{b}\,\bar{\mathrm{b}}$-case first emission comes mainly from the b-quarks, that we treat as massless, while in the $\mathrm{t}\,\bar{\mathrm{t}}$-case first emission comes from the heavy t-quarks. As a result the latter spectra are much harder.

In Fig. 1.b we show the distribution of azimuthal separation between the hardest isolated positron and the muon. This distribution is an example where the differences between the three cases were clearly visible in the LHE's. These differences are only slightly altered by the PS, or the full SMC. In particular, the effect of including the spin-correlation leads to an increase of the distribution for small azimuthal separation $\Delta\phi_{e^+\mu^-}$, where the distribution from the $\mathrm{t}\,\bar{\mathrm{t}}$+`DECAYER` computation, which includes the spin correlations in an approximate way, and from the $W^+W^-\mathrm{b}\,\bar{\mathrm{b}}$-prediction are similar in shape. Only the normalizations of the two predictions differ due to the the singly- and non-resonant graphs that are absent in the $\mathrm{t}\,\bar{\mathrm{t}}$+`DECAYER` computation. For small separations, these are both significantly larger than the distribution $\mathrm{t}\,\bar{\mathrm{t}}$-`PY1` obtained from the $\mathrm{t}\,\bar{\mathrm{t}}$ events if the decay of the t-quarks is performed by the SMC, where spin correlations are neglected. At large separations however, the latter becomes even larger than the predictions from the $W^+W^-\mathrm{b}\,\bar{\mathrm{b}}$ computation.

This research was supported by the LHCPhenoNet network PITN-GA-2010-264564, the TÁMOP 4.2.1./B-09/1/KONV-2010-0007 and 4.2.2/B-10/1-2010-0024 projects, the Hungarian Scientific Research Fund grant K-101482. We are grateful to G. Bevilacqua, M. Worek, A. van Hameren and P. Skands for useful discussions.

References

[1] P. Nason. JHEP **0411** (2004) 040, `arXiv:hep-ph/0409146 [hep-ph]`.

[2] S. Frixione, P. Nason, and C. Oleari. JHEP **11** (2007) 070, `arXiv:0709.2092 [hep-ph]`.

[3] S. Alioli, P. Nason, C. Oleari, and E. Re. JHEP **06** (2010) 043, `arXiv:1002.2581 [hep-ph]`.

[4] S. Frixione, Z. Kunszt, and A. Signer. Nucl.Phys. **B467** (1996) 399–442, `arXiv:hep-ph/9512328 [hep-ph]`.

[5] E. Boos, M. Dobbs, W. Giele, I. Hinchliffe, J. Huston, *et al.* `arXiv:hep-ph/0109068 [hep-ph]`.

[6] G. Bevilacqua, M. Czakon, M. V. Garzelli, A. van Hameren, A. Kardos, *et al.* `arXiv:1110.1499 [hep-ph]`.

[7] G. Ossola, C. G. Papadopoulos, and R. Pittau. Nucl.Phys. **B763** (2007) 147–169, `arXiv:hep-ph/0609007 [hep-ph]`.

[8] P. Draggiotis, M. V. Garzelli, C. G. Papadopoulos, and R. Pittau. JHEP **0904** (2009) 072, `arXiv:0903.0356 [hep-ph]`.

[9] Y. Hida, X. S. Li, and D. H. Bailey, "Quad-double arithmetic: Algorithms, implementation, and application", Tech. Rep. LBNL-46996, Lawrence Berkeley National Laboratory, Berkeley, CA 94720, October, 2000. Available at `http://www.nersc.gov/~dhbailey/mpdist/mpdist.html`.

[10] G. Ossola, C. G. Papadopoulos, and R. Pittau. JHEP **03** (2008) 042, `arXiv:0711.3596 [hep-ph]`.

[11] A. Kardos, C. G. Papadopoulos, and Z. Trocsanyi. Phys.Lett. **B705** (2011) 76–81, `arXiv:1101.2672 [hep-ph]`.

[12] M. V. Garzelli, A. Kardos, C. G. Papadopoulos, and Z. Trocsanyi. Europhys.Lett. **96** (2011) 11001, `arXiv:1108.0387 [hep-ph]`.

[13] S. Dittmaier, C. Mariotti, G. Passarino, R. Tanaka, *et al.* `arXiv:1201.3084 [hep-ph]`.

[14] A. Kardos, Z. Trocsanyi, and C. G. Papadopoulos. Phys.Rev. **D85** (2012) 054015, `arXiv:1111.0610 [hep-ph]`.

[15] M. V. Garzelli, A. Kardos, C. G. Papadopoulos, and Z. Trocsanyi. Phys.Rev. **D85** (2012) 074022, `arXiv:1111.1444 [hep-ph]`.

[16] T. Sjostrand, S. Mrenna, and P. Z. Skands. JHEP **0605** (2006) 026, `arXiv:hep-ph/0603175 [hep-ph]`.

[17] S. Frixione, E. Laenen, P. Motylinski, and B. R. Webber. JHEP **04** (2007) 081, `arXiv:hep-ph/0702198`.

Quarkonium Production in ATLAS

Sue Cheatham on behalf of the ATLAS Collaboration

McGill University, Montreal, Canada.

DOI: http://dx.doi.org/10.3204/DESY-PROC-2012-02/84

The production of Quarkonium is an important testing ground for QCD calculations. The J/ψ and Υ(1S) production cross-sections are measured in proton-proton collisions at the ATLAS detector at the LHC. Differential cross sections as a function of transverse momentum and rapidity have been measured. Charmonium states χ_{c1}(1P) and χ_{c2}(1P) have been observed through radiative decays, as well as a new χ_b state. Results are compared to perturbative QCD predictions.

1 Introduction

Despite being among the most studied of the bound quark systems, there is still no clear understanding of the production mechanisms for quarkonium states like the J/ψ and the Υ that can consistently explain both the production cross-section and spin alignment measurements in e^+e^-, hadron and heavy ion collisions. Data from the LHC allow tests of theoretical models of quarkonium production in a new energy regime. Details of the ATLAS detector may be found in [1]. The sub-detectors of greatest importance to the analyses presented here are the Inner Detector (ID) and Muon Spectrometer systems.

2 Measurement of the differential cross-sections of inclusive, prompt and non-prompt J/ψ production

The inclusive J/ψ production cross-section is measured at ATLAS in the di-muon decay channel using 2.3 pb^{-1} of 2010 data [2]. The number of J/ψ candidates are extracted from the observed di-muon pairs, applying event weights to unfold the response of the detector, reconstruction and trigger efficiency. The J/ψ yields are then determined in regions of the di-muon p_T and rapidity. The spin alignment of the J/ψ is unknown, as yet, at the LHC. An envelope of all possible spin alignment assumptions is taken as an additional theoretical uncertainty.

Prompt J/ψ are produced directly from the hard-scatter of the p-p collision, as well as through decays from higher charmonium states. Non-prompt J/ψ are produced via the decay of a B-hadron and can be distinguished experimentally due to the associated displacement of the J/ψ vertex in the transverse plane, due to the long lifetime of the B hadron.

Figure 1 shows the inclusive J/ψ production cross-section as a function of p_T, in two regions of J/ψ rapidity. The prompt and non-prompt J/ψ production cross-sections, as a function of p_T, are also shown in Figure 1. The non-prompt component is seen to be in good agreement

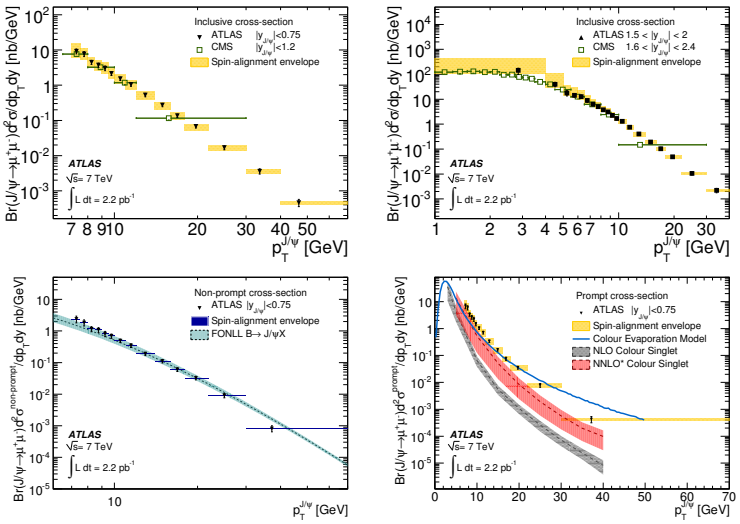

Figure 1: The inclusive J/ψ production cross-section as a function of J/ψ transverse momentum, for low J/ψ rapidity (top left) and higher J/ψ rapidity (top right). The equivalent results from CMS are overlaid. The non-prompt J/ψ production cross-section is shown (bottom left) and the prompt J/ψ production cross-section (bottom right), as a function of J/ψ p_T.

with the FONLL predictions. For the prompt component, the data are reasonably consistent with NNLO* Colour Singlet calculations at low p_T, but does less well at high p_T.

3 Observation of the $\chi_{c1}(1P)$ and $\chi_{c2}(1P)$ charmonium states

The $\chi_{c1}(1P)$ and $\chi_{c2}(1P)$ charmonium states in $\chi_c \to J/\psi\gamma$ decays are observed using an integrated luminosity of 39 pb^{-1} [3]. J/ψ candidates are reconstructed via the decay J/$\psi \to \mu^+\mu^-$ while photons are reconstructed with a calorimetric measurements. χ_c candidates are observed in the kinematic range $p_T^{\chi_c} > 10$ GeV and rapidity $|\, y_{\chi c}\, | < 2.4$. An extended unbinned maximum likelihood fit is performed to the invariant mass difference of the $\mu^+\mu^-$ and $\mu^+\mu^-\gamma$ systems to yield 2960 $\pm$ 120 (stat.) $\pm$ 90 (syst.) χ_{c1} and χ_{c2} candidates. The result of a simultaneous fit to the signal sample and background sample is shown in Figure 2. The small mass difference between the two χ_c states is comparable to the achievable mass resolution, which is dominated by the photon energy resolution.

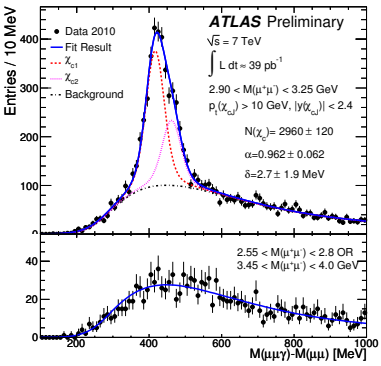

Figure 2: $\chi_c \to J/\psi\gamma$ decays. The result of a simultaneous fit to the signal selection (top) and background (J/ψ sideband) selection (bottom). The individual signal components are shown (dashed lines).

4 Measurement of the centrality dependence of J/ψ yields and observation of Z production in lead-lead collisions

A centrality-dependent suppression has been observed in the yield of J/ψ mesons produced in the collisions of lead ions in ATLAS [4]. In a sample of lead-lead collisions at a nucleon-nucleon centre of mass energy $\sqrt{s_{NN}} = 2.76$ TeV, corresponding to an integrated luminosity of about 6.7 μb^{-1}, J/ψ mesons are reconstructed via their decays to $\mu^+\mu^-$ pairs. The measured J/ψ yield, normalized to the number of binary nucleon-nucleon collisions, is found to significantly decrease from peripheral (glancing) to central (head-on) collisions, as shown in Figure 3. The centrality dependence is found to be qualitatively similar to the trends observed at previous, lower energy experiments. The same sample is used to reconstruct Z bosons in the $\mu^+\mu^-$ final state, and a total of 38 candidates are selected in the mass window of 66 to 116 GeV. No centrality-dependent supression is seen in the Z boson yield, as expected. This analysis provides the first results on J/ψ and Z production in lead-lead collisions at the LHC.

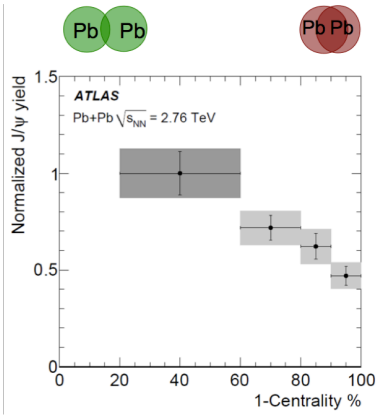

Figure 3: The measured J/ψ yield, normalized to the number of binary nucleon-nucleon collisions, is found to significantly decrease from peripheral to central collisions.

5 Measurement of the Υ(1S) Production Cross-Section

A measurement of the cross-section for $\Upsilon(1S) \to \mu^+\mu^-$ production is made as a function of the $\Upsilon(1S)$ transverse momentum, where both muons have $p_T > 4$ GeV and $|\eta| < 2.5$. The results, as shown in Figure 4, are based on an integrated luminosity of 1.13 pb^{-1} [5]. When the cross-section measurement is compared to theoretical predictions, it agrees to within a factor of two with a prediction based on the NRQCD model including colour-singlet and colour-octet matrix elements as implemented in PYTHIA while it disagrees by up to a factor of ten with the NLO prediction based on the Colour Singlet Model. This measurement is independant of the unknown Υ spin-alignment and as such offers a precise test of theoretical descriptions of quarkonium production.

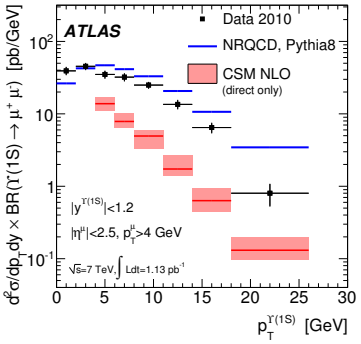

Figure 4: Υ(1S) cross-section as function of Υ transverse momentum for $|y_{\Upsilon(1S)}| < 1.2$

6 Observation of a New $\chi(b)$ State in Radiative Transitions to Υ(1S) and Υ(2S)

The $\chi_b(nP)$ quarkonium states are studied using a data sample corresponding to an integrated luminosity of 4.4 fb^{-1}. These states are reconstructed through their radiative decays to Υ(1S,2S) with $\Upsilon \to \mu^+\mu^-$ [6]. Photons are reconstructed with both calorimetric measurements (unconverted) and ID tracking (converted photons). In addition to the mass peaks corresponding to the decay modes χ_b(1P,2P)$\to \Upsilon(1S)\gamma$, a new structure centered at a mass of 10.530 ± 0.005 (stat.) $\pm$ 0.009 (syst.) GeV is also observed, in both the $\Upsilon(1S)\gamma$ and $\Upsilon(2S)\gamma$ decay modes. This is interpreted as the χ_b(3P) system. The mass difference $m(\mu^+\mu^-\gamma) - m(\mu^+\mu^-)$ distributions are shown in Figure 5.

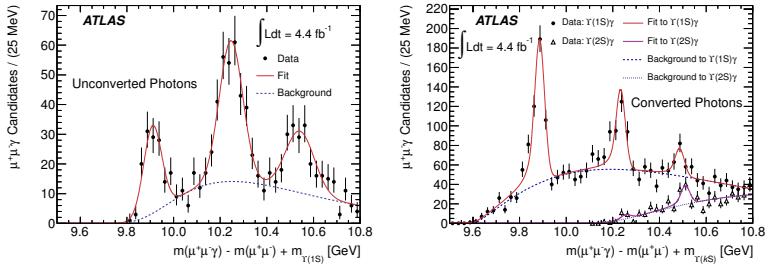

Figure 5: The mass distribution of $\chi(b)(nP) \to \Upsilon(1S)\gamma$ candidates for unconverted photons reconstructed using the electromagnetic calorimeter (left). The mass distributions of $\chi(b)(nP) \to \Upsilon(kS)\gamma$ (k = 1, 2) candidates formed using converted photons and been reconstructed in the ID (right).

7 Conclusions

In the first year of 7 TeV data-taking ATLAS has observed and measured charmonium and bottomonium states, including a new χ_b state. The production of heavy quarkonium provides particular insight into QCD theory as its mechanisms of production operate at the boundary of the perturbative and non-perturbative regimes. These measurements provide input towards an improved understanding and theoretical description of QCD.

References

[1] G. Aad *et al.* [ATLAS Collaboration], JINST **3** (2008) S08003.

[2] G. Aad *et al.* [ATLAS Collaboration], Nucl. Phys. B **850** (2011) 387 [arXiv:1104.3038 [hep-ex]].

[3] G. Aad *et al.* [ATLAS Collaboration], ATLAS-CONF-2011-136, https://cdsweb.cern.ch/record/1383839.

[4] G. Aad *et al.* [ATLAS Collaboration], Phys. Lett. B **697** (2011) 294 [arXiv:1012.5419 [hep-ex]].

[5] G. Aad *et al.* [ATLAS Collaboration], Phys. Lett. B **705** (2011) 9 [arXiv:1106.5325 [hep-ex]].

[6] G. Aad *et al.* [ATLAS Collaboration], Phys. Rev. Lett. **108** (2012) 152001 [arXiv:1112.5154 [hep-ex]].

Measurements of Quarkonium Production at CMS

Daniele Fasanella

University and INFN of Bologna

DOI: http://dx.doi.org/10.3204/DESY-PROC-2012-02/238

Recent quarkonium results obtained at the CMS experiment in proton-proton collisions at a centre-of-mass energy of 7 TeV are presented. These measurements include the differential production cross sections of prompt and non-prompt J/ψ and $\psi(2S)$ mesons in a wide range of transverse momentum and rapidity, which are compared to theory calculations. The measurement of the differential production cross sections of $\Upsilon(1S)$, $\Upsilon(2S)$, and $\Upsilon(3S)$ as a function of transverse momentum and rapidity. In addition, the reconstruction of the radiative decay of the $\chi_c(nP)$ states is demonstrated. Finally, results obtained from studies of the X(3872) state are described.

1 Introduction

The description of the process of quarkonium production is a challenge to theory, since it involves both the production of the quark system and the formation of the bound state. Significant progress has been made over the last decade, from both the experimental and the theoretical sides, and the experiments at the LHC provide great opportunities to further extend our understanding of quarkonia.

The Compact Muon Solenoid (CMS) has been collecting data for quarkonia using triggers based on the presence of two identified muons. In the year 2010 an integrated luminosity of 40 pb^{-1} at $\sqrt{s} = 7$ TeV was collected at peak instantaneous luminosities of up to 2×10^{32} cm^{-2} s^{-1}. The 2011 data taking period was characterized by a steep increase of the LHC instantaneous luminosity and the total integrated luminosity recorded was about 5 fb^{-1}. While in 2010 it was possible to operate an inclusive two-muon trigger configuration, in 2011, to cope with the higher instantaneous luminosity and event rates, dedicated trigger paths were implemented for each analysis.

2 S-Wave Quarkonium Production Cross Sections

In CMS, the S-wave charmonium states (J/ψ and $\psi(2S)$ and $\Upsilon(nS)$) are reconstructed in their decays into a pair of opposite-charged muons. The differential cross section is measured as

$$\frac{\mathrm{d}^2\sigma}{\mathrm{d}p_\mathrm{T}\mathrm{d}y}(Q\overline{Q})\cdot\mathcal{B}(Q\overline{Q}\to\mu^+\mu^-) = \frac{N_\mathrm{signal}(Q\overline{Q})}{\int L\,\mathrm{d}t\cdot A\cdot\epsilon\cdot\Delta p_\mathrm{T}\cdot\Delta y} \quad . \tag{1}$$

The yield $N_\mathrm{signal}(Q\overline{Q})$ is extracted using unbinned maximum-likelihood fits to the dimuon invariant mass spectra, separately in different intervals of transverse momentum (p_T) and

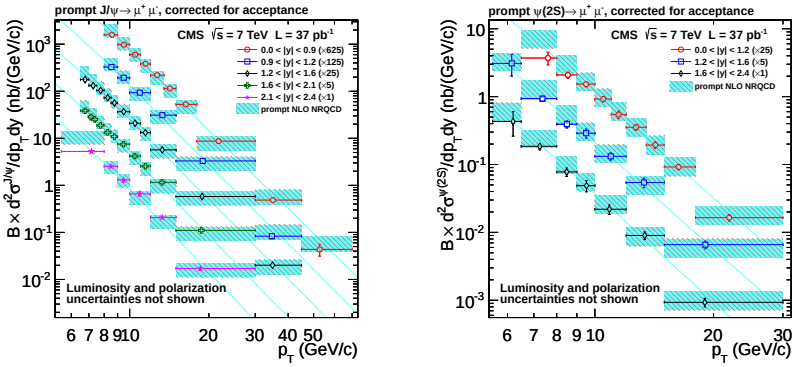

Figure 1: Measured differential cross section for prompt J/ψ and ψ(2S) production (left and right, respectively) as a function of p_{T} for different rapidity bins. The coloured (dark) bands indicate the theoretical predictions from NRQCD calculations.

rapidity(y). The acceptance correction A reflects the geometrical coverage of the CMS detector and the kinematic reach of the muon trigger and reconstruction. The muon efficiency ϵ is measured from data for muons in the acceptance, in several ($p_{\mathrm{T}}^{\mu}\eta^{\mu}$) bins, and is based on the tag-and-probe method, using independent triggers. Different assumptions of the - as yet unmeasured - polarization states of the quarkonia, lead to changes of the acceptance, and consequently the measured cross sections, of order 20%.

The J/ψ and ψ(2S) measurement [1] has been performed using 37 pb^{-1} of data collected in 2010. To estimate the prompt component, where the $c\bar{c}$ system is produced directly, from the non-prompt component, originating from B-hadron decays, two-dimensional fits to the lifetime spectra are performed [2]. In the fits the dimuon invariant mass and the "pseudo proper decay length" are used. The latter is defined as the most probable value of the transverse distance between the dimuon vertex and the primary vertex, corrected by the transverse Lorentz-boost of the charmonium.

The measured prompt and non-prompt cross sections for the J/ψ and the ψ(2S) states are shown in Figures 1 and 2 as a function of p_{T}, for the various rapidity bins. The measurements are compared with theoretical predictions from NRQCD [3] and from FONLL [4]. For the prompt case agreement is found for both J/ψ and the ψ(2S). This is remarkable as the contributions from feed-down from P-wave charmonia is expected to be significantly larger for the J/ψ.

In the non-prompt case, depicted in Figure 2, general agreement is found for the J/ψ at low values of transverse momentum, p_{T} <30 GeV/c. However, towards large p_{T} the predictions overestimate the measured differential cross sections. The shape of the ψ(2S) distribution is described over the entire p_{T} range, but an overall shift in normalization is observed.

The Υ(nS) production cross section measurement [5] is based on 3 pb^{-1} of 2010 data. The measured dimuon spectrum is shown in Figure 3-left. The measured differential Υ(nS) production cross sections are shown in Figure 3-center, for the rapidity interval $|y| < 2$. In the same figure (right) the corresponding cross section ratios of Υ(2S) and Υ(3S) with respect to Υ(1S) for the same rapidity region are presented.

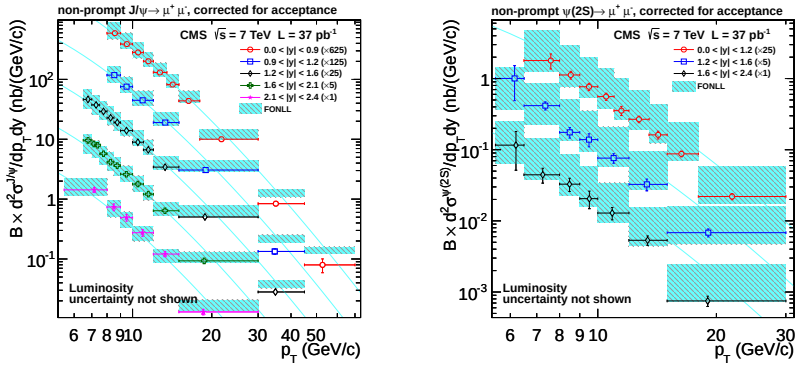

Figure 2: Measured differential cross section for non-prompt J/ψ and ψ(2S) production (left and right, respectively) as a function of p_{T} for different rapidity bins. The coloured (dark) bands indicate the theoretical predictions from FONLL calculations.

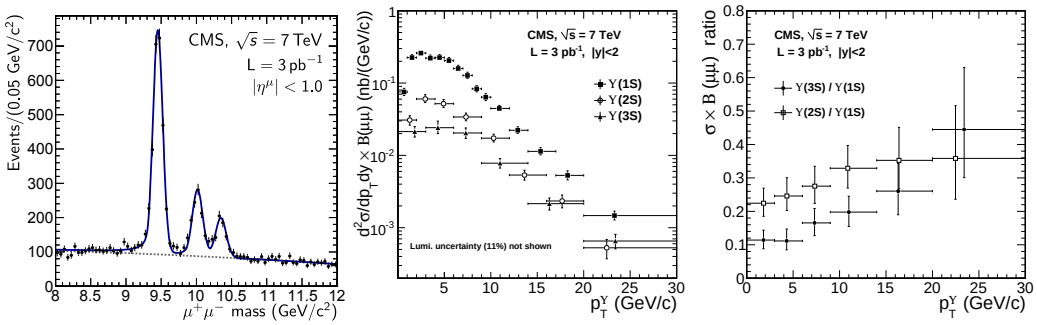

Figure 3: Left: The dimuon invariant-mass distribution in the vicinity of the Υ(nS) in the central region of the detector. Center: Υ(nS) differential cross sections for $|y| < 2$ Right: Cross-section ratios for Υ(nS) states as a function of p_{T} for $|y| < 2$

3 Reconstruction of χ_c states

The CMS experiment has also made measurements of the P-wave states χ_{c1} and χ_{c2}. These measurements are important for a more thorough understanding of quarkonium production as such, and, in particular, for the determination of the contribution from feed-down to the prompt production of S-wave states, presented above. The χ_c states are reconstructed in their radiative decays into a J/ψ and a photon, where the J/ψ further decays into two muons, and the photons are reconstructed through their conversions into electron-positron pairs. This photon reconstruction method yields a very good photon momentum resolution and consequently a separation of the χ_{c1} and χ_{c2} states in their invariant mass spectrum. This is demonstrated in Figure 4-left, showing a mass distribution of data corresponding to an integrated luminosity of 1.1 fb^{-1} recorded in 2011 [7].

4 Measurement of the $X(3872)$ state

The $X(3872)$ state is the first unexpected state discovered in the charmonium spectroscopy and is still the most intriguing. In CMS the state was measured in the decay channel $J/\psi\,\pi^+\pi^-$ using 40 pb^{-1} of 2010 data [6]. For the reconstruction of the $J/\psi\,\pi^+\pi^-$ system, the J/ψ meson candidates are combined with pairs of oppositely charged pion track candidates with transverse momentum larger than 400 MeV. The dimuon mass is constrained to the J/ψ one and candidates are kept in the kinematic region $p_{\rm T} > 8$ GeV and $|y| < 2.2$. The resulting $J/\psi\,\pi^+\pi^-$ spectrum is shown in Fig. 4.

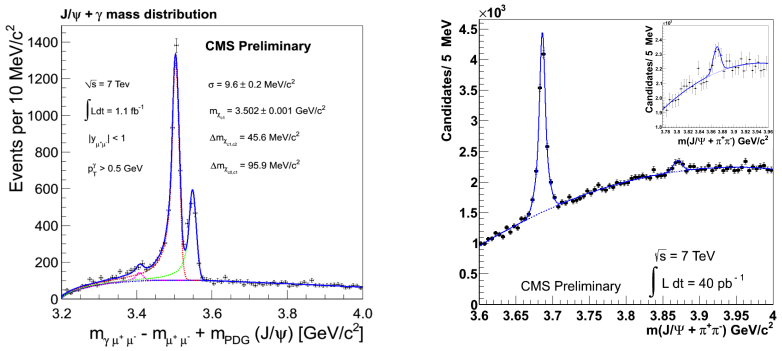

Figure 4: Left: Mass distribution of the $\chi_c \to J/\psi + \gamma$ candidates. Right: $J/\psi\pi^+\pi^-$ invariant mass spectrum. The insert shows the mass region around the $X(3872)$.

A measurement of the ratio of $\sigma \cdot \mathcal{BR}$ between X(3872) and ψ(2S) is performed correcting the observed signal yields for acceptance and efficiencies, as estimated from simulations. The measured ratio is $0.087 \pm 0.017(stat.) \pm 0.009(syst.)$. A more detailed measurement of this ratio, as a function of $p_{\rm T}$, using the 2011 dataset, is expected soon.

5 Summary

CMS has delivered a significant first set of quarkonium production results using the first-year run of the LHC and paved the way for a wide range of new studies with 2011 statistic.

References

[1] S. Chatrchyan *et al.* [CMS Collaboration], JHEP **1202**, 011 (2012) [arXiv:1111.1557 [hep-ex]].

[2] V. Khachatryan *et al.* [CMS Collaboration], Eur. Phys. J. C **71**, 1575 (2011) [arXiv:1011.4193 [hep-ex]].

[3] Y. -Q. Ma, K. Wang and K. -T. Chao, Phys. Rev. Lett. **106**, 042002 (2011) [arXiv:1009.3655 [hep-ph]].

[4] M. Cacciari, S. Frixione and P. Nason, JHEP **0103**, 006 (2001) [hep-ph/0102134].

[5] V. Khachatryan *et al.* [CMS Collaboration], Phys. Rev. D **83**, 112004 (2011) [arXiv:1012.5545 [hep-ex]].

[6] CMS collaboration, CMS-PAS-BPH-10-018 (2011).

[7] CMS collaboration, CMS-DP-2011-011 (2011).

Charmonium Production in pp Collisions with ALICE

Ionut-Cristian Arsene[1] for the ALICE Collaboration

[1]Research Division and ExtreMe Matter Institute EMMI, GSI Helmholtzzentrum für Schwerionenforschung, Darmstadt, Germany

DOI: http://dx.doi.org/10.3204/DESY-PROC-2012-02/152

The ALICE Collaboration studies the production of J/ψ meson in pp collisions at the center-of-mass energies of 2.76 and 7 TeV at mid- and forward-rapidity. Inclusive production cross-sections are presented as a function of the collision energy, rapidity and transverse-momentum. The J/ψ polarization measurements in the helicity and Collins-Soper frames is discussed. A novel result on the correlation between the collision charged particle multiplicity and J/ψ yield is also shown.

1 Introduction

Due to their large mass, the heavy quark pairs are considered to be produced in hard scatterings of partons which can be described perturbatively. However, the bound states of heavy quark pairs are formed via soft non-perturbative processes. Because of this interplay between the perturbative and non-perturbative aspects, quarkonium production is a unique and a very important testing case for QCD. Various theoretical approaches, recently reviewed in [1, 2] were proposed to describe the data. However the consistent description of both the differential production cross-sections and the polarization proved to be difficult to achieve.

2 Data analysis

	2.76 TeV	7 TeV
$\|y\| < 0.9$	1.1 nb^{-1}	5.6 nb^{-1}
$2.5 < y < 4$	19.9 nb^{-1}	15.6 nb^{-1}

Table 1: Integrated luminosity, L_{int}, used in the data analysis at mid- and forward-rapidity.

ALICE [3] studied the production of J/ψ mesons down to zero transverse-momentum, p_t, using their decays into e^+e^- at mid-rapidity ($|y| < 0.9$) and into $\mu^+\mu^-$ at forward-rapidity ($2.5 < y < 4$). In this report we present results on the J/ψ production in pp collisions at $\sqrt{s}$ =2.76 TeV and 7 TeV. The integrated luminosities of the analyzed data samples at the two different rapidity intervals are given in Table 1. A detailed description of the analysis and the detectors used for reconstructing the electron and muon candidates can be found in [4, 5]. The electrons and muons passing the analysis cuts are combined in opposite-sign (OS) pairs to construct an invariant mass distribution. In the di-electron channel (at mid-rapidity) the signal is obtained by subtracting the background which is estimated using the like-sign (LS) pairs [4] or track rotations [6]. In the di-muon channel (at forward-rapidity)

the signal shape is described by a Crystal Ball function while the background is parameterized using the sum of two exponentials [4].

In order to extract cross-sections, the raw signal counts extracted from the invariant mass distribution need to be corrected for triggering efficiencies, kinematical acceptance and reconstruction efficiencies. This is performed using a Monte-Carlo procedure based on generating a large sample of J/ψ mesons embedded in simulated pp events. All the particles are then transported through the realistic ALICE detector setup constructed in GEANT [7].

3 Results

Figure 1 presents the inclusive differential cross-section $d^2\sigma_{J/\psi}/dp_t dy$ in pp collisions at $\sqrt{s}$ =7 TeV [4] and 2.76 TeV [5]. At 7 TeV the p_t dependent cross-sections at mid-rapidity and forward-rapidity are shown together with the results from CMS [8] and ATLAS [9] at mid-rapidity and LHCb [10] at forward-rapidity. At mid-rapidity, the p_t coverage of the ALICE results is

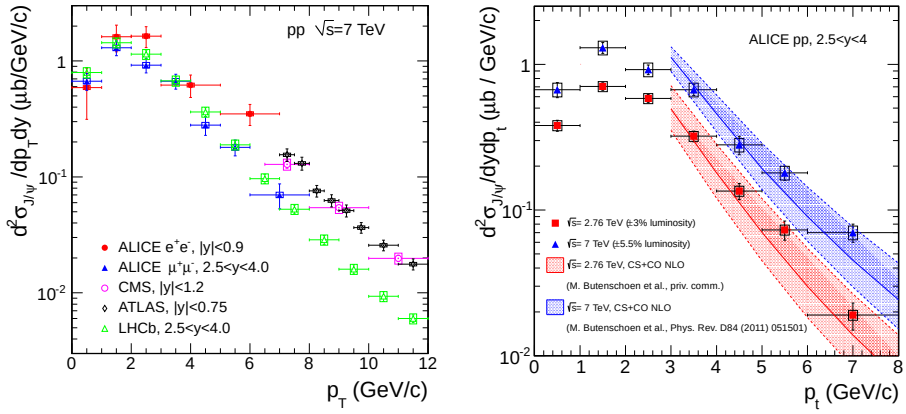

Figure 1: Differential cross-section $d^2\sigma_{J/\psi}/dp_t dy$ in pp collisions at 7 TeV [4] and 2.76 TeV [4]. The model calculations are from [11].

complementary to that from CMS and ATLAS. At forward-rapidity the ALICE results are in agreement with those from LHCb.

The inclusive cross-section at forward-rapidity in pp collisions at $\sqrt{s}$ =2.76 TeV and 7 TeV is shown in the right panel of Figure 1. The results at both energies are compared with the predictions of a NRQCD calculation [11] which includes both color singlet and color octet terms at NLO.

The wide kinematic coverage of ALICE, which is unique among the LHC experiments, allows the extraction of the p_t integrated J/ψ cross-section. In the left panel of Figure 2 we present the $d\sigma_{J/\psi}/dy$ at $\sqrt{s}$ =2.76 and 7 TeV. The results refer to the inclusive J/ψ production which is a sum of the direct component and of J/ψ resulting from decays of higher-mass charmonium states (mainly the χ_{c1}, χ_{c2} and $\Psi(2S)$ states) and from b-hadron decays. The contribution from higher-mass charmonium states measured at lower energies [12, 13] amounts to ≈33% while the contribution from b-hadron decays is 10-15% in the p_t range covered by ALICE [10, 14].

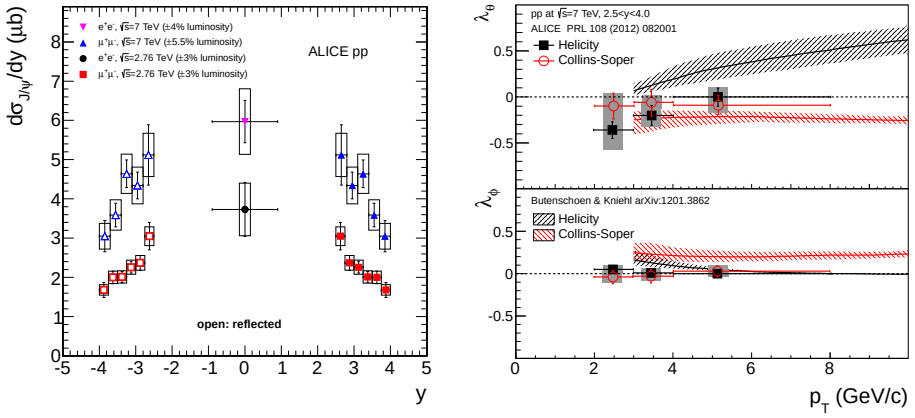

Figure 2: Left: $d\sigma_{J/\psi}/dy$ in pp collisions [5]. Right: Polarization parameters λ_θ and λ_ϕ as a function of p_t for inclusive J/ψ measured in the helicity and Collins-Soper frames [17].

The J/ψ is a spin-1 boson allowing for three degenerated states corresponding to projections of the angular momentum $J_z = \pm 1$ (transversal polarization) and $J_z = 0$ (longitudinal polarization).

The observed polarization is a superposition of the polarization from all the production mechanisms thus making this measurement a very important constraint for theoretical calculations. Existing models have difficulties in describing at the same time both the J/ψ production cross-section and the polarization. In particular NRQCD at leading order predicts for high-p_t J/ψ a large transverse polarization at CDF energies [15].

ALICE measured the J/ψ polarization at forward-rapidity in the helicity ($z-$axis is the J/ψ own momentum direction in the center-of-mass frame of the pp collision) and Collins-Soper ($z-$axis is the bisector of the angle between the direction of one beam and the opposite of the direction of the other one, in the rest frame of the J/ψ) frames. The measured angular distribution of the decay leptons is parameterized using the general form [16]

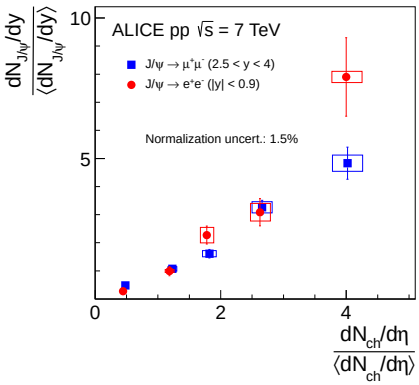

Figure 3: J/ψ yield as a function of the charged particle density at mid-rapidity [6].

$$W(\theta,\phi) \approx \frac{1}{3+\lambda_\theta}(1+\lambda_\theta \cos^2\theta + \lambda_\phi \sin^2\theta \cos 2\phi + \lambda_{\theta\phi} \sin 2\theta \cos\phi),$$

where θ (ϕ) are the polar (azimuthal) angles. The λ_θ, λ_ϕ and $\lambda_{\theta\phi}$ are parameters extracted from data which quantify the degree of polarization. The right panel of Figure 2 shows the ALICE results on λ_θ and λ_ϕ for inclusive J/ψ at forward-rapidity [17]. In both reference frames all the parameters are compatible with zero. Recent NLO calculations within the NRQCD factorization [18] have shown good agreement with the ALICE results.

To investigate further the J/ψ production mechanisms, the yield was measured as a function of the charged particle pseudo-rapidity density $dN_{ch}/d\eta$. Figure 3 presents the relative J/ψ yield at mid- and forward-rapidity as a function of the relative charged particle density at mid-rapidity [6]. The results indicate that the J/ψ production at both mid- and forward-rapidity tends to be accompanied by the production of many other charged hadrons. A possible reason for the observed results could be multiple partonic interactions [19, 20].

4 Conclusions

We presented results obtained by the ALICE Collaboration on J/ψ production in pp collisions at $\sqrt{s}$ =2.76 and 7 TeV. The inclusive cross-sections as a function of p_t and rapidity were shown. The NLO NRQCD calculations show a good agreement with the ALICE results at forward-rapidity. The measured polarization parameters λ_θ and λ_ϕ are compatible with zero. We have also shown that the relative J/ψ yields at mid- and forward-rapidity increase linearly with the charged particle density at mid-rapidity.

5 Acknowledgement

This work was supported by the Helmholtz Alliance Program of the Helmholtz Association, contract HA216/EMMI "Extremes of Density and Temperature: Cosmic Matter in the Laboratory".

References

[1] N. Brambilla *et al.* Eur.Phys.J. **C71** (2011) 1534
[2] J. P. Lansberg Eur.Phys.J. **C61** (2009) 693
[3] K. Aamodt *et al.* [ALICE Collaboration] JINST **3** (2008) S08002
[4] K. Aamodt *et al.* [ALICE Collaboration] Phys.Lett. **B704** (2011) 442-455
[5] B. Abelev *et al.* [ALICE Collaboration] arXiv:1203.3641
[6] B. Abelev *et al.* [ALICE Collaboration] Phys.Lett. **B712** (2012) 165-175
[7] GEANT - Detector description and simulation tool, CERN Program Library Long Write-up W5013, CERN Geneva
[8] V.Khachatryan *et al.* [CMS Collaboration] Eur.Phys.J. **C71** (2011) 1575
[9] G.Aad *et al.* [ATLAS Collaboration] Nucl.Phys. **B850** (2011) 387
[10] R.Aaij *et al.* [LHCb Collaboration] Eur.Phys.J. **C71** (2011) 1645
[11] M. Butenschoen and B. A. Kniehl Phys.Rev. **D84** (2011) 051501 and priv. comm.
[12] P. Faciolli *et al.* JHEP **0810** (2008) 004
[13] A. Adare *et al.* [PHENIX Collaboration] arXiv:1105.1966
[14] B. Abelev *et al.* [ALICE Collaboration] arXiv:1205.5880
[15] A. Abulencia *et al.* [CDF Collaboration] Phys.Rev.Lett. **99** (2007) 132001
[16] P. Faciolli *et al.* Eur.Phys.J. **C69** (2010) 657
[17] B. Abelev *et al.* [ALICE Collaboration] Phys.Rev.Lett. **108** (2012) 082001
[18] M. Butenschoen and B. A. Kniehl Nucl.Phys.Proc.Suppl. **222-224** (2012) 151-161 arXiv:1201.3862
[19] M. Strikman Phys.Rev. **D84** (2011) 011501
[20] E. G. Fereiro and C. Pajares arXiv:1203.5936

J/ψ Photoproduction in ultra-peripheral Au+Au collisions measured by RHIC-PHENIX

Akihisa Takahara[1,2] for the PHENIX collaboration

[1]University of Tokyo, Japan
[2]RIKEN,Japan

DOI: http://dx.doi.org/10.3204/DESY-PROC-2012-02/114

Ultra Peripheral collision is defined as heavy ion collision its impact parameter twice larger than the nuclear radius. Then there are no nuclear overlap. Strong interaction is impossible. Relativistic moving ions should emit quasi real photons to transverse direction with maximum energy γ/R. Ions can interact through photon-Ion (coherent) and photon-nucleus (incoherent), and photon photon collisions,

Measurement of vector meson photo production is a sensitive probe of gluon distribution in nuclei. At RHIC energy, measurement of J/ψ photo production corresponds to x $\cong$ 0.015 and Q^2 =2.5 GeV/c^2. In the kinematic region, nuclear shadowing plays an important role and that still have large uncertainty.

PHENIX measured J/ψ photo production in Au+Au collisions at $\sqrt{s_{NN}}$ = 200 GeV in 2004, 2007 and 2010. PHENIX has detectors at central (0.35> $|y|$) and forward (1.2< $|y|$ <2.2) rapidity. The 2004 integrated cross section result at central rapidity was already published. 2004 integrated cross section result is consistent with all theoretical predictions within 1σ statistical error.

2007 and 2010 higher statistics data make it possible to measure differential cross section and to improve statistical error associated with integrated luminosity Moreover improvement of trigger arrows forward rapidity UPC measurement. In this talk, integrated and differential cross section of UPC J/ψ at central rapidity preliminary results in 2007 and forward rapidity in 2010 will be shown.

1 Introduction

We present measurements of the photoproduction of J/ψ in ultra-peripheral Au+Au collisions at $\sqrt{s_{NN}}$ = 200 GeV at RHIC. An Ultra-Peripheral Collision (UPC) is a collision in which an impact parameter is greater than the sum of nuclear radii. Measurement of J/ψ in UPC serves as a considerable role for determining gluon density in nuclei at small Bjorken x, where the gluon density is expected to be suppressed due to gluon shadowing effect and has not been constrained by the theoretical calculation [1, 2, 3]. PHENIX has measured integrated cross section of J/ψ in UPC in 2004 [4]. However, due to small statistics, it was very difficult to constrain the theoretical calculations on gluon distribution in nuclei. In 2007 and 2010, PHENIX collected 527.45 ± 23 μb^{-1} and 1390.05 ± 37.3 μb statistics of Au+Au collisions, respectively. Measurement of J/ψ photoproduction in UPC as a function of transverse momentum p_T and rapidity y has been done by using data taken in 2007 and 2010, where 3 and 9 times larger

statistics were achieved compared to that in 2004.

2 Analysis

The requirement of UPC events selection are that there are only two electron (muon) tracks in central arms (forward muon spectrometer) and that at least one neutron is detected. Figure 1, 2 shows invariant mass spectra of dielectrons and dimuons in UPC events, respectively. The number of measured J/ψ is corrected by the detection efficiency, trigger efficiency, and integrated luminosity to extract the invariant cross section.

Figure 3 shows the preliminary results of the p_T distribution of J/ψ cross section in UPC, where black, blue and red correspond to the cross section at mid-rapidity with one neutron tagged by zero degree calorimeter(ZDC), -2.2<y<-1.2 and 1.2<y<2.2 with two neutron tagged at both sides of ZDC, respectively. From Fig.3 , cross section at mid-rapidity in low p_T is very large compared to that at forward-rapidity. This is due to the dominance of coherent J/ψ production at low p_T in mid-rapidity, while incoherent production is dominated at forward rapidity. The upper limit of integrated cross section for coherent J/ψ production was extracted to be 46.7±13±15 μb^{-1}. The value was found by integration from 0 to 0.4.

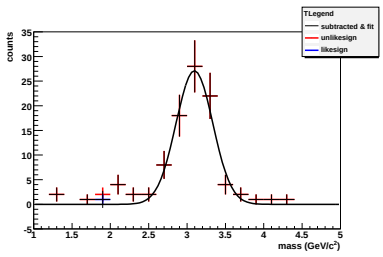

Figure 1: 2010 North arm (dimuon) invariant mass yields.

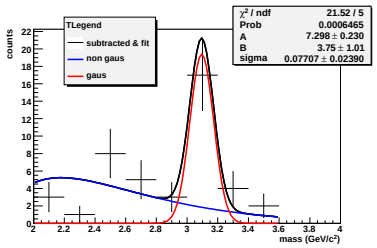

Figure 2: 2007 central arm (dielectron) invariant mass yields.

Since the cross section without any nuclear effects such as gluon shadowing is expected to be 118μb [5]. Figure 4 shows the cross section as a function of y, where both side neutrons are tagged. The comparison with the theoretical calculations is underway.

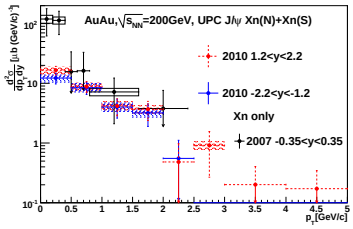

Figure 3: PHENIX 2010 dimuon (Red and Blue) and 2007 dielectron(black) UPC J/ψ $\frac{d^2\sigma}{dp_T dy}$. Dielectron distribution has significant 0 p_T peak, but same peak can't be find from dimuon distribution.

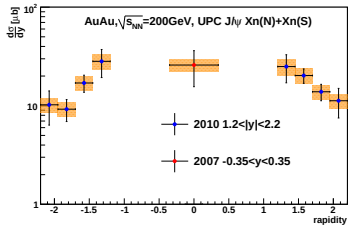

Figure 4: PHENIX 2010 RUN UPC J/ψ $\frac{d\sigma}{dy}$ distribution

3 Summary

Measurement of J/ψ in UPC has been performed by using 2007 and 2010 data. From the cross section as a function of p_T, the coherent production of J/ψ can be seen and integrated cross section is suppressed by a factor of 0.6 compared to the value without any nuclear effects. Further studies for both neutron tagging and theoretical understanding are on going.

4 Bibliography

References

[1] G. Baur, K. Hencken, D. Trautmann, S. Sadovsky, and Y. Kharlov: Phys. Rept. B, 359 (2002).

[2] C. A. Bertulani, and S. R. Klein, J. Nystrand, Ann. Rev. Nucl. Part. Sci. B, 271 (2005).

[3] A. Baltz et al.: Phys. Rept. B 171 (2008).

[4] S. Afanasiev PHENIX Collaboration: Phys. Lett. B 321(2009).

[5] A. L. Ayala Filho, V. P. Goncalves, and M. T. Griep Phys. Rev. C 78, 044904 (2008) G. Baur, K

Production of Heavy Flavor and Quarkonia at CDF

Manuel Kambeitz[1] on behalf of the CDF collaboration

[1]Karlsruhe Institute of Technology (KIT), Institut für Experimentelle Kernphysik, Campus Süd, Postfach 69 80, 76128 Karlsruhe, Germany

DOI: http://dx.doi.org/10.3204/DESY-PROC-2012-02/202

The production cross sections and polarizations of Υ mesons in hadron collisions are important observables with which to test different QCD models at low energy. This article describes the CDF measurement of the spin alignment of the $\Upsilon(1S)$, $\Upsilon(2S)$ and $\Upsilon(3S)$ states produced at the Tevatron using a data sample of 6.7 fb^{-1}. Compared to earlier CDF measurements, it extends the analysis technique in several ways. A new method to estimate the background angular distribution is used, a full angular analysis is performed for the first time and a consistency check is carried out by using two different reference frames. It is also the first measurement of the spin alignment of the $\Upsilon(3S)$.

1 Introduction

The decays of heavy quarkonia to $\mu^+\mu^-$ have been studied at hadron colliders for almost four decades. However, describing their production accurately based on QCD proved to be challenging and new models had to accommodate the surprisingly large measured J/ψ and Υ production cross sections [1, 2]. These models make specific predictions about the production polarization of the quarkonia, but these are generally in poor agreement with experimental measurements.
Moreover, there are discrepancies between results obtained by different experiments [3, 4]. The reason was thought to be possibly due to different detector acceptances, combined with the measurement of the distribution of only the polar angle of the positive muon in a reference frame that could not easily be transformed between different experiments [7].
In fact, the distribution of both polar and azimuthal angles of the positive muon from an Υ decay can be written as

$$\frac{dN}{d\Omega} \sim 1 + \lambda_\theta \cos^2\theta + \lambda_\phi \sin^2\theta \cos 2\phi + \lambda_{\theta\phi} \sin 2\theta \cos\phi \equiv w(\cos\theta, \phi; \vec{\lambda})$$

in the Υ rest frame. While previous experiments have only measured the parameter λ_θ, it is possible that Υ polarization is present and manifests itself by large values of λ_ϕ $\lambda_{\theta\phi}$, while λ_θ is close to zero.
Measuring Υ mesons instead of J/ψ has the advantage that they cannot originate for B meson decays, while limitations are imposed by χ_b feed-down.

2 Data sample

The dataset used in the analysis described here [5] corresponds to an integrated luminosity of 6.7 fb^{-1} of proton-antiproton collisions at the Tevatron at a center of mass energy of 1.96 TeV recorded by the CDF II detector [6] and contains 550 000 $\Upsilon(1S)$, 150 000 $\Upsilon(2S)$ and 76 000 $\Upsilon(3S)$ decays to $\mu^+\mu^-$ decays. It was collected with dimuon triggers, requiring a pair of oppositely charged muons in the invariant mass range $8 < m(\mu^+\mu^-) < 12$ GeV/c^2, among them one central muon with $p_T > 4$ GeV/c and an either central ($|\eta| < 0.6$) or forward ($0.6 < |\eta| < 1$) muon with $p_T > 3$ GeV/c.

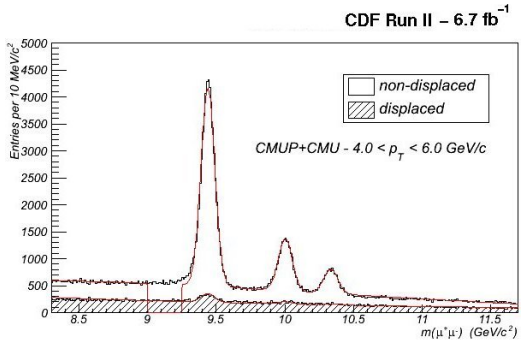

Figure 1: Dimuon mass spectra for the prompt and the displaced sample. The region from 9 to 9.25 GeV/c^2 is not fitted in order to reduce sensitivity to the modeling of final state radiation.

From this dataset, two samples are selected: the prompt or non-displaced sample, where both muons originate from the primary vertex, and the displaced sample, where at least one muon has an impact parameter of more than 150 μm. As can be seen from Fig. 1, the prompt sample contains most of the signal but also contains a significant level of background. The background is expected to be dominated by semileptonic decays of B hadrons which will have the same properties in the displaced sample, in which $\Upsilon(nS)$ decays are highly suppressed.
Furthermore, the shape of the background component in the dimuon mass is identical in both samples, so that the amount of background in the prompt sample can be constrained by scaling the background distribution observed in the displaced component by a linear function of mass. The displaced sample is more suitable than the mass sideband for extracting the angular distribution of the background, because there is evidence that the properties of muons in the background evolve rapidly with invariant mass and transverse momentum.

3 Analysis method

The analysis is performed separately in 8 ranges of dimuon transverse momentum. The events are analyzed in 12 separate ranges of invariant mass: the three $\Upsilon(1S)$, $\Upsilon(2S)$ and $\Upsilon(3S)$ signal regions and nine more regions containing background.
The number of expected signal events in the 20×36 bins of $(\cos\theta, \phi)$ is proportional to the product of the detector acceptance $\mathcal{A}$, which depends on the geometric coverage of the detector and on the kinematic requirements of the trigger, and the underlying angular distribution w: $dN/d\Omega \sim \mathcal{A}(\cos\theta, \phi) \cdot w(\cos\theta, \phi; \vec{\lambda})$. The signal acceptance is calculated from Monte Carlo

events using the full detector simulation, where the p_T distributions of the Υ states are tuned to match those in the data. Separate acceptance distributions are calculated for the background, where p_T, rapidity and invariant mass distributions are tuned to agree with the observed distributions in the background. The angular analysis is performed both in the s-channel helicity frame and in the Collins-Soper frame.

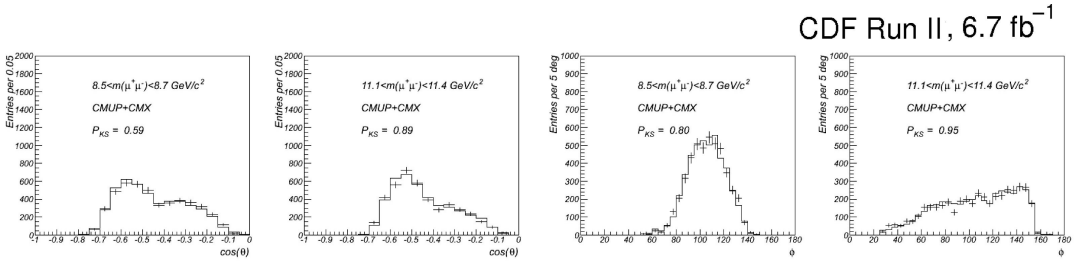

Figure 2: Projections of the angular distributions of prompt (histogram) and displaced samples (error bars) in the lower and upper mass sideband regions in the Collins-Soper frame. The agreement is quantified using the Kolmogorov-Smirnov P-value, shown with each distribution.

Figure 2 shows projections of the angular distribution of the background in the prompt and the displaced sample. They are found to be very similar in both sideband regions, so one can infer that the displaced sample provides a good background description also in the signal region.
The displaced sample is used to describe the background in the prompt sample, while it still contains some signal. Therefore, the fit to determine the polarization parameters $\vec{\lambda}$ is performed simultaneously to the two-dimensional angular distributions of the prompt and the displaced sample in the following way:

$$\frac{dN_p}{d\Omega} \sim \sigma_\Upsilon f_p \mathcal{A}_\Upsilon(\cos\theta,\phi)\cdot w(\cos\theta,\phi;\vec{\lambda}_\Upsilon) + \sigma_d s_p \mathcal{A}_{bkg}(\cos\theta,\phi)\cdot w(\cos\theta,\phi;\vec{\lambda}_{bkg})$$

$$\frac{dN_d}{d\Omega} \sim \sigma_\Upsilon (1-f_p) \mathcal{A}_\Upsilon(\cos\theta,\phi)\cdot w(\cos\theta,\phi;\vec{\lambda}_\Upsilon) + \sigma_d \mathcal{A}_{bkg}(\cos\theta,\phi)\cdot w(\cos\theta,\phi;\vec{\lambda}_{bkg})$$

with the Υ and displaced background yields σ_Υ and σ_d, the fraction of Υ events in the prompt sample f_p and the ratio of background yields in both samples s_p. The scale factor s_p is constrained by fits to the dimuon mass spectrum. In order to facilitate the background description in some p_T and invariant mass ranges, a phenomenological $\cos^4\theta$ term is added to the angular distribution functions for the background.

4 Results

Figure 3 shows the measured parameters λ_θ and λ_ϕ in the s-channel helicity frame. It demonstrates the significant difference between the angular distributions of signal and background and the significant variation of the angular shape of the background over the considered dimuon mass region.
The analysis is performed in both the Collins-Soper and s-channel helicity frames. The rotationally invariant quantity $\tilde{\lambda} = (\lambda_\theta + 3\lambda_\phi)/(1-\lambda_\phi)$ is calculated in each reference frame in bins of p_T for the three Υ states. Ensembles of Monte Carlo simulations indicated that the

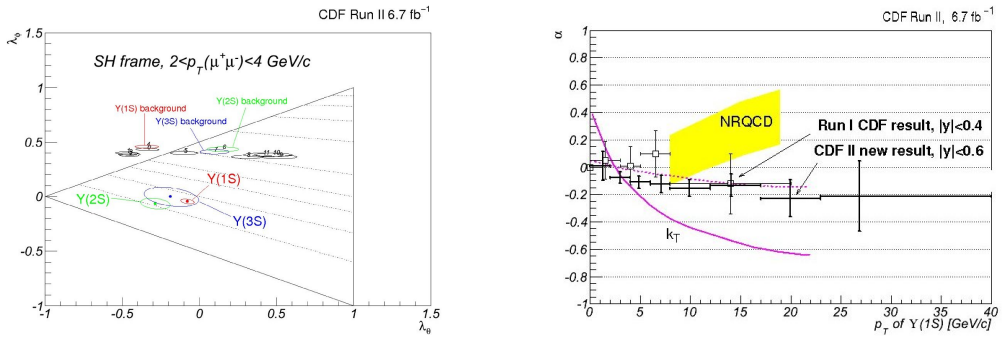

Figure 3: Left: 68% CL regions of λ_θ and λ_ϕ in the s-channel helicity frame for both signal and background in a given p_T range. The triangular region indicates the physical region. Right: Result for λ_θ for the $\Upsilon(1S)$ resonance and comparison with the CDF Run I result.

differences between measurements in both frames are consistent with statistical fluctuations. For the systematic uncertainties, a quadratic function with which to parameterize the prompt scale factor as a function of invariant mass was considered, the statistical contribution of Monte Carlo samples used to calculate the acceptance was calculated, and differences in $\tilde{\lambda}$ measured in the two coordinate frames were propagated into systematic uncertainties on λ_θ and λ_ϕ.

5 Summary

The complete angular distributions of muons from decays of $\Upsilon(1S)$, $\Upsilon(2S)$ and $\Upsilon(3S)$ mesons were analyzed and no evidence for strong polarization over a wide range of p_T has been found. It is the first measurement in three dimensions and the first measurement of the $\Upsilon(3S)$. The measurement for the $\Upsilon(1S)$ can be compared to previously published measurements. It is consistent with a Run I CDF analysis [3] and inconsistent at about the 4.5σ level with a Run II DØ measurement [4].

References

[1] E. Braaten and J. Lee, Phys. Rev. D **63**, 071501(R); P. Cho and A.K. Leibovich, Phys. Rev. D **53**, 150 (1996); **53**, 6203 (1996).

[2] S.P. Baranov and N.P. Zotov, JETP Lett. **86**, 435 (2007).

[3] D. Acosta, et al. (CDF Collab.), Phys. Rev. Lett. **88**, 161802 (2002).

[4] V.M. Abazov, et al. (DØ Collab.), Phys. Rev. Lett. **101**, 182004 (2008).

[5] T. Aaltonen et al. (the CDF Collaboration), Phys. Rev. Lett. **108**, 151802 (2012).

[6] F. Abe, et al., Nucl. Instrum. Methods Phys. Res. A **271**, 387 (1988); D. Amidei, et al., Nucl. Instum. Methods Phys. Res. A **350**, 73 (1994); F. Abe, et al., Phys. Rev. D **52**, 4784 (1995); P. Azzi, et al., Nucl. Instrum. Methods Phys. Res. A **360**, 137 (1995); The CDFII Detector Technical Design Report, Fermilab-Pub-96/390-E

[7] P. Faccioli, C. Lourenço, J. Seixas, and H. K. Wohri, Phys. Rev. Lett. **102**, 151802 (2009); Eur. Phys. J. C **69**, 657 (2010); P. Faccioli, C. Lourenço, and J. Seixas, Phys. Rev. Lett. **105**, 061601 (2010); Phys. Rev. D **81**, 111502(R) (2010).

Quarkonium results from LHCb

Giovanni Sabatino[1]

[1]Università degli studi di Roma "Tor Vergata" and INFN

DOI: http://dx.doi.org/10.3204/DESY-PROC-2012-02/144

During 2010 and 2011 the LHCb experiment [1] has collected a dataset corresponding to an integrated luminosity of 1 fb^{-1} in p-p collisions at $\sqrt{s}$ = 7 TeV. We present results of the quarkonium production studies recently performed at LHCb. The experimental findings are compared with the theoretical predictions and with measurements from other experiments. A good agreement is found with the theory predictions.

1 Introduction

The mechanism for the production of quarkonia in hadronic collisions is not yet completely understood. It is well known that the LO Colour Singlet Model (CSM) leads to predictions of the cross-sections which are in disagreement with the observations at high p_{T}. New theoretical approaches have been proposed in recent years. For example, the Non-Relativistic QCD factorisation formalism, in which Colour Octet diagrams are introduced. Another approach consists in extending the computation of the cross-sections in Colour Singlet Model up to the NNLO. In the Colour Evaporation Model (CEM) instead, the probability of forming a specific quarkonium state is assumed to be independent of the color of the $Q\bar{Q}$ pair. The debate is still open and experimental confirmations from the LHC experiments are needed to determine the reliability of the proposed models.

Open charm can be produced in p-p collisions in association to a J/ψ meson or in association to another open charm hadron. Predictions for the production cross-sections exist and are given by the LO perturbative QCD, where calculations are made for the processes gg $\rightarrow$J/ψJ/ψ [2], gg $\rightarrow$J/$\psi c\bar{c}$ and gg $\rightarrow c\bar{c}c\bar{c}$ [3, 4]. These predictions are affected by uncertainties that can amount to a factor of two due to the selection of the α_s scale. In p-p collisions contributions from other mechanisms are possible, such as Double Parton Scattering (DPS) in which the factorisation of the two PDF is assumed [5, 6], or the intrinsic charm content of the proton (IC) [7]. Since such theories lead to different predictions for double charm(onium) cross-sections, experimental results from the LHC can give helpful hints and strong indications.

2 $\psi(2S)$, χ_c and $\Upsilon(nS)$ production cross-sections

Promptly produced $\psi(2S)$ mesons have not appreciable feed-down from higher mass charmonium states. This facilitates the comparison between the measured cross-section and the theory prediction. $\psi(2S)$ cross-section has been measured at LHCb [8] with an integrated luminosity of 36 pb^{-1}, exploiting the decay channels $\psi(2S) \rightarrow \mu^+\mu^-$ and $\psi(2S) \rightarrow$J/$\psi(\mu^+\mu^-)\pi^+\pi^-$.

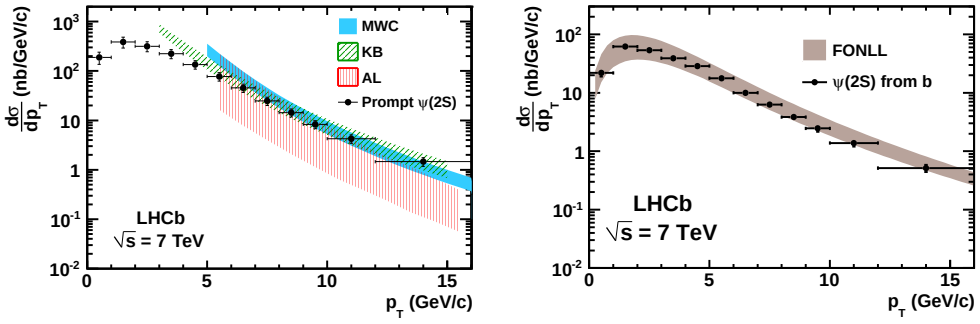

Figure 1: $\psi(2S)$ cross-section as a function of the transverse momentum for prompt mesons (left) and for $\psi(2S)$ originating from b-hadron decays (right) in the rapidity range $2 < y(\psi(2S)) < 4.5$. Experimental results are compared to theoretical predictions (see text).

Figure 1 (left) shows the measured cross-section for prompt $\psi(2S)$ as a function of the transverse momentum in the rapidity range $2 < y(\psi(2S)) < 4.5$. Since the polarisation state of the $\psi(2S)$ mesons is not measured yet, a systematic uncertainty is quoted and assigned to the cross-section. For comparison some theoretical predictions are also plotted: MWC [9] and KB [10] are NLO calculations including Colour Singlet and Colour Octet contributions. AL [11, 12] is a Colour Singlet model including the dominant NNLO terms. $\psi(2S)$ are also produced from b-hadron decays. They can be distinguished from promptly produced $\psi(2S)$ exploiting their finite decay time. Figure 1 (right) shows the measured cross-section for $\psi(2S)$ from b-hadrons as a function of the transverse momentum in the rapidity range $2 < y(\psi(2S)) < 4.5$. The shaded band is the prediction from a FONLL calculation [13, 14]. Combining these results with the LHCb J/ψ measurements given in Ref. [15] we determined the inclusive branching fraction $\mathcal{B}(b \to \psi(2S)X) = (2.73 \pm 0.06(\text{stat}) \pm 0.16(\text{syst}) \pm 0.24(\text{bf})) \times 10^{-3}$, where the last uncertainty originates from the uncertainties of the branching fractions involved in the measurement.
Feed-down from χ_c states provide a substantial contribution to prompt J/ψ through the decay $\chi_c \to$J/ψ γ, thus affecting the J/ψ cross-section and polarisation measurements. $\chi_{c1,2}$ have been selected at LHCb combining J/$\psi \to \mu^+\mu^-$ and $\gamma \to e^+e^-$ with converted photons in the tracking system [16]. Using a data sample corresponding to 370 pb^{-1}, the cross-section ratio $\sigma(\chi_{c2})/\sigma(\chi_{c1})$ has been measured as a function of the J/ψ transverse momentum and a good agreement with the NLO NRQCD predictions has been found for $p_{\rm T}$ above 8 GeV/c. Moreover LHCb has measured the prompt cross-section ratio $\sigma(\chi_c \to$J/ψ $\gamma)/\sigma($J/$\psi)$ with a data sample of 36 pb^{-1} [17]. In this case, good agreement with the NLO NRQCD predictions is found.
The bottomonium states $\Upsilon(1S)$, $\Upsilon(2S)$ and $\Upsilon(3S)$ are abundantly produced in p-p collisions. Their production cross-sections have been measured at LHCb [18] with a data sample of 25 pb^{-1} in the fiducial region $2 < y(\Upsilon) < 4.5$ and $p_{\rm T}(\Upsilon) < 15$ GeV/c. The signal yields obtained from the mass fits are 26410±212 for $\Upsilon(1S) \to \mu^+\mu^-$, 6726±142 for $\Upsilon(2S) \to \mu^+\mu^-$ and 3260±112 for $\Upsilon(3S) \to \mu^+\mu^-$. Figure 2 (left) shows the ratios $\Upsilon(2S) \to \mu^+\mu^-$ and $\Upsilon(3S) \to \mu^+\mu^-$ with respect to $\Upsilon(1S) \to \mu^+\mu^-$ as a function of the Υ $p_{\rm T}$. Since the polarisation state of the Υ mesons is not measured yet, a systematic error is quoted and assigned to the cross-sections.

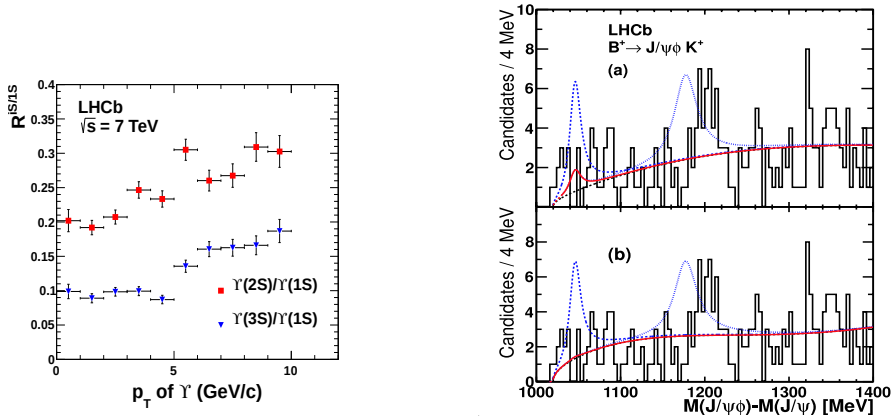

Figure 2: (Left) $\Upsilon(2S) \to \mu^+\mu^-$ and $\Upsilon(3S) \to \mu^+\mu^-$ to $\Upsilon(1S) \to \mu^+\mu^-$ production ratio as a function of the Υ transverse momentum. (Right) invariant mass difference $m(\mu^+\mu^- K^+K^-) - m(\mu^+\mu^-)$ for selected events at LHCb. The solid red line is the fitted curve while the dotted blue lines illustrate the expected X(4140) and X(4274) signal yields from the CDF measurement. The top and bottom plots differ by the background function definition.

3 Double charm production

As mentioned in the introduction, there is large theoretical interest in double charm production involving open charm. At LHCb, the J/ψC, CC and C$\bar{\text{C}}$ production cross-sections have been measured [19] in the fiducial region $3 < p_{\rm T}(\text{C}) < 12$ GeV/c, $p_{\rm T}(\text{J}/\psi) < 12$ GeV/c and $2 < y(\text{J}/\psi)$, $y(\text{C}) < 4$, where C=D^0,D^+,D_s^+,Λ_c^+. The analysis is based on a data sample of 355 pb^{-1}. Reconstructed and selected charmed hadrons are then required to be consistent with the same primary vertex. The pile-up has been accurately checked both with simulation and real data methods and it has been demonstrated to be negligible. Table 1 lists the measured cross-sections: the first uncertainty is statistical, the second is systematic. The dominant contribution to the systematic error comes from the hadron track reconstruction, with 2% error

Table 1: Double charm production cross-sections. The first uncertainty is statistical and the second is systematic.

Mode	σ [nb]	Mode	σ [nb]
J/ψD^0	161.0 ± 3.7 ± 12.2	D^0D_s^+	270 ± 50 ± 40
J/ψD^+	56.6 ± 1.7 ± 5.9	D^0D_s^-	1680 ± 110 ± 240
J/ψD_s^+	30.5 ± 2.6 ± 3.4	D^+D^+	80 ± 10 ± 10
J/$\psi\Lambda_c^+$	43.2 ± 7.0 ± 12.0	D^+D^-	780 ± 40 ± 130
D^0D^0	690 ± 40 ± 70	D^+D_s^+	70 ± 15 ± 10
$\text{D}^0\bar{\text{D}}^0$	6230 ± 120 ± 630	D^+D_s^-	550 ± 60 ± 90
D^0D^+	520 ± 80 ± 70	$\text{D}^+\Lambda_c^+$	60 ± 30 ± 20
D^0D^-	3990 ± 90 ± 500	$\text{D}^+\bar{\Lambda}_c^-$	530 ± 130 ± 170
$\text{D}^0\bar{\Lambda}_c^-$	2010 ± 280 ± 600		

per track. The predictions from gluon-gluon fusion, when available, are significantly smaller than the measured cross-sections, while better agreement is found with the DPS model.

4 X(3872), X(4140) and X(4274) production studies

X(3872) have been reconstructed at LHCb in the decay channel X(3872)→J/$\psi(\mu^+\mu^-)\pi^+\pi^-$ with a data sample corresponding to 35 pb^{-1} [20]. With a signal yield of 570 candidates, the production cross-section and the mass of the X(3872) have been measured. The obtained values are respectively $\sigma_{\mathrm{X(3872)}}\mathcal{B}_{J/\psi\pi^+\pi^-} = 4.7 \pm 1.1(\mathrm{stat}) \pm 0.7(\mathrm{syst})$ nb and $M_{\mathrm{X(3872)}} = 3871.95 \pm 0.48(\mathrm{stat}) \pm 0.12(\mathrm{syst})$ MeV/c^2. The dominant contributions to the systematic uncertainty on the mass measurement come from the momentum calibration scale ($\Delta m = 0.10$ MeV/c^2) and from the energy loss correction ($\Delta m = 0.05$ MeV/c^2). The mass value is a crucial input for the theory as it can help to understand the nature of the X(3872).

The CDF experiment has observed two narrow resonances in the J/$\psi\varphi$ system of the decay B$^\pm$ →J/$\psi\varphi$ K$^\pm$ [21]. Such resonances, generally referred to as X(4140) and X(4274), are very close to the J/$\psi\varphi$ kinematic threshold and their physical nature is not understood. LHCb searched for such resonances in the decay B$^+$ →J/$\psi\varphi$ K$^+$ and did not find evidence for the X(4140) nor for the X(4274) [22]. Figure 2 (right) shows the invariant mass difference $m(\mu^+\mu^-K^+K^-) - m(\mu^+\mu^-)$ for selected events at LHCb. The solid red line is the fitted curve while the dotted blue lines illustrate the expected X(4140) and X(4274) signal yields from the CDF measurement. The top and bottom plots differ by the background function definition. The following upper limits for the branching fraction ratios have been determined:

$$\frac{\mathcal{B}(B^+ \to X(4140)K^+) \times \mathcal{B}(X(4140) \to J/\psi\varphi)}{\mathcal{B}(B^+ \to J/\psi\varphi K^+)} < 0.07$$

$$\frac{\mathcal{B}(B^+ \to X(4274)K^+) \times \mathcal{B}(X(4274) \to J/\psi\varphi)}{\mathcal{B}(B^+ \to J/\psi\varphi K^+)} < 0.08$$

with 90% confidence level.

5 Conclusions

Quarkonia production studies performed at LHCb have been presented. The $\psi(2S)$, χ_c and $\Upsilon(nS)$ cross-sections are in good agreement with the theory predictions. Moreover LHCb has measured for the first time at a hadron collider, the charmed hadron pair production giving helpful hints to the theoretical models. Finally, the production of the exotic states X(3872), X(4140) and X(4274) has been studied: while the cross-section and the mass of the X(3872) have been measured with high precision, LHCb does not confirm the existence of the states X(4140) and X(4274) previously claimed by the CDF experiment.

References

[1] The LHCb collaboration, A. Augusto Alves Jr. *et al.*, *The LHCb Detector at the LHC*, JINST 3 (2008) S08005.

[2] A. V. Berezhnoy, A. K. Likhoded, A. V. Luchinsky and A. A. Novoselov, *Double J/ψ meson Production at LHC and 4c-tetraquark state*, Phys. Rev. D84 (2011) 094023, arXiv:1101.5881.

[3] A. V. Berezhnoy, V. V. Kiselev, A. K. Likhoded and A. I. Onishchenko, *Doubly charmed baryon production in hadronic experiments*, Phys. Rev. D57 (1998) 4385, arXiv:hep-ph/9710339.

[4] S. P. Baranov, *Topics in associated $J/\psi + c\bar{c}$ production at modern colliders*, Phys. Rev. D73 (2006) 074021.

[5] C. H. Kom, A. Kulesza, and W. J. Stirling, *Pair production of J/ψ as a probe of double parton scattering at LHCb*, Phys. Rev. Lett. 107 (2011) 082002, arXiv:1105.4186.

[6] S. P. Baranov, A. M. Snigirev, and N. P. Zotov, *Double heavy meson production through double parton scattering in hadronic collisions*, Phys. Lett. B705 (2011) 116, arXiv:1105.6276.

[7] S. Brodsky et al., *The intrinsic charm of the proton*, Phys. Lett. B93 (1980) 451.

[8] The LHCb collaboration, R. Aaij *et al.*, *Measurement of $\psi(2S)$ meson production in pp collisions at $\sqrt{s} = 7$ TeV*, LHCb-PAPER-2011-045, CERN-PH-EP-2012-094, arXiv:1204.1258v1 [hep-ex].

[9] Y.-Q. Ma, K. Wang and K.-T. Chao, *A complete NLO calculation of the J/ψ and ψ' production at hadron colliders*, arXiv:hep-ph/1012.1030.

[10] B. Kniehl and M. Butenschön, *Reconciling J/ψ production at HERA, RHIC, Tevatron, and LHC with nonrelativistic QCD factorization at next-to-leading order*, Phys. Rev. Lett. 106 (2011) 022003, and private communication.

[11] P. Artoisenet *et al.*, *Υ production at Fermilab Tevatron and LHC energies*, Phys. Rev. Lett. 101 (2008) 152001.

[12] J.-P. Lansberg, *On the mechanisms of heavy-quarkonium hadroproduction*, Eur. Phys. J. C61 (2009) 693.

[13] M. Cacciari, M. Greco, P. Nason, *The p_T spectrum in heavy-flavour hadroproduction*, JHEP 9805 (1998) 007.

[14] M. Cacciari, S. Frixione, M. Mangano, P. Nason and G. Ridolfi, *QCD analysis of first b cross-section data at 1.96 TeV*, JHEP 0407 (2004) 033.

[15] The LHCb collaboration, R. Aaij *et al.*, *Measurement of J/ψ production in pp collisions at $\sqrt{s} = 7$ TeV*, Eur. Phys. J. C71 (2011) 1645.

[16] The LHCb collaboration, R. Aaij *et al.*, *Measurement of the cross-section ratio $\sigma(\chi_{c2})/\sigma(\chi_{c1})$ for prompt χ_c production at $\sqrt{s} = 7$ TeV*, arXiv:1202.1080, LHCB-PAPER-2011-019, CERN-PH-EP-2011-227.

[17] The LHCb collaboration, R. Aaij *et al.*, *Measurement of the ratio of prompt χ_c to J/ψ production in pp collisions at $\sqrt{s} = 7$ TeV*, arXiv:1204.1462, CERN-PH-EP-2012-068, LHCB-PAPER-2011-030.

[18] The LHCb collaboration, R. Aaij *et al.*, *Measurement of Υ production in pp collisions at $\sqrt{s} = 7$ TeV*, arXiv:1202.6579, CERN-PH-EP-2012-051, LHCB-PAPER-2011-036.

[19] The LHCb collaboration, R. Aaij *et al.*, *Observation of double charm production involving open charm in pp collisions at $\sqrt{s} = 7$ TeV*, arXiv:1205.0975, CERN-PH-EP-2012-109, LHCB-PAPER-2012-003.

[20] The LHCb collaboration, R. Aaij *et al.*, *Observation of X(3872) production in pp collisions at $\sqrt{s} = 7$ TeV*, arXiv:1112.5310, LHCB-PAPER-2011-034, CERN-PH-EP-2011-216.

[21] CDF collaboration, T. Aaltonen *et al.*, *Observation of the Y(4140) structure in the $J/\psi\varphi$ mass spectrum in $B^{\pm} \to J/\psi\varphi K$ decays*, arXiv:1101.6058.

[22] The LHCb collaboration, R. Aaij *et al.*, *Search for the X(4140) state in $B^+ \to J/\psi\varphi K^+$ decays*, arXiv:1202.5087, CERN-PH-EP-2012-004, LHCB-PAPER-2011-033.

Charmonium and charmonium-like results from *BABAR*

Elisa Fioravanti[1]

[1]INFN Ferrara, Via Saragat 1, 44122, Ferrara, Italy

DOI: `http://dx.doi.org/10.3204/DESY-PROC-2012-02/195`

We present new results on charmonium and charmonium-like states from the *BABAR* experiment located at the PEP-II asymmetric energy e^+e^- storage ring at the SLAC National Accelerator Laboratory.

1 Study of the process $\gamma\gamma \to J/\psi\omega$

The charmonium-like state X(3915) was first observed by Belle [1] in two-photon fusion events decaying into $J/\psi\omega$. In addition, it was seen decaying into $J/\psi\omega$ in B decays by *BABAR* [2], along with the X(3872).
We study the process $\gamma\gamma \to J/\psi\omega$ at *BABAR* to search for the X(3915) and the X(3872) resonances via the decay to $J/\psi\omega$, using a data sample of 519 fb^{-1}. Figure 1 presents the reconstructed $J/\psi\omega$ invariant mass distribution after all the selection criteria have been applied. We perform an extended maximum likelihood fit to the efficiency-corrected spectrum. A large peak at near 3915 MeV/c^2 is observed with a significance of 7.6σ. The measured resonance parameters are $m[X(3915)] = (3919.4 \pm 2.2 \pm 1.6)$ MeV/c^2, $\Gamma[X(3915)] = (13 \pm 6 \pm 3)$ MeV. The measured value of the two-photon width times the branching fraction, $\Gamma_{\gamma\gamma}[X(3915)]$ x $\mathcal{B}(X(3915) \to J/\psi\omega)$ is $(52 \pm 10 \pm 3)$ eV and $(10.5 \pm 1.9 \pm 0.6)$ eV for two spin hypotheses $J = 0$ and $J = 2$, respectively, where the first error is statistical and the second is systematic. In addition, a Bayesian upper limit (UL) at 90% confidence level (CL) is obtained for the X(3872), $\Gamma_{\gamma\gamma}[X(3872)]$ x $\mathcal{B}(X(3872) \to J/\psi\omega) < 1.7$ eV, assuming J=2.

2 Study of the process $\gamma\gamma \to \eta_c\pi^+\pi^-$

This analysis has been studied for the first time and is performed to search for resonances decaying into $\eta_c\pi^+\pi^-$, using a data sample of 474 fb^{-1}. The η_c was reconstructed via its decay to $K^0_S K^+\pi^-$, with $K^0_S \to \pi^+\pi^-$. The signal yield for each X resonance is extracted from a two-dimensional fit to $m(K^0_S K^+\pi^-)$ and $m(K^0_S K^+\pi^-\pi^+\pi^-)$. Figure 2 presents the two dimensional fits around each of the resonances. No significant signal is observed in any of the fits. Table 1 summarizes these results. ULs are obtained on the branching fractions $\mathcal{B}(\eta_c(2S) \to \eta_c\pi^+\pi^-) < 7.4\%$ and $\mathcal{B}(\chi_{c2}(1P) \to \eta_c\pi^+\pi^-) < 2.2\%$ at 90% CL.

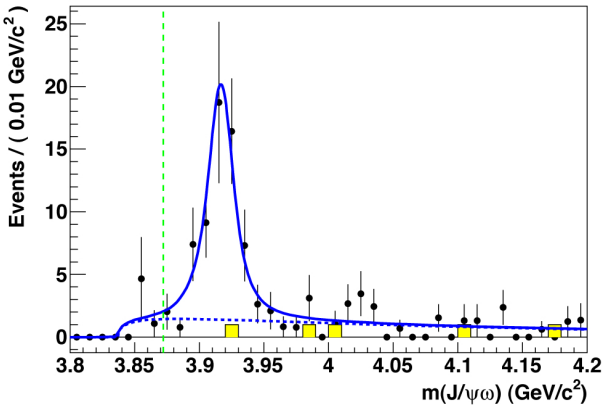

Figure 1: The efficiency-corrected invariant mass distribution for the $J/\psi\omega$ final state. The vertical dashed line is placed at the X(3872) mass.

Resonances	M_X (MeV/c^2)	Γ_X (MeV)	$\Gamma_{\gamma\gamma}\mathcal{B}$ (eV)	
			Central Value	UL
$\chi_{c2}(1P)$	3556.20±0.09	1.97±0.11	$7.2^{+5.5}_{-4.4} \pm 2.9$	15.7
$\eta_c(2S)$	3638.5±1.7	13.4±5.6	$65^{+47}_{-44} \pm 18$	133
$X(3872)$	3871.57±0.25	3.0±2.1	$-4.5^{+7.7}_{-6.7} \pm 2.9$	11.1
$X(3915)$	3915.0±3.6	17.0±10.4	$-13^{+12}_{-12} \pm 8$	16
$\chi_{c2}(2P)$	3927.2±2.6	24±6	$-16^{+15}_{-14} \pm 6$	19

Table 1: Results of the $\gamma\gamma \to \eta_c\pi^+\pi^-$ fits. For each resonance X, we show the peak mass and width used in the fit; the product of the two-photon partial width $\Gamma_{\gamma\gamma}$ and the $X \to \eta_c\pi\pi$ branching fraction, and the 90% CL upper limits on this product.

3 Search for the $Z_1(4050)^+$ and $Z_2(4250)^+$

Belle reported the observation of two resonance-like structures, $Z_1(4050)^+$ and $Z_2(4250)^+$ in the study of $\bar{B}^0 \to \chi_{c1}K^-\pi^+$, both decaying to $\chi_{c1}\pi^+$ [3].
BABAR studied the same final states [4] to search for the $Z_1(4050)^+$ and $Z_2(4250)^+$ decay into $\chi_{c1}\pi^+$ in $\bar{B}^0 \to \chi_{c1}K^-\pi^+$ and $B^+ \to K^0_S\chi_{c1}\pi^+$ where $\chi_{c1} \to J/\psi\gamma$, using a data sample of 429 fb^{-1}. The $\chi_{c1}\pi^+$ mass distribution, background-subtracted and efficiency-corrected, was modeled using the $K\pi$ mass distribution and the corresponding normalized $K\pi$ Legendre polynomial moments. Figure 3 shows the results of the fits done on the $\chi_{c1}\pi^+$ mass spectrum. The fit shown in Figure 3(a) includes both $Z_1(4050)^+$ and $Z_2(4250)^+$ resonances and the fit shown in Figure 3(b) includes a single broad $Z(4150)^+$ resonance. The Figures 3(c,d) show the $\chi_{c1}\pi$ mass spectrum fitted in the Dalitz plot region $1.0 \leq m^2(K\pi) < 1.75$ GeV^2/c^4 in order to make a direct comparison to the Belle results [3] (this region is labeled as "window" in Table 2). The results of the fits are summarized in Table 2 and in every case the yield significance does not exceed 2σ. The ULs on the 90% CL on the branching fractions are: $\mathcal{B}(\bar{B}^0 \to Z_1(4050)^+K^-)$ x $\mathcal{B}(Z_1(4050)^+ \to \chi_{c1}\pi^+) < 1.8$ x 10^{-5}; $\mathcal{B}(\bar{B}^0 \to Z_2(4250)^+K^-)$ x $\mathcal{B}(Z_2(4250)^+ \to \chi_{c1}\pi^+) <$ 4.0 x 10^{-5} and $\mathcal{B}(\bar{B}^0 \to Z^+K^-)$ x $\mathcal{B}(Z^+ \to \chi_{c1}\pi^+) < 4.7$ x 10^{-5}.

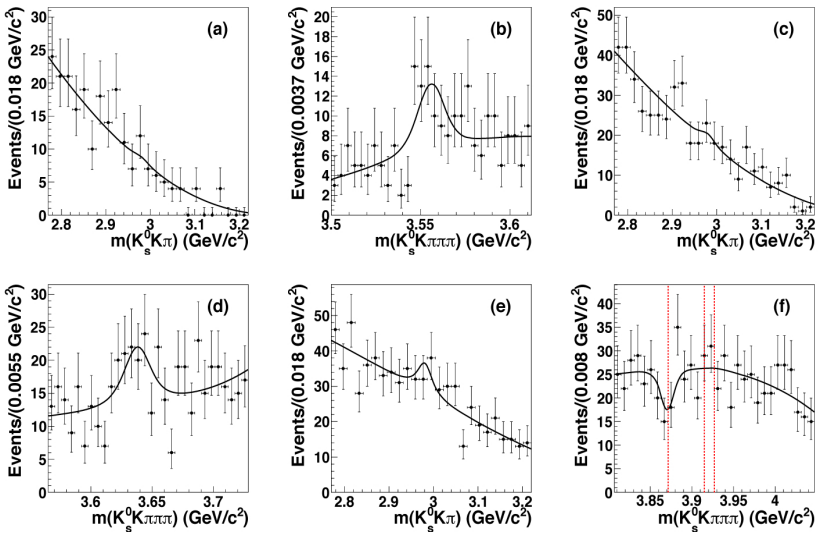

Figure 2: Distributions of (a,c,e) $m(K^0_S K^+\pi^-)$ and (b,d,f) $m(K^0_S K^+\pi^-\pi^+\pi^-)$ with the fit function overlaid for the fit regions of the (a,b) $\chi_{c2}(1P)$, (c,d) $\eta_c(2S)$, and (e,f) X(3872), X(3915) and $\chi_{c2}(2P)$. The vertical dashed lines in (f) indicates the peak mass positions of the X(3872), X(3915) and $\chi_{c2}(2P)$.

Data	Resonances	N_σ	Fraction (%)	χ^2/NDF
a) Total	$Z_1(4050)^+$	1.1	1.6±1.4	57/57
	$Z_2(4250)^+$	2.0	4.8±2.4	
b) Total	$Z(4150)^+$	1.1	4.0±3.8	61/58
a) Window	$Z_1(4050)^+$	1.2	3.5±3.0	53/46
	$Z_2(4250)^+$	1.3	6.7±5.1	
b) Window	$Z(4150)^+$	1.7	1.37±8.0	53/47

Table 2: Results of the $\chi_{c1}\pi$ fits. N_σ and Fraction give, for each fit, the significance and the fractional contribution of the Z resonances.

4 Study of the $J/\psi\pi^+\pi^-$ via Initial State Radiation (ISR)

The Y(4260) charmonium-like resonance was discovered by *BABAR* [5] in ISR production of $J/\psi\pi^+\pi^-$. A subsequent Belle analysis [6] of the same final state suggested also the existence of an additional resonance around 4.1 GeV/c^2 that they dubbed the Y(4008).
This analysis [7] is performed to study the reaction $J/\psi\pi^+\pi^-$ in ISR using a data sample of 454 fb^{-1}.
The $J/\psi\pi^+\pi^-$ mass region below ∼4 GeV/c^2 is investigated for the first time. In that region an excess of events has been observed and the conclusion, after a detailed study of the $\psi(2S)$ lineshape (to estimate the $\psi(2S)$ tail contribution to that region), is that it is not possible to discount the possibilty of a contribution from a $J/\psi\pi^+\pi^-$ continuum cross section in this region. From this study we obtain the cross section value 14.05 ± 0.26 (stat) pb for radiative return to the $\psi(2S)$ and the measurement of the width $\Gamma(\psi(2S)\to e^+e^-) = 2.31\pm0.05$ (stat) keV. Figure

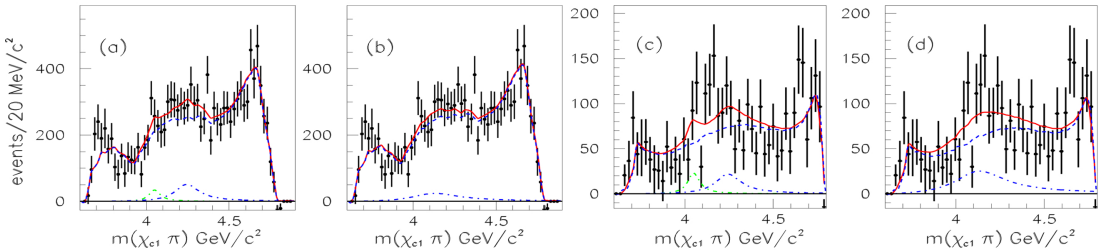

Figure 3: Fit on the background-subtracted and efficiency-corrected $\chi_{c1}\pi$ mass distribution. See text for more details.

4(a) shows the fit to the $J/\psi\pi^+\pi^-$ distribution. A clear signal of the Y(4260) is observed for which the values obtained are $m[Y(4260)] = 4244 \pm 5 \pm 4$ MeV/c^2, $\Gamma[Y(4260)] = 114^{+16}_{-15} \pm 7$ MeV and Γ_{ee} x $\mathcal{B}(J/\psi\pi^+\pi^-) = 9.2 \pm 0.8$ (stat) $\pm$ 0.7 (syst) eV. No evidence for the state at $\sim$ 4 GeV/c^2 reported by Belle [6] was seen. A study of the $\pi^+\pi^-$ system from the Y(4260) decay to $J/\psi\pi^+\pi^-$ is done. The dipion system is in a predominantly S-wave state. The mass distribution exhibits an $f_0(980)$ signal, for which a simple model indicates a branching ratio with respect to $J/\psi\pi^+\pi^-$ of 0.17 ± 0.13 (stat). The fit to the dipion invariant mass distribution is shown in Figure 4(b).

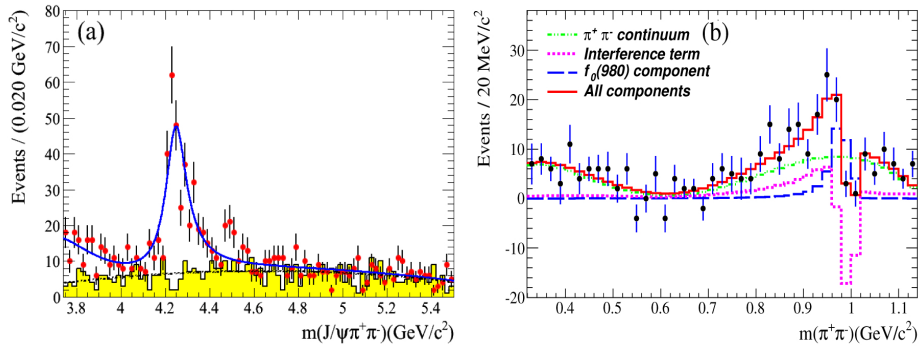

Figure 4: Figure (a) shows the fit to the $J/\psi\pi^+\pi^-$ invariant mass distribution. The Figure (b) shows the fit to the dipion invariant mass distribution.

References

[1] S. Uehara *et al.* (Belle Collaboration), Phys. Rev. Lett. **104**, 092001 (2010).

[2] P. del Amo Sanchez *et al.* (*BABAR* Collaboration), Phys. Rev. D. **82**, 011101(R) (2010).

[3] R. Mizuk *et al.* (Belle Collaboration), Phys. Rev. D **78**, 072004 (2008).

[4] J. P. Lees *et al.* (*BABAR* Collaboration), Phys. Rev. D **85**, 052003 (2012).

[5] B. Aubert *et al.* (*BABAR* Collaboration), Phys. Rev. Lett. **95**, 142001 (2005).

[6] C. Z. Yuan *et al.* (Belle Collaboration), Phys. Rev. Lett. **99**, 182004 (2007).

[7] *BABAR* Collaboration, `hep-ex/1204.2158v1`

Bottomonium(-like) Spectroscopy at Belle

Umberto Tamponi

Universitá degli Studi di Torino
INFN, Sezione di Torino

DOI: http://dx.doi.org/10.3204/DESY-PROC-2012-02/66

We report the recent progresses in bottomonium spectroscopy obtained with the $\Upsilon(1S)$, $\Upsilon(2S)$, and $\Upsilon(5S)$ samples collected by the Belle experiment. In particular, using the 121 fb^{-1} collected at the $\Upsilon(5S)$ resonance, the missing singlet states $h_b(1P)$ and $h_b(2P)$ are observed for the first time with high significance. The transition $\Upsilon(5S) \to \pi^+\pi^- h_b(1,2P)$ is found to be mediated by two new, bottomonium-like, charged state Z_b and Z_b', whose nature is still argument of discussion. We also report a new measurement of the hyperfine splitting in the $1S$ system, a new high significance observation of the $\eta_b(1S)$ state and a summary of the progresses archived in the study of the $\Upsilon(nS) \to \eta\Upsilon(mS)$ transition and in the Υ decay to charmonium and double charmonium.

1 New states observation in $\Upsilon(5S) \to \pi^+\pi^- X$

The Belle experiment [1] at the KEKB e^+e^- asymmetric collider [2] collected the world largest samples of $\Upsilon(1S)$, $\Upsilon(2S)$ and $\Upsilon(5S)$. The $\Upsilon(5S)$ sample revealed a totally unexpected potential for the study of the lower bottomonium resonances, in particular the singlet states h_b and η_b.

1.1 Observation of $h_b(1P)$ and $h_b(2P)$

The observation of $h_b(1P)$ and $h_b(2P)$ is made with an inclusive analysis [3], studying the distribution of the missing mass $M_{miss}(\pi^+\pi^-)$ from the $\pi^+\pi^-$ pair in $\Upsilon(5S) \to \pi^+\pi^- + X$ final states. Once the large combinatorial background is fitted and subtracted, the remaining distribution (Figure 1) shows different peaks, due to different dipion transitions: the $h_b(1P)$ and $h_b(2P)$ signals are clearly visible with a significance of 6.2 σ and 12.4 σ respectively, together with the $\Upsilon(5S) \to \pi^+\pi^-\Upsilon(nS)$ signals.
The measured masses of the h_b states are $M_{h_b(1P)} = 9898.3 \pm 1.1^{+1.0}_{-1.1}$ MeV/c^2 and $M_{h_b(2P)} = 10259.8 \pm 0.6^{+0.4}_{-1.0}$ MeV/c^2.

1.2 Observation of Z_b and Z_b'

The $\Upsilon(5S) \to \pi^+\pi^- h_b(1P)$ transition is expected to involve amplitudes related to a spin flip of the b quark, that are predicted by non-relativistic QCD (NRQCD) to be suppressed, while the dipion transition to a lower Υ resonance is not a spin flipping process and thus is predicted not to be suppressed. The measured ratio $\frac{\mathcal{B}(\Upsilon(5S)\to\pi^+\pi^- h_b(1P))}{\mathcal{B}(\Upsilon(5S)\to\pi^+\pi^- Y(1S))} = 0.77$, surprisingly indicates no significant suppression of the spin flip transition with respect to the non flipping processes. This unexpected behavior can be explained with the introduction of an intermediate charged

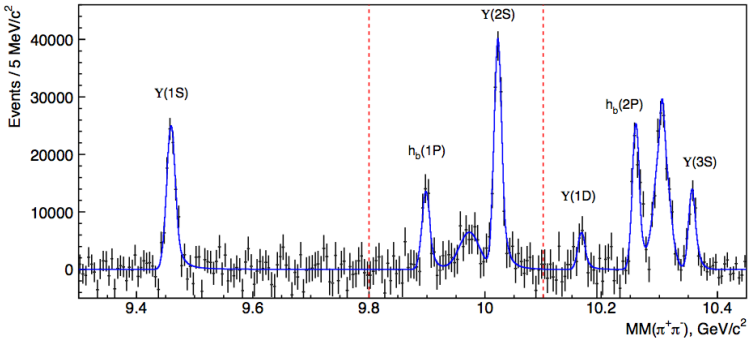

Figure 1: Missing mass in $\Upsilon(5S) \to \pi^+\pi^- + X$ events. The two peaks located at 9.95 GeV/c^2 and 10.3 GeV/c^2 are due to the known $\Upsilon(2,3S) \to \pi^+\pi^-\Upsilon(1S)$ transitions.

state that mediates the dipion transition; with this hypothesis the decay chain from the $\Upsilon(5S)$ to the h_b states should be $\Upsilon(5S) \to \pi^\pm Z_b^\mp \to \pi^+\pi^- h_b(1,2P)$, and the hypothetical Z_b state should be seen as a peak in the h_b yield distribution, when computed in bins of the missing mass form the single pion. A double peak observed in both the distributions of the $h_b(1P)$ (Figure 2) and $h_b(2P)$ (Figure 3) yields, is thus interpreted as a doublet of charged states Z_b and Z_b', with masses $M_{Z_b} = 10608 \pm 2.0$ MeV/c^2, $M_{Z_b'} = 10653 \pm 1.5$ MeV/c^2 and widths $\Gamma_{Z_b} = 15.6 \pm 2.5$ MeV, $\Gamma_{Z_b'} = 14.4 \pm 3.2$ MeV [4]. The same structures are also observed in the exclusive final states $\pi^+\pi^-\Upsilon(1,2,3S)$ where the Υ states are reconstructed in the leptonic final state $\Upsilon(nS) \to \mu^+\mu^-$. The Z_b and Z_b' parameters extracted in this five independent final states are in agreement, providing a strong observation of these states.

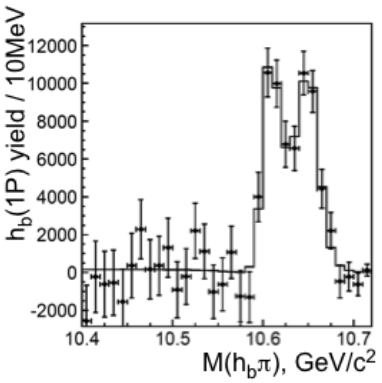

Figure 2: $h_b(1P)$ yield in bins of recoil mass against the single charged pion, in $\Upsilon(5S) \to \pi^+\pi^- + X$ events.

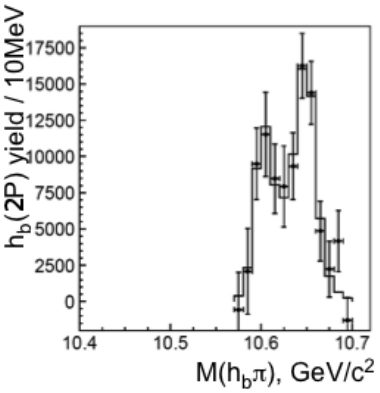

Figure 3: $h_b(2P)$ yield in bins of recoil mass against the single charged pion, in $\Upsilon(5S) \to \pi^+\pi^- + X$ events.

1.3 Observation of $h_b(1P) \to \gamma\eta_b(1S)$

The unexpected high number of h_b and the strong experimental signature provided by the observation of the Z_b allow, for the first time, the study of the radiative decay $h_b(1P) \to \gamma\eta_b(1S)$, opening new prospectives on the study of the $\eta_b(1S)$ itself [5]. This resonance, the ground state of bottomonium, was observed both by CLEO and BaBar studying the radiative transition $\Upsilon(2,3S) \to \gamma\eta_b(1S)$. This kind of studies are affected by large resonant background, mainly due to $\Upsilon(1S)$ ISR production, $\Upsilon(2S) \to \gamma\chi_b(1P)$ and $\Upsilon(2,3S) \to \pi^0\pi^0\Upsilon(1S)$ transitions. The $h_b(1P) \to \gamma\eta_b(1P)$ transition is studied requiring a single pion missing mass compatible with Z_b mass and fitting the h_b yield, extracted form the missing mass from the $\pi^+\pi^-$ system $M_{miss}(\pi^+\pi^-)$, in bins of ΔM_{miss}, where $\Delta M_{miss} = M_{miss}(\pi^+\pi^-\gamma) - M_{miss}(\pi^+\pi^-) + M(h_b)$, $M_{miss}(\pi^+\pi^-\gamma)$ is the missing mass from the $\pi^+\pi^-\gamma$ system, and $M(h_b)$ is the measured h_b mass. ΔM_{miss} peaks, by construction, at the η_b mass value, as shown in Figure 4.

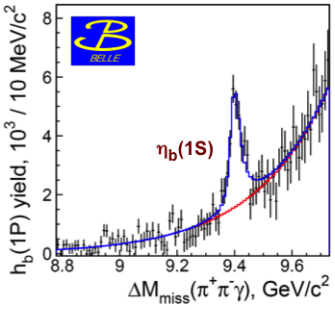

Figure 4: h_b yield in bins of ΔM_{miss}, in $\Upsilon(5S) \to \pi^\pm Z_b \to \pi^+\pi^- + X$ events.

The significance of the $\eta_b(1S)$ peak is 15 σ, and such a clean observation allows to measure with unprecedented precision the parameters of this resonance, obtaining $M_{\eta_b(1S)} = 9401.0 \pm 1.9^{+1.4}_{-2.4}$ MeV/c^2 and $\Gamma_{\eta_b(1S)} = 12.4^{+5.5+11.5}_{-5.6-3.4}$ MeV. The theoretical importance of such measurements is connected to the hyperfine splitting in the $1S$ system, defined as the mass difference between the $\Upsilon(1S)$ and the $\eta_b(1S)$. Previous measurement fixed this value slightly above the theoretical prediction obtained from both NRQCR and potential based models. The new value $\Delta M_{HF}(1S) = (59.3 \pm 1.9^{+1.6}_{-1.2})$ MeV/c^2 obtained by the Belle collaboration is lower than the previous ones and in agreement with the non-relativistic QCD predictions.

1.4 Observation of $\Upsilon(5S) \to \Upsilon(1D)\pi^+\pi^-$

A 2.5 σ $\Upsilon(1D)$ signal is visible in the dipion recoil mass distribution in $\Upsilon(5S) \to \pi^+\pi^- X$ events (Figure 1). Requiring the exclusive reconstruction of the double radiative decay $\Upsilon(1D) \to \gamma_1\chi_b(1P) \to \gamma_1\gamma_2\Upsilon(1S)$ an high significance signal of $\Upsilon(1D)$ is observed. The measured branching ratio for the complete decay chain is:
$\mathcal{B}[\Upsilon(5S) \to \pi^+\pi^-\Upsilon(1D) \to \pi^+\pi^-\gamma_1\chi_b(1P) \to \pi^+\pi^-\gamma_1\gamma_2\Upsilon(1S)] = (2.0 \pm 0.4 \pm 0.3) \times 10^{-4}$

2 Progresses in $\Upsilon(nS) \to \eta\Upsilon(mS)$

In the QCDME formalism [6] the η transitions between Υ states should be mediated either by two M1 gluons, or by one E1 and one M2 gluon: both cases imply a spin flip of the b quark. The corresponding amplitude should scale as $1/m_b$, leading to a suppression of these processes. By scaling from the $\psi' \to \eta J/\psi$ transition, one expects $\mathbf{B}[\Upsilon(2S) \to \eta\Upsilon(1S)] = 8 \times 10^{-4}$. $\Upsilon(2,3,4S) \to \eta\Upsilon(1S)$ branching ratios have been measured by BaBar [7, 8] and CLEO [9]: they are either unexpectedly large ($\Upsilon(4S)$), or too small ($\Upsilon(2S)$ and $\Upsilon(3S)$). We search for the $\Upsilon(2S) \to \eta\Upsilon(1S)$ process with the exclusive reconstruction of the η in both the $\gamma\gamma$ and the $\pi^+\pi^-\pi^0$ mode. The $\Upsilon(1S)$ is reconstructed in the leptonic modes e^+e^- and $\mu^+\mu^-$. The measured branching ratio is $\mathcal{B}[\Upsilon(2S) \to \eta\Upsilon(1S)] = (3.41 \pm 0.28 \pm 0.35) \times 10^{-4}$, with an high

significance η signal observed.
The isospin violating transition $\Upsilon(2S) \to \pi^0\Upsilon(1S)$ is investigated too, with the same technique, but no signal is observed and and upper limit is set: $\mathcal{B}(\Upsilon(2S) \to \pi^0\Upsilon(1S)) < 4.6$ (90% CL).
The η transition is observed for the first time from $\Upsilon(5S)$ too, requiring also in this case the exclusive reconstruction of $\Upsilon(1,2S) \to \mu^+\mu^-$. We measure the branching ratios $\mathcal{B}[\Upsilon(5S) \to \eta\Upsilon(1S)] = (7.3 \pm 1.6(stat) \pm 0.8(syst)) \times 10^{-4}$ and $\mathcal{B}[\Upsilon(5S) \to \eta\Upsilon(2S)] = (38 \pm 4(stat) \pm 5(syst)) \times 10^{-4}$.

3 Charmonium in $\Upsilon(1,2S)$ and $\chi_b(1P)$ decays

A large study of the charmonium production in bottomonium decays was carried on by Belle during last year. In particular intensive studies of the radiative transitions $\Upsilon(1,2S) \to \gamma c\bar{c}$ and of the double charmonium production $b\bar{b} \to (c\bar{c})(c\bar{c})$ led to a large set of upper limits. In details a systematic search for η_c, χ_{cJ}, $X(3872)$, $X(3915)$, $X(4350)$, and $Y(4140)$ signals in $\Upsilon(2S)$ radiative decays is performed by Belle [10], extending a previous work on the $\Upsilon(1S)$ transitions to charmonium states [11]. A search for new resonances is performed too, looking for the $\gamma_R\gamma\psi'$ final state where γ_R is the radiative photon from the $\Upsilon(2S)$ decay. No signal is observed and upper limits are set for all the transitions at the 10^{-4} level.
The second field of research is the double charmonium production, i.e. the $b\bar{b} \to (c\bar{c})(c\bar{c})$ decays [12]. Recent studies report theoretical prediction on $b\bar{b} \to J/\psi J/\psi, J/\psi\psi', \psi'\psi'$, where $b\bar{b} = \Upsilon(1S), \Upsilon(2S), \chi_{bJ}(1P)$, obtained with different frameworks: light cone formalism (LCF), potential QCD (pQCD), and non-relativistic QCD (NRQCD). The J/ψ candidates are reconstructed in the $\mu^+\mu^-$ and e^+e^- final states, while the ψ' is reconstructed in the dominant decay $\pi^+\pi^- J/\psi$. $\chi_{b0}(1P)$,$\chi_{b1}(1P)$, and $\chi_{b2}(1P)$ are distinguished by the energy of the photon from the radiative transition $\Upsilon(2S) \to \gamma\chi_{bJ}(1P)$. Signals are observed neither in the full reconstruction of the bottomonium decays, nor in the missing mass from the J/ψ candidate distribution, and stringent upper limits are set. This upper limits are in agreement with the NRQCD predictions, while they are significantly below the light cone formalism and pQCD ones.

References

[1] A. Abashian *et al.*, Nucl. Instrum. Meth. **A479**, 117-232 (2002).

[2] S. Kurokawa, E. Kikutani, Nucl. Instrum. Meth. **A 499**,1 (2003) and other papers included in this volume.

[3] I. Adachi *et al.* [Belle Collaboration], Phys. Rev. Lett. **108** (2012) 032001

[4] A. Bondar *et al.* [Belle Collaboration], Phys. Rev. Lett. **108** (2012) 122001

[5] Belle. Collaboration, arXiv:1110.3934 [hep-ex].

[6] T. -M. Yan, Phys. Rev. **D22**, 1652 (1980).

[7] B. Aubert *et al.* [The BaBar Collaboration], Phys. Rev. **D78**, 112002 (2008).

[8] J. P. Lees, *et al.* [The BaBar Collaboration], arXiv:1108.5874v1 [hep-ex].

[9] Q. He *et al.* [CLEO Collaboration], Phys. Rev. Lett. **101**, 192001 (2008).

[10] X. L. Wang *et al.* [Belle Collaboration], arXiv:1108.4514v1 [hep-ex].

[11] C. P. Shen *et al.* [Belle Collaboration], Phys. Rev. **D82**, 051504(R) (2010).

[12] C. P. Shen, C. Z. Yuan, T. Iijima and B. Collaboration, Phys. Rev. D **85** (2012) 071102

Properties and decays of b hadrons at DØ

Enrique Camacho-Pérez[1]

[1]Cinvestav, Av. IPN 2508, 07360 Mexico City, Mexico

DOI: http://dx.doi.org/10.3204/DESY-PROC-2012-02/311

The Tevatron, with $p\bar{p}$ collisions at $\sqrt{s} = 1.96$ TeV, can produce all flavours of b hadrons and allows several studies in the B physics sector. This paper presents a selection of recent results on heavy hadron physics using data up to 10.4 fb^{-1} of integrated luminosity collected with the DØ detector.

1 Results for Λ_b baryon

1.1 $\Lambda_b \to J/\psi\Lambda$ Branching Ratio

b-hadrons such as the Λ_b are currently the subject of much research in both the theoretical and experimental particle physics communities. Measurements of the production and decays of b-hadrons could improve understanding of the electroweak and strong interactions described by the Standard Model of particle physics, in addition to providing opportunities to search for physics beyond the Standard Model. The DØ Collaboration, using 6.1 fb^{-1} of $p\bar{p}$ collisions, reports an improved measurement on the relative production fraction [1], specifically

$$\sigma_{\rm rel} \equiv \frac{f(b\to\Lambda_b)\cdot\mathcal{B}(\Lambda_b\to J/\psi\Lambda)}{f(b\to B^0)\cdot\mathcal{B}(B^0\to J/\psi K^0_s)} = \frac{N_{\Lambda_b\to J/\psi\Lambda}}{N_{B^0\to J/\psi K^0_S}}\cdot\frac{\mathcal{B}(K^0_s\to\pi^+\pi^-)}{\mathcal{B}(\Lambda\to p\pi^-)}\cdot\epsilon.$$

For this analysis it is first necessary to find events with two oppositely charged reconstructed muons, forming a common vertex and invariant mass consistent with a J/ψ meson. The next step is to search in the dimuon selection for pairs of oppositely charged tracks with a common vertex, such as $p\pi^-$ or $\pi^+\pi^-$. Possible Λ_b and B^0 ($B^0 \to J/\psi\ K^0_s$ is the normalization channel) candidates are reconstructed by performing a constrained fit to a common vertex. Moreover, several conditions are imposed on the quality of the reconstructed objects (tracks, vertices and parent particles). To extract the yields of the observed Λ_b and B^0 hadrons, an unbinned likelihood fit is performed to each mass distribution assuming a double Gaussian function for signal and a second order polynomial distribution for background, as shown in Fig. 1.

Monte Carlo (MC) simulated data was analyzed in order to obtain the reconstruction efficiencies and several cross checks to ensure that the MC was correctly modeling the signal data. Studies of different sources of systematic uncertainty were performed: the determination of the Λ_b and B^0 yields, the determination of the relative efficiency, the contamination from Λ_b in B^0 and vice versa, and Λ_b polarization effects, with the final source being the most significant. As a final cross-check, lifetime measurements were performed for the Λ and K^0_S with results in agreement with the world average values.

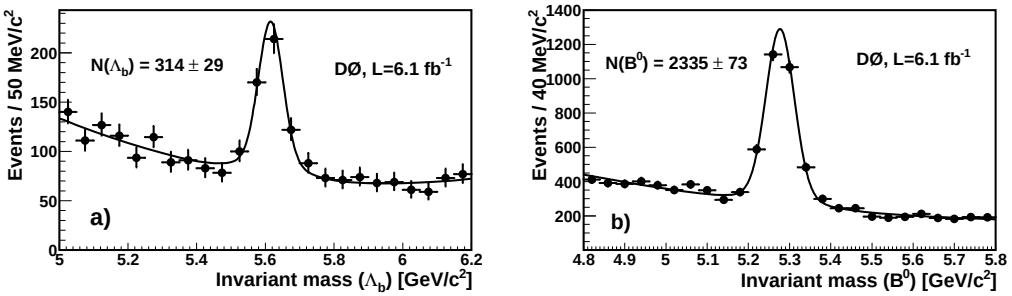

Figure 1: Invariant mass distribution in data for (a) $\Lambda_b \to J/\psi\Lambda$ and (b) $B^0 \to J/\psi K_s^0$ decays. Fit results are superimposed

The DØ Collaboration has obtained the production fraction multiplied by the branching fraction for the decay $\Lambda_b \to J/\psi\Lambda$ relative to that for the decay $B^0 \to J/\psi K_s^0$ to be

$$\sigma_{\rm rel} = 0.345 \pm 0.034 \text{ (stat.)} \pm \ 0.033 \text{ (syst.)} \pm 0.003 \text{ (PDG)}.$$

The measurement is the most precise to date and exceeds the precision of the current value reported as the world average, 0.27 $\pm$0.13 [2] . Using the PDG value $f(b \to B^0) \cdot \mathcal{B}(B^0 \to J/\psi K_s^0) = (1.74 \pm 0.08) \times 10^{-4}$ (from [2]),

$$f(b \to \Lambda_b) \cdot \mathcal{B}(\Lambda_b \to J/\psi\Lambda) = [6.01 \pm 0.60 \text{ (stat.)} \pm 0.58 \text{ (syst.)} \pm 0.28 \text{ (PDG)}] \times 10^{-5}$$

which can be compared directly to the world average value of $(4.7 \pm 2.3) \times 10^{-5}$ [2]. This result represents a reduction by a factor of $\sim$3 of the uncertainty with respect to the previous measurement [3]. With this result the CDF experiment was able to report the branching ratio $\mathcal{B}(\Lambda_b \to \mu\mu\Lambda^0)$, and they found no significant deviation from the Standard Model [4].

1.2 Λ_b lifetime in the exclusive decay $\Lambda_b \to J/\psi\Lambda$

Lifetime measurements of particles containing b quarks provide important tests of the significance of strong interactions between the constituent partons in the weak decay of b hadrons. These interactions produce measurable differences between b hadron lifetimes that heavy quark expansion (HQE) [5] predicts with good accuracy through the calculation of lifetime ratios, but currently there are remaining discrepancies between experimental results and theoretical predictions for b baryons.

The data used in this analysis were collected with the DØ detector during the complete Run II of the Tevatron Collider, from 2002 to 2011, and correspond to an integrated luminosity of 10.4 fb^{-1}. The main difference with the previous analysis is that events with J/ψ candidates are reprocessed with a version of the track reconstruction algorithm that increases the efficiency for tracks with low p_T and high impact parameter [6].

The samples of Λ_b and B^0 candidates have two primary background contributions: combinatorial background and partially reconstructed b hadron decays. In order to extract the lifetimes,

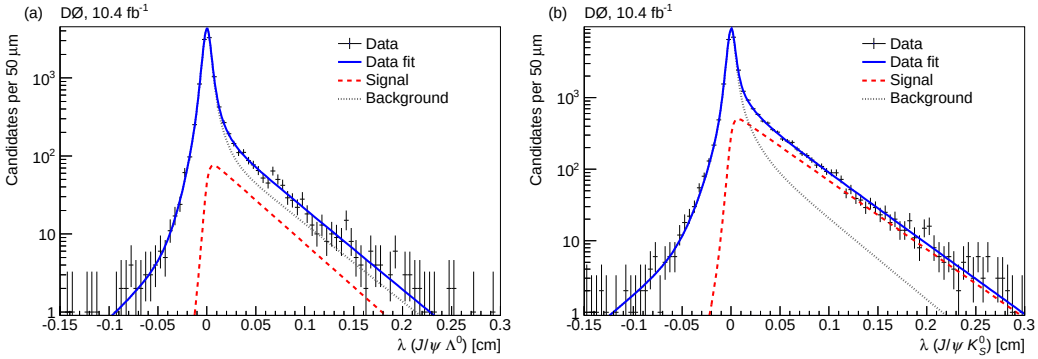

Figure 2: Proper decay length distributions for (a) $\Lambda_b \to J/\psi\Lambda$ and (b) $B^0 \to J/\psi K_s^0$ candidates, with fit results superimposed.

we perform separate unbinned maximum likelihood fits for Λ_b and B^0 candidates. The likelihood function ($\mathcal{L}$) depends on the probability of reconstructing each candidate event j in the sample with the mass m_j , the proper decay length λ_j and proper decay length uncertainty σ_j^λ:

$$\mathcal{L} = \prod_{j=1}^{N} [f_s \mathcal{F}_s(m_j, \lambda_j, \sigma_j^\lambda) + (1 - f_s)\mathcal{F}_b(m_j, \lambda_j, \sigma_j^\lambda)]$$

where f_s is the fraction of signal events, and $\mathcal{F}_s$ ($\mathcal{F}_b$) is the product of the probability distribution functions that model each of the three observables being considered for signal (background) events.

The maximum likelihood fits to the data yield $c\tau(\Lambda_b) = 390.7 \pm 22.4$ μm and $c\tau(B^0) = 452.2 \pm 7.6$ μm. The numbers of signal events, derived from f_s, are 755 ± 49 (Λ_b) and 5671 ± 126 (B^0). Figure 2 shows the λ distributions for the Λ_b and the B^0 candidates. Fit results are superimposed. Using the full data sample collected by the DØ experiment, we measure the lifetime of the Λ_b baryon in the $J/\psi\Lambda$ final state to be [7]

$$c\tau(\Lambda_b) = 1.303 \pm 0.075 \text{ (stat.)} \pm 0.035 \text{ (syst.) ps},$$

consistent with the world average, 1.425 ± 0.032 ps [2].

The method to measure the Λ_b lifetime is also used for $B^0 \to J/\psi K_s^0$ decays, for which we obtain

$$c\tau(B^0) = 1.508 \pm 0.025 \text{ (stat.)} \pm 0.043 \text{ (syst.) ps},$$

in good agreement with the world average, 1.519 ± 0.007 ps [2].

Using these measurements we calculate the ratio of lifetimes, $\tau_{\Lambda_b}/\tau_{B^0} = 0.864 \pm 0.052$(stat.)$\pm$ 0.033(syst.) The result, is in good agreement with the HQE prediction of 0.88 ± 0.05 [9] and compatible with the current world-average, 1.00 ± 0.06 [2], but differs with the latest measurement of the CDF Collaboration, 1.02 ± 0.03 [8] , at the 2.2 standard deviations level. These measurements supersede the previous DØ results of τ_{Λ_b}, τ_{B^0} and $\tau_{\Lambda_b}/\tau_{B^0}$ [10].

2 Measurement of the relative branching ratio of $B_s^0 \to J/\psi f_0(980)$ to $B_s^0 \to J/\psi\phi$

The decay $B_s^0 \to J/\psi f_0(980)$, offers an interesting probe of CP violation [14]. In particular, this channel allows us to search for CP-violating New-Physics contributions to $B_s^0 \bar{B}_s^0$ mixing, which is conventionally studied via the $B_s^0 \to J/\psi\phi$. The drawback of the $B_s^0 \to J/\psi\phi$ mode is that its final state contains two vector mesons and is thereby a mixture of CP-even and CP-odd eigenstates. Consequently, in order to disentangle the CP eigenstates, a time-dependent angular analysis of the decay products $J/\psi \to \mu^+\mu^-$ and and $\phi \to K^+K^-$ is necessary [15, 16]. In contrast, because the $f_0(980)$ is a scalar state with quantum numbers $J^{PC} = 0^{++}$ [17] , the final state of $B_s^0 \to J/\psi f_0(980)$ is a p-wave state with the CP eigenvalue -1 and thus an angular analysis is not needed [14].

Early in 2011, the LHCb Collaboration released an observation of the $B_s^0 \to J/\psi f_0(980)$ decay mode [11]. This was quickly followed by results from Belle [12] and CDF [13]. The results of these measurements are all in general agreement and point to a ratio of the fraction of $J/\psi f_0(980)$ decays to $J/\psi\phi$ decays.

Based on 8 fb^{-1} of data, DØ has extracted a measurement of the relative branching fraction [18]

$$\frac{\mathcal{B}(B_s \to J/\psi f_0(980); f_0(980) \to \pi^+\pi^-)}{\mathcal{B}(B_s \to J/\psi\phi; \phi \to K^+K^-\ )} = 0.275 \pm 0.041\ (\text{stat.}) \pm 0.061\ (\text{syst.})$$

This agrees with theoretical expectations and with previous measurements of the ratio of widths.

References

[1] V. M. Abazov *et al.* [D0 Collaboration], Phys. Rev. **D84**, 031102 (2011).

[2] K. Nakamura *et al.* (Particle Data Group), J. Phys. G **37**, 075021 (2010).

[3] F. Abe *et al.* [CDF Collaboration], Phys. Rev. D **55**, 1142 (1997).

[4] T. Aaltonen *et al.* [CDF Collaboration], [arXiv:1107.3753 [hep-ex]].

[5] G. Bellini, I. I. Y. Bigi, and P. J. Dornan, Phys. Rep. **289** , 1 (1997).

[6] V. M. Abazov *et al.* [D0 Collaboration], Phys. Rev. Lett. **99**, 052001 (2007).

[7] V. M. Abazov *et al.* [D0 Collaboration], [arXiv:1204.2340 [hep-ex]]

[8] T. Aaltonen *et al.* [CDF Collaboration], Phys. Rev. Lett. **106**, 121804 (2011)

[9] C. Tarantino, Nucl. Phys. B, Proc. Suppl. **156**, 33 (2006).

[10] V. M. Abazov *et al.* [D0 Collaboration], Phys. Rev. Lett. **99**,142001 (2007).

[11] R. Aaij *et al.* [LHCb Collaboration], Phys. Lett. B **698**, 115 (2011) [arXiv:1102.0206 [hep-ex]].

[12] J. Li *et al.* [Belle Collaboration], Phys. Rev. Lett. **106**, 121802 (2011) [arXiv:1102.2759 [hep-ex]].

[13] T. Aaltonen *et al.* [CDF Collaboration], Phys. Rev. D **84**, 052012 (2011) [arXiv:1106.3682 [hep-ex]].

[14] S. Stone and L. Zhang, Phys. Rev. D **79**, 074024 (2009) [arXiv:0812.2832 [hep-ph]].

[15] S. Stone and L. Zhang, arXiv:0909.5442 [hep-ex].

[16] A. S. Dighe, I. Dunietz and R. Fleischer, Eur. Phys. J. C **6**, 647 (1999) [hep-ph/9804253].

[17] I. Dunietz, R. Fleischer and U. Nierste, Phys. Rev. D **63**, 114015 (2001) [hep-ph/0012219].

[18] V. M. Abazov *et al.* [D0 Collaboration], Phys. Rev. D **85**, 011103 (2012)

Baryonic B Decay Results from *BABAR*

Marcus Ebert

SLAC National Accelerator Center, 2575 Sand Hill Road, 94025 Menlo Park, CA, USA

DOI: http://dx.doi.org/10.3204/DESY-PROC-2012-02/196

Decays of B mesons into final states containing baryons are much less understood than decays into mesons, and are useful for shedding light on baryon-production mechanisms and intermediate states. We report the results of recent and new studies of such decays, including $B^- \to \Sigma_c(2455)^{++}\overline{p}\pi^-\pi^-$, $\overline{B}^0 \to \Lambda_c^+\overline{p}p\overline{p}$, and $B \to D^{(*)}p\overline{p}(n\pi)$. Both the total decay rates and the resonant structure are reported.

1 Introduction

From what we know so far, $(6.8 \pm 0.6)\%$ of all B mesons decay to a final state with baryons and $(4.5 \pm 1.2)\%$ decay to a final state with a Λ_c^+ in there [1]. However, presently the sum of all exclusive branching fractions is only about 20% of all baryonic B-decays and also only very little is know about the decay mechanism. B mesons decay dominantly via $b \to c$ transitions while the c quark can be bound into a baryon or a meson. A common feature of processes with baryons in the final state is a threshold enhancement in the invariant baryon-antibaryon mass spectrum [2][3]. This feature may also explain the increase of the branching fraction with higher final state multiplicity and the suppression of two-body decays to baryons [4][5]. In the presented analyses we will measure the branching fraction, search for resonant subchannels and test for the enhancement in the baryon-antibaryon mass spectrum and the increase of the branching fraction with higher final state multiplicity.

2 Study of the decay mode $B \to D^{(*)}p\overline{p}(\pi)(\pi)$ [6]

We study 10 different decay modes and measure the branching fractions shown in table 1, while 6 of them are observed for the first time. The interesting conclusions from this measurements are:

- 4-body modes have a higher branching fraction than the corresponding 5-body modes $\mathcal{B}$(3-body)<$\mathcal{B}$(5-body)<$\mathcal{B}$(4-body)
- all branching fractions are of the same order of magnitude: $\mathcal{B} \approx \mathcal{O}(10^{-4})$

This is especially interesting given that for $B \to \Lambda_c^+\overline{p}\,(n\pi)$ with $n = 1, 2$, the branching fraction is around one order of magnitude higher when there is an additional pion in the final state, while the highest branching fraction is measured for $B^- \to \Lambda_c^+\overline{p}\pi^+\pi^-\pi^-$ [1] and $\mathcal{B}(B \to \Lambda_c^+\overline{p}\pi) \approx \mathcal{O}(10^{-4})$. The reason for this could be the influence of resonant substructures which are very important for the decay modes with a Λ_c^+ in the final state. While for the studied 5-body

decay mode	$\mathcal{B} \pm \sigma_{(\mathrm{stat})} \pm \sigma_{(\mathrm{syst})} (10^{-4})$
$\overline{B}^0 \to D^0 p\overline{p}$	$1.02 \pm 0.04 \pm 0.06$
$\overline{B}^0 \to D^{*0} p\overline{p}$	$0.97 \pm 0.07 \pm 0.09$
$\overline{B}^0 \to D^+ p\overline{p}\pi^-$	$3.32 \pm 0.10 \pm 0.29$
$\overline{B}^0 \to D^{*+} p\overline{p}\pi^-$	$4.55 \pm 0.16 \pm 0.39$
$\boldsymbol{B^- \to D^0 p\overline{p}\pi^-}$	$\mathbf{3.72 \pm 0.11 \pm 0.25}$
$\boldsymbol{B^- \to D^{*0} p\overline{p}\pi^-}$	$\mathbf{3.73 \pm 0.17 \pm 0.27}$
$\boldsymbol{\overline{B}^0 \to D^0 p\overline{p}\pi^-\pi^+}$	$\mathbf{2.99 \pm 0.21 \pm 0.45}$
$\boldsymbol{\overline{B}^0 \to D^{*0} p\overline{p}\pi^-\pi^+}$	$\mathbf{1.91 \pm 0.36 \pm 0.29}$
$\boldsymbol{B^- \to D^+ p\overline{p}\pi^-\pi^-}$	$\mathbf{1.66 \pm 0.13 \pm 0.27}$
$\boldsymbol{B^- \to D^{*+} p\overline{p}\pi^-\pi^-}$	$\mathbf{1.86 \pm 0.16 \pm 0.19}$

Table 1: Measured branching fractions for the different decay modes (decay modes observed for the first time are in bold).

decay modes the 2-body invariant mass distributions agree very well with simulated events using uniform phase space model, it is very different for the studied 3-body and 4-body decay modes.

2.1 3-body decay modes

Fig. 1 shows the 2-body invariant mass distributions for the studied 3-body B-decay modes. The diagrams (c) and (g) show a clear an enhancement in the $p\overline{p}$ mass distribution at threshold. In addition, we observe a clear difference between the invariant mass distributions $m(D^{(*)}p)$ for data and simulated 3-body phase space events, which is shown in (a) and (e).

2.2 4-body decay modes

Fig. 2 and Fig. 3 show the 2-body invariant mass distributions for the studied 4-body B-decay modes. In all decay modes we observe again an enhancement at threshold for the invariant mass distribution $m(p\overline{p})$. In addition we find a narrow structure in $m(p\pi^-)$ which is most prominent in Fig. 2 (d). For the mean and the width of this structure we measure $m = (1497.4 \pm 3.0 \pm 0.9)\,\mathrm{MeV}/c^2$ and $\Gamma = (47 \pm 12 \pm 4)\,\mathrm{MeV}/c^2$ where the first uncertainty is statistical and the second one the systematical uncertainty.

3 Study of the decay mode $\boldsymbol{B^- \to \Sigma_c(2455)^{++}\overline{p}\pi^-\pi^-}$ [7]

In this analysis we assume that $\mathcal{B}(\Sigma_c(2455)^{++} \to \Lambda_c^+\pi^+) = 100\%$ and reconstruct the Λ_c^+ candidate in the decay mode $pK^-\pi^+$ which has a branching fraction of $(5.0 \pm 1.3)\%$. The number of signal events is determined by a fit to a ΔE distribution, with $\Delta E = E_B^* - \sqrt{s}/2$ and the energy of the B-candidate in the e^+e^- rest frame (E_B^*) (Fig. 4). The fit finds $N_{\mathrm{sig}} = 787 \pm 43$ signal events which results in a branching fraction of $\mathcal{B}(B^- \to \Sigma_c(2455)^{++}\overline{p}\pi^-\pi^-) = (2.98 \pm 0.16 \pm 0.15 \pm 0.77) \times 10^{-4}$ where the uncertainties are statistic, systematic, and from

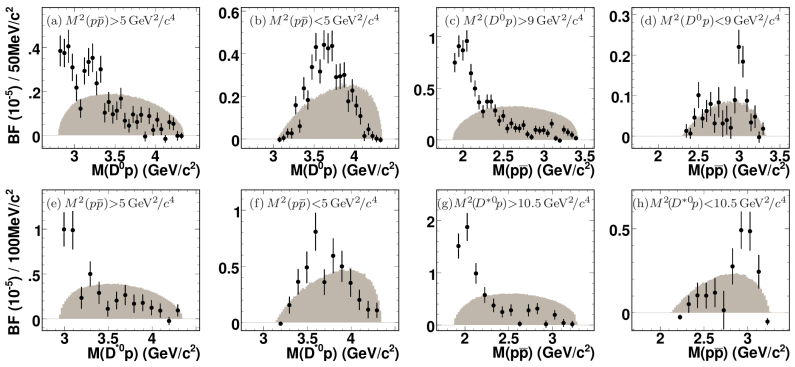

Figure 1: 2-body invariant mass distributions for $\overline{B}^0 \to D^0 p\overline{p}$ (top) and for $\overline{B}^0 \to D^{*0} p\overline{p}$ (bottom), the shaded histogram shows simulated 3-body phase space events

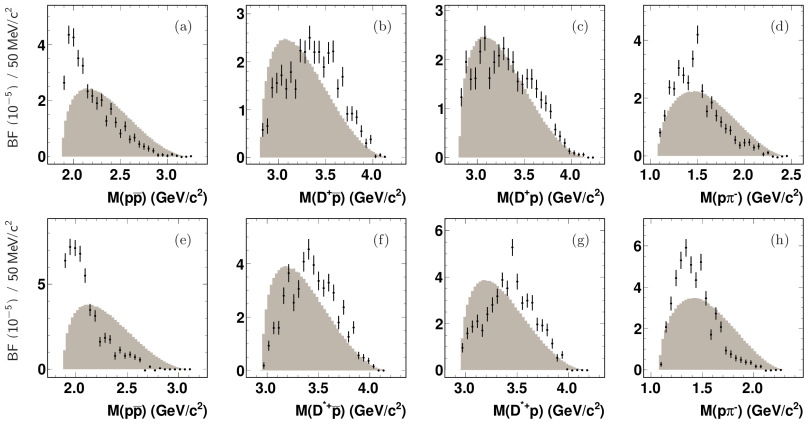

Figure 2: 2-body invariant mass distributions for $\overline{B}^0 \to D^+ p\overline{p}\pi^-$ (top) and for $\overline{B}^0 \to D^{*+} p\overline{p}\pi^-$ (bottom), the shaded histograms show simulated 4-body phase space events

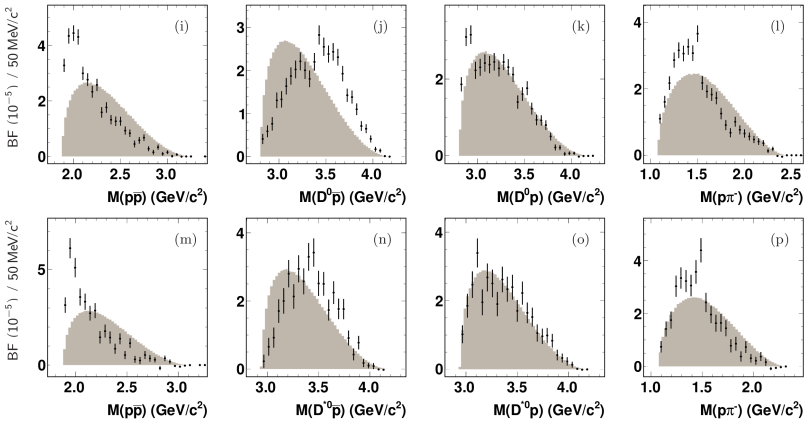

Figure 3: 2-body invariant mass distributions for $B^- \to D^0 p\overline{p}\pi^-$ (top) and for $B^- \to D^{*0} p\overline{p}\pi^-$ (bottom), the shaded histograms show simulated 4-body phase space events

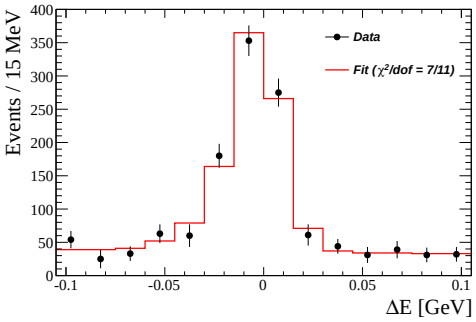

Figure 4: Points with error bars represent the number of Σ_c^{++} candidates obtained by a fit to $\Delta M = m(\Lambda_c^+\pi^+) - m(\Lambda_c^+)$ in every bin of ΔE; the red curves shows the binned fit to data

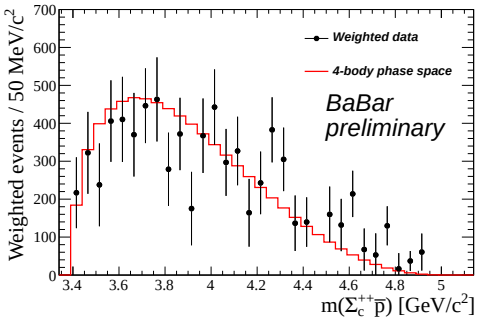

Figure 5: Baryon-antibaryon invariant mass distribution for data signal events after efficiency correction (points with error bars) and weighted simulated 4-body phase space events

the uncertainty on the Λ_c branching fraction. Although we see some structures in the invariant 2-body mass distributions as well as in the invariant mass distribution of $\Sigma_c(2455)^{++}\pi^-\pi^-$, there is no evidence for decays via resonant subchannels. Moreover, we do not observe an enhancement at threshold for the invariant baryon-antibaryon mass distribution (Fig. 5).

4 Study of the decay mode $\overline{B}^0 \to \Lambda_c^+\overline{p}p\overline{p}$

Since there are only baryons in the final state of this decay mode the possibilities for resonant subchannels are limited. However, the momenta of all particles are very low in the e^+e^- rest frame which could enhance the production rate of baryons and in this decay mode one can also look for the enhancement at threshold in the baryon-antibaryon invariant mass distribution using different combinations of the final state particles. As a preliminary result we observe two events after all selection criteria are applied and calculate an upper limit at 90% confidence level of $\mathcal{B}(\overline{B}^0 \to \Lambda_c^+\overline{p}p\overline{p}) \cdot \mathcal{B}(\Lambda_c^+ \to pK^-\pi^+)/0.05 < 6.2 \times 10^{-6}$ in which we divide the product branching fraction by the center value of the known Λ_c^+ branching fraction. This upper limit is already some orders of magnitude lower than the branching fraction for other 4-body baryonic B-decay modes.

References

[1] J. Beringer et al. (Particle Data Group), Phys. Rev. D**86**, 010001 (2012).

[2] B. Aubert *et al.* (*BABAR* Collaboration), Phys. Rev. D**78**, 112003 (2008).

[3] B. Aubert *et al.* (*BABAR* Collaboration), Phys. Rev. D**82**,031102 (2010).

[4] W. S. Hou and A. Soni, Phys. Rev. Lett. **86**, 4247 (2001).

[5] J. L. Rosner, Phys. Rev. D**68**, 014004 (2003).

[6] P. del Amo Sanchez *et al.* (*BABAR* Collaboration), Phys. Rev. D**85**, 092017 (2012).

[7] J. P. Lees *et al.* (*BABAR* Collaboration), arXiv:1208.3086

Part IX

Working Group 6
Spin Physics

Convenors:

Abhay Deshpande, Kresimir Kumericki, Marc Schlegel,

Sergei Yashchenko

Recent Results of Double Helicity Asymmetries from PHENIX

Scott Wolin

University of Illinois at Urbana-Champaign, 1110 W. Green St, Urbana, IL USA

DOI: http://dx.doi.org/10.3204/DESY-PROC-2012-02/108

The search for the gluon contribution to the proton spin, ΔG, is critical to understanding the proton spin puzzle. The PHENIX experiment at the Relativistic Heavy Ion Collider (RHIC) is able to directly probe gluon polarization using collisions between two polarized proton beams. ΔG is determined from the double longitudinal asymmetry, A_{LL}, for a final state to be observed between same and opposite sign helicity proton interactions. In this talk we will summarize the recent A_{LL} measurements. At mid-rapidity, $|\eta| < 0.35$, we can probe ΔG in the Bjorken-x range $0.05 < x < 0.2$. At forward rapidity we can probe ΔG down to $x \sim (1-3) \times 10^{-3}$.

1 Introduction

For more than two decades, it has been clear that the longitudinal spin structure of the proton cannot be described by quark spin contributions alone, as they account for only about 30% of its $\frac{1}{2}\hbar$ spin. The search for the remaining spin is deemed the "proton spin puzzle". The accounting is summarized by the spin-sum rule:

$$\frac{1}{2} = \frac{1}{2}\sum_q (\Delta q + \Delta\bar{q}) + \Delta G + L_{g,q}$$

The $\Delta q(\Delta\bar{q})$ represent the individual quark(antiquark) spin contributions which are measured from deep inelastic scattering (DIS) processes. The ΔG and $L_{g,q}$ terms represent the gluon spin and orbital angular momenta contributions from gluons and quarks, respectively. For a theoretical treatment of the spin decomposition, the reader is referred to Ref. [1] and [2].

The goal of the ΔG program in PHENIX is to determine how much of the missing spin comes from gluon polarization, and several measurements have been carried out using different final states. The observable that can be related to ΔG is the double longitudinal asymmetry, A_{LL}, measured from longitudinally polarized protons. It is defined as:

$$A_{LL} = \frac{\Delta\sigma}{\sigma} = \frac{1}{P_B P_Y}\frac{N^{++} - RN^{+-}}{N^{++} + RN^{+-}}$$

where σ is the total cross section for $pp \to \pi^0 + X$ and $\Delta\sigma = \sigma^{\overrightarrow{p}\,\overrightarrow{p}\to\pi^0+X} - \sigma^{\overrightarrow{p}\,\overleftarrow{p}\to\pi^0+X}$. P_B and P_Y are the beam polarizations. $N^{++(+-)}$ refers to the scaled yield from same(opposite) sign helicity interactions. $R = L^{++}/L^{+-}$ is the relative luminosity where $L^{++(+-)}$ is the luminosity for the same(opposite) helicity bunch crossings. The $\overrightarrow{p}\,\overrightarrow{p}$ indicates that the initial states of the

protons are either both positive helicity or both negative helicity. The notation $\overrightarrow{p}\overleftarrow{p}$ indicates that one proton has negative helicity while the other has positive helicity. We use the π^0 as the included particle in the final state, but it could be any measured state.

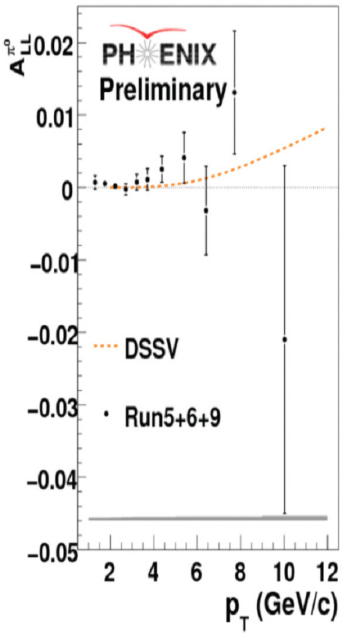

Figure 1: The measurement of the asymmetry for π^0 production at mid-rapidity is shown for the combined datasets from 2005,2006 and 2009. The red dashed line shows the prediction based on the DSSV model.

The unpolarized parton distribution functions (PDF) are denoted by $f(x)(\bar{f}(x))$ for each (anti-)quark flavor and $g(x)$ for the gluons, where x is the Bjorken-x. The polarized PDFs are denoted by $\Delta f(x), \Delta\bar{f}(x)$ and $\Delta g(x)$. The total gluon spin contribution is then $\Delta G = \int_0^1 \Delta g(x)dx$. By factorizing the cross sections as a product of PDFs, partonic cross sections, $\hat{\sigma}$, and fragmentation functions D_f^h, for parton f to fragment into hadron h, the cross sections can be written as convolutions:

$$\Delta\sigma^{pp\to h+X} = \sum_{a,b} \Delta f_a \otimes \Delta f_b \otimes \Delta\hat{\sigma}^{f_a f_b \to fX} \otimes D_f^h$$

$$\sigma^{pp\to h+X} = \sum_{a,b} f_a \otimes f_b \otimes \hat{\sigma}^{f_a f_b \to fX} \otimes D_f^h$$

2 Constraining ΔG by Measuring A_{LL}

In Figure 1 we show the combined result for the π^0 A_{LL} at central rapidity, $|\eta| < 0.35$. The de Florian, Sassot, Stratmann and Vogelsang (DSSV) prediction (Ref. [3] and [4]) is also shown. At low p_T this measurement is sensitive roughly equally to gluon-gluon and quark-gluon interactions, but when $p_T > 5$ GeV/c it is dominated by quark-gluon processes and $A_{LL} \propto \Delta g \Delta f$. The DSSV global analysis did not include these data sets. By running a modified analysis which includes this result the constraints on ΔG can be improved for the region of gluon sensitivity, $0.05 < x_g < 0.2$. The results are shown in Figure 2. Within the accessed x range, the uncertainty band has decreased and a once favored node in $\Delta g(x)$ at $x_g \sim 0.1$ is now disfavored. With no change in the sign of Δg, this result favors a more positive value for $\Delta G^{[0.05-0.2]} = \int_{0.05}^{0.2} \Delta g(x)dx$.

In addition to the π^0 measurement, A_{LL} has been measured in several other channels. The results are summarized in Figure 3. In Fig. 3a A_{LL} was measured for the inclusive $\pi^0 - \pi^0$ channel. Despite lower statistics, this final state constrains the inital parton x values better than a single inclusive measurement. In Fig. 3b we show the charged hadron A_{LL} incorporating the 2009 dataset. Due to the preferred fragmentation for $u \to \pi^+$ and $d \to \pi^-$, the sign of ΔG can be obtained. In Figure 3c we show the combined A_{LL} result for the η meson. The strangeness of the η allows the strange quark fragmentation functions to enter the ΔG extraction providing an independent cross check of the π^0 measurement. In Fig. 3d, the result from single electron detection from heavy quark mesons is shown. This channel is dominated by gluon-gluon fusion. Therefore, $A_{LL}^{pp\to e+X} \propto \Delta G^2$. The main advantage of this channel is the decreased uncertainty from the heavy quark fragmentation functions. This leads to less uncertainty when extracting ΔG from this channel.

In order to constrain $\Delta g(x)$ for $x < 0.05$, it is necessary to measure hadrons at forward rapidity using the Muon Piston Calorimeter (MPC). The MPC has 2π azimuthal coverage with $3.1 < |\eta| < 3.9$. Due to its segmentation, the two photons from π^0 decays are reconstructed as a single cluster due to merging if $p_{T,\pi^0} > 2$ GeV/c. Therefore, we measure $A_{LL}^{cluster}$ and from PYTHIA simulations we estimate that approximately 80% of this sample is from merged π^0's.

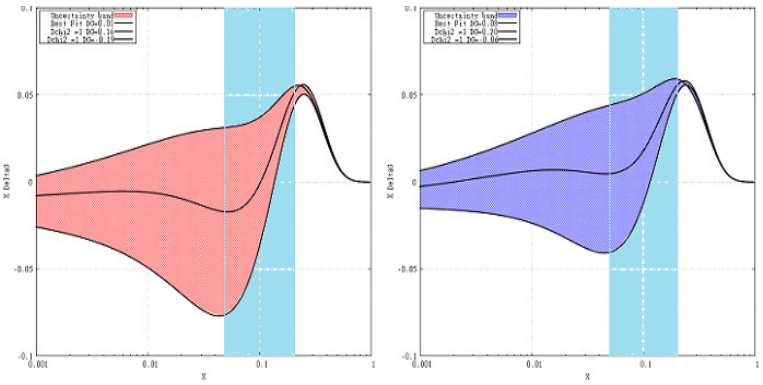

Figure 2: (Left) The DSSV curve before the results from the 2005,2006 and 2009 datasets are accounted for. The value of $\int_{0.05}^{0.2} \Delta g(x)dx$ is small but with large uncertainty. (Right) The best fit for ΔG using the DSSV framework shows the improved constraints on ΔG within the range of sensitivity.

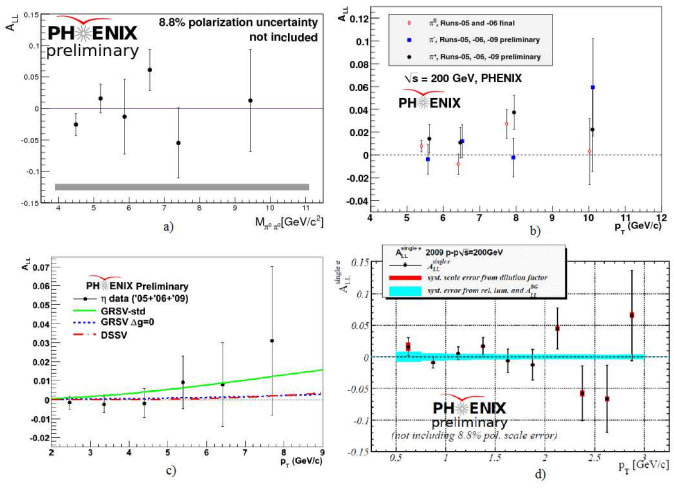

Figure 3: The A_{LL} results are shown for several final states measured at mid-rapidity. The measurements include (a) di-π^0 production, (b) identified charged pions, (c) η mesons, and (d) single electrons. Each measurement makes a specific contribution, as described in the text, toward constaining ΔG.

Unlike at mid-rapidity, where only at $p_T > 5$ GeV/c is the process fraction dominated by quark-gluon interactions, for the MPC this is already true at $p_T > 2$ GeV/c. The result for the measurement of the single cluster A_{LL} is shown in Figure 4. While the MPC single cluster measurement is most sensitive at $x_g \sim O(10^{-2})$ it also has very broad sensitivity. In order to be sensitive to more precise x_g ranges at low-x it is necessary to trigger on di-hadron events where, like in the mid-rapidity case, the event kinematics are better constrained. High-p_T di-hadron events are heavily dominated by an underlying highly asymmetric partonic interaction (with a heavily boosted center of mass) between a valence quark and gluon. This means that to good approximation, for the forward di-hadron measurement, $A_{LL} \propto \Delta f \Delta g$, and the measurement can distinguish between positive and negative values of $\Delta g(x)$ for the better constrained region of x that is involved.

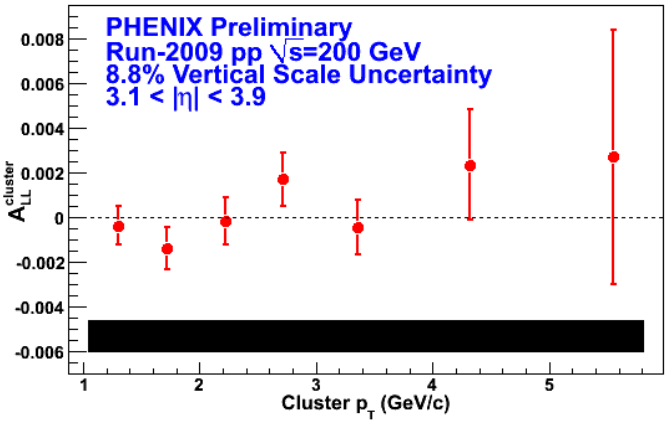

Figure 4: At forward rapidity, the MPC has the capability to be sensitive to gluons with significantly lower x than in the central arm. Here the A_{LL} result for forward single clusters is shown. The black systematic uncertainty band arises from the relative luminosity determination.

To measure this, however, it was necessary to commission a trigger upgrade. Since the previous trigger was only capable of triggering on a single high p_T cluster, the rejection power was too small. This was fixed in the new trigger by requiring two azimuthally separated hadrons each with a somewhat lower threshold than the single hadron case. The new trigger was commissioned successfully for the 2012 dataset, which has very recently concluded. PHENIX projections anticipate that this trigger has the potential to distinguish between some models of ΔG.

It is anticipated that the 2013 dataset for pp collisions at $\sqrt{s} = 500$ GeV will have up to 20 times more integrated luminosity that then the 2009 dataset. The most important issue for future high statistics measurements of A_{LL}, as demonstrated in Figure 4, is therefore to understand and minimize the systematic effects from relative luminosity that will start to dominate the overall uncertainty.

3 Acknowledgements

The author would like to thank the organizers of DIS2012 for the invitation to participate at this conference.

References

[1] Jaffe, Manohar Nucl. Phys. B 337, 509 (1990)

[2] X. Ji, Phys. Rev. Letters 78, 610 (1997)

[3] de Florian, et al., Phys. Rev. Lett. 101, 072001 (2008)

[4] de Florian, et al., Phys. Rev. D 80, 034030 (2009)

New COMPASS Results on Polarised Parton Distributions inside Nucleon

Marcin Stolarski on behalf of the COMPASS Collaboration
LIP-Lisboa, Av. Elias Garcia 14-1 1000-149 Lisboa Portugal

DOI: http://dx.doi.org/10.3204/DESY-PROC-2012-02/307

A selection of COMPASS results obtained in polarised deep inelastic scattering of polarised muons off longitudinally polarised proton and deuteron targets is presented. A LO flavour separation and two new measurements of the gluon polarisation $\Delta g/g$ are discussed.

1 Introduction

COMPASS is an experiment at CERN focusing on the spin structure of the nucleon and hadron spectroscopy. For analyses presented in this paper, a 160 GeV/c polarised muon beam and a two (three) cell polarised ^{6}LiD or NH_3 targets were used. The LO flavour separation is discussed with emphasis on ΔS distribution. The new $\Delta g/g$ results obtained in the open charm and in High-p_T hadron pairs analyses are also shown.

2 Flavour separation

COMPASS analysed the semi–inclusive asymmetries for kaons and pions on both proton and deuteron targets. In the LO approximation the hadron asymmetry can be expressed as

$$A_1^h(x,Q^2,z) = \frac{\sum_q e_q^2 \Delta q(x,Q^2) D_q^h(z,Q^2)}{\sum_q e_q^2 q(x,Q^2) D_q^h(z,Q^2)} \tag{1}$$

where e_q is quark electric charge, $(\Delta)q$ (polarised) parton distribution function and D_q^h is fragmentation functions (FF) of quark q into hadron h. With inclusive and semi-inclusive asymmetries one has 10 measured asymmetries and 5 unknown parameters $(\Delta u, \Delta d, \Delta\bar{u}, \Delta\bar{d}, \Delta s)$, The flavour separation of quark helicity distributions is possible using just a linear algebra. Some results were already published in [1] using FF from DSS parametrisation [2]. The results are summarised in Fig. 1. In general good agreement is observed between COMPASS results and DSSV parametrization [3].

From the inclusive asymmetries it is known that the strange sea polarisation is negative. This tend is so far not observed in COMPASS and HERMES semi-inclusive analyses where, in the measured rage of x, the value of ΔS is consistent with zero. However, as pointed out in [1], the ΔS obtained in semi-inclusive analysis strongly depends upon the choice of the fragmentation functions used. COMPASS try to extract these FF from data alone *cf.* [4].

3 Gluon polarisation

Information about gluon polarisation can be obtained indirectly from scaling violations in the structure function g_1 or in direct measurement studying photon-gluon fusion processes (PGF). Here only direct COMPASS measurements are discussed: *i*) open charm studies and *ii*) in the analysis of hadrons produced with high transverse momenta (HipT). In the former case the analysis is free from any physical background in the Leading order approximation. Unfortunately due to the large charm mass, in the COMPASS energy range the production cross section for charm mesons is small, and also branching ratio for the $D^0 \to K\pi$ is below 4%. Therefore the analysis has limited statistical precision. The HipT method has an advantage over open charm that the production cross-section is larger therefore the statistical error of $\Delta g/g$ will be reduced. On the other hand the HipT analysis is not background free.

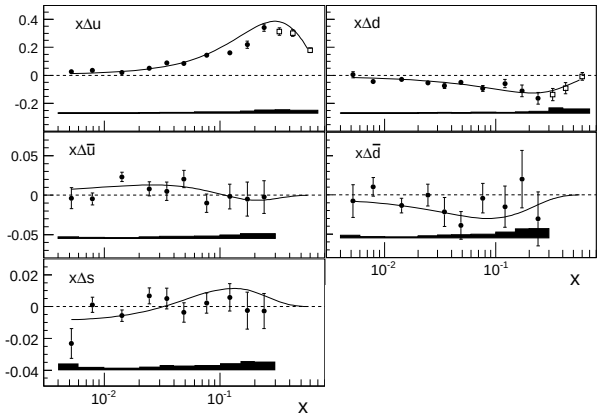

Figure 1: Results of LO flavour separation using COMPASS data [1]. The curves are from [3].

3.1 Open charm analysis

In the current open charm analysis all available data from 2002-2007 are used. In order to improve the statistical error of $\Delta g/g$ five different D mesons decay modes are studied. In total there are about 65000 D^0 candidates and about 29000 D^* candidates out of which 13000 are in the golden channel $D^* \to K\pi\pi_{slow}$. In a simplified approach the gluon polarisation $\Delta g/g$ can be obtained from:

$$\frac{\Delta g}{g} = \frac{1}{P_T P_b f a_{LL} \frac{S}{S+B}} A^{\mu N \to D^0 + X} \tag{2}$$

where $P_{T,b}$ are the target and beam polarisation, respectively, f is the dilution factor of the material which takes into account the fraction of polarisable nucleons in the target, including radiative corrections. a_{LL} is the so called analysing power which represents the polarisation transfer from muon to photon and from gluon to charm quarks. The $\frac{S}{S+B}$ is the ratio between signal and signal plus combinatorial background, and finally the $A^{\mu N \to D^0 + X}$ is the measured asymmetry. The method which is actually used in the analysis is much more complex *e.g.* it allows the simultaneous extraction of signal and background asymmetries, details can be found in [5]. To increase the statistical significance of the results the events are weighted on an event by event basis using a Neural Network approach. The preliminary result is $\Delta g/g = -0.08 \pm 0.21 \pm 0.11$. at average $x_g = 0.11$ and scale $\mu^2 = 13$ (GeV/c)^2.

The gluon polarisation in NLO approximation, based on [6], was recently extracted in COMPASS. The AROMA generator is used with active parton shower option. The parton shower simulates the phase-space for NLO correction, which can be calculated on the event by event

basis. Large differences are observed between a_{LL} and x_g for LO and NLO order. In addition, in NLO part of the D^0 doesn't come from PGF process, but is sensitive to inclusive spin asymmetries $A_1^{p,d}$. This correction was found to be small, but it is included in the analysis. The preliminary result of the NLO analysis is $\Delta g/g_{NLO} = -0.20 \pm 0.21 \pm 0.08$ at average $x_g = 0.28$ and scale $\mu^2 = 13$ (GeV/c)^2.

3.2 High-p_T hadron pair analysis

The results of $\Delta g/g$ analysis form $Q^2 > 1$ (GeV/c)^2 high-p_T hadron pairs are presented. Data come from 2002-2006 years when COMPASS used LiD target. As the Q^2 ensures perturbative scale the cut on hadron p_T can be low, here $p_{T_1} = 0.7$ and $p_{T_2} = 0.4$ GeV/c, for the first and the second hadron respectively. The total number of events in the selected sample is about 7.3 millions. The sample is strongly contaminated by a non–PGF processes. This background is related to Leading Process (LP) *i.e.* photon-quark scattering and QCD Compton process (QCDC), where the scattered quark emits in addition a gluon. It is expected that for higher p_T of hadrons the PGF fraction will grow while LP decreases. The observed asymmetry in a two hadron sample can be written as:

$$A_{LL}^{2h}(x_{Bj}) = R_{PGF}\, a_{LL}^{PGF} \frac{\Delta g}{g}(x_g) + R_{LP}\, D\, A_1^{LO}(x_{Bj}) + R_{QCDC}\, a_{LL}^{QCDC} A_1^{LO}(x_C) \qquad (3)$$

where $A_1^{LO} \equiv \frac{\sum_i e_i^2 \Delta q_i}{\sum_i e_i^2 q_i}$, Rs are fractions of the subprocesses (LO, PGF, QCDC) and a_{LL}s - analysing powers for PGF and QCDC. Unfortunately Rs and a_{LL}s cannot be determined from data they have to be taken from elsewhere *e.g.* MC simulation. Therefore a good agreement between data and MC is crucial for this analysis. In the above equation there are two unknowns $\Delta g/g$ and A_1^{LO}, to be obtain $\Delta g/g$ additional information is needed. This information is taken from the inclusive sample, where inclusive asymmetry is described in a similar way as the asymmetry of two hadron sample. Finally,

$$\Delta g/g = \frac{A_{LL}^{2h} + A^{corr}}{\beta} \qquad (4)$$

where β is a function of a_{LL}s, Rs and A^{corr} is in addition a function of inclusive A_1^d asymmetry. To reduce statistical error of $\Delta g/g$ the weighted method of the asymmetry extraction is used. All Rs and a_{LL}s have to be known on the event-by-event basis. We use a Neural Network trained on MC to obtain parametrizations of Rs and a_{LL}s.

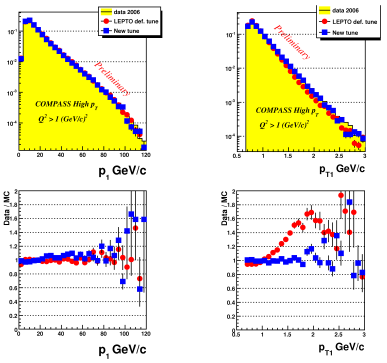

Figure 2: Data/MC agreement for different LEPTO tunings for longitudinal and transverse momenta of the first hadron.

The LEPTO generator is used with parton shower on, and MSTW08LO as a source of parton distribution functions. To improve data/MC agreement the intrinsic k_T of quarks inside nucleon and fragmentation parameters were adjusted. Example of data/MC agreement for p_{L_1}, p_{T_1} before and after adjustment is presented in Fig. 2. Clear improvement is seen for the HipT tuning.

COMPASS preliminary results of $\Delta g/g$ extracted in this analysis is $\Delta g/g = 0.125 \pm 0.060 \pm 0.065$ at average $x_g = 0.09$ and scale μ^2=3 $(\mathrm{GeV/c})^2$. The major contribution to the systematic error (0.045) comes from MC. In addition COMPASS for the first time obtained results in three bins of x_g. Within statistical errors these three results agree with each other.

The results of COMPASS $\Delta g/g$ analyses are summarised in Fig. 3. In all analyses extracted $\Delta g/g$ is small and consistent with zero. The results agree well with each other as well as with measurements from SMC and HERMES experiments. Currently the NLO analysis of a single high-p_T hadron is ongoing for $Q^2 < 0.1$ $(\mathrm{GeV/c})^2$ events *cf.* [7]. In the first step hadron cross-section as a function of p_T was compared with theoretical prediction [8].

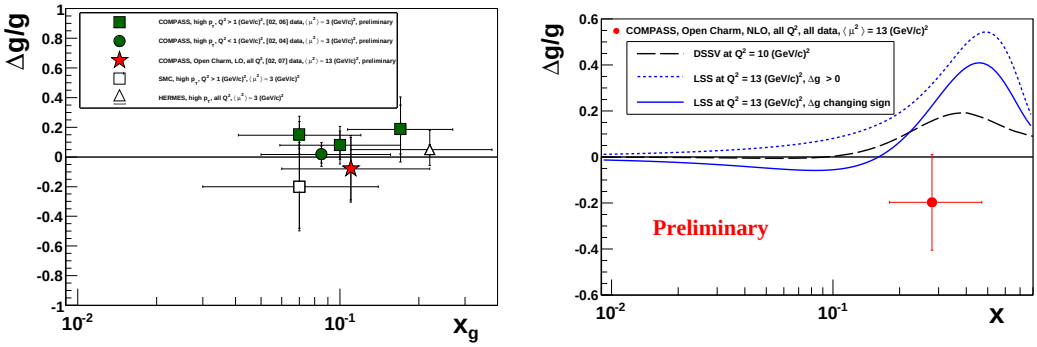

Figure 3: Summary of $\Delta g/g$ results obtained in LO and NLO analysis.

Acknowledgements

This research was supported by the Portuguese Fundação para a Ciência e a Tecnologia, grant SFRH/BPD/64853/2009.

References

[1] COMPASS, M. Alekseev *et al.*, *Phys. Lett.* **B693**, 227, (2009).

[2] D. de Florian, R. Sassot, M. Stratmann, *Phys. Rev.* **D75**, 114010 (2007).

[3] D. de Florian, R. Sassot, M. Stratmann, W. Vogelsang, *Phys. Rev. Lett.* **101**, 072001 (2008); *Phys. Rev.* **D80**, 034030 (2009).

[4] N. Makke, This proceedings.

[5] COMPASS, M. Alekseev *et al.*, *Phys. Lett.* **B676**, 31 (2009).

[6] I. Bojak, M. Stratmann, *Nucl. Phys.* **B540**, 345 (1999).

[7] C. Hoeppner, This proceedings.

[8] B. Jaeger, M. Stratmann and V. Vogelsang, *Eur. Phys. J.* **C44**, 533 (2005).

TMD Theory Overview

P.J. Mulders

Nikhef and Physics Department, FEW, VU University,
De Boelelaan 1081, 1081 HV Amsterdam, Netherlands

DOI: http://dx.doi.org/10.3204/DESY-PROC-2012-02/107

Transverse momentum dependent (TMD) distribution and fragmentation functions are described as Fourier transforms of matrix elements containing non-local combinations of quark and gluon fields. The x and p_T dependent TMD functions appear in the parametrization of light-front correlators including a transverse (space-like) non-locality. The TMD functions relevant at leading order include spin-spin densities as well as momentum-spin densities and they are able to describe single-spin and azimuthal asymmetries, such as Sivers and Collins effects in SIDIS. Their moments involve higher-twist operators evaluated at zero-momentum (gluonic poles). They appear in observables with process-specific gluonic pole factors such as the sign in SIDIS versus Drell-Yan, which can be traced back to having TMD's with non-trivial process-dependent past- or future-pointing gauge links.

To incorporate transverse momentum dependent (TMD) distribution functions (PDF) and fragmentation functions (FF), in short referred to as TMD's, the starting point are forward matrix elements of parton fields, such as the quark-quark correlator

$$\Phi_{ij}(p|p) = \int \frac{d^4\xi}{(2\pi)^4}\; e^{i\,p\cdot\xi}\; \langle P|\overline{\psi}_j(0)\,\psi_i(\xi)|P\rangle, \tag{1}$$

where a summation over color indices is understood. For a single incoming fermion one would have $\Phi \propto (\not{p} + m)$. The quark-quark-gluon correlator is defined

$$\Phi^{\mu}_{A\,ij}(p-p_1,p_1|p) = \int \frac{d^4\xi\,d^4\eta}{(2\pi)^8}\; e^{i\,(p-p_1)\cdot\xi}\; e^{i\,p_1\cdot\eta}\; \langle P|\overline{\psi}_j(0)\,A^{\mu}(\eta)\,\psi_i(\xi)|P\rangle. \tag{2}$$

The basic idea is to isolate these hadronic (soft) parts in a full diagrammatic approach and parametrize them in terms of PDFs. This requires high energies in which case the momenta of different hadrons obey $P\cdot P' \propto Q^2$, where $s \sim Q^2$ is the hard scale in the process. In that case one can for each hadron correlator employ light-like vectors P and n such that $P\cdot n = 1$ (for instance $n = P'/P\cdot P'$) and make a Sudakov expansion of the parton momenta,

$$p = xP + p_T + (p\cdot P - xM^2)n, \tag{3}$$

with $x = p^+ = p\cdot n$. In any contraction with vectors outside the correlator, the component xP contributes at order Q, the transverse component at order M and the remaining component contributes at order M^2/Q. This allows consecutive integration of the components to obtain from the fully un-integrated result in Eq. 1 the TMD light-front (LF) correlator

$$\Phi_{ij}(x,p_T;n) = \int \frac{d\xi\cdot P\,d^2\xi_T}{(2\pi)^3}\; e^{i\,p\cdot\xi}\; \langle P|\overline{\psi}_j(0)\,\psi_i(\xi)|P\rangle\Big|_{\xi\cdot n=0}, \tag{4}$$

the collinear light-cone (LC) correlator

$$\Phi_{ij}(x) = \int \frac{d\xi \cdot P}{2\pi}\, e^{i\,p\cdot\xi}\, \langle P|\overline{\psi}_j(0)\,\psi_i(\xi)|P\rangle\Big|_{\xi\cdot n=\xi_T=0 \text{ or } \xi^2=0}, \tag{5}$$

or the local matrix element

$$\Phi_{ij} = \langle P|\overline{\psi}_j(0)\,\psi_i(\xi)|P\rangle\big|_{\xi=0}. \tag{6}$$

The importance of integrating at least the light-cone (minus) component $p^- = p\cdot P$ is that the expression is at equal time, i.e. time-ordering is not relevant anymore for TMD or collinear PDFs [1]. For local matrix elements one can calculate the anomalous dimensions, which show up as the Mellin moments of the splitting functions that govern the scaling behavior of the collinear correlator $\Phi(x)$. We note that the collinear correlator is not simply an integrated TMD. The dependence on upper limit $\Phi(x;Q^2) = \int^Q d^2p_T\,\Phi(x,p_T)$ is found from the anomalous dimensions (splitting functions). One has a α_s/p_T^2 behavior of TMD's that is calculable using collinear TMD's and which matches to the intrinsic non-pertubative p_T-behavior [2]. We note that in operator product expansion language, the collinear correlators involve operators of definite twist, while TMD correlators involve operators of various twist.

In order to determine the importance of a particular correlator in a hard process, one can do a dimensional analysis to find out when they contribute in an expansion in the inverse hard scale. Dominant are the ones with lowest canonical dimension obtained by maximizing contractions with n, for instance for quark or gluon fields the minimal canonical dimensions $\dim[\overline{\psi}(0)\not{n}\,\psi(\xi)] = \dim[F^{n\alpha}(0)\,F^{n\beta}(\xi)] = 2$, while an example for a multi-parton combination gives $\dim[\overline{\psi}(0)\not{n}\,A_T^\alpha(\eta)\,\psi(\xi)] = 3$. Equivalently, one can maximize the number of P's in the parametrization of Φ_{ij}. Of course one immediately sees that any number of collinear $n\cdot A(\eta) = A^n(\eta)$ fields doesn't matter. Furthermore one must take care of color gauge invariance, for instance when dealing with the gluon fields and one must include derivatives in color gauge invariant combinations. With dimension zero there is $iD^n = i\partial^n + gA^n$ and with dimension one there is $iD_T^\alpha = i\partial_T^\alpha + gA_T^\alpha$. The color gauge-invariant expressions for quark and gluon distribution functions actually include gauge-link operators,

$$U_{[0,\xi]} = \mathcal{P}\exp\left(-i\int_0^\xi d\zeta_\mu A^\mu(\zeta)\right) \tag{7}$$

connecting the non-local fields,

$$\Phi_{q\,ij}^{[U]}(x,p_T;n) = \int \frac{d\xi\cdot P\,d^2\xi_T}{(2\pi)^3}\, e^{i\,p\cdot\xi}\, \langle P|\overline{\psi}_j(0)\,U_{[0,\xi]}\,\psi_i(\xi)|P\rangle\Big|_{LF}, \tag{8}$$

$$\Phi_g^{[U,U']\,\mu\nu}(x,p_T) = \int \frac{d(\xi\cdot P)\,d^2\xi_T}{(2\pi)^3}\, e^{ip\cdot\xi}\,\mathrm{Tr}\,\langle P,S|\,F^{n\mu}(0)\,U_{[0,\xi]}\,F^{n\nu}(\xi)\,U'_{[\xi,0]}\,|P,S\rangle\Big|_{LF}. \tag{9}$$

For transverse separations, the gauge links involve gauge links running along the minus direction to $\pm\infty$ (dimensionally preferred), which are closed with one or more transverse pieces at lightcone infinity. The two simplest possibilities are $U^{[\pm]} = U^n_{[0,\pm\infty]}\,U^T_{[0_T,\xi_T]}\,U^n_{[\pm\infty,\xi]}$, leading to gauge-link dependent quark TMDs $\Phi_q^{[\pm]}(x,p_T)$. For gluons, the correlator involves color gauge-invariant traces of field-operators $F^{n\alpha}$, which are written in the color-triplet representation, requiring the inclusion of *two* gauge-links $U_{[0,\xi]}$ and $U'_{[\xi,0]}$. Again the simplest possibilities are

the past- and future-pointing gauge links $U^{[\pm]}$, giving even in the simplest case four gluon TMDs $\Phi_g^{[\pm,\pm]}(x, p_T)$.

Using the dimensional analysis to collect the leading contributions in an expansion in the inverse hard scale, one will need the above quark and gluon TMDs for the description of azimuthal dependence. Taking the Drell-Yan process as an example, one can look at the cross section depending on the (small!) transverse momentum q_T of the produced lepton pair,

$$\sigma(x_1, x_2, q_T) = \int d^2p_{1T}\, d^2p_{2T}\; \delta^2(p_{1T} + p_{2T} - q_T)\, \Phi_1^{[-]}(x_1, p_{1T}) \overline{\Phi}_2^{[-^\dagger]}(x_2, p_{2T}) \hat{\sigma}(x_1, x_2, Q), \quad (10)$$

which involves a convolution of TMDs. What is more important, it is the color flow in the process, in this case neutralized in initial state, that determines the path in the gauge link in the TMDs, in this case past-pointing ones. In contrast in semi-inclusive deep inelastic scattering one finds that the relevant TMD is $\Phi^{[+]}$ with a future-pointing gauge link. In a general process one can find more complex gauge links including besides Wilson line elements also Wilson loops. In particular when the transverse momentum of more than one hadron is involved, such as e.g. in the DY case above, it may be impossible to have just a single TMD for a given hadron because color gets entangled [3, 4].

The correlators including a gauge link can be parametrized in terms of TMD PDFs depending on x and p_T^2. For quarks, these include not only the functions that survive upon p_T integration, $f_1^q(x) = q(x)$, $g_1^q(x) = \Delta q(x)$ and $h_1^q(x) = \delta q(x)$, which are the well-known collinear spin-spin densities (involving quark and nucleon spin) but also momentum-spin densities such as the Sivers function $f_{1T}^{\perp q}(x, p_T^2)$ (unpolarized quarks in transversely polarized nucleon) and spin-spin-momentum densities such as $g_{1T}(x, p_T^2)$ (longitudinally polarized quarks in a transversely polarized nucleon).

In many cases, it is convenient to construct moments of TMDs in the same way as one considers moments of collinear functions. For $\Phi(x)$ in Eq. 5 one constructs moments

$$\begin{aligned} x^N \Phi(x) &= \int \frac{d\xi \cdot P}{2\pi}\; e^{i\,p\cdot\xi}\; \langle P|\overline{\psi}(0)\,(i\partial^n)^N\, U^n_{[0,\xi]}\,\psi(\xi)|P\rangle\Big|_{LC} \\ &= \int \frac{d\xi \cdot P}{2\pi}\; e^{i\,p\cdot\xi}\; \langle P|\overline{\psi}(0)\,U^n_{[0,\xi]}\,(iD^n)^N\,\psi(\xi)|P\rangle\Big|_{LC}. \end{aligned} \quad (11)$$

Integrating over x one finds the connection of the Mellin moments of PDFs with local matrix elements with specific anomalous dimensions, which via an inverse Mellin transform define the splitting functions. Similarly one can consider transverse moment weighting starting with the light-front TMD in Eq. 4,

$$p_T^\alpha\, \Phi^{[\pm]}(x, p_T; n) = \int \frac{d\xi \cdot P\, d^2\xi_T}{(2\pi)^3}\; e^{i\,p\cdot\xi}\; \langle P|\overline{\psi}(0)\,U^n_{[0,\pm\infty]}\,U^T_{[0_T,\xi_T]}\,iD_T^\alpha(\pm\infty)\,U^n_{[\pm\infty,\xi]}\psi(\xi)|P\rangle\Big|_{LF}. \quad (12)$$

Integrating over p_T gives the lowest transverse moment, which appears in the q_T-weighted result of Eq. 10. This moment involves twist-3 (or higher) collinear multi-parton correlators, in particular the quark-quark-gluon correlator

$$\Phi_F^{n\alpha}(x - x_1, x_1|x) = \int \frac{d\xi \cdot P\, d\eta \cdot P}{(2\pi)^2}\; e^{i\,(p-p_1)\cdot\xi}\; e^{i\,p_1\cdot\eta}\; \langle P|\overline{\psi}(0)\,U^n_{[0,\eta]}\,F^{n\alpha}(\eta)\,U^n_{[\eta,\xi]}\,\psi(\xi)|P\rangle\Big|_{LC}. \quad (13)$$

In terms of this correlator and the similarly defined correlator $\Phi_D^\alpha(x-x_1,x_1|x)$ one finds

$$\int d^2p_T\ p_T^\alpha\,\Phi^{[U]}(x,p_T) = \tilde{\Phi}_\partial^\alpha(x) + C_G^{[U]}\,\pi\,\Phi_G^\alpha(x), \tag{14}$$
$$\tilde{\Phi}_\partial^\alpha(x) = \Phi_D^\alpha(x) - \Phi_A^\alpha(x) = \int dx_1\,\Phi_D^\alpha(x-x_1,x_1|x) - \int dx_1\ PV\frac{1}{x_1}\,\Phi_F^{n\alpha}(x-x_1,x_1|x),$$
$$\Phi_G^\alpha(x) = \Phi_F^{n\alpha}(x,0|x).$$

The latter is referred to as a gluonic pole or ETQS-matrix element [5, 6]. They are multiplied with gluonic pole factors $C_G^{[U]}$ (e.g. $C_G^{[\pm]} = \pm 1$), that tell us that new functions are involved with characteristic process dependent behavior [7, 8]. This behavior is for the single transverse moments also coupled to the behavior under time reversal. While $\tilde{\Phi}_\partial^\alpha$ is T-even, Φ_G^α is T-odd. Since time reversal is a good symmetry of QCD, the appearance of T-even or T-odd functions in the parametrization of the correlators is linked to specific observables with this same character. In particular single spin asymmetries are T-odd observables.

The analogous treatment for fragmentation functions is simpler because the gluonic pole matrix elements vanish in that case [9, 10]. Nevertheless, there exist T-odd fragmentation functions, but their QCD operator structure is T-even, similar as the structure of $\tilde{\Phi}_\partial^\alpha$. There is thus no process dependence, which comes from the factors $C_G^{[U]}$ multiplying the gluonic poles.

The use of transverse moments in the description of azimuthal asymmetries via transverse momentum weighting of the cross section can be extended to higher moments involving higher harmonics such as $\cos(2\varphi)$. Also here process dependence may come in from double gluonic pole matrix elements $\Phi_{GG}^{\alpha\beta}$, which are twist four operators. This affects studies that involve the quark TMD $h_{1T}^{\perp q}(x,p_T)$ (Pretzelocity distribution) or the gluon Boer-Mulders function $h_1^{\perp g}(x,p_T)$ (linear gluon polarization in unpolarized targets).

A largely unexplored territory is that of TMD factorization, the evolution of TMDs [11] and the possible link to kT-factorization as used for small-x physics [12]. It will be addressed in some of the other talks in this session.

References

[1] M. Diehl and T. Gousset. Phys. Lett. **B428** (1998) 359–370, arXiv:hep-ph/9801233.

[2] J. C. Collins, D. E. Soper, and G. F. Sterman. Nucl. Phys. **B250** (1985) 199.

[3] T. C. Rogers and P. J. Mulders. Phys. Rev. **D81** (2010) 094006, arXiv:1001.2977 [hep-ph].

[4] M. Buffing and P. Mulders. JHEP **1107** (2011) 065, arXiv:1105.4804 [hep-ph].

[5] A. V. Efremov and O. V. Teryaev. Phys. Lett. **B150** (1985) 383.

[6] J.-W. Qiu and G. Sterman. Phys. Rev. Lett. **67** (1991) 2264–2267.

[7] A. Bacchetta, C. J. Bomhof, P. J. Mulders, and F. Pijlman. Phys. Rev. **D72** (2005) 034030, hep-ph/0505268.

[8] C. J. Bomhof and P. J. Mulders. JHEP **0702** (2007) 029, hep-ph/0609206.

[9] S. Meissner and A. Metz. Phys. Rev. Lett. **102** (2009) 172003, arXiv:0812.3783 [hep-ph].

[10] L. P. Gamberg, A. Mukherjee, and P. J. Mulders. Phys. Rev. **D77** (2008) 114026, arXiv:0803.2632 [hep-ph].

[11] S. M. Aybat, J. C. Collins, J.-W. Qiu, and T. C. Rogers. Phys.Rev. **D85** (2012) 034043, arXiv:1110.6428 [hep-ph].

[12] E. Avsar. arXiv:1203.1916 [hep-ph].

One-Hadron transverse target spin asymmetries at COMPASS

Christoph Adolph on behalf of the COMPASS Collaboration

christoph.adolph@physik.uni-erlangen.de
Universität Erlangen Nürnberg, Physikalisches Institut 4
Erwin-Rommel-Str. 1, 91058 Erlangen, Germany

DOI: http://dx.doi.org/10.3204/DESY-PROC-2012-02/174

The measurements of single spin asymmetries in semi-inclusive deep inelastic scattering on a transversely polarized target are an important part of the COMPASS physics program. By measuring the spin dependent azimuthal asymmetries in hadron production one can access both transversity - using the Collins fragmentation function - and the Sivers distribution function. The COMPASS collaboration has measured these asymmetries in the scattering of a 160 GeV/c polarized μ^+ beam off a transversely polarized ^{6}LiD (deuteron) target in the years 2002–2004 and off a transversely polarized NH_3 (proton) target in 2007 and 2010. In this contribution we present the results from the 2010 data for the Collins and Sivers asymmetries.

1 Introduction

The quark content of the nucleon at twist-two level in the collinear case can be fully characterized by three independent parton distribution functions (PDF), namely the unpolarized distribution function $f_1(x)$, the helicity distribution function $g_1(x)$ and the transverse spin distribution function $h_1(x)$, also called transversity. Due to its chiral-odd nature, transversity cannot be accessed directly via deep inelastic lepton-nucleon scattering (DIS), but can be measured in semi inclusive DIS in combination with another chirally odd function like the Collins fragmentation function (FF) $H_1^h(z, p_T^2)$ [1] in single hadron production. Other possibilities to access transversity, which are also investigated at COMPASS, are the Λ hyperon polarization and the coupling to the interference FF $H_1^\sphericalangle$ for the production of hadron pairs [2, 3]. Taking the intrinsic transverse momentum of the quarks k_T into account, the nucleon structure at leading twist can be described by eight transverse momentum dependent distribution functions, which are all measured at COMPASS. One of these is the Sivers function [4], which gives the correlation between the transverse spin of a nucleon and the intrinsic transverse momentum of unpolarized quarks.

COMPASS is a fixed target experiment at the CERN M2 beam line where the nucleon spin structure is investigated using a 160 GeV/c polarized μ^+ beam and polarized solid state targets. For measuring transverse spin effects a transversely polarized ^{6}LiD (deuterium) target (years 2002–2004) [5] and a transversely polarized NH_3 (proton) target (years 2007 and 2010) [6] were used. The proton target consists of three target cells, where a polarization of the free protons of up to 95% can be achieved.

2 Collins asymmetry

The Collins mechanism leads to a modulation in the azimuthal distribution of the hadrons produced in the fragmentation of a transversely polarized quark, which is given by $N_h(\phi_C) = N_h^0[1 + f\ P_T\ D_{NN}\ A_{Coll}\ \sin(\phi_C)]$. Here f is the target dilution factor, P_T is the target polarization and $D_{NN} = \frac{(1-y)}{(1-y+y^2/2)}$ is the spin transfer coefficient. The Collins angle ϕ_C is defined as $\phi_C = \phi_h + \phi_s - \pi$, where ϕ_h is the azimuthal angle of the hadron transverse momentum p_T and ϕ_S is the azimuthal angle of the nucleon spin with respect to the scattering plane. The Collins asymmetry A_{Coll} is given by

$$A_{Coll} = \frac{\sum_q e_q^2 \cdot h_1(x) \otimes H_1^h(z, p_T^2)}{\sum_q e_q^2 \cdot f_1(x) \otimes D_q^h(z, p_T^h)},$$

where D_q^h is the unpolarized FF and $\otimes$ indicates the convolutions over transverse momenta. Here $z = E_h/(E_\mu - E_{\mu'})$ is the fraction of the virtual photon energy carried by the hadron and p_T^h is the transverse momentum of the hadron with respect to the photon direction. In order to select only events from the DIS regime, kinematic cuts on the photon virtuality $Q^2 > 1\,(\mathrm{GeV}/c)^2$, on the fractional energy transfer of the muon $0.1 < y < 0.9$ and on the invariant mass of the hadronic final state $W > 5\,\mathrm{GeV}/c^2$ are applied. Furthermore for the selection of the hadrons $z > 0.2$ and $p_T^h > 0.1\,\mathrm{GeV}/c$ are required.
Figure 1 shows the preliminary results for the Collins asymmetry from the 2010 measurement as function of x, z and p_T^h for both positive and negative hadrons. The asymmetries are compatible with zero for small values of x but they show a clear signal in the valence region ($x > 0.1$) of opposite sign for positive and negative hadrons. The results are in a very good agreement with the measurement of 2007 at COMPASS and the results from HERMES [7]. The good agreement with the HERMES experiment, where transversity was measured using an electron beam at lower energies compared to COMPASS, indicates a weak Q^2 dependence of the Collins asymmetry.

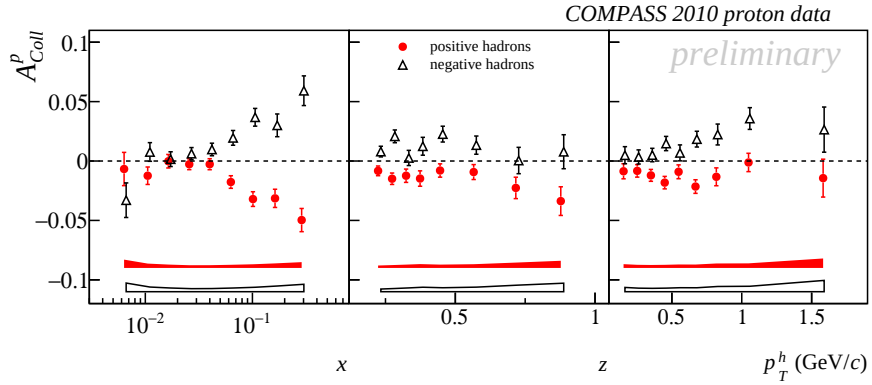

Figure 1: Collins asymmetries of 2010 proton data as a function of x, z and p_T^h for positive and negative hadrons. The bands correspond to the systematical error.

3 Sivers asymmetry

The Sivers effect is sensitive to the correlation of the transverse momentum of an unpolarized quark inside a transversely polarized nucleon and the transverse polarization of this nucleon. This effect is described by the Sivers function $f_{1T}^{\perp}(x, \vec{k_T})$. The number of produced hadrons $N_h(\phi_S) = N_h^0[1 + f\ P_T\ A_S\ \sin(\phi_S)]$ depends on the Sivers angle $\phi_S = \phi_h - \phi_s$. The Sivers asymmetry A_S is given by the convolution of the Sivers function and the unpolarized fragmentation function:

$$A_S = \frac{\sum_q e_q^2 \cdot f_{1T}^{\perp}(x, \vec{k_T}) \otimes D_q^h(z, p_T^h)}{\sum_q e_q^2 \cdot f_1(x) \otimes D_q^h(z, p_T^h)}$$

The preliminary results for the Sivers asymmetry from the 2010 run on a transversely polarized proton target are shown in Fig. 2 as a function of x, z and p_T. In contrast to the Collins asymmetry, for positive hadrons the Sivers asymmetry is clearly different from zero also for low values of x but it is small and compatible with zero for negative hadrons. The agreement with the previous COMPASS measurement from 2007 is again very good. In comparison with the results from the HERMES experiment [8] the Sivers asymmetries measured at COMPASS show the same trend but are smaller in absolute value, which indicates - in contrary to the Collins case - a possible Q^2 dependence.
For further investigation the asymmetries were also extracted for a y range of $0.05 < y < 0.1$. Since there is no data for $x < 0.032$ at this low-y selection, an additional cut $x > 0.032$ was applied on the standard sample for better comparison. Figure 3 shows the preliminary results for the low-y sample for the Sivers asymmetry together with the results from the standard sample for positive hadrons. A clear increase of the Sivers asymmetry is visible for the low-y data, which could be again explained by the smaller average Q^2 in this sample. Also latest extractions of the Sivers function with TMD evolution [9] indicate a large Q^2 dependence. For negative hadrons (not shown) no effect is visible for all three variables x, z and p_T^h.

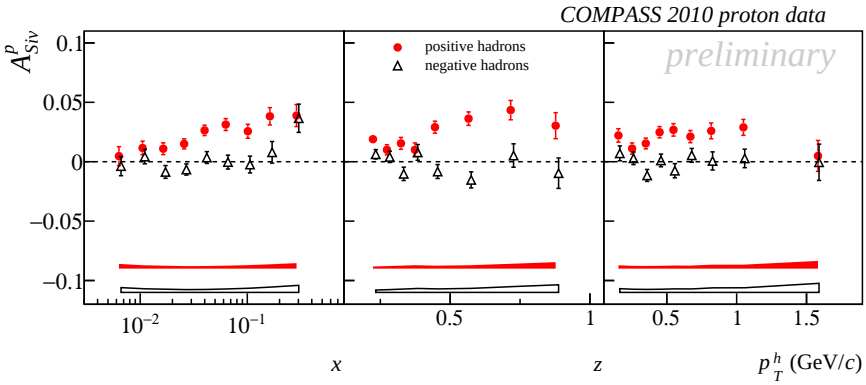

Figure 2: Sivers asymmetries of 2010 proton data as a function of x, z and p_T^h for positive and negative hadrons. The bands correspond to the systematical error.

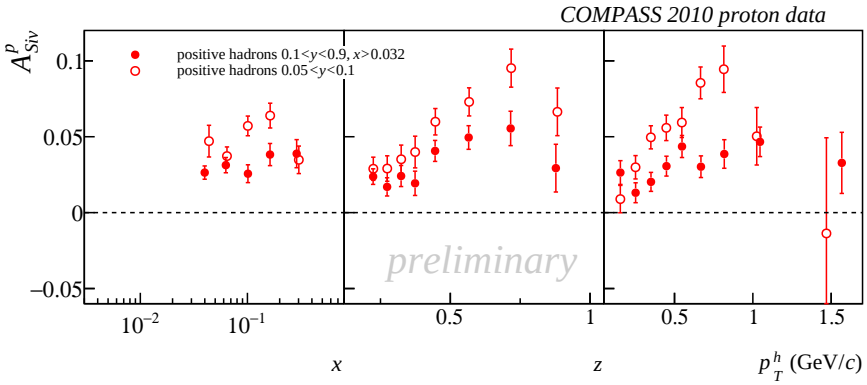

Figure 3: Sivers asymmetries of 2010 proton data as a function of x, z and p_T^h for $0.1 < y < 0.9$ and $0.05 < y < 0.1$ with $x > 0.032$, positive hadrons only.

4 Conclusion

The measurements on a transversely polarized proton target at COMPASS in 2010 show non-zero asymmetries for Collins and Sivers which are in very good agreement with the published results from the 2007 run. The higher statistics achieved in 2010 allows the investigation of different kinematical regions which show interesting results, especially for the Sivers asymmetries. The next steps will be the extraction of the asymmetries for identified hadrons making use of the COMPASS RICH detector as well as the other six transverse spin dependent asymmetries which are expected to be present in the expression of the SIDIS cross-section.

References

[1] J. Collins, Fragmentation of Transversely Polarized Quarks Probed in Transverse Momentum Distributions, Nucl. Phys. **B396** (1993) 161.

[2] C. Braun for the COMPASS Collaboration, COMPASS results on transverse spin asymmetries in two-hadron production in SIDIS, these Proceedings.

[3] COMPASS Collab., C. Adolph *et al.*, Transverse spin effects in hadron-pair production from semi-inclusive deep inelastic scattering, arXiv:1202.6150v1 [hep-ex] .

[4] D. Sivers, Single-spin production asymmetries from the hardscattering of pointlike constituents, Phys. Rev. **D41** (1) (1990) 83-90.

[5] COMPASS Collab., V. Alexakhin *et al.*, First Measurement of the Transverse Spin Asymmetries of the Deuteron in Semi-inclusive Deep Inelastic Scattering, Phys. Rev. Lett. **94** (20) (2005);

[6] COMPASS Collab., M.G. Alekseev *et al.*, Measurement of the Collins and Sivers asymmetries on transversely polarised protons, Physics Letters **B692** (4) (2010) 240-246.

[7] HERMES Collab., A. Airapetian *et al.*, Effects of transversity in deep-inelastic scattering by polarized protons, Physics Letters **B693** (1) (2010) 11-16

[8] HERMES Collab., A. Airapetian *et al.*, Observation of the Naive-T-Odd Sivers Effect in Deep-Inelastic Scattering, Phys. Rev. Lett. **103** (15) (2009)

[9] M. Boglione, Phenomenology of Sivers Effect with TMD Evolution, these Proceedings.

Flavor dependent azimuthal cosine modulations in SIDIS unpolarized cross section

Francesca Giordano[1], *Rebecca Truty*[2] on behalf of the HERMES Collaboration

[1] University of Illinois at Urbana-Champaign, Department of Physics, 1110 West Green Street, Urbana, IL 61801-3080, USA
[2] Gladstone Institutes, 1650 Owens Street, San Francisco, CA 94158-2261

DOI: http://dx.doi.org/10.3204/DESY-PROC-2012-02/137

The azimuthal $\cos\phi$ and $\cos 2\phi$ modulations of the distribution of hadrons produced in unpolarized semi-inclusive deep-inelastic scattering of electrons and positrons off hydrogen and deuterium targets have been measuread at the HERMES experiment. For the first time these modulations were determined in a four-dimensional kinematic space for positively and negatively charged pions and kaons separately, as well as for unidentified hadrons. These azimuthal dependences are sensitive to the transverse motion and polarization of the quarks within the nucleon via, e.g., the Cahn, Boer-Mulders and Collins effects.

1 Introduction

In lepton-nucleon deep-inelastic scattering (DIS), the structure of the nucleon is probed by the interaction of a high energy lepton with a target nucleon, via, at HERMES kinematics, the exchange of one virtual photon. If at least one of the produced hadrons is detected in coincidence with the scattered lepton, the reaction is called semi-inclusive deep-inelastic scattering (SIDIS):

$$l(\mathbf{k}) + N(\mathbf{P}) \rightarrow l'(\mathbf{k}') + h(\mathbf{P}_h) + X(\mathbf{P}_X), \tag{1}$$

where l (l') is the incident (scattered) lepton, N is the target nucleon, h is a detected hadron, X is the target remnant and the quantities in parentheses in equation (1) are the corresponding four-momenta.

If unintegrated over the hadron momentum component transverse to the virtual photon direction $P_{h\perp}$ (Fig. 1), the cross section can be written as [1]:

$$\begin{aligned} d\sigma \equiv \frac{d\sigma}{dx\,dy\,dz\,dP_{h\perp}^2\,d\phi_h} = \frac{\alpha^2}{xyQ^2}\left(1+\frac{\gamma^2}{2x}\right)\{A(y)\,F_{UU,T} + B(y)\,F_{UU,L} + \\ C(y)\,\cos\phi_h F_{UU}^{\cos\phi_h} + B(y)\,\cos 2\phi_h F_{UU}^{\cos 2\phi_h}\}, \end{aligned} \tag{2}$$

where $F_{UU}^{\cos\phi_h}$, $F_{UU}^{\cos 2\phi_h}$, are azimuthally dependent structure functions, and are related respectively to $\cos\phi_h$ and $\cos 2\phi_h$ modulations, with ϕ_h the azimuthal angle of the hadron production plane around the virtual-photon direction (Fig. 1). In equation 2, the subscripts UU stand for unpolarized beam and target, T (L) indicates the transverse (longitudinal) polarization of the virtual photon, α is the electromagnetic coupling constant, $\gamma = 2Mx/Q$ with M the target mass, $A(y) \sim (1 - y + 1/2y^2)$, $B(y) \sim (1 - y)$, and $C(y) \sim (2 - y)\sqrt{1-y}$.

Here Q^2 and y are respectively the negative squared four-momentum and the fractional energy of the virtual photon, x the Bjorken scaling variable and z the fractional energy of the produced hadron.

Among possible mechanisms, two are expected to give important contributions to the azimuthal dependence of the unpolarized cross section in the hadron transverse momentum range accessible at HERMES. The first one is called the *Cahn effect* [2, 3], a pure kinematic effect where the azimuthal modulations are generated by the non-zero intrinsic transverse motion of quarks. In the second mechanism, the *Boer-Mulders effect* [4], $\cos\phi_h$ and $\cos 2\phi_h$ modulations originate from the coupling of the quark intrinsic transverse momentum and intrinsic transverse spin, a kind of spin-orbit effect.

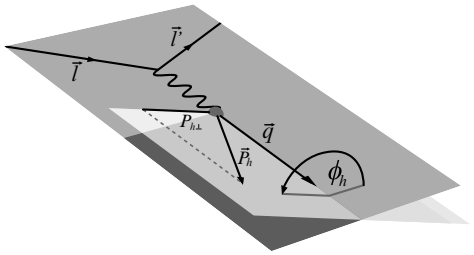

Figure 1: Definition of the azimuthal angle ϕ_h between scattering plane, spanned by the in- and out-going lepton three-momenta ($\vec{l}$, $\vec{l'}$), and the hadron production plane, defined by the three-momenta of the virtual photon ($\vec{q}$) and produced hadron ($\vec{P_h}$).

2 Multi-dimensional unfolding

In order to study the new structure functions $F_{UU}^{\cos\phi_h}$ and $F_{UU}^{\cos 2\phi_h}$ defined in Eq. (2), a measure of the azimuthal modulation of the unpolarized cross section is needed, which can be extracted via the so-called $\langle\cos n\phi_h\rangle$-moments:

$$\langle\cos n\phi_h\rangle \;=\; \frac{\int \cos n\phi_h \, d\sigma \, d\phi_h}{\int d\sigma \, d\phi_h} \tag{3}$$

with $n = 1, 2$ and $d\sigma$ defined in equation 2.

The extraction of these cosine moments from data is challenging because they couple to a number of *experimental sources* of azimuthal modulations, *e.g.* detector geometrical acceptance and higher-order QED effects (*radiative effects*). Moreover, in the typical case, the event sample is binned only in one variable (1-dimensional analysis), and integrated over the full range of all the other ones, but the mentioned structure functions and the instrumental spurious contributions depend on all the kinematic variables x, y, z and $P_{h\perp}$ simultaneously. Therefore a 4-dimensional analysis is needed to take into account the correlations between the physical modulations and those spurious contributions, where the event sample is binned simultaneously in all the relevant variables [1]. Therefore, a detailed Monte Carlo simulation of the experimental apparatus including radiative effects is used to define a 4-D unfolding procedure [6] that corrects the extracted cosine moments for radiative and instrumenthal effects.

The 4-D unfolded yields are fit to the functional form:

$$\mathcal{A}(1 + \mathcal{B}\cos\phi_h + \mathcal{C}\cos 2\phi_h) \tag{4}$$

where $\mathcal{B} = 2\langle\cos\phi_h\rangle$ and $\mathcal{C} = 2\langle\cos 2\phi_h\rangle$ represent the desired moments. One moment pair ($2\langle\cos\phi_h\rangle$, $2\langle\cos 2\phi_h\rangle$) for each of the 4-D kinematic bins is extracted, and the moment dependences on a single kinematic variable is obtained projecting the 4-D results onto the variable

[1] For a more detailed discussion about one- and multi-dimensional analysis see [5].

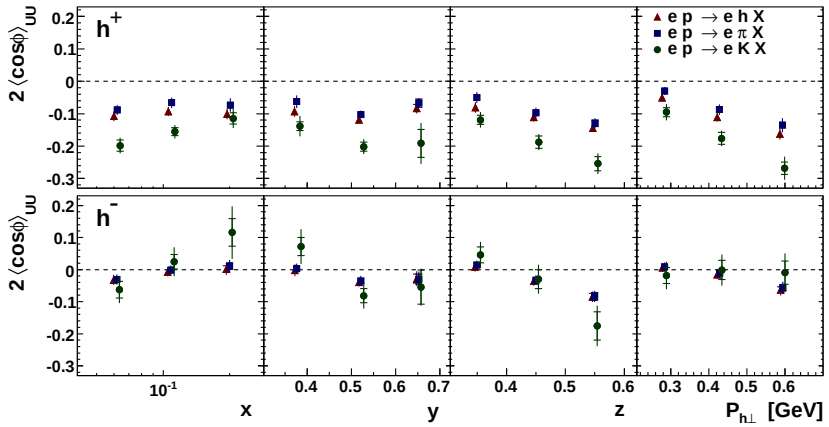

Figure 2: $\langle \cos \phi_h \rangle$ moments for positive (upper panel) and negative (lower panel) hadrons, extracted from hydrogen data projected versus the kinematic variables x, y, z and $P_{h\perp}$.

under study by weighting the moment in each bin with the corresponding 4π cross section obtained from a Monte Carlo calculation [2].

3 Results

The cross section unintegrated over hadron transverse momentum gives access to new exciting aspects of the nucleon structure, which are currently under intense theoretical investigations. To date, HERMES results [8] represents the most complete data set on the subject, and allows access to flavor dependent information on the nucleon internal transverse degrees of freedom.

The projected moments for pions (blue squares), kaons (green circles) and unidentified hadrons (red triangles) are shown projected in the relevant kinematic variables in figures 2 and 3 for $\langle \cos \phi_h \rangle$ (upper panel) and $\langle \cos 2\phi_h \rangle$ (middle panel) moments, respectively.

The $\langle \cos \phi_h \rangle$ moments are found to be negative for all positively charged hadron types, with a significative larger magnitude in the kaon case. All negative hadrons types present moments slightly negative, with a magnitude smaller than for the positive hadron case.

The $\langle \cos 2\phi_h \rangle$ moments show a different behavior in pions with respect to kaons. For pions, the $\langle \cos 2\phi_h \rangle$ moments have opposite sign for positive and negative pions: both modulations are clearly charge dependent, and this feature is considered as an evidence of a non-zero Boer-Mulders effect [9, 10, 11, 12].

The absolute value of kaon $\cos 2\phi_h$ modulations are found to be larger in magnitude than pions ones. Furthermore, while pion $\cos 2\phi_h$ modulations change sign between differently charged pions, kaon modulations are negative for both kaon charges.

The unidentified hadrons present similar trends as the pions but, particularly for the $\langle \cos 2\phi_h \rangle$ moments, the hadrons are shifted to lower values than the pions. The discrepancy between hadrons and pions is consistent with the observed kaon moments.

[2] Details on the full 4-D unfolding and extraction procedure as well as on the projection versus the single variable can be found in [7].

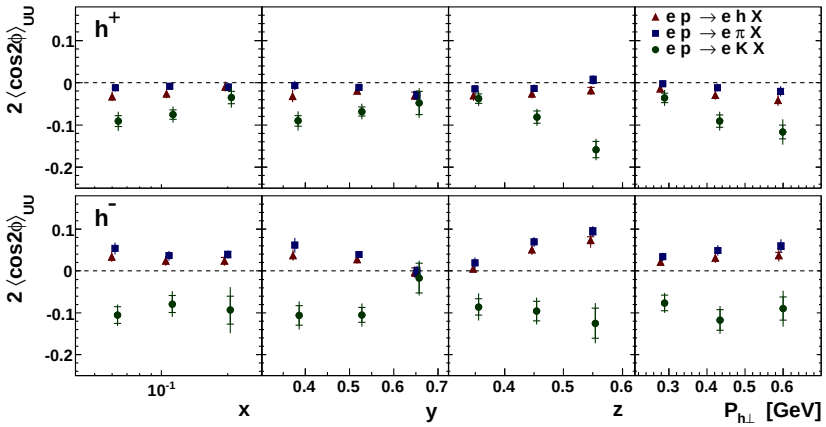

Figure 3: $\langle \cos 2\phi_h \rangle$ moments for positive (upper panel) and negative (lower panel) hadrons, extracted from hydrogen data projected versus the kinematic variables x, y, z and $P_{h\perp}$.

The cosine modulations have been extracted also for data collected with deuterium target, and they are found to be compatible with hydrogen results, both for unidentified hadrons, pions and kaons. This suggests that similar contributions arise from *up* and *down* quarks to the cosine modulations.

References

[1] Bacchetta A et al, 2007, *JHEP* **02** 093

[2] Cahn R N, 1978, *Phys. Lett.* B **78** 269

[3] Cahn R N, 1989, *Phys. Rev.* D **40** 3107

[4] Boer D and Mulders P J, 1998, *Phys. Rev.* D **57** 5780

[5] Giordano F, HERMES Collaboration, 2008, *Proc. of 2nd Int. Workshop on Transvers Polarisation Phenomena in Hard Processes (Transversity 2008)* Ferrara, Italy, May 28 - 31

[6] Cowan G, 1998, *Statistical Data Analysis* (Oxford:Clarendon Press)

[7] Giordano F and Lamb R, HERMES Collaboration, 2009, AIP Conf. Proc. **1149** 423 (*Preprint* hep-ph/0901.2438)

[8] A. Airapetian et al., HERMES Collaboration, 2012, arXiv:1204.4161v2 [hep-ex], submitted to PRD, in press.

[9] Gamberg L P, Goldstein G R and Schlegel M, 2008, *Phys. Rev.* D **77** 094016

[10] Barone V, Prokudin A and Ma B, 2008, *Phys. Rev.* D **78** 045022

[11] Zhang B, Lu Z, Ma B and Schmidt I, 2008, *Phys. Rev.* D **78** 094035

[12] Barone V, Prokudin A and Melis S, 2010, *Phys. Rev.* D **81** 114026

Unbiased Polarised Parton Distribution Functions and their Uncertainties

Emanuele R. Nocera[1], *Stefano Forte*[1], *Giovanni Ridolfi*[2], *Juan Rojo*[3]

[1]Dipartimento di Fisica, Università di Milano and INFN, Sezione di Milano,
Via Celoria 16 I-20133 Milano, Italy
[2]Dipartimento di Fisica, Università di Genova and INFN, Sezione di Genova,
Via Dodecaneso 33 I-16146 Genova, Italy
[3]CERN, PH Department, TH Unit, CH-1211 Genève 23, Switzerland

DOI: http://dx.doi.org/10.3204/DESY-PROC-2012-02/273

We present preliminary results on the determination of spin-dependent, or polarised, Parton Distribution Functions (PDFs) from all relevant inclusive polarised DIS data. The analysis is performed within the NNPDF approach, which provides a faithful and statistically sound representation of PDFs and their uncertainties. We describe how the NNPDF methodology has been extended to the polarised case, and compare our results with other recent polarised parton sets. We show that polarised PDF uncertainties can be sizeably underestimated in standard determinations, most notably for the gluon.

The interest in spin-dependent, or polarised, Parton Distribution Functions (PDFs) of the nucleon is mainly motivated by the desire to understand its spin structure in terms of its quark and gluon parton substructure. It largely originates from the first EMC results [1], originally interpreted as an indication that quark and anti-quark intrinsic angular momenta only contribute a small fraction of the full nucleon spin. A faithful knowledge of polarised PDFs is also an essential ingredient for exploring QCD beyond the helicity-averaged case and for studying the phenomenology of spin-dependent processes.

Polarised PDFs have been investigated with increasing precision in recent years. On one hand, several experiments have contributed a large amount of data for a variety of processes, mainly inclusive polarised deep-inelastic scattering (DIS) but also proton-proton collisions and semi-inclusive reactions. On the theoretical side, the interest has been ultimately focussed on the global reconstruction of PDFs, together with their uncertainties. At least four groups have constructed such polarised PDF sets recently: BB [2], AAC [3], LSS [4] and DSSV [5]. These sets slightly differ in the choice of datasets, PDF parametrisation and details of the QCD analysis (such as the treatment of higher-twist corrections). Nevertheless, they are all based on simple functional forms of the momentum fraction dependence of the PDFs at the refence scale (typically, a power-like behavior is assumed both at large and small momentum fraction) and on the Hessian approach for the estimate of uncertainties. Two main shortcomings are known to affect this methodology. The first one concerns how to propagate errors consistently from data to fitted parameters and then to observables: this is usually done by assuming Gaussian linear error propagation, which is not always adequate, in particular in those kinematical regions where few data are available. The second one consists in assessing the theoretical bias introduced by a fixed functional parton parametrisation. This is particularly delicate for polarised PDFs,

owing to the quantity and the quality of the data, which are respectively less abundant and less accurate than their unpolarised counterparts.

In order to overcome these difficulties, in recent years the NNPDF collaboration has developed a new approach to parton fitting (see, for example, [6, 7, 8, 9, 10] and references therein). This new technique, designed to provide a faithful representation of PDFs and their uncertainties, is based on robust set of statistical tools, including Monte Carlo and Neural Network methods.

In the NNPDF approach, experimental data are sampled by generating an ensemble of Monte Carlo replicas with data probability distribution; individual replicas are allowed to fluctuate in such a way that the mean value, standard deviation and correlation computed over Monte Carlo ensemble reproduce the experimental values, provided the sample is sufficiently large. Fitting an ensemble of parton distributions automatically propagates statistical fluctuations to the PDFs and then to observables. Hence, expectation values and uncertainties of PDFs (or of any observable) are obtained by considering their Monte Carlo integrals over the ensemble of replicas. Furthermore, in this approach neural networks are used as unbiased interpolants for PDF parametrisation. Since they provide functions depending on a large number of parameters, they are very flexible tools: this flexibility allows one to reduce the bias associated to the choice of some fixed functional form.

The NNPDF approach has been succesfully applied to the determination of unpolarised PDFs and these NNPDF sets are routinely used by Tevatron and LHC collaborations for data analysis and data-theory comparisons. We will present here some preliminary results obtained by extending the NNPDF approach to the determination of a set of polarised PDFs. After illustrating the main features of our analysis, we will compare our results to those obtained by other collaborations. Specifically, we will see that the uncertainty on some polarised PDFs, most notably on the gluon PDF, are rather larger than previously estimated.

The first NNPDF analysis of polarised PDFs, `NNPDFpol1.0` henceforth, is based on a comprehensive set of polarised DIS data. We exclude from our analysis data points with $Q^2 \leq Q^2_{\rm cut} = 1$ GeV^2, since below such energy scale perturbative QCD cannot be considered reliable. We also impose $W^2 \geq W^2_{\rm cut} = 6.25$ GeV^2 for the squared invariant mass $W^2 = Q^2(1-x)/x$, according to the study presented in Ref. [11]. This choice removes the dependence of results on possible dynamical higher-twist effects, which we do not include even though we do include target-mass corrections. The dataset used in the `NNPDFpol1.0` analysis is shown, after kinematic cuts, in Fig. 1.

The experimental data used in this fit do not allow a full separation of individual flavour and anti-flavour parton densities. Hence, we define, for each light flavour q, the net amount of quark-antiquark spin density

$$\Delta q(x,Q^2) = q^{\uparrow\uparrow}(x,Q^2) + \bar{q}^{\uparrow\uparrow}(x,Q^2) - q^{\uparrow\downarrow}(x,Q^2) + \bar{q}^{\uparrow\downarrow}(x,Q^2) \ ,$$

where the superscript $\uparrow\uparrow$ ($\uparrow\downarrow$) denotes that the parton spin is parallel (antiparallel) to the proton spin. We parametrise PDFs at the scale $Q_0^2 = 1$ GeV^2 by choosing, besides the gluon density $\Delta g(x,Q_0^2) \equiv g^{\uparrow\uparrow} - g^{\uparrow\downarrow}$, the following three linear combinations of light quarks: the flavour-singlet

$$\Delta\Sigma(x,Q_0^2) \equiv \Delta u(x,Q_0^2) + \Delta d(x,Q_0^2) + \Delta s(x,Q_0^2) \ ,$$

the non-singlet triplet and the non-singlet octet

$$\Delta T_3(x,Q_0^2) \equiv \Delta u(x,Q_0^2) - \Delta d(x,Q_0^2) \ , \qquad \Delta T_8(x,Q_0^2) \equiv \Delta u(x,Q_0^2) + \Delta d(x,Q_0^2) - 2\Delta s(x,Q_0^2) \ .$$

Each of these four combinations is parametrised by a neural network, with a total number of $\mathcal{O}(200)$ parameters, to be compared to $\mathcal{O}(10-20)$ used in other existing fits.

A fast and accurate evaluation of polarised parton distributions, as required by the fitting, is achieved with the `FastKernel` method [12]. The accuracy of polarised PDF evolution has been shown to be $\mathcal{O}(10^{-5})$ comparing with the `HOPPET` code.

Theoretical constraints are taken into account during the fitting procedure. We have imposed positivity of physical cross-sections, which implies that the polarised structure function g_1 is bounded by its unpolarised counterparts F_1, so that $\left|g_1(x,Q^2)\right| \leq F_1(x,Q^2)$ [13]. For consistency, the unpolarised structure functions have been computed from the recent NNPDF2.1 unpolarised PDF determination [10]. We have also used SU(3) symmetry to relate the first moments

$$a_3 \equiv \int_0^1 dx \Delta T_3(x,Q_0^2) \ , \qquad a_8 \equiv \int_0^1 dx \Delta T_8(x,Q_0^2) \ , \tag{1}$$

to the determination of a_3 and a_8 from baryon decay constants (allowing for large uncertainties). We have also performed a fit in which we have relaxed the first constraint in Eq. 1 and we have considered a_3 as a fit parameter, in which case we have found $a_3 = 1.21 \pm 0.08$ to be compared with the global average from experimental measurement of β-decay, $g_A = 1.2701 \pm 0.0025$ [14]. This result provides a consistency check of the fitting procedure and validates the Bjorken sum rule with an accuracy of about 10%.

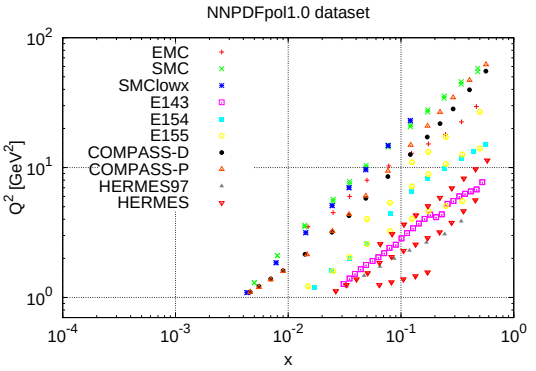

Figure 1: Experimental dataset after kinematic cuts for the `NNPDFpol1.0` analysis.

We show preliminary results for the `NNPDFpol1.0` set at initial scale $Q_0^2 = 1$ GeV^2 together with DSSV08 [5] and BB10 [2] determinations (Fig. 2). In general, we can see that all PDFs show larger error bands than previously estimated, in particular at very small- or high-x values, where no DIS data are available. This is especially the case for the polarised gluon PDF, which cannot be constrained by the available DIS data. We also notice that, at least for the non-singlet triplet, the `NNPDFpol1.0` analysis seems to agree better with DSSV08 than with BB10.

Finally, we compute the first momenta of polarised singlet and gluon PDFs

$$\Delta\Sigma(Q^2) \equiv \int_0^1 dx \Delta\Sigma(x,Q^2) \ , \qquad \Delta g(Q^2) \equiv \int_0^1 dx \Delta g(x,Q^2)$$

	NNPDFpol1.0	DSSV08 [5]	BB10 [2]	LSS10 [4]	AAC08 [3]
$\Delta\Sigma(Q^2)$	0.31 ± 0.10	0.37 ± 0.04	0.19 ± 0.08	0.21 ± 0.03	0.24 ± 0.07
$\Delta g(Q^2)$	-0.2 ± 1.4	-0.06 ± 0.18	0.46 ± 0.43	0.32 ± 0.19	0.63 ± 0.19

Table 1: The first momenta of the singlet and gluon polarised PDFs at the scale $Q^2 = 4$ GeV^2 in the $\overline{\text{MS}}$ scheme.

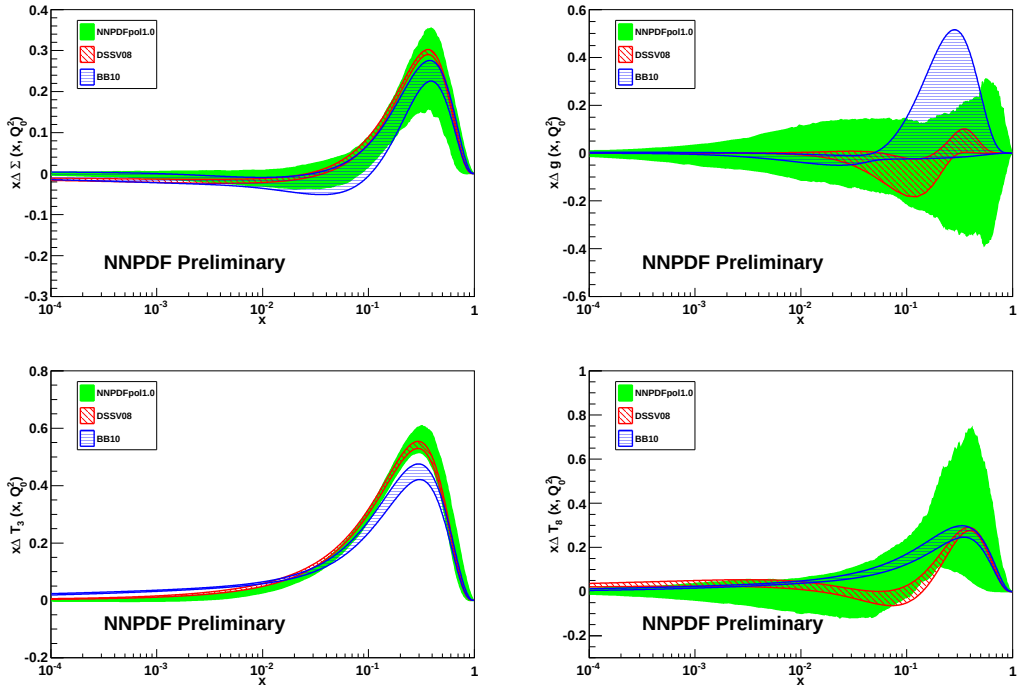

Figure 2: The `NNPDFpol1.0` parton set at the initial evolution scale $Q_0^2 = 1$ GeV^2 compared to DSSV08 [5] and BB10 [2] determinations. Uncertainties on `NNPDFpol1.0` parton distributions are computed at 68% confidence level (see Ref. [9] for details).

at the scale $Q^2 = 4\,\text{GeV}^2$ and compare with the results obtained by other collaborations (Tab. 1). Again, we notice the uncertainties of our results: the error on the singlet momentum is between two and four times larger than that from other collaborations, while the error on gluon momentum is almost one order of magnitude larger.

More precise determinations of polarised PDFs will have to resort to data coming from other processes but DIS, such as open charm and jet production in fixed target experiments or inclusive jet and W boson production in proton-proton collisions. We plan to extend our analysis to these data in the near future, and also to use our PDF set to determine the strong coupling constant α_s.

Acknowledgements

The research of J. R. has been supported by a Marie Curie Intra–European Fellowship of the European Community's 7th Framework Programme under contract number PIEF-GA-2010-272515.

References

[1] J. Ashman *et al.* Phys.Lett. **B206** (1988) 364.

[2] J. Blumlein and H. Bottcher. Nucl.Phys. **B841** (2010) 205–230, arXiv:1005.3113 [hep-ph].

[3] M. Hirai and S. Kumano. Nucl.Phys. **B813** (2009) 106–122, arXiv:0808.0413 [hep-ph].

[4] E. Leader, A. V. Sidorov, and D. B. Stamenov. Phys.Rev. **D82** (2010) 114018, arXiv:1010.0574 [hep-ph].

[5] D. de Florian, R. Sassot, M. Stratmann, and W. Vogelsang. Phys. Rev. **D80** (2009) 034030, arXiv:0904.3821 [hep-ph].

[6] L. Del Debbio, S. Forte, J. I. Latorre, A. Piccione, and J. Rojo. JHEP **03** (2007) 039, arXiv:hep-ph/0701127.

[7] R. D. Ball *et al.* Nucl. Phys. **B809** (2009) 1–63, arXiv:0808.1231 [hep-ph].

[8] R. D. Ball *et al.* Nucl. Phys. **B823** (2009) 195–233, arXiv:0906.1958 [hep-ph].

[9] R. D. Ball, L. Del Debbio, S. Forte, A. Guffanti, J. I. Latorre, *et al.* Nucl.Phys. **B838** (2010) 136–206, arXiv:1002.4407 [hep-ph].

[10] R. D. Ball *et al.* Nucl.Phys. **B855** (2012) 153–221, arXiv:1107.2652 [hep-ph].

[11] C. Simolo. arXiv:0807.1501 [hep-ph].

[12] G. P. Salam and J. Rojo. Comput. Phys. Commun. **180** (2009) 120–156, arXiv:0804.3755 [hep-ph].

[13] G. Altarelli, S. Forte, and G. Ridolfi. Nucl. Phys. **B534** (1998) 277–296, arXiv:hep-ph/9806345.

[14] K. Nakamura *et al.* J.Phys.G **G37** (2010) 075021.

Longitudinal semi-inclusive double-spin asymmetries at HERMES

Polina Kravchenko[1] on behalf of the HERMES collaboration

[1]DESY, Notkestraße 85, 22607 Hamburg, Germany

DOI: http://dx.doi.org/10.3204/DESY-PROC-2012-02/117

Final results are reported on the semi-inclusive double-spin asymmetries A_{LL} for charged hadrons and identified charged pions and kaons measured at HERMES longitudinally polarized hydrogen and deuterium targets and the longitudinally polarized 27.6 GeV HERA lepton beam. The kinematic dependences of the azimuthal $cos\phi$ moments of A_{LL} simultaneously on Bjorken-x, the hadron energy fraction z and hadron transverse momentum $p_{h\perp}$ are explored. The x, z and $p_{h\perp}$ dependencies of $A_{LL}^{cos\phi}$ asymmetry were found to be small, no dependence on the kinematic variables was observed.

1 Introduction

Longitudinal double-spin asymmetries in polarized deep inelastic scattering (DIS) have since many years provided a window to study the spin-structure of the nucleon by HERMES [1] and other experimental collaborations. At fixed beam energy, the inclusive virtual-photon nucleon asymmetry A_1 is defined in terms of the photoabsorption cross section in the two possible virtual-photon-nucleon spin configurations and is a function of only two kinematic variables:

$$A_1(x,Q^2) = \frac{\sigma_{1/2} - \sigma_{3/2}}{\sigma_{1/2} + \sigma_{3/2}}(x,Q^2) \ , \qquad (1)$$

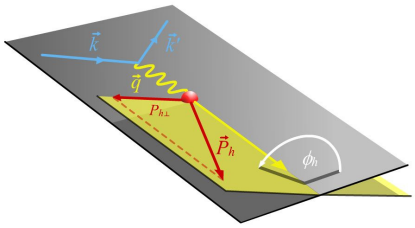

Figure 1: $p_{h\perp}$ and $\phi = \phi_h$ defined for SIDIS

where x is the Bjorken scaling variable and -Q^2 is the squared four-momentum transfer of the virtual photon Q^2. In leading order QCD, one can express this asymmetry as the ration of the charge-weighted sums of polarization-dependent to polarization-independent quark densities:

$$A_1(x,Q^2) \sim \frac{\sum_q \Delta q(x,Q^2)}{\sum_q e_q^2 q(x,Q^2)} \ . \qquad (2)$$

In semi-inclusive DIS (SIDIS), the measurement of a final state hadron in conjunction with the scattered lepton provides additional information about the flavor-dependence of the parton structure and about the fragmentation process through which these hadrons are produced. The presence of the hadron provides us with three additional possible kinematic degrees of freedom,

for which we will use z, the fraction of the virtual photon's momentum carried by the hadron, $p_{h\perp}$, the transverse momentum of the hadron with respect to the virtual photon direction, and ϕ, the azimuthal angle between the hadron production plane and the lepton sattering plane, depicted in Fig. 1.

The semi-inclusive asymmetry, A_1^h can then be expressed

$$A_1^h(x, Q^2, z_h, p_{h\perp}, \phi) = \frac{\sigma_{1/2}^h - \sigma_{3/2}^h}{\sigma_{1/2}^h + \sigma_{3/2}^h}(x, Q^2, z_h, p_{h\perp}, \phi) \ , \tag{3}$$

where h represent the hadron observed.

The decision to present the kinematic dependences is motivated be several factors. First, the additional kinematic dimensions contain information that could be used to extract information otherwise unavailable when semi-inclusive parameters, sensitive specifically to the fragmentation process, are integrated over. For example, the two sources of transverse momentum, the parton distribution related intrinsic $k_\perp$ and fragmentation related $p_\perp$ combine to make the $p_{h\perp}$ dependence of the asymmetry. A multidimensional dataset potentially provides additional leverage for disentangling these individual contributions as x for example resides exclusively in the parton densities and z in the fragmentation function. It is also increasingly clear that empirical results should be made available with as few model assumptions and model-related kinematic requirements as are reasonable in order to accommodate the broadest possible range of theoretical models and assumptions. Finally, the growing interest in unintegrated cross sections reminds us that providing fuller kinematic dependence only may simplity theoretical interpretation.

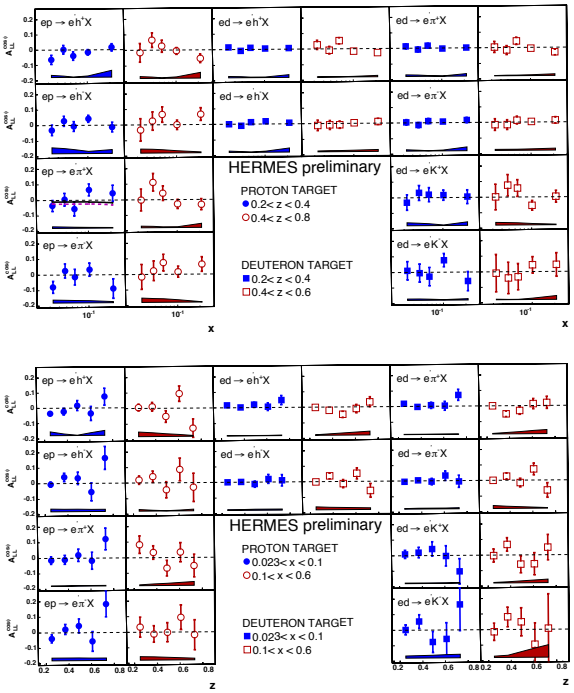

Figure 2: The asymmetries $A_{p,d}^{\cos\phi}$ as a function of x (top) in two z slices and z in two x slices (bottom) for positively and negatively charged hadrons, pions and kaons.

2 Measurement of asymmetries

The data presented here were collected using the HERMES spectrometer [2] at the HERA storage ring during the years 1996-2000. A longitudinally polarized lepton (electron or positron) beam was scattered off a longitudinally polarized hydrogen (H) or deuterium (D) gas target.

The polarization of the target was flipped approximately every 60(90) seconds foe H(D) to provide yields in both spin states and to reduce systematic uncertainties related to the stability of the experimental setup. The asymmetries are computed using the same procedure presented in prior papers on longitudinally polarized SIDIS asymmetries [3]. The Born lepton-nucleon asymmetry is constructed as follows:

$$A_{||}^{B} = \frac{C_{\phi_h}}{f_D}\Big[\frac{L^{\vec{}}_{\Rightarrow} N^{\vec{}}_{(h)}{}^{\Leftarrow} - L^{\vec{}}_{\Leftarrow} N^{\vec{}}_{(h)}{}^{\Rightarrow}}{L^{\vec{}}_{P}{}^{\Rightarrow} N^{\vec{}}_{(h)}{}^{\Leftarrow} + L^{\vec{}}_{P}{}^{\Leftarrow} N^{\vec{}}_{(h)}{}^{\Rightarrow}}\Big]_B \ , \tag{4}$$

where $N^{\vec{}}_{(h)}{}^{\Leftarrow}$ represent yields (hadron h tagged for SIDIS samples) containing events which meet the kinematic requirements and $L^{\vec{}}_{\Rightarrow}{}^{(\vec{}_{\Leftarrow})}$ and $L^{\vec{}}_{P}{}^{\Rightarrow}{}^{(\vec{}_{\Leftarrow})}$ represent the luminosity and the polarization weighted luminosity in the parallel (antiparallel) beam-target helicity configuration. The square brackets, $[]_B$, indicate that the experimental asymmetry is corrected to Born level, i.e. unfolded for radiative and detector smearing, using Born and smeared Monte Carlo simulations according to the essentially model-independent procedure described in [3]. The factor f_D represents the dilution of the polarization the nucleon with respect to that of deuterium the nucleus.

The factor C_ϕ is a correction applied to the semi-inclusive asymmetries that compensates for the influence of the spectrometer acceptance in the implicit integration over kinematic variables in the semi-inclusive yields. It is primarily the azimuthal integral (over ϕ), which combines a non-uniform acceptance with azimuthal modulations in the unpolarized yield which are contained in the denominator of the semi-incusive asymmetries. Such modulations are produced, for example, by the Cahn Effect [4]. In practice, the measured asymmetry that we measure, $\tilde{\mathrm{A}}$, involves a convolution with an acceptance function $\xi(\phi)$:

$$\tilde{A}_1^h(x, Q^2, z, p_{h\perp}) = \frac{\int d\phi \Delta\sigma^h(x, Q^2, z, p_{h\perp}, \phi)\xi(\phi)}{\int d\phi \sigma^h(x, Q^2, z, p_{h\perp}, \phi)\xi(\phi)}. \tag{5}$$

The ϕ modulation of the SIDIS cross section can be decomposed into $\cos(\phi)$ and $\cos(2\phi)$ moments as follows:

$$\begin{aligned}\frac{d\sigma}{dx\ dQ^2\ dz\ dp_{h\perp}\ d\phi} \propto\ & \sigma_{UU}(x, Q^2, z, p_{h\perp}) + \\ +\ & \sigma_{UU}^{\cos(\phi)}(x, Q^2, z, p_{h\perp})\ \cos(\phi) + \sigma_{UU}^{\cos(2\phi)}(x, Q^2, z, p_{h\perp})\ \cos(2\phi) + \\ & + P_B\ P_T\Big[\sigma_{LL}(x, Q^2, z, p_{h\perp}) + \\ +\ & \sigma_{LL}^{\cos(\phi)}(x, Q^2, z, p_{h\perp})\ \cos(\phi) + \sigma_{LL}^{\cos(2\phi)}(x, Q^2, z, p_{h\perp})\ \cos(2\phi)\Big].\end{aligned} \tag{6}$$

The subscript UU of the first three coefficient functions denotes unpolarized beam and unpolarized target, whilethe subscript LL denotes longitudinally polarized beam and longitudinally polarized target. P_b and P_t represent the longitudinal polarizations of beam and target – which are zero in the unpolarized case.

In order to correct for this effect in the unpolarized denominator of the asymmetry, a recent parameterization of the azimuthal modulation measured by HERMES [5] was used. This parameterization was produced by unfolding unpolarized semi-inclusive yields in all five kinematic

degrees of freedom simultaneously. The unfolding was conducted in 5000 ($5x \times 4y \times 5z \times 5p_{h\perp} \times 12\phi$) bins, correcting the unpolarized yields to 4π and avoiding any integration over the detector acceptance.

The unpolarized correction factor C_ϕ is formed by taking the ratio of two Monte Carlo asymmetries, A_1^h, where one contains no azimuthal cross-section dependence and the other is computed in acceptance and weighted event-by-event by the parameterized azimuthal modulation to reproduce the effect with the non-uniform azimuthal acceptance.

3 Result

Also the polarization-dependent numerator of the asymmetry is also subject to possible azimuthal modulations, i.e. the ϕ dependence σ_{LL} of Equation (5) , that can enter the cross section at subleading-twist [5]. Sizeble subleading twist effects have in fact been observed in the asymmetries A_{UL} [7], which accentuates the need to proceed with some caution. As statistics are limited in the longitudinally double-spin dataset for a complete five-parameter kinematic unfolding, a full parameterization of polarization dependent modulations is currently not possible, preventing a correction similar to that described for the unpolarized azimuthal acceptance. In order to address this, $A_{||}$ was unfolded simultaneously in $x - z$, $x - p_{h\perp}$, $z - x$ and ϕ and the $A_{LL}^{cos\phi}$ moments were found to be small. These moments are shown in Fig. 2 as a function of x in two z slices (top panel) and as a function of z in two x slices (bottom panel) and in Fig. 3 as a function of $p_{h\perp}$ in two x slices for charged hadrons and identified charged pions and kaons. No statistically significant dependence on the kinematic variables has been observed

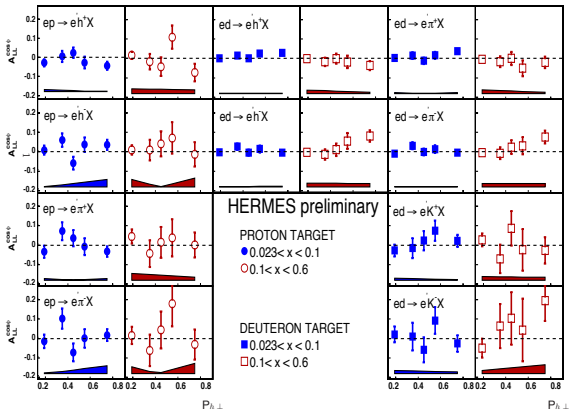

Figure 3: The asymmetries $A_{p,d}^{\cos\phi}$ as a function of $p_{h\perp}$ in two x slices for positively and negatively charged hadrons, pions and kaons.

References

[1] A. Airapetian et al. (HERMES), Phys. Rev., **D71**, 032004 (2005). hep-ex/0412027

[2] K. Ackerstaff et al. (HERMES), Nucl. Instrum. Meth., **A417**, 230 (1998). hep-ex/9806008

[3] A. Airapetian et al. (HERMES), Phys. Rev., **D71**, 012003 (2005). hep-ex/0407032

[4] R. N. Cahn, Physics Letters, **B78**, 269 (1978).

[5] A. Airapetian et al. (HERMES), submitted to Phys. Rev., **D**.

[6] A. Bacchetta, D. Boer, M. Diehl, and P. J. Mulders, JHEP, **0808**, 023 (2008).

[7] A. Airapetian et al. (HERMES), Phys. Lett., **B622**, 14 (2005). hep-ex/0505042

Insights into the Nucleon Spin from Lattice QCD

Sara Collins[1] for the QCDSF Collaboration

[1]Institut für Theoretische Physik, Universität Regensburg,
93040 Regensburg, Germany

DOI: http://dx.doi.org/10.3204/DESY-PROC-2012-02/123

Flavour singlet contributions to the nucleon spin are elusive due to the fact that they cannot be determined directly in experiment but require extrapolations to the small x region. Direct calculations of these contributions are possible using Lattice QCD, however, they pose a significant computational challenge due to the presence of disconnected quark line diagrams. We report on recent progress in determining these sea quark contributions on the lattice.

1 Introduction and Results

The distribution of the spin of the proton among its constituents has long been a topic of interest. The total spin can be decomposed into the contribution from the quark spins, $\Delta\Sigma$, the quark orbital angular momenta, L_ψ, and the gluon total angular momentum J_g [1],

$$\frac{1}{2} = \frac{1}{2}\Delta\Sigma + L_\psi + J_g, \tag{1}$$

where $\Delta\Sigma = \Delta u + \Delta d + \Delta s$ (heavier quarks are normally neglected). In this work, Δq ($q = u, d, s$) denotes the combined spin contribution of the quark and the antiquark. Using Lattice QCD, one can determine the Δq from first principles through the axial-vector matrix element,

$$\frac{1}{m_N}\langle N, s|\bar{q}\gamma_\mu\gamma_5\frac{1}{2}q|N, s\rangle = \frac{\Delta q}{2}\, s_\mu, \tag{2}$$

where m_N is the mass of the nucleon with spin s_μ ($s_\mu^2 = -1$). Thus, one can construct the axial charges, $a_3 = \Delta u - \Delta d = g_A$, $a_8 = \Delta u + \Delta d - 2\Delta s$ and $a_0(Q^2) = \Delta u + \Delta d + \Delta s = \Delta\Sigma(Q^2)$. $\Delta\Sigma$ acquires a scale dependence, Q^2, due to the axial anomaly. The axial-vector matrix element is related to the first moment of the quark helicity distributions. The second moment, $\langle x\rangle_\Delta$, and the second moment of the transverse helicity distribution, $\langle x\rangle_\delta$, can also be calculated on the lattice, higher moments are more challenging. Furthermore, the total angular momentum of quark q, $J_q = \frac{1}{2}\Delta q + L_q$ ($\sum_q J_q = \frac{1}{2}\Delta\Sigma + L_\psi$) can be obtained from the generalised form factors, $A_{20}^q(Q^2)$ and $B_{20}^q(Q^2)$, which parameterise the matrix element of the energy-momentum tensor for momentum transfer, Q. For a review of recent Lattice results of J_q, $\langle x\rangle_\Delta$ and $\langle x\rangle_\delta$ see [2, 3] and references therein.

In these proceedings we focus on Δq and Δs in particular. Lattice results for Δs have an important role to play in constraining fits of polarised parton distribution functions (PDF).

The spin structure function of the proton and neutron, $g_1^{n,p}(x,Q^2)$, is measured in deep inelastic experiments. The first moment is related to the axial charges via the operator product expansion. To leading twist:

$$\Gamma_1^{p,n}(Q^2) = \int_0^1 \mathrm{d}x\, g_1^{p,n}(x,Q^2) \quad = \quad \frac{1}{36}\left[(a_8 \pm 3a_3)C_{NS} + 4a_0 C_S\right] \tag{3}$$

where C_S and C_{NS} are the singlet and non-singlet Wilson coefficients, respectively. Model assumptions are made in order to extrapolate $g_1^{n,p}(x,Q^2)$ from the minimum $x = 0.02$ accessible in experiment down to $x = 0$. a_3 is known from neutron β-decay, while, assuming $SU(3)$ flavour symmetry, a_8 can be obtained from hyperon β-decays. Thus, in combination with $\Gamma_1^{p,n}(Q^2)$, a_0 and the Δq can be deduced. For example, HERMES find $\Delta s(5\mathrm{GeV}^2) = \frac{1}{3}(a_0 - a_8) = -0.085(13)(8)(9)$ [4]. However, if the range of x in the integral in Eq. 3 is restricted to the experimental range, $x > 0.02$, Δs is consistent with zero, indicating the large negative value arises from model assumptions in the low x region.

Semi-inclusive deep inelastic scattering (SIDIS) experiments offer a direct measurement of the Δq using pion and kaon beams. Results from COMPASS show the strangeness contribution is consistent with zero down to $x = 0.004$ [5]. A naive extrapolation to $x = 0$ gives $\Delta s = -0.02(2)(2)$, while using the parameterisation of De Florian et al. (DSSV) [6] gives $\Delta s = -0.10(2)(2)$. Present measurements via SIDIS are limited by the knowledge of the quark fragmentation functions, to which Δs is particularly sensitive. Another possibility of directly determining Δs combines νp, $\bar{\nu} p$ and parity-violating ep elastic scattering data [7]. Here, the MicroBooNE experiment will enable errors to be significantly reduced.

Considering the lattice approach, simulations are performed at finite volume (V) and lattice spacing (a) and typically with u and d quarks with unphysically heavy masses (m_q). Physical results are recovered in the continuum ($a \to 0$) and infinite volume ($V \to \infty$) limits at physical quark masses. The u, d and s quark masses used in simulations are normally expressed in terms of the pseudoscalar meson masses they correspond to ($M_{PS}^2 \propto m_q$). Developments in algorithmic techniques and computing power mean typical simulations now involve lattices with $a \sim 0.05 - 0.1$ fm, $V \sim 2.5 - 6$ fm and $M_{PS}(u/d) \sim 200$ MeV.

For any lattice prediction, the size of the main systematic errors, discretisation effects, finite volume and so on, must be investigated thoroughly. However, the systematic uncertainties should always be compared to the inherent statistical error, where for some quantities the latter dominates. Δs is one such example. Evaluating $\langle N|\bar{s}\gamma_\mu\gamma_5 s|N\rangle$ involves calculating a disconnected quark line diagram (for the strange quark). These types of diagrams are computationally expensive to calculate as they involve the quark propagator from all space-time lattice points to all points. In the past these diagrams were often not calculated and differences of quantities were quoted, for which the disconnected contribution cancelled assuming isospin symmetry, for example, $g_A = \Delta u - \Delta d$, J_{u-d} and $\langle x\rangle_{\Delta u - \Delta d}$. However, methods have been developed which enable the disconnected contributions to be calculated [8], in particular, also Δs. Note that for Δu and Δd a "connected" quark line diagram must also be evaluated in addition to the disconnected one.

In the following we present results for the quark spin contributions to the proton generated on configurations with two degenerate flavours of sea quarks[1], with $a \sim 0.072$ fm and u/d quark masses given by $M_{PS} = 285$ MeV. The quark action employed has leading order discretisation

[1]The number of sea quarks refers to the number of flavours of quark fields included in the Monte Carlo generation of an ensemble of representative quark and gluon field configurations.

effects of $O(a^2)$, which are not expected to be significant for this value of the lattice spacing. Two lattice volumes, with spatial dimensions of 2.3 fm and 2.9 fm, were used and no significant finite volume effects were found. Although the u and d quark masses are unphysically heavy, we varied the quark masses in the range corresponding to $M_{PS} = 285 - 720$ MeV and found no significant change in the results. This suggests our results may also apply to physical quark masses. Further details can be found in [9].

q	$\Delta q^{\rm lat}_{\rm con}$	$\Delta q^{\rm lat}_{\rm dis}$	$\Delta q^{\overline{\rm MS}}(Q)$	DSSV x_{min}	DSSV 0
u	1.071(15)	-0.049(17)	0.787(18)(2)	0.793	0.814
d	-0.369(9)	-0.049(17)	-0.319(15)(1)	-0.416	-0.458
s	0	-0.027(12)	-0.020(10)(1)	-0.012	-0.114
a_3	1.439(17)	0	1.105(13)(2)	1.21	1.272
a_8	0.702(18)	-0.044(19)	0.507(20)(1)	0.401	0.583
Σ	0.702(18)	-0.124(44)	0.448(37)(2)	0.366	0.242

Table 1: The bare (lattice) connected, $\Delta q^{\rm lat}_{\rm con}$, and disconnected, $\Delta q^{\rm lat}_{\rm dis}$, quark spin contributions of the proton. Renormalisation to the $\overline{\rm MS}$ scheme is performed for $Q \sim \sqrt{7.4}$ GeV, to obtain $\Delta q^{\overline{\rm MS}}(Q)$. The first error is statistical, the second is from the renormalisation. A comparison is made with the results of DSSV global fits to DIS and SIDIS data [10] (see this reference for the uncertainties on the values) for the cases where x is restricted to $[x_{min} = 0.001 \to 1]$ and where $x = [0 \to 1]$.

Table 1 displays the results for Δs and the axial charges and compares them to results from a DSSV global analysis [10]. We obtain a small, negative value for Δs, consistent with the result obtained from a truncated DSSV fit to experimental data. Notably, a_3 is significantly lower than the experimental value of $a_3 = g_A = 1.2695(29)$. This is a general feature of lattice calculations of g_A. A summary plot of recent simulations taken from [3] is shown in Fig. 1. Over the range of u/d quark masses available the results obtained using different lattice quark actions, volumes and lattice spacings, are fairly constant and lie approximately 10% below the experimental result. Simulations at smaller u/d quark masses are needed. Problems with excited state contaminations have also been suggested as a possible source of the discrepancy, see, for example, Ref. [11]. On the lattice an operator with the quantum numbers of the proton, creates all states of $J^P = \frac{1}{2}^+$ and one needs to ensure that the matrix element for the ground state has been extracted. Nonetheless, the uncertainty in the lattice determination of g_A seems to be multiplicative, as shown on the right in Fig. 1: the ratio of g_A/f_π tends to the experimental value.

Considering the underestimate of g_A, we add a 20% uncertainty to our results and obtain a final value of

$$\Delta s = -0.020(10)(4).$$

The first error is statistical, the second is due to the systematic uncertainty, which dominates. Other groups using similar methods, albeit at heavier quark masses and without renormalisation, obtain consistent results, see [12] and [13]. This is in contradiction to earlier exploratory work by, for example, the Kentucky group [14]. Note that this group have recently also calculated flavour singlet contributions to J_q [15].

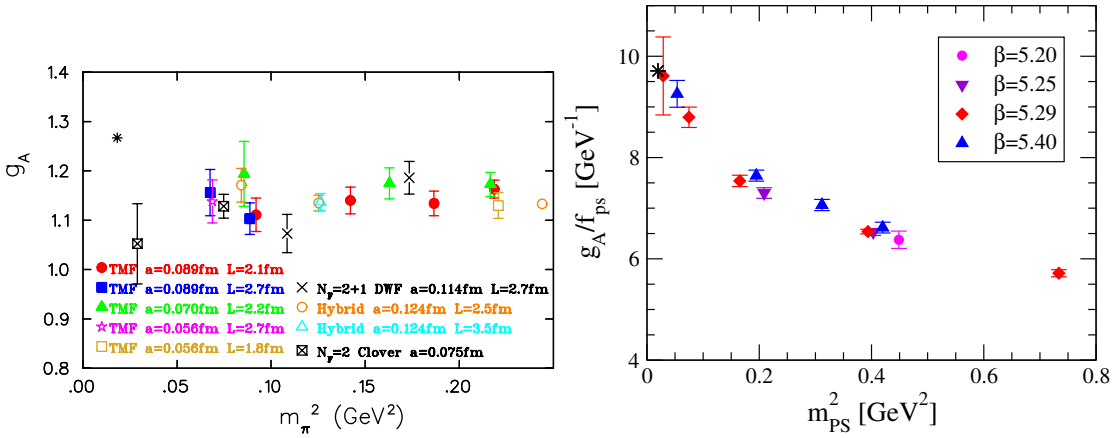

Figure 1: (left) A summary plot of $a_3 = g_A$ for different lattice simulations as a function of the u/d quark mass, expressed in terms of $M_{PS}^2 = m_\pi^2$ [3]. (right) The ratio of g_A/f_π as a function of M_{PS}^2 for different lattice spacings [16]. $\beta = 5.2 - 5.4$ corresponds to $a \sim 0.083 - 0.060$ fm.

2 Acknowledgements

This work is supported by the EU ITN STRONGnet and the DFG SFB/TRR 55. S.C. acknowledges support from the Claussen-Simon-Foundation (Stifterverband für die Deutsche Wissenschaft).

References

[1] X.-D. Ji. Phys.Rev.Lett. **78** (1997) 610–613, arXiv:hep-ph/9603249 [hep-ph].

[2] P. Hagler. Phys.Rept. **490** (2010) 49–175, arXiv:0912.5483 [hep-lat].

[3] C. Alexandrou. Prog. Part. Nucl. Phys. **67** (2012) 101–116, arXiv:1111.5960 [hep-lat].

[4] A. Airapetian *et al.* Phys. Rev. **D75** (2007) 012007, arXiv:hep-ex/0609039 [hep-ex].

[5] M. Alekseev *et al.* Phys. Lett. **B693** (2010) 227–235, arXiv:1007.4061 [hep-ex].

[6] D. de Florian, R. Sassot, M. Stratmann, and W. Vogelsang. Phys.Rev.Lett. **101** (2008) 072001, arXiv:0804.0422 [hep-ph].

[7] S. F. Pate. Phys.Rev.Lett. **92** (2004) 082002, arXiv:hep-ex/0310052 [hep-ex].

[8] G. S. Bali, S. Collins, and A. Schafer. Comput.Phys.Commun. **181** (2010) 1570–1583, arXiv:0910.3970 [hep-lat].

[9] G. S. Bali *et al.* arXiv:1112.3354 [hep-lat].

[10] D. de Florian, R. Sassot, M. Stratmann, and W. Vogelsang. Phys. Rev. **D80** (2009) 034030, arXiv:0904.3821 [hep-ph].

[11] S. Capitani, M. Della Morte, G. von Hippel, B. Jager, A. Juttner, *et al.* arXiv:1205.0180 [hep-lat].

[12] R. Babich, R. C. Brower, M. A. Clark, G. T. Fleming, J. C. Osborn, *et al.* Phys. Rev. **D85** (2012) 054510, arXiv:1012.0562 [hep-lat].

[13] M. Engelhardt. PoS **LATTICE2010** (2010) 137, arXiv:1011.6058 [hep-lat].

[14] S. Dong, J.-F. Lagae, and K. Liu. Phys.Rev.Lett. **75** (1995) 2096–2099, arXiv:hep-ph/9502334 [hep-ph].

[15] K. Liu, M. Deka, T. Doi, Y. Yang, B. Chakraborty, *et al.* arXiv:1203.6388 [hep-ph].

[16] D. Pleiter *et al.* PoS **LATTICE2010** (2010) 153, arXiv:1101.2326 [hep-lat].

Hard Exclusive ϕ meson leptoproduction at HERMES

Mayya Golembiovskaya[1], *Armine Rostomyan*[1], *Sergey Yaschenko*[1], *Denis Veretennikov*[2]

[1]DESY, Notkestraße 85, 22607 Hamburg, Germany
[2]PNPI, St.Petersburg, Russia

DOI: http://dx.doi.org/10.3204/DESY-PROC-2012-02/69

The HERMES experiment at DESY, Hamburg collected a set of data on hard exclusive vector meson (ρ^0, ϕ , ω) leptoproduction using the 27.6 GeV self-polarized lepton beam of HERA accelerator and a longitudinally or transversely polarized or unpolarized gas target. The latest results for spin density matrix elements of exclusive ϕ meson production using the full statistics collected at HERMES are presented. Conclusions on the helicity amplitudes, which are related to spin density matrix elements, are also presented.

1 Introduction

Electroproduction of vector mesons (V) from scattering the beam lepton (e) on the nucleon target (N) can be described by the equation $e + N \to e' + V + N'$, with the following decay of the vector meson to two oppositely charged kaons in case of ϕ meson production. In perturbative Quantum Chromo Dynamics (pQCD) exclusive meson production can be considered as an interaction with the target nucleon of a qq pair into which the virtual photon has fluctuated. Therefore, in the single photon approximation, the last equation can be represented as $\gamma^* + N \to V + N'$. The spin state of the final vector meson produced is determined by the spin density matrix. The decay angular distribution of the ϕ meson, which can be reconstructed via measurement of all the reaction kinematics, also can be decomposed in terms of the model-independent quantities - spin density matrix elements (SDMEs) [1]. With the HERMES experimental configuration (longitudinally polarized beam and unpolarized target) 15 so-called unpolarized SDMEs and 8 beam-polarization dependent SDMEs can be determined. The set of 23 SDMEs for the ϕ meson is presented here in the Wolf-Schilling representation [1]. Using the measured SDMEs, the hypothesis of s-Channel Helicity Conservation (SCHC), which is the conservation of helicity in the $\gamma^* \to V$ transition, can be tested. If SCHC holds, SDMEs responsible for helicity-flip transitions are zero. SDMEs can be expressed through bilinear products of helicity amplitudes, defined in the "hadronic" center of mass system of virtual photon and target nucleon [2]. Since the spin density matrix elements are dimensionless they may be expressed through ratios of amplitudes rather than amplitudes themselves. In contrast to SDMEs, the number of helicity amplitudes does not depend on the beam and target polarization. Therefore the helicity amplitudes provide more a general description of vector meson electroproduction than SDMEs.

2 Data

The exclusive ϕ meson event sample used in the analysis was selected by requiring the existence of three tracks: a lepton and two oppositely charged kaon tracks. Certain kinematic restrictions were applied to the momentum transfer Q^2, the inelasticity y and the invariant mass of the excited photon-nucleon system W. Exclusivity of the sample was achieved via restrictions on the invariant mass of the ϕ meson, the squared transverse 4-momentum transfer t', and the missing energy of the reaction ΔE, calculated as $\Delta E = (M_x^2 - M_p^2)/(2M_p)$, where M_x is the missing mass of the recoil particle, and M_p is target mass. The background fraction was estimated using the PYTHIA monte Carlo and was found to be of the order of 2-3%.

3 Extraction of SDMEs

The 3-dimensional angular distribution of the scattered lepton and the decay products can be expressed in terms of SDMEs and the following angles (see detailed definition in [3]): Φ which is the angle between φ meson production plane and the lepton scattering plane in the center of mass system of virtual photon and target nucleon; θ and ϕ which are the polar and azimuthal angles of the decay K^+ in the vector meson rest frame. The distribution of these angles is calculated for two sets - a measured data set, whose angular distributions are generated by SDMEs and therefore is not flat; and a data set generated by a Monte Carlo simulation whose angular distribution does not contain SDMEs and is affected by detector geometry only. Then the maximum likelihood function, which contains the Monte Carlo decay angular distribution for normalization and the data angular distribution, are fit by (for the present analysis MINUIT package was used), using the SDMEs are treated as fit parameters.

4 Results

In Fig 1 twenty three ϕ SDMEs for the ϕ (red) and ρ (black) mesons are presented. Usage of almost the whole HERMES statistics for the ϕ meson allow the separation for hydrogen and deuterium targets. SDMEs are divided into 5 classes according to the transition processes. Shadowed areas denote polarized SDMES. The inner error bars represent statistical uncertainties, while the outer error bars represent total uncertainties, obtained as the sum of squared statistical and systematic uncertainties. The average kinematics are $< Q^2 >= 1.956$ GeV^2, $< W^2 >= 21.89$ GeV^2, $< x >= 0.088$, $< t' >= -0.12$ GeV^2. The SDMEs are multiplied by certain kinematic factors in order to facilitate comparison with the corresponding helicity amplitude. The large SDME values of classes A and B corresponding to the helicity-conserving transitions, support the SCHC hypothesis. The SDMEs of class A have dominant contributions proportional to the helicity amplitudes $|T_{00}|^2$ or $|T_{11}|^2$. For the ϕ meson, the SDMEs of the class A are 10-20% larger than those of ρ meson, which implies that the corresponding amplitude ratio T_{11}/T_{00} is larger for ϕ meson than for ρ. Several relations between SDMEs of classes A and B allow conclusions to be drawn on the validaty of SCHC (see Eqs. (78-83) in Ref. [4]). The relations $r^1_{1-1} = -Imr^2_{1-1}$ and $Rer^5_{10} = -Imr^6_{10}$ are fulfilled for both the ϕ and ρ mesons. The relation $Rer^8_{10} = Imr^7_{10}$ is fulfilled for ρ, while for ϕ no conclusion can be made due to the large uncertainties. Class B SDMEs correspond to the interference of the class A SDMEs. SDMEs of classes C, D, E are responsible for SCHC-violating transitions. For both ϕ and ρ mesons the most significant deviations from zero are observed in C class. This class contains SDMEs with

dominant terms that are products of the s-chanel helicity non-conserving amplitude T_{01} and helicity conserving amplitudes T_{00} and T_{11}. In D and E classes ϕ and ρ meson SDMEs fluctuate about zero, supporting SCHC. They are composed of SDMEs in which the main terms contain a product of T_{10} (for single helicity flip) or T_{1-1} (for double helicity flip), respectively, with T_{11}^{*}. From the relations between SDMEs cited above a conclusion on the amplitudes hierarchy for the ϕ meson can be drawn, namely, $|T_{00}| \sim |T_{11}| >> |T_{01}|, |T_{10}| \approx |T_{1-1}| \approx 0$.

References

[1] K. Schilling, G Wolf, Nucl. Phys. B61, 381 (1973).

[2] M. Diehl, JHEP 0709, 064 (2007).

[3] P. Joos et al., Nucl. Phys. B 113, 53 (1976).

[4] HERMES collaboration, A. Airapetyan, et al., Eur. Phys. J. C62, 659 (2009).

[5] S. V. Goloskokov, P. Kroll, Eur. Phys. J. C42, 281 (2005).

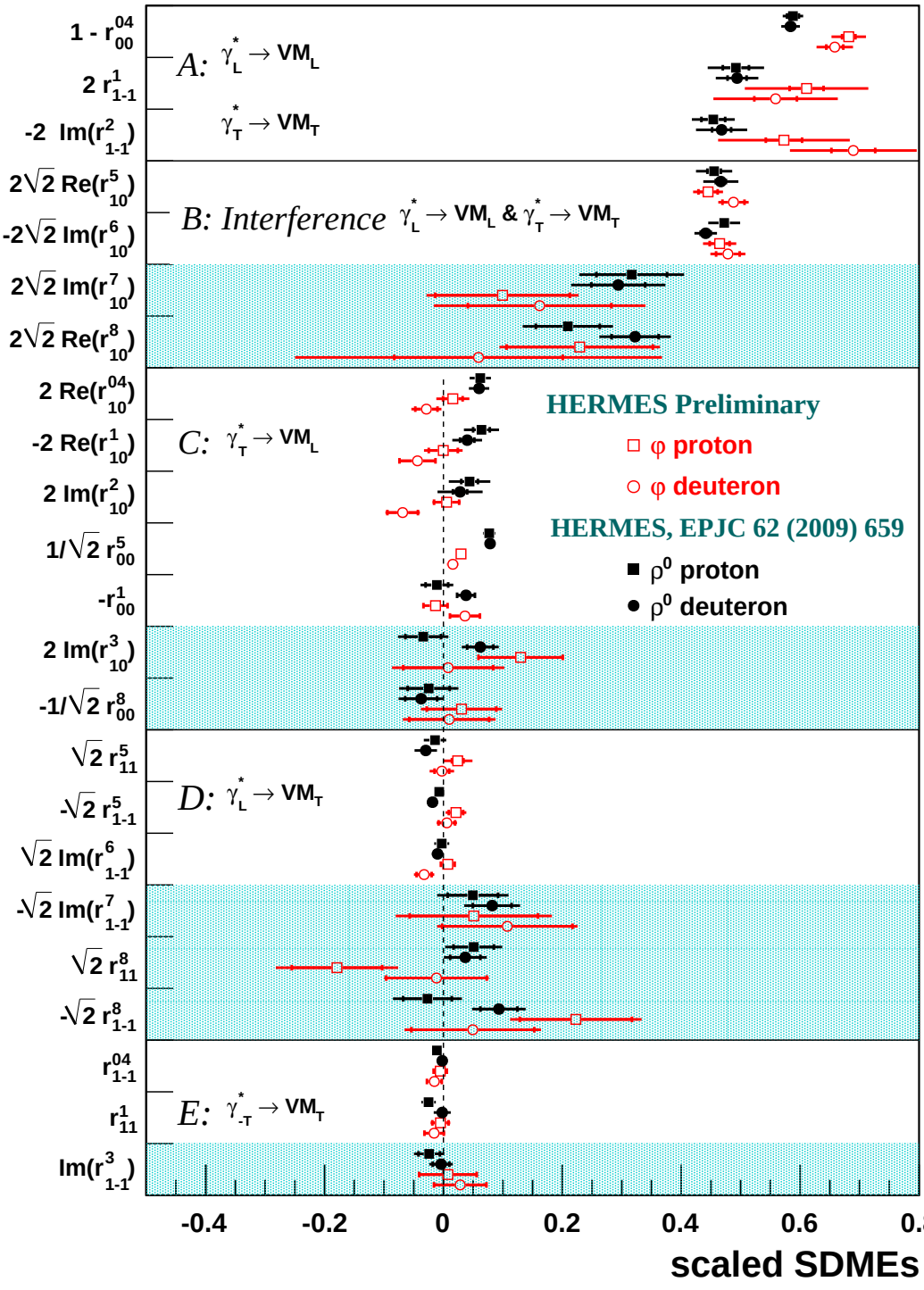

Figure 1: The 23 SDMEs for the ϕ and ρ mesons.

Fragmentation Functions at Belle

Martin Leitgab for the Belle Collaboration

University of Illinois at Urbana-Champaign, Department of Physics, 1110 West Green Street, Urbana, IL 61801, USA

DOI: http://dx.doi.org/10.3204/DESY-PROC-2012-02/64

Fragmentation functions (FFs) describe the formation of final state particles from a partonic initial state. Precise knowledge of these functions is a key ingredient in accessing quantities such as the nucleon spin structure in semi-inclusive deep-inelastic scattering and proton proton collisions. However, fragmentation functions can currently not be determined from first principles Quantum Chromodynamics and have to be extracted from experimental data. The Belle experiment at KEK, Japan, provides a large data sample for high precision measurements on e^+e^- annihilations allowing for first-time or more precise extractions of fragmentation functions. Analyses for extractions of spin-independent (unpolarized FFs) as well as spin-dependent fragmentation functions (interference FFs) at Belle are presented.

1 Precision measurement of charged pion and kaon multiplicities

1.1 Motivation and outline

A number of polarized Semi-Inclusive Deep-Inelastic Scattering (SIDIS) and polarized proton-proton scattering (pp) experiments are measuring quark and gluon distributions via QCD analysis. Unpolarized hadron fragmentation functions are input quantities for such analyses and currently limit the accuracy with which e.g. parton helicity distributions can be determined. Two recent studies have extracted hadron fragmentation functions from datasets of hadron production in e^+e^- [1], and from a combination of e^+e^-, SIDIS and pp datasets [2]. In both studies, the authors emphasize the need for a precision hadron multiplicity measurement from e^+e^- annihilation data at low center-of-mass energies, compared to the bulk of existing datasets taken at the Large Electron-Positron Collider (LEP) at CERN. This precision dataset is expected to improve in particular the knowledge of the gluon fragmentation functions.

Presented in this section is a precision measurement of hadron multiplicities on about 220×10^6 e^+e^- annihilation events taken with the Belle experiment at KEK, Japan, at a center-of-mass energy of 10.52 GeV, 60 MeV below the $\Upsilon(4S)$ resonance. The multiplicities are measured in dependence of $z = 2E_{had}/\sqrt{s} = E_{had}/E_{parton}$, the hadron energy relative to half of the center-of-mass energy, on an interval $0.2 \leq z < 1.0$. The measured hadrons are produced in reactions $e^+e^- \to q\bar{q}$, where $q = \{u,\ d,\ s,\ c\}$.

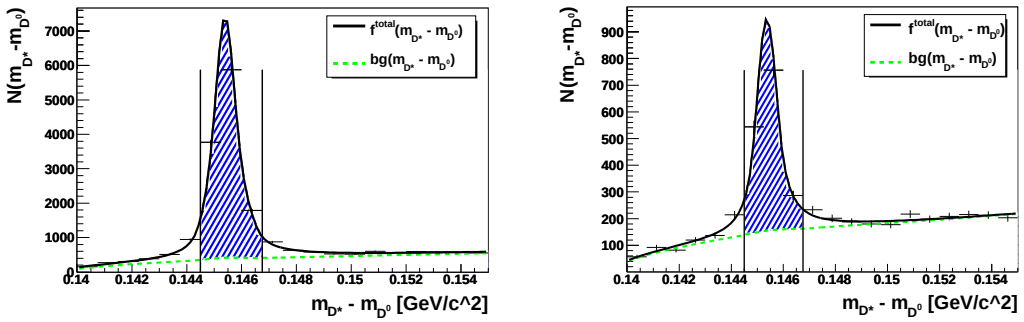

Figure 1: Fits of experimental invariant mass distributions $m_{D^*} - m_{D^0}$ from decays $D^* \to \pi + D^0 \to \pi + (K\pi)$. Figures a) and b) show distributions containing negatively-charged kaon candidate tracks with laboratory frame momentum $1.4 < p_{\rm lab} < 1.6$ GeV/c and laboratory frame azimuthal angle $77.9 < \theta_{\rm lab} < 89.0$ degrees. Figure b) shows all contributions to Figure a) where the kaon candidate additionally passes PID likelihood cuts to select pions. The PID misidentification of kaons as pions can be extracted from the ratio of the hatched areas, yielding the probability $p_{(K^- \to \pi^-)} = 0.111 \pm 0.004$.

1.2 Experimental-data-based calibration of the Belle particle identification

The Belle detector contains several subsystems which allow for particle identification (PID) by imposing cuts on likelihood values extracted from measurements of these subsystems. The likelihood cut selections yield fairly accurate PID but need to be calibrated in the context of a high precision measurement, such that measured hadron yields can be corrected for particle misidentification. Particle misidentification changes hadron yields up to 10% for pions and up to 20% for kaons, depending on hadron momentum. The correction is performed through an unfolding technique based on inverse 5×5 PID probability matrices.

PID probability matrices are obtained from analyzing decays of particles in which the species i of the decay products can be determined through purely kinematic means. In such a sample, additional cuts on track PID likelihood variables selecting a species j define a subsample of tracks. Comparing the number of cut-selected tracks to the total number of tracks in the sample allows to extract PID probabilities $p_{(i \to j)}$. Complete 5×5 matrices of PID probabilities are extracted from experimental data for species $\{i, j\} = \{e, \mu, \pi, K, p\}$ by analyzing decays of D^*, Λ and J/ψ particles. This data-driven PID calibration avoids the dependence on the modeling of Belle PID detectors in GEANT [3]. As an example, Figure 1 displays fits of invariant mass distributions $m_{D^*} - m_{D^0}$ from decays $D^* \to \pi + D^0 \to \pi + (K\pi)$. The kaon candidates in contributions to Figure b) fulfill an additional PID likelihood cut to select pions. The ratio of the hatched peak areas is equal to the PID probability $p_{(K^- \to \pi^-)}$.

For kinematic regions not accessible to this calibration method, an extrapolation algorithm is used to obtain PID calibration information. The PID probability matrices from all kinematic areas are inverted and then applied to the measured yields $\overrightarrow{N}_{meas} = (N_e, N_\mu, N_\pi, N_K, N_p)$ to

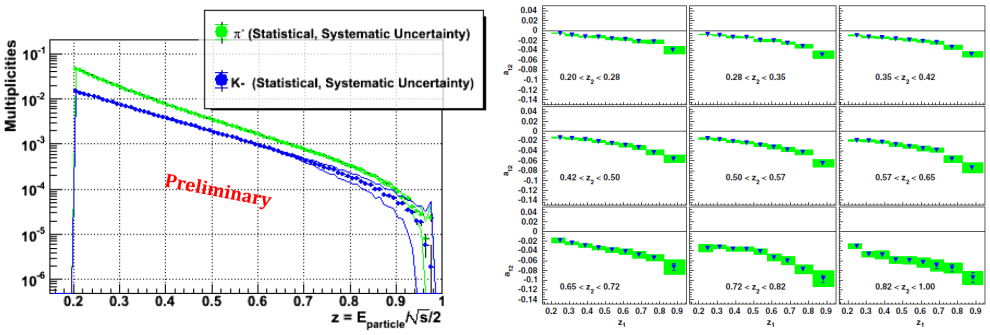

a) b)

Figure 2: a) Measurement of hadron multiplicities: Preliminary negatively-charged pion and kaon multiplicities including statistical and systematic uncertainties. An additional 1.4% normalization uncertainty is not shown. b) Measurement of the interference fragmentation function: Azimuthal modulations $a12$ of two-pion yields for a 9×9 z_1, z_2 binning, as a function of z_2 for all z_1 bins. Indices 1 and 2 refer to the respective reaction hemisphere.

obtain PID-corrected pion and kaon yields $N_{PID-corr}$. All uncertainties of the extracted PID probabilities are propagated through the inversion process using a Monte Carlo technique and are assigned to the PID-corrected yields as systematic uncertainties.

1.3 Other systematic corrections, preliminary results and outlook

In addition to particle misidentification, the measured experimental data yields are also corrected for sample purity, kinematical smearing, decay-in-flight, detector interaction/shower particles, detector and tracking efficiencies and analysis acceptance. The presence of initial state radiation is accounted for as well. Figure 2 a) shows preliminary negatively charged pion and kaon multiplicities including statistical and systematic uncertainties from about 220×10^6 e^+e^- annihilations. In Figure 3 a) and b) the relative size of preliminary statistical and systematic uncertainties is given. Final systematic uncertainties will likely remain below 2% (3%) for π (K) spectra for $z < 0.6$, and will increase with z up to 14% (50%) for π (K) spectra through $z \sim 0.9$, respectively. Currently, the last systematic studies are being finished and timely journal submission for publication is expected.

2 Measurement of the interference fragmentation function for charged pion pairs at Belle

Spin-dependent, chiral-odd fragmentation functions can be used to extract transverse spin quark distributions (so called transversity distributions) in the nucleon from polarized SIDIS and pp scattering experiments. One candidate for such a chiral-odd function is the interference fragmentation function (IFF). First proposed by Collins, Heppelman and Ladinsky [4], the IFF describes the fragmentation of a polarized quark into two hadrons correlated via partial wave interference. The corresponding observable is an azimuthal dependence in the production cross-

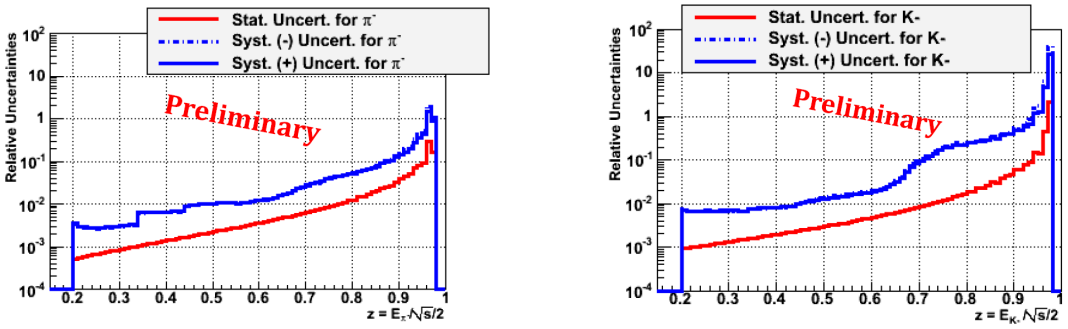

a) b)

Figure 3: Relative uncertainties of preliminary negatively-charged pion (a) and kaon (b) multiplicities. An additional 1.4% normalization uncertainty is not shown.

section of hadron pairs. At Belle, the product of two IFFs can be measured by identifying one hadron pair in either hemisphere in a two-jet event $e^+e^- \to q\bar{q} \to (hh)(hh)X$. The IFF does not depend on transverse momenta and therefore its factorization and evolution can be described in a collinear approach. This makes the IFF an attractive alternative compared to the usually used Collins fragmentation function (previously measured for pions at Belle, cf. References [5] and [6]) for the extraction of parton transversity distributions.

Azimuthal correlations between the planes spanned by two hadron pairs and the interaction plane defined by the incoming lepton momenta and the quark-antiquark momentum axis (approximated by the thrust axis) are extracted. The raw azimuthal yields are normalized to the average hadron pair yield and fitted. This approach is not susceptible to QCD radiative effects and the $cos(\phi_1 + \phi_2)$ azimuthal modulation a_{12} is directly proportional to the product of two IFF $H_1^{\sphericalangle}(z, m)$, where $z = E_{pair}/E_{parton}$ represents the fractional energy of the hadron pair and m its invariant mass. Analysis results on a dataset of 672 fb^{-1} containing 711×10^6 $\pi^+\pi^-$ pairs collected at the $\Upsilon(4S)$ resonance have been published in Reference [7]. Figure 2 shows azimuthal modulations rising with the fractional energy of the hadron pair to significant values of up to 10% for highest z.

The Belle Collaboration is currently also pursuing measurements of the kaon Collins FF, the kaon and π^0 IFFs and the di-hadron FF. In addition, measurements are being prepared to extract the k_t dependence of the unpolarized and the di-hadron FFs.

References

[1] M. Hirai, S. Kumano, T.-H. Nagai and K. Sudoh. Phys. Rev. **D75** (2007) 114010.

[2] D. de Florian, R. Sassot and M. Stratmann. Phys. Rev. **D75** (2007) 094009.

[3] For further reference about GEANT see `http://wwwasd.web.cern.ch/wwwasd/geant/index.html`.

[4] J. C. Collins, S. F. Heppelmann and G. A. Ladinsky. Nucl. Phys. **B420** (1994) 565.

[5] R. Seidl *et al*, Belle Collaboration. Phys. Rev. Lett. **96** (2006) 232002.

[6] R. Seidl *et al*, Belle Collaboration. Phys. Rev. **D78** (2008) 032011.

[7] A. Vossen *et al*, Belle Collaboration. Phys. Rev. Lett. **107** (2011) 072004.

Transverse single-spin asymmetries

Jian-Wei Qiu[1,2]

[1]Physics Department, Brookhaven National Laboratory, Upton, NY 11973, USA
[2]C.N. Yang Institute for Theoretical Phyics, Stony Brook University, Stony Brook, NY 11794, USA

DOI: http://dx.doi.org/10.3204/DESY-PROC-2012-02/30

In this talk, I will review the physics behind the measured large transverse single-spin asymmetries (SSAs) of cross sections with large momentum transfers in high energy collisions, and the twist-3 mechanism to generate the SSAs in perturbative QCD. I will also discuss the connection between the twist-3 collinear factorization approach and the transverse momentum dependent factorization approach to SSAs.

1 Introduction

Transverse single-spin asymmetry (SSA), $A_N \equiv (\sigma(s_T) - \sigma(-s_T))/(\sigma(s_T) + \sigma(-s_T))$, is defined as the ratio of the difference and the sum of the cross sections when the spin of one of the identified hadron s_T is flipped. Large SSAs of cross sections with a large momentum transfer in high energy collisions were once thought impossible in QCD [1]. With over 30 years of experimental as well as theoretical efforts, large SSAs are not only possible in QCD, but also carry extremely valuable information on the motion and structure of quarks and gluons inside a transversely polarized hadron. In this talk, I will briefly review our current understanding of the physics that is responsible for generating the measured large SSAs of cross sections with large momentum transfers in high energy collisions.

2 QCD factorization approaches to SSAs

Two complementary QCD-based approaches have been proposed to analyze the physics behind the measured SSAs: the transverse momentum dependent (TMD) factorization approach [2, 3, 4, 5, 6, 7] and the collinear factorization approach [8, 9, 10, 11, 12, 13, 14, 15]. In the TMD factorization approach, the asymmetry was attributed to the spin and transverse momentum correlation between the identified hadron and the active parton, and represented by the TMD parton distribution or fragmentation function. For example, the Sivers effect (Sivers function) [2] represents how hadron spin influences parton's transverse motion inside a transversely polarized hadron, while the Collins effect (Collins function) [3] describes how parton's transverse spin affects the parton's hadronization. On the other hand, in the collinear factorization approach, all active partons' transverse momenta are integrated into the collinear distributions, and the explicit spin-transverse momentum correlation in the TMD approach is now included into the high twist collinear parton distributions or fragmentation functions. The asymmetry in the collinear factorization approach is represented by twist-3 collinear parton distributions or

fragmentation functions, which carry the net effect of spin-transverse momentum correlations generated by QCD color Lorentz force [16]. The TMD factorization approach is more suitable for evaluating the SSAs of scattering processes with two very different momentum transfers, $Q_1 \gg Q_2 \gtrsim \Lambda_{\rm QCD}$, where the Q_2 is sensitive to the active parton's transverse momentum, while the collinear factorization approach is more relevant to the SSAs of scattering cross sections with all observed momentum transfers hard and comparable: $Q_i \sim Q \gg \Lambda_{\rm QCD}$. Although the two approaches each have their own kinematic domain of validity, they are consistent with each other in the perturbative regime where they both apply[17, 18].

Both factorization approaches necessarily introduce a factorization scale, $\mu \gg \Lambda_{\rm QCD}$, to separate the calculable short-distance perturbative dynamics from the long-distance nonperturbative physics of the observed cross sections or the asymmetries. Since the physical observables, the cross sections or the asymmetries, are independent of the choice of the factorization scale, the scale dependence of the nonperturbative distributions, either TMD distributions or twist-3 collinear distributions, must match the scale dependence of corresponding perturbative hard parts. That is, the factorization scale dependence of the nonperturbative distributions is perturbatively calculable and is a prediction of QCD perturbation theory when $\mu \gg \Lambda_{\rm QCD}$. For example, the scale dependence of the leading power parton distributions obeys DGLAP evolution equations whose evolution kernels are perturbatively calculable, and has been very successfully tested when the scale varies from a few GeV to the hundreds of GeV. The scale dependence of the Sivers function was recently evaluated [19, 20], while the scale dependence of twist-3 correlation functions and fragmentation functions were derived by several groups [21, 22, 23, 24, 25, 26, 27, 28]. In the rest of this talk, I will concentrate on the discussion of the collinear factorization approach to SSAs.

3 Collinear factorization approach to SSAs

With one large momentum transfer Q, the hard scattering is localized to a distance scale of $1/Q$. Since pulling an extra physically polarized parton from the colliding hadron into the localized collision point is suppressed by a power of $1/Q$, the cross section for a hadron A to scatter off a hadron B can be expanded in a power series in $1/Q$,

$$\sigma_{AB}(Q,\vec{s}) = \sigma^{\rm LP}_{AB}(Q,\vec{s}) + \frac{Q_s}{Q}\,\sigma^{\rm NLP}_{AB}(Q,\vec{s}) + ... \quad (1)$$

$$\approx H^{\rm LP}_{ab} \otimes f_{a/A} \otimes f_{b/B} + \frac{Q_s}{Q}\, H^{\rm NLP}_{ab} \otimes \mathcal{T}_{a/A} \otimes f_{b/B} + ... \quad (2)$$

where Q_s^2 represents a characteristic scale of the power corrections. The leading power contribution to the cross section can be factorized into a convolution of a localized and perturbatively calculable hard part $H^{\rm LP}_{ab}$ from the collision between partons a and b, and the universal twist-2 collinear parton distribution functions (PDFs), $f_{a/A}$ (and $f_{b/B}$), to find a parton of flavor a (and b) from the colliding hadron A (and B), as indicated in Eq. (2), and does not contribute to the SSA [1]. The leading contribution to SSAs in QCD collinear factorization approach comes from the quantum interference between a partonic scattering amplitude with one active parton and that with an active two-parton composite state [8, 9]. Such a quantum interference can be represented by the universal twist-3 quark-gluon correlation functions, and whose contribution is effectively the first power correction to the spin-dependent cross section and can be perturbatively factorized as in Eq. (2) [29]. Although the power correction to the cross section is formally

suppressed by a power of $1/Q$, its contribution to SSAs could be significant in a certain part of the phase space, such as forward region of the polarized hadron from the derivative of the correlation functions, $\frac{d}{dx}\mathcal{T}_{a/h}(x,x)$, which is a natural feature of twist-3 contributions[9]. The predictive power of the approach relies on the universality and our knowledge of the twist-3 correlation functions and fragmentation functions.

For SSAs of single particle inclusive cross section: $A(p_A, s_\perp) + B(p_B) \to h(p) + X$, there could be three potential sources of contributions [10],

$$\begin{aligned} A_N &\propto \sigma_{AB\to h}(Q, s_\perp) - \sigma_{AB\to h}(Q, -s_\perp) \\ &\propto \mathcal{T}^{(3)}_{a/A}(s_\perp) \otimes f_{b/B} \otimes \mathcal{H}^{(S)}_{ab\to c} \otimes D_{h/c} \\ &+ \delta q_{a/A}(s_\perp) \otimes \left[\mathcal{T}^{(\sigma)(3)}_{b/B} \otimes \mathcal{H}^{(BM)}_{ab\to c} \otimes D_{h/c} + f_{b/B} \otimes \mathcal{H}^{(C)}_{ab\to c} \otimes \mathcal{D}^{(3)}_{h/c}\right] \end{aligned} \tag{3}$$

where $\mathcal{T}^{(3)}_{a/A}$ and $\mathcal{T}^{(\sigma)(3)}_{b/B}$ are twist-3 quark-gluon correlation functions of a transversely polarized hadron and that of an unpolarized hadron, respectively, and $\mathcal{D}^{(3)}_{h/c}$ are twist-3 quark-gluon fragmentation functions. The $\mathcal{T}^{(3)}_{a/A}$ take care of the hadron spin flip of the first term, while the twist-2 quark transversity distributions $\delta q_{a/A}(s_\perp)$ take care of the hadron spin flip of the second and the third term. The superscripts, S, BM and C, of partonic hard parts indicate that the first, second, and third term corresponds to, respectively, the sources of SSAs for Sivers, Boer-Mulders, and Collins contribution in the TMD factorization approach.

The first term in Eq. (3) and the twist-3 quark-gluon correlation functions have been systematically studied and compared with data on SSAs, while limited effort has been devoted to the second and third term. With the potential sign conflict between the twist-3 quark-gluon correlation function directly extracted from data on SSAs in hadronic collisions and those indirectly derived from the moments of measured Sivers functions [30], it is very important to investigate the contributions to the SSAs from the second and third term in Eq. (3).

4 Evolution of twist-3 correlation functions

Much of the predictive power of perturbative QCD calculation relies on the factorization and the universality of non-perturbative distributions. An immediate consequence of the QCD factorization formalism for physical observables is that the factorization scale dependence of these universal non-perturbative distributions is also universal and perturbatively calculable, and is a prediction of perturbative QCD dynamics.

A complete and close set of evolution equations for the twist-3 quark-gluon and gluon-gluon correlation functions of a transversely polarized hadron, which are relevant to SSAs, was derived in terms of Feynman diagram approach [21], as well as in terms of the ultra-violet (UV) renormalization of composite operators defining the correlation functions [24]. Leading order evolution kernels for the correlation functions, relevant to the so-called gluonic pole contributions [9], were derived by several groups [21, 22, 23, 24, 26]. An apparent discrepancy between the Feynman diagram approach and that based on the UV renormalization was recently resolved [25, 27]. Leading order kernels for the distributions, relevant to the fermionic pole contribution [9], were recently derived [26].

In addition, the leading order flavor non-singlet evolution kernels for the twist-3 quark-gluon correlation function $\mathcal{T}^{(\sigma)}_{q,F}$ of a unpolarized hadron were derived [22, 27]. Leading order evolution kernels for twist-3 fragmentation functions are also available [28].

5 Summary

The collinear QCD factorization approach to the phenomena of SSAs of cross sections with one large momentum transfer has been well-developed in last thirty years. With the systematic derivation of evolution equations and kernels, the QCD description of the SSAs in terms of the collinear factorization approach is now much more mature. With more future data from RHIC spin program, the SSAs could provide new quantitatively tests of QCD dynamics that could not be explored by measurements of spin-averaged cross sections.

I thank Z.-B. Kang and G. Sterman for useful discussions. This work was supported in part by the US Department of Energy, Office of Science, under Contract No. DE-AC02-98CH10886.

References

[1] G. L. Kane, J. Pumplin and W. Repko, Phys. Rev. Lett. **41**, 1689 (1978).

[2] D. W. Sivers, Phys. Rev. D **41**, 83 (1990); Phys. Rev. D **43**, 261 (1991).

[3] J. C. Collins, Nucl. Phys. B **396**, 161 (1993).

[4] S. J. Brodsky, D. S. Hwang and I. Schmidt, Phys. Lett. B **530**, 99 (2002); Nucl. Phys. B **642**, 344 (2002).

[5] X. Ji and F. Yuan, Phys. Lett. B **543**, 66 (2002); A. V. Belitsky, X. Ji and F. Yuan, Nucl. Phys. B **656**, 165 (2003).

[6] J. C. Collins and A. Metz, Phys. Rev. Lett. **93**, 252001 (2004) [arXiv:hep-ph/0408249].

[7] A. Bacchetta, C. J. Bomhof, P. J. Mulders and F. Pijlman, Phys. Rev. D **72**, 034030 (2005); C. J. Bomhof, P. J. Mulders and F. Pijlman, Eur. Phys. J. C **47**, 147 (2006).

[8] A. V. Efremov and O. V. Teryaev, Sov. J. Nucl. Phys. **36**, 140 (1982); Phys. Lett. B **150**, 383 (1985).

[9] J. W. Qiu and G. F. Sterman, Phys. Rev. Lett. **67**, 2264 (1991); Nucl. Phys. B **378**, 52 (1992).

[10] J. W. Qiu and G. F. Sterman, Phys. Rev. D **59**, 014004 (1998).

[11] C. Kouvaris, J. W. Qiu, W. Vogelsang and F. Yuan, Phys. Rev. D **74**, 114013 (2006).

[12] Y. Koike and K. Tanaka, Phys. Lett. B **646**, 232 (2007) [Erratum-ibid. B **668**, 458 (2008)]; Phys. Rev. D **76**, 011502 (2007); Y. Koike and T. Tomita, Phys. Lett. B **675**, 181 (2009).

[13] J. W. Qiu, W. Vogelsang and F. Yuan, Phys. Lett. B **650**, 373 (2007); Phys. Rev. D **76**, 074029 (2007).

[14] Z. B. Kang and J. W. Qiu, Phys. Rev. Lett. **103**, 172001 (2009).

[15] Z. -B. Kang, F. Yuan and J. Zhou, Phys. Lett. B **691**, 243 (2010) [arXiv:1002.0399 [hep-ph]].

[16] J. -W. Qiu and G. F. Sterman, In *Brookhaven 1993, Future directions in particle and nuclear physics at multi-GeV hadron beam facilities* 212-216.

[17] X. Ji, J. W. Qiu, W. Vogelsang and F. Yuan, Phys. Rev. Lett. **97**, 082002 (2006), Phys. Rev. D **73**, 094017 (2006); Y. Koike, W. Vogelsang and F. Yuan, Phys. Lett. B **659**, 878 (2008).

[18] A. Bacchetta, D. Boer, M. Diehl and P. J. Mulders, JHEP **0808** (2008) 023.

[19] S. M. Aybat, J. C. Collins, J. -W. Qiu and T. C. Rogers, Phys. Rev. D **85**, 034043 (2012).

[20] S. M. Aybat, A. Prokudin and T. C. Rogers, arXiv:1112.4423 [hep-ph].

[21] Z. -B. Kang and J. -W. Qiu, Phys. Rev. D **79**, 016003 (2009) [arXiv:0811.3101 [hep-ph]].

[22] J. Zhou, F. Yuan and Z. -T. Liang, Phys. Rev. D **79**, 114022 (2009) [arXiv:0812.4484 [hep-ph]].

[23] W. Vogelsang and F. Yuan, Phys. Rev. D **79**, 094010 (2009) [arXiv:0904.0410 [hep-ph]].

[24] V. M. Braun, A. N. Manashov and B. Pirnay, Phys. Rev. D **80**, 114002 (2009) [arXiv:0909.3410 [hep-ph]].

[25] A. Schafer and J. Zhou, Phys. Rev. D85, 117501 [arXiv:1203.5293 [hep-ph]].

[26] J. P. Ma and Q. Wang, arXiv:1205.0611 [hep-ph].

[27] Z. -B. Kang and J. -W. Qiu, Phys. Lett. B713, 273 (2012) [arXiv:1205.1019 [hep-ph]].

[28] Z. -B. Kang, Phys. Rev. D **83**, 036006 (2011) [arXiv:1012.3419 [hep-ph]].

[29] J. -W. Qiu, G. F. Sterman, Nucl. Phys. **B353**, 137-164 (1991); AIP Conf. Proc. **223**, 249-254 (1991).

[30] Z. -B. Kang, J. -W. Qiu, W. Vogelsang and F. Yuan, Phys. Rev. D **83**, 094001 (2011) [arXiv:1103.1591 [hep-ph]].

Single and Double Spin Asymmetry Measurements in Semi-Inclusive DIS on Polarized ^{3}He

Vincent Sulkosky[1], *Kalyan Allada*[2] for the JLab E06-010 Collaboration

[1]Massachusetts Institute of Technology, Cambridge, Massachusetts 02139, USA
[2]Thomas Jefferson National Accelerator Facility, Newport News, Virginia 23606, USA

DOI: http://dx.doi.org/10.3204/DESY-PROC-2012-02/139

Jefferson Lab experiment E06-010 measured the target-single spin (SSA) and double spin asymmetries (DSA) in semi-inclusive deep inelastic $^3\mathrm{He}^\uparrow(\mathrm{e},\mathrm{e}'\pi^\pm)\mathrm{X}$ reactions on a polarized ^{3}He target. The measured asymmetry (A_{UT}) is sensitive to the nucleon transversity and Sivers distribution functions, whereas the measured A_{LT} asymmetry is related to the transverse momentum dependent PDF g_{1T}. The kinematics were chosen to be in the valence quark region with $x \sim 0.16$-0.35 and $Q^2 \sim 1.4$-2.7 $(\mathrm{GeV}/c)^2$. The Collins moment, which is sensitive to transversity, the Sivers and A_{LT} moments, which are sensitive to the orbital motion of the quarks, were extracted using the azimuthal angular dependence of the measured asymmetries. The final semi-inclusive results for the electroproduction of pions are presented and discussed.

1 Introduction

Over the past few decades, the study of nucleon spin structure has been an active field, both experimentally and theoretically. This endeavor has lead to our current knowledge of the unpolarized and polarized parton distribution functions (PDFs) f_1^q and g_1^q, which describe the longitudinal momentum and helicity of the quarks inside the nucleon. Only recently, the study has proceeded to study the aspects of quark transverse spin and transverse momenta. The transverse momentum dependent parton distribution functions (TMDs) [1] describe the nucleon structure in terms of quarks and gluons in all three directions of momentum space. Access to the transverse spin and momentum of the partons provides important information on the quark orbital angular momentum (OAM).

All of the eight leading-twist TMDs are accessible in semi-inclusive deep inelastic scattering (SIDIS) and can be separated by their azimuthal angular dependencies. For unpolarized lepton scattering from a transversely polarized target, the target spin-dependent asymmetry is

$$A_{\mathrm{UT}}(\phi_h,\phi_s) = \frac{1}{P_T}\frac{Y^{\uparrow}_{\phi_h,\phi_s} - Y^{\downarrow}_{\phi_h,\phi_s}}{Y^{\uparrow}_{\phi_h,\phi_s} + Y^{\downarrow}_{\phi_h,\phi_s}} \approx A_{\mathrm{C}}\sin(\phi_h+\phi_s) + A_{\mathrm{S}}\sin(\phi_h-\phi_s),$$

where ϕ_h and ϕ_s are the azimuthal angles of the produced hadron and the target spin as defined in the Trento convention [2], $Y^{\uparrow(\downarrow)}$ is the normalized yield for the up (down) spin direction of the target and P_T is the target polarization. The Collins moment is related to the convolution of the transversity distribution h_1^q and the Collins Fragmentation Function (FF), which are both

chiral-odd functions. The transversity distribution describes transverse polarization of quarks in a transversely polarized nucleon. The Sivers moment involves a convolution of the naive T-odd Sivers function $f_{1T}^{\perp}$ [3] and the unpolarized FF. The Sivers function is a correlation between the nucleon spin and the quark transverse momentum, which requires an interference between quark wave function components that differ by one unit of quark orbital angular momentum.

The beam helicity asymmetry, $A_{\rm LT}$, for a longitudinally polarized lepton beam and a transversely polarized target can be written in a similar manner. At leading twist, this asymmetry is proportional to the convolution of g_{1T}^{q} and the unpolarized FF [1, 4]. Recently, the Collins and Sivers moments and the $A_{\rm LT}$ asymmetry were published from data taken at Jefferson Lab on a polarized ^{3}He; the experiment and final results will be discussed in these proceedings.

2 The Experiment

Experiment E06-010 [5, 6] acquired data at Jefferson Lab in Hall A [7]. A longitudinally polarized electron beam was scattered from a transversely polarized ^{3}He target [7] to measure the semi-inclusive reaction $^3\mathrm{He}^{\uparrow}(e,e'h^{\pm})X$, where h is a charged hadron: either pion, kaon or proton. An electron beam with an energy of 5.9 GeV and an average current of 12 μA was used. A Møller polarimeter was used to periodically measure the beam polarization with an average polarization of (76.8±3.5)%. For the SSA, unpolarized beam was accomplished by summing together the two electron helicity states.

The scattered electrons were detected in the BigBite Spectrometer at an angle of 30° with momenta 0.6-2.5 GeV/c on the beam-right side. The BigBite detector package consisted of a dipole magnet, three multi-wire drift chambers (MWDC) for tracking, a scintillator plane for timing and a lead glass calorimeter for particle identification (PID). The solid angle acceptance was 64 msr. The coincident charged hadrons were detected in the left high resolution spectrometer (HRS) [7] with a central momentum of 2.35 GeV/c and at an angle of 16°. The HRS has a momentum acceptance of ±4.5% and a angular accepance of 6 msr. The spectrometer detector package contained drift chambers for tracking, two scintillator planes for triggering the data acquisition and time-of-flight, and a gas Cerenkov counter and a two layer electromagnetic calorimeter for PID. Additionally, a ring imagining Čerenkov (RICH) and an aerogel Čerenkov were used for hadron ID.

For this experiment, we used a polarized ^{3}He target as an effective polarized neutron target. This is possible due to the fact that the ground state ^{3}He wave function is predominately in an S state, where the two proton spins cancel. The ^{3}He nuclei were polarized by spin-exchange optical pumping with a Rb-K mixture [8], and the maximum polarization was significantly improved by using spectrally narrowed lasers, which aided in the laser absorption efficiency. An electron-polarized neutron luminosity of 10^{36} cm^{-2} s^{-1} was achieved with about 10 atm of ^{3}He gas contained within a 40 cm long target. The spin state of the nuclei were flipped every 20 minutes via adiabatic fast passage to reduce the systematic uncertainties. NMR polarimetry was used to measure the polarization with each spin flip, which was calibrated using electron paramagnetic resonance. The average in-beam target polarization was (55.4±2.8)%.

3 Results and Summary

From the measured data discussed in Section 2, the SIDIS event selection was chosen with PID and kinematic cuts, including $Q^2 > 1$ (GeV/c)^2, $W > 2.3$ GeV/c^2 and missing mass $W' >$

1.6 GeV/c^2. The extraction of the Collins, Sivers and $A_{\rm LT}$ moments were cross-checked by two independent methods: a local-pair binning-fitting [5] and a maximum likelihood method [6]. Reasonable consistency was achieved between the two techniques. The moments were corrected for the N_2 dilution of about 10%, where a small amount of nitrogen is used inside the target cells to reduce depolarization effects. The neutron Sivers and Collins moments and $A_{\rm LT}$ asymmetry were extracted from the ^{3}He results using the prescription discussed in [5].

The final results for the neutron Collins and Sivers moments are shown in Fig. 1 in the top and bottom panels, respectively. The left-hand side of the plot shows the results for the π^+ and the right-hand side shows the results for π^-. The error bars on the points indicate the statistical

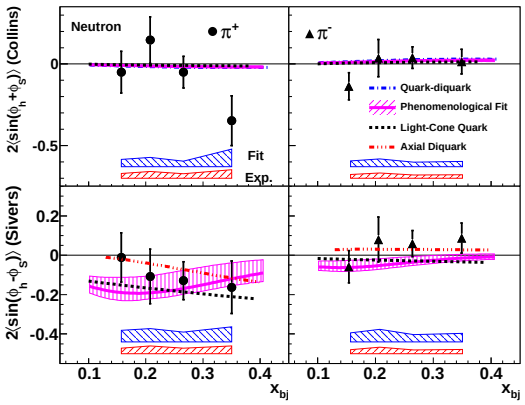

Figure 1: The Collins (top) and Sivers (bottom) neutron moments vs $x_{\rm bj}$ for the electroproduction of π^+ (left) and π^- (right). The bands below the data points represent the experimental and model uncertainties, which are labeled as `Exp` and `Fit`, respectively.

precision of the data, whereas the bands below the data show the experimental (`Exp`) and model (`Fit`) systematic uncertainties. The total experimental uncertainties are less than 25% of the statistical uncertainty in each bin. The fitting uncertainties result from ignoring other ϕ_h- and ϕ_S-dependent terms in the extraction of the moments. The data are compared with a phenomenological fit [9] and model calculations, which include a light-cone constituent quark model (LCCQM) [10] and quark-diquark calculations [11]. Both the data and the calculations indicate that the Collins asymmetries are small, though the data at $x_{\rm bj} = 0.34$ is more negative at the 2σ level. For the Sivers moments, the π^+ asymmetries favor negative values, whereas the π^- results are consistent with zero within the uncertainties.

The $A^n_{\rm LT}$ asymmetries are shown in Fig. 2 along with model calculations, which include Wandzura-Wilczek (WW)-type approximations using parameterizations from Ref. [12], a LCCQM [10] and a light-cone quark-diquark model (LCQDM) [13]. The extracted asymmetries are consistent with zero for positive pion production; however, the negative pion asymmetries are positive at the level of 2.8σ with all four bins averaged together. This observation is consistent with the model predictions though favoring larger magnitudes.

In summary, the first SSA and DSA results were reported for charged pion electroproduction on a polarized ^{3}He target in SIDIS. From this data, the neutron Collins and Sivers moments were extracted. The Collins moments were found to be small, which is consistent with the

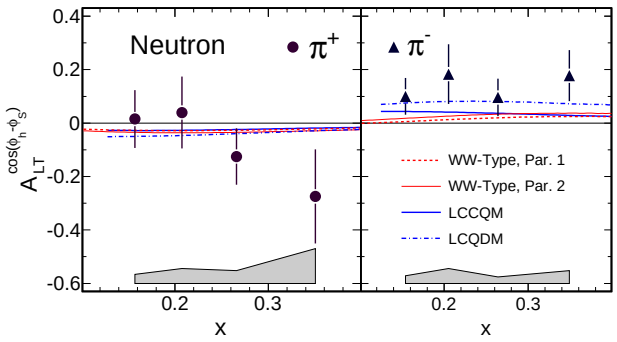

Figure 2: The neutron $A_{\rm LT}$ asymmetry for π^+ (left) and π^- (right) vs $x_{\rm bj}$ compared with model calculations.

model calculations. On the other hand, the π^+ Sivers moment favors negative values, while the π^- moments are close to zero. For the $A_{\rm LT}$ asymmetry, a positive value for π^- production is seen, which provides the first indication for a nonzero $A_{\rm LT}$ and infers a nonzero g_{1T} at leading twist. These measurements are the foundation for future high-precision measurements following the Jefferson Lab 12-GeV upgrade [14].

4 Acknowledgments

This work is supported by the U.S. Department of Energy. Jefferson Science Associates, LLC operates the Thomas Jefferson National Accelerator Facility under the contract DE-AC05-06OR23177.

References

[1] A. Bacchetta *et al.* J. High Energy Phys. **02** (2007) 093.
[2] A. Bacchetta *et al.* Phys. Rev. **D70** (2004) 117504.
[3] D. Sivers. Phys. Rev. **D41** (1990) 83.
[4] A. M. Kotzinian and P. J. Mulders. Phys. Rev. **D54** (1996) 1229.
[5] X. Qian *et al.* Phys. Rev. Lett. **107** (2011) 072003.
[6] J. Huang *et al.* Phys. Rev. Lett. **108** (2012) 052001.
[7] J. Alcorn *et al.* Nucl. Instrum. Meth. **A522** (2004) 294.
[8] E. Babcock *et al.* Phys. Rev. Lett. **91** (2003) 123003.
[9] M. Anselmino *et al.* Phys. Rev. **D75** (2007) 054032.
[10] S. Boffi *et al.* Phys. Rev. **D79** (2009) 094012;
B. Pasquini, S. Cazzaniga, and S. Boffi. Phys. Rev. **D78** (2008) 034025.
[11] J. She and B. Q. Ma. Phys. Rev. **D83** (2011) 037502;
B. Q. Ma, I. Schmidt, and J. J. Yang. Phys. Rev. **D65** (2002) 034010.
[12] A. Kotzinian, B. Parsamyan, and A. Prokudin. Phys. Rev. **D73** (2006) 114017.
[13] J. Zhu and B. Q. Ma. Phys. Lett. **B696** (2011) 246.
[14] H. Gao *et al.* Eur. Phys. J. Plus **126** (2011) 2.

Overview of Parton Orbital Angular Momentum

Feng Yuan[1]

[1]Nuclear Science Division, Lawrence Berkeley National Laboratory, Berkeley, CA 94720, USA

DOI: http://dx.doi.org/10.3204/DESY-PROC-2012-02/235

In this talk, I present the theory overview of recent developments on the parton orbital angular momentum in nucleon.

1 Introduction

Understanding the proton spin structure has been a driving motive for intense spin-physics activities in hadron physics in the last two decades. Much progress has been made both experimentally and theoretically [1, 2, 3]. Orbital angular momentum (OAM) has played a central role in all these studies. There have been many investigations from both theory and experiments [4]. In recent years, three major developments have been particularly emphasized to extract the quark OAM information: (1) GPDs measurements [5]; (2) TMD studies [6]; and (3) very recently the Wigner distributions. In this talk, we would like to present an overview for these developments based on recent publications [7]. Here, we focus on the partonic interpretation of the proton spin and the experimental measurability of the relevant distributions. We explain why a simple partonic sum rule exists only for the transverse polarization. We find that the gauge-invariant OAM contribution to the proton helicity is related to twist-two and three GPDs which are measurable in hard exclusive processes. Finally, the canonical OAM distribution in the light-cone gauge is related to a Wigner distribution [8], which is accessible through certain hard processes. Our discussions are mainly focused on quarks, but they can be easily extended to gluons.

The starting point is the matrix element of the QCD AM density $M^{\mu\alpha\beta}$ in the nucleon plane-wave state [2]

$$\langle PS|\int d^4\xi M^{\mu\alpha\beta}(\xi)|PS\rangle = J\frac{2S_\rho P_\sigma}{M^2}(2\pi)^4\delta^4(0)\left(\epsilon^{\alpha\beta\rho\sigma}P^\mu+\epsilon^{[\alpha\mu\rho\sigma}P^{\beta]}-(\text{trace})\right)+\cdots\ , \quad (1)$$

where ξ^μ is the space-time coordinates, P^μ and S^μ ($S\cdot P=0$, $S^2=-M^2$) are the four-momentum and polarization of the nucleon, and $J=1/2$ and M are the spin and mass, respectively. To seek the partonic interpretation, we consider the nucleon in the Infinite Momentum Frame (IMF) along the z-direction and take μ to be $+$ component. Because of the antisymmetry between α and β, the leading component of the angular momentum density comes from $\alpha=+$ and $\beta=\perp=(1,2)$. This is only possible if the nucleon is transversely polarized and the matrix element reduces to

$$\langle PS|\int d^4\xi M^{++\perp}|PS\rangle = J3(P^+)^2S^{\perp'}(2\pi)^4\delta^4(0)/M^2\ , \quad (2)$$

where $S^{\perp'} = \epsilon^{-+\perp\rho} S_\rho$ with convention of $\epsilon^{0123} = 1$. The longitudinal polarization supports the matrix element of the next-to-leading AM tensor component M^{+12},

$$\langle PS| \int d^3\vec{\xi} M^{+12} |PS\rangle = J(2S^+)(2\pi)^3\delta^3(0) \ , \tag{3}$$

which has one P^+-factor less. Thus the nucleon helicity J is a subleading light-cone quantity, and a partonic interpretation will in general involve parton transverse-momentum and correlations.

2 Transverse-polarization Sum Rule

According to Eq. (2), one expects a simple partonic interpretation of the transverse proton polarization from the leading parton distributions. Indeed, the quark AM sum-rule derived in terms of the quark distribution $q(x)$ and GPD $E(x,0,0)$ is exactly of this type [3],

$$J_q = \frac{1}{2}\sum_i \int dx x \left[q_i(x) + E_i(x,0,0)\right] \ , \tag{4}$$

where i sums over different flavor of quarks, and similarly for the gluon AM. We emphasize that this spin sum rule is frame-independent. To attribute the above sum rule with a simple parton picture, one has to justify that $(x/2)(q(x)+E(x))$ is the transverse AM density in x, i.e., it is just the contribution to the transverse nucleon spin from partons with longitudinal momentum xP^+. We can define the quark longitudinal momentum density $\rho^+(x,\xi,S^\perp)$ through

$$\rho^+(x,\xi,S^\perp) = x\int \frac{d\lambda}{4\pi} e^{i\lambda x} \langle PS^\perp|\overline{\psi}(-\frac{\lambda n}{2},\xi)\gamma^+\psi(\frac{\lambda n}{2},\xi)|PS^\perp\rangle \ , \tag{5}$$

where n is the conjugation vector associated with P: $n = (0^+, n^-, 0_\perp)$ with $n\cdot P = 1$. A careful calculation shows that beside the usual momentum distribution, it has an additional term

$$\rho^+(x,\xi,S^\perp)/P^+ = xq(x) + \frac{1}{2}x\left(q(x)+E(x)\right)\lim_{\Delta_\perp\to 0}\frac{S^{\perp'}}{M^2}\partial^{\perp\xi} e^{i\xi_\perp\Delta_\perp} \tag{6}$$

where the $\xi^\perp$-dependence comes from the slightly off-forward matrix element. The parton contribution to the transverse spin is just the transverse-space moment of $\rho^+(x,\xi,S^\perp)$,

$$S^q_\perp(x) = \frac{M^2}{2P^+S^{\perp'}(2\pi)^2\delta^2(0)}\int d^2\xi\xi^\perp\rho^+(x,\xi,S^\perp) = \frac{x}{2}(q(x)+E(x)) \ . \tag{7}$$

where we have included the contribution from the energy-momentum component $T^{+\perp}$ through Lorentz symmetry.

3 Helicity Sum Rule

For a longitudinal polarized nucleon, we consider the z-component of the quark AM,

$$J^3 = \int d^3\vec{\xi} M^{+12}(\xi) = \int d^3\vec{\xi}\left[\overline{\psi}\gamma^+(\frac{\Sigma^3}{2})\psi + \overline{\psi}\gamma^+\left(\xi^1(iD^2) - \xi^2(iD^1)\right)\psi\right] \ , \tag{8}$$

where the quark helicity is well-known to have a simple parton density interpretation. However, the quark OAM involves transverse component of the gluon field, and thus is related to three-parton correlations.

Thus a partonic picture of the orbital contribution to the nucleon helicity necessarily involves parton's transverse momentum. In other words, TMD parton distributions are the right objects for physical measurements and interpretation. In recent years, TMDs and novel effects associated with them have been explored extensively in both theory and experiment [1], where it was found that the physical parton represents a gauge-invariant object with a gauge link extended from the location of parton field to infinity along the conjugating light-cone direction n^μ,

$$\Psi_{LC}(\xi) = P\left[\exp\left(-ig\int_0^\infty d\lambda n\cdot A(\lambda n+\xi)\right)\right]\psi(\xi)\ . \tag{9}$$

where P indicates path ordering. Therefore, in perturbative diagrams, a parton with momentum $k^+ = xP^+$ represents in fact the sum of all diagrams with longitudinal gluons involved.

When considering parton's transverse momentum, we also need appropriate gauge links formed of gauge potentials. In practical applications, two choices stand out. First one uses the same light-cone gauge link as shown in the above. The second choice is a straightline gauge link along the direction of spacetime position ξ^μ,

$$\Psi_{FS}(\xi) = P\left[\exp\left(-ig\int_0^\infty d\lambda \xi\cdot A(\lambda\xi)\right)\right]\psi(\xi)\ , \tag{10}$$

The link reduces to unity in Fock-Schwinger gauge, $\xi\cdot A(\xi)=0$.

To investigate parton's OAM contribution to the proton helicity, one also needs their transverse coordinates. The most natural concept is a phase-space Wigner distribution, which was first introduced in Ref. [9]. A Wigner distribution operator for quarks is defined as

$$\hat{\mathcal{W}}_{\mathcal{P}}(\vec{r},k) = \int \overline{\Psi}_{\mathcal{P}}(\vec{r}-\xi/2)\gamma^+\Psi_{\mathcal{P}}(\vec{r}+\xi/2)e^{ik\cdot\xi}d^4\xi\ , \tag{11}$$

where $\mathcal{P}$ denotes the path choice of LC or FS, $\vec{r}$ is the quark phase-space position and k the phase-space four-momentum. The above quantity is gauge invariant although it does depend on the choices of the gauge link. The Wigner distribution can be define as the expectation value of $\hat{\mathcal{W}}$ in the nucleon state,

$$W_{\mathcal{P}}(k^+=xP^+,\vec{b}_\perp,\vec{k}_\perp) = \frac{1}{2}\int\frac{d^2\vec{q}_\perp}{(2\pi)^3}\int\frac{dk^-}{(2\pi)^3}e^{-i\vec{q}_\perp\cdot\vec{b}_\perp}\left\langle\frac{\vec{q}_\perp}{2}\left|\hat{\mathcal{W}}_{\mathcal{P}}(0,k)\right|-\frac{\vec{q}_\perp}{2}\right\rangle\ . \tag{12}$$

where the nucleon has definite helicity $1/2$.

The total OAM sum rule in term of parton's Wigner distribution,

$$\frac{\langle PS|\int d^3\vec{r}\,\overline{\psi}(\vec{r})\gamma^+(\vec{r}_\perp\times i\vec{D}_\perp)\psi(\vec{r})|PS\rangle}{\langle PS|PS\rangle} = \int(\vec{b}_\perp\times\vec{k}_\perp)W_{FS}(x,\vec{b}_\perp,\vec{k}_\perp)dxd^2\vec{b}_\perp d^2\vec{k}_\perp \tag{13}$$

which gives a parton picture for the gauge-invariant OAM [3], although the straightline gauge link destroys the straightforward parton density interpretation.

4 Canonical Orbital Angular Momentum

The quark contribution to the canonical orbital angular momentum was explored in Ref. [10],

$$l^q(x) = \frac{1}{(2\pi)^2 2P^+\delta^2(0)} \int \frac{d\lambda}{2\pi} e^{ix\lambda} d^2\xi \langle PS|\overline{\psi}(-\frac{\lambda n}{2},\xi)\gamma^+(\xi^1 i\partial^2 - \xi^2 i\partial^1)\psi(\frac{\lambda n}{2},\xi)|PS\rangle \ . \quad (14)$$

This definition represents the canonical OAM in the light-cone gauge $A^+ = 0$. Its matrix element is in principle related to the twist-three GPDs, and an infinite number of moments are involved due to non-locality. Therefore, we arrive at the interesting conclusion that $l_q(x)$ in light-cone gauge is actually accessible through twist-two and three GPDs.

A clear parton picture emerges through connections between $l_q(x)$ and TMDs and Wigner distributions [7, 8]. One can introduce a Wigner distribution with the gauge link in the light-cone direction, $W_{LC}(x,\vec{b}_\perp,\vec{k}_\perp)$. Integration over the impact parameter space $\int d^2\vec{b}_\perp W_{LC}$ generates quark-spin independent TMDs. It can be shown that the canonical AM distribution in $A^+ = 0$ gauge as defined in [10] can be obtained from the simple moment of a gauge-invariant Wigner distribution,

$$l_q(x) = \int (\vec{b}_\perp \times \vec{k}_\perp) W_{LC}(x,\vec{b}_\perp,\vec{k}_\perp) d^2\vec{b}_\perp d^2\vec{k}_\perp \ . \quad (15)$$

From the discussion of the previous paragraph, this also implies constraints on the moments of Wigner distributions from the GPDs. Finally, the canonical OAM in light-cone gauge acquires the simple but gauge-dependent parton sum rule in the quantum phase space [7, 8],

$$l_q = \frac{\langle PS|\int d^3\vec{r}\ \overline{\psi}(\vec{r})\gamma^+(\vec{r}_\perp \times i\vec{\partial}_\perp)\psi(\vec{r})|PS\rangle}{\langle PS|PS\rangle} = \int (\vec{b}_\perp \times \vec{k}_\perp) W_{LC}(x,\vec{b}_\perp,\vec{k}_\perp) dx d^2\vec{b}_\perp d^2\vec{k}_\perp \ . \quad (16)$$

The measurability of this Wigner distribution will be studied in a future publication.

To summarize, we reviewed parton pictures for the proton spin: For the transverse polarization, we found that it is simple to interpret in terms of parton AM density measurable through twist-two GPDs; For the nucleon helicity, the gauge-invariant parton picture can be probed through twist-two and three GPDs, and also calculable in lattice QCD. A simpler parton picture in the light-cone gauge can be established through the quantum phase space Wigner distribution, and can be measured through either twist-two and three GPDs or directly from Wigner distribution.

We thank X. Ji and X. Xiong for the collaboration on this project. This work was partially supported by the U.S. Department of Energy via grants DE-AC02-05CH11231.

References

[1] D. Boer, *et al.*, arXiv:1108.1713 [nucl-th].
[2] R. L. Jaffe and A. Manohar, Nucl. Phys. B **337** (1990) 509.
[3] X. Ji, Phys. Rev. Lett. **78** (1997) 610 [hep-ph/9603249].
[4] INT Workshop on "Orbital Angular Momentum in QCD", Seattle, February 6-17, 2012.
[5] D. Mueller, these proceedings.
[6] A. Bacchetta, these proceedings.
[7] X. Ji, X. Xiong and F. Yuan, arXiv:1202.2843 [hep-ph]; to be published.
[8] C. Lorce and B. Pasquini, Phys. Rev. D **84** (2011) 014015; C. Lorce, B. Pasquini, X. Xiong and F. Yuan, Phys. Rev. D **85** (2012) 114006; Y. Hatta, Phys. Lett. B **708** (2012) 186.
[9] A. Belitsky, X.Ji, F. Yuan, Phys. Rev. **D69** (2004) 074014
[10] S. Bashinsky and R. L. Jaffe, Nucl. Phys. B **536** (1998) 303.

Constraining quark angular momentum with the Sivers function

Alessandro Bacchetta[1,2], *Marco Radici*[2]

[1]Dipartimento di Fisica
[2]INFN, Sez. di Pavia, via Bassi 6, 27100 Pavia, Italy

DOI: http://dx.doi.org/10.3204/DESY-PROC-2012-02/50

Currently, the best way to determine quark total angular momentum requires the knowledge of the generalized parton distribution E in the forward limit. We present the results of a recent work where we assumed a connection between this function and the Sivers transverse-momentum distribution. Using this assumption, we fitted at the same time nucleon anomalous magnetic moments and semi-inclusive single-spin asymmetries. This allowed us to give an estimate of the total angular momentum carried by each quark flavor.

This talk describes the results of a recent work [1], where we proposed a nonstandard way to constrain the angular momentum J^a of a (anti)quark with flavor a. In order to do this, we adopted an assumption [2], motivated by model calculations and theoretical considerations, that connects J^a to the Sivers transverse-momentum distribution (TMD) [3] measured in semi-inclusive DIS (SIDIS). We showed that this assumption is compatible with existing data, and allows us to derive estimates of J^a in fair agreement with other "standard" extractions.

The total angular momentum of a parton a (with $a = q, \bar{q}$) at some scale Q^2 can be computed as a specific moment of generalized parton distribution functions (GPD) [4]

$$2J^a(Q^2) = \int_0^1 dx\, x \left(H^a(x,0,0;Q^2) + E^a(x,0,0;Q^2)\right). \tag{1}$$

The GPD $H^a(x,0,0;Q^2)$ corresponds to the familiar collinear parton distribution function (PDF) $f_1^a(x;Q^2)$. The forward limit of the GPD E^a does not correspond to any collinear PDF. It is possible to probe the function E^a in experiments, but never in the forward limit. Assumptions are eventually necessary to constrain $E^a(x,0,0;Q^2)$. This makes the estimate of J^a particularly challenging. The only model-independent constraint is the scale-independent sum rule $\sum_q e_{q_v} \int_0^1 dx\, E^{q_v}(x,0,0) = \kappa$, where $E^{q_v} = E^q - E^{\bar{q}}$ and κ denotes the anomalous magnetic moment of the parent nucleon.

Denoting the Sivers function by $f_{1T}^{\perp a}$, we propose this simple relation at a scale Q_L,

$$f_{1T}^{\perp(0)a}(x;Q_L^2) = -L(x)\, E^a(x,0,0;Q_L^2), \tag{2}$$

where $f_{1T}^{\perp(0)a}$ is the integral of the Sivers function over transverse momentum. This assumption is inspired by theoretical considerations [2] and by results of spectator models [5, 6, 7, 8, 9]. $L(x)$ is a flavor-independent function, representing the effect of the QCD interaction of the outgoing quark with the rest of the nucleon. The name "lensing function" has been proposed by Burkardt to denote $L(x)$ [10]. Computations of the lensing function beyond the single-gluon

approximation have been proposed in Ref. [11]. It is likely that in more complex models the above relation is not preserved. Nevertheless, it is useful and interesting to speculate on the consequences of this simple assumption.

The advantage of adopting the Ansatz of Eq. (2) is twofold: first, the value of the anomalous magnetic moment fixes the integral of the GPD E and allows us to constrain the valence Sivers function also outside the region where SIDIS data are available; second, our Ansatz allows us to obtain flavor-decomposed information on the x-dependence of the GPD E and ultimately on quark and antiquark total angular momentum. This is an example of how assuming model-inspired connections between GPD and TMD can lead to powerful outcomes.

To analyze SIDIS data, we use the same assumptions adopted in Refs. [12, 13]: we assume a flavor-independent Gaussian transverse-momentum distribution for all inolved TMDs and we neglect the effect of TMD evolution, which has been studied only recently [14, 15, 16].

Neglecting c, b, t flavors, we parametrize the Sivers function in the following way:

$$f_{1T}^{\perp q_v}(x, k_\perp^2; Q_0^2) = C^{q_v} \frac{\sqrt{2e} M M_1}{\pi M_1^2 \langle k_\perp^2 \rangle} (1-x) f_1^{q_v}(x; Q_0^2), e^{-k_\perp^2/M_1^2} e^{-k_\perp^2/\langle k_\perp^2 \rangle} \frac{1 - x/\alpha^{q_v}}{|\alpha^{q_v} - 1|} . \quad (3)$$

For the $\bar{q}$ functions, we use a similar function, excluding the last term. We used $\langle k_\perp^2 \rangle = 0.14$ GeV^2. M_1 is a free parameter that determines the transverse-momentum width of the function. We imposed constraints on the parameters C^a in order to respect the positivity bound for the Sivers function [17]. We multiply the unpolarized PDF by $(1-x)$ to respect the predicted high-x behavior of the Sivers function [18]. We introduce the free parameter α^{q_v} to allow for the presence of a node in the Sivers function at $x = \alpha^{q_v}$, as suggested in Refs. [9, 19, 20].

For the lensing function we use the following Ansatz

$$L(x) = K/(1-x)^\eta. \quad (4)$$

The choice of this form is guided by model calculations [5, 6, 7, 8, 9], by the large-x limit of the GPD E [18], and by the phenomenological analysis of the GPD E proposed in Ref. [21]. We checked *a posteriori* that there is no violation of the positivity bound on the GPD E^{q_v}.

We performed a combined χ^2 fit to the nucleon anomalous magnetic moments (for our present purposes we take $\kappa^p = 1.793 \pm 0.001$, $\kappa^n = -1.913 \pm 0.001$) and the Sivers asymmetry with identified hadrons from Refs. [22, 23, 24].

We set the gluon Sivers function to zero (the influence of the gluon Sivers function through evolution is anyway limited) and we chose $Q_0 = Q_L = 1$ GeV. We fixed $\alpha^{d_v, s_v} = 0$ (no nodes in the valence down and strange Sivers functions). We explored several scenarios characterized by different choices of the parameters related to the strange quark. In all cases, we obtained very good values of χ^2 per degree of freedom (χ^2/dof), around 1.35.

All fits lead to a negative Sivers function for u_v and large and positive for d_v, in agreement with previous studies [25, 26, 12, 13]. The data are compatible with vanishing sea-quark contributions (with large uncertainties). However, in the x range where data exist, large Sivers functions for $\bar{u}$ and $\bar{d}$ are excluded, as well as large and negative for $\bar{s}$. The Sivers function for s_v is essentially unconstrained. The parameter M_1 is quite stable around 0.34 GeV, as well as the strength of the lensing function K around 1.86 GeV. The parameter η is typically around 0.4. There is little room for a node in the up Sivers function, also because of the constraint imposed by the anomalous magnetic moments.

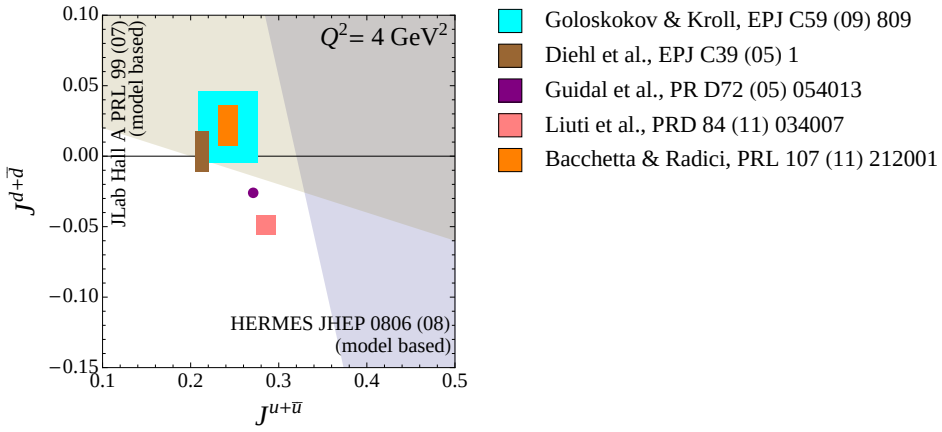

Figure 1: The results of our determination of $J^{u+\bar{u}}$ and $J^{d+\bar{d}}$ compared with other estimates based on GPD extractions from Refs. [21, 27, 28, 29] and measurements of Refs. [30, 31]. (For the extraction of Ref. [28], the values of J^q are quoted in Ref. [32].

Our results for the Sivers function are comparable with other extractions [25, 26, 12]. The results for the forward limit of the GPD E are also qualitatively similar to available extractions [21, 27, 28, 29].

Using Eq. (1), we can compute the total longitudinal angular momentum carried by each flavor q and $\bar{q}$ at our initial scale $Q^2_L = 1$ GeV^2. Using the standard evolution equations for the angular momentum (at leading order, with 3 flavors only, and $\Lambda_{\rm QCD} = 257$ MeV), we obtain the following results at $Q^2 = 4$ GeV^2:

$$J^u = 0.229 \pm 0.002^{+0.008}_{-0.012}, \qquad J^d = -0.007 \pm 0.003^{+0.020}_{-0.005}, \qquad J^s = 0.006^{+0.002}_{-0.006},$$
$$J^{\bar{u}} = 0.015 \pm 0.003^{+0.001}_{-0.000}, \qquad J^{\bar{d}} = 0.022 \pm 0.005^{+0.001}_{-0.000}, \qquad J^{\bar{s}} = 0.006^{+0.000}_{-0.005}.$$

The first symmetric error is statistical and related to the errors on the fit parameters, while the second asymmetric error reflects the uncertainty introduced by the other possible scenarios. In the present approach, we cannot include the (probably large) systematic error due to the rigidity of the functional form in Eqs. (3) and (4). The bias induced by the choice of the functional form may affect in particular the determination of the sea quark angular momenta, since they are not directly constrained by the values of the nucleon anomalous magnetic moments. Our present estimates (at $Q^2 = 4$ GeV^2) agree well with other estimates based on the study of the GPD E [21, 27, 28, 29]. Our study indicates a total contribution to the nucleon spin from quarks and antiquarks of $0.271 \pm 0.007^{+0.032}_{-0.028}$, of which 85% is carried by the up quark.

Our approach can be used also to estimate the size of the total angular momentum carried by the gluons. In this case, we expect the lensing function to be different from that of the quarks. However, our extraction leaves little room for a nonzero gluon Sivers function, since the quark Sivers function already saturate the so-called Burkardt sum rule [33]. If the Sivers function of the gluons is zero, our reasonsing allows us to conclude that E^g is also zero, independent of the details of the lensing function. This would lead to a value of $J^g = 0.215$ at 4 GeV^2. However, these considerations are strongly affected by the uncertainties on the sea-quark Sivers functions outside the x range where data exists. Direct measurements of the sea-quark and gluon Sivers

functions are therefore highly necessary.

At this point, we add a remark on the effect of TMD evolution on the Sivers function. The discussions in Refs. [14, 15, 16] suggest that the inclusion of TMD-evolution effects might lead to larger values of the Sivers function at the starting scale Q_0. If this were the case, we would need to compensate the effect by a smaller size of the lensing function in order to have an agreement with the anomalous magnetic moments. However, this will have a negligible net effect on the results for J^a.

References

[1] A. Bacchetta and M. Radici. Phys.Rev.Lett. **107** (2011) 212001, arXiv:1107.5755 [hep-ph].

[2] M. Burkardt. Phys. Rev. **D66** (2002) 114005, hep-ph/0209179.

[3] D. W. Sivers. Phys. Rev. **D41** (1990) 83.

[4] X. Ji. Phys. Rev. Lett. **78** (1997) 610–613, hep-ph/9603249.

[5] M. Burkardt and D. S. Hwang. Phys. Rev. **D69** (2004) 074032, hep-ph/0309072.

[6] Z. Lu and I. Schmidt. Phys. Rev. **D75** (2007) 073008, hep-ph/0611158.

[7] S. Meissner, A. Metz, and K. Goeke. Phys. Rev. **D76** (2007) 034002, hep-ph/0703176.

[8] A. Bacchetta, M. Radici, F. Conti, and M. Guagnelli. Eur. Phys. J. **A45** (2010) 373–388, arXiv:1003.1328 [hep-ph].

[9] A. Bacchetta, F. Conti, and M. Radici. Phys. Rev. **D78** (2008) 074010, arXiv:0807.0323 [hep-ph].

[10] M. Burkardt. Nucl. Phys. **A735** (2004) 185–199, hep-ph/0302144.

[11] L. Gamberg and M. Schlegel. Phys. Lett. **B685** (2010) 95–103, arXiv:0911.1964 [hep-ph].

[12] S. Arnold, A. V. Efremov, K. Goeke, M. Schlegel, and P. Schweitzer. arXiv:0805.2137 [hep-ph].

[13] M. Anselmino, M. Boglione, U. D'Alesio, S. Melis, F. Murgia, *et al.* arXiv:1107.4446 [hep-ph].

[14] S. M. Aybat, J. C. Collins, J.-W. Qiu, and T. C. Rogers. Phys.Rev. **D85** (2012) 034043, arXiv:1110.6428 [hep-ph].

[15] S. Aybat, A. Prokudin, and T. C. Rogers. arXiv:1112.4423 [hep-ph].

[16] M. Anselmino, M. Boglione, and S. Melis. arXiv:1204.1239 [hep-ph].

[17] A. Bacchetta, M. Boglione, A. Henneman, and P. J. Mulders. Phys. Rev. Lett. **85** (2000) 712–715, hep-ph/9912490.

[18] S. J. Brodsky and F. Yuan. Phys. Rev. **D74** (2006) 094018, hep-ph/0610236.

[19] Z.-B. Kang and A. Prokudin. Phys.Rev. **D85** (2012) 074008, arXiv:1201.5427 [hep-ph].

[20] D. Boer. arXiv:1105.2543 [hep-ph].

[21] M. Guidal, M. V. Polyakov, A. V. Radyushkin, and M. Vanderhaeghen. Phys. Rev. **D72** (2005) 054013, arXiv:hep-ph/0410251.

[22] A. Airapetian *et al.* Phys. Rev. Lett. **103** (2009) 152002, arXiv:0906.3918 [hep-ex].

[23] M. Alekseev *et al.* Phys. Lett. **B673** (2009) 127–135, arXiv:0802.2160 [hep-ex].

[24] X. Qian *et al.* Phys.Rev.Lett. **107** (2011) 072003, arXiv:1106.0363 [nucl-ex].

[25] W. Vogelsang and F. Yuan. Phys. Rev. **D72** (2005) 054028, hep-ph/0507266.

[26] M. Anselmino *et al.* Eur. Phys. J. **A39** (2009) 89–100, arXiv:0805.2677 [hep-ph].

[27] M. Diehl, T. Feldmann, R. Jakob, and P. Kroll. Eur. Phys. J. **C39** (2005) 1–39, arXiv:hep-ph/0408173 [hep-ph].

[28] G. R. Goldstein, J. O. Hernandez, and S. Liuti. Phys.Rev. **D84** (2011) 034007, arXiv:1012.3776 [hep-ph].

[29] S. Goloskokov and P. Kroll. Eur. Phys. J. **C59** (2009) 809–819, arXiv:0809.4126 [hep-ph].

[30] M. Mazouz *et al.* Phys.Rev.Lett. **99** (2007) 242501, arXiv:0709.0450 [nucl-ex].

[31] A. Airapetian *et al.* JHEP **0806** (2008) 066, arXiv:0802.2499 [hep-ex].

[32] S. K. Taneja, K. Kathuria, S. Liuti, and G. R. Goldstein. arXiv:1101.0581 [hep-ph].

[33] M. Burkardt. Phys. Rev. **D69** (2004) 091501, hep-ph/0402014.

Phenomenology of Sivers Effect with TMD Evolution

Mauro Anselmino[1], *Mariaelena Boglione*[1], *Stefano Melis*[2]

[1] Dipartimento di Fisica Teorica, Università di Torino,
and INFN - Sezione di Torino, Via P. Giuria 1, I-10125 Torino, Italy
[2] European Centre for Theoretical Studies in Nuclear Physics and Related Areas (ECT*),
Villa Tambosi, Strada delle Tabarelle 286, I-38123 Villazzano, Trento, Italy

DOI: http://dx.doi.org/10.3204/DESY-PROC-2012-02/256

Following the TMD evolution scheme recently proposed for the unpolarized and the Sivers distribution function, we propose a simple strategy to take into account this TMD Q^2 dependence in our phenomenological extraction of the Sivers function from SIDIS data. New results are presented and possible future applications are discussed.

The exploration of the 3-dimensional structure of the nucleon, both in momentum and in configuration space, is one of the major issues in high energy hadron physics. Information on this 3-dimensional structure is embedded in the Transverse Momentum Dependent distribution and fragmentation functions (TMDs). The Sivers function, which describes the number density of unpolarized quarks inside a transversely polarized proton, is particularly interesting, as it might provide information on the partonic orbital angular momentum.

So far, all phenomenological fits have either neglected the QCD scale dependence of TMDs (which was unknown) or limited it to the collinear part of the unpolarized PDFs, according to the DGLAP evolution. Here, we present the first attempt to take into account the TMD evolution as proposed by Aybat, Collins, Qiu and Rogers [1, 2, 3] in the analysis of the Sivers asymmetry data and show how these new results compare with the previous extractions. Eventually, such a scheme will provide a complete TMD factorization framework for a consistent treatment of all SIDIS data.

In Ref. [4] we showed how the QCD evolution equation of the TMDs in the coordinate space proposed in Refs. [2] and [3] can be expressed in a simplified way, taking the renormalization scale μ^2 and the regulating parameters ζ_F and ζ_D all equal to Q^2, as

$$\widetilde{F}(x, \boldsymbol{b}_T; Q) = \widetilde{F}(x, \boldsymbol{b}_T; Q_0)\, \widetilde{R}(Q, Q_0, b_T)\, \exp\left\{-g_K(b_T) \ln \frac{Q}{Q_0}\right\}\,, \tag{1}$$

where $\widetilde{F}$ can be either the unpolarized parton distribution, $\widetilde{F}(x, \boldsymbol{b}_T; Q) = \widetilde{f}_{q/p}(x, \boldsymbol{b}_T; Q)$, the unpolarized fragmentation function $\widetilde{F}(x, \boldsymbol{b}_T; Q) = \widetilde{D}_{h/q}(z, \boldsymbol{b}_T; Q)$, or the first derivative, with respect to the parton impact parameter b_T, of the Sivers function, $\widetilde{F}(x, \boldsymbol{b}_T; Q) = \widetilde{f}^{\prime\perp f}_{1T}(x, \boldsymbol{b}_T; Q)$; $g_K(b_T)$ is an unknown, but universal and scale independent, input function, while $\widetilde{R}(Q, Q_0, b_T)$ is the evolution kernel

$$\widetilde{R}(Q, Q_0, b_T) \equiv \exp\left\{\ln \frac{Q}{Q_0} \int_{Q_0}^{\mu_b} \frac{\mathrm{d}\mu'}{\mu'} \gamma_K(\mu') + \int_{Q_0}^{Q} \frac{\mathrm{d}\mu}{\mu} \gamma_F\left(\mu, \frac{Q^2}{\mu^2}\right)\right\}\,. \tag{2}$$

The anomalous dimensions γ_F and γ_K appearing in Eq. (2), are given, at order $\mathcal{O}(\alpha_s)$, by [2]

$$\gamma_F(\mu; \frac{Q^2}{\mu^2}) = \alpha_s(\mu)\,\frac{C_F}{\pi}\left(\frac{3}{2} - \ln\frac{Q^2}{\mu^2}\right) \qquad\qquad \gamma_K(\mu) = \alpha_s(\mu)\,\frac{2\,C_F}{\pi}\ . \tag{3}$$

The Q^2 evolution is therefore driven by the functions $g_K(b_T)$ and $\widetilde{R}(Q, Q_0, b_T)$. While the latter, Eq. (2), can be easily evaluated, numerically or even analytically, the former, is essentially unknown and will need to be taken from independent experimental inputs.

The appropriate Fourier transforms allow us to obtain the distribution and fragmentation functions in the momentum space:

$$\widehat{f}_{q/p}(x, k_\perp; Q) = \frac{1}{2\pi}\int_0^\infty \mathrm{d}b_T\; b_T\; J_0(k_\perp b_T)\; \widetilde{f}_{q/p}(x, b_T; Q)\;, \tag{4}$$

$$\widehat{D}_{h/q}(z, p_\perp; Q) = \frac{1}{2\pi}\int_0^\infty \mathrm{d}b_T\; b_T\; J_0(\mathrm{k}_T b_T)\; \widetilde{D}_{h/q}(z, b_T; Q)\;, \tag{5}$$

$$\widehat{f}_{1T}^{\perp f}(x, k_\perp; Q) = \frac{-1}{2\pi k_\perp}\int_0^\infty \mathrm{d}b_T\; b_T\; J_1(k_\perp b_T)\; \widetilde{f}_{1T}^{\prime\perp q}(x, b_T; Q)\;, \tag{6}$$

where J_0 and J_1 are Bessel functions, while $\widehat{f}_{q/p}$ is the unpolarized TMD distribution function for a parton of flavor q inside a proton, $\widehat{D}_{h/q}$ is the unpolarized TMD fragmentation function for hadron h inside a parton q and $\widehat{f}_{1T}^{\perp q}$ is the Sivers distribution describing unpolarized partons inside a transversely polarized proton.

The unknown input functions $g_K(b_T)$ and $\widetilde{F}(x, b_T; Q_0)$ inside Eq. (1) have to be appropriately parameterized. As already anticipated, $g_K(b_T)$ is a non-perturbative, but universal function, which in the literature is usually parameterized in a quadratic form: $g_K(b_T) = \frac{1}{2}\,g_2\,b_T^2$. As in Ref. [3] we will adopt the results provided by a recent fit of Drell-Yan data [5], and assume $g_2 = 0.68$ GeV^2. The input functions $\widetilde{F}(x, b_T; Q_0)$ are parameterized by requiring that their Fourier-transforms, which give the corresponding TMD functions in the transverse momentum space, coincide with the previously adopted $k_\perp$-Gaussian forms, with the x dependence factorized out. As shown in Ref. [4], one finds

$$\widetilde{f}_{q/p}(x, b_T; Q) = f_{q/p}(x, Q_0)\;\widetilde{R}(Q, Q_0, b_T)\;\exp\left\{-b_T^2\left(\alpha^2 + \frac{g_2}{2}\ln\frac{Q}{Q_0}\right)\right\} \tag{7}$$

$$\widetilde{D}_{h/q}(z, b_T; Q) = \frac{1}{z^2}D_{h/q}(z, Q_0)\;\widetilde{R}(Q, Q_0, b_T)\;\exp\left\{-b_T^2\left(\beta^2 + \frac{g_2}{2}\ln\frac{Q}{Q_0}\right)\right\} \tag{8}$$

$$\widetilde{f}_{1T}^{\prime\perp}(x, b_T; Q) \;\; = -2\,\gamma^2\,f_{1T}^{\perp}(x; Q_0)\,\widetilde{R}(Q, Q_0, b_T)\,b_T\,\exp\left\{-b_T^2\left(\gamma^2 + \frac{g_2}{2}\ln\frac{Q}{Q_0}\right)\right\} \tag{9}$$

with $\alpha^2 = \langle k_\perp^2\rangle/4$, $\beta^2 = \langle p_\perp^2\rangle/(4z^2)$, $4\,\gamma^2 \equiv \langle k_\perp^2\rangle_S = \frac{M_1^2\,\langle k_\perp^2\rangle}{M_1^2 + \langle k_\perp^2\rangle}$, and $\widetilde{R}(Q, Q_0, b_T)$ in Eq. (2).

Eqs. (7)-(9) show that the Q^2 evolution is controlled by the logarithmic Q dependence of the b_T Gaussian width, together with the factor $\widetilde{R}(Q, Q_0, b_T)$: for increasing values of Q^2, they are responsible for the typical broadening effect already observed in Refs. [2] and [3].

As $R(Q, Q_0, b_T)$ shows a weak dependence on (large) b_T (i.e. small $k_\perp$), we can assume $R(Q, Q_0, b_T)$ to be constant in b_T and compute the Fourier transforms of the evolution equa-

Table 1: χ^2 contributions corresponding to our three fits, for some experimental data sets of HERMES and COMPASS experiments.

	TMD Evolution (exact)	TMD Evolution (analyt.)	DGLAP Evolution
	$\chi^2_{tot} = 255.8$ $\chi^2_{d.o.f} = 1.02$	$\chi^2_{tot} = 275.7$ $\chi^2_{d.o.f} = 1.10$	$\chi^2_{tot} = 315.6$ $\chi^2_{d.o.f} = 1.26$
HERMES π^+	$\chi^2_x = 10.7$ $\chi^2_z = 4.3$ $\chi^2_{P_T} = 9.1$	$\chi^2_x = 12.9$ $\chi^2_z = 4.3$ $\chi^2_{P_T} = 10.5$	$\chi^2_x = 27.5$ $\chi^2_z = 8.6$ $\chi^2_{P_T} = 22.5$
COMPASS h^+	$\chi^2_x = 6.7$ $\chi^2_z = 17.8$ $\chi^2_{P_T} = 12.4$	$\chi^2_x = 11.2$ $\chi^2_z = 18.5$ $\chi^2_{P_T} = 24.2$	$\chi^2_x = 29.2$ $\chi^2_z = 16.6$ $\chi^2_{P_T} = 11.8$

tions (7), (8) and (9) analytically, to find

$$\widehat{f}_{q/p}(x,k_\perp;Q) = f_{q/p}(x,Q_0)\; R(Q,Q_0)\; \frac{e^{-k_\perp^2/w^2}}{\pi\, w^2} \tag{10}$$

$$\widehat{D}_{h/q}(z,p_\perp;Q) = D_{h/q}(z,Q_0)\; R(Q,Q_0)\; \frac{e^{-p_\perp^2/w_F^2}}{\pi w_F^2} \tag{11}$$

$$\Delta^N \widehat{f}_{q/p^\uparrow}(x,k_\perp;Q) = \frac{k_\perp}{M_1}\,\sqrt{2e}\,\frac{\langle k_\perp^2\rangle_S^2}{\langle k_\perp^2\rangle}\,\Delta^N f_{q/p^\uparrow}(x,Q_0)\, R(Q,Q_0)\,\frac{e^{-k_\perp^2/w_S^2}}{\pi w_S^4}\,, \tag{12}$$

where $f_{q/p}(x,Q_0)$ and $D_{h/q}(z,Q_0)$ are the usual integrated PDF evaluated at the initial scale Q_0, and $\Delta^N f_{q/p^\uparrow}(x,Q_0)$ gives the x dependence of the Sivers function [4] $[-(2k_\perp/M_p)\widehat{f}_{1T}^\perp = \Delta^N \widehat{f}_{q/p^\uparrow}]$. Most importantly, w^2, w_F^2 and w_S^2 are the "evolving" Gaussian widths, defined as:

$$w^2 = \langle k_\perp^2\rangle + 2\,g_2 \ln\frac{Q}{Q_0}\;, \qquad w_F^2 = \langle p_\perp^2\rangle + 2z^2 g_2 \ln\frac{Q}{Q_0}\;, \qquad w_S^2 = \langle k_\perp^2\rangle_S + 2g_2 \ln\frac{Q}{Q_0}\;\cdot \tag{13}$$

Notice that the Q^2 evolution of the TMD PDFs is now determined by the overall factor $R(Q,Q_0)$ and, most crucially, by the Q^2 dependent Gaussian width $w(Q,Q_0)$.

It is interesting to point that the evolution factor $R(Q,Q_0)$, controlling the TMD evolution, is the same for all functions (TMD PDFs, TMD FFs and Sivers) and is flavor independent: consequently it will appear, squared, in both numerator and denominator of the Sivers azimuthal asymmetry and, approximately, cancel out. Therefore, we can safely conclude that most of the TMD evolution of azimuthal asymmetries is controlled by the logarithmic Q dependence of the $k_\perp$ Gaussian widths $w^2(Q,Q_0)$, Eq. (13).

The aim of our paper is to analyze the available polarized SIDIS data from the HERMES and COMPASS collaborations in order to understand whether or not they show signs of the TMD evolution proposed in Ref. [3]. In particular we perform three different data fits of the SIDIS Sivers single spin asymmetry $A_{UT}^{\sin(\phi_h-\phi_S)}$ measured by HERMES and COMPASS: a fit (TMD-fit) in which we adopt the TMD evolution equations of Eqs. (7)-(9);a second fit (TMD-analytical-fit) in which we apply the same TMD evolution, but using the analytical approximation of Eqs. (10), (11) and (12); a fit (DGLAP-fit) in which we follow our previous work, as done so far in Ref. [6, 7], using the DGLAP evolution equation only in the collinear part of the TMDs.

Table I shows the main results of our fitting procedure. The best total χ^2_{tot}, which amounts to 256, is obtained by using the TMD evolution, followed by a slightly higher χ^2_{tot} of the analytical approximation, and a definitely larger $\chi^2_{tot} \simeq 316$ corresponding to the DGLAP fit. The difference of about 60 χ^2-points between the TMD and the DGLAP fits is heavily concentrated in the asymmetry for π^+ production at HERMES and for h^+ production at COMPASS, especially when this asymmetry is observed as a function of the x-variable. It is important to stress that, as x is directly proportional to Q^2 through the kinematical relation $Q^2 = x\,y\,s$, the x behavior of the asymmetries is intimately connected to their Q^2 evolution. While the HERMES experimental bins cover a very modest range of Q^2 values, from 1.3 GeV^2 to 6.2 GeV^2, COMPASS data raise to a maximum Q^2 of 20.5 GeV^2, enabling to test more severely the TMD Q^2 evolution in SIDIS. These aspects are illustrated in Fig. 1, where the SIDIS Sivers asymmetries $A_{UT}^{\sin(\phi_h-\phi_S)}$ obtained in the three fits are shown in the same plot. It is evident that the DGLAP evolution seems to be unable to describe the correct x trend, *i.e.* the right Q^2 behavior, while the TMD evolution (red solid line) follows much better the large Q^2 data points, corresponding to the last x-bins measured by COMPASS.

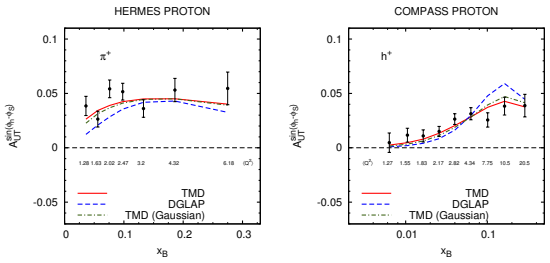

Figure 1: The results obtained from our fit of the SIDIS $A_{UT}^{\sin(\phi_h-\phi_S)}$ Sivers asymmetries applying TMD evolution (red, solid lines) are compared with the analogous results found by using DGLAP evolution equations (blue, dashed lines). The green, dash-dotted lines correspond to the results obtained by using the approximated analytical TMD evolution. The experimental data are from HERMES [8] (left panel) and COMPASS [9] (right panel) Collaborations.

In conclusions, we have analyzed the Sivers effect by up-grading old fits with the addition of the most recent HERMES and COMPASS SIDIS data, and by applying, for the first time, TMD evolution equations. We have compared the results obtained using TMD evolution equations with those found by considering only the DGLAP evolution of the collinear part of the TMDs. Our results give evidence that SIDIS data support the TMD evolution scheme, although further experimental data, covering a wider range of Q^2 values, are necessary to confirm this.

References

[1] J. C. Collins, Foundations of Perturbative QCD, Cambridge Monographs on Particle Physics, Nuclear Physics and Cosmology, No. 32, Cambridge University Press, Cambridge, 2011.

[2] S. M. Aybat and T. C. Rogers, Phys. Rev. D **83**, 114042 (2011) [arXiv:1101.5057 [hep-ph]].

[3] S. M. Aybat, J. C. Collins, J. -W. Qiu and T. C. Rogers, arXiv:1110.6428 [hep-ph].

[4] M. Anselmino, M. Boglione and S. Melis, arXiv:1204.1239 [hep-ph].

[5] F. Landry, R. Brock, P. M. Nadolsky and C. P. Yuan, Phys. Rev. D **67**, 073016 (2003) [hep-ph/0212159].

[6] M. Anselmino, M. Boglione, U. D'Alesio, A. Kotzinian, S. Melis, F. Murgia, A. Prokudin and C. Türk, Eur. Phys. J. A **39**, 89 (2009) [arXiv:0805.2677 [hep-ph]].

[7] M. Anselmino, M. Boglione, U. D'Alesio, S. Melis, F. Murgia and A. Prokudin, arXiv:1107.4446 [hep-ph].

[8] A. Airapetian *et al.* [HERMES Collaboration], Phys. Rev. Lett. **103**, 152002 (2009) [arXiv:0906.3918 [hep-ex]].

[9] F. Bradamante [COMPASS Collaboration], arXiv:1111.0869 [hep-ex].

Single Spin Asymmetry in $e + p^{\uparrow} \to e + J/\psi + X$

R. Godbole [1], *A. Misra*[2], *A. Mukherjee*[3], *V. Rawoot*[2]

[1] Centre for High Energy Physics, Indian Institute of Science, Bangalore, India
[2] Department of Physics, University of Mumbai, Mumbai, India
[3] Department of Physics, Indian Institute of Technology Bombay, Mumbai, India

DOI: `http://dx.doi.org/10.3204/DESY-PROC-2012-02/49`

We report on a recent investigation of the single spin asymmetry (SSA) in low virtuality electroproduction of J/ψ in color evaporation model. We show that this can be used as a probe for the still unknown gluon Sivers function.

1 Introduction

Large single spin asymmetries (SSA) observed when an unpolarized beam of electrons or protons is scattered off a transversely polarized target can be explained with the inclusion of $\boldsymbol{k}_\perp$ dependence in parton distribution functions (pdf's) and fragmentation functions(ff's) [1]. One is led to a generalized factorization formula called TMD factorization [2, 3], which in some processes has been proved at leading twist and leading order [4] and has been argued to hold at all orders. The inclusion of the effect of transverse momentum of partons in parton distribution (pdf) and fragmentation functions leads to a new class of parton distributions that include the effects of spin and transverse momentum of the partons. One of these functions is the Sivers function which describes the probability of finding an unpolarized parton inside a transversely polarized hadron. In this work, we propose charmonium production as a probe to investigate the Sivers function and as a first step, estimate SSA in photoproduction (low virtuality electroproduction) of charmonium in scattering of electrons off transversely polarized protons. At leading order (LO), this receives contribution only from a single partonic subprocess $\gamma g \to c\bar{c}$. Hence, SSA in $e + p^{\uparrow} \to e + J/\psi + X$, if observed, can be used as a clean probe of gluon Sivers function. In addition, charmonium production mechanism can also have implications for this SSA and therefore, its study can help probe the production mechanism for charmonium.

2 Estimate of the Sivers Asymmetry

There are several models for charmonium production. We use the color evaporation model (CEM) as its simplicity makes it suitable for an initial study of SSA in the charmonium production. This model was first proposed by Halzen and Matsuda [5] and Fritsch [6]. In this model, a statistical treatment of color is made and the probability of finding a specific quarkonium state is assumed to be independent of the color of heavy quark pair. In later versions of this model it has been found that the data are better fitted if a phenomenological factor is included in the differential cross section formula, which depends on a Gaussian distribution of

the transverse momentum of the charmonium [7]. We have used Weizsacker-Williams equivalent photon approximation for the photon distribution of the electron [8, 9], to calculate the cross section for the process $e + p^{\uparrow} \to e + J/\psi + X$ at low virtuality of the photon. The underlying partonic process at LO is $\gamma g \to c\bar{c}$ and therefore, the only $k_\perp$ dependent pdf appearing is the gluon Sivers function. For a complete calculation of photoproduction of J/ψ one has to consider higher order contributions and also the resolved photon contributions [7]. Also the gauge links or Wilson lines present in the TMD distributions are important at higher order [10].

According to CEM, the cross section for charmonium production is proportional to the rate of production of $c\bar{c}$ pair integrated over the mass range $2m_c$ to $2m_D$

$$\sigma = \frac{1}{9}\int_{2m_c}^{2m_D} dM \frac{d\sigma_{c\bar{c}}}{dM} \tag{1}$$

where m_c is the charm quark mass and $2m_D$ is the $D\bar{D}$ threshold, M^2 is the squared invariant mass of the $c\bar{c}$ pair.

To calculate SSA in scattering of electrons off a polarized proton target, we assume a generalization of CEM expression by taking into account the transverse momentum dependence of the Weizsacker-Williams (WW) function and gluon distribution function. The numerator of the SSA can be written as

$$\frac{d^4\sigma^{\uparrow}}{dydM^2d^2\boldsymbol{q}_T} - \frac{d^4\sigma^{\downarrow}}{dydM^2d^2\boldsymbol{q}_T} = \frac{1}{s}\int [d^2\boldsymbol{k}_{\perp\gamma}d^2\boldsymbol{k}_{\perp g}]\Delta^N f_{g/p^{\uparrow}}(x_g, \boldsymbol{k}_{\perp g}) f_{\gamma/e}(x_\gamma, \boldsymbol{k}_{\perp\gamma}) \times \delta^2(\boldsymbol{k}_{\perp\gamma} + \boldsymbol{k}_{\perp g} - \boldsymbol{q}_T)\hat{\sigma}_0^{\gamma g\to c\bar{c}}(M^2) \tag{2}$$

where y is the rapidity and q_T in the transverse momentum of the charmonium; $\Delta^N f_{g/p^{\uparrow}}(x_g, \boldsymbol{k}_{\perp g})$ is the gluon Sivers function, $f_{\gamma/e}(x_\gamma, \boldsymbol{k}_{\perp\gamma})$ is the photon distribution of the electron, given in the WW approximation. The denominator would have a similar expression involving the unpolarized gluon distribution of the proton; $f_{g/p}(x_g, \boldsymbol{k}_{\perp g})$, for which we use a gaussian form of $k_\perp$ distribution and a similar gaussian form for the transverse momentum dependence of the WW function. To extract the asymmetry produced by the Sivers function, we calculate the weighted asymmetry [11]

$$A_N^{\sin(\phi_{q_T}-\phi_S)} = \frac{\int d\phi_{q_T}[d\sigma^{\uparrow} - d\sigma^{\downarrow}]\sin(\phi_{q_T} - \phi_S)}{\int d\phi_{q_T}[d\sigma^{\uparrow} + d\sigma^{\downarrow}]} \tag{3}$$

where ϕ_{q_T} and ϕ_S are the azimuthal angles of the J/ψ and proton spin respectively. For the gluon Sivers function we have used a model in our analysis, which has been used in the literature to calculate SSA in semi-inclusive deep inelastic scattering (SIDIS) [12] and DY process [13] (see [14] for details). The parameters are taken from [15]. Other parameters we use are

$$\langle k_{\perp g}^2\rangle = \langle k_{\perp\gamma}^2\rangle = 0.25\, GeV^2.$$

Also it is to be noted that in the model we consider for charmonium production, namely the color evaporation model, the only relevant scale is M^2 which is the invariant mass of the heavy quark pair. This is integrated between a narrow region, from $4m_c^2$ to $4m_D^2$ irrespective of the center-of-mass energy of the experiment. So the scale evolution of the TMDs is not expected to affect the asymmetry too much.

In Fig. 1 we have shown a comparison of the y and q_T dependence of the asymmetry at JLab, HERMES, COMPASS and eRHIC. Model I refers to the parametrization in [13] and (a) refers to the parametrization of the gluon Sivers function in terms of an average of the u and d quark Sivers function [14]. Different experiments cover different kinematical regions, and our

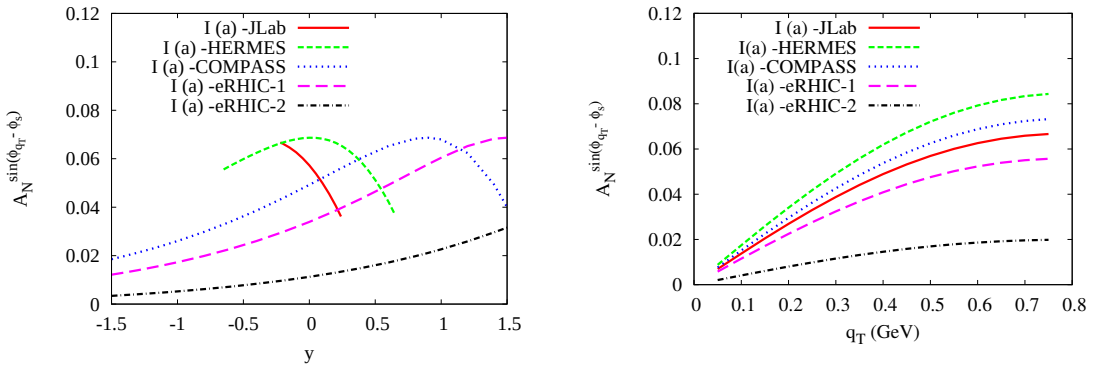

Figure 1: (Color online) The single spin asymmetry $A_N^{\sin(\phi_{qT} - \phi_S)}$ for the $e + p^{\uparrow} \to e + J/\psi + X$ as a function of y (left panel) and q_T (right panel). The plots are for model I (a) (see text) compared for JLab ($\sqrt{s} = 4.7$ GeV) (solid red line), HERMES ($\sqrt{s} = 7.2$ GeV) (dashed green line), COMPASS ($\sqrt{s} = 17.33$ GeV) (dotted blue line), eRHIC-1 ($\sqrt{s} = 31.6$ GeV) (long dashed pink line) and eRHIC-2 ($\sqrt{s} = 158.1$ GeV) (dot-dashed black line).

results clearly show that the asymmetry is sizable, and that it is worthwhile to look at SSA's in charmonium production in order to extract information on the gluon Sivers function.

3 Acknowledgements

A. Mukherjee thanks the organizers of XX th International Workshop of Deep Inelastic Scattering and Related Areas. R.M.G. wishes to acknowledge support from the Department of Science and Technology, India under Grant No. SR/S2/JCB-64/2007 under the J.C. Bose Fellowship scheme. A. Misra and V.S.R. would like to thank Department of Science and Technology, India for financial support under the grant No. SR/S2/HEP-17/2006 and to Department of Atomic under the grant No. 2010/37P/47/BRNS.

References

[1] P. J. Mulders and R. D. Tangerman, Nucl. Phys. B **461**, 197 (1996) [Erratum-ibid. B **484**, 538 (1997)] [hep-ph/9510301]; D. Boer and P. J. Mulders, Phys. Rev. D **57**, 5780 (1998) [hep-ph/9711485]; R. D. Tangerman and P. J. Mulders, hep-ph/9408305.

[2] D. W. Sivers, Phys. Rev. D **41**, 83 (1990);

[3] M. Anselmino, M. Boglione and F. Murgia, Phys. Lett. B **362**, 164 (1995) [hep-ph/9503290]; M. Anselmino and F. Murgia, Phys. Lett. B **442**, 470 (1998) [hep-ph/9808426]; M. Anselmino, M. Boglione and F. Murgia, Phys. Rev. D **60**, 054027 (1999) [hep-ph/9901442].

[4] J. C. Collins and D. E. Soper, Nucl. Phys. B **193**, 381 (1981) [Erratum-ibid. B **213**, 545 (1983)] [Nucl. Phys. B **213**, 545 (1983)]; X. -d. Ji, J. -p. Ma and F. Yuan, Phys. Rev. D **71**, 034005 (2005) [hep-ph/0404183].

[5] F. Halzen, Phys. Lett. B **69**, 105 (1997); F. Halzen and S. Matsuda, Phys. Rev. D **17**, 1344 (1978).

[6] H. Fritsch, Phys. Lett. B **67**, 217 (1977).

[7] O. J. P. Eboli, E. M. Gregores and F. Halzen, Phys. Rev. D **67**, 054002 (2003).

[8] C. F. von Weizsacker, Z. Phys. **88**, 612 (1934).

[9] E. J. Williams, Phys. Rev. **45**, 729 (1934).

[10] F. Yuan, Phys. Rev. D **78**, 014024 (2008) [arXiv:0801.4357 [hep-ph]].

[11] W. Vogelsang and F. Yuan, Phys. Rev. D **72**, 054028 (2005) [hep-ph/0507266].

[12] M. Anselmino, M. Boglione, U. D'Alesio, A. Kotzinian, F. Murgia a Phys. Rev. D **72**, 094007 (2005) [Erratum-ibid. D **72**, 099903 (2005)] [hep-ph/0507181].

[13] M. Anselmino, M. Boglione, U. D'Alesio, S. Melis, F. Murgia and A. Prokudin, Phys. Rev. D **79**, 054010 (2009) [arXiv:0901.3078 [hep-ph]].

[14] R. M. Godbole, A. Misra, A. Mukherjee, V. S. Rawoot, Phys.Rev. **D 85**, 094013 (2012); e-Print: arXiv:1201.1066 [hep-ph]

[15] M. Anselmino, M. Boglione, U. D'Alesio, S. Melis, F. Murgia and A. Prokudin, arXiv:1107.4446 [hep-ph].

Timelike Compton Scattering - New Theoretical Results and Experimental Possibilities

B. Pire[1], *L. Szymanowski*[2], *Jakub Wagner*[2]

[1] CPHT, École Polytechnique, CNRS, 91128 Palaiseau, France
[2] National Center for Nuclear Research (NCBJ), Warsaw, Poland

DOI: http://dx.doi.org/10.3204/DESY-PROC-2012-02/68

We review recent progress in the study of timelike Compton scattering (TCS), the crossed process of deeply virtual Compton scattering. We emphasize the need to include NLO corrections to any phenomenological program to extract Generalized Parton Distributions (GPDs) from near future experimental data. We point out that TCS at high energy should be available through a study of ultraperipheral collisions at RHIC and LHC, opening a window on quark and gluon GPDs at very small skewness.

1 Intoduction

Almost two decades after its first stages [1], the study of deeply virtual Compton scattering (DVCS), i.e., $\gamma^* p \to \gamma p$, and more generally of hard exclusive reactions in a generalized Bjorken regime, has now entered a phase where many theoretical and experimental progresses can merge to enable a sensible extraction of generalized parton distributions (GPDs). Indeed, the measurement of GPDs should contribute in a decisive way to our understanding of how quarks and gluons build hadrons [2]. In particular the transverse location of quarks and gluons become experimentally measurable via the transverse momentum dependence of the GPDs [3].

Timelike Compton scattering (TCS) [4]

$$\gamma(q)N(p) \to \gamma^*(q')N(p') \to l^-(k)l^+(k')N(p')$$

at small $t = (p'-p)^2$ and large *timelike* virtuality $(k+k')^2 = q'^2 = Q^2$ of the final state dilepton, shares many features with its "inverse" process, DVCS. The Bjorken variable in the TCS case is $\tau = Q^2/s$ with $s = (p+q)^2$. One also defines $\Delta = p' - p$ ($t = \Delta^2$) and the skewness variables $\xi = -\frac{(q+q')^2}{2(p+p')\cdot(q+q')} \approx \frac{-Q^2}{2s-Q^2}$, $\eta = -\frac{(q-q')\cdot(q+q')}{(p+p')\cdot(q+q')} \approx \frac{Q^2}{2s-Q^2}$ where the approximations hold in the extended Bjorken regime where masses and $-t$ are small with respect of Q^2 (s is always larger than Q^2).

2 Basic properties and first experimental results

In the region where the final photon virtuality is large, the Compton amplitude is given by the convolution of hard scattering coefficients, calculable in perturbation theory, and generalized

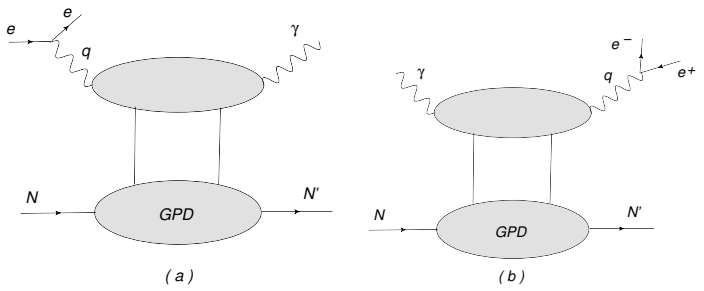

Figure 1: (a) Deeply Virtual Compton Scattering and (b) Timelike Compton Scattering

parton distributions, which describe the nonperturbative physics of the process. The physical process where to observe TCS, is photoproduction of a heavy lepton pair,

$$\gamma N \to \mu^+\mu^- N \qquad or \qquad \gamma N \to e^+e^- N \, .$$

A QED process, the Bethe-Heitler (BH) mechanism $\gamma(q)\gamma^*(-\Delta) \to l^-(k)l^+(k')$ contributes at the amplitude level. This latter process has a very peculiar angular dependence and overdominates the TCS process if one blindly integrates over the final phase space. One may however choose kinematics where the amplitudes of the two processes are of the same order of magnitude, and use specific observables sensitive to the interference of the two amplitudes. Since the amplitudes for the Compton and Bethe-Heitler processes transform with opposite signs under reversal of the lepton charge, it is possible to project out the interference term through a clever use of the angular distribution of the lepton pair [4].

First attempts to measure TCS, and to confront the theoretical predictions with data were already performed at JLab at 6 GeV[5], and may serve as a feasibility test for a proposed experiment with higher energy after upgrade to 12 GeV.

3 TCS at next to leading order

After proper renormalization, the Compton scattering amplitude reads in its factorized form:

$$\begin{aligned} \mathcal{A}^{\mu\nu} &= -g_T^{\mu\nu} \int_{-1}^{1} dx \left[\sum_q^{n_F} T^q(x) F^q(x) + T^g(x) F^g(x) \right] \\ &+ i\epsilon_T^{\mu\nu} \int_{-1}^{1} dx \left[\sum_q^{n_F} \tilde{T}^q(x) \tilde{F}^q(x) + \tilde{T}^g(x) \tilde{F}^g(x) \right] , \end{aligned} \tag{1}$$

where renormalized coefficient functions for the vector case are given by:

$$\begin{aligned} T^q(x) &= \left[C_0^q(x) + C_1^q(x) + \ln\left(\frac{Q^2}{\mu_F^2}\right) \cdot C_{coll}^q(x) \right] - (x \to -x) \, , \\ T^g(x) &= \left[C_1^g(x) + \ln\left(\frac{Q^2}{\mu_F^2}\right) \cdot C_{coll}^g(x) \right] + (x \to -x) \, . \end{aligned} \tag{2}$$

and similarily (but with different symmetry in x) for the axial quantities $\tilde{T}^q, \tilde{T}^g$. Results for TCS [6] compare to the well-known DVCS results [7], through a simple relation [8]:

$$^{TCS}T(x) = \pm \left(^{DVCS}T(x) + i\pi C_{coll}(x)\right)^* , \tag{3}$$

where +(-) sign corresponds to vector (axial) case. The NLO relation (3) tells us that if scaling

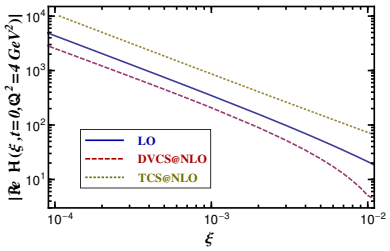

Figure 2: The real part of CFF $\mathcal{H}$ vs. ξ with $\mu^2 = Q^2 = 4$ GeV^2 and $t = 0$ at LO (solid) and NLO for DVCS (dashed). For TCS at NLO its negative value is shown as dotted curve.

violations are small, the timelike CFFs (TFFs) can be obtained from the spacelike ones by complex conjugations. Moreover, GPD model studies indicate that in the valence region, i.e., for $\xi \sim 0.2$, CFFs might only evolve mildly. This rather generic statement, which will be quantified by model studies [9], might be tested in future (after 12GeV upgrade) Jefferson Lab experiments. On the other hand we expect huge NLO corrections to $\Re\mathrm{e}^T\mathcal{H} \overset{\mathrm{LO}}{=} \Re\mathrm{e}\mathcal{H}$, induced by $\Im\mathrm{m}\mathcal{H}$. Utilizing Goloskokov-Kroll model for H GPDs [10], we illustrate this effect in Fig. 2 for $10^{-4} \leq \xi \leq 10^{-2}$, accessible in a suggested Electron-Ion-Collider [11], and $t = 0$. We plot $\Re\mathrm{e}\mathcal{H}$ vs. ξ, for LO DVCS or TCS (solid), NLO DVCS (dashed) and NLO TCS (dotted) at the input scale $\mu^2 = \mathcal{Q}^2 = 4$ GeV^2. In the case of NLO TCS $-\Re\mathrm{e}^T\mathcal{H}$ is shown, since even the sign changes. We read off that the NLO correction to $\Re\mathrm{e}^T\mathcal{H}$ is of the order of -400% and so the real part in TCS becomes of similar importance as the imaginary part. This NLO prediction is testable via a lepton-pair angle asymmetry, governed by $\Re\mathrm{e}^T\mathcal{H}$ [4].

4 Ultraperipheral collisions

As described in [12] the cross section for photoproduction in hadron collisions is given by:

$$\sigma_{pp} = 2 \int \frac{dn(k)}{dk} \sigma_{\gamma p}(k) dk \tag{4}$$

where $\sigma_{\gamma p}(k)$ is the cross section for the $\gamma\, p \to p\, l^+ l^-$ process and k is the photon energy. $\frac{dn(k)}{dk}$ is an equivalent photon flux (the number of photons with energy k). In Ref. [13] we analized the possibility to measure TCS at the LHC. The pure Bethe - Heitler contribution to σ_{pp}, integrated over $\theta = [\pi/4, 3\pi/4]$, $\phi = [0, 2\pi]$, $t = [-0.05\mathrm{GeV}^2, -0.25\mathrm{GeV}^2]$, $Q'^2 = [4.5\mathrm{GeV}^2, 5.5\mathrm{GeV}^2]$, and photon energies $k = [20, 900]$GeV gives $\sigma_{pp}^{BH} = 2.9\,$pb. The Compton contribution (calculated with NLO GRVGJR2008 PDFs, and $\mu_F^2 = 5\mathrm{GeV}^2$) gives $\sigma_{pp}^{TCS} = 1.9\,$pb.

We have choosen the range of photon energies in accordance with expected capabilities to tag photon energies at the LHC. This amounts to a large rate of order of 10^5 events/year

at the LHC with its nominal luminosity ($10^{34}\,\mathrm{cm}^{-2}\mathrm{s}^{-1}$). The rate remains sizeable for the lower luminosity which has been achieved in 2011. Figure 3 shows predictions obtained for

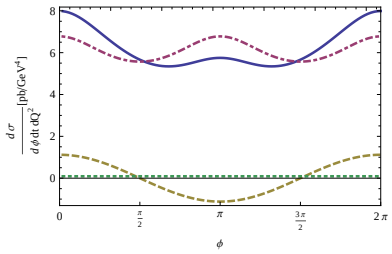

Figure 3: Total (solid), TCS (dotted), BH (dash-dotted) and intereference (dashed) differential cross section for ultraperipheral collisions at RHIC.

ultraperipheral collisions at RHIC, using KG model for $t = -0.1\mathrm{GeV}^2$ and $\sqrt{s_{pp}} = 500\mathrm{GeV}^2$. Only BH contribution gives 10^3 events for $10^7 s$.

Acknowledgements

This work is partly supported by the Polish Grant NCN No DEC-2011/01/D/ST2/02069 and the Joint Research Activity "Study of Strongly Interacting Matter" (acronym HadronPhysics3, Grant Agreement n.283286) under the Seventh Framework Programme of the European Community.

References

[1] D. Müller *et al.*, Fortsch. Phys. **42**, 101 (1994); X. Ji, Phys. Rev. Lett. **78**, 610 (1997); A. V. Radyushkin, Phys. Rev. **D56**, 5524 (1997); J. C. Collins and A. Freund, Phys. Rev. **D59**, 074009 (1999).

[2] M. Diehl, Phys. Rept. **388** (2003) 41; A. V. Belitsky and A. V. Radyushkin, Phys. Rept. **418**, 1 (2005); S. Boffi and B. Pasquini, Riv. Nuovo Cim. **30**, 387 (2007).

[3] M. Burkardt, Phys. Rev. D **62**, 071503 (2000) and Int. J. Mod. Phys. A **18**, 173 (2003); J. P. Ralston and B. Pire, Phys. Rev. D **66**, 111501 (2002); M. Diehl, Eur. Phys. J. C **25**, 223 (2002).

[4] E. R. Berger, M. Diehl and B. Pire, Eur. Phys. J. C **23**, 675 (2002).

[5] P. Nadel-Turonski *et al.*, AIP Conf. Proc. **1182**, 843 (2009); T. Horn *et al.*, AIP Conf. Proc. **1374**, 542 (2011).

[6] B. Pire, L. Szymanowski and J. Wagner, Phys. Rev. D **83**, 034009 (2011).

[7] A. V. Belitsky *et al.*, Phys. Lett. B **474**, 163 (2000); L. Mankiewicz *et al.*, Phys. Lett. B **425**, 186 (1998); X. D. Ji and J. Osborne, Phys. Rev. D **58**, 094018 (1998) and Phys. Rev. D **57**, 1337 (1998).

[8] D. Mueller, B. Pire, L. Szymanowski and J. Wagner, arXiv:1203.4392 [hep-ph].

[9] H. Moutarde, B. Pire, F. Sabatie, L. Szymanowski, and J. Wagner. Work in preparation.

[10] S. V. Goloskokov and P. Kroll, Eur. Phys. J. C **50**, 829 (2007).

[11] D. Boer *et al.*, arXiv:1108.1713 [nucl-th].

[12] C. A. Bertulani, S. R. Klein and J. Nystrand, Ann. Rev. Nucl. Part. Sci. **55** (2005) 271

[13] B. Pire, L. Szymanowski and J. Wagner, Phys. Rev. D **79**, 014010 (2009).

Conformal symmetry based relations between Bjorken and Ellis-Jaffe sum rules

A. L. Kataev

Institute for Nuclear Research of the Russian Academy of Sciences, 113112, Moscow, Russia

DOI: http://dx.doi.org/10.3204/DESY-PROC-2012-02/315

The identity between expressions for the coefficient functions of the Bjorken and Ellis-Jaffe sum rules is derived in the conformal invariant limit of massless $U(1)$ model, which is realised in the perturbative quenched QED (pqQED) approximation and in the conformal invariant limit of $SU(N_c)$ gauge group with fermions. The derivation is based on the comparison of the expressions for the triangle dressed Green functions of singlet Axial vector- Vector-Vector and non-singlet Axial vector-Vector-Vector fermion currents in the limit, when the conformal symmetry is not violated. In the case of pqQED its explicit cross-check at the third order of perturbation theory is discussed. The analytical order α_s^3 approximation for the non-singlet coefficient function, derived in the conformal invariant limit of $SU(N_c)$ group, is reminded. Its possible phenomenological application is outlined.

1 Introduction

The definitions of the massless perturbative expressions for the Bjorken and Ellis-Jaffe sum rules of the polarised lepton-nucleon DIS are well-known and have the following form

$$Bjp(Q^2) = \int_0^1 \left(g_1^{lp}(x,Q^2) - g_1^{ln}(x,Q^2)\right)dx = \frac{1}{6}g_A C_{NS}(A_s(Q^2)) \quad (1)$$

$$EJ^{lp(n)}(Q^2) = C_{NS}(A_s(Q^2))(\pm\frac{1}{12}a_3 + \frac{1}{36}a_8) + C_{SI}(A_s(Q^2))\frac{1}{9}\Delta\Sigma(Q^2) \quad (2)$$

where $a_3 = \Delta u - \Delta d{=}g_A$, $a_8 = \Delta u + \Delta d - 2\Delta s$, Δu, Δd and Δs are the polarised parton distributions and the subscript $lp(n)$ indicate the processes of the polarised DIS of charged leptons (l) on protons (p) and neutrons (n). In the $SU(N_c)$ colour gauge theory $A_s = \alpha_s/(4\pi)$. The order $O(A_s^3)$ and $O(A_s^4)$ perturbative expressions for the non-singlet (NS) coefficient function $C_{NS}(A_s)$ were analytically evaluated in [1] and [2] correspondingly, while the analytical expressions for the leading in the number of quarks flavours terms (renormalon contributions) were obtained in [3] (see [4] as well). The singlet (SI) contribution C_{SI} to Eq.(2) contains the coefficient function , calculated in [5] at the $O(A_s^3)$- level in the $\overline{MS}$-scheme, while the SI anomalous dimension term is known analytically from the $O(A_s^2)$ and $O(A_s^3)$ results of [6] and [5] respectively. In all these calculations the $\overline{MS}$-scheme was used. In this scheme the polarised gluon distribution ΔG does not enter into Eq.(2). Our main aim is to prove, that in the *conformal invariant limit* of the perturbative series, obtained in the $SU(N_c)$ quantum field theory model with fermions and in the $U(1)$ model with fermions (i.e. in the perturbative quenched QED (pqQED) approximation) the analytical expressions for C_{NS} and C_{SI}, defined in Eq.(2),

are identical in all orders of perturbation theory in the expansion parameters $A_s = \alpha_s/(4\pi)$ or $A = \alpha/(4\pi)$. While proving this identity we follow the studies, given in [7], where the classical Crewther relation [8], derived in the quark-parton era from the three-point Green function of the NS Axial vector-Vector-Vector(AVV) currents, is compared with the three-point Green function of singlet Axial vector-Vector-Vector currents. In the era of continuing understanding of the special features of the relations between NS characteristics of strong interactions, evaluated within perturbative approach in the the $SU(N_c)$ gauge group (see [3], [2], [10]), the detailed studies of the relations, which follow from the three-point Green functions of the NS AVV currents, were considered in [11], [12], [13]. The comment on possible phenomenological applications of the conformal-symmetry motivated expression for the Bjorken polarised sum-rule, which in QCD depends from the scale, fixed within *principle of maximal conformality* [14], [15], is given.

2 Proof of the identity

Theoretical considerations of [8] are based on the property that in the *conformal invariant limit* the dressed expression for the three-point Green functions of NS AVV currents is proportional to the *1-loop* expression of the related three-point diagram [16]. In the momentum space this means, that

$$T^{abc}_{\mu\alpha\beta}(p,q) = i\int < 0|TA^a_\mu(y)V^b_\alpha(x)V^c_\beta(0)|0 > e^{ipx+iqy}dxdy = d^{abc}\Delta^{(1-loop)}_{\mu\alpha\beta}(p,q) \tag{3}$$

where $A^a_\mu(y) = \overline{\psi}(y)\gamma_\mu(\lambda^a/2)\gamma_5\psi(y)$ and $V^b_\alpha(x) = \overline{\psi}(x)\gamma_\mu(\lambda^b/2)\psi(x)$ are the NS Axial-vector and Vector currents. In the same limit it is possible to write-down the similar expression for the three-point Green function of SI Axial vector-NS Vector-Vector currents [17]

$$T^{ab}_{\mu\alpha\beta}(p,q) = i\int < 0|TA_\mu(y)V^a_\alpha(x)V^b_\beta(0)|0 > e^{ipx+iqy}dxdy = \delta^{ab}\Delta^{(1-loop)}_{\mu\alpha\beta}(p,q) \tag{4}$$

where $A_\mu(y) = \overline{\psi}(y)\gamma_\mu\gamma_5\psi(y)$. The SI coefficient function of the Ellis-Jaffe sum rule is defined as the coefficient function of the SI structure in the operator-product expansion of two NS Vector currents,namely

$$i\int TV^a_\alpha V^b_\beta d^4x|_{p^2\to\infty} \approx i\delta^{ab}\epsilon_{\alpha\beta\rho\sigma}\frac{p^\sigma}{P^2}C^{SI}_{EJp}(A_s)\ A_\rho(0) + \dots \tag{5}$$

The expression should be compared with the definition of the NS coefficient function , which enters into operator-product of the three-point Green function of Eq.(4) as

$$i\int TV^a_\alpha V^b_\beta e^{ipx}d^4x|_{p^2\to\infty} \approx id^{abc}\epsilon_{\alpha\beta\rho\sigma}\frac{p^\sigma}{P^2}C^{NS}(A_s)\ A^c_\rho(0) + \dots \tag{6}$$

Taking now the limit $q^2 \to \infty$ in Eq.(4) and Eq.(3), we get the following Crewther-type identity in the SI channel [17], [7]

$$C_{SI}(A_s) \times C^{SI}_D(A_s) \equiv 1 \quad . \tag{7}$$

It should be compared with the classical NS Crewther identity, namely with

$$C_{NS}(A_s) \times C^{NS}_D(A_s) \equiv 1 \quad . \tag{8}$$

It follows from the x-space considerations of [8] (see [9] as well). In the momentum space it was re-derived in [11]. Note, that $C_D^{SI}(A_s)$ and $C_D^{NS}(A_s)$ are the coefficient functions of the massless axial-vector and vector Adler D-functions, defined by taking derivative $Q^2\frac{d}{dQ^2}$ of the mass-independent terms in the correlator of SI axial-vector currents

$$i\int < 0|TA_\mu(x)A_\nu(0)|0 > e^{iqx}d^4x = \Pi_{\mu\nu}^{SI}(Q^2) = (g_{\mu\nu}q^2 - q_\mu q_\nu)\Pi^{SI}(Q^2) \tag{9}$$

and of the correlator of NS axial-vector currents

$$i\int < 0|TA_\mu^{(a)}(x)A_\nu^{(b)}(0)|0 > e^{iqx}d^4x = \delta^{ab}\Pi_{\mu\nu}^{NS}(Q^2) = \delta^{ab}(g_{\mu\nu}q^2 - q_\mu q_\nu)\Pi^{NS}(Q^2) \tag{10}$$

where $Q^2 = -q^2$ is the Euclidean momentum transfer. The exact chiral invariance of the massless perturbative expressions for the coefficient functions implies, that $C_D^{SI}(A_s) \equiv C_D^{NS}(A_s)$. Keeping this in mind and comparing l.h.s. of Eq.(7) and Eq.(8), we get the following relation

$$C_{NS}(A_s) \equiv C_{SI}(A_s)|_{conformal\ invariant\ limit} \tag{11}$$

which is valid in the conformal-invariant limit of $SU(N_c)$ gauge model and in the pqQED model in all orders of perturbation theory. In the latter case Eq.(11) was proved in [7].

3 Conformal invariant limit of the third order perturbative series

In the pqQED model it is possible to demonstrate explicitly the validity of the identity of Eq.(11) at the level of third order corrections [7]. In these studies the following $O(A^3)$ pqQED expressions were used: order $O(A^3)$ expression for $C_{NS}(A)$, available from [1] and the following dimensional regularisation [18] expression for $C_{SI}(A_s) = \overline{C}_{SI}(A_s)/Z_5^{SI}(A_s)$ [6] where Z_5^{SI} is the finite renormalization constant of the SI Axial-vector current. In order to get the pqQED limit of all functions, contributing to $C_{SI}(A_s)$, in the work [7] $Z_5^{SI}(A)$ was determined from the pqQED limit of $Z_5^{NS}(A_s)$ renormalization constant, analytically evaluated in [1]. Using all these inputs and the validity of identity of Eq.(11) was explicitly demonstrated at the $O(A^3)$ -approximation of pqQED [7]. To fix the $O(A^4)$ pqQED correction to these functions, one can use the pqQED expression of the related analytical result from [2]. This result coincides with the one, obtained in [19] from classical Crewther relation of Eq.(8), supplemented with the pqQED $O(A^4)$ analytical approximation for $C_D^{NS}(A)$, first presented in [20]. The $O(A^4)$ pqQED expression for $C_{NS}(A)$ reads

$$C_{NS}(A) = 1 - 3A + \frac{21}{2}A^2 - \frac{3}{2}A^3 - \left(\frac{4823}{8} + 96\zeta_3\right)A^4 + O(A^5) \ . \tag{12}$$

It should coincide with the pqQED limit of still unknown $O(A^4)$ coefficient of $C_{SI}(A_s)$ contribution into the Ellis-Jaffe sum rule. In the case of $SU(N_c)$ gauge group with fermions the similar expressions for the coinciding SI and NS coefficient functions are known at present at the $O(A_s^3)$ level. They can be obtained from the $O(A_s^3)$ expression for the coefficient function $C_{NS}(A_s)$

$$C_{NS}(A_s) = 1 - 3C_F A_s + \left(\frac{21}{2}C_F^2 - C_F C_A\right)A_s^2 - \left[\frac{3}{2}C_F^3 + 65C_F^2 C_A + \left(\frac{523}{12} - 216\zeta_3\right)C_F C_A^2\right]A_s^3 \tag{13}$$

derived in the conformal invariant limit of $SU(N_c)$ in [10] using the β-expansion approach of [21]. Here C_F and C_A are the Casimir operators of the $SU(N_c)$ group. This result should coincide with the similar approximation of $C_{SI}(A_s)$-contribution into Eq.(2). Considering now the ratios of the corresponding approximations for the Ellis-Jaffe and Bjorken sum rule, namely

$$\frac{EJ^{lp(n)}(Q^2)}{Bjp(Q^2)} = \pm\frac{1}{2} + \frac{a_8}{6\ a_3} + \frac{2\Delta\Sigma}{3a_3} \tag{14}$$

where $a_8 = 3a_3 - 4D$, $a3$, a_8 and $\Delta\Sigma$ are defined through the polarised parton distributions below Eqs.(2) and D is the hyperon decay constant, we recover the massless quark-parton relations. Indeed, these ratios can be re-written as

$$\frac{EJ^{lp}(Q^2)}{Bjp(Q^2)} = 1 + \frac{2(\Delta\Sigma - D)}{3\ a_3} \quad ; \quad \frac{EJ^{ln}(Q^2)}{Bjp(Q^2)} = +\frac{2}{3}\frac{(\Delta\Sigma - D)}{a_3} \quad .$$

They lead to the quark-parton model definition of the Bjorken sum rule through and Ellis-Jaffe sum rule

$$Bjp \equiv EJ^{lp} - EJ^{ln} \quad . \tag{15}$$

Thus, one can see that our considerations are self-consistent.

4 Conformal symmetry and the Bjorken sum rule

To conclude the discussions presented above we note, we outline the ideas how the obtained in [10] $O(A_s^3)$ approximation for the coefficient function $C_{NS}(A_s)$ of the Bjorken sum rule, given in Eq.(13), can be used in the phenomenological studies. As mentioned above, this result was obtained with the help of formulated in [21] β-expansion approach, which prescribes to consider the following representations of the $O(A_s^2)$ and $O(A_s^3)$ coefficients

$$c_2 = \beta_0 c_2[1] + c_2[0] \quad , \quad c_3 = \beta_0^2 c_3[2] + \beta_1 c_3[0,1] + \beta_0 c_3[1] + c_3[0] \quad , \ldots \tag{16}$$

of the coefficient $C_{NS}(A_s)$ function of the Bjorken sum rule which is defined as

$$C_{NS}(A_s) = 1 + \sum_{l\geq 0} c_l A_s^{l+1}(Q^2) \quad . \tag{17}$$

In Eq.(16) β_i are the perturbative coefficients of the $SU(N_c)$ gauge group β-function, which can be written down as

$$\mu^2\frac{\partial A_s}{\partial \mu^2} = -\sum_{i\geq 0}\beta_i A_s^{i+1} \quad . \tag{18}$$

The conformal-invariant contribution $c_l[0]$ to the coefficients in Eq.(16) are obtained in the conformal-invariant limit of the $SU(N_c)$ group, which corresponds to the imaginable theory, which has all perurbative coefficients of the β-function identically equal to zero. They were obtained in [10] and are presented in the expression of Eq.(13). To relate this pure theoretical expression to the real world, one should fix absorb into the scale Q^2_{PMC} of the expansion parameter A_s the terms, proportional to the coefficients of the $SU(N_c)$ β-function. This can achieved using the concrete realisation of the principle of maximal conformality (PMC), introduced and applied in the works [14], [15]. This PMC approach should be considered as the analog of the

formulated in [22] generalization of the original BLM procedure [23]. The resulting expression coincide with Eq.(13), where all coefficients of the β-function in Eq.(16) should be absorbed into the scale of the expansion parameter $A_s(Q^2_{PMC})$ The details of the derivation of the related expressions the corresponding scales and possible phenomenological applications will be considered elsewhere.

5 Acknowledgements

This talk was presented at the 20th International Workshops DIS-2012 Bonn Univ., March 26-30 , 2012 and at the International Workshop "Holography: Applications to Technicolour, Condensed matter and Hadrons", INR RAS ,June 11-15, 2012. I am grateful to the OC of DIS-2012 Workshop for hospitality in Bonn and for the financial support. The material of this talk was discussed during 2 weak stay at Ruhr Univ. Bochum, prior DIS Workshop. It is the pleasure to thank M.V. Polyakov and N.G. Stefanis for useful comments. I am also grateful to S.V. Mikhailov, O.V.Teryaev and D. Mueller for the detailed discussions of the material, which was presented in this talk. The work is done within the scientific program of RFBR Grant N 11-01-00182 and was supported the Grant NS-5590.2012.2.

References

[1] S. A. Larin and J. A. M. Vermaseren, Phys. Lett. B **259** (1991) 345.

[2] P. A. Baikov, K. G. Chetyrkin and J. H. Kuhn, Phys. Rev. Lett. **104** (2010) 132004.

[3] D. J. Broadhurst and A. L. Kataev, Phys. Lett. B **315** (1993) 179.

[4] D. J. Broadhurst and A. L. Kataev, Phys. Lett. B **544** (2002) 154.

[5] S. A. Larin, T. van Ritbergen and J. A. M. Vermaseren, Phys. Lett. B **404** (1997) 153.

[6] S. A. Larin, Phys. Lett. B **334** (1994) 192.

[7] A. L. Kataev, Phys. Lett. B **691** (2010) 82.

[8] R. J. Crewther, Phys. Rev. Lett. **28** (1972) 1421.

[9] S. L. Adler, C. G. Callan, Jr., D. J. Gross and R. Jackiw, Phys. Rev. D **6** (1972) 2982.

[10] A. L. Kataev and S. V. Mikhailov, Theor. Math. Phys. **170** (2012) 139 [Teor. Mat. Fiz. **170** (2012) 174]

[11] G. T. Gabadadze and A. L. Kataev, JETP Lett. **61** (1995) 448 [Pisma Zh. Eksp. Teor. Fiz. **61** (1995) 439]

[12] R. J. Crewther, Phys. Lett. B **397** (1997) 137.

[13] V. M. Braun, G. P. Korchemsky and D. Mueller, Prog. Part. Nucl. Phys. **51** (2003) 311.

[14] S. J. Brodsky and L. Di Giustino, arXiv:1107.0338 [hep-ph].

[15] S. J. Brodsky and X. -G. Wu, Phys. Rev. D **85**, 034038 (2012)

[16] E. J. Schreier, Phys. Rev. D **3** (1971) 980.

[17] A. L. Kataev, "The Generalized Crewther relation: The Peculiar aspects of the analytical perturbative QCD calculations," in Proceedings of 2nd Workshop on Continuous advances in QCD, 28-31 March, Minneapolis, USA, pp. 107-132; World Scientific, 1996, ed. M.I. Polikarpov and Preprint INR- 0926.

[18] G. 't Hooft and M. J. G. Veltman, Nucl. Phys. B **44** (1972) 189.

[19] A. L. Kataev, Phys. Lett. B **668** (2008) 350

[20] P. A. Baikov, K. G. Chetyrkin and J. H. Kuhn, PoS RADCOR **2007** (2007) 023

[21] S. V. Mikhailov, JHEP **0706** (2007) 009 [hep-ph/0411397].

[22] G. Grunberg and A. L. Kataev, Phys. Lett. B **279** (1992) 352.

[23] S. J. Brodsky, G. P. Lepage and P. B. Mackenzie, Phys. Rev. D **28** (1983) 228.

Distribution of linearly polarized gluons inside a large nucleus

Jian Zhou[1] *Andreas Metz*[2]

[1]Institut für Theoretische Physik,Universität Regensburg, Regensburg, Germany
[2]Department of Physics, Barton Hall, Temple University, Philadelphia, PA 19122, USA

DOI: http://dx.doi.org/10.3204/DESY-PROC-2012-02/126

The distribution of linearly polarized gluons inside a large nucleus is studied in the framework of the color glass condensate. We find that the Weizsäcker-Williams distribution saturates the positivity bound at large transverse momenta and is suppressed at small transverse momenta, whereas the dipole distribution saturates the bound for any value of the transverse momentum. We also discuss processes in which both distributions of linearly polarized gluons can be probed.

1 Introduction

Recently, transverse momentum dependent parton distributions (TMDs) inside a nucleon have attracted a lot of interest. So far, the main focus of the field has been on quark TMDs. On the other hand, the available studies of (polarized) gluon TMDs are still rather sparse. Among them the distribution of linearly polarized gluons inside an unpolarized nucleon ($h_1^{\perp g}$ in the notation of Ref. [1]) is of particular interest. It is the only polarization dependent gluon TMD for an unpolarized nucleon, and is a time-reversal TMD implying that initial/final state interactions are not needed for its existence. This distribution, in principle, can be accessed through measuring azimuthal asymmetries in processes such as jet or heavy quark pair production in electron-nucleon scattering as well as nucleon-nucleon scattering, and photon pair production in hadronic collisions [2, 3, 4]. Moreover, it has been found that the linearly polarized gluon distribution may affect the transverse momentum distribution of Higgs bosons produced from gluon fusion [5, 6, 7]

It has long been recognized that the $k_\perp$ dependent unpolarized gluon distribution f_1^g plays a central role in small x saturation phenomena. Due to the presence of a semi-hard scale (the so-called saturation scale), $f_1^g(x, k_\perp)$ at small x can be computed using an effective theory which is also known as the color glass condensate (CGC) framework. There are two widely used $k_\perp$ dependent unpolarized gluon distributions with different gauge link structures: (1) the Weizsäcker-Williams (WW) distribution [8, 9, 10] describing the gluon number density, and (2) the so-called dipole distribution which appears, for instance, in the description of inclusive particle production in pA collisions [11, 12]. Moreover, it has shown that both types of $k_\perp$ dependent gluon distributions can be directly probed through two-particle correlations in various high energy scattering reactions [13, 14, 7].

In a recent paper [15], we extended the calculation of $f_1(x, k_\perp)$ to the case of $h_1^{\perp g}(x, k_\perp)$.

By following the procedure outlined in [13, 14] we further demonstrated that the WW distribution and the dipole distribution can be accessed by measuring a $\cos 2\phi$ asymmetry for dijet production in lepton nucleus scattering and for production of a virtual photon plus a jet in nucleon nucleus scattering, respectively.

2 Distribution of linearly polarized gluons at small x

We first introduce the operator definition of the Weizsäcker-Williams gluon distribution inside a large nucleus [16, 1],

$$\begin{aligned} M_{WW}^{ij} &= \int \frac{d\xi^- d^2\xi_\perp}{(2\pi)^3 P^+} e^{ixP^+\xi^- - i\vec{k}_\perp\cdot\vec{\xi}_\perp} \langle A|F^{+i}(\xi^- + y^-, \xi_\perp + y_\perp)\, L^\dagger_{\xi+y}\, L_y\, F^{+j}(y^-, y_\perp)|A\rangle \\ &= \frac{\delta_\perp^{ij}}{2}\, x f^g_{1,WW}(x,k_\perp) + \left(\frac{1}{2}\hat{k}_\perp^i \hat{k}_\perp^j - \frac{1}{4}\delta_\perp^{ij}\right) x h^{\perp g}_{1,WW}(x,k_\perp)\,, \end{aligned} \tag{1}$$

where $\hat{k}_\perp^i = k_\perp^i/|\vec{k}_\perp|$. Color gauge invariance is ensured by two (future-pointing) gauge links in the adjoint representation. We use

$$L_\xi = \mathcal{P}\, e^{-ig\int_{\xi^-}^{\infty^-} d\zeta^- A^+(\zeta^-,\xi_\perp)}\, \mathcal{P}\, e^{-ig\int_{\xi_\perp}^{\infty} d\vec{\zeta}_\perp\cdot\vec{A}_\perp(\zeta_\perp,\xi^-=\infty^-)}\,, \tag{2}$$

where $A^\mu = A^\mu_a t_a$ with $(t_a)_{bc} = -if_{abc}$, and f_{abc} denoting the structure constants of the $SU(3)$ group. We performed the calculation of the WW gluon distributions in the CGC framework in the light-cone gauge by following the standard procedure, and we obtained [15],

$$\begin{aligned} x h^{\perp g}_{1,WW}(x,k_\perp) &= \left(4\hat{k}_\perp^i \hat{k}_\perp^j - 2\delta_\perp^{ij}\right) M_{WW}^{ij} \\ &= \frac{N_c^2-1}{4\pi^3}\, S_\perp \int d|\xi_\perp| \frac{K_2(|k_\perp||\xi_\perp|)}{\frac{1}{4\mu_A}|\xi_\perp| Q_s^2} \left(1 - e^{-\frac{\xi_\perp^2 Q_s^2}{4}}\right). \end{aligned} \tag{3}$$

where K_2 is the second order Bessel function. Let us now discuss the above expression in the limit of high and low transverse momenta,

$$x h^{\perp g}_{1,WW}(x,k_\perp) \simeq 2S_\perp \frac{N_c^2-1}{4\pi^3}\frac{\mu_A}{k_\perp^2} \qquad (k_\perp \gg Q_s)\,, \tag{4}$$

$$x h^{\perp g}_{1,WW}(x,k_\perp) \simeq 2S_\perp \frac{N_c^2-1}{4\pi^3}\frac{\mu_A}{Q_s^2} \qquad (\Lambda_{QCD} \ll k_\perp \ll Q_s)\,. \tag{5}$$

On the other hand, in these limits the unpolarized gluon distribution takes the form [9, 10]

$$x f^g_{1,WW}(x,k_\perp) \simeq S_\perp \frac{N_c^2-1}{4\pi^3}\frac{\mu_A}{k_\perp^2} \qquad (k_\perp \gg Q_s)\,, \tag{6}$$

$$x f^g_{1,WW}(x,k_\perp) \simeq S_\perp \frac{N_c^2-1}{4\pi^3}\frac{1}{\alpha_s N_c}\ln\frac{Q_s^2}{k_\perp^2} \qquad (\Lambda_{QCD} \ll k_\perp \ll Q_s)\,. \tag{7}$$

From those results one immediately finds that for large $k_\perp$ the distribution of linearly polarized gluons saturates the positivity limit, which in our notation reads $h_1^{\perp g} \leq 2f_1^g$ [16]. In contrast, the ratio $h^{\perp g}_{1,WW}/f^g_{1,WW}$ is suppressed in the region of small $k_\perp$.

We now present the expression for the dipole distribution. In that case the operator definition reads [17, 13, 14]

$$\begin{aligned} M_{DP}^{ij} &= 2\int \frac{d\xi^- d^2\xi_\perp}{(2\pi)^3 P^+}\, e^{ixP^+\xi^- - i\vec{k}_\perp\cdot\vec{\xi}_\perp}\langle A|\mathrm{Tr}\, F^{+i}(\xi^- + y^-, \xi_\perp + y_\perp)U^{[-]\dagger}_{\xi+y} F^{+j}(y^-, y_\perp)U^{[+]}_{\xi+y}|A\rangle \\ &= \frac{\delta_\perp^{ij}}{2}\, x f^g_{1,DP}(x,k_\perp) + \left(\frac{1}{2}\hat{k}_\perp^i\hat{k}_\perp^j - \frac{1}{4}\delta_\perp^{ij}\right) x h^{\perp g}_{1,DP}(x,k_\perp)\,, \end{aligned} \tag{8}$$

where $U^{[-]}_\xi = U^n(0,-\infty;0)U^n(-\infty,\xi^-;\xi_\perp)$ and $U^{[+]}_\xi = U^n(0,+\infty;0)U^n(+\infty,\xi^-;\xi_\perp)$ are gauge links in the fundamental representation. In covariant gauge, the only nontrivial component of the field strength tensor is $F^{+i}(y_\perp) = -\partial^i_\perp\alpha(y_\perp)$, which can be viewed as the realization of the eikonal approximation in the McLerran-Venugopalan model. By noticing this fact, one may easily obtain,

$$x h^{\perp g}_{1,DP}(x,k_\perp) = 2x f^g_{1,DP}(x,k_\perp) = \frac{k_\perp^2 N_c}{\pi^2\alpha_s} S_\perp \int \frac{d^2\xi_\perp}{(2\pi)^2}\, e^{-ik_\perp\cdot\xi_\perp}\, e^{-\frac{Q^2_{sq}\xi_\perp^2}{4}}\,, \tag{9}$$

which means that the positivity bound is saturated for any value of $k_\perp$.

3 Observables

For the unpolarized case it has been shown that the results from the TMD factorization are in agreement with the results obtained by extrapolating the CGC calculation to the correlation limit [13, 14]. By applying a corresponding power counting in the correlation limit where the transverse momentum imbalance between two final state particles (or jets) is much smaller than the individual transverse momenta, we found a complete matching between the effective TMD factorization and the CGC calculation in the polarized case as well [15].

First, we discuss dijet production in lepton nucleus scattering. In fact, we consider the process $\gamma^* + A \to q(p_1) + \bar{q}(p_2) + X$ for both transversely and longitudinally polarized photons. The correct gluon TMD entering the factorization formula is the WW distribution. The calculation provides

$$\begin{aligned} \frac{d\sigma^{\gamma^*_T A\to q\bar{q}+X}}{dP.S.} &= \delta(x_{\gamma^*}-1)H_{\gamma^*_T g\to q\bar{q}}\Bigg\{ x f^g_{1,WW}(x,k_\perp) \\ &\quad - \frac{[z_q^2+(1-z_q)^2]\epsilon_f^2 P_\perp^2 - m_q^2 P_\perp^2}{[z_q^2+(1-z_q)^2](\epsilon_f^4+P_\perp^4)+2m_q^2P_\perp^2}\cos(2\phi) x h^{\perp g}_{1,WW}(x,k_\perp)\Bigg\}\,, \end{aligned} \tag{10}$$

$$\frac{d\sigma^{\gamma^*_L A\to q\bar{q}+X}}{dP.S.} = \delta(x_{\gamma^*}-1)H_{\gamma^*_L g\to q\bar{q}}\left\{ x f^g_{1,WW}(x,k_\perp) + \frac{1}{2}\cos(2\phi) x h^{\perp g}_{1,WW}(x,k_\perp)\right\}, \tag{11}$$

where $x_{\gamma^*} = z_q + z_{\bar{q}}$, with z_q, $z_{\bar{q}}$ being the momentum fractions of the virtual photon carried by the quark and antiquark, respectively. The phase space factor is defined as $dP.S. = dy_1 dy_2 d^2P_\perp d^2k_\perp$, where y_1, y_2 are rapidities of the two outgoing quarks in the lab frame. Moreover, $\vec{P}_\perp = (\vec{p}_{1\perp} - \vec{p}_{2\perp})/2$, and $\epsilon_f^2 = z_q(1-z_q)Q^2 + m_q^2$. The transverse momenta are defined in the $\gamma^* A$ *cm* frame. In the correlation limit, one has $|P_\perp| \simeq |p_{1\perp}| \simeq |p_{2\perp}| \gg |k_\perp| = |p_{1\perp} + p_{2\perp}|$. The (azimuthal) angle between $\vec{k}_\perp$ and $\vec{P}_\perp$ is denoted by ϕ. The hard partonic cross sections $H_{\gamma^*_{T,L}g\to q\bar{q}}$ can be found in Ref. [14]. The $\cos(2\phi)$-modulation of the cross section allows one

to address the distribution of linearly polarized gluons. For intermediate values of x this was already pointed out in Ref. [3].

Let us now turn to the dipole distribution at small x. From a theoretical point of view, the simplest process to address $h_{1,DP}^{\perp g}$ seems to be back-to-back virtual photon plus jet production in pA collisions, i.e., $p + A \to \gamma^*(p_1) + q(p_2) + X$. The differential cross section, obtained in the effective TMD factorization, reads

$$\frac{d\sigma^{pA\to\gamma^* q+X}}{dP.S.} = \sum_q x_p f_1^q(x_p) \Big\{ H_{qg\to\gamma^* q}^{UU}\, x f_{1,DP}^g(x,k_\perp) + \cos(2\phi) H_{qg\to\gamma^* q}^{\cos(2\phi)}\, x h_{1,DP}^{\perp g}(x,k_\perp) \Big\}, \tag{12}$$

where the partonic cross sections are given by

$$H_{qg\to\gamma^* q}^{UU} = \frac{\alpha_s \alpha_{em} e_q^2}{N_c \hat{s}^2} \left(-\frac{\hat{s}}{\hat{u}} - \frac{\hat{u}}{\hat{s}} - \frac{2Q^2\hat{t}}{\hat{s}\hat{u}} \right), \qquad H_{qg\to\gamma^* q}^{\cos(2\phi)} = \frac{\alpha_s \alpha_{em} e_q^2}{N_c \hat{s}^2} \left(\frac{-Q^2\hat{t}}{\hat{s}\hat{u}} \right). \tag{13}$$

Here we used the partonic Mandelstam variables $\hat{s} = (p_1 + p_2)^2$, $\hat{u} = (p_1 - p)^2$ and $\hat{t} = (p_2 - p)^2$, with p denoting the momentum carried by the incoming quark from the proton. Note that this effect drops out for prompt (real) photon production.

4 Summary

We derived both the WW distribution and the dipole distribution of linearly polarized gluons in a large nucleus by using the CGC formalism. We further demonstrated that the WW and the dipole gluon distribution can be probed by measuring a $\cos 2\phi$ asymmetry for dijet production in DIS, and for virtual photon-jet production in pA collisions, respectively. Such observables can, in principle, be measured at a future Electron Ion Collider, at RHIC and the LHC.

References

[1] S. Meissner, A. Metz and K. Goeke, Phys. Rev. D **76**, 034002 (2007).

[2] D. Boer, P. J. Mulders and C. Pisano, Phys. Rev. D **80**, 094017 (2009).

[3] D. Boer, S. J. Brodsky, P. J. Mulders and C. Pisano, Phys. Rev. Lett. **106**, 132001 (2011).

[4] J. -W. Qiu, M. Schlegel and W. Vogelsang, Phys. Rev. Lett. **107**, 062001 (2011).

[5] D. Boer, W. J. den Dunnen, C. Pisano, M. Schlegel and W. Vogelsang, Phys. Rev. Lett. **108**, 032002 (2012).

[6] P. Sun, B. -W. Xiao and F. Yuan, Phys. Rev. D **84**, 094005 (2011).

[7] A. Schafer and J. Zhou, arXiv:1203.1534 [hep-ph].

[8] L. D. McLerran and R. Venugopalan, Phys. Rev. D **49**, 2233 (1994); Phys. Rev. D **49**, 3352 (1994).

[9] Y. V. Kovchegov, Phys. Rev. D **54**, 5463 (1996).

[10] J. Jalilian-Marian, A. Kovner, L. D. McLerran and H. Weigert, Phys. Rev. D **55**, 5414 (1997).

[11] A. Dumitru and J. Jalilian-Marian, Phys. Lett. B **547**, 15 (2002); Phys. Rev. Lett. **89**, 022301 (2002).

[12] F. Gelis and J. Jalilian-Marian, Phys. Rev. D **66**, 014021 (2002).

[13] F. Dominguez, B. W. Xiao and F. Yuan, Phys. Rev. Lett. **106**, 022301 (2011).

[14] F. Dominguez, C. Marquet, B. -W. Xiao and F. Yuan, Phys. Rev. D **83**, 105005 (2011).

[15] A. Metz and J. Zhou, Phys. Rev. D **84**, 051503 (2011).

[16] P. J. Mulders and J. Rodrigues, Phys. Rev. D **63**, 094021 (2001).

[17] C. J. Bomhof, P. J. Mulders and F. Pijlman, Eur. Phys. J. C **47**, 147 (2006).

Linearly polarized Gluons and the Higgs Transverse Momentum Distribution

Wilco J. den Dunnen[1], *Daniël Boer*[2], *Cristian Pisano*[3], *Marc Schlegel*[4], *Werner Vogelsang*[4]

[1] VU University Amsterdam, NL-1081 HV Amsterdam, The Netherlands
[2] KVI, University of Groningen, Zernikelaan 25, NL-9747 AA Groningen, The Netherlands
[3] INFN, Sezione di Cagliari, C.P. 170, I-09042 Monserrato (CA), Italy
[4] Universität Tübingen, Auf der Morgenstelle 14, D-72076 Tübingen, Germany

DOI: http://dx.doi.org/10.3204/DESY-PROC-2012-02/51

We investigate the possible role of linearly polarized gluons in Higgs production from unpolarized *pp* collisions. The transverse momentum distribution of the produced Higgs boson is found to exhibit a modulation with respect to the naive, unpolarized expectation, with the sign depending on the parity of the Higgs boson. The transverse momentum distribution of a scalar Higgs will, therefore, have a shape clearly different from a pseudoscalar Higgs. We suggest that this effect can be used to determine the parity of the Higgs at the LHC, without the need to use challenging angular distributions.

Introduction

After a discovery of a new scalar particle at the LHC, the next task at hand is to determine its coupling to other particles. Not only the size, but also the type of coupling to fermions has to be determined, being either the P even $\overline{\Psi}\Psi$ or the P odd $\overline{\Psi}\gamma_5\Psi$. Relatively few suggestions to this end have been put forward for the LHC, e.g., using Higgs + 2 jet production [1] or τ pair decays [2]. We claim that the difference between a scalar and pseudoscalar coupling might also be visible in the transverse momentum distribution of the scalar particle.

The Higgs transverse momentum distribution has been calculated in the framework of collinear factorization at Next-to-Next-to-Leading Logarithmic (NNLL) accuracy for small q_T, matched to Next-to-Leading Order (NLO) accuracy for large q_T [3, 4]. It was noted [4, 5] that in NLO $\gamma\gamma$ continuum production there are "gluon spin-flip contributions" in the gg induced channel, which should be described by a "spin-flip distribution" $\mathcal{P}'$, that can, in principle, be as large as the unpolarized distribution. It was also noted [6] that in the NNLO radiative corrections to the Higgs boson q_T cross section "gluon spin correlations" become important, which cause the standard Drell-Yan transverse momentum resummation to fail for the gluon-gluon fusion process. We claim that the fact that these gluon polarization effects are only observed at NNLO in Higgs production, is due to the use of the collinear factorization framework in which the polarized gluons have to be generated from the unpolarized distribution by gluon radiation. Within the framework of Transverse Momentum Dependent (TMD) factorization, the effect of polarized gluons is already present at tree-level and described by a non-perturbative input function $h_1^{\perp g}$. Although dependent on its size, the effects of polarized gluons are, in principle, large and modify the q_T distribution of a scalar and pseudoscalar Higgs in a distinct way.

TMD factorization

The contribution of gluon fusion to Higgs production in the TMD framework reads [7] in leading order in q_T/m_H,

$$\frac{\mathrm{d}\sigma}{\mathrm{d}^3\vec{q}} \propto \int \mathrm{d}^2\mathbf{p}_T\, \mathrm{d}^2\mathbf{k}_T\, \delta^2(\mathbf{p}_T + \mathbf{k}_T - \boldsymbol{q}_T)\, \Phi_g^{\mu\nu}(x_a,\, \mathbf{p}_T) \Phi_g^{\rho\sigma}(x_b,\, \mathbf{k}_T) \left(\hat{\mathcal{M}}^{\mu\rho}\right) \left(\hat{\mathcal{M}}^{\nu\sigma}\right)^* \Big|_{p_a = x_a P_a}^{p_b = x_b P_b}, \quad (1)$$

in which the momentum fractions are given by $x_{a(b)} = q^2/(2P_{a(b)} \cdot q)$ and Φ_g is the gluon correlator [8, 9],

$$\begin{aligned}\Phi_g^{\mu\nu}(x, \boldsymbol{p}_T) &= \frac{n_\rho\, n_\sigma}{(p\cdot n)^2} \int \frac{d(\xi\cdot P)\, d^2\xi_T}{(2\pi)^3}\; e^{ip\cdot\xi}\, \langle P|\, \mathrm{Tr}\left[\, F^{\mu\rho}(0)\, F^{\nu\sigma}(\xi)\,\right] |P\rangle\, \big\rfloor_{\mathrm{LF}} \\ &= -\frac{1}{2x} \left\{ g_T^{\mu\nu}\, f_1^g(x, \boldsymbol{p}_T^2) - \left(\frac{p_T^\mu p_T^\nu}{M^2} + g_T^{\mu\nu} \frac{\boldsymbol{p}_T^2}{2M^2} \right) h_1^{\perp\, g}(x, \boldsymbol{p}_T^2) \right\} + \text{higher twist}, \end{aligned} \quad (2)$$

with $p_T^2 = -\boldsymbol{p}_T^2$, $g_T^{\mu\nu} = g^{\mu\nu} - P^\mu n^\nu/P\cdot n - n^\mu P^\nu/P\cdot n$, and M the proton mass. The function $f_1^g(x, \boldsymbol{p}_T^2)$ represents the unpolarized gluon distribution and $h_1^{\perp\, g}(x, \boldsymbol{p}_T^2)$ represents the distribution of linearly polarized gluons.

Size of the linearly polarized gluon distribution

As a first step, to study the effects of linearly polarized gluons, we follow a standard approach for TMDs in the literature and assume a simple Gaussian dependence of the gluon TMDs on transverse momentum:

$$f_1^g(x, \boldsymbol{p}_T^2) = \frac{G(x)}{\pi \langle p_T^2 \rangle}\, \exp\left(-\frac{\boldsymbol{p}_T^2}{\langle p_T^2 \rangle} \right), \quad (3)$$

where $G(x)$ is the collinear gluon distribution, $G(x) = \int \mathrm{d}^2\mathbf{p}_T\, f_1^g(x, \mathbf{p}_T)$. The width, $\langle p_T^2 \rangle$, depends on the energy scale, Q, and should be experimentally determined. We will estimate $\langle p_T^2 \rangle = 7\,\mathrm{GeV}^2$, at $Q = m_H = 120\,\mathrm{GeV}$, in rough agreement with the Gaussian fit to $f_1^u(x, \boldsymbol{p}_T^2)$ evolved to $Q = M_Z$ of Ref. [10].

No experimental data on $h_1^{\perp g}$ is available, but a positivity bound has been derived in Ref. [8]: $\frac{\boldsymbol{p}_T^2}{2M^2} |h_1^{\perp g}(x, \boldsymbol{p}_T^2)| \leq f_1^g(x, \boldsymbol{p}_T^2)$. We will use a Gaussian Ansatz for $h_1^{\perp g}$, with a width of $r\langle p_T^2 \rangle$,

$$h_1^{\perp g}(x, \boldsymbol{p}_T^2) = \frac{M^2 G(x)}{\pi \langle p_T^2 \rangle^2} \frac{2e(1-r)}{r}\, \exp\left(-\frac{\boldsymbol{p}_T^2}{r\langle p_T^2 \rangle} \right), \quad (4)$$

with a normalization such that it satisfies the bound for all $\boldsymbol{p}_T$.

Higgs transverse momentum distribution

Using the TMD factorization expression in Eq. (1), the parameterization of the gluon correlator in Eq. (2) and the Ansatz for the TMD distribution in Eqs. (3) and (4), the transverse momentum distribution for a scalar and pseudoscalar Higgs can be written as

$$\frac{1}{\sigma} \frac{\mathrm{d}\sigma}{\mathrm{d}q_T^2} = [1 \pm R(q_T)]\, \frac{1}{2\langle p_T^2 \rangle} e^{-q_T^2/2\langle p_T^2 \rangle}, \quad (5)$$

where $\pm$ stands for a scalar/pseudoscalar and $R(q_T) \equiv \mathcal{C}[w_H h_1^{\perp g} h_1^{\perp g}]/\mathcal{C}[f_1^g f_1^g]$, with

$$\mathcal{C}[w\, f\, f] \equiv \int \mathrm{d}^2\mathbf{p}_T \int \mathrm{d}^2\mathbf{k}_T\, \delta^2(\mathbf{p}_T + \mathbf{k}_T - \boldsymbol{q}_T) w(\mathbf{p}_T, \mathbf{k}_T)\, f(x_a, \mathbf{p}_T^2)\, f(x_b, \mathbf{k}_T^2) \tag{6}$$

and $w_H = [(\mathbf{p}_T \cdot \mathbf{k}_T)^2 - \frac{1}{2}\mathbf{p}_T^2 \mathbf{k}_T^2]/2M^4$. With our Ansatz for the distribution functions,

$$R(q_T) = \frac{r}{2}(1-r)^2 \left(1 - \frac{q_T^2}{r\,\langle p_T^2\rangle} + \frac{q_T^4}{8\,r^2\,\langle p_T^2\rangle^2}\right) \exp\left[2 - \frac{1-r}{r}\frac{q_T^2}{2\,\langle p_T^2\rangle}\right]. \tag{7}$$

The transverse momentum distribution in Eq. (5) for a scalar and pseudoscalar Higgs is plotted in Figure 1 for $r = 2/3$ and $r = 1/3$. As long as $h_1^{\perp g}$ is not measured, the absolute size of the effect is unknown, but it will always be such that a scalar has enhancement at low q_T, suppression at moderate q_T, followed again by enhancement at high q_T, whereas for the pseudoscalar this is reversed. Higher order perturbative corrections will modify the exact form and width of our tree-level q_T distribution, as well as the size of the modulation, but this qualitative behavior is expected not to change.

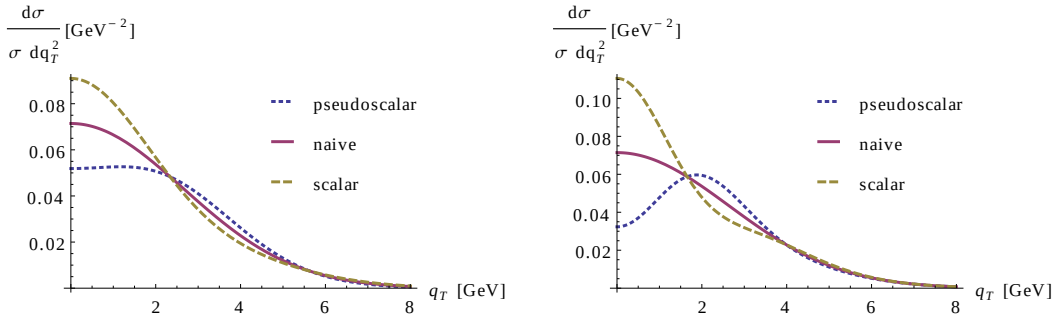

Figure 1: Transverse momentum distribution of the Higgs, using the parameterization of $h_1^{\perp g}$ in Eq. (4) with $r = 2/3$ (left) and $r = 1/3$ (right). The naive curve is the prediction for both scalar and pseudoscalar in case $h_1^{\perp g} = 0$.

Two photon decay channel

When the Higgs decays to, e.g., two photons, there will be irreducible background due to $gg \to$ quark box $\to \gamma\gamma$, which was recently investigated in the framework of TMD factorization [11]. Including this background, we come to the conclusion [7], that the transverse momentum distribution of the photon pair has the same form as Eq. (5), but with a Q and Collins-Soper angle, θ, dependent size, i.e.,

$$\frac{1}{\sigma}\frac{\mathrm{d}\sigma}{\mathrm{d}q_T^2} = \left[1 + \frac{F_2(Q,\theta)}{F_1(Q,\theta)} R(q_T)\right] \frac{1}{2\langle p_T^2\rangle} e^{-q_T^2/2\langle p_T^2\rangle}. \tag{8}$$

The ratio F_2/F_1 is plotted in the left graph of Fig. 2. At the Higgs mass we reproduce Eq. (5), i.e. $F_2/F1 \to \pm 1$, for a scalar/pseudoscalar, but away from the pole, the background quickly dominates. To mimic a finite detector resolution in the determination of Q, we also plot the ratio F_2/F_1 in which both numerator and denominator are separately weighted with a Gaussian distribution. From the graph we see that the continuum background reduces the effect to approximately 30% or 20% of the maximal size with a 0.5 or 1 GeV resolution, respectively.

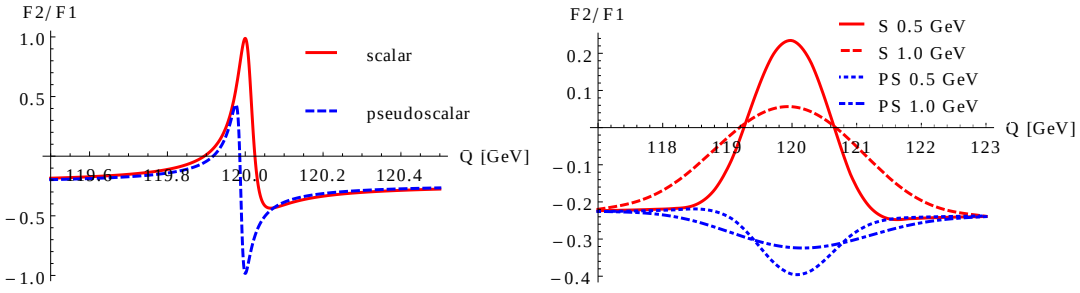

Figure 2: The ratio F_2/F_1 in Eq. (8) plotted as function of Q for $\theta = \pi/2$ assuming a 120 GeV Higgs (left) and the same curves including a detector resolution of 0.5 and 1 GeV (right).

Conclusions

The effect of gluon polarization in pp collisions is such that scalar and pseudoscalar particles, produced through gluon fusion, will have different transverse momentum distributions. Although the absolute size of the effect cannot be estimated without experimental input on $h_1^{\perp g}$, the qualitative features are such that this effect can, in principle, be used to distinguish scalar from pseudoscalar particles. In the two photon decay channel of the Higgs, the continuum background partially washes out the difference between scalar and pseudoscalar. Other decay channels are currently being investigated.

This work is part of the research program of the "Stichting voor Fundamenteel Onderzoek der Materie (FOM)" which is financially supported by the "Nederlandse Organisatie voor Wetenschappelijk Onderzoek (NWO)".

References

[1] T. Plehn, D. L. Rainwater and D. Zeppenfeld, Phys. Rev. Lett. **88**, 051801 (2002); F. Campanario, M. Kubocz and D. Zeppenfeld, Phys. Rev. D **84**, 095025 (2011)

[2] S. Berge and W. Bernreuther, Phys. Lett. B **671**, 470 (2009); S. Berge, W. Bernreuther, B. Niepelt and H. Spiesberger, Phys. Rev. D **84**, 116003 (2011)

[3] G. Bozzi, S. Catani, D. de Florian and M. Grazzini, Phys. Lett. B **564**, 65 (2003); G. Bozzi, S. Catani, D. de Florian and M. Grazzini, Nucl. Phys. B **737**, 73 (2006); G. Bozzi, S. Catani, D. de Florian and M. Grazzini, Nucl. Phys. B **791**, 1 (2008)

[4] C. Balazs, E. L. Berger, P. M. Nadolsky and C. P. Yuan, Phys. Rev. D **76**, 013009 (2007)

[5] P. M. Nadolsky, C. Balazs, E. L. Berger and C. P. Yuan, Phys. Rev. D **76**, 013008 (2007)

[6] S. Catani and M. Grazzini, Nucl. Phys. B **845**, 297 (2011)

[7] D. Boer, W. J. den Dunnen, C. Pisano, M. Schlegel, W. Vogelsang, Phys. Rev. Lett. **108**, 032002 (2012)

[8] P.J. Mulders, J. Rodrigues, Phys. Rev. D **63**, 094021 (2001)

[9] D. Boer, S. J. Brodsky, P. J. Mulders and C. Pisano, Phys. Rev. Lett. **106**, 132001 (2011)

[10] S. M. Aybat and T. C. Rogers, Phys. Rev. D **83**, 114042 (2011)

[11] J. W. Qiu, M. Schlegel and W. Vogelsang, Phys. Rev. Lett. **107**, 062001 (2011)

COMPASS results on transverse spin asymmetries in two-hadron production in SIDIS

Christopher Braun[1] on behalf of the COMPASS collaboration

[1]Physikalisches Institut IV der Universität Erlangen-Nürnberg, Erwin-Rommel-Strasse 1, 91058 Erlangen, Germany, e-mail: christopher.braun@cern.ch

DOI: `http://dx.doi.org/10.3204/DESY-PROC-2012-02/151`

COMPASS is a fixed target experiment at CERN where nucleon spin structure and hadron spectroscopy are investigated. An important part of its physics program are the measurements of single spin asymmetries in semi-inclusive deep inelastic scattering on transversely polarized targets. Data on a deuteron target were taken in 2002-2004. After taking the first data on a transversely polarized proton target in 2007, a full year of data taking followed in 2010 to increase precision. In this contribution we present the latest results for the azimuthal asymmetries in two-hadron production which allow to investigate the transversity distribution function coupled to the two-hadron interference fragmentation function.

1 Theoretical framework

The quark content of the nucleon at twist-two level can be fully characterized in the collinear case by three independent parton distribution functions (PDF): the quark distribution f_1, the helicity distribution g_1 and the transversity distribution h_1. The latter is chiral-odd and therefore is not accessible in inclusive deep inelastic scattering (DIS). h_1 can be observed in semi-inclusive DIS in combination with another chirally odd function *e.g.* the two-hadron interference fragmentation function (FF) $H_1^{\sphericalangle}$ in two-hadron production, which is one subject of this contribution. Other possible channels which have also been measured at COMPASS are the production of single hadrons using the Collins effect [1] and the Λ polarization. A schema of the reaction $lN^{\uparrow} \to l'hh$ is shown in fig. 1. The incoming lepton (in the COMPASS case a 160 GeV/c^2 polarized μ^+), the scattered lepton and the virtual photon γ with their 3-momenta $\mathbf{l}$,$\mathbf{l'}$ and $\mathbf{q}$ define the scattering plane. $\mathbf{R} = (z_2\mathbf{p_1} - z_1\mathbf{p_2})/(z_1 + z_2)$ is the normalized relative hadron momentum with the momenta of the two hadrons $\mathbf{p_1}$ and $\mathbf{p_2}$. The angle Φ_R between the two-hadron plane and the scattering

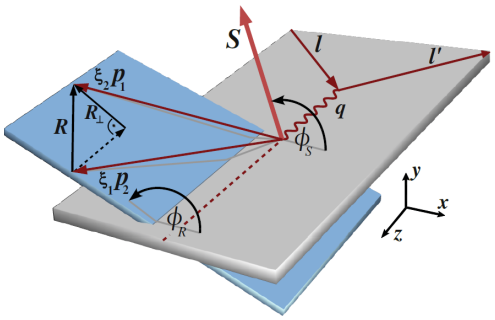

Figure 1: Definition of the azimuthal angles Φ_R and Φ_S in two-hadron production, where l, l', q and p_i are the 3-momenta of beam, scattered muon, virtual photon and hadrons.

plane is defined by $\frac{(\mathbf{q}\times\mathbf{l})\cdot\mathbf{R}}{|(\mathbf{q}\times\mathbf{l})\cdot\mathbf{R}|}\arccos\left(\frac{(\mathbf{q}\times\mathbf{l})\cdot(\mathbf{q}\times\mathbf{R})}{|\mathbf{q}\times\mathbf{l}||\mathbf{q}\times\mathbf{R}|}\right)$ [2]. In the SIDIS cross section of a transversely polarized quark into two unpolarized hadrons Φ_R and the azimuthal angle of the spin of the initial quark Φ_S appear in an azimuthal modulation as a function of $\Phi_{RS} = \sin(\Phi_R+\Phi_S-\pi)$ [3].

$$\frac{\mathrm{d}^7\sigma}{\mathrm{d}\cos\theta\ \mathrm{d}M_{inv}^2\ \mathrm{d}\Phi_R\ \mathrm{d}z\ \mathrm{d}x\ \mathrm{d}y\ \mathrm{d}\Phi_S} = \frac{\alpha^2}{2\pi Q^2 y}\Big((1-y+\frac{y^2}{2})\sum\nolimits_q e_q^2 f_1^q(x)D_1(z,M_{inv}^2,\cos\theta) + (1-y)S_\perp\sum\nolimits_q e_q^2\frac{|\mathbf{p_1}-\mathbf{p_2}|}{2M_{inv}}\sin(\Phi_{RS})\sin(\theta)h_1^q(x)H_1^\sphericalangle(z,M_{inv}^2,\cos\theta)\Big)\ . \tag{1}$$

Accordingly one gets the number of produced pairs $N_{2h}^{\pm}(\Phi_{RS}) = N_{2h}^0(1\pm f(x,y)P_T D_{NN}(y)A_{2h}\sin\Phi_{RS}\sin\theta)$, where the asymmetry amplitude A_{2h} can be written as

$$A_{2h} \propto \frac{|\mathbf{p_1}-\mathbf{p_2}|}{2M_{inv}}\frac{\sum_q e_q^2\cdot h_1^q(x)\cdot H_1^\sphericalangle(z,M_{inv}^2,\cos\theta)}{\sum_q e_q^2\cdot f_1^q(x)\cdot D_1(z,M_{inv}^2,\cos\theta)}\ . \tag{2}$$

The $\pm$ signs indicate the spin orientation of the nucleon, $f(x,y)$ gives the fraction of events originating from polarised protons or deuterons relative to all events, P_T the target polarization and $D_{NN}(y) = (1-y)/(1-y+\frac{y^2}{2})$ the transvers spin transfer coefficient. The latest results on the unpolarized dihadron fragmentation function D_1 can be found in ref. [4].

2 Data selection

In the description of the data selection we focus on the analysis of the 2010 proton (NH_3 target) data, which is very similar to that of the data collected in the previous years. To select DIS events, kinematic cuts on $Q^2 > 1$ GeV/c^2, the fractional energy transfer of the muon $0.1 < y < 0.9$ and the hadronic invariant mass $W > 5$ GeV/c^2 were applied. The hadron pair sample requires more selection *w.r.t.* the one-hadron asymmetry analysis [1], of which the requirement for a vertex with 3 outgoing tracks (a scattered μ^+ and two hadrons) is essential. All possible combinations of oppositely charged hadron pairs originating from the vertex are taken into account, each of these hadrons has to have a $z > 0.1$ and a $x_F > 0.1$, to exclude products of target fragmentation. Exclusively produced ρ^0 mesons are rejected by a cut on the missing energy $E_{miss} > 3$ GeV, which is the Lorentz invariant difference of the energy of the pair system *w.r.t.* the energy of the γ-nucleon system. Finally a cut of $|\mathbf{R_T}| > 0.07$ GeV/c, which is the absolute value of the component of $\mathbf{R}$ perpendicular to $\mathbf{q}$ ensures a good definition of the azimuthal angle Φ_R. After all cuts the 2010 statistics consists of $34.56\cdot10^6$ h^+h^--pairs.

3 Results from the deuteron and proton data until 2007

The two-hadron asymmetries for the data collected in 2002-04 for the deuteron (^{6}LiD) target are consistently small and compatible with zero within the error bars (fig. 2 upper part). Furthermore no specific trend is visible for their depenence on x, z and M_{inv}.
The first measurement of a two-hadron asymmetry on a proton target at COMPASS were performed using the data collected in 2007. The results [5] as a function of x, z and M_{inv} are shown in the lower part of fig. 2. A large asymmetry up to $5-10\%$ in the valence x-region has been measured. This implies a non-zero transversity distribution and a non-zero polarized two

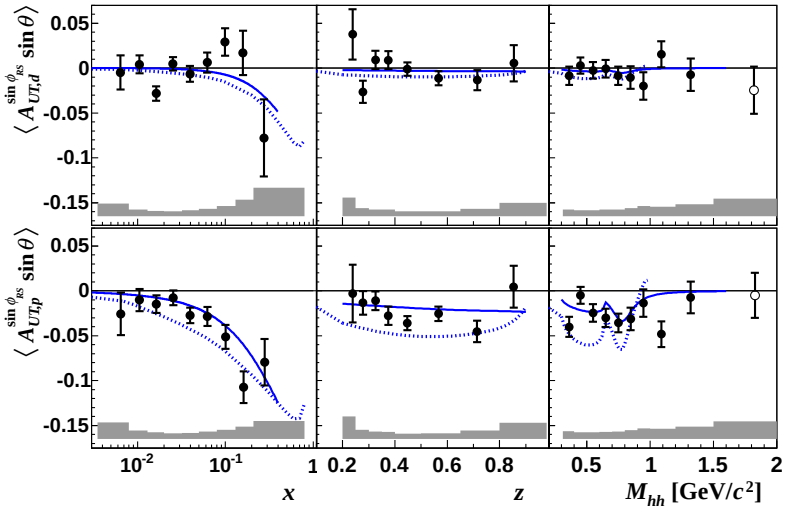

Figure 2: 2002-2004 deuteron (top) and 2007 proton (bottom) two-hadron asymmetries of h^+h^--pairs in comparison with model predictions from refs. [12] (solid lines) and refs. [13] (dotted lines). The systematical uncertainty is given by the error band.

hadron intereference FF $H_1^{\sphericalangle}$. A First extraction of h_1 for proton and deuteron targets can be found in ref. [6, 7, 8]. For the z-dependence no specific trend is visible, while for the invariant mass a negative signal around the ρ^0-mass of 0.77 GeV/c^2 is observed and the asymmetry is negative over the whole mass range.

4 Results from the proton data 2010

The whole COMPASS beam time in 2010 was dedicated to measure the spin asymmetries on transversely polarized protons with higher precision, resulting in a gain in statistics of ≈ 3.5 *w.r.t.* 2007. These two independent measurements of the two-hadron asymmetry by COMPASS are in good agreement. The signal in the x valence region is confirmed. Nearly constant with a negative asymmetry in z, and the structure in M_{inv} are congruent. The two-hadron asymmetry was also measured by the HERMES experiment [9]. HERMES published lepton-nucleon asymmetries, while COMPASS calculates photon-nucleon asymmetries. To allow a comparsion with their results for identified $\pi^+\pi^-$-pairs, their released asymmetry values have to be scaled with $\langle 1/D_{nn} \rangle \approx 3$ [10, 11] and multiplied by -1 due to an additional phase π in the angle definition of Φ_{RS} in the COMPASS analysis. The overall agreement between HERMES and COMPASS is good within the error bars (fig. 3) bearing in mind the larger kinematical range in x and M_{inv} of COMPASS. This is an important result, also because of the different $\langle Q^2 \rangle$ values in the valance region for the two experiments. The prediction for the two-hadron asymmetry from the model of Bachetta and collaborators [12] were scaled with this factor of about 3 to undo the adaptation made to fit the HERMES data, the result is shown in fig. 3. For the x dependence of the asymmetry the agreement is good and the trend is clearly visible, in the cases of z it implies a more linear behavior and for M_{inv} the agreement is fair. While the agreement between model predictions of Ma *et al.* [13] and the data is in general poorer.

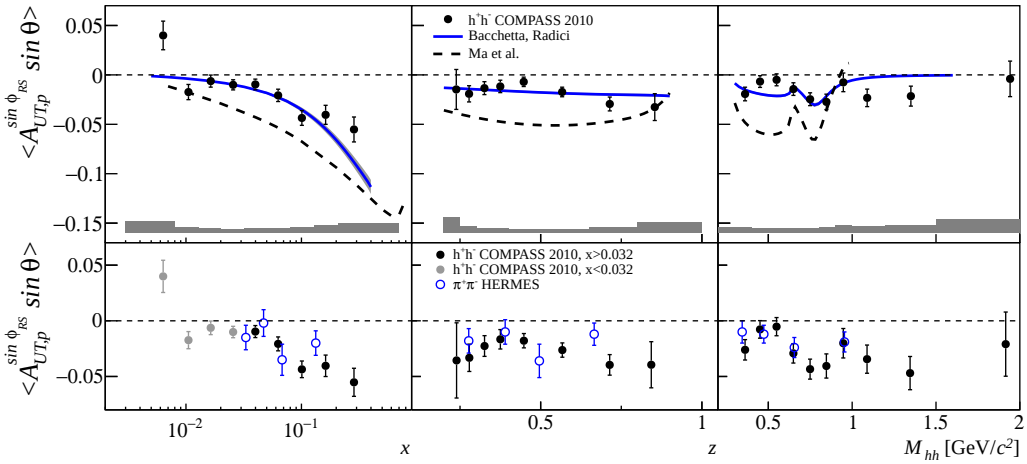

Figure 3: 2010 proton data two-hadron asymmetries of h^+h^--pairs in comparison with model predictions from refs. [12, 13]

5 Conclusions & Outlook

Now a large set of COMPASS two-hadron data on a transversely polarized target is available — deuteron data and two independent measurements on the proton. The presented preliminary results from 2010 data are in agreement with the previous COMPASS data, the HERMES data and the available model predictions in particular with the one of Bacchetta and Radici [12]. The small systematic uncertainties and high statistics of the data will allow more studies, in particular in a next step the extraction of the asymmetries for identified pion pairs and also pairs including charged kaons.

References

[1] F. Bradamante *o.b.o.* the COMPASS Collab. Nuovo Cimento C **035** (2012) 02 arXiv:1111.0869v1.

[2] X. Artru and J. C. Collins. Eur. Phys. J. C **69** (1996) 277-286 arXiv:hep-ph/9504220v2.

[3] A. Bacchetta and M. Radici. Phys. Rev. D **67** (2003) 094002 arXiv:hep-ph/0212300v1.

[4] BELLE Collaboration, A. Vossen *et al.*. Phys. Rev. Lett. **107** (2011) 072004 arXiv:1104.2425v3.

[5] COMPASS Collaboration, C. Adolph *et al.* `CERN-PH-EP-2012-053`

[6] M. Radici. Nuovo Cimento C **035** (2012) 02 69-77 arXiv:1111.3383v2.

[7] A. Courtoy. "Interference Fragmentation Functions and Transverse Spin Studies", these proceedings.

[8] C. Elia. PhD thesis, University of Trieste (2011) C. Elia PhD thesis.

[9] HERMES Collaboration, A. Airapetian *et al.*. J. High Energ. Phys. **06** (2008) 066 arXiv:0802.2499v2.

[10] L. Xiaorui. PhD thesis, Tokyo Institute of Technology (2008) L. Xiaorui PhD thesis.

[11] H. Wollny. PhD thesis, University of Freiburg (2010) H. Wollny PhD thesis.

[12] A. Bacchetta and M. Radici. Phys. Rev. D **74** (2006) 114007 arXiv:hep-ph/0608037v1.

[13] B.-Q. Ma, V. Barone, J.-S. Huang and Y. Huang Phys. Rev. D **77** (2008) 014035 arXiv:0711.0817v4.

Status on the transversity parton distribution: the dihadron fragmentation functions way

A. Courtoy[1], *Alessandro Bacchetta*[2,3], *Marco Radici*[2]

[1]IFPA, AGO Department, Université de Liège, Allée du 6 Août 17, 4000 Liège, Belgium
[2]INFN Sezione di Pavia, via Bassi 6, I-27100 Pavia, Italy
[3]Dipartimento di Fisica Nucleare e Teorica, Università di Pavia, via Bassi 6, I-27100 Pavia, Italy

DOI: `http://dx.doi.org/10.3204/DESY-PROC-2012-02/55`

We report on the extraction of dihadron fragmentation functions (DiFF) from the semi-inclusive production of two hadron pairs in back-to-back jets in e^+e^- annihilation. A nonzero asymmetry in the correlation of azimuthal orientations of opposite $\pi^+\pi^-$ pairs is related to the transverse polarization of fragmenting quarks through a significant polarized DiFF. A combined analysis of this asymmetry and the spin asymmetry in the SIDIS process $ep^\uparrow \to e'(\pi^+\pi^-)X$ has led to the first extraction of the u and d-flavor transversity parton distribution function in the framework of collinear factorization.

The distribution of quarks and gluons inside hadrons can be described by means of parton distribution functions (PDFs). In a parton-model picture, PDFs describe combinations of number densities of quarks and gluons in a fast-moving hadron. The knowledge of PDFs is crucial for our understanding of QCD and for the interpretation of high-energy experiments involving hadrons. At leading-twist, the quark structure of hadrons is described by three PDFs. The unpolarized distribution $f_1(x)$, the longitudinal polarization, *helicity*, distribution $g_1(x)$ and the transverse polarization, *transversity*, distribution $h_1(x)$. From the phenomenological point of view, the unpolarized PDF is a well-known quantity and the helicity PDF is known to some extent. On the other hand, the transversity distribution is poorly known. It is due to its chiral-odd nature. In effect, transversity is not observable from fully inclusive DIS. In order to measure the transversity PDF, chirality must be flipped twice. We can either have two hadrons in the initial state, e.g. proton-proton collision ; or one hadron in the initial state and at least one hadron in the final state, e.g. semi-inclusive DIS (SIDIS).

In these proceedings, we consider two-hadron production in DIS, i.e., the process

$$\ell(l) + N(P) \to \ell(l') + H_1(P_1) + H_2(P_2) + X \ , \tag{1}$$

where ℓ denotes the beam lepton, N the nucleon target, H_1 and H_2 the produced hadrons, and where four-momenta are given in parentheses. The transversity distribution function is here multiplied by a chiral-odd DiFF, denoted as $H_1^{\sphericalangle\, q}$ [1], which describes the correlation between the transverse polarization of the fragmenting quark with flavor q and the azimuthal orientation of the plane containing the momenta of the detected hadron pair. DiFFs are functions of the invariant mass of the pion pair, M_h, and the momentum fraction of the fragmenting quark carried by the pair, z. Since DiFFs are not TMD FF but collinear FF instead, this effect survives after integration over quark transverse momenta and can therefore be analyzed in the framework

of collinear factorization. Measurement of the relevant asymmetry has been presented by the HERMES collaboration for the production of $\pi^+\pi^-$ pairs on transversely polarized protons [2], and led to the first extraction of transversity in a collinear framework [3]. The COMPASS collaboration [4] has recently published similar measurements on proton and deuteron targets. The combination of these new data allows for a flavor separation of the transversity, which we present here for the first time.

In order to extract transversity for pion pair production in SIDIS, one has to determine independently the DiFFs. This can be achieved by studying the correlations between the azimuthal orientations of two pion pairs in back-to-back jets in e^+e^- annihilation [5]. The first analysis of the so-called Artru–Collins asymmetry [6], i.e.,

$$A_{e^+e^-}(z, M_h, \overline{z}, \overline{M}_h; Q^2) \quad \propto \quad \frac{\sum_q e_q^2 \, \frac{|\mathbf{R}|}{M_h} \, H_1^{\sphericalangle q}(z, M_h; Q^2) \, \frac{|\overline{\mathbf{R}}|}{\overline{M}_h} \, \overline{H}_1^{\sphericalangle q}(\overline{z}, \overline{M}_h; Q^2)}{\sum_q e_q^2 \, D_1^q(z, M_h; Q^2) \, \overline{D}_1^q(\overline{z}, \overline{M}_h; Q^2)} \ , \tag{2}$$

by the Belle collaboration [7] made possible a direct extraction of $H_1^{\sphericalangle}$ [1] for the production of $\pi^+\pi^-$. R is the relative momentum of the pair, it obeys the relation $2\,|\mathbf{R}|/M_h = \sqrt{1 - 4m_\pi^2/M_h^2}$. In the absence of a measurement of the unpolarized cross section for dihadron production in e^+e^- annihilation, the unpolarized DiFF, D_1, was parametrized to reproduce the two-hadron yields of the PYTHIA event generator, which is known to give a good description of data. Combining the parametrization of the unpolarized functions D_1 with the fit of the azimuthal asymmetry presented in Ref. [7], it was possible to extract the DiFF $H_1^{\sphericalangle}$ [8].

We have now all the ingredients at hand to extract transversity from the process (1). In a collinear framework, we can single out the DiFF contribution to the SIDIS asymmetry from the x-dependence coming from the transversity PDF. In particular, the x behavior of $h_1(x)$ is simply given by integrating the numerator of the asymmetry over the (z, M_h)-dependence, so that the relevant quantities for our purposes are

	HERMES range	COMPASS range
$n_u =$	0.5638	0.7848
$n_s =$	0.3033	0.4432
$n_u^\uparrow =$	0.0185 ± 0.0047	0.0206 ± 0.0039

Table 1: DiFF integrated over experimental ranges. We neglect the error coming from the determination of D_1.

$$n_q(Q^2) \quad = \quad \int dz \, dM_h \, D_1^q(z, M_h; Q^2) \ , \tag{3}$$

$$n_q^\uparrow(Q^2) \quad = \quad \int dz \, dM_h \, \frac{|\mathbf{R}|}{M_h} \, H_1^{\sphericalangle\, q}(z, M_h; Q^2) \ , \tag{4}$$

where the integral limits are defined in the physical range of validity, i.e. from $2m_\pi$ to $M_h \ll Q$ and $0.2 < z < 1$.

The asymmetry, expressed in terms of the integrated DiFFs, reads

$$A_{\rm SIDIS}(x, Q^2) \quad = \quad \frac{\sum_q e_q^2 \, h_1^q(x, Q^2) n_q^\uparrow(Q^2)}{\sum_q e_q^2 \, f_1^q(x, Q^2) n_q(Q^2)} \ . \tag{5}$$

[1] We call here $H_{1,sp}^{\sphericalangle}$ by $H_1^{\sphericalangle}$ to avoid clumsy notations.

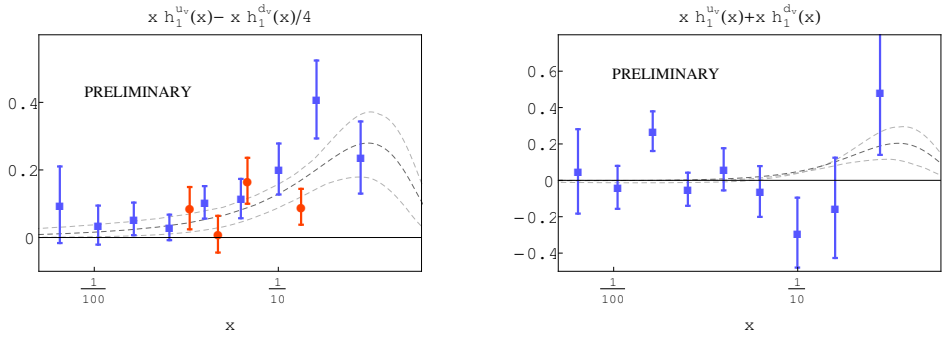

Figure 1: The combinations of Eq. (7), left panel, and Eq. (8), right panel. The circle red dots are the extracted transversities at HERMES ; the squared blue dots are the extracted transversities at COMPASS. The dashed lines correspond to Torino's transversity [9].

Asumming isospin symmetry and charge conjugation [10], i.e.

$$D_1^u = D_1^d = D_1^{\bar{u}} = D_1^{\bar{d}} \,, \quad D_1^s = D_1^{\bar{s}} \,, \quad D_1^c = D_1^{\bar{c}} \quad \& \quad H_1^{\sphericalangle u} = -H_1^{\sphericalangle d} = -H_1^{\sphericalangle \bar{u}} = H_1^{\sphericalangle \bar{d}} \,, \tag{6}$$

the only relevant quantities here are n_u, n_s and $n_u^\uparrow$, since the charm unpolarized PDF can be neglected. For phenomenological purposes, we evaluate the integrals (3, 4) over the corresponding kinematical ranges for the HERMES and the COMPASS data. The results are given in Table 1. Hence, for a proton target, Eq. (5) leads to the combination of transversity PDFs

$$x h_1^{u_v}(x,Q^2) - \tfrac{1}{4}\, x h_1^{d_v}(x,Q^2) \;=\; -\frac{A^P_{\rm SIDIS}(x,Q^2)}{n_u^\uparrow(Q^2)} \sum_{q=u,d,s} \frac{e_q^2}{e_u^2}\, n_q(Q^2)\, x f_1^{q+\bar{q}}(x,Q^2) \;, \tag{7}$$

and, for a deuteron target,

$$\begin{aligned} x h_1^{u_v}(x,Q^2) + x h_1^{d_v}(x,Q^2) \;=\; & -\frac{A^D_{\rm SIDIS}(x,Q^2)}{n_u^\uparrow(Q^2)}\, \frac{5}{3}\, x \Big(n_u(Q^2) \, \Big(f_1^{u+\bar{u}}(x,Q^2) + f_1^{d+\bar{d}}(x,Q^2) \Big) \\ & + \frac{2}{5} n_s(Q^2)\, f_1^{s+\bar{s}}(x,Q^2) \Big) \;. \end{aligned} \tag{8}$$

In Fig. 1, we show the extracted transversity combinations in the experimental x values, together with the parametrization of Ref. [9]. We have employed the MSTW08LO PDF set [11] for the unpolarized PDFs. The errorbands include both the error on the experimental data, $\Delta A_{\rm SIDIS}$, and the error coming from the fit of $H_1^\sphericalangle$, i.e. $\Delta n_u^\uparrow$.

Combining the proton and deuteron data, i.e. Eqs. (7-8), allows for a flavor separation, which results are shown in Fig. 2.

In summary, we have presented a determination of the transversity parton distribution for the u and d flavors in the framework of collinear factorization by using data for pion-pair production in DIS off transversely polarized targets, combined with data of e^+e^- annihilations into pion pairs. The final trend of the extracted transversity seems not to be in disagreement with the Torino's transversity [9], even though there is a large uncertainty due to the deuteron data. More data are needed to clarify the issue.

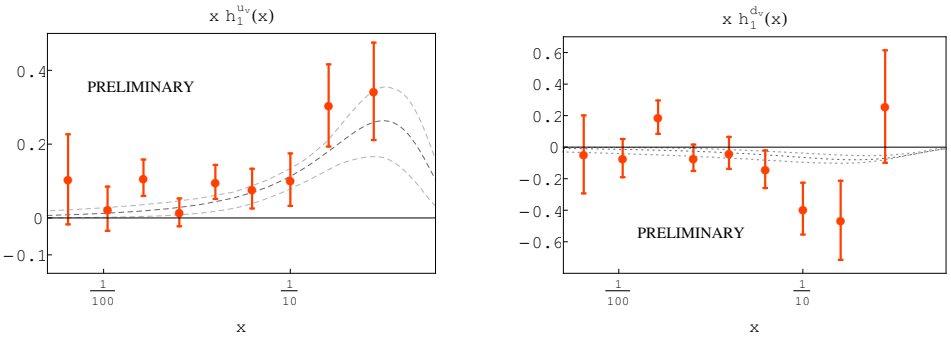

Figure 2: The extracted transversities at COMPASS for the u-flavor on the left panel, and for the d-flavor on the right panel.

Acknowledgments

This work is partially supported by the Italian MIUR through the PRIN 2008EKLACK, and by the Joint Research Activity "Study of Strongly Interacting Matter" (acronym HadronPhysics3, Grant Agreement No. 283286) under the 7th Framework Programme of the European Community and the Belgian Fund F.R.S.-FNRS via A. Courtoy's contract of Chargée de recherches.

References

[1] M. Radici, R. Jakob, and A. Bianconi. Phys. Rev. **D65** (2002) 074031, hep-ph/0110252.

[2] A. Airapetian *et al.* JHEP **06** (2008) 017, arXiv:0803.2367 [hep-ex].

[3] A. Bacchetta, A. Courtoy, and M. Radici. Phys.Rev.Lett. **107** (2011) 012001, arXiv:1104.3855 [hep-ph].

[4] C. Adolph *et al.* arXiv:1202.6150 [hep-ex].

[5] X. Artru and J. C. Collins. Z. Phys. **C69** (1996) 277–286, hep-ph/9504220.

[6] D. Boer, R. Jakob, and M. Radici. Phys. Rev. **D67** (2003) 094003, hep-ph/0302232.

[7] A. Vossen *et al.* Phys.Rev.Lett. **107** (2011) 072004, arXiv:1104.2425 [hep-ex].

[8] A. Courtoy, A. Bacchetta, M. Radici, and A. Bianconi. arXiv:1202.0323 [hep-ph].

[9] M. Anselmino, M. Boglione, U. D'Alesio, A. Kotzinian, F. Murgia, A. Prokudin, and S. Melis. Nucl. Phys. Proc. Suppl. **191** (2009) 98–107, arXiv:0812.4366 [hep-ph].

[10] A. Bacchetta and M. Radici. Phys. Rev. **D74** (2006) 114007, hep-ph/0608037.

[11] A. D. Martin, W. J. Stirling, R. S. Thorne, and G. Watt. Eur. Phys. J. **C63** (2009) 189–285, arXiv:0901.0002 [hep-ph].

Cross Section for High-p_T Hadron Production in Muon-Nucleon Scattering at $\sqrt{s} = 17.4\,\text{GeV}$

Christian Höppner[*1] for the COMPASS Collaboration

[1]Technische Universität München, Physik Department, 85748 Garching, Germany

DOI: http://dx.doi.org/10.3204/DESY-PROC-2012-02/112

The measurement of the cross section for quasi-real photoproduction of charged hadrons with high transverse momenta (high p_T) in muon-nucleon scattering at COMPASS ($\sqrt{s} = 17.4\,\text{GeV}$) is presented. The results are compared to a next-to-leading order perturbative QCD (NLO pQCD) calculation of the cross section to evaluate the applicability of pQCD to this process at the COMPASS energy. The calculation is found to reproduce the shape of the differential cross section well, but to underestimate the normalization of the cross section by a factor of three to four. It is shown that this underestimation increases with decreasing energy of the photon, which is emitted by the muon.

The measurement of the polarization of gluons in the nucleon has been a long-standing goal of hadron physics. Gluon polarization can be directly accessed in lepton-nucleon scattering experiments by measuring double-spin asymmetries of cross sections that have contributions from the photon-gluon fusion (PGF) process. The PGF is the interaction of a photon, emitted by the lepton, with a gluon inside the nucleon via the formation of a quark-antiquark pair. It dominates the cross section for the production of charmed mesons in lepton-nucleon scattering in the kinematic domain of the COMPASS experiment [1] and also has a considerable contribution to the cross section for the production of hadrons with high transverse momenta (high p_T) [2, 3]. The polarized and unpolarized cross sections for single-inclusive high-p_T hadron production in the quasi-real photoproduction limit, i.e. at low photon virtualities, Q^2, have been calculated in next-to-leading order perturbative QCD (NLO pQCD) [4] for the COMPASS kinematics. The calculations show that the gluon polarization can be constrained in the gluon-momentum-fraction range $0.1 \leq x_g \leq 0.3$ using the pQCD framework by comparing the calculated double-spin asymmetries of the cross section, using different input distributions for the gluon polarization, with the asymmetries extracted from the COMPASS data. This approach would be complementary to the gluon polarization measurements of Refs. [2, 3], which are based on the Monte Carlo (MC) generators PYTHIA [5] and LEPTO [6], respectively, for the quantification of the PGF contribution to the cross section. However, before the pQCD-based gluon-polarization analysis can be performed with confidence, the applicability of pQCD to this process at the COMPASS energy has to be proven by comparing the calculated and measured values of the unpolarized cross sections. In this contribution, the measurement of the

*supported by the German Bundesministerium für Bildung und Forschung and the DFG cluster of excellence "Origin and Structure of the Universe".

cross section for quasi-real photoproduction of high-p_T hadrons in muon-nucleon (μ-N) scattering at the center-of-mass system (c.m.s.) energy, $\sqrt{s} = 17.4\,\mathrm{GeV}$, at the COMPASS experiment is presented and compared to the NLO pQCD results.

The experimental data were recorded in 2004 with the COMPASS spectrometer at CERN [7]. In the experiment, a $160\,\mathrm{GeV}/c$ μ^+-beam scatters off a polarized, isoscalar target which consists of granulated ^{6}LiD in a liquid helium bath. The target is arranged in two oppositely polarized 60 cm long cells. The unpolarized cross section is obtained by averaging over the target polarizations. The integrated luminosity was determined via the direct measurement of the rate of beam muons crossing the target and is found to be equal to $142.4\,\mathrm{pb}^{-1} \pm 10\%$(syst.). As an independent check of the luminosity result, the structure function of the nucleon F_2 was determined from this data set and successfully compared [8] to the NMC parametrization of F_2 [9]. The high-p_T analysis is based on events that were recorded by the quasi-real photoproduction trigger systems [10], which are based on the coincidence between the detection of the scattered muon at low scattering angles and an energy deposit of at least 5 GeV in one of the hadronic calorimeters. Events are accepted if $Q^2 < 0.1\,(\mathrm{GeV}/c)^2$ and if the fractional energy of the virtual photon, emitted by the incident muon, is $0.2 \leq y \leq 0.8$, where the acceptance of the triggers is maximal. Hadrons with an energy in units of the photon energy $z < 0.2$ are rejected to ensure the applicability of current fragmentation, and exclusively produced hadrons are excluded by rejecting particles with $z > 0.8$. Moreover, hadron candidates are required to have momenta $p > 15\,\mathrm{GeV}/c$ and to hit one of the hadronic calorimeters to ensure full trigger efficiency. The angle of the hadron with respect to the direction of the virtual photon has to be in the range $10 \leq \theta \leq 120\,\mathrm{mrad}$, which corresponds to a range of c.m.s. pseudo-rapidities $2.4 \geq \eta_{\mathrm{c.m.s.}} \geq -0.1$.

The hadron-production cross section is measured in bins of p_T (with the width Δp_T) and is defined as

$$\frac{1}{2\pi p_T}\frac{\mathrm{d}\sigma}{\mathrm{d}p_T} = \frac{1}{2\pi p_T}\frac{N_h}{\Delta p_T \cdot L \cdot \epsilon} \quad , \tag{1}$$

where $p_T = p \cdot \sin\theta$ is the transverse momentum of the hadron with respect to the direction of the photon, L is the integrated luminosity, and N_h is the number of observed hadrons in the p_T bin. The cross section is integrated over the above-stated range of $\eta_{\mathrm{c.m.s.}}$. The acceptance-correction factor, ϵ, is determined with an MC simulation of μ-N scattering in the COMPASS experiment. Events are generated with PYTHIA [5], the response of the spectrometer is simulated with a GEANT3-based program [11], and the data are reconstructed with the same software as the experimental data [7]. ϵ is defined as the ratio of the number of reconstructed hadrons over the number of generated hadrons in each p_T bin. It corrects the number of observed hadrons for geometrical acceptance and detection efficiency of the spectrometer as well as for kinematic smearing.

A possible source of background for this measurement are hadrons which are created by secondary interactions of other hadrons in the rather thick target. The background contribution is estimated by fitting the shapes of particular vertex distributions [12] and is found to be consistent with zero. A cross check of this procedure with MC data shows that the background contribution can be underestimated by 6%. The systematic error band associated with the possibility of residual background is chosen to span between a background level of zero and $2 \times 6\%$. The central value for the acceptance factor is placed in the middle of the band. The second contribution to the systematic error of the acceptance factor is due to the fact that it is determined in a one-dimensional way, i.e. by integrating over all kinematic variables other

than p_T. This uncertainty is quantified by determining the acceptance correction and the cross section binned in two variables, p_T and each of the variables Q^2, y, x_{Bj} (Bjorken scaling variable), W (invariant mass of the hadronic system), z, and θ. The results are compared to the one-dimensional case and the deviations are below 3%. This uncertainty is added in quadrature to the uncertainty from background contamination, yielding a point-to-point systematic error of 7%. Another systematic uncertainty of the cross section is the 10% normalization uncertainty from the luminosity determination.

The cross section for quasi-real photoproduction ($Q^2 < 0.1\,(\mathrm{GeV}/c)^2$) of charged high-$p_T$ hadrons in μ-N scattering at $\sqrt{s} = 17.4\,\mathrm{GeV}$ is presented in Fig. 1. The cross section drops about four orders of magnitude over the measured p_T range and the only apparent feature is a slight hardening of the spectrum around $p_T = 2.5\,\mathrm{GeV}/c$. The presented cross section is not corrected for QED radiative effects. The data are compared to the updated [13] NLO pQCD calculation of Ref. [4]. The three curves correspond to different choices of the renormalization (μ_r) and factorization (μ_f) scales in the pQCD calculation. The scale uncertainty of the calculation is estimated by varying the scale $\mu = \mu_r = \mu_f$ in the range $2p_T \geq \mu \geq p_T/2$ with the central value $\mu = p_T$. The NLO pQCD results follow the shape of the differential cross section remarkably well, but the central result ($\mu = p_T$) underestimates the experimental cross section by a factor of three to four. This underestimation is of the same order of magnitude as the underestimation of cross sections for high-p_T hadron production in proton-proton (p-p) scattering at the energies of fixed-target experiments, $\sqrt{s} \sim 20\,\mathrm{GeV}$ [14]. It has been shown that this low-energy discrepancies in p-p scattering can be reconciled by the inclusion of all-order resummations of threshold logarithms beyond NLO, which are related to soft-gluon emissions [15]. Such calculations have not yet been published for the quasi-real photoproduction process, but preliminary results were presented at this conference [16]. They indicate that the normalizations of the pQCD cross section and the measured cross section agree with each other after the inclusion of the resummations.

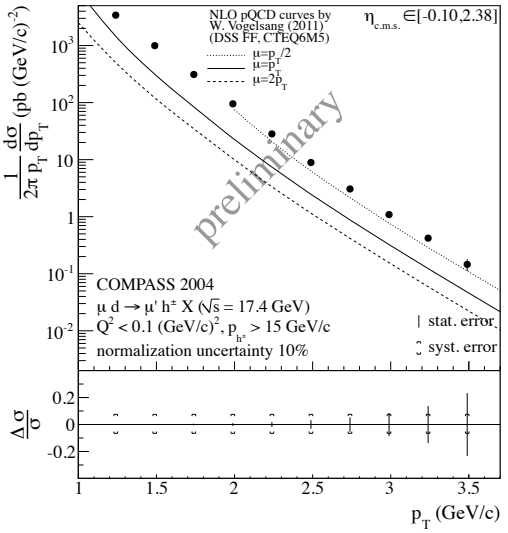

Figure 1: Cross section for high-p_T hadron production. The data are compared to the NLO pQCD calculation [4, 13]. The plot in the upper panel contains the total error bars and the lower panel shows the relative statistical and systematic errors of the measurement.

Figure 2 presents the ratio of the y-differential cross section measured in COMPASS over the cross section calculated in NLO pQCD ($\mu = p_T$) [13] in bins of p_T. It is clearly visible that the underestimation of the cross section by NLO pQCD increases with decreasing photon energy. This shows that the contributions to the cross section which are neglected in the NLO calculation become more significant with decreasing photon-nucleon c.m.s. energy. It will be an interesting test of the resummed calculations, once available, to check whether they can account for the energy dependence of the missing part of the cross section, visible in Fig. 2.

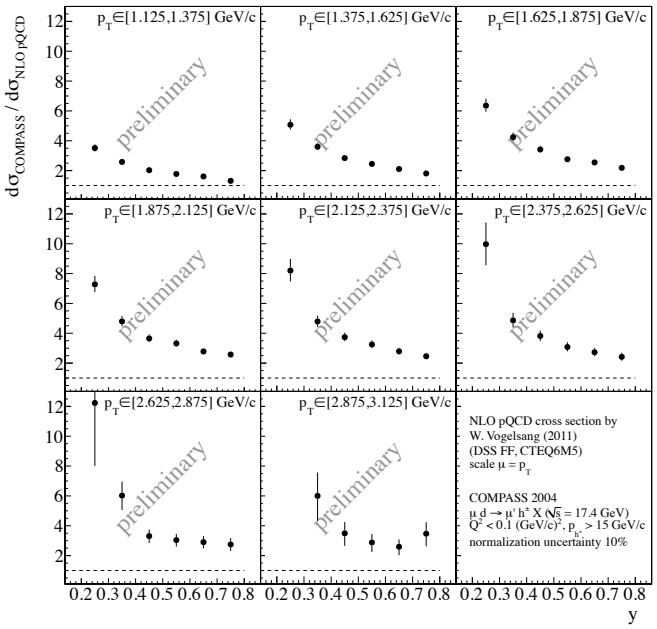

Figure 2: Ratio of the measured y-differential cross section over the NLO pQCD cross section (scale $\mu = p_T$) [13] in bins of p_T.

In conclusion, the measurement of the cross section for the production of charged high-p_T hadrons in μ-N scattering at $\sqrt{s} = 17.4\,\text{GeV}$ has been presented and compared to an NLO pQCD calculation. The calculated p_T-differential cross section follows the shape of the measured cross section well, but underestimates the normalization of the experimental result by a factor of three to four. The y-dependent comparison of the cross sections shows that the underestimation by NLO pQCD clearly increases with decreasing photon energy. Hence, the NLO pQCD calculation seems to be insufficient to fully describe the quasi-real photoproduction of high-p_T hadrons at the COMPASS energy. This discrepancy might be resolved by the inclusion of all-order resummations of threshold logarithms beyond NLO. Establishing an agreement between the cross sections is a prerequisite for the extraction of the gluon polarization in the nucleon from the COMPASS data with the pQCD framework.

References

[1] M. Alekseev *et al.* Phys.Lett. **B676** (2009) 31–38, arXiv:0904.3209 [hep-ex].

[2] E. Ageev *et al.* Phys.Lett. **B633** (2006) 25–32, arXiv:hep-ex/0511028.

[3] C. Adolph *et al.* submitted to Phys.Lett. **B** (2012) , arXiv:1202.4064 [hep-ph].

[4] B. Jäger *et al.* Eur.Phys.J. **C44** (2005) 533–543, arXiv:hep-ph/0505157.

[5] T. Sjostrand *et al.* Comput.Phys.Commun. **135** (2001) 238–259, arXiv:hep-ph/0010017.

[6] G. Ingelman *et al.* Comput.Phys.Commun. **101** (1997) 108–134, arXiv:hep-ph/9605286.

[7] P. Abbon *et al.* Nucl.Instrum.Meth. **A577** (2007) 455–518.

[8] C. Höppner *et al.* Proceedings of SPIN Praha 2010 (2011) , arXiv:1104.2926 [hep-ex].

[9] M. Arneodo *et al.* Phys.Lett. **B364** (1995) 107–115, arXiv:hep-ph/9509406.

[10] C. Bernet *et al.* Nucl.Instrum.Meth. **A550** (2005) 217–240.

[11] R. Brun *et al.* CERN Program Library Long Writeup W5013 (1993) .

[12] C. Höppner. PhD thesis, Technische Universität München, CERN-THESIS-2012-005 (2012).

[13] W. Vogelsang. Private communication, 2011.

[14] C. Bourrely and J. Soffer. Eur.Phys.J. **C36** (2004) 371–374, arXiv:hep-ph/0311110.

[15] D. de Florian and W. Vogelsang. Phys.Rev. **D71** (2005) 114004, arXiv:hep-ph/0501258.

[16] M. Pfeuffer *et al.* These proceedings, 2012.

Part X

Working Group 7
Future of DIS

Convenors:

Elke Aschenauer, Paul Newman

The ATLAS Upgrade programme

Claudia Gemme on behalf of the ATLAS Collaboration

INFN, Sezione di Genova, Via Dodecaneso 33, 16146 Genova, Italy

DOI: http://dx.doi.org/10.3204/DESY-PROC-2012-02/346

After the first successful years of LHC running, plans are actively advancing for a series of upgrades leading eventually to about five times the design-luminosity some 10-years from now. Coping with the high instantaneous and integrated luminosity will be a great challenge for the ATLAS detector and will require changes in most of the subsystems, specially those at low radii and large pseudorapidity, as well as in its trigger architecture. Plans to consolidate and improve the physics capabilities of the current detector over the next decade are summarized in this paper.

1 Introduction

ATLAS [1] is a general-purpose experiment designed to explore the pp collisions at the CERN Large Hadron Collider (LHC) [2] at center of mass energies up to $\sqrt{s} = 14$ TeV and a maximum peak luminosity of 10^{34} cm^{-2} s^{-1}.

ATLAS has been successfully collecting collision data at $\sqrt{s} = 7$ TeV since March 2010, recording an integrated luminosity of $\sim$5 fb^{-1} with a peak luminosity of 3.3×10^{33} cm^{-2} s^{-1}. In the next years, LHC will undergo a series of upgrades leading ultimately to five times increase of the instantaneous luminosity in the High-Luminosity LHC (HL-LHC) project. The goal is to extend the dataset from about 300 fb^{-1}, expected to be collected by the end of the LHC run (in 2020), to 3000 fb^{-1} by 2030. The foreseen higher luminosity at the HL-LHC is a great challenge for ATLAS. Meeting it will require significant but gradual detector optimizations, changes and improvements, which are subject of these proceedings.

2 LHC and ATLAS Upgrade Plans

The main motivation for the LHC upgrades is to extend and improve the actual machine physics programme. A major focus is on the Higgs boson. Using data from the 2011 running, the allowed mass range has already been greatly constrained. With increased statistics, the SM Higgs should be either discovered or excluded in the coming year. In the first case, with larger luminosity, it will be possible to observe the various Higgs decay modes first and then to make precision measurements of the Higgs boson properties, in particular its couplings to fermions and bosons, its rare decays and its self-couplings. If the Higgs is excluded, WW scattering measurements will become essential to unveil the electroweak symmetry breaking mechanism. Other physics items of interest will be: performing a complete supersymmetry spectroscopy; searching for new heavy gauge bosons; searching for a quark and lepton substructure.

In all cases, ATLAS capability to maintain an optimal trigger system as the luminosity increases beyond its nominal design value requires a strong reduction of the main source of backgrounds: jets mimicking electrons in the calorimeters and misidentified muons in the forward spectrometer. Otherwise, increased threshold cuts would have to be deployed to control rates, reducing significantly the signal efficiency. The harsher radiation environment and higher detector occupancies at the HL-LHC imply major changes to most of the ATLAS systems, specially those at low radii and large pseudorapidity. A general guideline for these changes is maintaining the same (or better) level of detector performance as at the LHC. The higher event rates and event sizes will be a challenge for the trigger and data acquisition (DAQ) systems, which will require a significant expansion of their capacity.

The ATLAS upgrade will be gradual and flexible to accommodate a possible evolution of LHC operational parameters and hints from new physics signals. It is planned in three phases, which correspond to the three long, technical shutdowns of the LHC towards the HL-LHC.

3 Phase-0 upgrades

The repair of the splices in the main accelerator during a long shutdown in 2013-2014 (LS1) will allow the LHC to continue its operation (Phase-0) close to its design parameters with a center of mass energy $\sqrt{s}$ =13-14 TeV, 25 ns bunch spacing and peak luminosities $\sim 1 \times 10^{34}$ cm^{-2} s^{-1}, which would bring ATLAS to collect a dataset corresponding to an integrated luminosity $\geq$50 fb^{-1}.

ATLAS will use the shutdown period mainly for detector consolidation works, including a new Inner Detector (ID) cooling system, new power supplies for the calorimeter, completion of the Muon Spectrometer (MS) and a new beam pipe, in the central and forward region. Other activities are still under evaluation as the replacement of the Pixel services, a new diamond beam monitor, a new neutron shielding of the MS, the replacement of the Minumum bias trigger scintillators. The main ATLAS upgrade activity in Phase-0 is the installation of a new barrel layer in the Pixel detector that is briefly described in the next section.

IBL. The Insertable B-Layer (IBL) [3] is an additional, 4^{th} pixel layer, that will be built around a new beam pipe and then slipped inside the present Pixel detector in situ or, if the Pixel package is removed for services replacement, on the surface. The IBL will be therefore placed between the actual innermost pixel layer (the B-layer) and the beam pipe, at a sensor average radius of 33 mm (50.5 mm is the radius of the B-layer). To make the installation of the IBL possible, a new beam pipe in the central region, with reduced by 4 mm radius (r=29 mm $\rightarrow$ r=25 mm), built of Beryllium, is envisaged.
IBL will help to preserve the tracking performance at high luminosity when the B-layer will suffer from radiation damage and high pile-up occupancies. Moreover, it will compensate for defects (irreparable failures of modules) in the existing detector, assuring tracking robustness. It is expected that the IBL will also improve the vertex resolution, secondary vertex finding and b-tagging, hence extending the reach of the physics analysis.
The IBL will consist of 14 pixel staves surrounding the beam-pipe, see Fig. 1. Each carbon-fibre stave carries and provides cooling to 32 read-out chips, which are bump-bonded to silicon sensors, corresponding to a pseudo-rapidity coverage of $|\eta|$ <3. Two types of sensors will be used: planar n-in-n sensors, similar to the present Pixel detector, and 3D silicon sensors. The staves are inclined by 14° with respect to the radial direction in order to achieve overlap of active area between staves and to compensate for (a) the Lorentz angle of drifting charges in

the 2 T magnetic field in case of planar sensors or (b) the effect of partial column inefficiency with perpendicular tracks in case of 3D sensors. There is no shingling of sensors along z due to the lack of radial space. To cope with a larger fluence and peak luminosity, higher hit rate and occupancy, a new generation of read-out chip, FE-I4, has been developed using a new architecture, IBM 130 nm CMOS process manufacturing and smaller pixel size (50×250 μm^2).

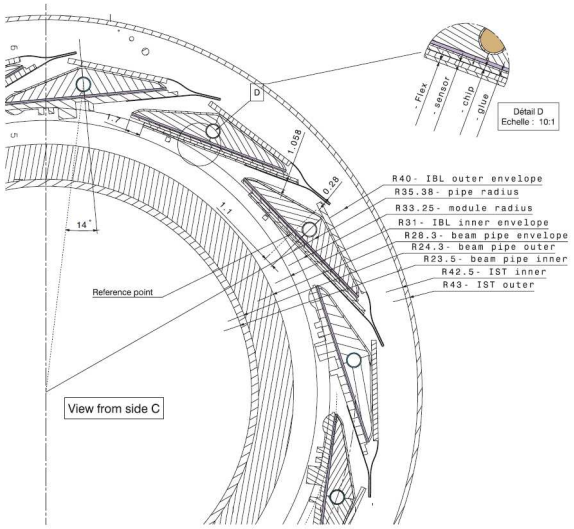

Figure 1: Section view of the IBL, the new beam-pipe and the IBL support tube (IST). Radii of envelopes are given in mm.

4 Phase-I upgrades

A second shutdown (LS2) is being planned in 2018 to integrate the Linac4 into the injector complex, to increase the energy of the PS Booster to reduce the beam emittance, and to upgrade the collider collimation system. When data taking resumes in 2019 (Phase-I), the peak luminosity is expected to reach $\sim 2-3 \times 10^{34}$ cm^{-2} s^{-1} corresponding to 55 to 80 interactions per crossing (pile-up) with 25 ns bunch spacing, well beyond the initial design goals. Phase-I will allow collection of an integrated luminosity of ~ 300 fb^{-1}, extending the reach for discovery of new physics and the ability to study new phenomena and states. In Phase-I, ATLAS proposes the installation of new Muon Small Wheels and new trigger updates (Fast TracK , topological triggers, improved L1Calo granularity) to handle luminosities well beyond the nominal values. Detailed plans are described in Ref. [4].

New Small Wheels. In the muon spectrometer trigger rates, detector occupancy and momentum resolution are strongly affected by the level of background present in the cavern, both from particles generated at the interaction point, and from halo particles in the proton beams. This effect will increase as the peak luminosity evolves. While the implementation of an aluminium beam pipe (Phase-0 upgrade) will reduce the background rate in the forward region by 30%, a replacement of the first endcap station of the Muon Spectrometer, see Fig. 2,

the Muon Small Wheel (MSW), is proposed. The new Muon Small Wheels must ensure efficient tracking at high particle rate (up to 5×10^{34} cm^{-2} s^{-1}) and larger $|\eta|$, with position resolution of < 100 μm. Furthermore, the new MSW will be integrated into the Level-1 trigger, resulting in a rate reduction to 20% with similar signal efficiency. Several detector technologies have been investigated: the final choice being Micro-MEsh GAseous Structures (MicroMEGAs) complemented with fast trigger chambers Thin Gap Chambers (TGC).

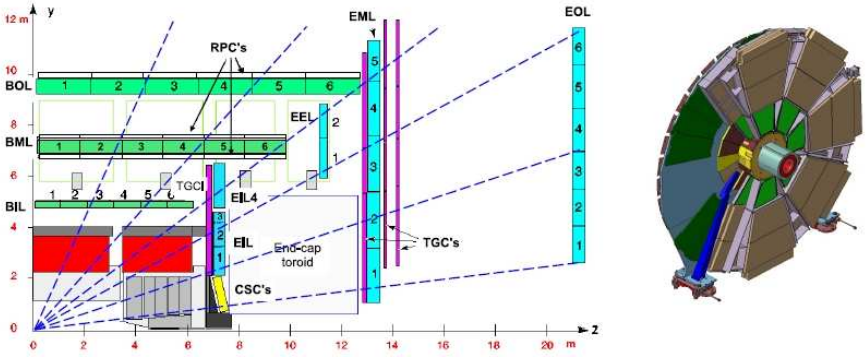

Figure 2: Left: A $z-y$ view of 1/4 of the ATLAS detector. The blue boxes indicate the end-cap MDT chambers and the yellow box CSC. Right: A view of a small wheel.

Level-1 Trigger calorimeter. Suggestions are also in place for combining trigger objects at Level-1 (topological triggers) and implementing higher granularity readout of the calorimeter. Preliminary studies show that shower shape algorithms based on finer granularity *Supercells* ($\Delta\eta \times \Delta\phi = 0.025 \times 0.1$) in the EM calorimeter's second layer achieve a background rejection factor for jets faking electrons similar to what is currently achieved in the Level-2 trigger with the full cell granularity.

Fast Track Trigger (FTK). The Fast TracKer Trigger [5] will perform the track finding and fitting at a hardware level, instead of the Level-2 software farm, which makes it extremely faster. FTK will then provide the track parameters at the beginning of the Level-2 processing thus releasing extra resources for more advanced selection algorithms, which ultimately could improve the b-tagging trigger performances. Commissioning of a barrel slice is on-going in the current data-taking.

5 Phase-II upgrades

The Phase-I upgrades are designed to be fully compatible with the physics program of the high luminosity HL-LHC (Phase-II), when the instantaneous luminosity should reach $\sim 5-7 \times 10^{34}$ cm^{-2} s^{-1}, up to 200 interactions per crossing (pile-up) and a total integrated luminosity of 3000 fb^{-1}. A third long shutdown (LS3) in 2022-23 will be necessary to upgrade the accelerator to this ultimate operation mode. ATLAS is being planning major updates in all its subsystems and trigger architecture.

New Inner Tracker. The present ATLAS Inner tracker will have several limitations in Phase-II when up to 200 pile-up events per bunch crossing are expected. The gas-based

TRT outer tracker has a limit due to instantaneous luminosity because of very high occupancy. The functionality of the silicon-based parts of the tracker will be deteriorated due to the total radiation dose affecting both sensors and read-out electronics and also by the instantaneous luminosity, too high for the present limited band-width. Because of all these factors, ATLAS has decided to replace the entire Inner Detector with a new, all-silicon Inner Tracker (ITk). The ITk must satisfy the following criteria (w.r.t. ID): higher granularity, improved material budget, increased radiation resistivity of the readout components. The current baseline design of the ITk, with a layout similar to the present detector, consists of 4 Pixel and 6 Si-strip double layers of variable length in the barrel part. The two endcap regions are each composed of 6 Pixel and 7 Si-strip double-sided disks, built of rings of modules. Other layouts are still under study.

Calorimeters upgrades. Instantaneous and integrated luminosity will create potential problems related to rates and average energy deposited in the Forward Calorimeter (FCal) and issues related to long-term radiation damage on the on-detector electronics in LAr Hadronic endcap (HEC). Since a replacement of the HEC cold electronics also requires an opening of the end-cap cryostat, which is a major high-risk intervention, it is essential to accumulate more experience on the level of radiation doses in this region. Three scenarios are envisaged: first, if HEC cold electronics needs replacement, the large cold cryostat cover will be opened and then also FCal will be replaced by a new cold sFCal; second, if HEC is fine, but the FCal lost performance, either replacement with a new sFCal or add a small warm calorimeter, MiniFCal in front of the present one; third, if performances are good enough, leave both as they are.

Trigger.

The planned trigger upgrades for Phase-II foresee applying full granularity of calorimeter at Level-1 and improving the muon trigger coverage. Moreover, work is underway to quantify the benefits of a Level-1 track trigger (L1Track) and to evaluate alternative designs. The main design challenge is to reduce the bandwidth of data coming out of the tracker, as it is unrealistic to read out the whole tracker for every bunch crossing. The architecture that is currently preferred is an region of interest-seeded L1Track, fitting into a two step hardware trigger.

6 Conclusions

A coherent overall upgrade program for ATLAS from Phase-0 through Phase-II has being planned to allow ATLAS to fully exploit the LHC energy and instantaneous luminosity at up to 5-7 times the design one. The planned approach is gradual and accommodates flexibility based on the experience and indication from physics results.

References

[1] ATLAS Collaboration, The ATLAS Experiment at the CERN Large Hadron Collider, J. Instr. 3 (2008) S08003.

[2] L. Evans and P. Bryant, LHC Machine, J. Instr. 3 (2008) S08001.

[3] ATLAS collaboration, Insertable B-Layer, Technical Design Report, CERN/LHCC-2010-013

[4] ATLAS collaboration, Letter of Intent for the Phase-I Upgrade of the ATLAS Experiment, CERN/LHCC-2011-012, LHCC-I-020

[5] M.S. Neubauer, A Fast Hardware Tracker for the ATLAS Trigger System, ATL-DAQ-PROC-2011-023, arXiv:1110.1910v1 [hep-ex]

The ALICE Upgrade Program

Thomas Peitzmann[1] for the ALICE collaboration

[1]Nikhef Amsterdam and Utrecht University, The Netherlands.

DOI: `http://dx.doi.org/10.3204/DESY-PROC-2012-02/345`

While groundbreaking measurements on the properties of strongly interacting matter in p+p, p+A and A+A collisions at the LHC are being performed, it is clear that many important questions in heavy-ion physics will remain unanswered in this first phase of beam times up to 2017. The ALICE is setting up a program of detector upgrades to be installed in the LHC shutdown planned for 2017/18, to address the new scientific challenges. We will discuss examples of the scientific frontiers and will present the corresponding upgrade projects under study for the ALICE experiment.

1 Introduction: the physics frontiers for ALICE

In the first years of operation ALICE has demonstrated its excellent capabilities to measure high-energy nuclear collisions at the LHC, delivering exciting results on *elliptic flow*, which appears to be even larger than at RHIC [1], strong *quenching* of high momentum hadrons including first measurements using *identified open charm* mesons [2] and intriguing results on the centrality dependence of charmonium production [3], to just name a few examples. Further data taking up to 2017 will improve the understanding of heavy-ion collisions significantly and will very likely yield comprehensive results on many experimental probes, as e.g. the details of anisotropic flow of light hadrons, inclusive momentum spectra of heavy flavor mesons including their nuclear modification, or the global features of jets in nuclear collisions, all-in-all the baseline program of the ALICE experiment.

Still, crucial measurements will not be possible. For illustration let us consider the study of collective motion of charm. While the measurement of spectra of open charm mesons is challenging, it has already been shown to be feasible, and a further increase in statistics to $1\,\mathrm{nb}^{-1}$ should allow precision measurements of the most abundant D mesons. However, anisotropic flow studies generally require an order of magnitude higher statistics, thus calling for $\approx 10\,\mathrm{nb}^{-1}$ in Pb+Pb collisions. In addition, it is known from light hadrons, that significant differences essential for theoretical understanding of collective flow are observed between mesons and baryons. This requires a measurement of charmed baryons, as e.g. the Λ_c. Furthermore, it is crucial for studies of equilibration properties to cover the lowest transverse momenta possible. Both, the measurement of the Λ_c, and a significant measurement at very low p_T will profit enormously from an improved background rejection and secondary vertex resolution of the tracking detectors. Similar arguments hold for other important physics signals of the quark-gluon plasma, that will not be accessible with the current apparatus and the available integrated luminosity up to the long shutdown in 2017/18. Overall, an upgraded ALICE setup at high luminosity should allow

1. precision studies of primary charm (open and hidden) including flow and correlations,
2. measurements of low mass lepton pairs and thermal photons,
3. studies of jet thermalization via gamma-jet and jet-jet correlations including particle ID, and
4. the search for heavy nuclear states.

In this context, ALICE is preparing an upgrade program to enhance the rate capabilities of the experiment to allow an inspection of Pb+Pb collisions at an interaction rate of 50 kHz and of p+p collisions at a rate adequate for reference measurements, and to develop and implement a significantly improved inner tracking system (ITS).

Other new detectors are being investigated to possibly further enhance the measurement capabilities for the signals mentioned above. Additionally, with an appropriate detector at large rapidity an opportunity arises for measurements, where the influence of small-x partons is more and more important. This is the region, where effects of gluon saturation [4] should be most prominent. Signals consistent with gluon saturation have been observed at RHIC [5], but the interpretation is hampered by the very limited kinematical reach. The larger beam energy of the LHC will allow us to enter a new physics regime with access to much smaller values of x and a larger phase space for saturation due to the expected larger saturation scale.

2 ALICE rate capabilities and the upgraded ITS

Within the current ALICE apparatus, the TPC with its long drift time is limiting the rate capabilities. Using the multi-wire readout chambers, a gated operation (at a maximum of 3.5 kHz) is necessary to limit ion feedback to the drift volume, which would otherwise lead to intolerable space-charge distortions. To be able to inspect a significantly higher interaction rate, new readout chambers based on triple-GEMs will be developed. These would be continuously read out (no gating) and should have small enough ion feedback to allow an operation at 50 kHz interaction rate. In a pipelined readout data would be shipped from the TPC front-end at 10 MHz for later inspection in a high level trigger system (HLT). This will be a major challenge to the DAQ as a maximum bandwidth of $\approx$ 60 Tbit/s will be required. R&D on the GEM readout chambers is ongoing with an emphasis on achieving the projected low ion feedback and in particular on demonstrating the necessary stability in a high multiplicity/high rate environment.

Such a system would also be ready to work with a significantly higher interaction rate for p+p reactions, which might be necessary to accumulate sufficient signals for reference measurements. The new ITS will be developed according to the rate specifications. The readout electronics of all existing detector systems will be modified to accommodate the rate capabilities. Some systems, like e.g. the TRD will likely share the pipelined electronics with the TPC, other detectors, e.g. the electromagnetic calorimeter (EMCal), might preferably be readout on L1 triggers provide by a hardware trigger unit.

A completely new Inner Tracking System (ITS) will be developed. The most important features of the new design will be:

- A decrease of the radial distance of the first layer to the beam to 22 mm (from 39 mm),
- a reduction of the layer thickness possibly down to 50 μm (from 350 μm), and

- a higher granularity with pixel sizes as small as 20x20 μm^2.

Two detector options are currently under investigation: a combination of the three inner layers consisting of pixel detectors (either hybrid silicon pixel detectors or monolithic active pixel sensors) with four outer layers of silicon strip detectors, or alternatively all seven layers implemented as pixel detectors. Independent of the specific design, the new ITS will improve the secondary vertex resolution by a factor of ≈ 3 and allow measurements down to much lower values of p_T. Furthermore the high efficiency and low contamination of the new ITS should allow for enhanced level 2 trigger capabilities. Examples of the estimated performance of the upgraded ITS are shown in Fig. 1: On the left the considerable improvement in the significance for the D^0 measurement, on the right the achievable statistical uncertainty on the Λ_c/D^0 ratio, which wouldn't be measurable with the current ITS.

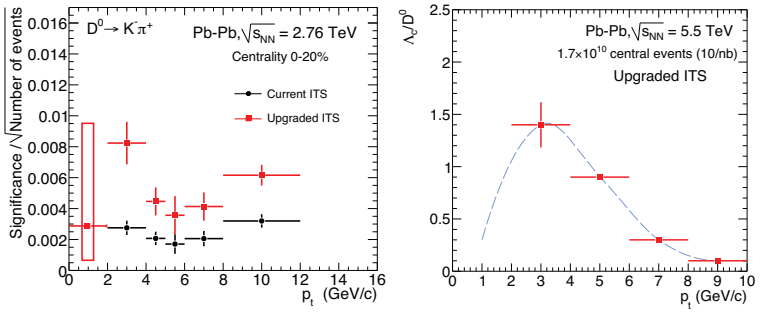

Figure 1: Left: Comparison of the significance for the D^0 obtained for the current and the upgraded ITS as a function of p_T in central Pb+Pb collisions. Right: Estimated statistical uncertainty on the measurement of the Λ_c/D^0 ratio using $1.7 \cdot 10^{10}$ central Pb+Pb collisions.

3 Additional Detector Upgrades

A number of additional upgrades further enhancing the ALICE detector setup is currently under study. The Muon Forward Tracker (MFT), adding tracking in front of the muon absorber, would allow us to reconstruct possible secondary vertices of muon tracks. This would remove the largest limitation of the current forward muon measurements, improving the performance for low mass dileptons and enabling the identification of J/ψ from B decays. The MFT would use silicon tracking with technologies very similar to those considered for the ITS upgrade.

The VHMPID[1], a new RICH detector, should be able to identify hadrons on a track-by-track basis up to $p_T = 25\,\mathrm{GeV}/c$. The detector would be placed in front of (part of) the electromagnetic calorimeter to allow efficient hadron identification in jets. It would consist of a focusing RICH with a pressurized gaseous C_4F_{10} radiator of ≈ 50 cm length, using spherical mirrors, a CsI-based photon detector and front-end electronics based on the Gassiplex chip.

An obvious candidate for forward measurement with the generally higher momenta of particles in the lab system is an electromagnetic calorimeter with its intrinsically better resolution at

[1]Very High Momentum Particle ID

higher energies and the possibility to identify photons and neutral hadrons. A possible location of such a detector would be on the A-side (opposite the Muon Spectrometer) at a distance of $\approx 3.5\,\mathrm{m}$. While the demands on energy resolution are moderate at this location, the small opening angle of neutral pion decays and the overall large particle density in Pb+Pb collisions will require good position resolution and two-particle separation power. To achieve this, the Molière radius of the material should be small and the granularity of the signal readout high. The favorite design for the Forward Calorimeter (FoCal) would use W ($R_M = 9\,\mathrm{mm}$) as absorber and Si-sensors as active material. This could provide a granularity $< 1\,\mathrm{mm}^2$ resulting in superior performance for γ/π^0 discrimination and high particle density measurements compared to existing calorimeters. As sensor technologies, conventional pad/pixel sensors with separate readout and monolithic pixels are being investigated. Fig. 2 shows the kinematic reach in x and Q^2 for different detectors at the LHC (assuming LO kinematics). With a direct photon measurement, FoCal would provide significant coverage for small x and a range of Q^2, which is crucial for measurements relevant for gluon saturation, but is not yet covered by existing experiments.

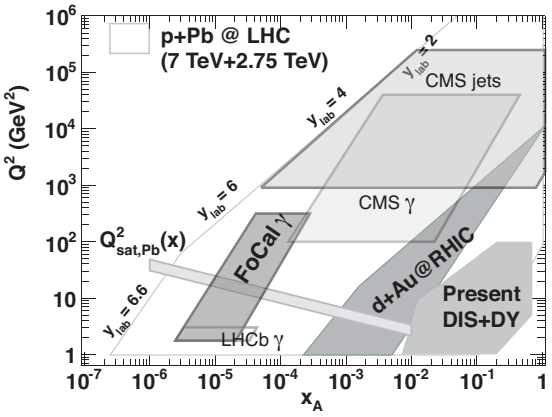

Figure 2: Kinematic coverage in Q^2 and Bjorken-x. Shown are regions where information is available from earlier measurements (DIS, Drell-Yan, and d+A at RHIC) [6], as well as estimates for existing LHC detectors and the ALICE FoCal upgrade.

References

[1] K. Aamodt et al. (ALICE), Phys. Rev. Lett. 105 (2010) 252302.

[2] B. Abelev et al. (ALICE), submitted to JHEP (2012), preprint arXiv:1203.2160

[3] B. Abelev et al. (ALICE), submitted to Phys. Rev. Lett. (2012), preprint arXiv:1202.1383

[4] L.V. Gribov, E.M. Levin, and M.G. Ryskin, Phys. Rept. 100 (1983) 1; A.H. Mueller and J.-W. Qiu, Nucl. Phys. B268 (1986) 427; L.D McLerran and R. Venugopalan, Phys. Rev. D50 (1994) 2225; Phys. Rev. D49 (1994) 3352.

[5] I. Arsene et al. (BRAHMS), Phys. Rev. Lett. 93 (2004) 242303; J. Adams et al. (STAR), Phys. Rev. Lett. 97 (2006) 152302.

[6] C.A. Salgado, J. Phys. G 38 (2011) 124036.

The LHCb upgrade

Renaud Le Gac

CPPM, Aix-Marseille Université, CNRS/IN2P3, Marseille, France

DOI: http://dx.doi.org/10.3204/DESY-PROC-2012-02/150

The LHCb experiment is running at the Large Hadron Collider to study *CP* violation and rare decays in the beauty and charm sectors. The motivation and the strategy of the upgrade envisaged for the long shutdown LS2 (2018) is presented with the expected performance for an integrated luminosity of 50 fb^{-1}.

1 LHCb

Studies of *CP* violation and more generally flavor changing neutral currents were essential in establishing the Standard Model (SM), as the theory describing the *CP* violation observed in the laboratory. Today, they appear as a powerful tool to reveal processes beyond the SM and to understand their nature. In this context, LHCb will play a key role.

The LHCb detector [1], shown in Fig. 1, is a single-arm forward spectrometer covering the forward region of the *pp* interaction. The detector geometry is driven by the kinematics of the $b\bar{b}$ pair production at the LHC energy where both b and $\bar{b}$ quarks mainly fly in the forward or backward direction.

The interaction point is surrounded by a silicon vertex detector (VELO). It measures precisely the position of primary and secondary vertices as well as impact parameters. The tracking system is composed of a magnet, deflecting particles in the horizontal plane, and two groups of tracking stations: the TT stations before the magnet and the T station after. On both sides of the tracking system, Ring Imaging Cerenkov counters (RICH) are used to identify charged particles. Further downstream, an electromagnetic calorimeter (ECAL) is used for photon detection and electron identification, followed by a hadronic calorimeter (HCAL) and a muon detector (M1- M5). The latter is composed of five stations interleaved with iron shield.

During 2011 both the LHC machine and the LHCb detector performed superbly, allowing LHCb to accumulate 1.1 fb^{-1} of $\sqrt{s} = 7$ TeV *pp* collisions that is available for physics analysis. The detector was running at an instantaneous luminosity of about 3.5×10^{32} cm^{-2} s^{-1}, constant during the fill duration, and with a number of *pp* interactions per crossing of ~ 1.4. The values of these running parameters are above the design values by a factor 1.8 and 3.5 respectively.

LHCb is expected to collect 6.5 fb^{-1} in 2018 at different centre of mass energies varying between $\sqrt{s} = 7$ and 13 TeV.

2 Performance in 2018

Among many observables accessible to LHCb, we will only discuss four key measurements selected for their potential to reveal physics beyond the SM:

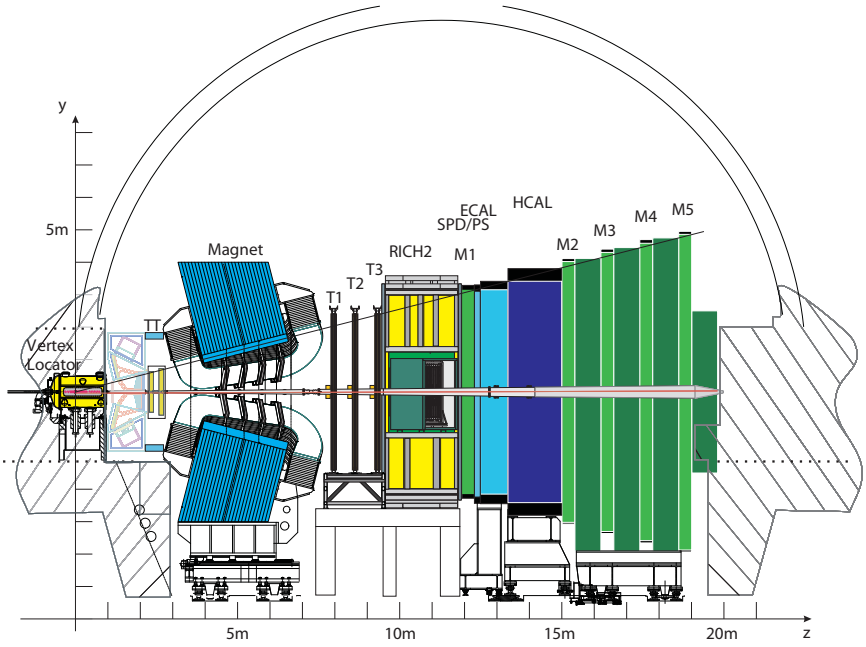

Figure 1: Vertical view of the LHCb detector.

- the branching ratio of the $B_s^0 \to \mu^+\mu^-$ probing new masses and new couplings,
- the weak phase $\phi_s \sim 2 \times \arg|V_{ts}|$ in the $B_s^0 \to J/\psi\,\phi$ decay, which probes new phases,
- the zero-crossing point (s_0) of the forward backward asymmetry $A_{\rm FB}(B^0 \to K^{*0}\mu^+\mu^-)$, which probes the Lorentz structure of the new coupling.
- the weak phase $\gamma \sim \arg|V_{ub}|$ in B^0 and B_s^0 decays to DK mediated by tree amplitudes since it is a reference measurement, not affected by new physics.

Observable	Sensitivity	SM prediction
$\mathrm{Br}(B_s^0 \to \mu^+\mu^-)$	0.5×10^{-9}	$(3.2 \pm 0.2) \times 10^{-9}$ [2]
ϕ_s	0.025 rad	(0.036 ± 0.002) rad [3]
$s_0 A_{\rm FB}(B^0 \to K^{*0}\mu^+\mu^-)$	6% of the SM value	4.36 GeV^2 [4]
γ (tree amplitude)	4 $^\circ$	$(67.1 \pm 4.3)^\circ$ [3]

Table 1: LHCb Sensitivity in 2018 [5]

.

The summary of the expected sensitivity in 2018 is given in Table 2 assuming a detector performance as achieved during 2011 data taking [5].

3 The LHCb detector upgrade

The aim of the LHCb upgrade is to run at $\mathcal{L} = 1 \times 10^{33}$ cm^{-2} s^{-1} with a fully flexible software trigger running at a readout rate of 40 MHz [6]. This increases the annual signal yields by a factor around ten for muonic B decays and twenty or more for heavy-flavour decays to hadronic final states, as compared to those obtained by LHCb in 2011. The upgraded experiment will collect a total sample of 50 fb^{-1}. For reason of flexibility, and to allow for possible evolutions of the trigger, we have decided to design those dectectors that need replacement such that they can substain a lumnosity of $\mathcal{L} = 2 \times 10^{33}$ cm^{-2} s^{-1}.

The challenge of this update is related to the number of pp interactions per crossing. The average number of interactions per crossing is about 2.3 at $\mathcal{L} = 1 \times 10^{33}$ cm^{-2} s^{-1} and reaches more than 4 interactions per crossing at 2×10^{33} cm^{-2} s^{-1}. In the latter case, all crossings have at least one interaction. These extreme conditions put heavy requirements on the tracking as well as on the trigger algorithms.

3.1 New trigger strategy

The current LHCb trigger contains two stages, the Level-0 (L0) and the High Level Trigger (HLT). The L0 reduces the rate from 40 MHz down to 1 MHz. It is based on custom electronics receiving dedicated information from the calorimeters and from the muon detector. It looks for lepton and hadron candidates with a high transverse momentum.

The HLT trigger reduces the rate down to a few kHz. The HLT is a software trigger running on a dedicated CPU farm and receiving the full detector information at 1 MHz. By running tracking and vertexing algorithms it selects leptons and hadrons with a high transverse momentum as well as a high impact parameters. More elaborate algorithms, close to the off-line selections, are then applied to select inclusive or exclusive heavy-quark decays.

The L0 saturates for hadronic channels when the luminosity increases [6]. At high luminosity we cannot rely only on the transverse momentum cut for efficient triggering. A software based trigger, however, allows use of many discriminants including track impact parameters and combinations of different criteria.

The more flexible way to trigger at high luminosity is to readout the whole detector at 40 MHz instead of 1 MHz and to select interesting events in the HLT.

3.2 Upgrading the tracking system

The VELO is a silicon strip detector with r and ϕ geometry. It will be replaced by either a pixel or a strip detector. The pixel version provides a very low occupancy for each channel, reducing the combinatorial for the tracking algorithm. The base line is a modified version of the TimePix readout chip [7] with a pixel size of 55×55 μm^2.

The TT station is a silicon-strip detector. It will be replaced by the same technology with an enlarge acceptance and an improved granularity.

The T stations are composed of an OT with straw tube detectors and an IT with silicon-strip detectors to cover the high occupancy area near the beam pipe. To account for the higher occupancy due to the increase in luminosity, we are investigating two options, a large area silicon-strip IT completed by OT straw tubes, or a Central Tracker made from scintillating fibres read by silicon photomultipliers.

3.3 Upgrading the particles identification

The RICH photon detector is an HPD with the readout frequency limited to 1 MHz. The replacement candidate is a multi-anode photomultiplier which can be readout at 40 MHz. The front-end electronics of the calorimeters will be replaced while the muon systems will almost remain unchanged.

4 Expected performance

The estimated sensitivities are given in Table 4 for an integrated luminosity of 50 fb^{-1}, taking into account all necessary trigger improvements [5].

Observable	Sensitivity	Theory uncertainty
$\text{Br}(B_s^0 \to \mu^+\mu^-)$	0.15×10^{-9}	0.3×10^{-9}
ϕ_s	0.008 rad	~ 0.003
$s_0 A_{\text{FB}}(B^0 \to K^{*0}\mu^+\mu^-)$	2% of the SM value	7%
γ (tree amplitude)	0.9 °	negligible

Table 2: LHCb Sensitivity with an upgraded detector and $\int \mathcal{L} = 50$ fb^{-1} [5].

Many more observables will be accessible with high statistics, like the measurement of ϕ_s in the B_s^0 decay to $\phi\phi$, the measurement of γ in decays mediated by loop amplitudes, or the fraction of longitudinal K^{*0} polarization, F_{L} in $B^0 \to K^{*0}\mu^+\mu^-$.

It must be emphasised that the upgraded experiment will have exciting opportunities to perform studies in the lepton flavour physics, electroweak physics, exotic search and QCD sectors.

5 Conclusions

The performance of the current detector and the purity of the samples already accumulated gives confidence that measurements of very hight sensitivity can be achieved with the upgraded LHCb detector. A challenging upgrade is under preparation, aiming at an integrated luminosity of 50 fb^{-1}. The detector TDRs will be published in 2013.

References

[1] LHCb Collaboration, A. A. Alves *et al.*, JINST 3 (2008) S08005.

[2] A. J. Buras *et al.*, JHEP 1010 (2010) 009.

[3] J. Charles *et al.*, Eur. Phys. J C41 (2005) 1. Updated results and plots available at http://ckmfitter.in2p3.fr.

[4] M. Beneje *et al.*, Eur. Phys. J. C41 (2005) 173.

[5] LHCb Collaboration, I. Bediaga *et al.*, Framework TDR for the LHCb upgrade, CERN-LHCC-2012-007

[6] LHCb Collaboration, R. Aaij *et al.*, Letter of Intend for the LHCb Upgrade, CERN-LHCC-2011-001

[7] Medipix web site (http://medipix.web.cern.ch/MEDIPIX/).

Neutrino Deep Inelastic Scattering with the MINERνA Experiment

Joel Mousseau on behalf of the MINERνA Collaboration*

University of Florida, 32611 Gainesville, FL USA

DOI: http://dx.doi.org/10.3204/DESY-PROC-2012-02/348

The MINERνA experiment, located in the NuMI beam at Fermilab, is in a position to significantly add to the world knowledge of DIS. Current neutrino DIS data contains poorly understood nuclear effects. In order to investigate these nuclear effects, MINERνA has installed nuclear targets of C, Fe and Pb in the same beam to measure the Fe/C and Pb/C ratios of DIS cross sections. While many uncertainties due to neutrino flux will cancel out in these ratios, MINERνA has developed three independent studies to better measure and constrain neutrino flux for total cross section measurements. MINERνA has begun a charged current inclusive neutrino analysis, which will serve as a basis as a more complete DIS analysis.

1 Motivation

Data from neutrino deep inelastic scattering (DIS) experiments are very helpful in forming a complete set of parton distribution functions, or pdfs. Neutrino DIS measurements probe a complementary set of quark flavors from those probed in charged lepton DIS interactions. Unfortunately, anomalies in current charged lepton and neutrino DIS datasets prevent the creation of global pdfs. For example, recent analysis from CTEQ suggests the nuclear effects in neutrino-nuclear deep inelastic scattering seen by the NuTeV experiment may be quite different in magnitude and shape from charged lepton DIS [1]. However, the NuTeV result is a statistics limited sample, and only engaged one type of nucleus. High statistics, multi-Z neutrino DIS measurements are needed to resolve this apparent discrepancy, paving the way for the full characterization of pdfs. MINERνA will provide these high statistic neutrino DIS measurements, across a wide range of targets.

2 Beamline Description and Flux Measurement

The NuMI neutrino beam, located at Fermi National Accelerator Laboratory in Batavia, IL, is one of the world's most intense source of accelerator neutrinos. The two experiments located in the NuMI beam line are MINERνA and MINOS. NuMI produces neutrinos by colliding 120 GeV protons with a thin graphite target. Two magnetic horns are used to sign-select positive or negative mesons from the p-C collisions. The horns and target are mounted on rails,

*http://minerva.fnal.gov/

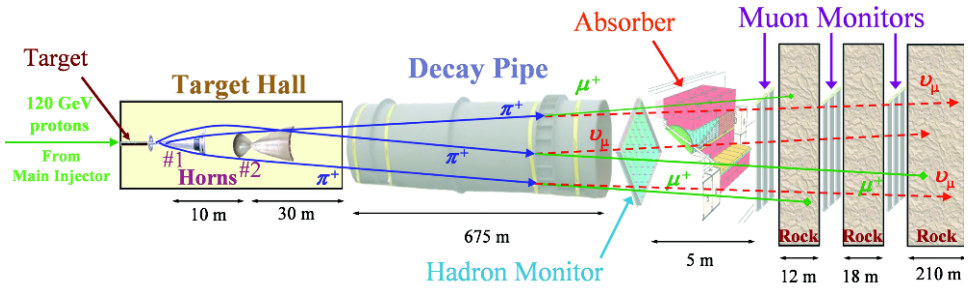

Figure 1: Diagram of the MINERνA beamline, showing the muon monitors and moveable magnetic horns.

allowing the experiments to select varying momentum ranges of the resulting mesons and their daughter neutrinos. The mesons are allowed to decay into ν (positive mesons) and $\overline{\nu}$ (negative mesons) in the decay pipe. The decay pipe terminates in a hadron absorber, allowing only muons and neutrinos to continue toward the detectors. The remaining muons are stopped by 240 m of rock located between the hadron absorber and the MINERνA detector hall.

Measuring the neutrino flux is vitally important for all of MINERνA's physics goals. The largest flux uncertainty arises from uncertainties in hadron production models of p-C collisions in the NuMI target. External hadron production data is used to reduce this uncertainty. Hadron production data from the NA49 experiment is used to re-weight the MINERνA Monte Carlo depending on the parent meson of the neutrino. The NA49 experiment used a similarly sized target and a proton beam of similar energy as NuMI. However, there is a proposal for MINERνA to conduct a dedicated hadron production experiment using the exact beam energy and target as NuMI. This work would be carried out with the SHINE collaboration at CERN.

MINERνA takes dedicated special runs with varying target positions and horn currents to constrain the neutrino flux. The resulting spectrum of neutrino events in the MINERνA main detector is used to fit a parametrized Monte Carlo of hadron production in the NuMI target. This procedure is repeated using data from the muon monitors interspersed in the 240 m of rock between the end of the decay pipe and the MINERνA detector hall. This gives the MINERνA experiment three handles on the measurement and constraint of the neutrino flux.

3 Detector and Performance

The MINERνA detector consists of a fine-grained scintillating tracking detector with position resolution of 3.00 mm. This design allows for excellent capability in reconstructing muons from DIS events. The tracking detector is followed by electromagnetic and hadron calorimeters with sufficient mass to contain final state hadron showers. Upstream of the tracker region are solid nuclear targets of graphite, iron and lead. In addition, MINERνA has installed a cryogenic liquid helium target as well as a liquid water target. The ensemble of nuclear targets exposed to the same neutrino beam will allow MINERνA to make the world's first systematic measurement of nuclear effects in neutrino scattering across a wide range of Z.

A DIS analysis in MINERνA will rely on accurate measurements of muon energy and angle, as well as final state hadron energy. Muon reconstruction in MINERνA currently relies on using the MINOS near detector to measure the final state energy and momentum of muons exiting

MINERνA. The final state muon track is matched to a track in MINERνA. The efficiency of this process is approximately 93%. Additional energy is added to the muon based on the material in the detector, until a production energy and angle is determined.

Hadronic energy in MINERνA is computed via calorimetry. Visible energy deposited in the detector is divided into muon and recoil energy. The visible recoil energy is weighted depending on the amount of passive material proximate to the event. The resolution of this process is determined using Monte Carlo. Energy deposited in the detector is compared to generated neutrino energy for neutral current events. This process determines the resolution of the calorimetric measurement for each bin of generated energy. The recoil energy is then fitted to a standard calorimetry resolution function (see Figure 2). Hadronic reconstruction in MINERνA will also be cross calibrated using data from a dedicated test beam experiment.

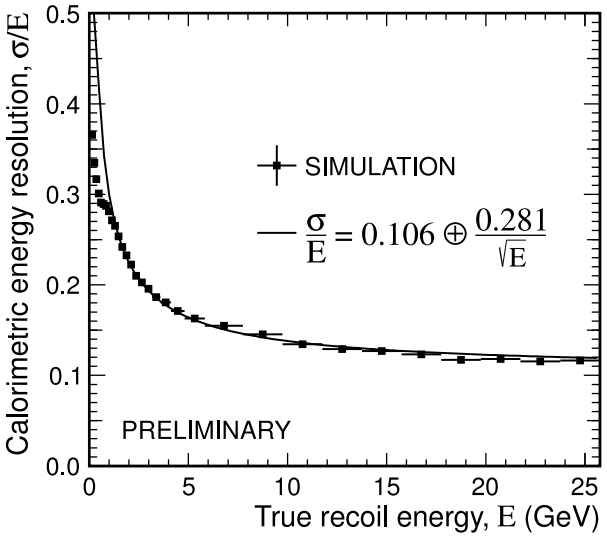

Figure 2: Calorimetric energy resolution vs. true recoil energy. The solid curve is the parametrized fit to the points.

4 Charged-Current Inclusive Analysis

The first step in a full DIS analysis is a charged current inclusive analysis. In this analysis, neutrino events are selected based on the location of the event vertex in the tracker region of the detector. The vertex must be inside a fiducial area of a 85 cm apothem hexagon. Outgoing muons from this vertex are then matched to tracks in the MINOS near detector, where their final state energy and momentum are measured. The number of CC inclusive events per POT recorded is plotted in Figure 3 for the neutrino exposure.

A DIS analysis will be derived from the inclusive analysis. Kinematic cuts will be placed on the events of $Q^2 > 1\,\mathrm{GeV}^2$ and $W > 2\,\mathrm{GeV}$. Events will also be restricted to the iron and lead regions of the nuclear targets. These samples will be compared to event rates in the tracker region of the detector in order to compute ratios of events. Likewise, the ratio of events from

iron to lead will be measured by dividing the iron to plastic ratio by the lead to plastic ratio. This method allows the measurement of nuclear effects independent of flux uncertainties and MINOS acceptance effects.

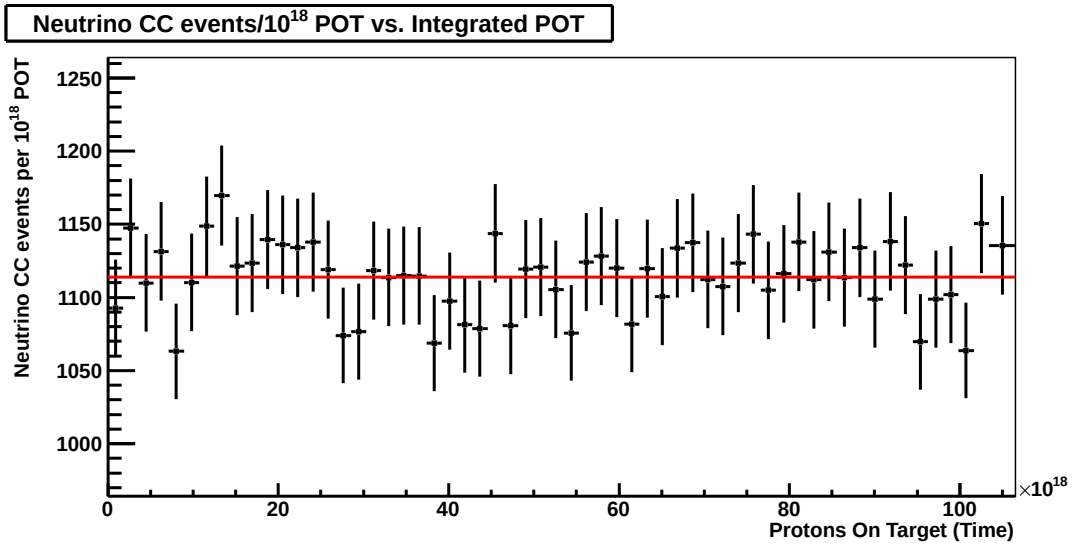

Figure 3: Number of CC Inclusive events vs. POT recorded by MINERνA.

5 Conclusion

The MINERνA collaboration has just completed collection of its low energy data set, and will soon be releasing results for a number of analyses. Using the reconstruction and flux measurements discussed in this note, a DIS analysis will be conducted in the near future based on the CC inclusive analysis. This DIS analysis will be complete but preliminary, and will lay a foundation for a more comprehensive analysis using the medium energy beam sample.

References

[1] K. Kovarik *et al.* Phys. Rev. Lett. **106** (2011) 122301, `arXiv:1012.0286 [hep-ph]`.

DIS with Neutrinos: Now and When

Jorge G. Morfín

Fermi National Accelerator Laboratory, Batavia, IL, USA

DOI: http://dx.doi.org/10.3204/DESY-PROC-2012-02/321

Neutrino scattering experiments have been studying QCD with DIS for around 40 years. An example of the more recent DIS studies of QCD with neutrinos is the NuTeV ν-Fe experiment that used the high-energy TeVatron neutrino beam. The problem the community faces in trying to study QCD with modern neutrino data is that there is no experimentally verified way to scale neutrino-nucleus (for example, Fe) results to the equivalent neutrino-nucleon values and there are now indications that nuclear effects in neutrino nucleus interactions might be different than those measured in charged-lepton nucleus scattering. To better understand this situation, the MINERνA neutrino-nucleus scattering experiment at Fermilab and eventually the much more precise neutrino factory scattering experiments will yield a more thorough A-dependent study of nuclear PDFs and these correction factors.

1 Introduction

Neutrino scattering plays an important role in extraction of fundamental parton distribution functions (PDFs) because only neutrinos can resolve the flavor of the nucleon's constituents: ν interacts with d, s, $\overline{u}$ and $\overline{c}$ while the $\overline{\nu}$ interacts with u, c, $\overline{d}$ and $\overline{s}$. The weak current's unique ability to "taste" only particular quark flavors significantly enhances the study of parton distribution functions. High-statistics measurement of the nucleon's partonic structure, using neutrinos, will complement studies with electromagnetic probes.

Large data samples, and dedicated effort to minimizing beam-related systematics will allow neutrino experiments to independently isolate all the structure functions $F_1^{\nu N}(x,Q^2)$, $F_1^{\bar{\nu} N}(x,Q^2)$, $F_2^{\nu N}(x,Q^2)$, $F_2^{\bar{\nu} N}(x,Q^2)$, $xF_3^{\nu N}(x,Q^2)$ and $xF_3^{\bar{\nu} N}(x,Q^2)$ for the first time. By taking differences and sums of these structure functions, specific parton distribution functions in a given (x,Q^2) bin can in turn be determined. With the manageable systematic uncertainties expected in current and future experiments, neutrino experiments can dramatically improve the isolation of individual PDFs by measuring the full set of ν and $\bar{\nu}$ structure functions. Extracting this full set of structure functions will rely on the y-variation of the structure function coefficients in the expression for the cross-section. In the helicity representation, for example:

$$\begin{aligned}\frac{d^2\sigma^\nu}{dxdQ^2} &= \frac{G_F^2}{2\pi x}\Big[\frac{1}{2}\left(F_2^\nu(x,Q^2)+xF_3^\nu(x,Q^2)\right)+ \\ &\quad \frac{(1-y)^2}{2}\left(F_2^\nu(x,Q^2)-xF_3^\nu(x,Q^2)\right)- \\ &\quad 2y^2F_L^\nu x,Q^2)\Big]. \qquad (1)\end{aligned}$$

By analyzing the data as a function of $(1-y)^2$ in a given (x, Q^2) bin, all six structure functions can be extracted.[1]

2 Neutrino Iron Scattering Results

Due to the weak nature of the neutrino interaction, to acquire significant statistics the use of heavy nuclear targets is unavoidable. This complicates the extraction of free nucleon PDFs because corrections must be applied to the data to convert from the nucleus A to a nucleon. The results of the latest study of QCD using neutrino scattering comes from the NuTeV experiment [1]. The NuTeV experiment accumulated over 3 million ν and $\overline{\nu}$ events in the energy range of 20 to 400 GeV off a manly Fe target. The main points are that the NuTeV cross section agrees with the CCFR values (obtained using the same detector) for values of $x_{Bj} \leq 0.4$ but is systematically higher for larger values of x_{Bj} culminating at $x_{Bj} = 0.65$ where the NuTeV result is 20% higher than the CCFR result. NuTeV agrees with charged lepton data for $x_{Bj} \leq 0.5$ but there is increasing disagreement for higher values. Although NuTeV F_2 and xF_3 agree with theory for medium x, they find a different Q^2 behavior at small x and are systematically higher than theory at high x. These results can be summarized in four main questions to ask subsequent neutrino experiments:

- At high x, what is the behavior of the valence quarks as x $\rightarrow$ 1.0?
- At low W, what is happening in the transition region between resonance production and the DIS regions?
- At all x and Q^2, what is yet to be learned if we can measure all six ν and $\overline{\nu}$ structure functions to yield maximal information on the parton distribution functions?
- At all x, how do nuclear effects with incoming neutrinos differ from nuclear effects with incoming charged leptons?

This last item highlights an overriding question when trying to get a global view of structure functions from both neutrino and charged-lepton scattering data. How do we compare data off nuclear targets with data off nucleons and, the associated question, how do we scale nuclear target data to the comparable nucleon data. In most PDF analyses, the nuclear correction factors were taken from $\ell^{\pm}$-nucleus scattering and used for both charged-lepton and neutrino scattering. Recent studies by a CTEQ-Grenoble-Karlsruhe collaboration have shown that there my indeed be a difference between the charged-lepton and neutrino correction factors.

The data from the high-statistics ν-DIS experiment, NuTeV summarized above, was used to perform a dedicated PDF fit to neutrino–iron data.[2] The methodology for this fit is parallel to that of the previous global analysis,[3] *but* with the difference that only Fe data has been used and no nuclear corrections have been applied to the analyzed data; hence, the resulting PDFs are for a proton in an iron nucleus - nuclear parton distribution functions.

By comparing these iron PDFs with the free-proton PDFs (appropriately scaled) a neutrino-specific heavy target nuclear correction factor R can be obtained which should be applied to relate these two quantities. The nuclear correction factors for $F_2^{\nu Fe}$ and $F_2^{\bar{\nu} Fe}$ at $Q^2 = 5$ GeV^2 and 20 GeV^2 derived in this analysis and labeled A2 are shown in Fig. 1.

[1] Note that for this type of parton distribution function study, anti-neutrino running will be essential.

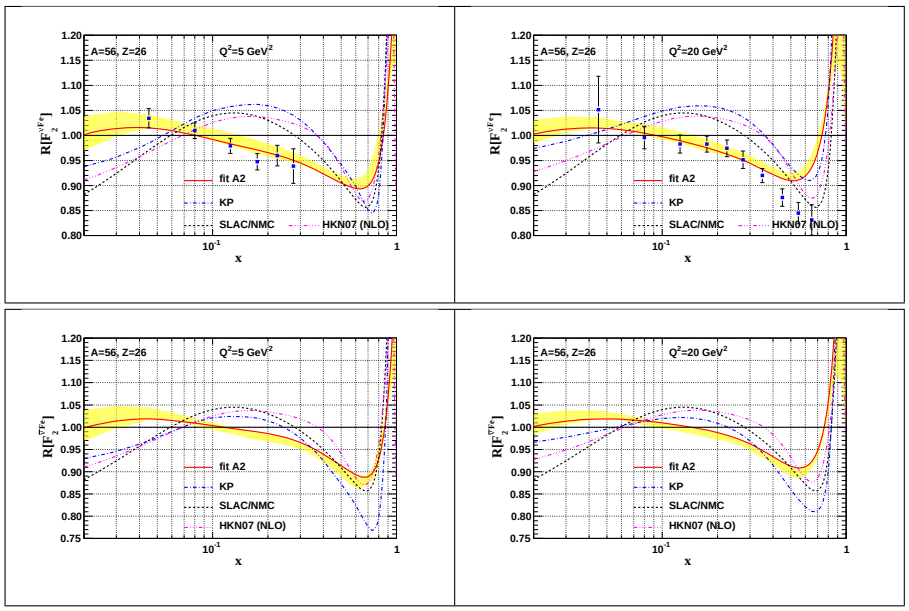

Figure 1: Nuclear correction factor R for the structure function F_2 in neutrino and anti-neutrino scattering from Fe for $Q^2 = \{5, 20\}\,\mathrm{GeV}^2$. The solid curve shows the result of the nCTEQ analysis of NuTeV data; the uncertainty from the fit is represented by the shaded (yellow) band. For comparison the correction factor from HKN07 (dashed-dotted line),[4] and the SLAC/NMC parametrization (dashed line) are shown.

The SLAC/NMC curve in the figures has been obtained from an A and Q^2-independent parameterization of calcium and iron charged–lepton DIS data.[3] Although the results of this analysis have general features in common with the SLAC/NMC (charged-lepton) parameterization, the magnitude of the effects and the x-region where they apply are quite different. The present results are noticeably flatter than the SLAC/NMC curves, especially at moderate-x where the differences are significant. The general trend is that the anti-shadowing region is shifted to smaller x values, and any turn-over at low x is minimal given the PDF uncertainties. More specifically, there is no indication of "shadowing" in the NuTeV neutrino results,particularly at low-Q^2 In general, these plots suggest that the size of the nuclear corrections extracted from the NuTeV data are smaller than those obtained from charged lepton scattering (SLAC/NMC).

3 Continuing the Study of DIS ν - A Interactions

To eventually be able to include neutrino-nucleus DIS scattering results in a global QCD fit, understanding the neutrino-nucleus nuclear effects is essential. The CTEQ study of the iron PDFs provides a foundation for a general investigation (involving a variable A parameter) that can address this topic. However the results from a much wider variety of nuclear targets will be needed to definitively answer this question. There is one experiment currently taking data and a future neutrino DIS experiment that will have the small statistical and systematic errors needed to measure all six of the neutrino structure functions mentioned at the beginning of this article.

3.1 The MINERνA Experiment

The MINERνA experiment [5, 6], a collaboration of elementary-particle and nuclear physicists, is performing a hight-statistics, systematic study of neutrino nucleus interactions. The overall goals of the experiment are to measure absolute exclusive cross-sections and study nuclear effects in ν - A interactions with He, C, O, Fe and Pb nuclear targets. For QCD oriented studies, they are planning systematic studies of the resonance-DIS transition region and the low Q^2 DIS region including the extraction of high-x_{Bj} parton distribution functions. The MINERνA experiment recently finished their low-E_ν exposure and will begin taking data with a higher energy beam (= higher percentage DIS events) next year. More details can be found in the contribution of Joel Mousseau to these proceedings.

3.2 A Neutrino Factory Study of DIS ν - A Interactions

The baseline design for a Neutrino Factory [7] includes the need for one or more near detectors. The near detectors must be designed to carry out measurements essential to the sensitivity of the oscillation-physics program. However, in addition, the intense neutrino beam delivered by the Neutrino Factory makes it possible to carry out a unique neutrino scattering physics program at a near detector. This program includes fundamental electroweak and QCD physics.

The unprecedented neutrino fluxes available for the Neutrino Factory program will allow the collection of a large number of inclusive neutrino charged current (CC) interactions. The combination of this substantial flux with a finely segmented near detector offers a unique opportunity to produce a range of neutrino scattering physics measurements, in addition to those needed by the long base line oscillation program.

4 Conclusions

The NuTeV ν-Fe experiment is the most recent high-statistics DIS experiment that also has produced a very detailed study of systematic errors in the form of a covariant error matrix. There are inconsistencies of the NuTeV results with other ν-nucleus experiments particularly at low- and high-x. To be able to combine these NuTeV results with other DIS experiments, a way of converting ν-Fe to ν-nucleon has to be determined. Using these results from the NuTev neutrino Fe experiment, nuclear effects of charged current deep inelastic neutrino-iron scattering were studied by the nCTEQ collaboration in the frame-work of a χ^2 analysis and a set of iron nuclear correction factors for iron structure functions were extracted. Comparing these results with correction factors for $\ell^\pm$-iron scattering it was determined that, except for very high x_{Bj}, the neutrino correction factors differ in both shape and magnitude from the correction factors for charged-lepton scattering. For the near future, the nuclear correction factors R are being measured over a wider range of A and with reduced errors by the MINERνA experiment in the NuMI beam. Further in the future, a neutrino factory with very intense and well-known neutrino beams will provide a direct comparison between nuclear targets and nucleon (liquid hydrogen and deuterium) targets.

References

[1] M. Tzanov *et al.* [NuTeV Collaboration], Phys. Rev. D **74**, 012008 (2006).

[2] As space is limited in this conference report, we refer the reader to the following for analysis details and a full set of references. I. Schienbein, J. Y. Yu, C. Keppel, J. G. Morfin, F. Olness and J. F. Owens, Phys. Rev. D **77**, 054013 (2008) [arXiv:0710.4897 [hep-ph]].

[3] J. F. Owens *et al.*, Phys. Rev. D **75**, 054030 (2007) [arXiv:hep-ph/0702159].

[4] M. Hirai, S. Kumano and T. H. Nagai, Phys. Rev. C **76**, 065207 (2007) [arXiv:0709.3038 [hep-ph]].

[5] D. Drakoulakos *et al.* [Minerva Collaboration], arXiv:hep-ex/0405002. http://minerva.fnal.gov/

[6] The MINERνA Technical Design Report, 1 December 2006, http://minerva-docdb.fnal.gov/cgi-bin/ShowDocument?docid=700

[7] S. Choubey *et al.*, **International Design Study for the Neutrino Factory, Interim Design Report**, IDS-NF-20, (2011). The chapter on the near detector written by Y. Karadzhov, R. Matev, J.G. Morfín, P. Soler, and R. Tzenov.

Future Programme of COMPASS at CERN

Gerhard K. Mallot on behalf of the COMPASS Collaboration
CERN, 1211 Genève 23, Switzerland

DOI: http://dx.doi.org/10.3204/DESY-PROC-2012-02/141

COMPASS at CERN is preparing for a new series of measurements on the nucleon structure comprising deep virtual Compton scattering and hard exclusive meson production using muon beams, as well as Drell-Yan reactions using a polarised proton target and a negative pion beam. The former will mainly constrain the generalised parton distribution H and determine the transverse size of the nucleon, while the latter measurements will provide information on transverse-momentum dependent parton distribution functions. The projected results of the programme and the necessary hardware upgrades are discussed.

1 Introduction

The COMPASS Collaboration at CERN proposed in 2010 new measurements on hadron structure [1]. The proposal was approved in December 2010 and experiments will start in 2012 with a pion/kaon polarisability measurement (not discussed here). The future programme starting 2014 after the accelerator shutdown focuses on transverse momentum dependent (TMD) distributions and generalised parton distributions (GPDs). A polarised Drell–Yan experiment will take place in 2014 and in 2015/2016 deeply virtual Compton scattering (DVCS) and hard exclusive meson production will be studied with a 160 GeV muon beam and an unpolarised hydrogen target. A pilot run for the latter experiment is planned already for late 2012. In parallel with the GPD programme, high statistics data for semi-inclusive DIS will be taken.

2 GPD programme

The GPDs are universal distributions which contain as limiting cases nucleon form factors on the one hand and parton distribution functions (PDFs) on the other. The GPDs H^f and $\widetilde{H}^f$ ($f = u, d, s, g$) describe processes where the nucleon helicity is preserved and contain as limiting cases the PDFs f_1 and g_1, respectively. Processes where the nucleon helicity is flipped are described by the GPDs E^f and $\widetilde{E}^f$ for which no such limiting case exists. GPDs correlate transverse spatial and longitudinal momentum and thus provide a kind of 'nucleon tomography'. They depend on four variables x, ξ, t, and Q^2. The cleanest process to assess GPDs is DVCS shown in Fig. 1, in which also the relevant momentum fractions x (not the Bjorken scaling variable) and ξ, and the momentum transfers t and Q^2 are defined.

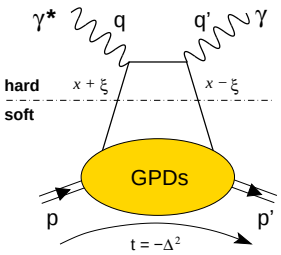

Figure 1: DVCS process.

The interest in these distributions was boosted, when X.-D. Ji showed that there is a sum rule for the total angular momentum J^f of a quark or a gluon and the corresponding GPDs [2].

The DVCS process interferes with the Bethe–Heitler (BH) process due to identical final states. The cross-section then contains five terms

$$\mathrm{d}\sigma^{\mu p\to\mu p\gamma} = \mathrm{d}\sigma^{\mathrm{BH}} + \mathrm{d}\sigma_0^{\mathrm{DVCS}} + P_\mu \mathrm{d}\Delta\sigma^{\mathrm{DVCS}} + e_\mu \Re\mathrm{e}\, I + P_\mu e_\mu \Im\mathrm{m}\, I, \tag{1}$$

where I denotes the DVCS–BH interference term. An important feature is that the BH contribution can be normalised at small x_B, where it dominates. From Eq. 1 one can build the sum $\mathcal{S}$ and difference $\mathcal{D}$ of the $\mu p \to \mu p\gamma$ cross-section for simultaneous change of lepton charge e_μ and polarisation P_μ of the incoming lepton beam (+ to − and ← to →)

$$\begin{aligned} \mathcal{D} &= \mathrm{d}\sigma^{\overleftarrow{+}} - \mathrm{d}\sigma^{\overleftarrow{-}} &&= 2(\mathrm{d}\sigma_0^{\mathrm{DVCS}} + \Re\mathrm{e}\, I) \\ \mathcal{S} &= \mathrm{d}\sigma^{\overleftarrow{+}} + \mathrm{d}\sigma^{\overleftarrow{-}} &&= 2(\mathrm{d}\sigma_0^{\mathrm{BH}} + \mathrm{d}\sigma_0^{\mathrm{DVCS}} + \Im\mathrm{m}\, I). \end{aligned} \tag{2}$$

The muon beam used at COMPASS has exactly this behaviour that negative muons have opposite polarisation than positive muons. Upon integration over the azimuthal angle ϕ the interference contribution to $\mathcal{S}$ vanishes [3] and after subtraction of the BH contribution one obtains the DVCS cross-section. This cross-section depends on the squared momentum transfer t from the initial to final nucleon (Fig. 1). At small x_B one has the relation $\langle r_\perp^2(x_B)\rangle \approx 2B(x_B)$ if the exclusive cross-section is parametrised as $\mathrm{d}\sigma/\mathrm{d}t \propto \exp(-B(x_B)|t|$. The transverse distance $r_\perp$ is measured between the struck quark and the centre of mass of the spectator system. Thus, independent of any GPD parametrisation, one obtains a measure of the transverse nucleon size as a function of x_B. Using a parametrisation of the type $B(x_B) = B_0 + 2\alpha' \log(x_0/x_B)$, one can characterise the t slope of the cross-section by the parameter α'. The projected precision of a t-slope measurement is presented in Fig. 2. A new electromagnetic calorimeter, ECAL0, will improve the precision of the measurement and enlarge the accessible range towards larger x_B. Combined with the HERA data and future JLab data a comprehensive picture of the evolution of the nucleon's transverse size with x_B will be achieved in a model-independent way. For the 2012 pilot DVCS run we project already a significant measurement combining the three central x_B bins of Fig. 2 into one large x_B.

The ϕ dependence of the difference $\mathcal{D}$, the sum $\mathcal{S}$ and the asymmetry $\mathcal{A} = \mathcal{D}/\mathcal{S}$ of the DVCS cross-sections defined in Eq. 2 allow for the extraction of quantities related to Compton form factors (CFF) which in turn depend on the GPDs. With an unpolarised target, COMPASS DVCS results will mainly provide information on the CFF $\mathcal{H}$ and thus constrain the GPD H. Results will be obtained in (x_B, Q^2) bins. An example for the projected precision in such a bin is shown in Fig. 3 for the beam charge-and-spin asymmetry $\mathcal{A}$.

Some handle on the flavour separation of GPDs may be obtained from hard exclusive meson production measured simulataneously with DVCS. Here the meson replaces the real photon. The GPD E can in principle be assessed using a transversely polarised target. Such measurements are under consideration for a later stage of the programme.

Another physics topic pursued in parallel with DVCS, is the study of spin-independent TMD distributions like the Boer–Mulders distribution and of fragmentation functions, in particular for strange quarks. Also the spin-averaged strange quark PDF needs further studies.

A major rearrangement of the spectrometer target region will be necessary for the GPD measurements. The polarised target has to be removed and a recoil proton detector, the Camera detector, will be installed. It consists of two concentric scintillator barrels of 3.6 m length and

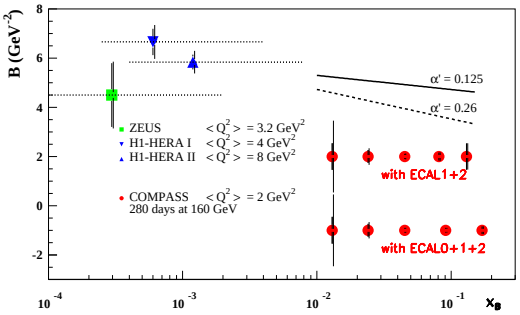

Figure 2: Projected measurements of the x_B dependence of the t-slope parameter $B(x_B)$ (red filled dots) using only ECAL1 and ECAL2 (upper row) and with an additional ECAL0 calorimeter (lower row).

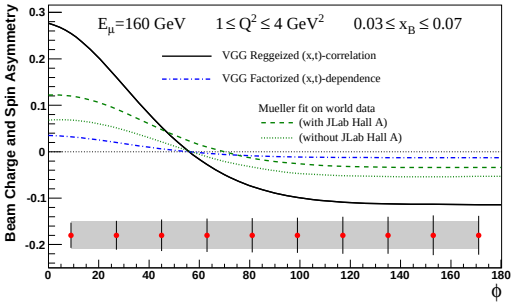

Figure 3: Projected measurements of the dependence of the beam charge-and-spin asymmetry on ϕ. compared to various models from Refs. [4, 5]

2.2 m diameter for the outer barrel. The photomultiplier signals will be digitised with 1 GHz to cope with the high rate and pile-up. Camera is essential to ensure the exclusivity of the observed reactions. It houses on the central axis a 2.5 m long liquid hydrogen target. In order to improve the acceptance of real photons, a third electromagnetic calorimeter, ECAL0, will be constructed and placed just downstream of the Camera detector. Multipixel avalanche photodiodes were chosen for the readout to avoid problems due the magnetic field of the close spectrometer magnet SM1. Furthermore the RICH photodetection will be improved.

3 Drell–Yan programme

The second approach to access transverse nucleon structure in the future COMPASS programme is via the Drell–Yan process (Fig. 4) using a 190 GeV negative pion beam impinging on a transversely polarised proton target (NH_3). The advantage of DY processes is that fragmentation functions are not involved. However, this has to be paid by a convolution of two distribution functions. The DY cross-section is given by $\sigma^{\mathrm{DY}} \propto \sum_f f_{\bar{u}|\pi^-} \otimes f'_{u|p}$, where f and f' are generic place holders of PDFs. For $\pi^- p$ scattering the process is dominated by the up quark distributions. Polarised DY experiments can study TMD distributions like the Sivers and Boer–Mulders distributions. Theory predicts that these naive T-odd TMD distributions obey a restricted universality and change sign when observed in SIDIS and DY

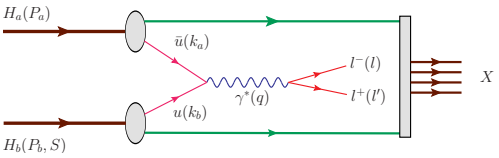

Figure 4: Sketch of the Drell–Yan process.

$$f_{1T}^{\perp}\big|_{DY} = -f_{1T}^{\perp}\big|_{DIS} \qquad \text{and} \qquad h_1^{\perp}\big|_{DY} = -h_1^{\perp}\big|_{DIS}\,. \tag{3}$$

This sign change is due to switching from final-state interaction in SIDIS to initial-state interaction in DY [6]. A violation of this prediction would imply drastic consequences on how cross-sections are calculated. This has generated wide-spread interest in a direct comparison of TMD distributions obtained from SIDIS and DY, respectively. Plans for future polarised DY

experiments exist at various laboratories, e.g. at RHIC, JPARC, GSI and at JINR. The COMPASS DY experiment is planned and approved for 2014 and primarily assess transversity h_1 and the T-odd Sivers and Boer–Mulders TMD distributions, $f_{1T}^{\perp}$ and $h_1^{\perp}$ for up quarks. For all of these COMPASS SIDIS measurements exist, showing non-vanishing asymmetries for the proton.

To avoid the J/ψ region and the region of background from charm decays, the experiments will focus on dimuon masses $4\,\text{GeV} < M_{\mu\mu} < 9\,\text{GeV}$. The azimuthal asymmetries depend on two azimuthal angles, ϕ_S of the target spin with respect to the transverse momentum of the virtual photon in the target rest frame and ϕ between the incoming hadron and outgoing lepton plane in the Collins–Soper frame, a the polar angle θ of the lepton pair (see Ref. [1]), as well as on the Feynman variable $x_F = x_\pi - x_p$. Here x_π and x_p are the momentum fractions carried by the involved quarks in the pion and proton, respectively. The projected $A_T^{\sin\phi_S}$ asymmetry measurement in the high-mass region $4\,\text{GeV} < M_{\mu\mu} < 9\,\text{GeV}$ is compared to predictions in Fig. 5 (top left). The measurement will certainly be able to answer the sign question of T-odd TMD distributions and allow for a comparison of the absolute size of the effects in SIDIS and DY. However, a determination of the shape of the Sivers TMD distribution in DY will only be possible with further measurements. The shaded grey area and the central line in Fig. 5 correspond to a calculation based on a TMD PDF fit to data [7]. The Boer–Mulders related asymmetry $A_T \cos 2\phi$ will be determined with high precision.

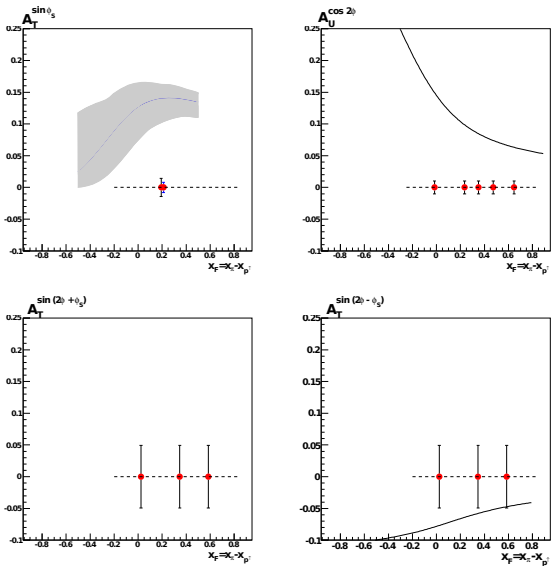

Figure 5: Projections for the asymmetries $A_T^{\sin\phi_S}$ (Sivers), $A_U^{2\cos\phi}$ (Boer–Mulders), $A_T^{\sin(2\phi+\phi_S)}$ and $A_T^{\sin(2\phi-\phi_S)}$.

As the measurement is statistics limited, optimising luminosity is mandatory. A massive hadron absorber downstream of the target reduces radiation and detector occupancy problems. Therefore the polarised target has to be moved upstream by about 3 m. The absorber consists of a tungsten core surrounded by alumina (Al_2O_3), which minimises multiple scattering. This is essential to disentangle the oppositely polarised target cells in the track reconstruction.

References

[1] COMPASS Collab., F. Gautheron *et al.*, CERN-SPSC-2010-014, SPSC-P-340, 17 May 2010.

[2] X.-D. Ji. Phys. Rev. Lett. **78** (1997) 610.

[3] A. V. Belitsky *et al.* Nucl. Phys. **B629** (2002) 323.

[4] M. Vanderhaeghen *et al.* Phys. Rev. **D60** (1999) 094017.

[5] K. Kumerički and D. Müller. Nucl. Phys. **B841** (2010) 1.

[6] J. C. Collins. Phys. Lett. **B536** (2002) 43.

[7] M. Anselmino *et al.*. In Proceedings of *II International Workshop on Transverse Polarization Phenomena in Hard Scattering Processes*, World Scientific, ed. by G. Ciullo *et al.*, April 2009, p. 138.

Precision Polarized SIDIS Experiments in Hall-A at 12 GeV JLab

Kalyan Allada[1], *Vincent Sulkosky*[2]

[1]Thomas Jefferson National Accelerator Facility, Newport News, Virginia 23606, USA
[2]Massachusetts Institute of Technology, Cambridge, Massachusetts 02139, USA

DOI: http://dx.doi.org/10.3204/DESY-PROC-2012-02/140

Single (SSA) and double spin asymmetries (DSA) in semi-inclusive DIS reactions using polarized nucleon targets provide a powerful method to probe transverse momentum dependent parton distribution functions (TMDs). The Jefferson Lab 12 GeV upgrade will provide a unique opportunity to perform precision measurements and to map out these multi-dimensional PDFs. Future plans for performing these measurements in Hall-A using the Solenoidal Large Intensity Device (SoLID) and polarized proton and ^{3}He (neutron) targets are discussed. The high luminosities from these targets and the large acceptance of the SoLID spectrometer will allow for a 4-dimensional (x, Q^2, z, P_T) mapping of SSA and DSA. These experiments will provide the most precise data to extract transversity (h_1), Sivers ($f_{1T}^{\perp}$) and Worm-gear (g_{1T} and $h_{1L}^{\perp}$) distributions of u and d-quarks and provide comprehensive information on the correlation between quark angular momentum and the nucleon's spin.

1 Introduction

In recent years, the study of transverse momentum dependent parton distribution functions (TMDs) has become one of the major goals in the investigation of nucleon spin structure. TMDs provide new and fundamental information about the structure of the nucleon by imaging its partonic structure, dynamics, and spin-orbital couplings in three-momentum space. At leading twist there are eight TMD quark distributions [1]: three of them, the unpolarized (f_1), the helicity (g_1) and the transversity (h_1) distributions are integrated over the transverse momenta of quarks, while the other five have an explicit dependence on the transverse momentum of quarks (k_T). While inclusive DIS experiments provide an access to the first two PDFs, semi-inclusive deep inelastic scattering (SIDIS) allows us to probe the other six TMDs. Of these eight TMDs, transversity (h_1), Sivers ($f_{1T}^{\perp}$), pretzelosity ($h_{1T}^{\perp}$), and g_{1T} can be accessed using a tranversely polarized target, while $h_{1L}^{\perp}$ can be accessed using a longitudinally polarized target.

The transversity distribution gives the probability of finding a transversely polarized parton inside a transversely polarized nucleon with certain longitudinal momentum fraction x and certain transverse momentum k_T. The Sivers function [2] provides the number density of unpolarized partons inside a transversely polarized proton, and it requires wave function components with nonzero orbital angular momentum and thus provides information about the correlation between the quark orbital angular momentum (OAM) and nucleon spin. Furthermore, it is a (naive) T-odd function which relies on the final state interactions (FSI) experienced by the

active quark in a SIDIS process. In contrast to $f_{1T}^{\perp}$, the functions g_{1T} and $h_{1L}^{\perp}$ are T-even, and thus do not require FSI to be nonzero. Nevertheless, they also require interference between wave function components that differ by one unit of OAM and thus require OAM to be nonzero. Finally, pretzelosity requires interference between wave function components that differ by two units of OAM (e.g. p-p or s-d interference). Combining the wealth of information from all these functions could thus be invaluable for disentangling the spin orbit correlations in the nucleon wave function, providing important information about the quark orbital angular momentum, and for imaging of the nucleon in full momentum space.

Single spin asymmetries (SSA) using SIDIS on a transversely polarized proton target were measured by both HERMES [4, 5] and COMPASS [6] collaborations. Non-zero asymmetries were observed for both Collins and Sivers moments in the π^+ channel. However, for the π^- channel the Collins asymmetry was non-zero, whereas Sivers asymmetry was small and consistent with zero within the statistical precision of these experiments. Recently, JLab measured these asymmetries on a polarized ^{3}He target and extracted Collins and Sivers asymmetry moments [7] using SSA and A_{LT} using double spin asymmetries (DSA) [8].

The target single spin asymmetry from the SIDIS reaction, in the leading twist, can be obtained by

$$\begin{aligned} A_{UT} &\equiv \frac{1}{|S_T|}\frac{Y^{\uparrow}(\phi_h,\phi_S) - Y^{\downarrow}(\phi_h,\phi_S)}{Y^{\uparrow}(\phi_h,\phi_S) + Y^{\downarrow}(\phi_h,\phi_S)} \\ &= A_{UT}^{\sin(\phi_h+\phi_S)}\sin(\phi_h+\phi_S) + A_{UT}^{\sin(\phi_h-\phi_S)}\sin(\phi_h-\phi_S) + A_{UT}^{\sin(3\phi_h-\phi_S)}\sin(3\phi_h-\phi_S) \end{aligned}$$

where ϕ_S and ϕ_h are the azimuthal angles of the produced hadron and the target spin as defined by the Trento convention [3], S_T is the transverse polarization of the target w.r.t the virtual photon direction, and $Y^{\uparrow\downarrow}(\phi_h,\phi_S)$ is the normalized yield for the up-down transverse spin direction of the target. The three terms correspond to the Collins, Sivers and pretzelosity asymmetries, respectively. Similarly, the beam-target double spin asymmetry, A_{LT}, gives access to the $\cos(\phi_h - \phi_S)$ term.

2 Proposed Experiment

The proposed experimental setup consists of the Solenoidal Large Intensity Device (SoLID) and a polarized target as shown in Fig. 1. The SoLID spectrometer has a full 2π azimuthal angular coverage, which is essential to control the systematic uncertainties in extracting various azimuthal moments from the measured asymmetries. Two SIDIS measurements using polarized ^{3}He (transverse and longitudinal) target [9, 10] and one with a transversely polarized NH_3 (proton) target were proposed [11]. The luminosity for the ^{3}He target is about 10^{36} nucleons/cm^2/s while that for NH_3 target it is 10^{35} nucleons/cm^2/s. Two different beam energies, 11 GeV and 8.8 GeV, will be used to measure the asymmetries. The lower beam energy will provide precision data on the radiative corrections along with increased Q^2 coverage.

The SoLID detector consists of two regions. The forward region with polar angle coverage of 8.5° to 16° has a total solid angle of 95 msr, and covers a momentum range from 1 GeV/c to 7 GeV/c for both electrons and pions. Tracking will be done by GEM detectors and particle identification will be provided by the combination of a gas Cerenkov, an aerogel counter, and an electromagnetic calorimeter. A thin layer of scintillator and one layer of Multi-gap Resistive Plate Chamber (MRPC) will be used for the timing information. The large angle region with

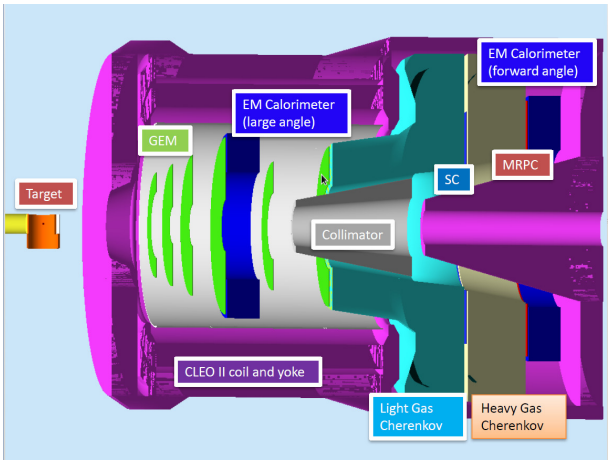

Figure 1: The experimental layout of the SoLID and polarized target in the proposed measurement. The subdetectors are labeled with colors corresponding to the detector regions.

polar angle coverage of 16° to 25° has a solid angle of 280 msr, and is mainly used for the electron detection in the momentum range of 4 to 6 GeV/c. GEMs and an electromagnetic calorimeter will be used in this region to provide accurate momentum and energy reconstruction of the scattered electron.

Figure 2 shows the projected results for the π^+ Collins asymmetry in one bin of Q^2 and z that can be obtained in 90 days with a ^{3}He target. The theoretical predictions of Collins asymmetries are from Anselmino *et al.* [12], Vogelsang and Yuan [13] and Pasquini [14]. The x-axis shows the bjorken-x, y-axis on the left side shows the P_T coverage, and y-axis on the right side shows the scale of the asymmetries. The overall kinematic coverage is as follows: P_T from 0-1.6 GeV/c, Q^2 from 1-8 (GeV/c)^2, z from 0.3-0.7, and x from 0.05-0.65. P_T and z coverage is divided into 8 bins each, and the Q^2 range is divided into 6 bins. The combined data from two beam energies will be divided into a total of 1400 bins for the SIDIS measurement with a ^{3}He target. This will allow us to study the measured asymmetries in 4 dimension (x, Q^2, z, P_T). Along with the SSA, the DSA data will allow us to measure A_{LT}, which is related to the g_{1T} distribution. Moreover, SIDIS with longitudinally polarized beam on a longitudinally polarized target will provide A_{LL} and A_{UL} data which will be used to extract g_{1L} and $h_{1L}^{\perp}$, respectively.

3 Summary

The proposed SIDIS measurements at Jefferson Lab will provide the most precise 4-D (x, Q^2, z, P_T) data of SSA and DSA on both proton and neutron targets. The combined analysis of the data from these measurements will help in extracting various TMDs for both u and d-quarks. This will also enable us to do a model independent extraction of the u and d-quark tensor charges within a 10% accuracy. Measurement of Sivers, pretzelosity and g_{1T} distribution functions will enable a comprehensive understanding of quark orbital angular momentum, its relativistic effects and spin-orbit correlations.

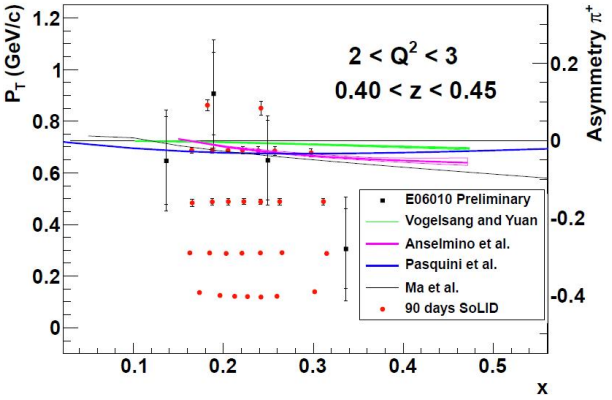

Figure 2: Projected results for π^+ Collins asymmetry in one bin of Q^2 and z. The y-axis on the left side shows P_T coverage and y-axis shows on the right side shows the scale of the asymmetry. The data from the Hall-A 6 GeV experiment (E06-010) is shown in black point with large errors.

4 Acknowledgements

This work is supported by U.S. Department of Energy. Jefferson Science Associates, LLC operates the Thomas Jefferson National Accelerator Facility under the contract DE-AC05-06OR23177.

References

[1] A. Bacchetta. *et al.* JHEP **02** 093 (2007).

[2] D. Sivers. Phys. Rev. **D41** (1990) 83.

[3] A. Bacchetta. Phys. Rev. **D70** (2004) 117504.

[4] A. Airapetian. *et al.* Phys. Rev. Lett. **94** (2005) 012002.

[5] A. Airapetian. *et al.* Phys. Lett. B **693** (2010) 11.

[6] M. Alekseev *et al.* Phys. Lett. B **692** (2010) 240.

[7] X. Qian. *et al.* Phys. Rev. Lett. **107** (2011) 072003.

[8] J. Huang. *et al.* Phys. Rev. Lett. **108** (2012) 052001.

[9] JLab proposal PR-12-10-006
`http://www.jlab.org/exp_prog/proposals/10/PR12-10-006.pdf`.

[10] JLab proposal PR-12-11-007
`http://www.jlab.org/exp_prog/PACpage/PAC37/proposals/Proposals/NewProposals/PR-11-007.pdf`.

[11] JLab proposal PR-12-11-108
`http://www.jlab.org/exp_prog/proposals/11/PR12-11-108.pdf`.

[12] M. Anselmino and A. Prokudin, *private communication.*

[13] W. Vogelsang and F. Yuan, *private communication*

[14] B. Pasquini, *private communication*

PHENIX Upgrade Plans for the Next Decade

Kieran Boyle for the PHENIX Collaboration

RIKEN BNL Research Center, Bldg. 510A, Upton, NY 11973, USA

DOI: http://dx.doi.org/10.3204/DESY-PROC-2012-02/158

Over its first twelve years, the PHENIX experiment has studied the spin structure of the proton, cold nuclear matter (CNM) in d+Au and discovered a strongly coupled quark gluon plasma in Au+Au collisions. We present the near- and long-term upgrades planned for PHENIX. The MPC-EX, a preshower for the forward calorimeter, is expected to be installed by 2014. A larger upgrade of PHENIX, envisions replacing the central arm with a compact jet detector, as well as adding a forward arm spectrometer to study the source of large single spin asymmetries in $p^{\uparrow} + p$ collisions, as well as measure Drell-Yan, to study both the proton spin structure and CNM effects in d+Au collision.

1 Introduction

During 12 years of operations, the PHENIX experiment has studied many aspects of QCD by utilizing the flexibility of RHIC, which can collide transversely and longitudinally polarized protons, an array of nuclei such as Au, Cu and U, and also have asymmetric collisions, such as d+Au and Cu+Au. Asymmetry measurements in longitudinally polarized proton collisions have significantly constrained the gluon spin contribution to the proton [1]. Unexpectedly large single spin asymmetries (SSA) have been measured in transversely polarized proton collisions at high $x_F = p_z/(\sqrt{s}/2)$ [2, 3, 4]. In Au+Au collisions, PHENIX has discovered a strongly-coupled quark-gluon plasma (sQGP) [5], and is continuing to study its properties. One of the requirements to understand the behavior of this hot, dense matter is to understand the initial state of cold nuclear matter (CNM), which has been probed in d+Au [6].

2 Completed and Near-Term Upgrades

Over the past several years, PHENIX has implemented an upgrade program to both extend and enhance our physics reach. A GEM-based Čerenkov detector, the Hadron Blind Detector, was installed in 2009-2010 to understand the background in the dielectron spectrum in Au+Au. In 2011, this was removed, and a barrel and (in 2012) endcap vertex detectors (VTX) were installed to separate charm and beauty quarks to understand how the mass of heavy quarks affects the suppression of related mesons in the sQGP.

Trigger electronics have been added to the existing muon tracker. These, along with recently installed resistive plate chambers, have extended the trigger capabilities of PHENIX so that it can record a sizable W-boson sample in longitudinally polarized $p + p$ at $\sqrt{s} = 500$ GeV. With this data, PHENIX will be able to access the poorly known sea quark helicities through a parity violating single spin asymmetry. The first results were shown at this conference [7].

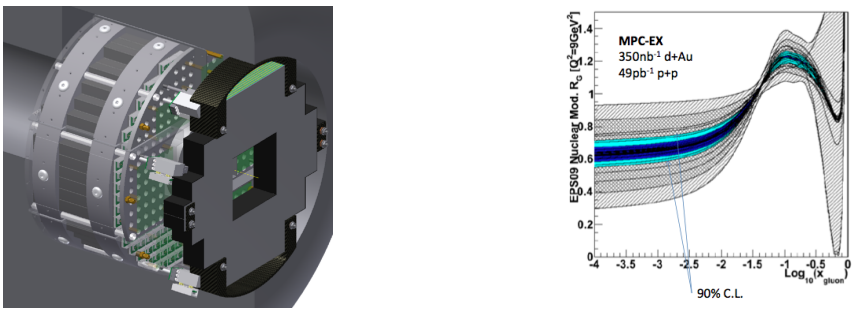

Figure 1: (Left) Drawing of MPC-EX. (Right) Nuclear modification factor for the gluon from EPS09. Grey band shows current uncertainty. Highlighted band shows uncertainty discriminating power of expected direct photon measurement from the MPC-EX based on the EPS09 best fit as input.

The final upgrade of the current PHENIX detector in this program is the MPC extention (MPC-EX). This detector (see Fig. 1), currently in the proposal stage, is a Si-W preshower which will be installed in front of an existing calorimeter, the MPC, which covers $3.0 < \eta < 3.8$. The detector is made of eight layers of Si "minipad" sensors between layers of tungsten absorber, allowing for π^0 identification separation up to 80 GeV. This then enables separation of π^0 and direct photons up to similar energies. Direct photons are primarily produced in photon-gluon Compton scattering, and, in d+Au, in the deuteron-going direction can probe the low x gluon distribution in the target Au nuclei. Measurements of the nuclear suppression factor, R_{dAu}, with identified π^0s and direct photons will be used to study gluon saturation in nuclei at low x, providing strong constraints on gluon parton distribution functions (PDF) in nuclei, as seen in Fig. 1. Assuming the best fit result from the EPS nuclear PDF [8], the expected sensitivity is shown in the highlighted region, as compared to the current uncertainty (larger shaded region).

3 sPHENIX

Over the last decade, PHENIX has answered many of the questions for which it was designed. However, many of these answers have generated further questions, such as what the source of the large transverse SSA is, or how the sQGP affects quarks traversing it. In order to fully address these and other important questions, PHENIX is planning a significant upgrade of it's detector capabilities for the latter half of this decade. This upgrade, named sPHENIX, consists of new azimuthally symmetric barrel covering $|\eta| < 1$ for measuring jet asymmetries in nuclei collisions, and a forward spectrometer ($1 < \eta < 4$) for measuring electrons and hadrons/jets in d+Au and transversely polarized $p + p$. The detector is also being designed with a possible upgrade path to an electron-ion collider detector at eRHIC [9].

3.1 Understanding the sQGP: Central Barrel Upgrade

Now that we know an sQGP is produced in heavy nuclei collisions, it is important to understand its behavior. By studying jets produced in hard scattering, and the energy asymmetries in back-to-back jets, we can learn how a colored particle is effected by the medium produced, as well

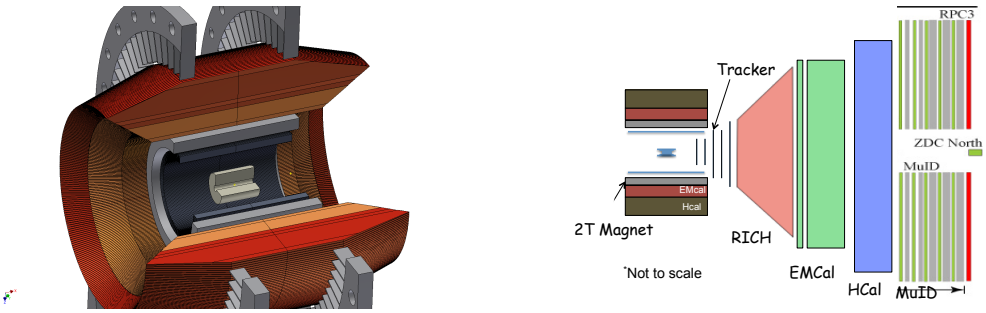

Figure 2: (Left) Engineering drawing of central barrel in sPHENIX. (Right) Conceptual design plan for sPHENIX forward upgrade.

as how the medium itself changes as it expands. In order to measure jets, one must fully reconstruct the jet energy. This requires full calorimetry, both hadronic and electromagnetic, over a sizable rapidity range. Therefore, the barrel upgrade will have full azimuthally symmetric calorimetry covering $|\eta| < 1$, as shown in the engineering drawing in Fig. 2. The detector will also retain the VTX detector in conjunction with a 2 T solenoidal magnet to continue the study of heavy flavor, with the added ability to study heavy flavor jets. The detector is being designed with possible upgrade paths, such as a possible preshower detector to select direct photons for γ-jet events, which are less sensitive to surface bias in heavy nuclei collisions.

3.2 Nucleon Transverse Spin Structure

The large transverse SSA found at RHIC can be generated by coupling between the proton spin and (1) the quark orbital motion, as in the Sivers effect, or (2) the quark transverse spin, as in transversity. In the case of transversity, a nonzero result requires a spin dependent fragmentation function (FF), such as the Collins FF. To understand how these two sources lead to the measured hadron SSA, it is important to separate jet asymmetries, which would be due to Sivers, from hadron asymmetries about the jet axis, which would be due to Collins. Therefore, we need to measure forward jets at RHIC. As the Collins effect can differ by hadron, it is also necessary to have particle identification (PID) in the forward region. As discussed below, the planned forward spectrometer will achieve both of these goals.

A second transverse spin measurement we are planning is polarized Drell-Yan (DY) production. DY is similar to Semi-Inclusive Deep Inelastic Scattering (SIDIS), but with the $\gamma*$ and quark legs interchanged. When color exchange between the remnant and the quark legs are considered, it is found that factorization is broken in the case of the Sivers distribution. However, it is broken in a unique way, namely that the Sivers function in DY has the same magnitude, but opposite sign, to the Sivers function in SIDIS. A number of experiments have plans to test this theory over the next several years. With sPHENIX, we expect to measure the Sivers function in polarized DY over a wide range in rapidity, and therefore determine the Sivers function over a wide range at large x currently not measured in SIDIS.

3.3 Cold nuclear matter (CNM) and low x gluons

A well known signal of the QGP is the suppression of quarkonia such as J/ψ due to color screening. However, separating the effects from cold nuclear matter and screening is not simple. The d+Au program at PHENIX, and the planned program with sPHENIX, will help unravel this puzzle. The first piece is to understand parton energy loss in CNM, which can be done by measuring DY. As the leptons do not interact strongly, they should exit the nuclei unaffected, and so any energy loss would be from the initial parton. The second piece is to understand quarkonia breakup in CNM, which can be done by comparing expected rates of $c\bar{c}$ vs. J/ψ production. However, to fully understand these results, the gluon and quark nuclear PDF (nPDF) must be know. The quark nPDF can be obtained from DY, while the gluon nPDF can be measured in direct photon production. Finally, effects of gluon shadowing can be studied by varying the $\sqrt{s}$ and measuring different quarkonia states. It is important to make these measurements over a wide range in η to fully understand the CNM effects.

3.4 Forward Spectrometer

A conceptual plan for the forward spectrometer is shown in Fig. 2. We envision both hadronic and electromagnetic calorimetry, required for jet reconstruction. For the electromagnetic calorimeter, we will restack our current central and forward arm calorimeters, which will give us coverage from $1 < \eta < 4$. For a number of the planned measurements, tracking will be required. We are investigating whether the central barrel magnetic field can be shaped to optimize particle bend without the need for additional magnets, though it is possible that one will be required for $\eta > 3$. Gas Electron Multiplier (GEM) detectors will provide charged particle tracking, required for both hadron asymmetries and DY measurements. Due to the high momenta of particles in this rapidity region, we expect to use Čerenkov based PID, and are looking at possible options. GEANT4 studies are underway to better define the detector requirements to achieve the ambitious physics goals described above.

.

References

[1] A. Adare *et al.* Phys.Rev.Lett. **103** (2009) 012003, arXiv:0810.0694 [hep-ex].

[2] J. Adams *et al.* Phys.Rev.Lett. **92** (2004) 171801, arXiv:hep-ex/0310058 [hep-ex].

[3] I. Arsene *et al.* Phys.Rev.Lett. **101** (2008) 042001, arXiv:0801.1078 [nucl-ex].

[4] J. Koster. Proc. of XVII Int. Workshop on Deep-Inelastic Scattering and Related Topics (April 2009) .

[5] K. Adcox *et al.* Nucl.Phys. **A757** (2005) 184–283, arXiv:nucl-ex/0410003 [nucl-ex].

[6] A. Adare, S. Afanasiev, C. Aidala, N. Ajitanand, Y. Akiba, *et al.* arXiv:1204.0777 [nucl-ex].

[7] Y. Kim. Proc. of XVIII Int. Workshop on Deep-Inelastic Scattering and Related Topics (March 2012) .

[8] K. Eskola, H. Paukkunen, and C. Salgado. JHEP **0904** (2009) 065, arXiv:0902.4154 [hep-ph].

[9] A. Bazilevsky. Proc. of XVIII Int. Workshop on Deep-Inelastic Scattering and Related Topics (March 2012) .

Accelerator Design of High Luminosity Electron-Hadron Collider eRHIC

Vadim Ptitsyn on behalf of the eRHIC Accelerator Design team
BNL, Upton, NY 11973, USA

DOI: http://dx.doi.org/10.3204/DESY-PROC-2012-02/125

The accelerator design of future high-energy high-luminosity electron-hadron collider at RHIC, called eRHIC, is presented. We plan adding energy recovery linacs to accelerate the electron beam to 20 (potentially 30) GeV and to collide the electrons with hadrons in RHIC. The center-of-mass energy of eRHIC will range from 30 to 200 GeV. The luminosity exceeding 10^{34} cm^{-2} s^{-1} can be achieved in eRHIC using the low-beta interaction region with a 10 mrad crab crossing. The important eRHIC R&D items include the high-current polarized electron source, the coherent electron cooling and the compact magnets for re-circulating passes. A natural staging scenario is based on step-by-step increases of the electron beam energy by building-up of eRHIC's SRF linacs.

1 eRHIC Design

Relativistic Heavy Ion Collider (RHIC) has been operating at BNL (USA) for more than decade, producing either polarized p-p collisions (with the proton energy up to 250 GeV) or unpolarized heavy ions collisions (with ions up to U and the ion energy up to 100 GeV/u). The future electron-ion collider eRHIC will take advantage of the existing RHIC ion complex. The layout of the future accelerator is shown in Figure 1. In order to keep the modifications to minimum, eRHIC will add an electron accelerator inside the present RHIC tunnel. To achieve high average electron beam current (50 mA) the energy recovery linacs (ERLs) are used for electron acceleration. Two ERLs (200m long and 2.45 GeV energy gain each) are placed in two straight sections in the RHIC tunnel. The electrons from the polarized source injector are accelerated to the top energy, first, by a 600 MeV pre-accelerator ERL, and then by passing six times through the main ERLs. After colliding with the hadron beam in up to three experimental detectors, the e-beam will be decelerated in the same linacs and dumped. The recirculations are realized with vertically stacked recirculation passes (the beam lines), which run along the RHIC circumference. The recirculation passes are composed from compact size magnets to minimize the construction and operation costs. Highest luminosity is achieved with the electrons at (or below) 20 GeV energy. In addition to ion species used in present RHIC, eRHIC will include also polarized $^3He^{++}$ ions.

The acceleration in the main linacs, as well as in the pre-accelerator ERL, will be done by using 5-cell 704 MHz SRF cavities, developed in BNL [1]. The cavity has been designed for high current applications, with the attention to minimizing and damping of high-order modes of RF electromagnetic field. In order to achieve the required beam acceleration in 200 m straight section of the RHIC tunnel the cavity cryomodule will be as compact as possible, with the

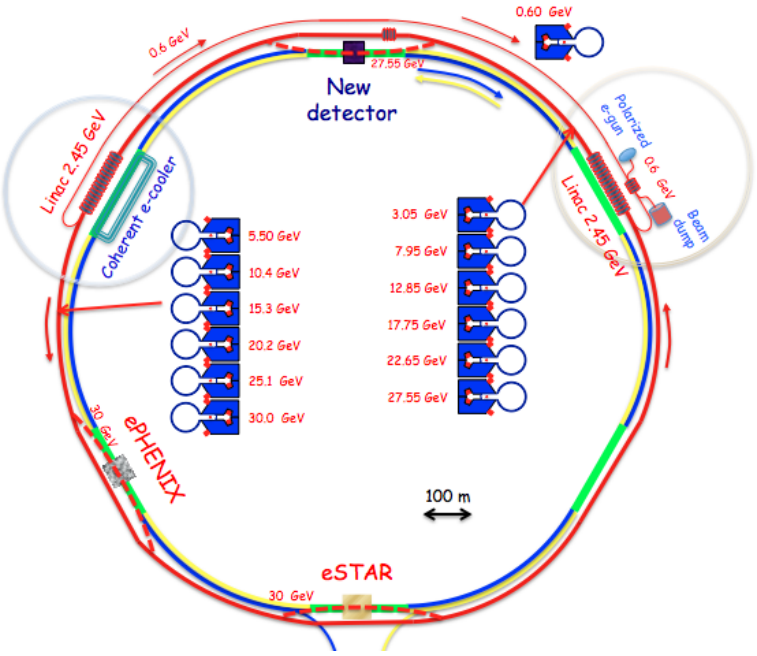

Figure 1: eRHIC Accelerator Layout.

average acceleration gradient reaching up to 12.3 MeV/m. The attractive feature of the eRHIC design is that the staging of this machine can be easily arranged. It is planned that, on the first stage, eRHIC will have shorter length ERLs and the maximum electron energy of 10 GeV. On later stages the linacs will be enlarged by adding SRF cavities, ultimately reaching 30 GeV energy of electrons. In the full staged design the collider will be able to do experiments in a wide range of center mass energies: from 30 to 200 GeV.

With the bunch repetition rate defined by the present RHIC hadron beam the electron beam has relatively low bunch frequency (9.4 MHz) and high charge per bunch (3-5 nC). The main luminosity limiting factors are the hadron space charge tune shift (< 0.035), hadron beam-beam parameter (< 0.015), the achievable value of the polarized electron current (50 mA) and synchrotron radiation power losses. The luminosity of collisions of 20 GeV electrons and 250 GeV protons reaches $2.7 \cdot 10^{34}$ cm^{-2} s^{-1}. Because of the space charge limit the luminosity would drop as the cube of the proton energy. In order to prevent this sharp drop of the luminosity with the proton energy, the space charge compensation (the electron columns) is utilized in the design. With the space charge compensation the luminosity decreases proportionally to the proton energy. The transverse and longitudinal cooling of the hadrons is required to reach high design luminosities. Above 20 GeV electron energy the luminosity decreases as $1/E_e^4$ due to the synchrotron radiation power limit (7 MW at 20 GeV). Further information on the beam parameters and the luminosities can be found on the eRHIC accelerator webpage [2].

2 eRHIC R&D program

In order to reach its luminosity and polarization objectives the eRHIC design intends to utilize advanced accelerator technologies. The list of eRHIC accelerator R&D items includes: high average polarized current source; efficient high energy cooling of hadron beams; high power energy recovery linacs; beam-beam effects for linac-ring collision scheme; compact magnets of electron recirculation passes; polarized $^3He^{++}$ production and acceleration; crab crossing and crab-cavities; the design of high gradient interaction region magnets.

The eRHIC polarized electron source has to be able to produce the average current up to 50 mA. The high current can be achieved by effectively increasing the cathode area, using standard cathode materials (strained GaAs or superlattice). The BNL group has been developing a so-called "Gatling gun" design where the high current is produced by merging the electron currents extracted from several small size cathodes [3]. The engineering design of the "Gatling gun" has been completed. The next planned step is building the gun prototype.

To efficiently reduce the transverse and longitudinal emittances of high-energy proton and ion beams by an order of magnitude, the novel technique of coherent electron cooling (CeC) has been proposed [4]. The calculation shows the cooling rates on the scale of tens of minutes can be achieved for the high-energy proton beam, which can not be done with traditional stochastic- or electron- cooling techniques. The proof-of-principle experiment for CEC, funded by DOE NP Office of Science, is being prepared in RHIC by the collaboration of BNL, JLab and Tech-X [5]. The experiment will take place in 2014-2016. The aim of the experiment is to demonstrate the longitudinal cooling of 40 GeV/u Au ion beam.

With the large number of electron recirculation passes, several thousand magnets are needed to guide and focus electron beam. Making the magnets as compact as possible is a major cost saving issue for eRHIC. The R&D effort of designing and prototyping efficient and inexpensive small-gap magnets and the corresponding vacuum chamber has been underway at BNL for the last three years [6]. The magnetic measurements done with the dipole magnet prototypes (with the gap as small as 5mm) demonstrated a magnetic field quality close to satisfying eRHIC requirements.

The high beam power ERL technology will be used in RHIC to accelerate the high average current electron beam. The ERL test facility has been built in BNL in order to test the key components of the SRF technology (with 704 MHz BNL cavity) and the energy recovery with high beam average current (up to 0.5 A) [7]. The beam dynamics issues, specific for the energy recovery machines will be also explored, They include the beam breakup, the beam emittance growth and the beam halo formation. The facility plans to start first tests with the electron beam, produced by the SRF gun, later this year.

The beam-beam interactions for the linac-ring collision scheme have been the subject of thorough studies. All diverse features of the beam-beam effects were explored with the beam simulations as well as analytically: electron beam disruption, proton kink instability, and electron beam parameter fluctuations. The beam halo created because of the beam disruption by the collisions defines the aperture of recirculation pass magnets. It was shown also, that the dedicated broadband feedback scheme can be successfully used against the kink instability [8].

The Interaction Region design is crucial for the luminosity gains. It faces the issues of strong focusing of beams at the collision point and the fast separation of beams after the collision. The detector integration issues are important: the design has to provide the good experimental acceptance and separate neutrons and off-momentum charged particles from the outgoing hadron beam. In the same time the synchrotron radiation fan produced by electrons in

the magnets has to be kept away from hitting the pipe inside and in the vicinity of the detectors and in superconducting magnets. Because of the proximity of the hadron and electron beam trajectories, special designs of IR magnets have to be developed. The application of Nb_3Sn superconductor technology is considered, following recent progress made for such magnets for the LHC luminosity upgrade. The details of the present interaction region scheme is described in [9]. It employs the 10 mrad crossing angle and the crab-crossing technique. Corresponding crab-cavity design has been developed on the basis of Quarter Wave Resonator cavity [10]. The main advantages of such crab-cavity design are its compactness and large separation of the fundamental mode from unwanted HOM modes. The present crab-crossing system for hadrons includes also higher harmonic cavities, which compensate for longitudinal nonlinearities induced by the main crab-cavities.

On the basis of EBIS ion source, recently built for RHIC, the polarized $^3He^{++}$ ions can be produced. The concept of such polarized $^3He^{++}$ ion source has been developed by the collaboration of MIT and BNL scientists [11]. The use of polarized $^3He^{++}$ ions is presently considered for the experiments at RHIC, that is on the time scale before eRHIC. Corresponding studies of the polarization preservation through the injector chain and at the acceleration in RHIC are underway.

The considerable progress has been already achieved on all major R&D items. Next 3-4 years will be critical for completing R&D work and finalizing the cost effective eRHIC accelerator design.

3 Acknowledgements

My acknowledgements are to scientists who contributed to various aspects of the eRHIC accelerator design: V. N. Litvinenko, S. Belomestnykh, I. Ben-Zvi, M. M. Blaskiewicz, K. A. Brown, J. C. Brutus, A. Elizarov, A. Fedotov, P. K. Feng, D. Gassner, H. Hahn, Y. Hao, P. He, L. T. Hoff, W. Jackson, A. Jain, Y. Jing, D. Kayran, R. Lambiase, C. Liu, Y. Luo, M. Mapes, G. Mahler, G. McIntyre, W. Meng, M. Minty, R. Michnoff, B. Parker, A. Pendzick, A. Pikin, I. Pinayev, T. Rao, E. Riehn, T. Roser, J. Sandberg, J. Skaritka, B. Sheehy, K. Smith, S. Tepikian, O. Tchoubar, Y. Than, C. Theisen, D. Trbojevic, E. Tsentalovich, N. Tsoupas, J. Tuozzolo, G. Wang, Q. Wu, W. Xu, A. Zaltsman, W. Zhang, A. Zelenski.

References

[1] Wencan Xu *et al.* PAC11, New York, (2011) FROBS6.

[2] www.bnl.gov/cad/erhic .

[3] X. Chang *et al.* PAC11, New York, (2011) WEP263.

[4] V. N. Litvinenko, Y. S. Derbenev, Physical Review Letters **102** (2009) 114801 .

[5] V. N. Litvinenko *et al.* IPAC11, San Sebastian, (2011) THPS009.

[6] Y. Hao *et al.* IPAC10, Kyoto, (2010) TUPEB040.

[7] D. Kayran *et al.* PAC11, New York, (2011) THP006.

[8] Y. Hao, M. Blaskiewicz, V. N. Litvinenko, V. Ptitsyn, IPAC'12, New Orlean, (2012) TUPPR083.

[9] D. Trbojevic *et al.* IPAC11, San Sebastian, (2011) THPZ020.

[10] Q. Wu *et al.* SRF11, Chicago, (2011) THPO007.

[11] C. Epshtein *et al.* PANIC'11, Cambridge, AIP Conf. Proceed., **1441** (2011) 643.

The STAR Experiment: The second decade and beyond

Matthew A. C. Lamont[1] for the STAR Collaboration

[1]Brookhaven National Lab, Upton, NY 11973, USA

DOI: http://dx.doi.org/10.3204/DESY-PROC-2012-02/157

The STAR experiment at RHIC has been running successfully for over 10 years. Over this time, many upgrades have been made to the detector configuration, driven by the physics requirements. In this presentation, I will review the upgrades in the near term with respect to A+A and p+p physics and review what STAR can contribute to an eRHIC era.

1 Introduction

The STAR experiment started taking data at the Relativistic Heavy Ion Collider at BNL in 2001. From the outset, STAR was designed as a large volume (acceptance) detector with a large array of physics capabilities, focussed on charged particle identification in its Time Projection Chamber (TPC). The TPC has uniform acceptance over 2 units of pseudo rapidity, centred at mid-rapidity, and provides particle identification through specific ionisation with up to 45 samples per track. Also in the first year, a small-volume mid-rapidity RICH detector was in use, together with a small-volume TPC in the forward region and a number of trigger detectors. The whole of the mid-rapidity part of the detector was situated in a magnetic field of up to 0.5 T.

Over the past decade, STAR has evolved from this initial setup and is now a much more complex series of detectors, comprising electro-magnetic calorimetry in both the barrel and the forward regions, a Time of Flight detector at mid-rapidity and a 3-layer silicon vertex tracker has come and gone, along with 2 forward TPCs. A detailed description of all these detectors mentioned above can be found elsewhere [1].

The STAR detector has performed admirably over the last decade and has produced a great wealth of physics results, resulting from the polarised p+p programme to the heavy-ion programme, where it is believed a "perfect liquid' of de-confined quark-gluon matter has been created. The page limit in these proceedings does not afford me room to discuss these further, so I refer the reader to the literature [2].

2 STAR upgrades in the near term

Despite the success of the STAR physics programme, STAR has not sat on its laurels but has been following an aggressive path of upgrades to its detector system, led by the questions arising from the RHIC data which so far remain unanswered. In the following section, I will describe

three of the upgrades planned in the near-term, which are aimed specifically at the heavy-ion and spin physics programmes.

2.1 Forward GEM Tracker

In order to study the spin dependence of the sea-quarks, STAR plans to make measurements using parity violating W production in the $e^{-(+)}$ decay mode in p+p collisions at $\sqrt{s} = 500$ GeV. First measurements of this effect have been made using the calorimeter currently in place in STAR and these are shown in the left-hand-side of figure 1 [3]. This preliminary measurement was made with 12 pb^{-1} of data. The right-hand-side of figure 1 shows a prediction of this measurement for 300 pb^{-1}, a polarisation of 70% and with precise tracking information.

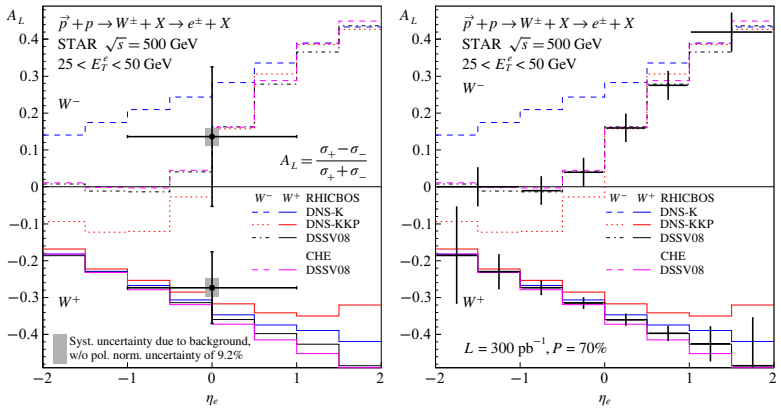

Figure 1: The current measurement (left) and future capabilities (right) for measuring A_L of W^+ and W^- in STAR.

This tracking information comes from a forward GEM tracker (FGT) which consists of six triple-GEM planar detectors currently under construction. The FGT sits around the beam pipe in the forward direction and covers the same pseudo-rapidity range ($1.1 < \eta < 2$) as the endcap calorimeter. The inner radius of the FGT is 10.5 cm and the outer radius is 39 cm. The GEM foils themselves have an inner hold radius of 50 µm, an outer radius of 70 µm and a 140 µm pitch. Each of the 6 rings are subdivided into 4 quadrants, 14 of which are installed in the current RHIC run and the rest will be completed in time for the 2013 run. The data from 2012 will allow for an evaluation of the detector performance.

2.2 Heavy-Flavour Tracker

One of the interesting questions to arise from the RHIC data is whether or not charm flows hydro-dynamically or not. Measurements of charm flow, via the flow of secondary non-photonic electrons have proved inconclusive. This is a very challenging measurement, partially due to the unknown contribution of bottom and charm to the electron spectra. To overcome this, it is desirable to measure the flow of D mesons themselves. In order to do this, STAR is building a Heavy-Flavour Tracker (HFT) - a very thin vertex detector which can measure the secondary decay vertex of the D meson. The HFT is a silicon detector consisting of 4 layers. The innermost layer is at a radius of 2.5 cm from the centre of the beam pipe and uses CMOS active pixel

Detector	Technology	Radius	Hit Resolution R-ϕ (μm)	Rad. Length
PIXEL	Active pixels	2.5, 8 cm	8.6-8.6	0.4 %
IST	Si strip pad sensors	14 cm	170 - 1700	1.2 %
SSD	Double-sided strips	23 cm	30 - 857	1.0 %

Table 1: Detector technologies used for the STAR Heavy-Flavour Tracker

sensors which are 50 μm thick. This radius is actually smaller than the radius of the current beam pipe so a new beam pipe, with radius 2 cm, will be installed along with the detector. The second layer of the detector also uses active pixel technology and sits at a radius of 8 cm. The next layer, at a radius of 14 cm utilises silicon strip pad sensors whilst the final layer, at a radius of 23 cm, uses double sided strips. Table 1 summarises the technology together with the corresponding radiation lengths and hit resolutions.

As well as charm flow, the HFT can be used to investigate the baryonic composition as a function of transverse momentum. In heavy-ion collisions, it was observed that at a few GeV/c, the ratio of p/π and Λ/K was significantly enhanced, leading to theories on quark coalescence of constituent quarks dominating over fragmentation at these momenta. If this is also true in the charm sector, it will lead to a re-interpretation of the non-photonic electron results as the branching ratios in the medium would be different to what was expected. The installation of the HFT will start ahead of the 2013 RHIC run.

2.3 Muon Telescope Detector

Due to the large mass of the charm and bottom quarks, heavy flavour measurements play an important role in heavy-ion collisions. Complementing the HFT, which will measure heavy-flavour particles by reconstructing their secondary decay vertex, it is also possible to measure those particles which decay through leptonic channels (e.g. J/ψ, Υ). It is desirable to measure these through the muon decay channels, rather than the electron, because this minimises the Dalitz decay background and importantly, the Bremsstrahlung radiation, allowing for the Υ 1S, 2S and 3S states to be distinguished.

To accomplish this goal, STAR is building a Muon Telescope Detector (MTD) which differs from conventional muon detector technology and instead uses the same Multi-Gap Resistive Plate Chamber (MRPC) technology that has been shown to work successfully in the STAR Time-of-Flight Detector. The MTD will consist of 118 modules and will sit outside the return iron bars of the STAR magnet system and will cover $\approx$ 45% in azimuth and $|\eta|$ <0.5. The MTD will be ready for operation in 2014.

3 eSTAR - can STAR be viably used in a future EIC?

Whilst the near-term upgrades in STAR, described above, are important in addressing the questions discussed, some of the remaining unknowns arising from the RHIC programme can only be addressed with the precision afforded by colliding lepton beams with ions. Therefore, a proposal to add an electron beam to the RHIC complex has been put forward (eRHIC) [4]. In order to fully address all the physics, it is clear that a new detector will need to be built [5].

However, as long as it remains feasible to run STAR in the eRHIC era, it is only natural to investigate the capabilities of an eSTAR detector.

It is envisaged that the building of eRHIC will be staged. Whilst there are no significant increases in ion-beam energy foreseen, the first stage of eRHIC will see a 5 GeV electron beam, increasing in later stages to 30 GeV. Figure 2 is a representation of the detector coverage in the $x - Q^2$ plane of the outgoing electron (left). The same plot is shown in the right-side of figure 2 for 30 GeV electrons. In the case of Deep-Inelastic Scattering (DIS), only the outgoing electron needs to be detected. As can be seen, for 5 GeV beams, the $x - Q^2$ coverage is good, with existing detectors covering everything above Q^2=10 GeV^2. However, this gets worse as the energy increases and as can be seen for 30 GeV, this coverage is very small and only for very high Q^s. Therefore, whilst STAR will be able to make strong contributions to the physics programme at eRHIC in stage-1, complementing a dedicated detector, it becomes more and more important that a dedicated detector is built, the higher the electron energy.

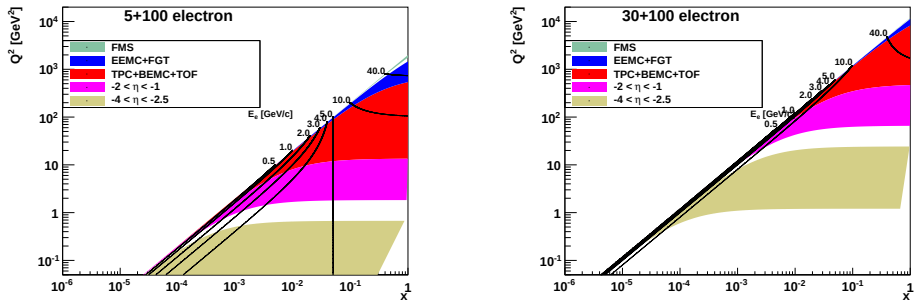

Figure 2: STAR detector coverage in $x - Q^2$ space and how it pertains to the outgoing electron in e+p(A) collisions for 5 GeV (left) and 30 GeV (right) electrons.

4 Summary and Conclusions

In summary, the STAR experiment has provided a rich set of results in heavy-ion and p+p collisions over the last decade and is well positioned to continue this in the near term with a strategy of detector upgrades. This process has already started with the partial construction of the Forward Gem Tracker in the current 2012 RHIC run. Looking to the long-term and the construction of an electron-ion collider (eRHIC), STAR is participating in the BNL-led R&D programme and investigating what is required to add to the current suite of detectors in order to be viable in this phase of RHIC's future.

References

[1] STAR Collab., K. H. Ackermann *et al.* Nucl. Intr. Methods **A 499** (2003) 624.
[2] STAR Collab., J. Adams *et al.* Nucl. Phys. **A 757** (2005) 102.
[3] STAR Collab., M. M. Aggarwal *et al.* Phys. Rev. Lett. **106** (2011) 62002.
[4] V. Ptitsyn, these proceedings
[5] K. Dehmelt, these proceedings

Very Forward/Backward Detectors at the LHeC

Armen Buniatyan

DESY, Notkestraße 85, 22607 Hamburg, Germany

DOI: http://dx.doi.org/10.3204/DESY-PROC-2012-02/332

This contribution briefly describes the possibilities for the measurements in the very forward and backward directions at the proposed future LHeC $e^{\pm}p$ collider. The ideas for the detector design for luminosity, polarisation and forward baryon measurements are presented.

1 Introduction

The Large Hadron Electron Collider (LHeC) is a proposed future deep-inelastic scattering facility at CERN, where protons or heavy ions from an existing LHC storage ring collide with electrons or positrons beam of energy 60 to 140 GeV from a newly built machine. The LHeC is presently being evaluated in the form of two options, 'ring-ring' (RR) and 'linac-ring' (LR), either of which operate simultaneously with proton-proton or heavy ion collisions at the existing LHC experiments. The conceptual design of the LHeC detector was presented in this workshop by A. Polini [1]. In this report I discuss the detector components which are located outside of the main apparatus, in the very forward and backward directions, and aimed for the measurement of luminosity, electron beam polarisation and the baryons scattered at very low angles. In order to finalise the study of the geometry of detectors, a detailed simulation of the LHeC interaction region and the beamline must be performed.

2 Luminosity measurements and Electron tagging

Luminosity measurement is a crucial issue for the LHeC, where precision measurements constitute a significant part of the physics programme. In addition to an accurate determination of integrated luminosity with the 1% precision for the normalisation of physics cross sections, the luminosity system should allow for fast beam monitoring for tuning and optimisation of ep-collisions and has to provide control of the mid-term variations of instantaneous luminosity.

An important lesson from HERA is that one has to prepare alternative methods for luminosity determination. The physics processes which are best suitable for luminosity determination are the electromagnetic Bethe-Heitler (BH) and QED Compton (QEDC) scattering processes $ep \to e + \gamma + p$, which have a large and well known cross sections. In addition, Neutral Current DIS events in a well understood (x, Q^2) range can be used for the relative normalisation and mid-term yield control. The methods are complementary, having very different systematics and providing useful redundancy and cross check for the luminosity determination.

The QEDC events, for which the scattered electron and photon are measured in the backward part of the LHeC main detector with stable and well known acceptance, are well suited

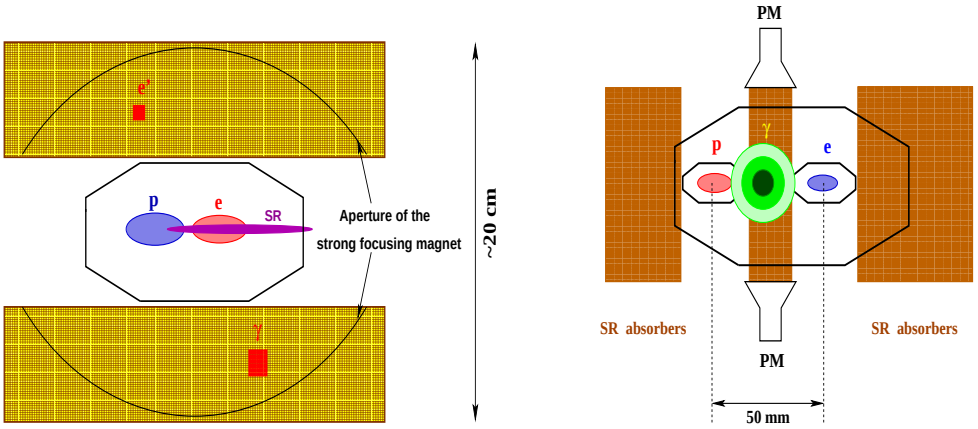

Figure 1: Options for the luminosity monitoring. (a) QEDC tagger at $z = -6$m; (b) active SR absorber and liminosity detector at $z = -22$m.

for global normalisation of the physics samples. The visible cross section of QEDC events can be increased by installing a dedicated small 'QEDC tagger' at $z = -6$m, consisting of two movable calorimeter sections approaching the beampipe from the top and the bottom (Figure 1a), supplemented by small silicon tracking detector for e/γ separation and background rejection.

The BH process has a very high cross section and can be measured in the dedicated 'tunnel detectors'. This method is, however, very sensitive to the details of the beam optics at the interaction point, requires a large and precisely known geometrical acceptance, and may suffer from synchrotron radiation (SR). In case of the RR-option the dominant part of the BH photons will end up at $z \simeq -22$m, between electron and proton beam-pipes. At this position measurement of photons is very difficult due to large SR flux. There is however an interesting possibility to use cooling water of SR absorber as an active media for Čerenkov radiation from electromagnetic showers initiated by the energetic photons. The Čerenkov light can be read out by two photomultipliers as sketched on Figure 1b. For the actual RR design the 90% acceptance to the BH photons can be reached, thus allowing fast and reliable luminosity monitoring with $3-5\%$ uncertainty. In case of LR-option the luminosity detector will be placed in the median plane next to the interacting proton beam. The major uncertainty will come from the knowledge of the limited geometric acceptance. This limitation is defined by the proton beam-line aperture. The geometric acceptance of the Photon Detector up to 95% is possible at the nominal beam conditions. The total 1% luminosity error can be achieved.

The BH reaction can be tagged also by detecting the outgoing electron. In order to determine the best positions for the electron taggers the LHeC beamline simulation has been performed. The best position for the electron tagger is at z=−62 m, which less suffers from SR flux and provide reasonable acceptance, reaching approximately $(20-25)\%$ at the maximum. The actual acceptance strongly depends both on the distance of the sensitive detector volume from the e-beam axis and on the details of the electron optics at the IP. Therefore a precise independent monitoring of beam optics and accurate position measurement of the e-tagger are required in order to control geometrical acceptance to a sufficient precision.

3 Polarimeters

The polarisation measurement of the electrons and positrons at the LHeC will be based on Compton polarimetry. This technique has been successfully used in the past at SLC [2] and at HERA [3], and is foreseen for the polarisation measurement at the future linear colliders [4]. The experimental setup consists of a laser beam, which scatteres off the lepton beam, and calorimeters, which measure the scattered photon and lepton. The longitudinal polarisation of lepton is obtained from a fit to the scattered photon and/or to the lepton energy spectra.

For the extraction of the longitudinal polarisation one may then distinguish between the single (or few) scattered photon regime, where the polarisation can be determined from a fit to the scattered photon energy spectrum, and the multi-photon regime, where the photons can not be distinguished in the calorimeter and the polarisation is calculated from an asymmetry between the average scattered energies corresponding to a circularly left and right laser beam polarisations [5]. Considering a very stable pulsed laser beam with adjustable pulse energy and operating in different regimes, one can calibrate the calorimeter in situ, optimise the dynamical regime and minimise the final uncertainty on the polarisation measurement.

The Compton interaction region will include a dedicated electron spectrometer followed by a segmented electron detector [4], which will measure the scattered electron angular spectrum. The measurements of both the scattered photon and leptons are complementary and allow for a precise control of the systematic uncertainties of the polarisation measurement [2].

4 Zero Degree Calorimeter (ZDC)

The position of the ZDC in the tunnel and the overall dimensions depend mainly on the space available for the installation. The geometry, technical specifications and proposed design of ZDC detectors are to large extent similar to the ZDCs of the LHC experiments [6, 7, 8]. The ZDC can be placed in a 90 mm narrow space available at about 100 m next to the interacting proton beam pipe. The detector has to be capable of detecting neutrons and photons produced with scattering angles up to 0.3 mrad and energies between some hundreds GeV to the proton beam energy (7 TeV) with a resolution of few percents. It must be able to separate neutrons from photons and to distinguish showers from two or more particles.

The ZDC can be built as a longitudinally segmented tungsten-quartz calorimeter with the electromagnetic and hadronic sections. The electromagnetic section with fine granularity is needed for precise determination of the position of the impact point, discrimination of the electromagnetic and hadronic showers and separation of the showers from two or more particles. The hadronic section of the ZDC can be built with coarser sampling. The longitudinal segmentation will allow the control of the change of energy response due to radiation damage.

Another possibility for the ZDC design is provided by the the Dual Readout calorimetry [9]. The detector will have tungsten absorber and equipped with scintillating and quartz fibres readout by the SiPM. Two kind of fibres are sensitive to the different components of the hadron shower, which leads to the improved hadronic energy resolution. The discrimination between neutrons and photons will be possible using the time structure of the signals.

In addition to the ZDC calorimeter for measurement of neural particles at 0°, a proton calorimeter positioned externally to the outgoing proton beam can be installed for the measurement of spectator protons from eD and eA scattering produced at zero degree. This calorimeter will be made using the same technique as the neutron ZDC.

Due to the hard radiation and temperature environment it is essential to control of the stability of the ZDC response. The stability of the gain of the PMTs and the radiation damage in fibres can be monitored using the laser or LED light pulses. The stability of absolute calibration can be monitored using the interactions of the proton beam and residual gas molecules in the beam-pipe, as used at HERA [10, 11]. A useful tool for absolute energy calibration will be the reconstruction of invariant masses, e.g. $\pi^0 \to 2\gamma$ or $\Lambda, \Delta \to n\pi^0$, with decay particles produced at very small opening angles and reconstructed in ZDC. It is therefore essential that several particles in the ZDC within the same event are reconstructed.

5 Forward Proton Spectrometer (FPS)

In diffractive *ep* interactions the proton may survive a hard collision and scatter at a low angle along the beamline while loosing a small fraction $\xi \approx \mathcal{O}(1\%)$ of its energy. The ATLAS and CMS collaborations have investigated the feasibility to install proton detectors along the LHC beamline [12]. The conclusions reached in these R&D studies are relevant for the LHeC detector.

The acceptance window in ξ is determined by the closest possible approach of the proton detectors to the beam for low ξ and by the distance of the beam pipe walls from the nominal proton trajectory for high ξ. The maximaum allowed four-momentum transfer squared t is defined by the radius of the LHC beam pipe, which is approximately 2 cm at the large distances from the interaction point. The acceptance for diffractively scattered protons as a function of ξ and t at 420 m from the interaction point, determined using the LHC proton beam optics, is shown in Figure 2. A quite good acceptnace is reached in the range $0.002 < \xi < 0.013$. The kinematics of diffractive interaction can be reconstructed from the accurate measurements of the proton's position and angle with respect to the nominal beam. However the resolution of the reconstructed variables will be determined by the intrinsic width and divergence of the proton beam.

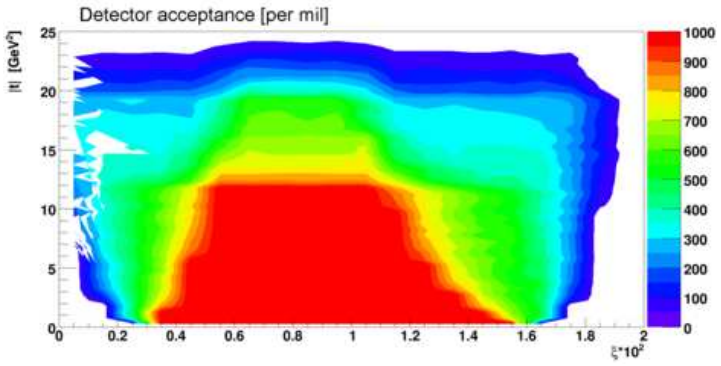

Figure 2: The acceptance for a proton detector placed at 420 m from the interaction point as a function of the momentum loss ξ and 4-momemtum transfer squared t.

A crucial issue in the operation of proton detectors is the alignment of the detectors with respect to the nonimal beam. The detectors have to be aligned for each accelerator run and the drifts have to be monitored. As at HERA, alignment constants will be determined by requirement that the observed cross section is maximal for forward scattering. This procedure

can be cross-checked using a physics process with a exclusive system produced in the central detector such that the proton kinematics is fixed by applying energy-momentum conservation to the full set of final state particles. The feasibility of various alignment methods at the LHeC has to be studied.

6 Summary

Forward and backward 'tunnel' detectors are the important parts of the future *ep* experiment at the proposed LHeC collider. The ideas for the detector design for luminosity, polarisation and forward neutron and proton measurements are presented.

Acknowledgements

I wish to thank the organisers for this interesting, stimulating and enjoyable workshop.

References

[1] A. Polini, *"The LHeC central detector", in these proceedings.*

[2] R. King. Nucl. Phys. Proc. Suppl. **37B** (1994) 23–31.

[3] D. P. Barber *et al.* Nucl. Instrum. Meth. **A329** (1993) 79–111.

[4] S. Boogert *et al.* JINST **4** (2009) P10015, `arXiv:0904.0122 [physics.ins-det]`.

[5] M. Beckmann *et al.* Nucl. Instrum. Meth. **A479** (2002) 334–348.

[6] N. De Marco *et al.* J. Phys. Conf. Ser. **160** (2009) 012060.

[7] ATLAS Collaboration, *"Zero degree calorimeters for ATLAS"*, CERN-LHCC-2007-01.

[8] O. Grachov *et al.*, *"Commissioning of the CMS zero degree calorimeter using LHC beam"*, `arXiv:1008.1157 [physics.ins-det]`.

[9] N. Akchurin and R. Wigmans. Nucl. Instrum. Meth. **A666** (2012) 80–97.

[10] S. Bhadra *et al.* Nucl. Instrum. Meth. **A394** (1997) 121–135, `[hep-ex/9701015]`.

[11] F. D. Aaron *et al.* Eur. Phys. J. **C68** (2010) 381–399, `arXiv:1001.0532 [hep-ex]`.

[12] M. G. Albrow *et al.* JINST **4** (2009) T10001. `arXiv:0806.0302 [hep-ex]`.

The LHeC Central Detector

Alessandro Polini[1]*, *Peter Kostka*[2], *Rainer Wallny*[3]

[1]INFN Bologna, via Irnerio 46, 40126 Bologna, Italy
[2]DESY, Platanenallee 6, 15738 Zeuthen, Germany
[3]Institute for Particle Physics, ETH Zurich, Zurich, Switzerland

DOI: `http://dx.doi.org/10.3204/DESY-PROC-2012-02/331`

The Large Hadron Electron Collider (LHeC) is a new project proposed at CERN to exploit the LHC for lepton-nucleon scattering at an unprecedented centre-of-mass energy and luminosity. The design of a detector for the LHeC is discussed along with the requirements coming from the physics and the boundaries from the accelerator options. A baseline layout is presented with some focus on the central detector components. Few options, which depend on later studies and choices in the overall project, are also discussed.

1 Introduction

At the LHeC [1], electrons of evergy from 60 GeV and up to 140 GeV collide with LHC protons of 7000 GeV with an *ep* design luminosity of about $10^{33}\,\mathrm{cm}^{-2}\mathrm{s}^{-1}$. The physics program is devoted to an exploration of the TeV energy frontier, complementing the LHC and its discovery potential for physics beyond the Standard Model with high precision deep inelastic scattering (DIS) measurements. These are projected to solve a variety of fundamental questions in strong and electroweak interactions continuing and extending the unique analysis of DIS lepton-hadron scattering by a factor of twenty in the four-momentum squared, Q^2, and in the inverse Bjorken x. A huge physics potential is opened also by the $(Q^2,\ 1/x)$ region accessible in electron-ion (eA) scatterings which at the LHeC is by four orders of magnitude larger compared to previous lepton-nucleus DIS experiments.

In this writeup the design of the main LHeC detector is described. In section 2 the overall requirements coming from the physics and the constraints from the accelerating machine are presented. The detector layout along with a description of the main detector components, are discussed in Section 3. An outlook on the project is given in 4.

2 Requirements and Constraints

The new ep/A detector at the LHeC has to be a precision instrument of maximum acceptance. The physics program depends on a high level of precision, as for the measurement of α_s, and in the reconstruction of complex final states, like the charged-current single-top production and decay or the precision measurement of the b-quark density.

*Corresponding author alessandro.polini@bo.infn.it

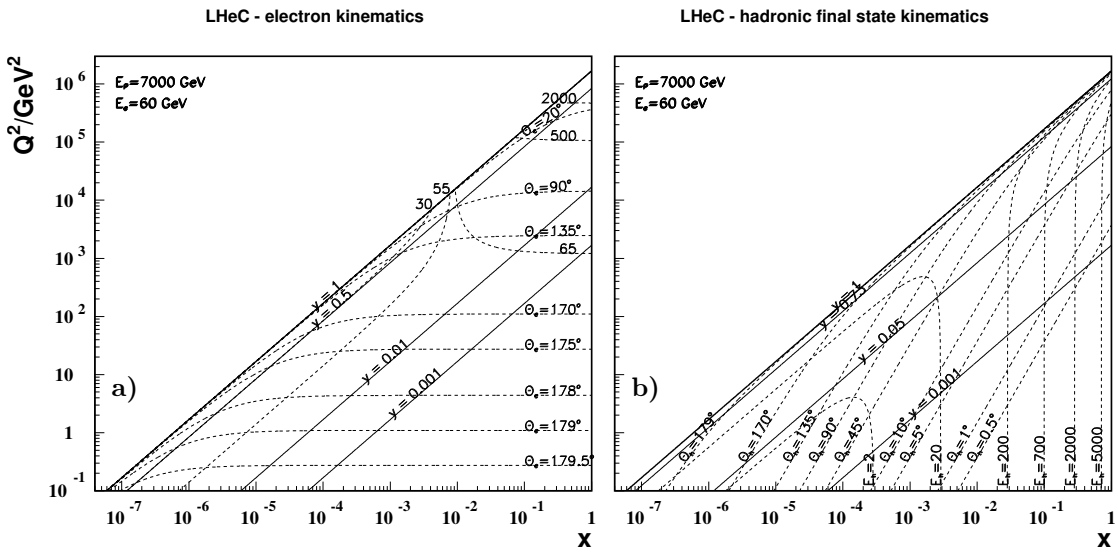

Figure 1: **a)** Kinematics of electron detection at the LHeC. Lines of constant scattering angle θ_e and energy, in GeV, are drawn. The region of low Q^2 ($\lesssim 10\,\mathrm{GeV}^2$), comprising the lowest x region, requires to precisely measure electrons scattered backwards with energies not exceeding E_e. **b)** Kinematics of hadronic final state detection at the LHeC. Lines of constant energy and angle of the hadronic final state are drawn, as represented by simple kinematics of the struck quark. One easily recognizes that the most demanding region is the large x domain, where very high energetic final state particles are scattered close to the (forward) direction of the proton beam.

Figure 1 shows the kinematics of scattered electron and of the interacting hadronic final state detection as a function of Bjorken x, and the fourmomentum trasfer squared Q^2. The acceptance has to extend as close as possible to the beam axis because of the interest in the physics at low and at large Bjorken x. The dimensions of the detector are constrained by the radial extension of the beam pipe in combination with maximum polar angle coverage desirably down to about 1° and 179° for forward (i.e. along the proton outgoing direction), final state particles and backward scattered electrons at low Q^2, respectively.

The LHeC interaction region [2] poses additional constraints coming from a complex optics which includes 3 beams (the interacting protons and electrons and the second spectator proton beam). Two options for providing the electron beam are presently being discussed. In the Ring-Ring design (RR), an electron ring is installed on top of the existing LHC requiring for high luminosity running additional strong focusing magnets located at 1.2 meters from the interaction point. In the Linac-Ring (LR) option an Energy Recovery Linac provides the electron beam. Special arrangement has to be done in order to avoid parasitic interactions which for the LHC bunch spacing of 25 ns requires either a non null crossing angle (RR) or an extra dipole field (LR) along the whole length of the central detector and beyond. A schetch of the interaction region for this second and more complex case is shown in Fig.2-a. Synchrotron radiation coming from the deflection of the electron beam will need an asymmetric beampipe to accomodate for the synchrotron fan which needs to pass the central detector area as depicted in Fig.2-b.

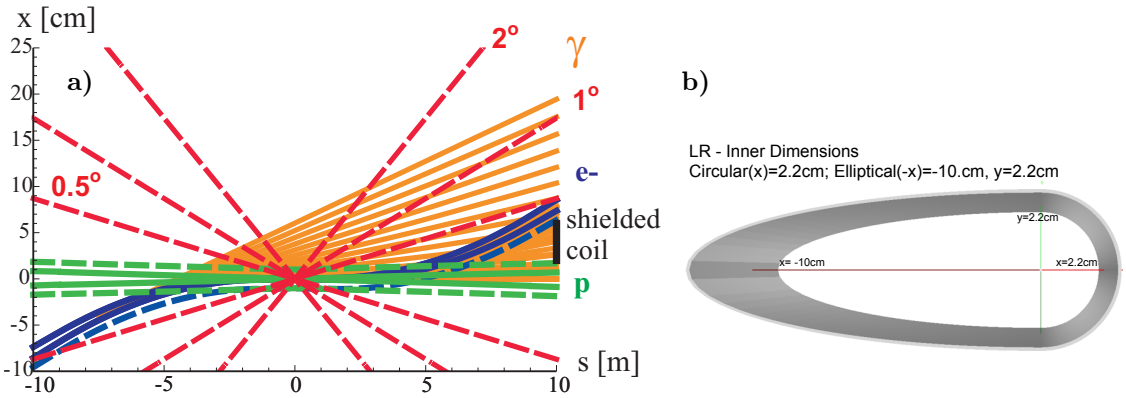

Figure 2: **a)** LR interaction-region layout. Shown are the beam enevelopes of 10σ (electrons) [solid blue] or 11σ (protons) [solid green], the same envelopes with an additional constant margin of 10 mm [dashed], the synchroton-radiation fan [orange], the approximate location of the magnet coil between incoming protons and outpgoing electron beam [black], and a 1° line. **b)** Perspective drawing of the beam pipe and its dimensions in the LR configuration. The dimensions consider a 1 cm safety margin around the synchrotron radiation envelope.

A further general requirement to the detector is a high modularity to enable the bulk of the construction phase to be performed above ground and therefore keep the installation time at a minimum, and allow to access inner detector parts within reasonable shutdown times. The time schedule of the project demands to have the detector ready within ten years from now, for the LHC phase II running (around year 2023). This prevents any significant R&D program to be performed although the project can still rely on the vast experience from HERA, the LHC, including its detector upgrades to come, and the ILC.

3 Detector Design

The LHeC detector has to be hermetic in order to maximize coverage especially in the forward and backward regions and provide precise energy and missing energy, the latter being the signature for charge-current processes where the incoming electron is converted into an outgoing neutrino. The LHeC detector is asymmetric in design, reflecting the beam energy asymmetry. Moving from the interaction region outwards, a light beampipe surrounded by a precision tracking detector with extended forward and backward parts is required before reaching the electromagnetic calorimetry. A strong solenoid (3.5 Tesla) is needed for momenta separation and long dipoles of 0.3 Tesla are required in the LR configuration along the whole interaction region from $z = -9m$ to $z = +9m$ providing a field in a region not too extended in radius. The requirement of a precise electron energy measurement and not too large beam-steering magnets, suggest to have the solenoid and the dipoles integrated in a single structure placed immediately outside of the electromagnetic calorimetry. The hadron calorimeter surrounds therefore the magnet system and is enclosed in a muon tracker system. The described detector layout is shown in Fig. 3. The inner detector dimensions along the beamline are constrained by the radial extension of the beam pipe in combination with maximum polar angle coverage

(1° and 179°) for forward going final state particles and backward scattered electrons at low Q^2, respectively. The outer radial size is mainly determined by the requirement of full energy containment of hadronic showers in the calorimeter. The main detector is complemented by hadron tagging detectors (not shown) in the forward direction and a polarimeter and luminosity measurement system backwards [3]. Below some details for the different central subdetectors are given.

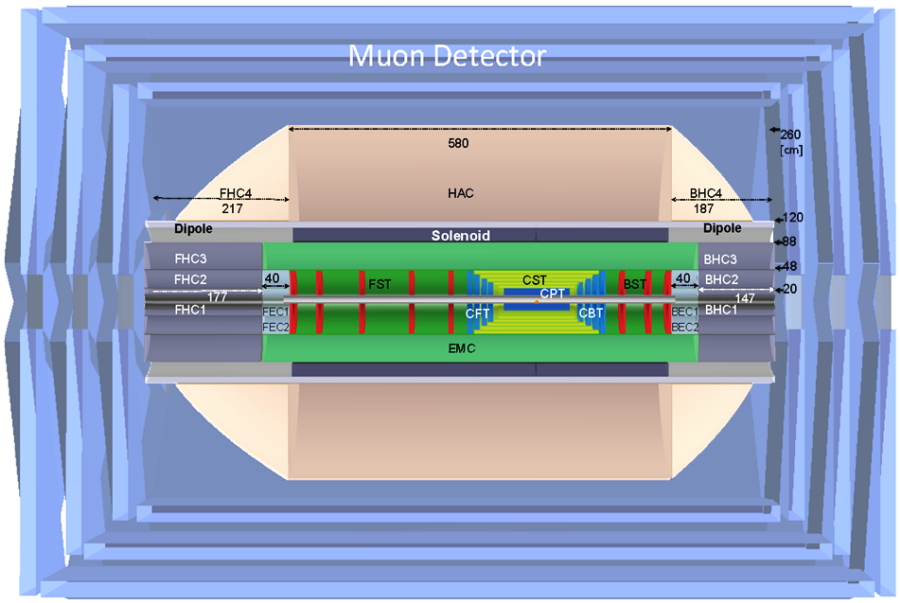

Figure 3: An rz cross section of the LHeC detector in its baseline configuration with the magnet configuration for LR with the solenoid and dipoles placement between the electromagnetic and the hadronic calorimeters. The proton beam, from the right, collides with the electron beam, from the left, at the IP which is surrounded by a central tracker system complemented by large forward and backward tracker telescopes followed by sets of calorimeters.

Tracking System

The constraints given by the magnet system (solenoid/dipoles) force the tracking detectors to be kept small in radius. The baseline layout is an all-Silicon detector, for high momentum resolution[1] and secondary vertices tagging extending over the pseudorapidity range of $-4.8 < \eta < 5.5$. Pixels are used in the inner layers and while strips or strixels are used in the external layers summing up to a total area of about 34 m^2 of Silicon sensors. All of the components need power and cooling, influencing the material budget of the tracker system which should be kept as low as possible. The technology used must be advanced at the industrial level, radiation hard and relatively cheap.

[1] Momentum resolution: $\delta p_t/p_t^2 \simeq 0.001\ c/\text{GeV}$ for $p_t = 100$ GeV and $4° \theta \leq 90°$; impact parameter resolution $\delta ip \simeq 10 \mu m$ for $4° \theta \leq 90°$. Data obtained using the LicToy simulation program.

Calorimetry

A modular structure of independent electromagnetic (EMC) and hadronic (HAC) calorimeter components is foreseen. The design of the EMC modules differs for the very forward region, where energies up to few TeV are expected and the barrel and backward regions where lower energies and a precise measurement of the scattered electron are paramount. Based on experience with H1 and ATLAS the EMC the default choice is a Liquid Argon (LAr) Calorimeter. The superconducting dipoles are placed in a common cryostat with the detector solenoid and the LAr EMC. The HAC is an iron-scintillator tile calorimeter which provides the required mechanical stability for the inner LAr and Magnet cryostat and guides the return flux of the magnetic field, as in ATLAS. The restrictive geometry of the forward/backward insert calorimeters requires a non-conventional and challenging design using silicon readout in conjunction with tungsten as the absorber material, in particular for the forward inserts. For the hadronic absorber, also copper might be considered as an alternative. The choice of the sampling calorimetry for all calorimeter parts is motivated by the good experience from past experiments along with considerations on the available technologies, and cost, although other approaches (dual readout or fully active calorimetry, etc.) could be considered. Preliminary simulations on all calorimeters parts including the dead material of the magnet system have been done using the GEANT4 and FLUKA programs and support a satisfactory performance [4].

Muon Detection

The two LHC general purpose detectors, ATLAS and CMS, combine Drift Tubes and Cathode Strip Chambers for precision measurements along with Resistive Plates Chambers and Thin Gap Chambers for Trigger and second coordinate measurements. A similar approach can also be considered for the LHeC although, for the baseline design, the muon detectors will not provide an independent momentum measurement since no strong magnetic field is present. The use of a forward toroid to improve the momentum measurement in the forward region where high energy muons are expected is beeing evaluated. Of particular interest is also the option where, by means of a second larger active return shielding solenoid surrounding the muon detector, an iron free area with almost constant field (1.5T) provides a precise muon tracking as was first proposed by the 4th concept detector collaboration for the ILC.

4 Conclusions and Outlook

The LHeC is a project with an ambitious physics program which complements the measurements of present and future *pp* and lepton collider experiments. A baseline design and some extensions for the LHeC detector have been presented. More studies and simulations supporting the proposed detector layout are now available in a recently published Conceptual Design Report [4]. A roadmap with an LHeC taking data concurrently with the other experiments during the LHC phase II program appears feasible.

References

[1] M. Klein, "The LHeC Project", DIS 2012, Bonn 2012, these proceedings.

[2] R. Thomas Garcia, "LHeC Interaction Region" DIS 2012, Bonn 2012, these proceedings.

[3] A. Bunyatian, "Forward/backward detectors at an LHeC", DIS 2012, Bonn 2012, these proceedings.

[4] The LHeC Study Group, *"A Large Hadron Electron Collider at CERN: Report on the Physics and Design Concepts for Machine and Detector"*, arXiv:1206.2913v1 [physics.acc-ph].

An eRHIC Detector: Design Consideration and its Realization by Means of Detector R&D

Klaus Dehmelt[1]

[1]Stony Brook University, Dept. of Physics & Astronomy, Stony Brook, NY 11794-3800, USA

DOI: http://dx.doi.org/10.3204/DESY-PROC-2012-02/138

eRHIC is a proposed high luminosity, polarized Electron Ion Collider, which would make use of the existing RHIC infrastructure. eRHIC is a collider with the possibility of using the two existing upgraded IP detectors and a dedicated eRHIC detector. This detector has to be designed making use of present knowledge and experience gained from the HERA detectors, but has to be adapted such that it is able to cope with the EIC physics program. The following will give an overview of the detector design, its IR and presently ongoing R&D activities for making technology choices towards such a detector.

1 Introduction

An Electron-Ion Collider (EIC) will be best suited for answering compelling questions in Quantum Chromodynamics (QCD). The EIC will be able to quantitatively probe the universality of strong color fields in electron-ion collisions. It will help to establish the existence of a saturation regime, will explore non-linear QCD, as well as measuring the momentum and space-time structure of glue.
The EIC will also play a vital role in determining answers for spin physics related questions with polarized electron-proton collisions. It will do so by precisely imaging the sea-quarks and gluons and thus determining spin, flavor, and the spatial structure of the nucleon. It will determine the quark and gluon contributions to the proton at last.
The eRHIC design requires a dedicated detector design that will be differing in various aspects from detectors such as ePHENIX, eSTAR, or an ELIC detector.

2 Detector Requirements

A detector has to be developed that can cope with the opportunities an EIC can deliver. Such a detector must be multi-purpose, i.e., one detector that is able to perform inclusive ($eh \to e'X$), semi-inclusive ($eh \to e'h'X$), as well as exclusive ($eh \to e'\pi p$) deep inelastic scattering (DIS) measurements, where eh can be either ep or eA collisions.
The detector must also be able to handle collisions with varying beam energies and therefore varying eh kinematics. It is anticipated that $\frac{E_h}{E_e}$ varies between 1 and 65, in contrast to HERA, where it varied between 17 and 34, with a fixed electron-energy of 27 GeV.
The impact on the detector configuration can be seen in terms of the various final state conditions: for inclusive DIS reactions the scattered lepton goes more and more into the original

beam direction when increasing its initial energy. High Q^2 events will be detected with the central detector. Low Q^2 events will have only small scattering angles and close to the original beam energy. One therefore needs a small angle, forward electron tagger. Moreover, the tracker has to be low-mass with a high resolution, covering a wide angular acceptance.
Semi-inclusive DIS reactions have a signature in hadrons that go from very forward to central and even backward directions, when the lepton energy increases. A good particle identification is required over the entire detector.
Exclusive DIS reactions require the measurement of decay products from $\rho - \phi - J/\psi$ particles, which will appear from very forward to central to even backward directions with increasing lepton beam energy.

3 Design Interaction Region

Due to the desired high luminosity at eRHIC the interaction region (IR) is designed to have a $\beta^* = 5$ cm and a field-free region of $l^* = 4.5$ m and a crossing angle of 10 mrad. This is required to achieve a luminosity of up to 10^{34} cm^{-2} s^{-1}.
The crossing angle will be combined with the *crab-crossing* technique so that a maximum overlap of the crossing bunches can happen. High gradient large aperture Nb_3Sn focusing magnets are planned for and a field-free region will be arranged where the electrons pass through the hadron triplet magnets.
The integration with the detector allows an efficient separation and registration of low angle collision products. Last but not least, a gentle bending of the electron-beam out of the the IR will avoid the synchrotron radiation impact in the detector.

4 Detector Concept

The generic detector concept for a dedicated eRHIC detector is shown in Fig. 1. It will be

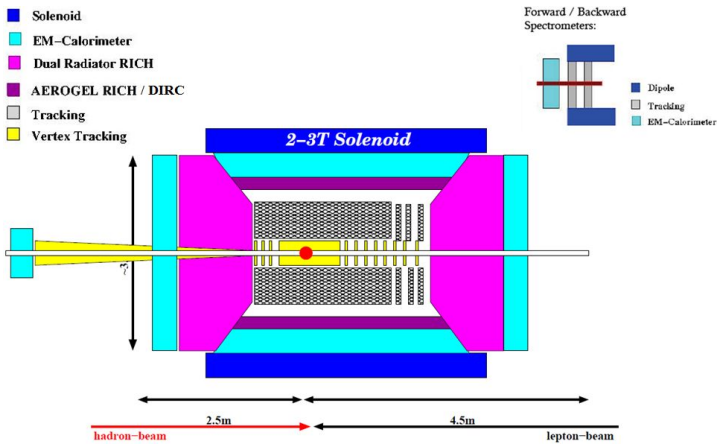

Figure 1: Concept for a dedicated eRHIC detector.

asymmetrically surrounding the IR and will consist of vertex tracking, barrel and forward

tracking, particle identification detectors and electromagnetic calorimeters. All is embedded in a solenoid, which is foreseen to deliver a magnetic field of 2-3 T. This detector concept is based on providing maximum hermecity.
The detector is planned to also have the least amount material so that multiple scattering and bremsstrahlung is avoided to the highest degree. A radiation length scan in a *GEANT4*-simulation is shown Fig. 2.

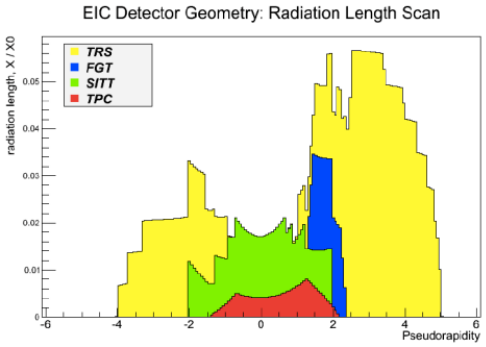

Figure 2: Radiation length distribution for a dedicated eRHIC detector.

4.1 Tracking-Vertex

For a vertex detector it is foreseen to make use of a Si-VTX device which is based on the MAPS-technology [1]. This technology is in an advanced R&D stage, mainly pursued by the IPHC group in Strasbourg/France. It found already use in the STAR-HFT, CBM, ALICE, to name a few.
The barrel will be equipped with four double sided layers at distances of 2.5/5.0/7.5/15.0 cm, subdivided in ten sectors in ϕ. The rapidity coverage should be at least $|\eta| = 1$. A dual sided readout with 60 µs readout time per column would result in a radiation length of 0.5 % per layer based on 5 µm Si and will have an excellent vertex resolution of better than 5 µm.
In the forward direction at least four single sided disks are foreseen, spaced in z from 20 cm. The radial extension makes from 3 to 12 cm with 19 respectively 75 µm pixel-size. The radiation length per layer is expected to be 0.3 %.

4.2 Tracking-Barrel and Forward

For the barrel tracking a Time Projection Chamber (TPC) with Micro Pattern Gas Detectors (MPGD) is a preferred technology. It provides low mass, particle identification ability e/h via dE/dx and the has a rather good position resolution in conjunction with pattern recognition.
Present MPGD-R&D is ongoing with the most promising technology being the Gas Electron Multiplier (GEM [2]) and Micro Mesh Gas Detectors (Micromegas [3]). Both offer transverse $\sigma_r < 150$ µm and longitudinal $\sigma_z < 300$ µm position resolution.
Forward tracking detectors are foreseen similar to the very small angle tracker (VSAT) in COMPASS or the Forward GEM Tracker at STAR.

4.3 Particle identification

The particle identification PID options for a dedicated eRHIC detector are manifold. In the barrel region one could deploy a combination of a TPC with dE/dx in conjunction of a Cerenkov detector with gaseous radiator, a detector of internally reflected Cerenkov light (DIRC [4]), time of flight detector (ToF) of the next generation with 10 ps time resolution [5], Aerogel as proximity focused Cerenkov detector plus ToF, proximity focused Cerenkov detector with liquid radiator, and/or electromagnetic calorimetry detectors (EmCal) In the forward region one is not as spatially constrained as in the barrel region. Therefore a combination of a Cerenkov detector with gaseous radiator and CsI-GEM photodectors plus tracking, ToF, and EmCal detectors would be suitable. In the very forward region EmCal detectors could be used.

4.4 Electromagnetic Calorimetry

In the backward as well in the barrel region PWO-crystal calorimeters are considered because of their good resolution and small Molière radius which enables them to provide good e/π-separation. It also gives the possibility to measure the scattered lepton from the *eh*-collision which is an important aspect for the measurement in Deep Virtual Compton Scattering (DCVS). In the forward direction the requirements are less demanding and one could think about the use of sampling calorimeters made out of scintillating fibers and tungsten powder. Preshower might find an application in form of the Si-W technology as proposed for the PHENIX MPC-EX detector.

5 Summary

The eRHIC is one of the possible EIC options and will be considering eSTAR, ePHENIX, and a dedicated eRHIC detector. This particular detector will be able to cover all EIC physics aspects and will have much more stringent requirements as previous detectors at HERA. There is a vast number of R&D activities that this detector will make use of: Tracking R&D efforts for the vertex, forward, and the barrel region, as well as for PID and calorimetry. All these aspect are going hand-in-hand with R&D efforts for various other detector projects. Furthermore, the Brookhaven National Lab has announced a generic detector R&D program for an EIC [6].

References

[1] R. De Masi, et al., Nucl. Instr. and Meth. A 628 (2011) 296.

[2] F. Sauli, Nucl. Instr. and Meth. A 386 (1997) 531.

[3] Y. Giomataris, et al., Nucl. Instr. and Meth. A 376 (1996) 29.

[4] D. Brown, et al., Nucl. Instr. and Meth. A 397 (1997) 261.

[5] M. G. Albrow, et al., `arXiv:0806.0302 [hep-ex]`

[6] EIC R&D. `Generic Detector R&D for an Electron Ion Collider.`

ePHENIX for eRHIC

Alexander Bazilevsky[1] for the PHENIX Collaboration

[1]Brookhaven National Laboratory, Upton, NY 11973, USA

DOI: http://dx.doi.org/10.3204/DESY-PROC-2012-02/105

Addition of a high intensity polarized electron beam facility which could realize Deep Inelastic Scattering (DIS) research with one of the RHIC beams is one of the future upgrades to the Relativistic Heavy Ion Collider (RHIC) presently under consideration. To take a full advantage of such machine evolution, after more than a decade of exciting physics results, both with heavy ion and polarized proton collisions, PHENIX Collaboration has launched a detector upgrade study consistent with the above collider upgrades, going in to the eRHIC era.

1 Introduction

One of the realization of the future Electron Ion Collider is eRHIC – by adding 5–30 GeV electron beam facility to the existing RHIC hadron beam facility, accelerating and colliding polarized protons and nuclei in wide range of masses [1]. In this presentation we consider possible Deep Inelastic Scattering (DIS) measurements with a future upgraded PHENIX detector (ePHENIX) at eRHIC.

Our goal is to fully utilize sPHENIX upgrade being proposed by PHENIX collaboration to further advance the study of cold and hot nuclear matter in nuclear collisions and nucleon spin structure in polarized proton collisions [2]. We discuss the requirements to ePHENIX detector imposed by DIS goals [3] to provide smooth evolution from sPHENIX to ePHENIX.

2 Physics goals and detector requirements

With ePHENIX we hope to perform a wide range of measurements summarized in [3] to greatly expand our knowledge in the following major themes:

- The spin and flavor structure of the proton
- Three dimensional structure of the nucleons in momentum and configuration space
- QCD matter in nuclei.

Another major topic of Electroweak physics and the search for physics beyond the Standard Model discussed in [3] requires higher energies and luminosities anticipated in the latter phase of eRHIC, and they are not discussed in this presentation.

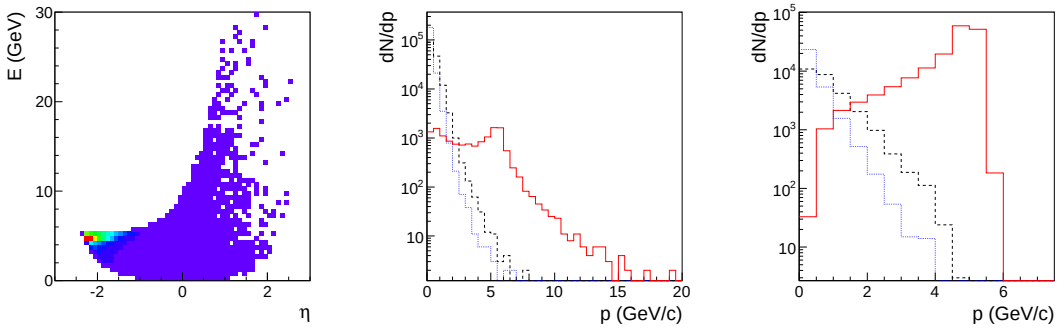

Figure 1: From PYTHIA for 5 GeV (electron) × 100 GeV (proton) beam energy configuration: scattered electron energy vs pseudorapidity distribution (left); momentum spectra for scattered electron (red), charged pions (black dashed) and decay photons (blue dotted) detected in central rapidity, $|\eta| < 1$ (middle) and backward rapidities, $\eta < -1$ (right).

2.1 Inclusive DIS and scattered electron measurements

Inclusive DIS measurements implies reconstruction of only the scattered lepton in the final state of a reaction. Measurements of energy and angle of the scattered lepton provide the reconstruction of the kinematics of the inclusive DIS, which is described by two independent variables, the Bjorken scaling variable x and square of the four momentum transfer Q^2.

Inclusive DIS provide "golden" measurements for the gluon polarization in the nucleon and its contribution to the nucleon spin via scaling violation of the structure function g_1, as well as quark and gluon distribution in nuclei via structure functions F_2^A and F_L^A.

In collider geometry the DIS electrons are scattered mainly in backward (electron beam direction) and central rapidities, see Fig. 1 left. Central rapidity selects scattering with higher Q^2 and higher x (due to its correlation with Q^2). The energy of the scattered electron varies in the range from zero to electron beam energy and even to higher values for electrons detected in central and forward rapidities.

Collider kinematics allows us to clearly separate scattered electrons from other DIS fragments - hadrons and their decay products, which are detected preferably in forward region (hadron beam direction), leaving much softer spectra in central and backward rapidities, see Fig. 1. Reasonable tracking and electromagnetic calorimetry will provide enough rejection through E/p matching and shower profile analysis to allow us to reliably identify electrons down to momentum at least 1 GeV/c. Photon conversion in material on the way from beam line to tracker ($\sim 10\%$ of radiation length looks affordable) also is not expected to contribute sizable background except for very low momenta (< 1 GeV/c). Lower momentum electrons (< 1 GeV/c) only modestly extend the $Q^2 - x$ phase space of DIS kinematics. In addition, these events are more contaminated by radiative effects, so other approaches (e.g. Jacquet-Blondel method with hadronic final states) are supposed to be used for DIS kinematics reconstruction in these cases.

The energy and angular resolution requirements are presented on the example of F_L measurements in Fig. 2, for the 1% systematic uncertainty in each 0.1×0.1 bin in $\log_{10}(x) \times \log_{10}(Q^2)$ space, assuming that 1/5 of the systematics due to bin migration would contribute to the final systematic uncertainty. In the backward and central rapidity regions, covering the

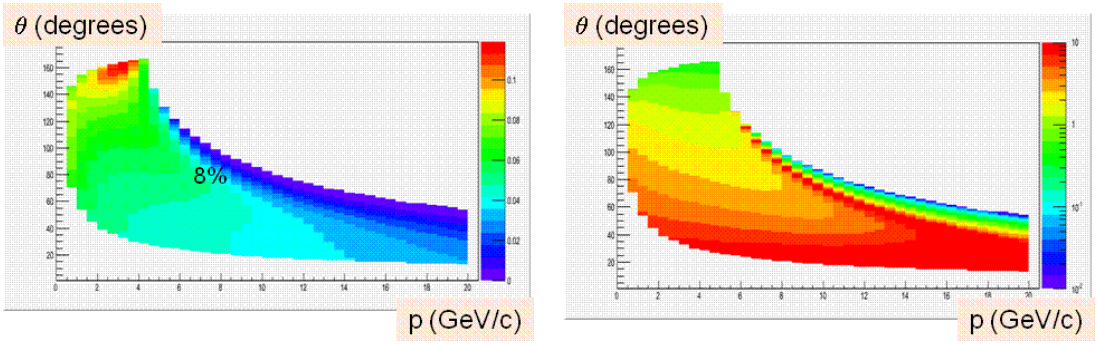

Figure 2: For 5 GeV (electron) × 100 GeV (proton) beam energy configuration: momentum, $\delta p/p$ (left) and angular (right) resolution requirements (z-axis, collor coded) for bins in scattered electron momentum and angle.

major of the DIS phase space (forward region corresponds to high x, while our main interest is in lower x) the detector resolution requirements are not strict and can be easily provided by tracking system with momentum resolution of $\delta p/p \sim 1\% \cdot p$. For higher electron beam energy the scattered electron energy is higher, and a combination of the tracking detectors with electromagnetic calorimetry with energy resolution of $\sigma_E/E \sim (10-15)\%/\sqrt{E}$ is expected to provide enough resolution for electron energy measurements.

2.2 Semi-inclusive DIS and hadron measurements

Hadron identification (pions vs kaons) is a requirement for flavor decomposition of quark and anti-quark polarization in the nucleon, as well as to study the transverse spin structure of the nucleon, in semi-inclusive DIS, when along with scattered lepton one measures one or more fragmented hadrons.

Charged hadrons are mainly scattered in central and forward (hadron beam direction) rapidities. A set of particular detectors is required for hadron identification in these regions. While in forward region we can consider various options, in central region we are limited by the space available inside the solenoid magnet [2], where only a compact detector in radial space can be affordable. Among other options, we consider DIRC with a very thin radiator ($\sim$ 5 cm), or proximity focused RICH, which can provide hadron identification up to momenta 4–5 GeV/c. It doesn't introduce any limitation on the accessible $Q^2 - x$ phase space in the central rapidity region, as can be seen from Fig. 3.

2.3 Exclusive DIS and DVCS

Exclusivity implies the reconstruction of the complete final state, which includes reconstruction of the scattered proton with small four momentum transfer $-t$ at about 1 $(\mathrm{GeV/c})^2$ or lower. Among exclusive processes, Deeply Virtual Compton scattering (DVCS) is of particular interest because it provides theoretically the cleanest access to Generalized Parton Distributions (GPDs), describing the correlation between parton momentum and (transverse) position within the nucleon. One of the important aspects of GPDs is that they are connected to the total quark and gluon angular momentum.

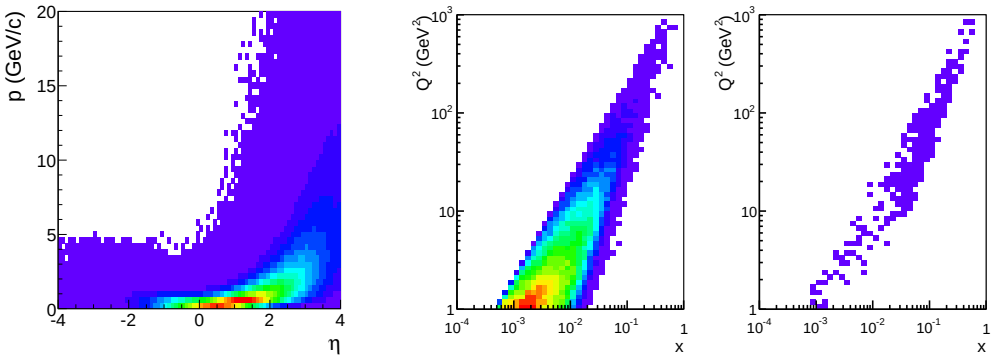

Figure 3: From PYTHIA for 5 GeV (electron) × 100 GeV (proton) beam energy configuration: charged pion momentum vs pseudorapidity distribution (left); Q^2 vs x coverage in DIS events with charged pions detected in central rapidity ($|\eta| < 1$) with $p < 4$ GeV/c (middle) and $p > 4$ GeV/c (right).

The produced DVCS photon momentum versus pseudorapidity distribution is shown in Fig. 4. For 5 GeV electron beam, near half of photons are detected in central rapidity. For higher electron beam energy more photons scatter in backward direction, still leaving about a third of photons scattered in central region with electron beam energy 20 GeV. The photon momentum in central rapidity varies in the range ∼1–4 GeV/c near independently on beam energy in the range considered for eRHIC. Photons in backward rapidity are more correlated with electron beam and have energy varied roughly from 1 GeV/c to electron beam energy.

3 Summary

The reasonably minimal detector configuration considered for ePHENIX should provide scattered electron and photon measurements in the central and backward (electron beam direction) rapidities, hadron identification and momentum measurements in central and forward (hadron beam direction) rapidities, and scattered proton measurements in very forward direction (within beam pipe) in exclusive reactions. Adding new detector systems should provide a smooth evolution from sPHENIX (as a *pp* and Heavy Ion detector) to ePHENIX (as a DIS detector).

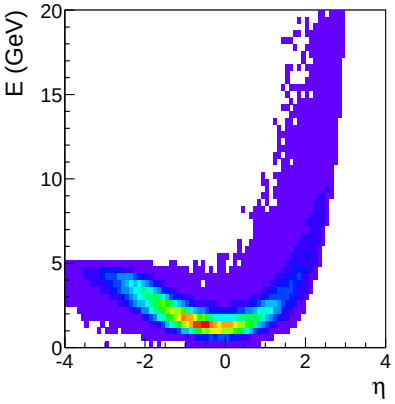

Figure 4: MILOU DVCS generator ([4]) for 5 GeV (electron) × 250 GeV (proton) beam energy configuration: DVCS photon energy vs pseudorapidity distribution.

References

[1] V. Ptitsyn, this proceedings.

[2] K. Boyle, this proceedings.

[3] BNL/INT/JLab report, arXiv:1108.1713.

[4] E. Perez, L. Schoeffel and L. Favarat, arXiv:hep-ph/0411389.

Medium-induced soft gluon radiation in DIS

Néstor Armesto[1], *Hao Ma*[1], *Mauricio Martínez*[1], *Yacine Mehtar-Tani*[2], *Carlos A. Salgado*[1]

[1]Departamento de Física de Partículas and IGFAE, Universidade de Santiago de Compostela E-15782 Santiago de Compostela, Galicia-Spain
[2]Institut de Physique Théorique, CEA Saclay, F-91191 Gif-sur-Yvette, France

DOI: `http://dx.doi.org/10.3204/DESY-PROC-2012-02/0`

We study color coherence effects on the medium-induced soft gluon radiation off an asymptotic quark hit by a virtual photon traversing a hot and dense QCD medium. The transverse momentum spectrum of the emitted gluon is computed at 1st order in opacity expansion. The interference effects between the initial and final state radiation modify the soft gluon spectrum when a finite angle between the incoming and outgoing quarks is considered, presenting a soft divergence. We comment on possible implications on observables in eA collisions which are sensitive to the initial state radiation.

1 Introduction

Color coherence effects in vacuum are found by TASSO and OPAL experiments [1, 2], by the depletion of particle energy spectrum in the soft part. Medium-induced soft gluon radiation off a single quark in the final state was also studied [3, 4, 5]. Our goal is to check color coherence between initial and final state quarks in the presence of a medium which could be of applicability in DIS on nucleus. This is a different setup complementary to the antenna in s-channel [6, 7, 8, 9]. One can imagine an energetic electron with very large forward rapidity scatters on an energetic nucleus with very large backward rapidity by exchanging a highly virtual photon. The photon scatters on one quark inside the nucleus to change its transverse momentum, and then such small-x quark can rescatter on the fields generated by the other components of the nucleus. The soft gluon radiation should be induced by the quark rescattering. The process we study happens in eA collisions [1], which is related to the future LHeC and EIC experiments. When the scattering angle between the incoming and outgoing quarks becomes 0, our calculation matches the one for gluon production in the totally coherent limit in the CGC framework [10].

2 The antenna spectrum in t-channel in vacuum

Antenna radiation in t-channel in vacuum is shown in Fig.1. We work in infinite momentum frame. Small scattering angle between incoming and outgoing quarks (p and $\bar{p}$, respectively) is assumed, i.e. $\theta_{p\bar{p}} \ll 1$. Eikonal approximation is employed, i.e. $p^+ \sim \bar{p}^+ \gg k^+ \gg |\mathbf{k}|$, where the relation between the forward light-cone momentum and the energy of the emitted soft gluon reads $k^+ = \sqrt{2}\,\omega$. The light-cone gauge $n \cdot A = A^+ = 0$ is chosen, with the axial

[1]If the exchanging particle is a highly virtual gluon, then one can consider the process as pA collisions.

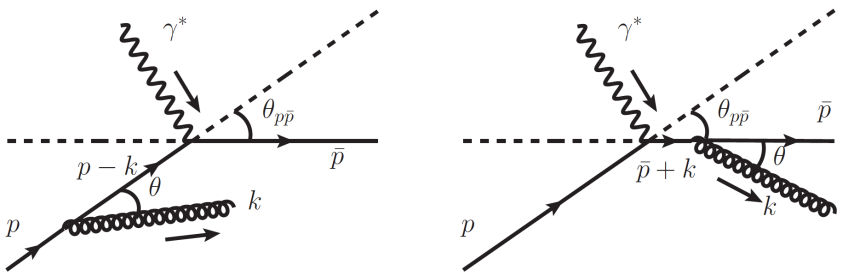

Figure 1: Antenna radiation in t-channel in vacuum

vector $n = (0, 1, \mathbf{0})$. Highly virtual photon γ^* is absorbed by an incoming quark with transverse size $|\Delta\mathbf{x}| \sim 1/|\bar{\mathbf{p}} - \mathbf{p}|$. The soft gluon spectrum off, e.g. outgoing quark in vacuum in which the azimuthal angle is integrated with respect to the direction of outgoing quark (analogously for the incoming quark) reads

$$dN^{\rm vac}_{\rm out} = \frac{\alpha_s\, C_F}{\pi}\,\frac{d\omega}{\omega}\,\frac{\sin\theta\, d\theta}{1-\cos\theta}\,\Theta(\cos\theta - \cos\theta_{p\bar{p}}), \tag{1}$$

where α_s is the strong coupling constant, C_F is the Casimir factor of the fundamental representation, $\theta \approx |\boldsymbol{k}|/\omega$ is the gluon emission angle, and the heaviside step function gives the angular constraint $\theta < \theta_{p\bar{p}}$, i.e. the soft gluon emission is constrained to be inside the cone set by the scattering angle between the incoming and outgoing quarks [11]. As long as $|\boldsymbol{\lambda}| = 1/|\boldsymbol{k}|$, i.e. the transverse wave length of the emitted gluon, is shorter than $|\boldsymbol{r}| \sim t_{\rm form}\,\theta_{p\bar{p}}$ (the change of position of the quark in the transverse plane due to the photon scattering when the gluon is formed [2]), the gluon resolves the color structure and the bremsstrahlung is therefore off either the incoming quark or the outgoing quark. In terms of angles, one gets immediately $\theta < \theta_{p\bar{p}}$ from the simple analysis above.

3 The medium-induced antenna spectrum in t-channel

Medium-induced antenna radiation in t-channel is shown in Fig.2. We work in the same setup as the one in vacuum. Medium is assumed to act right after the photon scattering. Note that there is no need to go into the details of how the medium is modeled in our study. We consider dilute medium scenario, i.e. one gluon exchange. The opacity is defined as L/λ, and when we say "opacity expansion", we mean the expansion in number of scattering centers. Hadronization is considered to occur outside the medium, therefore the process we consider is a pure perturbative process. The medium-induced antenna spectrum in t-channel at 1st order

[2] The formation time is defined as $t_{\rm form} \sim \omega/\boldsymbol{k}^2$.

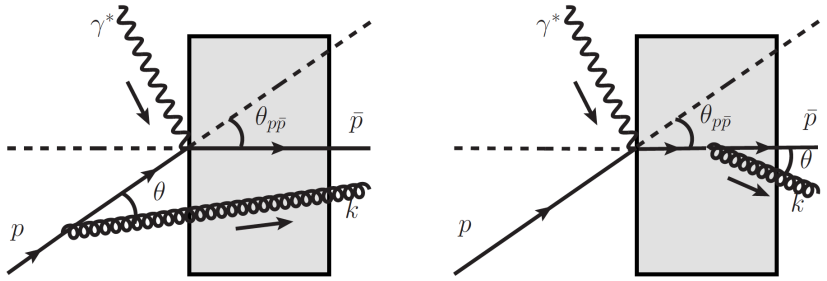

Figure 2: Medium-induced antenna radiation in t-channel

in opacity expansion reads:

$$\begin{aligned}\omega\frac{dN^{\rm med}}{d^3\vec{k}} =& \frac{\alpha_s C_F\,\hat{q}}{\pi}\int\frac{d^2\boldsymbol{q}}{(2\pi)^2}\mathcal{V}^2(\boldsymbol{q})\int_0^{+\infty}dx^+\\ &\left[\frac{\boldsymbol{\nu}^2}{x^2\,(p\cdot v)^2}-\frac{\boldsymbol{\kappa}^2}{x^2\,(p\cdot k)^2}\right.\\ &+\frac{2}{\bar{x}^2}\left(\frac{\bar{\boldsymbol{\nu}}^2}{(\bar{p}\cdot v)^2}-\frac{\bar{\boldsymbol{\kappa}}\cdot\bar{\boldsymbol{\nu}}}{(\bar{p}\cdot v)(\bar{p}\cdot k)}\right)\left(1-\cos\left[\Omega_{\bar{p}}x^+\right]\right)\\ &+\frac{2}{x\,\bar{x}}\left(\frac{\boldsymbol{\kappa}\cdot\bar{\boldsymbol{\kappa}}}{(\bar{p}\cdot k)\,(p\cdot k)}-\frac{\boldsymbol{\nu}\cdot\bar{\boldsymbol{\kappa}}}{(\bar{p}\cdot k)\,(p\cdot v)}\right.\\ &\left.\left.+\left(\frac{\boldsymbol{\nu}\cdot\bar{\boldsymbol{\kappa}}}{(\bar{p}\cdot k)\,(p\cdot v)}-\frac{\boldsymbol{\nu}\cdot\bar{\boldsymbol{\nu}}}{(\bar{p}\cdot v)\,(p\cdot v)}\right)\left(1-\cos\left[\Omega_{\bar{p}}x^+\right]\right)\right)\right],\end{aligned}\tag{2}$$

where $\hat{q}=\alpha_s C_A n_0 m_D^2$ denotes the medium transport coefficient and $\Omega_{\bar{p}}=(\mathbf{k}-\mathbf{q})^2/(2\,k^+)$ is the inverse of the gluon formation length. The second line in Eq.(2) is the contribution from the gluon radiation off the initial quark. The third line in Eq.(2) comes from the medium-induced gluon radiation off the outgoing quark, i.e. the independent spectrum [8]. The last two lines of Eq.(2) is the interference between the incoming and outgoing quarks. Note that when the scattering angle $\theta_{p\bar{p}}=0$, the spectrum becomes [3]

$$\omega\frac{dN^{\rm med}}{d^3\vec{k}}=\frac{4\,\alpha_s C_F\,\hat{q}\,L^+}{\pi}\int\frac{d^2\mathbf{q}}{(2\pi)^2}\mathcal{V}^2(\mathbf{q})\,\boldsymbol{L}^2,\tag{3}$$

where $\boldsymbol{L}=(\boldsymbol{\kappa}-\boldsymbol{q})/(\boldsymbol{\kappa}-\boldsymbol{q})^2-\boldsymbol{\kappa}/\boldsymbol{\kappa}^2$ is the transverse component of the Lipatov vertex in the light-cone gauge. The notations are $\boldsymbol{\kappa}=\boldsymbol{k}-x\,\boldsymbol{p}$ and $x=k^+/p^+$. The structure of the transverse component of the gauge invariant Lipatov vertex indicates that Eq.(3) is the genuine medium-induced gluon radiation off an on-shell quark which comes from the $-\infty$ and goes to the $+\infty$.

[3]The case of $\theta_{p\bar{p}}=0$ was studied in the multiple soft scattering approach in [10].

4 Soft limit

In the soft gluon emission limit ($\omega \to 0$), the antenna spectrum in t-channel in medium, adding the medium-induced and the vacuum contributions, reads

$$\omega \frac{dN^{\rm vac}}{d^3\vec{k}} + \omega \frac{dN^{\rm med}}{d^3\vec{k}} = \frac{4\,\alpha_s\,C_F}{(2\,\pi)^2}\left[(1-\Delta)\left(\frac{1}{\boldsymbol{\kappa}^2} - \frac{\boldsymbol{\kappa}\cdot\bar{\boldsymbol{\kappa}}}{\boldsymbol{\kappa}^2\,\bar{\boldsymbol{\kappa}}^2}\right) + \frac{1}{\bar{\boldsymbol{\kappa}}^2} - (1-\Delta)\,\frac{\boldsymbol{\kappa}\cdot\bar{\boldsymbol{\kappa}}}{\boldsymbol{\kappa}^2\,\bar{\boldsymbol{\kappa}}^2}\right], \qquad (4)$$

where the medium parameter at 1st order in opacity is $\Delta = \hat{q}\,L^+/m_D^2$ and the notations are $\bar{\boldsymbol{\kappa}} = \boldsymbol{k} - \bar{x}\,\bar{\boldsymbol{p}}$ and $\bar{x} = k^+/\bar{p}^+$. The first term in the brackets shows the angular constraint for a reduced number of soft gluon emission off the incoming quark if one performs the azimuthal angle integration for the emitted soft gluon. The reason for the reduction of the soft gluon multiplicity inside the cone is that, the emitted soft gluon off the incoming quark will suffer rescattering when it goes through the medium. Therefore, part of the soft gluon multiplicity is further "kicked" out of the cone, which causes a reduction of the soft gluon spectrum off the incoming quark. The rest in the brackets is the soft gluon emission off the outgoing quark in medium. When the medium is switched off, i.e. $\Delta \to 0$, one naturally gets the vacuum contribution only. In the opaque medium limit, i.e. $\Delta \to 1$, one has

$$\omega \frac{dN^{\rm vac}}{d^3\vec{k}} + \omega \frac{dN^{\rm med}}{d^3\vec{k}} = \frac{4\,\alpha_s\,C_F}{(2\,\pi)^2}\,\frac{1}{\bar{\boldsymbol{\kappa}}^2}. \qquad (5)$$

After comparing Eq.(5) with Eq.(4), one can see that the soft part of the medium-induced gluon energy spectrum off the incoming quark is suppressed, i.e. the gluon density is saturated, and the bremsstralung contribution between vacuum and medium-induced parts get canceled with each other. In Eq.(5), one gets complete color decoherence for the outgoing quark, i.e. in the opaque medium the outgoing quark loses the color coherence with the incoming quark, and then the soft gluon radiation off the outgoing quark is like the soft gluon radiation off a single quark in vacuum. A similar property was discovered in the antenna spectrum in s-channel [8, 9].

Generalizing the results to the multiple soft scattering limit is in progress.

References

[1] W. Braunschweig *et al.* [TASSO Collaboration], Z. Phys. C **47** (1990) 187.

[2] G. Abbiendi *et al.* [OPAL Collaboration], Eur. Phys. J. C **27** (2003) 467.

[3] R. Baier, Y. L. Dokshitzer, A. H. Mueller, S. Peigné and D. Schiff, Nucl. Phys. B **483**, 291 (1997) [arXiv:hep-ph/9607355].

[4] B. G. Zakharov, JETP Lett. **65**, 615 (1997) [arXiv:hep-ph/9704255].

[5] U. A. Wiedemann, Nucl. Phys. B **588**, 303 (2000) [arXiv:hep-ph/0005129].

[6] Y. Mehtar-Tani, C. A. Salgado, K. Tywoniuk, Phys. Rev. Lett. **106** (2011) 122002. [arXiv:1009.2965 [hep-ph]].

[7] J. Casalderrey-Solana, E. Iancu, JHEP **1108** (2011) 015. [arXiv:1105.1760 [hep-ph]].

[8] N. Armesto, H. Ma, Y. Mehtar-Tani, C. A. Salgado and K. Tywoniuk, JHEP **1201** (2012) 109 [arXiv:1110.4343 [hep-ph]].

[9] Y. Mehtar-Tani, C. A. Salgado and K. Tywoniuk, Phys. Lett. B **707** (2012) 156 [arXiv:1102.4317 [hep-ph]].

[10] Y. V. Kovchegov and A. H. Mueller, Nucl. Phys. B **529** (1998) 451 [hep-ph/9802440].

[11] Yu. L. Dokshitzer, V. A. Khoze, A. H. Mueller, and S. I. Troyan, *"Basics of Perturbative QCD", Gif-sur-Yvette, France, Ed. Frontières 1991.*

Low-x Physics in ep and eA Scattering at the LHeC: Inclusive and Final State Observables

Néstor Armesto[1] for the LHeC Study Group

[1]Departamento de Física de Partículas and IGFAE, Universidade de Santiago de Compostela, 15782 Santiago de Compostela, Spain

DOI: http://dx.doi.org/10.3204/DESY-PROC-2012-02/350

The opportunities for low-x physics studies at the proposed Large Hadron-electron Collider at CERN will be examined. After a brief introduction, the kinematical reach of the machine will be presented. Then I will focus on inclusive and final state observables, with special attention to the improvements on the determination of parton densities both in ep and eA and to the possibilities for establishing novel aspects of the dynamics at small-x.

1 Introduction

From our present experimental knowledge of DIS, it is widely accepted that inclusive and diffractive data at small-x can be described by several alternatives: non-perturbative models and, within perturbative QCD, different realizations of evolution equations - fixed-order perturbation theory (DGLAP), resummation schemes and non-linear approaches. Concerning the last item, saturation of partonic densities should occur at high energies or small Bjorken-x. The present discussion focuses on the relevant kinematical regime for such phenomena and the possibilities offered by existing or future experiments to discriminate between different schemes.

On a more practical level, our knowledge of partons distributions (PDFs) at small x in protons and nuclei does not suffice for the required predictive precision within collinear factorization at hadron colliders. Besides, in lepton-nucleus and in the semihard region for particle production, collinear factorization is not expected to work and other factorization schemes have been proposed. Both aspects are key for the study of hadronic and nuclear collisions.

The Large Hadron-electron Collider (LHeC [1, 2, 3]) is an electron-proton/ion collider currently under design, that will collide $20 \div 140$ GeV $e^{\pm}$ against the LHC beams. Besides EW and new physics investigations, this machine will perform precision QCD studies and should allow an unambiguous access to the novel regime of QCD in which non-linear effects are dominant - the dense region in Fig. 1. With the transition between the dilute linear region and the new phase characterized by high density, a two-pronged approach will be pursued: either decreasing x at fixed mass number A and negative photon virtuality Q^2, or increasing A at fixed x and Q^2. The LHeC will explore a completely new region of the Q^2-x plane, see Fig. 2. In this contribution I will mention some aspects: inclusive and final state observables, of the small-x studies that may be performed at the LHeC (for other aspects, see the contribution by A. Stasto [3]). Full information can be found in [2] to which I refer the reader for details and references, and in related work concerning the proposed Electron-Ion Collider in the USA [4, 5], see also [6].

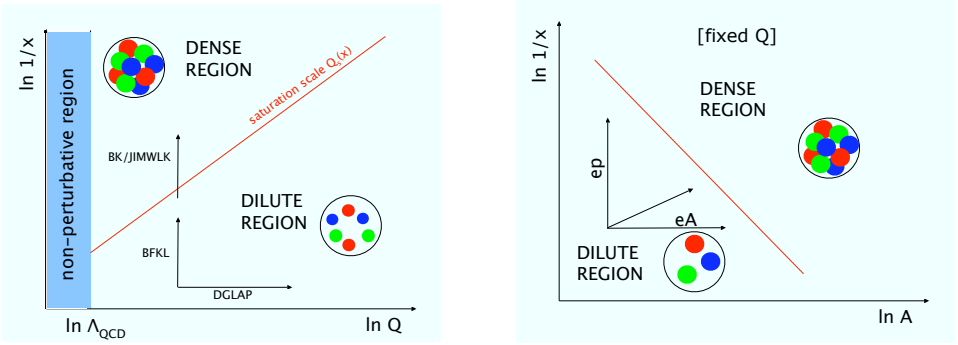

Figure 1: Sketch of the access to the dense partonic region where unitarity effects are essential, from the dilute one where linear evolution is valid. (From [2].)

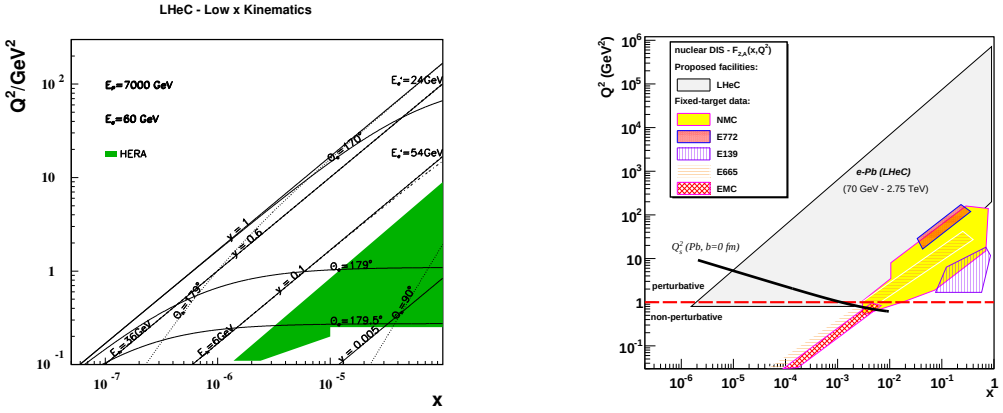

Figure 2: Left: kinematics of ep scattering at the LHeC at low x. Solid (dotted) curves correspond to constant polar angles θ_e (θ_h) of the scattered electron (hadronic final state). The polar angle is defined with respect to the proton beam direction. Dashed (dashed-dotted) curves correspond to constant energies E'_e (E_h) of the scattered electron (hadronic final state). The shaded (green) area illustrates the region of kinematic coverage in neutral current scattering at HERA. Right: region of the Q^2-x plane that will be explored with the LHeC in ePb, compared to those achievable at existing eA experiments. An estimation of the saturation scale indicating the dilute-dense transition is shown. (From [2].)

2 Inclusive observables at small x

With its huge kinematical lever arm and the possibility to measure not only the total structure function, F_2, but also its flavor decomposition and the longitudinal one, F_L (see Figs. 3 and 4 for examples of pseudodata for F_2 and F_L in ep and eA respectively), the LHeC offers rich possibilities for:
(a) Constraining PDFs in DGLAP analysis, both in ep and eA, particularly for sea quarks and gluons. For this purpose, the combination of F_2, F_L and $F_{2c,b}$ appears to be very promising. As shown in Figs. 3 and 4 for F_2 and F_L, the expected uncertainty of data is much smaller than the

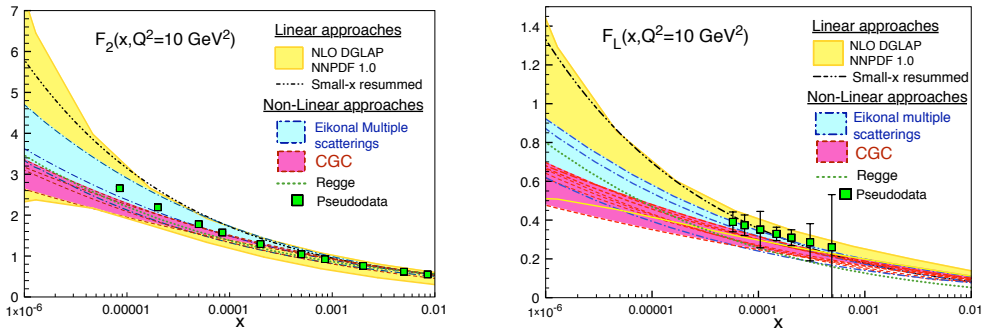

Figure 3: Predictions from different models for $F_2(x, Q^2 = 10\ \mathrm{GeV}^2)$ (plot on the left) and $F_L(x, Q^2 = 10\ \mathrm{GeV}^2)$ (plot on the right) versus x, together with LHeC pseudodata. (From [2].)

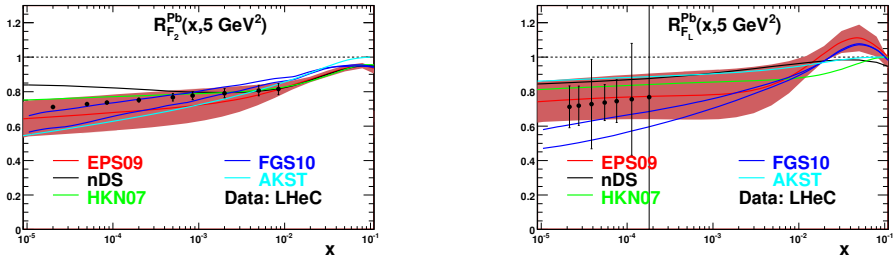

Figure 4: Predictions from different models for the nuclear ratio $R_{F_i}^{\mathrm{Pb}} = F_i^{\mathrm{Pb}}/(208\, F_i^{\mathrm{p}})$, $i = 2, L$, at small x, see the legend on the plots. Circles with error bars are LHeC pseudodata. (From [2].)

spread of existing models. This will have strong implications on the search of ultra-high-energy neutrinos in cosmic ray experiments.
(b) Disentangling fixed-order evolution schemes from resummation or non-linear ones. In this respect, the combination of data on F_2 and F_L is required.

As an additional aspect, the measurement of the γp cross section will help to constrain models for the high-energy behavior of hadronic cross sections.

3 Final states

The LHeC will offer huge possibilities for clarifying the dynamics of QCD radiation and hadronization. For example:
(a) The dynamics of QCD radiation at small x will be studied through forward jet and particle production, which will be abundant, see Fig. 5.
(b) The parton/hadron energy loss mechanism in semi-inclusive DIS will be tested by introducing a nucleus which would modify the hadronization pattern. Energies as high as 10^5 GeV in the rest frame of the nucleus will be accessible and the transition from low to high energies will be studied. As an example of the large yields, inclusive jet rates for $Q^2 = 0$ around 10^3 jets per GeV per year are expected with $E_{Tjet} \sim 95$ (80) GeV in ep (ePb).

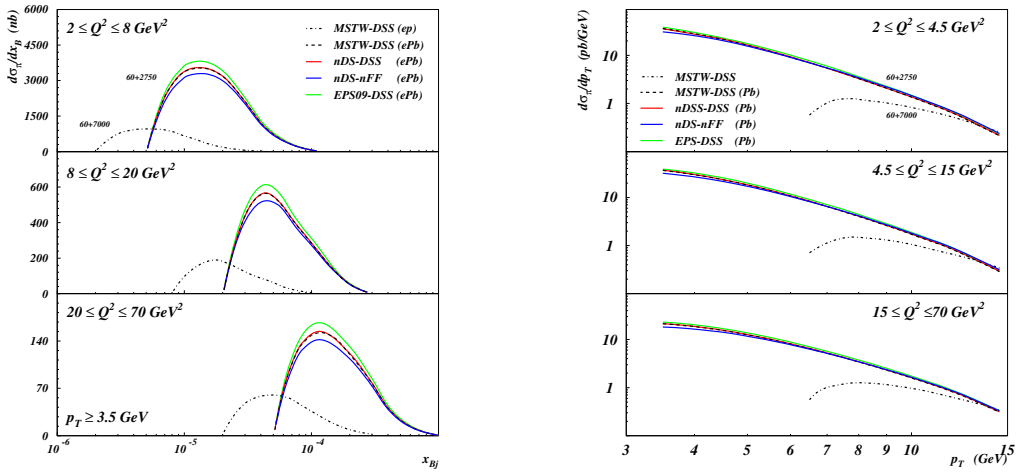

Figure 5: Cross section per nucleon for inclusive π^0 production versus $x_{Bj} = x$ for $p_T > 3.5$ GeV/c (left) and versus p_T (right), computed in NLO QCD. Dashed-dotted black lines refer to ep collisions. All other line types refer to ePb collisions: dashed black ones to standard nucleon PDFs and fragmentation functions (FFs), solid red and green ones to nuclear PDFs and nucleon FFs, and solid blue ones to nuclear PDFs and nuclear FFs. Cuts: $\theta_\pi \in [5°, 25°]$, $x_\pi = E_\pi/E_p > 0.01$, have been applied. (From [2].)

Acknowledgements

Financial suppport by the European Research Council grant HotLHC ERC-2011-StG-279579, by MiCinn of Spain grants FPA2008-01177, FPA2009-06867-E and Consolider-Ingenio 2010 CPAN CSD2007-00042, by Xunta de Galicia grant PGIDIT10PXIB 206017PR and by FEDER, is gratefully acknowledged.

References

[1] M. Klein *et al.*, Proceedings of *11th European Particle Accelerator Conference (EPAC 08)*, Genoa, Italy, 23-27 June 2008, preprint WEOAG01; `http://cern.ch/lhec`.

[2] J. L. Abelleira Fernández *et al.* [LHeC Study Group], *A Large Hadron Electron Collider at CERN: Report on the Physics and Design Concepts for Machine and Detector*, J. Phys. G39 (2012) 075001 [arXiv:1206.2913 [physics.acc-ph]].

[3] A. Bunyatyan, these proceedings; D. Schulte, *ibid.*; A.Stasto, *ibid.*; O. Behnke, *ibid.*; R. Godbole, *ibid.*; A. Polini, *ibid.*; R. Tomás García, *ibid.*

[4] The Electron Ion Collider Working Group Collaboration, C. Aidala *et al.*, *A High Luminosity, High Energy Electron Ion Collider*; `http://web.mit.edu/eicc/`; D. Boer *et al.*, arXiv:1108.1713 [nucl-th].

[5] F. Yuan, these proceedings; M. Stratmann, *ibid.*; C. Keppel, *ibid.*; K. Dehmelt, *ibid.*; J. H. Lee, *ibid.*; E. Nissen, *ibid.*; A. Bazilevsky, *ibid.*; V. Ptitsyn, *ibid.*

[6] M. Klein, these proceedings.

Physics with Electron-Ion Collisions at EIC

J.H. Lee

Brookhaven National Laboratory, Upton, NY11973, USA

DOI: http://dx.doi.org/10.3204/DESY-PROC-2012-02/338

Nuclei and nucleons probed in DIS and diffractive processes in the high-energy (small-x) regime open a new precision window into fundamental questions in QCD. The proposed Electron-Ion Collider (EIC) is a new high-energy and high-luminosity polarized electron-ion/polarized proton machine. The design offers an unprecedented access to explore the nature of QCD matter and strong color fields. In particular, the new collider will allow us to reach and explore the regime where the gluon density saturates, one of the fundamental outstanding questions in QCD, and test the validity of the Color Glass Condensate approach. Selected key measurements in eA collisions as probing and characterizing the gluonic matter are discussed.

1 Introduction

Quantum Chromodynamics has established itself as a successful theory of strong interactions, yet the details of the underlying mechanism of the theory have not been fully understood. Especially the dynamics of the gluons is still far from complete understanding, considering gluons are the mediator of the strong force and mostly responsible for the visible mass of the universe. The difficulty of the theoretical understanding lies mainly in the nature of self-coupling of gluons, which is conjectured to lead to the phenomenon of parton saturation at small parton momentum fraction (x) theorized as the Color Glass Condensate (CGC) [1]. The non-linear regime, where the increase of the number of gluons through gluon radiation and parton splitting is balanced by multi-gluon fusion between self-interacting gluons. The dynamic scale Q_s^2 characterizes onset of the saturation for the density of gluons in the target, and increases as x_g gets smaller as shown in Fig. 1. The proposed electron-ion collider (EIC) [2, 3] is designed to explore the nature of QCD matter and strong color fields with a unprecedentedly wide kinematic reach accessing deeply into saturation regime by utilizing nuclear enhanced saturation scale $(Q_s^A)^2 \approx A^{\frac{1}{3}}(Q_s^p)^2$. The kinematic coverages of the EIC for the planned electron and nucleon energy ranges from $5(e)$+$100(N)$ GeV (stage I) to 30+100 GeV (stage II) with predicted saturation scales are shown for ep and eA collisions in Fig. 1. Selected key measurements in eA collisions with the EIC as probing and characterizing the gluonic matter will be discussed. A more detailed description of physics capabilities and proposed machine designs of the EIC can be found in [4, 5, 6].

2 Key Measurements with the EIC

2.1 Nuclear Structure Functions

Nuclear structure functions $F_2^A(x,Q^2)$ and $F_L^A(x,Q^2)$ which characterize the partonic structure of nuclei are the most basic observables in eA, and they will be one of the first observables at the EIC. F_2 is sensitive to gluons via scaling violations, and F_L is directly proportional to the gluon momentum distribution. Extraction of nuclear F_L requires running at multiple beam energies, which can be accommodated by the flexibility of the EIC. Higher-twist effects [7] in non-linear evolution in x can be realized as variations of the nuclear modification factors of the structure functions defined as $R_{2,L}(x,Q^2) = F_{2,L}^A(x,Q^2)/(AF_{2,L}^p(x,Q^2))$. Various models with different treatment of the conventional QCD effects and the expected phenomenology of saturation, have a wide range of predictions for $R_{2,L}(x,Q^2)$. Within the expected precision of the measurements at the EIC, differentiation between the different models is clearly possible in the region $10^{-4} \lesssim x \lesssim 1$. In addition to inclusive DIS measurements for structure functions, nuclear diffractive structure functions F^D, which have never been measured in $e+A$, can be also accessed at the EIC. At the EIC energy regime, diffractive processes are expected to share a large ($> 30\%$) fraction of the total cross-section, and nuclear F^D will be a sensitive measurement of saturation [8].

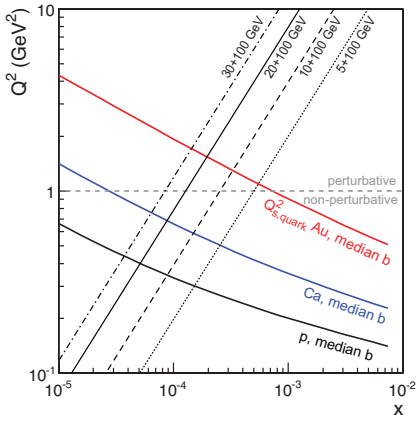

Figure 1: Kinematic coverage in x and Q^2 of the EIC for different beam energies, compared with predictions of the saturation scale, Q_s^2, in p, Ca, and Au.

2.2 Di-hadron Correlations

The nonlinear evolution of multi-gluon distributions are expected to be different from that of the single-gluon distribution, and it can be measured through modification of di-hadron correlations [9] in semi-inclusive DIS process $e + A \to e' + h_1 + h_2 + X$. Saturation physics allows us to compute the functional form of the gluon distribution as functions of gluon transverse momentum $k_\perp$ and saturation momentum $Q_s^2(x_g)$. Figure 2 shows the difference in azimuthal angle between a trigger- ($p_T^{trig} > 2$ GeV/c) and an associate- ($p_T^{trig} > p_T > 1$ GeV/c) hadrons. Precise measurements of these

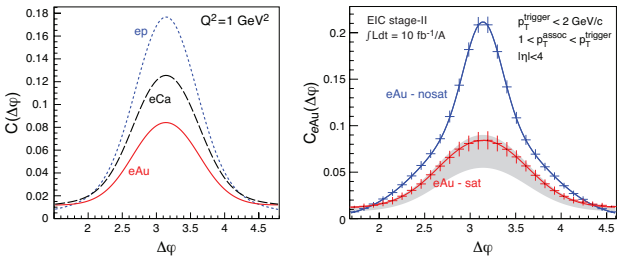

Figure 2: Saturation model [10] predictions of azimuthal angle difference ($\Delta\varphi$) between two hadrons in ep, eCa, and eAu (left), and comparisons with calculations from conventional non-saturated model (right).

di-hadron correlations at the EIC would allow one to extract the spatial multi-gluon correlations and study their non-linear evolution. Saturation effects in this channel correspond to a progressive disappearance of the back-to-back correlations of hadrons with increasing atomic number A.

2.3 Exclusive Diffractive Vector Meson Production

For precise transverse imaging of gluon distributions and how the small-x evolution modifies the transverse distributions, exclusive vector meson production, $e + A \to e' + V + A'$ where $V = \rho, \phi, J/\psi$ in coherent and incoherent diffractive processes will be studied. Coherent diffraction, where the nucleus stays intact, probes the space-time distribution of the patrons in the nucleus, while incoherent diffractive processes where the nucleus excites and breaks up, is sensitive to fluctuations of high parton densities at small impact parameter with large momentum transfer in the collision. The impact parameter dependence of the gluon distribution is obtained from the dependence of the squared momentum transfer (t) on the cross-section by Fourier transformation. The EIC allows to study how this changes with the non-linear QCD evolution towards small x in exclusive diffractive processes. Experimentally coherent processes can be tagged by measuring the neutrons emitted by the nuclear breakup of the nucleus in the incoherent diffractive eA collision. Figure 3 shows the $d\sigma/dt$ distribution for J/ψ on the left and ϕ mesons on the right, and they are compared with predictions of saturation and non-saturation models. The curves were generated with the Sartre [4] event generator.

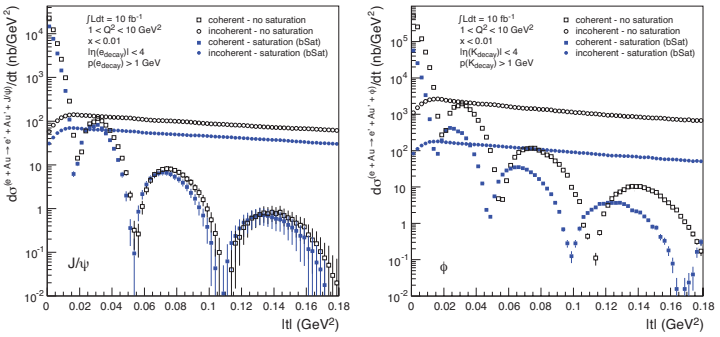

Figure 3: $d\sigma/dt$ distributions for exclusive J/ψ (left) and ϕ (right) production in coherent and incoherent events in diffractive eAu collisions. Predictions from saturation and non-saturation models are shown.

2.4 Energy loss, Fragmentation at Large x

The EIC can reveal the nuclear structure throughout the (x, Q^2) plane, from gluon saturation at low-x to the gluon EMC effect and its Q^2 evolution at high-x, which allows to estimate nuclear quark and gluon distributions and their uncertainties. The EIC will provide a wide $\nu = \frac{Q^2}{2Mx}$ range, which greatly extend the existing fixed-target measurements [11]. At small ν, studying in-medium hadronization can provide information on the dynamics of confinement: the stages of hadronization and their time scales. At large ν, parton propagation through the medium will allow us to study the energy loss and p_T-broadening of leading partons as well as jet-shape modifications. For the first time, the in-medium hadronization and propagation of heavy quarks can be also studied, and the pQCD description of cold nuclear matter can be tested. The EIC can provide the insight into how colorless hadrons emerge from the quarks and gluons and the dynamics governs color neutralization and hadron formation.

Table 1 shows a summary of the key measurements at the EIC.

to study	measurements	access to	stage-I	stage-II
nuclear wave function; saturation, Q_s	$F_{2,L}$	integrated gluon momentum distribution	gluons at $10^{-3}\lesssim x\lesssim 1$	exploration of saturation regime saturation
nonlinear QCD evolution/universality	di-hadron correlations	k_T-dependent gluons; gluon correlations	onset of saturation; Q_s	nonlinear small-x evolution
nonlinear small-x evolution; saturation dynamics	diffractive process; σ_{diff}, exclusive vector mesons	spatial gluon distributions	moderate x with nuclei Q_s	saturation regime; evolution
parton energy loss, shower mechanism and evolution	large-x SIDIS; jets	transport coefficients in cold matter	light flavors and charm; jets	rare probes and bottom; large-x gluons

Table 1: Key measurements in eA collisions at the EIC addressing the physics of high gluon densities.

3 Conclusion

The proposed EIC will be the world's first electron ion collider with high luminosity at high-energy. The versatility of the machine will allow systematic exploration of strong gluon fields in nucleons and nuclei with unprecedented precision and kinematic reach and reach/establish a new QCD phase - gluon saturation in eA collisions. The physics program of the EIC is toward a unified understanding of strongly interacting matter.

References

[1] F. Gelis, E. Iancu, J. Jalilian-Marian, and R. Venugopalan. Ann. Rev. Nucl. Part. Sci., **60** (2010) 463.

[2] V. Ptitsyn, these proceedings.

[3] E. Nissen, these proceedings.

[4] C. Aidala *et al.* "A Hign Luminosity, High Energy Electron Ion Collider", A white paper prepared for the NSAC LRP 2007.

[5] D. Boer *et al.*, "Gluons and the quark sea at high energies: distributions, polarization, tomography", A report on the joint BNL/INT/Jlab program on the science case for an Electron-Ion Collider, Sept. 13 to Nov. 19 2010, Institute for Nuclear Theory, Seattle, arXiv:1108.1713, 2011.

[6] V.N. Litvinenko *et al.*, "High-energy high-luminosity electron-ion collider eRHIC", arXiv:1109.2819, 2011.

[7] J. Bartels, K. Golec-Biernat, and L. Motyka. Phys. Rev., **D81** (2010) 054017.

[8] M.S. Kugeratski *et al.*, Eur. Phy. J., **C46** (2006) 413.

[9] D. Kharzeev, E. Levin, and L. McLerran. Nucl. Phys., **A748** (2005) 627.

[10] C. Marquet, B. Xiao, and F. Yuan. Phys. Lett., **B682** (2009) 207.

[11] A. Accardi *et al.*, Rivista del Nuovo Cimento, **32** (2009) 439.

List of Authors